Thermal, Power and Electrical Engineering III

Edited by
George Zhao, Guojun Ma,
Rutang Liao and Jianwen Wang

TRANS TECH PUBLICATIONS

Thermal, Power and Electrical Engineering III

Edited by
George Zhao
Guojun Ma
Rutang Liao
Jianwen Wang

Thermal, Power and Electrical Engineering III

Selected, peer reviewed papers from the
2014 3rd International Conference on
Energy and Environmental Protection
(ICEEP 2014),
April 26-28, 2014, Xi'an, China

Edited by

George Zhao, Guojun Ma,
Rutang Liao and Jianwen Wang

Trans Tech Publications Ltd
Kreuzstrasse 10
CH-8635 Durnten-Zurich
Switzerland
http://www.ttp.net

Volumes 960-961 of
Advanced Materials Research
ISSN print 1022-6680
ISSN cd 1022-6680
ISSN web 1662-8985

Full text available online at *http://www.scientific.net*

***Distributed** worldwide by*

Trans Tech Publications Ltd
Kreuzstrasse 10
CH-8635 Durnten-Zurich
Switzerland

Fax: +41 (44) 922 10 33
e-mail: sales@ttp.net

and in the Americas by

Trans Tech Publications Inc.
PO Box 699, May Street
Enfield, NH 03748
USA

Phone: +1 (603) 632-7377
Fax: +1 (603) 632-5611
e-mail: sales-usa@ttp.net

Preface

The International Conference on Energy and Environmental Protection provides a forum for accessing to the most up-to-date and authoritative knowledge from both industrial and academic worlds, sharing best practice in this exciting field. The first ICEEP was successfully taken place in Hohhot during the period 23-24 June, 2012 and the 2nd ICEEP was held in Guilin, from 19 to 21 April 2013. Following the success of the previous two conferences, the third ICEEP2014, held in Xi'an during April 26-28, 2014, was organized in four simultaneous tracks: "Applied Energy Technology", "Advances in Environmental Technologies", "Thermal, Power and Electrical Engineering" and "Resources and Sustainable Development".

The present volumes contain the selected papers from many submissions for this conference and provide up-to-date, comprehensive and worldwide state-of-the art knowledge in this field. All papers included in this collection had undergone the careful peer-review by the experts of international and domestic of China before it is selected for publications. Studies presented in this book cover these topics: Materials and Processing Technology, Engineering Thermophysics, Thermal Engineering, Fluid and Air Engineering and Machinery, HVAC, Air Conditioning and Refrigeration, Electrical Theory and New Technology, Smart Grid Technology, High Voltage and Insulation Technology, Power System, Control and Automation, Motor and Electrical Research, Power Electronics and Power Drives, Power Machinery and Engineering, Power Systems Management etc.

We would like to take this opportunity to thank many people. First and foremost we want to express my deep appreciation to invited keynote speakers, invited session chairs, invited session organizers and reviewers for their efforts and kind help in this congress. Final thanks go to all authors and participants at ICEEP2014 for helping to make it a productive and interactive meeting.

The Organizing Committee of ICEEP 2014

2014 3rd International Conference on

Energy and Environmental Protection

(ICEEP 2014)

Organized by:

Inner Mongolia University, China

Co-organized by:

Key Laboratory of Environmental Biotechnology, Research Center for Eco-Environmental Sciences, CAS

Conference Organization

Co-Chairmen

Prof. Lu Xixi, National University of Singapore

Prof. Ji Zhao, Inner Mongolia University, China

Prof. Aijie Wang, Harbin Institute of Technology, China

International Scientific Committee

Prof. Shuqing An, Nanjing University, China

Prof. Shahrum Abdullah, University Kebangsaan Malaysia, Malaysia

Prof. Jinglong Bu, Hebei United University, China

Prof. Heinz-Gunter, Brokmeier, Technische Universitat Clausthal,Germany

Prof. Wenbin Cai, Fudan University, China

Prof. Zhenqian Chen, Southeast University, China

Prof. Lam Kin Che, The Chinese University of Hongkong, HK

Prof. Haozhong Cheng, Shanghai Jiao Tong University, China

Prof. Shupei Cheng, Nanjing University, China

Prof. Carlos Caceres, The University of Queensland, Australia

Prof. Ming Dong, Shanghai Jiao Tong University, China

Prof. Renjie Dong, China Agricultural University

Prof. Boxue Du, Tianjin University, China

Prof. Huiwang Gao, Ocean University of China

Prof. Aijie Wang, Harbin Institute of Technology, China

Prof. Jingtao Han, University of Science & Technology Beijing, China

Prof. Minsheng Huang, East China Normal University

Prof. George A . O'Doherty, Northeastern University, USA

Prof. Jinping Jia, Shanghai Jiaotong University, China

Prof. Tetsuro Majima, Osaka University, Japan

Prof. Zhongyang Luo, Zhejiang University, China

Prof. Yunfeng Lu, University of California, Los Angeles, USA

Prof. Jummy C. Yu, The Chinese University of Hong Kong, HK

Prof. Zhengyi Jiang, University of Wollongong, AU

Prof. Yongguang Li, Shanghai University of Electric Power, China

Prof. Boqiang Lin, Xiamen University, China

Prof. Yongdi Liu, East China University of Science and Technology, China

Prof. Lianguang Liu, North China Electric Power University, China

Prof. Lubo Liu, California State, University, USA

Prof. Xiaoming Jia, Hebei United University, China

Prof. Jianmin Chen, Fudan University, China

Prof. Jinping Jia, Shanghai Jiaotong University, China

Prof. Xuesong Jin, Southwest Jiaotong University, China

Prof. Yongfa Zhu, Qinghua University, China

Prof. Yiming Xu, Zhejiang University, China

Prof. He Xu, Naikai University, China

Prof. Yun-Hae Kim, Korea Maritime University, Korea

Prof. Sagar Kamarthi, Northeastern University, USA

Prof. Shaojian Ma, Guangxi University, China

Prof. Christian Kloc, Nanyang Technological University, Singapore

Prof. Sihai Jiao, Research Institute,Baosteel, China

Prof. Yungang Li, Hebei United University, China

Prof. Shanqing Li, Research Institute,Baosteel, China

Prof. Xiaodong Li, Zhejiang University, China

Prof. Yongchen Lin, Central South University, China

Prof. Xianghua Liu, Northeastern University, China

Prof. Lianguang Liu, South China Electric Power University

Prof. Zifeng Ma, Shanghai Jiao Tong University, China

Prof. Nabukazu Nakagoshi, Hiroshina University, Japan

Prof. Shigang Sun, Xiamen University, China

Prof. Wenlei Sun, Xinjiang University, China

Prof. Zhonghua Tang, China University of Geoscience

Prof. Kaiming Wu, Wuhan University of Science and Technology, China

Prof. Jun Wang, Northeastern University, China

Prof. Fushuan Wen, Zhejiang University, China

Prof. Qiang Wang, Jinan University, China

Prof. Jiang Wu, Shanghai University of Electric Power, China

Prof. Yongyao Xia, Fudan University, China

Prof. Gang Xu, Guangzhou Institute of Energy Conversion, CAS

Prof. Yongping Yang, South China Electric Power University

Prof. Fenglin Yang, Dalian University of Technology, China

Prof. Jie Yang, Inner Mongolia University, China

Prof. Shaohui Yin, Hunan University, China

Prof. Takushi Yokoyama, Kyushu University, Japan

Prof. Bo Zhang, South China University of China, China

Prof. Hong Zhang, Nanjing University of Technology, China

Prof. Guohua Zhao, Tongji University, China

Prof. Feng Zhao, Institute of Urban Environment, CAS

Prof. Chuxin Zhou, Nanjing University of Technology, China

Prof. Jianmin Zeng, Guangxi University, China

Prof. Qi Zhou, Tongji University, China

Prof. Huisheng Zhuang, Shanghai Jiaotong University, China

Local Organizing Committee

Prof. Ji Zhao, Inner Mongolia University, China

Prof. Aijie Wang, Harbin Institute of Technology, China

Prof. Zhibin Jia, Inner Mongolia University, China

Prof. Lixin Wang, Inner Mongolia University, China

Associate Prof. Yixin Zhang, Inner Mongolia University, China

Table of Contents

Chapter 2: Engineering Thermophysics

Chapter 3: Thermal Engineering

Chapter 4: Fluid and Air Engineering and Machinery

Chapter 5: HVAC, Air Conditioning and Refrigeration

Chapter 6: Electrical Theory and New Technology

Chapter 7: Smart Grid Technology

Chapter 8: High Voltage and Insulation Technology

Chapter 9: Power System, Control and Automation

Chapter 10: Motor and Electrical Research

Chapter 11: Power Electronics and Power Drives

Chapter 12: Power Machinery and Engineering

Chapter 13: Power Systems Management

CHAPTER 1:

Materials and Processing Technology

Advanced Materials Research Vols. 960-961 (2014) pp 3-6

doi:10.4028/www.scientific.net/AMR.960-961.3

Fluoroimmunoassay Based on FITC-labeled Antibody for the Determination of Estradiol

Longjun Wang, Weili Xue and Lingyun Du*

College of chemistry and chemical engineering, Liaocheng university,

Liaocheng, 252059, China

*Corresponding author: lingyun_du@sohu.com

Keywords: Fluorescence immunoassay, Estradiol, FITC-labeled anti-E_2 antibody

Abstract. A new fluorescence immunoassay with high sensitivity, time-saving, good precision and reliablility was proposed for the determination of estradiol (E_2) in human urine. The complex of FITC-labeled anti-E_2 antibody was produced and regarded as a probe in this system. Ninety-six microplate was coated with ovalbumin conjugated E_2 antigen as solid phase for the immunoassay. The method parameters affecting the determination, such as the concentration of immunoreagents, pH, and other relevant variable conditions upon the immunoassay were studied and optimized systematically. Under the optimal experimental conditions, it was found that the proposed method exhibited high performance with the detection limit of 9.2 pg/mL, and the linear range of determination of 0.01-1000 ng/mL. The recoveries were 93.58-105.82% with the relative standard deviations (RSD) 5.52-7.09%. The proposed method has been used for the determination of E_2 in human urine with satisfactory results, and may be expected to find wide application in other environmental samples.

Introduction

With the development of industry, the pollution of the global environment due to various human activities is continuously increasing and becoming more and more complex. More and more attention was paid to the adverse effects of environmental endocrine which threaten endocrine systems of a great variety of organisms including our humans. Estrogens have been often identified as the major contributors to the endocrine-disrupting activity observed in environmental samples[1]. Since 17β-estradiol has the greatest estrogenic activity and even a very low concentration of exogenous estradiol can disturb the balance of it in vivo. So it is very necessary to establish a sensitive method for the detection of estradiol in the environment.

There were many analytical methods for the determination of estradiol in environmental samples. In contrast, immunoassay method[2] is highly sensitive and cost effective, so it is easy to use exhibiting good potential in widespread application. In recent years, radioimmunoassay (RIA)[3], enzyme-linked immunosorbent assay (ELISA)[4], fluoroimmunoassay (FIA)[5], chemiluminescence enzyme immunoassay (CLIA)[6] and electrochemical immunoassay (ECIA)[7] have been reported. FIA has been widely applied in environmental analysis, and the major advantages of FIA, as compared with conventional RIA, are the use of nonradioactive reagents, and increased reagent stability, and the short counting time, and the wide dynamic range[8].

The aim of this study was to establish a robust, reliable, speedy and sensitive fluoroimmunoassay method for the routine quantification of estradiol in urine sample, and the method can also be used for clinical diagnosis. In this study, it is reported that a FIA for the determination of estradiol based on indirect competitive reaction using E_2-OVA as solid phase and FITC-labeled anti-E_2 antibody conjugation as a probe, the FITC-labeled anti-E_2 antibody was produced in my laboratory. The competition assay took place in a conventional 96-well microplate. Up to now, the FITC-labeled primary antibody as direct detection signal has not been reported at home and abroad. Compared with other immunoassays, the proposed method has some advantages of simple steps, short detection time, high accuracy and sensitivity, and saving reagent. The reaction parameters of the present FIA were

studied and optimized. Applicability of the method was evaluated through analyzing human urine sample.

Experimental

Apparatus

All fluorescence intensity determinations were performed on a model M200 microplate reader (Tecan Genios, Switzerland). 96-well black polystyrene microplates (Costar) were purchased from Beijing Dingguo Biotech Co.. UV-Vis Spectrophotometer (UV2550, Shimadzu) was used for characterization. The pH values were controlled with pHs-3C precision acidity meter purchased from Shanghai Leici Apparatus Factory (P.R. China).

Chemicals and Immunoreagents

All chemical reagents used were of analytical grade. Estradiol, N,N-dicyclohexylcarbodiimide (DCC), N-hydroxysuccinimide (NHS), bovine serum album (BSA), ovalbumin (OVA) and fluorescein isothiocyanate (FITC) were purchased from Sigma Chemicals Co. (St. Louis, MO, USA). Dimethylsulfoxide (DMSO) was purchased from Tianjin Fuchen Chemical Reagent Factory (P.R. China). Tween-20 was purchased from Beijing bayer di biological Co.. Polyclonal anti-E_2 antibody and artificial antigen were obtained from my laboratory.

Buffers

Highly purified distilled and deionized water was used throughout this work. The coating solution was 0.01 mol/L carbonate buffer solution, pH 9.6. The dilution buffer (PBS) was 0.02 mol/L phosphate buffer solution containing 150 mmol/L NaCl, pH 7.4. The washing solution (PBST) was PBS containing 0.05% (v/v) Tween-20. The blocking buffer was PBST containing 0.4% (w/v) OVA.

Preparation of FITC-labeled Antibody Conjugates

Lyophilized antibody was dissolved in carbonate buffer solution (pH 9.2), and made it into 2 mg/mL solution. FITC was dissolved in dry dimethylsulfoxide (DMSO), and made it into 1 mg/mL solution. The antibody solution and a certain amount of FITC solution were mixed. The mixture was reacted at 4°C for 2 h in the dark. After that a certain amount of 1 M NH_4Cl was added to the above solution to 50 mmol/L and then incubated at room temperature for 2 h. The resulted solution was dialyzed with PBS (pH 7.4) under 4°C for 3-4 days until the dialysis fluid had no fluorescence, and then stored at 4°C for future use.

Sample preparation

The two urine samples were collected from the same pregnant woman. One sample is morning urine, another sample is the urine after meal three hours. Because the urine was packed with many other proteins, these proteins may seriously interfere with the detection of E_2, so it should be necessary to remove the proteins.The treatment process was as follows: 1 mL urine was added a little distilled water, and then added 2.5 mL 2 M HCl. The mixture was heated at 100°C for 30 mins, after that, cooled it at the room temperature. The obtained urine hydrolysate was added to 2.5 mL of 1 M sodium carbonate solution. After eliminating carbon dioxide, added HCl or Na_2CO_3 to adjust the pH value to 7.4, and then diluted the solution to 20 mL with PBS. The volume dilution ratio of urine was 1 : 20.

Fluorescence Immunoassay Procedure

The direct competitive fluorescence immunoassay procedure was shown as follows. 96-well polystyrene microplate was coated with 100 μL E_2-OVA in coating buffer. The microplate was kept at 4°C overnight and then washed three times with PBST. Then 150 μL blocking buffer was added to each well and incubated with gentle shaking at 37°C for 1 h in order to saturate the attachment sites on the microplate. After that, the microplate was washed as the described above. Then 50 μL serial dilutions of the E_2 or sample solution and 50 μL FITC-labeled anti-E_2 antibodies were added to the coated wells and incubated at 37°C for 1 h. And then the microplate was washed three times with PBST. An excitation wavelength of 485 nm and an emission wavelength of 525 nm were chosen to measure the fluorescence intensity.

Results and Discussion

The label ratio of FITC-labeled anti-E_2 antibody

The FITC-labeled anti-E_2 antibody was characterized by spectrophotometry using absorption bands at 280 nm and 495 nm. The single antibody has the characteristic absorption only in the 280 nm place, and the single FITC has the characteristic absorption only in the 495 nm place, but the conjugation of FITC-labeled antibody has two characteristic absorptions both in the 280 nm and 495 nm places. According to the change of characteristic absorption, the result of UV-Vis spectrum indicated that the conjugation of FITC-labeled anti-E_2 antibody was successfully produced. The absorbance ratio of FITC to antibody (A_{495}/A_{280}) can produce a big effect on the detection limit and linear range for the determination. In order to get a better ratio, the experiment synthetized three different FITC-labeled anti-E_2 antibody conjugations and compared with their impacts on the determination of the method. The three different label ratios were 0.53, 0.7 and 0.88 respectively.

Optimum Immunoassay condition

In general, the amounts of immunoreaction reagents are key parameter affecting the sensitivity and specificity of a competitive reaction. Therefore, in this experiment, the coating antigen and FITC-labeled anti-E_2 antibody concentrations were investigated and optimized. The fluorescence intensity increased gradually with increasing FITC-labeled anti-E_2 antibody concentration from 5 μg/mL to 60 μg/mL, and reached a plateau at 60 μg/mL. The fluorescence intensity showed a maximum at 20 μg/mL of the coating antigen. Finally, 20 μg/mL and 60 μg/mL were selected as the best concentrations of coating antigen and FITC-labeled anti-E_2 antibody respectively.

The non-specific adsorption can be reduced by adding blocking solution. Various concentrations of OVA solution were investigated and the result was shown that the fluorescence intensity showed a maximum at the concentration of 0.4%, so 0.4% was chosen as the optimum condition in this experiment.

pH of solution is one of the most important impact factors affecting the sensitivity of an immunoassay, which was investigated and the result was shown that the fluorescence intensity increased gradually to the peak, and then weakened with the increase of pH. The fluorescence intensity showed a maximum at pH 7.4. Therefore, in this experiment, pH 7.4 was selected as the optimum condition.

The label ratio of FITC-labeled anti-E_2 antibody is an important factor that influences the sensitivity and linear range of an immunoassay. Three different label ratios of FITC-labeled anti-E_2 antibody were investigated and the results were shown that the label ratio of 0.7 was shown greatly heightened sensitivity compared with the other two ratios. Thus the label ratio of 0.7 was used in this experiment.

Preparation of standard curve

Under the optimal conditions, the typical standard curve for E_2 with the proposed method was obtained. The calibration graphs were found to be linear over the concentration range 0.01-1000.0 ng/mL. The line equation for the calibration curve was $\Delta I = 198.3 \lg C_{E2} + 434.7$, the linearity of measurement resulted in a correlation coefficient of 0.9951, and the detection limit calculated from three times the standard deviation (SD) of the blank was 9.2 pg/mL.

Sample Analysis

To evaluate the application of the present method, one urine sample was investigated. Corresponding recoveries and the relative standard deviations (RSD) for urine samples at each concentration were presented. The recoveries were 93.58-105.82% with the relative standard deviations (RSD) 5.52-7.09%. It was found that the proposed method possessed high reproducibility, good precision, and was suitable for the detection of E_2 in urine and other environmental samples.

Conclusions

A new fluoroimmunoassay based on FITC-labeled anti-E_2 antibody was constructed to monitor E_2 in human urine samples. The label ratio of FITC-labeled anti-E_2 antibody has a large effect on the sensitivity of the proposed immunoassay. Under the optimal conditions, the linear range for

determination of E_2 was 0.01-1000 ng/mL, and the detection limit was 9.2 pg/mL. Compared with other methods, this technique only required small volumes of samples and did not need expensive equipment. This method has been shown to be advantageous in terms of sensitivity, accuracy, reliablility and simplicity of handling. The method could be further developed for determination of E_2 in other environmental samples, and may indicate its potential use in clinical diagnosis.

Acknowledgements

This work was financially supported by the National Natural Science Foundation of China (No. 20877037).

References

[1] V. Pacáková, L. Loukotokvá, Z. Bosáková and K. Štulík: J. Sep.Sci., Vol. 32 (2009), p. 867.

[2] M. Farre, M. Kuster, R. Brix and F. Rubio: J. Chromatogr., A, Vol. 1160 (2007), p. 166.

[3] F. Z. Stanczyk, I. Miyakawa and U. Goebelsmann: Am. J. Obstet. Gynecol., Vol. 137 (1980), p. 443.

[4] D.G. Cooke, J. E. Binnie and L. F. Blackwell: Steroids, Vol. 72 (2007), p. 580.

[5] D. Scalas, S. Squadrone, M. Gili, D. Marchis and M. Prearo: J. AOAC Int., Vol. 90 (2007), p. 1427.

[6] Y. Y. Qi, H. Chen, Z. Lin, and G. N. Chen and J. M. Lin: Chin.J.Chem., Vol. 29 (2011), p. 2520.

[7] S. H. Wang, H. S. Zhuang, L. Y. Du and S. L. Lin: Anal Lett., Vol. 40 (2007), p. 887.

[8] I. Hemmilä: Clin Chem, Vol. 31 (1985), p. 359.

Advanced Materials Research Vols. 960-961 (2014) pp 7-10

doi:10.4028/www.scientific.net/AMR.960-961.7

Study and Analysis On The High Temperature Performance of Calcined Bauxite

Binzheng Fang[1, a,*], Hui Li[1,b] , Jianwei Cao[1,c], Jianfeng Wu[2,d], Xiaohong Xu[2,e], and Xidong Wang[1,f,*]

[1]Institute of Engineering (Baotou), College of Engineering Peking University, Baotou 014030, China

[2]State Key Laboratory of Silicate Materials for Architectures, Wuhan 430070, China

[a]fangbz@ie.pku.edu.cn, [b]lih@ie.pku.edu.cn, [c]caojw@ie.pku.edu.cn

Keywords: Calcined bauxite, Physical and chemical properties, Thermal performance, Phase composition and microstructure

Abstract. In order to further broaden the application field of calcined bauxite, using XRF and other testing technology to study and analysis on the high temperature performance of calcined bauxite in this paper. The results showed that the sintering temperature range was 1300 ~ 1650℃, the firing line shrinkage, bulk density, bending strength, heat capacity and thermal conductivity was increased gradually, the water absorption and porosity was decreased, the water absorption, volume density and flexural strength of the sample fired at 1650℃ were 0.93%, 3.20 $g \cdot cm^{-3}$ and 182.23 MPa, the specific heat and thermal conductivity were 0.83 $kJ \cdot (kg \cdot K)^{-1}$ and 9.21 $W \cdot (m \cdot K)^{-1}$. Due to the thermal performance of calcined bauxite is optimal, and is expected to be used for the field of high temperature solar thermal heat storage material.

Introduction

Bauxite is the most important ore of aluminum which belongs to the family of lateritic rocks. It is characterized by the enrichment of aluminum hydroxide minerals, such as gibbsite [$Al(OH)_3$], boehmite [γ-AlO(OH)], and diaspore [α-AlO(OH)], together with the iron ore minerals hematite and goethite, the kaolinite and small amounts of anatase (TiO_2). The bauxite resource has been very scarce in recent years [4-7]. Therefore, it is necessary to improve the application value and further broaden the application field of the bauxite. In order to make full use of bauxite resource and improve utilization effectively, the bauxite must be pre-processed through sinter at high temperature. The bauxite is calcined at high temperature that is called calcined bauxite.

Bauxite was used as raw material for producing calcined bauxite by the following steps: Bauxite ores was crushed and dry milled to pass through a certain sieve, Then, the bauxite powdered sample was mixed with water as binder. After that, the obtained mixtures were packed into metal mould and processed into compacted shapes by a hydraulic pressing. The pressed samples were cured for some time. Finally, the samples were fired at high temperatures. The prepared calcined bauxite is a widely used homogenized synthetic clinker because of its good chemical stability and excellent physical properties, excellent homogeneous structure, dense microstructure, low thermal expansion coefficient and so on [8-10].

The objective of this study is to make better use of Xinmi bauxite through high-temperature calcination.

Experimental

Raw materials. Calcined bauxite was provided by Henan Xinmi. The total tonnage is more than 57 million tons and a further 0.3 billion tons can be estimated as possible resources with a mean value of Al_2O_3 content around 78.05%. The chemical compositions of the calcined bauxite is given in Table 1.

Table 1 The chemical composition of calcined bauxite（wt%）

Materials	SiO_2	Al_2O_3	Fe_2O_3	TiO_2	CaO	MgO	K_2O	Na_2O	I.L	Total
calcined bauxite	12.09	78.05	1.03	4.17	0.24	0.30	0.46	0.11	3.05	99.74

Experimental procedures. The calcined bauxite was ball milled in a zirconia pot with zirconia ball for 1 h and passed through 250 mesh sieve to get the desired powder. The ball to calcined bauxite weight ratio was kept at 2:1. Water mist was then added gradually to made the calcined bauxite homogenized. Then the sample was cured at room temperature for 24~48h. The samples were prepared by wet-pressing molding by using a NYL-500 pressing machine at 55 KN and 40KN, respectively (produced by Wuxi Machine Factory). Both rectangular bars (36 mm×6.5 mm×6.5 mm) and cylindrical pellets (30 mm in diameter and 4.5 mm in height) were made. Finally, the compacted samples were heated at various temperatures (1300-1650˚C) for 2 h.

Characterization techniques. The water absorbency（Wa）, apparent porosity（Pa）and bulk density（D）were measured by an AUY120 electronic analytical balance (Japanese Shimadzu) through Static Weighing methods. The bending strength of the samples were tested by using a computer-controlled electronic universal testing machine (REGER-4100, produced by Shenzhen Rui Geer).

Results and discussion

Physicochemical properties. In order to investigate the sintering property of calcined bauxite，the single calcined bauxite was studied through high-temperature calcination. The measured physicochemical properties (apparent porosity, Pa, water absorption, Wa, bulk density, D, bending strength, σ_b, and firing shrinkage coefficient, S_f) of the sintered samples were investigated over the temperature range 1300-1650˚C, and the results are shown in figures 1 and 2. It was shown that the water absorption and apparent porosity decreased with the sintering temperature increasing, on the contrary, the bending strength, bulk density and firing shrinkage coefficient increased with the sintering temperature increasing. After sintering at 1300˚C, the calcined bauxite had a higher water absorption and lower bulk density and bending strength, also had a little powder on the surface of the sample. That was because the main crystalline phases of the raw calcined bauxite were corundum and mullite, and there was no phase inversion or new phases were found when the sintering temperature reached 1300˚C. While the calcined bauxite was sintered at 1500˚C, there was no powder on the surface of the sample, the firing shrinkage coefficient was about 6%, the bulk density and bending strength reached 2.56g·cm^{-3} and 84.48MPa, respectively. When the sintering temperature reached 1650˚C, the water absorption of the sample could be reduced to 0.93%, the bulk density and bending strength reached 3.20g·cm^{-3} and 182.23MPa, respectively, and the firing shrinkage coefficient reached above 10%. It is because of the high - temperature resistance of raw calcined bauxite that it has enormous potential applications in the fire-resisting material industry and high-temperature ceramic field.

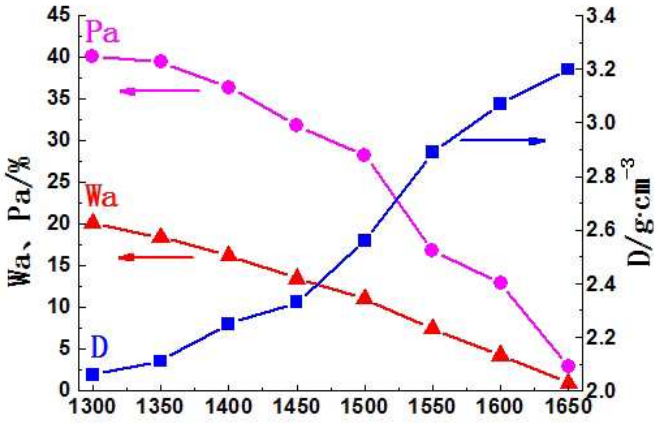

Fig. 1 Relationship of Pa, Wa, D and the firing temperature of samples

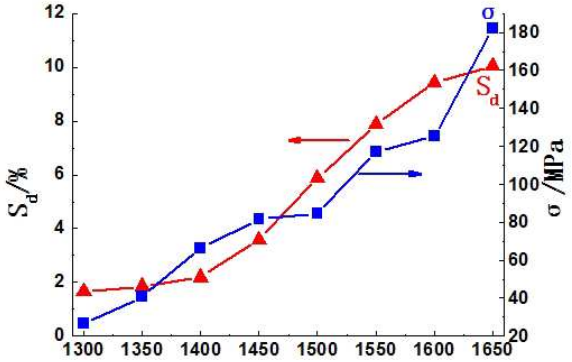

Fig. 2 Relationship of S_d, σ_f and the firing temperature of the samples

Thermophysical properties. The measured thermophysical properties of the sintered single calcined bauxite samples are listed in Table 2. It can be seen that the thermal conductivity coefficient increased from 0.61W/m·K to 2.02W/m·K at 600˚C, from 0.51W/m·K to 9.08W/m·K at 300˚C, from 7.93W/m·K to 8.15W/m·K at room temperature, respectively. With the temperature increasing from room temperature to 600˚C, the specific heat capacity increased from 0.37kJ·(kg·K)$^{-1}$ to 0.61kJ·(kg·K)$^{-1}$, from 0.31kJ·(kg·K)$^{-1}$ to 0.79 kJ·(kg·K)$^{-1}$ and from 0.55kJ·(kg·K)$^{-1}$ to 0.72kJ·(kg·K)$^{-1}$, respectively. Therefore, the calcined bauxite will be a promising material in the new energy resources ceramic field.

Table 2 The thermal properties test results of the samples

Firing temperature /˚C	Test temperature /˚C	Thermal diffusivity /cm^2·s^{-1}	Specific heat capacity /kJ·(kg·K)$^{-1}$	Thermal conductivity coefficient /W·(m·K)$^{-1}$
1400	25	0.02	0.55	1.93
	300	0.01	0.31	0.51
	600	0.01	0.37	0.61
1600	25	0.04	0.72	8.15
	300	0.04	0.79	9.08
	600	0.01	0.61	2.02
1650	25	0.05	0.83	9.21
	300	0.04	0.88	9.15
	600	0.02	0.71	3.24

Summary

(1) Results indicated that the main component of the calcined bauxite is Al_2O_3. The phase composition analysis shows that the main crystalline phases of the calcined bauxite samples are corundum and mullite, and the impurity content is low. Therefore, it has enormous potential applications in the fire-resisting material industry and high-temperature ceramic field.
(2) The results of investigations reveal that the calcined bauxite has high temperature resistance and the melting temperature could be above 1650˚C. With the increase of the sintering temperature, the main crystal phases of the calcined bauxite are corundum and mullite. With the temperature increased, the main crystalline phases of calcined bauxite are both corundum and mullite, and the the bulk density, bending strength, specific heat capacity, thermal conductivity coefficient are all increased gradually.
(3) After sintering at 1650˚C, the thermal conductivity coefficient of the calcined bauxite could reach 9.21 W/m·K (at room temperature), so the calcined bauxite would be expected to be used in the field of high-temperature solar thermal storage materials.

References

[1] Manivasakan P, Rajendran V, Rauta P R, et al. Nanomaterials and Devices: Processing and Applications (2009).

[2] Mondal A, Maitra S, Chandra S, et al. Transactions of the Indian Ceramic Society (2008).

Advanced Materials Research Vols. 960-961 (2014) pp 11-13

doi:10.4028/www.scientific.net/AMR.960-961.11

Study on Parrifine Removal Additive of High Wax Crude Oil

ZHANG HONG [1, a]

[1]Shanghai University of Engineering Science College of Chemistry and Chemical Engineering, Shanghai 201620, China

[a]zhanghonglindi@163.com

Keywords: high wax crude oil; parrifine removal additive; consist property;

Abstract. The consist property analysis of Shenbei and simulation high wax crude oil was carried on in the paper. The result showed the key factor of temperature lies in the wax crystal forming and growing. only when the heating temperature is high, the wax can be fully dissolved in crude oil drop dispersed, glial, asphaltene can be fully dissolved, agent and in crude oil.

Introduction

Most of China's crude oil are high waxy crude oil. According to the statistics, the wax content is higher than 10% in the 90% of total output of crude oil [1]. The high wax content of crude oil brings a lot of difficulties for the oil exploitation and transportation. The surface generates by wax deposition and attached on the pipe wall when the temperature access to the critical point. Also result to transport capacity greatly reduced, even serious blockage. It becomes the primary problem of oil transportation and exploitation [2]. At present, the chemical additive was added into the crude oil to solution the problem in the foreign countries use. The pour point depressant can change the original state of paraffin crystallization difficult to form network structure to improving the liquidity of the crude oil[3]. In China, research of the crude oil pour point depressant has made great progress and it has entered the practical using stage, such as, Lu Ning, Luo, Ma Huining long distance oil pipeline has been officially used crude oil pour point depressant [4].

The paper mainly aims at development of new high waxy crude oil pour point depressant. At the same time test the application the effect of improving the security of oil transportation and reducing the transportation and processing costs effectively.

Experiment

1.1 Simulation crude oil preparation

Paraffin wax (58# ~ 62#) with different proportion was added into n-octane, heating to melt to get simulation high waxy crude oil with different wax content.

1.2 Shenbei crude oil properties

Table 1 The crude oil properties

density	water	wax	pour point	wax precipitation
Kg/m³	（%）	（%）	℃	℃
839.1	0.30	24	44	49

1.3 Wax cleaning agent preparation

Preparation of long chain ester was got by ester reaction, distillation, solvent removal. Different long chain series was gained by transform different alcohols. The copolymer is prepared in the polymerization reaction, under the protection of nitrogen of polymerization was completed.

Results and discussion

2.1 Application performance testing

2.1.1 Additive on the depressive temperature effect

Temperature on the depressant effect has a great influence at the same additive conditions. The pour point depressant can change the crystalline morphology and coagulation function only above the wax precipitation temperature. The temperature is too low to prevent wax formation. So pour point depressant effect is unsatisfactory. However the temperature should not be too high the wax is dissolved, colloidal and other substances can be fully free. So pour point depressant can inhibit the three-dimensional network structure the low-temperature fluidity of crude oil was improved.

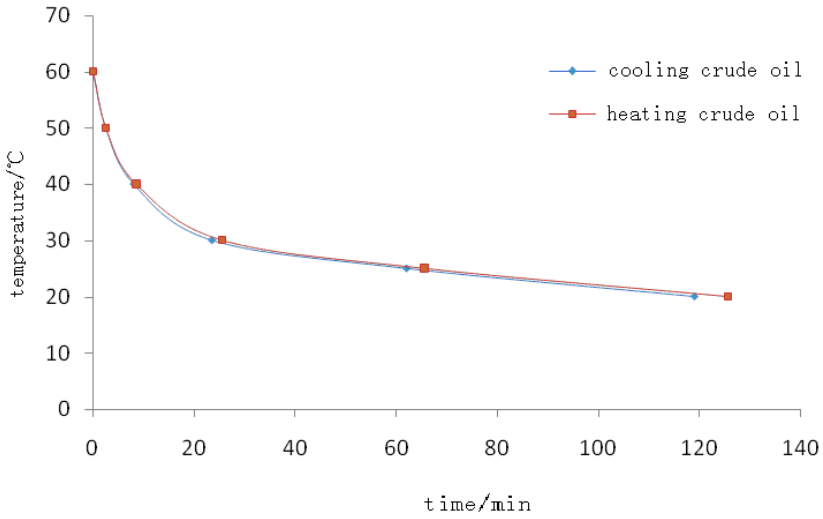

Fig. 1 Additive on the depressive temperature effect

In Figure 1 can be observed, whether cold or hot crude oil cooling preheating are quite fast from 60 ℃ to 40 ℃. It is slow cooling from 40 ℃ to 30 ℃ and below 30 ℃ more slowly. This is due to the thermal treatment temperature is an important factor of coagulation effect. Based on the theory of adsorption of eutectic, joining the intermediate temperature must be higher than the wax in the melt temperature, pour point depressant for crude oil pour point can effective better.

2.2 The solubility of wax in base oil

Wax solubility in crude oil is different with different composition of wax. The solubility of 54#, 56# and 62# three kinds of models of paraffin wax in base oil at different temperature were tested. The solubility change trend chart is as below fig. 2.

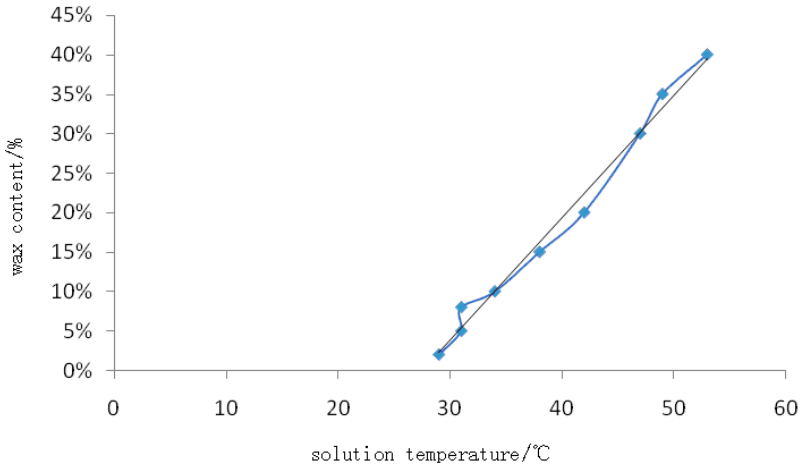

Fig. 2 The solubility of wax

The solubility of wax can been seen from graph 3 which increases the melting point of wax in crude oil with the solubility. On the other hand, for the wax was added to the base oil the wax melting point higher the wax precipitation at the same temperature will higher. Different molecular weight of alkane molecules in crude oil with different solubility, relative molecular mass is greater, the melting temperature is higher. Results also showed that solubility of wax and wax content are better conform to the exponential relationship.

Conclusion

Adding pour point depressant into crude oil the temperature factor is very important and the existence of a modified optimum range of heating temperature. This shows that only when the heating temperature is high, the wax can be fully dissolved in crude oil drop dispersed, glial, asphaltene can be fully dissolved, agent and in crude oil. Flow improver modification of wax crystal is better than that of the commercially available flow improver. Wax crystals have grow up and get well dispersed, which confirms the flow improver can enhance the crystalline wax wax crystals grow up point of view

References

[1] Siddhartha Seth, F. Brian and Towler: submitted to Journal of Petroleum Science and Engineering, Vol. 43 (2004), p. 13–23

[2] Guillaume Vinay, Anthony Wachs and Jean-FrancoisAgassant: submitted to Journal of Non-NewtonianFluidMech, Vol. 136 (2006), p. 93–105

[3] LI Hong-ying, ZHANG Jin-jun and GAO PENG: submitted to Journal of Oil Saving, Vol. 23 (2004), p. 19-22

[4] Ismayil Nurulla, Tanimoto Akitoshi and Shiraishi Kouichi: submitted to Polymer, Vol. 43 (2002), p. 1287-1293

Advanced Materials Research Vols. 960-961 (2014) pp 14-17

doi:10.4028/www.scientific.net/AMR.960-961.14

Study on the Produce Process and Electrical Resistivity of Carbon Fiber Conductive Concrete

Ting Ding[1, a], Yan Liu[1, 2, 3, b]

[1]Department of Civil Engineering, Beihang University, Beijing 100191, China

[2]China Airport Construction Group Corporation of CACC, Beijing, 100101, China

[3]Beijing Super-Creative Technology Co., LTD, Beijing, 100621, China

[a]dingtinn@gmail.com, [b]tjdoc@tom.com

Keywords: Carbon Fiber, Conductive Concrete, Electrical Resistivity, Produce Process

Abstract. This paper studied the produce process of carbon fiber concrete and the workability of carbon fiber conductive concrete (CFCC) by changing the fiber content as well. Based on a proper process, the electrical resistivity of CFCC in different CF continents was discussed and the percolation threshold was obtained.

Introduction

The research in the performance and application of conductive concrete has become a focus both at home and aboard in recent years.

Compared with the conventional concrete which has a high level of electrical resistivity about 10^5 - $10^9\Omega\cdot$cm, the conductive concrete has it much lower by adding some conductive materials such as carbon fiber, steel fiber and graphite. It is useful for cathodic protection, self monitoring of structure, deicing or snow-melting, etc. [1, 2]

Carbon fiber is widely considered the ideal conductive material，because of its high specific modulus, high rupture strength, fine corrosion resistance oxidation resistance and both high and low temperature resistance.

Carbon fiber conductive concrete (CFCC) is a new kind of intelligent concrete made by adding chopped carbon fibers into conventional concrete. It has a serious of fine properties as well. For example: electrical conductivity, compression sensitivity, thermo sensitivity.

On the other hand, it has been recognized as the most promising way for pavement deicing or snow-melting due to a good deal of advantages for instance: economic friendly, easy operation, high conductivity, good durability, etc.

In this paper, an advanced produce process is used to guarantee the CF can be fully dispersed. Besides, the workability and conductivity of CFCC is tested by changing the content of carbon fibers.

Experimental

1. Materials and electrode fabrication

1) Ordinary Portland cement was used.
2) Standard river sand was used as fine aggregates.
3) The largest stone size was 15 mm, the smallest was 5 mm, and the average stone size was 10mm.

4) The ratio of the high-range water-reducing agent to cement was 4% (by weight).
5) Hydroxypropyl Methyl Cellulose (HPMC) was used as dispersant in the amount of 0.1%-0.25% by weight of cement.
6) Defoamer was added to accompany HPMC; the defoamer-cement ratio was 0.3% by weight.
7) Carbon fibers of 7 μm in diameter and 10-15 mm in nominal length were used as the conductive filler. The carbon fibers were isotropic PAN-based and unsized. Other properties of CF are given in Table 1.

Table 1 Properties of CF

Tensile strength [MPa]	Tensile modulus [GPa]	Density [g/cm3]	Electrical resistivity[μΩ·m]	Content of carbon
2000-3000	175-215	1.74-1.77	30	93%

The electrode is made by 1 mm in thickness stainless steel plant in square ($130\times130mm^2$) with 9 circular holes in it which is shown in Fig.1. The diameter of the hole is 20mm, which is slightly larger than the aggregate particle size to ensure the electrical plate on both sides of the CFCC can be well connected.

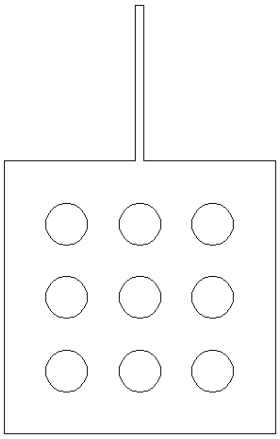

Fig.1 Electrode Plant

2. Mixing procedure

HPMC and defoamer were first added into water and stirred well for approximately 5 min. CF was then added into water and stirred gently. The rest of the mixing water was poured into the mixer followed by the high-range water-reducing agent.
Then the cement, sand and stones were added and stirred by a rotary mixer for 2 min. The mixer was stopped and the carbon fibers were spread into the mixer in several batches. Finally, ran the mixer for 5 min when all CF and mixed liquid were poured into the mixer.
The electrode was laid in oiled mold when fresh concrete was poured into an oiled mold. Then an external vibrator was used to facilitate compaction and decrease the amount of air bubbles. The samples were demolded after 24 hours and then cured at room temperature (temperature: 20℃; relative humidity: 50%). Fig.2 shows the samples were 150 mm length of side in cubes and $100 \times 100 \times 400\ mm^3$ in cuboids.

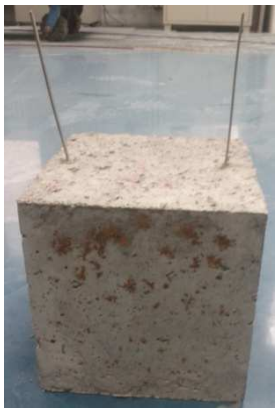


Fig.2 CFCC samples for electrical resistivity and rupture strength tests

Results and Discussion

1. The influence of carbon fiber content on workability

Slump was tested as an index of the workability of CFCC. The result proved the produce process in this paper is fantastic to guarantee the workability of CFCC. Since the increase of CF content and the water retention of HPMC, the fluidity of CFCC declined within a certain range.

2. The influence of carbon fiber content on rupture strength

Carbon fiber can prevent early plastic shrinkage crack of concrete from appearing and expanding, because CF fiber can absorb a part of tensile stress on the section, relieve the stress concentration of the concrete and thereby have good effect on rupture strength. When the crack appears, CF across the crack can still absorb and transfer tensile stress. It can not only delay the time of incipient crack, but also resist the expanding of crack. The experiment proved this idea well. Rupture strength was tested among samples in different CF content. All tests were taken after 28 days. The results are listed in Table 2

Table 2 Comparison of Rupture Strength and Slumps

Cement [kg/m$^{3]}$	Sand [kg/m^3]	Stone [kg/m^3]	Water [kg/m^3]	water-reducing agent [kg/m^3]	CF content (volume)	water cement ratio	28d rupture strength [MPa]	Slumps [mm]
500	525	1225	250	20	0.50%	0.50	5.49	177
500	525	1225	250	20	0.75%	0.50	6.24	149
500	525	1225	250	20	1.00%	0.50	6.63	143
500	525	1225	250	20	1.25%	0.50	7.03	132

3. The influence of carbon fiber content on concrete resistivity

The electrical resistivity of different CF contents was tested after 28d and the result was listed in the Fig.3. Each data is an average from 5 samples.

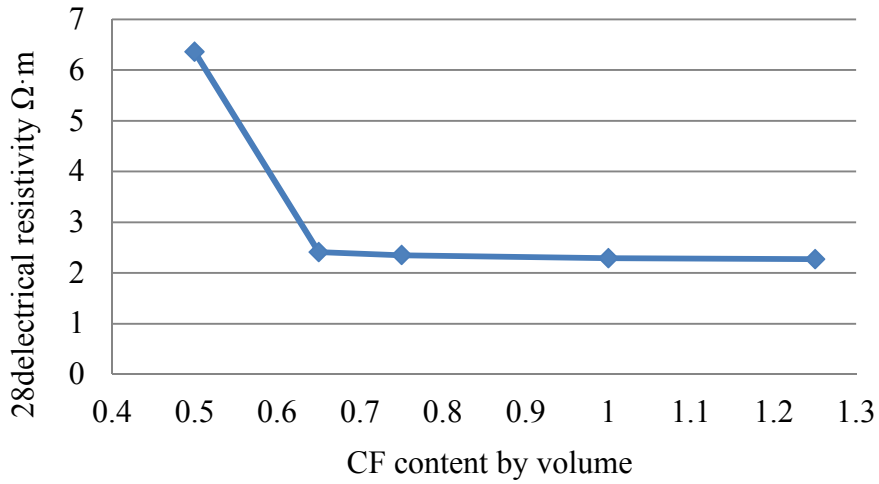

Fig.3 The effect of CF content on the electrical resistivity

Summing up the Fig.3, there is an obvious decrease in the electrical resistivity with the increasing CF content in the beginning stage. There is only a slight decrease in the electrical resistivity when the content varies from 0.65% to 1.25%.

It is concluded that low CF content in the beginning stage, the space between fibers is relatively large, so the fibers contribute less in electrical conduction than Ionic conduction in the concrete. While, a network of CF gradually formed with the increase of CF content, leading to an obvious decrease in the electrical resistivity.

When CF content was enough to form a stable conductive network, the electrical conductivity of CFCC became mainly depend on the CF network. The feature point of CF content is defined as the percolation threshold. After that, the electrical resistivity tends to be stable.

Fig.3 shows that the percolation threshold of CFCC is about 0.65%

Conclusions

The carbon fiber conductive concrete shows a good electrical conductivity and a superior mechanical strength. The workability of CFCC can be better since the CF content decreases in a certain range. CF content has an obvious influence on conductivity. When it reaches percolation threshold, the conductivity of CFCC tends to be stable. Percolation threshold of CFCC obtained is 0.65%

In this paper, CFCC of great workability, well fiber dispersion and stable electrical resistivity was produced, which laid a good foundation of CFCC practical application.

References

［1］Xuli Fu，D D L．Chung Carbon fiber reinforced mortar as an electrical contact material for cathodic protection［J］．Cement and Concrete Research，1995，25 (4) : 689－694．

［2］Xuli Fu，D D L．Chung Radio wave reflecting concrete for lateral guidance in automatic highways［J］．Cement and Concrete Research，1998，28(6) : 795－801．

Advanced Materials Research Vols. 960-961 (2014) pp 18-21

doi:10.4028/www.scientific.net/AMR.960-961.18

Chemical composition characteristics of calcite in gold and silver deposits in Jiaodong peninsula, China

Jinggui Tong[1,a], Yutong Yan[2,b], Na Zhang[3,c]

[1]Shenzhen polytechnic, Shenzhen 518055, PR China

[2]Faculty of City and Environmental Science, Xinyang Normal University, Xinyang 464000, China

[3]State Key Laboratory of Geological Processes and Mineral Resources, China University of Geosciences, Beijing 100083, PR China

[a]tongjinggui@163.com, [b]81089633@qq.com, [c]zhangna@biem.edu.cn

Keywords: Chemical composition; gold deposits; calcite; Jiaodong

Abstract. The largest gold district in China is the Jiaodong Peninsula. This study is based on chemical composition characteristics of calcite from gold deposits in Jiaodong. In this paper, a new formula was proposed to character the chemical composition characteristics of calcite in gold and silver deposits. The results showed that the chemical composition characteristics of calcite between gold and silver deposits were of great difference. And each data focused in each area. The spots of gold deposits located in the area of riched CO_2 areas. But the spots of silver deposits located in the area of riched CaO areas. The reason of these differences was mainly resulted from each different ore-forming condition.

Introduction

The Jiaodong Peninsula is the premier gold district in China with total measured gold reserves exceeding 1000t, and current annual production of over 30tonnes. There are conflicting views regarding the sources of ore-forming fluids in the Jiaodong gold province. the fact that most of the gold orebodies are hosted in 160 to 150 Ma Linglong-type biotite granite or 130 to 126 Ma Guojialing-type granodiorite has prompted a group of researchers to suggest that the ore-forming fluids were dominantly derived from granitic magma, which increasingly mixed with meteoric water during the late stages of hydrothermal activity[1,2]. Others, on the basis of stable isotope systematics and initial ratios of Sr isotopes, suggested that the major component of the ore-forming fluids was meteoric water, or that the meteoric water mixed with small amounts of magmatic fluid. Owing to the close spatial relationship between the orebodies and Cretaceous lamprophyre dykes, together with some evidence of mantle-derived components, other researchers argued that deep fluids or mantle-derived fluids were responsible for the gold deposits in the Jiaodong Peninsula.

One method to constrain the nature of ore-forming fluids is to study stable isotopes, such as those of hydrogen, oxygen, sulfur and nitrogen [3]. In the present work, a new formula was proposed to character the chemical composition characteristics of calcite in gold and silver deposits. The results showed that the chemical composition characteristics of calcite between gold and silver deposits were of great difference. The reason of these differences was mainly resulted from each different ore-forming condition in Jiaodong peninsula.

Regional geological setting

The Jiaodong peninsula is located along the southe-eastern margin of the North China carton and at the western margin of the Pacific Plate. It is bounded to the west by the NNE-trending Tanlu Fault zone that extends for thousands of km fom the Yangtze River north to Far East Russia. The peninsula is divided into two-Hurassic tectonic units: the Jiaobei terrane in the north and Sulu Terrane in the south. These terrane are separated by the Wulian-Yantai suture (Figure 1). The Sulu Terrane is at the eastern end of the Qinling-Dabie-Ulu diamond and coesite-bearing ultra-high pressure metamorphic belt. The Jiaobei Terrane consists of the Jiaobei uplift in the north and the jiaolai basin in the south.

The gold deposits can be classified into: 1) quartz vein type, as exemplified by the Linglong gold deposit; 2) altered-fracture type, as in the Jiaojia deposit, and interlayer slippage type as shown by the Dujiaya and Pengjiakuang deposits [4].

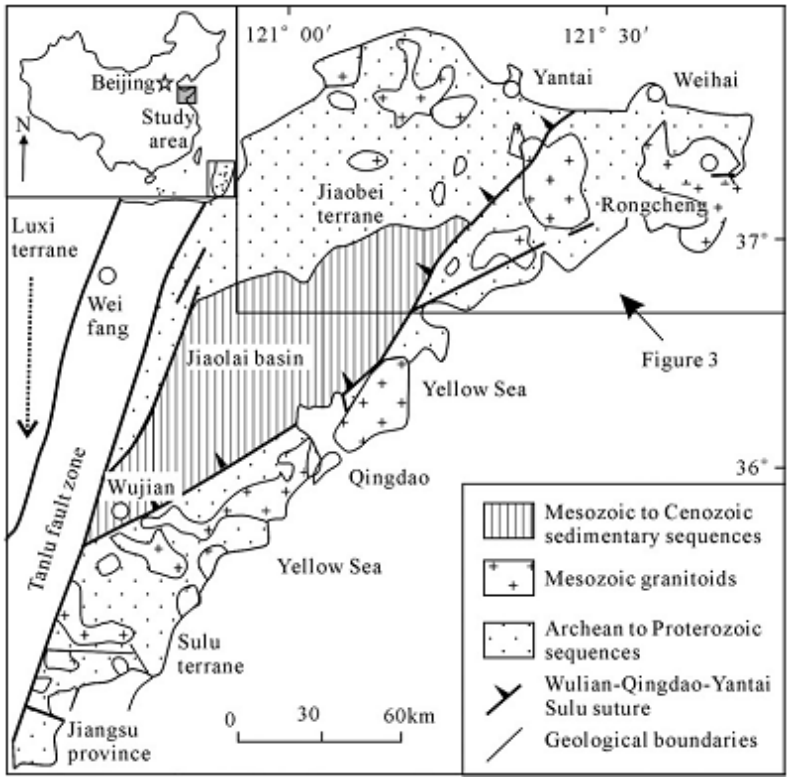

Figure 1 Simplified geological map of the Jiaodong Peninsula (according to [5])

Methods

The gold and silver chemical composition data is collected from the electronic probe analysis and previous literatures. And a new formula was proposed.

Results and Discussion

4.1 New formula of chemical composition characteristics of calcite in deposits

Until now, there are few method to character the chemical composition of calcite in gold and silver deposits. In this paper, a new formula was proposed as follows.

$$\delta CaO(\%) = \frac{100x - 52.0435}{52.0435} \times 100 \quad (1)$$

$$\delta CO_2(\%) = \frac{100y - 47.0565}{47.0565} \times 100 \quad (2)$$

x，y are signed for mass fraction of CaO and CO2。and δCO2

4.2 Chemical composition differences between gold and silver deposits

The calcite chemical composition data in Jiaodong gold and silver deposits are listed in Figure 2 and Table 1. Based on the data, the δCaO and δCO2 values changes little and have a narrow range of δCaO of -10.23 to -2.45 and of δCO2 of -0.07 to -5.69. The δCaO values changes bigger than the δCO2 values. The spots of gold deposits occupied riched δCO2 area. And the spots of silver deposits occupied reched δCaO area. The reason can be related to the ore-forming conditions between gold and silver deposits.

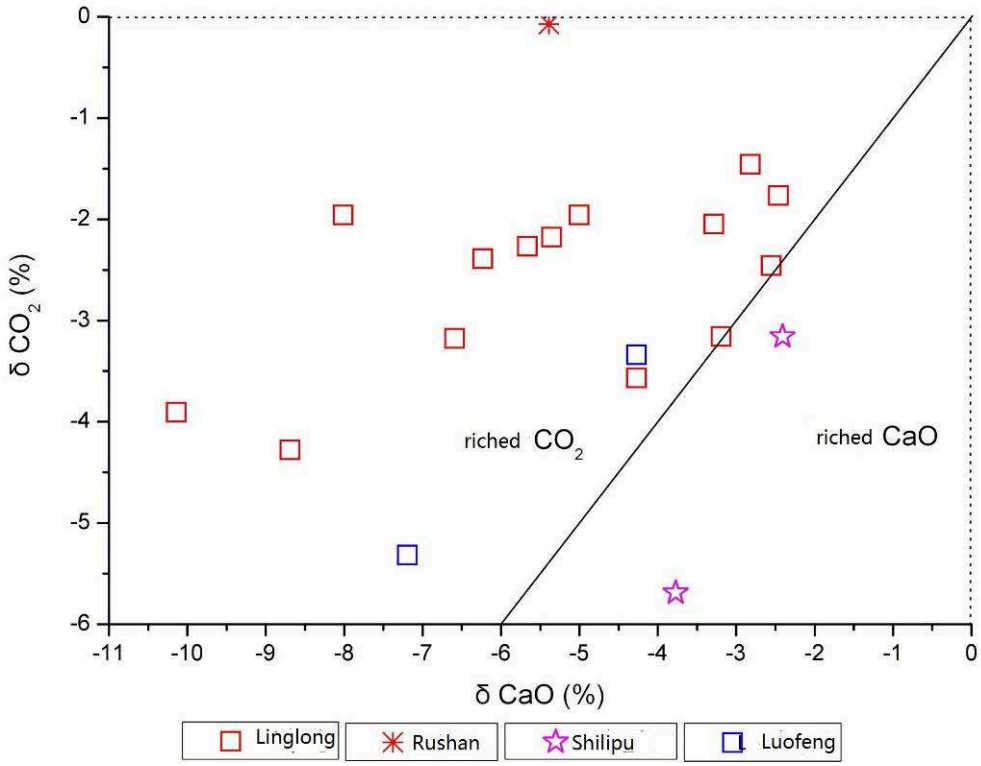

Figure 2 The spot of δ CaO— δ CO_2 of calcite in gold and silver deposits in Jiaodong. Red data stand for quartz-vein type gold deposit, blue data stand for alter type gold deposit, pink data stand for Shilipu silver deposit.

Table 1 Chemical composition of calcite in Jiaodong gold and silver deposits (%).

deposit	samples	mineral	Na2O	K2O	CaO	MgO	FeO	Fe2O3	MnO	Al2O3	SiO2	CO2	δCaO	δCO2
1	M10-206	Calcite			54.24		1.21	0.02	0.33	0.12	0.54	42.58	-3.19	-3.16
	M9-206-7	Calcite			54.45		0.92	0.01	0.17	0.27	0.17	43.33	-2.82	-1.46
	M4-130	Calcite			54.6		0.75		1.1	0.05	0.72	42.89	-2.55	-2.46
	M13-170	Calcite			52.34	1.04	1.95	0.02	1.42	0.02	0.6	42.57	-6.59	-3.18
	M52-255	Calcite			52.86	1.49	1.69	0.03	1.34	0.6	0.22	42.97	-5.66	-2.27
	M52-176	Calcite			51.54	1.09	1.63		0.71	0.12	1.24	43.11	-8.01	-1.96
	M52-10	Calcite			52.54	2.58	1.23	0.01	0.96	0.38	0.25	42.92	-6.23	-2.39
	M14-206	Calcite			50.35	2.15	2.01	0.01	1.67	0.38	0.19	42.25	-10.14	-3.91
	M51-262	Calcite			54.65	0.43	1.11	0.02	0.67	0.64	0.11	43.19	-2.46	-1.77
	M51-206	Calcite			54.19		1.63	0.02	0.99	0.52	0.1	43.07	-3.28	-2.05
	M45-206H	Calcite			53.03		1.84	0.01	1.54	0.82	0.09	43.01	-5.35	-2.18
	M45-206	Calcite			53.64	0.63	2.11	0.02	1.25	0.43	0.34	42.4	-4.27	-3.57
	M9-206	Calcite			53.23	0.51	1.06	0.14	1.15	0	0.44	43.11	-5.00	-1.96
	M108-300	Calcite			51.16		3.8	0.05	2.42	0.54	0.41	42.09	-8.69	-4.28
2	2--48	Calcite			54.68	0.17	0.49	0.58	0.46			42.58	-2.41	-3.16
	2--55	Calcite			53.92	0.13	0.42	0.05	0.62			41.47	-3.77	-5.69
3		Calcite	0.3	0.04	54.92	0.26	1.55		0.23	0	0.03		-1.98	
		Calcite	0	0	57.13	0.29	1.23		0.08	0.03	0		1.96	
4	31	Calcite			52	0.5	0.6	0.06	2.19			41.63	-7.19	-5.32
	224	Calcite			53.64	0.1	0.66	0.06	1.21			42.5	-4.27	-3.34
5		Calcite			53.01	0.39	1.64	0.32	0.57			43.94	-5.39	-0.07
6	2-4-18-2	Calcite	0.2	0.05	55.82	0.47	1.65		0.32	0.11	0.21		-0.37	
	H-2	Calcite	0.28	0.02	54.8	0.15	0.38		2.32	0	0.12		-2.20	
	H-3	Calcite	0.16	0	51.45	0.14	1.5		2.03	0.08	0.2		-8.17	

	1-1-22-③	Calcite	0.05	0	57.4	0.49	0.81		0.55	0.03	0.06		2.45	
	F-2	Calcite	0.2	0.04	55.85	0.39	1.13		1.15	0	0		-0.32	
	2-4-30-5	Calcite	0.07	0.04	57.29	0.54	1.04		0.09	0.02	0.21		2.25	
7	C-4	Calcite	0.21	0.08	54.69	21	0.44		0.08	0.33	0.67		-2.39	
8		Calcite	0.19	0	54.71	0.82	0..52		0.23	0.04	0.03		-2.36	
		Calcite	0	0	50.3	0.13	0.39		0.9	0.05	0		-10.23	
		Calcite	0	0.04	54.78	0.21	0.4		0.89	0.07	0		-2.23	
		Calcite	0	0.1	53.99	0.23	0.3		0.45	0.24	0.12		-3.64	
	X95-2	Calcite	0.03	0.03	53.1	0	0.28		1.92	0	0.11		-5.23	
9	14--2--14	Calcite	0.05	0.22	53.8	1.62	0.22		0	0	0		-3.98	
	Yj-1	Calcite	0.15	0	56.84	0.16	0.43		0.88	0.05	0.1		1.45	
	Jd-13	Calcite	0.02	0.1	54.07	1.71	0.81		0.27	0	0		-3.50	
10	YZ-7	Calcite	0.04	0	51.83	0	0		0.96	0	0		-7.50	

Note: 1 Linglong, 1988; 2 Shilipu, 1988; 3 Lingshangou, 1993; 4 Luofeng, 1988; 5 Rushan, 1990; 6 Muping,1992; 7 Fujia,1991; 8 Lujia,1994; 9 Jindoushan, 1999; 10 Nanzhangjia, 1990[9].

Conclusions

1) A new formula was proposed to character calcite in gold and silver deposits.

2) The spots of gold deposits occupied riched δCO2 area. And the spots of silver deposits occupied reched δCaO area. The reason can be related to the ore-forming conditions between gold and silver deposits.

References Cited

[1] Yang, J,Z., Shen, Y.C., Liu, T.B., et al. Geochemical characteristics of ore-forming fluids in the Pengjiakuang gold deposit, Shangdong provice. Mineral Deposits, 2000, 19:235-243. (in Chinese with English abstract).

[2] Wang, L.G., Qiu, Y.M., McNaughton, N.J., et al. Constraints on crustal evolution and metallogeny in the Northwestern Jiaodong Peninsula, China: from SHRIMP zircon studies of granitoids. Ore Geology Reviews, 2002, 13:275-291.

[3] Mao, J. W., Wang, Y.T., Li, H.M., et al. The relationship of mantle-derived fluids to gold metallogenesis in the Jiaodong Peninsula: Evidence from D-O-C-S isotope systematics. Ore Geology Reviews, 2008,33:361-381.

[4] Yan Y.T. Genetic and prospecting mineralogy studies of quartz-type and altered-type gold deposit in Jiaodong region. Beijing: China University of Geosciences, 2012.

[5] Qiu, Y.M., Groves, D.I., Mcnaughton, R.J., et al. Nature, age, and tectonic setting of granitoid-hosted, orogenic gold deposits of the Jiaodong Peninsula, eastern North China craton, China. Mineralium Deposita, 2002,37:283-305.

Advanced Materials Research Vols. 960-961 (2014) pp 22-26

doi:10.4028/www.scientific.net/AMR.960-961.22

Crack growth features in hydrogenating high-strength steel AISI 4340 under cycling

Georgy V. Shashurin[1,a], Pavel V. Tarakanov[2,b], Ludmila A. Rezchikova[1,c]

[1]BMSTU, 2nd Baumanskay str., h. 5, Moscow 105005, Russia

[2]IMASH RAS, Maliy Kharitonievsky per., h. 4, Moscow 101990, Russia

[a]goshasuper1@rambler.ru, [b]pashabeetle@yandex.ru, [c]var1950@gmail.com

Keywords: life, hydrogen embrittlement, cycling.

Abstract. There are various types of structural components, which are subjected to hydrogen aggressive environment and cycling. Their unexpected failure occurs suddenly and may entail serious consequences such as emergency stop of equipment, failure of the structure etc. The special engineering models are developed to predict the crack kinetics in structure components, which are subjected both to hydrogen environment and to cycling simultaneously. These models enable estimation of structure component life. The paper considers some features of such empirically specified special model giving emphasis to the one of them, namely to the prevailing fracture mechanism transition from fatigue to hydrogen embrittlement and back in crack kinetics process.

Introduction

Each structure, apparently, may have different metallurgical defects (cracks initial length of L_0, for instance). An aggressive hydrogen environment influence is supposed to accelerate a precipitateness of the fatigue fracture process in the structure component containing defects.

Numerous catastrophic failures of the important structure components have been reported. Most of them concern the steels of high yield strength for tubing and casing although there are also accidents with low alloy steels used in pipelines and pressure vessels [1]. The paper describes kinetics of central crack length of L in infinite plate [2] kinetics in the specimen made from the high-strength steel AISI 4340 using two different models, i.e. hydrogen cracking (HC) model and fatigue cracking (FC) one. Authors suppose that influence of cycling in combination with hydrogen environment leads to appearing some features in crack kinetics. Crack kinetics described till unstable cracking (UC) becomes the prevailing fracture mechanism.

Hydrogen cracking model

Hydrogen penetrates into material through the material-environment interface due to diffusion process. Eq. 1 describes hydrogen penetration into material for unidirectional diffusion and tension of a specimen [3]. Boundary and initial conditions are presented below too.

$$\frac{\partial C}{\partial t} = D\frac{\partial^2 C}{\partial x^2} + f\left([\Psi]\right)\frac{\partial C}{\partial x}\frac{\partial \tilde{\sigma}}{\partial x};\ C(0,t) = C^0;\ C(x,0) = C^0 G(x), \tag{1}$$

where x is a coordinate from the crack tip, t is time, $C = C(x,t)$ is hydrogen distribution function, $\tilde{\sigma}$ is stress distribution near the crack tip, C^0 is the current hydrogen concentration in the material-environment interface, $f([\Psi])$ is a function of environment and material parameters.

Mechanical characteristics in the hydrogenated region differ from those of in another part of the same body [4]. Hydrogen penetration into material lattice, for instance, results in decreasing fracture toughness. Therefore, *conditional stress intensity factor* (CSIF) and conditional fracture *toughness* (CFT) $\tilde{K}_I$ and $\tilde{K}_{Ic}$ are introduced instead of K_I and K_{Ic} in the hydrogenated region near the crack tip, and a criterion of the crack propagation is described by Eq. 2

$$\tilde{K}_I\left(\tilde{\sigma}^{\infty},l\right)\geq\tilde{K}_{Ic}\left(\bar{C}_a\right) \tag{2}$$

where $\tilde{K}_I=Y\tilde{\sigma}^{\infty}\sqrt{\pi l}$, $\bar{C}_a$ is an average hydrogen concentration in a *prerupture region a(l)* of the material. This region is much smaller than the hydrogenated one.

Crack growth rate in hydrogenated material depends on a *specific pair*, i.e. *environment and material* used in different experiments. Therefore, authors have introduced a new material-environment characteristic Ω to relate the current hydrogen concentration in the crack tip C^0 (*environment, initial condition of Eq. 1*) to the maximum solubility of the hydrogen in material C^* (*material*), in other words $\Omega=C^0/C^*$ [5].

CFT $\tilde{K}_{Ic}$ versus $\bar{C}_a$ is described by the Eq. 3:

$$\left(\left(\tilde{K}_{Ic}-\tilde{K}^*_{Ic}\right)/\left(\tilde{K}^0_{Ic}-\tilde{K}^*_{Ic}\right)\right)^{\alpha_1}+\left(\Omega\cdot\bar{C}_a/C^0\right)^{\beta_1}=1 \tag{3}$$

where $\tilde{K}^*_{Ic}$ - CFT of the material with uniform hydrogen concentration equals to C^0/Ω, $\tilde{K}^0_{Ic}$ - CFT of the non-hydrogenated material, α_1,β_1 - constants.

A crack propagation process is discrete in the given model. It is divided into three main stages:

- The first (incubation) stage may last quite long. It means an initial accumulation of hydrogen near the crack tip in the initial prerupture region. The length of this area depends on the metal lattice.
- The second stage is a stable crack growth. Here, the stable crack growth proceeds till the initial average hydrogen concentration does not exceed the critical one in the current prerupture region. The current prerupture region is longer as compared to the initial prerupture region length (Fig.1).

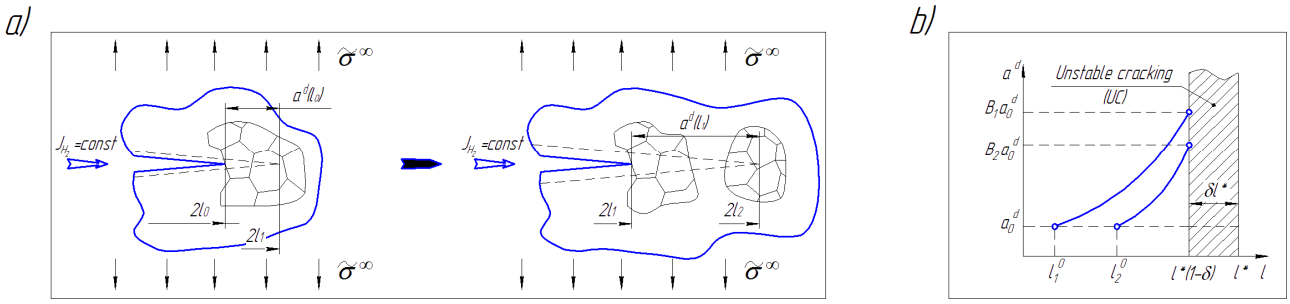

Fig. 1. (a) Crack growth; (b) The prerupture region length.

The length of initial prerupture region is supposed to be constant, and it does not depend on initial crack length. Eq. 4 describes a prerupture region length $a^d(l,\delta,l_0,l^*,a_0^d,A,\alpha_2,\beta_2)$ versus crack length l.

$$\left(\left[a_i^d-a_0^d\right]/\left[a_0^d\left(B-1\right)\right]\right)^{\alpha_2}+\left(\left[l^*\left(1-\delta\right)-l\right]/\left[l^*\left(1-\delta\right)-l_0\right]\right)^{\beta_2}=1 \tag{4}$$

where a_0^d is an initial prerupture region length, B,α_2,β_2 are parameters; l_0 is an initial half-length of the crack, l^*,δ are parameters, which defined below.

Using Eqs. 2-4 and a solution of Eq. 1 time $t^*(a_i^d)$ (i is a number of iterations) which is expanded to crack growth from l_i to $l_i+a_i^d(l_i)$, is defined as follows

$$t_d^*\left(a_i^d\right)=\frac{\int_{\Phi}\varphi(x)^2\,dx}{\int_{\Phi}\left(D\varphi''(x)\varphi(x)-\frac{\tilde{K}_I f\left([\Psi]\right)}{2\sqrt{\pi}}\frac{\varphi'(x)\varphi(x)}{x\sqrt{x}}\right)dx}\ln\left\{\frac{a_i^d\sqrt{1-\left(\frac{\tilde{K}_I-\tilde{K}^*_{Ic}}{\tilde{K}^0_{Ic}-\tilde{K}^*_{Ic}}\right)^{\alpha}}}{\Omega\int_0^{a_i^d}\varphi(x)\,dx}\right\} \tag{5}$$

where $\varphi(x)$ is a coordinate function, which appears after using Galerkin method with orthogonalizaiton of difference on the hydrogenated area $\Phi >> a_0$.

Crack growth rate $\dot{l}_{d\,i}$ at the i[th] regrowth caused both by hydrogen embrittlement of the material and by static loading is determined by the formula below

$$\dot{l}_{d\,i} \approx a_i^d \Big/ t_d^* \left(a_i^d\right) \tag{6}$$

- The third stage is an unstable cracking (UC). It occurs when the current initial average hydrogen concentration is greater than the critical one. In the other words, stable cracking lasts till the crack growth length L smaller than the L_{fr}^*:

$$L_{fr}^* = l^* \left(1-\delta\right) = \left[\left(\tilde{K}_{Ic}^0\right)^2 \Big/ \left(\pi \cdot Y^2 \cdot \tilde{\sigma}^{\infty 2}\right)\right] \cdot \left(1-\delta\right) \tag{7}$$

where $\delta = \delta(C)$ - parameter.

Fatigue cracking model

It is supposed that a crack growth rate is defined by two independent mechanisms. The first mechanism is accumulation of plastic strain near the crack tip due to cycling and another one is embrittlement structure component material especially near the crack tip caused by the aggressive hydrogen environment coming in contact with material. Also it is supposed that the incubation stage occurs only in case of hydrogen embrittlement and static loading. The Paris-Erdogan law, Eq.8, determines a crack growth rate due to fatigue:

$$\dot{l}_f = A\left(Y \Delta\tilde{\sigma}^{\infty} \sqrt{\pi l}\right)^n \tag{8}$$

where A, n are Paris-Erdogan constants, Y is a crack shape factor, $\tilde{\sigma}^{\infty}$ is a stress far from the crack. Time Δt_i^f a crack growth time from l_i to $l_i + a_i$ due to fatigue is defined by the formula below:

$$\Delta t_i^f = f^{-1} \cdot \Delta N_f \tag{9}$$

where f is a load frequency, ΔN_f is the number of cycles.

According to Eqs. 8 and 9, Eq. 10 determines the length of the crack regrowth a_i^f:

$$a_i^f = A \cdot \left(\Delta t_i^f \cdot f\right) \cdot \left(Y \Delta\tilde{\sigma}^{\infty} \sqrt{\pi l_i}\right)^n \tag{10}$$

The crack propagation in hydrogenating metal due to cycling

The Eq. 11 allows us to determine the crack growth rate $\dot{L}$ in structure components, which are subjected to cycling and hydrogen environment in case of $a_i^f = a_i^d = a_i$ [6].

$$\dot{L}_i \approx a_i \Big/ \min\left(\Delta t_i^f, \Delta t_i^d\right) = F\left([X],[Y],\tilde{\sigma}^{\infty}, l_0, t\right) \tag{11}$$

where Δt_i^d is the crack growth time from l_i to $l_i + a_i$ caused by the hydrogen embrittlement and static loading, $[X]$ and $[Y]$ are mechanical and environment parameters.

Diagram $L(t)$ and structure component life t^* is defined using Eq. 12.

$$L(t) \approx \int_0^t F\left([X],[Y],\tilde{\sigma}^{\infty},l_0,t\right)dt;\ L(t^*) = L^* \to t^* \tag{12}$$

Using Eqs. 11-12 is supposed to lead to appearing points $P\left(HC \xleftarrow{change} FC\right)$ to indicate the HC prevailing over FC (or vice versa). The curve to connect such points represents a borderline. The appeared borderline is a crack growth feature in hydrogenated material under cycling.

High-strength steel AISI 4340 has been examined using available empirically specified model. Table 1 gives specimen with the crack under mode I loading.

Table 1. Data for the specified specimen with crack under loading (mode I)

$\Delta\tilde{\sigma}^{\infty}$	f	A	n	$\tilde{K}^*_{Ic}$	$\tilde{K}^0_{Ic}$	α_1	β_1	a_0^d	α_2	β_2	B	δ	Ω	lg([Y])	L_0
[MPa]	[Hz]	$\left[\frac{\mathrm{m}\cdot\left(\mathrm{MPa}\cdot\sqrt{\mathrm{m}}\right)^{-n}}{\mathrm{cycle}}\right]$		$\left[\mathrm{MPa}\cdot\sqrt{\mathrm{m}}\right]$				[m]						$\lg\left[\frac{\mathrm{kg}\cdot\mathrm{m}}{s^2}\right]$	[m]
140	1.2	$1.095\cdot10^{-12}$	3.24	10	80	2	2	10^{-5}	2	2	10	0.05	1.5	-19.094	var.

Fig. 2 shows the crack growth versus life for various initial crack lengths. The initial crack length L_0 was varied beginning from $0.02\cdot l^*$ to L^*_{fr} in presented example.

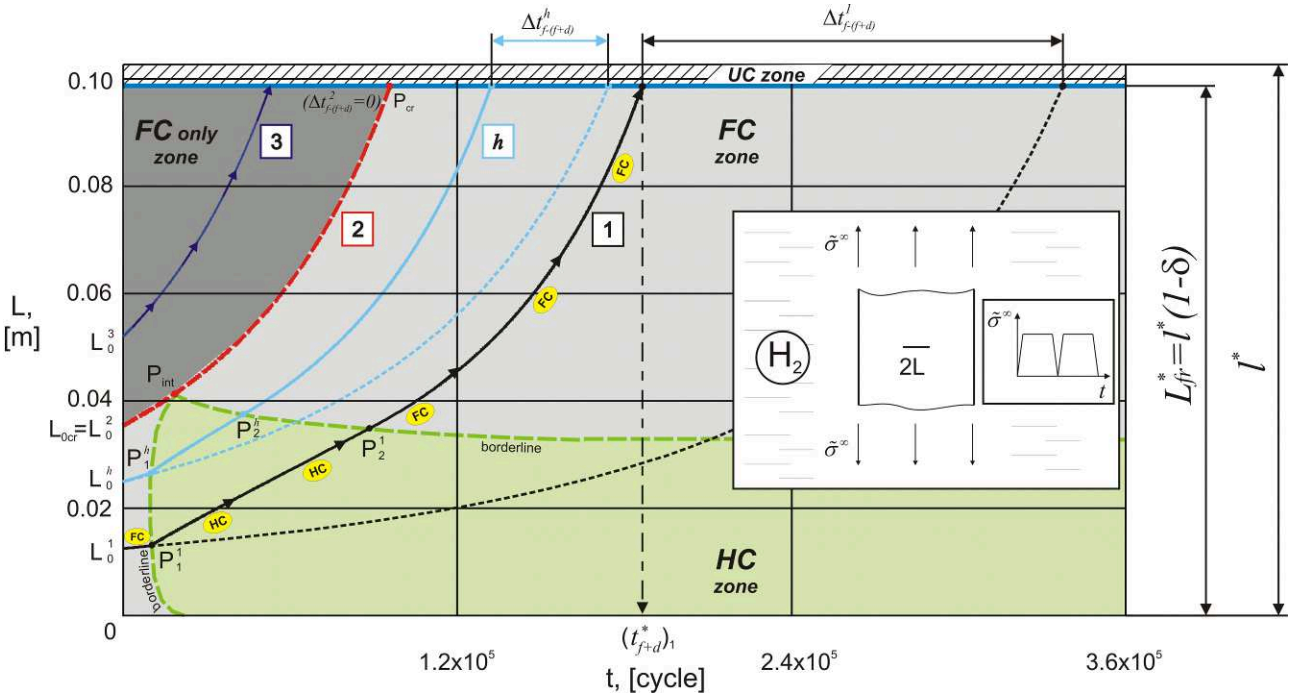

Fig.2. Crack kinetics features diagram (example)

The crack growth features description

Simulation results presented in Fig.2 illustrate appearing points P_i^j to indicate the HC prevailing over FC (or vice versa). A connecting these points borderline is shown in the diagram too. The mentioned borderline divides the diagram into two zones, namely the FC zone and the HC one.

The crack growth process with initial length L_0^1 is shown for two different loading conditions, i.e., hydrogen environment influence and cycling (solid curve 1) and only cycling (dashed curve 1). The growth process represented by the solid curve 1, starts due to fatigue. Then the crack continues growing to the point P_1^1. This point indicates that the prevailing fracture process changes, namely the mentioned solid curve transits to the HC zone. As time goes by the crack continue growing till it

reaches the point P_1^2 to indicate that the prevailing fracture process changes for fatigue. Afterwards, the solid curve 1 transits to the FC zone again. The proposed model allows us to follow the kinetic process till the moment when the crack reaches the value of $l^*(1-\delta)$; life t^*_{f+d} of the specimen under examination is exhausted. In other words, the crack growth process becomes unstable (UC zone).

Fig.2 presents the life difference of the specimen under two loading conditions mentioned above. Such difference $\Delta t^h_{f-(f+d)}$ is shown for curve h, which represents the crack growth with initial length $L_0^h > L_0^1$ under the same conditions. With increasing initial crack length the difference of the mentioned life $\Delta t^*_{f-(f+d)}$ decreases. The curve 2 describes the case, when life difference is zero ($\Delta t^2_{f-(f+d)} = 0$) thereby showing that the initial critical length L_{0cr} exists. Cracks with initial length $L_0 > L_{0cr}$ will grow just due to fatigue fracture process (only FC zone).

Summary

For high-strength steel AISI 4340 crack begins growing due to fatigue mechanism until hydrogen embrittlement does not prevail. As time goes by the fatigue mechanism becomes the prevailing one again. Borderline of HC zone in the diagram *L(t)* is defined by the proposed empirically-specified model. The determined zones could help to determine the prevailing fracture mechanism of the structure components with the cracks subjected to hydrogen environment influence and cycling.

Besides, the proposed empirically-specified model is a tool to define the life of the structure components under consideration.

References

[1] Uhlig's corrosion handbook, edited by W. Winston Revie. – 2nd edition, A Wiley-Interscience Publication John Wiley & Sons, New York (2000).

[2] British Energy Generation Ltd., R6: Assessment of the Integrity of Structures Containing Defects, Revision 4, British Energy Generation Ltd., (2001).

[3] V. Panasyuk, A. Andreykiv, V. Parton, in: Fracture mechanics and strength of materials, Naukova dumka Press, Kiev (in Russian) (1988).

[4] P. Tarakanov, G. Shashurin: 19th European Conference on Fracture, Kazan, Russia, Book of Abstracts, p. 231, (2012).

[5] P. Tarakanov, G. Shashurin, A. Romanov. Numerical life estimation of structure components subjected to hydrogen embrittlement and cycling. Key Engineering Materials, V 592-593, pp. 117-120, (2014).

[6] P. Tarakanov, G. Shashurin, M. Hruschov: Structural integrity and lifetime of NPP equipment, Kyiv, Ukraine, Book of Abstracts, pp. 202-203, (2012).

Advanced Materials Research Vols. 960-961 (2014) pp 27-31

doi:10.4028/www.scientific.net/AMR.960-961.27

Extrusion process and mould design for contact finger

Xuanrong Xin [1, a *], Ding Xu [2,b]

[1]Henan University of Science&Technology. Luoyang,Henan,471003,China

[2]Henan University of Science&Technology. Luoyang,Henan,471003,China

[a]xxr@qhforging.com, [b]xd@qhforging.com

Keywords: extrusion, stamping machine, contact finger, mould

Abstract. Extrusion process and mould design for contact finger by stamping machine is introduced in this paper. The structural design of the die is simple and practical, the productivity is improved significantly, the material consumption is reduced accordingly , the quality of products is very good and the production cost is low.

Introduction

As a near net shape technique, cold extrusion plays a more and more important role in the product manufacturing for its efficient high quality and low consumption characteristics .It can directly form the billet into net shape and near net shape products. Except for a small amount of mechanical processing, this technique does not need machining but just but also can improve the mechanical properties of the product and dimensional accuracy, and can improve the productivity. This paper introduces a technology using the cold extrusion to punch contact figure. Compared with the hydraulic press, it has high production efficiency, low cost, and high precision, good quality, and it has achieved good economic benefits.

The material of the contact finger is T2Y, which is a kind of hard copper. The part is as shown in Fig.1

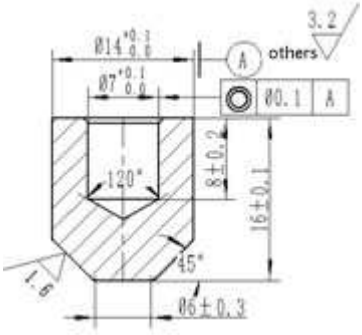

Fig.1 Part drawing

Process Analysis

From the shape of contact finger, this part belongs to the parts that are typical suitable for extrusion forming. On this occasion, if we use general lathe, drilling or some other methods for processing, the utilization rate of materials will be low and the labor time cost will be high. From the point of material characteristics, T2y copper's hardness is not high, which is suitable for cold extrusion forming. From the requirements of size tolerance, in addition to the requirements of the internal and external circular coaxial degree is high, which require the precision achieves 0.1, the general requirements are not high. After taking the appropriate measures, cold extrusion process can meet the requirements of the indicators. So the extrusion forming process is a better choice.

From the view of deflection, the deflection ε_A of backward extrusion hole in this contact is 25%, which is relatively smaller. While forward compression deformation condition also requires to being meet to fill the cone Ø6. The deflection ε_A of forward extrusion is 81.6%, which is relatively larger, but it is also within the decrement of 90~95% of forward extrusion allowable end face for fine copper. Thus it can be seen that the contact can be formed only once by using extrusion process.

The contact has holes of Ø7×8 and cone Ø6, the hole needs to be formed by backward extrusion and the cone needs forward extrusion, which is able to calculate forming extrusion force respectively. According to the algorithm of unit extrusion force diagram for nonferrous metals, unit extrusion force of backward extrusion hole can be figured out as p=965MPa, total extrusion force of backward extrusion hole as P=3.7T. Similarly, unit extrusion force of forward extrusion cone can be figured out as p=817MPa, total extrusion force of forward extrusion cone as P=12.6T.

Based on above forming forces, it can be judged that the backward extrusion forming of hole Ø7 has already completed prior to forward extrusion in pressure of 4T. However, after backward extrusion of forming hole, cone Ø6 is not able to completely take shape, which needs to control metal flow in direction of backward extrusion to force metal fill down. Finally, when the pressure reaches to 12T, the cone will form to required shape.

The extrusion forming force of contact finger is not much larger, as well as extrusion trip, equipment selection of hydraulic machine or punch is able to meet forming requirements. If extrusion forming is taken place in general oil press, mandrill can autonomously return after ejection, and the blank can be easily put in. and due to controllable pressure, the size of blank is not a big issue, this is just a matter of extrusion that whether it is longer or shorter. However, it is too slow in form by hydraulic machine to meet mass and low cost production requirements. Therefore, the punch is considered for production. Based on above calculations, the selection of punch 16t or 40 is favorable

In order to meet coaxiality of inner bore and encircle, some measures need to be taken to ensure coaxiality of 0.1when forming is completed in the punch with steeled terrace die.

According to the part drawing of finished products, we select the blank with a diameter of Ø 14. According to the principle of the invariability of volume constant in the process of compressional deformation, we can select the blank with a height of 12.5 mm and eventually determine the blank size for Ø14 x 12.5 mm.

Finite element software of DEFORM-3D will be used for simulation verification. Taking 1/12 blank to do numerical simulation and then getting the extrusion simulation diagram with intact forming (figure 2), its load curve of punch travel can be shown in Figure 3, and the total extrusion force is 15.36 T, which is close to the extrusion force calculated by algorithm of non-ferrous metal graph. Forming condition can be backward hole extrusion and meanwhile forward extrusion boss, but the hole accomplish forming in advance, and the boss accomplish forming later. At last, formed boss requires larger extrusion force.

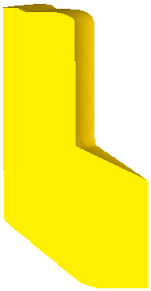

Figure 2: Mimetic diagram of the extrusion

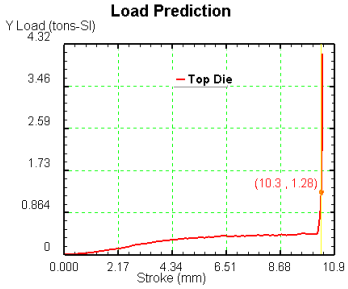

Figure 3: The lode curve of the punch

The mould structure and precision guarantee method

The mould structure formed by the extrusion of contact punch is shown in Figure 4. The mould structure has designed discharging mechanism consisting of guide sleeve for terrace die and kicker pin to ensure that after extrusion, extrusions can smoothly demould. Discharging mechanism is composed of Belleville spring 3, plate 4, plunger, kicker pin 5, and guide sleeve for terrace die 13. Lifter mechanism consists of kicker pin 21, pull rod 28, crown sheet 29, etc. which drives pull rod to lift upwards by return trip of punch sliding block. In order to ensure the accuracy requirement of coaxiality and parts for terrace die and die in the process of backward extrusion, guide sleeve 27 and guide pillar between up and down dies.

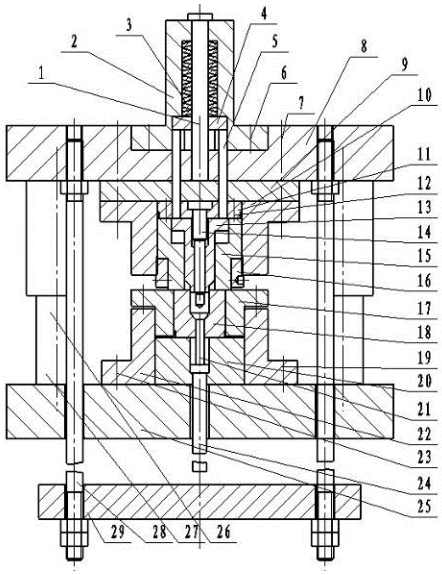

Fig.4 Structure schematic illustration of the die

n order to make it convenient to install mould in the punch, punch shank is used and mandril 5 inside of the punch shank uniformly configures by 120 °.

The die can be quickly replaced. Prestress circle of the die and the lower flange are connected by socket head cap screw, which is easy to assemble and unassembled, and the die replacement can be easier.

The extrusion is ejected by pull rod system [3], and the ejection distance should be strictly controlled within 17 ~ 19 mm. If the ejection distance is beyond the standard, the extrusion may knock terrace die or its guide sleeve; besides, another condition may be taken place that the next extrusion blank cannot put into the die cavity due to the overtop mandril. If the ejection distance is less than the standard, the ejected part of extrusion in the die cavity is too less to take the extrusion out.

Since the extrusion excircle doesn't process, while it directly require to reaching requirements of part, then only cavity Ø14 can be used. However bar-stock with negative tolerance of Ø14×12.5mm will be tense when putting into the die and the bar-stock will be easy to deflect resulting in punch broken when the punch is downriver in that the mandril places in a high position after ejection completion and little parts of the blank are put into the die. Besides the extrusion die is not flat but a sharp punch. The punch tends to partial, which makes the inner hole can not meet the requirement of the coaxiality. The way to solve this problem is to add a guide sleeve to the punch.

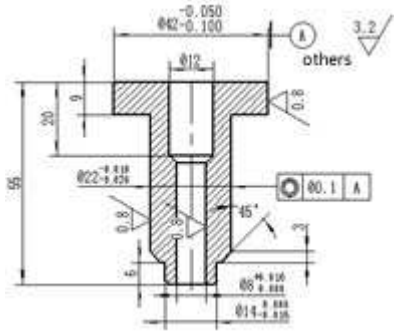

Figure 5: The punch guide sleeve

The punch guide sleeve as shown in figure 5, undeclared chamfer 1*45 degrees, unnoted fillet R2, materials GCr15, heat treatment requires HRC58~62. The punch guide sleeve in the mold structure played the following roles: (1) the punch guide sleeve extends a little beyond the tip, ensuring that before the semi-finished product is put into the die, it has already forced into the die cavity rough, which is used to avoid the punch guide sleeve partially slanting cut before entirely entrance. (2)The punch guide sleeve plays a role of guidance, which ensures coaxial requirements of the extrusion hole and ex-circle reach 0.1 degree. Since the inner hole is small, the head is cone, easily eccentric flow; pure reverse extrusion cannot guarantee the coaxial requirement of the contact finger. T he punch with the guide sleeve can ensure the requirements of it. (3) The punch guide sleeve plays a role of extruding punch when the backward extrusion finished, then it goes downward along with the hole punch to finish the Ø6 small platform extrusion forming. (4) The ex-circle of the punch guide sleeve is 1×45°,which can prevent the blank is so large that car will be stuffy, as well as releasing the excess metal to reach the design dimension when the blank volume is a little larger than the parts. (5) The punch guide sleeve ensures the extrusion release from the punch .In the interaction of the Belleville spring pressure and extrusion force, the punch guide sleeve retains the extrusion in the hollowing block and then push-out by the pull rod system.

It is simple and reliable by using the belleville spring to control the punch guide sleeve's movement. The application on the relatively smaller opening height of the punch is very convenient, because the belleville spring has the characteristics of big strength and compressible distance. It can not only ensure the mold, punch and extrusion part ejection, but also provide a lager pressure to force them into the blank.

Process experiment

The process flow diagram of this contact finger is as follows: cutting – cylinder deburring—smearing stearic acid zinc powder—extrusion forming—barrel burnishing—inspecting—warehousing.

Lubricant uses stearic acid zinc powder and the effect of lubrication is better when we use roller coated rather than use manual or simple rolling powder.

This method is feasible and can successfully produce qualified extruding contact finger, which has been proved by actual production, which is shown in the figure 6.

Figure 6: The part

Conclusions

(1)Using the forming technology of contact finger punching on extrusion is advanced feasible, and high efficient.
(2)It has reasonable extrusion process and high material utilization.
(3)The mould design is simple and practical. Besides it has reliable operation, long service life, and it can meet the requirement of mass production.

References

[1] Hong Shenzhang. Practical technology of cold extrusion [M]. Bei jing. Machinery Industry Press, 2005

[2] Jia Lili. Extrusion Technology and Mould Design [M]. Bei jing. Machinery Industry Press, 2004:56-62

[3] Hu Yamin. Forging molding Atlas [M]. Bei jing. Machinery Industry Press, 2002:78-81

Advanced Materials Research Vols. 960-961 (2014) pp 32-38

doi:10.4028/www.scientific.net/AMR.960-961.32

Fast detection of illegal sweeteners in liquor and wine by laser Raman spectroscopy

Da-you Fu [a], Dong Yuan[b], Xiao-fang Zhang[c] and Xin Zhao[d]

College of Material and Chemical Engineering, Sichuan University of Science and Engineering, Sichuan Zigong643000, China

[a]fdy888@263.net, [b]yuandong68@126.com, [c]446250525@qq.com, [d]zhaoxinzhaowuben@163.com

Keywords: Sweeteners, Qualitative Analysis, Micro-Laser Raman, Liquor and Wine

ABSTRACT. Efficient method was proposed for the qualitative detection of 6 illegal sweeteners in commercial liquor and wine by laser Raman spectroscopy. The method was based on the comparative analysis of Raman spectrogram of pure sweeteners and alcohol samples. For the 6 kinds of sweeteners tested, saccharin sodium, acesulfame potassium impurity and cyclamate, were present as additives in the samples. The results showed that the proposed method was fast and simple with high repeatability and sensitivity, and needed little samples and cost less.

Introduction

Laser Raman spectrometry, which uses laser as the powerful light sources, is theoretical based on Raman scattering. Raman spectrometry has been strongly applied in studying the composition and structure of material[1-5]. It was largely restricted due to the low sensitivity and weak signal processing techniques in the early stage of Raman. However, it has been quickly developed because of the introduction of laser, the improvement of weak signal processing techniques and the application of computers[6]. With the continuous development of Raman techniques, the application fields have been expanded from laboratory to storage and work site as a result of the appearance of portable Raman spectrometry, which is light and handy, more powerful and costs less on maintainance[6-8].

Micro-laser Raman spectrometry technology is a combination technology of microscopic analysis and Raman spectrum analysis. It adopts holographic CCD technology of high conversion efficiency, laser scanning confocal microscopy and low power laser in order to overcome the shortcomings of traditional laser Raman spectroscopy that had high powerful laser and low sensitivity. Micro-roman spectroscopy can do the in-situ testing, multiphase testing and microcosmic testing. It also has the advantages of high sensitivity, fast detecting, high spatial resolution and non-made sample technology, which allows it to achieve spectral information in different depth through point by point scanning[9].

Raman spectroscopy has been put into use in molecular biology[6], medicine[10], analytical chemistry[11] and nano-structure with the development of high sensitive analytical instruments, including in testing illegal and excess food additives[12]. Recently, Raman spectroscopy has been a significant instrument in qualitative determination of complex mixture[13]. The greatest difference of Raman spectroscopy from other analytical instruments is that it doesn't require dissolving or collecting samples, which simplifies the analysis procedure and shortens the time of analysis[1,12].

Sweetening agent is a kind of substance that can give food sweet taste and has high-sweetness but low heat and nutritional value. There are a large number of known intense sweeteners, but only

very few are allowed to be used in liquor and wine. The list of authorized artificial sweeteners varies from country to country[12]. It's reported that taking in high doses of artificial sweeteners can lead to the damage of liver and nervous system, even cancer[14]. However, many liquor-manufacturing enterprises add sweeteners into liquor to improve the taste regardless of the law, just because of the lack of detection methods of sweeteners in samples.

In this study, a rapid detection method of 6 illegal artificial sweeteners in liquor and wine was built by DXR micro-laser Raman, including Sodium cyclamate, Acesulfame potassium imputity, Aspartame, Saccharin sodium, stevioside and Neotame. The results show that the determination method is fast and simple with high repeatability and sensitivity and needs less samples and low costs.

Experimental

2.1 Instrumental

A DXR micro laser Raman spectrometer equipped with full scope grating, CCD array detector and auto-3D software was used to perform the measurements. The imaging software of OMNICTM AtlusTM was applied to collect and analyze imaging information.

Electronic balance (AR1140 from MET instruments) was used to weigh the solid sweeteners.

Electric heating water bath (DZKW-4) was employed to evaporate alcohols from liquid samples.

Ultrapure water polishing system (UPⅡ) was operated to obtain pure water.

2.2 Chemicals

Sodium cyclamate, Acesulfame potassium imputity, Aspartame, Saccharin sodium, stevioside and Neotame were of pharmacopoeial purity. The 10 kinds of liquor samples and 8 types of wine samples were bought at a local store. The liquid standard substance and samples were prepared using purified water.

2.3 Sample preparation

Sodium cyclamate, Acesulfame potassium imputity, Aspartame, Saccharin sodium, stevioside and Neotame were exactly weighed 50.08mg, 50.19mg, 50.23mg, 50.04mg, 50.03mg and 50.45mg in 6 volumetric flasks of 50mL respectively to prepare certain concentration solutions using pure water.

30mL of each samples were measured in 50mL beakers, and evaporated to a little solutions, then transferred to volumetric flasks of 5mL, volumed by pure water, then filtered through0.45μm filter membrane, contained in the vitric cuvette to be determined. In the full progress, alcohols were taken off from liquor and wine samples.

2.4 Determination of standard substances and samples

Solid reference sweeteners were tiled on the gold-plating glass sheet, which was put on the optical table of Raman spectrometer. Light should be hit exactly on the solid sweeteners by hand. The sample state would be clearly visible by coarse tuning and fine controlling to obtain Raman spectrograms of solid sweeteners. The wavelength of laser was 780nm under the power of 50mW, and the grating was 400gr/mm with 50μm slit.

The solutions contained in the vitric cuvette were put on the optical table, respectively and detected under the same conditions in the same way. The obtained Raman spectrograms were compared with the Raman spectrograms of solid reference sweeteners to confirm whether there was sweetener in liquor and wine samples.

Results and discussion

The qualitative analysis of sweeteners shows that 3 kinds of sweeteners, saccharin sodium, acesulfame potassium impurity and cyclamate, were present as additives. The Raman spectra of commercial samples in liquor and wine and the spectra of pure sweeteners (reference substance) are shown in the following figure.

3.1 Reference analysis

The spectrum of pure Sodium cyclamate, Acesulfame potassium imputity, Aspartame, Saccharin sodium, stevioside and Neotame, the Raman shift of which was revealed obviously, were shown in Fig.1-6. The 3075 cm^{-1} and 3058 cm^{-1} of Raman spectra were strongly expressed in saccharin sodium, aspartame and neotame, because of the stretching vibration of C-H in aromatic compound, and the signal of 1598cm^{-1} was powerful because of C=C. The signals of 1295 cm^{-1},1162 cm^{-1}, 1147 cm^{-1}, 1062 cm^{-1} and 1036 cm^{-1}were obvious in acesulfame potassium impurity, cyclamate and saccharin sodium owing to the structure of SO_2. And also there existed 1023 cm^{-1}and705 cm^{-1}(because of C=S) in saccharin sodium and 2968$cm^{-1}$and 2853 cm^{-1}(because of CH_2) in cyclamate and stevioside.

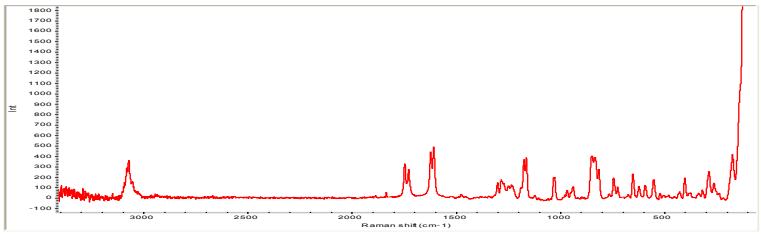

Fig.1 Raman spectrum of Sodium cyclamate (reference substance)

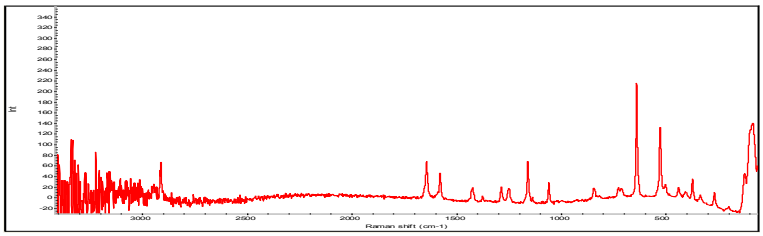

Fig.2 Raman spectrum of Acesulfame (reference substance)

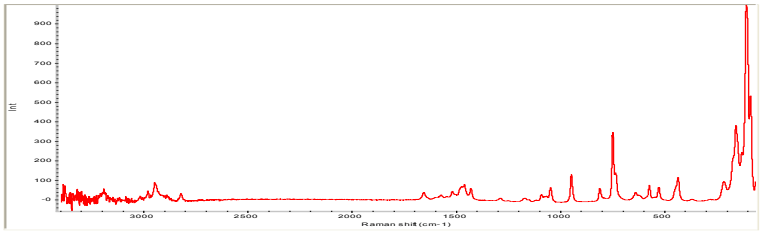

Fig.3 Raman spectrum of Aspartame (reference substance)

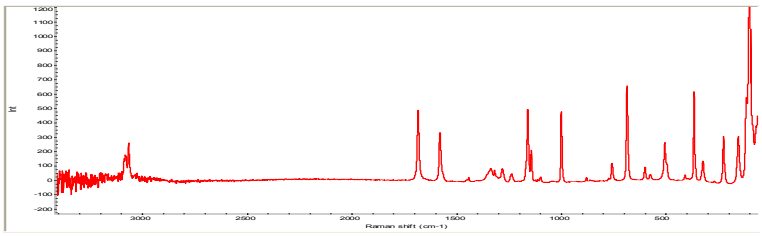

Fig.4 Raman spectrum of saccharin sodium (reference substance)

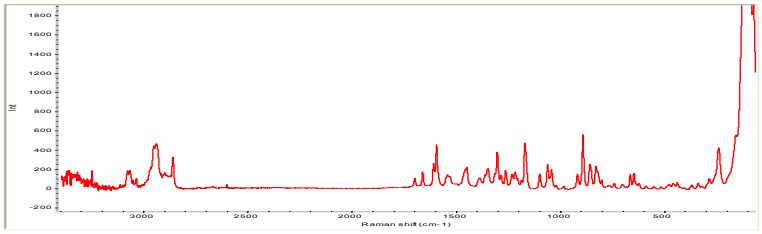

Fig.5 Raman spectrum of stevioside (reference substance)

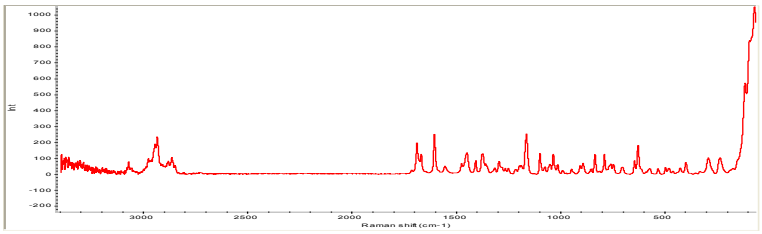

Fig.6 Raman spectrum of Neotame (reference substance)

3.2 The comparison of Raman spectra of reference substance and Liquor samples

The spectrum band width, the shift of spectral peak and the characteristic of peak shape is the obvious recognition information. According to the comparison of the Raman spectra of samples with that of pure sweeteners in the following figure, saccharin, sodium cyclamate, acesulfame were found in liquor and wine samples.

3.2.1 The comparison of Raman spectra of sodium cyclamate

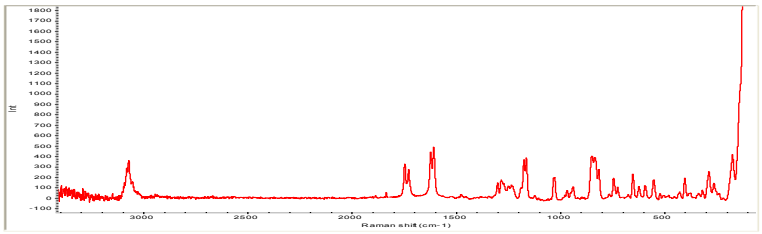

Fig.1 Raman spectrum of Sodium cyclamate (reference substance)

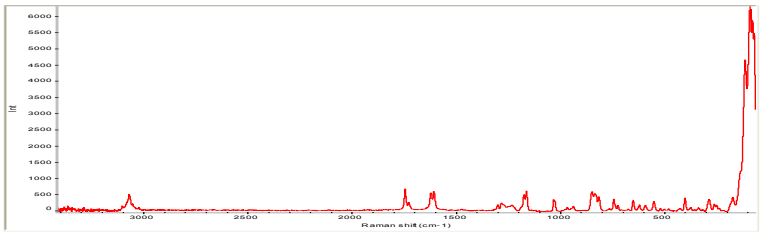

Fig.7 Raman spectrum of Liquor samples

According to the contrast of the Raman spectrun of reference(fig.1) and liquor samples(fig.7) of sodium cyclamate, the signals of 1295 cm^{-1}, 1162 cm^{-1}, 1147 cm^{-1}, 1062 cm^{-1} and 1036 cm^{-1} were both obvious because of the existence of SO_2. Also, there existed the signal of 2968cm^{-1} and 2853 cm^{-1} owing to the structure of CH_2. Therefore, Sodium cyclamate was obviously present in liquor samples, when compared the two Raman spectrums.

3.2.2 The comparison of Raman spectra of acesulfame

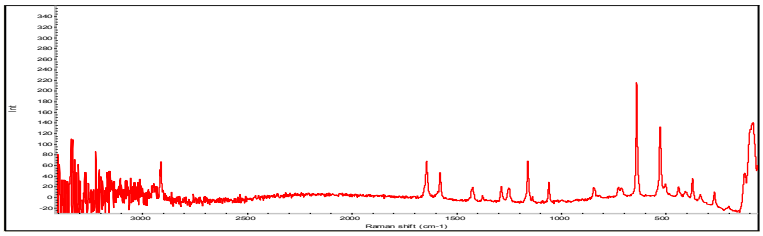

Fig.2 Raman spectrum of Acesulfame (reference substance)

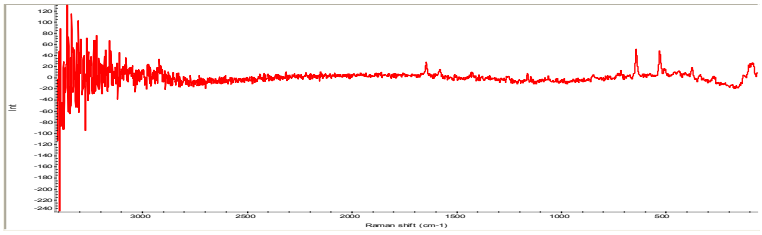

Fig.8 Raman spectrum of Liquor samples

The signals of 3075 cm^{-1} and 3058 cm^{-1} were strongly expressed in fig.2 and fig.8 because of the stretching vibration of C-H in aromatic compound, and the signal of 1598cm^{-1} was powerful because of C=C. Owing to the structure of SO_2, the signals of 1295 cm^{-1}, 1162 cm^{-1}, 1147 cm^{-1}, 1062 cm^{-1} and 1036 cm^{-1}were presented obviously. According to the comparative analysis of the Raman spectrum of acesulfame (Fig.2) and liquor samples (Fig.8), there exactly existed acesulfame in liquor samples.

3.2.3 The comparison of Raman spectra of saccharin sodium

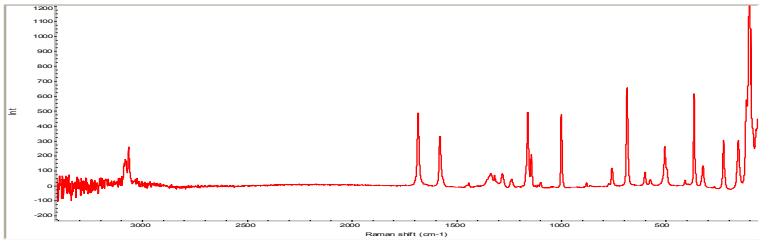

Fig.4 Raman spectra of saccharin sodium (reference substance)

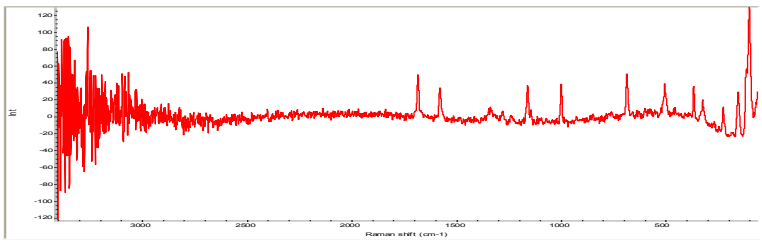

Fig.9 Raman spectra of liquor samples

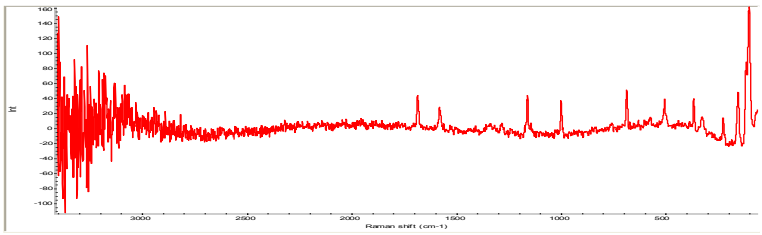

Fig.10 Raman spectra of wine samples

Based on the contrast of Raman spectra of liquor samples, wine samples and reference substance, there existed saccharin sodium in liquor samples and wine samples, respectively, according to the reasons below. Because of the stretching vibration of C-H and C=C in aromatic compound, the signals of 3075 cm^{-1} and 3058 cm^{-1} ,1598cm^{-1}were strongly conveyed respectively in fig.4, fig.9 and fig.10. And also there existed the signal of 1023 cm^{-1}and705 cm^{-1}(because of C=S) in saccharin sodium.

Conclusions

An method of rapid detection for sweeteners qualitative analysis via micro-laser Raman were presented in this paper. The proposed method can be a convenient alternative to the standard procedures of sweeteners qualitative determination[1]. In the 6 kinds of detected sweeteners, saccharin sodium, acesulfame potassium impurity and cyclamate were present as additives in liquor and wine samples. However there still remains the challenge of developing stable , reliable methods for the determination of artificial sweeteners in different kinds of liquor and wine. Analytical methods are essential to meet the needs of growing markets in quality control and consumer safety[12].

References

[1] Department of Chemistry, university of Wroclaw, Quantification of aspartame in commercial sweeteners by FT-Raman spectroscopy, Food Chemistry 125(2011)1051-1057

[2] Sergio Armenta, Salvador Garrigues, Miguel de la Guardia, Sweeteners determination in table top formulations using FT-Raman spectrometry and chemometric analysis, Analytica Chimica Acta 521(2004)149-155

[3] B.T. Bowie, B. Chase, P.R. Griffiths, Factors affecting the performance of bench-top Raman spectrometers. Part: I: Instrumental effects, Applied Spectroscopy, 54(2000)164A–173A

[4] R. Kizil, J. Irudayaraj, K. Seetharaman, Characterisation of irradiated starches by using FT-Raman and FTIR spectroscopy, Journal of Agricultural and Food Chemistry 50(2002)3912–3918

[5] R.A. Medeiros, A.E. De Carvalho, R.C. Rocha-Filho et al, Simultaneous square-wave voltammetric determination of aspartame and cyclamate using a boron-doped diamond electrode, Talanta 76 (2008)685–689

[6] Xuan Wei, Dengfei jie, Joel j. et al, Microalgal detection by Raman microspectroscopy, Trends in Analytical Chemistry 53(2014)33-40

[7] S.G. Skoulika, C.A. Georgiou, Rapid quantitative determination of ciprofloxacin in pharmaceuticals by use of solid-state FT-Raman spectroscopy, Applied Spectroscopy 55 (2001)1259–1265

[8] Debbie Lauwers, Anna Garcia Hutado, Vinka Tanevska, et al, Characterisation of a portable Raman spectrometer for in situ analysis of art objects, Spectrochimica Acta Part A: Molecular and Biomolecular Spectroscopy 118(2014)294-301

[9] Xiaotian Wang, Guangwei She, Haitao Xu, et al, The surface-enhanced Raman scattering from ZnO nanorod arrays and its application for chemosensors, Sensors and Actuators B: Chemical 193(2014)745-751

[10] Victor I. Mikia, Victor V. Mikia, 8-Raman Spectroscopy in Medicine, Medical Imaging Technology (2014)129-141

[11] Elena Avzianova, Sarah D. Brooks, Analysis of nickel(II) in particulate matter by Raman microspectroscopy, Journal of Aerosol Science 67(2014)207-214

[12] Agata Zygler, Andrzej Wasik, Jacek Namiesnik, Analytical methodologies for determination of artificial sweeteners in foodstuffs, Trends in Analytical Chemistry 28(2009)1082-1102

[13] Capitán-Vallvey, L. F., Valencia, M. C., Nicolás, E. A., et al, Resolution of an intense sweetener mixture by use of a flow injection sensor with on-line solid-phase extraction, Application to saccharin and aspartame in sweets and drinks, Analytical and Bioanalytical Chemistry 385(2006)385–391.

[14] Morando Soffritti, Fiorella Belpoggi, Eva Tibaldi, Davide Degli Esposti, et al, Life-Span Exposure to Low Doses of Aspartame Beginning during Prenatal Life Increases Cancer Effects in Rats, Environ Health Perspect 115(2007)1293-1297

Advanced Materials Research Vols. 960-961 (2014) pp 39-42

doi:10.4028/www.scientific.net/AMR.960-961.39

Optimum design of flexible microwave absorption fabrics

Sai-Nan Wei[1,a], Qian Li[1,b], Ji-Ming Yao[1,c], Rui-Fang Cui[1], Tian Sun[1]

[1]Hebei University of Science & Technology, Shi jiazhuang Hebei 050018,China

[a]wsn1009@sina.com, [b]liqianfz08@126.com,[c]yaojiming66@126.com,[d]736353244@qq.com

Keywords: reflectivity, microwave absorption, Ni-Fe fiber, stainless steel filament

Abstract. In order to develop flexible absorption fabric and study the effects of specifications on absorption properties, two-layer laminated fabrics were designed according to thickness matching and impedance matching. Stainless steel core-spun yarn fabrics were used as first layer which easily realized matching to the free space, Ni-Fe fiber consisted of second layer because its strong dielectric loss and magnetic loss. The reflectivity of fabrics were measured by the means of "arch testing method" in the range from 2~18 GHz. The results showed that the reflectivities of laminated fabrics can below -20 dB and the bandwidth <-10dB can reach 3.88 GHz with the change of fabric specifications**.**

Introduction

The wide application of electronic technology which has significant improved the quality of people's work and life, also produced a lot of negative effects at the same time, leading to electromagnetic pollution[1-3]. Absorbing material could transform the electromagnetic wave into other state of energy, not only can realize the stealth of aircraft, but also can use in electromagnetic pollution prevention which gained growing concern[4-5].

With technology development, metal fiber in textile level can be applied to the exploitation of flexible absorbing fabric because its anisotropic properties, and can be adjusted by its aspect ratio to achieve high absorption efficiency in wide range[6-7].

The main aim of this study is to optimum the design of flexible microwave absorption fabrics, which are fabricated by weaving technology with stainless steel filament and Ni-Fe fiber. And gain the good absorbing performances by optimizing fabric specifications.

Experiment

2.1 Theoretical background. Due to Ni-Fe fiber's low impedance, the difference between fabric wave impedance and free space impedance was larger when Ni-Fe fiber fabric as surface layer, and the reflection was high, unless the geometric structure designed specially such as pyramid. So, it needed to set a wave impedance between Ni-Fe fiber fabric and free space making the more electromagnetic wave into the absorption material.

$$Z_0 = \sqrt{\frac{\mu_0}{\varepsilon_0}} = 120\pi\Omega = 377\Omega \tag{1}$$

where Z_0 was the characteristic impedance of free space,

$$R = \frac{Z_L - Z_0}{Z_L + Z_0} \tag{2}$$

If the reflection coefficient was zero, medium impedance Z_L match with the free space wave impedance Z_0 was needed.

$Z_0 = \sqrt{\mu_0/\varepsilon_0}$,

$Z = \sqrt{\mu_r\mu_0/\varepsilon_r\varepsilon_0}$

Where Z was absorbing interface wave impedance, μ_0 and ε_0 were magnetic permeability and dielectric constant of free space, μ_r and ε_r were relative permeability and relative dielectric constant. By the formula (2), it was easy to calculate ideal impedance matching conditions:

$\mu' = \varepsilon'$, $\mu'' = \varepsilon''$

Stainless steel filament fiber conducted electricity well, resistivity was only $10^{-6}\ \Omega \cdot$ cm, had been widely used in electromagnetic radiation shield fabric. Stainless steel filament in the center of core yarn reduced the overall conductivity of fabric, which was conductive to achieve impedance matching and reduce electromagnetic reflections. Ni-Fe fiber blended fabric was used as the second layer with a strong dielectric loss and magnetic loss characteristics.

2.2 Measurement. GJB2038-94 wave absorbing material reflectivity test method 102"RAM reflectivity arch testing method" was used. Microwave scanning signal source was HP83751B and obtained the results by HP8757E network analyzer in the frequency range of 2~18GHz.

2.3 Single layer fabrics design and test. Single layer Ni-Fe fiber and stainless steel filament fabrics were fabricated and tested respectively, the results were shown in Fig.1 and Fig.2.

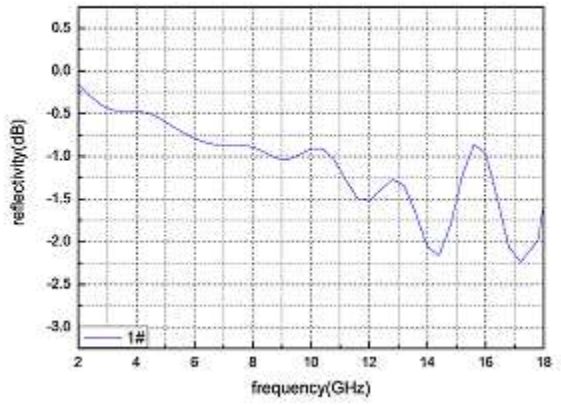

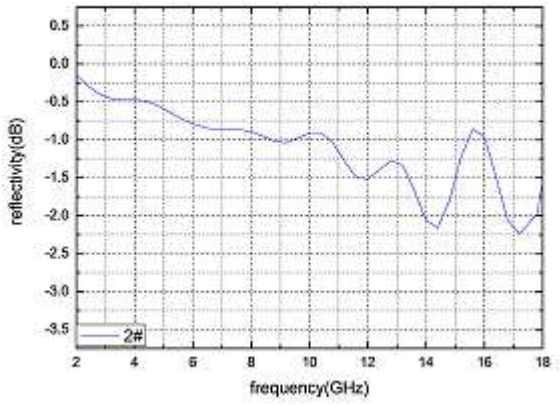

Fig.1 The reflectivity of stainless steel core-spun fabric Fig.2 The reflectivity of Ni-Fe fiber fabric

As shown in Fig.1 and Fig.2. , the reflectivity of designed single-layer were poor, because it was too thin to adjust electromagnetic parameters of single-layer fabric, difficult to meet the impedance matching.

2.4 Double layer fabrics design and test. According to absorbing material design principle, the single components was difficult to fully meet the "thin, light, wide, strong" and other requirements, double layer two-component absorption fabrics were designed. Ni-Fe fiber consisted of second layer due to its strong dielectric loss and magnetic loss, stainless steel core-spun yarn made up of first layer which easily realized matching to the free space.

In order to find the optimal laminated fabric, orthogonal experimental with three factors and three levels of the fabric specifications was shown in Tab.1. SU111-automatic sample loom was applied to fabricate 4 kinds of fabrics, the length and width were both of 30cm, the test results of absorbing properties were shown in Tab.2. Only one type of Ni-Fe fiber blended fabric was prepared as the underlayer, which blending ratio, warp density and weft yarn were 8.34%, 230/10cm and 18/10cm respectively.

Tab.1 Laminated fabric design

Levels	A The yarn core diameter （μm）	B warp density Pj(/10cm)	C Weft density Pw(/10cm)
1	18	260	210
2	28	280	230
3	34	300	250

Tab.2 The absorbing properties test

Number	The yarn core diameter（μm）	Pj (/10cm)	Pw (/10cm)	absorption peaks（GHz）	Minimum reflectivity R_L (dB)	bandwidth <-10dB f_w (GHz)
1	18	260	210	10.08	-13.68	2.02
2	18	280	230	11.24	-16.74	2.55
3	18	300	250	11.86	-14.50	2.35
4	28	260	230	14.56	-19.59	3.59
5	28	280	250	7.32	-28.50	4.10
6	28	300	210	16.32	-22.33	3.85
7	34	260	250	13.40	-20.02	3.88
8	34	280	210	7.48	-22.56	3.60
9	34	300	230	10.68	-23.12	3.16

Results and discussions

As shown in Tab.2, the optimal reflectivity of laminated fabrics can reach -21.10 dB and the bandwidth <-10dB was 3.08. The test results were studied with variance analysis method and shown in Tab.3. From the analysis, we can obtain that the yarn core diameter had significant influence on absorbing performance, the warp density and weft density also had effects on it.

Tab.3 The variance analysis of absorbing property of double composite fabric

（a）The variance analysis of minimum reflectivity

Variation source	deviation quadratic sum	freedom	variance	F	Fa	significance
core diameter	143.9606	2	71.980	13.9883	F0.05（2,6）=5.14335	**
Pj	61.1052	2	30.553	5.9375	F0.01（2,6）=10.9248	*
Pw	107.9054	2	53.953	10.485		*
null columns e*	26.0931	2	13.047	2.5354		
error	30.8746	6	5.146			
total	369.9389	8				

（b）The variance analysis of bandwidth of reflectivity less than -10dB

Variation source	deviation quadratic sum	freedom	variance	F	Fa	significance
core diameter	4.0178	2	2.009	23.260	F0.05（2,6）=5.14335	**
Pj	1.0592	2	0.530	6.132	F0.01（2,6）=10.9248	*
Pw	1.3072	2	0.654	7.568		*
null columns e*	0.3584	2	0.179	2.075		
error	0.5182	6	0.0864			
total	7.2608	8				

Conclusions

Different combinations of laminated fabrics were compared to find the main affect factors of absorbing performance. As the experimental results shown, the factors of yarn core diameter had significant effects, warp density P_j and weft density P_w both also had significant effects on absorbing performances. With optimized specifications, the fabrics can obtain good absorbing performances with a low areal density, wideband and thin characters.

Acknowledgments

This work was supported by the Natural Science Foundation of Hebei Province (E2013208122), The Natural Science Youth Foundation Project of Education Department of Hebei

Province(QN20131125) and Research Fund for the Doctoral Program of Hebei University of Science and Technology (010085).

References

[1] Heyun Zhao, Xiang Jingzhong, Xinghui Wu. Journal of Yunnan University (Natural Sciences: 2002, 24 (1A): 58~62
[2] Zili Yang. Heilongjiang Environmental Journal. 2010(34):19-26
[3] Yuling Zheng, Jianjun Yu , Jingliang Qin, et al. Occupation and Health. 2011(27):689- 691
[4] Guodong Yang, Yong Kang, Qianjin Meng. Applied Chemical Industry. 2003 (39):584–589
[5] Xiaofang Guo, Changzheng Wang, Shiyang Wu. Gansu Metallurgy. 2010(32):47-50
[6] Yan'an Yang, Wenyan Zhang, Wenfeng Bai. Rare Metals Letters. 2006(25):33-37
[7] Xiucheng Zhang, Huahui He. Journal of Huazhong University of Science and Technology. 2001 (29):14-15

Advanced Materials Research Vols. 960-961 (2014) pp 43-46

doi:10.4028/www.scientific.net/AMR.960-961.43

Research new waterproof agent of the particleboard

Zhao yan

Beihua University, Jilin, 1320132

Keywords: Non wood shavings; Molded sheet; Process parameters; Mechanical properties

Abstract: Modern society,with the rapid development of economy,people living standard increasing, for the plate demand continues to grow. Because the forest resources dwindling, To make full use of waste bagasse, corn straw and non wood fiber materials to produce an artificial plate material instead of wood man-made board has be imperative.Corn straw shavings can realize the recycling of waste materials, bring the economic value, so this topic with corn straw shavings as raw material, in the laboratory preparation of melamine resin adhesive, pressing flake molded sheet.Melamine plastic using M (melamine):U (urea) :F (formaldehyde) =1∶0.6∶2.5, adhesive solid content is 54%, the sizing, hot pressing temperature, hot pressing time as three factors orthogonal experiment, pressed sheet. On the plate thickness swelling, internal bond strength and surface plate bending strength test, on the analysis and summarization of results, the optimum process parameters: sizing quantity20%, temperature 150 ˚C, hot pressing time25min. The corresponding optimum mechanical properties: the absorbing water thickness expansion rate (2H) 9.76%, inner strength, bend strength of17.49Mpa,0.45MPa.

Introduction

In particleboard production process, in order to enhance the waterproof performance particleboard, widely used in the production method of a waterproofing agent was added to the plate. Currently the most used is water repellent wax emulsion. The paraffin emulsion quality directly affect the waterproof performance. So many domestic researchers waterproofing agent on paraffin emulsion stability, water resistance, etc. conducted extensive research.

For a long time, particleboard production is mainly used as a waterproofing agent paraffin, particleboard production of basic addition method using molten paraffin, particleboard production in the use of paraffin emulsion. Particleboard using conventional solid wax emulsion has a low content (usually less than 30%) and high moisture content.

Shavings molded integrally molded flat this subject, the package can be avoided, in order to enhance the tear waterproof particleboard, loaded material, adding new water repellent - paraffin. The product board formation, its carrying capacity in line with national standards, fairly flat with ordinary wood. Due to the production process particleboard center temperature exceeds 105 ˚C, and the final moisture content of the product is less than 9%, so the product can resist insects and decay fungi erosion, without further processing can be achieved by any other international organization Plant Protection Convention at No. 15, the international standard for phytosanitary measures enacted in 2002——"Wood Packaging Material in International Trade Management Guidelines" (International Standard for Phytosanitary Measures 15, referred to as ISPM 15) in particleboard materials for export quarantine requirements [1-6].

Physical and mechanical properties of this material particleboard meet structural requirements; smooth surface, excellent performance, environmental protection, fumigation, the economy, the furniture market is to meet the needs of the most ideal products [7]:

Experiment

2.1 Physical and chemical properties of the test urea-formaldehyde glue

2.1.1Viscosity measurement

The Tu 4 cup viscometer cleaning and keep it dry, adjust the horizontal screw in a horizontal position so viscometer, viscosity cup placed beneath 250ml beaker, hand blocked drain holes, filling the glue viscosity cup, with a glass rod the design of bubbles and excess scraped into the groove, and then

release your finger out of, and immediately start the stopwatch, the time when the entire sample flowing from the drain mouth is coated specimen 4 cup measuring viscosity. The difference between the two measured values should not exceed 3% of the average.

2.1.2 Determination of solid content

Take three glass dish, washed with water and put it into the oven removed after drying, labeling, pick a good analytical balance to be cleared in advance, the glass dish on the analytical balance, note the glass dish weight after cleared; taken with plastic dropper dropping resin, drop by drop on a glass dish, when the value reaches a certain date, note the weight of the resin and the glass dish, and then the weight of the glass dish, and then put the glass dish into the constant temperature of the drying oven 100 ˚C, after about three hours to remove, removed after cooling in the oven for some time, and then weighed on an analytical balance, note values. Averaging the three values, namely the solid content of the melamine resin.[8]

Tab1 Solid content measurement data

No.	m1（g）	m2（g）	m（g）	R(%)
1	13.9747	15.0630	14.5640	54.50
2	15.0018	16.1850	15.6390	53.85
3	12.6683	13.7478	13.2466	53.57

Therefore, the solids content of urea-formaldehyde glue: $R=(R_1+R_2+R_3)/3=53.97\%$。

2.2 Orthogonal design

In the packing sheet repression experiment, due to take into account the amount of glue, pressing temperature, pressing time three factors, if we make a three experimental factors and three levels, according to a comprehensive test requirements shall be 3×3 = 27 combination of experimental and has not yet considered the number of repetitions of each combination, and therefore adopt high efficiency, quick and economical method of orthogonal experimental design to volume sizing, pressing temperature, pressing time for three factors are the main factors, 3 levels L9 (3^4) orthogonal experiment, bit-level factors are shown in Table 2-2.

Tab2 Orthogonal table

Test No.	Factor		
	Content of glue/%	Thermal pressure temperature/˚C	Thermal pressure time/%
1	10	130	4
2	10	140	5
3	10	150	6
4	15	130	5
5	15	140	6
6	15	150	4
7	20	130	6
8	20	140	4
9	20	150	5

Determination of thickness swelling of particleboard

3.1 Experimental principle, instruments, methods

(1) Principle: Make sure the specimen before absorbing increased thickness than the thickness of the absorbent.

(2) laboratory equipment: water bath pot calipers

(3) Specimen size: 50×50mm

(4) experimental procedures and methods:

(a) measuring the center of the test piece thickness h1, accurate to 0.01mm;

(b) the specimen placed on the shelf, immersed in water for 20±2˚C, so that the specimen surface is higher than 2cm, all specimens that do not float on water, do not sink to the bottom, either free expansion of the specimen;

(c) soaking two hours, remove the specimen, and then measuring the thickness of the original measuring point h_2;

$$D = \frac{h_2 - h_1}{h_1} \times 100$$

Where: D - specimen water swelling (%)

h_1 - before soaking the specimen thickness (mm);

h_2 - after soaking the specimen thickness (mm)

3.2 Experimental results and analysis

The results are shown in Table 3-1, where α = 0.05, F0.1 (2,2) = 4.460. Response curve shown in Figure 3-1.

Tab. 3 Intuitive adsorption expanding of orthogonal table

Test No.	Factor			Adsorption expanding/%
	conten of glue/%	thermal pressure time/%	water-proofing addivice/%	
1	10	130	4	8.97
2	10	140	5	7.98
3	10	150	6	7.80
4	15	130	5	7.82
5	15	140	6	7.50
6	15	150	4	8.57
7	20	130	6	7.40
8	20	140	4	8.15
9	20	150	5	7.74
K1j	8.25	8.06	8.07	
K2j	7.96	7.88	7.98	
K3j	7.76	8.04	7.92	
Rj	1.46	0.56	0.44	

3.3 Experimental results and analysis

Table derived from visual analysis, static bending strength of the primary to the secondary factors as: the amount of glue, pressing temperature, pressing time. MOR optimal solution is: $A_3B_2C_2$, namely resin content of 20%, hot temperature of 140 ˚C, hot pressing time was 25min.[9-10]

ANOVA table can be drawn glue content, pressing time, pressing temperature were the significant factors. Effect curves can be drawn, the greater the amount of sizing, static bending strength increases; pressing temperature of 140 ˚C, hot pressing time 25min, the MOR maximum value. Pressing higher the temperature, the longer the pressing time, pallet board brittle, its bending strength decreases, the same as the above results and analysis. Therefore, the optimal process parameters $A_3B_2C_2$, namely resin content of 20%, hot temperature of 140 ˚C, hot pressing time was 20min.

According to GB / T 4897.1-2003, structural use in humid conditions required by board, the board thickness of 13 ~ 16mm, water expansion ratio less than or equal 8.0, because this time the water swelling of 7.40%, thus reaching the national standard.

Conclusion

Since the majority of particleboard in furniture applications, so it is important waterproof particleboard, adding waterproofing agent affect particleboard water swelling. Of water swelling, the resin content of 20%, pressing temperature 140 ˚C, when the pressing time 20min, its value reaches a minimum. From the table, when pressed to process parameters A3B2C2 particleboard, its water swelling, internal bond strength have reached the national standard.

In summary, pressed particleboard optimal process parameters A3B2C2, namely resin content of 20%, hot temperature of 140 ˚C, water repellent 6%. Mechanical properties of the corresponding value: 7.40% water swelling, internal bond strength 0.46MPa.

References

[1] Tang Chaofa, Shen Dejun straw board veneer isocyanate adhesive [J]. Timber industry, 2011,3

[2] Zheng Fengshan, Li Yuefen, Ding Zhanlai for. Corn stalks manufacture particleboard experiment [J]. Plywood communications, 2002,12

[3] Wang Qi,Li Jining, Shi Yuliang.Impact of corn stover particle shape on the physical properties of particleboard [J]. Agriculture and Technology,2005,12

[4] Feng Shan. Corn stover particleboard identified by experts in Shijiazhuang [J]. Plywood Communications, 2002,12

[5] Xu Meijun. Non-wood panel research attention [J]. Building Materials Industry Information[J].1995(04)

[6] Shang Deku,Li Zhanbo,Wang Maodi,Liu Ruoxing.A theory of determining mass transfer parameters for wood particle materials[J]. Forest Prod,1996

[7] Qin Tefu. Effect of wood particle size on the properties of wood/polypropylene composite I: Mechanical properties .Chinese forestry science and technology,2002,1

[8] Stark,N,M;Berger,M,J.Investigation of species effects in an injection-molding-grade, wood-filled polypropylene.The fourth international conference on woodfiber-plastic composites,1997,13(1):19~25

[9] Inge Johansson,Tobias Karlsson,Roland Wimmerstedt. Volatole organic compound emission when drying wood particles at hign dewpoints[J]. Forest products journal,2004,12(6)767~772

[10] Karlsson,T.“Terpene release during drying of wood flakes for particleboard manufacture”, Ph.D.Thesis, Lund University, Lund, Sweden.(2001)

Advanced Materials Research Vols. 960-961 (2014) pp 47-51
© (2014) Trans Tech Publications, Switzerland
doi:10.4028/www.scientific.net/AMR.960-961.47

The Comparison of Albumin Dialysis between Open- and Closed-Loop Dialysis Modes

Yingying Pei[1, a], Yize Sun[1], Sijie Sun[2], Dayong Gao[2, b, *], Weiping Ding[3, 4, c, *]

[1]Department of Mechanical Engineering, Donghua University, Shanghai 201620, China

[2]Department of Bioengineering, University of Washington, Seattle, WA 98195, USA

[3]Center for Biomedical Engineering, [4]Department of Electronic Science and Technology, University of Science and Technology of China, Hefei, Anhui 230027, China

[a] peiyingying@mail.dhu.edu.cn, [b] dayong@u.washington.edu, [c] wpdings@ustc.edu.cn

[*]Corresponding authors. Tel.: +86-55163600197

Keywords: albumin dialysis, artificial liver support system, protein-bound toxin, mass transfer

Abstract: The open-loop albumin dialysis mode (OLM) is usually used to remove protein-bound toxins from artificial liver support systems. However, there is still interest in closed-loop albumin dialysis mode (CLM) because this mode could enable the regeneration and reuse of albumin and minimize the physical size of liver support systems. In this paper, the two dialysis modes were theoretically compared under various theoretical conditions. Our results show that at the beginning of the dialysis period, in terms of detoxification efficiency, CLM is better. As the molar ratio of toxin to albumin in the blood (RTA) decreases, the overall performance of CLM approaches that of OLM in 4-hour dialysis. In certain cases, the clearance of albumin-bound toxins by CLM could be as effective as that by OLM; occasionally, CLM is even more effective.

Introduction

Liver failure, a common and serious public health problem, causes high mortality all over the world [1]. A shortage of donor organs is prompting the development of various extracorporeal artificial liver support systems [2-4].Currently, albumin dialysis is used in liver support systems, starting a new era of the treatment of liver failure [5].

Albumin dialysis is a detoxifying method that involves a hemodialysis system in which albumin solution is used as dialysate [6]. In the dialysis process, free toxins unbound to albumin are transferred out of fibers because of concentration and pressure differences across the fiber membrane, bind to albumin on the dialysate side and are eventually removed. Usually, there are two operating modes: one is called open-loop dialysis mode (OLM) [7, 8], the other is closed-loop dialysis mode (CLM) [9, 10]. For OLM, it requires a large volume of dialysate and is also not convenient for regenerating albumin. Therefore, there is still interest in closed-loop mode (CLM) for systems removing toxins only by albumin [11]. CLM is considered to be a possible way to help to reduce the use of dialysate (i.e., increasing the portability of devices) and to improve the regeneration of albumin (i.e., reducing the treatment cost), but there are still certain issues that need to be resolved in advance. The first issue is what factors affect the efficiency of CLM, the second is how to obtain a higher efficiency for CLM in practice, and the third is whether the efficiency of CLM is better than that of OLM.

In this work, CLM in albumin dialysis was investigated and then compared with OLM in term of their efficiency in removing albumin-bound toxins. The factors affecting the efficiency of CLM are also discussed. The results of this study are of great significance to the design of a portable extracorporeal artificial liver system.

Theory

In the solution, the concentration of the toxin is equal to the sum of the free toxin concentration and the albumin-bound toxin concentration. Under the condition of equilibrium, there exists an equilibrium binding constant k_B (l/mol) as follows [12]:

$$k_B = C_{a\cdot s} / (C_s \cdot C_a) \tag{1}$$

where the subscripts *a·s, s,* and *a* denote the albumin-toxin compound, the free toxin, and the free albumin, respectively; k_B (l/mol) the equilibrium constant; and C (mol/l) the concentration. For a given equilibrium constant, the above binding kinetic can be used to obtain the relationship of the free toxin concentration and the total toxin concentration.

According to the literature [13, 14], the equations for calculating the local ultrafiltration are:

$$dP_b / dz = -8\mu_b \cdot Q_b / (n\pi \cdot r_i^4) \tag{2}$$

$$dP_d / dz = 8\mu_d (R_M + nr_o)^2 \cdot Q_d / [\pi (R_M{}^2 - nr_o{}^2)^3] \tag{3}$$

$$dQ_b / dz = dQ_d / dz = -J_v \tag{4}$$

$$J_v = 2n\pi r_i \cdot L_P \cdot (P_b - P_d) \tag{5}$$

where the subscripts *b* and *d* denote the blood and dialysate sides, respectively; r_i (μm) the inner radius of hollow fibers; r_o (μm) the outer radius of fibers; Q (ml/min) the flow rate; P (P_a) the pressure;μ (N·s/m^2) the viscosity; L_P (cm/s/P_a)the hydraulic permeability; R_M (cm) the inner radius of the module; n the number of fibers; and J_v (ml/min/cm) the local ultrafiltration rate.

According to mass conservation, the mass transport of free toxins along the axial direction, considering the effect of local ultrafiltration, can be described as follows [15]:

$$d(Q_b \cdot C_{s,tl,b}) / dz = d(Q_d \cdot C_{s,tl,d}) / dz = [J_v (1-\sigma) f - kA / L] \cdot [C_{s,b} - C_{s,d}] - J_v (1-\sigma) C_{s,b} \tag{6}$$

where the subscript *tl* indicates the total amount; σ the toxin reflection coefficient; k (cm/min) the mass transfer coefficient; L (cm) the effective length of fibers; A (cm^2) the total membrane area and f a function of the Pe number: $f = 1/Pe\text{-}1/(e^{Pe}\text{-}1)$ and $Pe = Q_f \cdot (1\text{-}\sigma)/kA$ [15].

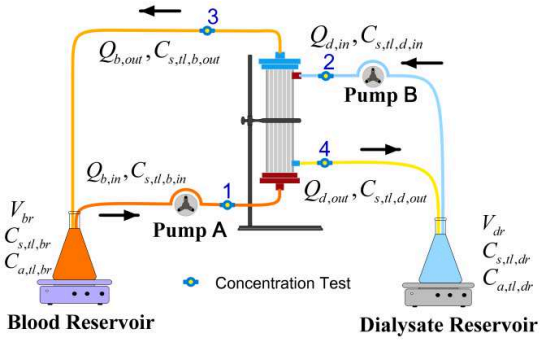

Fig. 1 Schematic of albumin dialysis in CLM

In the CLM experiment shown in Fig.1, the total toxin and albumin concentrations in blood and dialysate reservoirs are functions of dialysis time and can be written as

$$d(C_{s,tl,br} \cdot V_{br}) / dt = C_{s,tl,b,out} \cdot Q_{b,out} - C_{s,tl,b,in} \cdot Q_{b,in} \tag{7}$$

$$d(C_{s,tl,dr} \cdot V_{dr}) / dt = C_{s,tl,d,out} \cdot Q_{d,out} - C_{s,tl,d,in} \cdot Q_{d,in} \tag{8}$$

where the subscripts *br* and *dr* denote the blood and dialysate reservoirs, respectively; the subscripts *in* and *out* denote the inlet and outlet of a reservoir, respectively; and V (ml) is the solution volume.

In simulation, equations were solved by Runge-Kutta, and a regula-falsi method was used, according to the literature [13, 14]. A mesh refinement analysis was performed so that the error caused by the grids was less than 0.5%.

Results and Discussion

The Effect of Albumin Concentrations in CLM. In OLM, the concentration of albumin in the dialysate is low, and the volume of the dialysate is large; therefore, albumin regeneration is not convenient. However, CLM does not have such draw back. Fig. 2 shows the effect of albumin concentrations in dialysate on the clearance of toxins for a certain mass of albumin. If the albumin concentration is higher, more free toxins in dialysate will be bound to albumin molecules in dialysate, generating a higher driving force for the transport of free toxins from the blood side to the dialysate side. Therefore, a highly concentrated albumin dialysate results in a high toxin clearance.

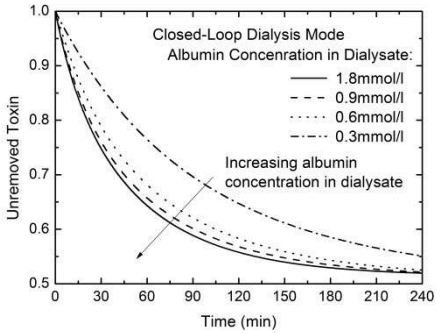

Fig.2 Effect of albumin concentrations in dialysate on toxin (k_B= 10^5 l/mol) removal in CLM with a fixed mass of albumin (1.8 mol) at Q_d= 30 ml/min, Q_b = 200 ml/min, and Q_f= 0 ml/min. Initial conditions: $V_{br}|_{t=0}$ = 3000 ml, $C_{a,tl,br}|_{t=0}$ = 0.6 mmol/l, $C_{s,tl,br}|_{t=0}$ = 0.684 mmol/l.

Comparison of Detoxification Efficiencies. In this work, we performed a comparison between CLM and OLM. To facilitate the comparison, the amounts of albumin used in both CLM and OLM were assumed to be equal, and the dialysis time was set at 4 hours. Our results show that the detoxification efficiency of CLM is higher than in OLM at the beginning and lower in the late stage (Fig. 3). If the molar ratio of toxin to albumin in the blood (λ) become smaller (Fig. 3 A vs. B and Fig.3 C vs. D), the difference in detoxification efficiency between CLM and OLM in the late stage could decrease. Based on the above analysis, there is possibly a turning point for λ for a certain toxin, under which CLM could be more effective and over which OLM could be more effective during 4 hours of dialysis. Both CLM and OLM have their own advantages and disadvantages; however, for the sake of albumin cost and the convenience of albumin regeneration, CLM is highly recommended.

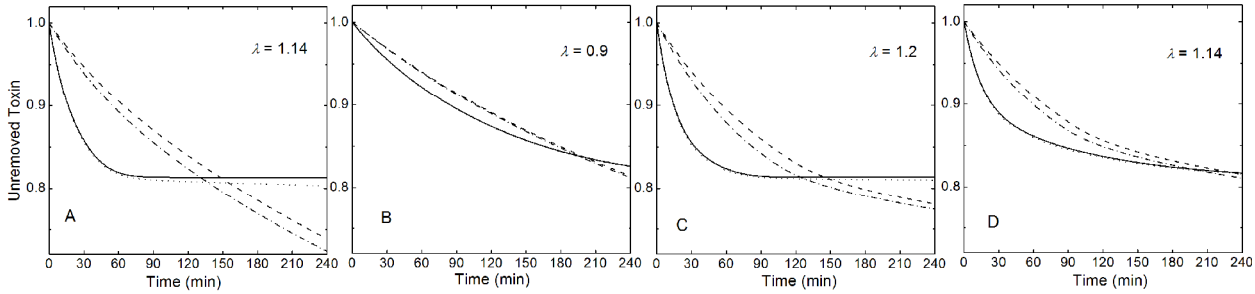

Fig. 3 Comparison of clearances for a toxin between CLM and OLM at Q_b = 200 ml/min(A, B: k_B = 10^6 l/mol; C,D: k_B = 10^7 l/mol)(Initial conditions: $V_{br}|_{t=0}$ = 3000 ml, $C_{a,tl,br}|_{t=0}$ = 0.6 mmol/l, $C_{s,tl,br}|_{t=0}$ = 0.684 mmol/l. In CLM, $V_{dr}|_{t=0}$ = 500 ml, $C_{a,tl,dr}|_{t=0}$ = 0.864 mmol/l, Q_d= 200 ml/min. In OLM, $C_{a,tl,dr}|_{t=0}$ = 0.06 mmol/l, Qd = 30 ml/min). Solid line: CLM, Q_f= 0 ml/min; dot line: CLM, Q_f= 10 ml/min; dash line: OLM, Q_f= 0 ml/min; dash-dot line: OLM, Q_f=10 ml/min.

Conclusions

The need for a large quantity of expensive albumin in albumin dialysis motivated us to find not only a more efficient but also a more economical mode of dialysis operation for artificial liver systems. In this work, the detoxification efficiencies for toxins in the blood in both CLM and OLM were compared theoretically. Our results show that for a fixed mass of albumin in CLM, a higher albumin concentration in the dialysate is helpful to remove toxins from the blood. As the molar ratio of toxin to albumin in the blood decreases, the overall performance of CLM approaches that of OLM in 4-hour dialysis. In certain cases, the clearance of toxins in CLM could be as effective as in OLM; occasionally, this clearance could be even better. Both CLM and OLM have their own advantages and disadvantages; however, due to the cost of albumin and the convenience of albumin regeneration, CLM is highly recommended. In addition, because a concentrated albumin solution is used, the volume of the dialysate is reduced, which will enable significant improvements in the design of portable extracorporeal liver supporting systems.

References

[1] J. Vienken and H. Christmann, *How can liver toxins be removed? Filtration and adsorption with the Prometheus system,* Therapeutic Apheresis and Dialysis, **10** (2006) 125-131.

[2] T.M. McCashland, B.W. Shaw Jr and E. Tape, *The American experience with transplantation for acute liver failure*, in Seminars in liver disease, 1996: Thieme Medical Publishers, Inc.

[3] J. Rozga, Y. Umehara, A. Trofimenko, T. Sadahiro and A.A. Demetriou, *A novel plasma filtration therapy for hepatic failure: Preclinical studies,* Therapeutic Apheresis and Dialysis, **10** (2006) 138-144.

[4] J. Stange, *Extracorporeal liver support,* Organogenesis, **7** (2011) 64-73.

[5] B. Kreymann, M. Seige, U. Schweigart, K.-F. Kopp and M. Classen, *Albumin dialysis: effective removal of copper in a patient with fulminant Wilson disease and successful bridging to liver transplantation: a new possibility for the elimination of protein-bound toxins,* Journal of hepatology, **31** (1999) 1080-1085.

[6] J. Patzer, *Principles of bound solute dialysis,* Therapeutic Apheresis and Dialysis, **10** (2006) 118-124.

[7] U. Boonsrirat, K. Tiranathanagul, N. Srisawat, P. Susantitaphong, P. Komolmit, K. Praditpornsilpa, K. Tungsanga and S. Eiam□Ong, *Effective Bilirubin Reduction by Single‐Pass Albumin Dialysis in Liver Failure,* Artificial organs, **33** (2009) 648-653.

[8] K.L. Collins, E.A. Roberts, K. Adeli, D. Bohn and E.A. Harvey, *Single pass albumin dialysis (SPAD) in fulminant Wilsonian liver failure: a case report,* Pediatric Nephrology, **23** (2008) 1013-1016.

[9] P. Krisper and R.E. Stauber, *Technology Insight: artificial extracorporeal liver support—how does Prometheus® compare with MARS®?,* Nature Clinical Practice Nephrology, **3** (2007) 267-276.

[10] S. Sen, R. Mookerjee, N. Davies, R. Williams and R. Jalan, *Review article: the molecular adsorbents recirculating system (MARS) in liver failure,* Alimentary pharmacology & therapeutics, **16** (2002) 32-38.

[11] I.M. Sauer, M. Goetz, I. Steffen, G. Walter, D.C. Kehr, R. Schwartlander, Y.J. Hwang, A. Pascher, J.C. Gerlach and P. Neuhaus, *In vitro comparison of the molecular adsorbent recirculation system (MARS) and single-pass albumin dialysis (SPAD),* Hepatology, **39** (2004) 1408-1414.

[12] J.F. Patzer and S.E. Bane, *Bound solute dialysis,* ASAIO journal, **49** (2003) 271-281.

[13] W. Ding, S. Heimfeld, J.-A. Reems, D. Gao and X. Zhou, *A steady-state mass transfer model of removing CPAs from cryopreserved blood with hollow fiber modules,* Journal of biomechanical engineering, **132** (2010) 011002.

[14] Y. Pei, Y. Sun, Y. Xu, G. Zhao, D. Gao and W. Ding, *A theoretical ultrafiltration model for albumin-bound toxin dialysis*, in Complex Medical Engineering (CME), 2013 ICME International Conference, 2013: IEEE.

[15] J.F. Patzer, S.A. Safta and R.H. Miller, *Slow continuous ultrafiltration with bound solute dialysis,* ASAIO journal, **52** (2006) 47-58.

Advanced Materials Research Vols. 960-961 (2014) pp 52-56

doi:10.4028/www.scientific.net/AMR.960-961.52

The research of high internal pressure forming process of variable cross-section elliptical tube

Jintao Wang, Jian Li

School of materials, Northwestern Polytechnical University, Shaanxi Xi' an China

15362282@qq.com

Keywords: TA2; high internal pressure forming; variable cross-section elliptical tube; finite element method

Abstract: Based on the ETA/DYNAFORM elastic-plastic explicit finite element platform, the finite element model of high internal pressure forming was established and the forming process was simulated. Through simulating, the forming process was researched. The distribution law of wall thickness, stress and strain was revealed in forming process. The results show that: the thinnest wall lies in the middle of forming part, and the thickest wall in the end of feeding areas. Both maximum equivalent stress and minimum equivalent strain lie in the forming fillet of the large elliptical cross-section. These play an important guiding significance on molding process.

Introduction

As a kind of advanced no-cutting plastic forming technology, high internal pressure forming has take more and more attention and development [1]. In recent years, Germany, the United States and Japan use the forming technology for the manufacture of machine parts, the forming pressure is generally greater than 500 MPa, sometimes more than 1, 000 MPa[2] .At present, it has been used in automobile, aviation and other machine manufacture field of practical production[3]. But on the other hand, it is a relatively new industry technology. Some key technical problems, such as forming mechanism of complex parts, have not been resolved and need further research. So, the research of high internal pressure forming technology has an important practical significance [4-7].

High internal pressure forming of variable cross-section elliptical tube is a complex multi-factor coupling deformation process ,including material, mould, process parameters, etc[5-9].In this paper, the internal high pressure forming process of varying cross-section elliptical tube is studied though the theoretical analysis and finite element numerical simulation. The forming law and deformation mechanism is revealed through stress and strain distribution, and laws of wall thickness development in the process of forming. These provide certain theoretical basis for the establishment of the forming process, thus reducing the time and cost for high internal pressure forming technology research and development, and increasing productivity and utilization rate of materials.

Build models

DYNAFORM pretreatment provides with modeling function. But because of its low efficiency, 3D modeling software UG is used to establish the geometric model. Here we only need to build mould, tube billet and punch on both ends. After building up the mold, output of IGES format file, and then input it to the former processor of DYNAFORM software. Because high internal pressure forming simulation usually adopt thin shell grid cell, block model is used in modeling. As shown in figure 1 is the geometry model.

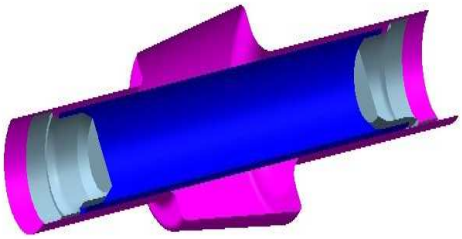

Figure1 Geometrical model

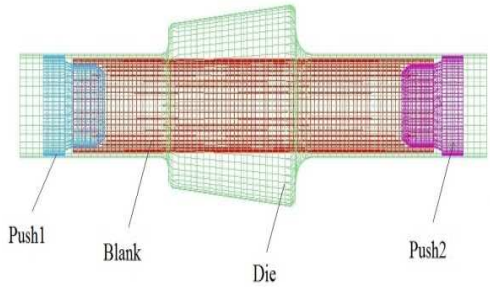

Figure2 The finite element model

In the EAT/DYNAFORM MESH generator, TOOL MESH is chose to divide grid for die and punch, because this type of grid has the highest fitting precision to mold. PART MESH is chose to mesh for the pipe, as it can obtain more uniform fine grid, which is convenient to subsequent calculation. In the process of meshing, try to ensure that all units are quadrilateral element, and make the triangle element distribution on the edge, so that the accuracy of the calculation can be ensured .Finite element model is shown in figure 2, the tube billet is BT shell element and other tools are treated as rigid body unit.

The simulation results and analysis

3.1 The variation law of wall thickness in the forming process

In the process of pipe high internal pressure forming, the stress distribution of each part is different. It will change with the increase of the swelling degree. Wall thickness distribution is an important indicator of internal high-pressure forming.

Figure 3 shows the distribution of wall thickness in four forming stages. As we can see: The wall thickness mainly thin in 0.04 ~ 0.05 s, because during this time, the materials of transition fillet accumulate, which causes materials flow into the mold cavity difficulty. At the end of the forming, the wall thickness of forming central area is thinnest, and the more to the sides, the thicker the wall thickness is, because internal pressure increases faster than the feeding speed; the feeding zone have a thickening , this is because of the friction between pipe material and mold. The wall thickness of large elliptical cross- section feeding area thickens bigger than small.

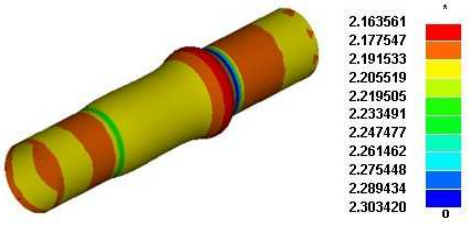

a) forming time 0.019s

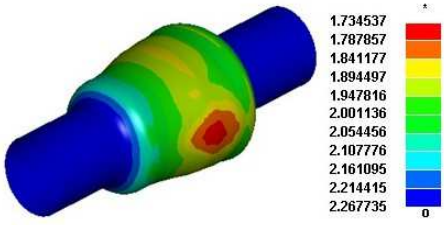

b) forming time 0.04s

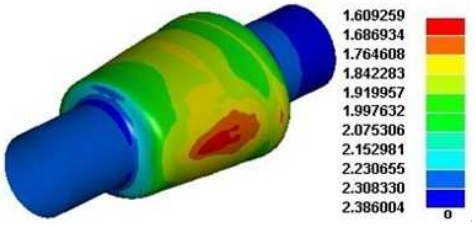

c) forming time 0.05s

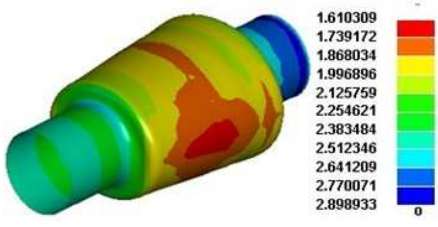

d) forming time 0.06s

Figure3 Thickness distribution of variable parameters elliptical Cross-section tube in internal high pressure forming (mm)

3.2 The distribution rule of equivalent stress

Assume that the pipe is a thin wall one, ignore the stress in the thickness direction, and only consider the axial and tangential stress, we can simplify stress state as a plane one. With the forming, the pipe of forming area bulges outward and stays at a two-way tensile stress state.

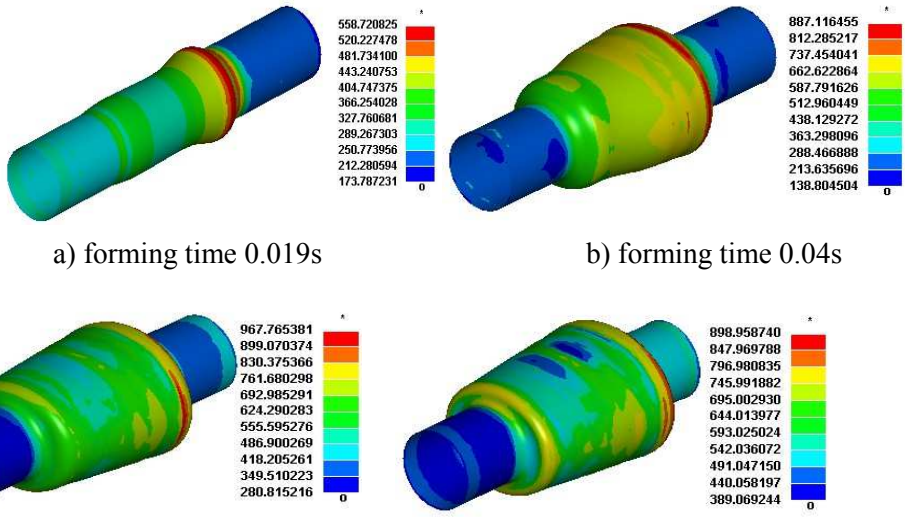

a) forming time 0.019s b) forming time 0.04s

c) forming time 0.05s d) forming time 0.06s

Figure4 Max equivalent stress distribution of variable parameters elliptical Cross-section tube in internal high pressure forming

As shown in figure 4 is equivalent stress distribution nephogram of forming process. at 0.019 s, the maximum equivalent stress locates in the forming rounded corner of large section, and forms a circular area; at 0.04 s, it is same with the previous stage but the area of maximum equivalent stress increases; at 0.05 s, the scope continues to increase, After the forming, the maximum equivalent stress still locates at the forming rounded corner of large section.

From above analysis we can see that in the whole forming process, the maximum equivalent stress always locates in the forming rounded corner of large elliptical cross-section, this is because the deformation of large cross-section forming rounded corner is maximum and deformation is most difficult.

3.3 The distribution rule of equivalent t strain

In forming process, the axial and tangential is tensile deformation, thick is compression deformation. As shown in figure 5 is equivalent strain distribution nephogram of forming process. At the beginning of forming, the equivalent strain presents a series of circular distribution, and the maximum equivalent strain locates in the forming rounded corner of large elliptical cross-section. Strain value of each part increases with the forming. At the end of the forming, the maximum equivalent strain still locates at the forming rounded corner of large section.

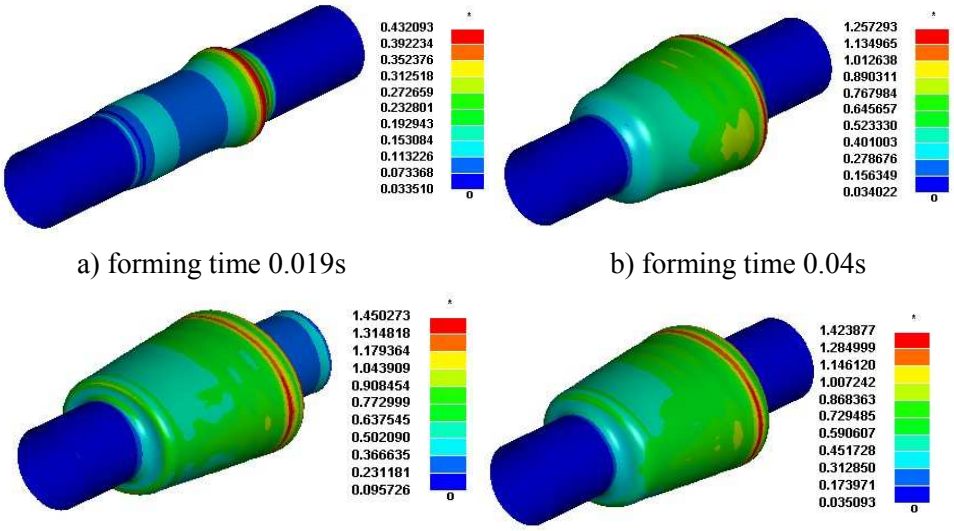

a) forming time 0.019s b) forming time 0.04s

c) forming time 0.05s d) forming time 0.06s

Figure5 Max equivalent strain distribution of variable parameters elliptical Cross-section tube in internal high pressure forming

From above analysis we can see that in the whole forming process, the maximum equivalent strain always locates in the forming rounded corner of large section. Deformation and flow are most sever in the maximum equivalent strain regions, so defects is easiest to appear in this place.

Conclusions

In this paper, through establishing the finite element model of TA2 varying cross-section elliptical tube high internal pressure forming, and simulating the forming process, we revealed the distribution rule of wall thickness, stress and strain in forming process:

1) The wall thickness mainly thin in 0.04 ~ 0.05 s. At the end of the forming, the wall thickness of forming central area thin and the more to the sides, the thicker the wall thickness is. The feeding zone thickens. The wall thickness of large elliptical cross- section feeding area thickens bigger than small.

2) The maximum equivalent stress and strain all locate at the forming rounded corner of large elliptical cross- section

References

[1] Baicheng Liu, The material forming technology of the 21st century. Aviation manufacturing technology. 2003, (6) 17 ~ 22

[2] Tonghai Wang, Tube plastic processing technology. Second edition. Beijing: mechanical industry press, 1998:102-115

[3] VOLLERTSEN F, PRANGE T, SANDER M. Hydroforming: needs, developments and perspectives Geiger M.Proceedings of 6th International conference on TechnologyPlaticity [C] . Berlin & Heidelberg: Springer verlag,1999. 1197□1210.

[4] Jie Tao, Gongbing Liu. Reviews and prospects of Metal pipe cold forming technology research progress. Machinery manufacturing and automation. 2009, 38:1 ~ 5

[5] M. Koe. Development and design guidelines for part, tooling and process in the tube hydroforming technology. Dissertation, The Ohio State University,1999

[6] LiHui Lang, Internal high pressure hydraulic processing technology and numerical simulation of its forming process. The Harbin industrial university postdoctoral outbound report, 2001

[7] F. Dohmann, Ch. Hartl. Research and practical application. Proceedings of 2th International Conference on Innovations in Hydroforming Technology. Ohio, USA, 1997:1~5

[8] F. Dohmann, Ch. Hartl. Hydroforming applications of coherent FEM simulation to the development of products and processes. Journal of Materials Processing Technology. 2004, 150: 18~24

[9] K.I. Manabe, M. Amino. Effects of process parameters and material properties on deformation process in tube hydroforming. Journal of Materials Processing Technology. 2002(123) : 285~291.

Advanced Materials Research Vols. 960-961 (2014) pp 57-60

doi:10.4028/www.scientific.net/AMR.960-961.57

The research progress of boron nitride nano-tubes in hydrogen storage

Ning Zhang, Feiyi Yang, Hongmin Kan, Huan Liu， Xiaoyang Wang

Key Laboratory of Advanced Materials and Manufacturing Technology of Liaoning Province,Shenyang University, Shenyang, Liaoning 110044, PR China

Zhangning5832@163.com

Keywords: Environmental protection; Nano-tubes; Hydrogen storage capacity

Abstract. There are a series of problems existing in global issues, such as the increasing energy demand, environmental pollution, haze and global warming. Thus, the hydrogen energy attracts more attention of new energy industry. The materials of hydrogen storage are ideal renewable energy carrier; the combustion of hydrogen forms water is pollution-free for the environment and releases large amounts of heat. This paper systematically introduces the structure, preparation methods, and hydrogen storage capability of boron nitride nano-tubes. It also highlights the importance of boron nitride nano-tubes, which we believe will play a promoting role for the hydrogen storage materials.

Introduction

With global economic development, human demand for oil, coal, natural gas and other fossil fuels are increasing. According to the existing world oil reserves and mining velocity, global oil resources will be depleted till 2050 year, and humanity will face an energy crisis.[1] It is noteworthy that fossil energy release large amounts of harmful gases in the combustion process. Nowadays, we are suffering serious pollution and ecological destruction. In addition, global warming and its effects are only worsening. Therefore, the development of new clean renewable energy is imminent, because of high efficiency and environmentally friendly hydrogen, which is honored as green renewable energy. However, hydrogen storage has become a major bottleneck of hydrogen energy technology development. For example, compared with the same energy of gasoline, the volume of liquid hydrogen(under pressure of 100bar) is 30 times that of gasoline. If its volume continues to compress until it exceeds the volume of gasoline by 10, one would need to pay a high cost, and there is a significant safety risk during the practical operation [2]. Thus, solid-state hydrogen storage materials has increased in importance and as an issue that needs to be addressed. Based on adsorption theory, hydrogen storage materials is divided into two sections chemistry adsorption and physical adsorpti：
Chemisorption of hydrogen storage materials include light metal alloys [3-5] and lanthanide hydrogen storage alloys [6-8]. Physical absorption of hydrogen storage materials include carbon nano-tubes [9-11] and boron nitride nano-tubes [12-14]. The hexagonal planar network structure of boron nitride is similar to graphite, which makes the preparation of boron nitride nano-tubes become possible. Boron nitride also shows a higher chemical and thermal stability, and its electrochemical properties has nothing to do with its diameter or helicity. Therefore, boron nitride nano-tubes could be ideal hydrogen storage materials, along with light quality and stability.

The structure of boron nitride

The structure of boron nitride(BN) is similar to the graphite(C), especially the hexagonal boron nitride (h-BN), its structure almost same to the layered structure of graphite. The cell parameters of hexagonal boron nitride (a=0.2504nm, c=0.6660nm) and graphite(a=0.2464nm, c=0.6708nm) is almost the same, so hexagonal boron nitride is also named white graphite. The comparison of crystal structure between hexagonal boron nitride and graphite is shown in Figure 1.

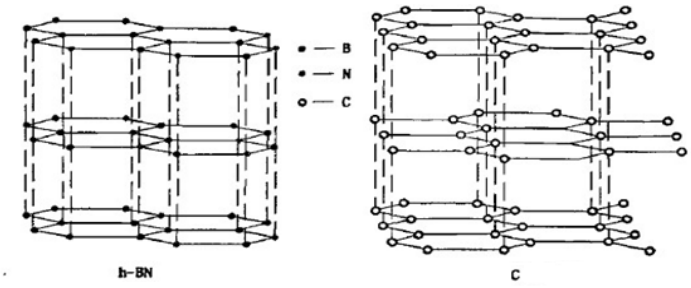

Figure1. The crystal structure of hexagonal boron nitride and graphite

The preparation of boron nitride nano-tubes

Currently, there are many different methods in preparing boron nitride nano-tubes, such as arc discharge method, laser evaporation method, arc melting method, and a carbon nano-tubes template method. Boron nitride nano-tubes were synthesized for the first time in a arc-discharged process[16]. Arc-discharge is a method to obtain nano-tubes by using a reactant as the electrode to discharge directly. In 1995, Chopra NG et al [16] made a bold improvement on the outer surface of a layer of BN coating, adding another refractory material(tungsten), and using tungsten as the positive electrode. With a water-cooled copper electrode as the anode electrode and helium as a buffer gas, multi-walled boron nitride nano-tubes are prepared by using a plasma arc method. Most of the pipe end of boron nitride nano-tubes have similar size and tube diameter of metal or metal boride particles by this method. Terrones et al.[17]. In addition, synthesized multi-walled boron nitride nano-tubes can be successful by using a similar method. Altoe et al.[18] This method can make the boron cast into ingots with a metal catalyst. Using these ingots as the electrode then can synthesize high-purity double-walled boron nitride nano-tubes. However, this method is too costly and it is almost impossible to apply it to industrialization.

Laser evaporation is a method of using laser that irradiates the block structure of boron nitride in the high pressure atmosphere of N_2 or Ar to prepare boron nitride nano-tubes. The diameter distribution of boron nitride nano-tubes prepared in this way is particularly small. In 1996, Golberg [19] used a 10Hz laser beam to prepare single-walled boron nitride nano-tubes, and D.P.Yu et al.[20] used 248nm laser beam to prepare single-walled boron nitride nano-tubes. Compared to other methods, boron nitride nano-tubes synthesized in this method show fewer layers, mostly single-walled tubes, and narrow the diameter distribution. However, the yield and purity of the boron nitride nano-tubes are not ideal.

The arc melting method is a way of preparing boron nitride nano-tubes in which the melting mixture of boron and the transition metal combine in a N_2 atmosphere. Tateo Oku et al.[21] Press the boron powder which is mixes Au and Fe_3O_4 into tablets, then the tablets are synthesized to boron nitride nano-tubes in the mixture atmosphere of Ar(0.025MPa) and N_2(0.025MPa). Recently, Zettl [22] wrote, using the non-equilibrium plasma arc method, melting BN ingots which mixed with cobalt and nickel, the current was 60A, the voltage was under the range of 30~45V, and then synthesized double layer of boron nitride nano-tubes. The inner diameter of the boron nitride nano-tubes was 2.2nm, and the outside diameter of the boron nitride nano-tubes was 2.9nm.

The carbon nano-tubes template method is also named carbon nano-tubes substitution method. This is because the preparation of carbon nano-tubes substitution method uses carbon nano-tubes as a template, replacing the boron atom of carbon nano-tubes with boron atom and nitride atom, and the boron nitride nano-tubes is formed. D. Golberg et al.[23] added when MoO_3 or V_2O_5 is mixed into the powder of the multi-wall carbon nano-tubes and B_2O_3, and then heat-treated at 1773℃ in nitrogen atmosphere, multi-walled boron nitride nano-tubes bundles are formed. SEM results showed that the top of the tube bundle is open, and the obtained tops are sealed when using the MoO_3 and V_2O_5 as raw material directly without the metal oxide inside.

Because of the higher reactivity, ammonia is envisaged to replace the nitrogen in reducing the reaction temperature. Deepak et al.[24] Does a lot of work on the ammonia and boric acid. The results showed that under the temperature of 1000~1300℃, an atmosphere with ammonia, and when mixture of boric acid and multi-walled carbon nano-tubes are heated, high yield boron nitride nano-tubes can be obtained, with close to a 100% conversion rate. When using arrayed carbon nano-tubes bundles as template, the boron nitride nano-tubes are also arrayed, indicating that the carbon nano-tubes template does play an important role during this reaction.

The hydrogen storage property of boron nano-tubes

The structure of boron nitride nano-tubes is very similar to that of carbon nano-tubes. Considering the chemical stability and thermal stability of boron nitride nano-tubes, boron nitride nano-tubes may become the most ideal lightweight hydrogen storage materials. Ma et al.[25] studied the hydrogen storage capacity of boron nitride nano-tubes. Studies have shown that, at room temperature, when pressure is gradually increased from 0 to 10MPa, boron nitride nano-tubes with hydrogen storage mass fraction corresponding increases. The mass fraction of hydrogen storage of multi-walled boron nitride nano-tubes and bamboo-like boron nitride nano-tubes are 118% and 216%. The mass fraction of hydrogen storage of bamboo-like boron nitride nano-tubes is higher than multi-walled boron nitride nano-tubes, which is due to the bamboo-like nanotubes that are composed of a variable diameter segment composition. With more defect structure, there are many openings edge layer around the outer surface, thus the mass fraction of hydrogen storage is much higher. The multi-walled boron nitride nano-tubes with capped ends hindered the entrance of the hydrogen molecules, thus the mass fraction of hydrogen storage is much lower. Tadao Sato[26] research group reported the hydrogen storage capability of boron nitride nano-tubes. When the boron nitride nano-tubes are placed between two platinum plates and then placed into a tube furnace, a heat treatment during hydrogen atmosphere at 1500℃, produces a vicious producet. Compared to the untreated boron nitride nano-tubes, the specific surface area of the treated boron nitride nano-tubes increased from 254.2 m^2/g to 789.1m^2/g. Through the thermal analysis, as the pressure increases, the ratio of the hydrogen storage increases. At the pressure of 10MPa, boron nitride nano-tubes collapse, the mass fraction of the collapsed hydrogen storage is 4.2wt%, which is higher than the traditional structure of multi-walled boron nitride nano-tubes. This may be due to the specific surface area of the boron nitride nano-tubes which is increased after heated-treating. In other words, after the heat treatment, the wall openings expand more hydrogen storage channels, thus, the boron nitride nano-tubes with surface defects shows a better hydrogen storage capacity.

Outlook

At present, the study of boron nitride nano-tubes is at the initial stage. Although there are many research achievements about the synthesis technology of boron nitride nano-tubes, the syntheses of highly pure and highly yield boron nitride nano-tubes are still difficult. Meanwhile, the growth mechanism of boron nitride nano-tubes is not very clear. The synthetic technology of highly pure, highly yield, and the growth mechanism of boron nitride nano-tubes will be the research emphases in future.

Boron nitride nano-tubes play an important role in the fields of structure materials for its potential advantages, and it also shows immeasurable advantages in the fields of functional materials, such as ferromagnetic materials, ferroelectric materials, piezoelectric semiconductors materials, and nano-superconducting materials. We believe that the application of boron nitride nano-tubes will make a significant contribution to the development of human civilization in the near future.

Acknowledgements

This work was financially supported by the National Natural Science Foundation of China (51372156 and 51101104), the Liaoning Province Nature Science Foundation (L2013455) and the Key Scientific and Technological Foundation of Shenyang City (F13-316-1-46).

References

[1] Z. L. Hu, Hydrogen storage materials: Beijing: chemical industry press(2003)

[2] C.M. Jensen, R. Zidan, N. Mariels, A. Hee, C. Hagen: Int, J. Hydrogen Energy.Vol. 24 (1999) , p.461.

[3] R. Griessen, T. Riesterer, Hydrogen in intermetallic compounds I, in: L. Schlapbach (Ed.), Topics in Applied Physics, Vol. 63(1988), p. 219.

[4] H. Buchener, R. Povel, Int. J. Hydrogen Energy Vol. 7 (1982),p. 259.

[5] G. Liang, J. Hout, S. Boily, A. Van Neste and R. Schulz: J. Alloys Compd. Vol. 292(1999) ,p.247.

[6] H. Wang, Z.Y. Liu : Rare Metal Materials and Engineering(2004).

[7] G. Liang, J. Huot, R. Schulz : Journal of Alloys and Compounds, Vol. 320(2001), p.133.

[8] Y.P. Liu, G. Zhao, R. Li, etc. Journal of Chongqing University. Vol. 26 (2003),p.144.

[9] S. Lee, Y. Lee:Appl. Phys. Lett. Vol.76 (2000),p.2877.

[10] D. Bae, J. Bok, Y. Choi, T. Frauenheim, N. Kim, S. Lee, Y. Lee, K. Nahm, K. Park, Y. PARK and S.Yu: Met. Vol. 113 (2000),p. 209.

[11] T. Bekkedahl, D. Bethune, A. Dillon, M, Heben, K. Jones and C. Kiang: Nature vol. 386(1997), p.377.

[12] X. Y. Liu, C. Y. Wang. :Acta Physica Sinica, Vol. 58(2009),p.1126.

[13] R. Ma, Y. Bando, H. W. Zhu, T. Sato, C. Xu and D. Wu: J. Am. Chem. Soc. Vol. 124(2002),p. 7672.

[14] C. C. Tang, Y. Bando, X. X. Ding, S. R. Qi, D. Golberg. J. Am. Chem. Soc. Vol. 124(2002),p.14550.

[15] G.Z.Zong, W.J.Chi :Modern ceramic,Tongji University Press (1988).

[16] M. Menon, D. Srivastava: Chem Phys Lett,Vol. 307(1999), p. 407

[17] X. Blase, A. Vita and J. C. Charlie :Phys Rev Lett,Vol. 80 (1998), p.1666.

[18] Y. Chen, J. Zou and S. J. Campbell: Appl Phys Lett, Vol. 84 (2004),p. 2430.

[19] X. Y. Lu, C. Y. Wang :Vol.58(2009),p. 1126.

[20] R. Ma, Y. Bando, H. W. Zhu, T. Sato, C. Xu and D. Wu: J. Am. Chem. Soc. Vol. 124(2002),p.7672.

[21] Y. F. Wang, J. C. Lin: Henan University of Science and Technology ,Vol. 6(1994),p.19.

[22]C. C. Tang, X. X. Ding and J. M. Gao, Chinese Patent: CN1931719A.(2007).

[23] R. T. Paine, C. K. Narula, O. Schaeffer, U S Patent: 5,188,757.(1993).

[24] X. S. Guo, C. H. Chen and Y. C. Xiang, : Journal of Xi'an Jiaotong University. Vol37(2003),p. 201.

[25] Dresselhaus M S, Dresselhaus G, Eklund P. Science of fullerenes and carbon tubes, Acadeic Press, New York(1996).

[26] X. Blase, A. Rubio and S.G.Lowie : Europhys Lett,Vol.28(1994),p. 335.

Advanced Materials Research Vols. 960-961 (2014) pp 61-64

doi:10.4028/www.scientific.net/AMR.960-961.61

Wetting Property of Cu-doped ZnO with Micro-/nano-Structures

S. Cao[1, a], C. H. Xu[1, b], Y. B. Huang[1,c], M. Liu[1], Z .H. Guo [1], B. W. Cheng[1], H. Y. Duan[1], L. G. Han [1], Y. N. Fan[1] and Y. F. You

[1] School of Materials Science & Engineering, Henan University of Science & Technology, Luoyang, Henan, P. R. China

[a]327029191@qq.com, [b]mmcjxu@haust.edu.cn, [c]1546158681@qq.com

Keywords: copper doping, zinc oxide, micro/nanostructure, wetting.

Abstract. ZnO with different morphologies were formed on Zn foils immersed in various concentrations of CuSO4 solutions. Then the specimens were heated at temperature of 200~600℃ in air for 3h. The morphologies of as-prepared specimens were characterized by a scanning electron microscope (SEM). Water wetting angles on the specimens were measured. The results indicate that the morphologies of ZnO on the Zn foils relate to the CuSO4 concentration of in solutions. The morphologies on the specimens with dual-scale (nano and micro) structure have higher wetting angles than those with flat structure. The water wetting angles can reduce with the increase in annealing temperatures of immersed specimens. The water wetting angles increase with keeping immersed specimens at room temperatures. The change of the wetting angle is explained by absorption of organic carbon on specimen surface and the geometric structure of the surface.

Introduction

Wettability of solid surfaces is a very important property and is governed by both the chemical composition and the geometric structure of the surface [1]. In order to increase in wetting angle, some spectral materials, such as heptadecafl uorodecyl-trimethoxysilane, were used to modify the materials surface, based on chemical modification [2]. A simple and effective way to achieve high wetting angle is preparation of dual-scale (nano and micro) structure on materials surface, based on physical modification [3]. The surface is superhydrophobic when the wetting angle in a solid–water–air system is larger than 150°, hydrophobic when the wetting angle is between 90~150° and hydrophilic when the wetting angle (θ) is <90° [4]. In recent years, one of the extensive researches on the material surface is hydrophilic/hydrophobic.Hydrophilic surfaces have been widely used in biological, chemical, solar, bio chip etc. Surperhydrophobic surfaces have important practical applications, such as self-cleaning, lubricity, resisting water coalescence, etc [5]. A fast and low cost method to fabricate ZnO nanosheets has been reported in our previous paper [6]. The morphologies of ZnO nanosheets with micro/nano structures can be controlled with different concentrations of CuSO4 in aqueous solutions. The effects of annealing temperatures on the morphologies of ZnO nanosheets are also studied [7] in our paper. The effects of the different morphologies of ZnO nanosheet surfaces and annealing temperatures on the wettability are studied in this paper.

Experimental procedure

Commercial zinc foil (300 μm in thickness and 99.0% in purity) was ground on 1000# emery paper, cleaned in acetone, ethanol and distillation water for 5min, respectively, by an ultrasonic machine (SYS5200). Cleared zinc foils were immersed into 1%CuSO4 and 5%CuSO4 aqueous solutions for 3 seconds, and finally dried at ambient condition for about 20 min in order to obtain ZnO micro- / nano-structures on the surface of Zn foils. All the chemicals in the experiment, including acetone (99.5%), ethanol (99.7%), CuSO4(99%) are analytic grade reagents without further purification. The immersed specimens were heated in a SYS-G-Z-13 tube furnace at 200˚C, 300 ˚C, 400 ˚C, 500 ˚C, 600 ˚C in air for 3 hours, respectively. Water wetting angles (WA) on the specimens was measured and recorded after cooling specimens to room temperature immediately and after keeping the specimens at room temperature for 3 to 100 days. Water wetting angles were measured on the using

the sessile drop method by deposition of 4~6μL droplets of DI water on a horizontal surface, and under their observation in cross-section. Each drop was observed directly with an Olympus BX-41 microscope objective lens, whereas its image was digitally captured using a 1.4 mega pixel computer-controlled digital CCD camera. Five water drops were placed at different locations on a horizontal surface, and the derivation of the WAs measured was within 2°. The morphologies of as-prepared specimens were observed by a field emission scanning electron microscope (JSM-6335F).

Results and discussions

The morphologies of as-prepared specimens show in Fig. 1. Fig. 1a shows uniformly distributed nanosheets on the specimen immersed in 1%CuSO4 aqueous solutions. The width and thickness of the nanosheets are about 1μm and 80 nm, respectively. Quasi-flowers assembled with nanosheets can be formed on the specimens immersed in 5%CuSO4 aqueous solution in Fig. 1b. The diameters of quasi-flowers are in the range of 1~2 μm. Morphology change in Fig. 1 suggests fast chemical reaction rate between zinc and CuSO4 in high concentration solutions. With the increase in the concentration of CuSO4 in the solution, uniformly distributed nanosheets become quasi-flowers.

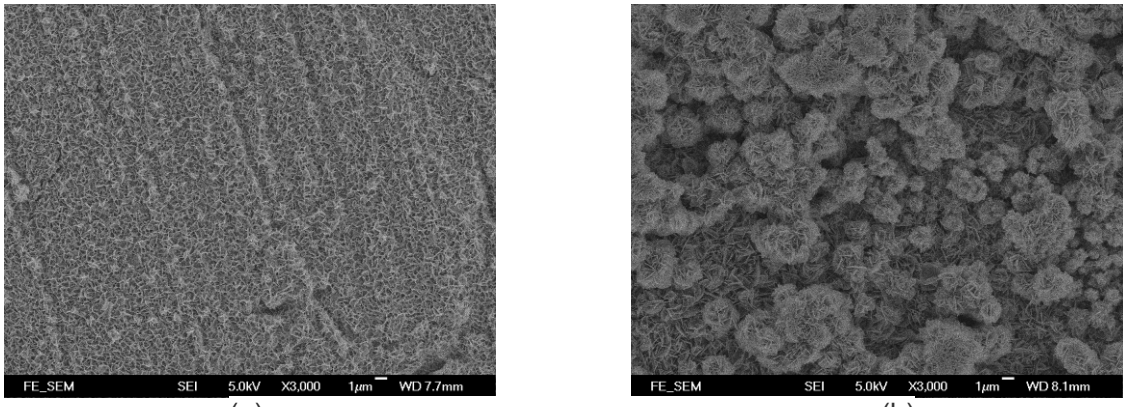

(a) (b)

Fig. 1 Morphologies of the specimens after immersing in (a) 1% and 5%CuSO4 aqueous solutions

Water wetting angles on the specimens were measured and recorded after immersing Zn foils in CuSO4 aqueous solution and drying immediately. Fig. 2 the exhibits a water wetting angle measured for the specimens with the morphologies in Fig. 1. The wetting angle on the specimen surface in Fig. 1a with uniformly distributed nanosheets (only nanostructure) is as small as 14.93°, as shown in Fig. 2a. The wetting angle on the immersed specimen in 5%CuSO4 solution with dual-scale (nano and micro) rough surfaces in Fig. 1b is 70.21°, as shown in Fig. 2b.

The combination of a dual-scale (nano and micro) roughness and an inherent low-surface energy coating material are an essential factors for the increase in water wetting angles on metallic surfaces. According to the Cassie model, increasing the proportion of water/air interfaces can greatly intensify the surface superhydrophobicity [8]. The Cassie wetting mechanism indicates that only the hills of the rough surfaces are wetted, while the water drop does not penetrate into the valleys. The morphology on the specimen immersed in 5%CuSO4 aqueous solution in Fig. 1b shows a dual-scale (nano and micro) roughness, which can trap more air, resulting in higher wetting angle 70.21°. There is low wetting angle 14.93° on the specimen immersed in 1%CuSO4 aqueous solution in Fig. 1b with nano structure only.

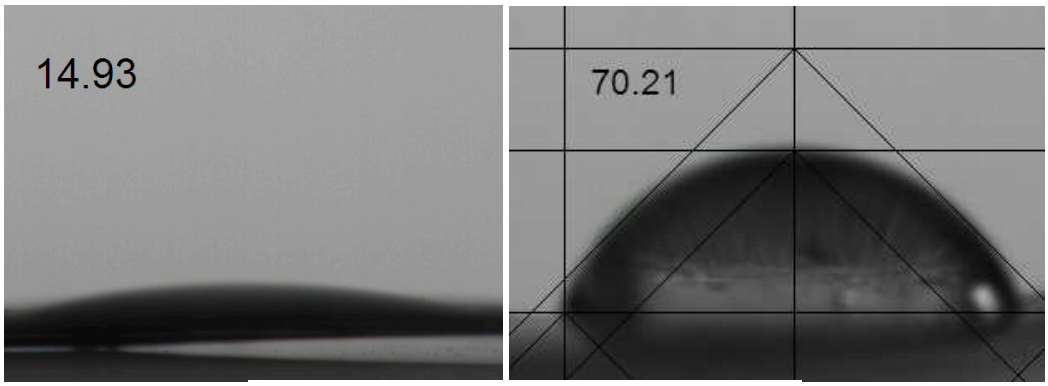

Fig. 2 Water contact angle measured on the specimens after immersing in (a) 1% and (b) 5%CuSO4 aqueous solutions

The immersed specimens were heated at different temperatures and wetting angle was measured on the specimens after cooling immediately. The results are shown in Fig. 3a. Generally, wetting angles decrease with the increase in temperatures. The reasons can be (1) the surface morphology changing form dual-scale (nano and micro) roughness to flat or (2) the changing chemical state on specimen surfaces. Based on our previous research, the surface morphologies nearly did not change after heating the specimens immersed in 1%CuSO4 aqueous solution at the temperatures less than 450˚C or after heating the specimens immersed in 5%CuSO4 aqueous solution at the temperatures to 600˚C [6]. This factor implies that the change in the chemical state on the specimen surface dominates the changing wetting angles.

Then the specimens after heating at 300˚C were kept at room temperature for various times (3, 17, 100 days) and wetting angles were measured as shown in Fig. 3b. Wetting angles increase with the increase in time. For the specimen immersed in 1%CuSO4 and heated at 300˚C, wetting angle increases form 12.8˚ measured at 0 day to 114.36˚ measured at 100 day.

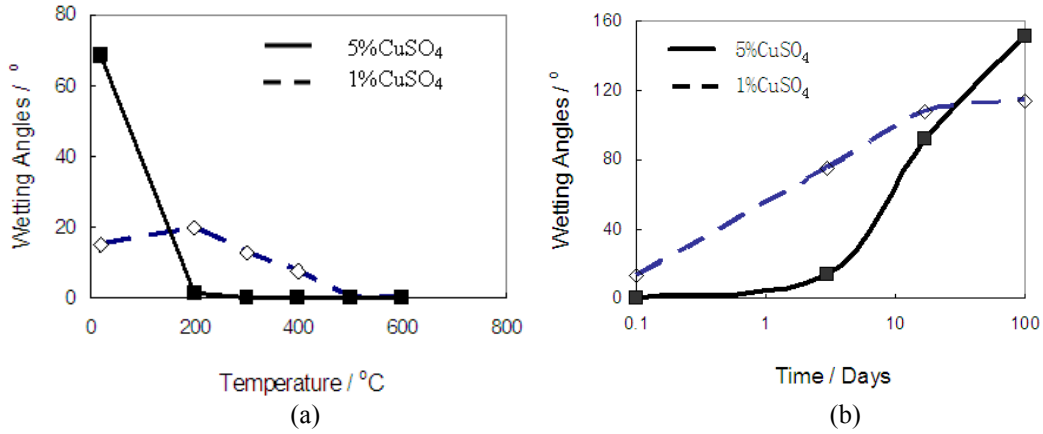

Fig. 3 Wetting angles versus of (a) annealing temperature and (b) time at room temperature

For the specimen immersed in 5%CuSO4 and heated at 300˚C, wetting angle increases form 0° measured at 0 day to 151.16° measured at 100 day. Theoretically speaking, ZnO is a hydrophilic material, wetting angle should be small. The samples can adsorb organic carbon in air and carbon is hydrophobic materials. The samples kept longer at room temperature and absorbed more carbon, resulting in the increase in wetting angle. When an annealed specimen at 300˚C was kept at room temperature for 17 days with the wetting angle of 107°, the wetting angle became 77° after specimen was heated again at 200˚C for 3 hour.

It can be concluded that ZnO surface can absorb organic carbon at room temperature and that heating specimen at high temperature can cause evaporation of organic carbon.

Conclusions

1. The morphology on the specimen immersed in 1%CuSO4 aqueous solutions shows uniformly distributed ZnO nanosheets with water wetting angle of 14.93°. The morphology on the specimen immersed in 5%CuSO4 aqueous solutions shows quasi-flowers assembled with ZnO nanosheets with water wetting angle of 70.21°.

2. Water wetting angles on the ZnO nanosheets decrease with the increase in temperatures of 200~600℃, due to evaporation of organic carbon.

3. After heating the immersed specimens at 300℃ and keeping the specimens at room temperature, the wetting angle on the specimen immersed in 1%CuSO4 increases form 12.8° measured at 0 day to 114.36° measured at 100 day and wetting angle on the specimen immersed in 5%CuSO4 increases form 0° measured at 0 day to 151.16° measured at 100 day.

Acknowledgements

This work was financially supported by NSRTP (201310464002) and by Program for Changjiang Scholars and Innovative Research Team in University（IRT1234）.

References

[1] R. N. Wenzel, “Surface roughness and contact angle” J. Phys. Colloid Chem., vol. 53, pp1466-1467, 1949.

[2] D. L. Tian, J. Zhai, Y. L. Song, and L. Jiang, “Photoelectric Cooperative Induced Wetting on Aligned-Nanopore Arrays for Liquid Reprography”, Adv.Funct.Mater.vol.21,pp4519–4526, 2011.

[3] M. E. Abdelsalam, ”Wetting of regularly structured gold surfaces”, Langmuir, vol. 21, pp1753, May 2005

[4] A. M. Gaudin, Flotation, McGraw-Hill Book Company Inc, New York, 1957, pp388.

[5] T. Sun, L. Feng, X. Gao, and L. Jiang, “Bioinspired Surfaces with Special Wettability” Acc. Chem. Res. Vol. 38, pp644-645, Oct. 2005.

[6] J. P. Wang, C. H. Xu, Y. F. You, Z. S. Si, D. L. Li, and S. Q. Shi, “Fast Synthesis of Cu-doped ZnO Nanosheets at Ambient Condition”, Cryst. Res. Technol. Vol. 48, pp 273–278, May 2013.

[7] Y L Liu, J. P. Wang, C. H. Xu, “The Effects of Annealing Temperature on Cu-doped ZnO Nanosheets”, unpublished.

[8] A. B. D. Cassie, “Wettability of porous surfaces”, Trans. Faraday Soc., vol. 40, pp 546, 1944.

Advanced Materials Research Vols. 960-961 (2014) pp 65-68

doi:10.4028/www.scientific.net/AMR.960-961.65

Development of SO_2 absorption materials having low temperature activity by base adducted complex method

Yugo Osaka[1, a], Fumiya Takahashi[2], Takuya Tsujiguchi[1], Akio Kodama[1], Hongyu Huang[3], Zhaohong He[3] and Huhetaoli[3]

[1] School of Mechanical Engineering, College of Science and Engineering, Kanazawa University, Kakuma, Kanazawa, Ishikawa, 920-1192, Japan

[2] Division of Human and Mechanical Science and Engineering, Graduate School of Natural Science and Technology, Kanazawa University, Kakuma, Kanazawa, Ishikawa 920-1192, Japan

[3] Chinese Academy of Science, Guangzhou Institute of Energy Conversion, No.2 Nengyuan Rd. Wushan, Tianhe District, Guangzhou 510640, P.R. China

[a]y-osaka@se.kanazawa-u.ac.jp

Keywords: DeSOx filter, dry-desulfurization, amorphous citric acid complex method, base adducted complex material

Abstract. Sulfur dioxide (SO_2) including combustion exhaust gas is must be clarified because of its air pollutant in middle-scale facilities or marine ships. In this study, dry $DeSO_x$ filter is developed to capture SO_2 within diesel exhaust. $CaCO_3$ is focused on as SO_2 absorption material. However, SO2 absorption materials has to be improved low temperature activity below 723 K. To improve the low-temperature desulfurization performance, physically and chemically modified $CaCO_3$ was synthesized using the amorphous citric acid complex method and base adducted complex method. Development of $CaCO_3$ having high specific surface area of 169 m_2/g (HSSA $CaCO_3$) by the amorphous citric acid complex method was succeeded. Then, Li or Na doped complex $CaCO_3$ by HSSA $CaCO_3$ was synthesized by base adducted complex method. It is found that these Li -doped complex $CaCO_3$ have higher SO_2 absorption performance than conventional $CaCO_3$ and HSSA $CaCO_3$. Its performance is reached 0.31 $g_{SO2}/g_{material}$ at reaction temperature of 723 K by TG experiment, as a comparison, that of conventional $CaCO_3$ is 0.02 $g_{SO2}/g_{material}$.

Introduction

Sulfur dioxide (SO_2) from combustion exhaust gas is one of the main air pollutants, and it affects human being harmfully in its small amount under 100 ppm. Moreover, it is reported that SO_2 from diesel exhaust deteriorates NO_x catalyst [1,2]. However, sulfur as a chemical substance is largely demanded, for example, fertilizer, source of sulfuric acid and neutralization solution of alkaline. Emission of SO_2 is improved by upgrading of fuels and clarification from exhaust gas. Exhaust clarification device is used only large-scale facilities because of its big size. In the recent social situation of Japan, demand of medium-scale power generator such as diesel power plant is rapidly used. Compact size SO_2 purification device is need for middle-scale facilities. SO_2 clarification device becomes large size because of a lot of water use. The initial cost of SO_2 capture device become bigger. So, we have focused on dry $DeSO_x$ filter by sulfate reaction of alkaline metal oxide ($M_xO_y + ySO_2 + 0.5xO_2 \rightarrow M_x(SO_4)_y$). This method has potential to be small size because it does not demand water treatment process. The concept of our study is developing dry $DeSO_x$ filter having good SO_2 capture performance for downsizing, simple SO_2 capture materials for sulfur reuse. In our past study, $CaCO_3$ having good reaction with sulfur dioxide at 923K is found by our past research [3]. However, in the low temperature conditions, there is problem that sulfate reaction rate decreases. In this study, in order to develop DeSOx filter having low temperature activation, physically modification such as making high specific surface area and chemically modification such as making low activation energy is desired. In this study, the amorphous citric acid complex method is focused on as a physically modification of $CaCO_3$ [4]. Then, base adducted complex method is focused on the chemically modification of $CaCO_3$ [5]. $CaCO_3$ having more low temperature activation is proposed by

combining both method. Physically and chemically modified $CaCO_3$ is synthesized and evaluated material characterizations, then SO_2 absorption performance of these synthesized $CaCO_3$ is investigated by TG experiment.

Material preparation

Synthesis of $CaCO_3$ having high specific surface area

For the synthesis of calcium carbonate having high specific surface area, commercial calcium hydrate was used as a starting material and citric acid (Kanto Kagaku Co. Ltd.) as the organic acid. Calcium hydroxide ($Ca(OH)_2$) was mixed with aqueous citric acid solution in a beaker, through which carbon dioxide gas was passed, and the mixture was stirred for about an hour. The intermediate product was then introduced into the calcination reactor, which is shown in Fig.1. The molar ratio of citric acid molecules to Ca^{2+} ions is changed from 0 : 1 to 4 : 1 as a parameter of specific surface area or mean pore diameter. It was desiccated at 393 K. Then, extra moisture was removed from the solid substance by pre-calcination at 473 K under vacuum at 4.0 kPa in a vacuum firing furnace. Finally, these dried materials was calcinated by high temperature of 873 K. The target calcium carbonate materials were obtained by repeating this procedure.

Synthesis of base doped composite materials of $CaCO_3$ by base adducted complex method

In previous experiment, several alkaline materials and concentrations of sorbents were investigated as a preliminary validation, including LiOH, LiCl, KOH, KCl, NaOH and NaOH. From these previous examinations, $CaCO_3$ doped NaOH or LiOH have a good SO_2 absorption performance. So, NaOH or LiOH is focused on in this study as a base materials. These base materials were diluted with ultrapure water to generate from 0 to 2.0 Molar aqueous of these base materials solution at room temperature, and 100 mL of these solution was mixed with 50 mg of synthesized $CaCO_3$ by amorphous citric acid complex method. The solution mixture was dried and crushed at 393 K and classified as a $CaCO_3$-based composite materials, i.e., "Na doped $CaCO_3$" or "Li doped $CaCO_3$."

Experimental procedure

Evaluation of SO_2 absorption performance by using TG experiment

The effectiveness of SO_2 absorption performance of synthesized materials was measured by using TG (TGA-50, Shimadzu Co. Ltd., resolution of 10μg) measurement. Schematic drawing of the TG measurement is shown in Fig.2. The simulated exhaust-gas composition used in the TG experiment is that 500 ppmv of SO_2, 10 wt% of O_2, 6.0 wt% of CO_2, and N_2 base, then, total flow rate is 300 mL/min. Reaction temperature is 723 K. These conditions are simulated real diesel engine.

The SO_2 absorption performance in terms of the reaction rate per single particle, as well as the sulfate reaction rate, were evaluated. The SO_2 absorption performance per unit mass X is expressed by the following equation:

$$X = \frac{M_{SO_2}}{M_{SO_3} - M_{CO_2}} \cdot \frac{m_t - m_0}{m_0} \left[g_{SO_2} / g_{material} \right] \qquad (1)$$

X is the SO_2 capture performance per unit mass [g_{SO2} / $g_{material}$], M_i is the molar mass of i [g/mol], m_0 is the initial weight [g], and m_t is the weight after t seconds [g].

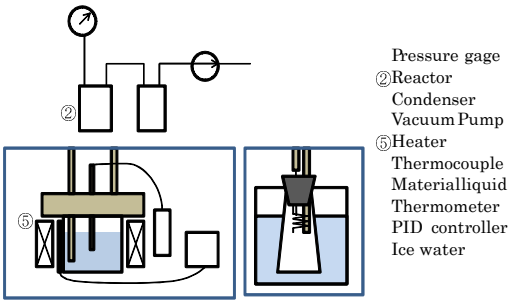

Fig.1 Schamatic drawing of calcination reactor

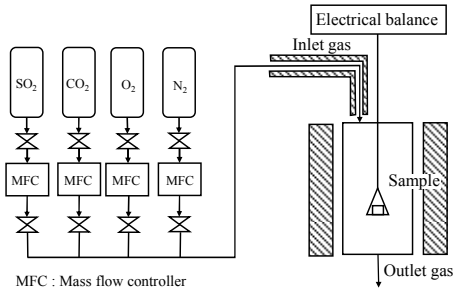

Fig.2 Schamatic drawing of TG experiment

Results and Discussions

Characterization of Na or Li doped composite $CaCO_3$ having high specific surface area

Pore distribution and BET specific surface area of synthesized $CaCO_3$ by amorphous citric acid complex method with changing citric acid concentration is shown Fig.3 .These characteristics were measured from BET method and BJH method by N_2 adsorption isotherm at N_2 melting point. From this result, $CaCO_3$ with a specific surface area of 169 m^2/g could be synthesized using the amorphous citric acid complex method with a molar ratio of organic acid molecules to Ca^{2+} ions of 4:1 and calcination temperature of 823 K. This $CaCO_3$ having high surface area is called "HSSA $CaCO_3$". However, mean pore diameter did no change in concentration of citric acid. It is thought that mean pore diameter depends on kind of doped acid. For comparison with influence of specific surface area, starting material of synthesis of composite $CaCO_3$ is selected two kind of $CaCO_3$ having different specific surface area having 16 and 169 m^2/g.

Then, Na or Li-doped $CaCO_3$ was synthesized with changing concentration of NaOH or LiOH aqueous solution. XRD patterns of synthesized composite $CaCO_3$ which concentration of each solutions is 1.0 M is shown Fig.4 and SEM photograph is shown in Fig.5. From the result of XRD pattern, it is found that main component is $CaCO_3$ however, Li-doped $CaCO_3$ is synthesized amalgam of Li_2CO_3 and $CaCO_3$, Na-doped $CaCO_3$ is synthesized $Na_2Ca(CO_3)_2$. It seems that these materials differ SO_2 absorption mechanism. From SEM photograph, $CaCO_3$ without citric acid mixing is formed cubic structure, on the other hands, $CaCO_3$ synthesized by amorphous citric acid complex method (HSSA $CaCO_3$) is formed complex surface structure. This complex surface structure increases specific surface area.

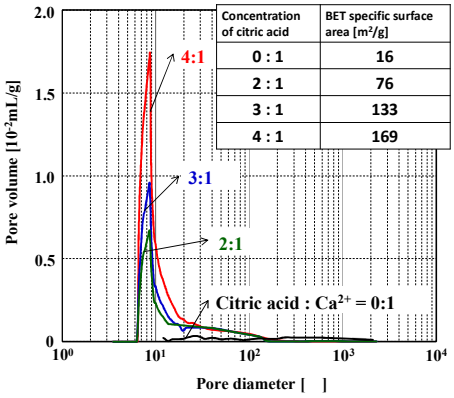

Fig.3 Pore distribution of $CaCO_3$ doped citric acid

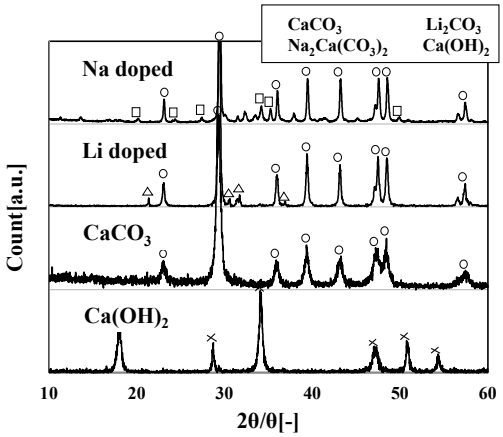

Fig.4 XRD patterns of chemically modifid $CaCO_3$

SO_2 absorption performance of Na or Li doped $CaCO_3$

The SO_2 absorption performance of Na or Li doped $CaCO_3$ was evaluated using TG. Influence of concentration of NaOH or LiOH aqueous solution and specific surface area of $CaCO_3$ against SO_2 absorption performance is investigated by using TG device. Result of Na doped $CaCO_3$ is shown in Fig.6 and that of Li doped $CaCO_3$ is shown in Fig.7. Summary of SO_2 absorption capacity after 2.0 h of TG experiment is shown in Fig.8. XRD analysis of products are also measured. From XRD analysis, products after SO_2 absorption of Li or Na doped material are all sulfate not including sulfite. From these results, SO_2 absorption performance of both doped $CaCO_3$ increase much more than that of $CaCO_3$. However, in Na doped $CaCO_3$, SO_2 absorption rate does not change with increasing specific surface area, but it does not change with increasing concentration of NaOH aqueous solution, on the other hands, in Li doped $CaCO_3$ it does not increase with increasing specific surface area, but it increase in high concentration

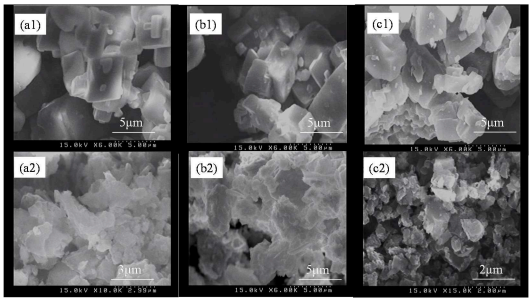

Fig.5 SEM photograph of chemically modifid $CaCO_3$
(a1) $CaCO_3$, (a2)HSSA $CaCO_3$,
(b1)Na doped $CaCO_3$, (b1)Na doped HSSA $CaCO_3$
(b1)Na doped $CaCO_3$, (b1)Na doped HSSA $CaCO_3$

of LiOH aqueous solution. In Li doped $CaCO_3$ synthesized by concentration of LiOH aqueous solution of 2.0 M, maximum performance which means SO_2 absorption capacity after 2.0 h in TG experiment at reaction temperature of 723 K is reached 0.31 $g_{SO2}/g_{material}$ as a comparison that of conventional $CaCO_3$ is 0.02 $g_{SO2}/g_{material}$. It is thought that SO_2 absorption mechanism of these materials is different. Na doped $CaCO_3$ is formed $Na_2Ca(CO_3)_2$ and $CaCO_3$, Li doped $CaCO_3$ is formed Li_2CO_3 and $CaCO_3$. Both materials increase SO_2 absorption capacity which is shown in Fig.8. Li^+ ions assist SO_2 absorption reaction in material surface at low temperature. For development of dry DeSOx filter, improvement of SO_2 absorption material is desired. Improvement of materials mean increase of SO_2 absorption rate and capacity. From this, Li doped $CaCO_3$ seems hopeful material for improving SO_2 absorption rate and capacity. In our future work, doping Li^+ ion will be focused on. Clarification of SO_2 absorption mechanism and roll of Li^+ ions will be investigated.

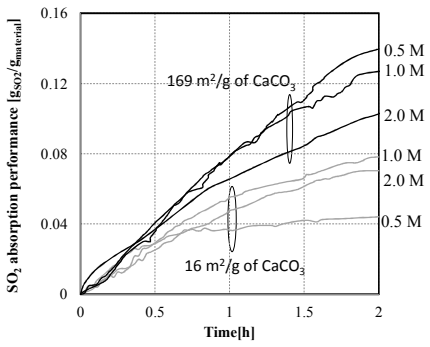

Fig.6 SO_2 absorption performance of Na doped $CaCO_3$

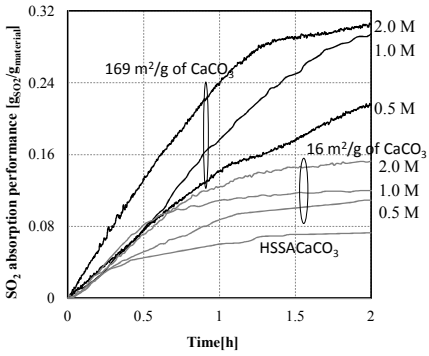

Fig.7 SO_2 absorption performance of Li doped $CaCO_3$

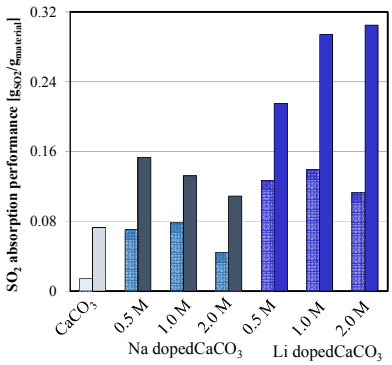

Fig.8 Summary of SO_2 absorption performance of physically and chemically modifid $CaCO_3$

Conclusions

Dry DeSOx filter is developed for purification of diesel engine exhaust. To improve SO_2 absorption material having more low temperature activation, physically and chemically modification of $CaCO_3$ is investigated. In this study, the following conclusions were obtained from this study.

- $CaCO_3$ with a specific surface area of 169 m^2/g could be synthesized using the amorphous citric acid complex method with a molar ratio of organic acid molecules to Ca^{2+} ions of 4:1 and calcination temperature of 823 K.
- Li-doped $CaCO_3$ is synthesized amalgam of Li_2CO_3 and $CaCO_3$, Na-doped $CaCO_3$ is synthesized $Na_2Ca(CO_3)_2$.
- SO_2 absorption performance of Na or Li doped $CaCO_3$ increase much more than that of $CaCO_3$.
- In Li doped $CaCO_3$ synthesized by concentration of LiOH aqueous solution of 2.0 M, maximum performance which means SO_2 absorption capacity after 2.0 h in TG experiment at reaction temperature of 723 K is reached 0.32 $g_{SO2}/g_{material}$.

References

[1] Jae-Soon Choi, William P. Partridge, Josh A. Pihl, C. Stuart Daw, Catalysis Today vol.136, 2008 p.173–182

[2] K. Yoshida, T. Asanuma, H. Nishioka, K. Hayashi, S Hirota, Proceedings of JSAE annual congress, No.40-07, p.27-31, 2007

[3] T. Kitou, Y. Osaka, N. Kobayashi, A. Matsuyama, Journal of Energy and Resources, vol.31, No.4, p.214, 2010

[4] Victoria M.L. Whiffen, Kevin J. Smith, Suzana K. Straus, Applied Catalysis A: General, Vol. 29, pp. 111-125, 2012

[5] Y. Osaka, S. Kurahara, N. Kobayashi, M. Hasatani, and A. Matsuyama, 2014, Heat transfer engineering, vol. 35, Issue 13

Advanced Materials Research Vols. 960-961 (2014) pp 69-72

doi:10.4028/www.scientific.net/AMR.960-961.69

Electron Beam Irradiation on Substrate for Precise Dielectrophoretic Assembly of Carbon Nanotubes - A Simulation

Yan Chen[a], Libao An[b*]

College of Mechanical Engineering, Hebei Provincial Key Laboratory of Inorganic Nonmetallic Materials, Hebei United University, Tangshan, Hebei 063009, China

[a]cheny19900807@163.com, [b]lan@heuu.edu.cn

[*]Corresponding author

Keywords: carbon nanotube, dielectrophoresis, electron beam irradiation, precise assembly, field simulation

Abstract. The effect of electron beam irradiation on permittivity of silicon dioxide insulate layer was investigated. Theoretical analysis indicates that electron beam irradiation will change the permittivity of SiO_2 through decreasing the molecular number per unit volume and increasing the polarizability of the sample. The escape of impurities during irradiation decreases the permittivity while the accumulation of space charge increases the permittivity. Simulation results show that with the change of permittivity, the electric field of the area irradiated by electron beam is strengthened locally and carbon nanotubes (CNTs) are more likely attracted to this area by dielectrophoresis. Therefore, the method could be used for precise positioning of CNTs for various applications in many areas including nano-electronics, sensors, and new energies.

Introduction

Due to their excellent electrical, thermal and mechanical properties, carbon nanotubes (CNTs) have become a candidate of nano materials for micro- and nano-sensors, energy storage and conversion devices, field emission displays, and many other applications [1-3]. Several approaches have been used to assemble CNTs such as utilizing directed CNT-growth techniques and by means of manual manipulations [4,5]. Dielectrophoresis (DEP) is a simple and efficient method for CNTs assembly since it does not require chemical reactions and expensive instruments [6]. However, there exist multiple influencing factors in DEP which include the magnitude of the applied voltage, the concentration of the CNT suspension, the duration of the electric field, the electrical properties of the CNTs and the dielectric liquid, and the geometry and spacing of the electrodes. Therefore, it is difficult to achieve precise positioning of assembled CNTs by DEP.

Several methods have been presented for precise positioning of CNTs such as using floating metal posts during DEP and chemically modifying substrates [7,8]. By using floating posts, it is possible to perturb and enhance the electric field in the vicinity of the posts, guiding the alignment of CNTs along the posts across the electrodes in the process of DEP assembly of CNTs [7]. In this paper, we will show an alternative way of precise positioning of CNTs by simulating the DEP force field with a change of permittivity of the dielectric layer on the selected area of the substrate after electron beam irradiation, which can strengthen electric field locally and attract CNTs to the irradiated area for precise positioning of CNTs by DEP.

Theory of Dielectrophoresis

During DEP, particles will be aligned to the field direction and attracted to the area of the highest DEP force [9]. When a particle is subject to an externally applied electric field, a dipole moment is induced. If the electric field is inhomogeneous, the DEP force acting on each side of the particle will be different, causing the particle to move with respect to the liquid medium [10]. The DEP force exerted by an electric field E on a particle is [11]:

$$F_{DEP} = \Gamma \cdot \varepsilon_m \operatorname{Re}\{K_f\} \nabla |E|^2 \tag{1}$$

where Γ is a factor depending on the geometry of the particle, ε_m is the permittivity of the suspending medium and E is the externally applied electric field. The factor K_f depends on the complex permittivities of both the particle and the medium.

In DEP manipulation, CNTs will be attracted to the area with the maximal field strength. When parallel electrodes are used, CNTs will tend to be evenly arranged between the electrode gap along the width of the electrodes. Electron beam irradiation on a selected area of the electrode gap will change the electrical properties of the substrate such as permittivity. A local permittivity change of the substrate could affect the distribution of the whole DEP electric field, strengthening the electric field locally and realizing a precise positioning of CNTs on the irradiated area. In order to explore the role of electron bean irradiation, we looked into the role of the electron beam and simulated the DEP force field respectively before and after irradiation.

Effect of Electron Beam Irradiation

When electron beam irradiates a dielectric material, the physical and chemical structure of the dielectric will change, leading to a change in its electrical properties. After electron beam irradiation, the relative permittivity of the dielectric ε_r is given by Clausius – Mossotti equation [12]:

$$\frac{\varepsilon_r - 1}{\varepsilon_r + 2} = \frac{N\alpha}{3\varepsilon_0}, \tag{2}$$

where N is the number of molecules per unit volume of the dielectric, ε_0 is the permittivity of a vacuum, α is the molecular polarizability of the dielectric. As shown in equation 2, ε_r is related to N and α, and only one or two polarizations among electronic polarization, ionic polarization, dipole polarization, and thermionic polarization dominate the magnitude of ε_r.

Impurities usually exist in dielectric materials such as SiO_2. After electron beam irradiation, these impurities would escape, causing some interspaces in the dielectric [13]. This implies that after irradiation the molecular number N in the dielectric would be decreased, causing permittivity ε_r decreased with it too. Another influence is that, after radiation, large number of negative charges will store in the SiO_2 substrate [14,15]. With the change of space charge distribution, the polarizability α is increased, causing ε_r increased too.

Simulation and Analysis

In order to evaluate the influence of local permittivity change of SiO_2 in the selected area due to electron beam irradiation on the CNT assembly by DEP, we calculated the DEP force distribution for parallel electrodes before and after electron beam irradiation by numerical simulation. Table 1 shows the electrical properties of the components of the DEP system in simulation.

Table 1 The electrical properties of the components in the DEP system for simulation

Components in the system	Conductivity [s/m]	Relative permittivity
Metallic CNT	1×10^{7}	1×10^{4}
IPA	6×10^{-16}	18.6
Aluminum electrode	3.774×10^{7}	1
Silicon dioxide	1×10^{-18}	3.8
Silicon	1.2×10^{-6}	11.7

Fig. 1 shows the schematic of parallel electrodes in (a) and DEP force field distribution before irradiation in (b). As shown in Fig. 1 (b), the biggest DEP force appears at one corner of the electrodes. This means that CNTs will deposit firstly in the corner area during DEP.

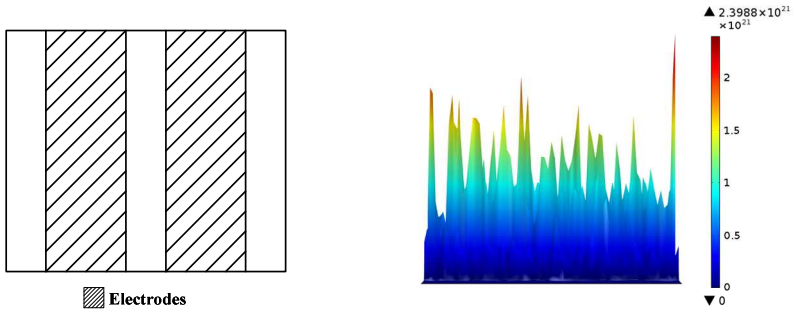

(a) (b)

Fig. 1 Schematic diagram of electrodes (a) and DEP force field (b) before irradiation

Fig. 2 shows the area of electron beam irradiation on SiO_2 layer in (a) and DEP force field distribution with permittivity ε_r increased to 4.3 in (b). Compared to Fig. 1 (b), the largest DEP force appears at the irradiation area, instead of the electrode corner area. Therefore, CNTs will take precedence to deposit in this irradiated area and realize precise positioning. When permittivity ε_r is decreased to 3.8, similar results were obtained by simulation. This indicates that the permittivity change in the selected area of SiO_2 layer influences the whole DEP electric field. A local enhancement of the field in the irradiated area will attract CNTs to deposit there first.

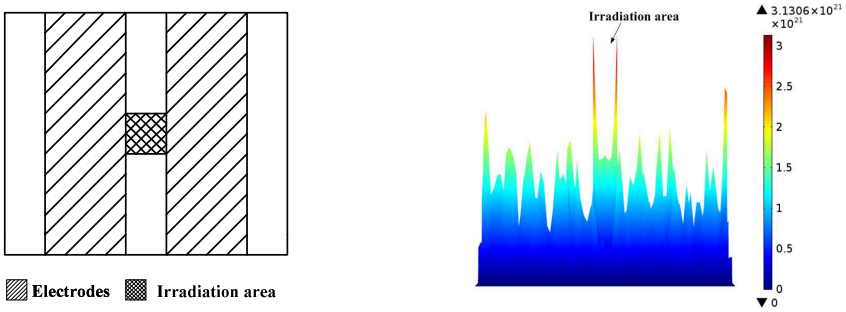

(a) (b)

Fig. 2 Schematic diagram of electrodes (a) and DEP force field (b) after irradiation

Summary

The permittivity of the dielectric layer on the substrate has an impact on electric field distribution when manipulating CNTs by DEP. Two factors will affect the permittivity of a dielectric after electron beam irradiation: molecules number N and polarizability α. After irradiation, molecule number per unit volume will decrease, making the permittivity decrease too. On the other hand, due to electron injection the permittivity is increased. Although these two factors have opposite influence on the permittivity, simulation results indicate that DEP force can be enhanced in the irradiation area under the both cases. It is possible to achieve precise assembly of CNTs by DEP through electron beam irradiation on a selected position between the electrodes. However, the roles of electron beam irradiation have not been clearly understood and further studies are still needed.

Acknowledgments

The research was jointly sponsored by the National Natural Science Foundation of China (51172062), the Scientific Research Foundation for the Returned Overseas Chinese Scholars from the Ministry of Education of China, the Natural Science Foundation of Hebei Province of China (E2012209017), and the Hundred Talents Program of Hebei Province of China (E2012100005).

Reference

[1] R.H. Baughamn, A.A. Zakhidov and W.A. de Heer: Science Vol. 297 (2002), p. 787.

[2] J. Li, Q. Zhang, N. Peng and Q. Zhu: Appl. Phys. Lett. Vol. 86 (2005), p. 153116.

[3] R. Li, H.B. Li and Q.W. Li: Mater. Rev. Vol. 27 (2013), p. 50.

[4] L. An, C. Friedrich: Appl. Phys. Lett. Vol. 92 (2008), p. 173103.

[5] A.M. Cassell, N.R. Franklin and T.W. Tombler: J. Amer. Chem. Soc. Vol. 121 (1999), p. 7975.

[6] Y.K. Ren, H.R. Ao, J.H. Gu, H.Y. Jiang and A. Ramos: Acta Physica. Sinica Vol. 58 (2009), p. 7869.

[7] S. Banerjee, B. White, L. Huang, B.J. Rego, S.O. Brien and I.P. Herman: Appl. Phys. A Vol. 86 (2007), p. 415.

[8] S. Auvray, V. Derycke, M. Goffman, A. Filorama, O. Jost and J.P. Bourgoin: Nano Lett. Vol. 5 (2005), p. 451.

[9] S.G. Kwon, S.H. Kim, K.H. Kim, M.C. Kang and H.W. Lee: Trans. Nonferrous. Met. Soc. China Vol. 21 (2011), p. 117.

[10] J.E. Kim, C.S. Han: Nanotechnology Vol. 16 (2005), p. 2245.

[11] M. Dimaki, P. Boggild: Nanotechnology Vol. 15 (2004), p. 1095.

[12] X.D. Liu, X.Q. Zheng, Y.Q. Zhang, S.S. Yang, X.G. Qin and L. Wang: Adv. Technol. Electri. Eng. Energy Vol. 26 (2007), p. 55.

[13] F.H. Zheng, Y.W. Zhang, C. Xiao and J.F. Xia: Journal of Sichuan University (Natural Science Edition) Vol. 42 (2005), p. 337.

[14] W.Q. Li, H.B. Zhang: Appl. Surf. Sci. Vol. 256 (2010), p. 3482.

[15] W.Q. Li, H.B. Zhang: Micron Vol. 41 (2010), p. 416.

Advanced Materials Research Vols. 960-961 (2014) pp 73-77

doi:10.4028/www.scientific.net/AMR.960-961.73

Preparation of novel membrane material 4',4''(5'')-di-tert-butyldicyclohexyl-18-crown-6

Alsamani A. M. Salih [1, a], Yingming Li [1,b], Juan Fan [1,c], Chunhai Yi [1,d], and Bolun Yang[1,e*]

[1]School of Chemical Engineering and Technology, Xi'an Jiaotong University, Xi'an shaanxi 710049, China

[a]samani15@hotmail.com, [b]lym2519@163.com, [c] juan.fan@stu.xjtu.edu.cn, [d]chyi@mail.xjtu.edu.cn, [e]blunyang@mail.xjtu.edu.cn

Keywords: 4',4''(5'')di-tert-butyl-dicyclohexyl-18-crown-6; Bimetallic Rh-Fe catalyst; MgO support; Crown ethers hydrogenation

Abstract. For preparing 4',4''(5'')di-tert-butyl-dicyclohexyl-18-crown-6 with high yield under low H_2 pressure, the support, active component, promoter, reduction time and reduction temperature were studied. The catalyst structure and composition were characterized by XRD, TEM and EDS. The experimental results showed that MgO was the most suitable catalyst support because of its weaker acidity than other supports. The higher hydrogenation activity and selectivity were observed when Rh was used as the active component and Fe was used as promoter owing to the cooperative interaction. The optimum reduction temperature and the reduction time were 500 ºC and 3h, respectively. The specific surface area of Rh-Fe/MgO was 133m^2/g, and the Rh-Fe was well dispersed on MgO with the particle size about 20 nm. Under a low H_2 pressure (4 MPa), the 4',4''(5'') di-tert-butyldibenzo 18-crown-6 conversion was 78% and 4',4''(5'')di-tert-butyl-dicyclohexyl- 18-crown-6 yield was 53% catalyzed by Rh-Fe/MgO, which were higher than that catalyzed by single metal catalyst.

Introduction

Crow ether, which has a cavity with precise size, has been seen as a promising membrane material for liquid membrane [1-3]. Singh S.K. [1] and Walkowiak W[2] reported liquid membrane using crown ether for removal of metal ions from water. Mona M. Naim [3] prepared dibenzon 18-c-6 liquid membrane for the desalination of sea water. Among the crown ethers, 4',4''(5'')di-tert-butyl-dicyclohexyl-18-crown-6 (DTDCH18C6) is of particular interest for it similar cavity size with Cs ion and low solubility in water.

Generally, DTDCH18C6 was prepared by the di-tert-butyldibenzo 18-crown-6 (DTBB18C6) hydrogenation catalyzed by mono-noble metal catalyst. Predersen [4] synthesized dicyclohexyl 18-crown-6 by Ru/ at 10 Mpa, 100 °C with the conversion about 90% and the yield about 70%. Gula [5] synthesized DTDCH18C6 by Rh/Al_2O_3 at 10 MPa, 120 °C with the conversion about 90% and the yield about 60%. Liu [6] reported preparing dicyclohexyl 18-crown-6 with Rh/CNTs at 10 Mpa, 50 °C with the conversion about 60% and the about 80%.

Due to the cooperative interaction between two different metals [7], using bimetallic catalyst may increase the DTDCH18C6 yield under lower hydrogen pressure compared to monometallic catalyst, the active component and promoter thus were studied in this work. The catalyst support was investigated too because its structure and acidity also affected the DTDCH18C6 yield under lower hydrogen pressure. Moreover, the mass ratio of active component to promoter, reduction temperature, and time were researched to define the preparing conditions of this catalyst. At last, the catalyst structure and composition were characterized by XRD, TEM, and EDS.

Experiments

2.1. Catalyst preparation

The catalysts were prepared by an impregnation method using $H_2PtCl_6 \cdot 6H_2O$ (Aldrich) as the Pt precursor, $RhCl_2$ (Aldrich) as the Rh source, $RuCl_2$ (Aldrich) as the Ru source, $Co(NO_3)_2 \cdot 6H_2O$ (Aldrich) as the Co source, $Fe(NO_3)_3 \cdot 6H_2O$ (Aldrich) as the Fe source, and $NiNO_3 \cdot 6H_2O$ (Aldrich) as the Ni source, respectively. In a typical procedure, a certain quality of the support and the precursor (the total percentage of active component and promoter is 5%) were stirred in deionized water 4h and dispersed in ultrasound 2h. After the mixture was immersed 48h, it was dried in a vacuum oven 110 ° C. Then, the mixture was calcined under nitrogen (60 mL/s) at 400-500 °C for 2-4h, and reduced under hydrogen (60 mL/s) at 400-500 °C for 2-4h.

2.2. Catalyst characterization

The contents of Rh and Fe were estimated using the Scanning electron microscope (JSM-6700F, JEOL, Japan).X-ray diffraction (XRD) patterns were obtained with a powder X-ray diffractometer (X'Pert Pro, Panalytica, Holland), using Cu as α radiation (1.5406 Å) at 40 kV, 40 mA. The measurements were recorded with a count time of 1 s in the 2θ range of 0^o-80^o.

Results and Discussion

3.1. Catalyst characterization

Fig. 1 showed the XRD patterns of MgO, Rh/MgO and Rh-Fe/MgO. Peaks at 36.1^o and 61.5^o were assigned to MgO. Peaks at 41.2^o detected in the XRD patterns of Rh/MgO were assigned to Rh (111). However, this peak was not detected in the XRD pattern of Rh-Fe/MgO, which may be due to the effect of Fe on Rh.

The TEM patterns of Rh-Fe/MgO were shown in Fig. 2. As can been seen from the TEM pattern of Rh-Fe/MgO, the Rh and Fe were dispersed on the support well with the size about 20 nm.

EDS results show that the the mass percentage of the Rh was 4.46% and the Fe mass percentage was 1.32%, which was agreed with the design mass ratio of Rh (4%) and Fe (1%)

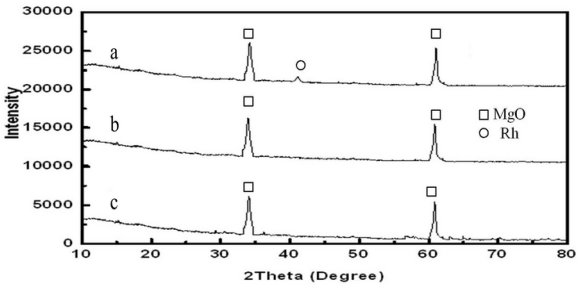

Fig. 1. XRD patterns of MgO, Rh/MgO and Rh-Fe/MgO

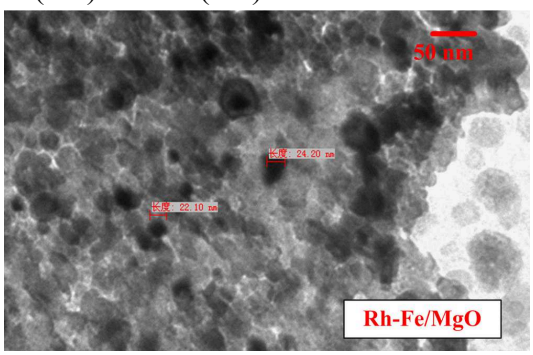

Fig. 2. TEM patterns of Rh-Fe/MgO

3.2. Catalyst activity and selectivity

3.2.1. The effect of the catalyst support on the reaction

Table 1 The effects of the catalyst support

Samples	ABET(m^2/g)	Pore Size (nm)	DTBB18C6 conversion	DTDCH18C6 yield
Rh/ Al_2O_3	238	22	75.3%	36.5%
Rh /MgO	133	43	72.2%	43.4%
Rh /TiO_2	108	15	49.6%	28.8%
Rh /CNTs	212	13	52.3%	33.4%

The effects of CNTs, TiO_2, Al_2O_3 and MgO as the catalyst supports were studied. As it shown in Table 1, owing to MgO can provide a more effective surface area and suitable pore structure than other supports, the DTBB18C6 conversion reached to 72.2% and the DTDCH18C6 yield was 43.4% when MgO was used as support. Although the activity of Al_2O_3 was slight higher than that of MgO, its selectivity was much lower than that of MgO. It may attribute to that Rh did not interact with Mg

and lose its catalytic activity when the catalyst was reduced by H_2 at high temperature [8]. Moreover, because the metal of group VIII was electron deficient, more strong adsorption bonds between reactants and active metal will formed and the reaction rate thus lowered if the metal was supported on an acidic support [9]. A strong interaction between the acidic sites of support and the reactants will also reduce the efficiency of the hydrogenation [10].

3.1.2. The effect of the active component on the reaction

Generally, the hydrogenation activity of the group VIII metals was highest than other group due to their lower chemical adsorption energy (100-120 kJ/mol). Therefore, Pt, Rh and Ru were selected in this work. Seen from Fig. 3, the following sequence for catalyst activity was founded: Pt>Rh>Ru**.** The selectivity was founded: Rh>Pt>Ru**.** It was believed that the metal activity was related to the arrangement of its outer electrons, and the activity sequence was 4d, 5d and 3d in succession[11]. The outer electrons arrangement of Pt, Rh and Ru are $5d^9 6s^1$, $4d^8 5s^2$ and $4d^7 5s^1$, respectively, which can explain the reason why the activity of Rh was higher than Ru and lower than Pt. In addition, some authors suggested that the hydrogenation activity of metal was associated with the acidity of the corresponding Lewis acid [11]. They indicated that the strong bond between a metal and reactants will be formed when the corresponding Lewis acid of this metal was hard acid, and weak bond will be formed if it was soft acid. The acidity of $RhCl_6^{3-}$ was lower than $PtCl_6^{2-}$, but higher than RuO_4^{2-}, that was why Rh showed a higher selectivity and activity for DTBB18C6 hydrogenation than Pt and Ru.

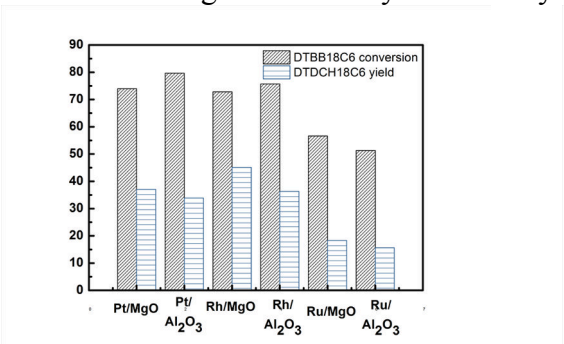

Fig. 3. The effect of the active component on the reaction.

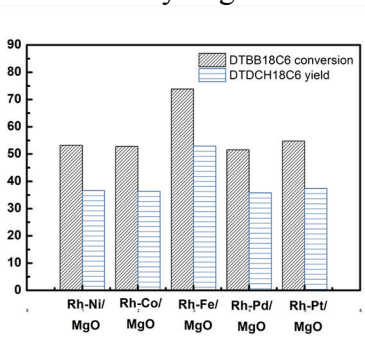

Fig. 4. The effect of promoter on the reaction.

3.1.3. The effect of promoter on the reaction

One role of promoter on the catalyst activity was group effect which can reduce the aggregation of the active component and improve its dispersity. Another was electronic effect which can affect the chemical bonds between the active component and the reactants. Ni, Co, Fe, Pd, and Pt were used as the promoter (its mass ratio to Rh was 1:4) in this works. As shown in Fig. 4, when Fe was used, DTDCH18C6 yield increased from 43% to 53%. Fe was able to influence the electron distribution of Rh d-orbital better than other metals, the Rh atoms were thus disordered on the crystal surface and the percentage of lattice defects was increased, which resulted the selectivity of catalyst increased.

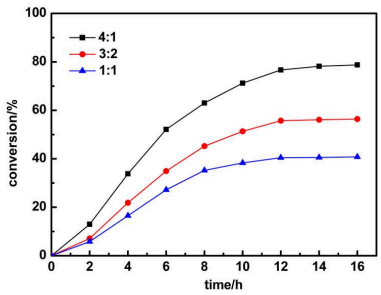

Fig. 5. The effect of Rh to Fe mass ratio on DTBB18C6 conversion

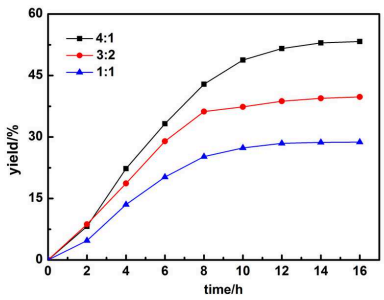

Fig. 6. The effect of Rh to Fe mass ratio on the DTDCH18C6 yield.

3.1.4. The effect of Rh to Fe mass ratio on the reaction

Since Fe was able to influence the electron distribution of Rh, the different mass ratio of Rh to Fe, the different electron distribution of Rh and different products yield, thus it was important to study the

mass ratios of Rh to Fe. Three different mass ratios of Rh to Fe (4:1, 1.5:1 and 1:1) were investigated, and the total mass percentage of Rh ang Fe was 5%. Seen from Fig. 5 and Fig. 6, the DTBB18C6 conversion (78%) and DTDCH18C6 yield (53%) both reached to its highest value when the Rh-Fe mass ratio was 4:1. The reason was that the mass percentage of an active component in a bimetallic catalyst must get to a certain value so as to ensure catalytic activity and the higher mass percentage of the active component the higher activity of catalyst generally. However, the selectivity of this catalyst was affect by the mass percentage of Fe, therefore Fe must be added moderately owing to the total mass percentage of Rh and Fe was constant.

3.1.5. The effect of impregnation sequence on the reaction

Rh and Fe were impregnated by three methods. As it Shown in Fig. 7 and Fig.8, the DTBB18C6 conversion and DTDCH18C6 yield were both highest when Rh and Fe were impregnated simultaneously. The reason was that the hydrogenation process carried out on the catalyst surface generally, if Rh and Fe were impregnated at different time, the two metals will easily form a structure similar to "core-shell" which was harmful to the surface reaction. While if Rh and Fe were impregnated simultaneously, the two metals may disperse randomly on the support surface and it was helpful for Fe influencing the *d*-orbital of Rh.

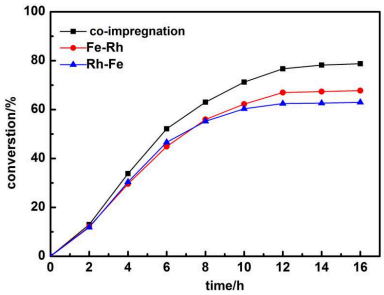

Fig. 7. The effect of Rh-Fe impregnation sequence on the DTBB18C6 conversion

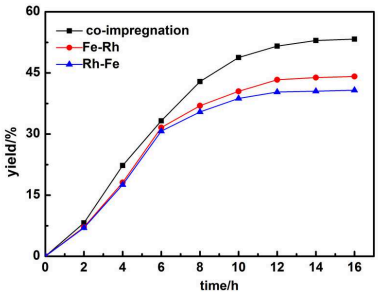

Fig. 8. The effect of impregnation sequence of Rh-Fe on the DTDCH18C6 yield.

3.1.6. The effect of reduction time on the reaction

Due to the large amounts of water vapor will be produced at a high reduction temperature, the active metal was easily oxidized and lost its activity if the reduction time was too long, the catalyst should be reduced as quick as possible. In this work, the catalyst was reduced for 2h, 3h and 4h， respectively. Shown in Fig. 9 and Fig. 10, although the activity of the catalyst reduced 3h was slightly higher than others, the activity difference of these catalysts was not distinguished. This result implied that the Rh^{+} and Fe^{3+} of the precursor could be completely reduced to Rh^{0} and Fe^{0} during 3h, and extending the reduction time was not helpful for increasing the catalytic activity under this condition.

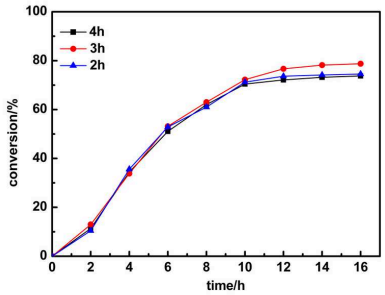

Fig. 9. The effect of reduction time on the DTBB18C6 conversion

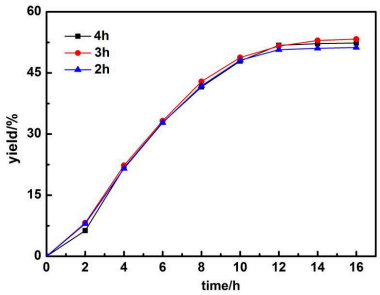

Fig. 10. The effect of reduction time on the DTDCH18C6 yield.

3.1.7. The effect of reduction temperature on the reaction

The reduction temperature directly affected the catalyst structure, and thus affected the catalyst activity. At low reduction temperature, the size of active metal particles was non-balance because of the gathering of water vapor on the metal surface. While at high reduction temperature, the metal

atoms rapidly diffused to the ligand center and its size was very stable due to the role of surface re-configuration [19]. However, if the reduction temperature was too high, the metal atoms will be sintered and lost its activity. The activity of catalysts reduced at 300 °C, 400 °C and 500 °C were studied. It can be seen from Fig. 9 and Fig. 10, the highest DTDCH18C6 yield and DTBB18C6 conversion were founded when the reduction temperature was 500 ^{o}C. Some papers reported that the relative percentage of the defects on Rh surface was less than 10^{-4} when the reduction temperature was below 500 °C, and the higher metal surface defects the higher catalyst activity.

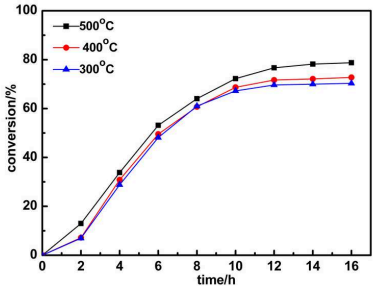

Fig. 11. The effect of reduction temperature on the DTBB18C6 conversion

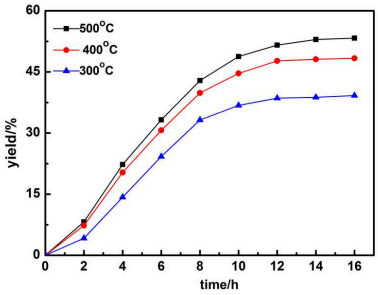

Fig. 12. The effect of reduction temperature on the DTDCH18C6 yield

Conclusion

The results of catalyst supports research indicated that the DTBB18C6 conversion and DTDCH18C6 yield were higher when MgO was used as a support. Pt, Rh and Ru were employed to study the use of active component, and it was founded that Rh was the proper active component for DTDCH18C6 preparation. When Fe was used as promoter, the DTDCH18C6 yield increased from 43% to 53%, which was the highest increase than other promoters. In addition, the optimal mass ratio of Rh to Fe was 4:1. When Rh and Fe were impregnated simultaneously, and reduced at 500 ^{o}C for 3h, the DTBB18C6 conversion and DTDCH18C6 yield reached to the highest values in this work. From the results of characterization, peak of Rh was not detected in the Rh-Fe/MgO XRD patterns which may be due to the effect of Fe on Rh. The EDS showed the mass ratio of the Rh (4.46%) to Fe (1.32%) was agreed with the design mass ratio of Rh (4%) to Fe (1%). The Rh and Fe were dispersed well on the support with the size about 20 nm from the TEM pattern of Rh-Fe/MgO.

Acknowledgements

This work is supported by the National Basic Research Program (No. 2009CB219906), the Natural Science Foundation of China (No. 21206131).

References

[1] Singh, S. K., Z. Asfari, et al. *Sep. Purif. Rev*.Vol. 42(2013), p. 28
[2] Walkowiak, W. and Kozlowski, C. *Desalination*, Vol. 240(2009), p.186
[3] Mona M. N., Abeer A. M., Mahmoud M. Elewac, *Dselin. Water Treat*. Vol.51 (2013), P.4350
[4] C.J. Pedersen, *Org. Synth.* Vol. 52 (1972), p.66
[5] M.J.Gula, R.A.Bartsch, , U.S. Patent 5,478,953. (1995)
[6] H.W. Liu, H.B. Pan and G.X. Tian, *et al*, *Synth. Commun*. Vol. 41 (2011) , p.624
[7] A. Stanislaus, B.H. Cooper, *Catal. Rev*. Vol. 36 (1994), p.75
[8] J. Santos, J. Phillips, J.A. Dumesic, J. Catal. Vol. 81 (1983), p. 147
[9] H.R. Sadeghi, V.E. Henrich, *J. Catal*. Vol. 87 (1984), p. 279
[10] S.J. Tauster, S.C. Fung, R.L. Garten, *J. Am. Chem. Soc*. Vol.100 (1978), p. 170
[11] H. Matsumoto, Y. Saito, Y. Yoneda, *J. Catal.* Vol. 19 (1970), p.101

Advanced Materials Research Vols. 960-961 (2014) pp 78-81

doi:10.4028/www.scientific.net/AMR.960-961.78

Study on influence of Snowmelt Agent to Performances of Asphalt

Yang Jin[1, a] ,Liu Lixia [2, b],Xiao Pengfei[1, b]

[1]Jinan Urban Construction Design ＆Research Institute Co.,ltd, Jinan 250000,Shandong, China

[2]Jinan Urban Construction Group,Jinan 250000,Shandong, China

[a] 369409986@qq.com [b]327254118@qq.com

Keywords: Snowmelt Agent; Asphalt; Performances; aging

Abstract: To study the influences of snowmelt agent to performances of asphalt,three snowmelt agents of NaCl，$CaC1_2$，$CH_3COONa·3H_2O$ were used to make asphalt sample and experiments about performances of high temperature and low temperature of asphalt were done.The results indicated that: temperature sensibility of 90# asphalt was reduced, softening point was increased ,dynamic viscosity was increased and ductility was reduced after being dealedwith snowmelt agent; Residual penetration ratio and residual ductility were also reduced after being dealedwith snowmelt agent.

As the development of the highway transportation, performances of roads are improved continuously[1]. However, snows of road hinder the normal transportation and also influence the traffic Safety, Even can cause a wide range of vehicles on the highway, Thus cause huge economic loss to the country. Therefore using the effective means to eliminate the road snow and ice quickly and maintain normal operation of transportation are very important. Snowmelt agent is the main way to snow melt in our country because of the low price and user-friendly control[2~3]。

Chlorine salt snowmelt agent is the most widely used snowmelt agent but which also can erode environment: Soil and groundwater, reinforced concrete structure and so on.The problems of chlorine salt snowmelt agent emergent after 1950s in the USA[4]. A large number of research reports of snowmelt agent impact on the environment and concrete structures at home and abroad has been reported but corrosion destruction to asphalt mixture do not form a unified understanding[5]. The influences of snowmelt agent to performances of asphalt was studyed in the paper to research the failure mechanism and degree to asphalt.

Test materials

Asphalt

SK90# asphalt was used,and the indexes is as table 1.

Table 1 The indexes of SK90# asphalt

Asphalt type	25℃needle penetration /0.1mm	10℃duc-tility /cm	softening point /℃	60℃dynamic viscosity/Pa·s	RTFOT (163℃,85min)		
					quality change /%	Residual penetration ratio /%	10℃Residual ductility /cm
SK90#	85.6	47	48.7	198.1	0.3	73.3	20.1

Snowmelt agent

three snowmelt agents of NaCl， $CaC1_2$， $CH_3COONa·3H_2O$ were used to make asphalt sample.

NaCl: white crystal, hygroscopy, can be dissolved in water and ethyl alcohol;

$CaC1_2$: white crystal, Strong moisture absorption, can be dissolved in water and ethyl alcohol;

$CH_3COONa·3H_2O$: white crystal, can be dissolved in water

Specimen preparation

1）NaCl,$CaC1_2$,$CH_3COONa·3H_2O$ of 0.2g/ml were made up in vessels and then heating and boiling it.;

2) Asphalt was heated to 155~165℃;

3)Heating ssphalt was poured into snow-melting Agent and then boiled 3min;

4) Thermal dehydration.

Test and results analysis

penetration index PI, softening point, dynamic viscosity, ductility,were done to test the performances of asphalt in high temperature, low temperature .

Temperature sensitive performance

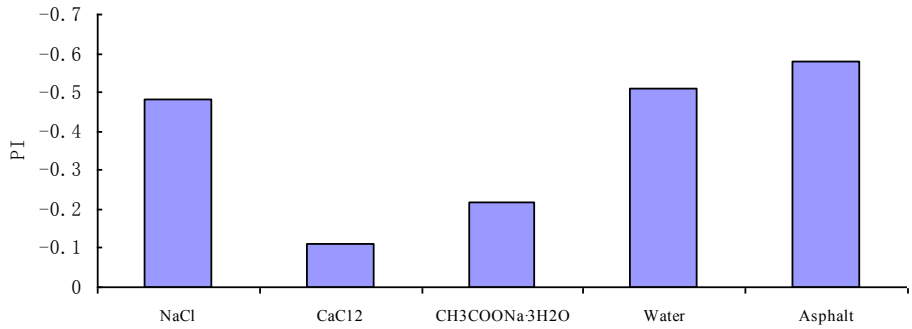

Fig. 1 The influences of snowmelt agent to temperature sensitive performanceof asphalt

The influences of snowmelt agent to temperature sensitive performanceof asphalt is shown like Fig. 1 which indicat that PI indexes of 90# matrix asphalt are increased after dealing with snowmelt agent.The order is that $CaC1_2$＞$CH_3COONa·3H_2O$＞NaCl.The reason is that snowmelt agent exist in asphalt as type of ionic crystal whiach share responsibility for temperature variation.

High-temperature behavior

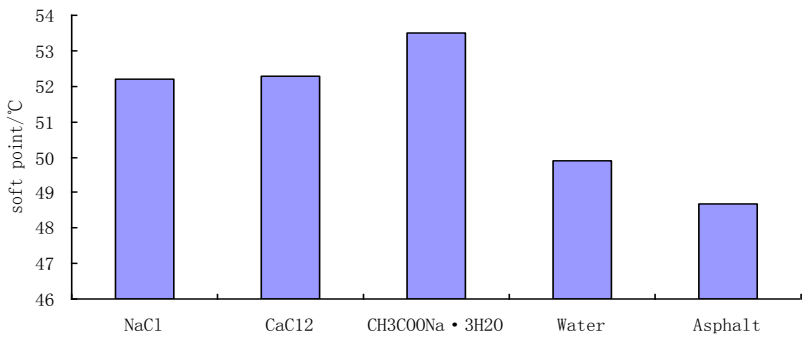

Fig. 2 The influences of snowmelt agent to softening point of asphalt

The influences of snowmelt agent to softening point of asphalt is shown like Fig. 2 which indicat that idexes of softening point are increased after dealing with snowmelt agent. The order is that $CH_3COONa \cdot 3H_2O > CaC1_2 > NaCl$.

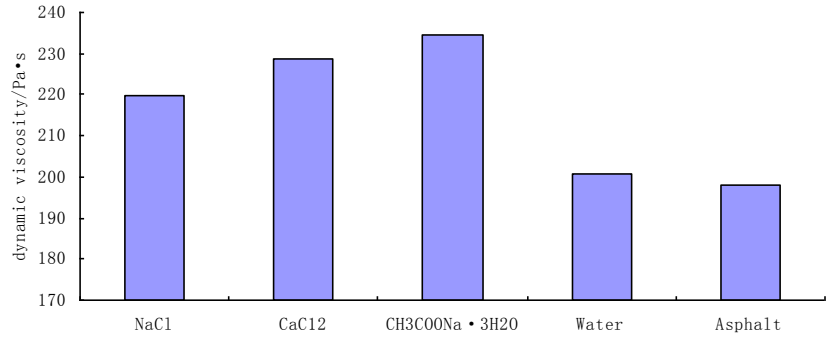

Fig. 3 The influences of snowmelt agent to dynamic viscosity of asphalt

The influences of snowmelt agent to dynamic viscosity of asphalt is shown like Fig. 3 which indicat that idexes of dynamic viscosity are increased after dealing with snowmelt agent. The order is that $CH_3COONa \cdot 3H_2O > CaC1_2 > NaCl$.The reason is that the molecular weight of asphalt is increased afte dealing with snowmelt agent which resulted in viscosity increased.

Low-temperature performance

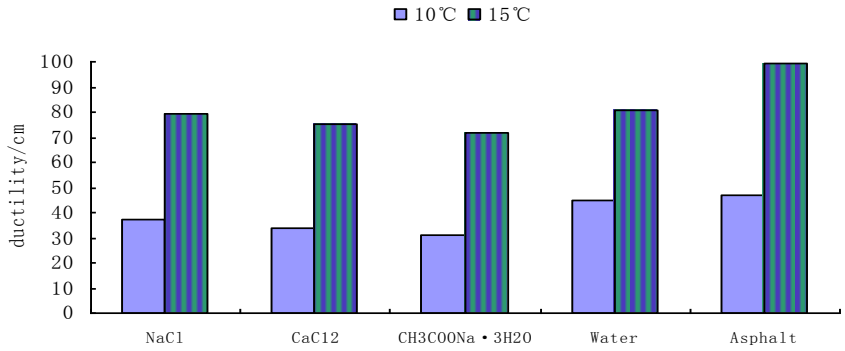

Fig. 4 The influences of snowmelt agent to ductility of asphalt

The influences of snowmelt agent to ductility of asphalt is shown like Fig. 4 which indicat that idexes of ductility are decreased after dealing with snowmelt agent. The order is that $NaCl > CaC1_2 > CH_3COONa \cdot 3H_2O$.

The influences of snowmelt agent to aging characteristic of asphalt

Residual penetration ratio

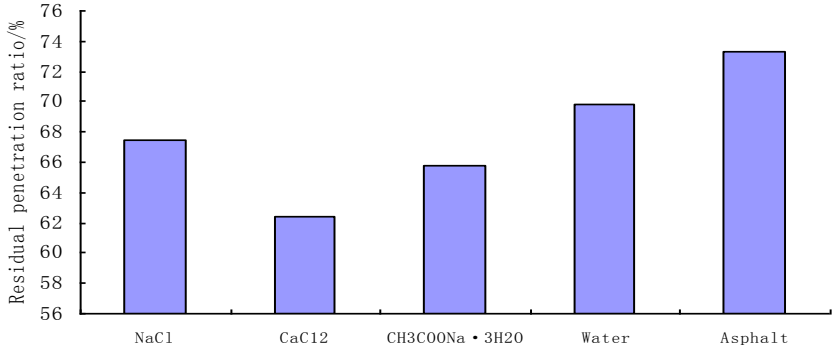

Fig. 5 Residual penetration ratio

Residual penetration ratio can reflect changes of asphalt after aging. the residual penetration ratio is greater ,the anti-aging performance of asphalt is the better. The influences of snowmelt agent to residual penetration ratio is shown like Fig. 5 which indicat that idexes of residual penetration ratio are decreased after dealing with snowmelt agent. The order is that NaCl＞ $CH_3COONa·3H_2O$＞$CaC1_2$.

Residual ductility

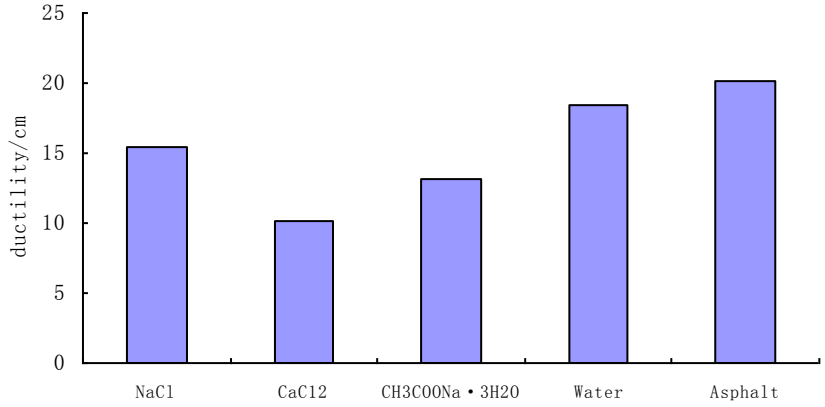

Fig. 6 10℃Residual ductility

The influences of snowmelt agent to 10℃residual ductility are shown like Fig. 6 which indicat that idexes of 10℃residual ductility are decreased after dealing with snowmelt agent. The order is that NaCl＞$CH_3COONa·3H_2O$＞$CaC1_2$.

Conclusion

The indexes of temperature sensibility are reduced, indexes of softening point are increased, dynamic viscosity are increased, ductility are reduced after the 90# asphalt dealing with snowmelt agent.

The indexes of residual penetration ratio and 10℃residual ductility are decreased after the 90# asphalt dealing with snowmelt agent which shows that aging characteristic of 90#asphalt is decreased by snowmelt agent.

References

[1]YuWen-bing, Li Shuang-yang, Snow and Ice Melting Techniques of Pavement:State of the Art andDevelopment Tendency[J]. JOURNAL OF GLACIOLOGY AND GEOCRYOLOGY,2011,33(8)

[2]Fu Guangwen.Research on Infiuence of Snowmelt Agent to Performances of Asphalt and Asphalt Mixture[D].Changsha University of Science and Technology,2010

[3] Xu Pengyu. Study and development direction s of snow melta-gents[J].Forestry Science and Technology Information, 2008(4)

[4] Cheng Gang, HanPing, Du Sujun . The discussion on the conditions and main problem of the dei cer [J] . Shanxi Science &Tech nology of Communications,2004,5

[5] CONG Pei –liang.Effects of Deicers on Properties of Asphalt Concrete[J].HIGHWAY,2011,6

Advanced Materials Research Vols. 960-961 (2014) pp 82-86

doi:10.4028/www.scientific.net/AMR.960-961.82

CT Analysis of Meso-structure Changes in Rock Salt with Brine Corrosion

Yandong Liu[1, a], Fanglong Yuan[1, b], Jianhua Dong[1, c]

[1]School of Civil Engineering,Lanzhou University of Technology,Lanzhou 730050,China

[a]649976471@qq.com, [b]184353256@qq.com, [c]415884371@qq.com

Keywords: rock salt; CT scan; corrosion;

Abstract: The roadbed base of railway in Qarhan Salt Lake area entirely consists of brine saturated rock salt formations. However, low salinity brine would cause corrosion for roadbed and the stability of rock salt roadbed would be directly affected. In this paper, physical and mechanical properties of brine-dissolved rock salt have been studied, as well as Computer Tomography was used to scan and analyze the meso-structural changes in rock salt before and after corrosion. The results show that density of rock salt would be changed obviously in the process of corrosion.The deriving or closing of meso-fissures in rock salt could been found with rock salt immigrating and corrosion damage.

Introduction

The brine saturated rock salt formations is adopted as the roadbed base of the Qinghai-Tibet railway, which goes across the largest Saline Lake called Qarhan Salt Lake in China[1]. The phenomena of brine corrosion appear in freshwater or low salinity brine, the solution and salt crystallization conditions of rock salt will be changed under conditions such as rainfall and brine deposits mining, these will cause diseases in rock salt roadbed. Therefore, studying of percolation, salting and changes of mechanical properties of salt rock under dissolution has become the governing problem to ensure stability of railway roadbed in salt area.

A lot of research on rock salt corrosion problems have been in progress at home and abroad. Results of mechanical and corrosion experiment of rock salt shows that a significant correlation exists between damage evolution and corrosion of rock salt. The corrosion characteristics of rock salt are obviously different under conditions of stressed and unstressed [2,3].

The technique of CT has received extensive attention, because of its advantages such as low disturbance, real-time and nondestructive analysis which make up for the defects of electron microscopy and many other means for observation [4,5]. This article analyzed CT scans of rock salt before and after corrosion, the aim is to discuss the mechanism of corrosion damage of rock salt from the micro level, provide test data for studying the macro corrosion properties of rock salt and the stability of rock salt roadbed.

Test situation

The samples were collected from the K740+200 transmission channel in crystalline rock salt specimen halogen, specimen is cylindrical, machined specifications: height 100mm, diameter 50mm. The samples are numbered and brine infiltration directions are marked. Because water has great influence on rock salt, so the specimens are processed using dry milling methods.

PHILIPS Brilliance 16 spiral CT of CAS Lanzhou Institute of Glaciology and Frozen State Key Laboratory of Engineering was utilized in the CT scan experiment of the rock salt before and after corrosion. Experimental coefficients is shown in figure. The spatial resolution of PHILIPS Brilliance 16 spiral CT system is 0.208mm, density resolution is 0.3%. The parameters about this test of CT scan: the scanning voltage :90~140kV, scanning current (the tube current):30~500mA, scan time: 4~10s, a magnification of 1, slice thickness: 3mm. Several layers are scanned each time, selected three layers as the test layer in random. Corrosion device for rock salt is designed by the author. It mainly made up by three parts, the infiltration of halogen water, the tank to undertake halogen water and corroded pipe.

Fig. 1 PHILIPS Brilliance 16 spiral CT machine

Procedure of this test: in order to obtain initial damage of the internal structure before rock salt corrosion, firstly, progress the initial CT scanning of rock salt as the basis to contrast the change image that rock salt corrosion. Scanning for 3 slice, the thickness is 3mm. Select a certain concentration of brine to progress corrosion test according to the corrosion mechanism of rock salt. After a certain time, remove the samples of corrosion rock salt, progress the second scan after drying the rock salt, scanning layer and layer thickness were consistent with the first scanning, so as to make a comparison with same position of the meso-structure damage changes before and after corrosion.

Analysis of test results

Generally speaking, it is difficult to reflect the meso-structure characteristics from density information in a CT images. If the CT images about samples of the same layer in different states are compared, we can get the meso-structure evolution information of the tested samples easily. Therefore, the same layer of the salt rock sample was scanned respectively before and after corrosion. In other words, CT scanning the sample for the first time, then carry on the second scanning after the corrosion test of rock salt samples. Three samples and three layers of each sample are scanned totally, there are 18 CT images before and after corrosion in all, limited by the length of the article, only 6 CT images of rock salt sample 2 are shown in Figure 4, 5, 6.

Figure 2 and Figure 3 are CT scanning location maps of 2# rock salt sample before and after corrosion. The pure salt rock is white, while the 2# rock salt sample presents hoar, it was caused by the internal impurities of rock salt, the surface presents granular, with teeth marks, and there is a visible fracture.

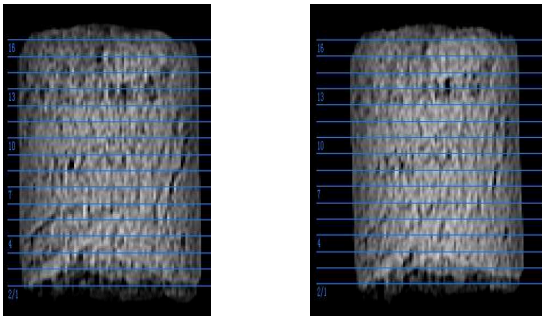

(a) before corrosion (b) after corrosion

Fig. 2 The sample location map

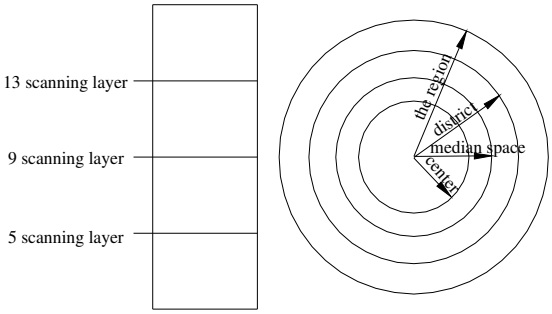

Fig. 3. 2# rock salt sample scanning horizon and measurement area

The CT images 5, 9, 13 layers of 2# rock salt sample before and after corrosion are shown in Figure 4-6, CT image is essentially a gray scale display of data image, and the gray values of each part can be displayed in the appropriate position of the image. In the course of rock salt dissolution, meso-evolutionary change will cause damage to the internal structure of the rock, which is expressed as diversification of gray values in CT images Gray shading indicates the gray size of CT images, the larger of the gray size, the higher the density of rock salt is, and vice-versa. The mean numbers and variances of CT image in each layer of 2# sample were given in Table 1, the mean number of the CT

image reflects the average density of all material points in the cross section, the variance value reflects the differences of density of material points in the cross section in degree. It reflects the structural strength of the rock salt rock salt indirectly.

The properties of CT images show that dark black region is low density area, which means in this area of the sample existing pores, cracks and other damage; bright white region in the image is high density area, in which rock salt particles are concentrated, which can be seen Figure 4~6. Three layers of 2# rock salt sample were taken before and after corrosion, each layer can be divided into four regions of interest (ROI) : respectively named the region, district, median space and center, the number of CT domain of interest is shown in table 1 and Figure 7.

It can be seen from the relevant data in Figure 4,5, 6,7 and Table 1 that :

It can be concluded from 5, 9, 13 (the first layer scanning) images of 2# rock salt sample before corrosion in Figure 4, Figure 5 and Figure 6 that, brightness level of each layer in the image was obviously uneven distributed, gray of rock salt was evenly distributed in 5, 9 layers before corrosion, there is only a small amount of abnormal low density area and internal structural damage is lesser. However, the image of rock salt sample in 13 layer before corrosion shows that most regions are abnormal low density area, even appear "cavity", it's the internal large holes and cracks within rock salt, thus structure is quite fragile. Longitudinally compare the three layers before corrosion.

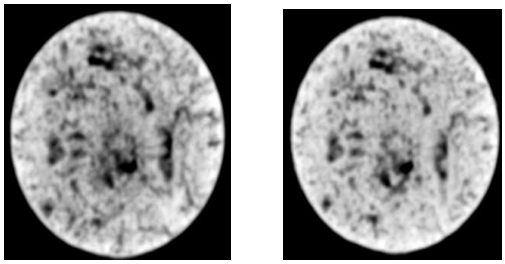

(a) before corrosion (b) after corrosion

Fig. 4 The 5 layer scanning corrosion image

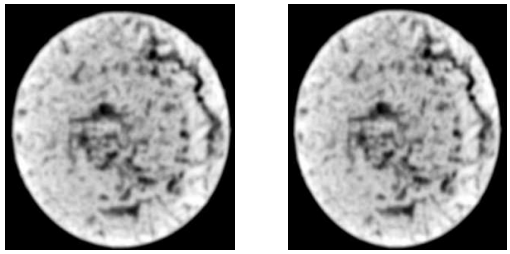

(a)before corrosion (b)after corrosion

Fig. 5 The 9 layer scanning corrosion image

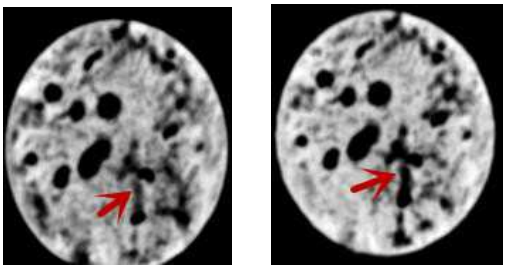

(a)before corrosion (b) after corrosion

Fig. 6 The13 layer scanning corrosion image

It can be found in CT images of 2# sample that the brightness of three different layers is markedly different , which means the density of rock salt sample in each layer is different ; it can be seen from Table 1 and Figure 7, the CT number of the same sample at different levels (Table 1) are different. In addition, the CT number within the same layer of each pixel is also different. Namely the density inhomogeneous distribution. It can be concluded that the internal structure of rock salt sample exists inhomogeneity before corrosion. Whole internal parts density of the rock salt shows a random distribution. That is to say, there is initial damage in rock salt.

In the course of rock salt corrosion test, brine which infiltrated into 2 # sample is unsaturated, internal meso-damage evolution of rock salt causes the internal structure changes which is shown as differences of gray values in CT images. It can be seen there's no significant change about integral gray scale of CT images on rock salt with corrosion from Figure 4, 5, and 6, abnormality only appears as increasing or decreasing in local areas of the rock salt. From Table 1 and Figure 7 we can see : ΔME increased in different regions of the three layers before and after corrosion, but the values added are extremely uneven. The number of value added in 13 layer is the smallest , SD increased greatly

and discrete is also increased among the three layers , the opening of the pores of areas in which indicated by the arrow is increased . We can conclude that integral density of rock salt increased but reduced in local areas, the phenomenon indicates that salt grow in rock salt in the course of corrosion integrally and corroded locally .

Table 1 2# rock salt specimen CT scanning CT number

CT number	5					9					13				
	ME		SD		ΔME	ME		SD		ΔME	ME		SD		ΔME
	B	A	B	A		B	A	B	A		B	A	B	A	
The region	1132	1278	406	368	146	1116	1262	410	382	145	843	991	593	631	148
district	1043	1193	387	361	150	1034	1176	387	366	141	774	909	598	652	135
Median space	928	1096	384	377	168	950	1104	339	343	153	760	848	618	685	88
Center	848	1037	390	387	189	829	1027	335	336	197	657	713	686	760	55

Note : B mean before corrosion ;A mean after corrosion ;AR is fault measurement area ; ME : mean number of the measurement area ; SD : the measurement of regional CT value standard deviation ; △ME : variation of the mean value of CT before and after immersion .

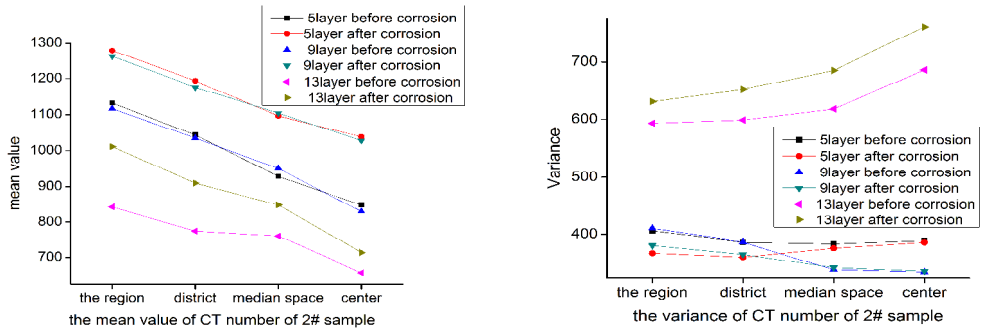

Fig. 7 Mean and variance of CT number of the 2# rock salt sample before and after corrosion

It can be seen from analysis the longitudinal of 5-9-13 layer: the brightness level of 5 and 9 layers of 2# sample changed little before corrosion, namely density is similar and tend to increase to the infiltration direction. Most of the regions in 13 layer are abnormal low density areas, while the low density band is essentially the micro crack development zone. A small amount of pores appear signs of rising and fracture began to run through after corrosion , shown as corrosion, part of rock salt soluble matter was taken away by brine and voids arise which is indicated by the arrow in figure 6. From table 1 and Figure 7, we can see that the mean CT values of each area have increased before and after corrosion, 5 layer and 9 layer show little fluctuation, and the 13 layers has a wider fluctuation range. The change of CT mean number is smaller but variance fluctuated greatly in the center of 13 layer before and after corrosion, especially in the core area. This demonstrates that the internal particles, they arrangements and fracture structures in 13 layer of rock salt are greatly uneven, and low density areas and dissolution increased the discretion of internal structure of rock salt that crack growth becomes possible, and all the results above are consistent with figure 6.

It can be seen in Figure 4 , 5 and 6: the higher brightness in the edge of the area it is, the higher density it will be . From Table 1, the initial means of CT value about 2 # rock salt sample decreased gradually from the region to center, which suggest that density of the edge of rock salt is bigger and more compact while density in center is smaller , the structure is more fragile. By comparing the differences of brightness of CT images about rock salt before and after corrosion, we can see that the gray-scale in each layer increased significantly in the edge region and changed a little in other areas. Comparing the 4 ROI, mean CT values decreased gradually from the edge to the center. It shows that the rock salt density reduced over the edge to the center, the marginal zone is fringe while the center

area is loosed texture. It can be seen from△ME of 5 layer and 9 layer in table 1. CT value increment increased from edge to center, Central areas the phenomenon of salt growth is obvious; In 13 layer mean CT value increment gradually reduced from edge region toward center zone, salt growth mainly occurred in edge of rock.

It can be seen from 6 CT images as well as in Table 1 and Figure 7: the mean CT values of 5 and 9 layers changed greatly, variances changed minimally, 13 layer CT number mean changed in large level and shows small change in the central area while the variance fluctuate dramatically. This illustrates materials moved into the edge in 5 and 9 layers of rock salt sample, so there appears salt growth ; but at the central and edge zone of 13 layer arises the phenomenon of local corrosion .

Conclusions

There are greater differences of meso-structure of rock salt sample and distribution unevenly. The internal particles and porosity of samples were arranged also unevenly. That means the internal structure of rock salt have initial damage, and fissure begin to develop.

The CT values changed regularly with corrosion, the values of CT were greater after corrosion. The growth rate is connected its internal micro-structure, solution concentration and immersion time. Solution migration occurs inside the sample when it was soaked. Then the external solution gets into the pore of the sample, a part of solution become crystallization, some remains in the pore, lead to density difference of samples and meso-structure changes.

The CT number of 2# sample increased in each layer after corrosion, showing that some substances moved into rock salt and caused increasing of the density in rock salt. The corrosion brine is unsaturated solution. The CT number of the 13 layer overall increased slightly after corrosion , but parts of the area occurs pore expansion and perforation which is shown that the CT number increased slightly, SD values increased obviously, which can account for the original crack of local area inside rock salt, with the new crack emergence, the amount of the fracture increased and connected,finally forming fissure network, namely produce corrosion phenomenon .

The corrosion liquid of 2# sample is unsaturated brine, the analyzed results show that 2# rock salt samples grow salt integrally and corrode locally. The probable reason should be that the concentration of unsaturated brine is too high, the local area fracture inside rock salt developed abnormally.

The density of rock salt is increased with the infiltration of saturated brine, internal cracks closed and holes were filled. The structure was repaired, but the structure that was repaired presents uneven distribution. The phenomenon of salt growth at the edge area of rock salt is obvious; However the phenomenon of salt growth is not appeared in the central area.

Reference

[1] Zengwang Fan,Chengjiang Zhao. *Subgrade Engineering*. Vol.1(2010),p.190-192(In Chinese).

[2] Zhewei Zhang. *Well and Rock Salt of China.*Vol.33 (2)(2002), p. 23-25(In Chinese).

[3] Jingnian Fang. Coupled Elasto-Plasto_Damage Mechanism and its Influence on Dissolving Property of Rock Salt[D]. Instiute of Rock and Soil Mechanics, Chinese Academy of Sciences, master thesis, 2009(In Chinese).

[4] Yanchun Tang. *Rock and Soil Mechanics.*Vol.29 (2)(2008),p. 296-302(In Chinese).

[5] Zaihua Lu. *Rock and Soil Mechanics.*Vol.23 (4)(2002) ,p.47-422(In Chinese).

Advanced Materials Research Vols. 960-961 (2014) pp 87-91

doi:10.4028/www.scientific.net/AMR.960-961.87

Effect of rare earth elements on Microstructure and Mechanical Properties of AZ91D Alloy

ZhichaoLiu[1], YaoLi[1,a,*] and JunjieYang[1]

[1]The school of electromechanical & architectural engineering, Jiang Han University, Wuhan, Hubei Province in China

[a,] *lylly111@sina.com

Keywords: AZ91D magnesium alloy; rare earth element; mechanical properties

Abstract: Rare earth Y, Gd, Nd were added to improve the tensile strength, elongation, hardness and microstructure of AZ91D magnesium alloy in this study. The investigation had been undertaken by 8 GWU type resistance furnace, RGM - 50 electronic machine , Vickers ,etc. Results show that a moderate amount of composite adding rare earth can effectively improve the tensile strength of AZ91D alloy, elongation, hardness and the organizational structure, as a rare earth content increased after the first performance decline. When rare earth content is 1.8%, the highest tensile strength up to 276.58mpa, 8.3% elongation. When rare earth content is 2.4%, the hardness is up to 99.36 HV1.96.

Introduction

In recent years，magnesium alloy has become the most commonly used light structural alloy, plays an important role in the automotive, aerospace, consumer electronics and so on. Magnesium alloy and the expansion coefficient of heat transfer is larger.AZ91D alloy is a kind of foundry magnesium alloy, it has high strength, good heat dissipation, etc. It is one of the hot topics in the study of magnesium alloy, and in terms of a large proportion in the use of magnesium alloy[1].

But in practice, AZ91D is difficult to completely replace the lightweight materials such as aluminum alloy. This is due to the strength and plasticity of magnesium alloys is difficult to meet the requirements of actual use. Existing research[2-4] shows that alloying of rare earth elements can make magnesium alloy get enough reinforcement.

This paper selects the AZ91D magnesium alloy and rare-earth yttrium, neodymium, gadolinium as research materials. With the aid of industrial production equipment, researched on compound added comprehensive effects of rare earth on microstructure and properties of AZ91D alloy.

Experimental materials and methods

Experiment chooses industrial AZ91D magnesium alloy ingot.Using mixed refrigerants YH134a and nitrogen gas,melting in 8 GWU type resistance furnace.Compound of adding different ratio of Mg - Y, Mg - Nd, Mg - Gd rare earth alloy and stirring When the temperature reached 690 ℃ ~ 720 ℃.Thermal insulation for 10 minutes,then making RE-AZ91 magnesium alloy experimental samples in the J1125B type of test die casting machine with a metal die-casting mold at 680 ℃~ 710 ℃.Die casting sample size and die casting process are according to the national standard GB/T 13822-13822 "die casting non-ferrous alloy specimen" regulation requirements.Tensile specimen size chart as shown in figure 1.The experiment using RGM-50 electronic universal testing machine,with tensile speed of 5 mm/min.

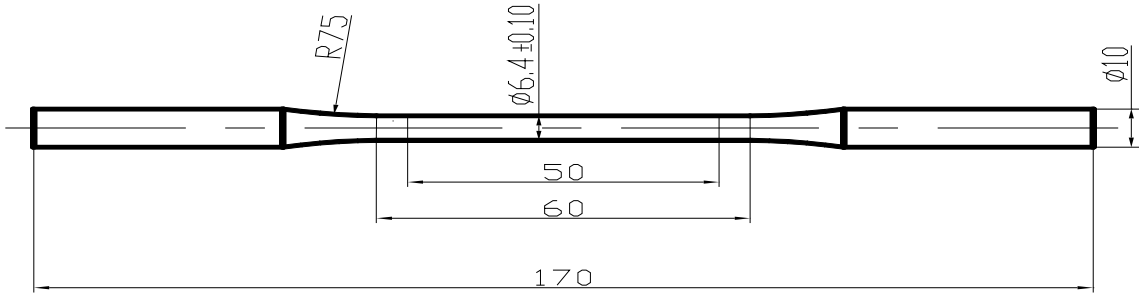

Fig.1 Tensile specimen size figure

Removed the burr of the sample surface, and numbered 10 groups of sample, each group contains three parallel samples. Zero group for not adding rare earth of AZ91D magnesium alloy, the rest of the group of rare earths such as shown in table 1.

Table 1 Adding rare earth elements table

number	Content of rare earth %			Amount of rare earth
	Y	Nd	Gd	(%)
0	0	0	0	0
1	0.2	0.2	0.4	0.8
2	0.2	0.4	0.4	1
3	0.4	0.4	0.6	1.4
4	0.6	0.6	0.6	1.8
5	0.6	0.6	0.8	2
6	0.8	0.8	0.8	2.4
7	1	1	1	3
8	1	1	1.5	3.5
9	1	1.5	1.5	4

The experimental results and analysis.

3.1Rare earth magnesium die casting organization and the performance impact

Figure 2 for the different content of rare earth 400 ratio of metallographic sample photos. Figure 2a is not adding rare earth alloy phase diagram, organized by figure known alloy by the matrix and eutectic of precipitation (Mg17Al12) phase. The alpha phase distribution uniformity, beta phase presents the coarse mesh intermittent or continuous irregular distribution, and a small amount of particulate matter exists. The figure 2b and 2c show that with the increase of the content of rare earth basic remains the same, alpha beta phase number, have great changes, and the distribution form by thick mesh gradient for the tiny granule. In addition, the organization of rare earth compounds, and the content is on the rise. By figure 2d, rare earth content is increased to a certain amount, the increase of the rare earths are not further promote the grain refinement, on the contrary make grain overgrowth of. In addition to the above two phase, after adding rare earth alloy, there is a new phase for rare earth compounds, its content increased with the increase of content of rare earth.

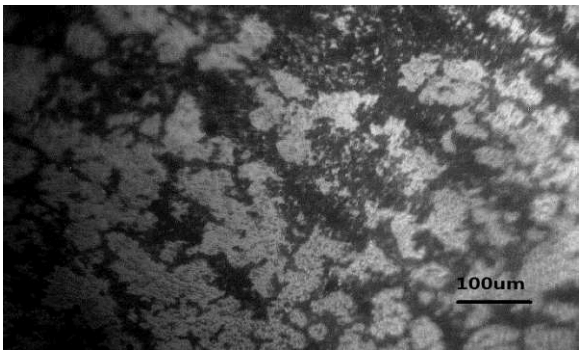

a 0%

b 1%

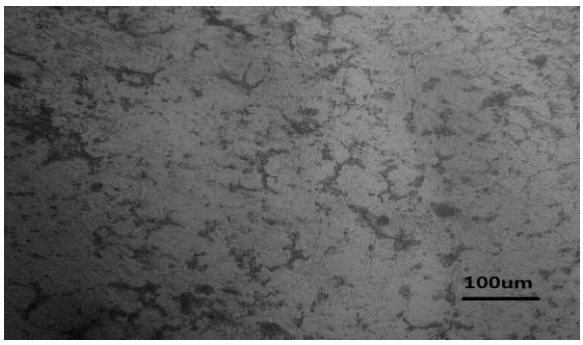

c1.8%

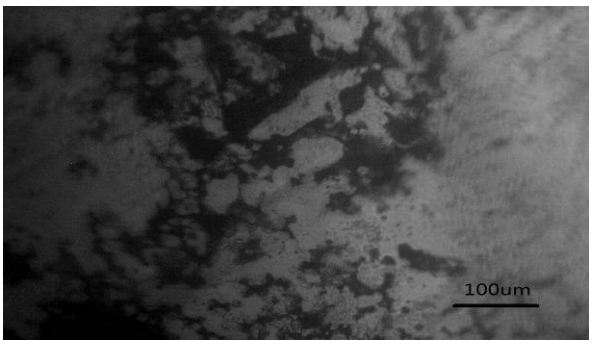

d 4%

Fig.2 Different content of rare earth 400 ratio photos

In addition to the above two phase, after adding rare earth alloy, there is a new phase for rare earth compounds, its content increased with the increase of content of rare earth. After adding rare earth magnesium alloy, because of the difference between element electronegativity, adding rare earth elements will be priority and Al element reaction, formation of rare earth compounds .The metallography theory shows that the new formation of the rare earth compounds from the elements affected the beta phase.

3.2Tensile experimental results.

The fig.3 shows that the RE (rare earth) content increased, the strength and elongation of the alloy were increased. With the increase of the content of rare earth alloy intensity present a first down later. When the adding amount of RE in the rang e of 1.8%, the strength of the alloy and elongation increase with the increase of rare earth, the highest can reach 276.58mpa and 8.3% respectively. Rare earth content is above 1.8%, , the alloy strength and elongation does not increase, instead of down.

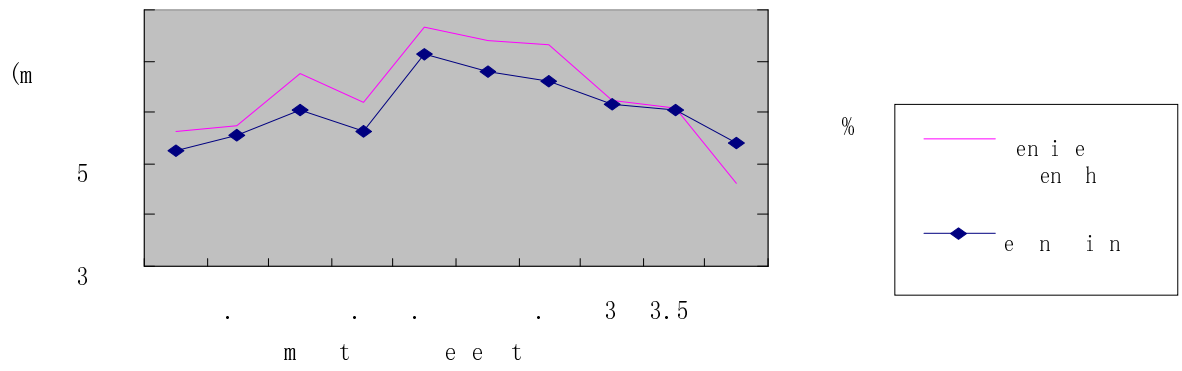

Fig. 3 Tensile strength and elongation of different rare earth content

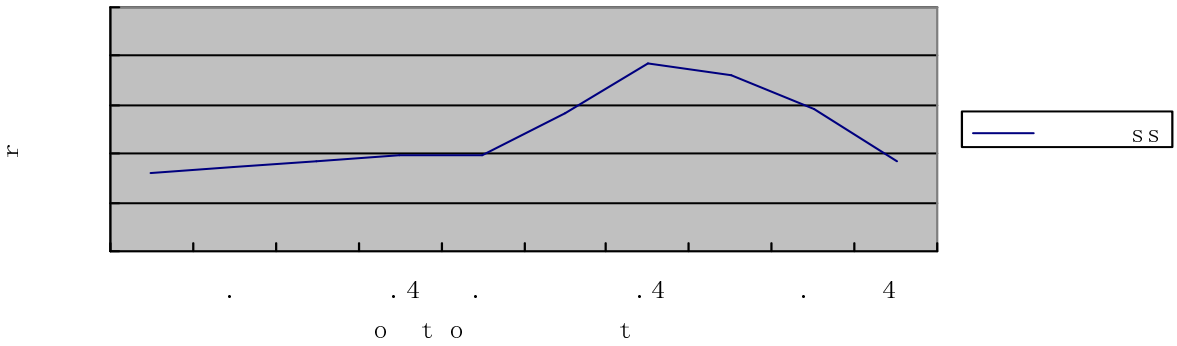

Fig. 4 Hardness

The hall-page formula shows that the size of the grain can affect the strength of the alloy. When adding rare earth alloy, organizations are obviously enhanced, the tensile strength and elongation were increased, surface hardness of alloy rose slightly. And when the organization fully refined grains and uniform distribution, the tensile strength of alloy achieves the best condition, it shows that the rare earth elements by influencing the grain size of the organization's size distribution and then change the performance of the alloy[5].When rare earth content continues to increase, the microstructure changed from spread evenly to part is linked together, and have obvious trend of bulky, the corresponding tensile strength and elongation decreased, and the hardness is increased. Can be thought that tensile strength and elongation are greatly influenced by grain size and distribution, and hardness are greatly influenced by content of rare earth compounds. When rare earth content continues to increase, alloy tensile strength and elongation decreased, and not as good as not adding rare earth, and the hardness and nominal tensile modulus when adding rare earth also dropped to less than not. The grain overgrowth of resulting in a decline in the tensile strength of the alloy at the same time reduce the hardness of the alloy.

Conclusion

1. Adding rare earth can be change alloy casting organization, with the increase of the content of rare earth group shows the tendency of refinement before coarsening.

2. The right amount of compound added rare earth magnesium alloys can be effectively increased the tensile strength, elongation, surface hardness. when rare earth content is 1.8%, the strength of the alloy and the highest elongation can be up to 276.58mpa and 8.3% respectively. When the content of 2.4%, up to 99.36 HV1.96 hardness.

3.Alloy strength and hardness increased with the increase of the content of rare earth were first after a downward trend, but the best rare earth content is different.

Acknowledgements

This work was financially supported by the Wuhan Planning Project of Science and Technology(201250499145-16，2013071004010467）.

References

[1] D. H. StJohnM. A. EastonM. QianJ. A. Taylor.Grain Refinement of Magnesium Alloys: A Review of Recent Research, Theoretical Developments, and Their Application[J],2013,44(7).

[2] Mordike.B.L Ebert.T.Magnesium properties application potential [J] .Mater Sci Eng.2001,A302 37-38.

[3] WANG Rongbin.Roles of R in Magnesium Alloys and Application of RE Magnesium[J].Nonferrous Metals Processing,36(1),27(2007).

[4] F. KabirianR. Mahmudi.Effects of Rare Earth Element Additions on the Impression Creep Behavior of AZ91 Magnesium Alloy[J],2009,40(9).

[5] TONG GUO-DONG, LIU HAI-FENG, LIU YAO-HUI. Effect of rare earth additions on microstructure and mechanical properties of AZ91 magnesium alloys[J]. 2010, 20:336-340.

Advanced Materials Research Vols. 960-961 (2014) pp 92-96

doi:10.4028/www.scientific.net/AMR.960-961.92

Study on preparation and properties of in situ composite of nano-SiO_2 and vinyl acetate-acrylate emulsion

Xiaohui Wang[1, a], Renli Wang[2,b], Limin Dong[3,c] and Hanfei Lu[4,d]

[1]School of Chemistry Engineering, Xuzhou Institute of Technology, Xuzhou, Jiangsu, 221111, China

[2] Department of I & E Engineering, Xuzhou Institute of Technology, Xuzhou, Jiangsu, 221111, China

[3] School of Chemistry Engineering, Xuzhou Institute of Technology, Xuzhou, Jiangsu, 221111, China

[4] School of Chemistry Engineering, Xuzhou Institute of Technology, Xuzhou, Jiangsu, 221111, China

[a] wxh2116@163.com, [b]dlm@xzit.edu.cn, [c]wxh2116@yeah.net, [d]wangxh@xzit.edu.cn

Keywords: Nano-SiO_2, Acetic Acid-Acrylate Copolymer, Situ Emulsion.

Abstract. Available nano-silica commercially was modified with silane coupling agent A-151, and then emulsion was synthesized with modified SiO_2, vinyl acetate, methyl methacrylate and butyl acrylate by polymerization reaction. Effects the amount of emulsifier, initiator and organic nano-SiO_2, etc factors on the performance of emulsion polymerization and latex film were investigated. The best test results of composite emulsion of SiO_2 and vinyl acetate-acrylate were obtained by theoretical research and experimental operation: modified nano-SiO_2 content of 3%, the content of 3% emulsifier OP, content of 0.5% potassium persulfate initiator.

Introduction

Vinyl acetate-acrylate emulsion as film forming material has low environmental pollution, good gloss, color retention and resistance to the aging, showing expansive prospects in many fields [1, 2] . However, its poor water resistance, cold resistance, storage stability and low drying rate had limited its development to some extent. It is necessary to study and solve these problems. Composite of nanoparticles/emulsion can improve the aspects of performance greatly. Because the added nano-materials could react with the monomer, emulsifier, and initiator, etc in situ polymerization process[3-6]. The way could allow a more uniform distribution of the nanoparticles in the polymer system. This could also allowa chemical effects and an interface interaction sufficiently and uniformly between the molecules of the polymer and nanoparticle, thus this would has an obvious effect of the performance of these polymers [7].

This paper has used the commercially available nano-SiO_2 modified by silane coupling agent A-151 to be added into the vinyl acetate, methyl methacrylate acrylate, and butyl acrylate, etc monomers and to synthesize vinyl acetate-acrylate emulsion by situ emulsion polymerization method. The effect of the amount of emulsifier, initiator and modifiednano-SiO_2 on performances of the emulsions was investigated.

Experimental Section

Experimental Materials and main test instruments. Toluene, Nano-SiO_2 (Q/RMHGI-2009), a silane coupling agent (A-151), ethanol, dilute hydrochloric acid, vinyl acetate, butyl acrylate, methyl methacrylate, polyvinyl alcohol, emulsifier(OP-10), potassium persulfate, ammonia. Electric mixer (JJ-1), shear emulsifying machine with high velocity(A300-70G-S), infrared spectroscopy (ALPHA), rotational viscometer (NDJ-1).

Preparation of modified SiO2. Nano-SiO2 with a silane coupling agent A-151 was modified at its surface. When content of the A-151 is 5%, effect of SiO2 air gel particle surface modification was the best.SiO_2 of 3 g was dispersed in 90 mL of toluene. A-151 of 5% content was dissolved in anhydrous ethanol of 6 mL. Then they were added into four-neck flask and ultrasonic dispersed by 10 min and stirred at 75 ˚C with constant temperature about 1.5 h. Finally they were cooled to room temperature,

and filtered. The precipitate was washed with ethanol and repeated 4 times to remove the excess of a-151 and byproducts and dried to obtain modified SiO_2.

Preparation of nano-SiO_2 and vinyl acetate-acrylate emulsion. Vinyl acetate of 12.5 mL, methyl methacrylate of 25 mL, butyl acrylate of 12.5 mLas monomers, emulsifier (OP-10, $C_8H_{17}C_6H_4O(CH_2CH_2O)_{10}H$), initiator(KPS, potassium persulfate). Distilled water of 400 mL (the ratio of it with monomer was 1:4), all of emulsifier, polyvinyl alcohol of 0.5 g, modified nano-SiO_2, and 1/5 of the monomer mixture were added into a beaker. They were dispersed about 15 min in a dispersion machine. When water bath is heated up to 80 ˚C, initiator was added to appear blue light. The remaining monomer mixture was added at 80-83 ˚Cdropwise. The reaction was warmed to 85 ˚C.After additional initiator of 0.1 g added, it was cooled to 40 ˚C. Using aqueous ammonia to adjust pH value as 7-8, the material was given out.

The types of experiments: 25% vinyl acetate, 50% butyl acrylate, 25% methyl methacrylate, emulsifier OP (contents of 1%, 2%, 3%, 4%, 5%, 6%), 0.5% initiator KPS and 3%modified nano-SiO_2.25% vinyl acetate, 50% butyl acrylate, 25% methyl methacrylate, 3% emulsifier OP, initiator KPS(contents of 0.3%, 0.4%, 0.5%, 0.6%, 0.7%) and 3%modified nano-SiO_2.25% vinyl acetate, 50% butyl acrylate, 25% methyl methacrylate, 3% emulsifier OP, 0.5% initiator KPS and 3%modified nano-SiO_2(contents of 0%, 1%, 2%, 3%, 4%).

Methods of analysis. Appearance is checked visually. Viscosity is measured by NDJ-1 rotary viscometer. Test method of stability of calcium ion: sample of 8mL composite emulsion was added into a tube with 10mL graduation. Then 3mL (concentration of $CaCl_2$ was 0.5%) added into solution. About 24h later, if lamination phenomena is not appeared, stability of calcium ion was considered as qualification. Condensation rate: after the reaction, the gel was collected, and dried to reach a constant temperature to calculate condensed material accounting mass percentage for monomer. Determination of solids content of the emulsion: approximately1.0gsample was placed in a small beaker to form an uniform film. The film was dried about 6hat100 ˚C and cooled to room temperature and weighed. The aqueous assay: take emulsion of 100 μL on glass pane to prepare dry film at 30 ˚C and then the dry film was soaked in deionized water, phenomenon was observed after a day. Film-forming: the prepared emulsion was coated on a clean glass surface at room temperature. The film formation conditions of the emulsion were observed.

Results and Discussion

Effect of the amount of emulsifier on properties and viscosity of the emulsion. From the table 1 it can be found that when the amount of emulsifier at 1% and 2%, the appearance of the emulsion would have a stratification phenomenon, mainly due to insufficient amount of the emulsifier, thus only a small part of the surface of particles of the monomer mixture was surrounded by emulsifier molecules. Less than enough emulsifier molecules were absorbed into surface of the monomer mixture particles, which cannot sustain a stable emulsion, and stability of the emulsion was not good and gloss of the liquid was not too good. The reactants were not fully reacted. When the amount of emulsifier is between 3% and 4%, sufficient emulsifier improved stability of the emulsion polymerization process. The polymerization rate became faster. Appearance of the resulting emulsion was uniform, good gloss, and no precipitation. Increasing the amount of emulsifier continuously to exceed 5%, emulsifier was too more, and the emulsions contained more coarse particles and agglomeration phenomenon, thus a little precipitate has formed.

Figure 1 shows that amount of the emulsifier increase the viscosity of the emulsion. An increase in the number of colloidal particles was caused by an increased probability of a single particle nucleation and decreasing of the large particle diameter, thus the surface area of the particles became larger, thus bind the particles together to increase the viscosity of the emulsion performance. However, when the viscosity is very large, the cohesion was increased, and stability of the emulsion was decreased. The optimum of amount of the emulsifier was 3%.

Effect of the amount of initiators on properties and viscosity of the emulsion. As shown in the table 2 and figure 2, when content of the initiator is at 0.3%, polymerization was not very stable, and the appearance of emulsion was gray. It was because of amount of the initiator was very less, and the

reaction rate would be smaller, and thus the conversion of monomers was low. The chemical reactions were not complete. The particles of the emulsion became unstable, thus resulted in the larger rate of aggregation. The amount of initiator of 0.7% produced violent polymerization. It was because more free radicals were formed to accelerate the rate of polymerization, thus the emulsion stability became lower. The amount of initiator at 0.5% made emulsion attain a best performance.

Table 1 Effect of the amount of emulsifier on properties of the emulsion.

Amount of emulsifier/%	Appearance	Viscosity	Gloss	Stability of Ca^{2+}
1	White, stratification	15	Poor	More precipitation
2	A little stratification	20	General	Little precipitation
3	White, blue	26	Good	No precipitation
4	White, blue	29	Good	No precipitation
5	White, a little blue	35	Good	Little precipitation

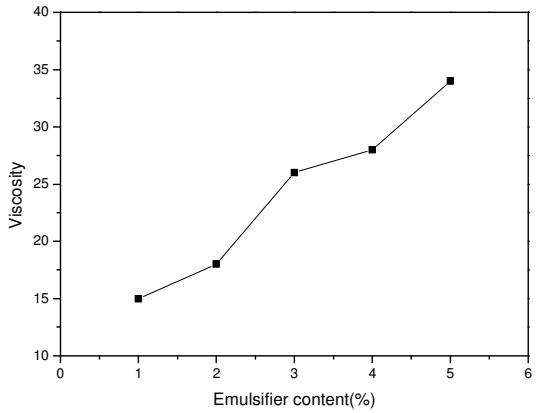

Figure 1 Effect of the amount of emulsifier on viscosity of the emulsion.

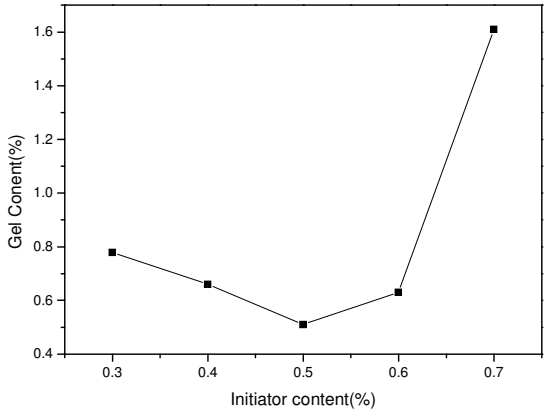

Figure 2 Effect of the amount of emulsifier on polymerization degree of the emulsion.

Table 2 Effect of the amount of initiators on properties of the emulsion.

The amount of initiator/%	Aggregation rate/%	Appearance
0.3	0.79	Gray
0.4	1.2	White
0.5	0.52	White, blue
0.6	0.67	White,a little blue
0.7	1.57	White, yellow

Effect of the amount of the modified SiO_2 on properties and solids content of the emulsion. Modifiednano-SiO_2 had better original dispersion to improve the properties of the emulsion. As can be seen from Table 3, with the increase of amount of the SiO_2 from 0 to 3%, water resistance changed better. When diameter of the SiO_2 particles is smaller, the surface area of the particles would be increased, thus chemical bind had more opportunities of binding between polymer chain and particles. However, excessive amount of SiO_2 led to worse water resistance. This was mainly result of agglomeration and lost of nano effects of air gel.

Table 3 Effect of the amount of nano-modified SiO_2 on properties of the emulsion.

Nano-modified SiO_2/%	Solid content/%	Water resistance	Film-forming
0	53.9	Better, white	Uniform, transparent
1	47.2	Well, white	Uniform, transparent
2	41.7	Well, white	Uniform, transparent
3	37.8	Well, no white	Uniform, transparent
4	32.5	Poor, no white	Fine lines, yellow

As can be seen from Figure 3, the solid content decreased with the increase of the use of SiO_2. The reason may be result of reactions of between the excessive charge on the surface of SiO2 and free radicals produced by the initiator. This decreased the efficiency of reaction of initiator. Usually for the polymer emulsion, the solids content is about 35%, latex particle size is prefer between 0.1 and 0.5 μm. If the polymer emulsion had an average particle diameter of 0.1μm, and an average particle diameter of the cores had 10μm, under suitable process conditions and the ratio of raw materials, and the reaction did not generate the new latex particles, the monomer would be seen as the seed particles of the polymerization. According to the theoretical calculation, the amount of SiO_2 as seeds should be less than0.14% of amount of the total monomers. The theoretical amount of SiO_2 as air gel should be less than 5% of amount of the total emulsion. Obviously, the amount of SiO_2 was too low to reflect the nano performance of it.

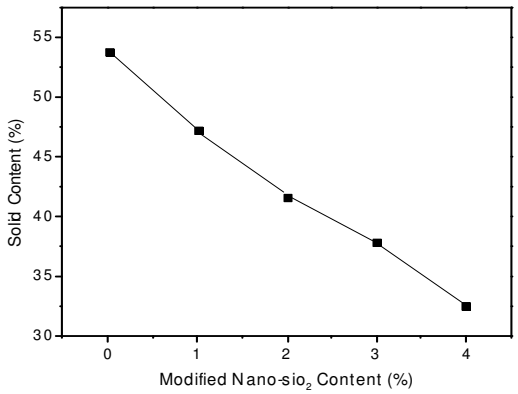

Figure 3 Effect of the amount of nano-modified SiO2 on solid content of the emulsion.

Analysis of IR spectrum. For understanding the change of structure and properties of vinyl acetate-acrylate emulsion, IR results them modified by nano-SiO2 before and after were characterized. After modification, at 1637 cm^{-1}, 1407cm^{-1}, 1115cm^{-1} and 544cm^{-1}, absorption peak moved to long wave direction respectively, showing structural change of the emulsion. At 3431 cm^{-1}, the absorption peak moved to 3449 cm^{-1}. The movement showed existence of -OH and -COOH groups and increased amount of them. Moreover, the absorption peak of 1115cm^{-1} approved existing of functional groups of –C=O and –C-O-C- etc.

Conclusions

When the amount of the silane coupling agent (A-151) is 5%, the effect of surface modification of surface of the SiO_2 was best and can achieve best dispersion effect in the emulsion, thus effectively prevent the occurrence of agglomeration of nano-SiO_2 particles with the effect of high surface energy.

In modified nano-SiO_2 and vinyl acetate-acrylate emulsion, under nano-SiO_2 content of 3%, emulsifier (OP-10) as 3% of total content, initiator of potassium persulfate as 0.5% of total content, the prepared vinyl acetate-acrylate emulsion showed good shiny, viscosity, solids content and stability and performance of emulsion had been significantly improved.

After modification by nano-SiO_2 based on the silane coupling agent (A-151), absorption peak moved to long wave direction respectively, showing structural change of the emulsion. Surface of modified emulsion were grafted by polymers.

Acknowledgement

This work was financially supported by the Agglomeration Program of Doctors of Jiangsu Province (2013), the Cultivation Project of Xuzhou Institute of Technology (4100716028) and Innovation Program of Jiangsu Province Natural Science Foundation (BK2012142).

References

[1] S. B. Zhou: Elastom Vol. 16 (2006), p. 27

[2] F. A. Zhang, C. L. Yu: Eur. Polym. J Vol. 43 (2007), p. 1105

[3] G. J. Liu: Chin. Adhes Vol. 15 (2006), p. 1

[4] Q. Y. Wang, S. S. Ge and Z. Q.Wang: Coll.PolymVol. 27 (2009), p. 21

[5] L. J. Chen, H. X. Shi and H. K. Wu: Polym. Mater. Sci. Eng Vol. 25 (2009), p. 5

[6] S. L. Shen, W.Wu andK. Guo: J. SilicaVol. 33 (2005), p. 304

[7] G. B. Li, Y. L. Ma and X. Y. Kang: New. Chem. Mater Vol. 39 (2011), p. 1

Advanced Materials Research Vols. 960-961 (2014) pp 97-102

doi:10.4028/www.scientific.net/AMR.960-961.97

Techniques of preventing subgrade from salinization for Qarham to Golmud expressway

Junyong Liu [1,2,a] , Liujun Zhang [1,b]

[1]CCCC First Highway Consultants Co. , Ltd. Xi'an ,Shan Xi, 710065,China

[2]School of Highway, Chang'an University , Xi'an ,Shan Xi, 710064,China

[a]liu88618@163.com,[b]zlj52208@163.com

Keywords: Qarham to Golmud expressway, saline soil, subgrade, technique of salinization prevention, Qarham salt lake

Abstract. Qarham to Golmud expressway is the first high-grade road in Qarham salt lake, which is regarded as the most enormous inland salt lake in China, moreover, it is the first expressway built on the inland salt lake in China. There is high and excessive saline soil distributed over this area whose thickness is no less than 20m, but the average subgrade height of the expressway is only 2m. A great many of measures are taken for the construction of the subgrade to prevent salt migrating from foundation to roadbed and pavement, which will cause disasters of secondary salinization in roadbed and pavement. By paving testing road at the site and detecting the efficiency of the measures in preventing salt, the paper put forward the technique of preventing subgrade from salinization for Qarham to Golmud expressway. The results of testing and detecting demonstrate that the height of salt migration is only 45cm in subgrade under the condition of brine supply, which is less than the height of subgrade. So it is efficient to keep the roadbed and pavement from the erosion of salt; The settlement of road surface was about 0~2mm among 3 months since the highways had been opened to traffic for two years, and uneven settlement and other diseases caused by the secondary salinization were not appeared, which showed that the measures of salinization prevention (salt resistance) were taken well to achieve the design purposes.

Introduction

Currently, the grades of domestic existing roads are limited to 2 to 3 in saline soil area, and the construction of high grade highway is lack of engineering practice and the corresponding support of technology. Qarham to Golmud expressway is the first high grade way in saline soil regions, while it is the first expressway in the field of inland salt lake in China. It used a variety of techniques of salinization prevention and achieved the desired effects, which provides practical experience and technical reference for the highway construction in saline soil regions.

The analysis of salt migration

In order to study the technique of salinization prevention of highway subgrade, we have to understand the migration of salt in subgrade and the factors that affecting this migration. According to massive relevant literatures[1-5], the primary methods of the migration involve that: 1) salt rises along with the rise of capillary water, the moisture evaporation or the temperature decrease, leading to the salt precipitation, which causes the secondary salinization; 2) the infiltration of surface water or rainfall leads to the invasion of salinity into roadbed; 3) salinity increasing is accompanied by

conflux rising, capillary water gathers from high temperature area to low temperature area, and moisture and salinity moves upward in embankment. The Qarham salt lake has a long time of droughts, with less rainfall, than which the evaporation is much greater. So the salinity move-up with capillary rise is overwhelmingly dominant.

The main factors that influencing the migration of capillary water (salinity)[6-9] include that: 1) soil particle size; 2) the salinity of capillary water; 3) types of salt.; 4) soil density. The greater the soil density, the smaller the migration of water and salt[10]; 5) The overlying conditions of surface [11]. In addition, soil permeability, temperature phase transition, and temperature gradients also have some effects on salt migration.

The measures of salinization prevention for subgrade in Qarham to Golmud expressway project

General situation of Qarham salt lake.

Qarham salt lake is the largest inland salt lake in China. The subsoil is mainly the chlorine excessive saline soil, and the salt content of topsoil is as high as 90%. The groundwater level is about 0 to 2.0m whose the salinity is 310 to 370g / L. The head height of pressurized brine layer is 2 to 5m, while the salinity of the water is 79 to 392g / L [12-13]. The embankment of Qarham to Golmud expressway is mainly low embankment, that the average filling height is 2.0m.

The measures of salinization prevention

Gravelly soil subgrade

Well-graded gravel soil reclamation was used as the subgrade filler in the Qarham to Golmud expressway, and the subgrade compaction was strictly controlled to reduce capillary water rising height. Subgrade filler adopted gravel soil, of which the natural moisture content was 1.4% to 1.6%, the optimum moisture content was 4.4% to 5.5%, and the maximum dry density was 2.22 to 2.30g/cm^3. The minimum intensity and maximum particle size of Subgrade were implemented according to the regulations in the " Specifications for design of highway subgrades " (JTG D30-2004)[14].

The analysis results of subgrade particle size are shown in Table 1. The particle size was mainly distributed among the range of 40mm ~ 2mm, which took up 70.4%, the uniformity coefficient Cu was 27.81> 5, and the curvature coefficient 1 <Cc was 1.7 <3; it was gravel type soil with good grading.

Table 1 Test results of particle size analysis of gravelly soil

Particle size range (mm)	100~60	60~40	40~20	20~10	10~5	5~2	2~1	1 0.5	0.5 0.25	0.25 0.075	≤0.075
Percentage (%)	0	3.20	58.00	3.50	4.30	4.60	3.60	5.80	12.90	2.80	1.30

The separation layer technique

In order to prevent capillary and gaseous capillary water rise, the gravel separation layer and impermeable geotextile barrier layer were set up between the embankment and roadbed.

The material selection of separation layer

The material selection of separation layer should be based on local materials, road grade, subgrade height and hydro-geological condition [15]. The gravel reserves are rich along the road that it is suitable for building the gravel separation layer. The particle analysis results of separation layer material are displayed in Table 2, the particle size was mainly distributed in the range of 2 mm

~ 40mm, which took up 99.06% and the uniformity coefficient Cu was 3.14 <5 , which was poorly graded gravel. The natural moisture content of gravel was 1.1%, the maximum dry density was 2.28g/cm3，and the void ratio was 1.38. The impermeable geotextile is laid in the top of separation layer, the indicators should be consistent with the specification [16].

Table 2 Test results of particle size analysis of gravel

Particle size range (mm)	100~60	60~40	40~20	20~10	10~5	5~2	2~1	<2
Percentage (%)	0.00	0.82	43.84	33.49	20.33	1.40	0.12	0.12

The separation layer set

The separation layer set and construction techniques were determined through a field trial road paving combining with the construction appropriate test in the barrier layer. The thickness of gravel separation layer was 30cm; the impermeable geotextile was laid on it, under which 10cm sandy gravel was laid as a protective layer. The separation layer set is shown in Fig.1.

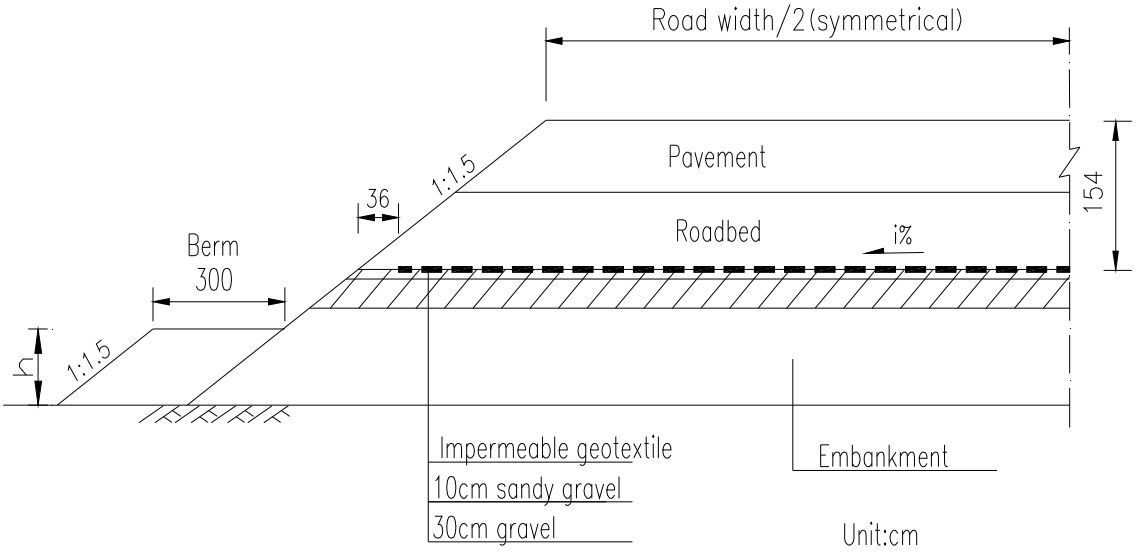

Fig.1. Separation layer set

The effect test of subgrade salt resistance

Subgrade soil was taken to measure the moisture and salinity after the embankment was completed, which as the initial value: the initial moisture was 0.4%, and the initial salt content was 1.321%. The period of the examination of salt resistance in roadbed was 2 years, the examination depth of subgrade was 0～1.5m.The test results of water and salt content of subgrade filling are shown in Table 3 and Fig.2.

Table 3 Test results of water and salt content of subgrade filling

Soil number	Height(cm)	Water content(%)	Salt content(%)
1—1	145	0.3	1.510
1—2	125	0.3	1.453
1—3	105	0.3	1.302
1—4	85	0.4	1.247
1—5	65	0.4	1.130
1—6	60	0.4	1.473
1—7	55	0.3	1.437
1—8	50	0.9	1.752
1—9	45	1.3	2.494

1—10	40	1.6	3.056
1—11	35	1.8	3.894
1—12	30	2.2	3.964
1—13	25	2.6	5.635
1—14	20	3.1	5.041
1—15	15	4.0	6.769
1—16	10	4.8	8.334
1—17	5	5.3	9.868

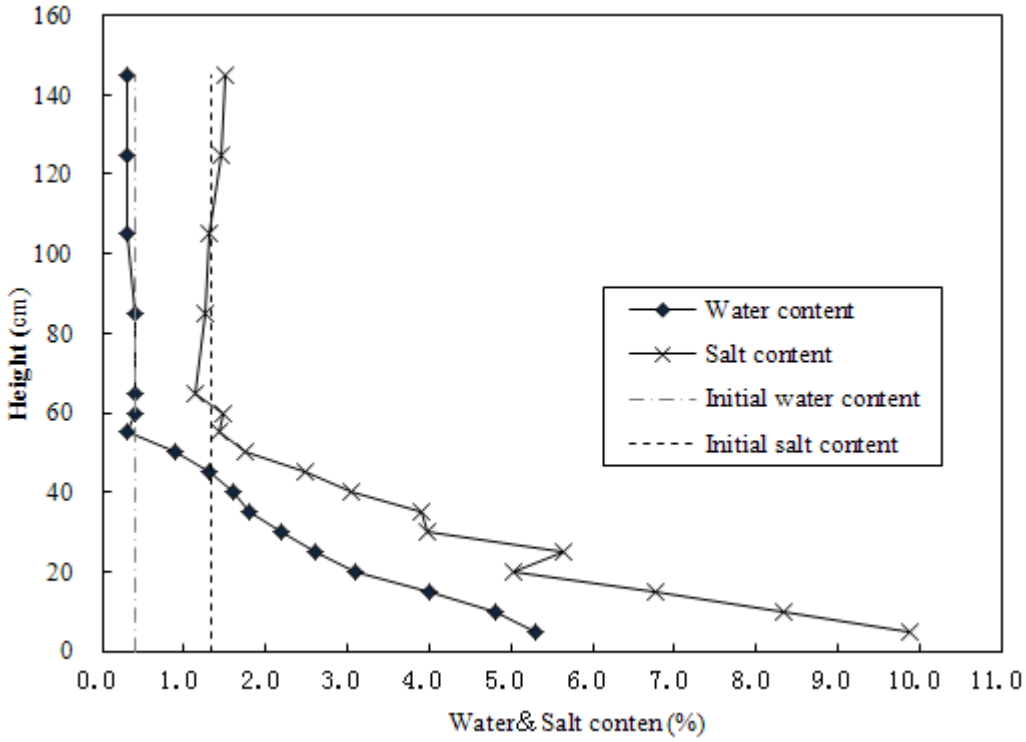

Fig.2. The height of rising capillary water and salt

(1) Moisture migration condition: As can be seen from the moisture curve, the water content decreased gradually from the bottom to up, and it was 0.9% at 50cm, 0.3% at 55cm. The curve come out a significant turning point at 50cm, and the height of capillary water rising was 50cm.

(2) Salt migration condition: As is shown in the salinity curve, the salinity decreased gradually from bottom to up, and at the height of capillary water rising, that is 50cm, the salt content was 1.752%, greater than the initial salt content, which illustrates that the capillary water rise brought out salt migration to make the salt content of the soil changed. The salt content was 2.494% at 45cm, greater than 2% of threshold salinity, which indicates that non-saline soil had been transformed into weak saline soil, and the critical height of salinization of good gravel was 45cm under the condition of brine supply.

Test results showed that: the internal migration height of water and salt were 50cm in gravel subgrade, the volume of migration gradually decreased with the height increasing, and the effect of salt blocking was obvious. The whole settlement of road surface was about 0~2mm among 3 months since the highways had been opened to traffic for two years, and uneven settlement and other diseases caused by the secondary salinization were not appeared, which showed that the measures of salinization prevention (salt resistance) were taken well to achieve the design purposes.

Conclusions

(1) The techniques of salinization prevention for highway subgrade were put forward depending on the project of Qarham to Golmud expressway: Coarse-grained materials such as gravel soil were used as subgrade filler; the gravel separation layer and geotextile barrier layer were set in subgrade structure;

(2) The separation layer trial road was built to finally determine the settings of the separation layer and the construction technology.

(3) According to the monitoring of road operation, the water and salt content within the scope of the structural layers were consistent with the initial value, the amount of settlement was small, and the salinization diseases were not found in the embankment since the highway was opened to traffic, which evidence that the measures of salinization prevention used in Qarham to Golmud expressway are effective.

(4) The research results can provide technical references and support for the new construction of expressway, the renovation and expansion project, the road maintenance and so on in saline soil area.

Acknowledgements

Funding for this study was provided by CCCC First Highway Consultants Co.,Ltd .

References

[1] XUE, M., ZHU,W,W., and JIN, Z,Z., “Salt moving protection and maintenance of salt soil subgrade”, *Technology of Highway and Transpor(Application technology)*, 07(2007), pp. 28-31.

[2] GAO,J,P., and YANG,R,S., “Study on the Moving Pattern of Water and Salt with Directional Temperature lowing in Suphate Salty Soil Containing NaCl”, *Journal of Xi'an Highway University* , 17(3) (1997), pp. 22-25.

[3] YAN,X,G., “Water and Salt Migration Analysis of and Strength Characteristics Saline Soil”, *Highway Engineering and Transportation* , (202) (2009), pp. 93-98.

[4] CHEN,Y,M., ZHANG,X,F., ZHANG,D,Q., et al. “An Integrated Experimental Study Water of Highway Subgrade in of Harmful Rising Height of Capillary Seasonally Frozen Ground Regions”, *Journal of Glaciology and Geocryology* , 30(4) (2009), pp. 641-645.

[5] BING,H and HE,P., “Experimental study of water and salt redistributions of saline soil with different freezing modes”, *Rock and Soil Mechanics* , 32(8) (2011), pp. 2307-2312.

[6] WENG,T., “Water capillarity effect and compaction characteristic of salty soil” .Xi’an: Chang’an University.,(2006).

[7] DONG,B., ZHANG,X,F., et al., “Comprehensive tests on rising height of capillary water”, *Chinese Journal of Geotechnical Engineering*, 30(10) (2008), pp. 1569-1574.

[8] TANG,S,F., FU,Q,L and YAO,R,J., “Research on Rising height of water capillarity in sulphate salty soil”, *Shanxi Science&Technology of Communications*, (4) (2007), pp. 10-11.

[9] BAO,W,X., XIE,Y,L and Xiao,H., “A laboratory test study on water and salt migration in natural saline soils and associated shear strength changes under freezing and thawing cycles”, *Journal of Engineering Geology*, 14(03) (2006), pp. 380-384.

[10] GW Aihong,GU Qiangkang and Li,W., "Experiment research on moving of water capillarity in airport salty soil", *Subgrade Engineering*, 141(6) (2008), pp. 137-138.

[11]DAN,X,H., "Research on rising height of water capillarity in graded broken stone", *Geotechnical Engineering World*, 10(5) (2007) , pp. 42-44.

[12] LONG,J,Y and CHU,Y,C., "First salt lake railway in China- Qinghai to Tibet Railway", *Journal of Railway Engineering Society*, (Supp) (2005), pp. 167-172.

[13] YANG,H,R., JIANG,F,Q., WANG.X et al., "Characteristics of Salt Rock and Salt-dissolution Engineering Geology and Subgrade Construction in Chaerhan Salt Lake Along Qinghai-Tibet Railway", *Journal of Railway Engineering Society,* (Supp) (2005), pp. 373-378.

[14] CCCC Second Highway Consultants Co., Ltd: "Specifications for Design of Highway Subgrades (JTG D30—2004)", Bei Jing, China Communications Press (2004).

[15] XinJiang Road Society: "Technical Guidelines for Highway Design and Construction in the Saline Soil Regions", Bei Jing, China Communications Press (2006).

[16] Chongqing Highway Traffic Science Research Institute: "Technical Specifications for Application of Geosynthetics in Highway (JTJ/T 019-98)", Bei Jing, China Communications Press (1998).

Advanced Materials Research Vols. 960-961 (2014) pp 103-108

doi:10.4028/www.scientific.net/AMR.960-961.103

The current situation and development trend of Electroforming

Wuxin Yu[1], Shiqian Zhou[1,a]

[1]The school of electromechanical & architectural engineering, JiangHan University, Wuhan, Hubei Province in China

[a]zhoushiqian0225@163.com

Keywords: electroforming, overpotential, micro fabrication, nanocrystalline

Abstract: Electroforming technology is an important part of micro fabrication andfine parts and composite materials prepared by the electroforming technology has broad application prospects. This paper describes the principle and method of electroforming, introduces the development and the basic elements of electroforming, then concludes the research status and main research direction and trend of this technology.

Introduction

Electroforming is based on electrochemical principle,which electrodeposited metal layer on cathode mold, and then separated the layer from the original mold for electroforming layer.Since 1838, Russian professor Jacobi developed copper electroforming, 1842 German scientist Professor Boettger invented the nickel electroforming[1-2],Electroforming process has 170 years of history. In early times, electroforming process was used to produce exquisite and complex crafts or apply in printing industry, the range of application is narrow. With the increasing profound understanding of electroforming technology, research on electroforming process has been more and more deeply. In the last 50 years,the applications of electroforming technology has had a greater degree of expansion which extends to mold, automotive, electronics, materials, aerospace, weapons and other manufacturing fields.

In the machinery industry, electroforming is used to make complex shapes and high precision machining or otherwise difficult to hollow parts, injection mold cavity, and other fine surface profile , electroforming material can also expand from copper to nickel, iron and its alloys (or other alloys) for the high replication accuracy, surface finish.

Principles and characteristics of electroforming technology

Electroforming principle: use the pre-made original mold which is according to the desired shape as a cathode, use electroforming material as an anode , then put them together into appropriate metal salt solution, through DC. In electrolysis, the original mold surface gradually deposited metal electroformed layer. After reaching the desired thickness we removed it from the solution, and separated the electroformed layers from the original mold to obtain a shape corresponding to the original copy of a metal. Electroforming technology consists of four basic elements:an anode, a cathode (to be plated original mold), the electrolyte, and the power. As electroplating technology, both are belong to the ion adsorption behavior under current effect.The difference is, purpose of electroplating is forming coating on the material surface to protect or decorative raw materials, but the purpose of electroforming is obtaining manufacture parts which is hard to made by machining method, the final deposition of metal can form an independent structure.

From the results we can see some differences, the thickness of the electroplated coating is generally about 1 to 30 microns, the thickness of the electroformed layer often greater than tens of microns, even to the millimeter. Judging from the expected results, we hope to combine raw materials and electroplating coating very closely, they can not appear peeling phenomenon, but we hope electroforming layer can separated from the original mold easily.

Compared to other processing methods, electroforming method has the following three main features:①Can quickly replicate the complex shape, deformation processing of large or difficult to machine parts.②Higher copy accuracy which can achieve sub-micron level, far beyond the ordinary machining methods. ③ Processing costs are relatively low, there is no waste of materials processing[3].

Development of electroforming basic elements

2.1 Effect of power on electroforming

For electroforming experiment using DC in normal circumstances, under different power the quality of cast layer, electroforming speed, energy consumption are different.When using ordinary DC power electroforming complex shape castings，Because the electric field e effect between the cathode and anode, casting surface and edges generate a lot of buildup, electroforming has disadvantages of effective rate, higher consumption, in some cases it cannot meet the requirements.

Using current pulse is an effective means to improve the quality of electroforming layer.Pulse electrodeposition change original current to periodic pulses current, the pulse power impact on the quality and physical properties of the deposited layer greatly.There is close relationship between the metal crystalline morphology, growth patterns and cathodic polarization overpotential. Increase the overpotential during electroforming can lead to fine-grain and cast layer of dense.

At the same time within the pulse interval, metal ions can quickly add at the cathode interface and significantly reduce the concentration polarization. So we can achieve higher electrochemical polarization by using pulse current which has higher electric potential than conventional DC, ultimately makes the cast layer of grain refinement, improved densification[4~5]. In addition, the pulse current can improve the dispersion of the electrolyte, improve ability to both plating, it also changes physical and mechanical properties of the electrodeposited layer.

2.2 Effect of anode on electroforming

The anode materials commonly used today has two types: One is a metal material that containing the cation in the electrolytic solution，This anode material can add the depletion of cationic in the electrolytic solution ，this method is commonly used in the LIGA technique, used for the preparation of micro and small parts. The basic process includes steam plating, using the metal layers below the photoresist as electrode for electroforming, then filling metal into the void of the three-dimensional structure of photoresist，at last forming a stable concave-convex metal that convex complementary to photoresist pattern. Removed the photoresist and the substrate material attached to it when the electroformed layer has a certain thickness and strength. Then we can obtain the casting mold[6~7].As it shown in Fig.1, soluble metal anode are also used in pictographic-anode electroforming[8]. This method can make the clearance between anode and original model of each corresponding point basically consistent, It ensures more uniform electric field, thereby cathode deposition rate remain basically the same.

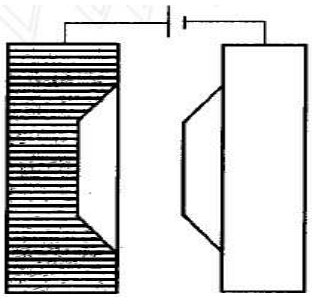

Fig.1 Soluble pictographic-anode Electroforming

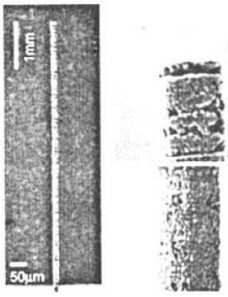

Fig.2 Electroforming of micro copper cylinder

The other is insoluble inert anode, typically platinum or graphite.It is commonly used to cast linewidth uniform, simple structure parts or do laboratory studies of metal ion electrodepositing behavior. For example：Dr.Said used a platinum wire anode to deposit fine copper cylinder in copper sulfate solution,the length diameter reached 282, the deposition rate reached 8 um/s(Fig.2)[9]。

2.3 Effects of electrolyte on electroforming

Usually electrolyte consist of the main salt, conductive salt, buffering agents, anode activator, complexing agents, additives, etc. Each components has different functions in electroforming process. Composition of electroforming liquid should not be too complex,for electroforming process is relatively long, the complex composition will easily change significantly, thereby increasing the difficulty of maintaining the solution.

For example, in nickel electroforming, we currently mainly use electrolytic solution of two types: Watt type and amino sulfonate type. Watt-type electrolyte solution has the advantages of low cost, easy maintenance, easy operation, but the disadvantage is coating of greater internal stress; electrolyte solution of amino sulfonate type has the advantages of less internal stresses, but the disadvantage is the higher cost of the electrolyte, a strong sensitivity to impurities.The solubility of nickel-sulfamate is much higher than nickel sulfate in aqueous solution, so that a high current density and high electrolyte concentration (300 ~ 650g / L) can be electroformed. Under these conditions, we can obtain electroformed casting that hardness range from HV200~750, strength up 340 ~ 1370MPa [10]。

Buffering agents effect mainly reflected in the stability of PH changes due to a variety of reactions during electroforming process, thereby stabilizing the electrode potential of each material. Such electroforming process lead to small change of current density and better quality of the electroforming layer.

Complex in electroforming has the following effects：

1. Promoting normal dissolution of the anode (soluble anode)
2. Preventing metal hydrolysis, stable plating solution
3. Increasing cathodic polarization,improving crystalline coating
4. Enhanced the activity of cathode surface
5. Masking metal impurities in plating solution

Additives have some influence on crystal grains size of the electroformed layer. By selecting appropriate additives and controlling the dosage can reach the objective of controlling the crystal grains size.

The development trends of electroforming process

Current research of electroforming technology to further the development of three aspects: 1. New materials and equipment of electroforming; 2. Explore the copy process for special type of parts; 3. Study of micro electroforming for precision and ultra precision machining.

In recent years, research of electroforming process mainly has following several aspects:Composite electroforming, Alloy electroforming and Nanocrystalline electroforming.

3.1 Composite electroforming

There are two types of composite electroforming：One is adding fine dispersed solid particles to the solution during electroforming,so that deposited metal layer is finally obtained with the fine solid particles,thereby increasing the hardness,strength and wear resistance of the electroforming metal,while improving the electroforming product's service life. Wang Xuran, Feng Xiaoming [11], et al. obtained composite electroforming layer of iron base SiC_p friction material on the surface of Q235 steel. They found that when the the concentration of SiCp is 35g/L, the current density is 3.5A/dm^2, the pH value is 1~1.5, temperature is 35 ℃, SiCp is uniformly dispersed in the composite electroforming layer(Fig3, Fig4), and crystallite size is more uniform.Composite electroforming friction layer's dry friction is 0.55 ~ 0.60, the wear rate is less than $0.42\times10\text{-}^7$ cm^3 / J, and the wear resistant property is good.

The second is winding high-strength fiber to the cathode of the original mold, so this high-strength fibers embedded in Electroforming metal layer ,thereby electroformed layer strength is greatly improved. High strength metal fibers, glass fibers and ceramic fibers are usually used as reinforcing fibers. Qian Wanghuan,Qu Ningsong[12] et al obtained composite nickel electroforming layer by using boron fiber. They found that when fiber volume fraction of 40%, the current density is 4A/dm^2, the tensile strength of the composite electroforming layer can reach 1255MPa at room temperature,Tensile strength relative to pure nickel electroforming layer (550Mpa) has improved significantly.

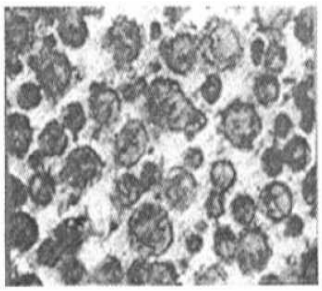

Fig. 3 Surface morphology of the composite electroforming layer650×

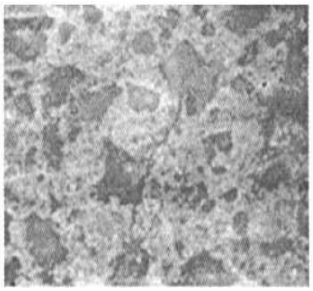

Fig. 4 Section morphology of the composite electroforming layer650×

3.2 Alloy electroforming

In alloy electroforming, there have been many research achievements on nickel-copper, nickel-iron, nickel-manganese,nickel-phosphorus and other binary alloy. The electroforming alloy often has many excellent properties, they are often used to product many important components. Nickel-copper, electroforming, for example, has been widely used in rocket nozzles cooling channels. There have been successful cases on rocket engine combustion chamber system by using electroformed Cu/ Re alloy with good weldability, high temperature resistance, high hardnessand high strength [13].

He Fengjiao, Zhang Yubin[14] studied the process of electrodeposition of iron-nickel alloy thin films and found that increasing the iron content or increasing the cathode rotational speed will both increase the iron content in the alloy film. The optimum process parameters for the preparation of iron nickel alloy: C_{Fe}=0.15mol/L, rotational speed V=300~800rpm, pH 2.5~3.0, complexing agents0.10-0.2mol/L, temperature 45-65℃, Boric acid 35-45g/l，current density15-25A/dm^2；In this case the iron content can reach 33-45%， the alloy films is smooth, bright, dense and of good flexibility.

Wang Ruiyong, Long Jinming[15] studied the electroforming process of copper content of 28 to 30% Ni-Cu alloys(Monel); Yang Dongfang, Pei Hezhong[16] used the response surface method to do further analysis of the factors influencing the Ni-Cu alloy electroforming coating grain size.

3.3 Nanocrystalline electroforming

Nanocrystalline electroforming is a research hotspot of domestic and foreign scientists. When the metal materials' grain refining to the nanoscale, they will have a quantum size effect, small size effect, surface effect and macroscopic quantum tunneling effect.

Canadian scientist Erb et obtained nano nickel, nickel-based alloys by using pulse current method with organic additives such in Watts electrolytic solution and studied the alloys' microstructure and properties[17]. Domestic research on nanocrystalline electroforming is relatively late. Zhu Di studied precision electroforming technology of nanocrystalline nickel, and obtained nanocrystals nickel electroforming layer at the size of 20 nm(Fig.5), inally studied the relationship between process parameters and microstructure of the electroforming layer[18]。

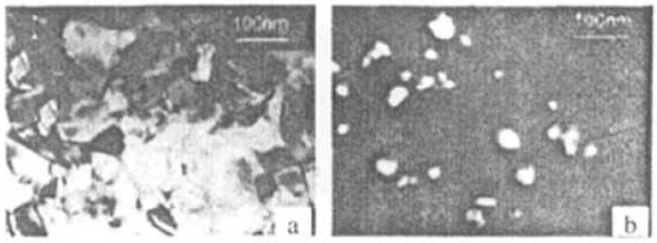

Fig.5 Electroforming nanocrystalline

Conclusion

Electroforming technology has been invented over 170 years. Electroforming materials have changed from copper, nickel, iron metal to today's composite, nano-crystalline alloy materials etc; From the early primary application, preparation of the print version, electroforming developed to various high-tech precision manufacturing and traditional manufacturing. With the continuous development of physical chemistry, materials science, mechanical engineering, electrical engineering, environmental science and other disciplines, will expand the application of electroforming and electroforming technology is bound to a further development.

References

[1] Zhu Baoguo, Wang Zhenlong. Development and application of electroforming technology. Electroforming & mold, 2006, 5

[2] Huang Chao, Li Hongyou, Jiang Kaiyong. Research and development of electroforming technology. Electroplanting & Pollution control, 2010,30(6):1-4

[3] Wang Wenzhong, Electroforming technology and the applications. Plating and Finishing, 1998,17(1):36-39

[4] Zhao Jianfeng, Zhu Di. Pulse current electroforming and Research on the quality of electroforming layer. Materials protection, 1997,30(3):3-5
[5] Liulan Bo, Wu Meng Hua. Ultrasound - Pulse electroforming process parameters effects on the grain size of the nickel electroforming layer. Mechanical engineering materials .2012,36(3):22-25
[6] Kong Xiangdong, Zhang Yulin, Song Huiying. Development and application of LIGA technology. Micro electronic technology, 2004(5):13-18
[7] Yi Futing, Wu Jianwu, Xi Dingchang. Microfabrication technology- LIGA technology. Microfabrication technology, 1993(4):1-7
[8] Yang Dachun, Yun Naizhang. Combined soluble conformal anode electroforming technology. New Technology & New Process, 2004(2):33-34
[9] Ra'a A.. Said. Adaptive tip-withdrawal control f or reliable micro fabrication by localized electrodeposition [J]. Journal of Microelectron mechanical Systems, 2004,13(5):822-832.
[10] Cheng Chen. The main components of electrolyte and its effect on mechanical properties of electro deposition. Chemical engineering and equipment, 2008(7):14-15
[11] Wang Xuran, Feng Xiaoming, Wang Zhong. Preparation process of Fe-SiC_p composite electroforming layer. Mechanical Engineering Materials .2006,30(9):32-43
[12] Qian Wanghuan, Qu Ningsong, Zhu Zengwei. Study on t continuous fiber reinforced composite electroforming metal. 15th National Special Processing Conference Proceedings (Next volume) 2013:18-22
[13] Malone GA, Winkelman DM. High Performance alloy Electroforming. NASA-N 89-16041, 206P
[14] Zhang Yubin. deposition of iron-nickel alloy film, Journal of Hunan University, 2009
[15] Wang Ruiyong, Long Jinming. Research progress of electroformed nickel alloy [J]. Plating and finishing, 2009(3)
[16] Yang Dongfang, Pei Hezhong. Development trend and application of chemical nickel plating [J]. Electroplating & Finishing, 2011,2:19-20
[17] Clark D, Wood D, Erb U. industrial applications of electrodeposited
Nanocrystals [J]. Nanostructured Materials ,1997(9)：755-758 .
[18] Lei Weining, Zhu Di. Study of nanocrystalline electroforming [J]. China mechanical engineering, 2003,14 (12): 1065-1068

Advanced Materials Research Vols. 960-961 (2014) pp 109-112

doi:10.4028/www.scientific.net/AMR.960-961.109

Influence of Si content on microstructure and erosion properties of Al-based Alloy

WANG Xiaoming[1, a], ZHU Sheng[1,b], Cui Jianzhong[2,c], CHANG Qing[1,d] and Zhu Qingfeng[2,e]

[1] National key Laboratory for Remanufacturing, Academy of Armored Force Engineering, Beijing 100072, China

[2] Key Laboratory for Electromagnetic Processing of Materials, Northeastern University, Shenyang 110001, China

[a]email, uwangxm@126.com, [b]email, zusg@sina.com,[c]email, cjz@163.com

[d]email, chang2008qing@163.com, [e]email,zqf@163.com

Keywords: Al-based alloy, Si-content, Chemical composition, Microstructure, Erosion property

Abstract. In order to develop new protective materials for magnesium alloy, Al-based alloys with different Si-content were fabricated by copper mold casting. Microstructure, erosion properties of the ingot samples were characterized or tested by using spectrum analysis, optical imcroscope, salt testing machine etc, respectively. The results indicated that the microstructure of Al-1.9Si-1.32Mg-0.40Mn was mostly dendritic crystal. That of Al-13Si consisted of α-Al, flaky eutectic silicon and primary crystal silicon. That of Al-18Si-0.01%P was consistent of a large proporation of primary crystal silicon phase, a part of eutectic silicon phase and a little of α-Al phase. With Si-content increasing, anti-corrosion properties of Al-based alloy gradually improved, which could provide theoretical principle to determine chemical elements of protective materials for magnesium alloy.

Introduction

With outstanding performance, called 21st century green engineering materials, magnesium alloys have been applied in aerospace, automotive, military weapon and equipment etc[1]. However, owing to be prone to be severely corroded, large scale application of magnesium alloys was still restricted[2]. Therefore, the development of surface protective materials for magnesium alloy had become an international research hotspot among materials field. Now, surface protective materials used for magnesium alloys included mainly commercial pure aluminium, Zn-Al alloy, Al-12%Si, Al356 and Al-Al_2O_3 mixed powder etc[3-5]. Application of the powders mentioned above might improve wear-resistant properties or anti-corrosion properties of magnesium alloy at certain extent. However, its features such as bond strength and erosion property etc, could not meet the requirements used in high temperature, high humidity and high salt-fog environment.Therefore, new type protective materials for magnesium alloy should be exploit, which could deposit effevtively and generate excellent coating with superior performance.

In the present work, Influence of Si content on microstructure and erosion properties of Al-based alloy was investigated, which laid a foundation for the further development of protective powders and preparation of coating on magnesium alloy.

Experimental method

Industrial pure aluminum, industrial pure silicon and industrial pure magnesium utilized as raw materials to generate ingots. Industrial pure aluminum was melted firstly in graphite crucible equiped at intermediate frequency induction coil; then the other raw materials were added in turn. At certain temperature measured by K-type thermocouple, fused mass was poured into water-cooled copper mold and solid into ingot.

The samples prepared as follows: the casting ingot cutted into given size by band saw, machined by lathe, preparatory grinded, fine grinded and polished; Then etched using 30%HNO_3-40%HCl-30%H_2O. FOUNDRY-MASTER PRO optical spectrometer adopted to analyze chemical composition of the sample. Leicae DMI5000M optical microscope applied to observe its microstructure.

Salt-fog corrosion experiment conducted in DCTC1200P type test case. The 50+5 g/L corrosion fluid with PH value 6.5-7.2 adopted, which made from the sodium chloride consistent with GB1266 dissolved into distilled water.Then the samples placed into salt-fog case. Experimental temperature kept at 35±2 ℃ and mist spray 12 hour interval.

Experimental results and discussion

2.1Chemical composition test. Table 1 presented chemical composition spectral analysis results of the casting ingot samples including Al-1.9Si-1.32Mg-0.40Mn, Al-13Si and Al-18Si-0.01%P. The chemical composition of each casting ingot was within setting scope, which proved the excellent melting process control. The testing value of Si and Mn content in Al-1.9Si-1.32Mg-0.40Mn and Si content in Al-18Si-0.01%P was higher than that of theorical value. The main reason is that, considering elements burning loss during melting, addition actual amount of each element was slightly higher than the theoretical value in design. Due to melting titanium alloy cap and doped into aluminum alloy flux during addition of raw silicon materials, Ti-content increased significantly in Al-18Si-0.01%P.

Table 1.Chemical composition spectral analysis results of alloy

	Al	Si	Fe	Ti	Mn	Mg	P
Al-1.9Si-1.32Mg-0.40Mn	95.9	1.91	0.215	0.019	0.426	1.32	-
Al-13Si	86.6	13	0.186	0.03	-	-	-
Al-18Si-0.01%P	80.9	18.6	0.205	0.124	-	1.32	0.0084

2.2 Macrostructure observation. Fig.1 (a)-(c) exhibited macrostructure of Al-1.9Si-1.32Mg-0.40Mn,Al-13Si and Al-18Si-0.01%P alloy,respectively. It was founded that the grains in Al-1.9Si-1.32Mg-0.40Mn casting ingot was coarse and no obvious defects such as porosity and loose; There existed fine equiaxed grains at top layer, and columnar crystal region grown vertical to the die wall in the middle region, and equiaxed crystal region in the core. Superiorsurface layer of Al-13Si ingot was composed of a little short columnar crystal, and there existed a large proportion of uniform isometric crystal enclosed by black eutectic structure. Al-18Si-0.01%P casting ingot possessed an obvious columnar crystal area at the edge and isometric crystal region in the core. Due to the increasing Si-content, black area increased in the core of casting ingot increased.

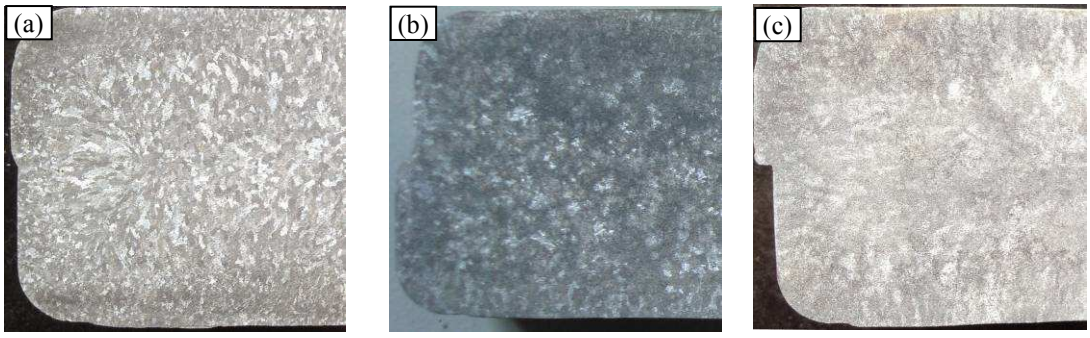

Fig.1. Macrostructure of different alloy

2.3 Microstructure observation. Fig.2 (a)-(c) displayed microstructure of Al-1.9Si-1.32Mg-0.40Mn casting ingot under different magnification. It was founded that the grains appeared rosette morphology and its size was about 200 um. Secondary dendrite arm spacing was smaller; and there existed an amount of strip mesophase. The most area was aluminum phase.

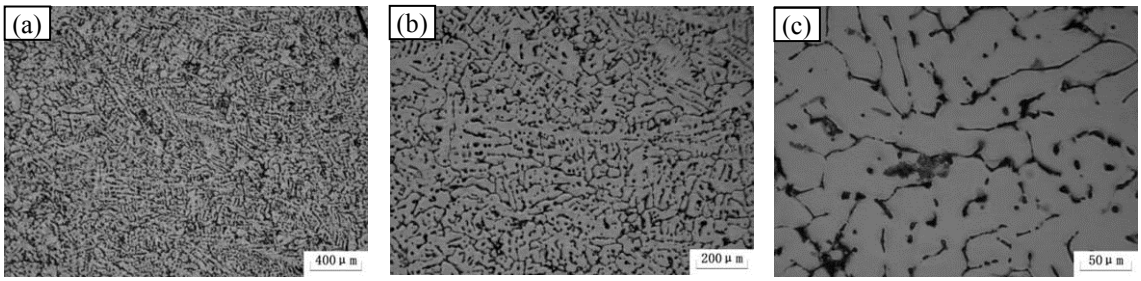

Fig. 2. Microstructure of Al-1.9Si-1.32Mg-0.40Mn casting ingot under different magnification

As seen in Fig.3 (a)-(c), The microstructure of Al-13Si casting ingot was composed of white bulky dendritic α-Al phase, black lamellar eutectic silicon phase and grey block primary silicon.Block primary silicon and lamellar eutectic silicon distributed around the dendritic α-Al. The area of aluminum phase decreased.

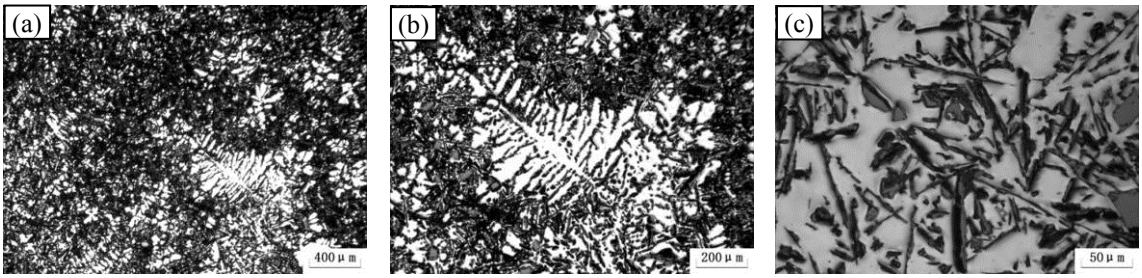

Fig.3. Microstructure of Al-13Si casting ingot under different magnification

Microstructure of Al-18Si-0.01%P ingot casting under different magnification, Fig.4 (a)-(c), depicts that there emerged a large proporation of block primary silicon, which presented grey, about 20μm, with irregular geometric shape and uniform distribution; while, there existed eutectic silicon phase and white α-Al phase. The area of white aluminum phases reduced furtherly.

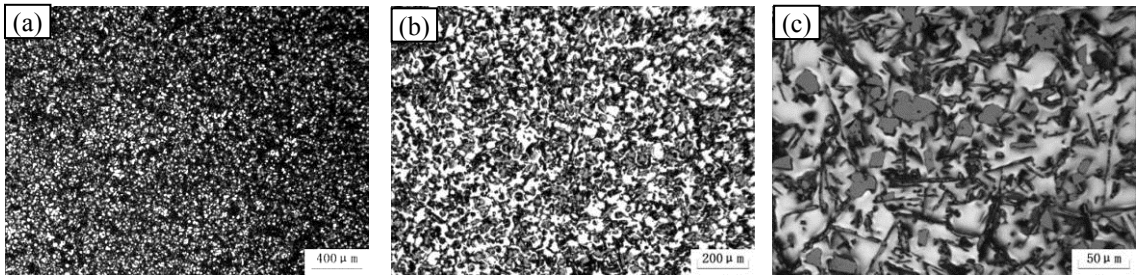

Fig.4.Microstructure of Al-18Si-0.01%P casting ingot under different magnification

2.4 Erosion properties test. Fig.5~Fig.7 presented the corrosion morphology of different aluminum alloy sample. It can be founded that the samples with difference Si-content educed different anti-corrosion properties. There emerged some deep corrosion pits on the surface of Al-1.9Si-1.32Mg-0.40Mn casting ingot attached by plenty of white grains. Al-13Si casting ingot sample had been covered entirely by a large number of white attachments, on which could not found any Al-substrate morphology. Al-18Si-0.01%P casting ingot sample exhibited excellent anti-corrosion properties, and emerging only a little of white flake induced by salt-fog corrosion.

6x） 24x） (40x)

Fig.5. Corrosion morphology of Al-1.9Si-1.32Mg-0.40Mn alloy

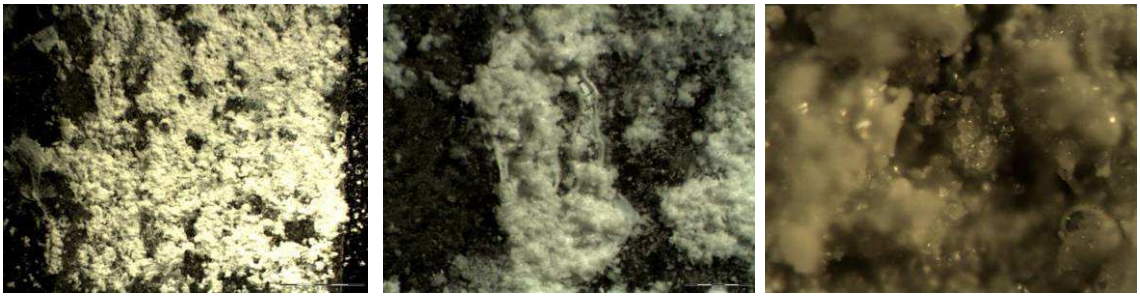

6x） 24x） (40x)

Fig.6. Corrosion morphology of Al-13Si alloy

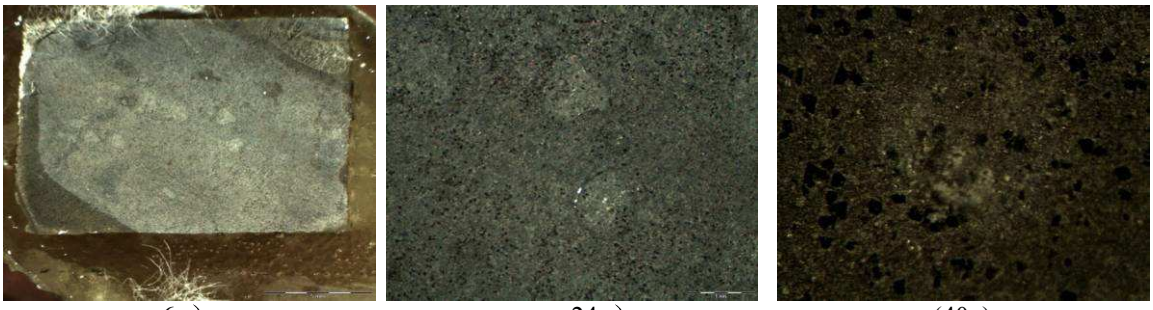

6x） 24x） (40x)

Fig.7. Corrosion morphology of Al-18Si-0.01%P alloy

Conclusions

(1) Al-1.9Si-1.32Mg-0.40Mn, Al-13Si and Al-18Si-0.01%P casting ingots were fabricated by water-cooled copper mold method. With the increasing percentage of Si-element, the sample exhibited different microstructure obviously. Microstructure of Al-1.9Si-1.32Mg-0.40Mn alloy was mianly dendritic crystal and most area was aluminum phase. That of Al-13Si alloy was composed of white dendritic α-Al phase, black lamellar eutectic silicon phase. Al-18Si-0.01%P possessed a large number of block primary silicon, eutectic silicon phase and a little of white α-Al phase.

(2) Erosion property was influenced seriously by Si-content in Al-based alloy. In the present work, with Si-content increasing, anti-corrosion properties of Al-based alloy gradually improved, which provided theoretical principle to determine chemical element of the protective materials for magnesium alloy.

Acknowledgements

The authors would like to acknowledge the financial support of the Presearch Foundation of China (No. 9140A27030312JB3501) and Research Project (No.51327040301).

References

[1] Z.H. Chen: *Magnesium Alloy*(Chemical Press, Beijing 2004)

[2] L.P. Liu, L.J. Li: Journal of Chongqing University Vol. 35(2012) , p. 47

[3] J.G. Qian, J.X. Zhang and S.Q. Li: Rare Metal Materials and Engineering Vol. 40(2012) , p. 359

[4] H. Feng, Z.Q. Cui and W.X. Wang: Applied Laser Vol. 32(2012) , p. 13-15

[5] Y.X. Liu, X.G. Yuan and H.J. Huang: Special Casting & Nonferrous Alloys Vol. 26(2006) , p. 204

Advanced Materials Research Vols. 960-961 (2014) pp 113-117

doi:10.4028/www.scientific.net/AMR.960-961.113

Preparation and Properties of CF/CNTs/NanoG Filled Polyacrylate Electrically Conductive Pressure-sensitive Adhesives

Huan Ma[1, a], Shuhua Qi[2, b], Fan Zhang[3,c] and Zhang He[4,d]

[1, 2, 3]Department of Applied Chemistry, School of Science, Northwestern Polytechnical University, Xi'an 710072, P.R. China

[a]mahuan2013@gmail.com,[b]qishuhua@nwpu.edu.cn,[c]zhang_fan2003@126.com, [d]hezhengnwpu@163.com

Key word: composite fillers; morphology; synergistic effects; electrically conductive adhesives

Abstract. With the 'Synergistic Effects' such as 'Bridging' and 'Intercalating' between fillers with different morphologies, we can get the CF/CNTs/NanoG filled polyacrylate electrically conductive adhesives(ECA). Through the study, we found that the comprehensive properties of the electrically conductive PSA reach the best when the composite fillers are made up of CF 3wt%, NanoG 5wt% and CNTs 5wt%. The conductivity of the electrically conductive PSA reaches 3.0×10^{-2} S/cm, the 180^{o} peel strength is 0.38KN/m and the shear strength is 0.42MPa.

Introduction

In the electronic packaging industry, lead-based solder alloys are frequently used to produce manufactures such as flexible printed circuit boards (PCBs) [1]. However, with the enhancement of people′s environmental consciousness, the harm of lead-based solder alloys is gradually attracted people′s attention [2]. As the alternative of solder alloys, electrically conductive adhesives (ECA) have many advantages, such as environment-friendly, low packaging temperature and so on [3]. ECA are made up of polymer resin (such as, an epoxy or a polyacrylate) that provides mechanical properties and fillers (such as silver or carbonaceous fillers) which conduct electricity [4]. Currently, the ECA on the market are made up of single-morphology fillers, such as silver powder and the proportion of filler is more than 30 percent [5]. Nevertheless, the considerable adding of single filler would reduce the mechanical properties significantly and serious agglomeration appears [6].

For solving these problems, ECA can be prepared by acrylate resin and composite carbonaceous fillers with different morphology.The fillers with different morphology would form "Intercalating effect" and "Bridging effect" with each other.

Experimental

Materials. MA and BA were washed with 10 wt% NaOH solution to remove the polymerization inhibitor. The initiator 2,2-azodiisobutyronitrile(AIBN)was recrystallized twice before use. 2-Butanone (MEK), KH-570, Carbon Nanotubes (CNTs, chopped Carbon Fiber (CF), Carbon Black (CB) were purchased from commercial suppliers and used received.

Preparation. Preparation of acrylate pressure-sensitive adhesive (PSA):The thermoplastic acrylate pressure-sensitive adhesive was synthesized in a 250ml, four-necked flask equipped with a thermometer, a reflux condenser, an efficient stirrer and N_2 purge. First, half of the solvent was added into the flask, mixing for 15 min with the efficient stirrer at the rate of 150rad/min. When the temperature of solvent reached about 70~75^{o}C, all the monomers mixed with half of the initiator

were added into the flask, and the reactant was heated to the 80~85°C. After 2.0h of polymerization, the mixture of the remaining solvent and initiator was added to raise the degree of polymerization. The reaction processed continuously for another 2.0h.

Preparation of ECA: The ECA was prepared by mixing the solvent-based acrylate PSA with the composite fillers at room temperature. The acrylate PSA was diluted with MEK regent, and then the composite fillers were added into the PSA in an ultrasonic bath for 30 min.

Characterization. The internal morphology of the composite fillers based ECA was analyzed by the transmission electron microscope (TEM; H-600 model, Japan). Megohmmeter (ZC-36 model, China) and Desktop digital multimeter (UT61E model, China) were used to measure the conductivity(σ) of the acrylate resin and composite fillers based ECA. The peel strength at the angle of 180° and the shear strength of the ECA were measured with computer controlled electronic tensile testing machine (CMT-8502 model, China). The thermal property of the acrylate resin and the composite fillers based ECA were analyzed by thermogravimetric analysis (TGA; Q50 model, America) at a heating rate of 10 K/min in the range from 50°C to 700°C under environment atmosphere.

Results and discussion

The acrylate resin has poor conductivity; the value is 10^{-16} S/cm. Many groups of samples could be got by changing the constituent and proportion of the composite fillers, and measuring the conductivity of each sample (showing in Tab.1)

Tab.1 Relationship between the constituent and proportion of the compesite fillers in the ECA and the conductivity of the compesite fillers based ECA

Sample	CF (ωt%)	NanoG (ωt%)	CNTs (ωt%)	CB (ωt%)	Total fillers (ωt%)	Conductivity(σ) (S/cm)	lgσ
1	/	/	/	/	0	10^{-16}	-16
2	/	/	/	15	15	8.3×10^{-8}	-7.1
3	/	/	/	30	30	5.3×10^{-7}	-6.3
4	/	/	10	30	40	1.7×10^{-3}	-2.8
5	10	/	/	30	40	7.5×10^{-2}	-1.1
6	/	10	20	10	40	4.5×10^{-3}	-2.3
7	/	5	5	20	30	1.4×10^{-4}	-3.9
8	/	5	5	15	25	3.6×10^{-4}	-3.4
9	5	/	/	15	25	6.7×10^{-4}	-3.2
10	3	10	/	10	23	4.1×10^{-3}	-2.4
11	3	5	/	10	18	2.9×10^{-3}	-2.5
12	3	/	10	10	23	2.9×10^{-2}	-1.5
13	3	5	5	/	13	3.0×10^{-2}	-1.5

Comparing sample 1 and sample 2, the conductivity of PSA increased dramatically from 10^{-16} S/cm to 8.3×10^{-8} S/cm. The results show that the electrical fillers could improve the conductivity of acrylate resin significantly. Comparing simple 2 and simple 3, which indicate 15wt% CB has formed a conductive path within the adhesive.

Comparing simple 3 and simple 4, the conductivity to increase from 5.3×10^{-7} S/cm to 1.7×10^{-3} S/cm. The change can be explained by the "Bridging Effect" between the CB caused by the CNTs. More conductive chain means higher electrically conductivity. Replacing the 10 wt% CNTs by CF (simple 5), the conductivity is 43 times higher than the simple 4, which indicates CF has advantage than CNTs in improving conductivity. The reason is a) CNTs is apt to agglomerate, uneasy to mix in the matrix homogeneously, and b) CF has larger aspect ratio and superior "Bridging Effect" (Fig.1).

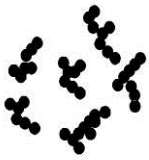

Fig.1(a) Imitative scattergram of CB15wt%

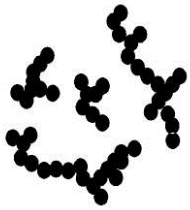

Fig.1(b) Imitative scattergram of CB30wt%

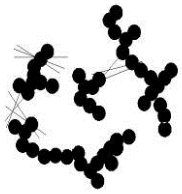

Fig.1(c) Imitative scattergram of CB+CNTs

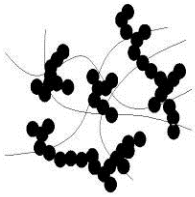

Fig.1(d) Imitative scattergram of CB+CF

The adding of 5wt% CF into the simple 2 lead the conductivity to increase; comparing simple 4 and simple 12, the tests show that 3wt% of CF is enough for bridging within the PSA. Comparing simple10 and simple 11, the decrease of NanoG to 5wt% has miniscule impact to the conductivity. The result indicates that 5wt% NanoG is enough to form the conductive chain within the PSA. There are bridging taking place in the PSA (Fig.2), and some CNTs intercalating into the NanoG(Fig.3). All the above weakens the agglomeration of CNTs and NanoG and promotes the conductive chains to form within the PSA.

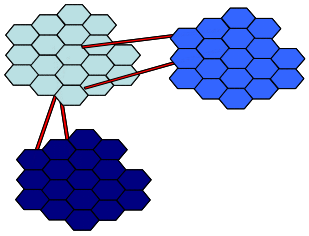

Fig.2 Bridging effect of NanoG+CNTs

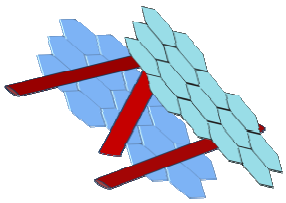

Fig.3 Intercalating effect of NanoG+CNTs

In the process of mixing within the PSA, owning to the “Bridging Effect” and “Intercalation Effect”, dissimilar fillers are apt to contact. Therefore hydrogen bonds form between the dissimilar fillers to prevent the agglomeration. Based on the experimental data(Tab.1), when the composite fillers are CF 3wt%, NanoG 5wt% and CNTs 5wt%, the conductivity of PSA is 3.0×10^{-2} S/cm, reaching the goal: low fillers(13%) and high conductivity(3.0×10^{-2} S/cm).

Fig.4 shows selected TEM image of ECA. The gray coshes, gray tubules, gray flakes represented the CF, CNTs and NanoG. The light coloring area was the acrylate resin. It can be seen from the TEM image that the composite fillers disperse among the acrylate resin homogeneously, less agglomeration can be observed obviously.

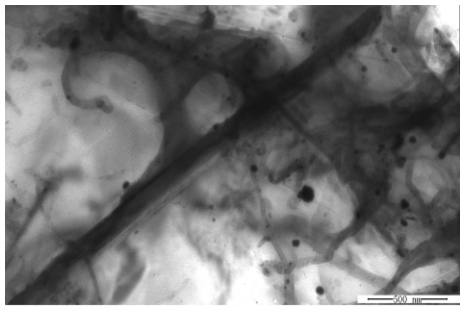

Fig.4 TEM micrograph of ECA

The tests of the 180° peel strength and shear strength of the ECA on the content of the fillers were shown in Tab.3. The 180° peel strength of ECA dropped down to 0.38 KN/m. The behavior is common for polymers filled with filler. The 180° peel strength is mainly related to the adhesion strength between the adhesive and the surface of the testing panel. The adding of filler to the PSA forms hydrogen bonds between acrylate molecular and filler, reducing the fluidity of polymer and wettability to the adherends. The adhesion strength between the adhesive and testing panel reduces sharply. Shear strength of ECA increased slightly which is in line with the other researchers' results [7]. As for shear strength, the shear strength is related to cohesive strength of the ECA. With the adding of composites fillers, the hydrogen bonds between acrylate molecular and filler strengthen the rigidity and cohesive strength of PSA.

Tab.3 Mechanical properties of the pure acrylate resin and composite fillers based ECA

Sample	180° peel strength from Al plate (KN/m)	180° peel strength from silicone rubber (KN/m)	Shear strength MPa）
Pure acrylate resin	0.70	0.42	0.35
ECA	0.38	0.38	0.42

The thermal stability is mainly dependent on the resin, but the addition of fillers would endow the composites with new characteristics. TG analysis is performed under air atmosphere at heating rate of 10K/min. Fig.5 shows the TG and DTG curves of the pure acrylate resin PSA and ECA. From the TG curve, it can be observed that both PSA and ECA show only one decomposition peak, they all start to decompose at 300°C which were as a result of the main-chain pyrolysis. The temperature of max weight loss rate for PSA and ECA were 405 °C and 433 °C. The reason is that a higher interaction between large numbers of surface atoms of composite fillers and acrylate molecule chains. The barrier character for the degradation of acrylate resin was then achieved.

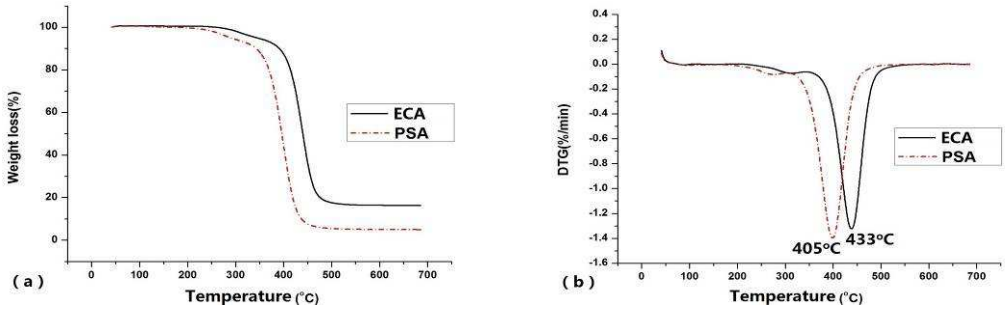

Fig.5 TG (a) and DTG (b) curves of the pure acrylate resin and composite fillers based ECA

Conclusions

A novel ECA consisted of acrylate resin and composite fillers with solution blending and ultrasonic dispersion method was obtained. The SEM and TEM images indicated a homogeneously dispersion of composite fillers in the acrylate resin and the "Intercalating effect" and "Bridging effect" were formed between the CF, CNTs and NanoG. The conductivity increased to 3.0×10^{-2} S/cm. The 180° peel strength was 0.38KN/m and the shear strength was 0.42 MPa. The thermal stability of ECA was also improved with acrylate resin from TGA.

Acknowledgements

The work is supported by graduate starting seed fund of Northwestern Polytechnical University (Z2014071).

References

[1] Cui HW, Fan Q, Li DS: *POLYMER INTERNATIONAL*. 2013,62(11):1644-1651.
[2] Fallahi H, Nurulakmal MS, Fallahi A, et al: *JOURNAL OF MATERIALS SCIENCE-MATERIALS IN ELECTRONICS*. 2012,23(9):1739-1749.
[3] Chen S L, Liu K H, Luo Y F, et al: *International Journal of Adhesion and Adhesives*.2013,45:138-143.
[4] Wang L; Wan C; Fu Y,et al: *JOURNAL OF ELECTRONIC MATERIALS*. 2014, 43(1):132-136.
[5] Zhang Y, Qi S H, Wu X M, et al: *Synthetic Metals*. 2011(161):516-522.
[6] M Zulkarnain, M Mariatti, I A. Azid: *J Mater Sci: Mater Electron*. 2013(24):1523-1529.
[7] Cai YB, Zong X, Zhang JJ, et al: *INTERNATIONAL JOURNAL OF GREEN ENERGY*. 2014,11(8):861-875.

Advanced Materials Research Vols. 960-961 (2014) pp 118-125

doi:10.4028/www.scientific.net/AMR.960-961.118

Study of garlic Extract as a Green Corrosion Inhibitor for Mild Steel in Acidic Media

Bo Yang [1, a]， Wu Chen [2,b] Mu Danhua[3,c]

[1]School of Chemistry and Environmental Engineering, Yangtze University, Jingzhou 434023, Hubei, China.

[2]School of Chemistry and Environmental Engineering, Yangtze University, Jingzhou 434023, Hubei, China.

[3]School of Chemistry and Environmental Engineering, Yangtze University, Jingzhou 434023, Hubei, China.

[a]email: ybby2008@126.com

[b]email:ccww91@126.com

[c]email: 897096620@qq.com

Biography: Bo Yang(1964-), male, Ph. D., Associate professor of Yangtze University.

Corresponding author: Wu Chen (1967–), male, Ph. D.，Professor of Yangtze University, Research direction: oilfield wastewater treatment.

Keywords: Garlics; corrosion inhibitor; corrosion inhibitive performance evaluation; electrochemical techniques.

Abstract: This paper studies extract as corrosion inhibitors extracted from garlic. The IR spectrum analysis of the extract shows that the main ingredient of extract is amino acids, and the better extracting condition is that 30˚C 50mL 10%$H_2SO_4$and 20g peeled garlic react for 120.0h, and composite amino acids content in the extract is 19.0mg/L. The result of corrosion inhibition performance using static weight loss shows that the dosage of the extract, temperature and concentration of acidic mediums have effect on corrosion inhibition remarkably. The corrosion inhibitive efficiency for A3 steel is 93.26% in 5% Hydrochloric acid and 79.2% in5% mud acid when the dosage of the garlic extract is 4.0%(V/V) and 6.0%(V/V),respectively. The investigated results of electrochemistry performance of the extract indicates that corrosion potential of A3 steel shift in negative direction both in Hydrochloric acid and in mud acid, which indicates that the extract are inhibitors of inhibiting cathodic corrosion, and circular-arc radius of alternating-current impedance spectroscopy increase notably in acidic medium, and corrosion inhibition effect is remarkable. Therefore, it is feasible to extract inhibitors from garlic.

Introduction

Using corrosion inhibitor is one of the best way to prevent corrosion. Along with the increasingly regard on the hazard which is produced by using chemicals, people have reduced the use of corrosion inhibitors of high-toxic or non-biodegradable. The researchers shifted their attentions to high efficiency, eco-friendly, low-toxic materials which called green corrosion inhibitors. The Chinese scholars Ying-Chu Tao[1],Zhi-Hu Guo[2],Zheng Lin [3],Wan-You Zhang[4] ,Zheng Liu[5],Xiu-Zhou Lin[6],Yan Li etc[7],Xiang-Hong Li[8], began the corrosion inhibitive performance evaluation research respectively from the plant stem and leaf extract, tea, camphor leaves, Chinese prickly ash, peel, orange peel, cork, baicalin, berberine, black pepper,

white pepper, tobacco and reed, water lotus, sweet potato, white magnolia, hibiscus rosa-sinensis, etc. The foreign researchers, like Salch[9], Farooqi etc[10], Vinod Kumar etc[11], Minha[12], Matamala etc [13], Martinez etc[14] , had studied the inhibitive efficiency and mechanism of the extract of the mango skin and aloe leaf , betel nut seed, plants of the genus eucalyptus leaves, pod jam of plant flowers and Jun Cao section plant and pine bark, gum Arabic tannins and chestnut tannin, natural plant extracts-hardwood alkaline, curcumin; another researchers, Xiu-Zhou Lin[6], Ying Han[15], Guang-Hua Zhang[16], Hai-Yan Du[17], also extracted the corrosion inhibitive components from waste rice bran, Chinese medicine residue, rapeseed meal, bean dregs bread. The literatures reveal that the effect of the corrosion inhibitor in different medium is remarkable. This paper will develop the study on the extract from garlics in acid medium for metal corrosion inhibition. Garlic Contains the active ingredient such as Diallyl Disulfide, Diallyl Trisulfid, amino acids, and the amino and carbonyl with more negative charge, can provide electrons to the empty orbital of metal, and adsorb the metal surface to form a protective film, which separated the metal surface and from corrosion medium and slow down the metal corrosion rate. To prepare inhibitor from garlic is low cost, non-toxic harmless, and no environmental pollution. The research in this field is seldom. Therefore, this research is significant for resource utilization, environment protection, and the development of green corrosion inhibitor.

Experimental section

Experimental material, reagent and instrument. Fresh garlic, concentrated hydrochloric acid, ninhydrin, dibasic sodium phosphate, potassium phosphate monobasic, sodium hydroxide, L-glutamic acid; A3 steel, soxhlet extractor, thermostat water bath, adjust electric heating set, electrothermal constant-temperature dry box, electronic balance, corrosion coupon instrument, electrochemical workstation (model:LK2005A1),Fourier transform infrared (FTIR) spectrograph.

Extraction and characterization. Taking a certain amount of peeled garlic, Mashed and soaked in 50ml certain concentration of H_2SO_4 at a certain temperature for 120.0h according reference[17], filtrating under suction, and the obtained filtrate storage standby, The concentration of the filtered liquor can be determined by colorimetric method according to the National Standard(GB/T8314-2002)[18]. With sodium hydroxide to adjust the pH of the filter liquor, then continue to add acetone until there are white precipitations in the solution. The solution was filtered, and the filter residue dried in electrothermal constant-temperature dry box at 60℃ to get the dry solid extractors which can characterizationed by Fourier transform infrared(model:UV2450) spectrograph.

Performance evaluation method. The experiment is on the basis of the standard of China petro and gas industry(SY/T5405-1996)[19],and reference[20,21]. Weight loss analysis were used for corrosion inhibition performance evaluation of the garlic extractors on mild steel in acid medium; the polarization and impedance studies of the system which consists of mild steel and acid medium(with or without extractors) were carried out by electrochemical workstation(model: LK2005A1),thereby we can discuss the mechanism of the corrosion inhibition. The acid medium is hydrochloric acid and mud acid with different concentration.

Results and discussion

Components analysis of amino acids in garlic extract. According to the GB8314-2002[18], we used the assay method of the free amino acid to determine the amino acid content. Firstly, 0.1g/L L-glutamic acid solution was prepared. Different volume of standard amino acid solutions mixed with 0.5mL Na_2HPO_4—NaH_2PO_4 buffered solution and 0.5mL ninhydrin. Put it into the

thermostat water bath 15min, then cool it at room temperature, transfer it to a 25mL volumetric flask and constant volume. After 15min, measure the absorbance with λ=570nm. The standard curve of the composite amino is A =20.957C+0.0625（r= 0.9979）. The amino acid content of the extract can be obtained using the equation after the absorbance of the garlic extracts was measured.

The effect of H_2SO_4 concentration on the extractor inhibition efficiency. Six copies of peeled garlic, each 20g, Mashed and soaked in 50ml different mass fraction H_2SO_4 at 30℃for 120.0h. The soaking solution was filtered, then operation according to the above method, the absorbance of 5ml filtrate was measured at λ=570nm ，according to the standard curve equation for calculating amino acid content in liquid, at the same time，Respectively taking extract，and adding to 50 ℃ 500ml 5% HCl by 1% (V/V), hanging pieces experiments was carried, hang time was 4.0h, calculate A3 steel corrosion rate and the corresponding inhibition rate, all results as shown in Fig.1.

Fig.1 show that with the increase of the H_2SO_4 concentration, and content of amino acid in the extract increased at first, then decreased. Due to the linear relationship between absorbance and amino acid concentration, When the H_2SO_4 mass fraction was 10%, the content of the amino acid in extractors is maximal, up to 19.0mg/L, At the same time, extract had the best corrosion inhibiting effect on A3 steel ， the inhibition efficiency was 89.08%. Therefore, it identified using 10% H_2SO_4 as extraction agent in the following experiment.

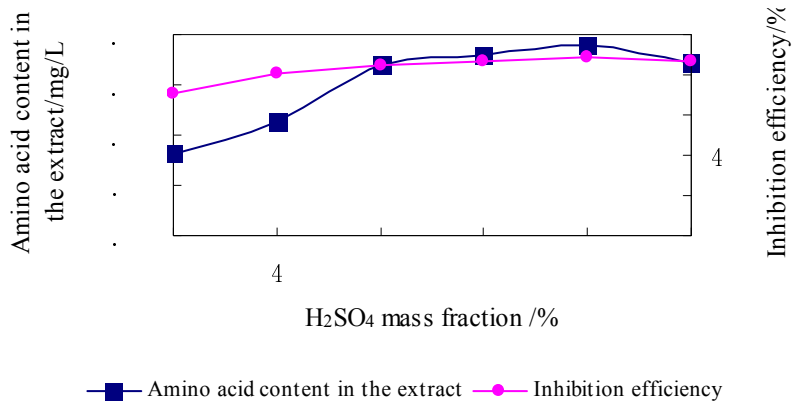

Fig.1 The effect of H_2SO_4concentration on the extractor inhibition efficiency

characterization of the extractors. The garlic leaching liquid with H_2SO_4 was filtered, sodium hydroxide is added to adjust the pH of the filter liquor, then continue to add acetone until there are white precipitations in the solution. and the filter residue dried in electrothermal constant-temperature dry box at 60℃ to get the dry solid extractors which can be characterizationed by Fourier transform infrared(model:UV2450) spectrograph. The results shown in Fig.2.

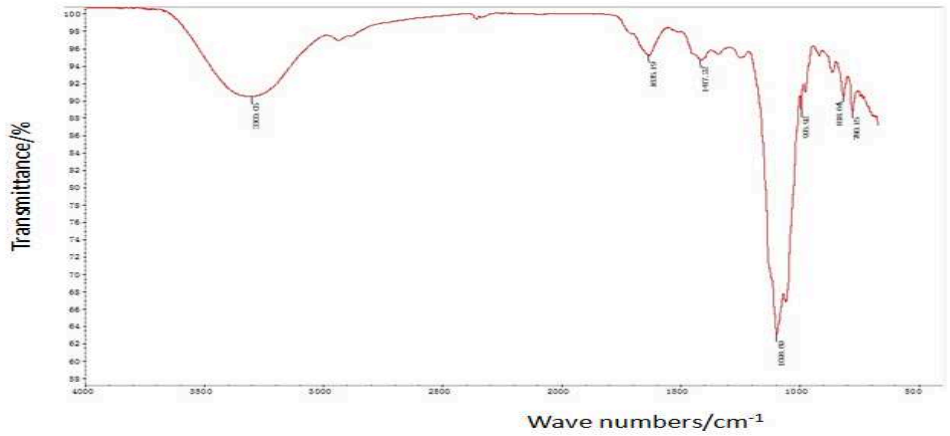

Fig.2 The infrared spectra of the extract

According to Fig.2,the infrared spectra absorption characteristic peak of the extract are3300.05cm^{-1} (V_{NH})，1635.19cm^{-1}($V_{C=O}$)，1098.69cm^{-1}(ν_{C-N})，995.92 cm^{-1},818.64 cm^{-1},780.15 cm^{-1}($V_{C=H}$).The result shows that the main ingredient of extractors from garlic is amino acids.

Corrosion inhibitive performance evaluation

The effect of dosage of the extractors on inhibitive efficiency. Three parallel specimens were completely immersed in an open beaker containing 500mL 5% HCl and mud acid with different dosages of extractors at 50℃for weight loss measurements, Respectively. For 4.0 h, take the specimens out, and wash and dry, and then weight accurately. The corrosion rate of A3 steel and corrosion inhibitive efficiency is presented in Fig.3 and Fig.4.

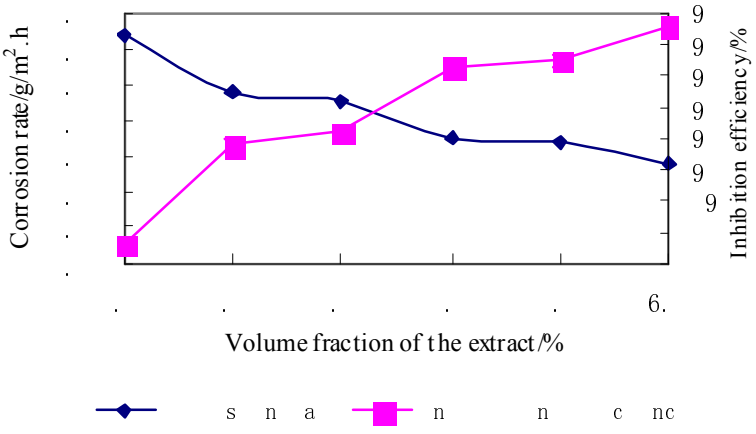

Fig.3 The effect of dosage of the extract on corrosion inhibitive efficiency for A3 steel in HCl

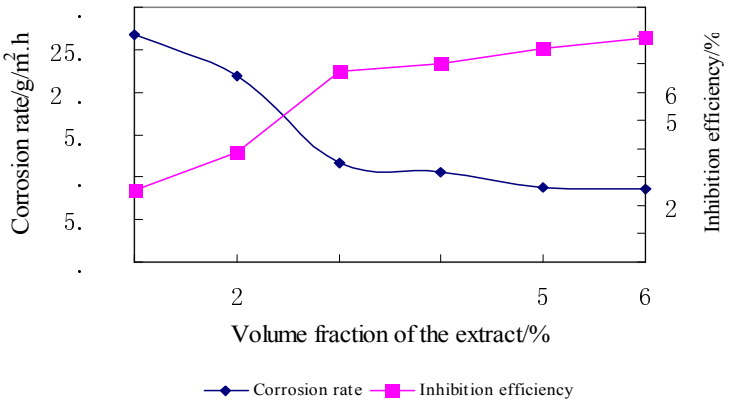

Fig.4 The effect of dosage of the extract on corrosion inhibitive efficiency for A3 steel in mud acid

Fig.3, Fig.4 shows, both in the medium of hydrochloric acid, or in the mud acid medium, garlic extract has good inhibition effect on the A3 steel in corrosion medium. The inhibition efficiency increase with the the dosage of extract increased. But the extract volume fraction is 4.0%-6.0% in the 5%HCl, the inhibition efficiency did not change significantly, therefore, the dosage of extract as corrosion inhibitor adding volume fraction is 4% in 5%HCl,and the inhibition efficiency is 93.26%,while the extract as corrosion inhibitor adding volume fraction is 6%in 5% mud acid, and the inhibition efficiency is 79.2%, therefore, adding extract corrosion inhibitor should follow appropriate amount principles.

Effect of temperatures on corrosion inhibitive efficiency. Three parallel specimens were completely immersed in an open beaker containing different temperatures 500mL 5% HCl and mud acid for 4.0h, when the dosage of the garlic extract is 1.0%(V/ V). The effect of corrosion inhibitive efficiency in different temperatures are given in Tab.1.

Tab.1 Effect of temperatures on corrosion inhibitive efficiency for A3steel in hydrochloric acid and mud acid

condition / index	The temperature of HCl/				The temperature of mud acid /			
	30	40	50	60	30	40	50	60
Corrosion rate/g/m^2·h	2.8298	7.0877	11.3985	16.002	8.9125	10.0497	11.6629	16.000
Inhibition efficiency/%	89.08	79.64	66.64	65.95	75.09	70.40	65.37	24.23

It is clear that (Tab.1) on increasing the temperature there is an increase in corrosion rate, so there is a decrease in inhibitive efficiency.

Effect of concentration of medium Three parallel specimens were completely immersed in an open beaker containing different concentration 500mL hydrochloric acid and mud acid at 50℃ for 4 h, when the dosage of the extract is 1.0%(V/ V). The results were given in Tab.2.

Tab.2 Effect of concentration of hydrochloric acid and mud acid on corrosion inhibitive efficiency for A3steel

condition / index	The concentration of HCl /%				The concentration of mud acid /%			
	5	10	15	20	5	10	15	20
Corrosion rate/g/m^2·h	4.4430	11.4778	17.4812	21.1837	8.4276	8.4968	8.6132	8.9125
Inhibition efficiency /%	76.79	51.36	22.23	20.91	75.09	60.89	16.86	15.68

Tab.2 present that with the rise of the concentration of hydrochloric acid and mud acid, the corrosion rate is increased and the corrosion inhibitive efficiency is decreased.

Evaluation of the electrochemical properties of extracts

(1) Polarization curve. An electrochemical workstation (model:LK2005A1) with a three-electrode assembly(platinum counter electrode(CE, Pt), saturated calomel electrode(SCE), working electrode(mild steel)) was used to study the corrosion inhibitive mechanical of the garlic extract at room temperature. The polarization curves for the A3 steel in the 5% hydrochloric acid and 5% mud acid when the dosage of the extract is 1.0%(V/V) are shown in Fig.5 and Fig.6,respectively.

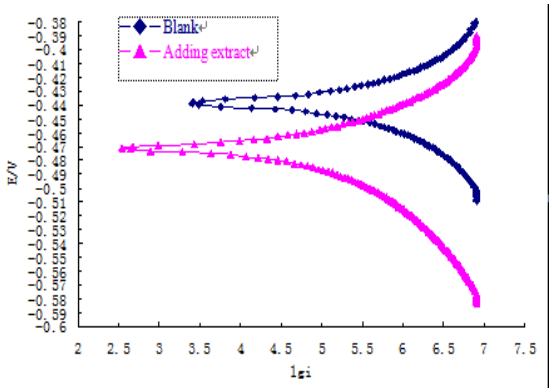

Fig.5 Polarization curve ofA3steel in 5%HCl solution with or without extract

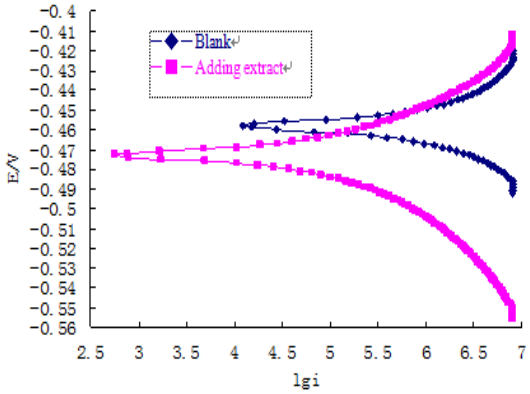

Fig.6 Polarization curve of A3 steel in 5%mud acid solution with or without extract

It is obvious from Fig.5 and Fig.6, that corrosion potential of A3 steel shifted in negative direction both in 5% hydrochloric acid and in 5% mud acid. It makes the Tafel slops increased, makes the cathodic polarization increased, and slows down the corrosion rate. This result is correspondence with the weight loss studies. Therefore, the garlic extract is cathodic corrosion inhibitor.

(2) Impedance analysis. In order to a further study on the corrosion inhibitive mechanical of the garlic extract,an electrochemical workstation (model:LK2005A1) was used to study the alternating-current impedance for the A3 steel in the 5% hydrochloric acid and 5% mud acid when the dosage of the extract is 1.0%(V/V). The electrochemical impedance spectroscopy (EIS) was carried out in the frequency range of 10^{-1} Hz to10^{5} Hz using a 10 mV peak-to-peak voltage excitation. The results are shown in Fig.7 and Fig.8.

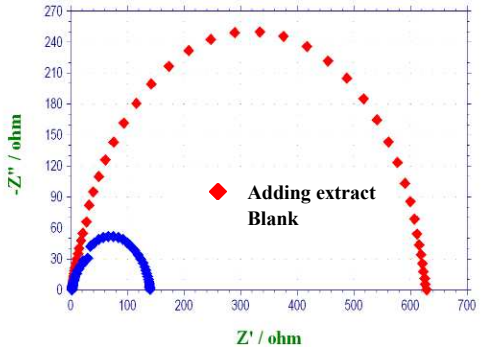

Fig.7 Impedance spectra of A3 steel in 5%HCl solution with or without extractors

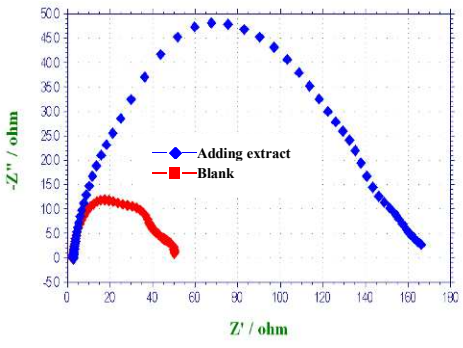

Fig.8 Impedance spectra of A3 steel in 5% mud acid solution with or without extractors

As it shown for us in Fig.7, Fig.8 , extractors make circular-arc radius of impedance spectroscopy increase notably for A3in acidic medium. The results indicate that after addition of the extract, the impedance increased, the corrosion current lower, and the corrosion inhibition effect is remarkable. Because of the semicircle is above the real axis, extract from garlic control the electrochemical process of the corrosion. This result is correspondence with the weight loss studies.

Conclusions

(1) The analysis IR spectrum of extract shows that the main ingredient of garlic extract is amino acids, and the better extracting condition is as follows: 30℃,50mL 10%H_2SO_4 and 20g garlic react 120.0h, and composite amino acids content in extract is19.0mg/L.

(2) The corrosion rate in 500mL 5% hydrochloric acid and mud acid decrease with the increase of the dosage of the garlic extract as inhibitor. The corrosion inhibitive efficiency for A3 steel is 93.26% in 5% Hydrochloric acid and 79.2% in5% mud acid when the dosage of the garlic extract is 4.0%(V/V) and 6.0%(V/V),respectively. On increasing the temperature and acidity, there is a increase in corrosion rate and a decrease in inhibitive efficiency.

(3) The corrosion potential shifted in negative direction both in hydrochloric acid and in mud acid after addition of the garlic extract. The results indicate that the garlic extract is cathodic corrosion inhibitors. The extract make circular-arc radius of impedance spectroscopy increase notably, which means that the impedance increased ,the corrosion current lower, and the corrosion inhibition effect is remarkable.

Acknowledgements

This work was financially supported by CNPC Innovation Foundation, China (2010D-5006-02-03).

References

[1] YingchuTao.A new type steel pickling inhibitor (LK45 phytic acid extract) for cleaning scale of boiler[J].Materials Protection,1987,28(4):26-30(In Chinese)

[2] Zhihu Guo，Heqing Tan.Inhibitive Effects of Extracts of Some Plants on the Corrosion of Carbon Steel[J].Materials Protection,1989,22(2):9-12(In Chinese)

[3] Zheng Lin. On Effects of Some Plant Corrosive Inhibitorson Cathodic Polarization of Steel[J].Journal of Fuzhou University(Natural Science),1999,27(4):108-110(In Chinese)

[4] Wanyou Zhang,，Yuefang Chen，XunLi. Inhibitive Effect of Some Natural-occuring Substance on Dissolution of A3 Steel in HCl Solution[J].North China electric power,2002,1:9-15(In Chinese)

[5] Zheng Liu, Gen liang Xiong. Preparation and application of plant inhibitors. Corrosion and Protection,2003,24(4):146-149(In Chinese)

[6] Xiu-zhou Lin, Min Gong, Jianping Wu.Study about use of abstracted oil from plant scrap as corrosion-inhibitor for hydrochloric acid cleaning. Corrosion science and protection technology,2006,18(3) : 222-225(In Chinese)

[7] Yan Li, Peng Zhao, Baorong Hou. Corrosion inhibition of mild steel by goldthread extractive in 1mol/L HCl solutions. Corrosion science and protection technology,2006,18(1)： 1-3(In Chinese)

[8] Xiang-Hong Li，Shu-Duan Deng，Hui Fu. Inhibition by Jasminum nudiflorum Lindl leaves extract of the corrosion of cold rolled steel in hydrochloric acid solution. J Appl Electrochem,2010,40:1641–1649(In Chinese)

[9] R M Salch. Corrosion inhibition by naturally occurring substances: The effect aqueous extracts of some leaves and fruit peels on the corrosion of steel Al， Zn and Cu in acid [J].British Corrosion Journal，1982,17(3):131-136(In Chinese)

[10] I H Farooqi，A Hussain，M A Quraishi,et a1. Study of low cost ecofriendly compounds as corrosion inhibitors for cooling systems [J] . Anticorrosion Methods and Materials，1999，46(50) : 328-331

[11] K P Vinod Kumar，M. Sankara Narayanan Pillai，G. Rexin Thusnavis. Green corrosion inhibitor from seed extract of Areca catechu for mild steel in hydrochloric acid medium[J]. J Mater Sci,2011,46:5208–5215

[12] A Minhale .The effect aqueous extracts of some leaves and fruit peels on the corrosion of steel in acid[J].Corrosion Prevent ion and Control 1999,4 :32-35

[13] G. Matamala. Comparison of steel anticorrosive protection formulated with natural tannins extracted from acacia and from pine bark[J] . Corrosion Science，2000,42:1351-1356

[14] S Martinez，Stadjar I. Correlation between the molecular structure and the corrosion inhibition efficiency of chestnut tannin in acidic solutions[J]. Journal of Molecular Structure，2003,640:167-171

[15] YingHan, Weidong Run .Preparation of corrosion inhibitor from wild natural plant[J].Chemical Engineer. 1994,5: 48(In Chinese)

[16] Guanghua Zhang,Yang Li.Research on picking inhibitor made by hydrolysis of papeseed cake[J].Fine Chemicals,1996,13(1) : 18.

[17] Hai-yan Du Xiao-hong,Peng,Yanfen,Zhang,Yan Gao.The process extraction amino acid from bean dregs and its corrosion mechanism. Anhui Chemical Industry, 2008,34（3）:35-37

[18] The determination of free amino acids content in tea[S].National standard of the People's Republic of China.GB/T8314-2002

[19] Performance test methods and evaluation indexes of Corrosion Inhibitor for Acidification[S],The People's Republic of China oil and gas industry standards SY/T 5405-1996

[20] Water quality standard and practice for analysis of oilfield injecting waters in clastic reservoirs [S],The People's Republic of China oil and gas industry standards SY/T 5329-2012

[21] Corrosion of metals and alloys——Removal of corrosion products from corrosion test specimens[S].National standard of the People's Republic of China GB/T16545-1996

Advanced Materials Research Vols. 960-961 (2014) pp 126-129

doi:10.4028/www.scientific.net/AMR.960-961.126

Ceramic Nano Composites for Thermal Insulators

Hae-Noo-Ree Jung [a], Yoon Kwang Lee[b] and Hyung-Ho Park[c]

Department of Materials Science and Engineering, Yonsei University, 50 Yonsei-ro, Seodaemun-gu, Seoul, 120-749, Republic of Korea

[a] nuri_j@yonsei.ac.kr, [b] yklee0330@yonsei.ac.kr, [c] hhpark@yonsei.ac.kr

Keywords: alumina xerogel, alumina whisker, Nanocomposite, Solvothermal drying

Abstract. In this research, nano pore composite had an effect on enhancing thermal property and mechanical property. The nano pore composite maintained the pore structure and enhanced mechanical property. Al_2O_3 xerogel was collapsed after heat treatment over 1000℃ and they had weak mechanical strength because of pores. For maintenance of pore at high temperature and improvement of mechanical strength, Al_2O_3 whisker was hybridized. The Al_2O_3 whiskers in nano pore composite play the role of pillar during heat treatment. The mechanical property of Al_2O_3 xerogel was improved through complexation with Al_2O_3 whisker. The elastic modulus of nano pore composite increased 225 % from Al_2O_3 xerogel.

Introduction

A porous structure is known to interrupt the thermal conduction of materials. For this reason, porous structure can apply for an insulator at ultimate environment. Especially, ceramic materials that have outstanding heat-resisting property are more helpful for porous structure. And nano meter sized pores made the structure have excellent insulating property as shown in Fig. 1. It means that porous structure made by ceramic material is suitable for an insulator. [1]

Fig. 1. Excellent thermal insulation property of nano pore structure [2]

Thermal conduction is largely occurred by solid conduction and gas convection. But nano-sized pore of ceramic nano pore structure can reduce a mean free path of gas and efficiently prevent the gas convection. Also solid conduction can be controlled by higher porosity. [3]

Ceramic nano pore structures that can apply for an insulator are ordered mesoporous, aerogel, xerogel materials. And these structures are made by sol-gel process.[4] The materials are divided by external conditions like a target temperature. It is useful for economical side and efficient side. In other words, under 1100℃ of low temperature, Silica is most widely used. Especially, silica is a lowest-cost oxide. Under 1400℃ of mid temperature, alumina is most widely used and above 1700℃ of high temperature zirconia is most widely used for. And a research for finding another ceramic matrix material is widely progressed.[5,6]

But nano pore structure has a weak mechanical strength because of the pores. Therefore overcoming of mechanical strength weakening is very important for an application of ceramic nano pore structure. In order to overcome of mechanical strength weakening, I.-K. Jung et al. studied about nano pore composite, such as doping of nano particles or CNT with xerogel. The complexation brought about an improvement of mechanical strength. But it is still imperfect for commercialization due to some problems. [7]

In this study, Al_2O_3 whisker was chosen for overcoming mechanical weakening problem and Al_2O_3 xerogel hybridized with Al_2O_3 whisker. Al_2O_3 whisker is known to have outstanding thermal and mechanical property. The changes of structural and mechanical properties were observed after high temperature treatment between Al_2O_3 xerogel and Al_2O_3 xerogel hybridized with Al_2O_3 whisker.

Experimental procedure

Formation of Al_2O_3 xerogel. One of the alkoxide precursor Aluminum sec-butoxide (ASB) was used as a precursor for formation of Al_2O_3 xerogel. And solvent for formation of Al_2O_3 xerogel was ethanol. Acetic acid and H_2O were used as catalyst for hydrolysis reaction. After hydrolysis reaction, highly polar agent N,N-dimethylformamide (DMF) was added for inducement of condensation reaction. After adding of DMF, the solvent was exchanged with n-hexane and surface modification was proceeded using HMDS(5 vol% in n-hexane). The final Al_2O_3 xerogel was synthesized through solvothermal drying in the autoclave. The total procedure was shown at Fig. 2.

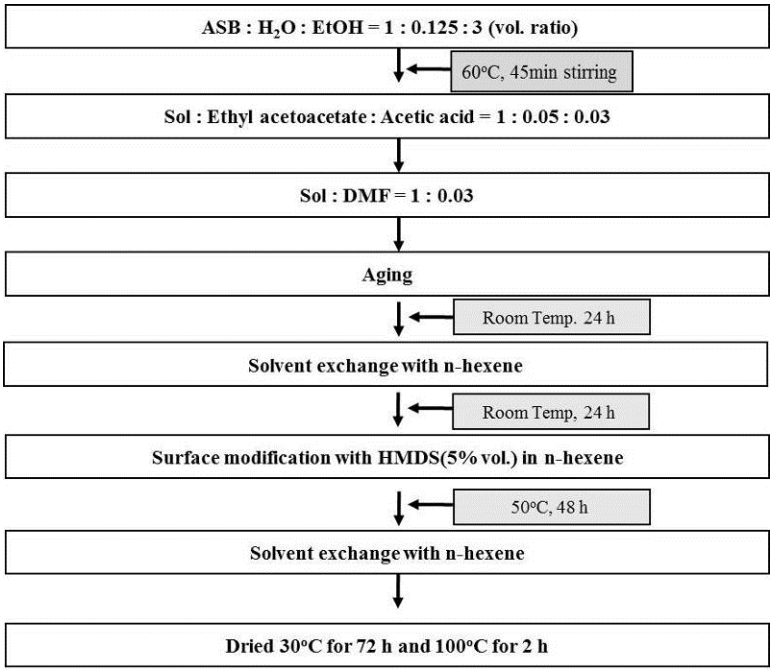

Fig. 2. Fabrication procedure of Al_2O_3 xerogel

Formation of Al_2O_3 whisker. Al_2O_3 whisker was synthesized using hot-wall chemical vapor deposition (CVD). The mixture of Al powder and Al_2O_3 powder was used as a source. During heating, evaporation and cooling process, Ar gas was flowed at 100 sccm for gas dilution and the pressure was fixed under 0.1 torr. At evaporation temperature 1400℃, reactant gas O_2 gas was flowed at 6 sccm during 10 m and cooled at room temperature. Scanning electron microscopy (SEM) image of Al_2O_3 whisker was shown in Fig. 3.

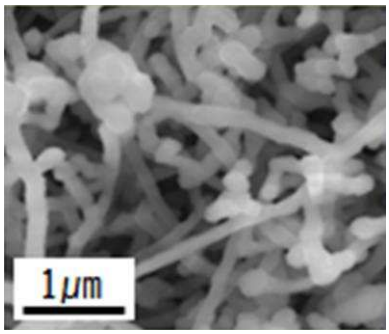

Fig. 3. Al_2O_3 whisker grown at 1400℃ [8]

Formation of nano pore composite. After formation of Al_2O_3 xerogel and Al_2O_3 whisker, the complexation was proceeded. For complexation of Al_2O_3 xerogel and Al_2O_3 whisker, Al_2O_3 whisker grown Al_2O_3 substrate was dip coated at Al_2O_3 xerogel solution during 15 m. After solvothermal drying at ambient pressure drying, the final composite was synthesized.

Results & discussion

The structural changes of composite after heat treatment. Al_2O_3 xerogel hybridized with Al_2O_3 whisker annealed at 1100℃ for 2 h. The structural analysis of composite was observed by SEM. The structural changes after exposing of high temperature were shown in Fig. 4. In the result of a comparison between Al_2O_3 xerogel and nano pore composite, Al_2O_3 xerogel has collapsed structure after heat treatment. It was confirmed that Al_2O_3 xerogel hybridized with Al_2O_3 whisker maintained pore structure after heat treatment at 1100℃. It was because that the existence of Al_2O_3 whisker increased thermal resistance of internal matrix for maintenance

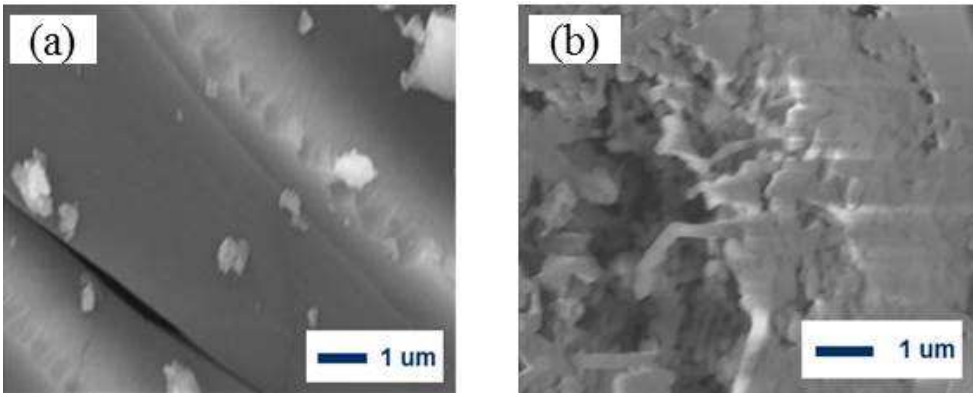

Fig. 4. SEM images after annealing of (a) Al_2O_3 xerogel, (b) nano pore composite

The mechanical changes of composite. The mechanical property of Al_2O_3 xerogel hybridized with Al_2O_3 whisker was analyzed using nano indentor. The result was shown in Table 1. In the mechanical properties of Al_2O_3 xerogel, the modulus of elasticity of Al_2O_3 xerogel was improved up to 225% after hybridization with Al_2O_3 whisker. The mechanical properties like modulus of elasticity and hardness coefficient of composite were even increased after heat treatment. Especially, composite of Al_2O_3 xerogel and Al_2O_3 whisker annealed at 1100℃, the composite had fine porous structure of xerogel and the modulus of elasticity was improved up to 114% after heat treatment. So it can be said that an improvement of thermal and mechanical property was obtained by complexation. With grain boundary densification occured at the interface, it was caused an increasing of the modulus of elasticity and hardness coefficient.

Table 1. Mechanical property of nano pore composite

	Modulus (GPa)	Hardness (GPa)
Al_2O_3 xerogel	0.4±0.2	0.02±0.01
Al_2O_3 xerogel+Al_2O_3 whisker before anneal	0.9±0.3	0.03±0.02
Al_2O_3 xerogel + Al_2O_3 whisker after anneal at 1000℃	1.15±0.5	0.03±0.02
Al_2O_3 xerogel + Al_2O_3 whisker after anneal at 1100℃	1.03±0.3	0.04±0.01
Al_2O_3 xerogel + Al_2O_3 whisker after anneal at 1200℃	2.3±0.2	0.06±0.01

Summary

In this study, a porous structure was formed by complexation of Al_2O_3 xerogel and Al_2O_3 whisker via solvothermal drying at ambient pressure. It was confirmed that nano pore composite had improved thermal stability with enhanced modulus of elasticity and hardness coefficient. As a result, it was verified that excellent mechanical property of Al_2O_3 whisker has an effect on the improvement of mechanical strength of Al_2O_3 xerogel.

Acknowledgements

This work was supported by the National Research Foundation of Korea (NRF) grant funded by the Korea government (MEST) (No. 2012R1A2A2A01011014).

References

[1] X.Y. Huang, Z. Xu, L.D. Chen and X.F. Tang : Key Eng. Mater. Vol. 249 (2003), p. 79

[2] Photograph courtesy of National Renewable Energy Laboratory, NREL

[3] D.M. Smith, A. Maskara, U. Boes, J. Non-Cryst. Solids. Vol. 225 (1998), p. 254

[4] J.F Poco, J.H Satcher Jr. and L.W Hrubesh : J. Non-Cryst. Solids. Vol. 285 (2001), p. 57

[5] Ward, D.A. and Ko, E.I. : Chem. Mater. Vol. 5 (1993), p. 956

[6] Suh, D.J. and Park, T.-J. : Chem. Mater. Vol. 8 (1996) , p. 509

[7] I.-K. Jung, J.L. Gurav, U.K.H. Bangi, S. Beck and H.-H. Park : J. Non-Cryst, Solids Vol. 358 (2012) , p. 550

[8] S.J. Park, Y.Y. Choi, J.G. Kim and D.J. Choi : Journal of Crystal Growth Vol. 361 (2012) , p. 189

Advanced Materials Research Vols. 960-961 (2014) pp 130-133

doi:10.4028/www.scientific.net/AMR.960-961.130

Inhibition of corrosion by dithiocarbamate in Oilfield water injection

Zuohua Wang

Sinopec Petroleum Engineering Corporation (SPE), Dongying 257000, P. R. China. E-mail: messias1015@163.com

Keywords: dithiocarbamate (DTC), corrosion inhibition, oilfield wastewater.

Abstract In this work, corrosion inhibition in steel water pipes, used in Shengli oilfieldis studied in different corrosive media by adsorption of dithiocarbamate (DTC) on the surface of the pipes. Electrochemical impedance spectroscopy (EIS), linear polarization resistance (LPR) and potentiodynamic was applied to determine the effection of this dithiocarbamate. And the result shows that this dithiocarbamate has high corrosion inhibition up to 90%.

Experimental principle and method

Electrochemical impedance spectroscopy (EIS) is an transient electrochemical technique. The characteristics as follows, each half cycle duration is very short and can not cause serious concentration polarization and surface state change while the frequency is high enough because of using the small amplitude symmetrical alternating current(<10 mV) for polarization of electrode. The process of cathode and anode alternate on the electrode without causing the accumulation of polarized development, which can avoid excessive impact on system. Secondly, it can be measured in wide frequency range to get impedance spectroscopy. Therefore, EIS can get more electrode kinetics information and electrode interface structure information than other conventional electrochemical methods.

In this experiment, electrochemical impedance spectroscopy test were performed using the classic three-electrode system. All electrochemical experiments were carried out by using an PARSTAT 2273 (AMETEK, USA).Working electrodes with a surface area of 1cm^2 are carbon steel material, and non-working surface sealed with epoxy resin, and the surface of the electrode were polished by DTC metallographic sandpaper, and washed with water, and then degreased with alcohol and washed with deionized water to soak in the solution. The reference electrode is a saturated calomel electrode and the counter electrode is a platinum electrode. The EIS measurements were carried out over a frequency range from 0.05 Hz to 100 kHz with sinusoidal potential perturbation 5 mV in amplitude. All the potential values in this paper are relative to the saturated calomel electrode (SCE).

Experiment

Fig.1 shows the Nyquist plots of the carbon electrodes immersed in oilfield water injection solution with different concentrations DTC inhibitor for 4d. Where the abscissa Z ' represents the real part of the impedance, and where the vertical axis-Z '' represents the imaginary part of the impedance. Fig.1 shows a flattened semicircular, semicircle in the chord Z 'axis corresponds to the electrode polarization resistance Rp. And the greater the value of Rp, the better corrosion inhibition effect [1].Compared to blank electrode, the polarization resistance of carbon electrodes increased obviously after added DTC corrosion inhibitor, and the polarization resistance of electrodes

increases with increasing inhibitor concentration.. And the polarization resistance at 20mg /L is greater than at 10mg/L. Fig.2 shows the Bode plots of the carbon electrodes immersed in oilfield water injection solution with different concentrations DTC inhibitor for 1d.. Corrosion inhibition effect can also be characterized by the impedance modulus value $|Z|_{0.05}$ at the low-frequency electrode point (f = 0.05Hz). And the greater the value of $|Z|_{0.05}$, the corrosion inhibition effect is better. The value of the $|Z|_{0.05}$ also increases with the increasing inhibitor concentration. And the impedance modulus $|Z|_{0.05}$ at 20mg/L is greater than at 10mg/L. It is also easy to find out from Fig.3 the phase angle only appears a maximum value, which illustrate in the system of corrosion electrochemistry reaction there is only one time constant. In the presence of inhibitor, it can consider that the corrosion system composed by basement metal and inhibitor film as a protective film was formed on metal surface. But in the neutral interface, because of the diffusion of oxygen molecules, EIS will be partially covered, and phase angle only appears a maximum value at the Bode phase angle θ-logf figure (Rs is the solution resistance, Rp is Polarization resistance, C is the capacitance between the electrode and the solution).

Admittance of a C is given by (1) [3]:

$$C = 1 / (2\pi f\theta max \, |Z|\theta max) \quad (1)$$

Where $f\theta max$ and $|Z|\theta max$ is corresponding with maximum phase angle θmax and the Bode figure.

The inhibition efficiency η can be calculated according to the following equation (2) [4]：

$$\eta = (R_p - R_p^\circ) / R_p \times 100\% \quad (2)$$

Where Rp is the polarization resistance of the electrode with inhibitor and Rp° is the the polarization resistance of the electrode without inhibitor.

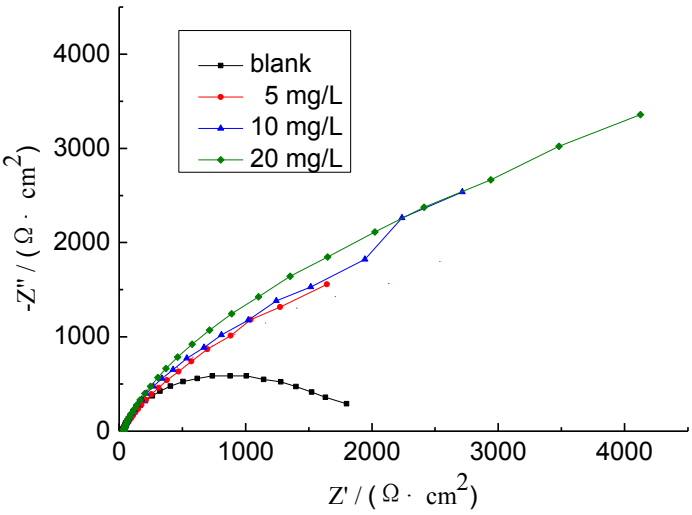

Fig. 1 Nyquist plots of the carbon electrodes immersed in oilfield water injection solution with different concentrations DTC inhibitor for 4d

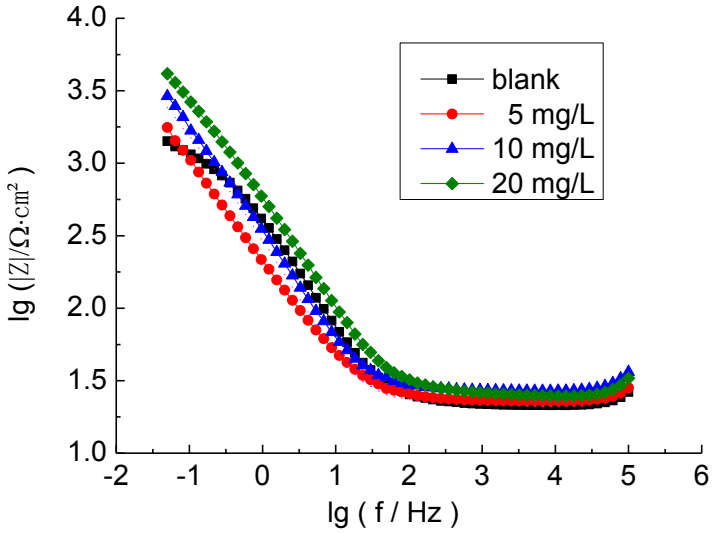

Fig. 2 Bode plots of the carbon electrodes immersed in oilfield water injection solution with different concentrations DTC inhibitor for 1d. （lg|Z|~lg f）

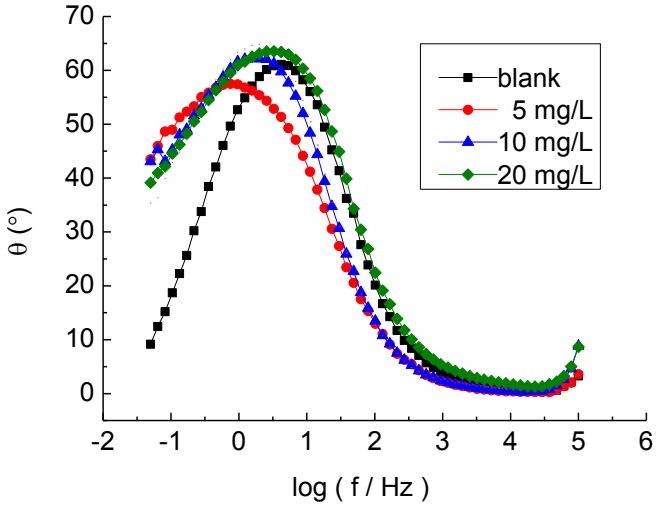

Fig. 3 Bode plots of the carbon electrodes immersed in oilfield water injection solution with different concentrations DTC inhibitor for 1d. （θ~lg f）

Table 1 $f_{\theta max}$ and $|Z|_{\theta max}$ corresponding with maximum phase angle θ_{max} and the Bode figure of DTC inhibitor

Concentration (mg/L)	θ_{max}(°)	$lgf_{\theta max}$	$f_{\theta max}$(Hz)	$lg\|Z\|_{\theta max}$	$\|Z\|_{\theta max}$(Ω·cm²)
blank	61.4	0.603	4.09	2.16	144.54
5	57.4	-0.109	0.79	2.40	251.19
10	62.4	0.282	1.91	2.32	208.93
20	63.7	0.518	3.30	2.38	239.88

Table 2 Fitted values of electrochemical impedance spectroscopy of carbon electrodes with DTC inhibitor.

Concentration (mg/L)	R_s /m^2	R_p/Ω·cm^2	C/μF·cm^{-2}	η_1/%
blank	23.72	1925	269.4	—
5	24.56	6284	802.4	69.37
10	24.28	15476	399.0	87.56
20	25.51	18482	201.2	89.58

Table 1shows the $f_{\theta max}$and $|_{\theta max}$corresponding with maximum phase angle θ_{max} and the Bode figure of DTC inhibitor. Table 2 shows the fitted value of electrochemical impedance spectroscopy of carbon electrodes with DTC inhibitor. Table 2 shows that the polarization resistance of carbon electrodes increased obviously after added another DTC corrosion inhibitor. And polarization resistance also increased with increasing of the inhibitor concentration. Inhibition efficiency can up to 89.58% when the concentration of inhibitor is 20mg/L.

Conclusion

DTC inhibitor has corrosion resistance for carbon steel in oilfield water injection. Inhibition efficiency can up to 89.58%.when the concentration of DTC inhibitor is 20mg/L.

References

[1] C.N. Cao., J.Q. Zhang. The Introduction of Electrochemical impedance spectroscopy[].Beijing: Science and Technology Press, 2002:68

[2] G. W. Walter. A review of impedance plot methods used for corrosion performance analysis of painted metals. Corrosion Science, 1986,26(9):681-703

[3] R.T. Tong., Z.CH.Ma.,G.D. Zhou.,SH.M. Cai. The method of electrochemical impedance spectroscopy reseach BTA and MBT for corrosion behavior of copper [J]. Chemical Research and Application,1996,8(3):331-333

[4] Quan Z. L., Chen S. H ., Li S L. Protection of copper corrosion by modification of self-assembled films of schiff bases with alkanethiol [J]. Corrosion Science, 2001,43(6): 1071-1080

Advanced Materials Research Vols. 960-961 (2014) pp 134-137

doi:10.4028/www.scientific.net/AMR.960-961.134

Monomethyl β-methylglutarate of new synthetic methods

Fengwei He[1,a] Tong Lui[1,b] and Yaqin Zhang[2,c]

[1]Department of biological medicine and chemical Engineering,
Liao Ning Institute of Science and Technology, Benxi, liaoning, 117004, China

[2]Benxi Chemical Industry School, Benxi,liaoning, 117019, China

[a]hfwdd@163.com, [b]ltong_78@163.com, [c]zhangyaqin@hotmail.com

Keywords: monomethyl β-methylglutarate; musk ketone; methyl malonate; butene Ethyl;heteropoly acid

Abstract. Malonate ethyl ester of butene in the presence of sodium hydroxide was synthesized by addition reaction of 2-methyl propane-1,1,3 tricarboxylic acid ester, by hydrolysis decarboxylation heatingβ- methyl glutaric acid. First with excess of methanol into methyl metaplasiaβ- methyl dimethyl glutarate, and then itsβ- methyl glutaric acid methylation, get high yield of monomethyl β-methylglutarate.

β-methyl glutaric acid monomethyl ester is an important intermediate by the stoll synthesized musk ketone [1]. Musk ketone is not only an excellent spice, but also is an important component of Chinese medicine musk. The natural musk contains musk ketone 1.2% to 1.4%,with exciting nerve center, respiratory center and heart, for the treatment of delirium, swelling pain, sore, bruises .

The method of synthesis of β-methyl-glutaric acid monomethyl ester as follows.

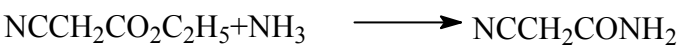

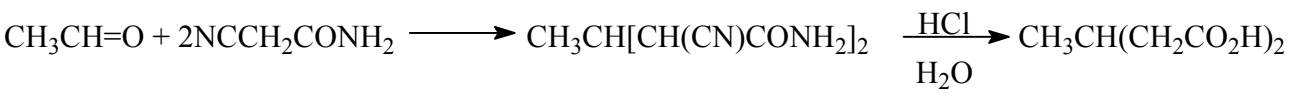

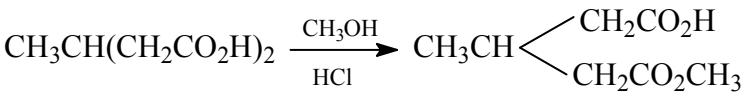

The total yield of this method is only 30%, ethyl cyanoacetate is bimolecular reactions, therefore, the total efficiency is only 15%.After repeated tests, we use the following route:

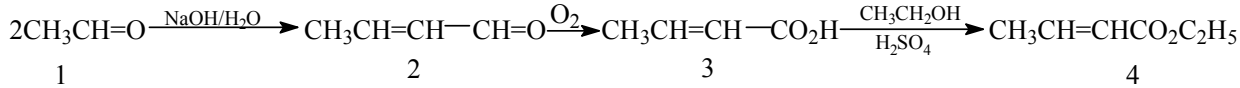

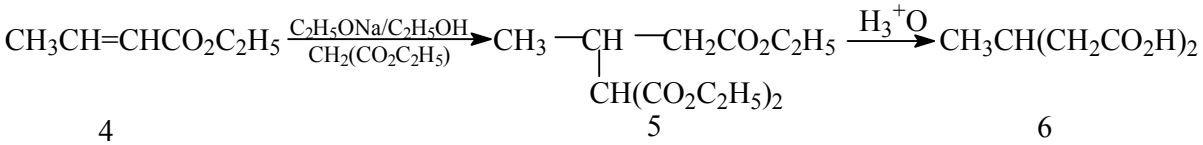

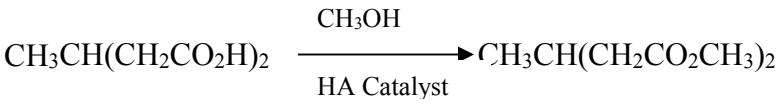

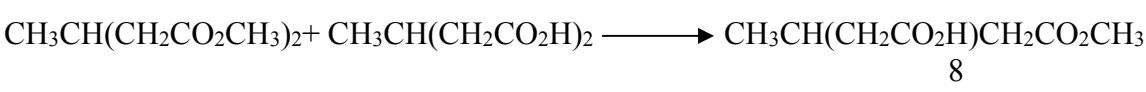

The reaction under mild conditions is less by-products, the unreacted raw materials are recovered, dimethyl malonate utilization rate is more than 90%. Heteropoly acid compound is a class of oxygen bridge polynuclear complexes, having the characteristics complex and a metal oxide, is a multifunctional catalyst. As catalyst of the esterification reaction, there must be sufficiently acidic, the weaker the oxidation. Experiments show, phosphotungstic heteropoly acid (PW) in organic solvent the acidity of $-8.2 \leq HO \leq -5.6$, while oxidation is very weak, is an ideal esterification catalyst,and load heteropolyacid has stronger catalytic activity in the reaction.

Experiment

1.1 Crotonic acid ethyl (2 - butenyl acetate) (4) Synthesis

Compound (2) according to the literature [5] synthesis, yield 72%, b•p 102~103℃, nD^{20} 0.8450 .compounds (3), according to the literature [6] synthesis, yield 50%, m•p 72 ℃. Compound (4) according to the literature [4] synthesis, yield 71%, b•p 137~140℃

1.2 2 - methyl-propane-1,1,3 - tricarboxylic acid ethyl ester (5) Synthesis

First,420 g (9.13 mol) of anhydrous ethanol was added 1 000 ml round bottom flask with stirrer and reflux apparatus, 35 g (1.52 mol) of pure sodium under stirring was added portionwise.Then, 220 g (1.50 mol) of diethyl and 161 g (1.50 mol) of ethyl crotonate malonate was gradually added .After 10 h of reflexing, the mixture was distilled off ethanol. The remaining liquid is cooled, addition of 50% sulfuric acid aqueous to acidic, separation of reservoirdistillation under reduced pressure, collecting fraction at 157~170℃/14 mmHg to obtain a colorless oily liquid 300 g, 73.0% yield. Elemental analysis: $C_{13}H_{22}O_6$ measured values (calculated value%): C, 56.68 (56.93); H, 8.10 (8.03), ^{1}HNMR, δ: 0.9 (d, 3H, CH_3); 1.3 (t, 9H, CH_2); 4.1 (q, 6H, 3 × CH_2)

1.3 β-methyl glutaric acid (6) Preparation

274 g (1.0mol) of 2 - methyl-propane-1 ,1,3 - 3-carboxylic acid ethyl ester and 280 g of 95% ethanol was added 1000ml round bottom flask with stirrer and reflux apparatus, was heated to reflux, 210 g of potassium hydroxide (content 82%, 3.0 mol) was gradually added . After 5h of reflexing, the mixture was distilled off ethanol. The remaining liquid was cooled, addition of 50% sulfuric acid aqueous to acidic, filtered potassium persulfate,dryed at 140 ℃ and pulverized. Extraction by 100 mL - acetone in five, the extract was distilled acetone. The remaining liquid was distilled under reduced pressure. Fractions was collected at 150~170℃/10mmHg. Recrystallized in ethyl acetate we get white solid 122.8 g was prepared, yield 83.0%, m•P 86 °C (literature values 86~87°C)

1.4 Synthesis of β-methyl glutaric acid monomethyl ester (8)

146 g (1.0 mol) of (6) and 192 g (6.0 mol) of anhydrous methanol, 200 g - anhydrous toluene, 5 g - heteropoly acid mixed , refluxed in flask 4 h, toluene and methanol was distilled off under reduced pressure, β-methyl glutaric acid dimethyl ester was prepared; 65.7 g (0.45mol) of (6) and 100g dioxane was added. After 2h of reflexing, dioxane was distilled off under reduced pressure.The remaining liquid was distilled under reduced pressure. Fractions was collected at 138~144℃/10mmHg and 148~152℃/10mmHg. The former was (7), obtained 81.8 g, bis esterification rate was 32.4%, and the latter was (8), obtained 132.9 g, single esterification rate was 60.0%. The conversion rate of (6) reached 90%. Elemental analysis:C7H12O4，measured values (calculated%)：C，52.15（52.17）；H，7.16（7.14）。^{1}HNMR，δ：0.96（d，3H，CH_3）；2.41（t，2H，CH_2）；2.53（q，2H，CH_2）；3.68（s，3H，CH_3）. B-methyl-glutaric acid

monomethyl esterβ-methyl glutaric acid dimethyl ester was prepared by the above method - main infrared spectroscopy σ is (liquid film method): 1146, 1740, 1450, 1326, 1170 cm-1, with the standard sample of the infrared spectra consistent σ. The product was confirmed by IR and 1HNMR data for the structure of β-methyl-glutaric acid monomethyl ester. The refractive rate of product was 1.440(nD^{20}), consistenting with the standard sample(nD^{20} 1.442).

Results and discussion

We found that synthesis of β-methyl-glutaric acid monomethyl ester (8) was the key step,so we focus on the step.

2.1 Orthogonal experiment

Selected five factors and four levels orthogonal experiment [10] table, - experiments are shown in Table 1:

Table 1 L16 (4^5) experimental factor level table

Reaction temperature /℃	acid and alcoholmolar ratio - mol/mol	Solvent	Reaction time /h	Catalyst
60	1:4	Benzene	2	PW
70	1:5	Toluene	3	CMA-PW
80	1:6	Tetrahydrofuran	4	C-PW
90	1:7	Dioxane	5	SiO_2-PW

By range analysis and Ri, We come to the influence factors on the experimental results: time> acid molar ratio > solvent> catalyst> temperature. L16 (4^5) orthogonal experimental results can - initially identified heteropoly acid catalyzed synthesis of β-methyl glutaric acid monomethyl ester optimal process parameters: reaction temperature: 80 °C; molar ratio: 1:6; solvent : toluene; reaction time: 4h; catalyst: CMA-PW.

2.2 Single factor experimental results

2.2.1 the effects amount of catalyst

Acid with methanol of the molar ratio was 1:6,200 ml of toluene as a solvent, the reaction temperature was 80 °C, the reaction time was 4h, in accordance with the synthesis method in reaction was carried out of the orthogonal experiments. CMA-PW were added to 3g, 4g, 5g, 6g, 7g as a catalyst. Analytical data of the drawing shown in Figure 1:

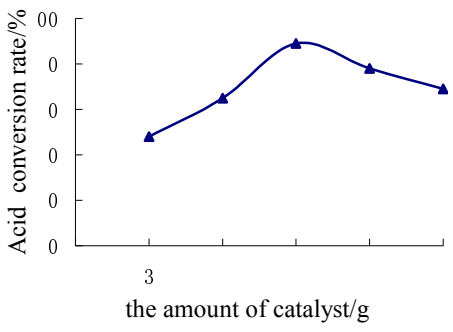

Fig.1 The effects of the amount of catalyst

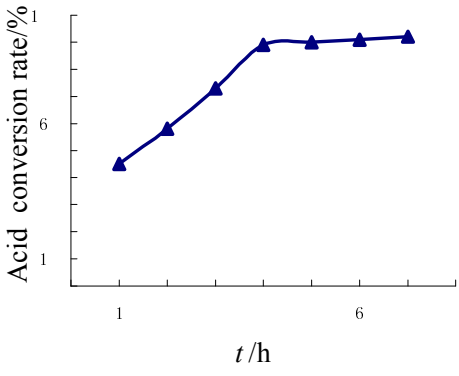

Fig.2 The effects of time

Figure 1 shows: the maximum of the catalytic efficiency is the amount of catalyst of 5g. When the the amount of catalyst less than 5 g, the catalyst amount the insufficient, not enough to make the reaction has reached the maximum reaction conversion rate; When the catalyst amount is more than 5 g, the conversion rate the diacid lower, may be due to the occurrence of side reactions. Therefore, the amount of catalyst 5 g is appropriate, that is 1.5% of the quality the the substrate.

2.2.2 Time factors

Acid with methanol of the molar ratio was 1:6,200 ml of toluene as a solvent, the reaction temperature was 80 °C, the reaction time was8h, in accordance with the synthesis method in reaction was carried out of the orthogonal experiments. When the reaction proceeds to 1h, 2h, 3h, 4h, 5h, 6h, 7h, 8h were measured by the conversion rate of the acid. Diacid conversion rate increasing with reaction time, it can be shown from Figure 2. But after 4h acid conversion rate rises slowly from 4 ~ 8 h reaction lasted for4 h, acid conversion rate rose only 5.0%. Consider of economic factors, reaction time is 4 h appropriately.

Conclusions

(1) Under basic conditions the addition reaction of crotonic acid ethyl ester and diethyl malonate to prepare β-methyl glutaric acid , the two sides are single molecule reactions, the relative production rate can be greatly improved, while also recovery to 20% of the reactants can be recycled.
(2) The use of β-methyl dimethyl glutarate and β-methyl glutaric acid reaction, single esterification rate can be improved. Diester can be recycled, so that of utilization rate of more of 90% of dicarboxylic acid.
(3) Optimal conditions of heteropoly acid catalyzed transesterification method is that acid and alcohol molar ratio of 1:6, solvent for anhydrous toluene, catalyst supported heteropoly acid dosage under of condition of 1.5% of of substrate, and the reaction time was 4h, of acid after of reactionof the conversion rate was 90%.
(4) All reaction conditions are mild, heteropoly acid catalyzed is reusable, non-corrosive, non-pollutant emissions, green line chemical cleaner production concept has important practical value.

References

[1] Stoll M，Commarmont A. A New synthesis of muscone [J].Helv Chin Acta.1947,31:1435-1438.

[2] Kozhevnikov I V,Matveev K I.Homogeneous catalys based on heteropolyacids(review) [J]. Applcatal,2000,5:136-149

[3] Yadav G D,Mistry C K. Oxidation of benzyl alcohol under a synergism of phase tranafer catalyis and heteropolyacids[J].Mol Catal A Chem.2001,172(1/2):140-143

[4] Pope M T,Muller A.Polyoxm et.al.ate Chemistry:Anold field and new dimeionsinseveral disciplines [J].Angew Chem Int EdEngl,2001,30:34-36

[5] Kennedy B. The hydration of unsaturated compounds. VI.The rate of hydration of trans-crotonaldehyde. The equilibrium between trans-crotonaldehyde and aldol in dilute aqueous solution. [J].Am Chem Soc.1937,59:146-149.

[6] Brtish Celanese. Manufacture of Crotonic acid [P]. GB 612346,1948-11-11.

[7] Wenqing Liu. Experimental design [M]. Beijing: Tsinghua University Press, 2005

Advanced Materials Research Vols. 960-961 (2014) pp 138-142

doi:10.4028/www.scientific.net/AMR.960-961.138

Preparation and properties of thiol-ene UV-curable fluorinated emulsion

Xiuzhen Hu, Huayun Cheng, Wenhua Deng, Changqing Fu[a]*

Jiangxi Key Laboratory of Organic Functional molecules, Jiangxi Science and Technology Normal University, Nanchang 330013, P.R.China

[a] 275341990@qq.com

Keywords: fluorinate; thiol-ene; SET-LRP; UV curable

Abstract. Single electron transfer living radical emulsion polymerization (SET-LRP) of allyl methacrylate (AMA) coupled with 2,2,3,4,4,4-hexafluorobutyl methacrylate (HFBA) was investigated in the presence of Cu(0)/N,N,N',N'',N''-pentamethyldiethylenetriamine (PMDETA) as catalyst and ethyl 2-bromoisobutyrate (EBiB) as initiator. Solid content of the emulsion and the amount of the catalyst, initiator and emulsifier were discussed for the optimal reaction conditions. Then, the emulsion was combined with thiol capped polyurethane (SHPU) under UV to form the UV curable fluorinated films. Mechanical properties and contact angle of the UV cured films were studied.

Introduction

Living radical polymerization (LRP) has come into the spotlight for synthesis of well-defined polymers from a versatility range of vinyl monomers via a reversible activation-deactivation process [1]. A variety of LRP techniques have been developed, such as atom transfer radical polymerization (ATRP), reversible addition-fragmentation chain transfer (RAFT), nitroxide-mediated polymerization (NMP) and SET-LRP. Among them, SET-LRP has emerged as a robust technique for the ultrafast synthesis of tailored and multifunctional polymers with excellent control of molecular weight and molecular distribution [2]. Cu(0) powder and Cu(0) wire or Cu_2X (X= Te, Se, S, O) combined with diversity of disproportionating N-ligands are used as catalyst in SET-LRP [3-5]. A wide range of polar solvents such as DMSO [6], DMF [7], alcohols [8], and water [9] were confirmed to be feasible in this versatility channel. In this work, we report a SET emulsion polymerization of AMA and HFBA. Optimal reaction conditions for SET-LRP emulsion polymerization including solid content of the emulsion and the amount of the catalyst, initiator and emulsifier were investigated. The illustration for synthesis of PAMA-co-PHFBA was shown in Scheme 1. Afterward, SHPU was synthesized in our previous research [10] was used to react with double bond containing of PAMA-co-PHFBA under UV to obtain the UV cured films.

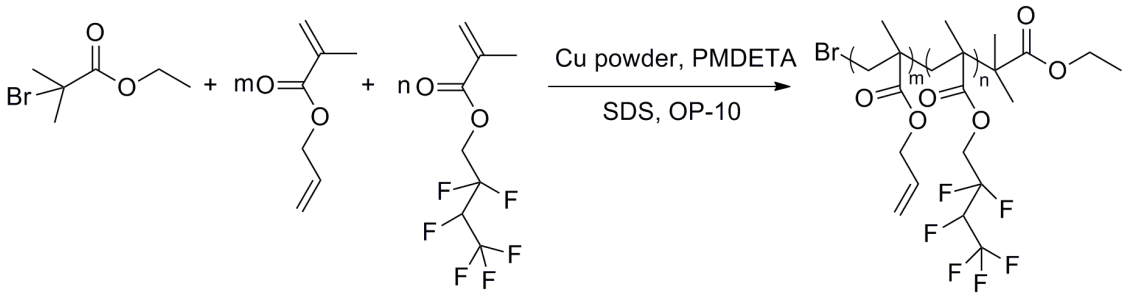

Scheme 1. SET emulsion polymerization of PAMA-co-PHFBA

Materials and methods

Allyl methacrylate (AMA), 2,2,3,4,4,4-hexafluorobutyl methacrylate (HFBA), 2-bromoisobutyrate (EBiB), sodium lauryl sulfare (SDS), polyoxy ethylene nonyl phenyl ether (OP-10) were purchased from Aladin China. photoinitiator 2959 (BASF), N,N,N',N'',N''-pentamethyldiethylenetriamine (PMDETA) (Alfa Aesar).

SET-LRP of PAMA-co-PHFBA. Cu(0) powder 0.15g, PMDETA 0.06g, SDS 0.01g, OP-10 0.02g and deinoized water 3g were charged into a 25mL three neck round flask, then the mixture was stirred vigorously with a speed of 1000rpm for 1h to obtain the emulsified catalyst system . On the other hand, AMA 0.755g, G02 1.5g, SDS 0.067g, OP-10 0.03g, EBiB 0.06g were charged into another 25 mL round flask, then the mixture was stirred vigorously for 30 min at 30°C under N_2 to obtain the pre-emulsion of the monomers. The emulsified catalyst system was transferred to the pre-emulsion with a stirring speed of 200rpm to initiate the polymer reaction. Conversion of the monomer was measured by weighting method.

Synthesis of UV curable films. UV cured films of PAMA-co-PHFBA and SHPU were prepared with the mole ratio of double bond and thiol of 1.5:1, 1:1, 1:2, 1:2.5 and 1:3, and the corresponding codes were 1, 2, 3, 4, 5 respectively, then the mixture was cured by UV in the presence of photoinitiator 2959.

Result and discussion

Optimal conditions for fluorinated SET emulsion. Solid content of the emulsions ranging from 10-30 wt% were investigated at the emulsifier content of 5 wt%, initiator loading of 1% and catalyst of 10% to the total monomer molar ratio, the results are shown in Fig.1. It was found that the shorter induction time of the polymerization was found in higher solid content, which may be ascribed to the higher monomer concentration in higher solid content system. However, in the solid content of 20%, the polymerization rate was much faster. Hence, solid content of 20 wt% was used in the next experiments. Effects of catalyst content on the conversion are revealed in Fig.2. Interestingly, 7% catalyst exhibited the fastest polymerization rate and 10% and 5% both prolong the induction time. This is due to reaction site is much less when polymerized at low catalyst and the generation of Cu(2)-ligand that lead to the passivation of the reaction, then 7% catalyst was used in the next experiments. Initiator content of 4%, 2%, 1%, 0.5% were studied and results are shown in Fig.3. It can found that the increment of initiator results in faster polymerization rate. However, at the point of 4%, the induction time became longer, which is attributed to the more activity centers were appeared and results in more time to obtain the same molecular weight. As a result, initiator of 1% was used in the next experiments. Emulsifier content of 3%, 5%, 7%, 9% were investigated and the results are shown in Fig.4. It can be figured out that emulsifier of 5% got the highest polymerization rate. This can be ascribed to the increased emulsifier resulted smaller particle size, which creates more particles and turn out to be faster polymerization rate. Thus 5% emulsifier was chosen as the best emulsifier content.

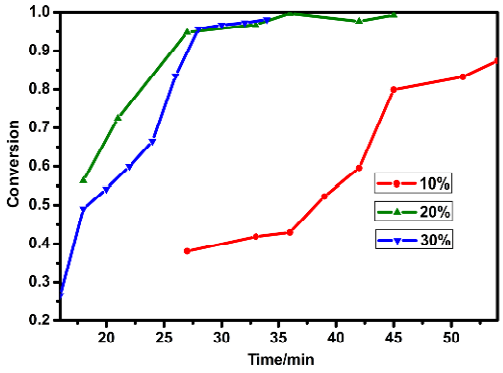

Fig. 1 Solid content vs the conversion

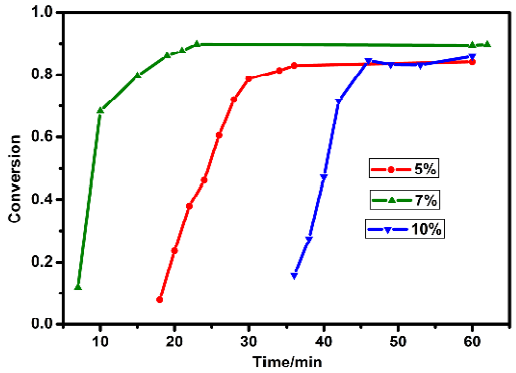

Fig. 2 The amount of catalyst vs the conversion

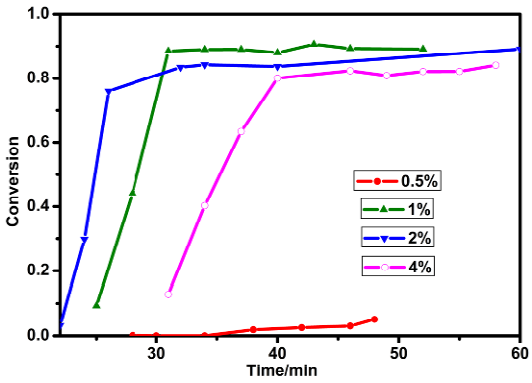

Fig. 3 The amount of initiator vs the conversion

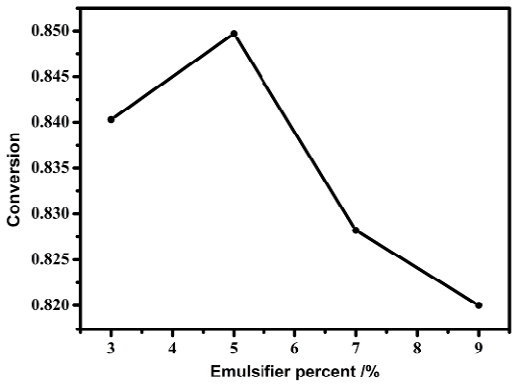

Fig. 4 The amount of emulfisier vs the conversion

FT-IR. FT-IR spectras of PAMA-co-PHBA, SHPU, and UV cured film are shown in Fig.5. It can be noted that 3060 cm^{-1} and 1654 cm^{-1} are attributed to ally hydrogen characteristic absorption peaks. 1295 cm^{-1}, 974 cm^{-1}, 745 cm^{-1}, 682 cm^{-1} were due to the C-F absorption peaks. In the spectra of SHPU, 1738 cm^{-1} was ascribed to carbonate vibration absorption and 2570 cm^{-1} was due to the thiol characteristic absorption. As expect, in the spectra of UV cured film, absorption of ally at 3060 $cm^{-1}$and thiol characteristic absorption at 2570 cm^{-1} was disappeared and the C-F absorption peaks were retained, which confirmed the thiol-ene photopolymerization between SET emulsion of PAMA-co-PHFBA and SHPU.

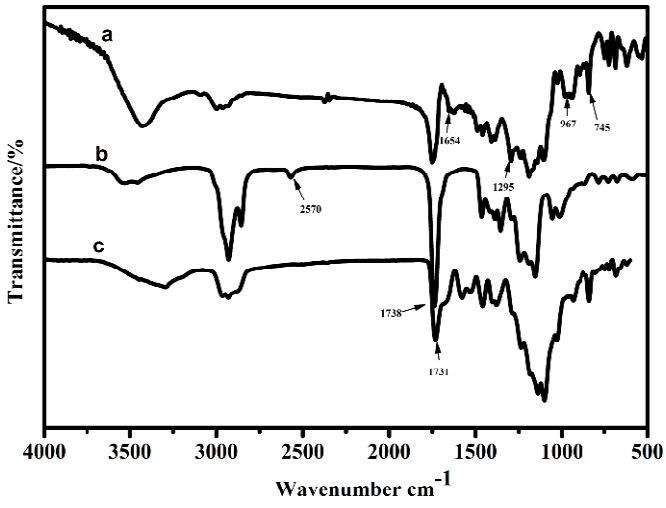

Fig. 5 FT-IR of a: PAMA-co-PHFBA, b: SHPU, c: UV cured film

Properties of UV cured films. Results of mechanical properties, gel rate and contact angle of UV cured polymer films are shown in Table 1. The gel rate of the films was inversely to the thiol and double bond ratio, which may be due to the high degree of crosslink between SHPU and PAMA-co-PHFBA when the double bond component was increased. In addition, pendulum hardness of film was also increase with the content of SET emulsion since PAMA-co-PHFBA was belongs to hard segment. Elongation at break and fracture deformation was increase followed by a little decline when thiol and double bond ratio increase, which may be attributed to the fact that SHPU was soft segment in UV curing films. The more composition of SHPU, the more flexible of the film was. As a result, tensile strength and elongation at break was increased. However, when SHPU was increased, the crosslink between thiol and double bond was saturated and the thiol residues was remained thus may impair the flexible of the final UV curing films. Contact angle of the UV curing films was decreased as thiol and double bond ratio increase, which can be ascribed to low surface energy fluorine atom in the PHFBA that can act as hydrophobic role in this UV curing films.

Table 1 Properties of UV cured polymers

Entry	1	2	3	4	5
Gel rate [%]	80.98	77.69	70.58	67.69	68.64
Pendulum hardness [s]	7.0	5.6	4.62	4.2	4.2
Elongation at break [%]	24.8	47.2	79.6	70	52.9
Fracture deformation [mm]	9.94	18.86	31.83	28.02	21.15
Contact angle [°]	83	81	80	78	75

Conclusions

SET emulsion polymerization of AMA coupled with HFBA were investigated in the presence of Cu(0)/PMDETA as catalyst and EBiB as initiator. Solid content of 20%, catalyst of 7%, initiator of 1% and emulsifier of 5% to the total monomer molar ratio was found to be the optimal reaction condition. And then the fluorated crosslink film were prepared under UV, Mechanical properties and contact angle of the UV cured films were investigated.

Acknowledgements

This work was supported by Science Funds of Education Office of Jiangxi Province (GJJ13575), the Youth Science Funds of Jiangxi Province (20122BAB213010), the Project of Jiangxi Youth Scientist (2011BCB23018) and the seventh University Student's Pioneering Work, Scientific Research Fund Project of Jiangxi Science and Normal University.

References

[1] M Kamigaito, T Ando, M Sawamoto. Chem. Rev. Vol. 101(2001), p.3689.
[2] V Percec, T Guliashvili, J S Ladislaw, A Wistrand, A Stjerndahl, M J Sienkowska, M J Monteiro, and S Sahoo. J. Am. Chem. Soc. Vol. 128(2006), p. 14156.
[3] N H Nguyen, B M Rosen, G Lligadas, V Percec. Macromolecules Vol. 42(2009), p.2379.
[4] B M Rosen, V Percec. J. Polym. Sci., Part A: Polym. Chem. Vol. 45(2007), p.4950.
[5] M J Monteiro, T Guliashvili, V Percec. J. Polym. Sci., Part A: Polym. Chem. Vol. 45(2007), p.1835.

[6] N H Nguyen, J Kulis, H J Sun, Z Jia, B Beusekom, M E Levere, D A Wilson, M J Monteiro, V Percec. Polym. Chem. Vol. 4(2013), p.144.
[7] N H Nguyen, B M Rosen, V Percec. J. Polym. Sci., Polym. Chem. Vol. 48(2010), p.1752.
[8] G Lligadas, V Percec. J. Polym. Sci., Polym. Chem. Vol. 46(2008), p.2745.
[9] N H Nguyen, B M Rosen, X Jiang, S Fleischmann, V Percec. J. Polym. Sci., Polym. Chem. Vol. 47(2009), p.5577.
[10] C Q Fu, H B Liu, Z Chen, C J Cheng, L Shen. Polyurethane Industry. Vol. 27(2012), p.5.

Advanced Materials Research Vols. 960-961 (2014) pp 143-147

doi:10.4028/www.scientific.net/AMR.960-961.143

The Effects of Magnetic Field on Micro-arc Oxidation Ceramic Coating on Magnesium Alloys

Jun Zhao[1, a], Jian Jun Xi[2,b]， ZhiGang Wang [3,c], Chun Ping Zhao[1,d]

[1]China and Russian Company of Harbin Institute of Technology, Harbin 150001, China

[2]Institute of Mechanical and Electrical Engineering, Harbin Institute of Technology, Harbin 150001, China

[3]Harbin Chenergy Hit Environmental Technology Co.LTD. Harbin 150001, China

[a]hit_zhaojun@163.com, [b]xjj63@163.com, [c]zgwang999@163.com, [d]13304512078@163.com

Keywords: Micro arc oxidation; Magnetism; Magnetic Field; Performance;

Abstract. Ceramic coatings were prepared on ZM5 magnetism substrate by micro-arc oxidation method with and without magnetism filed in silicate electrolyte. The morphology of the MAO coatings was investigated by scanning electron microscope (SEM). The friction coefficient of the MAO coatings prepared with magnetism is about 0.2 and more stable than the coatings prepared without magnetism. The polarization test indicated that the coating prepared with magnetism has better corrosion resistance.

Introduction

Micro-arc oxidation (MAO) is a complex thermo-chemical, electrochemical and plasma chemical process with combining concurrent partial processes of oxide film formation, dissolution and dielectric breakdown [1-3]. It is a new surface treatment technique developed from tradition anodic oxidation for aluminum, magnesium and titanium and their alloys to improve the performance of were resistant, corrosion, high temperature resistant and so on [4-6]. In recent years, vast investigations have studied on composition and concentration of electrolyte, oxidation time, electric parameters and it is with good performance of silicate solutions as environmental friendly electrolyte [7, 8]. Magnetic has the ability to increase the Lorentz force to affect particles in the electrolyte to move regularly [9, 10]. So this article is to investigate the MAO ceramic coatings performance with and without magnetism acting on both sides of the samples.

Experimental

A schematic of the experimental set-up used in this work is shown in Fig.1 (1-MAO power supply, 2-cyclied cooling water, 3-work sample, 4-electrolyte, 5- magnesium field, 6-insulate bracket). Samples made from a ZM5 magnesium alloy, which chemical composition is: 5.7% Al, 0.9% Zn, Fe, Si<0.01%, plus a small amount of rare metals with total surface area of 0.3dm^2. The samples were mechanically polished with waterproof abrasive paper up to 600 grits prior to micro-arc oxidation. The aqueous solution consists of 10g/l Na_2SiO_3 and adjusts pH to 10.5. An average current density of 1A/dm^2 was maintained on the surface with a frequency of 1200Hz and the duty of 10%. The oxidation process was conducted for 90min and electrolyte temperature for less than 40℃.

The surface morphologies of the oxide coatings were characterized by scanning electron microscopy (SEM, S2570). Friction and wear test was done on ceramic coatings produced by MAO with and without magnesium with CJS111B friction wear testing machine made by HIT. The relative grinding object is Si3N4 alloy with relative sliding speed of 0.377m/s and load of 1N. Friction coefficient is known directly on the testing machine. Potentiodynamic polarization was used to investigate the protective properties of the composite coatings and MAO film with CHI 660D at scan rate of 1mV/s in 3.5% NaCl solution.

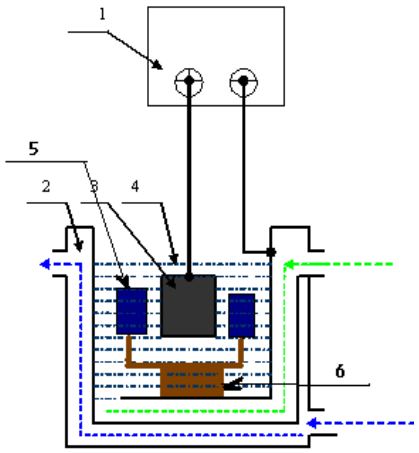

Fig.1 Typical arrangement of the equipment used for MAO treatment

Discussion

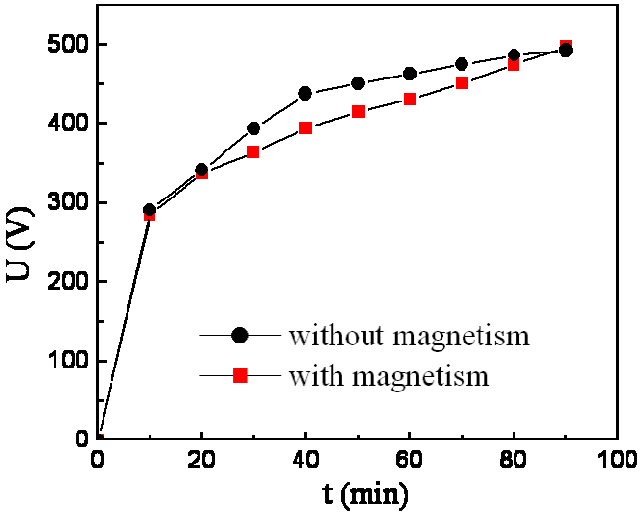

Fig.2 Voltage-time curves of MAO coatings progress

Fig.2 shows the voltage-time curves of ceramic coatings made with and without magnetism. From the picture it can be seen that the line with magnetism is smooth with voltage rising after 20min MAO course. This means as the increase of micro-arc oxidation time, conductive ions move intense disordered. The magnetism can lower the disordered movement of ions of the electrolyte but didn't affect the final voltage deeply. After 90min micro arc oxidation, the voltage without magnetism is 497V and with magnetism is 493V.

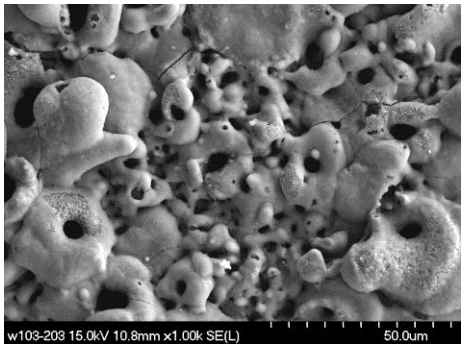

a) With magnesium×1000

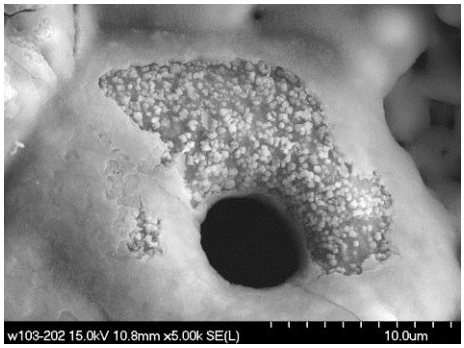

b) With magnesium×5000

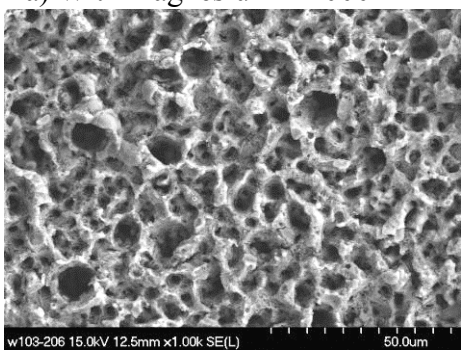

c) Without magnesium×1000

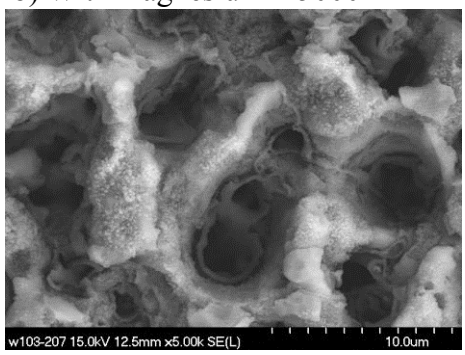

d) Without magnesium×5000

Fig.3 SEM images showing the surface morphology of MAO coatings prepared with and without magnetism

Fig.3 shows the picture of the surface morphologies of MAO coating prepared with and without magnetism. As can be seen in the picture, the ceramic coatings made with magnetism has lower porosity with a dense and flat outside layer and small particle as the inner layer. Compared to the magnetism sample, the samples without magnetism has relatively big pore as the net layer. So the magnetism has the ability to promote the good growth of ceramic coatings.

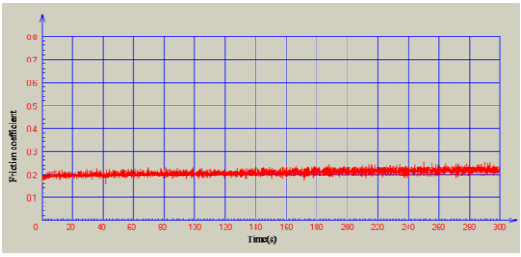

a) With magnesium

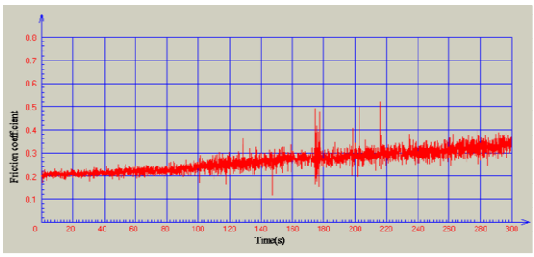

b) Without magnesium

Fig.4 Friction and wear testing of MAO coatings prepared with and without magnetism

Fig.4 shows the friction-wear tests of MAO coatings with and without magnetism field. Compared to the coatings without magnesium, the friction coefficient of MAO coatings prepared with magnesium is smaller and stable. According to SEM of the MAO structure, the coefficient is not a constant value due to the heterogeneous and inconsistency phases.

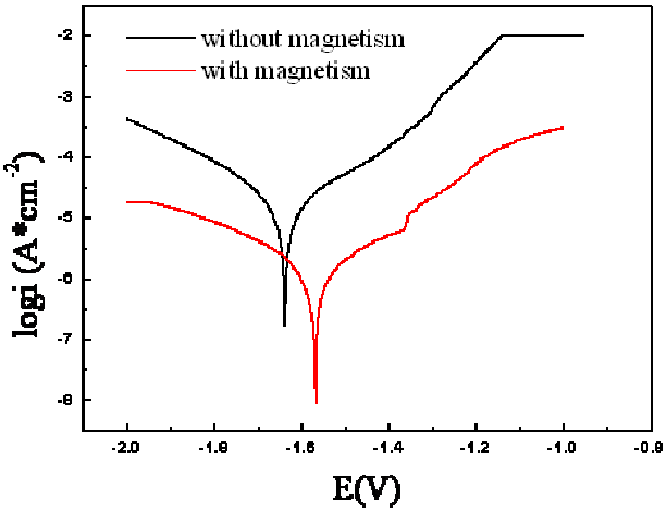

Fig.5 Potentiodynamic polarization curves of MAO films with different conditions

Fig.5 is the potentiodynamic polarization curves of MAO films with and without magnetism. With the same solution and same constant current density, MAO coating with the magnetism has the corrosion resistance with lower corrosion current 1.458×10^{-6} and higher corrosion resistance 31183.9Ωcm^2.

Table 1 Parameters of potentiodynamic polarization curves of

Samlpes	E_{corr}(V)	I_{corr}(A/cm^2)	R_p(Ωcm^2)
With magnetism film	-1.5683	1.458×10^{-6}	31183.9
Without magnetism film	-1.6389	1.533×10^{-5}	2578.0

Conclusions

In summary, we have demonstrated that magnetism has effect on the performance of MAO ceramic coatings of ZM5 magnetism alloys. The coating prepared with magnetism has small pore and a dense and flat outside layer. It has a better mechanical property and anti-corrosion performance of the MAO coatings prepared added in magnetism field.

References

[1] I.J. Hwang , D.Y. Hwang , Y.G. Ko , D.H. Shin: Surface & Coatings Technology. Sci. Forum Vol. 206 (2012), p.3360–3365

[2] L.L. Shi, Y.J. Xu, K. Li, Z.P.Yao, S.Q.Wu: Current Applied Physics. Sci. Forum Vol. 10 (2010), p.719–723

[3] C.Z. Wang, D. Zhang, Y.F. Jiang: Applied Surface Science. Sci. Forum Vol. 253 (2006), p.674–678

[4] Y.W. Song, K.H. Dong, D.Y. Shan, E.H. Han: Journal of Magnesium and Alloys. Sci. Forum Vol. 1 (2013), p. 82-87

[5] E. E. Demirci , E. Arslan, K.V. Ezirmik, Ö. Baran, Y. Totik, İ. Efeoglu: Thin Solid Films. Sci. Forum Vol. 528 (2013), p.116–122

[6] D.V. Renaux, E. Rocca, G. Henrion: Electrochemistry Communications. Sci. Forum Vol. 31 (2013), p. 42–45

[7] S. LU, Z.X.Wang, J.Chen, X.S.Zhou: Transactions of Nonferrous Metals Society of China. Sci. Forum Vol. 21(2011), p. 929-935
[8] F. Jin, P. K. Chu, G.D. Xu, J. Zhao, D.L. Tang, H.H: Materials Science and Engineering A. Sci. Forum Vol. 435–436 (2006), p. 123–126
[9] C. Wang, Y.B. Zhong , W.L. Ren, Z.S. Lei, Z.M. Ren, J. Jia, A.R. Jiang: Applied Surface Science. Sci. Forum Vol. 254 (2008), p. 5649–5654
[10] L. Wang, F. He, Y.Z. Wan: Journal of Alloys and Compounds. Sci. Forum Vol. 509 (2011), p. 4726–4730

Advanced Materials Research Vols. 960-961 (2014) pp 148-151

doi:10.4028/www.scientific.net/AMR.960-961.148

Preparation and Properties of Organosilicon-Modified Epoxy Esters Resin

Xiaojun Hu[1, a]; Yanan Chen[1,b]; Qing Bian[1,c]; Ming Chen[2,d] ; Wen Qin[1,e]; Jing Feng[3,a]

[1]Key Lab. of Regional Environment and Eco-Remediation(Ministry of Education), Shenyang University, Shenyang, 110044, China

[2]Beijing Jinhweili Applied Chemical Products Co., Ltd. Beijing，100036，China

[3]College of Computer Science and Technology, Shenyang University of Chemical Technology, Shenyang, Liaoning, 110142, China

[a]Hu-xj@mail.tsinghua.edu.cn, [b.c]cyntmac@163.com, [d,e]chenmab@126.com,

Keywords: Organosilicon; epoxy esters resin; silane coupling agent; solution polymerization

Abstract. Organosilicon-modified epoxy esters resin was successfully prepared by solution polymerization and the effect of content of silica sol and silane coupling agent (KH560) on the resistance to water, acid, alkali and film dry, the polymerization mechanism, structure were studied, respectively. The results showed that: compared with the properties of resistance to water, acid, alkali and film dry of pure epoxy esters resin, to some extent, those of organosilicon-modified epoxy esters resin had been improved a lot. The properties of resistance to water, acid, alkali and aging increased at first and then changed little with the increase of the content of organosilicon. Especially, the comprehensive performance of composite resin was relatively excellent when the content of silica sol and KH560 was 10%, respectively.

Introduction

As a new type of high performance coatings, epoxy esters resin coating have developed rapidly in recent decades. However, pure epoxy esters resin has some defects, for example, it exists high viscosity , poor coating.These cause bad properties of acid resistance ,alkali resistance and aging resistance, its application range is also limited [1-3].

After modified by organosilicon, epoxy esters resin contained Si-O-Si bonds, Si-C bonds, the bond energy of Si-O bonds can be greater than the C-O. It could effectively solve the epoxy esters resin coating and silicon sol coating defects, achieving the complementary advantages in the performance [4-8].In addition, the weatherability of organosilicon modified epoxy esters resin coatings can be comparable to those containing fluorine resin coating, but its cost is only one third of the fluoride resin coating. So organosilicon modified epoxy esters resin has become one of hot research topic in the field of coatings.

Experiment

2.1 Experimental raw materials and equipment

Epoxy resin,Oleic acid,Zinc oxide, maleic anhydride, triphenylphosphine ,ethanol：Sinopharm Chemical Reagent Co. ,Lt d, KH560: Nanjing nengde chemical Co., Ltd , Hydrochloric acid: Shenyang economic development zone reagent factory, Deionized water: homemade, Digital display temperature control electric heating; motor stirrer, Four flask, Constant pressure drop funnel. Straight type reflux condenser pipe, Electronic balance, beakers, etc.

2.2 Preparation

According to the proportion of the molar ratio of TEOS: anhydrous ethanol: water 1:5:3 to put into four flask with hydrochloric acid to adjust pH between 2~4, insulation 6 h under 50~60℃. KH560 was dropped according to 1molTEOS/0.2mol KH560 ratio after the reaction, and then keep the temperature between 50~60℃ 6h reaction, at last modified silica sol was achieved.The fatty acids was added to the molten, hot resin, and the esterification reaction was continued. The esterification was carried out at high temperatures (220 to 240℃),until the acid number is low, usually less than 5mg of KOH per gram of resin. Cool to 110℃to maleic anhydride and dripped silica sol into it，tir and heat preservation 2~3h in 100~110 ℃ in order to make fully react. In the end, organosilicon-modified epoxy esters composite resin had been prepared.

3.1 Synthetic process and mechanism analysis of organosilicon modified epoxy esters resin

Ethyl orthosilicate (TEOS) reaction in acidic system is placid and easy to control, and silicon alkoxide groups can exist stably in acid solution, the stability could be improved in this way. Therefore, modified silica sol was prepared under acid condition.

The silane coupling agent KH560 could hydrolyze in a certain degree Under the same principle, and produced R_1-Si$(OCH_3)_2$(OH), R1-Si$(OCH_3)$$(OH)_2$ and R_1-Si$(OH)_3$ (R_1=CH_2=C(CH_3)-COO$(CH_2)_3$), eventually converted into R1-Si$(OH)_3$. At the same time of hydrolysis reaction, polycondensation among hydrolysis product of TEOS and KH560 generated silanol and other compounds containing -Si-O-Si-bonds or cross-linked R_1-[Si-O-Si] n-R under the condition of acid catalytic. Modified silica sol was achieved eventually.

$$Si(OC_2H_5)_4+xH_2O \rightarrow Si(OC_2H_5)_{4-x}(OH)_x+xC_2H_5OH \quad (x=1,2,3,4)$$

$$R_1\text{-}Si(OCH_3)_3+xH_2O \rightarrow R_1\text{-}Si(OCH_3)_{3-x}(OH)_x+xCH_3OH \quad (x=1,2,3)$$

$$R_1\text{-}Si(OCH_3)_{3-x}(OH)_x+Si(OC_2H_5)_{4-x}(OH)_x \rightarrow R_1\text{-}[Si\text{-}O\text{-}Si]_n\text{-}O\text{-}R_{11}+H_2O$$

3.2 Structure analysis of organosilicon modified epoxy esters composite resin

The structural of organosilicon modified epoxy esters composite resin was characterized by using Fourier infrared spectrum. Fig.1 showed the infrared spectrogram of epoxy esters resin and organosilicon modified epoxy esters resin. 770$cm^{-1}$and 843cm^{-1} vibration absorption peaks were characteristic peak of Si-C bond, 972cm^{-1} was characteristic peak of Si-O bond, absorption peak at the near 1070 cm^{-1} was the stretching vibration characteristic peaks of Si-O-C bond in the samples,1027 cm^{-1} was characteristic peak of Si-O-Si, This suggests that the epoxy esters resin polymer containing silicone group.

From figure 1 and the above analysis, Due to the synthesis of epoxy esters resin monomer is roughly same, so the skeleton structure of organosilicon modified epoxy esters resin is similar to that of pure epoxy esters polymer, Just only vibration absorption peak intensity was different because of the introduction of organosilicon containing Si-O bonds and Si-C bonds. Thus the organic silicon have been graft copolymerization on epoxy esters polymer molecules.

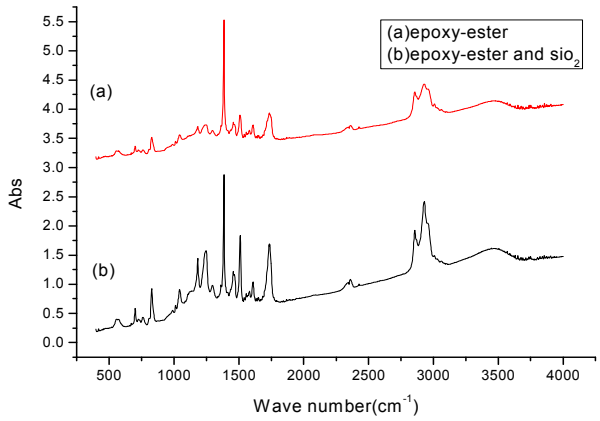

Fig. 1 The infrared spectrogram of the pure epoxy esters resin and organosilicon modified composite resin

3.3 Affect of silica sol content on the performance of composite resin coating

As is shown from tablel, Compared with pure epoxy esters resin coating, the performance of the organosilicon modified composite resin coating such as hardness, water resistance, acid resistance, alkali resistance and aging resistance had improved dramatically with the increase of silica content.

Table 1 Different silica sol content composite resin coating performance tests

Colloidal silica content	0%	5%	10%	15%
Hardness	HB	HB	HB	HB
Impact 500g cm	30	30	30	30
Water resistant 25	7h white	22h white	32h white	32h white
Acid resistant 0.05mol	9h white	15h white	48h normal	48h normal
Alkali resistant 0.1mol	3h hair bubbles	3h air bubbles	45h paint film falls off	50h paint film falls off
Film dry(h)	6	5	4	4

With the increase of organosilicon content water resistance, acid resistance, alkali resistance and aging resistance of composite resin showed a trend of first increases then changed little.Comprehensive consideration ,when colloidal silica content was 10%, the performance become better.

Conclusion

Compared with pure epoxy esters resin, water resistance, acid resistance, alkali resistance, ageing resistance, film dry and stability of organosilicon-modified epoxy esters resin had more improvement. When KH560 content remained invariant, water resistance, aging resistance and other comprehensive performance increased,but Especially, the comprehensive performance of composite resin was relatively excellent when the content of silica sol was 10%.

Acknowledgments

This research was financially supported by the National Natural Science Foundation of China (21277093, 20807029), Program for New Century Excellent Talents in University (NCET-13-0910) and the Science and Technology Program of Shenyang City of China (F13-062-2-00).

Reference

[1] L. Liu, Z. Qi, X. Zhu. Appl. Polym. Sci. 71 (7) (1999) 1133–1138

[2] Zhanguang Huang, Wenfang Shi. European Polymer Journal, 2007,43(4): 1302-1312

[3] Gaoyong Ye. Nano silicon dioxide/polyacrylate composite coating[D].Shanghai:Shanghai University,2005

[4] Wang Yan,Baoli Zhang,Zhu Ke. Coating Industry, 2000,30(10): 1-5

[5] Ahmad Dashtizadeh, Majid Abdouss, et al. Applied Surface Science,2011,257(6): 2118-2125

[6] S. Kojima, Y. Watanabe. Polym. Eng. Sci., 1993,33(5):253-259

[7] D.J. Mills, S.S. Jamali, K. Paprocka. Surface and Coatings Technology,2012,209(9): 137-142

[8] Frank Bauer, Roman Flyunt, Konstanze Czihal, et al. Progress in Organic Coatings, 2007, 60(2): 121-126

Advanced Materials Research Vols. 960-961 (2014) pp 152-156

doi:10.4028/www.scientific.net/AMR.960-961.152

Corrosion resistance of CrSiN coatings by cathodic arc deposition with different arc currents

Wei-Yu Ho*, Po-Yi Tsou, Yen-Shuo Chang, Cheng-Liang Lin

Department of Materials Science and Engineering, MingDao University, Taiwan

weiyuho@mdu.edu.tw

Keywords: Cathodic arc deposition, arc current, bipolar plate, corrosion resistance

Abstract. Recently, metallic bipolar plates, particularly different grades of stainless steels, have been increasingly considered due to excellent properties. Metallic bipolar plates are coated with protective coating layers to avoid corrosion. The corrosion behavior of the nanostructured CrSiN coatings on the stainless steel was studied to be potential application for the bipolar plate. In this study, CrSiN coating deposited by a modulated pulsed current arc process was achieved using the cathodic arc deposition process. The crystallographic structure of the CrSiN coatings does not affect with the different cathodic arc currents. The interfacial electrical resistance of CrSiN coatings deposited on AISI 304 stainless steel substrates similar with the blank substrate was confirmed. The improved corrosion behavior can be obtained by using the cathodic arc current of 90/120and 90/150 A modulated type.

Introduction

Bipolar plate with multiple functions is one of the essential components of the PEMFC (Proton Exchange Membrane Fuel Cells) stacks. Recently, metallic bipolar plates, particularly different grades of stainless steels, have been increasingly considered due to relatively low cost, good corrosion resistance, sufficient stiffness and excellent flexibility in thin forms, and easy manufacturability [1-3]. However, the major concerns with the use of stainless steel alloys as bipolar plates are their corrosion resistance and interfacial electrical resistance under long operation conditions. Development of advanced ternary nitride coatings such as chromium silicon nitride (CrSiN) has attracted significant industrial interest in recent years [4-11]. Si addition of CrN to form CrSiN films were prepared by cathode arc ion deposition technique and magnetron sputter technique, in order to improve the characterizations of the coatings from structure to corrosion behaviors. It is reported that with the additional element of Si, the hardness and corrosion resistance of the CrSiN coatings can be greatly improved compared to that of the CrN coating. A direct link between the microstructure and mechanical properties of CrSiN coatings with varying Si contents was established [8]. With increasing Si content, the structure of CrSiN coating exhibited the transformation from a columnar-grained structure to a nanocomposite structure, consisting of CrN nanocrystallites embedded in an amorphous matrix. A maximum hardness of 26.6 GPa was found for CrSiN coating with Si content of about 6.7 at.%, while that of pure CrN was 19.4 GPa [6]. Up to now, the CrSiN is yet thoroughly investigated.

The goal of this paper is to report a study on the corrosion behavior of nanostructured CrSiN coatings on the stainless steel in the H_2SO_4 solution. The cathodic arc deposition technique with deposition condition of various pulsed arc currents was conducted.

Experimental

AISI 304 stainless steel used as substrates were cleaned in acetone and then in alcohol ultrasonically for 15 min before deposition. CrSiN coatings were deposited at the temperature of 300°C using a commercial cathodic arc deposition unit. Two kinds of targets, Cr and $Cr_{0.8}Si_{0.2}$ were used as cathodic arc sources. The process is designed as CrN as an adhesive layer and then CrSiN as the top layer. Different arc currents of 90A and modulating pulsed current of a duty ratio 90/120, 90/150 A were used. The duty cycle of the modulating pulsed current of 90/120, 90/150 A was set at 1 ms. The thickness of the coatings is about 2 μm.

X-ray diffraction (XRD; model PAN analytical X'pert PRD (MRD)) with Cu Kα radiation were used to specify the existent phases and the orientation of the CrSiN coatings. The Cu Kα line at 0.15405 nm was used as the source for diffraction pattern analysis. Scanning electron microscopy (SEM; model JOEL JSM-5600) was carried out to observe the surface morphology of the various samples. Thickness was measured from SEM observation of the fractured cross-sections of coated samples. A surface roughness tester was used to measure the surface roughness of the coating and substrate surfaces. A four point probe is used to measure the resistivity of the coated samples. Polarization test was conducted to distinguish the corrosive behavior of the CrSiN coated AISI 304 stainless steel. The corrosive medium of 1M H_2SO_4 solution was used to simulate the aggressive aqueous environment. The electrode potential was scanned from −0.8 to 0.8 V at the scanning rate of 1.0 mV/s. The corroded surface was then examined by using SEM.

Results and discussion

Fig. 1 shows the cross-sections of the CrSiN coatings deposited with modulated arc currents 90/120 A. The thickness of 2 μm was obtained from the Fig. 1. It is interesting that the thickness of the coatings is not related to the modulated pulsed arc current from 90 A to 90/120 and 90/150A, but is dependent on the deposition time. It is clearly observable that the deposited CrSiN coatings were equiaxed grain instead of columnar grain structure. Fig. 2 shows surface morphologies of the SEM observation of the CrSiN coatings deposited with modulated arc currents 90/120 A. The grain size of CrSiN coating is estimated about 1 μm of nanocomposite structure which are similar with the other work, consisting of CrN nanocrystallites embedded in an amorphous matrix [8].

Fig. 3 shows the surface roughness of the CrSiN coatings deposited with different arc currents. It is found that the surface roughness of the CrSiN coating decreases from 0.3 μm to 0.1 μm with an arc current from 90 A to 90/120 and 90/150A. The reason may be from the higher mobility result that the higher arc current causes the Cr ion to arrive at the desired location, resulting in a smoother surface [12].

Fig. 4 shows the XRD patterns of the CrSiN coatings with different arc currents. The (1 1 1), (2 0 0) orientation can be clearly observed for all the deposited films, indicating a NaCl-type crystal structure. The crystallographic structure of the CrSiN coatings does not therefore affect by the different cathodic arc currents.

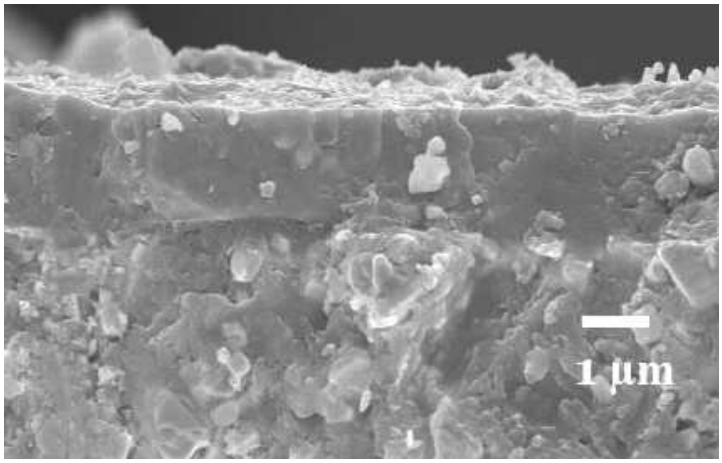

Fig. 1 Cross-section of CrSiN coatings with modulated pulsed arc currents 90/120A.

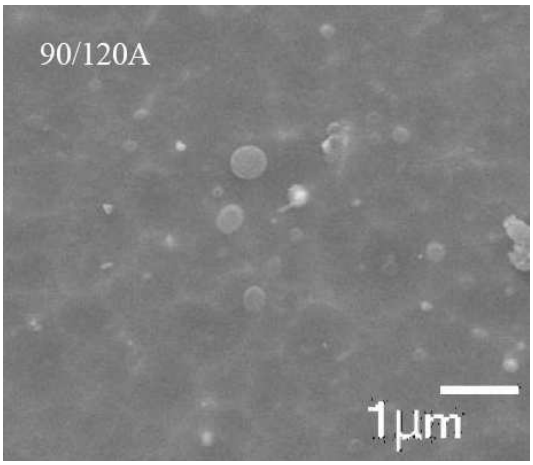

Fig. 2 SEM observation of the surface morphologies of CrSiN coatings deposited with modulated arc currents 90/120 A.

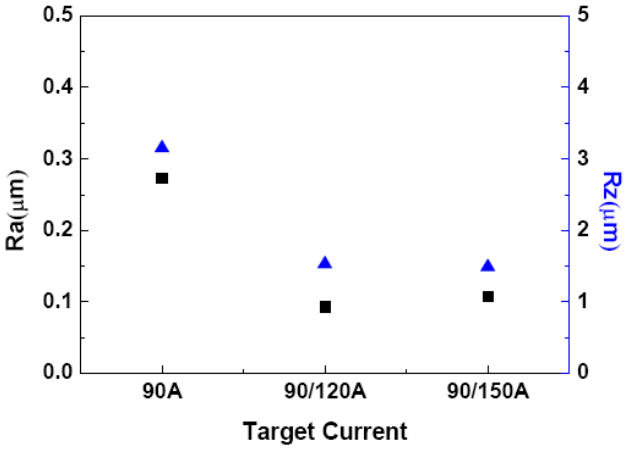

Fig. 3 Surface roughnes of CrSiN coatings with different arc currents.

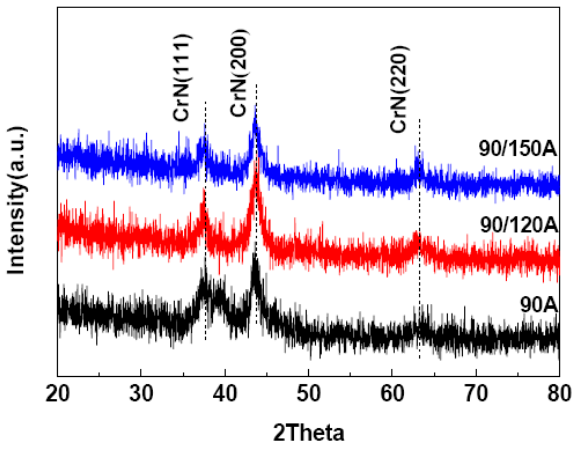

Fig. 4 XRD patterns of the deposited CrSiN coatings with different arc currents.

The interfacial electrical resistances of CrSiN coatings deposited on the AISI 304 substrates are examined by four-point probe measurement (Fig. 5). The CrSiN coatings are conductive and adhere to the base metal without exposing the substrate. The similar interfacial electrical resistance values of 2 $m\Omega.cm^2$ is observed for the CrSiN coating deposited at the different arc currents in this study. Generally, the CrSiN coatings have an average electrical resistance similar with the stainless steel substrate indicating electrical resistance low enough to meet the requirement of the bipolar plate for PEMFCs [13].

Polarization tests were carried out using 1M H_2SO_4 solution at room temperature. The polarization curves ($E_{corr.}$ vs. $I_{corr.}$) of CrSiN coated AISI 304 stainless steels are shown in Fig. 6. Compared with the blank stainless steel sample, the CrSiN coated specimens had evidently higher $E_{corr.}$ value. In particular, the film treated by 90/120 and 90/150 A showed a clear increase in $E_{corr.}$ value. A higher value implies that a stable electrode potential has been achieved, indicating an improvement in the corrosion resistance of the coated AISI 304 stainless steel. In addition, I_{corr} commonly utilized as an index of corrosion rate is determined by the extrapolation of cathodic Tafel lines. In this study, a significantly reduced I_{corr} was observed for the coatings with CrSiN deposition treated by 90/120 and 90/150 A. The treated specimens had an evident enhancement on the corrosion resistance as compared to the blank stainless steel and the one coated at 90A. It is expected that modulated pulsed arc current causes the reduction of defects in the coatings. A better corrosion resistance of the CrSiN coated AISI 304 stainless steel obtained by using the cathodic arc current of 90/120and 90/150 A is the potential application for the bipolar plate.

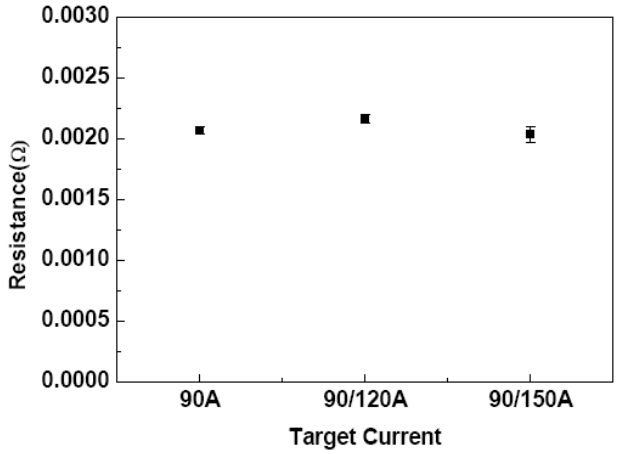

Fig. 5 Interfacial electrical resistances of CrSiN coatings deposited with different arc currents.

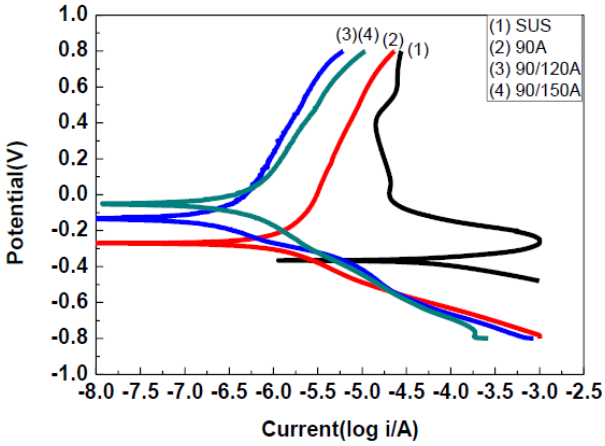

Fig. 6 Potentiodynamic curves for CrSiN coated stainless steel in 1M H_2SO_4 solution at room temperature.

Conclusions

CrSiN coating deposited by a modulated pulsed current arc process was achieved using the cathodic arc deposition process. The crystallographic structure of the CrSiN coatings does not affect with the different cathodic arc currents. The interfacial electrical resistance of CrSiN coatings deposited on AISI 304 stainless steel substrates similar with the blank substrate was confirmed. The improved corrosion behavior can be obtained by using the cathodic arc current of 90/120and 90/150 A modulated type.

Acknowledgement

Funding for this work was provided by the National Science Council, Taiwan, under contact no. NSC 102-2221-E-451 -002.

References

[1] D.P. Davies, P.L. Adcock, M. Turpin, S.J. Rowen, J Power Sources 86 (2000) 237.

[2] Dongming Zhang, Liangtao Duan, Lu Guo, Zaiyi Wang, Jun Zhao, Wei-Hsing Tuan, Koichi Niihar, Int. J Hydrogen Energy, 36 (2011) 9155.

[3] Cabir Turan, Ömer Necati Cora, Muammer Koc, Int. J Hydrogen Energy, 36 (2011) 12370.

[4] Y.H. Yoo, J.H. Hong, J.G. Kim, H.Y. Lee, J.G. Han, Surf. Coat. Technol. 201 (2007) 9518.

[5] Sang-Yul Lee, Yeh-Sun Hong, Surf. Coat. Technol. 202 (2007) 1129.

[6] E. Bousser, M. Benkahoul, L. Martinu, J.E. Klemberg-Sapieha, Surf. Coat. Technol. 203 (2008) 776.

[7] M. Azzi, M. Benkahoul, J.A. Szpunar, J.E. Klemberg-Sapieha, L. Martinu, Wear 267 (2009) 882.

[8] P.C. Wo, P.R. Munroe, Z. Li, Z.-T. Jiang, Z.H. Xie, Z.F. Zhou, K.Y. Li, Mater. Sci. Eng. A 534 (2012) 297.

[9] Hetal N. Shah, R. Jayaganthan, Avinash C. Pandey, Materi. Design 32 (2011) 2628.

[10] Jianliang Lin, Bo Wang, Yixiang Ou, William D. Sproul, Isaac Dahan, John J. Moore, Surf. Coat. Technol. 216 (2013) 251.

[11] Shaojian Yan, Tongcheng Fu, Ruyi Wang, Canxin Tian, Zesong Wang, Zhihong Huang, Bing Yang, Dejun Fu, Nuclear Instruments and Methods in Physics Research B 307 (2013) 143.

[12] Min-Hang Weng, Cheng-Tang Pan, Ru-Yuan Yang, Chun-Chih Huang, Ceramics International 37 (2011) 3077.

[13] Antunes R, Oliveira M, Ett G, Ett V., Int J Hydrogen Energy 35 (2010)3632.

Advanced Materials Research Vols. 960-961 (2014) pp 157-160

doi:10.4028/www.scientific.net/AMR.960-961.157

Synthesize of Mesoporous ZnO Thin Films and Gas Sensing Property

Min-Hee Hong[a], Yong-June Choi[b], Tae-Won Lee[c],
Hee Yoon Chung[d] and Hyung-Ho Park[e]

Department of Materials Science and Engineering, Yonsei University, Seoul 120-749, Republic of Korea

[a]minhee_hong@yonsei.ac.kr, [b]yongjune_choi@yonsei.ac.kr, [c]lvm1983@yonsei.ac.kr,
[d]hychung@yonsei.ac.kr, [e]hhpark@yonsei.ac.kr

Keywords: Zinc Oxide, Mesoporous structure, Sol-gel process, EISA process, pH value

Abstract. In this work, ordered mesoporous ZnO thin films was synthesized and gas sensor properties were introduced. Mesoporous ZnO thin films were successfully formed by sol-gel process. In ZnO structure, complex agent (MEA) was used for the hydration and condensation reaction. According to the change of MEA concentration, porosity and pore arrangement, specific surface area could be changed. As complex agent concentration decreased, pore ordering was increased and gas sensitivity has the high value (8.01).

Introduction

Mesoporous structures have pores with size ranging from 2 to 50 nm [1]. This pore structure causes low thermal conductivity, high specific surface area, and so on. Mesoporous structure could be used in gas sensor applications and thermoelectric devices, among many other applications. Metal oxide semiconductor gas sensor has merit due to their low cost and high sensitivity. Among many metal oxide semiconductors, zinc oxide (ZnO) was widely used for gas sensor application [2]. ZnO is an inexpensive, n-type semiconductor and it has been researched such as laser, thermoelectric, and gas sensor applications. ZnO thin films could be synthesized by RF sputtering, chemical vapor deposition (CVD), sol-gel process [3-5], and so on. In this work, sol-gel process was chosen because sol-gel process could be easily controlled the film thickness and composition. And, evaporation-induced self-assembly (EISA) process was progressed to synthesize ordered pore structure. In this paper, we investigated the effect of the molar ratio of MEA/Zn precursors on the formation of mesoporous ZnO thin films. Monoethanolamine (MEA) acts sol stabilizer and control pH value and viscosity. Because sol stability and pH could affect ZnO structure, pore arrangement and porosity could be affected by MEA addition. In this work, crystallization, pore structure, porosity, and gas sensing properties of mesoporous ZnO thin films were analyzed.

Experimental

Mesoporous ZnO thin films were synthesized by using sol-gel process. Zinc acetate dihydrate [$Zn(CH_3COO)_2 \cdot H_2O$], Brij-76, and n-propanol were used as ZnO precursor, surfactant, and solvent, respectively. MEA was used as complex agent that acts a ZnO sol stabilizer and pH controller. Addition of MEA to ZnO sol causes the ZnO matrix to adopt a rigid structure. So, because mesoporous structure could be changed by MEA addition, molar ratio of MEA/Zn precursors was changed from 0.8 to 1.2. In this work, the molar ratio of zinc acetate dihydrate : Brij-76 : MEA : n-propanol was 1: 0.05 : 0.8~1.2 : 34.5. MEA/Zn precursors molar ratios were 0.8, 1.0, and 1.2, which were indexed as MEA(0.8), MEA(1.0), and MEA(1.2), respectively.

Brij-76 was dissolved in n-propanol for solution preparation. After stirring for 1 hour, Zinc acetate dihydrate and MEA were added to the solution. The mixed solution was aged for 24 hours at room temperature to get stable solution. Mesoporous ZnO thin films were prepared by spin coating on SiO_2/Si substrate through the evaporation-induced self-assembly (EISA) process [6, 7]. After coating, thin films were preheated at 300°C for 10 min to pyrolysis of ZnO precursor and remove residual organics. After anneal at 450°C for 4 h under vacuum, mesoporous ZnO thin films were synthesized.

Pore arrangement could be confirmed by using small angle X-ray diffraction (SAXRD). SAXRD was performed with angles ranging from 1° to 5° using CuKα radiation (1.5418 Å). The refractive indices of mesoporous ZnO thin films were obtained by using an ellipsometer (Gatan L117 C, 632.8 nm He–Ne laser). Based on these refractive indices, the porosities were calculated using the Lorentz-Lorenz equation [8]. A gas sensor for sensing CO gas was fabricated using a SiO_2/Si substrate with 200 nm thick of Pt interdigitated electrodes (IDE) which electrode gap of 5 μm. IDE patterns were fabricated using photolithography and dry etching. The responses of the fabricated gas sensors to CO gas were measured at 350 °C by monitoring in change of sensor resistances with 100 ppm CO gas which was balanced with dry air. To eliminate interfering effects, a constant flow rate of 1000 sccm for dry air and the CO gas were used. Film resistance was measured under a DC bias voltage of 3 V using a source measurement unit (Keithley 2635A).

Results and discussion

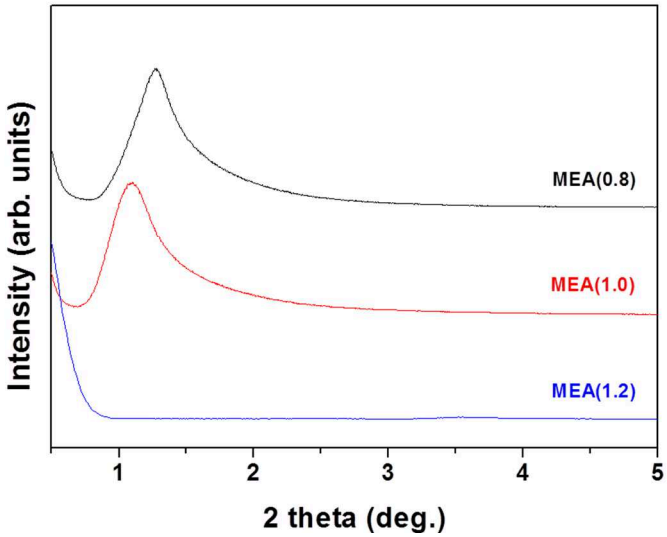

Fig. 1. SAXRD patterns of mesoporous ZnO thin films with various MEA/Zn concentrations.

Fig. 1 shows the SAXRD patterns of mesoporous ZnO thin films with various MEA/Zn precursor molar ratios. At SAXRD results, existence of diffraction peaks indicates a regular pore arrangement. As shown at Fig. 1, SAXRD peaks were observed at MEA (0.8) and MEA (1.0). However, in the case of MEA (1.2) sample, diffraction peak was not observed because ordered pore structure was collapsed. From the diffraction 2θ data, we confirmed that MEA concentration could affect regular pore arrangement. Because MEA has amine ligand and high viscosity, pH and sol viscosity were increased with MEA concentration. When MEA was added in excess, sol stability was decreased because hydration and condensation reaction rate was affected by pH value. It could affect pore structure arrangement, no diffraction peak was observed at MEA(1.2). Diffraction peaks were observed around 1.1 and 1.26° of 2θ for MEA (0.8) and MEA (1.0). From diffraction peaks, inter-planar distances were calculated as 8.03 and 7.01 nm for MEA (0.8) and MEA (1.0), respectively. From the SAXRD data, pore structure of mesoporous ZnO thin films could be analyzed. Crystallization of mesoporous ZnO thin films was shown in Fig. 2 of wide angle X-ray diffraction (WAXRD). As shown at Fig. 2, all mesoporous ZnO thin films have hexagonal wurtzite structure which diffraction peaks at 2θ of approximately 31.8°, 33.4°, and 36.2°. These WAXRD peaks could be indexed as (100), (002), and (101), respectively. Comparison of diffraction peak position and intensity, all samples has same crystallization although MEA concentrations affect pore arrangement.

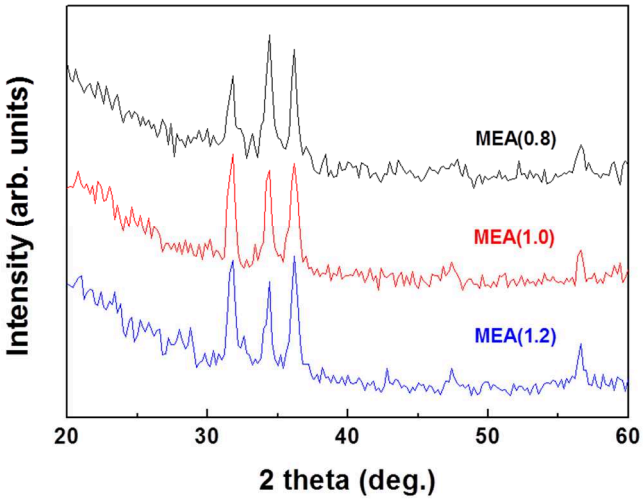

Fig. 2. WAXRD patterns of mesoporous ZnO thin films with various MEA/Zn concentrations.

$$1 - F_p = \frac{\frac{nf^2-1}{nf^2+2}}{\frac{na^2-1}{na^2+2}} \quad (1)$$

Fig. 3 shows the porosity behavior of mesoporous ZnO thin films with various MEA concentrations. Porosity was calculated by Lorentz-Lorenz equation (Eq. 1) where F_p is the pore volume fraction, n_f is the refractive index of the film, and n_a is the refractive index of air.

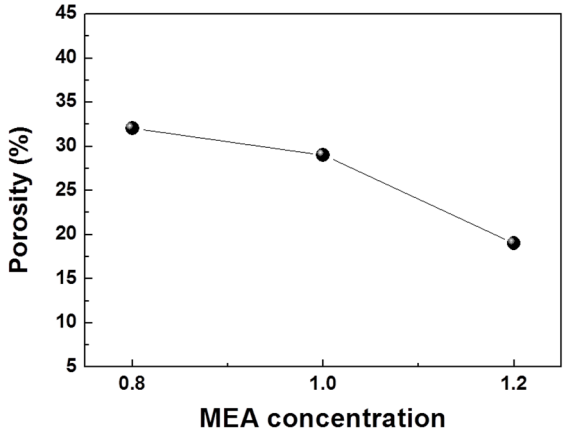

Fig. 3. Porosity behavior of mesoporous ZnO thin films with various MEA/Zn concentrations.

As shown at Fig. 3, porosity was decreased with increasing MEA concentration. The porpsity values of MEA (0.8) and MEA (1.0) were 32% and 29%, respectively and they were similar values. However, in the case of MEA (1.2) sample, porosity was decreased rapidly because ordered pore structure was collapsed as shown in Fig. 1. From Fig. 1 and Fig. 3, ordered mesoporous ZnO structure could be affected by an increase of MEA concentration.

Fig. 4 shows gas sensing properties of mesoporous ZnO thin films with various MEA/Zn precursors. During an exposure to 100 ppm CO at 350 °C, the sensor resistance decreased, which indicated that the ZnO thin films were n-type semiconductors. From the difference between the sensor resistance in air and the sensor resistance in CO, sensitivity of gas sensors could be calculated. Gas sensitivities of mesoporous ZnO with various MEA concentrations were 8.01, 5.64, and 4.41, respectively.

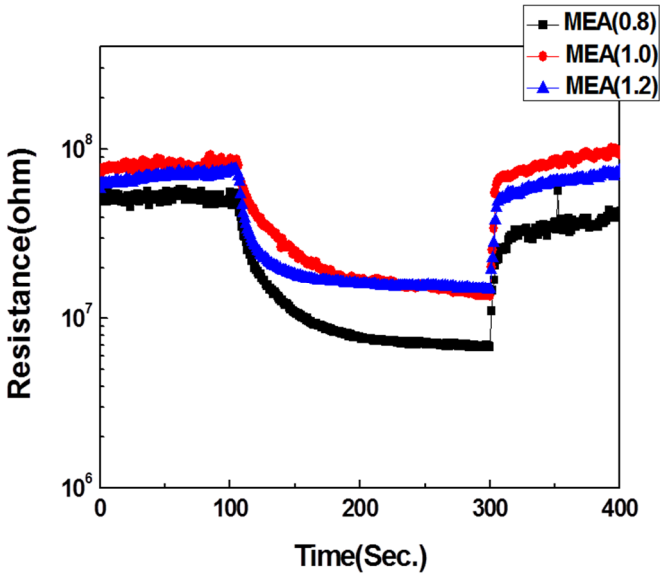

Fig. 4. Gas sensing properties of mesoporous ZnO thin films with various MEA/Zn concentrations.

As shown at Fig. 4, the sensitivity was decreased with increasing MEA concentration. The sensitivity of MEA(0.8) was higher than that of MEA(1.2) and this difference was followed by pore arrangement and porosity as MEA(0.8) has higher pore ordering and porosity.

Summary

In this work, mesoporous ZnO thin films were synthesized by using sol-gel and EISA process. Porosity of the thin films changed from 19% to 32% by adjusting the MEA/Zn precursors. Because pore arrangement and porosity were changed with MEA concentrations, specific surface area could be changed and gas sensor properties were also changed.

Acknowledgement

This work was supported by the National Research Foundation of Korea (NRF) grant funded by the Korean government (MEST) (No. 2012R1A2A2A01011014).

References.

[1] G. J. D. A. A. Soler-Illia, C. Sanchez, B. Lebeau, and J. Patarin, Chemical Reviews Vol. 102(2002) p. 4093.
[2] H. Ra, K. Choi, J. Kim, Y. Hahn, and Y. Im, Small Vol. 4(2008) p. 1105.
[3] Y.Natsume andH. Sakata, Thin Solid Films Vol. 372(2000) p. 30.
[4] M. Smirnov, C. Baban, and G. I. Rusu, Applied Surface Science Vol. 256(2010) p. 2405.
[5] T. Sahoo, M. Kim, M. Lee et al., Journal of Alloys and Compounds Vol. 491(2010) p. 308.
[6] C. J. Brinker, Y. Lu, A. Sellinger, and H. Fan, Advanced Materials Vol. 11(1999) p. 579.
[7] D. Grosso, F. Cagnol, G. J. D. A. A. Soler-Illia et al., Advanced Functional Materials Vol. 14(2004) p.309.
[8] M.R. Baklanov, K.P. Mogilnikov, Microelectronic Engineering Vol. 64 (2002) p.335.

Advanced Materials Research Vols. 960-961 (2014) pp 161-164

doi:10.4028/www.scientific.net/AMR.960-961.161

Glass forming ability and crystallization kinetics of Al-Mg-Ni-La metallic glasses

Juan Mu[1, a] and HaiFeng Zhang[2,b *]

[1] Key Laboratory for Anisotropy and Texture of Materials (MOE), Northeastern University, Shenyang 110004, China

[2] Shenyang National Laboratory for Materials Science, Institute of Metal Research, Chinese Academy of Sciences, 72 Wenhua Road, Shenyang 110016, China

[a]muj@atm.neu.edu.cn, [b]hfzhang@imr.ac.cn

Keywords: Al base alloys; glass-forming ability; thermal stability; crystallization kinetics.

Abstract. Glass forming ability and crystallization kinetics of Al-Mg-Ni-La alloys have been investigated by X-ray diffraction (XRD) and differential scanning calorimetry (DSC). The maximum thickness achievable in glasses of $Al_{76}Mg_{11}Ni_8La_5$ and $Al_{69}Mg_{18}Ni_8La_5$ ribbons were 200 and 120 μm, respectively. The crystallization temperature and peak temperature indicated by DSC measurements displayed dependence on the heating rate during continuous heating, and were coincident with Lanoka's relationship. The activation energies for the crystallization reaction E_x were obtained from the Kissinger's equation. The results show the Mg addition is beneficial to the thermal stability of the amorphous phase.

Introduction

Multi-component Al-based metallic glasses (MGs) are of significant interest as low-density and high-strength alloys. The limited glass forming ability of the present Al-based metallic glasses, however, is the bottleneck to constrain their application. Tremendous work has been devoted to pursuing the higher glass forming ability of Al-based MGs since their discovery. Up to date, most of Al-based MGs have high Al content of 85 at. % more or less [1], which is very different from that of other system MGs, in which the content of the base element is in the range of 40-60 at.% [2]. Many studies show that the poor glass forming ability of Al-based MGs is related to the easy formation of f.c.c.-Al thermodynamically and kinetically. These works shed light on improving the glass forming ability of Al-based MGs by suppressing the precipitation of f.c.c.-Al. Recently, some progresses that bulk amorphous sample with the size of 1mm was successfully prepared in the Al-Ni-La system have been made [3]. The formation of f.c.c.-Al was effectively hindered through melt treatment [4].

In other MG systems, minor alloying of the element with a large size mismatch with the base element favors stabilizing the supercooled melt and suppressing the nucleation of the crystals, which leads to the enhancement of glass forming ability[5]. Similarly, in the Al-based MGs, minor alloying is used to improve the glass forming ability and enhance the thermal stability as aforementioned. However, the effect of glass forming ability improvement is limited [6,7]. Because the Al content as high as 85 at.% leads to the nucleation ease of f.c.c.-Al in most of the present developed Al-based MGs. From this aspect, reducing the Al content is probable to restrain the precipitation of f.c.c.-Al, leading to elevating the glass forming ability. Simultaneously, the alloying element with the replacement of Al cannot increase the density of MGs. Based on such a consideration, Mg is selected as alloying element because of the low density, the negative mixing enthalpy of Al-Mg along with the large size difference between Al and Mg[8] in the present work. The glass forming ability and crystallization kinetics of Al-Mg-Ni-La alloys were investigated. It shows that MG samples can be prepared in the investigated range of Mg content and Mg addition obviously enhances the thermal stability by suppressing the formation of f.c.c.-Al.

Experimental

Intermediate alloy with the composition of $Al_{50}Mg_{50}$ (in atomic percentage, at.%) was prepared firstly using induction melting method. The ingots of $Al_{(87-x)}Mg_xNi_8La_5$ (x=11,13,15,18,20, at.%) were obtained by melting the intermediate alloy and the rest elements in a graphite crucible under high purity argon atmosphere using induction melting in order to reduce evaporation of Mg. All the raw materials have the purity more than 99.9 wt.%. Proper amount of ingots were then remelted under high vacuum in a quartz tube and injected through a nozzle with 0.5-1 mm in diameter onto surface of rotational copper wheel at different speeds to obtain ribbons with 70 to 200 μm thickness. The structure of the ribbons was examined by X-ray diffractometry (XRD; Rigaku, D/Max-2500PC, Tokyo, Japan, Cu Kα). Thermal behaviors were analyzed by differential scanning calorimetry (DSC; Netzsch DSC 204C, Germany) at different heating rates of 5, 10, 15 and 20K/min.

Results and discussion

Figure 1 shows XRD patterns of melt-spun Al-Mg-Ni-La alloys. The thicknesses of all the ribbons are about 70 μm. It can be seen that only for $Al_{76}Mg_{11}Ni_8La_5$ and $Al_{69}Mg_{18}Ni_8La_5$ alloys, broad peaks characteristic of amorphous structure and no sharp Bragg diffraction peaks corresponding to crystalline phases are observed on the patterns, indicating that the samples are fully amorphous. For the other three alloys, some sharp peaks, which are not identified in the present work, are imposed on broad peaks, meaning that the samples consist of a mixture of crystalline phase and amorphous phase. These results suggest that $Al_{76}Mg_{11}Ni_8La_5$ and $Al_{69}Mg_{18}Ni_8La_5$ alloys exhibit relatively higher glass forming ability.

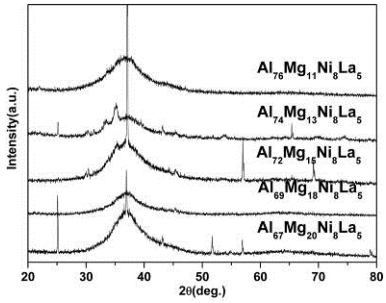

Figure 1 XRD patterns of melt-spun Al-Mg-Ni-La alloys with the thicknesses of 70 μm.

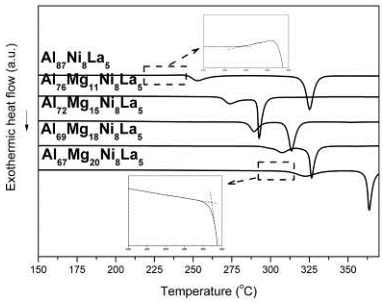

Figure 2 DSC curves of melt-spun Al-Mg-Ni-La alloys obtained at a heating rate of 20 K/min

The critical size for metallic glass formation was further examined for $Al_{76}Mg_{11}Ni_8La_5$ and $Al_{69}Mg_{18}Ni_8La_5$ alloys. For the $Al_{76}Mg_{11}Ni_8La_5$ alloy, when the sample thickness is 150μm or even 200μm, the patterns consist of only one broad diffraction peak, which shows the samples are in an amorphous state. When the sample thickness further reaches 220μm, some distinct diffraction peaks corresponding to crystalline phases are seen to appear on the XRD patterns, showing that the sample partially crystallized. This indicates that for $Al_{76}Mg_{11}Ni_8La_5$ alloy the critical thickness of glass formation is between 200 μm and 220 μm. For the $Al_{69}Mg_{18}Ni_8La_5$ alloy, it is found that the sample with a thickness of 140 μm contains some crystalline phase indicated by some sharp diffraction peaks imposed on a diffusive peak. That is to say, the critical size of the MG sample is smaller than 140 μm for this alloy. It indicates that the $Al_{76}Mg_{11}Ni_8La_5$ alloy shows a higher glass forming ability than the $Al_{69}Mg_{18}Ni_8La_5$ alloy.

Thermal properties of the investigated Al-Mg-Ni-La metallic glasses were evaluated using DSC measurements. Fig.2 shows the DSC curves obtained at a heating rate of 20 K/min. It clearly shows that the Mg addition obviously changes the thermal behaviors of the Al-based MGs. Although all the samples exhibit two-stage crystallization, the glass transition temperature (T_g) and on-set crystallization temperature (T_x) rise with the addition of Mg. With the increase of Mg content, T_g and T_x increase. It shows that Mg alloying favors thermally stabilizing the amorphous phase. The first crystallization peak on the DSC curve corresponds to the formation of f.c.c.-Al for $Al_{87}Ni_8La_5$

amorphous alloy. The rise of T_g and T_x with the Mg addition indicates that f.c.c.-Al is effectively suppressed. As aforementioned, it is beneficial to the improvement of glass forming ability. It is consistent with the results shown in Figure 1.

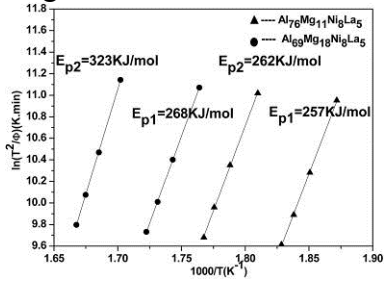

Figure 3 The Kissinger plots of crystallization peaks' temperatures for $Al_{76}Mg_{11}Ni_8La_5$ and $Al_{69}Mg_{18}Ni_8La_5$ alloys

Furthermore, the crystallization kinetics of $Al_{76}Mg_{11}Ni_8La_5$ and $Al_{69}Mg_{18}Ni_8La_5$ metallic glasses was studied. The continuous-heating DSC traces of $Al_{76}Mg_{11}Ni_8La_5$ and $Al_{69}Mg_{18}Ni_8La_5$ metallic glasses at heating rates of 5, 10, 15 and 20 K/min were tested. No clear glass transition phenomenon is observed in all DSC traces. Apparently, T_x and peak temperature T_{pi} of $Al_{69}Mg_{18}Ni_8La_5$ alloy are obviously higher than those of $Al_{76}Mg_{11}Ni_8La_5$ alloy, which indicates that the former should be more thermodynamically stable than the latter.The crystallization behavior is largely dependent on heating rate during continuous heating and presents kinetic nature. The activation energies E_x for crystallization reaction could be determined by Kissinger's equation [9],

$$\ln\frac{T^2}{\phi}=\frac{E_x}{k_BT}+C \tag{1}$$

Where k_B is Boltzmann's constant. The Kissinger plots of crystallization peaks' temperatures for $Al_{76}Mg_{11}Ni_8La_5$ and $Al_{69}Mg_{18}Ni_8La_5$ alloys are shown in Fig. 3. The E_{p1} and E_{p2} of $Al_{76}Mg_{11}Ni_8La_5$ are obtained to be 257 and 262 KJ/mol. For $Al_{69}Mg_{18}Ni_8La_5$, they are 268 and 323 KJ/mol, respectively. The E_{pi} of $Al_{76}Mg_{18}Ni_8La_5$ is higher than those of $Al_{69}Mg_{11}Ni_8La_5$, indicating that $Al_{76}Mg_{18}Ni_8La_5$ alloy has better thermal stability, which coincides with the case stated above.

As described by Inoue's three empirical rules for glass formation [10], Mg has a large size difference from Al, Ni and La, and the negative mixing enthalpy exists between them [8]. The Mg replacement of Al improves the atomic packing of the supercooled melt. The atom diffusion becomes harder in this case so that the competing crystals are difficult to form. In other words, the Mg alloying is expected to not only improve the thermal stability of the amorphous alloy, but also enhance glass formation. In the previous studies, the core-shell structure with the Al core and La-rich shell is formed when the f.c.c.-Al is formed in the Al-based metallic glass [11]. This structure shows that the atomic diffusion is needed in the process of f.c.c.-Al nucleation and growth. It is believed that the precipitated nanoscale Al crystal is the perfect one which will exclude other elements, such as Ni and La in the Al-Ni-La metallic glasses. Correspondingly, the similar process should occur upon the f.c.c.-Al formation in the Al-Mg-Ni-La system. From the Al-Mg binary phase diagram, the solubility of Mg in Al is quite small at room temperature [12]. In the precipitation of f.c.c.-Al, Mg should be rejected. Due to the high content and relatively large atomic size of Mg, this process is more difficult to occur. The higher activation energy is needed. As shown in Fig. 3, T_x is increased with the addition of Mg.

As shown in Fig. 2, without the addition of Mg, the $Al_{87}Ni_8La_5$ base alloy exhibits obvious glass transition, which is enlarged in the inset of Fig. 2. The width of supercooled region is about 30 K. With the addition of Mg, the alloys exhibit no clear glass transition phenomenon as shown by DSC traces in Fig. 2. Crystallization of metallic glasses is reported to be nucleation controlled or growth controlled. When crystallization of MGs is under growth control, the nuclei is supposed to be some small fraction of crystallization occurring initially in the rapid solidification process or atomic clusters with the size equivalent to the critical nucleation size retaining in the solidification process. In either case, once MG crystallizes upon heating, no nucleation is activated and the growth directly starts

based on the existing nuclei, which results in the coincidence of T_g and T_x. In this way, the addition of Mg changes the crystallization mechanism of the investigated Al-based MGs from the nucleation-controlled one to the grow-controlled one. As discussed above, the mixing enthalpy between Mg and Al is quite low. In the liquid state, Mg and Al tend to self-agglomerate, producing the atomic-scale chemical heterogeneities. Some Al-rich clusters with large size can serve as the nuclei in the crystallization of MGs upon heating, the further development of which is limited by the Mg-rich heterogeneities. This kind of chemical heterogeneities in the melt helps form the amorphous phase. At the same time, it helps stabilize the amorphous phase against heating, which is evidenced by the activation energy of crystallization of the present Al-Mg-Ni-La MGs higher than the base alloy. Furthermore, the atomic scale chemical heterogeneities are expected to benefit the mechanical properties of MGs, which makes Al-Mg-Ni-La metallic glasses in the present study exhibit good mechanical performance.

Conclusion

The glass forming ability, thermal properties and crystallization kinetics of Al-Mg-Ni-La MGs were investigated by using Mg partially replacing Al in the $Al_{87}Ni_8La_5$ alloy. The following conclusions can be drawn:

1. Among the investigated $Al_{87-x}Mg_xNi_8La_5$ (x=11, 13, 15, 18, 20) alloys, $Al_{76}Mg_{11}Ni_8La_5$ and $Al_{69}Mg_{18}Ni_8La_5$ have better glass forming ability. And the maximum thickness of $Al_{76}Mg_{11}Ni_8La_5$ and $Al_{69}Mg_{18}Ni_8La_5$ are 200 and 120μm.

2. The addition of Mg enhances the thermal stability though elevating the glass transition and onset crystallization temperature. The corresponding crystallization activation energies are calculated by Kissinger's plot and increases with the Mg addition. The values are 257 and 262 KJ/mol for $Al_{76}Mg_{11}Ni_8La_5$ amorphous alloy, and 268 and 323 KJ/mol for $Al_{69}Mg_{18}Ni_8La_5$ amorphous alloy.

Acknowledgement

The authors gratefully acknowledge the financial support from the Fundamental Research Funds for the Central Universities (Grant No. N120310002) and the China Postdoctoral Science Foundation (Grant No.2012M520638)

References

[1] A. Inoue, Prog. Mater. Sci. Vol.43 (1998) 365.
[2] W. Johnson, MRS Bull. Vol.24 (1999) 42.
[3] J. Mu, H. Fu, Z. Zhu, A. Wang, H. Li, Z. Hu and H. Zhang, Adv. Eng. Mater. Vol.11 (2009) 530.
[4] J. Mu, H. Fu, Z. Zhu, A. Wang, H. Li, Z. Hu and H. Zhang, Adv. Eng. Mater. Vol.12 (2010) 1127.
[5] W.H. Wang, Prog. Mater. Sci. Vol.52 (2007) 540.
[6] D. Kim and W. Kim, Mater. Sci. Eng. A Vol.385 (2004) 44.
[7] G. Li, X. Bian, K. Song, J. Guo, X. Li and C. Wang, J. Alloys Compd. Vol.471 (2009) L47.
[8] A. Takeuchi and A. Inoue, Mater. Trans. Vol.46 (2005) 2817.
[9] H. Kissinger, J. Res. Nat. Bur. Stand. Vol.57 (1956) 217.
[10] A. Inoue, T. Zhang and T. Masumoto, J. Non-Cryst. Solids Vol.156 (1993) 473.
[11] B. Radiguet, D. Blavette, N. Wanderka, J. Banhart and K. Sahoo, Appl. Phys. Lett. Vol.92 (2008) 103126.
[12] T.B. Massalski, J.L. Murray, L.H. Bennett and H. Baker, Binary Alloy Phase Diagram. (Am. Soc. Metals, Ohio, 1986).

Advanced Materials Research Vols. 960-961 (2014) pp 165-169

doi:10.4028/www.scientific.net/AMR.960-961.165

Motion Characteristics of Microbubble in Water

Kunfeng LIANG [1,a], Quanhai WANG [2,b] ,Chunlei RUAN [3,c] and Zhiwen TONG[4,d]

School of Vehicle and Motive Power Engineering

Henan University of Science and Technology

Luoyang 471003, China

[*]Corresponding author Email: liangkunf@163.com

Key words crystallization; microbubble; motion characteristics; force equilibrium

Abstract：The motion characteristics of microbubble in the water or solution have important influence to crystallization process. In the paper, the movement equation of single bubble was modeled based on force equilibrium, the mechanics factors influence on the single bubble motion were discussed, and the velocity of microbubble was analysed with the different bubble sizes. The results show that the velocity of microbubble in static water is increasing with time increasing, the influence of virtual mass force and Basset force caused by the acceleration on the velocity of microbubble must be considered in the initial stage of microbubble motion. In the processes of microbubble motion, compared with constant microbubble radius the variation laws of velocity fluctuations mean with microbubble radius changing are uniform.

Introduction

In recent years, people have made great progress in the relationship between crystallization, fluid mechanics and external factors intervention, and people have started to search all kinds of external factors to dynamically intervene crystallization process. Researches of plus ultrasonic strengthening water or solution crystallization are catching researcher's attention more and more[1-4]. Mathieu[3] studies the first nucleation process when a single bubble collapse into a plurality of microbubbles, the influence of the number of hole microbubbles on crystal nucleation in the nuclear. Therefore, there are still many hot issues in the study of ultrasonic cavitation to promote or reinforce water and solution crystallization.

As the microbubble widely exists in chemical industry, power plant, nuclear reactor, heat energy, biology, medicine and other fields, the research of motion law of microbubble has a great significance for actual production, fluid mechanics and development of multiphase. At present, the research of the bubble rising velocity, bubble distribution and gas-liquid mass transfer has been widely concerned by scholars both home and abroad. Chakraborty[5] researches on the coupling relationship of bubble radius change and upward movement, establishing the motion equation, and obtaining the influence of bubble radius change on the rising movement by numerical calculation. However researches mentioned above are still imperfect both in the influence of mechanical factors on the bubble rise process and in the influence of bubble radius change on the rising movement.

This paper researches the influence of various mechanical impact factors on the single bubble movement. The bubble velocity is discussed with the constant sizes or sizes changing by sine or sawtooth rule.

Simulation theory and Method

A. Motion control equation

1) Basical assumptions

Several simplified assumptions are adopted in the present analysis. a) Bubble keeps spherical state. b) The gas in the bubble keeps in constant temperature condition. c) The liquid keeps in stationary state.

2) Motion balance equation

Based on the above assumptions, analysis the forces of the bubble, we could obtain the motion balance equation for bubble:

$$m_b \frac{du}{dt} = F_g + F_b + F_d + F_A + F_B \tag{1}$$

Balance equations expression (1) could be rearranged as:

$$\int_0^t \frac{du/d\tau}{\sqrt{t-\tau}} d\tau = \frac{\Delta t}{2}(a(0) + 2\sum_{i=1}^{n-2} \frac{a(i\Delta t)}{\sqrt{t-i\Delta t}}) + \frac{3}{2} a(t-\Delta t)\sqrt{\Delta t} + \sqrt{\Delta t}\frac{du}{dt} \tag{2}$$

B. The calculation method of the equation

A singular point can be found from the basset force expression of the bubble motion differential equation (2), And when try to solve the differential equation, we need to deal with the generalized integral term properly. First estimate the convergence of generalized integral term, because when the acceleration of bubble is bounded, there will be a positive number $M < +\infty$, making $|du/dt| \leqq M$ establish. So according to the generalized integral limit review gathered method, this generalized integral item must be convergent.

$$\frac{du}{dt} = \frac{2(\rho_l - \rho_g)g}{\rho_l} - \frac{9u}{r}\cdot\frac{\mu}{\rho_l r}[1 + 0.168(\rho_l r u/\mu)^{0.75}] - \frac{9\sqrt{\pi\rho_l\mu}}{r\pi\rho_l}\left(\frac{\Delta t}{2}(a(0) + 2\sum_{i=1}^{n-2}\frac{a(i\Delta t)}{\sqrt{t-i\Delta t}}) + \frac{3}{2}a(t-\Delta t)\sqrt{\Delta t} + \sqrt{\Delta t}\frac{du}{dt}\right) \tag{3}$$

C. Solving method and parameter determination

In order to improve the accuracy of numerical results, the method is first to predict and second to correct, in other words it is modified Eular method. Then solve equation through the adaptive variable step size simultaneous. During solving the model, some key parameters are shown in table 1.

Table 1 Parameter determination

Parameter	Bubble density ρ_g [kg/m^3]	Water density ρ_l [kg/m^3]	Empirical coefficient K_m	Empirical coefficient K_B	Viscosity coefficient μ [Pa · s]	Radii R [m]
Value	1.29	1000	0.5	6	1.0042×10^{-3}	5×10^{-5}

Results and Analyses

A.The influence of force on the bubble rise process

Figure 1 is curve of the bubble rise velocity changing with time in the influence of force. We can see that the bubble rise velocity increases gradually with the time, and in late process bubble rising velocity tends to be stable. In the figure, black solid line expresses the curve of bubble rise velocity that considers virtual mass force and basset force , and the red dashed line expresses the curve that doesn't consider basset force. Contrast these two curves we can find that when not consider the basset force, the bubble rise velocity is bigger than that considers basset force. It makes clear that basset force not only continues to affect the movement of bubbles, but also plays the leading role. The virtual mass force on the influence of the bubble motion is very small in the late process. Meanwhile, when consider neither virtual mass force nor basset force and when just not consider virtual mass force, bubble rising velocity changes from 0 mutation to steady state velocity in the initial time.

B. The influence of particle size

1) The influence of constant particle size

Figure 2 shows bubble velocity changing with time when particle sizes are respectively taken 30μm, 50μm, 100μm, 200μm, 300μm in the rise process. From figure 2 we could see the bubble velocity is in increasing trend with time, and bubble velocity increases rapidly in the initial time. In

the late process bubble rise velocity tends to be stable. At the same time, bubbles of greater size has the greater velocity, conversely, bubbles of smaller size has the smaller velocity. In addition, the increasing trend of bubble velocity is not obvious with the increase in time when the bubble size is less than 50μm. According to figure 2, the bubble rise velocity is related directly with particle size, greater size bubble has the greater velocity. For the smaller size bubbles, for example bubble size is less than 50μm, if want to gain greater velocity, external force needs to be used.

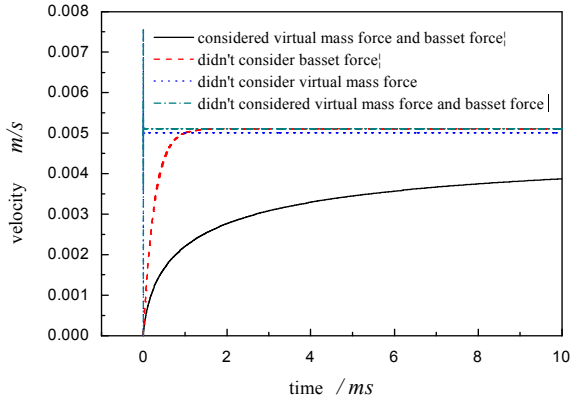

Figure 1. The influence of force during rising process

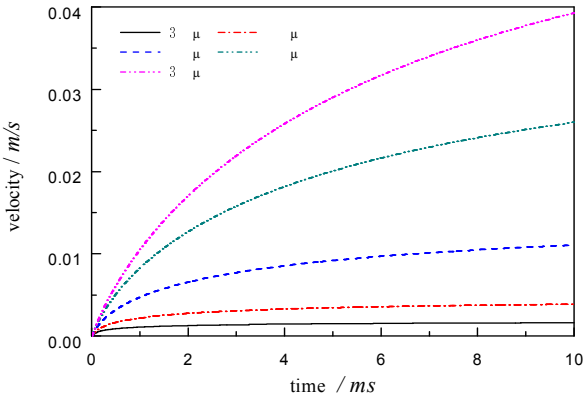

Figure 2. Velocity profile of constant size bubble

The table 2 is the experimental value and the simulation value of bubble velocity at the end of the rise motion. The experimental value could be obtained on literature[4].From table 2 we know that the changing rule of simulation value and experimental value is consistent. The error between experimental value and the simulation value is less than 8%. It demonstrates that the method proposed by this article is feasible.

Table 2 Experiment and simulation results

Item / Particle Size[μm]	experiment value [4] [m/s]	simulation value [m/s]	deviation [%]
30	0.0017	0.0016	5.9
50	0.0040	0.0039	2.5
100	0.0120	0.0111	7.5
200	0.0280	0.0260	7.1
300	0.0400	0.0393	1.7

2) The influence of changing particle size

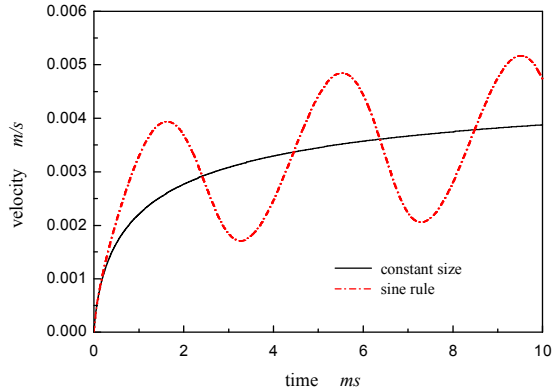

Figure 3 Velocity of bubble with sine rule

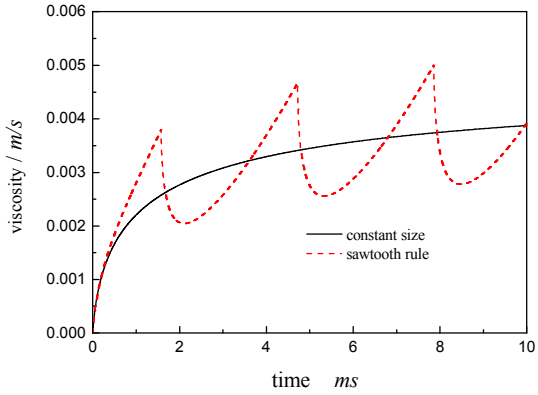

Figure 4 Velocity of bubble with sawtooth rule

Figure 3 shows the bubble rising velocity contrast curve. Where the red dashed line says the changing curve of bubble rise velocity when the bubble particle size changes in sine wave. Black solid line says the curve of bubble rising velocity when the size is constantly 50 μm . It is known

from figure 3 that when the bubble size changes in sine wave, the bubble rise velocity changing rule also presents the sine wave characteristic. The fluctuation mean is consistent with the changing rule of rising velocity for particle in 50μm size, and also has increasing trend. As time increases, rising velocity fluctuation amplitude and particle size changing by sine law has increase trend.

Figure 4 shows the bubble rise velocity contrast curve where the red dashed line says the changing curve of bubble rise velocity with the bubble particle size changing in sawtooth wave. Black solid line says the changing curve of rising velocity when bubbles are in constant size 50μm. It is known from figure 4 that when the bubble size changes by sawtooth law ,the bubble rise velocity change rule also presents the sawtooth wave characteristics. In a maximum size , the sawtooth changing law of bubble velocity is obvious, but in minimum size, the bubble velocity curve is more smooth. The fluctuation of mean is consistent with bubble rise velocity change rule when the particle size is 50μm, and also has an increasing trend. As time increases, the fluctuation amplitude of rising velocity for particles whose size change by sawtooth law has an increasing trend..

Conclusions

Velocity of the bubble increases gradually with the increase of time in static water, and the experimental values are consistent with the calculated values. The influence of virtual mass force and basset force caused by acceleration to float velocity in initial stage must be considered, When not consider the virtual mass force, float velocity has the characteristics of the shock and in late stage velocity tends to be stable .

In static water the greater size of bubbles has the greater velocity. When the bubble size changes in rising process by sine or sawtooth wave, the changing rule of bubble velocity fluctuation mean and the changing rule for bubbles in constant size, but in the turning point of the maximum radius the rising velocity changes abruptly and in minimum point the bubbles' rising velocity could change smoothly.

Acknowledgment

This work is supported by the Science Fund of State Natural (U1304521),science and technology project of Henan Province(102102210162) and major prophase of Henan science and technology university (2011CX007).

Symbol Description

$\mathbf{m_b}$	quality of the bubble [kg]	$\mathbf{r_0}$	the initial bubble radius [m]
u	velocity of the bubble [m/s]	$\mathbf{K_m}$	empirical coefficient of virtual mass force
t	time variable [s]	$\mathbf{K_B}$	empirical coefficient of the basset force
$\mathbf{F_g}$	gravity of the bubble [N]	$\mathbf{C_d}$ [6]	drag coefficient
$\mathbf{F_b}$	buoyancy of the bubble [N]	$\mathbf{P_0}$	the ambient pressure [Pa]
$\mathbf{F_d}$	viscosity resistance [N]	ρ_l	density of water [kg/m3]
$\mathbf{F_A}$	the virtual mass force [N]	ρ_g	density of the bubble [kg/m3]
$\mathbf{F_B}$	Basset force [N]	μ	viscosity coefficient of the water[Pa · s]
r	radii of the bubble [m]	γ	the polytropic constant

References

[1] Yu Deyang, Liu Baolin, Wang Bochun. The effect of ultrasonic waves on the nucleation of pure water and degassed water [J]. Ultrasonics Sonochemistry, 2012, 19(3): 459-463.

[2] Heneghan A F, Haymet A D J. Liquid-to-crystal heterogeneous nucleation bubble accelerated nucleation of pure supercooled water [J]. Chemical Physics Letters, 2003, 368(1-2): 177-182.

[3] Mathieu Saclier, Roman Peczalski, Julien Andrieu. A theoretical model for ice primary nucleation induced by acoustic cavitation [J]. Ultrasonics Sonochemistry, 2010, 17(1): 98-105.

[4] Thomas Leong, Muthupandian Ashokkumar, Sandra Kentish. The fundamentals of power ultrasound: a review [J]. Acoustics Australia, 2011, 39(2): 54-63.

[5] Chakraborty B B, Tuteja G S. Motion of an expanding spherical gas bubble in a viscous liquid under gravity[J]. Phys. Fluids A, 1993, 5(8): 1879-1882.

[6] Carrica P M, Bonetto F J, Drew D A, et al. The interaction of background ocean air bubbles with a surface ship[J]. Number. Meth. Fluids, 1998, 4(28): 571-600.

Advanced Materials Research Vols. 960-961 (2014) pp 170-175

doi:10.4028/www.scientific.net/AMR.960-961.170

Adaptability Evaluation of Conformance Control Agents in Low Permeability Reservoirs with Fractures

Fenglan Zhao[1, a], Shujun Cao [1,b] and Jirui Hou [1,c]

[1] Research Institute of Enhanced Oil Recovery, China University of Petroleum, Beijing, China

[a]zhaoflan123@163.com, [b] caoshujun1989@163.com, [c]houjirui@126.com

Keywords: preformed particle gel; emulsion microspheres; chromium gel; starch graft; fractures

Abstract. Several conformance control agents, including preformed particle gel, emulsion microspheres, continuous chromium gel and underground starch graft copolymer gel were evaluated. The properties such as gelation time and gel strength of gel, and expansion of particles and microspheres were tested at high temperature. Also, the injection pressure, plugging strength and resistance factor were measured using the artificial low permeability cores with fractures. It was shown that, for particle type conformance control agents, the particle size should be adaptable with the fracture width. Also, for continuous chromium gel, the added polymer concentration higher, the viscosity is higher, with higher plugging strength. The plugging and strength should be coordinated. The starch graft copolymer gel is easy to be injected into formation and has good plugging property. The results show that underground starch graft gel is more suitable for conformance control in low permeability formation with fractures.

Introduction

As for low permeability reservoirs with permeability under $50\times10^{-3}\mu m^2$ (Li, 1997), especially for the ultra-low permeability under $10\times10^{-3}\mu m^2$, it is common that there are fractures with high flow conductivity (Zhang, 2007). During water flooding, the water is prior flowing along fractures, leading to water breakthrough in short time (Hao et al., 2007; Pu and Yin, 2008). It has been proved that injecting chemical conformance control agents into formation to partly plug fractures is one of relatively effective and economic methods (Yang et al., 2006; An and Liu, 2004; Liu et al., 2012; Bai et al., 2013). Also, there are many challenges such as selection of agents with high plugging strength and good injectivity and injection parameters optimization (Yan et al., 2011), which are crucial for low permeability formation with low oil well production.

For preformed particle gels and emulsion microspheres, different sized particles/microspheres can plug fractures of different width (Tian et al., 2012). So, there is a need to study the adaptability of particle/microsphere size with fracture width. For continuous chromium gel, the added polymer concentration will affect the viscosity and plugging property of the gel (Perez et al., 2012). However, high polymer concentration will result in poor injectivity and high cost. Thus, it is important to coordinate the concentration and strength. Therefore, adaptability evaluation of the frequently-used conformance control agents in tight formation is essential for conformance control application.

Experiment

1.1 Materials

The formulation of continuous chromium gel includes polymer (0.3%~0.5%), cross-linker A (0.05%), cross-linker B (0.01%) and cross-linker D (0.3%). The underground starch graft copolymer gel basically consists of modified starch (2.5%~4%), cross-linker (0.05%-0.15%), control agent (0.1%~0.25%), unsaturated monomers (2.5%~4.0%), PAM (0.2%). The particle size of preformed particle gel KL-1 is 2~4mm, and the particle concentration is 5000mg/L. The polymer microspheres are of sub-millimeter, and the concentration is 3000mg/L. The experimental water used is produced water which can be used for sample preparation and water flooding after microfiltration.

1.2 Experimental methods

1.2.1 Static evaluation of chromium gel and underground starch graft copolymer gel

Put the formulated gel solutions into glass bottles, then place them in the constant temperature oven of 64℃. Measure the viscosity of gel solution using Brook Field viscometer at a regular time interval.

1.2.2 Dynamic performance evaluation

Different permeability sand-packs were filled in 100-cm or 50-cm long, 2.5-cm inside diameter tubes with different mesh sands to stimulate fractures. The core models were firstly vacuumed and saturated with formation water. Then, water was flowed into the core to calculate the absolute permeability of sand-pack. Next, conformance control agent was injected. At last, formation water was injected into the model until the pressure drop was stable. Thus, resistance factor, breakthrough pressure gradient and residual resistance factor were measured.

Results and Discussion

2.1 Static performance evaluation

Properties such as gelation time and gel strength of gel, and expansion of particles and microspheres were tested. The expansion time of preformed particle gel KL-1 is 3 days and the swelling ratio is more than 5(shown in Table1).

Table 1 Property of preformed particle gel KL-1

Particle Size and Roundness	Expansion Times	Expansion Velocity
2.0-4.0mm	≥5	6h-60%，24h-87%，48h-89%，72h-90%

The viscosity of continuous chromium gel with polymer concentration of 3000mg/L was measured. The results are shown in Figure 1. It can be seen that the viscosity of base fluid before gelation is only 423mPa•s, and the viscosity reaches maximum after 24 hours, then reduces slightly. So, the gelation time is about 24h, and the gel strength is more than 14000mPa•s.

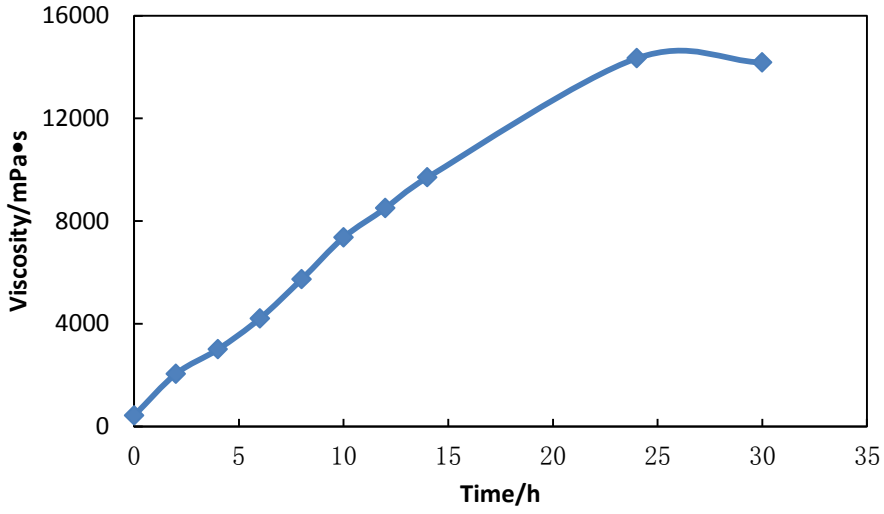

Figure 1 Viscosity of continuous chromium gel at different time

Figure 1 shows the viscosity of underground starch graft copolymer gel at different time. Note that the viscosity is very low before gelation, only 56.3mPa•s; after 8 hours, the viscosity sharply increases to 149871mPa•s. Then, viscosity changes very little. So, the gelation time is 8 hours, and the gel strength is more than 150000mPa•s.

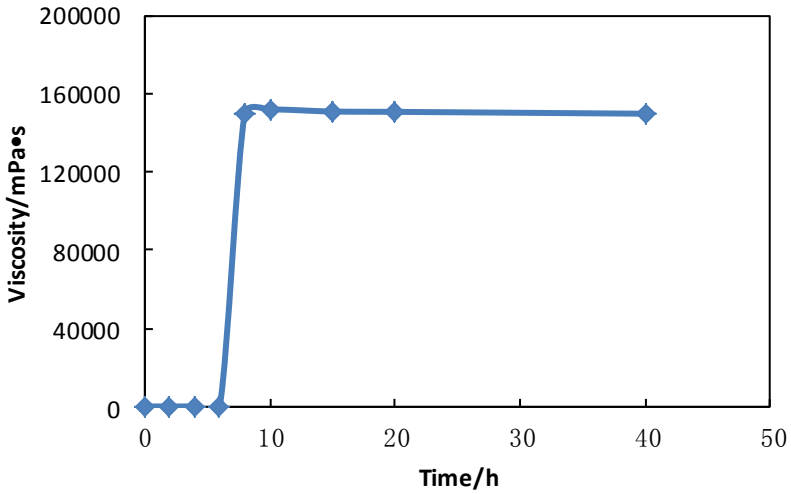

Figure 2 Viscosity of underground starch graft copolymer gel at different time

2.2 Dynamic Performance Evaluation

2.2.1 Preformed gel particles dynamic performance evaluation

The injection and plugging properties of preformed particle gels were studied in fractures of 10μm^2, 50μm^2 and 100μm^2. Figure 3(a) shows the injection pressure of preformed particle gel KL-1. After 3 days, the particles fully expanded; subsequently, the water was injected. Figure3 (b) is the water-flooding pressure curve. The resistance factor, residual resistance factor and plugging percentage are listed in Table 2. The results indicate that the particles have certain plugging property for these fractures, but the plugging ability is poor.

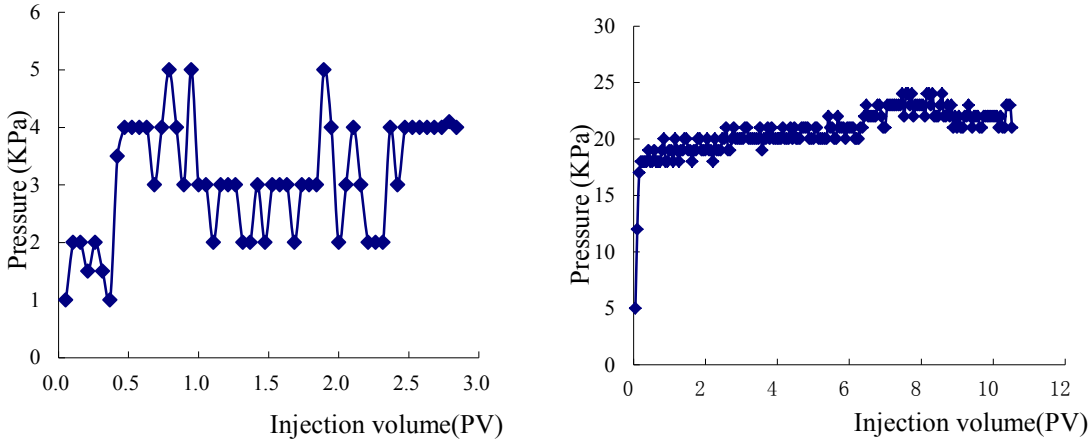

(a) (b)

Figure 3 Injection pressure and water flooding pressure curves (10μm^2)

Table 2 Plugging property of KL-1

Particle size (mm)	Permeability of Fracture (μm^2)	Resistance factor	Residual resistance factor	Plugging percentage (%)
2~4	11.7	1	5.71	82.5
2~4	51.6	1	3.95	74.7
2~4	98.6	1	1.88	46.9
2~4	150	15	5.68	91.5

To further determine the adaptability between particle size and fractures, the core of 150μm^2 was studied. The obvious increase of injection pressure (shown in Figure4 (a)) indicates that the particle size and the fracture have begun to match. Also, the water flooding pressure curve (shown in Figure4 (b)) after fully swollen has an obvious breakthrough pressure peak and the final average injection

pressure can maintain at a high value. So, for the core of 150μm^2, the preformed particle gel has good plugging adaptability.

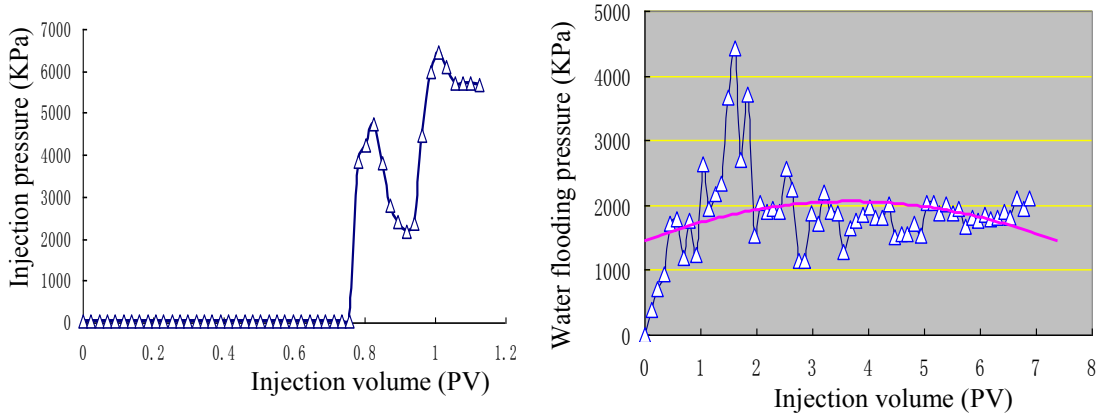

(a) (b)

Figure 4 Injection pressure and water flooding pressure curves (150μm^2)

2.2.2 Continuous chromium gel dynamic performance evaluation

Two formulations were selected to study the continuous chromium gel, and the polymer concentration was 3000mg/L and 5000mg/L respectively. The results are listed in Table 5. It can be found that, for continuous chromium gel, the added polymer concentration higher, the viscosity is higher, with higher plugging strength.

Table 3 Plugging properties of chromium gel

Polymer concentration (mg/L)	Permeability of Fractures(μm^2)	Injection volume(PV)	Plugging percentage (%)	Breakthrough Pressure Gradient(MPa/m)
3000	10	0.1	88.10	0.075
3000	100	0.1	77.78	0.000
5000	10	0.1	93.29	0.160
5000	100	0.1	81.48	0.031

2.2.3 Emulsion microspheres dynamic performance evaluation

After 1-day swelling at 64℃, the sub-millimeter sized microspheres were injected into models of 2μm^2, 3.5μm^2, 5.6μm^2 and 10μm^2. The pressures curves are shown in Figure5. The results show that for cores of 2μm^2, 3.5μm^2, 5.6μm^2, the microspheres can form plugging, but the plugging property becomes poorer with the increase of permeability. Figure 5 (b) indicates emulsion microspheres system is completely unable to form plugging in the pores of 10μm^2. Also, the resistance factor and residual resistance factor both are 1.0. So, emulsion microspheres system is not suitable to the formation of 10μm^2 or more.

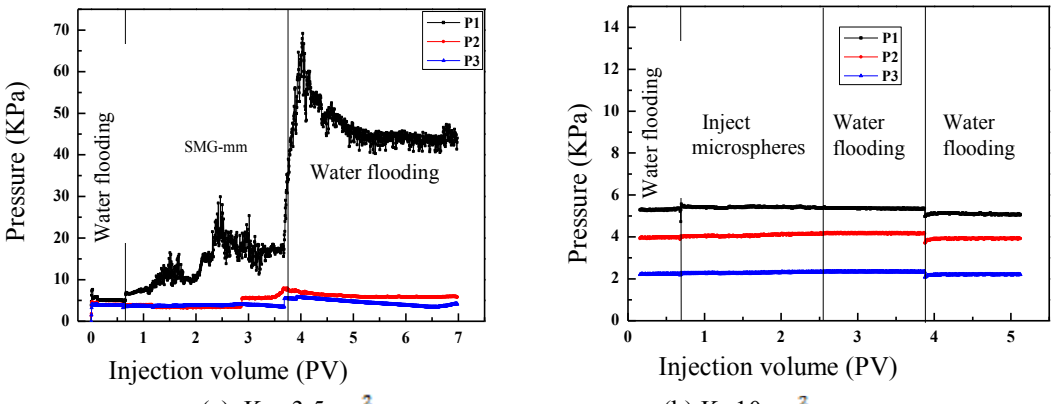

(a) K = 3.5μm^2 (b) K=10μm^2

Figure 5 Displacement pressures of different measuring points

2.2.4 Underground starch graft copolymer gel dynamic performance evaluation

The starch system was injected into different permeability models to test its resistance factor and residual resistance factor. The results are listed in Table 6 and the high residual resistance factor and high plugging percentage prove that the system has high plugging strength.

Table 4 Resistance characteristics of underground starch graft copolymer gel

Permeability of Fracture (μm^2)	Breakthrough pressure (MPa)	Resistance factor, Fr	Residual resistance factor, Frr	Plugging percentage (%)
213	7.06	2.2	54.3	98.16
196	28.28	13.8	73.4	99.03
88	30.77	14.4	106.3	97.22

Conclusions

(1) For the particle type water control agents, preformed particle gel KL-1(2~4mm) has good plugging adaptability to fractures of 150μm^2, while is not suitable for fractures of less than 100μm^2. The sub-millimeter emulsion microspheres system is not suitable to the formation of 10μm^{2}or more. So, the particle size should be adaptable with the fracture width.

(2) For continuous chromium gel, the added polymer concentration higher, the viscosity is higher, with higher plugging strength. Meantime, high polymer concentration will lead to poor injectivity (high viscosity on ground) and high cost. Therefore, the plugging and strength should be coordinated.

(3) The underground starch graft copolymer gel is easy to be injected into formation and has good plugging property.

(4) Underground starch graft copolymer gel is more suitable for conformance control in low permeability formation than the other three conformance control agents.

Acknowledgements

Financial supports for this work are gratefully acknowledged from the National Science and Technology Major Project (No.2011ZX05009-004) and Science Foundation of China University of Petroleum, Beijing (No.2462012KYJJ23).

References

[1] D.P. Li. *Development of low permeability sandstone oil field*. Beijing: Petroleum Industry Press, Beijing (1997) (In Chinese)

[2] Z.W. Zhang. *Study on the effect of fractures on the water flooding in low permeability reservoir at Ansai Oilfield*. Graduate School of Chinese Academy of Science (2007) (In Chinese)

[3]M.Q. Hao, Y.L. Hu and X.Q. Liu. *An overview on characteristics of low-permeability fractured reservoirs*. Special Oil and Gas Reservoirs, no.3 (2007), p12-15(In Chinese)

[4] H. Pu, D.Y. Yin. *Field practice of improvement of water flooding effect for a naturally fractured low-permeability field*. SPE 114200, 29 March-2 April 2008(In Chinese)

[5] L.M. Yang, J.R. Hou, and X.M. Song. *Plugging in-depth macro-porous flowage channels in low permeability and low temperature sandstone reservoirs*. Oil Chemistry, no.4 (2006), p337-339(In Chinese)

[6] X.R. An and R. Liu. *Application of organic chrome jelly profile control technique in Chaoyanggou oilfield.* Petroleum Geology & Oilfield Development in Daqing, no.6 (2004), p76-77(In Chinese)

[7] C. Liu, X.W. Liao, Y.L. Zhang,et al. *Field application of polymer microspheres flooding: a pilot test offshore heavy oil reservoir*. SPE158293, 8-10 October 2012

[8] B.J. Bai, M.Z. Wei and Y.Z. Liu. *Field and lab experience with a successful preformed particle gel conformance control technology*. SPE164511, 23-26 March 2013

[9] H.T. Yan, G.Y. Zhang, Q.C. Wang, et al. *Research and field application of low permeability reservoir gel water shutoff and profile control technology*. Advances in Fine Petrochemicals, no.8 (2011), p19-21

[10] Y.Q. Tian, L.S. Wang, Y.Y. Tang, et al. *Research and application of Nano polymer microspheres diversion technique of deep fluid*. SPE156999, 12-14 June 2012

[11] D. Perez, L.F. Munoz, W. Acosta and J. Falla. *Improving sweep efficiency in a mature waterflood: Balcon Field, Colombia*. SPE150955, 16-18 April 2012

Advanced Materials Research Vols. 960-961 (2014) pp 176-181

doi:10.4028/www.scientific.net/AMR.960-961.176

Effect of cordierite-modified on SCR commercial catalyst

Wenchang Xi[1,2] Qingcai Liu[1] Deliang Niu[1] Jian Yang[1]

Qiang Yang[1] Yuan Peng[2] Zhou Xiaoyan[2] Zhang Hekun[2] Hong Yan[3]

[1] Chongqing University, School of Material Science and Engineering,

Chongqing 400044,

[2] Chongqing YuanDa Catalyst Manufacturing Co., LTD, Chongqing 401336;

[3] China Power Investment YuanDa Environmental-Protection Engineering Co.,LTD,
Chongqing 401122

Key word V_2O_5-WO_3/ TiO_2; Cordierite; flue gas denitrification; NO_x; selective catalytic reduction (SCR)

Abstract: The V_2O_5-WO_3/TiO_2 honeycomb catalysts with cordierite modified were prepared by solid-liquid mixing method. Its thermal stability, crystal structure, abrasion resistance and activity were studied by XRD, abrasion equipment and simulated flue gas analyzer，respectively. The results indicated that V_2O_5-WO_3/Cordierite-TiO_2 honeycomb catalyst possessed a better thermal stability, mechanical property and activity at the higher temperature comparing to commercial catalyst. There was no rutile phase present after the catalysts were calcined at 700℃, and the vanadia and tungsten trioxide phases could be apparently visible on TiO_2.

Introduction

The selective catalytic reduction (SCR) of NOx by NH_3 is one of the most widely used methods of removing NOx from stationary sources of coal-fired power plant due to its efficiency, selectivity and economy [1-5]. V_2O_5-WO_3(MoO_3)/TiO_2 catalyst is well known for its high de-NOx activity, the good resistance against SOx and As poisoning[2-4]. Generally, SCR reactor is installed between the boiler economizer and air preheater, in which smoke ash content and temperature of the flow gas are both high, which inevitably makes the catalyst wore and tore easily and badly by smoke ash content and other impurities, thus its mechanical and chemical life are both shortened[4]. Accordingly if the thermal stability and corrosion resistance of the catalyst for SCR will be both improved, so is the catalyst's lifespan. It is reported that V_2O_5-WO_3(MoO_3)/TiO_2 supported on cordierite prepared by the coprecipitation method, the sol-gel method and the chemical vapor deposition have a large BET surface area and shows a remarkable acidity[6-14]. However, the stability and corrosion of the catalyst have not been investigated.

The purpose of this paper is to clarify the behavior of cordierite loaded with V_2O_5-WO_3/TiO_2 by XRD, mechanical properties and activity tested in comparison with commercial V_2O_5-WO_3/TiO_2.

Experiment

2.1. Catalyst preparation

Cordierite powder was immersed in sulfuric acid solution of 20 wt% at 60 ℃ for 6h and standby after 10h at 105 ℃ drying. Ammonium metatungstate and ammonium metavanadate were dissolved in a mixed aqueous of 10% oxalic acid at 80℃. The solutions, TiO_2 power and cordierite power mentioned above were thoroughly mixed under continuous addition of a suitable amount of distilled water, kneaded for a certain time and placed for 24h, then formed in an extrusion mold to produce a honeycomb monolith with 75mm×75mm in outer diameter. The obtained monolith was dried at 80℃ for 12h and then was calcined under the current of air at 600℃ for 4h.

The V_2O_5-WO_3/TiO_2 catalysts with cordierite contents (0.0, 5.0, 10.0, and 15.0wt. %) and 1%V_2O_5 and 7%WO_3 were obtained. This series of the catalysts are denoted as T, TC5, TC10 and TC15, respectively.

2.2. Characterization of catalysts

X-ray diffraction measurement (XRD) of the catalysts were carried out in the range of 2θ=10-90°at the scanning rate of 5°min^{-1} by a Spectris-diffractometer with Co Kα (Rigaku D/Max-2500pc). Mechanical properties (axial direction and lateral direction) of catalysts were examined by Shenzhen sans – at the rate of 0.7mm/min.

2.3. Abrasion performance of SCR honeycomb catalysts

The abrasion performance experiment was operated as follows. The catalyst samples (75mm×75mm×90mm) were placed into the tank of experimental sample and reference sample. And then quartz sand in the air was blown away by the blower and went through the samples in certain time. As a measure of weight change before catalyst was abrasion rate d . The definition of abrasion rate d is calculated by:

$$\delta = (1 - \frac{M2}{M1} \times \frac{M3}{M4}) / M5 \times 100\% \quad (1)$$

where M1 is the weight of the experimental sample; M2 is the weight of the experimental sample after being tested; M3 is the weight of the comparative sample; M4 is the weight of the comparative sample after testing; M5 is the weight of the collection of silica sand.

2.4. Catalyst performance measurement

Catalyst performance measurement for the SCR reaction of NO by NH_3 were carried out in a fixed bed reactor made of a stainless steel tube with 30mm×30mm in section orientation. The honeycomb catalysts samples were cut into a size of 9×9 cells and loaded in the reactor. The reaction gas mixture which consisted of 220 pm NO, 220 ppm NH_3, 1000ppm SO_2, 3.5% O_2, 10% H_2O (v/v) with N_2 as the carrier gas was fed into the reactor. The total flow through the reactor was 5Nm^3/h and the gas hourly space velocity (GHSV) was 15,000 h^{-1} for activity test of SCR reaction.

The inlet and outlet concentrations were measured by the CEMS NOx analyzer. The definition of NOx conversion is as follows:

$$\eta_{NO}(\%) = \frac{C_{NO,in} - C_{NO,out}}{C_{NO,in}} \times 100 \quad (2)$$

where η_{NO} is NO conversion rate; $C_{NO,in}$ is inlet NO concentration; and $C_{NO,out}$ is outlet NO concentration.

Results and discussion

3.1. XRD of catalysts

The XRD patterns of catalysts with cordierite contents, calcined at 600℃ and 700℃ are shown in Fig.1. The catalyst samples calcined at and below 600℃ possess only diffraction lines, such as 2θ=25°, 38°, 48° and 53°, all of which attribute to the phase of anatase. Although the calcinations temperature increases to 700℃, there is still no rutile TiO_2 appearing. Based on thermodynamic principles[15-18], the microcrystalline or crystalline material of V_2O_5 and WO_3 is not detected on TiO_2 due to the spontaneous heat, while at the high loaded of 15% V_2O_5 and WO_3, the vanadia and tungsten trioxide phases can be apparently visible on TiO_2. This indicates that V_2O_5, WO_3 are not changed or present a highly dispersion on supports as the increase of cordierite power. The catalyst samples overcome the deficiencies inherent due to the addition of whisker-like substance and then retain the crystal phase composition.

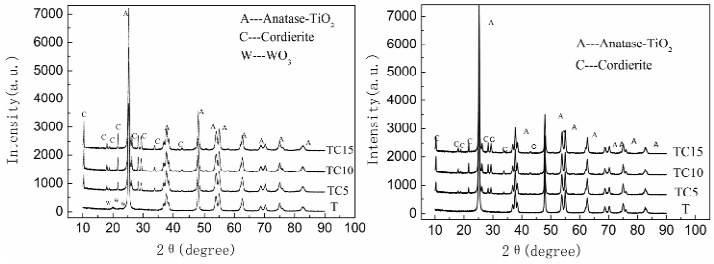

-600 -700

Fig.1 XRD spectra of catalytic samples

3.2. Mechanical properties

Tab.1 Mechanical properties of the catalysts

Catalysts	Transverse compressive strength (MPa)	Axial compressive strength (MPa)	Abrasion rate(%)
T	0.65	1.25	0.0650
TC5	0.45	0.79	0.0815
TC10	0.76	1.31	0.0559
TC15	0.56	0.37	0.0659

The mechanical properties of the catalysts were carried in the lab platform for commercial catalyst. The results are shown in Tab.1. It can be seen that transverse and axial compressive strength reaches a maximum when cordierite content is 10wt% while others decrease. Afterwards, the abrasion rate of catalysts slightly decreases.

It is well known that denitration catalyst is placed between the boiler economizer and air preheater, in which catalyst endure ash and high temperature erosion. Interspace of catalyst is filled by the addition of cordierite. Therefore, the ability of resistance of ash erosion should be improved. Meanwhile transverse and axial compressive strength of catalysts are also promoted. As cordierite content reaches 10%, mechanical properties of catalysts become lower. It seems that there are new defects on the surface of catalysts with cordierite content enhanced. Its mechanical properties will drop. It is considered that using 10 wt% cordierite and TiO_2 as a carrier of the catalyst can significantly resist ash and temperature erosion.

3.3. NO removal activity

It is well known that commercial SCR catalyst work between 300-400℃. The results of activity test are shown in Fig.2-4.

Fig.2 exhibits that NO conversation will be improved with the temperature ascend. NO conversation slightly increases at the higher temperature above 380℃(Formula 2). And at the temperature 450℃, NO conversation of commercial catalyst sharp drop in 52%. NO conversation of TC10 merely drop in 72%. It is reported NH_3 will occur oxidation reaction to NO or N_2O(Formula 3 and 4). Many other researchers[4]have reported that the content of N_2O in the atmosphere is very low, but the greenhouse effect of N_2O is 310 times of carbon dioxide.

Fig.3 shows that NO conversation increase with different molar ration of NH_3-NO. When molar ration of NH_3/NO is above 1, NO conversation has a slight increase. It is indicated that there are excessive NH_3 in the reaction mixture gas. Many researchers[19,20] have illuminated that the excess of NH_3 will react with SO_3 in the flue gas and generate a viscous substance ($(NH_4)_2SO_4$ or NH_4HSO_4). This substance is to be adhered to in the downstream equipment, making the system pressure increases and a bad effect on power plant operations.

The NO conversation is shown as a function of gas flow rate in Fig.4. When gas flow rate is gradually increases, the residence time of the reaction gas on the surface of the catalyst becomes short. The content of NH_4^+ or NH_2^- activated by active site is less corresponding; NO conversion rate is gradually falling off.

The reports suggest that cordierite added never change the N_2 selectivity of commercial catalyst. Therefore, it is considered that cordierite modified may be added into V_2O_5-WO_3/TiO_2 catalyst and replace a portion of TiO_2.

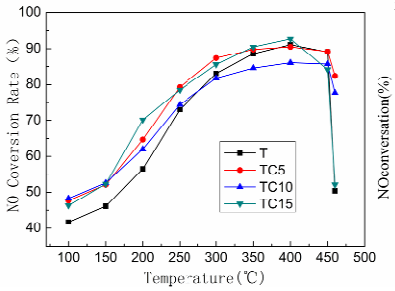

Fig.2 NO conversation vs. temperature

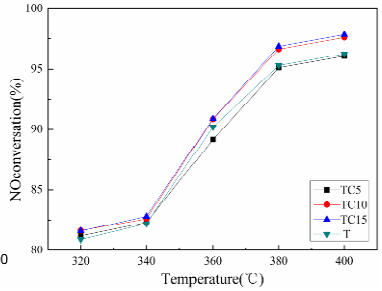

Fig.3 NO conversation vs. NH_3/NO

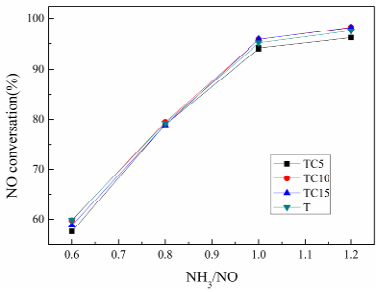

Fig.4 NO conversation vs. flow rate

Reaction condition O_2=6% C_{NO}=C_{NH3}=500PPM space velocity =10000H^{-1} N_2 =Balance gas

$$4NO + 4NH_3 + O_2 \rightarrow 2N_2 7 + 6H_2O \quad (2)$$

$$4NH_3 + 5O_2 \rightarrow 4NO + 6H_2O \quad (3)$$

$$2NH_3 + 2O_2 \rightarrow N_2O + 3H_2O \quad (4)$$

Conclusions

The TiO_2-cordierite support containing 10wt% of cordierite exhibits a good thermal stability ,activities and mechanical properties, as compared to TiO_2 support. With cordierite content increasing, the XRD spectra of V_2O_5/TiO_2-cordierite catalysts show anatase-TiO_2. V_2O_5 and WO_3 phases are not detected after catalyst samples were calcined at 700℃. The mechanical performance of V_2O_5/TiO_2-cordierite catalysts exhibits well as cordierite content increases.

The SCR activity and N_2 selectivity are found to be excellent over vanadia loaded on TiO_2 and cordierite carriers. In other words, cordierite addition will not change the dispersion of V_2O_5 and WO_3 on the support.

It is concluded that V_2O_5/TiO_2-cordierite is suitable as SCR catalysts for sulfur-containing coal and oil-fired SCR plants due to its lower abrasion, good mechanical performance and higher activity in SCR.

Acknowledgements

This work has been supported by Chongqing Integrated and demonstration projects (No. cstc2013jcsf20001), Science and technology correspondent projects (NO. 2009GJF10047) and Natural Science Foundation of China (No. 51204220 and NO. 51274263).

References

[1] Ha Heon Phil, Maddigapu Pratap Reddy, Pullur Anil Kumar., et al. SO_2 redidtant antimony promoted V_2O_5/TiO_2 catalyst for NH_3-SCR of NOx at low temperatures. Applied Catalysis B: Environmental, 2008, 78(3-4): 301-308.

[2] G. Busca. Chemical and Mechanistic aspects of the selective catalytic reduction of NOx by ammonia over oxide catalysts. A review[J].Applied Catalysis B: Environmental, 1998, 18(1-2): 1-36.

[3] P. Forzatti. Present Status and perspectives in de-NOx SCR catalysis[J]. Applied Catalysis A: General, 2001, 222(1-2): 221-236.

[4] Li Feng. Study of SCR Catalyst for Coal-fired Flue Gas Denitrification Grafted on Nanometer Titania, Doctoral Dissertation, Nanjing, Southeast University, 2006

[5] L. Lietti, J. L. Alemany, P. Forzatti, et. Al., Reativity of V_2O_5-WO_3/TiO_2 catalysts in the selective catalytic reduction of nitric oxide by ammonia[J], catalysis today, 1996, 29:143-148

[6] Liu . X. Y., Qian. D. F., Xie. J. G., et al., Study of Cordierite Horeycomb Ceramics Firing Process. Chinese Journal of Ceramic Engineering. 1999, 33(3) : 7-11（in Chinese）.

[7] Zeng Linke, Wang Hui, Luo Minhua et al., compilation. Preparation and Application of porous functional ceramics. Beijing: Chemical Industry Press, 2006.5

[8] Zhu X W,Jiang D L,Tan S H. Reaction bonding of open cell SiC-Al_2O_3 composites[J].Materials Research Bulletin,2001,36(11): 2003-2015.

[9] P.M. Then., P. Day. The Catalytic Converter Ceramic Substrate-An Astonishing and Enduring Invention[J]. Interceram, 2000, 49(1): 20-23.

[10] Li Landong, Zhang Fuxiang, Guan Naijia, et al. Metal-ZSM25 /Cordierite monolithic catalysts for purifying lean-burn engine exhaust [J]. Chinese Journal of Catalysis,2006, 27(1): 41- 44.

[11] Dong Guojun, Zhang Jie, Hao Shufu. Surface modification of cordierite support for V_2O_5-WO_3/SiO_2 catalystsof reducing NO. Industrial Catalyst, 2008, 5(16):20-23

[12] Liu Renlong, Lv Hanqing, Li Guoyun, et al,. Preparation of Novel V_2O_5-WO_3/TiO_2/Honeycomb Cordierite catalyst and Their Application in Selective Catalytic Reduction of NO. Journal of Wuhan University of Technology, 2011, 7(33):20-23

[13] Yang Mei, Liu Qingcai, Xue Qi et al,. Preparation and characterization of V_2O_5-WO_3/ TiO_2 catalyst by chemical vapor deposition. Functional Materials, 2010, 4(41):683-686

[14] Yang Mei, Liu Qingcai, Xue Qi et al,. Preparationof V_2O_5-WO_3/TiO_2 Catalyst by CVD Technology and Study on its Denitrification Property. Journal of Chinese Society of Power Engineering, 2010,1(30):52-56

[15] Seong Moon Jung, Paul Grange. Chatacterization and reactivity of V_2O_5-WO_3 supported on TiO_2-SO_4^{2-} catalyst for the SCR reaction[J]. Applied Catalysis B: Environmental 2001, 32(1-2): 123-131

[16] Vipul Kumar, Nathan Lee, Catherine Bothe Almquist,. An investigation of the thermal stability and performance of wet-incipient WO_3/V_2O_5/TiO_2 catalysts and a compatison with flame aerosol catalysts of similar composition for the gas-phase oxidation of methanol. Applied Catalysis B: Environmental. 2006, 69(1-2): 101-114.

[17] C U Ingemar Odenbrand, Ana Bahamonde, Pedro Avila, et al. Applied Catalysis B: Environmental [J]. 1994, 5(1-2): 117-131.

[18] Motonobu Kobayashi, Ryoji Kuma, Sinyuki Masaki, et al,. TiO_2-SiO_2 and V_2O_5/TiO_2-SiO_2 catalyst: Physico-chemical characteristics and catalystic behavior in selective catalytic reduction of NO by NH_3. Applied Catalysis B: Environmental [J]. 2005, 60(3-4):173-179

[19] J. Alemany，N. Ferlazzo, P. Forzatti，et. al. Oxidation of SO_2 to SO_3 over honeycomb DeNOxing catalysts[J]. Ind Eng. Chem. Res., 1993, 32(5): 826-834.

[20] L. J. Alemany，L. Lietti, N. Ferlazzo, et. al. Reactivity and physicochemical characrerization of V_2O_5-WO_3-TiO_2 De-NOx catalysts[J]. Journal of Catalysis, 1995:155(1), 117-130.

Advanced Materials Research Vols. 960-961 (2014) pp 182-188

doi:10.4028/www.scientific.net/AMR.960-961.182

Study of Hydrophobic Coating over Various Substrates Using an Industrial Coating-Bar Technique

Chih-Lin Hsu[a], Shyankay Jou[b], Ying-Ji Chuang[c], and Ching-Yuan Lin [d,*]

[a, c, and d] Department of Architecture, National Taiwan University of Science and Technology

[b] Department of Material Science and Engineering, National Taiwan University of Science and Technology

[a] d10113012@gmail.com, [b] sjou@mail.ntust.edu.tw, [c]chuang@mail.ntust.edu.tw, and [d]linyuan@mail.ntust.edu.tw

Keywords: Lotus effect, Super-hydrophobic surface, Dual-scale roughness, Silicon Wafer, TiZn-P, Al, Galvalume Steel.

Abstract. Si Wafer, pre-weathered TiZn alloy (TiZn-P), Aluminum (Al), and hot-dipped galvalume steel (G.L.) are chosen in this work for the study of hydrophobic coating to various substrates. Various amounts of TS-720 hydrophobic nano-particles were mixed into ITRI hydrophobic agent (H.A.), and this mixture liquid was applied onto different material surfaces by using a coating bar technique. High contact angle near 140^{o} are achieved in all samples with 2.5 wt% TS-720 in ITRI H.A. mixture.

Introduction

Lotus surface has a high hydrophobicity, which can significantly improve the ability of self-cleaning, anti-pollution and corrosion resistance by reducing the dielectric constant of the material surface, and decreasing the adhesion of dust [1 – 3]. The micro-nano dual-scale roughness surface structure is a crucial role for super-hydrophobic characteristic [4 – 6]. Coating bar (R.D.S. SUS304, No.5, wire diameter: 0.13 mm) is used to apply paint over metal substrate in coil coating industry. Cabot CAB-O-SIL® TS-720 is a medium surface area fumed silica which has been surface modified with polydimethylsiloxane, which diameter is 200 – 300 nm [7 – 9]. Zheng reported the ITRI, (C-B-HN-$(CH_2)_3$-$[A]_n$-$(CH_2)_3$-NH-B-C; $[A]_n$ is a composition of polysiloxane with fluoride oligomer, and B is isocyanate), which is a kind of hydrophobic agent (H.A.) [10], with the characteristics of high transparency, strong adhesion and abrasion resistance, that can be dissolved in the tetrahydrofuran (THF). This coating process study uses ITRI adding with TS720 as the hydrophobic composite agent in atmosphere condition, like the existing metal coil coating industry applying paints by using the coating-bar, achieves a surface with high hydrophobicity.

Experiment

There were various kinds of material chosen as the substrates, silicon wafer (MEMC), titanium-zinc (Ti-Zn alloy 710, 0.3 mm of thickness, with pre-weathered, TiZn-P), aluminum alloy (Al, 0.3 mm of thickness), and hot-dip galvalumed steel (GL, 0.3 mm of thickness). The substrates were degreased in ultrasonic with degreasing agent of 5 v% (Tanmax, No.928) at 50^{o}C for 5min, and rinsed with deionized water. In order to produce a surface with dual-scale roughness like lotus surface, we added the TS-720 nano-powder into ITRI H.A.

The ITRI/TS-720 composite was synthesized by two-step process. The first step, the ITRI THF solution was kept stirring for 30 min. The second step, various amount (0 – 2.5 wt %) of hydrophobic nano powder TS-720 were added into the ITRI THF solution, and dispersed by sonication for 5 min. We dripped the ITRI/TS-720 composite onto the cleaned si wafer and metal surfaces, and coated homogeneously by a coating bar (R.D.S. SUS304, No.5, wire diameter: 0.13 mm). The average thickness of wet film was 11.43μm, as shown in Figure 1 (a) – (c). The coated si wafer and metal substrates were dried in air for 20 s, and calcined at 130^{o}C for 5 min.

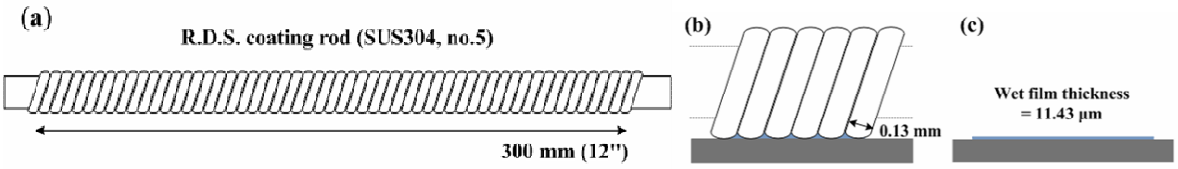

Fig 1 (a) Coating bar (R.D.S. SUS304, No.5, wire diameter: 0.13 mm), (b) The coating process by using coating bar, and (c) The wetted film thickness is 11.43 μm.

The schematic 1 illustrates the preparation process of hydrophobic coating to a sample.

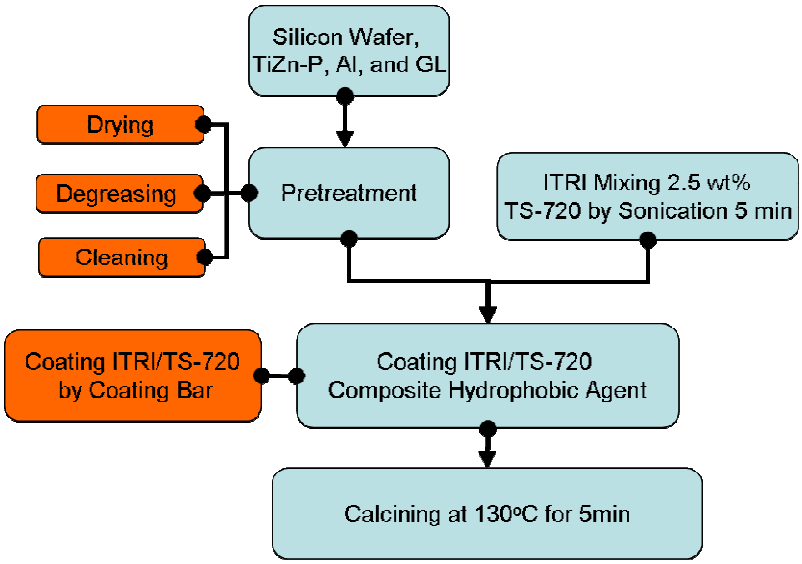

Schematic 1. The process of hydrophobic coating to a sample

Result and Discussion

The first experiment is using a Si wafer as the substrate. The morphology of the sample was via field-emission scanning electron microscope (FE-SEM, JEOL JSM-6500F). The specific contact angle of sample was calculated via static sessile drop method and contact angle goniometer (Sindatek, Model 100SB). Fig 2 demonstrates the SEM images of the Si wafer substrate when there is no hydrophobic coating, and the contact angle is 79.0°. Fig 3 demonstrates the SEM images of the Si wafer substrate coated with ITRI H.A. adding 2.5 wt% TS-720 which covered the Si wafer surface and observed a nanoporous structure, the inset fig presents the contact angle is 139.4°. After Si wafer coated with ITRI/2.5 wt% TS-720 composite, 60.4^{o} of contact angle is increased, with an enhancement of 76.5%.

The surface structure of sample was analysized by atomic force microscope (AFM, Veeco di-CP II). Fig 4(a) shows the 2D image of the wafer surface when there is no hydrophobic coating. Fig 4(b) shows the 3D image of wafer surface. The roughness was 2.5nm and the vertical height was 4.3nm, as shown in Fig 4(c). Fig 5(a) shows the 2D image of the wafer surface coated with ITRI H.A. adding 2.5 wt% TS-720. Fig 5(b) shows the 3D image of wafer surface coated with ITRI H.A. adding 2.5 wt% TS-720. The further observation of the surface morphology and roughness, the nanoparticle covered the entire sample surface. The roughness was 52.2nm and the vertical height was 228.5nm, as shown in Fig 5(c).

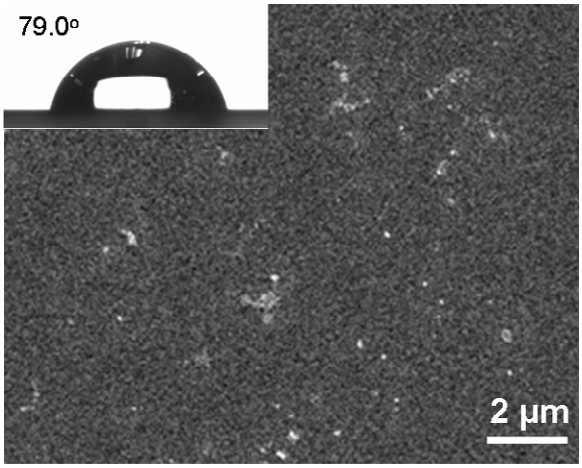

Fig 2 The morphology of Si wafer surface, and the inset presents the contact angle is 79.0° .

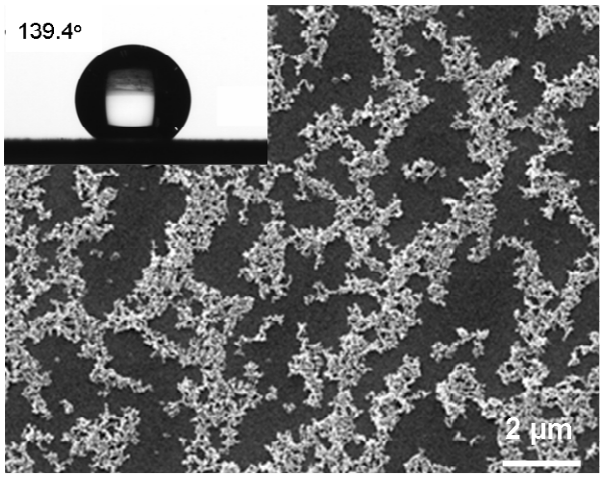

Fig 3 The morphology of Si wafer surface coated with ITRI H.A. adding 2.5 wt% TS-720, and the inset fig presents the contact angle is 139.4°.

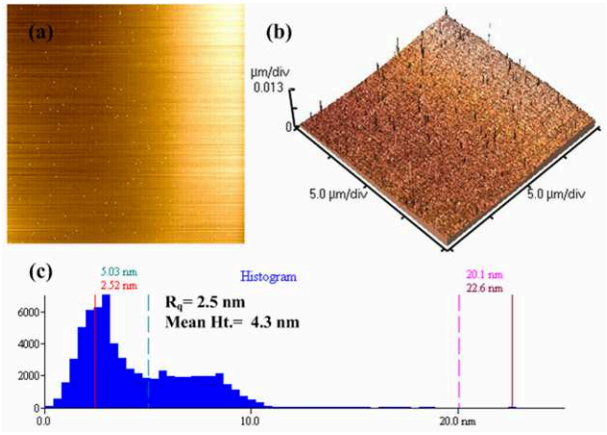

Fig 4. AFM image analysis of Si wafer surface, (a) 2D image, (b) 3D image, and (c) the roughness and the vertical height curve.

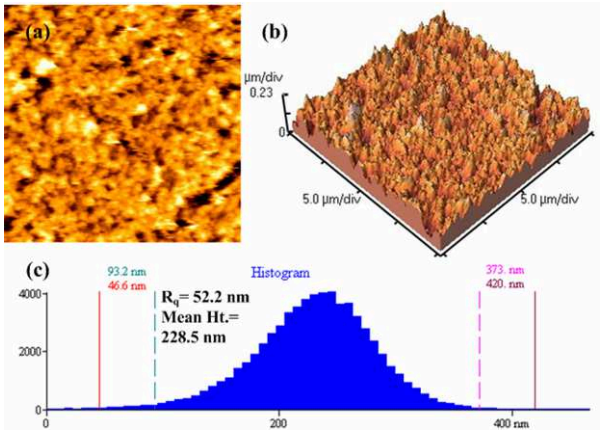

Fig 5. AFM image analysis of Si wafer surface coated with ITRI adding 2.5 wt% TS-720, (a) 2D image, (b) 3D image, and (c) the roughness and the vertical height curve.

Further experiment by using various metal substrates, the TiZn pre-weathered (TiZn-P), Al, and GL. Fig 6 demonstrates the SEM images of the TiZn-P surface with no hydrophobic coating and the contact angle is 97.6°. Fig 7 demonstrates the SEM images of the TiZn-P coated with the ITRI H.A. adding 2.5 wt% TS-720. The surface covered with microrods crystalline structure, and the TS-720 filled in the aggregate surface, and its contact angle is 142.1°. After TiZn-P coated with ITRI/2.5 wt%TS-720 composite, the contact angle increased 44.5°, with an enhancement of 45.6%.

Fig 8(a) shows the 2D image of the TiZn-P surface with no hydrophobic coating, . Fig 8(b) shows the 3D image of TiZn-P. The TiZn-P surface had micro crystalline structure, thus the surface roughness is higher. The surface roughness was 77.2nm and the vertical height was 329.0nm, as shown in Fig 8(c). Fig 9(a) shows the 2D image of the TiZn-P surface coated with ITRI H.A. adding 2.5 wt% TS-720. Fig 9(b) shows the 3D image of TiZn-P surface coated with ITRI H.A. adding 2.5 wt% TS-720. The further observation of the surface morphology and roughness, the nanoparticle fully covered the entire sample surface, and the aggregation of TS-720 can be observed clearly. The roughness was 107.5nm and the vertical height was 375.2nm, shown in Fig 9(c).

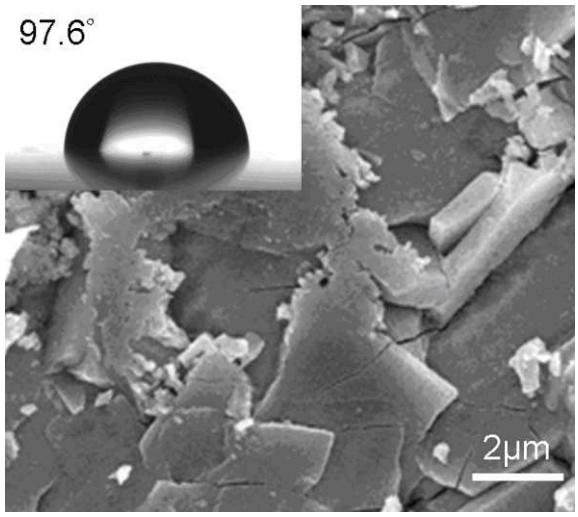

Fig 6 The morphology of TiZn-P surface, and the inset presents the contact angle is 97.6°.

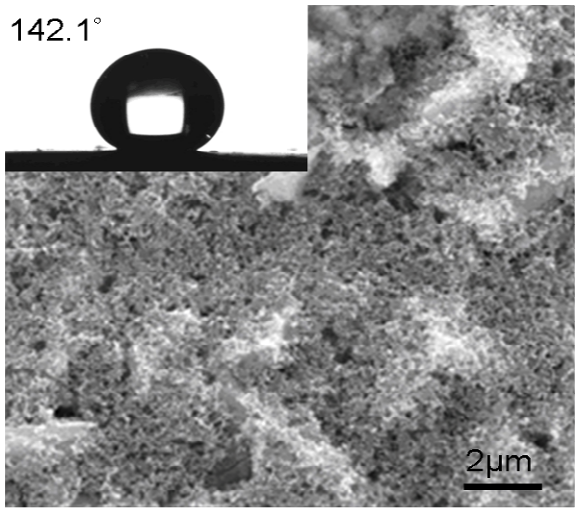

Fig 7 The morphology of TiZn-P surface coated with ITRI H.A. adding 2.5 wt% TS-720, and the inset presents the contact angle is 142.1°

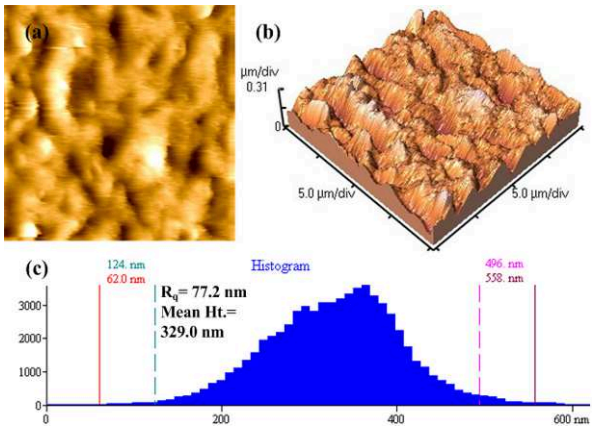

Fig 8 AFM image analysis of TiZn-P surface, (a) 2D image, (b) 3D image, and (c) the roughness and the vertical height curve.

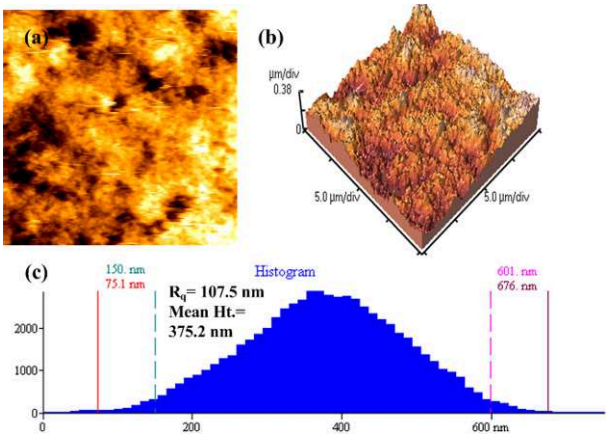

Fig 9 AFM image analysis of TiZn-P surface coated with ITRI adding 2.5 wt% TS-720, (a) 2D image, (b) 3D image, and (c) the roughness and the vertical height curve.

Fig 10 demonstrates the SEM images of the Al substrate when there is no hydrophobic coating. There were some fixed directional linear 4 – 10 μm width scratches on the surface, which were the mirroring roll machining mark from coil rolling, and the inset fig presents the contact angle is 76.4°. Fig 11 demonstrates the SEM images of the Al substrate coated with ITRI H.A. adding 2.5 wt% TS-720 which covered the Al surface completely, and the nanoporous structure was observed, the inset fig presents the contact angle is 141.3°. After Al coated the ITRI/2.5 wt%TS-720 composite, the contact angle increased 44.5°, with an enhancement of 84.9%.

Fig 12(a) shows the 2D image of straight rolling scratches on the Al surface with no hydrophobic coating. Fig 12(b) shows the 3D image of Al surface. The roughness was 15.9nm and the vertical height was 116.7nm, as shown in Fig 12(c). Fig 13(a) shows the 2D image of the Al surface coated with ITRI H.A. adding 2.5 wt% TS-720. Fig 13(b) shows the 3D image of Al surface coated with ITRI H.A. adding 2.5 wt% TS-720. Through further observation of the surface morphology and roughness, the nanoparticle covered the entire sample surface. The roughness was 89.6nm and the vertical height was 445.2nm, as shown in Fig 13(c).

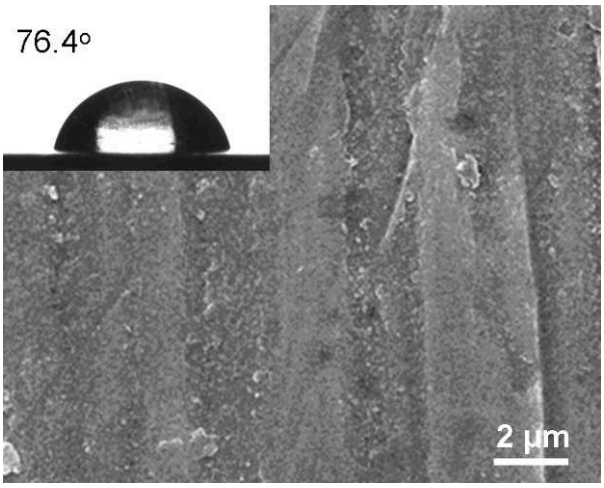

Fig 10 The morphology of Al surface, and the inset presents the contact angle is 76.4°.

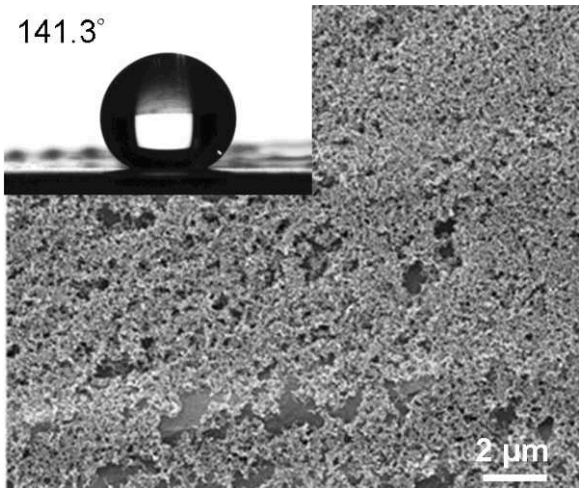

Fig 11 The morphology of Al surface coated with ITRI H.A. adding 2.5 wt% TS-720, and the inset fig presents the contact angle is 141.3°.

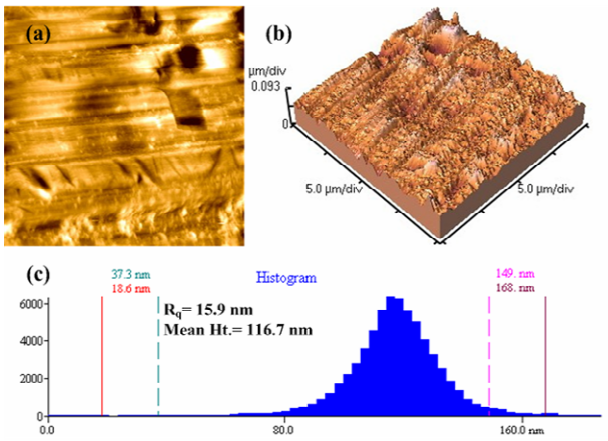

Fig 12. AFM image analysis of Al surface, (a) 2D image, (b) 3D image, and (c) the roughness and the vertical height curve.

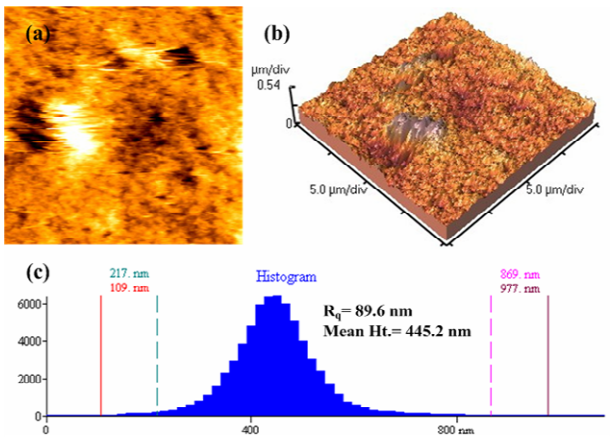

Fig 13. AFM image analysis of Al surface coated with ITRI adding 2.5 wt% TS-720, (a) 2D image, (b) 3D image, and (c) the roughness and the vertical height curve.

Fig 14 demonstrates the SEM images of the GL substrate with no hydrophobic coating. The island-like surface structure is from the hot-dipping galvalume (G.L.) process, which caused the zinc aluminum (Zn-Al) tends to the island-grow mode, the inset fig presents the contact angle is 93.6°. Fig 15 demonstrates the SEM images of GL coated with ITRI H.A. adding 2.5 wt% TS-720. The coated surface was covered by the TS-720 nanoparticle with an aggregation of nanoporous structure, the inset fig presents the contact angle is 138.6°. After GL coated the ITRI/2.5 wt%TS-720 composite, the contact angle increased 44.5°, with an enhancement of 48.1%.

Fig 16(a) shows the 2D image of the GL surface with no hydrophobic coating. Fig 16(b) shows the 3D image of GL surface. The GL surface roughness was 190.7nm and the vertical height was 1.121μm, as shown in Fig 16(c). Fig 17(a) shows the 2D image of the GL surface coated with the ITRI H.A. adding 2.5 wt% of TS-720. Fig 17(b) shows the 3D image of GL surface coated with the ITRI H.A. adding 2.5 wt% of TS-720. Through further observation of the surface morphology and roughness, the nanoparticle fully covered the entire sample surface. The roughness was 103.4nm and the vertical height was 380.0nm, as shown in Fig 17(c).

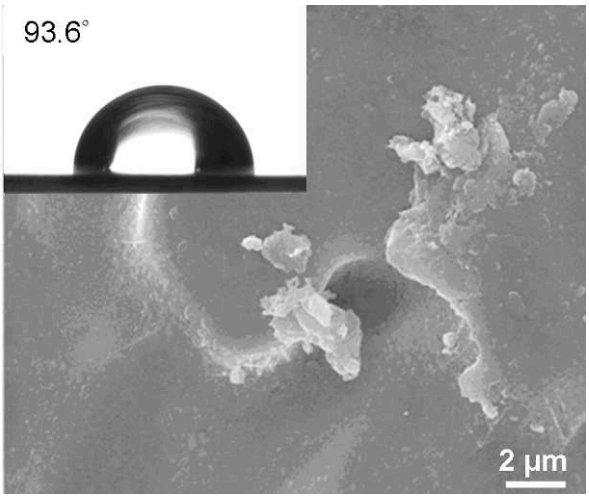

Fig 14 The morphology of GL surface, and the inset presents the contact angle is 79.0°.

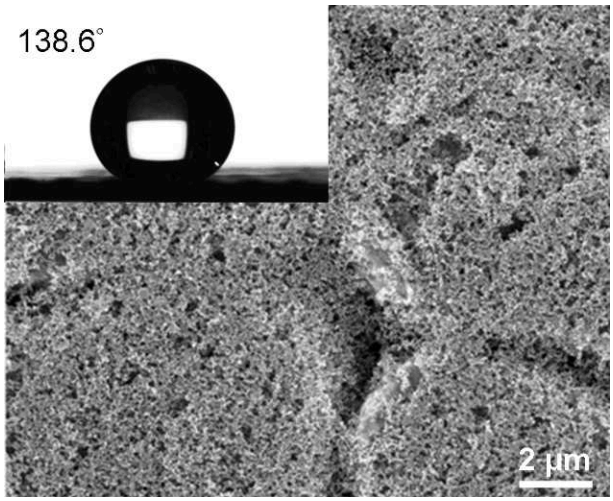

Fig 15 The morphology of GL surface coated with ITRI H.A. adding 2.5 wt% TS-720, and the inset fig presents the contact angle is 139.4°.

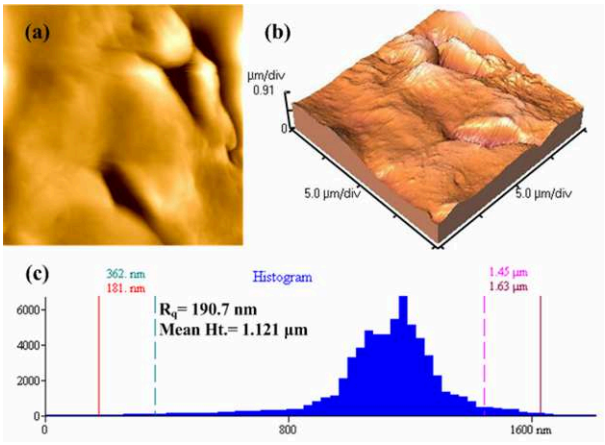

Fig 16. AFM image analysis of GL surface, (a) 2D image, (b) 3D image, and (c) the roughness and the vertical height curve.

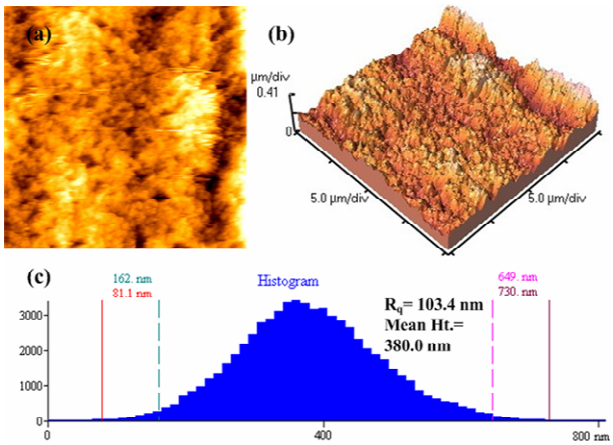

Fig 17. AFM image analysis of GL surface coated with ITRI adding 2.5 wt% TS-720, (a) 2D image, (b) 3D image, and (c) the roughness and the vertical height curve.

The original contact angles of various substrates were lower than 98° when the surface is without hydrophobic agent coating, which are shown on Table 1. After coating with the ITRI H.A. adding 2.5 wt% of TS-720, higher contact angles were generated which are between 138° – 142°. The enhancement of contact angle is above 45%. The best contact angle enhancement is from Al substrate (84.9%).

Table 1. The contact angle variation of various materials coated ITRI/TS-720 composite.

	Silicon Wafer	TiZn-P	Al	GL
No Coating	79°	97.6°	76.4°	93.6°
Coating ITRI/TS-720 Composite	139.4°	142.1°	141.3°	138.6°
Enhanced Contact Angle Ratio	45.6%	45.6%.	84.9%	48.1%

Conclusion

Making samples with a coating bar is an adopted mature process to current coil coating industry during color matching. This study, using the ITRI H.A. adding with TS-720 nanoparticle as the hydrophobic agent, operating the process in atmosphere parameters, demonstrates the possibility of using current facilities from coil coating industry to produce a hydrophobic surface with self-cleaning, anti-pollution and corrosion resistance for various substrates. Thus process is low cost and low technology threshold to current coil coating industry.

References

[1] W. Berthlott and C. Neinhuis, Purity of the Sacred Lotus, or Escape from Contamination in Biological Surfaces, Planta 202 (1997), No. 1, 1 – 8.

[2] R. N. Wenzel, Resistance of Solid Surfaces to Wetting by Water, Industrial and Engineering Chemistry 28 (1936), No.8, 988 – 994.

[3] A. Cassie and S. Baxster, Wettability of Porous Surfaces, Transactions of the Faraday Society 40 (1944), 546 – 551.

[4] T. Onda, S. Shibuichi, N. Satoh, and K. Tsujii, Super-Water-Repellent Fractual Surfaces, Langmuir 12 (1995), No. 9, 2125 – 2127.

[5] S. Shibuichi, T. Onda, N. Satoh, and K. Tsuji, Super Water-Repellent Surfaces Resulting from Fractal Structure, Journal of Physical Chemistry 100 (1996), No.50, 19512 – 19517.

[6] W. Ming, D. Wu, R. van Benthem, and G. de With, Superhydrophobic Films from Raspberry-like Particles, Nano Letters 5 (2005), No. 11, 2298 – 2301.

[7] X. Hou, F.Zhou, B. Yu, and W. Liu, Superhydrophbic Zinc Oxide Surface by Differential Etching and Hydrophobic Modification, Material Science and Engineering: A 452 – 453 (2007), 732 – 736.

[8] C.-H. Xue, S.-T. Jia, J. Zhang, L.-Q. Tian, H.-Z. Chen, and M. Wang, Preparation of Superhydrophobic Surfaces on Cotton Textiles, Science and Technology of Advanced Material 9 (2008), No. 3, 035008.

[9] Q. Xie, G. Fan, N. Zhao, X. Guo, J. Xu, J. Dong, L. Zhang, Y. Zhang, and C. C. Han, Facile Creation of a Bionic Super-Hydrophobic Block Copolymer Surface, Advanced Materials 16 (2004), No. 20, 1830 – 1833.

[10] Z. H. Zheng, Z. Y. Chen, C. F. Zheng, Proton Conducting Membrane of Sulfonated Fluorine-Free Polymer Blend Having Low Methanol Uptake and Low Methanol Permeability, Taiwan Patent 200,724,573. (2001).

Advanced Materials Research Vols. 960-961 (2014) pp 189-192

doi:10.4028/www.scientific.net/AMR.960-961.189

Porous aluminum titanate ceramics prepared using graphite as pore former

Genfa Zhao[1,a], Yang Bai[1,b], Lijie Qiao[1,c]

[1]Key Laboratory for Environmental Fracture (Ministry of Education), Advanced Material and Technology Institute, University of Science and Technology Beijing, Beijing 100083, China

[a]zhaogenfa@163.com, [b]baiy@mater.ustb.edu.cn, [c]lqiao@ustb.edu.cn

Keywords: Porous ceramic; Aluminum titanate; Thermal expansion; Porosity

Abstract: This paper described the properties of porous aluminum titanate (AT) ceramics. The AT samples with composition of 41 wt% Al_2O_3, 50 wt% TiO_2, 4.5 wt% MgO and 4.5 wt% Fe_2O_3 while 0~60 wt% graphite was used as pore former. The pore structures of the samples sintered at 1250~1350 ^oC were analyzed by scanning electron microscopy and Hg porosimetry, while the crystal phases of the aluminum titanate were analyzed by X-ray diffraction. After sintered at, the samples have open porosities of 25~51%, depending on the graphite amount and the sintering temperature. The porosity increases and the flexural strength decreases with the increasing amount of graphite.

Introduction

Aluminum titanate ceramic (Al_2TiO_5, AT) is promising material for many structural applications for their high melting point (1860 ^oCmatthew henrichsen), low thermal expansion coefficient (~1×10^{-6} $^oC^{-1}$), low thermal conductivity (0.9~1.5$Wm^{-1}K^{-1}$) and excellent thermal shock resistance.[1,2,3,4,5] However, its industrial applications are hindered by two drawbacks. One is the decompose into α-Al_2O_3 and TiO_2-rutile within the temperature range between 800 ^oC and 1280 ^oC.[6] The other is poor fractural strength due to microcracks.[7,8] In order to eliminate the drawbacks and improve the properties, much work has been done on doping additives into the raw materials.[9,10,11] This work is concerned with the fabrication of porous aluminum titanate ceramic materials using graphite as pore former, which endows the samples with different levels of porosity.

Experimental procedure

The raw materials were α-Al_2O_3(>99%, median particle size 53μm) and TiO_2(>99%, median particle size 0.8μm) powders on a molar ratio of 7:11 while 4 wt% MgO and 4 wt% Fe_2O_3 were added as additives. Then the mixtures were mixed with 25-55 wt% of graphite by planetary ball milling for 3 h. After that, the mixed powders with 5 wt% binder (PVA) was pressed uniaxially under a pressure of 3 MPa for disc samples (15mm diameter) and 15Mpa for rectangular samples (100 mm ×10 mm ×10 mm). Then, the dried samples were sintered at 1250 ^oC, 1300 ^oC, 1350 ^oC for 1h.

Linear dimensional changes of the sintered pellets were measured using a vernier caliper. The porosity and pore size distribution was measured by a mercury intrusion porosimeter (AutoPore IV 9500). Room temperature flexural strength was determined by the three-point bending method in a universal materials testing machine (CDW-5). The microstructure of the fracture surfaces of the

sintered samples was observed using a scanning electron microscopy (SEM, S440i). The linear thermal expansion coefficient were measured in a horizontal dilatmeter over the temperature range of 25-1100 °C at a heating rate of 10 °C /min. The phase composition was characterized using XRD (Cu Kα radiation; Rigaku DMAX-RB 12KW) for the sintered disc samples. The density of the specimens was measured using the Archimedes principle with water as medium. Thermogravimetric analysis (TGA) and differential scanning calorimetry (DSC) analysis were performed by TA instrument SDT 600 at a heating rate of 10 °C/min from 25 °C to 1350 °C.

Result and discussion

The XRD results (Fig. 1.) shows that the sintering at 1350°C for 1 h is enough to form nearly 100% Al_2TiO_5 with tiny Al_2O_3 and TiO_2 remnants, while the specimen sintered at 1250°C has a lot of Al_2O_3 and TiO_2 remnants.

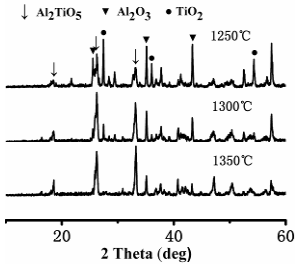

Fig. 1 XRD spectra of the samples sintered at 1250 °C, 1300 °C and 1350 °C for 1 h

Fig. 2 shows the linear shrinkage rate and bulk density as a function of the graphite content and the sintering temperature. Both the shrinkage rate and the bulk density increases with the increasing sintering temperature. The density decreases monotonically with the rise of the graphite amount, which tends to a steady value gradually. The shrinkage rate varies with graphite amount complexly. It decreases first, reaches a minimum at about 25wt% graphite, and then increases until 60wt% graphite. The thermal expansion curves of the samples with different graphite amount are shown in Fig. 3. The thermal expansion coefficient of the specimens varies between 0.76% and 0% in the temperature range 25~1100°C.

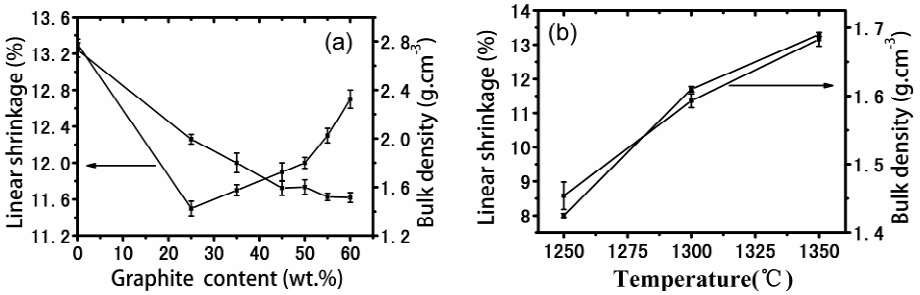

Fig. 2 Variation of linear shrinkage rate and bulk density of the porous AT ceramics with (a) graphite content (b) sintering temperature

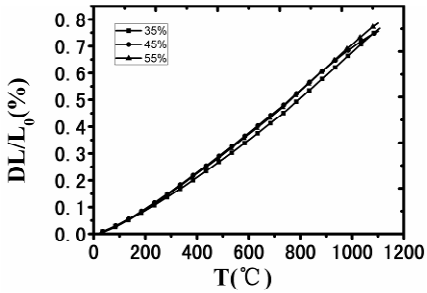

Fig. 3 Thermal expansion of the samples with 35-55 wt% graphite and sintered at 1300°C

The microstructures of the fracture surfaces of the porous AT ceramics are shown in Fig. 4(a-g). The specimens show obvious porous structure. The sizes of pores are in good agreement with the mercury porosimetry results. The pores of the sample without graphite addition are small. The number and size of the pores increase with the rise of graphite addition, while tends to steady as graphite amount is above 45wt%.

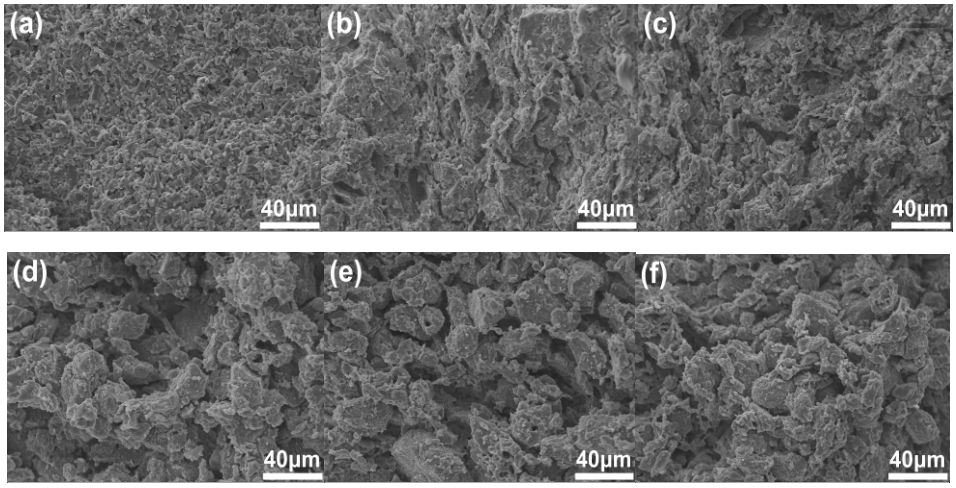

Fig. 4 SEM micrographs of the fracture surfaces of the porous AT ceramics with different graphite amount (a) 0 wt%; (b) 25 wt%; (c) 35 wt%; (d) 45 wt%; (e) 50 wt%; (f) 55 wt%

The open channels among pores result in an open porosity. Fig. 5 illustrated the effects of the graphite addition and the sintering temperature on the apparent porosity and median pore diameter. The apparent porosities increases from 25% to 51% as the amount of graphite increases from 0 wt% to 55 wt%. These results imply that the apparent porosity are determined by the amount of pore former. The apparent porosity and median pore diameter of the sample without graphite are 24.55% and 1.37μm, while those are 51.29% and 10.25μm for the sample with 55 wt% graphite. The median pore diameter increases with the rise of sintering temperature. The sample with 45 wt% graphite sintered at 1300°C has the highest apparent porosity and median pore diameter.

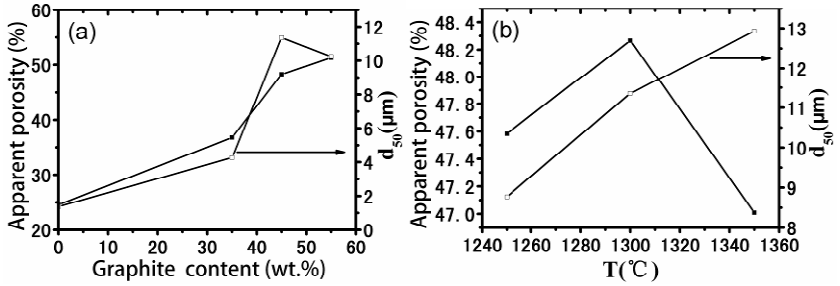

Fig. 5 (a) Influence of graphite content and (b) sintering temperature on the apparent porosity and the median pore diameter

Fig. 6 shows the pore size distribution for the samples with different graphite amount and sintered at different temperatures. The pore size distribution shows a sharp peak. The samples with 45 wt% and 55 wt% graphite have two types of pore size, one corresponding to the intrinsic pore size distribution and the other to those formed by burning-off of pore former[12]. he pore size distribution of the sintered samples is very uniform. With the rise of sintering temperature, median pore diameter is concentrated at 8.77μm, 11.35μm, and 12.94μm, respectively.

Fig. 7 shows the flexural strength of the sintered porous AT ceramics as a function of graphite amount. The strength decreases with the rise of graphite amount, especially from 25% to 35 wt%, because of the increase of porosity and pore size.

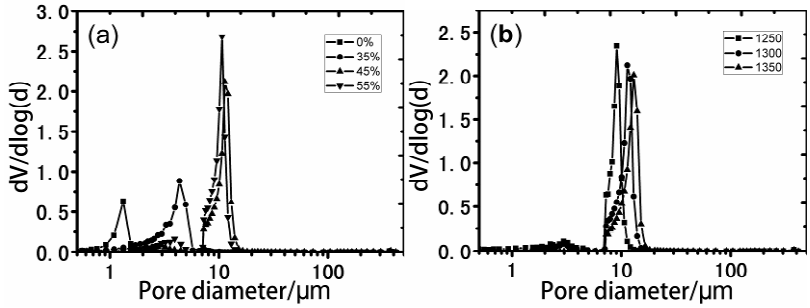

Fig. 6 Pore size distribution (a) different graphite amount (sintered at 1300°C for 1h); (b) different sintering temperatures (45 wt% graphite)

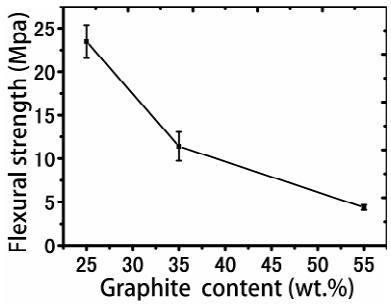

Fig. 7 The flexural strength of the porous AT sintered at 1300°C with graphite contents (25-55wt%)

Conclusions

The porosity increases and the flexural strength decreases with increasing graphite amount. The samples shows open porosities between 24.55% and 51.29% and median pore diameter between 1.37μm and 12.94μm with graphite within 0 wt% to 55 wt%. Flexural strengths of the samples with 25, 35 and 55 wt% graphite are 23.47±1.90, 11.41±1.66 and 4.38±0.29 MPa.

References

[1] Gurauskis J, Sánchez-Herencia AJ, Baudín C: J. Eur. Ceram. Soc., 2007, 27, 1389–1394.
[2] De Portu G, Bueno S, Micele L, Baudín C, Pezzotti G: J. Eur. Ceram. Soc., 2006, 26, 2699–2705.
[3] R. Uribe, C. Baudin: J. Am. Ceram. Soc., 2003, 86, 846–850.
[4] Rainforth WM: J. Mater. Sci., 2004, 39, 6705.
[5] Low, I. M., Lawrence, D. and Smith, R. I: J. Am. Ceram. Soc., 2005, 88, 2957–2961.
[6] Nagano, M., Nagashima, S., Maeda, H. and Kato, A.: Ceram. Int. 1999, 25, 681–687.
[7] Buscaglia, V., Battilana, G., Leoni, M. and Nanni, P.: J. Mater. Sci.,1996, 31, 5009–5016.
[8] Buscaglia, V., Nanni, P., Battilana, G., Aliprandi, G. and Carry, C.: J. Eur. Ceram. Soc., 1994, 13, 419–426.
[9] Buscaglia, V. and Nanni, P.: 1998,81, 2645–2653.
[10] Park, S. Y., Jung, S. W. and Chung, Y. B.: Ceram. Int.,2003, 29, 707–712.
[11] Bueno S, Moreno R, Baudín C: J. Eur. Ceram. Soc., 2004, 24, 2785–2791.
[12] Bahman Amini Horri, Cordelia Selomulya, Huanting Wang: Int. J. Hydrogen Energy, 2012, 37, 15311-15319.

Advanced Materials Research Vols. 960-961 (2014) pp 193-198

doi:10.4028/www.scientific.net/AMR.960-961.193

Research on changes of chemical compositions in the simulation of shark fin processing

Xiong ZHANG[1, a], Zhen-hua Duan[1, 2, b*] and Yi-wei Feng [1, c]

[1]College of Food Science and Technology, Hainan University, Haikou 570228, China

[2]Key Laboratory of Tropical Biological Resourced of MOE, Hainan University, Haikou 570228, China

[a]286517476@qq.com, [b] dzhwjl@hotmail.com (*corresponding author), [c]1124802945@qq.com

Keywords: Tilapia fishtail, byproducts, Chondroitin sulfate, Collagen, Simulation shark fin.

Abstract. The aim of this study is to investigate the changes of chemical compositions in the process of simulation shark fin. The simulation shark fin was produced by tilapia fishtail; whose main chemical compositions were collagen and chondroitin sulfate (CS). The study indicated that both of them had different change trend in the process of simulation. The process of softening had main effect on the content of collagen, the higher of ice acetic acid concentration, the lower of the level of collagen. The content of CS was related to the process of obtaining wings, and the high temperature would induce a reduction of CS. The content of collagen and CS could be maintained efficiently by improving the processing technology of simulation shark fin.

Introduction

In general, natural shark fin is made by shark's fin [1-2], and its main composition is protein, fat and minerals. With the improvement of people's living standard, there are more and more demands for shark fin. However, a large variety of sharks were slaughtered to get the shark fins. Therefore, it is essential to develop a technology of simulation shark fin to suppress the decline of shark. Nowadays, hybrid tilapias are used as the material of shark fin. At the same time, sodium alginate and gelatin are also used to make it [3].

The tilapia production in Hainan province accounted for 59% of all freshwater aquaculture production in China, which is the biggest export aquatic product. In the present, people focus their attention on the study of fish fillets and the extraction of pectin [4-9], and a large amount of byproducts are produced. Accumulating evidence suggested that tilapia fishtail could be used to prepare the simulation shark fin by the process of alkali treatment and acetic acid soften [10]. The simulated shark fin is similar to natural shark fin in appearance and taste, so this technology can take advantage of the tilapia byproducts effectively.

The utilization of byproducts can improve the additional value of products, whereas, the process of simulation shark fin will lead to the loss of collagen [11-15] and chondroitin sulfate[16-19], which is the main nutrients of fishtail. So it is critical to learn the tendency of nutrition change in the process of simulation, and it can provide theoretical basis for improving the quality of product.

Materials and methods

Materials. Tilapia(*Oreochromis niloticus*) fishtail was provided by Hainan Golden Spring Foods Co., Ltd. (China); standard chondroitin sulfate was purchased from Sigma-Aldrich (USA); compound protease (3.8×10^5 U/g) was bought from Novo. All the other reagents used in the experiment were analytical grade.

The tilapia fishtail were boiled in 80℃ water for 1h, removed the impurities and cleaned the bones, then dried in the constant temperature 65℃ for 4h, then stored at 4℃ in refrigerator until used.

Extraction of Collagen 0.5mL standard hydroxyproline added 1mL isopropyl alcohol, stir 2 minutes after added in oxidant A 0.2mL, placed 4 min after added chromogenic agent B 6.5mL at room temperature. Placed it under the condition of 60 ℃ keep 25 minutes, then cooled it to room temperature, determination the absorbance at 558 nm. Drawing standard curve with the Ammonia concentration (C) as the abscissa, absorbance (A) as the ordinate, the regression equation is that A=0.0355C+0.0024，R^2=0.9997.

The oxidant A was mixed by Sodium Citrate, Citric acid, Sodium acetate, and Isopropyl alcohol. Add the concentration of 7 g/100ml Chloramine-T, mixed them with the ratio of 1:4. The chromogenic agent B was mixed by p-dimethyl amino benzaldehyde and Isopropyl alcohol, with the ratio was 2:13. Put the samples (m_0) 4~6 mg in the block test tube, add 5mL, 6 mol/L HCl at 110 ℃ for 24 h, fix the capacity to 25mL with distilled water, using NaOH adjust pH value to 7, distilled water to 50mL. Take 0.2mL liquid sample under test, according to the standard curve of hydroxyproline in the standard liquid handling and measure its absorbance, the extraction rate of Collagen was calculated by the following formula:

$$\text{Collagen}(\%)=\frac{C\times V\times F}{m_0\times 1000}\times 100$$

Where C is the mass concentration of hydroxyproline; V was the volume of sample solution; F is 11.1; m_0 is the weight of raw materials. Every experiment was repeated three times, and averaged.

Extraction of Chondroitin Sulfate Take a certain volume chondroitin sulfate[20] standard or sample solution, put them in the two 10mL test tubes, respectively ,add distilled water to make the solution volume to 1.00mL, placed in ice water, then added 6 mL concentrated sulfuric acid, put in boiling water heating 20 min, then placed in ice water. One adds 0. 20mL carbazole solution, another one add 0.20mL ethanol without aldehyde as blank, put them in boiling water heating 15 min, then put in ice water to cool quickly. With blank solution for reference, determined the chondroitin sulfate's absorbance (A) under 520 nm, the regression equation is that A=1.2257C+0.0141, R^2=0.9942.

3.0g tilapia fishtail powder was soaked in 10mL petroleum ether for 5 minutes, poured out petroleum ether, add 10mL NaOH ultrasonic processing 25 min, then add 10mL again, extracted, put in water bath for 1h at 50℃(stirring once every 20 minutes). Adjusted the pH to 2~3, then adjusted it to 7 as soon as possible, filtered. Then it was necessary to measure the volume of the filtrate, added 2% compound protease into the filtrate, hydrolyzed it in water bath for 2h at 50℃. During that process keeping pH at 7.0, when the zymohydrolysis was accomplished, the solution would be heated to 85℃ for 5min to kill the enzyme, and decolorized with 2% activated carbon and removed protein and then filtered. Finally, the content of the chondroitin sulfate was measured by spectrophotometer. The extraction rate of CS was calculated by the following formula:

$$CS=\frac{C.N.V}{M\times 10^3}\times 100$$

Where C is the mass concentration of CS; N is the dilution time; V is the volume of sample solution; M is the weight of raw materials. Every experiment was repeated three times, and averaged.

Experimental design Take 50g dry fish tail, take wing by NaOH solution, then dip in black tea, filtering, dry in 30℃ constant temperature for 2 h. Soften, soak in the collagen solution, increase the simulation the taste of shark fin [21].

Measure the variation of collagen and chondroitin sulfate in the tail material, NaOH take wing, collagen optimization, and ice acetic acid softening after optimized and rehydrated.

The content of collagen and chondroitin sulfate were reduced more in the process of softening, in order to ensure the simulation of the shark fin's chemical composition, research the influence of the process of ice acetic acid concentration, softening time, and temperature in the shark fin's chemical composition content.

Results and Discussion

The Effect of Changes of Chemical Compositions in the Simulation of Shark Fin Processing. It can be seen from Figure 1a, the content of collagen was gradually reduced as the process going until reached to the ice acetic acid softening, then the yield increased when it reached to the collagen soaking the optimized fin, and then decreased little in rehydration, this might was because that collagen were extracted by NaOH and ice acetic acid treatment from the simulation shark fin, which lead to a drop of collagen content. The content of collagen in the simulation shark fin soaking by collagen solution will improve significantly; it can absorb part of the same kind of collagen. After rehydration, the collagen on the surface of the simulation shark fin will be lost to the solution.

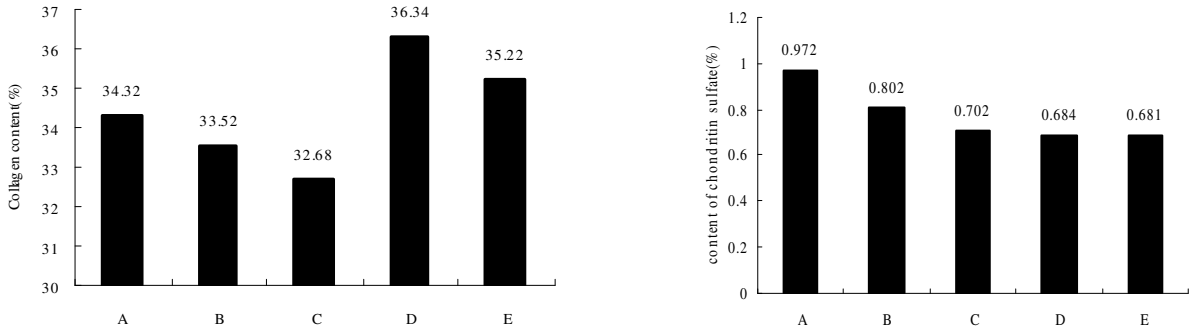

a **simulated process** **b** **simulated process**

Figure 1. Effects of simulated conditions on the chemical composition (a,collagen;b,chondroitin sulfate)

Figure 1 was the change of collagen content under different process conditions. A was the fish collagen content in the raw material; B was the collagen content in NaOH take wings; C was the collagen content in the ice acetic acid softening; D was the collagen content in soaking the optimized fin; E was the collagen content after product rehydration.

From figure 1b, the results showed that the content of chondroitin sulfate reduced greatly when it in the NaOH. It was because that the alkaline environment will extract part of the chondroitin sulfate[22] from the shark fin, resulted the decrease of chondroitin sulfate content in the shark fin. After softening technology, the content will reduce, too, this may be because part of chondroitin sulfate loss in the solution. Then it will remain stable in other conditions. It has no obvious change when it was soaked by collagen solution and rehydration. These results showed that the process of the ice acetic acid softening has the biggest change in these two chemical components.

The Effect of Concentration on Changes of Chemical Composition. When the time, temperature, ratio of solid to liquid were fixed at 120min, 45℃ and 1:20, respectively, the effect of different ice acetic acid concentration on change trend of chemical was showed in Figure 2.

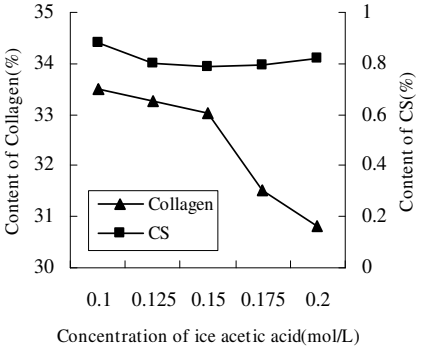

Figure 2. Effect of chemical composition content by different concentration

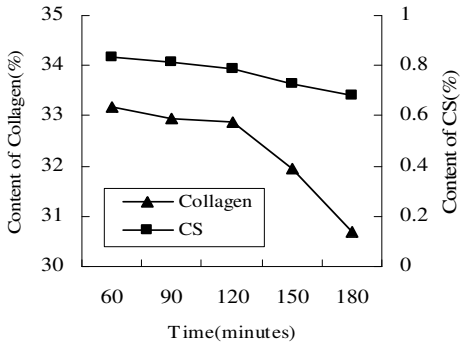

Figure 3. Effect of chemical composition content by different time

It reflected in Figure 2 that the content of collagen and chondroitin sulfate were significantly reduced with the increase of ice acetic acid concentration, and it showed a trend of rapid decline when the concentration higher than 0.15%, this is because that with the increase of acid concentration, the collagen will extracted from the shark fin, resulting in a loss of product in the content. The softening effect is better when the ice acetic acid concentration is higher than 0.1%, and the simulation of collagen in the shark fin will loss a lot when the concentration higher than 0.175%. In order to keep the chemical compositions of the simulation shark fin, and didn't damage the softening effect, we need to make sure the concentration of ice acetic acid is between 0.125% and 0.15%.

The Effect of Time on Changes of Chemical Composition. When the ice acetic acid concentration, temperature, ratio of solid to liquid were fixed at 0.15mol/L, 45℃ and 1:20, respectively, the effect of different time on change trend of chemical was showed in Figure 3. From the figure 3, the results showed that the content of collagen and chondroitin sulfate were significantly reduced. The content of collagen changed a little, but the content of CS declined rapidly when the time was higher than 120 min, this indicated that the increase of time would lead to a decrease of the nutrients in the stimulation shark fin, and the shark fin's softening effect has little change after 120 min, but the decrease of collagen is very obvious, this is not conducive to the production of the products.

The Effect of Temperature on Changes of Chemical Composition. When the ice acetic acid concentration, time and ratio of solid to liquid were fixed at 0.15mol/L, 120min and 1:20, respectively, the effect of different temperature on change trend of chemical was showed in Figure 4.

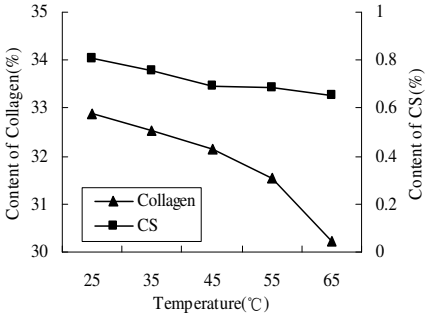

Figure 4. Effect of chemical composition content by different temperature

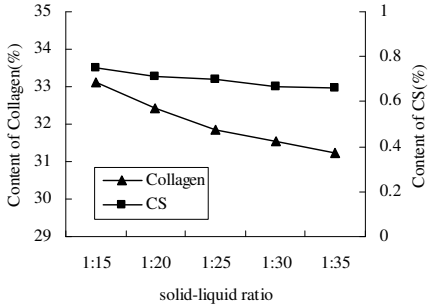

Figure 5. Effect of chemical composition content by different solid-liquid ratio

From the figure 4, the results showed that the content of collagen and chondroitin sulfate were significantly reduced. It kept stability when the temperature between 45 ℃ and 55 ℃. Collagen's downward trend is linear, which showed that the temperature will seriously affect the content of collagen, especially when the temperature is higher than 55 ℃.It showed that high temperature will lead to the dissolution of collagen in simulation shark fin. The content of CS is not obvious, when the temperature reached 45℃, it has a tread of steady. In order to keep the compositions, we need to keep the temperature less than 45℃, while the softening effect had no obvious change when the temperature higher than 45℃.

The Effect of Solid-liquid Ratio on Changes of Chemical Composition. When the ice acetic acid concentration, time and temperature were fixed at 0.15mol/L, 120min and 45℃, respectively, the effect of different ratio of solid to liquid on change trend of chemical was showed in Figure 5. From the figure 5, the results indicated that the content of collagen and chondroitin sulfate were significantly reduced. But the decline is not obvious, especially the change of CS, it's nearly without change, and the content of Collagen maintained a small amplitude stability reduce. While the softening effect was remain stable until the solid-liquid ratio is higher than 1:25. Generally speaking, the effect of solid-liquid ratio was not significant in the change of the content of chemical compositions.

Conclusion

The changes of the content of collagen and chondroitin sulfate were researched in the process of simulation shark fin. Results showed that: these two kinds of contents were decreased significantly in the process of ice acetic acid softening shark fin, the ice acetic acid concentration has the bigger influence in the content of collagen, when the concentration is higher than 0.15 mol/L, the content of collagen will decline rapidly. The time has the bigger influence in the content of CS, when the time is higher than 120 min, the content of CS will loss more. And the process of take wing has an effect on the content of CS, and the temperature has bigger influence, when the temperature is higher than 55 ℃, the content of CS drops rapidly.

Acknowledgements

This work was financially supported by the authors wish to thank the financial support provided by the National Key Technologies R&D Program (Grant No. 2012BAD28B06) for the research work.

Reference

[1] F. X. Xu, X. Gao, "The extract and qualitative analysis of shark fin," Science and Technology of Food Industry , vol. 28, pp. 225-228, June, 2007. (In Chinese)

[2] Z. P. Feng, X. L. Lin, "The culture thinking of shark fin's consumption" Oceanic society of China in 2007 academic essays, pp. 304-307, December, 2007. (In Chinese)

[3] R. Q. Deng, X. J. Su, "Development of imitate shark fin". Food Science, vol. 7, pp. 44-47, July, 2001. (In Chinese)

[4] Z. H. Duan, Lina Jiang, J. L. Wang, "Drying and quality characteristics of fresh tilapia fillets dried with hot air-microwave heating". Food and Bioproducts Processing, 89,pp . 472-476,May,2011.

[5] Z. H. Duan, L. Zhang, J. L. Wang, "Study on Characteristic of Isothermal Desorption of Tilapia Meats," Food Science, vol. 32, pp. 82-85, June, 2011. (In Chinese)

[6] Y. Yang, Z. H. Duan, "Characteristics of vacuum-microwave drying of tilapia fillets and its drying kinetics" Food Science and Technology, vol. 35, pp. 101-104, 2010. (In Chinese)

[7] Z. H. Duan, L. Liu, J. L. Wang, "Research on the osmotic dehydration of tilapia fillets in salt solution ," Fisheries Science, vol. 31, pp. 18-21, January, 2012. (In Chinese)

[8] S. K. Zeng, X. Y. Yan, "Optimization of extraction conditions and characteristics of skin gelatin from Nile tilapia," International Journal of Food Science Technology, vol 9, pp. 1807-1813, July, 2010.

[9] Z. H. Duan, L. J. Wang, "Tilapia processing technology,"Scientific Fish Farming, vol. 32, pp. 69-70, Tanuary, 2006. (In Chinese)

[10] Xiong Zhang, Z. H. Duan. "Preparation of Simulated Shark Fin from Tilapia Fish Tail ," Meat Research, vol. 27,pp 24-27,April,2013. (In Chinese)

[11] X. J. Lian, X. X. lu, "The research process of fish collagen," Meat Research, vol. 95, pp. 46-49, January, 2007. (In Chinese)

[12] Ogawa M , Portier R J , Moody M W , "Biochemical properties of bone and scale collagens isolated from the subtropical fish black drum and sheepshead seabream,"Food Chemistry, vol,8,pp.495-501,4,2004.

[13] C. H. Zhong, C. G. Lee, "The study of Grass carp fish soluble collagen enzyme viscosity characteristics and deformation temperature," Food and Fermentation Industries, vol 32, pp.64-68, July, 2006. (In Chinese)

[14] Z. W. Duan, X. R. Shen, "Extraction and Identification of Collagen from Tilapia Tail,"Food Science, vol. 33, pp. 59-64,March, 2012. (In Chinese)

[15] L. X. Hu, J. Cheng, "Research on collagen extraction and application in fish byproducts," Chemistry and Bioengineering, vol. 26, pp. 7-17, February, 2009. (In Chinese)

[16] C. Y. Cheng, Z. H. Duan, "Optimization of chondroitin sulfate extraction from tilapia byproduct with response surface methodology," Food Science and Technology, vol. 36, pp. 213-218, March, 2011. (In Chinese)

[17] C. Lee, Z. H. Duan, "Optimization of Extraction of Chondroitin Sulfate from Tilapia Skull," Food Science, vol.30, pp. 234-237, 2009. (In Chinese)

[18] Z. J. Pu, L. Ma, "The research of chondroitin sulfate prepared by ultrasound," Journal of Sichuan Normal University, vol. 23, pp. 640-642, 2000. (In Chinese)

[19] A. C. Gu, C. Li, "Study on the extraction and purification technology of the Chondroitin Sulfate from polyodon spashula," Food Research and Development, vol. 28, pp.30-33, December, 2007. (In Chinese)

[20] ISO: 3496—1994. Meat and meat products-determination of hydroxy proline content[S]

[21] Z. D. Yu, G. M. Yang, "The determination of chondroitin sulfate by Carbazole spectrophotometric," Journal of Qingdao University, vol. 18, pp. 41-44, 2005. (In Chinese)

[22] L. P. Wei, L. K. Jiang, "Research on the extraction of Chondroitin Sulfate" Journal of Biology, vol. 24, pp. 55-57, 2007. (In Chinese)

Advanced Materials Research Vols. 960-961 (2014) pp 199-203

doi:10.4028/www.scientific.net/AMR.960-961.199

Study on the process optimization for intermediate Magnesium Carbonate Tri-hydrate

Dan Wu [1, a], Bijun Luo [2, b], Wei Liu [3, c], Licong Wang [4, d], Ying Yao [5, e], Xiping Huang [6, f]

[1,2,3,4,5,6]Institute of Tianjin Seawater Desalination and Multipurpose Utilization, State Oceanic Administration, Tianjin scientific research east road No. 1, China

[a] wudan_jay@126.com, [b] luobj0222@163.com, [c] tjtdlw615@163.com, [d] wanglicong@eyou.com, [e] yaoying8778@126.com,[f] xipinghuang@163.com

Keywords: Magnesium Carbonate Tri-hydrate; magnesium oxide; optimal conditions; brine

Abstract. It is a kind of high efficiency and energy saving new method to prepare high purity magnesium oxide (MgO) with magnesium carbonate tri-hydrate ($MgCO_3 \cdot 3H_2O$) as intermediate. Our research group had already designed orthogonal experimental and got the optimal process conditions of $MgCO_3 \cdot 3H_2O$. The operating parameters such as temperature, pH and reaction time had been further optimized in this paper. Intermediate $MgCO_3 \cdot 3H_2O$ with high aspect ratio and good settling performance was synthesized at the optimal temperature 40-50°C， the optimal pH 8.8-9.0, the optimal reaction time70min, the optimal condition also applied to brine system.

Introduction

High purity active magnesium oxide (MgO) is an important chemical raw material. It is the necessary material in the production of high-temperature thermocouple, is the high quality material in made of refractory, is used as drilling mud additives and catalyst and desulfurizer in refining. What is more, it is widely used in the chemical industry, metallurgy, medical equipment, building materials; ceramics, etc [1-3].The production of MgO in our country is very large. However, High value-added production of magnesia products is very small and can't meet the requirements of the development of industrial production, which is long-term dependence on imports. Therefore, it is an urgent need to research new industrial production technology of high purity active MgO.

Magnesium brine resources are abundant in China. How to make rational utilization of the brine as raw material to produce high-grade magnesium series products are an important way for comprehensive utilization of brine resources. It not only is the strategic needs of national economic development, also is the need of protecting the environment sustainable development. Magnesium carbonate tri-hydrate（$MgCO_3 \cdot 3H_2O$）can be used as precursors for the preparation of high purity active MgO with low calcine temperature, energy and cost [4-5]. $MgCO_3 \cdot 3H_2O$ with high aspect ratio and good settling performance was synthesized in this paper.

Experimental Sections

2.1 Materials. $MgCl_2 \cdot 6H_2O$ and NH_4HCO_3 solution (reagent grade, Tianjin Guangfu fine chemical research institute) were used as starting materials. Also, ammonium water was used for the additive to control pH (reagent grade, Tianjin northern Tianyi chemical reagent factory).

2.2 Characterization

The morphology and size of particles obtained were observed by scanning electron microscope (SEM; Philips XL30ESEM). The crystal structures of as-prepared samples were characterized by X-ray diffraction (XRD; Rigaku D/max 2500v/pc, Cu Ka radiation).

Results and Discussion

Our research group had already designed orthogonal experimental and got the optimal process conditions: reaction temperature is 40-50°C, n (Mg^{2+}): n (HCO_3^-) =1:2.2, n (HCO_3^-): n ($NH_3 \cdot H_2O$) =1:1, stirring speed is 130 r/min; aging time is 3h. The optimization experiments were taken in this paper.

3.1 Effect of different reaction temperatures on crystal morphology

The reaction temperature parameters of crystal growth have a great effect on crystal morphology. The temperature of 25°C, 40°C, 50°C, 55°C, 60°C and 70°C was carried out respectively in the optimal conditions to the aim of optimize experiment. Different crystal morphologies of $MgCO_3 \cdot 3H_2O$ at different reaction temperatures are shown in Fig.1. XRD patterns are shown in Fig.2.

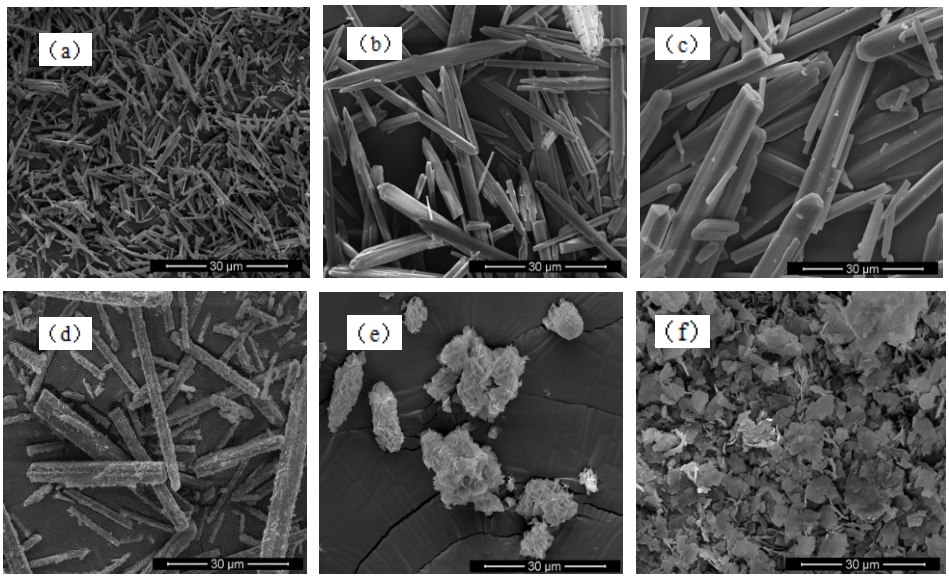

Fig.1 SEM images of $MgCO_3 \cdot 3H_2O$ with different temperature
(a)25°C,(b)40°C,(c)50°C,(d)55°C,(e)60°C,(f)70°C

It was possible to obtain different crystal morphologies of $MgCO_3 \cdot 3H_2O$ at different reaction temperatures. The reaction rate increased as the temperature rises. Only a few precipitations generated after 40 min in 25°C while a large number of precipitations generated after 15 min when the temperature was higher than 40°C. Needlelike or rod-like particles of $MgCO_3 \cdot 3H_2O$ were found to be formed when the temperature ranged from 40°C to 50°C [Figure 1(b) (c)]. $MgCO_3 \cdot 3H_2O$ deposited as a metastable phase in 55°C [Figure 1(d)], whereas no formation of $MgCO_3 \cdot 3H_2O$ was observed when the temperature was increased to 60°C.Figure 1(e) and 1(f) showed that flaky basic magnesium carbonate can be prepared at above 60°C.

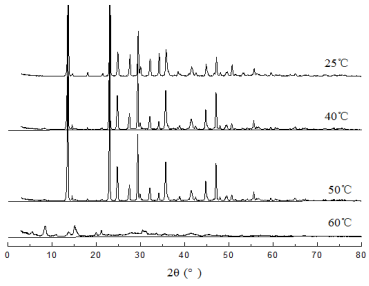

Fig.2 XRD patterns of $MgCO_3 \cdot 3H_2O$ with different temperature

Figure 2 showed that diffraction intensity of basic magnesium carbonate was far less than magnesium carbonate tri-hydrate.

3.2 Effect of different pH on the crystal morphology

The pH of 8.5, 8.8, 8.9, 9.0, 9.1, 9.3, 9.5, 9.8, and 10 was carried out respectively in the optimal conditions to the aim of optimize experiment. Different crystal morphologies of $MgCO_3 \cdot 3H_2O$ at different pH are shown in Fig.3. XRD patterns are shown in Fig.4.

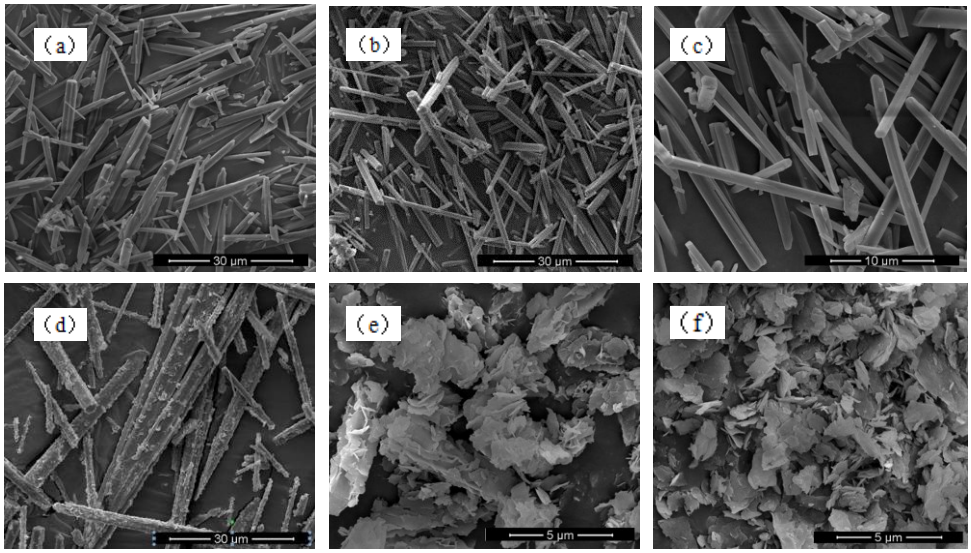

Fig.3 SEM images of $MgCO_3 \cdot 3H_2O$ with different pH
(a)pH=8.5,(b)pH=8.8,(c)pH=9.0,(d)pH=9.5,(e)pH=9.8,(f)pH=10

Observations were made on particles sampled at a specified period in the process of transformation from magnesium carbonate tri-hydrate to basic magnesium carbonate with pH range from 8.5-10 (Figure 3). The changing process of product morphology as the increase of pH value was: rod-like → needlelike → nest → flaky. There was no precipitation at pH=7.9-8.1 without adjust the solution pH value. The product was $MgCO_3 \cdot 3H_2O$ at pH=8.5-9.5 and was basic magnesium carbonate in pH=9.8-10. Especially in pH=9.8 could obtain $4MgCO_3 \cdot Mg(OH)_2 \cdot 5H_2O$ while in pH=10 could obtain $4MgCO_3 \cdot Mg(OH)_2 \cdot 4H_2O$. Aspect ratio of product could up to 29.60 while the section diameter was about 5-8μm in pH=8.8-9.0.

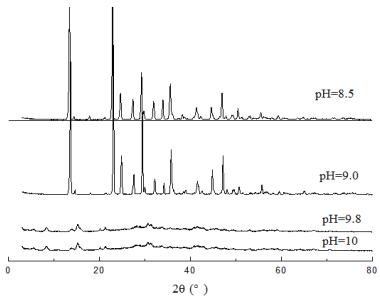

Fig.4 XRD patterns of $MgCO_3 \cdot 3H_2O$ with different pH

Regard to HCO_3^- ion, the ionization reaction ($HCO_3^- \rightarrow H^+ + CO_3^{2-}$) is greater than the hydrolysis reaction($HCO_3^- + H_2O \rightarrow H_2CO_3 + OH^-$) under the condition of weak alkaline, which contribute to form $MgCO_3 \cdot 3H_2O$. In conclusion, the optimal pH was 8.8-9.0.

3.3 Effect of different reaction time on the crystal morphology

The reaction time of 16.7min, 25min, 50min, 70min, and 100min was carried out respectively in optimal condition to the aim of optimize experiment. Different aspect ratio of $MgCO_3 \cdot 3H_2O$ at different reaction time is shown in Fig.5.

Table 5 Effect of reaction time on aspect ratio

Reaction time [min]	Dropping speed [ml·min^{-1}]	Aspect ratio
16.7	3	22.50
25	2	23.46
50	1	27.18
70	0.71	29.60
100	0.5	29.80

Table 5 showed that aspect ratio increased as the reaction time rose. However, unlimited extension of reaction time, the increasing of aspect ratio was not obvious. When reaction time was too short, namely titration speed too fast, it was possible to cause concentration super saturation partly and instantaneous nucleation in solution, crystal reunion and aspect ratio uneven. In contrast, the reaction time was too long, that was to say the titration speed too slow, the reaction efficiency was reduced. Aspect ratio of product could up to 29.60 while the section diameter was about 5-8μm in 70min.

SEM image of $MgCO_3 \cdot 3H_2O$ in optimum conditions is shown in Fig.5.

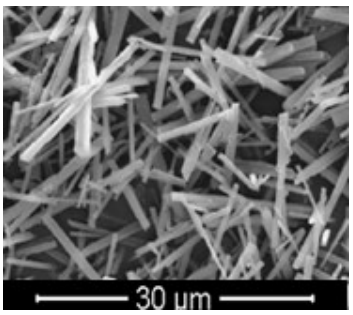

Fig.5 SEM image of $MgCO_3 \cdot 3H_2O$ in optimum condition

Conclusions

(1) The method of prepare high purity magnesium oxide (MgO) with magnesium carbonate tri-hydrate ($MgCO_3 \cdot 3H_2O$) as intermediate has very high popularization value. The process is reasonable and the conversion rate is higher.

(2) There are a lot of salt lake brine including carbonate salt lake, sulfate salt lake (including sodium sulfate and magnesium sulfate subtype), chloride salt lake in Tibet, xinjiang, qinghai and other regions in China. Resource utilization reasonable according to the intrinsic characteristics of each type of salt lake at the same time reduce the difficulty of the salt lake development alone is a new development direction of salt lake brine comprehensive utilization.

Acknowledgements

This work was financially supported by the Special Funds for Central Public Welfare Scientific Research Institutes (K-JBYWF-2013-G9), Special Research Funds for Marine Craft Industry (201005021-7) and Special Funds for Central Public Welfare Scientific Research Institutes (K-JBYWF-2013- T3).

References

[1] Weiqiang Yang, Gentu Xiao. Chemical Technology Market. Vol.32 (2009), p.20-23
[2] Wang X L. Materials Letters.Vol.60 (2006), p. 3160-3164
[3] Fereshteh M, Mehran R. Powder Technology. Vol. 196(2009), p. 85-88
[4] Mitsuhashi K, Tagami N and Tanabe K. Langmuir. Vol.21 (2005), p. 3659-3663
[5] Kloprogge JT, Martens WN and Nothdurft L. Letters. Vol.22 (2003), p. 825-829

Advanced Materials Research Vols. 960-961 (2014) pp 204-207

doi:10.4028/www.scientific.net/AMR.960-961.204

Synthesis and Characterization of Crosslinking Etherification Bagasse Xylan

Zutie Luo[1, a], Heping Li[1,2,b*]

[1]College of Chemistry and Bioengineering, [2]Key Laboratory of New Processing Technology for Nonferrous Metals and Materials, Ministry of Education, Guilin University of Technology, Guilin 541004, Guangxi, China

[a]zutiel@21cn.com, [b]lhpp2008@163.com

Keywords: Crosslinking Etherification Bagasse Xylan, Synthesis, Characterization

Abstract. The bagasse xylan is a polysaccharide that occurs in nature in enormous amount in various one year- and perennial plants. Versatile ways to generate bio-based functional polymers result from the chemical modification of this biopolymer. The crosslinking etherification bagasse xylan(CEBX) has been synthesized by using aqueous solution polymerization method. It implies the use of sodium hydroxide, chloroacetic acid as a carboxymethylating agent and epichlorohydrin as crosslinking agent. The DS values of Carboxymethylated xylan up to 0.59 can be controlled by adjusting the molar ratio in a two step syntheses. Crosslinking etherification bagasse xylan are water soluble at a DS of 0.3. The result showed that the final product had excellent surface activity. IR spectrometry were applied to characterize the carboxymethyl xylans in detail, and revealed characteristic absorption peaks at 1600, 1426 and 1324cm^{-1}.

Introduction

Xylans are the most abundant hemicelluloses. The hemicellulose xylan is most abundant in bagasse and other plants such as grasses, cereals, and herbs. Xylans of all higher plants possess β-(1→4) linked xylose units as the backbone, usually substituted with sugar- and *O*-acetyl groups. In the wood of dicots, only the typecontaining single side chains of 2-linked 4-*O*-methyl-α-D-glucopyranosyl uronic acid units was found[1]. In recent years, xylans as one of the most important renewable resources has received much attention because of its functional properties, such as antioxidant activity, anticomplementary activities, immunomodulating effects and anti-HIV activity[2]. Carboxy-methylation of polysaccharides is one of the most versatile functionalization procedures as it provides access to biobased materials with valuable properties like metal ion induced gel forming well studied for cellulose and starch.[3,4] Up to now, only a few papers describe carboxymethyl xylan (CMX) using AGX from corn cob, AX from oats and rice, and GX from beech wood with a degree of substitution(DS) lower than 1.0[5].

A problem that limits the use of xylans is their poor solubility. To get soluble polysaccharide derivatives, etherification in particular carboxymethylation, hydroxyalkylation, and methylation of the hydroxyl groups is a suitable way[6]. Carboxymethylation is one of the widest modified method of preparation of high-value biobased materials and seems to be an appropriate functionalization to get water-soluble products. [7~14]

The present paper describes the crosslinking etherification of bagasse xylans from bagasse applying different reaction conditions. Moreover, the derivative of xylan is water soluble. The aim of this work is the synthesis of crosslinking etherification bagasse xylan, as well as the characterization of this polymer by using spectroscopic and thermic analytical methods.

Experimental

Materials. Bagasse xylan was isolated from bagasse (all provided by Guilin institute of botany) washed with methanol. It had a water content of 6%. NaOH was obtained from Luoyang chemical reagent factory (Luoyang , China). Sodium monochloroacetate (SMCA) and epichlorohydrin were

obtained from Tianjin chemical reagent factory I (Tianjin, China). Ethylene diamine tetra acetic acid (EDTA) and Ammonia chloride were obtained from Xilong chemical plant (Shantou, China). Peroxyacetyl nitrate (PAN) was obtained from Kelong chemical reagent factory (Chengdu, China). Copper Sulfate was obtained from Xinyu chemical plant (Shantou, China). Ethanol, acetone, and acetic acid were reagent grade analyticals.

Measurements. The DS of the carboxymethyl groups was determined by complexometric titration using EDTA as the complexing agent and PAN as the indicator, according to carboxymethyl starch analysis.[15]

TG and DTG were performed with Netzsch STA 449C instrument. The measurements were recorded in an air atmosphere (flow rate: 20 mL/min). The sample mass was 20mg and it was heated from room temperature to 600 ℃at the heating rate of 10 ℃/min.

Complete Heterogeneous Synthesis of CEBX. For a typical synthesis of CEBX, 5.0g (38 mmole) of bagasse xylan was suspended in 25 mL 80% (v/v) aqueous ethanol. The reaction mixture was vigorously stirred at room temperature for 1 h, at the same time dropwise added NaOH solution (2.25 g, 56.7 mmole NaOH dissolved by 15 mL 80% (v/v) aqueous ethanol) slowly. Then SMCA solution (4.47 g, 47.25 mmole SMCA dissolved by 10 mL 80% (v/v) aqueous ethanol) and NaOH solution (3.02 g, 75.6 mmole NaOH dissolved by 20 mL 80% (v/v) aqueous ethanol) were dropwise added slowly and the temperature of the reaction bath was raised to 65℃. The etherification was performed for 3h. The product was filtered off, suspended in 80% (v/v) aqueous ethanol, neutralized with diluted acetic acid, and washed five times with 50 mL acetone. The product was dried at 60℃ in vacuum.

Effect of reaction parameters on crosslinking etherification

The xylan used is a commercial xylan isolated from sugarcane bagasse showing a yellow to brownish color. The molecular mass is 200,000 g/mole with a xylose content of 80% (related to the total sugar content). For the etherification of xylan a procedure according to the common method for carboxymethylation of the polysaccharides cellulose or starch was applied[7]. Thus, xylan was slurried in an aqueous ethanol followed by the addition of 15% NaOH solution and SMCA solution. The gelatinization was carried out for 2h at 45℃, and the etherification was reacted for 3h at 65℃(Table 1, sample 1~9). The epichlorohydrin as crosslinking agent was added to cross for 0.5h at 45℃.

Table 1 The compilation of reaction conditions used for the synthesis of CEBX

Sample	H_2O/solvent	$n_{NaOH}/n_{AGU(s)}$	$n_{SMCA}/n_{AGU(s)}$	DS
1	2/8	3.25	1.25	0.59
2	2/8	3.75	1.25	0.51
3	2/8	3.00	1.25	0.37
4	2/8	3.00	2.25	0.16
5	2/8	1.50	1.25	0.08
6	4/6	3.00	1.25	0.16
7	0.5/9.5	3.00	1.25	0.50
8	5/5	3.00	1.25	0.08
9	0/10	3.00	1.25	0.01

Infrared spectra

The infrared spectra of native and a representative CEBX derivative are presented in Fig. 1. The broad band between 3600 and 3000 cm^{-1} is assigned to O—H stretching and it is due to hydrogen bonding involving the hydroxyl groups on the xylan molecules. The band at 2925 cm^{-1} is assigned to C—H stretching vibrations. The band at 1643 cm^{-1} is attributed to the scissoring of two O—H bonds of water molecules, while the bands at ν = 860 and 767 cm^{-1} are due to skeletal stretching vibrations of xylan. The CEBX derivative revealed characteristic absorption peaks at ν = 1619, 1420 and 1320

cm^{-1}. These characteristic absorption peaks are assigned to carboxymethyl moieties and this indicates that the hydroxyl groups of xylan molecules were carboxymethylated. Besides, the band at 3430cm^{-1} grows wider due to the introduction of carboxyl enhancing the association of hydroxyl groups.

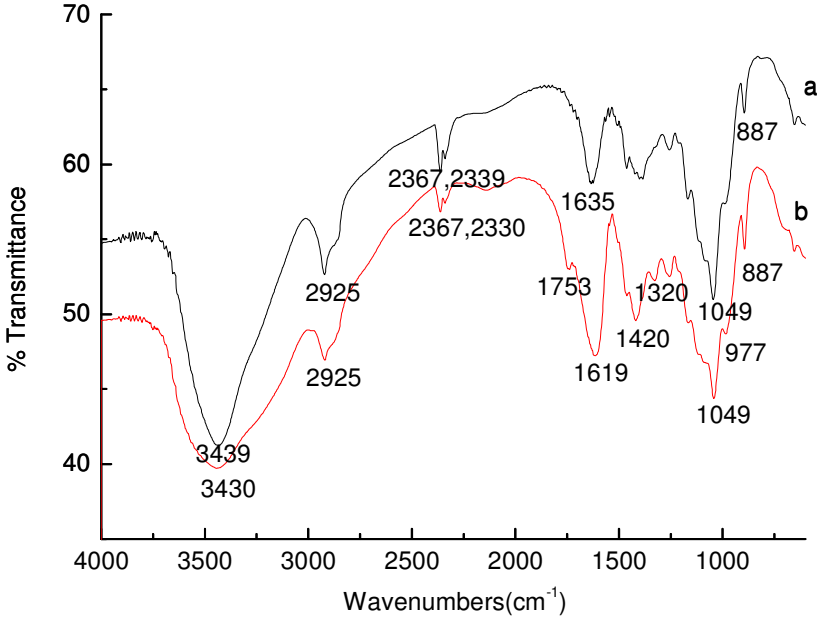

Fig.1 Infrared spectra of native and a representative CBEX (DS 0.59)

Thermogravimetry (TG) and derivative thermogravimetry(DTG)

Thermograms and derivatograms of native and a crosslinking etherification bagasse xylan are presented in Figs. 2 and 3, respectively. Native xylan showed a characteristic tow-step thermogram with 8.93% and 46.27% weight loss progressively. The derivatogram indicates that maximum decomposition occurred at the range 234~312 ℃. Representative CEBX showed tow decomposition stages with 9.72% and 30.58% progressively. In both native and carboxymethylated and crosslinking xyalns, the first thermal events are due to water evaporation. It is also instructive that only 32.64% of the total mass of the carboxymethyl starch was lost at 234~312 ℃ where maximum decomposition occurred. This is lower than 46.27% that was observed in the native starch within the same range. This information suggests that carboxymethylation and crosslinking improved the thermal stability of the xylan.

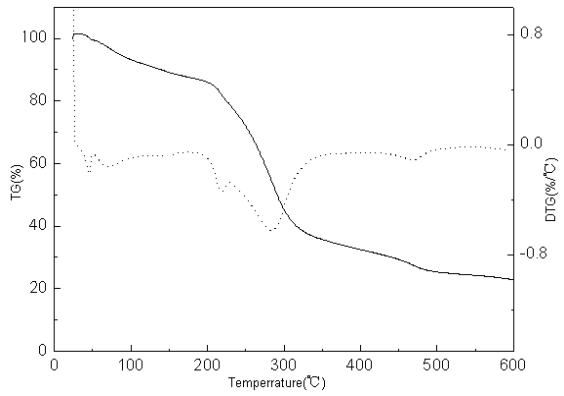

Fig. 2. Thermogravimetry (TG) and derivative thermogravimetry (DTG) of bagasse xylan.

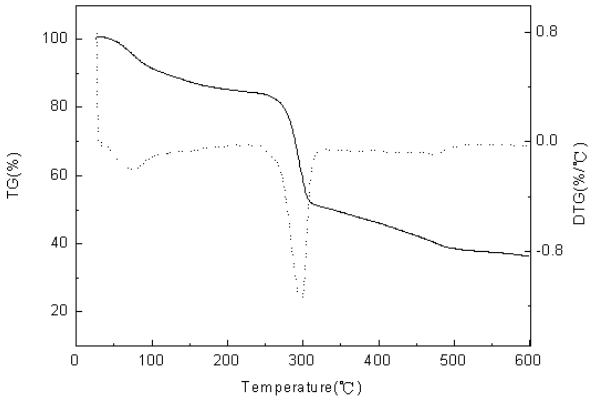

Fig. 3. Thermogravimetry (TG) and derivative thermogravimetry (DTG) of CBEX (DS 0.59)

A plausible explanation for this development is the replacement of the hydroxyl groups on the native xylan with carboxymethyl groups after modification. Since the main decomposition mechanism of xyaln is the dehydration reaction between xyaln hydroxyls, it is reasonable that the lower the amount of hydroxyl group that remained, the more the stability of the xyaln derivative.

Conclusions

In the present investigation, we report about the first synthesis of carboxymethylated and crosslinking bagasse xylan derivative. We investigated on the factors influencing the synthesis such as temperature, ratio of solvent to water in the reaction medium, amount of etherifying agent as well as the influence of the ratio of sodium hydroxide to xylan. All these are with a view to optimizing the synthesis conditions for high degree of substitution. The carboxymethylation and crosslinking of xylan represents a useful way to get water soluble bagasse xylans derivative with anionic functions.

The polymers contain more unsubstituted and di-*O*-carboxymethylated units and less mono-*O*-carboxymethylated units indicating a non-uniform distribution of the CEBX functions within the polymer chains. Further investigations will include some other derivatives in view of the biological activity, reactivity and the substitution pattern as well as the properties.

Acknowledgements

This work was financially supported by Scientific Research and Technology Development Project of Guilin City (20110105-3).

References

[1] A. Ebringerova, T. Heinze, Macromol. Rapid Commun. Vol.21(2000), p.542.

[2] D. R. Burton, P. Poignard, R. L. Stanfield, I. A. Wilson: Science, Vol. 337(2012), 183-186.

[3] B. Fatima-Zohra, P. Catherine, H. Patrick: Carbohydrate Research,Vol. 346(2011), p. 2896-2904.

[4] N.G.V. Fundador, Y. Enomoto-Rogers, A. Takemura: Polymer Degradation and Stability Vol. 98(2013), p. 1064-1071.

[5] A. Baar, W. M. Kulicke, K. Szablikowski, R. Kiesewetter, Macromol. Chem. Phys. Vol.195 (1994), p. 1483.

[6] S. Daus, K. Petzold-Welcke, M. Kötteritzsch: Macromolecular Materials and Engineering Vol. 296(2011), p. 551-561.

[7] M. Pinaki, A.P. Carlos, B.D. Elsa: International Journal of Biological Macromolecules Vol. 46(2010), p. 173-178.

[8] T.M. Mohammad, F. Yaghoub, J.S. Maryam: Food Chemistry Vol. 138(2013), p. 1028-1033.

[9] B. Tian , Y. Chen , S.J. Ding: Protein Expression and Purification Vol. 85(2012), p. 44-50.

[10] T. Heinze, K. Pfeiffer, Angew. Makromol. Chem. 1999, 266, 37.

[11] T. Marie-Christine, N. Audrey, D. Claude: Journal of Biotechnology Vol. 155(2011), p. 257-265.

[12] K. Toth, G.M.P. Van, H.A. Schols: BioEnergy Research Vol. 6(2013), p. 631-643.

[13] K. Petzold, K. Schwikal, T. Heinze: Carbohydrate Polymers Vol. 64(2006), p. 292-298.

[14] J.L. Ren, X.W. Peng, P. Feng, R.C. Sun: Fibers and Polymers Vol. 14(2013), p. 16-21.

[15] T. Heinze, K. Pfeiffer, Angew. Makromol. Chem. 1999, 266, 37.

Advanced Materials Research Vols. 960-961 (2014) pp 208-211

doi:10.4028/www.scientific.net/AMR.960-961.208

Experimental research on preparation of SiN films by magnetron sputtering

Zaiyu Zhang[1,4,a], Jianjun Yang[2,4,b], Yanhui Wu[3,c]

[1]College of Electronic and Information Engineering, Engineering Center of Avionics Electrical and Information Network,Anshun University, Anshun, Guizhou 561000, China

[2]School of Metallurgical Engineering, Hunan University of Technology, Zhuzhou, Hunan, 420007, China

[3]College of Finance and Economy, Hunan University of Technology, Zhuzhou, Hunan, 420007, China

[4]National Engineering Laboratory for Vacuum Metallurgy, Kunming University of Science and Technology, Kunming 650093, China

[a]1255309353@qq.com, [b]yjjsofc@qq.com, [b]yanfei.85@163.com

Keywords: magnetron sputtering; deposition rate; SiN.

Abstract. In this paper, the SiN film was deposited on Si wafer, and the deposition rate of the SiN film was discussed with different parameters such as the sputtering power, deposition temperature, deposition pressure and ratio of $N_2/(N_2+Ar)$. The result showed that the optimal parameter for SiN film were 60W, 300℃, 2.5% and 1Pa, respectively.

Introduction

The refractory metals and their nitrides were mostly polycrystalline structure, the grain boundary between the polycrystalline was become the rapid diffusion path to Cu atoms. To solve the problems, TaSiN, ZrSiN, WSiN and HfSiN et al[1-5] have become the hot topic for the barrier layer.

However, the resistivity of the ternary compounds constituting of Ta, Zr, W or Hf elements was 400μΩ·cm to 800μΩ·cm[1-5], which was not suitable for high speed operation of circuit. The barrier layer with low resistivity and good thermal stability has been demanded. The resistivity of CoSiN film is lower than 300μΩ·cm, and the crystal structure of CoSiN film were close-packed hexagonal at 350K, which were different with crystal structure of Cu. So the CoSiN film has become the research hot.

Magnetron sputtering[6] has been used to deposit various film on Si wafer. SiN film were deposited, which was benefited for depositing heterogeneity sandwich structure of $CoSiN/Cu/CoSiN/SiO_2/Si$[7]. In order to obtain the SiN film, the depositing parameter of sputtering power, depositing temperature, Ar pressure and the ratio of $N_2/(N_2+Ar)$ were discussed to analysis the SiN film.

Experimental

Si target with Ø60×5 was used to deposit SiN film, and the high purity N_2 and Ar with 99.999% were employed. Before depositing, the Si wafer was washed with HCl solution, ethanol, dilute HF solution and distilled water, respectively. The detail cleaning procedure was as follows. Firstly, the dilute HCl was used to remove the surface metal impurities, then the dilute HF was adopted to remove the surface organic impurities. Finally, distilled water was employed to wash the Si wafer under ultrasonic vibration, each process must be lasted 5min, the film can be deposited.

The cleaned Si wafer was shifted into the deposition chamber, and was placed onto the substrate. Then deposition chamber was turned off, and evacuated to a pressure of 1Pa by the mechanical pump, then the molecular vacuum pump was started to evacuate until the pressure under 9.0×10^{-4}Pa or less. At the same time, the substrate was heated, and the N_2 and Ar gases were imported into the chambers

with different proportions. After the gas flow was stable, the pre-sputtering of the target was started to remove the surface impurities or oxide, the process was lasted 10min.

After the pre-sputtering, the sputtering experiments were carried out with different depositing parameters, such as gas pressure, the ratio of $N_2/(N_2+Ar)$, sputtering power and substrate temperature, the detailed experimental parameters were in table 1. The samples can not take out immediately until the chamber pressure elevated to the Atmospheric pressure. And the samples have been sealed into a box to prevent film exposure to air and have been damaged.

Table 1 Deposition parameters

Experimental parameters					
Sputtering power/W	40	50	60	70	80
Deposition temperature/˚C	25	100	200	300	400
Ratio of $N_2/(N_2+Ar)$/%	2.5	5	10	15	20
Deposition pressure/Pa	1	2	3	4	5

Preparation of SiN films

The deposition rate is the important parameter for the film. The film thickness can be controlled by the deposition rate and the deposition time. The appropriate deposition rate and deposition time are in favor of the CoSiN film. The deposition rate are determined by the sputtering power, the ratio of $N_2/(N_2+Ar)$ and substrate temperature[7]. The film thickness of SiN was detected by SGC-10 measured thickness device.

Sputtering power for SiN film. In order to discuss the sputtering power for the film, five kinds of deposition power were explored to analyze the deposition rate. The deposition power were 40, 50, 60 and 80W, respectively. And the substrate temperature was 300˚C, the ratio of $N_2/(N_2+Ar)$ was 2.5%, and the deposition pressure was 1Pa. The deposition rate was calculated by the film thickness and deposition time, and the relationship of sputtering power and deposition rate of the SiN film was showed in figure 1.

From figure 1, it can be seen that deposition rate increased when the power enlarged from 40W to 60W. Then the power was further increased, the deposition rate decreased. At first, the sputtering power was increased, the ions amount of the target materials was enhanced, which was helpful for the film deposition. When the higher of deposition power, the greater of the Si ion power and the activity of the ion, the enhancer of the collision and the scattering of the ions, thereby the weaker the of deposition ions on the substrate.

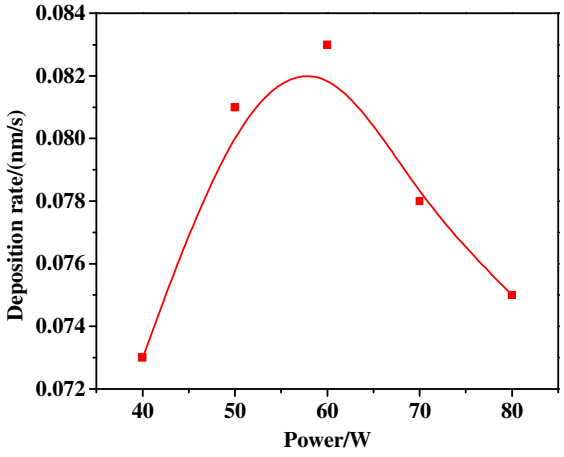

Figure 1 Relationship of the deposition rate of the SiN film and sputtering power

Deposition temperature for SiN film. In order to analyze the substrate temperature in the sputtering process, the SiN film was prepared at different substrate temperatures. And the deposition power was 50W, the ratio of $N_2/(N_2+Ar)$ was 2.5%, and the deposition pressure was 1Pa. The relationship of the substrate temperature and the deposition rate of the SiN film was showed in figure 2.

From figure 2, it can be seen that the deposition rate of the SiN film increased when the substrate temperature elevated from the room temperature to 300˚C, the deposition rate was descended while the substrate temperature further was increased. The highest of deposition rate appeared at 300˚C. The temperature was benefit for the growth of the film. When the substrate temperature increased, the surface diffusion of the adsorbed particles were increased, the number of the particle nucleation was enhanced, which were speeded up the deposition rate of the film. While increasing the substrate temperature was also raised the number of surface absorption and bonding capacity, which enhanced the film growth rate. On the other hand, the substrate temperature was proportional to the evaporation rate of the particle adsorption, the elevated temperature speeded up release of the target molecule in the surface reaction. The deposition rate of the film will fall if the substrate temperature was too high.

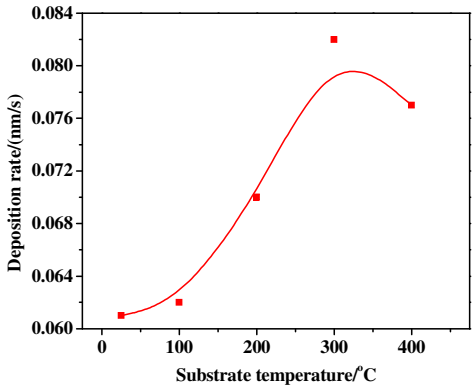

Figure 2. Relationship of substrate temperature and deposition rate of the film

Ratio of $N_2/(N_2+Ar)$ on SiN film. To explore the ratio of $N_2/(N_2+Ar)$ for the SiN film, the SiN film prepared by different ratio of $N_2/(N_2+Ar)$, and the sputtering power was 50W, the substrate temperature was 300˚C, the deposition pressure was 1Pa. The relationship of the deposition rate of the SiN film and the ratio of $N_2/(N_2+Ar)$ was showed in figure 3.

From figure 3, when increase of the ratio of $N_2/(N_2+Ar)$ from 2.5% to10.0%, the film deposition rate was elevated from 0.084nm/s to 0.092nm/s. If the ratio further increased, the deposition rate declined. At the stage of 2.5%-10%, the amount of the activity N_2 in the vacuum chamber enhanced, the phenomenon that the Si ion crashed with nitrogen ion has happened sharply, the deposition rate of the SiN film enhanced greatly. When the ratio of $N_2/(N_2+Ar)$ was greater than 10%, the amount of Ar was reduced, which caused the amount of the sputtered Si ion was declined gradually, and the deposition rate of the SiN film was decreased.

N_2 pressure on SiN film. In order to analyze the N_2 pressure influencing the SiN film, the different N_2 pressure was discussed, and the sputtering power was 50W, the substrate temperature was 300˚C, the ratio of $N_2/(N_2+Ar)$ was 2.5%. The relationship of the deposition rate of the SiN film and pressure was showed in figure 4.

It can be seen from figure 4, the deposition rate of the SiN film was reduced when the pressure was enlarged. If the pressure increased, the crash probability of the target ion and the residual gas was increased, the kinetic energy of the target ion decreased greatly, and the Si ion can not reached the substrate. The amount of Si ion on the substrate was reduced greatly, the deposition rate of the SiN film was decreased gradually.

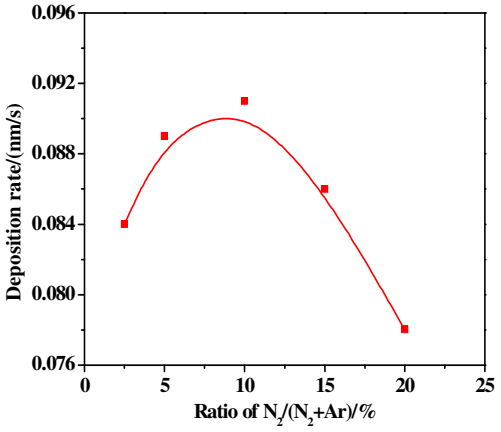

Figure 3 Relationship of deposition rate of SiN film and ratio of $N_2/(N_2+Ar)$

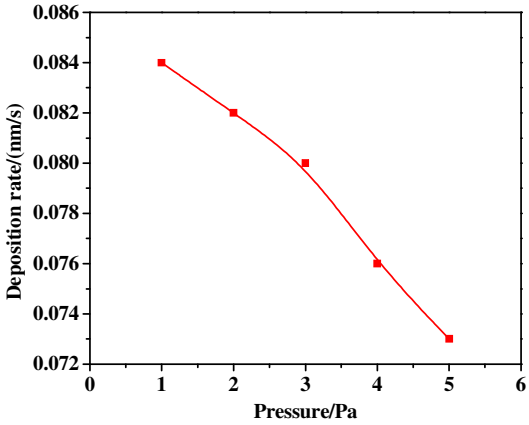

Figure 4 Relationship of deposition rate of the SiN film and the working pressure

Conclusions

The SiN film was deposited with different sputtering power, deposition temperature, ratio of $N_2/(N_2+Ar)$ and N_2 pressure. The deposition rate of the SiN film was increased and then decreased with increase of the deposition power, and the maximum deposition rate was 0.083nm/s. The substrate temperature was also seriously influenced the deposition rate of the SiN film, the deposition rate of the SiN film was enhanced when the temperature was below 400˚C. The ratio of $N_2/(N_2+Ar)$ was also affected the deposition rate of the film, the change trends o f the deposition rate was consistent with that of the ratio of $N_2/(N_2+Ar)$. The deposition rate of the film was declined with the N_2 gas pressure.

References

[1] R.Hübner, M.Hecker, N.Matter, et al. Influence of nitrogen content on the crystallization behavior of thin Ta-Si-N diffusion barrier [J].Thin Solid Films, 2004, 468(1-2):183-192.

[2] Wang Y, Cao F, Shao L, Ding M H. Diffusion barrier capability of Zr-Si films for copper metallization with different substrate bias voltage[J]. Thin Solid Films, 2009, 517(18):5593-5596.

[3] Zenglin Wang, Zonghuai Liu, Zupei Yang, Shoso Shingubara. Characterization of sputtered tungsten nitride film and its application to Cu electroless plating[J].Microelectronic Engineering, 2008, 85(2):395-400.

[4] Qi Xie, Yu-Long, Jan Musschoot, Jan Musschoot, et al. Ru thin film grown on TaN by plasma enhanced atomic layer deposition [J].Thin Solid Films, 2009, 517 (16): 4689-4693.

[5] Dung Ching Perng, Kuo Chung Hsu, Shuo-Wen Tsai, et al. Thermal and Electrical Properties of PVD Ru(P) Film as Cu Diffusion Barrier [J].Microelectronic Engineering, 2010, 87(3): 365-369.

[6] Chen Jianhui, Liu Baoting, Zhao Dongyue. Investigation of Barrier Layer for Cu Interconnection on Si-based Integrate Circuit[J]. Materials Review, 2010, 24(6):58-63.

[7] Liu Jiyan, Ma Shining, Sun Xiaofeng, Li Xin. Influence of Technique Parameters on Depositing Rate of SmCo Films Prepared by Magnetron Sputtering[J]. Journal of Materials Science & Engineering, 2011,29(3): 411-414.

Advanced Materials Research Vols. 960-961 (2014) pp 212-216

doi:10.4028/www.scientific.net/AMR.960-961.212

Application performance and mechanism of tea saponin in dyeing and finishing pretreatment

Jianhong Bai [1, a], Shuling Cui[2, b,*]

[1, 2] College of Textile and Garments，Hebei University of Science &Technology

No.26, Yuxiang Street, Shijiazhuang 050018, China

[a]mewhitesnow@163.com, [b]cuishulingling@126.com

*Author to whom correspondence be addressed

Keywords: tea saponin, cotton, pre-treatment, short process

Abstract. Combining the application of tea saponin in short pre-treatment of cotton fabric, the chemical reaction characteristics and mechanism of one-bath process were discussed. The impact of various parameters on the one bath process with tea saponin was analysed, and the optimum process prescription was obtained: tea saponin 40 g/L, penetrating agent JFC 5 g/L, scouring agent YS198 6 g /L and hydrogen peroxide stabilizing agent GJ-101 4 g/L. By tea saponin qualitative analysis, the action mechanism of tea saponin in one bath pretreatment was proposed.

Introduction

Tea saponin as a novel auxiliary for cotton fabric pretreatment of desizing-scouring-bleaching one-bath process was launched grandly in 2009. The tea soponin features replacing the caustic soda and hydrogen peroxide used in the conventional desizing scouring and bleaching three-step method, shortening the process, reducing the consumption of water and energy, decreasing wastewater BOD and COD emissions. It is an effective way to achieve high efficiency, energy-saving and environmentally friendly for low-carbon era cotton fabric pre-treatment process. If the role of the tea saponin is really as well as they said, this is undoubtedly a great reform for the cotton fabric pretreatment. However, this auxiliary is still in its beginning application period in pre-treatment, so its action mechanism, practical effect and operability need further research.

Experimental procedures

Materials and chemicals

Fabric: 122/127 cm 18.2tex * 18.2tex +19.5 tex 551 / 10cm * 315 pieces / cm cotton twill

Chemicals: 27.5% hydrogen peroxide (Xingtai Furunde Chemical), 395 g/L sodium hydroxide solution (Ji-heng Chemical stock company) , hydrogen peroxide stabilizing agent GJ-101 (around the city of Shijiazhuang biological), scouring agent YS198 (Xingtai Furunde Chemical), alkali resistant penetrating agent JFC (Shijiazhuang the Bang Ke-te Chemical), tea saponin (trade name Bugong tea saponin, Shanghai yuanna Fine Chemical Co., Ltd.)

Desizing-scouring-bleaching one-step process

Dipping and padding many times (at 50 ℃) → steaming (95-100 ℃，60 min) →hot water washing twice (100 ℃) → cold water washing →drying

Caustic soda and hydrogen peroxide one-bath prescription (g/L)

Hydrogen peroxide stabilizing agent GJ-101 4 g/L, sodium hydroxide solution 30 g/L, scouring agent YS198 6 g/L, alkali resistant penetrating agent JFC 5 g/L, 27.5% hydrogen peroxide 12 g/L.

Tea saponin one bath prescription(g/L)

Hydrogen peroxide stabilizing agent GJ-101 4 g/L, Scouring agent YS198 6 g/L, Alkali resistant penetrating agent JFC 5 g/L, Tea saponin 20 g/L.

Test procedure

Take a 20 cm×15 cm (warp and weft) cotton gray fabric, with a small amount of water wetting. After being squeezed, put into working bath to full wet. At about 50℃, dipping and padding many times (rolling over rate greater than 100%). After pad-batch, put the fabric on the surface of the dish, and

then put it on the pot grate, avoiding the cloth with the grates, pot wall and other metal contact. Steaming at 100 ℃ for 60 minutes, hot water (100 ℃) washing twice, followed by cold water washing, and then drying, reserved for semi-finished products index test.

Quality testing methods of semi-finished products

Whiteness

The whiteness of fabric after pretreatment is measured by the national standard FZ/T 01068-2009 on WD80 whiteness meter (Dong-guan City Wei-dun Test Equipment Co., Ltd.)

Capillary effect

By FZ/T01071-1999 standards with YGB871-capillary effect analyzer (the textile Wen-zhou city Da-rong instruments)

Strength

By ASTMD 50535-96 standards (strip method) with YGB026E-250 Electronic fabric strength tester (Wen-zhou Da-rong textile instruments)

Results and discussion

Effects of various process parameters on tea saponin one-bath process

Effects of tea saponin concentration

Respectively select tea saponin of 10, 20, 30, 40 and 50 g/l, to examine the effects of tea saponin dosage on pretreatment. The results were shown in table1.

Table1. Effects of tea saponin concentration

	1	2	3	4	5
Tea saponin concentration [$g.L^{-1}$]	10	20	30	40	50
whiteness	78.3	79.3	82.8	83.5	83.8
Capillary effect [cm]	7.3	7.4	10.1	10.0	9.7
Strength [N]	397	415	422	431	407

From Table 1, with the increase of tea saponin concentration, fabric whiteness and capillary effect and strength have increased. So select the tea saponin amount of 40 g / L better.

Effects of steaming time

Under the premise of the tea saponin dosage set at 40 g/L, respectively select steaming time as 40, 50 and 60 min, to examine the effects on pretreatment. The results were shown in Table2.

Table2. Effects of steaming time

	1	2	3
Steaming time [min]	40	50	60
whiteness	82.5	83.3	83.7
Capillary effect [cm]	8.7	9.3	9.8
Strength [N]	417	430	428

From Table2, with the change of steaming time, fabric whiteness, capillary effect and strength have hardly changed. Therefore, the steaming time can be chose between 50 to 60 minutes.

Effects of scouring agent

During tea saponin pretreatment found that oil processing effect was not very well. Scouring agent was added in tea saponin formulations, so as to achieve a better effect. The results were shown in Table3.

Table3. Effects of scouring agent

	1	2	3	4
Scouring agent [$mL.L^{-1}$]	2	4	6	8
whiteness	83.3	83.1	82.8	83.8
Capillary effect [cm]	9.7	9.8	11.1	11.0
Strength [N]	428	419	412	406

From Table3, adding scouring agent to tea saponin process, a better pretreatment effect can be achieved. The scouring agent improved the fabric capillary effect. Furthermore removes residual size, oil and the cotton fibers concomitant.

A better recipe of tea saponin steaming desizing –scouring-bleaching one bath process was elected by the above tests. Namely: the tea saponin 40 g/L, alkali resistant penetrating agent JFC 5 g/L, scouring agent YS198 6 ml/L,GJ101 hydrogen peroxide stabilizing agent 4 ml/L.

Comparative analysis of pure and composite tea saponin

Physical and chemical properties contrast

The pure tea saponin (Xin-yi City-imperial Chemical Co., Ltd., Fig.1) is light yellow solid, amorphous powder. It is easy to float so as to stimulate the nasal mucosa, making people sneezing. And it is insoluble in water, but after heating was dissolved in water and the aqueous solution was dark brown, pH value of 5-7. Composite tea saponin (Fig.2) as a white and small solid particles, is not soluble in cold water and heated gradually dissolved, the aqueous solution is strongly alkaline, pH value of 13-14.

Fig1. Pure tea saponin.

Fig2. Composite tea saponin.

One-bath pretreatment process test contrast

In accordance with the above process and the prescription concluded above. Respectively to do one bath pretreatment test with the two types of tea saponins and results were shown in Table 4.

Table 4. Pure and composite tea saponin semi-products test results

	Pure tea saponin			composite tea saponin		
whiteness	51.5	51.5	51.4	84.3	85.7	86.3
Capillary effect [cm]	6.8	6.9	6.1	8.9	9.3	8.6
Strength [N]	356	368	373	412	398	406

From Table 4, the gray fabric treated with pure tea saponin in whiteness, capillary effect and strength are far less than that treated with composite tea saponin. This shows that only the composite component was analyzed before understand the action mechanism of tea saponin in pretreatment.

Observed the cotton fabric treated with pure tea saponin found that it is some yellowing compared with gray fabric. After testing fabric whiteness, measured the data inTable 5.

Table 5. The whiteness contrast of gray fabric and pure tea saponin treated fabric.

	Whiteness		
Gray fabric	57.5	57.2	57.4

From Table 5, the cotton fabric whiteness treated with pure tea saponin but reduced, this indicated tea saponin almost no effect in bleached cotton fabrics.

Discussion of composite tea saponin action mechanism

(1) Composite tea saponin composition analysis

The composite tea saponin was reported to contain nano-TiO_2, tea saponin, chitosan and other materials. The above test shows that composite tea saponin contains strong alkali and bleaching materials.

A. Identification of the bleaching effect substances in composite tea saponin

Assuming the bleaching effect material is hydrogen peroxide. Then, added MnO_2 in tea saponin solution, the MnO_2 can catalyze H_2O_2 to produce oxygen.

Collect the gases produced and it can make the wood with spark resurgence. This shows that the composite tea saponin containing H_2O_2. But the composite tea saponin is solid, how the H_2O_2

presents in solid? By information knows that H_2O_2 and sodium carbonate can generate sodium percarbonate under certain conditions, which is commonly known as solid hydrogen peroxide. This substance is a white solid particle, dissolved in water and decomposition of hydrogen peroxide, which has bleaching effect.

Adding barium chloride in composite tea saponin solution, appearing precipitation, after added hydrochloric acid, precipitation disappeared, showing that composite tea saponin solution contains carbonate ions. Thereby further prove that bleaching effect substances should be sodium percarbonate.

B. Identification of the chitosan in composite tea saponin

Chitosan is the degradation products of chitin or chitosan, which is a oligomeric soluble sugars and linked by acetyl glucosamine or glucosamine through 1,4-glycosidic bond. The chitosan molecule containing amino and hydroxyl group, salting-out can occur. According to the salting-out nature, added a certain amount of salt in composite tea saponin solution, precipitate generated (Fig3). So preliminary concluded that composite tea saponin contains chitosan. To filter the precipitate and take its supernatant set aside.

To do pre-treatment using the salting tea saponin (the supernatant), and compared with the results of the composite tea saponin pretreatment. Test data were shown in Table 6.

Table 6. The test results of salting tea saponin and composite tea saponin semi-products

	whiteness		Capillary effect [cm]		Strength [N]
composite tea saponin process	85.6	83.9	84.4	9.7	420
after salting out of tea saponin process	84.3	83.7	83.8	8.6	415

From Table 6, the capillary effect of fabric treated with composite tea saponin is better than that treated with salting tea saponin in pre-treatment, and the whiteness and strength changes a little. This shown that the chitosan can improve the absorbency of the fabric in pretreatment.

C. Identification of the nano-TiO_2 in composite tea saponin

TiO_2 non-toxic, chemically very stable, hardly react with other substances at room temperature, not soluble in water, fatty acids and other organic acids and weak inorganic acid, slightly soluble in alkali and hot nitric acid, is an acidic amphoteric oxide. Only long time boiling can fully dissolve in concentrated sulfuric acid and hydrofluoric acid, the reaction of TiO_2 with sulfuric acid to produce $TiOSO_4$ precipitate. Add concentrated sulfuric acid, stirring results in white floc produced (Fig4.) in tea saponin after salting, indicating that the composite tea saponin containing TiO_2.

Fig3. The salting-out precipitation-chitosan.

Fig4. The white precipitation-$TiOSO_4$.

(2) Composite tea saponin action mechanism discussion

A. The role of sodium percarbonate

The case of sodium percarbonate in aqueous solution can be represented by the Eq.1 and Eq.2.

$$2Na_2CO_3 \cdot 3H_2O_2 = 2Na_2CO_3 + 3H_2O_2 \quad (1)$$

$$H_2O_2 = H_2O + [O]. \quad (2)$$

From the chemical equation, the sodium percarbonate has bleaching and alkaline dual nature; it is very suitable for scouring and bleaching process used in cotton.

B. The role of chitosan

According the test, chitosan can improve the moisture absorption capacity of the fabric in the pretreatment. And in theory, the chitosan has adsorbed flocculation function. Either by complexation and adsorbing the metal ions in the pretreatment liquid and thus play the role of the bleaching stabilizers, or by enclosing the flocculation of sizes and other impurities on the fabric serves to prevent secondary sizing pollution.

C. The role of TiO_2

Nanoscale titanium dioxide, the special catalytic action, removal of formaldehyde and other impurities, bactericidal antimicrobial effect, the health effects of the absorption of far infrared, ultraviolet shielding effect, so that it has a wide range of applications in a variety of areas, including textile printing and dyeing industry. In addition, TiO_2 has high reflectance, high opacity and whiteness. So it is speculated that TiO_2 may be used to improve the whiteness and glossiness of the cotton fabric in the pretreatment process, and is conducive to the removal of impurities.

D. The role of tea saponin

As the special chemical structure of tea saponin make its emulsifying, dispersing, wetting, foaming, foam stability, decontamination has good activity, and it is an excellent natural surfactant, so tea saponin can greatly enhance the absorption capacity of the cotton fibers, fabric luster and texture, and remove the fabric stain in the printing and dyeing pretreatment.

Conclusions

(1) The optimal formula of composite tea saponin in one step steaming pretreatment: Hydrogen peroxide stabilizing agent GJ-101 4 g/L, scouring agent YS198 6 g/L, alkali resistant penetrating agent JFC 5 g/L, tea saponin 40 g/L.

(2) The one step process of composite tea saponin steaming pretreatment:
Dipping and padding many times (at 50℃) → steaming (95-100℃, 50-60min) →hot water washing twice (100℃) → cold water washing →drying

(3) The speculated mechanism of composite tea saponin pretreatment: the alkali agent in the composite tea saponin has scouring effect; the sodium carbonate has bleaching effect; the chitosan has adsorption flocculation function, and can play the role of bleaching stabilizing agent; the real tea saponin has the function of emulsifying, dispersing, wetting, foaming, foam stabilization, decontamination effect. Pure tea saponin cannot replace caustic soda and hydrogen peroxide in the traditional pre-treatment process. It's the combined effect of each component in the composite tea saponin that makes the cotton fabric obtain a better whiteness, strength and capillary effect.

References (In Chinese)

[1] L. Y. Xiang, M. Y. Tang and B. Huang: Journal of Hunan Agricultural University 26 (2000) 218-220.
[2] Z. X. Liu, G. J. Chen and Y. L. He: Dyeing & Finishing 17 (2009) 17-20.
[3] J. P. Liu: Textile Dyeing and Finishing Journal 4 (2007) 34-36.
[4] Y. Zhang, l. Y. Hao, Y. Q. Cai and K. J. Fang: Textile Dyeing and Finishing Journal 3 (2007) 28-31. .
[5] Y. X. Huang and J. W. Xing: Textile Dyeing and Finishing Journal 5 (2007) 31-33.
[6] Z. C. Liu: Dyeing agents (volume one), Textile Industry Press publications, Beijing1997.
[7] W. J. Zhu and D. M. Gu, Dyeing & Finishing 6 (2003) 8-10.
[8] G. C. Xu: The development and application of the short process, in Xu Gucang Selected Papers.

Advanced Materials Research Vols. 960-961 (2014) pp 217-220

doi:10.4028/www.scientific.net/AMR.960-961.217

Ir/AlO(OH)/Fe_3O_4: A high active and selective catalyst for Hydrogenation of p-choronitrobenzene to p-chloroaniline

Jie Wu[1, a*], Chun Zhang[2,b]

[1]Vocational and technical college, China West Normal University, Nanchong 637002, China

[2] Chemical Synthesis and pollution control Key Laboratory of Sichuan Province, College of Chemistry and Chemical Engineering, China West Normal University, Nanchong 637009, China

[a]xiaowulaoshi@126.com, [b] chunzhang@163.com

[*] Corresponding author

Keywords: p-choronitrobenzene; p-chloroaniline; hydrogenation; magnetic catalyst

Abstract. Ir/AlO(OH)/Fe_3O_4 catalyst has been prepared and applied for the hydrogenation of p-choronitrobenzene(p-CNB) to p-chloroaniline(p-CAN) at 35 ^oC and balloon hydrogen pressure in ethanol/water mixture. The experiment results indicated that the catalyst Ir/AlO(OH)/Fe_3O_4 showed excellent catalytic properties for the hydrogenation of p-CNB to p-CAN. A complete conversion of p-CNB was achieved with a selectivity of 97.2 % to p-CAN. The catalyst was quite stable and can be recycled at least seven times without loss of any activity. Moreover, the magnetic property of the catalyst facilated the separation of the used catalyst from the reaction system without filtration.

Introduction

Hydrogenation of chloronitrobenzenes to chloroanilines is of great concern in synthetic chemistry since chloroanilines are important chemicals which are widely applied as end products or intermediates for producing herbicides, dyes, drugs, pesticides and fine chemicals[1, 2]. Compared to the traditional synthesis routes, catalytic hydrogenation has been demonstrated as an alternative avenue for the reduction of chloronitrobenzenes from the view of environment because it is considered to be a simple, safe, and effective technology. Especially, liquid hydrogenation of chloronitrobenzenes catalyzed by heterogeneous catalysts using molecular hydrogen as a reducing agent has attracted intensively attention in recent years. Up to now, catalytic hydrogenation of CNBs has been successfully achieved using catalysts based on noble metals, such as Ru, Pt, Au, Ag and Pd, with this last being the most active[2-5]. Nevertheless, the selectivity to chloroanilines is very low due to the extensive dehalogenation of C-Cl bond in the starting materials or the final products[4]. Apart from the metals that have been mentioned above, catalytic hydrogenation of CNBs catalyzed by iridium nanoparticles supported on commonly used carriers such as active carbon and Al_2O_3 is an emerging process due to its comparable catalytic activity. However, the selectivity to CANs is still not satisfied enough even though large amount of additives and modifiers are introduced into the reaction systems[6]. Therefore, it is a tremendous challenge to develop iridium based catalysts for the clean synthesis of CANs.

In a previous work, we synthesized catalyst Ir/$ZrO_2 \cdot xH_2O$ by a co-precipitation method and applied for the hydrogenation of haloaromatic nitro compounds in ethanol/water mixture at room temperature and atmospheric pressure[6]. The catalyst showed both 99.9 % conversion of p-CNB and selectivity to p-CAN, which was probaly attributed to the the formation of hydrogen bond between p-CNB and the hydroxyl groups on the surface of Ir/$ZrO_2 \cdot xH_2O$ or solvent water,faciliating the activation of the N=O bond in nitro group. Although superior catalytic properties have been obtain, the separation of the catalyst from the reaction mixture should be conducted by centrifugation with high speed. In the present work, Ir/AlO(OH)/Fe_3O_4 catalyst were prepared and used for the selective hydrogenation of p-CNB to p-CAN at 35 ^oC and balloon hydrogen pressure in ethanol/water mixture. The as-prepared catalyst exhibited excellent catalytic performace for the selective hydrogenation of p-CNB to p-CAN.

It can be easily separated from the reaction system by a magnet and can be recycled at least seven times without loss of any activity.

Experiment

Materials. $IrCl_3.nH_2O$ was purchased from Kunming Borui Preclous Metals. $Al(O\text{-}sec\text{-}Bu)_3$ were purchased from Alfa Aesar. PEG-400 (PEG with an average molecular weight of 400), p-CNB, ethanol, and 2-butanol are analytical grade and used without further purification. Hydrogen (H_2) with a purity of 99.99% were used as delivered, water was distilled and deionized before use.

Catalyst preparation. Synthesis of iron oxide nanoparticles[7]: $FeCl_3 \cdot 6H_2O$ (540 mg, 2.00 mmol) and ethylene glycol (16.0 g) were added to a 100 mL round bottom flask equipped with condenser. The mixture was stirred at room temperature for 10 min, then sodium acetate (1.60 g) and poly(ethylene glycol) (Mn =400; 400 mg) were added to the reaction mixture and was heated up to 200 ^oC for 6 h and cooled to room temperature. The black nanoparticles were isolated by centrifugation and washed several times with ethanol, and dried under vacuum to give iron oxide nanoparticles(165mg).

Synthesis of $Ir/AlO(OH)/Fe_3O_4$: $IrCl_3$ (50.0 mg) and THF (1.0 mL) were added to a 50 mL round bottom flask. The mixture was stirred at 23 ^oC for 10 min. $Al(O\text{-}sec\text{-}Bu)_3$ (4.0 g) and 2-butanol (1.0 mL) were added to the reaction mixture and the mixture was heated at 50 ^oC for 20 min. Magnetite nanoparticles (100 mg) dispersed in ethanol (2.00 mL) was added to the resulting black suspension. The mixture was stirred for 10 min at 50 ^oC. Then, water (3.0 mL) was added to form black gel. The gel was isolated by filtration, washed with acetone, and dried at 120 ^oC for 5 h to give dark brown powder.

Catalyst Characterization. X-ray photoelectron spectroscopy (XPS, Kratos XSAM800) spectra was obtained by using Al Ka radiation (12 kV and 15 mA) as an excitation source (hv = 1486.6 eV) and Au (BE Au4f = 84.0 eV) and Ag (BE Ag3d = 386.3 eV) as reference. All binding energy (BE) values were referenced to C1s peak of contaminant carbon at 284.6 eV. A Fourier transform infrared (FT-IR) spectrum was recorded with a Nicolet 6700 (resolution 0.4 cm^{-1}) infrared spectrometer and samples were dispersed in potassium bromide and compressed into pellets. All hydrogenation samples were analyzed by gas chromatography (Agilent 7890A) with a FID detector and PEG-20M supelco column (30m×0.25mm, 0.25 um film) and nitrogen was used as a carrier gas. The vented gas was detected with Agilent 7890A equipped with a thermal conductivity detector (TCP) and a plot carbon sieve column (25m×0.53mm) and hydrogen was used as a carrier gas.

The catalytic hydrogenation of p-CNB was carried out in a 50 mL round flask equipped with a balloon. Typically, p-CNB (1.0 mmol), catalyst (20 mg), ethanol (5 mL), and water (2 mL) were indtroduced to the round-bottom-flask. The reactor was treated under vacuum and charged with pure hydrogen. After the designated reaction temperature (35 ^oC) was reached, the stirring rate was adjusted to 1200 rmp, and the reaction time was accounted.

Results and Discussion

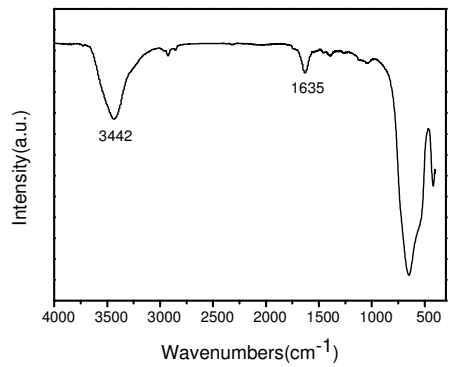

Fig.1 FT-IR spectrum of the catalyst $Ir/AlO(OH)/Fe_3O_4$

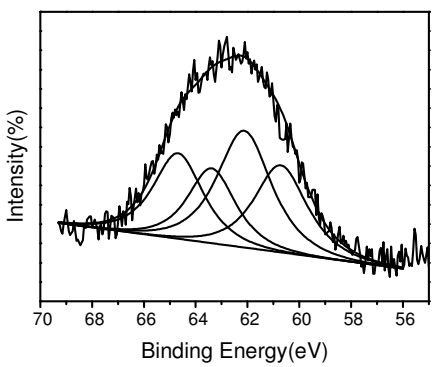

Fig.2 XPS pattern of the catalyst $Ir/AlO(OH)/Fe_3O_4$

The as-prepared catalyst Ir/AlO(OH)/Fe_3O_4 was firstly characterized by the FI-IR technique and the reuslt is shown in Fig.1. It can be seen that the intensive bands at 3442 cm^{-1} was blonged to the ν_{as}(Al)O-H stretching vibrations and the band at 1065 cm^{-1} was assigned to the δ_sAl-O-H mode of boehmite, respectively, indicating that the pre-prepared catalyst contained large amount of hydroxyl groups and structure water and can be dispersed well in ethanol/water mixture[8]. The band at 590 cm^{-1} was originated from the Fe-O bonds, confirming that Fe_3O_4 particles were sucessfully entrapped into the AlO(OH) matrix. In order to evaluate the electronic state of Ir in the Ir/AlO(OH)/Fe_3O_4 catalyst, the binding energy of Ir was determined and the reslut was illustriated in Fig.2. The peaks at 61.1 and 64.9 eV were assigned to the $4f_{7/2}$ and $4f_{5/2}$ peaks of metallic iridium, while the binding energy values at 62.7 and 65.8 eV were attributed to the $4f_{7/2}$ and $4f_{5/2}$ peaks of iridium dioxide, which was attributed to the oxidation of metallic iridium in the air or the incomplete reduction of Ir^{3+} ion[6]. However, the IrO_2 could be redcued by melecular hydrogen during the hydrogenation process and acted as the active sites for the hydrogenation of p-CNB.

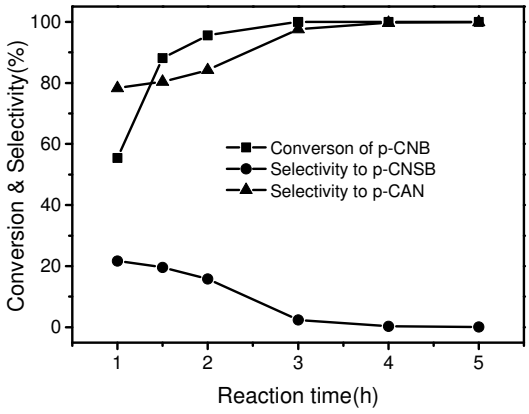

Fig.3 Hydrogenation of p-CNB catalyzed by Ir/AlO(OH)/Fe_3O_4

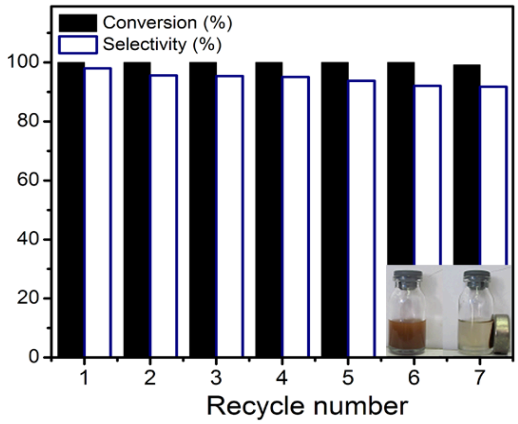

Fig.4 Reusability of Ir/AlO(OH)/Fe_3O_4 catalyst

Catalytic hydrogenation of p-CNB. The selective hydrogenation of p-CNB was employed as a model reaction to investigate the catalytic performance of the catalyst Ir/AlO(OH)/Fe_3O_4 and the results are illustrated in Fig.3. Blank test or the use of AlO(OH)/Fe_3O_4 as catalyst showed no conversion of p-CNB, showing that the iridium was indispensable for the high activity of the Ir/AlO(OH)/Fe_3O_4. During the reaction process, p-CAN, p-chloronitrosobenzene (p-CNSB), and a trace amount of aniline were detected as the main products. It can be seen that a complete conversion of P-CNB was obtained with a selectivity of 97.6 % to p-CAN in a reaction time of 3 h. Moreover, large amount of p-CNSB was detected as an intermediate at the beginning of the reaction; however it can be further hydrogenated to the desired product p-CAN with the elevation of reaction time. A high yield of 99.9 % can be observed at a reaction time of 5 h. The stability and reusability of the catalyst Ir/AlO(OH)/Fe_3O_4 was also studied and the reuslts are shown in Fig.4. Specifically, at the end of each run, the catalyst was separated from the reaction system by a magnet and the supernatant liquid was removed to determine the conversion of p-CNB and selectivity to p-CAN. The black catalyst was washed with ethanol three times and dried under vacuum at room temperature for 12 h for the next run. As shown in Fig.4, the catalyst Ir/AlO(OH)/Fe_3O_4 exhibited excellent catalytic activity and can be recycled at least seven times without loss of any acitivity with a slight decrease of the selectivity to p-CAN.

Summary

In summary, the magnetic nanocomposites Ir/AlO(OH)/Fe_3O_4 was synthesized and applied for the catalytic hydrogenation of p-CNB to p-CAN. The catalyst exhibited excellent catalytic properties at mild conditions in a ethanol/water mixture. Furthermore, it also exhibited showed substantial stability

and recyclibilty and can be easily separated from the reaction mixture by a extenal magnet and recycled at least seven times without loss of any activity

Acknowledgements

This work was financially supported by the National Natural Science Foundation of China (21207109), Scientific Research Fund of Sichuan Provincial Education Department (11ZA034).

References

[1] X. Xu, X. Li, H. Gu, Z. Huang, X. Yan, Appl. Catal., A Vol.429–430 (2012),p. 17-23
[2] J. Ning, J. Xu, J. Liu, H. Miao, H. Ma, C. Chen, X. Li, L. Zhou, W. Yu, Catal. Commun. , Vol.8 (2007),p.1763
[3] M. Liu, J. Zhang, J. Liu, W.W. Yu, J. Catal. , Vol.278 (2011),p. 1
[4] D. He, H. Shi, Y. Wu, B.-Q. Xu, Green Chemistry, Vol.9 (2007),p. 849
[5] F. Zhang, J. Jin, X. Zhong, S. Li, J. Niu, R. Li, J. Ma, Green Chemistry, Vol.13 (2011),p. 1238
[6] G.-Y. Fan, L. Zhang, H.-Y. Fu, M.-L. Yuan, R.-X. Li, H. Chen, X.-J. Li, Catal. Commun. , Vol.11 (2010),p. 451
[7] M.S. Kwon, I.S. Park, J.S. Jang, J.S. Lee, J. Park, Org. Lett. , Vol.9 (2007),p. 3417
[8] H. Hou, Y. Xie, Q. Yang, Q. Guo, C. Tan, Nanotechnology, Vol.16 (2005),p. 741

Advanced Materials Research Vols. 960-961 (2014) pp 221-224
© (2014) Trans Tech Publications, Switzerland
doi:10.4028/www.scientific.net/AMR.960-961.221

Selective hydrogenation of p-chloronitrobenzene catalyzed by Fe_xO_y@C supported Pt-catalyst

Jie Wu[1, a*], Guangyin Fan[2, b] and Wenjun Huang[2, c]

[1]Vocational and technical college, China West Normal University, Nanchong 637002, China

[2] Chemical Synthesis and pollution control Key Laboratory of Sichuan Province, College of Chemistry and Chemical Engineering, China West Normal University, Nanchong 637009, China

[a]xiaowulaoshi@126.com, [b]fanguangyin@cwnu.edu.cn, [c]wenjunhuang@cwnu.edu.cn

[*] Corresponding author

Keywords: catalysis; platinum; water; selective hydrogenation

Abstract. Fe_xO_y@C nanocomposites were synthesized and used as carriers for depositing Pt nanoparticles. Catalytic properties of the nanocomposites were investigated for the hydrogenation of p-chloronitrobenzene at room temperature and balloon hydrogen pressure. The catalyst Pt/Fe_xO_y@C was extremely active for the hydrogenation of p-chloronitrobenzene. Completely conversion of p-chloronitrobenzene was achieved with a selectivity of 99.7 % in ethanol-water mixture in a reaction time of 40 min. Moreover, it can be reused four times without loss of any activity.

Introduction

Selective hydrogenation of p-chloronitrobenzene(p-CNB) to p-chloroaniline(p-CAN) has attracted widely attention in recent years because of their useful application in the field of synthetic organic chemistry. As an atom-efficient and environment-friendly approach, catalytic hydrogenation is seen as one of the most promising avenues for the production of p-CAN from the hydrogenation of p-CNB. To this end, liquid catalytic hydrogenation of p-CNB over heterogeneous catalysts such as Pt, Pd, Ru, Ir, and Ni based catalysts are studied in recent years.[1-8] Among these catalysts, Pd has the highest catalytic activity but always generates various kinds of by-products. Ru exhibits lower activity but is more selective for this reaction. In view of Pt-based catalysts, although higher catalytic activity was achieved, the side reaction of dechlorination through the break-up of C-Cl bond should be inhibited to obtain a high selectivity of the desired product. As a result, many methods such as the addition of additives and modifiers have been adopted in order to overcome this disadvantage. However, extra efforts are needed to avoid the secondary pollution due to the addition of additives or modifiers. Despite this advances, it is still remains a big challenge to synthesize Pt based catalysts with high activities and selectivities.

Recently, the preparation of functionalized supports for immobilizing Pt nanoparticles are widely concerned especially the carbon based nanocomposites with the advantages of good stability, accessibility and porosity[4]. However, these catalysts are not steady due to the lack of organic groups on the surface of these nanocomposites. Very recently, it has been reported that the carbon spheres made from the hydrothermal of glucose has large amount of functional organic groups which can be used as robust anchor to stabilize the catalytic centers on the surface of the catalyst [9]. It is desirable to explore such a material as a support for catalysis. To the best of our knowledge, no attempt has yet been exerted to develop the catalytic performance of the platinum catalysts for the reduction of p-CNB by using carbon sphere nanocomposites as a carrier. In this work, we reported a facile route to synthesize the Pt/Fe_xO_y@C catalyst and investigated its catalytic properties for the hydrogenation of p-CNB.

Experiment

Catalyst preparation. All aromatic compound (A.R.), solvents (A.R.), and reagents (A.R.) were used as received. Fe_xO_y@C was prepared according to the reported literature[10]. Typically, glucose(11.250 g) and $Fe(NO_3)_3 \cdot 9H_2O$ (13.635 g) were dissolved in 60 and 30 mL distilled water respectively. The two solutions were mixed together and introduced to an autoclave (120 mL), which was heated at different temperatures for 12 h. The resulting black solid was washed with water and ethanol several times, and dried at 60 ^oC under vacuum for 12 h. Finally, the black solid was caclined at 400 ^oC for 8 h and then used as carrier to deposit platinum nanoparticles. Specifically, 200 mg of the pre-prepared Fe_xO_y@C was transferred into a 50 mL round-bottom-flask, followed by the addition of an aqueous solution of $H_2PtCl_6 \cdot 6H_2O$(0.55 mL,9.844 mg/mL). Then the mixture was reduced by an excess amount of aqueous solution of $NaBH_4$. The resulting products were washed several times with water and ethanol, and dried at 60 ^oC under vacuum overnight.

Activity test. The catalytic property of the Pt/Fe_xO_y@C catalyst was tested as follow: 10.0 mg of catalyst and 0.5 mmol of p-CNB, a mixture of ethanol and water (7 mL, volume ratio of 6:1) were introduced into a 25 mL round-bottom-flask equiped with a balloon. The reactor was treated under vacuum in order to remover air and then purge with pure hydrogen. After the designated temperature (30 ^oC) was reached, the stirring rate was ajusted to 1200 rpm and the reaction time accounted.

Results and Discussion

Catalytic hydrogenation of p-CNB. The catalytic performance of the catalyst Pt/Fe_xO_y@C was investigated using the selective reduction of p-CNB as a model reaction and the results are listed in Table 1. No conversion of p-CNB was detected without catalyst or with Fe_xO_y@C as the catalyst, indicating that Pt was the active site for the hydrogenation of p-CNB. P-chloronitrosobenzene (p-CNSB), P-CAN and a trace amount of aniline were detected as the main products during the hydrogenation process. Specifically, the applied support of the catalyst Pt/Fe_xO_y@C was prepared by heating the mixture at 80 ^oC. From the results illustrated in Table 1, it can be seen that the conversion of p-CNB increased with the elevation of the reaction time. The Pt/Fe_xO_y@C catalyst achieved an 18.2 % conversion of p-CNB within 5 min with a selectivity of 83.1 % towards p-CAN. The conversion of p-CNB and selectivity to p-CAN reached 100 % and 99.4 % respectively when the reaction time was increased to 35 min. The increasing selectivity of p-CAN was contributed to the further hydrogenation of the intermediate p-CNSB to the desired product p-CAN.

Table 1 Effect of reaction time on the hydrogenation of p-CNB catalyzed by Pt-Fe_xO_y@C

Reaction time (min)	Conversion (%)	Selectivity (%)	
		p-CAN	p-CNSB
5	18.2	83.1	16.9
10	33.8	89.9	9.9
15	52.5	90.1	9.9
20	66.5	92.9	7.1
25	79.5	94.8	5.1
30	89.9	96.4	3.5
35	100.0	99.4	0.5

Reaction conditions: catalyst, Pt/Fe_xO_y@C(10 mg) p-CNB,0.5 mmol; temperature, 30 ^oC; solvent, ethanol/water=6:1(total volume was 7 mL)

The heating temperature for the synthesis of the support Fe_xO_y@C was also investigated and the results are shown in Table 2. It can be seen that the catalytic properties of the Pt/Fe_xO_y@C catalysts decreased with the increase of the heating temperature. The conversions of p-CNB decreased from 34.4 to 13.1 % with the increasing temperature from 80 to 140 ^oC. On the contrary, the selectivity to

p-CAN was not affected with the increase of the heating temperature since the selectivity to p-CAN was higher than 96 % in all the investigated temperatures. However, we can see that the catalytic activities of the catalysts are relative low and a long reaction time is required. In order to improve the catalytic activity of the catalyst, NaOH was added to deposit the Pt precursor before it was reduced by $NaBH_4$. From the results listed in Table 2, we can see that the addition of NaOH can significantly increase the catalytic properties of the Pt/Fe_xO_y@C catalysts. Especially, the conversion of p-CNB achieved 100 % when the support of the catalyst was heated 80 ^oC. However, it should be noted that the addition of NaOH resulted in a slight reduction of the selectivity to p-CAN.

Table 2 Effect of heating temperature on the catalytic activities of the catalysts Pt/Fe_xO_y@C

Temperature	NaOH	Conversion (%)	Selectivity (%)	
			p-CAN	p-CNSB
80	No	34.4	98.0	2.0
	Yes	100.0	95.5	0.0
100	No	30.1	97.6	0.7
	Yes	50.4	95.3	0.9
120	No	21.2	100.0	0.0
	Yes	44.2	98.0	0.5
140	No	13.1	96.8	3.2
	Yes	30.3	90.5	0.0

Reaction conditions: catalyst, 10 mg; temperature, 30 ^oC; H_2 pressure, 1 atm; solvent, ethanol/water mixture (volume ratio=3:4, total: 7 mL); reaction time, 4 h.

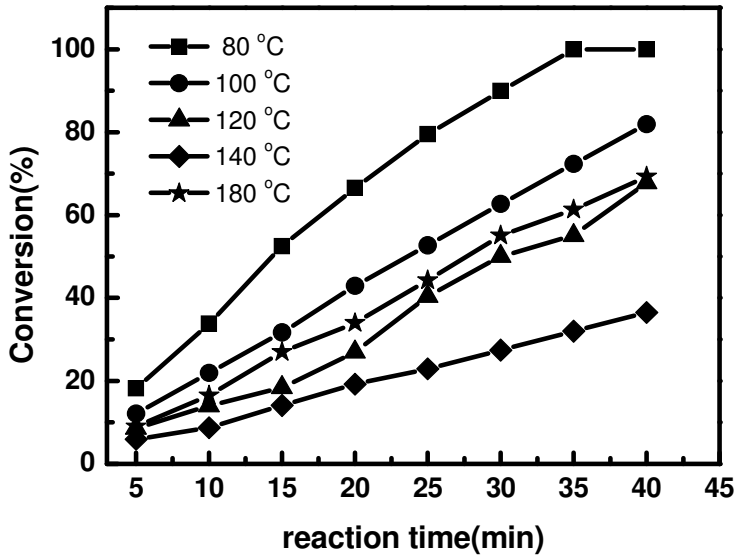

Fig.1 Hydrogenation of p-CNB catalyzed by the Pt/Fe_xO_y@C after calcination

Although the application of NaOH increased the activity of the catalyst to some extent, a long reaction time of 4 h was required to obtain a complete conversion of p-CNB. Therefore, the carriers were calcined at 400 ^oC to improve their crystallites with the aim of enhancing the catalytic activity of the catalysts. The results illustrated in Fig.1 showed that the catalytic activities of the catalysts were enhanced after the catalyst supports were treated. The conversion of p-CNB was 100 % within 35 min at the same reaction conditions compared to 34.4 % conversion of p-CNB within 240 min for the catalyst without calcination. Moreover, these catalysts also showed increased catalytic activities compared to the catalysts which were treated with NaOH during the procedure of catalyst reduction. For example, both of the catalysts (the carrier was obtained from heating mixture at 80 ^oC and the NaOH was used for depositing the Pt ion) achieved 100 % conversion of p-CNB, however the

reaction time for complete conversion was reduced 35 min with the catalyst support calcined at 400 ^{o}C compared to the catalyst treated with NaOH. From the results discussion above, it can be seen that the Pt/Fe_xO_y@C catalyst exhibits excellent catalytic activity and selectivity without the detection of any hydrodechlorination product. This advanced composite material provides a kind of novel and effective catalyst with great promise for catalytic hydrogenation of p-CNB in practical application.

Summary

Catalyst Pt/Fe_xO_y@C was prepared and used for the selective hydrogenation of p-CNB to p-CAN at 30 ^{o}C and balloon hydrogen pressure in ethanol/water mixture. The hydrothermal temperature played an important role in the catalytic performance of the catalyst. Furthermore, the calcination temperature also has a significantly effect on the catalytic activity of the Pt/Fe_xO_y@C catalyst. The complete conversion of p-CNB with a 99.4 % selectivity of p-CAN was achieved in a short reaction time of 35 min.

Acknowledgements

This work was financially supported by the National Natural Science Foundation of China (21207109), Scientific Research Fund of Sichuan Provincial Education Department (11ZA034).

References

[1] G.Y. Fan, and W.J. Huang: Chin. Chem. Lett., Vol.25 (2014), p. 359
[2] G.Y. Fan, W.J. Huang, C.Y. Wang, Nanoscale, Vol.5 (2013), p. 6819
[3] C. Antonetti, M. Oubenali, A.M. Raspolli Galletti, P. Serp and G. Vannucci: Appl. Catal.A: Vol.421 (2012), p. 99
[4] M. Oubenali, G. Vanucci, B. Machado, M. Kacimi, M. Ziyad, J. Faria, A. Raspolli-Galetti, P. Serp:ChemSusChem, Vol.4 (2011) , p.950
[5] X. Meng, H. Cheng, S.-i. Fujita, Y. Hao, Y. Shang, Y. Yu, S. Cai, F. Zhao, and M. Arai: J.Catal., Vol.269 (2010), p.131
[6] G.Y. Fan, L. Zhang, H.Y. Fu, M.L. Yuan, R.X. Li, H. Chen, and X.J. Li, Catal.Commun., Vol.11 (2010), p. 451
[7] J. Zhang, Y. Wang, H. Ji, Y. Wei, N. Wu, B. Zuo, and Q. Wang:J.Catal., Vol.229 (2005), p.114
[8] B. Zuo, Y. Wang, Q. Wang, J. Zhang, N. Wu, L. Peng, L. Gui, X. Wang, R. Wang, and D. Yu, J. Catal., Vol. 222 (2004), p. 493
[9] Q. Yang, J. Zhang, L. Zhang, H. Fu, X. Zheng, M. Yuan, H. Chen, R. Li, Catal.Commun.,Vol. 40 (2013), p. 37
[10] G. Yu, B. Sun, Y. Pei, S. Xie, S. Yan, M. Qiao, K. Fan, X. Zhang, B. Zong, J. Am. Chem. Soc., 132 (2009) 935-937.

Advanced Materials Research Vols. 960-961 (2014) pp 225-228

doi:10.4028/www.scientific.net/AMR.960-961.225

The Comparison of Au/C Catalyst and Au-Pd/C Catalyst for the Oxidation of Glyoxal to Glyoxylic Acid by Oxygen

Xiaoli Wang[1,2,a], Shuangcheng Bao[2,b] and Meilin Jia[2,c]

[1] Professional College, Inner Mongolia Vocational College of Chemical Engineering, Huhhot, 010070,China

[2] College of Chemistry & Environmental Science, Inner Mongolia Normal University, Huhhot 010022,China

[a]404782509@qq.com, [b]shuangcheng@imnu.edu.cn, [c]jml@imnu.edu.cn

Keywords: Bimetallic Catalyst, Glyoxal, Glyoxylic Acid

Abstract. In this paper, Au/C and Au-Pd/C catalysts were prepared respectively. The catalytic performance for the oxidation of glyoxal to glyoxylic acid has been investigated. Furthermore, these catalysts were characterized by XRD and XPS. The results demonstrate that, the conversion of glyoxal was 58.9% and the yield of glyoxylic acid was 13.7% at the optimum reaction time of 20h, which implied the bimetallic catalyst showed higher performance than the monometallic catalyst obviously.

Introduction

Au-Pd/TiO_2 catalyst has been found to be particularly effective for the liquid-phase oxidation of primary alcohols by Enache et al[1] In addition, there are some studies indicated that Au-Pd bimetallic catalyst has shown good catalytic activity for selective hydrogenation of Nitro compounds[2] and selective oxidation of organic compounds in liquid phase[3-4] reactions. It has also been reported that the addition of another metallic element to the monometallic catalysts can give rise to catalytic activity and stability, when compared to their monometallic catalysts due to the synergistic effect and coordination effect. The experiments by Rossi et al[5-6] confirmed that for the selective oxidation of alcohols, the catalytic activity of bimetallic catalyst such as Au-Pd and Au-Pt supported on activated carbon is better than a single metallic catalyst. Landon et al[7-8] found that the yields of the synthesis of H_2O_2 reaction was significantly enhanced over Au-Pd alloys catalyst compared with the Pd or Au monometallic catalysts, which related with the Synergistic effect between Au and Pd.

According to the literature[9], Au/C catalyst has shown catalytic properties for the oxidation of glyoxal to glyoxylic acid, but there are some shortcomings such as low yields and poor stability of catalyst. In this paper the catalytic performance of Au-Pd/C for the oxidation of glyoxal to glyoxylic acid has been investigated and the structure of the bimetallic catalyst was characterized by XRD, XPS.

Experimental

Materials. Activated carbon is provided by sheng-miao industry of fine chemicals company, glyoxal is provided by sinopharm group chemical reagent co, $HAuCl_4$ is provided by Shang Hai reagent company, $PdCl_2$ is provided by Bei Jing reagent company.

Pretreatment of carbon. Before use, the carbon was suspended in HCl 2mol/L for 6h, then washed several times with distilled water until the pH of the solution reached values of 7. At the end the carbon was filtered off and dried under vacuum at 120℃.

Catalysts preparation. Au/C catalyst: A certain amount of carriers, 20mL of lysine solution(0.1mol/L) and solution of $HAuCl_4$(2.43mol/L) were mixed for 30min under vigorous magnetic stirring in the cone-shaped bottle. $NaBH_4$ solution (0.1mol/L) which was freshly prepared was added, then after 2min, HCl solution (0.3mol/L) was immediately added. The system was left to

stand for 24h, filtered, washed with a small amount of anhydrous ethanol, dried under vacuum at 100℃ in for 6h, calcined at 200℃ for 2h.

Au-Pd/C catalyst: An aqueous solution of $PdCl_2$(0.0385mol/L) was added under vigorous stirring to 100ml distilled water which contains a certain amount of above-mentioned Au/C catalyst and reacted for 0.5h, then $NaBH_4$ solution (0.1mol/L) which was freshly prepared was added. The solution was left to stand for 24h, filtered, washed with a small amount of anhydrous ethanol, dried under vacuum at 100℃ in for 6h, calcined at 200℃ for 2h.

Catalytic test. Glyoxal (2.5ml, 40%) and 0.2g catalyst were mixed with 200ml distilled water in a 4-mouth flask(500ml) provided with an electric stirrer and reflux condensing tube. The reactor was pressurized at the desired pressure of O_2 and at the constant temperature of 323k. The pH of the reaction mixture was kept at a constant value of 7.7 by addition of a solution of NaOH(0.05mol/L). After the end of reaction the catalyst was filtered and the organic products were tested. According to literature[10], spectrophotometry is used to analyse the concentration of glyoxal and glyoxylic acid.

Catalysts characterization techniques. XRD patterns were obtained with a philips RW-1729 diffractometer using the Cu Ka radiation (λ =0.15405nm). XPS was performed on an Escalab-210 spectrometer from VG Scitntific, using the Mg Ka radiation.

Results and discussion

Comparison of catalytic activity of Au/C and Au-Pd/C for the oxidation of glyoxal to glyoxylic acid. At the reaction temperature of 50℃, oxygen flow of 0.4L/min, pH value of 7.7 and the catalyst of 0.2g, the catalytic activity of Au/C and Au-Pd/C for the oxidation of glyoxal to glyoxylic acid was compared. From fig.1 we can see that Au/C catalyst showed high activity at the reaction time of 10h, the yield of glyoxylic acid reached 9.7%. However the highest activity was achieved over Au-Pd/C catalyst at the reaction time was 20h, with 58.9% conversion of glyoxal and 13.7% yield of glyoxylic acid. The catalytic activity of bimetallic catalyst is sure to win out over the monometallic catalyst. This is determined by synergistic effect between Au and Pd[6].

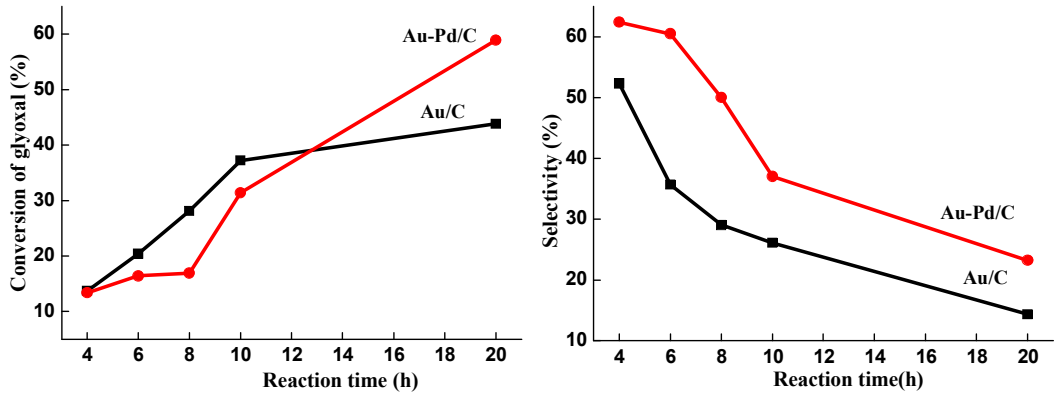

Fig.1 Comparing of the performance of Au/C and Au-Pd/C

XPS. In order to study the relationship between catalytic activity and active components of bimetallic catalyst, XPS test was used for Au/C and Au-Pd/C catalyst. We can see from Fig. 2, Au $4f_{7/2}$ binding energy of Au/C is 83.9eV which is similar to the reported literature[11], but Au $4f_{7/2}$ binding energy of Au-Pd/C is 84.3eV which is obviously increased. This means that the electronic structure of gold was changed because of introduction of Pd[12] and synergistic effect between these two metal elements. Yet, this result can impact the catalytic activity of bimetallic catalyst.

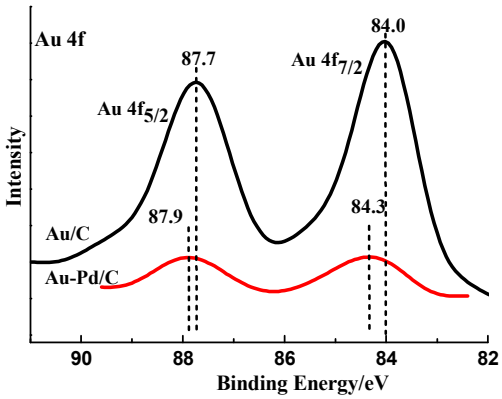

Fig.2 XPS spectra of Au4f in Au/C and Au-Pd/C

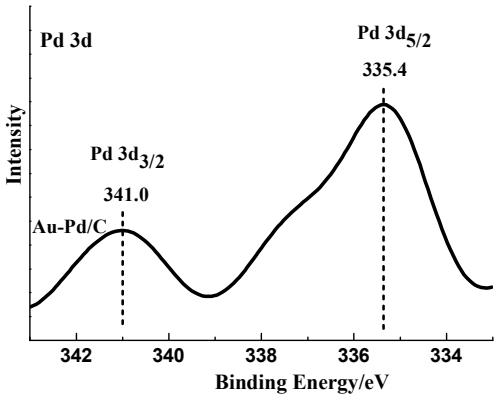

Fig.3 XPS spectra of Pd 3d in Au-Pd/C

Fig. 3 reports XPS spectra, in the Pd 3d region, of the Au-Pd/C catalyst. According to the literature reported[13], Pd $3d_{3/2}$ and Pd $3d_{5/2}$ binding energy of Pd^0 are 335.6eV and 341.3eV, respectively; Pd $3d_{3/2}$ and Pd $3d_{5/2}$ binding energy of PdO are 336.9eV and 342.3eV, respectively. Fig. 3 displays that Pd $3d_{3/2}$ and Pd $3d_{5/2}$ binding energy of Au-Pd/C catalyst are 335.4eV and 341.0eV which are consistent with Pd^0. This means that Pd existed as Pd^0 on the surface of Au-Pd/C catalyst.

XRD. Characteristic peaks of Au are normally considered as 2θ = 38.2°, 44.4°, corresponding to cubic Au crystal face of (111), (200). Pd characteristic peaks are considered as 2θ=40.2°, 46.3°, corresponding to Pd (111), (200). According to the literature[14-15], the characteristic peaks in the range of 38.18-40.18° and 44.20-46.35°should be attributed to Au-Pd alloy. If diffraction peak is close to 38.18° and 44.20°, Au-Pd alloy will be the rich gold alloy, if it is close to 40.18°and 46.35°, Au-Pd alloy will be rich of Palladium. XRD spectra of Au/C and Au-Pd/C are reported in Fig.4. We can find that there are diffraction peak of activated carbon besides characteristic peak of gold. This indicates the high dispersion of gold on carrier.

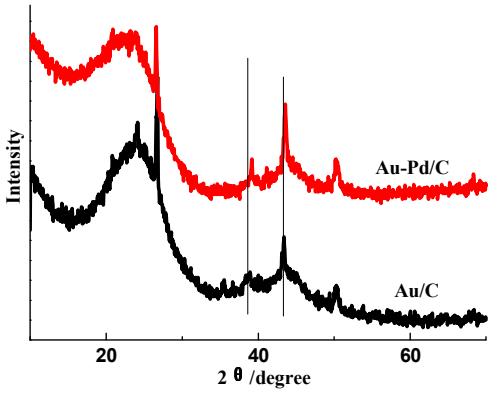

Fig.4 XRD patterns of Au/C and Au-Pd/C

Conclusion

In this paper we have shown that the Au-Pd/C catalyst was more active than the Au/C catalyst for the oxidation of glyoxal and glyoxylic acid. At the optimum reaction time of 20h. the conversion of glyoxal was 58.9% and the yield of glyoxylic acid was 13.7% over Au-Pd/C. This means that the synergistic effect between Au and Pd is better for this reaction.

Acknowledgements

1. This work was financially supported by Research Program of Science and Technology at Universities of Inner Mongolia Autonomous Region. (NJZZ14032).

References

[1] D.I. Enache,J.K. Edwards, G.J. Hutchings, et al. Science, 311:362-365(2006).

[2] A. Corma, P. Serna. Science, 2006, 313:332-334.

[3] T. Hayashi, T. Inagaki, N. Itayama, et al. Catalysis Today, 117(1-3): 210-213(2006).

[4] N. Dimitratos, F. Porta, L. Prati, et al. Catalysis Letters, 99(3-4):181-185(2005).

[5] M. Comotti, C.D. Pina, M. Rossi, et al. Applied Catalysis A: General, 291(1-2):204-209(2005).

[6] S. Demirel, K. Lehnert, P. Claus, et al. Applied Catalysis B: Environmental, 70(1-4): 637-643 (2007).

[7] P. Landon, P.J. Collier, A.F. Carley, et al. Physical Chemistry Chemical Physics, 5:1917-1923 (2003).

[8] B.E. Solsona, J.K. Edwards, G.J. Hutchings, et al. Chemistry of Materials, 18(11): 2689- 2695 (2006).

[9] Xiaoli Wang, Shuangcheng Bao, Tan Guo, et al. Chemical Reagent, 35(8):749-752(2013).In Chinese.

[10] Jialiang Xu, Chengyu Wang, Xiaodong Tang. Chinese Journal of Analytical Chemistry, (25):1086-1089(1995). In Chinese.

[11] J. hastain, Eden Prairie, MN:Perkin-Elmer Corp,(1992).

[12] Lingling Shi. Master's Thesis of Yan Tai University,(2009). In Chinese.

[13] S.H. Oh, G. Hoflund.Journal of Catalysis, 245(1):35-44(2007)

[14] A.M. Venezia, V.L. Parola, G.Deganello, et al. Journal of Catalysis, 215(2):317-325(2003).

[15] A.M. Venezia, L.F.Liotta, G. Pantaleo, et al. Applied Cata lysis A: General, 251(2): 359-368 (2003).

Advanced Materials Research Vols. 960-961 (2014) pp 229-233

doi:10.4028/www.scientific.net/AMR.960-961.229

Electrochemical Investigation of Myclobutanil as Corrosion Inhibitor for Copper in Acid Medium

Li zheng[1], Ji liu[1], Zhihua tao[1, a], wei he[1, b], Dingjun Xiao[2], Ze Tan[2]

[1]School of Microelectronics and Solid-State Electronics, University of Electronic Science andTechnology of China, Chengdu 610054

[2]Guangdong Guanghua Sci-Tech Co., Ltd., Shantou 515000, China

[a]email:Tzh3595@uestc.edu.cn, [b]email: Heweiz@uestc.edu.cn

Keywords: Inhibition efficiency, Copper, Polarization curves, Acid solutions.

Abstract. This paper is mainly to discuss that myclobutanil as corrosion inhibitor and its corrosion efficiency were evaluated via electrochemical impedance spectroscopy (EIS) and potentiodynamic polarization. The potentiodynamic polarization measurements showed that the inhibition efficiency increases sharply with the increasing of concentration of myclobutanil, and the highest inhibition efficiency of the myclobutanil reached 84.3% at 3.2×10^{-4} mol/L in 1 mol/L HCl. The result also indicated that myclobutanil belongs to the mixed type inhibitor. The results obtained from EIS measurements are in good agreement with that obtained from potentiodynamic polarization.

Introduction

Copper plays an indispensable role in daily life, but due to the characteristics of metal, when the copper is exposed in acid solution, corrosion will happen. It will cause huge economic loss. In recent years, corrosion inhibitor began raising concern as a new method for metal corrosion [1]. Now the most widely used inhibitor is benzotriazole (BTA). Thanks to its excellent corrosion resistance performance, BTA is used in the production of all aspects of life. But with the awareness of environmental protection rising, people are eager to find a more environmentally friendly corrosion inhibitor. Myclobutanil is a three azole compounds, and it has good biodegradation properties and low toxicity. In this work, the corrosion behavior of copper in 1mol/L HCl solution with addition of myclobutanil as inhibitor was investigated by EIS and potentiodynamic polarization.

Materials and methods

Materials

In this paper, the working electrode is a copper electrode, and the copper electrode is coated by epoxy resin with an exposed diameter of 3.0 mm. The structure of myclobutanil namely 2- (4-chlorophenyl) -2- (1H, 1, 2, 4- three -1- methyl) of adiponitrile are shown below (**Fig.1**). Before the experiment, the copper electrode need to be polished by metallographic sandpaper, then placed it in ethanol to ultrasound, acetone degrease, finally washed the electrode with deionized water. Corrosive medium used in this essay is 1mol/L HCl. Concentrations of myclobutanil are 0, 3.2×10^{-4}, 1×10^{-4}, 3.2×10^{-5}, 1.0×10^{-5}, 3.2×10^{-6}. The experiment was carried out in 293K water bath.

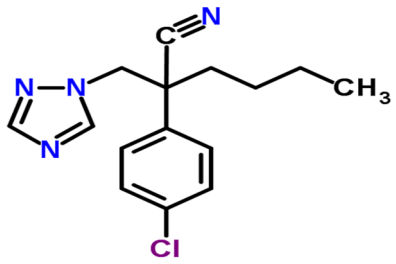

Fig.1 Molecular structure of the studied compound of myclobutanil

Methods

The experiment was conducted by using a three-electrode system with the electrochemical workstation CHI660D in this essay. The copper electrode is working electrode, reference electrode is saturated calomel electrode, a platinum foil of 1.5×1.5 cm as counter-electrode. The three electrodes are placed into a 250 mL solution for half an hour, and then measured the open circuit potential, the corrosion system is considered to have reached a steady state when the open circuit potential changes less than 2 mV in five minutes. In the measurement of polarization curve, the potential scan ranges from -250 to 250 mV SCE (relative to the open circuit potential), and the scanning rate is 0.5 mV/s. The frequency range of the measurements of EIS is 100 k Hz~10 mHz, and the excitation signal is a sine wave with its amplitude of 10mv. Then using specialized software analysis the measured data.

Results and discussion

Polarization curves

Fig. 2 shows the corrosion potentiodynamic polarization curves of copper electrode under different concentrations of the inhibitor in 293 K. From the picture, cathode and anode's potentiodynamic polarization curves with corrosion inhibitor have changed obviously, namely inhibitor has suppress both cathode and anode. And Tafel curve of cathode and anode move to the low current density area with the increase of the inhibitor concentration. That is, the inhibition efficiency increased with the concentration of the inhibitor.

The corrosion parameters of copper in 1mol/L HCl Solution with different concentrations of inhibitor determined by the Tafel extrapolation method- were listed in **Table**.1. From the charts, the corrosion current sharply reduced after adding the corrosion inhibitor, at the same time the concentration increased and corrosion current reduced, which also indicates that the inhibition efficiency increases with the concentration and the highest inhibition efficiency of the myclobutanil reached **75.9%**.Because the change of the open circuit potential is less than 85mV [2], myclobutanil belongs to mixed type inhibitor. The corrosion efficiency is calculated by the following formula [3]. $i_{coor(inh)}$ means the current density in the absence of myclobutanil.

$$IE\% = \frac{I_{coor} - I_{coor\ inh}}{I_{coor}} \times 100$$

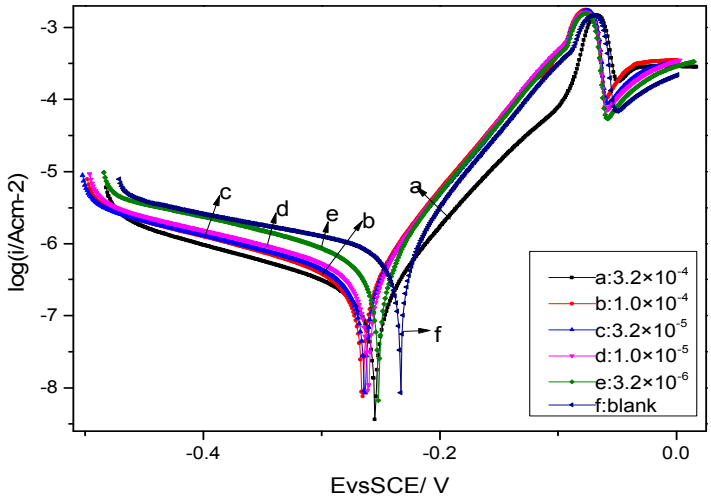

Fig.2. Potentiodynamic polarization curves of copper in 1mol/L HCl solution with different concentrations of myclobutanil

Table1 Potentiodynamic polarization parameters of copper in 1mol/L HCl solution with different concentrations of myclobutanil

Concentration (mol/L)	Ecorr (mV SCE)	Icorr (μAcm^{-2})	β c ($mVdec^{-1}$)	β a ($mVdec^{-1}$)	IE%
blank	-222	0.8613	320.0	50.6	--
3.2×10^{-6}	-234	0.5221	229.2	51.6	39.4
1.0×10^{-5}	-246	0.3828	233.4	49.9	55.6
3.2×10^{-5}	-252	0.3474	232.0	50.6	59.7
1.0×10^{-4}	-248	0.3205	213.4	51.1	62.8
3.2×10^{-4}	-233	0.2080	212.8	57.3	75.9

Electrochemical impedance spectroscope

Fig.3 shows the Nyquist diagram of copper electrode in the solution containing different concentrations of myclobutanil at 293K. Compared with the blank solution, the curves of the Nyquist diagrams with the myclobutanil shifted obviously and the impedance arc diameter get enlargement with increasing the concentration of myclobutanil.

Fig. 4 shows the equivalent circuit of the electrochemical impedance spectroscopy. R_s represents the resistance of the solution, R_{ct} is the charge transfer resistance, R_f stands for the film resistor, C_{dl} and C_f are double layer capacitance and film capacitor, respectively. W is the Warburg impedance which is caused by the diffusion of water soluble substances. Each element's data is in **Table 2**. The inhibition efficiency IE% with myclobutanil in different concentration is calculated by the following formula [4]:

$$IE\% = \frac{R_{ct} - R_{ct}^{0}}{R_{ct}} \times 100$$

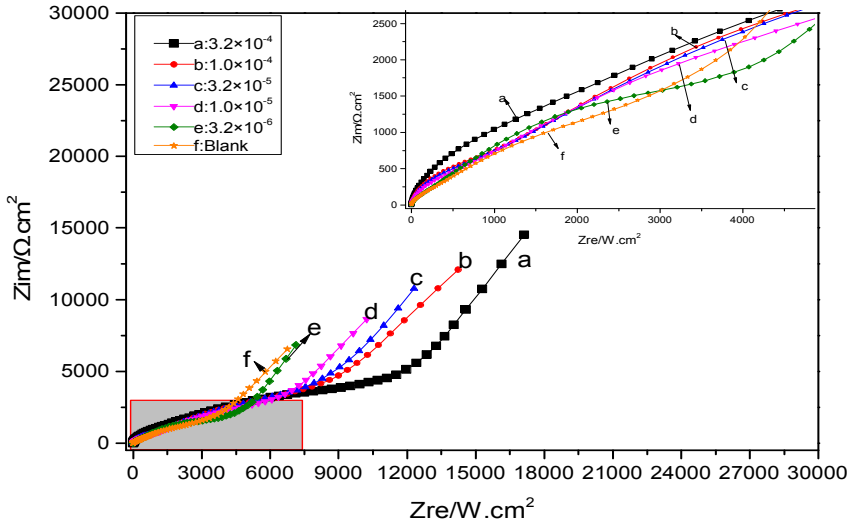

Fig.3. Nyquist diagrams for copper in 1mol/L HCl solution with different concentrations of myclobutanil

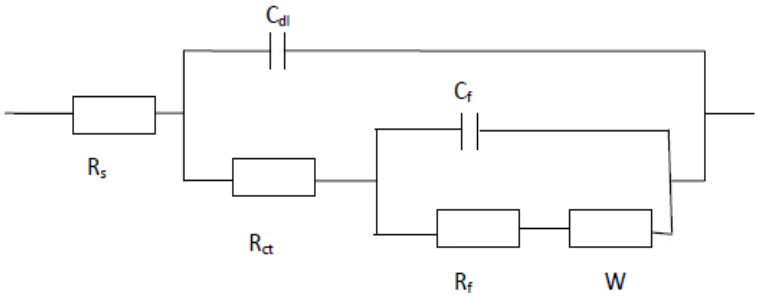

Fig.2. Equivalent circuit model used to fit the EIS experiment data

Table 2 Impedance parameters of copper in 1mol/L HCl solution with different concentrations of inhibitor at 293 K.

Concentration (mol/L)	R_s (Ωcm^2)	R_{ct} (Ωcm^2)	R_f (Ωcm^2)	C_{dl} ($\mu F/cm^2$)	C_f ($\mu F/cm^2$)	W×1000 ($S\ s^{0.5}cm^{-2}$)	IE%
Blank	5.908	201.4	795.8	1.120	7.67	0.3824	--
3.2×10^{-6}	3.701	248.8	1244.0	1.323	11.26	0.3851	19.1
1.0×10^{-5}	3.179	545.7	1588.0	1.268	8.73	0.2746	63.1
3.2×10^{-5}	3.132	672.5	1722.0	1.082	7.20	0.2259	70.1
1.0×10^{-4}	2.786	865.2	2269.0	0.831	7.22	0.2073	76.7
3.2×10^{-4}	3.045	1280.0	4026.o	0.755	4.68	0.1889	84.3

Conclusion

Myclobutanil is an effective inhibitor for corrosion of copper in acid medium at 293K.It can inhibit the copper corrosion by forming the adsorption protective film on metal surface [5]. The potentiodynamic polarization measurements showed that both cathodic and anodic processes of copper corrosion were suppressed and the myclobutanil acts as a mixed-type inhibitor. It is obviously that inhibition efficiency depended on inhibitor concentration and the corrosion efficiency reached the highest point at 3.2×10^{-4} mol/L in 1mol/L HCl solution.

Acknowledgments

The authors gratefully acknowledge the support of Guangdong Innovative Research Team Program (NO. 2013C092) and the Open Foundation of State Key Laboratory of Electronic Thin Films and Integrated Devices (KFJJ201211), and we also express our sincere thanks to the support of "Ph.D Programs Foundation of Ministry of Education of China" (No: 20120185110021).

Refrences

[1] H.O. Curkovic, E. Stupnisek-Lisac, H. Takenouti. Corros. Sci. Vol. 51(2009), p. 2342-2348.
[2] Ying Yana, Weihua Li, Lankun Cai, Baorong Hou. Electrochimica Acta, Vol.53 (2008), p. 5953-5960.
[3] Mohammed A.Amin, K.F.Khaled, Q.Mohsen, H.A.Arida, Corros. Sci. Vol. 52 (2010), p. 1684-1695.
[4] Mohammed.A. Amin, K.F. Khaled, Q. Mohsen, H.A. Arida, Corros. Sci. Vol. 52 (2010), p1684–1695.
[5] S. Zhang, Z. Tao, W. Li, B. Hou, Appl. Surf. Sci. Vol.255 (2009) ,p.6757–6763.

Advanced Materials Research Vols. 960-961 (2014) pp 234-239

doi:10.4028/www.scientific.net/AMR.960-961.234

Low temperature selective catalytic reduction of NO on CeO_2-Fe_3O_4/TiO_2,CeO_2 /TiO_2 catalysts prepared by coprecipitation method

Wenlong Zhen[1,a], Ruitang Guo[1,b], Weiguo Pan[1,c]

[1]Shanghai University of Electric Power (Shanghai) School of power and Mechanical Engineering, Shanghai 200090, China

[a]zhenwl317@163.com,[b]grta@zju.edu.cn,[c]pweiguo@163.com

Keywords: Selective catalytic reduction; NH_3; NO; coprecipitation method.

Abstract: CeO_2-Fe_3O_4/TiO_2 and CeO_2/TiO_2 catalysts were prepared by coprecipitation method, and their activities for selective catalytic reduction of NO with NH_3 were investigated. As can be seen from the experimental results, the CeO_2-Fe_3O_4/TiO_2 catalyst prepared showed the best SCR activity and SO_2 resistance. Based on the characterization results of BET, XRD, NH_3-TPD and XPS the excellent performance of CeO_2-Fe_3O_4/TiO_2 catalyst should be resulted from its large surface area, high NH_3 adsorption capacity and high concentration of surface chemisorbed oxygen.

Introduction

Selective catalytic reduction process is the main technique for controlling NO in the flue gas emitted from stationary sources such as coal fired boilers [1]. Now, vanadium based catalyst has been put into large scale commercial utilization. But the deactivation od this catalyst caused by dust and SO_2 in the flue gas make it necessary to develop low temperature SCR catalyst [2].

In recent years, much attention had been paid on Ce-Fe-based low temperature SCR catalysts because ceria oxides have high oxygen storage capacity and high activity and Fe have good SO_2 resistance in low temperature [3,7]. Fang et al. [4] found that highly dispersed CeO_2 on carbon nanotubes showed high NH_3-SCR activity and good SO_2 and H_2O resistance. Gu et al. [5] found that surface sulfation could enhance the NH_3-SCR performance of CeO_2 catalyst. Gao et al. [6] reported a Ce-Cu-Ti complex oxide catalyst with high activity and SO_2 resistance ability at the temperature lower than 350 ℃. However, very few reports on Ce-Fe-based catalysts over TiO_2 can be found in the literatures. It is well recognized that the difference of components and preparation conditions have great impact on the dispersion and existence state of active components[1,7], therefore, affecting the activity and SO_2 resistance of catalyst. So it is necessary to find the relationship between different components and the activity and SO_2 resistance of TiO_2 supported Ce-Fe-based catalysts.

In this study, CeO_2-Fe_3O_4/TiO_2 and CeO_2/TiO_2 catalysts prepared by coprecipitation method. The effect of different components on the SCR activity, SO_2 resistance and surface properties of catalysts samples was investigated and discussed.

Experimental

1.1 Catalyst preparation

The catalysts were prepared by coprecipitation method. Titanium sulfate (0.1 mol), ferric nitrate (0.05mol) and cerium nitrate (0.05mol) (or titanium sulfate (0.1 mol) and cerium nitrate (0.05mol)) were fully dissolved in deionized water(100ml), then ammonia solution(3mol/L) was added drop by drop into the solution under adequate mixing at room temperature until the pH value of the solution reached 11. After 3h, the sediment was filtered and washed throughly with deionized water. After dried at 100℃ in air for 12h, the sediment was calcined at 550℃ in air for 5h.

1.2 Characterization

The BET surface areas of the catalysts were measured N_2 adsorption at77 K on a Quantachrome Autosorb iQ instrument. The X-ray diffraction (XRD) measurement was performed on a Bruker D8advance X system with CuK α a radiation. The t temperature programmed desorption with ammonia (NH_3-TPD) was carried out on a chemisorption analyzer (ChemBET TPR/TPD, Quantachrome Instruments). The NH_3 signal was measured by a thermal conductivity detector.

1.3 Activity test

The SCR activity test was performed on a fixed bed reactor (13mm i.d.) with 2.4mL catalyst samples with particle size of 60-100 mesh. The simulated flue gas composition was as follows: 600ppmNH_3, 600ppm NO, 5%O_2, 200ppm SO_2(when used), and balance Ar. The concentrations of NOx before and after reaction was determined by a flue gas analyzer (Model 60 I, Thermo Fisher Scientific Inc.). X-ray photoelectron spectroscopy (XPS) was performed on an AXIS-NOVA (Kratos, Inc.) by using 300W AlK radiation.

Results and discussion

2.1 Characterizations

The textural properties of the catalyst samples are listed in Table 1. It is clear that Ce-Fe-TiO_2 and Ce-Fe-TiO_2-S(By Ce-Fe-TiO2 catalyst forming in the sulfur dioxide poisoning) is of the largest BET surface area and total pore volume among the three samples. And the difference in the average pore diameter is also obvious: Ce-TiO_2>Ce-Fe-TiO_2 and Ce-TiO_2-S(By Ce-TiO2 catalyst forming in the sulfur dioxide poisoning)>Ce-Fe-TiO_2-S. That is to say, different components catalysts have impact on the textural properties of catalysts .

Table 1. Textural properties of the catalyst samples

Samples	BET surface area (m^2/g)	Total pore volume (cm^3/g)	Average pore diameter (nm)
Ce-Fe-TiO_2	46.8713	0.035611	34.7913
Ce-TiO_2	31.5262	0.010775	38.9864
Ce-Fe-TiO_2-S	81.4939	0.246598	10.6511
Ce-TiO_2-S	80.0124	0.284306	12.7842

XRD patterns are shown in Fig.1. It is obvious that Ce-Fe-TiO_2 and Ce-TiO_2 is similar.So that the activity of Ce-Fe-TiO_2 and Ce-TiO_2 catalysts are similar.There are several peaks of CeO_2, Fe_2O_3,Fe_3O_4,rutile and TiO_2 can be observed in the spectrum of Ce-Fe-TiO_2 and Ce-TiO_2, but the Ce-Fe-TiO_2-S and Ce-TiO_2-S intensities are very low. Because, the surface of catalysts is encased by sulfur dioxide . As a whole, CeO_2, Fe_2O_3,Fe_3O_4 and rutile are well dispersed on the surface of TiO_2, which means strong interaction between the active components and the support. As for the two samples, the diffraction peaks of CeO_2, Fe_3O_4 and TiO_2 are more apparent compared , and the crystallinity of CeO_2, Fe_3O_4 and TiO_2 is very high. The amorphous CeO_2-TiO_2 and Fe-TiO_2 is believed to be beneficial to SCR reaction[6,7] .

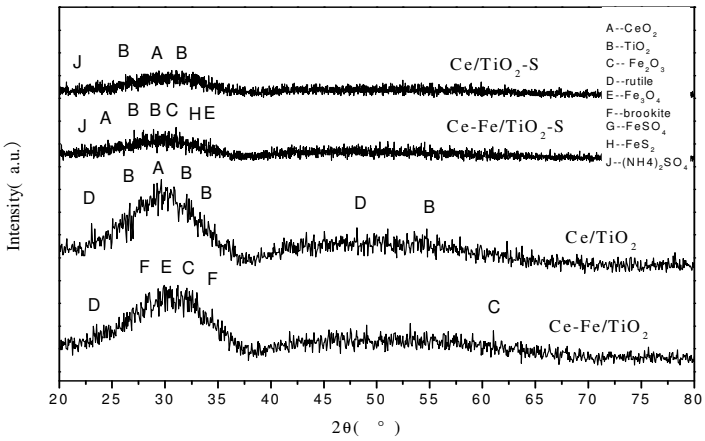

Fig.1 XRD Patterns of the Ce-Fe/TiO_2 and Ce/TiO_2 catalysts

NH_3-TPD profiles of the Ce-Fe/TiO_2 catalysts are shown in Fig.2. It is clear that there are different acid sites of different strength on each sample. Ce/TiO_2 has three desorption peaks, the first one centered at about 175℃ and the second one centered about 650℃ could be assigned to Brönsted acid sites[9]. And the third one may be linked to Lewis acid sites[5].As for Ce-Fe/TiO_2, desorption peaks belong to Brönsted acid sites and Lewis acid sites can also be observed in their NH_3-TPD profiles. In addition, the total surface concentration of acid sites of the two samples are calculated and the results are listed in Table 2. Table 2 shows that Ce-Fe/TiO_2 is of the strongest surface acidity, indicating its strongest NH_3 adsorption capacity. And high NH_3 adsorption capacity can promote SCR reaction[10].And the two catalysts have the similar characterizations after sulfur dioxide poisoning because of encased by sulfur dioxide.

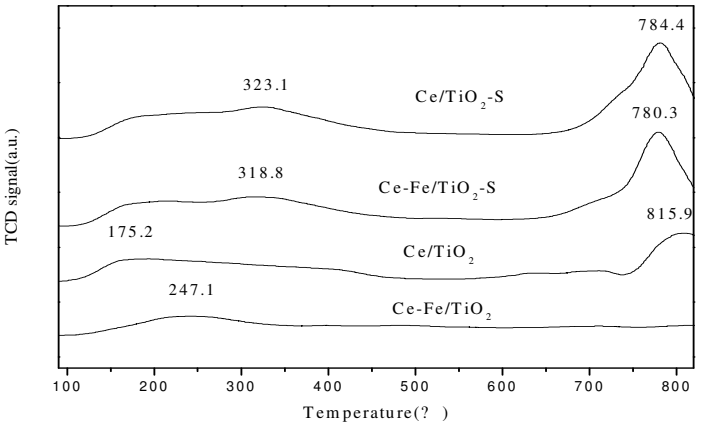

Fig.2 NH_3-TPD profiles of the Ce-Fe/TiO_2 and Ce/TiO_2 catalysts

Table 2. Surface acidity of the catalyst samples

Samples	Surface acidity(mmol/g)
Ce-Fe-TiO_2	5.57
Ce-TiO_2	4.97
Ce-Fe-TiO_2-S	8.69
Ce-TiO_2-S	8.38

H_2-TPR profiles of the four catalysts are shown in Fig.3. It could be seen that there is one reduction peak in the TPR profile of each catalyst sample. The reduction peak in the TPR profile of Ce/TiO_2 centers between 600-700℃ might be linked to the reduction of non stoichiometric ceria of type Ce^{3+}–O–Ce^{4+}[11]; the peak centered at about 500 ℃ in the profile of Ce-Fe/TiO_2 belongs to the

reduction of Fe_2O_3 and FeO. In addition, the Ce-Fe/TiO_2-S and Ce/TiO_2-S catalysts lead to a shift of reduction temperature to a higher value, which the process may be explained that sulfate species deposit on catalyst surface at low temperature, and catalytic active center is covered[12]. And the redox ability of the two catalyst samples is in the following order: Ce-Fe/TiO_2> Ce/TiO_2.

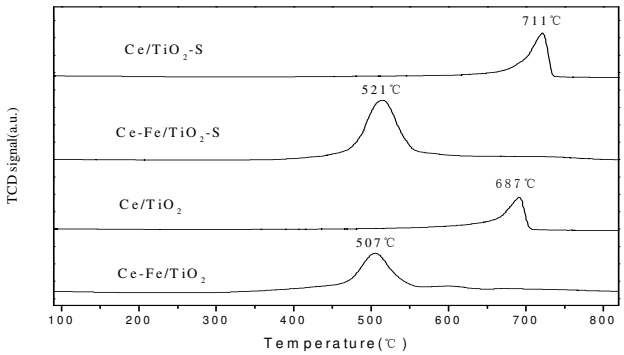

Fig.3 H_2-TPR profiles of the Ce-Fe/TiO_2 and Ce/TiO_2 catalysts

XPS:O1 s spectra of the two catalyst samples are shown in Fig.4. Fig.4 shows that the O1 s profiles of the two samples can all be fitted three peaks. The three peaks can be assigned to: lattice oxygen O_α (529.9-530.0eV), chemisorbed oxygen O_β (531.3-531.9eV) and hydroxyl groups O_γ (532.7-533.5eV)[13]. As can be seen from Fig.4, the concentration of chemisorbed oxygen is in the following sequence: Ce-Fe/TiO_2>Ce/TiO_2 . It has been reported that chemisorbed oxygen is of the highest activity among oxygen species in the SCR reaction[14]. The presence of so high concentration of chemisorbed oxygen in CCA(SG) would be helpful to enhancing its SCR performance.

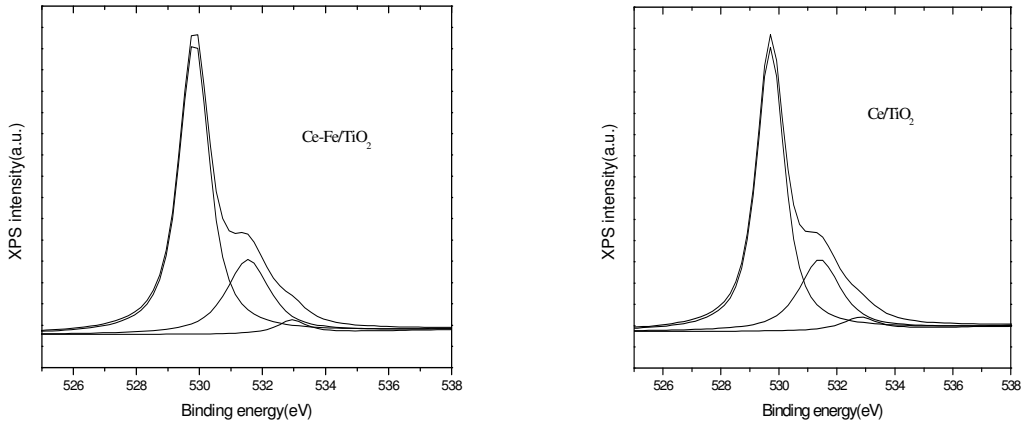

Fig.4 O1s spectra of the Ce-Fe/TiO_2 and Ce/TiO_2 catalysts

2.2 Catalytic activity

The NO conversions over the two catalyst samples at different reaction temperature are shown in Fig.5. It is obvious that the two catalyst samples show the best similar performance in the whole temperature range. And Ce-Fe/TiO_2 and Ce/TiO_2 , a decrease of NO conversion can be observed when the reaction temperature exceeds 330℃. A similar phenomenon was also found by Gao et al. [1] when they studied NO conversion over CeO_2/TiO_2 catalyst, which be may be caused by NH_3 oxidation to NO at high temperature. And the high NO conversion of the two catalyst samples maybe caused by CeO_2 ,and Fe_3O_4 maybe not influence the NO conversion. As shown in section 3.1, large surface area, well dispersion of CeO_2, high NH_3 capacity and high concentration of chemisorbed oxygen may be the main reasons for its best SCR performance.

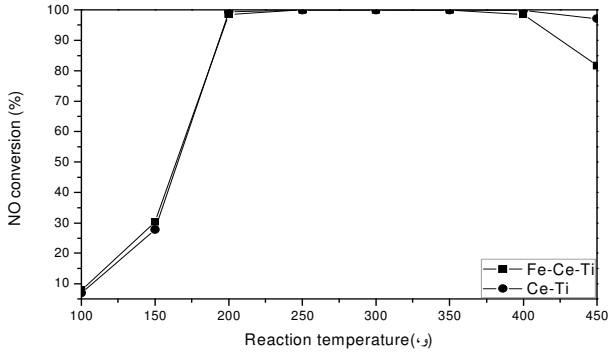

Fig.5 NO conversion as a function of reaction temperature for different catalysts
Reaction conditions: [NO]=[NH_3]=600ppm, [O_2]=5%, total flow rate =1L/min, GHSV=25,000h^{-1}

2.3 Effect of SO_2 on the catalytic activity

Effect of SO_2 on NO conversion over the two catalyst samples is shown in Fig.6. It is obvious that SO_2 has an inhibition effect on the performance of the catalysts, and the effect of SO_2 on the catalytic activities of the two samples is quite different. While Gao et al. [6] had reported that SO_2 can enhance the activity of Ce-Cu-Ti oxide catalyst, the difference may be caused by the presence state of Cu species in the catalysts. From Fig.6, it can be seen that NO conversion decreases about 41% in 5h for Ce/TiO_2, while the NO conversion of $Ce\text{-}Fe/TiO_2$ decrease after piped SO_2 between 60 and 90 minutes, after 90 minutes the NO conversion of $Ce\text{-}Fe/TiO_2$ rises to about 98%,and Liu et al.[7] had reported that the sulfate species was mainly formed on iron sites in a chelating bidentate conformation, resulting in the higher binding energies of Fe 2p and Ti2p due to the inductive effect of the S==O double bond . That is to say, $Ce\text{-}Fe/TiO_2$ has the best SO_2 resistance ability among the two sample. According to the results of BET and XRD, the inhibition effect of SO_2 on Ce/TiO_2 may be weakened by the strong interaction between active components.

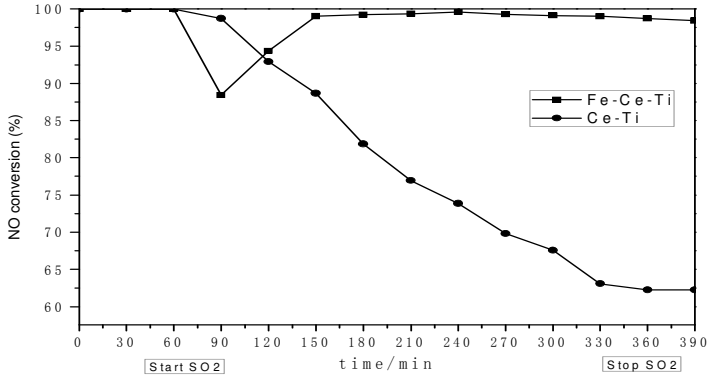

Fig.6 Effect of SO2 on NO conversion over different catalyst samples
Reaction conditions: [NO]=[NH_3]=600ppm, [O_2]=5%, [SO_2]=200ppm, total flow rate =1L/min, GHSV=25,000h^{-1}, reaction temperature 250℃

Conclusions

The performance of $Ce\text{-}Fe/TiO_2$ and Ce/TiO_2 catalysts were investigated and discussed based on the characterization results. It was found that the two catalysts showed the best SCR activity and $Ce\text{-}Fe/TiO_2$ showed the best SO_2 resistance. Large surface area, high NH_3 adsorption capacity and high concentration of surface chemisorbed oxygen should be the main reasons for its excellent performance.

Acknowledgements

This work was supported by Scientific Problem Tackling Program of Science and Technology Commission of Shanghai Municipality (11dz2281700).

References

[1] X. Gao, Y. Jiang, Y. Fu, Y. Zhong, Z. Luo, K. Cen. Catal. Commun. 2010, **11**, 465.
[2] B. Jiang, Y. Liu, Z. Wu. J. Hazard. Mater. 2009, **162**, 1249..
[3] Y. Shen, S. Zhu, T. Qiu, S. Shen. Catal. Commun. 2009, **11**, 20.
[4] C. Fang, D. Zhang, L. Shi, R. Gao, H. Li, L. Ye, J. Zhang. Catal. Sci. Technol. 2013,**3**,803.
[5] T. Gu, Y. Liu, X. Weng, H. Wang, Z. Wu., Catal. Commun. 2010, **12**,310.
[6] X. Gao, X. Du, L. Cui, Y. Fu, Z. Luo, K. Cen. Catal. Commun.2010, **12**,255.
[7] F. Liu, K. Asakura, H. He,W. Shan, X. Shi, C. Zhang. Catal. B: Environ.2011,01,044.
[8] P.J. Schmitz , R.K. Usmen, C.R. Peters, G.W. Graham , R.W. McCabe. Appl. Sur. Sci. 1993, 72, 181.
[9] R. Jin, Y. Liu, Z. Wu, H. Wang. T. Gu. Chemosphere 2010, **78**, 1160.
[10] E. Y. Choi, I. S. Nam, Y. G. Kim. J. Catal. 1996, **161**, 597.
[11] B. Murugan, A.V. Ramaswamy, J. Phys. Chem. C 112 (2008) 20429–20442.
[12] L. Chen, J. Li , M. Ge, R. Zhu.Catal.Today.2010.153.
[13] M. Kang, E.D. Park, J.M. Kim, J.E. Yie, Appl. Catal. A 2007, **327**, 261.
[14] L. Jing, Z. Xu, X. Sun, J. Shang, W. Cai, Appl. Sur. Sci. 2001, **180**, 308.

Advanced Materials Research Vols. 960-961 (2014) pp 240-244

doi:10.4028/www.scientific.net/AMR.960-961.240

Research on the Mobility of Polymer Flooding System for Xinjiang Conglomerate Reservoirs

Wu Yunqiang[1,2,a], Lou Qingxiang[1,2], Nie Xiaobin[1,2],Li Yiqiang[3], Xiang Jianan[3], Miao Junjie[3]

[1]Research Institute of Experiment and Detection, Xinjiang Oilfield Company, Karamay, 834000, China;

[2] Key Laboratory of Conglomerate Reservoir of Xinjiang Uygur Autonomous Region, Karamay, 834000, China;

[3]Enhanced Oil Recovery Institute, China University of Petroleum, Beijing, 102249, China.

[a]liuhualong0525@163.com

Keywords: conglomerate reservoir, mobility, compatibility, injection parameters

Abstract. The conglomerate reservoir is provided with strong heterogeneity and complex pore structure. To study the matching relationship between polymer flooding system and pore throat of the conglomerate reservoir and set up the flow matching relationship plate, this paper conducted natural core flow experiments at the true flow rate of the site formation based on constant pressure flooding method, considering the shear of the borehole and the formation. And several suitable polymers for different reservoirs permeability were given. The experimental results indicated that a positive correlation between the flow properties and the viscosity of the polymer solution, but a negative correlation between the mobility and the permeability of reservoir. Such as the natural core with the permeability = $30\times10^{-3}\mu m^2$ was suitable for the viscosity$\leqslant$16.0 mPa·s of the polymer solution in the formation, the natural core with the permeability = $60\times10^{-3}\mu m^2$ was suitable for the viscosity$\leqslant$35.2mPa·s of the polymer solution and the natural core with the permeability = $120\times10^{-3}\mu m^2$ was suitable for the viscosity $\leqslant$ 102.4mPa·s of the polymer solution. Using compatibility relationship, quickly and easily choose the right injection parameters of the polymer based on the reservoir permeability, providing a theoretical basis for program preparation and parameters adjustment of the polymer flooding.

Introduction

Compared with sandstone reservoirs, conglomerate reservoir with features of complex structure and uneven distribution of pore[1,2], small diameter of throat and big throat to pore ratio has bad physical property. So study on the compatibility between displacement system and conglomerate reservoir becomes difficult. The traditional research methods were mathematical method, atomic force microscopy (SEM) and dynamic light scattering (DLS) [3,4], but the results obtained from them have some limitations. The block of displacement system in farther formation occurs frequently because of serious permeability differences however the displacing phase was injected into immediate vicinity of wellbore easily. In this paper, natural core flow experiments under the condition of deep formation pressure gradient based on constant pressure flooding method were conducted to study on the matching relationship between displacement system and the father

formation, providing guidance and research methods for field application to select suitable polymer system for reservoir with different permeability.

Experimental materials and equipment

1.1 The experimental materials and conditions

(1) Polymer: XinJiang oilfield using polymer, molecular weight are 600×10^4, 1000×10^4, 1500×10^4, 2000×10^4, 2500×10^4 respectively, the solid content is 90%;

(2) Xinjiang oilfield injection water, water salinity and ion composition are shown in table 1;

Table 1 Ion composition of dilution water

water quality	Cl^-	$SO4^{2-}$	HCO^{3-}	K^++Na^+	Ca^{2+}	Mg^{2+}	Total salinity(mg/L)
injected water	103.0	33.7	146.7	55.3	58.0	8.4	405.2

(3) Experimental model: use natural core, The size isΦ3.8×10cm, core permeability are $30\times10^{-3}\mu m^2$, $60\times10^{-3}\mu m^2$and $120\times10^{-3}\mu m^2$;

(4) The experimental temperature: 34.3℃.

1.2 Experimental apparatus

(1) FY-3 type constant temperature box, the control precision of +/-1℃;

(2) Waring blender, speed is divided into 7 files;

(3) Precision pressure regulator, the adjusting range of 0.05 to 0.4 MPa, 0.0008 MPa accuracy;

(4) Pressure sensor: the maximum range is 0.2 MPa, precision to 0.001 MPa;

(5) Brookfield DV-typeII+Pro BROOKFIELD viscometer;

(6) Cylinders, container, etc.

Experimental methods

2.1 Shear simulation

Before it is injected into the deep reservoir area, the polymer solution goes through the high-speed shear of wellhead and the near-wellbore. This study using Waring blender, design a shear simulator of the near-wellbore, with the shear strength of viscosity 50% lost after shear, which is the same shear strength as the spot water compounding water diluting molecular weight of polymer solution after the shear of wellhead and the near-wellbore. All the polymer solution involved in the experiment is shared by the simulator, in order to simulate the spot which the polymer solution was shared in the wellhead and the near-wellbore before entering the deep reservoir.

2.2 Determine the constant pressure method

Due to the match object is deep reservoir area with low and little change pressure gradient value,and approximate it constant, so we use the constant pressure gradient method.

2.3 Quantify stable flow velocity of the producted end

According to field experience, in deep reservoir area polymer solution actual flow velocity is 0.2m/d.

2.4 Calculate the actual pressure gradient in deep reservoir

According to field experience, the actual field with the well spacing 200m of reservoir deep area，the average pressure gradient is about 0.12MPa/m.

2.5 The determination methods of liquidity

Use The nature core with the constant pressure gradient 0.12MPa/m, inject the polymer solution for evaluation, record the outlet volume with the injection PV, then calculate the matching flow velocity in the formation.

Experimental result

3.1 The influence of polymer molecular weight on the mobility

The results of the core flow experiments showed that the greater the molecular weight of the polymer, the more difficult the polymer flowed in the core because the polymer solution was a kind of viscoelastic fluid, the ability flow into the throat became worth with the molecular weight of the polymer increased[5,6].

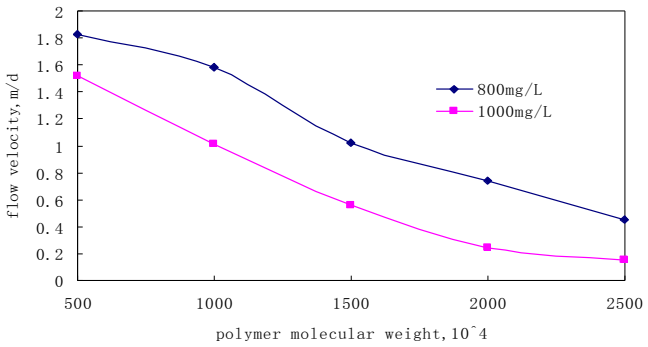

Figure1 Mobility experimental results in 100md cores

3.2 The influence of polymer concentration on the mobility

The results of the core flow experiments also showed that the greater the polymer concentration, the bigger the viscosity of the polymer solution was and the worse the ability of the polymer flowed into the throat was.

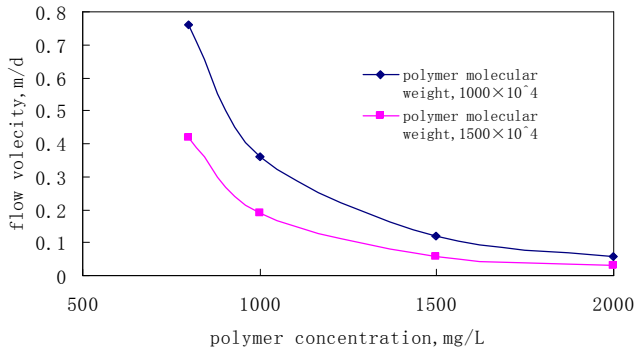

Figure2 Mobility experimental results in 50md cores

3.3 Establishing the matching relationship chart of the polymer system and reservoir permeability

Based on the real formation flow rate 0.2m/d, we establish the matching relation chart of different polymer system in effective permeability 30mD, 60mD and 120mD cores, with the polymer molecular weight of 600×10^4, 1000×10^4, 1500×10^4, 2000×10^4, 2500×10^4, at a concentration of 800mg/L, 1000mg/L, 1500mg/L, 2000mg/L, respectively. The result shows that Permeability of $30\times10^{-3}\mu m^2$ natural core requires polymer solution viscosity no more than 16.0mPa·s at formation, and the polymer solution viscosity should be equal or lesser than 35.2mPa·s at $60\times10^{-3}\mu m^2$ natural core, and the $120\times10^{-3}\mu m^2$ cores require polymer solution viscosity no more than 16.0mPa·s at formation, respectively. The results are shown in Table 2, Table 3, Table 4.

Table2 Different polymer system with $30\times10^{-3}\mu m^2$ mobility compatibility chart

water quality	Concentration, mg/L / Molecular weight, $\times10^4$	800	1000	1500	2500
injected water	600	1	1	0	0
	1000	0	0	0	0
	1500	0	0	0	0
	2000	0	0	0	0
	2500	0	0	0	0

Table3 Different polymer system with $60\times10^{-3}\mu m^2$ mobility compatibility chart

water quality	Concentration, mg/L / Molecular weight, $\times10^4$	800	1000	1500	2500
injected water	600	1	1	0	0
	1000	1	1	0	0
	1500	1	0	0	0
	2000		0	0	0
	2500	0	0	0	0

Table4 Different polymer system with $120\times10^{-3}\mu m^2$ mobility compatibility chart

water quality	Concentration, mg/L / Molecular weight, $\times10^4$	800	1000	1500	2500
injected water	600	1	1	1	
	1000	1	1	1	
	1500	1	1	1	0
	2000	1	1	0	0
	2500	1	1	0	0

(0 represents bad matching;1 represents good matching)

Conclusions

(1) To evaluation liquidity of flooding system in the core at the condition of deep formation, we adopt shear simulator and constant pressure gradient near wellbore area, which can better simulate the polymer solution flow state in deep reservoir.

(2) Under certain conditions of core permeability, with the increase of Polymer molecular weight and concentration, the mobility of polymer system turns bad. The mobility of polymer system depends on its molecular weight at a fixed permeability core.

(3) The matching relationship chart of the polymer system and reservoir permeability can guide the plan for polymer flooding program and adjustment of injection parameters, which can help to determine polymer injection parameters.

Reference

[1] Feng Huijie, Nie Xiaobin, Xu Guoyong,et al. Microscopic Mechanisms of Oil Displacement by Polymer Solution for Conglomerate Reservoir[J].Oilfield Chemistry,2007,24(3):232-237.

[2] Song Ziqi, Sun Ying, Liu Gang,et al. Characteristics and remaining oil distribution of heterogeneous conglomerate reservoir in Karamay Oilfield[J]. Journal of Petrochemical Universities, 2012,25(2):42-47.

[3] Han Xiuzhen, Li Mingyuan, Linmeiqin. Properties evaluation of linked polymer microspheres dispersed system.PGRE,2009,16(5):63-65.

[4] Lin Meiqin, Zuo Qingquan, Liu Gang, ea tl. Matching Relation Between HPAM and Pores of Nuclepore Film[J].Journal of Petrochemical Universities,2012,25(2):42-47.

[5] Zhao Fulin. Principle of EOR[M]. DongYing: China university of petroleum press,2006.

[6] Gao Zhenhuan, Lu Xiangguo. Experimental Study of Relationship Between Polymer Molecular Weight and Sweep Effciency[J]. Petroleum Geology & Oilfield Development in Daqing,1994,13 (2):54-57.

Advanced Materials Research Vols. 960-961 (2014) pp 245-248

doi:10.4028/www.scientific.net/AMR.960-961.245

Study on Plastic Strain and Plastic Strain Rate in Machining of Steel AISI 1020 using FEM Analysis

QIN Qi [1, a], MA Shizhong[1,b], LI Pengyun[2,c], WANG Mingwei [3,d]

[1] Geosciences College, Northeast Petroleum University, Daqing 163318, Heilongjiang Province, China

[2] Down Hole Opration Sub-Company of Daqing Oilfield Company Ltd., Daqing 163413, Heilongjiang Province, China

[3] Exploration and Development Research Institute of North China Oilfield Company Ltd., Renqiu 062552, Hebei Province, China

[a]qinqiqq777@sina.com, [b] szm6503@sina.com, [c]125478563@qq.com, [d]450185813@qq.com

Keywords: Heterogeneity, Fuyu Reservoir, Chao 45 block, Remaining oil

Abstract. Based on analyzing and testing the core samples of three inspection wells, we research in-layer heterogeneity of the main types monosandbody; in order to build macroscopic analysis on the difference of physical properties in reservoir interbedded, we can also draw distribution diagram of the interbedded sandstone's average porosity and permeability through the physical property data in the study area, meanwhile it is necessary to use statistic data of physical parameters including variation coefficient, mutation coefficient and range to draw tables, which can show the degree of heterogeneity of monosandbody in the reservoir become much stronger from top to bottom; In addition, according to the study of plane microfacies and monosandbody, the information relating to the heterogeneity of the main monosandbody can be acquired. In conclusion, it is clear to know the distribution characteristics of remaining oil deriving from FuYu oil layer in the Chao 45 Block, and the distribution area of residual potential of microfacies by reducing the heterogeneity of reservoir to improve the connectivity, and then increase the mining effect.

Introduction

Reservoir heterogeneity is refers to the basic properties of the reservoir (lithology, physical property, electric property and oiliness, etc.) on the 3D spatial distribution of heterogeneity[1-6]. Under the influence of structure, diagenesis and reservoir sedimentary environment, the interior of the reservoir physical properties and spatial distribution of non-uniform changes, which make the underground oil, gas, water sports and oil and gas recovery factor affected, so studying the reservoir heterogeneity has an important significance on oil and gas drilling and the evaluation of reservoir remaining oil.

General situation in the study area

Chao 45 block is located in south Chaoyang block oil field in pure oil region, exploited horizon is fuyu oil reservoir, oil bearing area is 2.0 km^2, geological reserves is 184×10^4t. Fuyu reservoir is in Songliao basin in middle-late development which as a predominantly fluvial-dominated delta deposits , the upper delta front subfacies and lower delta distributary plain subfacies.

Reservoir heterogeneity

Heterogeneity in reservoir layer upon layer. Through core observation description and on the basis of single well facies analysis, we draw the conclusion: The development of Fuyu reservoir is delta front subfacies, delta distributary is plain subfacies, sand body reservoir is mainly distributary channel, at the same time, it develops sedimentary microfacies of crevasse-splays and natural levees, including fuyu oil layer stranded at the bottom of the underwater distributary channel deposits in this

area is mainly calcium nodules[7], controls the sand body vertical permeability is positive and negative are more complex rhythm, also often appear positive rhythm. The following is the area of backward and forward in the small layer composite rhythm to be analyzed.

Typical analysis of the heterogeneity in single sand layer. For the 103-55 Coring Wells on F Ⅰ 2^2 depositional time unit as an example, F Ⅰ 2^2 depositional time unit representative microfacies types are high sinuosity distributary channel microfacies, delta front is a typical microfacies types. Property vertical sequence of sequence is controlled by sedimentary and lithology , the field logging data, the permeability sand body as a whole for a f positive and negative in the layer composite rhythm, 45 block in fuyu reservoir is the distributary channel micro phase extremely typical type of rhythm. According to mechanical analysis, the interior is divided into seven secondary rhythm (figure 1), with the thinnest 52 cm, upper and lower porosity is the rhythm of negative and positive , lower and upper permeability is the rhythm of negative and positive, secondary rhythm thin interbedded easily identified from the log.

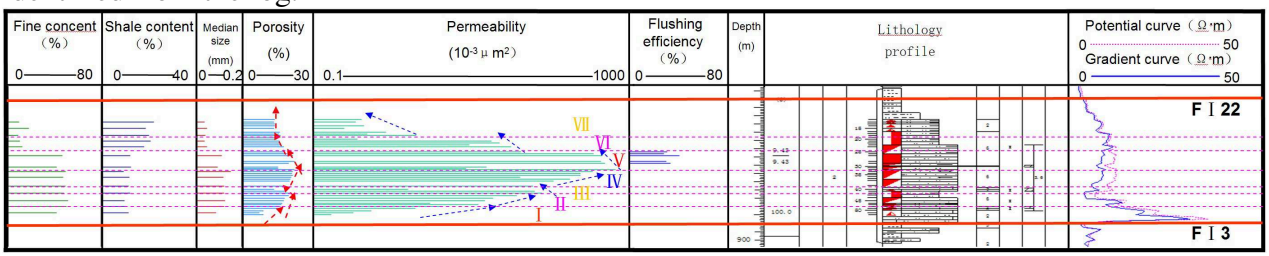

Fig. 1 Heterogeneity analysis of unit F Ⅰ 2^2

Within the depositional time unit, shale content showed a trend of positive and negative rhythm and silt content showed a trend of positive and negative rhythm and fine content was positively rhythm trend, medium sand content showed a trend of anyway, rhythm and the lower layer is thin coarsen and then gradually tapering upward, permeability showed a trend of anyway, a negative and positive rhythm, and the granularity has corresponding good rhythm, but no significant vertical variation of porosity, the layers of inner heterogeneity is strong.

The permeability in this layer shows the positive rhythm, water absorption on the lower layer is stronger than upper one in the permeability of positive rhythm on the above layer . Lots of injected water crashed into the lower part of the bottom quickly through the high permeability zone .At the same time, gravity and then put into the upper injection water sinks and more contributed to the level of the water flowing and water washing at the bottom of the reservoir . And the permeability of the in turn rhythm layer is Under the low high above , the layer of high permeability water absorption, upper infiltration gradually, but as a result of injected water by gravity makes less water washing to strengthen in the bottom of the reservoir .The result that the lower interval section water to wash up and down differences .In conclusion, the water in the small layer thickness distribution on the bottom, controlled by the heterogeneity, predict remaining oil throughout the layer on top of the underwater distributary channel.

Interlayer heterogeneity

Refers to the reservoir sand body on longitudinal and physical properties of the differences between distribution characteristics, on the other hand refers to the distribution and the change of the mudstone interlayer between each group .In the layers of mudstone interlayer distribution change law is not obvious, here we focus on physical differences between the study of sand body. The property differences between layers including the differences of porosity and permeability , the permeability differences between interlayer usually use parameters such as coefficient of permeability differential, coefficient of variation, dash coefficient to show[8]. The vertical distribution of oil and gas, the condition of water between the upper and remaining oil distribution are different due to the Interlayer heterogeneity.

Physical differences between the layers. Each layer of fuyu oil layer in the study area vertical relatively has little change of porosity, the average porosity is above 15%; Vertical permeability changes are very different, The property of two depositional time unit F Ⅰ 2^2 ,F Ⅰ 3^2 is best, Permeability in more than $20\times10^{-3}\mu m^2$, As the neutral pore of low permeability reservoir, Permeability of the adjacent vertical F Ⅰ 3^2 quickly reduced. The property the differences between the layers shows that F Ⅰ 2 and F Ⅰ 3 have a better ability to control the oil and gas gathering; The rest of the average permeability basic depositional time unit is less than $9\times10^{-3}\mu m^2$, as a neutral pore of low permeability reservoir. Depositional time unit property of F Ⅱ 1^1 is relatively poor, The average porosity is 13.3%, the average permeability is $4.9\times10^{-3}\mu m^2$,Under the influence of the neutral hole in the low permeability reservoir, by combining with valid for alloy layer sandstone thickness of the two vertical adjacent time units for the further investigation.

The main unit plane heterogeneity. Plane heterogeneity is due to the geometry of sand body, the size of continuity, porosity and permeability, the plane changes [9].Fuyu oil layer planar sand body and heterogeneity is mainly controlled by sedimentary microfacies distribution, so the characteristics of layer heterogeneity distribution basic consistent with the plane distribution of sedimentary microfacies, phased by the plane can further determine the distribution of remaining oil in the area of sedimentary units, which can be through the volume method to calculate geological reserves, residual oil reserves in the entire block, prediction and evaluation.

According to layer data of 103-55 well on Unite F Ⅰ 7^3 to make the contour map(figure 2).

Boundaries of the sand body is not necessarily strictly stuck in hierarchical boundary, the condition of the cross, this need split, sandstone finally get effective sandstone thickness 10.2 metres at the last(10C98-60 Wells), which is 4.56 meters thick, on average, value distribution in 3-5.2 meters, about 24%, low distribution at 0-0.8 m, about 15%, mainly distributed in 1.2-2.4 meters, about 61%. Figure sandstone in the high value area even lamellar distribution in all those places, 10C106-49, 10C106-50, 10C106-52, 10C106-54. Along the river, gradual trend, effective thickness change controlled by the river. Which can be further, effective sandstone thickness according to the channel boundary preliminary qualitative outlined the distribution of remaining oil in the sedimentary unit boundaries, to guide in the process of oilfield production, play an important role of remaining oil exploration and exploitation.

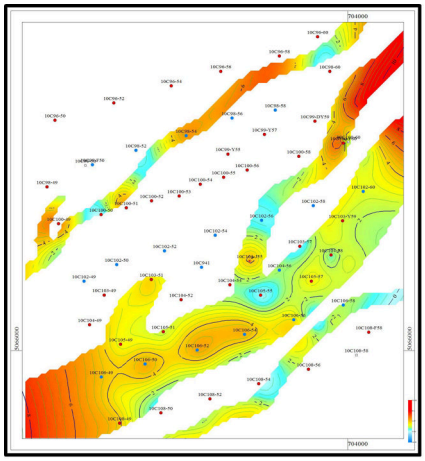

Fig. 2 Isogram of effective sand thickness with facies controlled on Unit F Ⅰ 7^3

Summary

The reservoir development of 45 block in Chaoyang ditch oilfield in delta front subfacies, delta distributary plain subfacies, reservoir mainly underwater distributary channel sand body. In which Fuyu oil layer stranded at the bottom of the underwater distributary channel deposits in this area is given priority to with calcium nodules, what controls the sand body vertical permeability is always backward and forward composite rhythm, also often appear forward rhythm. Thus controlled by the heterogeneity strongly, the remaining oil distribution in the top of the underwater distributary channel.

Intraformational heterogeneity of fuyu reservoir is mainly controlled by sedimentary facies, FⅠ oil reservoir group of delta front subfacies sand body heterogeneity is strongest. The other two reservoir group FⅡ and FⅢ delta distributary plain subfacies sand body heterogeneity more weak. Residual oil is generally a lot of focus on relatively strong heterogeneity and the horizon of relatively poor physical properties.Therefore, by the property differences between layer and interlayer heterogeneity parameters, The two layer FⅠ2, FⅠ7 is the main horizon of enrichment of remaining oil, as an important horizon for oilfields to explore.

For 103-55 wellblock on Unit FⅠ7^3 depositional time of sand body as an example, According to the purpose of effective sandstone layer logging data compiled river phased effective sandstone thickness contour map, depend on the river boundary and effective sandstone thickness boundary preliminary qualitative we can further outlined the distribution of remaining oil in the sedimentary unit boundaries, as the guidance in the process of oilfield production and remaining oil potential.

Aiming at Chaoyang ditch oilfield reservoir with characteristics of low porosity, low permeability and reservoir heterogeneity. such as fracturing, bentonite and separate injection measures should be taken, by lowering the reservoir heterogeneity, improving connectivity, we can improve the development effect.

Acknowledgements

This work was financially supported by the National Science and Technology Major Project of C hina (2011ZX05010-001).

References

[1] Wu Shenghe,Xiong Qihua. Geology In Gas-Oil Reservoirs[M].Beijing: Publishing House of Oil Industry,1998,155-172.

[2] Qiu Yinan, Xue Shuhao. Evaluation And Technique of Petroleum Reservoirs[M].Beijing: Publishing House of Oil Industry,1994.

[3] Wu Yuanyan, Chen Biyu. Industrial Geology of Petroleum[M]. Beijing: Publishing House of Oil Industry, 1995.268-326.

[4] Dai Qide, Ji Youliang. Geology in Gas-oil Reservoirs[M]. Beijing: University of Petroleum Press,1996.107-124.

[5] Zhang Houfu, Fang Chaoliang, Gao Xianzhi, et al. Petroleum Geology[M]. Beijing: Publishing House of Oil Industry, 1999.

[6] Peng Shifu, Huang Shuwang. Oilfield Development Geology[M]. Beijing: Publishing House of Oil Industry, 1998.

[7] Sun Yu.A Study On High-resolution Sequence Stratigraphy and Rule of Hydrocarbon Accumulations of Lithologic Reservoirs in Meandering River Delta[D]. Northeast Petroleum University, 2010.

[8] Yang Shaochun. A New Method For Quantitatively Studying Reservoir Heterogeneity[J]. Journal of The University of Petroleum: Natural Science Edition,2000,24(1):53-56.

[9] Yu Cuiling, Lin Chengyan.Petroleum Geology And Recovery Efficiency[J]. Petroleum Geology And Recovery Efficiency,2007,14(4):15-18.

Advanced Materials Research Vols. 960-961 (2014) pp 249-253

doi:10.4028/www.scientific.net/AMR.960-961.249

Rheological Properties of Sodium Metatungstate in Aqueous Solutions

Jiangang Ku[1, a *], Kui He[1, b], Huihuang Chen[2, c] and Wenyuan Liu[1, d]

[1]College of Zijin Mining, Fuzhou University, Fuzhou, Fujian, 350116, China

[2]College of Chemistry and Chemical Engineering, Central South University, Changsha, Hunan, 410083, China

[a]kkcc22@163.com, [b]243280330@qq.com, [c]chenhuihuang2012@gmail.com, [d]15146@163.com

Keywords: Sodium metatungstate, Rheological properties, Apparent viscosity, Herschel-Bulkley model.

Abstract. Sodium metatungstate (SMT) solution is an inorganic heavy liquid which is widely used in density fractionation. However, rheological properties of aqueous SMT solutions have never been fully researched. The objective of the present work was to study the rheological properties of aqueous SMT solutions and effects of temperature and density on the apparent viscosity. The steady flow experimental data was fitted using Herschel-Bulkley model. The results show that aqueous SMT solutions of different density are pseudoplastic fluids and the flow curves of SMT solutions were described by the Hershel-Bulkley equation. The apparent viscosity decreases monotonically with increasing temperature under the same density and increases exponentially with increasing density at the fixed temperature. Rheological properties of aqueous SMT solutions can be applied in the calculation of density fractionation efficiency and provides a theoretical basis for flow simulation.

Introduction

Sodium metatungstate (SMT) has the formula of $Na_6O_{39}W_{12}$ with a molecular weight of 2986.12 $g \cdot mol^{-1}$. It is extremely soluble in water giving neutral solutions and it is possible to achieve solution of very high density (3.12 $g \cdot cm^{-3}$ at 298.15 K). SMT solutions are nontoxic and tasteless inorganic heavy liquid with high stability [1]. SMT was started to be used in density fractionation of macromolecule in physical chemistry and cell separation in biological sciences from the mid-1980s [2,3], and then its application was expanded into various areas, such as density fractionation of organic matter in soil science [4-7], riverbed sediments in hydrology and water resources [8,9], marine microbes in marine science [10,11], and minerals in geology which is the most widely used application [12-15].

There are no special requirements on efficiency of density fractionation and the amount of SMT needed at the laboratory scale is very small. However, with the advancement of engineering in density fractionation and computer simulation of density fractionation, study on rheological properties of SMT solutions is becoming more and more important. The viscosity of aqueous solutions of SMT at the molalities (0.0055 to 1.73) $mol \cdot kg^{-1}$ were measured at 5 K temperature intervals from 288.15 to 308.15 K [16]. However, the measured viscosity values were dispersed and research on rheological properties of different substances in SMT solutions for their separation is far from enough. And rheological properties of SMT solutions were not researched in this paper as well.

In the present study, the rheological properties of SMT solutions were measured with Brookfield DV-Ⅱ+ viscosimeter and Ultra-low viscosity adapter. The effects of temperature and density of aqueous SMT solutions on the apparent viscosity were investigated. The research provides a theoretical basis for dynamic analysis in density fractionation process and flow field simulation of aqueous SMT solutions flowing in vessel and pipeline.

Experimental section

Materials. Sodium metatungstate hydrate 2.82 $g \cdot cm^{-3}$ density solution in water was obtained from J&K Chemical Ltd. Bidistilled water was used in all experiments.

Instruments. The rheological properties and viscosity were measured using Brookfield DV-Ⅱ Pro viscosimeter with ultra-low viscosity adapter. Accuracy of viscosity measurement was ± 1% of measurement range from 1 to 20 mPa·s and repeatability of viscosity measurement was ± 2%. The instrument has a built-in thermostat to maintain the temperature of solutions between -15 and 100 °C with a precision of ± 0.1 °C. The instrument required a liquid volume of about 16 ml and measured the viscosity after a thermal equilibration period of 10 min.

Densities were measured by Sartorius Cubis® MSA224S-000-DA electronic analytical balance, Shenzhen Ater DZF-6210 vacuum drying box, Blaubrand® volumetric flasks and transferpette® digital pipettor from Brand Tech Scientific Inc. The uncertainty of weighing data of balance is 0.1 mg and the repeatability and nonlinearity of balance is below 0.1 mg and 0.2 mg, respectively. Weighing capacity of balance is 220 g. Stability of temperature control to the volatility of vacuum drying box is within 1.0 ˚C from 10-250 ˚C in vacuum of below 133 Pa. The volumetric flask has a capacity of 10ml with the upper/lower mark is ± 0.07 ml. The pipettor has range of 5 ml with accuracy 30 μl and relative deviation 10 μl.

Preparation of aqueous SMT solutions. The mass of SMT and the volume of water in aqueous SMT solutions were calculated according to the data shown in Table 1 [17] and the volume of the desired aqueous SMT solutions. Firstly, distilled water was added to the SMT solution at a density of 2.82 $g \cdot cm^{-3}$ by stirring, and then the obtained aqueous SMT solutions were calibrated using the electronic analytical balance and the volumetric flask. A suitable amount of distilled water or stock solution might be added into the obtained solution according to the calibration to get the desired aqueous SMT solutions. The obtained desired SMT solutions of different density were stored in volumetric flasks. The density of the SMT solutions should be measured again before each use and distilled water or SMT solution might be added into the obtained solutions according to the measured density.

Table1
Composition of aqueous SMT solutions of different density

ρ/g·cm^{-3}	SMT/g	Distilled water/mL	ρ/g·cm^{-3}	SMT/g	Distilled water/mL
2.25	700	300	2.50	772	228
2.30	723	277	2.60	790	210
2.35	740	260	2.80	820	180
2.40	752	248	3.00	850	150

Rheological property testing. SMT solutions of different density were taken into low viscosity meter adapter outer cylinder. The desired temperature was adjusted in a water bath to maintain a constant temperature for at least 15 min. Then the rheological properties and viscosity were measured using Brookfield DV- Ⅱ Pro viscosimeter with ultra-low viscosity adapter.

Results and Discussion

Rheological curves and model of aqueous SMT solutions. The relationship between viscosity and shear rate of different fluids is various and thus the rheological curves are distinct as well. In the present work, a shear stress *vs.* shear rate plot for aqueous SMT solutions at different density and temperature is shown in Fig. 1.

Herschel-Bulkley model shown in Eq. (1) was adopted to fit the rheological curves in Fig. 1, where τ is shear stress (Pa), γ is shear rate(s^{-1}), τ_0 is the parameter defined as yield stress (Pa), K is consistency coefficient ($Pa \cdot s^n$), which indicates fluid flow property, and n is the flow property index. In general, a fluid is pseudoplastic fluid if its flow property index is less than 1.

$$\tau = \tau_0 + K\gamma^n \tag{1}$$

As shown in Fig. 1, the shear stress of SMT solutions of various density first increases sharply with the increase in shear rate, and then the rising rate is reduced gradually but still maintains positive in

the test shear rate range. Moreover, SMT solutions of greater density tend to have higher shear stress at the same shear rate, including when shear rate is zero. According to Fig. 1 and the above discussion, it can be concluded that SMT solutions exhibit the characteristics of pseudoplastic fluids.

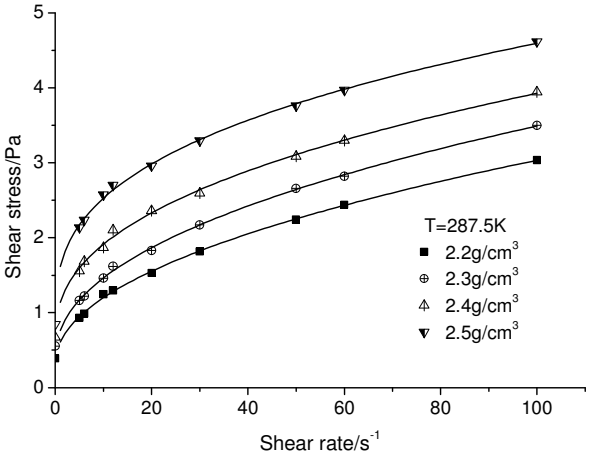

Fig. 1 Rheological curves of aqueous SMT solutions at different density

Using the measured shear stress and shear rate, fitting results of rheological curves in Fig. 1 of SMT solutions at 287.5 K can be obtained and are listed in Table 2. As can be seen from Table 2, the value of n decreases from 0.49132 to 0.35436 and the value of K increases from 0.28175 to 0.72461 with increasing density, which indicates that the non-Newtonian property of the system is intensified, the viscosity is higher and the mobility is worse. Due to the molecular attraction among molecules and ions in SMT solutions, the system is arranged in spatial structure. Only when fluid shear stress exceeds yield stress τ_0, intermolecular forces can be destroyed and the solution can flow. It can also be seen from Table 2 that the value of τ_0 for SMT solutions at different density is very small, which demonstrates that although molecular attraction exists in SMT solutions, the intensity of the formed spatial net structure is weak.

Table2
Fitting results of rheological curves of aqueous SMT solutions at different density at 287.5 K

ρ/g·cm^{-3}	$\tau_0 \pm \sigma_{\tau 0}$	$K \pm \sigma_K$	$n \pm \sigma_n$	r^2
2.20	0.03262±0.00086	0.28175±0.00473	0.49132±0.00304	0.99881
2.30	0.03909±0.00126	0.37097±0.00736	0.46106±0.00356	0.99839
2.40	0.06470±0.00247	0.48786±0.01576	0.41379±0.00558	0.99599
2.50	0.08892±0.00266	0.72461±0.01877	0.35436±0.00421	0.99768

Effects of temperature on the apparent viscosity of aqueous SMT solutions. The apparent viscosity was plotted against temperature in Fig. 2 and then the measured experimental data were regressed linearly respectively according to Eq. (2) to determine a, b parameters at each density studied. Linear fitting results are given in Table 3.

$$y=ax+b \tag{2}$$

It is observed from Fig. 2 that the temperature has a great influence on the apparent viscosity and the apparent viscosity decreases linearly with the increase in temperature. Moreover, the apparent viscosity increases with the increase in the density if the temperature is constant. As can be seen from the negative fitting straight slopes (parameter a) in Table 3, the greater the density, the faster the apparent viscosity falls with the increase in the temperature. It can also be seen from Fig. 2 that molecule structure or aggregate state in SMT solutions did not change in the range of test temperature. The decrease of the apparent viscosity resulted from the increase in intramolecular energy and the temperature, and the decrease of intermolecular forces.

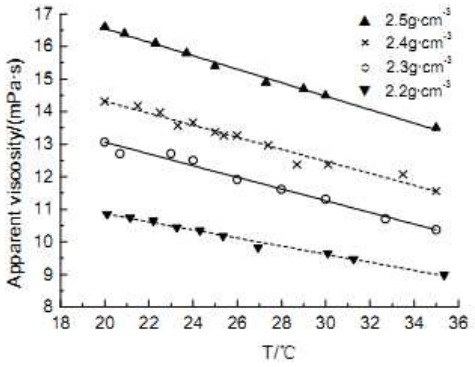

Fig. 2 Viscosity curves of aqueous SMT solutions at different density

Table 3
Linear fitting results of aqueous SMT solutions at different density and 287.5K

ρ/g·cm^{-3}	a	b	r^2
2.50	-20.6958±0.1457	0.2074±0.0055	0.994
2.40	-18.0409±0.2570	0.1846±0.0096	0.968
2.30	-16.6452±0.2454	0.1796±0.0091	0.980
2.20	-13.4168±0.1275	0.1308±0.0049	0.988

Effects of density on the apparent viscosity of aqueous SMT solutions. It is obvious from Fig. 3 that the density plays an important role in the apparent viscosity of SMT solutions. To be more specific, the apparent viscosity increases slowly first and then increases quickly with the increase in the density at different temperature. Additionally, if the density is fixed, the apparent viscosity decreases with the increase in the temperature, and the apparent viscosity decreases faster with the increase in the temperature at higher density. Fitting results of 5 curves in Fig. 3 are obtained and shown in Table 3 according to Eq. (2) using the measured experimental data;

$$y=a+bx^c \tag{2}$$

where a, b and c are the parameters.

From Table 3, it can be seen that the apparent viscosity grows exponentially with the increase in the density at the same temperature, and the apparent viscosity increases faster with the increase in the density at lower temperature based on the c parameter, which demonstrates that molecule structure or aggregate state in SMT solutions did not change in the range of test temperature, and the increase of the apparent viscosity resulted from the increase in the density and intermolecular forces, and the decrease in intermolecular distance.

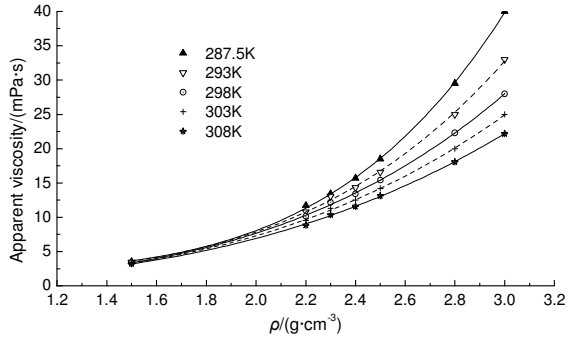

Fig. 3 Viscosity curves of aqueous SMT solutions at different temperature

Table 3
Fitting results of 5 curves ($y=a+bx^c$) in Fig. 2

T/K	a	b	c	r^2
287.5	2.0070	0.2628	4.5238	0.9983
293.0	1.5334	0.4134	3.9370	0.9942
298.0	0.7843	0.6543	3.3929	0.9994
303.0	0.6709	0.7200	3.2018	0.9994
308.0	0.5272	0.7879	3.0172	0.9996

Conclusions

Herschel-Bulkley model was adopted to fit rheological property curves of aqueous SMT solutions at different density with the fitting correlation coefficient r^2=0.99768~0.99881. Results show that SMT solutions at different density are pseudoplastic fluids.

At 287.5 K, the non-Newtonian property of SMT solutions increases with increasing density, the viscosity is higher and the mobility is worse. Molecules in SMT solutions attract each other and form spatial net structure of weak intensity.

The apparent viscosity of SMT solutions decreases with increasing temperature if the density is fixed and grows exponentially with increasing density if the temperature is constant.

Acknowledgements

This work is supported by the National Natural Science Foundation of China (Grant No. 51104048), for which the authors express their appreciation.

References

[1] M. R. Gregory, K. A. Johnston: New. Zesl. J. Geol. Geop. Vol. 30 (1987), p. 317

[2] G. Alexis, M. O. Charles, M. R. Tracy and M. O. Warrenton, U. S. Patent 8,231,006 (2012)

[3] B. Plewinsky and R. Kamps: Die makromolekulare Chemie Vol. 185(7) (1984), p. 1429

[4] K. Olivia, K. Angelika, S. Sandra, R. Thilo, K. Klaus and K. K. Ingrid: J. Plant. Nutr. Soil. Sc. Vol. 176(4) (2013), p. 509

[5] P. C. Conceição, M. Boeni, J. Dieckow, C. Bayer and J. Mielniczuk: Rev. Bras. Ciênc. Solo Vol. 32(2) (2008), p. 541

[6] E. G. Morgun and M. I. Makarov: EURASIAN SOIL SCI+ Vol. 44(4) (2011), p. 394

[7] P. L. Aberdeen: *Norse landnám and its impact on the vegetation of Vatnahverfi, Eastern Settlement, Greenland*. Unpublished PhD Thesis, University of Aberdeen College of Physical Sciences, 2013, 62–63.

[8] K. L. Plathe, F. von der Kammer, M. Hassellöv, J. N. Moore, M. Murayama, T. Hofmann, M. F. Hochella Jr: Geochim. Cosmochim. Ac. Vol. 102(1) (2013), p. 213

[9] S. T. Krukowski: J PALEONTOL Vol. 62(2) (1988), p. 314

[10] Y. Morono, T. Terada, J. Kallmeyer and F. Inagaki: Environ. Microbiol. Vol. 15(10) (2013), p. 2841

[11] Tiegang Li and Zhifang Xiong: Oceanologia Et Limnologia Sinica. Vol. 41(4) (2010), p. 645 (In Chinese)

[12] C. J. S. Bolch: Phycologia Vol. 36(6) (1997), p. 472

[13] Li Zhang, Zhenkun Wu, Shaohua Song, Hong Chang, Guoqing Zhao: Rock and Mineral Analysis Vol. 31(5) (2012), p. 780 (In Chinese)

[14] A. Decou, H. V. Eynatten, I. Dunkl, D. Frei and G. Wörnera: J. S. Am. Earth. Sci. Vol. 45 (2013), p. 6

[15] C. A. Corcea, D. Constantin, V. Anechitei, A. Timar-gabor and S. Filipescu: Carpath. J. Earth. Env. Vol. 8(1) (2013), p. 139

[16] M. Sahin, K. Ayranci, E. Kosun, E. Ayranci: Chem. Geol. Vol. 264(1-4) (2009), p. 96

[17] Tiyu Duan, Shiqi Wang and A. M. Faiia: Geology and Prospecting Vol. 37(5) (2001), p. 38 (In Chinese)

Advanced Materials Research Vols. 960-961 (2014) pp 254-257

doi:10.4028/www.scientific.net/AMR.960-961.254

Pore network simulation of two phase flow based on X-ray micro computed tomography images

Meiheriayi,Mutailipu[1,a], Yu Liu[2,b], Ling yu Chen[3,c] and Yong chen Song[3,d]

[1,2,3,4]Key Laboratory of Ocean Energy Utilization and Energy Conservation of Ministry of Education, Dalian University of Technology, Dalian116024, P.R.China

[a]mhriay@foxmail.com, [b]liuyu@dlut.edu.cn, [c]lingyu_chen165@163.com, [d]songyongchen@dlut.edu.cn,

Keywords: Pore-network; Digital core; Micro-CT; Maximal Ball algorithm; Pore-scale modeling

Abstract. In this paper, firstly, the X-ray micro computed tomography (micro-CT) is used for the analysis of internal structure of sand-packed beds. Binary data which are able to describe the pore structures of these beds were obtained from a series of imaging processing of rescaling, media filtering, and thresholding. Then a Maximal Ball (MB) algorithm is applied to these binary data to extract the equivalent pore networks. The parameters of the pore networks, such as radius, coordination number and shape factors of pore and throat are computed. The results demonstrate that the MB method can extract reasonable and faithful pore network of the different sand packed samples. Finally, the relative permeability and capillary pressure of drainage and imbibition cycle of water and oil are predicated. The numerical simulation results demonstrated good accordance with that of the experiments. Pore network simulation shows good results for two phase flow in porous media.

Introduction

The macroscopic properties of porous media such as porosity, permeability are related to their internal structures. In recent decades, pore network models that represent the void space of a rock by a lattice of pores connected by throats have been widely used as a platform of core analysis to predict multiphase flow. In this paper, an improved maximal ball method proposed by Dong et al. [1], has been used for pore network extraction. Because the parameters of extracted pore network have significant influence on the modeling of multiphase flow, it is necessary to investigate those influences of the pore network parameters. So this paper aims to compare the structure of pore networks of different sand packed samples, which are extracted from the micro-CT images using the maximal ball method. Through direct imaging, usually by micro-X-Ray computerized tomography (micro-CT), can obtain the pore-space geometry (i.e. digital cores) of rocks[2,3].The micro-CT imaging is considered the most direct and accurate way to construct pore geometry (digital core).Micro-CT allows samples a few millimeters across to be imaged nondestructively at a resolution of a few microns or submicron using nano-CT scanners[4].

Micro-CT scanning and imaging process

The parameters of samples are listed in Table 1.

Table 1 Parameters of four sand packed samples.

Samples	Diameter (mm)	Porosity (%)
BZ02	0.105-0.125	37.2
BZ04	0.350-0.500	37.5
BZ06	0.500-0.710	38.7

The images of samples are obtained through a desktop X-ray micro-CT. It is necessary to apply a series of filters to smooth the image, to reduce noise and improve the contrast between grain and void [5]. In this paper, the median filter is used to replace the gray scale value of a voxel by the median value of the nearest 26 surrounding cells. And then a threshold value based on the isodata algorithm

[6] is chosen to binarize or segment the gray scales into two phases: solid and void. At last, those black-white images are rescaled and normalize to be digital cores with the size of 248×248×248. The imaging process and all the reconstructed images of the three BZ sand packed samples and obtained digital cores from rescaling, median filtering, and segment are shown in Fig. 1.

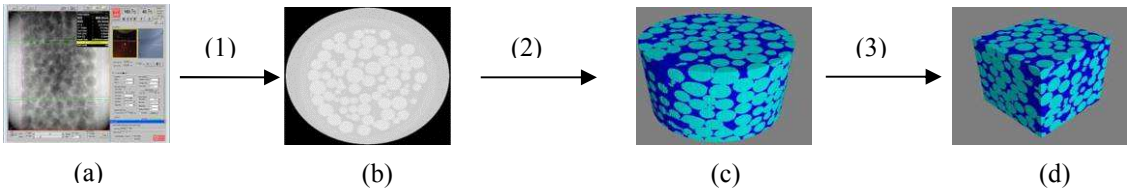

Fig. 1 The flow chart of image processing of BZ04 sand packed sample. (a) x-ray image, (b) CT image, (c) smoothing and segment, (d) rescaled digital core.

Pore-network extraction and flow simulation

In this study, the pore network extraction algorithm used to extract a topologically equivalent network of pores and throats from 3D micro-CT images is the Maximal Ball algorithm firstly used by Sillin et al. [7]. Flow simulation used to predicate the relative permeability and capillary pressure of the oil and water displacement is performed based on this pore network extraction[8]. The grade pore quasi static flow simulation model [9] was used for the flow simulation research. Pore-scale oil-water two phase flow simulation process is as follows: firstly, network model will be water saturated ,then oil drainage is performed until the experimental initial water saturation is reached; after the oil flooding process, oil and water contact angles of each pore and throat is adjusted, to simulate the changes of porosity wettability of cores after being invaded by oil. Finally, to simulate the process of water imbibition, inject water into the model, then calculate oil water relative permeability[10] .

In the simulation, single wetting system is used for all samples. To be specific, oil and water contact angles of all pores and throats are uniformly distributed. Decane is used in this flow simulation process. The parameters of two-phase fluid at room temperature are given in Table.2.

Table 2 Parameters of two-phase fluid in flow simulation

parameters	value
Water viscosity(cp)	1.005
Oil viscosity (cp)	0.93
Water density(kg/m^3)	998.2
Oil density(kg/m^3)	731.9
Interfacial tension(mN/m)	37.26*
Water wetting Angle	78.5*
oil wetting Angle	45.3*

* is laboratory measurements

Results and discussion

The properties of the extracted networks are listed in Table 3. In this part we compare the three samples in terms of connectivity (coordination number), size distributions (contains inscribed radii, volume, lengths of pores and throats), and shape factors.

Table 3 Properties of the pore networks extracted from four BZ sand packed samples.

Properties	Samples		
	BZ02	BZ04	BZ06
Porosity (%)	37.14	35.79	38.89
Ave. Coord. No.	7.60	6.86	6.20
Ave. pore radius 10^{-6}m	30.0	54.3	65.9
Ave. pore volume 10^{-12} m^3	1.36	6.96	16.7
Ave. pore shape facture (10^{-2})	2.28	2.11	2.22
Ave. throat radius 10^{-6}m	13.6	25.4	34.2
Ave. throat volume 10^{-15} m^3	37.4	230.0	489.0

By comparing Table 3 with Table 1, we can see that porosity of samples in pore-network extraction reaches basic agreement with results from CT scanning. Therefore, network modeling method established in this paper can preserve the fluid storage capacity ability of the core completely into the pore network model, which is of great significance in developing relative research based on network modeling with the aid of micro flow simulation technology (such as the remaining oil distribution, etc.).

Radii distribution of pore and throats for all the BZ samples are plotted in Fig. 2, respectively. There are two kinds of lengths of throat. The throat total length, is the distance measured form two pore centers that are linked by this throat. The throat efficient length is the length of a pure throat defined as equation calculated by Øren and Bakke [11]. Those two kinds of statistical data are shown in Fig. 3. The void space will become larger with the increase of diameters of sand packed samples. So the peaks of sizes (radii and length) of pores and throats have gradually shifted toward rights as the BZ02 to BZ06.

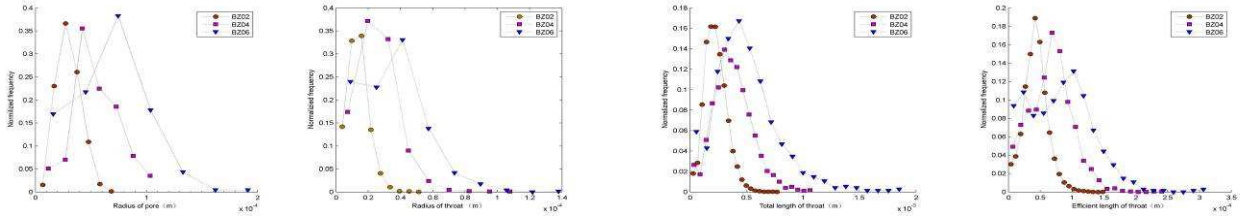

(a) (b) (c) (d)

Fig. 2 Distributions of inscribed radii of pores (a) and throats (b) for three BZ samples.

Fig. 3 Distributions of the total (c) and efficient (d) lengths of throats for three BZ samples.

The results of oil flooding and water flooding from pore scale flow simulation are listed in Fig. 4, Fig. 5 respectively. Capillary pressure of oil flooding and water flooding curved along with the water saturation are illustrated in Fig. 6(a) and Fig. 6(b) respectively.

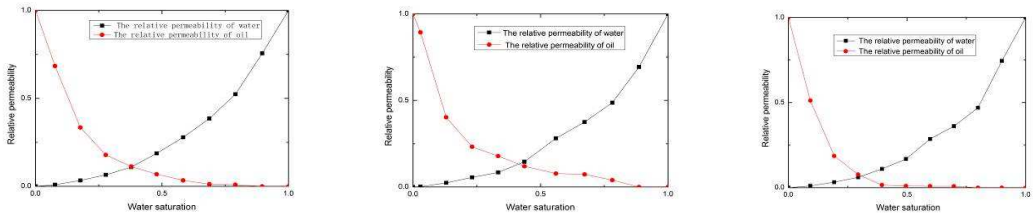

(a) BZ02 (b) BZ04 (c) BZ06

Fig. 4 Graphs of relative permeability (a), (b), (c) of oil flooding

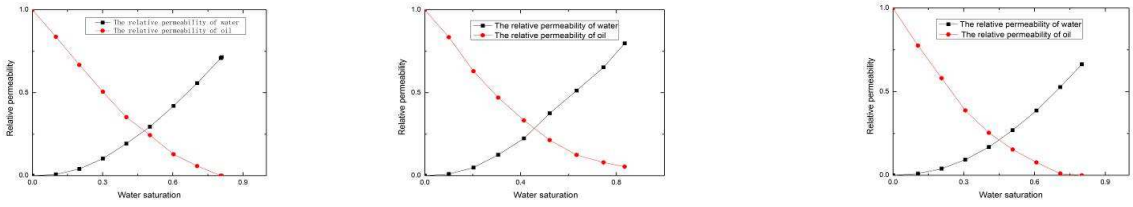

(a) BZ02 (b) BZ04 (c) BZ06

Fig. 5 Graphs of relative permeability (a), (b), (c) of water flooding

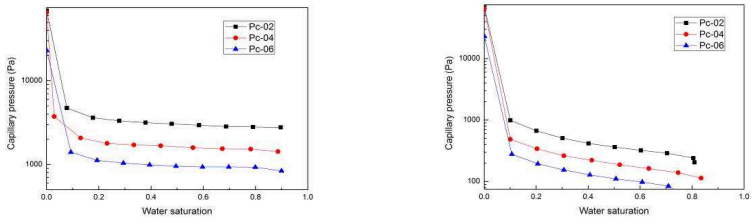

(a) Capillary pressure of oil flooding (b) Capillary pressure of water flooding

Fig. 6 Graphs of Capillary pressure (a) and (b) of oil flooding and water flooding

As seen in the Fig. 4 and Fig. 5, the pore-network modeling established in this paper predicated the experimental relative permeabilityof three BZ sand samples, as well as giving the prediction of oil and water two phase relative permeability changing along with the water saturation within the whole interval, which indicates that pore-network modeling established in this paper can reflect the real structure , in terms of Topology and geometry characteristics of the digital cores.

Summary

Pore space images of three BZ samples with high resolution can be obtained through Micro-CT scanning based on X-ray. Development characteristics of the pore space, such as size of pore and throat, connectivity and morphological characteristics are analyzed to construct the pore-network based on those reconstructed CT images. By comparing and analyzing properties of samples, we can see that porosity of samples in pore-network extraction reaches basic agreement with results from CT scanning. Therefore, network modeling method established in this paper can preserve the fluid storage capacity ability of the core completely into the pore-network model. In the end, the relative permeability and capillary pressure of three BZ sand samples are predicated based on pore network extraction, which demonstrated that pore network extraction algorithm—Maximal Ball (MB) algorithm cited in this article could extract reasonable and reliable pore network of different BZ sand packed samples. This simulation technology has great utility value in oil recovery.

References

[1] H. Dong and M. Blunt: Pore-network extraction from micro-computerized-tomography images, Physical Review E, vol. 80(2009), p. 036307

[2] R. I. Al-Raoush and C. S. Willson: Extraction of physically realistic pore network properties from three-dimensional synchrotron X-ray microtomography images of unconsolidated porous media systems, Journal of Hydrology, vol. 300(2005), pp. 44-64

[3] J. Coenen, et al.: Measurement parameters and resolution aspects of Micro X-ray tomography for advanced core analysis, Proceedings of the 2004 International Symposium of the Society of Core Analysts, AbuDhabi, UAE(2004)

[4] J. H. Dunsmuir, et al.: X-Ray Microtomography: A new tool for the characterization of porous media, SPE 22860 of the 1991 66th Annual Technical Conference and Exhibition of the Society of Petroleum Engineers, Dallas, Texas(1991)

[5] H. Dong, et al.: Pore network Modeling Analysis of Pore Size Distribution of Arabian Core Samples, SPE 105156, p. 5(2007)

[6] T. W. Ridler and S. Calvard: Picture thresholding using an iterative selection method, IEEE Trans. System, Man and Cybernetics, vol. SMC-8 (1978), p. 630-632

[7] D. Silin and T. Patzek: Pore space morphology analysis using maximal inscribed spheres, Physica A: Statistical Mechanics and its Applications, vol. 371(2006), p. 336-360

[8] Kovscek A.R., Wong H., Radke C.J.A : Pore-Level Scenario for the Development of Mixed Wettability in Oil Reservoirs [J]. AIChE. J. , Vol. 39(1993) , p. 1072-1085.

[9] Blunt M.J. : Physically-based network modeling of multiphase flow in intermediate wet porous media[J].Journal of Petroleum Science and Engineering(1998)vol. 20, p. 117-125.

[10] P. H. Valvatne and M. J. Blunt, Water Resour. Res. 40,W07406 2004.

[11] P.-E. Øren and S. Bakke: Reconstruction of Berea sandstone and pore-scale modelling of wettability effects, Journal of Petroleum Science and Engineering, vol. 39(2003), pp. 177-199

Advanced Materials Research Vols. 960-961 (2014) pp 258-261

doi:10.4028/www.scientific.net/AMR.960-961.258

Compare the Petrophysics of Formation Type I and II by Mercury Injection Curve Normalization

Lingyun Chen[1, a] , Yikun Liu[1,b], Lihua Xia [1,c], Qian Liu [2, d]

[1]Northeast Petroleum University, Daqing, Heilongjiang, China

[2] Daqing Oilfield Co., Ltd., Daqing, Heilongjiang, China

[a]462415985@qq.com, [b] liuyikun111@126.com, [c] 954507199@qq.com, [d] 271115437@qq.com

Keywords: Mercury Injection, Normalization, Petrophysics

Abstract. Study on Formation Type II is so few that affect on tapping the potential [2]. Analyzing petrophysics of Formation Type I and II by mercury injection curve normalization, it's vital to developing method choice on tapping the potential of Formation Type II.

Capillary pressure curves (Pc-curves) from conventional Mercury Injection are hard to analyze and compare because of various shapes. To get typical capillary pressure curves for Formation Type I and II, the curves from Mercury Injection is processed by Function J, and the J function curves and normalized Pc-curves for tabulated thin layers, tabulated thick layers and un-tabulated layers in Formation Type I and II, compare and analyze the influence of permeability on the shape of J function curves and normalized Pc-curves; compare the influence of different kinds of layers with the same permeability order of magnitude on the shape of J function curves and normalized Pc-curves, i.e. the influence of other factors except permeability, to get some visual identification methods and analyze the petrophysics difference between Formation Type I and II which is shown on Pc-curves.

Introduction

In mercury injection method each pressure point represents the pressure under which the mercury is injected into the pore with corresponding size [1]. The result of experiment shows that, the shape of Pc-curves is mainly determined by the wettability and pore structure property of the formation. The Pc-curves of formation with different permeability and porosity is different.

To get the J function curves and normalized Pc-curves for tabulated thin layers, tabulated thick layers and un-tabulated layers in Formation Type I and II, the Pc-curves from mercury injection is processed with J function; compare them and seek creative conclusion.

Principle of Normalized Pc-curves

Experiments proves that, the capillary pressure in the formation is the function of fluid saturation, which can be formulated as,

$$p_c = f(S_{Hg}) \tag{1}$$

The ratio of measured capillary pressure values and reference ones is defined as the J function of formation by M. C. Leverett, thus the expression of J function is gotten as following:

$$J(S_{wn}) = \frac{p_c}{\sigma}\sqrt{\frac{K}{\phi}} \tag{2}$$

Where, S_{wn} is the normalized saturation of core:

$$S_{wn} = \frac{S_{Hgmax} - S_{Hg}}{S_{Hgmax}}, \qquad 0 \le S_{wn} \le 1 \tag{3}$$

Where, S_{Hg} is core mercury saturation; S_{Hgmax} is the maximum mercury saturation.

Combining core data, the pc and S_{Hg} measured in laboratory is transformed to $J(S_{wn})$ function and data corresponding S_{wn} by equation (2) and (3). To get J (S_{wn}), the data can be fitting by least square method. The power function is chosen in fitting after observation on the Pc-curve features [3].

$$J(S_{wn}) = a\ S_{wn}^{b} \tag{4}$$

Where, a is dimensionless drainage pressure of J function; b is curve index of J function.
Solving the equations satisfied by the fitting curves, the expression of a, b is gotten.

$$c = \left[\sum_{i=1}^{m} \ln J_i \sum_{i=1}^{m} (\ln S_{wni})^2 - \sum_{i=1}^{m} S_{wni} \sum_{i=1}^{m} \ln S_{wni} \ln J_i\right] \Big/ \left[m \sum_{i=1}^{m} (S_{wni})^2 - \left(\sum_{i=1}^{m} \ln S_{wni}\right)^2\right] \quad (5)$$

$$b = \left[m \sum_{i=1}^{m} \ln S_{wni} \ln J_i - \sum_{i=1}^{m} \ln J_i \sum_{i=1}^{m} \ln S_{wni}\right] \Big/ \left[m \sum_{i=1}^{m} (S_{wni})^2 - \left(\sum_{i=1}^{m} \ln S_{wni}\right)^2\right] \quad (6)$$

$$a = e^c \quad (7)$$

Thus a, b of each core is calculated, substitute arithmetic mean of a, b values of all the core into equation (4), then the average J function curves of formation is determined. Average capillary pressure can be calculated from equation (8) and (9):

$$p_c(S_w) = \frac{\sigma}{\sqrt{K/\phi}} J(S_{wn}) = \frac{\sigma}{\sqrt{K/\phi}} a S_{wn}^b \quad (8)$$

$$S_{Hg} = S_{Hgmax}(1 - S_{wn}) \quad (9)$$

Where, P_c is average capillary pressure of formation, MPa, σ is the interfacial tension between oil and water, which is given as 0.033N/m, K is air permeability of core, μm^2, ϕ is porosity.
Based on the theory the core data from different type layers of Formation Type I and II is processed, from which their normalized Pc-curves are gotten and analyzed.

Pc-curves Normalization results

Contrast the capillary pressure and coring data according to depth, refer to net pay thickness, the core data is classified as tabulated thin layers（0<h<0.5）, tabulated thick layers(h≥0.5) and un-tabulated layers(h=0), which is taken normalization, from which normalized Pc-curves for different formation with different permeability. According contrasting between these curves, the relationship between shape of normalized Pc-curves and petrophysics of formation is discussed.
The normalization method for mercury withdrawal curve is revised. If small step length is given, the normalized mercury injection curve will meet with the normalized withdrawal curve, which is the same as original mercury curve.

Normalized Pc-curves with different permeability in Formation I

Thick layers in Formation I are analyzed by permeability magnitudes because of abundant coring.

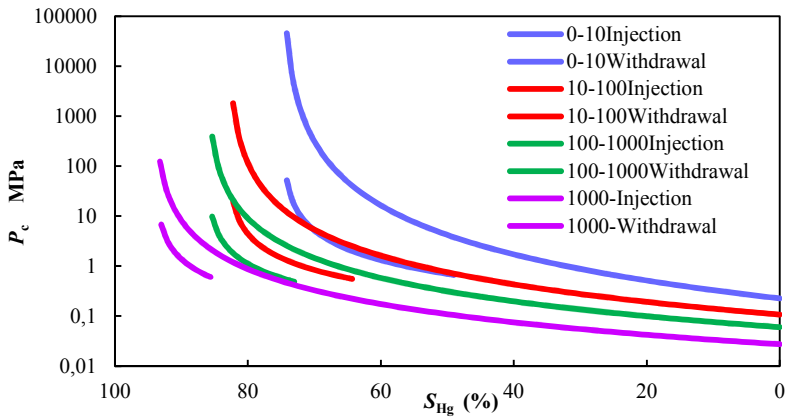

Figure 1 Normalized Pc-curves of thick layers with different permeability in Formation I

Larger is the permeability of thick layers in Formation I, Larger is the maximum mercury saturation and minimum mercury saturation in withdrawal curves, and the more normalized Pc-curve is closed to axis X and Y, which means better formation property.

Normalized Pc-curves with different permeability in Formation II

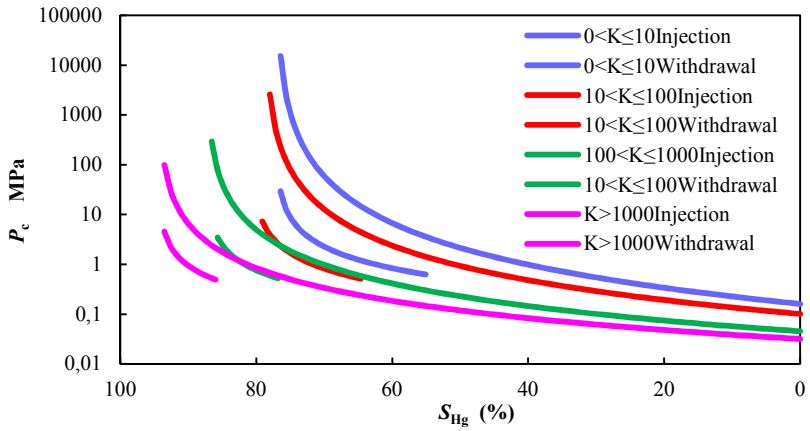

Figure 2 Normalized Pc-curves of thick layers with different permeability in Formation II

Normalized Pc-curves in Formation II follow the same law for permeability in Formation I. And it also can be seen that for different type of layers in Formation II, the shape of Pc-curves, that is the formation property, is different, from which provides visual means of distinguishing methods.

Normalized Pc-curves of thick layers in Formation I and II

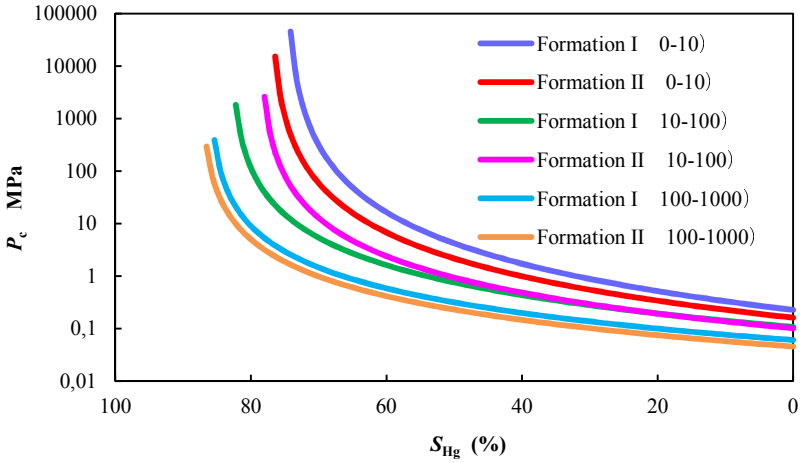

Figure 3 Normalized injection Pc-curves of thick layers in Formation I and II

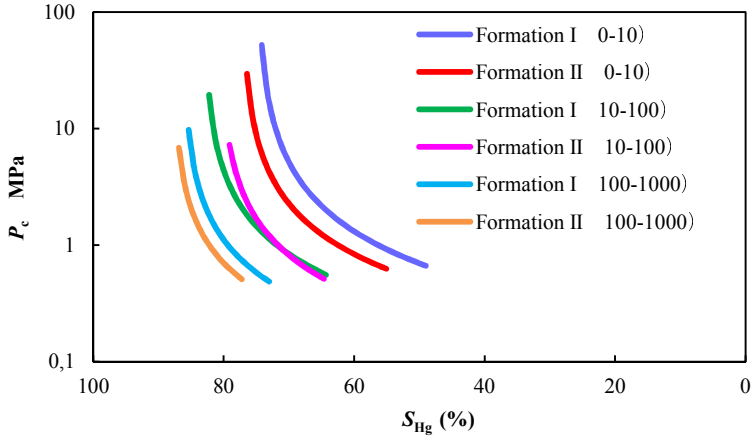

Figure 4 Normalized withdrawal Pc-curves of thick layers in Formation I and II

From Fig.3 and 4, it can be seen that in the permeability range (10-100) mD the property of Formation II is better than that of Formation I; while it's inverse for the other two ranges.

Summary

1. Normalization for original Pc-curve makes it easy to find and analyze the law of formation property;
2. Larger is the permeability of thick layers in Formation I, Larger is the maximum mercury saturation and minimum mercury saturation in withdrawal curves, and the more normalized Pc-curve is closed to axis X and Y, which means better formation property.
3. In the permeability range (10-100) mD, the property of Formation II is better than that of Formation I; while it's inverse for the other two ranges.
4. For the core in Formation I, higher is the permeability magnitude, smaller is the difference between the properties of cores with different permeability, that is, and more similar are the shapes of different cores.

Acknowledgements

This work was financially supported by the National Major Project "Large Oil Gas Field and CBM Development" (2011ZX05052), Special Fund （2011ZX05010-002）, Graduate Innovation Fund （YJSCX2012-050HLJ）, Innovation Fund of Heilongjiang Education Apartment " Development Optimization in Low Permeability Reservoir" (12511020) and National Natural Science Foundation (51074035).

References

[1] Chen Jie: Research Method Summary on character of pore structure in formation rock [J], Special Oil & Gas Reservoirs, 12 (4): 11-14, (2005).

[2] Gu Tuan: Further Understanding on Formation II in matured block [J], China Petroleum Exploration.

[3] Liao Jing: Normalization of Pc-curves and J function Processing [J], Special Oil & Gas Reservoirs, 15(6), (2008).

[4] Liu Xiaopeng: Pc-curves for formation drawing and application [J], Journal of Southwest Petroleum University (Science and Technology Edition), 30(6), (2008).

[5] Li Yanshan: Classification and Research on Formation Chang 6 at Changqing Area by Mercury Injection Data [J], lithologic reservoirs, 21(2):91-93,(2009).

Advanced Materials Research Vols. 960-961 (2014) pp 262-269

doi:10.4028/www.scientific.net/AMR.960-961.262

Effect of Compatilizers on Morphology and properties of Natural Rubber/Polyvinyl alcohol (NR/PVA) Blends

Ke Chen[1,a] , Rui Wang[1,2,b]

[1]Agricultural Product Processing Research Institute, Chinese Academy of Tropical Agriculture Science, Zhanjiang 524001, PR China

[2]Rubber Research Institute, Chinese Academy of Tropical Agricultural Sciences, Danzhou 571737, PR China

[a]ct-152@sohu.com, [b]wangruifly@163.com

Keywords: natural rubber, polyvinyl alcohol, blend, compatilizer.

Abstract. The natural rubber/polyvinyl alcohol (NR/PVA) blends containing various compatilizers grafted from NR were prepared using latex compounding techniques. The effects of various compatilizers on the morphology, mechanical properties and thermal behaviors were studied. The interface compatible performance of the blends were greatly improved with the presence of the compatilizers, and the phase dispertion of the blends achieved the best effect under the action of epoxidized natural rubber (ENR). The onset temperature of the thermal decomposition of ENR and graft copolymerization of methyl methacrylate (MMA) onto NR (NR-g-PMMA) increased obviously, but the maleic anhydride grafted onto NR (NR-g-MAH) drop obviously comparing to that of NR. The thermal stability of the blends were inferior to NR. With the presence of ENR, the tensile strength and elongation at break obtained great value which was ascribed the presence of the best phase dispertion, while the tear strength and shore A hardness obtained great value due to the addition of MAH-g-NR.

Introduction

With the development of modern science and technology, the wide range of material are required increasingly as the single material difficult to meet a variety of requirements, so the polymer blends have become indispensable a class important materials in industrial and agricultural production and life[1,2]. The interface modification technology is increasingly being studied for the performance of the blend to get the proper morphology and interfacial strength in order to obtain better properties of the blends.

The interface modification techniques developed after the 1970s, since then it facilitated numerous incompatible blends to achieve compatiblity, and a series of new polymer alloy were developed[3]. The natural rubber (NR) blends prepared based on NR and other polymers have been a very important modern industrial production technology in the modern industrial production of NR[4].

In this work, the natural rubber/polyvinyl alcohol (NR/PVA) blends containing various compatilizers grafted from NR were prepared using latex compounding techniques. The influence of various compatilizers on the morphology, mechanical properties and thermal behaviors were investigated systematically.

Experimental

Materials. Natural rubber latex, with dried rubber content (DRC) of 60 wt%, was obtained from Agricultural Processing Research Institute, Chinese Academy of Tropical Agriculture Science. Polyvinyl alcohol (PVA, molecular weigth of 13000～23000 and degree of hydrolysis 87～89 %) was supplied by Sigma-Aldrich company. Hydrogen peroxide(H2O2, 30 %), Benzoyl peroxide (BPO, minimum purity of 98 %), Patassium hydroxide (KOH) and sodium dodecylsulfate were obtained from Sinopharm Chemical Reagent Company. tert-butyl hydroperoxide (TBHP), Oleic acid and Ammonia solution (25 %) were obtained from GuangZhou Jinhuada Chemical Reagent Company. Formic acid was obtained from Guangzhou chemical reagent company. Maleic Anhydride (MAH) was supplied by Tianjin YongDa chemical reagent company. Tetraethylene pentamine (TEPA) was supplied by Tianjin Guangfu fine chemical research institute. Methyl methacrylate (MMA) was supplied by Xiya Reagent Company. Various additives such as the Peregal-O (99.5 %,), the sulfur, the zinc oxide (ZnO), and Zinc diethyl dithiocarbamaate (ZDC) were used as supplied. DI (deionized water) was used throughout.

Preparation of compatilizers.

Epoxidized natural rubber (ENR)[5]. 200 g of NR latex containing 30 % dried rubber content (DRC) was blended with the peregal-O as a non-ionic surfactant at ambient temperature while stirring for 1 h. The mixture was then acidified with 15 g of formic acid. After that, 100 ml of hydrogen peroxide was added at 30 °C within 10～15 min. The epoxidation process was carried out at 70 °C for 5 h and the resulting ENR processing a 30 % of epoxided content was used after calculation.

Graft copolymerization of methyl methacrylate (MMA) onto NR (NR-g-PMMA)[6]. NR latex (100 g, DRC 60 %) was placed in a reactor, and sodium dodecylsulfate (1 phr) was then added while stirring. The mixture was deoxygenated by passing through the nitrogen gas for approximately 15 min at room temperature. Oleic acid as the stabilizer was added. After 20 min of stirring, MMA monomer was then added continuously while stirring for 30 min to allow the latex particles to swell. The mixture was heated up to 60 °C. TBHP and TEPA were added at a ratio of 1:1. The reaction was then allowed to proceed for 8 h under continuous stirring to complete the polymerization. The final product could be determined by the Soxhlet extraction. The free natural rubber was extracted in a Soxhlet extractor by light petroleum ether for 24 h while free PMMA was extracted by acetone for 24 h. Then, the grafting rate was 61.4 % after calculation.

The maleic anhydride grafted onto NR (NR-g-MAH). The graft reaction was carried out in a three flask with reflux condensing tube and thermometer. NR latex (100 g, DRC 60 %) placed in the flask was blended with the peregal-O as a non-ionic surfactant. MAH and BPO were added in turn to the latex, respectively. The reaction was carried out by stirring the latex at about 60 rpm for 5 h at 80 °C. The final product was cast into a glass sheet and it was dried at 60 °C in a vacuum oven. The unreacted monomer and initiator were removed by using aceton for 24 h in a soxhlet apparatus. Then, the grafting rate was 44.3 % after calculation.

Preparation of NR/PVA blends. PVA was first dissolved into the saturated solution of 25 wt% at 90 °C, then the solution mixing with NR latex (DRC 60 %) was carried out in a beaker by stirring for 1 h at 35 °C. The compatilizer and vulcanizing system were added and then the blend was heated up to 55 °C to be precured for 2 h. After that, the blend was cast into the glass sheet to be molded into film which thickness was about 1～2 mm. The film was cured at 60 °C for 3 h after natural dring, and then taken to the next test after placed in the standard test environment for 16 h. The formulations shown in Table 1 were used in this study.

Tab 1 Sample composition and code of NR/PVA blends [phr]*

components	0#	1#	2#	3#
NR	100	100	100	100
ENR	-	3.09	-	-
NR-g-PMMA	-	-	3.09	-
NR-g-MAH	-	-	-	3.09
PVA	11.8	11.45	11.45	11.45
sulfur	1.67	1.72	1.72	1.72
ZnO	0.67	0.69	0.69	0.69
KOH	0.17	0.18	0.18	0.18
ZDC	0.83	0.86	0.86	0.86
Peregal-O	0.17	0.18	0.18	0.18

***ALL the components are in phr (weight per hundred weight of NR)**

Fourier Transform Infrared Spectroscopy Analysis (FT-IR). The FT-IR spectra of the samples were obtained from Perkin-Elmer (GX-1) measuring in the range of 4000-500 cm^{-1}. The samples were cut into strips of 50 mm, using attenuated total reflection (ATR) accessory, scanning 16 times.

Mechanical Testing. The tensile and tearing test were performed on Testing Mechine UT-2080 (Ucan Instrument, TaiWan) at a crosshead speed of 500 mm/min at room temperature. The dumbbell-shaped samples for tensile tests were cut from the molded sheets according to GB/T 528-2009. For the tearing test crescent-shaped die B were punched from the molded sheets according to GB/T 529-2008. Hardness of the samples was also measured using a Shore A durometer according to GB/T 531-1999.

Scanning Electron Microscope (SEM) Observation. The morphology of the NR/PVA blends was characterized by a Hitachi S 4800 SEM instrument. Molded samples were fractured in liquid nitrogen. Then the samples were dried under vacuum at 40 °C for 2 h. The samples were examined by scanning electron microscope after sputter coating with a thin film of gold.

Thermogravimetric Analysis. The thermogravimetry analysis was carried out in a NETZSCH STA449C (Germany) instrument. The sample was scanned from 25 to 700 °C at a heating rate of 10 °C min^{-1} in nitrogen atmosphere.

Results and Disscussion

Fourier Transform Infrared Spectroscopy Analysis (FT-IR). The FT-IR spectra of NR and comptilizers grafted from NR are shown in Fig 1. The absorptions at 876 and 1253 cm^{-1} from the ENR plot can be attributed to the epoxy group, and the weak absorption at 1735 cm^{-1} can be assigned to the carbonyl group of the easter. The absorption of the NR-g-PMMA is found at 1140 cm^{-1} (–C–O– stretching), 1390cm-1 (methy C–H deformation),and 1725 cm^{-1} (carbonyl group). The main peaks of NR-g-MAH shown at 3450 cm^{-1} which is strong and wide can be attributed to O–H stretching vibration (MAH hydrolyzate). The main peaks shown at 1630～1660 cm^{-1} and 1050～1250 cm^{-1} are attributed to carbon-oxygen double bond stretching and carbon-oxygen single bond stretching, respectively. The presence of characteristic peaks of the above describes MAH monomer has been grafted onto NR macromolecular chain.

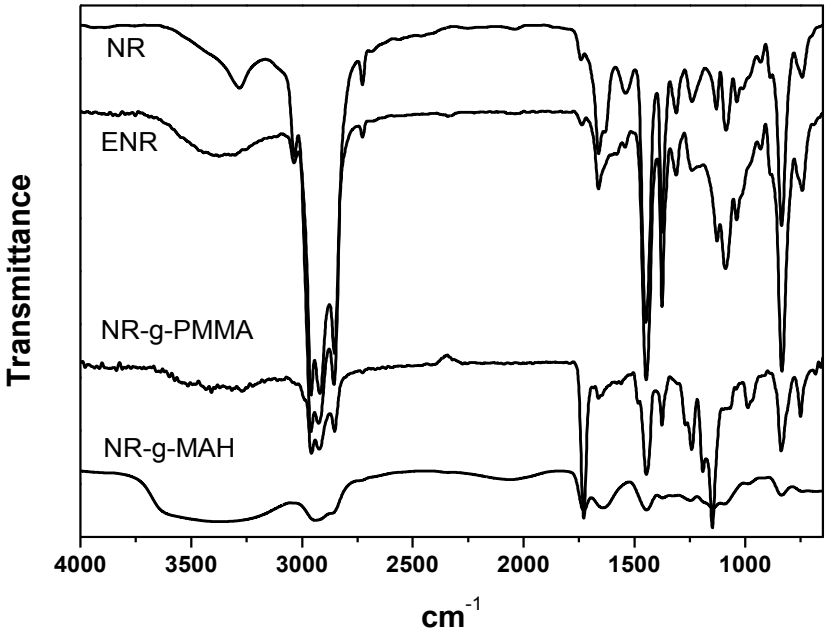

Fig.1. FT-IR spectra of NR, ENR, NR-g-PMMA and NR-g-MAH.

Phase Morphology. NR exists primarily as the matrix phase, and PVA exists primarily as the dispersed phase from NR/PVA blends composition. It can be found as shown at Fig 2 that the distribution of the dispersed phase disperses unevenly and the particles gather before the compatilizer added, while the distribution of the dispersed phase shows more regular domains after the compatilizer added. The interface compatible performance of the blends are greatly improved with the presence of the compatilizers, and the phase dispertion of the blends achieve the best effect under the action of ENR. Although the dispersed phase shows irregular shape in the NR-g-PMMA and NR-g-MAH blends, the dispersed phase presents a certain distribution due to the addition of the compatilizers. Thus, the compatilizer can greatly improve the interface compatibility of the NR/PVA blends.

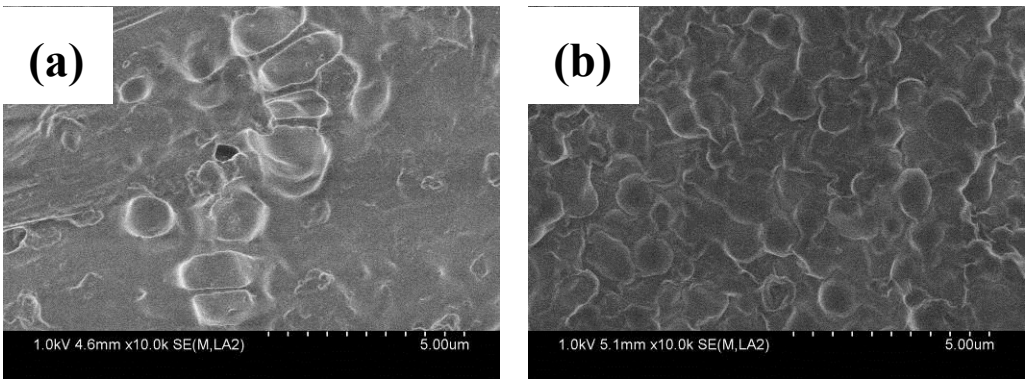

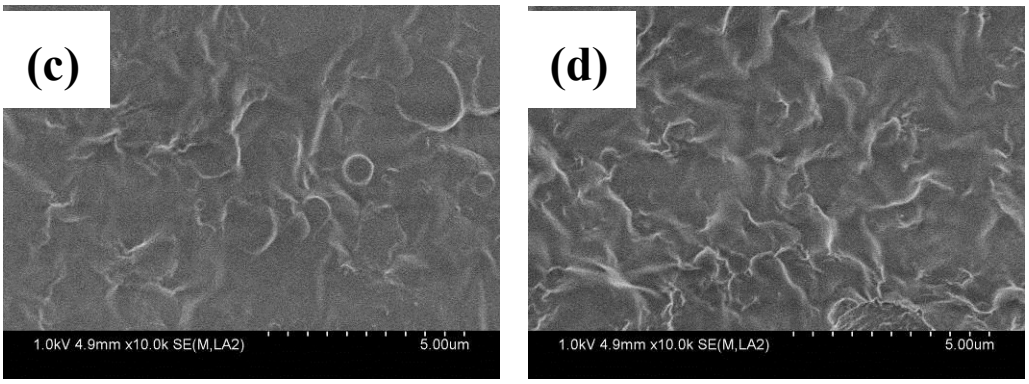

Fig.2. SEM micrographs of the NR/PVA blends:(a)sample 0#;(b)sample 1#;(c)sample 2#;(d)sample 3#.

Mechanical Properties. The effect of the compatilizers on the mechanical properties of NR/PVA blends are shown in Tab 2. The tensile strength, tear strength and hardness of the NR/PVA blends increase with the presence of the compatilizers. This is attributed to the compatilizers which results in the smaller particle size and improving the dispersion of the dispersed phase and enhancing the strength of the two-phase interface. With the presence of ENR, the tensile strength and elongation at break obtain great value which is mainly due to the presence of the epoxy group to active the adjacent double bonds, increasing the crosslink density, and thereby the mechanical properties increase. The tear strength and shore A hardness obtain great value due to the MAH-g-NR. The elongation at break of the blends decline after compatilizers added, which may be due to the compatilizers improving the toughness of the interface layer so that the elasticity of the material decreases.

Tab 2 Mechanical Properties of NR/PVA blends

Sample	Tensile strength [Mpa]	Elongation at break [%]	Tear strength [N/m]	Shore A hardness
0#	12.19	748.5	23.04	43
1#	18.27	716.0	36.28	52
2#	17.18	627.9	40.35	55
3#	15.84	574.4	52.16	55

Thermol behaviors. Thermograms results of the compatilizers are plotted in Fig 3. Thermograms and derivative thermograms results of the blends are plotted in Fig 4 and Fig 5. Both of the plots decomposed in one step.

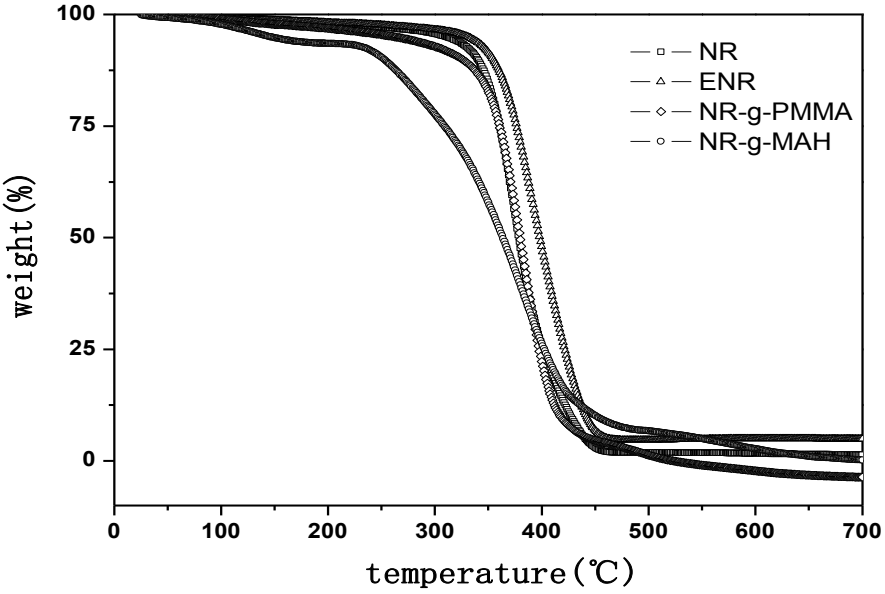

Fig.3. TG curve of the compatilizers

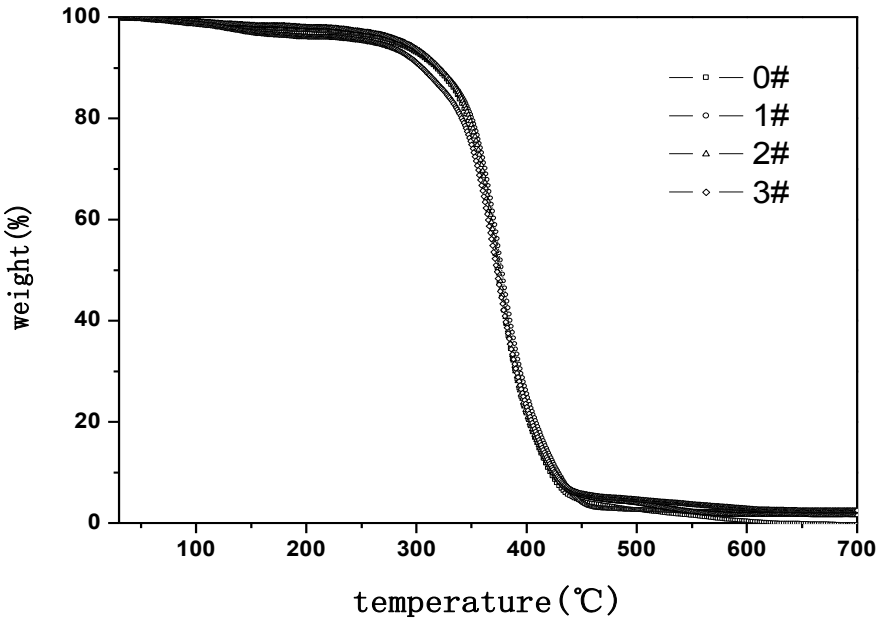

Fig.4. TG curve of NR/PVA blends

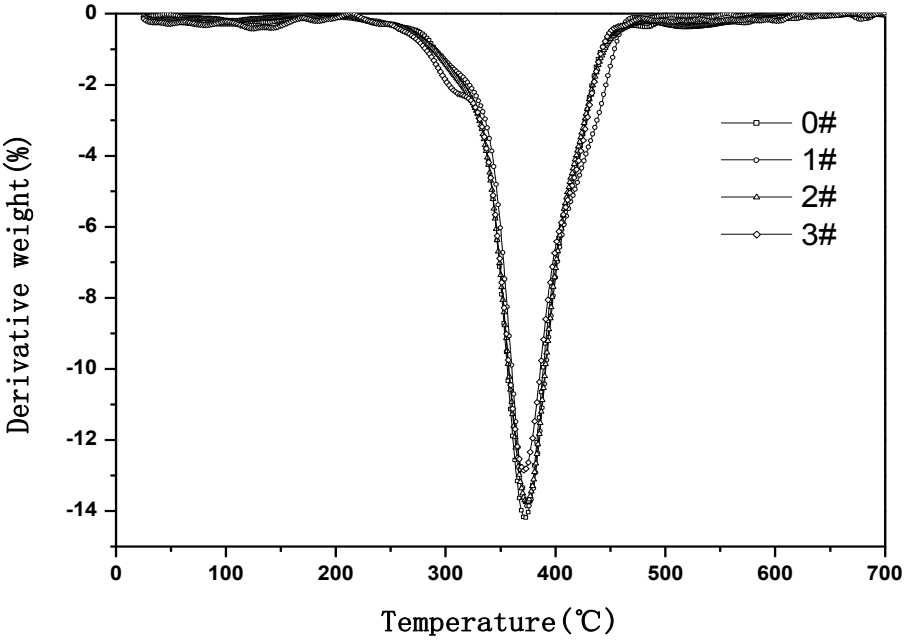

Fig.5. DTG curve of NR/PVA blends

The characteristics temperature of the thermol degradation process can be plotted through the double tangent curve method. The characteristics temperature of the thermol degradation process of the compatilizers and blends are summarized at Tab 3, of which To represents the onset temperature of the thermal decomposition, Tf representing the termination temperature of the thermol decomposition, Tp representing the temperature corresponding to the maximum rate of the thermal decomposition. The onset temperature of the thermal decomposition of ENR and NR-g-PMMA increase obviously, but that of the NR-g-MAH drops obviously comparing to NR. The thermal stability of the blends are inferior to that of the NR. This is due to the onset temperature of the thermal decomposition of the PVA is lower than that of the NR, so that the thermal stability decreases because of the oxidation induction time shortening. It can be observed that the temperatures corresponding to the maximum rate of the thermal decomposition show no significant change, indicating no significant effect on the temperatures corresponding to the maximum rate of the thermal decomposition after PVA added, but the maximum decomposition rate increasing gradually accelerates the thermal decomposition process.

Tab 3 Characteristic temperatures of compatiblizers and NR/PVA blends

Sample code	T_o [°C]	T_p [°C]	T_f [°C]
NR	347	374	411
ENR	358	392	438
NR-g-PMMA	351	382	411
NR-g-MAH	311	383	424
0#	341	372	406
1#	345	375	412
2#	343	374	407
3#	338	372	408

Conclusions.

The NR/PVA blends with various compatilizers were prepared and investigated. The interface compatible performance of the blends were greatly improved with the presence of the compatilizers, and the phase dispertion of the blends achieved the best effect under the action of the ENR. The onset temperature of thermal decomposition of ENR and NR-g-PMMA increased obviously, but that of the NR-g-MAH drop obviously comparing to NR. The thermal stability of the blends were inferior to NR. With the presence of the ENR, the tensile strength and elongation at break obtained great value which was ascribed the presence of the best phase dispertion, while the tear strength and shore A hardness obtained great value due to the addition of MAH-g-NR.

Acknowledgements.

This work was financially supported by the Fundamental Research Funds for Rubber Research Institute, CATAS(1630022013020).

References.

[1] Paul D R, Bucknall C B: *Polymer blends: formulation and performance* (John Wiley & Sons, Inc, 2000).

[2] Utracki L A, Favis B D: *Polymer alloys and blends*(Marcel Dekker, Inc, New York, 1989).

[3] Y uri S. Lipatov: Prog. Polym. Sci. Vol. 27(2002), p. 1721.

[4] Carrot C, Guillet J, May J F: Plast. Rubber Compos. Process. Appl. Vol. 16 (1991), p. 61.

[5] Heping Y, Sidong L, Zheng P: J. Therm. Anal. Calorim. Vol. 58 (1999), p. 293.

[6] Kochthongrasamee T, Prasassarakich P, Kiatkamjornwong S: J. Polym. Sci. Vol. 101 (2006), p. 2587.

Advanced Materials Research Vols. 960-961 (2014) pp 270-273

doi:10.4028/www.scientific.net/AMR.960-961.270

Preparation of the Scales Material Adsorption EGCG

Zhou-Wei Duan[1,a], Zhi-Hao Dou[1,b*], Hui Xie[1], Ai He[1], Zhu-Ning Wan[1]

[1] Institute of Processing&Design of Agroproducts,Hainan Academy of Agricultural Sciences, Haikou, China 571100

[a]universeduan@163.com, [b]513408658@qq.com

*Corresponding author

Keywords: scales; adsorption; EGCG

Abstract. Tilapia scale was used as the raw material to explore the preparation methods of EGCG adsorption material. Based on the results, the most reasonable interpretation of the data indicates that the EGCG adsorption material preparation process was as follows, particle size 0.30-0.45 mm , preparation temperature 110℃, pH 7, solid to liquid ratio (g/mL)1:6, time 20 min. Under this condition, the adsorption capacity of EGCG was 23.53mg/g.

Introduction

Epigalocatechin-3-gallate (EGCG) is one of the most important and main active ingredients derived from green tea, and has a broad spectrum of beneficial activity, for example strong antioxidant [1,2], tabacum [3], anticancer[4],antiaging[5],antiatherosclоresis[6,7]， antibacterial and antiinflammatory [8-10]activity in humans . EGCG is a natural antioxidant, has important applications in food industry, medicaments and chemical products for daily use. In generally, the conventional techniques for EGCG extraction are solvent extraction, precipitation and resin column chromatography [10], which are all limited by low extraction efficiency, large depletion of many kinds of reagents, heavy and complicated steps, high production costs and always using heavy metal salt as precipitator which pose some potential safety hazards. Therefore, recently, researches about safe and effective materials to extract and separate EGCG have received more and more attention from all over the world.

Tilapia is cultured as the main economic fish species in China and the yields in 2008 reached to 1.21 million tons [11] sharing 48.4% of the annual yield of Tilapia in the world. Hence there is a large number of fish head, fish skin, fishbone and fish scale and so on which are the waste of Tilapia processing. Hereinto, the amount of the fish scale accounts 2% allows an abundant and cheap source of biomaterial, such as extraction collage and hydroxyapatite. In present， the use of usually scales focus on the adsorption material research have reported less. This work used tilapia scales as raw materials, to prepare a new type of adsorption material with large adsorption capacity, low-cost, high security to extract and separate EGCG. More to the point, the preparation methods were investiged on EGCG adsorption of tilapia scale.

Experimental

Materials. The tilapia scales were provided by Hainan Golden Spring Foods Co., Ltd. EGCG (≥98%, Fu Zhou Corona Science & Technology Development Co., Ltd.). All other chemicals used in this study were of analytical grade.

Pretreatment of Tilapia scales. The raw tilapia scales were first washed in water to get rid of the surface impurity, and then contacted with 0.1mol/L NaOH solution for five hours. After that the scales was washed abundantly with deionized water until neutrality was reached and dried by naturally for reserve.

EGCG adsorption material preparation and appraisement. A certain amount of the pretreated scales treated with different griddle(below 0.30, 0.30-0.45, 0.45-0.90, 0.30-0.90mm), temperature(65, 80, 95, 110, 125℃), pH(3, 5, 6, 7, 9, 11), solid to liquid ratio（1:3, 1: 6, 1:12, 1:18, 1:24（g/mL））and time（10, 20, 30, 40, 50min） produced the adsorption materials.

When examined a single factor of the above, the factors as the variables, the others set as particle size 0.30-0.45 mm , preparation temperature 110℃,pH 7 , solid to liquid ratio (g/mL) 1:6, time 20 min. Then, the effect of the adsorption materials produced by different conditions determined by adsorption tests based on a batch reactor that 0.5g of the adsorption materials infused with 7mL of EGCG solution (0.004mol/L) at room temperature(25℃) was oscillated at 200r/min for 40min. Then after 10 min, the absorbance of supernatant was measured at 510nm by method for determining EGCG.

EGCG content test. The preparation of the sample liquid was produced by three steps. First, 1ml sample was immersed in 4 mL deionized water and 0.3ml 5% $NaNO_2$ for 5 min in a test tube. Second, adding 0.3 mL 10% $AlCl_3$ into that test tube and setting for other 1 min. At last, putting 2 mL 1mol/L NaOH into that test tube and adding enough deionized water making the volume of the liquid in the test tube reached exactly 10 mL. Then the absorbance of the sample liquid is measured at 510nm on the UV-4802.

Results and Discussion

Single factor experiment for EGCG adsorption material preparation. The results of the single factor experiment indicated that these facts are producing big influence on the adsorbance. The figure 1(a) shows, the material have the maximum adsorption capability with the particle size between 0.30 and 0.45 mm. That could be considered that the specific area of the scales is one of the key points for adsorption. When the particle size is too big the specific area is relatively small which counts against to adsorption. However, when the particle size is too small, the period of adsorption equilibria would be too long for the material to hold the EGCG that once adsorbed, hence, resulted in some of the adsorbed EGCG desorption, the final adsorbance is still decrease. So the particle size was set to 0.30-0.45 mm.

The figure1(b) shows, the adsorbance increased obviously with the temperature from 65℃ to 110℃. However, once the temperature exceed 110℃, the adsorbance would decrease. It could be own to the temperature which influenced the combinative state of the protein and hydroxyapatite of the scales. The fact is the materials prepared at 110℃ possess the optimal combination or existent pattern of ingredients in the scales to adsorb EGCG , therefore, the 110℃ is the optimal temperature in the preparation.

The figure1(c) indicated, with increasing of pH, the adsorbance for EGCG by the material increases first and then decrease.Under the pH value of 7, the scales had a maximum adsorbance for EGCG. Weak acids or weak bases environment are benefit for dissolving protein that is why the relationship between the rate that collagen to the scales decreased and the adsorbance being contacted like that. Therefore, we chose the pH 7 as the optimal processing pH value.

The figure1(d) shows, the material have a maximum adsorbance for EGCG, when the solid to liquid ratio (g/mL) is 1:6 to be used to processing the scales. And the adsorbance decreases with decreasing of solid to liquid ratio. This could be explain like this, for a certain amount of scales, the

increasing amount of the liquid could increase the apparent contact area for the scales and the liquid in the process, which would promote the dissolution of collagen, consequently, the amount of collagen has been occupied in forming a good structure to absorb EGCG would change too, so that the absorption level of EGCG by the scales has been influenced. So the solid to liquid ratio was set to 1:6.

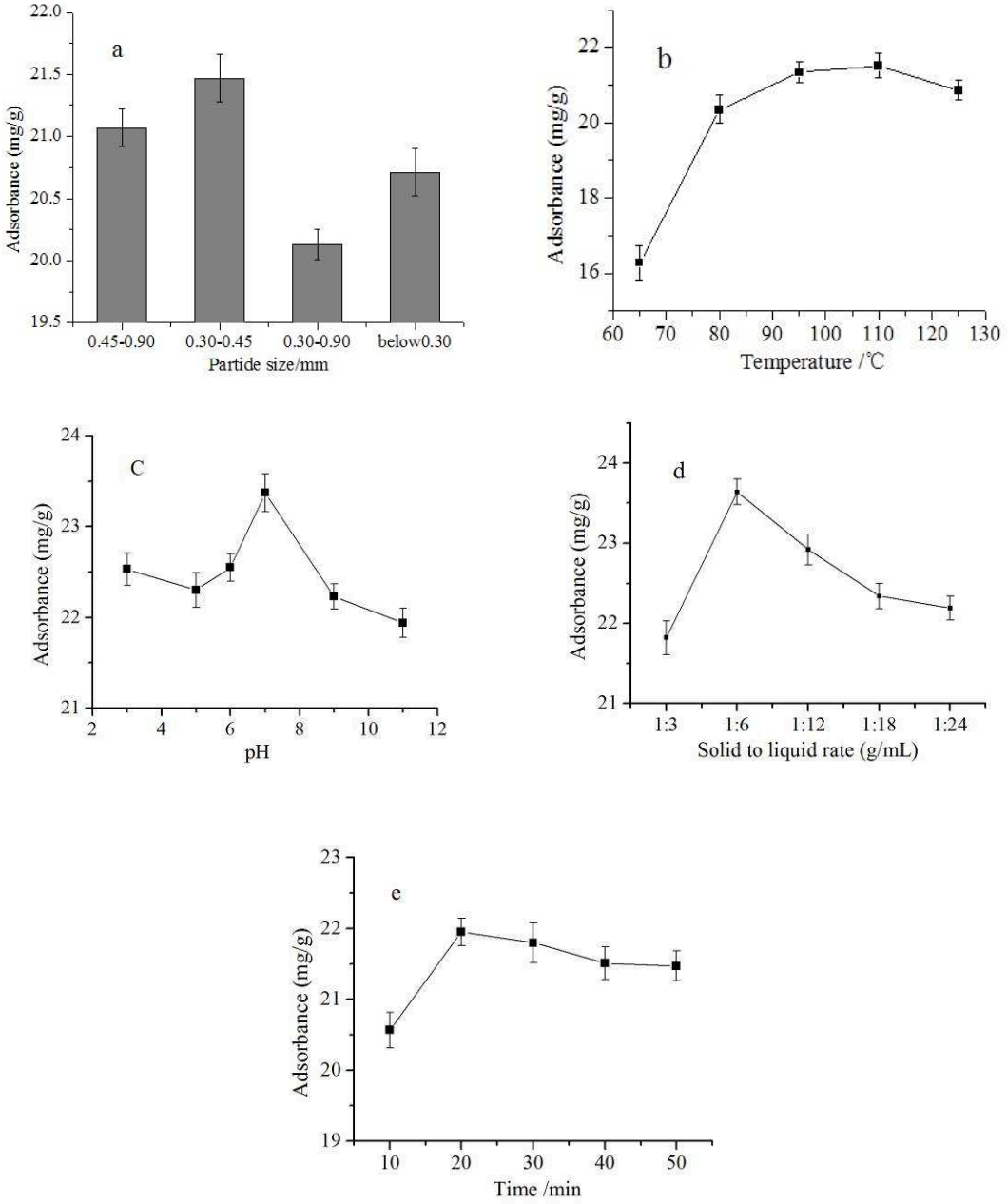

Fig.1 Variation curve of adsorption capacity vs sieve mesh(a) temperation(b) pH(c) solid to liquid ratio(d) time(e)

By figure1(e) knowable, there is little difference in adsorbance when the time of the scales preparation is longer than 20 min. By determination content of the protein dissolving from the scales we found the material achieved a dissolution balance for the collagen during the period, which indirectly demonstrated that the ingredients of the scales reached to a relatively stable state. Since the adsorbance of the scales for EGCG is relatively stable as long as the processing time surpassed 20 min, we chose the 20 min as the optimal processing time.

We did another experiment according the conditions of the particle size 0.30-0.45 mm , pH 7 , temperature 110℃, processing time 20 min, solid to liquid ratio (g/mL) 1:6. Under this condition,

the result showed the highest adsorbance for EGCG that is 23.53 mg/g, which is higher than the value that Wang RuiFang[12] and so on got though X-5, RA and RB resin. It demonstrated that tilapia scales possesses obvious potential to be as EGCG adsorption material. Since the tilapia scales have large adsorption capacity, low-cost, high security and easy to prepare, it would have a promising future applied in separation and purification of EGCG.

Summary

On the basis of above investigation of parameters in preparation of the scales material adsorption EGCG, it is confirmed that the tilapia scales process great ability to absorb EGCG and the optimal adsorption material preparation methods could be acquired when the particle size of 0.30-0.45 mm , pH of 7 , temperature of 110℃, processing time of 20 min, solid to liquid ratio (g/mL) of 1:6. Under this condition, we acquired the maximum adsorption capacity was 23.53mg/g.

Acknowledgements

The research was supported by the innovation of agricultural science and technology Foundation of Hainan Academy of Agricultural Science and Professor of Xuan Ri Shen of Hai Nan University.

References

[1] Rodents B,Fujiki H,Okabe S,Sueoka N,et a1.Mutation Research,Vol.402(1998),p,307-310

[2] Nakagawa T,Yokozawa T.Food and Chemical Toxicology,Vol.40,(2002),p,1745-1750.

[3] Khan N,Afaq F,Saleem M,et al.Cancer Reserch,Vol.66 (2006),p,2500-2505

[4] Howe IR, Leevers SJ, Gomez N, et a1.Cells,Vol.71(1992),p,335-342

[5] Esposito E,Rotilio D,Matteo,et al. Neurobiology of Aging,Vol.23(2002),p,719-735

[6] Zhao B L,Li X J,He R G,Jia W Y,Xin W J. Cell biophysics,V0l.14(1989),p,175-185.

[7] Rumpler W, Scale J, Clevidence B, Judd J, Wiley E, et al. Journal of Nutrition, Vol. 131(2001), p,2842-2852.

[8] Ahmad N,Mukhtar H. Skin Pharmacology and Applied Skin Physiology,Vol.14(2001),69-76.

[9] McKay DL,Blumberg J B.Journal of the American College Nutrition,Vol.21(2002),p,1-13.

[10] He P,Noda Y,Sugiyama K.Journal of Nutrition,Vol.131(2001),p,1560-1567.

[11] Yinzhe Jin,Chun Hua Jin,Kyung Ho Row.Biotechnology Journal,Vol.1(2006),p,209-213

[12] Wang Ruifang,Chen Fahe,Wu Guangbin,et al.Food Science,Vol.30(2009),p,40-42.(In Chinese)

Advanced Materials Research Vols. 960-961 (2014) pp 274-280

doi:10.4028/www.scientific.net/AMR.960-961.274

Classification and Morphological Structure of Scale in the Process of Alumina Production High Pressure Digestion

Haizhu Ma[1,a], Fang Huang[1,b], Shirong Liu[2,c] ,Bo Xu[3,d] ,Hualong Liu[4,e]

[1]College of Material and Metallurgy, Guizhou University, Guiyang, Guiyang, China

[2]State Key Laboratory of Deposit Geochemistry, Institute of Geochemistry, Chinese Academy of Sciences, Guiyang, Guizhou, China

[3]Guizhou Branch of CHALCO, Guiyang, Guizhou, China

[4]Wuchuan Alumina Branch of CPI Guizhou Zunyi Industry Development Company Limited, Zunyi, Guizhou, China

[a]137831464@qq.com, [b]hfcy_215@163.com, [c]liushirong@vip.gyig.ac.cn, [d]xu_bo@163.com, [e]363993784@qq.com

Keywords: scale; classification; alumina; morphological structure

Abstract. The chemical composition, phase component and morphology characteristics of scale were researched by chemical analysis, XRD, SEM and TEM. The results show that the scale can be divided into iron minerals, silicon minerals, Ca-Ti-Mg minerals and aluminum hydroxide. Alumogoethite and micro-fine sodium-silicon slag fill in the gaps between the neat and bulky hematite crystals. Microgranular hydrated garnet and olivine fill in the gaps between the goethite crystals with a dense layered structure, accompanied by a small amount of galena and apatite precipitation particles. Perovskite and magnesium hydroxide have five periodic sedimentary cycles, forming an alternating sedimentary layer structure. Aluminum hydroxide forms thick scale and presents two kinds of typical structures, spherulitic and laminated. The research provides the theoretical basis for preventing and controlling scale in high-pressure digester group.

Introduction

In Bayer process of high pressure digestion of diaspore, various scales form inevitably. A large number of scale results in pipeline blocking, reducing heat transfer coefficient of heat exchanger severely, thereby reducing the output of equipment, increasing energy consumption and production cost. If it is serious, normal production will be affected [1,2].

Scholars at home and abroad have done a lot of work towards the scale forming in alumina production and put forward methods of scale prevention and treatment, mainly from property [3], formation mechanism and influence of scale. In general, methods of scale prevention and treatment mainly include three aspects [4,5]. The first is the pretreatment [6] which means strengthening the pre-desilication process to slow down scale formation. The second is the handling during the production which means optimizing process conditions to reduce scale formation, by using new digestion technology such as two-stream process and so on [7,8,9,10,11]. The last is the handling after the production which means cleaning scale up by use of machining, fire, high-pressure hydraulic, acid-base, magnetic field, electric field, ultrasonic and so on [12,13,14]. But these studies have not yet formed a set of effectively preventive, efficient, scientific and reasonable practice in scale prevention and treatment. The reason is that they are lack of systematic research and comparative analysis on the morphological structures of scale forming during every scaling step in the whole high pressure digestion unit. Therefore, this paper combines with high pressure digestion process in alumina production, studying the morphological structures of scale in the high- pressure-digestion single tube preheater, autoclave, staying ladle and flash type evaporator in turn, then classifying the scale, in order to provide theoretical and practical basis for scale prevention and treatment.

Methods and analysis instruments

We used chemical analysis and XRD to measure and analyze the main chemical composition and phase component of each sample of scale, adopt spectrum selection component analysis technique of scanning electron microscopy to analyze the micro-zone of component of scale, and used backscattered electron imaging analysis technique of SEM to study the internal structure characteristics of scale.

The chemical composition and phase component of scale

The chemical composition. The scale sample was taken from high-pressure digester group of a certain alumina plan. The results of its chemical composition are shown in Table 1. From the table, the chemical compositions of scale forming in different parts are quite different. The scale in the single tube preheator and stay ladle primarily contains Fe_2O_3, accounting for 60 %. The scale in the autoclave primarily contains TiO_2, accounting for 40 %. The scale in the flash type evaporator primarily contains Al_2O_3 and Fe_2O_3, accounting for 24.91 % and 27.51% respectively.

Table 1 Chemical composition of scale in different parts

Scale sample	Al_2O_3	Fe_2O_3	SiO_2	TiO_2	CaO	MgO	Na_2O	K_2O
Scale in single tube preheator	6.79	67.66	7.42	2.13	6.66	3.18	0.84	0.0059
Scale in autoclave	0.69	3.52	10.83	39.44	16.91	4.09	4.16	0.0053
Scale in stay ladle	10.84	61.12	6.62	3.08	2.21	4.77	1.50	0.0074
Scale in flash type evaporator	24.91	27.51	9.87	2.82	5.00	1.50	5.10	0.050

The phase components. Through XRD, we analyzed the phase component of scale. It's known that the scale in the single tube primarily contains sodium-silicon slag, hematite and aluminum goethite. The scale in the autoclave primarily contains perovskite and magnesium. The scale in stay ladle primarily contains hydrate garnet, olivine and goethite. The scale in the flash type evaporator primarily contains Al_2O_3($Al_2O_3 \cdot 3H_2O$) and calcium titanate iron. Along with alumina production process, scale has changed greatly.

The classification and morphological structure of scale

Scale in the high pressure digestion unit could be divided into iron mineral, silicon mineral, calcium titanium magnesium mineral and Al_2O_3 ($Al_2O_3 \cdot 3H_2O$) .

Iron mineral scale. Iron mineral scale contains hematite, aluminum goethite and goethite. Scale of hematite and aluminum mainly exists in single tube. Its SEM backscattered electron image is shown in Fig.1. Adopt spectrum selection component analysis technique of scanning electron microscopy to analyze Fig.1a. From the analysis result, it's knowable that the fillings are aluminum goethite and micro-fine sodium-silicon residue.

From Fig.1a, hematite grows along pipe wall, forming dense crystal clusters, crystals of which are regular and big, in forms of plate and column. Aluminum goethite is needle-like and tiny, filling in the gaps between the hematite crystals together with micro-fine sodium-silicon slag, as shown in figure 1b. Compared with original pulp material, the scale in the single tube is mainly the deposition of hematite, and that aluminum goethite and sodium-silicon slag form in the process of dissolving and preheating.

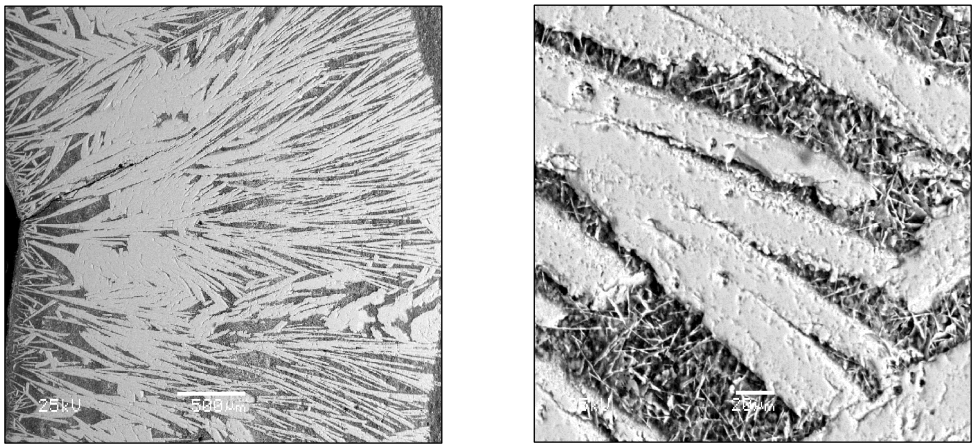

a b

Fig.1. SEM backscattered electron image hematite and aluminum scale

Scale of goethite mainly exists in stay ladle. The most important deposition is goethite containing aluminum and titanium. In the backscattered electron imaging of SEM, goethite appears to be gray-white contrast. Goethite crystals develop perfectly and big with columnar structure. The shape is clear and neat. A large number of goethite grows vertical to the pipe walls, forming thin scale with dense layered structure in the staying tank, as shown in Fig.2a. Use spectrum selective component analysis technique of scanning electron microscopy to analyze the material component in Fig.2b. The results show that aluminum and titanium accrete in the goethite, that the highest content of Al_2O_3 is up to 2.36% and that the highest content of TiO_2 is up to 6.49%. On the surface of scale and pipe walls, there is a small amount of particle-like deposition of bright white galena and gray apatite. Goethite crystal fillings primarily contains $Ca_3Al_2(SiO_4)_3$ and Mg_2SiO_4, also including a small amount of needle-like Na_2CO_3 and sodium silicate fillings.

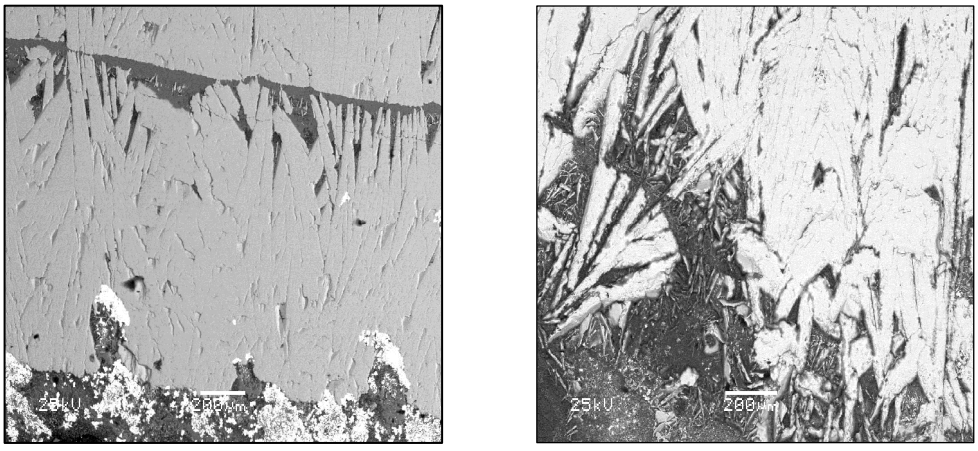

a b

Fig.2. Backscattered electron image of goethite and its fillings characteristic

Silicon mineral scale. Silicon mineral scale mainly composes of sodium-silicon residue ($Na_2O{\cdot}Al_2O_3{\cdot}xSiO_2{\cdot}nH_2O$), existing in single tube. Micro-fine sodium-silicon residue fills in the gaps between other scale crystals in the form of packing, as shown in Fig.1b. And silicon mineral scale has been forming during the whole alumina production process, as shown in Fig.2b.

Ca-Ti-Mg mineral scale. Ca-Ti-Mg scale mainly exists in autoclave. It's the deposition of titanium, calcium and magnesium. The most important is the deposition of titanium. Titanium separate out in the form of perovskite. Perovskite and magnesium hydroxide share five periodic cycles of sedimentation, forming sedimentary structure of perovskite and magnesium hydroxide in the form of layered alternation, as shown in Fig.3. Fig.3b is the element line distribution imaging

analysis of Fig.3, visually displaying the content change rule and correlation between elements which are Na, Mg, Al, Si, P, S, K, Ca, Ti and Fe in different sedimentary layers. The figure shows that the contents of Na, Mg, Al, K, Fe, P, S and Si is increasing in five depositions and that the content of Ca and Ti in the first deposition is significantly at lower level.

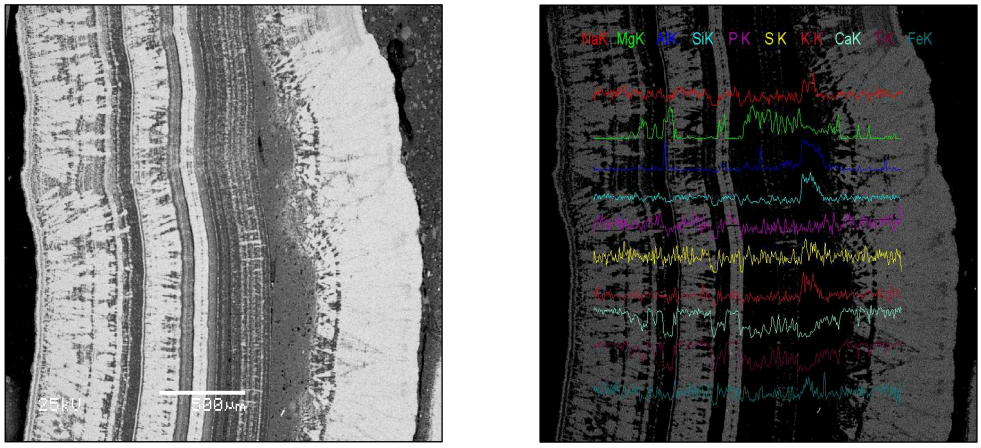

a. backscattered electron image b. element line distribution analysis image

Fig.3. Backscattered electron and element line distribution analysis image of Ca-Ti-Mg scale

Characteristics of five periodic sedimentary cycles of titanium are shown in Fig.4.

Perovskite which forms in the first cycle of sedimentation of titanium appears to be bright white contrast, and crystals are big and plate-like. The crystals of perovskite grow along the edge of pipe wall, forming perovskite crystal clusters which are perpendicular to the pipe walls. A large number of perovskite crystal clusters form dense structure. A little micro-fine calcium magnesium silicate scale deposits partially between interlamination.

Subhedral perovskite crystals which form in the second cycle of sedimentation of titanium are not only less than the one of the first deposition of titanium apparently, but also appear to be sparse, depositing in the micro-fine magnesium hydroxide matrix.

Dense enriched layers of perovskite form in the third cycle of sedimentation of titanium. In the early and advanced periods of the third cycle of sedimentation, fine-grained perovskite spread in the magnesium hydroxide.

The characteristics of enriched perovskite layer which forms in the forth cycle of sedimentation of titanium are similar to the one that forms in the first cycle of sedimentation of titanium. The crystals of perovskite are big in the form of dense crystal clusters which are perpendicular to sedimentary layer.

A large number of features of the last cycle of sedimentation of titanium appear to be platelike crystals of perovskite with euhedral and subhedral structure, locating in the fine-grained perovskite and magnesium hydroxide matrix, in the form of crystal clusters which are perpendicular to sedimentary layer.

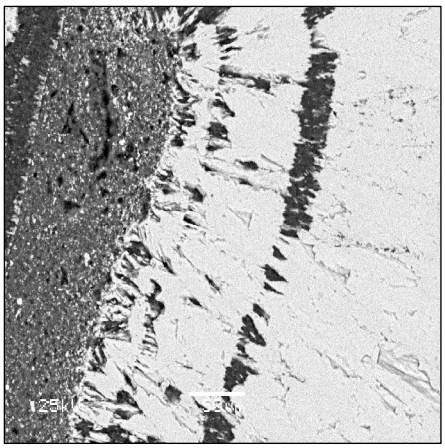

The first sedimentation

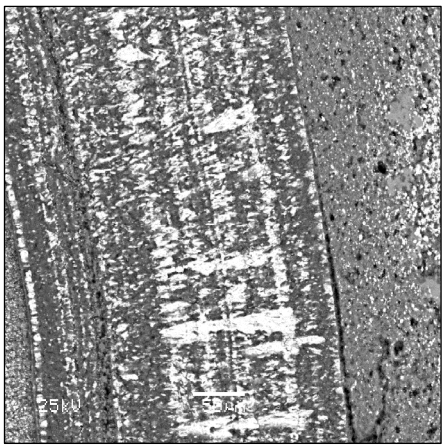

The second sedimentation

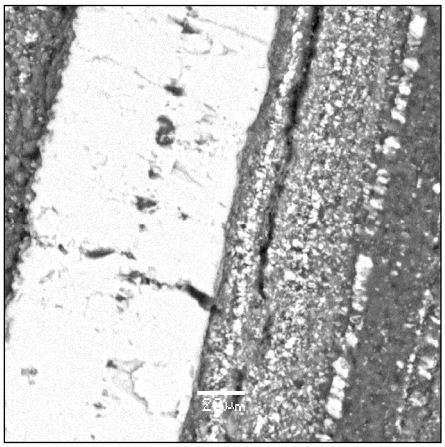

The third sedimentation

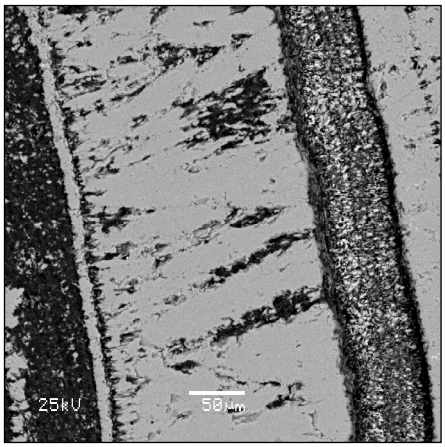

The forth sedimentation

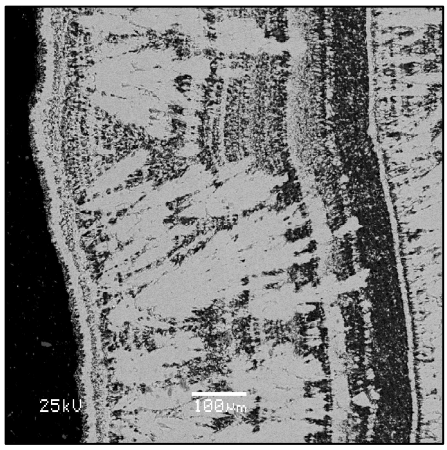

The last sedimentation

Fig.4. Backscattered electron image of the five cycles sedimentation of Ti

$Al_2O_3(Al_2O_3 \cdot 3H_2O)$ scale. It exists in flash type evaporator and has two major kinds of typical structures, spherulitic and laminated. Their backscattered electron image and structure characteristics are shown in Fig.5 and Fig.6, respectively.

The Fig.5a shows the spherulitic structure. Spherulite appears to be gray contrast with the size of 400 microns to 1300 microns, in forms of elliptical or irregular granular state. The core of it is often hollow. Component analysis shows that, the spherulite is mainly composed of $Al_2O_3(Al_2O_3 \cdot 3H_2O)$, in symbiosis with a small amount of Na, Mg, Si, Co, Ca, Cr, Fe. Between spherulites, there are gray-white fillings. The fillings is mainly composed of Al_2O_3 $(Al_2O_3 \cdot 3H_2O)$. But in the fillings, there

are a lot of bright white calcium titanate iron [$CaFe(Ti_2O_6)$] and iron garnet in all size in symbiosis. It makes the contents of Si, Ca, Ti, Fe and other elements of fillings higher than that of spherulite in chemical composition. In addition, $Al_2O_3(Al_2O_3 \cdot 3H_2O)$t, the crystallinity of the main content of fillings, is higher than that of spherulite. $Al_2O_3(Al_2O_3 \cdot 3H_2O)$ in the fillings appears to be sheet-like and fibrous micro-crystal structures, while the one in the spherulite appears to be dense aphanitic texture. As shown in Fig.6a, the composition of crust layer and the composition of dark crust layer are both relatively pure aluminum hydroxide phase.The composition of the outside edge of crust layer is iron garnet which is bright white particle like triangle. The composition of fillings is calcium titanate iron [$CaFe(Ti_2O_6)$] phase.

In the laminated structure, gray-white laminae winds, bypassing gray contrast aluminum spherulite and aluminum clusters, with a characteristic of liquidity, as shown in Fig.5b, Through component analysis, gray-white laminae has two kinds of component characteristics. One is more Na, Si, S and K and less Al than gray aluminum spherulite. Gray-white laminae form when the mixture of micro-fine aluminum hydroxide phase and $Na_2Ca_3Si_3O_{10}$ phase flows through the edge of gray aluminum hydroxide. The other is rich in Ca, Ti, Fe. Under the SEM, there are a number of small bright contrast particles. They distribute in the interior of aluminum hydroxide phase with the size of less than 20 microns. The bright particles consist of calcium titanate iron [$CaFe(Ti_2O_6)$] phase. As shown in Fig.6b, the composition of bright laminae are $Na_2Ca_3Si_3O_{10}$ enrichment phase and pure aluminum hydroxide phase with round dark mass composition.

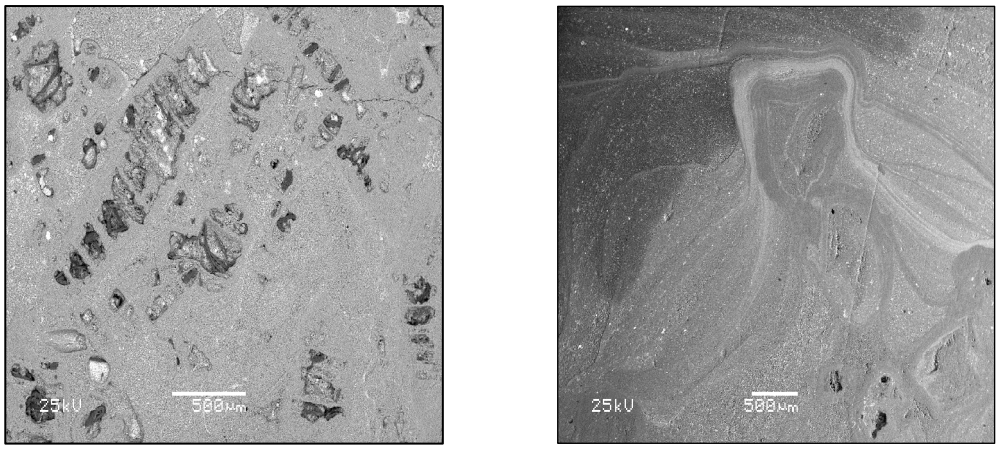

a. spherulitic structure b. laminated structure

Fig.5 Backscattered electron image of $Al_2O_3(Al_2O_3 \cdot 3H_2O)$ scale

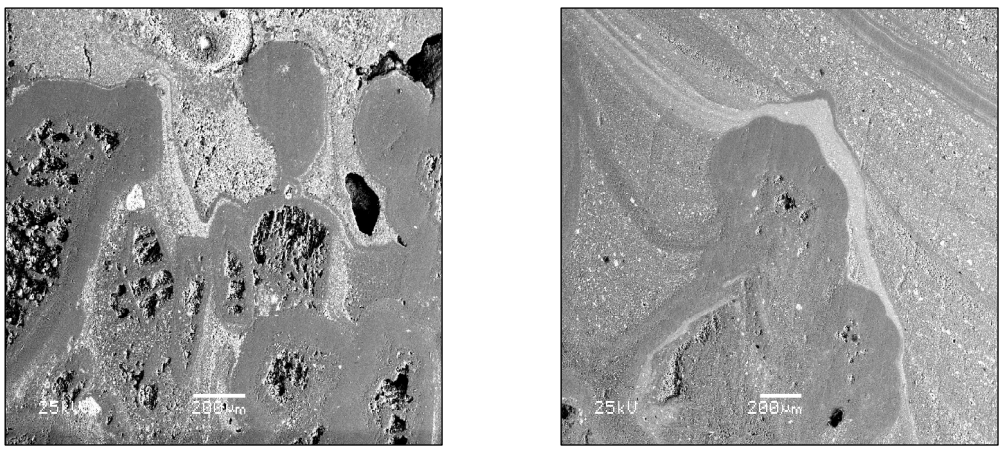

a. spherulitic structure b. laminated structure

Fig.6. SEM of structure characteristics of $Al_2O_3(Al_2O_3 \cdot 3H_2O)$ scale

Analysis and discussion

Scale in single tube preheater mainly contains hematite, aluminum goethite and sodium-silicon slag. It could be reduced by strengthening the pre-desilication process, changing the flow velocity and flow condition of pulp reasonably, embalming the surface of steel composites to reduce the nucleation of iron, adding chemical scale inhibitors and so on. The most important material of scale in autoclave is the deposition of titanium. Build a detitanation pot in temperature area where reaction is rapid and precipitation is violent, and most of calcium titanate will separate out in staying ladle. The scale in staying ladle primarily contains goethite containing aluminum and titanium with dense layered structure. It is suitable for adopting alkali cooking after fire. Flash type evaporator mainly contains thick $Al_2O_3 \cdot 3H_2O$ scale. Higher solution alkalinity is conducive to deposition of $Al(OH)_3$. It is suitable for adopting hot alkali dissolving, before considering other mechanical or chemical methods.

Conclusions

The mineral composition and morphological structure of scale changed persistently in high pressure digestion process of alumina production. Formation of scale could be divided into early and advanced sedimentation. The early sedimentation is a chemical crystallization mainly with coarse crystalline of hematite, perovskite and goethite. The advanced sedimentation is an effect of physical deposition which are $Al_2O_3 \cdot 3H_2O$, Na_2CO_3 and sodium silicon slag in forms of micro-fine particles and aphanitic texture with loose structure and liquidity. Therefore, controlling the grow of hematite, perovskite and goethite crystal clusters is the key to scale prevention and treatment in high pressure digestion process.

Acknowledgements

This work was financially supported by the Guizhou Science and Technology Plan Foundation ([2012]3011).

References

[1] Ping Zhou, Wangxing Li, Jiemin Zhou: Light Metals. (2001), p. 20(In Chinese)
[2] Songqing Gu, Lijuan Qi, Zhonglin Yin: Light Metals. (2007), p. 55(In Chinese)
[3] Fang Huang, Huajun Yuan, Fei Zhao: Journal of Guizhou University of Technology(Natural Science Edition). (2001). p. 18(In Chinese)
[4] wenjie Pang, ying Zhang: Sci/tech Information Development & Economy. Vol. 14 (2004), p. 266 (In Chinese)
[5] Huajun Yuan, Fang Huang, Yi Yuan: Light Metals. (2002), p. 24(In Chinese)
[6] Zhonglin Yin, Songqing Gu: China Journal of nonferrous metals. Vol. 11 (2001), p. 910(In Chinese)
[7] Qingjie Zhao, Qiaofang Yang, Qiyuan Chen: Transactions of Nonferrous Metals Society of China. (2010), p. 1(In Chinese)
[8] Bingan Xu, Peter Smith, Lynette De Silva: International Journal of Mineral Processing. (2013), p.22
[9] Brown N: Journals of Crystal Growth. (1988), p. 26
[10] Zhonglin Yin, Songqing Gu, Shiwen Bi: Light Metals. (2005), p. 24(In Chinese)
[11] Zongfu Jian: Journal of Xinxiang University(Natural Science Edition). Vol. 25 (2008), p. 42(In Chinese)
[12] Yong Yu, Wei Li: Chinese Nonferrous Metallurgy. Vol. 42 (2013), p. 54(In Chinese)
[13] Xinping Ren: Nonferrous Metals Design. Vol. 38 (2011), p. 29(In Chinese)
[14] Bingan Xu, Peter Smith, Christine Wingate, Lynette De Silva: Hydrometallurgy. Vol. 105 (2010), p. 75

Advanced Materials Research Vols. 960-961 (2014) pp 281-286

doi:10.4028/www.scientific.net/AMR.960-961.281

Economic Analysis of Buried Corrugated Steel Culverts considering Deterioration

Chunhong Zhi

School of Business/Collaborative Innovation Centre for State-owned Assets Administration
Beijing Technology and Business University, Beijing, China

zhi_chunhong@sina.com

Keywords: LCC analysis; Buried Corrugated Steel Culvert; Deterioration

Abstract. The characteristics of the corrugated steel culvert and the deterioration of the structure are analyzed. The Life Cycle Cost (LCC) approach is put forward to analysis the initial, maintenance and recycling cost of the different material culverts. The user delay costs are added to the typical LCC values considering the deterioration and the failure of structures. The analysis and the economic comparison results show that the total LCC values at the failure emergency situation is much larger than the situation when the deterioration is considered initiatively. Such economic analysis can help the project decision makers better understand the risks associated with deterioration and failure. The inspection and maintenance schedule should be formulated considering the culvert size, the environment in which the culvert is placed, and the characteristics of the soil and the backfill.

Introduction

As a pipe culvert structure with superior mechanical properties, buried corrugated steel culverts are getting more and more popular on roadway and drainage engineering [1]. They are more economical considering the Life Cycle Cost (LCC) compared to traditional concrete or masonry bridges and culverts [2]. It was widely built as highway structures in the USA, Canada, North Europe and such countries which have permafrost and deserts since 1950s and 1960s. In China, there were also many applications in highway engineering from the late 1990s [3]. Culverts were installed based on a 30-50 year expected life. In many western countries, many of these culverts have never been replaced and now their life expectancy is not only arrived but has passed in many locations and yet there are no plans for a replacement plan. However, corrosion protection is required for steel culverts to achieve their full-expected life. In some cases, corrosion will more than expected and this type of structure would not crack like concrete or masonry structure. Thus the deterioration of the buried corrugated culverts is relatively not easy to see. This is resulting in increased culvert failures and the replacements being handled haphazardly with emergency repairs often costing far more to replace and as an inconvenience to motorists than a scheduled repair would cost [4]. It can be a good reference for China to study the inspecting and maintenance strategies for this type of structures in these countries. With the increasing applications of buried corrugated steel structure in China recently, it is urgency to pay close attention to the deterioration of the structure and to avoid failure. In this paper, the economic analysis of the buried corrugated steel culverts considering the deterioration and the impact of the failure are present and some advice to the inspecting and maintenance strategies for this type of structures in China are proposed.

Deterioration of the Structure

The Durability is important for design and construction of all structures. The deterioration of the structure brought a lot of economic cost in many countries [5]. For pipe culvert structures, the United States Army Corps of Engineers identified recommendations on the design life by materials [6]:

Concrete: “Most studies estimated product service life for concrete pipe to be between 70 and 100 years. Of nine state highway departments, three listed the life as100 years, five states stated between 70 and 100 years, and one state gave 50 years.”

Steel: “Corrugated steel pipe usually fails due to corrosion of the invert or the exterior of the pipe. Properly applied coatings can extend the product life to at least 50 years for most environments.”

In many western countries, after nearly 90 years of practical experience with corrugated steel culverts installations, this type of structure has a proven durability for use as culverts and storm drains. Corrugated steel culverts can be designed for field conditions by using galvanizing, asphalt coating, paved inverts, and varying the metal thickness. Corrosion and abrasion are the major causes of corrugated steel culvert deterioration. Corrosion is a significant problem for underwater structures, particularly in environments where there are conditions that accelerate the process. Three dominant factors that cause deterioration of corrugated steel culvert are soil chemistry, water chemistry, and abrasion resistance of sediments. The abrasion potential of an environment can be evaluated by measuring the slope of installation, the velocity of the flow, and the size of the abrasive materials in the culvert. Erosion of corrugated steel culvert at the inverts can mechanically damage the invert surface. New Jersey Department of Transportation Maintenance has identified deterioration of corrugated steel culvert as a significant problem because many installed pipes are at or near the 30-year age mark. Most of these older culverts that are currently in the field exhibit 80-90% section losses, or in many cases 100% section losses at the inverts of the culvert [4]. If this deterioration is not addressed within the next several years, many areas will exhibit soil transfer from under the pipe resulting in erosion and/or collapse. A culvert collapse may result in the above roadway settling, or itself collapsing, which would prove very costly in terms of traffic delays and roadway repair. China is in the period of rapid applying this type of structure in highway engineering now. The design and construction specifications are most from the experience of abroad. The corrugated steel plates are generally galvanized to corrosion as the foreign standards. Although generally this method can avoid corrosion problems, the absence of in-depth study of durability for this type of structure will course extreme deterioration even the collapse after 10 or 20 years.

So not only the typical LCC, but also the structural deterioration or even failure must be considered when design (choose the materials) of the culvert. Such economic analysis can help the project decision makers better understand the risks associated with deterioration and failure. It would also help in identifying trends as well as quantifying the costs associated with failures. Based on this information, a risk factor could also be incorporated in future LCC calculations.

Economic Analysis Method

The concept of LCC is first proposed by the U.S. military in the 60s, 20th century. In 1980s, LCC method gradually applied to the road transport engineering [7]. For engineering, LCC models are used in business practice to determine an alternative by analyzing the structure type, the materials selected for it, the maintenance strategies and repair/rehabilitation engineering. From the analysis of various studies, the LCC analysis can be divided into two general categories: general LCC analysis model which using deterministic or probabilistic LCC approach and theoretical LCC analysis model which based on structural reliability approach. The theoretical LCC model can consider the risk (earthquake, typhoon, etc.) to structures that cannot be considered in a general LCC analysis model using time-invariant reliability or time-variant reliability. But it is more complicated. So the general LCC model is used more popular. However, it is difficult to determine whether a deterministic approach or a probabilistic approach is more accurate, as it is dependent on the type of the structure and cost-composition factors. For the large project that can be influenced by numerous environmental variables and has various cost-composition factors that are not clearly specified, probabilistic approach is more suitable. And for a specific structure, the cost-composition factors can be clearly specified, so the deterministic approach may be more accurate [8].

The deterministic approach is used to analyze the LCC of the culverts. Typical LCC mainly include three parts: that is the initial cost (design cost, supervise cost, construction cost, etc.), the maintenance cost and the recycling cost. The initial cost is assumed as happened at present and the maintenance

cost is assumed as happened in specific future points according to the usual maintenance strategies within the service life period of the culvert. The recycling cost is assumed as happened at the final points of the service life. So the total LCC present value of the culverts can be expressed as Eq. 1.

$$PV_{\mathrm{LCC}} = C_{\mathrm{ini}} + C_{\mathrm{mai}} - C_{\mathrm{rec}} \tag{1}$$

Where, PV_{LCC} is the present value of the LCC cost of the culvert, C_{ini} is the initial cost of the culvert, C_{mai} is the maintenance cost of the culvert and the C_{rec} is the recycling cost of the culvert.
The initial cost can be calculated according to the present standards and codes.
The maintenance cost can be calculated according to the ordinary cost of the maintenance and repair cost of the culvert and pavement. And then discount to present value. The maintenance cost can be expressed as Eq. 2.

$$C_{\mathrm{mai}} = \sum_{1}^{n} \frac{C_{\mathrm{mai1}}}{(1+q)^{y_n}} \tag{2}$$

Where, C_{mai1} is the cost of one ordinary maintenance and repair for the culvert and pavement, n is the number of times needed to be maintained and repaired during the service life, y_{n} is the years to the present when the maintenance and repair happened, q is the discount rate. Based on the general capitalization rate of the highway engineering in China, discount rate of the present value chooses 8%.

The recycling cost can be calculated according to the salvage value of the culvert. The salvage value is the value of the old material after demolition and take off the cost of the dismantle work. It always represent by a percent of the initial cost. Then it must be discount to the present value. So the recycling cost can be expressed as Eq. 3.

$$C_{\mathrm{rec}} = \frac{C_{\mathrm{ini}} \times q_{\mathrm{s}}}{(1+q)^{y}} \tag{3}$$

Where, q_{s} is the salvage value ratio, y is the expected service life of the culvert.

The traffic will be interrupted when the deterioration of the culvert needs to be fixed or the deterioration causing failure. The user delay costs (C_{ud}) are not considered in the LCC because user costs are experienced by traffic users and are not a direct expense to any agencies budget. However, these are in fact real costs and need to be considered in the economic analysis. Recent studies have shown that user delays are the primary benefit in the select of the structural and/or construction methods [9]. The cost of delay is experienced by the user during the culvert's re-installation. Such costs can be significant and consideration should be given to incorporate them in LCC. So the total LCC present value of the culverts should be expressed as Eq. 4.

$$PV_{\mathrm{LCC}} = C_{\mathrm{ini}} + C_{\mathrm{mai}} - C_{\mathrm{rec}} + C_{\mathrm{ud}} \tag{4}$$

The user delay cost C_{ud} can be expressed as Eq. 5.

$$C_{\mathrm{ud}} = \frac{1}{(1+q)^{y_d}} (C_{\mathrm{udd}} + C_{\mathrm{udi}}) \tag{5}$$

Where, C_{udd} is the direct cost of the user causing by the delay, C_{udi} is the indirect cost of the user causing by the delay, y_{d} is the years to the re-installation happened.

Generally, the direct cost of the user can be calculated using Eq. 6.

$$C_{\mathrm{udd}} = t \times u \tag{6}$$

Where, t is the increasing time for the delay or congestion when the culvert re-installation (in days), u is the unit cost of the user causing by the delay per day.

The unit cost can be expressed as Eq. 7.

$$u = u_{\mathrm{t}} + u_{\mathrm{d}} \tag{7}$$

Where, u_{t} is time cost of the user causing by the delay per day, u_{d} is detour cost of the user causing by the delay per day.

The u_{t} can be calculated according the local staff wage levers and the ud is relating to the cargo transportation costs and traffic flow of the road [10].

The indirect cost should consider the cost of the relevant industry sections and the social losses caused by traffic disruption. It is relate to the length of time and the generally correlation with the relevant industry sections. The calculation is more complex, generally can be derive using the analogy method under the same conditions [11].

Various types of culvert material have different life expectancies. A major concern is whether the road operating managers have a plan to monitor and replace culverts based on either inspection, or culverts reaching their expected life. Without a plan followed by action, failing culverts will have to be replaced at emergency rates instead of normal rates. The new relationship would likely include a risk factor cost as included in many risk assessment methodologies. So the total LCC present value of the culverts should be expressed as Eq. 8.

$$PV_{\mathrm{LCC}} = C_{\mathrm{ini}} + C_{\mathrm{mai}} - C_{\mathrm{rec}} + C_{\mathrm{eu}} \tag{8}$$

Where, C_{eu} is the cost of emergency.

It includes the emergency installation cost and emergency user delay cost. So the C_{eu} can be expressed as Eq. 9.

$$C_{\mathrm{eu}} = \frac{1}{(1+q)^{y_d}}[ERF \times C_{\mathrm{ini}} + (1+RF) \times C_{\mathrm{udd}}] \tag{9}$$

Where, ERF is emergency replacement factor for a certain culvert type, RF is the emergency user delay risk factor for a certain culvert type.

Obviously, the cost of installation in emergency situation when failure occurs would much larger than the normal situation. And the user delay cost, especially the indirect user delay cost also would much more than the planned arrangements in advance. The value of the factors ERF and RF should based on a national database. It also can be got using the analogy method if the database is not enough.

Example Analysis and Discussion of Results

The example is three reinforced concrete culverts with 5m span in Inner Mongolia changed design to the round corrugated steel culverts with the same span. According to the budget of the project, the initial cost of the reinforced concrete culverts are RMB 8 921 026 yuan. The initial cost of three corrugated steel culverts are RMB 9 774 155 yuan. The initial cost of the corrugated steel culverts is larger than the reinforced concrete because the corrugated steel is import from Korea. The import tariffs and the port charges is RMB 777 102 yuan. Subtract the import fee, if only the initial cost is considered, the cost increased by 0.9%.

But the reinforced concrete culvert need maintained or repaired regularly while the corrugated steel culvert hardly needs it. According to the Guidelines for Design of Highway Culverts of China [12], the design service life of culvert is 50 years. Assumed the ordinary cost of each maintenance or repair work is RMB 60 000 yuan for the three culverts, so the maintenance cost of the reinforced concrete culvert can be calculated using Eq. 2 and get the maintenance cost RMB 49 389 yuan.

The salvage value rate of the reinforced culvert is almost zero [13]. But the salvage value rate of the corrugated steel plate culvert is 80%, so the recycling cost of the corrugated steel culvert can be calculated using Eq. 3 and get the recycling cost RMB 166 717.6 yuan. Thus the typical total LCC present value of the reinforced culvert is: 8 921 026 + 49 389=8 970 415 yuan RMB. The total LCC present value of the corrugated steel culvert is: 9 774 155-166 717.6 =9 607 437.4 yuan RMB.

Taking off the import fee, the cost reduction of the corrugated steel culvert is 1.6%. So, it is can be seen that the cost is reduced when considering the typical LCC while it increased if only consider the initial cost as mentioned above.

But the above analysis has a prerequisite that all the culverts can achieve the design life. This is somewhat unrealistic. The deterioration of the corrugated steel culverts must be taken into account.

Now, considering the deterioration of the corrugated steel culverts, the user delay cost must be taken into account. Assuming the expected service life of the culvert is 25 years, the LCC cost during the design service life (50 years) can be calculated as follows:

The initial cost at 0 years is RMB 9 774 155 yuan; The recycling cost of the corrugated steel culvert at 25 years calculated using Eq. 3 is RMB 1 141 761.3 yuan; The initial cost at 25 years discount to present value is RMB 1 427 201.6 yuan; The recycling cost of the corrugated steel culvert at 50 years calculated using Eq. 3 is RMB 166 717.6 yuan.

The user delay is related to the population density and the economic develop lever of the district where the culvert constructed. Using the date of China from reference [14], for one breakage of the road, the direct cost of the user delay is RMB 2777.8 yuan per day, the indirect cost of the user delay is RMB 1111.1 yuan per day. The installation period of one corrugated culvert is about 20 days. So the user delay cost C_{ud} can be calculated using Eq. 5 and get the user delay cost RMB 102 212.8 yuan.

The total LCC value considering the deterioration initiatively is: 9 774 155-1 141 761.3+1 427 201.6-166 717.6+ 102 212.8= 9 995 090.5 yuan RMB.

But if the culvert not being replaced as it approaches its expected life, the failure may happen. According to reference [6], the re-installation cost in emergency is larger than the normal cost by times various from 4-140. Here we choose ERF =5 conservatively. According to reference [5, 11], the indirect cost of the user the delay in emergency is about 5-12 times as the direct cost. Here we also choose RF =5 conservatively. Thus the cost of emergency C_{eu} for corrugated steel culvert failure at the 25th service year can be calculated using Eq. 9 and get the cost of emergency RMB 7 574 065.4 yuan.

The total LCC value at emergency situation is: 9 774 155-1 141 761.3-166 717.6+ 7 574 065.4= 17 039 741.5 yuan RMB. It is much larger than 9 995 090.5, almost double the cost of considering the deterioration. The costs will much more if we take the risk factors larger. That is to say if agencies replaced culverts regularly once the expected service life was met, then most culvert failures could be prevented and the total LCC could be reduced. But this may best accomplished by initially constructing culverts with pipe materials with longer life expectancies and/or by providing an established inspection, maintenance, and replacement program.

Conclusions

According to the above analysis and the economic comparison, following conclusions can be obtained:

Deterioration of the corrugated steel culvert is objective. The inspection and maintenance schedule should be formulated considering the culvert size, the environment in which the culvert is placed, and the characteristics of the soil and the backfill.

The typical LCC approach can be used to choose the design plan. But the user delay cost should be added to the typical LCC value if the deterioration is considered.

The total LCC value at emergency situation is much larger than the situation when the deterioration is considered initiatively. Such economic analysis can help the project decision makers better understand the risks associated with deterioration and failure.

Acknowledgements

This work was financially supported by the Collaborative Innovation Centre for State-owned Assets Administration of Beijing Technology and Business University (GZ20130801) and the Construction of Accounting Professional Group of Beijing Education Committee (PXM2014_014213_000059).

References

[1] E.B.Flener, R. Karoumi, H. Sundquist: Structure and Infrastructure Engineering Vol. 3 (2005), p. 181-188.

[2] C. H. Zhi: Business Management and Electronic Information Vol. 4 (2011), p. 729-731.

[3] C. W. Chen: Highway Vol. 7(2000), p. 48-54. (In Chinese)

[4] Sinha, S.K., Fieguth, P.W. and Polak, M.A: Comput-Aided Civ . Inf. Vol. 18(2003), p. 95-112.

[5] N. F. Hong: Industrial Construction Vol. 3(2006), p. 76-79. (In Chinese)

[6] Joseph Perrin, Jr., Chintan S. Jhaveri: submitted to Transportation Research Board (2004).

[7] H. J. Wu, A. R. Chen: Highway Vol. 12(2004), p. 34-38. (In Chinese)

[8] Gu-Taek Kim, Kyoon-Tai Kim, Du-Heon Lee, et al.: Automation in Construction Vol. 19 (2010), p. 308-325.

[9] Joseph Perrin Jr., Rajesh Dwivedi: Journal of the Transportation Research Board Vol. 1957(2006), p. 8-15.

[10] Y. Y. Chen, G. Y. Wang: World Earthquake Engineering Vol. 1(2002), p. 18-22. (In Chinese)

[11] Y. M. Wang, B. H. Mao, W. Guan, et al.: Journal of Transportation System Engineering and Information Technology Vol. 2(2002), p. 134-140. (In Chinese)

[12] JTG/T D65-2007: *Guidelines for Design of Highway Culverts* (China Communications Press, Beijing 2007). (In Chinese)

[13] Sun Xing, Zhang Xun, Gao Jun: Energy and Building Vol. 40(2008), p. 1188-1193. (In Chinese)

[14] Y. Xu, T. L. Wu: Journal of Chang'an University (Natural Science Edition) Vol. 3(2004), p. 30-34. (In Chinese)

Advanced Materials Research Vols. 960-961 (2014) pp 287-291

doi:10.4028/www.scientific.net/AMR.960-961.287

The combination sewage treatment process of Nanofiltration and Photocatalytic Oxidation for the removal of Endocrine Disruptors

Feifan Deng[1, a], Lamei Yang[1,b], Zhengdong Deng[1], Guofu Xu[1,c]

[1]PLA University of Science and Technology,Nanjing 210007,China

[a]dengfeifanstudy@sina.com, [b]Yanglamei@sina.com, [c]xuguofu2007@163.com

Keywords: endocrine disrupting chemicals (EDCs);nanofiltration;photocatalytic oxidation

Abstract: The potential hazard effects of Endocrine Disruptors (EDCs) are drawing growing attention from the public,and the traditional sewage water treat process works in an unstable way in the removal of EDCs and can be influenced by many factors.The membrane technology shows good interception efficiency of EDCs,and the photocatalytic oxidation,with its wide application range of different types of polluted water,can thoroughly convert EDCs to inorganic materials.The combination process of nanofiltration and photocatalytic oxidation can easily extract EDCs from the water at first step,and decompose the EDCs in the concentrated polluted water and the back fluch water collected at the second step.The combination process is a reliable,practical and effective methods for EDCs removal.

Since the 1990s, scholars have discovered that many chemicals have the ability to interfere with the endocrine system of the human body and the animals',those chemicals are generally called endocrine disruptors (EDCs).Because EDCs behave similarly to hormones,traces of them can cause negative effects on the reproduction and growth process,neural and immune system,and can lead to cancers and bring damages to the eco-system,etc.which poses great potential hazardous threats on the health of human and wild lifes.

Because EDCs usually exist in our life in very small amount[1] and damage the body slowly but continuously,it took a very long time for the public to take notice of their harms.In 1960,the publication of Silent Spring by Carson drew worldwide attention to environmental issues and aroused concerns about synthetic hazardous chemicals.With the increasing reports of abnormal growth of fishes, birds and frogs,etc. people are becoming increasingly aware of harms caused by EDCs.EDCs can be found in many places in our daily lives,for example,plastics,pesticides and pharmaceutical agents,etc. all of them contain EDCs or are themselves EDCs,what's more,even foods may contain EDCs such as phytohormone[2].

Current treatment process for EDCs

Because of lacks of relevant regulations,control criteria,public attention as well as the treatment technology and other reasons to fight against the soil and air pollution, the current pollution treatment methods focus mainly on water body,therefore,the EDCs controlling project should and can only begins from water treatment.Water body is one of the main place where EDCs exist,in wastewater,surface water, groundwater, and even drinking water,there have been EDCs detected,so the water body is the main target for EDCs removal and relevant studies[3].

Conventional water treatment processes for the removal of EDCs can generally be divided into three categories:physically,chemically and biologically.The major physical removal methods for EDCs are membrane method and absorbent charcoal method.The absorbent charcoal method shows great absorption ability in the removal of organic pollutants with small solubility,high hydrophobicity and weak polarity under the experimental conditions,however,this method can be seriously influenced by water conditions,especially in wastewater where diverse pollutants exist,and the adsorption capacity of the absorbent charcoal can deteriorate dramatically which will in the end make the processed water disqualified[4].Chemical methods such as photocatalytic oxidation,ozonation and chlorination can decompose EDCs to some extent,however,the hard to create and maintain working conditions,high costs and the possibility to generate new poisonous chemicals make it impractical in EDCs removal[5].Biological method performs unstable EDCs biodegradation,at the same time it

produces large amounts of toxic sludge treatment which makes the process even more complicated.Nie Yafeng[6] studied the EDCs removal efficiency of sewage treatment plants in many countries and found in some cases that the EDCs concentration in the processed water were unexpectedly doubled or more when compared with the primary sewage,concluding that the biodegradation process is much complex and can produce metabolites more toxic than the original pollutants [7].

As mentioned above,the sewage water contains pollutants that are both diverse and complicated,on the other hand,the conventional water treatment processes mainly focus on the demineralization,sterilization and turbidity reduction rather than EDCs removal of the polluted water,therefore,advanced treatment processes need to be established on the basis of conventional sewage treatment facilities in order to remove the conventional pollutants as well as EDCs.

Advanced combination treatment process for EDCs

Water body,even the domestic water we use daily,may carry kinds of pollutants such as heavy metals,disinfection by-products and EDCs which may be trace in amount but tremendous in their harms.How to wipe those pollutants out of everyday life is a question needs to be answered instantly for the long-term human health and development.

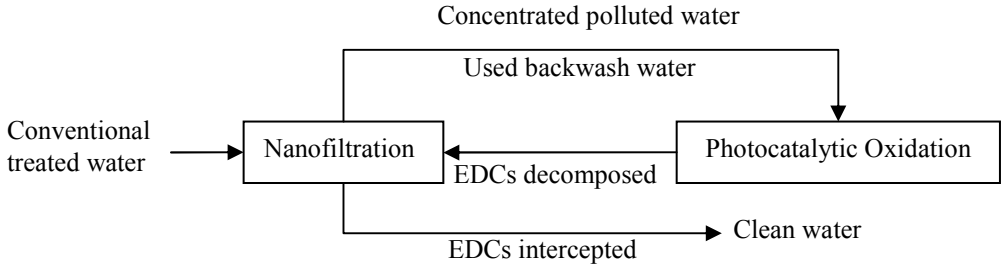

Fig.1 Advanced combination treatment process for EDCs

In order to remove the pollutants of trace amount from the water,an advanced treatment process is proposed as shown in Figure 1,this removal process can be interpreted as two steps:interception and decomposition.

2. 1 Interception

The interception of EDCs is necessarily the first step in the removal process,and in this step,the nanofiltration turns out to be effective and efficient with its unique advantages.As a membrane technology,nanofiltration performs better in the EDCs interception than ultrafiltration and microfiltration,and it needs lower operating pressure and is more energy saving than reverse osmosis,which makes it a ideal method for EDCs interception.

EDCs are mostly micromolecular organic pollutants,Figure 2 lists the relative molecular mass(MW) and dissolvability of 33 kinds of common EDCs,which are mostly pesticides,food additives and pharmaceuticals.

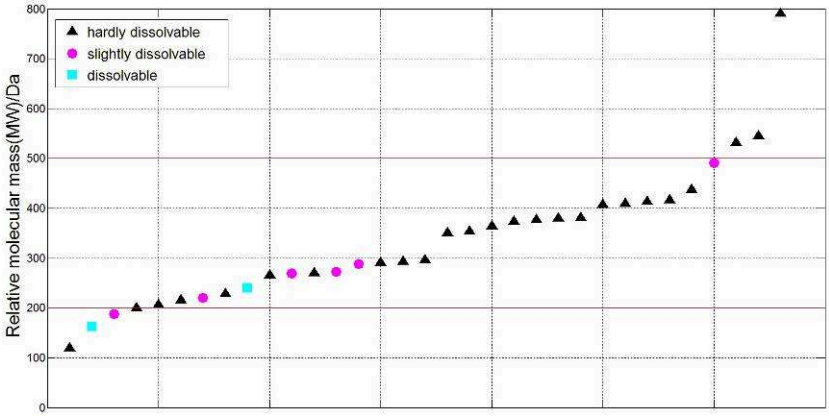

Fig.2 Features of 33 common EDCs

MWs of almost all the EDCs listed Figure 2 are greater than 200Da except 1,2-dibromoethane,methomyl and chloroform,and that of nearly 85 percent of the listed are ranging from 200Da to 500Da, according to the relationship between the Stokes radius and the MW of the organic molecules[8] [9]:

$$r_s = 0.0397 MW^{0.43}$$

It can be calculated that micromolecular organic pollutants with MW above 200Da have their stokes radius greater than 0.39nm,which are in the same order of magnitude with the nanofiltration membrane pore size.In fact,many studies have discovered that nanofiltration can effectively intercept the organic pollutants when their MWs are greater than 200Da,and sometimes the MW less than 200Da organic pollutants as well [10].

According to Figure 1,EDCs are mostly hydrophobic,and that many nanofiltration membrane are made from hydrophobic materials.It is similar to the principle 'like dissolves like' that adsorption occurs when the hydrophobic EDCs make contact with the surface of the membrane if it is also hydrophobic,and this adsorption reaction can be enhanced with the increase of the hydrophobicity of either the pollutant or the membrane[10].

The majority of EDCs are synthetic compounds that may be very possible to carry functional groups like amino and carboxyl,which can hydrolyze under certain pH condition so that the charged membrane surface will attract or repulse the ionized pollutants,for example,estriol,triadimefon and phthalate,etc.Other EDCs without hydrolysable functional groups may carry alcohol,aldehyde, ketone,ester or amine that can interact with the membrane due to the polar force.Thus,some of the EDCs are intercepted by nanofiltration.

In the light of the special properties of nanofiltration membrane and molecular characteristics of EDCs,it can be concluded that nanofiltration is an effective method in advanced sewage water treatment for EDCs interception.However,the membrane fouling will eventually happen during the working process due to concentration polarization and pollutants deposition,and this may lead to some serious problems such as disqualified processed water and shortened life span of the membrane, therefore,periodical backwash for the membrane is needed to ensure its proper functioning.The backwash water carries the pollutants away from the membrane so the membrane will be fresh again,then the used backwash water and the concentrated polluted water on the polluted side will be collected for further treatment to decompose the EDCs at last.

2. 2 Decomposition

The second step of EDCs removal process is decomposition.In this step, photocatalytic oxidation is applied to ensure the thorough decomposition of EDCs.It is a water treatment method using semiconductor as catalyst for the oxidation of pollutants.The semiconductor particles have energy band structure that consist of low-energy valence band (VB) filled by electrons and high-energy conduction band(CB) composition which is empty.When the light hit the semiconductor,photons in the irradiation light carrying certain energy also reach the surface of the semiconductor,and if the energy is greater than or equal to the energy the electrons needed for transition,electrons(e^-) in the VB will leap into the CB,leaving behind holes(h^+) in the VB.In the electric field,the holes will be ultimately transfered to the surface of the particle[11].Photocatalytic oxidation mechanism can be described by the following equations:

$$\text{semiconductor particle} \xleftrightarrow{h\nu} h^+ + e^-$$

$$H_2O + h^+ \longrightarrow \cdot OH + H^+$$

$$OH^- + h^+ \longrightarrow \cdot OH$$

$$O_2 + e^- \longrightarrow O_2^-$$

$$O_2^- + H_2O \longrightarrow \cdot OOH + OH^-$$

$$2 \cdot OOH \longrightarrow H_2O_2 + O_2$$

$$\cdot OOH + H_2O + e^- \longrightarrow H_2O_2 + OH^-$$

H_2O_2 and h^+ generated by the above process have very strong ability to steal electrons from the pollutants.These strong oxidizing intermediate products can snatch electrons of EDCs adsorbed on the surface of the semiconductor or in the water and make them completely decomposed.

TiO_2 is one of the most mommon photocatalysts applied in Photocatalytic oxidation,if the wavelength of the light strikes on TiO_2 is equal to 387.5nm or less, electrons will be motivated and leap into CB,creating the strong oxidizing holes and electrons structure.Nowadays,new techniques has made it possible for TiO_2 to be motivated by visible light,of which the wavelength is much longer than the 387.5nm ultraviolet light,these techniques include photosensitization and adding special reagents.Those techniques pave ways for the photocatalytic oxidation of pollutants under milder working conditions,making this water treatment method more practicable and easier to popularize.

Photocatalytic oxidation has many advantages over other methods in sewage water treatment.For example,it requires milder working conditions and it can be widely applied in different kinds of polluted water,most important of all,it can completely convert organic pollutants to CO_2 and H_2O,including recalcitrant and toxic chemicals[12].

The used backwash water and the concentrated polluted water collected from the nanofiltration facilities will be diverted directly to the photocatalytic oxidation facilities.In the coming period of a membrane backwash cycle,the EDCs and other contaminants in the water will be decomposed completely at last.Time is sufficient and chemical reaction is strong in this process,and that photocatalytic oxidation for EDCs removal is both effective and efficient.The decomposed water will then be delivered back to the nanofiltration facilities for recycling treatment,making sure that water coming out of the treatment plant will be clean water only.

Conclusions

From the theoretical standing point,the combination sewage treatment process of nanofiltration and photocatalytic oxidation,as an advanced treatment method,can work effectively in the control over EDCs.As for the selection of materials,the membrane with molecular weight cutoff 200Da and which is also hydrophobic is the optimum choice.Although to add advanced water treatment processes on the basis of conventional sewage treatment facilities will no doubt increase the operation cost and complicate the management,we should learn our lessons from the disadvantages of ‘economic development first,environmental protection second’ route,and take preventive measures before the crises emerge.In the long run,the advanced treatment program will benefit all the mankind.

The in-depth study of the EDCs control still has a long way to go,the comprehensive understanding and forward-looking research of EDCs is necessary and will certainly play a significant role in ensuring the cleaness of domestic water and safeguarding people’s the health. There arestill many questions of EDCs need to be answered now,before we solve all those problems,the most important things we can do right now are changing the way we lives,strengthening environmental protection consciousness,paying more attention to the way we produce life necessities especially pesticides and fertilizers and other chemical goods,encouraging cleaner production,safely usage and proper waste disposal,so as to prevent EDCs pollution.

References

[1] Xianyin Ping:Environment and Transportation Engineering.2011,6: 7086~7089.

[2] Kevin C. Knower,Sarah Q. To,Yuet Kin Leung,Shuk Mei Ho,Colin D. Clyne: Accepted Preprint first posted on 14 February 2014 as Manuscript ERC-13-0513.

[3] Zehua Liu,Wenfa Xiao,Sihao Chen, KANJO Yoahinori: Technology of Water Treatment. 2007,33(4): 6~10. In Chinese.

[4] Rui Wu: Industrial Water Treatment,2010,30(7):11~14. In Chinese.

[5] Li Ren,Weiben Yang:Yunnan Chemical Technology,2010, 37(2):63~65. In Chinese.

[6] Yafeng Nie, Zhimin Qiang,Heqing Zhang,Weiwei Ben:Acta Scientiae Circumstantiae, 2011, 31(7):1352~1360. In Chinese.

[7] Weiying Li, Jinbei Li, Qing Wang, Ming Zhang, Chunyan Guo: Science,2007, 59(4):18~20. In Chinese.

[8] Wang X L,Tsuru T,Nakao S, et al. Membrane Sci.,1997,135:19~32.

[9] Bowen W R,Mohammad A W,Hilal N:Membrane Sci.,1997,126:91~105.

[10] Han Zhang,Bingzhi Dong:Sicuan Environment,2011, 30(3) :104~108. In Chinese.

[11] Zidong Wei,Fei Yin,Jun Tan,Walter Z. Tang,Wanguo Hou :Chemistry, 2001,2:76~80. In Chinese.

[12] Ang Li,Yanqiu Zhang,Yan Li:Journal of Anhui Agriculture Sci.,2009,37(8) :3706~3707,3722. In Chinese.

CHAPTER 2:

Engineering Thermophysics

Advanced Materials Research Vols. 960-961 (2014) pp 295-298

doi:10.4028/www.scientific.net/AMR.960-961.295

Computer Simulation of Helium Adsorption in Argon Frost at Low Temperature

TANG Jiancheng[1, 2, a], XIONG Lianyou[1, b] and DONG Bin[1, c]

[1]State Key Laboratory of Technologies in Space Cryogenic Propellants （Technical Institute of Physics and Chemistry, Chinese Academy of Sciences）, Beijing 100190, China

[2]Graduate School of the Chinese Academy of Sciences, Beijing 100039, China

[a]tjc19822002@163.com, [b]lyxiong@mail.ipc.ac.cn, [c]dongbin@mail.ipc.ac.cn

Keywords: argon frost, cryogenic, helium adsorption, Grand Canonical Monte Carlo

Abstract. Fusion reactors require high-speed pumping of helium, deuterium and tritium while maintaining the inventory of tritium in the pumps at a low level. Cryopumping is potentially the most attractive method for this task. Cryosorption pump using rare-gas as sorbent is a good choice to satisfy the reactors for its special characters. Although a large number of works have been published in recent years on the properties of cryosorption pump using rare-gas as sorbent, it is hard to understand the behavior of fluid in a frost layer due to expensive and strict experiment conditions. Molecular modeling provides a convenient way to understand the principle of adsorption procedure in microscopic view. This paper applies the Grand Canonical Monte Carlo (GCMC) simulation method to study the adsorption behavior of Helium in argon frost. The HFD-B (HE) Aziz potential is used for the description of the interaction between two helium molecules. The adsorption behavior of helium in slit pore at T=4.3 K, 5 K, 6 K and 7 K is simulated. The simulation results show that the adsorption capacity increased rapidly as the bulk pressure smaller than 0.01 Pa, and the slop becomes slowly as pressure raised. The adsorption capacity is over 50% higher at lower temperature. The adsorption behavior agrees very well with experimental data in the public literature. The results show in this paper could be a guide for cryogenic workers to design cryosorption pump system. It is also provided a convenient method to predict the real adsorption procedure.

Introduction

Fusion power has the potential to provide sufficient energy to satisfy mounting demand with a relatively small impact on the environment. Fusion reactor which burn hydrogen isotopes (D/T) will produce neutrons and helium. It requires high-speed pumping of helium, deuterium and tritium while maintaining the inventory of tritium in the pumps at a low level. Cryopumping is potentially the most attractive method for this task. Cryosorption pump using rare-gas as sorbent is a good choice to satisfy the reactors for its special characters.

There are some gases, such as Ar, CO_2, SF_6 and N_2, exhibit large adsorption ability at low temperature for their porous structure [1]. The technology was applied in many large scientific projects. An argon frost continuous cryopumping system was carried out for Tokamak Fusion Test Reactor (TFTR) at the Princeton Plasma Physics Laboratory, and for DIII-D at General Atomics [2]. The TRAP (TRitium Argon frost Pump) was set up to study the performance of argon frost adsorption pump at Tritium Laboratory Karlsruhe in Germany [3].

Although a large number of works have been published in recent years on the properties of cryosorption pump using rare-gas as sorbent, it is hard to understand the behavior of fluid in a frost layer due to expensive and strict experiment conditions. The mechanism of the adsorption of gases on frost layers is best understood with computer simulation because detailed configurations of the adsorbed phase can be analyzed.

This paper applied the Grand Canonical Monte Carlo (GCMC) simulation method to study the adsorption behavior of spherical Helium molecule at 4.3 K, 5 K, 6 K and 7 K in argon frost pores.

Theory

The GCMC simulation is used to simulate the adsorption isotherms [4]. The slit pore model is used during the simulation (Fig. 1). The slit is bounded by argon walls of infinite area in the x-y plane. H is the internuclear distance (along the z-axis) between argon atoms in opposite walls. Δ is the internuclear distance of argon frost layers. Each pore wall comprises n parallel layers which represented the thickness of pore wall.

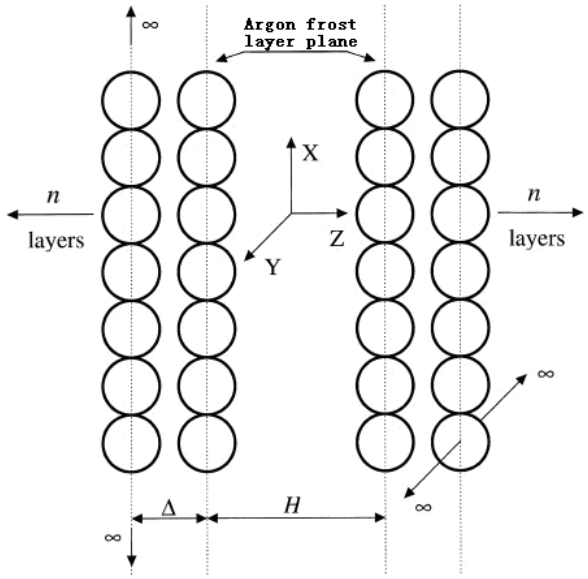

Fig. 1 The Schematic diagram of a slit pore

Periodic boundary conditions are applied in the x and y direction to simulate the infinite extent in that direction. Each of the equilibration and sampling stages has 50,000 cycles, with 3,000 steps in each cycle and equal probability between displacement, insertion and deletion.

Helium-Helium Potential Model. The HFD-B (HE) Aziz potential is adopted to represent the helium-helium interaction. The form of the HFD-B potential is [5]

$$U(r) = \varepsilon_{He} U^*(x) \tag{1}$$

where

$$U^*(x) = A^* \exp(-\alpha^* x + \beta^* x^2) - F(x)\sum_{j=0}^{2} c_{2j+6} / x^{2j+6} \tag{2}$$

with

$$F(x) = \begin{cases} \exp[-(\dfrac{D}{x} - 1)^2] & x < D \\ 1 & x \geq D \end{cases} \tag{3}$$

$$x = \frac{r}{r_m}$$

The parameters of the present potential are given in Table 1. ε_{He} is the depth of the potential minimum and σ_{He} is the collision diameter. The potential is cut off at a distance $r_c = 5.0\sigma_{He}$ during simulations to save computer time.

Table 1 HFD-B(HE) potential parameters

Parameter	Value	Parameter	Value
α	10.43329537	C_{10}	0.17473318
β	2.27965105	D	1.4826
C_6	1.36745214	r_m/A	2.963
C_8	0.42123807	A	184431

Argon-Helium Potential Model. The total interaction potential is the sum of the helium-helium interaction energy and the argon-helium interaction energy. This paper takes a simple model of surface, which is assumed to be homogeneous (structureless). The interaction potential energy between a helium molecule and the homogeneous flat argon frost wall is calculated by the well-known 10-4-3 Steele potential: [6]

$$U(z)=4\pi\rho\varepsilon_{sf}\sigma_{sf}^2\Delta\left\{\frac{1}{5}\left(\frac{\sigma_{fs}}{z}\right)^{10}-\frac{1}{2}\left(\frac{\sigma_{fs}}{z}\right)^{4}-\frac{\sigma_{sf}^4}{6\Delta(0.61\Delta+z)^3}\right\} \tag{4}$$

Where ρ is the volumetric argon atom density (27.5 nm^{-3}), and Δ is the spacing between two adjacent layers (2.628 A). The helium-argon molecular parameters are calculated from the Lorentz-Berthelot mixing rule with the values of $\varepsilon_{Ar}/k_B=119.8\,\mathrm{K}$ and $\sigma_{Ar}=0.34\,\mathrm{nm}$ for argon and $\varepsilon_{He}/k_B=10.948\,\mathrm{K}$ and $\sigma_{He}=0.26369\,\mathrm{nm}$ for helium. The cross collision diameter is:

$$\sigma_{sf}=(\sigma_{Ar}+\sigma_{He})/2 \tag{5}$$

The argon-helium interaction energy is:

$$\varepsilon_{sf}=\sqrt{\varepsilon_{Ar}\varepsilon_{He}} \tag{6}$$

Analysis of Simulation Data

The surface excess density is used to represents the adsorption amount. The excess amount is defined as the difference between the amount in the system and a hypothetical amount occupying the accessible volume of the system with adsorbate having the same density as the bulk gas phase.

$$\Gamma_{ex}=\frac{\langle N_{ex}\rangle}{A}=\frac{\langle N\rangle-N_G}{A} \tag{7}$$

where <> represents the ensemble average. N_G is the number of particles occupying the accessible volume of the system at the same density as the bulk gas phase. The accessible volume is the volume for which a molecule has a non-positive potential, and can be calculated by Monte Carlo method [7] as follows: a spherical helium particle is randomly inserted into the simulation model, and if its solid-fluid potential energy is negative or zero, it is counted as a success and then remove the particle from the box. This process is repeated 10 million times and the percentage of success is calculated and taken to be the ratio of the accessible volume to the simulation box volume.

Results and Discussions

Fig. 2 shows the isotherms of helium adsorption in argon frost at 4.3 K, 5 K, 6 K and 7 K. From the simulation results, it is seen that the adsorption capacity increased rapidly as the bulk pressure smaller than 0.01 Pa, and the slop becomes slowly as pressure rised. That's because the adsorption capacity increased with bulk pressure. It is difficult to adsorb more particles when the argon frost filled with

helium atoms. It is also seen that at the same helium pressure, the surface excess density increased as the temperature down. The adsorption capacity is over 50% higher at 4.3 K than that at 7 K. The results are in reasonable agreement with experiment conclusion in literature [8]. In the low pressure zone (less than 0.01 Pa), the higher the temperature the greater slop changed. As the temperature increased, the thermal motion of molecules makes it easer to release from the argon frost. So decrease the temperature of cryoplate can make the cryosorpsion pump more efficiet.

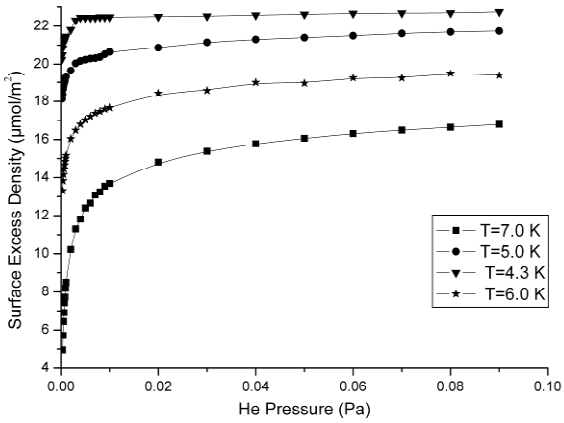

Fig. 2 Isotherms for helium adsorption in argon frost

Acknowledgements

This work is supported by the Chinese National Natural Science Foundations (Foundation No. 51076159) and the fund of the State Key Laboratory of Technologies in Space Cryogenic Propellants, SKLTSCP1203.

References

[1] R.I. Brackmann, W.L. Fite. 1961. Condensation of atomic and molecular hydrogen at low temperature. Journal of Chemical Physics 34: 1572-1579.

[2] Kamperschroer, J. H., et al. 1990. Cryosorption of helium on argon frost in Tokamak Fusion Test Reactor neutral beamlines. Journal of Vacuum Science & Technology A: Vacuum, Surfaces, and Films 8(3): 3079-3083.

[3] Kazachenkoa, O., et.al. 2008. TRAP-a cryo-pump for pumping tritium on pre-condensed argon. Nuclear Instruments and Methods in Physics Research A 587: 136–144.

[4] Frenkel, D., Smit, B. 1996. Understanding Molecular Simulation: From Algorithms to Applications, San Diego: Academic Press.

[5] Ronald, A. Aziz, Frederick, R.W.McCourt, Clement, C.K.Wong. 1987. A new determination of the ground state interatomic potential for He. Molecular Physics 61(6) :1487-1511.

[6] Steele W.A. 1973. The physical interaction of gases with crystalline solids I: Gas-solid energies and properties of isolated adorbedatoms. Surface Science 36: 317-352.

[7] D.D. Do, H.D. Do. 2006. Modeling of Adsorption on Nongraphitized Carbon Surface: GCMC Simulation Studies and Comparison with Experimental Data. Journal of Physics and Chemical B 110: 17531.

[8] J. H. Kamperschroer, M. B. Cropper1, H. F. Dylla, et al. 1990. Cryosorption of helium on argon frost in Tokamak Fusion Test Reactor neutral beamlines. Journal of Vacuum Science and Technology A 8(3): 3079-3083.

Advanced Materials Research Vols. 960-961 (2014) pp 299-303

doi:10.4028/www.scientific.net/AMR.960-961.299

Numerical Study of Laminar Flow and Convection Heat Transfer of Nanofluids Inside Circular Tube

Ningbo Zhao[1, a], Shuying Li[1, b], Jialong Yang[1], Zhitao Wang[1], Hui Meng[1]

[1]College of Power and Energy Engineering, Harbin Engineering University, Harbin 150001, China

[a]zhaoningbo314@hrbeu.edu.cn, [b]lishuying@hrbeu.edu.cn

Keywords: Nanofluids; Nanoparticles; Convection heat transfer; Laminar flow

Abstract. This paper presents a numerical study on laminar flow and convective heat transfer of nanofluids in a circular tube under constant wall heat flux boundary condition. Single phase model is used for simulating the heat transfer and flow behaviors of three different nanofluids. The effects of nanoparticle concentrations, nanoparticle diameter, nanoparticle material and Reynolds number on the Nusselt number and wall shear stress of nanofluids are determined and discussed in details. The comparison of Nusselt number of CuO-EG/water, SiO_2-EG/water and Al_2O_3-EG/water nanofluids are presented. The results show that Nusselt number clearly increases with an increase in the nanoparticle concentration and flow Reynolds number, while the nanoparticle diameter has an opposite effect on the Nusselt number. Compared to SiO_2-EG/water and Al_2O_3-EG/water nanofluids, CuO-EG/water nanofluids give higher Nusselt number with the same nanoparticle concentrations. The results also show that wall shear stress increases with increasing nanoparticle volume concentration.

Introduction

As a type of colloidal suspensions of nano-sized solid particles, nanofluids named by Choi [1] in 1995 have attracted much attention since extensively greater thermal conductivity and heat transfer performance as compared to the base fluids [2]. Since a decade ago, there were several experimental and numerical studies about flow and convective heat transfer performance of nanofluids. In the experimental aspect, Xuan and Li experimentally studied the convection heat transfer and friction coefficient of nanofluids in both laminar and turbulent flows [3]. Wen and Ding investigated the convective heat transfer characteristics in Al_2O_3-water nanofluids along a copper tube [4]. Sharma et al. experimentally studied the convective heat transfer coefficient and pressure drop in the transient region for Al_2O_3-water nanofluids under a constant heat flux [5]. As for as the numerical simulations for flow and convection heat transfer of nanofluids is concerned, only very recently a few papers have published. He et al. numerically studied the convective heat transfer in TiO_2 nanofluids flow through a straight tube under the laminar conditions by using both single phase method and combined Euler and Lagrange method [6]. Izadi et al. numerically investigated laminar forced convection in Al_2O_3-water nanofluids in an annulus by the single phase approach [7]. Moraveji et al. simulated Al_2O_3-water nanofluids through a tube under constant heat flux [8]. They all found that the heat transfer coefficient increased by increasing the nanoparticle concentration and Reynolds number.

Ethylene glycol and water (EG/water) based nanofluids are required for application in cold regions, which have not been studied widely thus far. In this study, the forced flow and convective heat transfer of the laminar flow containing EG/water based nanofluids under constant heat flux is simulated using the Computational Fluid Dynamics (CFD) tools. Three different nanoparticles (CuO, Al_2O_3 and SiO_2) in an EG/water mixture are used to investigate the effect of nanoparticle concentrations, size and their properties on convective heat transfer and flow.

Mathematical modeling

Governing equations. Compared to the two phase model, the single phase model is simpler to implement and requires less computational time. For the nanofluids, nanoparticles are much smaller

than micro particles and the relative velocity decreases as the particle size decreases. The fluid phase and nanoparticles are in thermal equilibrium with zero relative velocity, which means the nanofluids may be considered as a conventional single phase fluid [9]. Therefore, single phase model is adopted to describe the laminar flow and heat transfer characteristics of nanofluids through a straight circular tube under constant wall heat flux in this study.

On the basis assumptions of single phase model, the governing equations for nanofluids are given in the following [9].

$$\iint \rho_{nf} \vec{V} \cdot d\vec{A} = 0 \tag{1}$$

$$\int_{\forall} \rho_{nf} \frac{\partial \vec{V}}{\partial t} d\forall + \iint \vec{V} \rho_{nf} \vec{V} \cdot d\vec{A} = -\iint p\vec{n} \cdot d\vec{A} + \iint \mu_{nf} \vec{\nabla} \vec{V} \cdot d\vec{A} \tag{2}$$

$$\int_{\forall} (\rho C_p)_{nf} \frac{\partial T}{\partial t} d\forall + \iint (\rho C_p)_{nf} T\vec{V} \cdot d\vec{A} = \iint k_{nf} \vec{\nabla} T \cdot d\vec{A} \tag{3}$$

where $\vec{V}$, p , T , t , $\forall$, $\vec{A}$ and $\vec{n}$ are the velocity vector, pressure, temperature, time, volume, cross-sectional area vector and normal unit vector, respectively. The subscript nf means the effective thermophysical properties of nanofluids which are temperature dependent under the operating conditions.

The density and heat capacity of nanofluids can be calculated by Buongiorno [10].

$$\rho_{nf} = \phi\rho_p + (1-\phi)\rho_{bf} \tag{4}$$

$$C_{pnf} = \frac{\phi\rho_p C_p + (1-\phi)\rho_{bf} C_{bf}}{\rho_{nf}} \tag{5}$$

The thermal conductivity of nanofluids can be calculated by Hamilton and Crosser [11].

$$\frac{k_{nf}}{k_{bf}} = \frac{k_p + (n-1)k_{bf} - (n-1)\phi(k_{bf} - k_p)}{k_p + (n-1)k_{bf} + \phi(k_{bf} - k_p)} \tag{6}$$

where the subscript p and bf mean the effective thermophysical properties of nanoparticle and base fluid, respectively. n is the shape factor and is equal to 3 for spherical nanoparticle.

The viscosity of nanofluids can be calculated by Namburu et al. [12].

$$\log \mu_{nf} = Ae^{-BT} \tag{7}$$

where two parameters A and B are determined according to the experimental data .

Boundary conditions and grid optimization. In order to simulate the nanofluids flow, circular tube geometry with 0.004 m in diameter and 2 m long is adopted according to the flow geometry in the experimental work of He et al. [6] as shown in Fig. 1. As for boundary conditions, the uniform velocity and temperature (T_{in}=293K) profile are assumed at the tube inlet section. At the outlet section, the flow and temperature fields are assumed fully developed ((L/D) > 10). Wall boundary condition is subjected to nonslip velocity and a uniform heat flux of 4000 W/m^2.

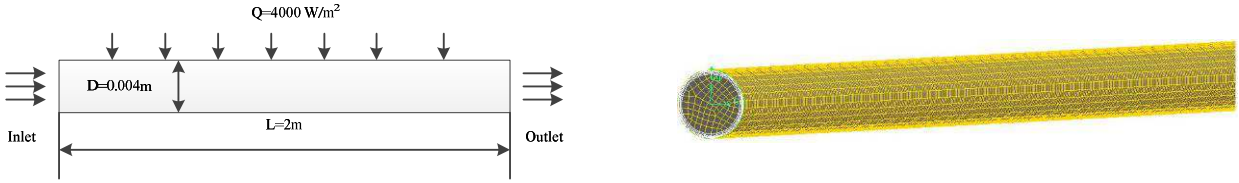

Fig.1 Flow geometry and numerical grid distributions

In order to identify the number of grid points that produce reasonably grid independent results, extensive computations have been performed. Fig. 2 presents the grid resolution effects on the axial variations of the centerline velocity and temperature for just four different mesh distributions. It is clear that both the grid 3 and grid 4 can resolve the velocity and thermal fields with reasonable accuracy. Considering computation time, grid 3 is used to describe the laminar flow and heat transfer characteristics of nanofluids in this study.

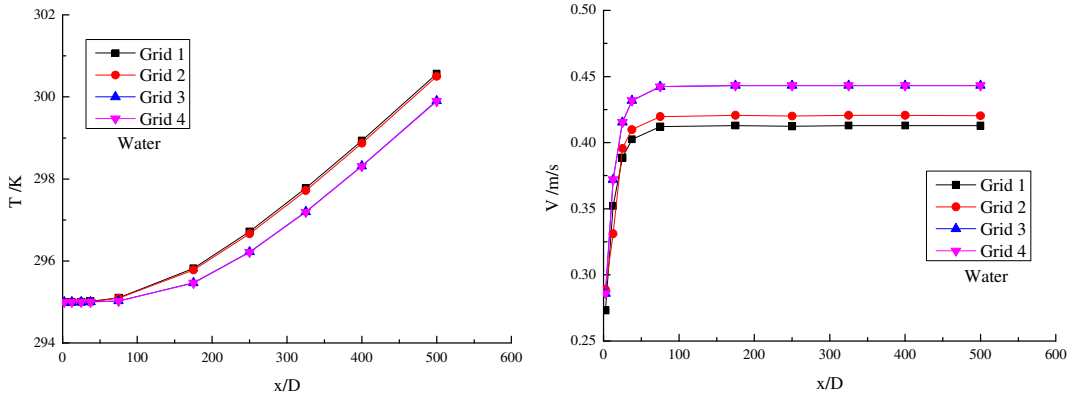

Fig.2 Axial variations of the centerline (a) velocity and (b) temperature of water for different grids at T_{in}=295K and Re=900

Results and discussion

Local heat transfer coefficient and Nusselt number are calculated using the following equations.

$$h(x)=\frac{Q}{T_w(x)-T_m(x)} \tag{8}$$

$$Nu(x)=\frac{h(x)D}{k_{nf}} \tag{9}$$

where T_w and T_m are tube wall temperature and nanofluids average temperature, respectively.

For checking the reliability and accuracy of the present numerical scheme, the numerical study is carried out on pure water firstly. As shown in Fig. 3, the axial variations of the local Nusselt number is compared with the experimental data of He et al. [6] and the results of the empirical expression by Shah [13]. It can be seen that reasonably good agreement is achieved.

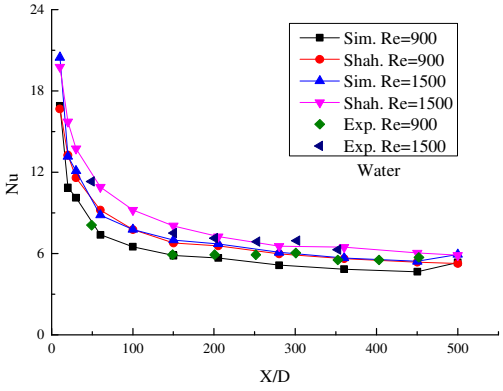

Fig.3 Comparison of axial variations of the Nusselt number with experimental data and empirical data

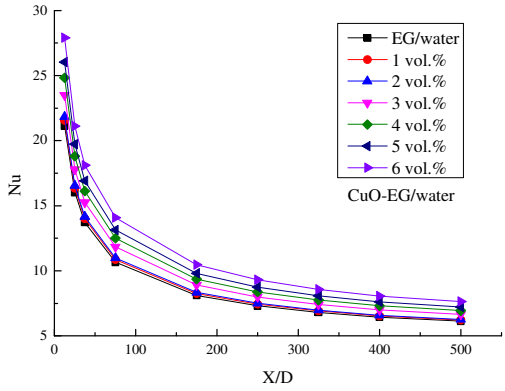

Fig.4 Axial variations of Nu for different nanoparticle volume concentrations

Effect of nanoparticle concentration on Nusselt number. Fig. 4 displays the effect of CuO nanoparticle (29nm) volume concentration on the Nusselt number along the tube for Reynolds number of 1000. The results indicate that the Nusselt number of nanofluids increases with increasing nanoparticle volume concentration. For example, in the case of 6 vol. %, the Nusselt number is about 24.76 % larger than EG/water at the end of tube.

Effect of nanoparticle diameter on Nusselt number. The effect of SiO_2 nanoparticle diameter (6 vol. %) on the Nusselt number along the tube for Reynolds number of 1000 is shown in Fig. 5. The results show that the nanofluids with larger nanoparticle diameter slightly decrease the Nusselt number as compared to the smaller nanoparticle diameter, especially at lower volume concentrations.

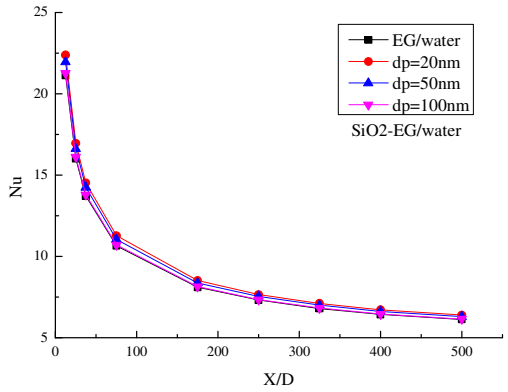

Fig.5 Axial variations of Nu for different nanoparticle diameter

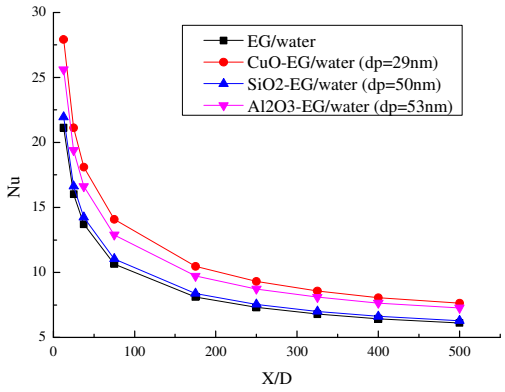

Fig.6 Axial variations of Nu for different nanoparticle material

Effect of nanoparticle material on Nusselt number. In order to study the effect of nanoparticle material, the Al_2O_3-EG/water and SiO_2-EG/water nanofluids are selected to compare with the results of the CuO-EG/water nanofluids. As shown in Fig. 6, CuO-EG/water nanofluids give higher Nusselt number than the Al_2O_3-EG/water and SiO_2-EG/water nanofluids with 6 vol. % nanoparticle concentration. This is because of the fact that the thermal conductivity of CuO nanoparticles is much larger than the thermal conductivity of Al_2O_3 and SiO_2 nanoparticles.

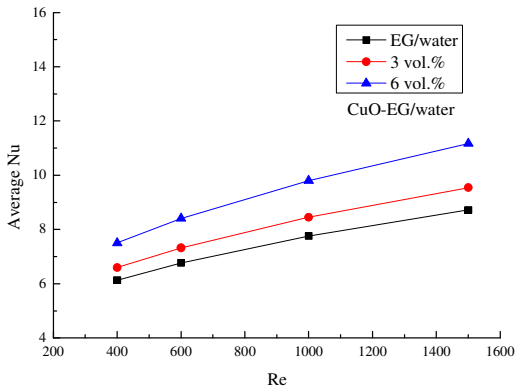

Fig.7 Variations of average Nu for different Reynolds number and nanoparticle concentrations

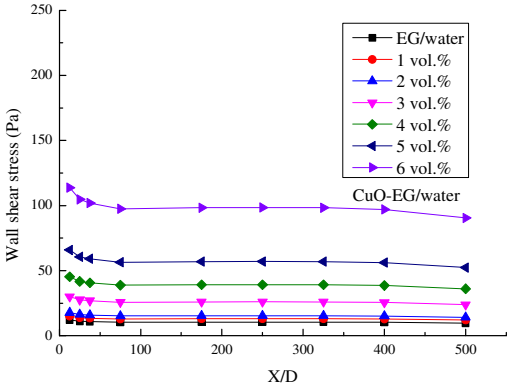

Fig.8 Axial variations of wall shear stress for different nanoparticle volume concentrations

Effect of Reynolds number on Nusselt number. Fig. 7 presents the effect of Reynolds number on the Nusselt number along the tube for CuO-EG/water nanofluid with nanoparticle diameter of 29 nm. The results indicate that the Nusselt number of nanofluid increases with increasing Reynolds number. This is due to the fact that higher Reynolds numbers lead to higher velocity and temperature gradients at the tube wall.

Effect of nanoparticle concentration on wall shear stress. Fig. 8 shows the numerical data obtained for the CuO-EG/water nanofluids with different nanoparticle (29nm) volume concentration on the wall shear stress along the tube for Reynolds number of 1000. From Fig. 8, it can be seen that wall shear stress increases with increasing nanoparticle volume concentration. Higher the wall shear stress, higher is the pumping power. Therefore, we should make a comprehensive decision the flow and convection heat transfer when selecting the nanofluids.

Conclusions

Numerical simulations have been performed by using a single phase model on the laminar flow and convective heat transfer of different nanofluids through a straight tube under constant wall heat flux boundary condition. The effects of some important parameters such as nanoparticle concentrations, nanoparticle diameter, nanoparticle material and Reynolds number on the Nusselt number and wall shear stress have been investigated. The results show that Nusselt number of

nanofluids increase with increasing in the nanoparticle concentration and flow Reynolds number and decreasing the nanoparticle diameter. At the Reynolds number of 1000, the Nusselt number for 6 vol. % CuO-EG/water nanofluids increases by 24.76 % over the base fluid at the end of tube. For the same nanoparticle concentrations of CuO-EG/water, SiO_2-EG/water and Al_2O_3-EG/water nanofluids, CuO-EG/water have highest heat transfer performance. The results suggest that we should make a comprehensive decision the flow and convection heat transfer when selecting the nanofluids because wall shear stress increases with increasing nanoparticle volume concentration.

References

[1] S. U. S. Choi, Enhancing thermal conductivity of fluids with nanoparticles, In Proceedings of the 1995 ASME International Mechanical Engineering Congress and Exposition, ASME, New York, (1995) 99-105.

[2] P. Keblinski, S. R. Phillpot, S. U. S. Choi, J. A. Eastman, Mechanisms of heat flow in suspensions of nano-sized particles (nanofluids), International Journal of Heat and Mass Transfer 45 (2002) 855-863.

[3] Y. M. Xuan, Q. Li, Investigation on convective heat transfer and flow features of nanofluids, Journal of Heat Transfer 125 (2003) 151-155.

[4] D. Wen, Y. Ding, Experimental investigation into convective heat transfer of nanofluids at the entrance region under laminar flow conditions, International Journal of Heat and Mass Transfer 47 (2004) 5181-5188.

[5] K. V. Sharma, L. Syam Sundar, P. K. Sarma, Estimation of heat transfer coefficient and friction factor in the transition flow with low volume concentration of Al_2O_3 nanofluid flowing in a circular tube and with twisted tape insert, International Communications in Heat and Mass Transfer 36 (2009) 503-507.

[6] Y. R. He, Y. B. Men, Y. H. Zhao, H. L. Lu, Y. L. Ding, Numerical investigation into the convective heat transfer of TiO2 nano fl uids flowing through a straight tube under the laminar flow conditions, Applied Thermal Engineering 29 (2009) 1965-1972.

[7] M. Izadi, A. Behzadmehr , D. Jalali-Vahid, Numerical study of developing laminar forced convection of a nanofluid in an annulus, International Journal of Thermal Sciences 48 (2009) 2119-2129.

[8] M. K. Moraveji, M. Darabi, S. M Hossein Haddad, R. Davarnejad, Modeling of convective heat transfer of a nanofluid in the developing region of tube flow with computational fluid dynamics, Int Commun Heat Mass Transfer 38 (2011) 1291-1295.

[9] E. Ebrahimnia-Bajestan, H. Niazmand, W. Duangthongsuk, S. Wongwises, Numerical investigation of effective parameters in convective heat transfer of nanofluids flowing under a laminar flow regime, International Journal of Heat and Mass Transfer, 54 (2011) 4376-4388.

[10] J. Buongiorno, Convective transport in nanofluids, Journal of Heat Transfer, 128 (2006) 240-250.

[11] R. L. Hamilton, O. K. Crosser, Thermal conductivity of heterogeneous two-component system, Industrial & Engineering Chemistry Fundamentals, 1 (1962), 187-191.

[12] P. K. Namburu, D. K. Das, K. M. Tanguturi, R. S. Vajjha, Numerical study of turbulent flow and heat transfer characteristics of nanofluids considering variable properties, International Journal of Thermal Sciences, 48(2009), 290-302.

[13] R. K. Shah, A. L. London, Laminar flow forced convection in ducts, Academic Press, New York, (1978).

Advanced Materials Research Vols. 960-961 (2014) pp 304-307
© (2014) Trans Tech Publications, Switzerland
doi:10.4028/www.scientific.net/AMR.960-961.304

Static and Dynamic Response of a Cu-Ni Thin Film Heat Flux Sensor

Shuo WU[a], Fang YE[b, *], Hang GUO[c], Chong Fang MA[d]

MOE Key Laboratory of Enhanced Heat Transfer and Energy Conservation and Beijing Municipal Key Laboratory of Heat Transfer and Energy Conversion, College of Environmental and Energy Engineering, Beijing University of Technology, 100 Pingleyuan, Chaoyang District, Beijing 100124, China

[a]wushuo@emails.bjut.edu.cn, [b]yefang@bjut.edu.cn (* Corresponding author), [c]hangguo@bjut.edu.cn, [d]machf@bjut.edu.cn

Keywords: thin film, heat flux sensor, thermopile, thermocouple, dynamic response.

Abstract. A Cu-Ni thin film heat flux sensor had been fabricated on a 0.05mm thick polyimide film substrate by vacuum coating technology. The overall dimension of the sensor was 8 mm long and 4 mm wide. A thermopile and a thermocouple were arranged on the substrate to measure both heat flux and surface temperature. The thermopile had 18 thermocouple junctions which formed 9 pairs of differential thermocouples and were covered by two different thickness of thermal resistance layers. This research carried out static and dynamic tests of the thin film heat flux sensor. Seebeck coefficient of thermocouple is 19.3761μV/(˚C). Sensitivity of the thermopile is 0.010121μV/(W/m^2). Steady-state tests of the thermopile and the thermocouple were taken separately. Time constant of the thermocouple is about 0.26s, which is faster the thermopile of 1.57s.

Introduction

Various types of heat flux sensors have been developed due to its small volume, quick response and high sensitivity, including thin film thermocouple arrays and thin film Wheatstone bridge design. Liu selected silicon dioxide as the substrate to fabricate a six layers thin film heat flux sensor. Its sensitivity was 0.05062 μV/(W/m^2) [1]. Christopher et al developed a compound thin film heat sensor, which could measure both the surface temperature and heat flux. Materials of the sensor were Pt and Pt/Rh [2]. Using the same layout, Xiao et al made a high temperature thin film sensor. Results showed that response time of the heat flux sensor was 0.1s [3]. Experiment had indicated that the intrinsic strength and adhesion of the films to the substrate had a significant effect on sensor itself [4]. NASA used semiconductor materials - Al:ZnO and N:ITO to make thin film heat flux sensor. Placed on a 250 °C hot plate with an estimated maximum heat flux of 2200 W/m^2, the senor got a maximum output of 0.015μV, and the fluctuation was ±0.0035μV [5].

So far, research is mainly focus on single thin film thermocouple [6] or single thin film heat flux sensor. In this investigation, a thin film heat flux sensor, which can measure both heat flux and surface temperature, is designed, fabricated and calibrated.

Design of Thin Film Heat Flux Sensor

The thin film heat flux sensor was placed on polyimide film with a dimension of 8mm long, 4mm wide, and 0.05mm thick (Fig.1). Using vacuum coating technology, four layers were deposited on the substrate step by step - Cu layer (0.1μm), Ni layer(0.1μm), thermal resistance layer 1(0.2μm)

and thermal resistance layer 2(1.2μm). Silicon dioxide was applied as the two thermal resistance layers to create a temperature gradient in the vertical direction to the thermal resistance layers. To get a large output, 9 pairs of thermocouples were connected in series to form a thermopile. What's more, there was a single thermocouple beside the thermopile, which was used as a temperature sensor to measure the surface temperature. Leg A and leg B were the output of thermocouple and the thermopile output was read between leg C and leg D (shown in Fig.1).

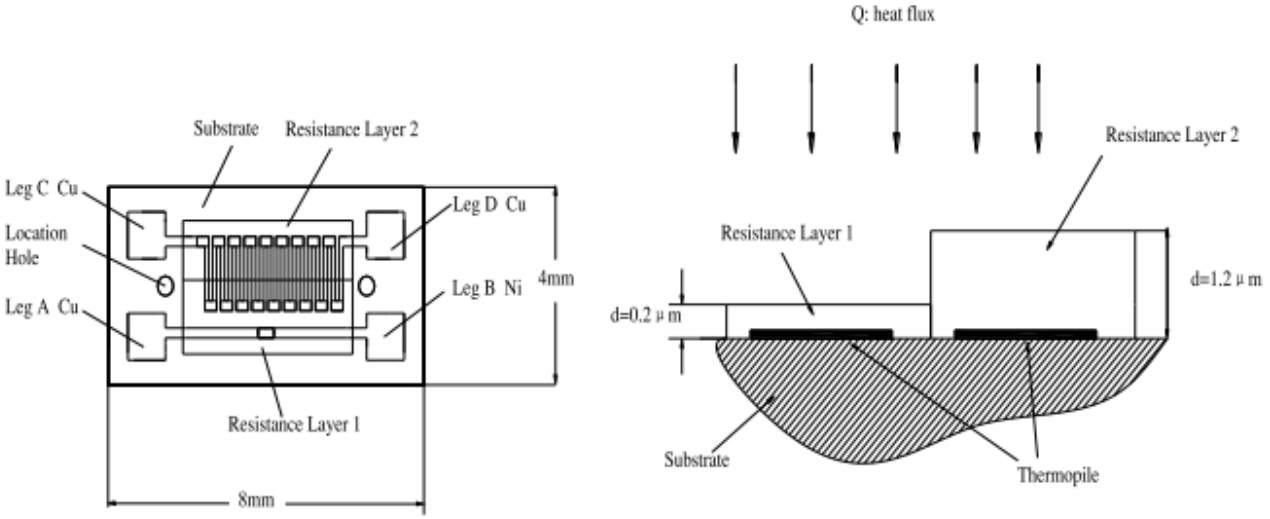

Fig. 1 Design layout of the thin film heat flux sensor

When a uniform heat flux is applied to the sensor, a temperature gradient will be created in the thermal resistance layer according to Fourier's conduction law. Therefore, the temperature difference measured by the thermopile is a function of the thickness of thermal resistance layer and the heat flux applied to the sensor, which can be shown s the following equation:

$$Q = \frac{\lambda}{d_1 - d_2}(T_1 - T_2) \tag{1}$$

Calibration of Thin Film Heat Flux Sensor

Static calibration is essential for the self-made sensor to obtain its sensitivity and performance. In fact, there are two sensors on the substrate: thin film heat flux sensor and thin film temperature sensor. Therefore, they have to be calibrated separately. First, the sensors were attached on the internal wall of a high-precision thermostatic water cabinet for temperature calibration. A K type thermocouple was placed at the same place. Output of the K type thermocouple is regarded as the reference temperature. The calibration was taken at a room temperature of 24.5˚C. Fig.2 shows the result of thermocouple's static calibration. As can be seen, correlation coefficient R is 0.94871.Result indicates that the output of thin film thermocouple has a relatively good linear relationship with the temperature. Moreover, Seebeck coefficient of the thin film thermocouple is 19.3761μV/(˚C), which is close to the standard Cu-Ni thermoelectric power 22.5μV/(˚C).

The heat flux calibration system is the same system with Liu [1]. The reason for choosing a halogen lamp as heat source is that it not only produce a wide range of heat flux values but also the heat flux values can be measured by a standard sensor. The standard heat flux sensor is HFM-201 in this paper. By adjusting the input power of halogen lamp we can get a series of heat flux values. Fig.3 is the calibration line between the heat flux and output voltage. Correlation coefficient R is 0.99759. The slope of the fitting line is 98.80643, thus the sensitivity is 0.010121μV/(W/m^2).

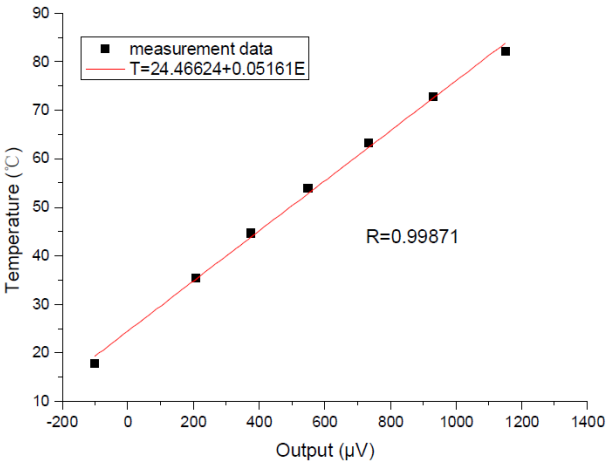

Fig.2 Static calibration of temperature

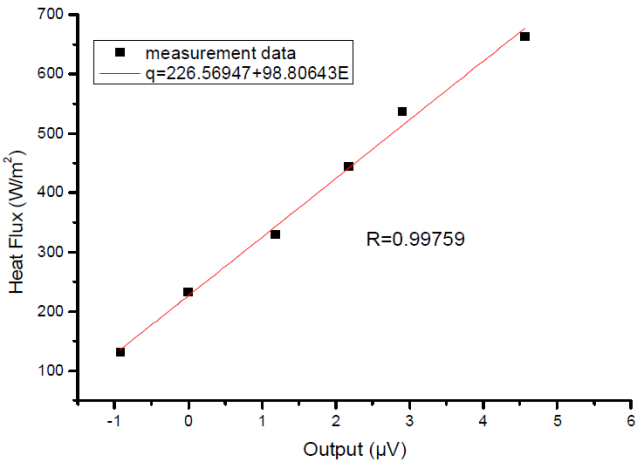

Fig.3 Static calibration of heat flux

Steady-State Response of Thin Film Heat Flux Sensor

To measure the steady-state response of the heat flux sensor, the halogen lamp is set at a constant output of 2kW and the sensor is irradiated until it reaches steady state. Results are show in Fig.4. It is observed that the heat flux increases rapidly when opening the circular shadow shield and stabilizes to an approximately constant value, same phenomenon emerges when heat source is disappeared. However, the temperature increases as a function of time. This behavior can be explained by that: the output of thermopile is the temperature difference between different thermocouples under different thickness of thermal resistance layers, while, the output of thermocouple is the temperature of substrate, which is increasing because of constant radiant heating during the test. Through this test, time constant of the thermopile can be calculated, which is 1.57s. In order to get the real dynamic response of the thin film thermocouple, we take the quickly throwing method as Yang [6] used. Fig.5 is the steady-state response of the thin film thermocouple when suddenly throwing the sensor into hot water. Time constant of the thermocouple is 0.26s, which is faster than the thermopile.

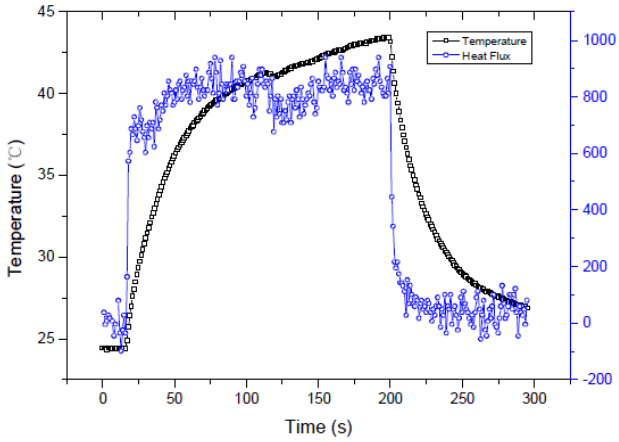

Fig.4 Steady-state responses of the sensor

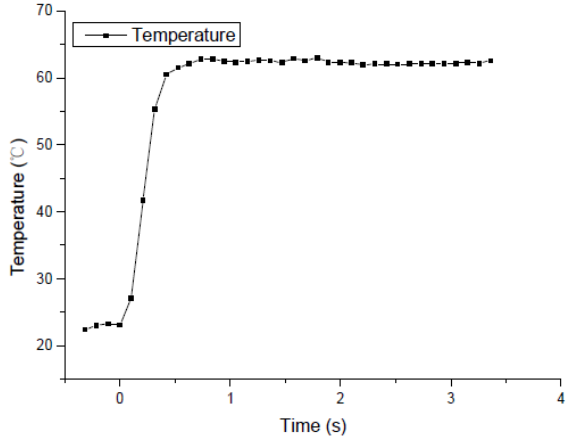

Fig.5 Steady-state responses of the thermocouple

Dynamic Response of Thin Film Heat Flux Sensor

During the dynamic calibration, the sensor get an intermittent heat flux by adjusting the circular shadow shield and the interval time is 10s. Dynamic response of the sensor is shown in Fig 6. As seen, responses of the thermopile and the thermocouple show two different tendencies. The heat

flux changes rapidly to the periodic heat flux. With a relatively high sensitivity of the heat flux sensor, its output fluctuates around a certain value. Surface temperature of the substrate is getting up and down when open and close the circular shadow shield. Different behaviors of heat flux and temperature once again demonstrate that heat flux has nothing to do with the substrate temperature.

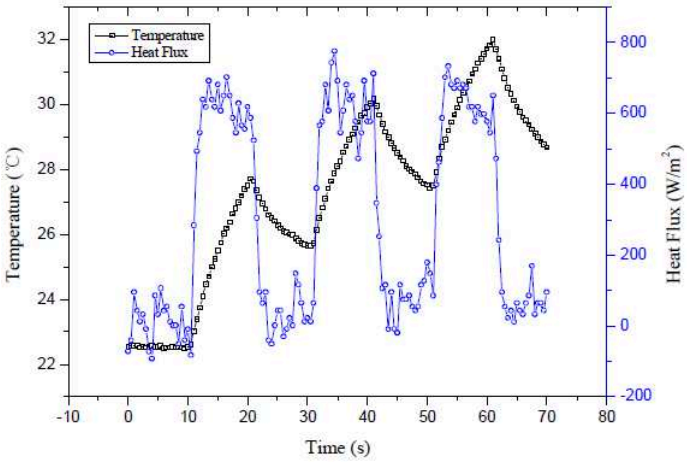

Fig.6 Dynamic response of the sensor

Conclusion

In this paper, a compound thin film heat flux sensor is developed and tested. It can measure both heat flux and temperature. Calibration results show that both thermopile and thermocouple have good linear relationship. Correlation coefficient R are 0.99759 and 0.99871, respectively. Using quickly throwing method, time constant of the thin film thermocouple is obtained and the value is 0.26s, which is faster than the thermopile. Dynamic test shows that the heat flux sensor responds fast to periodic radiant heat flux.

Acknowledgements

The authors are grateful to the National Natural Science Foundation of China (Grant Nos.: 50976006, 11102005), Program for New Century Excellent Talents in University (Grant No.: NCET-10-0006) and Specialized Research Fund for the Doctoral Program of Higher Education (Grant No.: 20121103110009) for the financial support.

References

[1] LIU J X, GUO H, JIANG J Y, et al. Fabrication and calibration of a thin film heat flux sensor [J]. Advanced Materials Research, 2013, 718-720:1181-1184.

[2] CHRISTOPHER S C, GUSTAVE C F, HEMANSHU D B. Steady State and Frequency Response of a Thin Film Heat Flux Gauge [J]. Journal of Spacecraft and Rockets, 1997, 34(6): 792-798.

[3] XIAO Y W, XIE G J. The Research of Heat Flux Film Sensor under High Temperature Environment [J]. Microprocessors, 2012(5): 1-3. (In Chinese)

[4] ZHAO W Y, JIANG H C, et al. Fabrication of Pt /ITO Thin Film Thermocouple on Metal Substrates [J]. Measurement & Control Technology, 2013, 32(4): 23-25. (In Chinese)

[5] WRBANEK J D, GUSTAVE C F, HUNTER G W. Thin Film Heat Flux Sensor Development for Ceramic Matrix Composite (CMC) Systems[C]//45th Joint Propulsion Conference and Exhibit, Denver, 2009: 1-10.

[6] YANG L H, ZHAO S Y. Study on Dynamic Characteristics of Cu/CuNi Thin-film Thermocouple Based on Theory and Experiment [J]. China Mechanical Engineering, 2013, 24(10): 1336-1339. (In Chinese)

Advanced Materials Research Vols. 960-961 (2014) pp 308-315

doi:10.4028/www.scientific.net/AMR.960-961.308

A Thermodynamic Analysis of the Fuel Synthesis System with CO_2 Direct Captured from Atmosphere

Tao Wang[a], Kun Ge, Jun Liu, Mengxiang Fang

State Key Laboratory of Clean Energy Utilization, Zhejiang University, Hangzhou 310007, Zhejiang, China

[a]oatgnaw@zju.edu.cn

Keywords: Syngas, CO_2 capture, Renewable energy, Thermodynamic analysis, Sensitivity analysis

Abstract. Hydrocarbon fuel synthesis with renewable energy and captured CO_2 is a promising option for CCU and an important approach to sustainable energy. Like photosynthesis of plants, the technology of CO_2 direct captured from atmosphere with CO_2 utilization would close the carbon cycle thoroughly. Because of the dilute CO_2 in the atmosphere, the air capture process faces the challenge of high energy penalty. However, integrated with fuel synthesis process, the air capture process can take advantage of the waste heat produced by syngas production process and the transportation of CO_2 can also be avoided. In this study, a thermodynamic model of the fuel synthesis system is built through energy and exergy analysis. The thermodynamic contribution of three typical CO_2 capture technologies, moisture swing air capture, high-temperature swing air capture and traditional amine-based flue gas capture, is studied using the model built. Furthermore, by the sensitivity analysis of the critical parameters of the capture, electrolysis and heat exchange process, the influence of each process on the performance of fuel synthesis system is examined and the approach to improve the efficiency of the total system is proposed.

Introduction

CCU (Carbon Capture and Utilization)[1] is a new concept developed from CCS (Carbon Capture and Sequestration), which could evade the risk and uncertainty of CO_2 storage. Meanwhile, the conversion of CO_2 into high value products offsets high energy penalty and cost of capture process, which will accelerate the application of the technology.

As an option of CCU, hydrocarbon fuel synthesis with renewable energy and captured carbon dioxide has been widely studied[2]. Among the different carbon capture technologies, air capture is a more suitable technology for fuel synthesis as it can provide a CO_2 source without constraints from location, timing and transportation. Meanwhile, thermodynamic analysis has shown that the energy cost of an air capture device should not be much larger than that of a flue gas scrubber[3,4], although the CO_2 concentration of atmosphere is 400 times lower than that of flue gas.

A fuel synthesis system with renewable energy and captured CO_2 from ambient air was put forward in previous work[5]. And preliminary analysis shows that the fuel synthesis system is a promising approach to the utilization of CO_2 and renewable energy. To obtain additional insight about the energy flow and exergy reduction of the system, an energy and exergy analysis is conducted in this study.

The Fuel Synthesis System

For the sake of comparison, during all the thermodynamic calculations, electricity is converted from high temperature heat which could come from either concentrated solar energy or nuclear energy. Fuel synthesis using several typical CO_2 capture technologies: moisture swing air capture (low temperature process), temperature swing air capture (high temperature titanate causticization process) and amine-based flue gas capture, are evaluated.

Process Description. A diagram of three hydrocarbon fuel pathways with different approaches of CO_2 feeding is presented in Fig.1. The system has been described in detail in previous work[5], here gives a brief description.

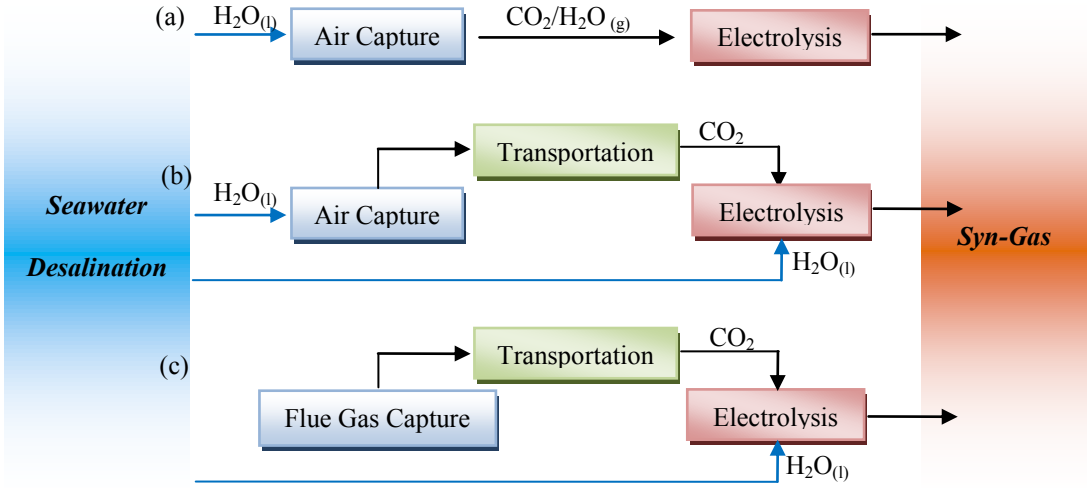

Fig.1 Hydrocarbon fuel synthesis from (a) integrated air capture, (b) transported CO_2 from air capture, (c) transported CO_2 from flue gas capture

The water consumed in the process of carbon capture and hydrogen production is provided from seawater desalination. As showned in Fig.1(a), the captured CO_2 from atmosphere could be directly fed to electrolysis process, which means the capture process is intergrated with eletrolysis process. As showned in Fig.1(b) and Fig.1(c), the captured CO_2 from atmosphere or flue is compressed, transported supplied to electrolysis process, which means the capture process is separated with eletrolysis process.

Efficient co-electrolysis under the same reversible potentials could avoid the excessive Joule heat production and the consequent complex heat management. The Gibbs free energy of dissociation corresponds to electrolysis reversible potential, which has the same value for CO_2 and H_2O at 850 ^oC. In this study, the SOEC (Solid Oxide Electrolyzer Cell), which is generally operated in the range of 700-1000 ^oC[6], is chosen for CO_2/H_2O dissociation and related thermodynamic analysis.

The MSAC (moisture-swing air capture) process employs an anionic exchange resin as the CO_2 sorbent, which absorbs CO_2 when dry and releases it when wet[7]. An optimum operating condition should consider the advantages from elevated temperature and the related energy penalty, which is about 45 ^oC[8] in this study. Since the partial pressure of regenerated CO_2 is on the order of several kPa, a vacuum condition for pure CO_2 production will be needed. In this study, liquid water is sprayed onto the sorbent to reduce the time for wetting. A moderate water consumption of 25 moles of water per mole of CO_2 is used[3].

Traditional high temperature processes for air capture is always energy intensive[9,10] and the temperature during the thermal decomposition process is usually at over 850 ^oC[11], which greatly reduces the feasibility of these technologies. However, since the regeneration temperature is close to the working temperature of high temperature electrolysis, the produced high temperature CO_2 gas could be directly fed to a HTE cell without additional heating. Nowadays, a titanate process technique developed by Mahmoudkhani et al.[10] requires a high-grade heat of 150 kJ/mol of CO_2, which is 50% less than conventional calcination. Considering the relatively low energy consumption, the titanate process with integrated high temperature electrolysis is analyzed as the other pathway for fuel synthesis.

Among the different post-combustion CO_2 capture technologies, systems based on amine solutions have been previously used industrially for more than half a century and are presently still one of the most suitable and widely employed technologies for high volume flue gas stream treatment[12]. The commonly used absorbents are typically 25–30 wt% aqueous solutions of alkanolamines such as monoethanolamine (MEA) and diethanolamine (DEA), which form carbamates and bicarbonates

with CO_2[13]. In this study, the amine regeneration is considered to have an energy requirement of 110 kJ/mol of CO_2 with 150 ^oC steam as the input heat source.

System and Parameters. Fig.2 shows the conceptual flow diagram of HTE for CO_2 and H_2O co-electrolysis and the gas parameters at the inlet and outlet of the heat exchangers and heater are given in Tab.1. System 1 is the fuel synthesis with integrated moisture-swing air capture (IFS-MSAC). Water vapor and CO_2 gas feeding to the electrolysis cell is provided simultaneously from the CO_2 stripper. System 2 is the fuel synthesis with integrated temperature-swing air capture (IFS-TSAC). High temperature CO_2 gas is generated through the 850 ^oC titanate process. High temperature water vapor is prepared in a separated heating device. System 3 is fuel synthesis with transported liquid CO_2 which could be captured from flue gas or ambient air. In systems 2 and 3, the exhaust steam is extracted from the turbine and then heated to 850 ^oC for electrolysis. By assuming the total electricity requirement of 1 MJ/Carbon for syngas generation, the steam consumption is around 0.13kg/kWh. The inefficiency of electricity generation due to low grade steam extraction should be insignificant.

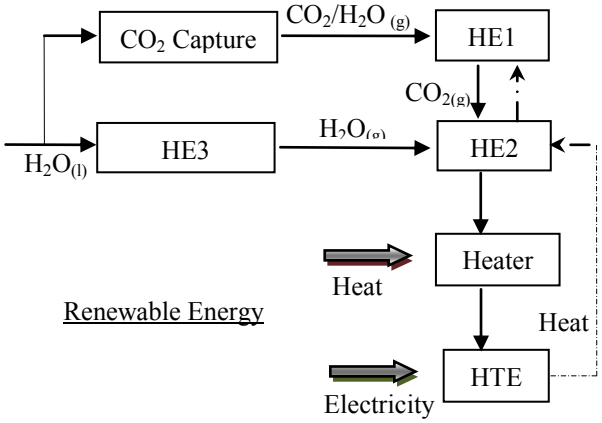

Fig.2 Conceptual flow diagram of HTE for CO_2 and H_2O co-electrolysis

Tab.1 System parameters for fuel synthesis

System		HE1	HE2	HE3	Heater
1	Feed Gas (in)[a]	14.25 kPa, 45 ^oC	100kPa, 100 ^oC	--	100kPa, 662 ^oC
	Feed Gas (out)	16.7 kPa, 100 ^oC	100kPa, 662 ^oC	--	100kPa, 850 ^oC
	Production Gas (in)	107 ^oC	850 ^oC	--	--
	Production Gas (out)	50 ^oC	107 ^oC	--	--
2	Feed H_2O (in)[b]	--	100 kPa, 100 ^oC	[c]	--
	Feed H_2O (out)	--	100 kPa, 850 ^oC	100 kPa, 100 ^oC	--
	Production Gas (in)	--	850 ^oC	--	--
	Production Gas (out)	--	240 ^oC	--	--
3	Feed Gas (in)	100 kPa, 25 ^oC	100kPa	[c]	100kPa, 670 ^oC
	Feed Gas (out)	100 kPa, 100 ^oC	100kPa, 670 ^oC	100 kPa, 100 ^oC	100kPa, 850 ^oC
	Production Gas (in)	102 ^oC	850 ^oC	--	--
	Production Gas (out)	70 ^oC	102 ^oC	--	--

[a] The feed gas (CO_2/H_2O : 1/2) is compressed to 100 kPa at 100 ^oC before entering HE2.
[b] The CO_2 gas is fed directly into the electrolyzer without additional heating.
[c] Water vapor for electrolysis is directly extracted from exhaust steam of turbine.

Thermal energy at 850 ^oC is provided from renewable energy to satisfy the heat requirement for power conversion, electrolysis and high temperature calcination. The modular helium reactor (MHR) and advanced high temperature reactor (AHTR) are candidate nuclear reactor technologies for achieving heat around or above 850 ^oC[14]. Solar thermal power plants with volumetric receivers have been successfully demonstrated to generate high temperature working fluids (800-1200 ^oC)[15]. Electricity is assumed to be converted at high efficiencies of 42-52% with current gas turbine technologies. The majority of the electricity is consumed by the electrolyzer, with the remainder

divided among desalination, CO_2 capture and CO_2 compression. A solid oxide electrolyzer cell is employed at an electrical efficiency of close to 100%[2]. Water vapor and CO_2 gas with a molar ratio of 2:1 are co-electrolyzed at 850 ^oC and 100 kPa. For fuel synthesis with isolated CO_2 capture, the CO_2 is compressed to liquid at 10 MPa for transportation. The net efficiency of heat exchangers or heater is designed as 70%.

Methodology

The energy analysis could be used to understand the energy flows in the system while exergy analysis could identify the components with high irreversibility. The reference environment for the gas phase process is taken to be 298 K and 100 kPa. The reference environment for seawater desalination is taken to be 298 K and 3.5% salinity. Thermodynamic parameters, such as heat capacity, standard change of enthalpy and entropy, are cited from literatures[16].

Energy Analysis. The first law of thermodynamics is the fundamental of the energy analysis. Five processes, including CO_2 capture, compression, heating, desalination and electrolysis, are considered to be main energy consumption processes. Reference [3] has discussed the required energy for MSAC process, whose data will be used for energy analysis in this study. The practical energy requirement for desalination is assumed to be 3.7 kWh/m^3 water[17]. The energy requirement for co-electrolysis could be considered as 780 kJ when 1 mole of CO and 2 moles of H_2 are produced at 850 ^oC. The compression process and heating process are basic thermal process, whose energy required could be calculated by corresponding formula.

Exergy Analysis. In thermodynamics, the exergy of a system is the maximum useful work possible during a process that brings the system into equilibrium with a reference environment[18]. The exergy ananlysis is based on the second law of thermodynamics, and the exergy reduction of a process is proportional to the entropy production of the process. The exergy could be divided into physical exergy and chemical exergy, which can be calculated by formula (1) and (2) respectively.

$$e_{ph} = (h_j - h_0) - T_0(S_j - S_0) \quad (1)$$

$$e_{ch,mix} = \sum_{i=1}^{n} X_i e_{ch,i} + RT_0 \sum_{i=1}^{n} X_i \ln X_i \quad (2)$$

where e_{ph} is physical exergy, h_j is enthalpy, S_j is entropy, h_0, S_0 are enthalpy and entropy in the reference environment respectively, $e_{ch,mix}$ is chemical exergy of mixture, X_i is mole percent of a certain component in mixture.

The exergy reduction could be calculated as the difference between inlet exergy and outlet exergy, which could be expressed as formula (3).

$$E_L = E_{in} - E_{out} \quad (3)$$

where E_L is exergy reduction, E_{in} is inlet exergy, E_{out} is outlet exergy.

Kinetic energy and potential energy are ignored in this study.

Results and Discussions

The thermodynamic analysis is based on parameters representative of typical industrial processes of electricity generation, heat exchange, CO_2 capture, electrolysis, etc (Tab.2).

Energy Analysis. Fig.3 shows the energy required in different processes when syngas is produced. As expected, the electrolysis dominates the total energy requirement. The implementation of air capture is evaluated to have significant uncertainty in economic assessments considering technique and market development[19,20]. However, from the thermodynamic point of view, it shows that the total energy requirement of fuel synthesis would not be sensitive to CO_2 capture technologies. Compared to separated fuel synthesis with moisture swing air capture (SFS-MSAC), the integrated fuel synthesis with moisture swing air capture (IFS-MSAC) has higher energy consumption on CO_2 capture, which is dominated by sorbent heating and enthalpy of water vaporization at 45 ^oC. The

required low grade heat can be provided from the waste heat during electricity generation (WH-1 in Fig.3). The WH-2 is the waste energy available from high temperature syngas at the exit of the electrolyzer. Due to the advantage of recycling low grade heat for CO_2 capture with the moisture swing process, the integrated fuel synthesis with MSAC technology has the highest energy efficiency. Compared to traditional high temperature process for air capture, TSAC of the titanate process has a relatively low energy consumption in the heating part. However, it still has a large high-temperature heat requirement of 150 kJ/mol of CO_2 during the capture process[10]. Moreover, due to the strong internal heat exchange in the titanate process, the dependence of energy consumption on heat recuperation efficiency is significant. In the long term, fuel synthesis utilizing a moisture-swing air capture technology could have greater potential because of the smaller energy cost and local CO_2 supply.

Tab.2 Parameters for thermodynamic analysis

Parameter	Deterministic Value	Uncertainty Distribution
Heat recuperator efficiency	70%	(60%, 80%)
Electrolyzer efficiency	90%	(80%, 100%)
Electricity generation efficiency	46%	(42%, 50%)
Water consumption (mol/mol CO_2)	25	(15, 35)
Electrolyzer conversion efficiency	50%	(40%, 60%)
Capture mode	IFS-MSAC	(SFS-MSAC, SFS-Amine)
Electrolyzer heat source	Electricity	Hybrid heat-electricity

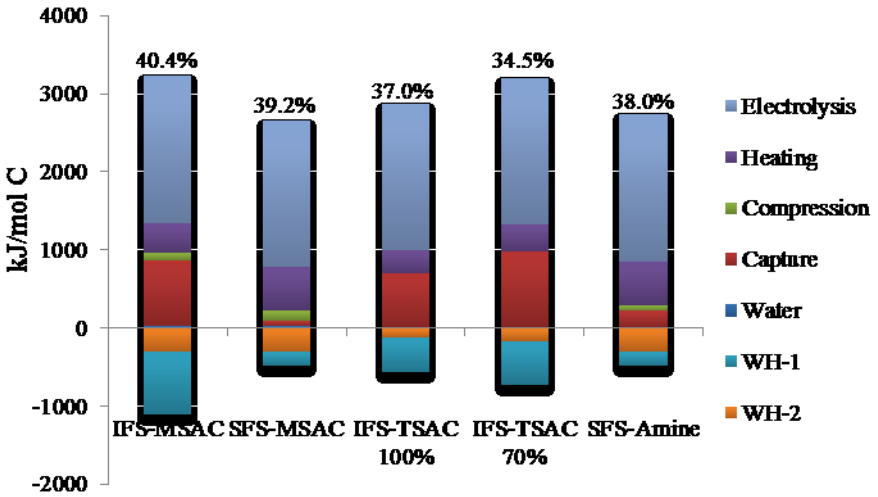

Fig.3 Energy requirement for fuel synthesis processes related to CO_2 capture technologies.

Exergy Analysis. The exergy analysis is based on three systems, IFS-MSAC, SFS-MSAC and SFS-Amine, with relatively lower energy consumption. Fig.4 shows the consumed exergy in the fuel synthesis processes. The minimum exergy requirement of the electrolysis is 780 kJ when producing 1 mole of CO and 2 moles of H_2 at 850 ^oC with electricity as the only input energy. The exergy output of syngas is 733 kJ with an ideal fuel cell at 25^oC. Fig.4 shows that the exergy consumption is dominated by the exergy output of syngas and exergy loss due to electricity generation. The electricity generation from high temperature heat consumes about one third of the total exergy requirement. From this point of view, for solar and nuclear energy, exploring fuel synthesis technologies with a lower electricity requirement (such as a hybrid sulfur cycle[21,22]) or direct chemical energy conversion without an electricity requirement (such as photosynthesis and phtoelectrolysis[23]) could be more exergy efficient.

The exergy consumptions related to CO_2 capture process, including the compression of CO_2, are listed in Tab.3. The moisture-swing air capture process generally has a larger energy consumption than that of an amine based flue gas capture as shown in Fig.3. However, the required exergy of MSAC could be smaller than that of an amine process. This is due to the consumption of high temperature steam when the amine sorbent is regenerated. The SFS-MSAC system has the largest

exergy consumption on CO_2 capture. For CO_2 transportation, additional electricity has to be consumed during air capture, such as water condensation and CO_2 compression. Waste heat is unavailable when air capture is isolated from the processes of fuel synthesis and electricity generation. Without the waste heat from electricity generation, the isolated moisture-swing air capture has to be conducted at room temperature rather than 45°C.

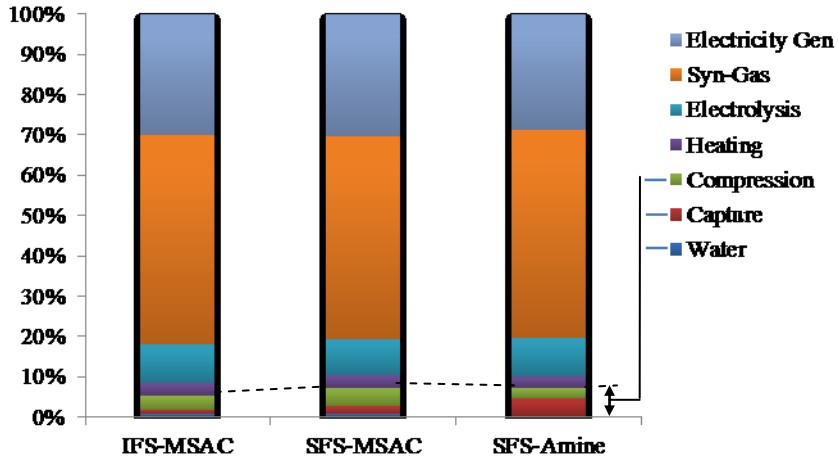

Fig.4 Exergy consumption and output for fuel synthesis processes related to CO_2 capture technologies.

Tab.3 Exergy consumption (kJ·mol^{-1} C) related to CO_2 capture

Parameter	IFS-MSAC	SFS-MSAC	SFS-Amine
Water	12.0	12.0	0.96
Capture	12.0	27.9	65.0
Compression	50.0	65.4	34.5
Total Exergy	74.0	105.3	100.5
Exergy Efficiency	52.0%	50.4%	51.7%

Although the CO_2 capture technology or process has a minor effect on the total exergy efficiency due to the huge exergy requirement for electrolysis and electricity generation, this exergy analysis on CO_2 capture is helpful for other CO_2 utilization processes. Tab.3 shows that for moisture swing air capture technology, the exergy requirement is dominated by compression of CO_2 from several kPa to 10 MPa for the goal of transportation. For the moisture-swing air capture, water is used as the only fuel to drive the gas separation. The free energy is provided from water evaporation and the use of heat for sorbent regeneration can be avoided. Therefore, the production of clean and low partial pressure CO_2 can be energy efficient and attractive for in-situ CO_2 utilization or conversion processes. For example, at CO_2 partial pressures of 5-10 kPa, the microalgae generally have the maximum growth rates[24-26]. The weathering process of minerals on the surface of the earth, especially the ultramafic tailing, can be enhanced when CO_2 partial pressure is elevated from atmospheric level to several kPa[27].

Sensitivity Analysis. To assess the sensitivity of the energy and exergy consumption to changes in CO_2 capture technologies and parameters of energy conversion and transfer, uncertainties were assigned to several parameters. The integrated fuel synthesis with moisture swing air capture technology was selected to study due to several advantages of independence on CO_2 source, requirement of low grade heat and no requirement of CO_2 transportation. The energy conversion parameters of interest are the electricity generation efficiency, conversion efficiency of electrolyzer, electricity efficiency of electrolyzer and heating source of high temperature electrolyzer. The carbon capture parameters of interest include water consumption and technological processes, such as separated air capture and amine based flue gas capture. The parameters of the electrolyzer were determined based on the current technical development of a solid oxide electrolyzer cell[7,28]. Values of the input parameters for the sensitivity analysis are shown in Tab.2.

Energy and exergy efficiencies obtained with deterministic values in Tab.2 are 40.4% and 52.0% respectively. The energy efficiency and exergy efficiency have similar sensitivity to the studied

parameters, shown in Fig.5. Electricity efficiency of the electrolyzer and efficiency of electricity generation have the most significant impact on thermodynamic performance. It is interesting to find that both the energy and exergy efficiency are very sensitive to the source of high temperature heat for the electrolyzer. With current technologies of HTE, the high temperature heat is generally provided from the ohm heat by consuming electricity[2]. However, by supplying heat directly from a heat source rather than from electricity, the system efficiency increase could reach the same level as that with very high electricity generation efficiency. It implies that, for this fuel synthesis system, the process optimization can be as important as innovation of technologies of electrolysis or electricity generation. For example, in order to have similar energy or exergy efficiency enhancement, one has to increase the efficiency of electricity generation from 42% to more than 50%, which would be very difficult for current or advanced power plants.

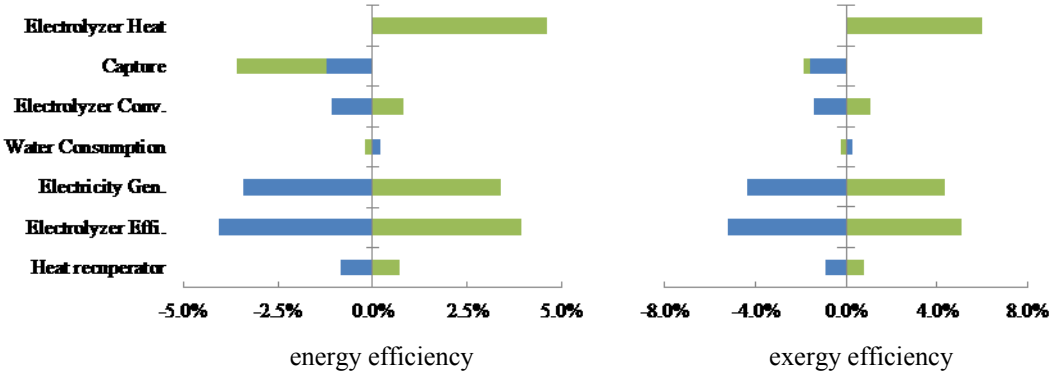

Fig.5 Sensitivity analysis on energy and exergy efficiency of the fuel synthesis system

The only exception, when comparing the sensitivities of energy efficiency and exergy efficiency, is the effect of the carbon capture process. As discussed above, the carbon capture process with amine has higher energy and exergy requirements compared to moisture swing air capture. However, the exergy efficiency is less sensitive to the CO_2 capture process due to heat consumption rather than electricity consumption when conducting amine based technology.

Conclusions

Energy and exergy analyses have been conducted to study the thermodynamic performance of fuel synthesis systems with heat from renewable energy, and CO2 captured from ambient air or flue gas. The results of the present investigation indicate that:

a) Compared to the energy consumed by electrolysis, the energy penalty from CO2 capture is insignificant. That is, the total energy requirement of fuel synthesis is not sensitive to CO2 capture technologies. This indicates the feasibility of air capture when integrated into the conversion of CO2 to high value products.

b) By choosing thermal energy, rather than electricity, from renewable energy as the direct heat source for high temperature electrolysis, the thermodynamic efficiencies could be enhanced greatly. This suggests the importance of process optimization for fuel synthesis with renewable energies. A system with lower electricity requirements is preferred, especially when using solar and nuclear energy.

c) Although energy and exergy analysis both show that fuel synthesis is not sensitive to CO2 capture technologies from the thermodynamic point of view, the advantages of direct air capture processes are still obvious, such as local CO2 capture and conversion. Moreover, the air capture unit can be integrated into renewable energy systems, both thermodynamically and physically.

Acknowledgements

This work was financially supported by the National Natural Science Foundation of China (51306161), the Natural Science Foundation of Zhejiang Province, China (LY13E060004) and the Doctoral Fund of Ministry of Education of China (20130101120143).

References

[1] Xie Heping, Xie Linzhi, Wang Yufei, Zhu Jiahua, Liang Bin, Ju Yang. [J]. JOURNAL OF SICHUAN UNIVERSITY, 2012, 44(4): 1-5 (In Chinese)
[2] Graves C, Ebbesen S D, Mogensen M, Lackner K S. [J]. Renewable and Sustainable Energy Reviews, 2011, 15(1): 1-23
[3] K. S. Lackner, Thermodynamics of the Humidity Swing Driven Air Capture of Carbon Dioxide, GRT LLC[C], Tucson, AZ ,2008
[4] Wang Tao, Lackner K S, Wright A B. [J]. Phys. Chem. Chem. Phys., 2013, 15: 504-514
[5] Wang T. Fuel Synthesis with CO2 Captured from Atmosphere: Thermodynamic Analysis//ECS Transactions[C], Boston: Volume 41, 2011
[6] Jensen S H, Larsen P H, Mogensen M. [J]. International Journal of Hydrogen Energy, 2007, 32(15): 3253-3257
[7] Wang T, Lackner K S, Wright A. [J]. Environmental Science Technology, 2011, 45: 6670-6675
[8] Lackner K S. [J]. The European Physical Journal Special Topics, 2009, 176(1): 93-106
[9] Zeman F. J]. Environmental Science Technology, 2007, 41: 7558-7563
[10] Mahmoudkhani M, Keith D W. [J]. International Journal of Greenhouse Gas Conversion, 2009, 3(4):376-384
[11] Nikulshina V, Ayesa N, Galvez M E, Steinfeld A. [J]. Chemical Engineering Journal, 2008, 140(1-3): 62-70
[12] Goeppert Alain, Czaun Miklos, Surya Prakash G K, Olah G A. [J]. Energy Environ. Sci., 2012, 5: 7833-7853
[13] Kohl A, Nielsen R. Gas Purification [M]. 5th edition. Houston: Gulf Publishing Company, 1997: 95-103
[14] Yildiz B, Kazimi M S. [J]. International Journal of Hydrogen Energy, 2006, 31(1): 77-92
[15] Avila-Marin A. L. [J]. Solar Energy, 2011, 85(5): 891-910
[16] Smith J M, Ness H C V, Abbott M M. Introduction to chemical engineering thermodynamics [M]. 6th edition. Boston: McGraw-Hill, 2001: 631-689
[17] Elimelech M, Phillip W A. [J]. Science, 2011, 333: 712-717
[18] Rosen M A, Scott D S. [J]. International Journal of Hydrogen Energy, 1992, 17(3): 199-204
[19] M. Ranjan and H. J. Herzog[J]. Energy Procedia, 2011, 4: 2869-2881
[20] Direct Air Capture of CO2 with Chemicals [M], The American Physical Society, College Park, MD, 2011.
[21] Hinkley J T, O'Brien J A, Fell C J, Lindquist S-E. [J]. International Journal of Hydrogen Energy, 2011, 36(18): 11596-11603
[22] Takai T, Kubo S, Nakagiri T, Inagaki Y. [J]. International Journal of Hydrogen Energy, 2011, 36(8): 4689-4701
[23] Khaselev O, Turner J A. [J]. Science, 1998, 280(5362): 425-427
[24] Hanagata N, Takeuchi T, Fukuju Y, Barnes D J, Karube I. [J]. Phytochemistry, 1992, 31(10): 3345-3348
[25] Kodama M, Ikemoto H, Miyachi S. [J]. J. Mar. Biotechnol., 1993, 1: 21-25
[26] Kativu E, Hildebrandt D, Matambo T, Glasser D. [J]. ENVIRONMENTAL PROGRESS & SUSTAINABLE ENERGY, 2012, 31(1): 24-28
[27] Wilson S A, Barker S L L, Dipple G M, Atudorei V. [J]. Environmental Science Technology, 2010, 44(24): 9522-9529
[28] Zhan Z, Kobsiriphat W, Wilson J R, Pillai M, Kim I, Barnett S A. [J]. Energy & Fuels, 2009, 23: 3089-3096

Advanced Materials Research Vols. 960-961 (2014) pp 316-321

doi:10.4028/www.scientific.net/AMR.960-961.316

Heat transfer characteristics of MEPCMS in turbulent flow: a review

Mei He [1, a], Zhongzhu Qiu[2,b] and Pan Zhang [3,c]

[1,] College of Energy and mechanical engineering, Shanghai University of Electric Power, 2103 Pingliang Road, Shanghai, China

[a]hemei90328@126.com, [b] 1050079260@qq.com

Keywords: heat transfer coefficient, degree of turbulence, heat transfer correlations

Abstract. This article mainly makes a brief introduction about Microencapsulated Phase Change Material Slurries(MEPCMS) and its preparations， the research status and several correlations of heat transfer in turbulent flow of MEPCMS are also listed.The influencing factors of turbulent heat transfer are mainly the degree of turbulence, the mass fraction and wall heating rate,particle size effects weakly. Several heat transfer correlations under different degrees of turbulence are also presented.

Introduction

Energy is the motive force of social development and the foundation of human survival.With the development of science and technology and the increasingly prominent energy and environment problems, the problems of heat transfer,heat and cold storage have emerged in the fields of power, metallurgy, chemical engineering and technology.Since the limited heat transfer ability of ordinary fluid can not meet the actual needs, in this case, the functional fluids with higher heat transfer capability are needed[1，2].

Microencapsulated Phase Change Material(MEPCM) is the new material which is fabricated by the PCM(Phase Change Material) as core material and polymer as wall material[3，4].The diameter varies from 1μm to 1000μm. Microencapsulated particles can be mixed with fluids(water,ethylene glycol ect.) to form MEPCMS.Since they can store or reveal a lot latent heat and they have very large specific surface area, MEPCM can effectively hance the process of heat transfer.

Due to the complex heat transfer mechanisms of the MPCM slurry flow and narrow ranges of experimental conditions applied for each investigation.Only a few correlations were proposed to describe the melting heat transfer characteristics of MPCM slurry flows in a circular pipe.

The requirements of material

The MEPCM chosen should satisfy the following requirements:

1) High latent heat so that can be stored or released more heat in the phase change process ;

2) It has small reversibility and expansion shrinkage ratio,the same to the undercooling and overheating in the phase change process;

3) Appropriate phase change temperature can satisfy the need to control the specific temperature;

4) Large heat conductivity coefficient,density and specific heat;

5) It should be innocuous, non-corrosive,low costing and easily manufactured.

Compared with the traditional fluids,MEPCMS has higher heat transfer coefficient. The comparison of some microencapsulated PCMS from literature and prepared microencapsulated PCM are given in table 1.

Manufacturing

There are several methods which can be used to produce microencapsulated particles, such as spray-drying and fluidized bed process for physical approaches; and there are also chemical processes which can be used for microencapsulation, such as simple and complex coacervation, interfacial polymerization，in situ polymerization and so on.[5，6] The appearance is shown in fig 1.

Table 1 The comparison of some microencapsulated PCMS from literature and prepared MEPCM

Microcapsule shell	Core material	Encapsulation ratio wt%	Microcapsue diameter. μm	T_m	ΔH_m J/g	Method
Polyurea	n-Eicosane	75	—	35.7	55.5	Interfacial polymerization
Melamine-formaldehyde	n-Octadecane	59	2.2	40.6	144.0	In situ polymerization
Polyurea	Hexadecane	-	2.5	15.5	66.1	Interfacial polycondensation
Polyurea	Butyl stearate	66	20-35	28.6	76.3	Interfacial polycondensation
Melamine-formaldehyde	n-Octadecane	70	9.2	30.5	169.0	In situ polymerization
Urea-melamine-formaldehyde	n-Octadecane	72	0.8	36.5	167.0	In situ polymerization
Urea-melamine-formaldehyde	n-Nonadecane	69	—	30.3	233.0	In situ polymerization
Urea-melamine-formaldehyde	n-Eicosane	71	—	45.3	172.0	In situ polymerization
Melamine-formaldehyde	n-Octadecane	40	1.6	—	166.0	Emulsion polymerization
Melamine-formaldehyde	Lauryl alcohol	75	9.2	—	—	In situ polymerization
Polymethylmethacrylate	n-Docosane	28	0.16	41.0	54.6	Emulsion polymerization
Polymethylmethacrylate	n-Eicosane	35	0.7	35.2	84.2	Emulsion polymerization

Fig 1 The appearance of MEPCMS

Research status and heat transfer correlations

Several researchs have been conducted to explore the flow and heat transfer properties of MEPCMS.

Kasza and Chen[7] conducted an analytical study to investigate the heat transfer performance of solar energy or waste heat utilization system using phase change slurries and explored the potential benefits in reducing the pumping power and the storage tank size. They claimed that heat transfer performance of slurry flow in both laminar and turbulent conditions would increase because of the microconvective enhancement of thermal conductivity and latent-heat-induced heat capacity. Charunyaorn et al.[8] developed a model to predict the laminar MPCM slurry flow in a heated circular duct and showed about 2–4 times increase of the Nusselt number compared with single phase fluid flow. Goel et al.[9] conducted the heat transfer test of laminar MPCM flow in a heated circular pipe and confirmed the validity of numerical results of Charunyaorn et al. Other related numerical investigations of laminar MPCM slurries flow include the works of Zhang and Faghri,[10] Alisetti and Roy,[11] Hu and Zhang,[12] and Ho et al.[13]. All previous investigations in laminar MPCM slurry flow showed that the particle concentration and latent heat were dominating parameters in heat transfer enhancement, whereas the effects of specific heat ratio ($C_{P,P}/C_{p,f}$), thermal conductivity ratio k_p/k_f), and particle size were relatively weak.

Choi et al.[14] measured the local pressure drop and heat transfer coefficient of turbulent phase change emulsion flow (mixture of water and PCM with additive of emulsion) with 10% particle mass concentration in a horizontal tube with constant heating rates. They observed a significant enhancement in heat transfer performance because of the latent heat effect when PCM melted. They also found that both the local heat transfer coefficients and pressure drop along flow direction varied significantly when PCM melted, which made it difficult to determine the heat transfer coefficient. Yamagishi et al.[15] measured the pressure drop and local convective heat transfer coefficients of turbulent microencapsulated octadecane($C_{18}H_{38}$) slurry flow in a horizontal circular pipe with constant heating rates, and reported that heat transfer performance of MPCM slurry was influenced by the particle fractions, the degree of turbulence, and the heating rates on the tube wall.

Due to the reliable heat transfer data derived by former researchers in a horizontal circular pipe with constant heating rates. Several empirical correlations have been reported to predict the heat transfer characteristics of solid–liquid flow without phase change in the pipes.

Choi and Cho[16] calculated the local Nusselt number for the turbulent convective heat transfer of a single-phase fluid with combined thermal developing and hydraulic developed regions at the constant heating rates.

$$Nu_x = 0.00425\,\mathrm{Re}_{lb}^{0979}\,\mathrm{Pr}_{lb}^{0.4}(\mu_{1w}/\mu_{1b})^{-0.11} \tag{1}$$

where water dynamic viscosity μ_{1b} was evaluated based on the local mean temperature of the fluid and water dynamic viscosity, μ_{1w}, was calculated based on the local wall inner surface temperature.

Salamone and Newman [17] investigated the heat transfer of the water suspensions of solid particles of copper, carbon, chalk, and silica with various size ranges from 1.5 to 56 lm and with concentrations varying from 2.3% to 10.7% (by volume) in a horizontal pipe and derived the following correlation:

$$Nu = 0.131\mathrm{Re}^{0.62}\,\mathrm{Pr}^{0.72}(\frac{k_p}{k_f})^{0.06}(\frac{D}{d_p})^{0.05}(\frac{C_{P,P}}{C_{p,f}})^{0.35} \tag{2}$$

for 14,000≤Re≤140,000，3.4≤Pr≤12.7,0.53≤k_p/k_f≤12.7，282≤D/d_p≤10,500,and 0.09≤$C_{P,P}/C_{p,f}$≤0.22,where $C_{P,P}$ is the specific heat capacity of the MPCM particles, k_p is the thermal conductivity of the MPCM particles

Xichun Wang and Jianlei Niu [18]presented the heat transfer characteristics of MEPCMS flow in a horizontal tube,they proposed a new heat transfer correlation for the slurry under slightly turbulent condition.

$$Nu_m = 4.8527\times10^{-4}\,\mathrm{Re}_m^{0.7733}\,\mathrm{Pr}_m^{2.7941}\,Ste^{0.3159}\times[(L_1+L_2)/D]^{-0.333}(\mu_m/\mu_w)^{-2.4349} \tag{3}$$

for 2100<Re<3500，13<Pr<15，and 0.05<w_p<0.1,where w_p is the mass fraction of MPCM particles in the slurry, phase change region length $[(L_1+L_2)/D]$, μ_m is the average dynamic viscosity of the slurry in the phase change region and μ_w the average dynamic viscosity of water calculated based on the inner tube wall temperature.

Conclusions

Turbulent slurry flows are not only affected by the mass fraction and wall heating rate, but are greatly influenced by turbulent degree. About 1–2.5 times higher average Nusselt number relative to pure water was found for turbulent slurry flow, whereas a degradation of heat transfer performance was found at a higher particle load of the slurry.

Several turbulent heat transfer correlations were proposed by other researchers,which predicts the average heat transfer data. The new correlations, derived based on the series of experiments covering in both laminar and turbulent flow conditions, should be useful for the design of the new compact heat exchangers with MPCM slurry applications.

In adition, turbulent heat transfer correlations under different degree of turbulence should be proposed to meet the needs of practical engineering.

Acknowledgements

The author appreciate the financial support from the Shanghai Engineering Research Center of Power Generation Environment Protection

References

[1] P. Zhang, Z.W. Ma，R.Z. Wang. Renewable and Sustainable Energy Reviews 14 (2010) 598–614.

[2] Lazarus Godson, B. Raja， D. Mohan Lal， S. Wongwises. Renewable and Sustainable Energy Reviews 14 (2010) 629–641.

[3] Cho J, Kwon A, Cho C. Colloid. Polym. Sci. 2002，280(3): 260–266

[4] Hawlader M N A, Uddin M S, Khin M M. Appl. Energ., 2003, 74: 195–202

[5] Jianli Li,Ping Xue,Jinmin Han. The preparation and evaluation method of microcapsulated phase change materials [J]．2007，34(9), In Chinese

[6] Fan Yang,Guigen Fang,Lin Xing.Refrigeration technology，2007，34(5), In Chinese

[7] Kasza KE, Chen MM. J Solar Energy Eng. 1985;107:229–236.

[8] Charunyaorn P, Sengupta S, Roy SK. Int J Heat Mass Transfer. 1991;34:819–833.

[9] Goel M, Roy SK, Sengupta S. Int J Heat Mass Transfer. 1994;37:593–604.

[10] Zhang Y, Faghri A. J Thermophys Heat Transfer. 1995;9:727–732.

[11] Alisetti EL, Roy SK. J Thermophys. 1999;14:115–118.

[12] Hu X, Zhang Y. Int J Heat Mass Transfer. 2002;45:171–190.

[13] Ho CJ, Lin JF, Chiu SY. Numer Heat Transfer A. 2004;45:171–190.

[14] Choi E, Cho YI, Lorsch HG. Int J Heat Mass Transfer. 1993;37:207–215.

[15] Yamagishi Y, Takeuchi H, Pyatenko AT. AIChE J. 1999;45:696–707.

[16] Choi E, Cho YI. Heat Transfer. 1995;7:283–288.

[17] Salamone JJ, Newman M.. Ind Eng Chem. 1955;47:283–288.

[18] Xichun Wang ,Jianlei Niu, Yi Li. Heat Transfer of Microencapsulated PCM Slurry Flow in a Circular Tube.[J] AIChE Journal,2008,54(4)1110-1120.

Advanced Materials Research Vols. 960-961 (2014) pp 322-326

doi:10.4028/www.scientific.net/AMR.960-961.322

The effects of surface shape of microchannels on methane/moist air catalytic combustion

Jingyu Ran[1,2,a], Ruirui Wang[1,2,b] ,Wenjie Qi[1,2,c] and Junlei Wang[1,2,d]

[1] Key Laboratory of Low-Grade Energy Utilization Technologies and Systems of Ministry of Education,Chongqing University,Chongqing,400044,China

[2] College of Power Engineering, Chongqing University,Chongqing,400044,China

[a]ranjy@cqu.edu.cn, [b]wangruirui2324@gmail.com,[c]407059331@qq.com,[d]just4pipi@126.com

Keywords: microchannel, groove, shape factor, Catalytic combustion.

Abstract. This paper studied the methane/moist air combustion characteristics in smooth microtube and microtubes with five different shape grooves and proposed the microtube groove dimensionless shape factor $F=4\pi S/L^2$. The results show that the appearance of five grooves make combustion components and velocity occur jumping change and the vortex flow appears. The highest methane conversion rate is for the microtube with triangle grooves, which also indicates that the smaller shape factor is more in favor of methane conversion.

Introduction

At present, the micro-scale combustion problem has become the forefront of international research, the study has not only academic value, but a guiding significance for the corresponding areas[1]. Due to the decrease of the scale, the residence time of fuel in combustion chamber is sharply reduced, it is difficult to ensure that the fuel can complete combustion. What's more, the increased surface-to-volume ratio of micro-reactors leads to thermal and radical quenching of reactions and the heat loss is even serious. Catalytic microcombustor exhibits wider stability than homogeneous micro-combustor[2].The catalytic layer deposited on the reactor walls may sustain chemical reactions at lower temperatures and in the presence of higher heat losses, thus reducing the impact of thermal quenching.

Recently, most research activities in the field of catalytic combustion has emphasized on the use of methane, mainly for its nature of clean fuel, widely available world-wise. Nonetheless, methane is inherently the most stable, difficult-to-oxidize hydrocarbon with outstanding characteristics that its catalytic ignition occurs at relatively high temperature even on the most active and expensive PdO-based catalysts. Some strategies were proposed to overcome the shortcoming, such as preheating the fuel-air gas, adding hydrogen in methane-fuel and proposing new catalyst layout to improve hetero and homo-geneous reaction in a confined space. Undoubtedly, a proper combustor configuration and a well designed catalyst bed can improve the reaction and reduce heat and radical loss. Federici et al.[3]demonstrated that the thermal properties of reactor materials play a vital role in the overall thermal stability of micro-reactors. The reactor walls not only contribute to heat loss through conduction, but they are often responsible for the majority of heat transfer from upstream, which is necessary to preheat the feed to ignition temperature. Yueh-Heng Li et al.[4] proposed a configuration of catalyst segmentation with cavity to accelerate the methane conversion in a microreactor.

To extend the operation range and to study the interplay of methane/moist air reactions in microchannel-reactors, this paper simulated the methane/moist air catalytic combustion with fluent software in mirochannels with different wall shapes and analyzed the impact of different surface shape factors on the methane/moist air catalytic combustion .

Numerical Model and Chemical Mechanical

Physical Model. The physical model adopted diameter 1mm, long10mm microtubes with the wall owning different grooves. Fig.1 only shows a schematic diagram of a smooth tube and microtubes with five small groove of different shapes. The groove shapes and size are rectangular (0.1mm×0.2mm), triangle (two right-angle side: 0.1mm,0.2mm),isosceles trapezoid (bottom 0.2mm, lower base 0.1mm, height 0.1mm),respectively. The shape of each tube channel was calculated separately by groove number from zero to five, and the groove laid along the wall by way of groove spacing arithmetic increments, i.e. 0.5mm, 1.0mm, 1.5mm, 2.0mm. The wall thickness of each microtube is 1mm. To study the catalytic combustion of methane/moist air heterogeneous reaction, all of the walls were coated with Pt catalyst inside, ignoring its effect on the reactor volume.

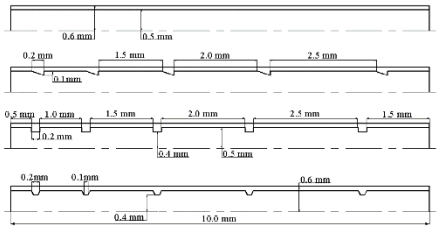

Fig. 1 Schematic diagram of a smooth tube and microtubes with five grooves of different shapes

Catalytic combustion mechanism. Surface catalytic reactions used a 24-step methane catalytic reaction mechanism on the Pt surface proposed by Deutschmann et al.[5], the mechanism includes nine kinds of gaseous components (CH_4, H_2, O_2, H_2O, CO_2, CO, O, H, OH) and eleven surface species (C(s), CH(s), CH_2(s), CH_3(s), CO(s), CO_2(s), H(s), H_2O(s), O(s),OH(s), PT(s)). The reaction mechanism has been widely used by numerical study of CH_4, H_2 and CO catalytic combustion,its accuracy has been demonstrated by literature[6].

Calculation methods and working conditions. According to the structure of the micro cavity, we used the structured grids and the grid size was taken as 0.01mm, the wall grids were handled with encryption processing. Grid sensitivity test should be carried out for combustion cases before the numerical simulation starts, the total number of mesh grid cells was 34033-35000 for microtubes with and without grooves. Laminar flow and species transport models were used and the solving method was the SIMPLE algorithm. Velocity inlet and pressure outlet boundaries were setted. The outer wall was insulating, while the inner wall surface was coupled with the flow region. This article is simulated at 573K, 0.1MPa environment, methane/moist air inlet equivalence ratio (0.5,0.8,1.0,1.2) and the inlet velocity (0.5m/s, 0.8m/ s, 1.0m/s, 1.2m/s) were changed separately in turn for different microchannels.

Results and discussion

To investigate the influence of different groove shape on the combustion characteristics of the microtubes, according to the microtube dimension characteristics, this article assumes microtube groove dimensionless shape factor $F=4\pi S/L^2$,where S is the area of a single groove, L is the

perimeter of a single groove. i.e., the shape factor of a single groove is a triangular groove F1=0.37,a rectangular groove F2=0.70, a trapezoidal groove F3=0.69, respectively.

Combustion characteristics of microtubes with different groove shapes.

When the methane/moist air equivalence ratio is 0.5 and inlet velocity of 1m/s, the combustion characteristics of smooth microtube and microtube with one single different groove are as follows:

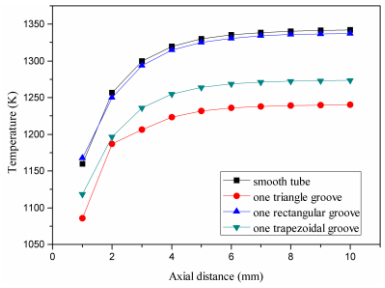

Fig. 2 Temperature along axial distance for smooth tube and tube with one groove

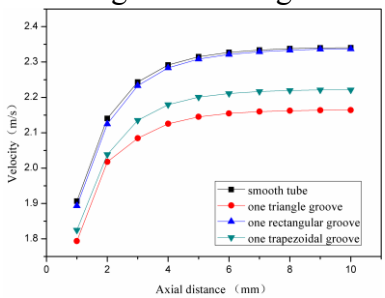

Fig. 3 Velocity along axial distance for smooth tube and tube with one groove

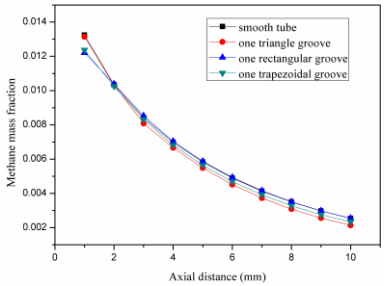

Fig. 4 Methane mass fraction along axial distance for smooth tube and tube with one groove

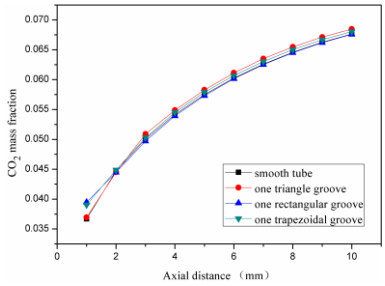

Fig. 5 CO_2 mass fraction along axial distance for smooth tube and tube with one groove

From Fig.2 and Fig.3 we can see that the variation tendency of methane/moist air combustion temperature and velocity along axial distance for different microchannels is basically the same. Fig.2 shows the outlet temperature is different: the smooth tube has the highest temperature of about 1350K, tube with a rectangular groove followed, and the tube with a triangular groove has the lowest temperature. This is because the groove in the microchannel increased wall roughness, thereby affecting the residence time of the combustion gas. Fig.3 shows that the velocity of smooth microtube is the maximum, and the microchannel with a triangular groove has the minimum velocity. As shown in Fig.4 and Fig.5, the average cross-sectional mass fraction of methane decreases along the axial distance, while the mass fraction of CO_2 is gradually increased. The methane mass fraction of the microchannel with a triangular groove is the lowest, which means small shape factor is in favor of methane conversion. A single groove on the overall average mass fraction of each component is not affected.

Impact of multiple grooves on catalytic combustion.

The paper studied the effects of multigroove microtubes (as shown in Fig.1) on the combustion characteristics under the inlet velocity is 1m/s and equivalence ratio is 0.5. Fig. 6 shows that the cross-section temperature gradually increased along the axial distance, the temperature of microtube with five triangular groove whose shape factor is also the lowest is still the lowest . As can be seen in the vicinity of 6mm occurs temperature jump because the appearence of grooves here makes the cross-sectional area decreases, the residence time is reduced and fuel combustion is not sufficient,

all of which lead to the temperature reduces. Fig. 7 shows that the appearance of five grooves make significant changes in the fuel flow lines, the horizontal velocity decreases near the grooves, increasing the vertical velocity, and the vortex flow appeares.

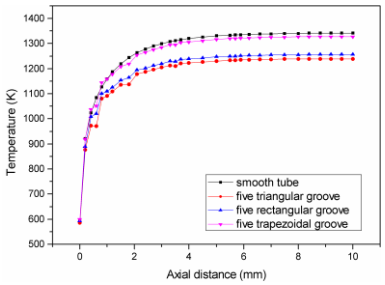

Fig. 6 Temperature along axial distance for smooth tube and tube with five grooves

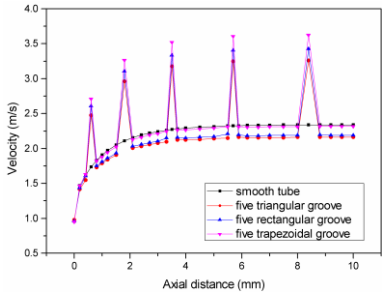

Fig. 7 Velocity along axial distance for smooth tube and tube with five grooves

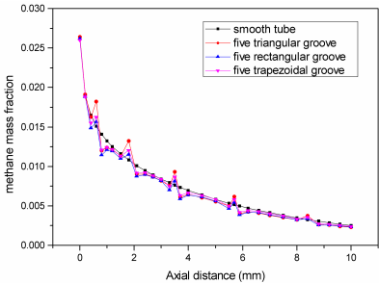

Fig.8 Methane mass fraction along axial distance for smooth tube and tube with five grooves

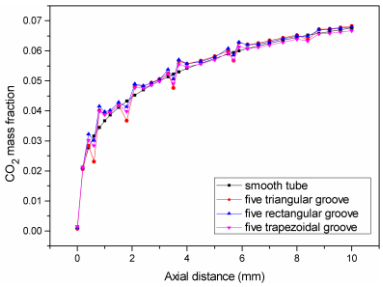

Fig.9 CO_2 mass fraction along axial distance for smooth tube and tube with five grooves

Fig.8 and Fig.9 show that the appearance of tiny grooves inside the microchannels making the combustion components occur jumping change, the overall trend is consistent of the smooth microtube. As for the tubes with five grooves, the area of fuel contact with the catalytic surface is increased, which promotes the methane conversion rate. The methane conversion of tube with five triangular groove (shape factor is the lowest) is the highest .

Effect of the shape factor on methane conversion rate.

Fig.10 and Fig.11 show methane conversion rate decreases with the increase of inlet velocity in the smooth microtube under the same equivalence ratio. When the inlet velocity increased, the residence time of fuel will be reduced, which leads to incomplete combustion and the methane conversion rate decreases. Methane conversion rate first decreases and then increases with the increase of equivalence ratio in the smooth microtube under the same inlet velocity. This is because the change of equivalent ratio leads to the change of mass fraction of inlet component, equivalent ratio less than 1 is oxygen-enriched combustion, the smaller equivalent ratio, the more oxygen, methane conversion rate is higher.

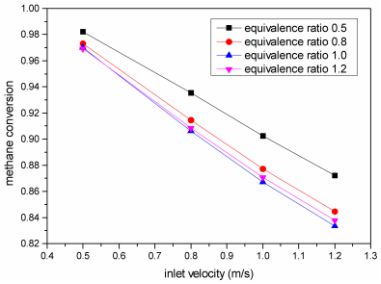

Fig.10 Schematic of methane conversion rate variation with inlet velocity in smooth tube

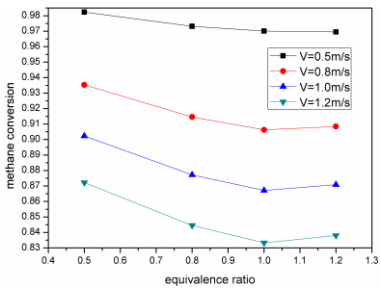

Fig.11 Schematic of methane conversion rate variation with equivalence ratio in smooth tube

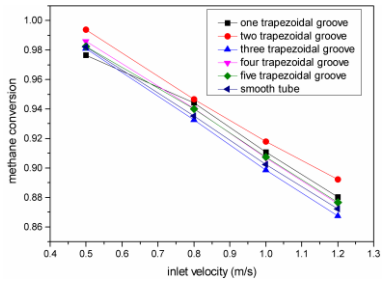

Fig.12 Influence of the groove number on methane conversion(equivalence ratio = 0.5)

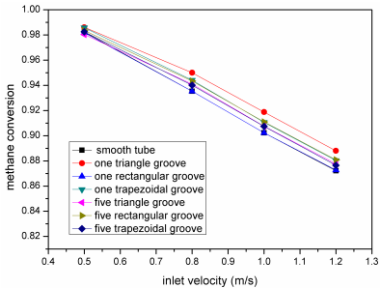

Fig.13 Influence of different shape factor on methane conversion (equivalence ratio = 1)

Fig.12 shows that the methane conversion rate decreases with the increasing of inlet velocity , and first increases then decreases with the decreasing of the groove number for the mirochannel with the same groove shape. The highest conversion rates is in microtubes with two trapezoidal groove. But the groove number has no significant impact on conversion rate.Fig.13 shows that for all of the microtubes, methane conversion rate decreases with the increasing of inlet velocity under the same equivalence ratio. That is the highest methane conversion occurs in the microchannels with the smallest shape factor (the microtube with a triangle groove), which indicates that the smaller shape factor is more favorable for the conversion of methane.

Conclusions

1.The variation tendency of combustion temperature and velocity along axial distance for different inner wall shape microchannels is the same. The mass fraction of methane decreases along the axial distance, while the mass fraction of CO_2 is gradually increased.

2.The appearance of five grooves makes significant changes in the fuel flow lines and it makes the combustion components occur jumping change, but the overall trend is consistent of methane and CO_2 mass fraction with the smooth microtube.

3.For all of the microtubes, methane conversion rate decreases with the increasing of inlet velocity under the same equivalence ratio. The smaller shape factor is more favorable for the conversion of methane.

Acknowledgements

This work was financially supported by the National Natural Science Foundation of China (51276207) and the National Natural Science Foundation of China (50876118).

References

[1] Loy Chuan Chia and Bo Feng: J. Power Sources Vol.165(2007),p.455

[2] N.S. Kaisare,S.R. Deshmukh and D.G. Vlachos: Chem. Eng. Sci. Vol.63 (2008),p.1098

[3]J.A. Federici, E.D. Wetzel, B.R. Geil , D.G. Vlachos: Proc. Combust. Inst.Vol.32(2009), p.3011

[4] Y.-H. Li,G.-B. Chen, H.-W. Hsu and Y.-C. Chao: Chem. Eng. J.,Vol.160 (2010), p.715

[5]Deutschmann O, Maier LI, Riedel U,et al. : Catal. Today, Vol.59(2000),p.141

[6]Norton D. G and Vlachos D. G.: P. Combust. Inst. Vol. 30(2005),p.2473

Advanced Materials Research Vols. 960-961 (2014) pp 327-331

doi:10.4028/www.scientific.net/AMR.960-961.327

Numerical Simulation on Separation Characteristic of an Elbow Bias-Oriented Rich-Lean Burner

Nan He[1, a], Xinghai Zhao[1, b]

[1]College of energy and power engineering, Northeast Dianli University, Jilin, Jilin, 132012, China

[a]angle_310_618@126.com, [b]ZXHDY2000XS@163.com

Keywords: Rich-Lean Burner, Bias Current Stopper, Partition Plate, Concentration Ratio, Speed Difference.

Abstract. In order to solve the problem of that the boiler burns inferior coal but cannot guarantee the combustion stability, the rich-lean burner divides primary wind pulverized coal airflow into two stocks of airflows containing different amounts of pulverized coal and sends the airflows into coal-fired furnace for improving the ignition characteristics. By the numerical simulation of the pulverized coal flow characteristics in an elbow bias-oriented rich-lean burner, regarding the "concentration ratio" and "speed difference" as the standard of evaluating the separation characteristic of the burner, considering the influence of the partition plate length, bias current stopper height and primary wind velocity to the separation effect of pulverized coal so as to provide technical assistances for the elbow bias-oriented rich-lean burner's practical application and improvement.

Introduction

According to Chinese current energy policy, as far as possible the inferior coal used in coal-fired power plant, and now for the coal and coal blending system has many shortcomings, power plant boiler burning coal quality is difficult to guarantee, coal-fired variable and high ash content, calorific value has a tendency to decrease. Lower grade of coal lead to boiler combustion instability and caused not broken oil in boiler start-up and low load operation, even appear put out the flame [1]. Therefore, we should take effective measures to solve the problem of stability of the boiler burning inferior coal combustion.

For the corners of our country generally used direct flow burner arrangement tangential firing way, because of duct layout produce pulverized coal concentration differences in horizontal direction, and only two angles of burner can satisfy the conditions of pulverized coal strong combustion. Therefore, can be add partition plate and bias current stopper to adjust the pulverized coal flow direction in the other two angles of burner [2].

A power plant 2# furnace use HG - 670/140-7 boiler is a production of Harbin boiler factory. In the power plant unit overhaul in 2012, the two layers of middle burner were transformed into elbow bias-oriented rich-lean burner [3]. See Fig.1.In diameter of 480 *mm* wind pipe bending export add bias current stopper and 1/2 partition plate, make the primary air flow in the burner outlet is divided into two strands of airflow, two air flow deviate their respective stoichiometric ratio, and this form of pulverized coal on the rich side is ignition area "Three Highs" [4]. So rich-lean combustion on the horizontal direction is come true in the furnace, which is beneficial to improve the combustion stability and reduce NO_X formation.

The Mesh and Calculation Condition

Mesh. The model is divided into three regions, elbow and mixing chamber adopt Hex /Wedge mesh, main burner use Tet/Hybrid grid and encrypted. See Fig.2.The model use a lot of structured grids are helpful to speed up the operation and iteration convergence. Based on different order of magnitude of grid and grid sensitive independence test, determine the grid conform to the requirements of the calculation precision.

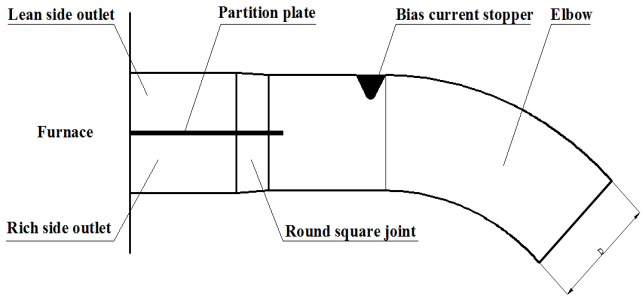

Fig.1 Structure diagram of the elbow bias-oriented rich-lean burner

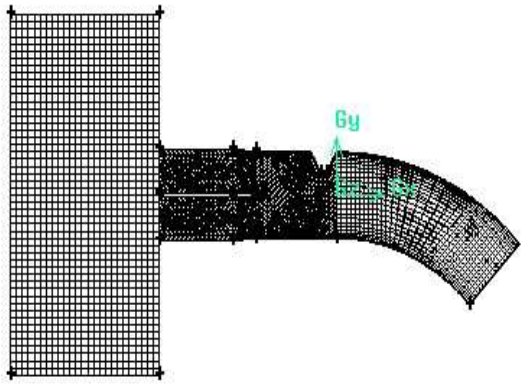

Fig.2 Schematic diagram of the mesh division of a burner

Calculation Condition

- Based on an equilateral triangle bias current stopper height of D/4 and angle 45 °of the elbow, add a partition plate from elbow (L)0.5D, 0.8D, D, 1.5D, 1.8D respectively, conduct particle trajectory tracking and numerical simulation analysis. Calculate conditions use the actual design conditions: the primary air velocity for 23*m/s*, the primary air pulverized coal concentration is 0.5 *kg*C/*kg*A, 60 μm of pulverized coal particle diameter, 1350 kg/m^3 of pulverized coal density.
- Based on distance elbow D partition plate, change the bias current stopper height of D/3 and D/4, conduct numerical simulation comparison.
- For the bias current stopper height of D/4 and partition plate from elbow length of D, simulate different primary air velocities effect on the separation result and contrast with the original design conditions of 23*m /s*.

Results and Discussion

Partition plate lengths effect on the separation result. No matter how far the partition plate distance elbow, the velocity of rich side outlet is always higher than the lean side outlet air flow, which is consistent with the result of the scene. Strong secondary flow of pulverized coal in the elbow generated by the centrifugal force, the mainstream high-speed fluid flow along the outside of the elbow, but the effect of the bias current stopper of the guide, high-speed air tent to concentrated side outlet and cause the rich side outlet flow velocity higher than the lean side. When the partition plate distance elbow length is 0.5D, pulverized coal of the rich side outlet is less than the lean side amount, which is due to the bias current stopper on the guiding role of coal particles is not fully realized, pulverized coal has separated by the partition plate, result in concentration ratio is less than 1. The result of particle phase movement trajectories at different partition plate lengths is shown in Fig. 3.

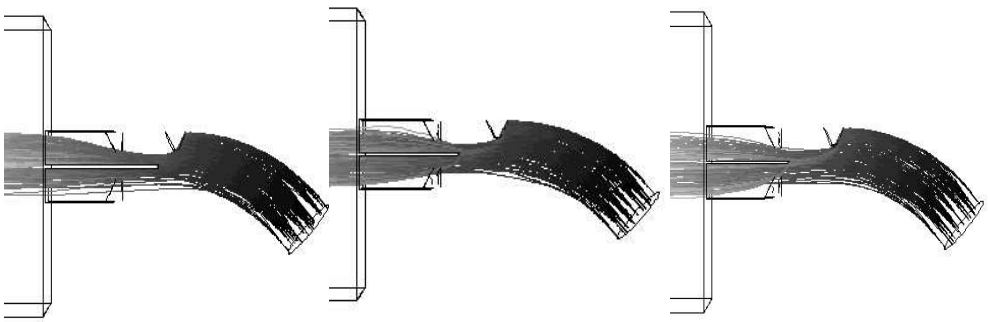

(a) (b) (c)

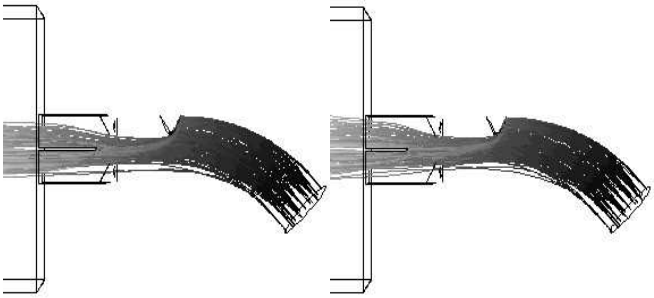

(d) (e)

Fig.3 Schematic drawing of the particle phase movement trajectories at different partition plate lengths

(a) L=0.5D*mm* (b) L=0.8D*mm* (c) L=D*mm* (d) L=1.5D*mm* (e) L=1.8D*mm*

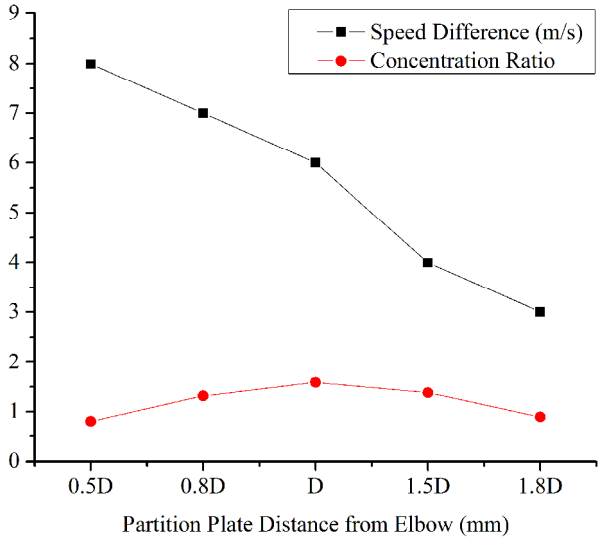

Fig.4 Law governing the change of speed difference and concentration ratio at the rich and lean outlet sides of burner with the plate lengths

Fig. 4 shows that with increasing partition plate and elbow distance, the both sides of export airflow speed difference is decreased, concentration ratio is increased then decreased after the first, when partition plate from elbow for D, concentration ratio reaches a maximum. This is because the partition plate is too far from elbow, the pulverized coal restore to the lean side that after guiding role of bias current stopper has been tented to the rich side, so the pulverized coal amounts of rich side outlet is decreased and the both sides of export airflow speed difference is decreased too.

Bias current stopper heights effect on the separation result. The bias current stopper height of D/3, a large number of coal particles flow from the rich side exit, both sides pulverized coal concentration ratio as high as 1.975, but with increasing the height of bias current stopper, both sides outlet air speed difference would increase to 14 *m/s* and increase the resistance significantly. Resistance of the burner increases with the height of bias current stopper. When the bias current stopper height of D/3, burner pressure drop of 1500*Pa*, when the bias current stopper height D/4, burner pressure drop of only 1000*Pa*. Therefore, excessive bias current stopper height although can get better pulverized coal concentration ratio, but weakened the ability primary air pulverized coal flow capacity and the speed difference of burner outlet is bigger, which is unfavorable to improve the life of burner nozzles and coal combustion stability. The result is shown in Fig. 5.

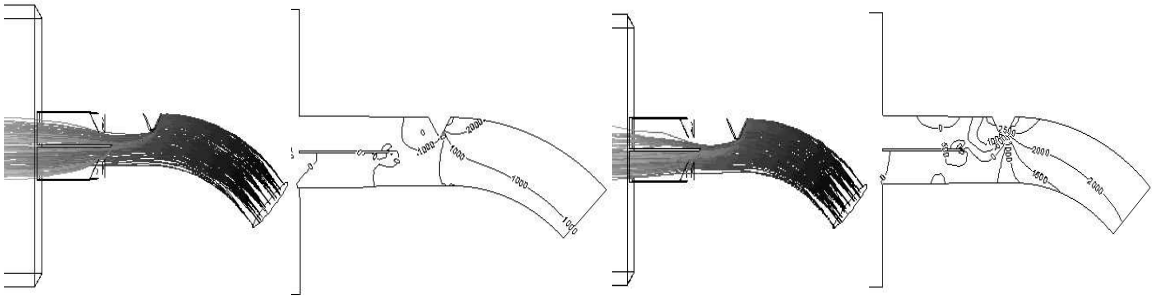

(a) (b)

Fig.5 Schematic drawing of the particle phase movement trajectories and static pressure distribution chart at different bias current stopper heights (a)H=D/4*mm* (b)H=D/3*mm*

Primary air velocities effect on the separation result. By condition 1, condition 2 simulation results show that within the burner equipped with the partition plate from elbow D and bias current stopper height of D/4 is combined, which is the best to improve the comprehensive performance of burner. In this combination of conditions, adjust the primary air velocity. A relationship between primary air velocity and concentration ratio is shown in Fig. 6.

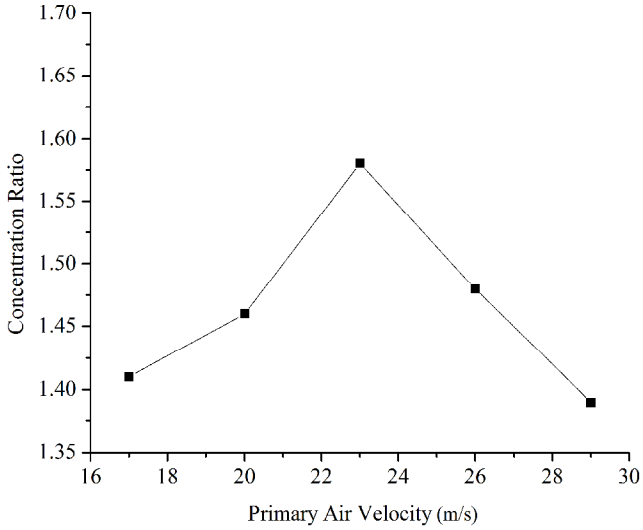

Fig.6 Law governing the change of the concentration ratio at the rich and lean outlet sides of burner with the primary air velocities

When the primary air velocity is less than 23*m /s*, coal particles momentum and inertia increase with the primary air velocity advances at the same time, and the airflow is better to follow. After the effect of bias current stopper adjust the airflow direction is easy to form a higher concentration ratio. Primary air velocity more than 23 *m/s*, concentration ratio would turn down, which is due to the different structure of the flow around the air flow when the air flows through the bias current stopper.

Conclusion

The partition plate from elbow too close will cause the both sides outlet of the burner speed difference bigger and pulverized coal concentration ratio less than 1, which is unable to guarantee the rich side pulverized coal combustion; the partition plate from elbow too far distance will lead to the rich side of pulverized coal to the lean side recovered and concentration ratio reduced, but the speed difference is decreased, which is conducive to protect the burner nozzle. The higher bias current stopper can enhance pulverized coal separation effect, but the burner resistance than normal run time increases by 500*Pa*, and the both sides outlet speed difference attains 14 *m/s*, which is disadvantageous to burner operation. Too low or too high primary air velocity will lead to poor

concentration ratio, when 23 *m/s* of primary air velocity for the design conditions, the pulverized coal concentration ratio than most, so should be as possible as to ensure sustained winds in the actual operation with the design value.

References

[1] Pei Li, Zengtong Liang, Yonggang Zhou, "Optimization Adjustment of Pulverizing System for a 600MW Unit Boiler Burning Mixed Inferior Coal" Thermal Power Generation In Chinese, Vol.42, NO.5, 64-68, 2013

[2] Hao Zhou, Kefa Cen, Jianren Fan, "Numerical Simulation Study of the Influence of the Elbow on the Operating Characteristics of a Pulverized Coal Bias Combustion Separator" Proceedings of China Electric Machinery Engineering In Chinese, Vol.23, NO.1, 132-135, 2003

[3] Guohua Xin, Yinping Hu, Huiguang Lei, "Rich-Lean Burner" Chinese Patent, CN93204272.4, 26-01-1994.

[4] Shunlin Yan, Huagang Chen, Biao Dong, "'Three High One Strong Principle' Analysis of Inferior Coal Stable Combustion" Boiler Technology In Chinese, Vol.43, NO. 5, 46-49, 2012

Advanced Materials Research Vols. 960-961 (2014) pp 332-336

doi:10.4028/www.scientific.net/AMR.960-961.332

Study of Hot Surface Aviation Fuel Thermal Ignition Pattern

Boyun Liu[1, a], Minlin Liu[1,b],Yanhong Liu[1,c]

[1]College of Power Engineering, Naval University of Engineering, Wuhan ,430033,China

[a]boyunliu@163. Com, [b]minlinliu@163. Com, [c]yanhongliu@163. Com

Keywords: Aviation Fuel; Hot Surface; Boiling pattern; Thermal ignition

Abstract. Fuel evaporation and ignition process on the high-temperature hot surface are difficult to be predicted accurately. The rule of fuel evaporation and ignition delay that various with hot wall temperature have been obtained by utilizing the simulated experiment to study the evaporation and ignition process of aviation fuel on hot surface. This study complements the related content of the fuel ignition mechanism on hot wall， at the same, reference method for fuel fire engineering practice has been provided.

Introduction

Fuel leaks onto the hot surface is quite a common fire accident of warship. Due to the damaged high pressure fuel pipe of diesel engine in the engine room, fire is caused by fuel sprays to high temperature of the body shell, etc[1]. A series of phenomena occur when aviation kerosene flows to the hot wall involving many theoretical problems in the field of engineering thermal physics: fuel film is formed after the flowing fuel expand on hot wall; fuel film conduct boiling heat transfer with the hot wall; the produced vapour flow and diffuse in the air and exchange heat with the surrounding air and occur ignition; etc.

According to the findings of the pool boiling heat transfer [2-4], when the hot wall temperature was different, the boiling pattern of fuel leakage on the hot wall was different, and heat that transferred from hot wall to liquid was also different. The boiling heat transfer can be divided into natural evaporation region, nucleate boiling region and film boiling region in accordance with the different temperature difference(or called degree of superheat, namely the temperature difference between the wall temperature and liquid saturation temperature)[5]. The ignition process of warship's fuel that leaked into the hot surface in engine-room was studied by Li Yuanlong, Lu Shouxiang, etc [6]. Furthermore, the evaporation pattern of leaked fuel on the hot surface was analyzed and the motion process of fuel vapour above the horizontal hot wall was described by them. Because of the complexity of fuel leakage conditions, it may generate all kinds of various boundary conditions. In addition, the space distribution and temperature distribution of fuel-gas that changed with time were caused by evaporation process. These factors make it difficult to predict the process of fuel evaporation and ignition. In this paper, the rule and the influence factors of the leaked aviation kerosene on horizontal hot wall were studied and analyzed through utilizing experiment to simulate the whole ignition process of the leaked aviation kerosene on horizontal hot wall.

Experimental platform

The thermal ignition experiment of aviation fuel could be carried out in early fire test platform. The platform was composed of environmental control system and data acquisition control system.

(1)Environmental control system

Environmental control was composed of simulation of high-temperature thermal environment, hot wall and atmospheric environment.

The conical electric heater above the combustion chamber was utilized to simulate high-temperature thermal environment. The radiant heat source of actual fire field could be simulated by conical electric heater. In this experimental platform, the conical electric heater could provide arbitrary heat radiation intensity ranging from 0 to 80kW/m2.

Hot surface was simulated by placing a copper plate at the bottom of combustion chamber. The area of the copper plate was 25 cm × 50 cm and the thickness was 3 cm. A control thermocouple and a 6 kW heat ring were embedded respectively in plate. The heat capacity of plate should be large so as to ensure the temperature have little changed after plate contacted with cold liquid. The temperature of hot plate was controlled by using a temperature controller to control the hot wall temperature. Temperature controller should adjust automatically and control temperature, ranging from 0 °C to 1000 °C. The resolution and temperature control precision was set as ± 2 °C. Furthermore, it had an automatic cold junction compensator with a thermocouple.

The atmospheric environment was controlled by a high pressure cylinder to connect the gas access to rotor flow meter. The flow meter was adjusted to connect the valve below pipeline for providing the requirement changes of atmosphere. Gas supply system of test platform could change the oxygen content of gas ranging from 0 to 21% arbitrarily.

(2)Data acquisition and control device

Test platform of early fire characteristics was mainly utilized to measure the characteristic parameters of combustible materials. The main measured parameters included: flame temperature, the shape and the size of flame, smoke composition, smoke temperature, smoke flow rate, smoke density, weight loss rate of sample, sample ignition temperature, thermal radiation temperature rise curve of sample surface, etc.

The full flame image acquisition and analysis system could be realized by installing industrial endoscope, CCD camera, optical system, filter, lens connecting, close-up lens and other optical measuring device on high-temperature hot wall. And then ignition temperature and ignition delay of fuel on high temperature hot wall could be analyzed.

Main performance parameters were shown in table 1

.

Table 1. Performance parameters of test bench

Shape size	600mm×800mm×2500mm
Gas composition	Atmospheric oxygen content 0～21% (random variable)
Gas flow rate	0～30L/s random variable
Experimental object	Solid, liquid fuel
Electronic balance weighing range	0. 01～3000g
Radiation heat flux	0～80kW/m^2 random adjustable
Maximum temperature limit of heater	1100^{0}C

Experimental results and test results

2. 1 Boiling pattern of aviation fuel on hot surface

From the experimental records, when the surface temperature of aviation kerosene ranged from 400K to 600K on horizontal hot wall , nucleate boiling dominated ;when the surface temperature of aviation kerosene ranged from 600K to 800K on horizontal hot wall, transition boiling dominated; when temperature was above 800K on horizontal hot wall surface, the film boiling dominated.

When the temperature of horizontal hot wall was approximately 600K, under this temperature condition, the boiling pattern of fuel sample was the most severe. At the same time, it also showed that heat transfer mechanism between nucleate boiling and transition boiling were not the same.

The temperature of fuel vapour surface could reflect the variation of heat flux density on hot surface from the other side. The fundamental reason lied in that heating region in the nucleate boiling stage was larger than that in the transition boiling stage. Because heating surface which was covered with film had a greater proportion, heat flux density from hot wall to fuel decreased when temperature was increased, resulting in the decline of vapour surface temperature.

According to the findings of Xiong and Yuen, the boiling pattern of diesel fuel is nucleate boiling below 356 °C ;that is transition boiling ranging from 356 °C to 440 °C ; that is film boiling above 440 °C . The boiling evaporation experiment that fuel sprayed into hot surface for twelve alkyl was conducted by Vaivids, etc [7]. The experimental results showed that nucleate boiling dominated

within 470K temperature for twelve alkyl. The boiling pattern was transitional boiling ranging from 470K to 550K. The boiling pattern is film boiling pattern in a higher temperature range for twelve alkyl. It can be seen that the experimental study that is carried out by utilizing aviation kerosene has a similar conclusion, only the transformation temperature of different boiling pattern is different.

2. 2 Ignition mode and ignition delay time

Through the analysis of 200 cases ignition experimental process, ignition mode could be divided into two types as following:

The first mode was when plume began to rise, fuel vapour formed a combustible mixture gas reaction through entraining the around oxygen mixture, and after a certain time, ignition occurred. With the increase of height, vapour accelerated entraining the around fresh air, and the maximum reaction rate of mixed gas was also moving up with the movement of plume and was almost near the position where the entrainment velocity was larger. This moment, the high temperature region of flammable vapour was located at the top of plume. Oxygen had also entered plume, and combustible gas mixture was formed at the top of plume, and the reaction rate had been accelerated to a certain value. Therefore, ignition occurred, called center ignition.

The second ignition mode usually occurred in the lower heat flux density condition, and ignition did not occur in the vapour just rising. However, after a period of time, it occurred in the full development of the plume. Furthermore, due to the mixed reaction between continuous flowing of vapour and air, ignition occurred when the condition was suitable. At the moment, the high temperature region distributed on the two sides of plume, while the vapour velocity was larger than that of the initial stage of plume. Combustible mixed gas could be formed through fast motion of vapour that entrained around air on both sides. If the mixed gas reaction rate was increased to a certain value, ignition occurred, called surrounding ignition.

Test records of ignition delay time, as shown in table 2:

Table 2. Ignition test records

Surface temperature（K）	660	670	680	690	700	710	720	730	740	750
Ignition delay time（S）	11	10. 9	10. 3	9. 7	8. 6	8. 5	8. 2	7. 9	7. 8	7. 8
Ignition height（mm）	1. 8	1. 9	2. 1	2. 5	2. 7	2. 7	2. 8	2. 9	2. 9	3
Surface temperature（K）	760	770	780	790	800	810	820	830	840	850
Ignition delay time（S）	8	8. 1	8. 3	8. 4	8. 4	8. 5	8. 6	8. 7	8. 9	9
Ignition height（mm）	3	3	2. 9	2. 7	2. 6	2. 5	2. 4	2. 3	2. 1	2

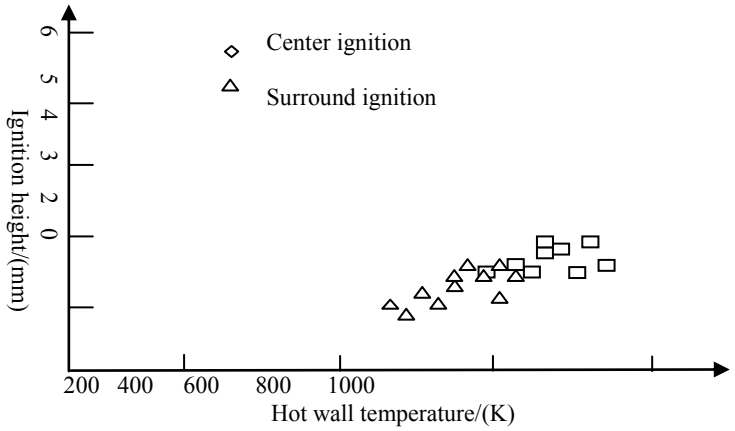

Fig. 1 Fuel ignition height under different surface temperature

Comparing the three kinds of boiling pattern, aviation kerosene could not be ignited within the nucleate boiling temperature range; within the transition boiling temperature range, ignition mode of aviation kerosene was mainly center ignition; while within the film boiling temperature range, ignition mode of aviation kerosene was mainly surrounding ignition. The average value of ignition

delay time was 9. 2S within the transition boiling temperature range. However, the average value of ignition delay was 8. 4S within the film boiling temperature range. As can be seen, the hot wall surface temperature had a direct relationship with the form of boiling evaporation; while the ignition morphology and ignition delay time mainly depended on the concentration and temperature distribution of combustible mixture vapour on hot wall.

Influence of boiling heat flux

After fuel leaked into the hot wall, the first occurrence was boiling heat transfer, then the generated vapour occurred ignition over the hot wall. Because there were a lot of key factors that influenced ignition delay over the hot surface, such as temperature, pressure, turbulent state, time scale, mixing degree between fuel and oxidizer , high temperature fuel pyrolysis and additional factors. The given factors of different literature such as ignition delay time definition, experimental equipment, experimental method were also different. Furthermore, the fitting relationship between ignition delay time and these parameters were also different. It may even appear more than one order of magnitude difference. The fitting relationship of ignition delay time was utilized in combustion chamber flow field calculation program, which provides possibility for ignition delay comparison under different parameters condition and also had a guiding significance for the selection of experimental conditions. Therefore, it was necessary to fit the ignition delay time. This paper attempted to analyze the key influence factors of ignition delay from experimental angle.

Based on the Arrhenius theory and Experimental Research on dynamic characteristics of aviation kerosene, the reaction system of aviation kerosene under the action of hot surface can be expressed as:

$$\tau_{ig} = A[Fuel]^{a}[O_2]^{\beta}[M]^{\gamma}\exp(\frac{E}{RT}) \quad . \tag{1}$$

where A is the pre-exponential factor. [Fuel], [O2], [M] are respectively the molar concentration of gas fuel, oxidant and other gas in air. α, β, γ are the impact factors. E is the activation energy. R is the universal gas constant. T is the ignition temperature.

Taking the logarithm of equation, there is:

$$1/\tau_{ig} = (M_{evap})^{1/4} C_1 + \ln[Fuel] + \frac{E}{RT} \quad . \tag{2}$$

In the Eq. (2), $\ln A$ is not related to temperature, while the atmospheric environmental is the natural environment under test condition. The oxygen concentration depends directly on the mixture concentration of combustible gas . Therefore, the formula can be simplified as:

$$\ln \tau_{ig} = C_1 + \ln[Fuel] + \frac{E}{RT} \quad . \tag{3}$$

Utilizing the Eq. (3) to attempt to fit out the relationship between ignition delay time and temperature are serious discrepancies with the experimental data. The reasons are because the above theories derivation foundation are based on some experimental data which are obtained through dynamic characteristics of aviation kerosene test, and the ignition conditions are obtained in a closed container. Furthermore, the temperature and concentration distribution are relatively consistent in reaction system. In this experiment, upward plume was generated for the combustible mixture gas and the surrounding air were mixed with each other. Fuel evaporation rate was also varying with the temperature, resulting in the complexity of distribution gradient of temperature and concentration above the liquid surface. Therefore, it cannot reflect the changes of ignition delay through the temperature this parameter.

The experimental results showed that boiling heat transfer size of hot wall was an important factor to influence ignition, however, boiling heat transfer leaded to a direct result that is the changes of the fuel surface heat flux density. Because the heat flux is not easy to be measured. So, the evaporation rate was utilized to express the changes of heat flux density in test. Fig. 2 shows the relationship between fuel evaporation rate and ignition delay time on hot wall surface. Through function fitting to make it meet:

$$1/\tau_{ig} = (M_{evap})^{1/4} \quad . \tag{4}$$

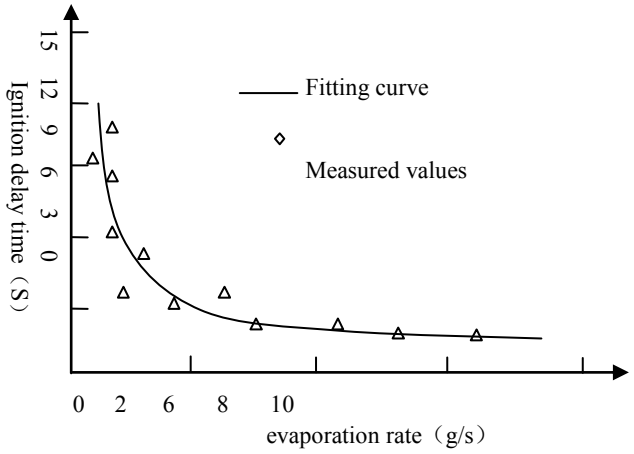

Fig. 2 Relationship between ignition delay and evaporation rate

Conclusions

Evaporation and ignition process of aviation kerosene on horizontal hot wall are studied, and the rule of ignition delay variation with hot wall temperature is obtained by utilizing the simulated experiment. The relationship between heat flux on hot wall and ignition delay time is analyzed and established to obtain the prediction model of ignition delay time by utilizing plume theory. This study not only complements the related content of hot wall fuel ignition mechanism, but also provides reference method for hot wall safety protection engineering practice.

References

[1] Chen Guoqing, Lu Shouxiang, Zhuang Lei. Study on the development process of marine engine fuel fire [J]. Journal of University of Science & Technology China, 2006, 36 (1): 93 ～ 95

[2]OKOYA S S. Disappearance of criticality in a branched-chain thermal explosion with heat loss[J]. Combustion and Flame, 2006(144): 410-414.

[3]Stephan K. Dieter G， Elisabeth D, et al. Heat Transfer and Bubble Formation in Pool boiling: Effect of Basic Surface Modifications for Heat Transfer Enhancement [J], International Journal of Thermal Sciences, 2006, 45:217-236.

[4]Yagov V V. Generic features and puzzles of nucleate boiling [J]. International Journal of Heat and Mass Transfer, 2009, 52: 5241-5249.

[5]Gradeck M. Kouachi A. Lebouche M. et al. boiling curves in relation to quenching of a high temperature moving surface with liquid jet impingement [J]. International Journal of Heat and Mass Transfer, 2009. 52: 1094-1104.

[6] Li Yuanlong, Lu Shouxiang. The numerical simulation of leakage fuel evaporation and fire on horizontal hot wall[J]. Journal of combustion science and technology，2005，11(2)：159～162.

[7] Vaivads R H, Bardon M F, Bttista V. A computational study of the flammability of methanol and gasoline fuel spills on hot engine manifolds [J]. Fire Safety Journal, 1997, 28:307~322.

Advanced Materials Research Vols. 960-961 (2014) pp 337-340

doi:10.4028/www.scientific.net/AMR.960-961.337

Thermal transport in hotspots using the Lattice Boltzmann method with application to Silicon-on-insulator transistors

Y.D. Mao[a], M.T. Xu[*]

Department of Engineering Mechanics, School of Civil Engineering, Shandong University, Jinan, China

[a]maoyudong@aliyun.com, [*]mingtian@sdu.edu.cn

Keywords: hotspots, Lattice Boltzmann method, Silicon-on-insulator.

Abstract. Silicon-on-insulator (SOI) transistors have been widely used in the micro-electronic devices. The Lattice Boltzmann method (LBM) is employed to simulate the heat conductions of hotspots appeared in a SOI transistor. The results show that a thermal wave effect is appeared in micro-region, and it can not be found in Fourier prediction. Comparing the results obtained by the Fourier law and LBM, we find that the LBM solution shows approximately 22% higher energy density than the Fourier prediction. When two thermal waves form different hotspots meet together, a significant energy enhancement will be appeared.

Introduction

SOI devices are fabricated in a thin silicon layer that is electrically isolated by a buried oxide layer. It is well known that localized energy emission may result in hotspot with dimensions on the order of 10nm and it would challenge the stabilities and service life of devices [1, 2].

Thermal transport in semiconductor devices is modeled usually using diffusion theory based the Fourier law. However, some problems appear when the Fourier law is applied to micro-scale heat conductions, which has been mentioned in the past studies [3-5]. As a powerful tool, Boltzmann transport equation (BTE) is used to solve the thermal transport problems in micro-scale systems [6, 7]. However, it is too difficult to solve BTE by the direct mathematic methods because of its complex nonlinear integral item. Therefore the numerical methods are significant for us to resolve this problem. Having the obvious and delighted advantages in resolving the boundaries, achieving the programming and dealing with the complex multi-scale coupling problem, lattice Boltzmann method had been used to deal with the BTE in the last papers, and it has received considerable attention during the recent years [8-10].

In the present work, 2D heat conduction models based on LBM are built to simulate the energy distribution in hotspots of SOI transistors.

Theoretical analysis

In SOI transistors, phonon is the dominant energy carriers. Based on the BTE, 2D heat conduction model in hotspots can be expressed as Eq. (1)

$$\frac{\partial e_i}{\partial t} + v_i \nabla e_i = -\frac{e_i - e_i^0}{\tau} + S(x, y, t), i = 1, 2 \ldots \mathrm{m} \tag{1}$$

where e is energy density, e^0 is the equilibrium energy density, v is phonon group velocity, τ is the phonon relaxation time, and S is the energy source induced by hotspot. Here we consider a D_2Q_m lattice model with specular reflection boundary conditions and constant temperature initial condition, and define one-dimensional quantities in Eqs. (2-5).

$$x^* = x / L; \quad y^* = y / L; \quad t^* = t / \tau \tag{2}$$

$$e(T_0) = N_0 = C_v T_0 \tag{3}$$

$$e_i^*(x^*, y^*, t^*) = \frac{e_i(x, y, t) - N_0 / m}{N_0} \tag{4}$$

$$e^*(x^*, y^*, t^*) = \sum_{i=1}^{m} e_i^*(x^*, y^*, t^*) = \frac{e(x, y, t) - N_0}{N_0} \tag{5}$$

where L is the length of transistor medium, C_v is the volumetric heat capacity of silicon. Using LBM to discretize Eq. (2) and neglecting the high order terms, then the dominant equation can be written as Eq. (6)

$$e_i^*(x^* + \alpha\Delta x^*, y^* + \beta\Delta y^*, t^* + \Delta t^*) \approx (1-w)e_i^*(x^*, y^*, t^*) + we_i^{0*}(x^*, y^*, t^*) + \frac{w\tau}{N_0} S(x^*, y^*, t^*) \tag{6}$$

where $w = \Delta t^* = \Delta x^* / Kn$, $Kn = l / L$ is the Knudsen number, and l is the phonon mean free path. α and β are parameters which can be composed of a matrix B. For example, in the D_2Q_4 lattice model, the matrix B can be expressed as, $\mathbf{B} = [\boldsymbol{\alpha}, \boldsymbol{\beta}] = [1, 0; 0, 1; -1, 0; 0, -1]$.

Based on the Fourier law, the hotspots self-heating problem discussed above is described by the heat conduction equation with heat source expressed in Eq. (7):

$$C_v \frac{\partial T}{\partial t} = k_F \nabla^2 T + S \tag{7}$$

Introduce the notations in Eq. (2), the Fourier solution can be written as Eqs. (8-10)

$$e^*(x^*, y^*, t^*) = \sum_{n=1}^{\infty} \Gamma_n(t^*) \cos\alpha_n x^* \cos\alpha_n y^* \tag{8}$$

$$\Gamma_n(t^*) = \exp(-qt^*)\left[C + \int \exp(qt^*) \cdot 2\int_0^1\int_0^1 S(x^*, y^*, t^*) \cos\alpha_n x^* \cos\alpha_n y^* dx^* dy^* dt^* \right] \tag{9}$$

$$q = \frac{k_F \tau}{C_v L^2} \alpha_n^2, \quad \alpha_n = n\pi, \quad C = -2\int\int_0^1\int_0^1 S(x^*, y^*, t^*) \cos\alpha_n x^* \cos\alpha_n y^* dx^* dy^* dt^* \,|_{t=0} \tag{10}$$

Numerical results and Discussion

Now we consider a SOI transistor with the following parameters: $C_v = 1.66\times10^6$ J/m3K, $T_0 = 300$ K. The size of hotspot is *h*h*, and the proportion of *h* and *L* is kept 1:20. The phonon mean free path of silicon l is 40nm, and the phonon relaxation time τ is 6.53ps. The thermal conductivity of bulk silicon k_F is 148W/mK. In the following computation of LBM, the grid size Δx^* is taken as 0.01, and the time step $\Delta t^* = \Delta x^* / Kn$ which is required by the relation of the two parameter. The values of the parameters given above will be used throughout the following discussion, unless stated otherwise.

At first, the validity of LBM in solving macroscopic heat conduction problems is discussed by comparing with the Fourier law. We set the characteristic length value of transistor *L*=4000nm, then Knudsen number is equal to 0.01 and *h*=200nm. The hotspot is set at the center of transistor, and the system here is in diffusive region. Then the sectional view of comparison between Fourier law and LBM solutions at the middle of y-axis is present in Fig. 1. It can be found that the solution of LBM is very agreement with the prediction of Fourier law. Therefore, the LBM is verified to validate in dealing with macro-thermal transfer problems.

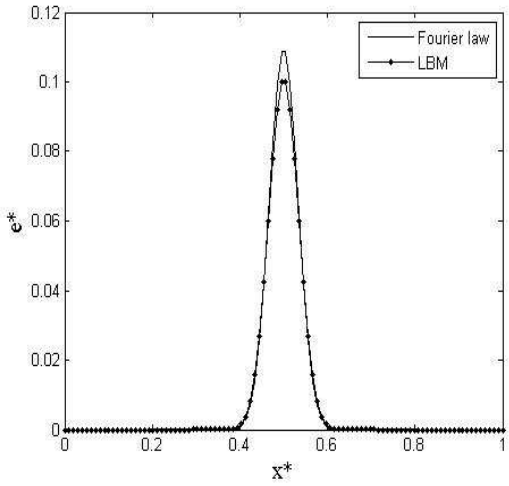

Fig. 1 Comparison between LBM solution and the Fourier law at the middle of y-axis

Energy density distributions obtained by Fourier law and LBM with $Kn=1$ are presented in Figs. 2 and 3. The system length

L here is 40nm, and the hotspot width h is 2nm. Thermal transport in ballistic region makes great difference between the Fourier law solution and LBM prediction. In Fig. 2, the energy density peak value obtained by Fourier law at the center of hotspot is 0.072. As illustrated in Fig. 2(b), the Fourier law only shows a diffusive energy propogation.

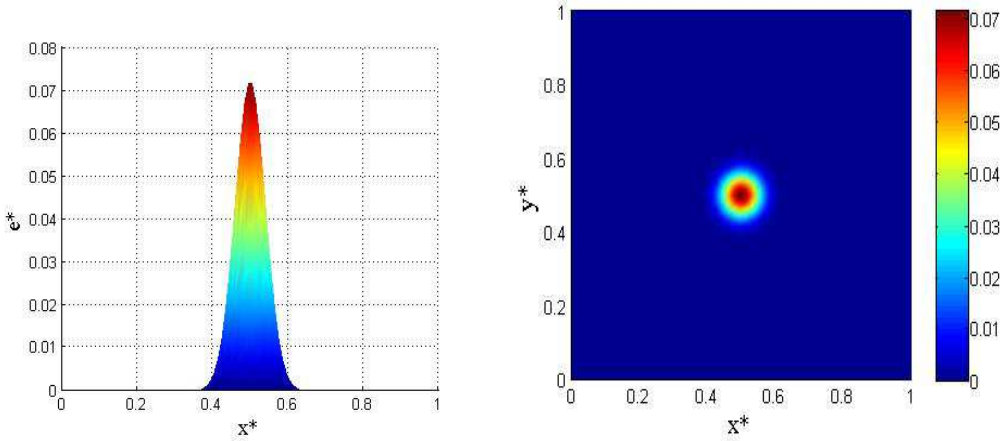

(a) (b)

Fig. 2 Energy density distribution obtained by the Fourier law with Kn=1, (a) X-O-Z lateral view, (b) X-O-Y bottom view.

However, the peak value in LBM solution is 0.088, as is shown in Fig. 3. This value is approximately 22% higher than which obtained by Fourier law. In Fig. 3(b), we can see that the energy are no longer abiding by diffusive track, but travels a wave-like movement from center to boundaries. This wave-like energy propogation can capture the ballistic characters with $Kn=1$. It is worth note that the energy in LBM prediction, not like the Fourier solution, no longer has its peak value in the center of hotspot. This means that the energy travels at a limited velocity.

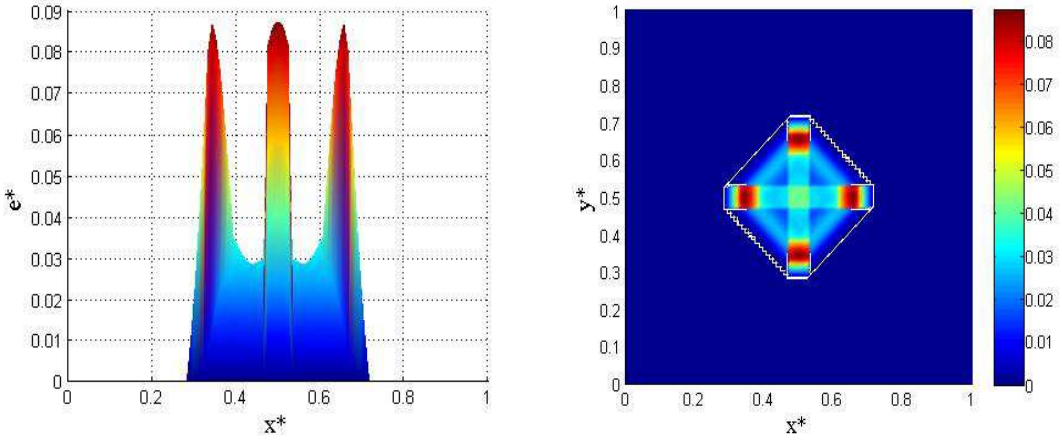

(a) **(b)**

Fig. 3 Energy density distribution obtained by LBM with Kn=1, (a) X-O-Z lateral view, (b) X-O-Y bottom view.

The energy density distribution of two hotspots in the transistor obtained by LBM is present in Fig .4. The conditions of this problem is same with which has been discussed in Fig. 3. Comparing the two graphs, one can see that when the thermal waves from different hotspots meet at the center of system, as is illustrated in Fig. 4, the energy has a significant enhancement. The peak value of

energy density at the middle of system is about 0.14 predicted in Fig. 4 (b), and it is approximately 60% higher than the peak value of one hotspot.

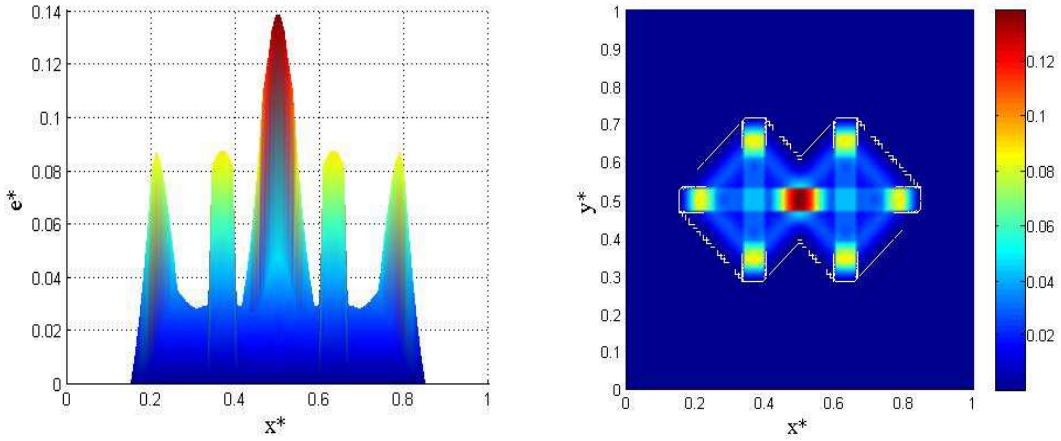

(a) (b)

Fig. 4 Energy density distribution of two hotspots obtained by LBM, (a) X-O-Z lateral view, (b) X-O-Y bottom view.

Conclusion

(1) The LBM is a valid method to simulate thermal transport problems in diffusive regions.
(2) In ballistic regions, the LBM solution can capture the thermal wave character, which can not be seen in the classical Fourier's solution.
(3) In the hotspot self-heating problems, the LBM solution illustrates about 22% higher energy density than the Fourier prediction.

Acknowledgements

The support of our research by the National Natural Science Foundation of China (Project No. 50876054) is greatly appreciated.

References

[1] S. Sinha, K. E. Goodson. Thermal conduction in sub-100nm transistors. Microelectronics Journal [J], 2006, 37: 1148-1157.
[2] S. Sinha, E. Pop, K. E. Goodson. Non-equilibrium phonon distributions in sub-100 nm silicon transistors. ASME. J. Heat Transfer [J], 2006, 128: 638-648.
[3] D.Y. Tzou, Macro- to Microscale Heat Transfer: The Lagging Behavior, Taylor & Francis, Washington, DC, 1996.
[4] A. A. Joshi, A. Majumdar, Transient ballistic and diffusive phonon heat transport in thin films, Journal of Applied Physics [J], 1993, 74: 31–39.
[5] S. S. Ghai, W. T. Kim, M. S. Jhon, A novel heat transfer model and its application to information storage systems, Journal of Applied Physics [J], 2005, 97: 703.
[6] S. Pispati et al. Multiscale thermal device modeling using diffusion in the Boltzmann Transport Equation [J], 2013, 64: 286-303.
[7] S. Pisipati et al. A novel alternate approach for multiscale thermal transport using diffusion in the Boltzmann Transport Equation [J], 2011, 54: 3406-3419.
[8] R. A. Escobar, B. Smith, C. H. Amon. Lattice Boltzmann modeling of subcontinuum energy transport in crystalline and amorphous microelectronic devices. ASME. J. Heat Transfer [J], 2006, 128: 115-125.
[9] R. A. Escobar, C. H. Amon. Thin film phonon heat conduction by the dispersion lattice Boltzmann method. ASME. J. Heat Transfer [J], 2008, 130: 092402.
[10] A. Homayoon, A. H. Meghdadi Isfahani, E.Shirani, M. Ashrafuzadeh. A novel modified lattice Boltzmann method for simulation of gas flows in wide range of Knudsen number. Int. J. Heat Mass Transfer [J], 2011, 38:827-832.

Advanced Materials Research Vols. 960-961 (2014) pp 341-348

doi:10.4028/www.scientific.net/AMR.960-961.341

Numerical study on the interaction mechanism between swirl and reverse flow rate in a twin swirl combustor

Yinli Liu[1, a], Hao Tang[1, b]

[1]College of Energy and Power Engineering,

Nanjing University of Aeronautics and Astronautics, Nanjing 210016, China

[a]yinli.liu@nuaa.edu.cn, [b]hao.tang@nuaa.edu.cn

Keywords: Twin swirl; Swirl number; Reverse flow rate; Numerical simulation

Abstract. An isothermal flow in a Twin Swirl Combustor (TSC) was simulated with the Renormalized Group (RNG) k-ε turbulence model. The swirling and recirculation intensity was studied under different structures and inlet conditions. The results confirmed that there was a significant negative correlation between the trend lines of the swirl number (S) and reversed flow rate (X_r). The gradient of reversed flow rate was larger in the front and middle parts of the combustor than that of swirl number. The end-surface-inlet structure had a better swirl and recirculation enhancement effect. With the end-surface-inlet structure, the internal swirl and reverse intensity could be flexibly adjusted by switching the swirl intensity of the primary air. Under the structure of staggered-inlet, there was a critical distance between primary and secondary air inlets. When exceeded, it would be more difficult to enhance the swirl and reverse flow effect by increasing the swirl intensity of the secondary air.

Introduction

Confined swirling flows are widely used in most the industrial instruments, i.e. internal combustion engines and industrial burners. A strong swirling airflow in the chamber will cause negative-pressure effects, generating internal recirculation zones (IRZ). The existence of recirculation is beneficial for both premix and non-premixed combustion. In pulverized coal combustion, it can help increase the gas recirculation for flame stabilization, and prolonging the travelling time of the coal particles, which is beneficial for reaching high-level burnout rate.

Many experiments have been done to better understand the flow properties of swirling and recirculation in pulverized coal burner. Wang [1] observed the gas-particle flow properties in a vertical-layout cyclone coal combustor using the visualization method and LDA system. The isothermal results showed there is strong internal recirculation in the spouting zone and strong swirling effect in the cyclone zone. A typical Rankine-vortex was observed in the cyclone zone. Li [2] and Chen [3] both studied the air-particle flows in a swirling pulverized coal burner in an isothermal condition with a three-dimension particle-dynamics anemometer(PDA). The experiment results revealed the relationships between the recirculation intensity and the air flux ratio. IRZ could generate while proper air flux ratio and swirl intensity were adopted.

Numerical simulation is another powerful method to better understand the properties of swirling flows, because there are always limitations for a few discrete positions for the sensors and cannot get the whole three-dimensional structure. This method also saves more time and is more cost-effective Weber [4, 5] used the RANS k-ε turbulence model and a second order Reynolds stress model (RSM) to simulate the isothermal expanding swirling flows into divergent burner with different expansions The results showed that anisotropic turbulent closure provided Reynolds stress transport model was better in the research case than that the k-ε model, due to the non-homogeneous and highly anisotropic turbulence in the swirling flows. Jawarneh [6] adopted the RANS RSM to simulate the strong confined swirling flow in a vortex chamber. The simulation results of velocities and pressure profiles were compared with the measurement data obtained from the experiment. The forced-vortex inside the core and the free-vortex outside the core were revealed by the mean tangential velocity profiles, which agreed well with the experiment data. Wang [7] used the Large Eddy Simulation (LES) to study the swirling air flow properties in a model dump combustor. The time averaged mean

velocity and Reynolds sheer stresses under three different swirling numbers were calculated and agreed well with the experiment data. LES succeed in simulating the vortex breakdown, the internal recirculation zones and the anisotropic turbulence structures in different levels of swirling intensity.

Hou [8] carried out a numerical simulation on a swirling flow tundish with different turbulence models. For the different treatment toward effective viscosity, the RNG k-ε is valid for both low and high Reynolds number flows. The standard k-ε however, was only for fully turbulent flows with high Reynolds number. The results prove that the RNG k-ε model is more suitable, because compared with standard k-ε model it has a faster convergence. Gupta [9] calculated the dynamics of the turbulent swirling flow in a cylinder with a tangential inlet and a tangential exit. The standard k-ε and RNG k-ε turbulence models were used and the simulation results were compared with the experiment data. The RNG k-ε model yield better results to the experiment because it modifies the standard k-ε model by adding a swirling factor into its model. It is better to use RNG k-ε model when simulating the flow under strong swirling conditions.

Comparisons between LES and RANS have proved LES predicts the flow properties more accurately, especially for transient and anisotropic flows, but tremendous time and calculation resources are required compared to RANS to get the result converged. While the RANS is still able to offer satisfied simulation results for the swirling flows with a reasonable calculation time, if modifications are adopted to the standard k-ε model.

It could also be concluded that the internal recirculation flow in the chamber is adjusted mostly by the outer swirling secondary air or the bluff body equipped inside the chamber, while the primary air is non-swirling. With the twin swirling air flow, both the primary and secondary air are swirling so that the recirculation and swirling intensity inside the chamber could be flexibly adjusted by either of them. The structure could be further simplified if no bluff body is installed in the chamber. While the interaction mechanism of recirculation and swirling between twin swirling flows is not clear yet, it is important to look inside the flowing characteristics in the chamber of the Twin Swirl Combustor (TSC).

In this paper, the renormalization group (RNG) k-ε model is used to predict the airflow in a confined TSC with a contraction in the rear, near the exit. Validation case has been implemented using RNG k-ε model on a swirling airflows in a smooth straight pipe done by Rocklage-Marliani [10], which is similar to the current chamber. A 2d mesh with an "axisymmetric swirling axis" is used according to the geometry and flow conditions. The results match favorably with the experiment data, which means the RNG k-ε model is qualified in predicting the internal swirling flow with appropriate mathematic method and high-quality 2d meshes (y^+<=1 for the grids adjacent to the wall and axis).

Case illustration

The properties of the co-axial swirling airflow in a dump combustor with a construction have been studied in this article. The simulation model setup is shown schematically in Fig.1. H is used as a scale and is equivalent to 0.125 m. The length of the chamber (L) is 8H, with an inner diameter (D) of 4H. The diameter of the exit is 2H. The primary air and secondary air enter the chamber through toroidal cross-sections respectively and then leave from the exit. Swirling airflow could be generated after travelling through the vanes equipped in the air inlets (not shown in the schematic Fig.1). The vane inclination for both inlets is 60°. The inner and outer diameters of the primary air inlet are 0.64H and 0.96H, and remain unchanged. The co-annular width is 0.16H for both primary and secondary air inlets. An IRZ can be generated in the vortex breakdown regions due to the swirling effect and the construction part [7].

The flux rate of the primary air remains at a constant of 0.02 m^3/s in all simulation cases, while that of the secondary air alters according to different flux ratios (β) between primary and secondary air. The structure of the model changes with different axial position (Δx) and radial position (α) of the secondary air inlet. Combining different flux ratio (β) between primary and secondary air, 4 simulation cases are calculated and analyzed, which is shown in Table 1. It is worth noting that when referring the end-surface-inlet structure, it means Δx=0, as is shown in Fig.2 (a); while the

staggered-inlet structure means $\Delta x \neq 0$, as are shown in Fig.2 (b) and (c). The inlet boundary conditions can be determined by the flux ratio β and the primary air flux, as well as the inclination angle of the vanes.

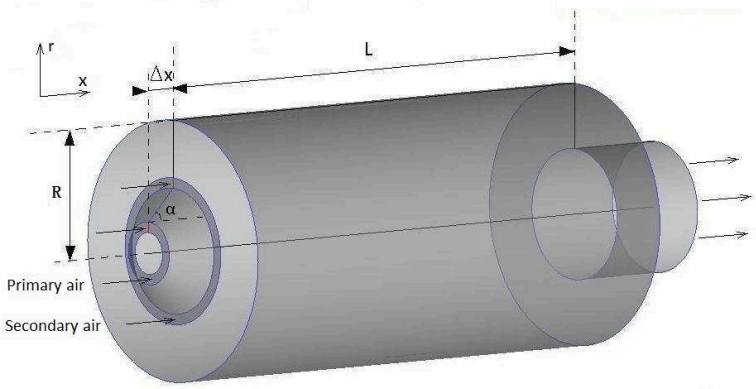

Fig.1 A schematic plot of the simulation model

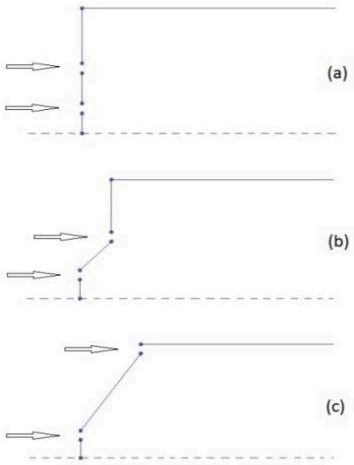

Fig.2 A schematic plot of the inlet structures

Table.1 Computational cases

Case	Δx	α (°)	β
C1	0	90	1:1
C2	0.48H	45	1:3
C3	0.48H	45	1:5
C4	0.96H	55	1:5

Note: in C1, the radial position for secondary air inlet is the same as that in C2 and C3

Numerical method

Governing Equations

The steady state Reynolds average Navier-Stokes continuity and momentum equations can be described as follows:

$$\frac{\partial U_i}{\partial x_i} = 0 \tag{1}$$

$$\rho \frac{\partial}{\partial x_j}\left(U_i U_j\right) = -\frac{\partial P}{\partial x_i} + \frac{\partial}{\partial x_j}\left[\mu\left(\frac{\partial u_i}{\partial x_j} - \rho\overline{u_i' u_j'}\right)\right] \tag{2}$$

Where ρ is the fluid density, U_i is a mean velocity component for the different direction X_i, P is the pressure, μ is the dynamic viscosity, and u' is a fluctuating component of velocity. The repeated indices represent summation from one to three for 3D problems and one to two for 2D problems.

The RNG k-ε model is based on the instantaneous Navier-Stokes equations using a mathematical technique called the "renormalization group" (RNG) methods. It contains modifications for the swirling flows by modifying the turbulent viscosity appropriately. The modification takes the following functional form:

$$\mu_t = \mu_{t0} f\left(\alpha_s, \Omega, \frac{k}{\varepsilon}\right) \tag{3}$$

Where μ_{t0} is the value of turbulent viscosity calculated without the swirl modification using the equations described above. Ω is a characteristic swirl number. α_s is a swirl constant, which equal to 0.07 while it's mildly swirling flows and can vary depend on the swirling intensity.

Mesh, boundary conditions and numerical methods

In the current simulation, 2D structured quadrilateral mesh cells are used according to the validation case. Three different numbers of grids (0.1 million, 0.2 million and 0.4 million) with the same meshing strategies have been implemented for the case C1 for the mesh independence check.

Results have proved that the predicted results match each other with few differences. So the minimum number of approximately 0.1 million is adopted. For other cases, the same meshing strategies are applied with a number of around 0.1 million in total. In the near-wall and near-axial regions, refined meshes are placed.

In this study, the commercial code ANSYS FLUENT 13.0 is used with the ICEM CFD for the mesh generation. The finite-volume method is applied while the governing equations are solved. The pressure based segregated solver solves the equations separately and sequentially. The SIMPLE scheme is applied for the pressure-velocity coupling. A second-order upwind scheme is used for spatial discretization of momentum, swirl velocity, turbulent kinetic energy and turbulent dissipation rate. Convergence criteria are set to five orders of magnitude reduction and at least 20,000 iterations have been carried out to insure the convergence.

The flowing parameters inside the chamber of TSC change with different structures and swirling intensities. It is hoped that from different cases, the characteristics of reverse and swirling flow under the condition of co-axial twin-swirl flow in a dump combustor could be better understood, and beneficial could be gained from the well-organized airflow structure for ignition and flame stabilization.

Results and Discussion

During coal combustion, the IRZ could be created by swirling air flow in the chamber. The combustion stabilization can be realized when appropriate swirl and reverse intensity is applied in the chamber. The intensity of swirling and flow reversals in the chamber will be analyzed, and the interaction mechanism will be illustrated below.

In the current research, the intensity of swirling in a given cross section can be evaluated by swirling number S. For any circular cross-section, S could be given by:

$$S = \frac{\int_0^R \rho u w \cdot 2\pi r^2 dr}{\int_0^R \rho u^2 \cdot 2\pi R r \, dr} \tag{4}$$

Here, R is the inner diameter of the chamber, ρ is the density of the fluid (here it is air), u is the axial velocity component and w is the tangential velocity component.

For any circular cross-section, the intensity of reverse flow can be assessed by reverse flow rate (X_r), given as follows,

$$X_r = \frac{|Q_{neg}|}{Q} = \frac{\left|\int_0^R u_{neg} \cdot 2\pi r dr\right|}{\int_0^R u \cdot 2\pi r dr} \tag{5}$$

Here, Q_{neg} is the net reflux through the cross-section, and Q is the flux in the given section. U_{neg} is the negative axial velocity component and u is the axial velocity component.

The swirling and recirculation features under the twin-swirl conditions

According to Eq. 4 and 5, the swirl number S and reverse flow rate X_r in different cross-sections which are perpendicular to axis x can be calculated by integration. Fig. 6 shows the trend lines of S and X_r in different simulation cases.

The interaction of inner and outer swirling flows make the internal swirl and reverse flow inside the combustion chamber more complicated than common single swirl cases, as is shown in Fig. 3. It is obvious to see that the trend lines change in a completely opposite way between swirl number S and reverse flow rate X_r, i.e., while S increases, X_r decreases; vice versa. When S increases to its local maximum or minimum, X_r is in its local minimum and maximum, correspondingly. The gradient of X_r is larger than S in the front and central of the chamber. In all 4 cases, the variance trends for both S and X_r are almost the same respectively, though different axial and radial inlet positions as well as the inlet flux ratio have been applied. In the front of the chamber, the swirl number S decreases initially and gets its global minimum at x/H=0.5 ~ 1.0. After that, it increases gradually along the axial direction downstream and gets its global maximum at x/H=6.5 ~ 7.0, then decreases rapidly as it approaches the end of the chamber.

Though the magnitude and range for the average S is almost the same, the X_r for C1 is notably larger than C2. A conclusion could be drawn that even though the flux ratio for C1 is smaller than C2 (which means the swirl momentum brought in by secondary air in C1 is smaller than that of C2), the recirculation effect for the end-surface-inlet structure (C1) is greater than staggered-inlet structure (C2). This is believed to be mainly due the fact that in the end-surface-inlet structure, the distance between primary and secondary inlet is smaller, which means that the mutual synergistic effect between primary and secondary air is better and the stronger swirling effect can be created under a greater negative pressure gradient and centrifugal forces.

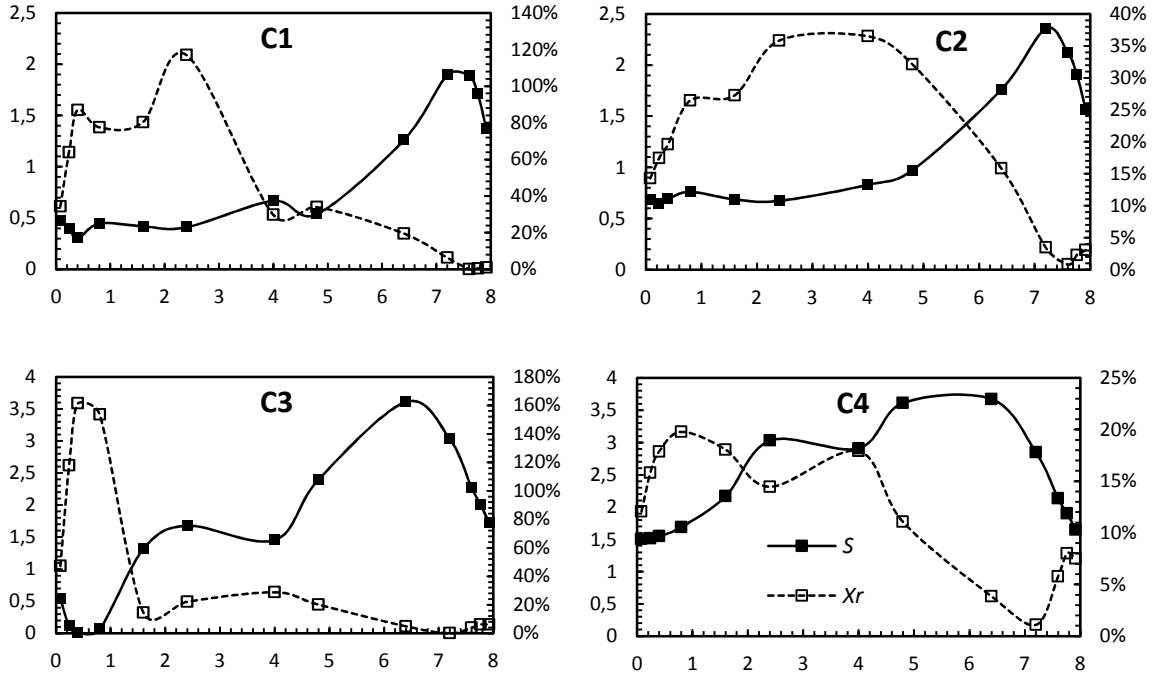

Fig. 3 Variances of S (straight lines with filled nodes) and X_r (dashed lines with unfilled nodes) in different axial positions (left vertical axis: S; right vertical axis: X_r)

With the same inlet structure (C2 and C3), when the flux ratio is increased (which means the secondary and total air flux are increased), both the swirl number S and reverse flow rate X_r increase. This can be explained that the swirl momentum brought in by the secondary air increases as the secondary air flux increases, which makes swirling effect inside the chamber enhanced. The stronger swirling airflow intensifies the reverse flow effect.

Even with the same air flow ratio while the distance between primary and secondary air inlets is further increased (C3 and C4), the range for the swirl number differs a little, while the reverse flow rate is significantly reduced. This is consistent with the former conclusion drawn from the comparison between C1 and C2. This comparison shows that increasing the distance will not help generating better recirculation effect. Besides, it is possible that there is a critical distance between primary and secondary air inlet. When exceeded, it would be difficult to enhance the recirculation effect by increasing the swirl intensity of the secondary air.

Comparative analysis on the swirling and recirculation features under the twin/single swirl conditions

The airflow in the TSC chamber can be flexibly adjusted and organized by both inner primary air and outer secondary air. For better understanding the influence of primary swirling air on the flow field in the chamber, a comparative analysis on the twin or single swirl was implemented. By turning the tangential velocity component of the primary airflow to zero while keep the axial velocity component unchanged, the former simulation cases C1 ~ C4 are named C1' ~ C4', respectively. The comparative results of swirl number S along the axis x for both twin and single swirl are illustrated in Fig. 4 (a) and (b), while those of the reverse flow rate X_r are shown in Fig. 4 (c) and (d).

As is shown in Fig 4 (a) and (c), the trend lines of swirl number S and reverse flow rate X_r are more similar between C2 and C2', compared with that of C1 and C1'. In most of the positions, both S and X_r in C1 are larger than C1'. This could attribute to the more "effective" enhancement of the swirling and recirculation in the twin swirl inlet conditions with the end-surface-inlet structure. When the primary air is turned from swirling into non-swirling, the average swirl number is slightly increased, while the average reverse flow rate is significantly decreased, which is not beneficial for combustion stability and intensification. As is mentioned before, with the end-surface-inlet structure, twin swirl airflows have a better superposition on swirling enhancement. When it comes to a single swirl, the enhancement effect is decayed so that the recirculation effect is receded correspondingly. When the staggered-inlet structure is applied in C2 and C2', the swirl number S in C2 is slightly smaller in the front chamber but marginally larger in the rear; while the reverse flow rate slightly enlarged, compared with C2'.

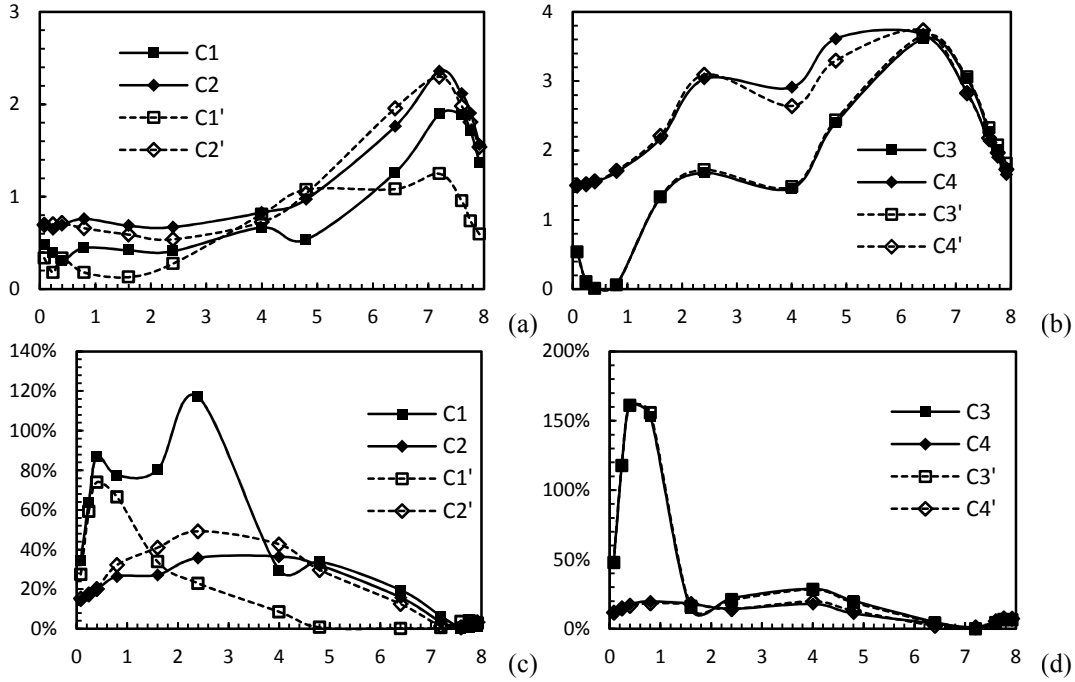

Fig. 4 Variances of S (straight lines with filled nodes) and X_r (dashed lines with unfilled nodes) in different axial positions (left vertical axis: S; right vertical axis: X_r)

Table 2 Average of swirl number $\bar{S}$ and reverse flow rate $\overline{X_r}$ for different cases

Cases	$\bar{S}$	$\overline{X_r}$ (%)	Cases	$\bar{S}$	$\overline{X_r}$ (%)
C1	0.9058	42.40	C3	1.5556	45.11
C1'	0.6103	23.42	C3'	1.5839	45.23
C2	1.2030	18.07	C4	2.3204	11.87
C2'	1.1721	20.64	C4'	2.3023	11.53

When the flux ratio β is further enlarged (C3 and C3'), and/or the distance between primary and secondary inlets is further increased (C4 and C4'), the differences of the trend lines for both swirl number and reverse flow rate between twin/single swirl are quite subtle, as it shown in Fig 4 (b) and (d). This could be explained by the relatively limited influence of the swirl momentum generated by the primary air, when β was changed from 1:3 to 1:5. Furthermore, the larger Δx weakens the swirl superposition effect. Compared with the secondary air, whether the primary air is swirling or not, there is less impact on the internal swirl flow and recirculation, with a relatively small β and large Δx.

The arithmetic means for both swirl number S and reverse flow rate X_r in 13 different axial positions are demonstrated in Table. 2. The dimensionless axial positions (x/H) for these cross-sections which perpendicular to the axis x are 0.24, 0.8, 1.6, 2.4, 4.0, 4.8, 6.4, 7.2 and 7.92. The quantitative analyses confirm the conclusions from the qualitative study of Fig. 7, as is mentioned above.

Conclusion

The confined swirling flow inside the chamber of the co-axial Twin Swirl Combustor (TSC) is studied with the RNG k-ε turbulence model. The validation case has proved that with qualified mesh and adequate mathematic method, RNG k-ε model is able to yield reliable results which could meet the requirements for industrial design and modifications. The swirling and recirculation characteristics in the chamber of TSC have been analyzed and discussed under different flux ratio of primary and secondary air, as well as the inlet structure. Conclusions can be made from the comparison on the trend lines of swirl number S and reverse flow rate X_r:

1) There is a notable negative correlation between the trend lines of swirl number (S) and reversed flow rate (X_r). The extreme values appear in the same axial location for S and X_r, when maximum or minimum is allocated to either of them.

2) The end-surface-inlet structure has a better swirl and recirculation enhancement effect when both the primary and secondary air are swirling. The gradient of reverse flow rate X_r is larger in the front and middle part of the combustion chamber than that of swirl number S. The swirl and recirculation intensity could be flexibly adjusted by regulating the swirling primary air.

3) With the staggered-inlet structure, the swirling and recirculation enhancement created by increasing the flux of swirling secondary air is not more notable than end-surface-inlet structure. Few differences are observed on the swirling and recirculation features inside the chamber when the primary air was turned from swirling to non-swirling. There is a critical distance between primary and secondary air inlets. When exceeded, it is more difficult to enhance the swirl and reverse flow effect by increasing the swirl intensity of the secondary air.

Acknowledgements

This work was financially supported by China Scholarship Council, Funding of University-industry Cooperation and Innovation of Jiangsu (BY2012020) and Funding of Jiangsu Innovation Program for Graduate Education (CXLX11_0193). Thanks also go to Dr. Zhaofeng Tian and Prof. Bassam Dally from the University of Adelaide, for their patient and helpful instructions and advice on the CFD simulations.

References

[1] D. Wang, Z. Ma, X. Wang, and L. Zhou, "Experimental studies on gas—Particle flows and coal combustion in new generation spouting—Cyclone combustor," *Journal of Thermal Science,* vol. 5, pp. 132-137, 1996.

[2] Z. Qi Li, R. Sun, Z. X. Wan, S. Z. Sun, S. H. Wu, and L. Z. Chen, "Gas-particle flow and combustion in the near-burner zone of the swirl-stabilized pulverized coal burner," *Combustion Science and Technology,* vol. 175, pp. 1979-2014, 2003/11/01 2003.

[3] Z. Chen, Z. Li, F. Wang, J. Jing, L. Chen, and S. Wu, "Gas/particle flow characteristics of a centrally fuel rich swirl coal combustion burner," *Fuel,* vol. 87, pp. 2102-2110, 2008.

[4] R. Weber, F. Boysan, J. Swithenbank, and P. A. Roberts, "Computations of near field aerodynamics of swirling expanding flows," *Symposium (International) on Combustion,* vol. 21, pp. 1435-1443, 1988.

[5] R. Weber, B. M. Visser, and F. Boysan, "Assessment of turbulence modeling for engineering prediction of swirling vortices in the near burner zone," *International Journal of Heat and Fluid Flow,* vol. 11, pp. 225-235, 1990.

[6] A. M. Jawarneh and G. H. Vatistas, "Reynolds Stress Model in the Prediction of Confined Turbulent Swirling Flows," *Journal of Fluids Engineering,* vol. 128, pp. 1377-1382, 2006.

[7] P. Wang, X. S. Bai, M. Wessman, and J. Klingmann, "Large eddy simulation and experimental studies of a confined turbulent swirling flow," *Physics of fluids,* vol. 16, p. 3306, 2004.

[8] Q. Hou and Z. Zou, "Comparison between Standard and Renormalization Group k & epsilon; Models in Numerical Simulation of Swirling Flow Tundish," *ISIJ International,* vol. 45, pp. 325-330, 2005.

[9] A. Gupta and R. Kumar, "Three-dimensional turbulent swirling flow in a cylinder: Experiments and computations," *International Journal of Heat and Fluid Flow,* vol. 28, pp. 249-261, 2007.

[10] G. Rocklage-Marliani, M. Schmidts, and V. I. Vasanta Ram "Three-Dimensional Laser-Doppler Velocimeter Measurements in Swirling Turbulent Pipe Flow," *Flow, Turbulence and Combustion,* vol. 70, pp. 43-67, 2003.

Advanced Materials Research Vols. 960-961 (2014) pp 349-352
© (2014) Trans Tech Publications, Switzerland
doi:10.4028/www.scientific.net/AMR.960-961.349

Optimization design and analysis of heat pipe internal factors based on the orthogonal test method

Shouguang Yao[1, a], Jiangwei Deng[2,b], Dong Sheng[3,c], Xinwang Jia[4,d] and Sheng Lu[5,e]

[1] School of Energy and Power Engineering, Jiangsu University of Science and Technology. Zhen Jiang, 212003, China

[5] School of Material and Science Engineering, Jiangsu University of Science and Technology. Zhen Jiang, 212003, China

[a]zjyaosg@126.com, [b]624195379@qq.com

Keywords: Heat pipe; Orthogonal test method; Optimization levels; Heat transfer performance

Abstract. In order to study the influence of various factors on the heat pipe heat transfer performance, the heat transport limit was taken as test index, nine groups of heat pipe factors matching experiments were carried out based on the orthogonal test method. Four heat pipe internal factors including wick, work media, mass concentration and filling ratio were studied. The results show that the wick has the greatest influence, filling ratio ranks the second, while the work media and mass concentration are not so obviously; the wick and work filling ratio both have significant influences on test index, while work media and mass concentration have little significance.

Introduction

Working media and the wick are two important parts of heat pipe, which are closely related to the heat pipe heat transfer performance due to its structure and characteristics [1-4]. However, it is always confused to select the optimization factors and levels when study heat pipe heat transfer performance, such as the optimal combination among the wick, work media, mass concentration and filling ratio [5]. It must be considered how to find the optimal levels and main factors for heat pipe heat transfer performance with fewer test as possible.

In this paper, synthesizes the effects of heat pipe internal factors, such as wick, work media, mass concentration and filling ratio on heat transfer performance, and heat transport limit P was taken as test index in the test. The heat pipe tasted in this paper was copper tube (wall thickness 0.7 mm, outer diameter 12 mm).

The principle of orthogonal test method

Orthogonal test is a design method by using orthogonal table to arrange multi-factor and multi-level experiment [6]. Its core idea is through some typical combination to illustrate the information of the total test combination, and find out the optimal combination.

For example, a three factors three levels test, factor A have three levels: A 1, A 2, A 3; factor B have three levels: B 1, B 2, B 3; factor C have three levels: C 1, C 2, C 3, the possible combination is 27. As shown in Fig. 1, 27 points on the cube stand for the total test, 9 test points marked with "1" to "9" on the cube were selected by orthogonal table L_9 (34). Seen from the cube, each plane has three test points and each line has one test point, 9 test points are evenly distributed, every factor level has the same combination chance with other factor levels. These 9 points are very representative, can fully reflect the the total test characteristics and so reliable. According to the results and analysis of orthogonal test, the influence of various factors on the index, the significant, the optimal combination of different factors can be studied.

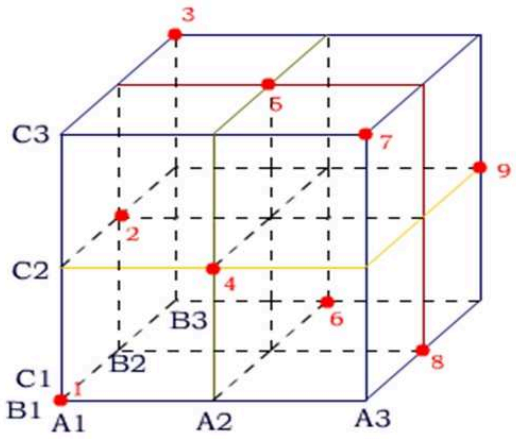

Fig. 1 The principle diagram of the orthogonal test

The orthogonal experiment design and arrangement

The wick, work media, mass concentration and work filling ratio are the major factors that influence heat pipe heat transfer. Different combination results in different heat transfer performance, we try to find the best combination of the four major factors to reach the maximum heat transfer potential: heat transport limit P. As show in Table 1, A stands for different wick form, PPI (pores per inch) is the porosity of the wick; B stands for filling ratio; C stands for work media; D stands for the mass concentration, 0% in the table means the work media is water. Each factors has three levels, regardless of the the factors interaction, an orthogonal $L_9(34)$ table [7-8] was used to find the best combination of heat transport limit. And the test plan and results was shown in Table 2.

Results and discussion

Range analysis and variance analysis are two common methods of orthogonal experimental design. Range analysis method can distinguish the primary and secondary order of various factors, and can find out the optimum level combination. But this method cannot distinguish the difference between the corresponding test results of difference factor level, also has no standard to make a judgement whether the factors have significant effect on the test index results,so variance analysis was uesd as a complement.

Range analysis. Range value reflects the changes of test index if a certain factor level changes, the more, the greater influence on index. Range analysis table is shown in Table 3. Attention: K_i is the sum value of the test index, k_i is the average value of the test index, R is the range of factors, is equal to the difference between maximum k and minimum k.

Table 1 Table of factor levels

Factors	Levels		
A: Wick	1(300 PPI mesh)	2(160 PPI copper foam)	3(160 PPI copper foam)
B: Filling ratio	1(40%)	2(50%)	3(60%)
C: Work media	1(SiO_2)	2(Al_2O_3)	3(CuO)
D: Mass concentration	1(0%)	2(0.3%)	3(0.5%)

Table 2 Analysis of the test data

Test number	Factor A	B	C	D	Index P
1	1 300 PPI mesh）	1(40%)	1(SiO_2)	1(0%)	105.8
2	1	2(50%)	2(Al_2O_3)	2(0.3%)	134.7
3	1	3(60%)	3(CuO)	3(0.5%)	126.3
4	2(160 PPI copper foam)	1	2	3	95.4
5	2	2	3	1	124.9
6	2	3	1	2	100.2
7	3(200 PPI copper foam)	1	3	2	136.3
8	3	2	1	3	156.4
9	3	3	2	1	136.4

Table 3 The table of ranges analysis W

Range	Factors A	B	C	D
K_1	366.8	337.5	362.4	367.1
K_2	320.5	416	366.5	371.2
K_3	429.1	362.9	387.5	378.1
k_1	122.3	112.5	120.8	122.4
k_2	106.8	138.7	122.3	123.7
k_3	143.0	120.9	129.2	126.0
R	36.20	26.20	8.37	3.67

As can be seen from Table 3, the maximum average index value of factor A is k_3(143.0 W), factor B is k_2(120.9 W), both factor C and D are k_3(129.2 W and 126.0 W). According to the results, 200 PPI copper wick has the greatest influence on heat pipe heat transfer limit, 160 PPI has the minimum influence; 50% filling ratio has the greatest influence on heat pipe heat transfer limit, 60% ranks second, while 40% has minimum influence; when compared the influence of work media, CuO- water nanofluids have a heat transfer advantages than that of other three work media; mass concentration has no obvious influence on heat transfer limit, but using nanofluids can make a difference on heat transfer limit, the value of 0.5% is the best. It can also be found that the influence on the heat transfer limit in the order of A>B>C>D. The conclusion can be reached from the discussion above: the important order of influence on test index is A B C D, Factors A 3, B 2, C 3, D 3's influence is the greatest. The optimal combination is A 3 B 2 C 3 D 3; that is, the wick 200 PPI copper foam, the filling ratio is 50%, work media is CuO-water nanofluids, mass concentration is 0.5%. When cooling water flow is 9 L/h, heat pipe heat transfer limit is the highest.

Variance analysis. The basic idea of variance analysis is total changes of test index value can be divided into two parts: changes caused by factors level, changes caused by test error. By F-statistics, significant effect of factors on test index shall be determined. Variance analysis of test results are listed in Table 4. And the principles of determine are as follows:(1)$F>F_{0.01}$, the factor has a very significant influence on the test index value, even a small changes in factor will results in big difference on test value; (2) $F_{0.01}>F>F_{0.05}$, the factor has a significant influence on the test index value; (3) $F<F_{0.05}$, the factor has little significant influence on the test index value.

Table 4 The table of variance analysis

Source	Sun of squares	Mean square	Freedom degree	F
A	1979.88	989.94	2	96.1
B	1069.67	534.8	2	51.9
C	120.87	60.43	2	5.8
D	20.6	10.3	2	1
Error	20.6	10.3	2	1

Check from the F statistic distribution table, $F_{0.05}$=19, $F_{0.01}$=99, while in this test, F_A=96.1, F_B=51.9, F_C= 5.8, F_D=1. According to the principle, factor A and B are the primary factors, have great significant influence on hear pipe heat transfer limit, factor A is more evidently than factor B; both factor C and D are secondary factors, have little significant influence on heat transfer limit.

Conclusions

(1)Various internal factors have influence on heat transfer performance, by orthogonal test, wick and filling ratio are the two primary factors, which have great significant influence on heat transfer limit .

(2) work media and mass concentration have little significant influence on heat transfer limit, but reasonable choice can also improve heat transfer performance.

(3) The optimal combination is: the wick is 200 PPI copper foam, the filling ratio is 50%, work media is CuO, mass concentration is 0.5%. When cooling water flow is 9 L/h, heat pipe heat transfer limit is the highest.

Acknowledgements

This work was financially supported by National Natural Science Foundation of China through Grant （NO .51176069. We warmly thank Luobin Duan for helpful discussions.

Reference

[1] T.Shu and Z.H,Liu: Journal of Aerospace Power,Vol.23(2008) No.10, p.1623-1627[in Chinese].

[2] L.Zheng, J.X. Li and M.Zhu: CIESC Journal,Vol.62(2012) No.12, p.3861-3866[in Chinese].

[3] Y.X. Zhang, H.D. Dong and J.Q. Qi: Chemical Equipment Technology, Vol.34(2013) No.1,p.47-49 [in Chinese].

[4] S.G. Yao, Z.S. Ma, L.Luo and R.B. Chen: Journal of East China Shipbuilding Institute(National Science Edition),Vol.17(2003) No.4, p.9212[in Chinese].

[5] S.G. Yao, Q.F. Chen, G.L. Wang, D.Sheng and S.Lu: Journal of East China Shipbuilding Institute (National Science Edition),Vol.27(2013) No.6, p.556-560 [in Chinese].

[6] Y.C. Chen, Y.M. Sun and J.M. Mou: ISIJ International, Vol.49(2009) No.5, p. 743-748.

[7] M.H. Wang, K.D. Woo, T.P. Lou, Y.C. Zhai and D.K. Kim: International Journal of Hydrogen, Vol,30(2005) No.4, p.381-384.

[8] Z.X. Liu, R.H. Huang and A.M. Tian: *Experimental Design and Data Processing*(Chemical Industry Press, China, 2005) [in Chinese].

Advanced Materials Research Vols. 960-961 (2014) pp 353-357

doi:10.4028/www.scientific.net/AMR.960-961.353

Research of Dirt Growth Pattern Based on the different heat exchanger pipe

Li Bai[1,a] Tan Liu[1,b]

([1]Jilin Universality of Architecture and Civil Engineering, School of Municipal and Environment Engineering, Changchun, China)

[a]baili0308@163.com,[b]ltmapro@163.com,

Keyword: Different materials; different times; the unit area of dry dirt mass; Growth pattern analysis

Abstract: This experiment wastewater treatment plant set up a device of researching different periods of dirt on the different heat exchanger tubes. The moisture test of dirt were derived from tubes of different materials (copper alloy tube, stainless steel pipe, polyethylene-aluminum composite pipe) is between 92.50% and 96.70%, This shows that the quality of per unit area of dry dirt to describe variation is feasible. The induction period of dirt on the copper alloy is between the 0d and 35d, the growth cycle is longer. In the mature period, the quality of per unit area of dry dirt is 2.031 mg/cm^2. The induction period of dirt on the stainless steel is between the 0d and 20d, the growth cycle is shorter. In the mature period, the quality of per unit area of dry dirt is 2.627 mg / cm^2. The induction period of dirt on the polyethylene-aluminum composite pipe is between the 0d and 35d, the growth cycle is shorter. In the mature period, the quality of per unit area of dry dirt is 2.863 mg/cm^2.

Foreword

The characteristics of heat transfer tube surface are different, the roughness, the surface free energy of the surface will affect the adhesion property of the dirt[1]. The literature mentioned in recent years, sewage source heat exchanger tubes are mainly three kinds, namely, copper alloy tube, stainless steel pipe, polyethylene-aluminum composite pipe [2]. In this experiment, the sewage is regarded as the heat source, combining the growth situation of three kinds of pipe , making dynamic experiments and comparative analysis.

Experimental introduction

In order to studying of three dirt's growth pattern, building three experimental pipe respectively, DN 20mm copper alloy tube, DN 20mm stainless steel pipe, the DN 20mm polyethylene-aluminum composite pipe, flow velocity V = 0.78m/s, a sewage influent water to plant secondary sewage effluent. The feed water come from a sewage treatment plant secondary effluent in changchun. According to the sampling date, name the experiment section numbers. Such as T - 12/06/04 for sampling date is on June 4, 2012 copper tube section. as shown in figure 1,put a row of experimental section as an example, the S0 valve is open, S1, S2, S3 valve is in the closed position, the sewage through the bypass valve and meter, loop through T3, T2, T1 and T1 ', T2 ', T3 ' ,flow to the next unit, sampling time period is t1,t2, t3 ••• tn, at the time when the t1 in, all of the experimental section's bio-film growth period is the t1 time. After t1 time ,close T0 valve, open the S1 valve, S2, S3 remain closed, removal the T1 number section, S0 valve, T1' number section for

sampling and analysis. When after t2 time, close S1 valve, open the t2 valve, the experimental section of bio-film growth within the t1 and t2 time, then use the same principle of regular sampling and records, to observe the different periods bio-film growth situation.

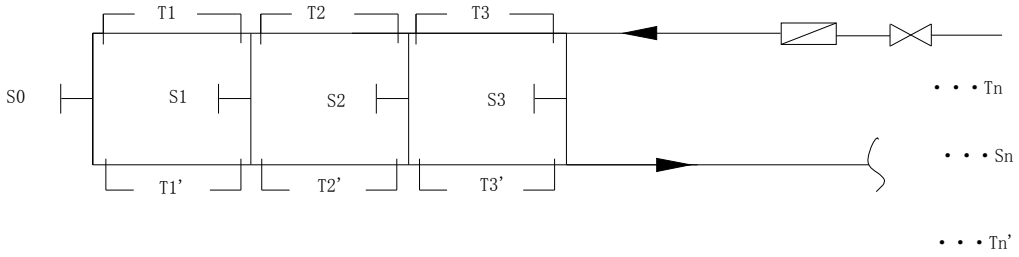

Figure 1 Experimental principle diagram

Moisture content analysis of the different dirt

Analysis result of moisture and burning weightlessness as table 1 shown, in 105 ~ 110 ℃ drying to constant weight loss is water. Moisture content at 92.50% ~ 96.60%,in the 550 ℃ burning to constant weight, the weight loss of the part is the biological sticky mud, combined water, organic matter [4]. In 950 ℃ calcination to constant weight, the weight loss part is CO2. The dirt in the 550 ℃ and 950 ℃ calcination weight value was 68.45% ~ 85.53% and 0.77% ~ 1.86%. Dirt moisture content is very high, dry dirt of the composition is mainly organic matter.

Table 1 The dirt moisture content and burning weightlessness analysis

Numbers	Sample quality	moisture (%)	550 ℃ calcination lost weight(%)	950 ℃ calcination lost weight(%)
T-11/06/19	1.0221	96.5689	72.896	0.7698
B-11/06/19	1.0125	92.4616	68.452	0.7952
L-11/06/19	1.0098	95.4212	85.527	1.8564

The different material exchanger pipe's dirt growth record

Respectively collect the three tube dirt samples, sample records such as table 1:

Table 2 Sampling site record

number	run days	scale sample description	dry biomass mg/cm2
T-11/04/20	5d	Smooth, no bio-film	0.221
B-11/04/20	5d	Smooth, no bio-film	0.398
L-11/04/20	5d	Smooth, little bio-film	1.232
T-11/05/05	20d	Smooth, no bio-film	0.245
B-11/05/05	20d	Smooth, no bio-film	0.532
L-11/05/05	20d	little bio-film	1.354
T-11/05/20	35d	Smooth, no bio-film	0.286
B-11/05/20	35d	Smooth, little bio-film	1.487
L-11/05/20	35d	thin, not easy peeling off	2.654
T-11/06/04	50d	thin	1.454
B-11/06/04	50d	thin, dense, not easy peeling off	2.627
L-11/06/04	50d	have fibrous macro creatures, thick,	2.863

		not easy peeling off	
T-11/06/19	65d	thick, dense, not easy peeling off	2.031
B-11/06/19	65d	have fibrous macro creatures, thick, easy peeling off	1.334
L-11/06/19	65d	have fibrous macro creatures, thin, easy peeling off	2.231

From the table 1, Because the quality of dry dirt keep increasingly, we know that copper tube dirt growth cycle period is longer than 65d. stainless steel tube's fouling growth cycle is about 65d, polyethylene-aluminum pipe's dirt growth cycle is almost 65d .The copper dirt growth cycle is long, polyethylene-aluminum tube dirt growth cycle is short. This is because:(1) copper tube surface is smooth, the crack is scattered and small, and polyethylene-aluminum tube surface crack arrange closely, heat transfer surface area is far greater than other pipe surface area; (2) copper tube surface is the presence of copper ion, which have certain inhibition function to the growth of microorganism.

Copper alloy tube fouling growth variation analysis

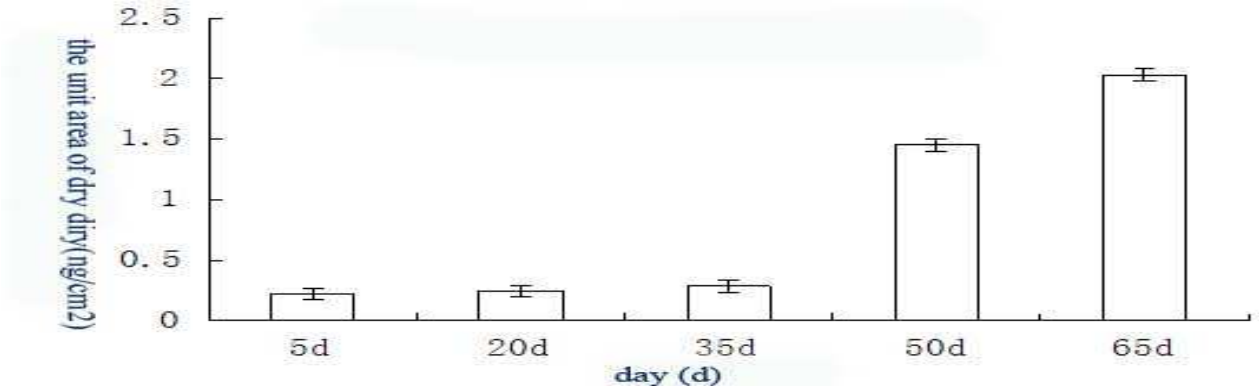

Figure 2 The increase regularity of copper alloy tube surface dirt

From Figure 2, the copper alloy tube fouling growth cycle is longer, the copper alloy tube fouling growth induction period is between 0d and 35d, 35d-65d is the logarithmic growth phase. The quality of dry dirt in induction period and maturity period is 0.286 mg / cm ^{2} and 2.031mg/cm ^{2}. This shows that the copper alloy tube is not easy to adhere dirt.

Stainless steel tube fouling growth variation analysis

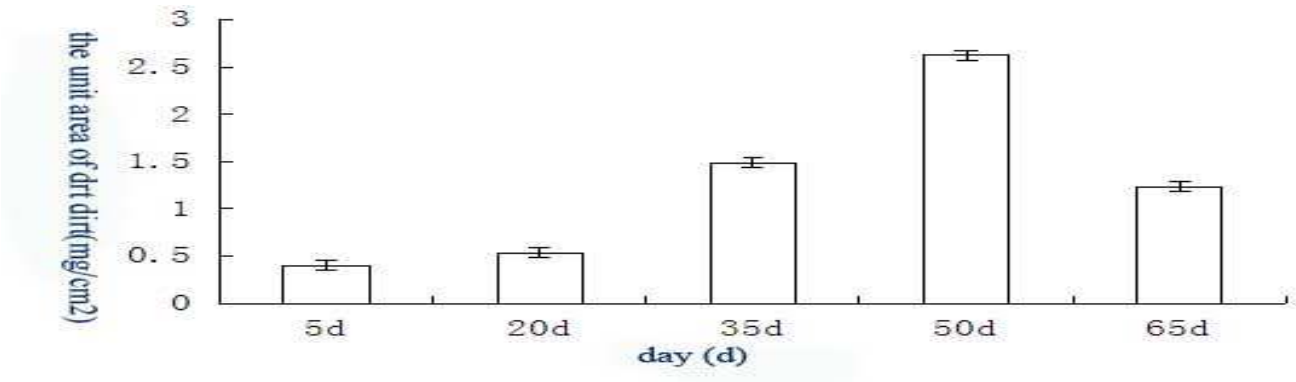

Figure 3 The increase regularity of stainless steel tube surface dirt

At the figure 3, the stainless steel surface dirt induction period is between 0d and 20d, the stain logarithmic growth phase is from the 20d to 50d. The amount of dirt shedding larger before the 65d, because stainless steel pipe surface is smooth, and have little adhesion of dirt.

Aluminum tube fouling growth variation analysis

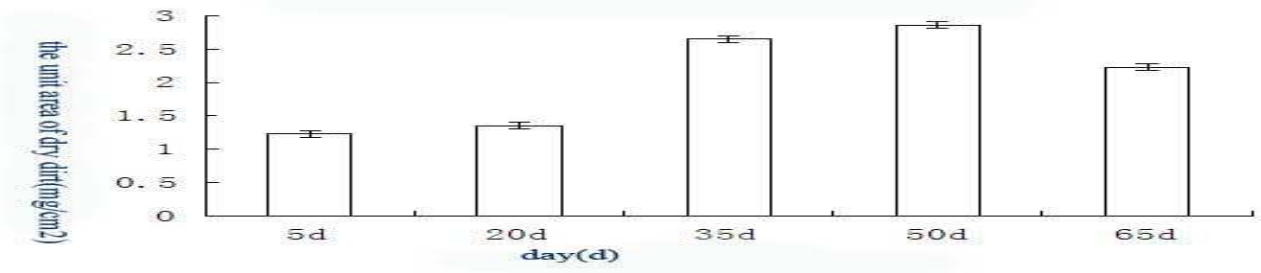

Figure 4 The increase regularity of the polyethylene-aluminum composite pipe surface dirt

Figure 4 shows that the growth cycle is short aluminum pipe. Induction period is from 0d to 20d, and the induction period is greater than 1mg/cm^2.this is because the specific surface area aluminum tube, resulting in the induction phase of the large surface dirt. Dirt grow into the stable period at 35d, and at 50d into the off period. The dirt on the maturity of the mass per unit area is more than 2.5mg/cm^2, and less dirt shedding, it is because of the larger surface area of the stain of solid foundation, can resist the erosion of sewage and shear force.

Conclusion

(1) The moisture content of the three pipes showed that the stain ignition moisture content 92.50% ~ 96.70%, the weight loss at this time is mainly water, the remain is compound water and organic matter. Dirt moisture is in a certain range, and keep stability. Therefore, the use of the area of the stain dry dirt to research quantity description rule is feasible.

(2) This experiment use urban sewage to be heat source. Dirt drawn copper alloy tube growth induction period between the 0d and 35d, stainless steel tube fouling induction period is at 20d. The aluminum tube induction period is at the 30d. Dirt within the copper alloy tube fouling growth cycle is longer, aluminum pipe dirt have a short growth cycle. Probably because the surface of the copper alloy tube is smooth, and copper ions give the dirt an early microbial growth inhibition, resulting in copper alloy surface dirt's growth cycle is longer.

(3) Copper alloy tube induction period and maturity dirt dry mass per unit area was 0.286 mg/cm^2 and 2.031mg/cm^2, stainless steel pipe induction period and maturity dirt dry mass per unit area were 0.532 mg/cm^2, and 2.627 mg/cm^2, aluminum tube induction period and maturity dirt dry mass per unit area was 1.354 mg/cm^2 and 2.863mg/cm^2.The specific surface area of copper alloy tube is much bigger than the specific surface on the polyethylene-aluminum composite pipe surface area, the uneven surface of copper alloy pipe provides habitat for microbial growth, resulting in a specific surface area become smaller than polyethylene-aluminum composite pipe's dirt.

Acknowledgment

The authors gratefully acknowledge the financial support from the National Science Foundation of China.(Grant Nos.50978120).

References

[1] Tianqing Liu.Ruihong Yu, [J] ACTASCIENTIAE CIRCUMSTANTIA ,2001-21-4 ,491-494.
[2] Bai Li,Yin Jun, Liao Zi-sheng based aluminum pipe improved urban sewage heat energy heating systems [J]. Jilin University, 200 6, 36 (2) :269-273.
[3] Li Xin, Sun Dexing, sewage source heat pump system, heat exchanger fouling growth characteristics, Harbin Institute of Technology Engineering Thesis .2005.
[4]Bhosle N, Suci PA, Baty AM, et al. Influence of divalent cations and pH on adsorption of a bacterial polysaccharideadhesion [J].Journal of Colloid and Interface Science,1998,205: 89-96.

Advanced Materials Research Vols. 960-961 (2014) pp 358-365

doi:10.4028/www.scientific.net/AMR.960-961.358

Research on the initial features and spreading rules of large scale oil fire

Xinsheng Jiang[1, a], Guojun Sun[1, b], Biao He[1, c], Yihong Ou[1, d], Dong Wang[1, e] and Jianzhong Zhou[1, f]

[1] Department of Military Oil Supply Engineering,

National Engineering Research Center for Disaster and Emergency Rescue Equipment,

Logistical Engineering University,

Chongqing, P.R.China 401311

[a] jxs_dy@163.com, [b] sgj66@vip.qq.com, [c] 993612061@qq.com,

[d] oyh1219@163.com, [e] eletterbox@126.com, [f] zmeim@tom.com

Keywords: oil fire; temperature distribution; thermal radiation; gaseous pollutant component.

Abstract. The initial features of large scale oil fires were studied through combustion experiments in oil basins. Four basins were prepared, the diameters of two of them were 2.5m, and another two were 2m. Oil in the basins was ignited simultaneously, and the experiments were conducted twice. The thermal radiation, temperature distribution and components of pollutants were detected and analyzed. Then, some initial features and instructive rules of large scale oil fire disasters were concluded. Known from the experiments, the temperature is high in center areas and low around, in the vertical direction the temperature is high both in upper part and bottom and low in the middle. In addition, the density values of gas pollutants sampled during the experiments can reach to several hundred times of the standard values.

Introduction

Oil is a kind of important but flammable and explosive strategic resource, thus oil depot safety has always been the most concerned and urgent subject of relevant departments at all levels[1, 2].

Statistics show that noxious gas released from oil combustion is the key factor leading to casualties, thus the evaluation and forecast of gas components in fires are important subjects in the field of fire risk assessment. The analyzing methods and principles of gas composition based on Fourier transform infrared spectroscopy (FTIR) are introduced in literature [3]. Smoke extraction in case of fire in a tunnel is investigated experimentally in literature [4]. The producing mechanisms and the component detection methods of smoke are summarized in literature [5].

When oil depot fires break out, masses of oil catch fire and release lots of heat into the atmosphere, the heat extend outwards continuously in the form of radiation and convection. Suppose that there were combustible substances, trees and weeds for example, near the fire, they might be ignited simply by the energy delivered from heat radiation and convection, which results in worse situation and greater loses. Therefore, when evaluating the danger and pollution of oil fires, not only harmful gases and dusts in combustion need to be researched, but also the thermal pollution during combustion and the diffusion ability of the disaster need to be evaluated and analyzed[6, 7]. A systematic procedure for the quantitative assessment of the risk caused by domino effect is developed in literature [8]. The minimum fire suppression distance considering the safety of fire fighters is studied under the condition of 5 meter high flame and different critical heat radiation flux in literature [9]. The variation of flame temperature with time and height is studied in hydrocarbon pool-fires in literature [10]. Two synthetic 30 cm-diameter pool fires, generated from experimental data, are used to assess different radiative properties models in literature [11].

The literatures mentioned above have obtained certain achievements, but due to the complexity of fire itself; the difficulty in numerical modeling; great inaccuracy and weak similarity and different characteristics presented in different kinds of fires, more experimental data are needed

for further research. To this end, this article simulated the initial features of oil fire through experiments, collected the data of heat radiation, temperature, pollution components of the simulated fire, and concluded the initial features and rules of large scale oil fires.

The experimental system in this article mainly consists of experimental bench, data acquisition system and auxiliary experimental devices.

Experimental bench

The bench mainly consisted of oil basins, sampling system, supports of test devices, etc.

Oil basins. Oil basins were containers for the oil fire burning, welded from A3 steel plates with thickness of 3mm, including four basins with height of 0.3m, and the diameters of two of them were 2.5m, another two were 2m, some water was added into the basins before experiment for avoiding deformation caused by high temperature. Thin wire nettings were covered on the basins to ensure the homogeneity and constancy of burning. The arrangement plan of the experiment is shown in Figure 1.

Figure 1. Basins arrangement

Sampling system. The temperature of combustion products and atmosphere around the fire was so high after ignition that detection equipments could not get close to the fire and sampling could not be conducted directly. Thus the pollutants in high temperature needed to be cooled and sampled far away. The sampling system consisted of the sampling equipment, the cooling equipment, air pump and pipes. The sampling equipment consisted of Φ0.25×3m steel pipe and support, which could sample pollutant air in fixed points, high-temperature fields and flaming areas. The cooling equipment was a Φ0.08×1.5m brass pipe immersed in water, the air pump was a kind of diaphragm type air compressor pump, which could deliver sample gas into detection devices.

Data acquisition system. Data acquisition system mainly consisted of temperature online detection system, pollutant density test system, radiation heatflowmeter and live video capture system, etc.

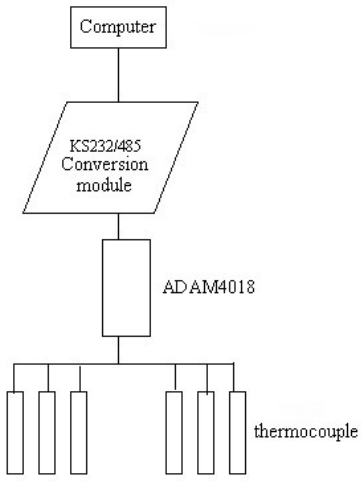

Figure 2. Structure of temperature online detection system

Individual protection facilities and emergency equipments. To meet the demand of close monitoring in experimental field simulating oil depot fires and handling sudden fire spread in emergency, protective and emergency equipments like fire-proof suit, fire-smothering blanket and fire extinguisher were prepared.

Experimental parameters and process

In the process of experiment, ten temperature and one thermal radiation measuring points were set around the fire to collect environment temperature and thermal radiation value during the burning process in real time, the arrangement plan of the temperature measuring points is shown in Figure 3.

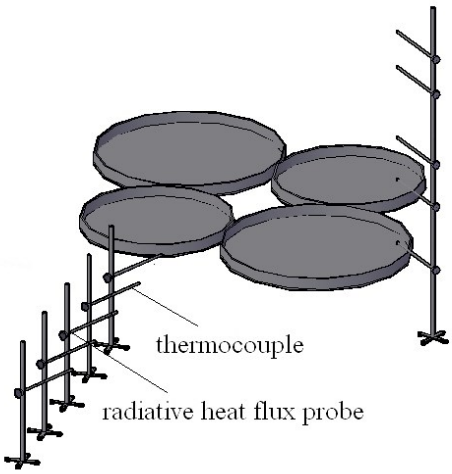

(a) General arrangement of experimental field

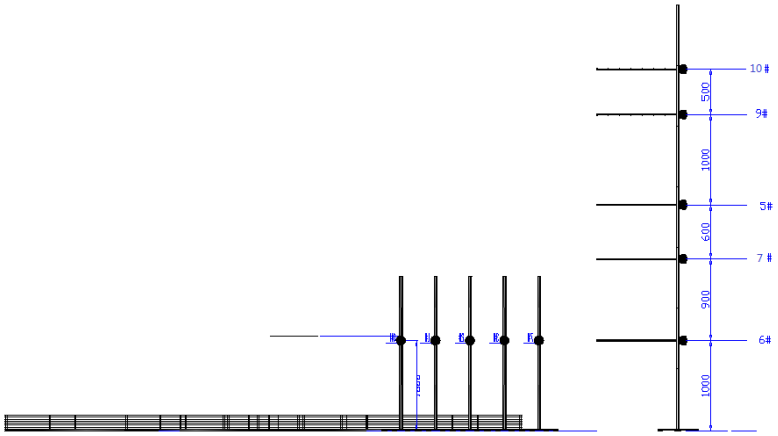

(b) Temperature measuring points arrangement

Figure 3. Experimental field and temperature measuring points arrangement

The environment temperature during the experiment was 11℃ and the atmospheric pressure was 98.6 kPa. The experiment was conducted twice, for each time every basin was filled with 25L $0^{\#}$ diesel separately, and 4 basins with 1L gasoline in total for the use of ignition. Wind speed in the first experiment was about 1.4～2 m/s, wind direction was about north by east 22.5～45 °. In the second experiment the wind speed was about 1.4～1.6 m/s and the wind direction was about north by east 0～30 °.

Data analysis

Thermal radiation and temperature data analysis. Experimental data from temperature measuring points and thermal radiation measuring points are shown in Figure 4. Seen from the graph,

the temperature gradient in the horizontal direction gradually decreases as the distance increases, the temperature of the measuring point closest to the fire was far higher than the one of other points, but in the vertical direction the temperature did not decline progressively. Together with the position of sensors shown in Figure 3, we can see the temperature was high in top and bottom and low in middle. This was mainly decided by the shape of fire and smoke, as shown in Figure 5.

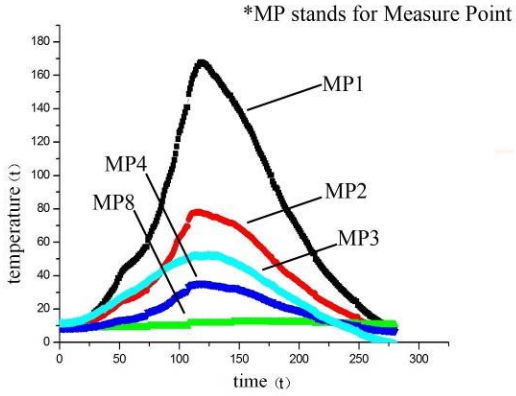

(a) Temperature data of the first experiment in the horizontal direction

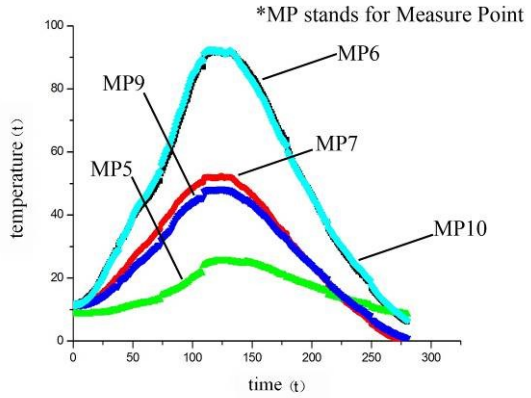

(b) Temperature data of the first experiment in the vertical direction

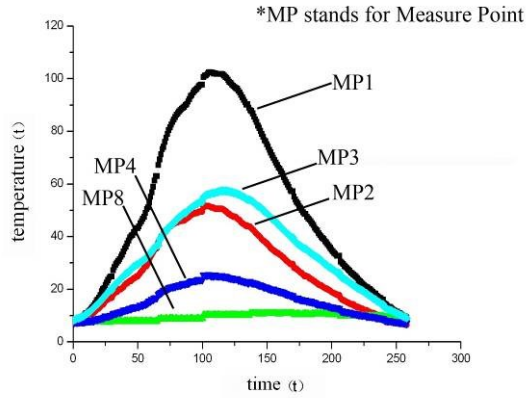

(c) Temperature data of the second experiment in the horizontal direction

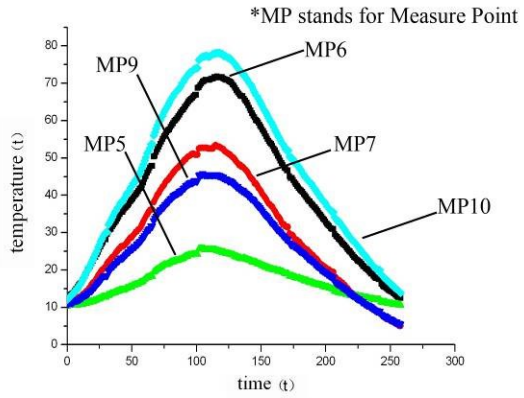

(d) Temperature data of the second experiment in the vertical direction

Figure 4. Experimental data of each temperature measuring points

Figure 5. Shape of fire and smoke during combustion

It can be seen from the picture, the lower part of fire was naked flame and the upper part was dense smoke. Consider the temperature distribution in vertical direction, the flame in lower part released heat without limit, so the nearest measuring point, No.6, received more heat and which temperature was higher than the others. In middle part of the flame, dense smoke took in flux heat from flame and resulted in temperature rise, but the temperature and heat radiation of the smoke was far lower than that of the flame, so measuring points in the middle got less heat. In the upper part, measuring point No.10 was surrounded by dense smoke with the help of wind, in this condition, heat convection between smoke and the measuring point rose sharply, which resulted in similarly high temperature. In summary, in vertical direction, temperature was high in lower and upper part and low in the middle.

In terms of radiation, owing to the relatively large quantity of gasoline, the oil burned quickly, the radiation value reached its peak at 100 seconds or so, but the general level of radiation and its influence to temperature field were equivalent to former experiments, as shown in Figure 6.

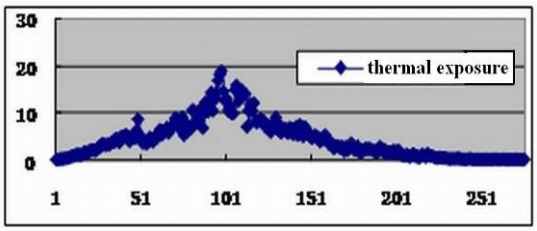

(a) Radiation in the first experiment

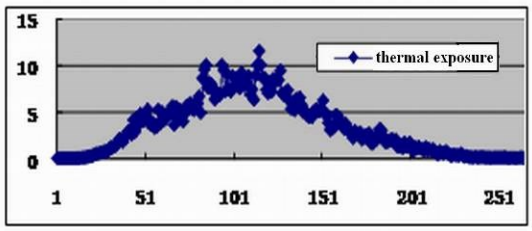

(b) Radiation in the second experiment
Figure 6. Radiation data

Test result and Analysis of gas pollutants. Two experiments both lasted for about 5min and during which samplings lasted for 3min, samples were taken every 5s. Test results of gas pollutant components near the fire source in two experiments are shown as follows.

CO.As shown in Figure 7, the density of CO gradually rose after ignition, in the first experiment, release of CO reached its peak at about 1.5min after ignition, and in the second at about 2min, then the release value dropped with the abatement of fire after the peak. The same quantity of oil was burned in two experiments, the production law of CO agreed basically, the gas sampling process might be influenced by wind, which resulted in that the peak value of CO in the second experiment only equaled to a half of that in the first experiment.

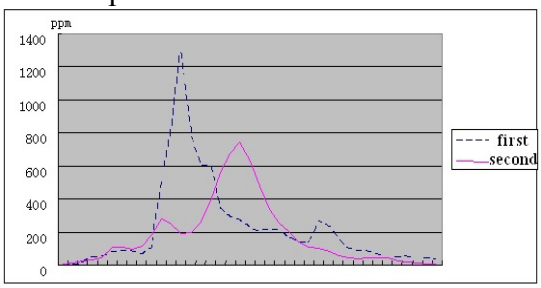

Figure 7. Density variation trend of CO

Known from results, the instantaneous maximum density of CO in the first experiment was 1290ppm, the average density during sampling process was 315ppm, comparing with the second level limit of average density of CO in one hour in *GB3095-2012 Ambient Air Quality Standard* [12], the instantaneous maximum density was 161 times of the standard value and the average density was 24 times of the standard value. The instantaneous maximum density in the second experiment was 744ppm, the average density during sampling process was 264ppm, the instantaneous maximum density was 93 times of the standard value and the average density was 19 times of the standard value.

NO. In both experiments, NO started to be detected at 0.5min after ignition, and its release peak appeared at about 1.5min, then release value dropped with the abatement of fire, this illustrated that NO had its regularity during burning process, as shown in Figure 8.

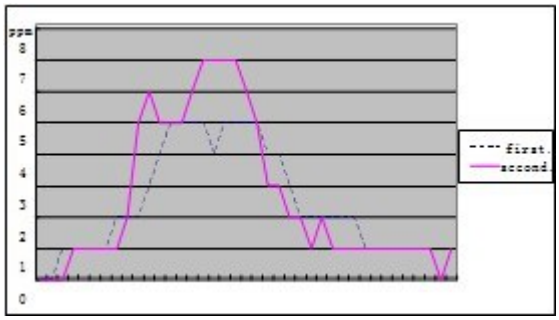

Figure 8**.** Density variation trend of NO

Known from results, the instantaneous maximum density of NO in the first experiment was 7ppm, the average density during sampling process was 2ppm, since NO can be quickly transformed

into NO_2 in air, the density of NO during the burning process can be seen as the density of produced NO_2, comparing with the second level limit of average density of NO_2 in one hour in GB3095-2012 Ambient Air Quality Standard, the instantaneous maximum density of NO_2 was 72 times of the standard value and the average density was 20 times of the standard value. The instantaneous maximum density of NO in the second experiment was 5ppm, the average density during sampling process was 2ppm, the instantaneous maximum density was 51 times of the standard value and the average density was 20 times of the standard value.

SO_2. In the first experiment, SO_2 started to be detected no long after ignition, and its release peak appeared at about 1.5min and reached 120ppm, then decreased rapidly, while in the second experiment, the density of SO_2 basically stabilized below 8ppm besides little rises and falls, as shown in Figure 9.

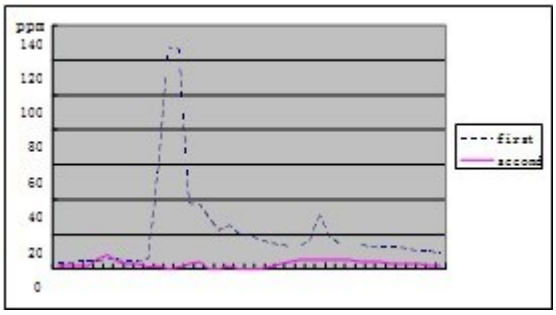

Figure 9. Density variation trend of SO_2

Known from testing results, the instantaneous maximum density of SO_2 in the first experiment was 127ppm, the average density during sampling process was 19ppm, comparing with the second level limit of average density of SO_2 in one hour in *GB3095-2012 Ambient Air Quality Standard*, the instantaneous maximum density was 725 times of the standard value and the average density was 108 times of the standard value. The instantaneous maximum density of SO_2 in the second experiment was 8ppm, the average density during sampling process was 3ppm, the instantaneous maximum density was 46 times of the standard value and the average density was 17 times of the standard value.

HC. In the first experiment, HC started to be detected no long after ignition, and its release peak appeared at about 1.5min and beyond 2200ppm, then release value decreased rapidly, while in the second experiment, HC density curve rose gently, and its release peak appeared at about 2min and reached 440ppm, as shown in Figure 10.

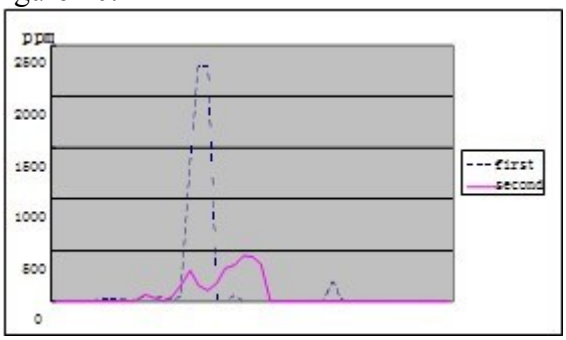

Figure10. Density variation trend of HC

Known from the results, at 1.5min after ignition the instantaneous density of HC reached the peak of 2298ppm in the first experiment, the average density during sampling process was 145ppm. At 2min after ignition, the instantaneous density of HC reached the peak of 436ppm in the second experiment, the average density during sampling process was 66ppm.

Under the condition of the same quantity of oil, the peak density values of all kinds of pollutants in the second experiment were apparently lower than that in the first experiment, it might result from some changes of wind direction meanwhile the location of inlet port of gas sampling

device was left unchanged, which leaded the peak density of pollutants during sampling to variation, but the variation trend of density agreed basically.

Conclusions

The experiments and research mentioned above can be concluded that:

- The temperature field around fire mainly influenced by heat radiation and convection, and direction of wind determines the location of fire radiation center. Temperature is centered by the center of flame radiation, which is regularly high in center areas and low in surroundings, and the temperature gradient gradually reduces from center to surrounding, in the vertical direction, the temperature appears high both in upper part and bottom and low in the middle.
- 2m away from radiation center, the heat radiation peak value reaches 10～20kW/m^2, it is mainly influenced by the oil burning velocity and has little to do with wind direction.
- Experiments indicate that with fire and explosion of oil depot, a great quantity of gas pollutants such as CO, NO, SO_2 and so on are produced, their instantaneous maximum density values far exceed the standard values, in dense smoke the density of CO is enough to stifle a man suddenly. In the initial period of fire, density of pollutants will rise rapaidly with the development of fire and diffuse to surroundings within several minutes, the release value usually reaches its peak 2min after ignition and then drops with the abatement of fire.

In experiments above, it lasted for about 5min from ignition to end, high level diffusion of pollutants lasted for about 3min. In real process of fire and explosion, burning usually lasts much longer than that in the experiment and production of pollutants is higher, as a consequence, its threat to man and environment is more conspicuous.

Acknowledgment

This work was sponsored by Chongqing Science and Technology Key Projects Fund (CSTC, 2012gg-sfgc00002), supported by Construction of Fire and Explosion Safety Protection Key Laboratory of Chongqing (CSTC, 2010CA0005).

References

[1] W.H. Wang, Z.S. Xu, B.J. Sun: Procedia Engineering ,52 (2013) 395 - 400.
[2] D.Q. Wang, P. Zhang, L.Q. Chen: Journal of Loss Prevention in the Process Industries, 26 (2013): 1390-1398
[3] Hakkarainen, Mikkola, Laperre, et al: Fire and Materials, 24 (2000): 101 - 112.
[4] O. Vauquelin, O. Mégret: Fire Safety Journal ,37 (2002): 525 - 533.
[5] Q. Li, Q.H. Liu, H. Zhang, C.Z. Lian, L.P. Zhan, Z. Lv: Journal of natural disasters, 12(3), (2003): 69-74 (in Chinese).
[6] M. Muñoz, J. Arnaldos, J. Casal, E. Planas: Combustion and Flame ,139 (2004): 263–277.
[7] Gunnar Heskestad: Fire Safety Journal, 5(2) (1983): 103-108
[8] Cozzani V, Gubinelli G, Antonioni G, et a: Journal of Hazardous Materials, A127 (2005): 14 – 30.
[9] L. Xiao: Safety, health and the environment, 11(11) (2011): 20-22 (in Chinese).
[10] Eulàlia Planas-Cuchi, Joaquim Casal: Journal of Hazardous Materials, 62 (1998): 231–241.
[11] J.L. Consalvi, R. Demarco, A. Fuentes, S. Melis, J.P. Vantelon. On the modeling of radiative heat transfer in laboratory-scale pool fires. 7th Mediterranean Combustion Symposium, Sardinia, Italy, 11-15 September, 2011. *Fire Safety Journal*, 60 (2013) 73 - 81.
[12] GB3095-2012. Ambient air quality standard. Environmental protection department of P. R. China; State Administration for Quality Supervision and Inspection and Quarantine.

Advanced Materials Research Vols. 960-961 (2014) pp 366-369

doi:10.4028/www.scientific.net/AMR.960-961.366

Numerical simulating the ground coefficient of thermal conductivity in severe cold region

BAI Li [1a], WANG Yan[1b] , HUA Yawei[1c]

[1]School of Municipal & Environmental Engineering ,Jilin Jianzhu University, Changchun, China 130118

[1a] baili0308@163.com;[1b] wangyan2387@163.com; [1c] 15943041867@163.com

Keywords: thermal conductivity; temperature field; moisture content; porosity

Abstract. The ground coefficient of thermal conductivity is one of the most important parameters of simulating the ground temperature field. The ground coefficient of thermal conductivity of the severe cold region is investigated in this article. Firstly, calculating the ground thermal conductivity with considering the moisture content and porosity; then measuring the thermal conductivity of the 1.5 Meter depth; finally, simulating the unsteady heat transfer model of the shallow buried pipe and the ground with the Matlab software; it founded that the calculation data and the actual data differ only 0.31,but the corresponding ground temperature field vary widely. Thus, it can be concluded that the more precise temperature field of the ground can be simulated with the actual data of ground coefficient of thermal conductivity.

Introduction

Soil is a typical muti-phase medium, which consists of mineral substance, moisture and gases. The climate factor of the seasonal exchange and rainfall will induce the change of underwater level. With the variation of moisture content and porosity, the coefficient of thermal conductivity will change. Thus, it is necessary and important to carry out the investigation of the coefficient of thermal conductivity.

In past research, there are three mainly method to navigated the soil coefficient of thermal conductivity.

The heat probe method is applied to test the soil coefficient of thermal conductivity[2] ,the structure is shown in figure 1.With this experimental method, the values of it can be more accurate, but the initial investment of the engineering will increase.

It is believed that the values are constant, when assuming that: (1) soil is a semi infinite and uniform object ;(2) Ignoring the moisture migration ;(3)Ignoring the heat-moisture migration caused by moisture migration ; which is 1.2W/(m.k)～1.5 W/(m.k).

It is assumed that there is only exists porosity effect on coefficient of thermal conductivity but no heat transfer between the component of liquid and solid, whose calculation is below[3]:

$$\lambda = \varepsilon\lambda_f + (1-\varepsilon)\lambda s \tag{1}$$

Among that , λ_f and λ_s are representatively on behalf of soil coefficient of thermal conductivity with moisture and solid; ε is soil porosity. Because the soil structure is relatively complex, the influential factors include moisture migration, which results the heat-moisture migration, the type of soil and the porosity [4]. Thus, in order to simulate the soil temperature field more accurate, the factors above should be under consideration.

$$\lambda_{dry} = \frac{0.135\rho_b + 64.7}{2700 - 0.947\rho_b} \tag{2}$$

Among that: ρ_b is the density of bulk soil, kg/m^3.

Lu Sen semi-experience formula

LuSen improved Johansen O.'s mathematical model in 2007[5] ,mainly amended for Kersten coefficient and the thermal conductivity of dry soil.

$$K_e = \exp\{\alpha[1 - S_r^{(\alpha-1.33)}]\} \tag{3}$$

Among that, α is constant related to the soil geology, when soil sand content greater than 40%,the value adopt 0.96, whereas is 0.27.

$$\lambda_{dry} = -a\varepsilon + b \tag{4}$$

In the formula, a, b are empirical parameters values 0.56 and 0.51 respectivel

$$\lambda = \{[\lambda_q^{\alpha}\lambda_0^{1-\alpha}]^{1-\varepsilon}\lambda_w^{\varepsilon} + 0.56\varepsilon - 0.51\}\exp\{\alpha[1 - S_r^{(\alpha-1.33)}]\} - 0.56\varepsilon + 0.51 \tag{5}$$

Numerical calculation and experimental verification.

The test base of the group is located in Daqing City, Heilongjiang Province, the mainly soil components of the region are silver sand, light loam, loam and a handful of clay, the original porosity of the soil is 0.6～0.7, the dry density of soil is 1.5 g/cm ～1.6g/cm[6] the thermal conductivity of soil under the condition of unfrozen is 1.11 w/(m.k), saturated soil moisture content is 0.80, the initial moisture content is 0.2, the measured values of soil thermal conductivity[7] is shown in table one, Johansen O.semi-empirical formula are shown in figure 2 and figure 3.

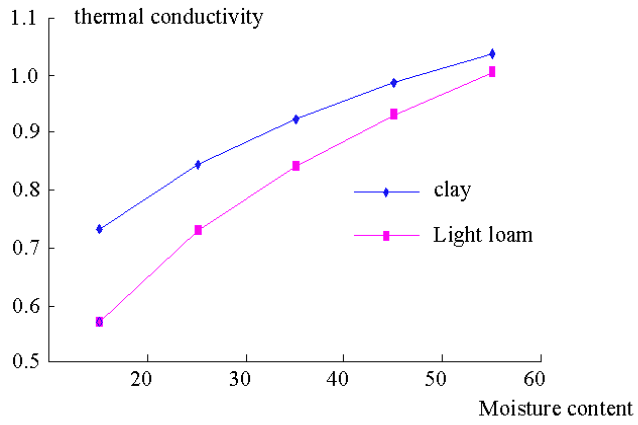

Fig. 2 Effects of moisture on the thermal conductivity

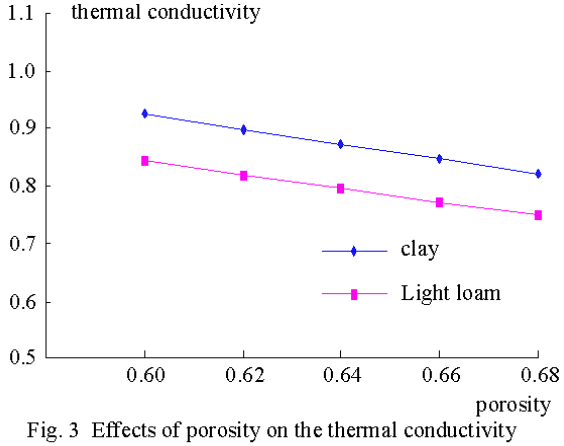

Fig. 3 Effects of porosity on the thermal conductivity

Table 1 The measured soil thermal conductivity

Sampling number	Wet soil density	Dry soil density	water content/%	saturation/%	Non-frozen soil thermal conductivity
1	1.7	1.34	26.5	70.4	1.3
2	1.84	1.46	26.1	82.2	1.5
3	1.91	1.57	21.8	80.7	1.43
4	1.47	1.23	20	44.6	1.32
5	1.73	1.31	32.3	80.8	1.49
6	1.73	1.35	27.6	74.3	1.38
7	1.66	1.42	17.3	51	1.25
8	1.48	1.28	15.9	38.3	0.98

The results with improved method of calculating of Lu Sen are shown in figure 4 and 5:

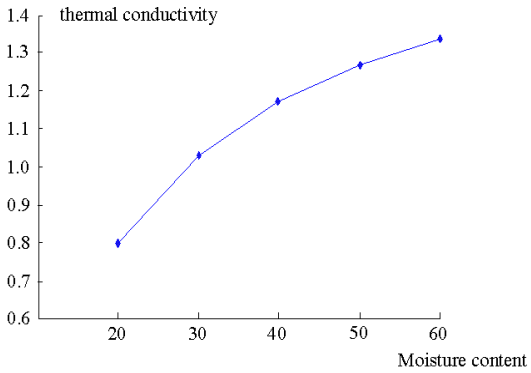

Fig. 4 Effects of moisture on the thermal conductivity

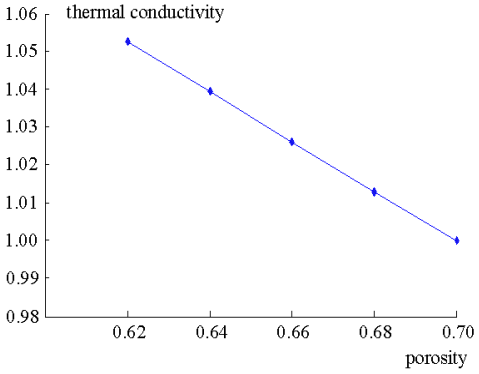

Fig. 5 Effects of porosity on the thermal conductivity

From above figures we can see, with the empirical formula of Johansen O, the calculated thermal conductivity of soil in Daqing area is 0.5w/(m.k)~1.1 w/(m.k), with an average of 0.8w/(m.k), with the empirical formula of Lu Sen , the calculated thermal conductivity of soil in Daqing area is 0.8 w/(m.k)~1.3w/(m.k), with an average of 1.05w/(m.k), the measured soil thermal conductivity is measured soil thermal conductivity, with an average of 1.24w/(m.k), Using matlab to simulate different coefficient of thermal conductivity of soil temperature field, as shown in figure6~figure8.

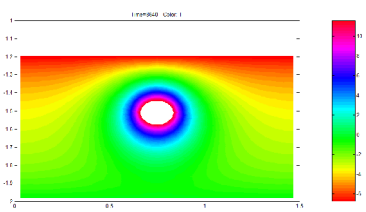

Fig. 6

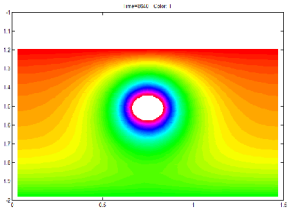

Fig. 7

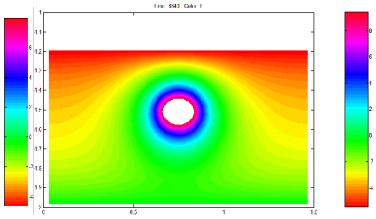

Fig. 8

Fig.6 soil temperature field around the DN100 pipeline when the thermal conductivity is 1.24w/(m.k);

Fig.7 soil temperature field around the DN100 pipeline when the thermal conductivity is 1.24w/(m.k);

Fig.8 soil temperature field around the DN100 pipeline when the thermal conductivity is 1.24w/(m.k).

Conclusion

(1)The soil thermal conductivity increase with the moisture content increase. This is mainly because the migration of moisture will induce the heat-moisture migration. Thus, soil in the region of long-term of rainfall has a good performance of good heat transfer conductivity.
(2) With the soil porosity increasing, the thermal conductivity shows a decreasing trend, because the increase of porosity leads to the increase of air content. The thermal conductivity of air is lower than soil, so that the thermal conductivity of the soil becomes small.

(3) In comparison with the measured values, the experimental results Obtained from the improved empirical formula of Lu Sen are close to the measured values. Therefore, when calculating the thermal conductivity of the soil ， It is recommended to use Lu Sen empirical formula. The larger the thermal conductivity, the greater the buried pipeline ambient temperature gradient, the greater the exchanged heat and moisture between soil.
(4) When the coefficient of thermal conductivity changing greatly, the temperature gradient around the buried pipeline will vary.

References

[1] Liu Mingzhi Influence of water content on soil thermal conductivity and the mechanism[J]Journal of Shandong Jianzhu University 2012(2):152-153.
[2] YANG Wen- bing, DING Yun- fei, GUAN Ling- jun Measurement of Thermal Conductivity of Wet Soil by the Heated Probe Method[J] Refrigeration Air Conditioning & Electric Power Machinery, Vol.133(31) 2010
[3] XIA Chen,YU Yue-jin,WANG Tao . The Computation of Water Content Soil T herma l Conductivity in the Vertical Bore hole Geothermal Heat Pumps Building Energy & Environment,2010,29(6): 20-21.
[4] Johansen O. Thermal Conductivity of soil [D]. Trondheim:University of Trondheim, 1975.
[5] Lu Sen. An improved model for predicting soil thermal conductivity from water content at room temperature [J]. soil.Sci.Soc, 2007,71(1):8-14.
[6] Hongju Jiang, Enyuan Cheng,in:Research of Frost Heave Property of Soil in Daqing Region, in Journal of Glaciology and Geochronology,(15)272-276.(1993)
[7] Liu Xiaoyan，Liu Jiajia，Guo Lin，Liu Lijun，Li Xiaoqing[J] Study on effect of phase transition on natural soil temperature field ,acta enlarger souaris sinical .Vol32，No6,2011

Advanced Materials Research Vols. 960-961 (2014) pp 370-374

doi:10.4028/www.scientific.net/AMR.960-961.370

Dependence of the distribution law parameters of the annual run-off of rivers in Primorsky region on the soil thermal conductivity

S.A. Lobanov, E.E. Kholoden

Far-Eastern Federal University, Vladivostok, Russia

lobanov.sa@dvfu.ru

Key words: Watershed area, annual run-off, distribution law, statistical parameters, polymodality of distribution laws, thermal conductivity of watershed area soil.

Abstract

The empirical investigation of the dependence of the statistical characteristics of annual run-off of Primorsky region rivers - modulus of flow, variation coefficient, asymmetry ratio, polymodality degree – on the weighted average values of the soil thermal conductivity coefficients within their watershed areas was carried out. The physico-statistical interpretation of the general form of correlation dependences obtained is provided.

Problem statement

The thermal-physical properties of soils are the most important energy factor determining their water-thermal regime, microclimate of the surface layer of the atmosphere, character of thermal interaction of the land underlying surface with atmosphere on scale of synoptic processes. The soil cover transforms the absorbed solar radiation into its other kinds and, eventually, into the kinetic energy of atmosphere motion. It is characterized by high spatial nonuniformity of mechanical and mineralogical compositions, thermal conductivity, temperature conductivity and heat capacity and, as a result, conditions of forming the hydrometeorological processes. These questions were not adequately investigated and were reflected in the monograph [1]. The authors of this paper have developed a paleogeologic method of calculating the soil thermal conductivity coefficients [2]. Based on this method, a mapping of the thermal conductivity coefficients of the southern Russian Far East soils was executed [1]. The maps constructed provided a possibility to evaluate the effect of soil thermal conductivity on the water balance elements. As a result of researches performed, it was shown that the spatial variations of the long-time annual average values of evaporation, annual precipitation and annual run-off of rivers are determined, to a great extent, by the spatial variation of the soil thermal conductivity coefficient. The strongest correlation of the value of soil thermal conductivity is noted with modulus of annual flow (R = 0.94, Primorsky region), evaporation coefficient (R = -0.81, Khabarovsk region), annual precipitation (R = -0.85, Amur region) [3]. These and other results show that the soil thermal conductivity can be considered as the important climate forcing having a geological interpretation. The obtained dependences of the water balance equation components on the soil thermal conductivity coefficient offer the possibility to evaluate their mathematical expectations. Hereafter we propose also to consider the dependence of other parameters of the distribution law (DL) of the annual run-off of rivers – variation coefficient C_v, asymmetry coefficient C_s as well as polymodality degree Pl of the annual run-off of rivers DL on the soil thermal conductivity coefficient within the watershed areas of the Primorsky region rivers.

Materials and research methodology

In papers [1.3] in the course of investigating a dependence of the water balance elements on the soil thermal conductivity, the maps of the thermal conductivity of soils in the territory of the southern Russian Far East were placed in correspondence with maps of the water balance elements. At that, the territory was subdivided by the grade grid into cells. Then, the weighted average values

of the water balance elements and soil thermal conductivity were determined in each of these cells. Hereafter a correlation between the values of water balance elements and soil thermal conductivity for the cells having the same name was found. In this paper we propose to compare the soil thermal conductivity for the watershed areas and statistical characteristics of their annual run-off. For this purpose, the weighted average values λ of the soil thermal conductivity for the watershed areas were estimated with consideration for a weight proportional to an area f_i occupied by each value λ_i of the soil thermal conductivity for the watershed area:

$$\lambda = \frac{\sum_{i=1}^{m} \lambda_i f_i}{F}, \qquad (1)$$

where F is the watershed area.

The parameter values of the distribution laws of the annual run-off – long-time annual average modulus of run-off M, variation coefficient of the annual run-off C_v, asymmetry coefficient C_s as well as polymodality degree Pl of the DL of annual run-off – were determined using streamflow records in the main-stream station of watershed areas. A criterion Pl was calculated by formula

$$Pl = - lg (P_k), \qquad (2)$$

where P_k is the probability of accidental appearance of the identified empirical polymodality which is as follows [4-6]:

$$P_k = \frac{n!\, k_1!\, k_2!}{\prod_{i=1}^{k} m_i!} \prod_{i=1}^{k} p_i^{m_i}, \qquad (3)$$

where n is the sample size; ! is the factorial symbol; k_1 and k_2 is the number of intervals with reduced and, respectively, alternating increased density of points in them ($k_1+k_2=k$) ; k is the number of all identified intervals; Π is the product symbol; p_i is the probability of entry of the random variable into the identified interval with quantity m_i of the random points within it read from the analytic probability curve approximating the empirical curve. A writing of the polymodality criterion in the form of (2) was taken for the sake of convenience in order to avoid a cumbersome writing of small number in the demonstration form. The calculations of statistical parameters were carried out by the procedure recommended by the set of rules SR 33-101-2003 for determination of basic estimated hydrological characteristics [7]. For approximation of the empirical probability curves, the Pearson type III distribution curve was used. The coefficients of variation and asymmetry were determined using method of moments.

The study was carried out for the following rivers of Primorsky region (within the brackets the watershed area are shown in square kilometers): Avvakumovka river –Vetka village (1740), Arsenyevka river –Yakovlevka village (5180), Bikin river - Zvenyevaya village (21400), Bikin river - Krasny Yar village (13100) , Bolshaya Ussurka river - Melnichnoye village (6750), Zhuravlevka river - Zhuravlevka village (3190), Ilistaya river - Khalkidon village (4030), Malinovka river - Rakitnoye village (4730), Melgunovka river –Lugovoy settlement (3450), Partizanskaya river –Partizansk town (3120), Samarga river - Unty village (7280), Ussuri river – Kirovsky settlement (24400), Ussuri river –Koksharovka settlement (9340).

Results and discussion

Hereafter a non-linear correlation dependence of the long-time annual average modulus of annual run-off of the rivers under consideration on the weighted average coefficient of thermal conductivity for soils of watershed areas with the correlation ratio $\eta = 0.86$ is presented (Fig. 1). The similar dependence with coefficient of linear correlation $R = 0.94$ was obtained in paper [1] when determining a correlation between the modulus of run-off and thermal conductivity coefficient of soils for cells of grade grids. A closeness of the presented correlation measures points to the equal significance of these methodological approaches to examination of dependence of the distribution law parameters of the annual run-off on the thermal-physical properties of soils. A form

of dependence $M = f(\lambda)$ is determined by the following physical mechanism: the smaller is the soil thermal conductivity, the higher is a heating of its upper layer at the expense of the inflow of solar radiation and the more is approach of the evaporation value to the amount of precipitation.

The thermal conductivity of the soil cover, as the climate forcing, can influence not only on the long-time annual average value of the annual run-off but also determine other parameters of its distribution law. The most important of them is variation coefficient C_v. The inverse non-linear correlation dependence $C_v = f(\lambda)$ in Fig. 2 with correlation ratio $\eta = 0.78$ confirms the theoretically substantiated conclusion [8] that the variation coefficient is inversely proportional to the quantity of days in the year with the flood-forming rainfalls. The less is the soil thermal conductivity coefficient, the higher is the air temperature and the souther is the watershed, the less is the quantity of such days. Dependence $C_s=f(\lambda)$ does not reveal such high correlation due to great accidental errors when evaluating C_s.

A dependence of the polymodality degree Pl of the annual run-off DL on the soil thermal conductivity coefficient is emphasized by the high correlation ratio $\eta = 0.87$. It allows us to conclude that the DL polymodality has an especially wide occurrence in the areas with high air temperature and small amount of precipitation where an insignificant variety of the atmospheric circulation types with intense cyclones is observed. The similar result was also obtained in paper [9] where it was shown that the biggest inconsistency between empirical and analytic probability curves is observed on the southern European territory of Russia.

Conclusions

1. The close correlation dependences of the modulus and variation coefficient of the annual run-off as well as polymodality degree of its DL on the soil thermal conductivity in the watershed areas with correlation ratios of 0.86, 0.78 and 0.87 respectively were obtained.
2. The regression equations of these dependences can be used for evaluation of parameters of the DL of annual run-off of the rivers of Primorsky region in the absence of the hydrometric observation data.
3. The dependences of the values of the annual run-off modulus and variation coefficient on the watershed altitude and area are known but none of these physic-geographical characteristics determines the polymodality degree of the distribution laws. The exception is provided by the soil thermal conductivity.

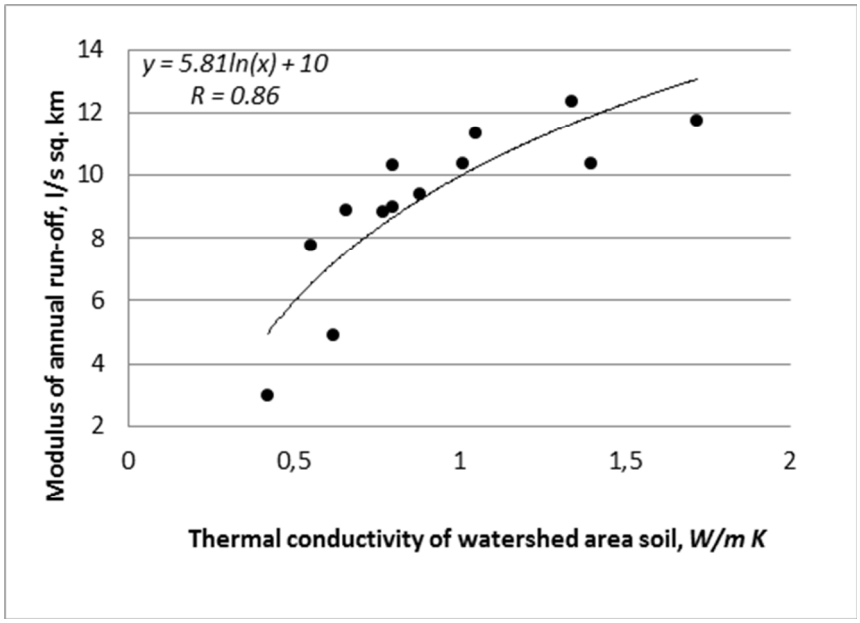

Fig. 1. Diagram of dependence of the modulus of annual run-off of rivers of Primorsky region on thermal conductivity of watershed area soil

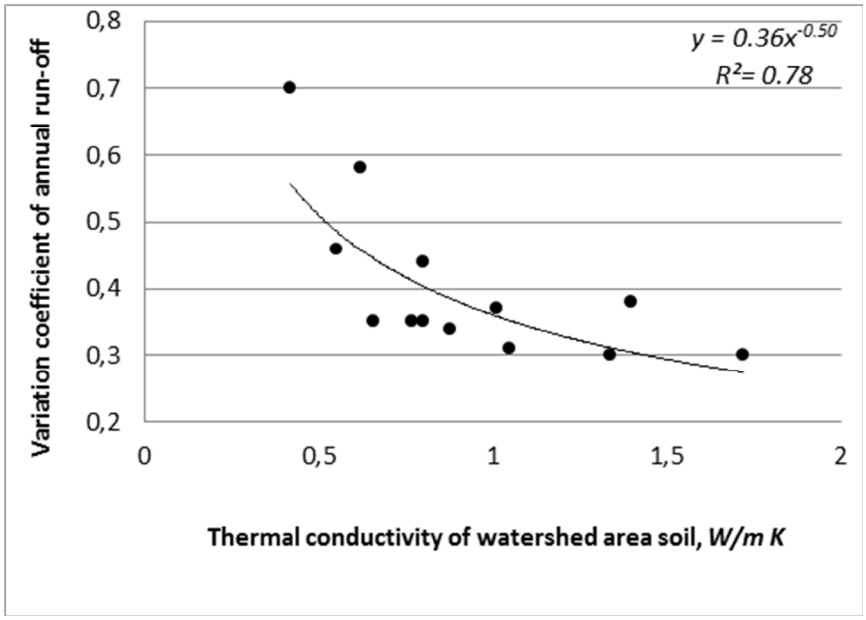

Fig. 2. Diagram of dependence of the variation coefficient of annual run-off of rivers of Primorsky region on thermal conductivity of watershed area soil

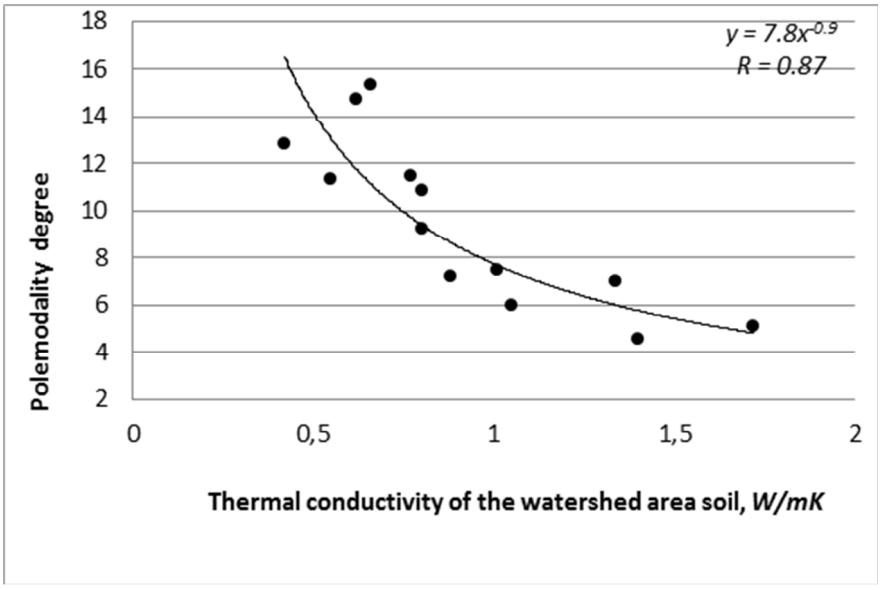

Fig. 3. Diagram of dependence of the polymodality degree *Pl* of distribution laws of the annual run-off of Primorsky region rivers on the soil thermal conductivity coefficients within watershed areas

References

[1] Lobanov S.A., Kholoden E.E. Thermal-physical properties of soils and their role in formation of hydrological processes. – Vladivostok: Publ. by Far-Eastern University, 2009, 216 p.

[2] Lobanov S.A., Kholoden E.E. Paleogeologic method of calculation of the heat conductivity coefficient of soils. References: 13th SGEM GeoConference on Water Resources. Forest, Ocean Marine Ecosystems And, www.sgem.org , SGEM2013 Conference Proceedings, ISBN 978-619-7105-02-5 / ISSN 1314-2704, June 16-22, 2013, 603 - 610 pp. DOI: 10.5593/SGEM2013/BC3/S13. 017.

[3] Lobanov S.A., Kholoden E.E. Effect of the soil thermal conductivity on the water balance elements. – Ecological systems and instruments, No.7, Moscow, Nauchtekhizdat, 2011, 13 – 17 pp.

[4] Lobanov S.A. Polymodality of distribution laws of the river run-off. Vladivostok: Publ. by Far Eastern State Academy of Economics and Management, 2004, 104 p.

[5] Lobanov S.A. The phenomenon of poly-modality of the laws of distribution of annual discharge, maximum discharge and water levels. International Symposium on Stochastic Hydraulics 2005. 23 and 24 May 2005. Nijmegen – The Netherlands. ISSH.v12.

[6] Lobanov S.A. The phenomenon of general spread of poly-modality of the distribution laws annual rivers runoff. Materials Research Vols. 864-867 (2014) pp 2312-2317 © (2014) Trans Tech Publications, Switzerland. doi:10.4028/www.scientific.net/AMR.864-867.2312.

[7] SR 33-101-2003 Determination of basic estimated hydrological characteristics // Gosstroi of Russia, Moscow: FGUP TsIP, 2004.

[8] Lobanov S.A. Method of calculation of variation coefficient of the annual run-off of rivers. Moscow, Nauchtekhlitizdat, Ecological systems and instruments. No.10, 2012, 73-76 pp.

[9] Kovalenko V.V. Non-linear aspects of the partially infinitary modeling in the evolutional hydrometeorology. St. Petersburg: Publ. by RGGMU, 2002, 158 p.

Advanced Materials Research Vols. 960-961 (2014) pp 375-381

doi:10.4028/www.scientific.net/AMR.960-961.375

Operational Efficiency Evaluation of Cogeneration Central Heating System Based on Improved Matter-element Model in North China

REN Feng

School of Business and Administration, North China Electric Power University, Baoding, China, 071003

renfeng2002@126.com

Keywords: Cogeneration; Central heating; Comprehensive evaluation; Matter-element model

Abstract. In order to assess the operational efficiency of cogeneration heating system and measure the system's social, economic, energy-saving and environmental protection benefits in North China, an evaluation index system is built up after analyzing the influence factors which may impact the heating system operation. The association degree function of classical matter element method is improved. And then, an improved matter-element evaluation model is established, which not only can figure out the evaluation grade that heating system belongs to, but also can point out the direction of the further improvement work. Besides, the model has other merits, such as uncomplicated operation, good scalability and so on. Example indicates that this evaluation model has excellent applicability and operability.

Introduction

In the last decade, in order to protect human survival environment, voluntary environmental programs have increased considerably in number and scope in many countries in the world [1]. Today, energy conservation, emissions reduction and environmental protection gradually become the focus issues under the background of energy depletion and environmental degradation in China. At present, there are about 6.5 billion m2 heating areas in the north of China, of which about 70% using different types of central heating. China's exceptional national condition decides that cogeneration central heating will continue dominating city heating in the future. This paper mainly focuses on the evaluation of cogeneration central heating system operational efficiency. The evaluation of heating system efficiency is closely related to the related parties: for heat users, they hope to be able to get more high-quality services; for heating enterprises, they need to measure the heating system efficiency; for relevant supervision departments, they also hope to measure and sort the heating enterprises, so as to provide separate supporting policies. Therefore, it has very important practical significance to use accurate models and methods to evaluate the efficiency of cogeneration heating system, and assess the societal benefit, economic benefits, energy saving and environmental protection benefits of the heating system.

Now there are limited researches done regarding the heating system operational efficiency. Existing literature mainly focused on the economy and reliability of the heating system. Based on the particularity of the thermal power plant system, Zhang established a comprehensive economic quantitative mathematical model for thermal power plant, and solved the problem of simplified the process of partial quantitative analysis by introducing a concept of "generalized heating extraction"[2]. According to the characteristics of the secondary network load of heating systems, Zheng, et al., proposed the heat supply network system reliability index calculation method, and analyzed the effects of peak shaving heat sources to the reliability index of heat supply network [3]. Based on climate data, Gao, etc., analyzed the three principal energy saving measures (indoor temperature control, system climate compensation, variable flow rate systems running) of heat metering system respectively. The analysis results showed that the energy-saving benefits of metering heating are remarkable; reasonable heating price enabled users to benefit at the same time; heat metering shall abide by the principle of the market [4]. Jiang analyzed the reasons for low efficiency and high energy

consumption of the central heating system in China, and discussed the reform of heat metering and charging [5]. Zhang, et al., defined a comprehensive index, and applied it to the evaluation of heating system efficiency [6]. Ferreira, et al., presented an idea that in the building sector, an emerging pathway was the decentralized power production via small thermal units, and micro-cogeneration offered a valuable opportunity for studying the potential of Combined Heat and Power (CHP) production for the residential sector[7]. Rong, et al., presented an improved unit decommitment algorithm to research the relative cost-efficiency of CHP, considering the possibility to trade power on the spot market[8]. In addition, there are some literature concerning the heating efficiency, economic operation of heat and power system and other issues[9-14].

These studies mainly discussed the reliability of the heating system with a single index from the technical perspective. we improve the matter-element method, and establish a simple and practical evaluation model. Based on these, we can conduct a comprehensive analysis and discussion on the operational efficiency of central heating system.

Influence factors analysis

Heating system reliability（C1）

Stable operation of cogeneration heating system is the precondition of efficient evaluation, because only when the system reliably operates, the demand of all kinds of heat load can be met. The index values find themselves in the range of 0 ~ 100% and the optimum is 100%..

Heating system operation regulation abilities（C2）

In order to make the temperature of each user in a heating system meet the design requirements, the parameters of supply and return water temperatures and the circulating flow rate should be adjusted along with the change of outdoor temperature at any time. It will make the whole system more effectual in saving energy and reducing consumption on the premise of meeting the heating demands. The index values find themselves in the range of 0 ~ 100% and the optimum is 100%.

The qualified rate of room temperature（C3）

This index is measured with the specific value between the number of qualified household and the total number of tested household. It is the result of the heating piping on the imbalances, reflecting the heat distribution situation of a heating system. If the room temperature is lower than the specification requirements, then users need to use additional auxiliary heating methods. Therefore, inefficiency of thermal imbalance reflects at least in two aspects: in poor social benefit and poor energy saving benefit. So, we can think that the qualified rate of room temperature is the quantitative representation of the collective benefit and energy saving benefit. According to the relevant provisions, the qualified rate of room temperature should not be less than 97%.

Energy efficiency of heating（C4）

It refers to civilian residential heating floor areas that a ton of steam heating load (0.7 MW) can burden under the design condition. The index is utilized to measure the utilization ratio of the heating system. In accordance with the pertinent provisions, the technical standard of heating energy efficiency is 8000 ~ 10000 square meters per ton steam.

Coal consumption for heating（C5）

It is the principal index of the energy saving effect. It refers to the coal consumption quantity for unit quantity of heat, and it shows the thermal efficiency of the heat source or heat supply system. For a definite heating area, due to the constant heating period, the unit coal consumption of heating area can also be used as an evaluation index. In accordance with the related regulations, coal consumption amount should not be more than 19kg per heating area in a winter. The standard of coal consumption quantity is 17kg per square metre in Hohhot, Inner Mongolia, China.

Circulation flows（C6）

It refers to the circulating water quantity per heating area. The significance of this index is as follows: (1) increase the circulating pump power utilization; (2) is an essential means of overcoming the enormous flow operation; (3) can prevent the vertical imbalance of indoor thermal system. In accordance with the pertinent provisions, for 95/70 type of hot water heating system, the parameter value should be controlled in the range of 2-3kg per square metre per annum.

Perfect degrees of system operation and management（C7）

The index can be utilized to measure the operation and management level of the heating system. Stable and proficient operation of the heating system is due to the perfect rules and regulations. The value of this index is restricted in the range of 0 to 100%, and 100% means the optimal level of operation and management.

The matter-element evaluation model

Dividing the evaluation grades

According to the authentic situation, the system to be evaluated is divided into p kinds of evaluation grades. The following expression is used to denote the value intervals of these kinds of grades: $V=\{[a_{j1},b_{j1}],[a_{j2},b_{j2}],\cdots,[a_{jp},b_{jp}]\}$. In this paper, the heating system is separated into three kinds of evaluation grades, respectively is superior heating system, qualified heating system and unqualified heating system.

Constructing the matter-element evaluation model

Based on the above evaluation index system, the matter-element model is constructed as follows:

$$R_k=(N_k,C,V_{kj})=\begin{bmatrix} N_k & c_1 & V_{k1} \\ & c_2 & V_{k2} \\ & \vdots & \vdots \\ & c_n & V_{kn} \end{bmatrix}=\begin{bmatrix} N_k & c_1 & <a_{k1},b_{k1}> \\ & c_2 & <a_{k2},b_{k2}> \\ & \vdots & \vdots \\ & c_n & <a_{kn},b_{kn}> \end{bmatrix}$$

Where, N_k denotes the kth evaluation grade, C denotes the characteristic collection of the evaluation grade N_k, and V_{kj} devotes the value range of $c_j(j=1,2,\cdots n)$ in the evaluation grade N_k, which is the so-called classical domain.

The joint domain is described as follows:

$$R_p=\left[P,C,V_{pj}\right]=\begin{bmatrix} P & c_1 & v_{p1} \\ & c_2 & v_{p2} \\ & \vdots & \vdots \\ & c_n & v_{pn} \end{bmatrix}=\begin{bmatrix} P & c_1 & <a_{p1},b_{p1}> \\ & c_2 & <a_{p2},b_{p2}> \\ & \vdots & \vdots \\ & c_n & <a_{pn},b_{pn}> \end{bmatrix}$$

Where, P denotes the collection of all evaluation grades, v_{pj} denotes the value range of P with respect to the attribute $c_j(j=1,2,\cdots n)$.

The matter-element to be evaluated is described as follows:

$$R_0=\begin{bmatrix} P_0 & c_1 & x_1 \\ & c_2 & x_2 \\ & \vdots & \vdots \\ & c_n & x_n \end{bmatrix}$$

Where, P_0 is the system to be evaluated, x_j is the value of $c_j(j=1,2,\cdots,n)$.

Improving correlation functions of each grade

Here is the definition of general correlation function. The correlation degree of the ith evaluation object with respect to the jth index in the kth evaluation grade is described as follows:

$$\mu_{ijk} = \begin{cases} -\dfrac{\rho(x_{ij}, V_{jk})}{|V_{jk}|}, x_{ij} \in V_{jk} \\ \dfrac{\rho(x_{ij}, V_{jk})}{\rho(x_{ij}, V_{jp}) - \rho(x_{ij}, V_{jk})}, x_{ij} \notin V_{jk} \end{cases}$$

Where, $V_{jk} = [a_{jk}, b_{jk}], V_{jp} = [a_{j1}, b_{jp}]$, $\rho(x_{ij}, V_{jk}) = \left| x_{ij} - \frac{1}{2}(a_{jk} + b_{jk}) \right| - \frac{1}{2}(b_{jk} - a_{jk})$, $\rho(x_{ij}, V_{jp}) = \left| x_{ij} - \frac{1}{2}(a_{j1} + b_{jp}) \right| - \frac{1}{2}(b_{jp} - a_{j1})$.

In order to solve the illogical problems above, we the correlation function of the ith evaluation object with respect to the jth index in the kth evaluation grade should be corrected as follows:

$$\mu_{ijk} = \frac{\frac{1}{2}(b_{jk} - a_{jk}) - \left| x_{ij} - \frac{1}{2}(a_{jk} + b_{jk}) \right|}{\sqrt{(b_{jk} - a_{jk}) \left| b_{jp} - a_{j1} \right|}}$$

The larger the correlation degree, the closer to the midpoint of the classification interval the attribute value is. If the correlation degree is positive, then the attribute value is in classification interval; if the correlation degree is negative, then the attribute value is outside the classification interval; if the correlation degree is zero, then the attribute value is at the critical point of the classification interval.

Improving the weights of the original model

The index weights are treated equally in the original matter-element model, without considering the relative importance of different index. Therefore, in this paper, we consider using the analytic hierarchy process (AHP) to improve the original matter-element model, to the effect that we can get more reasonable index weights.

Analytic hierarchy process (AHP) can decompose various factors in the complex problem into an interconnected ordered hierarchies, and integrate the information, such as objective data, experts' advices, subjective judgement of analysts, et al., directly and effectively. Then, the relative importance of each index is quantified, and finally, the weights of all the indexes are determined.

Determining the evaluation grade

If the weight of the jth index is α_j, then the correlation degree of the ith evaluation object with respect to the kth evaluation grade is as follows:

$$\mu_{ik} = \sum_{j=1}^{n} \alpha_j \mu_{ikj} (i = 1, 2, \cdots, m)$$

If $\max_{1 \le k \le l} \mu_{ik} = \mu_{ik^*}$, then the ith evaluation object is belong to the k^* th evaluation grade. If for all values of k, $\mu_{ik} \le 0$, then the evaluation grade of the ith evaluation object is beyond the scope of all evaluation levels set in the research, and should be discarded.

Case analysis

Thinking certain thermal power plant in northern China, the maximum capacity of heating of each generating unit is to provide steam 200t/h, and total heating ability is 250MW(900GJ/h).

Peak-shaving boiler rooms in heating area are responsible for the gap between the maximum heat load of 328 MW (1182 GJ/h) and the maximum heating supply capacity. The information of peak-shaving boiler rooms is shown in TABLE1.

TABLE I. THE INFORMATION OF PEAK-SHAVING BOILER ROOMS

Number	Scale	Heating areas ($\times 10^4 m^2$)	Heating supply capacity (MW)
1	4×20t/h	12	56
2	4×10.5t/h	26	42
3	3×10.5t/h	40	31.5
Total		78	129

As can be seen from the table1, the heating supply capacity of three boiler rooms is up to 129.5MW, and can fully meet the needs of heating peak. During the outage of one boiler in the power plant, the maximum heating supply capacity of another boiler and that of the peak boiler can meet more than 65% of the maximum heat demand load. The thermalization coefficient is $C_5 = 250/328 = 0.76$. Here, we use the improved matter-element model to evaluate the performance of the heating systems.

Step1, the heating system is divided into three levels: excellent heating system, qualified heating system and unqualified heating system.

$$R_1 = \begin{bmatrix} \text{excellent} & c_1 & (98.0,100) \\ & c_2 & (96.0,100) \\ & c_3 & (97.5,100) \\ & c_4 & (9500,10000) \\ & c_5 & (16.0,17.0) \\ & c_6 & (2.00,2.40) \\ & c_7 & (98.0,100) \end{bmatrix}, R_2 = \begin{bmatrix} \text{qulified} & c_1 & (96.0,98.2) \\ & c_2 & (94.0,96.2) \\ & c_3 & (95.5,98.0) \\ & c_4 & (8500,9600) \\ & c_5 & (16.8,18.0) \\ & c_6 & (2.38,2.80) \\ & c_7 & (95.0,98.2) \end{bmatrix}, R_3 = \begin{bmatrix} \text{unqualified} & c_1 & (90.0,96.2) \\ & c_2 & (90.0,94.2) \\ & c_3 & (90.0,96.0) \\ & c_4 & (8000,8600) \\ & c_5 & (17.8,19.0) \\ & c_6 & (2.79,3.00) \\ & c_7 & (90.0,95.2) \end{bmatrix}$$

The joint domain of reliability of the heating system:

$$R_p = \begin{bmatrix} \text{efficiency} & c_1 & (90,100) \\ & c_2 & (90,100) \\ & c_3 & (90,100) \\ & c_4 & (8000,10000) \\ & c_5 & (16,19) \\ & c_6 & (2.0,3.0) \\ & c_7 & (90,100) \end{bmatrix}$$

Step2, determining the matter-element to be evaluated. The data of the evaluation index system is expressed in the form of matter-element as follows:

$$R_1 = \begin{bmatrix} \{p_0\} & c_1 & 98.5 \\ & c_2 & 97.3 \\ & c_3 & 98.3 \\ & c_4 & 9580 \\ & c_5 & 16.6 \\ & c_6 & 2.56 \\ & c_7 & 96.5 \end{bmatrix}$$

Step3, determining the correlation degree.

$$Q = \begin{bmatrix} \mu_{111} & \mu_{121} & \mu_{131} & \mu_{141} & \mu_{151} & \mu_{161} & \mu_{171} \\ k_{112} & \mu_{122} & \mu_{132} & \mu_{142} & \mu_{152} & \mu_{162} & \mu_{172} \\ k_{113} & \mu_{123} & \mu_{133} & \mu_{143} & \mu_{153} & \mu_{163} & \mu_{173} \end{bmatrix} = \begin{bmatrix} 0.112 & 0.206 & 0.160 & 0.080 & 0.239 & -0.253 & -0.335 \\ -0.067 & -0.174 & -0.060 & 0.020 & -0.116 & 0.285 & 0.335 \\ -0.514 & -0.490 & -0.460 & -0.980 & -0.693 & -0.364 & -0.291 \end{bmatrix}$$

Step4, using analytic hierarchy process (AHP) to determine the weight vector.

$\alpha = (\alpha_1, \alpha_2, \cdots, \alpha_7)^T = (0.058, 0.090, 0.178, 0.286, 0.290, 0.060, 0.038)^T$ After computation, the consequences passed the conformity test. Evaluation matrix was calculated as follows:

$$U = \left[u_{kj}\right]_{3\times 7} = \begin{bmatrix} 0.0065 & 0.0185 & 0.0285 & 0.0229 & 0.0670 & -0.0152 & -0.0128 \\ -0.0039 & -0.0157 & -0.0107 & 0.0057 & -0.0335 & 0.0171 & 0.0127 \\ -0.0298 & -0.0441 & -0.0819 & -0.2803 & -0.2009 & -0.0218 & -0.0111 \end{bmatrix}$$

Where, $u_{kj} = \mu_{1kj} \times \alpha_j$. As can be seen from the evaluation matrix, the cyclical flow control index and management level of this heating system have reached qualified level, and need to be further improved. The other five indexs are up to the excellent level, but it is not difficult to see that the index of heating energy efficiency will come back to the qualified level if not strengthen the management. In addition, the reliability of the heating system should also be strengthened. Moreover, $u_{3j} < 0 (j = 1, 2, \cdots, 7)$, so you can determine the heating system does not belong to the unqualified heating supply system.

Step5, the calculated correlation degrees corresponding to different grade are as follows:

$K = Q\alpha = (k_1, k_2, k_3)^T = (0.115, -0.028, -0.670)^T$

Obviously, 0.115 is the largest, so the heating system is rated as excellent heating system.

Conclusions

The improved matter-element model has many merits. For example, it does not need to consider the type of evaluation index (positive index, reverse index or moderate indexs); it does not need to do dimensionless treatment, its computation process is succinct; its calculation workload is very small, and et al. For the evaluation of complex structure with multiple indicators, it can be processed by a specialized computer program with higher efficiency.

It is worth mentioning that, although the matter-element model has its unique merits, but it is not a panacea by any means, so, in solving practical problems, you should choose the appropriate method based on the characteristics of the problem.

Acknowledgements

This work was supported by the Fundamental Research Funds for the Central Universities and the Soft Science of Hebei Province (12457301).

References

[1] Ferrara A, Lange I. Voluntary Programs to Encourage Diffusion: The Case of the Combined Heat-and-Power Partnership[J]. ENERGY JOURNAL. 2013, 35(1): 161-173.

[2] Xiaohui Z. Research on Thermo-economics Diagnostic Method for the Combined Heating Cooling and Power Plant[J]. Proceedings of the CSEE. 2009(11): 8-13.

[3] Xue-Jing Z, Shi-Jun Y, Nan J. Operational Regulation Schedule of District Heating System with Peak-Load Boiler in the Secondary Network[J]. Journal of Tianjin University(Science and Technology). 2007, 40(12): 1511-1516.

[4] Xiang G, Jun D A, Zhao F X. Analysis on Economy and Energy -efficiency of the Measurable Heating System[J]. Journal of Chongqing Jianzhu University. 2006, 28(6): 91-94.

[5] Yi J. Problems in improvement of central heating systems in China and possible solutions[J]. Journal Heating Ventilating and Airconditioning. 2006, 36(3): 37-41.

[6] Hua-Bin Z, Xiao-Xia W, Ping-Hua Z, et al. Failure rate statistics and spectrum analysis of heating network components based on an investigation[J]. Journal Heating Ventilating and Airconditioning. 2004, 34(1): 15-18.

[7] Ferreira A, Nunes M, Martins L, et al. Innovation of Decentralised Power Production: The Sustainability of Micro-Cogeneration for the Portuguese Market[J]. PROCEEDINGS OF THE 7TH EUROPEAN CONFERENCE ON INNOVATION AND ENTREPRENEURSHIP, VOLS 1 AND 2. 2012: 217-225.

[8] Rong A, Lahdelma R, Grunow M. An improved unit decommitment algorithm for combined heat and power systems[J]. EUROPEAN JOURNAL OF OPERATIONAL RESEARCH. 2009, 195(2): 552-562.

[9] Pohl E, Diarra D. A method to determine primary energy savings of CHP plants considering plant-side and demand-side characteristics[J]. APPLIED ENERGY. 2014, 113(SI): 287-293.

[10] Ranjbar M R, Mohammadian M, Esmaili S. Economic analysis of hybrid system consists of fuel cell and wind based CHP system for supplying grid-parallel residential load[J]. ENERGY AND BUILDINGS. 2014, 68(A): 476-487.

[11] Gladysz P, Ziebik A. Complex analysis of the optimal coefficient of the share of cogeneration in district heating systems[J]. ENERGY. 2013, 62: 12-22.

[12] Coskun C, Oktay Z, Dincer I. Performance assessment of a novel hybrid district energy system[J]. APPLIED THERMAL ENGINEERING. 2012, 48: 268-274.

[13] Kusch W, Schmidla T, Stadler I. Consequences for district heating and natural gas grids when aiming towards 100% electricity supply with renewables[J]. ENERGY. 2012, 48(1): 153-159.

[14] Wu J Y, Wang J L, Li S. Multi-objective optimal operation strategy study of micro-CCHP system[J]. ENERGY. 2012, 48(1): 472-483.

Advanced Materials Research Vols. 960-961 (2014) pp 382-385

doi:10.4028/www.scientific.net/AMR.960-961.382

The Utilization of Genetic Algorithm on High Temperature Superconducting Magnet Design

Meng Song[1], Hao Liu[2,a], Xuzhi Deng[2], Yi Zhang[2], Li Ren[2], Shifeng Shen[2], Nannan Hu[1]

[1]Yunnan Electric Power Research Institute, Kunming, P. R. China

[2]State Key Laboratory of Advanced Electromagnetic Engineering and Technology, Huazhong University of Science &Technology, Wuhan, P. R. China

[a]suplabnote@hotmail.com

Keywords: Superconducting magnets, HTS, Genetic algorithm.

Abstract. In high temperature superconducting (HTS) magnet design, it well known that the critical current (I_c) is sensitive to the direction of the local magnetic field. The perpendicular magnetic field component to the face of tape have a larger effect on the I_c of a HTS tape than the parallel component. Thus in HTS magnet design, the magnetic field distribution is the first considering factor. This work presents a HTS magnet design using genetic algorithm to obtain the object. When the length of the tape is certain, the results show that the process gives the optimal number of the double pancake and the inner radius of the magnet.

Introduction

High temperature superconducting wire has provide a significant benefit from operating in liquid nitrogen, which lower the cost of the cryogenic facilities. However, the obvious anisotropy electromagnetic character makes the design of the HTS magnet is different with the LTS magnet design. It is well known that in HTS materials are more sensitive to magnetic fields perpendicular to the wide face of the HTS tape than to fields parallel to the wide face of the HTS tape [1].

For a HTS SMES magnet, the energy storage efficiency is crucial for the performance of the facilities. When the length of the tape is certain, the geometry of the magnet (number of the double pancake and the inner radius of the magnet) determines the I_c of the coils as well as the energy storage capacity. Fig.1 shows a cross section of a uniformed-current-density solenoid.

The magnet is optimized with the help of using genetic algorithm. After the optimization, the magnetic field distribution are calculated to confirm the result. At last, we using two different types of conductor in the same length in design, results shows the maximum energy storage capacity efficiency of the magnet.

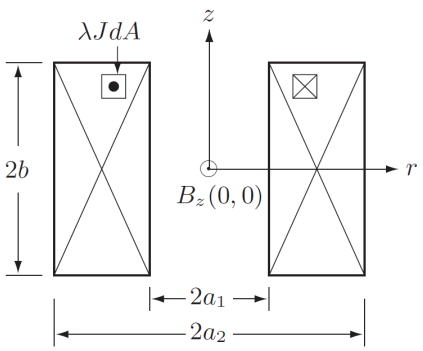

Fig.1 Cross section of a uniformed-current-density solenoid

Magnet Model

A SMES magnet consists single or multi solenoid magnet. Tape are winded as a double pancake coil type there insulation between each turn of the coil. Generally, the maximum magnetic field value is in the inner side center of the magnet and the perpendicular component maximum value is located in the top and bottom edge of the magnet.

The center magnetic field could be calculated by the equation (1)

$$B_0 = J\lambda\alpha F(\alpha,\beta) \tag{1}$$

$$F(\alpha,\beta) = \mu_0\beta\ln\{\frac{\alpha+\sqrt{\alpha^2+\beta^2}}{1+\sqrt{1+\beta^2}}\} \tag{2}$$

$$\alpha = a_2 / a_1, \beta = b / a_1 \tag{3}$$

As Fig. 1 shows, the a_1 is the inner radius and the a_2 is the outer radius. The b represents the total length of the magnet. The dimensionless number λ, is the space factor.

Conductor Characteristic

HTS materials are more sensitive to magnetic fields perpendicular to the wide face of the HTS tape than to fields parallel to the wide face of the HTS tape.

Fig. 2 illustrated the uniformed $I_c - B_\perp$ curve of the tapes in 20K. The Ic will be calculated by using this data and the load line of the magnet.

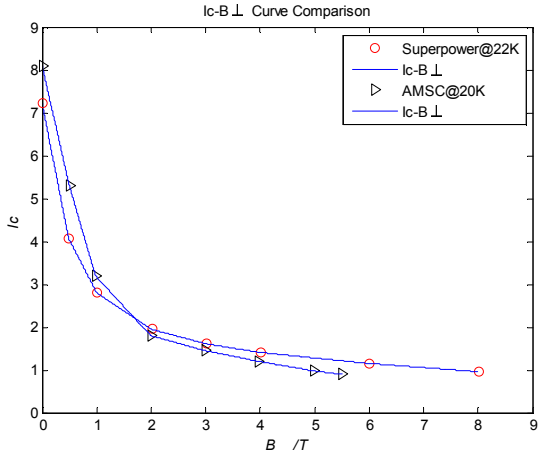

Fig. 2 Uniformed $I_c - B_\perp$ curve of the tapes

Optimization

Generally, due to there are many variables in a design problem, it can be very complex especially when they are interacted with each other. Many efforts have been made to find out an optimal solution investigation several approaches. Genetic algorithm is an efficient way to get the best results in multi variable condition.

The energy storage capacity efficiency is defined as follow:

$$\xi = \frac{E_{\max}}{V} = \frac{L\cdot I_{op}^2}{2V} \tag{4}$$

where the E_{max} is the energy storage capacity of the magnetic and the V represents the volume of the magnet by using $V = \lambda 2\pi a_1^3(\alpha^2-1)\beta$ to obtain. L is the inductance of the magnet and the I_{op} is the working current of the magnet.

The object of the optimization is find the maximum value of ξ. The Optimization Toolbox of the MATLAB is used to call the FEM software to obtain the perpendicular component of the magnetic field.

Fig. 3 shows the flow diagram of the optimization process as well as the program calling step in which the MATLAB is used as a optimize tool.

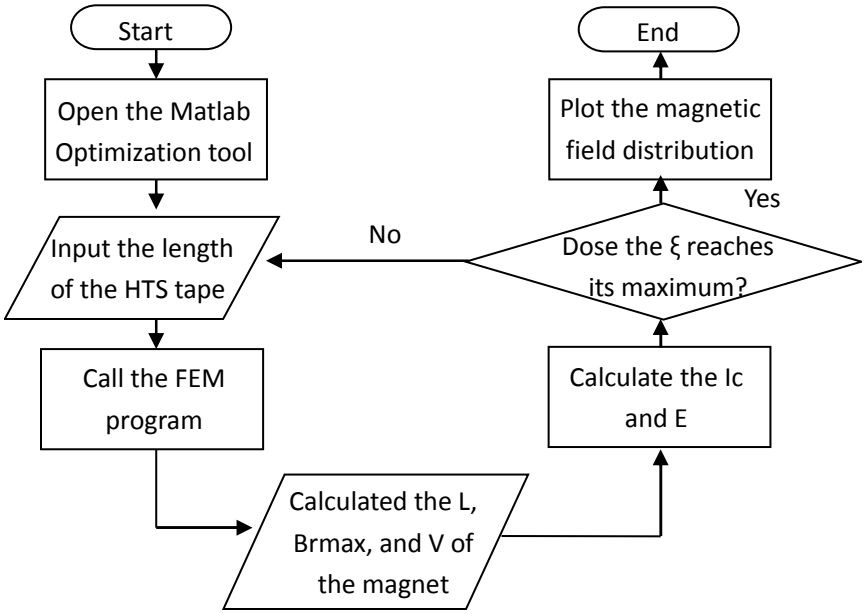

Fig. 3 The flow diagram of the optimization process

Result and Analysis

The result of the optimization has shown in Table 1. It suggests that in 20K and the same length of the tape, SCS4050 could get a larger ξ, which means for a SMES magnet, regardless the magnetic force sustainability the SCS4050 could be a better choice of the magnet.

Table 1 Parameters of the optimized magnet

	SCS4050	Amperium8501
Inner radius mm）	71	88
Outter radius mm）	192	228.7
Turns of each pancake	968	804
Energy Storage Capacity kJ）	41.929	39.331
Critical current A）	160.7	168
Working current A）	112.49	117.6
Inductance	6.627	5.688
ξ	4569.3	3085.7

Fig. 4 shows the magnetic field distribution of the optimized magnet. The magnet made by SCS4050 have a higher magnetic field because of the smaller inner radius as well as less thickness. Thus the energy storage capacity efficiency could be significant larger than the magnet make by Amperium8501.

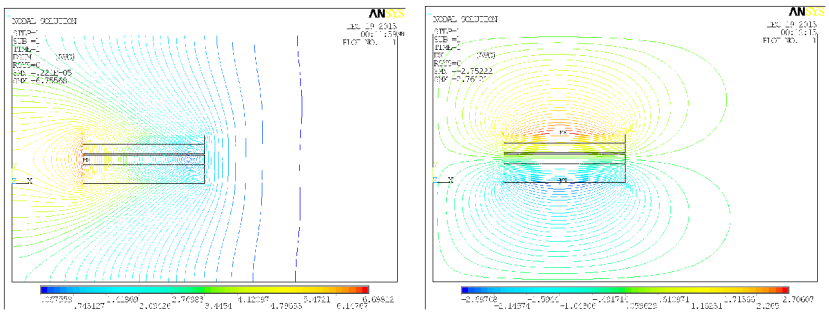

(a) (b)

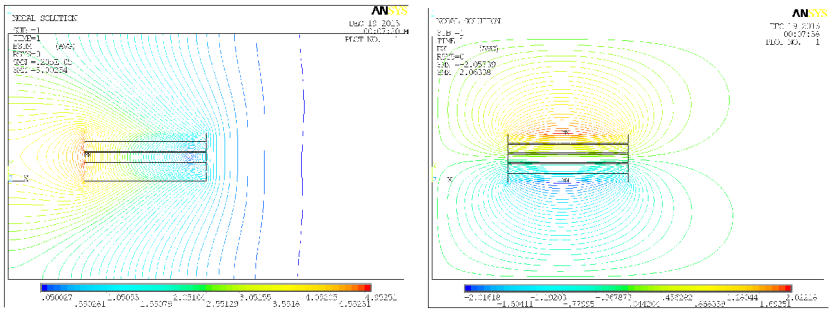

(c) (d)

Fig. 4 Magnetic field distribution of the optimized magnet with 1000m HTS tapes
(a) SCS4050, absolute value (b) SCS4050, racial component
(c) Amperium8501, absolute value (d) Amperium8501, racial component

Conclusions

In this paper, we presents a HTS magnet design using genetic algorithm to obtain the maximum value of the energy storage capacity efficiency. When the length of the tape is certain, the results show that the process gives the optimal number of the double pancake and the inner radius of the magnet. The result gives the parameter of the optimized magnet which made by SCS4050 and Amperium8501 respectively. It shows that regardless the magnetic force sustainability the SCS4050 could be a better choice of the magnet.

References

[1] J. F. Picard, et al., "Technologies for high field HTS magnets," IEEE Trans. Appl. Supercond., vol. 9, no. 2, pp. 535–540, 1999.

[2] Y. K. Kim, Y. S. Jo, J. P. Hong, and J. Lee, "Approach to the shape optimization of racetrack type high temperature superconducting magnet using response surface methodology," Cryogenics, vol. 41/1, pp. 39–47, 2001.

[3] L. Ren, Y. Tang, J. Li, J. Shi, L. Chen, F. Guo *et al.*, Physica C, 470 (2010) 1717-1720.

[4] T. Dai, J. Li, Y. Tang, Y. Zhou, S. Chen, P. Yuan, IEEE Trans. Appl. Supercond., 15 (2005) 1679-1682.

[5] J. Shi, Y. Tang, Z. Li, L. Ren, J. Li, S. Chen., IEEE Trans. Appl. Supercond., 19 (2009) 2044-2047.

CHAPTER 3:

Thermal Engineering

Advanced Materials Research Vols. 960-961 (2014) pp 389-393

doi:10.4028/www.scientific.net/AMR.960-961.389

Integrated flat plate heat pipe-pulsation heat pipe for the high-flux electronics cooling

Y.P Zhang, J.G Wang,

School of Energy, Xi′an University of science and technology , Xi′an 710054, China

Keywords: Heat pipe; Heat dissipation, Thermal characteristic; Electronics cooling

Abstract. A trend towards increasingly dense and compact architectures has led to unmanageably high heat fluxes in electronic components. A novel heat pipe will be developed. Heat pipe designed is based on the flat plate heat pipe and pulsation heat pipe effective combination. Channel quantity is greatly increased ,as well as compact and homogeneous red copper pulsation plank is severed as the wick, dense and connected channels are served as the passage of the working fluid.

Introduction

As the power densities of power components continue to grow, thermal issues ars becoming extremely important and vital for the product quality. The primary causes of failures in electronic equipment are the excessive temperatures of the critical components, such as semiconductors and transformers. The current trend for increased integration, faster speed, and small die size means both increased raw power and power density resulting in greatly increased heat fluxes. Furthermore, the need for higher performance encourages the clustering of high power devices on a die. The collected electronic component have given rise to the hot spot in certain locations of a die far exceeding the surface-averaged heat flux. This complicates the adoption of cooling solutions in regards to placement of the cooling device on a die. This creates a challenge to provide the thermal solution without compromising the power module size and weight. The processor's die surface where most heat generated is usually small approximates 10mm×10mm. For effective cooling the heat must spread to a larger surface area and away from the processor. Extended surface devices, such as heat sinks, coupled with forced air convection are a reliable thermal solution for many applications. Heat sinks are a passive technology, simply manufactured and mass produced, requiring little to no maintenance and are relatively easily attachable to the desired components. These features have made the heat sink and fan a popular cooling system for many years, even though higher power dissipating options have been available. Heat pipe in phase change heat transfer bring new hope for the greater power electronics cooling since they make use of a circulating liquid-vapor phase change to transfer heat rather than generate heat. Its equivalent thermal conductivity can be several hundred times than that of a solid copper of the same dimensions [1]. Heat pipe are very effective heat transfer devices and can be used to raise the thermal conductive path in order to spread a concentrated heat source over a much larger surface area. The heat pipe has been widely used, and evidently acceptable to preserve. Because of the high ratio of heat transfer capacity to weight, the heat pipe takes a predominant position in the aeronautics and electronic cooling applications. Heat pipe emerged as the most appropriate technology and cost effective thermal solution due to its excellent heat transfer capability, high efficiency and its structure simplicity. It has many advantages compared to other cooling devices such as fans, thermoelectric module, liquid pump loop device are that it has simple structures, no moving parts and does not use electricity [2].

In the heat pipe development, the wick structure and material are of major concern. It is classified into four categories: convective heat pipe, flat plate heat pipe, separated liquid and vapor channel heat pipe and pulsating heat pipe. In addition, several novel heat pipe structure were developed at present. Yaxiong Wang et al.[3] presented a novel flat heat pipe to assist in meeting the high thermal design requirements in high power microelectronics, sintered copper screen mesh was used as the primary wicking structure, in conjunction with a series of parallel wires, which formed liquid arteries.

In this investigation, a novel heat pipe is proposed, The advantage of this kind of heat pipe is the integration of the plate heat pipe with pulsating heat pipe, which eliminates the existence of a thermal interface between the device and the cooling system.

Design heat pipe

A flat plate heat pipe has many advantages, such as flexible shape ,low resistance and lay out the heat source. However, dry out still occurs due to the opposing and interacting vapor and liquid flows, causing the same problems as suffered by convectional heat pipe.

A pulsating heat pipe(PHP) consists of a micro channel that meanders back and forth between a cooling section and heating section many times. After injection, the working fluid naturally forms liquid plugs and vapor bubbles distributed along the channel length. Pulsating flow enhances heat transfer because it breaks the thermal boundary layer on the channel wall, reducing thermal resistance [4]. Performance of a heat pipe improved with an increase in the number of channels. The heat pipes performed well at both the horizontal and vertical orientations. Heat pipe with smallest internal diameters is responded more quickly to change in the heat input. And therefore improving heat pipe performance by limiting the effect of the side channels should be an achievable goal. The channel diameter must be small enough to allow the vapor bubble, liquid plug configuration to develop. Akachi et al.[5] determined the maximum tolerable internal channel diameter (dmax) to be:

$$d_{\max} = 2\sqrt{\frac{\sigma}{g(\rho_l - \rho_v)}} \tag{1}$$

Where σ is the surface tension of the working fluid, g is the gravitational acceleration, and ρ is the density of the liquid/vapor. For internal diameters less than dmax surface tension dominates the stable liquid slugs' form. For internal diameters greater than dmax the working fluid will stratify and the meandering channel will function as an interconnected array of thermosyphons. In practice, internal channel diameters greater than dmax have resulted in slug formation in channels oriented vertically while stratifying in the horizontal orientation[6].Therefore this guideline on channel diameter is important for fabricating pulsating heat pipes that can function in any orientation. There have also been many observations of an increase in performance with an increase in internal diameter[7].This observation coupled with the requirement of a small enough channel diameter in order to form stable liquid slugs suggests the existence of an optimum channel diameter.

An argument for an optimum number of channels was made by Khandekar et al. [7]. Because of the small channel size, and small liquid inventory and thermal cross section per channel, increasing the number of channels reduces the heat load on any individual channel. Therefore, increasing the number of turns increases the performance of the pulsating heat pipe. Increasing the number of turns also increases the number of perturbations in the pulsating heat pipe which helps initiate and sustain the oscillating flow.

The most challenging aspect in convectional heat pipe design is the return of the liquid to the evaporator. Vertical, bottom heated heat pipe can use gravity for condensate return. A more effective mechanism is the use of a wick or micro-channels to induce capillary action. Capillary action is improved by increasing the surface area of the material which the fluid must travel relative to the volume of the fluid. Micro heat pipe arrays (MHPA) typically consist of a fine grooves machined into flat plates. Heat transport is improved because of the large quantity of fluid, and the plate geometry which allows better contact with the heat source. Construction and charging of MHPAs, however, is very complicated and thus cost prohibitive. A method of reducing the cost is to make the channels interconnected. This makes the charging of the channels much easier, as they can all be charged at once. Optical observations and theoretical studies of such arrays showed that the interconnection of the channels led to balance effects between the channels, resulting in even fluid distributions and even heat transport[8].

Heat pipe designed is based on the flat plate heat pipe and pulsation heat pipe effective combination. Channel quantity is greatly increased in the novel heat pipe structure. Compact and homogeneous red copper pulsation plank is severed as the wick, working medium is heated and then bubble generated in the evaporation face channel continuously expands, bring about working medium goes through the center pore ,arrive at the condensation section. Rapidly pass though the positive channel circulate the evaporation face and then finish the circulation, where air plug and liquid column were produced continually in the nature of excellent even heat transfer capacity (as shown in Fig.1). The novel heat pipe designed is integrated the micro channel of high heat transfer with phase change of even temperature.

The purpose of the heat pipe channels is to transfer heat from the evaporator to the condenser end with a minimal fluid temperature drop. It is expected that the thermal performance would increase as the number of capillaries increases because that the heat distributed to each capillary channel decreases as the number of capillaries increases. When the evaporator capillary channels is too big to transport a liquid back to the evaporator section by the capillary force in the channel, and the liquid in large capillaries might be depleted and caused bad evaporation performance. One can improve the design by reducing the channel size at the evaporator for the heat pipe. If the evaporation and condenser heat transfer coefficients in the capillaries are equal, then a vapor pressure drop would be the next factor to be considered. More capillaries would work to reduce the vapor pressure drop. Therefore, we adopt the dense and petty micro channel wick for the design of heat pipe.

Figure 2 is a configuration of the novel heat pipe. （1-Interconnected hole 2-Positive groove 3-Back groove 4- Screw hole 5-Rubber insert）.

The heat pipe was 99 mm in length, 83 mm in width, and 60 mm in height. The heat pipe walls were made of 1.5mm thick red copper plate. Attached to the inner surfaces of the heat pipe wall are porous wicks, In addition, vertical wicks are used to provide a secondary return mechanism for the condensate. 40 wide 1.5mm deep 1mm channel are layout separately in the wick of the front and back side,80 pylome are connected the close passage from beginning to end. The channel is layout denser in the evaporation side due to thermal resistance of heat pipe the evaporation side wick are the majority [14]. With the increase of heat flux, boiling and phase change take place and working medium is reflow rapidly, thus dry out limit is enhanced and pulsation channel make the condensation side temperature even in order to strengthen heat dissipation efficiency. Brazing welding was used to link fins and condensers. This technique can help reducing the contact thermal resistance between the evaporation

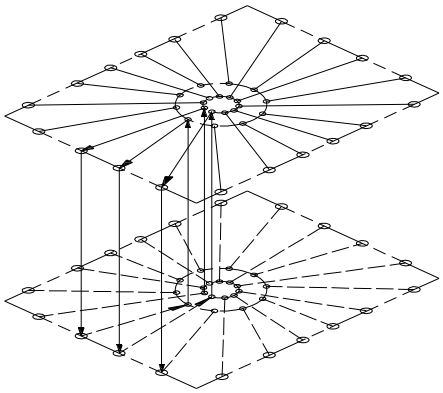

Fig.1. Working fluid passage

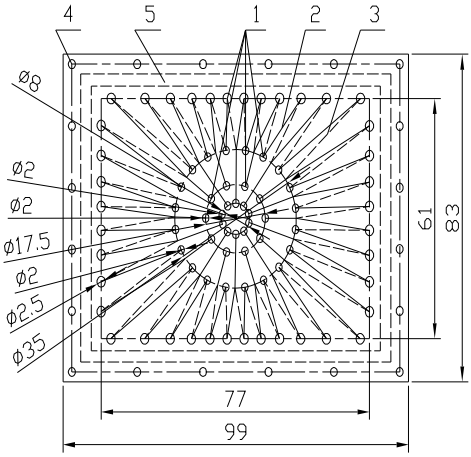

Fig.2. Heat pipe configuration

and the outside surfaces of the condenser. One of the main advantages of a heat pipe is that single or multiple heat sources can be located at any point on the evaporator surface, and generated heat would be spread out across the entire surface of the evaporator to achieve a near isothermal condition on the surface.

The features of the novel heat pipe are:

1) no contact resistance between the heat and the heat spreading plate;
2) quick-turn customization of the flow passage pattern to accommodate varying CPU location
3) combine flat plate heat pipe with pulsation heat pipe

dense channel is served as the passage of the working fluid in order to enhance the dry out limit. The wick structure is simple and high capillary force.

Conclusions

In the present heat pipe, which is designed on the base on the flat plate heat pipe and pulsation heat pipe effective combination. Channel quantity is greatly increased ,as well as compact and homogeneous red copper pulsation plank is severed as the wick, dense and connected channels are served as the passage of the working fluid. It makes temperature uniform distribution,corresponding improvement of the heat dissipation efficiency.

Acknowledgments

This paper and its related research are supported by Scientific Research Program Founded by Shanxi Provincial Education Department (Program No. 12JK0786).

References

[1]Peterson,G.P.,An introduction to heat pipes: Modeling,Testing,and Applications,John Wilek & Sons,Inc.New Yok,2000

[2]Z.J.Zuo,M.T.North,L.Ray,Combined pulsating and capillary heat pipe mechanism for cooling of high heat flux electronics,Thermacore Inc.white paper.2000

[3]Yaxiong Wang, G. P. Peterson.Investigation of a Novel Flat Heat Pipe, journal of heat transfer, 127.(2005)165-170

[4]Z.Jun,Z.Danling,W.Ping,G.Hong,An experimental study of heat transfer enhancement with a pulsating flow,Heat Transfer-Asian Research,33(2004)279-286

[5] H.Akachi,S.Motoya,Thermal performance of capillary tunnel type flat plate heat pipe.Proceedings of the 7th international Heat pipe Conference,Albuquerque,New Mexico,1995

[6]L.Shemer,Hydrodynamic and statistical parameters of slug flow,International journal of Heat transfer and Fluid Flow,24(2003) 334-344

[7]M.B.Shafii,A.Faghri,Analysis of heat transfer in non-looped and looped pulsating heat pipes,International Journal of Numerical Methods for Heat & Fluid Flow,12(2002) 585-609

[8]S.Khandekar,M.Groll,An insight into thermo-hydrodynamic coupling in closed loop pulsating heat pipes, International Journal of Thermal Sciences 43(2004)13-20

[9]M.Schneider,M.Yoshida,M.Groll, Investigation of interconnected mini heat pipe arrays for microelectronics cooling,1999

Advanced Materials Research Vols. 960-961 (2014) pp 394-398
© (2014) Trans Tech Publications, Switzerland
doi:10.4028/www.scientific.net/AMR.960-961.394

Non-pressure Heater Utilization on low-capacity Industrial Boiler

Guanghua Li[1, a *], Qunfeng Yang[2,b]

[1] Shandong Electric Power College, Taian City, Shandong province, China

[2] Special Equipment Inspection Institute Jining Branch, Jining City, Shandong province, China

[a]leegh195@sohu.com, [b]fenzl@126.com

Keywords: Coal-fired Industrial Boiler, Non-pressure Heater, Heat Recycling, Boiler Efficiency

Abstract. A new non-pressure waste heat recycling system was designed and arranged on KHSS0.5-0.7-AⅡ industrial coal-fired boiler to decrease the exhausted gas temperature about 35℃, improve the boiler efficiency about 3.2%. Results showed that this system can avoid low-temperature sulfur corrosion and operate in normal and intermittent water supply condition safely and economically.

Introduction

There are about 550,000 unit coal-fired industrial boilers in china accounted for one-third of the total national annual coal consumption, and an objective fact is that the coal burned inefficiently in most of these boilers [1]. There are significant gaps between small industrial boilers and large industrial boilers, in terms of design efficiency, the operational level, the user's awareness of energy conservation, etc. which means great energy saving potential [2]. And one of the main reasons of low thermal efficiency of industrial boilers is that exhaust gas temperature is too high. According to statistics, a great number of general industrial boilers flue gas temperatures are nearly 200 ℃.

For example: According to 2010 statistics in Jining city Shandong province, there are about a thousand units coal-fired industrial boilers, in which 705 units' capacity are less than or equal to 4t / h, 257 units are more than 4t / h. We found that many boiler flue gas temperatures is designed as 160 ℃ during the daily inspection, while the actual exhaust gas temperature are close to 200 ℃, and to some small rated output boiler flue gas temperature is higher. Jining is the main coal producing areas with coal sulfur content typically 0.6%, yet most of the sulfur content of coal used are less than 1%. In order to avoid low temperature corrosion at tail heating surface area, its ideal exhaust gas temperature is preferably maintained at 130℃ [3].

Analysis of Industrial boiler status

Many reasons that cause high exhausted temperature problems are discussed as follows.

1.1 The poor adaptability of coal boiler

A particular coal boiler is generally designed for using a special coal and it can run under good operating efficiency [2]. The reality is that it is difficult to ensure stable quality for the vast majority of coal boilers. To meet the design requirements blending coal is necessary, yet for most coal-fired industrial boilers no proper blending system to qualify the calorific value, ash content etc. all of these makes the combustion conditions change, the combustion incomplete and the exhaust gas temperature high.

1.2 Poor operating conditions of boiler

To most coal fired low capacity industrial boilers, cleaning are not timely or convenient after boiler fouling because of lack boiler water treatment equipment. Serious fouling also makes boiler efficiency decreases, the exhaust gas temperature high.

1.3 Poor use of new technology

Energy-saving technologies and products that used in energy-saving industrial boilers include: condensing heat recovery technology, the transformation layer fired boiler combustion system, steam accumulator in the heating system and so on [4]. These technologies focused on the transformation of

the combustion system, furnace arch reconstruction, the use of new refractory materials, auxiliary transformation, optimized air distribution, regulation, and self-control. Some energy-saving technological transformation test running effects are good, but the transformation is more complex, with higher cost of renovation, more difficult reconstruction work, long recovery period, and the operating level of staff required which has failed to achieve the expected energy savings.

1.4 The existing reducing flue gas temperature methods

To reduce exhaust gas temperature, heat pipe technology, composite phase change heat transfer technology such as the installation of air preheater rehabilitation programs has been used in large oil boiler or large power station boiler [5]. As for the small boiler users the transform price is too high, the whole project is difficult to carry out and also the relatively complex operation, the long cycle energy recovery device which limited the application of these technologies.

For small industrial boilers, as managers, a simple low price and easy operating energy saving device is needed. To overcome the deficiencies of the higher exhaust temperature, providing a practical new industrial boiler energy-saving device is the main purpose of the project.

Research of Waste Heat Utilization on low-capacity Industrial Boiler

2.1 Selected samples

In Jining city, 73% boiler capacity is less than or equal to 4t / h. To make the experiment more typical, according to the current boiler situation of Jining city, one type of boilers KHSS0.5-0.7-AⅡ with horizontal tube, with economizer, forced ventilation is chosen. The economizer outlet water temperature is tested to compare the impact of the using of the new heat transfer equipment.

2.2 Parameters of KHSS0.5-0.7-AⅡ Horizontal boiler model:

Evaporation capacity: 0.5t / h
Design pressure: 0.7MPa
Working pressure: 0.5MPa
Designed exhausted Temperature: 158 ˚C
Design efficiency: 70%
Ventilation mode: induced draft fan

2.3 Tested data of operating sample boiler

The exhaust gas temperature, water temperature, water temperature, fan opening status of the normal operation of the boiler was tested and shown in Table 1.

Table 1. Data of the operating boiler (before transformation)

Serial number	Pump operating time		economizer（˚C）		Exhaust temperature	Water treatment operating	notes
	on	off	Inlet temperature	Outlet temperature			
1	9:10		20	65	221	on	Water tank area :1.76 m^2 Water tank height: 0.5m Induced draft fan: on Operating pressure: 0.5MPa
2	9:15		20	67	223		
3	9:20		20	67	223		
4	9:25		20	67	222		
5	9:30		20	68	223		
6		9:31	20	70	227	off	
7		9: 35	34	93	238		
8		9:40	50	115	245		
9	9:41		57	120	245		
10	9:45		24	77	238		
11	9:50		20	68	234		

From the test results, under stable and normal operating conditions, the exhaust gas temperature is about 223 ˚C, far above designed temperature 158 ˚C. The economizer outlet water temperature in normal operation is about 67 ˚C. However, if the pump stops, the water flow in the economizer stops, an over-temperature condition happened.

2.4 The design of non-pressure heat exchanger

The design efficiency of the small industrial boiler means enormous energy saving potential. The high exhausted gas temperature means a device can be used to reduce the heat exhaust. During the implementation of the project, to reduce the changing investment, the original boiler pressure structure was not changed; a non-pressure design heat exchanger is adopted. The water flowing after the heat exchanger was sent to the entrance of the pump directly which ensure the safety performance of the equipment, and avoid the risk of explosion. Considering the possible intermittent operation of industrial boilers, water in the tank was used to store the heat. Even the pump stops, the water was heated by the high temperature exhausted gas which is helpful to reduce exhausted gas temperature and also helpful to improve the boiler efficiency.

The flue gas flow chart of the waste Heat Utilization and the water flow chart are shown as follows. And the system is shown in Fig. 1.

Transformed flue gas flow is from furnace →Convection tubes →economizer → Non-pressure heat exchanger→ filter →draft fan→ chimney.

Water flow is from Water treatment equipment →water tank →Non-pressure heat exchanger → pump → economizer →boiler drum

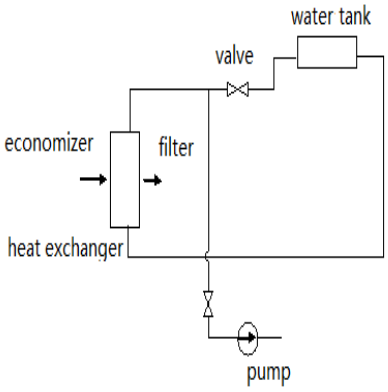

Fig. 1 Non-pressure energy-saving system

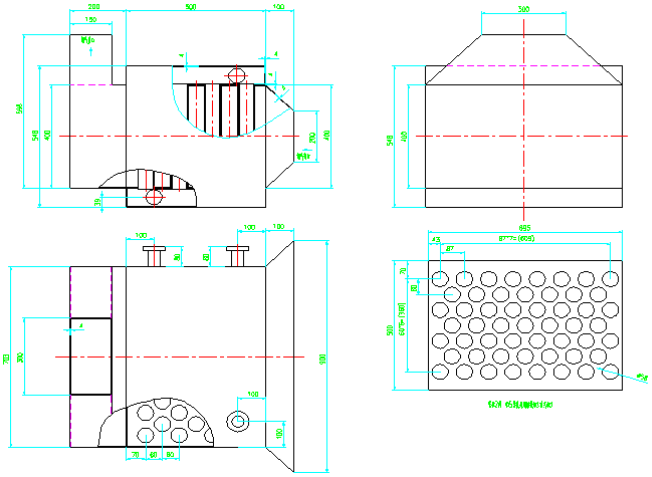

Fig. 2 The contracture of non-pressure heater

In this system, taking into account the normal use of industrial boilers with intermittent water supply, so that the valve connected the tank and the pump was designed as automatically open and close linkage. When the pump starts, the valve automatically shut off, the water was sucked by the pump, flow through the economizer and the non-pressure heat exchanger; when the pump stops the valve automatically open, the water tank, the cold water pipe, hot water pipes and non-pressure heat exchangers form a closed system, tank water cooling heat exchanger through natural circulation to reduce the exhaust gas temperature. Considering the sulfur content of Jining area coal, to avoid the low temperature area corrosion the heat exchanger area was designed to keep exhausted gas temperature as 173℃. After calculation non-pressure heater required transfer area is 3.9m^2. The actual design of the tube heat transfer area is 3.8m^2, and the tube sheet heat area is 0.4m^2.

In order to reduce the non-pressure heat exchanger manufacturing costs, and improve the heat transfer effect, in favor of the natural cycle principles, a vertical pipe structure for the staggered arrangement of the water flowing in the pipes up and down the tank tube sheet and plate has formed. The heater structure is shown in Fig. 2, to ensure the effective establishment of the natural cycle, the bottom of the tank is above the top of the heat exchanger. In the actual test unit the actual height of the tank bottom is flush with the top of the heat exchanger.

2.5 Results after use of waste heat utilization

2.5.1 Test Conditions

To demonstrate the feasibility and energy efficiency of the system, a stable load operating condition was considered. In order to compare the test results, reduce human error the operations are carried out by the same fireman. The test results are shown in table2. Operating conditions are: continuous water supply, fan operating, water treatment operating, the pressure stabilized at about 0.5MPa.

Table2 Test record in stable operation condition (after transformation)

num	Pump condi-tion	No pressure heat exchanger（˚C）				economizer（˚C）		Water treatment device condition	notes
	on	Inlet water temperature	Outlet water temperature	Flue gas inlet temperature	Flue gas outlet temperature	Inlet water temperature	Outlet water temperature		
1	9:00	24	61	195	165	67	116	on	Operat time:8:50 Stable operation
2	9:05	20	54	220	185	54	103		
3	9:10	20	52	231	189	52	97		
4	9:15	20	52	230	190	52	95		
5	9:20	20	52	229	189	52	95		
6	9:25	20	52	230	189	52	95		

Results and Discussion

Compare data shown in table1 and table2, the use of non-pressure waste heat device decrease the boiler exhaust temperature from 223 ˚C decreased to 189 ˚C, while the economizer outlet flue gas temperature increased which can protect the economizer form sulfur corrosion. The water temperature through the heater improves 32 ˚C. The water temperature flow into the economizer increase is 28 ˚C. The operating pressure is 0.5MPa, the saturated steam enthalpy is 2747.5KJ/Kg, the saturated water enthalpy is 640.115KJ/Kg, and the quality of the wet saturated steam is 4% by experience. The 20˚C feed water enthalpy is 84.476 KJ/Kg. The boiler efficiency improvement's about 3.2% and the coal saving rate is about 4.3% after the use of heater.

Conclusion

According to the results of the test and calculation, the evolution succeeded to achieve the expected energy savings. The temperature difference between the input and the output exhausted gas through is 41 ˚C deviate the design temperature difference 50 ˚C. The deviation is caused by the coal change, which means the actual gas enthalpy is lower than the calculated one. And also in the design calculation the ignored influence of the economizer inlet water change caused the bias. Actually if we want to modify the whole design, we can add 5~10˚C on non-pressure heater. If we give 10˚C modification to the non-pressure heater we tested, the outlet temperature will be 183˚C, very close to the actual tested value.

The flue gas resistance increased because of the improvement of boiler no pressure heat exchanger which will cause the power increased of the induced draft fan. And the calculation results is 23Pa, the actual test is about 40Pa. From the actual application perspective, the baffle opening of induced draft fan before transformation is 60%, after installation, no further adjustment is needed to the fan baffle opening which means the power increase of induced draft fan can be ignored.

To avoid boiling phenomena happen we must keep sufficient safety margins, keep the outlet temperature not close to the saturation temperature and in this project the temperature is 67 ˚C which is a reasonable choice.

To keep the pump safe operation we need consider the heat resist temperature which is 80 ˚C got form the pump factory manual. That means the pump can operate in the evolution project perfect. The following actual operation verified this.

Non-pressure heater can decrease the exhaust temperature and increase the efficiency of coal-fired industrial boilers. While the boiler feed water running intermittently, after the pump stops, the water in the tank can flow through economizer to absorb waste heat reducing the exhaust gas temperature. The heater run without pressure, so it is a safe, reliable, easy installation equipment which can also effectively reduce exhaust gas temperature, increase water temperature, saving energy. This non-pressure heater has been used in several industrial boiler and Tests data show that it can get a good energy saving effect.

Acknowledgement

This work was financially supported by the AQSIQ Technology Projects (Foundation No. 2011QK234).

References

[1] Boqiang Lin: China's Energy Strategy Adjustment and the Energy Policy Optimize. [J] Electric Grid and Clear Energy, 2012(1):1-3.

[2] Ke Zhang, Dezu Yu: China's Industrial Boiler Status and Development. [J] Boiler and Pressure Vessel Safety in China, 2014(2):17-21.

[3] Fengrong Wang: A New Boiler Flue Gas Dew Point Temperature Calculation Method. [J] Boiler Technology, 1997(6):19-20.

[4] Hongkui Lian, Yan Li: Overview of Industrial Waste Heat Recycling Technology in China. [J] Energy conservation technology, 2011(3):123-128.

[5] Qunfeng Yang, Ying Cao: New Technology for Waste Heat Utilization of Low-capacity Industrial Boiler. [J] Energy Conservation Technology, 2012(4):342-345.

Advanced Materials Research Vols. 960-961 (2014) pp 399-404

doi:10.4028/www.scientific.net/AMR.960-961.399

Optimized Operation of Boiler

Chang Liu[1, a]

[1]North China Electric Power University, Baoding, Hebei, China, 071003
[a]balejuju@163.com

Keywords: Optimization Boiler efficiency Excess air coefficient Fitting and interpolation Principal components analysis Correlative analysis

Abstract. This paper studies the problem of optimal operation of 300MW boiler. We combine the actual situation of the device and the theory of heat together, and improve the operating efficiency of the boiler through adjustment of device parameters, thus improving the economic benefit of thermal power plants. Firstly, according to coal characteristics and the theory of heat, we establish an improved utility model to calculate the heat loss of exhaust - gas, chemical incomplete combustion heat loss and heat loss of mechanical incomplete combusting. Then, we use fitting and interpolation, which is always applied to problems of Discrete Mathematical Statistics, to analyze discrete form of experiment data record, and give the relationship between 300MW boiler efficiency and excess air coefficient, which leads us to a new way to ascertain optimal excess air coefficient. And then, we use Principal Components Analysis (PCA) and Correlative Analysis (CA) to study the affection of operation parameters on boiler efficiency. Finally, we combine local optimization with global optimization, and establish an optimal operational model.

Background Information

In actual operation of the boiler, In order to ensure that the fuel completely combust, the amount of air supply is always greater than theory. Excess air coefficient refers to the ratio of tangible air volume to theoretical air volume. Excess air coefficient directly affects the heat loss of exhaust – gas (q_2), chemical incomplete combustion heat loss (q_3) and heat loss of mechanical incomplete combustion (q_4) [1].

When excess air coefficient increases, $q_2+q_3+q_4$ firstly increases and then decreases, and it has a minimum value. The excess air coefficient corresponding to this minimum value is called the optimal excess air coefficient. Because excess air coefficient has little effect on the chemical incomplete combustion heat loss, it can be regarded as constant. According to experiment, carbon content in fly ash (C_{fh}) is in one to one correspondence with excess air coefficient. Their relationship is given in Table 1.

Table 1: Excess air coefficient and carbon content in fly ash

α	1.1	1.15	1.2	1.25	1.3	1.35	1.4	1.45	1.5
C_{fh}/%	5.90	5.10	4.75	4.6	4.55	4.50	4.45	4.43	4.50

Sub problems to be solved

In this paper, on the basis of above background data and experimental results, following problems are put forward and solved.

Firstly, we have to determine the optimal excess air coefficient of boiler operation.

Secondly, we have to establish a model to describe the relationship between boiler efficiency and excess air coefficient.

Thirdly, we have to study the effect of boiler operation parameters on boiler efficiency.

Finally, we have to explore the method of optimal operation of 300MW boiler.

Model1: A simplified calculation model of mechanical incomplete combustion heat loss

The calorific value of coal is defined as the amount of heat evolved when a unit weight of the coal is completely burnt, which is divided into gross calorific value (GCV) and net calorific value(NCV) in practical application. GCV is applied when latent heat of vaporization which is generated by steam condenses is included. In this paper, we use Q_g^y on behalf of GCV, and we use Q_r on behalf of NCV.

In modern large capacity boiler, the water vapor in flue gas doesn't condense under atmospheric pressure, which means that latent heat of vaporization is not included. Therefore, NCV is used when it comes to calculation related to boilers. However, GCV is of great significance in practical application, so we give the relationship between GCV and NCV as follows:

$$Q_r = Q_g^y - 206H_{ar} - 23W^y . \tag{1}$$

In this equation, H_{ar} is Hydrogen content, and W^y is inorganic water content. We use Q_r to behalf NCV.

The conventional calculation formula to calculate heat loss of mechanical incomplete combustion (q_4) uses NCV. For certain coal, different ash and moisture will cause the change of NCV, which will be a great trouble when calculating. As a consequence, we introduce net calorific value on combustion basis (NCVB) to simplify calculating.

The relationship between NCV and NCVB is:

$$Q_r = Q_r^D(100 - A^y - W^y)/100 - 6W^y . \tag{2}$$

In this equation, we use Q_r^D to behalf NCVB.

Then, we introduce another parameter: dry ash content. Since NVCB has nothing to do with moisture, dry ash content is of great importance when it comes to correspondence. The relationship between dry ash content and ash content is

$$A^y = A^j(100 - W^y)/100 . \tag{3}$$

In this equation, A^j is dry ash content.

After arranging the above four equations, we come to a conclusion:

$$q_4 = a\frac{C_{fh}}{100 - C_{fh}} \bullet \frac{7.8A^j}{Q_r(B - A^j)} \bullet 10^5\% . \tag{4}$$

In this equation, B is an intermediate variable:

$$B = [100 - (1 + 600/Q_r)W^y]100/(100 - H_{ar}) . \tag{5}$$

This is the simplified calculation of mechanical incomplete combustion heat loss. For certain coal, different ash and moisture will cause the change of NCV, but it will not affect NCVB. Not like the traditional model, where we have to make a calorific analysis whenever the situation is changed,

in the simplified model, most of parameters stay unchanged. In this model, B is related to water content and net calorific value on combustion basis. Calculation shows that their effect on B is so little that it can be ignored. According to the actual situation, the value of B can be chosen as 99.5 [2]. Take experimental results for example, we get $Q_r = 24041.98KJ/kg$ [3].

After discussion above, we obtain the discrete mapping between excess air coefficient α and mechanical incomplete combustion heat loss (q_4), which is shown in Table 2.

Table 2 Discrete mapping between α and q_4

α	1.1	1.15	1.2	1.25	1.3	1.35	1.4	1.45	1.5
q_4	8.3672	7.1717	6.6550	6.4347	6.3614	6.2882	6.2151	6.1859	6.2882

Using exhaust enthalpy [4], we get the discrete mapping between excess air coefficient (α) and exhaust – gas heat loss (q_2), which is shown in Table 3.

Table 3: Discrete mapping between α and q_2

α	1.1	1.15	1.2	1.25	1.3	1.35	1.4	1.45	1.5
q_2	5.5511	5.7821	5.9643	6.1190	6.2542	6.3791	6.4930	6.5926	6.6710

We can see from the values of these discrete points that with α increasing, q_2 ascends monotonically. Under actual situation, the more air enters, the more smoke emissions, which increase heat loss. Moreover, the entry of cold air will also cause heat loss [5].

Model2: Calculation model of optimal excess air coefficient based on the least squares fit

As excess air has little effect on chemical incomplete combustion heat loss, it can be regarded as constant, according to actual situation, the value of q_3 can be chosen as 0.5. As a result,

$$q_2 + q_3 + q_4 = (100 - q_4)(h_{py} - \alpha h_{lk}) / Q_r + q_4 + 0.5 . \tag{6}$$

Then, we get $(q_2 + q_3 + q_4)_k$ at discrete points when α takes discrete values from 1.1 to 1.5, which is shown in Table 4.

Table 4: Discrete mapping between α and $q_2 + q_3 + q_4$

α	1.1	1.15	1.2	1.25	1.3	1.35	1.4	1.45	1.5
$q_2 + q_3 + q_4$	14.41	13.45	13.11	13.05	13.11	13.16	13.20	13.27	13.45

Using the least squares fit, we change discrete mapping into a continuous function:

$$f(\alpha) = 21.2155\alpha^2 - 56.5173\alpha + 50.6286 . \tag{7}$$

The function's minimum point is 1.33, so the optimal excess air coefficient is 1.33.

Model 3: Causal model of boiler efficiency and excess air coefficient

We use indirect balance method in this paper to estimate boiler efficiency. When this method is utilized, we need to know all kinds of heat loss that can't be ignored. Among them, radiation loss (q_5) and cinder heat loss (q_6) haven't been discussed yet.

When boiler rated evaporation increases, its fuel consumption is directly proportional to the increase, but the radiating area of boiler increases more slowly, which is equivalent to the reduction of radiating area .Therefore radiation loss increases as the amount of evaporation increases.

$$q_5 = 5.82(D)^{-0.38} \tag{8}$$

is used to determine q_5. In this formula, D represents the main steam flow of a 300MW boiler under rated operation. Since we can't get the data under rated operation exactly, we measure the main steam flow near rated point several times, and get D by interpolation. By applying the equations and conducting experiments, we get $q_5 = 0.4494$.

In actual situation, cinder heat loss can be neglected. So,

$$\eta_{gl} = \frac{Q_1}{Q_r} \times 100 = 100 \quad (q_2 + q_3 + q_4 + q_5 + q_6) = 100 - (21.2155\alpha^2 - 56.5173\alpha + 50.6286 + 0.4494). \tag{9}$$

When excess air coefficient is 1.33, efficiency of a boiler is the highest, with the value of 86.56%.

Model 4: Rational model of boiler operation parameters and boiler efficiency.

Boiler operating efficiency, different kinds of heat loss and specific operating parameters affect each other hierarchically [6].

According to background data, temperature of boiler water has little effect on boiler efficiency, which means that it can be neglected. With boiler mechanical parameters stay unchanged, there is a positive correlation between load and exhaust gas temperature, moreover, load and main steam flow are also positively related. That is to say, when load is given, exhaust gas temperature and main steam flow are fixed.

Exhaust gas temperature and heat loss of exhaust – gas are in positive correlation, while main steam flow and radiation loss are inversely correlated. So，load affects boiler efficiency in two distinct ways, and the trends in these two aspects are totally opposite. We use principal component analysis method, and extract two primary factors: excess air coefficient and load. We get the experimental data of a boiler when load is 298MW, 245.3MW, 215.8MW, and 192.3MW. Using methods and theory discussed above, we get four functions concerning boiler efficiency and excess air coefficient, which is shown in Fig.1.

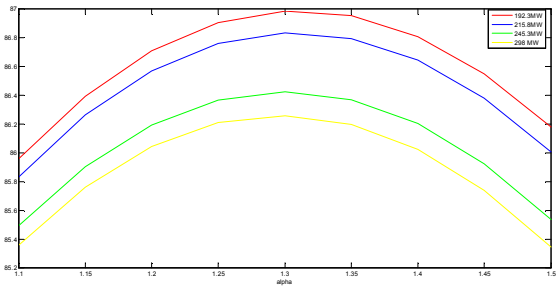

Fig.1: Functions of boiler efficiency and excess air coefficient

In summary, water temperature has negligible impact on boiler efficiency, while load and excess air coefficient have significant impact on the efficiency of the boiler. If load is given, main steam flow and exhaust temperature are fixed, and therefore the function of excess air coefficient and operating efficiency is also fixed. Furthermore, different values of the load result in different corresponding optimal excess air coefficient. Under the constant excess air coefficient, the more the load tends to 280MW, the higher the efficiency.

Model 5: Calculation of the most efficient operation based on layered optimization model

We combine local optimization with global optimization, and determine different variable in different layers.

On the basis of experimental data, we discuss such circumstances as loads are 298MW, 245.3MW, 215.8MW, 192.3MW and of 300MW. Using least squares fit, we change the discrete correspondence between excess air coefficient and carbon content in fly ash in Table 1 into a continuous function:

$$C_{fh} = 16.743\alpha^2 - 46.2271\alpha + 36.3229 . \tag{10}$$

With the help of enthalpy-temperature table, we use interpolation to obtain function of flue gas enthalpy and excess air coefficient under different load conditions. Then, we get

$$\eta_{gl} = 100 - [(100 - q_4)(h_{py} - \alpha h_{lk}) / Q_r + q_4 + 0.5 + q_5 + q_6] = f_k(\alpha) \text{ (k=1...5)} . \tag{11}$$

By derivation, we get the maximum values of the five functions, which are shown in Table 5.

Table 5: Loads and their corresponding optimal excess air coefficient of each load

Load	Corresponding optimal excess air coefficient of each load	Operation efficiency
192.3 [MW]	1.3103	85.9886
215.8 [MW]	1.3075	86.8362
245.3[MW]	1.3004	86.4248
298 [MW]	1.2971	86.2593
300 [MW]	1.2960	85.1952

It shows that different loads correspond to different optimal excess air coefficient, and when load increases, optimal excess air coefficient decreases.

Owing to the fact that we can't obtain experimental data under every load circumstances, we draw a function curve of load and boiler efficiency under its corresponding optimal excess air coefficient with the use of cubic spline interpolation, which is shown in Fig.2.

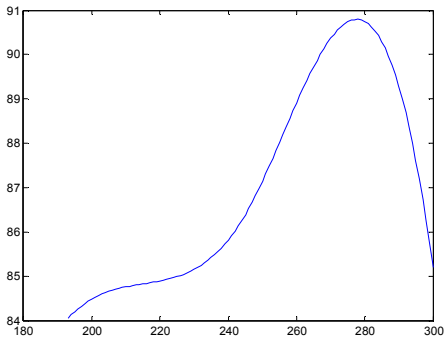

Fig.2: Function of load and boiler efficiency

When the load is 280MW, its efficiency is the highest, which is 90.79%. Its corresponding optimal excess air coefficient is 1.2982, and this is the result of global optimization.

With the help of models that have been discussed above, we get the optimal operation parameters, which are shown in Table 6.

Table 6: Optimal operation parameters

Load	280[MW]
Excess air coefficient	1.2982
Oxygen content	4.8238%
Main steam flow	789.3214[t/h]
Exhaust-gas temperature	136.5031[˚C]
Carbon content in fly ash	4.5282%
Exhaust – gas heat loss	5.89%
Incomplete combustion heat loss	2.36%
Radiation loss	0.46%
Operation efficiency	90.79%

Conclusions

It can be seen from Table 6 that layered optimization successfully improves the boiler efficiency. In this paper, a reasonable combination of the theory of heat and actual operational parameters is applied to establishing utility models of heat loss. Additionally, mathematical statistical methods are fully utilized to achieve a transformation of discrete domain to continuous domain.

Reference

[1] Quangui Fan, Principles of Boiler, China Electric Power Press (2008), p.36-57. (In Chinese)
[2] Shici Liu, Electric Power, Vol.1 (1981), p.2. (In Chinese)
[3] Jiahu Li, Course Project of Principle of Steam Boiler, China Electric Power Press (2007), p.11-12. (In Chinese)
[4] Shunlin Yan, Bin Zhang, Huanying Wu, and Qinyuan Wu, Power Equipment, 2010, Vol. 24(4),p.238. (In Chinese)
[5] Yonghua Li, Hongwei Chen, Fanjun MengProceedings of the Chinese society for electrical engineering, Vol.24 (1) (2004), p.217. (In Chinese)
[6] Jinzhi Wang, Ming Xiao, Chunmin Jiang, Shandong Electric Power, Vol.2 (2008), p.36. (In Chinese)

Advanced Materials Research Vols. 960-961 (2014) pp 405-409

doi:10.4028/www.scientific.net/AMR.960-961.405

ORC System Development Using Diesel Engine Waste Heat

DONG Junqi[a], WANG Jiangzhang and Zhang Rongyou

Zhejing Yinlun Machinery Co.,LTD, Zhejiang, China,

[a]dongjunqi2008@163.com

Keywords: Organic Rankince cycle（ORC）, engine, generator, exhaust gas

Abstract: Based on the waste heat characteristics of the coolant and exhaust gas from diesel engine, the Organic Rankine Cycle (ORC) commercial plant had been developed. The working fluid was the R245fa, and the plate type heat exchangers were used as the condenser and evaporator in the ORC systems. The performance of condenser and evaporator had been simulated and developed using the effective-NTU method. Using the engine jacket coolant as the heating media, the coolant absorbs the waste heat from the exhaust gas and engine cylinders. The ORC system and engine can stably run for a long time without frequent control acting. The ORC systems can bring the 14.6 kw electric energy in the stable condition. The efficiency based on the first law of thermodynamics is 7.2%; complete generating efficiency is 6.25%.

Introduction

The invention of the electric power is the core impetus of the second industrial revolution, and the steam Rankine cycle driven by fossil fuels is still the dominant power supply method. As is known to all, the accelerated consumption of fossil fuels has caused many serious environmental problems such as air pollution, global warming, ozone layer depletion and acid rain. Energy conservation and environmental protection have been the main issues in the word in the past twenty years [1]. How to effectively utilize low and medium temperature energy which is vast but undeveloped is one of the solutions to alleviate the energy shortage and environment pollution problems [2].

The organic Rankine cycle (ORC) in the past 10 years has gotten more and more attentions of the researchers, engineers and entrepreneurs for its obvious good characteristics [3-8], which lie in the absorption of low level temperature heat resource and simple structure. The ORC is similar to a typical Rankine cycle in principle structure, but it uses the organic fluid as the working fluid instead of water. Organic fluids are selected in the new Rankine systems (ORC) because their specific vaporization heat is much lower than that of water used in the classics Rankine cycle. This enables the ORC systems to produce electricity by using the low-temperature heat sources, with the temperature range 80~200℃. The technologies of ORC have been become more and more mature in the high power field in the past 15 years, such as the industry waste heat recovery, geothermy and biomass. Due to economic reason, the ORC power stations' ranges are almost the MW power level or more than 100kw power level. However, there very few ORC plants existing in the world with the kW power range [9].

And the development of higher efficiency ICE (internal combustion engine) will be most key task for the ICE researcher after the exhaust gas pollution problem has been solved. And the ORC technology will be one of methods in increasing engine efficiency because the engine have much waste heat and discharge to atmosphere, such as the in high temper exhaust gas, coolant and charge air. The waste heat discharged from the engine is about 60% in all the fuel energy [10-11]. However, there are very few ORC plants or systems using the ICE waste engine in the real products from the public literature or newspaper. There are some researchers doing the ORC plants using the ICE engine, but still in the testing and studying phase.

The authors developed the 10kw power range ORC commercialization of prototype based on the ICE waste heat in this paper. The waste heat is from the exhaust gas and coolant in the ICE.

ORC Principle

2.2 Thermo-physical property of the working fluid

Because affecting the efficiency of system, the size of the systems components, the design of expansion machine, the system stability and safety and environmental concerns, the selection of working fluids is very important for the ORC system performance economy. Except for the structural point of view and type of atoms in the fluid molecule, the working fluids could be categorized according to the saturation vapor curve. This saturation vapor curve is one of the most crucial charateristics of the working fluids in ORC. The character affects the fluid applicability, the system's efficiency and arrangement of the associated equipment in a power generation systems. As shown in the Fig.1, there are three types of vapor saturation curves in the temperature-entropy (T-S) diagram: a dry fluid with positive slopes, a wet fluid with negative slope, and an isentropic fulid with nearly infinitely large slope [2]. If the working fulid is the dry fluid, then the working fluid could not enter in the two-phase zone in the expander. This is very useful for the life of expander in ORC systems. If the working fluid beome the liquid or condense at the end of expaner, this is an unfavorable and unacceptable phenomenon for the expander during the ORC working process. While because the working fulid R245fa has the good thermo-physical property and has the dry fulid characterics, it has been accepted widely as one of working fulids in the ORC systems

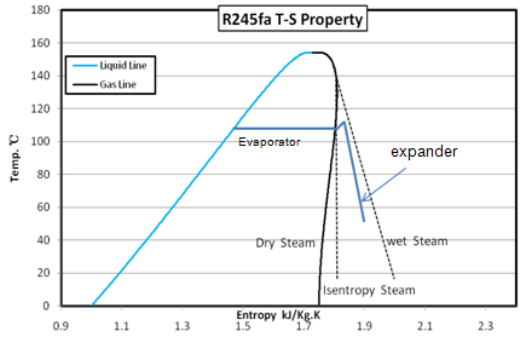

Fig.1 The T-S plots in ORC system

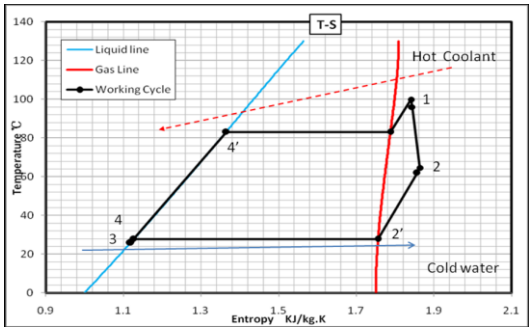

Fig.2 T-S process of working fluid of ORC system

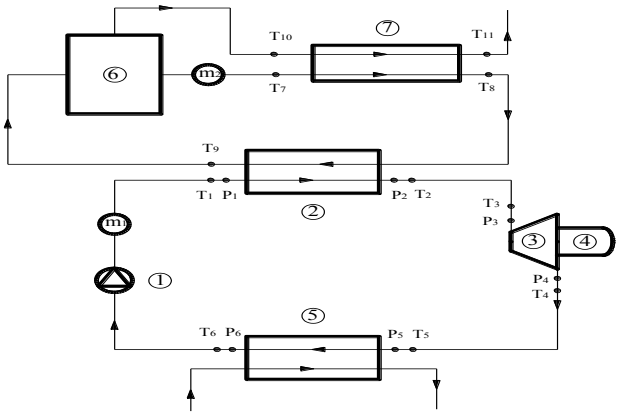

① Pump
② Evaporator
③ Expander
④ Generator
⑤ Condenser
⑥ Engine
⑦ Heat recoverer

T, Temperature
P, Pressure abs.
m, mass flow rate

Fig.3 Test principle diagram for ORC systems and Engine waste heat

Engine Waste Heat ORC systems development

3.1 ORC systems for Engine waste heat

In the engine, the fuel is the total heat source. One part is used to do useful work , which is about only 40% of total heat source, while the other part is rejected to atmosphere as various waste heat, such as exhaust gas, radiation and coolant heat in radiator. The Fig.3 give the ORC systems based on

the Engine waste heat, which is the high temper exhaust gas and coolant heat from the cyclinders. The Engine rate power is 200kw with 6 cylinders. In the engine, there is much waste heat rejected to atomosphere. This part of heat can be used as ORC heat source and generate electricity by ORC systems generator. At first, the coolant which is used to cool the engine cylinder is pumped to the exhaust gas heat recoverer from engine. In the recoverer, the coolant is heated by the high temperature exhaust and absorb the heat energy of exhaust gas, then the coolant enters the evaporator and engine. In the ORC system, the coolant is used as the media of heat source, which absorbs the heat energy from the engine cyclnder and exhaust gas.

The working fulid absorb the heat from the coolant in the evaporator, and then the vapor directly exnpand in the expander to do work and generate electricity. Other part are similar to the basic ORC systems, which include the pump, condenser, evaporator and expander,generator. At same time, the Fig.2 also gives the temperature and pressure sensor location. The temperature, pressure and mass flow parameters are very imporatnt for the systems analysis. The temperature sensor is the RTD type, whose accuracy is 0.1˚C.

3.2 Systems analysis for ORC

The temperature entropy diagram(T-S) is used to analyze the thermodynamic systems of ORC. The Fig.3 is the T-S diagram of the ORC working process, including the 4 main processes. 1-2 process is the working fulid expand in the expander, 2-3 process is the condensing in the condenser which the working fulid become the subcooled liquid from the superheat vapor; 3-4 process is the pressure raised by pump, in which frequency pump is used to adujst the working fluid flow rate according to the control order. The process 4-1 is the working fluid absorbing heat, evaporating and bringing phase exchange process. The working fluid become the high temperature and high pressure vapor which had much energy, and then enter in the expander. Then the whole Rankine cycle 4 basic processes are realized.

3.3 Data reduction and analysis

The whole ORC systems was taken for reaching the steady condition when all the sensors do not change. The test data are recordered by data acquisition systems, in which the sample rate is 0.2HZ. To more clear analyze the thermodynamic process, the data reduction are expressed by the list equation:

1）The total quantity of engine waste heat ,Q

$$Q=Q_w+Q_e \quad (1)$$

2）The working fluid absorb heat quantity, Q:

$$Q = m \times (h_1 - h_4) \quad (2)$$

3）The work expander do ,W：

$$W = m \times (h_1 - h_2) \quad (3)$$

4） Isentropic efficiency of expander ：

$$\eta s = \frac{h1-h2}{h1-h2s} \quad (4)$$

5) Heat rejection for the condenser, Qc：

$$Qc = m \times (h_3 - h_4) \quad (5)$$

6) Generating efficiency of ORC:

$$\eta = \frac{E}{Q} \quad (6)$$

7) Net generate efficiency of ORC systems

$$\eta_e = \frac{\dot{E} - E_1}{Q} \quad (7)$$

In the above equation, the Qw,Qe are the heat quantity of coolant and exhaust gas; the h_1, h_2, h_3, h_4, hs are respectively the enthalpy of the corresponding locations. In the Fig.3, the m is the mass flow rate of working fulid. The E and E1 are the elecrity of generation and consuming elecrity of ORC systems,such as the pump and control systems .

Test results and discussion

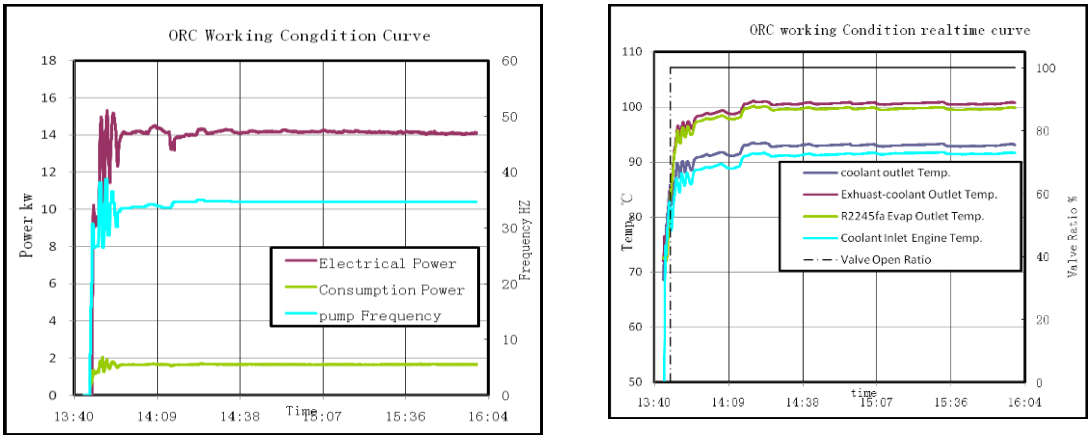

(a) (b)

Fig.4 The realtime working condition of ORC system

To clearly descibe the test process and working conditon of ORC systems and Egine. The Fig.4 gives the realtime working condition for the ORC systems and Engine. From the ORC systems beginning to generate elecrity to the steady condition, the test data recording time is about 2 hours and 24minutes. From the Fig4.(a), we can see the electricity generating power, consumtion power and pump frequency achieved a very stable condition after about 20 minutes. The steady elecric quantity of generator is about 14.6 kW, and the consumption power is about 1.9kw. And during the 2 hours, the speed of working fulid pumb almost no change, this shows the ORC systems based on the engine waste heat using the coolant as the media heat trasnfer is very right and effective. From the Fig.4(b), it can be seen that the engine coolant temper in the inlet and exit position are very stable, and it can control the suitable temperature according to the ORC systems effective and no frequently control is required from the control system of ORC.

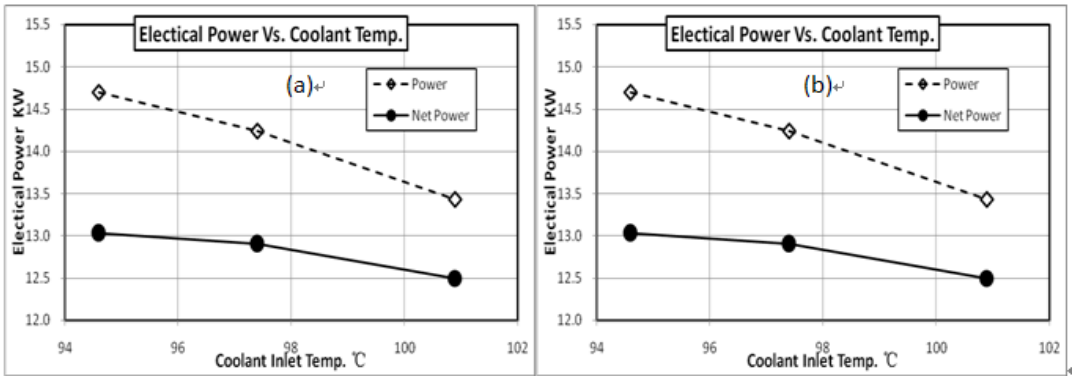

Fig.5 Generate Energy and Efficiency

Also, it can be seen clearly from the Fig.5 that the inlet and exit of engine coolant, and the exhaust gas valve open ratio have much effects on the R245fa temperature in expander inlet. The reason is the engine has a big thermal inertia, the control sofware of ORC systems must be considered.

Fig.5(a) give the curves for the generate electricity power and net power of ORC system under the different exit temperature of the engine coolant. From the plots change, we can see that the generator power reduces with the coolant exit temperature rising. However the net power has no obvious reducing with the coolant exit temperature rising. From the Fig.9(b), the generator electricity efficiency and Net power efficiency are respectively 7.4% and 6.4% under the coolant temperature with 94.4˚C; and the two efficiency are 6.7% and 6.2% under the coolant temperature with 100.9 ˚C

Conclusions

There are much waste heat is discharge in the engine and the ORC technology is a very attractive scheme in improving the engine efficiency and reduce fuel consumption ratio . In the study, the 10kw level ORC commercial plant had been developed based on the engine waste heat.

1. Using the engine coolant as the ORC heat source is a very right choice from the technology and economy point, which can make the ORC systems compact and reduce power consumption of whole ORC systems.
2. The condenser and evaporator are very imporatant components in the ORC systems. The thermal performance calculation are very key in the early development stage.
3. The control systems and control principle are very improtant for the ORC systems, especically for the ORC systems based on engine waste heat because the engine has much thermal inertia.
4. The big stable generator power is 14.6KW and the Net power is 13kw based on 200kw engine waste heat. The efficiency of ORC system is 7.4%.

Reference

[1] Qiu G. Selection of working fluids for micro-CHP systems with ORC. Renewable Energy 48(2012)565–70

[2] Junjiang Bao, Li Zhao，A review of working fluid and expander selections for organic Rankine cycle；Renewable and Sustainable Energy Reviews 24 (2013) 325–342

[3] Roy JP, Mishra MK, Misra A. Parametric optimization and performance analysis of a waste heat recovery system using Organic Rankine Cycle. Energy 2010, 35(12)5049–62

[4] Maraver D, Uche J, Royo J. Assessment of high temperature organic Rankine cycle engine for poly generation with MED desalination: A preliminary approach. Energy Conversion and Management 2012; 53(1):108–17.

[5] Sébastien Declaye, Sylvain Quoilin, Experimental study on an open-drive scroll expander integrated into an ORC (Organic Rankine Cycle) system with R245fa as working fluid[J]，Energy 55 (2013) 173-183

[6] Seok Hun Kang，Design and experimental study of ORC (organic Rankine cycle) and radial turbine using R245fa working fluid [J], Energy 41 (2012) 514-524

[7]Musbaudeen Bamgbopa, Eray Uzgoren, Quasi-dynamic model for an organic Rankine cycle [J], Energy Conversion and Management 72 (2013) 117–124

[8] Noboru Yamada, Md Nor Anuar Mohamad, Trinh Trung Kien, Study on thermal efficiency of low- to medium-temperature organic Rankine cycles using HFO1234yf [J], Renewable Energy 41 (2012) 368-375

[9] S. Quoilin, S. Declaye, Organic rankine cycle systems: a techno-economic overview, Proceedings of EMC 2013

[10] Tom Howel，Development of an ORC system to improve HD truck fuel efficiency, DEER 2011 CONFERENCE

[11] Paola Bombarda, Costante M. Invernizzi， Claudio Pietra，Heat recovery from Diesel engines: A thermodynamic comparison between Kalina and ORC cycles [J]，Applied Thermal Engineering 30 (2010) 212–219

Advanced Materials Research Vols. 960-961 (2014) pp 410-413

doi:10.4028/www.scientific.net/AMR.960-961.410

Research on Recovering Waste Heat from Liquid Produced in Heavy Oil Exploitation by SAGD Technology

Zhongzheng Xiao[1, a], Shuzhong Wang[1,b] and Jianping Yang[2,c]

[1]School of Energy and Power Engineering, Xi'an Jiaotong University, Xi'an, Shaanxi, China

[2] SAGD Development Project Management Department of Liaohe Oilfield Company, Panjin, Liaoning, China

[a]zzxiao@stu.xjtu.edu.cn, [b]szwang@mail.xjtu.edu.cn, [c]yangjianp@petrochina.com.cn

Keywords: steam assisted gravity drainage (SAGD); waste heat recovery; heat exchanger; boiler feed water; fuel consumption

Abstract. In order to enhance the economy of steam assisted gravity drainage (SAGD) technology, researches were conducted on the technology for recovering heat from liquid produced from oil wells. In this study, spiral-plate heat exchanger has been chosen after comparison and analysis, which is used to recover the heat from the produced liquid and raise the temperature of the softened water used in steam injection boilers. The procedures are liquid produced from the wellhead enters a metering and transfer station for degasification and then enters a centralized heat exchanger station where its temperature is reduced to 100°C from 170°C and the temperature of softened water used as boiler feed water is increased to 110°C from 70°C. The result shows that the fuel gas consumption will drop by 907200Nm^3 for each boiler annually when the liquid heat recovery technology is adopted.

Introduction

Steam assisted gravity drainage (SAGD) is an effective technology to extract heavy oil petroleum. Steam is injected through vertical boreholes into the oil reservoir and forms a "steam chamber" that grows vertically and horizontally in the formation. The heat from the steam reduces the viscosity of the crude oil which allows it to flow together with condensate water down into the horizontal segments of the wellbore where it is pumped out [1]. Since 2004 SAGD technology trial has been conducted in Liaohe Oilfield, lots of significant breakthroughs were made so far and the current oil production can reach 150-300 t/d per well. As the SAGD technology matures, SAGD technology has already been an important technology to extract heavy oil petroleum after the steam flooding technique.

Although SAGD technology can improve the oil recovery efficiency substantially, it generates a large amount of waste heat [2]. Based on the current application of SAGD technology, the amount of high temperature produced liquid is 200-400 t/d for each oil well and its temperature can be 170°C, which contains a large amount of waste heat. If the energy of the high temperature produced liquid could be used, it may lower the energy consumption of oil exploitation and improve the economic benefit of SAGD technology.

The design of the process for recovering heat from liquid produced by SAGD Technology

In order to meet the needs of gathering and dehydration and lower the cost of SAGD technology, we can use high efficiency heat exchanger to recover the heat from the high temperature liquid produced from oil wells and raise the temperature of the softened water used in steam injection boilers.

The flow chart of using the produced liquid's heat is shown in Fig. 1. The liquid blended with heavy oil produced from the oil well enters a metering and transfer station for degasification and then enters a centralized heat exchanger station to undergo heat exchange. When its temperature is reduced to 100°C from 170°C, the produced liquid enters a multipurpose station and is dehydrated. While, the

softened water enters the centralized heat exchanger station from the softened water station and after its temperature rises through heat exchange, it's fed into the steam injection boiler as boiler feed water.

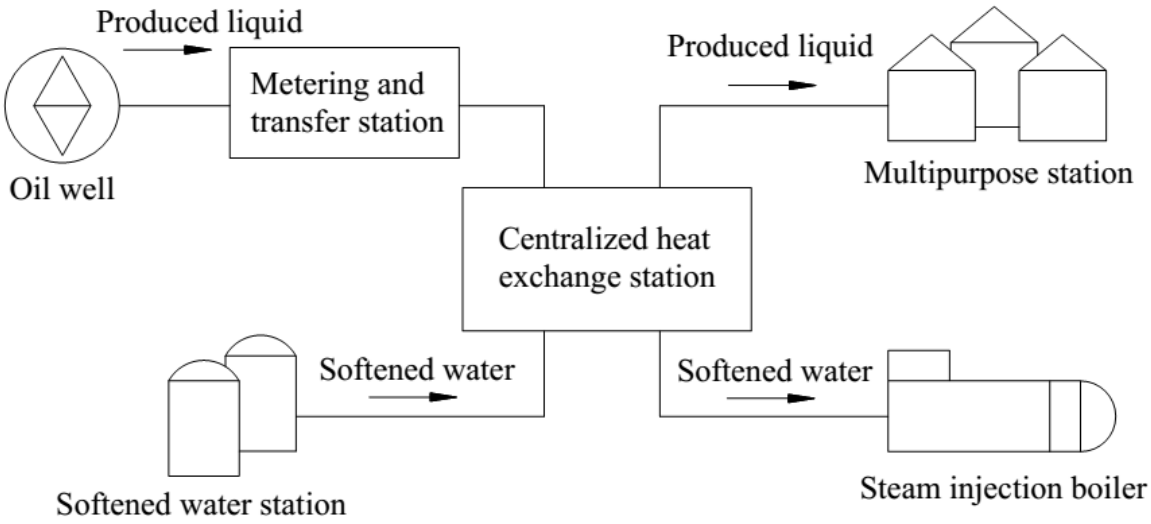

Fig. 1. The flow chart of using the heat of the produced liquid

The analysis on the physical and chemical properties of the produced liquid

In order to recover the waste heat of the liquid produced from oil well efficiently, we should measure and analyze physical and chemical properties of the liquid at first, which is the key to the design of the heat exchanger. So, we took samples of the liquid produced from the oil well in Liaohe Oilfield, which was measured and analyzed on the physical and chemical properties.

The analysis of physical properties. To design a proper heat exchanger, three characteristics (viscosity, specific heat at constant pressure and thermal conductivity) of the produced liquid was measured at two states at 1.6MPa with the temperature of 135°C and 170°C, respectively. The result is shown in Table 1.

Table 1. The result of physical properties analysis

State point	μ [Pa·s]	C_p [kJ/(kg·K)]	λ [W/(m·K)]
1.6MPa, 135°C	0.105	3.818	0.844
1.6MPa, 170°C	0.060	3.923	0.574

The analysis of chemical properties. Some researchers found that the heavy oil heat exchanger had serious corrosion [3]. Therefore, to avoid serious corrosion and reduce the economic loss as possible, the chemical properties analysis of the produced liquid is very important. The major ions in the high temperature produced liquid and the pH value were measured quantitatively. Before the test, oil was removed from the produced liquid. The quantitative analysis is mainly about pH of the produced liquid and the highly corrosive ions, such as Ca^{2+}, Mg^{2+}, Cl^-, HCO_3^-, SO_4^{2-}. The result is shown in table 2.

Table 2. The result of chemical properties analysis

Item	Ca^{2+} [mg/L]	Mg^{2+} [mg/L]	Cl^- [mg/L]	HCO_3^- [mg/L]	CO_3^{2-} [mg/L]	SO_4^{2-} [mg/L]	pH
Value	106	28	125	145.8	None	325	7.2

Comparison of alternative heat exchanger [4]

In Liaohe Oilfield, the pressure of the produced liquid ranges from 1 to 1.6MPa and the temperature is about 170°C when using SAGD technology. Considering the working condition of different heat exchangers and the needs of actual operation, the suitable heat exchanger can be plate heat exchanger or spiral-plate heat exchanger. The comparison and analysis about the characteristics of these two kinds of heat exchanger is shown as follows.

The characteristics of plate heat exchanger:

1) It has high heat-transfer coefficient, which can generate turbulence with low Reynolds number (Re=50-200). Generally speaking, its heat-transfer coefficient ranges from 3000-6000W/(m^2·K) which is 3-5 times to that of shell-and-tube heat exchanger.

2) Its logarithmic mean temperature difference is large and the terminal temperature difference is small.

3) It has compact structure so that it occupies a limited area. Its heat exchanger area per unit volume is 2-5 times to that of shell-and-tube heat exchanger.

4) It has long service life. It's punched with stainless steel sheet or titanium alloy sheet, so that it has high corrosion resistance against many working fluids.

5) Its operating pressure is less than 2.5MPa generally and the working temperature ranges from -40°C to 260°C.

6) The flow path is easily blocked due to the small space between sheet plates. Moreover, the flow path is more likely to be blocked when the working fluid contains large-size solid particle or fibrous matter.

The characteristics of spiral-plate heat exchanger:

1) It has high heat-transfer coefficient which is 1-3 times to that of shell-and-tube heat exchanger. When the hot and cold working fluids are both water, the maximal heat-transfer coefficient can reach 3000W/(m^2·K).

2) The spiral-plate heat exchanger is rolled of two stainless steel sheets so that two even spiral channels are formed and the both working fluids are flowing as complete counter current. So the mean temperature difference between the two working fluids can be as small as 1°C and the heat recovery efficiency may be over 99%.

3) It runs reliably. The sealing performance of non-detachable spiral-plate heat exchanger is fine. So it ensures that two working fluids will not be mixed.

4) It's free of clogging. Because of the spiral flowing, the dirt is not easy to be deposited, so it's easy to clean by using steam or alkali liquor as working fluid.

5) It has compact structure, small size and small external surface area. What's more, if the room temperature fluid flows in the outer channel, the thermal loss can be very low so that it doesn't need heat preservation.

Above all, plate heat exchanger is appropriate for operating when the pressure is lower than 2.5MPa and the temperature is not more than 260°C. It features compact structure and high heat-transfer coefficient. However, due to the narrow winding flow path (3-5mm) and a large amount of suspended solids and impurities mixed in the produced liquid, the flow path will be easily clogged. So, plate heat exchanger is inappropriate.

Not only does spiral-plate heat exchanger have the properties of compact structure, excellent seal and high heat-transfer coefficient, but also it's free of clogging and easily to clean without being disassembled. So, spiral-plate heat exchanger will be the best choice.

The results of design and calculation

The calculation results showed that, when the temperature of 12.5t/h of the produced liquid was reduced to 100°C from 170°C, the temperature of 18.5t/h of the softened water could be increased from 70°C to 110°C. During the design calculation of the spiral-plate heat exchanger, we denote the produced liquid's flow velocity as 0.6m/s and the softened water's flow velocity as 1.0m/s. The major

structures sizes of the spiral-plate heat exchanger are as follows: the produced liquid's passage interval is 10mm; the softened water's passage interval is 5mm; the plate width is 0.6m and the outer diameter is 1.32m. In addition, the overall heat transfer coefficient is 370W/(m^2·K) and the total heat exchange area is 59.7m^2.

In this process, the fuel consumption of the boiler will decrease with the increase of the boiler feed water's temperature. Referring to the report of SAGD project department of Liaohe Oilfield, the steam injection boiler uses natural gas as fuel and the original boiler feed water temperature is 70°C. According to our calculation, by adopting this process, the feed water temperature will be raised to 110°C. As a result, the gas consumption will be reduced to 1587Nm^3/h from 1713Nm^3/h, which means 2976Nm^3 of natural gas will be saved in one day. According to the local price of natural gas (3yuan/Nm^3), assuming the annual working time as 300 days, 2.72 million will be saved for each boiler per year.

Conclusions

1) This research shows that, by using spiral-plate heat exchanger to recover the waste heat of the liquid produced from the oil well, the temperature of the softened water will be raised to 110°C from 70°C which can meet the needs of the gas-fired boiler's technical specifications. So it is a feasible process to recover the waste heat of the produced liquid.

2) When this process is implemented, 3024Nm^3 of natural gas will be saved in one day corresponding that 2.72 million will be saved for each boiler annually. Therefore, this new technology has yielded remarkable economic and social benefits.

References

[1] H.C. Zhang: Sino-Global Energy, Vol. 03 (2011), p. 101-103.(In Chinese)

[2] Y. Zhang, J.C. Xie, Y.B. Bi, etc: Chemical Industry and Engineering Progress, Vol. S1 (2011), p. 669-672. (In Chinese)

[3] L.P. Zhang, Q.B. Zhang, Y.J. Zhang: Modern Paint & Finishing, Vol. 09 (2008), p. 16-18. (In Chinese)

[4] C.L. Yang, in: *Handbook of Heat Exchanger*, edited by S.W. Qian, Beijing, Chemical Industry Press (2006). (In Chinese)

Advanced Materials Research Vols. 960-961 (2014) pp 414-421

doi:10.4028/www.scientific.net/AMR.960-961.414

Analysis on the Calculation Methods of Acid Dew Point of Flue Gas

Chen Zong[1, a], Xiaohui Zhang[2,b] and Qimin Wang[3,c]

[123]Shenyang Institute of Engineering,No.18,Puchang Road,Shenbeixin District,Shenyang City,Liaoning Prov,China

[a]490305827@qq.com, [b]z333777@126.com, [c]123400878@qq.com

Keywords: flue gas; calculation of acid dew point;formula of acid dew point in the thermal calculation from the former U.S.S.R; sulfur dioxide

Abstract. At present, there are lots of calculation methods of acid dew point of flue gas; formula of acid dew point in the thermal calculation from the former U.S.S.R has been widely applied in China. But this formula still has some problems, such as the desulphurization ability of different fuels, classification of sulfur content in fuel and the factors of SO_2 transferred into SO_3.In order to solve these problems,the formula of the acid dew point in the thermal calculation from the former U.S.S.R is adjusted. It was found that the precision of A.G.O kkes formula is the highest by comparing several formulas. So the last will be the compilation of the new formula and A.G.O kkes formula, the former Soviet union formula and the calculation of burning lean coal,bituminous coal and lignite typical instance of 600 MW,it was found that the precision of new formula calculation has improved.

Foreword

So far ,there is sulfur (S) in the composition of the fossil fuels (coal, oil, natural gas, etc.)which the boiler used ,combustion of sulfur in the boiler produce SO_2,a few of SO_2 will generate SO_2 with the catalysis of Fe_2O_3 and V_2O_5,SO_2 and SO_3 combined with water vapor and produce sulfuric acid vapor,its dewpoint is the acid dew point of flue gas. When the temperature of the boiler heating surface is lower than that of acid dew point of flue gas, sulfuric acid vapor will be condenses on the surface heating surface and it has low-temperature corrosion on the heating surface[1].Therefore, calculate and determine the acid dew point of flue gas is significant to avoid the low temperature corrosion of heat exchangers and improving the boiler thermal efficiency. The acid dew point of flue gas is influenced by many factors (such as boiler combustion characteristics, sulfur content and ash content of fuel, moisture content, and excess air coefficient, etc), it is difficult to get accurate formula in theory.According to their own results of research, numerous research institutions get some empirical formula[2].As different starting point, they had different results.Therefore, analysis and comparison of the formula which frequently used to determine the applicable experience formula are necessary.

Commonly used calculation methods of the acid dew point of flue gas

Main methods follow:

(1)Formula of Japan Electric Power Research Institute[3]

$$t_{sld} = 20\lg\Phi_{so_3} + a - 80 \quad (1)$$

In the formula: Φ_{SO_3} is the volume fraction of SO_3 in the flue gas,%; a is water constant,when the volume of water constant in the flue gas is 5%,10% and 15%, a is 184,194 and 201.

(2)Formula of Experience method[3]

$$t_{sld} = 186 + 20\lg\Phi_{H_2O} + 26\lg\Phi_{SO_3} \quad (2)$$

In the formula: Φ_{H_2O} , Φ_{SO_3} is the volume fraction of Water vapor and SO_3 respectively,%.

(3)Muller curve[4]

$$t_{sld} = 116.5515 + 16.06329\lg V_{SO_3} + 1.05377(\lg V_{SO_3})^2 \quad (3)$$

In the formula: V_{SO_3} is the hundred million volume of SO_3 in the flue gas.

(4)A.G.Okkes formula[5]

According to experimental data,Dutch scholar A.G.Okkes put forward the following equation:

$$t_{sld} = 10.8809 + 27.6 \lg p_{H_2O} + 10.83 \lg p_{SO_3} + 1.06(\lg p_{SO_3} + 2.9943)^{2.19} \quad (4)$$

In the formula: p_{H_2O} is the partial pressure of water vapor in the flue gas,Pa; p_{SO_3} is the partial pressure of SO_3 in the flue gas,Pa.

(5)Formula of the acid dew point in the thermal calculation from the former U.S.S.R.1973[6]

$$t_{sld} = t_{ld} + \frac{\beta \bullet \sqrt[3]{S_n}}{1.05^{a_{fh} \bullet A_n}} \quad (5)$$

In the formula: t_{ld} is the dew point temperature of water vapor,℃; S_n is reduced sulfur content of fuel,10～kg / 4186． 8 kJ; A_n is the convert ash of fuel,10～kg / 4186． 8 kJ; a_{fh} is how many percent of fly ash in the convert ash of fuel,it generally takes 0.9 for domestic pulverized coal fired boiler; β is the coefficient about a'' (excess air coefficient at Chamber of furnace exit),when a''=1 ． 2～1． 5, $\beta = 121$～129.

(6)Correction formula of formula (5)[7]

$$t_{sld} = t_{ld} + \frac{1.1 \bullet \beta \bullet \sqrt[10]{S_n}}{1.05^{a_{fh} \bullet A_n}} \quad (6)$$

$$t_{ld} = -1.2102 + 8.4064 \bullet \phi_{H_2O} - 0.4749 \times (\phi_{H_2O})^2 + 0.01042 \bullet (\phi_{H_2O})^3$$

In the formula: ϕ_{H_2O} is the volume fraction of water vapor,%.

(7)Formula is based on the concentration of SO_2 in the flue gas[8]

$$t_{sld} = t_{ld} + \beta \bullet \sqrt[n]{4.2 S_n} \quad (7)$$

$$t_{ld} = -1.2102 + 8.4064 \bullet \phi_{H_2O} - 0.4749 \times (\phi_{H_2O})^2 + 0.01042 \bullet (\phi_{H_2O})^3$$

In the formula:n is conversion coefficient of SO_3, it takes 3 commonly,it can take 4-5 after installation of SCR denitration device; $S_n = S_{SO_2} / Q_{net.ar}$, $Q_{net.ar}$ is the low calorific value of fuel as received basis,MJ/kg; S_{SO_2} is sulfur content in fuel,%; $S_{SO_2} = 0.5 Q_V \bullet \rho_{SO_2} / B_M$, Q_V is the volume flow of flue gas, m^3 / s ; ρ_{SO_2} is the concentration of SO_2 of flue gas at desulfurization tower entry, mg / m^3 ; B_M is the amount of fuel,t/h.

Analysis on the calculation methods

Both formulae of Japan Electric Power Research Institute and the formula of Experience method need to measure the concentration of SO_3 in the flue gas. It is therefore difficult to measure accurately.These formulas are unfit for being applicable to the actual engineering.

Muller curve loses sight of the influence of water vapor,so it has certain limitations.

A.G.Okkes formula born of Muller data regression.It allowed for the impact of SO_3 and water vapor concentration in the acid dew point temperature.In the estimating of the acid dew point,it can be serve as a basis for the evaluation of other formula.

The current formula (5) is more widely applied in China,its data source (fuel element analysis and determination of calorific value)is easily got during the design and operation stages.This formula has the following problems:(1)It allowed for the influence of self-desulfurization of ash,but it is difficult to quantitatively the actual amount of desulfurization of fly ash ,different coal has different capacity of self-desulfurization[8];(2)The sulfur content in fuel was used in the calculation of this formula,actual sulfur content in fuel was divided into elemental sulfur, organic sulfur and sulfate sulfur and pyrite sulfur,organic sulfur also was divided into many kinds, there is a world of different between their releasing characteristics.For example,precipitation of SO_2 in the lean coal is divided into two stages:Stage one is produced by combustion of organic sulfur which easy to decompose and precalcining combustion of part of the pyrite sulfur(H_2S),stage two is produced by the organic sulfur which is difficult to decompose, pyrite sulfur and a small amount of sulfate sulfur[9].So the calculation of sulfur content is not accurate.(3)This formula loses sight of influence of SO_2 transferred into SO_3 to the acid dew point.

A large number of research results show that,acid dew point temperature rise accordingly when the generation of SO_3 increases.SO_3 in the flue gas usually accounts for 0.5%-5% of all SO_2,the flue gas which has different content of SO_3,its change of acid dew point temperature can reach 20 ℃[10].In this case, the consequences of formula (5) will be less than the actual acid dew point temperature.Literature [7] find the same conclusion after comparing with foreign acid dew point test measurements.

A new formula

According to the problems in the above formula,it put forward a method which uses the actual concentration of SO_2 in the flue gas to calculate the acid dew point on the basis of high precision correction formula. The methods follow:

(1)Fig.1 is the curve of acid dew point temperature change with the concentration of SO_3 comes in three kinds of formulas when the water vapor content is 8%.Among them,the Muller curve was verified by experiment[7].As we can see in the Fig.1,the calculation results of the former Soviet Union formula are quite far away from experimental data,and the slope of its curve is too large.So it changes the conversion coefficient from 3 to 10,and multiplies by 1.36 before $\Delta t(\Delta t = t_{sld} - t_{ld})$ to slow the increasing of the curve trend.

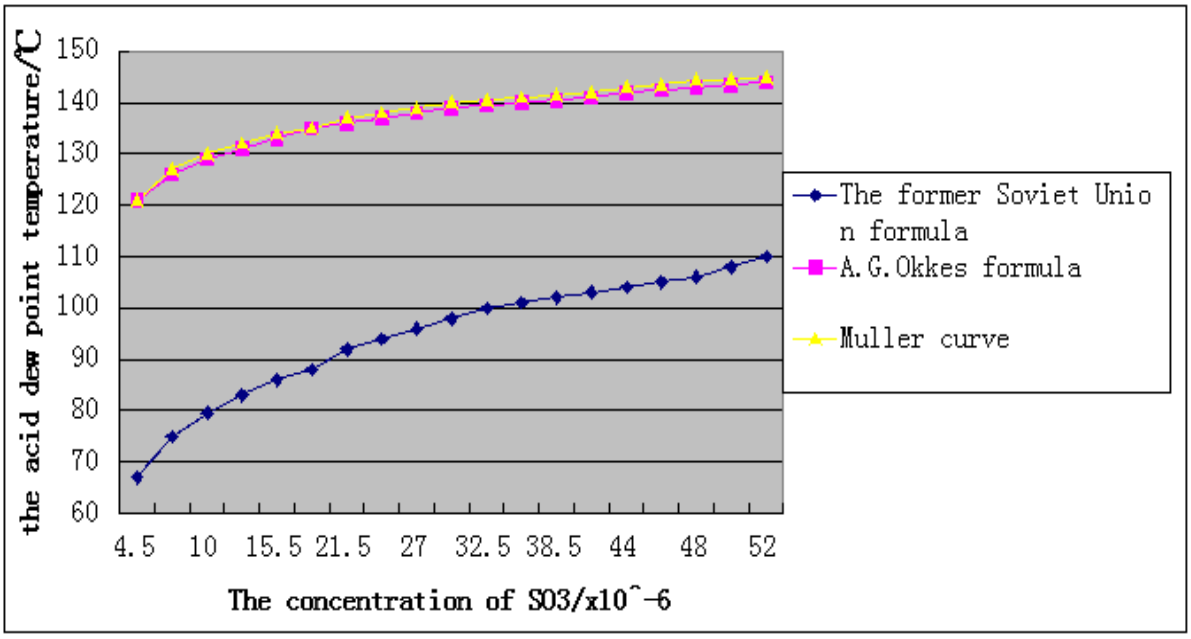

Fig.1 The curve about acid dew point temperature Change with the concentration of SO_3 when the water vapor content is 8%

(2)Based on the actual concentration of SO_2 in flue gas at desulfurization tower entrances(the smoke flow here is relatively stable and the difficulty of concentration of SO_2 measurement is smaller)[8],and combined with the actual boundary conditions to get the amount of actual flue gas,it gets the content of sulfur of SO_2 which is produced with coal in the grate.

(3)Changed type of coal have different ability of desulfurization and ash composition.The new formula performs the calculation of the actual concentration of SO_2 in flue gas.It needs not to reflect upon removal part of fly ash.

(4)Coal-fired power plants are widely equipped with SCR denitration system in recent years.The metal oxide of the main active ingredient in SCR catalysts will improve the proportion of SO_2 transferred into SO_3.Thus,improving the acid dew point of flue gas[11].Replacing the conversion coefficient of SO_3 is based on whether installed SCR denitration device.

The new formula is:

$$t_{sld} = t_{ld} + 1.36\beta\sqrt[n]{S_n}$$

$$t_{ld} = -1.2102 + 8.4064 \bullet \phi_{H_2O} - 0.4749 \times (\phi_{H_2O})^2 + 0.01042 \bullet (\phi_{H_2O})^3 \quad (8)$$

In the formula:n is conversion coefficient of SO_3, it takes 10 commonly,it can take 11-12 after installation of SCR denitration device; $S_n = S_{SO_2} / Q_{net.ar}$, $Q_{net.ar}$ is the low calorific value of fuel as received basis,MJ/kg; S_{SO_2} is sulfur content in fuel,%; $S_{SO_2} = 0.5Q_V \bullet \rho_{SO_2} / B_M$, Q_V is the volume flow of flue gas, m^3/s ; ρ_{SO_2} is the concentration of SO_2 of flue gas at desulfurization tower entry, mg/m^3 ;B_M is the amount of fuel,t/h.

Verification of formula

(1)Validated theoretically

In the estimating of the acid dew point,A.G.Okkes formula can serve as a basis for the evaluation of other formula.We get the Fig.2 after the comparation of the new formula,the former Soviet Union formula and A.G.O kkes formula,the change in trend of the new formula is slower than the former Soviet Union formula and its result is closer to the A.G.Okkes formula.

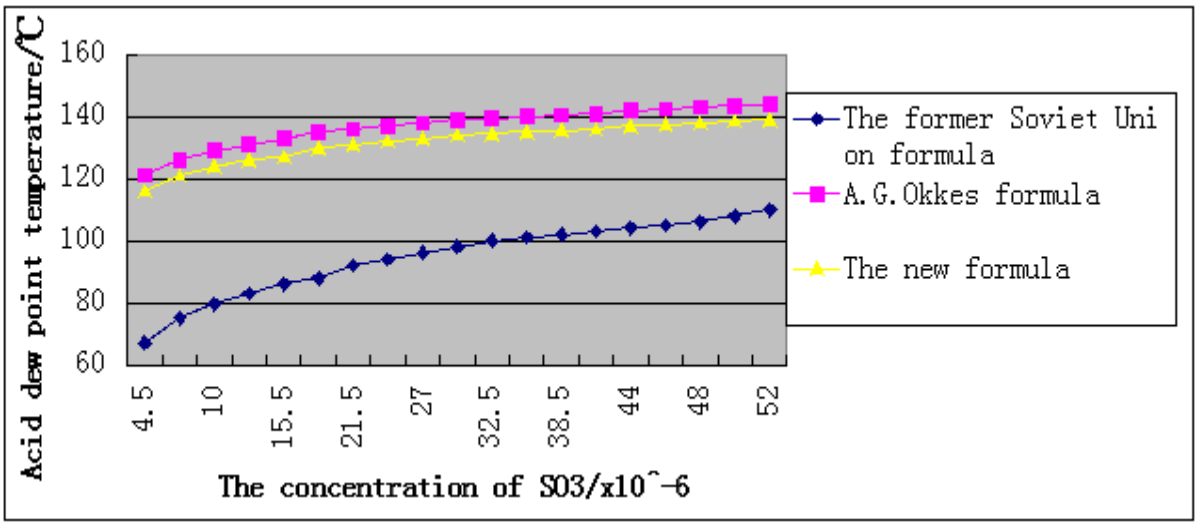

Fig.2 Comparison of the new formula,the former Soviet Union formula and A.G.O kkes formula

(2)Validated by calculation

According to the boundary conditions of the actual operation(Table 1),calculate the acid dew point temperature of the 600MW units firing lean coal,bituminous coal and lignite coal with the new formula.Specific steps are presented in Table 2.

We can see from Table 2:The result of the new formula is higher than formula(5) and formula(7),and close to the result of formula(6).The precision of the new formula can be guaranteed after the comparison with A.G.O kkes formula[7].

Table 1

Project		Lean coal unit	Bituminous coal unit	Lignite coal unit
Coal quality parameters	Carbon C_{ar}/%	55.15	62.41	32.74
	Hydrogen H_{ar}/%	2.21	3.63	2.43
	Oxygen O_{ar}/%	0.91	9.47	11.34
	Nitrogen N_{ar}/%	0.83	0.71	0.36
	Sulfur S_{ar}/%	2.31	0.77	0.16
	Moisture M_{ar}/%	10.31	10.92	40.61
	Ash A_{ar}/%	30.21	14.14	10.76
	Lower heating value $Q_{net.ar}$ / $MJ \bullet kg^{-1}$	19.51	22.82	11.62
Air parameters	Relative humidity φ/%	80.0	80.0	40.0
	The environment temperature t/°C	20.1	30.4	30.2
	Environmental stress p/Pa	87400	102000	94270
	Absolute humidity d / $g \bullet kg^{-1}$	13.7	22.4	11.2
Operation parameters	The total amount of fuel B_M / $t \bullet h^{-1}$	252.3	230.1	433.2
	Excess air coefficient of furnace exit a	1.1	1.1	1.2
	Air preheater and air leakage rate of electrostatic precipitation A/%	8.0	8.0	7.0
	Exhaust temperature t_{py}/°C	138.0	139.6	150.4
	Concentration of SO_2 in flue gas at desulfurization tower entrances (Standard state)/ $mg \bullet m^{-3}$	5700	1600	600
	Concentration of SO_2 in flue gas at desulfurization tower entrances （Actual status）/ $mg \bullet m^{-3}$	3106	1089	291

Table 2

Project		Formula	Lean coal unit	Bituminous coal unit	Lignite coal unit
Theoretical amount of dry air/ $m^3 \bullet kg^{-1}$		$V^0 = 0.0889(C_{ar} + 0.375S_{ar}) + 0.265H_{ar} - 0.0333O_{ar}$	5.5	6.2	3.2
The completed combustion product when $a = 1$	Theoretical volume of nitrogen/ $m^3 \bullet kg^{-1}$	$V_{N_2}^0 = 0.008N_{ar} + 0.79V^0$	4.4	4.9	2.5

	Theoretical volume of three atomic gas/ $m^3 \bullet kg^{-1}$	$V_{RO_2}^0 = 1.866(C_{ar} + 0.375S_{ar})/100$	1.0	1.2	0.6
	Theoretical volume of dry flue gas/ $m^3 \bullet kg^{-1}$	$V_{gy}^0 = V_{RO_2} + V_{N_2}^0$	5.2	6.0	3.2
	Theoretical volume of water vapor/ $m^3 \bullet kg^{-1}$	$V_{H_2O}^0 = 0.0124M_{ar} + 0.112H_{ar} + 0.0016dV^0$	0.5	0.8	0.8
	Theoretical volume of wet flue gas/ $m^3 \bullet kg^{-1}$	$V_y^0 = V_{gy}^0 + V_{H_2O}^0$	5.7	6.8	4.0
The completed combustion product when $a \geq 1$	Actual volume of dry flue gas/ $m^3 \bullet kg^{-1}$	$V_{gy} = V_{gy}^0 + (a-1)V^0$	5.8	6.6	3.8
	Actual quality of dry flue gas/ $kg \bullet kg^{-1}$	$m_{gy} = 0.0367(C_{ar} + 0.375S_t) + 0.9879aV^0 + 0.01N_{ar} + 0.3(a-1)$	8.2	8.9	5.2
	Actual volume of water vapor/ $m^3 \bullet kg^{-1}$	$V_{H_2O} = 0.0124M_{ar} + 0.112H_{ar} + 0.0016daV^0$	0.5	0.8	0.9
	Actual quality of water vapor/ $kg \bullet kg^{-1}$	$m_{H_2O} = 0.01(9H_{ar} + M_{ar} + 0.129adV^0)$	0.4	0.6	0.7
	Actual volume of wet fuel gas/ $m^3 \bullet kg^{-1}$	$V_y = V_{gy} + V_{H_2O}$	6.3	7.4	4.7
	Actual amount of flue gas produced by combustion of 1kg coal/	$m_y = m_{gy} + m_{H_2O}$	8.6	9.5	5.9

$kg \bullet kg^{-1}$				
Standard density of actual flue gas/ $kg \bullet m^{-3}$	$\rho_y^0 = m_y / V_y$	1.4	1.3	1.3
Density of actual flue gas/ $kg \bullet m^{-3}$	ρ_y ,conversion to the actual condition.	0.8	0.7	0.7
Amount of flue gas at air preheater entrance/ $kg \bullet s^{-1}$	$M_{y.in} = m_y \bullet B_M$	602.7	607.2	710.0
Amount of flue gas at air preheater exit/ $kg \bullet s^{-1}$	$M_{y.out} = M_{y.in} \bullet (1 + A)$	650.9	655.8	759.7
Volume flow of flue gas/ $m^3 \bullet s^{-1}$	$Q_V = M_{y.out} / \rho_y$	813.6	936.9	1085.3
The total of sulfur in SO_2/ $kg \bullet s^{-1}$	$M_{S.SO_2} = 0.5 Q_V \bullet \rho_{SO_2}$	1.30	0.52	0.16
The share of sulfur in SO_2//%	$S_{SO_2} = M_{SO_2} / B_M$	1.86	0.81	0.13
Reduced sulfur content/ $10g \bullet MJ^{-1}$	$S_n = S_{SO_2} / Q_{net.ar}$	0.10	0.04	0.01
Volume fraction of water vapor in flue gas/%	$\phi_{H_2O} = V_{H_2O} / V_y$	8.0	10.8	19.1
The dew point temperature of water vapor in flue gas/°C	t_{ld} ,look-up table or calculated by type (8)	41.0	47.3	58.7
Conversion coefficient of SO_3	n	10	10	10
Δt （Factors of sulfur content）/°C	$1.36\beta\sqrt[n]{S_n}$	135.0	123.2	107.3
The acid dew point temperature of flue gas/°C	$t_{sld} = t_{ld} + \Delta t$	176.0	170.5	166.0
Result of calculation of formula without correction/°C	Formula(5)	113.3	100.5	92.2
Result of calculation of formula based on the concentration of SO_2/°C	Formula(7)	134.6	116.3	102.2
Result of calculation of the former Soviet Union formula/°C	Formula(6)	177.0	171.4	166.7

Conclusions

(1)The acid dew point temperature in flue gas increase with the concentration of SO_3,in the formulas that considering the influence of SO_3,the former Soviet union formula after revised and A.G.Okkes formula are accurate.The error of former Soviet union formula and formula of Japan Electric Power Research Institute are large.There are still some certain errors in the formula based on the concentration of SO_2(formula (6)).

(2)The former Soviet Union formula loses sight of the influence of different desulfurization ability of different fuels,the classification of sulfur in coal and SO_2 transferred into SO_3 to the acid dew point of flue gas.Its result in low and slope of the curve is greater.

(3)The new formula which based on the actual concentration of SO_2 in the flue gas at desulfurization tower entrances combines with the actual boundary conditions to make calculations.It is more suitable for engineering application than the former Soviet Union formula without correction.

References

[1] Liguo SHI,Ligong SHI,Changquan WANG,Shupo ZHANG.*Total Corrosion Control*,2009, 4:32-35(in Chinese).

[2] Jian WANG,Xiguo ZHANG,Youxi LUO,et al.*Thermal Power Generation*,2011,40(4):57-61(in Chinese).

[3] Zhiyong TANG,Baosheng JIN,Keqin SUN,et al.*Journal of Power Engineering*, 2005, 25(S): 18-21(in Chinese).

[4] Müller P.A. *Chem. Eng. Technol*. 1959,31:345-350.

[5] A.G.Okkes,Badger B.V.*Hydrocarbon Processing*,1987(7):53-55.

[6] Junkai FENG,Youting SHEN.*The principle and the calculation of boiler*[M].Beijing:Science Press,1992:378-379(in Chinese).

[7] Pengfei LI,Huiling TONG.*Boiler Technology*,2009,4(6):5-8(in Chinese).

[8] TianXIE,Yang LI,Yuanyang ZHOU, Hao JIANG. *Thermal Power Generation*, 2013, 12(12): 120-134 (in Chinese).

[9] Yingjie LI,Chunmei LU,Hantao LIU,et al.*Journal of Shandong University*,2005(6):38-39(in Chinese).

[10] Jun LI,Weiping YAN,Baotong GAO,et al.*Boiler Technology*,2009,40(5):14-17(in Chinese).

[11] Yan GAO,Tao LUAN,Jiwei PENG,et al.*Ciesc Journal*,2013(7):2611-2617(in Chinese).

[12] Jianzhong ZHANG.*Boiler Technology*,2013,3(2):10-16(in Chinese).

Advanced Materials Research Vols. 960-961 (2014) pp 422-426

doi:10.4028/www.scientific.net/AMR.960-961.422

Coal and Wood Chips Co-pyrolysis Study

WANG Qi-min [1, a], WANG Hao [2, b], HAO Jia [3, c] and GUO Shuo [4, d]

[1,2,3,4] Shenyang Institute of Engineering, NO.18 Puchang road, Shenbei new area, Shenyang, Liaoning province, China

[a]123400878@qq.com, [b]644375189@qq.com, [c]hj258hj@163.com, [d]guoshuo2007@sina.com

Keywords: Coal, Wood chips, Co-pyrolysis, Interaction

Abstract. As a clean, renewable energy, rational use of biomss can effectively solve the problem of energy shortage and environmental pollution. Co-combustion and Co-gasification of biomass and coal are important ways of biomass utilization. Co-pyrolysis reaction is one of the most important processes in the co-combustion and co-gasification. In order to study the different mix ways of coal and wood chips affections on the co-pyrolysis process, TGA was used to study the co-pyrolysis characters of wood chips and coal mixed by different methods with mass ratio 1:1. it is founded out that there is certain interaction between wood chips and coal by the comparison of TGA curves and calculation curves. There is promoting affection at the high temperature if wood chips and coal had been mixed up. There is inhibiting affection if wood chips and coal are tiering distributed.

Introduction

With the rapidly growth of energy consumption in our country, it is primary energy coal resources are sharply declining. According to the proved reserves and production capacity, China's coal mining life of just only 80 years the data shows. Therefore, it is urgent developing and looking for a new, clean renewable energy for need to sustainable development. Biomass resources are rich in our country, though the annual crop waste is equivalent to more than 600 million t of standard coal, and forestry waste of standard coal equivalent to about 300 million t. In burning power generation and use of renewable biomass to replace part of gasification coal can not only alleviate energy crisis, but also can reduce environmental pollution, implementation technology, economic and environmental win-win [1-2].

Although biomass which abundant in China, is a renewable energy, it's energy density low, separately used in the low temperature pyrolysis, and the process is not easy to control, equipment corrosion, generate the tar is much, not only reducing its efficiency, and may cause secondary pollution, so make the size of the individual pyrolysis is restricted. Mixing biomass with coal in a certain proportion pyrolysis already separately overcome various problems of biomass pyrolysis; also can make up for the shortage of coal resources, and biomass ashes metal and alkaline substance content is higher, can increase the reactivity of coal and the sulfur removal ability. So no matter from the angle of ecology and economics analysis, this is one of the feasible way so fusing [3].

Pyrolysis is coal and biomass thermal conversion process of the initial stage and with reaction, in the aspect of comprehensive utilization of coal and biomass in the foundation status. For coal and biomass pyrolysis process, scholars at home and abroad are analyzed under different operating conditions. Foreign scholars M.Yilgin etc. [4] by lignite with beet ratio 1:1 fast pyrolysis experiments show that the lignite pyrolysis with beet synergies; Wei ping Yan [5] by lignite and biomass pyrolysis research shows that in the process of biomass with coal pyrolysis, biomass mixing proportion, composition and properties and mineral composition of coal ash pyrolysis volatilization analysis the influence of both promotion and inhibition. When biomass adding amount of more than 50%, a large number of biomass can occur before the Samples volatilization of precipitation in coal softening melting, then adhesion, covering the surface of coal, coal blockage wool stoma, suppress the volatile evolution and diffusion, which play the role of inhibition of lignite pyrolysis; Wen Lee [6] in pressurized with non isothermal weight on the heat balance method for total biomass (sawdust, rice husk) and coal pyrolysis research, think of biomass with coal pyrolysis temperature difference is very big, so no interaction in the pyrolysis process. Thus, for biomass pyrolysis process with coal blend for how to influence and influence mechanism has not unified conclusion.

This experiment using thermogravimetric analyzer with 1:1 proportion, according to different methods of mixed with sawdust pyrolysis process of coal property research, for the coal and wood pyrolysis process design and operation to provide theoretical basis.

Experimental study

Raw material and the analysis of nature

Wood chips with high-speed multi-function crusher (BL - 100 type, voltage 220 v, power 650 w, rotating speed of 22000 r/min) grinding particle size was less than 0.2 mm samples, coal sample grain size is less than 0.105mm.Samples of industrial analysis, element analysis to see the table.1below.

Tab.1 Proximate analysis and ultimate analysis of samples

Samples	Proximate analysis/ %*				Ultimate analysis/ %				
	M_{ar}	V_{ar}	A_{ar}	FC_{ar}	C	H	N	S	O
Wood chips	4.942	79.848	1.128	14.082	41.9	5.17	0.19	0.16	46.51
Coal	6.735	35.242	27.516	30.507	46.40	3.44	0.76	0.47	14.68

* Percent of weight.

Thermogravimetric analysis experiment

Experiment using TGA/DSC Switzerland Mettler Toledo - company - type 1 thermogravimetric analyzer, it analysis with high purity nitrogen as the carrier gas, flow rate of 60 ml/min, use PC - 85 MT type thermostatic bath cooling at low temperature. Experiments with each quantity of sample (10 + / - 0.1 mg), coal and wood chips under 1:1 ratio in three way mix, temperature range 50-1000˚C, the heating rate of 40˚C / min. Experiment explores different ways of mix influenced on coal pyrolysis characteristics with sawdust. Coal mixed with wood of three kinds of ways: 5 mg of coal sample with 5 mg sawdust by coal on sawdust, wood chips under coal mixed arrangement of stratification and the mixing coal and wood chips.

The results and discussion

Sawdust and coal pyrolysis alone

Figure1 and figure 2 respectively, sawdust and coal pyrolysis alone when the curve of the weight percentage change with temperature, Can be seen from the diagram, there are large differences in the process of pyrolysis between coal and wood chips alone; sawdust pyrolysis of coal pyrolysis temperature is higher; basic don't coincide with sawdust pyrolysis temperature range.

Sawdust pyrolysis process can be divided into three phases: preheating, volatile, analyzed a carbonized. From room temperature to 200 ˚C, sawdust mainly lose moisture, due to the moisture content in the wood is less, so the curve downward trend is not obvious. 200-400˚C is the main stage, the wood pyrolysis process of wood thermal decomposition under anoxic conditions, volatile precipitation, mass loss is as high as 70%. This phase of the important reactions include: dehydration reaction, decarboxylate and containing xylan of hemicellulose polymer. When the temperature is lower, coke formation reaction plays a leading role. As temperature rises, produce the sinistral glucan depolymerization reaction were dominated. The changes of biomass in low temperature pyrolysis have part of hemicellulose, lignin and cellulose decomposition (cellulose fiber shortening). Usually, hemicellulose decomposition during 200-250 ˚C, cellulose decomposition temperature range of 240-350 ˚C and lignin decomposition occurs in the within the range of 280-500, the decomposition rate of slow [1]. Hemicellulose and cellulose decomposing main produce volatile substances, and decomposition of lignin mainly for carbon [7]. Temperature of 400 ˚C above, mainly carbocoal decomposition is thought to be composed of C - C key and C - H key fracture caused by further, in this phase, sawdust volatile internal diffusion, slowly towards the outer quality change is relatively flat, a longer duration of [8]. Non-volatile solid residue into sawdust pyrolysis process carbocoal residue, generally does not generate gum body, and no bond phenomenon.

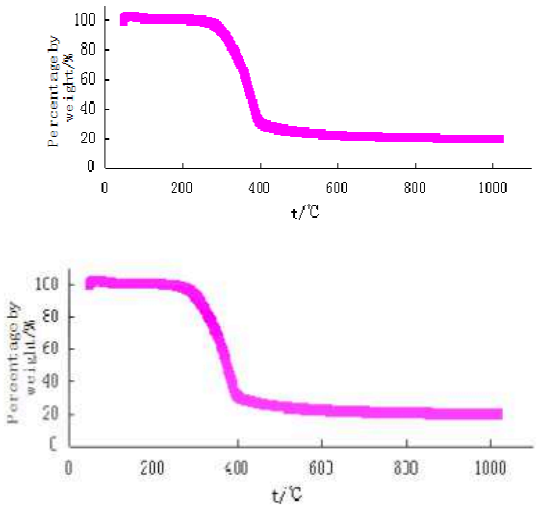

Fig.1 TGA curve of coal separate pyrolysis process

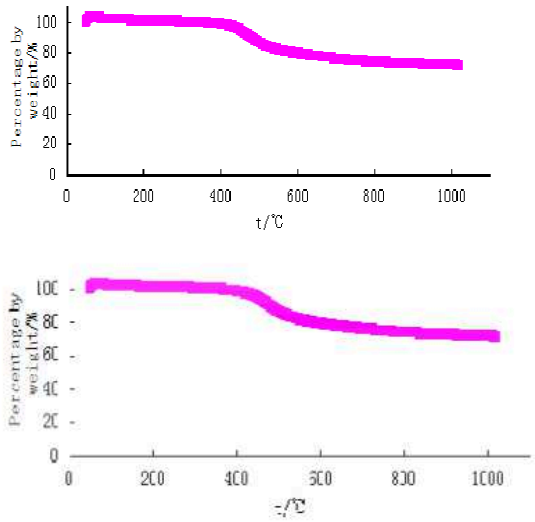

Fig.2 TGA curve of wood chips separate pyrolysis process

Coal compared with sawdust pyrolysis process, also has a powerful weightlessness, but the quality loss value are much smaller than wood, this industry analysis of volatile higher quality to score. With the increase of temperature, coal pyrolysis process is complex, gas during coal successively removing moisture and gap (350-400 ˚C); it is given priority to with depolymerization and decomposition reaction in a gas (400-550 ˚C); Polycondensation reaction gases and minerals decomposition gas (550-1000 ˚C), also known as secondary degassing [9]. Pyrolysis process of the TGA curve is consistent with the existing theory.

Sawdust mixed with coal pyrolysis

Analysis of coal mixed with sawdust pyrolysis synergy, need to draw the mixed pyrolysis process is the actual weight percentage and the difference between the theoretical values is calculated with the temperature change of the curve. Difference value greater than zero, the actual weight loss value is less than the theoretical value calculated, the pyrolysis process of mixing of coal and wood chips has played a certain inhibitory effect. On the other hand, the difference is less than zero, mixed with sawdust role to the improvement of the pyrolysis process of coal. Theoretical weight percentage of the total pyrolysis process is equal to the actual weight percentage of the coal and wood chips alone pyrolysis of 1/2, namely assume that when mixed with sawdust has no impact on the pyrolysis process of coal weight percentage.

Figure 3 to figure 5 for coal and wood chips in three different arrangement of mixed pyrolysis total actual weight percentage and the difference between the theoretical values is calculated with the temperature change of the curve, can be seen by the figure of coal mixed with sawdust in three ways, did not show obvious synergy before250 ˚C, after 250 ˚C inhibition enhanced obviously, peaked at about 350˚C, but far less evenly mixed inhibition enhanced amplitude fluctuation layered hybrid. The author concluded that produce inhibition to begin at about 250 ˚C was the main reason is that in the wood pyrolysis, volatile precipitation, at the same time a large number of biomass could occur in the coal volatile analysis before the softening melting, then adhesion, covering the surface of coal, coal blockage wool stoma, in both cases can inhibit the volatile matter in coal spillover and diffusion, which play the role of inhibition of coal pyrolysis [10]. Pyrolysis is a very complex physical and chemical reaction process, low temperature occurs mainly from coal pyrolysis decomposition, deployerization, generating a large amount of tar and gas. General bridge bond between the structural unit of coal when heated to above 250 ˚C are some weak bond began to break, with the increase of temperature, bond energy high bridge key will break. Bridge bond fracture generated on the basis of the structural unit of free radicals, is a kind of free radical molecules with unpaired electrons fragments, generally in bridge key on the breakup of a carbon atom, such as H +, CH3 -,

CH3CH2 - and C6H6 - etc. Temperature rises, the low temperature pyrolysis tar occurred secondary cracking, decomposed to solid carbon, gas, and free radicals reaction and most of these free radicals have the aromatic. Free radicals are unstable, baseband unpaired electrons has high reactivity, with adjacent unpaired electrons on the free radicals of pairs of trend, if these free radicals can not get hydrogen and its concentration is large, the free radical fragments will be combined with each other and generate greater molecular weight compounds and coke. Hydrogen atoms are the smallest and simplest of free radicals, rich in hydrogen atmosphere, free radicals hydrogenation can generate stable low molecular products (tar, a small amount of gas and water). In the process of pyrolysis of biomass and coal, biomass, ahead of coal pyrolysis, pyrolysis biomass pyrolysis release a large number of free radicals and small molecular hydrogen, makes coal pyrolysis of a large number of radicals stable low tar and gas molecules, speeding up the coal pyrolysis [11]. Due to the hierarchical hybrid coal mixed with sawdust even when fully contact, may offset the inhibition in a larger extent, so mixing showed inhibitory effect than layered mixed up and down.

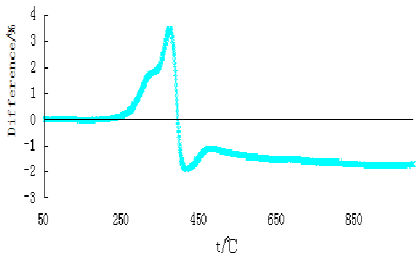

Fig.3 Differences of TGA measured value and calculated value with uniformly mix co-pyrolysis

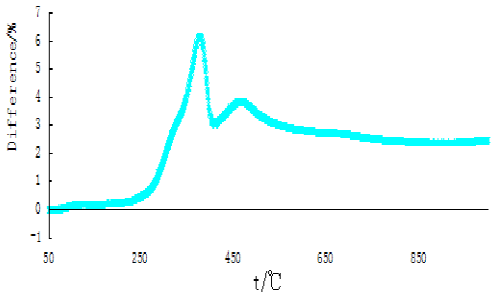

Fig.4 Differences of TGA measured value and calculated value with tiering distributed co-pyrolysis (toal in the upper

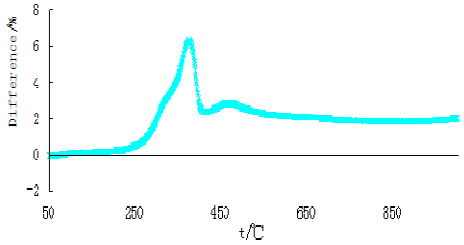

Fig.5 Differences of TGA measured value and calculated value with tiering distributed co-pyrolysis wood chips in the upper

Three ways that produce inhibitory effect began to decline after 350 ℃, it may on the one hand due to sawdust pyrolysis began to form the ash content, ash wood pyrolysis of alkali metal (K_2O, CaO,Na_2O) mass fraction is higher, the pyrolysis of coal play a catalytic role; Second, rice husk of H/C ratio greater than coal, pyrolysis process fracture C - H keys to produce hydrogen in part will be assigned to the coal carbon atoms, increase the quality of the coal pyrolysis process loss value. [8]At the same time it due to contact fully mixing, promoting effect is stronger, so the decline range is larger, after 400 ℃ has shown obvious role in promoting [1].

About 450 ℃, the curve has a modest rise, it may be due to the wood pyrolysis produced a large number of ash adsorption on the surface of coal particles, hindered the evolution of volatile matter in coal and diffusion, the pyrolysis process of coal to produce inhibition [12]. Using mixed coal on sawdust under stratified way, less ash wood pyrolysis will only part of the adsorption on contact with the underlying coal sample, and the rest of the coal samples pyrolysis has not been the impact of wood ash, compared with another two kinds of hybrid methods due to its smaller curve rises. After the curve of the three kinds of mixed mode relatively smooth, but there are varying degrees of decline, a longer duration. The authors concluded that may be because the adhesive on the surface of the coal, wood ashes and produce CO_2 reduction reaction occurred in the process of pyrolysis, reduced the

inhibitory effect of coal pyrolysis [13]. Using coal mixing way on the sawdust, sawdust pyrolysis of ash content accumulation in upper samples mostly, it is easier to contact fully with CO_2, there will be more adhesive on the surface of coal ash in response, so that this way of mixing the curve of the larger drop.

Conclusion

Through the above research and analysis to the following conclusion:

Coal mixture with sawdust pyrolysis rule is integrated embodiment of its single coal and wood pyrolysis regularity, but with sawdust pyrolysis characteristics of coal is not the simple sum of single coal and wood pyrolysis characteristics both in the process of coal pyrolysis with sawdust mixture has certain synergy.

Coal mixed with sawdust according to three different methods of TGA curves measured values compared with the theoretical value of curve trends are similar, but the range of the rise and fall is slightly different. When the temperature is higher, the mixing pyrolysis showed obvious synergy.

Coal mixed with sawdust pyrolysis of synergy and its hybrids, compared to the top and bottom layered hybrid, mixing may be more conducive to synergy.

References

[1] Yong Shi. Hybrid straw biomass low-temperature pyrolysis and gasification [J]. Shanghai chemical industry, 2010, 35 (8): 6-11, In Chinese.

[2] Shiguang Lee, Shaoping Xu. Coal and biomass pyrolysis [J]. Coal conversion, 2002, 25 (1): 7-11.M.A. Green: *High Efficiency Silicon Solar Cells* (Trans Tech Publications, Switzerland 1987), In Chinese.

[3] Qiaoling Hao, Yonghui Bai, Fan Lee. The research progress of biomass with coal gasification characteristics [J]. Chemical industry progress, 2011, 30 (supplement: 68-70, In Chinese.

[4] M.Yilgin, N. Deveci Duranay, D . Pehlivan Co - pyrolysis of ligniteand sugar beet pulp [J]. Energy Conversion and Management, 2010, 51: 1 060-1 060.

[5] Weiping Yan, Chenying Yin. The mixture of biomass with coal pyrolysis characteristics of experimental study [J]. Power engineering, 2006, 26 (6): 865-893, In Chinese.

[6] Baoqing Lee, Chenggong Sun. Biomass pyrolysis, hydrogenated pyrolysis and with coal pyrolysis thermogravimetric study [J]. Fuel chemical journal, 1996, 24 (4): 341-347, In Chinese.

[7] Li Sun, Xiaodong Zhang. The industrialization of biomass power generation technology [M]. Beijing: chemical industry press, 2011. 3, In Chinese.

[8] Dong Yan , Min Zhou, Liqiang Song. The pyrolysis kinetics of thermogravimetric analysis and by coal and rice husk [J]. Chemical engineering, 2012, 40 (9): 60-63, In Chinese.

[9] Liqiang Song , Min Zhou, Lei Meng , etc. Rice husk with coal pyrolysis characteristics [J]. China's agricultural mechanization, 2011, (4): 2011-118, In Chinese.

[10] Liqiang Song, Jiali Lei, Guozhang He, etc. The influence of adding biomass with coal gasification [J]. Guangzhou chemical industry, 2011, 33 (10): 6 52-53 on conversion, In Chinese.

[11] Peng Wang, Fang Wen , edge, etc. Coal and biomass pyrolysis characteristics of preliminary study [J]. Coal conversion, 2008, 31 (4), 40-44, In Chinese.

[12] Xue Zhang, Xuefeng Bai, Huijuan Fan. The synergy of coal and biomass pyrolysis research progress [J]. Chemical and glue, 2011 (3): 48-52, In Chinese.

[13] Linzhuan Ma, Ping He, Hua Wang. Coal and biomass pyrolysis [J]. Chemical industry in guizhou, 2004, 29 (1): 20-23, In Chinese.

Advanced Materials Research Vols. 960-961 (2014) pp 427-432

doi:10.4028/www.scientific.net/AMR.960-961.427

Experimental Investigation on Heat Transfer Characteristics of Thin Film Evaporation

Jingming Dong[1,a], Xinxiang Pan[1,b], Zhitao Han[1,c] and Zhijian Liu[1,d]

[1]Marine Engineering College, Dalian Maritime University, Dalian, 116026, China

[a]dmudjm@hotmail.com, [b]panxx@dlmu.edu.cn, [c]hanzht@yahoo.com.cn, [d]liuzhijian861231@163.com

Keywords: Thin film evaporation, heat transfer characteristics, Rectangular groove

Abstract. Thin film evaporation is a kind of high efficiency heat transfer. A thin film evaporator with rectangular micro groove has been designed, constructed and tested. The heat flux, superheat and thermal resistance of the thin film evaporator were investigated under different evaporating temperatures. Compared with the regular evaporator at the same condition, the thin film evaporator with rectangular micro groove has a better heat transfer performance and good temperature uniformity. The experimental investigation presented in this paper can be used as a reference to promote the engineering application and development of the thin film evaporator.

Introduction

With the rapid development of science and technology, instrument and equipment required total power and power density are significantly increasing. Thin film evaporation as a highly efficient heat transfer device has been concerned more and more. Fig.1 illustrates a schematic of an evaporating thin film formed in a rectangular micro groove. The heat transfer in the rectangular micro groove can be divided into two parts. Some of the heat is transferred through the bulk region, which is controlled by surface tension. While the rest of the heat through the thin film evaporating region, which is controlled by the disjoining pressure.

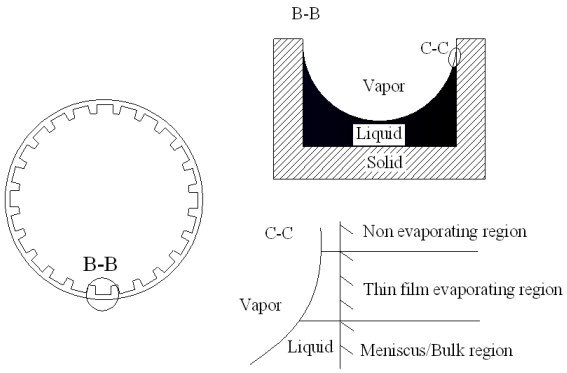

Fig.1 Schematic of an evaporating thin film formed in a rectangular micro groove

The description of the evaporation and fluid flow from an extended meniscus by expanding the Derjaguin-Landau-Verwey-Overbeek (DLVO) theory was reported by Potash and Wayner [1] as early as in 1972. Following this work, several investigations [2–5] were conducted to further understand the mechanisms of thin film evaporation, and found that thin film evaporation plays an important role in phase-change heat transfer. Xu and Carey [2] conducted investigations on the liquid flow in triangular grooves both theoretically and experimentally, and found the importance of disjoining pressure on the overall heat transfer. Ha et al. [3] investigated heat transfer in the evaporating thin film region in triangular micro grooves with non-uniform heat flux applied. It was found that the average and local heat transfer coefficients decreased as the ratio of film conduction resistance over ideal interfacial resistance increased. Still for triangular grooves, Ma and Peterson [4, 5] proposed a mathematical model involving the variation of heat transfer coefficient and temperature along the thin film region. They studied the thin film profile, heat transfer coefficient, and

temperature variation along the axial direction of a triangular groove with capillary induced liquid flow. All these investigations were limited to the evaporation and fluid flow in thin film regions occurring on a flat surface. More recently, Jiao et al. [6] proposed an analytical model which could predict the effects of contact angle on the thin film profile and meniscus radius within a micro-trapezoidal groove. It was found that the thin film evaporation governed the maximum heat transfer capability in a grooved heat pipe. Ma et al. [7] developed a mathematical model for the fluid flow and heat transfer in the thin film region, considering the effect of inertial force, disjoining pressure and temperature-dependent surface tension, which offered a better understanding of the thin film evaporation. Most recently, Cheng et al. [8] developed a mathematical model to determine heat transfer through both the thin film and bulk regions of a liquid in a rectangular micro groove. The result showed that the portion of heat transfer through the bulk region was found to be as high as 22%; hence heat transfer in this region should not be neglected. However, the temperature distribution within the meniscus bulk region was first found via a coordinate transformation and the Galerkin Method. Yan and Ma [9] proposed a mathematical model to predict heat transfer and film thickness in thin-film region. The analytical solutions show that the maximum dimensionless heat flux is constant which is independent of the superheat.

In the current investigation, a thin film evaporator with rectangular micro groove and a regular evaporator with regular pipe have been designed, constructed and tested in the same format and dimension. The evaporating temperature effects on the heat flux, superheat and thermal resistance were investigated for the two evaporators at the same condition. The experimental results presented in this paper will be used as a reference to promote the engineering application and development of the thin film evaporator.

Experimental Setup

The experimental setup is shown schematically in Fig. 2. The experimental system consists of an evaporator, a reservoir, a thermostatic water tank, a vacuum device and a NI-DAQ system. The evaporator is assembled by evaporation tubes, fins, inlet and outlet manifold and standard compression tube fittings. The fin pitch is 180 per meter. The length of the evaporation tubes is 330mm, the diameter is 10mm and wall thickness is 1mm. The total heat transfer area is 0.8822m^2. Two evaporators with different evaporation tubes were fabricated. One is the thin film evaporator, which use the rectangular grooved tubes. The other one is the regular evaporator, which use the regular tubes. The groove width and depth of the rectangular groove are 185μm and 320μm, respectively. The reservoir with a control valve is used for adjusting the flow rate into the evaporator. The thermostatic water tank was carefully wrapped by thermal insulation materials to eliminate the heat loss. The vacuum device was used to provide a certain degree of vacuum. Twenty T-type thermocouples (T1~T20) were placed at both inlet and outlet of the evaporator to monitor the temperature history and the accuracy of the T-type thermocouples is ±0.1 °C. The EJA310A type absolute pressure sensor was used for measuring the evaporation pressure of the evaporator. The range of the pressure sensor is 0~30kPa and the accuracy is 0.065%. The heating power of the thermostatic water tank was measured by the PZ200P-5K1 type wattmeter. The range of the pressure sensor is 0-2000W and the accuracy is 0.1%. A NI (National Instruments) high speed data acquisition system was used and a LabVIEW project was developed for the ejector test.

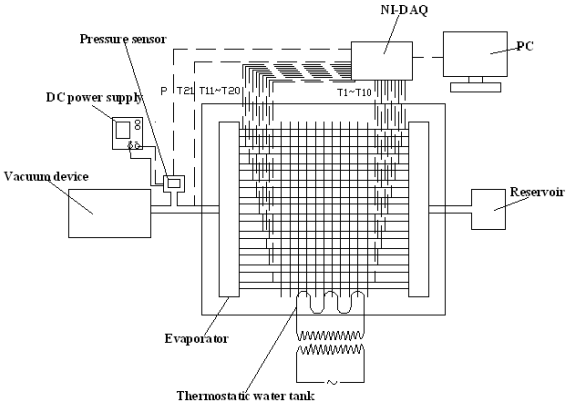

Fig.2 Schematic of thin film evaporation system

Results and Discussion

In this paper, the working fluid used in the test is water. The experimental contrast results of the heat transfer performance for the thin film evaporator and regular evaporator were shown in the Fig. 3 to Fig. 7.

Figure 3 illustrates the comparison result of the superheat at the inlet for the thin film evaporator and the regular evaporator under different evaporation temperature. The superheat at the inlet is defined as the temperature difference between the outer surface temperature at the inlet of the evaporator and evaporation temperature, $\Delta T_i = T_{i,w} - T_e$. Referring to Fig. 3, for the evaporation temperature at the range of 25～60℃, the superheat at the inlet of the thin film evaporator is 1.0~1.8℃. While the superheat at the inlet of the regular evaporator is 1.0~2.0℃. The superheat at the inlet of the two evaporators has less difference. The superheat at the inlet of the regular evaporator is a little bit higher than the thin film evaporator at some evaporation temperature.

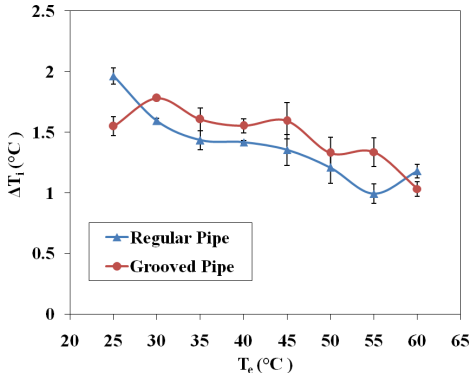

Fig. 3 The comparison result of the superheat at the inlet for two evaporator under different evaporation temperature

Figure 4 shows the comparison result of the superheat at the outlet for the thin film evaporator and the regular evaporator under different evaporation temperature. The superheat at the outlet is defined as the temperature difference between the outer surface temperature at the outlet of the evaporator and evaporation temperature, $\Delta T_o = T_{o,w} - T_e$. According to Fig. 4, for the evaporation temperature at the range of 25～60℃, the superheat at the inlet of the thin film evaporator is 1.3~2.0℃. While the superheat at the inlet of the regular evaporator is 1.8~3.0℃. The superheat at the outlet of the regular evaporator is much higher than the thin film evaporator.

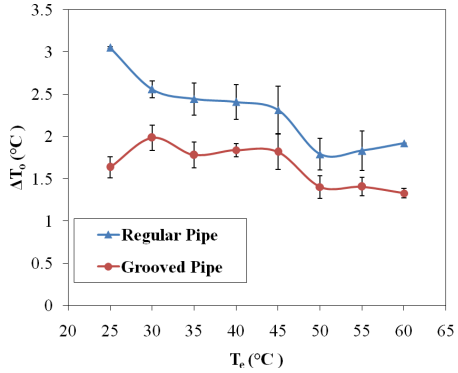

Fig.4 The comparison result of the superheat at the outlet for the thin film evaporator and regular evaporator under different evaporation temperature

Figure 5 shows the comparison result of the temperature difference between the inlet and outlet for the thin film evaporator and regular evaporator under different evaporation temperature. The temperature difference between the inlet and outlet is defined as the difference between the outer surface temperature at the inlet and outlet of the evaporator, $\Delta T_{i,o} = T_o - T_i$. From Fig. 5, it is clearly observed that the temperature difference between the inlet and outlet for the thin film evaporator is 0.1~0.3℃ for the evaporation temperature at the range of 25～60℃. While the temperature difference between the inlet and outlet for the regular evaporator is 0.7~1.1℃. The temperature difference between the inlet and outlet for regular evaporator is much higher than the thin film evaporator at the same evaporation temperature, which indicated that the thin film evaporator has good temperature uniformity.

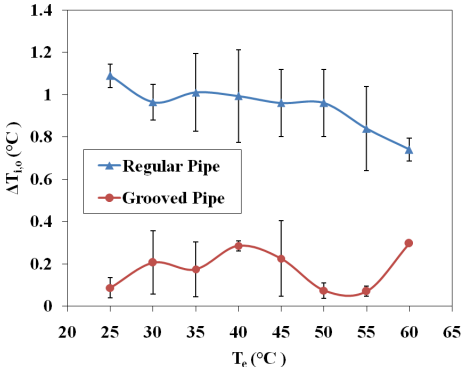

Fig.5 The comparison result of the temperature difference between the inlet and outlet for the thin film evaporator and regular evaporator under different evaporation temperature

Figure 6 shows the comparison result of the heat flux of the thin film evaporator and the regular evaporator under different evaporation temperature. In Fig. 6, the heat flux of the evaporator will increase with the increase of evaporation temperature, which is in a linear relation. From Fig. 9, it appears that the heat flux of the thin film evaporator increased from 193.6W/m2 to 827.3W/m2 for the evaporation temperature at the range of 25～60℃. While the heat flux of the regular evaporator increased from 173.2W/m2 to 501.1W/m2. The heat flux of the thin film evaporator is far above the regular evaporator at the same evaporation temperature, which showed that the thin film evaporator has a better heat transfer performance.

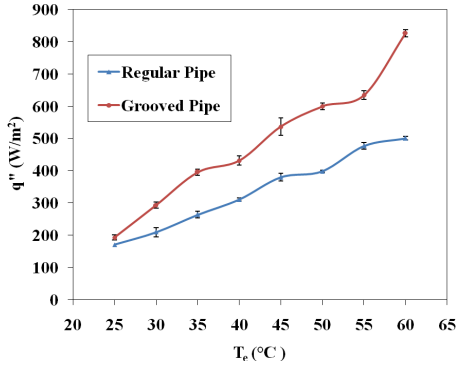

Fig.6 The comparison result of the heat flux of the thin film evaporator and regular evaporator under different evaporation temperature

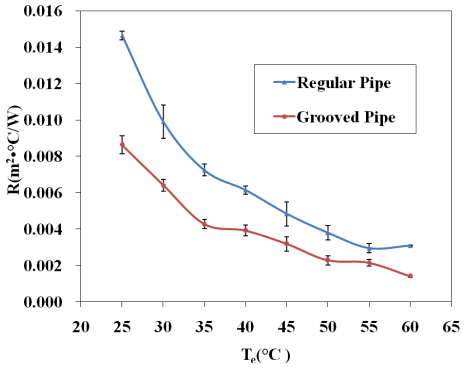

Fig. 7 The comparison result of the thermal resistance of the thin film evaporator and the regular evaporator under different evaporation temperature

The comparison result of the thermal resistance of the thin film evaporator and the regular evaporator under different evaporation temperature is shown in Fig. 7. The thermal resistance of the evaporator is defined as the ratio of temperature difference between the inlet and outlet into the heat flux, $R = \Delta T_{i,o} / q''$ .In Fig. 7, the thermal resistance of the evaporator will decrease with the increase of evaporation temperature, which is leveling off gradually. The thermal resistance of the thin film evaporator decreased from $0.086\,m^2 \cdot ℃/W$ to $0.0014\,m^2 \cdot ℃/W$ for the evaporation temperature at the range of $25 \sim 60$℃. While the thermal resistance of the regular evaporator decreased from $0.0146\,m^2 \cdot ℃/W$ to $0.0031\,m^2 \cdot ℃/W$. The thermal resistance of the thin film evaporator is lower than the regular evaporator at the same evaporation temperature, which showed that the thin film evaporator has a better heat transfer performance.

Conclusions

In the current investigation, a thin film evaporator with rectangular micro groove has been designed, constructed and tested. The evaporating temperature effects on the heat flux, superheat and thermal resistance were investigated. Compared with the regular evaporator at the same condition, the thin film evaporator with rectangular micro groove has a better heat transfer performance and good temperature uniformity. For the thin film evaporator, the heat flux increased from 193.6W/m^2 to 827.3W/m^2 and the thermal resistance decreased from $0.086\,m^2 \cdot ℃/W$ to $0.0014\,m^2 \cdot ℃/W$ for the evaporation temperature at the range of $25 \sim 60$℃. The experimental results presented in this paper will be used as a foundation to boost the engineering application and development of the thin film evaporator in the future.

Acknowledgment

This research work was supported by the National Natural Science Foundation of China under Grant No. 51079012 and the Fundamental Research Funds for the Central Universities No.3132014046.

References

[1] Jr., M., Potash and Jr., P. C. Wayner: International Journal of Heat and Mass Transfer, Vol. 15 (1972), p. 1851
[2] X. Xu and V.P. Carey: Journal of Thermophysics and Heat Transfer, Vol. 4 (1990), p. 512
[3] J.M. Ha and G.P. Peterson: ASME Journal of Heat Transfer, Vol. 118 (1996), p. 747
[4] H. B. Ma and G. P. Peterson: Journal of Thermophysics and Heat Transfer, Vol. 11 (1997), p. 90
[5] H. B. Ma and G. P. Peterson: Microscale Thermophysical Engineering, Vol. 2,(1998), p. 283
[6] A.J. Jiao , H.B. Ma, and J.K. Critser: International Journal of Heat and Mass Transfer, Vol. 50 (2007), p. 2905
[7] H.B. Ma, P. Cheng, B. Borgmeyer and Y.X. Wang: Microfluidics and Nanofluidics, Vol. 4 (2008), p. 237
[8] P. Cheng, J.M. Dong, S.M. Thompson and H.B. Ma: Journal of Thermophysicsand Heat Transfer, Vol.26 (2012), p.108
[9] C.J. Yan and H.B. Ma:ASME Journal of Heat Transfer,Vol. 12(2013), p. 0315011

Advanced Materials Research Vols. 960-961 (2014) pp 433-437

doi:10.4028/www.scientific.net/AMR.960-961.433

Influence of Inlet Mass Flow Rate on Heat Transfer of Supercritical Liquefied Natural Gas in Horizontal Tubes

Haiyu Meng[a], Shuzhong Wang[b *], Lu Zhou[c], Zhiqiang Wu[d], Jun Zhao[e] and Lin Chen[f]

Key Laboratory of Thermo-Fluid Science and Engineering, Ministry of Education ,School of Energy & Power Engineering, Xi'an Jiaotong University, Xi'an, 710049, P.R. China

[a]hymeng321@163.com, [b]szwang@aliyun.com, [c]zhoulu.1987@stu.xjtu.edu.cn, [d]frank.vipoy@gmail.com, [e]zhaojun1st@gmail.com, [f]mumuxin09@163.com

Keywords: Submerged combustion vaporizer, LNG, Horizontal tube, Heat transfer, Large specific heat region.

Abstract. The submerged combustion vaporizer (SCV) is a new kind of vaporizer for liquefied natural gas (LNG). In this paper, a numerical study has been carried out to investigate the heat transfer characteristics of supercritical LNG in horizontal tubes. The thermo-physical properties of supercritical LNG were used for this study, and the influence of inlet LNG mass flow rate on heat transfer was investigated. Numerical results showed that the LNG flow in horizontal tubes included two stages. In the first stage, the surface heat transfer coefficients increased significantly with the increase of the fluid bulk temperature and reached a maximum value when the fluid bulk temperature equaled the pseudo-critical point. After the maximum, the surface heat transfer coefficients fell rapidly with the increase of the fluid bulk temperature. With increasing the inlet LNG mass flow rate, the surface heat transfer coefficients increased due to the increased fluid velocity in horizontal tubes.

Introduction

Natural gas (NG) owns the advantages of safety and cleanness, and its demand is expected to increase in future energy market considering the global energy crisis and the serious environment contamination worldwide. Liquefied natural gas (LNG) is practical approach for large quantity of NG transportation for its mass storage. NG volume can be reduced by about 1/600 by liquefaction, which allows long distance transportation using LNG carriers. Upon arrival at an LNG receiving terminal, LNG is stored in insulated atmospheric LNG storage tanks. The LNG must be vaporized to natural gas before it is used as fuel gas for industrial and domestic purposes. Therefore, efficient and reliable vaporizers for LNG receiving terminals are important. Four types of LNG vaporizers are mainly used in the LNG receiving terminals, namely, open rack vaporizer (ORV), super ORV, submerged combustion vaporizer (SCV), and intermediate fluid vaporizer (IFV) [1].

The SCV's have high thermal efficiency, easy start-up, and are capable of long-terms continuous operation. The structure of SCV is mainly composed of water tank, serpentine tube coils inside the water tank, and burner. The low-temperature NG and the boil off gas (BOG) from the LNG terminals are burned to flue gas as high-temperature heat source. The flue gas is injected into the water tank to keep the temperature of water bath constant, and the LNG is vaporized inside the serpentine tube coils located inside the water tank. The serpentine tube coils are mainly composed of horizontal circular tubes, and the thermal performance of supercritical LNG in horizontal circular tubes has not been reported.

Base on the above preview, the heat transfer performance of supercritical LNG in horizontal tubes were studied computationally in this paper. The influence of inlet LNG mass flow rate on heat transfer was investigated.

Mathematical models

Physical descriptions. The heat transfer of supercritical LNG in horizontal circular tubes is considered here. Fig. 1 shows the schematic diagram of the calculation model which consists of eight horizontal tubes. The outside diameter of the tube is 32 mm with a stainless steel wall thickness of 2.5

mm and the length of the tube is 6308 mm. This tube has been widely utilized in supercritical pressure treatment. In the present study, it was assumed that the working fluid was incompressible, and a constant pressure of 9.85 MPa was used for the physical properties since the pressure drop along the pipe was very small.

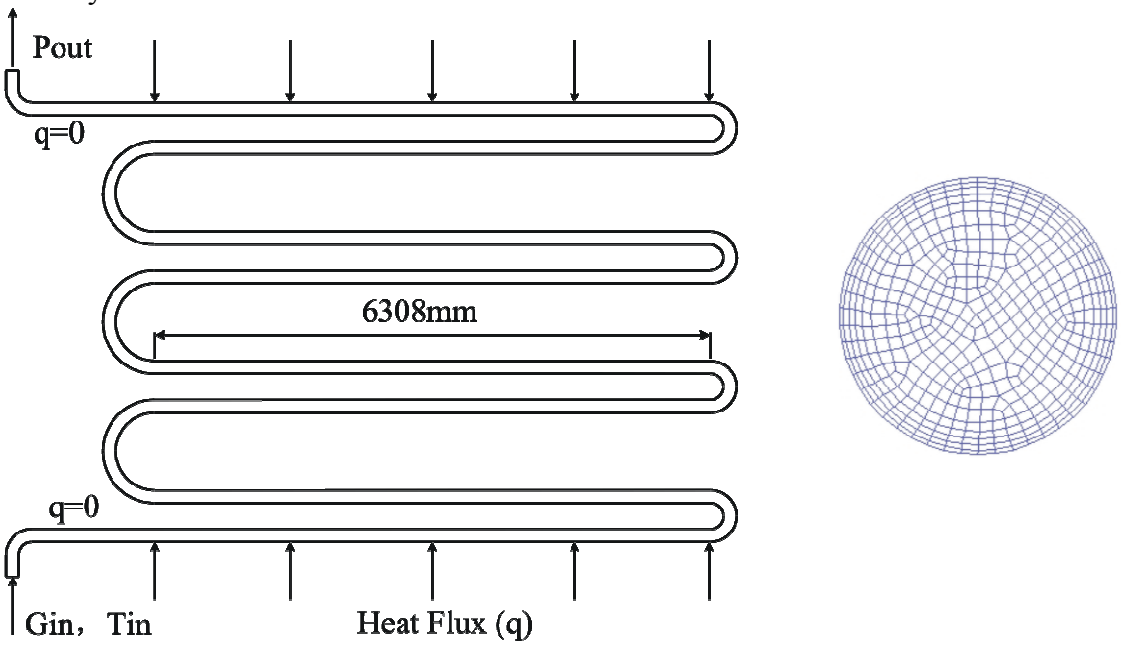

Fig. 1 Schematic diagram of the tubes and the grid configuration in the cross-sectional slice

Thermal properties of the working medium in SCV. Typical compositions of LNG or NG in the present study were (molar ratio): $Y_{CH_4}=89.39\%$, $Y_{C_2H_6}=5.76\%$, $Y_{C_3H_8}=3.3\%$, $Y_{C_4H_{10}}=1.44\%$, $Y_{N_2}=0.11\%$. Therefore, the thermal properties of mixture were used in the present study. The properties of working fluids varied with temperature and pressure. The thermal properties of each component of LNG or NG were calculated by the REFPROP developed by the National Bureau of Standards.

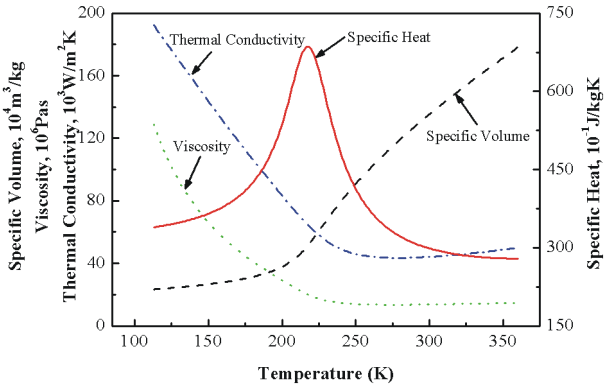

Fig.2 Thermo-physical properties variations of LNG at 9.85 Mpa

The major component of LNG or NG was methane. Fig. 2 shows the values of specific volume, viscosity, and specific heat and thermal conductivity of methane at a pressure of 9.85 MPa. It can be concluded from the variation trend of specific volume that the density decreased continuously with increased temperature, and the decreased trend was relatively significant near the critical temperature. However, the density variation was in the range of the same magnitude and no step variation was found. The specific heat changed sharply and had a maximum value near the critical point. The viscosity and thermal conductivity decreased with the increasing of temperature. The variation trends of thermal properties of other LNG components were as same as methane. The thermo-physical properties of the LNG were calculated by maxing-law based on the properties of each component.

LNG gasification differed from liquid evaporation, in which sharp density deduction and specific heat approaching infinite occurred with phase change. The LNG flow in tubes was consequently considered as single-phase flow rather than two-phase flow with reduced density.

Basic governing equations and Turbulence models. The governing equations of the continuity, momentum and energy [2] were used in the present study. The accuracy of numerical simulations of heat transfer in supercritical fluid may depend on turbulence models. Previous CFD study [3] using the Fluent code revealed the RNG $k-\varepsilon$ turbulence model gives reasonable results in predicting heat transfer of supercritical water, therefore the RNG $k-\varepsilon$ turbulence model was used in this study. **u** is the velocityvector, while u_i is velocity component in special direction $i(i=1,2,3)$. The transport equations for turbulence kinetic energy (k) and its dissipation rate (ε) are [4]:

$$\frac{\partial}{\partial t}(\rho k)+\frac{\partial}{\partial x_i}(\rho u_i k)=\frac{\partial}{\partial x_i}\left[\left(\alpha_k \mu_{eff}\frac{\partial k}{\partial x_i}\right)\right]+G_k+G_b-\rho\varepsilon-Y_M+S_k \tag{1}$$

$$\frac{\partial}{\partial t}(\rho \varepsilon)+\frac{\partial}{\partial x_i}(\rho u_i \varepsilon)=\frac{\partial}{\partial x_i}\left[\left(\alpha_\varepsilon \mu_{eff}\frac{\partial \varepsilon}{\partial x_i}\right)\right]+C_{1\varepsilon}\frac{\varepsilon}{k}\left(G_k+G_{3\varepsilon}G_b\right)-C_{2\varepsilon}\rho\frac{\varepsilon^2}{k}-R_\varepsilon+S_\varepsilon \tag{2}$$

where, G_k represents the generation of turbulence kinetic energy due to mean velocity gradients. G_b is the generation of turbulence kinetic energy due to buoyancy. Y_M represents the contribution of the fluctuating dilatation in compressible turbulence to the overall dissipation rate. The quantities α_k and α_ε are the inverse effective Prandtl numbers for k and ε, respectively. S_k and S_ε are user-defined source terms. The main difference between the RNG and standard $k-\varepsilon$ models lies in the additional term in the ε equation given by

$$R_\varepsilon=\frac{C_\mu \rho \eta^3\left(1-\eta/\eta_0\right)}{1+\beta\eta^3}\frac{\varepsilon^2}{k} \tag{3}$$

where $\eta=Sk/\varepsilon$, $\eta_0=4.38$, $\beta=0.012$. S is the modulus of the mean rate-of-strain tensor, $S=\sqrt{2S_{ij}S_{ij}}$. The effective viscosity μ_{eff} is determined by a differential equation:

$$d\left(\frac{\rho^2 k}{\sqrt{\varepsilon\mu}}\right)=1.72\frac{v}{\sqrt{v^3-1+C_v}}dv \tag{4}$$

where, $v=\mu_{eff}/\mu$, $C_v\approx 100$. In the high-Reynolds-number limit. Eq. (4) gives

$$\mu_t=\rho C_\mu\frac{k^2}{\varepsilon} \tag{5}$$

where $C_\mu=0.0845$.

Boundary conditions. Fig. 1 also shows boundary conditions of the computational domain. At the inlet of the tube, mass flow rate, temperature, turbulence intensity and hydraulic diameter were specified. The outlet boundary condition of the domain was specified as pressure-outlet, and the wall surfaces of tubes were set as heat flux boundary. In order to ensure a fully developed velocity profile before flowing into the heat transfer test section and also no backflow at the outlet, a certain length of tube wall surface was set to be adiabatic in the entrance and exit section. The inlet LNG mass flow rate varied in the range of 0.58-0.81 kg/s, and the inlet LNG temperature were kept constant of 118 K. The heat flux of the tube wall surface was 107 kW/m^2, and LNG outlet pressure was 9.55 MPa. The turbulence intensities at the inlet and outlet were both set to be 10%.

Numerical computations

Numerical methods. In this paper, a finite volume method [2] was used to solve all the governing equations above. Standard scheme was used for pressure treatment. A second-order upwind scheme was used for the discretization of the equations in the current work. The SIMPLE algorithm was used

for the velocity-pressure coupling. Numerical computations were carried out using the popular CFD package Fluent 6.3.26 [5]. For convergence monitoring, residual level for energy equation was less than 10^{-6} and for the other transport equations were less than 10^{-4}. Computations were stopped when all residuals became unchanged with iterations. Default under relaxation factor values were lowered to improve numerical stability. Global mass balances and LNG temperature at the outlet were also checked to ensure convergence.

Computational mesh. Gambit was used to generate the computational mesh as shown in Fig. 1. Most of the cells were of hex or wedge types with low skewness. To reduce computational cost, standard wall functions by Launder-Spalding [6] were utilized for turbulent flows. A further grid independence study has been carried out using several grid sizes. It was found a grid size of 1.5 million cells was fine enough to obtain grid-independent results, and the aspect ratio was 3.68. Using this grid size, all numerical computations were carried out using parallel computing techniques.

Results and Discussion

Heat transfer characteristics of supercritical LNG in horizontal tubes. Fig. 3 (a) shows the LNG

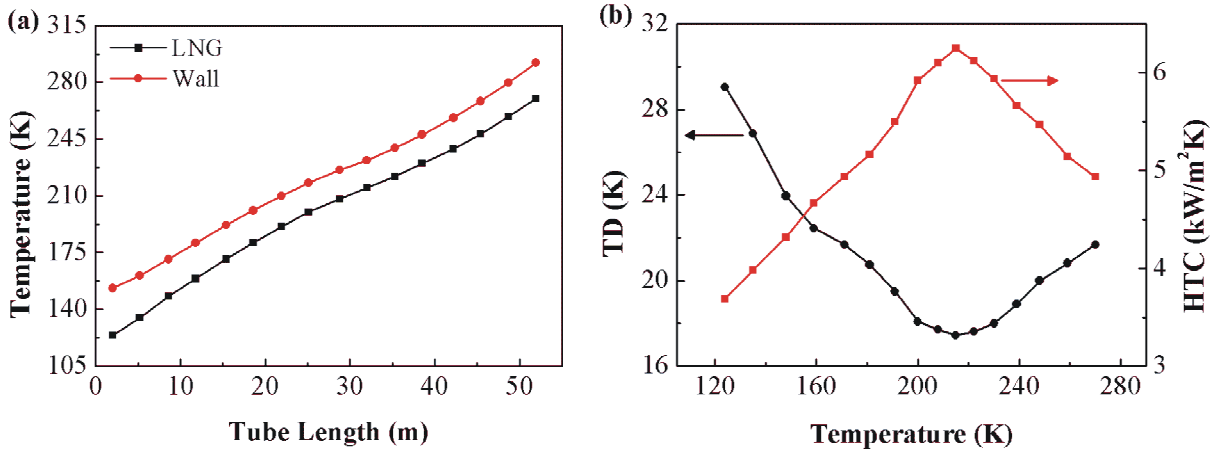

Fig. 3 Heat transfer characteristics of supercritical LNG in horizontal tubes, (a) LNG and inner wall temperature distributions along the ducts, (b) temperature difference between LNG and inner wall , and variation of HTCs with fluid bulk temperature.

and inner wall temperature along the ducts. The temperature of LNG increased along the ducts, and the LNG flow inside the tubes was composed of two stages, as shown in Fig. 3 (b). In the first stage, the temperature was below the critical point, whereas the pressure was above the critical point. The LNG flow was strictly supercritical flow in the second stage when the pressure and temperature were both above the critical point. The discharged NG was a supercritical fluid with large density, and only single-phase was encountered when the LNG was changed to NG during “gasification”. The temperature difference between LNG and inner wall showed different variation trends. The temperature difference decreased with increased fluid temperature when the fluid bulk temperature was below the pseudo-critical point T_{pc}, while the temperature difference increased when the fluid bulk temperature was above the pseudo-critical point T_{pc}, as shown in Fig. 3 (b). Fig 3 (b) also shows the influence of fluid bulk temperature on surface heat transfer coefficients. It can be observed that the surface heat transfer coefficients first increased and then decreased with the fluid bulk temperature, which reached a maximum value when the fluid bulk temperature equaled the pseudo-critical point T_{pc}. et alThe reasonable explain was that the physical properties of supercritical LNG varied sharply with the change of temperature and pressure in regions near the thermodynamic critical and pseudo-critical temperature. The specific heat of supercritical fluid at constant pressures in so-called large specific heat region was generally greater than that in other regions, which resulted in heat transfer enhancement, as previously described by other researches [7].

Influence of the inlet LNG mass flow rate. Fig. 4 shows the influence of the inlet LNG mass flow rate on the surface heat transfer coefficients. Increasing the inlet LNG mass flow rate can significantly improve the surface heat transfer coefficients in the horizontal tubes. The increased velocity of LNG caused by the increased inlet LNG mass flow rate contributed to the increasing of the surface heat transfer coefficients in the horizontal tubes. The surface heat transfer coefficients reached a maximum value in the pseudo-critical temperature point when the mass flow rate was kept constant.

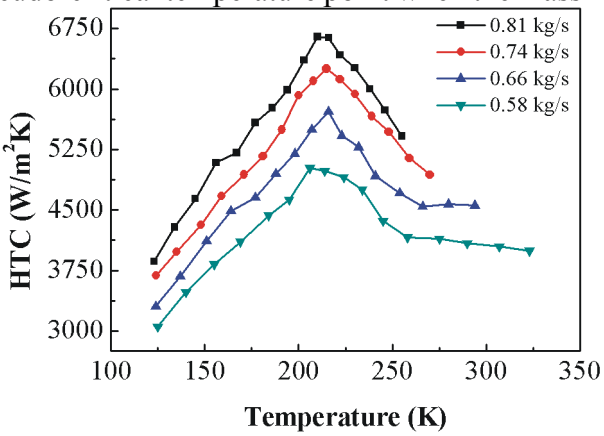

Fig. 4 Variation trends of surface HTCs with the inlet LNG mass flow rate

Conclusions

Three-dimensional computational fluid dynamics (CFD) based modeling and simulation have been conducted to investigate the influence of inlet mass flow rate on heat transfer of supercritical LNG in horizontal tubes. It has been found that the LNG flow in tubes included two stages, the surface heat transfer coefficients first increased and then decreased with the fluid bulk temperature. The surface heat transfer coefficients reached a maximum value when the fluid bulk temperature equaled the pseudo-critical point T_{pc}. Increasing the inlet LNG mass flow rate can significantly improve the surface heat transfer coefficients between supercritical LNG and the horizontal tubes.

References

[1] L. Pu, Z.G. Qu, Y.H. Bai, D. Qi, K. Sun and P. Yi, Thermal performance analysis of intermediate fluid vaporizer for liquefied natural gas, Applied Thermal Engineering. 65 (2014) 564-574.

[2] W.Q. Tao: *Numerical Heat Transfer, second* (Xi'an Jiaotong University Publishing Company, Inc., Xi'an, China, 2001).

[3] J.K. Kim, H.K. Jeon, J.Y. Yoo and J.S. Lee, in: Proc. of the 11th NURETH-11, Avignon, France, 2005.

[4] C.X. Lin, D.X. Wang and A.N. Bao, Numerical modeling and simulation of condensation heat transfer of a flue gas in a bundle of transport membrane tubes, International Journal of Heat and Mass Transfer. 60 (2013) 41-50.

[5] Fluent Inc., FLUENT 6.3.26, 2007. http://www.fluent.com

[6] B.E. Launder, D.B. Spalding, The numerical computation of turbulent flows, Comput. Methods Appl. Eng. 3 (1974) 269-289.

[7] S.Q. Yu, H.X. Li, X.L. Lei and Y.C. Feng et al, Influence of buoyancy on heat transfer to water flowing in a horizontal tubes under supercritical pressure, Applied Thermal Engineering 59 (2013) 380-388.

Advanced Materials Research Vols. 960-961 (2014) pp 438-441

doi:10.4028/www.scientific.net/AMR.960-961.438

Numerical Simulation of Heat Transfer of Liquefied Natural Gas in Horizontal Circular Tubes under Supercritical Pressure

Haiyu Meng[a], Shuzhong Wang[b *], Lu Zhou[c], Zhiqiang Wu[d], Jun Zhao[e] and Lin Chen[f]

Key Laboratory of Thermo-Fluid Science and Engineering, Ministry of Education, School of Energy & Power Engineering, Xi'an Jiaotong University, Xi'an, 710049, P.R. China

[a]hymeng321@163.com, [b]szwang@aliyun.com, [c]zhoulu.1987@stu.xjtu.edu.cn, [d]frank.vipoy@gmail.com, [e]zhaojun1st@gmail.com, [f]mumuxin09@163.com

Keywords: Submerged combustion vaporizer, LNG, Heat transfer, Supercritical pressure.

Abstract. The submerged combustion vaporizer (SCV) is a kind of equipment used for liquefied natural gas (LNG) vaporization. In order to get insights into the heat transfer of supercritical LNG, numerical simulations were carried out in this paper for investigating heat transfer of LNG in horizontal circular tubes under supercritical pressure. Numerical results showed that LNG temperature at the outlet under the design parameters was 276 K which met the demands of application. The velocity of LNG at the outlet was 12 m/s, and the pressure drop along the ducts was 120 kPa.

Introduction

Natural gas (NG) owns the advantages of safety and cleanness, and its demand is expected to increase in future energy market considering the global energy crisis and the rapid deterioration of the environment worldwide. Liquefied natural gas (LNG) is practical approach for large quantity of NG transportation for its mass storage. The LNG must be vaporized to natural gas before it is used as fuel gas for industrial and domestic purposes. Therefore, efficient and reliable vaporizers for LNG receiving terminals are important. Four types of LNG vaporizers are mainly used in the LNG receiving terminals, namely, open rack vaporizer (ORV), super ORV, submerged combustion vaporizer (SCV), and intermediate fluid vaporizer (IFV).

The structure of SCV is mainly composed of water tank, serpentine tube coils inside the water tank, and burner. The low-temperature NG and the boil off gas (BOG) from the LNG terminals are burned to flue gas as high-temperature heat source. The gas is injected into the water tank to keep the constant temperature of water bath, and the LNG is vaporized inside the serpentine tube coils located inside the water tank. The serpentine tube coils are mainly composed of horizontal circular tubes, and the thermal performance of supercritical LNG in horizontal circular tubes has not been reported.

Base on the above preview, heat transfer performance of supercritical LNG in horizontal circular tubes were studied computationally in this paper. The fields of LNG temperature, velocity and pressure along the ducts under constant inlet temperature, mass flux and wall heat flux were investigated.

Mathematical models

Physical descriptions. The heat transfer of supercritical LNG in horizontal circular tubes is considered here. Fig. 1 shows the schematic diagram of the calculation model which consists of eight horizontal tubes. The outside diameter of the tube is 32 mm with a stainless steel wall thickness of 2.5 mm and the length of the tube is 6308 mm. This tube has been widely utilized in supercritical pressure treatment. In the present study, it was assumed that the working fluid was incompressible, and a constant pressure was used for the physical properties since the pressure drop along the pipe was very small.

Basic governing equations and Turbulence models. The governing equations of the continuity, momentum and energy were used in the present study. The accuracy of numerical simulations of heat transfer in supercritical fluid may depend on turbulence models. Previous CFD study [1] using the Fluent code revealed the RNG $k-\varepsilon$ turbulence model gives reasonable results in predicting heat transfer of supercritical water, therefore the RNG $k-\varepsilon$ turbulence model was used in this study. **u** is the velocity vector, while u_i is velocity component in special direction $i(i=1,2,3)$. The transport equations for turbulence kinetic energy (k) and its dissipation rate (ε) are:

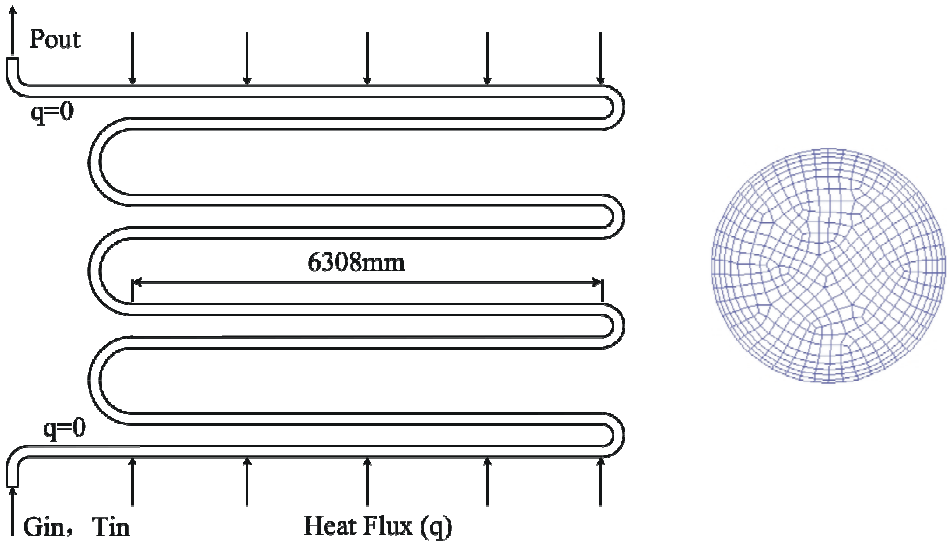

Fig. 1 Schematic diagram of the tubes and the grid configuration in the cross-sectional slice

$$\frac{\partial}{\partial t}(\rho k)+\frac{\partial}{\partial x_i}(\rho u_i k)=\frac{\partial}{\partial x_i}\left[\left(\alpha_k \mu_{eff}\frac{\partial k}{\partial x_i}\right)\right]+G_k+G_b-\rho\varepsilon-Y_M+S_k \tag{1}$$

$$\frac{\partial}{\partial t}(\rho \varepsilon)+\frac{\partial}{\partial x_i}(\rho u_i \varepsilon)=\frac{\partial}{\partial x_i}\left[\left(\alpha_\varepsilon \mu_{eff}\frac{\partial \varepsilon}{\partial x_i}\right)\right]+C_{1\varepsilon}\frac{\varepsilon}{k}(G_k+G_{3\varepsilon}G_b)-C_{2\varepsilon}\rho\frac{\varepsilon^2}{k}-R_\varepsilon+S_\varepsilon \tag{2}$$

where, G_k represents the generation of turbulence kinetic energy due to mean velocity gradients. G_b is the generation of turbulence kinetic energy due to buoyancy. Y_M represents the contribution of the fluctuating dilatation in compressible turbulence to the overall dissipation rate. The quantities α_k and α_ε are the inverse effective Prandtl numbers for k and ε, respectively. S_k and S_ε are user-defined source terms. The main difference between the RNG and standard $k-\varepsilon$ models lies in the additional term in the ε equation given by

$$R_\varepsilon=\frac{C_\mu \rho \eta^3(1-\eta/\eta_0)}{1+\beta\eta^3}\frac{\varepsilon^2}{k} \tag{3}$$

where $\eta=Sk/\varepsilon$, $\eta_0=4.38$, $\beta=0.012$. S is the modulus of the mean rate-of-strain tensor, $S=\sqrt{2S_{ij}S_{ij}}$. The effective viscosity μ_{eff} is determined by a differential equation:

$$d\left(\frac{\rho^2 k}{\sqrt{\varepsilon\mu}}\right)=1.72\frac{v}{\sqrt{v^3-1+C_v}}dv \tag{4}$$

where, $v=\mu_{eff}/\mu$, $C_v\approx 100$. In the high-Reynolds-number limit. Eq. (4) gives

$$\mu_t=\rho C_\mu \frac{k^2}{\varepsilon} \tag{5}$$

where $C_\mu=0.0845$.

Boundary conditions. Fig. 1 also shows boundary conditions of the computational domain. At the inlet of the tube, mass flow rate, temperature, turbulence intensity and hydraulic diameter were specified. The outlet boundary condition of the domain was specified as pressure-outlet, and the wall surfaces of tubes were set as heat flux boundary. In order to ensure a fully developed velocity profile before flowing into the heat transfer test section and also no backflow at the outlet, a certain length of tube wall surface was set to be adiabatic in the entrance and exit section. LNG inlet mass flux and temperature were 0.74 kg/s and 118 K, respectively. The heat flux of the wall surface was 107 kW/m^2, and LNG outlet pressure was 9.55 MPa. The turbulence intensities at the inlet and outlet were both set to be 10%. Typical compositions of the LNG at the inlet were (molar ratio): $Y_{CH_4} = 89.39\%$, $Y_{C_2H_6} = 5.76\%$, $Y_{C_3H_8} = 3.3\%$, $Y_{C_4H_{10}} = 1.44\%$, $Y_{N_2} = 0.11\%$.

Numerical computations

Numerical methods. In this paper, a finite volume method [2] was used to solve all the governing equations above. Standard scheme was used for pressure treatment. A second-order upwind scheme was used for the discretization of the equations in the current work. The SIMPLE algorithm was used for the velocity-pressure coupling. Numerical computations were carried out using the popular CFD package Fluent 6.3.26 [3]. For convergence monitoring, residual level for energy equation was less than 10^{-6} and for the other transport equations were less than 10^{-4}. Computations were stopped when all residuals became unchanged with iterations. Default under relaxation factor values were lowered to improve numerical stability. Global mass balances and LNG temperature at the outlet were also checked to ensure convergence.

Computational mesh. Gambit was used to generate the computational mesh as shown in Fig. 1. Most of the cells were of hex or wedge types with low skewness. To reduce computational cost, standard wall functions by Launder-Spalding [4] were utilized for turbulent flows. A further grid independence study has been carried out using several grid sizes. It was found a grid size of 1.5 million cells was fine enough to obtain grid-independent results, and the aspect ratio was 3.68. Using this grid size, all numerical computations were carried out using parallel computing techniques.

Results and Discussion

Temperature, velocity and pressure fields. Fig. 2 shows typical temperature fields of the horizontal tubes on symmetric plane under the design parameters. As can be seen from the figure, the temperature of LNG increased along the ducts, and the mass-weighted average temperature at the outlet was 276 K. Since the LNG temperature needs of industrial application is above 273 K, the design parameters are reasonable.

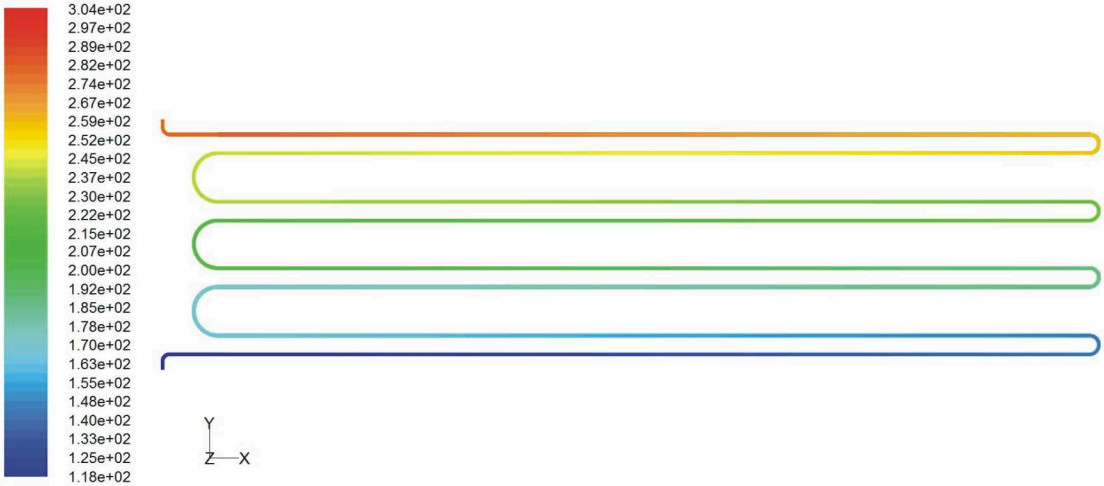

Fig. 2 Temperature distributions on the tube symmetric plane

Fig.3 shows the velocity fields on tube symmetric plane. It can be observed from the figure that the velocity of LNG increased from 3 m/s at the inlet to 12 m/s at the outlet under the constant inlet mass flow rate of 0.74 kg/s. The increasing of LNG velocity was attributed to the decreasing of supercritical fluid density caused by the increasing of temperature. Fig.4 shows the pressure fields on tube symmetric plane, which reveals the total pressure drop from inlet to outlet was 120 kPa.

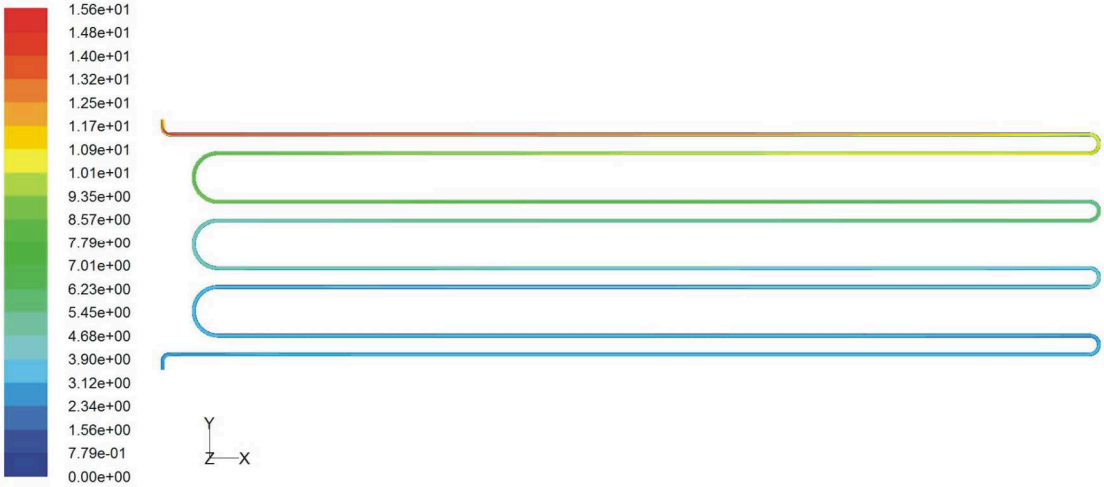

Fig. 3 Velocity distributions on the tube symmetric plane

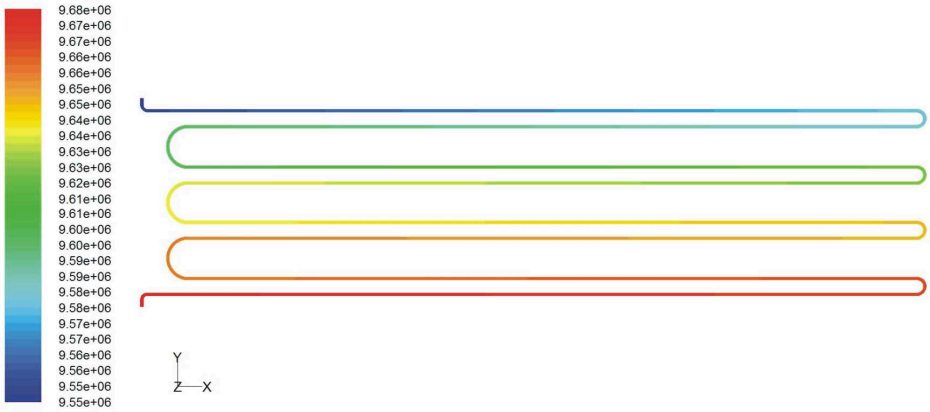

Fig. 4 Pressure distributions on the tube symmetric plane

Conclusions

Three-dimensional computational fluid dynamics (CFD) based modeling and simulation have been conducted to investigate the heat transfer and flow performances of supercritical LNG in the horizontal circular tubes for application in LNG vaporization. It has been found that LNG temperature increased from 118 K to 276 K under the design parameters, which met the requirements of application. The LNG velocity increased due to the decreasing of fluid density with the increasing of the temperature. The LNG velocity at the outlet was 12 m/s, and the pressure drop along the ducts was 120 kPa.

References

[1] J.K. Kim, H.K. Jeon, J.Y. Yoo and J.S. Lee, in: Proc. of the 11th NURETH-11, Avignon, France, 2005.

[2] W.Q. Tao: *Numerical Heat Transfer, second* (Xi'an Jiaotong University Publishing Company, Inc., Xi'an, China, 2001).

[3] Fluent Inc., FLUENT 6.3.26, 2007. http://www.fluent.com

[4] B.E. Launder, D.B. Spalding, The numerical computation of turbulent flows, Comput. Methods Appl. Eng. 3 (1974) 269-289.

Advanced Materials Research Vols. 960-961 (2014) pp 442-446

doi:10.4028/www.scientific.net/AMR.960-961.442

Pyrolysis kinetics and characteristics of wood-based materials from Municipal Solid Waste

Lin Chen[1, a], Shuzhong Wang[1, 2, b], Zhiqiang Wu[1, c], Haiyu Meng[1, d], and Jun Zhao[1, e]

[1]School of Energy & Power Engineering Xi'an Jiaotong University Xi'an, 710049, P.R. China

[2]Guangdong Shunde Academy of Xi'an Jiaotong University, Shunde, 528000, P.R. China

[a]xjtu_chenlin@163.com, [b]szwang@aliyun.com, [c]frank.vipoy@gmail.com, [d]hymeng321@163.com, [e]zhaojun1st@gmail.com

Keywords: Municipal solid waste, Pyrolysis, Characteristics, Kinetics analysis

Abstract. Wood-based materials from Municipal Solid Waste have the potential of covering a significant part of the future demand on gasification capacities. However, their pyrolysis kinetics and gasification behavior has not yet been fully investigated. This paper describes the pyrolysis characteristics of typing paper and Chinese parasol from municipal solid waste applying the non-isothermal thermogravimetric analysis, the apparent activation energy and the pre-exponential factor were obtained by kinetics analysis at the heating rate of 10/20/40 $^{o}C \cdot min^{-1}$.

Introduction

Municipal solid waste has become a serious environmental issue due to the increase of the produced waste quantities and the recently discovered limitations and impacts of the existing waste treatment concepts. In 2012, there are 160 million tons Municipal Solid Waste (MSW) being collected in a mixing way and cleaned out in China [1]. There are two major ways to dispose waste, which are landfill and incineration. A lot of flammable gases were generated in landfill, which led to explosions. The dioxins are inevitable under current techniques in combustion process of Chinese waste with high moisture content and complex substances. Concerning the usage of wastes as a substitute fuel for coal, it is important to have knowledge on its thermal properties and reaction kinetics.

Experimental

2.1 Materials. Materials tests included wood-based products, which represent two different qualities: typing paper and Chinese parasol. The biomass that was shattered to 74μm mainly consists of cellulose, hemicellulose and lignin. The pyrolysis and combustion processes of the cellulosic materials are complex because of the simultaneous degradation of the three components.

Table 1 Proximate analysis of Materials [wt. %, ad]

variety	moisture	volatile matter	ash	fixed carbon	Qgr.ad[$MJ \cdot kg^{-1}$]
Typing Paper	4.75	79.37	12.24	7.99	13.19
Chinese parasol	9.88	84.09	0.89	13.54	17.72

2.2 Apparatus and Procedures. Experiments were carried out in a TGA system (WCT-2C) produced by Beijing Optical Instrument Factory. The experimental apparatus is schematically shown in Fig. 1. The reactor consists of a quartz tube (22mm internal diameter) placed in an oven, which can be operated at a temperature up to 1400°C. The sample holders are two ceramic pans (5mm in diameter and 8mm in height). The inlet gas, of which the flow rate is controlled by a flow meter, is introduced to the reactor from the upper of the tube, whereas the outlet gas emits from the middle of the tube. The measurements of sample weight and reaction temperature are continuously recorded in a computer. A more detailed description of the apparatus can be found in [2].

In order to identify the behavior of selected fuels, thermo gravimetric tests were performed under inert atmosphere, at ambient pressure and different heating rates. The flow rate of inlet gas was kept at 60 ml·min^{-1}.

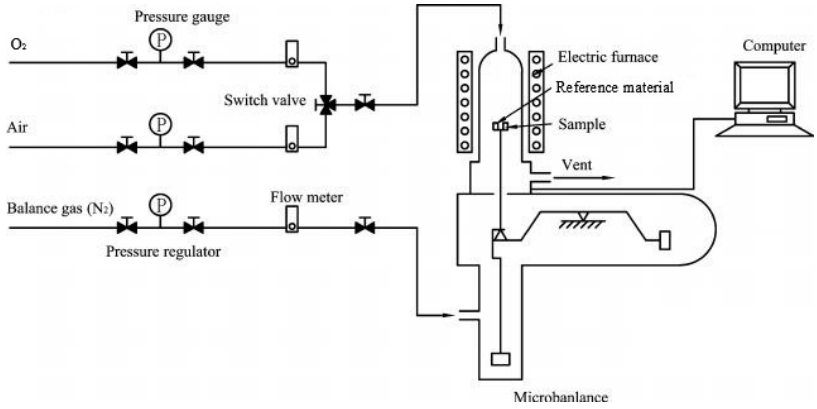

Fig. 1 Schematic diagram of the experimental apparatus

2.3 Evaluation Criteria. Pyrolysis involves a series of chemical and physical processes that contribute to the overall empirical weight loss in thermo gravimetric analysis. Differential method and integral method are two main methods to determine the apparent activation energy and pre-exponential factor. Coats-Redfern integral method is widely used to analysis the kinetic parameters of the non-isothermal pyrolysis process [3, 4, 5].

According to the Arrhenius law:

$$\frac{\mathrm{d}\alpha}{\mathrm{d}t} = A\exp(-E/RT)(1-\alpha)^n \tag{1}$$

where A and E are the apparent pre-exponential factor and activation energy, respectively. α is the conversion (reacted fraction) which can be expressed by:

$$\alpha = (m_0 - m)/(m_0 - m_\infty) \tag{2}$$

Where m_0, m_∞ and m represent the initial, ultimate and instantaneous mass of sample, respectively.

In the TGA experiments, $\beta = \mathrm{d}T/\mathrm{d}t$ represents the heating rate, so Eq. (1) can be transformed as follows:

$$\frac{\mathrm{d}\alpha}{(1-\alpha)^n} = \frac{A}{\beta}\exp(-E/RT)\mathrm{d}T \tag{3}$$

Coats-Redfern equation can be derived through integral transformation from Eq. (3) as follows [9]:

$$\text{if } n=1,\quad \ln\left|\frac{\ln(1-\alpha)}{T^2}\right| = \ln[\frac{AR}{\beta E}(1-\frac{2RT}{E})] - \frac{E}{RT} \tag{4}$$

$$\text{if } n\neq 1,\quad \ln\left|\frac{1-(1-\alpha)^{(1-n)}}{T^2(1-n)}\right| = \ln[\frac{AR}{\beta E}(1-\frac{2RT}{E})] - \frac{E}{RT} \tag{5}$$

For the temperature range of reaction, $E/RT \gg 1$, so $\ln[AR/\beta E(1-2RT/E)]$ is almost constant. In order to obtain kinetic parameters, PVC and PP can be assumed as first-order reaction using the Coats-Redfern equation above to evaluate the apparent activation energy and per-exponential factor. Thus a plot of $\ln\left|\ln(1-\alpha)/T^2\right|$ versus $1/T$ should be result in a straight line with the slope equal to $-E/R$ for the first order kinetics.

Results and Discussion

3.1. Paper samples

Experiments were carried out in different heating rates. A comparative analysis of the obtained TG(weight loss)and DTG(weight loss rate) curves for paper samples is presented Fig.2.

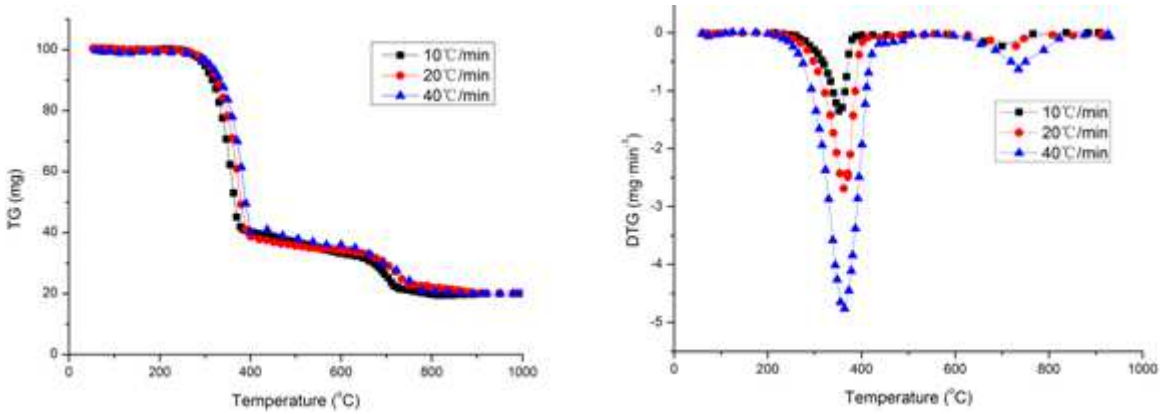

(a)TG of Paper in N_2 atmosphere (b) DTG of Paper in N_2 atmosphere

Fig. 2 TG/DTG analysis curves of paper pyrolysis in different heating rates

The paper samples include many complex additives. Fig.2 shows the TG and DTG curves of typing paper. The decomposition pattern reveals two distinct peaks on the DTG curves: (1)low temperature regions (290-490℃), which could be volatile release from cellulose, hemicellulose and lignin and (2)medium temperature regions (650-750℃), which could be volatile from additives. Between the two reactions, no decomposition zone is observed.

Fig.2 shows the effect of heating rate on the paper pyrolysis behaviors with the particle size of 74μm. It can be observed that, the derivative thermogravimetric (DTG) curves indicating the paper pyrolysis rate during the non-isothermal experiments shift to higher temperature zone with the increase of heating rate. This is due to more obvious thermal hysteresis at higher heating rate [6]. The characteristics of Typing Paper pyrolysis are presented in Table 2. With the increase of heating rate, the peak temperature and maximum DTG of both the two phase were increased.

Table 2 Characteristics of Typing Paper Pyrolysis

Heating rate[$^{o}C \cdot min^{-1}$]		10	20	40
First phase	Temperature range[^{o}C]	268-385	289-389	295-397
	Peak temperature[^{o}C]	352	362	364
	Maximum DTG[$mg \cdot min^{-1}$]	1.35	2.69	4.76
Second phase	Temperature range[^{o}C]	669-717	681-748	692-779
	Peak temperature[^{o}C]	700	730	735
	Maximum DTG[$mg \cdot min^{-1}$]	0.23	0.23	0.63
Total weight loss [%]		80.12	80.21	80.23

3.2. Chinese parasol samples

A comparative analysis of the obtained TG(weight loss)and DTG(weight loss rate) curves for Chinese parasol samples is presented in Fig.3. The major composition of Chinese parasol is volatile matter, which consists of cellulose, hemicellulose and lignin. It can be observed from Fig. 3(a, b) that the TG process of Chinese parasol consists of just one phase between 250-410℃, because of the simultaneous degradation of the three components. The total weight loss is about 85.7% for each test. The characteristics of Chinese parasol pyrolysis were presented in Table 3. Thermal hysteresis phenomenon also exists in pyrolysis of Chinese parasol in different heating rate as Typing paper, which is observed in the table 3.

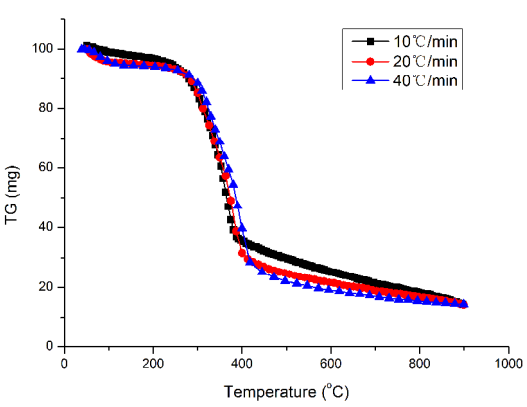

(a)TG of Chinese parasol in N_2 atmosphere

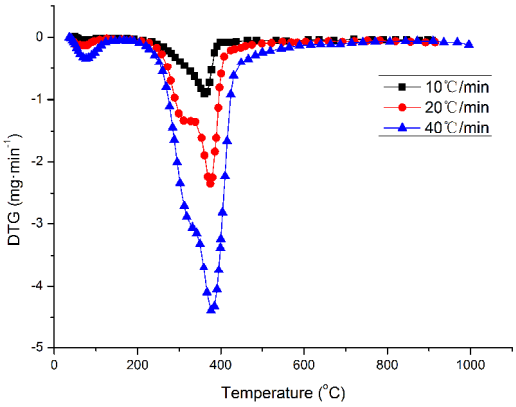

(b) DTG of Chinese parasol in N_2 atmosphere

Fig. 3 TG/DTG analysis curves of Chinese parasol pyrolysis in different heating rates

Table 3 Characteristics of Chinese parasol Pyrolysis

	Heating rate[°C·min^{-1}]	10	20	40
phase	Temperature range[°C]	296-399	289-400	295-405
	Peak temperature[°C]	361	375	376
	Maximum DTG[mg·min^{-1}]	0.91	2.35	4.39
	Total weight loss [%]	85.57	85.71	85.72

3.3 Kinetic Analysis.

Fig.4 shows the straight line of Y-ln|ln(1-α)/t^2| versusX-1/t for two weight loss of typing paper pyrolysis at different heating rates. The kinetic analysis results of typing paper pyrolysis are presented in Table 4.

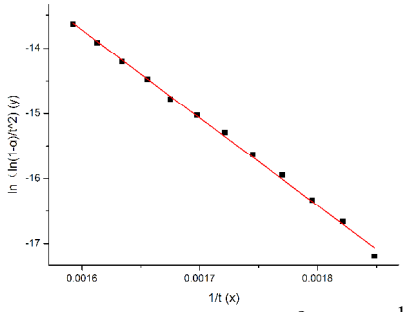

(a)The first phase at 10 °C•min^{-1}

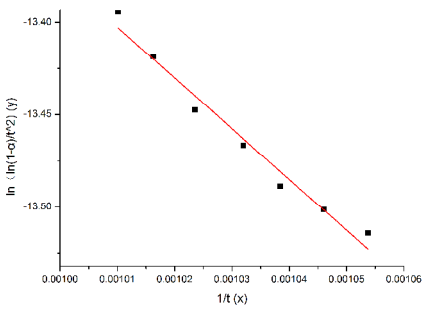

(b)The second phase at 10 °C•min^{-1}

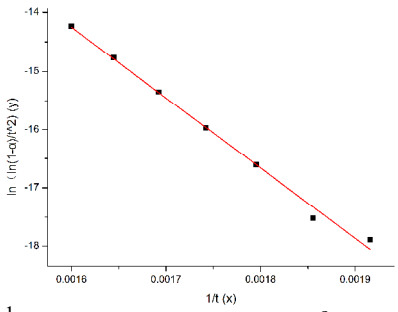

(c)The first phase at 20°C•min^{-1}

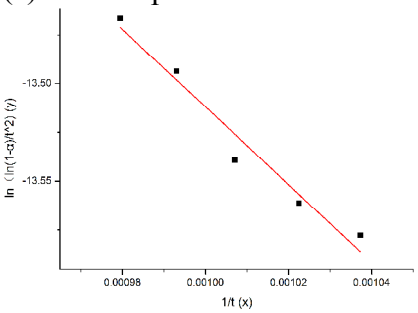

(d)The second phase at 20°C•min^{-1}

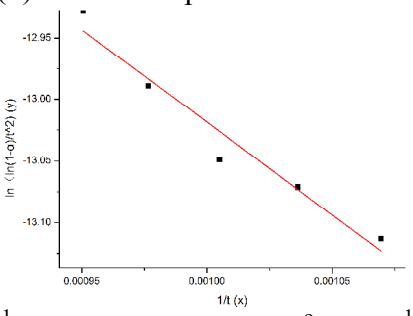

(e)The first phase at 40°C•min^{-1}

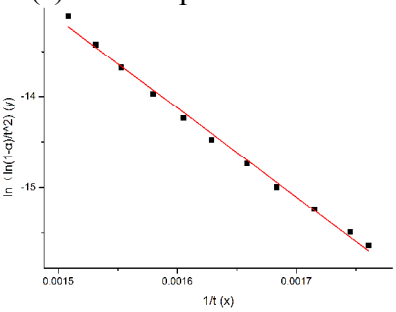

(f)The second phase at 40°C•min^{-1}

Fig.4. Arrhenius plots for typing paper pyrolysis

Table 4 Kinetic analysis of typing paper pyrolysis

Heating rate[°C·min^{-1}]	10				20				40			
	E[kJ·mol^{-1}]		A[min^{-1}]		E[kJ·mol^{-1}]		A[min^{-1}]		E[kJ·mol^{-1}]		A[min^{-1}]	
First phase	1.12	10^5	9.99	10^{11}	1.00	10^5	3.17	10^5	0.81	10^5	1.62	10^6
Second phase	2.28	10^4	7.77	10^{-8}	1.65	10^4	1.44	10^{-8}	1.25	10^4	2.21	10^{-8}

Fig.5 shows the straight line of Y-ln|ln(1-α)/t^2| versus X-1/t for two weight loss of Chinese parasol pyrolysis at different heating rates. The kinetic analysis results of Chinese parasol pyrolysis are presented in Table 5.

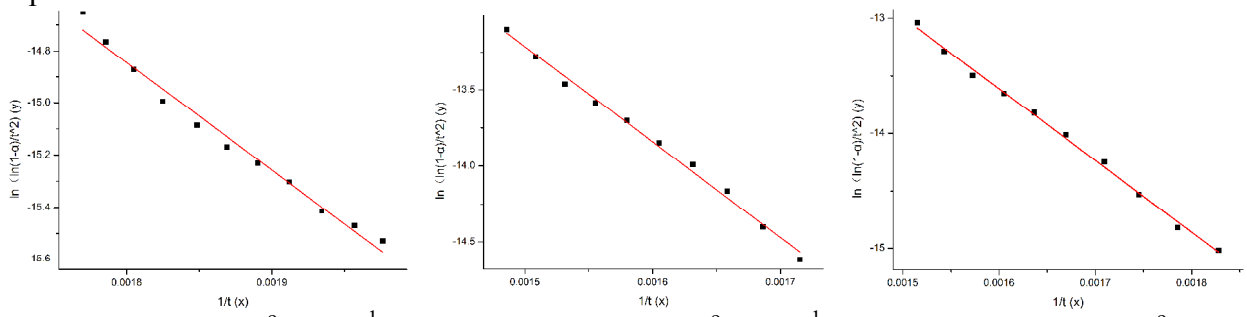

(a) The phase at 10 ^{o}C•min^{-1} (b) The phase at 20 ^{o}C•min^{-1} (c) The phase at 40 ^{o}C•min^{-1}

Fig.5. Arrhenius plots for Chinese parasol pyrolysis

Table 5 Kinetic analysis of Chinese parasol pyrolysis

Heating rate[^{o}C·min^{-1}]	10		20		40	
	E[kJ·mol^{-1}]	A[min^{-1}]	E[kJ·mol^{-1}]	A[min^{-1}]	E[kJ·mol^{-1}]	A[min^{-1}]
phase	34279	0.0002	51667	1.6790	52163	1.2212

It can be observed that both the apparent activation energy and pre-exponential factor stay at the same magnitude for one sample in different heating rates.

Conclusions

The pyrolysis of Typing paper and Chinese parasol were studied applying the non-isothermal thermogravimetric analysis. It is found that there are two weight loss phases in Typing paper TG curse, while Chinese parasol just one weight loss phase, which are in accordance with their composition. The DT curves indicating the wood-based samples pyrolysis rate during the non-isothermal experiments shift to higher temperature zone with the increase of heating rate. The peak temperature and maximum DTG of all phases were increased with the increase of heating rate.

Acknowledgements

This research was financially supported by the Low-carbon development special fund of Guangdong Province, China.

References

[1] National Bureau of Statistics of China: China Statistical Yearbook 2013. Published by China Statistics Press

[2] S. Z. Wang, M. Luo, G. X. Wang, L. F. Wang and M. M. Lv: Energy & Fuels 26 (2012), p. 3275.

[3] S. Y. Yorulmaz and A. T. Atimatay: Fuel Processing Technology 90 (2009), p. 939.

[4] H. Sutch and S. Piskin: Combust Science and Technology 181 (2009), p. 264.

[5] C. S. Li and K. Suzuk: Energy Fuels 23 (2009), p. 2364.

[6] C. A. Wang, X. M. Zhang, Y. H. Liu and D. F. Che: Applied Energy 97 (2012), p. 264.

Advanced Materials Research Vols. 960-961 (2014) pp 447-450

doi:10.4028/www.scientific.net/AMR.960-961.447

Research and Improvement of The Difficulties of FCB Function of Subcritical Units

Pengcheng Fei[1, a], Li Wang[1,b], Yunfeng Qi [1,c]

[1]Electric Power Research Institute of State Grid Liaoning Electric Power Co., Ltd,

Shenyang, Liaoning, 110006, China

[a]aaapengcheng@126.com, [b]innet_wl@163.com, [c]6283025@qq.com

Keywords: FCB, 35% bypass, Subcritical units.

Abstract. Power plant will be threatened in the blackout, a tiny carelessness could result in serious damage to the equipment. FCB (FastCutBack) refers to the function that during the normal operation, because of the internal fault or external fault the unit take the moment to get rid of all external power supply instantaneously, and keep the boiler continue running at the lowest load to supply the auxiliary power. In this paper, the new designed FCB control strategy has been applied in a 350MW subcritical coal-fired unit. Through some control logic optimization and debugging, the viable control parameters is obtained, the result of unit FCB function test is excellent and the safety of unit are effectively improved.

Introduction

With the rapid development of the national economy, the social demand for electric energy is increasing gradually. The grid is getting large day by day, and the security of electric network becomes important more and more. All over the world there have been some occurrence of severe balckouts, Natural disaster is a serious threat to the safe operation of power grid, and it may cause some power plant in the state of blackour in some areas[1].

During the state of the blackout, power plants will face a threat. A tiny carelessness may cause large damage of equipment, and the status and parameters of the unit will change dramatically, and the power of the cooling water, compressed air equipment will be lost. Most of the equipment of the unit will lost control. The safe operation of major equipment relies solely on the battery or backup diesel generators, and the safety factor of power plant decreased significantly. From the blackout accident of domestic power plant, we can find that there will be some bad effects on the equipments more or less, and even severe damage of the equipment. If the unit realize the FCB function, the unit could supply the auxilary power by itself in the most dangerous time, we can safely shutdown the unit or wait for the recovery of power grid. So there exist the following benefits for power plant[2] [3].

To unit security, FCB function can make the unit continuesly running after load rejection, and guarantee that system parameters will not exceed the limits in the whole process. The power plant can choose shutdown, or waiting for the recovery of grid, which inhance the security of the unit.

To reducing cost of unit, Comparing with the normal control strategy, the FCB can reduce times MFT, The boiler will be in the state of high parameters. After the cause of the accident is confirmed and solved, units can make a hot restart, so we can save a lot of time and energy, it is beneficial to reducing the operation cost.

When the unit realizes FCB function, the unit has the ability to supply the auxiliary power by itself. It could help the grid to return to normal as soon as possible, and also could safely shutdown the unit. So the FCB function has become an urgent topic of research.

Improvement of the difficulties of FCB functions

The overpressure of boiler. After the FCB action, turbine valve quickly turn down, while the boiler has larger inertia for the thermal storage, and the capacity of steam production will reduce slowly, which could cause the serious load imbalance of boiler and turbine [4]. Bypass capacity is only 35%,

so overpressure of boiler must happen. The solution is opening the bypass as soon as possible, quickly reducing the thermal load as much as possible. It is important to make short-term pressure relief with the PVC and safety, and then to use the bypass system to control pressure decreases slowly to a target value.

The rapid reduction of load of boiler. In the process of FCB, the bypass capacity is 35% , so it is needed to rapidly reduce of boiler load under 35%. Considering the unit characteristics, it is determined that during the FCB action two mills still run, rate of reduction load of boiler automatically changes to 100%/min, load target automatically changes to 35%. Considering the rapid reduction of the boiler load, furnace pressure fluctuation, and the unstable working condition of furnace, immediately boiler burner should be shut down from top to bottom automatically, and retained two coal mill running at least[5]. The FCB signal in fig. 1 is used by the load control system of the boiler.

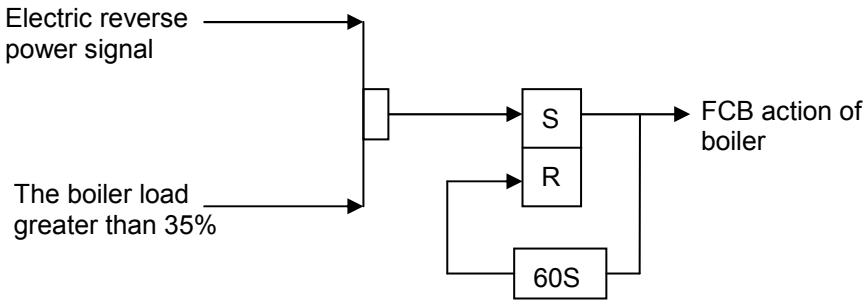

Fig. 1 FCB signal for boiler

DEH speed control. PLU is the function that when load rejection occurs, this circuit is used to avoid turbine overspeed. When the imbalance happens between turbine power and turbine load, it will cause overspeed of the turbine. When the PLU loop detect the situation, CV and CIV will be closed quickly to control the speed of turbine. ACC is acceleration control loop that When the turbine speed is greater than 3060rpm, the acceleration is greater than 49rpm, ACC will take an action to quickly close IV to control the speed of turbine.

Supplement of working fluid. After the FCB take an action, even if all the mills except 2 mills shut down, it still need some time to reduce the load to 35% for boiler, because the time delay of boiler and inertia of fuel system exit[6]. At this period, the surplus steam must be discharged by superheated steam safety valve and the PCV to the atmosphere. It caused a certain degree of imbalance of refrigerant cycle in perspective.

Switch of steam source of steam feedwater pump. During normal operation, steam source of feedwater pump is from four stage extraction of turbine. After load rejection, pressure of extraction steam falls. To maintain operation of feedwater pump, the steam source must quickly be cut into standby steam source. And it must meet 2 requirements during the steam source switch. One is the coal and water ratio imbalance is still within the allowable range, that is the overtemperature will not happen. The other is to maintain the hydrodynamic stability of boiler, that means superheat control of water cool wall is within the permitted value[7]. Switch to standby steam source can be in two ways, one is from four stage extraction of turbine to the auxiliary steam supply, the other is switch to the high pressure steam source from low pressure steam source

The logic of boiler, turbine and generator. The original design of the unit contains forward and reverses function that is boiler MFT action interlock ETS action, turbine ETS action interlock protection for generator; and generator protection action interlock turbine ETS action, ETS action interlock boiler MFT action (load greater than 35%). According to the purpose of FCB function, the reverse-power device to the generator protection circuit should be canceled.

Engineering Application

In this paper, the new designed FCB control strategy has been applied in a 350MW subcritical coal-fired unit. Through some control logic optimization and debugging, the viable control

parameters is obtained, the result of unit FCB function test is excellent and the safety of unit is effectively improved. The curve of 50% FCB result is shown in Fig. 2. The curve of 100% is shown in Fig. 3.

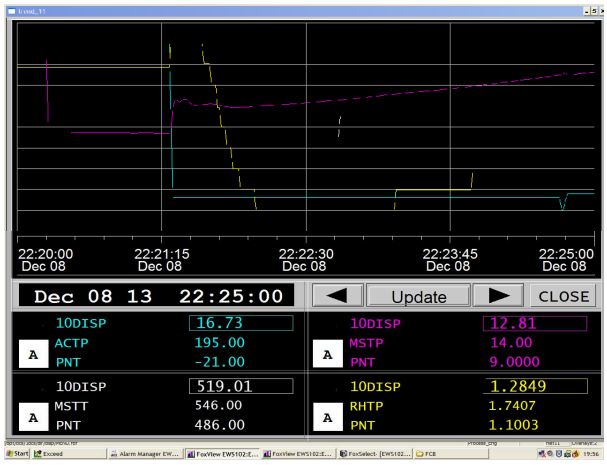

(a)

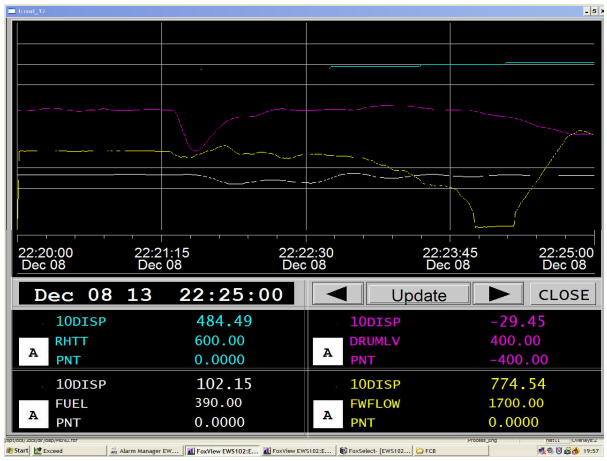

(b)

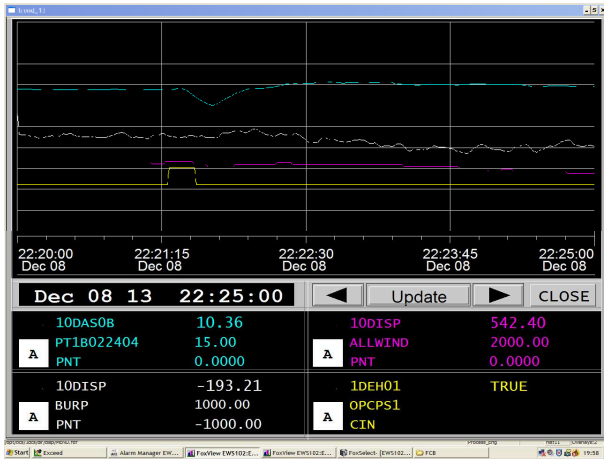

(c)

Fig. 2 50% FCB parameter curve

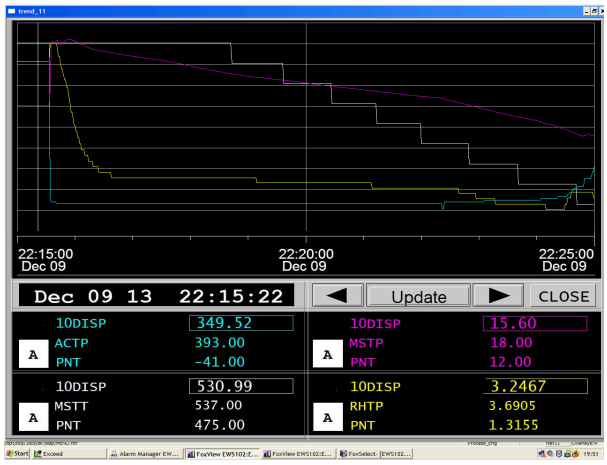

(a)

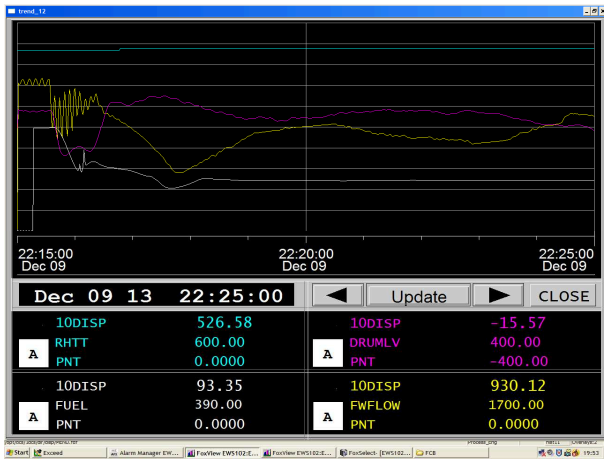

(b)

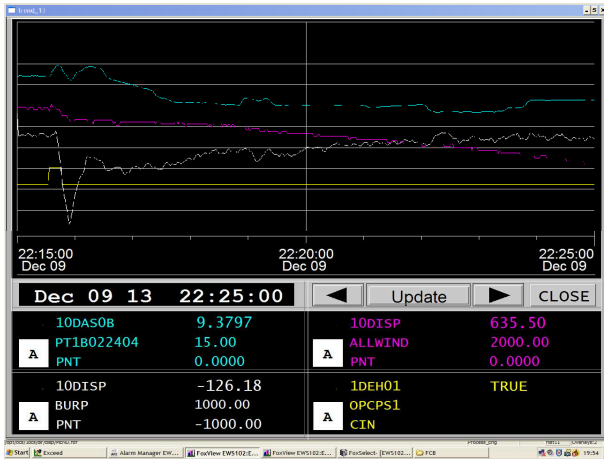

(c)

Fig. 3 100% FCB parameter curve

Conclusion

According to the result of the 50% load and 100% load FCB test, we can get the conclusion that in the process of the FCB test the 350MW unit with the bypass system of 35% BMCR could be stable at 3000rpm quickly through effective the control strategy. During the FCB test of 50% load and 100% load the OPC take action only once, and it effectively prevent the overspeed of the turbine. During the test all the main parameters are also in a stable state.

References

[1] Z. X. Lu, "Thoughts of reliability of power from 8.14 blackouts of US and Canada", *China Power*, no. 12, 2003, pp. 1-5.

[2] L. D. Wang and J. H Yao, "Successful application of FCB and new implementation scheme", *Process Automation instrumentation*, , no. 6, 2004, pp. 48-52.

[3] W. Z. Feng, "FCB test of 900MW supercritical unit", *China Power*, no. 2, 2005, pp. 74-77.

[4] X. K. Wen and P. Kang, "Exploration of FCB function of the units in Guizhou Province", *Guizhou Electric Power Technology*, no. 4, 2005, pp. 1-3.

[5] H. Chen, "Processing experience of 600MW supercritical unit FCB", *Thermal Power Generation*, no.6, 2006, pp. 62-63.

[6] J. H. Yao, "Discussion on several problems in FCB", *China Power*, no. 5, 2007, pp. 59-62.

[7] C. Q. Shen and X. Y. Zhou, "FCB function and its application in power grid recovery", *Shanghai electric power*, no. 3, 2007, pp. 251-254.

Advanced Materials Research Vols. 960-961 (2014) pp 451-455

doi:10.4028/www.scientific.net/AMR.960-961.451

The experiment for vertical rectangular micro-channel flow boiling

Dianxun LI[1, a], Shusheng ZHANG[2,b]

[1,2] School of Energy and Power Engineering, Shandong University, Jinan 250061, P.R. China

[a]6277237@163.com, [b]15005313009@139.com

Keywords: micro-channel, flow boiling, experimental system

Abstract. To further deepen exploration of boiling in micro-channels a set of experiment system for micro-channel flow boiling is homemade, which includes experimental equipment required and experimental pieces of the design process. The channel is width of 100mm, length of 1200mm, and the groove depth of 95mm. The gasket thickness is 0.5mm, 1.0mm, 1.5mm or 2.0mm.

Introduction

Flow boiling phenomenon in micro-channels has aroused widespread concern of scholars home and abroad. After many efforts, scholars have got a lot of experimental data of flow boiling in micro-channels, which is about heat transfer, pressure drop and the identification. Due to the particularity of the micro-channels, the experiment is affected by many factors, such as the machining precision, measurement error, etc.. So the experiment conclusions of different scholar's will often be different or even opposite [1-8]. So far the research of boiling heat transfer and resistance properties about micro-scale flow, we still do not have a mature and consistent conclusion. In order to further deepen exploration of boiling in micro-channels, we have established a set of micro channel flow boiling experiment system.

The experimental system

We have established a set of experimental units, used to study the flow boiling heat transfer and pressure drop characteristics of vertical rectangular micro-channels. The experimental station apparatus is composed by many devices, such as metering pumps, filters, pre-heating means, the volumetric flowmeter, a thermocouple, pressure gauge, a differential pressure transmitter, data logger, computer, image processing apparatus, electrically heated sheet, condenser, accumulator, etc..

What we used the working fluid in this experiment is deionized water, which is boosted by diaphragm metering pump and is circulated in the system. The de-ionized water is preheated by pre-heating means and its temperature is stabilized at between 35℃~40℃. Through the flowmeter it enters the test section inlet, where absorbs heating of sides of the heating plate, the temperature of which increases up to a boiling state. The steam or steam - water mixture generated in the boiling process flows through the condenser and is condensed into a low-temperature water, which flows back to the tank and completes a cycle.

The flow boiling test section length is 1200mm, in which the effective heating length is 1100mm. In the course of experiments we adjust the inlet flow rate and the inlet temperature of the deionized water to observe different flow pattern. The two surfaces of the test section are transparent plexiglass plate of 5.0mm thickness to facilitate visualization observations.

The experimental section of the present experiment system is based on two-channel non concave relative composition. The channel is width of 100mm, length of 1200mm, and the groove depth of 95mm. Front and rear sides with plexiglass seal are to achieve the visual observation. Heating plate is added to the tank, which is length of 1100mm, width of 90mm, the maximum heating power of 500W per piece. By changing the thickness of the gasket of the channel end portion, we obtain the desired width of the channel. The gasket thickness is 0.5mm, 1.0mm, 1.5mm or 2.0mm. In order to meet the requirements of the experimental precision, the composed two faces of channel are strictly machined,

precisely grinding treated, after channel after surface treatment finish of 20 microns. Finish of the channel after surface treatment can be up to 20 microns. The range of parameters is shown in Table 1.

Table1. Microchannel flow boiling range of experimental parameters

Project and No.	Channel size (mm)	Left heating power (W)	Right heating power(W)	Volume flow L/h
Exp. pieces 1#	0.5	0~500	0~500	0~10
Exp. pieces 2#	1.0	0~500	0~500	0~13
Exp.l pieces 3#	1.5	0~500	0~500	0~16
Exp. pieces 4#	2.0	0~500	0~500	0~20

Laboratory instruments and precision required

FMC-8DLiquid volume flow meter. Hefei Forstar Measurement and Control Technology Co., Ltd.. 24V voltage supply, range:0~20L/h, the measurement accuracy of 0.2. In addition to the measurable general uniform fluid viscosity, also measured high viscosity fluid (honey, oil, pulp, etc.). It can measure not only a single solution of fluid parameters, and can also measure multiphase flow. Whether the medium is laminar or turbulent flow, and do not affect the measurement accuracy.

JWM20/1.0 Diaphragm metering pump (with pulse damper). The Shanghai RONGXING Pump Co., Ltd. production. Maximum displacement 20L / h, the itinerary can be in the range of 0 to 100% stepless adjustment. The transport medium maximum stroke measurement accuracy of ± 1%. Suitable for conveying a temperature of -30 to 120°C, a kinematic viscosity of 0.3 ~ 800mm2/s without solid particles of the medium.FMC8201Pressure transmitter. Hefei Forstar Measurement and Control Technology Co., Ltd.. It uses differential pressure-sensitive chips and other key components of Switzerland HUBA production, can be used to measure small pressure. Range: 0 to 50 kPa and an accuracy of ± 0.25% Operating temperature range: -10 to 120 ° C, resistance to static pressure up to 20MPa.

FLUKE2625A Data collection instrument. Fluke company. Built-in non-volatile memory can save up to 2000 scans data for stand-alone applications, with RS-232 interface, 21 analog input channels, ± 0.1 ° C resolution. XMX618 Smart single-channel communications controller. Beijing Huibang Technology Co., Ltd. production, the supply voltage of 24V with RS485 output, accuracy class 0.2. CT488 Vacuum pressure gauge. Zhuji City, Zhejiang Hongsen Machinery Co., Ltd. production, range 0 ~ 0.5MPa, an accuracy of ± 2.5%. T-type thermocouples. The homemade, base metal thermocouples, the temperature range of -200 to 400°C. Tube-fin air-cooled condenser. Boxing County Shandong Province Jn Yue refrigeration equipment factory production. Air volume 8.04m3/min. Temperature adjustable pre-heating device. The maximum heating power 2KW, the temperature can be adjusted between 0~100°C.

Experimental Procedure

Check various parts of the opening and closing of the correct state to open a total power. Start the refrigeration unit, to ensure the normal work of the condenser.Turned on each instrument, and start the data collection instrument and differential pressure transmitters.Start diaphragm metering pumps, and regulate the flow, observed each instrument is working in the expected value. Turn on the power of the heating plates, heating the test pieces of the microchannels. Stable when the expected value for a period of time required for recording data. Adjust parameters, enter the next condition. Repeat steps 1-7 until you have tested all conditions.

Measurement of the experimental parameters

5.1 The flow boiling experiments need to measure the following parameters

Water temperature in the preheater and experimental pieces of the import and export of the temperature of the working fluid. Axial wall temperature distribution along the test section.

Differential pressure and the pressure of the import and export of the test section. Electric heating power. Heating current and voltage. Volumetric flow rate of the working conditions.

5.2 Thermocouple arrangement

The measurement of the temperature of the wall is completed by uniformly arranged in both sides of the wall surface 10 of the thermocouple. The thermocouples are respectively arranged in a position of a distance entrance 100, 200, 300, 400, 500, 600, 700, 800, 900, 1000 mm. Both sides of the wall surface at the same position disposed thermocouple is in order to prevent damage to the thermocouple measurement error and the heating process may occur. There are also two thermocouples used to measure the inlet and outlet of the test section temperature of the working fluid.

Because of the smaller channel size of this experiment, we directly in the flow channel into the thermocouple measurement will result in the destruction of the shape of the flow channel. Will also affect the distribution of gas-liquid two-phase flow. That it can not obtain accurate experimental results. Therefore, in the experimental process will thermocouple disposed in the inside of the channel concave. In order to ensure the system operating pressure and control the deformation of the test pieces, we used in the experiments of the channel having a thickness of 5.0mm. If the thermocouple is arranged directly on the inner surface of the recess for temperature measurement, and this is bound to cause a large temperature gradient, resulting in inaccurate temperature of the fluid in the measurement channel. In order to minimize the temperature gradient, we punch on the channel and then put into the thermocouple. In a predetermined place of the thermocouple location, we use the drill 4.0mm deep blind holes. First thermocouple probe into the hole, then solder thermocouple probe is close to the channel surface welding.

5.3 Heating uniformity test

Before the formal experiment, we first make heating uniformity testing of heat chip to ensure that the experimental results are accurate and reliable. The heated film is a self-made by heating wire evenly wound on mica. Mica sheet has a certain toughness, if its not close enough contact with the inner surface of the channel groove will form the thermal contact resistance, which leads to the heating effect can not meet experimental requirement. To avoid this situation, we must test for its heating uniformity.

Taking into account the inner surface of the channel groove finish is not enough to reduce the contact thermal resistance used in this experiment to ensure the tightness with the heater chip bonded smear high temperature thermal silica in the inner surface of the channel groove. After the completion of the heating plate laying, placed three aluminum silicate insulation materials for thermal insulation and fire retardant. The first installation of the cover, and then the insulation materials and heating plate is pressed against the inside surface of the channel groove.

After completion of the assembly of test pieces, test its heating uniformity. Heating with 220V AC power supply. Installation of leakage protection system to ensure the experiment safety. The test by FLUKE2625A. The data acquisition system has data-logging, real-time access to the temperature of the measuring point data. Some of the test data as shown in Table 2. Through the analysis table within the data, the maximum deviation of the temperature of 20 measurement points are located within ± 1.5℃, indicating that whether the heater chip mounting method or temperature measurement point arrangement are feasible.

5.4 System heat balance calculations

The heat loss in the experimental result is mainly due to the convective heat transfer between the test section and the environment. Despite insulation measures, this heat loss can not be ignored. To obtain reliable results, we must make the calculation of the heat balance. Taking into account the thermal equilibrium of multiphase flow calculation is more complicated, and many factors are difficult to determine, we have adopted a single-phase flow heat balance to calculate the heat loss Q_{loss} of the test section. Included in the heat flux heat loss formula is as follows.

$$q=(Q-Q_{loss})/A \ . \quad (1)$$

The boiling incipience is an important turning point in the flow boiling heat transfer and has an extremely important role for the study of the role of boiling heat transfer enhancement. Get to start boiling length is calculated as follows by thermal equilibrium.

$$C_pG(T_{L,sat}-T_{L,in})=q_SZ_{sat}\ . \quad (2)$$

Before boiling incipience of subcooled boiling phenomena have emerged. Through flow visualization method to determine the location of the cold boiling incipience Z_{ONB}.

According to the experimental data the rate of heat loss of the present experiment is about 9% by Formula 1 and Formula 2 calculations.

Table 2 Heating uniformity test temperature data recorded

Item No.	Temperature ℃				
	5 min	**10 min**	**15 min**	**20 min**	**25 min**
1	44.2	58.9	76.9	93.2	117.5
2	44.7	60.2	77.5	93.8	118.2
3	44.9	59.9	77.2	93.5	117.9
4	45.2	60.1	77.3	93.6	117.6
5	45.1	60.0	77.4	94.2	118.5
6	45.6	60.5	77.5	94.3	118.4
7	45.2	60.1	77.6	95.0	118.0
8	45.0	60.3	77.4	95.1	117.8
9	44.7	60.0	76.9	94.8	118.9
10	44.8	59.9	77.0	94.6	119.0
11	44.5	59.8	77.3	94.2	118.3
12	44.3	59.2	76.7	93.6	118.0
13	44.7	59.3	77.0	94.7	118.2
14	44.7	59.7	77.1	94.5	118.4
15	44.8	59.6	77.1	94.6	118.2
16	44.6	59.5	77.4	93.8	118.3
17	44.3	59.8	77.2	94.3	118.1
18	44.5	59.8	76.8	93.9	118.1
19	45.0	60.2	76.6	93.8	118.0
20	44.4	60.0	76.5	93.4	117.8

Conclusion

This paper describes the experimental system, experiment equipment and experimental procedures, focusing on the composition and installation method of temperature measurement system, the five experimental parameters such as temperature, pressure, heating power, flow, and pressure differential measurement methods and precaution sand heating uniformity testing system heat balance calculation.

Reference

[1] Tran T N, Wambsganss M W, and France D M. Small circular and rectangular- channel boiling with two refrigerants[J]. International Journal of Multiphase Flow, 1996, 22(3): 485-498

[2] Ruey-Tay Lin. Boiling heat transfer [M] Beijing: Science Press, 1988: 20-29

[3] Sun Zhongning, heat exchanger, D'Souza. Ray tube and the narrow annulus liquidity pool boiling heat transfer experimental study [J] Engineering Thermophysics, 2001, 22 (4): 485-487

[4] Xiaofeng P, Peterson G P. Convective heat transfer and flow friction in microchannel structures[J]. International Journal of Heat Mass Transfer, 1996, 39(12): 2599-2608

[5] Nguyen N T, Bochnia D, Kiehnscherrf R, et al. Investigation of forced convection in microfluid systems[J]. Sensors Actuators, 1996, 55(A): 49-55

[6] Sajith V, Haridas D, Sobhan C B, et al. Convective heat transfer studies in macro and mini channels using digital interferometry[J]. International Journal of Thermal Sciences, 2011, 50(3): 239-249

[7] Guo Lei, et al. Effect of Air Outflow Angle of Wall mounted Air-conditioner on the Indoor Thermal Environment. 6TH International Symposium on Heating, Ventilating, and Air Conditioning, Nov 14-16, 2009: 1023-1030

[8] Guo Lei, et al. Comparative Analysis of Mixing Performance and Pressure Loss of Three Types of Passive Micromixers. 9TH International Conference on Electronic Measurement & Instruments, Aug 16-18, 2009: 538-542.

Advanced Materials Research Vols. 960-961 (2014) pp 456-461

doi:10.4028/www.scientific.net/AMR.960-961.456

Preparation of SiO_2–TiO_2 Nanocomposite and Its Application on Elemental Mercury Removal in Simulated Flue Gas

Xue Shi[1,a], Bu Ni[2,b], Chaoen Li[2], Xian Li[2], Chong Zhang[2], Tao Hu[2], Jiang Wu[2,*]

[1]Industrial Management Office, Shanghai University of Electric Power, Shanghai 200090, P.R. China

[2]College of Energy and Mechanical Engineering, Shanghai University of Electric Power, Shanghai 200090, China

[a]shixue427@yahoo.com.cn, [b]1210557923@qq.com, [*] wjcfd2002@sina.com,

Key Words: SiO_2–TiO_2 nanocomposite; flue gas mercury; ratio of TiO_2 / SiO_2; UV irradiation

Abstract: SiO_2–TiO_2 nanocomposite was synthesized by an ultrasound-assisted pure physical method to oxidize elemental mercury (Hg^0) in simulated flue gas. Due to its low cost and photocatalytic ability, SiO_2 was used to dope TiO_2 to modify the TiO_2 photocatalyst. We put different ratio of TiO_2 / SiO_2 under the UV irradiation to get a low Ti/Si doping ratio and high flue gas mercury removal efficiency of SiO_2–TiO_2 nanocomposite catalyst. It was found that the photocatalytic activity of nanocomposite materials did not significantly improve, or even decline. This is mainly because that the presence of too much porous SiO_2 may affect TiO_2 on the effective absorption of light and direct adsorption of contaminants. When Ti: Si ratio was 2:1, SiO_2–TiO_2 nanocomposite catalyst reached its highest elemental mercury removal efficiency in the simulated flue gas.

Introduction

In recent years, with the rapid development of social economy, people's living standards frequently improves and people pay more and more attention to the influence of environment on the quality of life. Year after year all kinds of laws, regulations and policies on modern industrial pollutants emission standards has also improved, and the power plant emissions of heavy metal mercury is increasingly brought the attention of people. A lot of scholars have done much research on limiting the emissions of the metal mercury [1-4], In which photocatalytic technology is an emerging and rapid development in science and technology. At present, the materials in the field of photocatalytic technology adopted by the photocatalyst are N type semiconductor materials, such as TiO_2, ZnO, Fe_2O_3, SnO_2 and WO_3, etc.TiO_2 has been widely accepted because of its chemical and biological inertness, strong oxidizing power, non-toxicity and long-term stability against photo and chemical corrosion(Li et al,2011; Ghanbary et al,2012).

As the development of nanotechnology, titanium dioxide (TiO_2) nanocomposite has been widely used in photocatalysis field. Due to the character of nanomaterials (the surface effect, volume effect and quantum size effect and macroscopic quantum tunneling effect), make the nano TiO_2 have different physical and chemical properties compare to other block solid. It has big specific surface area, high density surface lattice defects, and high surface energy. What's more, because the nano SiO_2 [5] possesses small particle size, large specific surface area , carrying a small amount of catalyst active ingredients can achieve high catalytic activity, effectively reduce the cost of catalyst, improve the catalytic efficiency, and can extend the life of the catalyst. Such as TiO_2 - SiO_2 nanocomposite mixed with proper amount of SiO_2 is not only reduced the amount of TiO_2, reduces the cost but also to some extent improve the photocatalytic activity of TiO_2 [6-9]

In this paper, we make power plant flue gas emissions of mercury contamination can be reasonably and efficiently reduced as the research target. We design a method that it use TiO_2-SiO_2 nanocomposite materials to perform photocatalytic experiments in the simulated flue gas to achieve Hg^0 removal effect of simulated flue gas.

Experimental

Preparation of catalysts

A certain amount of TiO_2 and SiO_2 was dissolved in anhydrous ethanol and mixed in ultrasonic mixer for hours. The preparation of samples immersed in the processed glass fiber mat, dried in the oven and calcined in muffle furnace, to remove water and free alcohol of the gel adsorption. Six groups of sample set value as shown in table 1.

Catalytic activity measurement

The catalytic activities were evaluated using a bench-scale experimental system as shown in Fig1.The simulated flue gas was divided into two branches A and B and each of them passed through the mass flow controllers A and B. Mass flow controllers control the mass flow. The stream of B passed through a mercury generator to introduce the saturated Hg^0 vapor into the mixing tank and mixed with A. Gas after mixing valves are controlled by valves A and B into the main road or bypass. Valve A opens into the photocatalytic gantry system for photocatalytic reaction in the reactor; valve B opens into bypass. After leaving the reactor experiment, the gas went into mercury species conversion system and went through KCl fluid absorption, silica gel desiccant removal of oxidized Hg^{2+}, then entering the gas sampling system VM3000 mercury tester.

Special mercury generator generated certain concentration of elemental mercury Hg^0, carried by the simulated flue gas into the mixing tank whose flow controlled by a mass flow controller. Simulated flue gas is compressed air. TiO_2-SiO_2 and flow gas reacted in the photocatalytic reactor under UV light catalytic role. VM3000 mercury analyzer was used to test real-time measurement of the mercury concentration in flue gas.

Measurement of photocatalytic activity

Sample experiment time was 80 minutes in each group and was under the condition of 300W. The process for each experiment was 20 minutes of UV light, UV lamp close 20 minutes, 20 minutes of UV light, UV lamp closed for 20 minutes. Because before mercury into VM3000 tester installed KCl absorbing liquid, so finally only Hg^0 went into VM3000 mercury gas load, it can also be reflected on the line chart. When close the UV lamp, mercury value can back to the initial value.

Removal rate calculation formula

$$\eta_n = \frac{C_O - C_n}{C_O} \times 100\% \quad (1)$$

where C_0 is mercury initial value(μg/Nm^3); C_n is mercury instantaneous value(μg/Nm^3); η_n is removal rate(%).

Table 1 The sample set point

sample	Ti:Si	UV light intensity
1# sample	1:0	300W
2# sample	1:2	300W
3# sample	1:5	300W
4# sample	1:1	300W
5# sample	5:1	300W
6# sample	2:1	300W

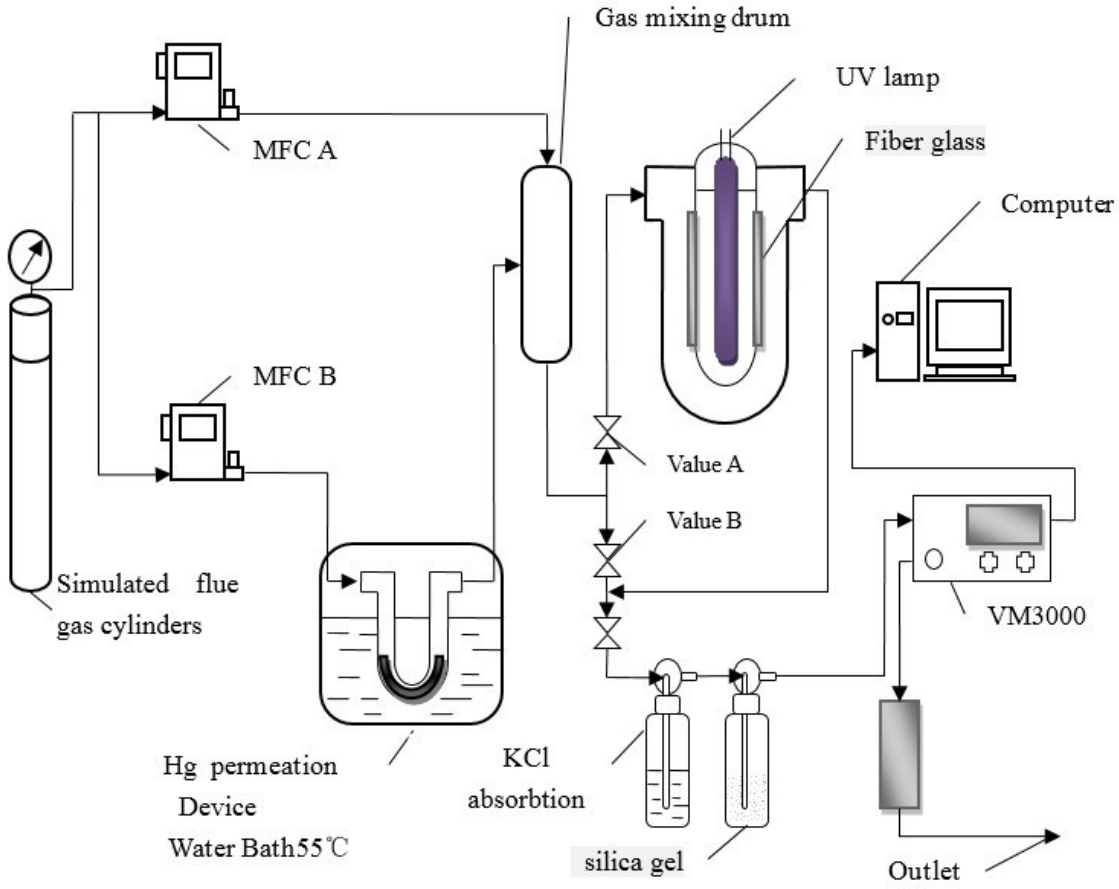

Fig 1 Bench-scale experimental system

Results and Discussion

Results

The removal rate of mercury under different ratio of Ti/Si is shown in Fig2 to Fig7.

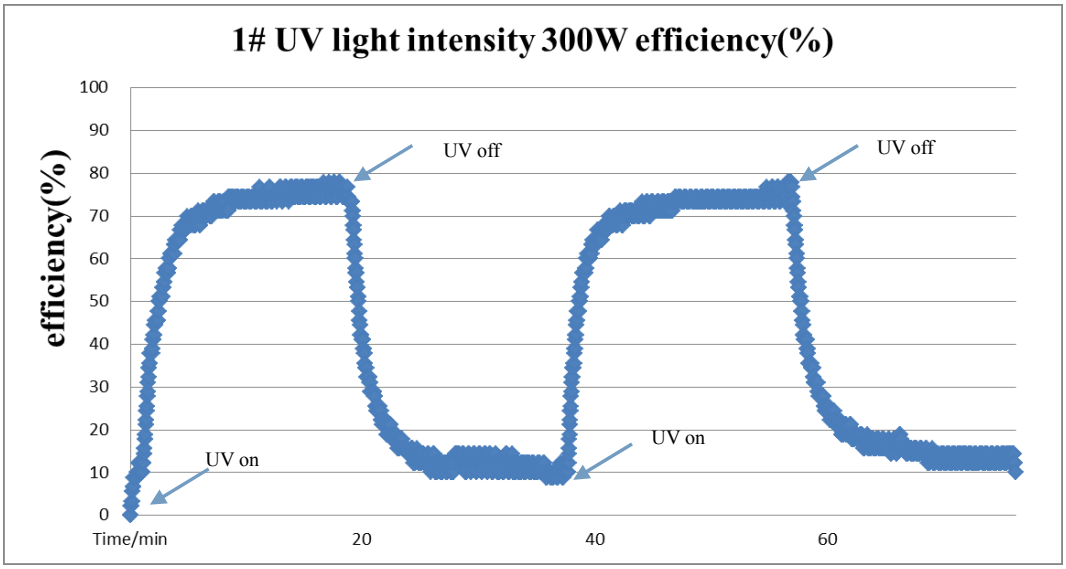

Fig 2 1#sample pure TiO_2

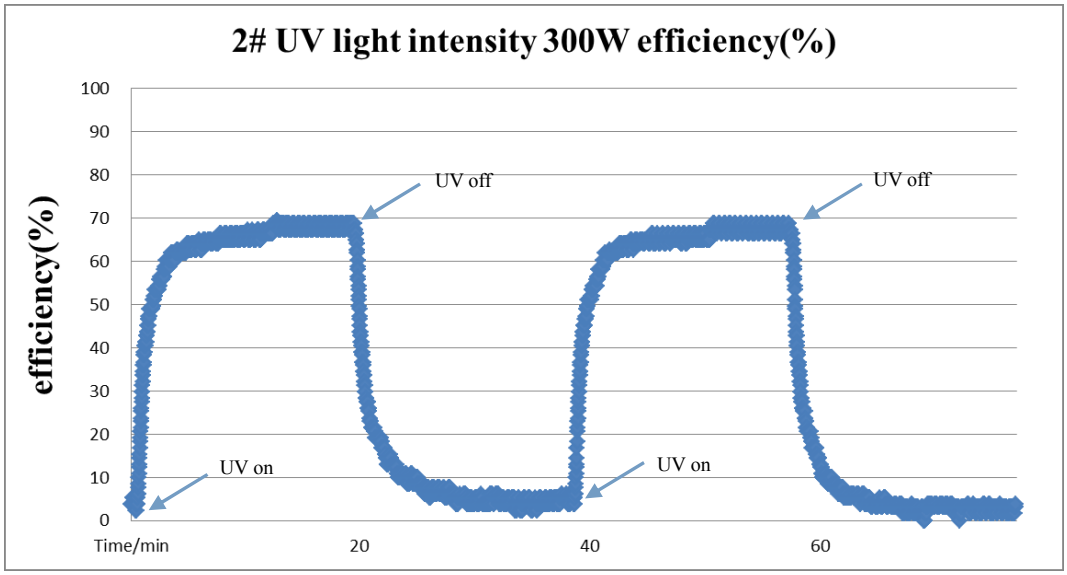

Fig3 2#sample Ti:Si=1:2

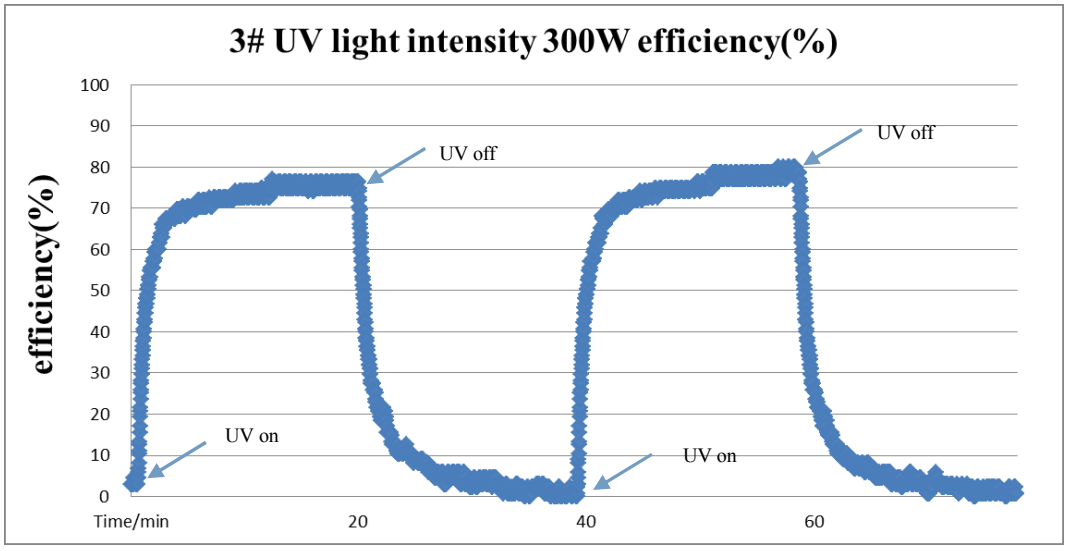

Fig4 3#sample Ti:Si=1:5

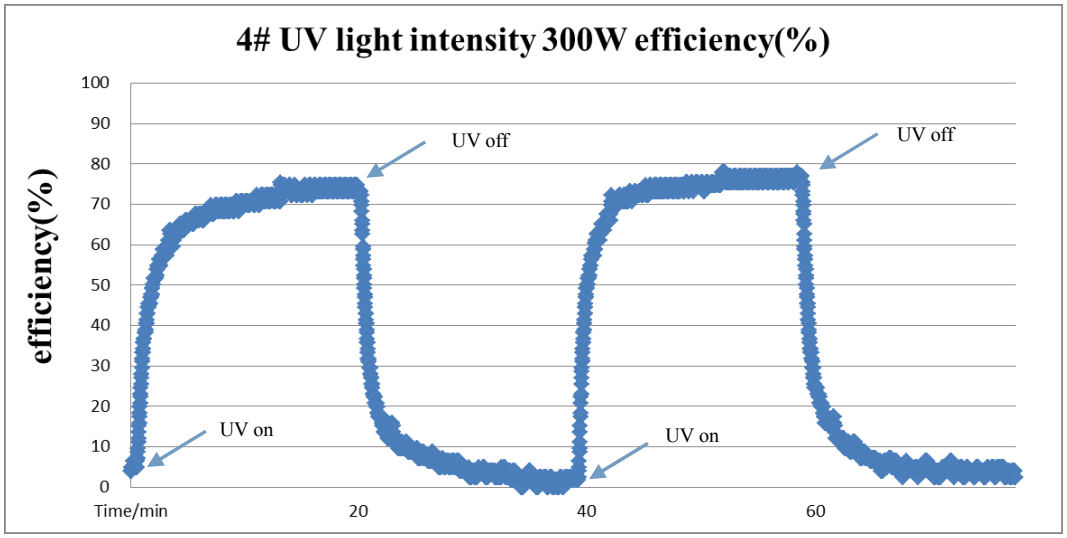

Fig5 3#sample Ti:Si=1:1

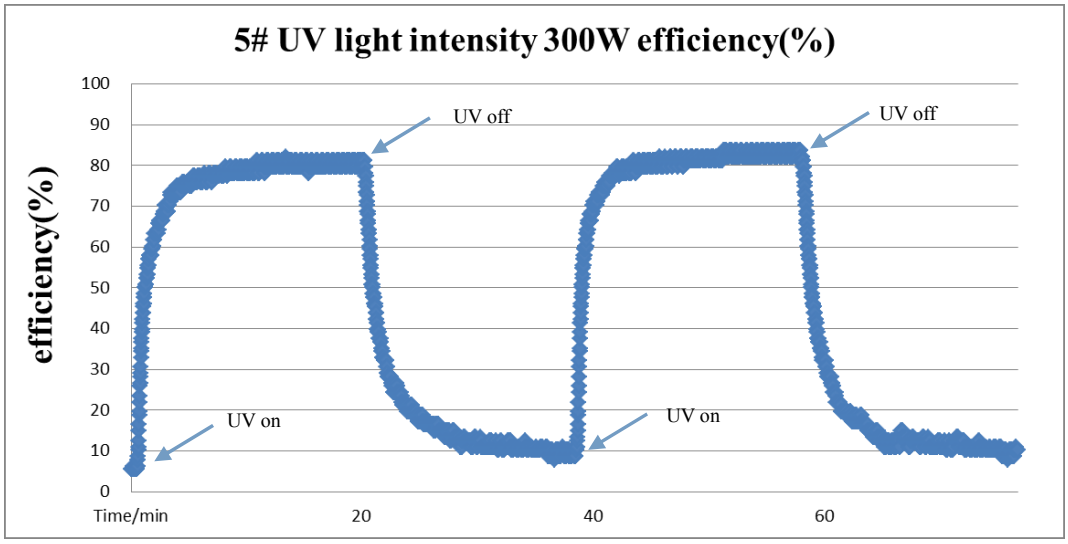

Fig6 5#sample Ti:Si=2:1

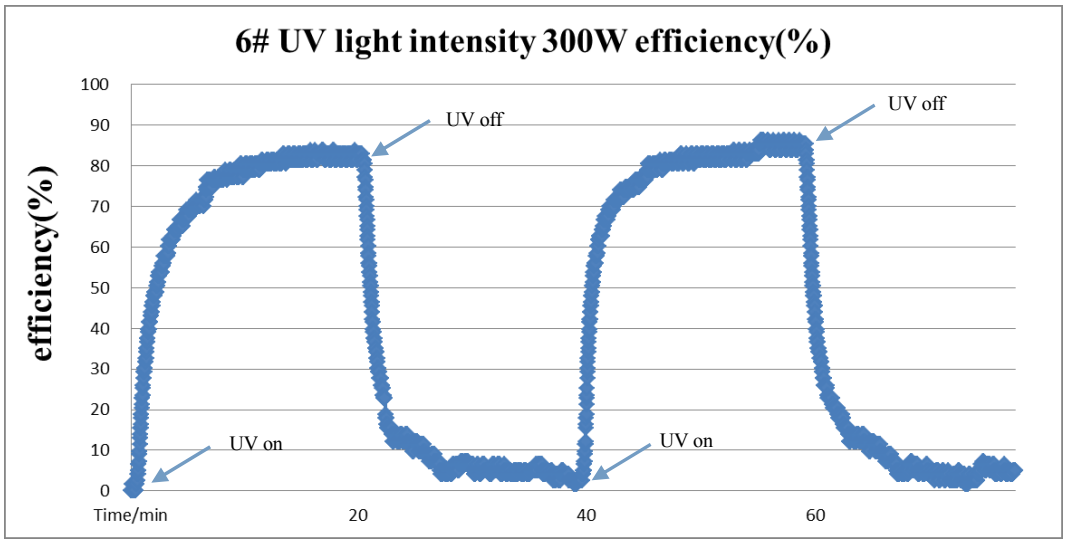

Fig7 6#sample Ti:Si=5:1

Discussion

The mercury removal efficiency of six samples was shown in Table 2, the results shown: the removal efficiency of Ti: Si ratio 1:0, 1:2, 1:5, 1:1, 5:1, 2:1 were 77.80%, 69.50%, 80.00%, 77.78%, 83.69%, 86.18% respectively. when Ti: Si ratio was 2:1,it reached the highest removal efficiency of elemental mercury.

The high photocatalytic nanoparticles of catalyst are mainly related with the anatase's high thermal stability and large specific surface. Porous SiO_2 on anatase TiO_2 nanocomposite surface effectively inhibit direct contact with TiO_2 nanocrystals. Thus significantly improve the thermal stability of anatase, and the improved thermal stability conducive to the crystallization of TiO_2 nano-titanium dioxide, thus contributing to the separation of photo-generated charge. Small crystallite size of TiO_2 and SiO_2 composite porous silica nanoparticles showed a larger surface area. However, preliminary results showed that: the photocatalytic activity of nanocomposite materials did not significantly improve, or even decline. This is mainly because that the presence of too much porous SiO_2 may affect TiO_2 on the effective absorption of light and direct adsorption of contaminants.

Table2 Experiment Results

sample	Ti:Si	Removal rate
1#sample	1:0	77.78%
2#sample	1:2	69.50%
3#sample	1:5	80.00%
4#sample	1:1	77.78%
5#sample	5:1	83.69%
6#sample	2:1	86.18%

Conclusion

This is based on the premise exploratory experimental studies and took into account the practical application, i.e, in view of the flue gas emissions from coal-fired power plants in the process of mercury removal process. Taking purely physical doping methods and draws close to the expected results of the experimental data. the results shown that the removal efficiency of Ti: Si ratio 1:0,1:2,1:5,1:1,5:1,2:1 were 77.80%, 69.50%, 80.00%, 77.78%, 83.69%, 86.18% respectively. When Ti: Si ratio was 2:1, it reached the highest removal efficiency of elemental mercury.

Acknowledgment

This work is support by supported by Shanghai Science and Technology Development (11dz1203402, 12dz1201702).

Reference

[1] Jie Zhang, Weiguo Pan, Guosong Wei. Control and Emissions of Mercury from Coal-fired Utility Boilers. Boiler Technology, 2007, 38 (1): 32 -35.(In Chinese)

[2] Thomas D Brown,Dennis N Smith,Richard A Hargis,et a1．Mercury measurement and its control：what we know, have learned, and need to further investigate．Journal of the Air & Waste Management Association, 1999, 6．(In Chinese)

[3] Yi Zhao, Zili Zhang. Research reviews of mercury control technology in the coal - fired power-plants. Electric Power Technology and Environmental Protection, 2010, 26 (4): 31-33.

[4] XU Wen-ding, SHI Lin, GENG Man. Research Reviews of Mercury Control Technologies for Coal-fired Power Plants. Power System Engineering, 2006, 22 (6): 1 -4. (In Chinese)

[5] Zhang Yuefeng, Zhang Yuqing Applica tions and Research Progress of Composite Nano - SiO_2. Journal of Tarim University. 2012, 22 (1): 151 -156. (In Chinese)

[6] YING LI, CHANG-YU WU. Role of Moisture in Adsorption, Photocatalytic Oxidation and Reemission of Elemental Mercury on a SiO_2-TiO_2 Nanocomposite. Environ. Sci. Technol. 2006, 40, 6444 -6448. (In Chinese)

[7] YANG Yi,WANG QiWei,WANG LianJun. Catalyst of Nanometer TiO_2/SiO_2 Composite. Environmental Science & Technology. 2009, 4: 9 -13. (In Chinese)

[8] ChinSan Wu. Synthesis of Polyethylene-Octene Elastomer/ SiO_2-TiO_2 Nanocomposites via In Situ Polymerization: Properties and Characterization of the Hybrid. Published online in Wiley InterScience (www.interscience.wiley.com).

[9] Ying Li,Chang-Yu Wu.Kinetic Study for Photocatalytic Oxidation of Elemental Mercury on a SiO_2/TiO_2 Nanocomposite. Environmental Engineering Science. 2007, 1: 3 -11. (In Chinese)

Advanced Materials Research Vols. 960-961 (2014) pp 462-468

doi:10.4028/www.scientific.net/AMR.960-961.462

Effects of pH on Hg^0 re-emission in WFGD

Yong Qiu[1,a], Hui Wu[1,b], Guangqian Luo[1,c*], Hong Yao[1,d]

[1]State Key Laboratory of Coal Combustion, Huazhong University of Science and Technology, Wuhan 430074, China

[a]qiuyong1990hust@163.com, [b]hwu@hust.edu.cn, [c]luoice@163.com, [d]hyao@hust.edu.cn

Keywords: WFGD, mercury, desulfurization slurry, flue gas, oxy-fuel

Abstract: Gaseous oxidized mercury (Hg^{2+}) in the flue gas is soluble in waterand can be captured effectivelyby Wet flue gas desulfurization (WFGD) system.But in some extent Hg^0 re-emission happens due to the reduction of absorbed Hg^{2+},and the pH of slurry is an important factor affecting Hg^0 re-emission. In this study, the theoretical formulas of slurry pH were derived through the conventional solution theoryand then were used to evaluate the factors determining the pH of slurry. A series oflaboratory experiments were carried out under N_2, CO_2 and O_2/N_2 atmosphere to measure the Hg^0 re-emission tendency at different pH values. The results show that the higher the pH, the less Hg^{2+} reduced by S(IV), resulting in the decrease of Hg^0 re-emission. Under N_2 atmosphere, the Hg^0 re-emission was mild at pH>4 while it was dramatic at pH<4. Under O_2/N_2 atmosphere, the addition of O_2 extended the time span of Hg^0 re-emission at low pH and increased Hg^0 re-emission unexpectedly in the latter part of the experiments at high pH. CO_2 atmosphere almost did not affect Hg^0 re-emission because of its little effect on the slurry pH.

Introduction

Mercury is one of the most toxic heavy metals in the environment. Coal-fired power plant is one of the largest stationary sources of anthropogenic mercury emission. Currently, mercury removal by existing air pollution control devices is the main strategy of mercury control in China. Wet flue gas desulfurization (WFGD) is the most widely used desulfurization unit which can simultaneously remove divalent mercury (Hg^{2+}) because of its water solubility. But the re-emission of Hg^0 generated by the reduction reaction of Hg^{2+} dissolved in the slurry, leading to atmospheric mercury pollution[1].

The slurry pH in WFGD not only influences the desulfurization efficiency, but also affects mercury removal efficiency[2]. The pH value is generally maintained at 5-6[3]. Previous studies showed that under N_2 or O_2/N_2 atmosphere Hg^0 release varied at different pH values. N.Omine, C.L.Wu and J.Schuetze[4-6]found that Hg^0 was re-emitted significantly at the higher pH values, which was completely opposite to the findings of R.Ochoa-González and J.J.Wo[7,8].J.J.Wo suggested that $Hg(OH)^+$ and $Hg(OH)_2$ inhibited Hg^0 release at high pH values[8], While J.Schuetze considered athigh pH values the reaction of $Hg(OH)_2$ with SO_3^{2-} and the $Hg_2(OH)_2$ decomposition led to Hg^0 re-emission[6].N.Omine found that the sulfite-Hg^{2+}reduction began to act at pH>5[4], but R.Ochoa-González thought $HgHSO_3^+$ formed at low pH was less stable than other S(IV)-Hg^{2+}complexes[7]. C.L.Wu considered at low pH the H^+ concentration was high so that Hg^{2+} reduction reaction could be inhibited[5]. Therefore, under N_2 or O_2/N_2 atmosphere the explanations of Hg^0 re-emission at different pH values are controversial and incomprehensive. Additionally, in their experiments $HgCl_2$was used as the source of mercury, the formed $ClHgSO_3^-$and $Cl_2HgSO_3^{2-}$could stabilize Hg^{2+}[9].In some of these experiments $CaCO_3$ or $CaSO_4$were added in the slurry, such solids introduced interfering substances[6]. Although O_2 had been contained in some

experimental atmospheres, there was no discussion about the effects of S(IV) oxidation by O_2 on the pH values and its further impact on the Hg^0 re-emission. On the other hand, because of adding fresh slurry, the pH of slurry in regionof circulationpumpsis above 6, oxidation and gypsum seed crystalscause abnormal decrease in pH values [10]. The pH of slurry changes under oxy-fuel flue gas condition[11], the pH of forced oxidation region may fluctuate. In all of these exceptional regions or circumstances Hg^0 re-emission is unclear.

In this study, the theoretical formulas of slurry pH were deduced to evaluate the decisive factor of pH values, and then the lab-scale experiments were performed under N_2, CO_2, O_2/N_2 atmosphere to test Hg^0 re-emission at different pH values. The objective of this work is to reveal the intrinsic mechanisms of Hg^0 re-emission from sulfur scrubbing slurry at different pH values, then provides some suggests for controlling Hg^0 re-emission in WFGDs.

Theory and experiments

Slurry pH theory

According to the solution chemistry theory, the pH value is directly determined by the concentration of H^+ ion generated by electrolyte ionization. The WFGD slurrypredominantly contains SO_4^{2-}, Ca^{2+}, SO_3^{2-} and HSO_3^-.Because SO_4^{2-} and Ca^{2+} are strong electrolyte ions which are hardly hydrolyzed, the pH value of slurry is mainly decided by weak electrolyte ions such as SO_3^{2-} and HSO_3^-. In order to study pH in single factor and conveniently, theoretical and experimental object of this study was the univariate solution consisting of SO_3^{2-} and HSO_3^-, which was abbreviated as S(IV)-H_2O solution.According to equilibration of S(IV)-H_2O solution[12], when the S(IV)consists of SO_3^{2-} and HSO_3^-,the formula (1) is used for calculating pH. When the S(IV) consists of H_2SO_3 and HSO_3^-, the formula (2) is used for calculating pH.

$$pH=lg[SO_3^{2-}]- lg[HSO_3^-]+(17780/T_0+1585T_1+114T_2+0.59T_0T_3)/R. \quad (1)$$

$$pH=lg[HSO_3^-]- lg[H_2SO_3]+(4604/T_0+7730T_1+118T_2+0.37T_0T_3)/R. \quad (2)$$

Where R=8.31448J/(mol·K), T_0=298.15K, $T_1=1/T_0-1/T$, $T_2=T_0/T-1+\ln(T/T_0)$ and $T_3=T/T_0-T_0/T-2\ln(T/T_0)$.

Experiment

A lab-scale scrubber was used to simulate a WFGD system, shown in Fig.1. The reactor containing S(IV)-H_2O solution was kept at 55℃in the water bath. A magnetic stirrer was put in the reactor and was kept stirring at the constant speed of 200r/min. The pH value was measured by a pH meter (PHS-3C, China). The concentration of Hg^0 at the outlet of the reactor was measured by an online mercury analyzer (VM3000, Mercury Instruments GmbH, Germany) based on cold vapor atomic absorption spectrometry (CVAAS). The detection limit of the mercury analyzer is 0.1 μg/m^3.

The experimental operational conditions were shown in Table 1. The reactive atmospheres were CO_2, N_2 and O_2/N_2. The total gas flow rate was set to 2 L/min by mass flow controllers. In preliminary experiments, 1N KCl and 4%$^W/_V$ $KMnO_4$ +10%$^V/_V$ H_2SO_4 were used for collecting Hg^{2+} and Hg^0 respectively, to evaluate mass balance of mercury.The results showed that the mercury recovery were between 79.95%and 106.94%, indicating the system was reliable.In the

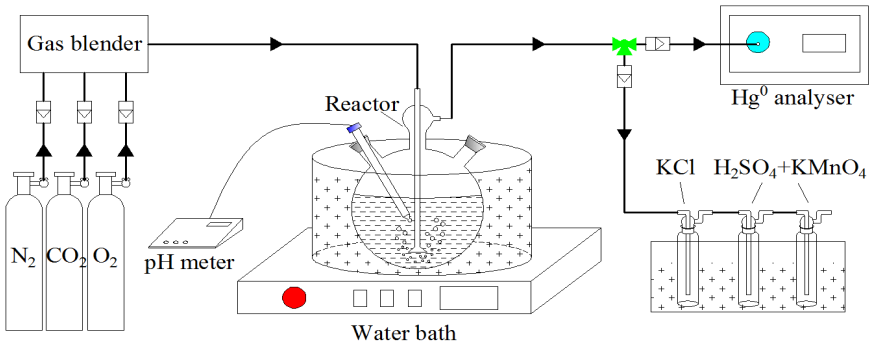

Fig.1 Schematic of lab-scale scrubber

formalexperiments, 1L 5mmol/L S(IV)-H_2O solution was added to the reactor and heated to 55℃. The pH value was adjusted to the expected value with 10% $^{V}/_{V}$ HNO_3 and 1mol/L NaOH. Afterwards, the standard mercury solution which composed of $Hg(NO_3)_2$ was added in the reactor. During the experimental process, the gas was continuously introduced in the solution in the reactor. When the Hg^{2+} was reduced to Hg^0 in the reactor, the gas would carry Hg^0out of the reactor.The Hg^0concentration in the outlet gas was recorded continuously.

Table 1 Experimental conditions

Experimental conditions	Parameters
O_2/N_2 [vol.%]	0/100,5/95
O_2/CO_2 [vol.%]	0/100
pH	3, 4, 6, 8
Hg^{2+} [μg/L]	100

Results and discussion

Simulation and experiments of S(IV)-H_2O solutionpH law

Relationship between theoretical pH and S(IV) species. The relationship between pH and S(IV)species in S(IV)-H_2O solution was calculated using the formula (1) and (2) , see Fig. 2. The total amount of S(IV) was 1mol, The temperature was 55℃. When pH is 2-5, S(IV)speciesare mainly in the form of HSO_3^- ions When pH is greater than 8, S(IV) speciesare mainly in the form of SO_3^{2-} ions. when pH is 5-8, S(IV) speciesare existed simultaneously as HSO_3^- and SO_3^{2-} ions.

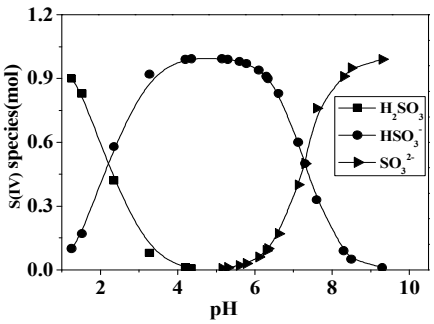

Fig.2 Relationship between pH with S(IV) species

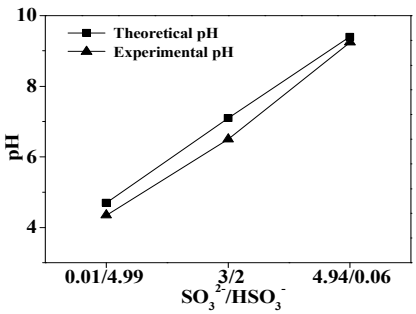

Fig.3 Comparison of experimental pH and theoretical pH(5mmol/L S(Ⅳ))

Comparison of experimental and theoretical pH. In order to evaluate the validity of the pH formulas, the pH values in the solutions with different SO_3^{2-}/HSO_3^- ratio were measured at 55℃. The experimental pH values are very close to the theoretical ones when the SO_3^{2-}/HSO_3^- ratio in the

solutions is the same (see Fig.3). The calculated pH value is less than 10% higher than the measured one. The comparison proved that the derived formulas could be used to judge the distribution ratio of S (Ⅳ)species in solutions at different pH value.

Relationship between pH and SO_3^{2-}/HSO_3^- ratio. The relationship between pH and SO_3^{2-}/HSO_3^- ratio is shown in Fig. 4. Seen from the simulation results the two curves were obtained at the same temperatures (25 or 55℃) are almost overlapped, showing that the S(IV) concentration has no effect on the pH values. At the same SO_3^{2-}/HSO_3^- ratio, the pH values slightly increase with the temperature increase from 25℃ to 55℃. Thetemperature has a little effect on the pH values. The pH values are strongly related with S(IV) species distribution ratio. Therefore, most likely it is the differentS(IV) species distribution ratio that causes the diversity of Hg^0 re-emission at different pH values.

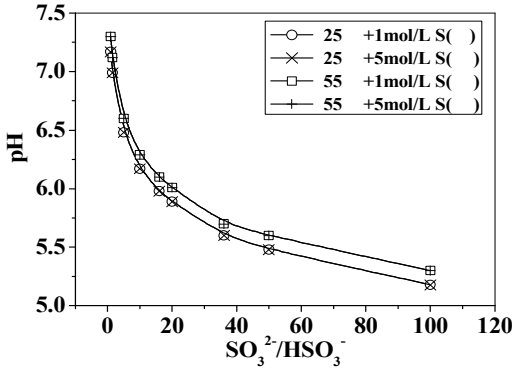

Fig.4 Relationship between pH and SO_3^{2-}/HSO_3^- ratio

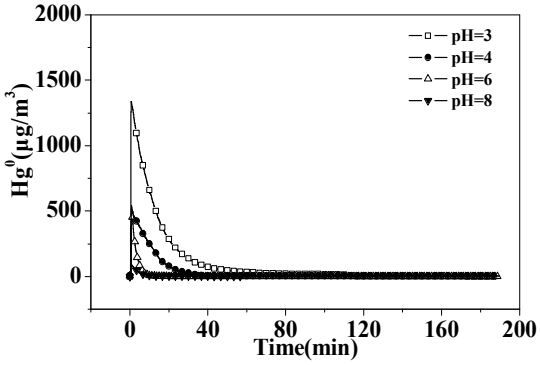

Fig.5 Hg^0 re-emission at different pH values under N_2atmosphere(5mmol/L S(Ⅳ))

Experimental study of the effects of pH on Hg^0 re-emission under different atmospheres

N_2 atmosphere. Fig. 5 shows the re-emission behavior of Hg^0 at different pH values under N_2 atmosphere. As shown in Fig.5, the lower the pH, the more Hg^0 reemitted under N_2 atmosphere.When the pH was 8, Hg^0reemitted gently. Although the peak height at pH 6 was much higher than that at pH 8, it decreased rapidly. Hence, the amount of Hg^0 re-emission was relatively small. Whereas the Hg^0 re-emission at pH 4 lasted for 30 minutes, which peak height was 541.2μg/m^3. When pH was 3, The Hg^0 re-emission sustained for about 50 minutes, which peak height was 1338.6μg/m^3. Therefore, under N_2 atmosphere when the pH is less than 4,Hg^0re-emissionis severe, Increasing the pH can remarkably inhabit the re-emission, lowering the peak height and shortening the time of duration.

The pH theory reveals that when the pH is between 5 and 8, S(IV)species are mainly in the form of HSO_3^- and SO_3^{2-}. SO_3^- is ready to react with Hg^{2+} and form $HgSO_3$. Because the concentration of SO_3^{2-} was much higher than Hg^{2+}, $HgSO_3$ which formedby the reaction of SO_3^{2-} and Hg^{2+} would further form $Hg(SO_3)_2^{2-}$ through the reactions expressed by Eq.(3) and (4). J. Munthe et al[13] demonstrated that $Hg(SO_3)_2^{2-}$ is relatively stable and difficultly hydrolyzed in the dynamics, so when the pH were 6 and 8, Hg^0 reemitted rarely. When pH is below 4, S(IV) species is in the form of HSO_3^- which can generate $HgSO_3$ and $HgSO_3H^+$ with Hg^{2+} through Eq.(5) and (6). $HgSO_3$ and $HgSO_3H^+$ are unstable resulting in increaseof Hg^0 re-emissionthrough Eq.(7) and (8), consistent with conclusion of R.Ochoa-González[7]. Because the pH of the plant WFGD is 5-6, once accidents of abnormal decrease in pH occur, the pH will be less than 5, the amount of Hg^0 re-emission should be increased.

$Hg^{2+}+SO_3^{2-}\leftrightarrow HgSO_3$. (3)

$HgSO_3+SO_3^{2-}\leftrightarrow Hg(SO_3)_2^{2-}$. (4)

$Hg^{2+}+HSO_3^{-}\leftrightarrow HgSO_3+H^{+}$. (5)

$Hg^{2+}+HSO_3^{-}\leftrightarrow HgSO_3H^{+}$. (6)

$HgSO_3+H_2O\rightarrow Hg^0+SO_4^{2-}+2H^{+}$. (7)

$HgSO_3H^{+}+H_2O\rightarrow Hg^0+SO_4^{2-}+3H^{+}$. (8)

O_2/N_2 atmosphere. Fig. 6 shows the re-emission behavior of Hg^0 at different pH values underO_2/N_2 atmosphere. Comparing the Hg^0 re-emission behavior curves in Fig. 5 with Fig. 6, great changes occurred when O_2 was added to the atmosphere. When the initial pH was 3, the time duration was extended from 50 minutes (under N_2 atmosphere) to about 90 minutes(O_2/N_2 atmosphere) due to the addition of O_2. When the initial pH was 6 or 8, the newly added O_2 caused a sudden increase of Hg^0 re-emission in the latter part of the experiments. The measured pH value decreased with the inflow of oxygen, once the pH was reduced to about 4, the outlet Hg^0 concentration began to rise.

The changes to the release behavior of Hg^0were possible due to the oxidation of the S(IV) species in solution by added O_2. According to previous study[14], the oxidation rate of S(IV) grows with the pH increases, which means the oxidation rate of SO_3^{2-} ions is greater than that of HSO_3^{-} ions. When pH was 6 or 8, through Reaction (9) and (10) the SO_3^{2-}ions were consumed faster than HSO_3^{-} ions, resulting in the decline of the ratio of SO_3^{2-}/HSO_3^{-}. The pH drop was caused by such SO_3^{2-}/HSO_3^{-}ratio decline, which was proved by the trend of pH curves in Fig. 6. Because the reactions (5) and (6) are reversible reactions in solution based on chemical equilibrium, When SO_3^{2-} concentration was reduced to the critical value for the maintenance of the chemical equilibrium, the reverse reactions would predominate. Finally the pH value dropped to less than 4, The insufficient SO_3^{2-} could not sustain the existence of $Hg(SO_3)_2^{2-}$. Then relatively stable $Hg(SO_3)_2^{2-}$ would be transformed into unstable $HgSO_3$ and $HgSO_3H^{+}$, resulting in the massive Hg^0 re-emission.

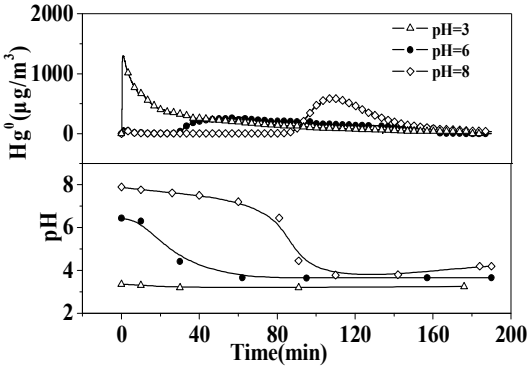

Fig.6 Hg^0 re-emission at different pH values under O_2/N_2 atmosphere (5mmol/L S(Ⅳ))

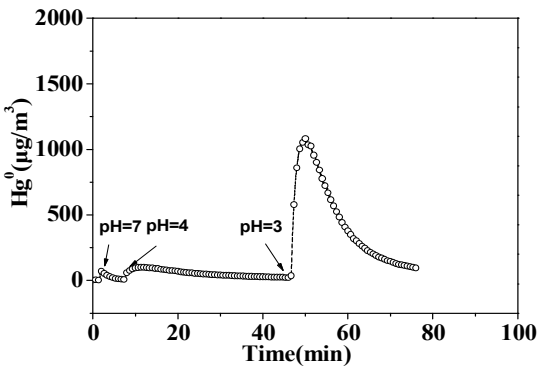

Fig. 7 Hg^0 re-emission at various pH values adjusted by HNO_3 (N_2,5mmol/L S(Ⅳ))

Direct oxidization of $Hg(SO_3)_2^{2-}$ by O_2 was another possible reason for Hg^0 re-emission. To exclude such a possibility, the effects of the pH drop on the Hg^0 re-emission under pure N_2 atmosphere were investigated by simply adjusting the pH value with $10\%^{V}/_{V}HNO_3$ (see Fig.7).

when the pH was adjusted down to 4, there was a Hg^0 re-emission peak which lasted for 15 minutes. when the pH was continuously adjusted down to 3, a high peak of Hg^0 re-emission turned up and sustained for more than 30 minutes. This indicated that no matter what O_2 exists or not, a large amount of Hg^0 will reemit as soon as the pH value of the solution decreases to less than 4. Hg^0 re-emission caused by O_2 addition was by consuming SO_3^{2-} to decrease the pH value. Therefore, massive Hg^0 re-emission may occur in the forced oxidation zone of WFGD system due to the unexpected low pH values produced by the sulfite oxidation during air bubbling.

$$O_2 + 2SO_3^{2-} \rightarrow 2SO_4^{2-}. \quad (9)$$

$$O_2 + 2HSO_3^{-} \rightarrow 2HSO_4^{-}. \quad (10)$$

CO_2 atmosphere. Fig. 8 shows that the Hg^0 re-emission at different pH values under CO_2 atmosphere. When the pH was 8, the behavior of Hg^0 re-emission under CO_2 atmosphere was similartothat under N_2 atmosphere which meant that CO_2 has no effect on Hg^0 re-emission. When the pH was 3, the peak of Hg^0 re-emission under CO_2 atmosphere was higher than that under N_2 atmosphere. The Hg^0 re-emission is sensitive to the pH values when the pH value is close to 3. CO_2 caused a little drop of the pH, leading to a slight increase of Hg^0 re-emission. The results are consistent with N. Omine's consequenceabout Hg^0 re-emission at different CO_2 concentration[4]. Because the solubility of CO_2 is low to0.017mol/L•atm at 50℃[15]and H_2CO_3 is weaker than H_2SO_3, CO_2 atmospherejust can slightly decrease the pH value of S(IV)-H_2O solution. As shown in Fig.8, when the pH is 3, for Hg^0 re-emissions underbothCO_2 and N_2 atmosphere, the durationisalmost identical and the amount has a little difference. As a result, no matter under CO_2 or N_2 atmosphere, Hg^0 re-emission is almost the same at same pH value. Based on above discussion, we believe that the enrichment of CO_2 in flue gas during oxy-fuel combustion has little effect on Hg^0 re-emission.

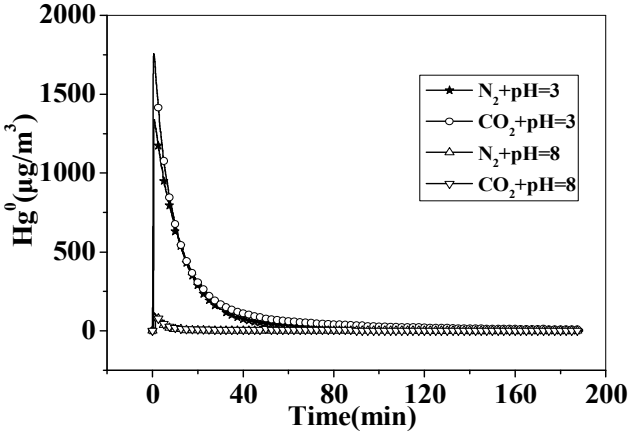

Fig.8 Hg^0 re-emission at different pH values under CO_2 atmosphere (5mmol/L S(Ⅳ)

Conclusions

A pH variation calculation method was established and a series of experiments were carried out to evaluate pH influences on Hg^0 re-emission in WFGD slurry under N_2,CO_2, O_2/N_2 atmosphere. The higher the pH value, the less Hg^{2+} reduced by S(IV), resulting in Hg^0 re-emission decrease. Under N_2 atmosphere,the Hg^0 re-emission wasmild at pH>4 while it was severe at pH<4.Under O_2/N_2 atmosphere, the addition of O_2extended the time span of Hg^0 re-emission at low pH and

increasedHg^0 re-emission unexpectedly in the latter partof the experiments at high pH.Hg^0 re-emission caused by O_2addition was to decrease the pH valueby consuming SO_3^{2-}. Under CO_2 atmosphere, CO_2 almost did not affect Hg^0 re-emission because of its little effect on the slurrypH.

Acknowledgments

The National Natural Science Foundations of China (U1261204, 51161140330 and 51306064) are gratefully acknowledged.

References

[1] C.L.Wu, Y. Cao, Z.B.Dong, C.M.Cheng, H.X.Li and W.P.Pan: Journal of Coal Science & EngineeringVol.16(2010),p. 82-87.

[2] M.Díaz-Somoano，S.Unterberger and K.R.G. Hein: Fuel Processing TechnologyVol.88(2007), p.259-263.

[3] Q.W.Hou,R.G.Shi,Y.C.Li and S.B.Gao: Journal of Shandong University (Engineering Science) Vol. 35(2005), p.37-38.

[4] N.Omine, C.E.Romero, H.Kikkawa, S. Wu and S.Eswaran: FuelVol.91(2012), p.93-101.

[5] C.L. Wu, Y. Cao, W.P. Pan, Z.B. Dong and W.P. Pan: Fuel Vol. 89(2010), p.2072-2080.

[6] J. Schuetze, D.Kunth, S.Weissbachand H.Koeser: Environ. Sci. Technol. Vol. 46 (2012), p.3008-3013.

[7] R. Ochoa-González, M.Díaz-Somoano and M.R.Martínez-Tarazona: Chemical Engineering JournalVol.214(2013),p.165-171.

[8] J.J.Wo, M. Zhang, X.Y. Cheng, X.H.Zhong, J. Xu and X.H. Xu:Journal of Hazardous MaterialsVol.172(2009),p.1106–1110.

[9] Y.Liu, Y.J.Wang, Z.B.Wu,S.Y.Zhou and H.Q.Wang: FuelVol.90(2011), p.2501-2507.

[10] W.Shao: Zhejiang Electric Power(2009),p.82-83, in chinese.

[11] B.B.Hansen,F.Fogh,N.O.Knudsenand S.Kiil: Ind. Eng. Chem. Res.Vol.50(2011), p.4238-4244.

[12] W.Pasiuk-Bronikowska and K.J.Rudzinski: Chemical Engineering ScienceVol.46(1991), p.2281-2291.

[13] J.Munthe, Z.F.Xiao andO.Lindqvist:Water: Air, and Soil PollutionVol.56(1991),p.621-630.

[14] W.Huo: Mechanism of oxidation, absorption and crystallization in limestone-gypsum wet desulfurization process [D]. PhD thesis, Zhejiang University(2009).

[15] H.Kong: Experimental and theoretical studies in limestone FGD technology [D]. PhD thesis, Zhejiang University(2001).

Advanced Materials Research Vols. 960-961 (2014) pp 469-474

doi:10.4028/www.scientific.net/AMR.960-961.469

Impact of changing combustion of Shenhua coal to boiler operation

Yipeng Sun [1, a], Liang Cheng [1,b] and Qingfeng Zhang [1,c]

[1] North China Electric Power Research Institute Co., Ltd，Beijing100045, China

[a]ypsun1103@gmail.com, [b]cheng.liang@ncepri.com.cn, [c]zhang.qingfeng@ncepri.com.cn

Keywords: Shenhua coal; blending combustion; slagging; coal pulverizing system; operation parameter.

Abstract. Experimental study of changing and blending combustion of Shenhua coal on boiler operation was carried out, while the furnace slagging during the experiment, the coal pulverizing system adjustment and the boiler operation oxygen control issues were analyzed. The results show that: the boiler can operate in safety blending Shenhua coal and Zhungeer coal with the ratio of 7:3 based on the strengthening laboratory analysis of coal as fired, the safety and economy of the boiler and coal pulverizing system can be ensured with the pulverized coal fineness R90 in 30%, and selecting the lower mill combinations and setting the coal pulverizer outlet temperature at 73℃, the reasonable exhaust gas oxygen content should be 4.0%, and the boiler thermal efficiency has an 1% increase compared with the condiation of burning inferior Shanxi bituminous coal, the nitrogen oxide emissions are significantly reduced.

Introduction

Shenhua coal is the major steam coal of China. Cheng and Zhao studied the characteristics of coal quality, coal combustion and slagging of Shenhua coal, showed that Shenhua coal had the characteristics of high calorific value, high volatile matter, high calcium in ash, low ash content and low sulfur content, which determined the Shenhua with good ignition and stable combustion performance[1,2]. The economic analysis showed that boiler burning Shenhua coal presented great economy and environment protection of high thermal efficiency and low NOx, dust and SO2 emissions[3]. But it was found that the characteristics of low ash melting point and easy to slag would easily cause several issues directly affecting the unit safe operation, such as coal pulverizing system explosion and boiler slagging, which severely restricted the applications of Shenhua coal in power plant. Many scholars have conducted in-depth analysis of Shenhua coal slagging characteristics. Yu studied the fouling and slagging characteristics with coal reburning and injected calcium in 2.11 MW boiler with four-cornered combustor[4]. Zhou identified the morphology and mineralogy characteristics of deposits sampled at different loacations in the 0.25MW combustion facility furnace burning Shenhua coal using the SEM(SED) and XRD techniques, and presented two indices, viz. shedding periodicity of the deposition and the decaying amplitude of the heat flux to quantificationally evaluate the deposition propensity of differernt coals[5]. Zhang analyzed the slagging characteristics of 660MW supercritical boiler burning Shenhua coal[6]. Ren presented two methods to judge the slagging of large-capacity pulverized coal boilers burning Shenhua coal[7]. In practice, many plants improved the ash fusion temperature of coal as fired by blending the coal with high ash fusion temperature to reduce the boiler slagging. Li and Liang carried out the blending combustion simulation study of Shenhua coal and other difficult slagging coals on a 800MW supercritical swirling combustion boiler and a 1025 t/h double-furnace tangential drum boiler respectively, and analyzed the furnace temperature and speed distributions of different conditions, and verified by experiments[8,9]. Yan investigated the slagging performance of the blended heavy slagging coals for 100MW and 200 MW boilers, and predicted the main slagging parameters and tendency of the coal quality index of different blending ratios[10]. Chen analyzed the variation regularity of ignition, burnout, slagging and contamination of blended coals of Shenhua coal and other bituminous coals in different ratios systematically[11]. Gao carried out an experimental study

on the mixed combustion of Shenhua coal with Huolinhe lignite in a 1000 MW unit, and analyzed the effect of blending ratio on the maximum mill output, maximum unit output and the unit performance, and performed combustion optimization tests at an optimal blending ratio[12].

In recent years, with the increasing of coal prices year by year, the phenomenon of burning non-designed coal has been more common. The major coal of a power plant has been transferred from inferior bituminous coal of Shanxi province to Shenhua coal since 2012, and the blend program of Shenhua coal and Junger coal blended outside the furnace was used. Due to the obvious changes of coal feature, such as coal calorific value, ash and sulfur, the produced flue gas and cinder also change significantly, which will impact the boiler, dust collector and desulfurzation system operation probably. The experimental research of changing combustion of Shenhua coal was carried out in this boiler, the effects of changing combustion to boiler operation were analyzed in three aspect: slagging control, pulverizing system adjustment and furnace oxygen adjustment.

Set-up

It is a pulverized coal-fired boiler with sub-critical pressure, controlled circulation, single hearth, once reheat, and dry ash extraction, which adopts burner wiggling temperature adjusting, four corner arrangement, tangential firing, and direct blowing coal-pulverizing system with positive pressure. The primary and secondary air nozzles are spaced with the OFA secondary air nozzle at top. The burners are horizontal bias combustion pulverized coal burners using V blunt width adjustment ratio nozzle.

Table 1 shows the coal quality testing data of coals burning during the experiment, including inferior Shanxi bituminous coal, Shenhua coal, Zhungeer coal, blended coal of Shanxi coal and Zhungeer coal with the blending ratio 5:5 (blended coal 1) and blended coal of Shenhua coal and Zhungeer coal with the blending ratio 7:3 (blended coal 2).

Table 1 Coal quality testing data of coals burning during the experiment

coal quality testing data	Shanxi coal	Shenhua coal	Zhungeer coal	blended coal 1	blended coal 2
M_{ar}[%]	20.60	18.60	11.00	11.35	13.20
A_{ar}[%]	17.67	10.03	27.46	21.78	19.02
V_{ar}[%]	22.35	25.89	22.89	23.44	24.18
FC_a[%]$_r$	39.38	45.48	38.65	43.63	43.60
C_{ar}[%]	47.56	57.60	47.74	53.84	54.97
H_{ar}[%]	2.75	3.37	2.92	3.21	3.25
N_{ar}[%]	0.54	0.65	0.76	0.84	0.80
$S_{t,ar}$[%]	0.49	0.50	0.32	0.85	0.59
O_{ar}[%]	10.37	9.25	9.80	8.13	8.17
$Q_{net,ar}$kJ/kg$_l$	17670	21760	17830	20380	20590
DT[℃]	/	1180	>1500	/	1260
ST[℃]	/	1190	>1500	/	1300

Problems in changing combustion of Shenhua coal

Slagging problem

Any coal has a certain slagging tendency, but the slagging and fouling tendency of Shenhua coal are strong because of its coal characteristic, so more attention should be paid to slagging and fouling problems in changing combustion and blending combustion. As can be seen in the table 1, DT and ST temperatures of Shenhua coal are lower compared to Zhungeer coal, which indicate the strong slagging and fouling tendency, and the ash fusion temperatures of blended coals have a certain improvement compared to Shenhua coal.

Risk of pulverizing system explosion

The Shenhua coal is easy to fire and explosive because of its high volatile. Coal volatile and pulverized coal concentration are internal reasons of pulverizing system explosion, while running out of coal in coal mill, too high outlet temperature of coal mill, too small coal fineness, loose hot air

distributor and external ignition sources are external reasons. Measures should be taken to prevent pulverizing system explosion in changing combustion of Shenhua coal, such as eliminating accumulated pulverized coal, eliminating air leakage, controlling mill outlet temperature, controlling coal fineness, strengthening coal testing and controlling external ignition sources.

Boiler operation parameter control

Because of the great difference between the active coal and the original one, the original boiler operation control method requires a corresponding change, especially the furnace oxygen control.

Results and analysis

Furnace slagging analysis

To analyze the furnace slagging, the flame temperatures at different boiler elevations were measured through the hole on the furnace using an infrared pyrometer, while the furnace slagging conditions were also observed through the hole on the furnace. The flame temperatures of 36 points at 6 elevations were measured during the test, and averaging the temperatures of different points at the same elevation as the elevation temperature, and averaging the temperature of 6 elevation temperature as the furnace temperature. A serious furnace slagging situation was occurred during July 17 and July 18 when the blending ratio of Shenhua coal and Zhungeer coal was 7:3, resulting slag dragging machine stuck. The serious furnace slagging situation will be analyzed according to the furnace flame temperature test results as shown in Table 2.

Table 2 The furnace flame temperature test results during July 17 and July 18 [℃]

elevation	Condition 1	Condition 2	Condition 3	Condition 4	Condition 5
45m	1067.6	1056.1	1098.7	1134.3	1090.8
40.3m	1230.0	1183.5	1246.5	1247.0	1264.0
36m	1254.7	1216.0	1280.3	1279.0	1282.7
34.2m	1327.0	1287.8	1354.5	1361.8	1345.7
31m	1369.0	1348.4	1384.3	1390.9	/
28.6m	1408.3	1389.4	1415.0	1428.1	/
average	1276.1	1246.9	1296.6	1306.9	/

As shown in table 2, the furnace average temperature was 1276.1℃ in condition 1 in July 17 when the boiler operated normally and the load was 280 MW, while the test time was 4 hours after soot blowing. The flame temperatures of every elevation were reduced when soot blowing just ended in condition 2 in July 18, the furnace average temperature was reduced about 30℃, which showed that soot blowing had obvious effect on the control of slagging. At condition3, which was 3 hours after condition 2, comparison with condition 1, the flame temperatures of every elevation increased significantly, the furnace average temperature increased 20.5℃, especially in the elevation of 34m or more, the temperature rise 31.1℃ to about 1100℃ at elevation of 45m, which indicated that serious slagging was occurred at elevation of 34m or less, resulting in lower water wall reducing heat absorption, then flue gas temperature above 34m rise. The increasing 10℃ of inlet flue gas temperature of the air preheater and increasing 2℃ of boiler flue gas temperature also indicated the conclusion. At condition 4, which was 45 minutes after conditon3, the flame temperature at the elevation of 45m showed a rapid rise, the heating rate was close to 1℃/min, which showed the rapid growth of furnace slagging in the upper area. Although trying to reduce slagging by adjusting the air distribution and mill output, but the effect was not obvious. The load was reduced to 260 MW at condition 5 for safety, and then the furnace slag blocks fall. The flame temperature of every elevation showed significant decreasing trend, and the amount of slag increased sharply at the slag dragging machine, and then the slag dragging machine stuck. The cooling slag blocks were hard and bright black, and the visible veins of water wall heating surface indicated that some slags were adhered to the water wall heating surface in a molten state, which was extremely harmful to the safe operation of the boiler.

Comparison of the normal condition and the serious slagging condition showed that the boiler operation modes were basically the same, while the ash test results of Shenhua coal in July 18 were significantly different from the previous one, as shown in Table 3, and differences of the ash test results of blending Zhungeer coal in July 18 and the previous ones were small.

Table 3 Ash test results of previous Shenhua coal and Shenhua coal in July 18

coal	Ash composition[%]									Ash fusion temperature[℃]			
	SiO_2	Al_2O_3	TiO_2	Fe_2O_3	CaO	MgO	K_2O	Na_2O	SO_3	DT	ST	HT	FT
previous Shenhua coal	40.7	19.31	0.77	7.58	16.84	1.22	1.28	1.01	6.63	1180	1190	1200	1240
Shenhua coal in July 18	35.4	14.25	0.65	13.45	22.01	0.9	0.67	2.06	8.65	1080	1080	1090	1100

As shown in table 3, the softening temperature (ST) of Shenhua coal in July 18 was smaller than that of previous one, which indicated that the slagging characteristics of Shenhua coal was more serious, while the coal change was the key reason of the serious furnace slagging and slag dragging machine sticking in July 18. So in the future, it is necessary to strengthen the coal quality test of coal as received and coal as fired, especially the test of ash composition and fusion temperature. It is recommended that the Shenhua coal blending ratio reduced to no more than 40% encountering the similar one as that of July 18.

Adjustment of pulverizing system

Adjustment of coal fineness

Because of the high volatile of Shenhua coal, larger coal fineness was need to prevent pulverizing system from firing and exploding in view of security, and larger coal fineness could extend combustion distance, reduce heat load of burner area and slow slagging of burner area, but may result in the upper furnace and convection heating surface slagging in view of slagging. The coal fineness R90 was about 25% with burning the inferior bituminous coal of Shanxi province which was difficult to burn, while the coal fineness R90 increased to about 30% during the test. Table 4 shows the results of the coal fineness before and after adjustment.

Table 4 The results of the coal fineness before and after adjustment

Mill	Before adjustment		After adjustment	
	R_{90}[%]	Separator opening [%]	R_{90}[%]	Separator opening [%]
A	25.06	45	32.54	50
B	26.98	45	31.72	50
C	23.28	45	29.08	50
D	25.46	40	31.52	47
E	25.24	45	29.62	50

Adjustment of mill combination

By changing the mill combination mode and adjusting the input coals of every mill to change the burner load distribution of every layer, the burner region load will be distributed uniformly, and to avoid the problem of too high local heat load, the burner declination angle could be reduced, and ultimately the purpose of slowing the furnace slagging could be achieved. Table 5 shows the flame temperature distributions of several mill combinations.

Table 5 The flame temperature distributions of several mill combinations [℃]

elevation	Mill combinations					
	Condition 6 -ABCDE	Condition 7 -ABCE	Condition 8- ABDE	Condition 9 -ABCD	Condition 10 -ABCD	Condition 11 -ABCD
45m	1108.4	1104.6	1147.3	1068.3	1085.9	1084.1
40.3m	1235.0	1258.0	1289.0	1200.0	1220.0	1232.0
36m	1279.7	1277.0	1327.7	1263.3	1280.3	1291.0
34.2m	1355.2	1375.2	1416.7	1325.2	1345.7	1328.5
31m	1379.0	1401.9	1455.1	1358.0	1373.0	1368.4
28.6m	1409.5	1434.6	1493.5	1397.8	1412.0	1405.4
average	1294.5	1308.5	1354.9	1268.8	1286.1	1284.9

Conditions 6, 7 and 8 give out the furnace flame temperature results of three different mill combinations, and the interval of each test was 2 hours after soot blowing. As shown in the table, the flame temperatures of each condition were increased gradually, while the flame temperature of condition 8 was increased of 60℃ compared to condition 6, which increased the possible of slagging. Conditions 9, 10 and 11 give out the furnace flame temperature results under mill combination ABCD, and the interval of each test was also 2 hours after soot blowing. Under this combination, the center of furnace flame was lower, and furnace temperature decreased significantly, which was helpful to reduce the slagging tendency and exhaust gas temperature. So, it is recommended to choose the lower mill combination under normal situation of pulverizing system.

Control of mill outlet temperature

Increasing the mill outlet temperature could effectively improve the performance of pulverized coal ignition, while the Shenhua cola is easy to fire and explosive, so it is necessary to control the mill outlet temperature to prevent spontaneous combustion and explosion of pulverizing system. The mill outlet temperature should not exceed 75℃ according to the empirical formula. At first, the mill outlet temperature of burning Shenhua coal was decreased to 68℃ from 80℃ which was the temperature of burning inferior bituminous coal of Shanxi province. The mill outlet temperature was improved to 73℃ in condition 11. Comparing with the condition 10 and condition 11, it is found that the furnace flame temperature decreased, especially in the area of elevation 28.6m to elevation 34.2m, where the temperature decreased for about 10℃. The results showed that the pulverized coal into the furnace presented earlier fire trend. In addition, the hot primary air temperature and the exhaust gas temperature were both decreased for 3℃ based on the same primary air fan output, which indicated that the primary air into the air preheater was increased and the air preheater heat transfer efficiency was improved. So the moderate increase of mill outlet temperature could reduce exhaust gas temperature and improve boiler efficiency. After operating for one day in condition 11, setting the mill outlet temperature as 73℃ could guarantee the security and economy of the boiler.

Control of furnace oxygen

Generally the low oxygen combustion was considered to cause burner regions to be in a reducing atmosphere, which was not conducive to reduce boiler slagging trend, while the Shenhua coal belong to easily slagging coal, so most boilers firing Shenhua coal run with high oxygen. The higher oxygen for tangentially fired boilers may make tangentially larger and lead the primary air against the water wall, which will increase slagging. The higher oxygen operation mode will increase the power consumption of the fan and be conducive to control NOx concentration of the exhaust gas.

Some plans tried to adopt the operation mode of low oxygen combustion based on the above disadvantages of high oxygen combustion[13]. The results showed that low oxygen combustion had effect on reducing power consumption of air fans and NOx emission concentration on the premise of safe operation of the boiler, but it may cause incomplete combustion of coal or prolong the coal burn time, which may increase the combustion temperature and slagging trend of the upper region of furnace. So it is necessary to detect the co of exhaust gas and carbon content of fly ash timely to eliminate or reduce the reducing atmosphere in the furnace.

Table 6 shows the boiler operation parameters, the boiler thermal efficiency and NOx emission results of three kinds of coal.

Table 6 Boiler operation parameters, thermal efficiency and NOx emission results of three kinds of coal

Items	Shanxi province coal	Shanxi coal and Zhungeer coal	Shenhua coal and Zhungeer coal
Load [MW]	328.0	300.3	329.0
Duty[t/h]	1093.8	996.7	1098.6
Coal[t/h]	159	138.7	139
Inlet air temperature of forced draft fan[℃]	2.18	27.3	23.55
Atmospheric pressure[Pa]	100980	101700	101700
Relative air humidity[%]	69.66	32.53	72.51

Exhaust gas oxygen[%]	4.83	4.82	3.98
Exhaust gas co[ppm]	1	4	2
Exhaust gas temperature[℃]	138.09	150.83	144.28
carbon content of fly ash[%]	1.26	1.56	1.56
carbon content of slag[%]	2.38	7.62	1.73
Thermal efficiency[%]	92.06	92.38	93.04
NOx emission concentration [mg/Nm^3]	1040	1060	712

As can be seen from the table, the exhaust gas oxygen of burning blended coal of Shenhua coal and Zhungeer coal was smaller than that of the other two coals for 1%, but the co concentration of exhaust gas was also very small, while the boiler thermal efficiency was the highest, and the NOx emission concentration was the smallest. So setting the exhaust gas oxygen as about 4.0% at full load condition was reasonable to burn blended coal of Shenhua coal and Zhungeer coal.

Conclusions

The major coal of a power plant has been transferred from inferior bituminous coal of Shanxi province to blended coal of Shenhua coal and Zhungeer coal, which will challenge the safe and economic operation of the boiler and related systems. The boiler combustion adjustment research was carried out, the changes and adjustments of slagging characteristic, pulverizing system and furnace oxygen after burning the blended coals were analyzed to determine the reasonable operation parameters. The results showed that:

1) When burning blended coal containing Shenhua coal, it is necessary to strengthen the coal quality test of coal as received and coal as fired, especially the test of ash composition and fusion temperature, and the Shenhua coal blending ratio should be reduced encountering severely slagging Shenhua coal.

2) The coal fineness could be a little large when burning the Shenhua coal, the coal fineness R90 of 30% was suitable for blended coal of Shenhua coal and Zhungeer coal, and it is recommended to choose the lower mill combination under normal situation of pulverizing system, and setting the mill outlet temperature as 73℃ could guarantee the security and economy of the boiler.

3) When burning blended coal of Shenhua coal and Zhungeer coal, the furnace oxygen could be reduced, and setting the exhaust gas oxygen as about 4.0% at full load condition was reasonable.

References

[1] Z.Q. Cheng, Z.H. Li, C. Liu: East China Electric Power, 2002(02): 52-54(in Chinese).
[2] Y. J. Zhao, H.F. Zhou, Z.S. Li: Thermal Power Generation, 2005(06):5-7, 4(in Chinese).
[3] J.G. Han, Y. Meng, Z.Q. Cheng, et al: Thermal Power Generation, 2003(02): 5-7(in Chinese).
[4] H.M. Yu, X.Y. Cao, J.H. Zhou, et al: Journal of Zhejiang University: Engineering Science, 2006(7): 1187-1191(in Chinese).
[5] J.H. Zhou, X.H. Zhao, W.J. Yang, et al: Proceedings of the CSEE, 2007, 27(8): 31-36(in Chinese).
[6] Z.Y. Zhang: Boiler Technology, 2011, 42(01): 60-63(in Chinese).
[7] R. Ren, W. Yao: Thermal Power Generation, 2012, 41(02): 8-11(in Chinese).
[8] Y.H. Li, H.W. Chen, J.Z. Liu, et al: Proceedings of the CSEE, 2002, 22(06): 102-105 (in Chinese).
[9] S.H. Liang, X.Y. Ning, E.X. Zhang, et al: Proceedings of the CSEE, 2011, 31(26): 9-15(in Chinese).
[10] W.P. Yan, Y.Y. Chen, D.S. Xing, et al: Proceedings of the CSEE, 2006, 26(14): 93-97(in Chinese).
[11] H.Z. Chen, D.Z. Gu, N. Xue, et al: Thermal Power Generation, 2007(10): 23-26(in Chinese).
[12] J.L. Gao, T.S. Zou, Z.S. Li, et al: Journal of Chinese Society of Power Engineering, 2012, 32(06): 430-434, 475(in Chinese).
[13] Z.L. Chen: Thermal Power Generation, 2011, 40(01): 55-57(in Chinese).

Advanced Materials Research Vols. 960-961 (2014) pp 475-478

doi:10.4028/www.scientific.net/AMR.960-961.475

Suitable for cold area soil GSHP system thermal compensation method argument

BAI Li[1, a], WANG Peng-xuan[1,b]

[1] Key Laboratory of Songliao Aquatic Environment Ministry of Education ,ilin Jianzhu University, Changchun China 130118

[a]baili0308@163.com, [b]wpx890307@163.com

Keywords: Ground-source heat pump; ground heat; thermal equilibrium;

Abstract. In order to study the issue of heat imbalance while the ground-source heat pump using in cold regions,this thesis adopts a technology with independent intellectual property rights which is called “thermal compensation control area partition method”.

Introduction

GSHP system as a reliable, efficient, economic and environmental protection air conditioning mode, cause the extensive concern of hvac industry in recent years, has become one of the frontier research topic in the field of building energy efficiency.[1-3] In cold region, however, due to the limitation of climate condition, soil source heat pump system in the operation process of "thermal imbalance" phenomenon, has become the bottleneck problem of its large-scale application.

In this thesis, A teaching in colleges and universities library in cold region Changchun heat pump project as an example, the project of six layers framework structure of large public energy saving building, a total construction area of about 27492 ㎡, the project adopts the "thermal compensation control area partition method" the winter use soil source heat pump system for heating of the building is 5000 ㎡, the rest of the use of city pipe network heating, in summer to building 10000 ㎡ (including winter heating area) and cooling way, to keep the soil source heat pump system take put the balance of heat from the soil, so as to maintain the stable operation of the heat pump system.According to using GAMBIT software to establish physical model for parts of the well group, and hourly simulate the 5 years operation of some heat exchanger of the well group by using FLUENT software, so that the simulation results of applicability of the thermal compensation method in severe cold area can be demonstrated.

Changchun natural conditions

Changchun City is located in the northern hemisphere mid latitude zone, east longitude 124 ° 18 ′ ~ 127 ° 02 ′, latitude 43 ° 05 ~ 45 ° 15 ′. Dry and windy spring, rainy summer, autumn is cool and windy, and the long cold winter are about the four seasons there. Changchun City, the annual average temperature of 4.8 ˚C, the highest temperature is 39.5 ˚C, the lowest temperature of -39.8 ˚C, belongs to the cold area[4]. HVAC design parameters of outdoor meteorological for Changchun are shown in Table 1.

Table1 , HVAC design parameters of outdoor meteorological for Changchun

The average temperature of heating period(˚C)	Heating period Z (d)	Degree days (˚C. d)	The annual average temperature (˚C)	Calculation of heating outdoor dry bulb temperature (˚C)	Calculation of the relative humidity of outdoor heating	The lowest temperature (˚C)
-8.3	170	4471	4.8	-23	69	-39.8

Underground penstock heat exchanger heat transfer model

Due to the underground heat transfer is a very complex process, the model of simplified assumptions are as follows:

1) The soil is uniform, the thermal properties of soil unchanged at the heat transfer process;

2) Ignore the soil moisture migration and influence of groundwater;

3) Ignore the surface temperature fluctuation effects on soil temperature, and soil temperature uniform;

4) Ignore the U type pipe wall and backfill, backfill material and the thermal contact resistance between the soils.

1 The determine of the heat conduction differential equation

$$\frac{\partial T_g}{\partial_t} = \frac{\lambda_g}{\rho_g c_g}\left(\frac{\partial^2 T_g}{\partial r^2} + \frac{1}{r}\frac{\partial T_g}{\partial r}\right) \quad (1)$$

In the way, T_g —The temperature of Soil,˚C; t—Time，S;

λ_g —Soil thermal conductivity/(m·˚C); ρ_g —Soil density, kg/m³; c_g —Specific heat capacity of soil, J/(kg·˚C); r—The radius of the U tube,m.

2 The determine of Equivalent diameter.

Cause of the Underground penstock with vertical U tube, tube spacing is close, and two adjacent wall will produce the influence each other, so the heat transfer surface and the soil is not uniform, in order to simplify the calculation, A equivalent tube instead of the equivalent radius of the U tube two.

$$r_{eq} = \sqrt{2}r \quad (2)$$

In the way, r- The radius of the U tube

3 Definite condition

(1) The initial conditions: the earth is regarded as isothermal body, according to the formation of thermal test measured initial ground temperature is 12 ˚C.

(2) Boundary condition: the equivalent pipe wall boundary conditions for the second boundary condition, when the heat pumps operation

$$-\lambda_g \frac{\partial T_g}{\partial_r}\Big|_{r=r_{eq}} = \frac{q}{2\pi r_{eq}} \quad (3)$$

In the way, q- The Unit amount of Borehole heat removal, W/m

When the heat pumps stop

$$-\lambda_g \frac{\partial T_r}{\partial r}\Big|_{r=r_{eq}} = 0 \quad (4)$$

Well drilling soil for adiabatic conditions

$$-\lambda_g \frac{\partial T}{\partial r}\Big|_{r=\infty} = 0 \quad (5)$$

4 The establish of the heat transfer model

The ground source heat pump project of the library according to the building in winter heat flux and soil heat exchanger calculation need heat hole 104, and then consider the drilling safety margin of 15%, the project for the heat transfer hole 120 single hole depth 100m, aperture 180mm, arrangement of hole spacing is divided into 4m, 5m, 6m. Heat pump in this project is show in Figure 2.

In this thesis, The total of 16 well group with the 5m distance will be simulated, and as shown in Figure 3, in a rectangular area is 35m * 35m, according to the 4 rows of 4 columns, evenly spaced 16 buried tube heat exchanger, drilling depth is 100m, the hole diameter 0.18m, buried pipe for 32mm, the heat exchanger spacing and heat exchanger and the soil boundary distance was 5m. Tube group drilling depth is 100m, aperture r=0.018m, equivalent radius of =0.025m, U type tube diameter is 32mm. Heat exchanger spacing and the heat exchanger and the soil boundary distance was 5m, initial ground temperature is 12 ˚C. By using CFD what is a special pre-processing software Gambit to

establish model and dividing grid as show in Figure 4, the simulation software to read the grid using Fluent heat pump operation, for five years the change of soil temperature field. The simulation runtime system physical parameters show Table 2**.**

Table 2, The thermal parameters of Ground-source heat pump system

The initial temperature of soil（˚C）	The initial temperature of soil W/(m·˚C)	Soil density (kg/m³)	Soil specific heat capacity J/(kg·˚C)	Thermal conductivity of water W/(m·˚C)	Water density kg/m3	Water specific heat capacity J/(kg·˚C)	The single well heat (w/m)
12	2.573	2200	950	0.61	996	4200	25

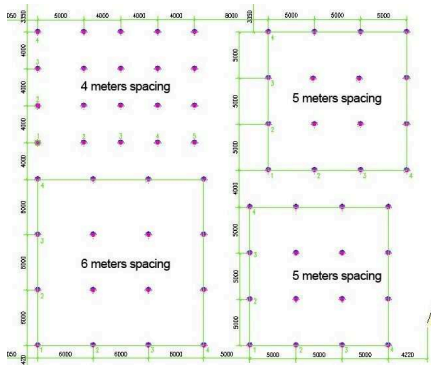

Fig. 2, Engineering heat pump system for well group arrangement

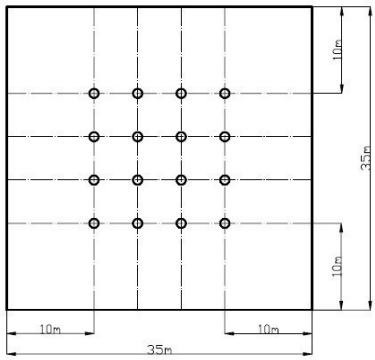

Fig. 3, The calculation area tube group layout

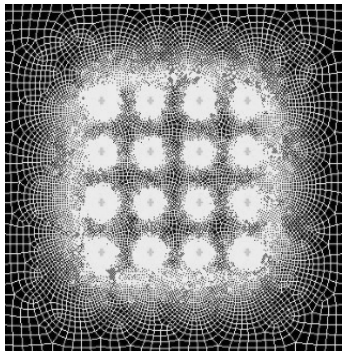

Fig. 4, Tube group soil around the unit grid

The simulation and analysis of dynamic

The simulation time of ground source heat pump system for five years, according to the characteristics of climate and load of the Building in Changchun City, operation process of every year is divided into four stages, the first stage for heating conditions (October 25th - April 15th), the second stage is the heating conditions after the end of the natural recovery (April 16th -5 months 31), the third stage is the cooling condition (June 1st -8 months 31), the fourth stage is the cooling after the end of the natural recovery (September 1st -10 months 24).The simulation and analysis of dynamic show figure5,figure6,figure7,figure8,figure9 and figure10.

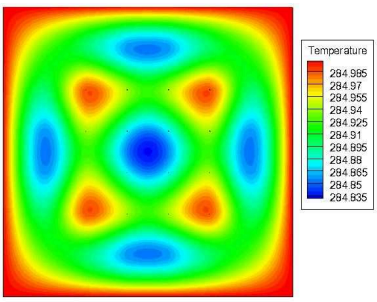

Fig.5, The temperature field Changes during one year

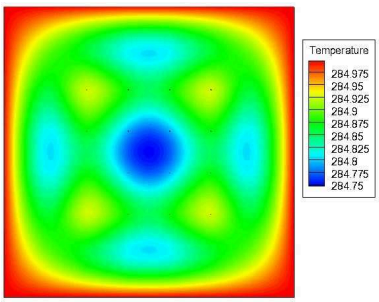

Fig.6, The temperature field Changes during two years

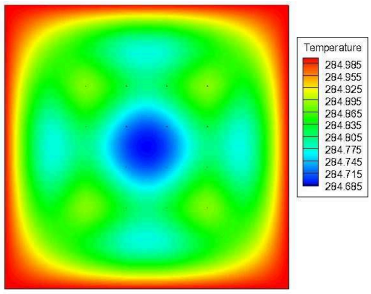

Fig.7, The temperature field Changes during three years

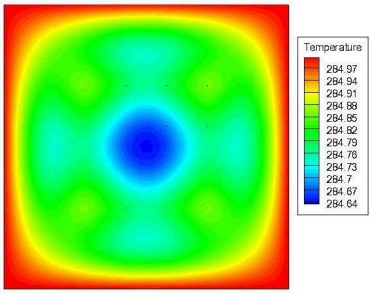

Fig.8, The temperature field Changes during four years

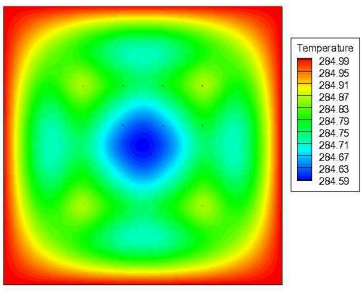

Fig.9, The temperature field Changes during five years

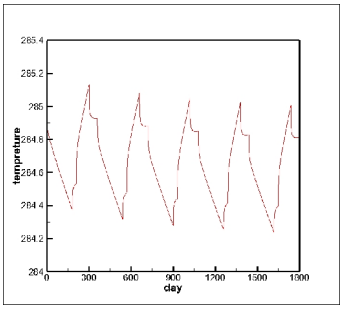

Fig.10, The average soil temperature variation

According to the simulation results, in the heat pump system after 1 years of operation, the soil after heating condition and the transition season in the heat exchanger will continue to absorb heat from the soil, the soil heat is not fully complementary, so the intermediate in the formation of the heat exchanger area cold accumulation, and well group Center "low temperature pit" is the heat exchanger area at low temperature in the soil is the most concentrated in a region. Through the heat pump system in operation, tube group around the soil temperature 0.15 ˚C lower than the initial soil temperature, soil temperature field system change after 2 years, the central area to reduce soil temperature 284.75K, 0.25 ˚C lower than the initial soil temperature. The system runs well group center temperature area expansion after 3 years, the central area to reduce soil temperature 284.68K, 0.32 ˚C lower than the initial soil temperature, the system to run for 4 years after the change of the soil temperature field, well group center soil temperature decreased, the temperature is lowered to 284.64K, than the initial soil temperature is 0.36 ˚C lower. Variation of system operation of soil temperature field in 5 year, reduce soil temperature well cluster center to 284.59K, 0.41 ˚C lower than the initial soil temperature. The soil temperature field can be balanced, and the soil temperature can be restored.

Conclusions

According to the simulation analysis on the operation of ground-source heat pump system: the soil temperature field has been basically balanced as the Ground-source heat pump system in 1 year operation, and as that proved the control area partition thermal compensation method for the proposed is feasible in severe cold regions. The system run for 5 years in the process of soil temperature decreased year by year, 5 years after the operation of the heat pump system, soil center temperature lower than the initial soil temperature as 0.41 ˚C,This shows, the thermal compensation method have a certain effect of resolving on the soil temperature which is used by the GSHP system, and this kind of mode is feasible.

References

[1] LI Yuan dan, ZHANG Xu .Domestic and foreign research and application status of GSHP Construction Machinery For Hydraulic Engineering & Power Station,Vol.23(2002), P.04-07.

[2] M.Y. Zheng, Y.S. Zhi, Y.Lin. Study of Heating and Cooling System with Solar Heat Soil Storage in Severe Cold Area[C]. Proceedings of the 2003 4th International Symposium on Heating, Ventilation and Air Conditioning. Beijing, 2003.

[3] M.Y. Zheng, D.M. Wang，Y.S. Zhi. The Study of Heating and Cooling Technique with Solar Energy in Severe Cold Area[C]. Energy and the Environment.Proceedings of the International Conference on Energy and the Environment,Shanghai, 2003.

[4] Information on http://baike.sogou.com/v11495.htm.

Advanced Materials Research Vols. 960-961 (2014) pp 479-484

doi:10.4028/www.scientific.net/AMR.960-961.479

Experimental Research of Heat Transfer Enhancement of the tube with disturbed flow components plug-in

Changfa JI [1, a], Rui QU[2, b] and Guoxin HE [3, c]

[1] School of Energy and Resource, Xi'an University of Science and Technology, Xi'an 710054, China
[2] School of Energy and Resource, Xi'an University of Science and Technology, Xi'an 710054, China
[3] School of Energy and Resource, Xi'an University of Science and Technology, Xi'an 710054, China

[a]jicf121@sohu.com, [b]qurui330@163.com, [c]heguoxin123@163.com

Key words:field synergy principle; metal-wire inserts; heat transfer enhancement; experiment study

Abstract. Based on Field Synergy Principle and orthogonal experiment design, nine arranged metal-wire inserts(that is high porosity porous inserts) is determined to experiment. The results showed that heat transfer performance of the pipe that metal-wire inserts is rooted at the core region of pipe is better than the pipe that metal-wire inserts is rooted at the edge region of pipe., location and curve radian can impact heat exchange significantly. Under the given experimental condition, the heat transfer quantity increased by 120 - 520%, overall heat transfer coefficient increased by 126 - 610%. Through enhancing heat transfer performance evaluation criterion (PEC) comprehensive evaluation, it is concluded that when the Reynolds number Re changes in 338 ~ 6931, the PEC value of 0.89 ~ 5.97.The calculation formula of the drag coefficient is obtained by regression analysis.

Introduction

At present,more energy has been converted and used through heat energy,which has reached more than 90% in China.Heat exchangers accounted for more than 70% only in the equipments of petrochemical enterprise[1].Our country keep in a low level in energy utilization.How to improve the energy utilization and develop new energy become an important topic under the circumstances of the global energy crisis, Research of heat transfer enhancement of heat exchanger has become an important means of engineering energy-saving in China under the background in the "energy conservation and emissions reduction" and the construction of economical society. The disturbed flow device Which has been inserted into the tube has low cost relatively,meanwhile,it has simple process and easy cleaning,and is especially good for innovation of old equipment[2].This device can effectively prevent dirt generated, therefore this device has been widely applied in engineering.

Field Synergy Principle of inserts heat transfer enhancement.

Field Synergy Principle. At present, flowing and heat transfer of porous medium involves in many engineering application fields,which has become one of the forefront in the active research areas in the engineering of thermal physics discipline.Inserts which is rooted in the pipe is regarded as heat transfer enhancement of porous medium (porosity $\varepsilon \geqslant 95\%$) in the pipe. When flowing liquid in the tube through inserts, the dispersion effect obviously generate in the flow channel. Under the condition of low Reynolds number ($Re \geqslant 300$), the flowing of liquid in the tube change into turbulence by promotion of dispersion flowing[3]. Total thermal resistance of flowing liquid under

the condition of turbulence is minimum at all flow patterns. Because thermal resistance of flowing liquid in the tube under the condition of turbulence is very small, heat transfer coefficient (K) of heat exchanger will greatly increase. Under the condition of high heat transfer coefficient (K), the effect of inserts heat transfer enhancement will be very obvious.

Academician in China named Zengyuan Guo analysis the energy equation to the boundary layer flow,re-examined mechanism of convective heat transfer from the angle of mutual coordinate of velocity field and temperature field, and put forward Field Synergy Principle[4] of heat transfer enhancement.

For situation of Steady-state incompressible flowing, introducing variable into expression of convective heat transfer energy equation, thus obtain the equation:

$$Nu = \mathrm{Re}\,\mathrm{Pr}\int_0^1 \left(\left|\overline{U}\right|\left|\nabla\overline{T}\right|\cos\beta\right)d\overline{y} \tag{1}$$

Among them, β express the angle between velocity vector and heat flow vector.

We can see it is the effective measures of strengthening heat transfer by inducing this angle.

According to Field Synergy Principle, we can achieve the purpose of heat transfer enhancement by organizing flowing of fluid in the heat exchanger effectively to reduce included angle between velocity field and temperature field.Based on this principle,this paper insert meal-wire into heat exchange tube and reorganize flowing of fluid to achieve the purpose of heat transfer enhancement with smaller flow resistance increase.

The analysis of metal-wire inserts. For heat transfer of laminar flow in The tube, the drop of the temperature mainly occur at the radial direction of tube[5], included angle between velocity and temperature gradient close 90°, integral value close 0 by Eq.(1.1), so heat transfer ability is poorer. As long as we produce a smaller velocity along the radial direction of tube, it can influence heat transfer significantly.

Inserting metal-wire network structure of organization according to specific rules into tube, constructing large porosity porous inserts,which can construct porous aisle in the tube.However the fluid of porous medium inner have the dispersion effect, which is similar to eddy of turbulence, it makes fluid to mixing along the radial direction under low Reynolds number (Re ≥300), and makes temperature distribution of radial direction to uniform, which can enhance heat transfer. It is important that flow resistance increase is small.

Experimental research

The experimental device and Process. Test device is mainly composed of casing tube heat exchanger, cold and hot water tank and a series of measurement and control instrument, The main process is described as follow: hot water is supplied into tube from heating water tank by circulating pump, and return heating water tank through rotameter, electric heater offset heat loss of hot water in the water tank, which keeping the temperature of hot water constant. Running water is inducted into casing tube heat exchanger as cold water, exchanging heat with hot water, and is exhausted to sewer. Flow direction of hot and cold fluid is contrary, so the experiment is convective heat transfer.The experiment process is shown in Fig.1.

Comparing casing tube heat exchanger with metal-wire network structure to plain tube heat exchanger in the experiment, so that we can validate heat transfer performance of heat exchange tube with metal-wire inserts. Changing velocity of hot fluid in the tube in different experiments, Keep velocity of cold fluid larger, so that obtain relatively stable test section temperature.The

measured data include temperature both at the inlet and at the outlet of cold and hot fluid, and test section pressure drop. Get heat transfer performance coefficient of heat exchange tube with metal-wire inserts, and criterion equation of heat exchange by calculated.

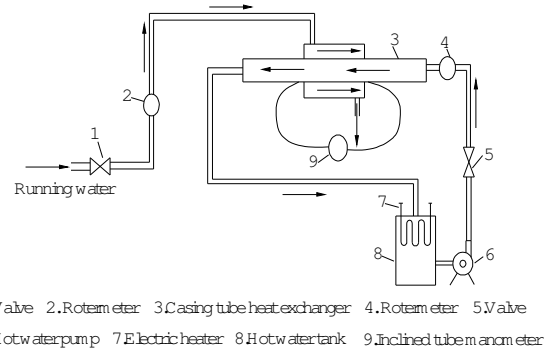

Fig. 1. Schematic drawing of experimental system

Results and analysis

Orthogonal experiment result analysis. By simulation analysis, this paper select 3 levels by location of metal-wire in the tube (A), metal-wire horizontal spacing (B) and curve radian (C). This paper make overall heat transfer coefficient K as experiment index and analyze orthogonal experiment[6] result of heat exchanger. We can get the most influential factor to experiment index and predict the optimal experiment combination. The range of 3 factors is obtained by orthogonal experiment range analysis, and demonstrated is shown in Fig.2,

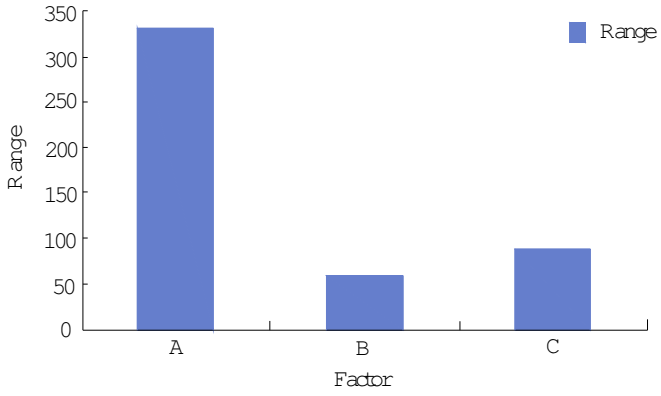

Fig. 2. The range of 3 factors

Through orthogonal design in the experiment,we summarize the poor and variance analysis to the 3 three parameters influence the heat pipe heat exchanger, The results show that location and curve radian can impact heat exchange significantly, the order according to ability of 3 factors impact heat exchange is: location > curve radian > spacing (A>C>B). Orthogonal experiment range analysis show that heat transfer performance of the pipe that metal-wire inserts is rooted at the core region of pipe is better than the pipe that metal-wire inserts is rooted at the edge region of pipe., this is because the full development period of equivalent thermal boundary layer is constructed in the tube, heat transfer enhancement main occur at the core region of flow.

Performance analysis of the heat transfer. Using the 50˚C hot water in the casing tube to exchange heat with constant 14˚C running water in the outer tube,taking average water temperature as qualitative temperature, When the heat hot water release equal to the heat cold water absorb (difference between the two<<5%), measuring temperature both at the inlet and at the outlet of fluid

and flow of cold and hot fluid. Getting convective heat transfer film coefficient of metal-wire porous tube by Wilson Principle, and criterion equation of heat exchange:

$$Nu = C \cdot \mathrm{Re}^{m} \cdot \mathrm{Pr}^{n} \tag{2}$$

the relation curve of overall heat transfer coefficient *(K)* and Nusselt number (*Nu*) versus Reynolds numbers (Re) are shown in Fig.3 and Fig.4.

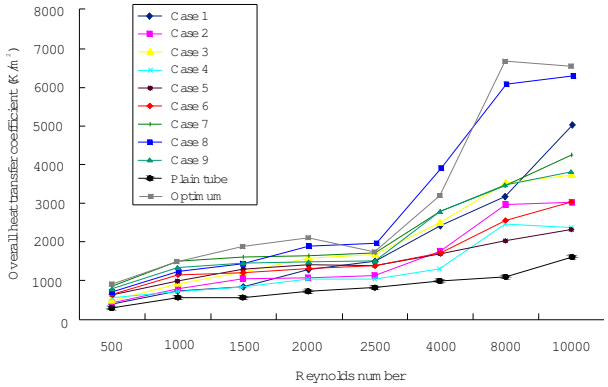

Fig. 3.Overall heat transfer coefficient versus Reynolds number

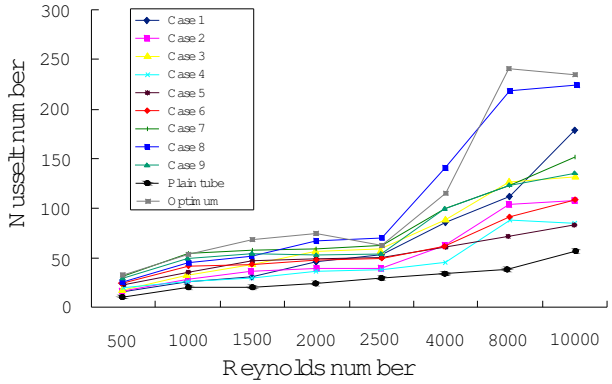

Fig. 4. Nusselt number versus Reynolds number

K and *Nu* gradually increase with increasing of Reynolds numbers, which consistent with change trend of plain tube. Under the same Reynolds numbers, overall heat transfer coefficient of tube with metal-wire is obviously bigger than plain tube, it show that metal-wire inserts can enhance heat transfer significantly. By calculating heat transfer quantity and overall heat transfer coefficient of tube with metal-wire, we know that heat transfer quantity increased by 120 - 520%, overall heat transfer coefficient increased by 126 - 610%.

Flow performance of heat exchanger analysis. Resistance coefficient of fluid in the tube is as follows:

$$f = \frac{2\Delta p}{\rho v^{2}} \cdot \frac{d_e}{l} \tag{3}$$

In the formula, $\triangle p$——the pressure drop of test section,Pa;

d_e——the hydraulic diameter of test section;

ρ ——heat density, kg/m^3;

v—— average flow velocity, m^2/s;

l—— the length of test section, m(200mm in the experiment).

We obtain the resistance coefficient by measuring pressure drop of test section, and draw resistance coefficient regression equation. The pressure drop $\triangle p$ versus Reynolds number Re is shown in Fig.5. As shown in the figures, pressure drop $\triangle p$ increase with increasing of Reynolds number Re, the pressure drop $\triangle p$ of tube with metal-wire is bigger than plain tube. It indicate that fluid resistance increase after metal-wire is inserted into heat exchange tube.

It can be seen from Fig. 5. After metal-wire is inserted into heat exchange tube, pressure drop $\triangle$p increase with increasing of Reynolds number Re, and the pressure drop $\triangle$p of tube with metal-wire is bigger than plain tube. It indicates that fluid resistance increase after metal-wire is inserted into heat exchange tube. The resistance coefficient is regressed, which obtain resistance coefficient regression equation:

$$f = 0.1476\,\mathrm{Re}^{-0.9653} \cdot \varepsilon^{-0.328} \tag{4}$$

Applicable conditions of the equation include: ① the hydraulic diameter of rectangular section tube is equal to 41.27; ② Re is among 300-1.3×10^4; ③ the porosity of metal-wire inserts ε is among 93.7-98.1

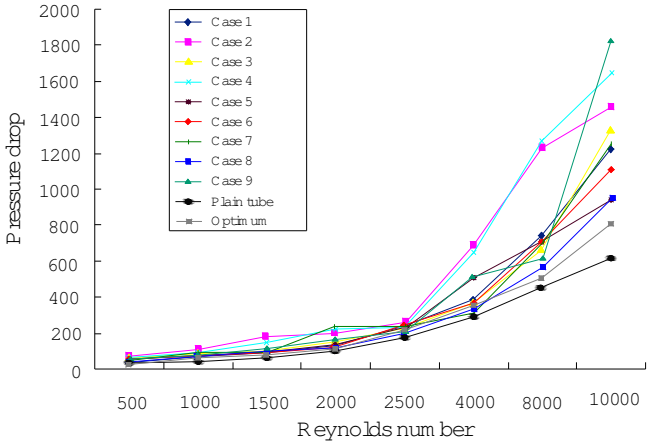

Fig. 5.Pressure drop versus Reynolds numbers

Comprehensive performance evaluation of heat exchanger. When heat exchanger is enhanced heat transfer, resistance will increase with increasing of heat exchange[7]. Some incremental of resistance is bigger than incremental of heat exchange, such measures is obviously unrealistic, we can also see that when the metal-wire inserted to enhance the heat transfer, Resistance is higher,So it is necessary that comprehensive evaluate heat transfer enhancement technology.

This paper adopt PEC as evaluation criteria of heat transfer enhancement performance according to paper[8]:

$$PEC = \left[\frac{Nu}{Nu_0}\right] \Big/ \left[\frac{f}{f_0}\right]^{\frac{1}{3}} \tag{5}$$

PEC>1 denotes that heat transfer enhancement is valid. The bigger PEC value, the better heat transfer enhancement effect. Comprehensive evaluation index PEC versus Reynolds number Re is shown in Fig.6. When $300 < Re < 1500$, the change of PEC value is small with increasing of Re; When $1500 < Re < 4000$, PEC value is monotonic rise with increasing of Re; When Re=6931, PEC value is maximum and up to 5.97; When Re=338, PEC value is minimum and up to 0.89. The heat transfer performance of all 9 cases experiment is enhanced, their heat transfer enhancement effect is obvious.

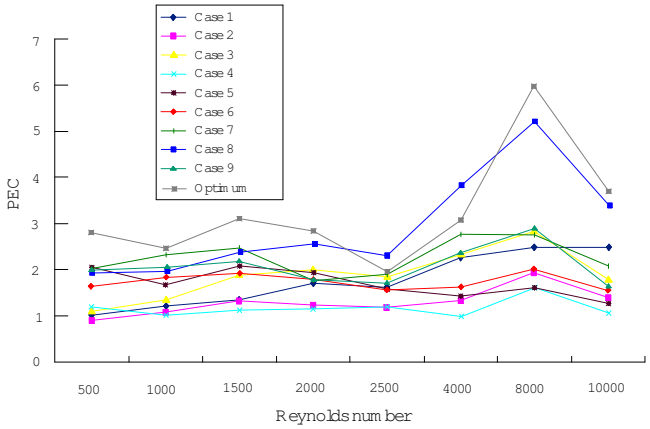

Fig. 6. PEC versus Reynolds numbers

Conclusions

(1) Orthogonal experiment range analysis show that heat transfer performance of the pipe that metal-wire inserts is rooted at the core region of pipe is better than the pipe that metal-wire inserts is rooted at the edge region of pipe., location and curve radian can impact heat exchange significantly, the order according to ability of 3 factors impact heat exchange is: location > curve radian > spacing.

(2) By calculating heat transfer quantity and overall heat transfer coefficient of tube with metal-wire, we know that heat transfer quantity increased by 120 - 520%, overall heat transfer coefficient increased by 126 - 610%. It show that metal-wire inserts can enhance heat transfer significantly.

(3) After metal-wire is inserted into heat exchange tube, pressure drop $\triangle p$ increase with increasing of Reynolds number Re, and the pressure drop $\triangle p$ of tube with metal-wire is bigger than plain tube. The resistance coefficient is regressed, which obtain resistance coefficient regression equation.

(4) When Re are change from 338 to 6931, PEC value also change from 0.89 to 5.97. The heat transfer enhancement effect of all 9 cases experiment is obvious.

References

[1] Bergles.A.E.， Junkhan.G.H and Webb.R.L.. *Energy conservation via heat transfer enhancement[J]*.Paper No.EGY 205,1978

[2]V.V.Wadekar.*Improving industrial heat transfer-compact and not-so-compact heat exchangers Enhanced Heat Transfer[J]*.1998,5: 53～69

[3]Eastman J A, Choi U S. *Novel thermal properties of nanostructured materials. Mater Sci Forum*, 1999,313: 629～634

[4] Zengyuan Guo,Suyi Huang. *Field Synergy Principle and New Technology of Heat Transfer Enhancement [M]*. Beijing: China Electric Power Press,(2004).,p.2~10

[5] S Wang，Z Y Guo, Z X Li. *Heat Transfer Enhancements by Using Metallic Filament Insert in Channel Flow. Int. J. of Heat and Mass Transfer*, 2001, 44(7): 1373～1378

[6] Shaohua Zheng,Fenghua Jiang. *Experimental Design and Data Processing [M]*. Beijing: China Building Materials Industry Press, (2004), p.58~60

[7]Agrawal K N,Kumar A,Akhavan M A,et al.*Heat transfer augmenttation by coiled wire inserts during forced convection condensation of R-22 inside horizontal tubes.Int.J.Multiphase Flow*,1998,24(4):635 ～650

[8] T.Kuppan. *Heat Exchanger Design Handbook.*Beijing: China Petrochemical Press,(2004)

Advanced Materials Research Vols. 960-961 (2014) pp 485-487

doi:10.4028/www.scientific.net/AMR.960-961.485

Problems and improvement measures of ash conveying system in coal economizer

Xueying Zhang[1, a],Jianxiao Zhang[2,a],Xueqin Wang [2,b]

[1]Electric Power Research Institute of Henan Electric Power Company,Zhengzhou 450052 P.R.China

[2] Datang Sanmenxia Power Generation Limited Liability Company,sanmenxia 472143 P.R.China

[1a]hnzhangxueying@163.com, [2a] ssy6357@126.com @126.com , [2b]qqqwdq@163.com

Keywords: Ash conveying system for economizer ; Pneumatic ash handing ; Blockage;Technological retrofit

Abstract：The power economizer of 600MW boiler in ash pipeline system of ash clogging, vibration, resulting in problems of ash conveying device is not running, the causes are analyzed, put forward the optimization scheme. Transformation through a series of Economizer Ash Conveying System, effectively eliminate the ash conveying pipeline vibration, clogging problems, ensure the economizer ash conveying system.

Introduction

Economizer ash conveying system is an important part of the normal operation of the boiler, economizer unit pneumatic ash conveying system, will reduce the pollutant discharge of atmospheric pollution, ensure the stable and efficient operation of the follow-up equipment safety unit[1-2]。Economizer of boiler in a power plant 2×600MW unit pneumatic ash conveying system, the dense phase conveying compressed air. The system consists of the discharging water dome valve, pump, ash transport pipeline, dense phase air supply device, dry ash storage. 7 below the boiler economizer hopper, fly ash of large particles collected in flue gas, in the control of ash conveying control system, 7 pump a falling ash, uniform delivery to the dry ash storage. The grey rough and ash conveying system without fluidizing device, dense phase stabilizer frequent blockage, causing blockage ash pipeline economizer, causing the pipe vibration.

Transformation of the former system problems

The economizer. The main problem of the following respects grey system running in time:

(1)A large number of dense phase stabilizer air conveying system (every 3 meters set 1), dense phase stabilizer for quality, wear or compressed air quality low, lost the check function, so the ash pipeline ash clogging check valve, ash transport pipeline lose the compressed air supply, no method to complete the normal transportation.

(2)Ash bin pump using the AV pump, pump bottom without fluidizing device, economizer hopper for ash, crude ash grey, falling ash accumulation in the bin pump bottom, by ash blowing compressed air, dry ash easily in the bin pump to form embolism.

(3)Economizer Ash from line 24 meters vertically downward through the pipeline 6 meters high, the stent delivery to 350 meters far, 20 meter high dry ash storage. Because the ash conveying pipeline elbow, the gap between large, extremely easy to cause the ash in the pipeline settling and accumulate, form a blockage.

(4)The system adopts water cooling type dome valve, pneumatic seals with dome valve, to ensure that the seals are not hot cement burns, the ball using water-cooled cooling. Economizer hopper as low boiler the flue, construction of the remaining debris and heating surface falling components (welding rod, wire) stuck in dome valve, extremely easy to cause the wear of the sealing ring and the dome of the rock, grinding cooling waterway wear dome, can lead to the cooling water into the ash falling pipe, ash bucket, ash change caused by the ash wet, compaction; at the same time the wet ash into the ash conveying pipeline and the ash storehouse, causing ash pipeline blockage and ash silo unloading difficulties.

(5)No row blocking device of ash conveying system. Pipeline plugging, manual cleaning, through the pump on the small ash discharge valve pressure relief or along the pipeline on pipeline, find the choke point. High altitude operation danger and environmental pollution.

System optimization design

Economizer design points of Grey System Optimization:

(1)Design capacity. Considering the current coal supply, coal and ash conveying system, design output should be appropriately increased, prevent the undercapacity, ash bucket full of accidents. This works by coal-fired boiler 320t/h, calculation of ash content 35%, ash content is 112t/h, Economizer Ash (according to the total ash content 5% consider) for 5.6t/h.

(2)Pump capacity design. Pump should have sufficient capacity to minimize the valve action time, but also shoulds not be too big, economizer hopper volume is generally not more than $0.5m^3$, if the tank volume is too large, the charging time increased, will cause the instantaneous conveying capacity is too large and plugging. This system conveying tank volume is provided with $0.5m^3$, can satisfy the need of ash, do not change. Pipeline installation of 57 5mm in the bin pump at the bottom of the inner sleeve and the pump casing (double reference ash transport double casing), improve the stem initial liquidity ash.

(3)Valve selection. The economizer ash temperature up to 400 ℃, the transformation, the inlet valve, outlet valve selection using high temperature double metal seal valve, effectively improve the reliability of the equipment.

(4)Design of blanking pipe expansion volume. Economizer hopper downward expansion amount is 250mm, about the expansion 150mm. Three installation of expansion joint expansion to the pulverized coal ash, compensation in different directions.

(5)Pipeline design. Between the ash conveying pipeline to the economizer hopper dredging pipeline installation, and installed exhaust valve and draining pipe metal compensator (absorption economizer hopper hot when the downward expansion). Ash conveying pipe blockage can be opened when the line block valve, reduce the labor intensity of manual dredging the blockage of the pipeline, also with the blanking valve exhaust valve pump work[2]. Increased Paidu manipulator valve in the control room of CRT picture, discharging valve for manual control.

Conveyance ash system transformation of economizer

4.1 Selection of an ash conveying system

At present, economizer hopper of dry ash conveying system piping layout are: economizer hopper ash conveying to ESP entrance; ash conveying pipe economizer hopper ash transportation pipeline with esp an electric field or electric field of two common; economizer hopper ash through the ash pipeline separate to the ash storehouse.

Considering the wide source, power plant coal coal quality change, esp a field itself ash conveying pressure, the electric dust dry ash removal system into consideration, should not be economizer hopper ash conveying to ESP electric field; considered from the cost point of view, is still based on the original system, through the ash transportation pipeline, uniform delivery to the dry ash storage.

4.2 Ash conveying system

The specific reform areas:

(1) The ash storage pump pipeline pump is changed into a double casing, and at the same time, the reform of AV pump, pump bottom mounted inner casing, improve dry transport mobility gray early.

(2) Economizer tube ash pipeline transmission vertical downward and horizontal pipe elbow joint, installing a set of internal air supply device, improving liquidity in grey; ash silo pipeline, site bend, vibration blocking concentrated mounting an air supply device, reduce the blockage of the pipeline, the degree of oscillation.

(3) Discharge valve before the installation of a DN80 pipeline to the economizer 7, an ash conveying pipe in the economizer, as ash conveying system draining device.

(4) Blanking valve and outlet valve adopts high temperature double metal seal valve, replace water-cooled dome valve.

(5) The blanking pipe expansion serious, failure of the bellows expansion joints for three to replace coal compensator deformation section.

Conclusions

Ash conveying system in thermal control logic unchanged, an automatic operation or operation manual. The operating personnel by controlling the feeding time, falling blanking valve waiting time, feeding amount adjusting pump to guarantee output ash conveying system. Based on a series of grey system in transformation, Economizer Ash Conveying in normal operation, to achieve the desired results.

References

[1]Luxin.Li,Yuesan.Qiu,Sanghu.Meng:Journal of Jilin Electric Power Vol. 3(2009).In chinese

[2]Bo.Jiang,Fuqiang.Su,Liang.Guo,Xiaoyong.Xu: Journal of Refrigeration Air Conditioning & Electric Power Machinery Vol.2(2013). In chinese

[3]Jianguo.Liang:Journal of Electric Power Construction Vol.7(2002). In chinese

Advanced Materials Research Vols. 960-961 (2014) pp 488-492

doi:10.4028/www.scientific.net/AMR.960-961.488

Study of Automatic Temperature Measurement of Foundation Ditch and Froze Soil's Retaining wall and System of Wireless Transmission

Huang fei[1,a,*] and Zhao Da Jun[2,b]

JiLin University, College of Construction Engineering, ChangChun,Jilin;China

JiLin University, College of Construction Engineering, ChangChun,Jilin;China

Huangfei1121@126.com , 1729333689@qq.com

Keywords: Frozen soil foundation wall, automatic temperature measurement, wireless transmission.

Abstract: Supporting of deep foundation of ditch has become outstanding issues. As a kind of effective supporting measurement, independent development of automatic temperature measuring system and wireless transmission system. Foundation ditch and froze soil's retaining wall has been taken into account. According to study of automatic temperature measurement of foundation ditch and froze soil's retaining wall and system of wireless transmission, this paper gets its own result. It plays an important role in temperature in foundation ditch and froze soil's retaining wall and survey in change of froze soil's retaining wall. And at the same time, we can transfer information and reduce the possibility of damage wire in engineering site. Foundation ditch and froze soil's retaining wall is a kind of environmental. It has an important meaning in deducing cost of foundation ditch and environmental construction.

Preface

Frozen soil wall as special method that it used in foundation pit soil retaining wall method as used in the construction of the special method, freezing process lasts about to frozen section of the building structure has been completed, foundation pit soil retaining wall technology gradually began as a subject to be studied in the construction site, but due to the detection of line is overmuch, can cause damage, causing the construction the phenomenon of pause, so this research is foundation pit soil retaining wall automatic temperature measuring and wireless receiving system, independently developed a set of automatic temperature measurement system with wireless transmission system, reducing cost and construction time vandalism.

Multi point temperature measurement and wireless transmission into the 9 probe, a square stereo in three horizontal longitudinal three, a total of three row. The recorded data by wireless transmission equipment transmission, will display the data with other panel insert can directly read sensor light statistics of wireless transmission of data (through the wireless transmission of data effects is very small, neglected) changes, and the actual direct test results are compared, find out the deviation, and indirect test data are corrected.

Development of multi point automatic temperature measuring system and wireless transmission equipment

1.1 Multi point automatic temperature measuring system

Multi point automatic temperature measuring system comprises a main processor, a temperature sensor, LCD monitor, PC.the main processor is AT89S52 of processor made.

The digital temperature sensor DS18B20 temperature sensor is a new generation of single bus digital temperature sensor, the single bus is the address line, data line, the line of control in three for a signal line, a signal line for bidirectional data transmission, so that the maximum to minimize the number of communication lines, make the system more simple. The system is based on PC as a host computer, microcontroller as the core of data acquisition for PC, SCM needs only one port line can with multiple DS18B20 series connection and communication, microcontroller through the serial port and PC machine together, constituted distributed three-in-one control system. The system uses DS18B20 to complete the temperature sampling and conversion work, while the microcontroller 89C51 always control and communication function. When in use, multiple DS18B20 and single chip microcomputer is connected with a line, the formation of the multi-point temperature measurement.

Liquid crystal display chooses 1602 character LCD module, LCD monitor with its low power consumption, small size, show many advantages of rich content, thin and light, it is widely used in the portable instrument and low power application system.

Host computer using RS232 interface, its full name is "data terminal equipment (DTE) and data communications equipment (DCE) between serial binary data interchange standard interface technology". The standard DB25 connector using a 25 foot, each pin connector signal content to be defined, but also for various signal level to be provided. With the continuous improvement of equipment, the DB9 interface instead of DB25, now the RS232 interface called DB9.

The assembly of each component:

(1) The main processor program, nine probes also can measure temperature.

(2) In the upper computer, the need and software combination, using serial debugging genies degree.

(3) In the temperature sensor, should be waterproof, the temperature measurement system used in engineering field, must be waterproof.

(4) For liquid crystal displays, seriously each connection, to ensure that the correct.

1.2 wireless transmission equipment.

This design is the core of NRF9E5 radio frequency chip, NRF9E5 is composed of a core of 8051 and a 433/868/915 MHz wireless transceiver chip NRF905. The equivalent of enhanced MCU integrates the wireless transceiver chip.

Engineering practice in the field of complex environment, the wireless part must have strong anti-jamming capability and the data transmission efficiency. In general, in the data transmission distance of 100~200m construction. The wireless data transmission module (NRF9E5) can completely meet the transmission distance. In the device of sensor nodes and main control unit using NRF9E5. So that the sensor nodes and the main control unit is formed between the point to point link, and a plurality of sensor node and a main control unit for data transmission, the formation of a star network structure. Because each node has a unique address, the main control unit to select the corresponding nodes to communicate, so that each node in a controlled state, everything in good order and well arranged to transmit data.

For low power implementation of the main control unit, the system adopts 1.9~3.6 V power supply voltage, if only use two No. 5 batteries or 3V batteries can work for 1~2 years, fully meet the requirements of low power. The main control unit of the display part due to general I/O NRF9E5 module on the mouth is very limited, so this system uses DM12232F LCD module, its connection with MCU to serial mode, need only 3 data lines, effectively avoids the problem of insufficient port.

Each communication node and data monitoring module uses NRF9E5,NRF9E5 8051 kernel is enhanced 51 MCU cores, with 4 input 10 bit A/D converter 80ksps, the four A/D converters can be used to the standard signal conversion on the sensor nodes. Can fully meet the requirement of the design of the host computer data processing. The main module and each node using time division multiple access TDMA the way to avoid the point to multipoint wireless communication data collision, through RXD and TXD serial port settings, connected to each node of the data collected from the MAX232 level conversion and PC, and through the module sends control command and effective data for each node set of sensor nodes control.

This design is for the measurement and wireless transmission of permafrost retaining wall of low temperature expansion. To detect temperature must adopt appropriate sensor. The sensor task will transmit the data to the data acquisition system, and the data acquisition system transfers the data to the host computer for analysis and processing.

At present, the reliability measure is used in sensor performance is good, high reliability to use under the condition of sensor parts often work under the bad environment, such as thermocouple and thermal resistance often working in corrosive and fluid erosion environment requirements, temperature measuring element capable of continuous trouble free working time longer, and puts forward mounted on the measuring element in the design of the structure. In the recent twenty years, considering the possibility of replacement components without stopping the machine, because of platinum thermal resistance of the production technology has made a major breakthrough, the range of temperature measurement platinum thermal resistance increased from 650 ˚C to 850 ˚C, temperature measurement precision and reliability (life) have greatly improved, and prices significantly lower.

Through one corresponding key, the first key, the first light receiving end of the light, followed by the two, third, the receiving end lights are bright, enough to prove to the signal transmission in the past, after some of the procedures and A/D converter, the analog signal into a digital signal, it can realize the wireless transmission temperature. The spot has been test, distance is received in 100~200 meters.

Equipment connection

2.1Connect to a wireless transmitting equipment and measuring system

The wireless transmitting device plug and the connector can be connected to a wireless transmitter and temperature measurement system, connected to a wireless transmitting and receiving devices enter the program, so that it can be measured temperature transmission to the receiving modules, after obtaining the temperature value through equipment and computer wireless connection.

2.2 Connecting devices and computer wireless receiver

This is used by the PC machine as the position machine to realize data display, so to the communication interface appropriate system configuration is necessary. Communication of parallel communication and serial communication, parallel data communication transmission capacity, but requires a large number of wiring, not suitable for long distance transmission. The serial communication with the characteristics of convenient connection, widely used for remote communication. In the serial communication with RS232 and RS485, the most widely used.

NRF9E5 and PC to realize the hardware interface communication by RS232. Since the PC series microcomputer serial interface for RS232C standard interface, input and output are used, TTL level of 89C51 MCU inconsistencies in the interface specification, so converting to TTL level to RS232 interface level using AXIM Company’s MAX232 standard RS232 interface chip P02 for the simulation of the receiver.

Temperature field simulation experiment device and the measuring point

3.1 Temperature field simulation test device measuring point

Longitudinal tube of frozen wall temperature field control simulation test device is composed of 4 parts: model test chamber, temperature control system, control system and test system .In order to ensure the simulation boundary conditions and foundation pit engineering similarity model test, insulation box consists of 150 mm thick insulation effect of sand layer two 9mm thick organic glass plate combination, internal test space net size is 0.8 m× 0.8m×0.8 m. Vertical tube wall temperature field of frozen soil control simulation test device is composed of 4 parts: model test box, temperature control system, control system and testing system. In order to ensure the simulation boundary conditions and the foundation pit engineering similar sand model test, insulation box is composed of 150 mm thick insulation layer two 9mm thick organic glass plate, internal test space net size is 0.8 m × 0.8m × 0.8 m.

3.2 Select the point position

Mainly for multi-point temperature measurement in order to form a relatively well, taking the center of the model as a benchmark pipe freezing tube section hydraulic arrangement of 9 measuring points in the center of the frozen. Square three-dimensional into horizontal three vertical three, a total of three rows. Depth from surface calculated distance, horizontal distance of center pipe starting distance. (Figure 1)

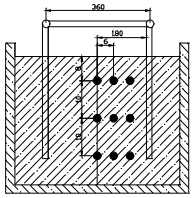

1-1	8	6
1-2	8	12
1-3	8	18
2-1	18	6
2-2	18	12
2-3	18	18
3-1	28	6
3-2	28	12
3-3	28	18

Fig.1 Measuring point parameters

Through long time data recording, a plurality of single probe sensor is inserted with the other groups can be directly read (relative to the experimental group, the sensor layout are 9 and have same position). Statistical measurement device reads the change rule of data, are compared with the actual test results to find out where the direct, deviation, then the indirect test data was modified.

Data acquisition and contrast

Foundation pit soil retaining wall cooling experiment, a cycle is 72 hours. In the beginning, middle, end of the three stages into the sensor probe, temperature measured by the multi-point temperature measurement system design. Compared with a single probe and measured the temperature of the temperature sensor. (Table 1)

	A	B	C	D	E	F	G	H	I	J	K
1						0h	5h	36h	36h	72h	72h
2			1-1	8	6	14.2	13.9	-6.3	-4.9	-6.3	-4.7
3			1-2	8	12	14.4	14.0	-3.8	-3.2	-5.4	-4.8
4			1-3	8	18	14.2	13.8	-2.4	-2.0	-5.4	-4.9
5			2-1	18	6	14.0	13.5	-5.3	-4.8	-5.4	-5.0
6		-10	2-2	18	12	14.0	13.4	-3.9	-3.3	-5.3	-4.7
7			2-3	18	18	14.1	13.8	-2.5	-2.0	-5.4	-4.9
8			3-1	28	6	14.4	13.9	-2.3	-1.9	-5.2	-4.6
9			3-2	28	12	14.4	13.9	-2.8	-2.2	-5.3	-5.0
10			3-3	28	18	14.3	13.7	-0.6	-0.2	-6.3	-4.8
11	-5		1-1	8	6	13.0	12.8	-15.6	-15.0	-15.6	-15.0
12			1-2	8	12	13.2	12.6	-17.4	-17.0	-15.3	-14.8
13			1-3	8	18	13.4	12.7	-5.0	-4.6	-15.2	-14.9
14			2-1	18	18	13.2	12.8	-15.6	-15.2	-15.6	-14.9
15		-20	2-2	18	12	13.1	12.6	-17.4	-16.7	-15.3	-14.8
16			2-3	18	18	13.4	13.0	-5.0	-4.4	-15.2	-14.8
17			3-1	28	6	14.0	13.7	-14.9	-14.2	-15.2	-14.7
18			3-2	28	12	14.0	13.4	-7.6	-7.0	-15.2	-14.8
19			3-3	28	18	14.2	13.4	-4.1	-3.5	-15.1	-14.7

Ps.: G, I, K as the developed equipment measured temperature; F, H, J as the single probe measured temperature.

Conclusions and suggestions

5.1Conclusions

By analyzing the data, we can be inferred from the rules:

The temperature is collecting temperature lower than measured temperature is the temperature is collected; in temperature must be higher than the measured temperature when negative. In fact, sampling and testing temperature difference, and repeated comparison of data, the correction results are: the measured temperature is positive, then on the basis of 0.5 °; the measured temperature is negative, then on the basis of minus 0.5 °.

5.2Suggestions

The test for the indoor test, due to limitations of the model device size, there are some differences in the foundation pit engineering thermal insulation and stratigraphic simulation and actual, not considering the influence of groundwater and geothermal, in future experiments suggest, can take the field of small pit simulation form, more practical.

Reference

[1] Xi Jianrong, 51 MCU-based Multipoint Ttemperature Control System, Modern Electronics Technique, vol．289(2): pp．186-188,2009 (In Chinese)

[2]Gao Min, Tong Boliang, Lin Jingfang, FrozenSand mining Gold and Methods, Journal of Glaciology and Geocryology, vol．16（3）, 1994 (In Chinese)

[3]Ma Qinyong, Artificially Frozen Soil Uniaxial Tensile Test of Strength, Rock and Soil Mechanics, vol．17（3）, pp．76-79, 1996(In Chinese)

[4] Pan Dianqi, permafrost drilling test study of influence factors and classification [J]

[5] Youhe Ma, 1996, physical and mechanical characteristics of saturated silty soil, electric power survey,12

[6] Zhou Youwu, Guo Dongxin, Qiu Guoqing, China frozen soil, Beijing: Science press,2000, 1-3

[7] Xu Zhongyan. Artificial freezing method〔M〕. Shanghai: College of civil engineering of Tongji University,2005

Advanced Materials Research Vols. 960-961 (2014) pp 493-497

doi:10.4028/www.scientific.net/AMR.960-961.493

The design of intelligent electric heating oil heater control system

Jin Li[1, a]

[1] School of Internet of Things, Wuxi Professional College of Science and Technology

[a]794142283@qq.com

Keywords: electric heating oil heater MCU temperature humidity

Abstract. An intelligent electric heating oil heater control system is designed in this paper. It takes the single chip microcomputer as the core controller; detects environmental temperature using the temperature sensor; controls opening and closing of electric heating oil heater according to the temperature user set; checks whether there is person indoor using the body detection sensor, if there is no, the oil heater is power off automatically; detects environmental humidity using the humidity sensor ,deciding whether the oil heater is turned on according to the current humidity sends out the alarm; detects oil heater placement using the angle sensor for detecting oil heater placement, Unable to start the oil heater. When the electric oil heater stands upside down or is set flat or inclined, it will send out the alarm. At the same time, the system is provided with keyboard and display circuit, which are used to set the various functions, such as setting the child lock and displaying the corresponding information.

Introduction

Oil heater is also called oil filled heater, is a space heater which is popular in recent years, its heat conduction oil is needed not to be changed and its long service life is also its advantage, besides, there is no noise, no light, no dust, no odor at the working state. However, at present, the control of the electric oil on the market is relatively simple and mainly using the switch and knob to control, the intelligent degree is low, unable to effectively save energy, and the security is low, unable to deal with the various things in family. We design and improve the system on the basis of this to improve the safety of electric heating oil heater then a multifunction and high security intelligent electric oil heater is designed.

The design of overall system

2.1 The design of the system function

2.1.1 Intelligent temperature control function

The control device can detect and display the current temperature indoor, adjust the heating power of electric oil heater automatically combining with the temperature the user set, which can effectively save energy;

2.1.2Auto induction of human body function

If there is some person in room, the oil heater works normally, otherwise, it will be Automatic power off, in order to achieve safe and energy-saving effect;

2.1.3The child lock function

The user can set the child lock function available, so that the children can't open the oil heater without the adults indoor;

2.1.4The dumping detection and control function

When the electric oil heater stands upside down or is set flat or inclined, it will not start and send out the sound and light alarm;

2.1.5 Humidity detection and control functions

Electric oil heater can't be used in the high-humidity environment, once the control device detects the environment humidity exceeds the limit range, oil heater will not start, and sends out the alarm.

2.2 System construction

Electric oil heater control system mainly consists of a main controller, a key detection module, body detection module, the ambient temperature detection module, humidity detection module, tilt angle detection module, LED display module, sound alarm module, heating control module, which collaborate with each other under the control of MCU to ensure the implementation of the various functions of the electric oil heater, the system construction is shown in Figure.1.

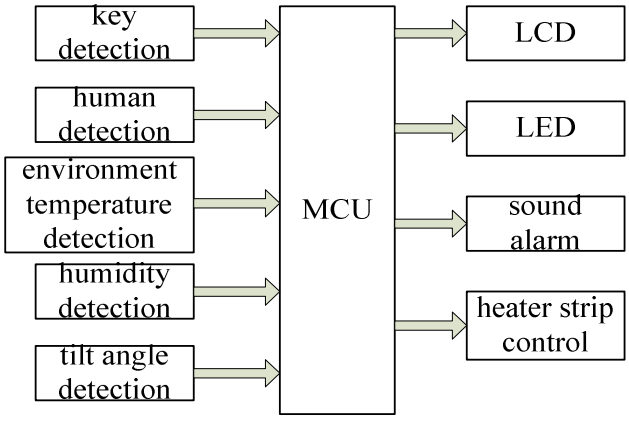

Fig.1 The block diagram of system construction

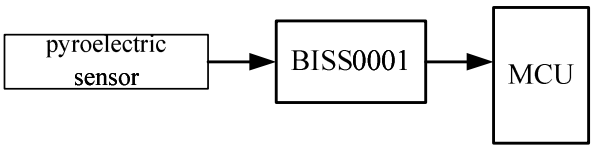

Fig.2The human detection diagram

The hardware design of the control system

3.1 The circuit of the MCU module

The controller of the electric heating oil heater uses STC12C5410AD microcontroller produced by domestic macro Crystal Technology Company, which has Wide 3.4V-5V working voltage range, 4K-FALSH program memory, 23 I/O ports, 2 16-bit timers, 4 PWM output. Based on the characteristics of the chip pins of STC12C5410AD, in actual design, human detection, temperature detection, humidity detection, angle detection, liquid crystal display, LED indicator, a voice alarm module are connected with the microcontroller I/O port and oil heater heating control module is connected with the MCU PWM port.

3.2 The human body detection

In this system, body detection is detected by the pyroelectric infrared sensor. Pyroelectric infrared sensor is mainly composed of a kind of high pyroelectric-coefficient material. Detecting signal of infrared radiation element is converted to the weak voltage signal, and then is output through the field effect transistor amplifier. The system uses the pyroelectric sensor BISS0001 as the processing chip, when there is some person, the pyroelectric sensor signal output high level after being treated by BISS0001, then is input an I/O port of the microcontroller, when the MCU detects that the falling edge of the signal, it shows that there is some person, the MCU decides whether the oil heater is started. Human body detection module schematic diagram is shown in figure 2.

3.3 The humidity detection module

Humidity detection module is used for detecting the environmental humidity oil heater located, when the humidity is greater than the threshold, the system will stop working. The system uses the HS1101 capacitance sensor as the humidity sensing element, HS1101 is placed in the 555 oscillation circuit, which transform the change of capacitance into voltage frequency signal inversely

proportional to it, and then the output signal is collected through the MCU. The circuit is shown in Figure 3.

The HS1101 and NE555 are connected to the circuit simultaneously. the function of NE555 circuit is summarized simply: When the pin 6 and the pin 2 is "1" at the same time, the pin 3 is output "0"; When the pin 6 and the pin 2 is "0" at the same time, the pin 3 is output "1". In this circuit, the 555 timer is used as multi state flip-flop output frequency signal just according to this function. When the power supply is switched on, the pin 6 and the pin 2 is input "0", then the pip 3 is output "1 ",because the voltage of the two ends of C1 is 0, C1 is recharge by VCC through R2 and R3. When the voltage of the two ends of C1 reached 2 /3VCC, the timer over reverses and is turned "0".Now, the base voltage of discharged BJT which is in the 555 timer is “1”, discharged BJT is conducted, so that the capacitor C1 discharge through R3 and internal discharged BJT, when the voltage of ends of C1 reduces to 1/3 VCC, the timer turns over again, and the output is "1", the internal discharged BJT is cut off, VCC begin charging on the C1 through R2 and R3, so go round and begin again, the oscillation is formed.

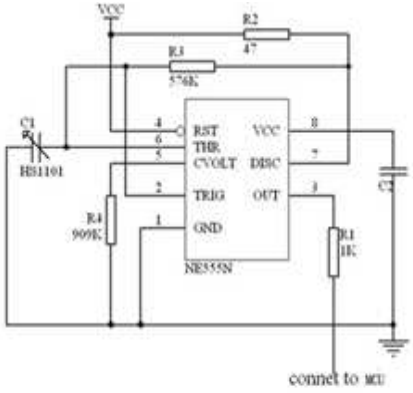

Fig.3The humidity detection circuit

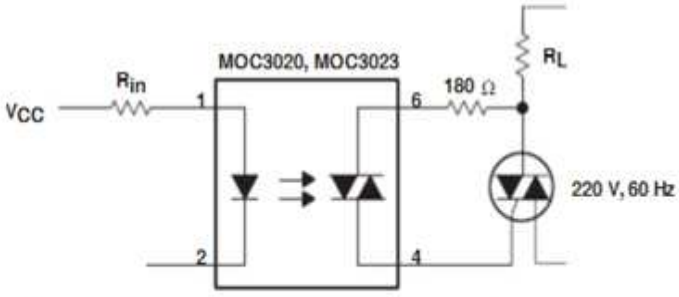

Fig. 4 The heating control module circuit

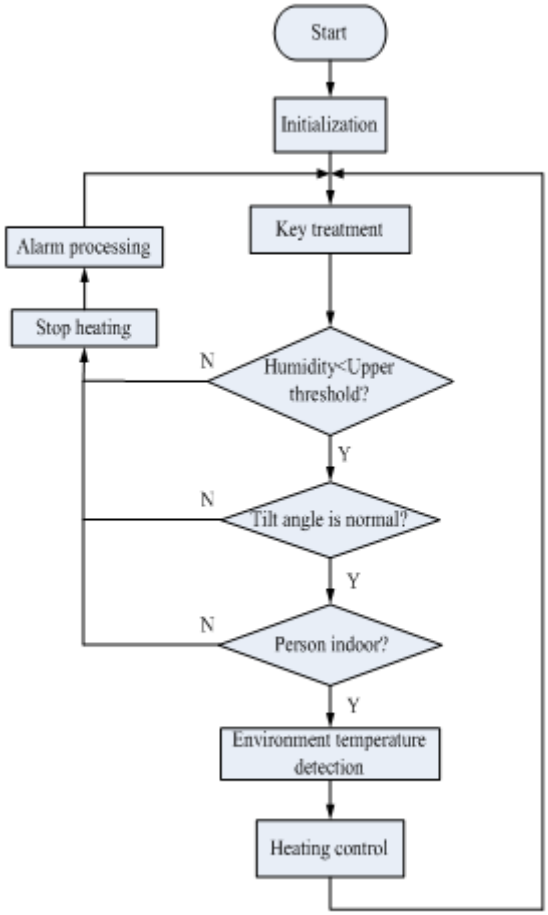

Fig.5 The flowchart of the software

The charging time in working cycle is T_h=0.7 (R2+R3) C1, the discharging time is T1= 0.7R3*C1, the duty cycle of the output pulse is q=(R2+R3)/(R2+2R3). In order to make the output pulse duty ratio is close to 50%, the R2 should be far less than R3. When the humidity changes outside, the capacitance value of both ends of the HS1101is changed, thus the output frequency of the timing circuit is changed. So as long as output frequency of 555 timer is measured, and according to the relationship between humidity and output frequency, we can obtain the humidity.

3.4 The temperature detecting module

The temperature detection module is used for detecting the temperature of the environment, and comparing to the temperature the user set to adjust the heating power of oil heater dynamically through the PID control algorithm. The system uses single bus temperature sensor

DS18B20 produced by DALLAS to detect the temperature, whose hardware circuit is very simple, here we say no more.

3.5 The heating control module

Oil heater uses the with heating wire heating, according to the different environment temperature detected ,combining with the temperature user set, adjusts heating power of the oil heater using PID algorithm dynamically, the circuit as shown in figure 4.

MOC3020 is the photoelectric coupler in figure. When the output of the SCM I/O is low-level, the photoelectric coupler is conducted, the port G of the bidirectional silicon controlled rectifier SCR1 gets trigger signals, the silicon controlled rectifier is conducted, and the voltage of two ends of the heating is 220V; When the output of the SCM I/O is high-level, the photoelectric coupler outputs no signal, the bidirectional silicon controlled rectifier is turned off, and the voltage of two ends of the heating is 0V. Accordingly, the PWM signal is output from n the SCM I/O ranging from low-level to high-level, conducted angle of the bidirectional silicon controlled rectifier can be changed by adjusting the duty cycle of the PWM signal, so as to achieve the purpose of regulating the heating power.

There are also the display module, keyboard module, and alarm module of hardware circuit in the system, which are much simpler, we say no more here.

The design of the hardware system

The design of System software follows the intelligent principle, when the control system is turned on, it is in the working status. The specific process is shown in figure 5. After power on, at first the system performs the initialization of program and variable, then tests whether the button is pressed, receives the information the user set (such as the setting of objective environment temperature),after this, it test whether the environment temperature and tilt angle is normal through the humidity sensor and angle switch. If the humidity value is over upper threshold or the angle switch is closed, it will stop heating program immediately, at the same time, send out the alarm. If the above are all normal, then it will test whether there is some person indoors. If there is someone, it will start the temperature detection sensor and collect the environment temperature, and then adjust the heating power through PID algorithm dynamically in order to the temperature maintain in the range of the value the user set. If there is no one indoors, it will stop heating the oil heater.

Conclusion

Intelligent electric oil heater control system designed in this paper, through testing and practical application, it is showed that the system has the characteristics of low cost, high intelligent degree and so on. Electric oil heater products have been applied in a company, the market reflects well. The system can accurately control the temperature according to the user set, provide a number of intelligent control and safety protection function for electric oil heater. It is the convenient to users at the same time saving electric energy to the full extent.

Reference

[1]Ding xiangxiang. Design and implementation of SCM system. ShuZiHua YongHu. 2013(15)

[2] Liu Jinzhen. Discussion on control system of temperature. Science & Technology Information. 2013, (14)

[3]Tan Haoqiang. C language program design[M]. Tsinghua University press.2008-11-1

[4]Shao Beibei. Online development method for embedded MCU[M]. Tsinghua University press.2004

[5]Sun Huiqin. SCM project design tutorials. Electronics industry press.2009

[6]Chen Linggui. Application of single chip microcomputer temperature control system of resistance furnace. Coal Technology. 2005, 24(6)

[7]Yang Qianli. The design of closed loop digital temperature control system based on PID algorithm. Computer and Digital Engineering. 2013, 41(12)

[8]Chen Yifei. Boiler temperature observation and control system design. Manufacturing Automation. 2011, 33(2)

[9]Liu Chenggang, Li Changfeng. Research and reform of sensor project teaching. China Education Innovation Herald. 2013(32)

Advanced Materials Research Vols. 960-961 (2014) pp 498-502

doi:10.4028/www.scientific.net/AMR.960-961.498

Optimal performance of the irreversible heat pump driven by steam turbine

Qi Zhao [1,a*] , Chen Wang [2,b] , Lixin Liu [1,c]

[1]College of Energy and Power, Changchun Institute of Technology, China

[2]Design and Research Institute of Changchun Institute of Technology, China

[a]email:hithot2@163.com, [b]chenchen0620_09@126.com, [c]962929719@qq.com

Key words: heat pump driven by steam turbine; irreversibility; optimal relation; thermal coefficient

Abstract: In this paper, a generalized irreversible heat pump driven by steam turbine cycle model was established by taking account of the heat resistances, heat leak and irreversibility due to the internal dissipation of the working substance. The heat transfer between the heat reservoir and the working substance is assumed to obey the linear (Newtonian) heat transfer law, and the overall heat transfer surface area of the assumed to be constant. The fundamental optimal relations between the heat load, the thermal coefficient of the system and the temperature difference of the evaporator are obtained. Moreover, the effects of the cycle parameters on the characteristics of the cycle are studied by numerical example. The results obtained herein have realistic significance and may provide some theoretical guidance for the performance improvements and optimizations of heat pumps driven by steam turbine.

Introduction

In recent years, the finite time thermodynamics has been developing rapidly, and many significant results have been obtained. Sahin and Kodal [1] have introduced a new finite time thermoeconomic performance criterion, defined as the cooling load for refrigerators and the heating load for heat pumps per unit total cost (total of investment and energy consumption costs). Based on this criterion, they investigated the economic design conditions of single stage and two stage vapor compression refrigerators and heat pumps [1–2].Some researchers established four-heat-reservoir absorption heat pump cycle with the loss of heat resistance and internal irreversibility [3], and with the loss of heat resistance, heat leakage and internal irreversibility [4,5]. In the studies of the internal irreversibility, almost just one internal irreversibility parameter is introduced, which could not distinguish the generator–absorber assembly and evaporator–condenser assembly.

Nomenclature

Q	heat transfer rate (kW)	A	heat transfer area (m^2)
k	heat transfer coefficient (kW/m^2)	T_H	the temperature of the steam input (K)
T_L	the temperature of the steam output (K)	T_c	the temperature of the condenser (K)
T_e	the temperature of the evaporator (K)	Q_L	rate of heat leak(kW)
K_L	heat leak coefficient(kW K)	a	heat exchange ratio
I	irreversibility factor		
Greek symbols			
τ	cycle period	π	the heat load(kW)
Ψ	the thermal coefficient		

In this paper, a generalized irreversible heat pump driven by steam turbine cycle model is established by taking account of the heat resistances, heat leak and irreversibility due to the internal dissipation of the working substance. At the condition of the total heat transfer area is constant, the fundamental optimal relations between the heating loads, the coefficient of the system's performance and the temperature difference of the evaporator are obtained.

System Model

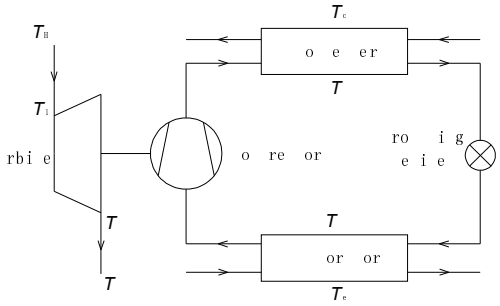

Fig.1 Schematic of heat pump system driven by turbine

It can be seen from Fig.1, the heat pump system driven by turbine is composed of two parts, the power cycle and the compression heat pump cycle, including the steam turbine, the compressor, the evaporator, the condenser and the throttling device. The temperature of the heat source and the working media in the cycle are shown in Fig.1.

According to the law of heat transfer, we can obtain:

$$Q_1 = k_1 A_1 (T_H - T_1)\tau, Q_2 = k_2 A_2 (T_2 - T_L)\tau, Q_3 = k_3 A_3 (T_3 - T_c)\tau, Q_4 = k_4 A_4 (T_e - T_4)\tau \quad (1)$$

Q_1, Q_2, Q_3 and Q_4 are the heat exchange on the high temperature side of the steam turbine, the low temperature side of the steam turbine, and in the condenser and the evaporator. k_1, k_2, k_3 and k_4 are the heat transfer coefficient and A_1, A_2, A_3 and A_4 are the heat transfer area respectively.

τ is the cycle time. According to the first law of the thermodynamics:

$$Q_1 + Q_4 = Q_2 + Q_3 \quad (2)$$

Introduce total heat transfer area A, which is determined by the following formula, and remains constant:

$$A = A_1 + A_2 + A_3 + A_4 \quad (3)$$

Define a as the heat exchange ratio between the condenser and the absorber,

$$a = Q_3 / Q_2 \quad (4)$$

Assume the thermal heat leakage between the space and the environment following the linear heat transfer law, the heat leakage can be expressed as:

$$Q_L = K_L (T_L - T_e + T_c - T_e)\tau \quad (5)$$

According to the second law of the thermodynamics, introduce the irreversible factor I, which is expressed as:

$$I = \frac{Q_2 / T_2 + Q / T}{Q_1 / T_1 + Q_4 / T_4} \geq 1 \quad (6)$$

When I=1, the cycle is reversible; I > 1, the cycle is irreversible.

Performance optimization

According to Eq.(6), we can obtain that

$$\frac{Q_1}{T_1} + \frac{Q_4}{T_4} - \frac{Q_2}{IT_2} - \frac{Q_3}{IT_3} = 0 \quad (7)$$

According to the definition of the heat load:

$$\pi=\frac{Q_3-Q_L}{\tau}=aA(\frac{(IT_2)^{-1}+a(IT_3)^{-1}-(1+a)T_4^{-1}}{k_1(T_1^{-1}-T_4^{-1})(T_H-T_1)}+\frac{1}{k_2(T_2-T_L)}+\frac{a}{k_3(T_3-T_c)}+\frac{(1+a)T_1^{-1}-(IT_2)^{-1}-a(IT_3)^{-1}}{k_4(T_1^{-1}-T_4^{-1})(T_e-T_4)})^{-1}-q_L \quad (8)$$

where $q_L=Q_L/\tau$.

The thermal coefficient of the system can be expressed as:

$$\psi=\frac{Q_1-Q_2}{Q_1}\cdot\frac{Q_3-Q_L}{Q_3-Q_4}=\frac{Q_3-Q_L}{Q_1}=\frac{Q_3}{Q_1}(1-\frac{Q_L}{Q_3})=a\frac{T_1^{-1}-T_4^{-1}}{(IT_2)^{-1}+a(IT_3)^{-1}-(1+a)T_4^{-1}}(1-\frac{q_L}{q_L+\pi}) \quad (9)$$

For the sake of convenience, let $T_L^*=IT_L$, $T_c^*=IT_c$, $k_2^*=k_2/I$, $k_3^*=k_3/I$, $x=T_4/T_1$, $y=T_4/IT_2$, $z=T_4/IT_3$, the heat load and the thermal coefficient can be written as:

$$\pi=aA(\frac{1-y+a(1-z)}{k_1(1-x)(T_H-T_4x^{-1})}+\frac{1}{k_2^*(T_4y^{-1}-T_L^*)}+\frac{a}{k_3^*(T_4z^{-1}-T_c^*)}+\frac{y-x+a(z-x)}{k_4(1-x)(T_e-T_4)})^{-1}-q_L \quad (10)$$

and

$$\psi=\frac{a(1-x)}{1-y+a(1-z)}(1-\frac{q_L}{q_L+\pi}) \quad (11)$$

Lagrangian functions are introduced:

$$L_1=\psi+\lambda_1\pi \quad , \quad L_2=\pi+\lambda_2\psi \quad (12)$$

Where λ_1 and λ_2 are two Lagrangian coefficients. Combining Eq. (12) and the extremal conditions $\partial L_1/\partial x=0$, $\partial L_1/\partial y=0$, $\partial L_1/\partial z=0$, $\partial L_1/\partial T_4=0$, $\partial L_2/\partial x=0$, $\partial L_2/\partial y=0$, $\partial L_2/\partial z=0$, $\partial L_2/\partial T_4=0$ yields a general relation

$$\sqrt{k_1}(T_Hx-T_4)=\sqrt{k_2^*}(T_4-T_L^*y)=\sqrt{k_3^*}(T_4-T_c^*z)=\sqrt{k_4}(T_e-T_4) \quad (13)$$

Let $u=T_e-T_4$,the thermal coefficient and the heat load after optimization are:

$$\pi=ak_4(b_1(T_eT_H^{-1}-(1-b_1)T_H^{-1}u)(1+a-T_eT_L^{*-1}-aT_eT_c^{*-1}+((1+b_2)T_L^{*-1}+a(1+b_3)T_c^{*-1})u)/((1-T_eT_H^{-1}+(1-b_1)T_H^{-1}u)u)+b_2(T_eT_L^{*-1}-(1+b_2)T_L^{*-1}u)/u+ab_3(T_eT_c^{*-1}-(1+b_3)T_c^{*-1}u)/u+(T_eT_L^{*-1}+aT_eT_c^{*-1}-(1+a)T_eT_H^{-1}-((1+b_2)T_L^{*-1}+a(1+b_3)T_c^{*-1}-(1+a)(1-b_1)T_H^{-1})u)/((1-T_eT_H^{-1}+(1-b_1)T_H^{-1}u)u))^{-1}-q_L$$

and

$$\psi=\frac{a(1-T_eT_H^{-1}+(1-b_1)T_H^{-1}u)}{1+a-T_eT_L^{*-1}-aT_eT_c^{*-1}+((1+b_2)T_L^{*-1}+a(1+b_3)T_c^{*-1})u}(1-\frac{q_L}{q_L+\pi}) \quad (14)$$

where $b_1=\sqrt{k_4/k_1}$, $b_2=\sqrt{k_4/k_2^*}$, $b_3=\sqrt{k_4/k_3^*}$.

Results and discussion

Numerical example is introduced to analyze the system. Conditions of the example are listed in Tab.1.

Tab.1 Parameters of the numerical example

k_i (kW/m^2)	A （m^2）	T_H(K)	T_I(K)	T_e(K)	T_c(K)
0.5	10	623	534	293	333

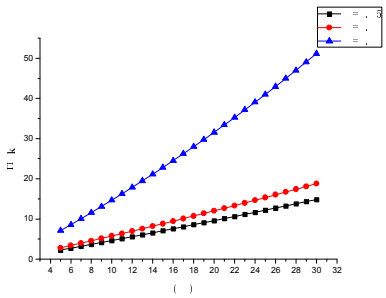

Fig.2 The effect of I on π

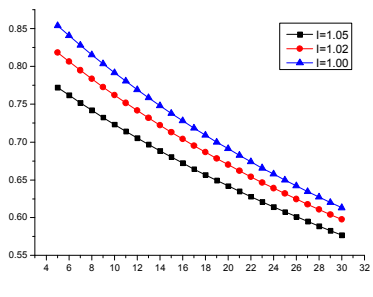

Fig.3 The effect of I on ψ

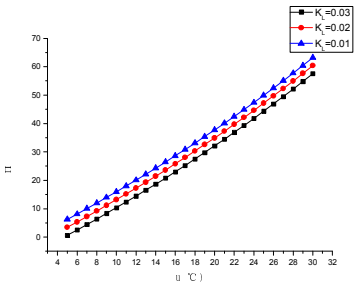

Fig.4 The effect of K_L on π

The Fig.2 and Fig.3 are the effect of I on π and ψ with the different of u when K_L=0, a=1. The heat load increases and the thermal coefficient decrease with the growth of u. When u is constant, the greater the irreversibility, the smaller the heat load and the thermal coefficient. As the temperature difference rises from 5℃ to 30℃(I=1), the heat load increase 6.21 times and the thermal coefficient decrease 28.22%, if I=1.05, the heat load increase 5.52 times and the thermal coefficient decrease 25.29%. When I = 1.05, compared to I=1.00, the heat load and the thermal coefficient decrease 69.34% and 7.39% at the temperature difference of 18℃.

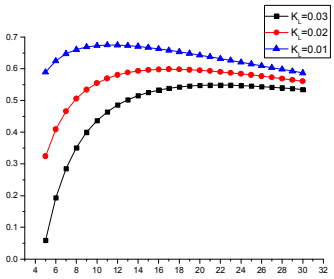

Fig.5 The effect of K_L on ψ

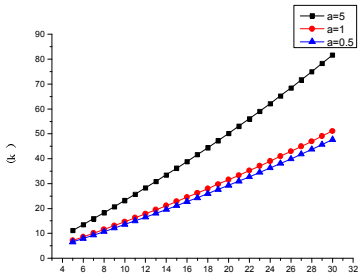

Fig.6 The effect of a on π

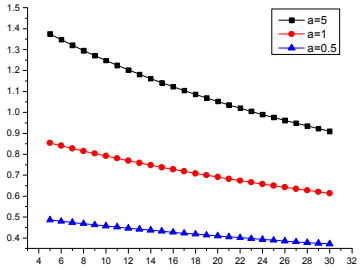

Fig.7 The effect of a on ψ

It can be seen from Fig.4, the heat load increases with the growth of u. When u is constant, the greater the heat leak, the smaller the heat load. As the temperature difference rises from 5℃ to 30℃(I=1,a=1), the heat load increase 16.56 times, when K_L=0.02. When the heat leak increases from 0.01 to 0.03, the heat load decreased 16.98% at the temperature difference of 18℃. The Fig.5 shows the thermal coefficient increases first then decreases with the increase of temperature difference in the presence of heat leakage. The thermal coefficient achieves maximum at u=15℃, u=17℃ and u=22℃, corresponding to K_L=0.01, K_L=0.02 and K_L=0.03, the maximum values are 0.667,0.599 and 0.549 respectively. The Fig.6 and Fig.7 show the heat load and the thermal coefficient increases with the growth of a(K_L=0，I=1). When the temperature difference rises from 5℃ to 30℃(a=5), the heat load increase 86.28% and the thermal coefficient decrease33.84%. When a= 5, compared to a=0.5, the heat load and the thermal coefficient increase 41.63% and 159.57% at the temperature difference of 18℃.

Conclusion

A generalized irreversible heat pump driven by steam turbine cycle model is established by taking account of the heat resistances, heat leak and irreversibility due to the internal dissipation of the working substance. Numerical example is introduced to analyze the effect of the cycle parameters on the heat load and the thermal coefficient. The heat load increases and the thermal coefficient decrease with the growth of u. The thermal coefficient increases first then decreases with the increase of temperature difference in the presence of heat leakage. The heat load and the thermal coefficient increases with the growth of a. These conclusions can provide some theoretical guidance for the improvement and the optimization of the heat pump driven by steam turbine.

References:

[1] Sahin B, Kodal A. Energ Convers Manage 1999;40:951–60.

[2] Sahin B, Kodal A, Koyun A. Energ Convers Manage 2001;42:451–65.

[3] Yasin Ust. Performance analysis and optimization of irreversible air refrigeration cycles based on ecological coefficient of performance criterion. Applied Thermal Engineering. 2009 (29): 47-55.

[4] Brice Le Lostec,Jocelyn Millette, Nicolas Galanis. Finite time thermodynamics study and exergetic analysis of ammoniaewater absorption systems. International Journal of Thermal Sciences.2010 (49):1264–1276.

[5] Paiguy Armand Ngouateu Wouagfack,Re´ne´ Tchinda. The new thermo-ecological performance optimization of an irreversible three-heat-source absorption heat pump. International Journal of Refrigeration.2012 (35):79–87.

Advanced Materials Research Vols. 960-961 (2014) pp 503-509

doi:10.4028/www.scientific.net/AMR.960-961.503

China's Thermal Power Generation Forecasting Based on Generalized Weng Model

Xibo Wang[1, a], Yalin Lei[1,b] and Min Yao[2,c]

[1] School of Humanities and Economic Management, China University of Geosciences, Beijing 100083, China

[2] Dept of Mechanical and Environmental Protection, Shandong Electric Power Consulting Institute Corp, Ltd, China

[a] wangxibo406@gmail.com, [b] leiyalin@cugb.edu.cn, [c] yaomin_@163.com

Keywords: thermal power generation; generalized Weng model; electrical energy

Abstract. Since the 21st century, China's power industry has been developing very quickly, and the generated electrical energy has been growing rapidly. Although nuclear power, wind power, solar power generations have been increased, thermal power generation still accounts for more than 80% of the total generating capacity. Thermal power provides an important material basis for the development of the national economy. Therefore, the prediction research on China's thermal power generation trend is becoming a topic of great interest.

The fuel of thermal power generation-coal, is an exhaustible resource. Due to the exhaustible constraints the fuel, thermal power generation trend is bound to show a similar trend bell curve as the coal production trend, similar to a bell-shaped curve—a gradual increase to maximum output and then a short peak and a gradual decline. To get more accurate results of future thermal power generation, this paper applies the generalized Weng model to forecast China's thermal power generation peak and trend.

The result indicted that the peak of China's thermal power generation appears in 2022 with generating capacity of 51,702 TWh. The generating capacity of thermal power will decrease gradually after 2022. Based on the results, the paper proposes some policy recommendations for the sustainable development of China's electrical energy. China should decrease the percentage of the capacity which comes from thermal generation and reduce the dependence on thermal power generation. Moreover, nuclear, hydraulic, wind and solar power should be developed before the thermal power generation peak.

Introduction

The electricity industry, which is gaining more attention from various countries, has become the most important factor impacting the development of socioeconomic status worldwide. China's electricity industry has been developing very quickly, and the generated electricity energy has been growing fast with the rapid development of economy. Although nuclear power, wind power, solar power generations have increased in recent year, thermal power generation is still considered as the most important source of China. Since 1949, the average of annul increase rate of electricity generation has been 12.5%, similar to the annul average increase rate of thermal power generation[1].By the end of 2012, China's total electricity power generation had been 49,377 TWh and more than 80% of power generation was thermal (see Fig. 2) [1]. Therefore, accurate thermal power generation forecasting can provide a reliable basis for a reasonable plan for an adjustment of power policy and structures to avoid electricity shortages.

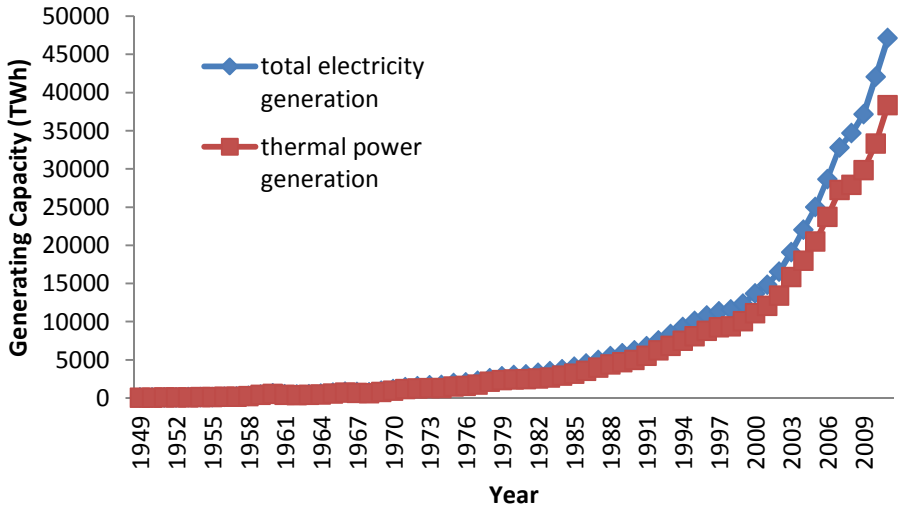

Fig. 1 China's historical Electricity generating capacity

Source:[1]

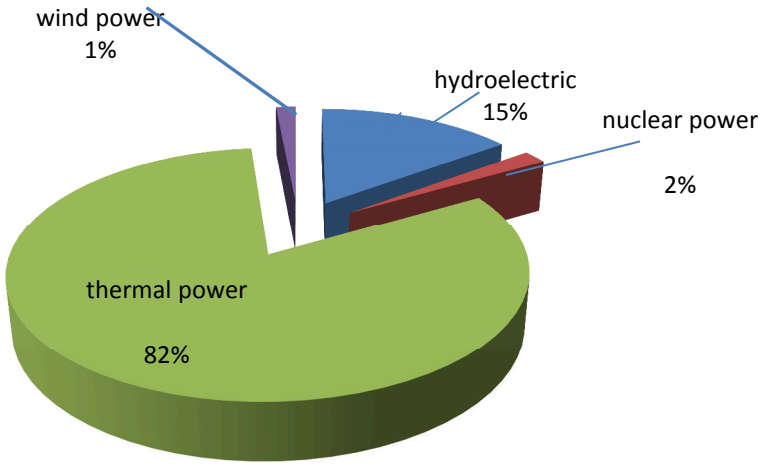

Fig. 2 The Source of China's Power Generation

Source: [1]

Different from the nuclear, wind and solar power generation, the major energy source of thermal power is coal, an exhaustible resource. Based on exhaustible property of the thermal power generation fuel, China's thermal power generation can also be seen as a kind of exhaustible resource. As most exhaustible resource production levels have already reached peaks or are approaching to peak levels, regardless of technological advances and price rising, China's thermal power generation peak which is based on coal-fired is inevitable. It is difficult to deny that a finite resource must at some point reach a maximum in extraction rate, after which production will decline [2].

Based on the production characteristics of nonrenewable resources, there are a number of commonly used forecasting techniques. Many scholars have adopted generalized Weng model (a typical bell curve model) which was first proposed by Chen [3] based on Weng model. Scholars have used the generalized Weng model to predict exhaustible resource supply trend and peak in China and obtained reasonable results [4-7].

The previous scholars have done a lot of research contributions by using Generalized Weng model.And the most of their study field is predictingthe peak production of oil and natural gas. Wang et.al,.[8] did some research on the production of China's natural gas by using Hubbert model and Generalized Weng mode and indicted that the gap between gas production and demand will reach 210.4 bcm by 2020.Feng et.al,.[9] did some research on the production of China's and world's oil by using Hubbert model and Generalized Weng model.Tang et al,. [10] researched on the peak production of oil in the North America, Central and South America, Europe, Middle East, Africa and Asia Pacific areas base on Generalized Weng model. And they pointed out hat the future oil pattern would become increasingly dependent on the Middle East, while Asia-Pacific region would become the most serious inbalanced between oil supply and demand. Feng Lianyong et al. [11] summarized the differences between domestic and foreign methods for predictingthe peak production of oil. As it can be seen in the development of predictive models, they considered that in foreign countries the methods are developed from a single-cycle model to a multi-cycle model, focusing on the vertical development of models; while in China the methods are developed from the Weng model to a series of predictive models, focusing on horizontal development of models. The study used the Generalized Weng model to predict the peak of world oil production, and indicated that the peak time would appear in 2020. Feng Lianyong et al [12] used Hubbert model, HCZ model and Generalized Weng model to predict the peak production of China's oil, without a reasonable plan for oil production.

In view of the exhaustibility of thermal power resources and the excellent performance of generalized Weng model in the field of exhaustible resource supply forecast, this paper proposes to use generalized Weng model to predict the thermal power generation in China and tries to provide some policy recommendations based on our forecasting results.

Methodology and Data Description

Methodology

Generalized Weng model is proposed by Chen Yuanqian [4] after deriving and expanding Weng model, which is proposed by Weng Wenbo [13], a Chinese famous geophysicist and member of Chinese Academy of Sciences.

$$Q_t = at^b e^{-(\frac{t}{c})} \quad (1)$$

The parameters referred in the equation include: the model predictive parameters a,b, c, and the time periods parameter t. The forecasting parameters of Generalized Weng model calculated by binary regression method is proposed by Zhao Lin, Feng Lianyong in 2009 [14]. It is calculated as follows:

The Equation (1) take the natural logarithm of both sides

$$\ln Q = \ln a + b\ln t - t/c \quad (2)$$

Set

$$Y = \ln Q \quad (3)$$

$$X_1 = \ln t \quad (4)$$

$$X_2 = t \quad (5)$$

$$B_0 = \ln a \quad (6)$$

$$B_1 = b \quad (7)$$

$$B_2 = -1/c \quad (8)$$

So Equation (12) can be written as

$$Y = B_0 + B_1X_1 + B_2X_2 \quad (9)$$

Using multiple linear regression we can obtain B_0, B_1, B_2, and after putting them into Equation (6), (7), (8), we can obtain B_0, B_1, B_2.

Table 1 Main Equations of Generalized Weng Model

Peak model	Basic Equations	Peak Production	Peak Time
Weng's Model	$Q = at^b e^{-t/c}$ $N_R = ac^{b+1}\Gamma(b+1)$	$Q_{max} = a(bc/2.718)^b$	$t_{max} = bc$

Data Sources

The historical data of China's thermal power generation 1949-2011 is taken from the *The National Bureau of statistics of PRC* [1].

Results and Disscussion

A systematic elaboration on the generalized Weng model has been presented previously in the paper. In this section, the generalized Weng model is employed to predict the trends and peaks of China's thermal power generation.

Results

Binary regression of the data from 2002 to 2011 was run on the EViews software according to Equation (19), and the reported F-test and DW test were all satisfying. In this way, we obtained B_0=-95.13, B_1=32.19, B_2=-0.44 (See Table 2). The prediction coefficients for the generalized Weng model were obtained from Equations (6), (7) and (8): a=4.83559E-42, b=32.19, c=2.27. Then a, b and c were substituted into the model, and predictions can thus be made.

The results which are predicted by generalized Weng model indicate that China's thermal power generation peak will appear in 2021 with the peak production 51,702 TWh.

Table 2 The results of Prediction Parameters

Variable	Coefficient	Std. Error	t-Statistic	Prob.
C	-95.13257	32.29350	-2.945873	0.0215
X1	32.19198	10.53118	3.056824	0.0184
X2	-0.440172	0.180320	-2.441058	0.0447

R-squared	0.991491	Mean dependent var	10.06849
Adjusted R-squared	0.989060	S.D. dependent var	0.339170
S.E. of regression	0.035475	Akaike info criterion	-3.596655
Sum squared resid	0.008809	Schwarz criterion	-3.505879
Log likelihood	20.98327	Hannan-Quinn criter.	-3.696235
F-statistic	407.8425	Durbin-Watson stat	1.526705
Prob(F-statistic)	0.000000		

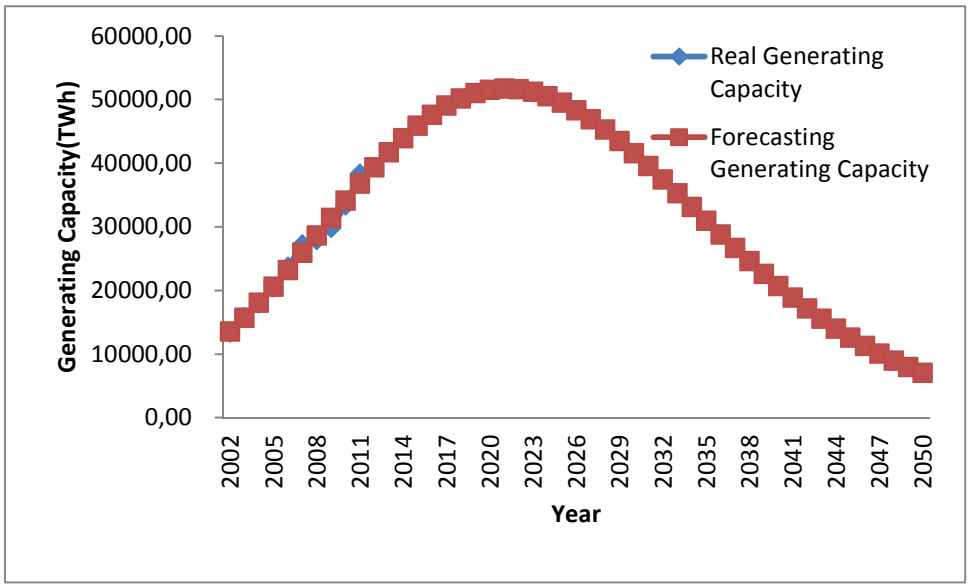

Fig. 3 China's Power Generation Forecasting

Discussion

This paper uses generalized Weng model to predict China's thermal power generation . The forecasting parameters of Generalized Weng model are calculated by binary regression method. In this paper, based on 2002-2011 China's thermal power annul generation data, we use the predictive parameter calculating method which is illustrated in last chapter to get the value of predictive parameter. The reason why we set the start year is 2002, because of the reformation of electric power system in the year of 2002. The power production and transmission are separated in the reformation. The aim of separation of power production and transmission is to break up the monopoly, to improve the efficiency, and to control the price of the electricity by impartial competition. Since then, the marketization of electric power in China is in a greater degree. Moreover, the data from market are more reliable than those from macro-control.

According to the comparison between the real generating capacity and forecasting generating capacity of thermal power from 2002 through 2011 in China, we find that the average difference rate is very small with the average difference rate of the results as less than 10%. R-squared is more than 99%. So we may judge that generalized Weng mode is considerable and suitable for China's thermal power generation forecasting.

Table 3 The Difference between Real and Forecasting Generating Capacity

Year	Real Generating Capacity	Forecasting Generating Capacity	Error
2002	13381.36	13513.39	0.99%
2003	15803.61	15708.54	0.60%
2004	17955.88	18066.94	0.62%
2005	20473.36	20567.17	0.46%
2006	23696.03	23182.53	2.17%
2007	27229.33	25881.56	4.95%
2008	27900.78	28628.79	2.61%
2009	29827.80	31385.69	5.22%
2010	33319.28	34111.63	2.38%
2011	38337.00	36765.10	4.10%

Conclusions and Recommendations

Conclusions

Electricity is indispensable energy in modern industry and society development. Thermal power generation account for about 80% of the total power generation in China. Based on the important position of China's thermal power generation in economy development, China's thermal power generation trends and peak prediction are increasingly the target of interest of researches. To achieve more accurate results, this paper applies the generalized Weng model to simulate China's thermal power generation peak and trends. Conclusions have been drawn based on the forecasting results.

(1) The generalized Weng model can be applied in the field of thermal power supply issues.

The generalized Weng model as a peak predictive model is widely used in forecasting exhaustible resource production peaks and trends. Because the coal of China's thermal power fuel is exhaustible, the thermal power in China also can be seen as an exhaustible resource. As an exhaustible resource, the curve of China's thermal power generation, a bell-shaped curve that is a gradual increase to maximum output and then a short peak and a gradual decline, is similar to other exhaustible resources. Once the output reaches the peak, regardless of efforts, thermal power generation cannot increase any more. In this study, the generalized Weng model is also used to study China's thermal power generation peaks and trends. According to the comparison between the real generating capacity and forecasting generating capacity of thermal power from 2002 to 2011 in China, we find that the average difference rate is less than 10%. We may judge from the small average difference rate that generalized Weng model is rational and suitable for China's thermal power generation forecasting.

(2) China's thermal power generation peak will appear by the year 2021.

According to the simulation, the peak of thermal power generation in China will occur in 2021 with peak generating capacity of approximately 51,702 TWh. Chinese thermal power generation will grow 7% annually before peaking and decrease afterwards.

Policy Recommendations

Based on the conclusions above, some policy suggestions are proposed as follow.

With the continuous development of China's macro-economy and urbanization, the demanding for electricity will rise. Nowadays, thermal power provides more than 80% China's electricity supply. However, the forecasting result indicates that China's thermal power generation will grow by 7% annually before peaking and decrease afterwards. If the electricity supply structure is still dominated by thermal power, then the gap between electricity supply and demand will certainly appear after peak generating capacity. The electricity shortage that may occur in the near future is certainly slowed down by China's economic and social development. Based on the consideration above, we suggest China's government, two major power grid companies and five major power generation companies adjust the structure of power supply as soon as possible to reduce the probability of electricity gap between supply and demand after thermal power generating peak.

Acknowledgement

The authors express thanks for the support from the National Natural Science Foundation of China under Grant No.71173200 and the support from the Development and Research Center of China Geological Survey under Grant No.1212011220302.

References

[1]. Yearbook C S. National Bureau of statistics of China[J]. China Statistical Yearbook, 2012.
[2]. Brecha R J. (2013) Ten reasons to take peak oil seriously[J]. Sustainability, 5(2): 664-694.
[3]. Chen, Y.Q., 1996. Derivation and application of Weng's Predication model. Natural Gas Industry 16 (2), 22–26 (in Chinese)
[4]. CHEN Y Q and HU J G. Weng's model for review and the new derived. China's Offshore Oil and Gas (Geology). 1996. 10 (05): 317-324 (in Chinese).
[5]. LvM Y, Shi H F, Zheng N and Zhou G Y. Coalbed Methane Production Forecast Method Based on Generalized Weng's Model. China Coal bed Methane. 2012, 6: 010 (in Chinese).
[6]. Tang X, Feng L, Zhao L. Prediction and analysis of world oil supply Pattern based on generalized Weng'smodel[J]. Resources Science,2009, 31(2): 238e42.
[7]. Qiang S U N, Bing D, Limei M. Application of generalized Weng's model and rayleigh model in recoverable reserves. Journal of Oil.1995. 16 (1): 79-86 (in Chinese).
[8]. Wang J, Feng L, Tverberg G E. An analysis of China's coal supply and its impact on China's future economic growth[J]. Energy Policy, 2013.
[9]. Feng L, Li J, Pang X. China's oil reserve forecast and analysis based on peak oil models[J]. Energy Policy, 2008, 36(11): 4149-4153.
[10]. Tang Xu, Feng Lianyong, Zhao Lin. Prediction and Analysis of world Oil Supply Pattern based on Generalized Weng's Model[J]. Resources Science, 2009, 31(2).(in Chinese)
[11]. Feng Lianyong, Zhao Lin, Zhao Qingfei, Wang Zhipeng. Model of Peak Oil Theory and Forecast of World Oil Peak[J]. ACTA PETROL EI SINICA, 2006, 27(5).
[12]. Tang X, Feng L, Zhao L. Prediction and analysis of world oil supply Pattern based on generalized Weng'smodel[J]. Resources Science,2009, 31(2): 238e42.
[13]. Weng, W.B., 1984. The Foundation of the Forecasting Theory. Published by Petroleum Industry Press in Beijing, China (in Chinese).
[14]. Zhao Lin, Feng Lianyong, Lu Xiangan, Tong Xiaoguang. Comparison of Two Methods for Generalized Weng Model[J]. XIJIANG PETROLEUM GEOLOGY, 2009, 30(5): 658-660.

CHAPTER 4:

Fluid and Air Engineering and Machinery

Advanced Materials Research Vols. 960-961 (2014) pp 513-516

doi:10.4028/www.scientific.net/AMR.960-961.513

Experiment Study of Dredger Fill Using Different Consolidation Methods

Huan Yan[1, a], Qing Wang[1, b], Dong-yan Sun[1, c]

[1] College of Construction Engineering, Jilin University, Changchun 130026, China

[a]parents456@126.com, [b]wangqing@jlu.edu.cn, [c] 865320605@qq.com

Keywords: Dredger fill; Vacuum preloading consolidation; Self-weight consolidation

Abstract. At present, there are many methods of the dredger fill foundation treatment, in which the most widely used application of vacuum preloading method. The dredger fill for test was taken from the Tianjin Binhai new area center fishing port area, separately carried on the self-weight consolidation and vacuum preloading consolidation. Through the indoor test of soil test physical and chemical parameters, comparing the moisture content, soluble salt amount and component, caption exchange capacity, PH value and physical and chemical index. The results show that: the clay content of soil sample in the central fishing port area is higher, degree of aggregation is high, liquid limit is less than 60%, Ip is more than 10, belongs to the low liquid limit clay. Relative self-weight consolidation, soluble salt content of soil samples after vacuum preloading drainage treatment are low, but the particle size composition change less. It is said that parts of salt in the soil samples discharge with water discharge in vacuum preloading process, vacuum preloading effect is better.
Introduction
All manuscripts must be in English, also the table and figure texts; otherwise we cannot publish your paper.

Introduction

Because the developing demand of coastal cities and the scale of the project construction, the requirements for land resource are increasingly urgent, it is become one of the effective ways to relieve the tense of land resources using silt dredged out for sea reclamation. In the process of sea reclamation in Tianjin region, sand source is nervous, so take the silt of offshore as blow packing. However, reclaimed materials not only include sandy soil, also include cohesive soil. Its source difference is one of the main reasons which influence the project treatment [1]. The soil also have characteristics of the short deposit time, high water content, high compressibility and low strength, therefore strengthening the reclaimed land base has become inevitable difficult technical problems [2]. A large number of engineering practices found that: the reinforcement of dredger fill site still exist questions that the curing effect is not uniform, engineering geological properties are complex and post-construction settlement is large [3].

Based on these, take the dredger fill in the Center Fishing Port, Binhai District, Tianjin as the object, and make a general analysis about the grain size composition, physical chemistry properties of the dredger fill via different reinforcement methods, it also can provide a sharp mental basis for furthering study on the reinforcement mechanism of the dredger fill.

Testing program

Soil samples for testing were taken from two holes at Center Fishing Port, Tianjin, one of which was taken the vacuum preloading drainage treatment and the other was taken gravity consolidation. The depth of the drilled hole was 60 m, because the depth of the drainage board was about 12 m, so take the soil samples of this depth for analysis. The samples after the vacuum preloading drainage were labeled ZY01 - ZY04, and the others are labeled ZK11 - ZK14, with the depth of 4 m, 7 m, 10 m and 12 m, then tested the grain size composition, physical chemistry properties of the two groups of samples separately. By comparing the testing results, analyzing the changes of the properties in the dredger fill under different reinforcing conditions, so as to provide some solid basis for the study of the reinforcing mechanism.

Granulometric

The granularmetric measurement adopts the method of densimeter B and refers to the specification requirements [4]. Before the test, the samples need to be washed if the soluble salt content is greater than 5‰. Through the cumulative curve method, the variation of granularity ingredients can be found. And the testing of the total content of the soluble salt in the Center Fishing Port turns out that the content are all greater than 5‰, so the samples are totally to be washed. And the results are showed in Fig.1: the particle distribution curve, where the samples are within the dispersant, is obviously above the curve where those without the dispersant, and it turns out that the soil particles are affected by the dispersant greatly. Because of some clay particles which have flocculation to form greater particles in the soil, we call these "false particulates". After adding the dispersant into the samples, the false particulates will be restored to the normal particles and finally disappear. Due to the more false particulates in the soil which are assumed as hydrotropism in the engineering and its value is relatively lower compared with the granularmetric composition, the mineral composition and the organic matter, the soil in the study area can be solidified to be ideal foundation via the gravity consolidation method in which the drainage consolidation (vacuum preloading) can be in a very ideal state within a very short time. Therefore, this method is feasible in Tianjin Area.

The soil samples are mainly classified referred to the DT-92 Regulations of the Ministry of Geology, and the results of the experiment are shown in Table 1 (due to the fine-grained soil used in the testing, the content whose grain size lower than 0.25mm is listed. It can be seen that: the uniformity coefficients of the soil are totally higher than 5, which turns out that the particle grading composition is good [5]. And the distribution and composition of the soil reflect that the possibility of the pores decreasing after being compacted is greater. Because the geological properties in the soil engineering are the overall performance of the various fraction properties, the fraction which has more content will be in charge.

Table 1 Granum analysis data

Samples	Content of various fractions (%)			d60 / mm	d10 / mm	d60 / d10	Name
	0.075 ~ 0.25 mm	0.005 ~ 0.075 mm	< 0.005 mm				
ZY01	0.891	44.841	45.351	0.015	0.003	5	Powder light clay
ZY02	0.891	86.196	10.65	0.048	0.005	10	Powder light sub-clay
ZY03	0.89	39.966	49.551	0.05	0.004	11.4	Powder light clay
ZY04	1.579	80.816	17.209	0.051	0.002	24.3	Powder medium clay
ZY11	0.863	57.922	41.16	0.012	0.0024	5	Powder light clay
ZY12	0.585	74.861	24.473	0.032	0.003	10.7	Powder heavy clay
ZY13	10.643	83.939	5.359	0.052	0.009	5.8	silt
ZY14	7.054	51.66	41.16	0.029	0.0024	12.1	Powder light clay

Chemical composition

The chemical composition of the soil refers to the chemical elements, compound types and the relative content in the solid phase, liquid phase and the vapor phase in the soil [5]. The content of the soluble salts in the soil is high, and these salts are solid when the soil is dry which play the role of cementing soil particles; Containing more moisture in the soil, the soluble salts dissolve into ions, and interact with the charged soil particles, and meantime affect the engineering geological properties of the soil [6,7].

Ion exchange effect occurs between the anti-ion layer and the ions with the same symbol in the solution, which are totally called exchangeable ion. Because the ion composition determines the thickness of the thin film of water on the surface of the clay particles, and the film determines the degree of the consolidation of the soil drainage, the exchange capacity of the positive ion affect the efficiency of the consolidation and also the engineering geological properties.

In this experiment, mainly take the test of the amount of the soluble salts, PH, the exchange capacity of the ion. The specific results are shown in Table 3.

From the Table 3, the content of sodium and chloride is the highest in the vacuum preloading soil in the Center Fishing Port, and magnesium and sulfate higher while the others lowest. Generally speaking, the content of the soluble salts, chloride salt and the sodium salt decrease with the depth of the samples increasing, which is due to silt and sediment on the bottom of the ocean on the casing body, therefore, the content of the shallow soluble is higher; The PH of the sample consolidated via vacuum preloading is 6.83-6.97 with the soil acidic while the PH of that consolidated via gravity is 7.43-7.65 with the soil weak base.

Table 2 Chemical composition test results

Name	Testing methods	ZY01	ZY02	ZY03	ZY04	ZY11	ZY12	ZY13	ZY14
Soluble salt (‰)	Steam seasoning	15.52	12.12	8.51	7.22	31.70	21.94	10.29	9.28
Chloridion ion (‰)	Silver nitrate titration method	7.03	5.72	4.09	3.77	15.37	11.25	4.93	5.08
Bicarbonate radical (‰)	Hydrochloric acid titration method	0.27	0.18	0.14	0.12	0.31	0.37	0.43	0.55
Calcium ion (‰)	EDTA	0.13	0.10	0.07	0.08	0.15	0.12	0.13	0.16
Calcium and magnesium (‰)	EDTA	0.85	0.77	0.23	0.27	1.38	1.13	0.61	0.54
Sulfate radical (‰)	EDTA	2.57	2.59	2.13	1.33	2.77	2.71	2.50	2.65
Potassium ion (‰)	flame photometry	0.67	0.52	0.42	0.49	0.70	0.56	0.55	0.50
Sodion ion (‰)	flame photometry	6.84	5.52	5.04	5.99	7.07	5.87	5.75	6.15
PH	electrometric methods	6.93	6.97	6.83	6.83	7.46	7.43	7.65	7.64
CEC (mmol/100g)	Ammonium acetate leaching method	6.09	3.79	1.88	4.81	6.25	4.32	2.56	5.71

Fig.2 shows the contrast of the content of various ions of the two consolidation methods: whether the total amount or the respective component, the content of the soil via vacuum preloading drainage processing is lower, which means the vacuum preloading method is better for consolidation.

Physical properties

The physical properties of soil is properties of three-phase material that is shown in the mutual proportional relationship between the mass and volume or the mutual effect of Solid-liquid two-phase, That is the basic physical properties and hydrological properties. Based on soil test specification, Dry and wet conditions， consistency and plasticity of dredger fill that have Different consolidation modes are tested. The results are shown in Table 4. And it shows that: the moisture content of dredger fill that have the same consolidation mode decreases with increasing depth. The moisture of dredger fill that has the vacuum preloading drainage processing is lower than that is gravity consolidation. Eight groups of soil's plasticity index greater than 10, which are divided into low liquid limit clay according to plasticity chart. That can't be contrasted because different consolidation modes don't affect granulometric composition of dredger fill. Table 4 basic physical properties

Table 3 Physical property indexes

Samples	Moisture content	Liquid limit	Plastic limit	liquidity index	Plasticity index（%）	Designation
ZY01	0.347	0.490	0.238	0.432	25.2	Low liquid limit clay
ZY02	0.259	0.398	0.150	0.439	24.8	Low liquid limit clay
ZY03	0.252	0.268	0.164	0.846	10.4	Low liquid limit clay
ZY04	0.251	0.274	0.164	0.790	11.0	Low liquid limit clay
ZY11	0.371	0.429	0.230	0.497	19.9	Low liquid limit clay
ZY12	0.314	0.330	0.180	1.066	15.0	Low liquid limit clay
ZY13	0.239	0.290	0.142	1.104	14.8	Low liquid limit clay
ZY14	0.290	0.338	0.195	1.085	14.3	Low liquid limit clay

Conclusion

(1) Dredger fill in the areas of central fishing port of Tianjin is mainly cohesive soil. Due to the flocculation, a large number of cosmids get together and form "fake silt", a large number of "fake silt" show hydrophobicity in engineering, which is very low. Therefore, the soil in study area reaches ideal foundation by gravity consolidation. But it can reach ideal foundation by vacuum preloading in short time.

(3) Content of disguise salt is high in the areas of central fishing port of Tianjin and greater than 5 ‰ on average. Content of sodium salt and chloride salt is huge, magnesium salt and sulfate followed by. The single approach soluble salt content is decreasing with increasing depth, because the covering soil is silt and sediment of the bottom of the ocean. Comparing the content of the various ions in the two reinforcement manner, Soil samples of the vacuum preloading drainage processing is higher than soil samples of gravity consolidation processing. A part of soluble salt in the soil samples discharge along with water in the vacuum preloading process. This fully illustrated that reinforcement effect of vacuum Preload process is better than gravity consolidation drainage process.

(4) It can be seen from the plastically Figure, Selected soil samples are low liquid limit clay. Denominating the soil only through granularity can’t reflect engineering geological properties of dredger fill, and result of Joint use of the plasticity index and liquid limit (plastically Figure) is more accurate.

Therefore, it can be known that vacuum Preload process can shorten the consolidation time comparing with gravity consolidation drainage process, through researching physical and chemical properties of dredger fill in the areas of central fishing port of Tianjin. The researches of the physical and chemical properties provide the necessary foundation for the research of Consolidation.

Reference

[1] Hang Xuan-jiang. Large circumferences of the land reclamation dredger fill base processing technology principle and application [M]. Beijing: China building industry press. 2009, 3.

[2] Yan Shu-wang, Liu Ke-jin, et al. Study of creep properties of soft clay in Tianjin Binhai New Area and no-yield-surface constitutive model [J]. Rock and Soil Mechanics. 2010, 31 (5): 1431-1436.

[3] Yang Fu-lin, Zhang Zhi-xian. Effect analysis of surface hydraulic soil′s reinforcement by vacuum preloading method in Nansha [J]. Port & Waterway Engineering. 2009 (3): 132-135.

[4] Ministry of water resources of the People's Republic of China. GB/T 50123-1999 The soil test method standard[S].Beijing: China building industry press, 1999

[5] Tang Da-xiong, Wang Qing, Zhang Wen-shu, et al. Engineering geotechnics [M]. Beijing: Geological Publishing House. 1999.

[6] Song Jing. Laboratory Simulation Test and PFC3D numerical analysis of high clay dredger fill in the consolidation process of step vacuum preloading [D].Chang Chun: Jilin university, 2011

[7] Liu Ying, Wang Qing, Xiao Shu-fang. The comparative researches on fundamental properties of dredger fill in different areas [J]. Geotechnical Engineering Technique，2003 (4): 197-200.

Advanced Materials Research Vols. 960-961 (2014) pp 517-522

doi:10.4028/www.scientific.net/AMR.960-961.517

Numerical Analysis of Welding in Fillet Weld for High-pressure Pipeline In-service

Zhang Lei[1,2,3,a], Zhang Jinzhou[4,b], Li Wenchun[4,c]

[1] Chemical Engineering Institute, Xuzhou College of Industrial Technology, Xuzhou 221140, China.

[2] JIANGSU JINMEI HENGSHENG Chemicals Co.Ltd., Xuzhou 221400, China.

[3] China University of Mining and Technology, Xuzhou 221000, China.

[4]College of Mechanical Engineering, Yangtze University, Jingzhou 434023, China.

[a]89202974@qq.com.

[b]87221914@qq.com,ctsdxyc@163.com.

[c]1280076717@qq.com.

Key Words: in-service welding, Software simulation, heat input, medium

Abstract: With the numerous applications of high-pressure pipeline, it is very important to simulate the in-service welding of the pipeline.The flow state of the medium in the pipeline can be analyzed, the temperature field and the stress field also can be simulated by applying sysweld software. The medium flow can reduce the welding residual stress and reduce welding stress range during in-service welding. Meanwhile, with the increase of flow rate of the medium, the maximum temperature of inner wall drops and the maximum weld residual stress increases by a slow growth. At the same time, the highest temperature of pipe wall increases rapidly with the increase of heat input, whereas the maximum residual stress of welded joint decreases by a slow trend.

Introduction

A type of high-pressure pipeline was used to transport the solid wastes(wet-ash) in JIANGSU JINMEI HENGSHENG Chemicals Co.Ltd. In order to guarantee the safe operation of the pipeline, we need to repair local corrosion of pipeline in-service. Obviously, the technology can ensure the continuity of the operation of the pipeline. Meanwhile, the repair time can be short. As a result the technology has a huge economic efficiency and broad application prospects. But because of the dangers of pipeline transport medium, guaranteeing the quality of welding in-service should be a priority. And numerical simulation of pipeline welding in-service is one of the necessities to ensure the welding quality[1-3].

Numerical analysis for fillet welding of transmission pipeline in-service

1.1 Establishment of the geometric model

Casing repair is the main method of pressure pipeline welding repair in service. This article uses the casing repair technology to illustrate, as shown in fig.1.

In the study, fillet welds of casing repairs is simulated, using pipe model symmetry build one-second when welding fillet welds, weld mesh refinement, other parts of mesh over the thick.

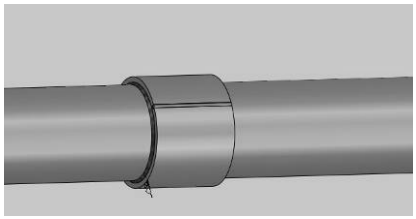

Fig.1 The diagram of Casing repair welded joints

The study is only the simulating of the fillet weld for casing repair, taking advantage of the symmetry of 1/2 fillet weld model for pipe welding. Refining the weld grid, and the rest of the meshing is coarser[4]. Its mesh generation of two-dimensional and three-dimensional model section is shown in Fig.2.

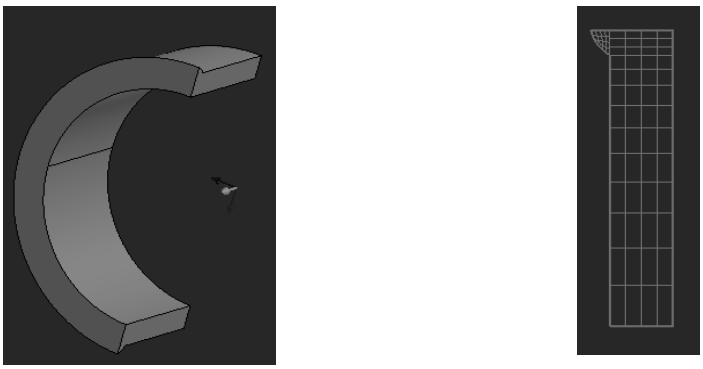

(a) Three dimensional model **(b) Two-dimensional meshing**

Fig.2 Weld model and meshing

1.2 Thermo-physical properties and mechanical properties of pipeline steel

The material of this simulation is X70 pipeline steel, more details about material performance parameter refer to references [5].

1.3 Welding heat source model

In terms of manual arc welding, the authors make use of double-ellipsoidal power density distribution model[6-7] based on Gaussian-Distribution-Function, the mathematical expressions are as follows Eq.1 and Eq.2:

$$q_1(x,y,z) = Qf \bullet \exp\left(-\frac{x^2}{a_f{}^2}\right) \bullet \exp\left(-\frac{y^2}{b^2}\right) \bullet \exp\left(-\frac{z^2}{c^2}\right) \quad (1)$$

$$q_2(x,y,z) = Qr \bullet \exp\left(-\frac{x^2}{a_r{}^2}\right) \bullet \exp\left(-\frac{y^2}{b^2}\right) \bullet \exp\left(-\frac{z^2}{c^2}\right) \quad (2)$$

Where:

q1, q2: heat flux, J.m-2s-1

x, y, z: coordinates that are relative to the heat Center, dimensionless.

Qf: the energy density of heat in the front of hemisphere, J. m-2.

Qr: the energy density of heat in the back of hemisphere, J. m-2.

af, ar, b, c: shape parameter, mm.

1.4 Welding parameters

The welding simulation uses electric arc welding, and choose the thermal efficiency of 0.8.

1.5 Heat transfer boundary conditions

The heat transfer between the pipe wall and the fluid is mainly forced convection heat transfer fluid inside the tube, the heat transfer coefficient is as follow Eq.3:

$$\alpha = 0.027\frac{\lambda}{d}\mathrm{Re}^{0.8}\,\mathrm{Pr}^{1/3}\left(\frac{\mu}{\mu_u}\right)^{0.14} \quad (3)$$

Where:

λ: thermal conductivity of wet-ash, W·m-1K-1.

Re: Reynolds number of wet-ash, dimensionless.

Pr: Prandtl number of wet-ash, dimensionless.

μ: dynamic viscosity of wet-ash, N s·m-2.

d: the inner diameter of the pipe, m.

μu: dynamic viscosity of wet-ash at wall temperature, N s·m-2.

Simulation results analysis

2.1 influence of the media

Fig.3 shows the welding residual stress distribution（MPa in SI units）. As can be seen, due to the forced convection of tube media, the stress distribution in-service area is small, and the welding stress reduces during the welding.

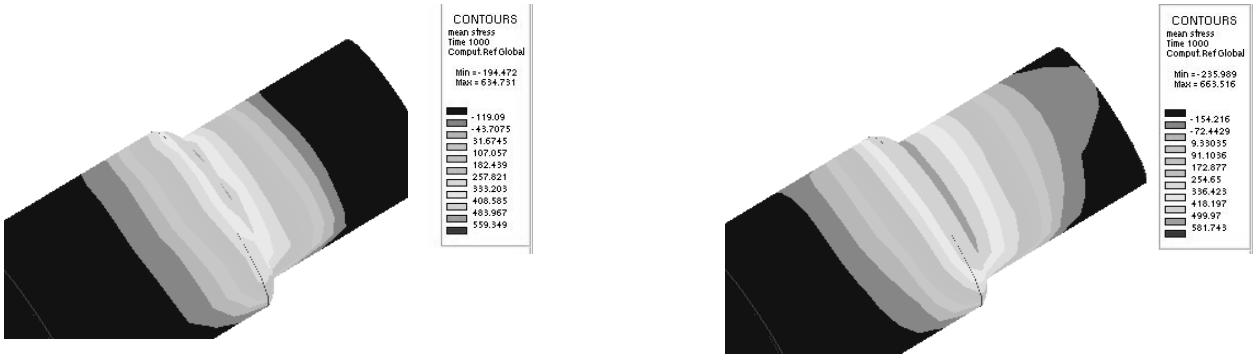

(a) with medium **(b) without medium**

Fig.3 Residual stress contours after welding

2.2 Effect of heat input

The heat input index of this simulation is welding heat input. Welding heat cycle area varies with the welding heat input, and leading to the change of welding thermal stress. When the pipe structure (the wall-thickness is 10mm) and medium flow rate (2m/s) remain the same at the medium temperature 200℃, taking 4 types of welding heat input respectively in Tab.1 to conduct simulation calculations, thus, different heat input acquisition versus the maximum temperature of inner wall, the maximum residual stress of welded joint, as shown in Fig.4.

Tab.1 Welding parameters

process planning	welding current I/A	welding voltage U/V	welding speed v/(cm·s-1)	heat input E/(J·cm-1)
A	85	28	4	595
B	110	28	3.3	933
C	130	29	3.4	1110
D	150	30	3.5	1320

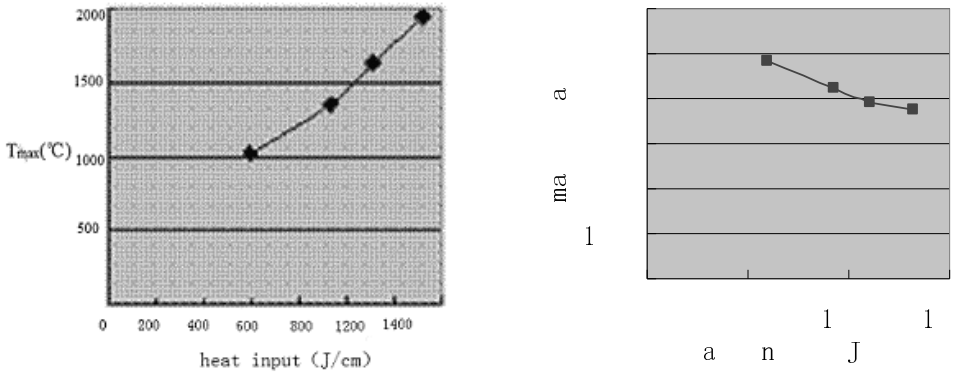

Fig.4 The maximum temperature of the inner wall and the maximum residual stress of welded joint at different line energy

The curve for maximum temperature of inner wall and welding heat input has a linear relation,and rising trend accelerated as welding heat input growth , as shown in Fig.4. However, the maximum residual stress of welded joint decreases with welding heat input growth, and at the same time, the descending trend slows. Therefore, low welding heat input should be input to prevent burn-through in the case of the welding residual stresses in not to exceed the yield strength during welding.

2.3 Influence of medium's velocity

The flow rate of the medium inner tube has a great influence on heat transfer coefficients during high-pressure pipeline in-service welding , and as a result, the welding thermal cycle will change, which also leads to the variation of welding thermal stress. Tab.2 shows the heat transfer coefficients between Medium and the pipe wall at different flow rate. The curses for different medium velocity versus the maximum temperature of inner wall and the welding residual stresses, as shown in Fig.5.

Tab.2 Heat transfer coefficient under different flow rates

flow rate/(m·s^{-1})	2	2.5	3	3.5	4	4.5
heat transfer coefficients /(W·m^{-2}℃$^{-1}$)	560.32	621.35	743.86	836.42	923.45	1053.96

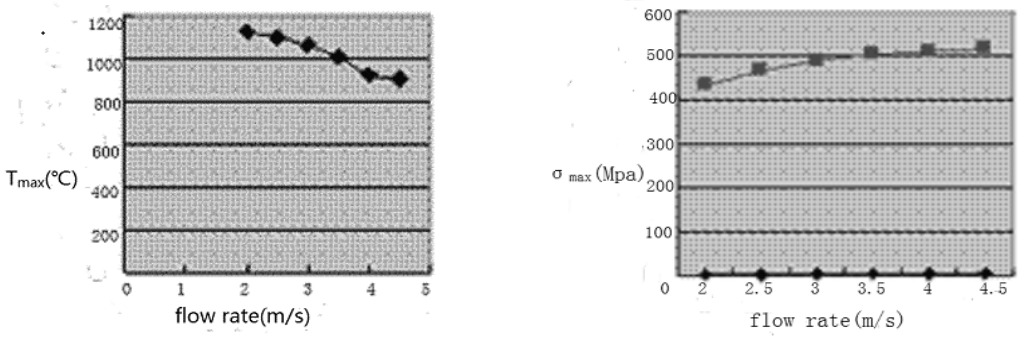

Fig.5 The maximum temperature of the inner wall and the maximum residual stress of welded joint at different medium flow velocity

It can be seen from Fig.5 that the maximum temperature of the inner wall falls with the medium flow rate increase, which is the result of the medium flow increases the convective heat transfer in tube that takes away the heat generated by the welding. And the increase of flow rate can lower the highest temperature of pipe wall in terms of preventing burn-through. As a consequence, the value of the welding heat input can be improved properly for high velocity pipeline welding in- service. The maximum residual stress of welded joint increases with an increase in medium flow rate is also shown in Fig.5, and the growth rate of the maximum residual stress slows down when it gets a fast speed, which indicates that the impact of flow rate on the maximum residual stress of welded joint will decrease gradually.

Conclusion

(1) Double ellipsoid heat source can be used for the fillet weld of high pressure transmission pipeline in-service, and the simulation has a good effect.

(2) The medium flow can reduce the welding residual stress and reduce welding stress range during in-service welding.

(3) With the increase of heat input, the highest temperature of pipe wall increases rapidly, whereas the maximum residual stress of welded joint decreases by a slow trend.

(4) With the increase of flow rate of the medium, the maximum temperature of inner wall drops and the maximum weld residual stress increases by a slow growth.

Acknowledgment

The authors would like to thank Xuzhou science & technology Research Fund Project (XM13B015) , and Jiangsu Postdoctoral Research Fund Project（1101056C）, and JIANGSU JINMEI HENGSHENG Chemicals Co.Ltd., and National "Twelfth Five-Year" Plan for Science & Technology Support)(2011BAB05B02), and National science and technology major special project 36, topic 6（2011ZX05036-006）, for financial support for this research. The authors would also like to thank Mechanical Engineering college of Yangtze University and China University of Mining and Technology for chemical analysis and numerical simulation.

Foundation item: Xuzhou science & technology Fund Project (XM13B015); Jiangsu Postdoctoral Fund Project（1101056C）; National "Twelfth Five-Year" Plan for Science & Technology Support)(2011BAB05B02); National science and technology major special project 36, topic 6 (2011ZX05036-006）;

Author Biography: Zhang Lei(1972-), Phd., Mainly engaged in solid waste resource utilization. E-mail:89202974

References

[1] Guo Haiyun, Li Heng, Li Guohua. the long distance oil pipeline construction[J]. Chinese Engineering Science, 2001,3(12):99-100

[2] Zhang Guodong, Liu Tao, Qi Wenxuan. Present situation and prospects of the welding method of long distance transmission pipeline[J]. Inner Mongolia Petrochemical Industry， 2006,19(9):58-60

[3] Zhang lei. Numerical Analysis Of Liquid Ammonia Storage Tank Welding Stress, 2nd International Conference on Advanced Design and Manufacturing Engineerin,2012. vol.206:1532-1537;

[4] Xue Xiaolong, Zhu Jiagui, Sang Zhifu. The influence of welding pipeline design pressure in-service[J]. Chinese science and technology subject，2006,36(9):991-1001

[5] Zhang Jinzhou, Xiong Hegen, Yang Xiong. numerical analysis of welding stress deformation based on hybrid welding of X70 pipeline[J]. hot working process, 2012(3):128-130

[6] Chen Yuhua, Wang Yong. pipe numerical simulation of welding thermal cycle in-service based on sysweld software[J]. Journal of welding, 007,28(1):86-88

[7] Claudio Ruggieri, Fernando Dotta. Numerical modeling of ductile crack extension in high pressure pipelines with longitudinal flaws [J]. Engineering Structures,2011,17 (6):515-522

Advanced Materials Research Vols. 960-961 (2014) pp 523-527

doi:10.4028/www.scientific.net/AMR.960-961.523

Numerical simulation of jet and cross-flow mixing in Tee pipe

Guobing Kang[1,a]

[1]Department of Packaging & Printing Engineering,

Guangdong Industry Technical College , Haizhu District, Guangzhou City, China

[a]kanggb@sina.com

Key words: Tee pipe; turbulent jet; mixing effect; numerical simulation

Abstract: In the present paper we investigated the mixing effect of uncompressible jet and cross-flow in Tee pipe based CFD, the model of Realizable $k-\varepsilon$ was employed as the tool to simulate the flow field, and the model was validated by experimental result of relative research. The mixing effect of jet and cross-flow in various configuration of Tee pipe at different inlet velocity of jet was discussed. The result shows jet and cross-flow mix quickly in near field of injection point, but in the downstream, the mixing effect keeps comparatively steady when $z>7d$, and there is power relation between the mixing parameter M and $r_1 \times r_2$. And r_1 is the ratio of jet pipe diameter to cross-flow pipe diameter, r_2 is the ratio of jet velocity to cross-flow velocity.

Introduction

Mixing processes in turbulent fluid motion are of fundamental interest in many engineering applications such as pollutant formation, heat and mass transfer and chemical reactions. The need for the efficiency of two kinds of fluid mixing systems and optimization of mixing processes has strongly increased. Transverse jets, or jets in cross-flow are generic flows which are often employed in technical applications where fast mixing is desired. In the chemical process industries jet and cross-flow mixing in Tee pipe are widely used for mixing miscible liquids.

Early stages of experimental work focused on the mixing effect for different combinations of flow parameters such as jet-to-cross-flow velocity ratios performed by SMITH and MUNGAL [1]. Fric and Roshko described the different vortical features of this flow in detail [2]. Flow phenomena resembling the interaction of a jet with a cross-flow such as ring-like vortices, interlocking vortex loops, shear layer structures, and vortex breakdown were observed [3-5]. Some numerical studies have been performed on two- or three-dimensional turbulent mixing with mass or heat transfer for simple geometries [6-7]. A round jet penetrating normally into a cross-flow is described through large-eddy simulation (LES) and the jet-to-cross-flow velocity ratio is 2.3 at a Reynolds number of 46,700, based on the jet bulk velocity and the jet diameter [8]. However, very few studies are available for dealing with the influence of the jet-to-cross-flow diameter ratio on the mixing effect. In this paper, we present a series of computational simulations of three-dimensional turbulent mixing in conditions of different jet-to-cross-flow diameter ratios and velocity ratios. In order to get the optimum mixing effect of the jet-to-cross-flow. The simulations are carried out with the ANSYS FLUENT software.

Turbulence model and verification

Turbulent flows are characterized by fluctuating velocity fields. These fluctuations mix transported quantities such as momentum, energy, and species concentration, and cause the transported quantities to fluctuate as well. Since these fluctuations can be of small scale and high frequency, they are too computationally expensive to simulate directly in practical engineering

calculations. Instead, the instantaneous (exact) governing equations can be time-averaged, ensemble-averaged, or otherwise manipulated to remove the resolution of small scales, resulting in a modified set of equations that are computationally less expensive to solve. For RANS (Reynolds Averaging Navier-Stokes equations), ANSYS FLUENT provides three choices of turbulence models: Standard k-ε turbulent model, Renormalization-group k-ε turbulent model and Realizable k-ε turbulent model. If just want to know the average physical quantity of flow field, the RANS is very effective [9]. The Realizable k-ε turbulent model was adopted to simulate mixing of jet-to-cross-flow successfully [10-13]. The current study uses Realizable k-ε turbulent model to simulate the mixing of jet-to-cross-flow.

In this study, the mixture model was adopted to investigate the mixing of jet-to-cross-flow. The mixture model is a simplified multiphase model that can be used in different ways. It can be used to model multiphase flows where the phases move at different velocities and the mixture model also can model n phases (fluid or particulate) by solving the momentum, continuity, and energy equations for the mixture, the volume fraction equations for the secondary phases, and algebraic expressions for the relative velocities [14]. The cross flow was defined as primary phase and the jet was defined as secondary phase. The materials of cross flow and jet both are liquid water.

The simulation was based on the following conditions: (1) the diameter of jet pipe is 10mm (d=10mm) and the diameter of cross-flow pipe is 60mm (D=60mm) ; (2) the materials are Non compressible fluid and there is no chemical reaction in flow field; (3) in mixture model, the primary phase and secondary are both defined as liquid water, there is no energy transfer and conversion during the process; (4) the velocity of jet is 847mm/s and the velocity of cross-flow is 277mm/s [5]. The configuration and grids of pipelines considered in this study are shown in Figure 1.

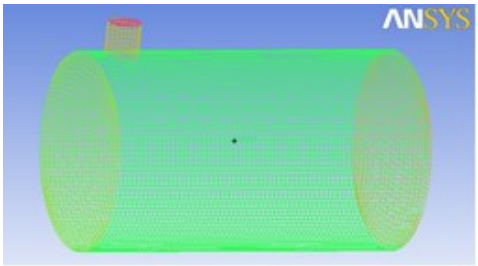

Fig.1 Configuration and grids of pipelines

Figure 2 shows examples of the side-view instantaneous concentration (mixture fraction) field on the center plane represented by 256 gray levels for this case. Figure 3 shows the contours of mean concentration of secondary phase on the center plane.

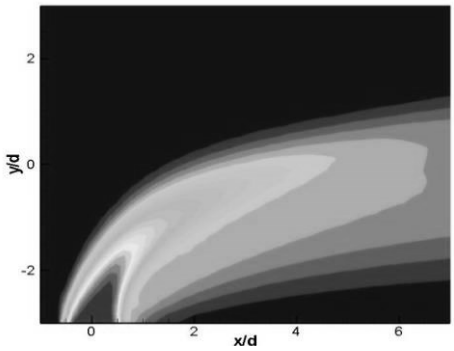

Fig. 2 Gray level images of the side-view instantaneous concentration field

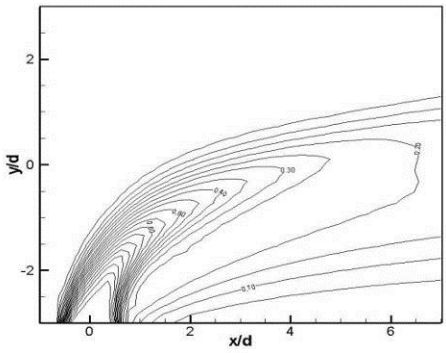

Fig.3 Contours of the side-view instantaneous concentration field (numerical simulation result)

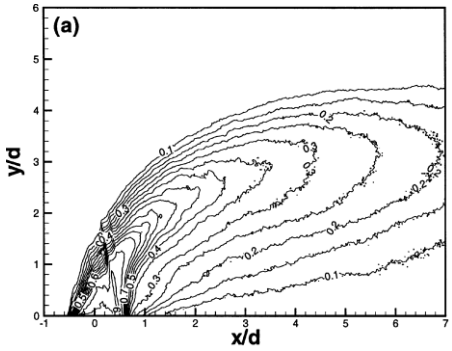

Fig.4 Contours of the side-view instantaneous concentration field (experimental result)

The result of numerical simulation shows a small difference as compared with the experimental result [5] showed in Figure 4, meaning that the turbulence model and simulation is effective.

Results and discussion

The mixedness of the flow can be computed for each cross-sectional plane. The average passive scalar $\bar{c}$ in a cross-sectional plane is defined by (1), its spatial variance σ_c by (2). The mixing parameter is M defined as the normalized square root of the spatial variance, as given by (3).

$$\bar{c} = \frac{1}{A}\int c dA \tag{1}$$

$$\sigma_c = \frac{1}{A}\int \left(c - \bar{c}\right)^2 dA \tag{2}$$

$$M = \sqrt{\sigma_c} / \bar{c} \tag{3}$$

The smaller the mixing parameter, the more homogeneous the mixture. If the spatial variance and hence the mixing parameter are zero, the mixture is perfectly homogeneous. The ratio of jet pipe diameter to cross-flow pipe diameter is defined as r_1, $r_1=d/D$. The ratio of jet velocity to cross-flow velocity is defined as r_2, $r_2=v_j/v_c$. Figure 5 shows the relation between the mixing parameter and distance of the measurement plane along the cross-stream line. In these cases, the diameter of jet pipe is 10mm and the diameter of cross-flow pipe is 60mm. The velocity ratios are 1, 2, 3 respectively (r_2=1,2,3). Figure 5 shows that the mixing parameter decreased slowly in the region where $z>3d$ especially $z>7d$ (z is the downstream distance from the injection point and d is the diameter of jet pipe). The relation between the mixing parameter and the product of r_1 and r_2 on the plane of $z=7d$.

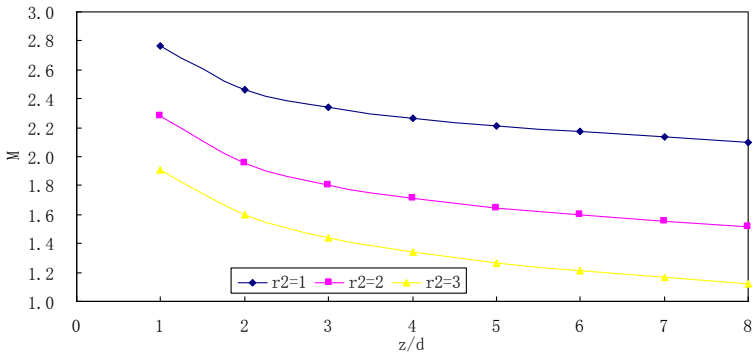

Fig.5 The mixing parameter on each cross-sectional plane

Table 1 $r_1 \times r_2$ and corresponding M value

r_1	r_2	$r_1 \times r_2$	M
0.167	2	0.334	2.133
0.167	3	0.501	1.551
0.167	4	0.668	1.166
0.167	5	0.835	0.912
0.167	6	1.002	0.821
0.200	2	0.400	2.055
0.200	3	0.600	1.411
0.200	4	0.800	1.031
0.200	5	1.000	0.794
0.250	2	0.500	1.500
0.250	3	0.750	0.922
0.250	4	1.000	0.760
0.333	1	0.333	1.981
0.333	2	0.666	1.032
0.333	3	0.999	0.826

The data in the Table 1 are fitted by power function as showed in Figure 6.

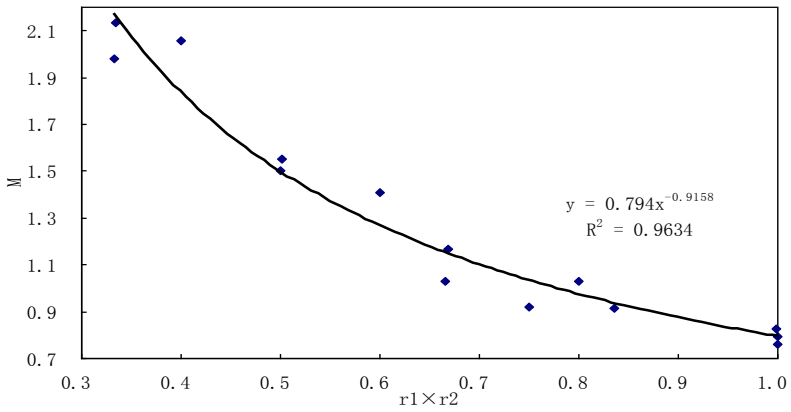

Fig. 6 The mixing parameter M on the plane of z=7d

Figure 6 shows on the plane of z=7d the mixing parameter M does eventually decline with the value of $r_1 \times r_2$. Further, the mixing parameter M has a power function to the product of r_1 and r_2. The power function can be expressed as :

$$M = a(r_1 \times r_2)^b \tag{4}$$

where a and b are linked to the downstream distance from the injection point.

Conclusion

In this paper, a numerical study of Tee pipe mixers has been conducted with the FLUENT software. To summarize, we obtain the following information pertaining to the design of the considered mixing arrangements:

1. Realizable *k-ε* turbulent model can be used to simulate the mixing of jet-to-cross-flow. The result of simulation does correspond with the existing experimental data.
2. The process of mixing happens quickly in zone of near the injection point, the mixing parameter decreased slowly in the region where z>3*d* especially *z*>7*d*.
3. In a certain plane where *z*>7*d*, the mixing parameter *M* has a power function to the product of r_1 and r_2. The power function can be expressed as $M = a(r_1 \times r_2)^b$.

Reference

[1] S. H. SMITH a1 and M. G. MUNGAL . Mixing, structure and scaling of the jet in crossflow. Journal of Fluid Mechanics, 1998,357, p.83-122.

[2] T. F. Fric and A. Roshko. (1994) Vortical structure in the wake of a transverse jet. Journal of Fluid Mechanics, 279, p.1–47.

[3] R. M. Kelso , T. T. Lim and A. E. Perry. An experimental study of round jets in cross-flow. Journal of Fluid Mechanics, 1996, 306, p. 111-114.

[4] Li Yuliang, Chen Chaoquan, Jiang Chunbo. Fractal characteristics of round jets in steady crossflow. Chinese Science Bulletin, 1999, 44(15), p.1366-1369

[5] Gang Pang, Hui Meng. Experimental study of turbulent mixing in a tee mixer using PIV and PLIF. AIChE Journal, 2001, 47 (12), p.2653-2665.

[6] Luis A. Monclova , Larry J. Forney. Numerical simulation of a pipeline tee mixer. Ind. Eng. Chem. Res, 1995,34(4), p.1488-1493

[7] Aklilu T.G. Giorges, Larry J. Forney, Xiaodong Wang. Numerical Study of Multi-Jet Mixing. Chemical Engineering Research and Design, 2001,79(5), p.515–522

[8] Petri Majander , Timo Siikonen. Large-eddy simulation of a round jet in a cross-flow. International Journal of Heat and Fluid Flow, 2006, 27, p.402-415.

[9] Zhang Zhaoshun, Cui Guixiang, Xu Chunxiao. Theory and application of large eddy numerical simulation of turbulent flow, Beijing: Tsinghua University Press (2008), p.54-59.

[10] Guo Tingting, Li Shaohua, Xu Zhong. Numerical analysis of three-dimensional turbulent jet in crossflow. Power Engineering, 2004, 24(2), p.244-248

[11] Bi Rongshan, Ma Lianxiang, Cheng Hua etc. Multi-scale simulation of turbulent mixing in ejector. CIESC Journal, 2009,60(1), p.157-162.

[12] Ma Lianxiang, Bi Rongshan, Zheng Shiqing. Multi-scale simulation of turbulent mixing in Tee mixers. Chemical Reaction Engineering and Technology , 2008,24(2),p.103-107.

[13] Bian Xiaojing. Numerical simulation of vertical momentum jet in cross-flow. Journal of Hohai University Natural Sciences,2006,34(5), p. 530-533.

[14] ANSYS Fluent Incorporated, Computational Fluid Dynamics Software, ANSYS Inc (2009).

Advanced Materials Research Vols. 960-961 (2014) pp 528-533

doi:10.4028/www.scientific.net/AMR.960-961.528

Effect of Design Parameters on Air Entrainment and Oxygen Transfer of Central-Driven Ejector

Dongjun Kim[1, a], Huiwei Du[2,b], Kyuho Kim[3,c], Lu Peng[4,d] and Heicheon Yang[5,e*]

[1, 2, 3]Graduate School of Chonnam National Univ., 50 Daehak-ro, Yeosu, Chonnam, 550-749, Korea

[4, 5]School of Mechanical Design Engineering, Chonnam National Univ., 50 Daehak-ro, Yeosu, Chonnam, 550-749, Korea

[a]dj3220@jnu.ac.kr, [b]duhuawei21@hotmail.com, [c]terfuone@nate.com, [d]bryant-1988@hotmail.com, [e]hcyang@jnu.ac.kr

Keywords: Air entrainment, Oxygen transfer, Dissolved oxygen concentration, Ejector, Design parameter.

Abstract. The objective of this study is to investigate the air entrainment and oxygen transfer characteristics of central-driven ejector with various ejector design parameters. The ejector design parameters are primary nozzle diameter, mixing tube length and diffuser angle. The entrainment ratio decreased with the primary nozzle diameter and diffuser angle, while the ratio increased with the mixing tube length. The trend of dissolved oxygen concentration with the diffuser angle and mixing tube length is equal to the result of entrainment ratio, however, the trend with the primary nozzle diameter is different to the result of entrainment ratio.

Introduction

An ejector works like a vacuum pump without usage of piston, rotor or any other moving components. In general, there are two configurations of ejector. The first is the central-driven ejector, in which the primary fluid passes through the inner nozzle inside the ejector and the suction fluid passes through the annular periphery surrounding the nozzle. The second is the annular-driven ejector, in which the suction fluid passes through the inner tube of the ejector and the primary fluid passes through the annular nozzle on the periphery of the suction tube [1-3].

Ejectors are being used as gas-liquid dispersion devices for many purposes in many industries since they have high mass transfer and mixing rate. Many reports have researched the gas-liquid flow and mixing in ejectors, but the results are different and have individual scope of application due to the different ejector geometries, study methods and the species of fluids [4,5].

There are many studies describing the hydrodynamic and mass transfer characteristics concerning multi-phase fluids with the conventional central-driven ejector [6]. The effects of various parameters such as primary nozzle area ratio, mixing tube length, diffuser angle and length on the ejector performance have been investigated by Sharma et al.[7], Kim et al.[8], Kumar et al.[9], Rogdakis and Alexis [10], Rainer et al. [1].

Mass transfer occurs in mixtures containing local concentration variation. Mass is transferred from one place to another under the influence of a concentration difference or concentration gradient in the system. Rate of mass transfer is directly proportional to the driving force for transfer, and the area available for the transfer process to take place. The solubility of oxygen within a water tank is very poor. Therefore, the enhancement of gas-liquid mass transfer during gas-liquid contacting processes is always put into priority. Mass transfer characteristics of ejectors using air or water as the primary fluid or the entrained fluid have been investigated by Park and Yang [11], Balamurugan et al.[12], Cramers and Beenackers [13] and Havelka et al.[14].

The development of new gas-liquid contacting systems for high-efficiency oxygen transfer at low operating costs is a very important issue in many applications. Because of the low solubility and transfer rate of oxygen, to achieve a higher oxygen transfer rate, it is necessary to have a large amount of entrainment air and to increase the contact time and area of the air-water bubbles by decreasing the

size of the entrained air bubbles. However, few experimental studies examining the effect of design parameter in central-driven on the flow and oxygen transfer characteristics have been reported in the literature [11]. The objective of this study is to investigate the flow and mass transfer characteristics of central-driven ejector with the primary nozzle diameter, diffuser angle and mixing tube length.

Experimental Setup and Method

The schematic diagram of central-driven ejector with screw pitch for movable primary nozzle is shown in Fig. 1, and the specifications of the ejector are listed in Table 1. The key components of the ejector are a primary fluid nozzle, a suction fluid tube, a parallel mixing tube, a diffuser and a screw apparatus. The primary fluid nozzle position could be adjusted by the screw apparatus. As the nozzle tip moves backward (as the screw pitch increases), the distance between the nozzle tip and the inlet of the parallel mixing tube increases. One pitch of the screw is 1.5mm. All experiments were carried out in a 0.48 m^3 (0.4 m wide × 1.5 m long × 0.8 m height) water tank system which was closed loop circulation type as shown in Fig. 2.

In the hydrodynamic experiments, the tank was filled with tap water which was circulated through the central-driven ejector by means of an electric motor-pump (Wilo, HL 8051-1). The volumetric water flowrate Q_p supplied by the motor-pump was regulated manually with a valve and measured by an electromagnetic flowmeter (Kometer, KTM-800) at the primary flow inlet with the accuracies of ±1.0% of full scale. The suction air flowrate Q_s was measured with an air flowmeter (Kometer, DPE-S) at the air suction inlet of the ejector with the accuracies of ±2.0% of full scale.

For the oxygen transfer measurements, the water in the water tank was deaerated by addition of sodium sulphite (Na_2SO_3) with a cobalt chloride($CoCl_2$) catalyst until the dissolved oxygen (DO) concentration fell to zero and then reaerated back to steady state (saturation) conditions. The total amount of sodium sulphite required for each test run was calculated based on the theoretical demand for sodium sulphite [11, 15]. The changes of the DO concentration with time were recorded until the water became saturated with air. The temperatures of the circulation water and the suction air were 14.3±1.0℃ and 14.4±0.5℃. The saturated dissolved oxygen concentration with the temperature of circulation water at standard atmospheric conditions is 10.24 mg/L. The dissolved oxygen concentration (C_t) was measured at 10 second time intervals with a DO meter (YSI model 5B). In each experiment, measurements were repeated three times at each operating condition. Percentage dissolved oxygen is defined by the ratio of actual dissolved oxygen concentration against saturated dissolved oxygen concentration at the water temperature.

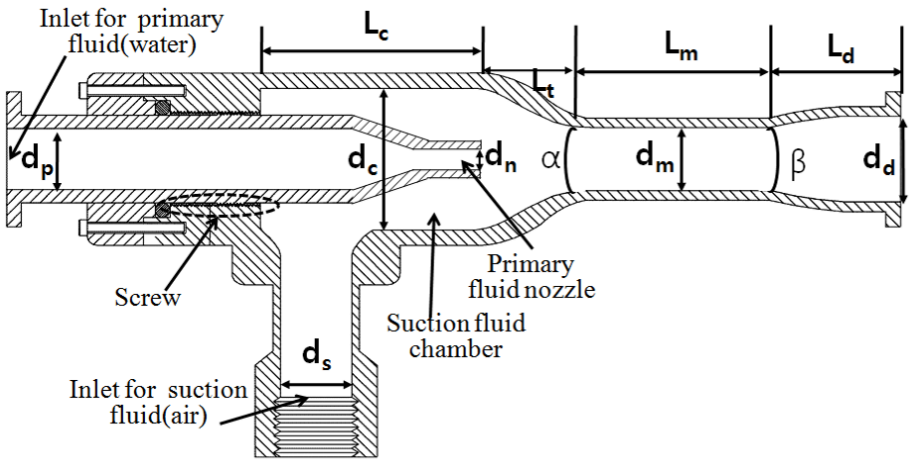

Fig. 1 Schematic diagram of the central-driven ejector

Table 1 Specifications of the central-driven ejector

Parameter	d_p, d_s	d_m	d_n	d_d	d_c	L_c	L_t	L_m	L_d	α	β
Values [mm]	28	30	8.7 11.4 15.2	36 42 47	65	110	36	130 213 350	128	51.6	2.7 5.1 7.5

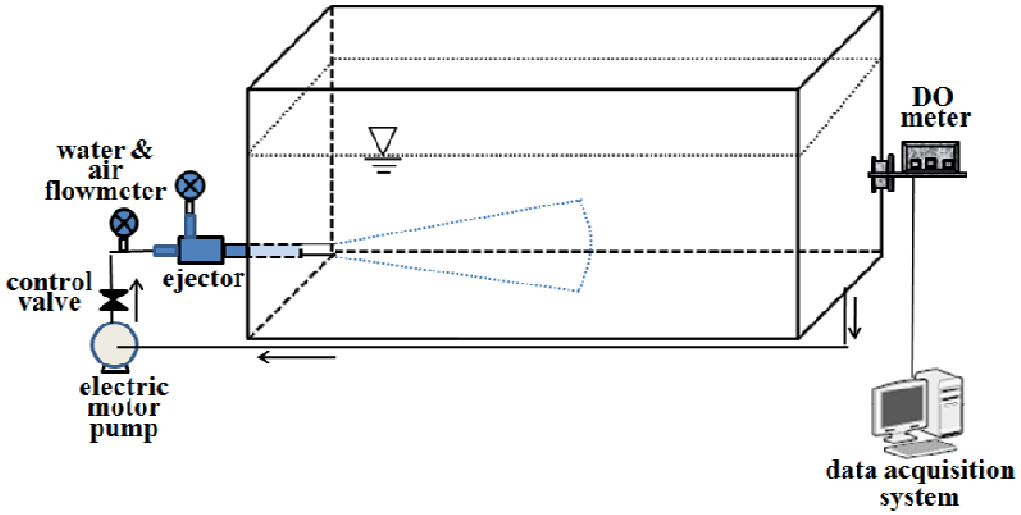

Fig. 2 Schematic diagram of experimental setup

Results and Discussion

The measured variables are the flow rates of the primary and suction fluids (water and air) and dissolved oxygen concentration. The entrainment ratio is the amount of suction air flow that can be sucked by a given primary flow. The entrainment ratio is calculated by $M=Q_s/Q_p$, where Q_s is the suction air flow rate and Q_p is the primary water flow rate.

Fig. 3 show the effects of primary nozzle diameter, diffuser angle and mixing tube length on the entrainment ratio with the screw pitch in the central-driven ejector. Generally, as the screw pitch increases (or as the nozzle exit tip is moved backward), the entrainment ratios increase. This is due to the fact that as the screw pitch increases the primary water flow rate is nearly constant, while the suction air flow rate increases. The nearly constant primary flow rate is owing to the constant primary nozzle area regardless of the screw pitch and the increasing suction air flow rate is owing to the variation of suction inlet vacuum pressure with the screw pitch. As the primary nozzle diameter reduces, the air entrainment ratio increases due to the increase of the vacuum pressure near the primary nozzle exit resulting from the increase of primary flow velocity. As the diffuser angle decreases, the entrainment ratio increases owing to decreasing vortical loss in the diffuser. As the mixing tube length decreases, the entrainment ratio reduces owing to the energy loss resulting from the incomplete mixing of primary fluid and suction air in the mixing tube and the vortical mixing in the diffuser.

Figs. 4, 5 and 6 show the effect of primary nozzle diameter, diffuser angle and mixing tube length on the percentage dissolved oxygen concentration with the aeration time at pitch 0, 7, 17 and 27 respectively. As can be seen in the percentage dissolved oxygen concentration results, dissolved oxygen concentrations increase with aeration time. The increase of dissolved oxygen concentration with aeration time may be attributed to the longer contacting time of air bubbles in aerating water [11].

As shown in Figs. 5 and 6, as the diffuser angle decreases and the mixing tube length increases, the dissolved oxygen concentrations increase with the aeration time. The trend is equal to the result of entrainment ratio as shown in Fig. 3. An increase in dissolved oxygen concentration with increasing the entrainment ratio may be ascribed to the increase in interfacial area between air bubbles and aerating water. At the minimum nozzle diameter the air entrainment ratios exhibit the highest values, however, the dissolved oxygen concentration exhibit the smallest values. This result may be attributed to the shorter persistence of air bubbles due to the increased buoyancy force resulting from their larger size.

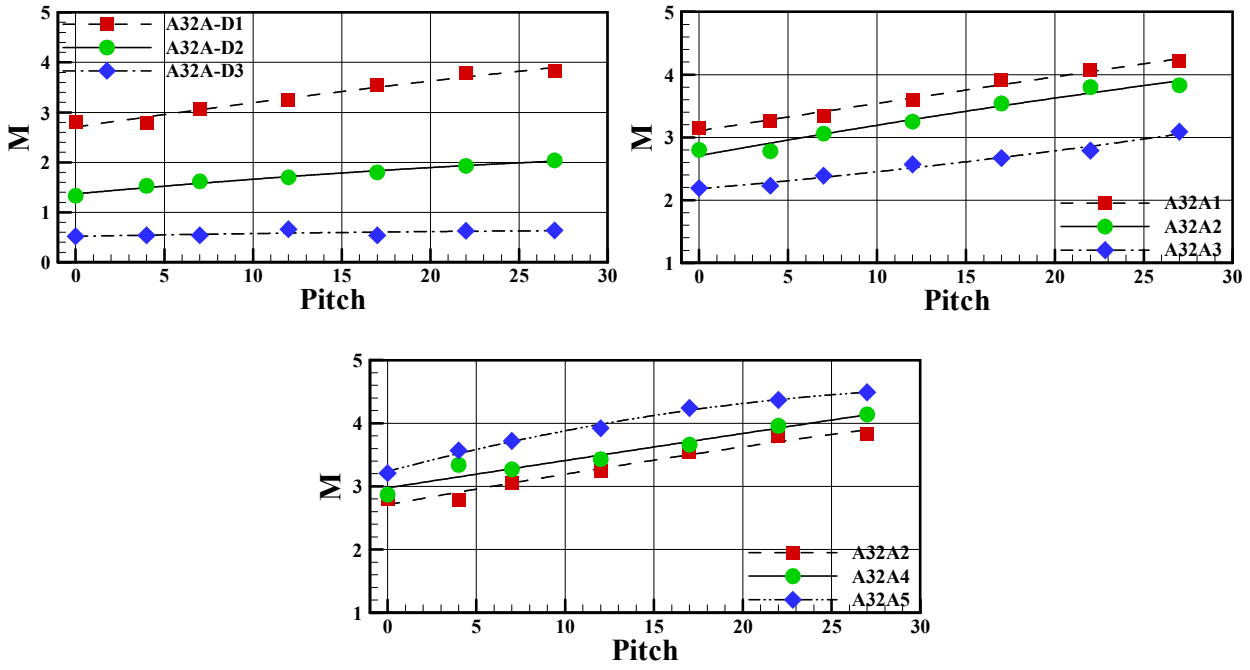

Fig. 3 Effect of design parameters (d_n, β, L_m) on the air entrainment ratio with screw pitch

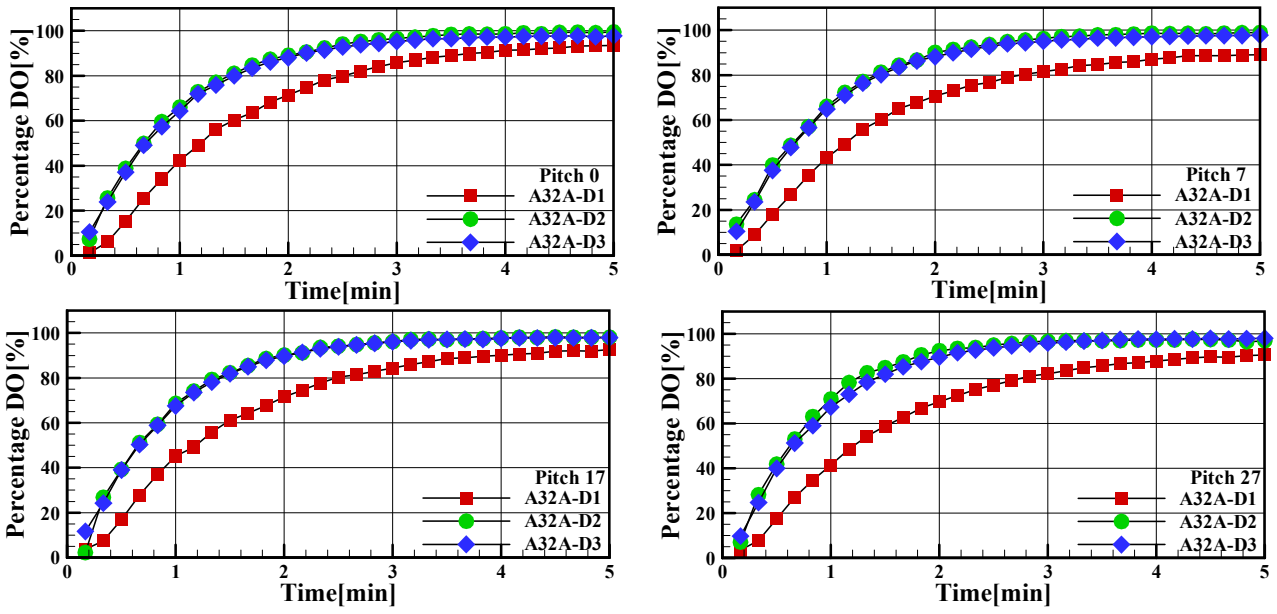

Fig. 4 Effect of primary nozzle diameter (d_n) on the percentage dissolved oxygen concentration with aeration time

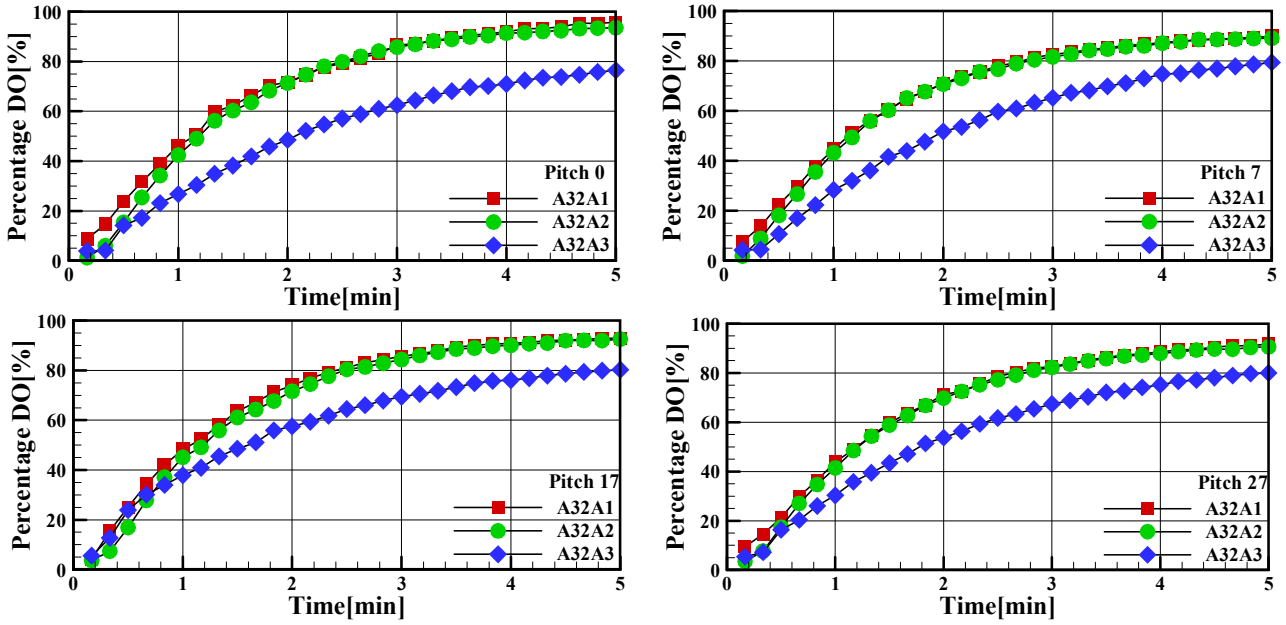

Fig. 5 Effect of diffuser angle (β) on the percentage dissolved oxygen concentration with aeration time

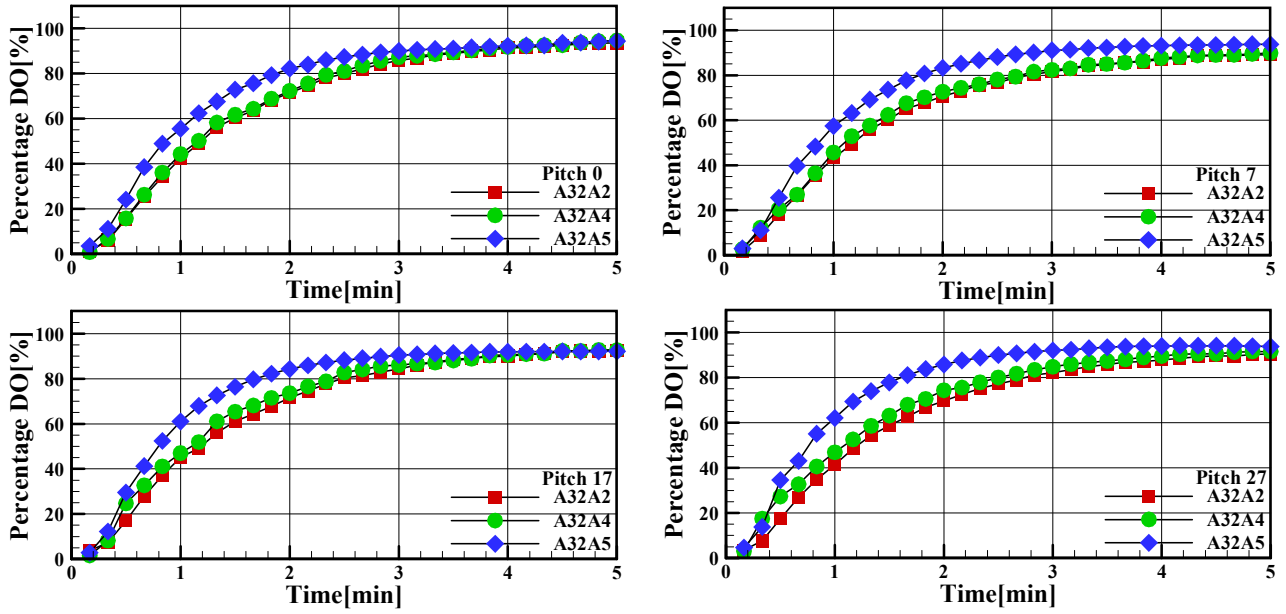

Fig. 6 Effect of mixing tube length (L_m) on the percentage dissolved oxygen concentration with aeration time

Conclusions

For the central-driven ejector, the entrainment ratios increase with the screw pitch. As the primary nozzle diameter reduces, the air entrainment ratio increases due to the increase of the vacuum pressure near the primary nozzle exit resulting from the increase of primary flow velocity. As the diffuser angle decreases, the entrainment ratio increases owing to decreasing vortical loss in the diffuser. As the mixing tube length decreases, the entrainment ratio reduces owing to the energy loss resulting from the incomplete mixing of primary fluid and suction air in the mixing tube. As the diffuser angle decreases and the mixing tube length increases, the dissolved oxygen concentrations increase with the aeration time. At the minimum nozzle diameter the air entrainment ratios exhibit the highest values, however, the dissolved oxygen concentration exhibit the smallest values due to the shorter residence time of air bubbles resulting from their larger size.

Acknowledgements

This research was supported by Basic Science Research Program through the National Research Foundation of Korea (NRF) funded by the Ministry of Education (No. 2013R1A1A4A01010854).

References

[1] B. Rainer, C. Fonade and A. Moser: Bioprocess Engineering, Vol. 13 (1995) p. 97.

[2] G. Park, S. Kim and S. Kwon: Journal of Propulsion and Power, Vol. 24 (2008) p. 631.

[3] D. H. Jang, H. Du, D. J. Kim and H. C. Yang: 5th Int. Sympsium on Fluid Machinery and Fluid Eng, ISFMFE 2012, Jeju, Korea, (2012) p. 2.

[4] K. K. Kim, E. S. Kim, S. M. Kang, J. K. Lee and B. J. Rho: Transactions of KSAE, Vol. 16 (2008) p. 49.

[5] R. Yapici: Energy Conversion & Management, Vol. 49 (2008) p. 953.

[6] M. EL-Ghandour, I.A. EL-Sawaf and F.M. EL-Ottla: 6th Int. Water Technology Conference, IWTC6 2001, Alexandria, Egypt, (2001) p. 328.

[7] V. P. Sharma, S. Kumaraswamy and A. Mani: World Academy of Science, Engineering and Technology, Vol. 61 (2012) p. 546.

[8] O. S. Kim, Y. Lee and D.H. Lee: Korean Journal Chemical Engineering, Vol. 26 (2009) p. 288.

[9] R. S. Kumar, S. Kumaraswamy and A. Mani: Desalination, Vol 204 (2007) p. 437.

[10] E.D. Rogdakis and G.K. Alexis: Energy Conversion & Management, Vol. 41 (2000) p. 1841.

[11] S. K. Park and H. C. Yang: Industrial & Engineering Chemistry Research, Vol. 52 (2013) p. 1756.

[12] S. Balamurugan, M. D. Lad, V. G. Gaikar and A. W. Patwardhan: Industrial & Engineering Chemistry Research, Vol. 46 (2007) p. 8505.

[13] P. H. M. R. Cramers and A. A. C. M. Beenackers: Chemical Engineering Journal, Vol. 82 (2001) p. 131.

[14] P. Havelka,V. Linek, J. Sinkule, J. Zaharadnik and M. Fialova: Chemical Engineering Science, Vol. 55 (2000) p. 535.

[15] J. M. Chern and S. P. Yang: Industrial & Engineering Chemistry Research, Vol. 42 (2003) p. 6653.

Advanced Materials Research Vols. 960-961 (2014) pp 534-538

doi:10.4028/www.scientific.net/AMR.960-961.534

The Influence of Pressure Pipe Diameter and Orifice Size of Surge Chamber Optimization on the Pressure at Volute

Peng Yang[1,a], Jian Zhang[1,b], Sheng Chen[1,c], Di Miao[1,d]

[1]Hohai University, Nanjing, China 210098

[a]1072134762@qq.com, [b]jzhang@hhu.edu.cn, [c]124461871@qq.com, [d]249580906@qq.com

Keywords: pressure pipe diameter, upper room of surge chamber, the size of orifice, volute pressure

Abstract: For a long-distance convey tunnel hydropower station, the changes of its convey tunnel diameter will impact on the pressure at the turbine volute, due to the influence of upper room of surge chamber, surge pressure is difficult to be the controlling value of the pressure at volute, the results also indicate that the influence of pressure pipe diameter on the pressure is more significant than the diversion tunnel diameter. This paper focuses on the pressure pipe diameter by the calculation of a numerical example, the increasing of the pressure at volute caused by the reduction of pressure pipe diameter can be adjusted for security requirements by optimizing the orifice size of surge chamber. Combined with the calculation of the combinational conditions, optimization results are satisfactory. That will reduce the investment of pressure pipe, so it has a certain reference value to the project.

Introduction

With the rapid development of China water utilities, more and more hydropower projects are coming into the research and development. Due to geological and topographical constraints, some stations built diversion power plants. For the long-distance convey tunnel system, because the water inertia is large, wave cycle of the surge chamber is long, the attenuation is slow and the amplitude is large, so the maximum pressure at volute is controlled by water hammer pressure and surge pressure [1]. But when the surge chamber has an upper chamber, its surge pressure is difficult to become the controlling value, the maximum pressure at volute is decided by water hammer pressure. To reduce water hammer pressure for the purpose, we can reduce the water flexibility of the pressure pipe. However, its diameter is often larger than the economic pipeline diameter that is designed in the preliminary design stage by Peng Deschutes formula [2], it will increase the project investment. Reducing the pressure pipe diameter will increase the pressure at volute, but the increasing of the orifice size of surge chamber can effectively reduce the pressure at volute, combined with the interactional relationship of them, we present a viable optimization program, that can make the results meet the calculation range.

Numerical example

Water diversion system of a hydropower station is composed of diversion tunnel, throttled surge chamber with upper room and pressure pipe, the diversion way is that two units share a diversion tunnel. The length of diversion tunnel between water inlet and surge chamber is 6045.6m, the diversion tunnel diameter is 8.5m, the length of pressure pipe between surge chamber and units bifurcation point is 326.87m, the pressure pipe diameter is 7.5m, the orifice diameter of surge chamber is 4.0m, rated flow of two units is 111.2m^3/s, rated head is 176.5m, rated output is 178.61MW. Its layout diagram is shown in Figure 1.

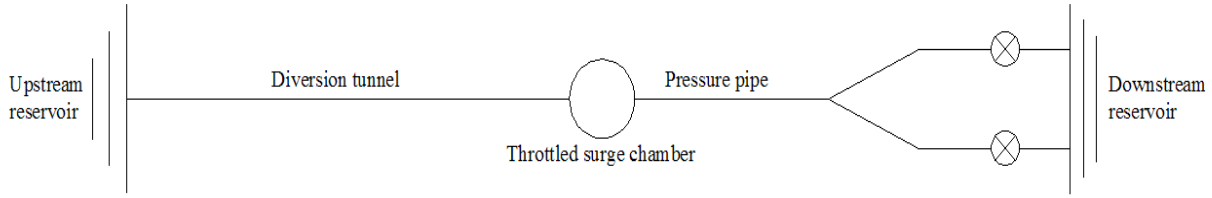

Fig. 1 Schematic of hydropower station layout

Effect of the water pipe diameter on the pressure in volute

Here, we have transitional process calculation for the numerical example, and respectively adjust the diameter of diversion tunnel and pressure pipe, then we can study its effects on the pressure at volute. Calculation condition is upstream reservoir high water level, the downstream reservoir normal tail water level, rated output, and two machines simultaneously loading rejection, this condition may be the controlled condition of the maximum pressure at volute, guide vanes turn off by straight at a fixed time. Diversion tunnel diameters are respectively taken 7.0m, 7.5m, 8.0m, 8.5m, 9.0m. Pressure pipe diameters are respectively taken 6.0m, 6.5m, 7.0m, 7.5m, 8.0m. The results are shown in Table 1, Table 2, Figure 2 and Figure 3.

Tab.1 Calculation results of the pressure at volute under different diversion tunnel diameters

Diameter of diversion tunnel (m)	7.0	7.5	8.0	8.5	9.0
Volute pressure (m)	264.13	265.50	265.05	264.38	264.37

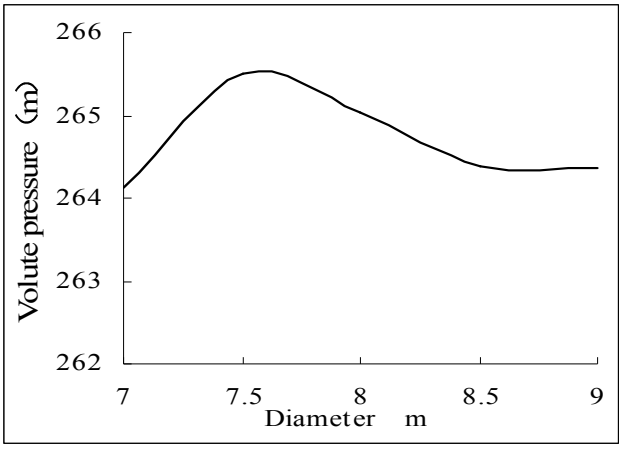

Fig.2 Relationship between the pressure at volute and diversion tunnel diameters

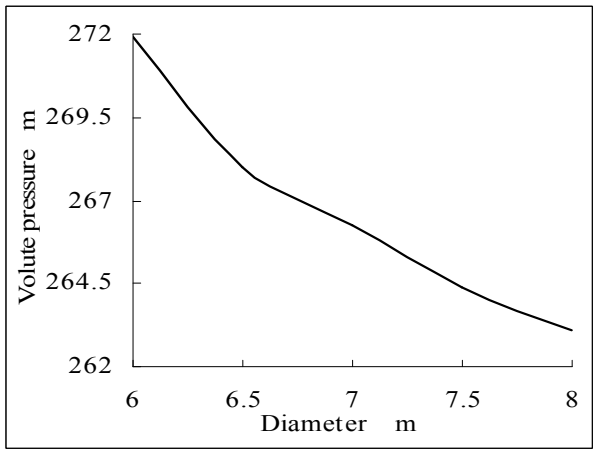

Fig.3 Relationship between the pressure at volute and pressure pipe diameters

Tab.2 Calculation results of the pressure at volute under different pressure pipe diameters

Diameter of pressure pipe (m)	6.0	6.5	7.0	7.5	8.0
Volute pressure (m)	271.96	267.97	266.25	264.38	263.12

We can see in Fig.2 the pressure at volute increases first and declines with the increasing of the diversion tunnel diameter, but the pressure amplitude changes little. In Fig.3, the pressure gradually decreases with the diameter increase of the pressure pipe, and the amplitude changes significantly. The reduction of diversion tunnel diameter makes its water inertia (∑LV) increased, the impact of the surge pressure on the volute will also increase. Due to the effect of the upper chamber, the flow rate rapidly decreases after water flowing into the upper room, it is difficult to form a higher surge to make it to be the controlling value of the maximum pressure at volute, so the change of the diversion tunnel diameter has little effect on the pressure at volute. Reduction of the pressure pipe diameter makes the water flexibility increased, the maximum pressure at volute is controlled by water hammer pressure so that it shows a significant change.

Effect of the orifice size of surge chamber on the pressure at volute

The water hammer wave reflectivity of the throttled surge chamber is not only related to the surge chamber diameter, but also its orifice area and throttle coefficients [3]. In general, the optimization of the surge chamber diameter only have an impact on the magnitude of the surge, compared to the orifice of surge chamber, its impact on the pressure at volute is not obvious. Keeping other parameters constant, we can study the impact of different diameters of the orifice of surge chamber on the pressure at volute. The results are shown in Table 3 and Figure 4.

Tab.3 Calculation results of the pressure at volute under different diameters of the orifice of surge chamber

Diameter of the orifice (m)	3.2	3.6	4.0	4.4	4.8	5.2
Volute pressure (m)	296.05	277.65	264.38	256.57	253.67	251.63

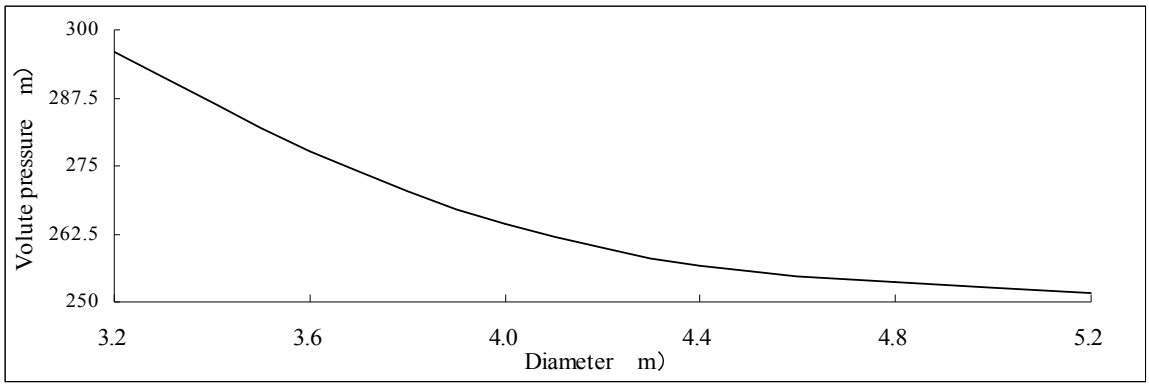

Fig. 4 The influence of different sizes of the orifice on the pressure at volute

By analyzing Table 3 and Figure 4, with the increasing of surge chamber orifice diameter, the pressure at volute gradually reduces. Thus, to increase the orifice diameter is an effective measure to reduce the water hammer pressure. While the curve in Figure 4 also reveals that when the orifice diameter increases to a certain extent, the reduced speed of the pressure at volute becomes slow. If we further increase the orifice diameter, its impact on the pressure will be getting smaller and smaller. In this case, increasing the area of the orifice will only lead to the increase of the surge and the adverse effect of delaying the decay time of the surge. Therefore, the orifice optimization is in a certain range.

Pressure pipe diameter and orifice size of surge chamber optimization

By the calculation above, reducing pressure pipe diameter will bring the rise of the pressure at volute, while increasing orifice diameter will effectively make the pressure reduced, combined with the optimization of them for their interactional relationship, so the pressure at volute is controlled in the calculation range that is possible. In general, at the feasibility study and preliminary design stage, the economic diameter of the pressure pipe is determined by Peng Deschutes formula [2], the formula is $D=(5.2Q^3_{max}/H)^{1/7}$, where, Q_{max} is the maximum design flow of the pressure pipe , H is the design head. The pressure pipe diameter of the example is 7.5m, but the calculated diameter is 6.12m by the Peng Deschutes formula in the same example, in comparison, to reduce the diameter of the original proposal has a certain space to explore. In the example, the design value of the pressure pipe diameter is 7.5m, the orifice diameter is 4.0m, the calculated value of the pressure at volute is 264.38m, we treat them as a benchmark, then the pressure pipe diameters are respectively taken 8.0m, 7.0m, 6.5m, 6.0m for the calculation of hydraulic transition process. To ensure the pressure is controlled in about 264.38m, orifice diameter is bound to be adjusted to meet the standard. The results are shown in Table 4.

Tab.4 Optimization of the orifice diameter of surge chamber under different pressure pipe diameters

Diameter of pressure pipe (m)	8.0	7.5	7.0	6.5	6.0
Diameter of the orifice (m)	3.96	4.00	4.06	4.30	4.90
Area of the orifice (m^2)	12.31	12.56	12.94	14.51	18.85
Volute pressure (m)	264.24	264.38	264.61	264.21	264.48

The following conclusions can be obtained by analyzing Table 4: the reduction of the pressure pipe diameter causes the increasing of the pressure at volute, with the increasing of orifice diameter, the reference value is controlled in about 264.38m by their interactional relationship. And when the pressure pipe diameter reduces at the same range, the orifice diameter only adjusts in a small extent to make the pressure controlled in the calculation range. So we can reduce the pressure pipe diameter without increasing construction costs, which provides a reference to reduce engineering investment. While the results in Figure 4 also reveal that when the orifice diameter increases to a certain extent, the effect of the reduction of the pressure at volute gradually becomes weak, thereby the orifice diameter is larger and larger with reducing the same diameter of the pressure pipe.

Combinational working conditions reviewing

Since the diversion tunnel of this hydropower station is long, the water inertia is large, wave cycle of the surge chamber is long, combinational working conditions often occur when the hydropower station works, so it may exacerbate the pressure at volute in the process of load shedding. Combined with conventional conditions, we draw up the following combinational conditions: upstream is the checking flood level and downstream is the normal tail water level, one unit is rated output, another unit normally starts to rated output, when the flow rate flows into the surge chamber to be the largest, two units suddenly load rejection, it may be the maximum pressure at volute. We select the original design (A-Program: pressure pipe diameter is 7.5m, orifice diameter is 4.0m) and two optimization programs (B-Program: pressure pipe diameter is 7.0m, orifice diameter is 4.06m;

C-Program: pressure pipe diameter is 6.5m, orifice diameter is 4.30m) to calculate in combinational working conditions. The results are shown in Table 5.

Tab.5 Check of combination conditions under different programs

Combinational program	The time of maximum flow (s)	The maximum volute pressure (m)
A-Program	237.44	275.38
B-Program	237.35	275.40
C-Program	236.02	270.15

By comparing the original program and the optimization programs in combinational conditions, the results indicate that the optimization programs have a good stability, even in C program, it achieves better results than the original program.

Conclusions

a. Due to the effect of the upper room of the surge chamber in the long-distance convey tunnel hydropower station, its surge is difficult to increase largely to be the controlling value of the maximum pressure at volute, and it leads to that the impact of diversion tunnel diameter on the pressure is also not obvious. With the function of the water flexibility in pressure pipe, the pressure at volute shows a growth trend by the decreasing of pressure pipe diameter.

b. With the increasing of the orifice diameter, the pressure at volute gradually decreases. But when the orifice diameter increases to a certain degree, its function on the pressure at volute gradually becomes weak.

c. By the interaction law between the pressure pipe diameter and orifice diameter, we reduce the pressure pipe diameter while increase the orifice diameter, so that the pressure at volute can be controlled within the scope of the guaranty calculation, that will be a feasible optimization program. And the optimization program has a good stability in combination conditions, so there will be a certain reference to the actual engineering design.

Acknowledgement

This work is supported by the National Natural Science Foundation of China (51379064).

References

[1] Lu Weihua, Zhang Jian, Fan Boqin, Hu Jianyong. Optimization of Body-type of Surge Tank and Vane Closure Law under the Long-distance Convey Tunnel of Hydropower Station [J]. Water Resources And Power, 2007, (04):90-93.

[2] Liu Qizhao. Hydropower Station. Third edition [M]. Beijing: China Water Power Press, 1998.

[3] Wang Liqing, Ma Yuexian, Wu Hao, Yuan Wenlin. Influence of Throttle of Surge Tanks on Water Hammer [J]. Water Power, 2007, (12):38-39.

Advanced Materials Research Vols. 960-961 (2014) pp 539-542

doi:10.4028/www.scientific.net/AMR.960-961.539

Simulation of effect of structural parameters on the ejector

Bin Li[1,a], Haixia Li[1,b]

[1]School of Mechanical and Power Engineering, Henan Polytechnic University, Jiaozuo 454000, China;

[a]libin457500@163.com, [b]lihx@hpu.edu.cn

Keywords: Ejector; Structural parameters; Simulation; Dimensionless

Abstract. The effect of structure size on the flow field in the ejector was investigated by simulating structural parameters of ejector. Simulation results show that the shock occurred in the flow field of the ejector. The entrainment coefficient shows different trends as different structure parameters change. The effects of nozzle position, inlet diameter and nozzle exit ratio were studied respectively. The simulation result revealed that the structural parameters impact the performance of the gas ejector, having certain engineering application value.

Introduction

The ceramic filter has been considered to be one of the most promising technology of particle separation from gas at high temperature owing to its high filtration efficiency, heat-shock resistance, and gas erosion resistance[1-5] However, it has been pointed out that commercialization of these technologies is critically hindered by the problems with the dust removal system operating at high temperature and high pressure[6,7] The effect of the pulse cleaning system is one of the important factors influencing the stability of ceramic filter with long period. Excellent ejector design has an important impact on the quality of blowback effect. Therefore, to find the optimal structure dimension of venturi diffuser to obtain a larger injection coefficient and achieve better cleaning results. As the experiment restrictive and numerical simulation has the advantage that the distribution of the ejector flow field is displayed. Numerical simulations of full-size gas ejector using computational fluid dynamics software FLUENT carried [8,9].

Methods

An ejector is shown in Fig.1. The main structural member comprises work nozzle, tapered section, throat and diffuser. High pressure purge gas ejected from the nozzle. In the role of suction and shear stress of high pressure blowback gas surrounding gas was sucked into the mixing chamber volume. Then, they exchange momentum, energy with ejector airflow. Gradually uniform mixing and form a single gas stream. Mixed gas pressure begins to rise. In the diffuser, the mixing air pressure continues to rise, the speed is reduced. In the general, airflow pressure in the diffuser is higher than that in the reception room[8,9].

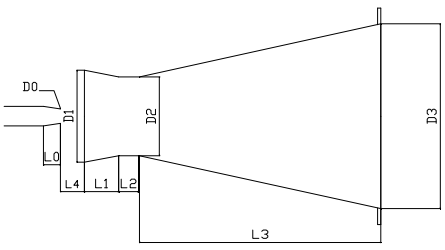

Fig.1 Schematic diagram of diffuser

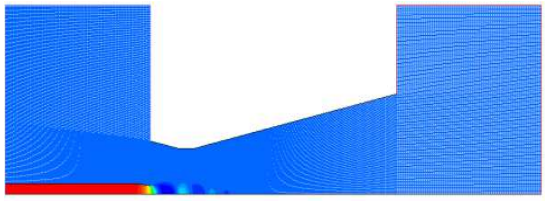

Fig.2 Schematic diagram of pressure distribution diffuser

Performance indicators used in this simulation is the injection coefficient. Referring to a certain conditions, Unit mass of high voltage pulse inverse blow air through ejector can inhale the quality of the low pressure gas. The entrainment coefficient is equal to the ratio of the low pressure gas mass flow Q_a to the mass flow Q_p of high pressure working gas.

The entrainment efficient can be calculated using the following equation:

$$n=Q_a/Q_p \quad (1)$$

Where n--Entrainment coefficient

Q_a--Low-pressure gas mass flow rate, kg/s

Q_p--High-pressure gas blowback mass flow rate, kg/s

The turbulent flow was described by using standard k—ε model which has a high stability, economy, accuracy and wide range of applications considering the flow rate inside the ejector is likely to exceed the speed of sound and the emergence of shock waves, the fluid was set as ideal-gas. Its viscosity is calculated using the law Sutherland. All the walls is taken as a standard wall function; For Pressure, Momentum, Turbulent Kinetic Energy, Turbulent Dissipation Rate and so on, first use of a First-order upwind discretization, After about a hundred iterations changed to second order upwind. Blowing gas entrance is set as pressure-inlet, its value is 0.6Mpa;Low pressure gas entrance is also set as pressure-inlet boundary condition, the pressure value is also 101325Pa. Export is pressure-outlet, The same value of the pressure is taken as 101325 Pa. The structured grid was used to compute the discrete area.

The structure parameters of injector were changed to determine the optimizing structural parameters of the ejector which can have a larger entrainment coefficient.

Results and discussion

The pressure distribution was checked after calculating stability. Pressure distribution was shown in Figure Fig.2. It can be clearly seen from the fig.3 that internal flow field has emerged shock. It showed the accuracy of the simulation is qualified.

Taking into account the structural parameters of ejectors have a lot of size, the non-dimensional method was used to analysis the results of simulation to obtain the main influence factor. The inlet diameter is set as the characteristic length to make other length parameter dimensionless. The structure size of ejector was changed to determine their impact on the entrainment coefficient respectively by observing the change trend of ejector coefficient.

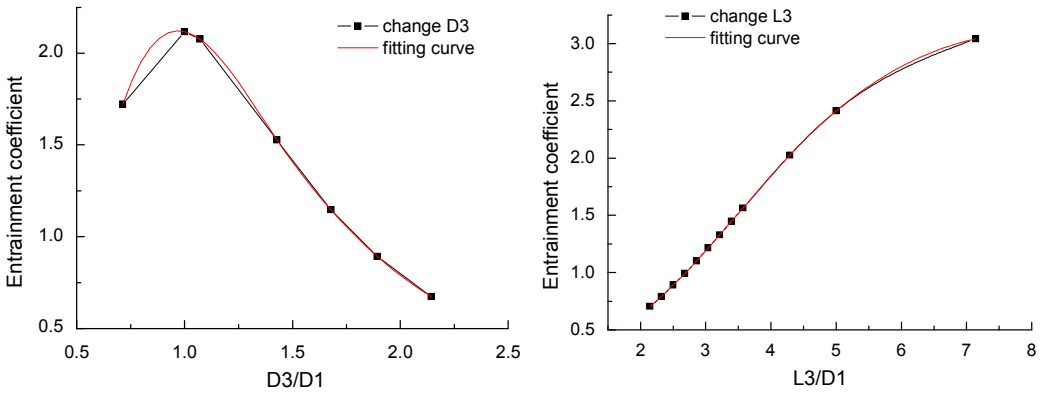

(a) (b)

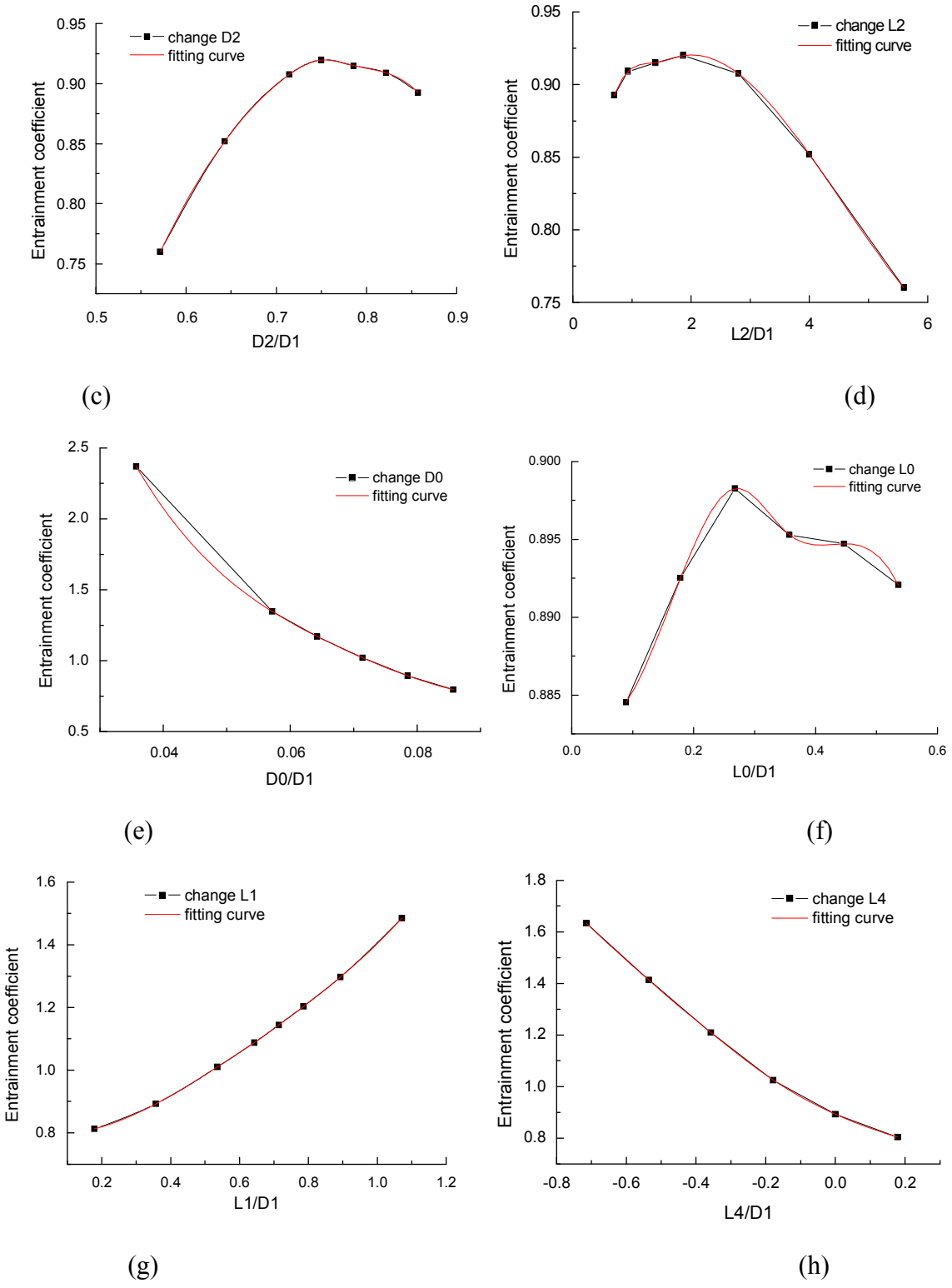

Fig.3 The variation of entrainment with the dimensionless length parameter

The length parameters were changed respectively, such as the ejector outlet diameter D3, the Diffuser length L3, the mixing chamber diameter D2, the mixing chamber length L2, the nozzle diameter D0, the nozzle length L0, contraction length L1 and the distance L4. The trend of the injection coefficient was observed to determine which structural parameter is the preferred. Figure 3 (a), (c), (d) and (f) show that entrainment coefficient variation with D3/D1, D2/D1, L2/D1, L0/D1 increase, but after the first increases and then decreases. The maximum value of 2.12172 occurred when the D3/D1 is 0.9663. The maximum value of 0.9198 occurred when D2/D1 is 0.75. The

maximum value of 0.92006 occurred when the L2/D1 is 2.1411. The maximum value of 0.89828 occurred when the L0/D1 is 0.2740. Furthermore, the slope of curve is sharper in the left side of the peak in figure 3 (a), figure 3 (c) and the right side of the peak in Figure 3(d). When design the value of D3/D1, D2/D1 and L2/D1 should be avoided in this interval when design ejector. This is to avoid the small change will cause a larger ejector coefficient changes.

Although in figure 3(b), (e), (g) and (h) did not appear peak value. Change trend clearly illustrates a situation. In the case of other conditions are met, L3/D1, L1/D1 should set as larger value and D0/D1, L4/D1 set as smaller values to get a larger coefficient ejector. Comparing figure 3(b), (e), (g), and (h), we can see that the slope of the curve is steeper in figure (e). This suggests that D0/D1 has a greater impact on entrainment coefficient. The value of the nozzle diameter D0/D1 should be key consideration in the design.

Conclusions

In this work, the relationship between the structure size and the coefficient of the ejector was obtained. Entrainment coefficient first increased and then decreased, along with the D3/D1, D2/D1, L2/D1, L0/D1 increase. The entrainment coefficient first increased and then decreased at first. While With the L3/D1, L1/D1 increase, it becomes larger. And it gradually becomes smaller as the D0/D1, L4/D1 increases. The ratio of the structure size should be taken to avoid the entrainment coefficient curve slope larger premises. Under the same condition, the part of the relatively steep curve should be considered in the design of ejector.

Acknowledgements

This work was financially supported by Scientific and technological project of Henan Province(102102210209) and Natural Science Foundation of Henan Province (2010B470005).

References

[1] Ji, Z.L., Shi, M.X., Ding, F.X.. Transient flow analysis of pulse-jet generating system in ceramic filter, *Powder Technol.*, 139 (3), 200-207 (2004).

[2] Fei, J.Y., Gao, T.Y., Yao, Y.P., Li, F.. Experimental study of filter flowing characteristics for candle ceramic filter elements, J. *Dalian railway inst.*, 27 (4), 31-34 (2006).

[3] Schimidt, E., Experimental investigations into the compression of dust cakes deposited on filter media, *Filter. Sep.*, 3, 789-793 (1997).

[4] Wu, J.H.,Wang, Y.. Study on an integrated sintered metal screen moving granular bed filter, *Chin.J. Chem. Eng.*, 12 (3),458-462(2004).

[5] Li Haixia, JI Zhongli, WU Xiaolin and CHOI Joo-Hong.Numerical Investigation of Coupling Effect in Multipipe Ceramic Filter Vessel, *Chin. J. Chem. Eng.*, 16(4) 558-563 (2008).

[6] Haixia Li, Zhongli Ji, Xiaolin Wu, Joo-Hong, Choi. Numerical analysis of flow field in the hot gas filter vessel during the pulse cleaning process, *Powder Technology* 173 (2007) 82–92

[7] H. Sasatsu, N. Misawa, M. Shimizu, R. Abe. Predicting the pressure drop across hot gas filter (CTF) installed in a commercial size PFBC system, *Powder Technology* 118 (2001) 58–67.

[8] Kunpeng Zhang, Fei Xue, Weiming Pan, Zhihua Fan. Experimental study and numerical simulation of high-pressure gas ejector, *Thermal Science and Technology* 1671-8097 (2004)

[9] Jianfeng Tang, Minggeng Shi, Yang Liu, Dengdeng Wang. Effect of structural parameters on the performance of the gas ejector, *Fluid Machinery* 005—0329(2012).

Advanced Materials Research Vols. 960-961 (2014) pp 543-546

doi:10.4028/www.scientific.net/AMR.960-961.543

The Research Progress of Steam Jet Pump Design Method

Dong Yang[1, a], Xiaojie Zhang[1,b] and Meng Zhang[1,c]

[1]Shandong Jianzhu Uinversity, Jinan

[a]ydc178@163.com, [b]1098751539@qq.com, [c]476665085@qq.com

Keywords: steam jet pumps, calculation model, design method

Abstract. The use of steam steam ejector is formed in a Laval nozzle entrained flow speed airflow to the power unit of the body, has a simple structure, easy maintenance, stable and reliable, pumping capacity, etc.which is widely used in metallurgy, chemical, pharmaceutical , food and other industries. Based on the comprehensive domestic steam jet pump theory and design based on the results of its variety of design methods reviewed, and in accordance with design features and compare their design processes, raise steam jet pump design trends.

Introduction

Steam jet pump is a low pressure fluid using high pressure fluid pumping fluid machine, usually consists of four parts: Working nozzles, receiving room (absorption chamber), the mixing chamber and diffuser chamber (diffusion chamber). A working fluid energy (pressure and velocity) imported into the injector from the work, through the nozzle at sonic or supersonic flow after, a negative pressure near the exit of the nozzle, under the action of the pressure ejector (low pressure) fluid into the absorbent room, two different pressures stocks mixed fluid mixed in the mixing chamber, resulting in the exchange of mass and energy, and then enlarged mixed fluid pressure chamber pressurized flow. The structure shown in Figure 1:

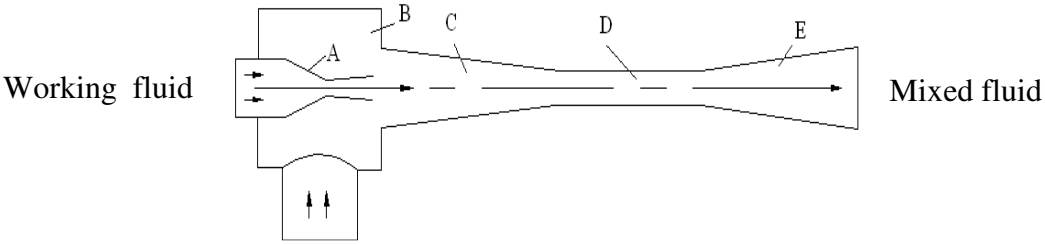

Fig.1 Ejector diagram. A—nozzle section, B—absorbing section, C—mixing section(conical), D—mixing section(cylinder) , E—diffuser section

Steam jet pump has no mechanical energy consumption, simple structure, no moving parts, low running costs, ease of operation and maintenance, and for toxic, flammable, corrosive and contain impurities or condensable gases entrained flow body apply. At home and abroad in the power, petrochemical, metallurgy, textile, refrigeration, industrial thermal engineering and other fields are widely used.

Steam ejector simple structure, but it involves the entrainment speed compressible flow, supersonic mixing, and the shock wave, boundary layer shear layer interactions, complex flow pattern, it is difficult to conduct a detailed flow process mathematical description. In industrial design, mostly used to check the chart method to determine injection coefficient, using the experience of rough estimation methods to determine the structure of the critical dimensions. Using this method injector design work often less than ideal performance, or even a vacuum degree of instability, thus affecting the stability of the entire production, continuity, security. Therefore, the structural design of steam ejector direct impact on the entire production process whether the normal and safe operation.

Calculation of Steam jet pump Model Research

One-dimensional Model. Keenan and Neumann section of a simplified without diffusion studied injector that the injector mixing process is a constant pressure , the injector is first given a complete theoretical analysis and experimental study , the formation of injector a wiki this theory . They assume that the working fluid and entrained flow body has the same molecular weight and the specific heat capacity of the working fluid and entrained flow body and the mixed fluid in any cross-section has a uniform physical distribution of the nozzle and the diffuser inside the process is such entropy process , without the wall resistance of the injector , without export of speed, ideal gas , based on the one-dimensional mass, momentum , and energy conservation equations , derived with a maximum compression ratio or the maximum coefficient of the injection jet geometric parameters optimization formulas and the ejector efficiency is defined as the actual and the ideal jet injection coefficient ratio coefficient . Keenan , also did not take into account the impact resistance , they were considered at constant pressure mixing phase working fluid in a very short distance to accelerate to supersonic speed , the impact resistance is negligible ; Similarly, when supersonic gas flows through the same pipe cross-section , the friction effect is extremely slight . Takashima In this method , based on the various parts of the jet pump friction loss calculations were classified and calculated according to this calculation the optimal performance parameters. However, these calculations are very complicated, and calculated and experimental values of the comparison is very narrow on the basis of the experimental results , it is not a large pressure range are able to set up , so that is not a perfect approach.

Obrine Simplified Model. Obrine put Keenan et al converted into a simple formula generalized equation , obtained by pumping gas is air , the working vapor steam (adiabatic index unchanged) , diffuser throat in the presence of shock steam jet pump design theory, the compression ratio and the entrainment ratio and the expansion ratio is a function . This model assumes that : (l) working steam and was pumping gas at the nozzle outlet to inlet diffuser throat between the isobaric mixing ; (2)ideal gas ;（3）one -dimensional flow . Wei Shiying first two based on the theory proposed by pumping gas is air , the working vapor is wet steam (steam during the expansion of the adiabatic index change), the shock diffuser throat more consistent with the presence of the actual operation of the steam jet pump design theory . Hayami Hui inferior water vapor jet pump also many theoretical problems have been studied , discussed the various factors that affect the pumping performance parameters as well as the state of the law on the pumping performance . Application of these theories is not only computationally intensive design calculations , but also in the practical application of the process by which some of the parameters , the coefficient is difficult to obtain exact values, resulting in theoretical calculations and the pump than the difference between the actual performance .

Cokonob Computational Model. Cokonob can summing the former Soviet Institute of Thermal Engineering Theory and practice based on the results of the working medium is pumped media with the states of matter, the different states of matter, as well as work in the process of change of state analysis of the situation, put forward a different compression ratio, the structural characteristics of the jet pump, design theory and design methods. Cokonob assumptions: (1) the mixing chamber pressure increases linearly; (2) ideal gas; (3) one-dimensional flow. Since the law does not consider the diffuser throat generate positive shock case, and did not fully consider the diverging section of the diffuser role in the calculation of the entrainment ratio decreases, thereby increasing the throat area ratio.

Design of a steam jet pump

Empirical Coefficient Method. Empirical coefficient method is the use of empirical coefficient and experimental investigations taking charts for injector design calculations . Because of this design method is simple , fast , many designers have taken this approach, but this method ah requires designers with rich experience in the design , such as different types, different structures and different working conditions ejector ejector coefficients are different , should the improper selection , it will seriously affect the working performance of the ejector can not even work properly.

Classical Thermodynamics. The first method is based on classical thermodynamics thermodynamics , second law -based , theory , be able to calculate the nozzle section humidity changes each case , but the compression ratio and the entrainment coefficient of the intrinsic link between not limited, can only rely on experience to solve, and classical thermodynamics method ejector key parts of the size , is also a major empirical approach to computing , it is difficult to get accurate results . However, after long-term improvements, part of his experience has been improved , the development has been more mature. Classical thermodynamic method is based on the fluid ejector thermodynamic process design calculation , calculation is relatively simple and convenient. But mostly based on classical thermodynamics law constant pressure hybrid model , simplifying the fluid mixing process, and multi-processing model based on adiabatic manner , and even ignored the impact of the model geometry , as is the mixing chamber and other cross-sectional hybrid model .

Gas Dynamics Function Method. Gas dynamics function method is based on kinetic theory of gases , according to the law of conservation of energy , the introduction of the relative pressure, relative hematocrit , converted isentropic speed dynamical functions , the theoretical analysis and empirical correction method perfected methods of calculation and solve the compression ratio and the entrainment ratio between the calculation of qualifying relationships, injector design calculations rationality has been greatly improved. However, this method are complex and cumbersome formula derivation , calculation of the gas injector is more accurate , but the saturated gas phase flow or humidity changes in the model can not resolve , calculation errors.

Computer Programming and Numerical Simulation. To improve water economy of the steam jet pump , the water vapor jet pump is necessary to optimize performance , and reduce the working steam consumption is particularly important. Current development of computer technology and the industry are closely related , in the steam jet pump jet pump theory based designers to work a minimum of steam consumption design objectives , and consider setting the condenser , condensate water flow and other factors, the compression ratio allocation to optimize the design to determine the objective function , using VB language, C language , Matlab and other writing optimized design process steam jet pump and two examples are calculated with the use of conventional design jet pump, can indeed save working steam .

As a new method of fluid flow , computational fluid dynamics (Computational Fluid Dynamics, CFD) in various industrial areas to be more widely used, at present , CFD methods have started to become enlarged engineering plant optimization and quantitative design tools. It not only gives approximate flow field within the device structure , but also provide some experimental information can not or difficult to measure . We can use existing models and CFD software flow jet pump the fluid simulation to simulate and study the different working media , was pumping gas state, the pump outlet conditions , gas mixing conditions and other factors on the jet pump performance effects and in-depth analysis of fluid flow within the jet pump status , according to the simulation results , and then the steam jet pump design optimization. Thus saving the financial and human resources and time investment. For the numerical simulation of steam jet pump the basic flow is (1) to establish computational model , formulating hypotheses ; (2) to establish the boundary conditions ; (3) for the discrete equations , numerical calculation .

Conclusion

Steam jet pump from the current domestic and international research status view, single-stage jet pump study design methods have matured, but multi-stage steam jet pump is not much research and application. The actual operation of the jet pump automatic detection automatic control needs to be improved. The jet pump theory, along with the continuous development of computer technology, CFD will become mainstream, its rich visualization predict the result will be complex fluid flow jet pump understanding of the issues and the analysis provides great help.

Literature References

[1] Alhussan,K.,Garris,C.. Study the Effect of Changing Area Inlet Ratio of a Supersonic Pressure-Exchange Ejector[C]. 43rd AIAA Aerospace Science Meeting and Exhibit, Paper No. AIAA-2005-519, Reno, NV, USA, 2005.
[2] E. Rusly, A.Lu, W.W.S.Charters, A.Ooi and K. Pianthong.CFD analysis of ejector in a combined ejector cooling system[J]. International Journal of Refrigeration, 28 (2005) ,p.1092-1101.
[3] S. B. Riffat, and S. A. Omer, CFD modeling and Experimental investigation of an ejector refrigeration system using methanol as the working fluid, International Journal of Energy Reservation, 2001, 25,p.115~128.
[4] Deng Guihua. The Mathematical Modeling and Structure Optimization for a Steam Ejector[D]. Shandong：Shandong Jianzhu University，2012.
[5] T. Sriveerakul, S. Aphornratana and K. Chunnanond, Performance prediction of steam ejector using computational fluid dynamics: Part 1. Validation of the CFD results[J]. International Journal of Thermal Sciences, The SCI.2553, Article in press (2006)
[6] H. M. Jeong, H. S. Chung,K. Y. Bae,et al. Water cooling characteristics in an enclosed vacuum tank by water driven ejector[J]. Journal of Mechanical Science and Technology. 2005,19 (1) ,p.164-172.
[7] Guihua Deng, Dong Yang, Riliang Sun, esc. Using the Ejector Technology to Recycle the Steam Exhaust and Its Application in the Engineering Project[J]. Advances in Sciences and Engineering, 2012,Vols.92-96.
[8] Pianthong K., Seehanam K., et al. Investigation and improvement of ejector refrigeration system using computational fluid dynamics technique[J]. Energy Conversion and Management, 2007(48),p.2556-2564.
[9] Eames I.W., Aphornratana S., et al. A theoretical and experimental study of a small-scale steam jet refrigerator [J]. International journal of refrigeration, 1995, 18(6):378-386.
[10] H. D. Kim and B. G. Choi. An experimental study of sonic/supersonic ejector flow[J]. Trans. of KSME, 26 (5) (2002),p. 640-647.
[11] Kun Zhang, Shengqiang Shen, et al. Experimental Investigation of Adjustable Ejector Performance[J]. Journal of Energy Engineering,2012(9)
[12] Chen, Y. M., and Sun, C. Y. .Experimental study of the performance characteristics of a steam-ejector refrig- eration system[J]. Exp.Therm. Fluid Sci., 1997,15(4), 384–394.
[13] Utomo T, Jin Z, Rahman MS,et al. Investigation on hydrodynamics and mass transfer characteristics of a gas-liquid ejector using three-dimensional CFD modeling[J]. Mech Sci Technol. 22(2008):1821–1829.
[14] Zheng SQ, Yao Y, Guo FF, et al. Local bubble size distribution, gas-liquid interfacial areas and gas hold ups in an up-flow ejector[J]. Chem Eng Sci. 2010(65),5264–5271.
[15] Li C, Li YZ, Wang L. Configuration dependence and optimization of the entrainment performance for gas–gas and gas-liquid ejectors[J]. Appl Therm Eng 48 (20 12),p.237–248.
[16] Wu WF, Feng QK, et al. Analysis of inner flow patterns in gas–liquid ejector[J]. Nucl Power Eng 06(2007),p. 34–38.
[17] V. Lijo, H.D. Kim, S. Matsuo, et al. A Study of the Supersonic Ejector-Diffuser System with an Inlet Orifice [J]. Aerospace Science and Technology. 31 August, 2011.
[18] X. Yang, X. Long, X. Yao. Numerical Investigation on the Mixing Process in a Stream Ejector with Different Nozzle Structures[J]. International Journal of Thermal Sciences, vol.56, 2012,p.95–106.

Advanced Materials Research Vols. 960-961 (2014) pp 547-550

doi:10.4028/www.scientific.net/AMR.960-961.547

Air Pressure Reducer Modeling by CFD Methodology

Ranran Wu, Ding Fan

School of Power and Energy, Northwestern Polytechnical University, Xi'an 710072, China

wrr_1120@163.com

Key words: Air pressure reducer; computational fluid dynamics; CFD methodology; displacement-pressure characteristics; SST k-omega turbulence model

Abstract. In this paper, the computational fluid dynamics (CFD) methodology as well as the shear-stress transport (SST) k-omega turbulence model was adopted to model the air pressure reducer (APR). Changing the gas needle's displacement of APR continuously, the writer obtains the displacement-pressure characteristics of APR. In order to demonstrate the validity of these characteristics, a physical experiment was conducted, which generates another displacement-pressure characteristic. Comparing the two characteristics with a good agreement, it is indicated that the CFD methodology is suitable to study the displacement-pressure characteristics of APR.

Introduction

The APR, one key component of afterburner state control system of aero engine, plays a very important role in the afterburner state control system. It can regulate the turbine pressure ratio, making the aero engine operate steadily as expected. However, some problems are still sustained in design, production and manufacture of the APR. These problems hinder its normal use and performance improvement. Therefore, investigating the APR's characteristics is vitally necessary.

In the past decades, little research was carried on about the APR, especially the simulation studies. In this paper, the writer is going to split the computational domains, obtain the relationships between structure parameters and characteristic curves, and study the flow field characteristics. The experimental data obtained by physical experiment are employed to assess the CFD model.

Mathematical model

A 3-D CFD methodology is developed in this paper to investigate the displacement-pressure characteristics of the APR. The Reynolds averaged Navier-Stokes (RANS) equations with the SST k-ω turbulence model are adopted. In the present simulation, the shear-stress transport (SST) k-ω turbulence model is usually adopted as the turbulence model. This turbulence model has been demonstrated to have a better prediction generally in the flow conditions, including large normal strain, separating flow, strong acceleration, etc., which may occur in the flow characteristics of the APR [1,2].

Boundary condition

As shown in Fig. 1(a), the APR has only single inlet and single outlet. As the Mach number in the throat of Laval pipe reaches 1, and becomes greater later, the part of flow outlet as well as the working chamber can be removed, as shown in Fig. 1(b). The essential boundary conditions are listed in Table 1.

Table 1 Boundary conditions of the APR model.

Material Name	Air
Wall Roughness Constant	0.5
Total Pressure of Inlet [MPa]	1.674
Total Temperature of Inlet [K]	300
Specific Dissipation Rate [1/s]	1
Turbulent Kinetic Energy [m^2/s^2]	1
Gauge Pressure of Outlet [Pa]	101325
Backflow Total Temperature [K]	300
Backflow Turbulent Kinetic Energy [m2/s2]	1
Backflow Specific Dissipation Rate [1/s]	1

Mesh model and numerical treatment

Fig. 1(b) schematically shows the simplified mesh model for simulating the APR model. Considering the complexity of its structure, an unstructured mesh is adopted.

There are 1.5 million tetrahedral cells and 2.8 million nodes approximately. In order to simulate the model better, the cell size where the gradient of flow parameters are rather great is set to be shorter. Calculations with different mesh distributions and quantities are carried out to demonstrate that the simulation results are grid independent.

The mathematical model describing the SST k-ω turbulence model belongs to the partial differential equations (PDEs), which can be calculated after discretization. The density-based solver is chosen for the calculation, since it is more suitable to simulate the high velocity flow fluid than the pressure-based coupled solver [1,3]. The multigrid levels are set to 5, which contributes to iteration convergence dramatically [4,5]. The second order upwind scheme is adopted in the flow, turbulence kinetic energy and specific dissipation rate discretization.

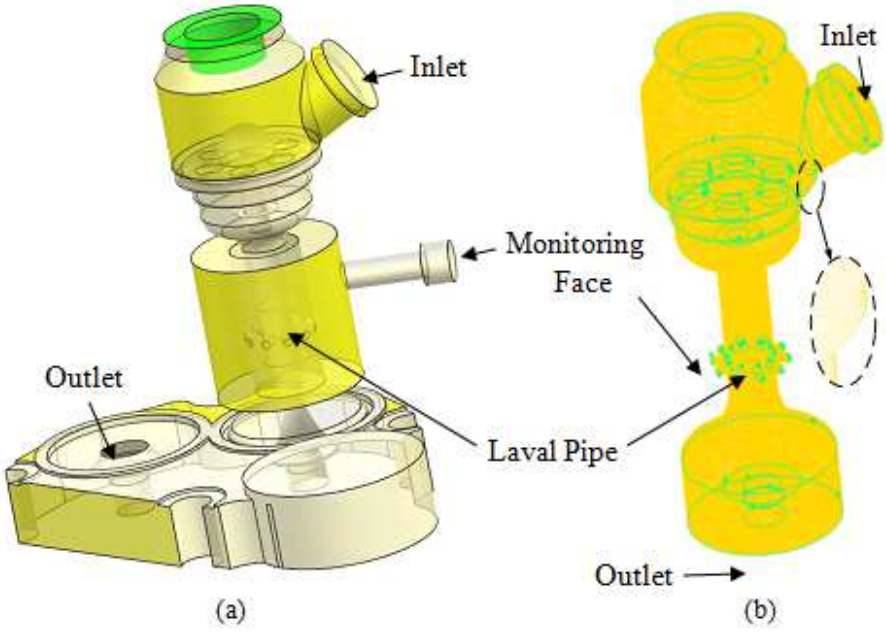

Fig. 1 Schematic of the APR model (a); Simplified mesh model (b)

Results and discussion

In order to validate the present CFD model, a physical experiment is conducted. Therefore, two sets of data are achieved, i.e., the measured data and the predicted data, as shown in Fig. 2. As seen in Fig.2, the predicted displacement-pressure characteristics show a good agreement with the measured'. The pressure monitored increases with an increase of the APR needle's displacement. When the needle's displacement is less than 5.6 millimeters, the pressure monitored increases linearly; then nonlinearly with a greater and changing increasing rate. This phenomenon can be explained by the characteristics of Laval pipe [6]. In addition, all the predicted data are slightly greater than the measured data, from the Fig. 2, since the heat transfer between the inside and outside of fluid field is omitted. Another reason is that, as known to all, there exists variance in the CFD simulation. However, the CFD methodology is often accepted, as long as it is utilized properly.

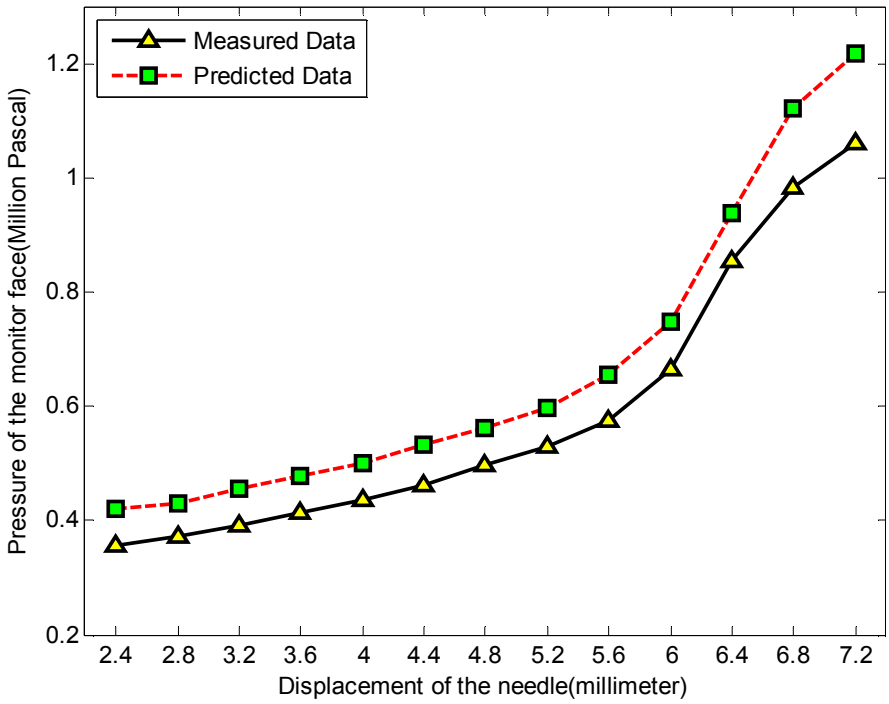

Fig. 2 Comparison of the displacement-pressure characteristics between measurements and predicts

The pressure nephogram and the Mach number nephogram of a symmetrical plane of the APR are obtained by TECPLOT software, as shown in Fig. 3. The air flows into the APR with a high pressure and low velocity. The parameters at the outlet of the top portion are almost the same as that at the inlet of the whole model. The flow fluid runs through the Laval pipe later, with the pressure from 1.6MPa to 0.1MPa, and the Mach number from 0.2 to 3.6. The Mach number reaches to 1 near the throat of the pipe. As the pressure of the outlet of the pipe is about 0.1MPa, which is slightly high, there is a shock wave before the fluid runs out of the pipe. The shock wave decreases the velocity of the fluid, but increases the pressure. The interface between the red color and the blue color in the Fig. 3(b) is the shock wave face. This indicates that the original outlet portion omitted is not essential. Near the outlet, there exist some small swirls.

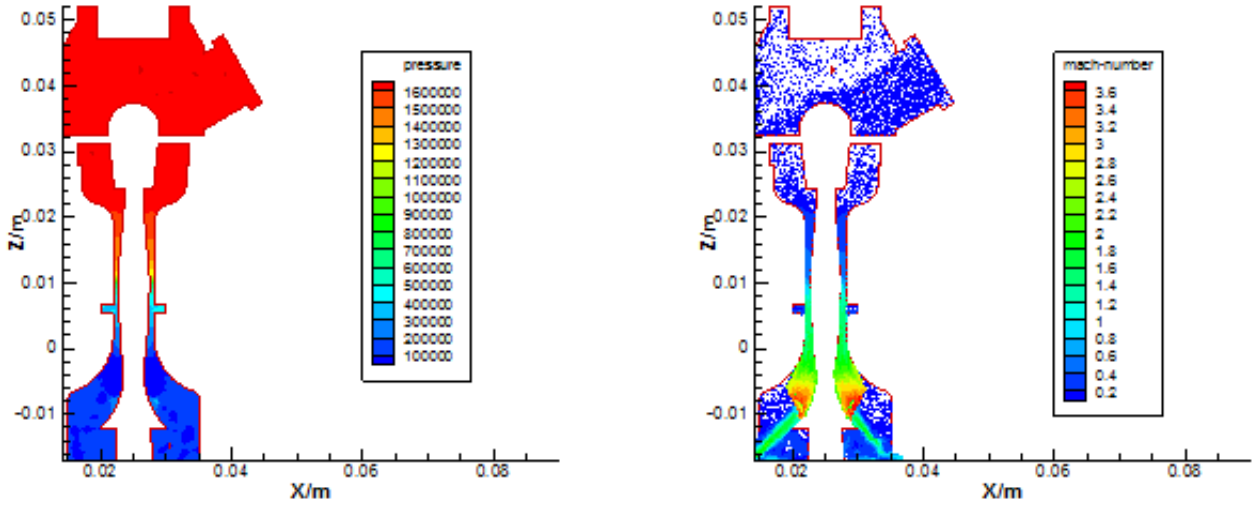

Fig. 3 The pressure nephogram of the APR (a); The Mach number nephogram (b)

Conclusions

In this paper, a 3-D CFD methodology is developed to simulate the displacement-pressure characteristics. A few conclusions can be drawn based on the simulation results and shown as follows:

1. Compared with the measured displacement-pressure characteristics, the present predicted results show a good result. These comparisons indicate that the RANS equation with the SST k-ω turbulence model can be adopted to reasonably simulate the flow behaviors for the APR.
2. The flow characteristics, including flow swirling as well as shock wave, can be reasonably captured by the RANS CFD model with the SST k-ω turbulence model.
3. The outlet portion which has no effect on pressure monitored, can be omitted when simulated.

References

[1] Y.S. Tseng, Y.M. Feng and C.H. Lin. Investigating flow and heat transfer characteristics in a fuel bundle with split-vane pair grids by CFD methodology. Annals of Nuclear Energy, 2014, 64: 93-99.

[2] F.R. Menter. Improved two-equation k-omega turbulence models for aerodynamic flows. NASA STI/Recon Technical Report N, 1992, 93: 22809.

[3] FLUENT 6.3 User's Guide.

[4] B. R. Hutchinson and G. D. Raithby. A Multigrid Method Based on the Additive Correction Strategy. Numerical Heat Transfer, 9: 511-537, 1986.

[5] P. Wesseling. Theoretical and practical aspects of a multigrid method. SIAM Journal on Scientific and Statistical Computing, 1982, 3(4): 387-407.

[6] J. D. Anderson. Fundamentals of Aerodynamics (3rd), 2001, 566-576.

Advanced Materials Research Vols. 960-961 (2014) pp 551-554

doi:10.4028/www.scientific.net/AMR.960-961.551

Numerical Analysis of Flow and Heat Transfer Characteristics on Micro Couette Flow

Lei Huang[1, a], Yang Cui [2,b]

[1]Luoyang Institute of Science and Technology Architectural Engineering,Luoyang 471023 China

Henan Luoyang ,China

[2]Luoyang Institute of Science and Technology Architectural Engineering,Luoyang 471023 China

Henan Luoyang ,China

[a]shuiyishan@163.com,[b]cuiyang0307@163.com

Keywords: Micro-fluidcs, Couette flow,shear stress,velocity slip,temperature jump

Abstract. In this paper, Couette flow is mainly discussed by studying the general flow behaviour mechanism and importing the velocity slip and temperature jump boundary condition. By analyzing velocity, temperature and pressure profiles at different Knudsen numbers, we concluded that Couette flow is driven by shear stress. The shear stress lies in stream direction. Viscous heat causes the increasing of the fluid's temperature. With the increasing of Knudsen numbers, the increasing speed increases. It's in the beginning of transition region that the heat flux has the maximum.

Introduction

In recent years, an important feature of scientific research is the development direction of the micro scale. Because of the mean free path feature size and molecular flow system in the same order of magnitude, gradient change of macro parameters, the traditional theory of fluid dynamics based on the continuum assumption is no longer applicable, The flow and heat transfer in micro scale must be improved. The study of microscale gas flow including three kinds of methods such as the experimental study, numerical calculation and the theoretical analysis . Numerical simulation study mainly includes two aspects: the numerical solution of the Boltzmann equation and Direct simulation Monte Carlo method[1]. Direct solution of the analytical solution is difficult because of the presence of differential and integral complex on Boltzmann equation. Therefore, the theoretical framework of the flow and heat transfer in a suitable for the development of micro scale gas is very meaningful.

This paper mainly discusses a common flow system named Couette flow[2]. This flow system choice argon as flowing medium to calculate the rarefied gas in slip and transitional flow. This establishment of mathematical model based on the Navier-Stokes equations[3], the Fourier Heat transfer law[4] and the state equation of ideal gas[5] considering the rarefied gas effect and boundary conditions. The calculation results using the direct simulation Monte Carlo method (DSMC) to verify its effectiveness.

Control Equation

The calculation is concerned with the gas flow between infinite plates as shown in Fig.1. The distance between the two plates is 1 μm with upper plate is fixed, at the same time the lower plate movementlower plate moving at a certain speed. This flow is called the Couette flow.

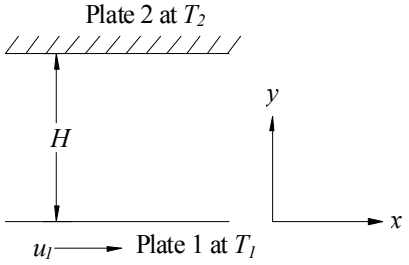

Fig.1 Couette Flow Coordinate Systerm

The flow can be considered as one-dimensional compressible steady flow，the suitable control equations is:

$$\frac{d}{d\tilde{y}}\left(\tilde{\mu}\frac{d\tilde{u}}{d\tilde{y}}\right)=0 \tag{1}$$

$$(\gamma-1)Ma^2\tilde{\mu}\left(\frac{d\tilde{u}}{d\tilde{y}}\right)^2+\frac{1}{\mathrm{Pr}_0}\frac{d}{d\tilde{y}}\left(\tilde{K}\frac{d\tilde{T}}{d\tilde{y}}\right)=0 \tag{2}$$

$$\tilde{p}=\tilde{\rho}\tilde{T} \tag{3}$$

In the formula: $\tilde{y}=\frac{y}{H},\tilde{u}=\frac{u}{u_0},\tilde{T}=\frac{T}{T_0},\tilde{p}=\frac{p}{p_0},\tilde{\rho}=\frac{\rho}{\rho_0},\tilde{\mu}=\frac{\mu}{\mu_0},\tilde{K}=\frac{K}{K_0}$

It will be occur velocity slip and temperature jump [6] phenomenon In the gas solid interface when the number of Kn exceeds 0.001. Schaaf and Chambre[7] indicates the dimensionless velocity slip conditions for single atomic gas:

$$\tilde{u}_s-\tilde{u}_w=\frac{2-\sigma_v}{\sigma_v}\lambda\left(\frac{d\tilde{u}}{d\tilde{y}}\right)_w \tag{4}$$

The dimensionless temperature jump boundary conditions is:

$$\tilde{T}_s-\tilde{T}_w=\frac{2-\sigma_t}{\sigma_t}\frac{2\gamma}{\mathrm{Pr}(\gamma-1)}\lambda\left(\frac{d\tilde{T}}{d\tilde{y}}\right)_w \tag{5}$$

The number of σ_v is a dimensionless quantity and its meaning the tangential momentum accommodation coefficient in the formula(4) . The numerical size of its representation momentum exchange between the degree of perfection of the incident gas molecules and wall: that is

$$\sigma_V=\frac{P_i-P_r}{P_i-P_w} \tag{6}$$

In the formula: the number of P_i is the incident to the wall surface of the momentum flux($kg.m/s^2$); the number of P_r is from the momentum flux wall reflection; the number of P_w as the momentum flux to the wall temperature out of the wall reflection.

The number of σ_t is a dimensionless quantity and its meaning the tangential energy accommodation coefficient in the formula(5). The numerical size of its representation energy exchange between the degree of perfection of the incident gas molecules and wall: that is

$$\sigma_t=\frac{E_i-E_r}{E_i-E_w} \tag{7}$$

In the formula: the number of E_i said the incident to the energy wall molecular flow(*J/s*); the number of E_r said from the molecular energy wall reflection out flow; the number of E_w said the molecular energy to wall temperature out of the wall reflection flow.

Numerical Method

The numerical methods used in this paper is the generalized differential quadrature method[8] (GDQ: Generalized Differential Quadrature Method): this method starting directly from the governing differential equation and take the node parameters as the corresponding time series In the time domain, also use the Lagrange polynomial approximation in the spatial domain to derive algebraic equations in the whole region. The amount of each time point were calculated independently and does not appear cumulative error in this method.

Rsults and Analysis

Velocity distribution. Fig.2 shows the Ma=1.0 under different Kn numbers speed distribution curve. The velocity distribution curve shows a linear distribution with a constant velocity gradient, it also shows shear stress is uniform along the groove height. With the increase of Kn number, the near the wall 2 (stationary flat) fluid velocity increases gradually, and the near the wall 1 (treadmill) fluid velocity gradually decreased. Because of as the Kn number increases, Knudsen layer would be thickened, and slip velocity is greater.

Temperature distribution. The curves of temperature distribution in Fig.3 shows clearly the dimensionless temperature elevation along the channel to the parabolic distribution. For the gas flow of Kn<1.2, the two kinds of model basically coincide. The figure also shows when the Kn number is increased, the more severe the temperature jump. The jump of the theoretical model and the DSMC model is the same to predict the temperature distribution when the Kn number is 0.01and 0.1. With the increase of Kn number, DSMC model to predict the temperature jump is bigger than predicted by the theoretical model.

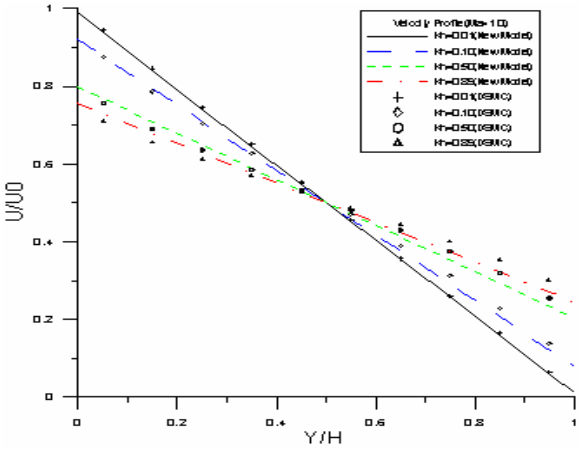

Fig.2 Velocity profiles at Mach 1.0

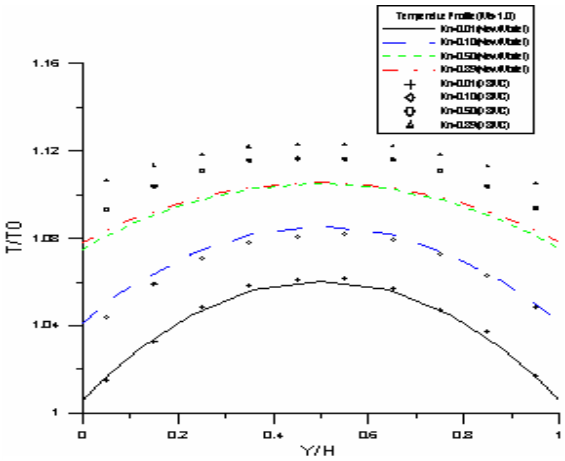

Fig. 3 Temperature profiles at Mach 1.0

Pressure distribution. Fig.4 shows the pressure distribution curve of pressure distribution curve of different under Kn. It shows that it exist larger error between the two models when the Kn number is larger. The DSMC model predicts an uneven pressure distribution, however the theoretical pressure hypothesis model distribution is uniform. And this difference increases gradually with the increase of Kn number.

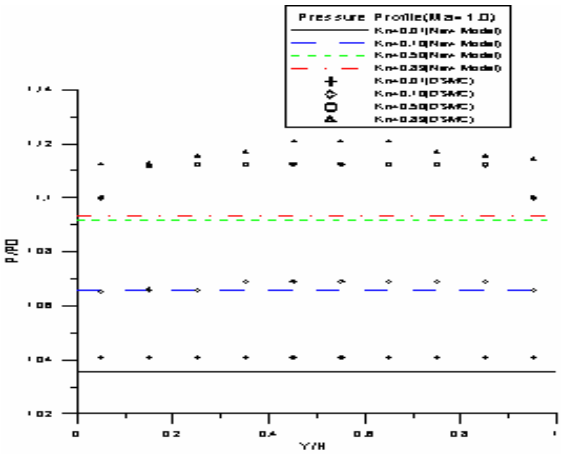

Fig. 4 Pressure profiles at Mach 1.0

Heat flow. The function relation between the dimensionless heat flux and Kn number of the new model and the DSMC model were plotted in Fig.5 and Fig.6. There is a big deviation about the dimensionless heat flux between the theoretical model and the DSMC model in the slip flow region and this deviation flow becomes more obvious when Kn>0.1 in transitional flow. This is because there is a corresponding deviation when use a slip velocity boundary and temperature jump boundary conditions to simulate the interface the actual velocity and temperature. The slip boundary condition was not applicable when Knudsen layer becomes thicker with the increase of Kn number. The prediction of flow line model in Kn>0.04 begins to bend in Fig.5. The deviation appeared in Kn>0.02 when the Maher number Ma=3.0 in Fig.6. With the increase of Kn number the molecules of a gas between two plates almost does not exist collision, so the heat conductivity between the molecules reduced to zero gradually, at the same time, heat transfer rely mainly on the radiation. The result of DSMC model showes that with the increase of Kn number, some characteristics of heat flux changes when the flow becomes more rarefied. The results of theoretical model and DSMC model are not very good agreement for the dimensionless heat flux.

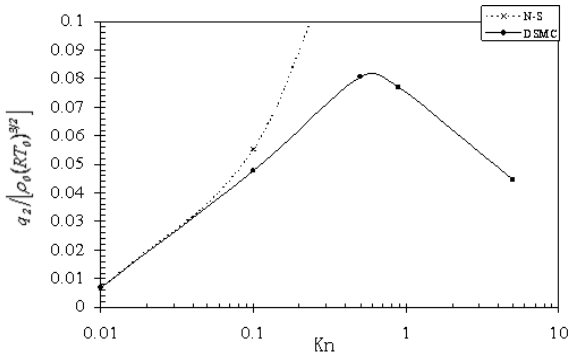

Fig.5 Non-dimensional shear stress at Mach 1.0

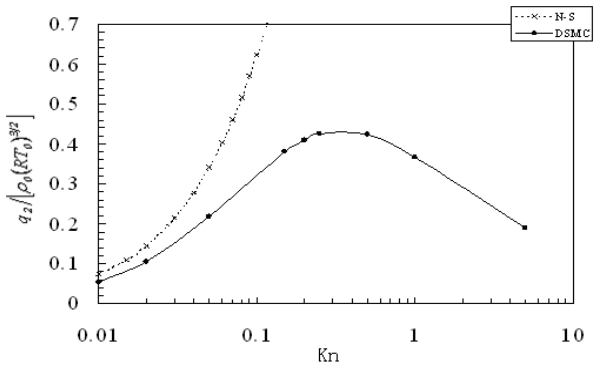

Fig.6 Non-dimensional shear stress at Mach 3.0

Conclusion

This paper discusses the physical mechanism of general micro flow use the macro method for simulation of gas flow and presents a mathematical model about the flow velocity,temperature and pressure distribution of rarefied gas micro Couette flow. This model is based on the N-S equation, also introduces the velocity slip and temperature jump boundary conditions. The theoretical model can be extended to the slip zone and the transition flow region based on the continuum hypothesis. The theoretical framework to analyze the micro Couette flow has been established. The precision of the model was verified through the contraction of direct simulation and Monte Carlo (DSMC). The comparison of the simulation results shows that: this model can reflect the change trend is consistent with DSMC model, but only can predict more accurately when Kn<1.2, the large deviation appears when *Kn*>1.2. Therefore it is still necessary to study the flow characteristics more in-depth about the flow mechanism of micro Couette flow.

References

[1] Devienne F M. Low Density Heat Transfer Advanced In Heat Transfer[J].Acedemic Press, 1965, 2:271-356.

[2] M. Gad-HI-Hak, The MEMS Handbooks, CRC Press (2001), p35-1.

[3] Kong Long.E ngineering Fluid Mechanics(The second edition) [M]. Beijing: Water conservancy and electric power press，1990：249-262.

[4] Yu Zuo-ping. Heat transfer[M]. Beijing: Higher Education Press,1988:3-19.

[5] Shen Wei-dao, Zheng Pei-zhi,Jiang Dan-an. Engineering Thermodynamics(The second edition) [M]. Beijing: Higher Education Press,1990:66-72.

[6] Arklic E.B, Breuerk.s, Schmidt M.A. Gaseous Flow in Microchannels.ASME FED-Vol.197,99.

[7] S . A. Schaaf, P. L. Chambré, Flow of Rarefied Gases, Vol. 8, Princeton Aeronautical Paperbacks, Princeton University Press, Princeton, New Jersey, 1961.

[8] C . Shu, B. C. Khoo, K.S. Yeo, Numerical Solutions of Incompressible Navier-Stokes Equations by Generalized Differential Quadrature, Finite Elements in Analysis and Design, 18 (1994) 83-97.

Advanced Materials Research Vols. 960-961 (2014) pp 555-558

doi:10.4028/www.scientific.net/AMR.960-961.555

The research on the influence law of the fluid temperature in ground heat exchange on system operation

Zishu Qi [1, 2, 3, a], Qing Gao [2, 3, *b], Zhenhai Gao[2], Yan Liu[2, 3] and Li Bai[1]

[1] Key Laboratory of Songliao Aquatic Environment of Ministry of Education, Jilin Jianzhu University, Changchun 130118, PR China

[2] State Key Laboratory of Automotive Simulation and Control, Jilin University, Changchun 130025, PR China

[3] Department of Thermal Energy Engineering, Jilin University, Changchun 130025, PR China

[a]senior00685@163.com, [b] gaoqing@jlu.ed.cn

[*] Corresponding author. Fax: +86 431 85094241.

E-mail address: gaoqing@jlu.ed.cn (Qing Gao).

Keywords: ground heat exchanger; fluid; temperature; power consumption

Abstract. In the paper, by studying the underground heat exchanger heat transfer mode, the computing platform for ground source heat pump system was established. Through a engineering case, the influence character of the fluid temperature at the outlet of ground heat exchange on the length of system, the fluid temperature in ground heat exchange, and the heat pump power consumption were analyzed, which provide an approach for engineering design and operation prediction, and for the thermodynamic analysis of performance of system year by year and prospective study to guide the engineering practice.

Introduction

Renewable energy is the inevitable choice for the future sustainable energy development, and earth energy utilization as well as its underground shallow as good heat reservoir to provide application space for heat pump technology, have aroused great attention in the world. Earth energy utilization is promising in fields of building HVAC (Heating, Ventilation and Air Conditioning) engineering, and melting snow and deicing in road traffic [1]. However, imbalance problem between cooling load and heating load in the HVAC system has long plagued heat pump engineering application of using earth energy in severe cold region. People have been seeking a solution for best efficiency.

In the paper, through a engineering case, the influence character of the fluid temperature at the exit of ground heat exchange on the length of system, the fluid temperature in ground heat exchange, and the heat pump power consumption were analyzed, which provide an approach for engineering design and operation prediction

The model

The fluid temperature in ground heat exchange. In the paper [2]**,** it systematically explored the establishment of modules, module scarf and coupling call based on Matlab/Simulink calculation control platform, established the basic analysis method of heat pump system. The calculation diagram of the fluid temperature at the outlet of ground heat exchange is shown in Fig.1. Eskilson developed an approach to determine the temperature distribution around a borehole based on a hybrid model combining analytical and numerical solution techniques called G function[3] [4]. The theory of G function of ground heat exchange is used to compute the borehole temperature and the thermal resistance of borehole by entering relevant parameter of ground heat exchange and thermophysical property date of ground, and output of the fluid temperature at the outlet of ground heat exchange.

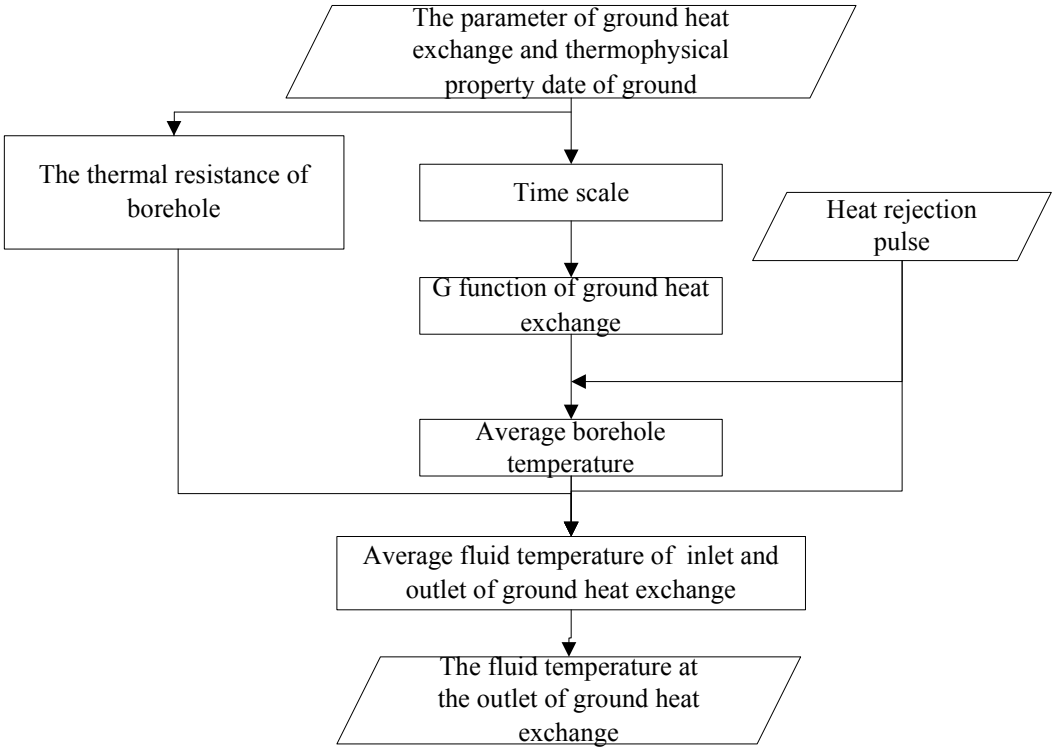

Fig. 1 The calculation diagram of the fluid temperature at the outlet of ground heat exchange

This provided hourly data for the space heating loads or cooling loads for the building in Changchun, China, a summary of the loads are shown in Fig.2. The purpose of this case is to research the influence character of the fluid temperature at the outlet of ground heat exchange on the length of system, the fluid temperature in ground heat exchange, and the heat pump power consumption for the space heating loads or cooling loads for 20 years.

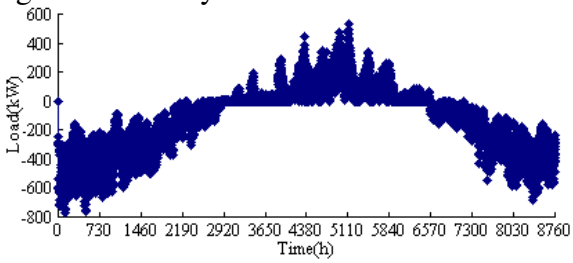

Fig. 2 Building loads

Results and discussion.

The design depth of borehole. The design depth of borehole is limited to the minimum fluid temperature at the outlet of ground heat exchange, and it decides initial cost and the life of project directly. In this case, we respectively select the minimum fluid temperature at the outlet of ground heat exchange of 0℃,-4℃,-6℃,-10℃. The deepest depth of borehole and biggest initial cost are caused by the increment of the minimum fluid temperature at the outlet of ground heat exchange. The longest life of project is caused by the decrement of the minimum fluid temperature under the same depth of borehole. In the Fig.3, a relationship diagram for the depth of borehole and the minimum fluid temperature at the outlet of ground heat exchange. Under this design conditions, we have to redesign the system for optimal solution for the minimum fluid temperature.

The average fluid temperature of GHE. As can be seen from the Fig.2, in Changchun, the heat load significantly greater than cooling load annual and the average fluid temperature of GHE declines year by year. After 20 years, we respectively select the minimum fluid temperature at the outlet of ground heat exchange of 0℃，-4℃，-6℃，-10℃ for the different depth as Fig.3. The average fluid

temperature of GHE can be calculated in Fig.4.After 20 years, the minimum average fluid temperature is -7.74℃ during operation time for when temperature is set at -10℃.

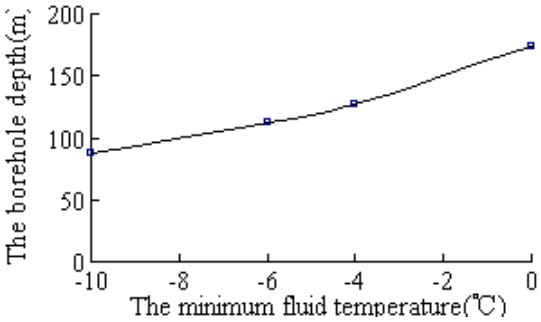

Fig. 3 The depth of borehole

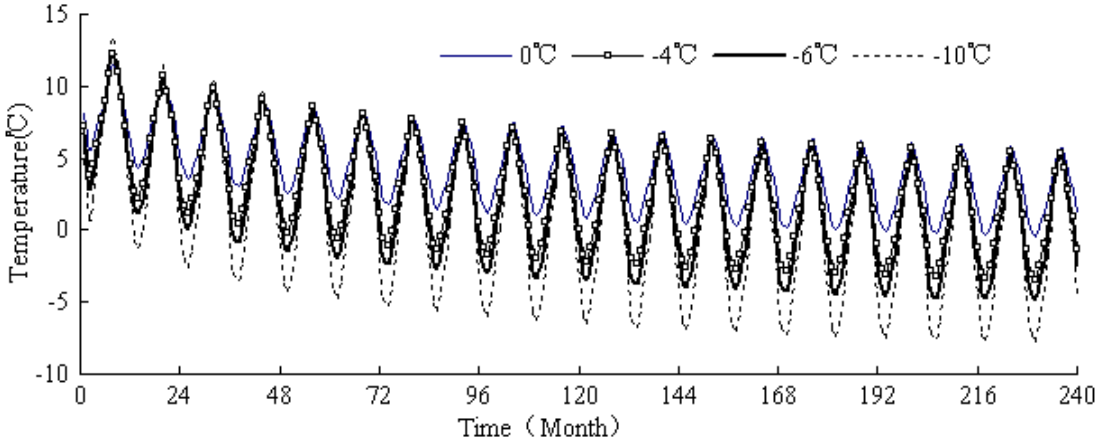

Fig. 4 The average fluid temperature of GHE

Power consumption. The power consumption for heat pump can be calculated in four conditions in Fig.5. In Changchun, the power consumption for heat pump is increase especially temperature is set at -10℃, due to the fluid temperature is low year by year. With lower fluid temperature, the energy consumption is increase. The power consumption only rises 4.25% when temperature is set at 0℃, after 20 years. When temperature is set at -10℃, because of the imbalance of heating and cooling load, the average fluid temperature of GHE decreases year by year, power consumption for heat pump rises 6.27% for 20 years.

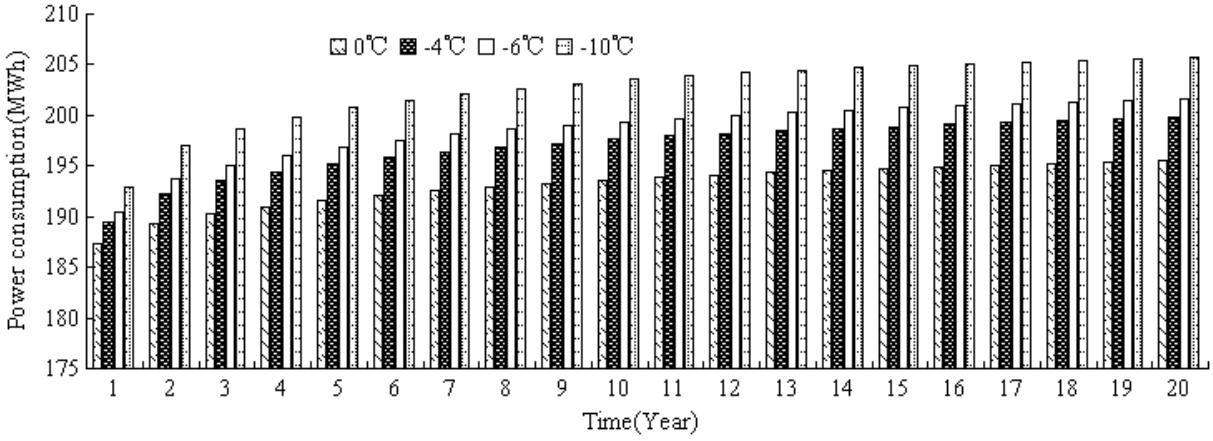

Fig. 5 Power consumption

Conclusion

In the paper, it is to study of underground heat exchanger heat transfer mode and calculate fluid temperature at the outlet of ground heat exchange. Through a engineering case, the influence character of the fluid temperature at the outlet of ground heat exchange on the length of system, the

fluid temperature in ground heat exchange, and the heat pump power consumption were analyzed, which provide an approach for engineering design and operation prediction

Acknowledgements

The authors gratefully acknowledge the financial support from the NSFC (National Natural Science Foundation of China) under the grant No. 51376080, 51076059, 41072198, Key Laboratory of Songliao Aquatic Environment of Ministry of Education, Department of Education of Jilin Province under the grant No.237(2014), Ministry of Housing and Urban-Rural Development of the People's Republic of China, Doctor Scientific Research Staring Foundation of Jilin Jianzhu University.

References

[1] Q Gao, M Li, M Yu, J D. Spitler, Y.Y. Yan. Review of development from GSHP to UTES in China and other countries [J]. Renewable and Sustainable Energy Reviews, 2009，13（6-7）：1383-1394.

[2] Zishu Qi. Diversity and Efficiency on Energy Mechanism of Heat Pump System by Using Earth Energy, Doctoral Dissertation. Jilin University, China, 2012.

[3]Xiaowei Xu. Simulation and optimal control of hybrid ground source heat pump systems, PhD Dissertation. Oklahoma State University, Oklahoma, USA, 2007.

[4] Spitler, J.D. 2000. GLHEPRO -- A Design Tool For Commercial Building Ground Loop Heat Exchangers. Proceedings of the Fourth International Heat Pumps in Cold Climates Conference, Aylmer, Québec. August 17-18, 2000.

Advanced Materials Research Vols. 960-961 (2014) pp 559-567

doi:10.4028/www.scientific.net/AMR.960-961.559

Total energy consumption optimization design of surface-water source heat pump systems

Min Liu[1, a], Ronghua Wu[1,b] and Qirong Yang[1,c]

[1]Institute of Mechanic and Electronic Engineering,Qingdao University,

308 Ningxia Road, Qingdao,Shandong,China 266071

[a]lm664083242@sina.com, [b] wuronghua18@126.com, [c] luyingyi125@163.com

Keywords: Transmission and distribution energy consumption(TDEC), Optimization design, Variable Flow(VF), Constant Flow(CF)

Abstract. This paper deals with the study of transmission and distribution energy consumption (TDEC) optimization design about surface-water source heat pump system. Three mathematical model have been established. The fitted polynomials of *COP*, N_e, N_c were obtained by the MATLAB curve fitting toolbox according to datum from product samples. The differences between two operating states which are constant flow and variable flow were analyzed and compared. Under variable flow operating state it was found that there exists an maximum energy conversation rate12.68% of TDEC; the heat pump unit will consume more than average 8.41% energy, while *COP* will decline average 7.61%, the mean energy conversation rate of N_e and N_c are 49.38% and 38.86%, the average declination rate of t_{ein} and t_{cout} are 17.09% and 5.73% compared with constant flow operating state.

Introduction

With the rapid development of global economy, energy and environment problems are becoming more and more serious. In the whole energy consumption, building energy consumption possess a large proportion, and Heating Ventilation and Air Conditioning(HVAC) part occupies a lot[1]. As a kind of energy consumption and environment protection technology, SWSHP(Surface-water source heat pump) can greatly reduce air conditioning energy consumption, taking into consideration of a tendency that people pay more and more attentions to the indoor environment quality, SWSHP will get more and more applications. However in the current SWSHP systems there exist " two low and one high " phenomenons: low efficiency of heat pump units, low water pump efficiency and high operating energy consumption. In order to solve the above problems, it is necessary to optimize TDEC(transmission and distribution energy consumption) of SWSHP system so that it will truly realize energy saving and environment protection goal.

This paper will analyze the energy consumption difference between two operating conditions of SWSHP system: constant flow and variable flow. When heat pump unit keeps operating in a constant flow state, it will maintain high *COP* compared with variable flow state[2,3], however this will lead more pump energy consumption. Reference[4] put forward that under variable flow state it will be more energy efficient compared with constant flow state. It is filled with contradiction between high *COP* and low water pump energy consumption, the purpose of this paper is to solve this contradiction through optimization to TDEC by MATLAB optimization toolbox.

SWSHP system components

A integral SWSHP system contains there subsystems: Refrigerant cycle system, chilled water system, cooling water system, the flow chart of SWSHP system is shown in Fig.1.

- Refrigerant cycle system: it includes the following four components: compressor, condenser, evaporator, expansion value. The compressor needs to consume energy in order to maintain system cycle.

• Chilled water system: chilled water pump, evaporator and pipeline are the main components. Chilled water pump provides hydraulic press to overcome resistance of evaporator and pipeline.

• Cooling water system: cooling water pump, condenser make a loop through pipeline. The cooling water from surface water with lower temperature can absorb heat from high temperature refrigerant vapor so that the surface water can be regarded as one kind of environment protection heat sink.

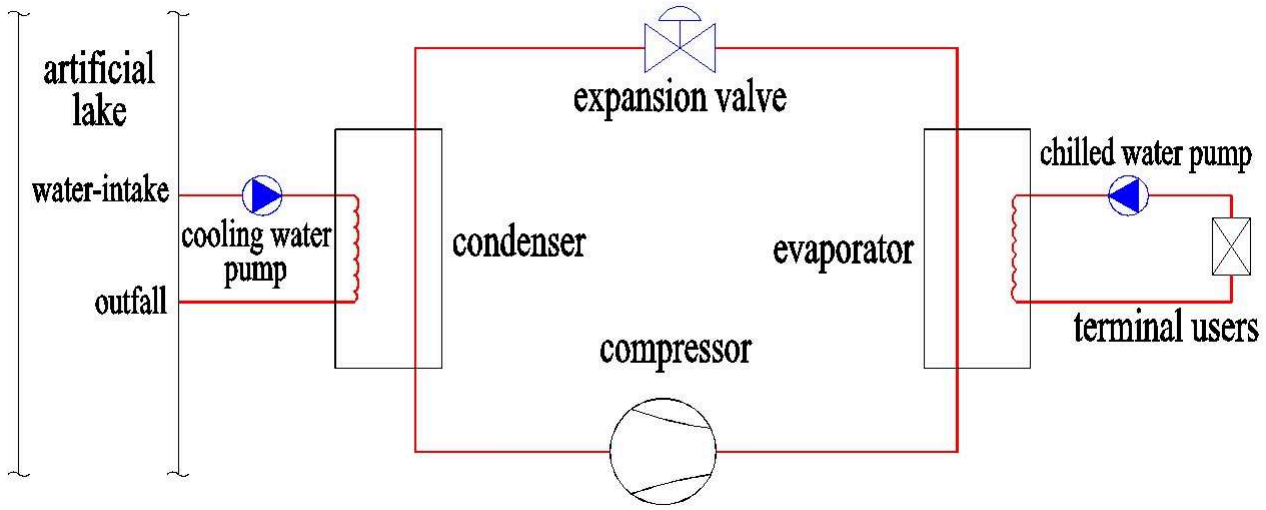

Fig.1 Flow chart of SWSHP system

Model establishment

Heat pump model. In summer air conditioning conditions, heat pump carries through reverse Carnot cycle, *COP* (Coefficient of performance) is proportional to t_0 and inverse proportional to t_k[5], when V_e and V_c keep constant, the mathematical model of *COP* can be described by formula (1):

$$COP_1 = \alpha_1 \exp(\alpha_2 t_0 + \alpha_3 t_k) + \alpha_4 t_0/t_k + \alpha_5. \quad (1)$$

When t_0 and t_k keep constant, *COP* can be described by formula (2):

$$COP_2 = \beta_1 \exp(\beta_2 V_e + \beta_3 V_c) + \beta_4 V_e/V_c + \beta_5. \quad (2)$$

Where, t_0 and t_k are chilled water outlet temperature and cooling water inlet temperature respectively, V_e, V_c are flow rate of chilled water and cooling water respectively, α_1-α_5 andβ_1-β_5 are fitted coefficients.

Under the actual operating conditions, the above parameters t_0, t_k, V_e, V_c are not always keep constant, their values can be changed according to load rate of users. Taking into account the variation of users' load rate–*R*, the mathematical model of *COP* can be described by formula (3):

$$COP = [\alpha_1 \exp(\alpha_2 t_0 + \alpha_3 t_k) + \alpha_4 t_0/t_k + \alpha_5] \cdot [\beta_1 \cdot \exp(\beta_2 V_e + \beta_3 V_c) + \beta_4 V_e/V_c + \beta_5]/\beta_6. \quad (3)$$

Where α_1-α_3 , β_1-β_6, represent fitted coefficients.

Chilled water pump model. In theory, energy consumption of chilled water system concludes water pump energy consumption, cooling loss etc. In order to simplify calculation, it can only consider the major energy consumption—chilled water pump energy consumption. In general, chilled water system is closed system. It needs a minimal differential pressure ΔH_{emin} to ensure that the most unfavorable terminal device can work normally. The pipeline characteristic curve, chilled water pump energy consumption and volume flow rate can be expressed respectively by formula (4), (5) and (6):

$$H_e = \Delta H_{emin} + S_e V_e^2. \quad (4)$$

$$V_{\mathrm{e}}=\frac{Q_{\mathrm{e}}}{\rho C_{\mathrm{p}}\left(t_{\mathrm{ein}}-t_0\right)}. \tag{5}$$

$$N_{\mathrm{e}}=\frac{\rho g V_{\mathrm{e}} H_{\mathrm{e}}}{\eta_{\mathrm{e}}}. \tag{6}$$

Where, H_{e}, N_{e}, η_{e} are lift, power and total efficient of chilled water pump respectively. Q_{e} is cooling load in the evaporator side. ρ and C_{p} are density and specific heat capacity of water. g is gravitational acceleration, S_{e} is impedance of chilled water pipeline. t_{ein} is inlet water temperature of evaporator.

For a given actual project, ΔH_{emim}, Q_{e} and S_{e} can be approximately regarded as constant, and it will satisfy the engineering demand. Meanwhile η_{e} is the function on V_{e}. Through above simplification it was found that N_{e} is only connected with V_{e}. So it is easy to get a polynomial of N_{e} on V_{e} through taking advantage of cftool (curve fitting toolbox) of MATLAB. The polynomial can be shown by formula (7):

$$N_{\mathrm{e}}=\gamma_0+\gamma_1 V_{\mathrm{e}}+\gamma_2 V_{\mathrm{e}}^2+\gamma_3 V_{\mathrm{e}}^3. \tag{7}$$

Where γ_0-γ_3 represent fitted coefficients.

Cooling water pump model. It is known that cooling water system is a open system, there exists a height difference ΔH_0 between water intake surface and water drainage surface. it is feasible that water pump energy consumption is only considered after ignoring energy dissipation and other loss. According to energy conservation principal the function of V_{c} on Q_{e} and COP can be deduced. The pipeline characteristic curve, chilled water pump energy consumption and volume flow rate can be expressed respectively by formula. The following formula(8), (9), (10),(11) can be used to calculate N_{c}:

$$H_{\mathrm{c}}=\Delta H_0+S_{\mathrm{c}} V_{\mathrm{c}}^2. \tag{8}$$

$$V_{\mathrm{c}}=\frac{Q_{\mathrm{e}}+W_{\mathrm{co}}}{\rho C_{\mathrm{p}}\left(t_{\mathrm{cout}}-t_{\mathrm{k}}\right)}. \tag{9}$$

$$W_{\mathrm{co}}=\frac{Q_{\mathrm{e}}}{COP}. \tag{10}$$

$$N_{\mathrm{c}}=\frac{\rho g V_{\mathrm{c}} H_{\mathrm{c}}}{\eta_{\mathrm{c}}}. \tag{11}$$

Where, H_{c}, N_{c}, η_{c} are lift, power and total efficient of cooling water pump respectively. S_{c} is impedance of cooling water pipeline. t_{cout} is outlet water temperature of condenser. W_{co} is energy consumption of heat pump unit.

For a given actual project, ΔH_0, Q_{e} and S_{c} can be approximately regarded as constant, and it will satisfy the engineering demand, meanwhile η_{c} is the function on V_{c}. Through above simplification it was found that N_{c} is only connected with V_{c}. The polynomial of N_{c} on V_{c} can be obtained by curve fitting toolbox of MATLAB. The polynomial can be shown by formula (12):

$$N_{\mathrm{c}}=\lambda_0+\lambda_1 V_{\mathrm{c}}+\lambda_2 V_{\mathrm{c}}^2+\lambda_3 V_{\mathrm{c}}^3. \tag{12}$$

Where λ_0-λ_3 represent fitted coefficients.

TDEC model. Through above three mathematical model TDEC of SWSHP system can be expressed by formula (13):

$$N_{\mathrm{t}}=W_{\mathrm{co}}+N_{\mathrm{e}}+N_{\mathrm{c}}. \tag{13}$$

Where N_t is the sum of heat pump unit, chilled water pump and cooling water pump energy consumption.

It is obvious that N_t is determined by six parameters: V_c, V_e, t_{ein}, t_0, t_k, t_{cout}, through analyzing formula (13), it is a multi-parameter function which includes some nonlinear and linear constraints such as mass conservation, energy conservation and flow limit of heat pump unit etc. And this optimization problem can be solved by MATLAB optimization toolbox.

Optimization function analysis. In the MATLAB optimization toolbox the fmincon function can solve such problems very well[6,7]. It contains four optimization algorithm: Trust region reflective, Active set, Interior point and SQP. It needs to create two M-file which stand for objective function and constraints respectively. The invoking format is shown as formula (14):

$$[x, fval, exitflag, output]=\text{fmincon}(@myfun, x0, A, b, Aeq, beq, lb, ub, @mycon). \quad (14)$$

Where, x represents variations, *fval* represents function value, *exitflag* represents the optimizing final state, *output* represents outputting the optimization message, *myfun* represents objective function expression, *x0* is a initial value so that the calculation can begin, A and b represent linear inequality, *Aeq* and *beq* represent linear equality, *lb* and *ub* represent the lower and upper bound, *mycon* represents nonlinear inequality.

Project case analysis. Here an actual project case was analyzed. This building which is used to office and dormitory is located in Qingdao China. In the northwest of the building there is an artificial lake whose dimensions are 80m long × 30m wide × 6m deep, annual mean water yield is roughly 8600 cubic meter, the maximum and minimum water temperature of the lakebed are 3℃and 28℃.

The total construction area of this project is 3750 square meter. Air conditioning cooling load is 300kW, the water-source heat pump unit is TECKA SRSW-90-1，the cooling water pump is KQB 80-125, and chilled water pump is KQB 80-160B.In the air conditioning water system variable flow primary pumps form is adopted, the terminal devices is fan coil. The design parameters of this SWSHP system are shown in Table.1.

Table.1 Design parameter

Parameter	Value	Parameter	Value
Q_e[kW]	300	Q_c[kW]	354.4
H_e[m]	22.17	H_c[m]	17.77
S_e[h^2/m^5]	0.0072	S_c[h^2/m^5]	0.0037
ΔH_{emin}[m]	3	ΔH_0[m]	4
t_0[℃]	7	t_k[℃]	27
t_{ein}[℃]	12	t_{cout}[℃]	32
V_e[m^3/h]	51.6	V_c[m^3/h]	61

According to formula (3) and correction coefficients Table.2 and Table.3 of heat pump unit sample, fitted values of α_i and β_i (i=1~6) were obtained as follow:the row vector of $\boldsymbol{\alpha}$=[-0.06178 -0.02769 0.1266 1.98909 5.455514], $\boldsymbol{\beta}$=[-5.9920 -0.02963 -0.00319 -0.6669 8.05699 5.511]. The variation tendency of COP_1 with t_0, t_k and COP_2 with V_c, V_e can be obtained which were shown in Fig.2 and Fig.3 respectively.

Table.2 Cooling performance correction coefficient table of variable temperature

t_{ein} [℃]	t_0[℃]	t_k [℃]									
		10		14		18		21		25	
		t_{cout}[℃]									
		21		25		29		32		36	
		Q_e	W_{co}	Q_e	W_{co}	Q_e	W_{co}	Q_e	W_{co}	Q_e	W_{co}

		[kW]	[kW]	[kW]	[kW]	[kW]	[kW]	[kW]	[kW]	[kW]	[kW]
10	5	0.97	0.90	0.94	0.96	0.92	0.98	0.89	1.04	0.85	1.07
12	7	1.05	0.91	1.02	0.97	1.00	1.00	0.96	1.06	0.93	1.10
14	9	1.13	0.92	1.10	0.99	1.07	1.02	1.03	1.08	0.99	1.14
16	11	1.20	0.93	1.17	1.01	1.15	1.04	1.11	1.10	1.05	1.16
18	13			1.22	1.02	1.20	1.05	1.17	1.12	1.10	1.19
20	15			1.25	1.03	1.24	1.06	1.24	1.13	1.15	1.20

Table.3 Cooling performance correction coefficient table of variable flow

V_e[m^3/h]	V_c[m^3/h]				
	31.04	43.45	55.87	68.28	80.70
28.96	0.9272	0.9839	1.0180	1.0417	1.0592
34.74	0.9693	1.0286	1.0642	1.0890	1.1073
40.25	1.0030	1.0643	1.1012	1.1268	1.1458
46.30	1.0303	1.0934	1.1312	1.1576	1.1770
52.09	1.0524	1.1168	1.1555	1.1824	1.2023

By observing Fig.2 and Fig.3 it was found that COP_1 will increase with increase of t_0, t_k, and COP_2 will increase with increase of V_c, V_e. It can be explain by that when flow rate increases, it can improve the fluid velocity, thus it will enhance heating transfer effect which is beneficial to improving *COP*.

According to the samples of chilled water pump and pipeline characteristic curve, the values ofγ_0-γ_3 can also be calculated, then put the results into formula (7):

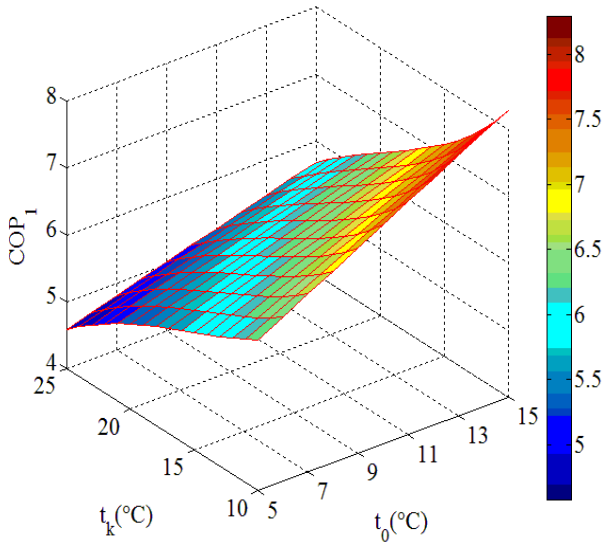

Fig.2 COP_1 with different t_0, t_k

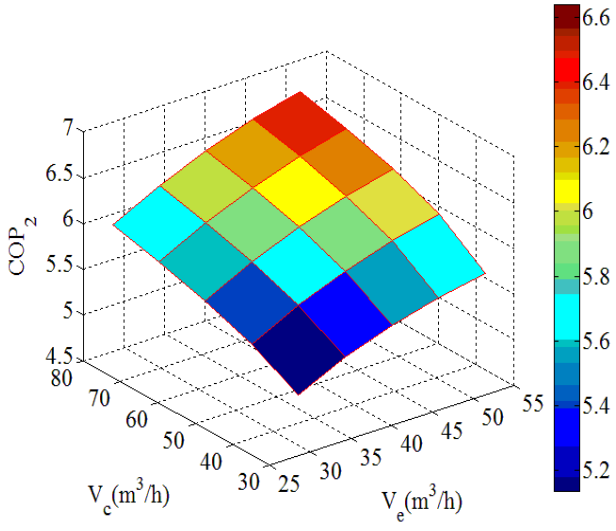

Fig.3 COP_2 with different V_e, V_c

$$N_e = 0.11 + 0.0066V_e + 0.00034V_e^2 + 2.6e-05V_e^3. \quad (15)$$

Similarly λ_0-λ_3 can be obtained by cooling water pump sample and pipe characteristic curve, then put the results into formula (12):

$$N_c = 0.11 + 0.012V_c + 0.00015V_c^2 + 1.4e-05V_c^3. \quad (16)$$

The variation tendency of N_e and N_c are shown in Fig.4.

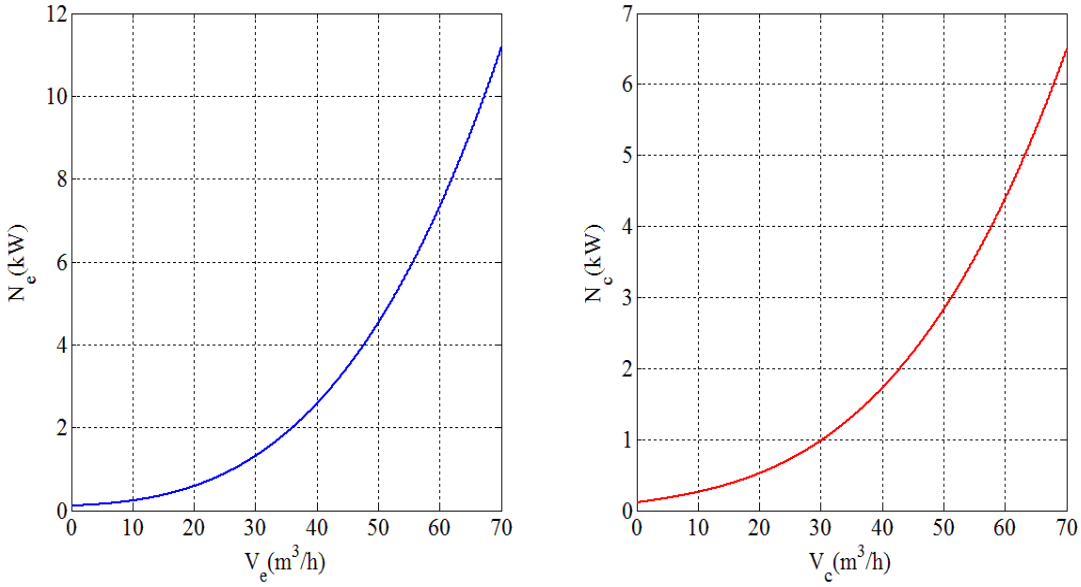

Fig.4 N_e and N_c with different V_e and V_c

It is obvious that both N_e and N_c reduce with the decrease of V_e and V_c respectively, it can illustrate that when variable flow condition was adopted there will save quite lots of energy consumption when terminal load of users begins to decrease.

Comprehensive optimization. According to above results, firstly it is necessary to create two M-file, then list various kinds of equality constraints and inequality constraints. The range of the six parameters V_c, V_e, t_{ein}, t_0, t_k, t_{cout} are shown in Table.4.

Table.4 Parameter range

Parameter	Range	Parameter	Range
V_c[m^3/h]	20-62	t_k[°C]	20-30
V_e[m^3/h]	15-52	t_{cout}[°C]	28-40
t_{ein}[°C]	8-15	t_{ein}- t_0[°C]	0-10
t_0[°C]	5-9	t_{cout}- t_k[°C]	0-11

COP, W_{co}, N_e, N_c under constant flow rate condition can be obtained by Table.1,and the energy consumption results are shown in Table.5.

Table.5 Energy consumption under constraint flow(CF)

R[%]	N_e[kW]	N_c[kW]	W_{co}[kW]	N_t[kW]
100	4.959	4.596	58.254	67.809
90	4.959	4.596	52.428	61.983
80	4.959	4.596	46.603	56.158
70	4.959	4.596	40.777	50.332
60	4.959	4.596	34.952	44.507
50	4.959	4.596	29.127	38.682
40	4.959	4.596	23.301	32.856
30	4.959	4.596	17.476	27.031

Taking into account of indoor temperature and humidity requirements t_0 and t_k should be regarded as constant whose values are 7°C and 27°C respectively, meanwhile the load rate R need to be 30% at least.

The optimization results are shown in Table.6.

Table.6 Energy consumption under variable flow(VF)

R[%]	N_e[kW]	N_c[kW]	W_{co}[kW]	COP	V_e[m^3/h]	V_c[m^3/h]	t_{ein}[ ]	t_{cout}[ ]	N_t[kW]
100	4.175	3.273	59.926	5.006	48.405	53.147	12.3	32.8	67.374
90	3.921	3.048	54.388	4.964	47.236	51.571	11.9	32.4	61.357
80	3.653	2.817	48.819	4.916	45.946	49.861	11.5	32.0	55.288
70	3.369	2.578	43.203	4.861	44.503	47.986	11.1	31.5	49.149
60	3.066	2.331	37.540	4.795	42.868	45.902	10.6	31.1	42.937
50	2.740	2.073	31.816	4.715	40.974	43.544	10.2	30.6	36.629
40	2.385	1.801	26.014	4.613	38.719	40.809	9.7	30.1	30.199
30	1.990	1.510	20.103	4.477	35.916	37.510	9.2	29.5	23.603

The differences between two operating conditions VF and CF are shown in Fig.5.

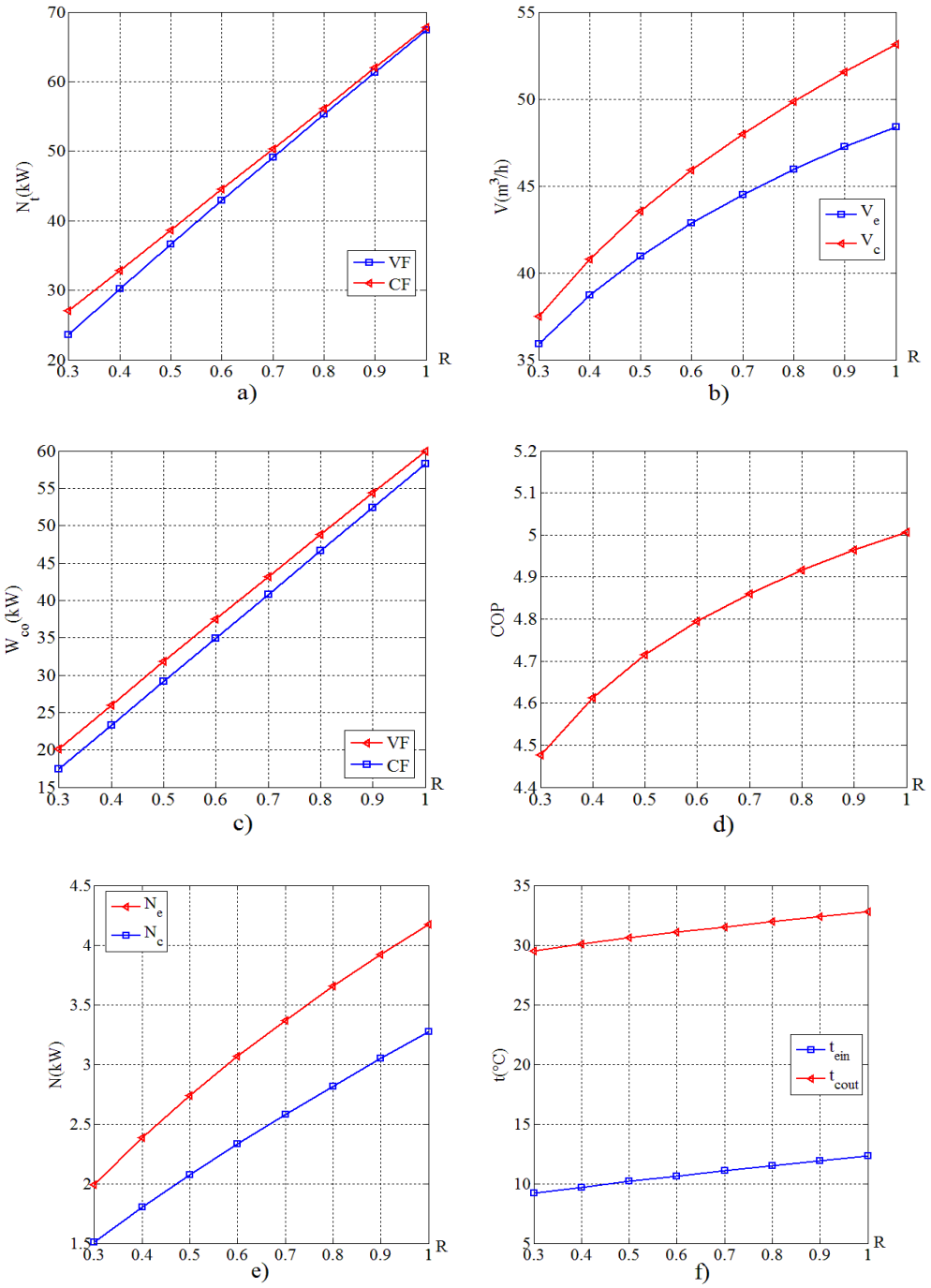

Fig.5. a)Comparison of N_t under constant flow and variable flow; b)The change of V_e and V_c with load rate R; c) Comparison of W_{co} under constant flow and variable flow; d)The change of COP with load rate R under variable flow; e)The change of N_e and N_c with load rate R; f)The change of t_{ein} and t_{cout} with load rate R.

Figure analysis. a)via optimization the total energy consumption of SWSHP system get a decrease compared with constant flow state, the maximun decrease percentage reaches 12.68%, it is proved that variable flow water system can save energy consumption; b)when load rate R reduces, V_e and V_c also go down which will lead a declination to heat exchange amount of evaporator and condenser so that the system can adapt the change of R; c), d)as load rate R reduces, it will lead a declination to COP, while W_{co} has a rising tendency, and it will consume more energy of heat pump unit compared with constant flow, it is because that when volume flow reduces, it will weaken heat-exchanging effect which will lead a declination to COP; e)as load rate R reduces, energy consumption of water pump will have a huge decrease, the smaller R is, the more energy will save, the reason is that both of N_e and N_c are proportion to V_e^3 and V_c^3 respectively; f)as load rate R reduces, both of t_{ein} and t_{cout} get reduced, this can be explained by that the temperature difference will reduce with the declination of water flow which is proportion to R.

Conclusions

In this paper, through the establishment of three mathematical model which are heat pump unit, chilled water pump and cooling water pump respectively, the curve fitting box was used to get fitted coefficients as well as an minimal TDEC through optimization tool box. Under the condition of that t_0 and t_k keep constant as 7℃ and 27℃ respectively, the results were shown as following:

(1)Under the variable flow operating state there exists an maximum energy conversation rate 12.68% of TDEC compared with the constant flow operating state, moreover with the decrease of R, it has more scope to save energy.

(2)With the reduction of R, under variable flow operating state the heat pump unit will consume more than average 8.41% energy, while COP will decline average 7.61% compared with constant flow.

(3)With the reduction of R both of the V_e and V_c will decrease so that there will have a energy saving of N_e and N_c.When R ranges from 30% to 100%, the mean energy conversation rate of N_e and N_c are 49.38% and 38.86%.

(4)With the reduction of R, both of t_{ein} and t_{cout} decrease due to the declination of temperature difference. When R ranges from 30% to 100%, the average declination rate of t_{ein} and t_{cout} are 17.09% and 5.73%.

Acknowledgements

This work was financially supported by the National Science & Technology Program during the 12th Five-year-plan period of China (sq2011sf14b00503sq) and Science & Technology Benefiting People Program of China (s2013gmc620002).

References

[1] Yi Zhang,in: *Building energy efficiency management textbook*. Beijing: China building industry press, In Chinese

[2] Caihua Liang, Xiaosong Zhang, Kui Mei, Xing Jin, Building Science Vol.24, No. 6,pp.40-44, 2008, In Chinese

[3] Binbin Meng, Yingxin Zhu, Borong Lin, HV&AC Vol.32, No. 6, pp.108-110, 2002, In Chinese

[4] Ahnfleth W, Peyer E.Comparative analysis of variable and constant primary-flow chilled-water-plant performance.HPAC Engineering. Vol.73, No. 4, 2001

[5] Yang Liu, Jinxiang Liu, Gao Ding, HV&AC Vol.37, No. 3, pp.21-24, 2007, In Chinese

[6] Byrd, R.H, Mary E. Hribar, and Jorge Nocedal, "An Interior Point Algorithm for Large-Scale Nonlinear Programming," *SIAM Journal on Optimization*,Vol. 9, No. 4, pp. 877-900,1999

[7] Byrd, R.H, J. C. Gilbert and J. Nocedal, "A Trust Tegion Method Based on Interior Point Techniques for Nonlinear Programming," *Mathematical Programming*, Vol. 89, No. 1, pp. 149-185,2000

Advanced Materials Research Vols. 960-961 (2014) pp 568-573

doi:10.4028/www.scientific.net/AMR.960-961.568

Experiment and simulation on pressure drop of pleated air filters

Fu Hai-ming[1]; fu yu[2], Xu Fang

[1:]College of environmental science and engineering, Shanghai, 201620

[2:] Wescon Controls (Shanghai),Inc. Building 6, 471 Guiping Road, Shanghai 200233, P.R. China

Key words: filtration medium; pressure drop; numerical simulation; air filter; pleated structure

Abstract: In order to reduce pressure drop of filtration process and increase filtration area, filtration media would usually made into pleated shape. The designs of pleats numbers and pleats height in the unit length have greatly impacted on pressure drop of the filtration process. In this paper, filter pressure drop of pleated air filters were examined by theoretical, experimental and simulation studies. By solving pressure drop from the Navier-Stokes equation on basis of velocity function assumption, by using the concept of average pressure drop in wind gap width, pressure drop in pleated filters was calculated. The numerical simulation of pleated filtration media was developed via using FLUENT software package and flow field variation in gap of pleated media was simulated. The results of theoretical calculations were in agreement with experimental results. It was confirmed that reducing pleat spacing or increasing pleats height could increased the area of filtration media and reduce the overall pressure drop of filters, although structure pressure drop increased. There were best value between pressure drop of pleated air filters and pleat numbers in the unite length.

INTRODUCTION

Air quality has become the attention Hotpoint due to the worsening environmental pollution and people's awareness of environmental protection. Air filtration devices were widely used in various industrial and residential rooms [1]. In order to improve the performance of air filtration, most of the filter materials were made into pleated structures [2], this kind of structure such as pleated shapes was shown in Fig.1. It could increase the filtration area and the amount of dust accumulation via reducing filtration velocity of media. It may reduce the cost of operation [1].However, the air entering into or leaving out from the pleated and tilted filtration media, the gas flow direction varied rapidly, which will spin off the flow and flow, causing an additional loss of energy [2]. In this paper, the pressure drop of filter structure and tilted media were calculated via solving Navies-Stokes equations and air flow variation in the pleated filtration media was simulated by computer.

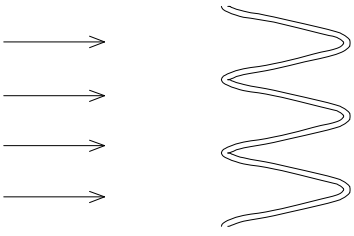

Fig. 1. Schematic of pleated air filter

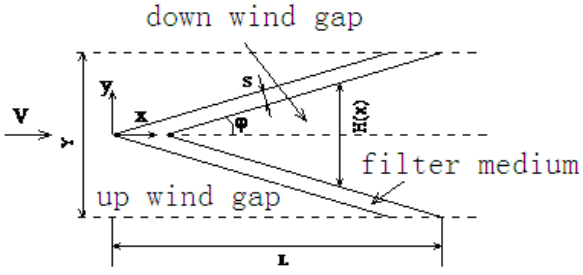

Fig.2. Schematic of pleat parameters

THE PRESSURE DROP OF PLEATED AIR FILTER

The pressure drop of pleated air filter was made up of two parts: that, is, structure pressure drop and media pressure drop. The structure pressure drop and media pressure drop were calculated as follows.

A. The pressure drop of pleated structure

The basic geometry and some of the parameters of pleated air filter was defined in Fig.2, Where, V is face flow velocity; Y is distance between two pleats, m ; L is pleats height, m ; s is filtration medium thickness, m ; j is pleats angle (angle between the center line and pleats); H (x) is distance between x and pleat. For the interest of simplicity, it is assumed for the pleated air filters that:

(1) Compressing of air was neglected, air density ρ is constant;

(2) The air dynamic viscosity μ is constant;

(3) No external force existed in x component direction (the direction of the pleat center line), according to the conservation of momentum equation:

$$V_x \frac{\partial V_x}{\partial x} + V_y \frac{\partial V_x}{\partial y} = -\frac{1}{\rho}\frac{\partial p}{\partial x} + \nu\left(\frac{\partial^2 V_x}{\partial^2 x^2} + \frac{\partial^2 V_x}{\partial^2 y^2}\right) \tag{1}$$

The pressure drop was obtained by solving equation (1) as follow:

$$\begin{aligned}\Delta p'_g = {} & \frac{\mu}{\rho V}\frac{\cos^2\varphi \sin\varphi}{s}\left[1-\left(\frac{s}{L\sin\varphi}\right)^3\right] + \frac{3\mu}{\rho V}\frac{\cos^2\varphi}{tg^2\varphi}\frac{\sin\varphi}{s}\left[1-\left(\frac{s}{L\sin\varphi}\right)\right] \\ & + \frac{1}{2}\cos^2\varphi\left(1+\frac{1}{2}\cos^2\varphi\right)\left[1-\left(\frac{s}{L\sin\varphi}\right)^2\right] - \frac{9}{40}\cos^4\varphi\left[1-\left(\frac{s}{L\sin\varphi}\right)^4\right] \\ & + \frac{1}{4}\cos^4\varphi\left[1-\left(\frac{s}{L\sin\varphi}\right)^3\right]\end{aligned} \tag{2}$$

$$\Delta p_g = \left|\ \Delta p'_g\ \right| \cdot \rho V^2 \tag{3}$$

B. Pressure drop caused by fluid across pleated medium

For Analysis calculation of the pressure drop of tilt filtration media, a microelement in tilt filtration medium was shown in Fig. 3 [2].

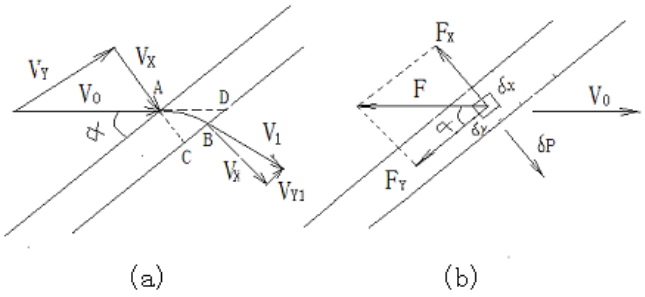

Fig. 3 Fluid flow and forced analysis of tilt filtration media

As the filtering occurs in low velocity flow, Darcy law was generally applicable, and pressure drop flowed across the tilt filtration medium could be expressed as [1]:

$$\begin{aligned}\Delta p_m &= \frac{\mu\cdot s}{K}V\sin\varphi\left[1+\left(\frac{1}{\sin^2\varphi}-1\right)\Big/\left(\frac{2\mu s}{K\rho V\sin\varphi}\right)\right] \\ &= \frac{\mu\cdot s}{K}V\sin\varphi\left(1+\frac{\cos^2\varphi K\rho V}{\sin\varphi 2\mu s}\right) \\ &= \frac{\mu\cdot s}{K}V\sin\varphi+\frac{\cos^2\varphi}{2}\rho V^2\end{aligned} \tag{4}$$

C. Overall pressure drop of pleated aerosol filters

The pressure drop of pleated air filters could be expressed as:

$$\Delta p = \Delta p_g + \Delta p_m = \left| \Delta p'_g \right| \cdot \rho V^2 + \Delta p_m \quad (5) \qquad \Delta p = f_1(\varphi, V, L, \mu, \rho, K, s) \quad (6)$$

Since $Y = \dfrac{1 - 2 \cdot s \cdot N}{N}$

The pleat angle in equation (6) could be expressed as ：

$$\varphi = arctg\left(\frac{Y}{2L}\right) = arctg\left(\frac{1 - 2 \cdot s \cdot N}{2LN}\right)$$

Therefore: $$\Delta p = f_2(N, V, L, \mu, \rho, K, s) \quad (7)$$

Where, K is permeability of filtration medium, m^2; α is tilt angle of filtration medium, V_0 is face flow velocity, m/s

PRESSURE DROP SIMULATION IN PLEATED FILTRATION MEDIUM

Fluid field flow was simulation calculated by CFD software package in this paper. In order to save computer resources, from the 80 pleats to select the four parts of them to conduct simulation. The filtration medium used triangle mesh to expressing porous region. The test parts used non-uniform rectangular grid. The total numbers of mesh were 2391.The results of the simulation do not changed with grid numbers increasing, that is, "grid independence." Selection of the calculation domain was considered as follows:

Inlet position (the position of experimental test points) was set in the distance which was less than 15 mm far to lower edge of filtration media, outlet position was set in the distance which was more than 67mm far to upper edge of filtration media. Boundary condition was velocity inlet, porous domain and freedom flow.

In order to minimize calculation errors, the impact of air leakage test was carried out and the velocity value was measured by the test and it was set up as entrance velocity of simulation calculation. Comparison of simulation results and experimental results was shown in table 1.The results of the simulation were different from the results of literature [3], but the simulation results were relatively close to results of experimental tests, it indicating that the simulation method of this paper was acceptable. It was found that the standard $k-\varepsilon$ turbulence model was a greater difference with results of the experimental test. The result of RNG $k-\varepsilon$ turbulence model was in agreement with result of RSM turbulence model and all of them were agreement with results of experimental test. However, RSM turbulence model was fitted better than RNG $k-\varepsilon$ turbulence model. This conclusion was in agreement with the literature [3].

Table 1 Comparison of experimental test and simulation on pressure drop of pleated filtration media

Entrance velocity，m/s	Experimental pressure drop，Pa	Simulation pressure drop，Pa	Relative error
0.6	12.0	7.2	40%
1.1	24.8	16.9	32%
2.1	50.9	44.2	13%
2.8	68.3	69.0	-1%
3.1	73.9	81.5	-10.3%

From Table 2, it could be seen that pressure drop relative error of simulation and experimental induced firstly and then increased, there were air leakages in experimental test and smaller of entrance velocity causing measure error of hot-wire anemometer, which could lead to bigger error of experimental results and simulation result. When the entrance velocity increasing, the calculation error between experimental results and simulation results become larger, this may be due to amount of air leakage increasing.

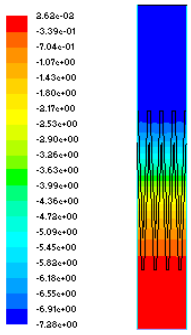

(a) The static pressure at $V = 0.6 m/s$

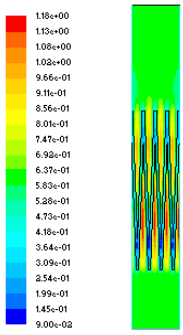

(b) The velocity at $V = 0.6 m/s$

Fig. 4 Simulation result of static pressure and filtration velocity and pressure drop on 80 pleated filter

The static pressure chart was similar with velocity chart at different face flow velocity (Fig.4). The static pressure chart (a) shows that pressure drop was gradual changing like wave layers, and velocity chart (b) shows that fluid gradually expands when it's flowed cross the pleated medium. The filtration velocity increases firstly and then decreased to smaller value..

The three impact factors such as medium thickness, porosity and the average particle diameter, affected on medium pressure drop were studied through the orthogonal experimental tests. It could be seen that the bigger the porosity and particles diameters were, the smaller the medium thickness were and larger pressure drop were.

COMPARISON OF CALCULATION RESULTS AND EXPERIMENTAL RESULTS

Filtration Media parameters was described as follows:

$K = 11.89 \times 10^{-12} m^2$, $s = 0.406 \times 10^{-3} m$;Air parameters: $\mu = 18.40 \times 10^{-6} Pa \cdot s$, $\rho = 1.185 kg/m^3$

Structural parameters: $L = 40 \times 10^{-3} m$

The pleated numbers N were 333 pleat/m, 250 pleat/m, 200 pleat/m, which were remarked by F-1, F-2, F-3, respectively. The face flow velocity varied from 0.45m/s to 2.25m/s and the face flow velocity of the air filter rated flow was 1.50m/s in this experimental test.

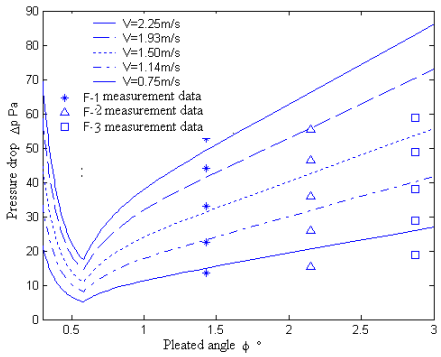

Fig.5. Comparison of pressure drop calculation results with experimental results

As shown in Figure 5: there was difference between theoretical results and experimental results, possible reason may be due to:
1. The fluid flowed into and leaved out from the filtration medium vertically was assumed, which made the path of flow into short, whereas the filtration velocity was calculated as average value.
2. The velocity was expressed by a special-second order polynomial.
3. Heterogeneity of the media and instability of media could cause measure error.

CONCLUSIONS

The pressure drop of pleated filtration medium was studied by experimental test and simulation in this paper. The factors such as filtration velocity, pleat numbers and pleat height impacting on pressure drop were discussed and main conclusions were described as follows:

1. The pressure drop of pleated air filters was obtained via solving the Navier-Stokes equation with concept of average velocity of gap width.
2. Calculation results were in agreement with results of experimental test.
3. The simulation results of RSM turbulence model were in agreement with results of experimental test.
4. There were best pleat numbers in unite length, minimum filtration pressure drop could be obtained according to this pleat numbers.

ACKNOWLEDGMENT

This paper was supported by National natural science foundation of China Project No..51178094 and Project No.41371445.

REFERENCES

[1] Liu lai-hong, Wang Shi-hong, development and application of air filter [J], filtration and separation, 2000, l0 (4): 8-9.China.

[2] Cai Jie, air filtration ABC [M], China Building Industry Press, 2002, China.

[3] Tobias Lucke and Heinz Fissan, The prediction of filtration performance of high efficiency gas filter elements [J], Chemical Engineering Science, April 1996, 51(8): 1199-1208.

[4] Paolo Tronville, Ph.D. Riccardo Sala, Ph.D. Minimization of Resistance in Pleated-Media Air Filter Designs: Empirical and CFD Approaches. HVAC&R RESEARCH. JANUARY 2003, 95-106.

[5] Feng Chao-yang, Zhang Zhen-zong, Jiang-feng, eatl, explore the relationship between the structure and pressure drop in high-level nuclear air filters [J], Journal of Environmental Science, 2008,28 (6): 1041-1046.China.

[6] L Del Fabbro，J C Laborde，P M erlin．Air flows and pressure drop modeling for different pleated industrial filters[J]．Filtration+Seperation，2002,2：35~40．

[7]Thomas Caesar，Thomas Schroth．The influence of pleat geometry on the pressure drop in deep-pleated cassette filters[J]．Filtration+Seperation，2002,2：49~54．

[8]V Nassehi，N S Hanspal，A N Waghode，etal．Finite-element modeling of combined porous regimes: Simulation of flow through pleated cartridge filters[J]，Chemical engineering science，2005，60：995~1006．

[9]Fu Hai-ming, SIMULATION AND PREDICTION ON PRESSURE DROP DURING FIBROUS FILTERS CLOGGED BY MICROBIOLOGY PARTICLES . International Conference on Biomedicine and Pharmacology (ICBP) : Beijing, PEOPLES R CHINA : APR 19-21, 2013 .JOURNAL OF INVESTIGATIVE MEDICINE : 61 : 4 : S24-S24 : APR 2013

[10] Fu Hai-ming, 3D MODEL FOR PREDICTING PRESSURE DROP AND PERMEABILITY IN FIBROUS POROUS MEDIA : International Conference on Biomedicine and Pharmacology (ICBP) : Beijing, PEOPLES R CHINA : APR 19-21, 2013 .JOURNAL OF INVESTIGATIVE MEDICINE: 61 : 4: : S22-S23 : APR 2013.

[11] Fu Hai-ming; Zhao You-jun. Experimental Study on Flow Field Characteristic of Bag Filter :9th International Conference on Measurement and Control of Granular Materials, MCGM 2011: Shanghai, PEOPLES R CHINA : OCT 27-29, 2011

Advanced Materials Research Vols. 960-961 (2014) pp 574-579

doi:10.4028/www.scientific.net/AMR.960-961.574

Nonlinear Hydro Turbine Model for Medium and Long Term Power System Stability Analysis with Sharing Long Common Tunnel

TANG Fan[1, a]，DING Li-jie[1, b]，and TENG Yufei[1, c]，WEI Wei[1, d]

[1]State Grid Sichuan Electric Power Research Institute，Chengdu 610072，China

[a]tangfance@163.com, [b]ding_lijie@163.com, [c]185873103@qq.com, [d]weiwei_6898825@163.com

Keywords: hydro turbine model long term stability power system simulation hydraulic coupling; structure coefficient

Abstract. Based on the theoretical derivation of hydraulic coupling relationship between the hydropower units sharing long common tunnel，the non-linear hydro turbine model with sharing long diversion tunnel system is established and order-reduced in accordance with the demand of power system simulation. And according to the complex structure characteristics of surge tank，a method of correcting surge tank storage constant with surge tank structure coefficient is proposed. This hydro turbine model can reflect the influence of surge tank and sharing common tunnel in the power system long term process，the accuracy of model is proved by comparison of simulation results and actual recording data in power system.

Introduction

Special geographic conditions make some hydropower stations connecting to upstream reservoir with long tunnel, and sharing bifurcation pressure steel pipe at the end of tunnel. The hydro turbine's mechanical power is determined by water head and flow, so there's association between the mechanical power and regulating characteristics of hydroelectric units sharing common conduit. That will affect AGC control precision, safety control effect and some other long term stability process in power system.

Accurate analysis of hydro turbine's dynamic response and its influence on power system, must rely on the model accuracy of dynamic elements and control & protection equipment[1]. In some practical applications, it is important to model the hydraulic coupling process in the long common tunnel and surge tank. But it is still a lack of accurate calculation model for hydro turbine with sharing long common tunnel in power system stability analysis. The ideal turbine model and non-elastic water column turbine model in widely used power system transient simulation program are only suitable for hydro turbine with single tunnel[2]. Although IEEE working group, power system full dynamic simulation program and other literatures [3-6] provided some hydro turbine models with sharing common tunnel, but these models can't take account of surge tank effects, which may be critical in some long term stability process in power system.

Based on theoretical derivation, this paper puts forward a new nonlinear model for hydro turbines with sharing long common tunnel, which can accurately reflect the influence of surge tank and sharing common tunnel in the power system long term process.

Non-linear model of multiple penstocks and turbines supplied from common tunnel--Non-Elastic water column including surge tank effects

For any section of diversion pipe, considering the flexibility of pipe, the hydraulics equation[7] is

$$\begin{aligned} H_b &= H_a \sec h(T_e s) - Z_0 Q_b \tanh(T_e s) \\ Q_a &= Q_b \cos h(T_e s) + \frac{1}{Z_0} H_b \sinh(T_e s) \end{aligned} \tag{1}$$

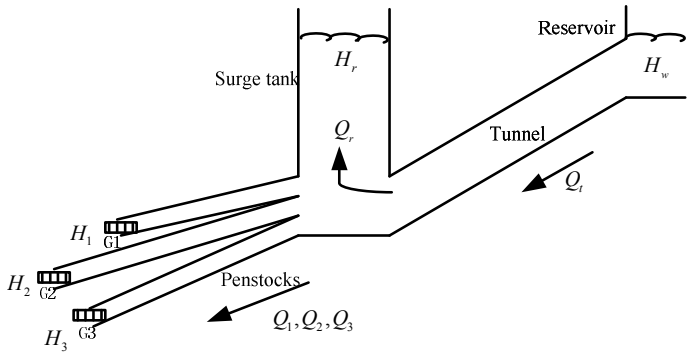

Fig.1 Hydraulic system sharing long common tunnel

Here, H_a, H_b are water head of the pipe; Q_a, Q_b are rate of flow, T_e is elastic time constant of pipe. So H_r in Fig.1 can be described in per unit as:

$$h_r = h_w \sec h(T_{eT}s) - Z_T q_T \tanh(T_{eT}s) \tag{2}$$

The water deviation of tunnel upstream side is zero, so h_w=1, then

$$h_r = 1 - Z_T q_T \tanh(T_{eT}s) \tag{3}$$

With n=0, tanh(T_s) can be expressed as:

$$\tanh(Ts) = \frac{1-e^{-2Ts}}{1+e^{-2Ts}} = \frac{sT\prod_{n=1}^{n=\infty}\left[1+(\frac{sT}{n\pi})^2\right]}{\prod_{n=1}^{n=\infty}\left[1+(\frac{2sT}{(2n-1)\pi})^2\right]} \approx Ts \tag{4}$$

That means ignoring elasticity of water column, so Eq.2 can be expressed as:

$$H_r = H_w - Z_T Q_T T_{eT} s \tag{5}$$

Considering the relationship between water head and flow in surge tank, as well as the flow relationship between tunnel, surge tank and penstocks, then

$$H_r = \frac{H_w - Z_T(Q_1+Q_2+Q_3)T_{eT}s}{1+Z_T T_s T_{eT} s^2} \tag{6}$$

The water head deviation of tunnel upstream side is zero, so

$$H_w - H_r = \frac{Z_T(Q_1+Q_2+Q_3)T_{eT}s}{1+Z_T T_s T_{eT} s^2} \tag{7}$$

For any penstock,

$$H_r - H_i = \frac{L_i}{S_i g}\frac{dQ_i}{dt} \qquad (i=1,2,3) \tag{8}$$

Here, Q_{i0}(i=1,2,3) is rate flow of penstocks, defining q_i(i=1,2,3) as per unit value for Q_i(i=1,2,3)

$$q_i = \frac{Q_i}{Q_{i0}} (i=1,2,3) \tag{9}$$

Then, from Eq.7, Eq.8 and Eq.9, we can see that

$$H_w - H_i = \frac{Z_T T_{eT} s}{1+Z_T T_s T_{eT} s^2}(Q_{10}q_1 + Q_{20}q_2 + Q_{30}q_3) + \frac{L_i}{S_i g} s(Q_{i0}q_i) \qquad (i=1,2,3) \tag{10}$$

Defining H_B as rate water head, and H_B=H_W, Eq. 10 divided by H_B, then

$$\begin{bmatrix} 1-h_1 \\ 1-h_2 \\ 1-h_3 \end{bmatrix} = \begin{bmatrix} \dfrac{T_{wT1}}{1+T_{wT1}C_{s1}s^2}+T_{wp1} & \dfrac{T_{wT2}}{1+T_{wT2}C_{s2}s^2} & \dfrac{T_{wT3}}{1+T_{wT3}C_{s3}s^2} \\ \dfrac{T_{wT1}}{1+T_{wT1}C_{s1}s^2} & \dfrac{T_{wT2}}{1+T_{wT2}C_{s2}s^2}+T_{wp2} & \dfrac{T_{wT3}}{1+T_{wT3}C_{s3}s^2} \\ \dfrac{T_{wT1}}{1+T_{wT1}C_{s1}s^2} & \dfrac{T_{wT2}}{1+T_{wT2}C_{s2}s^2} & \dfrac{T_{wT3}}{1+T_{wT3}C_{s3}s^2}+T_{wp3} \end{bmatrix} \begin{bmatrix} sq_1 \\ sq_2 \\ sq_3 \end{bmatrix} \tag{11}$$

Where T_{wti}, T_{wpi}, C_{si} represent the time constant of tunnel, penstock and surge tank.

$$\begin{aligned} T_{wTi} &= Z_T T_{eT} \frac{Q_{i0}}{H_B} \\ C_{si} &= T_s \frac{H_B}{Q_{i0}} \qquad (i=1,2,3) \\ T_{wpi} &= \frac{L_i Q_{i0}}{S_i g H_B} \end{aligned} \tag{12}$$

So, nonlinear hydro turbine model with sharing long common conduit can be described as

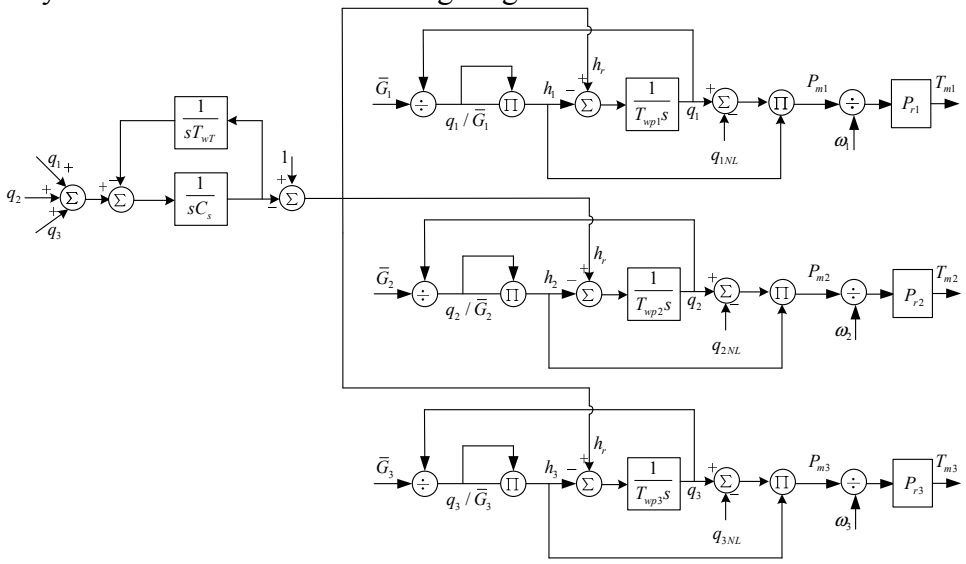

Fig.2 Nonlinear hydro turbine model with sharing long common conduit

Model of surge tank with complex structure

Some surge tank may consist of vertical shaft and upper chamber, where diameter of connecting pipe and shaft may be different, as shown in fig.3. Because the impedance orifice consumes some energy in hydraulic dynamic process, that can reduce water fluctuations amplitude in surge tank. But at the same time, the impedance may make tunnel under the influence of water hammer pressure.

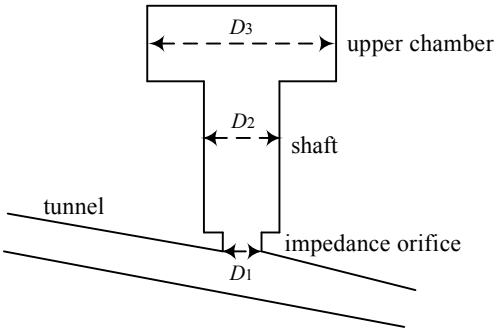

Fig.3 Impedance type surge tank model

Special structure makes it is difficult to calculate the impedance coefficient of surge tank, which is changing with flow and water level in the transition process. In hydraulic transient calculation, the surge tank impedance coefficient can be calculated by Gardel formula, model test or CFD[8-10]. For power system time domain simulation, using explicit formulation not only too complicated but also can't accurately represent some surge tank with special structures. Surge tank structure coefficient k is proposed in this paper, which can modify storage constant of surge tank according to the change of water head. The structure coefficient can simulate the pressure changing in tunnel which is caused by impedance orifice.

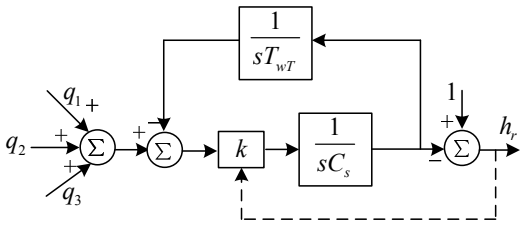

Fig.4 Tunnel and surge tank model with structure coefficient

The simulation model of tunnel and surge tank with structure coefficient is shown in fig.4. Where, C_s is the storage constant of shaft, accurate values of k can be gain by load rejection test or fluid mechanics calculation. Simplicity, we can use a piecewise function to approximate k:

$$k \approx \begin{cases} K_1 & (h \le h_1) \\ K_2 & (h_1 < h \le h_2) \\ K_3 & (h_2 < h) \end{cases} \tag{13}$$

Here, h_1 and h_2 respectively represent the water head at different cross-sectional area of surge tank.

Comparison of simulation results and recording data

Example 1: A hydraulic station with three units sharing long common tunnel, the rated head is 92m, rated flow of single unit is 62m^3/s, length of common tunnel is 22.975km, cross –section of tunnel is 45.3m^2, cylinder type surge tank diameter is 22m, pressure steel pipe inner diameter 5.8 m, total length is 391.3 m. The test operation condition is: Unit 3 was shutdown, governors of Unit 1 and 2 worked in opening regulation mode, primary frequency regulation was put into operation, Unit 1 AGC shutdown and Unit 2 AGC was put into closed-loop operation.

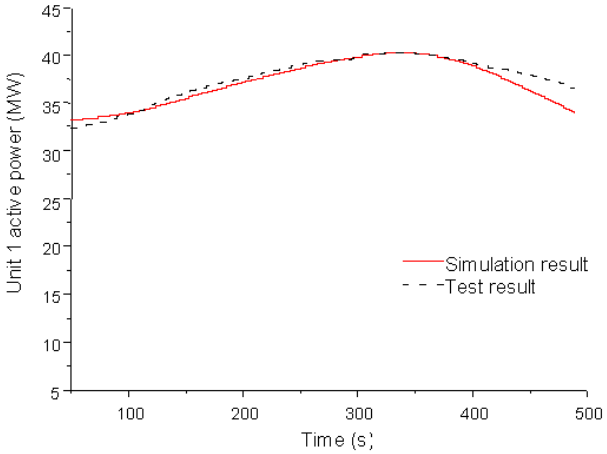

Fig.5 Active power curve of Unit 1

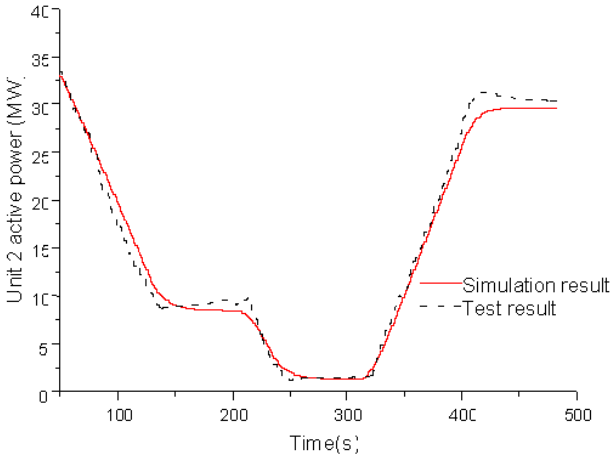

Fig.6 Active power curve of Unit 2

Because Unit 1 and Unit 2 sharing common tunnel, Unit 2 power reduction resulted in water pressure rising, then active power of Unit 1 increased almost 20% in opening regulation mode. Due to

AGC of this plant issued only one AGC command in active power regulation process, the active power closed-loop logic in monitoring and control system exit once actual power equals to command. So, the hydraulic correlation between turbines will affect AGC control precision.

Because primary frequency regulation didn't participate in active power adjustment, so the power curve in figure 5 can reflect dynamic characteristics of water diversion system and turbines. As shown in figure 5 and 6, simulation results are in good agreement with the measured curve.

Example 2: Another hydraulic station with two units sharing long common tunnel, the rated head is 288m, rated flow of single unit is 232.5m^3/s, length of common tunnel is 16.67km, cross –section of tunnel is 100.1m^2, vertical shaft diameter of its impedance type surge tank is 21m, pressure steel pipe inner diameter 6.5 m, total length is 584 m. This plant is a main power station of Jin-Su UHVDC, which special structure of tunnel and surge tank may have great influence on power system dynamic process.

The active power curve of Unit 1 after Unit 2 shutdown under the DC bipolar fault is shown in figure 7. Due to valve of Unit 2 was quickly closed, the hydraulic pressure of Unit 1 increase observably, that make active power increased almost 21%. Because of the status in system, the dynamic response characteristics of Unit 1 increased AC section power in the AC-DC hybrid power system after the accident. If Jin-Su UHVDC takes island operation mode, the dynamic process of the water diversion system may also have great influence on frequency stability in the island system.

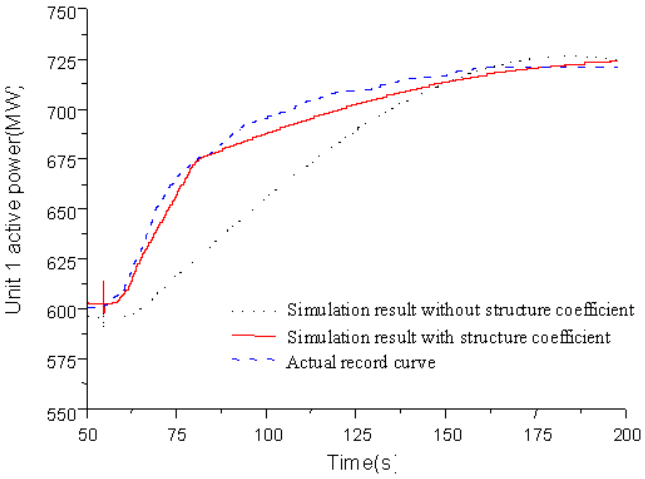

Fig.7 Active power curve of Unit 1

Tunnel and surge tank model considering structure coefficient which approximatively described by piecewise function was used in the simulation, and the simulation results and record curve are shown in figure 7. We can see that the simulation model has high precision. For the impedance type surge tank, if impedance coefficient of surge tank is ignored, although the active power fluctuation peak value is consistent, but the dynamic process will be different from the actual situation, as shown in figure 7.

Conclusions

(1) A nonlinear hydro turbine model for medium and long term power system stability analysis with sharing long common conduit was setup.

(2) For the difficult to determine impedance coefficient of surge tank with complex structure, the surge tank structure coefficient was put forward to dynamic correcting surge tank storage time constant. This method can improve accuracy of simulation model obviously.

(3) Contrast analysis with measured disturbance data shows that this model can correctly reflect the medium and long term process dynamic response of the hydro units sharing long common conduit.

(4) This model can be applied to prophase planning research and long term stability analysis in power system easily. And the water hammer constant testing in prime mover modeling test can improve the accuracy of this model further.

References

[1] Gao Hui-min，Liu Xian-lin，Xu Zheng．Effect of detailed hydro turbine models on analysis results of power system transient stability[J]．Power System Technology， 2005，29(2)：5-9．

[2] Li Hua，Shi Ke-qin，Fan Yue，et al．Structure analysis of water turbine governor model for stability calculation of power system[J]．Power System Technology，2007，31(5)：25-30．

[3] Working Group on Prime Mover and Energy Supply Models for System Dynamic Performance Studies．Hydraulic turbine and turbine control models for system dynamic studies[J]．Transactions on Power System，1992，7(1)：167-179．

[4] Tang Yong，Song Xin-li，Liu Wen-zhuo et al．Power system full dynamic simulation part III:Long term dynamic models[J]． Power System Technology，2002，26(11)：20-25．

[5] Hannett L.N，Feltes J.W，Fardanesh B ，et al．Modeling and control tuning of a hydro station with units sharing a common penstock section[J]．IEEE Transactions on Power Systems, 1999 , 14(4)：1407-1414．

[6] Zeng Yun，Zhang Lixiang，Guo Yakun，et al．Hydraulic Decoupling and nonlinear hydro turbine model with sharing common conduit[J]．Proceedings of the CSEE，2012, 32(14): 103-108.

[7] Kunder P. Power system stability and control[M]. New York：McGraw-Hill，1994．

[8] Ministry of Power Industry East China Investigation and Design Institute．Hydropower surge chamber design specifications（DL/T5058-1996）[S]．Beijing：China Electric Power Press，1996.

[9] Cheng Yong-guang, Yang Jian-dong．Hydraulic resistance coefficient determination of throttled surge tanks by means of computational fluid dynamics[J]．Journal of Hydraulic Engineering，2005, 36(7)：787-792．

[10]Fu liang，Wang Yi-guo．Load shedding test and simulation analysis of hydropower station with surge shaft[J]．Water Resources and Power，2012，30（6）：154-157．

Advanced Materials Research Vols. 960-961 (2014) pp 580-585

doi:10.4028/www.scientific.net/AMR.960-961.580

Study on the Transient Power Angle Characteristic of Doubly-Fed Induction Generator

Qiang Yu[1, a], Canping Yu[2, b], Huadong Sun[1], Jun Yi[1], and Xuzhi Luo[1]

[1] China Electric Power Research Institute, Haidian District, Beijing, China

[2] Guodian Nanjing Automation Co., Ltd., Jiangning District, Nanjing, China

[a]yuqiang2010@epri.sgcc.com.cn, [b]canping-yu@sac-china.com

Keywords: DFIG; transient characteristics; voltage dip; power angle.

Abstract: Doubly-fed induction generator (DFIG) wind turbine has become a mainstream machine of wind generators in China. As the different operational characteristics between the DFIG and synchronous generator (SG), the large amount of DFIG-based wind generators installed in the grid may bring a series of impacts on the dynamic behaviors of power system. In order to study the DFIG transient characteristics on the condition of the voltage dips happening in the power system, a definition of the DFIG power angle is given and the effects of the converters on the DFIG power angle are discussed. On this basis, the transient angle characteristic of the DFIG is derived. The DFIG transient characteristics are performed by Matlab/Simulink software, the simulation results demonstrate that the DFIG has the resemble power angle characteristic of SG and prove the effectiveness of the derivation process, which lay a foundation for the study on the interactions between the DFIG and power system.

Introduction

In recent years, the variable-speed and constant frequency (VSCF) wind turbine has replaced the constant-speed one to be the most popular generator in the area of wind generation. As an important type of the VSCF, the doubly-fed induction generator (DFIG) has advantages of a smaller capacity voltage-source converter, lower cost and flexible power control, which has occupied a large proportion of the installed wind generation capacity.

Different from the SG, the DFIG utilized a wound rotor induction generator and realized independently control of the active and reactive power through vector excitation control strategy. It demonstrates different operational characteristics from the SG during the faults. With the increasing capacity of the DFIG-based wind generation in the grid, the power system dynamic characteristics which are mainly decided by the SG will get a change and undertake a challenge on the stability. And therefore, it is very necessary to study the transient characteristic of the DFIG.

Currently, most of the literatures on the DFIG transient characteristics are concentrated in the DFIG stator and rotor current transients [1-8] and its own electromagnetic transients[9-11] during the grid faults, however, the dynamic process of the DFIG external characteristics and the interactions between the DFIG and power system are merely studied. In reference [12] and [13], the author proposed a definition of the DFIG power angle and suggested that the wide variation of the DFIG angle cause the deep dip of the terminal voltage. However, the definition of the DFIG power angle is simply the direct transplant of the synchronous generator's concept of the power angle, which didn't consider the DFIG transients during the fault and the effects of the DFIG vector orientation control strategy. Hughes, F.M and Anaya-Lara, O[14] addressed the design and implementation of a novel control scheme for a DFIG which provided a DFIG-based wind farm with the similar characteristics with the conventional generator. The authors focused on the improvement of the DFIG control strategy but ignored the effects of the DFIG transients on the power system dynamic behaviors.

The paper gives a definition of the DFIG power angle through the theoretical derivation, explores the influence mechanism of the DFIG control system on the power angle and analyzes the angle's

dynamic process. The paper lays a foundation for the future study on the transient stability of the power system with large amount of the DFIG integrated.

The models of the DFIG

The DFIG utilizes a wound rotor induction generator with the rotor windings connected with grid through a back-to-back voltage-source converter. The converters and its control system can regulate the rotor currents to satisfy the DFIG with a large-scale operation. The positive reference directions of the stator and rotor windings are both in the light of motor convention. The models of the DFIG under the synchronous rotating coordinate system are as follows:

The voltage equations:

$$\begin{cases} u_{ds}=R_s i_{ds}-\omega_s \psi_{qs}+\dfrac{d\psi_{ds}}{dt} \\ u_{qs}=R_s i_{qs}+\omega_s \psi_{ds}+\dfrac{d\psi_{qs}}{dt} \\ u_{dr}=R_r i_{dr}-s\omega_s \psi_{qr}+\dfrac{d\psi_{dr}}{dt} \\ u_{qr}=R_r i_{qr}+s\omega_s \psi_{dr}+\dfrac{d\psi_{qr}}{dt} \end{cases} \quad (1)$$

The flux equations:

$$\begin{cases} \psi_{ds}=L_s i_{ds}+L_m i_{dr} \\ \psi_{qs}=L_s i_{qs}+L_m i_{qr} \\ \psi_{dr}=L_m i_{ds}+L_r i_{dr} \\ \psi_{qr}=L_m i_{qr}+L_r i_{qr} \end{cases} \quad (2)$$

Where the symbols u_{ds} and u_{qs} are stator voltages, u_{dr} and u_{qr} are stator voltages, i_{ds} and i_{qs} are stator currents, i_{dr} and i_{qr} are rotor currents; ψ_{ds} and ψ_{qs} are stator fluxes; ψ_{dr} and ψ_{qr} are rotor fluxes; R_s is stator resistance; R_r is rotor resistance; ω_s is synchronous rotating angular speed; s is rotor slip; L_s is stator inductance; L_r is rotor inductance; L_m is mutual inductance between the stator and rotor; the subscripts d, q, s and r respond direct-axis component, quadrature-axis component , stator and rotor components respectively.

The definition of the DFIG power angle

SG is the main generation form in the system and its characteristics have a tremendous impact on the gird. As a new generaion form, the DFIG demonstrates different characteristics. Making an deeply investigation of the DFIG operatioal theory is of huge sense.

The steady-state characteristics of the DFIG. When the DFIG operates at steady state, the stator fluxes maintain constant and the components of $d\psi_{ds}/dt$ and $d\psi_{qs}/dt$ are both zero. According to the equation (1), it can be derived the equation (3).

$$\begin{cases} \psi_{qs}=-\dfrac{u_{ds}-R_s i_{ds}}{\omega_s} \\ \psi_{ds}=\dfrac{u_{qs}-R_s i_{qs}}{\omega_s} \end{cases} \quad (3) \qquad \dot{\psi}_s = \frac{\dot{U}_s - R_s \dot{I}_s}{j\omega_s} \quad (4)$$

Choose the direct-axis as the real axis and quadrature axis as imaginary axis, the equation (3) can be transformed as the equation (4), where the symbols $\dot{\psi}_s$, $\dot{U}_s$ and $\dot{I}_s$ are flux , voltage and current of stator vectors respectively. Similarly, according to the fluxes equation (2), it can be derived the equation (5) and make the equation (5) substituted into the equation (4) we can get the equation (6).

$$\dot{\psi}_s = L_s \dot{I}_s + \frac{L_m}{L_r}(\dot{\psi}_r - L_m \dot{I}_s) \quad (5) \qquad \dot{U}_s = \left[R_s + j\omega_s \left(L_s - \frac{L_m^2}{L_r} \right) \right] \dot{I}_s + j\omega_s \frac{L_m}{L_r} \dot{\psi}_r \quad (6)$$

Then, make the replacement $x' = \omega_s (L_s - \dfrac{L_m^2}{L_r})$ and $E' = \omega_s \dfrac{L_m}{L_r} \psi_r$, where the symbol E' is the DFIG internal voltage and x' is its equivalent internal inductance. We can get the equation (7) and equaivalent circuit in the figure 1.

$$\dot{U}_s = (r_s + jx')\dot{I}_s + \dot{E}' \tag{7}$$

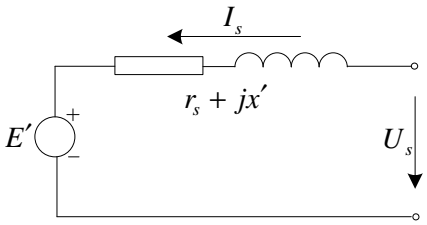

Fig. 1 DFIG steady-state equivalent circuit

The DFIG power angle. The SG is excited by a DC excitation system, which can produce a magnetic field that is stationary relatively to the rotor. When the rotor rotates at a synchronous speed under the dragging of the prime mover, a synchronous rotating magnetic field can be formed in the air gap of the generator and a constant 50 Hz AC voltage. As there is no relative motion between the rotor and the excitation magnetic field of the SG, the spatial position of the excitation field is the same as that of the direct axis of rotor. The vector diagram of the SG is shown in the figure 2, where the symbol δ_g is the relative angle between the internal voltage *E'* and the machine's terminal voltage U_s, φ is the power factor angle and ψ is the inner power factor angle.

However, the excitation currents through the DFIG rotor windings are a group of symmetrical three phase currents. According to the theory of AC motor, the equivalent excitation field rotates at a certain speed relative to the rotor with the speed determined by the frequency of the rotor currents. Similarly, under the adjustment fo the DFIG control system, a similar synchronous rotating field will appear in the air gap, whcih can induce a constant stator voltage with a frequency of 50Hz.

From the above literature we can conclude that the DFIG and SG are both have a synchronously rotating magnetic field in the air gap. So the DFIG can also be called an synchronous motor with an AC excitation.

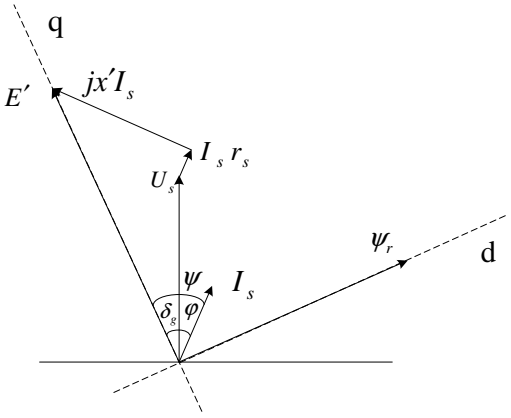

Fig. 2 The vector diagram of the SG

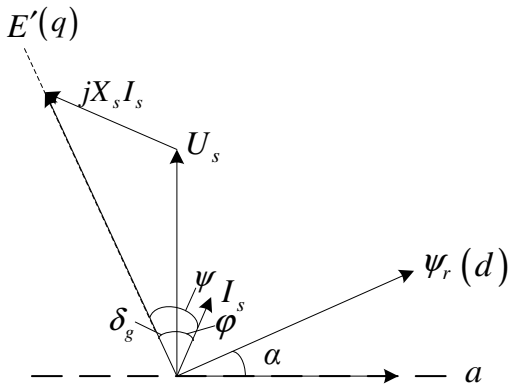

Fig. 3 The DFIG vector diagram

According to the AC motor theory, the magnitude and phase of the internal voltage E' is depended on the rotor flux ψ_r. With the consideration that the induced voltage is lead forward 90 space angle of the rotor flux, the real location of the SG internal voltage is the same with that of rotor's quadrant axis. However, for the DFIG, the real location of the rotor flux is not static relatively to the rotor. If making the location of the rotor flux as the imagined rotor direct axis, the DFIG vector diagram can be acquired in the figure 3. the angle α represents the relative angle between the space location of the rotor windings and the rotor flux vector. Ignore the effect of stator resistance on the DFIG power. The DFIG electric power can be expressed in the equation (8).

$$P_{em} = U_s I_s \cos\varphi = U_s I_s \cos(\psi - \delta_g) = U_s \cos\delta_g I_q + U_s \sin\delta_g I_d \tag{8}$$

Take the consideration of the equation (9), the equation (8) can be simplified to the equation (10).

$$\begin{cases} I_q = \dfrac{U_s \sin\delta_g}{x'} \\ I_d = \dfrac{E' - U_s \cos\delta_g}{x'} \end{cases} \quad (9) \qquad P_{em} = \frac{E'U_s}{x'} \sin\delta_g \quad (10)$$

Concluded from the equation (10) that the DFIG has the analogous power angle characteristics to the SG and its equivalent power angle is angle δ_g in the figure 3.

The effect of the converters on the DFIG power output

The DFIG has a back-to-back voltage-source converter (VSC), the rotor-side converter and the grid-side converter; the converters are important components in the doubly-fed wind generation system. With the controls of the DFIG converters, the DFIG realized the stable power output under the different wind velocity and the fast power exchange between the rotor windings and the power grid. The power flowing through the rotor windings can be illustrated in the equation (11).

$$\begin{cases} P_g = sP_s \\ Q_g = sQ_s \end{cases} \quad (11)$$

It can be conclude that the total exchange active power between the DFIG and the grid can be evaluated by the DFIG stator active power P_g.

Transient characteristics of the DFIG power angle

When the DFIG suffers a voltage dip by the faults happening in the power system, there will be a series of dynamic processes in the DFIG. The stator and rotor fluxes will both vibrant at a certain degree, which can affect the power angle of the DFIG. In order to make a detail analysis of the change rule of the DFIG power angle, it is very necessary to take the consideration of the flux vibrancy. The equation (6) can be expressed in the equation (12) during the transient process.

$$\dot{U}_s = \left[R_s + j\omega_s \left(L_s - \frac{L_m^2}{L_r} \right) \right] \dot{I}_s + j\omega_s \frac{L_m}{L_r} \dot{\psi}_r + \frac{d\dot{\psi}_s}{dt} \quad (12)$$

Thus, it can be derived the dynamic process of the DFIG internal voltage in the equation (13). Similarly, the dynamic stator voltage can also be expressed in the equation (14).

$$\dot{E}' = j\omega_s \frac{L_m}{L_r} \dot{\psi}_r + \frac{d\dot{\psi}_s}{dt} \quad (13) \qquad \dot{U}_s = j\omega_s \dot{\psi}_s + \frac{d\dot{\psi}_s}{dt} \quad (14)$$

By the comparison of the equation (13) and (14), the angle between the internal voltage *E'* and the terminal voltage U_s are as same as that between rotor and stator flux. So we can observe the angle α between the rotor and stator flux instead of the DFIG power angle. In addition, the equation (14) and (15) both have the component $d\psi_s/dt$, which represents the vibrant characteristics during the transient process. So the angle α can exactly substitute the DFIG power angle both in the steady and transient conditions. the total output power of the DFIG can be demonstrated in the equation (15).

$$P_G = (1-s) P_s = (1-s) \frac{E'U_s}{x'} \sin\alpha = \frac{(1-s)\omega_s L_m \psi_r \psi_s}{L_s L_r - L_m^2} \sin\alpha \quad (15)$$

Simulation example

To analyze the transient behaviors of the DFIG, a single machine and infinite bus system is modeled in the Matlab/Simulink environment. The diagram is showed in the figure 4. The established DFIG model includes two converters and its dual closed-loop control system model, the phase-locked loop model and flux observer model. Besides, the stator flux oriented control is utilized by the rotor-side converter control system. At the time 0.15 seconds, the terminal voltage of the DFIG suffers from voltage dips of 0.3 p.u, 0.5 p.u and 0.7 p.u respectively. The durations are both 0.1

seconds. After filtering stator flux oscillations, the simulation results are showed from the figure 5 to figure 9.

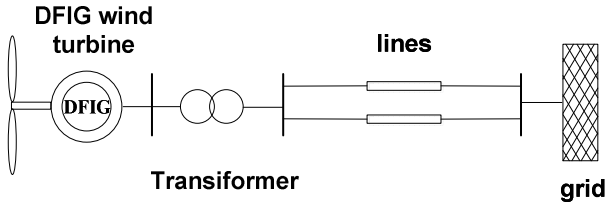

Fig. 4 Single DFIG infinite bus system

With the increase of the DFIG terminal voltage drop degree, the DFIG power angel also becomes greater, which is similar to the SG power angle. However, the DFIG power angel can restore to stability rapidly once the voltage dip disappeared, as shown from Figure 5 to Figure 6.

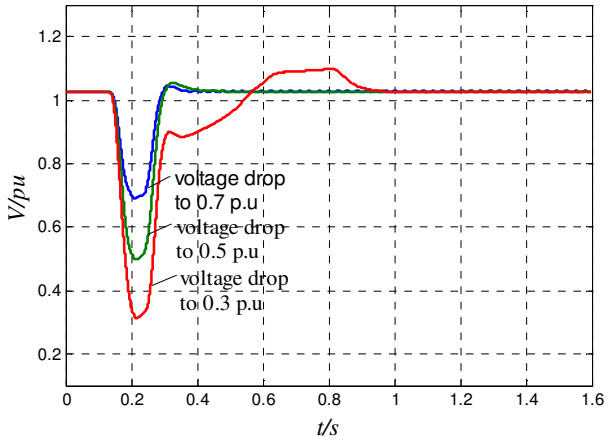

Fig. 5 The voltage dips of the DFIG stator terminal

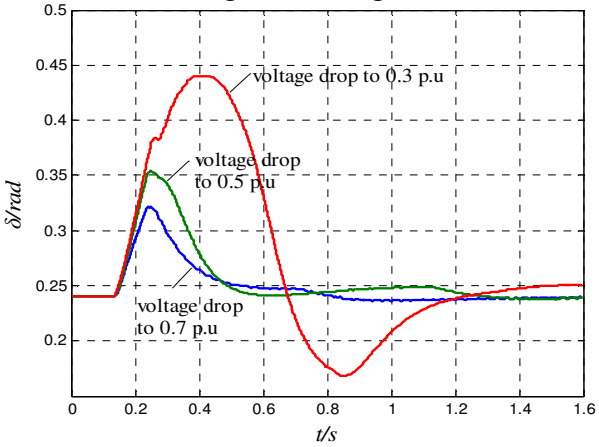

Fig. 6 The DFIG power angle under voltage dips

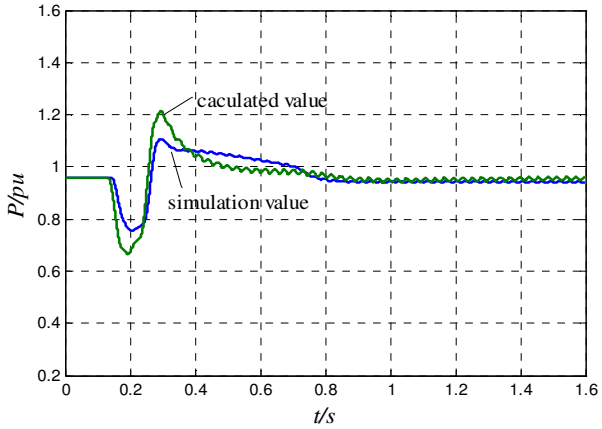

Fig. 7 The power output of the DFIG under 0.3 p.u voltage dip

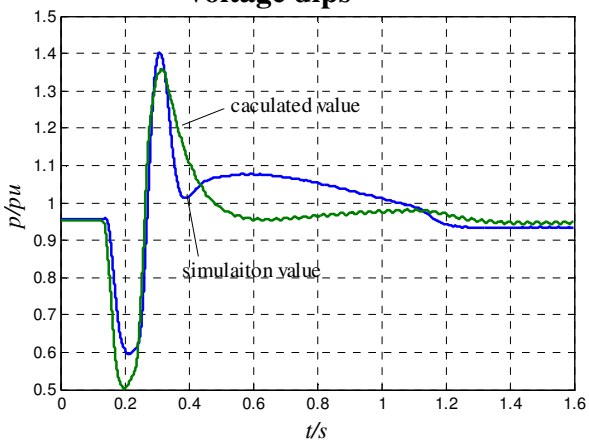

Fig. 8 The power output of the DFIG under 0.5 p.u voltage dip

Figure7 to8 demonstrates the comparison of the DFIG active power between the simulation result and the calculated active power defined on the basis of power angle characteristic equation 15. It can be seen from the Figures that the calculated power curve and the simulation curve are very close. The only difference is caused by the error and the time-delay of the regulation system. Wherefore, the DFIG power angle characteristics can make a better representation of the DFIG active power, which can illustrates the DFIG power angle defined in the paper are reasonable and accurate.

Summary

With the increasing capacity of the DFIG, the power system may appear a series of new features. The paper gives a definition of the DFIG power angle on the basis of its operational principle and

transients, analyzes the effects of the converters on the power angle and its transient characteristics. The study demonstrates that the DFIG has its own power angel characteristics. The simulation results verify the conclusions of this paper and prove the correctness of the derivation process.

References

[1] Simulation Study on Dynamic Response of Doubly Fed Induction Generators During System Voltage Sag Caused by Power Grid Faults[J]. Power System Technology, 2010, 34(8): 170-175(in Chinese).

[2] Jia Junchuan, Liu Jin, Zhang Yigong. Dynamic Characteristics of Stator Flux of Doubly-fed Induction Generator During Grid Voltage Fault[J]. Proceedings of the CSEE, 2011, 31(3): 90-96(in Chinese).

[3] Analysis on Low Voltage Ride-Through Techniques for Wind Turbines Using Doubly-Fed Induction Generator[J]. Power System Technology, 2010, 33(9): 72-77(in Chinese).

[4] Crowbar control strategy for doubly fed induction generator of wind farm during power grid voltage dips[J]. Power System Technology, 2008, 32(12): 84-89(in Chinese).

[5] Yang Shuying, Zhang Xing, Zhang Chongwei, et al. Electro-magnetic Transition of Doubly Fed Wind Turbines Initiated by Voltage Dip [J]. Automation of Electric Power Systems, 2008, 32(19): 85-91(in Chinese).

[6] Li Qin, Zhang Xing, Yang Shuying, et al. Dynamic Behavior of DFIG Rotor During Low Voltage Ride-Through[J]. Proceedings of the CSU-EPSA, 22010, 22(5): 19-24(in Chinese).

[7] Guo Jiahu, Zhang Luhua, Cai Xu. Dynamic Response of Wind Power Generation Based on DFIG Under Grid Fault [J]. Acta Energiae Solaris Sinica, 2010, 31(8): 1023-1029(in Chinese).

[8] Lopez J, Sanchis P, Roboam X, et al. Dynamic behavior of the doubly fed induction generator during three-phase voltage dips[J]. IEEE Trans on Energy Conversion, 2007, 22(3): 709-717.

[9] Li Hui, Zhao Meng, Ye Renjie, et al. Evaluation and analysis of transient current of a DFIG wind generation system under grid fault[J]. Electric Machines and Control, 2010, 14(8): 45-51(in Chinese).

[10] Zhang Xueguang, Xu Dianguo, Li Weiwei. Analysis of three-phase short circuit current of doubly fed induction generator[J]. Electric Machines and Control, 2008, 12(5): 493-497(in Chinese).

[11] Shi Yihui, Lu Zongxiang, Min Yong, et al. Practical Calculation Model of Three-phase Short-circuit Current for Doubly-fed Induction Generator [J]. Automation of Electric Power Systems, 2011, 35(8): 38-43(in Chinese).

[12] Hao Zhenghang, Yu Yixin, Zeng Yuan. Transient performance of DFIG power angle in wind farm and its control strategy [J]. Electric Power Automation Equipment , 2011, 31(2): 79-83 (in Chinese).

[13] Hao Zhenghang, Yu Yixin. The influence of doubly-fed induction generator on stability of power system [J]. Relay, 2011, 39(3): 7-11 (in Chinese).

[14] Hughes F.M, Anaya-Lara O, Jenkins N, et al. Control of DFIG-Based Wind Generation for Power Network Support [J]. IEEE Trans on Power Systems, 2005, 20(4): 1958-1966.

[15] Tang Yunmiao. Motor Theory[M]. Beijing: Tsinghua University Press,2002:179-193.

Advanced Materials Research Vols. 960-961 (2014) pp 586-591

doi:10.4028/www.scientific.net/AMR.960-961.586

Design of a Pressurized Circular Pipe with Benches Using the Rough Model Method (RMM)

Mohammed RIABI[1,a], Bachir ACHOUR[2,b]

[1]Department of Hydraulics, University of Chlef, 02000, Algeria

[2]Research Laboratory in Subterranean and Surface Hydraulics (LARHYSS) University of Biskra, PO Box 145, RP 07000, Biskra, Algeria

[a]mohammedriabi@hotmail.com, [b]bachir.achour@larhyss.net

Keywords: Rough Model Method, Pressurized conduit, circular pipe with benches, Turbulent flow, Discharge, Energy slope.

Abstract: The rough model method (RMM) is explained through its application to the design of a pressurized circular shaped conduit with benches, widely used in practice. The three basic equations of turbulent flow are firstly applied to define explicitly the geometric elements of a referential rough model characterized by an arbitrary assigned relative roughness value. The required linear dimensions of the studied conduit are then easily deduced by multiplying the homologues linear dimensions of the rough model by a non-dimensional correction factor. Friction factor is not indispensable when applying the RMM, unlike current design methods. Resulting RMM equations are not only explicit but are also valid in the entire domain of turbulent flow.

Introduction

In the field of hydraulic practice, the problem of designing pipes and channels is acute because current methods are laborious and difficult to handle for practical use [1, 2, 3]. For particular case of pressurized conduits, designing uses Darcy-Weisbach equation, expressing the energy slope, which is one of the three basic equations of turbulent flow. The major problem in this equation lies in the fact that it uses the friction factor which is himself implied regarding to Colebrook-White relationship [4, 5, 6]. The solution involves many trials and tedious computations or laborious graphical procedure due to the fact that linear dimensions of the conduit are unknown. To solve the problem, some authors have proposed in the past approximate relationships for designing conduits, especially circular pipe [7, 8, 9]. These relationships cause errors more or less acceptable, depending on the practical requirements. Despite the fact that the three basic relations of the turbulent flow are complete, they do not, however, allow an explicit solution to the design problem of conduits or channels. Referring to the literature, we can affirm that no explicit method is currently available for designing conduits, especially circular shaped conduit with benches subject of the present study, despite its extensive use in practice as water supply lines, sanitary sewers, culverts and storm drains or penstocks as well. For this reason, this article is a real enrichment of the literature by studying this type of conduit under pressurized condition of the flow. The problem of design will be solved by a rigorous theoretical development based on the three basic relations of the turbulent flow, especially Darcy-Weisbach relationship. To avoid the problem of friction factor, this relationship will be applied to a referential rough model whose friction factor is imposed in the rough turbulent domain. This helps provide explicit linear dimensions relationships of the rough model that are subsequently used to derive the required dimensions of the studied conduit, thanks to a non-dimensional correction factor of linear dimensions. This is the rough model method (RMM) that has been proven in recent past [10, 11] by its simplicity and effectiveness. We will observe that the equations resulting from the RMM are not only explicit but they are also applicable in the whole domain of the turbulent flow, corresponding to Reynolds number greater or equal to 2300 and relative roughness varying in the wide range [0; 0.05].

Basic equations

The relationships on which the study is based are simple well known hydraulic equations namely, Darcy-Weisbach equation, Colebrook-White equation and Reynolds number formula.
The energy slope of a conduit or channel is given by the Darcy-Weisbach relationship as:

$$J = \frac{f}{D_h}\frac{Q^2}{2gA^2}\cdot \quad (1)$$

where Q is the discharge, g is the acceleration due to gravity, A is the water area, D_h is the hydraulic diameter and f is the friction factor given by the well known Colebrook-White formula as:

$$\frac{1}{\sqrt{f}} = -2\log\left(\frac{\varepsilon / D_h}{3.7} + \frac{2.51}{R\sqrt{f}}\right)\cdot \quad (2)$$

ε is the absolute roughness and R is the Reynolds number which can be expressed as :

$$R = \frac{4Q}{P\nu}\cdot \quad (3)$$

ν is the kinematic viscosity and P is the wetted perimeter.

Geometric and hydraulic characteristics of the circular pipe with benches.

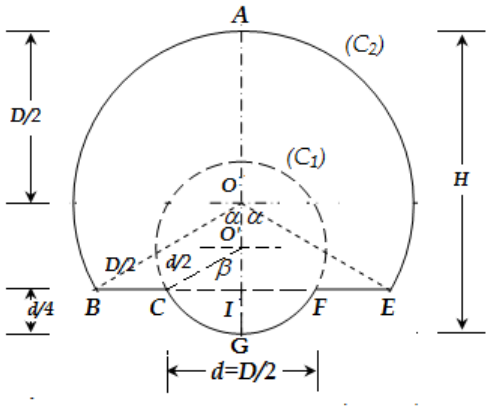

Fig. 1: Geometric elements of the pressurized circular pipe with benches

The circular pipe with benches is characterized by the vertical dimension H representing its height and the diameter D of the circle forming its top. The lower part is formed by a central circular culvert of diameter d and two benches of length $\overline{BC}$ and $\overline{FE}$.
The distance OO' between the two centers of the circle (C_2) of diameter D and the circle (C_1) of diameter d is equal to $D/4$. The diameter d of the circle (C_1) is the half of the diameter D of the circle (C_2).
From a geometrical point of view, Fig. 1 allows to write that:

$$\cos(\alpha) = \frac{\overline{OI}}{\overline{OB}} = \frac{0.5d}{0.5D} = \frac{d}{D} = 0.5\cdot$$

$$\cos(\beta) = \frac{\overline{O'I}}{\overline{O'C}} = \frac{0.25d}{0.5d} = 0.5\cdot$$

We can therefore deduce that: $\alpha = \beta = \pi/3$.
Moreover, one can write from Fig. 1:

$$tg(\beta) = \frac{\overline{CI}}{\overline{O'I}} = \frac{\overline{CI}}{0.25d}\cdot$$

Leading to:

$$\overline{CI} = 0.25\times d\times tg(\beta) = 0.25\times\frac{D}{2}\times\sqrt{3}\cdot$$

Or

$$\overline{CI} = \frac{D\sqrt{3}}{8}\cdot$$

$$tg(\alpha) = \frac{\overline{BI}}{\overline{OI}} = \frac{\overline{BI}}{0.5d} = 4\frac{\overline{BI}}{D}\cdot$$

Leading to :

$$\overline{BI} = \frac{D}{4}tg(\alpha) = \frac{D\sqrt{3}}{4}\cdot$$

The length of the benches is as:

$$\overline{BC} = \overline{BI} - \overline{CI} = \overline{FE} = \frac{D\sqrt{3}}{4} - \frac{D\sqrt{3}}{8} = \frac{D\sqrt{3}}{8}\cdot$$

The length of the arc $\widehat{BAE}$ is given by what follows:

$$\widehat{BAE} = D(\pi - \alpha) = D\left(\pi - \frac{\pi}{3}\right) = \frac{2\pi}{3}D\cdot$$

The length of the arc $\widehat{CGF}$ is as:

$$\widehat{CGF} = \frac{d}{2}(2\beta) = \frac{D}{4}\left(2\times\frac{\pi}{3}\right) = \frac{\pi}{6}D\cdot$$

The total water area A is calculated as follows:

$$A = A_0 - A_1 + A_2\cdot$$

Where:

A_0 is the area of the circular section of diameter D, given by :

$$A_0 = \pi D^2/4 = 0.7854D^2\cdot$$

A_1 is the area of the circular segment of the diameter D of center O and of central angle 2α. Hence:

$$A_1 = \frac{D^2}{4}\left[\alpha - \sin(\alpha)\cos(\alpha)\right] = \frac{D^2}{4}\left[\frac{\pi}{3} - \frac{\sqrt{3}}{4}\right] = 0.1535D^2\cdot$$

A_2 is the area of the circular segment $\widehat{CIFGC}$ belonging to the circle of diameter d of center O' and of central angle 2β. Hence:

$$A_2 = \frac{d^2}{4}\left[\beta - \sin(\beta)\cos(\beta)\right] = \frac{D^2}{16}\left[\frac{\pi}{3} - \frac{\sqrt{3}}{4}\right] = 0.0384D^2\cdot$$

The total water area is then equal to:

$$A = A_0 - A_1 + A_2 = 0.7854D^2 - 0.1535D^2 + 0.0384D^2\cdot$$

Or :

$$A = 0.6703D^2\cdot \qquad (4)$$

On the other hand, the total wetted perimeter P can be written as :

$$P = P_0 + P_1 + P_2\cdot$$

Where:

P_0 is the length of the arc $\widehat{BAE}$, given by :

$$P_0 = \frac{2\pi}{3}D = 2.0944D\cdot$$

P_1 is the length of the segments $\overline{BC}$ and $\overline{FE}$, expressed as:

$$P_1 = 2\overline{BC} = 2\times\frac{D\sqrt{3}}{8} = \frac{D\sqrt{3}}{4} = 0.4330D\cdot$$

P_2 is the length of the arc $\overset{\frown}{CGF}$, given by :

$$P_2 = \overset{\frown}{CGF} = \frac{\pi}{6} D = 0.5236D \cdot$$

The total perimeter P is therefore:

$$P = P_0 + P_1 + P_2 = 2.0944D + 0.4330D + 0.5236D \cdot$$

Or :

$$P = 3.0510D \cdot \quad (5)$$

Accordingly, the hydraulic diameter D_h is:

$$D_h = 4A/P = 4 \times 0.6703/3.0510\, D \cdot$$

Or:

$$D_h = 0.8788D \cdot \quad (6)$$

According to Fig. 1, the height H of the conduit can be expressed as:

$$H = \overline{AO} + \overline{OO'} + \overline{O'G} = \frac{D}{2} + \frac{d}{4} + \frac{d}{2} = \frac{D}{2} + \frac{D}{8} + \frac{D}{4} = \frac{7D}{8} \cdot$$

Or:

$$H = 0.875D \cdot \quad (7)$$

Referential rough model

Both of geometric and hydraulic characteristics of the rough model are distinguished by the symbol "$\bar{}$". Thus, its height is representing by $\overline{H}$, its diameter is $\overline{D}$ and the wetted perimeter is $\overline{P}$…etc. The rough model we consider is a pressurized circular conduit with benches characterized by $\overline{\varepsilon}/\overline{D}_h = 0.037$ as the arbitrarily assigned relative roughness value. The selected relative roughness value is so significant that the prevailed flow regime in the model is fully rough. Thus, the friction factor is $\overline{f} = 1/16$ according to Eq. 2 for $\overline{R} = R$ tending to infinitely large value. Applying Eq. 1 to the rough model leads to:

$$\overline{J} = \frac{\overline{f}}{\overline{D}_h} \frac{\overline{Q}^2}{2g\overline{A}^2} \cdot \quad (8)$$

Bearing in mind that $\overline{D_h} = 4\overline{A}/\overline{P}$ and $\overline{f} = 1/16$, Eq. 8 can be rewritten as:

$$\overline{J} = \frac{1}{128g} \frac{\overline{P}}{\overline{A}^3} \overline{Q}^2 \cdot \quad (9)$$

Introducing Eq. (4) and Eq. (5) into Eq. 9, one may deduce:

$$\overline{J} = 0.0791 \frac{\overline{Q}^2}{g\overline{D}^5} \cdot \quad (10)$$

Let us assume $\overline{Q} = Q$ and $\overline{J} = J$, implying obviously $\overline{D} \neq D$. Thus, Eq. 10 gives:

$$\overline{D} = 0.6021 \left(\frac{Q^2}{gJ} \right)^{1/5} \cdot \quad (11)$$

Eq. 11 allows computing explicitly the diameter $\overline{D}$ of the rough model for the given values of the discharge Q and the energy slope J.

Non-dimensional correction factor of linear dimension

The RMM states that any linear dimension "L" of the conduit is related to its homologue "$\overline{L}$" of the rough model by the following fundamental relationship:

$$L = \psi \overline{L} \cdot \quad (13)$$

Where ψ is a non-dimensional correction factor of linear dimension, less than unity, which is governed by the following explicit relationship [1, 10]:

$$\psi = 1.35\left[-\log\left(\frac{\varepsilon/\overline{D}_h}{4.75}+\frac{8.5}{\overline{R}}\right)\right]^{-2/5}. \tag{14}$$

In which $\overline{R}$ is the Reynolds number characterizing the flow in the rough model, which can be simply expressed as:

$$\overline{R}=\frac{4Q}{\overline{P}\nu}. \tag{15}$$

Computation steps of the linear dimensions of the conduit

Knowing the discharge Q, the energy slope J, the absolute roughness ε and the kinematic viscosity ν, the following steps are recommended to compute the required value of the linear dimensions of the conduit:

1. Compute the diameter $\overline{D}$ of the rough model using Eq. 11.
2. Knowing $\overline{D}$, compute the wetted perimeter $\overline{P}$ and the Reynolds number $\overline{R}$ in the rough model, using Eq. 5 and Eq. 15 respectively.
3. Compute the hydraulic diameter $\overline{D}_h$ of the rough model using Eq. 6.
4. Applying Eq. 14, the non-dimension correction factor of linear dimension ψ is then worked out.
5. The required value of the diameter D of the conduit is finally $D=\psi\overline{D}$ according to Eq. 13.
6. Once the diameter D of the conduit determined, the diameter d is then $d=D/2$ and the height H is directly deduced from Eq. 7.

Example:

Compute the linear dimensions of the pressurized circular pipe with benches schematised in Fig. 1, for the following data: $Q=1.225\,m^3/s$, $J=4\times10^{-4}$, $\varepsilon=0.002m$, $\nu=10^{-6}m^2/s$

1. According to Eq.11, the diameter $\overline{D}$ of the conduit is:

$$\overline{D}=0.6021\left(\frac{Q^2}{gJ}\right)^{1/5}=0.6021\times\left(\frac{1.225^2}{9.81\times10^{-4}}\right)^{1/5}=1.9778\,m.$$

2. According to Eq. 5, the wetted perimeter $\overline{P}$ of the rough model is as:
   $\overline{P}=3.0510\overline{D}=3.0510\times1.9778=6.0343\,m.$
   Using Eq. 15, the Reynolds number $\overline{R}$ is then:
   $$\overline{R}=\frac{4Q}{\overline{P}\nu}=\frac{4\times1.225}{6.0343\times10^{-6}}=812025.$$
3. Applying Eq. 6, the hydraulic diameter $\overline{D}_h$ is:
   $\overline{D}_h=0.8788\overline{D}=0.8788\times1.9778=1.7381\,m.$
4. According to Eq. 14, the non-dimensional correction factor of linear dimension is given as:
   $$\psi=1.35\left[-\log\left(\frac{\varepsilon/\overline{D}_h}{4.75}+\frac{8.5}{\overline{R}}\right)\right]^{-2/5}$$
   $$=1.35\times\left[-\log\left(\frac{0.002/1.7381}{4.75}+\frac{8.5}{812025}\right)\right]^{-2/5}=0.8090.$$
5. Finally, the required diameter D of the conduit is given by Eq. 13 as:
   $D=\psi\overline{D}=0.8090\times1.9778=1.6\,m.$
6. Consequently, the diameter d is:
   $d=D/2=1.6/2=0.8\,m.$

Using Eq. 7, the height H of the conduit is then:

$$H = 0.875D = 0.875 \times 1.6 = 1.4\,m \cdot$$

We can continue the calculation by writing that the length of the benches is:

$$\overline{BC} = \overline{FE} = \frac{D\sqrt{3}}{8} = \frac{1.6 \times \sqrt{3}}{8} \cong 0.3464\,m \cdot$$

7. This step aims to verify the validity of the calculations. To do this, determine from Eq. 9 the energy slope $\overline{J}$ which must be equal to J for $\overline{Q} = Q$. Determine first the value of the water area $\overline{A}$ using Eq. 4:

$$\overline{A} = 0.6703\overline{D}^2 = 0.6703 \times 1.9778^2 = 2.6220\,m^2 \cdot$$

Hence:

$$\overline{J} = \frac{1}{128g}\frac{\overline{P}}{\overline{A}^3}\overline{Q}^2 = \frac{1}{128 \times 9.81} \times \frac{6.0343}{2.6220^3} \times 1.225^2 = 0.00040006 \cong 4 \times 10^{-4} \cdot$$

It is indeed the value of J given in the problem statement.

Conclusions

To explain the advantages of the rough model method in the design of hydraulic structures, the case of circular shaped conduit with benches was considered. This conduit is characterized by three linear dimensions that we have explicitly determined by a new theoretical rigorous approach. The theory is mainly based on the Darcy-Weisbach equation in which friction factor can not be directly determined without a laborious process. To avoid this drawback, a rough model was used to the sake of calculation. Its hydraulic characteristics have been previously defined in the rough domain, more particularly the friction factor whose value is constant. As a result, the Darcy-Weisbach equation has explicitly expressed the geometric diameter of the rough model which can easily be calculated from the known values of the discharge Q and the energy slope J. The required diameter of the studied conduit was simply obtained by multiplying the diameter of the rough model by a non-dimensional correction factor, in accordance with the fundamental relationship of the RMM. The others linear dimensions of the conduit, such as its height, were determined according to the same principle.

References

[1] R.O. Sinniger, W.H. Hager, Constructions Hydrauliques, 1ère Ed., Ed. Lausanne, Suisse: Presses Polytechniques Romandes, 1989.
[2] V.T. Chow, Open channel hydraulics, McGraw Hill, New York, 1973.
[3] R.H. French, Open Channel Hydraulics, McGraw Hill, New York, 1986.
[4] Colebrook, C.F. and White, C.M., Experiments with fluid friction in roughened pipes, Proc. R. Soc. London, Ser. A, 161 (1937) 367-381.
[5] L.F. Moody, Friction factors for pipe-flow, Transactions ASME (1944).
[6] P.K. Swamee, A.K. Jain, Explicit equations for Pipe-flow Problems, J. Hyd. Engrg., ASCE 102(5) (1976) 657-664.
[7] B. Achour, A. Bedjaoui, Computation of Friction Factor in Pipe, Larhyss Journal, 5 (2006) 197-200.
[8] B. Achour, A. Bedjaoui, Turbulent Pipe-Flow Computation Using the Rough Model Method, J. Civil Engineering and Science, 1(1) (2012) 36-41.
[9] P.K. Swamee, N. Swamee, design of noncircular sections, J. Hyd. Res., 46(2) (2008) 277-281.
[10] B. Achour, Design of Pressurized Vaulted Rectangular Conduits Using the Rough Model Method, Advanced Materials Research, 779-480 (2013) 414-419.
[11] B. Achour, A. Bedjaoui, Discussion of Explicit Solutions for Normal Depth Problem, by P.K. Swamee, P.N. Rathie, J. Hyd. Res., 44(5) (2006) 715-717.

CHAPTER 5:

HVAC, Air Conditioning and Refrigeration

Advanced Materials Research Vols. 960-961 (2014) pp 595-598

doi:10.4028/www.scientific.net/AMR.960-961.595

Development of a condensation refueling gas recovery system based on turbo Brayton refrigeration technique

XIONG Lianyou [1, a], LU Wenhai[1, b], HUO Zhiyong[2, c], PENG Nan[1, d]

[1]State Key Laboratory of Technologies in Space Cryogenic Propellants (Technical Institute of Physics and Chemistry, Chinese Academy of Sciences), Beijing 100190, China

[2]Key Laboratory of Cryogenics, Technical Institute of Physics and Chemistry, Chinese Academy of Sciences, Beijing 100190, China

[a]lyxiong@mail.ipc.ac.cn, [b]luwenhai@mail.ipc.ac.cn, [c]zhiyonghuo@mail.ipc.ac.cn, [d]pengnan@mail.ipc.ac.cn

Keywords: Condensation, Refueling gas recovery, Turbo Brayton refrigeration

Abstract. Volatile organic compounds (VOCs) are emitted from the refueling of gasoline vehicles and trucks. Controlling these emissions has been an important issue since the late 2000s in China. We have recently developed a condensation refueling gas recovery system to recover the VOCs from gaseous wastes at a bulk gasoline terminal. In this system VOC vapor is condensed by a reversed turbo-Brayton cycle refrigerator. The recovery system has a capacity of 100 Nm^3/hr at the lowest condensation temperature of 190K. It has been put into use since 2008. The achieved recovery efficiency is 96% and the emission of VOCs is less than 8 g/m^3 at the exit of the recovery system.

Introduction

In China, there are more than 1500 bulk gasoline terminals, 90,000 gasoline filling stations and 20,000 tanker trucks until 2012. The emission of gasoline vapor containing volatile organic compounds (VOCs) from the filling, unloading and transportation of gasoline at the gasoline service stations is more than 600,000 tons per year. Controlling these emissions has been an important issue since the late 2000s in China. Several regulations have been enacted to limit the discharge of gasoline vapor to the environment. According to these VOC emission regulations and standards of China, the emission of total organic compounds loaded for gasoline storage and distribution facilities is specified to be less than 25g per cubic meter [1,2,3,4].

There are several techniques for recovering VOCs from gaseous wastes, such as activated carbon adsorption, condensation using refrigerants and membrane separation [5,6,7]. VOC-condensation processes use refrigerants to reduce the temperature of the emission stream to the level necessary for the VOCs to condense out of the stream. Two refrigeration cycles, the vapor-compression refrigeration cycle and Brayton refrigeration cycle, could be used to cool down the gasoline vapor. As compared with the vapor-compression refrigeration cycle, the Brayton refrigeration cycle can achieve very high recovery efficiencies. The reason is that it uses high efficiency turbo expanders to produce the necessary cooling power; the very low cooling temperature can be obtained by using different gas cryogen such as nitrogen, argon or dried air.

In order to meet the requirements of VOC emission regulations, Beijing Longyu Petroleum & Chemical Company had to develop a stage I vapor recovery system to control the VOC emissions during the transfer of gasoline from the cargo tank to the underground storage tank. This paper presents a condensation refueling gas recovery system based on turbo Brayton refrigeration technique.

Composition of VOC Vapor

In general, stage I vapors are created due to the high volatility of gasoline at atmospheric conditions. Emissions from the vent of underground storage tank include filling losses, breathing losses, and empting losses. The vapor evolved from the fuel tank contains a mixture of hydrocarbons and air. The concentrations of VOC vapors stream on user site are tested and listed in Table 1.

Table 1. Composition of VOCs vapors stream

compound	N_2	O_2	H_20	CO_2	C_2H_6	C_3H_8
Concentration (vol%)	62.1	16.5	1.1	0.8	1.1	2.3
compound	iC_4H_{10}	nC_4H_{10}	iC_5H_{12}	nC_5H_{12}	C_6H_{14}	C_7H_{16}
Concentration (vol%)	4.2	4.7	3.0	1.6	1.4	1.2

Condensation Temperature and Pressure

Owing to stringent environmental regulations imposed on the emission of VOCs, the gaseous wastes must be cooled to very low temperatures so as to condense the VOCs to the required level. Taking the VOC vapor with composition as listed in Table 1 as the inlet flow, the recovery efficiency of vapor gas of gasoline and the emission of VOCs by condensation is calculated based on the phase equilibrium theory. The simulation results are illustrated in Fig. 1 and Fig. 2. The results indicate that the values of percent removal of total VOCs of inlet gasoline vapor by condensation are about 89, 93, and 95.8 wt% at condensation temperature of 200, 190, and 180K, respectively. To reduce the VOC emissions to the level of 25g/m^3, the condensation temperature of less than 205K will be required at the pressure of 130 kPa. For the safety operation of VOC vapor, the low pressure of 130 kPa is considered as the condensation pressure, although the higher the condensation pressure (Pc) is, the higher the recovery efficiency may be achieved.

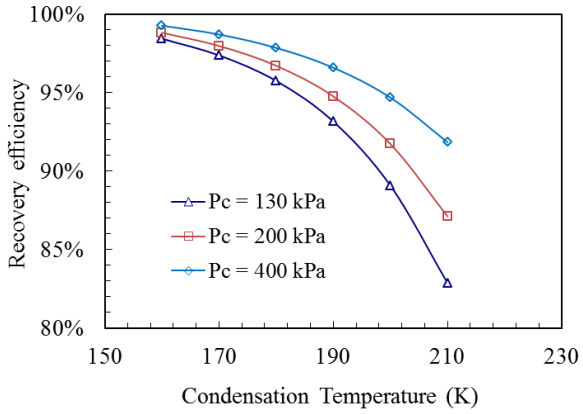

Fig. 1. Recovery efficiency at various condensation temperature

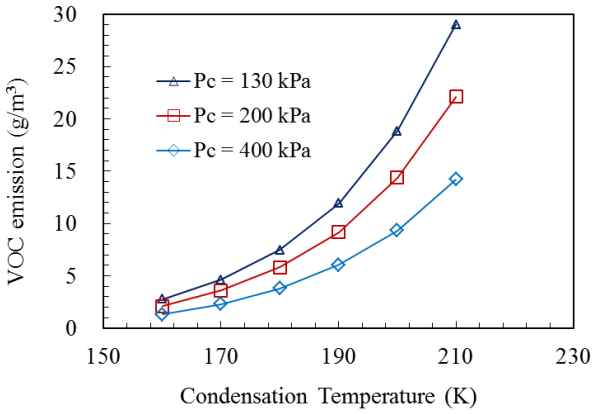

Fig. 2. VOC emissions at various condensation temperature

Condensation System Based on Reverse Turbo Brayton Refrigeration Cycle

Based on the above computation, we specified 190 K as the condensation temperature of the refueling gas recovery system. To condense the VOC vapor and remove the most VOCs at such low temperature, the reverse Brayton refrigeration technique was applied to the VOC condensation system.

As shown in Fig. 3, this system consists of a refrigeration loop and a VOC vapor flow loop. The refrigeration loop is a reverse Brayton refrigeration cycle, which is composed of a screw nitrogen compressor, an oil remove system, a gas nitrogen buffer tank, an air turbine expander and a two-stage aluminum plate-fin heat exchanger unit. The capacity of condensation recovery system is 100 Nm^3/hr at the lowest condensation temperature of 190K. The flow rate of the nitrogen compressor is 10 m^3/min, the discharge pressure is 800 kPa and the drive rated motor power is 55 kW. The high speed gas bearing turbine expander, working at 80000 rpm, is the key component to provide cooling capacity for the condensation of VOC vapor.

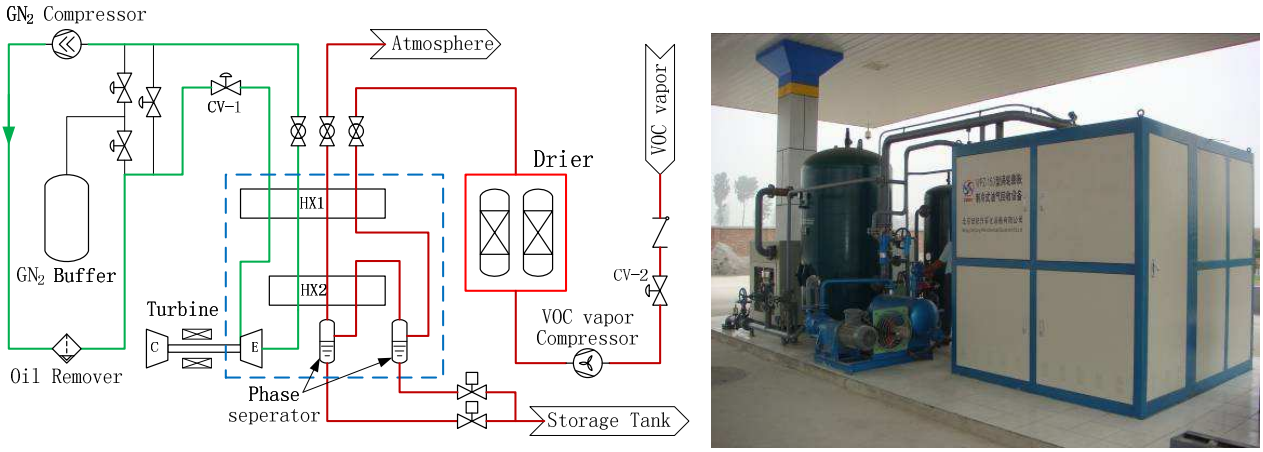

Fig. 3. Condensation recovery System

The VOC vapor flow loop is an isobaric heat exchanging process attached by phase separation at *the cold ends of heat exchangers, which includes a VOC vapor compressor, a VOC vapor dryer and* two gas-liquid phase separators. The condensation process occurs in the two-stage heat exchanger unit which avoids contamination due to the contacting of the VOC gas stream with other streams. The VOC vapor compressor is a liquid ring compressor equipped with a variable frequency drive and a control valve to match the VOC vapor flow and to avoid the subatmospheric pressure occurring inside the underground storage tank. The VOC vapor dryer consists of dual drying chambers alternately cycled through drying and regeneration.

Operation

This system has been put into use since 2008. The temperature at the outlet of the turbo-expander and the temperature at the outlet of the second stage phase separator are measured by two PT100 sensors which are located on the outside surfaces of pipes near the expander and phase separator.

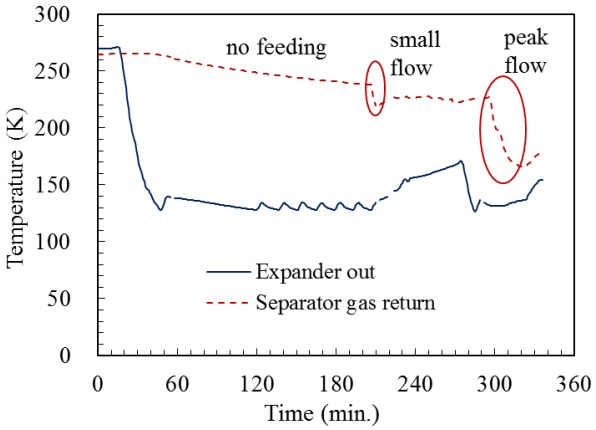

Fig. 4. Temperature change during Cool-down process

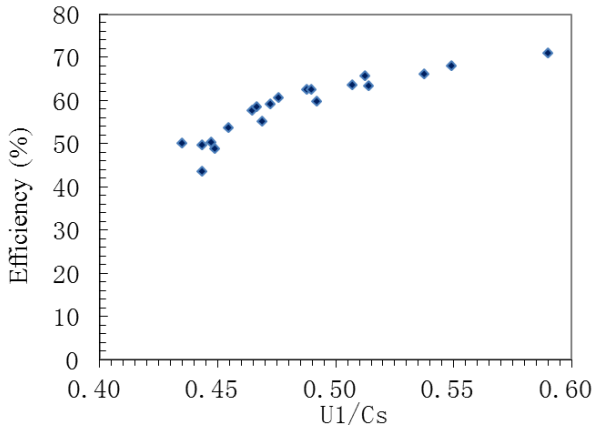

Fig. 5. Efficiency of turbo-expander at different isentropic velocity ratio

The variations of these two temperatures with the cool-down time are illustrated in Fig. 4. The cool-down time for the gas nitrogen refrigeration cycle as well as for the VOC vapor condensation loop is less than 30 minutes. Since the VOC vapor flow is not stable on the site of gasoline dispensing facility, the peak flow rate appears at heavy traffic period while the minimum flow rate is zero. The peak flow rate and a small flow rate are marked in the Fig. 4 with two ellipses. The condensation temperature at the peak flow is 170K which is lower than the design temperature. The reason is that the peak flow rate of VOC vapor is less than the capacity of condensation recovery system. In order to

match the lower peak flow rate, the working speed of turbo expander was controlled and adjusted to a lower speed. As a result, only the lower isentropic efficiencies had been achieved as shown in Fig. 5, the maximum efficiency of expander is about 70%.

The recovery efficiency of 96% and the VOC emission level of 8 g/m^3 at the exit of the recovery system had been detected and confirmed by authority in Nov. 2008.

Conclusion

The condensation refueling gas recovery system based on reverse turbo Brayton refrigeration technique was developed. The operation results indicate that such system meet the stringent requirement of VOC emission regulations of China. However, further work should be done to match the unstable flow of VOC vapor stream, and the cost effective analyses are expected to be carried out in details.

Acknowledgement

This work is supported by the Beijing Shijixing Petrochemical Equipment Company.

References

[1] Ministry of environmental protection, P.R. China.2007. GB 20950-2007 Emission standard of air pollutant for bulk gasoline terminals.

[2] Ministry of environmental protection, P.R. China.2007. GB 20951-2007 Emission standard of air pollutant for gasoline transport.

[3] Ministry of environmental protection, P.R. China.2007. GB 20952-2007 Emission standard of air pollutant for gasoline filling stations.

[4] Jun F. Research and Application of Condensation Unit for Oil Vapor Recovery. Low Temperature and Specialty Gases, 26 (2008) 21-23.

[5] Tsai W T, Chang C Y, Ho C Y, et al. Simplified description of adsorption breakthrough curves of 1, 1-dichloro-1-fluoroethane (HCFC-141b) on activated carbon with temperature effect. Journal of colloid and interface science, 214 (1999) 455-458.

[6] Dunn R F, El-Halwagi M M. Optimal design of multicomponent VOC condensation systems. Journal of Hazardous Materials, 38 (1994) 187-206.

[7] Ohlrogge K, Peinemann K V, Wind J, et al. The separation of hydrocarbon vapors with membranes. Separation Science and Technology, 25(1990) 1375-1386.

Advanced Materials Research Vols. 960-961 (2014) pp 599-602

doi:10.4028/www.scientific.net/AMR.960-961.599

Analysis of the Heating and Energy Saving Effect of Capillary Radiant Ceiling in Hot Summer and Cold Winter Area

Dong Yang[1,2],Qingmei Wen[1,2,a],Mingjiu Chen[1,2],Yongan Li[1,2],Shijun Wei[1,2]

[1]Key Laboratory of Renewable Energy Utilization Technologies in Buildings of the National Education Ministry, Jinan 250101, China

[2]School of Thermal Energy Engineering, Shandong Jianzhu University, Jinan 250101, China

[a]wenqingmei713@163.com

Key Words: Capillary, roof radiation, heating, Exergy Theory.

Abstract. This paper introduces the advantages of capillary roof radiant heating system, by using finite element numerical method, the indoor temperature distribution of capillary radiant roof and underfloor supply air composite system is simulated, using the theory of exergy to analysis the energy saving of the system, the result proves that the system can well satisfy indoor comfort requirements, and compared with the floor radiation heating system can saving energy 65.8%, has great research value.

Introduction

Existing air conditioning system through continuous improvement and perfection, but still has some problems such as: temperature and humidity coupling loss, difficult to adapt to changes in temperature and humidity, the cold surface mildew, convection wind feeling, coil air noise and indoor repeat installed two sets of environmental control system and so on[1]. Heating also have the problems such as the low heat exchange efficiency, nonuniform indoor temperature distribution, difficulty pipe installation and repair of the buried radiant floor heating system ,fouling and cleaning and other aspects etc. Therefore put forward higher request to the HVAC industry: in addition to the optimization of building periphery structure to strengthen heat preservation and heat insulation, research and development of high comfort, energy saving, low cost indoor environment control system is very necessary.

In twentieth Century 70 years scientists in Germany according to the principle of bionics invented the capillary radiation air conditioning system, but has not been seriously, while with the global energy crisis, environmental pollution and greenhouse effect is more serious, governments around the world to improve the energy-saving emission reduction standards, the capillary radiation heating refrigeration technology has become a hot research in recent years at air-conditioning industry.American Stanley A. Mumma[2] provides a design procedure of modern plane radiation air conditioning combined with ventilation system, and the system used in the commercial buildings are described. Stanley A. Mumma[3] discuss the dehumidifying measures in full consideration of capillary grille and displacement ventilation system investment and operation conditions. Wei Bing and Jiang Lu[4,5]of the North China Electric Power University studied model of capillary air-conditioning system, mainly for the numerical simulation of indoor thermal environment and micro environment between capillary tubes.

The advantage of capillary radiant ceiling

There was comprehensive study of cooling effect of capillary radiant ceiling at home and abroad, but the study of heating effect of capillary radiant ceiling is not enough . A complete air conditioning system which was propagable and energy-efficient must has the function of cooling and heating. In terms of human feelings, the capillary radiant ceiling is less comfortable than floor radiant heating, but it has its own advantage. For instance, in function, the capillary radiant ceiling system can both provides the function of heating and cooling; in installation, according to the structure of building the

capillary radiant ceiling system can be installed in the roof, wall, cylindrical and ground ;in energy saving effect, it used low grade energy, combined with heat pump it could save energy 40-70% ; in safety, even if destroyed, capillary diameter is small, no flooding accident, find the leak and repair is very simple.

Study on heating and energy saving

Calculation and analysis of the indoor temperature field in winter: In an office of Ji'nan city as an example, the room size is 4.85m×3m×3.9m, winter indoor temperature is 18℃, the average temperature of capillary radiant panel is 27℃, studies have shown that[7], using floor side air ways during winter, indoor vertical temperature difference is small, can well meet the requirements of comfort. According to the minimum fresh air and air speed 0.3m/s, determine the outlet size: 600mm×100mm, supply air temperature 21℃, office mesh as shown in Fig.1.

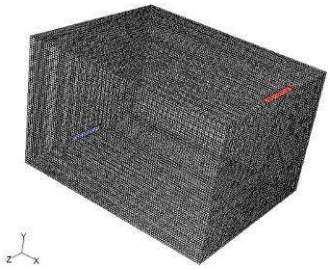

Fig.1 Room model meshing

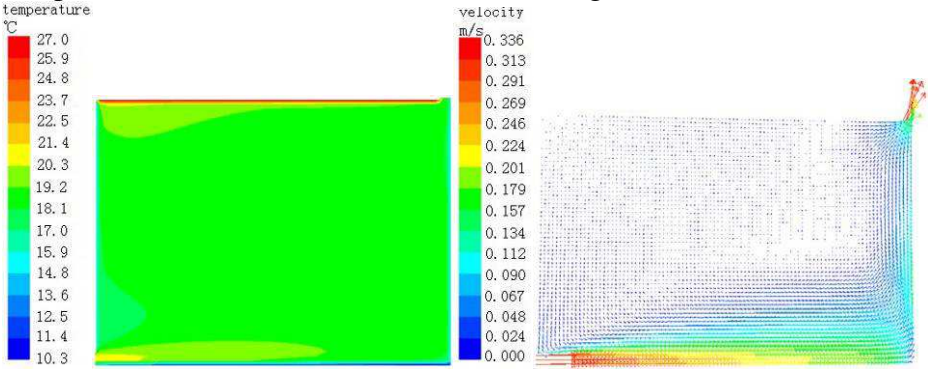

Fig.2 Temperature and velocity field of the Z = 1.95 cross-section

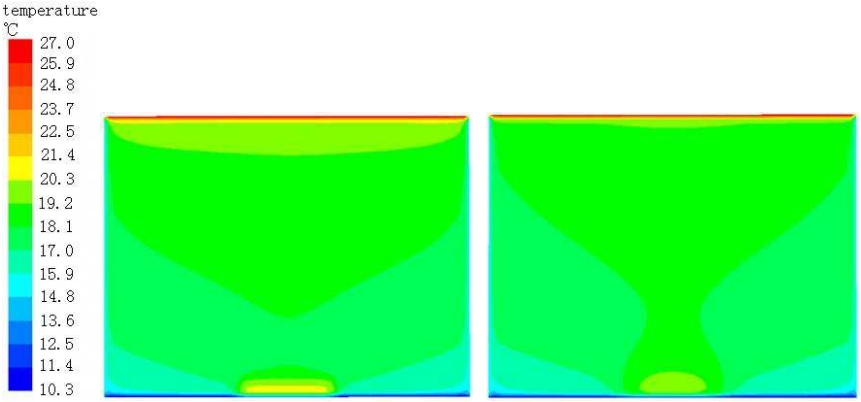

Fig.3 Temperature distribution of the X = 0.35m, X = 2m

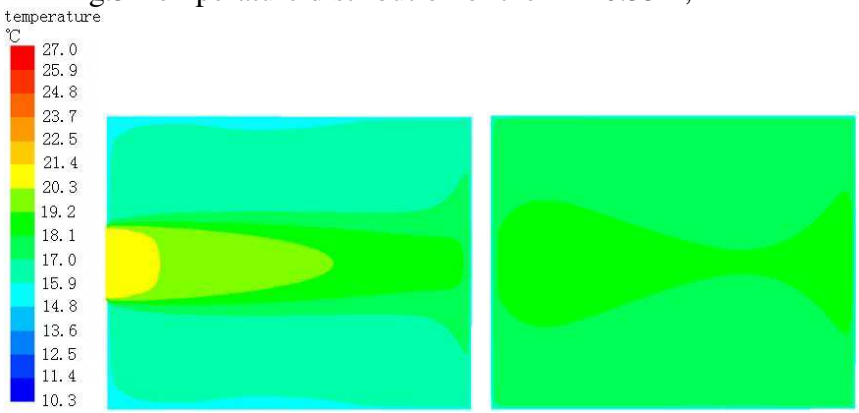

Fig.4 Horizontal temperature field of the Y = 0.1m, Y = 1.2m height

After the cross-section(Z=1.95) of heat source such as staff and computer, room temperature and velocity distribution as shown in Fig.2 when the outlet disposed on the ground. Fig.3 is the vertical temperature distribution close to the outlet(X=0.35) and the central(X=2) of the room, Fig.4 is the horizontal temperature distribution at a height of a human ankle(Y=0.1) and sitting(Y=1.2). In

addition to the outlet and close to the surface of the radiating plate, from the ankle (about 0.1m) to human activity area (2m or less), the indoor vertical temperature distribution is between 18.1℃ to 19.2℃, does not exceed 2℃. At the horizontal height of 0.1m close to the outlet, the temperature stratification, but not obvious, the horizontal temperature distribution at a height of 1.2m substantially consistent, the heating temperature reaches the set requirements and indoor temperature distribution is very uniform. Air flow in the room at 0.1m/s or less basically, no significant hair feeling, can well meet the requirements of comfort.

The results can be seen from the above simulation, capillary radiation plate has a good effect not only in terms of cooling, but also make the room temperature reaches requirements when heating, and have a high degree of comfort.

Exergy analysis theory: Seen by the thermodynamic principles: for 1kg working fluid, the maximum useful work for the opening lines of a steady flow from imports state into the state of the environment through the irreversible process is:

$$\mathrm{ex} = w_{\max} = (h-h_0) - T_0(s-s_0) = C_{\mathrm{p}}(T-T_0) - T_0\left(Cp\ln\frac{T}{T_0}\right) \tag{1}$$

Where, ex is the Exergy of the working fluid, kJ/kg; W_{max} is maximum useful work for the working fluid, kJ/kg; T_0 is the ambient temperature, K; T is working fluid inlet temperature, K; Cp is the specific heat, kJ/(kg • K).

Analysis of energy saving compared with floor heating

Capillary ceiling radiant heating and radiant floor heating are opening steady flow systems. Following as the radiant floor heating system and capillary ceiling radiant heating system example, supply water temperatures were 50℃and 30℃respectively, the temperature difference between supply and return water both were 5℃, calculation of the efficiency of the two systems is as follows (assuming the ambient temperature is 18 ℃):

Heat exergy for the supply water temperature of 50℃ is:

$$ex = 4.19\times(50-18) + (18+273)\times 4.19\times\ln\frac{18+273}{50+273} = 6.87kJ/kg \tag{2}$$

Heat exergy for the return water temperature of 45 ℃ is:

$$ex = 4.19\times(45-18) + (18+273)\times 4.19\times\ln\frac{18+273}{45+273} = 4.94kJ/kg \tag{3}$$

Heat exergy for the supply water temperature of 30℃ is:

$$ex = 4.19\times(30-18) + (18+273)\times 4.19\times\ln\frac{18+273}{30+273} = 1.01kJ/kg \tag{4}$$

Heat exergy for the return water temperature of 25 ℃ is:

$$ex = 4.19\times(25-18) + (18+273)\times 4.19\times\ln\frac{18+273}{25+273} = 0.35kJ/kg \tag{5}$$

Both are low-temperature radiant heating, and therefore take the two systems the same cooling load per unit area, the system's refrigerant mass flow rate can be calculated by the following formula:

$$Q = C_p m\Delta t \tag{6}$$

Mass flow ratio of the two systems working fluid is m1: m2 = 1:1.

For the radiant floor heating system 50/45℃, the exergy consumption for unit area of air conditioning per unit time is:

$$\Delta E_1 = m_1(ex_1 - ex_2) = m_1(6.87-4.94) = 1.93m_1 \tag{7}$$

For the radiant floor heating system 30/25℃, the exergy consumption for unit area of air conditioning per unit time is:

$$\Delta E_2 = m_2(ex_1 - ex_2) = m_2(1.01-0.35) = 0.66m_2 \tag{8}$$

Therefore, based on the same amount of heating, energy saving percentage of capillary roof radiant system are：

$$\eta = \frac{\Delta E_1 - \Delta E_2}{\Delta E_1} \times 100\% = \frac{1.93m_1 - 0.66m_2}{1.93m_1} \times 100\% = 65.8\% \quad (9)$$

Not difficult to see from the above results, on the basis of considering the heat "quality" and "amount", the capillary ceiling radiant heating system compared with radiant floor heating system can save energy about 65.8%. Capillary roof radiant energy saving system is reflected in saving not only the amount of energy, but also the high-grade energy. Thus, the capillary radiant system can take advantage of solar energy, geothermal energy and other low-grade renewable energy, better to reflect its energy efficiency superiority.

Conclusion

In this paper, an Office of Jinan City as an example, the indoor temperature and velocity field simulation shows that the use of capillary roof radiant heating, indoor temperature uniform, vertical temperature difference does not exceed 2 ℃, air velocity in addition of the outlet , were 0.1m/s or less, to meet the requirements of comfort. And use the exergy theory analysis the energy consumption of the system, the capillary radiant heating system can save 65.8% energy than radiant floor heating system at the same conditions, energy-saving effect is remarkable.

Although radiation capillary system has other conventional air conditioning systems incomparable advantages, but there are many problems, such as indoor dehumidification, cooling / heating capacity insufficient, air quality and other issues. This article only simulated and analyzed on the capillary heating and energy saving effect, without considering indoor air quality and other issues, I will continue to work in the relevant direction, get more valuable research results.

Acknowledgements

This work was financially supported by the Doctor Foundation of Shandong Jianzhu University (XNBS1223) and Ministry of housing and urban rural development project (K12014035).

References:

[1] Ma Yuqi, Liu Xuelai, Li Yongan,etc. Analysis of Energy Efficiency of Capillary Tube Air-conditioning System[J]. Low Temperature Architecture Technology, 2008,01:111-112.

[2] Stanley A. Mumma, Jae-Weon Jeong. Direct digital temperature, humidity and condensate control for a dedicated outdoor air-ceiling radiant cooling panel system [G]//ASHRAE Trans, 2005, 111:547-558.

[3] Stanley A. Mumma. Dedicated outdoor air system and desiccants [I]. Engineered Systems, http//:www.esmagazine.com, 2007-8-24.

[4] Wei Bing, Jiang Lu, Li Li,ect. Numerical Simulation of Air Distribution in A Residential Building with Capillary Plane HVAC Terminal System[S]. ASME ,2007.

[5] Jiang Lu. Numerical Simulation for the Indoor Thermal Environment of Capillary Plane HVAC System[D]. North China Electric Power University, 2007.

[6] Chen Peng.Thermal Comfort Investigation and Heat Transfer Analysis of Capillary Network Radiation Refrigeration[D]. Donghua University, 2013.

[7] Liu Xuelai. Dynamic models and experimental study on capillary grating plane air-conditioning system[D]. China University of Petroleum (EastChina), 2011.

Advanced Materials Research Vols. 960-961 (2014) pp 603-608

doi:10.4028/www.scientific.net/AMR.960-961.603

Analysis on Heat Transfer Energy Efficiency of U-Tube Buried Pipe under Variable Entering Water Temperature Conditions

Yuzhou Cui [1,a]

[1]China Railway First Survey and Design Institute Group Co.,Ltd.

No.2 Xiying Road, Yantadistrict, Xi'an City, Shanxi Province, 710043 China

[a]yuzhou.cui2014@gmail.com

Keywords: buried pipe, variable temperature inflow, energy efficiency coefficient, coefficient of heat accumulation

Abstract. Taken as the carrier of heat extraction between rock-soil body and ground source heat pump systems, U-tubed pipe heat transfer efficiency was the key for ensuring the long-term and high-performance operation of ground source heat pump systems by means of improving the heat transfer effect. The efficiency coefficient, E, is defined as the ratio of the actual heat transfer capacity to the theoretically maximal heat transfer capacity from the U-tube into rock-soil body, which illustrated the effect of heat transfer ability and the variable heating or cooling loads. Aim at Variation characteristics of heat transfer coefficient of energy efficiency under the variable temperature inflow condition, decomposed into the product of the ratio of biggest buried tube heat transfer temperature difference φ and heat pump outlet water temperature difference σ. Use of u-shaped buried pipe three-dimensional heat transfer model which based on the multipole theory, the influence law of its change which caused by the construction load, buried pipe flow and the unit performance were analyzed, it can provide technical support to optimize the design of ground source heat pump system.

Introduction

Nowadays, in Ground source heat pump engineering, the calculation, design and equipment selection of the buried tube heat exchanger is usually based on the maximum cold or heat load of the building, due to the difference of building function and the ways of using, Difference would inevitably be generated. Even the design of ground source heat pump system is very reasonable, Because most of the time it running in the part load, the actual heat exchange of the buried tube heat exchanger in a rock mass will produce a great influence[1]. The heat transfer process of buried pipe is decided by the result of the changes between building load and geotechnical heat regenerative ability. As the change of inlet temperature of buried pipe, the heat exchange efficiency is decided by the result of many factors of the whole ground source heat pump system, and has its own characteristics and change rules.

When the loop fluid velocity stays the same, U-buried pipe outlet temperature not only reflects the heat exchange efficiency between buried pipe and the rock and soil mass, is also an important characteristic parameters of buried tube heat exchange process. Based on heat transfer coefficient of energy efficiency concept from literature [2] in which the inlet temperature remains constant, the rule indicates some typical conditions. The change rule of buried tube heat exchange efficiency characteristics under the variable temperature inflow which change with the construction load is analyzed close to the actual situation.

Heat Exchange Efficiency Characteristic Parameters of Buried Tube

Outlet Temperature Model of the Buried Pipe. During the heat exchange process of the buried tube, in order to realize the heat exchange, the Circulating fluid flow from a u-shaped tube to the

bottom of the drilling pipe, then flow out from another tube. According to the buried tube heat transfer model based on the theory of the multipolar, the two tube temperature distribution $T_{f1}(Z,t)$ and $T_{f2}(Z,t)$ can be expressed as follows[3]:

$$T_{f1}(Z,t)=T_{f1}(0,t)f_1(Z)+T_{f2}(0,t)f_2(Z)+\int_0^1 T_0(\eta,t)f_4(Z-\eta)d\eta \quad (1)$$

$$T_{f2}(Z,t)=-T_{f1}(0,t)f_2(Z)+T_{f2}(0,t)f_3(Z)-\int_0^1 T_0(\eta,t)f_5(Z-\eta)d\eta \quad (2)$$

In the formula: $f_1(Z)=e^{\beta Z}\left[\cosh(\gamma Z)-\delta\sinh(\gamma Z)\right]$ $f_2(Z)=e^{\beta Z}\frac{\beta_{12}}{\gamma}\sinh(\gamma Z)$

$$f_3(Z)=e^{\beta Z}\left[\cosh(\gamma Z)+\delta\sinh(\gamma Z)\right] \quad f_4(Z)=e^{\beta Z}\left[\beta_1\cosh(\gamma Z)-\left(\delta\beta_1+\frac{\beta_2\beta_{12}}{\gamma}\right)\sinh(\gamma Z)\right]$$

$$f_5(Z)=e^{\beta Z}\left[\beta_2\cosh(\gamma Z)+\left(\delta\beta_2+\frac{\beta_1\beta_{12}}{\gamma}\right)\sinh(\gamma Z)\right]$$

$$Z=\frac{z}{H} \quad \beta_1=\frac{H}{R_1^{\Delta}\rho_f c_f V_f} \quad \beta_2=\frac{H}{R_2^{\Delta}\rho_f c_f V_f} \quad \beta_{12}=\frac{H}{R_{12}^{\Delta}\rho_f c_f V_f} \quad \delta\ \frac{1}{\gamma}\left(\beta_{12}+\frac{\beta_1+\beta_2}{2}\right)$$

$$\beta=\frac{\beta_2-\beta_1}{2} \quad \gamma\ \sqrt{\frac{(\beta_1+\beta_2)^2}{4}+\beta_{12}(\beta_1+\beta_2)}$$

Where, ρ_f is the density of fluid; c_f is the specific heat of fluid; V_f is the volume flow of the fluid in the buried tube; R^{Δ}, R_2^{Δ} can be regarded as the Integrated thermal resistance between a branch of the fluid and he infinite boundary of the soil; R_{12}^{Δ} is the integrated thermal resistance between the two branch pipe.

By the boundary conditions $T_{fin}(t)=T_{f1}(0,t)$, $T_{f1}(1,t)=T_{f2}(1,t)$, the fluid outlet temperature of the u-shaped tube can be expressed as:

$$T_{fout}(t)=\frac{f_1(1)+f_2(1)}{f_3(1)-f_2(1)}T_{fin}(t)+T_0(t)\int_0^1\frac{f_4(\eta)+f_5(\eta)}{f_3(1)-f_2(1)}d\eta=\frac{\cosh(\gamma)-\frac{\beta_1}{\gamma}\sinh(\gamma)}{\cosh(\gamma)+\frac{\beta_1}{\gamma}\sinh(\gamma)}T_{fin}(t)+\frac{2\frac{\beta_1}{\gamma}\sinh(\gamma)}{\cosh(\gamma)+\frac{\beta_1}{\gamma}\sinh(\gamma)}T_0(t) \quad (3)$$

The basic simulation conditions can be found in table 1.

Table1. Properties related to the buried pipes

k_s	$\rho_s c_s$	k_p	k_f	$\rho_f c_f$	V_f	υ	k_b
[w/(m·℃)]	[J/m^3·℃]	[w/(m·℃)]	[w/m·℃]	[J/m^3·℃]	[m^3/h]	[m^2/s]	[W/(m·℃)]
1.78	2.8×10^6	0.45	0.618	4.1×10^6	1.2	8.1×10^{-7}	1.9

r_i	r_o	r_b	D	H
[m]	[m]	[m]	[m]	[m]
0.013	0.016	0.096	0.064	80

Heat Transfer Coefficient of Energy Efficiency under the Variable Temperature Inflow. In view of the u-shaped buried pipe structure and heat transfer characteristics, define the heat exchanger efficiency coefficient E, which is the ratio between actual heat exchange amount Q of the buried heat pipe heat exchanger and the biggest theory heat exchange amount Q ', its expression is [2]:

$$E=\frac{Q}{Q}=\frac{Gc(T_{in}-T_{out})}{Gc(T_{in}-T_0)}=\frac{T_{in}-T_{out}}{T_{in}-T_0} \quad (4)$$

In the formula, T_{in}, T_{out}, T_0 are inlet temperature of the u-shaped ground heat exchanger, outlet temperature and the initial temperature of geotechnical. G, c are Mass flow rate, specific heat capacity of buried pipe cycle medium.

Inlet temperature of the buried pipe water changes with the change of building air conditioning load, according to the commonly used Bury pipe side water temperature of the heat pump units

35℃, buried tube heat transfer coefficient of energy efficiency can be expressed as the product of the ratio of biggest buried tube heat transfer temperature difference φ and Heat pump outlet water temperature difference σ, that is:

$$E = \frac{Q}{Q} \quad \frac{T_{in} - T_{out}}{T_{in} - T_0} = \frac{T_{in} - T_{out}}{T_{35} - T_0} \times \frac{T_{35} - T_0}{T_{in} - T_0} = \phi \times \sigma \tag{5}$$

In the formula, type of T_{35} is the constant import water temperature 35℃ under design conditions[4].

As the instantaneous value of the dimensionless, parameters φ is related to the heat exchange performance of the buried tube, Characterization the capacity of the Import and export temperature difference of the buried tube heat exchange that can reach the maximum. Parameter σ is related to building air conditioning load and running efficiency of heat pump, which characterization of the impact of Building air conditioning load intensity and unit performance to buried tube heat exchange system. The two parameters common affecting the heat exchange coefficient of energy efficiency of the buried tube.

Model of Heat Pump Unit. Heat pump unit as the core component of ground source heat pump system, its' running conditions directly affect the performance of the heat pump system and energy consumption. For a given heat pump unit, inherent characteristics such as size, structure remains the same, the buried tube inlet water temperature T_{in} (the outlet water temperature of the Condenser) are mainly related to building air conditioning load and the unit performance coefficient, can be represented as:

$$T_{in} = \mathcal{F}(Q,\ COP) \tag{6}$$

Base on the experimental data of the ground source heat pump units product samples that use in actual project, the unit model under the summer conditions are fitting out, the expression is as follows:

$$COP = 0.001T_{out}^2 - 0.2016T_{out} + 10.108 \tag{7}$$

$$T_{in} = T_{out} + \frac{Q}{GC_p}\left(1 + \frac{1}{COP}\right) \tag{8}$$

Analysis of Heat Exchange Efficiency under Variable Temperature Inflow

Compared with constant buried pipe inlet fluid temperature, the generation of Variable temperature inflow conditions mainly depends on the change of building air conditioning load and the performance change of the heat pump unit, energy efficiency of heat transfer process also has its own characteristics, therefore it is necessary to analyze the influence law of buried tube heat exchange efficiency.

Influence of Structure Load Characteristics of Air Conditioning on Heat Exchange Efficiency. Building air conditioning load have big differences in load intensity and time because of the different use function, Selection of office buildings, hotels and residential air conditioning system which running 15 days in the summer as analysis object, the exhaust heat load of a single buried tube in a typical day shown in Fig.1, changes of buried tube heat exchange coefficient of energy efficiency, ratio of φ and σ under the variable temperature inflow are shown in Fig.2 ~ Fig.4.

It can be seen from Fig. 2 ~ 4, buried tube heat transfer efficiency E value, values of φ and σ changed with the cycle change of air conditioning load, the value of E and φ gradually reduce with the increase of running time, while the value of σ is increased. This is due to the increase of the geotechnical heat accumulation around the buried pipe which caused by the increases of the exhaust heat, this will reduce the thermal efficiency of the buried pipe. With the inlet water temperature of buried pipe gradually increased to design point (35℃), and then gradually greater than the design temperature, this will leads to the deterioration of the heat transfer condition; Although Increase the buried tube heat transfer temperature difference between water and rock mass around, to some

extent, can increase the heat exchanger (values of φ increase), the value of σ gradually weakened with the increase of time, therefore, the buried tube heat exchange effect reduced gradually with the increase of running time. Compared with office building and residential, load duration time of hotel building keep more intense, although at the beginning of the heat exchange, the coefficient of heat transfer efficiency keep basically the same, after five hours, the heat exchange efficiency of the hotel is below the offices and homes. And as there has no natural recovery time, long time running makes the thermal efficiency of the buried pipe lower. This suggests that the building load characteristics had a great influence on buried pipe heat exchanger, especially the projects which have long continuous running time. In order to ensure the running efficiency of the ground source heat pump system, it's need to guarantee a certain time to recover, so the composite ground source heat pump system is adopted.

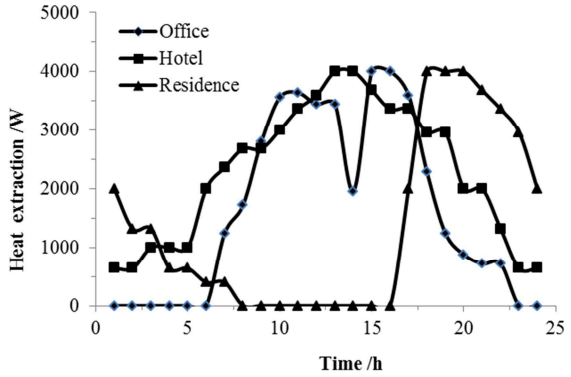

Fig.1 Characteristic curve of building air conditioning load

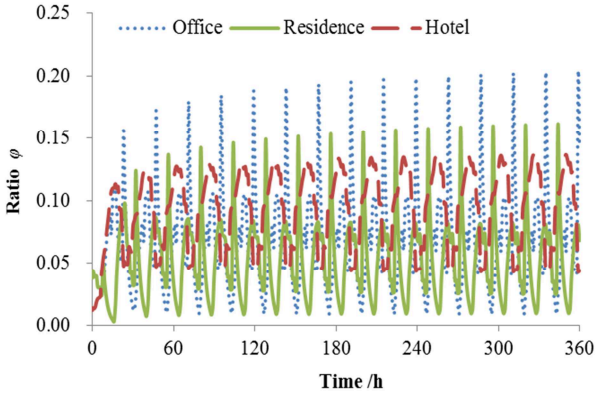

Fig.3 Effects of building load on values of energy efficiency φ

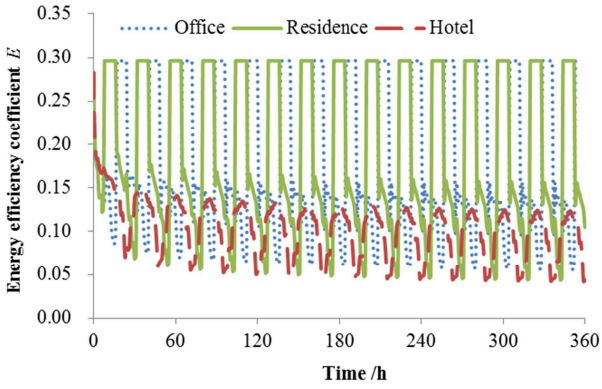

Fig.2 Influence of Building load to heat exchange efficiency of the buried pipe

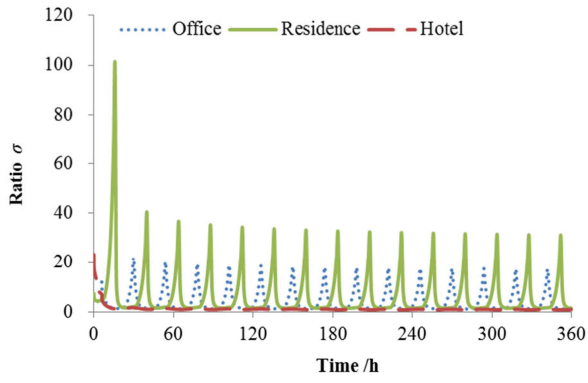

Fig.4 Effects of building load on values of energy efficiency σ

Influence of Flow on Heat Exchange Efficiency. In the process of buried pipe design, flow is one of the main parameters affecting the heat transfer effect. When the depth of the buried tube remains unchanged, the buried pipe inlet and outlet fluid temperature changed as the buried tube fluid flow changed. Fig.5 ~ Fig.7 shows the influence of circulating fluid flow velocity to the heat transfer coefficient, the ratio of φ and σ, the simulation operation condition is 0.6 m/s, 0.8 m/s and 1.0 m/s.

As can be seen from Fig.5 ~ Fig.7, the change rule of the buried tube heat exchange efficiency E value keep consistent under the conditions of velocity change, this is due to the change of velocity changing only import water temperature of the buried pipe, did not changes the heat resistance of the rock mass (different with the construction load intensity and duration time), it reveal the Consistent changing law with the literature [2].

The values of heat exchange efficiency φ gradually reduce with the increase of running time, while the value of σ is increased, this is due to the increase of the geotechnical heat accumulation around the buried pipe which caused by the increases of the exhaust heat, and the product is on the decline. When flow velocity under the working condition of 1.0 m/s, the water temperature that run

into the buried pipe is relatively low, the heat transfer temperature difference between buried pipe fluid and surrounding rock mass is reduced, the heat exchange intensity of buried tube is also weakened, the part of φ value is less than 0.6 m/s and 0.8 m/s conditions, and the part of σ value is on the contrary.

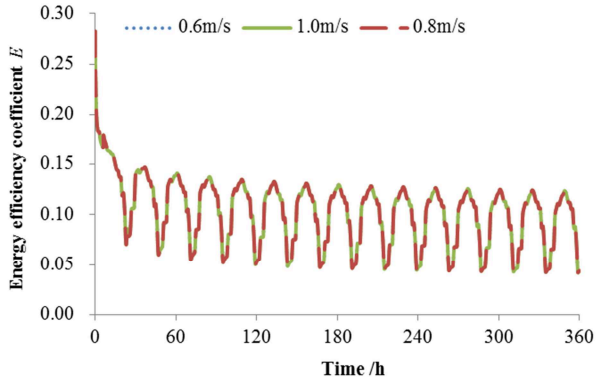

Fig.5 Velocity's influence on the buried tube heat exchange efficiency

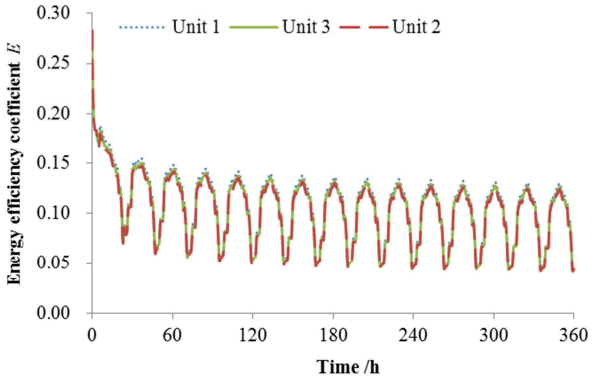

Fig.8 Unit performance's influence on the buried tube heat exchange efficiency

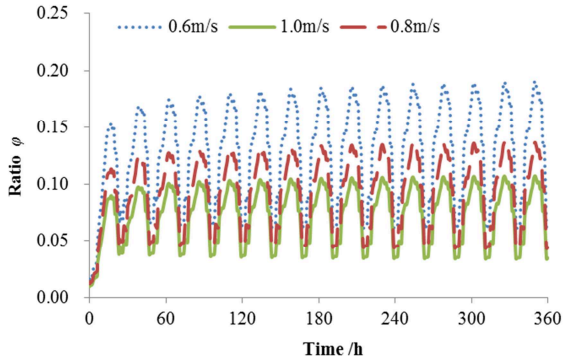

Fig.6 Velocity's influence on φ value of the energy efficiency

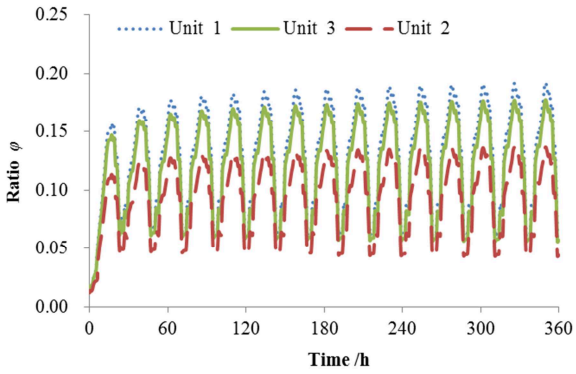

Fig.9 Unit performance's impact on φ value of energy efficiency

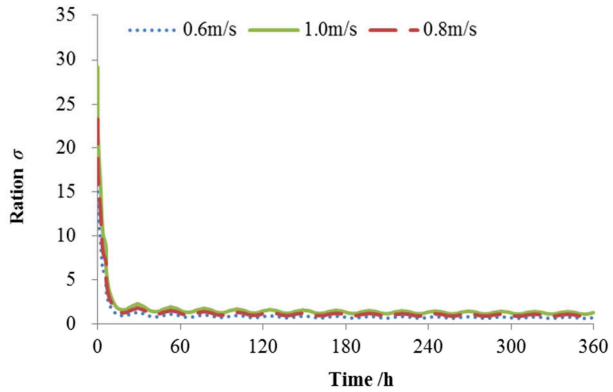

Fig.7 Velocity's influence on σ value of the energy efficiency

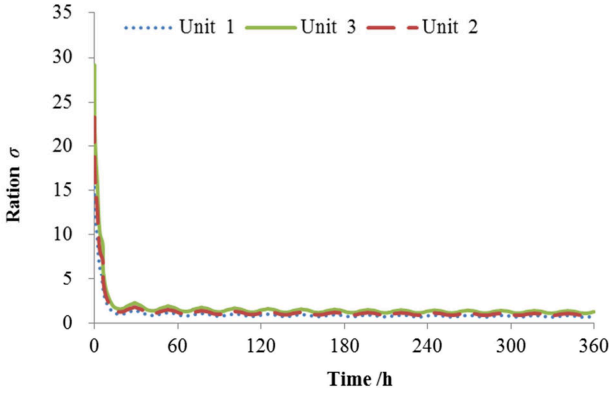

Fig.10 Unit performance's impact on σ value of energy efficiency

Influence of Heat Pump Unit Performance on Heat-Exchange Efficiency. Under different conditions of heat pump unit in type, cooling & heating capacity and manufacturer, its running efficiency is different, the buried pipe heat load are also different, which will affect the heat transfer process of buried pipe. Fig.8 ~ Fig.10 shows the influence of the performance of Heat pump unit on the heat transfer coefficient, the ratio of φ and σ, the simulation operation condition is unit 1: performance curve of formula (9), the unit 2: performance curve of formula (7), unit 3: performance curve of formula (10).

$$COP = 0.0012T_{out}^2 - 0.2347T_{out} + 11.768 \quad (9)$$

$$COP = 0.0009T_{out}^2 - 0.2346T_{out} + 11.763 \quad (10)$$

It can be seen from Fig.8 ~Fig.10, the change trend of the buried tube heat exchange efficiency E value keep consistent under the conditions of velocity change, but the values of the three conditions have small differences, this is due to the change of performance change the amount of the heat that released by buried pipe. For example, the changing of building load intensity and duration time change the heat resistance of the rock mass, this can lead to energy efficiency coefficient value is different. The values of heat exchange efficiency φ gradually reduce with the increase of running time, while the value of σ is increased, Just because the unit 1 is in better performance conditions, the heat transfer resistance of rock- soil is small, the heat transfer effect of buried tube Higher than that of unit 2 and unit 3 conditions are enhanced, so the unit performance is also the concerns during the design process of the buried tube heat exchanger.

Conclusion

Base on variation characteristics of heat transfer coefficient of energy efficiency under the variable temperature inflow condition, decomposed into the product of the ratio of biggest buried tube heat transfer temperature difference φ and heat pump outlet water temperature difference σ. Select the reasonable simulation conditions, three-dimensional heat transfer model of the u-shaped buried pipe that based on the theory of the multipolar are used to simulate the buried tube heat transfer process, the buried tube heat transfer coefficient, ratio of φ and ratio of σ main influence factors including the construction load, buried pipe flow, the unit performance are analyzed, and the changing rule with the time is also be study. The results show that the buried pipe flow does not affect the heat transfer coefficient of energy efficiency, only the ratio of φ and ratio of σ, and the intermittent changes of building air conditioning load, high efficiency of the unit can effectively enhance the heat transfer effect of buried tube, improve the running efficiency of ground source heat pump system.

Acknowledgements

This work was financially supported by The National Natural Science Foundation of China (51078160).

Reference

[1] Xianying Liu, Mingming Hu and Tangdi Wei. Journal of Chongqing Jianzhu University，Vol.4 (1999)，P.106 in Chinese

[2] Zhongyi Yu, Yanhua Chen and Pingfang Hu. HV&AC，Vol. 41 (2010)，P.93 in Chinese

[3] Pingfang Hu, Zhongyi Yu, Na Zhu, Fei Lei, et al. Energy and Buildings，Vol.65 (2013)，P.231

[4] China Academy of Building Research. Technical Code for Ground-Source Heat Pump System (GB50366-2005). Peking: China Building Industry Press.（2009）in Chinese

Advanced Materials Research Vols. 960-961 (2014) pp 609-613

doi:10.4028/www.scientific.net/AMR.960-961.609

Design of Virtual Corolla 1.6AT Automatic Air Conditioning Experiment Bench

Wenzi Gong

Wuxi Institute of Commerce Jiangsu Wuxi China 214153

gongwenzi1968@sina.com

Keywords: virtual; auto automatic air conditioning; experiment bench; working process; design

Abstract: This paper introduces a virtual experiment bench for automotive air conditioning. In the experiment bench based on the experiment bench for Corolla 1.6AT automatic air conditioning, the refrigeration, heating, gas distribution and other mechanical systems are removed and the electrical control system is reserved using the virtual and simulation theory. The experiment bench has the features, such as simple structure, low production and operation cost, safety and environmental protection; its main sensor signals are simulated through a variable resistance, the working processes of some actuators are shown by light bulbs, so that it is easy to operate the experiment bench, and the working process is visual and direct. The experiment bench can be self-developed, designed and produced by students under the guidance of teachers, thus to promote the comprehensive ability of students to use knowledge and innovate.

Introduction

With the wide application of electronic control technology in automobiles, automotive air conditionings in more and more automobiles, especially cars are controlled by microcomputer, and data transmission and communication between automobile control systems are done by buses, in order to achieve the coordinated operation of automotive air conditioning system and other systems [1]. At present, the experiment bench for automotive air conditioning is produced by real parts and components, not only including refrigeration, heating, gas distribution and control systems, but containing a motor system used to drive the compressor, so that the entire experiment bench is large, with high production costs, and has also an impact on the safety and environmental protection in experiment. The virtual experimental system can better address these problems above, and it is also easy to combine more than one system in a experimental platform, so that the interactive relationship between the systems can be clearly shown [2].

1 Basic working principle of microcomputer-controlled auto automatic air conditioning

Automotive air conditioning refers to the unit for control over the quality of air in cars. Its main function is to adjust the air temperature, humidity, flow rate, cleanliness, airflow pattern and intake patterns in cars, in order to improve comfort; its essential task is temperature adjustment. An automotive air conditioning is mainly composed of refrigeration system, heating system, gas distribution system and control system. The automotive air conditioning's refrigeration system enables the refrigeration medium stored in the confined refrigeration system through the engine driving the compressor to constantly circulate and makes its phase change to produce refrigeration effect, and each circulation has four processes: compression process, condensation process, expansion process, and evaporation process; in the condensation process, the refrigeration medium in the condenser turns into liquid from gas to dissipate heat outward; in the evaporation process, the

refrigeration medium in the evaporator turns into gas from liquid to absorb heat, thus reducing the temperature around the evaporator, while the blower blows the air through the evaporator into the car, so as to achieve the purpose of reducing the interior temperature [3]. The waste heat of the engine cooling water is generally used as a heat source of the automotive air conditioning's heating system; in buses or limousines, the waste heat from the engine cooling water and fuel or electrical interaction is used as a heat source, in order to improve the reliability of the heating system, and thus to achieve the purpose of quick heating.

The mechanical part of the microcomputer-controlled automatic air conditioning is consistent with ordinary air conditioning, and the main distinction is the control system of air conditioning. Its basic control theory is as follows: the interior set temperature, interior temperature, environment temperature, evaporator temperature, sun radiation strength, and pressure of the refrigeration system at high pressure end, engine water temperature and other signals are detected through various sensors or control panels; the displacement of the compressor at work (for electric controlled changed displacement compressor) or the pull-in and cutoff of compressor electromagnetic clutch is automatically controlled, and the blower speed and airflow way are regulated; meanwhile, data transmission and communication are completed through CAN-H line, CAN-L line and engine ECU and other control units, to enable the systems can coordinate, and thus to ensure that all the systems are in the optimum working conditions [4].

2 Overall programme and composition of the experiment bench

The experiment bench is a virtual integrated experiment bench for automotive air conditioning, and it is based on Corolla 1.6AT automatic air conditioning, without the complex mechanical systems such as refrigeration, heating and gas distribution, but with the air conditioning controller, engine ECU, air conditioning amplifier, sensors and actuators and other electrical components. The electrical components are installed at the positions as close as possible to the original places in cars, and a set of automotive air conditioning system with complete electrical systems and normal function displays is built. The entire system has the advantages, such as simple structure, small size, low costs, convenient detection and pollution-free[2].

As shown in Fig.1, this experiment bench is composed of slide rheostat 1, storage battery 2, DC motor 3, ignition switch 4, normally opened relay 5, indoor temperature sensor 6, air conditioning sunshine sensor 7, evaporator temperature sensor 8, pressure sensor 9, air mixing throttle servo motor with smart controller at driver side 10, air mixing throttle servo motor with smart controller at passenger side 11, vent throttle control servo motor with smart controller 12, intake throttle control servo motor with smart controller 13, water temperature sensor 14, speed sensor (crankshaft position sensor) 15, EFI main relay 16, No.1 PTC heating relay 17, blower motor with speed controller 18, No.2 PTC heating relay 19, No.2 PTC heater indicator light 20, No.1 PTC heater indicator light 21, No.3 PTC heating relay 22, No. 3 PTC heater indicator light 23, measuring terminal 24, CAN-H line 25, CAN-L line 26, air conditioning compressor indicator light with duty cycle controller 27, Lin line 28, air conditioner controller, engine ECU, and air conditioning amplifier[5]. The original installation positions of its main sensors and the roles are in the following: the pressure sensor 9 is installed on the high pressure end the refrigeration pipeline and is used for detection of the pressure of the refrigeration system at the high pressure end; the indoor temperature sensor 6 is installed inside the car and is used to detect the real temperature inside the car; the air conditioning sunshine sensor 7 is installed on the front windshield glass and is used to detect sunlight strength; the evaporator temperature sensor 8 is installed on the surface of the evaporator and is used to detect the temperature on the evaporator surface [5].

The indoor temperature sensor 6, air conditioning sunshine sensor 7, evaporator temperature sensor 8, pressure sensor 9, and water temperature sensor 14 are replaced by a variable resistor with an appropriate range of resistance value, and different resistor values can simulate corresponding signals. No.2 PTC heater working indicator light 20, No.1 PTC heater working indicator light 21, and No.3 PTC heater working indicator light 23 simulate the working process of the heater, and the heater is working when the lights are on. The air conditioning compressor indicator light with duty cycle controller 27 simulates the working process of the control electromagnetic valve of air conditioning compressor, and a different period of time for the indicator light in a cycle represents a different duty cycle. (Note: the compressor is an electrically controlled variable displacement compressor, the air conditioning amplifier controls the opening of the electromagnetic valve by the duty cycle, and different duty cycles enable the control electromagnetic valve to have a different opening, and the compressor has a different displacement.) CAN-H line 25 and CAN-L line 26 carry out data communication between the engine ECU and air conditioning amplifier; Lin 28 line conducts data communication between the air conditioning controller and air conditioning amplifier [5].

DC motor 3 turns through a homemade shaft-driven crankshaft signal gear, and the rotating crankshaft signal gear through the speed sensor (crankshaft position sensor) 15 provides the engine ECU engine with speed signal; the slide rheostat 1 is arranged below the throttle pedal, and interlocks with the throttle pedal; when stepping on the accelerator pedal, its resistance decreases, which in turn, its resistance increases, and the crankshaft signal gear speed that is, the engine speed rises; instead, its resistance increases, and the engine speed declines.

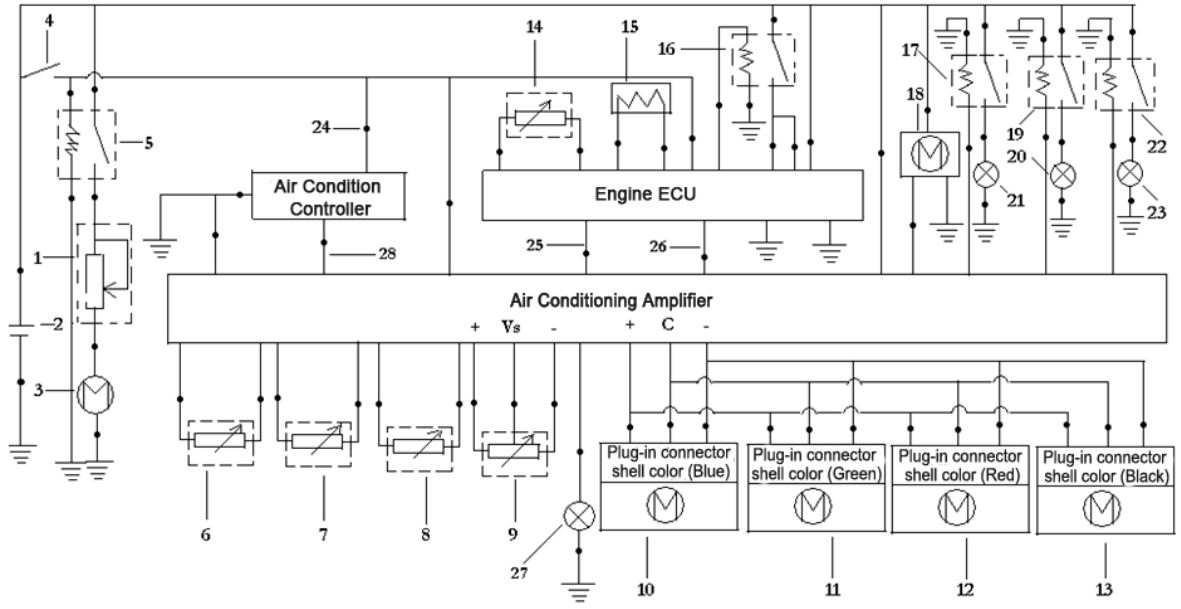

1-slide rheostat; 2-storage battery; 3-DC motor; 4-ignition switch; 5-normally opened relay; 6-indoor temperature sensor; 7-air conditioning sunshine sensor; 8-evaporator temperature sensor; 9-pressure sensor; 10- air mixing throttle servo motor at driver side; 11- air mixing throttle servo motor with smart controller at passenger side; 12- vent throttle control servo motor with smart controller; 13- intake throttle control servo motor with smart controller; 14-water temperature sensor; 15-speed sensor (crankshaft position sensor); 16-EFI main relay; 17- No.1 PTC heating relay; 18-blower motor with speed controller; 19- No.2 PTC heating relay; 20- No.2 PTC heater indicator light; 21-No.1 PTC heater indicator light; 22-No.3 PTC heating relay; 23-No.3 PTC heater indicator light; measuring terminal 24-; 25-CAN-H line 26-CAN-L line; 27-air conditioning compressor indicator light with duty cycle controller; 28-Lin line

Fig.1 Control schematic diagram

The air conditioning controller and the control panel with digital display are integrated, the function keys of the control panel are shown in Fig.2, and the information of the function keys is directly conveyed to the air conditioning controller and is transmitted to the air conditioning amplifier by the air conditioning controller through Lin line 28, to provide the air conditioning amplifier with driver's operating information; the related digital information is also transmitted by the air conditioning amplifier through Lin line 28 to the air conditioning controller and is displayed by the control panel with digital display[5].

Fig.2 Control Panel with digital display

3 Control functions of the experiment bench

This experiment bench takes Toyota Corolla 1.6AT automatic air conditioning as a template, by which the working processes of the automotive air conditioning systems and the intrinsic causal relationship between the systems can be displayed in an intuitive and eye-catching manner. It is very convenient to debug and detect this equipment, along with safety, economy and environmental protection.

3.1 Startup of the experiment bench

As shown in Fig.1, after the ignition switch 4 is closed, the engine ECU, air conditioning controller and air conditioning amplifier receive the signal of the ignition switch closed, and the control units begin to work. The engine ECU controls the switch touch of EFI main relay 16 to pull in, and to provide the engine ECU with working power supply; meanwhile, the switch touch of the normally opened relay 5 is pulled in, the DC motor 3 according to the position of throttle pedal turns with a certain speed, and the rotating crankshaft signal gear through the speed sensor (crankshaft position sensor) 15 provides the engine ECU engine with speed signal; the water temperature sensor 14 according to its adjusted resistance provides the engine ECU with engine water temperature signal. These signals above are passed to the air conditioning amplifier by the engine ECU through the CAN-H line 25 and CAN-L line 26.

3.2 Working process of the experiment bench

As shown in Fig.2, press down the AUTO key on the control panel and adjust the set temperature within the car through the TEMP key, and then the air conditioning controller through the Lin line 28 transmits the control key signal to the air conditioning amplifier; the indoor temperature sensor 6, air conditioning sunshine sensor 7, evaporator temperature sensor 8, and pressure sensor 9 according to their adjusted resistance provide the air conditioning amplifier with indoor temperature signal, sun radiation strength signal, evaporator temperature signal, and system pressure signal at high pressure end. According to the AUTO signal, TEMP control key signal and sensor signals, through analysis, calculation and processing, the air conditioning amplifier determines the optimal compressor displacement, temperature-regulated valve position, blower speed, airflow way, air intake mode and whether the heater works, and controls various actuators and indicator lights to work according to the set procedures, while the relevant digital information is displayed on the digital display on the control panel. Other keys on the control panel can shift from automatic mode to manual mode.

3.3 Measuring terminals are used for testing of relevant data, convenient for fault judgment, and detection and teaching needs[2].

Concluding remarks

This experiment bench takes Toyota Corolla 1.6AT automatic air conditioning as a template, the refrigeration, heating, gas distribution and other mechanical systems are removed and the electrical control system is reserved using the virtual and simulation theory. The experiment bench has the features, such as simple structure, low production and operation costs, and safety, environmental protection and economy in use; the main sensors are simulated with a variable resistance, so that it is more direct and convenient for teachers to teach and students to learn; light bulbs as actuators enable the whole process to be more visual and direct, thus improving the teaching effect [(2)]. Under the guidance of teachers, students participate in the design and production of the experiment bench, which can stimulate and improve students' innovative consciousness and ability.

References

[1] Wenzi Gong. Automotive air conditioning (M). Beijing: Chemical Industry Press, 2010. (In Chinese).

[2] Wenzi Gong. Design of virtual automotive automatic air conditioning experiment bench based on SCM controller (J). Chinese Agricultural Mechanization, 2011. (6): 118-121. (In Chinese).

[3] Jiang Yue. Maintenance of automobile air-conditioning system (M). Beijing: Posts and Telecom Press, 2009. (In Chinese).

[4] Wangnian Ji. Stucture and maintenance of automotive air conditioning (M). Beijing: Publishing House of electronics industry, 2007. (In Chinese).

[5] Qiwen Luan. Corolla/Corolla/Vios car intensive repair manual (M). Beijing: Mechanical Industry Press, 2010. (In Chinese).

Advanced Materials Research Vols. 960-961 (2014) pp 614-620

doi:10.4028/www.scientific.net/AMR.960-961.614

Experimental research on heat transfer of closed cooling tower with packing

Yasu Zhou[a], Xiao Ding[b] and Wei Xie[c]

College of Environmental Science and Engineering, Donghua University, Shanghai 201620, China

[a]zhouys@dhu.edu.cn, [b]982389098@qq.com, [c]516253599@qq.com

Keywords: closed cooling tower; packing; structure; thermal performance

Abstract. Three different structural types of closed cooling tower (CCT) and two cooling water flow directions were considered. The experimental study were done on the cooling performance of influences of inlet air dry and wet bulb temperature, cooling water flow rate and inlet temperature, air flow rate and spray density. The experimental results show that the cooling performance of CCT with packing is obviously better than non-packing cooling tower in 7%~18.4%. And the cooling performance of CCT with packing on top and coil underneath is slightly better than CCT with coil on top and packing underneath in 4.9%. In the same conditions the cooling performance of CCT with packing under cooling water cocurrent-flow is better than that cooling water countercurrent-flow in 3.2%~9.6%. Therefore, the closed cooling tower structure with the cooling water path in bottom and out top, and with packing on top and coil underneath is recommended.

Introduction

Compared with other conventional heat transfer equipment, cooling tower is a relatively inexpensive and dependable heat rejection device combined with energy-saving water cooling type cooler and cooling tower. Therefore, it is widely used for dissipating heat from the system of water-cooledrefrigeration, air-conditioning, power plants and other industries[1.2.3].

The closed cooling tower (CCT) maintains an indirect contact between the cooling water and the atmosphere. Many researchers have made great progress in the theoretical and experimental study of CCT. Sarker et al.[4] hintedthatthe heat and mass transfer process in a CCT was dominated by the moisture exchange between water and air to give out the medium heat inside coil. A.Hasan and K.Sirén [5] claimedthat the heat and mass transfer coefficient of finned tubesin CCT was greater than that of plain circular tubes. A.Hasan and K.Sirén[6]also obtained the empirical formulas of mass transfer which were suitable for plain circular tube and oval tube in CCT. However most of the researches are about non-packing cooling tower, the related research literature about CCT with packing and coil is rare. P.J.Erens [7] added plastic packing into the evaporative type cooler and found that it could significantly enhance the thermal performance of evaporative type cooler with smooth round tubes. In comparison with conventional non-packing cooling tower, experimental study will be done on the performance of CCT with packing and coilin this paper.

Experimental apparatus and CCT structures

The schematic of the experimental installationis shown in Fig.1. It is mainly composed of air dispose system, experimental apparatus and automatic data acquisition system. The air dispose system supplies appropriate air parameters during experiment. It consists of surface air coolers, heater, fan, vapor humidifier and so on.

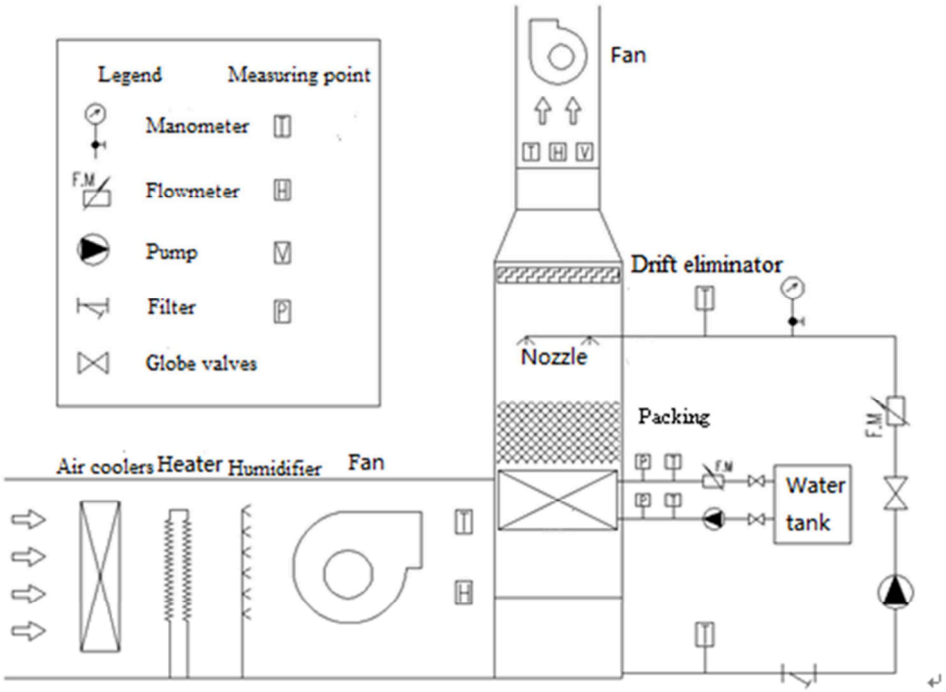

Fig.1 Principle diagram of the CCT experimental installation

The shell of CCT unitwas made of transparent organic glass so that one can clearly observe water distribution and water film flows inside the CCT. In order to improve the heat and mass transfer efficiency, PVC plastic oblique wave alternating packing was chosen inthis experiment.

Three different structural types of CCT were discussed in the experiment. Shown in Fig.2,Tower 1 isCCT with packing on top and coil underneath, Tower 2 is CCT with coil on top and packing underneath, and Tower 3 is non-packing cooling tower.

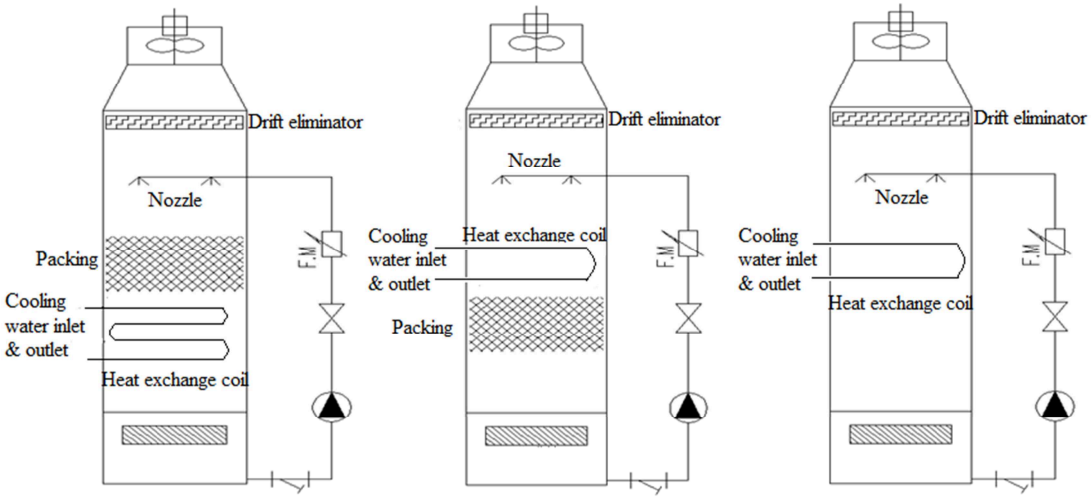

(a) Tower 1 (b) Tower 2 (c) Tower 3

Fig.2 Three structural types of CCT

The heat exchange process of CCT is complex, involving heat and mass transfer and flow, which are affected by many factors.In this paper the influence of the factors such as the dry and wet bulb temperatures of inlet air, cooling water flow rate and direction and its inlet temperature, air flow rate, spray density on the process of CCT is investigated. The research method was that keeping other parameters constant and only set one of the varying parameters at different values.

Results and discussions

The effects of cooling capacityand cooling efficiency were investigated experimentally. Cooling capacity can be analyzed and calculated according to following equations:

$$Q_c=m_c c(t_{c,in}-t_{c,out}) \quad (1)$$

$$Q_a=m_a (h_{a,out}-h_{a,in}) \quad (2)$$

$$\varepsilon =(Q_c-Q_a)/Q_c \times 100\% \quad (3)$$

The heat balance of the apparatus could be claimed to be satisfactory whenthe thermal equilibrium error ε is inhered within ±15%.

The cooling efficiency is defined as following [8]:

$$\eta=(t_{c,in}-t_{c,out})/(t_{c,in}-t_{a,wet}) \quad (4)$$

The influence of air wet bulb temperature. The cooling water flow , air flow and spray density were kept inconstant, and the inlet temperature of cooling water was kept in 38.4℃,changing the air web bulb temperature, the cooling water outlet temperature, cooling capacity and cooling efficiency were observed. If inlet air relative humidity was kept in 76.7%, experimental results were shown in Fig. 3. If inlet air temperature was kept in 31.5℃,experimental results were shown in Fig.4.

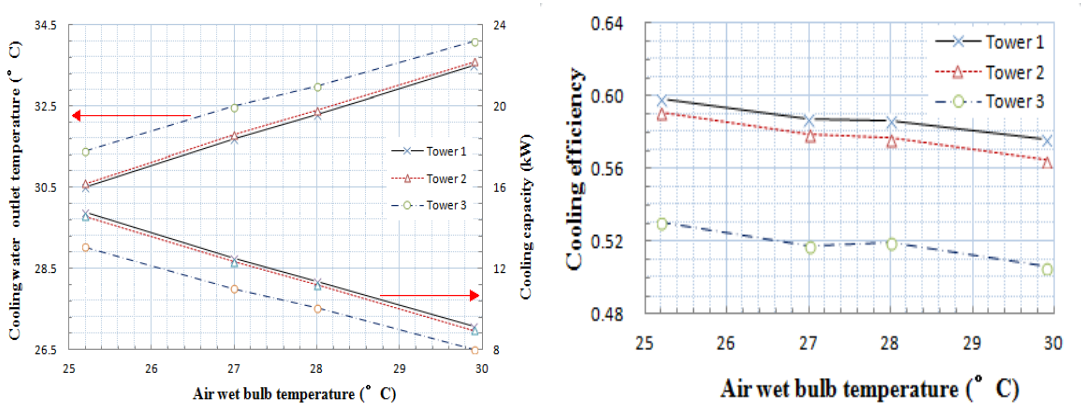

Fig.3 Cooling water outlet temperature, cooling capacity, cooling efficiency w.r.t. air wet bulb temperature (inlet air relative humidity constant)

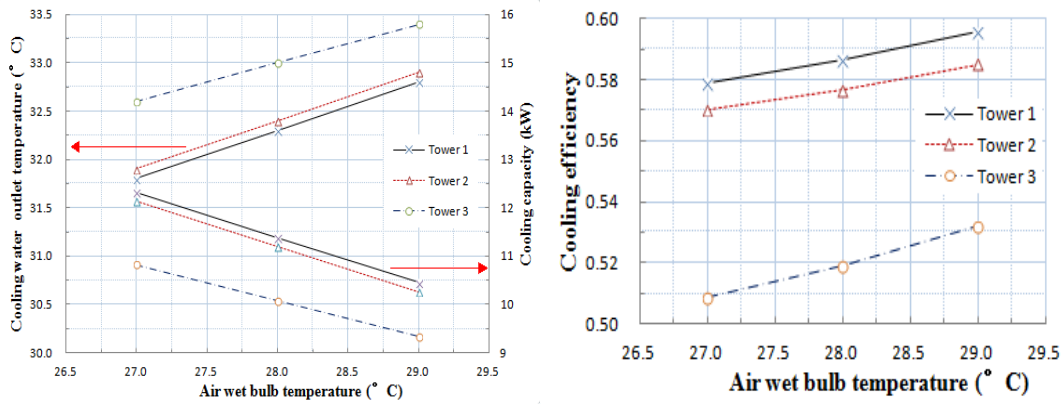

Fig. 4 Cooling water outlet temperature, cooling capacity, cooling efficiency w.r.t. air wet bulb temperature (inlet air temperature constant)

The influence of air dry bulb temperature. Keeping the air wet bulb temperature in 28℃. Other conditions same as above. Changing the air dry bulb temperature, the cooling water outlet temperature, cooling capacity and cooling efficiency were observed. Experimental results were shown in Fig.5.

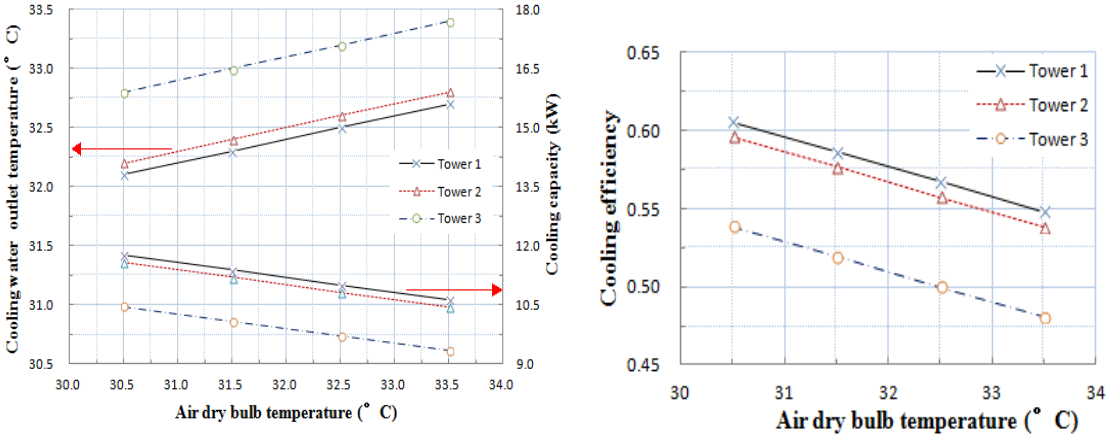

Fig. 5 Cooling water outlet temperature, cooling capacity, cooling efficiency w.r.t. air dry bulb temperature

The influence of cooling water flow rate and inlet temperature. Keeping the inlet air temperature in 31.5℃, air wet bulb temperature in 28℃. The cooling water flow rate and inlet temperature were changed respectively. Experimental results were shown in Fig.6 and Fig.7.

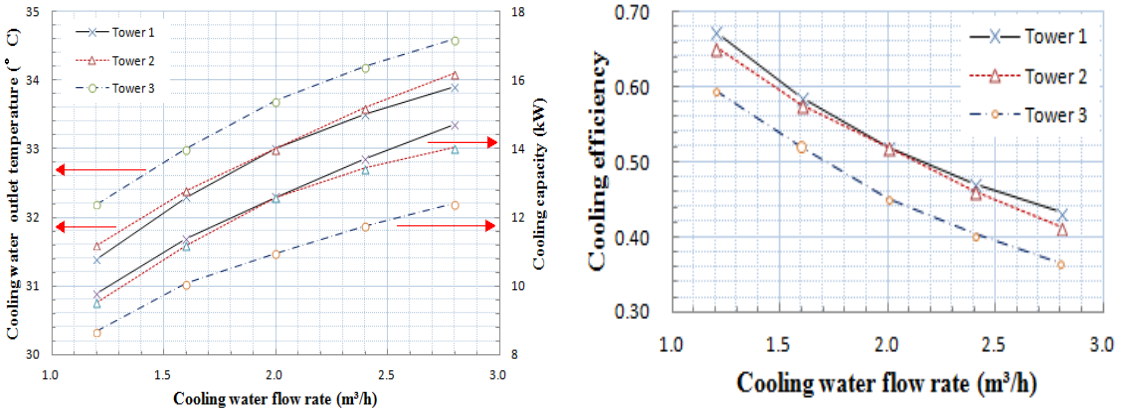

Fig. 6 Cooling water outlet temperature, cooling capacity, cooling efficiency w.r.t. cooling water flow rate

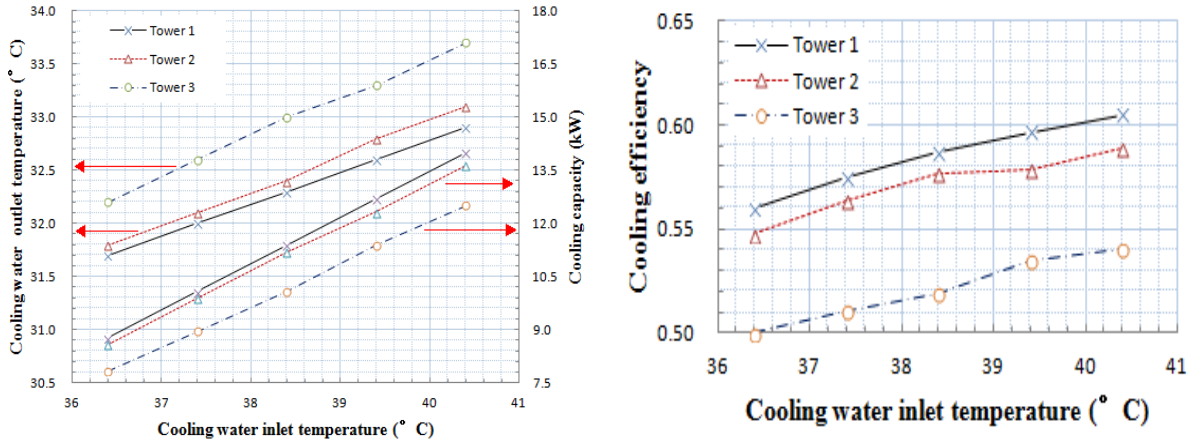

Fig. 7 Cooling water outlet temperature, cooling capacity, cooling efficiency w.r.t. cooling water inlet temperature

The influence of air flow rate. The air flow rate was changed by fan frequency changer. The other conditions were kept as the same as the above. Experimental results were shown in Fig.8.

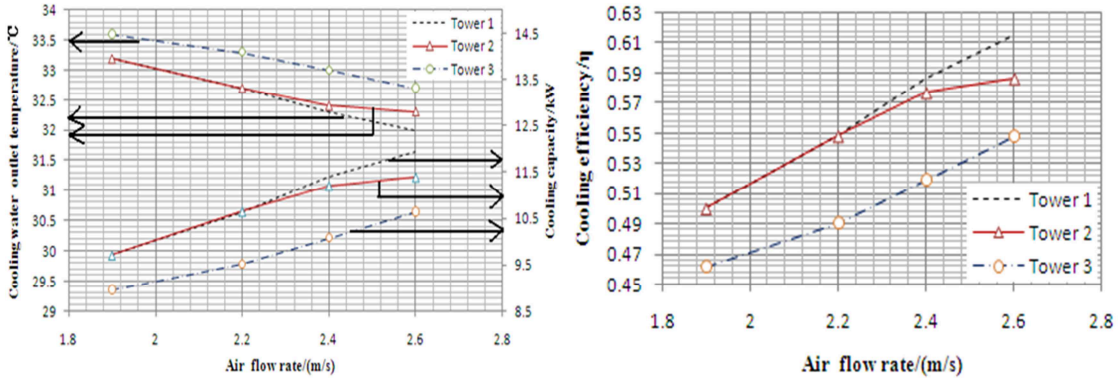

Fig. 8 Cooling water outlet temperature, cooling capacity, cooling efficiency w.r.t. air flow rate

The influence of spray density. The spray water was controlled by pump. The spray density was changed by changing pump frequency. The other conditions were kept as the same as the above. Experimental results were shown in Fig.9.

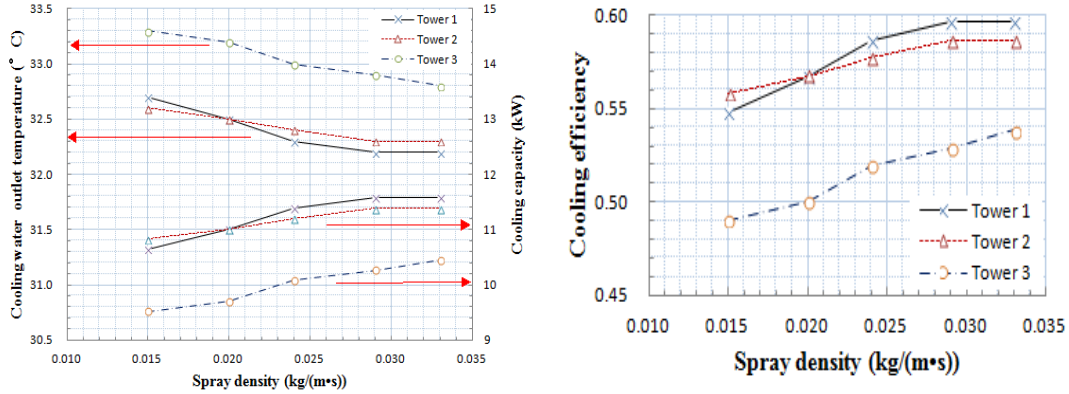

Fig. 9 Cooling water outlet temperature, cooling capacity, cooling efficiency w.r.t. spray density

Fig.3 to Fig.9 shows that decreasing the air dry and wet bulb temperature are good for enhancing the cooling capacity as well as cooling efficiency, while increasing cooling water inlet temperature, air flow rate and spray density. The air flow rate and air wet bulb temperature are the most important influence on cooling capacity.And the air dry bulb temperature is the least. As to the spray density, when it is low, the influence is relatively great, and with the spray density is increasing to an optimal value, the influence is getting to be neglected. The optimal spray density is about 0.025~0.035kg/m.s.

Fig.8 shows that the air flow rate is greater, the cooling performance of Tower 1 is better. But the fan power is also increased. Therefore air flow rate 2.5~3.5m/s is better.

It is worth noting that the cooling water outlet temperature, cooling capacity and cooling efficiency of Tower 1 and Tower 2 have alternating process, as shown in Fig.9. For example, when the spray density is 0.015 kg/(m·s), the cooling performanceof Tower 1 is slightly worse than that of Tower 2, when the spray density is about 0.020kg/(m·s), the cooling performance of Tower 1 and Tower 2 is approximately the same, but if the spray density goes on increasing, the cooling performance of Tower 1 is slightly better. Therefore, Tower 1 works better than Tower 2 when the spray density more than 0,020 kg/(m·s), and Tower 3 is the worst in all cases because of lack of packing.The cooling performance of Tower 1 and Tower 2 is better than Tower 3 in 7%~18.4%. And the cooling performance of Tower 1 is slightly better than Tower 2 in 4.9%. Therefore, Tower 1 is considered the best in cooling performance.

The influence of cooling water flow direction. According to the type of flow directions of thecooling water inside the heat exchange coil and air outside the coil, closed cooling tower can be divided into two types, i.e. countercurrent-flow and cocurrent-flow. Countercurrent-flow refers to the type that flow directionof cooling water is just the opposite of the air flow, so the cooling water pathway is of top in and bottom outas shown in Fig.2 Tower 1;while cocurrent-flow refers to the typethat cooling water and air flow in parallel with the same direction, andthe cooling water path is of bottom in and top out.

The influence of the cooling water flow direction on the cooling capacity is observed on Tower 1, under the condition of differentair dry and wet bulb temperature, cooling water flow rate, cooling water inlet temperature, air flow rate and spray density. The experiment is also operated in the sameexperiment platform, the experimental data of countercurrent-flowhas been obtained from the aboveexperiments, and the experimental results of cocurrent-flow were shown in Fig.10 ~ Fig.12.

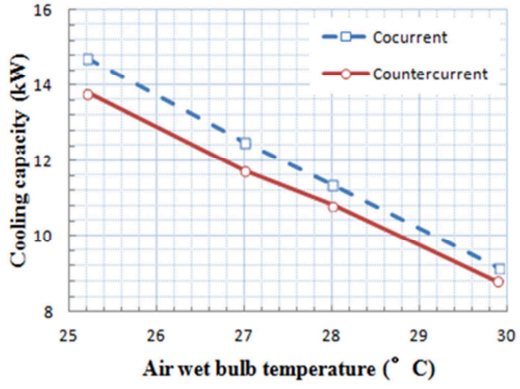

Fig. 10 The influence of air wet bulb temperature

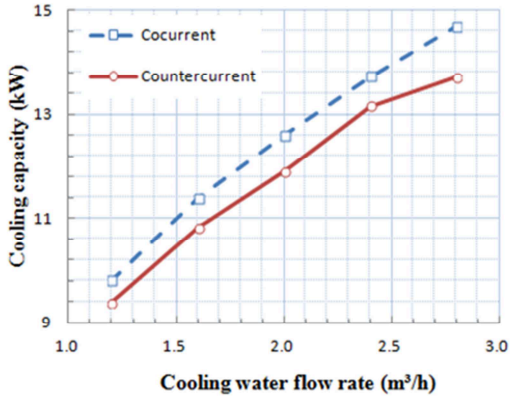

Fig.11 The influence of Cooling water flow rate

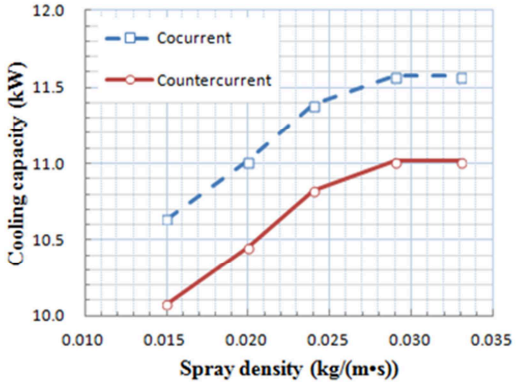

Fig.12 The influence of spray density

From Fig.10 to Fig.12 shows that, in the same conditions, the cooling capacity of concurrent-flow is greater than that of countercurrent-flow 3.2%~9.6%. Therefore, cocurrent-flow is better than countercurrent-flowfor enhancingcooling performance.

Conclusions

Based on three structural types of closed cooling tower, the effects of seven parameters on cooling performance are investigated. Theresults as follows:

a) To enhance the cooling performance in the three types of closed cooling tower, the air flow rate and wet bulb temperature contribute the most, and the air dry bulb temperature contributes the least. The optimal spray density is about 0.025~0.035kg/m.s. And 2.5~3.5m/s air flow rate is better.

b) The cooling performance of CCT with packing is obviously better than non-filler cooling tower in 7%~18.4%. And the cooling performance of CCT with packing on top and coil underneath is slightly better than CCT with coil on top and packing underneath in 4.9%.

c) The cooling water flow direction has a great influence on cooling performance. The cooling capacity of concurrent-flow is greater than that of countercurrent-flow 3.2%~9.6%.

Therefore, the best structure of closed cooling tower is the cooling water path in bottom and out top, and with packing on top and coil underneath.

Nomenclature	
c	specific heat capacity, J/kgK
h	enthalpy, J/kg
m	mass flow rate, kg/s
Q	heat transfer rate, W
t	temperature, K
$\mathcal{E}$	thermal equilibrium error
η	cooling efficiency
Subscripts	
a	air
c	cooling water
in	inlet
out	outlet
wet	wet-bulb temperature

References

[1] R.C. Rosaler, The Standard Handbook of Plant Engineering, seconded.,McGraw-Hill, New York, 1995.
[2] D.W. Green, R.H. Perry, Perry's Chemical Engineers Handbook, sixth ed.,McGraw-Hill, New York, 1984.
[3] M.M.A. Sarker, E. Kim, C.G. Moon, J.I. Yoon, Performance characteristics of the hybrid closed circuit cooling tower. Energy and Buildings,2008,40 (8): 1529–1535.
[4] M.M.A. Sarker, E. Kim, C.G. Moon, J.I. Yoon, Thermal performance characteristics of closed-wet cooling tower. Journal of Korean Society forPower System Engineering, 2005,9 (2): 88–92.
[5] A.Hasan, K.Sirén, Performance investigation of plain and finned tube evaporative cooledheat exchangers. Applied Thermal Engineering, 2002, 23(3): 325~340.
[6] A.Hasan, K.Sirén, Performance investigation of plain circular and oval tube evaporative cooled heat exchangers. Applied Thermal Engineering, 2004, 24(3): 777~790.
[7] P.J.Erens, Comparison of some design choices for evaporative cooler cores. Heat transfer engineering, 1988, (9): 29~35.
[8] T. Ravi Kiran, S.P.S. Rajput, An effectiveness model for an indirect evaporative cooling (IEC) system: Comparison of artificial neural networks (ANN), adaptive neuron-fuzzy inference system (ANFIS) and fuzzy inference system (FIS) approach. Applied Soft Computing, 2011, 11(4):3525–3533.

Advanced Materials Research Vols. 960-961 (2014) pp 621-624

doi:10.4028/www.scientific.net/AMR.960-961.621

Numerical Analysis of Air Measuring Station Location Optimization in Underground Mine Airway

Jingzhao ZHANG[1,a], Yongsheng YAN[2,b], Zhenguo YAN[1,c] and Fengliang Wu[1,d]

[1]Key Laboratory of Western Mine Exploitation and Hazard Prevention Ministry of Education, School of Energy Engineering, Xi'an University of Science and Technology, Xi'an 710054, China

[2]School of Energy Engineering, Xi'an University of Science and Technology, Xi'an 710054, China

[a]zhangjz98@126.com, [b]yanys98@126.com, [c]393826629@qq.com, [d]15038537@qq.com

Keywords: coal mine, air fully developed, air measuring station, numerical simulation

Abstract. The optimized air measuring station location of mine airway based on air fully developed was proposed and numerical tests were conducted with six models. The independence of air fully development and inlet velocity was analyzed which validated the models and the numerical methods. The results show that optimized air measuring station location in head entry is 132m-198m after the airway turning while 5.0m-10.1m before the airway turning in tail entry.

Introduction

Mine ventilation is one of the important technical means to ensure production safety of coal mine, in which the accurate determination of ventilation parameters is the basic work [1]. Air measuring uses the combination of artificial measuring with mechanical air flow meter and real-time monitoring with air velocity transducer in China's coal mines. In order to obtain the more accurate ventilation parameters, air measuring stations are installed in the main mine airways. According to the method described about air measuring station in reference [2], the main mine airways shall establish air measuring station, and air measuring station should be located in the flat airway; in order to ensure the measuring accuracy of air, the partial resistance may not be around the air measuring station within the range of 10m, such as obstacles, airway turning, etc.

Field air measuring show that some air measuring station' locations are not reasonable. Without any other changes, there have different results with the same air measuring worker in the different locations of an air measuring station. Fluid dynamics show that the flow parameters are changeless along the flow direction in the fully developed region. When the air measuring station is located in the fully developed region of the mine airway, there can obtain the consistent data in arbitrary cross section of the airway in air measuring, which can improve the measurement accuracy of air flow. Based on this idea, numerical tests of air measuring station location optimization in head entry and tail entry of coal face are conducted in order to obtain more reasonable air measuring station location.

Physical Models

The physical model based on some actual coal mine faces is shown in Fig.1. The model consists of two vertical airways, No.1 and No.2. When simulating the airway turning after the air measuring station, No.1 airway is regard as tail entry and No.2 airway as section outtake. When simulating the airway turning before the air measuring station, No.2 airway is regard as head entry and No.1 airway as section intake. The lengths of the two airways are 250m and 300m which are shown in Fig.1, and there have the same width (W) and height (H) of the two airways. Six models are designed, and whose sizes of width and height are shown in Table 1.

Table 1 Sizes of the six models

Model	Width[m]	Height[m]	Model	Width[m]	Height[m]
model 1	3	3	model 4	5	3.6
model 2	4	3	model 5	5	4.2
model 3	5	3	model 6	6	4

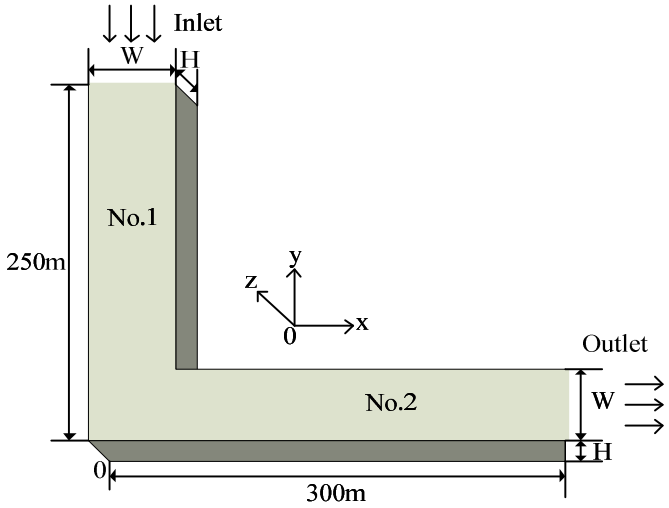

Fig.1 Schematic of physical model

Numerical Methods

Numerical tests are conducted using FLUENT software.

Mesh Generation. Mesh is generated by GAMBIT. A uniform structured grid with grid step 0.2m is used in airway cross section. A boundary layer non-uniform structured grid is used in air flow direction with the minimum grid step 0.2m, and the grid numbers in y and x direction are 250 and 300, respectively.

Parameter Setting. The fluid of the airway is air. Based on field testing data, the air density is set as 1.2kg/m^3 with the dynamic viscosity 1.44×10^{-5}kg/(m.s). The roughness height of the airway inner wall is set as 0.04m with roughness constant 0.8.

Boundary Conditions. Inlet condition: air velocity v=constant; Roof, floor and side wall of airways: wall; outlet condition: outflow.

Computational Model and Algorithm. The k-e turbulence model is used in air flow computation. The coupling between pressure and velocity is implemented by the SIMPLE algorithm and the convection term is discretized by the SUD (Second-order Upwind Difference) scheme. The convergence criteria is residual values of all variables are reduced to less than 2×10^{-6}.

Model and Methods Validation

Numerical tests of model 3 are conducted at different inlet air velocity which are 0.75m/s, 1.0m/s, 1.25m/s, 1.5m/s, 1.75m/s, 2.0m/s, 2.25m/s. The horizontal center line's velocity gradient of each node at different airway cross sections(x=20m, x=70m, x=120m, x=170m, x=270m) in different inlet air velocity are extracted to analyze the results. Taking the results at x=270m as the benchmark (where in the fully developed region), the velocity gradients of same location's relative deviation comparison at different air inlet velocity are shown in Fig.2.

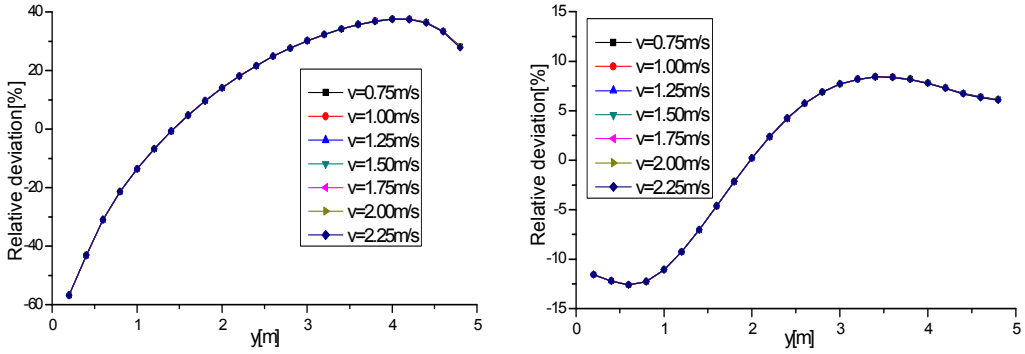

(a) x=20m (b) x=70m

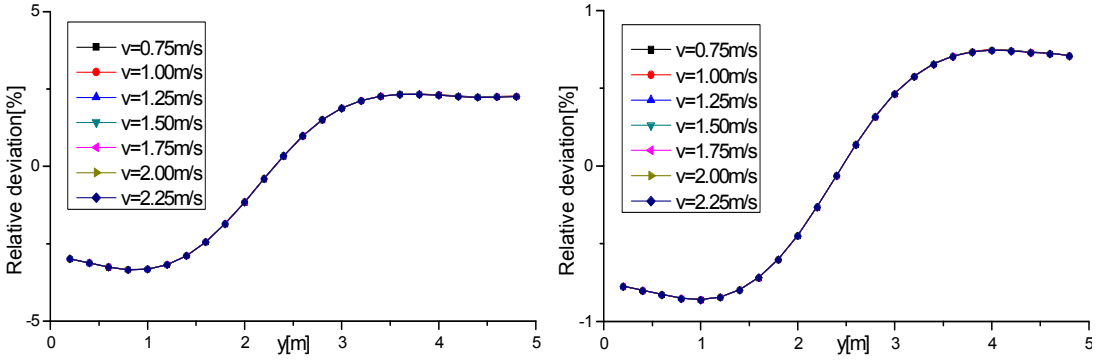

(c) x=120m (d) x=170m

Fig.2 Relative deviation VS inlet air velocity

Fig.2 show that there have the consistent relative deviation at different inlet air velocity and the relative deviations decrease gradually along the air flow direction. The independence of air fully development in airway and inlet air velocity validates the physical model and the numerical methods.

Results

Numerical tests are conducted with the inlet air velocity v=1.5m/s in different models. According to the actual situations of coal mine airway, air fully developed flow is defined as Eq.1.

$$|\max((vx-vf)/vf)|<1\%. \quad (1)$$

Where, vx is the velocity gradient of one of the node in analysis cross section, while vf is the corresponding node in reference cross section which in air fully developed region.

Results of head entry and tail entry are shown in Fig.3 and Fig.4, where the abscissa is the distance between analysis cross section and the corner in Fig.1.

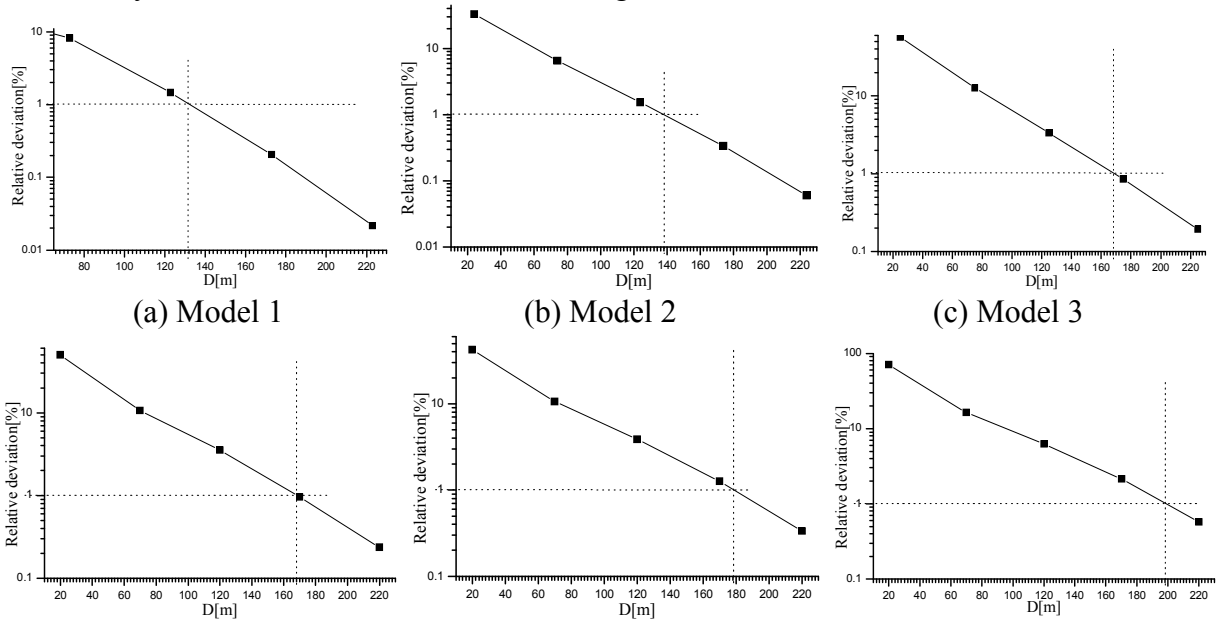

(a) Model 1 (b) Model 2 (c) Model 3

(d) Model 4 (e) Model 5 (f) Model 6

Fig.3 Results of air measuring station location in head entry

In Fig.3, the reference cross section is the cross section x=270m and the analysis cross sections are x=25m, x=75m, x=125m, x=175m and x=225m. In Fig.4, the reference cross section is the cross section y=70m and the analysis cross sections are y=7m, y=9m, y=11m, y=13m, y=15m, etc.

Fig.3 and Fig.4 show that the distance between the optimized air measuring station and air inlet/outlet increase with the increasing cross-sectional area, and air fully developed location at head entry in different models are range from 132m to 198m after the airway turning while range from 5.0m to 10.1m before the airway turning in tail entry.

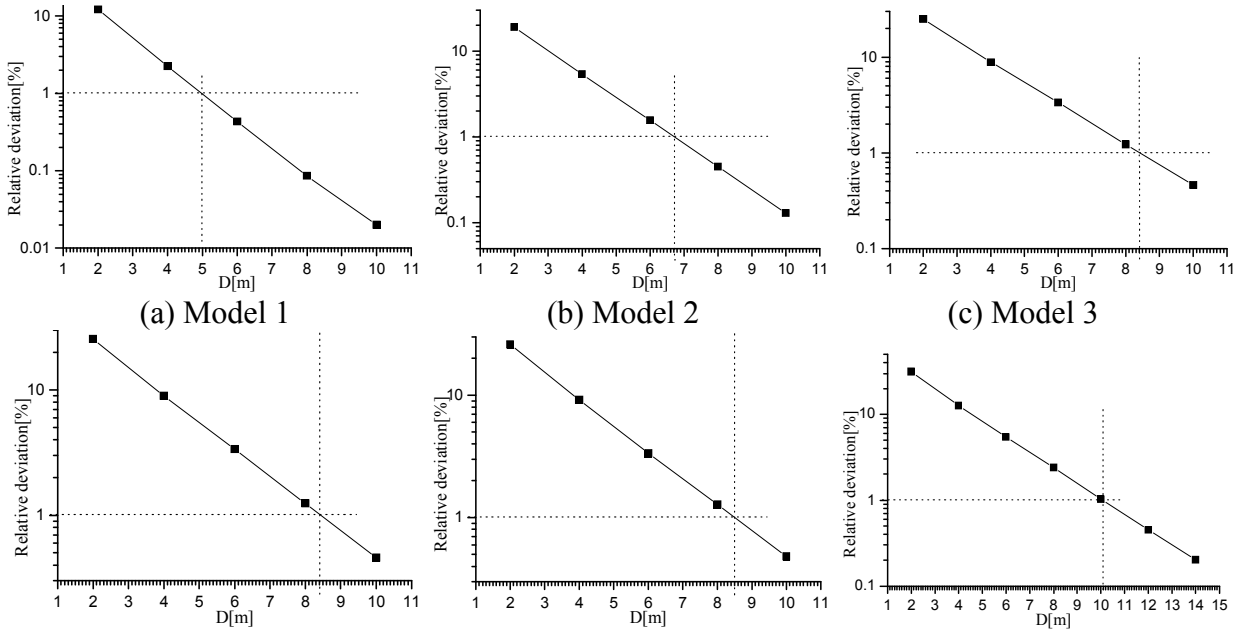

(a) Model 1 (b) Model 2 (c) Model 3

(d) Model 4 (e) Model 5 (f) Model 6

Fig.4 Results of air measuring station location in tail entry

Conclusions

The major findings are summarized as follows.

1) The air measuring station of mine airway should be located in air fully developed region.

2) The optimized air measuring station location at head entry in computational models are range from 132m to 198m after the airway turning while 5.0m-10.1m before the airway turning in tail entry.

Acknowledgements

This work was financially supported by the National Natural Science Foundation of China (51104116, 51104117).

References

[1] G.S. Zhang: Ventilation and Safety (China University of Mining and Technology Publications, Xuzhou, 2011). (In Chinese).

[2] Coal mine safety regulation expert interpretation Committee: Coal mine safety regulation expert interpretation (China University of Mining and Technology Publications, Xuzhou, 2011). (In Chinese).

Advanced Materials Research Vols. 960-961 (2014) pp 625-630

doi:10.4028/www.scientific.net/AMR.960-961.625

Numerical Simulation of UFAD Conditioned Space under Summer Part-load Conditions

Qiaoyan Ma [1, a], Shuxing Zhao [1,b *], Long Huang [1,c] and Cheng Deng [1,d]

[1]School of Energy and Safety Engineering, Tianjin Institute of Urban Construction

Jinjing Road No.26,Xiqing district, Tianjin 300384

[a]maqiaoyan723@163.com, [b]zhaoshuxing@126.com, [c]18579111286@163.com, [d] asixxx@sina.com

Keywords: UFAD, part-load, Fluent simulation, maximum (minimum) limit, optimal air parameters

Abstract. The air conditioning system did not run as the design conditions in most of the time. Therefore, how to rationally adjust air parameters under part-load conditions caused by changes in the outdoor environment is an important issue, which is crucial to people's comfort and energy systems. This paper introduces the part-load rate α to distinguish among different load-part conditions. And by taking the typical conditioned space of underfloor air distribution (UFAD) system in perimeter zone of New Tianjin Library as the object and using Fluent for simulation analysis, we get the conclusion that there is a maximum limit of supply air temperature and a minimum limit of supply air velocity under summer part-load conditions. For each condition, there is a set of optimal air parameters to make the indoor personnel achieve the most comfortable condition. Finally, we acquire this set of optimal air parameters by simulating and analyzing.

Introduction

In recent years, underfloor air distribution (UFAD) system has been widely studied and gradually used in office buildings, commercial buildings and other public buildings in China due to its advantages of high flexibility, comfort and energy efficiency. However, as the later application of this system in China and incomplete design specifications, there are still some problems in engineering design, operation of regulation and so on. This paper aims to estimate the best energy saving operational parameters of supply air and meanwhile ensuring comfort by simulating reasonable air parameters under part-load operating conditions with CFD simulation software. The simulation is carried out on a selected typical conditioned space of UFAD system which combines the actual project in Tianjin.

Typical room selection

Tianjin New Library is a comprehensive large public library. With consideration of the air conditioning energy efficiency and decorative effects, the library uses the UFAD air conditioning system in the study room, reading area and shared space in the public areas where are tall and diverse [1].

A typical conditioned room in the perimeter zone on the third floor was selected for simulation study. This room is a reading area, its east facade is glass curtain wall, and rest of the other walls is interior wall (adiabatic wall treatment). The master drawing of this room model is shown in Fig. 1, and the specific parameters are as follows:

The room is rectangular with dimensions of 10.2m × 10.2m × 5.85m (length × width × height); there are 20 air outlets on the floor, and the diameter D = 200mm; there are 2 air inlets in the ceiling with the size of 0.8m × 0.32m. The left air inlet is of 4.5m from the west exterior wall and 6.4m from the north exterior wall; the right air inlet is of 8m from the west exterior wall and 4m from the north exterior wall. We assume that there are total 15 staffs in the room: 10 people sit near eastern exterior wall and the other 5 people stand at the rest of the area. 10 fluorescent lamps have been situated at a height of 4.5m of the room. We also assume that the body heat quantity Q = 75W / person, and the fluorescent lamp heat quantity Q = 200W / light [2].

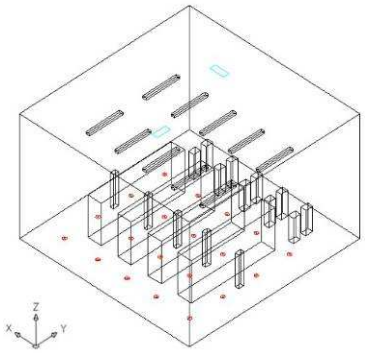

Figure.1 Master drawing of external room model

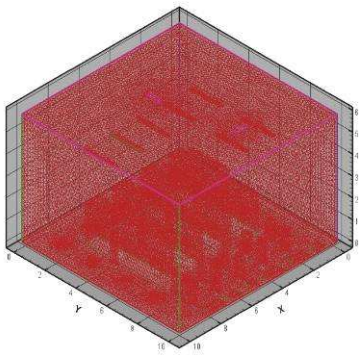

Figure. 2 Meshing Schematic of external room

Boundary conditions settings

It is difficult to build detailed models as the shapes of bodies, shelves and lamps in the actual room are complex. Therefore, in order to derive the simulation result, they are simplified to reduce the number of the mesh division to decrease computing cost and maintaining accuracy. The simplified models and the corresponding thermal boundary conditions are shown in Tab. 1.

Table.1 Simplified model and the thermal boundary layer settings

Type	Size	Setting boundaries	Remark
fluorescent lamp	2 m×0.2 m×0.1 m	q(heat flux)= constant	161.29 W/㎡
People standing	0.3 m×0.2 m×1.6 m	q = constant	45.18 W/㎡
People sitting	0.4 m×0.3 m×1.2 m	q = constant	41.67 W/㎡
Bookcase	5 m×0.8 m×2 m	q = constant	—
East exterior wall	—	q = constant	Setting based on the specific circumstances of different load
Interior wall	—	Adiabatic treatment	—

Establishment of radiation and numerical model

In the numerical simulation of the room, the radiation model is used to make the model closer to reality. DTRM model is used in this paper.

Tetrahedral mesh structure has been used to divide bodies, fluorescent lamps, air outlets and air inlets with refined mesh. Hybrid mesh has been used to divide the rest parts. The mesh division diagram of typical room at conditioned perimeter zone is shown in Fig. 2. As the problem in this study is incompressible flow problem, it can be solved with Segregated solver. Second Order Upwind format is used to deal with the discrete processing equation and SIMPLE algorithm is used to solve the discrete equations. Standard k-ε model, standard wall function and Bohemia Metalurh (Boussinesq) assumptions are also used. In the room model, boundary conditions of air outlets are velocity-inlet, and the air velocity of all the outlets are the same. Boundary conditions of air inlets are outflow. The rest of the facades are insulated walls. At the same time, each wall meets the no-penetration conditions and no-slip condition

Numerical simulation of summer part-load operating conditions

Under a certain load, the relationship between supply air volume and temperature difference of supply air is as follow：

$$V = \frac{Q_x}{c_p \rho \Delta t} \quad (1)$$

where V (m^3/h) is calculation supply air volume of the room; Q_x (kw) is calculation cooling load of the room; ρ (=1.2kg / m^3) is air density; c_p (=1.01 KJ/(Kg • ℃) is specific heat at constant pressure and Δt (℃) is the temperature difference between supply air and return air.

From the equation (1), it can be seen that there is a certain functional relation between supply air temperature and supply air volume. When outlet density and cooling load are determined, the change of supply air temperature can cause the change of supply air velocity. In summer, when the system is under part-load conditions, in order to meet the indoor environment and people's comfort when the load decreases, it is necessary to reduce supply air velocity to maintain the supply air temperature constant, or increase supply air temperature to maintain supply air velocity constant. And when maintaining supply air velocity as designing supply air velocity v_{design}, the correspond supply air temperature is the maximum supply air temperature t_{max} under this load condition; similarly, when maintaining supply air temperature as designing supply air temperature t_{design}, the correspond supply air velocity is the minimum supply air velocity v_{min}, under this load condition. The design supply air temperature of New Tianjin Library in summer is 19.2℃, the design supply air velocity in summer is 0.96m/s; based on these, this paper studies the effects of indoor environment and people's comfort under different supply air parameters and part-load conditions in summer.

Part-load operating conditions settings

In the study of system in part-load conditions, the part-load rate is used to distinguish among different load-part conditions, where the part-load ratio is the ratio of the actual running load and the design load, expressed by α, where $0 < \alpha \leq 1$. Assume that $0.4 \leqslant \alpha \leqslant 1$, operating point is established on each interval of 0.5 and there are total of 13 kinds of conditions. From equation (1), the maximum air supplying temperature t_{max} and the minimum air velocity v_{min} in the part-load conditions can be obtained. Then supply air parameter ranges in summer part-load can be also obtained, which is shown in Tab. 2.

Simulation parameters of supply air are chosen based on Tab. 2. Taking condition 7 for an example, supply air parameter is shown in Tab. 3, where the part-load factor α is set to be 0.70. The other 12 conditions are all set in the same way based on Tab. 2.

Table.2 Supply air parameter limits and ranges in summer part-load conditions

Conditions	Part-load ratio α	t_{max} (℃)	v_{min} (m/s)	Temperature ranges (℃)	Velocity ranges (m/s)
1	1.00	19.20	0.96	—	—
2	0.95	19.38	0.94	19.20—19.38	0.94—0.96
3	0.90	19.47	0.92	19.20—19.47	0.92—0.96
4	0.85	19.53	0.90	19.20—19.53	0.90—0.96
5	0.80	19.66	0.88	19.20—19.66	0.88—0.96
6	0.75	19.73	0.86	19.20—19.73	0.86—0.96
7	0.70	19.84	0.84	19.20—19.84	0.84—0.96
8	0.65	19.97	0.815	19.20—19.97	0.815—0.96
9	0.60	20.02	0.805	19.20—20.02	0.805—0.96
10	0.55	20.12	0.78	19.20—20.12	0.78—0.96
11	0.50	20.25	0.76	19.20—20.25	0.76—0.96
12	0.45	20.36	0.74	19.20—20.36	0.74—0.96
13	0.40	20.48	0.72	19.20—20.48	0.72—0.96

Simulation analysis of typical room under summer part-load operation

To be used as reference, temperature field and velocity field of the typical room under the design condition were firstly simulated. In order to facilitate the analysis of the flow field, profile of Y=4.2m is selected to analyze indoor temperature field and the result is shown in Fig.3. Profile of X=5.05m is selected to analyze indoor velocity field and the result can be seen in Fig.4.

Table.3 Supply air parameters setting of condition 7 (α=0.70)

Group number	Supply air temperature (℃)	Supply air velocity （m/s）
1	19.2	0.84
2	19.45	0.88
3	19.68	0.92
4	19.84	0.96

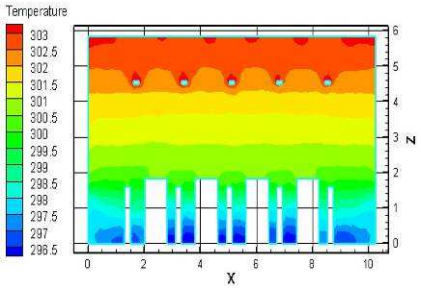

Figure.3 Temperature distribution profile of Y=4.2m under the design condition

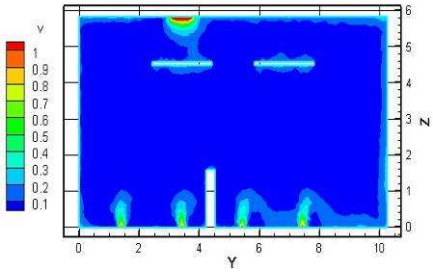

Figure.4 Velocity distribution Profile of X=5.05m under the design condition

In order to provide some guiding opinions to the actual adjust of the summer UFAD system, numerical simulation research is carried out to analyze changes of indoor air temperature field and velocity field under different supply air parameters based on the parameter combinations of condition 2 to condition 13. Supply air parameter combinations are represented with (t, v).

Research of correlation will be divided into the following three aspects:

1. Variable Air Volume conditions analysis

When the system is running under part-load conditions, with the load changing and the supply air temperature (t = 19.2℃) maintaining constant, only by changing the air outlet velocity (i.e.: supply air volume) can meet the indoor environment and people's comfort. Selected parameter combinations under 12 conditions are (19.20,0.94), (19.20,0.92), (19.20,0.90), (19.20,0.88), (19.20,0.86), (19.20,0.84), (19.20,0.815), (19.20,0.805), (19.20,0.78), (19.20,0.76), (19.20,0.74) and (19.20,0.72), respectively.

For comparative analysis, profile of Y=4.2m is selected to conduct temperature field analysis of various indoors conditions and profile of X = 5.05m is selected to conduct velocity field analysis of various indoors conditions. Taking the simulated figures of condition 2 with load factor α = 0.95 as an example, the profile of temperature field is shown in Fig. 5, and the profile of velocity field is shown in Fig. 6. Other simulation profiles of 11 conditions are omitted here.

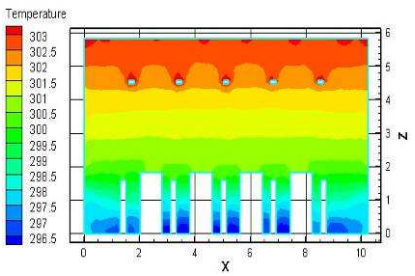

Fig.5 Temperature distribution profile of Y=4.2m under case 2

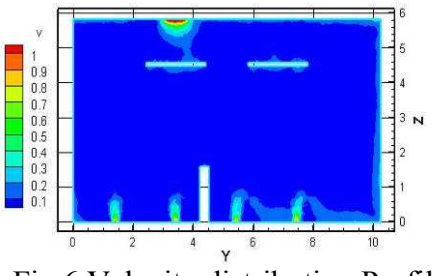

Fig.6 Velocity distribution Profile of X=5.05m under case 2

2. Constant air volume, variable temperature conditions analysis

When the system is running in part-load conditions, with the load change, maintaining the supply air velocity v = 0.96m / s constant, only by changing the air outlet temperature to meet the indoor

environment and people's comfort. Selected parameter combinations under 12 conditions are (19.38, 0.96), (19.47,0.96), (9.53,0.96), (19.66,0.96), (19.73,0.96), (19.84,0.96), (19.97,0.96), (20.02,0.96), (20.12,0.96), (20.25,0.96), (20.36,0.96）and（20.48,0.96), respectively.

For comparative analysis, temperature and velocity distribution profiles are selected in the same way as variable air volume conditions. The temperature distribution profile is shown in Fig. 7, and the velocity distribution profile is shown in Fig. 8. Other simulation profiles of 11 conditions are omitted here.

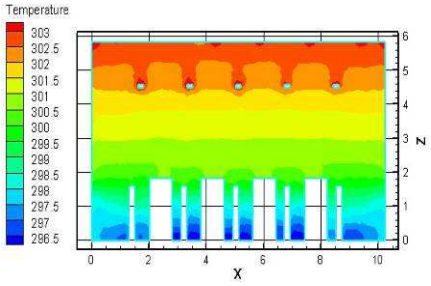

Figure.7 Temperature distribution profile of Y=4.2m under case 2

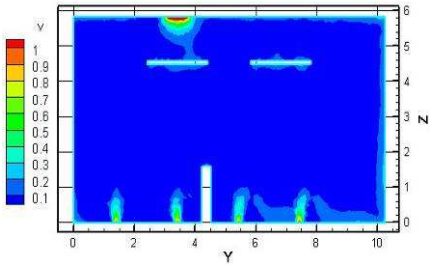

Figure.8 Velocity distribution profile of X=5.05m under case 2

3. Analysis of working conditions when air temperature and air volume change simultaneously

The impact of different supply air parameter sets for the indoor air environment and people's comfort have been analyzed when the system is under a certain part-load condition. Taking the condition 7 as an example, where the load factor α is set to be 0.70 and the supply air parameter combinations are shown in the Tab.3. Profiles of Y=4.2m are used to analyze the temperature and the results are shown in Fig. 9.

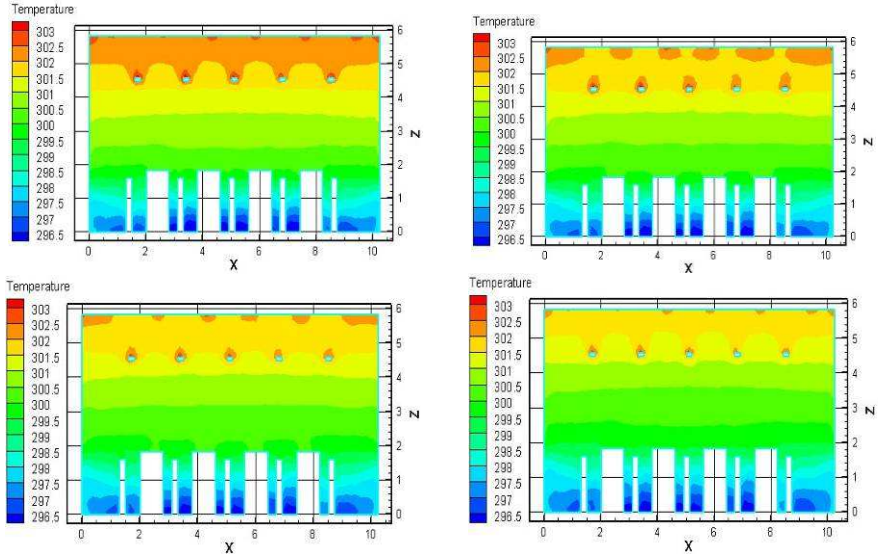

Figure.9 Temperature distribution profile of Y=4.2m under design condition

Analysis of the temperature and velocity distribution profiles in each condition, we can get the conclusions:

1)When the system is under part-load operations with changing load, it is feasible to maintain the supply air temperature t = 19.2 ℃ constant while only by changing the supply air velocity of the air outlet to meet the indoor environment and personnel comfort needs; it is also feasible to maintain supply air velocity v_{outlet} = 0.96m / s constant while only by changing the supply air temperature to meet the indoor environment and personnel comfort needs. The temperature and velocity distribution meet the requirements of ISO7730 [3], American Standard ASHRAE 55-1992[4] and Chinese specification [5]. Thus, as the indoor load reduces with the outdoor temperature declines in the summer, we can achieve the purpose of energy saving by changing the parameters of air supply.

2) For the summer part-load conditions, there is a maximum limit of supply air temperature and a minimum limit of supply air velocity. For a certain load condition, the design supply air velocity v_{design} should relate to the maximum limit of supply air temperature t_{max} and the design supply air temperature t_{design} should correspond to the minimum limit of supply air velocity v_{min}. Supply air parameter set (supply air temperature, supply air velocity) should satisfy the following relationship: t_{design} (19.2 ℃) $\leqslant t \leqslant t_{max}$, $v_{min} \leqslant v \leqslant v_{design}$ (0.96 m/s).

3) The average indoor temperature in work area and non-work area will both decrease in these three cases: Both of the two parameters of the supply air parameter set (air temperature and air velocity) increase; Supply air temperature maintains the design supply air temperature while supply air velocity decreases; Supply air velocity maintains design supply air velocity while supply air temperature increases.

4) The rational design of UFAD system can make people achieve a better comfortable condition [6].In the UFAD system, the indoor environment is more ideal, and the people's comfort is better in these conditions:

Average temperature of the indoor work area is closer to the design temperature;
Less temperature stratification of work area;
More temperature stratifications of non-work area;
Smaller height of the jet.

Therefore, for a certain summer part-load condition, there will be an optimum air parameter set to make the indoor environment most ideal, and to make people most comfortable. Through the above simulation analysis of each group, we can get that the first group of part- load parameter of each group (design supply air temperature t_{design}, the minimum supply air velocity v_{min}) is the best air parameter set. Therefore, variable air volume operation mode should be used in the actual operation of the project to achieve energy efficient operation, and to ensure the best comfort of the personnel.

Conclusion

A maximum limit of supply air temperature and a minimum limit of air velocity in the summer part-load conditions have been presented by simulation analysis. And it comes to the conclusion that for each condition, there is a set of optimal air parameters (t_{design} , v_{min}) to make the indoor personnel achieve the most comfortable condition. However, since the limited number of conditions, the α is not fully given. Therefore, there are some limitations of guidance for the actual operation of the complex working conditions. This section will be follow-up study in the future work.

References

[1] Zhihong An, Lei Liu: Air conditioning system design for New Tianjin Library, HV & AC, Vol. 42 (2012), p. 36-41. (In Chinese)

[2] Bin Fan: Simulation and Experimental Study of underfloor air distribution system. (2012) (In Chinese)

[3] ISO International Standard 7730. Moderate thermal environments — determination of the PMV and PPD indices and specification of the conditions for thermal comfort. International Standards Organization, Geneva (1994).

[4] ANSI/ASHRAE Standard 55—1992. Thermal environmental conditions for human occupancy. ASHRAE, Atlanta (1992).

[5] Design code for heating ventilation and air conditioning of civil buildings. GB 50736-2012. (In Chinese)

[6] Fountain M, Arens E, de Dear R, et al: Locally controlled air movement preferred in warm isothermal environments. ASHRAE Trans, Vol. 100 (1994), p. 937-952.

Advanced Materials Research Vols. 960-961 (2014) pp 631-634
© (2014) Trans Tech Publications, Switzerland
doi:10.4028/www.scientific.net/AMR.960-961.631

Study of Multivariable PID Neural Network Control for the Compression Station of Large-scale Helium Refrigerator

Peng Nan[1, a], Xiong Lianyou[1, b *] and Lei Linglong[1, 2, c]

[1]State Key Laboratory of Technologies in Space Cryogenic Propellants, Technical Institute of Physics and Chemistry, CAS, Beijing, 100190 China

[2]Graduate School of the Chinese Academy of Sciences, Beijing 100039, China

[a]pengnan@mail.ipc.ac.cn, [b]lyxiong@mail.ipc.ac.cn, [c]leilinglong10@mails.gucas.ac.cn

Keywords: Neural Network, PID Control, Multivariable Controller, Large-scale Helium Refrigerator

Abstract. With the fast development of superconducting, nuclear-energy and high-energy physics, further requirement of the system of large-scale helium refrigeration is brought forward by some associated subjects. The present controlling system of the system abovementioned is not well able to deal with the interruption such as the heat pulse impact. Thus, it leads to a new challenge that must be confronted with by the system of large-scale helium refrigeration.This paper aims at the control of gas management panel (GMP) in compression station of large-scale helium refrigerator. The neural network PID control of GMP in the system is introduced and simulated.

Introduction

Large-scale helium refrigerators at 4.2 K are used to cool down superconducting magnet systems, nuclear-energy and high-energy physics. These superconducting magnetic systems generate heat load that are pulsed in nature and helium refrigerators have to handle such heat loads [1-3]. The proposed control scheme can be used to have precise control of every pressure in normal operation or to stabilize and control the cryoplant under high variation of thermal loads. The strategy intends to replace all the PID loops controlling the GMP, by neural network PID controller.

A refrigerator based on modified reverse Brayton cycle has been developed recently [4]. This refrigeration cycle consists of an oil lubricated screw compressor, a GMP, a buffer tank, a counter-flow heat exchanger, a heater (dummy user) and a turbine expander as shown in Fig. 1. In the commercial helium refrigerator control system, the usual PID controller is used. The control strategy for the existing plant is that the suction pressure (P1) is controlled by the bypass valve V1 and the outlet pressure (P2) for compressor is controlled by using V2, V3 [5] as shown in GMP part of Fig. 1. According to this control strategy, the control loops for P1 and P2 are independent, which can't satisfy the control purpose to the object sometimes. This paper will introduce a way to improve the PID control for the compression station of large-scale helium refrigerator.

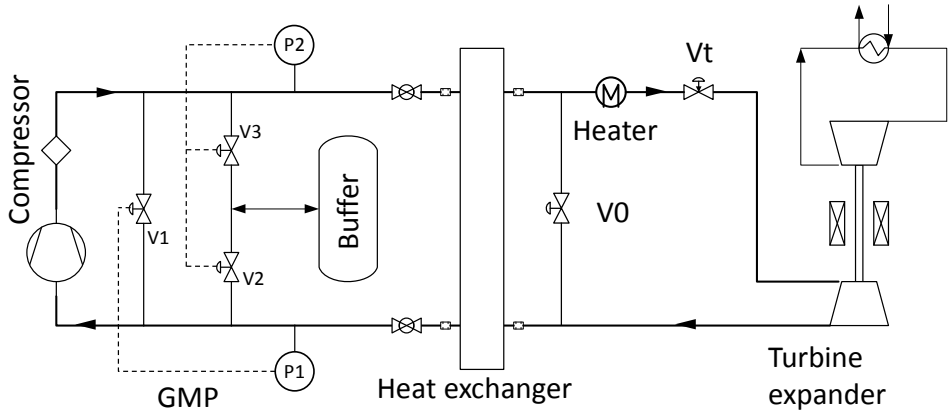

Fig. 1. Flow scheme of the modified reverse Brayton refrigerator.

Neuromorphic control structure

The function of V2 and V3 is charge valve and discharge valve, respectively. For the traditional control strategy, V2 and V3 can be opened at the same time, which is not rational in principle. In the new multivariable PID neural network (NN) control, the V2 and V3 will be considered as one regulator. When the system need more helium the V2 will be open and V3 will be closed. Conversely, when there is too much helium in the system the V3 will be open and V2 will be closed.

The multivariable PID neural network controller structure has been shown in Fig. 2. And the error1 is denoted by e1(t)=r1(t)-y1(t) where r1(t) is the desired signal of low pressure P1 and y1(t) is the actual P1; while the error2 is denoted by e2(t)=r2(t)-y2(t) where r2(t) is the desired signal of high pressure P2 and y2(t) is the actual P2. In the discrete-time control system, the PID algorithm can be given as Eq. 1:

$$u(t)=u(t-1)+K_P\left(e(t)-e(t-1)\right)+K_I e(t)+K_D\left(e(t)-2e(t-1)+e(t-2)\right) \tag{1}$$

where K_P, K_I, and K_D are respectively, the proportional, integral and derivative gains of PID controller which should be adjusted. The part of a NN block is build in order to adjust the gains of PID controllers adaptively by using the back propagation (BP) method with measurement data of u(t), y(t) and r(t).

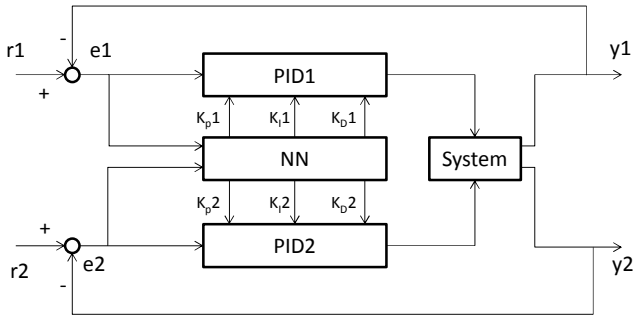

Fig. 2. Multivariable PID neural network controller structure.

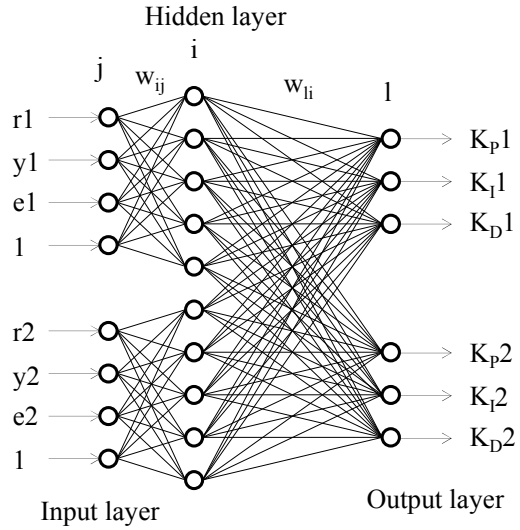

Fig. 3. Configuration of BP neural network.

The BP is a multilayered network which consists of an input layer, an output layer and several hidden layers of nonlinear processing elements [6]. For the new NN controller, the controller has three layers and the number of output layer neurons is K_P, K_I and K_D and the configuration of BP neural network is shown as Fig. 3. The input-output neurons relationship of BP NN can be expressed as follows:

$$net_p^{(m)}=\sum w_{pq}^{(m)}O_q^{(m-1)} \tag{2}$$

$$O_q^{(m)}=f\left(net_q^{(m)}\right) \qquad (pq=ij,li),(m=2,3) \tag{3}$$

where $w_{pq}^{(m)}$ is the weights of hidden layer, the upper number m = 1,2,3 denotes input layer, hidden layer, output layer, $net_p^{(m)}$ is the input of neuron p in the layer m, $O_q^{(m)}$ is the output of a neuron q,

$f(\cdots)$ is the neuron activation function, for hidden layer $f_1(x)=\tanh(x)$, for output layer $f_2(x)=\frac{1}{2}(1+\tanh(x))$. The learning goal of PID neural network is to minimize the average value of system output square error J which can be expressed as Eq. 4.

$$J=\frac{1}{2}\left(e_1(t)^2+e_2(t)^2\right) \tag{4}$$

where J is to modify the weights by the fastest descend mean, which is searched and tuned toward the negative gradient and added on a inertia coefficient to make faster constringency.

$$\Delta w_{li}^{(3)}(k)=-\eta\frac{\partial E(k)}{\partial w_{li}^{(3)}}+\alpha\Delta w_{li}^{(3)}(k-1) \tag{5}$$

where η is the learning rate and α is the smoothing coefficient. And Eq.5 can be rewrited as follows:

$$\begin{aligned}&\Delta w_{li}^{(3)}(k)=\eta\delta_l^{(3)}O_i^{(2)}(k)+\alpha\Delta w_{li}^{(3)}(k-1),\\&\delta_l^{(3)}=e(k)\operatorname{sgn}\left(\frac{\partial y(k)}{\partial u(k)}\right)\frac{\partial u(k)}{\partial O_l^{(3)}}f_2'\left(net_l^{(3)}\right),\qquad l=1,2,3.\end{aligned} \tag{6}$$

And the weights of hidden layser can be written as Eq. 7

$$\begin{aligned}&\Delta w_{ij}^{(2)}(k)=\eta\delta_i^{(2)}O_j^{(1)}(k)+\alpha\Delta w_{ij}^{(2)}(k-1),\\&\delta_i^{(2)}=f_1'\left(net_i^{(2)}(k)\right)\sum_l^3\delta_l^{(3)}w_{li}^{(3)}(k),\qquad i=1,2,3,4,5.\end{aligned} \tag{7}$$

Analysis and results

A dynamic simulator has been carried out, which provide a way to study and optimize control strategies of the refrigerator [7]. The numerical model comprises the typical components of the refrigerator: compressor, valves, heat exchangers, expander and heater. This simulator is based on the oriented-object approach and each component is represented by a set of differential and algebraic equations. The control logic of the refrigerator is also embeded in the simulator.

The initial pressure of the system is 0.2 MPa and the initial pressure in the buffer tank is 0.4 MPa. The setting pressure of high pressure is 0.55 MPa and that of low pressure is 0.105 MPa. The traditional PID parameters for V1 are $K_P = 2.0$, $K_I = 20$, $K_D = 0$; those for V2 and V3 are $K_P = 1.0$, $K_I = 30$, $K_D = 0$. For neural network PID in the simulation, the learning rate is 0.1 and the smoothing coefficient is 0.2 and the initial weights is the random number in the extent (-1,1).

The simulation results of nerual network PID control and traditional PID control in the starting stage have been obtained as shown in Fig. 4. The simulation results show that the high pressure and low pressure can be controlled to the setting point in shorter time by using NN PID control. It can be found that the overshooting of these two control loop is very similar, but the governing time of NN PID control is shorter than traditional PID control.

When the high pressure and low pressure is built up and kept to a steady state. The V0 should be turned on to start the self-circulation stage. The V0 is opened to 50 % at 400 s and then keep this opening. This operation is a typical disturbance to the GMP control system. Fig. 5 shows the simulation results of NN PID control and traditional PID control when V0 is turned on. The simulation results shows that the overshooting of the NN PID control is smaller than traditional PID control. And the governing time of NN PID control is much shorter than traditional PID control. The

simulation results indicate that the NN PID control can increase the performances and stability of the compressor station.

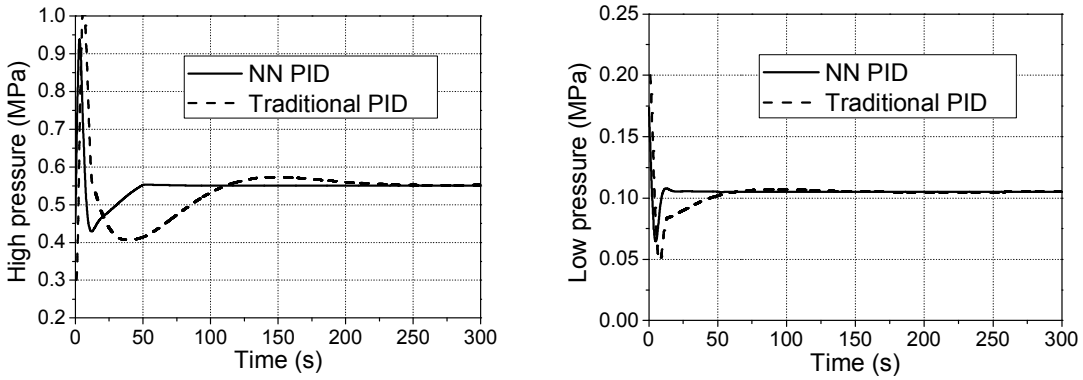

Fig. 4. Simulation results of NN PID control and traditional PID control in the starting stage.

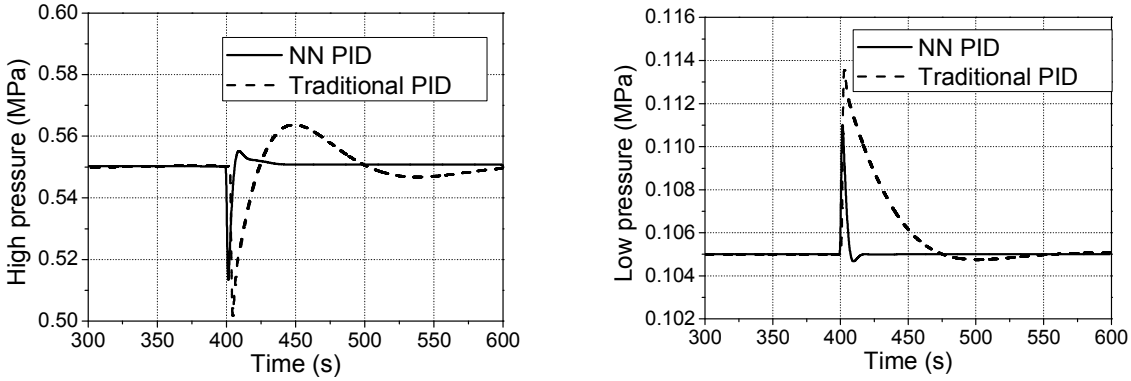

Fig. 5. Simulation results of NN PID control and traditional PID control when V0 is turned on.

Conclusions

A neural network PID controller, which is a method for adaptively adjusting the PID gains using a BP neural network, are introduced to GMP of the large-scale helium refrigerator. The neural network PID control has self-learning and self-adapting abilities. The neural network PID control and traditional PID control are applied to the pressure control for refrigerator. The simulation results indicate that the neural network control system has better robustness and higher precise than traditional PID control. For future work, the neural network PID controller will be applied to the control of turbine which is the key component of the helium refrigerator.

Acknowledgements

This work is supported by the Chinese National Natural Science Foundations (Foundation No. 51106169) .

References

[1] L. Serio. Adv. Cryog. Eng. Vol. 55, (2010), p. 651-662.
[2] B. Xiao, P. Weng, Cryogenics, Vol. 43, (2003), p. 173-178.
[3] P. Briend, C. Deschildre, Y. Icart, S.E. Sequeira. Adv. Cryog. Eng. Vol. 55, (2010), p. 1453-1459.
[4] L. Y. Xiong, Z. Y. Huo, Y. C. Jiang, W. H. Lu, N. Peng, L. R. Sun, L. L. Lei, B. Dong, J. Li, J. C. Tang, L. Q. Liu and X. J. Liu. In: Proceedings of ICEC 24-ICMC 2012, p. 477-480.
[5] L. R. Sun, L. Y. Xiong and L. Q. Liu, Cryogenic Engineering, Vol. 186, (2012), p. 55-59.
[6] H. L. Shu, Y. G. Pi. Computers and Chemical Engineering, Vol. 24, (2000), p. 859-862.
[7] N. Peng, L. L. Lei, L. Y. Xiong, J. C. Tang, B. Dong and L. Q. Liu. Adv. Cryog. Eng. AIP Conf. Proc. 1573, (2014), p. 1764-1769.

Advanced Materials Research Vols. 960-961 (2014) pp 635-638

doi:10.4028/www.scientific.net/AMR.960-961.635

The Analysis of Comfortable and Energy Saving of Ice-Storage Low Temperature Air Supply System

Li Bai[1, a], Xuezhi Zhou[2,b], Yan Wang[3,c], Yawei Hua [4,d]

[1,3,4]School of Municipal & Environmental Engineering ,Jilin Jianzhu University,.Changchun ,China

[2]The Chinese academy of sciences,Beijing,China

[a]baili0308@163.com, [b]23689849@qq.com, [c]wangyan2387@163.com, [d]1207495678@qq.com

Keywords: Low temperature air supply, Ice-storage, Energy saving, Indoor environmental quality.

Abstract. More and more attentions have been paid on ice-storage low temperature air supply system because of its notable energy saving effects and comfort. The paper expatiate on that ice-storage low temperature air supply system brings a series of especial superiority to modern air-condition cause. The results show that low temperature air supply system can exert the potential advantage of ice-storage further. The combination of ice-storage and low temperature air supply system can obtain an “integrated approach”, which can save energy resources and improve human body comfort and indoor air quality.

Introduction

China's air-conditioned buildings total energy consumption account for 60% to 70% . In this energy shortage situation, ice-storage technology, as a power load management measure to effectively alleviate the power shortage and ease the contradiction between power distribution and load capacity ,has played a "peak load shifting" effect successfully .

With the ice-storage technology being more sophisticated, cold air can be applied in air-conditioning possibly. Cold air from the air-conditioning is the focus of processor for sending low-temperature primary air, after inducing air at the high end of the room air-conditioning unit into the air supply system. With the rise of ice-storage air-conditioning technology, the advantage of the ice-storage system to provide cold water, has low investment and operation cost, high efficiency, less demand for electricity and so on. More importantly, it can reduce indoor air humidity and improve indoor thermal comfort and air quality, so it can prevent "air-conditioning disease". In the meantime, because lower air temperature slows the growth of bacteria, people have a healthy space.

Ice-storage cold air distribution system not only can improve the effective utilization rate of building space, lower operating costs, but also improve indoor comfort and indoor air quality. Therefore, the development of low-temperature ice-storage air conditioning systems in China and the world has become a popular trend and the focus of research .Ice-storage cold air distribution system will also become widespread central air-conditioning system in the 21st century.

Low-temperature ice-storage air supply system and characteristics of classification.

Low-temperature ice-storage air supply system classification. Cold air, being usually based on the level of air temperature, can be divided into three categories: Super-cold air. Air temperature is 4 ~ 6 ℃; because the supply of such air is special, it is generally less recommended.

Lower air temperature. Air temperature is 6 ~ 8 □.Only when ice-storage air supply technology work closely together, it can get a better effect of air-conditioning and has good economic returns, so the best choice is to be a wide range of promotion and application.

Cold air distribution. Air temperature of 9 ~ 12 □, Cold air distribution. Air temperature of 9 ~ 12 ℃, the air supply of such ice-storage air-conditioning can also be combined with conventional air-conditioning, more flexibly, less access to economic benefits; it also has less ice in cold air conditioning system application.

Ice-storage characteristics of cold air distribution system. As the ice make full use of the frozen water of 1.1 ℃ to 3.3 ℃ , the combination of ice-storage and cold air distribution system often use the primary air which is 6.6 ℃ to 8.8 ℃. This system has a number of advantages:
Low-temperature air conditioning system, applying of ice-storage technology to achieve the success of "peak load shifting," reduces peak electricity demand.
The air temperature increases, making air supply reduce, reducing the air-handling equipment size, making power blower axis wind pipe size become smaller , can save building space, which is favorable for commercial high-rise building. Operating mode, as a result of the reduction of air flue, makes equipment reduce capacity, which reducing power consumption and improve the performance

Ice-storage air-conditioned indoor air quality

Ice-storage air-conditioned indoor air quality
With the deepening of the study, it finds that indoor air quality is different from indoor pollution. The pollutant level of the individual indicators can accurately reflect the indoor air quality. Low concentration of indoor pollutants is difficult to detect, so indoor air quality is also relate to temperature and humidity.

The impact of air flow to the human body comfort. At present, the cold air distribution technology is not widely applied in China. The main reason is that this not belongs to the length of cold jet, so that there is a sense of staff hair in room to reduce the volume of air. So that poor indoor air flow, results in the emergence of air trapping zone. International briefing on the effectively use of the main sense of cold air temperature on air conditioning systems performance evaluation. Effective temperature briefing include that the air temperature, relative humidity and air flow on the human body's physiological effects of a comprehensive. it can be expressed:

$$EDT = (tx-tc)-8(vx-0.15) \quad (1)$$

Where, EDT - a briefing for the effective temperature ℃;
t_x - a point of the indoor air dry bulb temperature ℃;
t_c - the average indoor dry bulb temperature ℃;
v_x - a point of the indoor air center wind speed m / s.

Comparing with conventional air conditioning systems, cold air distribution system has the following characteristics: first, because of reducing the air supply amount, leading to the room air flow rate is too low, it is possible to affect the indoor air quality. The second, it is caused by the low-temperature air supply device. Third, because air temperature goes down easily, people have a sense of cooling. To deal with the problem, take the following measures:
Low-temperature air mix with the indoor air before gets into the room.
A good performance converter scatters into the air indoors, to prevent the occurrence of the phenomenon of sinking.
Strengthen the pipeline insulation to reduce the amount of cold and prevent the loss of the condensation phenomenon.
At the same time, this also shows that: the indoor air flow rate, comfort are great relate to device structure. The apparatus is not only a very high degree of induction than the connection end portion in the same length of time long enough to improve indoor quality and comfort of air jets.

Low relative humidity of indoor air. Indoor air quality of the human body's feeling good or bad is mainly affected by indoor air temperature and humidity. When the indoor air temperature and relative humidity increase, air quality acceptability for the human body will markedly decline. Experimental results show: low humidity, the subjects feel more comfortable and cool. The fresh air determines indoor air quality, which is more acceptable. The cold air distribution system, it is precisely because of
its low relative humidity, which has a strong capacity dehumidifier, which makes an increase of fresh air and an increase of people's comfort.

Temperature impact the indoor air quality. As the cold air conditioning systems is relate to low temperature of the air supply, cold air of air-conditioning directly get into the region, causing cold air and heterogeneous indoor temperature drop, which affects the thermal comfort. If the air temperature has not been took any special measures, then sent it to the area below the dew point temperature of the air-conditioning, it is easy to produce the phenomenon of sending "fogging" or water and make indoor environmental damage. At present, for China's production induced device, this problem has been successfully solved. Essentially eliminating the "fogging" and "water", only ending the device's low degree of automation, it needs to further improve.

On the other hand, due to the cold air distribution system, ice-storage temperature is very low. It is able to effectively overcome the central air-conditioning syndrome, which is much better than the conventional air-conditioning.

The fresh air determines indoor air quality. Using the way of VAV air, the indoor cooling load in air flue can be decreased. When outdoor air has a certain minimum volume, with the reduction of air supply the amount of fresh air will decrease than to improve. In some cold air distribution system, when the cooling load is in a low state, the fresh air rate even close to 100%. As a result, the system design and selection，should use VAV way to determine a minimum volume of outdoor air, so as to improve the indoor air quality.

The overall evaluation of the indoor environment. Indoor air temperature, humidity and air distribution are the three major factors impacting indoor air quality and thermal comfort, which are interactional. Cold air distribution ice-storage air conditioning system reduces relative humidity and temperature of the region to improve the comfort of environment. Dry bulb temperature of coil exports can reach 5.5 ℃ and relative humidity can reach 36%, while the conventional system is 50% to 60%. Lower relative humidity and 25 ℃ indoor conditions can be used in the region making a cool and refreshing feeling . Jet attached at the end of the device to ensure a reasonable indoor air, air-conditioned rooms can maintain a good indoor environment.

Ice-storage air-conditioning has energy-saving effect. When cold air distribution system and ice-storage technology apply to the building's air-conditioning, the electricity supply will achieve the "peak load shifting "of the user side from its peak during the day shift to night-time. At the same time, it can reduce transmission and distribution facilities, so it can lower all the cooling system capacity requirements and capacity of mechanical and electrical equipment costs.

As the air temperature increasing, air flue and air power accordingly reduce significantly. At the same time, coil road and wind section size can be significantly reduced, thus the initial investment can be reduced. Also it accordingly reduces the floor area occupied and raises the utilization rate of the building. The ice-storage system with low temperature evaporation of the ice, leads to decline the COP which is usually higher than the energy storage system for non-ice systems. Ice-storage and using of a combination of cold air distribution system, due to the reduction of air supply volume and reduction energy consumption of fan, so the total energy consumption could be lower than the storage of non-conventional air supply system.

Cold air distribution system ,comparing to the general air supply system, reduces the temperature of air of air-conditioned room , which is usually 3 ~ 11 ℃. Because it sends the low-temperature air, it has significant energy-saving effect. Cold air distribution systems and air supply systems in all aspects of more conventional parameters list in the table below:

Table 1 Aspects of conventional parameters

Item	Cold air distribution system	Conventional air supply system
Air temperature (℃)	10 to 20	8 to 10
Air temperature (℃)	3 to 11	10 to 15
Air-conditioning units to reduce the size ratio (%)	20 to 30	0
Duct size reduction ratio (%)	30	0
Fan power to reduce the ratio (%)	30 to 50	0

From the above we can see: ice-storage cold air distribution system, although increases storage devices and accordingly increases investment, but the units, pumps and pipes accordingly reduce in size to a large extent ,which can make up for the increased costs. Due to the reduction of air supply, water pump and power unit can significantly reduce running costs. As a result, low-temperature ice-storage air supply system both in the way of investment and in the early running costs has significant energy-saving effect.

Conclusion

Not only in the energy-saving, but also to ensure indoor air quality and improve human comfort , the low-temperature ice-storage air supply system, particularly the low-temperature ice-storage air supply system outside the office building has become a popular air-conditioning program. China's scientific and technological workers who look at the technology research prove: cold air and ice-storage technology, which can transfer peak load electricity, save energy consumption and improve indoor air quality, have special advantages and far-reaching significance in promoting China's HVAC cause.

References

[1] Yin Ping, Ice-storage cold air distribution system design (1): indoor parameters, comfort, indoor air quality. C. HVAC, 5, 58-59, 2004.

[2] Cheng Jian Jie, Chen Ru dong, Optimize the air-conditioning systems-low-temperature ice-storage air conditioning system. C. Energy, 6, 7-8, 1999.

[3] Xu Ya juan, Ice-storage at the end of the cold air distribution and application of a comparative analysis. C. Refrigeration and air-conditioning, 2, 19-20, 2002.

[4] Pan Yu shun, Zhi Yuan Lin, Most modern air-conditioned - ice-storage air temperature. C. Refrigeration, 4, 21-22, 2000.

[5] Pan Yu shun, Wu Jian guo, Gu Yan fang, Low-temperature ice-storage air conditioning technology research and development strengths. C. With special low-temperature gas, 19, 1-3, 2001.

Advanced Materials Research Vols. 960-961 (2014) pp 639-642

doi:10.4028/www.scientific.net/AMR.960-961.639

Research on Central Air Conditioning System of Intelligent Buildings

Xuejing Sun

School of Civil and Environmental Engineering, Jilin JianZhu University

Metro Street, Changchun City, Jilin Province, China 130118

sunxuejing2002@sina.com

Keywords: Intelligent building; Central conditioning system; LCD screen; PID parameter;

Abstract. In this paper, microcontroller is applied in the central air conditioning control system. Firstly, microcontroller controller is used as controlling core to control temperature and humidity of central air conditioning control system. Secondly, PID algorithm parameters are set up for improving traditional PID control principle. Lastly, input and output values can be set and displayed by LCD screen.

Introduction

At present, architecture consumption can account for about 70% of the total power consumption according to statistics. The architecture air-conditioning consumption can account for about 50% of the total architecture consumption [1-2]. Therefore, improving the management of central air conditioning is imperative. With the development of China's economy, people's living standards are improving. Their requirement for more comfortable air condition environment has become the first problem. How to control the air conditioner functioning to make its temperature within the human comfort range and how to improve the quality of system functioning to save operation energy consumption, has become a problem that should not be ignored [3]. This paper mainly elaborates the hardware of the central air-conditioning control system, PID parameter optimization problem and input and output problems.

The design of hardware of the central air-conditioning control system

Hardware selection. The hardware selection of this text mainly includes microcontroller, temperature and humidity sensor, regulating valve, frequency converter, air valve actuator and selection of related hardware. The list is shown in Table 1.

Table 1.The hardware list

sequence	type	hardware
1	micro controller	8051
2	temperature sensor	LM335
3	humidity sensor	HIH3610
4	regulating valve	V230
5	frequency converter	FR-A700
6	air valve actuator	CDH2019

Design principle. people can adjust the indoor temperature and humidity through remote control because of microcontroller inside instructions. Central air conditioning indoor temperature and humidity can make people get more comfortable office environment. 8051 microcontroller will drive the temperature sensor, humidity sensor to detect the air inlet temperature and humidity of new outlet.

When the control valve receives the feedback signal detection, it can automatically adjust the opening size. At this time, new entrants into the fresh air will be the same as the indoor return air mixing, forming a hybrid wind. When the wind pipe mixed air temperature is too high, the motor will drive the surface cooler for cooling treatment, hot and cold water will PID adjustment. In the precondition of ensuring the load demand, achieve the maximum energy saving central air conditioning. After A/D conversion, the humidity and temperature value is displayed on the LCD screen for people to confirm. The central air conditioning design principle is shown in Fig 1.

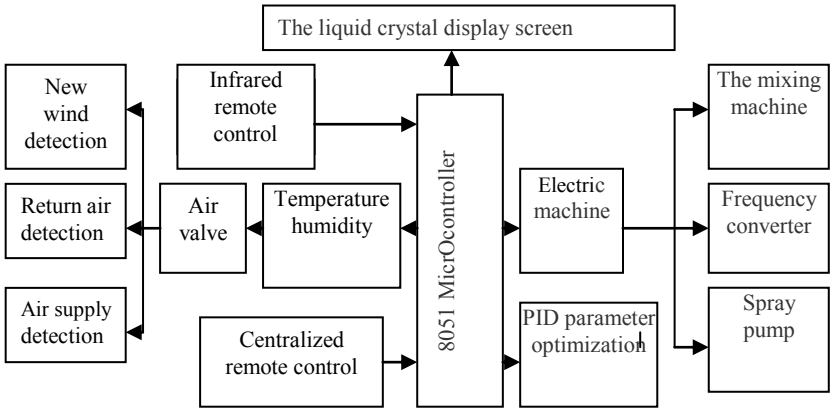

Fig 1. The design principle of central air conditioning

The PID parameter optimization

PID control algorithm is widely used in the intelligent architecture. The central air conditioning cold and hot water regulating control can also use PID control algorithm. The central air conditioning temperature and humidity sensor can build current signal of the fresh air temperature and humidity. The 8051 MCU and A/D conversion unit can transform the analog signal into digital signal. It can achieve PID control through software programming. Therefore, mixing unit for temperature and humidity treatment can satisfy the people' requirements. The fresh air is driven by single chip microcomputer. The traditional PID control principle is simple, strong robustness, adaptability. But the central air conditioning system is large, the control loop is more, the traditional PID algorithm parameters setting are difficult to meet their requirements. This design adopts the ant colony algorithm to optimize the parameters of PID control. Ant colony algorithm is a heuristic algorithm for discrete optimization problems. It is by a group of artificial ants cooperating to find the best solution. Its main part is the computer resource allocation to a group of relatively simple artificial ants, indirect communication between artificial ants through media. Ant colony algorithm with embedded operating system is the framework, after several times of iterative approaches the optimal results, the parameters of PID algorithm on the shortcomings of traditional setting lag, not precise. Application of PID in central air conditioning in the parameter optimization, the main algorithm is as follows:

First, Combinatorial optimization problems PID control parameters is transformed into the problem of ant colony algorithm applicable, Make a set of parameters(k_p, T_i, T_d),andA length of 15 digits correspond, The objective function is established:

$$J = \sum_{i=0}^{\infty} (w_1 |e(i)| + w_2 u^2(i) + w_4 |e(i)|) + w_3 t_w \tag{1}$$

Secondly, construct the desired path. Suppose that each artificial ant in the initial point($x_i - 1, y_i^{'}$),and in accordance with the probability of a random proportional rule behavior to choose rules, suppose climb to the next node(x_i, y_i),Until each ant at(15, $y_i^{''}$)as a cycle, The random proportional rule:

$$P_k(x_i,y_i,t)=\frac{\tau^{\alpha}(x_i,y_i,t)\eta^{\beta}(x_i,y_i,t)}{\sum_{j=0}^{9}\tau^{\alpha}(x_i,y_i,t)\eta^{\beta}(x_i,y_i,t)} \quad (2)$$

Finally, Conduct the pheromone update. Ants from the initial point to complete one cycle after the node information will change, Information update cable according to the following formula:

$$\tau(x_i,y_j,t+15)=\rho\tau(x_i,y_j,t)+\Delta\tau(x_i,y_j) \quad (3)$$

$$\Delta\tau(x_i,y_j)=\sum_{k=1}^{m}\Delta\tau_k(x_i,y_j) \quad (4)$$

$$\Delta\tau(x_i,y_j)=\frac{Q}{F_k} \quad (5)$$

The flow chart shown in Fig 2.

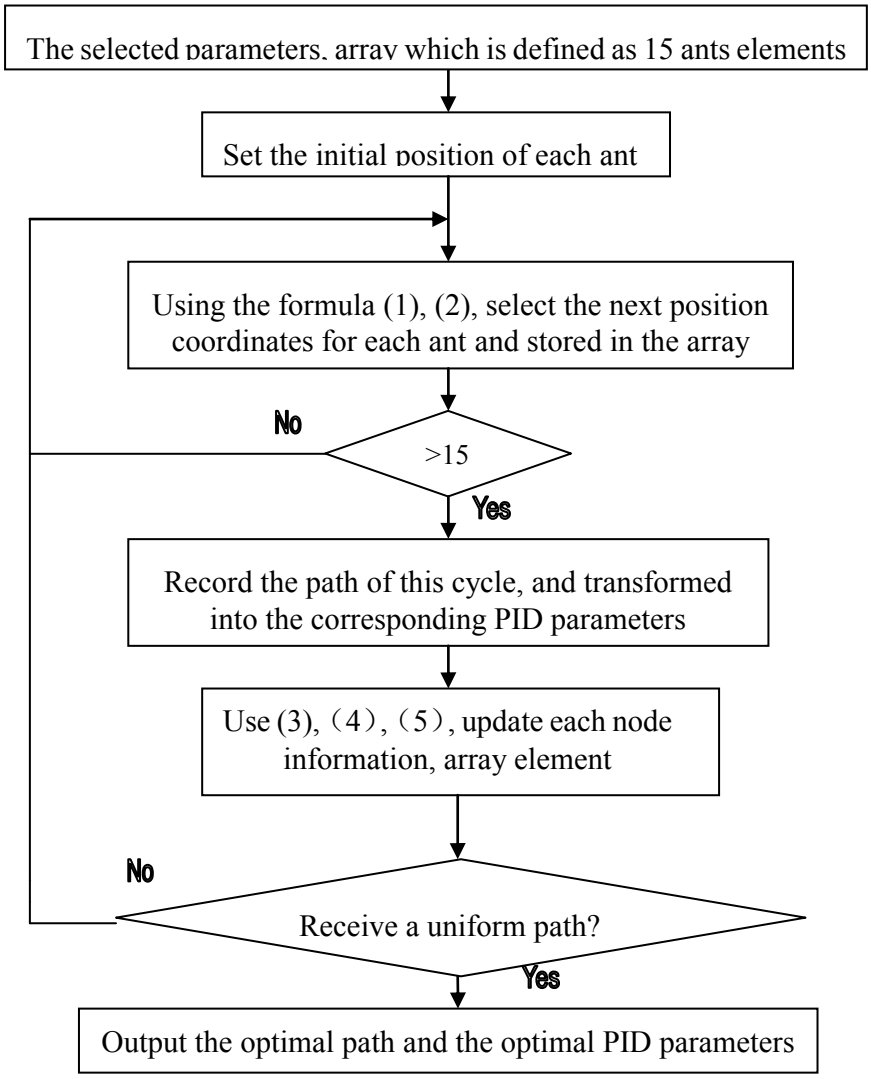

Fig 2. PID parameter optimization of ant colony algorithm

Design and display of input and output values

With the progress of society，more and more devices are equipped with remote control. The design of the infrared remote control can control the central air conditioning of 8051 single-chip operation. The motor can start and stop the temperature and humidity detection. Of course, the infrared remote control to be equipped with an infrared emission tube,when the electric infrared

receiving end to form on the radio state,then reach the remote control function. The infrared remote control by the 555 circuit generates a pulse signal, produced by the oscillating circuit characteristic frequency pulse through the drive signal of infrared emission tube emits the same frequency, complete the infrared control. The central air conditioning ventilation is good, the fresh air into the room. The temperature and humidity of air is displayed by LCD. LCD screen is composed of two plates, when an electric field is applied to the liquid crystal,then change the internal molecular arrangement,so that the droplets of liquid crystal layer formed in the pixel on the screen. This design allows the LCD display and the temperature and humidity detection circuit board, coordination the software can read the temperature and humidity of indoor. The temperature and humidity testing physical map is shown in Fig 3.

Fig 3. The physical map of temperature and humidity testing

Conclusions

This paper designs the hardware and software of the central air-conditioning control system using Siemens S7-200 programmable controller in the office. In the control algorithm, it adopts the traditional PID control and fuzzy control method to realize the combination of central air conditioning of the temperature and humidity and hot and cold water control. At the same time, it uses touch screen on the correlation parameter setting and information display. The central air conditioning system simulation control lays a certain theoretical basis for the intelligent central air conditioning.

Acknowledgements

This work was financially supported by the Educational Research Project of Jilin Province Department of Education (2013. No. 233).

References

[1] Xu Jinbiao: Research on Building Intelligent Technology .Vol.12 (2012), p. 22.

[2] Liang Qingjun: Science and Technology Innovation Herald. Vol.22(2013),p.120.

[3] Wu Li: Industrial Control Computer. Vol.23 (2010), p.114.

[4] Sui Fang: PLC Application Technology. Vol.28 (2009), p.66.

[5] Wei Ping: Design of Central Air Conditioning System. Vol.12 (2013),p.210.

Advanced Materials Research Vols. 960-961 (2014) pp 643-647

doi:10.4028/www.scientific.net/AMR.960-961.643

Experimental investigation on flow characteristic of stepped capillary tube for heat pump type air conditioner with R410A

Yansheng Xu[1,a]

[1]Guangdong University Heat Pump Engineering Technology Development Center, Shunde Polytechnic, Foshan Guangdong 528333, China

[a]jdxuys@163.com

Keywords: stepped capillary tube, heat pump type air conditioner, flow characteristic, R410A

Abstract. A stepped capillary tube consisting of two serially connected capillary tubes with different diameters is invented to replace the conventional expansion device. The mass flow rate of refrigerant R410A in stepped capillary tubes with different size were tested. The model of stepped capillary tube is proposed, and its numerical algorithm for tube length and mass flow rate is developed. The experimental results show that the performance comparing between stepped capillary tube system and capillary tube assembly system, the cooling capacity is reduced by 0.3%, the energy efficiency ratio(EER) is equal to each other, the heating capacity is increased by 0.3%, the coefficient of performance(COP) is decreased by 0.3%. That is to say, the performance index of the two kinds of throttle mechanism is almost identical. It indicates that the stepped capillary tube can replace the capillary tube assembly in the R410A heat pump type air conditioner absolutely. The model is validated with experimental data, and the results show that the model can be used for sizing and rating stepped capillary tube.

Introduction

The mass flow rate of refrigerant in heat pump type air conditioner is different under heatingand cooling mode. The mass flow rate of cooling mode is more than that of heating mode. In order to realize it, the capillary tube assembly is used in the heat pump type air conditioner. Fig.1 shows the the schematic diagram of the Capillary tube assembly. The length of capillary tubes are different under heating and cooling mode（for cooling mode, the refrigerant only goes through auxiliary capillary tube along the flow the path of A—B—E, for heating mode, the refrigerant goes through two capillary tubes sequentially along the flow the path of E—D—C—B—A）. The cost of capillary tube assembly is increased about $1 for adding the check valve. According to the performance of gas-liquid two phase flow in the capillary tube, Xu[1] invents a stepped capillary tube(as shown in Fig.2). It is composedof two tubes with different diameter, and it can replace the capillary tube assembly so as to reduce the expense as well as simplify the structure.

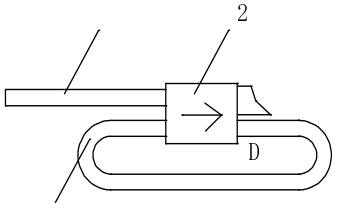

1-main capillary tube, 2-check valve, 3-auxiliary capillary tube

Fig.1 Capillary tube assembly

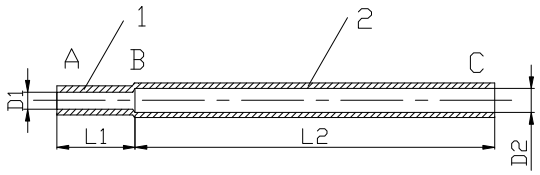

1-auxiliary capillary tube, 2-main capillary tube

Fig.2 Stepped capillary tube

Xu[1] performed the experiments of the stepped capillary tube replaced the capillary tube assembly in a heat pump type air conditioner (KFR-32GW) with R22. The ideal results were obtained, but the refrigerant R22 will be eliminated step by step due to the environmental problems. The refrigerant R410A as one of the most important substitute refrigerant will be applied to air conditioner widely[2]. Hence, the investigation on flow characteristic of stepped capillary tube for heat pump type air conditioner with R410A has an important significance.

Experimental program and equipment

Experimental program. The critical problem for stepped capillary tube replaces the capillary tube assembly is the matching problem of the stepped capillary tube in air conditioner. That is to say, how to design the pipe diameter and length of the capillary tube. At present, the theoretical and experiential models are used widely only for the structure size calculation of a constant diameter capillary tube[3-5]. The stepped capillary tube must meet the need of flow under heating and cooling mode. Two pipes diameter and length must be designed. On the one hand, the existing experiential models are not suitable for stepped capillary tube. On the other hand, the theoretical models have a low accuracy and a complicated calculation[6-8]. Hence, they are not suitable for the engineering application. In order to reduce the matching workload for stepped capillary tube used in R410A air conditioner, the experimental programs were set up as following.

(1)The performance index (refrigerating capacity, heating capacity, EER and COP) and operation condition(condensing pressure, degree of supercooling, evaporating pressure, degree of superheat) of the R410A heat pump type air conditioner used the capillary tube assembly were tested in the standard environmental condition.

(2)The flow of R410A refrigerant under heating and cooling modes were tested with the capillary tube assembly on a test bench for measuring mass flow characteristics of the throttle mechanism.

(3)A few of stepped capillary tubes with different structures dimension were made. The flow of R410A refrigerant under heating and cooling modes were tested with those stepped capillary tubes on the same test bench. The experiential models were then set up.

(4) According to the experiential models, the initial configuration size of the stepped capillary tube was calculated. In the end, the configuration size of the stepped capillary tube was determined after the matching test on the air conditioner.

Experimental rig. The flow of refrigerant in the stepped capillary tube was tested on the experimental rig for measuring mass flow characteristics of the throttle mechanism. Fig.3 is the schematic of the experimental rig. This rig contained a compressor, an oil separator, a water-cooling condenser, an evaporator, a subcooler and a test section.

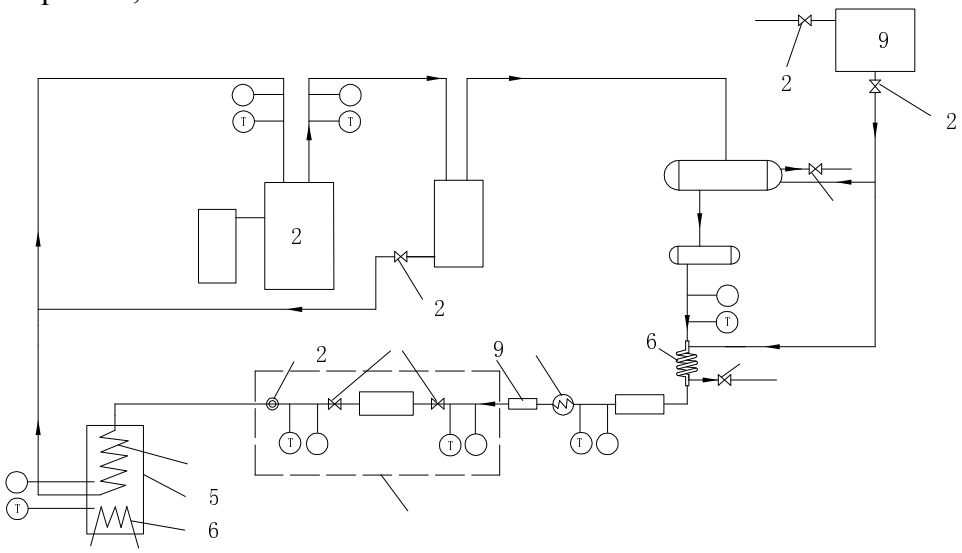

1.converter 2.compressor 3.oil separator 4.condenser 5.reservoir 6.subcooler 7. mass flow meter; 8.heater 9. dryer 10.stepped capillary tube 11.ball valve 12. sight glass 13.test section 14.evaporator 15. pressure vessel 16.electric heater; 17.control valve for condoner water flow 18. control valve for subcooler water flow 19.condensate water tank 20.float valve 21. ball valve

Fig. 3 Test rig for mass flow rate in step capillary tube

The condensing pressure was controlled by adjusting flow rate of water in the condenser, the evaporating pressure was controlled by adjusting the frequency of compressor, and the subcooling temperature was controlled by adjusting the water flow rate in the subcooler. The mass flow rate was measured by a Coriolis type mass flow meter with the uncertainty of ±0.2%. The inlet and outlet pressures of the test stepped capillary tube were measured by pressure sensors with the

uncertainty of ±0.2%, and the inlet and outlet temperatures were measured by T-type thermal couples with uncertainty of ±0.2 °C.

Flow experiment and modeling

Air conditioner performance test of capillary tube assembly. A heat pump type air conditioner with R410A(KFR-32GW) was chosen as the testing object. The inner diameter and length of the main capillary tube and auxiliary capillary tube are 1.6mm, 1350mm and 1.6mm, 400mm, respectively. Table.1 shows the air conditioner performance index and operation condition of the capillary tube assembly.

Table.1 Performance index and operation condition of the capillary tube assembly

Working mode	Environmental conditions		capacity W	COP	condensing temperature ˚C	supercooling temperature ˚C	evaporating temperature ˚C	Mass flow rate kg/h
	dry bulb/wet-bulb temperature indoor ˚C	dry bulb/wet-bulb temperature outdoor ˚C						
cooling	27/19	35/24	3250	3.26	46	41	7	70.8
heating	20/15	7/6	3630	3.40	47	43	4	63.1

Throttling characteristic model of stepped capillary tube

Foundation model. The flow resistance of the stepped capillary tube as shown in Fig.2 is composed of three portions. It includes the on-way resistance of the auxiliary capillary tube(ΔP_1), the main capillary tube(ΔP_2) and local resistance of the mutations place(ΔP_ξ). The local resistance is very small, so it can be ignored. When the pressure difference of import and export of the stepped capillary tube is a definite value, the dimensionless linear relationship between the mass flow rate and the structure size can be set up according to the impedance calculation under heating and cooling mode.

$$\begin{cases} a_1+b_1\left(\frac{L_1}{{D_1}^5}\right)+c_1\left(\frac{L_2}{{D_2}^5}\right)=\frac{1}{{G_C}^2} \\ a_2+b_2\left(\frac{L_1}{{D_1}^5}\right)+c_1\left(\frac{L_2}{{D_2}^5}\right)=\frac{1}{{G_H}^2} \end{cases} \quad 1)$$

Where a_1, a_2, b_1, b_2, c_1, c_2 is the non-dimensional coefficient. L_1, D_1 is the length and inside diameter of the auxiliary capillary tube, respectively, mm. L_2, D_2 is the length and inside diameter of the main capillary tube, respectively, mm. G_C, G_H is the mass flow rate under cooling and heating mode, respectively, kg/h.

Mass flow testing of stepped capillary tube. The orthogonal experiment scheme was adopted in this experiment. We made 16 stepped capillary tubes(D_1=1.2, 1.3, 1.4, 1.5mm，D_2=1.6, 1.7, 1.8, 1.9 mm，L_1=100, 200, 300, 400mm, L_2=300, 400, 500, 600mm). The mass flow of stepped capillary tubes were tested on the experimental rig for measuring mass flow characteristics of the throttle mechanism. The 16 mass flow values of cooling and heating were linear regressed. The experience calculation model for the physical dimension of stepped capillary tube is shown in Eq. (2).

$$\begin{cases} 62.5+0.953\left(\frac{L_1}{{D_1}^5}\right)+0.883\left(\frac{L_2}{{D_2}^5}\right)=\frac{10^6}{{G_C}^2} \\ 97.8+1.14\left(\frac{L_1}{{D_1}^5}\right)+0.59\left(\frac{L_2}{{D_2}^5}\right)=\frac{10^6}{{G_H}^2} \end{cases} \quad (2)$$

Model analysis. according to the Eq. (2), the cooling mass flow G_C and flow ratio G_C/G_H were calculated under different $\frac{L_1}{D_1^5}$ and $\frac{L_2}{D_2^5}$. The results were shown in Fig.4. It can be seen from Fig.4, the cooling mass flow G_C decreases with increasing $\frac{L_1}{D_1^5}$ and $\frac{L_2}{D_2^5}$, and the trend of decrease slow down. The influence of $\frac{L_1}{D_1^5}$ is greater than that of $\frac{L_2}{D_2^5}$. The flow ratio G_C/G_H decreases with increasing $\frac{L_2}{D_2^5}$ (when the $\frac{L_2}{D_2^5}$ is not more than 50), and the trend of decrease also slow down. But when the $\frac{L_2}{D_2^5}$ is more than 50, The flow ratio G_C/G_H increases with increasing $\frac{L_2}{D_2^5}$.

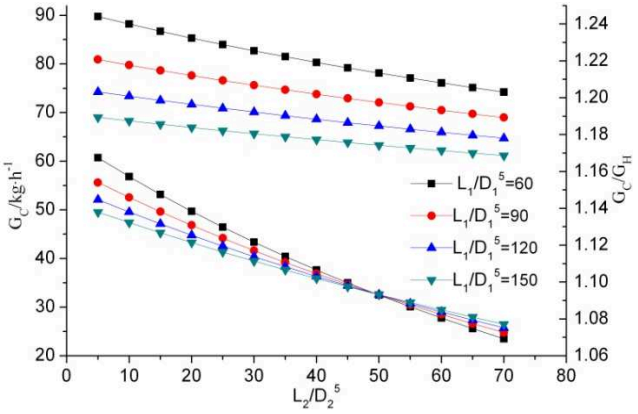

Fig.4 The calculated value of cooling mass flow and flow ratio

Case study on heat pump type air conditioner with stepped capillary tube

To study the effectiveness of stepped capillary tube in heat pump type air conditioner, the capillary tube assembly in a heat pump type air conditioner was replaced by a sized stepped capillary tube; and the air conditioner performances before and after replacement were experimentally tested. The mass flow of cooling and heating is G_C=70.8 kg/h and G_H=63.1 kg/h, respectively. In accordance with Eq. (2), $\frac{L_1}{D_1^5}$ is 123 and $\frac{L_2}{D_2^5}$ is 21.8. The length of capillarity tube is about in the range 500~1500mm, which in order to meet the need of working condition. Hence, the diameter of the auxiliary capillary tube and the main capillary tube is designed as 1.4mm and 1.8mm, respectively. The length of the auxiliary capillary tube and the main capillary tube is calculated as 661mm and 412mm, respectively. Based on these data, the further accurate match for stepped capillary tube can be carried out. In the case of D_1 and D_2 is a constant, the length of the auxiliary capillary tube (L_1)was chosen as 630, 660, 690mm, the length of the main capillary tube(L_2) was chosen as 380, 410, 440mm. All the 9 stepped capillary tubes with different size were tested in the air conditioner. The performance indicators of cooling and heating mode are shown in Fig.5 and Fig.6, respectively.

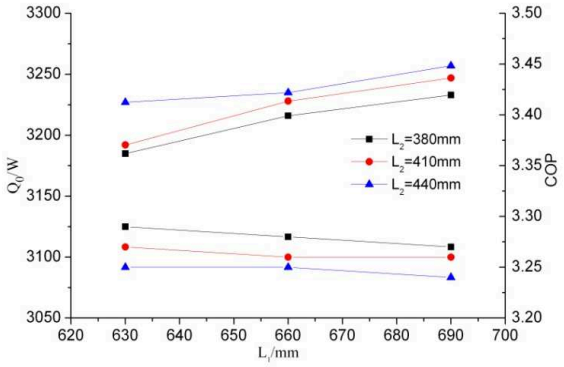

Fig.5 The performance indicators of cooling mode with different size stepped capillary tube

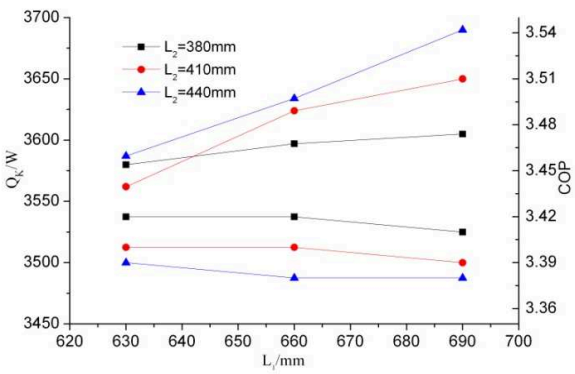

Fig.6 The performance indicators of heating mode with different size stepped capillary tube

The total cooling capacity change of the 9 stepped capillary tubes is 2.3%, and the change of EER is 1.5%. The total heating capacity change is 3.1%, and the change of COP is 1.7%. the experimental results show that the change of the capillary tube length has a less influence on the air conditioner performance. The structure size of the stepped capillary tube was confirmed after the testing, the diameter of the auxiliary capillary tube and the main capillary tube is 1.4mm and 1.8mm, respectively. The length of the auxiliary capillary tube and the main capillary tube is 690mm and 410mm, respectively. Table.2 shows the performance comparing between stepped capillary tube system and capillary tube assembly system.

As can be seen from Table.2, the performance comparing between stepped capillary tube system and capillary tube assembly system, the cooling capacity is reduced by 0.3%, the EER is equal to each other, the heating capacity is increased by 0.3%, the COP is decreased by 0.3%. As mentioned above, the performance index of the two kinds of throttle mechanism is almost identical.

Table.2 Performance comparing between stepped capillary tube system and capillary tube assembly system

Mode	Performance	Air conditioner with stepped capillary tube (NEW)	Air conditioner with capillary tube assembly (ORG)	Performance deviation (NEW-ORG)/ORG
Heating	Capacity W	3650	3630	0.5%
	COP	3.39	3.40	-0.3%
Cooling	Capacity W	3240	3250	-0.3%
	EER	3.26	3.26	0%

Conclusion

(1)The model of stepped capillary tube is proposed, and its numerical algorithm for tube length and mass flow rate is developed. The model is validated with experimental data, and the results show that the model can be used for sizing and rating stepped capillary tube.
(2)The change of the stepped capillary tube length has a less influence on the air conditioner performance.
(3) The performance index of stepped capillary tube system and capillary tube assembly system are almost identical, hence, the stepped capillary tube can replace the capillary tube assembly in the R410A heat pump type air conditioner absolutely.

Acknowledgments

This work was supported by Natural Science Fundation of Guangdong province (No.S2012010010199), the science and technology planning project of Shunde district (No.20120202087)and the science and technology planning project of Ronggui town of Shunde district (No.RGKJJH2013008)

Reference

[1]Yansheng Xu, Qinbo He, Mianchang Li, et al.: Fluid Machinery.,Vol.41(2013),p.62[In Chinese]
[2] Payne, W. V., O'Neal, D. L: ASHARE Transactions: Research. Vol.105(1999),p.66
[3] Khan M:Appl Therm Eng.Vol.29(2009),p.1426
[4] Bittle R R,Wolf D A,Pate M B.: HVAC&R Res.Vol.4(1998),p.27
[5] Choi J, Kim Y, Kim H Y. : International journal of refrigeration.Vol.26(2003),p.881
[6] Melo C, Ferreira R, Neto C B, et al.:Applied Thermal Engineering.Vol.19(1999),p.669
[7] Mitta M, Kumar R, Gupta A.: International journal of refrigeration.Vol. 33(2010),p.840
[8] C J L Hermes, C Melo, F T Knabben: Applied Thermal Engineering.Vol.30 (2010),p.449

Advanced Materials Research Vols. 960-961 (2014) pp 648-653

doi:10.4028/www.scientific.net/AMR.960-961.648

Model investigation on coupled throttling flow characteristic of stepped capillary tube with R22

Yansheng Xu[1,a]

[1]Guangdong University Heat Pump Engineering Technology Development Center, Shunde Polytechnic, Foshan Guangdong 528333, China

[a]jdxuys@163.com

Keywords: R22, stepped capillary tube, throttle,model

Abstract. In order to calculate the structure size of stepped capillary tube, the experiments of flow characteristic of it were performed. The experience benchmark model of flow characteristics of R22 was set up through experimental method in specific reference conditions based on the impedance calculation method. The variable working condition model suitable for a range of conditions was obtained through fixing the condition based on the reference model. The mass flow rate of refrigerant R22 in two stepped capillary tubes with different size was tested. The experimental results show that the stepped capillary tube model has a high precision and working condition of certain flexibility. The deviation of cooling and heating flow between the calculated values and measured values are less than±10%. The model can meet the need of matching for stepped capillary tube on the heat pump type air conditioner with R22.

Introduction

The mass flow rate of refrigerant in heat pump type air conditioner is different under heating and cooling mode. The mass flow rate of cooling mode is more than that of heating mode. In order to realize it, the capillary tube assembly is used in the heat pump type air conditioner. Fig.1 shows the schematic diagram of the Capillary tube assembly. The length of capillary tubes are different under heating and cooling mode（for cooling mode, the refrigerant only goes through auxiliary capillary tube along the flow the path of A—B—E, for heating mode, the refrigerant goes through two capillary tubes sequentially along the flow the path of E—D—C—B—A）[1]. The cost of capillary tube assembly is increased about $1 for adding the check valve. According to the performance of gas-liquid two phase flow in the capillary tube, Xu[2] invents a stepped capillary tube(as shown in Fig.2). It is composed of two tubes with different diameter, and it can replace the capillary tube assembly so as to reduce the expense as well as simplify the structure.

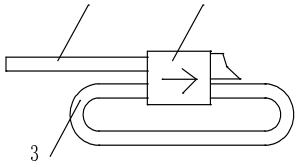

1-main capillary tube, 2-check valve, 3-auxiliary capillary tube

Fig.1 Capillary tube assembly

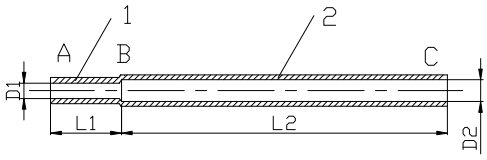

1-auxiliary capillary tube, 2-main capillary tube

Fig.2 Stepped capillary tube

Xu[2] performed the experiments of the stepped capillary tube replaced the capillary tube assembly in a heat pump type air conditioner (KFR-32GW) with R22. The ideal results were obtained. The stepped capillary tube must meet the need of flow under heating (the flow direction of refrigerant is C—B—A) and cooling mode (the flow direction of refrigerant is A—B—C) in refrigeration system matching. Two pipes diameter and length must be designed. The workload of experiment will be very large if the structure sizes are confirmed only through the air conditioner matching test. Hence, in order to reduce the matching workload, the model for calculating the structure sizes of the stepped capillary tube should be set up.

Modeling and solving

The flow region of refrigerant in capillarity tube can be divided into supercooled liquid region, metastable liquid area, metastable gas-liquid two phase zone and thermal equilibrium state of gas liquid two phase zone. The throttling theoretical model is very complex. At present, the models for calculating the capillary are all based on the one-way flow and a single diameter. Their calculation error is general within ±10％[3-5]. Few researchers study the flow characteristic of stepped capillary tube. The theoretical and empirical models of stepped capillary tube are not appearing. If the theoretical model of stepped capillary tube was set up based on the model of capillarity tube, its difficulty will be larger, and calculation accuracy is limited[6-8]. Hence, we try to establish a semi-empirical model through experimental method, which can be suitable for specific refrigerant, a range of operating conditions and refrigerant mass flow rate. The aim is to solve the application problem of stepped capillary tube in practical engineering.

Reference model. The flow resistance of the stepped capillary tube as shown in Fig.2 is composed of three portions. It includes the on-way resistance of the auxiliary capillary tube (ΔP_1), the main capillary tube (ΔP_2) and local resistance of the mutations place (ΔP_ξ). The local resistance is very small, so it can be ignored. When the pressure difference of import and export of the stepped capillary tube is a definite value, the dimensionless linear relationship between the mass flow rate and the structure size can be set up according to the impedance calculation under heating and cooling mode. It is expressed in Eq. (1).

$$\begin{cases} a_1 + b_1\left(\frac{L_1}{D_1^5}\right) + c_1\left(\frac{L_2}{D_2^5}\right) = \frac{1}{Q_C^2} \\ a_2 + b_2\left(\frac{L_1}{D_1^5}\right) + c_1\left(\frac{L_2}{D_2^5}\right) = \frac{1}{Q_H^2} \end{cases} \quad (1)$$

Where a_1, a_2, b_1, b_2, c_1, c_2 is the non-dimensional coefficient. L_1, D_1 is the length and inside diameter of the auxiliary capillary tube, respectively, mm. L_2, D_2 is the length and inside diameter of the main capillary tube, respectively, mm. G_C, G_H is the mass flow rate under cooling and heating mode, respectively, kg/h.

Non-dimensional coefficient

Experimental parameter. The Eq. (1) is the mathematical model that the working conditions of stepped capillary tube and refrigerant type is given. The relevant data of cooling and heating flow with different structure size of stepped capillary tube can be obtained by experimental method. Then the specific value of dimensionless coefficient can be gained through linear regression. Under the standard working condition of refrigeration and heating of heat pump type air conditioner (KFR-32GW), the parameters of inlet and outlet of the capillary tube assembly were chosen as the working condition parameter of stepped capillary tube. Table.1 shows the benchmark condition parameters of stepped capillary tube. The cooling capacity of heat pump type air conditioner (R22 is as the refrigerant) is from 2000W to 5000W, and the corresponding mass flow rate of cooling and heating is from 40 kg/h to 100 kg/h. So the structure size of the stepped capillary tube is decided as follows: D_1=1.1, 1.2, 1.3, 1.4,1.5,1.6 mm, D_2=1.6, 1.7, 1.8,1.9, 2.0,2.2 mm, L_1 =50～1000 mm, L_2=300～1000 mm.

Table.1 Benchmark condition parameters of stepped capillary tube

Mode	P_{CO} kPa	T_{CO} ˚C	P_{EO} kPa	T_{EO} ˚C	T_{SCO} ˚C
Cooling	1770	46	622	7	5
Heating	1810	47	566	4	5

Where P_{CO}, P_{EO}, T_{CO}, T_{EO}, ΔT_{SCO} is the condensing pressure, kPa, evaporating pressure, kPa, condensing temperature,˚C, evaporating temperature and supercooling degree, ˚C, under benchmark conditions, respectively.

Experimental rig. The flow of refrigerant in the stepped capillary tube was tested on the experimental rig for measuring mass flow characteristics of the throttle mechanism. Fig.3 is the schematic of the experimental rig. This rig contained a compressor, an oil separator, a water-cooling condenser, an evaporator, a subcooler and a test section. The condensing pressure was controlled by adjusting flow rate of water in the condenser, the evaporating pressure was controlled by adjusting the frequency of compressor, and the subcooling temperature was controlled by adjusting the water flow rate in the subcooler. The mass flow rate was measured by a Coriolis type mass flow meter with the uncertainty of ±0.2%. The inlet and outlet pressures of the test stepped capillary tube were measured by pressure sensors with the uncertainty of ±0.2%, and the inlet and outlet temperatures were measured by T-type thermal couples with uncertainty of ±0.2 ºC.

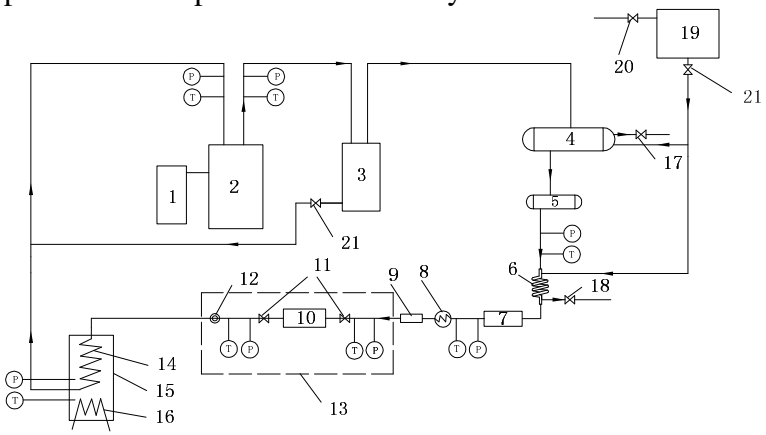

1.converter 2.compressor 3.oil separator 4.condenser 5.reservoir 6.subcooler 7. mass flow meter; 8.heater 9. dryer 10.stepped capillary tube 11.ball valve 12. sight glass 13.test section 14.evaporator 15. pressure vessel 16.electric heater; 17.control valve for condoner water flow 18. control valve for subcooler water flow 19.condensate water tank 20.float valve 21. ball valve

Fig. 3 Test rig for mass flow rate in step capillary tube

Linear regression. The orthogonal experiment scheme(four factors, four level) was adopted in this experiment. We made 16 stepped capillary tubes. The mass flow of stepped capillary tubes was tested on the experimental rig for measuring mass flow characteristics of the throttle mechanism. The 16 mass flow values of cooling and heating were linear regressed. The experience calculation model for the physical dimension of stepped capillary tube is shown in Eq. (2).

$$\begin{cases} 115+1.77\left(\frac{L_1}{D_1^5}\right)+1.08\left(\frac{L_2}{D_2^5}\right)=\frac{10^6}{Q_C^2} \\ 187+1.54\left(\frac{L_1}{D_1^5}\right)+0.849\left(\frac{L_2}{D_2^5}\right)=\frac{10^6}{Q_H^2} \end{cases} \quad (2)$$

Variable working condition model. Throttling flow characteristic semi-empirical model of stepped capillary tube was set up by correction method of working condition. The variable working condition model is shown in Eq. (3).

$$\begin{cases} k_1\left[115+1.77\left(\frac{L_1}{D_1^5}\right)+1.08\left(\frac{L_2}{D_2^5}\right)\right]=\frac{10^6}{Q_c^2} \\ k_2\left[187+1.54\left(\frac{L_1}{D_1^5}\right)+0.849\left(\frac{L_2}{D_2^5}\right)\right]=\frac{10^6}{Q_H^2} \end{cases} \quad (3)$$

Where k_1, k_2 is the correction factor of cooling and heating mode, respectively. The change of condensing pressure, evaporating pressure and supercooling degree has a different sensitive degree of influence on the flow characteristic of the stepped capillary tube. Hence, the ratio of condensing pressure, evaporating pressure and degree of supercooling were introduced as the influence factor. Eq.(4)shows the correction factor of the working conditions.

$$k = m\left(\frac{P_C}{P_{CO}}\right)^r \cdot \left(\frac{P_E}{P_{EO}}\right)^s \cdot \left(\frac{\Delta T_{SC}}{\Delta T_{SCO}}\right)^t \quad (4)$$

Where m is the comprehensive effect coefficient of working condition. r, s, t is the influence factor of condensing pressure ratio, evaporating pressure ratio and supercooling degree ratio, respectively. P_C, P_E, ΔT_{SC} is the condensing pressure, kPa ,evaporating pressure, kPa, and supercooling degree, ˚C. The range of condensing pressure and supercooling degree of heat pump type air conditioner under cooling and heating mode with R22 is from 1600 kPa to 2200 kPa and from 3˚C to 9˚C, respectively. The corresponding condensing temperature is from 41.6˚C to 51.3˚C. The range of evaporating pressure is from 550 kPa to700 kPa and from 500 kPa to 650 kPa under cooling and heating mode, respectively. The corresponding condensing temperature is from 41.6˚C to 51.3˚C and from 0˚C～8.5˚C, respectively. The orthogonal experiment scheme was designed with the P_C, P_E, ΔT_{SC} as the influence factors. It can be seen from Table.2.

The stepped capillary tube (D_1=1.4mm，L_1=300mm，D_2=1.9mm，L_2=400mm) was chosen for testing. The cooling and heating capacity is 68.4 kg/h and 59.1 kg/h under the benchmark condition, respectively. 16 groups of cooling and heating mass flow data were obtained under 16 different cooling and heating conditions. The parameter of m, r, s, t is 0.983, -1.11, -0.0672, -0.284 under cooling mode, respectively, and 0.933, -1.12, -0.0319, -0.272, under heating mode, respectively, after the data regression processing. Thereby, the correction coefficient of working condition of cooling (k_1) and heating (k_2) flow is shown in Eq. (5) and Eq. (6).

$$k_1 = 0.983\left(\frac{P_C}{1770}\right)^{-1.11} \cdot \left(\frac{P_E}{622}\right)^{-0.0672} \cdot \left(\frac{\Delta T_{SC}}{5}\right)^{-0.284} \quad (5)$$

$$k_2 = 0.933\left(\frac{P_C}{1810}\right)^{-1.12} \cdot \left(\frac{P_E}{566}\right)^{-0.0319} \cdot \left(\frac{\Delta T_{SC}}{5}\right)^{-0.272} \quad (6)$$

As can be seen from Eq. (5) and Eq. (6), condensing pressure has a major effect on the mass flow rate, while evaporating pressure and supercooling degree has a little effect on it. But the change of the supercooling degree in air-conditioner is large, which make the supercooling degree has a obvious effect on the flow. This is accordance with literature [2]and [6].

Table.2 Testing program of cooling and heating mode

No	P_C kPa	P_E(Cooling) kPa	P_E(Heating) kPa	ΔT_{SC} ˚C
1	1600	550	500	3
2	1600	600	550	5
3	1600	650	600	7
4	1600	700	650	9
5	1800	550	500	5
6	1800	600	550	3
7	1800	650	600	9
8	1800	700	650	7
9	2000	550	500	7
10	2000	600	550	9
11	2000	650	600	3
12	2000	700	650	5
13	2200	550	500	9
14	2200	600	550	7
15	2200	650	600	5
16	2200	700	650	3

Solution of the variable working condition model. The model has no fixed results because there are four unknown numbers (D_1, D_2, L_1, L_2) in Eq. (3). It is suppose that the inner diameter of auxiliary capillary tube and main capillary tube are constant (D_1 is designed as 1.1,1.2,1.3,1.4,1.5,1.6 mm; D_2 is designed as1.6,1.7,1.8,1.9,2.0,2.2mm), then the length of tube can be acquired. If L_1 and L_2 are between 0 and 1000, so the value of D_1, D_2, L_1, L_2 are the needed results. If L_1 and L_2 is beyond the scope, then the value of D_1 and D_2 must be supposed again and recalculate until $L_1$and L_2 is in the scope of the above. If D_1, D_2, L_1, L_2 has no result in the range, which indicates that the stepped capillary tube can not be used on this heat pump type air conditioner.

Model verification

Flow verification of stepped capillary tube. Two kinds of stepped capillary tube were tested in the experiment. The diameter and length of the stepped capillary tube (D_1=1.5 mm, L_1=200 mm, D_2=2 mm, L_2=700 mm) is for "A" group. The parameter of "B" group is D_1=1.4 mm, L_1=500 mm, D_2=1.8 mm, L_2=500 mm. The testing program is in accordance with Table.2. The measured value and calculated value of cooling and heating flow for "A" type stepped capillary tube is shown in Fig.4a and Fig.4b. Fig.5a and Fig.5b show the results of "B" type stepped capillary tube. In the drawing, Q_c is the calculated value of flow, Q_t is the measured value of flow.

As can be seen from Fig.4 and Fig.5, the deviation of the measured value and calculated value for the two type stepped capillary tube is less than $\pm 10\%$, it indicates that the variable condition experience model has a high precision.

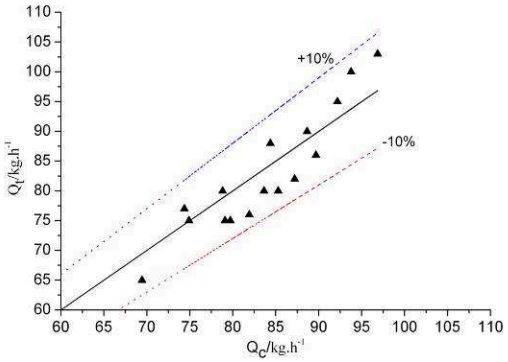

Fig.4a The measured value and calculated value of cooling flow for type "A"

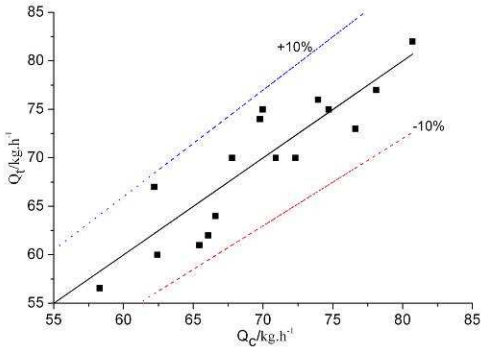

Fig.4b The measured value and calculated value of heating flow for type "A"

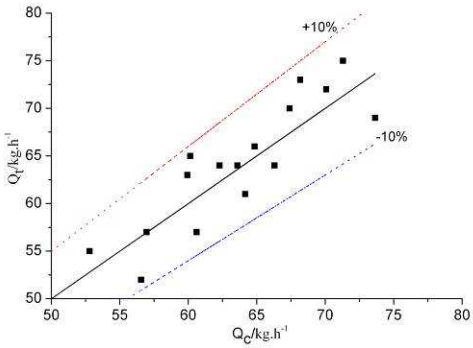

Fig.5a The measured value and calculated value of cooling flow for type "B"

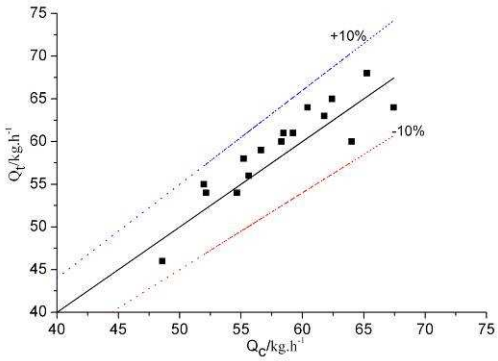

Fig.5b The measured value and calculated value of heating flow for type "B"

Conclusion

(1) The experience benchmark model of flow characteristics of R22 was set up through experimental method and based on the impedance calculation method. It has a high precision and working condition of certain flexibility. The deviation between the calculated values and measured values is less than±10%. The model can meet the need of matching for stepped capillary tube on the heat pump type air conditioner with R22.

(2) The condensing pressure has a major effect on the mass flow rate. The evaporating pressure and supercooling degree have a little effect on the mass flow rate. But the change of supercooling degree is larger in the design of air conditioner, which make the supercooling degree has a obvious effect on the mass flow rate.

Acknowledgments

This work was supported by Natural Science Fundation of Guangdong province (No.S2012010010199), the science and technology planning project of Shunde district (No.20120202087) and the science and technology planning project of Ronggui town of Shunde district (No.RGKJJH2013008)

Reference

[1]C.L. Zhang, G.L.Ding: Journal of Shanghai Jiaotong University.Vol.35(2001),p.1178[In Chinese]

[2] Y.S. Xu, Q.B.He, M.C. Li, et al.: Fluid Machinery.,Vol.41(2013),p.62[In Chinese]

[3] Khan M:Appl Therm Eng.Vol.29(2009),p.1426

[4] Bittle R R,Wolf D A,Pate M B.: HVAC&R Res.Vol.4(1998),p.27

[5] Choi J, Kim Y, Kim H Y. : International journal of refrigeration.Vol.26(2003),p.881

[6] Melo C, Ferreira R, Neto C B, et al.:Applied Thermal Engineering.Vol.19(1999),p.669

[7] Mitta M, Kumar R, Gupta A.: International journal of refrigeration.Vol. 33(2010),p.840

[8] C J L Hermes, C Melo, F T Knabben: Applied Thermal Engineering.Vol.30 (2010),p.449

Advanced Materials Research Vols. 960-961 (2014) pp 654-657

doi:10.4028/www.scientific.net/AMR.960-961.654

Gas Load Characteristics and Calculation

Lei Zhao

Jilin Jianzhu University, Changchun, Jilin, China

Zhao0438@126.com

Keywords: Gas Load, Curve of Load Characteristics, Non-uniform Coefficient Method, Load Coefficient Method.

Abstract. Gas Load Characteristics of different users are analyzed in this paper. Different types of load charts which is drawn according to the statistical data may provide certain guidance for gas companies. Non-uniform coefficient method that continues to be used for calculation of gas load in China has limitations. It is more reasonable to calculate gas load with load coefficient method.

Introduction

China is in an age when gas demand is growing rapidly; in addition to gas consumed by residents and business users for cooking and industrial production, gas is applied more and more frequently in heating, air conditioning, vehicles and other fields. In particular, users for gas heating have stronger seasonal characteristics and their load characteristics are obviously different from other users. Load characteristics have a relatively big influence on gas storage and peak shaving measures adopted by urban gas transmission and distribution system, therefore it is necessary to carry out in-depth researches on load characteristics and their calculation methods.

Gas Load Characteristics

Gas Load Characteristics. Gas load is determined by gas consumption and there are different methods for classification of users based on the classification of gas consumption. Some countries classify gas consumption into gas for domestic use in residential houses, gas for commercial use and gas for industrial use and each of them includes gas for heating. In China, gas users are categorized into residents, users of commercial and industrial enterprises (excluding heating), heating users, air conditioning users, vehicle users, etc.

Residents and business users require continuous supply, so rule of load change is almost identical between them. For them, gas consumption is non-uniform in different seasons, days and hours, in which non-uniform gas consumption in different hours is relatively obvious and its obviousness is related to type and number of users, type and capacity of gas appliances used by users, structure of buildings where users live and their lifestyles. Generally, the more the users, the more uniform gas consumption will be.

Gas consumption for industrial production is less non-uniform than that for residents and business users, and non-uniformity mainly depends on shift systems of industrial enterprises.

Gas consumption of large-scale gas-fired boilers shows smaller fluctuation when there is no big change in air temperature, while gas consumption for household heating shows bigger fluctuation in one day. Number of such users is relatively small in China, so there is no complete statistical data about this aspect yet. Household heating is very common in America, Europe and other western countries and their experiences indicate that heating load peak often occurs between 6:00 and 9:00 a.m. in cold seasons and there exist obvious peak and valley. Daily load of gas heating is mainly influenced by outdoor temperature and wind speed, which is not generally a constant. However, it can be predicted by statistical data of urban climate unless extreme weather emerges.

Curve of Load Characteristics. For curve of load characteristics, time (month, day or hour) serves as horizontal ordinate, indicating changes of load in one or various user groups within one period. Load charts can be categorized into yearly, weekly and daily load chart, which are the basis for

designing gas transmission and distribution system. Different types of load charts may provide certain guidance for gas companies in production scheduling.

Figure 1 is the yearly load chart of 2001 in Huangpi District of Wuhan City. This figure indicates that there are four types of users in this region and their gas consumption in different seasons is non-uniform, in which the variation between winter and summer are most obvious. Gas supply plan can be worked out based on this figure. If gas supply units cannot increase or decrease gas supply according to seasonal variation, gas storage facilities are required to maintain the balance between supply and demand.

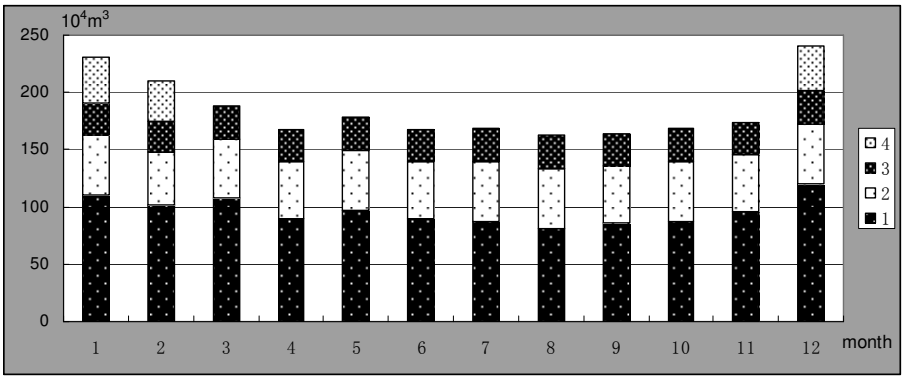

Figure 1 Yearly Load Chart of 2002 in Huangpi District of Wuhan City
1—Residents and business users 2—Industrial users
3—Vehicle users 4— Heating users

Figure 2 are respectively the hourly load chart in the week when gas consumption of residential users, business users and industrial users in Huangpi District of Wuhan City reaches the peak. This figure indicates that the largest gas consumption of residential users and business users doesn't occur in the same time period. Moreover, load characteristics in work days and holidays are also different because of lifestyles of residents.

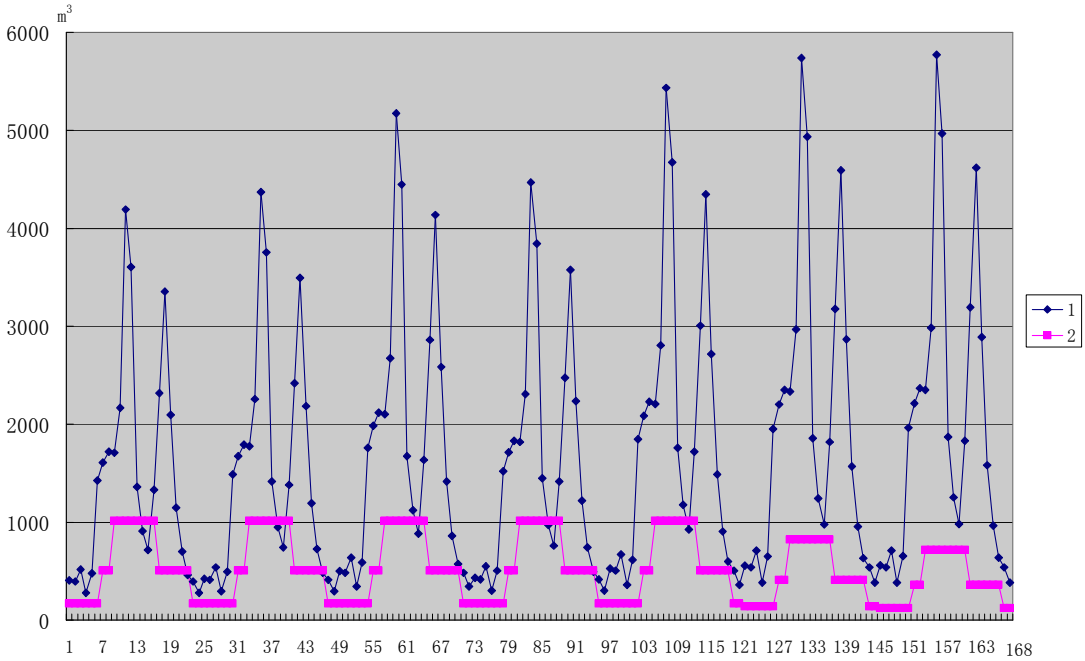

Figure 2 Daily Load Chart of users
1—Residents and business users 2—Industrial users

Heating is not taken into consideration in the above figures. When natural gas is applied in heating and such application reaches a certain scale, the maximum load of transmission and distribution system is often closely related to heating users. Therefore, it is very important to make a research on the load characteristics of gas heating and draw the load curve. There is a close relationship between

heating load and outdoor temperature. Figure3 is the daily load chart of heating users in a city in the US, in which different curves indicate different outdoor temperatures[1]. Although load increases along with decrease in outdoor temperature, the rule of load changes is basically identical.

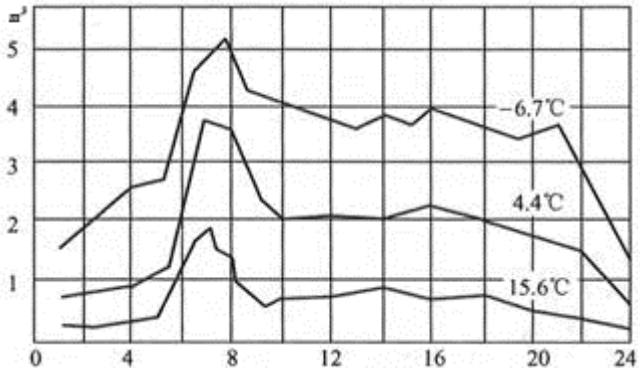

Figure3 Daily Load Chart of Heating users

Calculation of Gas Load

The method adopted by the former Soviet Union, namely non-uniform coefficient method, continues to be used for calculation of gas load in China, and changes in gas consumption of gas users are expressed with non-uniform coefficient. Firstly, yearly gas consumption of various types of users should be determined and then the peak hourly gas consumption can be calculated through three non-uniform coefficients, namely monthly, daily and hourly non-uniform coefficient. Herein, the month in which monthly non-uniform coefficient reaches the maximum is called month for calculation. Peak hour consumption is calculated as given blow[2].

$$Q_h = \frac{Q_y}{365\times 24} K_m^{\max} \bullet K_d^{\max} \bullet K_h^{\max} \tag{1}$$

Where, Q_h is hourly calculated flow (Nm^3/h), Q_y is yearly gas consumption (Nm^3/a), $K_m^{\max}$ is the maximum monthly non-uniform Coefficient, $K_d^{\max}$ is the maximum daily non-uniform Coefficient, $K_h^{\max}$ is the maximum hourly non-uniform Coefficient.

The premise for the formula being applicable is that the maximum daily peak coefficient occurs in the month for calculation, and the maximum hourly non-uniform coefficient and daily non-uniform coefficient occur in the same day, namely that month for calculation and peak day and peak hour coincide with each other. It is apparently that this assumption is unreliable.

In fact, gas companies in various regions draw yearly-daily load chart and yearly-hourly load chart based on statistical data in several years, in which the maximum daily gas consumption and maximum hourly gas consumption can be obtained. Many practices have proven that the concept of month for calculation is meaningless. For example, month for calculation of Changchun City in 2011 occurs in December, but the peak day occurs in January. Actually the maximum daily gas consumption in cities around China usually occurs on the New Year' Eve, so it is very important to ensure that sufficient gas can be supplied in this day. Therefore, data obtained through Formula (1) are inaccurate.

It is more reasonable to calculate gas load with load coefficient method. Load coefficient can be defined as the ratio of actual gas consumption in a certain period to the maximum short-term gas consumption in the same period.

Generally speaking, if load coefficient is based on Period a and Period b and Period b should be longer or cross Period a, then in the same climatic conditions, load coefficient can be expressed as

$$L_{a,b} = \frac{Q_{b,n}}{Q_{b,n}^{\max}} \tag{2}$$

If b stands for year and a stands for day, then daily load coefficient should be $L_{d,y}$, and herein $Q_{b,n}$ is annual average daily gas consumption and $Q_{b,n}^{\max}$ is the maximum of $Q_{b,n}$, namely the maximum daily gas consumption.If b stands for year and a stands for hour, then hourly load coefficient is $L_{h,y}$, $Q_{b,n}$ is annual average hourly gas consumption and $Q_{b,n}^{\max}$ is the maximum of $Q_{b,n}$, namely the maximum hourly gas consumption[3].

It can be known from definition of the two coefficients that non-uniform coefficient is always more than or equal to 1 and load coefficient is always less than 1. The larger the difference between 1 and these two coefficients, the more non-uniform the gas consumption will be.Table 1 can be filled out through an analysis on the statistical data of Changchun City in 2011 with the two methods.

Table 1 The statistical data of Changchun City in 2011

Type of Users	Residential Users	Business Users	Industrial Users	Vehicle Users
$K_m^{\max}$	1.65	1.65	1.0	1.1
$K_d^{\max}$	1.1	1.1	1.1	1.1
$K_d^{\max}$	2.2	2.2	1.5	1.5
$L_{h,y}$	0.35	0.40	0.89	0.50

It can be obtained through non-uniform coefficient method that peak hourly gas consumption is 145000m^3/h; it can be obtained through load coefficient method that peak hourly gas consumption is 126000 m^3/h; and the difference between them is 13%. It is obvious that the latter is more accurate. Therefore, adopting load coefficient method to calculate gas load can save project investment.

Conclusion

Heating users and non-heating users have different load characteristics and gas consumption peaks for them present different trends. Drawing curves of load characteristics for various types of users can better reflect characteristics of users and thus provide basic data for the optimization of urban gas transmission and distribution system. Climatic conditions, such as temperature and wind speed, have relatively big influence on heating user load.

Non-uniform coefficient method commonly used in China may lead to relatively big deviation, while load coefficient method doesn't require month for calculation to calculate peak hourly gas consumption. It is easier to obtain data for this method and its calculation results are accurate, so it is a method worth promotion.

References

[1] Gerald G.Wilson, Distribution Book D-1.System Design, The American Gas Assoeiation, Arlington Virginia 1990

[2] Changgui Duan, Gas Transmission and Distribution (Edition 4) (In Chinese), China Architecture and Building Press, Beijing 2011

[3] Youjia Li, Design of Gas Transmission and Distribution System and Practices(In Chinese), China Architecture and Building Press, Beijing 2007.

Advanced Materials Research Vols. 960-961 (2014) pp 658-661

doi:10.4028/www.scientific.net/AMR.960-961.658

Research on Central Air Conditioning Control System in Office Buildings Based on STC Microcontroller

Liming Wei[1, a], Chen Li[1, b]

[1]School of Electrical and Electronics Information Engineering, Jilin JianZhu University

Metro Street, Changchun City, Jilin Province, China 130118

[a]weiliming_1@sina.com, [b]1119672013@qq.com

Keywords: Central air-conditioning; STC11F08XE; PID optimization; Infrared control

Abstract: In this paper, hardware and software of the central air-conditioning control system is researched by STC series of enhanced 8051 microcontroller. The STC11F 08XE is the main control of the hardware part. Temperature and humidity sensor regulating valve and all kinds of motor are used as external equipment to complete the temperature and humidity of building the internal control of central air conditioner. In terms of software, the program is described by protel99SE software. Microcontroller program is compiled by Microcontroller development tools keil u and STC-ISP. The temperature and humidity control and optimization of central air conditioning are completed by PID parameters. Infrared control unit is operated and liquid crystal is displayed to show the operation results.

Introduction

Today's rapid development of intelligent building, central air conditioning is one of the main monitoring objects of building automation system. The reaction is slow, lagging more serious resulting in its annual power consumption accounts for about 50% -60% of the total electricity consumption of buildings [1-2]. Central air conditioning system is currently more widely, almost all large new buildings are equipped with central air-conditioning system, its development is more and more like energy, health, excessive. In this paper, According to the internal resources of traditional microcontroller less, performance and working slow defects, put to use the STC series enhanced 8051 microcontroller hardware design and software design of the central air conditioning.

The design of hardware of the central air-conditioning control system

Design principle. Central air conditioning indoor temperature and humidity make people get more comfortable office environment. When people adjust the indoor temperature and humidity through an infrared remote control for central air-conditioning inside the core of STC microcontroller instructions, STC microcontroller will mobilize the temperature sensor (18B20), humidity sensor (SHT11) to detect the new outlet, air inlet temperature and humidity. When the control valve receives the feedback signal detection, can automatically adjust the opening size. At this time, new entrants into the fresh air will be the same as the indoor return air mixing, forming a hybrid wind. When the wind pipe mixed air temperature is too high, the motor will drive the surface cooler for cooling treatment, hot and cold water will PID adjustment. In the precondition of ensuring the load demand, achieve the maximum energy saving central air conditioning. After A/D conversion, the humidity and temperature value is displayed on the LCD screen for people to confirm. The central air conditioning design principle is shown in Fig 1.

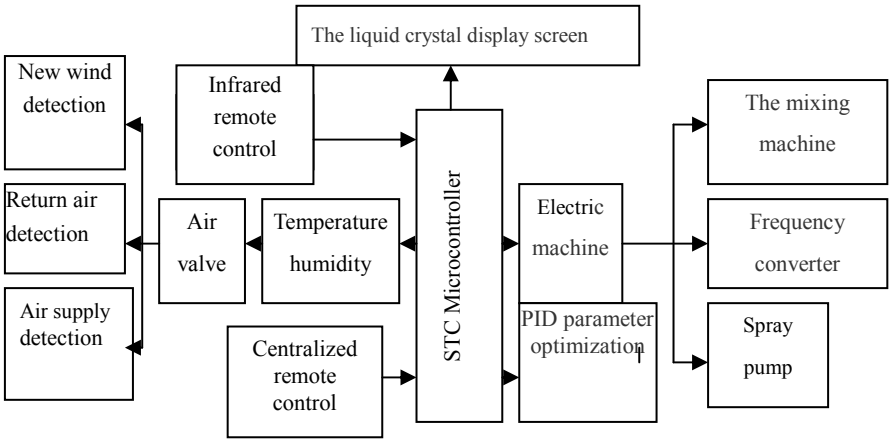

Fig 1. The design principle of central air conditioning

Hardware selection. The hardware selection of this text mainly includes micro controller, temperature and humidity sensor, regulating valve, frequency converter, air valve actuator and selection of related hardware. The list is shown in Table 1.

Table 1.The hardware list

sequence	type	hardware
1	micro controller	STC11F08XE
2	temperature sensor	DS18b20
3	humidity sensor	SHT11
4	regulating valve	Danfoss
5	frequency converter	MICROMASTER430
6	air valve actuator	GBB161.2E

The microcontroller used in this design is STC11F08XE. Resources on chip, performance and work speed have a great improvement compared with the traditional 8051 microcontroller core. Especially a Flash-based online system programming ISP technology is used. While the choice of on-chip resources is automatically follow the "good enough" principle to ensure the performance and reliability of the STC microcontroller system. STC11F08XE microcontroller incorporates enhanced 8051 CPU, 8KB Flash program memory, 1280 bytes of RAM, full-duplex asynchronous serial interfaces UART and MAX810 circuit and a dedicated hardware watch dog. Temperature sensor DS18b20 is all digital conversion and output temperature sensor. Having a single bus data communication of advanced, the highest resolution can reach 12. MICROMASTER430 inverter model has 6 programmable with potential isolation digital inputs, 2 analog inputs, 2 programmable analog output, 3 editable contact electrical output, has captured in the start-up and slip compensation function, senior PID built-in regulator.

The PID parameter optimization. PID control is widely used in the central air conditioning cold and hot water regulating control systems. When the central air conditioning temperature and humidity sensor built-in of the fresh air temperature and humidity, transformed into (4~20) mA current signal, through the STC11F08XE MCU A/D conversion unit, the analog signal into digital signal, and achieve PID control through software programming, thus mixing unit for temperature and humidity treatment to reach the people satisfied the requirements of fresh air is driven by single chip microcomputer. The traditional PID control principle is simple, strong robustness, adaptability. But the central air conditioning system is large, the control loop is more. The traditional PID algorithm parameters are difficult to meet requirements. This design adopts the ant colony algorithm to optimize the parameters of PID control. Ant colony algorithm is a heuristic algorithm for discrete

optimization problems. Its main part is the computer resource allocation to a group of relatively simple artificial ants, indirect communication between artificial ants through media.

Central air conditioning control system software design

The main part of the software design is to control the temperature and humidity of central air conditioner. The flow chart is shown in Fig 3 for motor control and analog digital conversion temperature and humidity detection software programming. Firstly, software design principle diagram mainly includes the main circuit part, USB download section, expanding pin part and power supply. Secondly, selection of the temperature and humidity control programming software Keil vision. They include temperature detection, humidity detection, PID regulation and each motor start stop. Finally, use ISP-STC burning software will be edited program recorded to calculate. The selected models in ISP-STC single chip microcomputer, click "open file" and in the dialog box to find the compiled program files to download, press the power switch to manual executable file write monolithic internal. The design of the software using C language and assembly language combining programming, the A/D conversion part of the program code is shown in Fig 2.

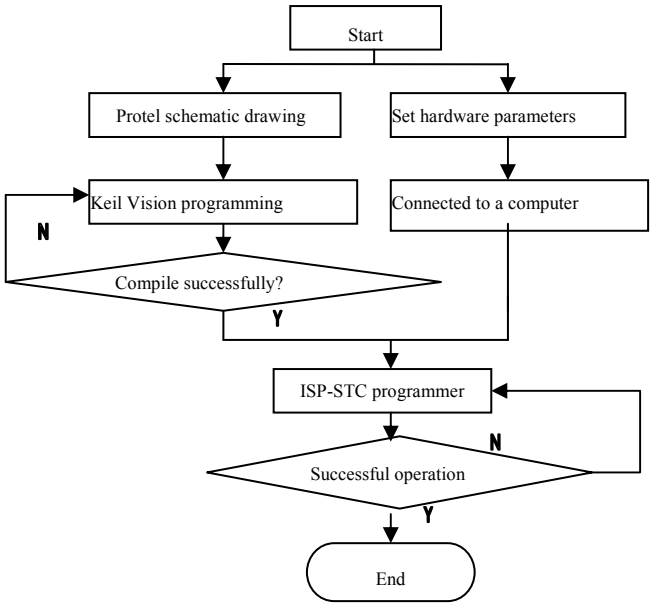

Fig 2. The software design flow chart of central air conditioning control system

Design and display of remote control

With the progress of society，more and more devices are equipped with remote control. The design of the infrared remote control to control the central air conditioning of STC11F08XE single-chip operation, it is the motor start and stop and the temperature and humidity detection. Of course, the infrared remote control to be equipped with an infrared emission tube, when the electric infrared receiving end to form on the radio state. The infrared remote control by the 555 circuit generates a pulse signal, produced by the oscillating circuit characteristic frequency pulse through the drive signal of infrared emission tube emits the same frequency, complete the infrared control. The design diagram is shown in Fig 3.

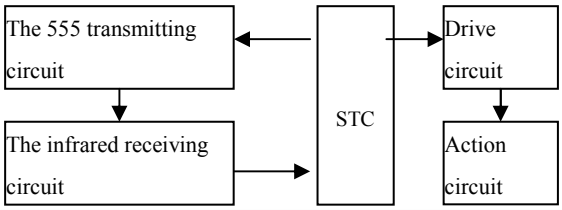

Fig 3. The design diagram of infrared remote control

Conclusions

The design is based on STC11F08XE single chip microcomputer as the control core. The design of hardware and software of central air conditioning are completed. The improved PID algorithm is adopted. The algorithm is combined with ant colony algorithm embedded traditional PID regulator. The control of hot and cold water of central air-conditioning temperature and humidity detection are completed. LCD screen display of central air-conditioning control results.

Acknowledgements

This work was financially supported by the Educational Research Project of Jilin Province Department of Education (2014. No. 224), and Changchun Science and Technology Project (122X56).

Reference

[1] An mei: Low Temperature and Special Gas.Vol.30(2013),p.12.
[2]Liang Qingjun: Science and Technology Innovation Herald. Vol.22(2013),p.120.
[3] Xing Lijuan: Electrical Application. Vol.39(2013),p. 98.
[4] Fan Xinglong: Power and Air Conditioning. Vol.33(2012),p.80.
[5] Deng Shoulu, Analysis of Central Air Conditioning System Energy. Vol.27(2013),p.224.

CHAPTER 6:

Electrical Theory and New Technology

Advanced Materials Research Vols. 960-961 (2014) pp 665-669

doi:10.4028/www.scientific.net/AMR.960-961.665

The Characteristic Analysis of Electromagnetic and AC Loss for A High Temperature Superconducting Adjustable Reactor with Considering the Structure of Superconducting Winding

Meng Song [1], Shifeng Shen[2,a], Nannan Hu [1], Kunnan Cao[1], Li Ren[2]

[1] Yunnan Electric Power Research Institute, Kunming City, Yunnan Province, P.R. China, 650217

[2]State Key Laboratory of Advanced Electromagnetic Engineering and Technology, Huazhong University of Science and Technology, Wuhan City, Hubei Province, P.R. China, 430074

[a]849588993@qq.com

Keywords: High-temperature superconductor (HTS), controllable reactor, structure, reactive power

Abstract. The power equipments made of high-temperature superconductor (HTS) widely applied in power system in the recent years. A HTS adjustable reactor (HTS-AR) is a novel controllable reactor with the controllable windings made of HTS tapes. Shunt HTS-AR can regulate the reactive power of power and reduce the transmission loss. However, the leakage magnetic flux of the superconducting windings is relatively large, which may restrict the application of the HTS-AR in high-voltage transmission line. Basing on the research of the structure design for HTS winding, the characteristic analysis of magnetic and AC loss of HTS-AR with considering the structure of superconducting winding is shown in this study. The results show that the HTS winding with the ladder-like structure has a better performance compares with HTS winding with the solenoid structure.

Introduction

A controllable reactor can automatically and smoothly adjust its inductance and thus provide a continuous reactive power compensation to suppress system over voltage [1]. There are mainly two types of controlled reactors applied in power system: saturable reactor (SR) and thyristor controlled reactor (TCR). Reactance of SR is changed by regulating the DC flux component in core [2-3]. TCR is controlled by triggering the thyristor valve [4]. What's worse, most of traditional reactors have serious harmonic components which limit their application [2]. Hence, a new method of reactive power adjustment is proposed, which contains partly and step adjustment, thus the reactive power variation range is quite large [5-6].

With the development of high temperature superconductivity (HTS) technology, the power equipments made of HTS tapes are widely applied in power systems. A HTS adjustable reactor (HTS-AR) is a novel controllable reactor with the controllable windings made from HTS tapes [7]. A HTS-AR with two HTS controllable windings has been developed in [8]. However, the structure of the HTS windings is solenoid, which makes leakage magnetic flux and the AC loss of the HTS windings are large. So it is necessary to improve the structure of the HTS windings to improve the characteristic of the HTS-AR. Basing on the research of the structure design for HTS winding, the characteristic analysis of magnetic and AC loss of HTS-AR with considering the structure of superconducting winding is show in this study.

Structure and principle of HTS-AR

The HTS-AR has a gapless core, main winding, and two HTS windings. Both of the HTS windings are wound concentrically inside the main winding, as shown in Fig. 1. The main winding is connected to the AC power line. The leakage reactance of the HTS-AR is large, which mainly represent the reactance of this controllable reactor. The reactance can be adjusted by alternatively open and short HTS windings. The HTS windings are wound by Sumitomo BSSCO wire Type H [9]. Considering

both the HTS windings have the same structure and principle, the structure of one HTS windings is researched. Table 1 shows the parameters of the HTS-AR.

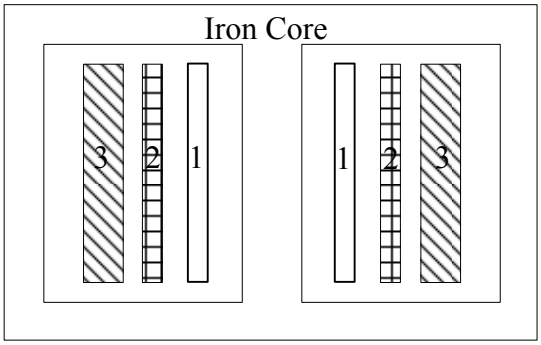

Fig. 1. Structure of HTS-AR
1-HTS-1 winding, 2-HTS-2 winding, 3-main winding

Table 1 The parameters of HTS-AR

rate voltage	380 V	Height of HTS winding	319.5 mm	Turns of HTS winding	426
rate current	100 A	Height of main winding	415 mm	Turns of main winding	190

Characteristic analysis of electromagnetic and AC loss

Calculation of magnetic and AC loss of HTS winding. The magnetic and current of HTS winding can be calculated by ANSYS [10]. Considering the anisotropy of BSCCO tape, we only research the vertical magnetic of HTS winding. The HTS winding of this HTS-AR is working in AC source. The HTS winding will generate AC loss, which will increase the cost of refrigeration and decrease the working reliability and safety. Based on equations provided by Carr [11], Muller [12], and simplified in [13], we use equations (1)-(5) to calculate the AC loss of HTS winding.

$$Q_{//} = \frac{2B_{a//}^2}{\mu_0}\left[\frac{i^3}{3\beta_{//}^2} + i\right] \qquad for \quad \beta_{//} \le 1 \tag{1}$$

$$Q_{//} = \frac{2B_{a//}^2}{\mu_0}\left[\frac{i^2}{\beta_{//}} + \frac{\beta_{//}}{3}\right] \qquad for \quad i \le \beta_{//} \le 1 \tag{2}$$

$$Q_{//} = \frac{2B_{a//}^2}{\mu_0}\left[\frac{3+i^2}{3\beta_{//}} - \frac{2(1-i^3)}{3\beta_{//}^2} + \frac{6i^2(1-i)^2}{3\beta_{//}^2(\beta_{//}-i)} - \frac{4i^2(1-i)^3}{3\beta_{//}^2(\beta_{//}-i)}\right] \qquad for \quad \beta_{//} \ge 1 \tag{3}$$

$$Q_{\perp} = \frac{2B_{a\perp}^2}{\mu_0}\frac{\pi w}{2\beta_{\perp} d}\left[\frac{2}{\beta_{\perp}}\ln(\cosh\beta_{\perp}) - \tanh\beta_{\perp}\right] \tag{4}$$

$$Q = Q_{//} + Q_{\perp} \tag{5}$$

Where $Q_{//}$ and $Q_{\perp}$ is the AC loss which is generated by the parallel magnetic and vertical magnetic of HTS winding, respectively. Table 2 shows the maximum vertical magnetic and AC loss of HTS winding with the parameter shown in Table 1.

Table 2 Magnetic and AC loss of HTS-AR

Maximum vertical magnetic	945 Gs	AC loss of parallel magnetic	54.33 W
AC loss of vertical magnetic	15.87 W	Total AC loss	70.20 W

Structure design of HTS Winding. A ladder-like structure of HTS winding is designed to analysis the characteristic of HTS-AR, as shown in fig 2. The current of HTS-AR, the leakage magnetic and AC loss of HTS winding are mostly affected by the parameters of the ladder-like structure. In Fig. 2, h_c is the total height of HTS winding, h_{c2} is the height of bulge, and $h_{c2}=h_c-2\times h_{c1}$. d_c is the total thickness of HTS winding, d_{cc} is the thickness of the bulge.

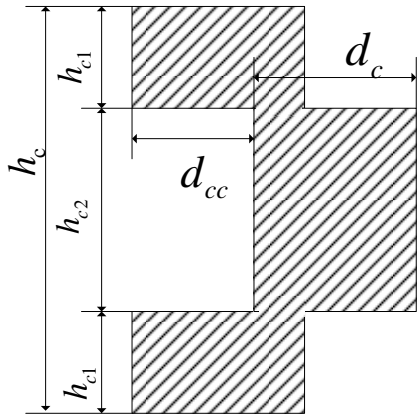

Fig. 2. The ladder-like structure of HTS winding

Electromagnetic characteristic analysis. The results of the electromagnetic characteristic of HTS-AR with ladder-like structure are shown in Figs. 3-4. Fig. 3. Shows the current of HTS-AR with h_{c1}/h_c is from 0.1 to 0.4 when d_{cc}/d_c is from 0.1 to 0.9. Fig. 4. Shows the maximum vertical magnetic field of HTS winding with h_{c1}/h_c is from 0.1 to 0.4 when d_{cc}/d_c is from 0.1 to 0.9.

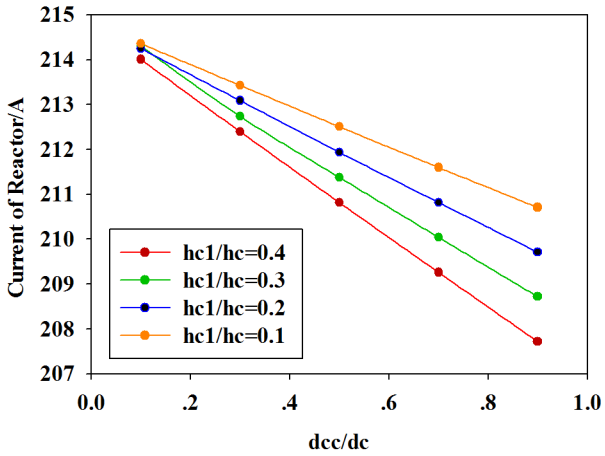

Fig. 3. The current of HTS-AR

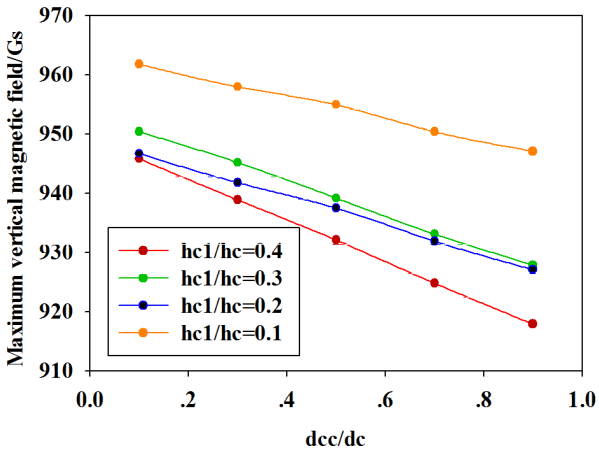

Fig. 4. The maximum vertical magnetic field

The current of HTS-AR is linearly reduces as d_{cc}/d_c increase from 0.1 to 0.9. When d_{cc}/d_c is 0.9, the current of HTS-AR reduce from 211 A to 207.5 A when h_{c1}/h_c is from 0.1 to 0.4. The attenuation rate is 1.66%. When d_{cc}/d_c is 0.1, the current of HTS-AR is almost no change. These results show that the height of the bulge will affect the work characteristic of HTS-AR when the thickness of the bulge is various. The effect will be weak when the thickness of the bulge is small. The effect will be strong when the thickness of the bulge is large. The effect caused by the height of the bulge will increase obviously when the thickness of the bulge increases.

The maximum vertical magnetic of HTS winding will linearly reduce when the thickness of the bulge increase. When d_{cc}/d_c is 0.9, the maximum magnetic of HTS winding reduce from 952 Gs to 917 Gs as h_{c1}/h_c is from 0.1 to 0.4. The attenuation rate is 3.68%. When d_{cc}/d_c is 0.1, the maximum magnetic of HTS winding reduce from 963 Gs to 946 Gs as h_{c1}/h_c is from 0.1 to 0.4. The attenuation rate is 1.76%. The maximum magnetic of the HTS winding will decrease when both the height and

thickness of the bulge increases. The attenuation rate of the maximum magnetic of HTS winding will slightly increase when the thickness of the bulge increases.

AC loss analysis of HTS winding. Figs. 5-7 show the total AC loss and AC loss in vertical magnetic, parallel magnetic of HTS winding. The total AC loss and the AC loss of vertical magnetic and the AC loss of parallel magnetic will nearly linearly decrease. When d_{cc}/d_c is 0.9, the total AC loss, the AC loss of vertical magnetic, and the AC loss of parallel magnetic reduce from 66.84 W, 15.03 W, and 51.8 W to 63.29 W, 14 W, and 49.27 W, respectively, as h_{c1}/h_c is from 0.1 to 0.4. The attenuation rate of the total AC loss, AC loss of vertical magnetic, and the AC loss of parallel magnetic is 5.31%, 6.85%, and 2.15%, respectively. When d_{cc}/d_c is 0.9, the total AC loss, the AC loss of vertical magnetic, and the AC loss of parallel magnetic are nearly no change. This indicates that the AC loss of HTS winding is mainly affected by the thickness of the bulge. The effect of AC loss caused by the height of the bulge is restricted by the thickness of the bulge. The attenuation rate rich the highest value when the height and the thickness of the bulge is large.

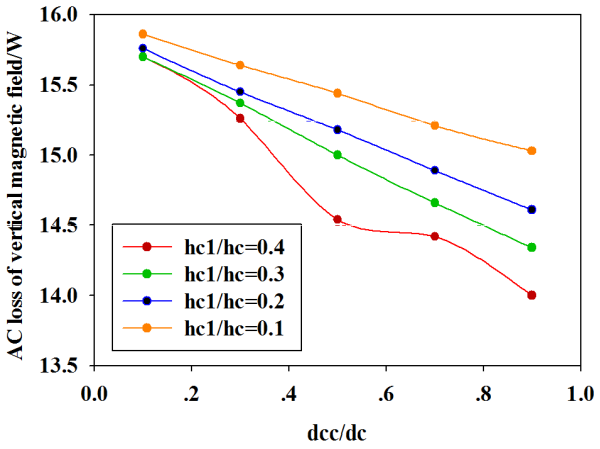

Fig. 5. AC loss of vertical magnetic field

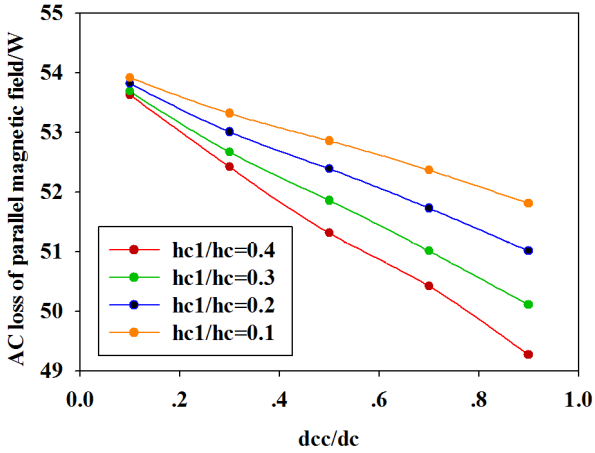

Fig. 6. AC loss of parallel magnetic field

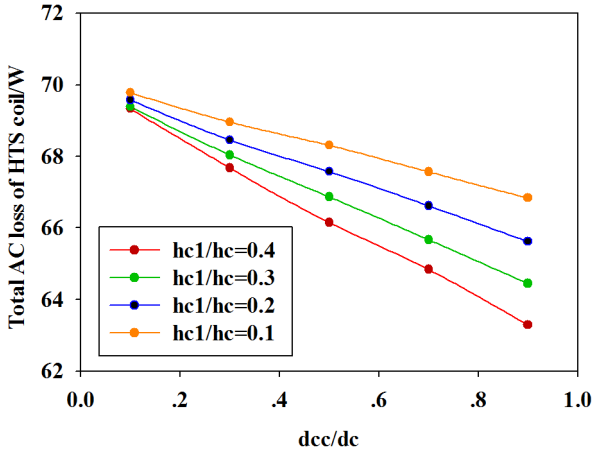

Fig. 7. The total AC loss of HTS winding

Conclusion

Basing on the ANSYS, the characteristic of electromagnetic and AC loss of a high temperature superconducting adjustable reactor (HTS-AR) with considering the structure of HTS winding is analyzed in this paper. The results show that the structure of the HTS winding will affect the work characteristic of HTS-AR, the maximum magnetic and the AC loss of the HTS winding. The current of main winding will reduce 1.66% when the sizes of the bulge are large. However, the attenuation rate of the AC loss is 6.85% when the sizes of the bulge are large. With the considering of the economy that the efficiency of the refrigerant is 0.05%, the larger AC loss will dramatically increased the cost of refrigeration and decrease the working reliability and safety. This indicates that the HTS

winding with the ladder-like structure has a better performance compares with HTS winding with the solenoid structure. The research in this study will provides some valuable reference for developing ultrahigh voltage and large capacity level HTS-AR.

Acknowledgements

Thank Miss Hu Xiaoming for the suggestions about my paper.

References

[1] X. Mu, X. Wei, and Y. Ji, in: Electric Power Automation Equipment, Vol. 27 (2007), No. 3, pp. 14-17 (in Chinese).

[2] M. Tian, Q. Li, in: IEEE Trans. on power delivery, Vol. 19 (2004), No. 4.

[3] T. Wass, S. HÖrnfeldt, and S. Valdemarsson, in: IEEE Trans. on Magnetics, Vol. 42 (2006), No. 9, pp. 2196-2200.

[4] L. J. Bohmann, R. H. Lasseter, in: IEEE Trans. on Power Delivery, Vol. 4 (1989), No. 3.

[5] Y. Zhang, Q. Chen, adn L. Cheng, in: ICEMS. (2007), pp. 1286-1290

[6] Y. Zhang, Q. Chen, and J. Tian, in: Proceedings of the CSEE, Vol. 29, No. 18 (2009), pp. 113-118 (in Chinese) .

[7] S. Shen, Y. Tang, and M. Song, in: Cryogenics and Superconductivity, Vol. 41, No. 9 (in Chinese).

[8] K. Cao, M. Song, and S. Shen, in: Cryogenics and Superconductivity, Vol. 41, No. 5 (in Chinese).

[9] Information on http://www.ansys.com/

[10] Information on http://global-sei.com/super/htse/type h.html

[11] W. J. Carr, in: IEEE Trans. Magnetic, Vol. Mag-15, No. 1, pp. 240-243, January 1979.

[12] K. H. Muller, in: Phys. C, Vol. 247, pp. 74-82, 1995.

[13] M. P. Oomen, in: Ph.D. dissertation, Dept. Eng. Tech., Univ. Twente., Enschede, Netherlands, 2000.

Advanced Materials Research Vols. 960-961 (2014) pp 670-675

doi:10.4028/www.scientific.net/AMR.960-961.670

The Design of a New Signal Handing Circuit of Seismic Geophone

Li Liang[1,*], Tuo Xianguo[1, 2], Mao Xiaobo[1] and Mingzhe Liu[1, a]

[1]State Key Laboratory of Geohazard Prevention and Geoenvironment Protection, Chengdu University of Technology, Chengdu 610059, China;

[2]Key Subject Laboratory of National Defense for Nuclear Waste and Environmental Safety, Southwest University of Science and Technology, Mianyang 621010, China;

[a]liumz@cdut.edu.cn

Keywords: MEMS Geophone; Signal handing circuit; DC elimination;

Abstract. This paper aims at the problem that how to isolation the DC component of the MEMS geophone in the acquisition and processing of Seismic signal. Put forward to design a new circuit in the signal handing system. Design a new type of DC elimination circuit to eliminate the DC component through low-pass filter, reverse and other modules. The experiment result shows that, this new DC elimination circuit is easier to realize and has a large advantage than other existing DC elimination circuits.

Introduction

The sensors which were made by MEMS technology have a better performance than other traditional sensors. They have too many advantages such as the wider frequency band, the better LF response, lower noise, higher sensitivity, better linearity and so on. As result, researching the geophone base on the MEMS technology, improving the precision of the signal detection has important practical significance. The geophone base on the MEMS technology consists of the part of power supply, MEMS sensors and the signal handing circuits. What's more, the signal handing circuits consist of DC elimination, pre-amplifier, program control amplifier and filter circuit. Fig 1 shows the function diagram of this type of geophone.

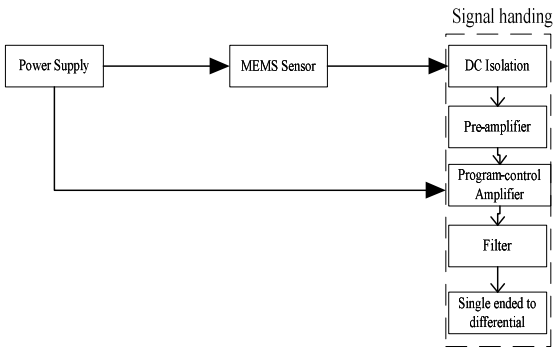

Fig. 1. Geophone function diagram

In the geophone system, signal handing circuit is the most important part of all. If the output error of any part in this circuit is larger than ever can inflect the later control system and the final seismic signal monitor and the system will affect the serious impact. As result, to design a reliable MEMS geophone's signal handing circuit occupies an important place in the whole system design. This

paper design a new type of DC elimination circuit apply to the Seismic acquisition and processing, this new type of DC elimination circuit has a lower response delay, higher precision and more reliable than other existing DC elimination circuit. It has a larger practicality and promotion value in Seismic signal processing.

Sensor, Amplifier and Transform Circuits Design

1.1 Sensor circuit design

This design chooses model1221L-002 accelerometer as the MEMS sensor, it manufacture by Silicon Designs Inc. it's a low noise capacitive accelerometer, its gravity block is the mobile heat convection nitrogen, it measure the acceleration by measure the inner temperature change cause by the acceleration. Model1221L-002 accelerometer owns a temperature sensor, which can measure the real temperature of the sensor inside; the senor is two way difference analog output, the difference analog output can eliminate the internal disturbance, reduce the impact cause by system error. In this design, if we let the sensor output the difference signal and use difference amplifier later, in that way, the signal in difference output unable to superposition. If we set it as in-phase input then there's none output signal, otherwise, if we set one output inverse and superimpose the output, then the DC offset will twice the value. In that way, it's very inconvenient in signal processing. So, this system must add a differential ended to single circuit to make the sensor output transform to single input of later signal handing circuit. We can see the detail circuit of sensor in figure 2.

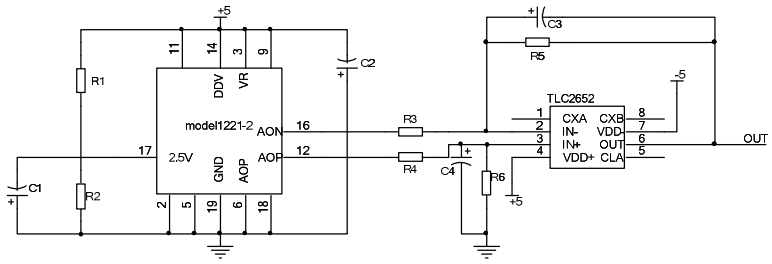

Fig. 2. Sensor circuit design

1.2 Pre-amplifier and signal transform circuits design

Analysis with exiting Seismic signal handing circuit, the circuit structure is almost the same. The signal processing circuits always use DC elimination part, pre-amplifier part and program-control amplifier part. Because of the follow-up ADC is differential output, so it must design a single ended to differential signal output to ADC. As result, this design use AD8138 chip and four same-arm resistances to transform the single signal output to differential output what the ADC needs.

In the signal handing circuit design, it use TLC2652 as the pre-amplifier and set the gain as 10 to amplifies the signal ten times in order to fit the PGA205 the program-control amplifier's picking request for the weak signal. Thus this paper underlines to analysis the new type of DC elimination circuit with existing circuits, so the follow-up handing circuits of all the experiment design as the same as above to obey the Single Variable Theory and analysis the different DC elimination result better.

DC Isolation Circuit Design

2.1 Existing DC Isolation Circuits analysis

There are two design methods of existing DC elimination circuit. The first is that using capacitance with pull-down resistor to eliminate the DC component of MEMS sensor; this design can basically complete the elimination work. But by the characteristic of the capacitance itself, the capacitance would bring the unexpected ripple wave noise to this system probably.

Reference [4] gives out a new method that using amplifier to complete the DC elimination work. It chooses instrumentation amplifier to isolation the DC component, because of the great performance in restrain the CMRR and the noise of instrumentation amplifier is small. So it selects AD620 to build up the DC elimination circuit and the gain is set to 1.because of it doesn't amplify the signal so the gain is 1. In accordance with the gain formula: $R_G = \frac{49.4\text{k}\Omega}{G-1}$ as we can conclude that, when the gain is set as to 1, the R_G goes to infinity so Pin1 and 8 set as dangling, Fig 3 shows the detail circuit of this method.

It must be informed that as we can conclude from the sensor character that when the sensor is vertical, there's 2V DC offset, but in experiment, it's hard to keep the sensor being absolute vertical, there must be a dip between the sensor and horizontal plane, so it cannot keep the offset value as 2V. Thus Pin2 must connect a potentiometer(R1) to precision fine adjust the input voltage to keep the DC offset as 2V in experimental stage.

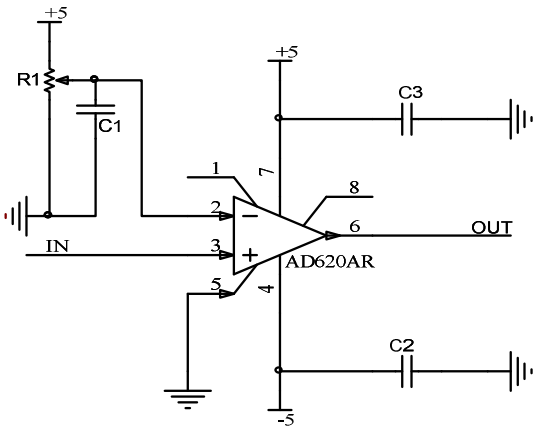

Fig. 3. AD620 DC elimination design

2.2 New Design of DC Isolation Circuit

In the condition of using MEMS technology in Seismic geophone signal processing, this paper comes up with a new type of DC elimination circuit. This design using four operation amplifiers which act as four different functions to complete the DC isolation work. The input signal will reduce the AC component through LPF(amplifier A); then back-ward processing by the invertor(amplifier B); the amplifier C act as a follower and output the input signal in the same potential; the amplifier D is a summator to sum the output of B and C. Then the DC component in the output signal of C will counteract by the B and complete the DC elimination work. The function diagram is Fig. 4.

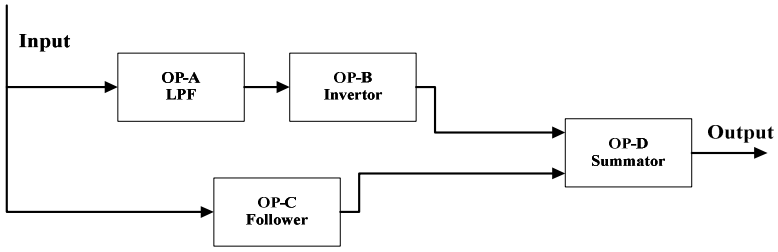

Fig. 4. Circuit function diagram

In the choice of operation amplifier, with the consideration of the complex of weak signal and the request of the signal handing. This circuit chooses OPA2735 from TI Inc as the four different function amplifier. This chip's zero offset is only 0.05μV/°C; maximum input offset voltage is 5μV. In the design of precision Seismic instruments, the request of offset voltage is 5μV max too, OPA2735 can fit the request of that. And OPA2735 is two operation amplifiers integrated in one chip, it can save the room in the circuit. Fig. 5 is the circuit diagram.

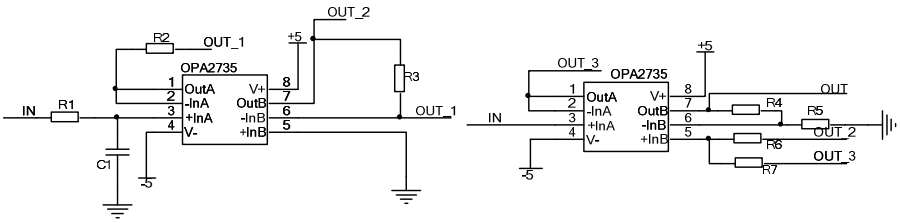

Fig. 5. Op-am DC elimination circuit diagram

Results Analysis and Conclusion

3.1 Result Analysis

Build the experiment circuits which consist of these three type of DC elimination methods, the sensor we choose Model1221L-002 to keep the input signal as the same. Using oscilloscope to observe the outputs of these three different DC elimination circuits when there's a slight shake.

For the DC elimination circuit which using AD620, Instrumentation amplifier notwithstanding has a great effect on CMRR but different types of the sensor the DC component of output is different, then this circuit need to adjust the potentiometer manually at the input (pin 2) to reset the reference voltage. If it need to satisfy the accuracy requirement or replace the sensor at the specific environment, we also need to adjust the potentiometer manually. It's very adverse for system automation of data collection and processing, and it's inconvenient to update the sensor type for this geophone.

As we can see, the DC elimination circuits build by four Op-Amps can avoid the problem what the AD620 DC elimination circuit brings, the result of this circuit is very perfect. But for the seismic transient signal, this momentary signal cannot make the capacitance saturated, then the output signal has a phase difference with the input signal, this phase difference is inevitable. Through analyzing low-pass filter amplitude-frequency characteristic we can launch that the filter instantaneous signal phase delay roughly 2ms. Then we use oscilloscope to observe the input and output signal showed in Fig. 6, we can conclude that the phase difference is almost 2ms, the calculated results approximately equal with the fact. And this phase difference is also within the range allowed by the system accuracy requirement.

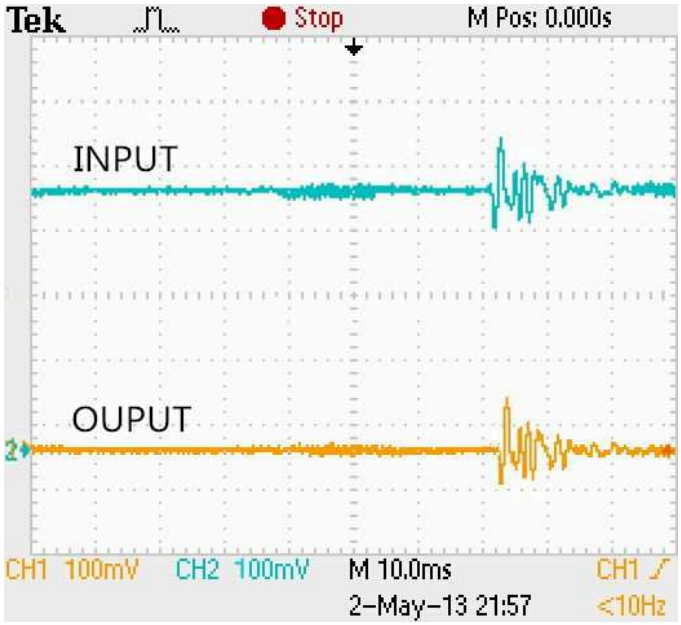

Fig. 6. Four op-ams DC elimination effect

3.2 Conclusion

This paper, based on the characteristic of the Seismic signal. Contrasts and analyzes the existing circuits of Seismic signal handing precisely, faces to the DC elimination problem to come up with a new circuit of DC elimination, breaks the traditional DC elimination method and solves the problems what the capacitance DC elimination circuit brings, using op-am to combine the circuit to finish the isolation work. Through the experiments contrast analysis, this new circuit of DC elimination has the advantages of better LP filter effect, short response delay, eliminate the DC component as much as possible in the condition of fitting the system requests. It has a great advantage by compared with other circuits. This design can widely be used in the further seismic instruments design and improve for production practice.

Acknowledgement

This paper is supported by The Major Research Equipment of National Natural Science Fund Development Projects (41227802) and The National Natural Science Fund (41025015, 41274109).

References

[1] Yang Hai- ping, Shi Yi- bing, Zhang Wei, Liu Xi- en, Study on Improving Technological Index of MEMS Geophone, China Measurement and Testing technology VOL. 2, No.2, 2012: 12~14. In Chinese.

[2] Yang Zhong-hua, Wang Shu-jun, Chen Hai-bo, Wang Yi-jiang, Tang Xiao-gang, Niu De-fang, Study on Improving Technological Index of MEMS Geophone, Instrument Technique and Sensor, VOL. 2, No.2, 2012: 12~14. In Chinese.

[3] S. Shariat Panahi, Sergi Ventosa, Javier Cadena, Antoni Mànuel-Làzaro,Antoni Bermúdez, Valentí Sallarès, and Jaume Piera, A Low-Power Data logger Based on Compact Flash Memory for Ocean Bottom Seismometers, Transactions On Instrumentation and Measurement, VOL. 57, No.10, 2008: 2297~2303.

[4] Jian Li, Jinjie Yao, Yan Han. Design of Wireless Vibration Detection Node. International Conference on Computing, Measurement, Control and Sensor Network (2012). In Chinese.

[5] Jiandong Wang, Yunhui Liu. Mems sensor intertial meaturement of module design and initial calibration. Sensor and micro system, Vol. 10, PP.82-85, 2006. In Chinese.

[6] Huai-Liang Li, Xianguo Tuo, Ming-Zhe Liu. Key techniques of wireless telemetry digital seismograph. Chinese Journal Geophysics, 2013,56(11): 3673-3682.

Advanced Materials Research Vols. 960-961 (2014) pp 676-679

doi:10.4028/www.scientific.net/AMR.960-961.676

A Combined AC+DC Distribution Network Interconnected with Renewable Energy

Dongxin Hao [1,a], Li Zhang [2,b], Mengqi Liu [3,c], Panting Dong [4,d], Hao Wu [5,e]

School of Electrical Engineering, Shandong University, Jinan 250061, China

[a]email: 15289379343@163.com, [b]email: zhlieee@gmail.com

Keywords: AC+DC distribution network, Renewable energy, Simulink simulation, Z transformer

Abstract: The combined AC+DC distribution network in this study provides a coupling and decoupling strategy of renewable energy in DC mode by using zig-zag transformer, which makes each line transmit AC electrical power and DC power simultaneously. The proposed scheme is digitally simulated with the help of Simulink software package. Simulation results indicate lower line voltage drop and less active and reactive power loss in steady state; almost similar or even better transient effects in transient state, which demonstrates the feasibility of combined AC+DC distribution network of single line interconnected with renewable energy.

Introduction

Renewable energy witnesses rapid development in recent years. However, its lower utilization and uncertain interconnection with grid raises the study of about it. One of way to connect renewable energy into the grid is to construct a DC micro gird[1]. However, considering high economical investment and limited line corridor , its sparkling advantage remains open to question. H.Rahman and B.H.Khan have ever put forward a simultaneous AC+DC power transmission mode through a transmission line[2-4]. Their research mainly focused on the power upgrading by simultaneous AC+DC power transmission.

In this paper, the configuration of combined AC+DC distribution network interconnected with renewable energy is given. From theoretical analysis and simulation results, the feasibility of combined AC+DC distribution network of single line interconnected with renewable energy is demonstrated.

Combined AC+DC distribution network

System Configuration. As is shown in Fig 1, AC is required from AC system through zig-zag transformer, while renewable energy in DC mode is superposed on each distribution line from the neutral line of zig-zag transformer. DC chopper circuit is used to get needed DC voltage value.

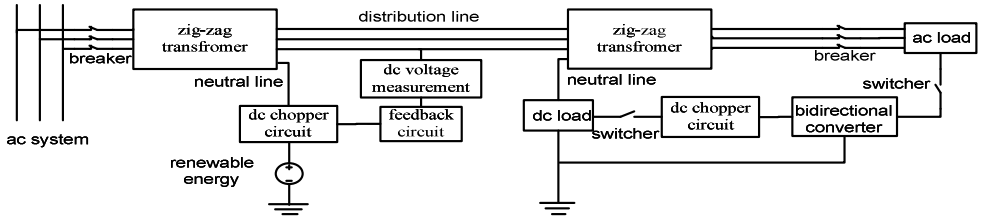

Fig.1 Configuration of combined AC+DC distribution Network interconnected with renewable energy

AC and DC power are separately supplied to AC load and DC load by zig-zag transformer. In order to guarantee reliability of power distribution to loads, bidirectional converter is used.

Zig-zag Transformer. Three-phase, nine windings transformer with six identical secondary windings can be used to zig-zag connection shown in Fig 2. Because of its special structure, on one hand, there is no zero-sequence flux in 3-phase core limb. On the other hand, the flux of 3-phase core limb doesn't change due to mutual offset of produced flux when DC current injects from neutral point.

DC Chopper Circuit and Control Strategy. In this study, the chosen DC chopper circuit is DC-DC full bridge chopper circuit with isolation shown in Fig.3.

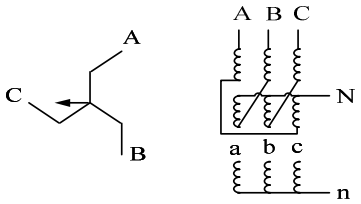

Fig.2 Zig-zag winding connection

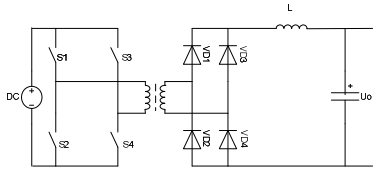

Fig 3. DC-DC full bridge chopper circuit

As is shown in Eq.1, the error of target value *ref* with output value e_r is integrated and then amplified by K times. Input current i_1 is amplified by f_1 times. The sum of two amplified value serves as input d (duty circle).

$$d = -f_1 i_1 + K\int (ref - e_r)dt \tag{1}$$

Theoretical Analysis

Steady State Analysis. Because DC component is superposed on 3 lines simultaneously, the line-to-line voltage remains unchanged. Line-to-ground voltage lifts to some extent. However, as long as the DC value is appropriate, the request of insulation margin of traditional AC distribution line can be meet. In order to simplify analysis, because of the symmetry of each line, the single line schematic diagram of AC+DC distribution is shown in Fig.4. The total power of node B of distribution line conforms to Eq.2.

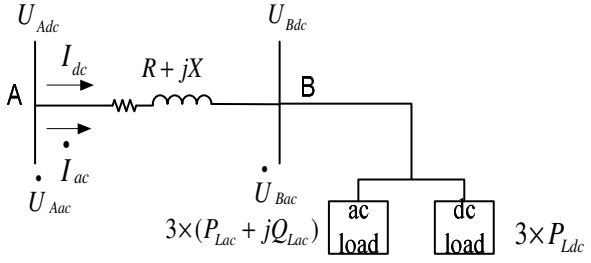

Fig.4 Single line schematic diagram of AC+DC distribution

$$S_B = P_B + jQ_B = 3\times(P_{Lac} + jQ_{Lac} + P_{Ldc}) \tag{2}$$

If provides S_B in traditional AC mode, the power loss ΔS_{ac} of distribution line and amplitude variation ΔU_{ac} of voltage vector of node A and B are as follows:

$$\Delta S_{ac} = \frac{3[(P_{Lac} + P_{Ldc})^2 + Q_{Lac}^2]}{U_{Bac}^2}(R + jX) \tag{3}$$

$$\Delta U_{ac} = U_{Aac} - U_{Bac} \tag{4}$$

If provides S_B in combined AC+DC mode, ΔS_{ac+dc} and ΔU_{ac+dc} are as follows:

$$\Delta S_{ac+dc} = \frac{3(P_{Lac}^2 + Q_{Lac}^2)}{U_{Bac}^2}(R + jX) + \frac{3P_{Ldc}^2}{U_{Bdc}^2}R \tag{5}$$

$$\Delta U_{ac+dc} = U_{Aac+dc} - U_{Bac+dc} \tag{6}$$

From Eq.2~6, $|\Delta Q_{ac+dc}| < |\Delta Q_{ac}|$, $|\Delta U_{ac+dc}| < |\Delta U_{ac}|$ can be get. Further, the theoretical analysis of comparison of active power is given. Supposing $\Delta P_{ac+dc} = k\Delta P_{ac}$, then get Eq.7:

$$U_{Bdc} = \frac{U_{Bac}}{\sqrt{k(1+2\frac{P_{Lac}}{P_{Ldc}}) + (k-1)\frac{P_{Lac}^2 + Q_{Lac}^2}{P_{Ldc}^2}}} \tag{7}$$

k is proportionality coefficient of active power loss, if $k \in (0,1)$, then $\Delta P_{ac+dc} < \Delta P_{ac}$. That means AC+DC distribution mode has less active loss.

Instance of Steady State and Transient State. Supposing a 10kV distribution line with AC load S_{ac}=3×(900+j240)=2700kW+j720kVar and DC load 3×300kW, if proportionality coefficient k is 0.8, U_{Bdc} is about 3kV from Eq.7. Distribution line is made of TJ70 sterepsinema. Resistance per unit length is r=0.28 Ω/km while reactance per unit length is x=0.37 Ω/km. Short-circuit fault occurs in 20km distance, then $R = 5.6\Omega$, $X = 7.4\Omega$.

Simulation Results

In this part, the simulation results are given by using simulink package of MATLAB. Model parameter uses the data of corresponding instance in last part.

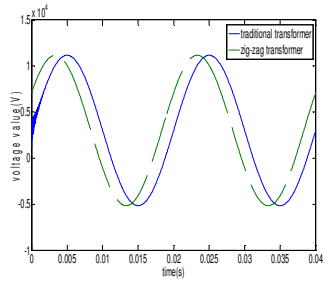

Fig.5 Comparison of zig-zag with traditional transformer

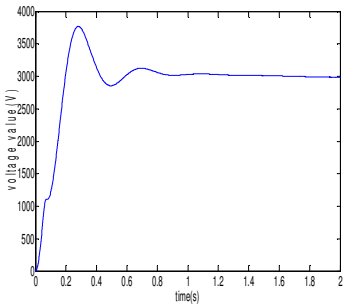

Fig.6 DC chopper circuit feedback result

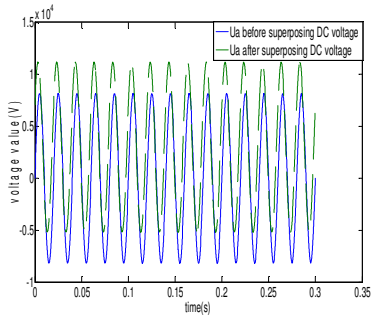

Fig.7 Comparison of u_a before superposing DC voltage with after

Fig.5 separately shows secondary side output voltage waveform by using zig-zag and traditional transformer. It can be seen that traditional transformer occurs saturation obviously while zig-zag transformer works properly. The simulation result of DC chopper feedback circuit is shown in Fig.6. The superposed DC voltage stabilizes 3kV effectively. Fig.7 shows that line-to-ground voltage of A phase uplifts after superposing 3kV DC voltage. The peak value is about 11160V, which corresponds to theoretical value.

From table 1, when works in AC+DC mode, active, reactive loss and voltage drop of distribution line are all less than AC mode, which corresponds to theoretical analysis. It can be seen from table 2 that the fault parameter of AC+DC distribution mode is similar to, or even better when three-phase symmetrical short-circuit occurs by adjusting parameter of zig-zag transformer. When other fault type occurs, simulation results also indicate the advantage of DC+AC distribution mode.

Table1 Comparison of steady state of two modes when R=5.6Ω ,L=0.02356H

	AC	AC+DC
Active loss（W）	6900	6200
Reactive loss（W）	9211	6030
Voltage drop（V）	116	115

Table 2 Comparison of three-phase symmetrical short-circuit impulse and RMS current when $L_{zig-zag}$ changed (A)

$L_{zig-zag}$ (H)	0.0445	0.05724	0.06996
i_{ac+dc}	960	907	865
I_{ac+dc}	609	591	580
i_{ac}	990		
I_{ac}	622		

Conclusion

The combined AC+DC distribution network realizes the coupling and decoupling of renewable energy. By using DC chopper circuit, the DC voltage can be kept to needed value. AC+DC distribution mode has lower line voltage drop and less active and reactive power loss in steady state; almost similar or even better transient effects in transient state, which demonstrates the feasibility of combined AC+DC distribution network of single line interconnected with renewable energy.

Acknowledgements

Financial support by the National Natural Science Foundation of China (51207084) and Science and State Key Laboratory of Alternate Electrical Power System with Renewable Energy Sources (LAPS13017) is here all acknowledged.

References

[1] Lasseter, Robert H., and Paolo Paigi. "Microgrid: a conceptual solution", Power Electronics Specialists Conference, 2004. PESC 04. 2004 IEEE 35th Annual. vol. 6. IEEE, 2004.

[2] K.P.Basu and B.H.Khan, "Simultaneous ac-dc power transmission ", Inst. Eng.(India) J.-EL,vol.82,32-35,Jun.2001.

[3] H.Rahman and B.H.Khan, "Power upgrading of transmission line by combining ac-dc transmission", IEEE Trans.Power Syst.vol.22(1),(2007),459-466.

[4]H.Rahman and B.H.Khan, "Enhanced power transfer by simultaneous transmission of AC-DC: a new FACTS concept", IEEE conference on Power Electronics, Machines and Divers,vol.1,(2004),186-191.

Advanced Materials Research Vols. 960-961 (2014) pp 680-683

doi:10.4028/www.scientific.net/AMR.960-961.680

A novel method of core saturation suppression for the AC+DC distribution network transformer

Mengqi Liu[1,a], Li zhang[1,b], Jie Lou[1], Liang Zou[1], Tong Zhao[1]

[1]School of Electrical Engineering, Shandong University, Jinan 250061, China

[a]lmqsdu2013@gmail.com, [b]zhlieee@gmail.com

Keywords: AC/DC distribution network, distributed renewable energy, inductive filtering, core saturation

Abstract. With the rapid development of smart grids, the interconnection between the grid and distributed renewable energy is the inevitable trend of future study. Because of the existence of the DC source in the combined AC-DC distribution network, the transformer iron core is easily saturated generating lots of harmonics and increasing the loss of the transformer. This paper presents a novel method based on inductive filtering technology of core saturation suppression of the transformer in the combined AC-DC distribution network, this novel method can suppress the harmonics caused by the flux saturation and forbid the harmonics intruding into the ac grid. In the end we build the simulation model to prove the correctness and practicability of this novel method.

Introduction

With the rapid development of smart grid, the way that how to access the distributed renewable energy to the distribution network has attracted more and more attention [1]. There are many types of new energy including wind power, photovoltaic power, fuel cell, tidal power and so on, but it still can be summed up as two types, that is the ac power and dc power. Connecting the ac sources to the grid is relatively simple. The difficulties of the study lies in the integration of dc source of distributed energy. There are two main existing approaches, one is converting the dc source to ac source through the rectifier, another is to construct a micro grid [2, 3]. There are two impacts of these two methods, on one hand the cost is very high, on the other hand they will form a certain degree of impact to the power grid. Therefore, the need of combined AC-DC power transmission is more and more urgent.

Because of the existence of the ac source, the transformer iron core is easily saturated. When the iron core is saturated, it will course the distortion of the voltage and the current also it will course the raise of the iron core loss. These phenomena are referred to as ac magnetic bias [4]. DC magnetic bias makes the core flux saturation generating lots of harmonics. This paper presents a novel method of flux saturation suppression of combined AC-DC distribution network transformer based on inductive filtering technology. That is applying the inductive filtering transformer to the combined AC-DC power transmission system, through the use of superconductor flux conservation principle to suppress the core flux saturation of the transmission system.

The topology of the combined AC-DC power transmission

To apply the new mode of inhibiting the flux saturation based on inductive filtering, we need a new topology of combined AC-DC distribution network. This network contains ac source, dc source, inductive filtering transformer, boost chopper circuit and distribution line. The ac source and the inductive filtering transformer stands for the ac distribution network, the dc source stands for the distributed new energy sources. The schematic diagram is shown in Fig.1.

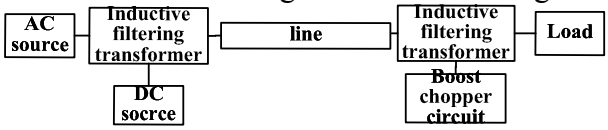

Fig.1 New topology of combined ac and dc distribution network

In Fig.1 the inductive filtering transformer is the special transformer used to inhibit the core flux saturation of the transmission system; the boost chopper circuit is a voltage conversion circuit.

Inductive filtering transformer. Inductive filtering transformer is a transformer with three windings, the LC filter is accessed to the third winding so as to inhibit the harmonic closing to the harmonic source. The spatial arrangement of the three windings and the number of the turns of the windings are all designed and arranged specially. The most important character of the special arrangement is that the equivalent impedance of the filtering winding is zero. The advantages of the inductive filtering transformer is that it can reduce the noise and vibration of the transformer and it can inhibit the harmonic coursed by the flux saturation [5].

The connection of the inductive filtering transformer windings and the connection of the inductive filtering device are shown in Fig.2.

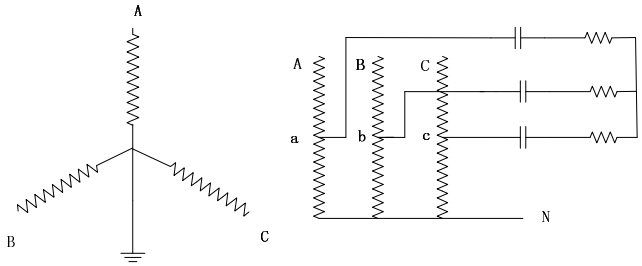

Fig.2 The connection of the inductive filtering transformer windings

The difference of the windings connection between the traditional transformer and the inductive filtering transformer is that the secondary is cut as two parts. Three taps a,b,c led out from the middle which is treated as public winding. We access the inductive filtering device in the light of the 2th,5th,7th,11th,13th harmonic to the three taps. The inductive filtering device can inhibit the harmonic right at the secondary side which can suppress the effect to the transmission line caused by flux saturation effectively.

Boost chopper circuit. Boost chopper circuit is a dc-dc conversion circuit whose output voltage is higher than input voltage. The angular phase difference courses the flow of the ac power, the voltage difference courses the flow of the dc power, so the voltage circuit is very necessary for maintaining the stability of voltage difference. In addition, boost chopper circuit unifying the rated voltage of every node of this topology in order to connect the ac source an ac load to the distribution network [6, 7].

Harmonic model and theoretical analysis

According to the connection of inductive filtering winding, the equivalent circuit diagram of the inductive filtering transformer is shown in Fig.3.

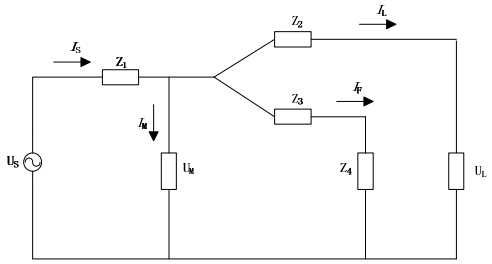

Fig. 3 Equivalent circuit diagram of the inductive filtering transformer

In this diagram, I_M contains a lot of 2th harmonic, I_L contains lots of 5th,7th,11th,13th harmonic, so the inductive filtering device accessed to this circuit is aimed at 2th,5th,7th,11th,13th harmonic.

According to the Kirchhoff law we can know:

$$\begin{cases} I_S = I_L + I_F + I_M \\ U_M = I_F(\mathrm{Z}_3 + \mathrm{Z}_4) \\ \mathrm{U_S} = \mathrm{I_S Z_1} + I_F(\mathrm{Z}_3 + \mathrm{Z}_4) \\ \mathrm{U_L} = \mathrm{I_F}(\mathrm{Z}_3 + \mathrm{Z}_4) - \mathrm{I_L Z_2} \end{cases} \tag{1}$$

In the above equations, U_S is the voltage source of the ac grid side, I_S is the current of the ac grid side, U_L is the voltage drop of the load, Z_1 is the impedance of the primary winding, Z_2 is the impedance of the secondary winding, Z_3 is the impedance of the inductive filtering winding, Z_4 is the impedance of the inductive filtering device.

We can get the current of the ac grid side I_S from the transform of the equations (1):

$$I_S = \frac{U_S}{Z_1 + Z_3 + Z_4} + \frac{I_L + I_M}{\frac{Z_1}{Z_3 + Z_4} + 1} \tag{2}$$

Also, we can get the current flowing through the inductive filtering winding branch I_F:

$$I_F = \frac{U_S}{Z_1 + Z_3 + Z_4} - \frac{I_L + I_M}{\frac{Z_3 + Z_4}{Z_1} + 1} \tag{3}$$

In this paper we have mentioned that through the special spatial arrangement the impedance of the inductive filtering winding $Z_3 \approx 0$, additionally under the specific harmonic frequency the impedance of the inductive filtering device $Z_4 \approx 0$. From the equations (2) and (3) we can know I_M and I_L are important elements of I_F but they have nothing to do with I_S which means the harmonic current is mostly shunted to the inductive filtering branch.

Meanwhile, we can get the current of the load side I_L from the change of equations (1) :

$$I_L = -\frac{U_L}{Z_2 + Z_3 + Z_4} + \frac{I_S - I_M}{\frac{Z_2}{Z_3 + Z_4} + 1} \tag{4}$$

We have known that $Z_3 + Z_4 \approx 0$, so the current I_L is only effected by U_L and the impedance of the windings.Through the harmonic shunting of the inductive filtering branch, the inductive filtering transformer achieve the target of inhibiting the iron core flux saturation.

Simulation and result analysis

In this paper we build the simulation model of combined AC-DC power transmission by matlab/simulink, and also we compare the result with the combined AC-DC distribution network applied with traditional transformer. In this model, the equivalent impedance of the load is 20+j31.4Ω. The rated capacity, voltage, frequency of the ac source is 100MVA, 10KV, 50HZ. The length of the line is 30km. The transformer ratio is 1:1. The rated voltage of the dc source is 3KV.

The simulation results are shown in Fig.4 and Fig.5:

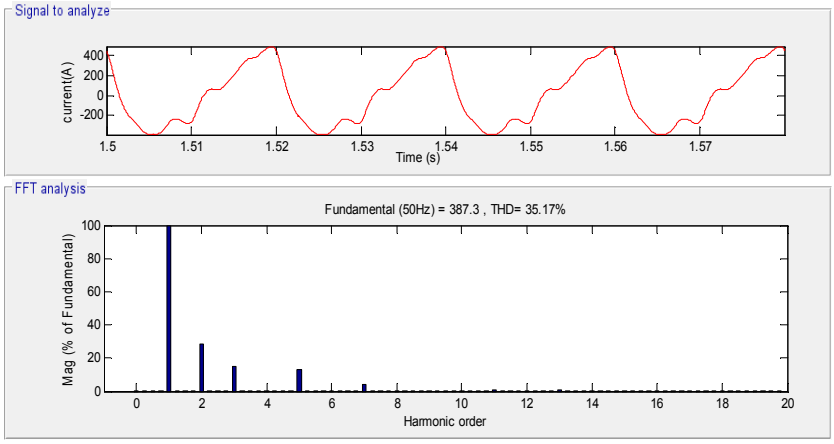

Fig.4 Current on line side in combined ac-dc distribution network with traditional transformer

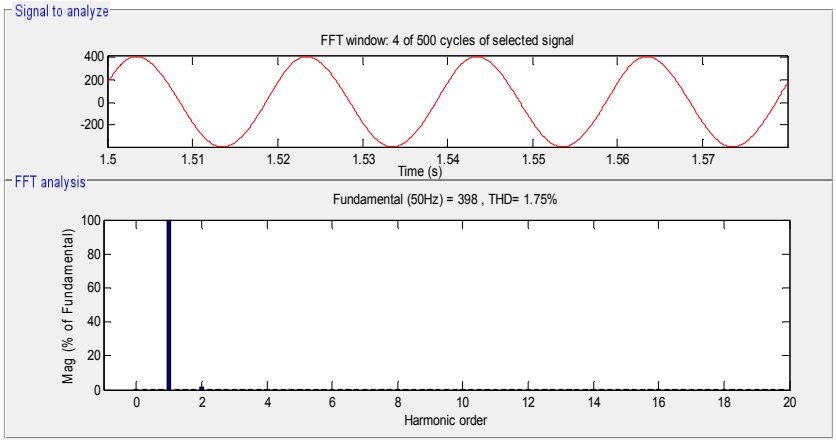

Fig.5 Current on line side in combined ac-dc distribution network with inductive filtering transformer

Fig. 4 and Fig. 5 show the simulation result of the current on line side in the two topologies of combined AC-DC power transmission. The waveform in Fig.4 has seriously distorted, meanwhile, the waveform in Fig.5 is much more smooth. From the two figures we can know:1. The core flux saturation generates many times of harmonic which leading to the distortion of the current on line side. The waveform in Fig.4 isn't asymmetrical, that is because of the effect of 2th harmonic generated by flux saturation. 2. When the inductive filtering transformer accessed to the combined AC-DC distribution network the current on line side becomes smooth and asymmetrical which means the inductive filtering transformer has good effect on the harmonic suppression.

Conclusion

Because of the existence of the dc source, the transformer of combined AC-DC distribution network is easily saturated. When the transformer is saturated it will generate many times of harmonics. When these harmonics intrude into the primary side, they will lead to the distortion of current on line side. The simulation result proves this phenomenon. This novel method of flux saturation suppression presented in this paper can suppress the harmonics on the secondary side. It can prevent the distortion of the current on line side caused by the flux saturation. The simulation result proves that this novel method has good effect on inhibiting the flux saturation. All of the theoretical analysis and the simulation results prove the correctness and practicability of this novel method.

Acknowledgements

Financial support by the National Natural Science Foundation of China (51207084) and Science and State Key Laboratory of Alternate Electrical Power System with Renewable Energy Sources (LAPS13017) is here all acknowledged.

References

[1] L. Zhang, H. Wu, L. Cao, Automation of Electric Power Systems, Vol.38 (2014), p. 85"In Chinese".
[2] Y.W. Liang, Z.J. Hu, Y.P. Chen, Power System Technology, Vol.27 (2003), p. 71 "In Chinese".
[3] Katiraei F, Iravani M R. IEEE Transactions on Power Systems, Vol. 21 (2006), p. 1821.
[4] Z.Y. Wang, L.F. Luo, Computer Simulation, Vol. 28 (2011), p. 325 "In Chinese".
[5] X.D. Cui, J.L. Yu, Electric Machines And Control, Vol. 11 (2007), p. 6 "In Chinese".
[6] Inaba C Y, Konishi Y, Nakamura M, Nakaoka M, High frequency PWM boost chopper-fed DC-DC converters with coupled-inductors [C]. VIII IEEE International Power Electronics Conference, (2002), p. 134-138.
[7] Kakigano H, Miura Y, Ise T, Uchida R. DC voltage control of the DC micro-grid for super high quality distribution [C]. Power Conversion Conference, (2007), p. 518-521.

Advanced Materials Research Vols. 960-961 (2014) pp 684-688

doi:10.4028/www.scientific.net/AMR.960-961.684

Design and prototype test of a high leakage reactance transformer-based HTS controllable reactor

Wentao Huang[1,2], Meng Song[1,a], Nannan Hu[1], Kunnan Cao[1],Dongdong Lu[1], Jiao Du[1,3], Chao Liu[2], Renkai Niu[2]

[1]Yunnan Electric Power Research Institute, Kunming City, Yunnan Province, P.R. China, 650217

[2]School of Electrical Engineering, University of Chongqing, Chongqing, P.R. China, 400044

[3]School of Electrical Engineering, Kunming University of Science and Technology, Kunming, Yunnan Province ,P.R. China, 650500

[a] 5487100@qq.com

Keywords: Controllable reactor, high temperature superconductor, reactive power compensation, electromagnetic design, DC critical current

Abstract. With the development of high voltage long distance transmission and expansion of the grid, continuous reactive power compensation devices, such as controllable reactor, become more and more important. This paper describes the design and prototype test of a high leakage reactance transformer-based high temperature superconducting controllable reactor (HLRT-HTSCR). Characteristics test results show the excellent impedance regulation characteristic of the prototype. DC critical current test of the superconducting winding shows that attention should be paid to the critical current of superconducting coil, avoiding over-current condition. This paper reveals the characteristics of HLRT-HTSCR by experiment, and will be of important practical significance to promote its development.

Introduction

As an important element of power system, controllable reactor has a broad application prospect, especially in the long-distance EHV/UHV transmission systems for the use of reactive power compensation [1]. Controllable reactor can adjust the line voltage and change the transmission power on condition that line voltage does not exceed the allowable value. The loss of traditional controllable reactor made of conventional materials is large in the case of high voltage and high current. Superconductor is a new type of material. Controllable reactor which is made of superconductor has the advantages of low loss, large capacity and rapid regulation and its characteristics are almost ideal [2]. High leakage reactance transformer-based HTS controllable reactor, which is one of the controllable reactor, has the characteristics of broad reactive power regulation range and very small output current harmonic and can be used in the occasion of high voltage level. This paper will analyze the characteristics of its operation by prototype experiments to promote the process of research and practicality.

Structure and principle

The structure and operation principle of HLRT-HTSCR is similar to the traditional power transformer [3]. It has a E-type core, main winding and two control windings which are made of high temperature superconducting (HTS) wire to reduce AC loss. Both of the two HTS windings are wound concentrically inside the main winding, as shown in Fig.1.

When HLRT-HTSCR works, the main winding is connected in parallel with the load on the line. By changing the operating state of HTS-A and HTS-B wingdings, capacity and the reactance of the reactor can be adjusted [4]. Here is the adjustment mechanism: HTS winding is shorted magnetic lines of flux is expelled from the HTS windings, then the flux area is reduced reactance decreases.

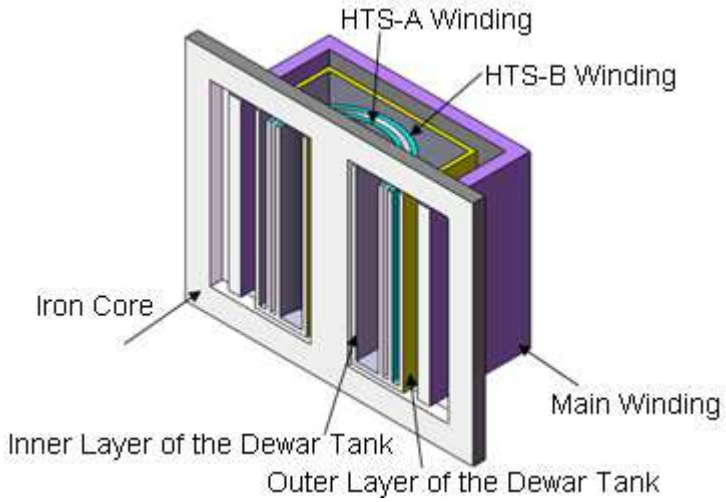

Fig.1. Structure of HLRT-HTSCR

Prototype design and calculation

A single-phase 380V/100A HLRT-HTSCR prototype is designed. The prototype has two superconducting windings, named HTS-A and HTS-B. Each of the windings has two operating modes. Therefore, the prototype has four operating states from M1 to M4, just as shown in the following table 1, where "0"represents open circuit and "1" represents short circuit.

Table 1. Operating modes of HLRT-HTSCR prototype

Mode	M1	M2	M3	M4
HTS-A	0	0	1	1
HTS-B	0	1	0	1

Prototype design includes the designs of windings, electromagnetic parameters, cryogenic system, control system and measurement and protection system. The following description focuses on the design of the electromagnetic parameters of superconducting windings, which is also the core of the prototype design.

Method of electromagnetic parameters design. The design principle is to fully consider the effect of the air gap length between superconducting winding and main winding, the superconducting winding parameters and space asymmetry coefficient on the reactor and electromagnetic characteristics of superconducting windings. The tool of analysis is ANSYS, using 2D symmetric electromagnetic unit to analysis the coupling field of magnetic and electric.

The flow chart of prototype electromagnetic design is shown in Figure 2. Use the methods of setting the parameters and then calculate and check whether the regulation performance of the reactor is good and whether there is enough critical current margin. If the check is not met, then correct the parameter to continue calculation and verification until meeting the requirements.

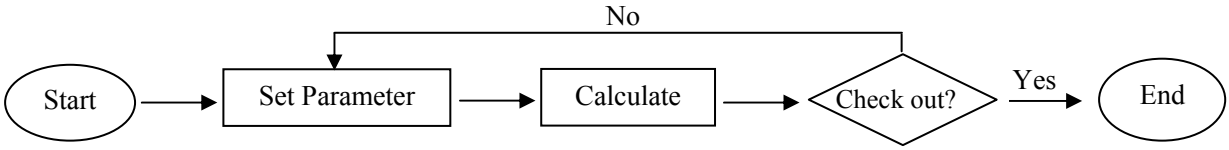

Fig.2 Flow diagram of the electromagnetic design

According to the design method in the previous section, a 380V/40kVar HLRT-HTSCR prototype is designed. Parameters and labels are shown in Table 2 and Figure 3:

Table 2. Parameters of HLRT-HTSCR prototype

Rated voltage /V			380	Rated Current /A			100	Turns of main winding			170
Turns of HTS-A winding			460	Turns of HTS-B winding			352	Height of iron core/mm			571
a/mm	85	a0/mm	45	a1/mm	55	a2/mm	75	a3/mm	125	a4/mm	129
a5/mm	160	a6/mm	168.8	a7/mm	185	a8/mm	205	a9/mm	215	a10/mm	285.5
a11/mm	310	h1/mm	50	h2/mm	220	h3/mm	80	h4/mm	410	h5/mm	450

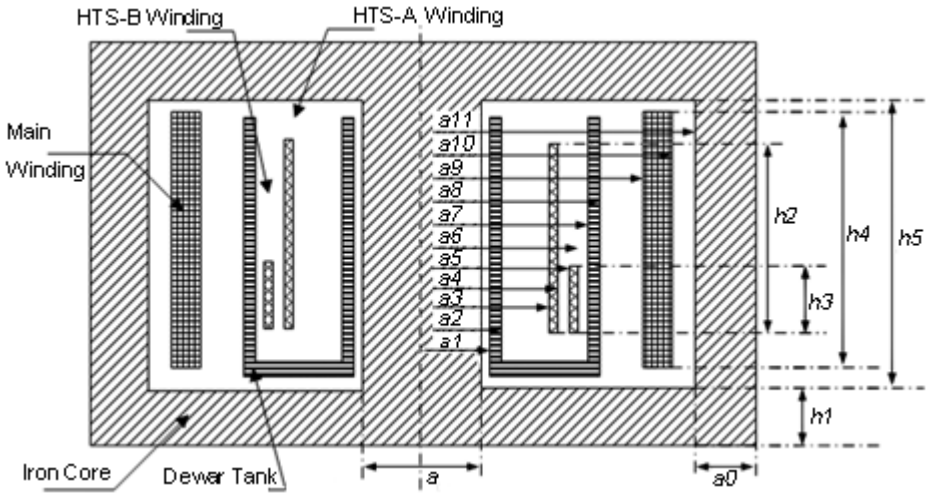

Fig.3. Marking of the electromagnetic parameters

Calculation of the reactance in M1-4. When the superconducting winding A and B are open, reactor can be seen as a conventional reactor which is made of iron core wound by normal conducting coils. In general, the relationship between reactor's inductance and structure size can be expressed by the following equation:

$$L_1=N^2A \tag{1}$$

$$A=\mu A_c/l_c \tag{2}$$

So，the reactance in M1 is given by Equation(3):

$$L_1=W^2\mu A_c/l_c \tag{3}$$

In order to approximately get the expression of inductance when the LFCR works from M2 to M4, we use the following approaches:1) The magneto motive force fully drops on reluctance of air space between short-circuit HTS winding and main winding;2) Leakage-flux density is homogeneous. So L2 is approximately represented by using the following equations:

$$\psi_2 =N\Phi_2 \tag{4}$$

$$\Phi_2 =B_2A_2 = \mu_0H_2A_2 = \mu 0N_iA_2/l_2 \tag{5}$$

$$L_2 =\psi_2/i = \mu_0N_2A_2/l_2 \tag{6}$$

The same as above, we use (7)–(8) to approximately represent L3 and L4, respectively.

$$L_3 =\mu_0N_2A_1/l_1 \tag{7}$$

$$L_4 =\mu_0N_2A_2/l_1 \tag{8}$$

Where,μ_0=4π×10^{-7}H/m; A_c: Equivalent flux area(m^2), l_c: Equivalent length of magnetic path(m).Ψ_2: flux linkage of main winding in M2; Φ_2: magnetic flux of LFCR in M2; N: turns of main winding; A_1:cross-section area between HTS-A and main winding; A_2:cross-section area between HTS-B and main winding; l_1:height of HTS-A winding; l_2:height of HTS-B winding.

Experiment and results analysis

Two relevant experiments are designed to test the performance of the prototype. Photograph of the prototype is shown in Fig.4&5.

Fig.4&5. Photograph of the prototyped HLRT-HTSCR

DC critical current test of the superconducting windings. This Experiment is to measure the maximum DC current which the prototype's superconducting windings can bear. Once the current exceeds this limit, the superconducting windings quenches. The measured data will be basis of the quench protection. The experimental data to be recorded is current and voltage of the two superconducting windings.

When the experiment starts, pay close attention to the data waveform of data acquisition system. Stop the experiment when the winding voltage offset exceeds the criterion (Taking 1uV/cm as a reference, the voltage offset is 35mV because the wire length of the superconducting winding is about 350 meters).

Since the acquisition of the voltage value includes superconducting coil voltage, superconducting coil induced voltage (current uniformly increases), and voltage drop across the welding point resistance and conventional wire resistance. We must subtract this part of the pressure drop when setting quenches criterion. This part of voltage drop increases linearly with the increase of current before superconducting coil quenches. Therefore, the voltage and current of the two loops of the superconducting coils A and B can be calculated and the voltage drop on the superconducting coil equals to the total voltage minus the linear-increasing voltage. The IV-curves are shown in Figure 6.

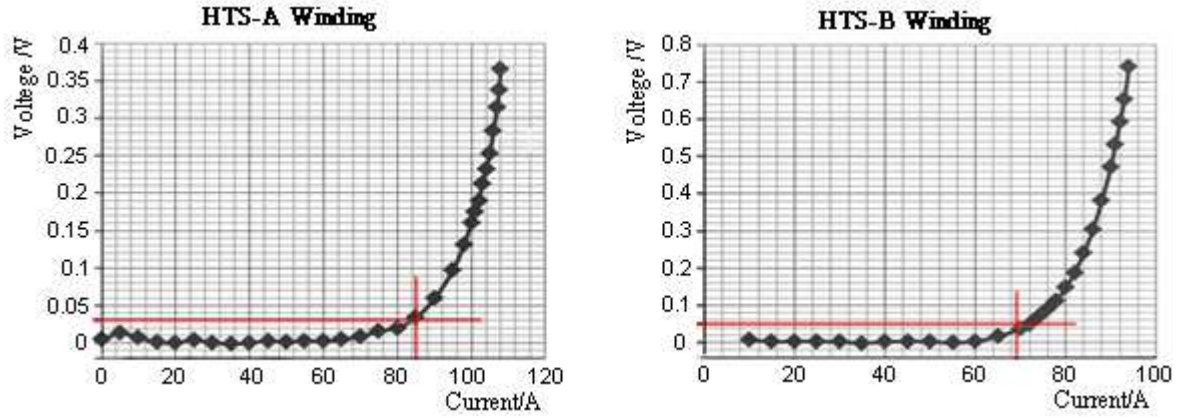

Fig.6. Processed volt-ampere characteristic curve

Making a judgment by 35mV offset voltage line, the DC critical current of HTS-A and HTS-B winding is 86A and 70A, respectively.

Test of reactance regulation. The test is to verify whether HLRT-HTSCR can realize four kinds of reactance adjustment rates in M1-4, and observe whether the adjusting effect is good enough.

The relationship between the main winding side current and voltage, which is worked out by original data, is shown in Figure 7.

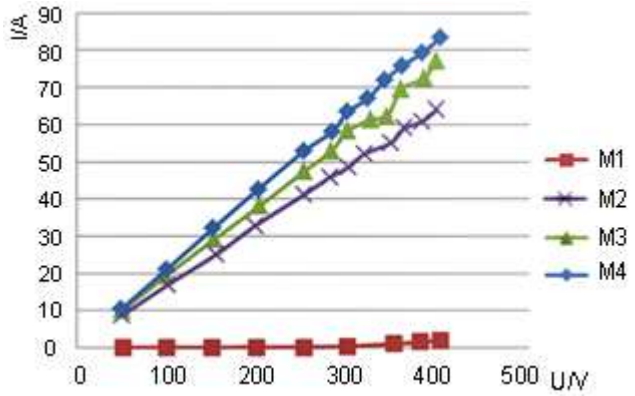

Fig.7. Characteristics of reactance regulation

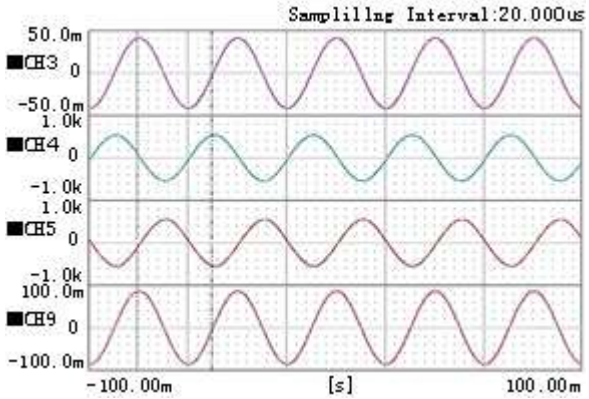

Fig.8. Waveforms of related U&I(M2,380V)

Fig 7 shows the main winding current harmonics and nonlinear relationship between the main winding voltage and current when HLRT-HTSCR works in M1. However, when a HTS winding is short-circuited, the voltage and current has good linearity. The ratio of main winding voltage and current can be considered the reactance. Because of the linearity, it can be considered that the reactance is constant in the test range of main winding voltage.

The prototype is rated at 380V/100A.It can be calculated that the four reactance adjustment rates is 1.94%, 76.6%, 91.7% and 100%. As can be seen from the results, the adjusting effect is good enough.

When the prototype works in M2 and the input voltage is 380V, the waveforms of main winding voltage(CH4), main winding current (CH9), HTS-A winding voltage (CH5), HTS-B winding current (CH3) are shown in Figure 8.It can be seen from Fig.8 that the harmonic is very small, calculated as THD=0.1%. Due to space limitations, waveforms in M1, M3 and M4 is not listed. Those waveforms are similar, containing very small harmonic components.

Experiment results analysis. Experimental results show that the HLRT-HTSCR can realize four kinds of reactance adjustment rates and has the characteristics of flexible control and small harmonic. So it can be used as reactive power compensation device to increase transmission capacity and improve grid stability and reliability.

Moreover, it is important to set the quench-protection action value according to the DC critical current of superconducting winding to avoid reactor damage caused by the quench. When measuring the DC critical current, attention should be paid to exclude the effects of the superconducting coil induced voltage and voltage drop across the welding point resistance and conventional wire resistance.

Conclusions

A single-phase 380V/100A HLRT-HTSCR prototype is developed. Based on the prototype test and analysis, the advantages of HLRT-HTSCR are summarized below:

1) Its structure is the same as traditional transformer, there are no problems on the production processes when used in the case of 500kV or 1000kV high voltage and large capacity;

2) The main reactance of HLRT-HTSCR is leakage reactance while the magnetizing reactance is very small. So, it has the advantages of fast response, stable reactance, no harmonic;

3) This type of reactor is controlled by thyristor-controlled secondary windings, so its response is very fast .As a result, it has the function of limiting line operation overvoltage.

The disadvantage is that the leakage flux is large at the ends of superconducting winding. So, there are strict requirements to the superconducting material. Overall, HLRT-HTSCR has many advantages, and there are a wide range of applications for it in the power system.

References

[1] Meng Song, Hongda Dong, Dada Wang, Kunnan Cao, Li Ren, S. Shen, Research on a Novel Hybrid Adjustable Reactor, Advanced Materials Research, 2013.8, Vols.732-733: 988-992.

[2] Hongda Dong, Li Ren, Ying Xu, Yuejin Tang, Meng Song, Dada Wang, Kunnan Cao, Prototype Test for Confirming the Concept of HTS Magnetically Controlled Saturable Reactor, 2013, Advanced Materials Research, Vols.732-733 , 1090-1094.

[3] Shifeng Shen, Yuejin Tang, Li Ren, Meng Song, Kunnan Cao, Dada Wang, Hongda Dong, et al., Development of A Leakage Flux-Controlled Reactor, accepted for publication in IEEE Transactions on Applied Superconductivity,2013.11, Volume:24 , Issue: 3.

[4] Shen Shifeng,Tang Yuejin,Song Meng,Cao Kunnan,Wang Dada,Ren Li,Dong Hongda. Cryogenics and Superconductivity. 2013, Vol. 41 No. 9, 1-5. (In Chinese)

[5] Cao Kunnan, Song Meng, Shen Shifeng, Tang Yuejin, Wang Dada, Ren Li, Dong Hongda. Cryogenics and Superconductivity,2013, Vol. 41 No. 5, 26-30.(In Chinese)

Advanced Materials Research Vols. 960-961 (2014) pp 689-694

doi:10.4028/www.scientific.net/AMR.960-961.689

The enhancement of a chronically implanted microwire electrode performance

Li Shi[a], Jian wei Chen[b], Song wei Wang[c]

School of Electrical Engineering, Zhengzhou University, Henan Zhengzhou, 450001, China

[a]email:xiaosheng581@sina.cn, [b]email:chenjianwei581@126.com ,[c]email:xiaosheng581@126.com

Keywords: microwire electrode; electrode tip; recording longevity; biocompatibility

Abstract. Electrodes are expensive consumables of electrophysiological experiments. Cheap and homemade microwire electrodes have been widely applied, but their implantation performance is not good. To fabricate low cost and acceptable performance of microwire electrode, first, we analyzed the key factors affecting the long-term recording performance and determined the direction of the enhancement of electrode. We improved the existing fabrication process through electrode fabrication and the electrode tip surface modification, and systematically evaluated its properties, signal acquisition ability and biocompatibility. The result shows that the improved electrode tip surface is smooth and tidy, and its impedance decreased by 56.1% on average; record signal-to-noise ratio is higher; recording longevity reached 45 days; biocompatibility is better. It can meet the use of the general electrophysiological experimental, and electrode fabrication cost is less than 58 yuan.

Introduction

The brain is the most complex organisms[1]. To study the brain to complete the complex mechanism of information processing, must obtain sufficient number of electrical activity information of neurons in the living brain environment. Microelectrode array recording technology can obtain a large number of electrical activity information of neurons[2].

Implanted electrodes are mainly silicon substrate electrode and the microwire electrode. The advantage of implanted electrode is its rich information bandwidth, but it has strong tissue reaction. The fabrication cost of silicon substrate electrode is complex and high, however, we can accurately control the electrode size, shape etc.. The fabrication cost of microwire electrode preparation is relatively simple. This paper uses nickel-cadmium alloy microwire electrode arrays by self-made.

Electrodes are expensive consumables. At present, there are 3 typical commercial electrodes price as follows: The Microprobe electrode is about $586, about $350 of the Michigan electrode, and the Plexon electrode is about 537 yuan. The homemade electrode fabrication cost is less than 58 yuan. Especially the cost is strictly limited circumstances ,self-made electrode is more significance. And the self-made electrode has the advantages of small volume, multiple recording points, stable and reliable performance, can meet the general electrophysiological experiments. In addition, from the literatures of recent years, the ability of long-term recording signal of microwire electrode is more than silicon electrode's [3].

However, after implantation of electrodes in vivo, as time increases, the recording performance of electrode will gradually become bad until failure. Using the operation scissors cutting electrode tip method, recording longevity of electrode is generally too short. Previous electrode problems mainly include two aspects: firstly, the uniformity can not be guaranteed, and the irregular increases implantation tissue damage and affects the long-term performance. Secondly, the tip can not guarante. Therefore, the urgent need is improvement of the performance of electrode. Mainly includes the fabrication of electrode and the electrode tip surface modification.

As a long-term implanted device in the brain cortex, the electrode need a stable electrode-tissue interface to ensure the selective neuronal population record, also need to avoid electrode or peripheral neural tissue degeneration. The study of its properties is related to the electrode and the electrode tissue. When the electrode was implanted into the brain tissue, it can cause injury or death of neurons and glial cells. And they stimulate the neighbor microglias and astrocytes[4,5,6,7]. At the

electrode-tissue interface, there is sustained inflammation, a lot of activated macrophages and damaged neurons[8]. The long-term reaction will reduce the recording performance of long-term application.

The electrode tissue interface has been studied many years. In 1968, DAVIDA proposed the equivalent model of the electrode tissue interface, and described the influence of the tip exposed of metal surface and platinum plating effect on electrode properties[9]. In 2003, L. A. Geddes selected for common electrode materials and insulating layer materials according to tissue reaction, allergic reaction, the electrode-tissue interface impedance[10]. Some literatures considered that electrode size, shape and cross-section affected tissue reaction[11]. But some studies keep skeptical, in 2003, Szarowski made different sizes, shapes, texture of the electrode compared to chronic experiment, and found the former 1-3 weeks of different electrode tissue reaction causes slight difference, and 6-12weeks of tissue reaction did not differ[12]. However, in 2011, Jonas Thelin's study showed that electrode size and fixed mode would strongly affect the nervous system tissue response [13]. In 2006, Sanchez J C studied the site and insulation layer damage of the electrode [14]. In 2011, Erin Patrick studied the electrode surface corrosion changing process of implantation process[15].

Review on the current status of the research can be found, the factors of affecting electrode chronically implanted performance included the electrodes and the tissue. In detail, there are the destruction of insulation layer, electrode tip corrosion, and the implantation site of acute and chronic tissue reaction. They pointed out our electrode improvement direction, so we should improve the tip. Another improvement is the arrangement of electrodes. Irregular arrangement will increase implanted tissue damage, the damage will affect their long-term performance, and we systematically evaluated its properties, signal acquisition ability and biocompatibility.

The design of experiment

The electrode fabrication. The electrode existing fabrication process: (a) Disinfect the experimental platform and the instruments. (b)Cut the wire. (c)Take the circuit board, fix, and glue. (d) Arranging the wire, punching, and welding. (e) The opposite side, repeat(c) and (d). (f)The circuit board welding pins and the Semtec pins are welded together, gluing electrode. (g)According to the need of experiment, the electrode was clipped to the appropriate length.

The fabrication process of modified electrode: (a) Disinfect the experimental platform and the instruments. (b) The micro-assembly: cut wire, into the ceramic piece, epoxy glue fixed, polyethylene glycol shaping. (c)Micro-welding (d) The opposite side, repeat (b). (e) Micro-cutting: according to the requirements, cut electrode wire with a professional tool.

The home-made electrode material of the paper is nickel cadmium alloy wire, diameter of 40 μm, and electrode tip point size was about 706.5 μm^2. Fig.1 shows the 16 recording channel electrode array, and electrode axial space is about 300 μm.

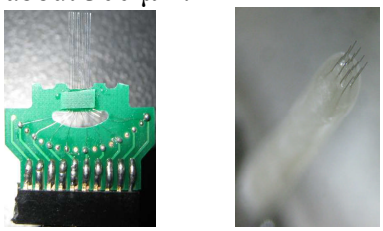

(a) (b)

Fig.1 (a) The electrode of the existing fabrication (b) the electrode of the modified fabrication

The electrode tip as the measuring point, its impedance and morphology is closely related to electrode recording performance. Because of the electrode wire with a diameter of 40 μm, the tip of the electrode was not observed in ordinary optical microscope; therefore, the electrode tip was observed in the scanning electron microscope (SEM). Fig.2 shows the images of the electrode tips in the SEM.

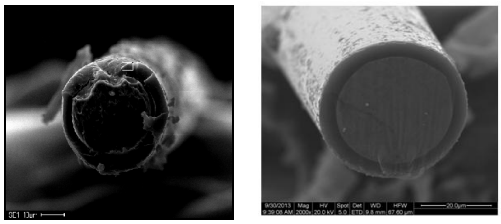

(a) (b)

Fig.2 (a) Using the operation scissors cutting (b) Using micro-cutting

From Fig.2, when using the scissors cutting, it would appear adhesion around the electrode tip. Using micro-cutting, its surface is smooth and tidy and the insulating layer is good around the electrode tip. Compared with the scissors cutting, micro-cutting could improve the electrochemical performance of electrode; and improve the electrode stability and biocompatibility.

The electrode tip modification and impedance measuring in vitro. Conductive polymer polypyrrole has the advantages of good conductive performance and biocompatibility, using polypyrrole on electrode tip modification. Using the NeuroNexus niPOD coating modification on electrode tip and impedance measuring in vitro, and the electrode performance is modified. The modified electrodes include 5, respectively G1, G2, G3, G4, G5. The unmodified electrodes also comprise 5, respectively W1, W2, W3, W4, W5. The modified electrode and unmodified electrode have same material, fabrication process and cutting method. Impedance test experiment was carried out in standard saline solution, temperature control in 25 ℃, the impedances of modified electrodes and unmodified electrodes in the 1kHz value is shown in table1.

Table 1 The impedance values of modified electrodes and unmodified electrodes at 1 kHz [MΩ]

Channel number	1	2	3	4	5	6	7	8	9	10	11	12	13	14
unmodified electrodes	0.85	0.85	0.86	0.87	0.88	0.89	0.95	0.99	0.86	0.87	0.88	0.89	0.90	0.93
modified electrodes	0.37	0.38	0.38	0.39	0.39	0.40	0.42	0.45	0.37	0.38	0.39	0.40	0.40	0.41

The unmodified electrode all channels (80) impedance values at 1kHz and modified electrodes all channels (80) impedance values at 1kHz made t test, so H=1, $P=3.08 \times 10^{-15} < 0.05$, therefore, there is a significant difference between the modified electrode impedance and the unmodified electrode impedance. Modified electrode impedance decreased by 56.1% on average.

The electrochemical impedance spectroscopy[13] of the modified electrode and unmodified electrode is shown in Fig.3.

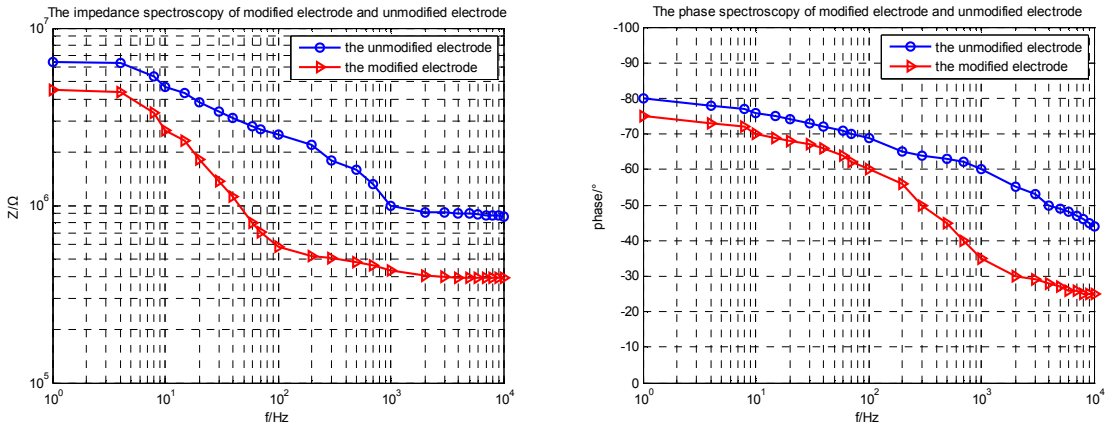

(a) (b)

Fig.3 (a) The impedance spectroscopy of modified electrode and unmodified electrode
(b) The phase spectroscopy of modified electrode and unmodified electrode

From Fig.3, as the frequency increases, the electrode impedance and phase decrease. Compared to the unmodified electrode, the impedance spectroscopy and the phase spectroscopy of modified electrode are lower. They are good for the modified electrode working.

Chronically implanted operation. The weights of 200-300 grams of LE (Long Evans) rats were used as experimental objects. The unmodified group and modified group electrodes (10) were implanted into the primary visual cortex (V1) of 10 rats. Each rat has the same sex and similar physical state. Inject anti-inflammatory drugs after operation.

The result of experiment

Signal acquisition and analysis. The ability of long-term acquisition signal electrode has important significance for evaluation of electrode performance. Using signal-to-noise ratio and recording longevity evaluates electrode signal acquisition ability.

After the implantation operation, after the rat body state recovery (about 1-2 weeks), we regularly (2-3 times per week) record signal by using Cerebus multi-channel data acquisition system .The modified electrode implantation signal acquisition situation is shown in Fig.4.

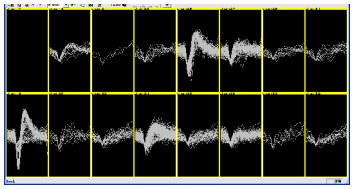

Fig.4 The modified electrode implantation signal acquisition graph

The signal-to-noise ratio (SNR) points out that the electrode differentiates the usable dynamic range of real neuron action potential from the random background noise. The signal-to-noise ratio is calculated by half of peak-to-peak of action potential divided by root mean square(RMS) of the noise base value[16]. The formula is as follows:

$$SNR = \frac{V_{P\_P}}{2V_{n\_std}} \tag{1}$$

Where, V_{P_P} represents the peak-to-peak of action potential, and V_{n_std} represents RMS of the noise base value. The SNR of the unmodified electrode and modified electrode recording signal is shown in Fig.5.

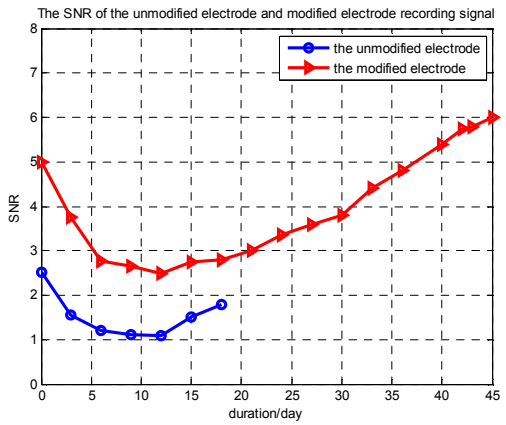

Fig.5 The SNR of the unmodified electrode and modified electrode recording signal

From Fig.5, as the duration increases, the changing trends of SNR of the unmodified electrode and modified electrode acquisition signal are first decreased and then increased. And the SNR of the modified electrode is higher than unmodified electrode's. Thus, the signal acquisition ability of modified electrode is better than unmodified electrode's.

The recording longevity of an electrode is the electrode recording a lot of action potentials duration[17]. The recording longevity of the unmodified electrodes and modified electrodes is shown in Fig.6.

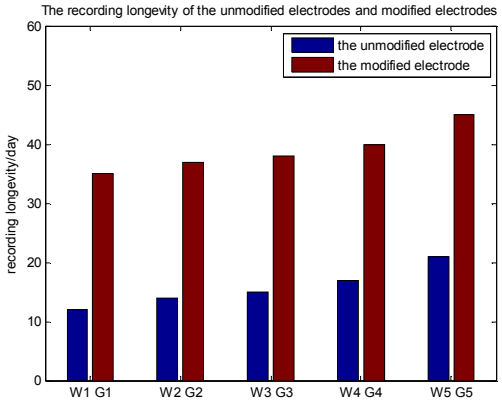

Fig.6 The recording longevity of unmodified electrodes and modified electrodes

From Fig.6, the recording longevity of unmodified electrodes is shorter, the average is 17 days, and the recording longevity of modified electrodes is longer, the average is 40 days.

The electrode biocompatibility

The glial fibrillary acidic protein (GFAP) is a marker of astrocyte activation. When an electrode implanting into the brain regions, it will cause the astrocyte proliferation and accumulation. The brain tissues of modified electrode implanting rats and unmodified electrode implanting rats were separately labeled with GFAP. They were observed under the fluorescence microscope, as shown in Fig.7.

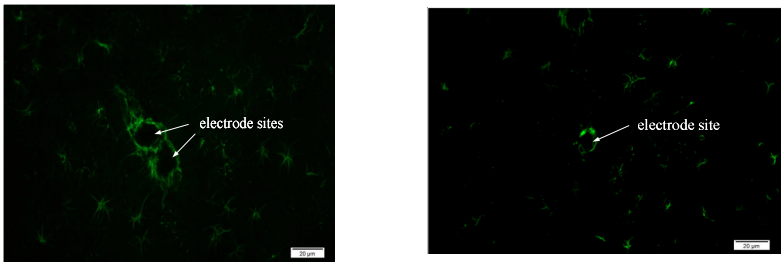

(a) (b)

Fig.7 (a) The unmodified electrode implanting rats GFAP labeled graph
(b) The modified electrode implanting rats GFAP labeled graph

From Fig.7, the aggregation degree of the unmodified electrode site surrounding glial cells is higher than the modified electrode's. So, the unmodified electrode to tissue damage is more serious than the modified electrode to tissue damage. It indicates that the compatibility of modified electrode is than the unmodified electrode's.

Conclusions

This paper improved the existing fabrication process through electrode fabrication and the electrode tip surface modification, and systematically evaluated its properties, signal acquisition ability and biocompatibility. The result shows as follow: (a) Compared to the unmodified electrode, the size of the modified electrode becomes smaller and electrode tip surface becomes smooth and tidy and its uniformity degree increases. (b) Compared to the unmodified electrode, the modified electrode impedance is reduced by 56.1% on average, increasing the recording SNR. (c) The recording longevity of modified electrode is up to 45 days and it is increased about 1.4 times compared to the unmodified electrode. (d)Modified electrodes implanted in the brain region, tissue reaction is smaller and they have better biocompatibility.

At present, the modified electrode fabrication cost is low, and its performance can meet the use of general electrophysiological experiment. But the recording longevity of modified electrode is not long. Factors which cause the electrode failure may be that electrode fabrication technology is not perfect, electrode tip modification is not good and the level implantation operation is low. Further, optimize the electrode design, and improve the level of electrode implantation. Thereby, improving the electrode performance and the recording longevity of electrode is the direction of next research.

Acknowledgement

This work was financially supported by the National Natural Science Foundation (U1304602), Henan Key Scientific and Technological Project (122102210102), The innovation of science and Technology Talents Support Plan of Henan Province Universities (124200510016) and Science and Technology Innovation Team Support Program of Henan Province Universities (2012IRTSTHN001).

References

[1] Pei ji Liang, Ai hua Chen: *Multi-electrode Recording and Neural Information Processing Activity of Neurons* (Beijing University of Technology press, China 2003). (In Chinese)

[2] Zhou yan Feng, Jing Wang: Chinese Journal of Electronics. 1,153-154. (2009) (In Chinese)

[3] Brent D.Winslow, Patrick A.Tresco: Biomaterials. 31,1558-1567. (2010)

[4] Kozai, T. D., Kipke, D. R: Neurosci. Methods. 184,199-205. (2009)

[5] Lee, H., Bellamkonda, R. V., Sun, W., Levenston, M. E: Neural Eng. 2, 81-89. (2005)

[6] Polikov, V. S., Tresco, P. A., and Reichert, W. M: Neurosci. Methods.148, 1-18. (2005)

[7] Grill, W. M., Norman, S. E., Bellamkonda, R. V: Annu. Rev. Biomed. Eng. 11, 1-24. (2009)

[8] Biran, R., Martin, D. C., Tresco, P. A: Exp. Neurol. 195, 115-126. (2005)

[9] David,A.Robinson: Proceedings of The IEEE. 56,1065-1067. (1968)

[10] L. A. GEDDES: Annals of Biomedical Engineering. 31,879-890. (2003)

[11] Rousche PJ, Pellinen DS, Pivin DP: IEEE Trans Biomed Eng. 48,361-371. (2001)

[12] Szarowski DH, Andersen MD: Brain Res. 983,23-35. (2003)

[13] Thelin J, Jo¨ rntell H, Psouni E, et al: PLoS ONE. 6,1~9. (2011)

[14] Sanchez J C, Alba N, Nishida T, et al: Neural Sys. Rehabil. Eng.14, 217-221 (2006)

[15] Erin Patrick, Mark E. Orazem, Justin C. Sanchez, et al: Journal of Neuroscience Methods. 198,158-171. (2011)

[16] E.Huigen, A.Peper C.A.Grimbergen: Med.Biol.Eng.Comput. 40,332-338. (2002)

[17] Xindong Liu, Douglas B.McCreery,et al: IEEE TRANSACTIONS ON REHABILITATION ENGINEERING. 7,315-325. (1999)

Advanced Materials Research Vols. 960-961 (2014) pp 695-699

doi:10.4028/www.scientific.net/AMR.960-961.695

Low-frequency nanotesla resolution of magnetic field detection in Metglas/magnetostrictive/piezoelectric laminates

Jiagui Tao[a], Yongyong Jia[b] Hao Wu[c] and Jinggang Yang[d]

State grid jiangsu electric power research institute nanjing 210003 china

[a]email: taojiagui@163.com

Key words: low-frequency nanotesla, magnetic field, detection, high-permeability materials

Abstract. We report nanotesla resolution in a three-phase Metglas/FeNi/PZT-5A multiferroic composite with one end rigidly clamped operating in the first-order bending resonant mode for low-frequency magnetic field detection. Strong bending magnetoelectric(ME) couplings induced by the ununiform strain distribution in the free-clamped magnetostrictive beam are achieved without the benefit of nonmagnetic tip mass, and its natural resonant frequency is much lower than that in operating free-free mode. In addition, high-permeability materials Metgals are attached on the magnetostrictive beam for magnetic flux concentrating and resolution improvement. Experimental results reveal that the three-phase ferromagnetic/magnetostrictive/piezoelectric composite with a cantilever beam structure exhibits a high bending ME coefficient of ~32.17 V/cm·Oe at the resonant bending frequency of 819Hz under Hdc=175Oe. At the resonant excitation, the maximum resolution of 7nT is acquired under Hac=1Oe. The proposed ME cantilever structure with high resolution provideds a promising application in low-frequency magnetic transducer and sensors.

Introduction

Multiferroic composites composed of magnetostrictive and piezoelectric phases simultaneous have drawn significant focus in recent years due to their multifunctional applications, such as memory devices, resonators, energy harvesters, phase shifters and magnetic sensors[1,2] Among these multiferroic structures, magnetoelectric (ME) laminate composites exhibit a stronger ME coupling through the product property at room temperature than that of the single-phase ME materials[3] In general, the magnetostrictive/piezoelectric laminate composites can be divided into bilayer, trilayer and multilayer architectures[4], and these ME laminate composites may be symmetric (e.g., Terfenol-D/PZT/Terfenol-D trilayer laminates[5]) or asymmetric (e.g., Metglas/PVDF, Terfenol-D/PZT bilayer laminates[6,7]. It is established that both the symmetric and asymmetric ME composites all have improved sensitivity at the mechanical resonant frequencies, where the mechanical losses are the smallest and more mechanical variation energies are transferred from magnetostrictive layer to piezoelectric layer via strain between layers[8]. Generally, the natural longitudinal resonant frequencies of such symmetric composites are quite high, approximately hundreds kHzs. In comparison, the bending resonant frequencies in such asymmetric composites are as low as ~5kHz[9]. Moreover, the resonant frequency will be much lower in the thin-film structures, but ribbons of higher thickness are not available due to partial crystallization during synthesis and resulting degradation of magnetic parameters. In recent reports, to match the ambient operating vibration frequency, the ME composites have to work at the frequencies of just several Hz while with their resonant frequencies of several hundreds kHz[10] In this case, working at the nonresonant conditions result in an inefficient ME energy conversion as well as the sensitivity is severely limited. In view of this, the theoretical and experimental investigations bending resonant ME response have attracted an ever-increasing focus and triggered a great number of research activities for the low-frequency magnetic field detection[9,11]. Meanwhile, great efforts have been devoted to decreasing the bending resonant frequency by various solutions such as applied tunable load biases, resorting torque, changing dimensions and magnetic fields[12-15]. However, most of these schemes

with tip mass would greatly increase the volume in the expense of energy conversion efficient, which is disadvantageous and difficult to deploy in practical situations

Experiments and main Results

In this study, an asymmetric ME composites of Matglas/FeNi/PZT-5A with on end rigidly clamped operating at the bending resonant frequency is fabricated and characterized. In this scheme, FeNi plate is designed as a magnetostrictive cantilever beam with no mass by its robust rigidity over the commonly used PZT cantilever. With one end rigidly clamped. In our proposed ME cantilever, the bending frequency mode is easily chieved due to the ununiform strain distribution of the magnetostrictive beam. Consequently, the clamped-free ME laminate works in the bending mode, and a lower natural resonant frequency and a higher sensitivity at lower operating frequencies can be achieved. Therefore, the proposed architecture offers potentials of an ultrasensitive magnetic sensor at low frequencies.

Here, we provide experimental details of our studies on ME effects in the presented structure. Permalloy (alloy of FeNi) plates with high magnetostriction (~21ppm) and high piezomagnetic coefficient (~23nm/A) are selected as ferromagnetic phase in the composites, and the easy-magnetized axis oriented along its longitudinal direction with dimensions of 25×6×0.6mm3. We use transversely-polarized ceramics PZT-5A plates with high permittivity (~0.6) and resisitivity for the piezoelectric layer, which has dimensions of 25×6×0.2mm3. In order to concentrate more magnetic flux to FeNi plate and enhance the sensitivity, the high-permeability material of Metglas is used in our experiment with its 25×6×0.03mm3. Non-magnetic epoxy α-cyanoacrylate with thickness of ~10μm is used for bonding together between ferromagnetic and ferroelectric layers, and cured for more than 6h at room temperature is required. In experimental setup, an electromagnet was used to provide a dc bias from 0 to 1000Oe, and Helmholtz coil powered by a signal generator (Agilent 33220A, USA) is used to generate a small required ac magnetic field, which was superimposed on the dc bias. The ME voltage induced from the PZT plate was monitored by a lock-in amplifier (Stanford SR844, USA).

The dynamic properties of the proposed structure are characterized by measuring the vibration characteristics and the ME characteristics around resonant frequency. The end vibration amplitude of the FeNi beam in responds to ac magnetic field and its resonance frequency dependence of the end vibration amplitude are measured by using a laser Doppler vibrometry (Sunny Instrum LV-S01, Singapore). Fig. 1 shows the strain coefficient spectrum of the FeNi plate under optimal dc bias magnetic field of 200 Oe. In Fig.1, the induced vibration amplitude induced strain spectrum of the FeNi beam in response to Hac=1Oe for no mass attached at the free end. Under nonresonant excitation (1kHz) the strain coefficient d33 of ~ 0.2nm/A for the sample is obtained, which achieves 23.12nm/A at its natural resonance frequency of 84.8 kHz. The resonant strain coefficient exhibits approximately 116 times higher than the nonsonant coefficient.

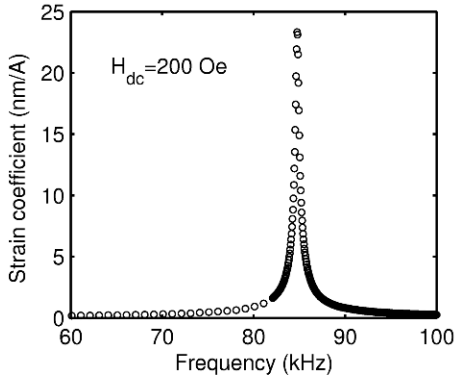

Fig. 1 Strain coefficient spectrum of the ferromagnetic alloy around resonant frequency.

Moreover, Fig. 2 shows the ME coefficient of the composite as a function of frequency at the bending resonant frequency, which is performed under the optimum dc bias magnetic field of 175 Oe.

The frequency dependence of ME coefficient is measured with the samples rigidly clamped at one end, and the optimum bias field is set to the values corresponding to maximum ME coefficient. The data show a resonance in ME vs f curve with a peak of ~32.17 V/cm·Oe for trilayers with Metglas, FeNi and PZT-5A, and the resonant frequency of 819 Hz occurs at the bending mode. The maximum ME response at such low frequencies exhibits ~0.6 times higher than that for 10Hz, which can be attributed mainly to the bending strain in a magnetic field associated with sample asymmetry. For a clamped-free cantilever composite, its natural resonant frequency is given as[16]

$$f_n = \frac{\pi d}{4\sqrt{3l^2}}\sqrt{\frac{\overline{E}}{\overline{\rho}}}\beta_n^2 \tag{1}$$

where d is the thickness of the cantilever, l is the length, $\overline{\rho} = v_m\rho_m + v_p\rho_p$ the average density, $\overline{E} = (v_m s_{33}^H + v_p s_{11}^E)/s_{33}^H s_{11}^E$ is the equivalent elastic modulus, and βn=n+0.5(n is the order of the bending mode). Taking advantage of the parameters list in Table.1, the first order bending mode resonance frequency can be estimated by Eq. 1 to be ~551Hz for the proposed cantilever. Predicted value is slightly lower than that of the experimental value, and this discrepancy at resonance mainly results from the decrease of the effective mechanical Q-factor of the clamped-free mode scheme.

Table.1 The material characteristics of FeNi and PZT-5A

Index	ρ_m or $\rho_p(kg/m^3)$	s_{33}^H or $s_{11}^E \times 10^{-12} m^2/N$	n_m or n_p	Q_m
FeNi	8000	5.22	0.6	1892
PZT-5A	7600	16.4	0.2	500

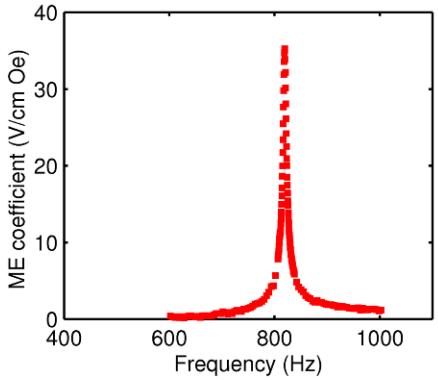

Fig. 2 ME coefficient as a function of frequency around bending resonance under 175Oe

The dependence of ME coefficient αv on Hdc at bending resonant frequency of 819Hz for the composite is demonstrated in Fig. 3. A rapid increase in αv with Hdc to its maximum value of ~32.17 V/cm·Oe is obtained and subsequent by a decrease to a minimum for higher bias fields. It is well known that the ME coefficients αv are directly proportional to the piezoelectric coefficient d33 (d33∞αv), hence we can predict that the H-variation in αv vs Hdc curve essentially tracks the change in piezoelectric coupling (d33=dλ/dH). In order to evaluate the capabilities of magnetic field detection by using our proposed architecture at low frequencies, the sample is placed in a μ-metal shield chamber for resolution measurement and superimposed with an alight ac magnetic field provided by Helmholtz coil. Figure 4 shows the induced ME voltage as a function of Hac under a magnetic bias. The induced ME voltage exhibits a linear function of Hac and increases progressively with applied ac field. The induced ME voltages at Hac=1Oe for 819Hz and 10Hz are 624mV and 0.7mV, respectively. The maximum resolution for detecting a small ac magnetic field is found to be 7nT under Hdc=175Oe at the first bending resonant frequency of 819Hz. When we change the

exciting frequency to the nonresonant frequency 10Hz, 400nT resolution is obtained under Hdc=175Oe at 10Hz.

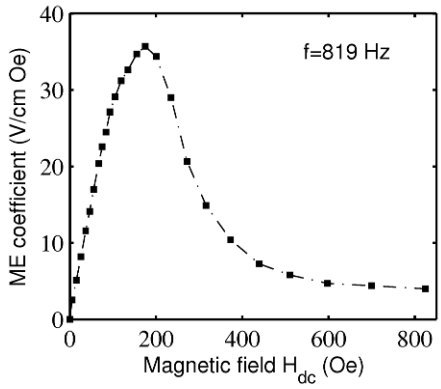

Fig. 3 Magnetic bias field dependence of the ME coefficient under the bending resonant frequency of 819 Hz

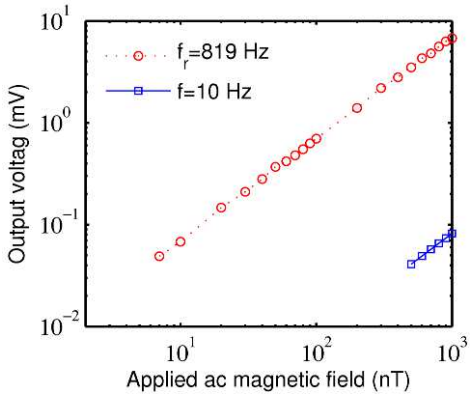

Fig. 4 The change in ME response with increasing applied ac voltage at resonant and nonresonant frequencies

Conclusions

In summary, a three-phase ferromagnetic/magnetostrictive/piezoelectric composite exhibiting high resolution for magnetic field detection at low frequencies is presented, which operates at the first bending resonant frequency with one end rigidly clamped. Without mass in our proposed ME cantilever, the bending frequency mode is easily realized due to the ununiform strain distribution of the magnetostrictive beam. In addition, more magnetic flux can be concentrated into the beam through the high-permeability materials of Metgals ribbons. Consequently, an enhancement of sensitivity and resolution can be achieved in the proposed structure for low-frequency magnetic field detection. Experimental results show that the ME coefficient and the resolution can reach 32.17 V/cm·Oe and 7nT at the first-order bending resonance frequency of 819 Hz, respectively. The strong bending-mode ME coupling with enhanced resolution in this three-phase composite will definitely offers a potential application in low-frequency magnetic transducer and sensors.

References

[1] C. W. Nan, M. I. Bichurin, S. X. Dong, D. Viehland, and G. Srinivasan, J. Appl. Phys. 103, 031101 (2008).
[2] J. Ryu, A. V. Carazo, K. Uchino, and H. E. Kim, J Electroceram 7, 17 (2001).
[3] J. Ryu, S. Priya, K. Uchino, and H. E. Kim, J Electroceram 8, 107 (2002).
[4] J. Jiao, L. Y. Li, B. Ren, H. Guo, H. Deng, W. N. Di, X. Y. Zhao, W. P. Jing, and H. S. Luo, J. Appl. Phys. 111, 043909 (2012).
[5] S. X. Dong, J. F. Li, and D. Viehland, IEEE Trans. Ultrason. Ferr 51, 794 (2004).

[6] X. W. Dong, B. Wang, K. F. Wang, J. G. Wan, and J. M. Liu, Sens. Actuators. A 153, 64 (2009).
[7] J. G. Wan, Z. Y. Li, Y. Wang, M. Zeng, G. H. Wang, and J. M. Liu, Appl. Phys. Lett. 86, 202504 (2005).
[8] S. X. Dong, J. R. Cheng, J. F. Li, and D. Viehland, Appl. Phys. Lett. 83, 4812 (2003).
[9] Z. P. Xing, S. X. Dong, J. Y. Zhai, L. Yan, J. F. Li, and D. Viehland, Appl. Phys. Lett. 89, 112911 (2006).
[10] S. D. Moss, J. E. McLeod, I. G. Powlesland, and S. C. Galea, Sens. Actuators. A 175, 165 (2012).
[11] V. M. Petrov, G. Srinivasan, M. I. Bichurin, and T. A. Galkina, J. Appl. Phys. 105, 063911 (2009).
[12] T. Wu, M. Emmons, T. K. Chung, J. Sorge, and G. P. Carman, J. Appl. Phys. 107, 09D912 (2010).
[13] J. R. Petrie, J. Fine, S. Mandal, G. Sreenivasulu, G. Srinivasan, and A. S. Edelstein, Appl. Phys. Lett. 99, 043504 (2011).
[14] K. Bi, Y. G. Wang, and W. Wu, Sens. Actuators. A 166, 48 (2011).
[15] J. Y. Zhai, S. X. Dong, Z. P. Xing, J. Q. Gao, J. F. Li, and D. Viehland, J. Phys. D: Appl. Phys. 42, 122001 (2009).
[16] B. L. Fu, New theory of thin bending plates.(Science Press, Beijing, China, 2003).

Advanced Materials Research Vols. 960-961 (2014) pp 700-703

doi:10.4028/www.scientific.net/AMR.960-961.700

Power Transformers Fault Diagnosis based on DRNN

Huida DUAN [1,a], Qiaosong LI[1,b]

[1]School of Electric and Information Engineering, Beihua University, ji lin, 132021

[a]huida_duan@126.com, [b]707110999@qq.com

Keywords: Diagonal recurrent neural network; Fault diagnosis; Dissolved gas analysis; Recursive prediction error algorithm

Abstract. In recent years, improved three-ratio is an effective method for transformer fault diagnosis based on Dissolved Gas Analysis (DGA). In this paper, diagonal recurrent neural network (DRNN) is used to resolve the online fault diagnosis problems for oil-filled power transformer based on DGA. To overcome disadvantages of BP algorithm, a new recursive prediction error algorithm(RPE) is used in this paper.In addition, to demonstrate the effectiveness and veracity of the proposed method, some cases are used in the simulation. The simulation results are satisfactory.

Introduction

At present, DL/T2000 has recommended improved three-ratio method for the main transformer fault diagnosis method of internal fault [1] in china. It is one kind of fault diagnosis methods based on Dissolved Gas Analysis (DGA) [2,3]. DGA is an analysis method which is used to detect and diagnose different types of faults occurring in oil-filled power transformers. The method tests and samples the insulation oil of transformers periodically to obtain the different interpretations of dissolved gases in the mineral oil-insulation of such transformers. Now, in order to obtain online monitoring and fault diagnosis, transformer fault diagnosis requires an accurate model under fault conditions, particularly toward internal faults. Recently, many intelligence methods such as artificial neural network [4], Bayesian classifier and rough set [5], expert system [6], fuzzy theory and other some mixed new methods [7] have been investigated for transformer fault diagnosis and produced useful conclusions. Thus, in this paper, the diagonal recurrent neural network is used in the transformer fault diagnosis to increase diagnosis accuracy.

In recent years, the research of DRNN [8, 9] has made great development. Compared with BP neural network, DRNN is a dynamic neural network, it has simple structure. It can approximate any regular function and it has faster convergence speed. This faster convergence speed comes from the fact that DRNN has just three layers of weights and each layer can be determined sequentially. So DRNN is widely used in the fault diagnosis, functional approximation, modeling and classifying. In this paper, to further reduce the training time of DRNN, a new Recursive Prediction Error algorithm is used in this paper.

Diagonal recurrent neural network

DRNN is a dynamic neural network. It consists of three layers, one input layer , one middle layer and one output layer. The input layer corresponds to the input vector space and the output layer to the pattern classes. The architecture of DRNN is shown in Fig.1.

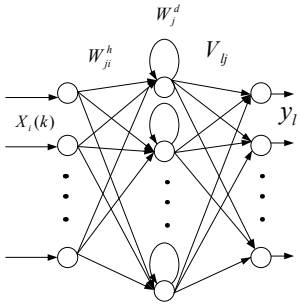

Fig.1 Architecture of DRNN

The DRNN equations between the input and output are as follows:

$$\begin{aligned} S_j(k) &= \sum_{i=1}^{M} W_{ji}^{h} * X_i(k) + W_j^d O_j(k-1) + b_{1j}(k) \\ O_j(k) &= f(S_j(k)) \\ y_l(k) &= \sum_{j=1}^{H} V_{lj} * O_j(k) + b_{2l}(k) \end{aligned} \tag{1}$$

Where, $X_i(k)$ is the input vector, $y_l(k)$ is the output, $S_j(k), O_j(k)$ are the input and output vectors of the hidden layer. W_{ji}^{h} is the weight vector between input layer and hidden layer. V_{lj} is the weight vector between output layer and hidden layer. W_j^d is weight of recurrent neuron. b_{1j} and b_{2l} are thresholds of hidden layer and output layer. $f(\bullet)$ is the excitation function of hidden neuron.

Recursive Prediction Error algorithm

The BP algorithm is a well-known method of training a multilayer feed-forward ANN. Although the algorithm is successful, it has some disadvantages. BP algorithm has a slow learning convergent velocity and easy convergence to local minima, which cannot be avoided. In addition, the selection of the learning factor and inertial factor affects the convergence of the BP neural network, which is usually determined by experience. To overcome disadvantages of BP algorithm, a Recursive Prediction Error algorithm is used. RPE algorithm is a method for parameter estimation based on the recursive prediction error minimizes principle.

Define the objective function:

$$\begin{aligned} E(\Theta) &= \frac{1}{2N} \cdot \sum_{k=1}^{N} [y_d(k) - \hat{y}(k)]^2 \\ &= \frac{1}{2N} \cdot \sum_{k=1}^{N} e^T(k,\Theta) \cdot e(k,\Theta) \end{aligned} \tag{2}$$

Where, e (k,Θ) is recursive prediction error vector. Θ is parameter vector(weights and thresholds of DRNN).

Then , the parameter vector revised formula is given :

$$\begin{aligned} &\Theta(k) = \Theta(k-1) + \alpha(k) \cdot \mu[\Theta(k-1)] \\ &\mu(\Theta) = -[H(\Theta)]^{-1} \nabla E(\Theta) \\ &\nabla E(\Theta) = -\frac{1}{N} \cdot \sum_{k=1}^{N} \psi(k,\Theta) \cdot e(k,\Theta) \\ &H(\Theta) = \sum_{k=1}^{N} \psi(k,\Theta) \cdot \psi^T(k,\Theta) \\ &\psi(k,\Theta) = [d\hat{y}(k,\Theta)/d\Theta]^T \end{aligned} \tag{3}$$

Where , $\alpha(k)$ is study velocity, μ(Θ)is the search direction of Gauss-Newton, ▽E(Θ) is gradient about Θ, H(Θ)is the Hessian array of E(Θ) .Then the RPE of DRNN can be given as follow functions.

$$\begin{aligned} &e(k) = y(k) - \hat{y}(k) \\ &P(k) = \frac{1}{\lambda(k)} \cdot \{P(k-1) + P(k-1) \cdot \psi(k)[\lambda(k) + \psi^T(k) P(k-1) \psi(k)]^{-1} \psi^T(k) \cdot P(k-1)\} \\ &\Theta(k) = \Theta(k-1) + \alpha(k) P(k) \psi(k) e(k) \\ &\lambda(k) = \lambda_0 \cdot \lambda(k-1) + (1-\lambda_0) \end{aligned} \tag{4}$$

Where, $\lambda(k)$ is forgetting factor.

Compared with the BP algorithm, RPE algorithm increases the amount of calculation for each-step training, but it uses second-order gradient effective accelerating the algorithm convergence speed, thus reduces overall training time. In addition, RPE algorithm of changed the algorithm adopted and the sensitivity of the initial momentum factors, and avoid the poor training effect of BP algorithm.

Improved three-ratio method

Among many DGA approaches, the normal three-ratio method is most commonly used because of its effective and convenient. It uses 3 gas ratios, C2H2/C2H4, CH4/H2 and C2H4/C2H6. Each ratio is quantized to a classification code 0, 1, or 2. So in total there is to be 27 possible combinations (fault types) but IEC 599 defines only 11 combinations leading to non-decision diagnosis, when falling within the invalid group of 16 remaining combinations. Improved three-ratio method overcomes the shortcomings of three-ratio method. Now, it is recommended fault diagnosis method based on DGA in china. Fault characters and fault diagnosis table of improved three-ratio method is given in Table 1.

Table 1. Improved three-ratio of DGA

Type of fault			
C_2H_2/C_2H_4	CH_4/H_2	C_2H_4/C_2H_6	Fault type code
$X_1<0.1$	$X_2<0.1$	$X_3<1$	1.Partial discharge
	$0.1<X_2<1$	$1 \le X_3<3$	2.Thermal fault with temperature(≤150℃)
	$1 \le X_2$	$X_3<1$	3.Thermal fault with temperature(150℃ 300℃)
	$1 \le X_2$	$1 \le X_3<3$	4. Thermal fault with temperature(300℃ 700℃)
	random	$X_3 \ge 3$	5. Thermal fault with temperature(≥700℃)
$X_1 \ge 3$	$X_2<1$	random	6.partial discharge with low energy density
	$X_2 \ge 1$	random	7.partial discharge with low energy density and thermal fault
$0.1 \le X_1<3$	$X_2<1$	random	8.Arc discharge
	$X_2 \ge 1$	random	9.Arc discharge and thermal fault

Neural network model and simulations

According to the improved three-ratio method, the structure of DRNN can be determined. The number of inputs of DRNN is three, respectively represent three inputs of C_2H_2/C_2H_4, CH_4/H_2 and C_2H_4/C_2H_6. The number of outputs of DRNN is nine, respectively represent nine different fault types (type 1-type 9). The nodes number of hidden layer is adaptive, meaning that the output of each node to the next node depends on the internal parameters pertaining to that particular node, which are modified during the learning process.

In order to evaluate the performance of the proposed algorithm, some simulation has been made. The diagnosis data of fault transformer contained 50 samples achieved from Jilin electrical science institute. With these samples, train the DRNN based on the RPE algorithm. Fig. 2 is the mean square error convergence curve of DRNN trained with RPE algorithm. Some fault diagnosis results with proposed method are list in the Table 2. From the simulation diagnosis results, it can be seen that the accuracy of this proposed method is satisfactory.

Conclusions

In this paper, a neural network fault diagnosis method based on DRNN is used to predict the internal fault for power transformers .In addition, to improve the convergence speed and improve the fault diagnosis accuracy, RPE algorithm is used. From the analysis of the results, it can be seen that the proposed method can provide an accurate approximation for fault diagnosis. It can detect the main fault type and provide useful information for future fault trends and multiple faults analysis systems.

Table 2. Diagnosis results

	H_2	CH_4	C_2H_4	C_2H_6	C_2H_2	CO	CO_2	type
1	2781	1293	23	248	84	750	—	Type 6
2	259	863	994	393	6	974	7038	Type 4
3	66	86	7	100	8	310	1800	Type 9
4	328	73	73	3	65	636	1023	Type 8
5	260	130	84	26	92	260	7400	Type8
6	58	55	110	10	70	71	9990	Type 9
7	610	1200	1800	300	6	180	2000	Type 5
8	133	466	502	70	9	107	1271	Type 5
9	73	520	1230	140	7	410	5500	Type 5
10	980	73	12	0	58	190	500	Type 1

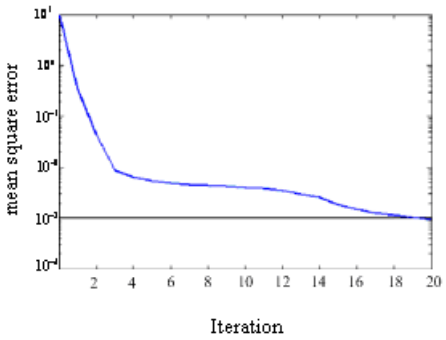

Fig. 2 Convergence curve with RPE

Acknowledgements

This work was financially supported by the Fund Project of Jilin education department (2011118).

References

[1] D.K. Cao, gas analysis diagnosis and fault inspection in transformer oil, China Electric Power Press,2005.

[2] Roers, R., IEEE and IEC codes to interpret incipient faults in transformer, using gas in oil analysis. IEEE Trans. On Electr. Insul., Vol. 13, No. 5, pp. 349-354, (1978).

[3] J.J.Kelly, Transformer fault diagnosis by dissolved-gas analysis, IEEE Trans. on Industry Applications, Vol. 16, No. 6, pp. 777-782, (1980).

[4] Zhang, S.L., A Fuzzy Logic and Neural Network Approach to Power Transformer Incipient Fault Detection, B Eng Final-year Project Thesis, National University of Singapore, (2003).

[5] Z. Wang, Y. Liu, and P. J. Griffin, A combined ANN and expert system tool for transformer fault diagnosis, IEEE Trans. on Power Delivery, Vol. 13, No. 4, pp. 1224-1229, (1998).

[6] Lin, C.E., Ling, J.M., and Huang, C.L., An Expert System for Transformer Fault Diagnosis Using Dissolved Gas Analysis, IEEE Transactions on Power Delivery, vol. 8, no. 1, pp 231-238,(1993).

[7] Su, Q., Mi, C., Lai, L.L., and Austin, P., A Fuzzy Dissolved Gas Analysis Method for the Diagnosis of Multiple Incipient Faults in a Transformer, IEEE Transactions on Power Systems, vol. 15, No.2 pp 593 – 598, (2000).

[8] Alex Aussem. Dynamical recurrent neural networks towards prediction and modeling of dynamical system. Neurocomputing,28(1999):207.

[9] H. D. Duan, D. L. Zheng, C. Liu. Modeling and application based on diagonal recurrent neural network, Journal of University of Science and Technology Beijing, (in Chinese) Vol. 26, No. 1, pp. 103-105, (2004)

Advanced Materials Research Vols. 960-961 (2014) pp 704-709

doi:10.4028/www.scientific.net/AMR.960-961.704

Cubic Spline Interpolation Method for the Envelope Tracking of Middle and Low frequency Voltage Flicker

Xiufang Jia[1,a] , Haiqing An[1,b], Shaoguang Zhang[1,c]

[1]State Key Lab of New Energy Power System (North China Electric Power University) Baoding 071003 China

[a]xiufangjia@163.com, [b]anhaiqing1990@163.com [c]shaoguang.z@163.com

Keywords: power quality; voltage flicker; cubic spline interpolation; envelope tracking

Abstract. Flicker envelope tracking is the key of analyzing voltage flicker signal. A novel method, i.e., cubic spline interpolation method is applied in the detection of the voltage flicker envelope. The typical flicker signals, such as one or multi-frequencies and frequency time-varying flicker signal are selected and analyzed by this method. Simulation results indicate that this method is effective in the detection of the envelope of voltage flicker signal. Results of one or multi-frequencies flicker signal simulation show that, when flicker frequency is less than 15Hz , the error of this method is quite tiny. The detection precision of this method is higher, especially in the scope of low frequencies of flicker and this method makes up for the disadvantage of square demodulation. Furthermore, results of frequency time-varying flicker signal simulation show that, the occurrence and recover time of voltage flicker signal can be accurately detected by cubic spline interpolation method.

Introduction

In various power quality problems, voltage fluctuation and flicker is considered as one of the major power quality disturbances [1-2]. With the development of the national economy, larger quantities of high-power impulsive, fluctuating and nonlinear loads, such as arc furnaces, arc welders, spot welders, resistance welders and repetitive operation machinery are used in power networks. The active power and reactive power change rapidly and violent during these equipments operate, which results in voltage fluctuation at the point of common coupling (PCC) [3]. In order to minimize voltage fluctuation, numerous reactive power compensation devices are applied in the power system. However, these devices are required to provide accurate tuning flicker parameters to make the right suppression decisions. The amplitude and frequency information of the voltage fluctuation is contained in the envelope of voltage flicker signal. Therefore, the key to analyze voltage flicker signal is the detection of flicker envelope. After separation of the flicker envelope, flicker-related parameters can be easily calculated according to selected criteria [4-5].

At present, square demodulation, rectifier detection and RMS detection are three main methods to be selected to detect voltage flicker by flicker meter at home and abroad [6]. However, these three methods are not suitable for detecting multi-frequency flicker signal and time-varying flicker signal. Especially, square demodulation is the method which based on the IEC recommended [7]. References [8-9] proposed that the error of square demodulation method to extract the envelope of flicker increases with the flicker frequency decreasing. In the vicinity of the most sensitive flicker frequency 8.8Hz, the detection error reduces to a minimum, and then increases again. In a word, the detection precision of square demodulation method is high, only in the scope of low frequencies.

The interpolation method is one of the important numerical approximation methods [10], which is based on the given variable value and function value to get the approximate value of unknown function. The task of interpolation is known by the observation points to set up a simple, continuous analytical model, in order to be able to deduce the physical quantities in the non observation points according to the characteristics of the model. However, in practice, there are many interpolation function curve with high smoothness. In the whole curve, curve can not be a turning point, but also can not have the mutation of curvature. Therefore, the interpolation functions must be continuous and constant micro No. two times; this requires cubic spline interpolation which has the best smoothness.

For this feature of cubic interpolation method, and considering the flicker signal characteristic, this method is used in this paper for the first time to track voltage flicker envelope.

The cubic spline interpolation method

The definition of cubic spline interpolation. For an interval $[a,b]$, $a=x_0<x_1<\cdots<x_n=b$, the corresponding function values are $y_0<y_1<\cdots<y_n$. If function $S(x)$ meets the following three conditions, $S(x)$ is called cubic spline interpolation on interval $a\le x_i\le b, i=0,1,\cdots n$.

(1) $S(x_i)=y_i$,$i=0,1,\cdots n$;(2)$S(x)$ is not more than three times polynomial on interval [x_{i-1}, x_i](i=1,2,…n);(3) $S(x)$ is continuous second-order derivative on interval $[a,b]$.

In constructing the cubic spline interpolation function, requiring $S(x)$ only determined a cubic polynomial on the each sub-interval [x_{i-1}, x_i], set:

$$S_i(x)=a_ix^3+b_ix^2+c_ix+d_i, i=0,1,\cdots,n \tag{1}$$

In which a_i,b_i,c_i,d_i are undetermined coefficients, and $S(x_i)=y_i$; $S(x_i-0)=S(x_i+0), i=1,2,\cdots,n-1$; $S'(x_i-0)=S'(x_i+0), S''(x_i-0)=S''(x_i+0), i=1,2,\cdots,n-1$ .There is 4n-2 conditions, so 4n coefficients need to be determined. To uniquely identify a cubic spline interpolation, additional two boundary conditions are also needed and they are usually given by the endpoints status of cubic spline interpolation in practical.

The construction of cubic spline interpolation function. Cubic spline interpolation function $S(x)$ approaches to the real function $y=f(x)$ through piecewise cubic polynomial, and satisfies three conditions mentioned above.

To make $M_i=S''(x_i)$, the interpolation condition $S(x_i)=y_i, i=1,2,\cdots,n$ and formula (2)

$$S''(x)=\frac{x-x_{i-1}}{h_{i-1}}M_i-\frac{x-x_i}{h_{i-1}}M_{i-1}, i=1,2,\cdots,n \tag{2}$$

By two continuous integration, you can get the cubic spline interpolation function $S(x)$ expressed as formula (3):

$$\begin{aligned}S(x)&=\frac{M_i}{6h_{i-1}}(x-x_{i-1})^3-\frac{M_{i-1}}{6h_{i-1}}(x-x_i)^3\\&+(\frac{y_{i-1}}{h_{i-1}}-\frac{M_{i-1}}{6}h_{i-1})(x_i-x)+(\frac{y_i}{h_{i-1}}-\frac{M_i}{6}h_{i-1})(x-x_{i-1})\end{aligned} \tag{3}$$

Where $x_{i-1}\le x\le x_i, i=1,2,\cdots,n$, $h_{i-1}=x_i-x_{i-1}, i=1,2,\cdots,n$.

The function $S(x)$ has a continuous second derivative at the sample point x_i , and according to cubic spline interpolation method principle, besides, increasing the natural boundary conditions:

$$\begin{aligned}S''(x_0)&=y_0''=0\\S''(x_n)&=y_n''=0\end{aligned} \tag{4}$$

Obtain the following equations represented by the matrix:

$$\begin{bmatrix}2 & j_0 & & & \\ \lambda_1 & 2 & j_1 & & \\ & \ddots & \ddots & \ddots & \\ & & \lambda_{n-1} & 2 & j_{n-1}\\ & & & \lambda_n & 2\end{bmatrix}\cdot\begin{bmatrix}M_0\\M_1\\\cdots\\M_{n-1}\\M_n\end{bmatrix}=\begin{bmatrix}J_0\\J_1\\\cdots\\J_{n-1}\\J_n\end{bmatrix} \tag{5}$$

Where $\begin{cases}j_i=\dfrac{h_{i+1}}{h_i+h_{i+1}}\\ \lambda_i=1-j\\ J_i=\dfrac{6}{h_i+h_{i+1}}(\dfrac{y_{i+1}-y_i}{h_{i+1}}-\dfrac{y_i-y_{i-1}}{h_i})\end{cases}$, and i=1， 2， …， n-1， j_0=0， J_0=0， λ_n=0.

To solve the equations above, obtained by M_i(i= 0, 1, 2,…,n) into formula (3), then get the cubic spline interpolation function on each sub-interval [x_{i-1},x_i](i= 1, 2,…,n).

The envelope tracking of voltage flicker based on this method

Voltage flicker is caused by voltage fluctuation. The analytical expression of periodic voltage flicker signal can be expressed by formula (6).

$$u(t) = A(1+\sum_{k} m_k \cos\Omega_k t)\cos(\omega t+\theta) \tag{6}$$

Where, A—the amplitude of power frequency carrier voltage;

ω—the angular frequency of power frequency carrier voltage;

m—the coefficient of amplitude modulation(AM) wave, i.e. AM wave voltage amplitude and power frequency carrier wave voltage amplitude ratio.

Ω_k—the angular frequency of amplitude modulation wave.

As power frequency voltage is the carrier of flicker signal, its peak value or root mean square voltage fluctuation component is modulated in amplitude as the waves, flicker frequency is generally between 0.5~25Hz. The amplitude and frequency information of the voltage fluctuation is contained in the envelope of voltage flicker signal. Therefore, the key to analyze voltage flicker signal is the detection of flicker envelope [11].

The steps of envelope tracking using cubic spline interpolation method are as follow:

1) For voltage flicker signal $u(t)$, high frequency sampling and the frequency of 3200Hz;

2) Determined all the coordinates of maximum points $p_i(x_i, y_i)$ and minimum points $q_j(x_j, y_j)$;

3) Regarded p_i and q_j as the interpolation nodes which have been known.

4) In order to avoid the end effect, adding the boundary condition and regarding the endpoints of flicker signal $u(t)$ as the maximum points.

5) Fitting the upper and lower envelope, respectively, using cubic spline interpolation.

6) The sum of the upper and lower envelope averaging to obtain the final envelope, i.e. to extract flicker envelope.

This method is simple and fast, just to get extreme points of flicker signal, you can quickly extract flicker envelope with a cubic spline interpolation method.

To reflect the cubic spline interpolation method to extract flicker envelope is valid, using the formula (7) to calculate the detection error of this method, which the relative error extracts flicker envelope is defined is:

$$e = \left|\frac{a(t)-a'(t)}{a(t)}\right| \times 100\% \tag{7}$$

In the formula (7), $a(t)$ is the real instantaneous amplitude, $a'(t)$ is the instantaneous amplitude extracted by cubic spline interpolation method.

Here the use of MATLAB software cubic spline interpolation method for programming method to extract flicker envelope, to verify the validity of this method. In the following case study, the voltage amplitude was represented by per-unit value. The extracted envelope is instantaneous amplitude of the results which the DC component has been filtered out.

Case study

Flicker signal with one frequency. In order to show test results more intuitively, set the example of the signal parameters calculated as follows: The frequency of AM wave: 8.8Hz, the coefficient m is 5%, carrier frequency:50Hz, Initial phase:0, sampling frequency: 3200Hz, sampling duration: 0.5s.

The example signal was shown as formula (8):

$$u(t) = (1+0.05\cos 17.6\pi t)\cos(100\pi t) \tag{8}$$

8.8Hz flicker signal waveform was shown in Figure 1, with cubic spline interpolation method to extract flicker envelope was shown in Figure 2. Figure 2 shows that the two envelopes are almost coincident. The method analyzing the detection error in this paper is that remove the anomalous data which in zero-crossing and endpoints and use the least squares to fit the data points. Take the average of fitting date as detection error of cubic spline interpolation method. Due to space limitations, only the results of a single frequency flicker detection error is shown in figure 3. Fitted by least-squares, it is a straight line parallel to the abscissa of the coordinate. The mean of detection error was 0.2772%.

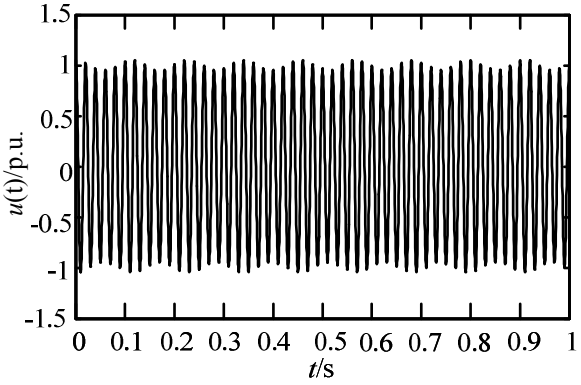

Fig.1 The one-frequency flicker signal

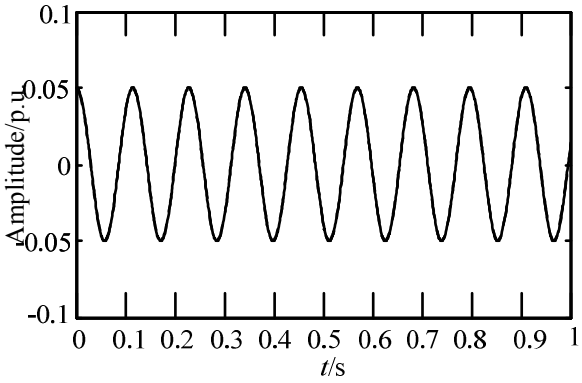

Fig.2 The detection result (dotted line) compare with real value (solid line) of multi-frequency

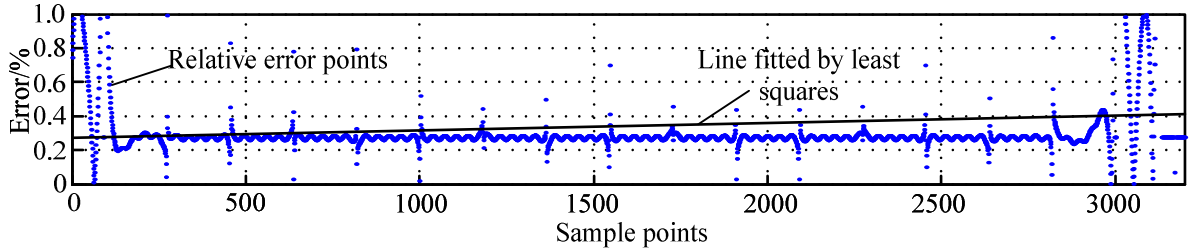

Fig.3 The relative value of detection errors

To get close to actual, take the voltage fluctuation parameters of instantaneous visual sensitivity $S(t)$=1 proposed in literature [6] for analysis. The errors detected by cubic spline interpolation method were shown in table 1.

Tab. 1 The detection errors of cubic spline interpolation method

f/Hz	Δ*V*/%	error/%	*f*/Hz	Δ*V*/%	error/%	*f*/Hz	Δ*V*/%	error/%	*f*/Hz	Δ*V*/%	error/%
0.5	2.340	2.2×10^{-6}	5.0	0.398	0.0241	**8.8**	**0.250**	**0.2772**	12.0	0.312	1.1900
1.0	1.432	3.5×10^{-5}	6.0	0.328	0.0518	9.5	0.254	0.3943	13.0	0.348	1.7692
2.0	0.882	5.6×10^{-4}	6.5	0.300	0.0730	10.0	0.262	0.4937	14.0	0.388	2.5771
3.0	0654	0.0029	7.0	0.280	0.1002	10.5	0.270	0.6268	15.0	0.462	3.6958
4.0	0.500	0.0095	7.5	0.266	0.1357	11.0	0.282	0.7817	**16.0**	**0.480**	**5.2105**

Analysis of the data in Table 1 shows that the detection error becomes larger and larger with flicker frequency increasing using the proposed method. When the frequency is greater than 15Hz, the error is more than a 5%. Using this method to extract the flicker envelope of which the frequency is below 12Hz, the detection error is small, maintained at 1.5%. And the lower the frequency is, the smaller the error is. In particular, when the flicker frequency is at 3Hz or less, the detection error is less than 0.003%. And this band is exactly in the test frequency range of low frequencies of IEC flicker meter. Literature [8] pointed out: IEC flicker meter for detection error of low-frequency flicker is large, so the cubic spline interpolation method is applicable to the detection of low-frequency flicker caused by wind power connected to grid (1~3Hz). Thus, this method is more suitable for flicker in low-mid frequency envelope detection.

Flicker signal with multi-frequencies. Formula (7) represents multi-frequency flicker signal.

$$u(t) = (1+0.075\cos 10\pi t + 0.05\cos 20\pi t + 0.025\cos 30\pi t)\cos(100\pi t) \tag{7}$$

The frequency of AM wave: 5Hz, 10Hz and 15 Hz; the coefficients are corresponding to 7.5%, 5% and 2.5%, respectively. Sampling frequency: 3200Hz, sampling duration: 0.5s.

Multi-frequency flicker signal waveform was shown in Figure 4, with cubic spline interpolation method to extract flicker envelope was shown in Figure 5. Since the endpoint effect, the two envelopes not coincide except for the envelope at the endpoint, and the rest almost coincide. Detection error is 1.2917% and the detection is ideal.

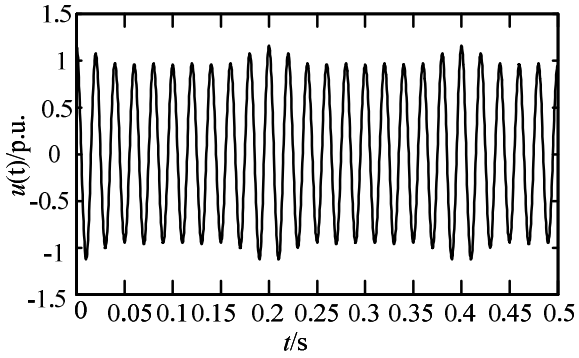

Fig.4 The multi-frequency flicker signal

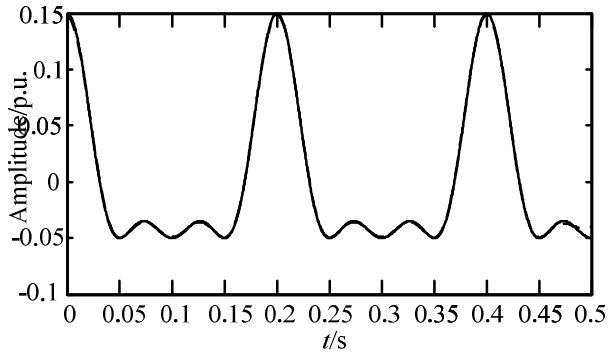

Fig.5 The detection result (dotted line) compare with real value (solid line) of multi-frequency

Flicker signal with time-varying frequency. EAF is one of the main equipment leading to voltage fluctuations and flicker. The frequency of each frequency component is roughly inversely proportional to the amplitude of the signal caused by it. Formula (7) simulates the flicker signal caused by EAF.

$$u(t)=\begin{cases}\cos(100\pi t); & 0\le t<0.3 \text{ or } 1.7\le t\le 2\text{s}\\ (1+0.1\cos(20\pi t))\cos(100\pi t); & 0.3\le t<1s\\ (1+0.075\cos(20\pi t)+ & \\ 0.05\cos(30\pi t))\cos(100\pi t); & 1\le t<1.7s\end{cases} \tag{7}$$

Time-varying frequency flicker signal waveform was shown in Figure 6, with cubic spline interpolation method to extract flicker envelope was shown in Figure 7.

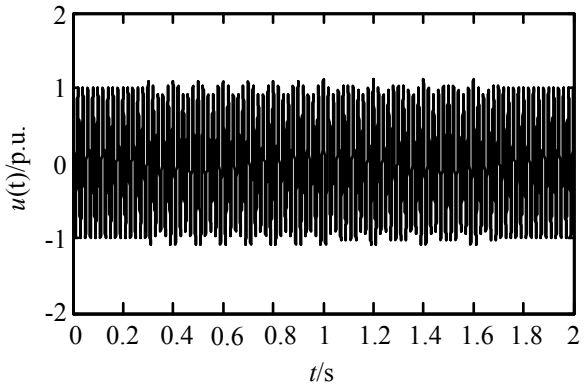

Fig.6 Time-varying frequency flicker signal

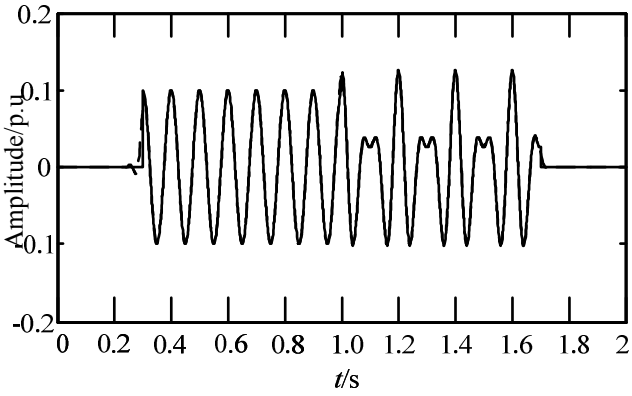

Fig.7 The detection result (dotted line) compare with real value(solid line) of Time-varying frequency

As shown in figure 7, Single frequency flicker occurred at moment 0.28s, changed into a multi-frequency flicker at 1.09s and continued to 1.73s, lastly changed into a power frequency signal. Thus this shows that this method can accurately detect the starting time and end time when flicker frequency component signal changes. Detection error is 1.5094% and the detection is ideal.

Conclusions

The key to analyze voltage flicker signal is to track envelope which contains the amplitude and frequency information of voltage fluctuation. The cubic spline interpolation method was applied in envelope tracking of voltage flicker and a new way was provided to analyze voltage flicker. Simulation examples show that the interpolation method in detecting single-frequency and multi-frequency flicker signal whose flicker frequency is 12Hz or less, the detection error is small. Especially in the low flicker frequency (0.5~3Hz), the error is smaller, making up for the disadvantage that the error is greater in detecting low frequency using square demodulation method.

Therefore, it is suitable for flicker envelope extraction caused by arc furnaces and grid connected wind power. Furthermore, results of frequency time-varying flicker signal simulation show that, the occurrence and recover time of voltage flicker signal can be accurately detected by this method.

References

[1] Dong Weijie，Bai Xiaomin，Zhu Ninghui，et al．Discussion on the power quality under Grid-connection of intermittent power sources[J]．Power System Technology，2013，37(5)：1265-1271 (in Chinese).

[2] A.Elnady，Yan-Fei Liu．A practical solution for the current and voltage fluctuation in power systems[J]．IEEE Transactions on Power Deliever，2012，27(3)：1339-1349．

[3] Ma Yongqiang，Zhou Lin，Wu Jian，et al．A new approach to measure voltage flicker caused by interharmonics[J]．Power System Technology．2010，34(5)：117-121 (in Chinese).

[4] Li Heming，Kang Wei，Yan Xiangwu，et al．Voltage flicker measurement based on Chirp-Z transform[J]．Transactions of China Electrotechnical Society，2009，24(3)：209-215 (in Chinese).

[5] Li Tianyun，Zhu Lei，Dang Guoying，et al．Application of total least squares-estimation on signal parameters via rotational invariarce technique in extraction of voltage flicker parameters[J]．Power System Technology，2009，33(13)：58-63 (in Chinese).

[6] Sun Shuqin．Voltage fluctuation and flickers[M]．Beijing：China Electric Power Press，1998，36-40(in Chinese).

[7] Xiao Xiangning．Analysis and control of power quality[M]．Beijing：China Electric Power Press，2010，112-115(in Chinese).

[8] Jia Xiufang，Chen Qing，Zhao Chengyong，et al．Comparison of the flicker detection methods[J]．High Voltage Engineering，2009，35(9)：2126-2132 (in Chinese).

[9] Jia Xiufang，Zhao Chengyong，Xu Guoyi，et al．Error analyzing of IEC flickermeter and its improving Design[J]．Transactions of China Electrotechnical Society，2006，21(11)：121-126．(in Chinese).

[10] Yang Hushan．The application and realization in actual problem of cubic spline interpolation [J]．Journal of Xinzhou Teachers University，2008，24(2)：47-49．(in Chinese).

[11] Jia Xiufang，Chen Qing．Teager energy operator for tracking the envelope pf voltage flicker produced by integrated wind power[J]．Acta Energiac Solaris Sinica，2010，31(7)：885-890(in Chinese).

Advanced Materials Research Vols. 960-961 (2014) pp 710-715

doi:10.4028/www.scientific.net/AMR.960-961.710

Partial Linear Method for Background Harmonic Voltage Estimation

Xiufang Jia[a], Shaoguang Zhang[b], Haiqing An[c]

State Key Lab of New Energy Power System (North China Electric Power University) Baoding 071003 China

[a]xiufangjia@163.com, [b]shaoguang.z@163.com, [c]anhaiqing1990@163.com

Key words: power quality; harmonic contributions; partial linear method; background harmonic voltage

Abstract. The linear regression method which will be influenced by fluctuations could only calculate constant background harmonic voltage. To make up the limitation, this paper studies partial linear method. The method expands fluctuant background harmonic voltage at a time in accordance with Taylor series. On the basis of least sum of square error, the objective function selected by the method considers the influence of weight and uses bandwidth control each size of weight. This method can calculate fluctuant background harmonic voltage accurately. A case study based on the IEEE 14-bus test system is conducted and the results indicate that fluctuant background harmonic voltage can be obtained effectively and accurately by the proposed method.

Introductions

In recent years, some large-capacity and non-linear equipment, such as electric locomotives, electric arc furnaces etc, have caused a large number of harmonic problems [1-3]. In order to improve the level of harmonic management and control the harmonic pollution in the grid effectively, National quality supervision bureau promulgate the《Quality of electric supply Harmonics in public supply network》(GB/T 14549-93) in 1993. The standard provides specific provision about the threshold [4], but it can not scientifically settle the dispute between power supplies and consumers. In order to implement the principle of " who pollution, who control " , it is necessary to quantify harmonic contributions on both sides at the PCC.

The key to quantify the harmonic contributions at the point of common coupling is evaluating equivalent harmonic impendence of the system and background harmonic voltage at PCC accurately. Equivalent harmonic impendence is related with operation modes of electrical system and the topology of the grid, which can be approximated as a constant in short monitoring period. However, considering the fluctuation brought by non-linear loads at the PCC, background harmonic voltage can not regarded as a constant. In recent years，linear regression method become a research focus. On the basis of Norton equivalent circuit, linear regression method establishes corresponding functions. Scholars have proposed several linear methods such as binary linear regression method [5], robust regression method [6], partial least-square regression method [7] and complex least squares method [8]. From [5-7], we acquire that basically unchanged harmonic impendence and background harmonic voltage at the PPC is the premise of approaching ideal harmonic contributions caused by each harmonic source. Therefore, the limitations are as follows: If the background harmonic voltage is not a constant, the assessment of harmonic contributions is inaccurate. In view of fluctuating background harmonic voltage in the specific period, subdividing monitoring period into uniform pieces and taking each section as a constant has been proposed in [8-9].However, it is difficult to choose the agreeable scale to subdivide the period.

In order to qualify the harmonic voltage contributions, kernel estimation in partial linear method is applied in the mathematical model presented by [10]. Compared with common linear

method, the method can calculate fluctuant background harmonic voltage accurately without doing too much data processing.

The definition of harmonic voltage contribution

As is shown in Fig.1. Bus X is the concerned bus, which are respectively connected with the power system and several nonlinear loads.

If monitoring equipments detect that severe harmonic voltage distortion exists, it is necessary to determine the harmonic voltage contribution of each nonlinear load quantitatively. Without loss of generality, assuming that load A is of concern. $\dot{U}_{h\mathrm{X}}$ is the h-th harmonic voltage at bus X, $\dot{I}_{h\mathrm{A}}$ denotes *h*-th harmonic current injected by load A. $\dot{U}_{h\mathrm{X}}$ is composed of two parts, the one is background harmonic voltage expressed as $\dot{U}_{h0}$, which can be explained as a compound amount including the system and the other loads except A; the other is $\boldsymbol{Z}_{hX,A}\dot{\boldsymbol{I}}_{hA}$ provided by load A.

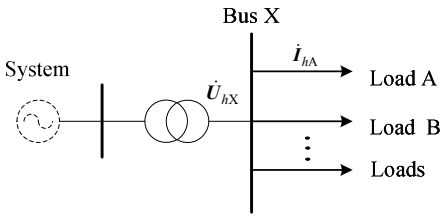

Fig. 1 Multiple loads connected with the same bus of concern

Due to the sampling measurement error, the relationship between $\dot{\boldsymbol{U}}_{h\mathrm{X}}$ and $\dot{\boldsymbol{I}}_{h\mathrm{A}}$ can be expressed in equation (1).

$$\dot{\boldsymbol{U}}_{hX} = \boldsymbol{Z}_{hX,A}\dot{\boldsymbol{I}}_{hA}+\dot{\boldsymbol{U}}_{h0}+\boldsymbol{\varepsilon} \tag{1}$$

Where $\boldsymbol{\varepsilon}$ is complex error. $\boldsymbol{Z}_{h\mathrm{X,A}}$ represents the *h*-th equivalent harmonic impendence, including the other loads and system side.

Detailed deduction about harmonic contribution calculation formula has been given in [10]. The final formula is shown in equation (2):

$$\mu_h = \frac{U_{h\mathrm{X}}^2 + \left|Z_{h\mathrm{X,A}}\right|^2 I_{h\mathrm{A}}^2 - U_{h0}^2}{2U_{h\mathrm{X}}^2} \tag{2}$$

From (2), we acknowledge that the essence of quantifying the harmonic contributions caused by concerned load is assessing equivalent harmonic impedance and background harmonic voltage accurately.

The paper attempts to apply a set of data $\dot{\boldsymbol{U}}_{h\mathrm{X}}$ and $\dot{\boldsymbol{I}}_{h\mathrm{A}}$ processed by Fourier transform and partial linear method to regress fluctuating background harmonic voltage $\dot{\boldsymbol{U}}_{h0}$ and equivalent harmonic impedance $\boldsymbol{Z}_{h\mathrm{X,A}}$.

Kernel estimation in partial linear method

Both $\dot{\boldsymbol{U}}_{h\mathrm{X}}$ and $\dot{\boldsymbol{I}}_{h\mathrm{A}}$ are plurals. Equation (3) can be derived by expanding complexes in equation (1).

$$\begin{cases} \boldsymbol{U}_{h\mathrm{X,r}} = R\boldsymbol{I}_{h\mathrm{A,r}} - X\boldsymbol{I}_{h\mathrm{A,x}} + \boldsymbol{U}_{h0,\mathrm{r}} + \boldsymbol{\varepsilon}_{\mathrm{r}} \\ \boldsymbol{U}_{h\mathrm{X,x}} = X\boldsymbol{I}_{h\mathrm{A,r}} + R\boldsymbol{I}_{h\mathrm{A,x}} + \boldsymbol{U}_{h0,\mathrm{x}} + \boldsymbol{\varepsilon}_{\mathrm{x}} \end{cases} \tag{3}$$

Subscript r and x respectively represent the real and the imaginary part of the complex. *R* is equivalent harmonic resistance, *X* denotes equivalent harmonic reactance.

Supposing there are n samples and taking the real part of voltage for example, we have:

$$\begin{cases} U_{hX,r}(1)=RI_{hA,r}(1)-XI_{hA,x}(1)+U_{h0,r}(1)+\varepsilon_{r1} \\ U_{hX,r}(2)=RI_{hA,r}(2)-XI_{hA,x}(2)+U_{h0,r}(2)+\varepsilon_{r2} \\ \vdots \\ U_{hX,r}(n)=RI_{hA,r}(n)-XI_{hA,x}(n)+U_{h0,r}(n)+\varepsilon_{rn} \end{cases} \tag{4}$$

The equation (4) can be described as follow:

$$\boldsymbol{U}=\boldsymbol{IZ}+\boldsymbol{U}_0+\boldsymbol{\varepsilon} \tag{5}$$

Where the elements R and X in matrix $\boldsymbol{Z}$ are constants while the elements in column vector $\boldsymbol{U}_0$ fluctuant with time. Therefore the mathematical mode is called partial linear model. The complex measurement error is ε_i which obeys normal distribution $N(0, \sigma^2)$.

Taking the background harmonic voltage at time t_k (k=1,2…， n) for example, $U_0(t)$ can be expressed approximately as follow at the time of t_k:

$$U_0(t)\approx U_0(t_k)+U_0'(t_k)(t-t_k) \tag{6}$$

Where $t_k=k$。For convenience, we assumed that $\alpha_k=U_0(t_k)$ and $\beta_k=U_0'(t_k)$. In order to calculate $U_0(t_k)$, the objective function selected by the method makes least square sum of error and considers the influence of weight.

$$\min\sum_{i=1}^{n}\left[U(t_i)-\boldsymbol{I}(t_i)\boldsymbol{Z}-\hat{\alpha}_k-\hat{\beta}_k(t_i-t_k)\right]^2K_b(x_i) \tag{7}$$

Where $\hat{\alpha}_k$ and $\hat{\beta}_k$ denote the estimation of α_k and β_k respectively, $K_b(x_i)=b^{-1}K(x_i/b)$, $x_i=(t_i-t_k)/n$. $K(x_i/b)$ represents kernel function which is a bounded symmetric density function. Parameter b represents bandwidth, a positive real number, which is associated with sample size. In this paper, we definite $b=n^{-1/5}$ [11]。Kernel function plays a role in weights which is controlled by parameter b.

Epanechnikov function is commonly used as optimal kernel function [12]:

$$K(x_i/b)=0.75\times\left(1-(x_i/b)^2\right)\qquad |x_i|\le b \tag{8}$$

The derivation shows that $\hat{\alpha}_k$ meets the equation (9):

$$\begin{bmatrix}\hat{\alpha}_k\\ \hat{\beta}_k\end{bmatrix}=\left(\boldsymbol{D}_{tk}{}^{\mathrm{T}}\boldsymbol{W}_{tk}\boldsymbol{D}_{tk}\right)^{-1}\boldsymbol{D}_{tk}{}^{\mathrm{T}}\boldsymbol{W}_{tk}(\boldsymbol{U}-\boldsymbol{IZ}) \tag{9}$$

Where:

$$\boldsymbol{D}_{tk}=\begin{bmatrix}1 & 1 & \cdots & 1\\ x_1 & x_2 & \cdots & x_n\end{bmatrix}^{\mathrm{T}},\qquad \boldsymbol{W}_{tk}=diag\left[K_b(x_1),K_b(x_2),\cdots,K_b(x_n)\right]$$

Therefore:

$$\hat{\alpha}_k=[1,0]\left(\boldsymbol{D}_{tk}{}^{\mathrm{T}}\boldsymbol{W}_{tk}\boldsymbol{D}_{tk}\right)^{-1}\boldsymbol{D}_{tk}{}^{\mathrm{T}}\boldsymbol{W}_{tk}(\boldsymbol{U}-\boldsymbol{IZ}) \tag{10}$$

According to earlier assumption $\hat{\alpha}_k=\hat{U}_0(t_k)$, $\hat{\boldsymbol{U}}_0$ can be described by equation (11):

$$\hat{\boldsymbol{U}}_0=\begin{bmatrix}[1,0]\left[\left(\boldsymbol{D}_{t1}{}^{\mathrm{T}}\boldsymbol{W}_{t1}\boldsymbol{D}_{t1}\right)^{-1}\boldsymbol{D}_{t1}{}^{\mathrm{T}}\boldsymbol{W}_{t1}\right]\\ \vdots\\ [1,0]\left[\left(\boldsymbol{D}_{tn}{}^{\mathrm{T}}\boldsymbol{W}_{tn}\boldsymbol{D}_{tn}\right)^{-1}\boldsymbol{D}_{tn}{}^{\mathrm{T}}\boldsymbol{W}_{tn}\right]\end{bmatrix}(\boldsymbol{U}-\boldsymbol{IZ})\triangleq\boldsymbol{S}(\boldsymbol{U}-\boldsymbol{IZ}) \tag{11}$$

Substituting (11) into (5), we have:

$$(\boldsymbol{E}-\boldsymbol{S})\boldsymbol{U}=(\boldsymbol{E}-\boldsymbol{S})\boldsymbol{IZ}+\boldsymbol{\varepsilon} \tag{12}$$

Where: $\boldsymbol{E}$ is unit matrix.

$\hat{\boldsymbol{Z}}$ can be obtained by least squares method.

$$\hat{\boldsymbol{Z}}=\left[\left((\boldsymbol{E}-\boldsymbol{S})\boldsymbol{I}\right)^{\mathrm{T}}(\boldsymbol{E}-\boldsymbol{S})\boldsymbol{I}\right]^{-1}\left((\boldsymbol{E}-\boldsymbol{S})\boldsymbol{I}\right)^{\mathrm{T}}(\boldsymbol{E}-\boldsymbol{S})\boldsymbol{U} \tag{13}$$

Case study

The proposed method is tested by the standard IEEE14 bus system shown in Fig.2. We select the 5th harmonic for explanation. Bus 11 which supplies three loads as our concern. HL1 and HL2 are nonlinear loads which could launch harmonic voltage into the concerned bus, and L3 is linear load. Without loss of generosity, we assume that load HL1 is of concern. Determining the harmonic impact of HL1 on bus 11 is commonly seen in engineering.

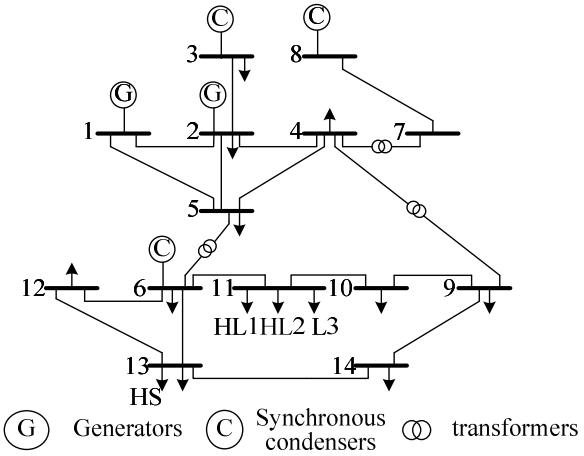

Fig. 2 IEEE14-bus system

Typical harmonic current spectrums given in [13] are used for HL1 and HL2 shown in Fig.3 andFig.4 respectively. Fluctuating background harmonic voltage is simulated by HL2. Harmonic source at system side is simulated by HS, which is a constant. The amplitude and initial phase angle is 114.80 amperes and -76.56 degrees. The background harmonic voltage is composed by HL2 and HS. The simulation process takes during a 24-h period, and each minute one sample is collected, resulting in 1440 data points for physical quantity that was measured.

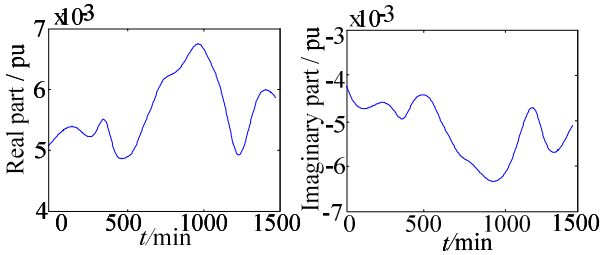

Fig.3 5th harmonic current injected by HL1

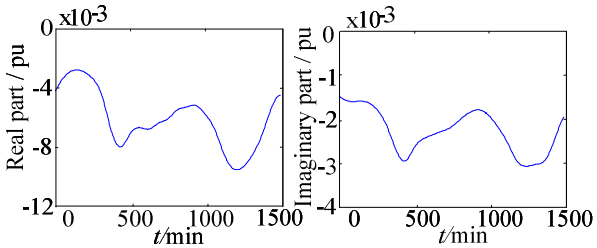

Fig.4 5th harmonic current injected by HL2

Curves of the effective value of the fifth harmonic voltage at bus 11 and effective value of the 5th harmonic current at bus 11 injected by HL1 are shown in Fig.5 and Fig.6.

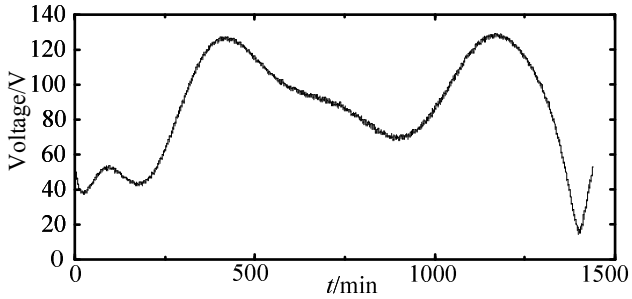

Fig.5 The 5th harmonic voltage at bus 11

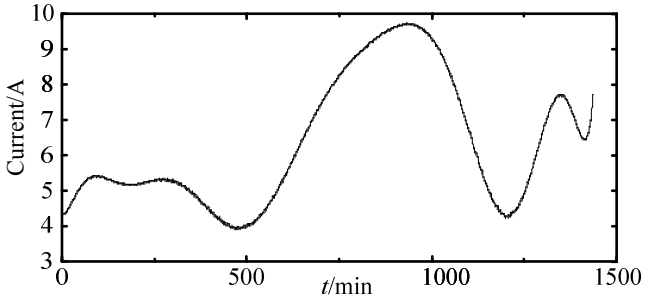

Fig.6 The 5th harmonic current injected by HL1

Kernel estimation in partial linear method is applied for calculating background harmonic voltage. The parameter bandwidth is 0.23. Comparing the real and imaginary part of the background harmonic voltage respectively with its true value achieved by case study is of importance. For the purpose of demonstrating the superiority of the method, we use the complex least squares

method to regress background harmonic voltage as well. Because of its nature that it could only regress constant coefficient, we subdivide the period of sampling time and regard that background harmonic voltage is unchanged in every piece of divided period. In this paper, the sampling time will be divided into 144 parts evenly. As is shown in Fig.6, the result has been compared among the true value and the two methods.

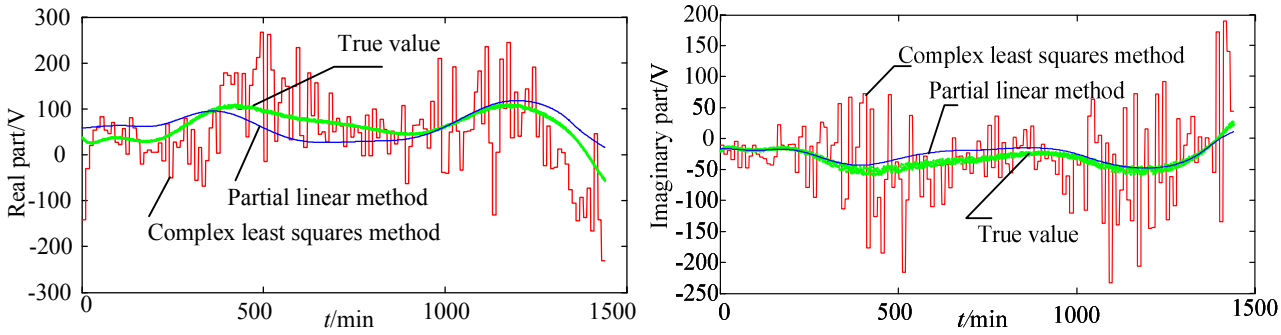

Fig.7 The real and the imaginary part of background harmonic voltage

Fig 7 shows that background harmonic voltage obtained by the method is close to the true value. Therefore, the complex least squares method can just return to the overall trend of the background harmonic voltage. Error analysis is displayed in Table 1. According to the data, equivalent harmonic impendence can be achieved by the two methods in the table 2.

Tab. 1 Error analysis of background harmonic voltage between the two methods

	Real part		Imaginary part	
	The absolute error /V	The relative error /%	The absolute error /V	The relative error /%
Complex least squares method	20.32	13.67	1.62	-72.49
Partial linear method	3.24	3.97	2.05	-1.46

Tab. 2 Error analysis of harmonic impedance results between the two methods

	Harmonic impedance/Ω	absolute error	relative error /%
True value	2.866∠79.75°	—	—
Complex least squares method	1.984∠173.06°	3.5784	124.86
Partial linear method	2.956∠70.70°	0.1650	5.76

Conclusions

For the purpose of solving fluctuant background harmonic voltage, this paper studies the kernel estimation in partial linear method, which is superior to linear method in several aspects. Kernel estimation in partial linear method can regress background harmonic voltage more accurately than complex least squares method in case of its fluctuation. Research for this article also requires the following instructions.

The equation (6) requires that background harmonic voltage is changing slowly. How to calculate the non-smoothing background harmonic voltage remains to be further studied.

References

[1] Lin Haixue. Some problems in national standard for harmonics in public supply network[J]. Power System Technology, 2003, 27(1): 65-70.(In Chinese)

[2] Deng Shujuan, Lei Longfu, Li Yong. Characteristic analysis on inter-harmonics and sub-harmonics in the new type of industry converting system[J]. Power System Technology, 2009, 33(5): 28-33. (In Chinese)

[3] Yang Shaobing, Wu Mingli. Assessing harmonic emission levels of traction substations based on simulated annealing algorithm[J]. Automation of Electric Power Systems, 2011, 35(11): 60-64. (In Chinese)

[4] GB/T 14549-1993, power quality Quality of electric supply Harmonics in public supply network[S].

[5] Zhang Wei, Yang Honggeng. A method for assessing harmonic emission level based of binary linear regression[J]. Proceedings of the CSEE, 2004, 24(6): 50-54. (In Chinese)

[6] Che Quan, Yang Honggeng. Assessing the harmonic emission level based on robust regression method[J]. Proceedings of the CSEE, 2004, 24(4): 39-44. (In Chinese)

[7] Huang Shun, Xu Yonghai. Assessing harmonic impedance and the harmonic emission level based on partial least-squares regression method[J]. Proceedings of the CSEE, 2007, 27(1): 93-97. (In Chinese)

[8] Jia Xiufang，Hua Huichun, Cao Dongsheng, et al. Determining harmonic contributions based on complex least squares method[J]. Proceedings of the CSEE, 2013, 33(4): 149-155. (In Chinese)

[9] Hua Huichun, Jia Xiufang, Cao Dongsheng, et al. Practical method to determine the harmonic contribution of a specific harmonic load[C]//15th IEEE International Conference on Harmonics and Quality of Power. Hong Kong: IEEE Power & Energy Society, 2012: 769-773.

[10] Hua Huichun, Jia Xiufang, Zhang Shaoguang. Neighborhood multi-point measurement method for harmonic contribution determination[J]. Power System Technology, 2014, 38(2): 502-508. (In Chinese)

[11] M.P. Wand, M.C. Jones. Kernel smoothing[M].CRC Press, 1995, 70-72.

[12] Meng Jiafu, Zhang Riquan, Lv Shiqin. Estimation of semivarying-coefficient models with the correlated random errors[J]. Applied probability and statistics, 2010, 26(5):477-479. (In Chinese)

[13] Gursoy E, Niebur D. Harmonic load identification using complex independent component analysis[J]. IEEE Trans on Power Delivery, 2009, 24(1):285-292.

Advanced Materials Research Vols. 960-961 (2014) pp 716-719

doi:10.4028/www.scientific.net/AMR.960-961.716

Simulation on Current Efficiency of Electrolytic Cleaning for cold rolled strip

Xiaokui Liu [1, a], Shuaifang Li[1,b] , Pengfei Gao[1,c] and Nan Qiao[1,d]

[1] Faculty of Materials and Energy, Southwest University, Chongqing 400715, PRC

[a]xiaokui@swu.edu.cn, [b]lshf860428@126.com, [c] raygaoswu@126.com, [d]qiaonan@swu.edu.cn

Keywords: Simulation, Electrolytic cleaning, Cold rolled strip, Current efficiency

Abstract. The model of electrolytic cleaning for cold rolled strip was established, and the simulation of cleaning process was carried out in the finite element method with the software(Ansoft). The influence of processing parameters was investigated. The results show that, the processing parameters, such as the current efficiency, the electrode plate intervals and the insulation board have intense influence on current efficiency, which is significant for improving cleaning efficiency and energy conservation.

Introduction

Compared with traditional cleaning technologies, electrolytic cleaning is a rapid and effective cleaning technology in the pretreatment of the cold-rolled steel. Lots of studies have been done on the processing parameters, such as current density, electrolysis time, temperature and concentration of electrolyte and so on. At present, the parameters of processing are mainly chosen through experience, not only wasting the resources but also having a low efficiency[1-6].

In the process of electrolytic cleaning, the cold-rolled steel strip acts as electrode, experiencing cathodic and anodic cleaning respectively. the total input current(I_t) for the device can be divided into two parts: the first part (I_1)is from electrode to electrode, as shown in dotted lines in Fig.1, and the second part(I_2) is from electrode to steel strip, as shown in solid lines in Fig.1. Hydrogen or oxygen evolution reaction takes place on the surface of electrode and steel strip separately, and the gas evolution on the surface of cold-rolled steel strip plays the main role of cleaning, which means that only the current from the electrode of electrolytic cleaning device to cold-rolled steel is effective for cleaning.

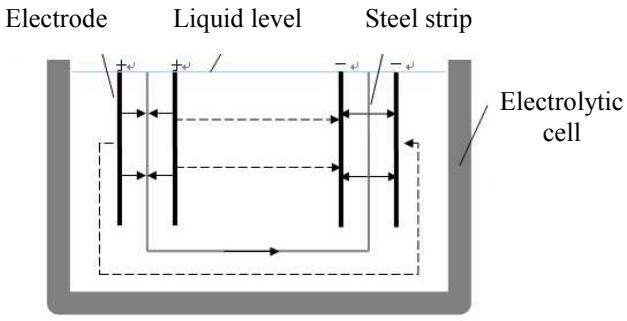

Fig.1 Current path in electrolytic cell

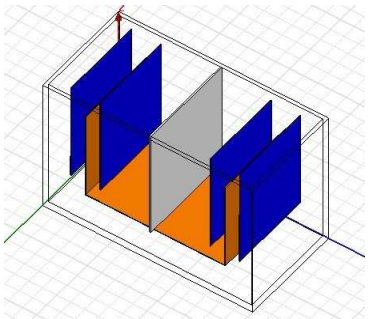

Fig.2 Simplied model of electrolytic cleaning

Up to now, there is no report studied on the distribution of electric current in the electrolytic cleaning device. In the paper, the current efficiency of electrolytic cleaning is defined as $\eta = \frac{i_2}{I_t}$, and the influencing factors were investigated in the method of simulation for the purpose of improving the efficiency of cleaning.

Establishment of Model and Simulation Principle

According to the process of electrolytic cleaning for cold rolled strip in practice, a simplified 3-dimention cleaning model with a insulation clapboard was established, which is shown in Fig.2. The conditions of boundary and initialization are set as follows:
Initial conditon:

$$\varphi_0 = C \tag{1}$$

φ is electric potential, and C is a constant.
Boundary condition:

$$\frac{\partial \varphi}{\partial n} = 0 \tag{2}$$

n is the normal line of the point on the electrolytic cleaning cell.
The distribution of electric potential in the cleaning cell can be calculated with laplace equation:

$$\frac{\partial^2 \phi}{\partial x^2} + \frac{\partial^2 \phi}{\partial y^2} + \frac{\partial^2 \phi}{\partial z^2} = 0 \tag{3}$$

Electric field intensity(E) and current density(j) can be obtained with such equations:

$$E = -\nabla \varphi \tag{4}$$

$$j = kE \tag{5}$$

∇ is laplacian, and k is the conductance.
The finite element software(Ansoft) was adopted for the calculation of electric field intensity(E). Using the values of current density(j), current can be calculated an follows:

$$I_e = \oiint_{S_e} j_e dS \tag{6}$$

$$I_s = \oiint_{S_s} j_s dS \tag{7}$$

I_s is the current through the surface of strip, which is useful for washing. I_e is the current through the electrode, which is equal to the total input current(I_t).
Then the current efficiency of electrolytic cleaning can be expressed as Eq.8:

$$\eta = \frac{I_s}{I_e} \times 100\% = \frac{\oiint_{S_s} j_s dS}{\oiint_{S_e} j_e dS} \times 100\% \tag{8}$$

Results and Discussion

Distribution of equipotential surface and current flow diagram calculated with Ansoft are shown in Fig.3 and Fig.4 respectively. It can be seen that, the equipotential surface and current density vary distinctly at the different part of the electrolytic cleaning cell. The distribution is most intensive in the areas close to the electric plate, and the potential reaches the maximum. The variance of electric potential and current density means there is leak current from electrode to electrode more or less, which would induce waste of electric energy.

The effect of processing parameters was investigated at different conditions, and the current efficiencies of electrolytic cleaning under different processing parameters were calculated with Eq.8, and contrasted separately.

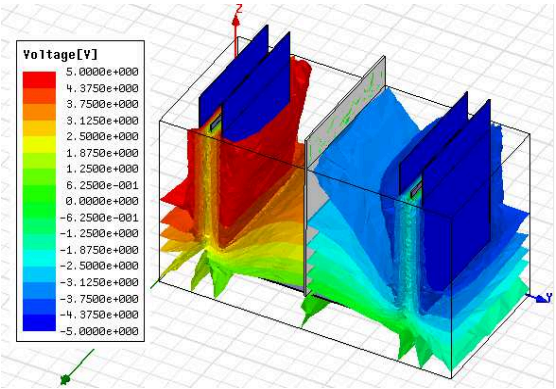

Fig.3 Stereogram of potential distribution

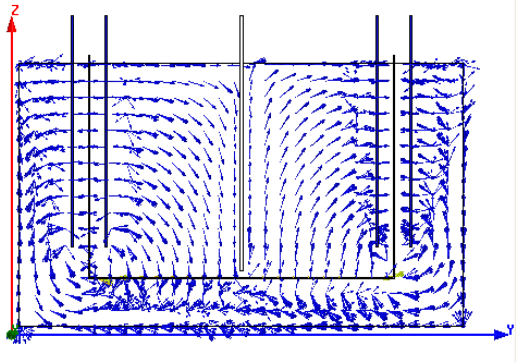

Fig.4 Current flow diagram

The influence of current density on current efficiency calculated at the conditions of different electrode plate intervals is shown in Fig.5. It can be seen that, the current density has remarkable effect on current density. The current efficiency increases almost 20% when the current density changes from 5A/dm^2 to 25A/dm^2. In addition, the larger is the electrode plate interval, the higher is the current efficiency with the same current densities(The current efficiency increases about 15% when the plate interval changes from 2.4cm to 6.4cm). It can be referred that, this is the reason that the high current density (beyond 100A/dm^2) electrolytic cleaning is more popular than ordinary current density (less than 50A/dm^2) electrolytic cleaning at present.

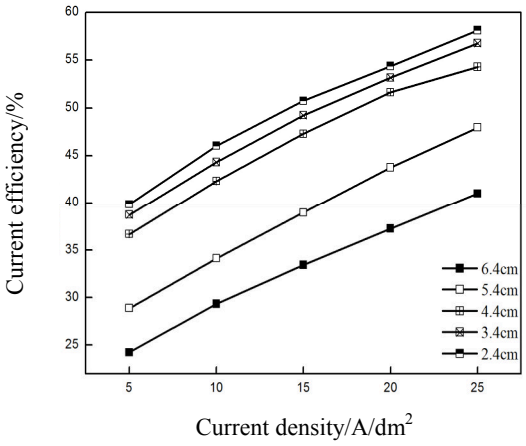

Fig.5 Current efficiency as a function of the current density

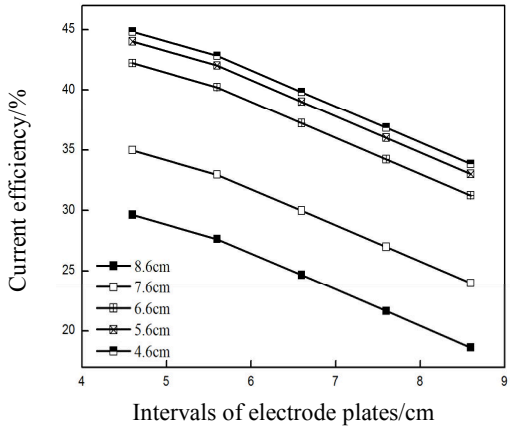

Fig.6 Current efficiency as a function of the electrode plate

Fig.6 illustrates the relationship among the current efficiency, the electrode plate interval and the length of electrode plate. It was shown that, there is a obvious decrease of about 10% of current efficiency when the interval changes from 4.5cm to 8.5cm. At the same time, the current efficiency reaches higher value when the length of electrode plate is shorter(There is a decrease of about 15% when the length of electrode plate increases from 4.6cm to 8.6cm). It can be inferred that, decreasing of electrode intervals can prevent the electric current from leaking to electrode plate directly.

The influence of insulation board on current efficiency with different current densities is presented in Fig.7. It indicates that, the insulation board is important for higher current efficiency. The current efficiency increases about 10% when the length of insulation board changes from 4.5cm to 8.5cm. It is

believed that the longer insulation board can separate the electrodes, which can significantly reduce the parallel discharge between positive and negative electrode, and induces a larger current focus flowing to the bottom of the strip.

Fig.8 reveals the relationship between the current efficiency and the electrolyte concentration. It can be learnt that, the current efficiency is unchangeable when the current density is fixed, and It can be learnt that, the current efficiency don't alter with electrolyte concentration. The reason is that, the electrolyte concentration can't induce the change of Electric field intensity(E). Though the conductance(k) increases with the concentration, the ratio of I_e to I_s would not alter according to Eq.4, Eq.5 and Eq.8. For the same reason, both the temperature and the conductance(k) have no effect on the current efficiency, which is confirmed by the results of simulation.

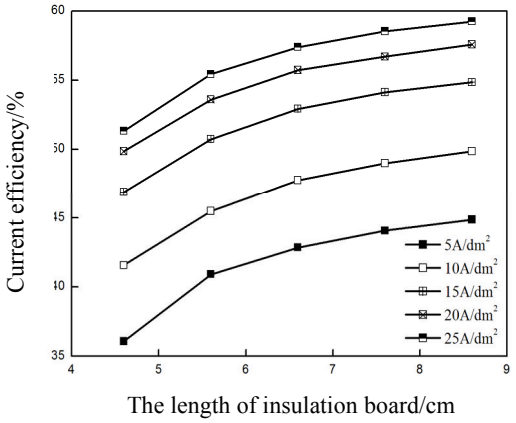

Fig.7 Current efficiency as a function of the length of insulation board

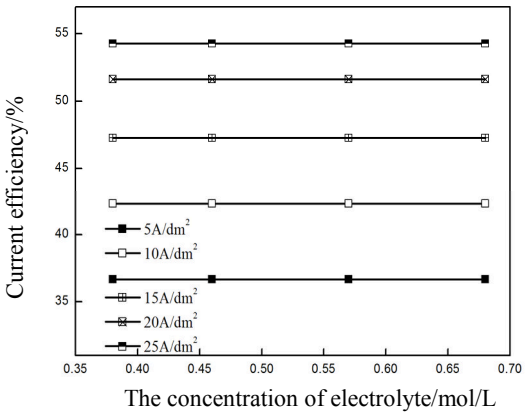

Fig.8 Current efficiency as a function of the concentration of electrolyte

Conclusions

Model of electrolytic cleaning for cold rolled strip was established, and the simulation of cleaning process was carried out with finite element method. The influences of processing parameters are studied, and the results show that:

(1) The current efficiency increases almost 20% when the current density changes from 5A/dm^2 to 25A/dm^2;

(2) The current efficiency decreases obviously with the increasing of the electrode plate intervals;

(3) The insulation board is important for higher current efficiency;

(4) The electrolyte concentration has no effect on current efficiency.

Acknowledgement

This work was financially supported by the Fundamental Research Funds for the Central Universities (XBJK2009B002) and the Chongqing Natural Science Foundation of China(CSTC,Grant No.2010BB 4128).

References

[1] Tianliang Zheng: Chinese Journal of Aeronautics, vol.16(2003),p.123.

[2] Wutian Li: Steel Wire Products, vol.31 (2005), p.7.

[3] Xuecheng Dai: Shanghai Metals, vol.29 (2007), p.48-53.

[4] Hailin Wang, Zhenlin Zhang: Steel Rolling, vol. 26 (2009), p.51.

[5] Yeke Wang: Steel Rolling, vol.18 (2001), p.30-32.

[6] Pengfei Gao: Applied Mechanics and Materials,Vols. 44-47 (2011),p 2954.

Advanced Materials Research Vols. 960-961 (2014) pp 720-725

doi:10.4028/www.scientific.net/AMR.960-961.720

Simulation Study on Core Material of Weak DC Current Sensor

Pengfei Meng[1, a], Min Wan[1,a], Han Yang[1,a], Runzhou Ge [2,b]

[1]Hongshen Honor College, Chongqing University, China

[2]College of Electrical Engineering, Chongqing University, China

[a]mengpfcqu@gmail.com, [b]runzhouge@gmail.com

Keywords: Weak DC Current, Sensor, Magnetic Core Material, Ansoft,Simulation

Abstract. ZnMn ferrite, cold-rolled silicon steel, permalloy and nanocrystalline alloy can be used as magnetic cores of current sensors. And based on these four materials' inherent characters of electromagnetic, this paper presents closed loop simulation model of them using Ansoft which is a finite element analysis software. In simulation, the measuring currents are set to DC currents ranging from 0 to 1mA. And different amplitudes of variation of currents are set for each material. The simulation of each material produces 280 sets of data and with these data a series of curves of magnetic field changing with currents can be plotted using Matlab. The simulation results show that permalloy and nanocrystalline alloy have good characters of electromagnetic and they are suitable for detecting weak DC currents. When these two materials are used as magnetic cores of sensors, thetheoretical detecting accuracy can be up to 0.001mA, meanwhile, detecting accuracy of ZnMn ferrite is about 0.1mA to 0.01 mA.

Introduction

On-line monitoring ofinsulationand leakage current of electrical equipment has been a significant method through which can we find security risk timely and through which can we improve the reliability of electrical equipment. In the processing of monitoring, collecting data of leakage current is the most important aspect. Insulation leakage current of electrical equipment which is collected as important signal by on-line monitoring equipment is one of the main features which could reflect insulation ageing and flaw directly or indirectly [1-2]. As for detecting current, the key technique is to study current sensor with high performance which can be used in on-line monitoring [2]. Meanwhile we should consider various kinds, such as the variously strong noise around power substations and the small leakage current. When equipment is running well, the leakage current ranges from several tenths of a milliampere to decadesmilliamperes and about one thousandth of dielectric is lost. Taken together, the requirement of accuracy, angle error, stability and SNR of sensor is very high [2]. Therefore, the core material of sensor not only should have high resolving power and linearity, but also should have high sensitivity and strong antijamming capability. Selecting material of high differential permeability to make magnetic core is a method through we can reducemeasurement error efficiently. But we should also consider the strength of hysteresis effect of magnetic core when we are measuring low-frequency current [1-2]. As the requirement of precision of detection for current is improving continuously in the industry, many researches and comparison on permeability of different core material have sprung up [2]. But now, we will carry out a more quantitative study on permeability, resolving power, linearity of different magnetic core.

Analysis on Material Characteristics of Sensor

With the information industry developing constantly, performances and measurement accuracy of electric measuring instrument is improving continuously [4]. At present many materials, such as ZnMn ferrite, cold-rolled silicon steel, permalloy, nanocrystalline alloy and so on have been used as ferromagnetic materials widely. Comparison of typical parameters of ferromagnetic materials which is commonly used in the core of current sensors is shown in Table 1.

Table 1. Comparison of typical parameters of ferromagnetic materials

Basic parameters	ZnMn ferrite	Silicon steel	Nanocrystalline alloy	Permalloy
Saturation magnetic induction *Bs* *T*	0.5	2.0	1.25	0.75
Initial permeanceμ_0 $\mu H \cdot m^{-1}$	$2\sim2.5\times10^3$	$\sim10^3$	$4\sim8\times10^4$	$5\sim8\times10^4$
Maximum permeanceμ_m $\mu H \cdot m^{-1}$	5×10^3	4×10^4	6×10^4	6×10^4
Curie temperatureT ^{0}C	230	740	570	400
Density d g·cm^{-3}	4.8	7.65	7.25	8.75
CoercivityA/m	>4.4	>29.8	>0.8	>0.8

The value of magnetic induction of magnetic core materialsvaries with the magnetic field intensity. Meanwhile magnetic induction of magnetic core of sensor varies with the current of sensor. But in view of the small current which is needed to be detected and the value of which only ranges from several tenths of a milliampere to a dozen milliamperes. So we should consider the value of magnetic induction which ranges from 0 to 0.5T when we are selecting magnetic core materials [1]. We havesimulated four materials as sated above for seeking the best material which is suited for detecting weak DC Current very well.

Simulation Model and Theoretical Analysis

Based on inherent electromagnetic properties of permalloy and nanocrystalline alloy, we build closed loop simulation model with Ansoft Software.

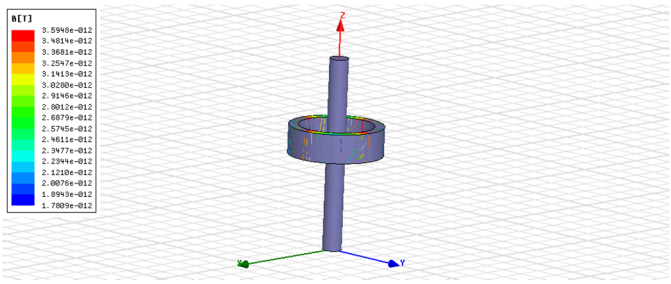

Fig. 1. Schematic diagram of Ansoft simulation model

Schematic diagram of Ansoft simulation modelis shown in Fig.1. We optimally choose magnetic ring's outer radius R2=25mm, inside radius R1=20mm and thickness h=5mm in Ansoft software. At center of the ring there is a cylindricalwire of which the diameter is 1mm and the length is 500mm and which is much larger than the thickness of the ring. In the model, the material of wire is copper. According to the references in Table 1, we put these four into material library of Ansoft. In this procedure, main parameters, such as differential permeability, coercivity, and state of materials should be set. As for ZnMn ferrite, we set the parameter of differential permeability to 5000, coercivity to –4.4A/m; for cold-rolled silicon steel, we set the parameter of differential permeability

to 10000, coercivity to –29.8A/m; for permalloy, we set the parameter of differential permeability to 200000, coercivity to –0.8A/m; for Nanocrystalline alloy, we set the parameter of differential permeability to 60000, coercivity to –29.8A/m. And we set the states of them to solid. Simulation result is shown in the left of the Fig. 1 through which we can see the magnetic induction B of different parts of the magnetic ring when a certain current is applied to the wire. From each time of simulation we can get 17 sets of data which respectively represent the magnitudes of magnetic induction of different parts between center and edge of the ring. We record the ninth set of data in order to make the mean value of magnetic inductionmore representative. In the processing of simulating, we set the range of current from 0.001mA to 1mA.

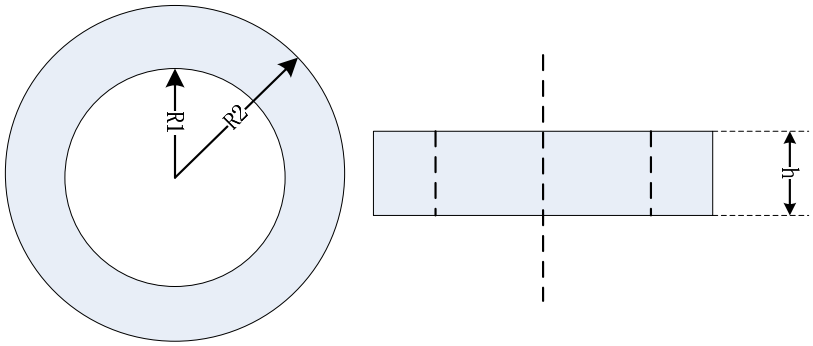

Fig.2. Schematic diagram of magnetic ring's structure

As Shown in Fig. 2, magnetic ring's outer radius is represented by R2; inside radius represented by R1; thickness is represented by h. Based on electromagnetic induction principle, when current flows in the center of the ring there should be magnetic induction B in the ferromagnetic material, and we have

$$\Phi = \int B.h.d_R (R_1 < R < R_2) \tag{1}$$

When the length of the wire is much larger than the thickness of the ring, the relationship between current and magnetic induction is approximately

$$B = \frac{\mu_r \mu_0 . I_0}{\pi \cdot (R_1 + R_2)} \tag{2}$$

Therefore, we can get corresponding relation of current and magnetic induction when we change the current magnitude in the wire and record corresponding magnitude of magnetic induction at the same time. And their relations are approximately linear.So as to determine whether we could detect various currents which range from 0.001mA to 1mA, we should set smaller step when we are collecting the data of small currents.

Simulation Results and Analysis

Among range of 0.00100–0.0100mA, we set step to 0.00005mA to collect 180 sets of data. Then we set step to 0.001mA to collect 90 sets of data among range of 0.01–0.1mA. Finally, we set step to 0.1mA to collect 10 sets of data among range of 0.1–1mA.Via this approach we could analyze whether the every material can reflect the various weak currents and determine the scope of accuracy. And in this way, we can make sure that the smallest current we detect is in our research scope. Because there always are electromagnetic interferences which produces higher magnetic induction than a 0.0005mA current does in the environment where the equipment is used.

3.1 Closed Loop Simulation Model of ZnMn Ferrite

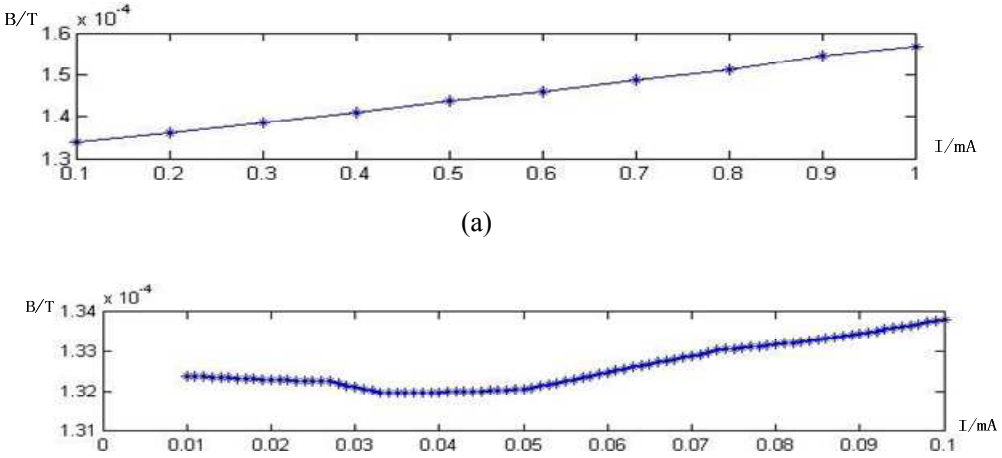

Fig. 3. ZnMn ferrite's change relation between magnetic induction and current

ZnMn ferrite's change relation between magnetic induction and current is shown is Fig. 3. When the step is set to 0.1mA, the relationship between magnetic field and current is approximately linear. And magnetic field can reflect variety of current as shown in Fig.3 (a). But when we set step to 0.01mA, we could find there is a nonlinear change of magnetic field in a certain scope as shown in Fig. 3 (b). Perhaps that phenomenon is led by hysteresis effect of ZnMn ferrite.

3.2 Closed Loop Simulation Model of Cold-rolled Silicon Steel

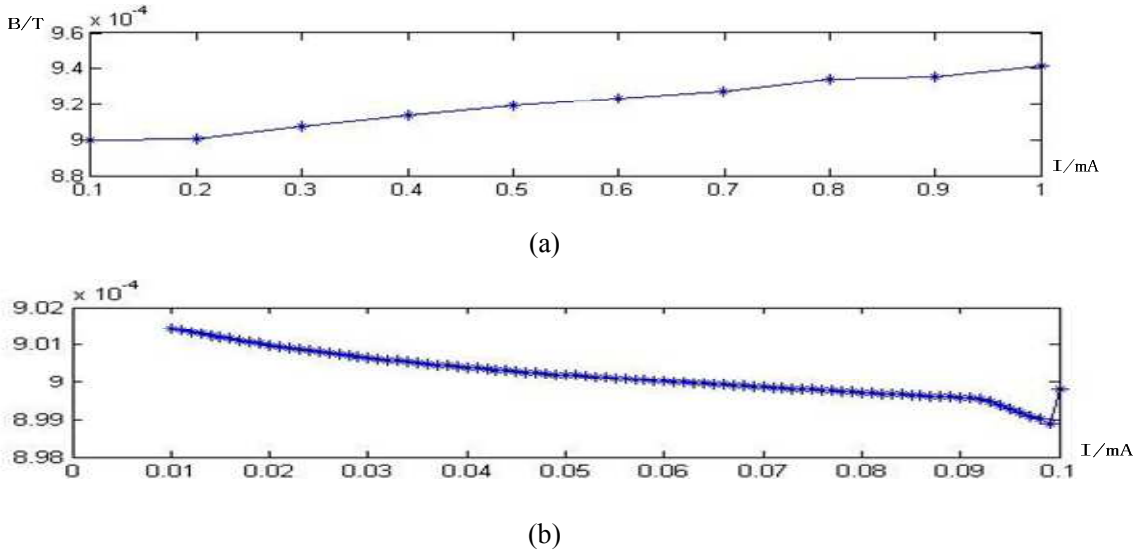

Fig. 4. Cold-rolled silicon steel's change relation between magnetic induction and current

Cold-rolled silicon steel's change relation between magnetic induction and current is shown in Fig.4. When the step is set to 0.1mA, the relationship between magnetic field and current is approximately less steadily linear. And magnetic field can reflect variety of current as shown in Fig. 4 (a). But when we set step to 0.01mA, we could find there is a nonlinear change of magnetic field which is led by variation of current in a large scope considering that ZnMn ferrite's nonlinear change only appears in a certain scope as shown in Fig. 4 (b). Perhaps that phenomenon is led by stronger hysteresis effect of cold-rolled silicon steel when we compare it with ZnMn ferrite.

3.3 Closed Loop Simulation Model of Permalloy (1J85)

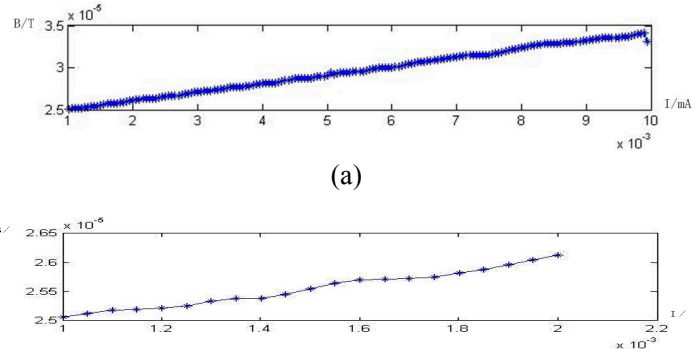

Fig. 5. Permalloy's change relation between magnetic induction and current

Permalloy's change relation between magnetic induction and current is shown in Fig.5. When the step is set to 0.1mA or 0.02mA, the relationship between magnetic field and current is steadily linear. When we set step to 0.01mA, the magnetic field has a relatively steady fluctuation with the change of current as shown in Fig.5 (a). Magnetic field can also reflect variety of current accurately. But when the step is set to 0.0005mA, the magnetic field has an unsteady fluctuation with the change of current as shown in Fig.5 (b). In this case magnetic field cannot reflect variety of current accurately. When we use permalloy (1J85) as the core material, the precision of detecting current is increased by at least two orders of magnitude comparing with ZnMn ferrite or cold-rolled silicon steel.

3.4 Closed Loop Simulation Model of Nanocrystalline alloy

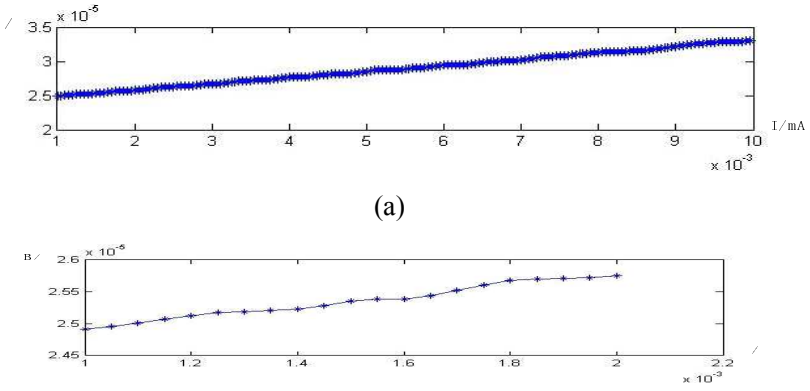

Fig. 6. Nanocrystalline alloy's change relation between magnetic induction and current

Nanocrystalline alloy's change relation between magnetic induction and current is shown in Fig.6. When the step is set to 0.1mA, 0.02mA or 0.001mA, the relationship between magnetic field and current is steadily linear similar to the relationship of permalloy. And magnetic field can reflect variety of current accurately as shown in Fig. 6(a). But when we set the step to 0.0005mA, the magnetic field has an unsteady fluctuation with the change of current as shown in Fig. 6 (d). In this case magnetic field cannot reflect variety of current accurately.

3.5 Simulation Analysis

In view of the closed loop simulation results of four materials, we could find that magnetic induction which are produced by different materials keep good linearities when the amplitude of variation of currents is 0.1mA. But when we reduce the amplitude of variation of currents by two

orders of magnitude (The step is 0.001mA), magnetic induction which is produced by ZnMn ferrite does not keep linearity because of its high coercivity and hysteresis effect. Similarly, the reason why cold-rolled silicon steel's magnetic induction appears abnormal is that it has the highest coercivity among four materials. At present, permalloy (1J85) and nanocrystalline alloy can keep their linearities of magnetic induction with the change of current well. But when the amplitude of variation of currents is set to 0.00005mA, with the change of current the magnetic field has an unsteady fluctuation which is not linear certainly.

Conclusions

Simulation data and analysis indicate that cold-rolled silicon steel can detect the variation of current which is smaller than 0.1mA and ZnMn ferrite can detect the variation of current which is smaller than 0.01mA. Permalloy (1J85) and nanocrystalline alloy can keep their linearities when magnetic induction is changing with smaller current relative to ZnMn ferrite and cold-rolled silicon steel. And when the measuring accuracy is set to 0.0001mA, these two materials can also keep good linearities. But when we set the measuring accuracy to 0.00005mA, the changing curve of magnetic induction of two materials is not linear. It is because differential permeability is not high enough and there exists coercivity and hysteresis effect. Hence, permalloy and nanocrystalline alloy is suitable for weak DC current sensors with high accuracy. By using the latter two materials, the highest accuracy of the sensor can be up to 0.0001mA without considering external interferences. But its real accuracy is less than 0.00005mA because of the deficiency of differential permeability and existence of coercivity and hysteresis effect. Considering that there are electromagnetic interferences of environment of which value is higher than this, so the detecting accuracy can reach 0.001mA in practical engineering field.

References

[1] Sun Heyi, Zhao Xuezeng, Nie Peng. Study on transducer used in on-line monitoring of insulation of high voltage electric equipment under low temperature conditions [J]. High Voltage Engineering, 2001, 27(5): 64-66

[2] BaoBinghao, Zhao Zhan. On weak current sensor using MnZnFeO-based material toroidalcore [J]. Chinese Journal of Sensors and Actuators. 2005, 18(3): 507-509

[3] Gong Jie, Yang Du, Zhou Lixing. Improvement of pulse current sensor for powertransformer partial discharge monitoring [J].Journal of Electric Power Science and Technology. 2007, 22(4): 68-71

[4] Hu Xin. Design and implementation of a train hall current sensor [J].Science & Technology Information. 2013 (7): 115-117

[5] Wang Hongxia, Liu Zongbin, You Pei. Application of nanocrystallinealloy toroidalcores for power measuring current transformer [J]. Metallic Functional Materials. 1999, 6 (3): 122-127

[6] Chai Yuhua, Zhao Xuetao. Research on measuring small current sensor in low temperature [J].Electrical Measurement & Instrumentation. 2002, 39(10): 35-38

[7] Zhukov A, Gonzalez J. Amorphous and nanocrystalline soft magnetic materials: tailoring of magnetic properties, magnetoelastic and transport properties[M]//Handbook of Advanced Magnetic Materials. Springer US, 2006: 1091-1157.

[8] Volchkov S O, Lepalovskii V N, Svalov A V, et al. Magnetic properties and huge magnetic impedance of permalloy/copper/permalloy film elements[J]. Russian Physics Journal, 2009, 52(10): 1092-1097.

Advanced Materials Research Vols. 960-961 (2014) pp 726-729

doi:10.4028/www.scientific.net/AMR.960-961.726

Influential Factors of suspension insulator AC Pollution flashover voltage: A Survey

SHEN Qing

School of Electrical Engineering, Wuhan University, Wuhan, China
d-q-j-0@163.com

Keywords: Insulator, Suspension, Pollution, Insulator structure, Pollution flashover voltage

Abstract: To make up insufficient of ESDD in insulator flashover voltage analysis, and A more comprehensive assessment of antifouling properties of insulators. This paper discusses the factors of suspension insulator flashover voltage of the AC, analyzed the influence of these factors on the flashover voltage, found the reason for large differences of the current test results of research institutions at home and abroad, and proposed future research directions.

Introduction

In recent years, with increased Pollution of industrial development, environmental degradation, the voltage increases, network expansion and interconnection of AC and DC, pollution flashover accident growing, threat to the safe operation of power transmission equipment. Therefore, the analysis of factors affecting the discharge of insulator flashover is conducive to seek administrative and technical measures to prevent flashover occurs, to minimize the occurrence of flashover accident. [1]~[3]

External insulation pollution discharge is a "product Pollution - wet - dry area and local arcing occurs - partial arc sent to flashover" [4]. The process is affected by filthy composition, degree of Pollution, insulator structure, weather conditions, and filthy uniform and so on.

The influence of the nature and amount of Pollution

The Pollution deposited on the insulator surface can be divided into industrial and natural. Whether it be industrial or natural filthy dirty, accumulate on the insulator Grimes actual solubles mainly is $CaSO_4$, $MgSO_4$, $ZnSO_4$ and $NaNO_3$, KNO3, KCl, NaCl etc. In these salts, $CaSO_4$ and NaCl influence the flashover voltage insulator pollution greater. The former makes flashover voltage rises. The latter makes flashover voltage decreases. Other salts such as $NaNO_3$, KNO_3, KCl, etc. can be incorporated in NaCl as Na salt. The little effect $MgSO_4$, $ZnSO_4$ and other salts of flashover voltage can not be considered [5].

Insulators withstand voltage or flashover voltage with different degrees of Pollution can be determined by artificial or natural Pollution experiment. Operating experience and a lot of test results show that flashover voltage insulators related to the degree of Pollution, its means that flashover voltage insulators related to salt density and non-soluble density.

According to a large number of experimental data, researchers establish a flashover voltage and salt density, non-soluble density equation:

$$U_f = K_{AB} S^{-a} G^{-b} \tag{1}$$

Where K_{AB} is the coefficient related with insulator string length, type and atmospheric conditions, and it can be calculated by the experiment.

Take the seven strings XP-160 insulators for example, the relationship between its flashover voltage and salt density, non-soluble density can be expressed as [7]:

$$U_f = 34.4S^{-0.237}G^{-0.139} \tag{2}$$

$$U_f(1) = 4.913S^{-0.237}G^{-0.139} \tag{3}$$

Analysis shows that, with the increase in salt and non-soluble density, U_f decreased; and U_f decreased rapidly when the salt and non-soluble density is small, with salt density and ash density increasing U_f decline slows, which are similar with the impact effected of salt and non-soluble density separately.

For composite insulators, Flashover voltage is much higher than the flashover voltage of the ordinary porcelain insulators; the non-soluble density impact characteristic index of composite insulators are not very different, and its salt density impact characteristic index is less than the non-soluble density impact characteristic index.

The influence of structure and the length of the insulator string

(1)The influence of structure

The Pollution situation of insulator surface depends primarily on the material and structure of the insulator.

Canadian theoretically derived that the insulator creepage distance is related with the insulator structural parameters and the degree of Pollution.

$$L_s = d_c D_e^{3r} SDD^r \tag{4}$$

Where, De is the average diameter of the insulator, cm; dc is vector constant; $r = n_a/(1-n_a)$, n_a is Static constant along the surface of the arc, $0 < n_a < 1$; SDD is the salt density, mg / cm2.

There are five main structure of anti-fog suspension insulator: Bell structure, ordinary suspension insulator with semiconductor glaze layer, flow lines umbrella structure, double or triple umbrella and large diameter, large creepage, lower height structure. Flashover Performance comparison of different types of insulators curve shows: In 0.1mg/cm^2 salt density, 70kN anti-fog insulator flashover voltage is 15% to 33% higher than the ordinary insulator flashover, and the double umbrella structure (XWPl-70) is 17% ~ 32% higher. Small height double umbrella structure(XWP2—70) is 15%～33%. Bell structure(XHPl-70) is 30%～60% higher. Meanwhile the 100kN or 160kN anti-fog insulator flashover voltage is similar. [8]

(2)The influence of the length

Whether a linear relationship is a very important unresolved issue between the insulator string length and AC flashover voltage. The problem for high voltage power transmission engineering filthy insulation design has important engineering significance. Since the test conditions, the test results are not uniform at home and abroad.

Experimental results in China show that the string length is proportional to the flashover voltage while the string less than 30 pcs. Experimental results in USA and Japan show that: the string length is proportional to the flashover voltage while the string length less than 6m. Voltage distribution of composite insulators under wet filthy conditions is very uneven, so nonlinear relationship can occur at lower voltages. Normally, natural Pollution insulator flashover voltage

higher than the artificial pollution tests, so it can be considered linear, when chosen the string according to the data from artificial pollution tests [5].

(3)The influence of Installation

Different insulator string installation, which flashover voltage is also significant differences. The test results show that the flashover voltage of dual string insulator is 5% ~ l0% lower than the single-string. When the distance between the double string insulator increases, the impact on flashover voltage is significantly reduced.

V-shaped installation can increased flashover voltage of ordinary suspension insulator by 25% to 30% [9], but the improvement is much less on anti-fog insulator.

The influence of weather conditions

Insulator flashover voltage depends not only on the type and degree of Pollution of the insulator, but also on the meteorological conditions, such as humidity, barometric pressure, temperature, and other acidic wet deposition.

(1) Wet condition

Wet weather condition is a necessary condition for the occurrence of flashover, such as fog, dew, drizzle and fog rain, snow and sleet. Wide range of fog occurred long duration, can insulators uniform moisture, concentration of fog, the lower visibility, the greater the harm; Dew is often seen in summer morning, for most industrial Pollution, short wet is not dangerous. Drizzle on the insulator surface is not as humid mist evenly. The duration of the long drizzle risk is very big. Fog, snow and sleet in the melting temperature of the insulator which constitute a serious hazard; Rain generally conducive to clean the surface of the insulator, but may make small pitch insulator flashover occurred in the rain; Direct splashing seawater, salt spray occured in saline areas etc. easily lead to flashover.

(2) Temperature

Mizuno et. deduced relations between insulator flashover voltage and ambient temperature is[10]:

$$U_f \propto \left[1+0.02(t-20)\right]^{-w_t} \tag{5}$$

where, t is Ambient temperature; w_t is ambient temperature impact characteristic index, AC w_t=0.2, DC w_t=0.33. The field test results of Chongqing university verify the validity of the derived results.

(3) Air pressure

The relation between flashover voltage and air pressure is:

$$U_f = U_0 \times \left(P / P_0\right)^n \tag{6}$$

Where, U_f is the flashover voltage under pressure (P, kPa), kV; U_0 is the flashover voltage under standard pressure(P_0=101. 3kPa), kV; n is the pneumatic impact characteristic index, between 0~1. Pneumatic impact characteristic index obtained by different researchers are quite different [11]. In general, n is about 0.5 while the structure of insulator is simple [12]. But in the actual operation, n has a relationship with the voltage type, degree of Pollution, the shape of the insulator.

(4) Rainwater acidity

In insulators artificial pollution tests, clean fog (vapor mist) or salt spray is used, and its acidity does not consider. Actually wet deposition of acidity in many areas has greatly increased, which will induced insulator flashover voltage drop. When ESDD of 0.015~0.1mg/cm^2, pH of 3.0~4.0,

insulator flashover voltage AC decreased by approximately 2.1%~21.7%. The decreased of different types of insulators is different. The decline of porcelain and glass insulators are larger than composite insulators and post insulators.

The influence of non-uniform Pollution

Under natural conditions, the Pollution of the insulator is always uneven. This uneven including upper and lower surfaces of the insulator, different fan on the same surface, and different components of one bunch. Numerous experiments show that, much uneven higher flashover voltage. Artificial pollution tests result is lower than the natural Pollution test, is a manifestation of the uneven.

Summary

Many domestic and foreign research institutions did a large number of experimental in insulator flashover characteristics area, but the test results obtained by various research institutions vary greatly. After analysis it can be seen, these differences are due to the influence of insulator structure, filthy type of experimental ambient temperature and humidity. So need to find a method to correct test results of the research institutes to the same type of insulator, salt density and non-soluble dense composition and temperature were analyzed to verify its legitimacy. Meanwhile, in order to obtain accurate insulator flashover characteristics, need to strengthen the natural contamination experimental study and insulator contamination degree online monitoring.

References

[1] Yutao Wang. Talk about Insulator Pollution Flashover Technology. Power and Electrical Engineering, 2012,(13): 122.

[2] Chao Xu, Jianwang Wang, Zhengjun Jin. Research on pollution flashover High-voltage transmission line insulator. Science & Technoligy Information,2008,(19): 318.

[3] Yumin Ge. Summary of Grid pollution flashover causes and prevention method. Electrical Engineering, 2006, (8): 11-13.

[4] Power Industry Bureau of Sichuan Province, Sichuan Electric Power Education Association. Grid Pollution Flashover Prevention Technology. BEI Jing: China Electric Power Press, 1998.

[5] Xingliang Jiang, Lichun Shu, Caixin Sun. Power Systems Insulation for Pollution and Icing. BEI Jing: China Electric Power Press, 2009.

[6] GB/T 4585—2004Atificial Pollution Test on High-voltage Insulator to be Used on AC Systems[S]. BEI Jing: China Standard Press, 2004.

[7] Yongji Zhang. Study on AC Flashover Performance of Artificially Polluted XP-160 Insulators at Various ρ_{ESDD} and ρ_{NSDD}. Chongqing University, 2006.

[8] Qipeng Ran. Study on AC flashover performance and valid coefficient of creepage distance for different types of artificially polluted insulators. Chongqing University, 2006.

[9] LI Zhen-yu,CUI Ji-feng,ZHOU Yuan-xiang. Influence of Insulator Installation Form on ITS Pollution Flashover Voltage. Power System Technology, 2005, 29(16): 52-55.

[10] Mizuno Y, Kusada H, Naito K. Effect of climatic conditions on contamination flashover voltage of insulators. IEEE Transactions on Dielectrics and Electrical Insulation, 1997, 4(3): 286–289.

[11] Caixin Sun,Wenxia Sima,Lichun Shu. Atmospheric Environment and outside Electrical insulation. BEI Jing: China Electric Power Press, 2002.

[12] Mercure H P. Insulator pollution performance at high altitude: major trends. IEEE Transactions on Power Delivery, 1989, 4(2): 1461–1468.

Advanced Materials Research Vols. 960-961 (2014) pp 730-733

doi:10.4028/www.scientific.net/AMR.960-961.730

The Design of Intelligent Pressure Detection and Alarm System

Yu Fan[1, a] and Xuefeng Wu[1,b]

[1] School of mechanical and power engineering, Henan polytechnic university, Jiaozuo, Henan, 454000, China

[a]fanyu@hpu.edu.cn, [b]wuxuefeng@hpu.edu.cn

Keywords: Pressure detection,Three topologies amplification, Differential amplifier

Abstract. An application of intelligent pressure detection and alarm system are studied in this paper . it is consists of the high integration, powerful function new microprocessor control, the internal integration of a large number of analog and digital peripheral module. The system has strong data processing ability. multifunctional intelligent hardware is not only realized in circuit necessary configuration,but also is a small size device. it ensure the intelligence function,and has the advantages of small volume, low cost, integration and strong anti-interference ability .

Introduction

Water resources is an uneven distribution in China, it is rich in some areas and very scarce in the others. Related equipment is often used for water supply I and water pump is now widely used. However, in the water pump water supply system, the pressure which water pipe wall can bear is a very important question [1].

This system is designed specifically for this issue. Pressure detection and alarm are realized in this system. Detecting pipeline pressure is easily real time carried out, if the pressure exceeds a certain value, the alarm system will be worked, and outputing some signal, controlling water pump motor speed to reduce the water flow, thereby the pressure on pipeline wall is reduced [2]. It provides automated and intelligent engineering self protection, avoiding the occurrence of a series of Engineering accident [3].

It is consist of supply circuit, amplifier circuit, A/D conversion and data processing, pressure display and alarm circuit in this paper.

The design of the system

The system principle. Three terminal voltage regulator chip LM7815,is used for voltage conversion from 24V to 15V, Three terminal voltage regulator chip LM7805,is used for voltage conversion from 15V to 5V. The requirement of the magnification is high in the amplifying circuit [4]. The performance of a single integrated or modular operational amplifiers can't meet the requirements generally. It can only be used in less demanding occasions. Operational amplifier input and signal amplification must be used in the system. Taking into account the A/D precision, and the amplified voltage up to 5-7V, A/D574 conversion is used, which can support the unipolar 0-10V and 0-20V the input voltage.

The design of the main work as follows: When the pipe wall subjected to liquid pressure, it makes the piezoresistive pressure sensor bridge unbalance, unbalanced bridge triggers weak electrical signal. The weak signal through three operational amplifier topology instrument for signal amplification is amplified by A/D converter,then is converted to digital signal.When the voltage signal is no more than a certain value, the signal display pressure value in LED [5].When this signal exceeds a certain value, it will make the alarm signal started by the MCU, prevent the occurrence of accidents, at the same time, MCU sends a signal input external frequency converter, adjusting the speed of the pump motor,then the motor speed and the water flow are reduced. The Work flow chart is shown in Fig. 1.

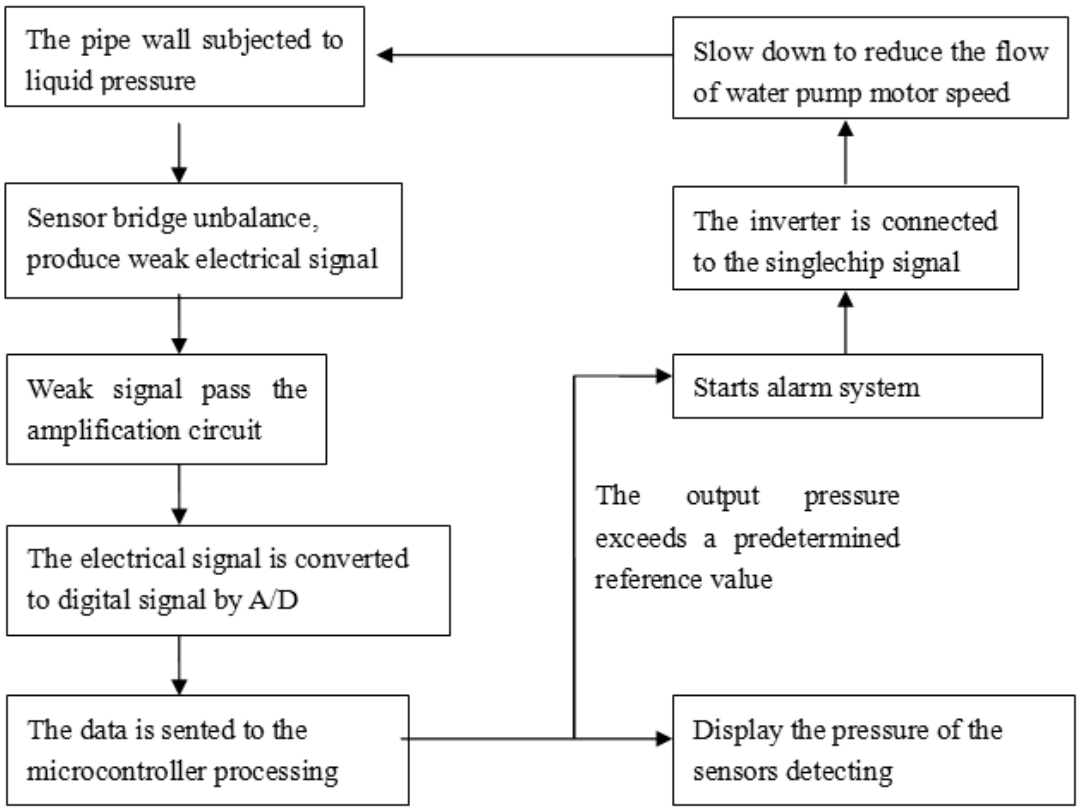

Fig. 1. The work flow chart

The System of Power Supply. It needs 24V, ± 15V and ± 5V supply voltage in the system, while the power supply can not provide more power, so the chips of LM7815 and LM7915 is used to conversion the voltage voltage supply system. The power supply circuit is shown in Fig. 2.

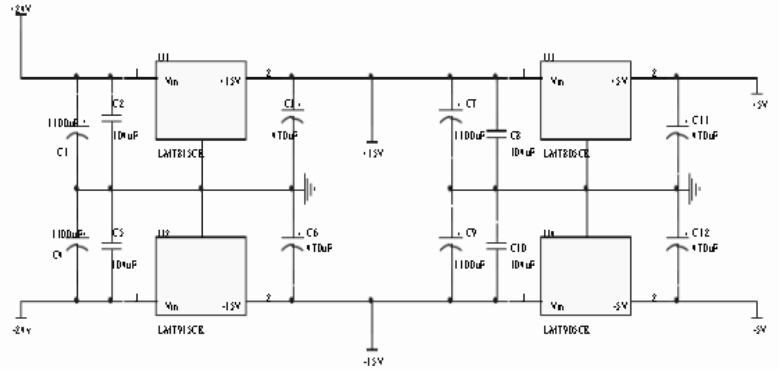

Fig. 2. The power supply circuit

The amplifying circuit. Three topologies amplification circuit is used in the system, and sensitive element is two output mode. It output a voltage signal with two induction of the sensor [6]. It should adopt double signal amplification method. The two signal is shaping and amplification, and then output the data signal processing, The amplifying circuit is shown in Fig. 3.

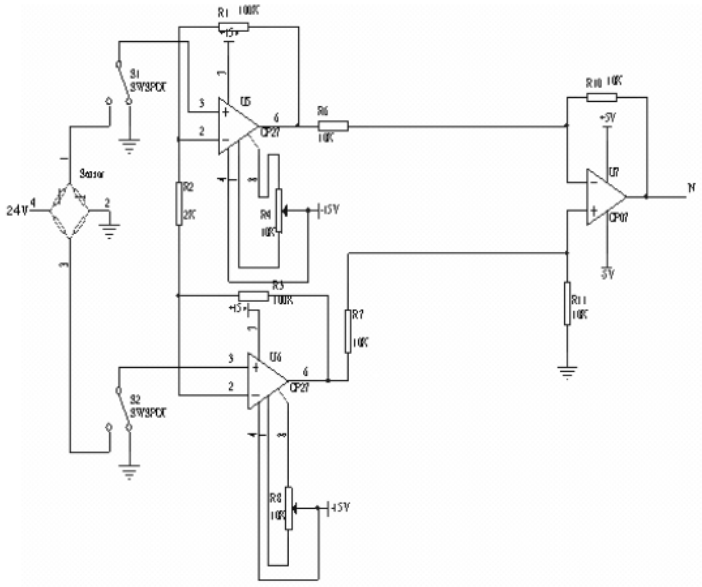

Fig. 3.The amplifying circuit

The real advantage of three topologies not only can get the performance the real difference measurement, but also has very high input impedance. Especially in the occasion of high impedance signal source. And the amplifier gain can be selected resistance by user. Therefore, it is particularly suitable for precision measurement in abominable environment, its main used as a common mode signal superimposed small differential signal preamplifier [7].

The circuit is suitable for special instrumentation amplifier circuit. An instrumentation amplifier is a differential voltage gain device precision, it has some advantages ,such as differential input, single output, high input impedance, low offset current and high rejection ratio. Basic component of the operational amplifier is same in differential amplifier and an instrument amplifier. And a differential amplifier and an instrument amplifier with common mode signal conditions can amplify the weak differential signal, so it has very high common mode rejection ratio. It do not require external feedback network.

A/D conversion and data processing. The task of input channel is converting the analog signal (such as temperature, liquid level, speed, current, voltage, phase, composition) into binary code .The channel is consists of multiple switch, amplifier, sample and hold circuit, analog / digital converter, interface and control circuit. Due to unlike the analog signals, digital signals that form is simple .The characteristics of digital signals are strong anti-jamming and not easy to distortion. It is easy processing, and widely used in digital signal. The A/D conversion intelligent pressure sensor system and microcomputer data processing circuit are shown in Fig. 4.

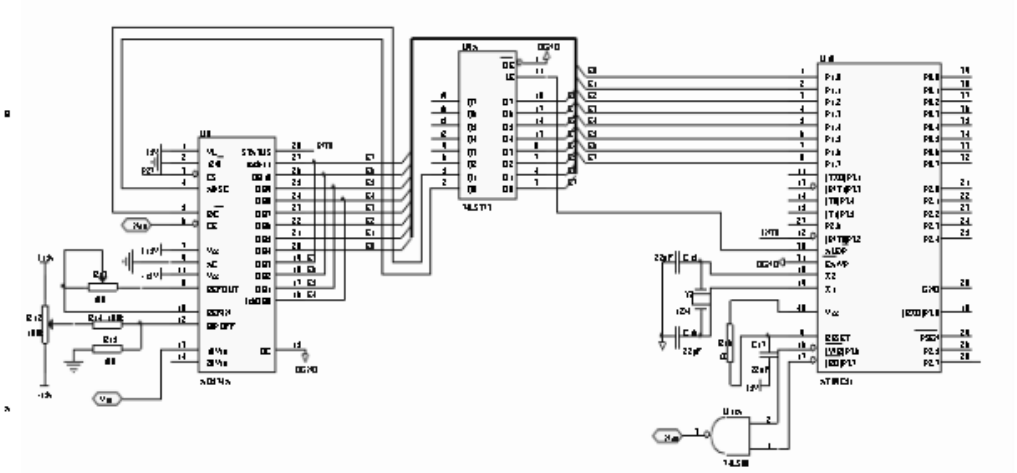

Fig. 4. A/D conversion and AT89C51 MCU circuit diagram

Conclusions

The application of intelligent pressure detection and the theory of alarm system in pressure measurement are studied in this paper. The high integration powerful function and new microprocessor are used in the system. Its internal integrates a number of analog and digital peripheral module, with strong data processing ability. The system configuration is necessary for the realization of multifunctional intelligent hardware within a circuit, and all of the low price, small size devices, it has the advantages of small volume, low cost, integration and strong anti-interference ability.

Acknowledgements

This work was financially supported by Henan Polytechnic University the doctor Foundation (72515/040, 64998544).

References

[1]D.B.Gennery:*Fiber Bragg Grating Pressure Sensor Based on Corrugated Diaphragm*,IEEE. Trans. Acoust. Speech.Signal Process. Vol. 25 (2008), p. 1263

[2]N.McGlamery:Design,Fabrication and Test of a VEM Pressure sensor,FBG Pressure Sensor Based on Corrugated Diaphragm Vol. 53-58(2004), p. 86

[3]D.B.Stockham:A new touch mode pressure sensor with two deformable diaphragms, Proc.IEEE. Vol. 73-77(2003), p. 582 [4] T. M.Cannon, R.L.Lagendijk, and G.Hertzmaun: *Principle and application of single chip microcomputer technology*, Electronic. Soc. Amer. Vol. 56-70 (2011), p. 321-332

[5] P.K. Cannon: *Application of electronic measuring instrument intelligent instrument*, Association for Computer Machinery(2006), p. 256

[6] T.A. Biemond and J. Tekalp: *Design of stable and practical circuit power supply: A Unifying Approach,* IEEE Transactions on Consumer Electronics,Vol. 58(2004),p. 72-76

[7] Pang Boon, Jaik Poon Pi and Tim Kae Ketm: *Detection technology and its application of pressure sensors*, electronic. Eng. Vol. 39-42 (1990), p. 574

Advanced Materials Research Vols. 960-961 (2014) pp 734-737

doi:10.4028/www.scientific.net/AMR.960-961.734

Anomalous Commutation Failure Phenomenon in Multi-infeed HVDC Systems

Mingchao Lv[1,a], Tong Zhao[1,b], Jie Lou[1,c], Liang Zou[1] and Li Zhang[1]

[1]School of Electrical Engineering, Shandong University, 17923 Jingshi Road, Jinan 250061, China

[a]lvmingchaooo@163.com, [b]zhaotong@sdu.edu.cn, [c]loujie00@sdu.edu.cn

Keywords: Commutation failure(CF), anomalous, faults levels, effective short circuit ratio(ESCR), coupling impedance.

Abstract. Commutation failure theory of HVDC system is proposed and its reason is analyzed. Faults at inverter bus in multi-infeed HVDC system can cause local commutation failure and even concurrent commutation failure. Anomalous commutation failure is simulated with six kinds of ac system strength, and it is more and more serious at first as the system strength increases then become less serious as the strength becomes stronger. Coupling impedance is changed to get its relationship with anomalous commutation failure.

Introduction

COMMUTATION FAILURE(CF) is an adverse dynamic event that occurs when a converter valve that is supposed to turn off, continues to conduct without transferring its current to the next valve in the firing sequence. Its occurrence causes temporary interruption of transmitted power, and stresses the converter equipment[1] . When the converter fails to regain breakdown capacity in the inverse voltage duration after breakover or commutation process doesn't complete during the time, commutation failure occurs. CF mainly happens at the inverter for the rectifier valve can have inverse voltage in a long time after its current shutoff. CF is one of the most common fault types at the inverter in HVDC system[2]. CF may lead to decline of dc voltage and increase of dc current. If measures haven't been taken properly, it can trigger concurrent commutation failure, which will cause shutting of whole dc system in some serious occasion. This will break up the dc power and influence the safe operation of Grids.

The essence of CF is that the valve extinction angle γ bellows the critical extinction angle γ_{min}. Traditional discriminant method for CF is the measurement of minimum voltage drrop. This method estimates whether CF happened or not by comparing commutation voltage drop with the critical voltage drop, and the latter one is the appraised standard of CF. However, this method neglects the influence of wave distortion, which will cause error in estimating CF. This essay use the extinction angle as the standard of CF, and if $\gamma < 7°$, CF happens.

Commutation failure theory

The converter valve voltage variation is the main reason of CF. Voltage variation can change the voltage zero drift as well as decline the voltage amplitude. The process of commutation can be expressed by commutation area in voltage-time graphic, which is shown in Fig. 1. There are some parameters at the inverter that are firing angle α, commutation angle μ and extinction angle γ, and they satisfy the equation $\alpha + \mu + \gamma = \pi$. Converter commutation area is S_1 which guarantee successful commutation when normally running, related to curve 1. When fault comes (take three phase fault as examples), the commutation voltage amplitude declines, showed as curve 2. As commutation area and firing moment keep constant, commutation duration have to be extended. According to Fig. 1,there gives new parameters μ' and γ'.

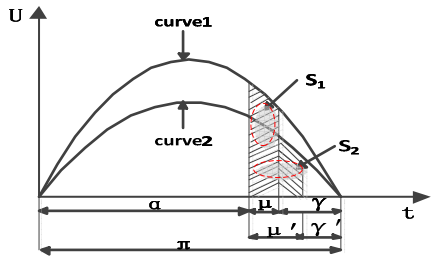

Fig. 1. Decrease of γcaused by voltage amplitude drop.

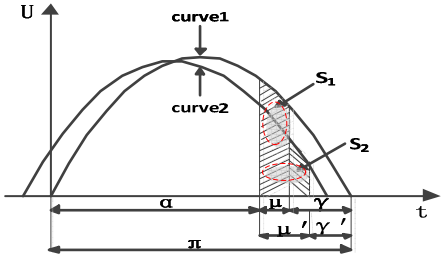

Fig. 2. Decrease of γcaused by voltage zero drift

When commutation voltage is below a certain value, $\gamma < \gamma_0$, and CF happened. The critical voltage drop ΔU is given by

$$\Delta U = 1 - \frac{I_d'}{I_d}\frac{(I_d/I_{dFL})\cdot X_{cpu}}{\left(\frac{I_d}{I_{dFL}}\right)\cdot X_{cpu}+\cos\gamma_0-\cos\gamma}. \quad (1)$$

where

I_d prefault dc current;
I_d' postfault dc current;
I_{dFL} nominal dc current;
X_{CPU} transformer per-unit impedance;
γ minimum extinction angle;
γ_0 extinction angle below which commutation fails.

Voltage zero drift

When asymmetrical faults happens, not only the voltage amplitude declines but also its zero crossing point moves which may also cause decline of γ, and then commutation failure happens. The zero crossing point moving can be called as zero drift, and only the forward moving of zero crossing point can cause CF. Fig. 2 shows the zero crossing point moves forward.

Similarly, here gives another critical voltage,

$$\Delta U = 1 - \frac{I_d'}{I_d}\frac{(I_d/I_{dFL})\cdot X_{cpu}}{(I_d/I_{dFL})\cdot X_{cpu}+\cos(\gamma_0+\varphi)-\cos\gamma} \quad (2)$$

There exists a new character 'φ' at the denominator of formula (2) compared to formula (1), which causes decline of ΔU and increase the probability of commutation failure.

Anomalous Commutation Failure phenomenon in Multi-Infeed HVDC Systems

Electrical coupling relationship exists between different dc system in multi-infeed system. When one of the dc systems encounters CF, other dc systems may be caused concurrent or successive CF. Here gives an example containing two dc systems showed as Fig. 3. Both of the two HVDC system are rated as in the "CIGRE First HVDC Benchmark Model" in PSCAD.

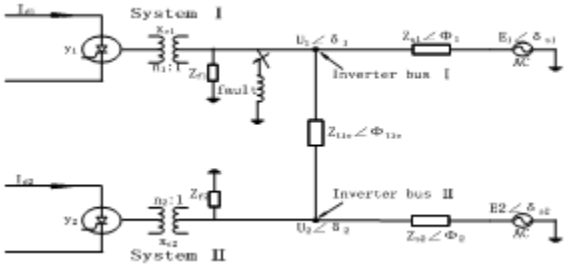

Fig. 3. Schematic diagram of double-infeed system

Suppose that inverter bus Ⅰ has a fault, which causes CF in inverter Ⅰ, the effect of fault can spread to inverter bus Ⅱ through coupled line. Thus inverter Ⅱ will encounter CF too. This concurrent CF has relation to fault level, fault situation and ac system strength. However, the CF of second inverter doesn't follow the first one, but comes out with some anomalous phenomena.

In order to elaborate these phenomena, first we introduce a concept called effective short circuit ratio (ESCR), which can represent the ac system strength. The effective short circuit ratio is an indicator of the performance of a given inverter without any other inverter in operation. Thus the ESCR for the inverter is given by

$$ESCR = \frac{SCL - Q_f}{P_{dc}} \quad (3)$$

SCL is the short circuit level at the given inverter bus due to the entire ac system. Q_f is the reactive power generated by filters and capacitors connected at the bus and P_{dc} is the rating of the given dc system. When calculating ESCR, other inverters must be blocked while their filter banks are in service.

Anomalous commutation failure phenomenon is showed in Fig. 4. The effective short circuit ratio are selected : ESCR1 = 2.5, ESCR2 = 4.5 and the tie line length is 80 km.

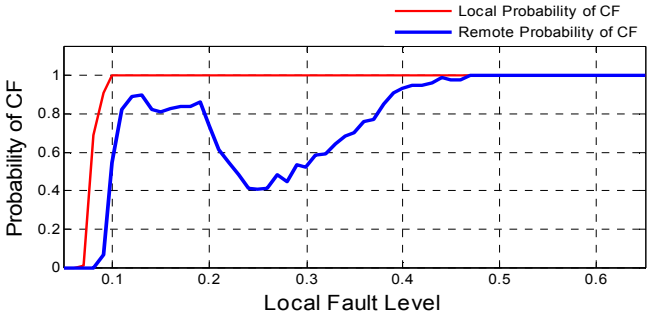

Fig. 4. Anomalous CF in double-infeed system

The local fault level is the level which converter bus encounters fault. Since inductive fault is more serious than capacitive and resistive fault, and it causes CF more easily, so this article just only analysis the inductive fault.

$$\text{Fault Level} = \frac{U^2}{Z_{fault} \cdot P_{dc}} \quad (4)$$

in which $Z_{fault} = \omega \cdot L_{fault}$, U is the nominal voltage of converter bus, Z_{fault} is ground impedance, and P_{dc} is the nominal power delivered by dc system.

Commutation failure is a random event, and we must grasp the statistical magnitude that reflect CF essence to know about the random event[3]. For each fault level, the probability of CF is calculated as the fraction of faults of a total of 100 applied at different points on wave within a cycle that resulted in CF[4]. We can get to know from Fig. 4 that the probability of CF becomes 1 at the 0.47 fault level. This essay set 61 fault levels, from 0.05 to 0.65, the interval is 0.01.

Analysis of anomalous CF phenomenon when changing ac system strength.

Paper [4] promoted anomalous commutation failure phenomenon but did not take deeper exploration. According to Fig. 3, this paper will make a probing analysis of anomalous CF phenomenon, by changing the second effective short circuit ratio and the coupling relationship of the two ac systems. Local CF happens at converter Ⅰ, while remote CF probability is the probability that converter Ⅱ encounters. From Fig. 4, we can see that when the fault level is low, about 0.1-0.2, remote CF probability is at 0.8 or so. As the fault level increase, the remote CF probability decreases at first and then increases. This is called anomalous CF phenomenon. Fig. 4 is the situation of ESCR1=2.5 and ESCR2=4.5, now change the effective short circuit ratio (ac system strength) of ac system Ⅱ, and analysis its influence on anomalous CF. This text gives out six ratios from 2.5 to 5.0

Sixty one times of fault level simulation are needed in each ac system strength, and each fault level needs 101 tines of simulation, so each ac system strength needs 6161 times of simulation in total.

Figure 5 shows the anomalous CF of six kinds of ac system strength. From the figure we can see that anomalous CF phenomenon of inverter Ⅱ are more and more obvious when ESCR2 increases from 2.5 to 4.5. At 0.1 fault level or less than it, the probability from 2.5 to 4.5 has little difference,

but as fault level increases, if the ac system is more stronger, its curve declines more seriously. Look at the curve of ESCR=4.5, when the fault level is between 0.1 and 0.2, the CF probability of inverter Ⅱ is between 0.8 and 0.9, but when the fault level is 0.25, the CF probability of inverter Ⅱ is 0.4. This is the most serious situation, and when ESCR2 equals 5.0, the anomalous commutation failure phenomenon is no longer obvious.

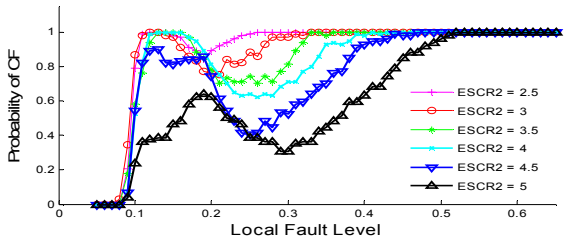

Fig. 5. Anomalous CF of six ac system strength types.

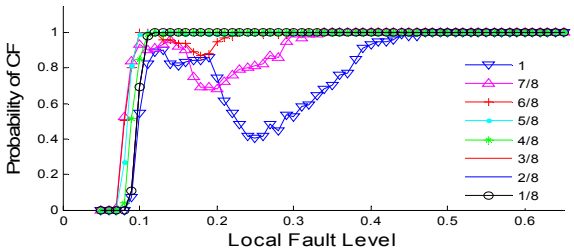

Fig. 6. Anomalous CF phenomenon when changing coupling impedence

Analysis of anomalous CF phenomenon when changing electrical coupling relationship.

Change the coupling impedance value of the double-infeed HVDC system. Take the value 1, 7/8, 6/8, 5/8, 4/8, 3/8, 2/8, 1/8 of original impedance at the most serious situation of ESCR1=2.5, ESCR2=4.5. The result is shown in Fig. 6.

As is shown in Fig. 6, the anomalous CF phenomenon is disappearing with the impedance decreasing. When the coupling impendence is less than 5/8 of original value, converter Ⅱ and converter Ⅰ are encountered concurrent CF almost at the same fault level. And three curves of 3/8, 2/8 and 1/8 coincide totally, and what's more, their probability of CF is 1 when the local fault level is more than 0.1. So the anomalous CF phenomenon has positive correlation with coupling impedance.

Conclusions

1). The paper shows commutation failure phenomenon and gives its detailed analysis. Two reasons of CF is proposed, one is the decline of voltage amplitude and the other is the voltage zero drift. Both are calculated by equations and can be used in practice.

2). Anomalous CF phenomenon is simulated with six ac system strength and eight kinds of coupling impedance. For ESCR1=2.5, ESCR2=4.5, the anomalous phenomenon is most serious and it is less serious when ESCR2 is less than 4.5 or more than 4.5. In addition, as the coupling impendence decreases, this phenomenon also weakens.

References

[1] J. Arrillaga. High Voltage Direct Current Transmission, 2nd ed. London, U.K.: Inst. Elect. Eng. Publ., 1998.

[2] Zhiyuan Sun. Simulation study of Commutation Failure in multi-infeed HVDC system based on EMTDC [D]. Guangxi University, 2007(in Chinese).

[3] Jian Liu, Xingyuan Li, Chong Wu, et al. Power System Technology, 2009, 33(8): 8-12(in Chinese).

[4] Ebrahim Rahimi, A.M.Gole, J.B.Davies, et al. IEEE Transactions on Power Delivery, 2011, 26(1): 378-384.

Advanced Materials Research Vols. 960-961 (2014) pp 738-741

doi:10.4028/www.scientific.net/AMR.960-961.738

Diagnosis of Commutation Failures in HVDC System Based on Voltage or Current of the Converter Valve

Tao Liu[1,a], Tong Zhao[1,b], Liang Zou[1,c], Li Zhang[1] and Mengqi Liu[1]

[1] School of Electrical Engineering, Shandong University, 17923 Jingshi Road, Jinan 250061, China

[a]ltxingyu@126.com, [b]zhaotong@sdu.edu.cn, [c]zouliang@sdu.edu.cn

Keywords: HVDC, commutation failure, diagnosis, valve voltage, valve current.

Abstract. Commutation failure is one of the most common typical faults of HVDC, and it may result in subsequent commutation failures, even the outage of the HVDC system if without timely and effective regulatory measures. Trigger of the control measures depends on the rapid and accurate diagnosis of commutation failure. In-depth analysis of the commutation failure mechanism indicates its new substantive characteristics: valve voltage being continuously zero and valve current being continuous with high amplitudes, according to which a novel method for fault diagnosis of commutation failure based on voltage or current of the converter valve is proposed in this paper. Simulation results prove the accuracy and effectiveness of this method.

Introduction

Commutation failure is one of the most common typical faults of HVDC. It can cause obvious drop of DC voltage, fast-rising of DC current and decrease of DC power, even subsequent commutation failures if no effective regulatory measures are taken, which may leads to the outage of the HVDC system, and then affects the safe and stable operation of the entire AC-DC power system.

Start of the effective control measures depends on the rapid and accurate diagnosis of commutation failure. Currently, diagnostic methods for commutation failure mainly include extinction angle, minimum voltage drop, minimum commutation voltage-time area, wavelet analysis method, etc. Formula for computation of the minimum voltage drop corresponding to commutation failure under symmetrical and asymmetrical AC faults was derived in reference [1]; however, this derivation was based on an infinite bus system and the quasi steady state equation of converter, and ignored the influence of voltage waveform distortion, which means low accuracy. Combined with influence analysis of commutation angle on commutation process, literature [2] gave the quantitative relation between commutation voltage-time area and commutation failure, considering that the commutation voltage was sinusoidal, DC current and the firing angle was constant during commutation process. According to reference [3], wavelet analysis of DC current and converter bus voltage can not only diagnose the occurrence of commutation failure, but also distinguish the corresponded fault types; But, setting of the threshold value and criterion is related to the structure and parameters of the entire system, and this method is difficult to achieve in engineering practice due to the complexity of the algorithm.

With deep analysis of the commutation failure mechanism, and from the perspective of substantive characteristics of commutation failure, a novel diagnostic method for commutation failure based on valve voltage or valve current is presented. Detailed simulation results based on the CIGRE HVDC standard test system also testify the accuracy and effectiveness of the proposed method.

Commutation Failure Mechanism

Definition of Commutation Failure. When the two valves of converter, for the commutation process can't be completed, or expected valve turns off, the valve fails to restore blocking capacity during the reverse voltage, if voltage on the valve is positive, it immediately re-turns, and inverted commutation occurs, this phenomenon is known as commutation failure.

That is, commutation occurs when the extinction angle γ is less than its critical value γ_{min}, where γ_{min} is the corresponding time for the thyristor to restore forward-voltage blocking capacity, and its value varies between 7 and 10 degrees due to the parameters of thyristors, the magnitude of loaded voltage and current.

Analysis of Commutation Failure Process. Fig. 1 shows the schematic diagram of 6-pulse inverter, where V1-V6 represent the six converter valves triggered in turns; u_a, u_b and u_c denote the power-frequency fundamental wave phase voltage of equivalent AC system; i_a, i_b and i_c represent three-phase alternating current respectively; L_r is the equivalent commutation inductance; L_d is the inductance value of smoothing reactor.

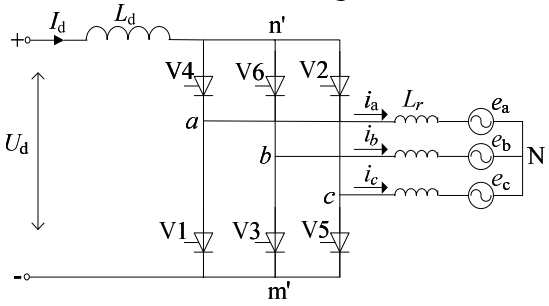

Fig. 1 Schematic diagram of 6-pulse inverter

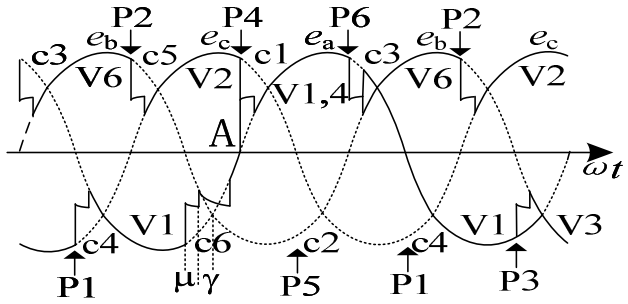

Fig. 2 Waveform of commutation failure of inverter

Taking commutation from V1 to V3 shown in Fig. 2 as an example, after valve voltage zero-crossing point, if V1 can't restore forward blocking capacity due to biggish commutation angle μ when V3 is triggered, thus V1 will re-conduct under forward voltage even without trigger pulse, which means inverted commutation from V3 to V1 will occur and V3 will turn off at point A. Sometimes μ is excessively big so that the commutation can't be completed even by point C6, and then followed by inverted commutation to V1, after which V1 and V2 will keep conducting continuously.

The following valves will be triggered in turns as originally planned if there are no effective measures in action. After conduction of V4, short circuit at the DC side will be caused by V1 and V4, which will inevitably result in fast-rising of DC current, drop of DC voltage and DC power. Because V5 is unable to turn on at point P5 due to backward voltage, the short circuit will continue until the successful commutation from V4 to V6. Then HVDC return to normal operation if no commutation failure happens again. V1 keeps conducting in a cycle during this process, and it is three times of the conducting time of V1 under normal conditions. The electrical degree corresponding to the short-circuit time is $120°+\mu$.

Restricted by the response time of DC current and extinction angle regulator, generally the short-circuit current can't be restrained completely by point P6, so μ is still very big, which means commutation from V4 to V6 will fail and short circuit at the DC side will continue to exist. Usually after 20ms from the moment of commutation failure, the short-circuit current will reach its maximum instantaneous value, which is 2 times of the rated DC current. About 50ms is needed for the DC current regulator at the rectifier side to diminish the DC current to set value or zero. After that, V6 or V4 will be trigged successfully and the short circuit will disappear.

When the value of commutation voltage drop or DC current rise is big, commutation from V2 to V4 may also fail after the failure of commutation from V1 to V3, in other words, two continuous commutation failures. In this case, V1 and V2 will keep conducting state nearly in a cycle, and inverse DC voltage at the inverter side will last 180° (about 10ms), bring down the counter electromotive force at the inverter side and enlarging the DC current.

Seen from the analysis above, if v4 is triggered successfully after the failure of commutation from V1 to V3, then short circuit at the DC side will be resulted in via V1 and V4, lasting about 50ms, and V1 and V4 will keep conducting in more than two cycles; otherwise, V1 and V2 will keep conducting nearly in a cycle.

Criterion for Commutation Failure

Currently, there are various criteria of commutation failure, but most of them are based on the γ_{min}, and derived on condition that some factors are constant during the commutation process, which is unreasonable and leads to low accuracy, limited application range. Commutation failure is the result from interactions among many factors, like DC current, set value of β or γ, converter bus voltage, equivalent commutation reactance, converter transformer transmission ratio, etc. Only considering the influence from some of these factors is likely to cause misjudgment, while it is impractical to take every factor into account. Hence, only by the substantive characteristics can realize the rapid and accurate diagnosis of commutation failure.

Although extinction angle method is based on the essence of commutation failure ($\gamma < \gamma_{min}$), and is the most commonly used method, two points need to be paid attention: first, γ can't be measured directly in practical engineering, and can only be acquired by indirect computing from operating parameters of the DC system, which means it is unable to trace the real-time variations of γ; second, γ_{min} is not constant, varying with the intrinsic parameters of thyristors, loaded voltage and current. In consideration of the two reasons, extinction angle may result in misjudgment in some cases, such as the state adjacent to commutation failure.

From above analysis of commutation process, it can be seen that commutation failure is always accompanied by the continuous conduction of certain valves — at least one cycle, with valve voltage being continuously zero and valve current being continuous with high amplitudes — about two times of the rated DC current, which can be regarded as two new substantive characteristics of commutation failure. Besides, measurement of valve voltage or valve current is very easy in practice. Therefore, the two substantive characteristics both can be used as a new criterion for commutation failure.

Fault Simulation and Analysis

The simulation model is based on the monopolar 12-pulse CIGRE HVDC standard test system, whose rated DC voltage is 500kV, DC current is 2kA and transmitted power is 1000MW. Inductive grounding short circuit is the most common fault in power system. Firstly, a three-phase inductive grounding fault is set in the inverter bus, and the fault occurs at 0.6s, the time of duration is 0.05s, the value of fault inductance is 0.2H, and the total simulation time is 1.2s. Simulation results are shown in Fig. 3-Fig. 6.

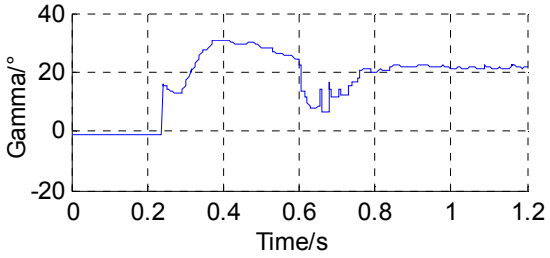

Fig. 3 Waveform of extinction angle

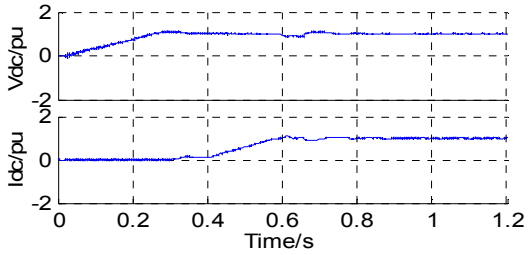

Fig. 4 Waveform of DC voltage and current

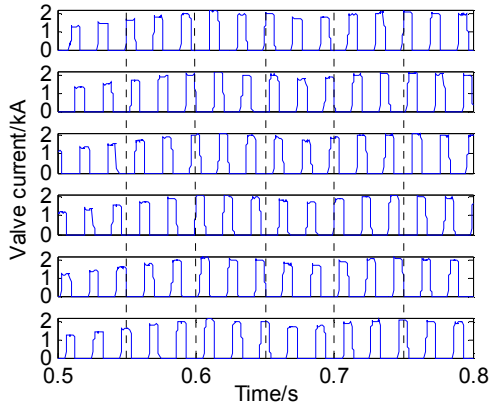

Fig. 5 Waveform of valve voltage

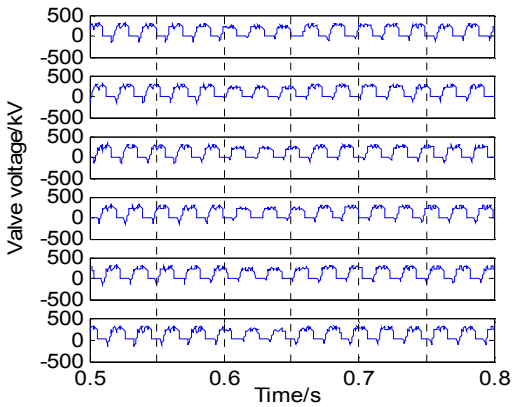

Fig. 6 Waveform of valve current

Fig. 3 shows that the minimum value of γat the inverter side is 6.2° during the fault. A conclusion of commutation failure can be drawn according to extinction angle method, which conflicts with the phenomenon in Fig. 4, for no drop to zero of DC current and fast-rising of DC current happens. Further analysis of valve voltage waveform shown in Fig. 5 and valve current waveform shown in Fig. 6 indicates that each valve is triggered successfully in normal turns; there are merely some small numerical fluctuations caused by the grounding fault; phenomenon of being continuously zero of valve voltage and being continuous with high amplitudes does not appear. Hence, we can come to the conclusion that commutation failure does not occur after the grounding fault, and this agrees with the waveform of DC voltage and current in Fig. 4.

Secondly, fault inductance of the three-phase inductive grounding fault is decreased to 0.1H, and other fault parameters are the same as the first case. Simulation results are shown in Fig. 7-Fig. 9.

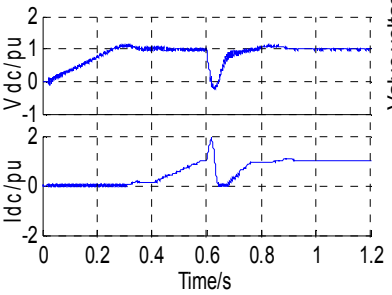

Fig. 7 Waveform of DC voltage and DC current

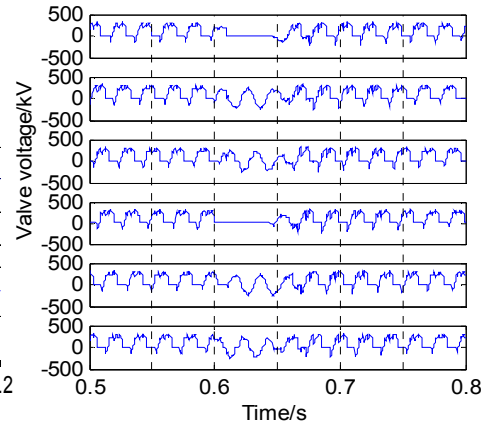

Fig. 8 Waveform of valve voltage

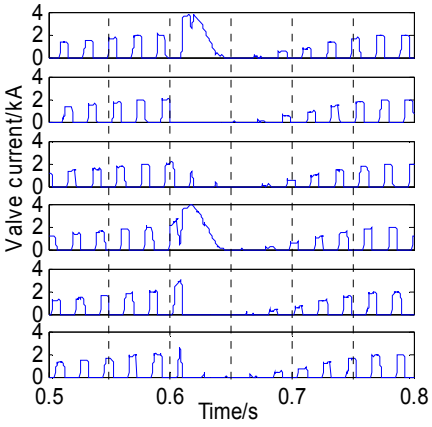

Fig. 9 Waveform of valve current

As shown in Fig. 8 and Fig. 9, V1 and V4 keep conducting during the fault and the duration time is about two cycles for valve voltage being continuously zero and valve current being continuous with high amplitudes which are about two times of the rated DC current. Therefore, commutation failure happens after the grounding fault, and this conclusion is coincident with the drop to zero of DC voltage and fast-rising of DC current shown in Fig. 7.

Simulation and analysis of other two typical faults — single phase grounding fault of AC system at the inverter side and loss of inverter trigger pulse, is also carried out. Simulation results also prove that it is accurate to diagnose whether commutation failure of HVDC occurs or not.

Conclusions

(1) Commutation failure is always accompanied by the continuous conducting of certain valves, and this makes the corresponding valve voltage being continuously zero, valve current being continuous with high amplitudes, which can be regarded as the substantive characteristics of commutation failure besides $\gamma < \gamma_{min}$.

(2) Extinction angle method may result in misjudgment in some cases such as state that is adjacent to commutation failure, due to the influence from calculation errors of $\gamma$and variations of γ_{min}.

(3) A new method for the diagnosis of commutation failure based on valve voltage or valve current is proposed in this paper. Simulation results prove the accuracy and effectiveness of this method.

References

[1] C.V. Thio, J.B. Davies and K.L. Kent: IEEE Trans on Power Delivery. Vol. 11 (1996), p. 946.

[2] G. Wang, Z.J. Li, M. Huang, et al: Automation of Electric Power Systems. Vol. 34 (2010), p. 49.

[3] L.X. Lin, Y. Zhang, Q. Zhong, et al: Automation of Electric Power Systems. Vol. 31 (2007), p. 49.

Advanced Materials Research Vols. 960-961 (2014) pp 742-745

doi:10.4028/www.scientific.net/AMR.960-961.742

The Models of Superconducting Power Facilities: The Effect of Different Tape

Meng Song[1], Lushun Su[2,a], Xuzhi Deng[2], Li Ren[2], Shifeng Shen[2], Yi Zhang[2], Nannan Hu[1]

[1]Yunnan Electric Power Research Institute, Kunming, P. R. China

[2]State Key Laboratory of Advanced Electromagnetic Engineering and Technology, Huazhong University of Science &Technology, Wuhan, P. R. China

[a]sulushun@qq.com

Keywords: Numerical Model, Superconducting Power Facilities, HTS.

Abstract. Due to the high current density in 77K, the high temperature superconducting facilities are expected to improve the efficient in power transmission. Superconducting facilities electromagnetic design is highly dependent on the characteristic of the superconducting tape. As a result, the comparison of the effect of different tape in electromagnetic design should be studied. In this paper, several facilities model are used as example to analyze the effect of different tape utilization. The result shows in different application conditions, or, specific benefits are considered, there is a specific tape will be the best choice.

Introduction

Superconductor have many advantage in power applications, such as power cable, fault current limiter as well as power transformer and reactor due to the high current density in superconducting state. In last years, many research in these area have achieved significant improvement especially in DC superconducting cable [1]-[3]. Because of the deeper research of the HTS Roebel cable in the Karlsruhe Institute of Technology [4], the AC losses in the AC applications could be expected to be reduced to a much lower level. Thus, the HTS will be used in more and more power facilities.

Electromagnetic model of the superconducting power facilities, for example, the FEM model, are widely used to analysis the performance of the superconductor and they could be used in the design superconducting magnet. In the magnet design, the tape character has a huge impact on the result, so we need to investigate this kind of effect.

In this paper, we present several electromagnetic models of the superconducting facilities and analyzed the effect on the represent of the device with different tape. The result could help us choose the type of tape when we design the superconducting magnet to obtain a specific function.

HTS Cable

Superconducting cable is expected to solve the limited channel space in the transmission system by using the high current density of the superconductor.

Table 1. HTS Tapes Properties

Type Name	Type-H (Sumitomo)	SCS4050 (Superpower)
Tape thickness	0.35[mm]	0.1[mm]
Tape wideness	4.2[mm]	4[mm]
Critical Current	180[A]	120[A]

Using a double layer (24 tapes each layer) cable as an example in order to analysis the magnetic field distribution. As to compare the different tapes effect, two kinds of tapes are applied as Table 1.

Fig.1 gives the magnetic distribution when a $I = 12 \times 80 \times 0.8A$ current has applied, the axial component and the racial component of the magnetic field have been illustrated in this figure.

The results show that when SCS 4050 tape applied to the model, the maximum of the racial component is 141Gs, while it is 94.9Gs when Type H tape used in this model.

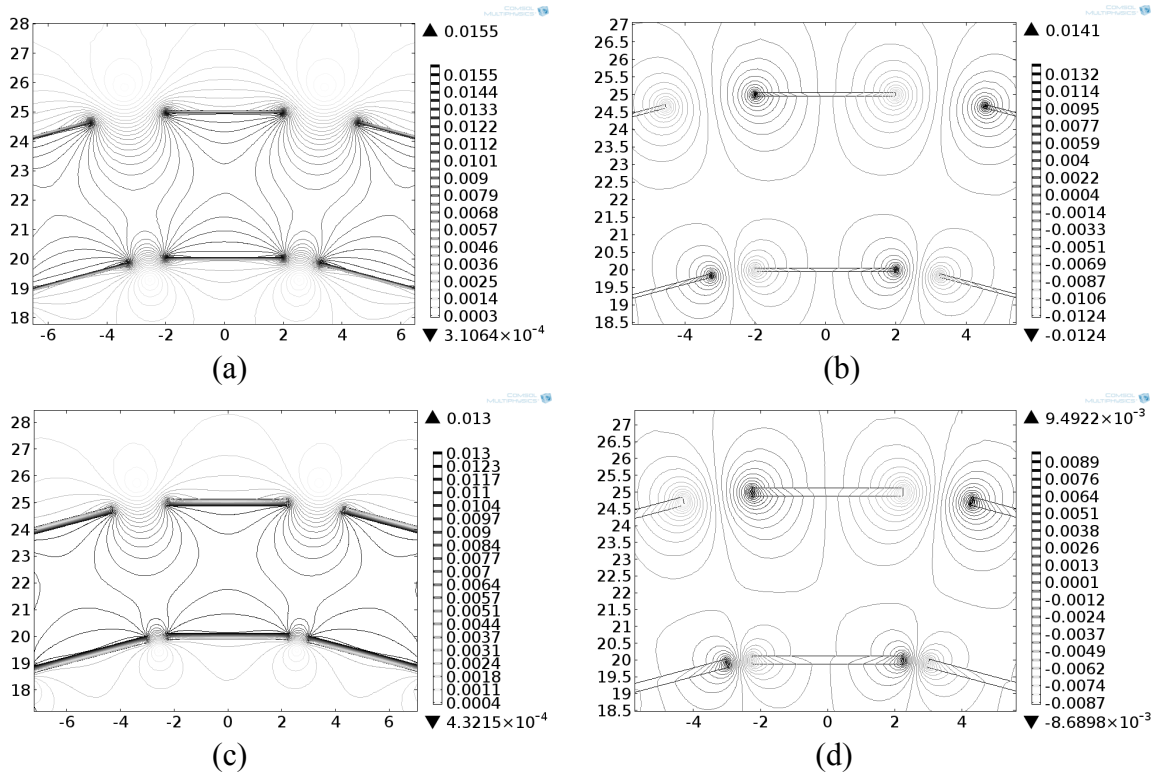

Fig. 1 The magnetic field density distribution of the cable
(a) SCS4050, absolute value (b) SCS4050, racial component
(c) Type H, absolute value (d) Type H, racial component

By using the load line and the B-T relationship of the HTS tapes, the critical current of the superconducting magnet could be obtained. Usually there should be a margin of the working current and the critical current, in this analysis, this margin is set to 0.7. Fig.2 shows the B-I curve and the load line with its cross point.

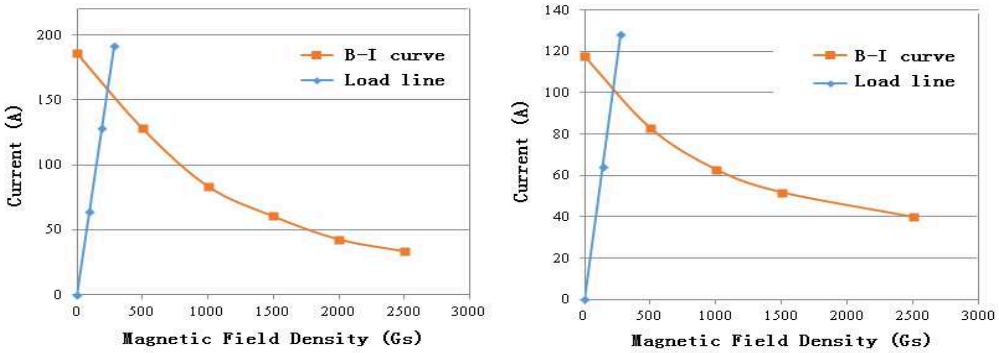

Fig. 2 The calculation of the critical current

The working current of the cable made by SCS4050 tape is 1696.8A and made by Type H is 2721.6A. Both of them have used tape data in 77K. This result indicates the type H type is more efficient for fabricate the power cable.

HTS Transformer

Transformers using HTS tapes are attractive because they are much smaller and have enormous overload capacity. Moreover, the operation of the superconducting transformer do not need insulation oil, that's make it become a more environmentally friendly facility.

To know which kind of tape is more suitable in this application, different types of tapes have been used in a Single Phase HTS transformer model, whose capacity is 110kVA.

The Table 2 listed the specification of the singe phase transformer. Fig 3 shows the geometry model as well as the magnetic field distribution of the calculation result. This general result shows the leakage flux in the transformer is the key factor which determine the critical current of the windings.

Table 2. Specification of a Single Phase HTS Transformer

Specification	Value
Phase	1
Capacity	110kVA
Rated voltage	25kV/365V
Number of turns	Primary 2092/ Secondary 72
Parallel conductors	Primary 1/ Secondary 12

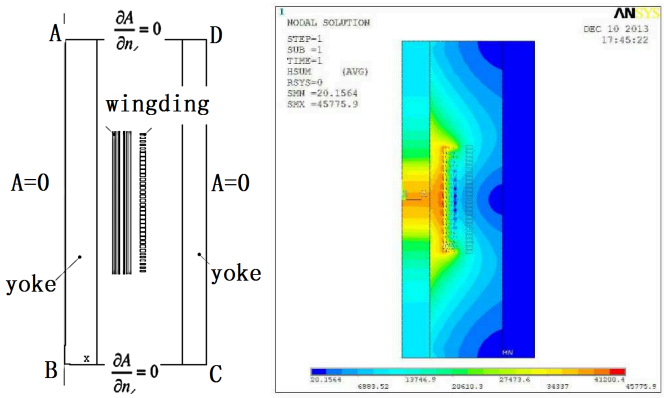

Fig. 3 Geomertry model (left) and the general magnetic field distrbution (right) of a HTS trasformer

In the Secondary winding, the conductor is consist of 12 parallel conductors. Although the current could transfer in these conductors when the winding is quenched, we still using the load line and the B-T relationship of single tape to calculate the critical current.

Fig 4 illustrates the racial component of the magnetic field density in the condition of using the AMSC-copper tape. It shows the maximum magnetic field density is in the third layer of the winding.

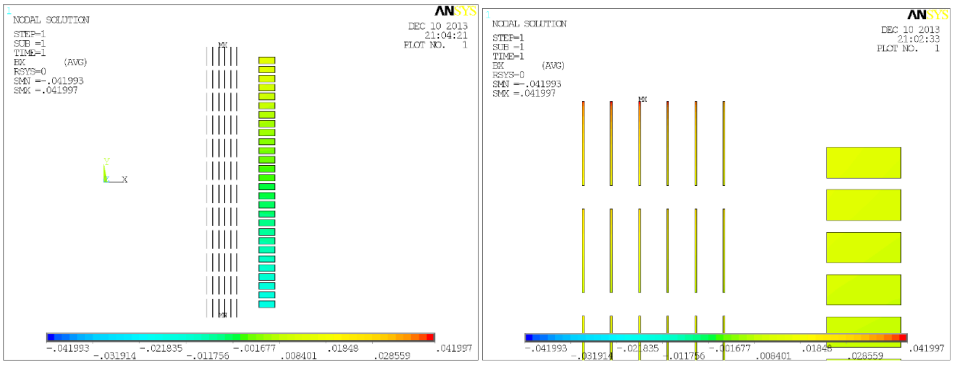

Fig. 4 The racial component of the magnetic field density of a transformer (left: whole windings; right: top of the windings)

The calculation could get the minimum critical current of the winding tape, which is determined the overload capacity: the bigger the critical current is, the larger the overload capacity will be. Table 3 gives the result and it indicates that the FYSC-SC05 has the highest minimum critical current value, so it is the best choice for the transformer.

Table 3 Simulation Result

Types	B_max T）	Br_max T）	Bz_max T）	Ic_min A）
AMSC-Copper	0.050158	0.041993	0.049108	95.84
SP-SCS4050	0.056298	0.047298	0.054786	81.08
Type HT-SS	0.05165	0.043167	0.050951	128.42
FYSC-SC05	0.047957	0.040112	0.047039	207.72
SUNAM	0.055686	0.046665	0.05467	138.82

Conclusions

In this paper, a HTS cable model and a HTS transformer model are analyzed by using different tape, and the result could guide researcher choose the type of conductor. For the cable, the result shows in 77K condition, the 1st generation HTS have significant advantage because of the high current density. As to the HTS transformer, the overload capacity is what we are aimed for and Simulation results shows that the FYSC-SC05 has the highest minimum critical current value, so it is the best choice for the transformer.

References

[1] T. Hamajima, N. Hu, N. Ozcivan, S. Soeda, T. Yagai, and M. Tsuda, "Balanced three-phase distributions of tri-axial cable for transmission line," IEEE Trans. Appl. Supercond., vol. 19, pp. 1748–1751, Jun. 2009.

[2] J. Cho, K. D. Sim, J. H. Bae, H. J. Kim, J. H. Kim, K. C. Seong, H. M. Jang, C. Y. Lee, and D. Y. Koh, " Design and experimental results of a 3 phase 30 m HTS power cable," IEEE Trans. Appl. Supercond., vol. 16, pp. 1602–1605, Jun. 2006.

[3] P. W. Fisher, M. J. Cole, J. A. Demko, C. A. Foster, M. J. Gouge, R. W. Grabovickic, J. W. Lue, J. P. Stovall, D. T. Lindsay, M. L. Roden, and J. C. Tolbert, "Design, analysis, and fabrication of a tri-axial cable system," IEEE Trans. Appl. Supercond., vol. 13, pp. 1938–1941, Jun. 2003.

[4] D. C. Van der Laan, "YBCO coated conductor cabling for low ac-loss and highfield magnet applications," Supercond. Sci. Technol., vol. 22, no. 6, pp. 065013-1–065013-5, Jun. 2009.

Advanced Materials Research Vols. 960-961 (2014) pp 746-754

doi:10.4028/www.scientific.net/AMR.960-961.746

A New Method of Evaluating the Sensitivity of Sensitive Load to Voltage Sag

Ruibin Luo[1, a]

[1] Dongguan power supply bureau, Guangdong grid corporation, China

[a]469569945@qq.com

Keywords: sensitive load; voltage sag; load sensitivity; sensitivity evaluation; probability density function

Abstract. This paper proposes a new method to evaluate the voltage sag sensitivity (VSS) of the sensitive load by the combination of several probability density function models, which can fully describe the randomness of load sensitivity. Firstly, five common probability density functions were respectively used to build the mathematical model of voltage tolerance curve (VTC) of sensitive load in uncertainty region. Secondly, the VSS of sensitive load was respectively evaluated by five models, and the weighted sum of five models' results was calculated by unbiased variance method. In the end, the proposed method was verified to be rational according to an application example.

Introduction

With the wide application of sensitive equipments, the voltage sag may cause sensitive equipments fail to work, which arouses the concern of the industrial circles. The probability of sensitive load breaking down in uncertainty region of voltage tolerance curve (VTC) is named voltage sag sensitivity evaluation. Current evaluation methods of voltage sag sensitivity for distribution network loads mainly includes the ITIC curve method, CBEMA curve method [1-3], the fuzzy evaluation method[4,5], the stochastic assessment method[6-9], the combination of fuzzy and stochastic theory method, the evaluation method based on cloud model [10,11] and the evaluation method based on maximum entropy theory [12-14].ITIC and CBEMA curve are fixed. Their duration lasts 0.5 cycle to 1 minute and voltage RMS value lasts 0.1 to 0.1 times the rated voltage, which does not include a full range of voltage sag. The two curves are both experimental curves, and need to have a lot of historical data, therefore the application's performance is not good enough. The fuzzy evaluation method makes use of membership degree that equipment belongs to the normal state to describe the transition state of equipment shifting from safety state to failure state during voltage sag event, and assumes that these verity probability of voltage sag follow Gaussian distributions, so this method is much affected by the selected samples, and the error depends on the number of samples.

The probability density function is used by stochastic assessment method to characterize the randomness of the load's voltage in uncertainty region of voltage tolerance curve, and to evaluate the sensitivity of the voltage sag directly. An appropriate probability density function is the key to improve the accuracy of the results of this method. The accuracy of the method based on cloud model depends on the accuracy of the characterization of voltage tolerance ability of the equipment, so it needs enough field experience. The evaluation method based on maximum entropy theory fully describes the randomness of voltage sag sensitivity. However, compared to the probability density function model, it's relatively complicated because of the computing process.

Probability density functions include uniform distribution, exponential distribution, Gaussian distribution, Rayleigh distribution, Weibull distribution and so on. The current probability evaluation methods use only one probability density function. However, in practice, it is very hard to fully describe the randomness of voltage sag sensitivity by a single probability density function model due to its one-sidedness, which cannot avoid error evaluation results.

This paper proposes a new method of evaluating voltage sag sensitivity, with five probability density functions respectively used to build the sensitivity evaluation model, and the assessed values of five models are added by mean square error method. This method highlights the consistency of the

conclusions of all of the models, meanwhile combines the different information of those models. This method makes full use of all the evaluated information, and the evaluation results are optimized combination, which can adapt to a more general stochastic environment.

This paper is organized as follows: Section II introduces the stochastic model of the voltage tolerance curve. Section III introduces the algorithm principles. Section IV introduces the algorithm design. And the cases are analyzed in section V. Section VI is the conclusions and the end is references.

Stochastic Model of the Voltage Tolerance Curve

Voltage tolerance curve of sensitive load and its uncertain region . The voltage tolerance ability of sensitive load changes along with the change of time and space. Usually, the sensitive equipments mainly include Programmable Logic Controller (PLC), Personal Computer (PC) and AC Speed Drive (ASD) and so on. Thevoltage tolerance curves (VTC) of PLC, PC and ASD are generally rectangular, their uncertain region is shown in Fig.1, and divided by Umin, Umax, Tmin and Tmax, among them, Umin and Umax are the minimum and maximum values of the amplitude of voltage tolerance; Tmin and Tmaxare the minimum and maximum values of duration of load voltage sag. In figure1,the normal operation region is the region that the actual amplitude of a voltage sagU>Umax or duration of load voltage sagT<Tmin,the fault region is the region that the actual amplitude of a voltage sagU<Umax or duration of load voltage sagT>Tmin. Uncertain region is between the two regions, and it can divided into three sub-regions (A, B and C), in which, A zone is the range of U <Umin and Tmin<T <Tmax;B zone is the range ofUmin<U<Umax and T>Tmax;C zone is the range ofUmin<U<Umax andTmin<T<Tmax. The Thresholds of different resistance curves of sensitive loads are shown in Table 1.

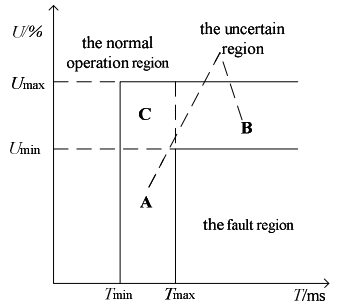

Fig.1 Uncertain region of sensitive load isVTC

Table 1 Threshold of sensitive load VTC

Type	Voltage Amplitudes p.u.		Duration ms	
	U_{min}	U_{max}	T_{min}	T_{max}
PLC	30	90	20	400
ASD	59	71	15	175
PC	46	63	40	205

Probability expression of the voltage tolerance curve of sensitive load. In fact, the position of load voltage tolerance curve is random, that is, U and T are random variables. Suppose that U and T are independent random variables, the probability density of random variables T and U in A zone and B zone are $f_a(T)$ and$f_b(T)$,so that the joint probability density of random variables U and T in C area is:

$$f_c(T,U) = f_a(T) f_b(U) \tag{1}$$

in which, Umin<U<Umax ,Tmin<T<Tmax.

Algorithm Principles

The commonly used probability density function. The commonly used probability density function includes 5 kinds of function, which are Uniform distribution function,Exponential distribution function, Normal distribution function,Rayleigh distribution function and Weibull distribution function.

In which， Uniform distribution is the ideal probability distribution.Exponential distribution belongs to thepartial type function;its characteristic is that it has value in the unilateral interval.Normal distribution, Rayleigh distribution and Weibull distribution belong to the middle type function;their characteristic is the interval symmetry. The characteristics and disadvantages of these 5 kinds of probability density function can be summarized as shown in Table 2.

Table 2 Comparison between five common probability density functions

Density functions	Characteristics	Disadvantages	Remarks
Uniform distribution	Equal probability distribution, in a given area in every point is equal to the probability of the event.	Belongs to the ideal situation; Lack of flexibility,can't fit the actual situation very well.	—
Exponential distribution	Belongs to the monotonically decreasing,the starting point has the maximum of probability density, then backward gradually decreases.	Monotone function,sometimes the error is larger when compared with the actual situation.	—
Normal distribution	There exists a maximum probability density point, the rest probability density values decrease to both sides,from the near to far distance the center, the change is slow down after,and the rate of change is controlled by parameters.	Difficult to determine theParameters.	The difference between these three kinds of function model is the decreasing speed,by selecting different parameters to determine the decreasing speed,to adapt to different practical problems.
Rayleigh distribution	There exists a maximum probability density point, the rest probability density values decrease to both sides,from the near to far distance the center, the change is slow down after,and the rate of change is controlled by parameters.	Difficult to determine theParameters.	
Weibull distribution	There exists a maximum probability density point, the rest probability density values decrease to both sides,from the near to far distance the center, the change is slow down after,and the rate of change is controlled by parameters.	Difficult to determine theParameters.	

Unbiased variance method. Unbiased variance method is one kind of objective method of endow with weight, which determines the weight coefficient in evaluating sensitivity based on variation of evaluating value between various evaluation methods. Assumed that there are n kinds of evaluation methods s_1, s_2, s_3, …, s_n. And m evaluating values x_{i1}, x_{i2}, x_{i3}, …, x_{im} can be obtained by method s_i. Steps of mean square error method to determine the weight coefficient are as follows:

(1)The mean of evaluating value of various evaluation methods is :

$$\overline{x_i} = \frac{1}{m}\sum_{k=1}^{m} x_{ik} \tag{2}$$

In this equation, xik represents kth evaluating value by method si, $\overline{x_i}$ represents the mean of evaluating value by method s_i, i=1, 2,..., n, k=1, 2,..., m.

(2)The variance of evaluating value of various evaluation methods is:

$$s_i^2 = \frac{1}{m}\sum_{k=1}^{m}(x_{ik} - \overline{x_i})^2 \tag{3}$$

In this equation, s_i^2represents the variance of evaluating value by method s_i.

(3)Weight coefficient of various evaluation methods is:

$$a_i = \frac{s_i}{\sum_{i=1}^{n} s_i} \tag{4}$$

In this equation, ai represents the degree of importance of evaluation method sirelative to evaluating object which is called weight coefficient, i=1, 2, ..., n.

Now, use the weighted sum of method s1 and s2 to analyze the reliability of the method.

Assume that the real VSS of the sensitive load is p0, and the evaluating values obtained by s1 and s2 are p1 and p2. So the weighted sum p is:

$$p = \alpha p_1 + (1-\alpha) p_2 \tag{5}$$

In this equation, α is a weight coefficient.

Let the error of evaluation be E=p-p0, then the square error of evaluation is:

$$E^2 = (p - p_0)^2 = [\alpha(p_1 - p_2) + p_2 - p_0]^2 \tag{6}$$

Take a derivative of E2 for optimal results:

$$\frac{\partial(E^2)}{\partial\alpha} = 2E(p_1 - p_2) \tag{7}$$

Then the iterative formula of α is as follows according to steepest descent method.

$$\alpha(n+1) = \alpha(n) - \lambda\frac{\partial(E^2)}{\partial\alpha} \tag{8}$$

In this equation, λ is a control coefficient.

The difficulty of this optimization algorithm is to determine p_0 and control the convergence. In order to simplify calculations, p_0 is defined as:

$$p_0 = (p_1 + p_2)/2 \tag{9}$$

In practical application, especially in the occasion where high control requirement of computing resource is preferred, the direction and number of iterations can be controlled as required.

The random estimation model of VSS. As shown in Fig.2, M_1-M_5 represents 5 different features of voltage sag: the voltage sag events happen in normal operation region, fault region, A region, B region and C region. When M_1 happens, all loads work well, while M_2 happens, all loads are broken. Assume that $T_3$is the duration of voltage sag when M_3 happens. Then when M_3 happens and $T_{min}<T<T_3$, the sensitivity of load is:

$$p_T = \int_{T_{\min}}^{T_3} f_a(T)dt \tag{11}$$

Assume that U_4 is the amplitude of voltage sag when M_4 happens. Then when M_4 happens and $U_4<U<U_{max}$, the sensitivity of load is:

$$p_U = \int_{U_4}^{U_{\max}} f_b(U)du \tag{12}$$

Assume that T5 and U4 are the duration and the amplitude of voltage sag when M5 happens. Then when M5 happens and Tmin<T<T5,U5<U<Umax, the sensitivity of load is

$$\int_{U_5}^{U_{\max}}\int_{T_{\min}}^{T_5} f_{ab}(T,U)dudt \tag{13}$$

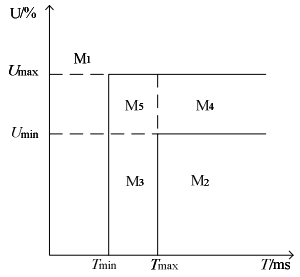

Fig.2 Schematic of sensitive load voltage sag event

Algorithm Design

The processes of weighted comprehensive evaluation algorithm in this paper are as follow:

(1)According to the category of load, identify the uncertain regions of VTC (Tmin, Tmax, Umin, Umax), and classify them into 3 uncertain subregions shown in Fig.1.

(2)Use five common probability density functions to build the evaluation model, and valuate the VSS of sensitive load running in different uncertain subregions according to 5 different features of voltage sag and equations (11)-(13).

(3)According to equations (2)-(4), use unbiased variance method to obtain the evaluation results' weighted value of various probability density function models. For region A, let the weight coefficient of probability density function models si be ai. For region B, let the weight coefficient of probability density function models si be bi. And the weight coefficients satisfy the following conditions:

$$\begin{cases} \sum_{i=1}^{5} a_i = 1 \\ \sum_{i=1}^{5} b_i = 1 \end{cases} \tag{14}$$

(4)According to the weight coefficients ai and bi, the VSS of sensitive load is evaluated by five probability density functions evaluation models, and the weighted sums of these five models in region A, B and C are:

$$p_A = \sum_{i=1}^{n} a_i p_{Ti} \tag{15}$$

$$p_B = \sum_{i=1}^{n} b_i p_{Ui} \tag{16}$$

$$p_C = \sum_{i=1}^{n} c_i p_{TUi} \tag{17}$$

In these equations, p_{Ti}, $_{Ui}$ and p_{TUi} represent the VSS of sensitive load in subregion A, B and C by probabilitydensity functions evaluation model si, respectively. a_i, $_i$ and c_i represent the weight coefficient of model si in subregion A, B and C. And $\sum_{i=1}^{n} a_i = 1, i = 1,2,\cdots,n$, $\sum_{i=1}^{n} b_i = 1, i = 1,2,\cdots,n$, $c_i = \frac{a_i + b_i}{2}, i = 1,2,\cdots,n$.

Simulation Analysis

The paper used Matlab as the auxiliary tool for simulation analysis, and made the evaluation of voltage sag sensitivity of sensitive load of PC. According to the research of literature [7], setting $U_{\min}$, $U_{\max}$, $T_{\min}$, $T_{\max}$ of the model as 46%p.u., 63%p.u., 40ms and 205ms[7] and calculating each weight of probability density function of evaluation model based on unbiased variance method, which was shown in the Table 3.

Table 3 Weights of probability density functions

Probability density functions	Weights		
	Region A	RegionB	Region C
Normal distribution	0.324	0.284	0.304
Uniform distribution	0.165	0.151	0.158
Exponential distribution	0.105	0.145	0.125
Rayleigh distribution	0.246	0.241	0.244
Weibull distribution	0.160	0.179	0.169
Total	1	1	1

According to the result of the weight distribution of Table 3,the evaluation functions of PC voltage sag sensitivity of region A and region B could be obtained:

$$P_A = 0.324P_{T1} + 0.165P_{T2} + 0.105P_{T3} + 0.246P_{T4} + 0.160P_{T5} \quad (18)$$

$$P_B = 0.284P_{T1} + 0.151P_{T2} + 0.145P_{T3} + 0.241P_{T4} + 0.179P_{T5} \quad (19)$$

Where PT1, PT2, PT3, PT4 and PT5 are respectively evaluation values of voltage sag sensitivity of sensitive load PC of each evaluation model.

Therefore, when voltage sag took place in region A and region B，the evaluation values of PC's voltage sag sensitivity were shown in the Fig. 3(a) and Fig. 3(b).It could figure out that the valuation values of various probability density function models were different comparatively and the bias between valuation values, which had been weighted and synthesized, and the evaluation values of various models was smaller.

Similarly, when voltage sag took place in region C, the evaluation function of PC sensitivity was:

$$P_C = 0.304P_{T1} + 0.158P_{T2} + 0.125P_{T3} + 0.244P_{T4} + 0.169P_{T5}$$

According to the comprehensive evaluation value getting from formula (20),we could describe the possibility of trouble happening when loads worked in region C.

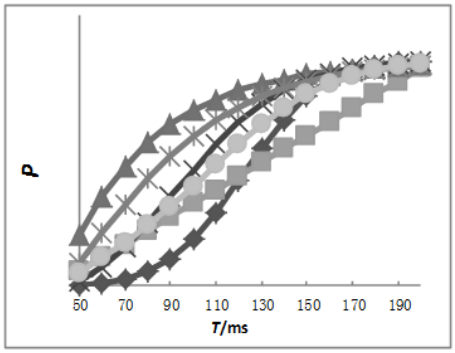

Fig.3(a) The voltage sag sensitivity of PC in region A

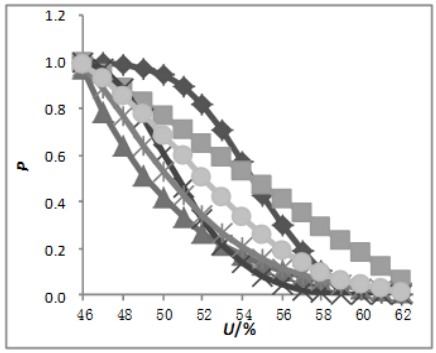

Fig.3(b) The voltage sag sensitivity of PC in region B

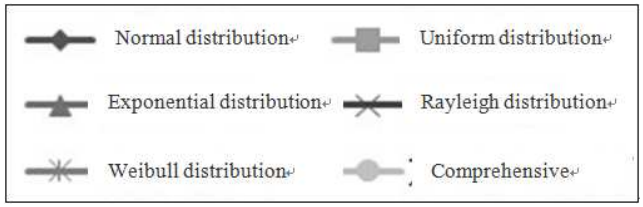

Fig.3(c) Legend

Table 4 Bias and variance between evaluation values and average values in region A

T/ms	Bias					
	Normal distribution	Uniform distribution	Exponential distribution	Rayleigh distribution	Weibull distribution	Weighted comprehensive evaluation algorithm
50	-0.074	-0.016	0.145	-0.057	0.023	-0.022
60	-0.148	-0.037	0.235	-0.081	0.070	-0.038
70	-0.214	-0.059	0.286	-0.076	0.114	-0.050
80	-0.265	-0.082	0.307	-0.051	0.146	-0.056
90	-0.291	-0.106	0.305	-0.015	0.164	-0.057
100	-0.287	-0.130	0.284	0.020	0.167	-0.053
110	-0.253	-0.153	0.249	0.047	0.155	-0.045
120	-0.195	-0.174	0.206	0.063	0.133	-0.033
130	-0.127	-0.188	0.161	0.069	0.106	-0.021
140	-0.061	-0.192	0.119	0.066	0.079	-0.010
150	-0.011	-0.185	0.084	0.059	0.055	-0.002
160	0.019	-0.166	0.057	0.051	0.036	0.003
170	0.032	-0.137	0.036	0.041	0.023	0.005
180	0.031	-0.101	0.021	0.031	0.012	0.005
190	0.023	-0.059	0.008	0.021	0.003	0.004
200	0.012	-0.015	-0.003	0.009	-0.006	0.002
Variance	0.015	0.004	0.013	0.003	0.004	0.001

According to the simulation analysis of Fig. 3(a), (b) and Table 4,we could obtain the following conclusions:

(1) The algorithm bias are smaller in this paper. The evaluation bias getting from Weighted comprehensive evaluation algorithm are up to 10-2, 10-3 order of magnitude. These minimum bias is -0.002 and maximum bias is -0.057,which is smaller than far the valuation bias of evaluation model of each single probability density function.

(2) The algorithm has preferable stability. In Table 5,the evaluation bias range of normal distribution is from -0.011 to -0.291, the evaluation bias range of uniform distribution is from -0.015 to -0.192, the evaluation bias range of exponential distribution is from -0.003 to -0.307, the evaluation bias range of rayleigh distribution is from -0.009 to -0.069, the evaluation bias range of weibull distribution is from -0.003 to -0.167, and the evaluation bias range of Weighted comprehensive evaluation algorithm is from -0.002 to -0.057 and its mean square error is only 0.0006,which is up to 10-4order of magnitude. It is thus clear that the fluctuation of sensitivity evaluation value of each single probability density function model is superior. However, the bias of weighted comprehensive evaluation value is smaller relatively and has better stability so that it can work better for the evaluation of voltage sag sensitivity of different sensitive loads.

Conclusion

1) The stochastic evaluation method of voltage sag sensitivity of sensitive load can gain the evaluation value of sensitivity by the probability density function. If we only choose a sort of probability density function, it will be difficult to overcome its one-sideness and possibly get the evaluation value with larger bias.

2) The stochastic evaluation method of voltage sag sensitivity in this paper gains the final comprehensive evaluation value by means of building five models of probability density function respectively and using unbiased variance method for weighting comprehensively the evaluation values of this five models. What the consistent conclusions of each model this algorithm emphasizing remains the different parts to a lesser extent among the valuation results of probability density functions so that it can comprehensively describe the sensitivity's randomness better than single probability density function model.

3) Finally, by the simulation analysis, the proposed method is verified to be rational in the application of random evaluation of voltage sag sensitivity of sensitive load.

4) It is because the method increase the calculated amount that it might cause problems of more space occupation in memory and longer calculation time. Therefore, the method in this paper applies to the occasions which not require accurate calculated results or strongly-real-time calculation.

Reference

[1] TanRodneyH.G，RamachandaramurthyVigna K.. Voltage sag acceptability assessment using multiple magnitude-duration function[J]. Power Delivery， 2012，27(4)：1984-1990.

[2] Elphick Sean，Smith Vic. The 230V cbema curve—preliminary studies[C]//Proceedings of Universities Power Engineering Conference(AUPEC). Christchurch：IEEE，2010：1-6.

[3] Abdullah M.Z., Ariffin R.. Power quality analysis of Residual Current Device [RCD] nuisance tripping at commercial buildings[C]. Industrial Electronics and Applications (ISIEA), IEEE, 2013: 122 - 125.

[4] XianYong Xiao, Chao Ma, Honggeng Yang, Wu Chen, Hua-Qiang Li. Failure Probability Analysis of Sensitive Equipment Due to Voltage Sags Using Fuzzy-Random Assessment Method[J]. Power Delivery, IEEE, 2010, 25(4) : 2970 - 2975.

[5] Ning Ding, Guodong Li, Yonghai Xu. Recognition of VoltageSag Disturbance by Mamdani Fuzzy Inference[C]. Energy and Environment Technology (ICEET), 2009, 2: 205 – 208.

[6] Gengyin Li, Xiaodong Yang, Ming Zhou. Probabilistic estimation of PCC loss due to voltagesags in large power systems[C]. Sustainable Power Generation and Supply(SUPERGEN), 2009: 1 – 6.

[7] Manjula M., Sarma A.V.R.S., Mishra, S.. Detection and classification of voltagesag causes based on empirical mode decomposition[C]. India Conference (INDICON), IEEE, 2011: 1 –5.

[8] Yong Liu, Lipin Chen, Zhijian Yuan. Affection of power system relay cooperation to voltage sag and sensitive equipment[C]. Electricity Distribution (CICED), China: 2012: 1 - 5.

[9] Khanh B.Q. Assessment of voltageSAG in distribution system regarding the uncertainty of wind-based distributed generation[C]. Electrical and Computer Engineering (CCECE), Canada: 2011: 000896 - 000899.

[10] XiaoLu Sun, YuanBo Li, Ying Wang, XianYong Xiao. Equipment Failure Probability Evaluation Due to VoltageSag Using CloudModel[C]. Future Power and Energy Engineering (ICFPEE), 2010: 83 - 86.

[11] Hong Zhao, Ying Wang, XianYong Xiao, HengGui Wang. Cloud Model Based Evaluation of Equipment Sensitivity to Voltage Sag[C]. Power and Energy Engineering Conference (APPEEC), 2011: 1 –4.

[12] Da Yang, Ying Wang, Xianyong Xiao, Wei Xu. The uncertainty assessment of sensitive equipment voltagesags ride-through ability based on maximum hybrid entropy[C]. Energy Conversion Congress and Exposition (ECCE), IEEE, 2012: 2022 – 202．.

[13] Xianyong Xiao, Chao Ma, Honggeng Yang. Voltagesag assessment based on maximumentropy principle[C]. Electricity Distribution (CIRED), 2009: 1 - 5．

[14] Ying Wang, Wei Xu, Xinghuo Yu, Xianyong Xiao. An interval probability maximum hybrid entropy assessment method of equipment sensitivity due to voltagesag[C]. IEEE Industrial Electronics Society(IECON), 2011: 825 - 830．

[15] Da Yang, Ying Wang, Xianyong Xiao, etal．The uncertainty assessment of sensitive equipment voltage sags ride-through ability based on maximum hybrid entropy[C]//Proceedings of the Energy Conversion Congress and Exposition(ECCE)．Raleigh：IEEE，2012：2022-2029．

[16] Zhuolin Zeng, Peidong Xu, Jing Ma, etal．Maximum hybrid entropy interval probability assessment of equipment failure due to voltage sags[C]//Proceedings of Power and Energy Engineering Conference (APPEEC)．Wuhan：IEEE，2011：1-5．

[17] Wagner Kevin T.，Doroslovački Miloš I.．Proportionate-type normalized least mean square algorithm with gain allocation motivated by minimization of mean-square-weight deviation for colored input[C]//Proceedings of Acoustics，Speech and Signal Processing (ICASSP)．Prague：IEEE，2011：4124-4127．

Advanced Materials Research Vols. 960-961 (2014) pp 755-758

doi:10.4028/www.scientific.net/AMR.960-961.755

Fault Line Selection in Resonant Grounded System Based on IMEn

Meng Zhang[1, a *], Jianwen Ren[1, b]

[1]School of Electrical and Electronic Engineering, North China Electric Power University, Baoding, Hebei, 071003, China

[a]zhang5538136@126.com, [b]rjw219@126.com

Keywords: Resonant Grounded System, Fault Line Selection, Single Phase Ground Fault, Sample Entropy (SampEn), Empirical Mode Decomposition (EMD), Intrinsic Mode Entropy (IMEn).

Abstract. When the single phase ground fault occurs in resonant grounded system, there are significant differences in the components of fault phase current between fault line and non-fault line. This feature can be reflected by intrinsic mode entropy (IMEn) of fault current. IMEn is a new signal analysis over multiple oscillation levels. It corresponds to the sample entropy (SampEn) and the empirical mode decomposition (EMD). The results of fault simulations in different conditions indicate that the method is reliable.

Introduction

Fault line selection in resonant grounded system has not been well solved yet. The traditional fault features applied to dealing with this problem contain amplitude, phase, energy and so on. It's a growing trend to uncover the new fault features to improve the traditional methods. The approach to fault line selection using similarity recognition based on time-frequency spectrum is presented in [1]. The method based on energy entropy measure is proposed in [2]. The approach using empirical mode decomposition and Duffing oscillator is proposed in [3].

Intrinsic mode entropy (IMEn) is able to quantify the degree of regularity and complexity in time series over multiple oscillation levels [4]. There are differences in the frequency components of fault phase current between fault line and non-fault line [5]. Then IMEn can be used to indicate these differences and select the fault line. Digital simulations verify the reliability of the proposed method.

Concept of Intrinsic Mode Entropy

IMEn is a combination of Sample entropy (SampEn) and empirical mode decomposition (EMD). Firstly, give the definition of SampEn. Give a time series $x(n)=\{x(1),x(2),\cdots,x(N)\}$, where N is the total number of data points. SampEn algorithm can be summarized as follows:

1) Define m-vectors, from $X_m(1)$ to $X_m(N-m+1)$:

$$X_m(i)=\left[x(i),x(i+1),\cdots,x(i+m-1)\right] \quad i=1,\cdots,N-m+1 \tag{1}$$

2) Define the distance $d_m\left[X_m(i),X_m(j)\right]$ between $X_m(i)$ and $X_m(j)$:

$$d_m\left[X_m(i),X_m(j)\right]=\max_{k=0,\cdots,m-1}\left[\left|x(i+k)-x(j+k)\right|\right] \tag{2}$$

3) Calculate the number of $d_m\left[X_m(i),X_m(j)\right]\le r$ and then divide it by $N-m+1$. The result is defined as $B_i^m(r)$.

4) Define m+1-vectors, and repeat the prior steps. The result is defined as $A_i^m(r)$.

5) Define $A^m(r)$ and $B^m(r)$:

$$\begin{cases} A^m(r) = \dfrac{1}{N-m}\sum_{i=1}^{N-m} A_i^m(r) \\ B^m(r) = \dfrac{1}{N-m}\sum_{i=1}^{N-m} B_i^m(r) \end{cases} \tag{3}$$

6) Calculate SampEn:

$$SampEn(N,m,r) = -\ln\left(A^m(r)/B^m(r)\right) \tag{4}$$

The parameter m determines the length of the sequences to be compared and the recommend value is 2. The parameter r is the tolerance threshold for accepting similar patterns between two segments and is recommended to be within 0.1–0.2 times the standard deviation of the data.

The EMD is an intuitive signal-dependent decomposition of a time series into several intrinsic mode functions (IMF) of different time scale and residual.

$$x(t) = \sum_{i=1}^{n} imf_i(t) + r_n(t) \tag{5}$$

The proposed IMEn consists in computing the SampEn of the cumulative sums of the IMFs obtained by the EMD decomposition. The cumulative IMF sum up to order k is noted C_{IMF}^k and defined by:

$$C_{IMF}^k = \sum_{j=1}^{k} imf_j(t) \tag{6}$$

If n is the total number of intrinsic mode function (IMF), the residual can be regarded as the n+1 mode. So C_{IMF}^{n+1} corresponds to the original signal. The IMEn is then defined as:

$$IMEn(k,m,r) = SampEn\left(C_{IMF}^k(t), m, r\right) \tag{7}$$

The Principle of Fault Line Selection

To be convenient for explanation, single phase ground fault in a resonant grounded distribution network with two outlets is shown in Fig.1.

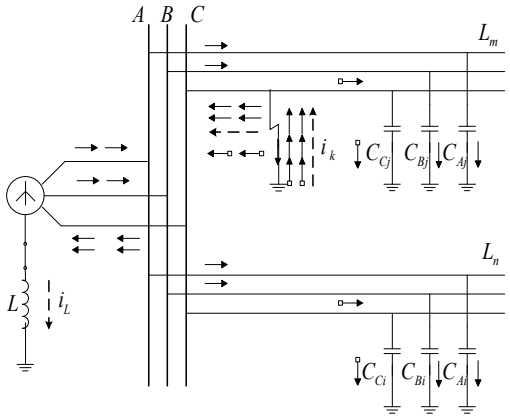

Fig.1 Fault current distribution

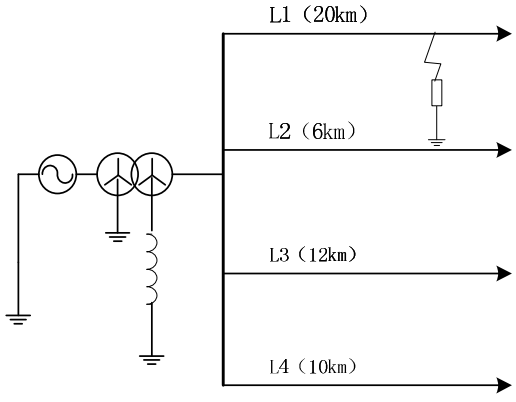

Fig.2 The simulation model of resonant grounded system

As shown in Fig.1, fault phase current in non-fault line contains only transient capacitance discharge current. However, fault phase current in fault line contains not only transient capacitance discharging current but capacitance charging current. The former results from the sudden voltage drop

of fault phase, and its oscillation frequency can reach several Kilohertz. The latter results from the sudden voltage increase of non-fault phase, and its oscillation frequency can just reach hundreds of Hertz [5].

In essence, IMEn is obtained by computing the SampEn of the cumulative sums of each of the IMF. This algorithm is robust to changes in low-frequency components of a signal. As is mentioned above, there are significant differences in the components of fault phase current between fault line and non-fault line. Therefore, the method is very appropriate for fault line selection in the resonant grounded distribution network.

The fault line selection of resonant grounded distribution networks using IMEn contains the following steps:

1) Collect the data of three phase voltage and current. The sampling rate is 10kHz. The sampling time of all signals is 60 ms from the time the fault occurs.

2) Extract the fault current. N stands for the number of sampling time per cycle. $\Delta i(k) = i(k) - i(k-3N)$.

3) Determine the fault phase by the change of phase voltage. If there is remarkable increase in one phase voltage, this phase is selected as fault phase.

4) Fault phase current of all outlets is decomposed by EMD. Determine the number of IMF as 9, with one residual regarded as the tenth IMF, for a total of 10 components.

5) Calculate the IMEn of the 10 IMFs. Finally, ten sets of results will be generated.

6) For each set of IMEn results, choose the minimum $IMEn_i^{\min}$ .Define the reliability index as K_{rel}. Through analysis of the effect of IMEn fault line selection, taking 1.1 for K_{rel} is proper. If the computed result of K_{rel} is less than 1.1, $IMEn_i^{\min}$ of this set of IMEn results does not exist.

$$K_{rel} = IMEn_i^{se\min} \Big/ IMEn_i^{\min} \quad i = 1, 2, \cdots, 10 \tag{8}$$

7) Count the number of $IMEn_i^{\min}$ belonging to the same outlet, and the results are normalized by dividing them by 10. Then some criterion is received.They are P_{L1}, P_{L2}, P_{L3}, P_{L4}.

8) Find the maximum of the criterion. It should belong to the fault line.

If busbar fault occurs, the method above can still be used to select one outlet. Then cut it off from the system. If the fault still exists, busbar fault will be confirmed.

Simulation Analysis

Firstly, establish a 10kv feeder system with 4 outlets. In order to simulate actual system better, this feeder system contains not only 3 overhead lines, but only one cable. Different fault conditions considered are grounding resistance, fault inception angle and fault position. The simulation model is established under the circumstance of MATLAB/SIMULINK. The parameters of overhead lines are shown as follow:

$r_0 = 0.34\Omega / km$, $r_1 = 0.19\Omega / km$; $l_0 = 4.93mH / km$, $l_1 = 1.22mH / km$; $c_0 = 0.0055\mu F / km$, $c_1 = 0.009\mu F / km$.

The fourth line is a 10km-long cable . The parameters of the cable are shown as follow:

$r_0 = 2.5\Omega / km$, $r_1 = 0.27\Omega / km$; $l_0 = 1.12mH / km$, $l_1 = 0.255mH / km$; $c_0 = 0.19\mu F / km$ $c_1 = 0.31\mu F / km$.

The inductance and resistance of the arc suppression coil can be given by formula(9) and (10). P stands for compensation degree and its value is 0.05. Q stands for active power loss and its value is 0.03. According to formula (9) and (10), the value of L and R is 1.54H and 14.5Ω. L1 and L4 are selected as the fault line. The simulation result is shown in Table 1. The simulation result shows that IMEn fault line selection fits for all these situations perfectly.

$$L = 1 \Big/ (1+\mathrm{P}) \times 3\omega^2 C_{\Sigma} \tag{9}$$

$$R_L = Q\omega L \tag{10}$$

Table 1 The results of fault line selection

Fault line	l_f / km	θ/(°)	R_f / Ω	criterion				Result of fault line selection
				P_{L1}	P_{L2}	P_{L3}	P_{L4}	
L1	18	90°	1000	1.0	0	0	0	L1
		45°	500	0.9	0	0	0.1	L1
		0°	0	0.9	0.1	0	0	L1
	9	90°	1000	0.7	0	0.3	0	L1
		45°	500	0.9	0	0	0.1	L1
		0°	0	0.6	0.1	0.1	0.2	L1
	2	90°	2000	1.0	0	0	0	L1
		45°	0	0.9	0	0	0	L1
		0°	1000	0.7	0	0	0.3	L1
L4	9	90°	0	0	0	0	1.0	L4
		45°	500	0.1	0	0	0.5	L4
		0°	1000	0.1	0	0.1	0.8	L4
	4.5	90°	2000	0.1	0.2	0.1	0.6	L4
		45°	1000	0	0.2	0	0.6	L4
		0°	500	0.2	0	0.1	0.7	L4
	1	90°	1000	0.2	0	0	0.5	L4
		45°	2000	0	0	0	0.8	L4
		0°	1000	0.1	0.1	0	0.7	L4

Conclusions

This paper presents a method for fault line selection in resonant grounded system based on IMEn. Firstly, select the fault phase. Then calculate the IMEn of fault phase current of each line and get the criterion. Choose the biggest one and select the fault line. The simulation results demonstrate that the algorithm is well adapted in resonant grounded system containing overhead lines and cables. For different fault conditions, the accuracy and reliability can be ensured.

References

[1] Yaming Sun, Youzhong Miao: 'A new principle of transient current grounded relay for feeder in resonant-grounded distribution systems', Proceedings of the CSEE, 2004, Vol.24, (3), p.62-66

[2] Qingliang Wang, Zhouxing Fu: 'An adaptive method for single-phase-to-ground fault line selection based on energy entropy measure', Automation of Electric Power Systems, 2012, Vol.36, (5), p.103-107

[3] Shuqing Zhang, Xinpei Zhai, Xuan Dong, et al: 'Application of EMD and Duffing oscillator to fault line detection in un-effectively grounded system', Proceedings of the CSEE, 2013, Vol.33, (10), p.161-167

[4] Amoud H, Snoussi H, Hewson D, et al: 'Intrinsic mode entropy for nonlinear discriminant analysis', IEEE Signal Processing Letters, 2007, Vol.14, (5), p. 297-300

[5] Xianyong Xiao, Wenhai Zhang, Ying Wang, et al: 'Two-dimensional fault line detection based on transient signal features of fault phase', Power System Technology, 2012, Vol.36, (5), p.178-184

Advanced Materials Research Vols. 960-961 (2014) pp 759-762

doi:10.4028/www.scientific.net/AMR.960-961.759

Partial Discharge Detection of on-line cables Based on Hilbert Huang Transform

Li Fang

Henan Haihua Engineering Construction Supervision Company ,Zhengzhou,Henan,450003, China

tf2006tf2006@126.com

Keywords: Lock-in amplifier, Cable , Hilbert-Huang transform , Partial discharge .

Abstract. Hilbert-Huang transforms calculation method was used in the study on signal of partial discharge from on-line cable. The partial discharge signal was made to be intrinsic mode function (IMF) by empirical mode decomposition (EMD).The cubic spline interpolation was selected as the interpolation function and ideal envelope curve was achieved to eliminates defects such as overshoot and undershoot effectively. Appropriate lock-in amplifier was choosed and pre-amplifier and phase-sensitive detection circuit was designed to determine the calculation programs. The results showed that the test system can effectively capture the weak PD signals in cable under complex environmental conditions and the PD signal waveform obtained was improved through Hilbert-Huang transforms.The state of insulation and the remaining life of the cable can be judged effectively,which has practical significance for improving the grid security.

Introduction

XLPE cables was introduced into the country in the late of 1980s. Because of the excellent performance and good processing properties of insulating materials, it was widely adopted and gradually replaced the paper insulated power cables in power transmission lines in the country. However, cross-linked polyethylene (XLPE) is a kind of polymer, its purity was easily affected by the synthesis,bubbles could be generated in the manufacture or operation.The electric field strength is much higher than the surrounding medium, due to the small dielectric constant. While in the manufacturing and installation, defects will also be caused.All this factors will cause partial discharge after a few years under work environment of high electric field. Statistics showed that the cable partial discharge was one of the main reasons which damaged the power cable or reduced its operation life. Therefore, timely on-line detecting could monitor cable insulation state,so as to maintain and timely replac defected cable, thus avoiding significant losses. [1] In order to prevent sudden failure and blackouts or damaging of circuit and terminating equipment, reducing losses to the power companies or the user,on-line monitoring of the cable must be used.

In order to get good results, it is important to timely capture the relevant partial discharge signal and calculate its value more accurately. At present, a lot of exploration studies on detection of on-line XLPE cable has been done in domestic and abroad. However, there is not much good practice effect. The main reason is that the actual workig environment of cable is relative complex and bad . The discharge signal is difficult to capture the signal so that the amount of discharge can not be accurately determined. Considering above factors, we designed test systems with digital lock-in amplifier during the partial discharge test , so the weak PD signal was easy to extract.meanwhile Hilbert-Huang conversion was applied, and the relevant calculation program was prepared. [2]Thus partial discharg could be emeasured during the cable was in operation and good results were achieved.

Hilbert - Huang Transform

Basic principle of Hilbert - Huang transform. Because the collected signal contained a lot of nonlinear signals, the effect of calculation according to the traditional Fourier transform was far from ideal. Therefore, the collected signal function should be processed by Hilbert - Huang Transform. Hilbert - Huang algorithm contains two parts. first, the signal could be turned into intrinsic mode function (IMF) by means of Empirical Mode Decomposition (EMD).Second,Hilbert spectrum was

available in the time-frequency plane and could be displayed on the instrument by using Hilbert transform. The maximum and minimum of signal should be fitted during process of Empirical mode decomposition,ensure that the fitted curve contained all the signals. So both envelope curves of the signal was available. [3] During this process, in order to eliminate overshoot and undershoot defects, cubic spline interpolation should be taken as an interpolation function, so the desired envelope curve could be gotten.

Calculation about Hilbert - Huang Transform. Function of acquired signal was set as m(t).Then the envelope curve of starting sequence data could be obtained by taking cubic spline function.After calculating its mean n (t),the difference between the both value is the function without low frequency. namely:

$$u(t) = m(t) - n(t) \tag{1}$$

Repeating the above calculation process until the u (t) was in line with IMF component characteristics,the first IMF component obtained at this time of was the most high-frequency component among signals.namely:

$$f_1(t) = u_{1(n-1)}(t) - n_{1n}(t) \tag{2}$$

Then the difference signal component can be obtained without high-frequency component.

$$v_1(t) = m(t) - f_1(t) \tag{3}$$

So a number of IMF components could be gotten successively.

$$v_n(t) = v_{(n-1)}(t) - f_n(t) \tag{4}$$

When vn (t) was a monotonic function, the process was over.

$$m(t) = \sum_{j=1}^{n} f_j(t) - v_n(t) \tag{5}$$

Then spectrum of the signal obtained by using Hilbert - Huang transform was as follows:

$$H(\omega,t) = \mathrm{Re}\sum_{i=1}^{n} m_i(t)e^{j\omega_i(t)dt} \tag{6}$$

Howevwe spectrum of the signal obtained by using Fourier algorithms was as follows:

$$F(\omega,t) = \mathrm{Re}\sum_{i=1}^{\infty} a_i e^{j\omega t} \tag{7}$$

It is not difficult to see that processing of instantaneous frequency changes for signals with Hilbert - Huang transform is more reasonable. [4]

Partial discharge test. The measuring principle of partial discharge was shown in Figure 5. The pulse could be achieved through the detection resistor when the discharge took place.The reason was that after the partial discharge,the charge which was generated due to the charge exchange effect at both ends of the cable would formed pulse current. [5]When the test loop parameters were certain, the voltage across the sample was as follow:

$$u_x = \frac{q}{C_x + \dfrac{C_k C_d}{C_k + C_d}} \tag{8}$$

The voltage on the detection resistor was:

$$U_{do} = \frac{q}{C_T} \tag{9}$$

Where:

$$C_T = \frac{q}{C_x(1 + \dfrac{C_d}{C_k}) + C_d} \tag{10}$$

The voltages on the detected impedance usually change exponentially with time, i.e.

$$u_d = u_{d0}e^{-\frac{t}{\tau_1}}t = U_{d0}e^{-\beta_1 t} \tag{11}$$

Therefore, the voltage response on the detection impedance was:

$$\int_0^{\infty} u'_d(t)dt = u_{d0}\frac{\alpha_0}{\alpha_0-\beta_1}(\frac{1}{\beta_1}-\frac{1}{\alpha_0}) = u_{do}/\beta_1 \tag{12}$$

Through integral transform, the frequency spectrum could be obtained and partial discharge was shown on the oscilloscope. The frequency spectrum was:

$$\phi(\omega) = \left|S(\omega) = U_{do}\right|(\beta_1^2+\omega^2)^{-\frac{1}{2}} \tag{13}$$

On-line partial discharge simulation test

Partial discharge test. When on-line partial discharge was tested,six cables with different voltage level and size were selected as samples.Before the test,the accelerated aging test was done for the cable samples so as to make them equivalent to the normal operation of 4-8 years.Meanwhile, in order to make sure the samples were in line with the real operating condition as probably as possible the state of the cable run under environmental, the applied voltage was that of the cables working at full capacity. [6]

Results and analysis.

The measured partial discharge waveform from unimproved and improved tester was shown in figure 1 and figure 2 respectively. We can clearly see from the figures that in the the improved waveform obtained, the pulse polarity can be easily judged. [7]It was very convenient to exclude non-discharge point. The waveform was clear and amplitude difference was obviously, helps to analyze reflexing and starting point of discharge and exclude secondary reflection waveform, the accuracy of the test can be improved.

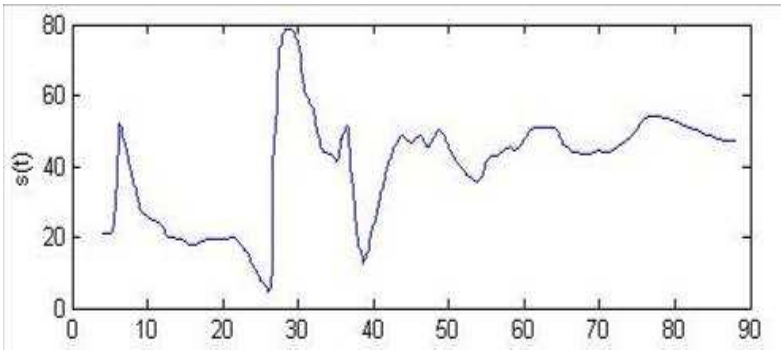

Figure 1 Discharge waveform obtained from Fourier transform

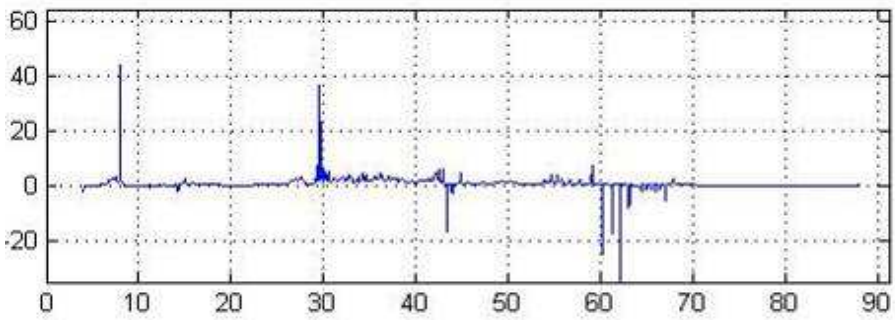

Figure 2 Discharge waveform obtained from Hilbert-Huang transform

The comparative results are shown in table 1 by testing of samples taken from the cable.

Conclusion

1.Lock-in amplifier can reduce efficiently the effect on discharge signal of environmental and cable itself. The weak partial discharge signal of cables can be capture in the complex conditions.
2.The waveform signal of partial discharge processed by Hilbert - Huang was clearer and distinguishable.The polarity and the amplitude of the waveform were determined easily.So the measurement results were more accurate.
3.Based on this study and accumulation of experimental data, the relationship between PD data, insulation condition and remaining life of cable will be deduced.

Table 1 Comparison of test results between the system with conventional test methods

No.	Cable Type	Voltage level kV	Cable length m	Discharge capacity	
				Unimproved	Improved
1	YJV	6	165	6.6	2.8
2	YJV_{22}	6	198	6.8	3.8
3	YJV_{22}	15	230	7.3	3.4
4	YJV_{22}	15	250	6.9	4.7
5	YJV	35	220	8.8	5.5
6	YJV	35	230	9.3	6.8

References

[1] Zhong-yuan ZHAO,Zheng-yu LV,Nai-xin,DUAN, et al. *Research and Development of On-line Monitoring System with Partial Discharge in XLPE Power Cables* [J].Automation of Electric Power Systems,2004,28(5):59-62.

[2] Jose M Grima Palop,Jose M Andres Teruel. *Virtual Work Bench for Electroic Instrumentation Teaching*[J]. IEEE Transactions on Education,2000,43(1):14-15.

[3] Tianyun LI, Siyong CHENG, Mei YANG.*Power system harmonic analysis based on Hilbert-Huang transform*[J].Proceedings of the CSEE, 2008,28 (4):109-113.

[4] AKKE M,THORP J T. *Some improvements in the three-phase differential equation algorithm for fast transmission line protection* [J]. IEEE Transactions on Power Delivery,1998,13(1):66-72.

[5] Sedding H G,Campbell S R,Stone G C. *A new sensor for detecting partial discharges in operating turbine generators*[J]. IEEE Transactions on Energy Conversion, 1991,6(4):700-706.

[6] Yigang ZHANG,Weiyong YU, ChengJun HUANG, et al. *Research status of on-line partial discharge monitoring system for generators* [J]. High Voltage Engineering,2002,28(12):32-35.

[7] Ying XIANG, Xianqu WU. *Realization of lock-in-amplifier software and parameter measurement* [J]. Computer and Modernization, 2007, 138(2): 19-21.

Advanced Materials Research Vols. 960-961 (2014) pp 763-768

doi:10.4028/www.scientific.net/AMR.960-961.763

Step Response Measurement System for Impulse Voltage Dividers Based on Labview

Li Wenting[1, a], Zheng Yan[2,b], Liu Shao-bo [1, a], Long Zhao-zhi [1, a] and Xiao Kai[1, a]

[1]State grid electric power research institute, Wuhan 430074, Hubei Province , China

[2]Wuhan Ordnance N.C.O Academy, Wuhan 430075, Hubei Province , China

[a]wohaio@126.com, [b]zy397037172@163.com

Keywords: impulse measurement system; step response; parameter extraction

Abstract: A measurement system used for step response of impulse voltage dividers has been designed. This software can be used for various kinds of step response waveforms and can calculate them accurately. The calculation methods used in this system are in full compliance with the requirements in DL/T992-2006 and IEC60060-2. When the software used for the step response of impulse divider，the calculation results meet the requirements of stepwave response parameters with good accuracy. This software is simple to calculate and it can greatly enhance the efficiency of the step response parameter extraction calculations.

Introduction

The step response parameters of impulse voltage measurement system are important to represent the dynamic performance of Impulse voltage divider, shock oscilloscope or digital recorder. In the past people usually extract these parameters by manual measurement, but this method is time consuming and the accuracy is not high. With the rapid development of computer digital processing application, now the waveform is collected by computer and the parameters are extracted by computer with data processing. Formerly automatic analysis processing for step waveform is more focused on the step response wave[1] whose front part is relatively smooth, such as figure 1 (a) and (b), the related introduction of step wave analysis processing for rising part with oscillation (figure 1 (c)) or distortion (figure 1 (d)) is less. In this paper, waveforms which are often encountered in actual measurement are analyzed and researched. Then a measurement system for calculating all kinds of step response waveform is compiled. The measurement system can real-time collect response waveform of impulse voltage divider and do calculation analysis, then output the parameters defined in IEC60060-2[2]: partial response time, test response time, stability time and overshoot, and save the collected waveform data.

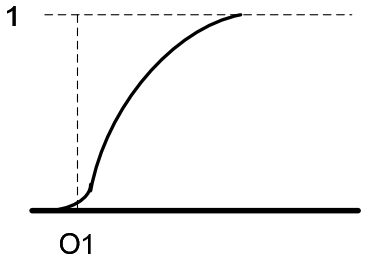

(a)exponential type Step response wave

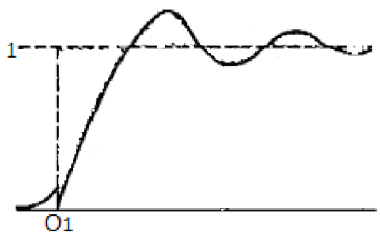

(b)exponential type Step response wave with oscillation

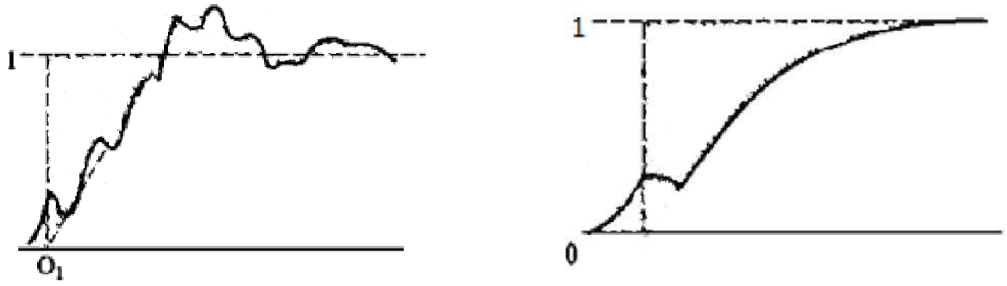

(c)step response wave with oscillation on the front waveform (d)Step response waveform with distortion

Fig.1 The waveform diagram of all kinds of step response

The key processing steps of the impulse step response measurement system including:

1. For the signal transformed from oscilloscope, the noise signals were filtered and the waveform was processed by removing to the first quadrant. Then the benchmark level and actual origin can be determined;

2. Determine the apparent origin. For the different types of step response waveform, methods to determine the origin of the apparent are as follows:

A) For the step response waveform with smoothly rising, the calculation program firstly determines the point of maximum slope, tangent and the apparent origin;

B) For the step response waveform with distortion rising , the calculation programs firstly find out the distortion ending point and eliminate distortion part. Then looking back from the distortion point for the maximum slope point, determining the apparent origin by draw the tangent line form the maximum slope point;

C) For the step response waveform with shocking increasing, calculating average cure of the shocking part, then the average curve was used instead of the shocking part . Then determining the apparent origin by draw the tangent line form the maximum slope point.

3. Calculating the reference level of the waveform, then determine the various parameters of step wave response.

The procedures to realize the method to calculate the various parameters of step response based on the Labview will be described in detail as follows.

1.Prcess of Software calculation

In practical application, sometimes real-time impact voltage divider step response waveform was needed to be analyzed, sometimes step response waveform preserved for ever was analyzed. so the calculation software should be used both for real-time response of impulse voltage measurement system and existing waveform data. Figure 2 is a block diagram for the calculation software of process.

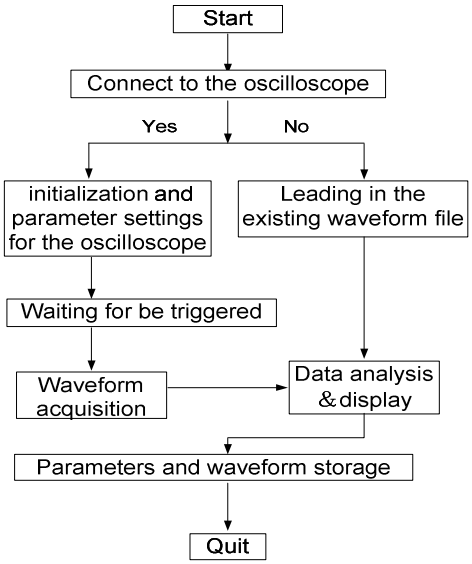

Fig.2 Flow chart of step response of impulse voltage measurement system calculation software

Determination of response parameters

2.1 Waveform acquisition and filtering. For the response waveform transformed from the oscilloscope collecting form impulse voltage divder， firstly the noise should be filtered. Usually the method of noise filtering is wavelet and cubic spine function method[3]. The method used in this calculation program is zero phase filter method based on Labview [4]-[5]. The principle of zero phase filter for the input sequence is firstly forward filter, then the filter sequence is reversal. Finally the results were reversely output. The time-domain said zero phase filter can be expressed as (1) - (4) :

$$y1(n) = x(n) * h(n) \quad (1)$$

$$y2(n) = y1(N-1-n) \quad (2)$$

$$y3(n) = y2(n) * h(n) \quad (3)$$

$$y4(n) = y3(N-1-n) \quad (4)$$

In equation (1) - (4), x (n) indicates the input data, h (n) is the impulse response digital filter used in the program. y4 (n) is the reverse sequence data after the second filtering ,namely zero phase filter output sequence data. Its implementation is mathematical "reverse" on the time signal sequence processing. Essentially h (n) and h (-n) these two links were used to construct zero phase filter.

In Labview, the filter module can construct the zero phase filter easily. figure 3 (a) is a waveform without zero phase filtering, figure 3 (b) is the waveform filtered with the zero phase filter , so zero phase filter is effective on the waveform visible smooth processing.

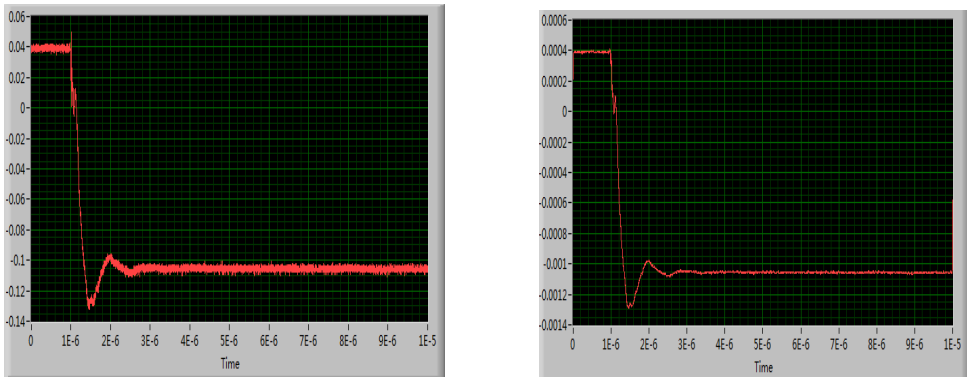

(a)Without filtering smoothing waveform (b)After smoothing waveform measurement system

Fig.3 Software for waveform smooth processing

2.2 Reference level. The methods to find out the starting point of step response waveform are slightly different[6] . The method to determine the starting point of the waveform used in this measurement system is as follows:firstly， find out the the peak value point P, then find the point A, when the D-value of point A and the initial point O is m times less than he D-value of point A and the initial point P, that is when $|U_A - U_O|$ J m$|U_P - U_A|$（m is about 0.1%~0.5%）， the point A is the cutoff point of the flat part of the waveform and the start rising point of the waveform. This method is simple and quite correct by verification and successfully meets the needs of subsequent calculation accuracy.

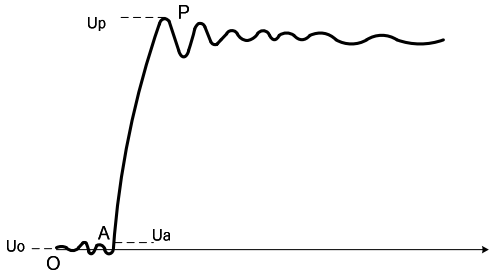

Fig.4 Determination of starting point of waveform

2.3 To calculate the apparent origin. Apparent origin zero point O_1 is the start calculation point of step response waveform. It is the intersection point of the tangent line form the front steep place and the zero line. If there is oscillation in the front part of the response waveform, drawing a tangent line form the steepest place on the center line of the oscillation. If the starting distortion part in the waveform is big, then the distortion part should be ignored when drawing the tangent line. In the impulse response calcultion program, the determination of the oscillation center line is quite important.

For the general step response waveform, as shown in figure 1 (a) and (b), firstly intercepting the voltage value array from the cutoff point of flat part to a maximum point, and then calculating the derivative of all the points in the array , the maximum derivative point is the point of tangency P. Then draw a line with the slope at the tangency P, and the intersection with the horizontal axis is the apparent zero point. Updating the voltage value to 0 before the Apparent zero point .

For the step response waveform with front oscillation , as shown in figure 5, according to the methods in DL/T992-2006[7]: first finding out the each oscillation peak value point in the oscillation waveform , then determine the corresponding time value of each peak point, summing up the time value of the peaks points, determining the average time point.

After finding out corresponding points to the average time value, these average points will be connected in chronological order to form a line. This line can be regarded as the oscillation curve of the center line. And then calculate the maximum slope point P in this line, then update the array before the point P.

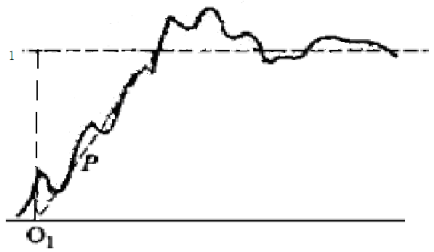

Fig.5 The determination of apparent zero point in response waveform with front oscillation

When there is aberration on the front part of the waveform, as shown in figure 6, first, the ending point of aberration part A should be found out. Then, finding out the point of tangency on the waveform form point A to another point whose value is unit amplitude and update the point array before P.

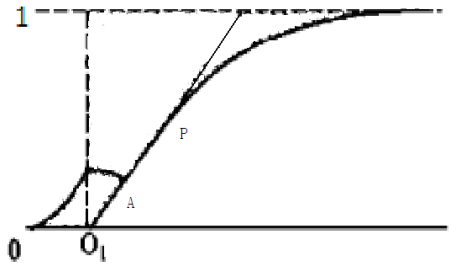

Fig. 6 Determination for Apparent Origin of Waveform with oscillation and aberration

When oscillation and aberration both existed on the front part of the step response waveform, the waveform should be firstly processed by the oscillation calculation program and then be processed by the aberration calculation program to ensure of the accuracy of calculation.

2.4 Calculation of step response parameters. After determination of the apparent origin point and the reference level of the response waveform, the partial response time, experiment response time, stabilization time and the overshoot can be calculated according to IEC60060-2.

Calculation of the measured step response waveform

In order to verify the calculation accuracy of the measurement system, we use the software for daily testing various step wave and calculating response waveform, then compared the software calculation results with manual calculation, to estimate the reliability of the software calculation.

This paper calculated three types of impulse step response waveform, as shown in figure 7, 8, 9, the used square wave power supply is the falling edge square wave, the calculation results are shown in table 1.

Figure 7 is a 200 kV impulse voltage divider step wave response waveform figure. There is no oscillation in the falling part of the waveform. It is the general type of step wave response waveform.

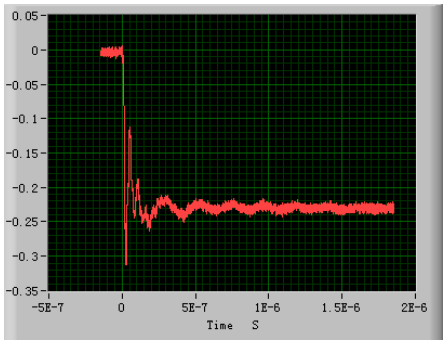

Fig. 7 a 200kV impulse voltage divider step wave response waveform figure

Figure 8 is a 1800 kV impulse capacitive voltage divider step response waveform figure. The falling part of the waveform is with obvious distortion.

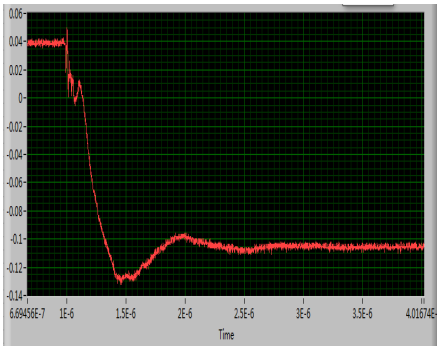

Fig. 8 a 1800kV impulse capacitive voltage divider step response waveform figure(wavefront with distortion)

Figure 9 is a 800 kV capacitive voltage divider step response waveform figure, the falling part of the response waveform is with obvious oscillation.

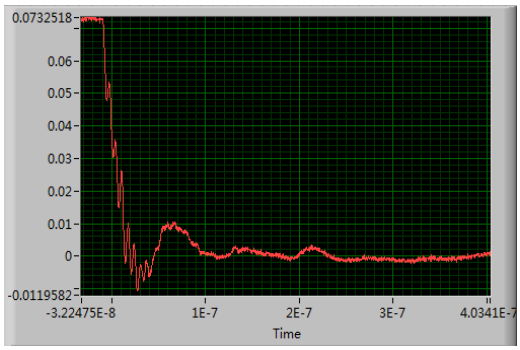

Fig. 9 800kV capacitive voltage divider step response waveform figure(wavefront with oscillation)

Because there is not standard waveform data in IEC60060-1 to evaluate step wave program calculation accuracy, so in this article we judge the calculation accuracy of the software by comparing the software calculation with manual calculation. The compared calculation results are shown in table 1.

Table 1 Comparing the software calculation with manual calculation

Figures	Calculation by	Partial response time ns	Experimental response time ns	Settleing time ns	Overshoot %
Fig7	software	4.56	10.8	51.8	33.19
	manual	4.32	12.0	49.0	33.5
Fig8	software	49	34.7	89.2	17.99
	manual	47	35.2	91.9	17.63
Fig9	software	8.0	14.8	125	13.38
	manual	9.1	16.2	131	13.45

By the computing results of the above three kinds of step response waveform using software compared with the results of manual, you can see the calculation results using step wave response calculation software and manual calculation results are comparable. It shows that the software can calculate accurately according to different types of step response waveform, and can greatly simplify the artificial calculation time.

Conclusion

1) the impulse step wave response measurement system is developed based on Labview platform. It can calculate three different types of impulse step wave response waveform.

2) the calculation processing of the measurement system is completely in accordance with the requirements of the DL/T992-2006 and the processing method is accurate and concise. They guarantee the calculation speed of the software.

3) the computation results using the measurement system to measure impulse step wave response, is comparable to a certain extent with manual calculation results. It can be used to analysis the character of impulse voltage divider in practice and can greatly simplify the computing time, improve work efficiency.

References

[1] HeYi, Liu Wei-guo, Wang Guo-li, Algorithm Study on Extracting The Step Response Parameters. High Voltage Apartment [J], 2001, 37(1)：1-4

[2] International Standard IEC60060-2. High-Voltage Test Techniques. Part 1: Part 2: Measuring systems [S] . 3 rd ed . ,Geneva, Switzer-land, 2010.

[3] Li Chen-guang, Zhang Wen, Xing Haiying, Research of a New Type High Impulse Voltage Measurement System. CHINA RURAL WATER AND HYDROPOWER [J] 2011, 3: 136-139.

[4] Wen Guilin, Xiao Yong. Application of Zero-Phase Digital Filter Based on LabView in Impact Test[J] Journal of Hunan University: 2007, 34(10):35-38.

[5] Ji Yue-bo, Qin Shu-ren, Tang Bao-ping. Digital Filtering with Zero Phase Error[J] . Journal of Chongqing University: Natural Science Edition, 2000, 23(6): 4-7.

[6] Guo Hong, Wu Peng, Guo Zhi-feng etc, Parameter Extraction of Lighting Impulse with Overshoot or Oscillation. High Voltage Apartment[J] 2010,46 (1): 76-79.

[7] DL/T 992-2006. The standards of the power industry Chinese people's Republic of China: Detailed implementation guide for impulse voltage measurement[S]. 2006, 5, 6.

Advanced Materials Research Vols. 960-961 (2014) pp 769-773

doi:10.4028/www.scientific.net/AMR.960-961.769

PIC/MCC simulation of glow discharge in N_2

Fang Cheng[1,a]，Aihua Gao[2,b]

[1,2] Department of Physics, Northwest University, Xi'an 710069, China

[a]819072060@qq.com, [b]gaoaihua@nwu.edu.cn

Keywords: PIC/MCC simulation, Glow discharge, Electric field, charged particles

Abstract. The simulation of glow discharge in N_2 in a needle-plane configuration with PIC/MCC method is presented. In the discharge channel the electric field driven by space charges is solved by PIC method, and various collisions between particles are described with MCC method. The electric field intensity, the electric potential and the net charge distribution in the discharge area are obtained. The numerical results are consistent with the corresponding features of glow discharge. This work can provide references to further study of glow discharge.

Introduction

Discharge plasma technology has attracted more and more attention due to its extensive applications in the industrial processing fields such as surface modification, highly pure and ultra-fine material preparations and very large-scale integrated circuit micro fabrication. Researchers in the environmental protection field recently show their interest in sewage treatment using the discharge plasma [1,2,3]. Discharge plasma technology is a new advanced oxidation technology for wastewater treatment. It can degrade the organic macromolecule compounds in the wastewater into non-toxic micro molecules, even directly into carbon dioxide and water. Using discharge plasma to degrade wastewater has many advantages such as potent oxidation, high degradable ratio and simple operation, etc. But the mechanism of this application is not very clear. With the development of computer technology, numerical simulation has become a powerful tool in revealing the physical nature in the process of a certain physical chemistry. We carried out the numerical simulation of some fundamental characteristics including electric field and charged particles distribution for a given glow discharge. N_2 is the dominant presence in the atmosphere and is widely used in many technical and industrial applications. And it is abundant, cheap, inert, non-toxic and non-flammable. As the result, in this paper N_2 is chosen as the working gas. At present, there are three main kinds of physical models used by researchers in doing the simulation. They are named particle model, fluid model and hybrid model. In particle model, electrons, ions and neutral particles are treated as individual particles. In principle, we can get some exact information including the dynamic behavior of charged particles, plasma physical quantities and so on. It can truly reflect the practical move of plasma. In this paper, MCC (monte carlo collision) [4] method is used to describe the interaction between particles. Meanwhile, PIC (particle in cell) is introduced to calculate the space electric field driven by space charges.

Simulation method

As the discharge begins, initial electrons are emitted from the needle cathode. The entry angles are shown as following.

$$\theta = \frac{1}{2}\arccos(1-2R_1), \tag{1}$$

$$\phi = 2\pi R_2, \tag{2}$$

where θ is the polar angle with respect to the axial direction (z-axis) and ϕ is the angle of the projection of the velocity vector in the xy plane, with respect to the x-axis. R_1 and R_2 are random numbers uniformly distributed between 0 and 1. Due to the existence of cosmic radiation, there are some electrons and ions in the space. In the simulation, electrons and ions are uniformly distributed in the space between the needle cathode and plane anode. The velocities of these charged particles follow the Maxwell Speed Distribution Law. The space field driven by the space charge is calculated using PIC method. The total electric field is the sum of the field driven by the applied voltage and the space charge. In the effect of the total field, charged particles follow the Newton's laws of motion.

The collision processes are resolved by MCC method. With it, whether a collision happens or not and which kind of collision will happen can be decided.

PIC method. The space between electrodes is divided into 1D cells. The cell size Δz is calculated:

$$\Delta z = \frac{d}{N}, \tag{3}$$

where d is the gap length and N is the cell number. Before the discharge, the space is electrically neutral. In every time step, the charge density of the charged particles in cells will be allocated to corresponding cell points using the linear interpolation method [5]. Then the electric potentials and the electric field intensities of cell points driven by space charges can be given as following.

$$\frac{\varphi_{i+1} + \varphi_{i-1} - 2\varphi_i}{(\Delta z)^2} = -\frac{\rho_i}{\varepsilon}, \tag{4}$$

$$E_i = \frac{\varphi_{i+1} + \varphi_{i-1}}{2\Delta z}, \tag{5}$$

where φ_{i-1}, φ_i and φ_{i+1} are the electric potential values of the (i-1)th to the (i+1)th three continuous cell points, ρ_i and E_i are the charge density and the electric field intensity of the ith cell point, respectively. From the electric field intensities of cell points, the field intensities of charged particles can be solved.

$$E_c = \frac{E_i(z_{i+1} - z_c) + E_{i+1}(z_c - z_i)}{\Delta z}, \tag{6}$$

where E_c is the electric field intensity of a certain point in the ith cell, E_i and E_{i+1} are the electric field intensities of the ith and (i+1)th two adjacent cell points, respectively. Because the external field value driven by the applied voltage is known from the reference [8], so the total field is obtained by the sum of the charge field and the external field.

MCC method. In every time step, the possibility of collision is calculated:

$$p = 1 - \exp[-n\sigma(\varepsilon)v\Delta t], \tag{7}$$

where n is the gas number density, $\sigma(\varepsilon)$ the total collision cross section and v is the velocity of the charged particle. The collisions considered in this paper are the elastic, excitation, dissociation,

ionization and dissociative ionization collisions [6] for electrons, the elastic and charge transfer collisions for both N_2^+ molecular ions and N^+ atomic ions. The cross sections used in this paper are from Tatsuo's study [7].

At the beginning of every time step, the random number R_3 that is uniformly distributed in the interval [0,1] is generated and compared with the possibility of collision P. If $P>=R_3$, a collision happens; or it does not. To determine what type of collision happens, the total cross section is split up into the fractional cross section for all possible collisions. The possibility of a certain fractional collision is given as following.

$$p_j = \frac{\sigma_j}{\sigma_T}, \tag{8}$$

where P_j is the possibility of the jth type collision. The sum of all possible collision possibilities is equal to 1. Another uniformly distributed random number R_4 in the interval [0, 1] is used to determine the jth type of collision in the formula below.

$$P_1 + P_2 + \cdots + P_{j-1} \le R_4 < P_1 + P_2 + \cdots + P_j. \tag{9}$$

Results and discussion

In this paper, the electrodes are the needle-plane configuration. The needle is cathode and the plane is anode. The simulation is performed with a gas number density of $N_2=2.69\times10^{24}/m^3$ at 1kV.

The external electric field at any point along the z-axis is the formula below [8].

$$E(z) = \frac{2V_0 d}{ln[4d/r][d(2z+r)-z^2]}, \tag{10}$$

where V_0 is the applied voltage, d the gap length, r the tip radius and z is the distance from the needle tip. The values are $d=5\times10^{-3}$m, $r=5\times10^{-3}$m, $\Delta z=2\times10^{-5}$, $N=250$. According the mean flight time, the time step $\Delta t=5\times10^{-13}$s.

A lot of initial electrons are emitted from the cathode. These electrons move to the anode under the influence of strong electric field near the cathode accompanying their kinetic energy increase. Assume that the electron average energy is 0.1eV at $t=0$. In the process of the electron drift motion, various collisions between particles will happen. Inelastic collisions such as ionization and dissociation collisions between electrons and neutral molecules generate a large number of charged particles including electrons and ions. Meanwhile, the velocity of the electron slows down because of the energy loss in the inelastic collisions with N_2 molecules. But it is easy for electron to obtain the energy from the electric field because its mass is far less than that of the ions. As the inelastic collisions process, the avalanche of electron and ions is produced. Due to the opposite drift motion directions of electron and ions they separate. Thus, the net charges appear in different areas between electrodes and drive a space electric field, which distort the external field obviously.

The evolution of two electric field profiles in the gap is shown in Fig. 1. The profile at time $t=0$ is the external field used to make a contrast. In Fig. 1, it is clear that there is an obvious distortion for the electric field at $t=4$ns compared with that at $t=0$. Especially the field in the cathode zone ($z=0.3\sim1.0$mm) has been greatly reduced due to the existence of space charged particles. The field in the positive column area ($z=1.3\sim5.0$mm) is evenly distributed and slightly increased comparing

with that at t=0. In this region the concentrations of electrons and positive ions are approximately equal, that is known as the plasma region.

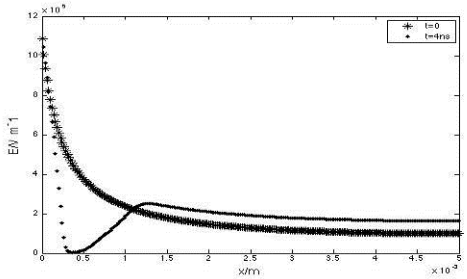

Fig. 1. Total field distribution in the gap at t=4ns

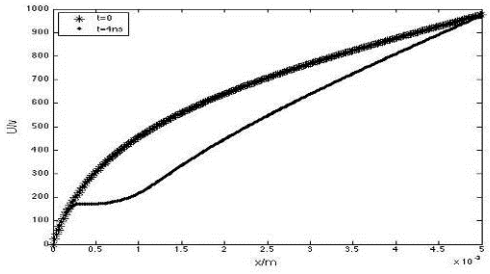

Fig. 2. The electric potential in the gap at t=4ns

The electric potential distribution at two different times is shown in Fig. 2. Similarly the potential drop in the cathode zone has a big change at t=4ns compared with that at t=0 because of the effect of the space charges. The profile at time t=4ns develops slowly even changelessly in the area where electrons stay. And then a linear growth comes in the plasma region. The physical nature embodied from Fig. 1 is consistent with that from Fig. 2，and conforms to the corresponding property of glow discharge.

Fig. 3 shows the net charges distribution in the gap at time t=4ns. Many charged particles are produced from the ionization collisions. Ions are almost stationary in the time scale of motion of the electron avalanche and remain behind. The electron avalanche moves to the anode and achieves a great loss of energy in the inelastic collisions. The downturn of the total field due to the electron avalanche will slow down the electrons further. Finally, net positive charges stay near the cathode (z=0.0~0.3mm) and net negative charges remain far from the cathode (z=0.3~1.0mm) as Figure. 3 shows. The net charges in the plasma region are roughly equal to 0.

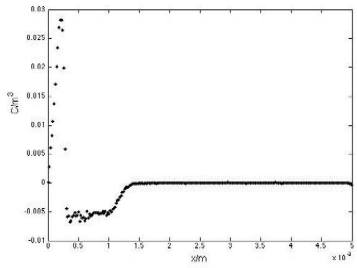

Fig. 3. Net charges distribution in the discharge channel at t=4ns

Summary

Some basic features of glow discharge in N_2 are simulated with PIC/MCC method. In the simulation, the velocity, angles, coordinates and energies of charged particles are calculated. The electric field distribution, the electric potential distribution and the net charge distribution are obtained from Poisson equation. The results show the detailed propagation of charged particles and the variation of the electric field under the influence of charged particles. The glow discharge mainly relies on ionization collisions in the discharge space. The numerical results may provide further understanding of the mechanism of the discharge process and some practical applications such as sewage treatment.

Acknowledgments

This work was supported in part by the Scientific Research Fund of Education Department of Shaanxi Province of China under Grant 09JK742 and in part by NWU graduate innovation and creativity Funds under Grant 10YJC16 and JX12022.

References

[1] Yuezhong Wen, Chensi Shen, Yanyan Ni. Glow discharge plasma in water: A green approach to enhancing ability of chitosan for dye removal. Journal of Hazardous Materials. 201-202(2012) 162-169.

[2] Xiaoyan Wang, Minghua Zhou, Xinglong Jin. Application of glow discharge plasma for wastewater treatment. Electrochimica Acta. 83(2012) 501-512.

[3] Nishioka H, Saito H, Watanabe T. Decomposition mechanism of organic compounds by DC water plasmas at atmospheric pressure. Thin Solid Film 2009; 518(3): 924-928.

[4] W Yu, LZ Zhang, JL Wang. Monte Carlo Simulation of the Fast Electrons and Heavy Particles in the CDS of Nitrogen DC Glow Discharge. Journal of Applied Physics, 2001, 34(3): 3349-3355.

[5] Fuqiu Shao. The simulation of particles in plasma. Beijing: Science Press, 2002,11.29.

[6] Guerra V, Loureiro J. Electron and heavy particle kinetics in a low-pressure nitrogen glow discharge [J]. Plasma Sources Sci. Techn, 1997, 6:361-372.

[7] Itikawa Y. Cross section for electron collisions with nitrogen molecules [J]. J. Phys. Chem. Ref. Data, 2006, 35(1): 31-52.

[8] K.Adamiak, V.Atrazhev, P. Atten, Corona discharge in the hyperbolic point–plane configuration: direct ionization criterion versus approximate for- mulations, IEEE Trans. Dielectr. Electr. Insul. 12(2005) 1025-1034.

Advanced Materials Research Vols. 960-961 (2014) pp 774-779

doi:10.4028/www.scientific.net/AMR.960-961.774

The fault diagnosis of a class of time-delay switched systems

Na Wang[1, 2,a], Laijun Lu[1,b]

[1]College of Earth Science, Jilin University, Changchun, China

[2] Jilin Teachers Institute of Engineering and Technology,Changchun Jilin 130052,China

[a] 30721394@qq.com,[b]284901934@qq.com

Keywords: Index Terms - Time-delay, Switched systems,Fault diagnosis

Introduction

The actual engineering control systems are nonlinear[1-2] and uncertainty[3-4] at the same time, so the robustness and fault diagnosis of systems are more meaningful[5-6]. Sometimes the system is with switching characteristics, which makes the study of switched systems more meaningful. As one of the nonlinear systems, switched systems exist in the practical systems widely, and the phenomenon of delay exists in industrial control nature, or in the life of people widely[7-8]. So the fault diagnosis research[11-12] of nonlinear switched systems with time-delay [9-10]has attracted the attention of many scholars. Motivated with the above issues, the general form of a class of switched systems with time-delay is described in detail, which also mentioned lemma 1 (Schur complement lemma)and lemma 2, the two lemmas will be applied to the proof process of the conclusion. The core part is observer design for time-delay systems fault, which puts forward the uniformly bounded stable condition of fault estimation error system expressed as the linear matrix inequality, and Lyapunov stability is applied to the strict proof. At last, the simulation of MATLAB in a numerical example proved the validity of the conclusion.

System description

Time-delay switched systems can be described as

$$\begin{aligned}\dot{x}(t) &= A_{\sigma(t)}x(t) + A_{d\sigma(t)}x(t-d(t)) + g(x(t)) + B_{\sigma(t)}u(t) + E_{\sigma(t)}f(t)\\ y(t) &= C_{\sigma(t)}x(t)\end{aligned} \tag{1}$$

where $x(t)\in\Re^n$ express the state vectors of system, $u(t)\in\Re^m$ expresses the system input, $y(t)\in\Re^p$ is the system output, $f(t)\in\Re^r$ is the actuator fault of the system, $A_{\sigma(t)}, A_{d\sigma(t)}, B_{\sigma(t)}, C_{\sigma(t)}, E_{\sigma(t)}$ are the system matrixes with appropriate dimension, for switching signal, $\sigma(t):[0,+\infty)\to\psi=\{1,\cdots,N\}$, where $N\geq 1$, especially, when $N=1$, system become ordinary time-delay systems, when $N>1$,it is supposed that the i subsystem work, that is $\sigma(t)=i$, so the formula was established

$$A_{\sigma(t)}=A_i, A_{d\sigma(t)}=A_i, B_{\sigma(t)}=B_i, C_{\sigma(t)}=C_i, E_{\sigma(t)}=E_i$$

where $(A_i \quad C_i)$ is observable, the matrix E_i is a line full rank matrix, that is $rank(E_i)=r$,the time-varying delay $d(t)$ satisfies $0<d(t)\leq h, \dot{d}(t)\leq\tau$

where h,τ are known constants, actuator fault satisfies the norm bounded condition $\|\dot{f}(t)\|\leq f_1, \|f(t)\|\leq f_2, \phi(\theta)$ is the initial function.

Lemma 1 (Schur Complement lemma), for a given symmetric matrix $\boldsymbol{Q}=\begin{bmatrix}\boldsymbol{Q}_{11} & \boldsymbol{Q}_{12}\\ \boldsymbol{Q}_{12}^{T} & \boldsymbol{Q}_{22}\end{bmatrix}<0$

Where $\boldsymbol{Q}_{ii}$ is a symmetric matrix of $r_i\times r_i$, r_i is a positive integer, $i=1,2$, the following conditions are

(1) $\boldsymbol{Q}<0$; (2) $\boldsymbol{Q}_{11}<0$ and $\boldsymbol{Q}_{22}-\boldsymbol{Q}_{12}^{\mathrm{T}}\boldsymbol{Q}_{11}^{-1}\boldsymbol{Q}_{12}<0$; (3) $\boldsymbol{Q}_{22}<0$ and $\boldsymbol{Q}_{11}-\boldsymbol{Q}_{12}\boldsymbol{Q}_{22}^{-1}\boldsymbol{Q}_{12}^{\mathrm{T}}<0$ 。

Lemma 2 For definite matrix composed of any positive constant $\boldsymbol{Z}\in\Re^{n\times n}$, $\boldsymbol{Z}=\boldsymbol{Z}^{\mathrm{T}}>0$,the scalars are $b>a\geq 0$,the vector function is $\boldsymbol{w}:[a,b]\to\Re^{n}$,the integral inequality was established:

$$(b-a)\int_a^b \boldsymbol{w}^{\mathrm{T}}(s)\boldsymbol{Z}\boldsymbol{w}(s)\mathrm{d}s\geq\left(\int_a^b \boldsymbol{w}(s)\mathrm{d}s\right)^{\mathrm{T}}\boldsymbol{Z}\left(\int_a^b \boldsymbol{w}(s)\mathrm{d}s\right)$$

Time-delay system fault observer design

If there are positive definite symmetric matrices P_i,Q_i and an arbitrary matrix Y_i satisfy the follow matrix inequality $\Xi<0$,then the fault estimation error system is uniformly bounded stable, where

$$Y_i=P_iL_i,\ E_i^TP_i=F_iC_i\quad \dot{\hat{f}}=-\Gamma^{-1}\left(Fe_y+F\dot{e}_y+\sigma\hat{f}\right)$$

The residence time of switching signal meets: $T_a>T_a^*=\dfrac{\ln(\mu)}{\alpha}$

Then the system is asymptotically exponentially stable and there is $\mu\geq 1$, $P_i\leq\mu P_j, Q_i\leq\mu Q_j, Z_i\leq\mu Z_j$

Where:

$$\Xi_{11}=A_i^TP_i+P_iA_i-C_i^TY_i^T-Y_iC_i+Q_i+\alpha P_i-e^{-\alpha h}\frac{1}{h}P_i+D_i+hA_i^TP_iA_i-hC_i^TY_i^TA_i-hA_iY_iC_i$$

$$\Xi_{12}=C_i^TY_i^T\quad \Xi_{13}=P_iA_{di}+hA_i^TP_iA_{di}-hC_i^TY_i^TA_{di}+e^{-\alpha h}\frac{1}{h}P_i$$

$$\Xi_{14}=P_i+hA_i^TP_i-hC_i^TY_i^T\quad \Xi_{15}=(h-1)A_i^TP_iE_i-(h-1)C_i^TY_i^TE_i$$

$$\Xi_{22}=-\frac{1}{h}P_i\quad \Xi_{33}=-(1-\tau)e^{-\alpha h}Q_i+hA_{di}^TP_iA_{di}-e^{-\alpha h}\frac{1}{h}P_i$$

$$\Xi_{34}=hA_d^T\quad \Xi_{35}=hA_{di}^TP_iE_i-A_{di}^TP_iE_i\quad \Xi_{44}=hP-D\quad \Xi_{45}=hP_iE_i-P_iE_i\quad \Xi_{55}=hE_i^TP_iE_i-2E_i^TP_iE_i$$

Proof: Lyapunov function is selected as following

$$V_i(t)=V_{1i}(t)+V_{2i}(t)+V_{3i}(t)+V_{4i}(t)$$

Where $V_{1i}(t)=e_x^T(t)P_ie_x(t)$ $V_{2i}(t)=e^{-\alpha t}\int_{t-d(t)}^{t}e^{-\alpha s}e_x^T(s)Q_ie_x(s)ds$

$$V_{3i}(t)=he^{-\alpha t}\int_{-h}^{0}\int_{t+\sigma}^{t}e^{\alpha s}\dot{e}_x^T(s)Z_i\dot{e}_x(s)dsd\sigma\quad V_{4i}(t)=e_f^T(t)\Gamma e_f(t)$$

Along (1), take the derivative of Lyapunov function :

$$\dot{V}_{1i}(t)\leq e_x^T(t)\left(\left(A_i-L_iC_i\right)^TP_i+P_i\left(A_i-L_iC_i\right)\right)e_x(t)+2e_x^T(t)P_ie_g(t)+2e_x^T(t)P_iA_{di}e_x\left(t-d(t)\right)$$

$$\dot{V}_{2i}(t)\leq-\alpha V_{2i}+e_x^T(t)Q_ie_x(t)-(1-\tau)e^{-\alpha h}e_x^T\left(t-d(t)\right)Q_ie_x\left(t-d(t)\right)$$

$$\dot{V}_{3i}(t)\leq-\alpha V_{3i}+h\dot{e}_x^T(t)Z_i\dot{e}_x(t)-e^{-\alpha h}\int_{t-h}^{t}\dot{e}_x^T(s)Z_i\dot{e}_x(s)\,ds$$

Because of the system so that there is:

$$h\dot{e}_x^T(t)Z_i\dot{e}_x(t)=he_x^T(t)(A_i-L_iC_i)^TZ_i(A_i-L_iC_i)e_x(t)+he_x^T(t)(A_i-L_iC_i)^TZ_iA_{di}e_x(t-d(t))$$
$$+he_x^T(t)(A_i-L_iC_i)^TZ_ie_g(t)+he_x^T(t)(A_i-L_iC_i)^TZ_iE_ie_f(t)$$
$$+he_x^T(t-d(t))A_{di}^TZ_i(A_i-L_iC_i)e_x(t)+he_x^T(t-d(t))A_{di}^TZ_iA_{di}e_x(t-d(t))$$
$$+he_x^T(t-d(t))A_{di}^TZ_ie_g(t)+he_x^T(t-d(t))A_{di}^TZ_iE_ie_f(t)$$
$$+he_g^T(t)Z_i(A_i-L_iC_i)e_x(t)+he_g^T(t)Z_iA_{di}e_x(t-d(t))$$
$$+he_g^T(t)Z_ie_g(t)+he_g^T(t)Z_iE_ie_f(t)+he_f^T(t)E_i^TZ_i(A_i-L_iC_i)e_x(t)$$
$$+he_f^T(t)E_i^TZ_iA_{di}e_x(t-d(t))+he_f^T(t)E_i^TZ_ie_g(t)+he_f^T(t)E_i^TZ_iE_ie_f(t)$$

According to the lemma, it can be obtained:

$$-e^{-\alpha h}\int_{t-h}^{t}\dot{e}_x^T(s)Z_i\dot{e}_x(s)ds\le-e^{-\alpha h}\frac{1}{h}e_x^T(t)Z_ie_x(t)+e^{-\alpha h}\frac{1}{h}e_x^T(t)Z_ie_x(t-d(t))$$
$$+e^{-\alpha h}\frac{1}{h}e_x^T(t-d(t))Z_ie_x(t)-e^{-\alpha h}\frac{1}{h}e_x^T(t-d(t))Z_ie_x(t-d(t))$$

Along (1), take the derivative of Lyapunov function $V_{4i}(t):\dot{V}_{4i}(t)=2e_f^T(t)\Gamma\dot{e}_f(t)$

Because of $FC=E^TP$ and for the system the following inequality exists:

$$-2\sigma e_f^T(t)(e_f(t)+f^*)\le-2\sigma e_f^T(t)e_f(t)+2\sigma e_f^T(t)f^*\le-\sigma e_f^T(t)e_f(t)+\sigma f^{*T}f^*$$

Select $\alpha=\sigma\lambda_{\min}(\Gamma^{-1})$,so it can be obtained:

$$\dot{V}_{4i}(t)\le-\alpha V_{4i}-2e_f^T(t)E_i^TP_ie_x-2e_f^T(t)E_i^TP_i(A_i-L_iC_i)e_x(t)-2e_f^T(t)E_i^TP_iA_{di}e_x(t-d(t))$$
$$-2e_f^T(t)E_i^TP_ie_g(t)-2e_f^T(t)E_i^TP_iE_ie_f(t)+\sigma f_2^2$$

Because $\|g(x_1)-g(x_2)\|\le\|x_1-x_2\|$ is established, so for any positive definite diagonal matrix D_i there is $e_x^T(t)D_ie_x(t)-e_g^T(x(t))D_ie_g(x(t))>0$ As a result: $\dot{V}_i(t)\le-\alpha V_i(t)+\xi^T\Theta_1\xi+\delta$

According to the Schur lemma and the skill of matrix elementary transformation, you can get $\Theta_1<0$ is equivalent to $\Xi<0$, where

$$\Xi=\begin{bmatrix}
A_i^TP_i+P_iA_i-C_i^TY_i^T & & & & \\
-Y_iC_i+Q_i+\alpha P_i & & & & \\
-e^{-\alpha h}\frac{1}{h}P_i+D_i & C_i^TY_i^T & P_iA_{di}+hA_i^TP_iA_{di} & P_i+hA_i^TP_i & P_iE_i \\
+hA_i^TP_iA_i & & -hC_i^TY_i^TA_{di} & -hC_i^TY_i^T & +(h-1)A_i^TP_iE_i \\
-hC_i^TY_i^TA_i & & +e^{-\alpha h}\frac{1}{h}P_i & & -(h-1)C_i^TY_i^TE_i \\
-hA_iY_iC_i & & & & -P_iE_i \\
* & -\frac{1}{h}P_i & 0 & 0 & 0 \\
 & & -(1-\tau)e^{-\alpha h}Q_i & & \\
* & * & +hA_{di}^TP_iA_{di} & hA_d^TP & hA_{di}^TP_iE_i-A_{di}^TP_iE_i \\
 & & -e^{-\alpha h}\frac{1}{h}P_i & & \\
* & * & * & hP-D & hP_iE_i-P_iE_i \\
* & * & * & * & hE_i^TP_iE_i \\
 & & & & -2E_i^TP_iE_i
\end{bmatrix}$$

$\delta=\alpha f_2^2$ So that, there is $V_i(t)\le-e^{-\alpha(t-t_0)}\mu^\beta V_i(t_0)+\frac{\delta}{\alpha}\le-e^{-\left(\alpha-\frac{\ln\mu}{T_a}\right)(t-t_0)}\mu^\beta V_i(t_0)+\frac{\delta}{\alpha}$

Fault estimation error system is uniformly bounded stable. The theorem is proven.

Simulation experiment

In order to verify the feasibility and effectiveness of the theoretical results, a two dimensional time-varying delay system is given, and then the MATLAB/SIMULINK software is used in simulation. In this paper, all the results are given in the form of linear matrix inequality (LMI), they can be solved by LMI toolbox of Matlab, but in the theorem $E^T P = FC$ is required, if the matrixes E, C are square matrixes, they can be solved through the matrix inverse operation, but if when the matrixes are not square matrixes, especially, when the output gain matrices $rank(C) = r < n$ not all of the E, C, P exist the matrix F to meet the condition. To solve $E^T P - FC = 0$ .Through a small enough positive number η, $E^T P - FC = 0$ can be realized. Known matrix and the related parameters of the system are selected :

Subsystem 1:

$$A_1 = \begin{bmatrix} -1 & 0 \\ 0.2 & -0.8 \end{bmatrix}, A_{d1} = \begin{bmatrix} 0.1 & 0.1 \\ 0.1 & 0.2 \end{bmatrix}, B_1 = \begin{bmatrix} 1 \\ 1 \end{bmatrix}, E_1 = \begin{bmatrix} 1 \\ 1 \end{bmatrix}, C_1 = \begin{bmatrix} 0 & 1 \end{bmatrix}$$

Subsystem 2:

$$A_2 = \begin{bmatrix} -5 & 2 \\ 2 & -5 \end{bmatrix}, A_{d2} = \begin{bmatrix} 0.5 & 1 \\ 1 & 2 \end{bmatrix}, B_2 = \begin{bmatrix} 1 \\ 1 \end{bmatrix}, E_2 = \begin{bmatrix} 1 \\ 1 \end{bmatrix}, C_2 = \begin{bmatrix} 0 & 1 \end{bmatrix}$$

$d(t) = 0.3 + 0.2\sin(t)$ $f(t) = 0.4\sin(t-30),$ $0 \le t \le 100$

we can get:

$$P_1 = \begin{bmatrix} 0.6615 & -0.6620 \\ -0.6620 & 3.0555 \end{bmatrix} \quad Q_1 = \begin{bmatrix} 0.0148 & -0.0170 \\ -0.0170 & 0.2375 \end{bmatrix} \quad D_1 = \begin{bmatrix} 0.6127 & 0 \\ 0 & 1.9210 \end{bmatrix} \quad Y_1 = \begin{bmatrix} 0.4334 \\ 3.4081 \end{bmatrix}$$

$F_1 = 2.3935$

Calculating $L_1 = P_1^{-1} Y_1$ can obtain $L_1 = \begin{bmatrix} 2.2619 \\ 1.6055 \end{bmatrix}$;

$$P_2 = \begin{bmatrix} 0.0176 & -0.0084 \\ -0.0084 & 0.0145 \end{bmatrix} Q_2 = \begin{bmatrix} 0.0197 & -0.0183 \\ -0.0183 & 0.0197 \end{bmatrix} D_2 = \begin{bmatrix} 0.0107 & 0 \\ 0 & 0.0108 \end{bmatrix} Y_2 = \begin{bmatrix} -0.0075 \\ 0.0211 \end{bmatrix}$$

$F_2 = 0.0061$ Calculating $L_2 = P_2^{-1} Y_2$ can obtain $L_2 = \begin{bmatrix} 0.3694 \\ 1.6628 \end{bmatrix}$.

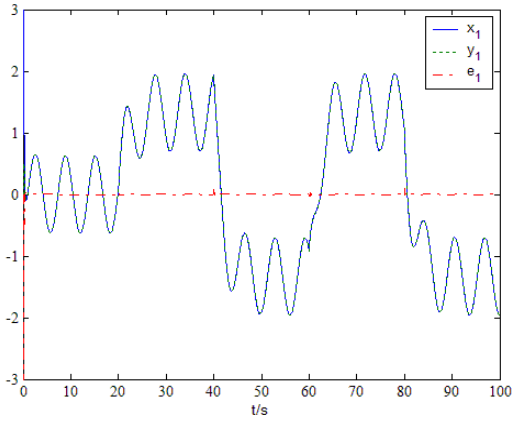

Fig. 1 State and error of the system

As can be seen from the simulation graph 1, in the 30 s before, the simulation is in the absence of fault, the state of the observer y_1 can track the system state x_1 soon. After the 30 s, the system has the fault, but the state of the observer y_1 can also track the system state x_1 very well. Through the error of the simulation e_1, it can be seen clearly that the error between the state of the system and the observer state in the whole simulation process.

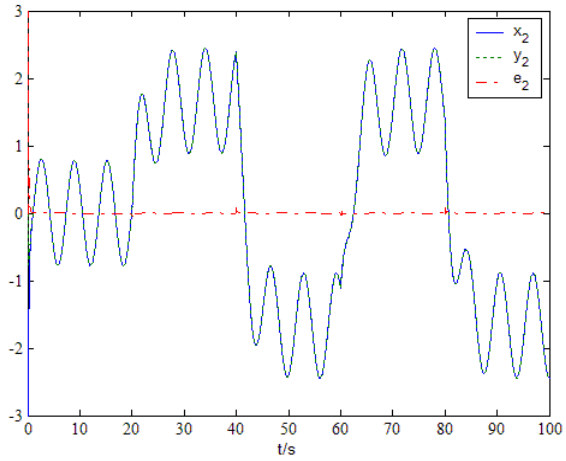

Fig.2 State and error of the system

As can be seen from the simulation graph 1, in the 30 s before,the simulation is in the absence of fault,the state of the observer y_2 can track the system state x_2 soon.After the 30 s,the system has the fault, but the state of the observer y_2 can also track the system state x_2 very well.Through the error of the simulation e_2 ,it can be seen clearly that the error between the state of the system and the observer state in the whole simulation process.

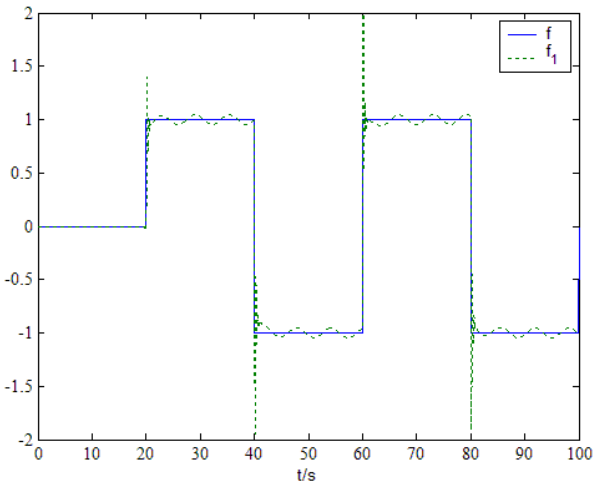

Fig. 3 Error and estimate of the system

As can be seen from the simulation graph 1, in the 30 s before,the simulation is in the absence of fault, the system failure f keeps zero,the state of fault observer f_1 also keeps zero.After the 30 s,the system has the fault, at the same time, the observer of system fault can also track the fault very well.

Conclusion

The fault diagnosis of a class of lag switched systems is studied in the paper. For such a system, the algorithm of adaptive fault estimation algorithm is adopted, through the observer design to the time-delay system fault, it is given in the form of linear matrix inequality (LMI) the uniformly bounded stable condition of the fault estimation error system. And the Lyapunov boundedness theory verify the effectiveness of the conclusion.Then a numerical example is given ,the SIMULINK toolbox of MATLAB give system simulation to verify the correctness and effectiveness of the proposed algorithm.

Acknowledgment

This work is partially supported by NSFC 61273188.

References

[1] Li W, Li YJ, Liu WR. Robust fault-tolerant control of networked control systems based on LMI method, Journal of the air force engineering university(natural science edition),2007， 8(4)：27-31.

[2] V. Venkatasubramanian, et al. A review of process fault detection and diagnosis Part II: Qualitative models and search strategies [J]. Computers and Chemical Engineering vol.27,2003.

[3] V. Venkatasubramanian, et al. A review of process fault detection and diagnosis: Part III: Process history based methods [J]. Computers & chemical engineering, vol. 27, pp. 327-346, 2003

[4] Peng FB, Yan DC, Wang GM, Yuan CH. Asymmetric six phase permanent magnet fault-tolerant motor operation research,Journal of the air force engineering university(natural science edition),2009， 10（3）：73-77.

[5] S. G. Mallat. A theory for multiresolution signal decomposition: The wavelet representation PatternAnalysis and Machine Intelligence [J]. IEEE Transactions on, vol. 11, pp. 674-693, 1989.

[6] I. Daubechies. Orthonormal bases of compactly supported wavelets [J]. Communications on pure and applied mathematics, vol. 41, pp. 909-996, 1988.

[7] Hao YH, Wang FM.Application of wavelet transform in mechanical failure signal analysis[J]Modern Electronics Technique, 2008,(31):110-112.

Advanced Materials Research Vols. 960-961 (2014) pp 780-785

doi:10.4028/www.scientific.net/AMR.960-961.780

A Method of Introducing PMU Current Measurement to Nonlinear State Estimation

Kun Zhao[1,a], Lei Yan[2,b], Li Li[1,c], Qiang Li,Yansheng Lang, Peiyu Jia

[1]China Electric Power Research Institute, China

[2]North China Electricity Power University, China

[a]zhaokun@epri.sgcc.com.cn, [b]yancuo.123@163.com, [c]lili2010@epri.sgcc.com.cn

Keywords: state estimation current measure RPM PMU

Abstract. Aiming at the problem that the current measurements provided by phasor measurement unit (PMU) is difficult to introduce to traditional state estimation, a new method to solve the compatibility problems of PMU and supervisory control and data acquisition (SCADA) is presented in this paper. By the rotated-pseudo-measurement (RPM) method, current measurements are transformed into the pseudo measurements and decoupled in polar coordinates, so that they could taken into nonlinear state estimation. Then the RPM method is simulated compared with the current transformation (CT) method. According to the result, it is showed that the RPM method has many advantages compared with the CT, such as independence of other measurements, small error in propagation and more significant in improving estimation accuracy. Moreover, the RPM method has the compatibility with traditional nonlinear state estimation and the fast calculating speed, which have good prospects of practice.

Introduction

In recent years, phasor measurement technology has been widely used. The PMU makes node voltage phasor and branch current phasor become measurable. Based on Wide Area Measurement System (WAMS), PMU measurement device is considered to bring some significant changes to traditional state estimation in power grid[1~7].

Compared with the traditional measurement devices on the types of measurements, PMU can not only obtain the measurement of the magnitude of voltage and power, but also the phase angle of voltage and current can be collected to measure voltage and current; PMU can be collected within a 50-second section of the data, and each measurement are marked with a time scasle to ensure the synchronization of the measurement. Therefore, compared to SCADA measurements, the PMU measurements are fast and accurate, and can well reflect the dynamic of the power system.

Among the existing power grid state estimation methods, the linear state estimation method and the non-linear method are both widely recognized. They are respectively based on decomposition of Cartesian coordinates and polar decomposition. Since the current measurement can be decomposed and analyzed in Cartesian coordinates easily, its technologies in linear state estimation have been mature.

However, considering the aspects of price and technique, it is impossible for all the nodes in power grid system equipped with PMU. Thus in a long period of time, only a small amount of nodes of the grids are observable in terms of PMU measurements. So it is of practical significant to take SCADA as the main measurement and PMU as a supplement to improve the accuracy of state estimation. In existing study on introduction of PMU, the methods of introduction of voltage and power measurement has been discussed widely, but a better approach to the introduction of the current does not exist yet. For the reason that the current measurement will be complex if decomposed directly in polar coordinates. And we cannot use some features of grid conditions decoupled it, which bring many difficulties to the introduction of the rapid decomposition.

STATE ESTIMATION WITH CURRENT MEASUREMENT

To introduce current measurement, quite a few articles use the equivalent-current -measurement-transformation method. In articles [13], the current measurements are directly changed to other to estimation measurements such as power measurements. The disadvantages are the amplification of transmission error and the decrease of the weighting factor, which lead to the loss of estimation accuracy. In article [15], the current measurement is directly decomposed into the real and the imaginary parts under the assumption that the whole network, voltage phase angle is zero. However, some phase angle may be large in the large power grid, which would bring to large errors to estimation.

To solve the problems the two current measurement methods bring, this article will use the rotation-pseudo-measurement (RPM) method.

It is difficult to introduce branch current measurement $\dot{I}_{ij}$ directly into the non-linear state estimation, because a branch current is the function of the voltage phase angle of both ends of the branch in polar coordinates. In other words, branch current vector will change when the voltage phase angle changes. Generally, the angle θ_i and θ_j, the voltage angle of bus i and bus j respectively, cannot be simply considered as zero. Therefore, function cannot be calculated using the PQ-decoupled method.

Since voltage phase angle of nodes equipped with PMU is know, and take into account that the branch current vectors change with voltage phase angles θ_i and θ_j of both ends of branch, we can construct a pseudo-measurement $\dot{I}_{ij}e^{-j\theta_i}$,where current measurement rotates an angle of $-\theta_i$, and the variable θ_i of the individual branch currents $\dot{I}_{ij}$ is changed to 0. So that we can the fixed angle bus i of a end of the branch current and construct θ_{ij} .By this method, we can use the condition of $\theta_{ij} \approx 0$ in high-voltage transmission network to decouple. Thus derivation is followed:

$$\begin{aligned} \dot{I}_{ij.0} &= \dot{I}_{ij}e^{-j\theta_i} = \left[y_{ij}(\dot{V}_i - \dot{V}_j) + y_{i0}\dot{V}_i \right] e^{-j\theta_i} \\ &= y_{ij}(V_i - V_j e^{-j\theta_{ij}}) + y_{i0}V_i \\ &= (g + jb)\left[V_i - V_j(\cos\theta_{ij} - j\sin\theta_{ij}) \right] + jy_{ic}V_i \end{aligned} \tag{1}$$

Where:

$\dot{V}_i$ and $\dot{V}_j$ is the voltage vector of both ends of branch respectively,

θ_{ij} is voltage phase angle difference of the both ends of the branch,

y_{ij}, g and b are admittance, conductance and susceptance of the branch respectively,

y_{ic} is the line-to-ground admittance.

The pseudo-measurement $\dot{I}_{ij.0}$ of the pseudo-measurement can be decomposed into two variables under Cartesian coordinates: the real part $I_{ij.0}^{re}$ and the imaginary part $I_{ij.0}^{im}$. As is showed followed:

$$\begin{cases} I_{ij.0}^{re} = gV_i - gV_j\cos\theta_{ij} - bV_j\sin\theta_{ij} \\ I_{ij.0}^{im} = gV_j\sin\theta_{ij} + bV_i - bV_j\cos\theta_{ij} + y_{ic}V_i \end{cases} \tag{2}$$

Then we take the partial derivative of the pseudo-measurements real and imaginary parts to V and θ:

$$\begin{cases} \dfrac{\partial I_{ij.0}^{re}}{\partial\theta_i} = gV_j\sin\theta_{ij} - bV_j\cos\theta_{ij} \\ \dfrac{\partial I_{ij.0}^{re}}{\partial V_i} = g \\ \dfrac{\partial I_{ij.0}^{im}}{\partial\theta_i} = gV_j\cos\theta_{ij} + bV_j\sin\theta_{ij} \\ \dfrac{\partial I_{ij.0}^{im}}{\partial V_i} = b + y_{ic} \end{cases} \qquad \begin{cases} \dfrac{\partial I_{ij.0}^{re}}{\partial\theta_j} = -gV_j\sin\theta_{ij} + bV_j\cos\theta_{ij} \\ \dfrac{\partial I_{ij.0}^{re}}{\partial V_j} = -g\cos\theta_{ij} - b\sin\theta_{ij} \\ \dfrac{\partial I_{ij.0}^{im}}{\partial\theta_j} = -gV_j\cos\theta_{ij} + bV_j\sin\theta_{ij} \\ \dfrac{\partial I_{ij.0}^{im}}{\partial V_j} = g\sin\theta_{ij} - b\cos\theta_{ij} \end{cases} \tag{3)(4}$$

In the high-voltage transmission system, the resistance of the transmission line is generally much smaller than its reactance, and the difference of amplitude of the voltage as well as the difference of the phase angle of the both ends of branch is not so large. That is $r \ll x$, $V_i \approx V_j = V_0$ and $\theta_{ij} \approx 0$ .Therefore, it is easy to draw the following conclusions : $g \ll b$, $\cos\theta_{ij} \approx 1$ and $\sin\theta_{ij} \approx 0$. If the formula is further deduced, we get that $g\sin\theta_{ij} \ll b\cos\theta_{ij}$, $\left|g\cos\theta_{ij} \pm b\sin\theta_{ij}\right| \ll \left|g\sin\theta_{ij} \pm b\cos\theta_{ij}\right|$.

Using these two deductions, we can simplify the formula (3)(4). The simplification for two formula (3)(4) are as follow:

$$\begin{cases} \dfrac{\partial I_{ij.0}^{re}}{\partial\theta_i} = -bV_0 \\ \dfrac{\partial I_{ij.0}^{re}}{\partial V_i} = 0 \\ \dfrac{\partial I_{ij.0}^{im}}{\partial\theta_i} = 0 \\ \dfrac{\partial I_{ij.0}^{im}}{\partial V_i} = b + y_{ic} \end{cases} \qquad \begin{cases} \dfrac{\partial I_{ij.0}^{re}}{\partial\theta_j} = bV_0 \\ \dfrac{\partial I_{ij.0}^{re}}{\partial V_j} = 0 \\ \dfrac{\partial I_{ij.0}^{im}}{\partial\theta_i} = 0 \\ \dfrac{\partial I_{ij.0}^{im}}{\partial V_i} = -b \end{cases} \tag{5)(6}$$

According to the formulas (5) (6), we can changes them into Jacobian matrix as follow：

$$\begin{pmatrix} \Delta I_{ij.0}^{re} \\ \Delta I_{ij.0}^{im} \end{pmatrix} = \begin{pmatrix} -B' & 0 \\ 0 & B' \end{pmatrix} \begin{pmatrix} V_0\Delta\theta \\ \Delta v \end{pmatrix} \tag{7}$$

Where

B' and B'' , are the corresponding coefficient matrix for $V_0\Delta\theta$ and Δv respectively, being constants if the network topology and parameter remain unchanged.

As can be seen from the above, the rotation pseudo-measurement method can achieve a decoupling. $I_{ij.0}^{re}$ can be classified as active and compute together with P, while $I_{ij.0}^{im}$ can be classified as reactive and compute together with Q.Therefore, this method can be carried out in conjunction with traditional state estimation based on PQ decomposition method. Through the above transformation, we achieve the introduction of PMU current measurement.

METHODS TO ACHIEVE

The weight of real and imaginary parts by the pseudo-rotation transformation can be determined by the relative error propagation equation:

$$R_{Ire} = \sqrt{\left(\frac{\partial \ln I_{ij.0}^{re}}{\partial I_{ij}}\right)^2 \sigma_{Iij}^2 + \left(\frac{\partial \ln I_{ij.0}^{re}}{\partial\theta_{Iij}}\right)^2 \sigma_{\theta Iij}^2 + \left(\frac{\partial \ln I_{ij.0}^{re}}{\partial\theta_i}\right)^2 \sigma_{\theta i}^2}, \quad R_{Iim} = \sqrt{\left(\frac{\partial \ln I_{ij.0}^{im}}{\partial I_{ij}}\right)^2 \sigma_{Iij}^2 + \left(\frac{\partial \ln I_{ij.0}^{im}}{\partial\theta_{Iij}}\right)^2 \sigma_{\theta Iij}^2 + \left(\frac{\partial \ln I_{ij.0}^{im}}{\partial\theta_i}\right)^2 \sigma_{\theta i}^2} \tag{8)(9}$$

Where:

R_{Ire} is the weight coefficients of the real part of the pseudo-measurement.

R_{Iim} is the weight coefficients of the imaginary part of the pseudo-measurement.

σ_{Iij}^2 , $\sigma_{\theta Iij}^2$ and $\sigma_{\theta i}^2$ are respectively the variance of amplitude of current measurement, the variance of the angle of current measurement, and the variance of phase angle of voltage measurement.

Thus the pseudo-measurement of the real and the imaginary parts of the weight is determined.

In the iteration, the PMU voltage phase angle θ_i^{PMU} ,if precise enough, can be taken directly to construct a pseudo measurement $\dot{I}_{ij}e^{-j\theta_i}$; if not, we can take improved-dynamic estimation method instead: take the rotation phase angle as θ_i^{PMU} before taking a few iterations； after than in each iteration, get the latest state estimation value $\theta_i^{(n)}$ to compose pseudo-measurement together with the original measurement $\dot{I}_{ij}$ .Therefore, the pseudo-measurement values are updated in subsequent

iterations (only a different in angle of rotation). The amount of computation with dynamic improved estimation method is small, which can reduce the error of state estimation when the error of phase angle PMU phase angle error is large.

ALGORITHM PROCESS

The process of mixed nonlinear state estimation is generally the same as the one of traditional nonlinear state estimation. Therefore we just have to make some modifications in the original process. As it is shown as Fig1:

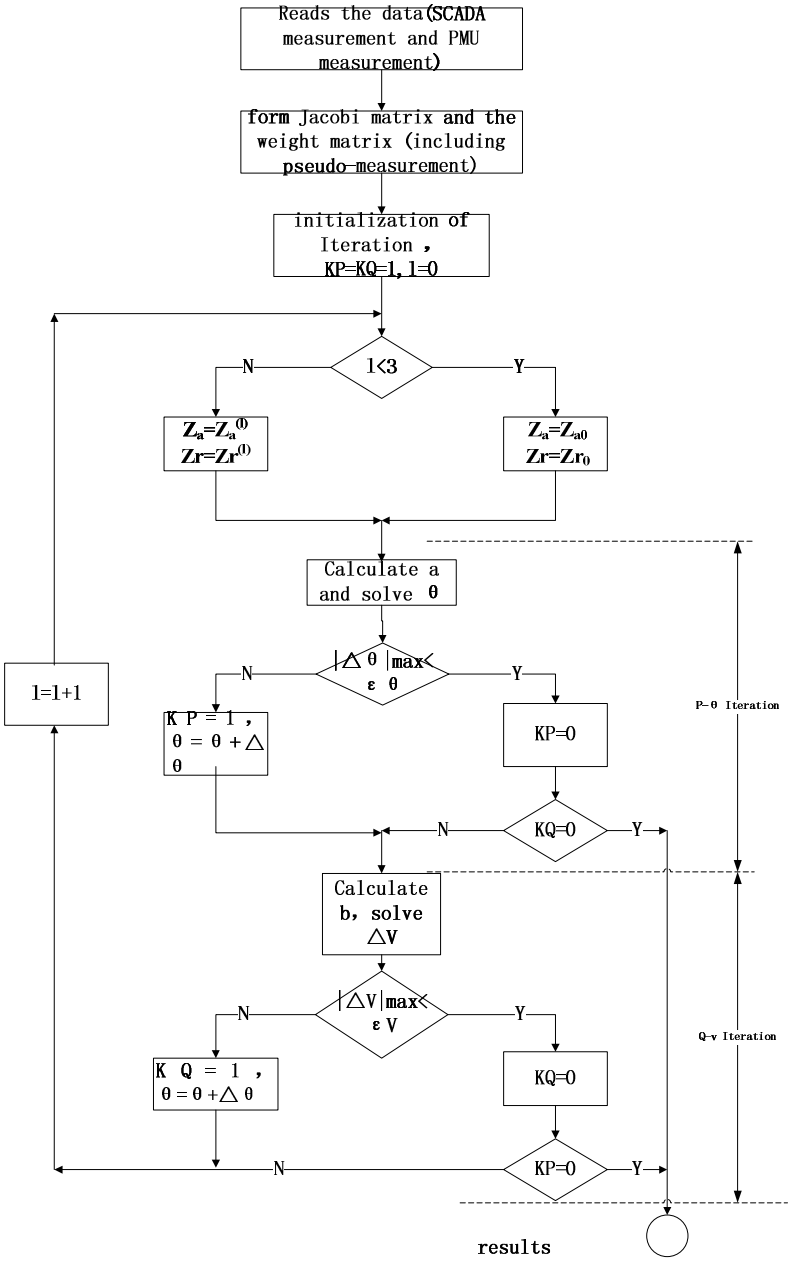

Fig.1 Process of RPM method

ANALYSIS OF EXAMPLE

In this paper, we take IEEE 39 node system as an example, and assume that all nodes are equipped with voltage PMU and all branches with power and current PMU. That is to say each branch of the current is known. Assume that all measurements are normally distributed with mean zero, and that standard deviation of the voltage measurements and power measurements is 0.2,while current measurements' standard deviation is 0.01. The convergence criterion is 10-5.

Table 1 Calculation results of the RPM method and other traditional non-liner estimations method in 39-bus system

Method	The RPM method	The CT method	The traditional method(without current measurement)
Times in multi-iteration	5	4	4
J(x)	34.3175	40.5590	25.7007

As can be seen from Table 1, although there is one more time in multi-iteration the RPM method than the CT method, the former's objective function J (x) is smaller than the latter's, revealing a better estimate performance.

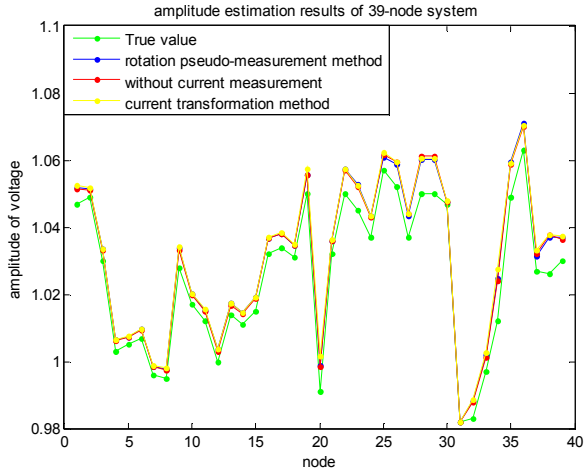

Fig.2 The voltage amplitude of estimation results

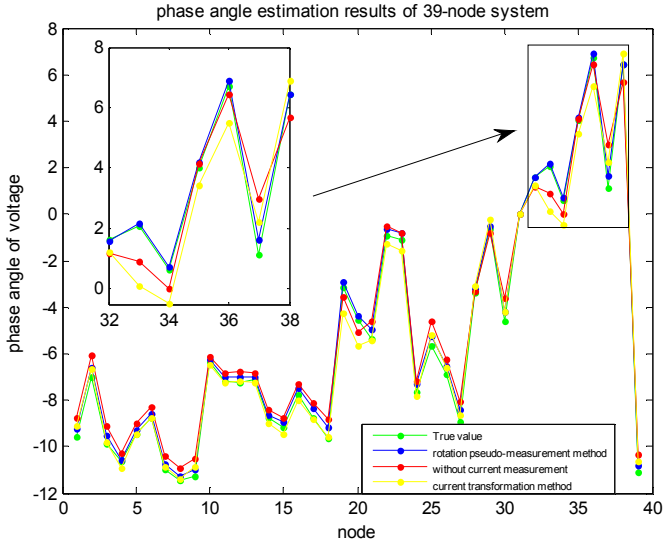

Fig.3 The voltage amplitude of estimation results

As can see from Fig.2, both of the performances of the RPM and the CT method have little influence on the result of the state estimation voltage amplitude. Among the result of the voltage phase angle estimation, the estimation result of the RPM is the closest to the true value in general, meaning a good estimation result. Because of some large errors in the voltage measure, the performance of the CT method is not so satisfying, in which some nodes estimation results are further from the true value. As it is shown in the box in Fig 3.While the RPM method only takes use of voltage phase information, and transmits smaller errors. Moreover, after multiple simulations, it is showed that the performance of RPM is not sensitive to the accuracy of voltage phase angle measurements. In other words, the accuracy of initial voltage measures has little impact on the effect of RPM.

CONCLUSION

This paper presents a method that current measurement is introduced into the nonlinear state estimation by constructing a pseudo-rotation current measurement with PMU voltage phase angle information. And its transmission error is calculated as well. Then IEEE 39 node system with a numerical example to calculate quantitative and qualitative analysis. Simulation results show that the method is simple and effective , with an estimated effect, accuracy higher than the average current transformation method and can be fully integrated into the nonlinear state estimation along with other characteristics. The disadvantage of this method is that if used alone without the other measurements, may result in an estimated without convergence.

About the Author

Kun Zhao(1984-),male,master,engineer,research on power system and Automation, WAMS. zhaokunfx@126.com.

Lei Yan (1988-),male, Studying for his master's degree, is engaged in WAMS and micro-grids

Li Li(1983-), master, majored in electrical engineering and automation, is mainly engaged in security constraints scheduling of real-time power system

REFERENCES

[1] Xu Shukai, Xie Xiaorong, Xin Yaozhong. *Present application situation and development tendency of synchronous phasor measurement technology based wide area measurement system* [J]. Power System Technology, 2005, 29(2):44-49.

[2] Wu Jingtao, Xie Xiaorong, Wang Liding, et al. *Development and prospect of WAMS in power system. Electrical Equipment*, 2006, 7(3):46-49.

[3] Xue Yusheng, Xu Wei, Zhaoyang Dong, et al. *A review of wide area measurement system and wide area control system[J], Automation of Electric Power Systems*, 2007, 31(15):1-5.

[4] Xue Yusheng, Li Haifeng. *A review of CIGRE 2008 on power system operation and control*[J]. High voltage Engineering, 2008, 34(11):2253-2258.

[5] He Jiang, Zhou Jingyang, Wang Mingjun. *Application of wide area phasor measurement technology in smart grid* [J]. Power System Technology, 2009, 33(15):16-19.

[6] Li Qiang, Yu Erkeng, Lu Shichao, et al. *An improved optimal PMU placement algorithm* [J]. Power System Technology, 2005, 29(12):57-61.

[7] Zhou Jie, Ding Xiaohua, Sun Guocheng, et al. *New distributed PMU substation system* [J]. Automation of electric power system, 2009, 33(17): 105-108.

[8] Zhang Sheng, Wang Jian, He Chun. *Evaluating standard and test Method on function of phasor measurement unit*. Automation of Electric Power systems, 2007, 31(21):102-105.

[9] Mai Ruikun, He Zhengyou, Bo Zhiqian, *Research on synchrophasor estimation algorithm based on taylor expansion*[J]. Automation of electric power system, 2008, 32(12)：22-26.

[10] Tang Yong. *Fundamental theory of forced power oscillation in power system* [J]. Power System Technology, 2006, 30(10):29-33.

[11] Xue Yusheng, Hao Sipeng, Liu Junyong, et al. *A review of analysis methods for* low-*frequency oscillations* [J]. Automation of Electric Power Systems, 2009, 33(3):1-8.

[12] Ding Junce,Cai Zexiang, *Wang Keying. Quickly transform state* estimation *with equivalent current measurement methods in polar coordinate system* [J]. Electric power system automation ,2005,05:31 -33 +96.

[13] Zhao Gahong, Xue Yusheng, Wang Derxing, Ge Minhui, Li Bijun. *Branch current state estimation model in account with PMU phasor* [J]. Electric power system automation ,2004,17:37-40.

[14] Qin Xiaohui, BI Tianshu, Yang Qixun, *New method of mixed nonlinear state estimation accounting PMU* [J]. Electric power system automation ,2007,04:28-32.

[15] Li Weiguo, Li Hong, Fu Hongjun, Yu Weicheng, Yang Jianrong. *Power system state estimation based on wide-area measurement system* [J]. Grid technology, 2008, S2 :124-127.

Advanced Materials Research Vols. 960-961 (2014) pp 786-789

doi:10.4028/www.scientific.net/AMR.960-961.786

A fast Search Algorithm for Transmission Section Based on K shortest paths

Xianchao Liu[1, a *], Jianwen Ren[1, b] Weidong Qu[1, c]

[1]School of Electrical and Electronic Engineering, North China Electric Power University, Baoding, Hebei, 071003, China

[a]imyelifu@sina.com, [b]rjw219@126.com, [c]qwdgeg@163.com

KEY WORDS: transmission section; shortest paths; Adjacency matrix

Abstract. A new algorithm based on K shortest paths is presented for quick search of the transmission section, and then the timely electricity network topology is transferred into a directed graph. Using this new algorithm, k shortest paths would be directly searched for; the transmission section influenced greatly by the power flow shift is then obtained quickly. To avoid leaving part of the search because criteria are too small tributary drain election when using a single path to ensure the integrity of the transmission section. Finally CEPRI36 nodes system simulation is analyzed, and the effectiveness of the algorithm is demonstrated.

Introduction

In recent years, a number of major power outages have occurred in domestic and international power systems caused by cascading failures. Economic losses and social impacts are extremely serious, such as the 2003 U.S. / Blackout. After removal of overload branches, the power flows of the entire system will be reallocated, which would determine the transfer of power flows on each overloaded element. Then the recalculation of the whole network power flows is needed, but it will cost too much time. In fact, after resection of overload only a few branches of the branch circuit would be influenced by the power flow shift [2]. So in the large power system if branches influenced greatly by power flow shifts can be searched out quickly, then the analysis of whether the overload will cause the action of backup protection, which is much simpler and faster than the whole network analysis. After breaking off the overloaded branches, branches with the shortest electrical distance would be influenced more greatly than those with long distances. According to the basic principles of the circuit, current and power can only run in the closed loop, which has the lowest impedance.

Analysis of power flow transfer characteristics

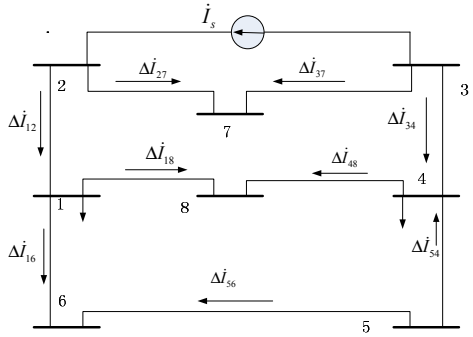

Fig.1 Equivalent network of flow transferring component

An 8-node network diagrams is shown in Fig. 1, when lines are cut off due to overload, active power of each generator and system load stay unchanged, without the consideration of nonlinear components in the system, such as power electronics. According to superposition theorem of the circuit theory, power flows in other lines after removal can be divided to two parts, one is power flows before the removal and the other is transferring components caused by the removal, which could be induced by

$$\dot{I}'_{ij} = \dot{I}_{ij} + \Delta\dot{I}_{ij} \tag{1}$$

Where, $\dot{I}_{ij}$ is the current before removal of L_{23}, $\dot{I}'_{ij}$ is the current after of L_{23}, and $\Delta\dot{I}_{ij}$ is the transferring component caused by the removal of L_{23}, a equivalent network where the L_{23} is replaced with a constant current source I_S (which current is equal in magnitude and opposite in direction before removal of the line L_{23}).

Knowledge of graph theory

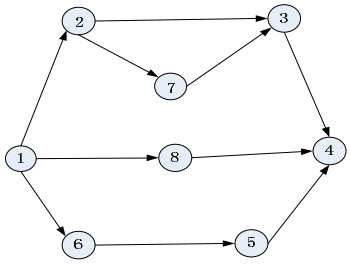

Fig.2 The weighted directed path

If physical characteristics of each component of the power system can be ignored and only research network topology counts, the power system can be abstracted into a graph, which can be expressed as $G(\mathrm{V},\mathrm{E})$, where V means node collections and E represents the line collections. When each line in the graph has a direction, the graph then becomes a directed one. As for a directed line: $E=\{\mathrm{e}_i \mid \mathrm{e}_i =< v_p, v_q >, v_p, \mathrm{v}_q \in \mathrm{V}\}$, G is a weighted graph, graph nodes represent the system buses, while lines represent transmission lines, transformers and other branches. If the edges in the graph not only represents the links between nodes, but also was given a numerical meanings such as length, price, reactance values, etc. The weighted directed path is shown in Fig. 2, the weighted directed adjacency moment can be got from a weighted directed graph, which is expressed as follows

$$a_{i-j} = \begin{cases} 0 & i = j \\ w_{i-j} & i \to j \\ \infty & \end{cases} \tag{2}$$

Where w_{i-j} represents weight between v_i and v_j, and the direction is determined from v_i to v_j, and ∞ means that there is no branch between v_i and v_j, or have a branch but the direction is from v_j to v_i. In this article the branch reactance represents value, G is a directed graph, and A is a N order square matrix.

Connect two nodes v_i and v_j in the graph , and directed edges could be obtained, which constitutes a path between v_i and v_j. The path does not contain any reverse branches, if a branch value e_{i-j} stands for length of the edge, then a path length is the path length of all edges and denoted

$$d(l) = \sum_{e_{i-j} \in l} w_{i-j} \tag{3}$$

Think that there are several paths Between two nodes, if the paths are arranged with length, just as $l_1, l_2, l_{3,} \cdots, l_k$,and which satisfied $d(l_1) \le d(l_2) \le \cdots \le d(l_k)$, they are called the shortest (1 short) path , the second short (2 short) paths, $\cdots$,the first K shortest paths. This article is to find out the K shortest path between two nodes, in order to quickly find the lines influenced mostly by the power flow transfer.

Transmission section search algorithm steps

According to the timely power flow information and the network parameters, the electricity network can be converted into a weighted topology.

(1) Eliminate the grounding branches and the power supply branches ,the power supply nodes and load nodes can be seen as the vertices, branch can be seen as edges and reactance value can be seen as a weight of the edges;

(2) Eliminate the suspension node, which can be expressed in Fig.3.

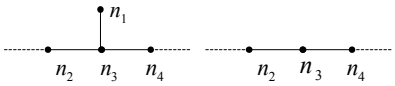

Fig.3 n_1 and n_3 can be merged

(3) Forming a weighted directed adjacency matrix A, if the weighted directed graph has n nodes, then the directed weighted adjacency matrix A is $n \times n$ non-symmetric matrix.

1）for all nodes $v_j(< v_s, v_j >\in E(G))$, $d(v_{j(1)}) = A(s, j)$, $pre(v_{j(1)}) = s$, $prs(v_{j(1)}) = 1$;

2）The end nodes is defined as v_e, if all $v_{e(m)} \in S$, then turn to 7）, if not ,turn to 4）;

3）for all nodes $v_{i(m)} \in \overline{S}$, calculate the $\min(d(v_{i(m)}))$, we call it $\min_{tep}$, which's $v_{i(m)}$ is $v_{p(q)}$,then $S = S \bigcup v_{p(q)}$;

4）for all nodes v_k （$< v_p, v_k >\in E(G)$）,

①if $d(v_{k(q)}) > \min_{tep} + A(p,k)$,then

$d(v_{k(K)}) = d(v_{k(K-1)})$, $d(v_{k(q+1)}) = d(v_{k(q)})$, $pre(v_{k(K)}) = pre(v_{k(K-1)})$,

$d(v_{k(q)}) = \min_{tep} + A(p,q)$, $pre(v_{k(q)}) = p$, $prs(v_{k(q)}) = q$

If not we use $q+1$ replace the q, turn to step1; Turn to step 4;

5）if for all nodes $v_{e(m)}, m = 1,2,\cdots,K$, $v_{e(m)} \in S$, then it has K shortest paths, turn 6）if not ,over;

6）Back from the end node to the source node to find the K shortest paths .

Simulation example

In order to verify the correctness of the algorithm, CEPRI36 node system is used for a simulation. Example 1: branch L_{19-21} simulation, part of the power flow of the transfer coefficients are shown in Table 1, and then use the algorithm searches the first K shortest paths, K value is 4,the search path information is shown in Table 2.

Tab.1 Distribution factors of part line to L_{19-21}

Line	power flow Transfer	Line	power flow Transfer
L_{15-12}	0.6871	L_{13-17}	0.2752
L_{14-15}	0.4308	L_{17-16}	0.2406
L_{19-14}	0.3963	L_{28-13}	0.2363
L_{22-21}	0.2867	L_{23-22}	0.1643
L_{27-28}	0.2824	L_{16-19}	0.1628
L_{12-27}	0.2752	L_{31-33}	0.1124

Tab.2 Path search data of L_{19-21} removal

path	paths	Transmission section
P1	21-16-17-13-28-27-12-15-14-19	L_{15-12}, L_{14-15}, L_{19-14}, L_{22-21}
P2	21-22-20-16-17-13-28-27-12-15-14-19	L_{12-27}, L_{13-17}, L_{28-13}
P3	21-22-23-9-10-11-25-26-12-15-14-19	
P4	21-22-9-10-11-25-26-12-15-14-19	

From the table, we can conclude that the branches which has larger power flow transfer coefficient are contained within the first six shortest path, and we can see that the branches with a larger distribution coefficient are concentrated in the first shortest paths L_{15-12}, L_{14-15}, L_{19-14}, L_{22-21}.

Epilogue

Reasons for the chain overload trip accident are summarized, and then characteristics of overloaded circuit after resection are analyzed. A new K shortest path algorithm based on K shortest paths is presented which is less complex. Multi-path search method avoids leakage election situations caused by only a single one line search. Finally, the simulation verified feasibility and rapidity of the algorithm.

References

[1] Larsson M, Rehtani C. Increase of Transfer Capability Through OPF-based Wide Area Control of FACTS[J]. Automation of Electric Power System, 2005, 29(16): 56-59

[2] Rasmussen J, Jrgensen P. Synchronized Phasor Measurements of a Power System Event in Eastern Denmark [J]. IEEE Transactions on Power Systems, 2006, 21(1): 278-284

[3] Chaudhuri B, Majumder R, Pal B. Wide-Area Measurement-Based Stabilizing Control of Power System Considering Signal Transmission Delay [J]. IEEE Trans on Power Systems, 2004, 19(4): 1971-1979

Advanced Materials Research Vols. 960-961 (2014) pp 790-795

doi:10.4028/www.scientific.net/AMR.960-961.790

Design and Implementation of a Rotary Inverted Pendulum Using Model-Based Design

Yunhao Pan[1, a], Pengfei Meng[1, b], Runzhou Ge[2, c], Zeyu Mao[2, d]

[1]Hongshen Honor College, Chongqing University, China

[2]College of Electrical Engineering, Chongqing University, China

[a]promisepan@gmail.com, [b]runzhouge@gmail.com, [c]mengpfcqu@gmail.com, [d]mao.mzy@gmail.com

Keywords: TMS320F28335, Rotary Inverted Pendulum, Double-loop PID control, Matlab Model-Based Design

Abstract. Aiming at the characteristic of nonlinear and natural unsteadiness in rotary inverted pendulum system. This kind of system uses the DSP TMS320F28335 of TI as the control and testing core of this system, adopts DC motor JGB37-3530 and motor drive L298, high precision potentiometer WDY35D4 as sample controller. Angle-to-resistance-to-voltage conversion is achieved by potentiometer, sensors export analog voltage to the first-order filter for filtering noise and transmit signal to the interior of TMS320F28335 and take ADC sample, then use digital filter algorithms to filter the signal again. Finally using double-loop PID control scheme to control motor precisely. Both DSP algorithm and program are implemented by Model-Based Design in Matlab, according to the process of model-simulation-code generation, this rotary inverted pendulum realizes the function of pendulum inverted and rotated. Experiments show this system has a stable and rapid transient process, possesses good stability and resisting disturbance.

Introduction

Inverted pendulum system is typical multi-variable, nonlinear, strong-coupling and instability naturally, as a typical control target, it has been subjected to many experts and scholars' concern [1]. Method and technology of control theory of inverted pendulum will serve as a significant role in processing of semiconductor and precision instrument, robotics, servocontrol field, control system of missile intercepts, control technology of aircraft docking [3]. The future for development and utilization is therefore bright. Generally, the analysis and calculation of inverted pendulum motion use physical feedback analysis and movement trace navigation by camera. The complex structure, higher requirements to the sensors and the disadvantages of time complexity are the main shortcomings of physical feedback analysis [3]. While the extremely complex structure, the highly design cost and the disadvantages in practical application are the main shortcomings of movement trace navigation by camera [3]. As for fuzzy control method, highly complex algorithm, lag of response time and bad simulation effect are it main shortcomings [2]. At present, many researches are aimed at the simulation control and researches on real control are most based on linear inverted pendulum. To avoid such advantages that stated above, we start from setting the physical model of Rotary Inverted Pendulum, and then design a control system with relatively low complexity and shorter response time aiming at the problem of balance control of inverted pendulum, which are based on conventional PID control of classical control theory and on linear quadratic regulator (LQR) of optimal control theory. Basing on the simulation test, we also develop experimental study on that system.

Model-Based Design is a front technology of the 21st century and with the help of that technology the development time and cost only has the tradition 1/5 to 1/2 about [13]. This technology has a main feature: the developers only have to care about the algorithm and test case so that they do not need to program or debug code which is done by computer automatically and the whole design is realizing on a uniformly virtual software platform. Therefore, we choose Matlab 2013a as our instrument of Model-Based Design. We link it with CCS which is a software developed by Texas Instruments to develop embedded software. Through Matlab, we also realize continuous test on code and generate code model after simulation.

Establishment of mathematical model

The Rotary system pendulum model, as shown in Fig.1, consists of a base 1, a stent 2, a DC motor 3, a rotary arm 4, an angular displacement sensor 5 and a vertical pendulum 6. The system measures real-time states of vertical pendulum via the angular displacement sensor and sends the states of position, angular velocity and angular acceleration of vertical pendulum to the main control chip. Main control chip adjusts the states of vertical pendulum and then keeps it standing upside down through controlling DC motor's current and torque.

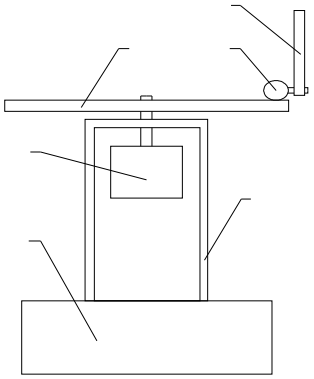

Fig. 1. Rotary Inverted Pendulum model

As shown in Fig.2, simple Rotary Inverted Pendulum consists of a rotary arm and a vertical pendulum. In Fig. 2, l_1 represents the length of rotary arm and l_2 represents the length of vertical arm. We choose counterclockwise direction as the reference direction. θ_1 is the angle of rotation of the rotary arm and θ_2 is the angle of rotation of the vertical pendulum in the plane perpendicular to the arm [12].

This system has 2 DOF motion, in which rotary arm can rotate flatly about z axis so that the rotary arm can make the pendulum into working state in which θ_2 is kept in a small range. We select a minimal length whose distance is l from hinge O and coordinates of this minimal length are

$$x = l_1 \cos\theta_1 - l \sin\theta_2 \sin\theta_1 \tag{1}$$

$$y = l_1 \sin\theta_1 + l \sin\theta_2 \cos\theta_1 \tag{2}$$

$$z = l \cos\theta_2 \tag{3}$$

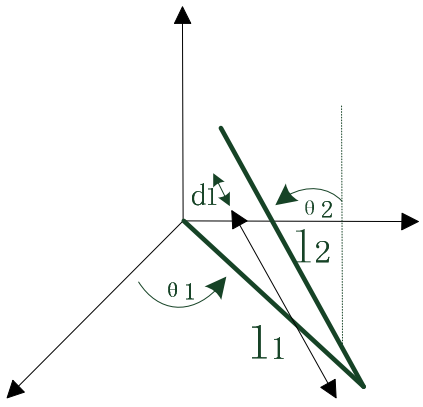

Fig. 2. Mathematical model of Rotary Inverted Pendulum

Suppose that the mass of the vertical pendulum is m_2 and kinetic energy of the pendulum is

$$T_{l_2} = \int_0^{l_2} dT = \frac{1}{6} m_2 [(\theta_1^2 - \theta_1^2 \cos^2\theta_2 + \theta_2^2) l_2^2 + 3 l_1 l_2 \theta_1 \theta_2 \cos\theta_2 + 3 l_1^2 \theta_1^2] \tag{4}$$

There is only kinetic energy on rotary arm and its kinetic energy is

$$T_{l_1} = \frac{1}{2} J_1 \omega_1^2 = \frac{1}{6} m_1 l_1^2 \theta_1^2 \tag{5}$$

The total kinetic energy of the system is

$$T = T_{l_1} + T_{l_2} \tag{6}$$

We select the plane of rotary arm as the reference plane of the zero of potential energy and the total potential energy which is also the potential energy of pendulum is

$$V = \frac{1}{2} m_2 g l_2 \cos\theta_2 \tag{7}$$

The Lagrange's operator is L=T-V. Generalized coordinates of the system are $q=\{\theta_1, \theta_2\}$ and there is no external force on generalized coordinate θ_2. Suppose that F_1 is generalized force and from Lagrange's equations we can get

$$\frac{d}{dt}\frac{\partial L}{\partial q_i} - \frac{\partial L}{\partial q_i} = F_i (i = 1, 2) \tag{8}$$

Thus we get the nonlinear mathematical model as follows:

$$M\ddot{q} + N = F_q \tag{9}$$

Where

$$M = \begin{bmatrix} (J_1 + m_1 l_1^2 + m_2 l_2^2 \sin^2\theta_2) & 2m_2 l_1 l_2 \cos\theta_2 \\ 2m_2 l_1 l_2 \cos\theta_2 & J_2 + m_2 l_2^2 \end{bmatrix} \tag{10}$$

$$N = \begin{bmatrix} -2m_2 l_1 l_2 \sin\theta_1 \theta_2^2 + 2m_2 l_2^2 \theta_2 \theta_1 \sin\theta_2 \cos\theta_2 \\ -m_2 l_2^2 \theta_1^2 \sin\theta_2 \cos\theta_2 - m_2 g l_2 \sin\theta_2 \end{bmatrix} \quad F_q = \begin{bmatrix} u \\ 0 \end{bmatrix} \tag{11}$$

J_1 is the rotational inertia of rotary arm when arm is rotating around Z axis as follows:

$$J_1 = \frac{1}{3} m_1 l_1^2 \tag{12}$$

J_2 is the rotational inertia of vertical pendulum when pendulum is rotating around hinge as follows:

$$J_2 = \frac{1}{3} m_2 l_2^2 \tag{13}$$

Double-loop PID control in inverted pendulum system and simulation by Matlab

After the establishment of the physical model, we can get the module chart of inverted pendulum system as follow in Fig. 3.

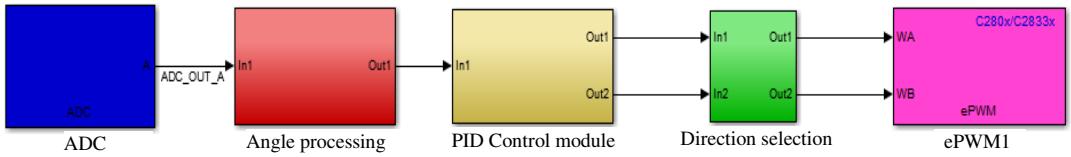

Fig. 3. The module chart of inverted pendulum system

We use double-loop PID control in PID Control module. The structure chart and inner structure chart of this system as shown in Fig. 4 and Fig. 5：

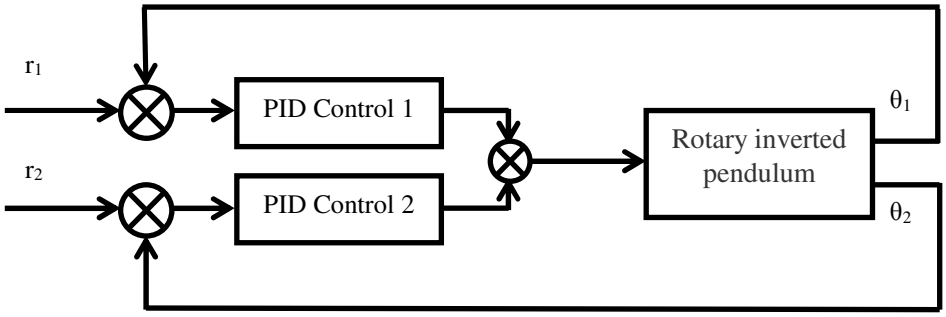

Fig. 4. Double-loop PID control

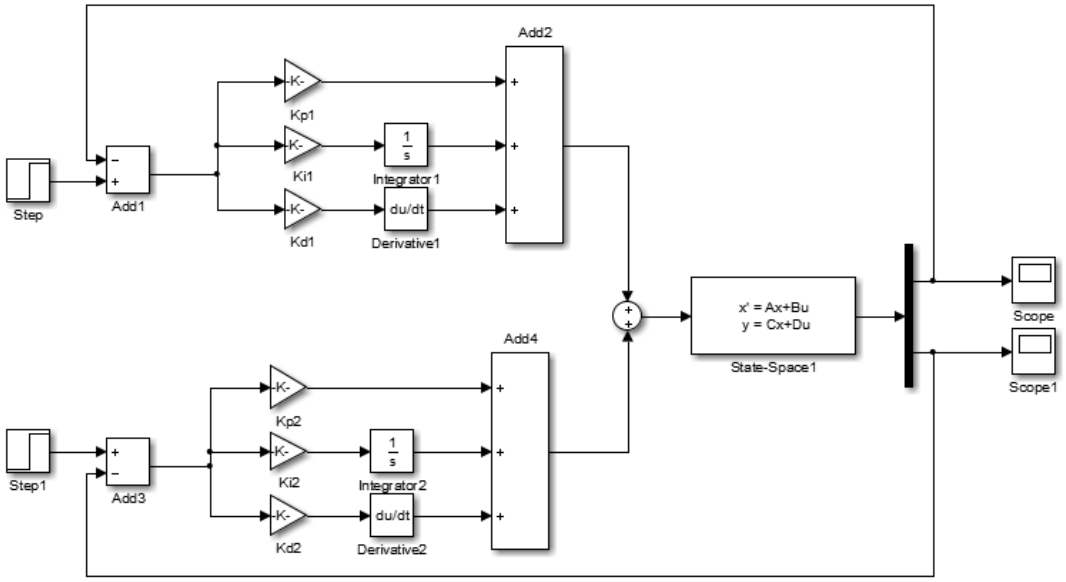

Fig. 5. Simulation of double-loop PID control by simulink

When a proper perturbation is given, by adjusting the parameters continuously, we can determine the parameters in the two PID controller in Table 1.

Table 1. The parameters in the two PID controller

	K_p	K_i	K_d
PID1	-90	-78	-63
PID2	220	50	45

The result of simulation can be seen in Fig. 6 and Fig. 7:

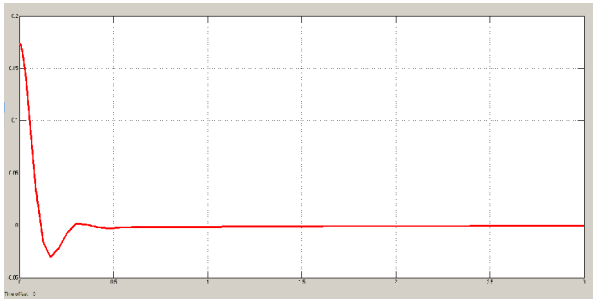

Fig. 6. Rotary arm

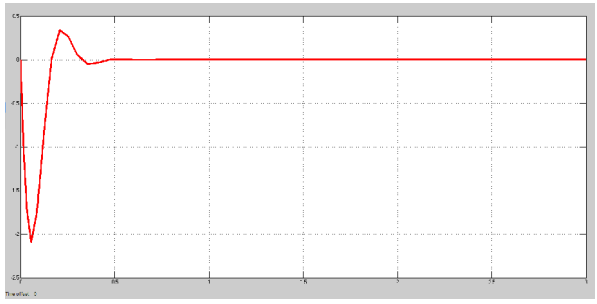

Fig. 7. Pendulum

Finally we make conclusion from those figures: double-loop PID control has basically achieved stabilization of radial arm and pendulum rod. Besides, we also find out that this inverted pendulum system has a low sensitivity to the parameters in PID controller, which means our parameters in PID controller are able to have a appropriate variation range.

Systematic design

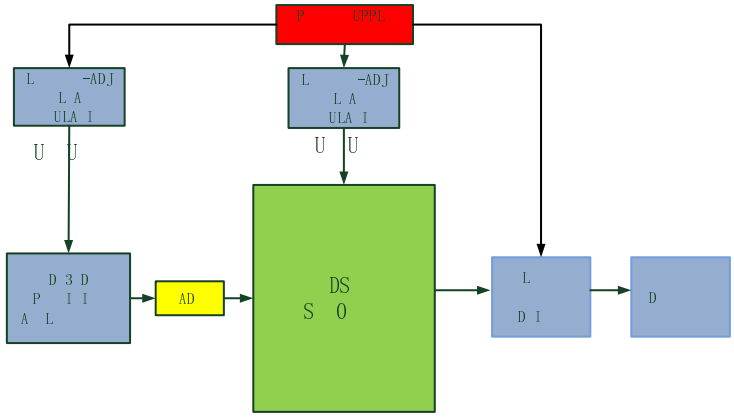

Fig. 8. System structure

We choose TMS320F28335 which is a DSP of Texas Instruments as our main chip of our system. TMS320F28335 has lots of advantages: it has a high computing power, many enhanced modules, many General-Purpose Input/Output ports, a 12-bit ADC with 16 input channels, as well as high freedom. And it can also realize code generation and code debugging with the help of CCSlink kit of Matlab, through which can we link Matlab with CCS. Model-Based Design can reduce the work of developers sharply because developers do not need to program laboriously.

We choose a DC motor as the driving motor and the model of motor is JGB37-3530. The voltage rating of the motor is 12V and its no-load speed is 531r/min. When the motor is running under rated load, its load current is 400mA and its torque is 0.00686 Nm. L298N which is a motor diver ship has many advantages, such as simplicity of its peripheral circuit, high reliability, capability of controlling speed and displacement of DC motors by software, and capability of being driven by DSP directly. We choose WDY35D4—angular displacement sensor of conductive plastics of which the resistance is 10K—as angular displacement sensor of vertical pendulum and we bond the senor to the pendulum tightly so that the axis of the sensor can rotate together with the pendulum without any slide. We should know that the sensor has one-to-one relationship between resistance and pendulum's position. By applying 3V electric voltages to the total resistance of the sensor, we can get voltage signal which is caused by the changing of resistance of the sensor and which is corresponding to the current position of the pendulum. As for power supply module, we choose LM2596S-ADJ which is a 3A step-down voltage regulator. The LM2596-ADJ is capable of driving a 3A load with excellent line and load regulation and of outputting adjustable voltages from 1.2V to 37V. LM2596S-ADJ has packaged a fixed-frequency oscillator and a voltage-reference regulator in it. Thus, using LM2596S-ADJ to build an efficient step-down circuit, we only need little peripheral devices. And yet the conversion efficiency is greater than 75%. We use ePWM module to control the DC motor precisely and test the encoder which is fixed with DC motor's axis to get the status information of the DC motor at the same time. The DC motor has many advantages, such as its stable operation, small vibration, and convenience to maintain and use. Besides those, the DC motor not only has a large range of revolving speed, but also has a high torque. System structure is shown in Fig. 8 and experimental device is shown in Fig. 9.

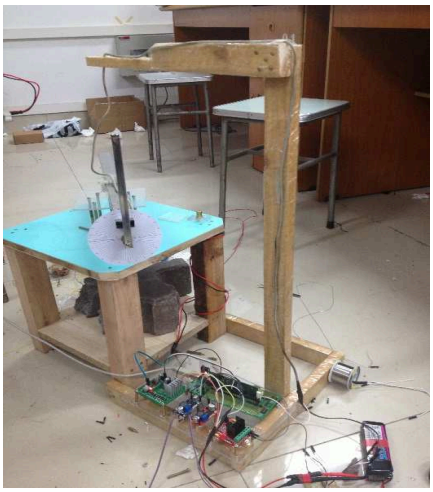

Fig. 9. Experimental device with pendulum standing vertically

Conclusion

After establishing simulation by Matlab, we use TMS320F28335 DSP controller and motor drive to exert control over this kind of rotary inverted pendulum. Besides, using high precision potentiometer WDY35D4 can adjust return signal of position, double-loop PID control can let pendulum rod achieve the function of inverted quickly. As a result, this kind of rotary inverted pendulum has a high ability to achieve inverted stably under partly interference of external environment.

References

[1] Mei H, He Z. Study on stability control for single link rotary inverted pendulum[C]//Mechanic Automation and Control Engineering (MACE), 2010 International Conference on. IEEE, 2010: 6127-6130.

[2] Xueli Y, Hanhong J. Control method study on a single inverted pendulum in simulation environment[J]. Measurement & Control Technology, 2005, 24(7): 37-39.

[3] Nan W. The Movement modeling and simulation of the scheme of angle movement controllmg of the simple inverted pendulum[J]. Journal of System simulation, 2003, 15(9): 1333-1336.

[4] Shuang C, Dongjun Z, Henghua W. Comparative study on three control methods of the single inverted-pendulum system[J]. Systems Engineering and Electronics, 2001, 23(11): 47-49.

[5] Xudong D, Ke X. Modeling and control simulation of single-rotational inverted pendulum[J]. Robot Technique and Application, 2002 (5): 43-46.

[6] Xianglin H, Lizhong G, Xinhe X. Swing up control of a circular rail single inverted pendulum[J]. Control and Decision, 2003, 18(4): 483-486.

[7] Ping Y, Chunmei X, Jingjing Z. PID Controller of inverted pendulum real-time control system[J]. Microcomputer Information, 2006, 22(19): 83-85.

[8] Gexiang Z, Zhongli L, Xiaohui B. Inverted pendulum system and research on automatical technique[J]. Journal of Southwest Institute of Technology, 2001, 16(3): 12-16.

[9] Eltohamy K G, Kuo C Y. Real time stabilisation of a triple link inverted pendulum using single control input[C]//Control Theory and Applications, IEE Proceedings-. IET, 1997, 144(5): 498-504.

[10] Furuta K, Kajiwara H, Kosuge K. Digital control of a double inverted pendulum on an inclined rail[J]. International Journal of control, 1980, 32(5): 907-924.

[11] Åström K J, Furuta K. Swinging up a pendulum by energy control[J]. Automatica, 2000, 36(2): 287-295.

[12] Al-Jodah A, Zargarzadeh H, Abbas M K. Experimental verification and comparison of different stabilizing controllers for a rotary inverted pendulum[C]//Control System, Computing and Engineering (ICCSCE), 2013 IEEE International Conference on. IEEE, 2013: 417-423.

[13] Jie L, Yubo Z. Model-Based Design–MSP430/F28027/F28335 DSP[M]. Beijing: National Defense Industry Press.2011.8

Advanced Materials Research Vols. 960-961 (2014) pp 796-800

doi:10.4028/www.scientific.net/AMR.960-961.796

The design of electronic weighing control system based on proteus

Rongxia Sun[1] Xingwang Feng[2] Xing Hao[3] Yingchang Zhou[4]

Shuonan Wang[5]

College of Electronic and Informational Engineering, Hebei University, Baoding 071002）

Key words: AT89C51MCU;A/D exchange;Sensor

Abstract: The control core of this design is MCU AT89C51,with the sensor MPX4115,it can complete the detection of weighting signal.Use the ADC0832 chip to achieve signal conversion, the input use a square 4*4 keyboard,the output display use the LCD LM4229.Use C Language Programing to achieve the modular design of software,use proteus simulation system to achieve the measure of weight of nine kinds of goods,The weighing range from 0.546Kg to 4.980Kg;Its resolution is 0.001Kg;This system has the function of calculating total price,storing single price,alarming when the goods overweights.

Introduction

To measure the weight of the object simply and easily，in this paper,we use proteus simulation method to design the software and hardware of electronic scale whose control core is AT89C51MCU.

Hardware system design

This design system use three modules to design the program of the electronic scale.They are data collection,human-computer interraction and minimum system.The system structure is shown in Figure 1.

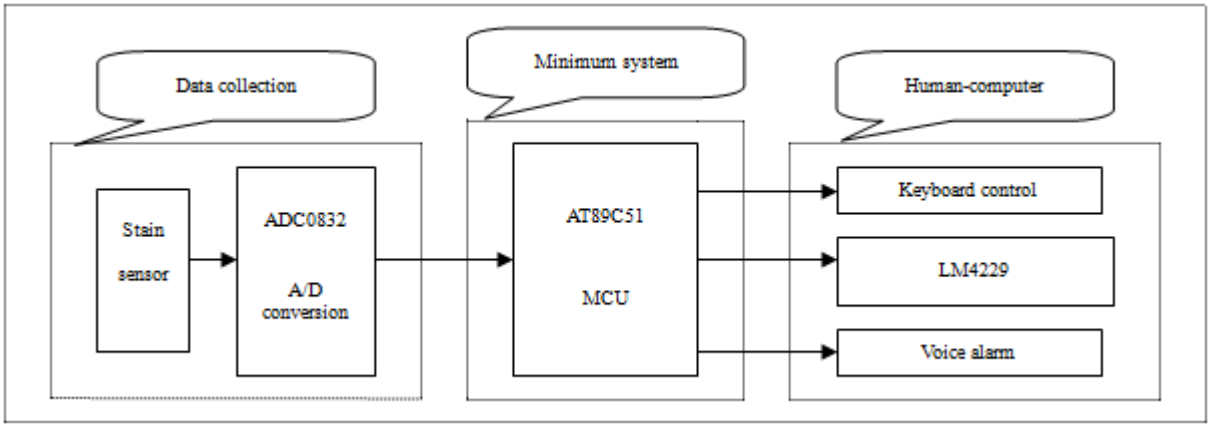

Figure 1 The electronic scale system block diagram

Working principle：firstly,use the sensor to detect the weight of the object and convert it into a voltage signal.Then use amplifier circuit enlarge linearly voltage precisely.Then convert the amplified analog voltage signal to digital signal through A/D converter circuit and take it to MCU.Then through MCU control LCD display and finally it shows the weight of the object in the LCD display.

Data collection

1.1.1 Data input detection

In the proteus simulation，The data input detection use the sensor MPX4115.Its pin 1 is connected with the pin CH0 of the chip ADC0832,input the signal which is detected by the sensor to the chip ADC0832,and it attach DC voltmeter.Pin 2 and pin 3 connect ground and power respectively.

1.1.2 Signal conversion

Use the chip ADC0832 to achieve A/D conversion.Its port VCC and GND connect ground and power respectively.The pin CS is the enable pin,the low is effective and it links the port P3.5.Pin CH0 links the pin 1 of the sensor,receive the signal which comes from sensor.Pin D0 and D1 link the port P3.7.Pin CLK links the port P3.6,receive the clock signal came from MCU.

1.2 MCU controlling

Use AT89C51MCU to achive weight control.The port P1 links keyboard,receives keyboard signals and makes corresponding control.The port P0 links LM4229 data terminal to output data.The port P2 links LM4229 control terminal and control its display.The port P3.0 links alarm circuit.It will control LS1 alarm when the weight is excessive.

Human-computer interaction

1.2.1 Display module

The display section use LM4229 in human-computer interaction module.The pin D0-D7 link the port P1,it receives data came from MCU.CE is the enable pin, the low is effective and it links the port P2.7.The pin RST links the port P2.3.V0 links the power.The C/D, RD, WR function as follows: WR=0, C/D=1 Write Command， WR=0, C/D=0 Write Data,RD=0, C/D=1 Read Command,RD=0, C/D=0 Read Data,the low is effective.FS1 controls the size of the display font. The effect of HALF is to stop vibration.

1.3.2 Keyboard Input

The keyboard input use the 4×4 matrix keyboard,its test is divided into two groups,one group is row line,one group is column line,the button is on the intersection of the row and column lines.The matrix keyboard need less I/O interfaces,One M×N matrix keyboard only need M+N pieces of test lines when it connects with host computer.

Software System Design

The software design part of the weighing system mainly includes main program,display subroutine,data acquisition subroutine,keyboard Subroutine and overload alarm subroutine.

2.1 The main program design

The design of the weighing system adopts modular design method,the main program is divided into several small modules,then draw the procedure flow charts of each module respectively, compile each module applications respectively according to the structure of the procedure flow charts,finally connect each module into a complete program.The procedure flow chart of the main program is shown in figure 2.

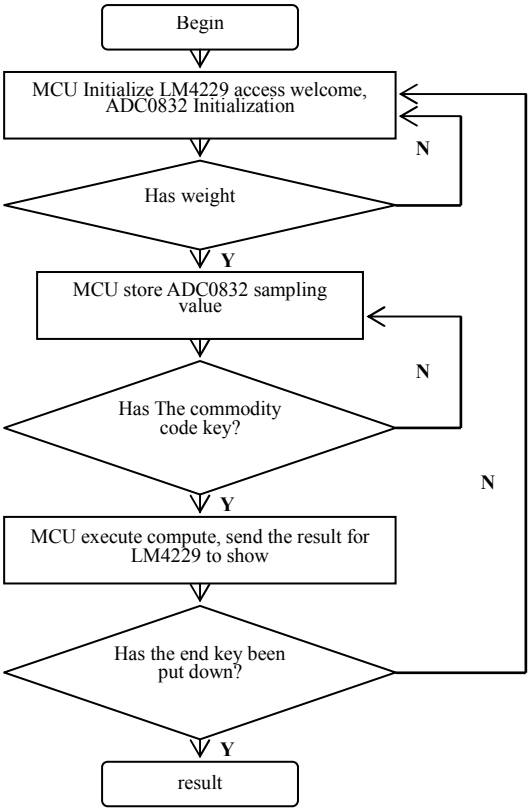

Figure2 The flow chart of the main program

2.2 The display subroutine design

Firstly, write control operation words in the display.Then write the initial row address, move the pointer to the left, until all the data is finished. The show subroutine flow chart is shown in Figure 3.

```
write_data(place&0xff); //Written to address high
write_data(place/256); //Written to address low
write_com(0x24); //Set address
write_com(0xb0); //Set data is automatically written
write_data(ASC_MSK[(c1-0x20)*16+k]);
write_com(0xb2); // Reset automaticly
```

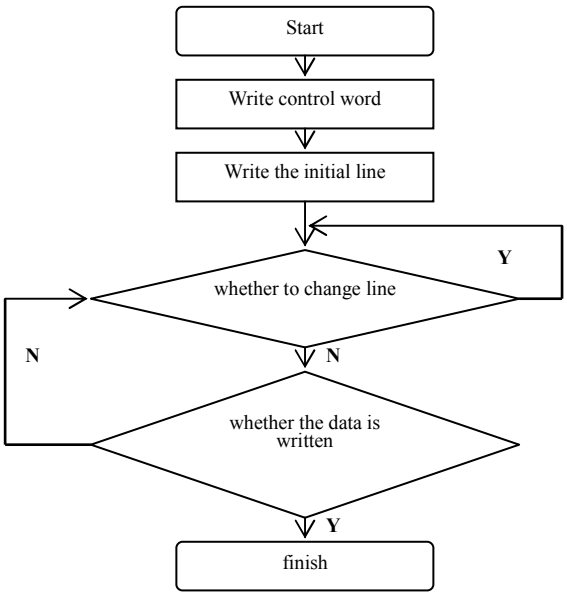

Figure 3 The display subroutine flow chart

2.3 The sampling subroutine design

MCU switchs on ADC0832 through swigging down CS and swigging up CLK , then it can take sample to the voltage signal . Once start up 8 CLK pulses ,DATA get a full 8bit data .At this point the MCU sends an interrupt request，the level of CS is set high, the level of CS is set low and the data is returned.Data collection section is finished by ADC0832 with the main four parts of initial, reading data, returning data and ending. After the ADC0832 initialized, convert the 0~7 analog signal of one channel to digital signal 00H-FFH.Then store it into specified unit in the internal RAM of the 8051.The sampling subroutine flow chart is shown in Figure 4.

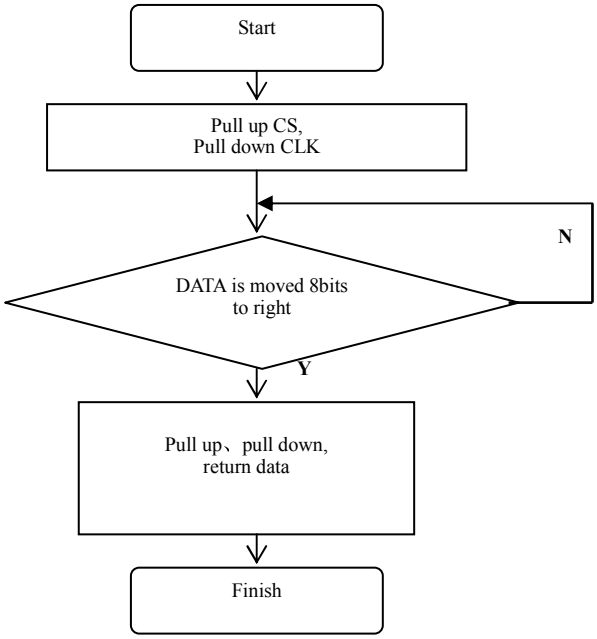

Figure 4 The sampling subroutine flow chart

2.4 The keyboard control subroutine flow chart

Adopt a 4 * 4 matrix keyboard,MCU queries timely.Firstly,The MCU transmits line scan code, and then scan the column, when a low level has been found in a column, the corresponding value is returned to the keyboard. If you did not find the description of the current line,then it means no key is pressed and line scan right one, proceeding column scanning.According to the corresponding key value, MCU can determine the pressed key. Analyzing button code in the program can be in the first place, and sends it to the corresponding numeric keypad representative memory cell according to the code, and then select functions or data processing. Keyboard control subroutine flowchart is shown in Figure 5.

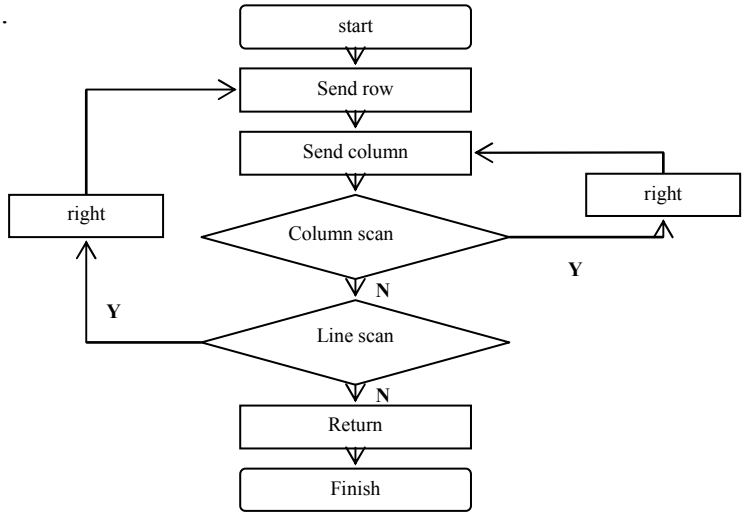

Figure 5 The keyboard control subroutine flow chart

The Simulation Experiment

The result of proteus simulation is shown in the figure 6.

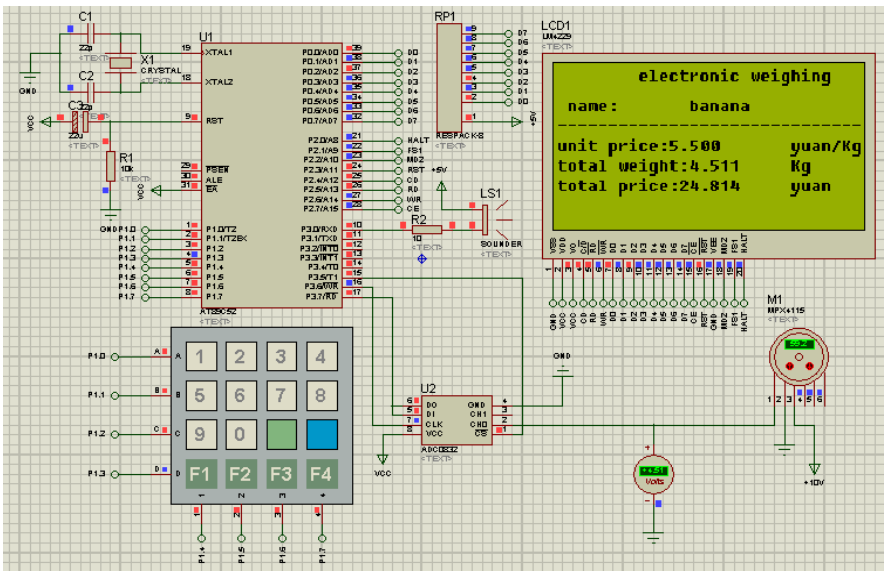

Figure 6 The proteus simulation

The electronic scale sets 16 keys,of which the "0"means cancel,and "1"～" 9 "reprsent the different prices of different comodities,each of them stands Banana, apple, orange, mango, pear, watermelon, orange, peach, sugar cane,and other keys can support the service of chosing the price of comodities.When the input voltage of sensor is +10V,the circuit will work normally, regulating the value of MPX4115 will change the weight of the comodities,and when the value of the voltmeter is greater than 4.980V, the alarm circuit will start to work.

Conclusion

The following functions have achieved though the simulation experiments weighing system: Weighing range 0.546Kg ~ 4.980Kg; Controlling the keyboard can display the unit price of banana, apple, orange, mango, pear, watermelon, orange, peach, sugar cane.Its resolution is 0.001Kg; When weight measured exceeds 4.980Kg, the alarm circuit would keep going until the weight dropped into 4.980kg.The total price of the product can calculate automatically according to the weight and unit price that 4 * 4 matrix keyboard selects.

[1]This project is funded by open project of Hebei University Lab.item number: 2012035

References:

[1] Xiaolei Wu;Feng Wang;Wei Han.The 24 bit A\D conversion data collection system. Electronic Design Engineering 2009. "In Chinese"

[2] Yu Zheng;Peng Guo.The Sensitivity characterization of Resistance strain sensor. Lanzhou Jiaotong University(2012-10). "In Chinese"

[3] Zicheng Zhu. The weighing system design of new MCU[D].2011 "In Chinese"

[4] Reginald C. Adiele, Don Stevens, Collins Kamunde.Features of cadmium and calcium uptake and toxicity in rainbow trout (Oncorhynchus mykiss) mitochondria[J].Toxicology in Vitro, 2012,9(26): 164~173

CHAPTER 7:

Smart Grid Technology

Advanced Materials Research Vols. 960-961 (2014) pp 803-807

doi:10.4028/www.scientific.net/AMR.960-961.803

Fuzzy Comprehensive Assessment of Smart Grid Maturity

WANG Ming-dong[1, a], SU Wen-xia[2,b], KONG Bin[1,c]

[1]School of Electrical Engineering, Zhengzhou University, Zhengzhou 450001, China;

[2] School of Information Engineering, Zhengzhou University, Zhengzhou 450001, China

[a]wangmingdong@zzu.edu.cn, [b]d894@163.com, [c]suwenxia@zzu.edu.cn

Keywords: Smart grid, Maturity, Fuzzy comprehensive assessment

Abstract: Smart grid must be evaluated correctly so that its development stage is determined and weak links, restrict factors in development are found. Based on it, the path from the stage to the next stage is planned for power enterprises. In view of the poor accuracy of conventional assessment methods, caused by subjective factors and uncertainty, the fuzzy comprehensive assessment method is applied to assess smart grid. Firstly, a smart grid assessment system is founded based of IBM's smart grid maturity model, and then method and procedure of fuzzy comprehensive assessment method are introduced. The study on an example shows that this approach is effective and feasible.

Introduction

Smart grid is the inevitable development trend of modern power grid and it has played an important role in response to the energy crisis and environmental degradation. Smart grid construction is a great and complex system engineering. The comprehensive and scientific assessment on smart grid have important theoretical significance and practical value for smart grid planning, construction, operation and management because by the assessment the difference from the goal and the direction needed to be readjusted can be identified.

Accurate assessment of power grid needs a correct evaluation system. Amounts of research have been done in this respect at home and abroad. The study focuses on assessment system founding in many research institutions, which shows that the assessment plays an important role in guiding and promoting of smart grid development[1]. Many smart grid assessment systems have been proposed which include IBM Smart Grid Maturity Model (SGMM)[2], Smart Grid Development Evaluation Index System of the U.S. Energy Department[3], the EU's Smart Grid Revenue Assessment System[4] and Resource-saving and Environment-friendly Grid Index system of Beijing State Power Economic Research Institute[5]. Due to different national circumstances and different power development situations, a variety of smart grid evaluation systems all have respective focus. As one of the earliest famous institutions to promote the smart grid development, IBM proposed SGMM in 2009 and the model has been applied to more than 50 power companies in the world.

Traditional scoring method is often used in smart grid evaluation. The evaluation procedure is simple, but the method is arbitrary and the results are inaccurate. In addition, some uncertainties in the evaluation process of the smart grid may also lead to big error between the evaluation results and the actual data. A dynamic evaluation method based system dynamics model for smart grid is proposed in reference [6]. Because its starting point is the smart grid investment, the rationality and validity has yet to be verified if other factors are considered. Fuzzy theory is one of the uncertain system theory and the fuzzy evaluation method has been widely used in many fields[7~9]. In order to decrease the error caused by subjectivity and uncertainty, the fuzzy evaluation method is employed to access smart grid in this research and the effectiveness of the method is proved through an instance.

Smart Grid Maturity Model

SGMM, proposed by IBM mainly, is an index system to measure the level of smart grid construction. By using the model, the current stage of smart grid can be determined, the difference from goals can be identified and the direction can be readjusted. The clear business model and the detailed plan can be guided to found for grid enterprises and the development path from this stage to the next maturity stage can be established.

A. Five Stages of Smart Grid Construction

According to planning, construction, operation and management of the power grid, SGMM divides smart grid development into five stages as follows.

Stage 1-Awareness and Starting: The stage is smart grid conceptual stage. Smart grid is paid attention and the grid enterprise has an aspiration to develop it. The smart grid is not yet planned but the construction of non-system business module may have been started.

Stage 2-Independent Business Investment: At least one of major business areas of smart grid began to be invested and constructed. The areas are electrical information collection, Demand Side Management (DSM) or the deployment of a distributed intelligent monitoring network which can improve the reliability of the power grid.

Stage 3-Business Integration: Many parts of smart grid began to be integrated with each other. The integration of two or more business areas is achieved, or the industry chain is upgraded.

Stage 4-Enterprises Optimization: Role and effectiveness of smart grid are understood profoundly. Enterprise-wide comprehensive observation and integrated control can be achieved across business, and then a new economic or business model may be founded.

Stage 5-Innovation and Promotion: Enterprises have the ability to take full advantage of the opportunities such as new business, operation and environment to grow and develop.

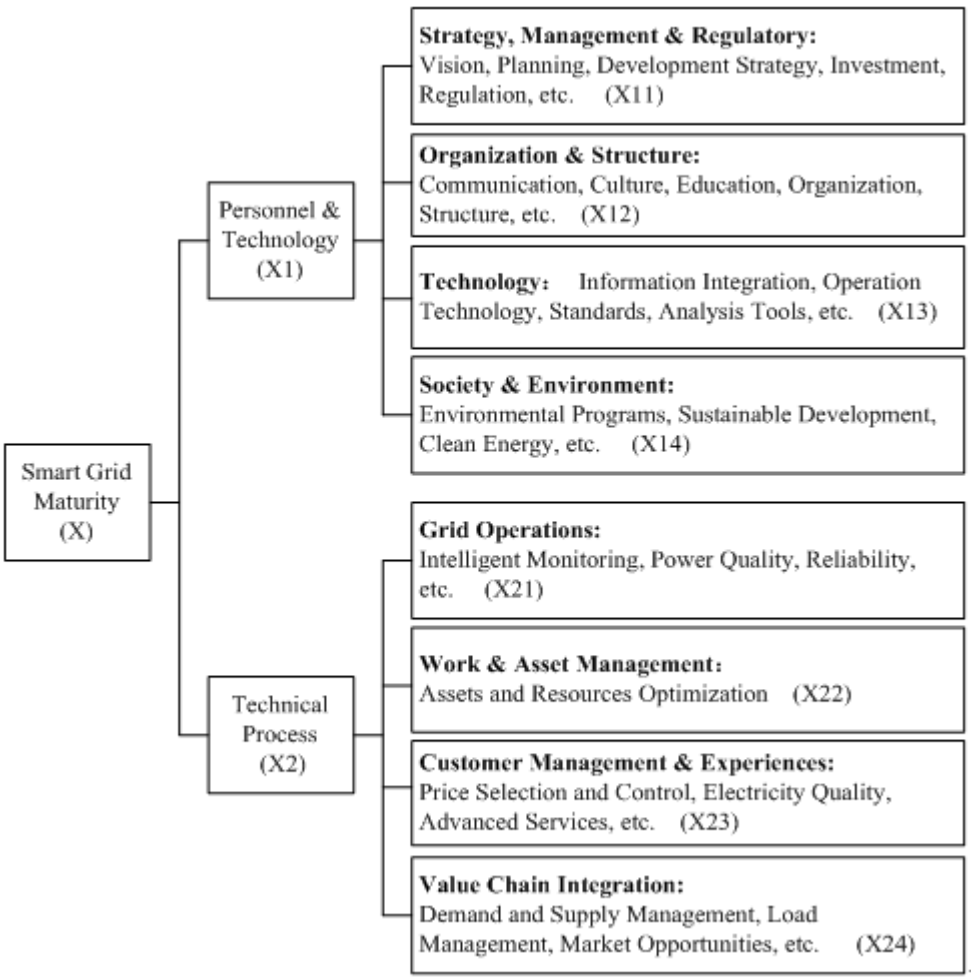

Fig.1 IBM smart grid maturity model

B. Smart Grid Maturity Assessment System

For SGMM, maturity of smart grid is analyzed comprehensively from two areas of Personnel & Technology and Operational Processes, eight dimensions (indexes) of Strategy & Regulatory, Organization & Structure, Technology, Society & Environment, Grid Operations, Work & Assets

Management, Customor Management & Experience, Value Chain Integration. The number of specific technical indexes of eight dimensions is up to 200 and the system is still improved. IBM Smart Grid Maturity Evaluation System is shown in Figure 1 (only some main technical indexes are given due to space constraints).

From Figure 1, it is shown that the system includes three levels of the total target level (first-level index), the criterion level (second-level index) and the sub-criteria level (third-level index), and the system is a comprehensive hierarchical structure evaluation model which is composed of one first-level index, two second-level indexes and eight third-level indexes.

1) Factors set of all levels

In the index system shown in Figure 1, the factors set of the first-level (the total target level) is {X}; the factors set of the second-level (the criterion level) is {X1,X2}; the factors set of the third-level (the sub-criterion level) is {X11,X12,X13,X14; X21,X22,X23,X24}.

2) Weights set of all factors

In general, the importance of various indexes in same level is different, and the weights of important indexes should be bigger. Weight values may be assigned directly according to experience, and can also solve by use of Analytic Hierarchy Process or entropy method. For the system shown in Figure 1, the weight set is expressed as following.

The criterion level: $A=\{a_1, a_2\}$

The sub-criterion level: $A_i=\{a_{i1}, a_{i2}, a_{i3}, a_{i4}\}$, $i=1,2$

Which, a_{ij} is the weight of No.j factor in the sub-criterion level, No.i factor in the criterion level. The weights satisfy the following equation.

$$\begin{cases} a_1 + a_2 = 1 \\ \sum_{j=1}^{4} a_{ij} = 1, \quad i = 1,2 \end{cases} \tag{1}$$

3) Remark set

Evaluation results of each factor can be represented with 5 stages of SGMM, and stage 1~5 are indicated v_1~v_5 respectively.

Fuzzy Comprehensive Assessment of Smart Grid Maturity

A. Determination of Fuzzy Assessment Set

An assessment team which consists of m experts evaluates eight third-level indexes by using fuzzy evaluation method. Suppose that the number of experts who believe the sub-criterion level factor X_{ij} as v_1~v_5 is p_1~p_5, then the fuzzy evaluation set of factor X_{ij} is following:

$$\begin{aligned} R_{ij} &= \left\{ \frac{p_1}{m}, \frac{p_2}{m}, \cdots, \frac{p_5}{m} \right\} \\ &= \left\{ r_{ij1}, r_{ij2}, \cdots, r_{ij5} \right\} \end{aligned} \tag{2}$$

the fuzzy evaluation set of criterion level factor X_i is following:

$$R_i = \begin{bmatrix} r_{i1.1} & r_{i1.2} & \cdots & r_{i1.5} \\ r_{i2.1} & r_{i2.2} & \cdots & r_{i2.5} \\ r_{i3.1} & r_{i3.2} & \cdots & r_{i3.5} \\ r_{i4.1} & r_{i4.2} & \cdots & r_{i4.5} \end{bmatrix} \tag{3}$$

B. The First-level Fuzzy Evaluating

All sub-criterion level factors for the No.i factor of criterion level are evaluated and the evaluating result (i.e., equation(3)) is the fuzzy matrix of the factors. The matrix is multiplied by weight matrix of all sub-criterion level factors, and then the membership degree matrix that the evaluation results belong to v_1~v_5 can be obtained.

$$B_i = \begin{bmatrix} b_{i1} & b_{i2} & \cdots & b_{i5} \end{bmatrix} = A_i \bullet R_i \tag{4}$$

Which, b_{ij} is the membership degree that the evaluating result of Criteria i (i=1,2) belongs to Stage j (i.e. v_j, j=1,2,…,5).

C. The second-level fuzzy evaluating

The result of the first-level evaluating (i.e. equation (4)) is multiplied by weight matrix of all criterion level factors, and then the membership degree matrix that the evaluation results belong to v_1~v_5 can be obtained.

$$B = \begin{bmatrix} b_1 & b_2 & \cdots & b_5 \end{bmatrix} = A \bullet B_i \tag{5}$$

Which, b_1~b_5 is the membership degree that the smart grid maturity belongs to v_1~v_5.

Case Study

Maturity of a regional power grid is analyzed. All indexes are assessed by 15 experts and the number of experts who believe that eight sub-criterion level factors belong to v_1~v_5 is shown in Table 1.

Table1 The assessment results for every factors

Index Number	Index Name	The number of votes for various stages				
		Stage 1	Stage 2	Stage3	Stage4	Stage5
X_{11}	Strategy, Management & Regulatory	5	5	4	1	0
X_{12}	Organization & Structure	4	6	3	2	0
X_{13}	Technology	6	5	4	0	0
X_{14}	Society & Environment	4	5	6	0	0
X_{21}	Grid Operations	5	5	4	1	0
X_{22}	Work & Assets Management	4	5	3	2	1
X_{23}	Customor Management & Experience	6	6	3	0	0
X_{24}	Value Chain Integration	5	4	5	1	0

Two factors of the criteria layer are weighed equally, that is A={0.5,0.5}. Each factor weight of the sub-criteria level is worked out by entropy method:

$$A_1=\{0.252,0.217,0.366,0.165\}$$
$$A_2=\{0.364,0.216,0.229,0.191\}$$

The fuzzy evaluation sets of criterion level factors X_1 and X_2 are determined according to equation (2), (3):

$$R_1 = \begin{bmatrix} 0.333 & 0.333 & 0.267 & 0.067 & 0 \\ 0.267 & 0.4 & 0.2 & 0.133 & 0 \\ 0.4 & 0.333 & 0.267 & 0 & 0 \\ 0.267 & 0.333 & 0.4 & 0 & 0 \end{bmatrix}$$

$$R_2 = \begin{bmatrix} 0.333 & 0.333 & 0.267 & 0.067 & 0 \\ 0.267 & 0.333 & 0.2 & 0.133 & 0.067 \\ 0.4 & 0.4 & 0.2 & 0 & 0 \\ 0.333 & 0.267 & 0.333 & 0.067 & 0 \end{bmatrix}$$

The sub-criteria layer factors are evaluated according to equation (4) and the membership matrixes that the evaluation results belong to v_1~v_5 are worked out:

$$B_1 = A_1 \bullet R_1 = [0.332, 0.348, 0.274, 0.046, 0]$$

$$B_2 = A_2 \bullet R_2 = [0.334, 0.336, 0.25, 0.066, 0.014]$$

The criteria layer factors are evaluated according to equation (5) and the membership matrix that the evaluation results belong to v_1~v_5 are worked out:

$$B = A \bullet B_i = [0.333, 0.342, 0.262, 0.056, 0.007]$$

Because $\max_{1\le i\le 5}\{b_i\} = b_2$, the maturity of the regional power grid is stage 2(v_2), that is the independent business investment stage according to the principle of maximum degree of membership. However, it is only in the initial stage of v_2 because of the very close between b_1 and b_2.

Conclusion

The subjectivity of traditional evaluation methods and some uncertain factors in the evaluation process make the evaluation results inaccurate. Based on IBM's smart grid maturity model, fuzzy comprehensive evaluation method is employed to evaluate Smart Grid Maturity. From the calculation and analysis results on an example, it is proved that the method is simple and the smart grid can be evaluated objectively, scientifically and accurately.

References

[1] SUN Qiang, GE Xu-bo, LIU Lin, et al, "Review of Smart Grid Comprehensive Assessment Systems", *Proceedings of the CSU-EPSA*, Vol: 23, No:6, pp.105-110, 2011.(in Chinese)

[2] IBM Corporation, "Smart Grid Method and Model", Beijing: IBM Corporation, 2010.

[3] U.S. Department of Energy, "Smart Grid System Report Annex A and B", New York: U.S. Department of Energy, 2009.

[4] European Smart Grids Technology Platform, "Strategic Deployment Document for Europe's Electricity Networks of the Future", Brussels: European Commission, 2008.

[5] State Power Economic Research Institute, "Resource-saving and Environment-friendly Grid Index system", Beijing: State Power Economic Research Institute, 2007.(in Chinese)

[6] HAN Dong, YAN Zheng, SONG Yi-qun, et al, "Dynamic Assessment Method for Smart Grid Based on System Dynamic", *Automation of Electric Power Systems*, Vol:36, No:3, pp.16-21, 2012. (in Chinese)

[7] JIN Zhi-ping, "Fuzzy Comprehensive Evaluation of Ways of Turbine's Quickly Cooled", *Turbine Technology*, Vol:46, No:4, pp.298-301, 2004. (in Chinese)

[8] SU Wen-xia, WANG Zhan-wei, "Fuzzy Integrated Evaluation for Operational Level of Laboratories", *Research and Exploration in Laboratory*, Vol:25, No:6, pp.722-724, 2006. (in Chinese)

[9] WANG Ming-dong, Su Wen-xia, "Fuzzy Integrated Evaluation for scheme of substation main electrical connections", *Electric Applications*, Vol:31, No:7, pp.54-56, 2012. (in Chinese)

Advanced Materials Research Vols. 960-961 (2014) pp 808-812

doi:10.4028/www.scientific.net/AMR.960-961.808

Modeling and Control of Solid Oxide Fuel Cell Generation System integrated in Microgrid

Wenqiang Xu[1, a], Zhiyong Dai[2, b], Qianggang Wang[3, c], Shu Pan[3, d *] and Niancheng Zhou[3, e]

[1]Guiyang Power Supply Bureau, Guiyang, 550002, Guizhou, China

[2]Planning center of Shenzhen Power Supply, 518001, Shenzhen China

[3]State Key Laboratory of Power Transmission Equipment & System Security and New Technology, Chongqing University, Chongqing, 400044, China

[a]123087948@qq.com, [b]123087948@qq.com, [c]qianggang1987@cqu.edu.cn, [d]panshu_19900904@126.com, [e]cee_nczhou@cqu.edu.cn

Keywords: Solid oxide fuel cell (SOFC), microgrid; mode transition, bi-directional DC-DC converter, droop control.

Abstract. This paper presents a control strategy of solid oxide fuel cell (SOFC) generation system integrated into microgrid. To enhance the dynamic response of SOFC, storage battery is paralleled via a DC bus, and the hysteretic control of bi-directional DC-DC converter is adopted. The common DC-AC inverter adopts an improved droop control. The active synchronization control is applied to ensure the smooth mode transition of microgrid. The simulation results show the dynamic performance of SOFC generation system in different operation modes.

Introduction

Microgrid is a controllable unit containing distributed generation (DG), load and energy storage device. Solid oxide fuel cell (SOFC) has been widely concerned due to the characteristic of leak-tightness, high efficient comprehensive utilization and long service life, etc [1]-[3]. The electrochemical characteristics and models of SOFC have been widely researched in many articles. References [4] and [5] study the model of grid-connected fuel cells, whereas the research about inverter control strategy is relatively simple. The proposed SOFC model in [6] doesn't consider about controlling the output power by adjusting the fuel flow. With the deepening research, the studies about fuel cells for distributed generation and its application in microgrid increase gradually. But in most of the recent studies, the control method of SOFC is taken to be simple and the fuel cells are usually combined with other micro source. Furthermore, there is less research about the transition of micro-grid operation modes.

The SOFC generation system model and its control strategy adapting to grid-connected, islanded and transition between the two modes is proposed in the paper. DC-AC inverter adopts loop control with synchronization control for reconnection to realize the grid-connection smoothly. At the DC bus side, the storage battery (BESS) is in parallel with fuel cells through the bi-directional DC-DC converter. The hysteretic charging and discharging control is adopted to improve the dynamic response of SOFC. At last, Simulation of microgrid containing SOFC generation system in PSCAD/ EMTDC is conducted to analyze the response characteristics of SOFC in different modes and mode transition.

Modeling of SOFC

The constant fuel utilization control mode of SOFC is adopted in this paper. To remain the fuel utilization unchanged, the load current feedback is used to control the rate of fuel flow which is inputted into the fuel processor, thus a link between load and fuel input quantity is built. The block diagram of SOFC is shown in Fig. 1.

The load current I_{fc} of SOFC is taken as feedback. After a first-order inertia link with time constant T_e (T_e=0.8s), representing the electric dynamic response time of fuel cells, stack current I of SOFC is produced. Through the first-order inertial link (T_f = 5 s), which stands for the fuel processor chemical reaction process, the hydrogen flow $q_{H_2}^{in}$ is generated by stack current I, fuel efficiency u_{opt} and hydrogen reaction coefficient K_r. Then obtain the oxygen flow $q_{O_2}^{in}$ according to the oxygen-hydrogen ratio r_{HO}, and the unit of $q_{H_2}^{in}$ and $q_{O_2}^{in}$ is mol/s. p_{H_2} , p_{O_2} , p_{H_2O} and are the pressure of hydrogen, oxygen and water vapor. E_0, η_{ohm}, η_{act} and η_{con} are separately battery unit standard electromotive force, ohmic polarization loss, activation polarization loss and concentration polarization loss.

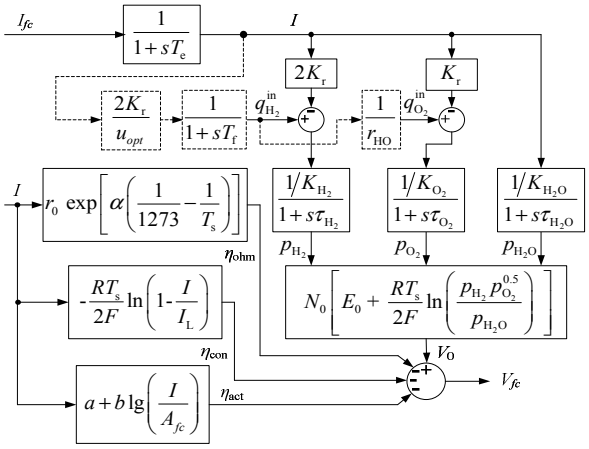

Fig. 1 SOFC dynamic model

Control of SOFC Generation System

The structure of SOFC generation system is shown in Fig. 2, which contains SOFC module, boost converter, DC-AC inverter, storage battery, bi-directional DC-DC converter.

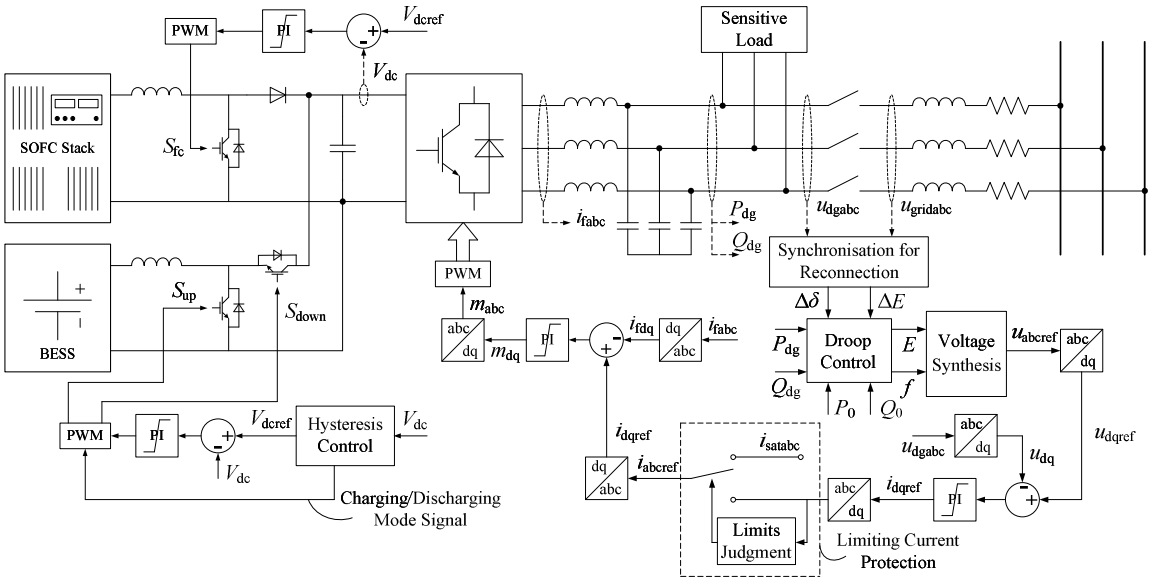

Fig. 2 Structure of SOFC generation system

According to the electrochemical properties of fuel cell, its output DC voltage has a large variation range with the change of load or temperature. Therefore, a boost conversion circuit is contacted at the DC output terminal of SOFC to satisfy the stable operation of inverter for the need of DC bus voltage. As the power regulative speed of fuel cells is slow, which cannot bear the rapid change of load, a storage battery is paralleled in the DC side of SOFC system, and bidirectional DC-DC converter is

used to realize the charging and discharging control of energy storage battery. SOFC module and storage battery are connected to the AC network through the common inverter, and its *LC* filter is used to filter high frequency harmonic.

Boost Converter Control. Based on the DC voltage deviation signal, the duty ratio can be obtained through PI link to control the operation of power switch S_{fc} through PWM modulation. Fig. 3 is the closed-loop transfer function block diagram of the boost converter, where the voltage feedback control function $G_c(s)$ uses PI hysteretic compensation and V_m is the amplitude of the sawtooth wave of PWM modulator.

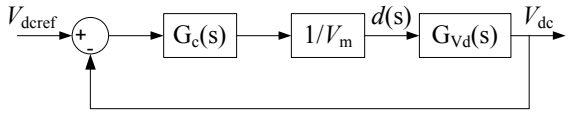

Fig. 3 Block diagram of the close-loop for the boost converter

Bi-directional DC-DC Converter Control. In order to improve the power regulation speed of SOFC system, storage batteries as quick response power source is paralleled with the SOFC in the DC bus side through bi-directional DC-DC converter to ensure the voltage of dc bus satisfy inverter. When the battery is charging, DC converter works in buck mode with power switch S_{up} shutting off and S_{down} working; otherwise, when discharging, the converter works in boost mode with power switch S_{dowm} shutting off and S_{up} working.

Voltage feedback PI control is also used in bi-directional DC-DC converter. The operating lifetime of storage battery has close relations with its charging/discharging frequency. The hysteretic charging/discharging control strategy of dc bus voltage is adopted in this study, which can reduce the redundancy charging/discharging times and extend the whole life of the system. Fig. 4 shows the block diagram of voltage hysteretic charging/discharging mode, where the time constant T_u of low-pass filtering link is 0.02s.

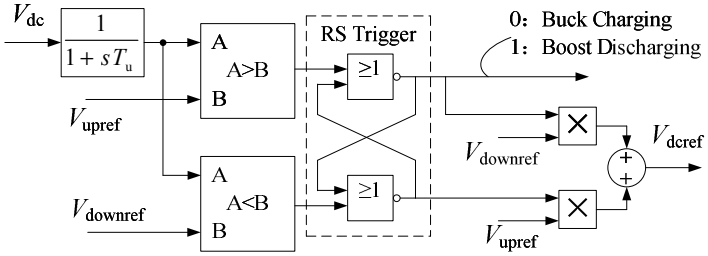

Fig. 4 Control block of voltage hysteretic charging/discharging strategy

DC-AC Inverter Control. To ensure the normal operation and smooth switch of the SOFC system under the grid-connection and islanded modes of microgrid, *E-f* droop control strategy is adopted for DC-AC inverter. By setting droop coefficient reasonably, the output voltage magnitude and frequency of SOFC system under different operation conditions is ensured change in a smaller range. The module of inverter control contains a synchronization block for safe reconnection between islanded microgrid and large power system illustrated in Fig. 2. Synchronization can by achieved by inputting the amplitude difference of voltage ΔE and phase difference $\Delta\delta$ on both sides of PCC node through synchronization link, and then being added to the output E and *f* of droop control link after the PI regulation.

Simulation Analysis

A microgrid model is established in the PSCAD/EMTDC shown as Fig. 5, where SOFC is the micro source and BESS as storage. The dynamic simulation in grid-connected mode, islanded mode and switch between the two modes is analyzed.

At *t*=6s, microgrid switches from grid-connected mode to islanded mode. In islanded mode, SOFC provides electrical energy and storage battery charges and discharges through bi-directional DC-DC converter automatically. Stable power supply of the local load is guaranteed by the coordinate of both of them. At *t*=7.7s, the voltage amplitude and phase of PCC of the microgrid side begin to be synchronized with those of the grid side. At *t*=8s, microgrid returns to the grid-connected mode.

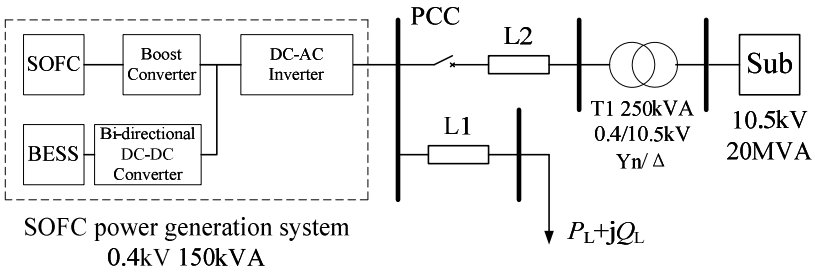

Fig. 5 Microgrid structure

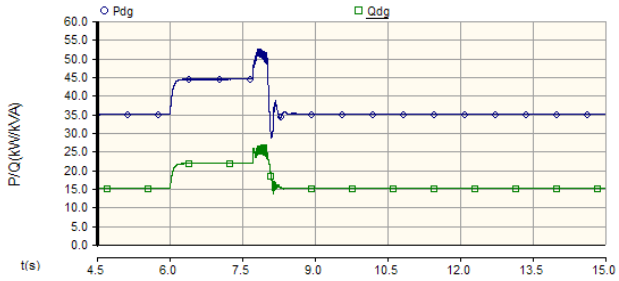

Fig. 6 Output power of generation system

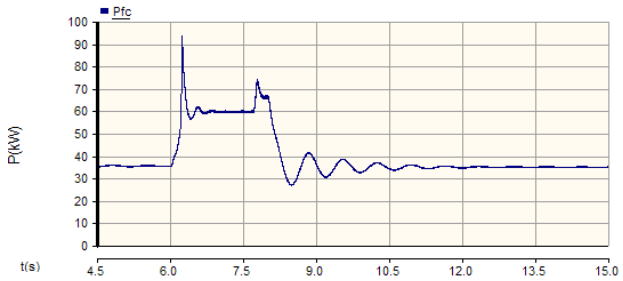

Fig. 7 Output active power of SOFC stack

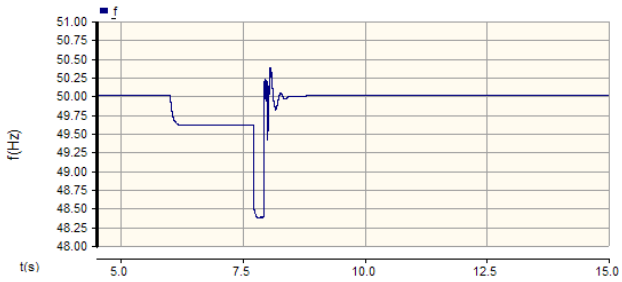

Fig. 8 Frequency response of the modes transition

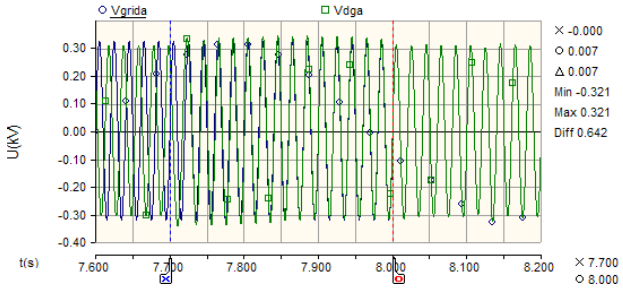

Fig. 9 Synchronization progress of voltage at PCC

Fig. 6 reflects the changes of output power of SOFC power generation system from *t*=6s when the system disconnects with the power grid to *t*=8s when it re-connects. Under grid-connected mode, the local load of microgrid absorbs part of the power from the large power grid. Therefore, after decoupling and turning to the islanded mode, the output active and reactive power of SOFC generation system increases thus the output power P_{fc} of SOFC battery stacks also increases, as shown in Fig. 7.

The variation of the system frequency when operation mode switches is shown in Fig. 8. Under the islanded mode, although losing supports from the large power grid, the islanded microgrid can operate stably with the help of the coordination of SOFC battery-stacks and storage battery. The microgrid frequency decreases slightly according to the active power increment and the droop coefficient. When reconnection synchronization, since the origin values of the phase angle deviation $\Delta\delta$ on both sides of the PCC is negative, the frequency drops for a short time at the beginning of synchronous process. After 0.3s synchronous process, the voltage phase and amplitude of PCC at microgrid side keeps consistent with those at the large power grid side, shown as Fig. 9. The output power of SOFC generation system comes back to the value before islanded after successful reconnection.

Conclusion

The SOFC model with constant fuel utilization rate control is proposed in this paper. Paralleled with SOFC at DC bus through bi-directional DC-DC converter, the storage battery makes up the shortcoming of the slow dynamic response speed of SOFC. The droop control mode adopted by DC-AC inverter ensures the microgrid containing SOFC operate stably under the islanded and grid-connected modes, and switch between the two modes. Simulation results show that the proposed SOFC generation model is able to reflect the electrochemical properties of SOFC correctly and its control strategy can ensure the stable operation of the microgrid in various operation conditions.

References

[1] A. M. Murshed, Biao Huang and K. Nandakumar: Journal of Power Sources. Vol. 163 (2007), p. 830

[2] D. J. Hall and R. G. Colclaser: IEEE Transactions on Energy Conversion. Vol. 14 (1999), p. 749.

[3] Tiejun Zhang and Gang Feng: IEEE Transactions on Fuzzy Systems. Vol. 17 (2009), p. 357.

[4] C. J. Hatziadoniu and A. A. Lobo: IEEE Transactions on Power Delivery. Vol. 17 (2002), p. 467

[5] Wang Li and Dongjing Lee: IEEE Transactions on Energy Conversion. Vol. 25 (2010), p. 128

[6] E. M. Stewart, R. Tumilty, J. Fletcher, etc: IEEE Transactions on Power systems. Vol. 25 (2010), p. 497

Advanced Materials Research Vols. 960-961 (2014) pp 813-817

doi:10.4028/www.scientific.net/AMR.960-961.813

Modeling and Testing of Hybrid Energy Microgrid with Wind Turbine and Photovoltaic Power

Yufeng Zhang[1, a], Wenqiang Xu[1, b], Zhiyong Dai[2, c], Qianggang Wang[3, d *] and Niancheng Zhou[3, e]

[1]Guiyang Power Supply Bureau, Guiyang, 550002, Guizhou, China

[2]Planning center of Shenzhen Power Supply, 518001, Shenzhen China

[3]State Key Laboratory of Power Transmission Equipment & System Security and New Technology, Chongqing University, Chongqing, 400044, China

[a]673293028@qq.com, [b]123087948@qq.com, [c]dzy13808800925@163.com, [d]qianggang1987@cqu.edu.cn, [e]cee_nczhou@cqu.edu.cn

Keywords: microgrid, microsource, wind energy, photovoltaic (PV), modeling.

Abstract. Modeling of the wind and PV hybrid microgrid is carried out by PSCAD/EMTDC. The model includes direct-drive wind power generator, Single-stage photovoltaic power generation system and storage battery. Simulate and analyze the operating characteristics of the microgrid running in grid-connected and islanding mode, which take into account the actual wind speed and light intensity. The simulation results show that the battery is able to regulate the voltage of the point of common coupling and smooth the power fluctuation of wind generator and PV generation system in the grid-connected mode. The microgrid can isolate itself from the grid in a rapid and seamless fashion when the battery adopting P/V and Q/f control strategy based on the droop characteristics.

Introduction

Microgrid is an independently controllable system which composed of distributed generators (DG), energy storage devices and load, and in situ to provide electricity and heat [1]. The microsource includes microturbines, fuel cell, PV panel, wind generator and so on. Among them, the wind and PV power generation are the fastest growing DG technologies in recent years. They have become the most potential for development of renewable energy technologies.

The reliability of wind and PV hybrid microgrid is higher than that of independent wind or PV microgrid due to they have a natural complementation, and it can also deploy the capacity of storage device rationally [2]. Reference [3] established a model for wind and PV hybrid grid system that connected with DC bus. Reference [4] designed a power control strategy for a wind, PV and fuel cell hybrid and independent system. But they all didn't consider whether the microgrid can isolate itself from the grid or not.

This paper proposes a control strategy of energy storage batteries running in grid-connected and islanding mode. The operating characteristics of the microgrid running in grid-connected and islanding mode have been verified and analyzed by the model of the wind and PV hybrid microgrid that carried out by PSCAD/EMTDC, which take into account the actual wind speed and light intensity.

Modeling of Wind and PV Hybrid Microgrid

The structure of wind and PV hybrid microgrid, which consists of PV array, wind power and storage battery, is shown in Fig. 1, In which, the direct-drive variable speed wind power generator access to the common frequency AC bus via the rectifier inverter device and transformer T1, the PV arrays incorporated into the distribution network by PV inverter, the energy storage device that uses batteries can achieve active power flow in both directions through the interface inverter.

PV Inverter Control. The voltage of the DC capacitor should be regulated properly, so that the PV array will be able to work at the maximum power point under different light intensity and ambient temperature, and therefore we need the maximum power point tracking (MPPT) module. In this paper, the incremental conductance method is used for tracking and calculations, reference [5] provided the specific algorithms and processes. The block diagram of PV inverrter control is shown in Fig. 2.

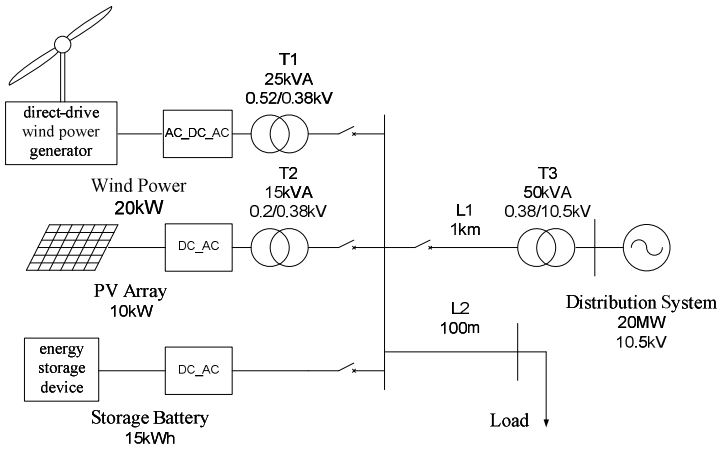

Fig. 1 Structure of wind and PV hybrid microgrid

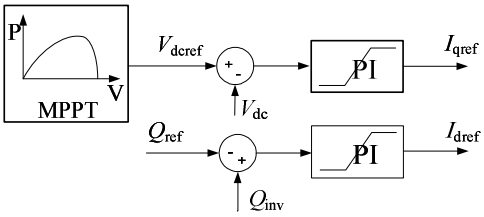

Fig. 2 Block diagram of PV inverter control

Wind Power Generator Converter Control. The wind power generator uses PQcontrol strategy. Track to the maximum output power $P_{\max}$ [6], its active power reference P_{ref} can be obtained in which the maximum use of renewable energy can be ensured. The active power reference P_{ref} can be written as,

$$P_{ref} = \eta \cdot P_{\max} = \eta \cdot \frac{1}{2} \cdot \rho \cdot A \cdot C_P^{\max} \cdot \frac{\omega_w^3}{\lambda_{OPT}^3} \tag{1}$$

where, ω_w is the rotational speed of the wind turbine, ρ is the air density of wind farms, A is the area of the blade. As a result of the fixed-pitch wind turbine, set the pitch angle β=0º, and then the optimum tip speed ratio λ_{OPT}=2.3875 [3] when wind energy utilization factor $C_p(\lambda_{OPT}) = C_{p\max}$.

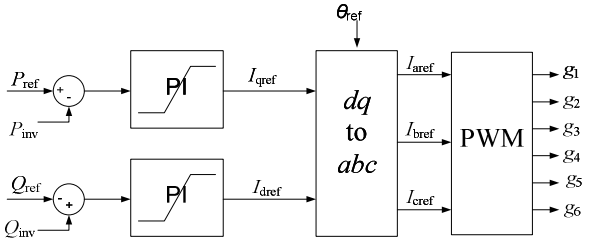

Fig. 3 Block diagram of wind power generator converter control

The block diagram of wind power generator converter control is shown in Fig. 3. The delivery, direct axis current reference I_{qref}, I_{dref}, which are generated by the active and reactive power error signal through the PI controller, and then through the Park transformation to get the three phase reference current I_{aref}, I_{bref}, I_{cref}, finally the voltage source inverter trigger signal can be obtained from

the PWM trigger pulse generator, as a result the decoupling control of the active and reactive power of wind turbine can be achieved.

Battery Inverter Control. To simplify the analysis, use DC voltage source as the battery model, and dodn't consider the charge-discharge process of the battery. Due to the frequency depends on the reactive power and voltage depends on the active power in the low voltage network, the battery adopting P/V and Q/f control strategy based on the droop characteristics. The block diagram of battery inverter control is shown in Fig. 4.

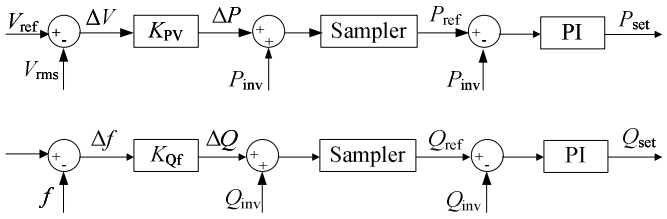

Fig. 4 Block diagram of battery inverter control

Note that, in order to maintain the stability of system frequency, we need to simulate the reference sine wave of phase voltage of distribution system as the input of the phase-locked loop (PLL) of battery inverter when it is running in islanding mode [7].

Simulation of Wind and PV Hybrid Microgrid

The structure of wind and PV hybrid microgrid is shown in Fig. 1. Assume that the local load is constant power load, and treat impedance elements as the models of lines L1 and L2 that the unit impedance parameter is 0.642+*j*0.083Ω/km. The specific parameters of hybrid microgrid are shown in Tab. 1 [3].

Tab. 1 Hybrid microgrid parameters

PV array			
Rated power [kW]	53	Rated power [kW]	20×9×53=9.54
The series number	20	Open circuit voltage [kV]	434
The parallel number	9	Short circuit current [kA]	26.8
Battery			
Capacity [kW·h]	15	Rated voltage[V]	400
Wind turbine		**Synchronous generator**	
Blade radius [m]	3.7	Rated voltage [kV]	0.52
Air concentrations [kg·m^{-3}]	1.225	Rated Capacity [kVA]	25
Rated speed [m·s^{-1}]	12	Motor poles	42
Cut-in speed [m·s^{-1}]	4	Rated frequency [Hz]	25.9
Cut-out speed [m·s^{-1}]	25	Inertia constant [s]	0.4

Grid-connected Mode. The active power of wind and PV work at the maximum power point and their constant reactive power reference is 0, the battery only participate in the regulation of active power, so the reactive power is also 0, and the local load is 15+*j*3kVA, in which the system is running in grid-connected mode.

The active and reactive power of microsources and DG in connection mode is shown in Fig. 5. From Fig. 5, the output active power of wind and PV fluctuate according to the time, the battery can adjust its output active power and maintain the stability of the load voltage when it adopting *P/V* and *Q/f* control strategy based on the droop characteristics, and its active power that injected in distribution system will change. Because of the reactive power of wind and PV microsource is 0, the reactive power that consumed by load, and transformer and line are all come from distribution system.

The RMS voltage and frequency of load bus are shown in Fig. 6. Due to the regulation of voltage of battery, the RMS of load bus voltage remains at 1.0 when the output active power of wind and PV change. The frequency of the load bus is around 50Hz, which varies range is ±0.06Hz.

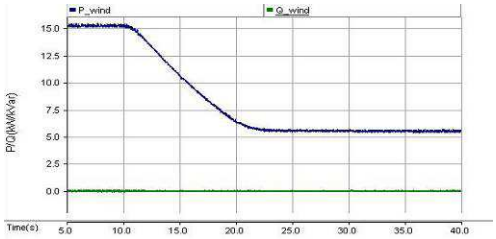

(a) Active and reactive power of Wind turbine

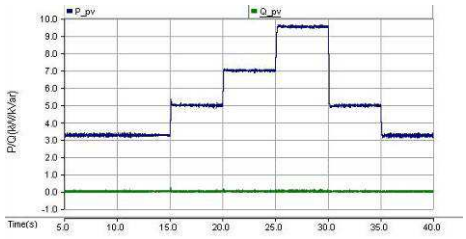

(b) Active and reactive power of PV

(c) Active and reactive power of battery

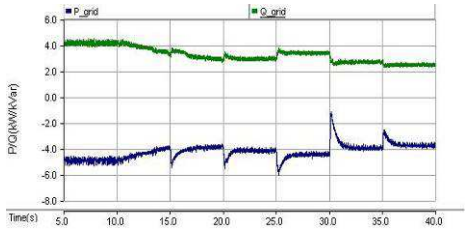

(d) Active and reactive power of distribution system

Fig. 5 Active and reactive power of distribution grid and microsources in connection mode

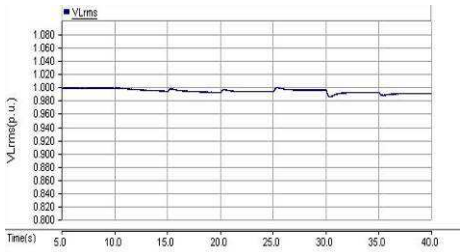

(a) RMS voltage of load bus

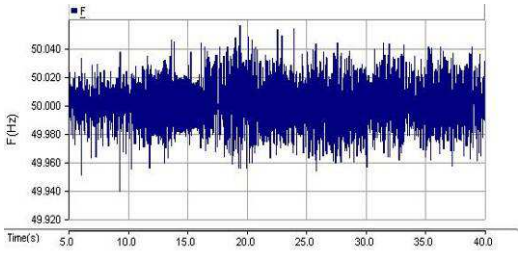

(b) Frequency of load bus

Fig. 6 Voltage and frequency of load bus in grid-connected mode

Islanding Mode. In order to maintain the stability of the voltage and frequency when the microgrid operated on islanding mode, the battery is regarded as the main control unit. Active and reactive power of distribution grid and microsources during islanding are shown in Fig. 7.

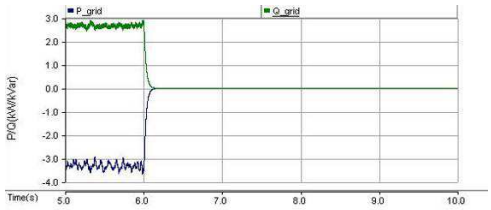

(a) Active and reactive power of distribution system

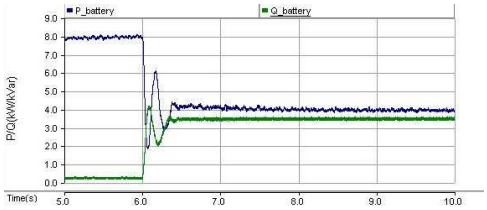

(b) Active and reactive power of battery

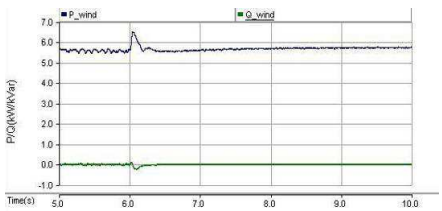

(c) Active and reactive power of Wind turbine

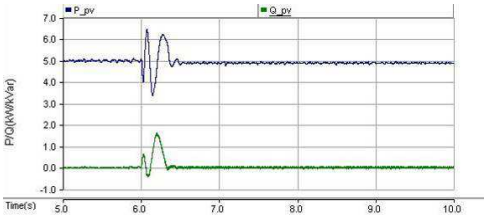

(d) Active and reactive power of PV

Fig. 7 Active and reactive power of distribution grid and microsources during islanding

Before switching into islanding mode, the local load is 15+*j*3kVA. And the figure shows that the output of the wind, PV and battery are 5.6kW, 5.0 kW and 8.0kW. After meeting the local load, the excess active power of the wind and PV hybrid microgrid will be injected into distribution system.

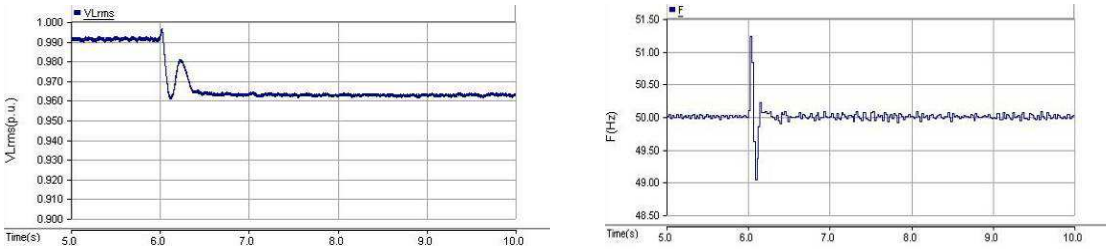

(a) Voltage of load bus (b) Frequency of load bus

Fig. 8 Voltage and frequency of load bus during islanding

Assuming the load remains unchanged when the microgrid switching into islanding mode at which t=6s. The regulation of voltage switch to voltage/frequency of battery. The battery adopt *P/V* and *Q/f* control strategy based on the droop characteristics and its active power is reduced to 4.0 kW. The RMS voltage and frequency of load bus are shown in Fig. 8 when it operated on islanding mode. According to the figure the per unit of voltage of load bus is about 0.96. During thd switching process, the maximum frequency of the load bus doesn't exceed 51.5Hz and the lowest was 49.0 Hz, eventually, after 0.5s, it stabilizes in the vicinity of 50 Hz. And its varies range is ±0.1Hz when the microgrid operated on islanding mode.

Conclusions

This paper established the model of the wind and PV hybrid microgrid by PSCAD/EMTDC. Simulate and analyze the operating characteristics of the microgrid running in grid-connected and islanding mode, which take into account the actual wind speed and light intensity. As is demonstrated in the test result, the battery is able to smooth the power fluctuation of wind generator and PV generation system in the grid-connected mode and the microgrid can isolate itself from the grid in a rapid and seamless fashion when the battery adopting *P/V* and *Q/f* control strategy based on the droop characteristics.

References

[1] Information on http:// certs.lbl.gov/pdf/50829-app.pdf

[2] Kellogg W D, Nehrir M H and Venkataramanan G: IEEE Transactions on Energy Conversion. vol. 13(1998), p. 70.

[3] Kim S K, Kim E S, Ahn J B: Proceedings of IEEE PES Transmission and Distribution Conference and Exhibition, Dallas, USA. vol. 5(2006), p.1202.

[4] Wang C, Nehrir M H: IEEE Transactions on Energy Conversion. vol. 23(2008), p.957.

[5] Hussein K H, Muta I, Hoshino T: IEE Proceedings on Generation Transmission and Distribution. vol. 142(1995), p. 59.

[6] Kim S K, Kim E S: IEEE Transactions on Energy Conversion. vol. 22(2007), p. 421.

[7] Laaksonen H, Saari P, Komulainen R: Proceedings of International Conference on Future Power Systems, Amsterdam, Holand. vol. 11(2005), p.1.

Advanced Materials Research Vols. 960-961 (2014) pp 818-822

doi:10.4028/www.scientific.net/AMR.960-961.818

An Improved Droop Control Strategy for Microgrid Inverter

Jihong Zhang[1, a], Zhiyong He[1,b], Chuan Li[1,c]

[1]Information Engineering School, UST Inner Mongolia, Baotou China

[a]zjh00318@163.com, [b]helong10013113@163.com, [c]lichuanmvp@163.com

Keywords: microgrid, inverter, droop control, feed-forward current.

Abstract. This paper proposes an improved droop control strategy. Its principle is an introduction of feed-forward bias currents based on conventional droop control, which makes the inverter work as grid supporting sources in the grid connected mode. When the main grid voltage suffers any variation, the inverter will respond with variation of active power and reactive power, so that it can restore the main grid voltage and frequency and increase stability of the main grid. In the island mode, the proposed control method can allocate load power proportionally as expected and make soft changes between island mode and grid connected mode. At last, verify the effectiveness and reasonableness of the proposed control strategy through simulation.

Introduction

With the energy and environmental issues increasingly severe, and users more demanding for power quality, distributed generation (DG) is paid widely attention for its advantages of renewable energy sources and little environmental pollution [1]. But a large number of distributed power generations connecting the grid can cause some problems, which can influence grid reliability and deteriorate power quality, like as voltage flicker generation or increase of harmonics [2]. In order to solve the difficulties and problems brought by distributed generations and improve the power quality, the concept of microgrid is proposed. The microgrid is considered to be composed of kinds of distributed generations, loads, monitoring and controlling devices, and can run in the island mode and the grid connected mode [4].

The control structures of microgrid are classified into three types, which are master-slave control, peer control and hierarchical control. Master-slave control and hierarchical control need communication between DGs, once the communication fault occurs, the microgrid system won't run normally. In the peer control structure there is no need communication between DGs, droop control based on local information is used as the control strategy[6]. The advantages of droop control are low cost and easy to expand while the disadvantage is easy to lose stability when the voltage and frequency of the main grid suffers any excursion from the normal value.

The improved droop control proposed by this paper is based on the conventional droop control. In the island mode, the proposed control method can allocate load power proportionally as expected, and make soft changes between island mode and grid connected mode. In the grid connected mode, when the main grid suffers any variation, the voltage and frequency will differ from the normal value, the control strategy will play a role in restoring the grid voltage and frequency to make sure the whole system is stable.

Study of control strategy

Droop control is widely used in uninterruptable power paralleled systems, its basic principle is in imitation of the external characteristics of synchronous generator to achieve uniform distribution for load power between inverters of DGs, this method uses the microgrid voltage and frequency as communication link, which make the inverters share load demand without physical connections, so this control method is used in peer control strategy for the control of inverters of DGs.

Conventional droop control can be expressed as:

$$f - f_n = -k_p(P - P_n). \quad (1)$$

$$U - U_n = -k_q(Q - Q_n). \quad (2)$$

Where K_p and K_q are respectively the droop characteristics constants, f is the output frequency of the inverter, U is the output voltage of the inverter, f_n and U_n are respectively the rated frequency and voltage of the inverter, P_n and Q_n are respectively the rated active power and reactive power of the inverter.

The main control scheme of the voltage source inverter in microgrid system used for both island mode and grid connected mode is presented in Fig.1. The outer voltage loop is used for determining the current reference used in inner current loop and stabilizing the voltage magnitude of AC side of the inverter. The inner current loop is used for current control in order to track current quickly. It can be observed that this method adds feed-forward bias currents I_{d_bias} and I_{q_bias}, compared to the conventional droop control. These bias currents can allow the inverter to make a grid supporting labor in the grid connected mode, which can make microgrid system more stable. In this case, the inverter works as inverse droop control that active power and reactive power is respectively a function of voltage and frequency. In the island mode, I_{d_bias} and I_{q_bias} are set to zero. Voltage reference of q-axis U_{qref} is set to zero for both working modes, while voltage reference of d-axis U_{dref} and frequency reference f_{ref} will depend on the working mode.

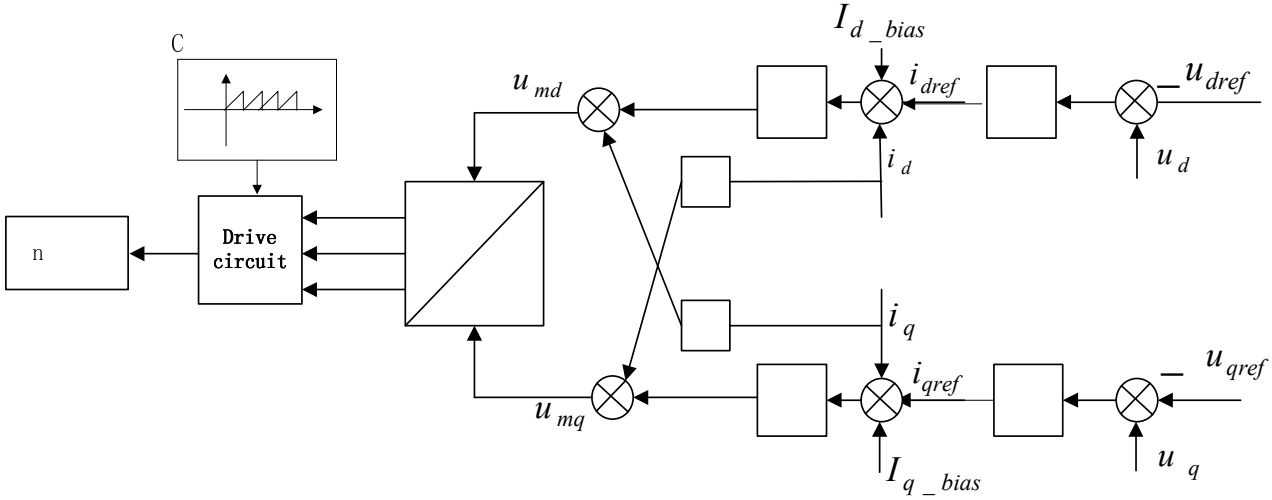

Fig.1 Main control scheme

The island mode

Firstly, voltage and frequency are obtained according to following formulas (3) and (4).

$$U_{dref} = U_0^* - K_p(Q - Q_n). \quad (3)$$

$$f_{ref} = f_0^* - K_q(P - P_n). \quad (4)$$

Where P and Q are the measured active power and reactive power, P_n and Q_n are the rated active power and reactive power, the droop characteristic slope K_p and K_q are calculated by following formulas (5) and (6).

$$K_p = \frac{U_{\max} - U_n}{Q_{\max} - Q_n}. \quad (5)$$

$$K_q = \frac{f_{\max} - f_n}{P_{\max} - P_n}. \quad (6)$$

Where $U_{\max}$ and $f_{\max}$ are the maximum allowable voltage and frequency, $P_{\max}$ and $Q_{\max}$ are the maximum output active power and reactive power of the inverter. The value of droop characteristic slope can affect the stability of system. Generally, the larger the droop characteristic slope is, the smaller the stability margin of system is.

In conventional droop control, U_0^* and f_0^* are respectively the rated active power and reactive power, which respectively equal to 380V and 50Hz.

This paper proposes the sync control based on conventional droop control when the microgrid system is in the island mode. In this case, U_0^* voltage and frequency f_0^* can be calculated by equations (7) and (8). This control method can regulate the difference of the voltage and frequency of the main and the microgrid before connecting the grid, which can make soft changes at the time of connection to the grid. So it should be used in the island mode before connecting the grid.

$$U_0^* = U_n - (K_{p1} + \frac{K_{i1}}{s})(U_g - U_{mg}) \text{ .} \tag{7}$$

$$f_0^* = f_n - (K_{p2} + \frac{K_{i2}}{s})(\theta_g - \theta_{mg}) \text{.} \tag{8}$$

Where U_g is the magnitude of the main grid voltage amplitude. U_{mg} is the magnitude of the microgrid voltage amplitude. θ_g is the phase of main grid voltage and θ_{mg} is the phase of microgrid voltage. K_{p1} and K_{p2} are the proportional parameters of PI controllers, K_{i1} and K_{i2} are the integral parameters of PI controllers, these parameters are very important since there exists a large displacement between voltages, high value of these parameters can result in a large variation of the microgrid frequency. So the output of PI controller must be limited in order to maintain the frequency within a specific band.

The grid connected mode

In this mode, the voltage reference U_{dref} and frequency reference f_{ref} mentioned in the main control scheme are equal to the values of the main grid voltage and frequency which are obtained by measuring. The feed-forward bias currents I_{d_bias} and I_{q_bias} are enabled, and the values are obtained according to equations (9) and (10).

$$I_{q\_bias} = \left[K_{p3} + \frac{K_{i4}}{s} \right] \left[(Q - Q_n) - \frac{1}{k_q}(U_d - U_n) \right]. \tag{9}$$

$$I_{d\_bias} = \left[K_{p4} + \frac{K_{i4}}{s} \right] \left[(P - P_n) - \frac{1}{k_p}(f - f_n) \right]. \tag{10}$$

In this case, the microgrid inverter works as grid supporting source, the active power and reactive power of the inverter vary with the value of the main grid voltage and frequency excursion from the normal value. If the value of the main grid voltage and frequency are 380V and 50Hz at the time of island connecting to the main grid, the inverter will output the rated active power and reactive power. If the voltage and frequency of the main grid suffer any variation, the reactive power and active power of the inverter will change because of this control method, so as to restore the main grid voltage and frequency to the normal value, as a function of supporting the main grid. This control method can mitigate the instability when the problems arise at connection to the main grid, otherwise, under those situations any attempt of connecting to the grid can lead to the loss of the main grid stability.

Simulation results

This section will present the simulation results to verify the proposed control scheme in PSCAD. The values of the main grid voltage and frequency are respectively 380V and 50Hz. At the beginning, the microgrid system is in island mode, the control method is conventional droop control, the load active power and reactive power are respectively 14kW and 0kVAr.

At 0.1s, activate the sync control. At 0.3s, change the load to 17kW and 4kVAr. At 0.5s, the microgrid and the main grid get connected. At 0.7s, the load power changes to 19.2kW and 6.5kVAr. At 0.9s, the value of grid voltage changes from 380V to 376V. The simulation results are presented in Fig.2.

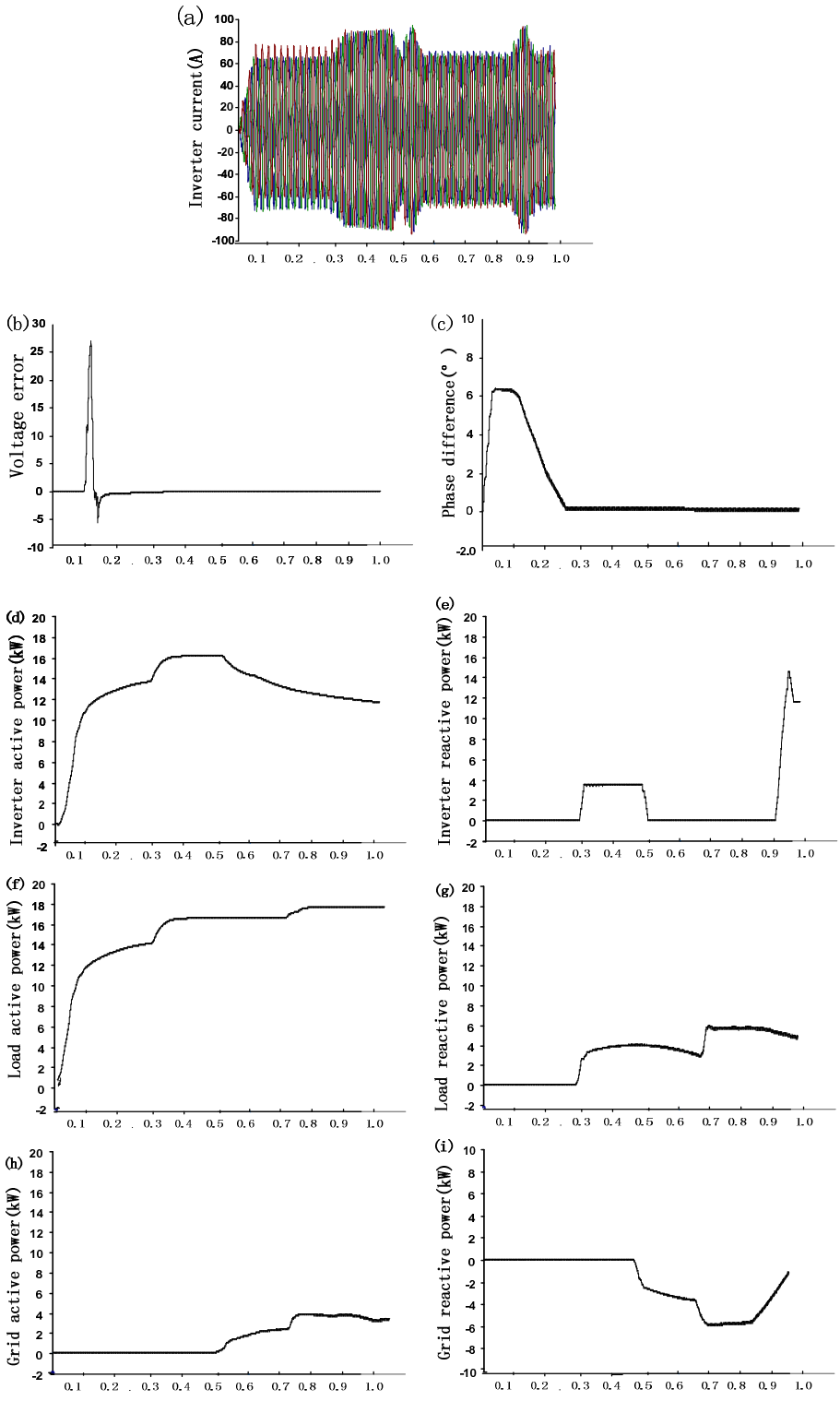

Fig.2. Simulation results

It can be observed that:
(1) At the beginning, no voltage errors but 6°phase shift between the microgrid and the main grid. After activate the sync control (0.1s), the phase shift is regulated to 0°before connection to the main grid. After the load change (0.3s), we can see that only the inverter changes correspondingly from Fig.2b-i.
(2) At the time of connection (0.5s), the main grid voltage and frequency are the rated values, 380V and 50HZ, and the inverter outputs the rated power, 14kW and 0kVAr, the other power 2kW and 4kVAr is provided by the main grid, observed in Fig.2d-i.
(3) After the load changes (0.7s), the main grid voltage and frequency are still the rated values, and the inverter still outputs the rated power, now the main grid increases the power to 5.2kW and 6.5kVAr, which is shown in Fig.2d-i.
(4) When the value of the main grid voltage decreases to 376V (0.9s), now the inverter working as a grid supporting source increases the reactive power to 12kVAr, of which 6.5kVAr is consumed by load, 5.5kVAr is absorbed by the main grid to restore the voltage, which can be observed in Fig.2d-i. Similarly, if the value of the main grid frequency increases, the active power of the inverter would decrease to restore the frequency. Under these situations, if the conventional droop is used, the power of inverter would not change, thus could result in instability of the main grid.

Conclusions

In the island mode, the sync control can regulate phase shift between the voltages of microgrid and the main grid and can make soft changes between island mode and grid connected mode. The main benefits of this control scheme arise when the microgrid is connected to the grid, when the main grid suffers any disturbance, the feed-forward bias currents will make the active power and reactive power of the inverter vary with the value of the main grid frequency and voltage excursion from the rated value, which make a grid supporting labor and increase the stability of the microgird system.

Acknowledgements

This work was financially supported by Inner Mongolia Department of Education Science and Technology Research Project (NJZY14170).

References

[1] F. Bastiao, P. Cruz, R. Fiteiro, Impact of distributed generation on distributionnetworks, in: 2008 5th International conference on the European electricitymarket, vols. 1 and 2, 2008, pp. 315–320.
[2] N. Hatziargyriou, H. Asano, R. Iravani, C. Marnay, Microgrids, IEEE Power &Energy Magazine 5 (4) (2007) 78–94.
[3] R.A. Walling, R. Saint, R.C. Dugan, J. Burke, L.A. Kojovic, Summary of distributedresources impact on power delivery systems, IEEE Transactions on Power Delivery23 (3) (2008) 1636–1644.
[4] KIM J,JEON J,JIM S.Cooperative control strategy of energy storagy system and microsources stabilizing the microgrid during islanded operation[J].IEEE TRANS.POWER ELCTRON.,2010,25(12):3037-3048.
[5] KANCHEV H,LU D. Energy management and operational planning of a microgrid with a PV-based active generator for smart grid application[J].IEEE TRAN. POWER ELCTRON.,2011 58(10):4583-4592.
[6] CHEN C,DUAN S,CAI T.Smart nergy management system for optimal microgrid economic operation[J].IET Renew.Power Gener.,2011,5(3):258-267.
[7] European research project micro grids. EB/OL. (2008)
[8] CHEN C,DUAN S,CAI T.Smart nergy management system for optimal microgrid economic operation[J].IET Renew.Power Gener.,2011,5(3):258-267.

Advanced Materials Research Vols. 960-961 (2014) pp 823-827

doi:10.4028/www.scientific.net/AMR.960-961.823

Smart Metering for Applications

Ying Pan [1, a *], Bo Jiang [2,b]

[1]Harbin University Engineering Institute Harbin ,China

[2]Harbin University Engineering Institute Harbin, China

[a]64271449@qq.com, [b]623013565@qq.com

Keywords: smart meter; remote monitoring; distribution grid; power industry; energy efficiency.

Abstract. As an important part of Smart Grid, smart metering attracts more and more attention all over the world. It is the way for energy consumer to sense the benefit of smart grid directly. Smart meter is an advanced energy meter that measures consumption of electrical energy providing additional information compared to a conventional energy meter. This paper discusses various applications and technologies that can be integrated with a smart meter. Smart meters can be used not only from the supply side monitoring but also for the demand side management as well. It plays an important role to monitor the performance and the energy usage of the grid loadings and power quality. In addition, This paper gives a comprehensive view on the benefit of smart metering in power network such as energy efficiency improvement.

Introduction

Nowadays, Smart Grid and Smart Metering are both the hot topics [1-3]. They are driven by the climate change and the reduction of carbon emission. Smart meter is an advanced energy meter that measures the energy consumption of a consumer and provides added information to the utility company compared to a regular energy meter. Smart meters can read real-time energy consumption information including the values of voltage, phase angle and the frequency and securely communicates the data. The ability of smart meters for bidirectional communication of data enables the ability to collect information regarding the electricity fed back to the power grid from customer premises.

Smart meters can be used to monitor and also to control all home appliances and devices at the customer's premises. They can also collect diagnostic information about the distribution grid, home appliances, and can communicate with other meters in their reach. They can measure electricity consumption from the grid, support decentralized generation sources and energy storage devices, and bill the customer accordingly. Data collected by smart meters is a combination of parameters such as a unique meter identifier, timestamp of the data, and electricity consumption values. Smart meters can be programmed such that, only power consumed from the utility grid is billed while the power consumed from the distributed generation sources or storage devices owned by the customers are not billed.

Remote Monitoring

By using smart meter and basic software for monitoring the low voltage grid, energy supplier can monitor their grid easily and find the place of illegal energy usage in their grid.

A. History detection of illegal electricity usage

In October 2004 Hakki cavdar suggest a new method for detection of illegal usage based on automatic meter reading. First we talk about his hypothesis to describe better of his new method. He assume that illegal usage of electricity may be happened in following ways [4].

1) Using the mechanical objects: A subscriber can use some mechanical objects to prevent the revolution of a meter, so the disk speed is reduced and the recorded energy is also reduced.

2) Using a fixed magnet: A subscriber can use a fixed magnet to change the electromagnetic field of the current coils. As we know, the mechanical energy meter is based on the electromagnetic field.

3) Using the external phase before meter terminals: This method gives subscribers free energy without any record.

4) Switching the energy cables at the meter connector box: In this way, the current does not pass through the current coil of the meter, so the meter does not record the energy consumption.

As Cavdar said first two methods are valid for mechanical meter and in digital meter subscriber cants use energy in illegal way, but the last two methods are valid for both mechanical and digital energy meters. The proposed system for detection of illegal usage of electricity is shown in fig. 1 power line carrier signal can transfer only in low voltage side of distribution transformer, and PLC signal's that blocked in transformer cant' pass it, so this topology must be repeated for each transformer. In his method each energy meter is equipped with PLC modems and digital energy meter IC. PLC modem must be send and receive data via power line by modulating or demodulating data over or from carrier frequency that travel over power line 220V signal, PLC signaling must be in CENELEC or FCC standards, EN50065-1 is formed by CENELEC, and frequency bands and signaling level for each usage is shown. [5]

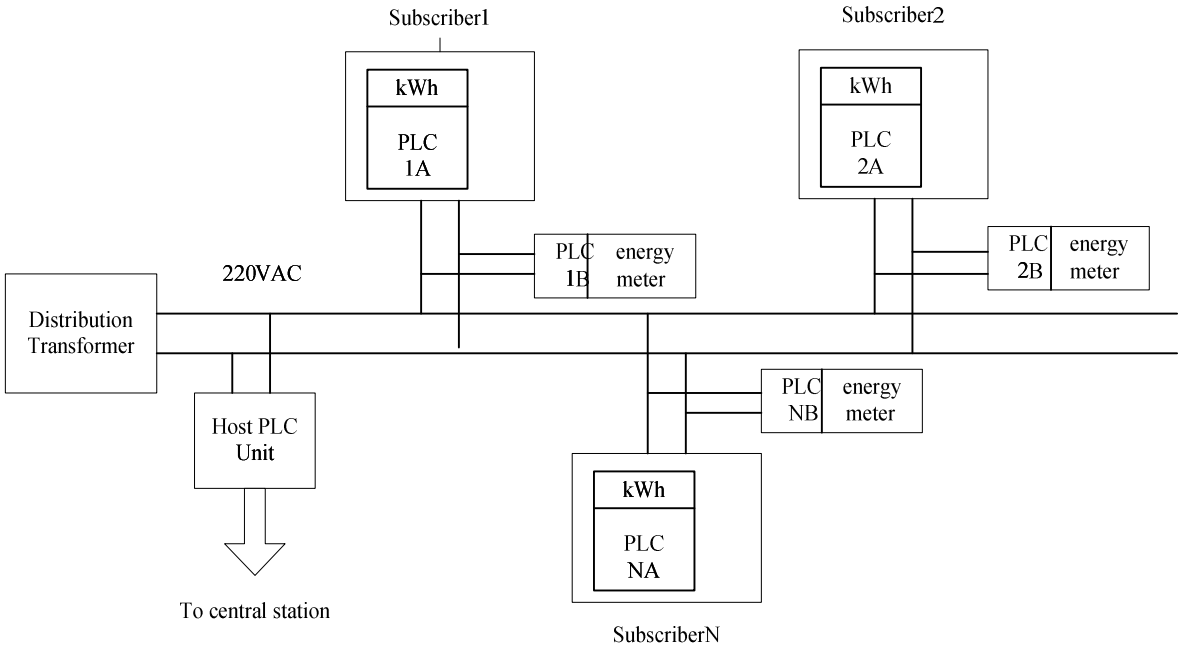

Figure 1. Cavdar's method for illegal usage of electricity.

In many cases, in which some one using extra cable before mechanical part terminal, if we assume that the digital unit be before this illegal connection his method can show the illegal connection, but in many cases and many countries such India the illegal node in many cases connect directly to power line of street and the load feed directly from main power line without any energy meter and any record of energy consumption data. From a reality point cavdar's method is only valid for detecting illegal usage of electricity in one low voltage grid, but for showing the place of illegal connection this method in many cases has now usage, in this effort we want to introduce new way for finding a place of illegal electricity usage based on smart metering.

B. New method for finding an illegal connection

The new method that we want to describe is based on smart metering.In fig. 2 the basic block diagram of smart meter is shown, as you see in fig. 2. this kind of energy meter has more ability than just automatic meter reading, one unit of smart meter act as traditional AMR, this unit measure energy consumption based on mechanical measuring or digital measuring. In mechanical kind measurement is based on disk and electromagnetic field. In mechanical AMR an optical sensor use for detection of disk movement, this sensor send digital pulse to microcontroller unit, and a counter

in microcontroller of energy meter counts disk routing, by counting the disk routing system can measure energy consumption. In digital AMR the energy meter IC such ade7751 calculates energy consumption based on voltage and current data that received from current and voltage transformer. Relay is another part of smart meter, by using this unit energy suppliers can turn on or off energy meter from distance without any physical attempting, the control command send from energy supplier via power line carrier signal.

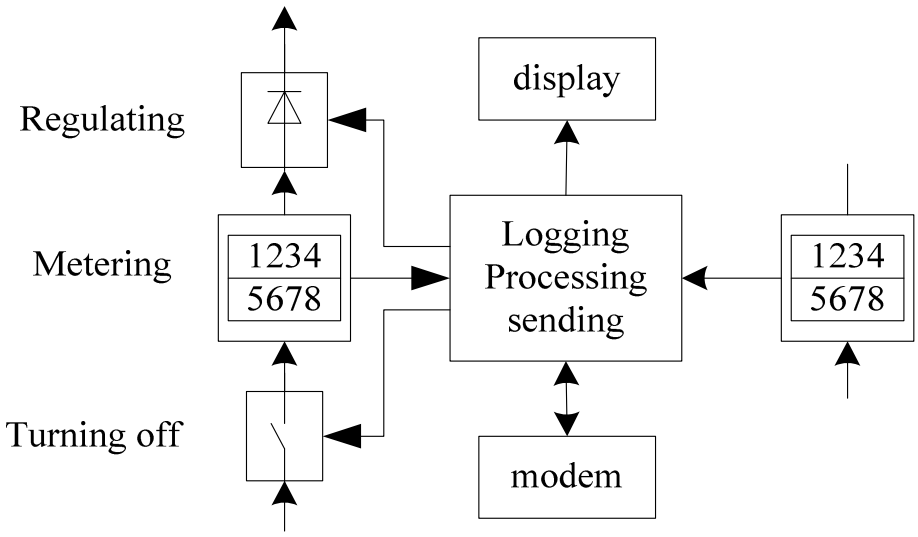

Figure 2. Smart metering block diagram.

Low voltage distribution grids

According to low cost smart meters requirements a simple method providing weekly basic statistical information about voltage levels at costumer's sites was applied. Lowest minimum but also highest maximum voltage values were observed at sites away from stations. Especially the increase of voltage is caused by unbalanced load. The results presented demonstrate that such observations are useful for the planning of low voltage grids. Further investigations are ongoing and more detailed analysis tools for better understanding the behavior of low voltage grids are planned[6].

The voltage level is one of the most important criteria for planning and operating rural distribution grids especially incase of decentralized generation. Changes in the European Standard EN 50160 and its meaning to regulation in European countries are currently discussed. In rural distribution grids reduced availability of voltage tolerance(e.g. preserved part of voltage tolerance for decentralized generation) results into decreasing transmission capacity of the distribution network. Today's methods of managing voltage levels in low voltage grids are simple estimations and reinforcing measures in case of customers complaints. The gap between estimation results and real conditions could be used for operating low voltage grids more cost-efficiently. To identify this gap and deliver adequate solutions, measurement results from several representative nodes of such low voltage grids are needed. Further on this will be the basis for the development of intelligent controlling of active grid components(e.g. active loads, plants, voltage regulators).

Because of striking costs, periodic observations or even monitoring of voltage levels on several points of each LV-grid branch cannot be done by extra installation. But each meter of an automated metering system has a three phase voltmeter and is set up for communication (e.g. power line).The idea is to use these options for permanent voltage level observations.[7]

1) A fully automated organization and presentation of data

2) A compression of data for transmission and storage.

3) Further it is presupposed that a standard meter can be programmed for these functions without any additional costs for extensions of hardware.

Further investigations in respect to voltage unbalance measurements and phase separated 15-min-average value seem to be necessary. For detailed low voltage grid analysis a concept supporting trigger functions was set up. The implementation of these tools and the verification of practical use are part of a planned research project. For put into practice the presented methods standardized procedures for determining voltage band reserve have to be developed. Future options of the smart metering system can be used as an effective tool for analyzing low voltage grids and the implementation of a smart grid low voltage distribution management, control and documentation system. Such functions are also very important for increased integration of decentralized generation to the grid. Nevertheless setting up and operating such systems is some effort and therefore a cost benefit analysis has to be performed.

Power industry & energy efficiency

Over the next five years, smart metering will be installed with all Norwegian electricity customers. The Norwegian energy sector moves toward a significant technology shift, perhaps one of the most extensive projects in the history of Norwegian grid operation. The stakes are high, but with careful planning and good technology choices the project has good chances of success. Even though only 11 % of the country's households currently have smart metering installed, nearly 60% of all electricity customers are positive or very positive towards not having to read the meter themselves in the future, and the general trust in the new technology is high. Most customers (83%) are of the opinion that readings will be at least as accurate as manual readings. However, the willingness to pay for the new technology is very low, but it is increasing over time. Many consumers are of the opinion that the rationalization the grid operators achieve though smart metering and communication automatically should benefit the customers. This could make it difficult for suppliers to request payment for the services, and is a challenge the grid operators need to prepare themselves for[8].

It is highly uncertain whether the new technology would lead the electricity customers to switch consumption to off-peak periods, when the prices are lower. Norwegian consumers are used to low prices and want to use the power when they need it. The interests in utilizing the services opened for by the new technology are moderate at the moment. In time, however, selling value added services might be a good opportunity for the grid operators to maintain and strengthen the customer relation. This is one way to avoid becoming one of the many invisible providers of necessary goods. A strong and distinct customer relation contributes to strengthening the individual company and the sector's reputation, and makes the customers feel that the power sector is making everyday life easier.

Nowadays, more and more people are encouraged to adopt Renewable Energy in order to reduce in greenhouse gas emission, and also the very important issue of climate change. And the smart meter provide knowledge, increase awareness and affect customers' behavior and attitude in using renewable energy. In the future, renewable energy is the trend to reduce the carbon emission and gas emission from the power generation. Although, it may not be cheap from the generation cost at the moment but customer can try our best to reduce the impact due to climate change. Hence, if every household can use electricity and gas efficiently, there is a need to minimize power generation as well.[9]

In the view of current abilities in smart metering, new meters are only expanded in providing real-time information without giving any constructive suggestion to consumers. The smarter meter not only provides services on real-time information, but also helps in establishing an optimal energy-consuming plan for a specific user by the AI technologies integrated into the meter. The introduction of AI technology offers chances in recognizing energy consuming patterns automatically and accurately other than consumers themselves [10].

A smart meter that deals with different energy-supplying forms will be required in the future. AI technology to find out an optimal plan for complex usage from different types of energy resources is necessary. This smart meter will form an instrumentation part of a micro-grid which further

aggregates together to develop a smart grid. It is foreseen that the cost of smart meters could be reduced significantly; therefore it will be widely used by many countries.[11,12]

Conclusion

The most important application of smart metering system is smart meter. Smart meter is fundamentally different from ordinary meters. It can provide a real-time, accurate, record of the gas and electricity you are using, different times and different costs. Smart meters allow people to see clearly how much electricity and gas they are using and send the data to energy firms automatically. As a part of smart grid technology, smart metering is the expanding of electricity and gas meters. Instead of the meter readings and bill-estimation, the data of the amount of electricity and gas could be collected real-time and accuracy for customers and source suppliers. Customers will benefit from this application on leaning how much energy they used at once and choice of optimal energy consumption could be made.The work is partially supported by the science and technology project of Harbin city under Grant 2002AFCXJ001.

References

[1] Smart Meters, Ministerial Council on Energy, Australia, Jan 2007.

[2] Afroz K. Khan, “Monitoring Power for the Future”, Power Engineering Journal, April 2001, IEE, pp. 81-85.

[3] Ringo P K Lee and L L Lai, A practical approach to wireless power quality, energy and facilities monitoring System. IEEE Power &Energy Society 2008 General Meeting 20-24 July 2008 Pittsburgh, Pennsylvania USA.

[4] H.Cavdar, “A solution to remote detection of illegal Electricity usage via power line communications,” IEEE Trans. Power delivery, vol. 19,N). 4, October 2004.

[5] M.Tang, “Optimal topology discovery for automatic meter reading using power line carrier,” B.S. thesis, Dept. Electrical & Electronic. Eng., Auckland Univ., 2003.

[6] Smart Meters, Ministerial Council on Energy, Australia, Jan 2007.

[7] S.V. Vadari, J. Taft, 2008, “Smart AMI Solutions Enable the Smart Grid”, Grid–Interop Forum 2008-Paper_Id-1.

[8] Han Chen, Paul Chou, Sastry Duri, Hui Lei, Johnathan Reason, “The Design and Implementation of a Smart Building Control System,” E-Business Engineering, IEEE International Conference on, pp. 255-262, 2009 IEEE International Conference on e-Business Engineering

[9] Lee.P.K., Lai. L.L, “A practical approach of smart metering in remote monitoring of renewable energy applications”, Power & Energy Society General Meeting, 2009. PES, 26-30 July 2009 pp1-4.

[10] Rob van Gerwen, Saskia Jaarsma and Rob Wilhite, “Smart Metering”, Distributed Generation, pp.7, July2006.

[11] G. Deconinck and B. Decroix, “Smart metering tariff schemes combined with distributed energy resources,” in Proc. Fourth International Conference on Critical Infrastructures,Linkoping, Sweden, Mar. 2009, pp.1 – 8.

[12] C.D. Suriyakala and P.E. Sankaranarayanan, "Smart multiagent architecture for congestion control to access remote energy meters," in Proc.International Conference on Computational Intelligence and Multimedia Applications, Sivakasi, India, Dec. 2007, pp. 24-28.

Advanced Materials Research Vols. 960-961 (2014) pp 828-831

doi:10.4028/www.scientific.net/AMR.960-961.828

Development and Application of Smart Distribution Grid Self-healing Control System

Shanshan Li[1,a*], Hongdan Li[2,b], Huiquan Zou[2,c], Yaoqiang Liu[2,d] and Xiang He [1,e]

[1]HAEPC Electric Power Research Institute, China

[2]HeNan EPRI Electric Technology Co. Ltd, China

[a]lishanshan@ha.sgcc.com.cn, [b]lihongdan_20081107@126.com, [c]zhqdas@sohu.com, [d]liuyaoqiang12@163.com, [e]hexiang@ha.sgcc.com.cn,

Keywords: Smart distribution grid; Distribution automation; Self-healing; Power supply capacity; Power supply quality

Abstract. Self-healing is an important feature of smart distribution grid. Self-healing control for smart distribution grid covers risk prevention and operation optimization before accidents, in addition, it covers fault location, fault isolation and power restoration. The research of self-healing control theory, risk assessment, fault diagnosis and safety warning for smart distribution grid provides technical supports to help build a safe, reliable, efficient, high-quality, flexible and compliant smart distribution grid.

Introduction

Distribution network is located in the end of power system, responsible for important tasks of power distribution and customer service[1]. Power supply capacity and power supply quality to users must be guaranteed and achieved through distribution network, which makes smart distribution grid the focal point of smart grid research[2]. Smart distribution grid differs from traditional distribution grid in that the former contains distributed generation, and has characteristics such as large-scale, complex and multi-point wide surface[3,4]. Operation modes and control strategies of smart distribution grid changed from that of traditional distribution grid, which proposed the needs of "self-healing" control technology[5].

Self-healing control technology

Distribution network self-healing control serves for smart distribution grid, transports by sensing collection and communication technology, bases on data mining, condition monitoring and grid early-warning, takes status assessment and analysis decision as core, controls with distribution equipment, in order to achieve optimal operation of the system, risk prevention and fault disposal[6,7]. The whole self-healing control technology contains two main lines and three major tasks. Structure diagram of self-healing control strategy is illustrated in fig.1.

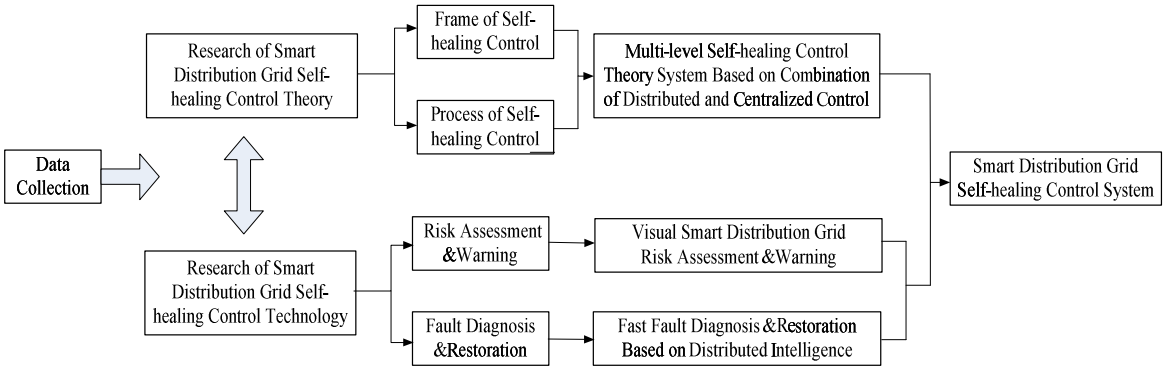

Fig.1 Structure diagram of self-healing control strategy

The two main lines contain research of self-healing control theory for smart distribution grid and research of self-healing control technology for smart distribution grid. The three major tasks contain research of multi-level self-healing control theory system based on combination of distributed and centralized control, research of visual smart distribution grid risk assessment and warning, and research of fast fault diagnosis and restoration based on distributed intelligence. The first task belongs to Line One, the second and third tasks belong to Line Two. The research of Line One and Line Two is non-independent, in the research of theory system, the main function and key technology of self-healing must be well considered. The established theory system of multi-level self-healing control theory system based on combination of distributed and centralized control must integrate risk control and emergency control (including fault diagnosis and power restoration) proposal. In the research of technology, the key technology must be consistent with the self-healing theory, combines the advantages of distributed control and centralized control framework, to achieve multi-level risk control and emergency control.

Main tasks of self-healing control technology

Self-healing control theory system for smart distribution grid. Self-healing control technology for smart distribution grid adopts a hierarchical distributed control system, is composed of multiple parts nested within each other. Various parts such as information system, dispatching automation system, substation automation system and distribution system combine self-healing control system for smart distribution grid. The service stream contains operation assessment, optimization control, coordinated control, risk control, emergency control and restoration control. Top-level structure diagram of self-healing control for smart distribution grid is illustrated in fig.2.

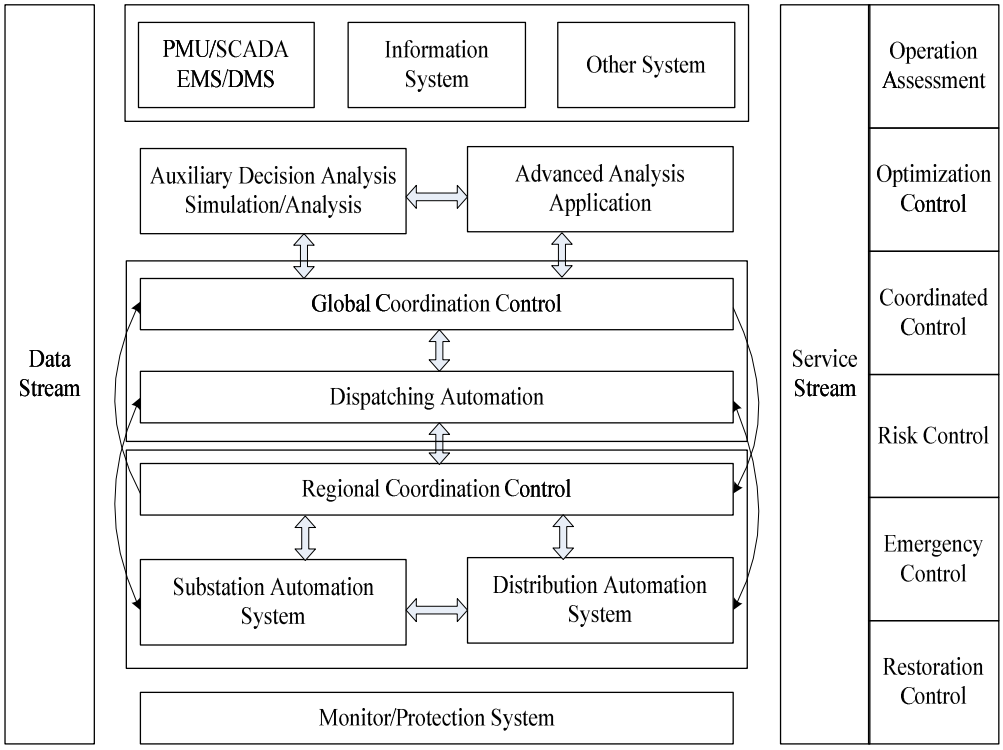

Fig.2 Top-level structure diagram of self-healing control for smart distribution grid

Smart distribution grid risk assessment and warning technology. In this task, first step, historical data of actual distribution network operation in the past 20 years should be collected from production management department of distribution network. The important collection data contains distribution network component reliability, various types of abnormal events/ operating characteristics before distribution network accident, distribution network component outage reasons, outage duration, outage consequences and other historical operation data. Study smart distribution

grid online risk assessment index system, evaluation methods, probabilistic characteristics of distribution network operation risk factors, risk assessment models, quantitative indicators and calculation methods based on data collection. Second step, generate smart distribution grid risk warning and location technology. Accordingly, study automatic configuration and calculation methods of reducing smart distribution grid risk strategy. Third step, integrate these research results above-mentioned, complete the "smart distribution grid risk assessment and safety warning technology research" report, and develop visual smart distribution grid risk assessment and warning subsystem. The subsystem should be able to display risk assessment and early warning indicators / information in a reasonable manner online and visual. Roadmap of smart distribution grid risk assessment and warning technology is illustrated in fig.3.

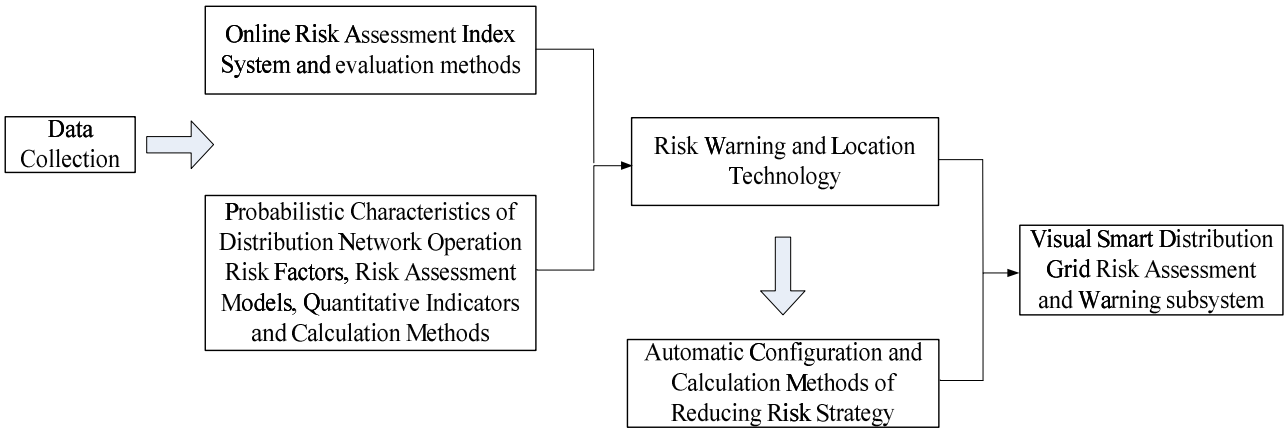

Fig.3 Roadmap of smart distribution grid risk assessment and warning technology

The research results of this task can be used in risk assessment index calculation, risk assessment warning/ location and identification of risk status, judgment, prevention, and control function of smart distribution grid self-healing system.

Smart distribution grid fault diagnosis and power restoration technology. In this task, first of all, historical data during distribution network fault in the past 20 years, switch type, common fault isolation and power restoration mode should be collected from production management department of distribution network. Accordingly, summarize the common faults of distribution network and the fault isolation methods/power restoration modes based on existing equipment. Study the spatial and temporal characteristics caused by various types of faults in order to get the diagnosis criterion. According to existing equipment information, such as switch type and installation location, study multi-level protection configuration and online tuning methods. By integrate the two above-mentioned points, generate fast fault identification, location and isolation methods based on combination of distributed and centralized control. Therefore, study the fast power restoration methods in non-fault region adapted to distribution network structure. Based on the study of traditional grid fault diagnosis method, analyze the impact on fault characterization of the introduction of distributed power, study the fault diagnosis technology of distribution network including distributed power. At last, integrate these research results above-mentioned, complete the "smart distribution grid fault diagnosis and power restoration technology research" report, and develop multi-level emergency control subsystem. Roadmap of smart distribution grid fault diagnosis and power restoration technology is illustrated in fig.4.

The research results of this task can be used in emergency/restoration status evaluation and control function of smart distribution grid self-healing system.

Application

Self-healing control system adopts centralized structure, makes full use of sophisticated network management technology, database middleware, object-oriented and component technology for construction. Follow the IEC 61968-1 standard system interface information exchange model (IEM), in strict accordance with message transport mechanism for information exchange through information exchange bus with other systems.

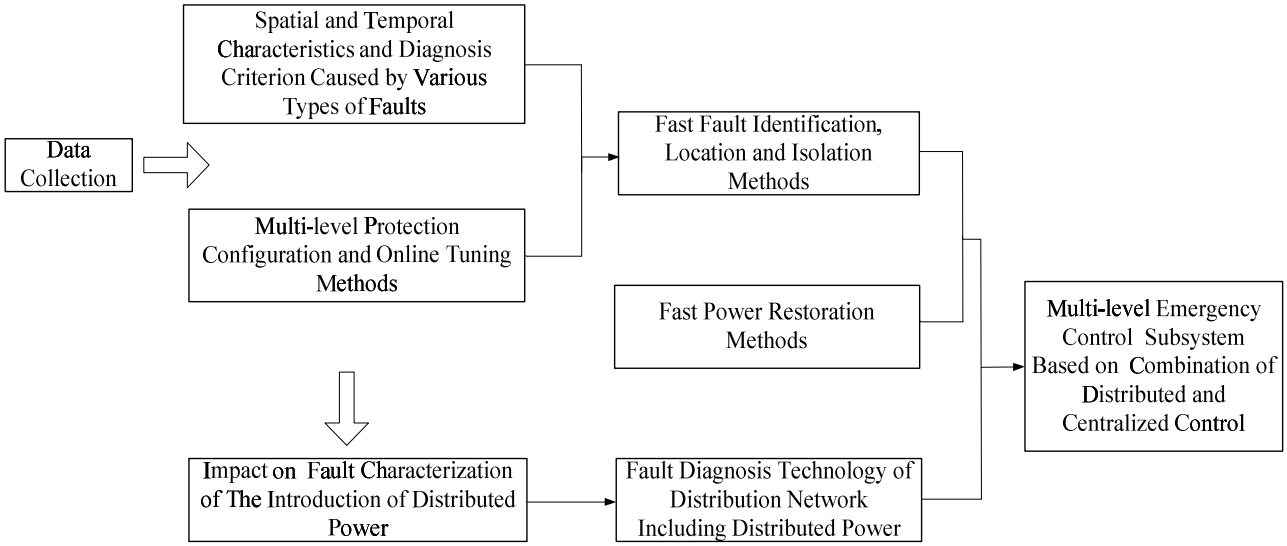

Fig.4 Roadmap of smart distribution grid fault diagnosis and power restoration technology

Conclusions

Distribution network occupies a significant position in power system. Self-healing is an important feature of smart distribution grid. Compared with the emphasis on fault handling in distribution automation system, self-healing control not only focuses on status while and after the accident, but also emphasizes the risk prevention, self-organization, adaption and operation optimization capabilities before accidents. Self-healing control has great significance for the protection of reliable, high-quality and efficient smart distribution grid.

References

[1] Karen NanMiu, Hsiao-Dong Chiang and Bentao Yuan: Fast service restoration for large-scale distribution system with priority customers and constraints. Power Systems 1998, 13(3):789–795.

[2] Dong Xuzhu, Huang Shaoyuan, Chen Rouyi, Li Peng and Zhang wenfeng: self-healing control technology for smart distribution system. Automation of Electric Power System 2012, 36(18):17–21.

[3] Kleinberg, M. R. , K. Miu and H. D. Chiang: Improving service restoration of power distribution systems through load curtailment of in-service customers. Power Systems 2011, 26(3):1110–1117.

[4] Guo Zhizhong: Scheme of self-healing control frame of power grid. Automation of Electric Power System 2005, 29(10):85–91.

[5] Bailing Zhang and Zhaoyang Dong: An adaptive neural-wavelet model for short term load forecasting. Electric Power Systems Research 2001, 59(1):121–129.

[6] Yu Yixin: Intelli-D-Grid for the 21st century. Southern Power System Technology Research 2006, 2(6):14–16.

[7] AMIN M: Energy infrastructure defense systems. Proceedings of the IEEE 2005, 93(5):861–875.

Advanced Materials Research Vols. 960-961 (2014) pp 832-835

doi:10.4028/www.scientific.net/AMR.960-961.832

The Scheme of Identity-based Aggregation Signcryption in Smart Grid

Jie Chen[1, a *] and Yueyu Zhang[1,b]

[1] State Key Laboratory of Integrated Service Networks, Xidian University, Xi'an, Shaanxi, 710071, China

[a]jchen@mail.xidian.edu.cn, [b]yy_zhang@mail.xidian.edu.cn

Keywords: Smart Grid, Aggregation Signcryption, Identity-based Signcryption, Batch Verification.

Abstract. Smart grid puts forward high requirements for the equipment to access authentication, which achieves openness and real-time performance in mart grid. The users' identities need to protect, in the meanwhile, identity authentication and data encryption should be efficient. According to the characteristics of smart grid, this paper proposed an identity-based aggregation signcryption scheme which combined pseudonymous ID with batch verification. The scheme adopted the pseudonym technology to achieve the user identity anonymity, and adopted the signcryption to complete digital signature and encryption in one time. This paper presented the aggregation signcryption for different multiple users by dynamic equation, which can compromise the security and computation overhead to meet the requirements of smart grid. This scheme can reduce the computational burden of aggregators with security of communication data. Moreover, this scheme solved the difficult problem of the management of pseudonymous ID, and improved the efficiency of the whole system. Therefore, this scheme meets the requirement of real time and high efficiency in smart grid.

Introduction

Different from the traditional power grid, smart grid can achieve elaborate and intelligent management based on lots of interactive data. And smart grid can achieve the data transmission and information control in two-way, high-speed and real-time parameter sampling [1]. Equipment to verify will bring tremendous computational pressure to the authentication server, so that it cannot be timely response, which will lead to delay for authentication with sharp increase. In smart grid, periodic data collection activities are faced with the risk of sensitive personal information leakage [2]. The existing privacy protection for real-time electricity data mainly achieves through data aggregation and homomorphic encryption [3,4,5,6], but all these programs do not provide protection for user identity from the access. Based on the above characteristic in smart grid, this paper proposes an identity-based aggregate signcryption scheme which combines pseudonymous ID and batch signature verification. The scheme adopts the pseudonym technology to meet users' privacy protection in the access terminal, the signcryption technique complete digital signature and encryption at a time. The scheme aggregates multiple users' signcryption which makes use of dynamic equation. This scheme can reduce the computational burden at the same time ensure communication data security.

In 1997, the signcryption technique is first proposed by Zheng[7] to complete digital signature and encryption in the same logical steps. Compared with the traditional signature then encryption, signcryption has higher efficiency in computation and communication and more secure in the whole scheme. In 2002, Malone-Lee presents Identity-based signcryption[8] which combines identity-based cryptography with signcryption. In 2010, identity-based signcryption scheme for smart grid was proposed by Hayden et. al [9]. The next section describes an identity-based aggregation signcryption scheme which combines pseudonymous ID and batch signature verification.

The Scheme of Identity-based Aggregation Signcryption in Smart Grid

The system of smart grid includes service provider (SP), central aggregator (CAG), local aggregator (LAG), trusted third party (TTP) and users (US). US need first register their smart meters (SM) in SP.

In the course of data collection, SM directly send data to LAG, then LAG collect the data from SM and send aggregated data to CAG.

System Initialization

SP selects parameters and sends it to key generating server (KGS) to generate desired parameters.

(1) KGS generates additive group G and G' with prime order q and multiplication group G_T. P is a generator of G and P' is a generator of G'. e: $G \times G \to G_T$ is a bilinear map of Weil pair.

(2) SP selects five hash function, H_0:$\{0,1\}^* \times G \to Z_q^*$, H_1: $G_T \to \{0,1\}^l \times G$, $H_2 : \{0,1\}^l \times \{0,1\}^* \times G \times G_T \times \{0,1\}^* \times G \to G$, $H_3 : \{0,1\}^* \to G'$.

(3) SP selects two random number $s_1, s_2 \in Z_q$ as its master key (s_1, s_2), and its public keys are $P_{pub1} = s_1 \cdot P$ and $P_{pub2} = s_2 \cdot P$. (s_1, s_2) is embed in equipment with tamper resistant, and P' and P_{SP} are embed in SM ahead of schedule.

With the above steps, SP publicizes the common public parameter *param*=(q, G, G_T, G', e, P, P', P_{pub1}, P_{pub2}, P_{SP}, H, H_0, H_1, H_2, H_3), and itself public key P_{sp}.

Register

Every US must register in SP before their SM join to smart grid at the first time, so US need provide their real identity *RID*. SP generates and sends a *permit* to US, and SP saves *RID* and *permit* at user information table (UIT). In the meantime, LAG and CAG also need register in order to obtain their public key certificate *Cert*.

Pseudonym and Key Generation

When US input correct *RID* and valid *permit*, SM will start and generate pseudonym $ID=ID_1 \| ID_2$ with $ID_1 = r \cdot P'$ and $ID_2 = RID \oplus H(r \cdot P_{sp})$, r is a random number with time variable. Then US randomly selects $x_i \in Z_q^*$, and computes $X_i = x_i P$, $SK_1 = s_1 \cdot X_i$, $SK_2 = (x_i + s_1 \cdot q_i)$, $q_i=H_0(ID,X_i)$, with its secret key $SK=<SK_1,SK_2>$ and public key $PSK=<X_i,q_i>$. LAG randomly selects $y \in Z_q^*$, with its secret key $SK_{LAG}=y$ and public key $P_{CAG}=yP$.

Signcryption

SP need periodically gather statistic information of electric consumption, and US sends information to SP including electric consumption information $m_{\text{Statistics}}$ and real-time electricity request m_{Request}.

(1) When user U_i sends message $m_{\text{Statistics}}$, LAG verifies the user's signature of $m_{\text{Statistics}}$ and then signs and transmits verified $m_{\text{Statistics}}$ to CAG. The step is as follows.

(*a*) U_i selects a random number $u_i \in Z_q^*$, and computes $W_i = u_i P$, $w_i = (P_{pub1}, P_{LAG})^{u_i}$, $h_{1i} = H_1(w_i)$, $R_i = H_2(m_{\text{Statistics}}, ID_i, X_i, w_i, ID_{LAG}, P_{LAG})$, $V_i = u_i P_{pub2} + \text{SK}_2 \cdot R_i$;

(b) Assume $m_{1i} = m_{\text{Statistics}} \| t_1$, with timestamp t_1. U_i computes ciphertext $c_i' = (m_{1i} \| V_i) \oplus h_{1i}$;

(c) U_i sends the signcryption ciphertext $\sigma_i' = (c_i, W_i, V_i, X_i, t_1)$ to LAG.

(2) When user U_i sends message m_{Request}, LAG verifies the user's signature of m_{Request}. Then LAG aggregates all the m_{Request} to M_{Request}, and then signs and transmits M_{Request} to CAG. The step is as follows.

(*a*) U_i selects a random number $u_i \in Z_q^*$ and computes $W_i = u_i P$, $w_i = (P_{pub1}, P_{LAG})^{u_i}$, $h_{2i} = H_1(w_i)$, $R_i=H_2(m_{\text{Request}}, ID_i, X_i, w_i, ID_{LAG}, P_{LAG})$, $V_i = u_i P_{pub2} + \text{SK}_2 \cdot R_i$.

(b) Assume $m_{2i} = m_{\text{Request}} \| t_2$, with timestamp t_2. U_i computes ciphertext $c_i'' = (m_{2i} \| V_i) \oplus h_{2i}$.

(c) U_i sends the signcryption ciphertext $\sigma_i'' = (c_i, W_i, V_i, X_i, t_2)$ to LAG.

Signcryption Aggregation

Since the interval time is short in real-time electricity request, LAG will receive lots of signcryption information at the same time. In order to speed up the verification and increase efficiency, LAG

should aggregate the signcryption. LAG computes $V_{agg}=\sum_{i=1}^{n}V_i$, signcryption aggregation is $\sigma_{agg}=<\{c_i,W_i,X_i,ID_i\}_{i=1}^{n},V_{agg}>$ for *n* different users with message $(m_{21},m_{22},\cdots,m_{2n})$.

Unsigncrypt and Transmit

When LAG receives electric consumption information (*c*, *W*, *V*, *X*), LAG first check the validity of timestamp *t*, that is LAG computes $\Delta t=t_T-t$, of which t_T is the system time with messages received. If Δt does not conform to the requirements of the system rules, (*c*, *W*, *V*, *X*) will be considered invalid. If Δt conforms to the requirements of the system rules, LAG will unsigncrypt and then signcrypt and transmit message to CAG. The step is as follows.

(1) LAG computes $w_i=e(W_i,SK_{LAG}\cdot P_{pub1})$ using LAG's secret key SK_{LAG} and TTP's public key (p_{pub_1},p_{pub_2}). Then LAG recovers $m_{1i}\|V_i=c_i\oplus H_1(w_i)$.

(2) LAG computes $R_i=H_2(m_i,ID_{1i},X_i,w_i,ID_{LAG},P_{LAG})$.

(3) LAG verifies whether or not $e(V_i,P)=e(W_i,P_{pub2})\ e(R_i,X_i+q_iP_{pub1})$. If equation is established, LAG selects a random number $a\in Z_q^*$ and computes

(*a*) $k_1=hash(aP)$, $(k_2,k_3)=hash(aP_{CAG})$;

(*b*) $c=E_{k_2}(\sigma'\|t_3)$, $w=kH_{k_3}(c\|k_1\|ID_{LAG}\|ID_{CAG})$;

(*c*) $s=a(w+SK_{LAG})^{-1}\bmod q$, $T=wP$.

LAG sends (c,T,s) to CAG as signcryption of message σ_i'. After CAG receives message, it first computes $k_1=hash(sT+sP_{LAG})$ and $(k_2,\ k_3)=hash(SK_{CAG}\cdot sT+\ SK_{CAG}\cdot sP_{LAG}\ )$, $r=kH_{k_3}(c\|k_1\|ID_{LAG}\|ID_{CAG})$. Signed message is availably if and only if $rG=T$ with $\sigma_i'\|t_3=D_{k2}(c)$.

When LAG receives real-time electricity request, LAG first checks the validity of timestamp *t* the same as the step above. When timestamp *t* is available, LAG will verify and aggregate the signcryption. The step is as follows.

(1) LAG computes $w_i=e(W_i,SK_{LAG}\cdot P_{pub1})$ using LAG's secret key SK_{LAG}. Then LAG recovers $m_{2i}\|V_i=c_i\oplus H_1(w_i)$.

(2) LAG computes $R_i=H_2(m_{2i},ID_i,X_i,w_i,ID_{LAG},P_{LAG})$.

(3) LAG verifies whether or not $V_{agg}=\sum_{i=1}^{n}V_i$ and $e(\sum_{i=1}^{n}V_i,P)=e(\sum_{i=1}^{n}W_i,P_{pub2})\cdot\prod_{i=1}^{n}e(R_i,X_i+q_iP_{pub1})$. If two equations are both established, LAG outputs m_{2i}. If not, LAG verifies the signcryption one by one.

Since batch verification of signatures has forgery attack, Ref.[10] presented dynamic equation which can resist forgery attack. So the scheme in this paper makes use of dynamic equation of batch verification. The step is as follows.

(1) LAG selects $k_i\in Z_7$ with dynamic change, for *n* messages $(m_{21},...,m_{2n})$ with signatures $(V_1,...,V_n)$. LAG computes $e(\sum_{i=1}^{n}k_iV_i,P)=\prod_{i=1}^{n}e(k_iV_i,P)=\prod_{i=1}^{n}k_i\cdot\prod_{i=1}^{n}e(V_i,P)$.

(2) LAG verifies the equation $e(\sum_{i=1}^{n}k_iV_i,P)=\prod_{i=1}^{n}k_i\cdot e(\sum_{i=1}^{n}W_i,P_{pub2})\prod_{i=1}^{n}e(R_i,X_i+q_iP_{pub1})$. If the equation are verified, LAG aggregates all users' electricity request $M_T=\sum_{i=1}^{n}m_{2i}$ at time *T*. Then LAG signcrypts M_T and transmits it to CAG.

Security Analysis

The scheme in this paper combines pseudonym with signcryption, which can realize identity authentication for SM in smart grid. The security of this scheme is based on difficult problem of

Computer Differ-Hellman. Therefore, this scheme can resist replay attack and has the character of unlinkability, traceability, and unforgeability.

In [9], when n users send n messages using signature verification one by one, there are $4n$ pairing operation in all. There are only n+3 pairing operation in the scheme of this paper. The signcryption can improve efficency compared with signature then encryption. Aggregation signcryption can verify multiple different messages in the meantime. Thus LAG and CAG can quickly and effectively to respond, which can greatly save the compute and storage consumption. The data transmission scheme proposed in this paper adopts to pseudonym technology when US communicates with LAG. At the same time, signcryption key is generated based on the pseudonym. Therefore, the proposed ID based aggregation signcryption scheme is simple in calculation, low in overhead, fast in transmission speed.

Summary

In this paper, an identity-based aggregation signcryption scheme is proposed in smart grid. The scheme adopts pseudonymous ID to achieve the users' privacy protection in the access terminal. The scheme uses the aggregation signcryption for different multiple users by dynamic equation, which can compromise the security and computation overhead to meet the requirements of smart grid. This scheme can reduce the computation burden for aggregator at the same time to ensure communication security, which can meet the requirement of real time and high efficiency in smart grid.

Acknowledgements
This work was financially supported by the Natural Science Foundation of China (61102056, 61201132), Fundamental Research Funds for the Central Universities of China (K5051301013, K5051201038) and the 111 Project of China (B08038).

References

[1] H. Khurana, M. Hadley, L. Ning, D. A. Frincke. Smart-grid security issues. IEEE Security and Privacy. 2010, Vol.8, pp. 81-85.
[2] J. Liu, Y. Xiao, S. Li, W. Liang, C. Chen. Cyber security and privacy issues in smart grids. IEEE Communications Surveys & Tutorials. 2012, 14(4), pp.981-997.
[3] A. Bartoli, J. Hernandez-Serrano, M. Soriano, et.al. Secure lossless aggregation for smart grid M2M networks. In Proc. 2010 IEEE Conference Smart Grid Communication. 2010, pp. 333-338.
[4] F. Li, B. Luo, P. Liu. Secure information aggregation for smart grids using homomorphic encryption. Proc. 2010 IEEE Conference Smart Grid Communication. 2011, pp.327-332.
[5] E. Shi, T. Chan, E. Rieffel, et.al. Privacy-Preserving aggregation of time-series data. Conferences & Talks in Proc. of NDSS 2011, San Diego, California, 2011.
[6] R.Q. Hu, Y. Qian, H.-H. Chen, H.T. Mouftah. Cyber security for smart grid communications: Part I. IEEE Communications Magazine, 2012, 50(8), pp.16-17.
[7] Yuliang Zheng. Digital signcryption or how to achieve cost(signature & encryption) ≪ cost(signature) + cost(encryption). Advances in cryptology — CRYPTO '97. August 17–21, 1997, Santa Barbara, California, USA. Springer Berlin Heidelberg LNCS1294, Springer-Verlag, 1997, pp 165-179.
[8] J. Malone-Lee. Identity based signcryption. Cryptology ePrint Archive. Information on http://eprint.iacr. org/2002/098, 2002-07-20/ 2011-11-22.
[9] Hayden K.-H. So, Sammy H.M. Kwok, Edmund Y. Lam and King-Shan Lui. Zero-configuration identity-based signcryption scheme for smart grid. Smart Grid Communications (SmartGridComm), 2010 First IEEE International Conference on. 4-6 Oct. 2010, pp.321–326.
[10] X. Boyen. Multipurpose identity-based signcryption: a swiss army knife for identity-based cryptography. Advances in Cryptology- CRYPTO 2003, August 17-21, 2003, Santa Barbara, California, USA. Springer Berlin Heidelberg LNCS 2729, Springer-Verlag, 2003, pp. 383-399.

Advanced Materials Research Vols. 960-961 (2014) pp 836-840

doi:10.4028/www.scientific.net/AMR.960-961.836

A Wide-area Backup Protection Algorithm for Multi-Fault Location in Complex Large Power Grid

Bingyang Xia[1, a] and Jing Ma[1, b]

[1] State Key Laboratory of Alternate Electrical Power System with Renewable Energy Sources, North China Electric Power University, Beijing 102206, China

[a]hdmajing@aliyun.com, [b]hdmajing@ncepu.edu.cn

Keywords: multi-fault location; equivalent fault model; fitting degree; wide-area measurement system; least square method; virtual fault location

Abstract. This paper presents a fitting degree-based multi-fault location algorithm for complex large power grid utilizing wide-area information. Firstly, fault injection current of the equivalent fault points is used in the equivalent model. Then the correlation matrix is formed by the network topology and associated nodal injection current and a network is formed to determine the location of faults. When multiple faults occur, the addition of the current of each two fault lines is calculated and the real-time current is measured. Then by calculating the minimum of fitting degree between two current values, fault line and virtual fault location can be determined. The simulation results of 10-generator 39-bus system verify the validity and feasibility of this algorithm.

Introduction

In recent years, with the continuous development of the power grid and the reinforcement of its main structure, the trip of a single element under normal operation mode is generally not a strong impact on the grid. However, frequently, there are various types of fault, i.e. more than one fault occurred in a short time. It will pose serious threat to the safety and stable operation of power grids, and it will become a failure mode which may lead to significant loss of load and result in serious damage to electrical components .The complexity of the power grid structure makes the traditional protections which are based on the amount of local backup settings more difficulty. The uncertainty of power grid structure and operating conditions has intensified the contradiction among selectivity, sensitivity and reliability of backup protection. It is necessary to improve the adaptability and intelligence of back-up protection levels for the rapid development of grid. Thus, the study on wide-area backup protection of multiple faults is of significance.

With wide-area synchronized phasor measurement technology, the information resources of the relay system have changed fundamentally. It makes a big change to relay on the configuration, the principle of setting and achieving technology and other aspects. Wide-area backup protection system can collect more information, but do not have to sacrifice time to ensure the selective action. According to wide-area information, we can locate the fault, in such cases of the main protection tripping and breaker fault. It can not only overcome the problem of too much time consuming, but also will prevent protection malfunction caused by overload of adjacent lines after a fault backup.

Presently, the research on backup protection is focused on the fault location methods based on wide area measurement. Reference [1] presents a new fault location method for transmission network using sparse (phasor measurement unit) PMU measurements. A new concept of fault location factor is defined to reflect the location of the fault. Then the matching based fault location method is presented. The fault location is estimated by matching measured factors with the calculated ones. Reference [2] presents a general fault location approach utilizing only voltage measurements from one or more terminals by taking advantage of network analysis based on bus impedance matrix technique. Reference [3] proposes fault location algorithms by utilizing sparse current measurements. Bus impedance matrix techniques are utilized to find a direct solution and the need of iterative searching of the fault location is eliminated. Algorithms for scenarios where current phasors or current magnitude are available from one or two branches are developed. In reference [4], global information

has been introduced into the backup protection system. By analyzing and computing real-time PMU measurements, basing on cluster analysis theory, hierarchical cluster analysis technology is used to locate fault line.

In order to further enrich and improve the fault location methods this paper presents a fitting degree-based branch of the faults location method. Firstly, fault injection current of the equivalent fault points is used in the equivalent model. Then the correlation matrix is formed by the network topology and associated nodal injection current and a network is formed to determine the location of faults. When multiple faults occur, the addition of the current of each two fault lines is calculated and the real-time current is measured. Then by calculating the minimum of fitting degree between two current values, fault line and virtual fault location can be determined. 10-generator 39-bus New England system simulation results verify the effectiveness and validity of the algorithm.

Multi-fault location

In the fault network, the model of fault branch b_0 is shown in Fig.1.The model uses lumped parameters, and the branch impedance is z. y1, y2 are the admittances to ground. K1 and K2 are two terminals of the line. The distance between failure point and the node K1 is a times of the total line. $\dot{I}_{\mathrm{f}}$ is the fault injection current. $\dot{U}_{\mathrm{f}}$ is the voltage of fault point. $\dot{I}_{\mathrm{K1}}$ and $\dot{I}_{\mathrm{K2}}$ are the currents inject into the terminals. $\dot{U}_{\mathrm{K1}}$ and $\dot{U}_{\mathrm{K2}}$ are the voltage of K1 and K2.

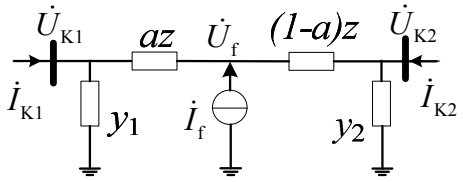

Fig. 1. Fault transmission line

By solving the nodal voltage equation, we can draw the following equivalent circuit as Fig.2 shows:

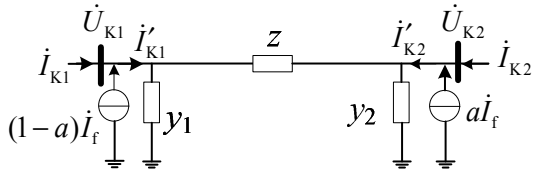

Fig. 2. Equivalent model of fault transmission line

Fig.2 shows that the equivalent model distributes the additional current to the terminals of the branch. The structure and parameters of the branch remain unchanged, so the admittance matrix does not change and then the computation is reduced. According to superimpose theorem, node of the branch current configuration PMU column vector can be expressed as follows:

$$\vec{\mathbf{I}} = \mathbf{P}\vec{\mathbf{R}} - (1-a)\dot{I}_{\mathrm{f1}}\vec{\mathbf{g}}_{\mathbf{K1}} - a\dot{I}_{\mathrm{f1}}\vec{\mathbf{g}}_{\mathbf{K2}} - (1-b)\dot{I}_{\mathrm{f2}}\vec{\mathbf{g}}_{\mathbf{K3}} - b\dot{I}_{\mathrm{f2}}\vec{\mathbf{g}}_{\mathbf{K4}} \tag{1}$$

$$\mathbf{P} = (\mathbf{Y_B}\mathbf{A}^T + \mathbf{Y_{B1}}\mathbf{A}_1^T)\mathbf{Y}^{-1} \tag{2}$$

where P is the correlation matrix, $\mathbf{Y_B}$ is the branch admittance matrix, $\mathbf{A}$ is the node-to-branch incidence matrix, $\mathbf{Y_{B1}}$ is branch-to-ground admittance matrix, $\mathbf{A_1}$ is node-to- branch incidence matrix and T represents the matrix of transpose.

From the previous analysis, the matrix can be formed in the system during normal operation. The fault location process remains the same. $\vec{\mathbf{g}}_{\mathbf{K1}}$ is a column vector and its element corresponding to K1-K2 (from K1 to K2) is 1, and the remaining elements are zeros. $\vec{\mathbf{g}}_{\mathbf{K2}}$ is a column vector and its element corresponding to K2-K1 (from K2 to K1) is 1, and the remaining elements are zeros. $\mathbf{Y}$ is the admittance matrix of network, $\vec{\mathbf{R}}$ is current column vector which inject into network nodes.

Basis of the preceding additional fault current distribution principle, steady-state fault slip faults at both ends of the network nodes only in K1 and K2 are the injection currents, which can get into the current node column vector:

$$\vec{\mathbf{R}} = [0 \cdots (1-a)\dot{I}_{f1} \cdots a\dot{I}_{f1} \cdots (1-b)\dot{I}_{f2} \cdots b\dot{I}_{f2} \cdots 0] \tag{3}$$

$\vec{\mathbf{g}}_{K1}$ and $\vec{\mathbf{g}}_{K2}$ represent K1th and K2th column of matrix **P** respectively.

$$\vec{\mathbf{I}} = [\vec{\mathbf{P}}_{k1} - \vec{\mathbf{g}}_{k1}\ \vec{\mathbf{P}}_{k2} - \vec{\mathbf{g}}_{k2}\ \vec{\mathbf{P}}_{k3} - \vec{\mathbf{g}}_{k3}\ \vec{\mathbf{P}}_{k4} - \vec{\mathbf{g}}_{k4}] \bullet [(1-a)\dot{I}_{f1}\ \ a\dot{I}_{f1}\ \ (1-b)\dot{I}_{f2}\ \ b\dot{I}_{f2}]^T \tag{4}$$

Equation (4) is always effective to the fault line and it is not effective to the normal branch. For the location of fault is random, the fault line and fault position are unknown before the fault point is located. The fault line and fault location can be found by solving the equation (4) of each branch. For any two branches b (k1-k2) and b (k3-k4), assume the fault occurs where the distance between the fault point1 and k1 is a times of the total line b (k1-k2), point2 and k3 is b times of the total line b(k3-k4). Solve (5):

$$\vec{\mathbf{I}} = [\vec{\mathbf{Q}}_{K1}\ \vec{\mathbf{Q}}_{K2}\ \vec{\mathbf{Q}}_{K3}\ \vec{\mathbf{Q}}_{K4}][(1-a)\dot{I}_{f1}\ \ a\dot{I}_{f1}\ \ (1-b)\dot{I}_{f2}\ \ b\dot{I}_{f2}]^T \tag{5}$$

$$\begin{cases} \vec{\mathbf{Q}}_{K1} = \vec{\mathbf{P}}_{K1} - \vec{\mathbf{g}}_{K1} \\ \vec{\mathbf{Q}}_{K2} = \vec{\mathbf{P}}_{K2} - \vec{\mathbf{g}}_{K2} \\ \vec{\mathbf{Q}}_{K3} = \vec{\mathbf{P}}_{K3} - \vec{\mathbf{g}}_{K3} \\ \vec{\mathbf{Q}}_{K4} = \vec{\mathbf{P}}_{K4} - \vec{\mathbf{g}}_{K4} \end{cases} \tag{6}$$

Equivalent transformations are made as follows:

$$\mathbf{M} = [\vec{\mathbf{Q}}_{K1}\ \vec{\mathbf{Q}}_{K3}\ \vec{\mathbf{Q}}_{K2} - \vec{\mathbf{Q}}_{K1}\ \vec{\mathbf{Q}}_{K4} - \vec{\mathbf{Q}}_{K3}] \tag{7}$$

$$\vec{\mathbf{N}} = [h_1\ h_2\ h_3\ h_4]^T \tag{8}$$

$$\begin{cases} h_1 = \dot{I}_{f1} \quad h_2 = \dot{I}_{f2} \\ h_3 = a\dot{I}_{f1}\ \ h_4 = b\dot{I}_{f2} \end{cases} \tag{9}$$

$$\vec{\mathbf{I}} = \mathbf{M}\,\vec{\mathbf{N}} \tag{10}$$

For the number of branch current is more than the number of variables, so the equation can be solved by least square method:

$$\vec{\mathbf{N}} = (\mathbf{M}^T\mathbf{M})^{-1}\mathbf{M}^T\,\vec{\mathbf{I}} \tag{11}$$

$$\begin{cases} a = h_3 / h_1 \\ b = h_4 / h_2 \end{cases} \tag{12}$$

If $a \notin [0,1]$ or $b \notin [0,1]$, it indicates that the according lines are not the right combination, but if $a \in [0,1]$ and $b \in [0,1]$, then the combination is considered as a suspected one. Substitute all the suspect lines to (5) and calculate $\vec{I}_m$ of these lines which are equipped with PMU. The relative distance between $\vec{I}_m$ and the measured current $\vec{I}$ by PMU is defined as the fitting degree *T*:

$$T = \frac{\left\| \vec{\mathbf{I}}_{\mathbf{m}} - \vec{\mathbf{I}} \right\|_2}{\left\| \vec{\mathbf{I}} \right\|_2} \tag{13}$$

Theoretically, the fitting degree of the fault combination is zero. However, for the existence of errors, the actual fitting degree is not zero. From plenty of simulations, it is reliable to set T=1 as the boundary value. If fitting degree of a combination is smaller than 1, the combination can be considered as a suspect one. For the normal combination, the fitting degree should be bigger than 1. So the fault line and the fault location can be defined.

Example Test System

This algorithm is tested on a 10-generator 39-bus New England system. A comprehensive analysis of the algorithm and its validation are given.

The faults are set in the branch8 and branch35 at 0.25s. Two fault types are analyzed.

Case1: Three-phase short circuit in both branch8 and branch35 and the fault points are set 40% length of each line.

Three of all the combinations are analyzed. The simulations of T of these combinations are shown in Fig.3.

Firstly both *a* and *b* are judged whether they are in the interval of [0, 1]. In mode2, both *a* and *b* are bigger than 1, so mode 2 is not a suspect combination. Mode1 and mode3 are suspect combinations because they satisfy the conditions that both *a* and *b* are in the interval of [0, 1]. Then the fitting degree T of each mode is compared to the boundary value. The fitting degree of mode1 is 0.2667 which is smaller than 1 and the fitting degree of mode 3 is 2.368 which is bigger than 1. So mode1 is judged as the fault combination.

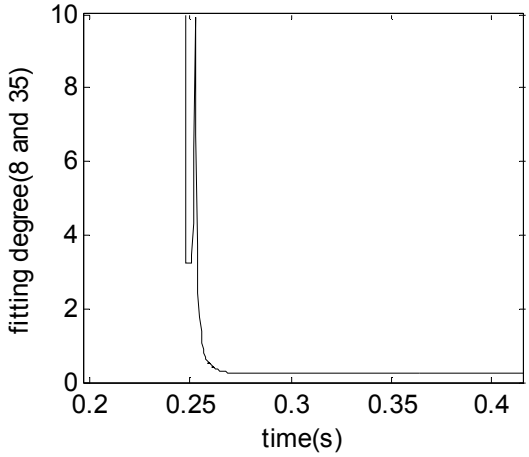

Fig.3. Fitting degree T (8 and 35)

Case2: AB two-phase short circuit in branch 8 and three-phase short circuit in branch 35. And the failure points are set 60% of each line.

The analysis process is the same as case1 and the simulations of T of these combinations are shown in Fig.4.

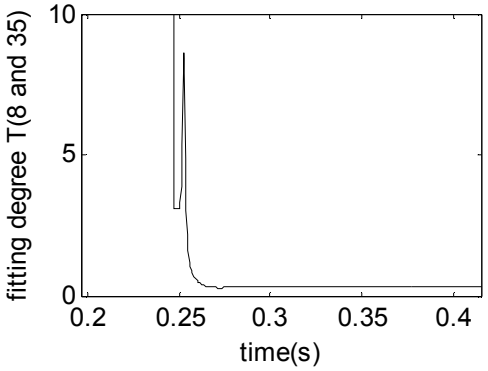

Fig.4. Fitting degree T (8 and 35)

Conclusion

The nodal admittance matrix Y and the correlation coefficient of the network can be formed when the system runs normally. The two matrixes remain unchanged and are applied to define the fault line and fault location after the fault occurs. Compared to searching the fault location based on traverse,

there is no need to change the matrix by the method proposed in the paper. So the recalculation of the admittance and its inverse matrix is voided. The algorithm is applied to each combination directly and there is no need to search by each step, so the computation is reduced enormously.

References

[1] Wang Bo, Quanyuan Jiang, Yijia Cao. Transmission Network Fault Location Using Sparse PMU Measurements[C]. 978-1-4244-4934-7 2009 IEEE

[2] Yuan Liao. New Fault Location Approach Using Voltage Measurements[C]. 1-4244-1029-0/07 2007 IEEE. 407

[3] Yuan Liao. Fault Location Using Sparse Current Measurements[C]. 978-1-4244-1726-1/07 (X) 2007 IEEE

[4] ZHANG Yagang, MA Jing, ZHANG Jinfang, WANG Zengping[C]. Fault Diagnosis Based on Cluster Analysis Theory inWide Area Backup Protection System. 978-1-4244-2487-0/09 2009 IEEE

[5] Zhiqin He,. Wide-Area Backup Protection Algorithm Based on Fault Component Voltage Distribution[C]. IEEE TRANSACTIONS ON POWER DELIVERY, VOL. 26, NO. 4, OCTOBER 2011

[6] J. C. Tan, P. A. Crossley, P. G. McLaren. Application of a Wide Area Backup Protection Expert System to Prevent Cascading Outages[C]. IEEE TRANSACTIONS ON POWER DELIVERY, VOL. 17, NO. 2, APRIL 2002 375.

[7] Y. Serizawa, M. Myoujin, K. Kitamura, et al. Wide-area current differential backup protection employing broadband communications and time transfer systems[C]. IEEE Transactions on Power Delivery, 1998, 13(4): 1046 – 1052

[8] R. Ciovanini' ,D.V. Couryl, K. M. Hopkinson', I. S. Thorp. IMPROVING LOCAL AND BACKUP PROTECTION USING WIDE AREA AGENTS[C]. 2004 The Institution of Electrical Engineers. Printed and published by the IEE, Michael Faraday House, Six Hills Way, Steven age, SGI 2AY.

[9] J. Tang, P. G. McLaren. A wide area differential backup protection scheme for shipboard application[C]. IEEE Transactions on Power Delivery, 2006, 21(3): 1183 - 1190 .

[10] K. Mazlumi, H. Askarian Abyaneh, S. H. H. Sadeghi, and S. S. Geramian. Determination of Optimal PMU Placement for Fault-Location Observability[C]. DRPT2008 6-9 April 2008 Nanjing China

[11] Zhiqin He, Zhe Zhang, Xianggen Yin, Hua Wang. A Novel Algorithm of Wide Area Backup Protection Based on Fault Component Comparison. 2010 International Conference on Power System Technology

[12] Mladen Kezunovic, A Novel Method for Transmission Network Fault Location Using Genetic Algorithms and Sparse Field Recordings[C]. 0-7803-7519-X/02 2002 IEEE

Advanced Materials Research Vols. 960-961 (2014) pp 841-844

doi:10.4028/www.scientific.net/AMR.960-961.841

Application credibility theory in the smart grid information network security assessment

Li Yanbin[1, a], Li Yun[2,b]and Li Weiguo[2,c]

[1] School of Economics and Management, North China Electric Power University,Changping District, Beijing102206, China

[2] School of Electrical and Electronic Engineering,North China Electric Power University,ChangpingDistrict,Beijing 102206,China

[a]gslyb2000@sohu.com, [b]leal_ly@hotmail.com, [c]lwglixi@tom.com

Keywords:credibility theory,information network,smart grid,security assessment,countermeasure

Abstract. With the development of the smart grid , information network security assessment affects the safe operation of the smart grid . In this paper, the improved credibility theory and analytic hierarchy process , combined with structural features of the smart grid network , From the wide area network , access network, enterprise local network , local area network and the CPN-site and home users to assess the impact of the five aspects of information networks for smart grid security operation. And make the case for more security strategy to improve the reliability of the smart grid operation , thus providing a basis for guiding the development and safe use of electricity grid users .

Introduction

Due to the rapid growth of China's future demand for electricity , smart grid development trend of China's power grid [1] . Different countries and different institutions for their own understanding and their own business, economic interests , such as the smart grid concept has a different understanding [2-4] . But the smart grid is still roughly the same basic idea , the use of modern communications , computing, control technology , power grid can adapt to optimize the operation of a variety of normal operation, the operation mode adjustment , and can take the initiative and respond to grid disturbances predictive method [5] .

Information network will go deep into the smart grid , electricity production efficiency and management level will be greatly improved , and for power users , there will be a better user experience and more economical electricity [6] . However, while the benefits , we must consider the level of information in the process of rapid development, it also brings a lot of security risks. In recent years , more and more hackers use information networks for business , industry and other institutions malicious intrusion , eavesdropping , tampering and information [7,8] . This information along with the development of the smart grid , also significantly increased their security risks and may even lead to a chain of large area blackout [9,10] . Therefore, the smart grid information network security assessment is essential.

Firstly, through a wide area network, access network , enterprise local network , local area network and the CPN -site and home users to establish a security assessment of five system , the introduction of smart grid credibility theory of information network security evaluation. Finally, the smart grid information network to improve the safety level of security and defense measures for the safe operation of the smart grid to provide a reference .

Smart Grid Information Network Security Assessment Index System

In traditional grid, the grid is to communicate through a dedicated network , and its main source of danger from the threat of internal network. The smart grid is an open system , there is a public communication network of information between the various aspects of the interaction , and links within itself also has an internal communications network . The interaction between the user information can be the grid . In this case, the information network itself has vulnerabilities , the impact on the smart grid hazard is greatly increased. In this paper, the establishment of a smart grid information network security evaluation index system based on network components , shown in Table 1 .

Table 1 Smart Grid information network security evaluation syste

Index	Use
WAN	1.Providing power data network , Internet networking and routing functions; 2.Label Switching backbone network to provide isolation of different business flow.
AN	1.To access WAN , MAN provides physical channel; 2.Available metropolitan Ethernet access Through wireless access WAN; 3.Available fiber access.
LAN	Power company intranet.
FAN	1.Production control area power plant and interconnection equipment; 2.Used to transmit data, such as data collection instrument; 3.Transmission, distribution, consumption data collection , monitoring and surveillance;
HAN	1.Provide fiber access to intelligent residential quarters users; 2.Remote meter reading, Internet access; 3.Smart home, smart meters and appliance control.

Safety assessment model based on credibility theory

Smart grid uncertainty , fuzziness and randomness , so the past are analyzed separately using probability theory and fuzzy theory, which caused the result is often one-sided. The use of credibility theory , can be a combination of random and fuzzy safety assessment for random fuzzy optimization modeling uncertainties dual problem solving work can be carried out smoothly laid a theoretical foundation , making the results more accurate.

Credibility Theory. According to the credibility theory four axioms [11-12] get triangular fuzzy variables $\xi = (r_1, r_2, r_3), r_1 < r_2 < r_3$ the membership function and the distribution of credibility are:

$$\mu(x) = \begin{cases} \dfrac{x - r_1}{r_2 - r_1}, r_1 \le x \le r_2 \\ \dfrac{x - r_3}{r_2 - r_3}, r_2 \le x \le r_3 \\ 0, \qquad Other \end{cases} \tag{1}$$

$$\Phi(x) = \begin{cases} 0, & x \le r_1 \\ \dfrac{x - r_1}{2(r_2 - r_1)}, & r_1 \le x \le r_2 \\ \dfrac{x + r_3 - 2r_2}{2(r_3 - r_2)}, & r_2 \le x \le r_3 \\ 1, & x \ge r_3 \end{cases} \tag{2}$$

Improved AHP. AHP weighting method for solving first evaluated in accordance with the internal logic to evaluate the indicators form an ordered hierarchy model ; followed by judgment matrix , using expert assessment of the index compared with each other . Solving the characteristic equation of the maximum eigenvalue of the corresponding feature quantity ; normalized eigenvector weight vector can be obtained .

Factors for a layer , the relative importance of the various factors associated with the level is expressed as the judgment matrix . By comparing the elements to be marked scale of 1-9 .

As can be seen from the table to determine the characteristics of the matrix P as follows :

1) $u_{ij} > 0$

2) $u_{ij} = \dfrac{1}{u_{ji}}, i, j = 1, 2, \cdots, n$

3) $u_{ii} = 1$

Definition, reciprocal matrix P, symmetric matrix $B = \lg P(b_{ij} = \lg u_{ij})$, and A is the optimal transfer matrix B . Therefore, by definition, intended to optimize the matrix P obtained transfer matrix P^*:

$$P^* = 10^{A_{ij}} \tag{3}$$

$$A_{ij} = \sum_{k=1}^{n} (u_{ik} - u_{jk}), \forall i, j \tag{4}$$

Based on the above , the optimal transfer matrix P^* is the same, so the consistency test may be directly obtained weights .

Algorithm steps. This paper has two levels indicators for more level indicators can be so :

First, $A = \{A_1, A_2, \cdots, A_n\}$ target layer were determined by an index layer improved AHP, Right weight vector $A_i = \{A_{i1}, A_{i2}, \cdots, A_{im}\}$, $P = (P_1, P_2, \cdots, P_n)$ and $P_i = (P_{i1}, P_{i2}, \cdots, P_{im})$.

The second step can be obtained membership of the index factor $A_{ij}(i = 1,2,\cdots,n; j = 1,2,\cdots,m)$ review of d_l （l=1, 2, …, k） h_{ijl} according to the Delphi method.

The third step is the introduction of the credibility of the above theory, solving the fuzzy expected triangular fuzzy variables $E[f(\xi)]$, then use the credibility inversion theorems formula for solving univariate A_{ij} measure to assess the credibility of the vector r_{ij} , and its be normalized .

$$C_r\{\xi \in B\} = \frac{1}{2}\left(\sup_{x \in B} \mu(x) + 1 - \sup_{x \in B^C} \mu(x)\right) \tag{5}$$

$$r_{ijl}^{k} = \frac{r_{ijl}'^{k}}{\sum_{l=1}^{n_k} r_{ijl}'^{k}} \tag{6}$$

By solving the above , r_{ij} in accordance with the sequence number order, constitute a layer of factor A_i on the credibility of the evaluation matrix :

$$R_i = (r_{ijl})_{m \times k} \begin{bmatrix} r_{i11} & r_{i12} & \cdots & r_{i1k} \\ r_{i21} & r_{i22} & \cdots & r_{i2k} \\ \cdots & \cdots & \cdots & \cdots \\ r_{im1} & r_{im2} & \cdots & r_{imk} \end{bmatrix} \tag{7}$$

The use of fuzzy linear transformation, the credibility measure to assess the credibility of the assessment matrix into vector about A_i , s_{il} indicates the status of the objective merits of the extent of A_i 's .

$$S_i = P_i * R_i = (s_{i1}, s_{i2}, \cdots, s_{ik}) \tag{8}$$

Measure to assess the credibility of the target layer matrix A can be arranged through the n- index layer A_i fuzzy subsets , we get:

$$R = (s_{ij})_{n \times k} \begin{bmatrix} s_{11} & s_{12} & \cdots & s_{1k} \\ s_{21} & s_{22} & \cdots & s_{2k} \\ \cdots & \cdots & \cdots & \cdots \\ s_{n1} & s_{n2} & \cdots & s_{nk} \end{bmatrix} \tag{9}$$

Finally, the evaluation matrix R fuzzy linear transformation , you can get the target layer A comment on the credibility of the assessment of vectors:

$$S = P * R = (s_1, s_2, \cdots, s_k) \tag{10}$$

According to the principle of maximum credibility measure , s_l maximum , this time to assess the results of d_l reviews .

Defensive countermeasures and suggestions

Smart grid security hazard a huge impact on the grid , in order to avoid harm, should establish a complete set of smart grid information network security defense system.

1) Security Policy

As a smart grid security policy on the basis of the rapid development of smart grid information network security compared to traditional grid , with network wide , interactive and more features , requiring new features for the national grid to develop a " dual network dual machine, partition Fenwick , secure access , dynamic perception, lean management , comprehensive protection , "the defense strategy , and therefore should be based on this , the smart grid hazard defense.

2) Security Technology

Strongly support smart grid security needs and technology, strengthen research and development from the information collection, interaction , and processing sectors . Smart meters , sensors , gateways and other equipment, which widely used in smart grid , to ensure their physical security, information security is essential ; adopt effective anti-intrusion systems and data encryption technologies will effectively protect network security ; operating system security updates, vulnerability scanning ; improve early warning, emergency response mechanism , the formation of effective protection security technology platform .

Conclusion

While the rapid development of smart grid , smart grid hazard also changed . This paper analyzes the network structure of the smart grid , from wide area networks, access networks, enterprise local area network , local area network and the CPN -site and home users the information analyzed five aspects of the smart grid network hazard . And protection against the above proposed strategy in terms of security policy, security technology, security training , to provide a reference for the security and defense of the smart grid , smart grid wish to be more stable operation.

Acknowledge

This work is supported by the Natural Science Foundation of China (51277063), the Beijing Central Universities in Beijing to build the project funding.

References

[1] Dongxia Zhang, Liangzhong Yao, Wenyuan Ma:Proceedings of the CSEE.Vol.33(2013),p.1

[2] Guangyu He, Yingyun Sun, Shengwei Mei, et al:Automation of Electric Power Systems. Vol.33(2009),p.1.

[3] Yixin Yu, Wenpeng Luan:Proceedings of the CSEE.Vol.29(2009) ,p.1

[4] Jiandong Wu: Power System and Clean Energy.Vol.25(2009) ,p.5

[5] Yixin Yu, Wenpeng Luan:Journal of Tianjin University. Vol.44(2011) ,p. 377

[6] Zhenya Liu.Smart grid technology[M].Beijing:China Electric Power Press,2010:1-11.

[7] Laijun Chen, Shengwei Mei, Ying Chen:Control Theory&Applications. Vol.29(2012) ,p.240

[8] Jietao Guan, Li Yan, Jietao He, Tao Ding:Shanxi Electric Power. Vol.06(2010) ,p.5

[9] BOMPARD E, NAPOLI R, XUE F:European Transactions on Electrical Power. Vol.18(2008) ,p. 820

[10] BULDYREV S V, PARSHANI R, PAUL G, et al:Nature, Vol.464(2010) ,p.1025

[11] Pishvaee M. S,Torabi S. A, Razmi J: Computers & Industrial Engineering. Vol.62(2012) ,p. 624

[12] Mao Jiaan,HeJin:Power System Protection and Control. Vol.39(2011) ,p.80

Advanced Materials Research Vols. 960-961 (2014) pp 845-848

doi:10.4028/www.scientific.net/AMR.960-961.845

Study on Improving Microgrid Transient Power Quality by Super-capacitor

Dan Wei[1, a], Wei Zhang[1,b], Zhijie Wang[1,c], David Zheng[2,d]

[1]College of Electrical Engineering Shanghai DianJi University, Shanghai 200240, China

[2]Goldwind science and Etechwin electric Co., Ltd, Beijing 100176,China

[a]weidande@sina.com, [b]WeiZhang147258369@126.com, [c] wzjsdstu@163.com, [d]zhengdehua01@hotmail.com

Keywords: Micro-grid, Transient power quality, Energy storage, Super-capacitor, Power compensation

Abstract. Massive applications of the power electronic devices and non-linear loads lead to various power quality problems during the microgrids grid-connecting. Aiming at improving power quality of micro-grid, the structure of SCs' main circuit and control circuit are designed. The model of super-capacitor energy storage system (SCESS) is established. A simulation model of micro-grid is also built up by using MATLAB and the simulation is conducted for different situations. Moreover, under Goldwind micro-grid platform, according to the result of MATLAB modeling and simulation, the SCESS effectively improves the transient power quality of the system.

Introduction

With the development of power system, the micro-grid has received much attention in recent years, which is expected to become competitive with conventional energy sources. As the functional part of energy buffering in micro-grid, energy storage systems is taking more and more effect in improving power quality and system operational stability. The super-capacitor (SC) energy storage device is considered as an auxiliary power source to compensate the energy gap when needed. Super-capacitors are attractive as they have a higher power density (kW/kg) than batteries, appropriate energy density, high charge and discharge rate. In addition, SCs has many advantages, such as convenient control, high conversion efficiency, wide working temperature range and no pollution [1].

The super-capacitor energy storage device is composed of several groups of super-capacitors, storing the electric energy as electric-field energy. When system voltage fluctuating, the device is accurate and efficient for supporting active power and compensating reactive power to micro-grid and power grid, which promotes a smooth transition of system and improves the power quality[2].
In this paper, the structure of SCs' main circuit and control circuit are designed. The model of super-capacitor energy storage system (SCESS) is established. A simulation model of micro-grid is also built up by using MATLAB and the simulations are conducted for different situations. Moreover, under Goldwind micro-grid platform, according to the result of MATLAB modeling and simulation, the SCESS effectively improves the power quality of the system.

Principle and Model of SCESS

Super-capacitor energy storage system consists of super-capacitors, AC-DC rectifier, bi-directional DC-DC converters, DC-AC inverter and controller. The corresponding topological structure chart of SCESS is shown in Fig. 1. SCESS is parallel on DC bus of micro-grid. The operating principle of SCESS is that the three-phase alternating current turns into direct current through rectifier. After that, the inverter converts DC to a controllable AC. SCs stores DC power from rectifier while the system operates properly. If the system fails or fluctuates, SCs feed power to the system through inverter rapidly and accurately, achieving balanced and stability control of electric energy [3]. For example, SCs provide power to system while the inverter voltage being higher the system voltage; otherwise SCs absorb power.

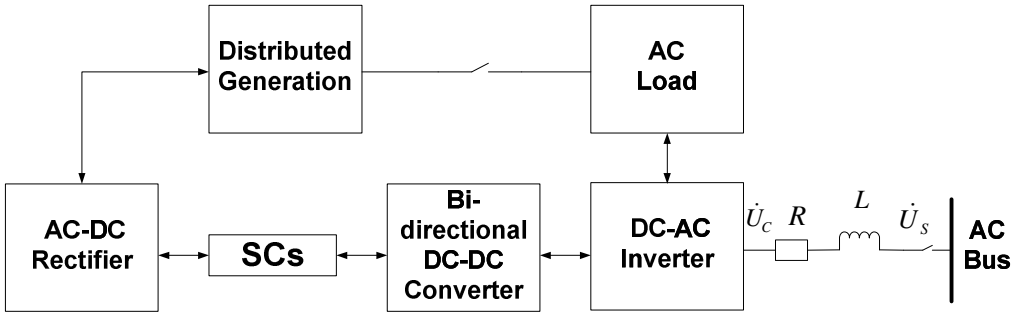

Fig. 1 Topological structure chart of SCESS

The super-capacitors group is supposed to be consist of m×n single super-capacitors, in which there are n branches. Each branch includes m single super-capacitors connected in series. C_F is the equivalent capacitance of single super-capacitor, and r_{ESR} is its equivalent resistance. The equivalent resistance of super-capacitors group is calculated applying equation (1).

$$r_i = \frac{m}{n} r_{ESR} \tag{1}$$

The equivalent capacitance of super-capacitors group is calculated applying equation (2).

$$C_{SC} = \frac{m}{n} C_F \tag{2}$$

The stored energy of super-capacitors group is calculated applying equation (3).

$$E = \frac{1}{2} CV^2 \tag{3}$$

Where, C is the capacitance of super-capacitors, V is the operating voltage of super-capacitors.
Given the voltage variation range of single super-capacitor at (U_{SC1}, U_{SC2}) during the discharge process. U_{SC1} is the minimum DC bus voltage when inverter operates normally, and U_{SC2} is the minimum DC bus voltage at the initial time of failure. Then total energy the super-capacitors group releases is calculated applying equation (4).

$$E = \frac{n}{2m} C_F \left[(mU_{SC2})^2 - (mU_{SC1})^2 \right] = mnC_F \left(U_{SC2}^2 - U_{SC1}^2 \right) \tag{4}$$

In this way, the total energy the super-capacitors group releases is irrelevant to the approach of series and parallel while quantity and voltage of single super-capacitor don't change. And the time that SCs could support power to the system after interruption of power supply can be calculated applying equation (5). Where, P is the load power.

$$t = \frac{1}{2} \frac{C}{P} (U_{SC2}^2 - U_{SC1}^2) \tag{5}$$

Case study description and hardware design

As the basis for this study, the experimental domestic microgrid of Goldwind Science & Technology Microgrid platform has been considered. The microgrid model is established based on MATLAB , which comprises micro turbine, wind turbine (WT), photovoltaic cell (PV) as generation units, thermal loads as consumption units, lithium ferrous phosphate battery (LFP), all vanadium flow battery (VRB) and SCs as energy storage units. The model is validated through the test under the Goldwind platform, as depicted in Fig. 2. In addition, the rated power of micro turbine, WT , PV, (LFP) , VRB and SCs are 130 kW, 2.5 MW, 150 kW, 100 kW, 100 kW, 100 kW respectively. The normal power output of WT is 1MW, and the total load value is about 1.2 MW.

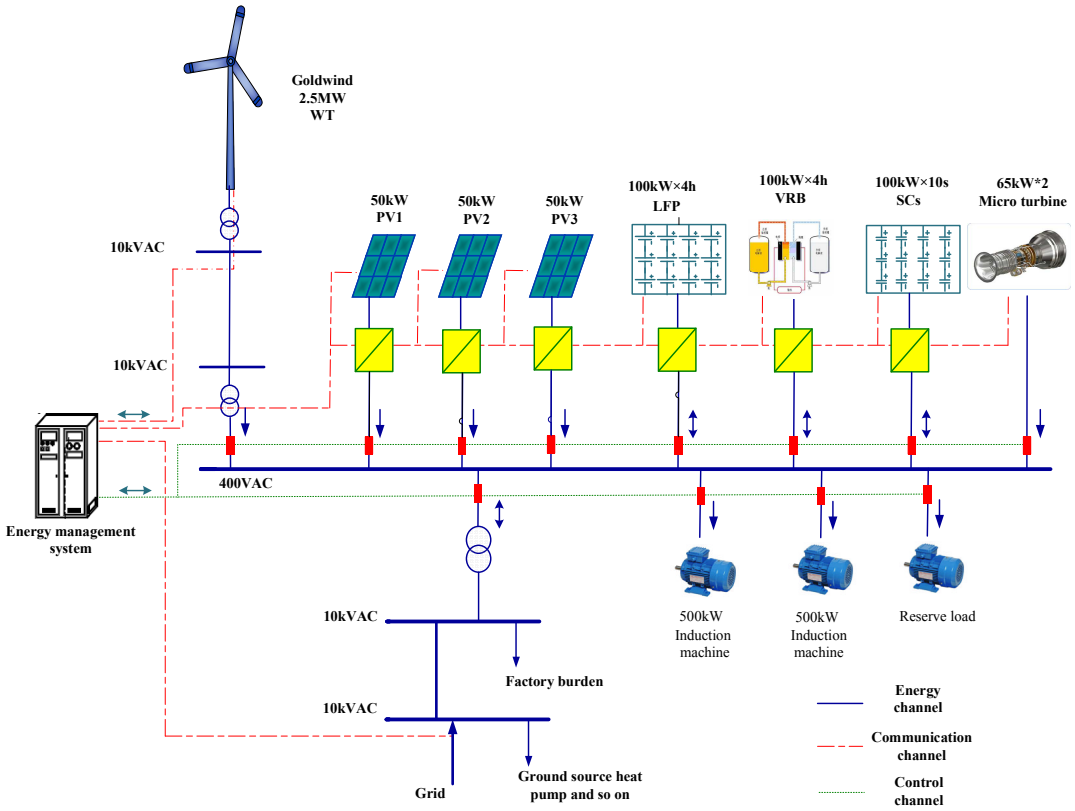

Fig.2 The hardware model of Goldwind microgrid

During the grid- connected operation, the control strategy used to be P/Q control method, while some DGs are under V/f control model during islanding operation, such as WT, PV and so on.

It's important to selecting the parameter of SCs. According to the quantity and the minimum discharge voltage of single super-capacitor applied to equation (3) and (4), the capacity of SCs will be settled.

The simulation results and analyses

Grid-connected operation and stand-alone operation are two typical operation modes in microgrid. Microgrid operation mode smooth transition is the key technique to guarantee the system working well. When the operation switch from Grid-connected operation to stand-alone operation, voltage sag will take place. Then the SCESS is used to improve the transitions between operating modes.

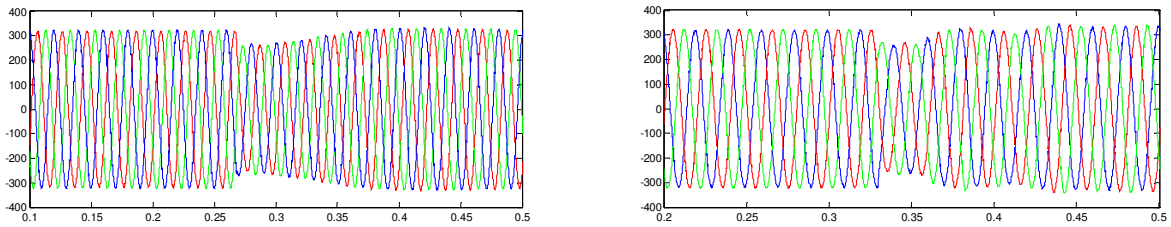

(a) Without SCs compensation (b) With SCs compensation

Fig.3 Detail of the triphase voltage during switching operation

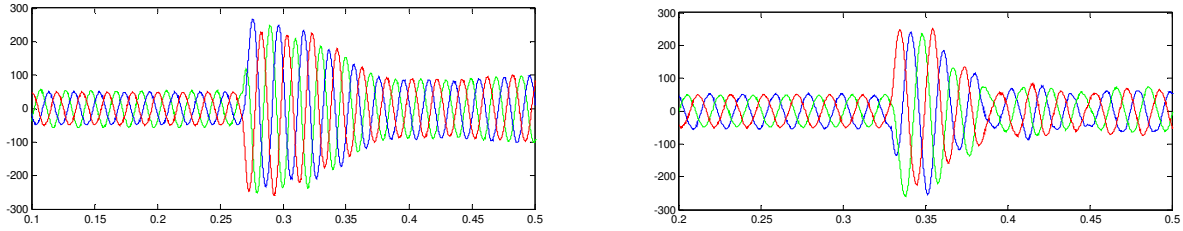

(a) Without SCs compensation (b) With SCs compensation

Fig.4 Detail of the three-phase current during switching operation

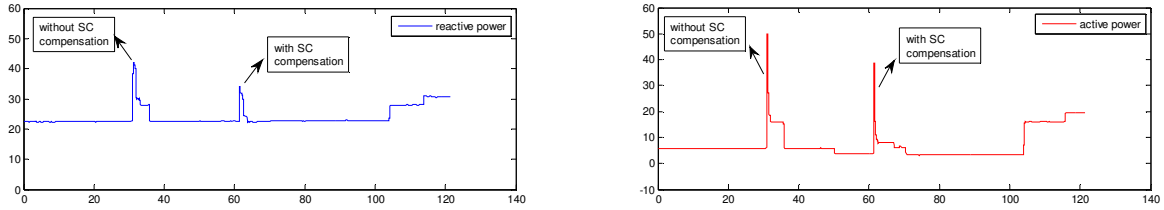

Fig.5 Inhibition effect on reactive power and active power when without SCs or with SCs compensation

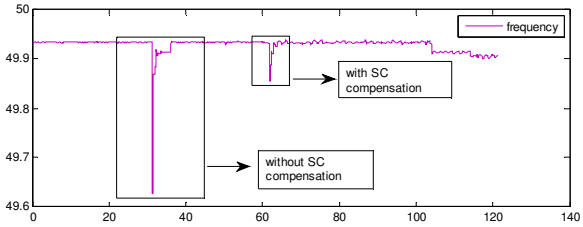

Fig.6 Inhibition effect on frequency when without SCs or with SCs compensation

In order to validate the whole hardware design, the prototype has been experimentally tested both in the condition of that without SCs compensation and with SCs compensation.

The Fig. 3 shows that the three-phase voltage returns to a new stable states in about 0.15 s without SCs compensation during switching operation, while it returns to a new stable states in about 0.05 s with SCs compensation. Similarly, the three-phase current with SCs compensation reaches a new stable condition faster than without SCs compensation during switching operation as depicted in Fig. 4. Moreover, Fig. 5 and 6 present waveforms that are also obtained during switching operation, which show that the SCs compensation contributes to reducing major fluctuations of reactive power, active power and frequency.

Conclusions

From Figs. 3, 4, 5 and 6, it is concluded that SCESS could improve the power quality and system operational stability, and conduce to promoting the microgrid to attaining new equilibrium. In a word, the super-capacitor energy storage system will take more and more effect in microgrid, as the indispensable energy buffer.

Acknowledgements

This work was financially supported by the Shanghai Natural Science Foundation (12ZR1411600), Natural Science Foundation (11201267).

References

[1] Conway B E. Transition from supercapacitor to battery behavior in electrochemical energy storage[C]. Power Sources Symposium, 1990: 319-327.

[2] Huiyan Zhang. Study on ultracapacitor Energy Storage [J]. Power system Technology, 2006 .Vol.30 (8):92-96. (in Chinese)

[3] Wenbo Xia, Mingbo Liu, Zhiwen Liu. Control method and strategy for smooth Switching of microgrid operation modes based on complex energy storage)[J]. Power system technology, 2012, Vol.4 (36): 1-8. (in Chinese)

CHAPTER 8:

High Voltage and Insulation Technology

Advanced Materials Research Vols. 960-961 (2014) pp 851-855
© (2014) Trans Tech Publications, Switzerland
doi:10.4028/www.scientific.net/AMR.960-961.851

A discussion on optimal wavelet basis for data de-noising of Insulator leakage current

Yicong Wang [1, a]

[1] North China Electric Power University, Baoding,Hebei,071000, China

[a] love-snow26@163.com

Keywords: Insulator leakage current; wavelet transform; optimal wavelet basis

Abstract. Insulator leakage current contains important information which can reflect the condition of insulators. However, it is always swallowed by many other noises which hinder us to get precise signals. Wavelet transform is a kind of new method which has been widely used in signal-de-noising because of its good frequency effect. However, suitable wavelet bases should be used to guarantee better effect. In this paper, we compared three groups of wavelet basis: db/coif/sym in hunt for the most relative suitable wavelet basis for insulator leakage current signal. Experiment results prove the conclusion later.

Introduction

Insulator Leakage Current (ILC) is one of the most important monitoring parameters of transmission line safety. It contains important information such as insulator state, leakage current state, hydrophobicity, aging state and many other key information which can be used to evaluate insulator contamination and make predictions ahead of time. Hence, it is of great importance to evaluate pollution flashover. However, ILC is often mixed with many noises in the process of collection and detection, which causes greater difficulty to extract further information. Therefore, to get ILC de-noised is essential. To get the best de-noising signal method, many experts and scholars have made great attempts, thus many methods appeared and are used gradually in our daily life, including: Empirical Mode Decomposition de-noising method[1], self-adaptation eliminating-noise-method based on HHT transform[2], EMD decomposition and time-frequency analysis method for de-noising and wavelet de-noising.

Among these methods, wavelet de-noising is one of the most popular methods that has been widely used in the field of signal processing in the past 10 years. It has good characteristics of multi-resolution analysis, thus it has advantages to present the local feature of the signal in time domain and frequency domain. Besides, it is very flexible, different results will be got if different wavelet basis will be chosen when dealing with the same signal. Hence, to select the optimum wavelet base according to the specific signal is a tough problem [3]. In the field of wavelet de-noising, many experts and scholars had attempted in depth and expressed different views on choosing suitable wavelet bases, yet a complete study on choosing the optimal wavelet basis for insulator leakage current development is vacant. In this paper, we try to find the proper wavelet basis among three classic groups of wavelet basis function: db/coif/sym; them make a comparison between those wavelet basis according to the subtraction of the original signal and the decomposed signal, and eventually draw the conclusion of the optimal wavelet basis for leakage current signal. Finally, an experiment is conducted to test the result.

Principle of wavelet transform in de-noising

Discrete wavelet transform

According to reference [4], the integral transform can be described as

$$W_f(a,\tau) = \int_R f(t)\overline{\varphi_{at}(t)}dt = (f, \varphi_{at}(t)) \tag{1}$$

Where signal $f(t)$ is known as the continuous wavelet transform, where

$$\varphi_{at}(t) = \frac{1}{\sqrt{a}}\varphi(\frac{t-\tau}{a}) \tag{2}$$

is known as the wavelet basis function, which is translated and scaled by a mother function. If the following function is satisfied, then $f(t)$ can be called as wavelet basis function.

$$\int_R \frac{|\hat{\varphi}(w)|^2}{w} dw < \infty \tag{3}$$

Where $\hat{\varphi}(w)$ can be got after the Fourier transform of $\varphi(t)$. In the discrete case, discrete wavelet function is defined as

$$\phi_{j,k}(t) = 2^{-j/2}\phi(2^{-j}t - k) \tag{4}$$

Then the discrete wavelet transform of the signal is defined as

$$D[W_f(j,k)] = 2^{-j/2}\int_R f(t)\overline{\phi(2^{-j}t-k)}dt \tag{5}$$

Wavelet decomposition and reconstruction method of de-noising

Suppose $f(i)$ is the real signal; $c(i)$ is the noise; $s(i)$ is the collect signal compounded with real signal and the noise. Then, $s(i)$ can be described as:

$$s(i) = f(i) + \sigma \times c(i), \quad (i = 0,1,2,\cdots,n-1) \tag{6}$$

In actual project, low frequency or more smoothly signals are always helpful whereas high frequency signals are noises which should be wiped out. De-noising procedure can be described as:

(1) Decompose the signal according to wavelet principle by choosing proper wavelet basis function and the number of decomposition layers N.
(2) Quantify the decomposition of the high frequency coefficient according to the threshold.
(3) Reconstruct the signal according to the principle of inverse transformation of wavelet, ultimately we can achieve the goal of eliminating noise.

Select the wavelet base

Since select the best wavelet base is of great importance in the process of signal de-noising, several characteristics of wavelet base should be taken into consideration: the orthogonality, symmetry, regularity, compactly supported, smoothness, vanishing moments and so on. Among them, the symmetry related to whether the filter characteristic of wavelet has linear phase, furthermore it can be used to test signal distortion; regularity is used to ensure the smoothness of the signal; compact support ensures excellent local time-frequency features, and are also conducive to the possibility of algorithm; smoothness is related to the frequency resolution. However, these characteristics mentioned above cannot be guaranteed thoroughly, for example: symmetry and orthogonality of wavelet bases is not compatible. Therefore, simulations of optimum wavelet base of leakage current should be conducted after theoretical analysis.

TABLE I. CHARATERISTICS OF THE THREE DIFFERENT WAVELET BASIS

Wavelet base	representation	orthogonality /Double orthogonality	symmetry	Compactly supported	Vanishing Moments	Support length	Filter length
Daubechies	db N	Yes	approximate symmetrical	Yes	N	2N-1	2N
Coiffets	coif N	Yes	approximate symmetrical	Yes	2N	6N-1	6N
Symlets	SymN	Yes	approximate symmetrical	Yes	2N	2N-1	2N

Table1 lists all the properties of the three kinds of wavelet bases, from which we can see that they all have orthogonality and symmetry, and are compactly supported.

Simulation and analysis

In this experiment, Matlab is used for simulation. First the origin clear signal (2500 sampling points) is added with a white noise, then the default threshold is generated according to the function *ddencmp*. Next, the function *wdencmp* is used for de-noising. Eventually, the effect of the de-noising can be judged by making a comparison between the deviation of the noised-signal and the original signal. The number of decomposition layer N is set to 3 to 5 according to a reference[5] , therefore, we finally determine by experiment that N is 5. Because the simulation process has a certain randomness, we take 5 times for each wavelet and get the average as the final result. Two different scales of noise: light noise and heavy noise are discussed repectively.

We choose Signal Noise Ratio(SNR) to evaluate the residuals. SNR can be defined as follows:

$$SNR = 10 * \lg(\sum s^2(n) / \sum p^2(n)) \tag{7}$$

Where $s(n)$ is the amplitude of de-noised signal, $p(n)$ is the amplitude of noise. SNR shows the proportion of denoised-signal and noise: a larger SNR promotes a better effect of wavelet de-noising. Figure 1 is the result of de-noising simulation.

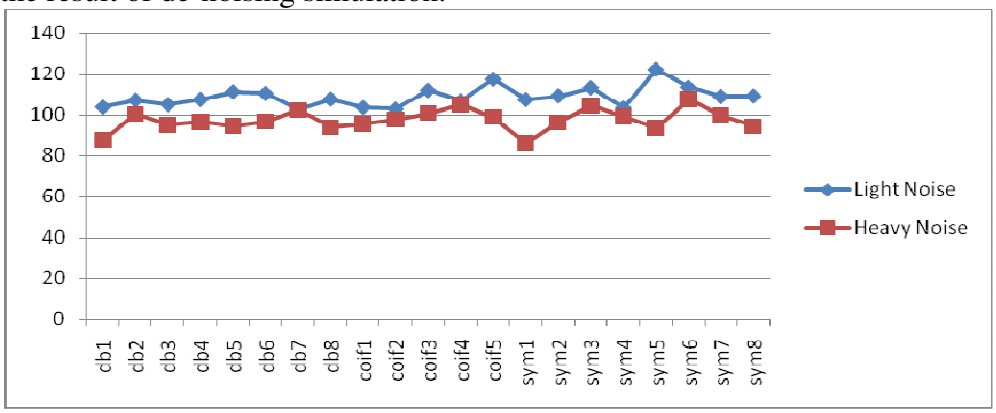

Figure 1. SNR of signal de-noising based on different wavelet basis

TABLE II. SNR OF DIFFERENT SCALE NOISES

order	Light Noise		Heavy Noise	
	Wavelet base	SNR	Wavelet base	SNR
1	sym5	122.2494	sym6	107.6558
2	coif5	117.4651	coif4	105.235
3	sym6	113.5321	sym3	104.5024
4	sym3	113.3299	db7	102.4369
5	coif3	112.0206	coif3	100.8336

According to SNR, Table2 list the best five wavelet bases in light and heavy noise environment respectively. Next the image of de-noising effect is shown by Matlab as Figure 2. Sym6 and db2 are chosen to denoise the signal in heavy noise as an example. It is obvious that the de-noised signal is smoother if the optimal wavelet base (sym6) is chosen.

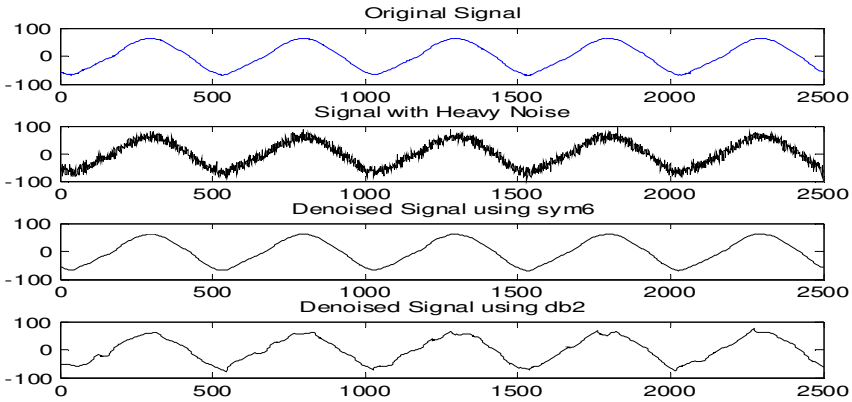

Figure 2. Image of de-noising effect based on sym6/db2

Experiment based on real signal

In this section, the actual leakage current signal is collected and tested according to the conclusions above. However, as the phenomenon of point discharge is very important in this issue, the effect of both signal de-noising and point discharge keeping are both important. Therefore, we choose sym5 as the wavelet base to denoise the collected signal.

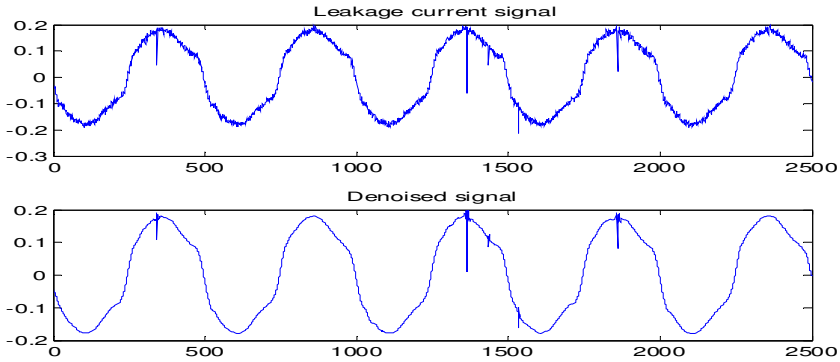

Figure 3. The real collected leakage current signal and de-noised signal using sym5

Figure 3 shows that denoised signal is smoother and point discharges have been kept well. Therefore, sym5 is a suitable wavelet base.

Summary

Based on the principle of discrete wavelet transform, this paper explores for the optimal base of insulator leakage current signal de-noising. Through simulation of the contamination of insulator leakage current de-noising, result shows that sym5 is the best wavelet base in light noise environment while sym6 is the best wavelet base in heavy noise environment. Experiments proved our conclusion later.

Acknowledgment

The author gratefully acknowledges North China Electric Power University for financial support for the research projects, meanwhile, sincerely thank for the colleagues who offered plenty powerfully technical support.

References

[1]Zhu Yong-li, Huang Yuan-qing. Application of EMDin the de-noise of insulator leakage current[C] //International Forum on Information Technology andApplications, 2009: 85-88.

[2]Liu Di-chen, Xia Li-min, SHANG Zhi-hui. Study of adaptive noise cancellation used in measuring HV insulator's leakage current[J]. Engineering Journal of Wuhan University, 2001, 34(4): 96-99.

[3]Gao Yu-bao, Zhang Dai-feng, Jiang jin-long,Selecting Criteria and Application of Optimal Wavelet Basis Regarding Stable-distribution Signals[J]. Communications Technology, 2008, 41(11):185-187.

[4]Zhang Xu-dong, Zhan Yi, Ma Yong-qin. Approaches of de-noise by wavelet transform of different signals.OGP, 2007,42 (supplement):118-123

[5]Huang Jian-cai, Zhu Yong-li. Insulator Leakage Current De-noising Using Wavelet Transform. High Voltage Engineering,2012,38(8):1981-1987

Advanced Materials Research Vols. 960-961 (2014) pp 856-862

doi:10.4028/www.scientific.net/AMR.960-961.856

The Analysis of Induced Voltage from AC Submarine Cable to Adjacent Communication Cable

Yang Wang [1]; Guangzhou Zhang [2], Guozhi Chen [1]; Xiaoqin Zhang [2,a *],

Xinlong Zheng [1]; Jian Zhang [1]

[1.] State Grid Zhoushan Power Supply Company, Zhoushan 316021, China;

[2.] State Grid Electric Power Research Institute, Wuhan 430074, China

[a]zxq850627@126.com

Keywords: AC Submarine Cable; induced voltage; shielding effect; horizontal arrangements; laying length

Abstract: The induced voltage generated by AC submarine cables would effect the normal operation of communication cables nearby. The paper calculated the induced voltage generated by AC submarine cable according to formula and procedures related to magnetic induction. The maximum parallel length between submarine cable and communications table was calculated under horizontal arrangement, and shielding effect was taken into account to the impact of the results. The causes of various induced voltage on communication cable were analysed under normal operation and various fault conditions. The results show that the induced voltage on communication cable is proportional to the parallel length and inversely proportional to parallel spacing. When the parallel length does not exceed a certain value, the induced voltage is in the allowable range and will not affect the normal operation of the communication cable.

Introduction

Submarine cables have been laid in more and more areas recently. Faraday's law of electromagnetic induction shows that AC transmission line will produce an alternating magnetic field in the adjacent areas, which induces vertical electromotive force in the adjacent communication cables and affecting the normal operation of communication cables. The induced voltage from submarine cables in fault states to the nearby communication cables would endanger the personal safety of telecommunications maintenance staff and telecommunications equipment[1,2].

For engineering applications, induced voltage communication lines from submarine cables to adjacent parallel communication cables was calculated under normal operation and fault states, and the maximum length of submarine cable in parallel with the communication cable was calculated in the paper.

Calculation Method

Communication cables generally use coaxial cable, which is consist of a center conductor and shield. When a current in the shield, induced voltage is generated on the center conductor, the magnetic flux generated by current of the shielding would linkage with the center conductor and magnetic coupling interference cannot be suppressed if the shield is grounded at both ends. The

shield has no current path when shield is grounded at one end, so the charge induced on the shield can be vented into the ground and magnetic coupling be eliminated.

Magnetic shielding effect of AC cable sheath is related with the sheath grounding mode. Sheath single-point grounding at one end and protective grounding on other end for short single-core cables, the induced current in the sheath is substantially zero in this case, without shielding to the magnetic field generated by core wire. When both ends of sheath are directly grounded, the magnetic field on the sheath can be offset by the magnetic field generated by the core wire in this case. However, the efficiency of transmission line will be reduced greatly and the loss generated by sheath current heat is very large. It is not allowed in the case of normal operation. When protection is breakdown under short fault state, both ends of sheath are grounded and the sheath has the magnetic shielding effect.

The actual frequency shielding factor of 220kV cross-section 600mm^2~800mm^2 cable corrugated aluminum sheath is probably between 0.05 and 1. For the short-circuit current, the center frequency of standard 8/20 lightning current wave is 25 KHz, and the actual shielding factor is probably between 0.05 and 0.1. The shielding factor in the paper is 0.7 referring to related date of inherent shielding factor of communication cables[3].

The formula calculating mutual inductance between the two insulated single conductors under the ground recommended by "The electromagnetic coupling between AC transmission line and telecommunication lines " is as follows[4,5]:

$$M = \frac{\mu_0}{4\pi}\left[2\ln\frac{D}{d} + 2\ln(\frac{2}{j^{1/2}\gamma\alpha a}) + 1 + \frac{4(b+c)}{a} - j^{1/2}\frac{4}{3}(\alpha|b+c|) \right] \quad (1)$$

In the formula: A is a close distance between the two cables (m); b and c respectively sensor cable and induced cable depth (m); σ is earth apparent conductivity (s / m); γ equals 1.7811;

$d = \sqrt{a^2 + (b-c)^2}$ (m); $D = \sqrt{a^2 + (b+c)^2}$ (m); $\alpha = \sqrt{\omega\mu_0\sigma}$ (1/m).

The formula of vertical magnetic induction electromotive force on the telecommunication lines from "design rules of dangerous effects from cable to telecommunication lines" is as follows:

$$Es = \sum_{i=1}^{n} \omega M_i L_{pi} I_s K \quad (2)$$

In the formula, ω is the current angular frequency of transmission line (rad/s), ω=2πf, *Mi* is the mutual inductance in paragraph *i* between cable and telecommunication line at 50Hz(H/km), L_{Pi} is the proximity length in paragraph *i* between cable and telecommunication line(A), *Is* is short-circuit current (A), K is integrated electromagnetic shielding factor of various grounding conductor in close paragraph at 50Hz, *f* is current frequency of cable(Hz).

Longitudinal magnetic induction EMF from AC submarine cable to communication line

The impact on the coax cable was considered under normal operation and fault conditions.

There are generally three arrangement types of power cables: horizontal arrangement, vertical arrangement and triangle arrangement. The induced voltage from AC submarine cable to communication cable was calculated under three types of arrangement when normal operating. For example of horizontal arrangement, induced voltage on communication line was calculated under fault state. Figure 1 shows horizontal arrangement of submarine cable.

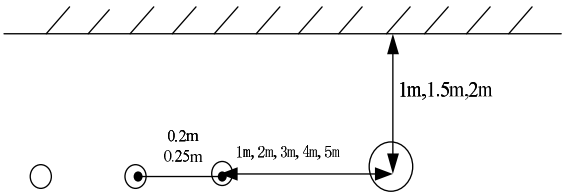

Fig.1 Submarine horizontal arrangement schematic

Normal operation

Calculation conditions: fixing center space between electrical cables and communication cables at 1m, submarine cables normal operating current at 1kA. Considering slightly different of induced voltage along the communication cable, maximum value was analyzed[6].

For the most serious cases, the communication cable shield was not grounded and there was no magnetic field on the communication cable. The relationship of induced voltage and parallel length of communication cable under three arrangements is shown in figure 2.

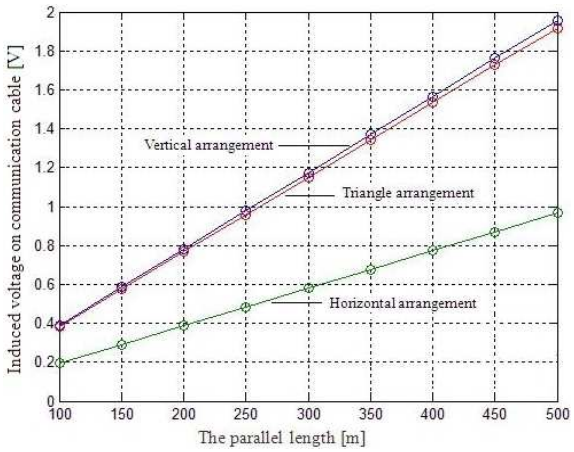

Fig.2 The relationship of induced voltage and parallel length under three arrangements

In figure 2, the induced voltage on communication cable is proportional to the parallel length. Comparing the three arrangements, the induced voltage on parallel communication cable is the minimum under horizontal arrangement and is very close under vertical arrangement and triangular arrangement.

The induced voltage variation with parallel length considering shielding is shown in figure 3. Considering the shielding effect of the communication cable, the overall level of induced voltage on communication cable decreased 0.7 times as the induced voltage not considering shielding.

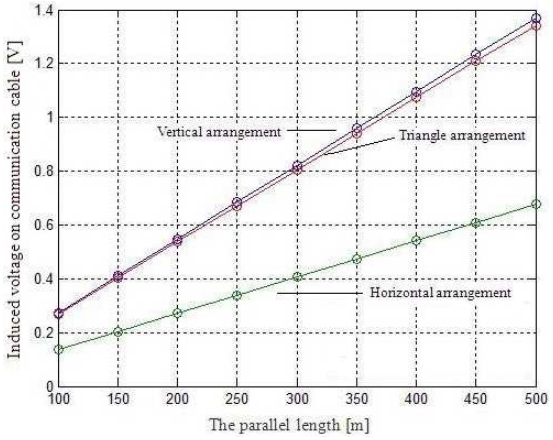

Fig.3 The relationship of induced voltage and parallel length considering shielding

Submarine cable in fault

When submarine cables were in fault, the variation of induced voltage was calculated at horizontal arrangement.

Calculation conditions: fault phase short-circuit current at 20kA, normal operating phase current at 1kA[7,8]. Calculation model is shown in figure 4.

When the protection of power cable acted and the cable sheath grounded at both ends, the circuit current in core wire and sheath would form a loop, and the sheath made better effort of shielding. The shielding factor was taken as 0.1. The distribution of induced voltage in communication cable is shown in figure 5 when submarine cable in different fault state at horizontal arrangement.

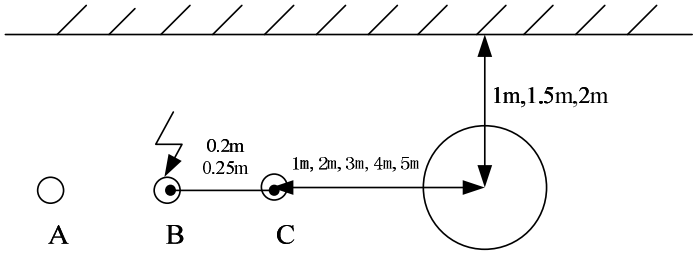

Fig 4 Horizontal arrangement schematic of submarine in fault state

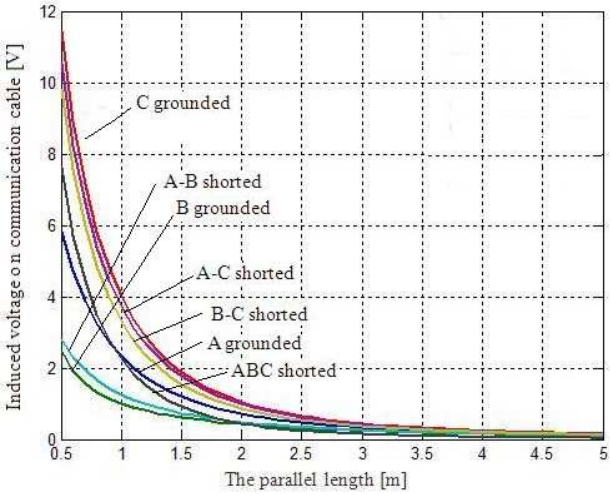

Fig.5 Induced voltage under horizontal arrangement in different fault states

The induced voltage on communication cable at different parallel spacing is shown in table 1, voltage unit, V.

Tab.1 Induced voltage on communication cable under horizontal arrangement at different spacing

short-circuit condition	different parallel spacing of submarine cable and communication cable				
	0.5m	1m	1.5m	2m	2.5m
A grounded	5.8	2.3	1.2	0.7	0.5
B grounded	2.5	1.0	0.6	0.4	0.3
C grounded	11.5	4.0	1.9	1.0	0.7
A-B shorted	2.8	1.3	0.7	0.5	0.3
A-C shorted	10.6	3.7	1.8	1.0	0.6
B-C shorted	9.8	3.3	1.5	0.9	0.5
ABC shorted	7.6	2.3	0.9	0.4	0.2

In table 1, the transient induced voltage is the largest when C-phase grounded under horizontal arrangement. This is mainly due to that the transient magnetic field generated by short circuit current cancels each other out at two-phase or three-phase short-circuit state. The C-phase is the closest to communication cables, there is no magnetic field generated by other phase circuit current to offset magnetic field generated by C-phase.

The impact of spacing between Submarine cables and communication cables on induced voltage

Fixing the parallel length of submarine cable and communication cable at 100m, depth at 1m and current 1kA, the variation of induced voltage under different parallel spacing is shown in figure 6.

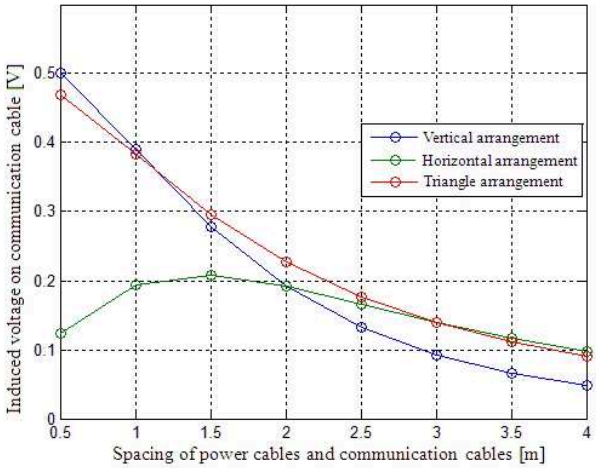

Fig.6 Induced voltage under different parallel spacing

The induced voltage on communication cable is inversely proportional to parallel spacing. Considering the mutual influence of three phases[9], the variation of induced voltage will change in case of small spacing. In figure 6, the induced voltage on communication cable is inversely proportional to the parallel spacing when parallel spacing is over 2m.

The maximum laying length

The allowable voltage on communication lines caused by magnetic is provided in CCITT "protective guidelines" and GB6830-86 "the tolerable limits of danger on telecommunication lines from power lines": when power lines operation normally, the allowable voltage on core line is 60 V; when power lines in fault, (1)430V, non-high reliability transmission lines, fault clearing time in less than 3s; (2)650V, high reliability circuit, fault clearing time in less than 0.5s. When power lines operation normally, the maximum induced voltage is approximately 2V at 500m parallel length without considering shielding[10,11].

Taking the proportional relationship among induced voltage with parallel length and current, the maximum parallel length between submarine cable and communication cable is 15km. After considering shielding, the maximum parallel length is up to 21km.

When submarine cables in fault, the maximum transient induced voltage on communication cable is 11.5V, the maximum parallel length between submarine cable and communication cable is 5.65km. After considering shielding, the maximum parallel length is up to 8km.

The impact of parallel spacing on submarine cable and communication cable is shown in table 2.

Table.2 Parallel induced voltage at depth 1m and current 1kA

Spacing [m]	Maximum induced voltage at parallel 100 m [V]	Maximum parallel length [km]
0.5	0.5	12
1	0.4	15
1.5	0.3	20

Conclusion

The paper calculated the vertical induced voltage from submarine cables to communication cable and the maximum length of submarine cable in parallel with the communication cables. The results show that the induced voltage is inversely proportional to spacing length of submarine cables in parallel with the communication cable.

Fixing center spacing between electrical cables and communication cables at 1m, submarine cables normal operating current at 1kA, the maximum parallel length between submarine cable and communication cable is up to 21km in the shielding. When submarine cables in fault and current at 20kA, the maximum parallel length between submarine cable and communication cable is 8km.

The calculating of induced voltage on communication cable adjacent submarine cable and the parallel length between submarine cables and communication cable can provide a reference for the laying of submarine cables.

References

[1] Stratton J. A. Electromagnetic theory. McGraw-Hill Book Co. ,1941.

[2] CCITT, Directives concerning the protection of telecommunication lines against harmful effects from electricity lines, 1963.

[3] Jin Yufeng. Discussion on Composite Shielding Factor of Multiple Shields[J]. Jilin Electric Power, 2010, （5）：29-31. In Chinese.

[4] Zhang Wenliang, CUI Dingxin. Electromagnetic coupling between AC transmission line and telecommunication line[M]. China electric power press. Beijing, 2013. In Chinese.

[5] China electricity Council. DL/T5033-2006: The design rules of telecommunication lines against danger and interference effects from power transmission lines[M]. China Electric Power Press. Beijing, 2006. In Chinese.

[6] Sun Jianming, Lu Tiecheng. Electromagnetic effect of Railway 10 kV Power Line on Signal Cable[J]. Power System Technology, 2007,31（6）: 93-94. In Chinese.

[7] Jiao Chaoqun, Li Lin, Zhao Zhibin, et al. Calculation of induced voltage on communication line in case of a short circuit fault on transmission line[J]. Journal of North China Electric Power University, 2003,30（3）：25-29. In Chinese.

[8] CCITT. Directives concerning the protection of telecommunication lines against harmful effects from electricity lines, ITU, Geneva, 1963 (1978).

[9] CIGRE. K. saf-Guidance on establishing limit for people safety related to induction from power and electrified traction lines in fault conditions. ITU-T D. 22,1995.

[10]CCITT. Directives concerning the protection of telecommunication lines against harmful effects from electric power and electrified railway lines. ITU, Geneva, 1989.

[11] PRC National Standard. GB6830-86: The tolerable limits of danger on telecommunication lines from power lines, 1986.

Advanced Materials Research Vols. 960-961 (2014) pp 863-866

doi:10.4028/www.scientific.net/AMR.960-961.863

An Experimental Study of Simplified Model for Air-core Reactors

Gan XU[1,a], Liang ZOU[1,b] , Li ZHANG[1,c] , Tong ZHAO[1,d], Qingquan LI[1,e]

[1]School of Electrical Engineering, Shandong University, Jinan 250061, China

[a]xugan0805@163.com, [b]zouliang@sdu.edu.cn, [c]zhlieee@gmail.com, [d]zhaotong@sdu.edu.cn, lqq@sdu.edu.cn

Keywords: Air-core reactor; magnetic field; scaling rules; simplified model

Abstract: With the development of electric power system, Power-frequency Magnetic Field (MF) has become a matter of concern recently. In order to speed up the computation and modeling process, the small-scale experimental technique and simplified model for air-core reactors are introduced as a novel way to assess the MF of air-core reactors in this paper. Firstly, the scaling rules of the parameters for air-core reactors are summarized. Then, the scaling rules modification is put forward to reduce the error. Thirdly, three simplified models were established for air-core reactors, including one loop model, two loops model and three loops model. It is concluded after that the two loops model in configuration 2 can be considered as the optimal simplified model.

Introduction

With the fast development of electric power technology in China, especially the increased construction of distributed generation and modern systems, the reactive power compensation is needed to improve voltage quality and reduce power loss. Dry-type air-core reactors, due to its uniform distribution of starting voltage, good linearity, small loss and low noise, have been widely used in electric power system. However, air-core reactors generate Power-frequency Magnetic Field (PFMF) in its normal operation threating the safe and stable operation of some other equipment in substation. Besides, the space MF of air-core reactors may put a potential threat to the health of the working staff and general public. Thus, air-core reactors have become the main source of electromagnetic contamination in substations[1-2].

Aiming at the problem of MF distribution of the air-core reactors, masses of work have been done at home and abroad. Many accurate calculation methods for evaluating the MF of air-core reactors have been proposed, including analytical, semi-analytical and numerical methods[3]. Besides, experimental method is widely used in the MF calculation. Among them small-scale experiment method is more accurate and convenient method. But in the practical application, it is difficult to make precise small-scale model, which greatly limits the application of small-scale experimental method.

In this paper, the scaling rules of parameters of air-core reactor are summarized firstly, then put forward three typical corresponding correction strategy under the premise of magnetic induction intensity keeps unchanged. Beyond this range, it is necessary to develop a new simplified model replaced the accurate small-scale model to save computation time.

Scaling rules of air-core reactor

It is assumed that the sources and devices of a system are purely conductive with high σ and $\mu=\mu_0$. Meanwhile, the sources operate within a quasi-static frequency range. Dry-type air-core reactor of coating parallel structure has been widely used in practice when considering the heat radiation and other problems. The reactor of coating parallel structure is equivalent completely to simplified single envelopment model which can be obtained by single conductor linear superposition. In the engineering practice, superposition principles are used in the calculation of MF generated by reactor neglecting adjacent effect and end effect. On these grounds, an air-core reactor model was set up by the single wire winding, as is shown in Fig.1 (a). According to the scaling rules, with the scaling factor k ($0<k<1$), the original reactor can be shrunk to a small-scale one, namely small-scale model I (Fig.1(b)). The parameters of theoretical scaling rules of air-core reactor are shown in Tab.1.

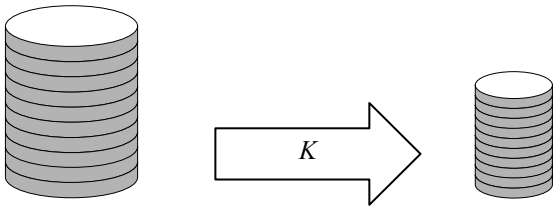

(a) The original model (b) The small-scale model I

Fig.1 The origin model and The small-scale model I

Tab.1 Parameters of theoretical rules of air-core reactor

	Wire thickness	Wire surface	Model height	Model radius	frequency
The original model	W	A	H	D	f
Small-scale model	kW	k^2A	kH	kD	k^2f
	Voltage	Current	Resistance	Inductance	MF
The original model	U	I	R	L	B
Small-scale model	kU	k^2I	$k^{-1}R$	kL	kB

Scaling rules modification

With the scaling rules, it is possible to build the small-scale models for air-core reactors and measure the MF in interested area around them. However it is often been affected by many objective conditions in the scaling process, modifications for scaling rules are needed. For three typical cases on the small-scale models, by maintaining the MF, puts forward corresponding correction strategy.

(1) According to the scaling rules introduced, with the scaling factor k, the wire thickness around the model is too thick to bend, and it is difficult to build model in lab. There are two methods to reduce the wire thickness. The first one is to leave space between wires (shown in Fig. 2(a) model II). The second one is to make the coil with two or more same wires in parallel, then join their terminals together (shown in Fig.2(b) model III). The above two models, the number of turns of the coil remains unchanged, and the current flowing through the coil is equal to model I (Fig 1(b)), thus the MF B keeps unchanged.

(a) The small-scale model II (b) The small-scale model III

Fig.2 The second and third model made with thin wires

(1) In some cases, the wire thickness may be too thin or there may be many turns in the original model, then a thicker wire will be easier to be built. In order to keep the same B, a factor will be multiplied to the original current, then the current should be twice as the original value.

(2) It is not necessary to apply a current as it is scaled by the scaling rules, because when the scaling factor is small, the scaled current is low. In order to reduce the error and to prevent the problems that caused by a low current, a larger current can be used, based on different situations. If the current is k times the scaled current, then the MF measured under this current will multiply k^{-1}.

Experiments of Simplified Models for Air-core Reactors

Based on scaling rules and scaling model of air-core reactor, it is possible to find an optimal simplified model using small-scale experimental technique to speed up the computation and modeling process. The simplified and the original model are shown in Fig.3.

(a) The original model (b) One loop model (c) Two loops model (d) Three loops model

Fig.3 Simplified models of the air-core reactor

The original model was shown in Fig.3 (a). The height of this coil is *l=134mm,* the diameter is *D=138mm,* number of turns is *N=120,* and the current flowing through the coil was 0.03 A, frequency of the power was 50 Hz. Then the MF around the original coil was measured in radial and axial direction respectively. Fig.4 shows the hardware set-up of the instrument.

As is shown in Fig.3 (b), the first model is to concentrate all the coils in one loop to represent the original coil. In this experiment, a loop of 40 turns was made for simplicity, which has the same diameter with the original coil. In order to keep the same current density flowing through the coil with the original reactor, a current of 0.09 A was used in the experiment.

The second simplified model is to use two circular current loops to represent the original coil, as shown in Fig.3 (c). In the experiment, each loop had 40 turns. In order to keep the same current density flowing through the coil, a current of 0.045 A was applied in the experiment. The two loops were placed at two types of separations with each other, as shown in Fig.4.

(a) Configuration 1 (b) Configuration 2

Fig.4 Two loops model of different configurations

The third simplified model is to use three circular current loops to represent the original coil, as shown in Fig.3 (d). In the experiment, each loop had 40 turns. In order to keep the same current density flowing through the coil, a current of 0.03 A was applied in the experiment. The three loops were placed at three types of separations with each other, as shown in Fig.5.

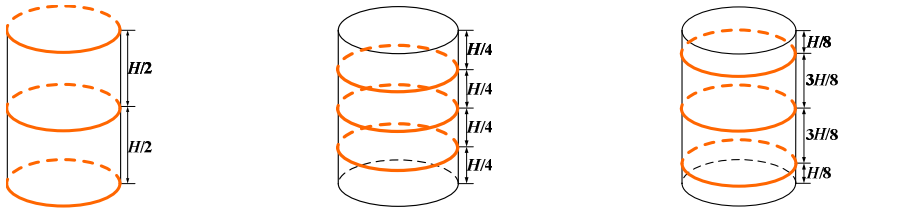

a）Configuration 1 (b) Configuration 2 (c) Configuration 3

Fig.5 Three loops model of different configurations

Based on the measurement results, the curves of MF versus distance from center can be drawn in the radial direction and axial direction respectively, as shown in Fig.6. In 200 mm, six simplified model can replace the original model approximately in the radial direction and axial direction. However, in the range of 200mm, the measurement error is large, and the main reason is the large size measurement instrument probe.

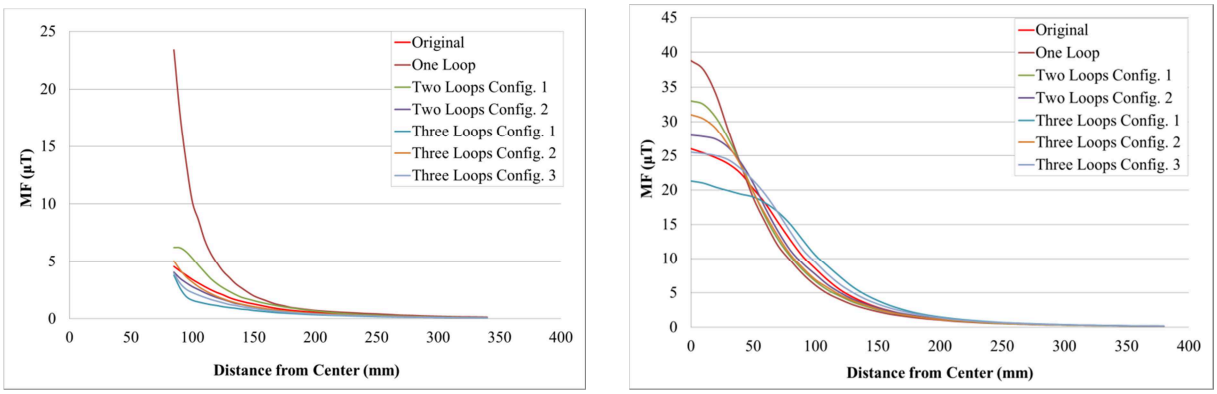

(a) MF in the radial direction (b) MF in the axial direction

Fig.6 Comparison of MF of different simplified models

Considering the simplicity of model establishment and the accuracy, the configuration 1 of two loops is the optimal model of the six configurations. It is much easy to establish the structure in a short time to simulate the MF around the air-core reactor. In this configuration, measurement results are more accurate in the distance of 1.5 times the diameter of the reactor. In engineering practice, reactor diameter and height were 1m~2m, while the public scope of activities is usually more than 1.5 times the diameter of the reactor. Therefore, the simplified model has an important practical significance in the prediction of MF distribution of air-core reactor.

Conclusion

In this paper, the scaling rules for air-core reactors is summarized first and three typical corresponding correction strategies are put forward according to different situation. Then, three simplified models were built for air-core reactors , including one loop model, two loops model and three loops model, and they all match the original model well. Especially when the current loops are placed at the position of 1/3 and 2/3 of the length of the coil, a simplified model (configuration 1) is of the highest accuracy. The results provide a basis for simplifying the computation process and speeding up the operation of experiment.

References

[1] Directive 2004/40EC of the European Parliament and of the Council of 29 April 2004 on the minimum health and safety requirements regarding the exposure of workers to the risks arising from physical agents (electromagnetic fields) (18th individual Directive within the meaning of Article 16(1) of Directive 89/391/EEC)[S], 2004, Official Journal of the European Union, L 159/1-26.

[2] U.S. Department of Energy, National Institute of Environmental Health Sciences (NIEHS) and National Institutes of Health, Assessment of health effects from exposure to power-line frequency Electric and magnetic fields, EMF Working Group (EMF RAPID Program) Report. 1999.

[3] Yu, Q., and Sebo, S. A., Simplified Magnetic Field Modeling and Calculation of Large Air-Core reactor Coils, IEEE Transactions on Magnetics, 1996, 32 (5), pp. 4281-4283.

Advanced Materials Research Vols. 960-961 (2014) pp 867-870

doi:10.4028/www.scientific.net/AMR.960-961.867

FEM Simulations of Permanent-magnet-biased Saturation Based Fault Current Limiter

Shouxiang Song[1,a], Liang Zou[1,b], Tong Zhao[1,c], Li Zhang[1,d],

Qingquan Li[1,e], Mengqi Liu[1,f]

[1]School of Electrical Engineering, Shandong University, Jinan 250061, China

[a]ssxall@gmail.com, [b]zouliang@sdu.edu.cn, [c]zhaotong@sdu.edu.cn, [d]zhlieee@gmail.com,

[e]lqq@sdu.edu.cn, [f]lmqsdu2013@gmail.com

Keywords: Permanent-magnet-biased saturation based fault current limiter (PMFCL), modeling, simulation, experiment

Abstract. The fault current limit technology based on the principle of permanent-magnet-biased saturation has several outstanding advantages in both economy and technology. A modeling method of PMFCL based on the finite element analysis platform – Maxwell is presented in this paper. The current limiting mechanism of line-type PMFCL is analyzed, on the basis of which the 2D and 3D models are established in Maxwell, and the corresponding experiments are designed as well. Comparisons between the simulation and experimental results indicate that the modeling method is reasonable. Research achievements of this paper provides theoretical basis for further studies of PMFCL.

Introduction

The short-circuit current level of power system is rising because of the growing scale of power grid, the rapid growth of power system load, etc. The power system voltage and frequency will be unstable with large circuit, and equipment insulation will be damaged because of high temperature and strong electrical force sent out by itself. At present, PMFCL is a means of effective implementation with excellent technical and economic characteristics.

The study of PMFCL design of large capacity and magnetic fluid thermal coupling field is desperately needed in high voltage power system. However, a reasonable simulation is the basis of it. The 2D and 3D models are firstly established by ANSOFT software based on the current limiting mechanism of PMFCL. Then the results of these two models are obtained by solving the analysis. Afterwards, the prototype experiments are done and a series of data is available naturally. Finally, the simulation results are compared with that of the prototype experiments.

Current Limiting Mechanism Analysis of PMFCL

The curves reflect the relationship between the core flux of PMFCL named φ_e and the winding current I in Fig. 1.The broken line –ABCDE is the work trajectory of half- wave current limiting in iron-cores, among AB represents the positive saturation zone of PMFCL while BD denoting the desaturation zone and DE is the negative saturation zone respectively. Under normal conditions, the strong magnetic field generated by permanent magnet makes the iron-cores stay in the saturated zone in which the winding characterize as low impedance. When there are short-circuit fault occurs

in system, magnetomotive force generated by the fault current will offset the magnetic force of permanent magnet gradually, and the work state of iron-cores will enter into the desaturation zone in which the winding characterize as high impedance. The magnetic force generated by strong alternating current makes the core into negative saturation zone if the current is still increase to greater than i_{max}, PMFCL is in loss of current limiting capability at this time.

In Fig. 1 , two stages are employed to denote the change of flux distribution of PMFCL in the current limiting area: 1) current limiting stage Ⅰ which corresponding to the point B to point C; 2) current limiting stage Ⅱ which corresponding to the point C to point D. Furthermore, the material parameters of PMFCL are shown in Table 1.

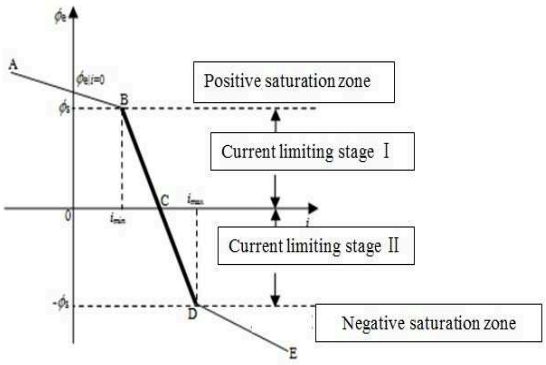

Fig. 1 The φ_e-i curve of linear PMFCL

Table 1 Material parameters of PMFCL

Components Materials	Magnetic parameters	Structure parameters
Iron-cores (ferrite,R2K3D)	B_s=1.78T	l_e=3×10^{-1}m
	μ_s=6.28×10^{-5}Wb/(A·m)	S_e=9×10^{-4}m^2
	μ_u=3.14×10^{-3}Wb/(A·m)	W=3×10^{-2}m
Permanent Magnet (NdFeB, N35)	B_r=1.22T	l_m=3.2×10^{-2}m
	H_c=8.68×10^{5}A/m	S_m=9×10^{-4}m^2
	μ_m=1.4×10^{-6}Wb/(A·m)	W=3×10^{-2}m
Winding	None	D=1.1×10^{-3}m
		N=300

Study of 2D Modeling

The 2D model of PMFCL is built by Maxwell release 15.0; there are four pictures of magnetic field distribution in current limiting stage Ⅰ as shown in Fig. 2. The figure indicates that permanent magnet can impact the magnetic flux of iron-cores through the area of winding package, the reverse magnetic field enhanced gradually while the winding current is increasing, and the magnetic flux of PMFCL is distorted, hence the biased magnetic field is greater than the reverse magnetic field of winding when iron-cores are working at extreme saturation stage.

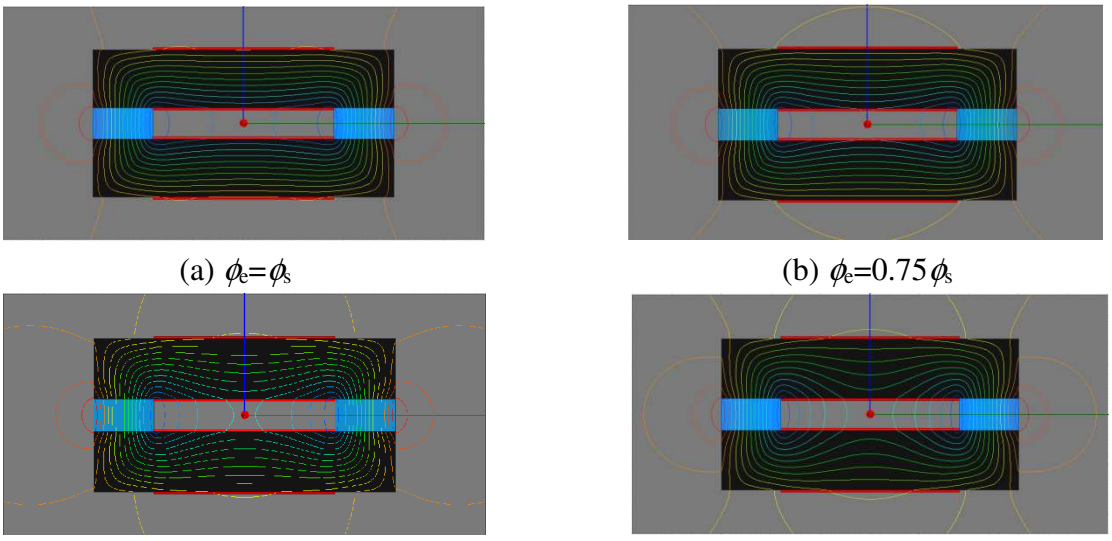

(a) $\phi_e=\phi_s$ (b) $\phi_e=0.75\phi_s$

(c) $\phi_e=0.5\phi_s$ (d) $\phi_e=0.25\phi_s$

Fig. 2 Magnetic field of PMFCL in current limiting stage Ⅰ

There are four pictures of magnetic field distribution in current limiting stage Ⅱ as shown in Fig. 3. The reverse magnetic field is inside the two dotted lines while permanent magnetic field is outside of them. The reverse magnetic field enhanced gradually and the area through by reverse magnetic flux is being larger as shown in the figure, the reverse magnetic field of winding is greater when iron-cores are working at negative saturation stage.

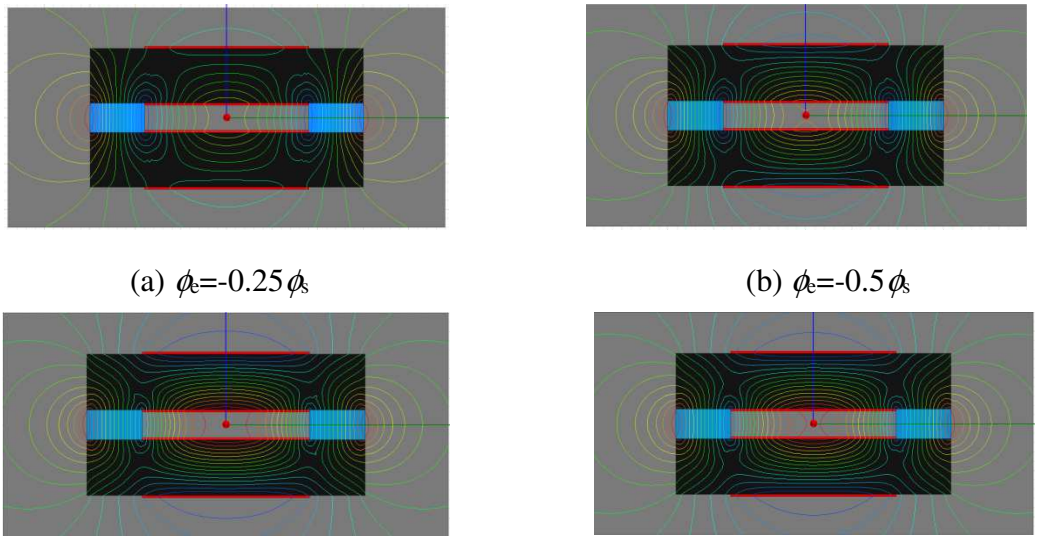

(a) ϕ_e=-0.25ϕ_s (b) ϕ_e=-0.5ϕ_s

(c) ϕ_e=-0.75ϕ_s (d) ϕ_e=-ϕ_s

Fig. 3 Magnetic field of PMFCL in current limiting stage Ⅱ

Study of 3D Modeling

The process of both 2D and 3D model is almost similar but the construction of 3D model should be paid attention to a few respects like mesh operation, solution region and design of boundary conditions, the 3D model is shown as Fig. 4, in addition the excitation of 2D and 3D model is realized by import external circuits, the external circuit is shown in Fig. 5. There are about 8 groups of external circuits to simulate the two current limiting stages shown in Fig. 2 and Fig. 3, and the difference between them is the magnitude of current, the waveform of current which flow through the winding as Fig. 6. At last, the 3D model is solved after confirming the correct.

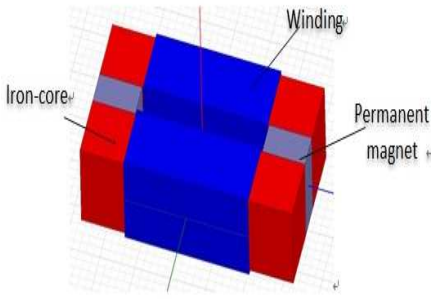

Fig. 4 3D geometric model

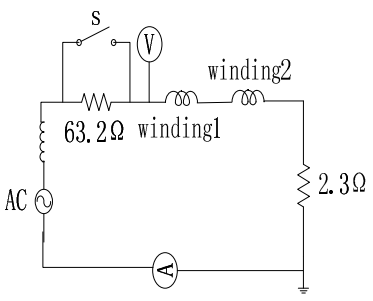

Fig. 5 External circuit

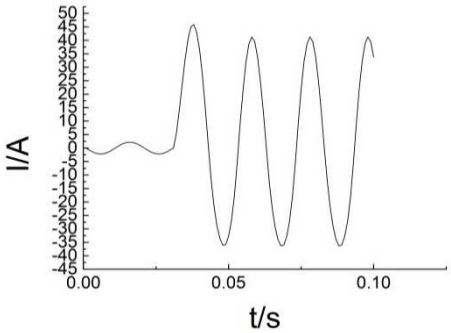

Fig. 6 Waveform of current

Experimental Verification

Experiments are important to verify the rationality of modeling. The values of circuits are the same no matter in experiment or in simulation, and there are also several groups of experiments to correspond the simulation. The parameters of external circuits are as follow: the internal inductance of power source is 6.5mH, the resistance of winding is 2.3 Ω, the resistance of the load is 63.2 Ω, the wiring diagram is shown as Fig. 7.

Fig. 7 Experimental wiring diagram

(1) The experiments indicate that the maximum value of magnetic flux in iron-cores are just zero when the voltage value of power source U_{ss} is 137.9V, and measure the data to draw curves that represent the relationship between the magnetic induction intensity B_e and time t as shown in Fig. 8(a), thereby the source voltage 137.9V is brought into the simulation models and gets the curve B_e-t as shown in Fig. 8(a). When the short current can't make the core flux in reverse, the error between simulation result and experimental results is 13.3%.

(2) The experiment indicated that the maximum value of magnetic flux in iron-cores are just reverse saturation when the voltage value of power source U_{ss} is 206.9V, and measure the data to draw curves that represent the relationship between the magnetic induction intensity B_e and time t as shown in Fig. 8(b), thereby the source voltage 206.9V is brought into the simulation model and gets the curve B_e-t as shown in Fig. 8(b). When the short current is enough to make the core flux in reverse, the error between simulation result and experimental results is 4.9%.

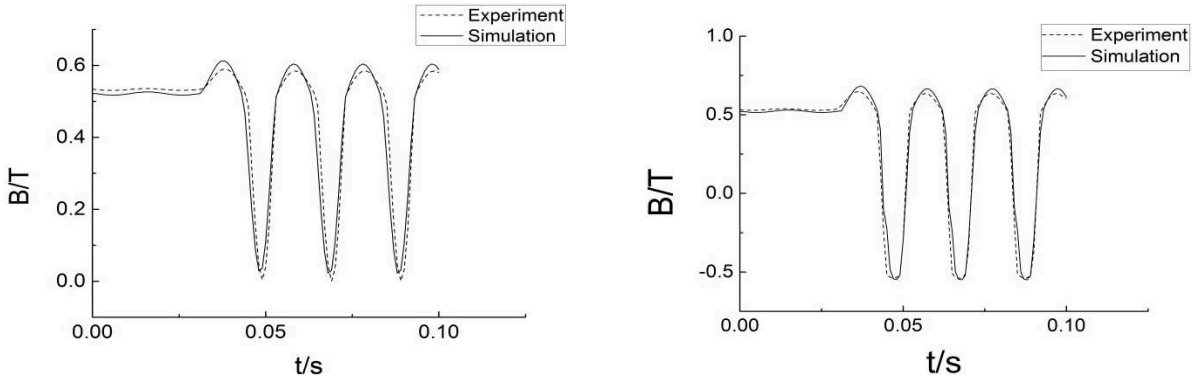

Fig. 8 The B_e-t curves of PMFCL

Conclusions

The analysis result of the 2D model shows that PMFCL has two working stages with the increasing short current: permanent magnet will play a role in limiting the current when the magnetic road is made of permanent magnet and the whole iron-cores; permanent magnet can't effect the current when the magnetic road is formed by air gap and iron-cores which are wrapped in winding. The modeling method is effective because of the small errors between the two kinds of results by comparing the simulation results with experimental results. Thereby it provides basic basis for the PMFCL design of large capacity and the study of magnetic fluid thermal coupling field, etc.

References

[1] L. Zou, Q.M. Li, H.S. Liu, High Voltage Engineering, Vol. 35 (2009), p. 2568
[2]M. Nagata, K. Tanaka, H. Taniguchi, IEEE Trans on Appl. Supercond, Vol. 11 (2001), p. 2489
[3]H.L. Xiao, J. Qiu, S.H. Wang, Q.H. Zhang, IEEE Trans on Magnetics, Vol.47 (2011), p. 2620

Advanced Materials Research Vols. 960-961 (2014) pp 871-876

doi:10.4028/www.scientific.net/AMR.960-961.871

Analysis and Thoughts on a 500kV H-GIS equipment failure

Wang Xiaodan[1, a], Xu Dongsheng[1, b], Wang Yi[1, c], Li Lu[1, d],

Zhang Qingjun[1, e], Lan Qi[1, f], Lu Yong[1, g], Li Hao[1, h]

[1]State Grid Henan Electric Power Corporation Maintenance Company,

No.206, Zhongyuan West Road, Zhengzhou, China, 450000

[a]wangxiaodan.zz@163.com, [b]xdszz@qq.com, [c]wangyi@qq.com, [d]104226976@qq.com,
[e]zhangqjhb@163.com, [f]iamlqlyl@163.com, [g]42118887@qq.com, [h]lihao@126.com

Keywords: H-GIS, SF_6, analysis of gas composition, internal discharge

Abstract: Analysis the 500kV H-GIS equipment failure, determine for the circuit breaker chamber internal discharge fault according to the protection action and the use of the analysis of SF_6 gas composition, a detailed analysis of the possible causes of failures, and according to the disintegration test results, to confirm the final reason for internal foreign bodies caused by discharge. Finally, put forward some prevention measures and suggestions for the accident.

Introduction

Because the cost of GIS bus is higher, and the future expansion inconvenience, etc, combine the advantages of open bus bar and GIS, H-GIS (Hybrid GIS) arises at the historic moment. Besides using traditional external tube bus, H-GIS completely consistent with the rest component of GIS. Domestic or foreign research and practical operation experience shows that, compared with using traditional AIS, GIS/H-GIS have higher reliability, maintenance cycle is longer, the maintenance cost is lower[1]. But if the internal failure, due to its complex structure, fault accurate positioning and maintenance is difficult.

5053 interval of the 500 kV substation G is the product of T company, model is GSR-500R2B, in August 2008, the production, in July 2009, putting into operation. The trip happened without any operation, this paper analyzes the accident.

After the accident

1.1 The operation mode before the failure

500 kV substation G system wiring diagram is shown in Fig.1. 500 kV bus I, bus II was running; The first string 5011, 5012 breakers and ZG I loop were running; The second string 5021, 5022, 5023 breakers and G 1 # main transformer , ZG II loop were running; The fourth string 5041, 5042 breakers were in the hot standby state; The fifth string 5051, 5052, 5053 breakers and G 3 # main transformer, GX line were running; The sixth string 5062, 5063 breakers were in the hot standby state.

Before failure, there was no operation; It cloudy, wind 4 ~ 5 level, the highest temperature was 23 ˚C, minimum temperature was 13 ˚C.

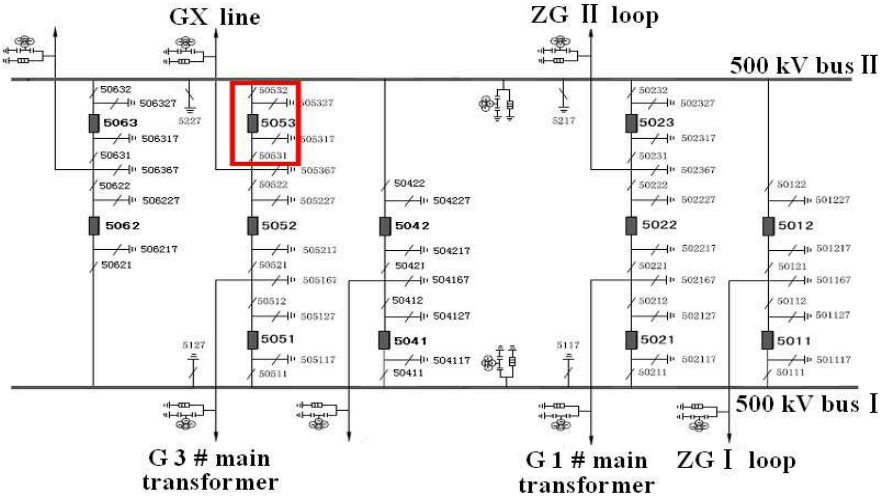

Fig.1 500 kV substation G system wiring diagram

1.2 The fault and protection action situation at the scene

03:32:53 on September 24, 2013, 500 kV substation G 5053 breaker tripping, 500 kV GX line tripping reclosing after success, the load current is 582 A, the voltage of 500 kV bus II was 0. Optical differential protection (WXH803, RCS931)of the GX line action, two sets of bus differential protection (BP2B, WMH800)of the bus II action, the first and second group of the breakers(5052, 5023,5053,5012) tripping exports, 5052 breaker reclosing protection action. On-site inspection by the operation personnel, find the appearance without exception.

The fault location

Due to the complicated structure of GIS/H-GIS, it is difficult to maintenance. Through the fault location, we can find the faulty air chamber, and maintenance it only, which can greatly reduce the maintenance time.

2.1 The method of the fault location

There are two kinds of method for the fault location in general. One is using UHF to monitor the GIS/H-GIS partial discharge on-line; Another is using the SF_6 gas composition analysis technology. This time we choose the second.

2.2 The introduction of the SF_6 gas composition analysis technology

When the discharge and overheating fault are occurring in SF_6, it will produce a series of gaseous impurities, such as SOF_2, SO_2F_2, SO_2, H_2S, CO, HF and CF_4, etc[2-4]. Detecting the characteristic components content (especially SOF_2+SO_2) is sensitive, accurate, and the advantages of small interference by external environment, so the technology can provide accurate and reliable diagnostic basis for fault location after the accident.

2.3 The results of the SF_6 gas composition analysis

September 24, 2013 morning, the test personnel had analyzed the SF_6 gas composition of the 5053, 50531, 50532, 50531 breakers' phase C air chamber and the 5053 breaker's phase B air chamber. The mode of the test instrument is RA500FAP. The specific test data is as follows:

number	air chamber	phase	SO_2 （uL/L）	H_2S （uL/L）	CO （uL/L）	humidity （uL/L）	Purity （%）	result
1	50531	C	0	0	17	——	——	qualified
2	50532	C	0	0	7	——	99.43	qualified
3	5053	C	564	0	8	78	99.80	unqualified
4	5053	B	0	0	6	——	——	qualified
5	5052	C	0.9	0	6	56	99.98	qualified

Test result: According to GB/T8905-2008<The guidelines for the gas management and maintenance in SF_6 equipment >, the content of SO_2 ,in the 5053 breaker's phase C air chamber, is 564 uL/L , greater than normal (2 uL/L), exceeding bid badly. It can be identified as the gas discharge in the 5053 breaker, causing the trip.

Analyze the possible cause of the gas discharge

1) Overvoltage

External overvoltage, such as Lightning overvoltage, and internal overvoltage, such as operating over-voltage, could cause spark discharge inside the equipment. However, there was no thunderstorm, no operation, no signs of overvoltage, before the accident, so this reason could be eliminated.

2) Operating at low pressure

In the case of SF_6 gas pressure is low, its insulating performance degradation. If operating at this time, it will cause internal discharge, because the ability of extinguishing arc is insufficient. According to the site condition, the air chamber pressure is normal and without any operation, it can eliminate the cause.

3) Internal conductor surface has sharp corners

Due to poor manufacturing process, the conductor surface has sharp corners, triggering point discharge. Such problems can be found in factory test. However the test is qualified, so we can rule out the reason.

4) The internal insulation materials have defects

There are a variety of insulation materials in the GIS/H-GIS, such as basin-type insulator, insulating rod, support insulating tube, etc. If there are air gaps or impurities in the insulation materials, its insulating performance will gradually decline, in the process of the running, until they are breakdown. According to the last experiment records before the failure, there is not any problem. But it cannot be ruled out that, the changes of external conditions make its rapid degradation in a relatively short time. Therefore, we need to detect to further confirmation.

5) The internal parts are loose or fractured

Due to the product assembly or parts quality have problems, making the shake in the running or normal operation. The shake will loosen or fracture its internal parts (fixed bolts, etc.) and make them the displacement. It makes the insulating distance between the conductor and the grounding shell not enough, causing the internal discharge. We need to disassembly for further judgement, according to the traces of the discharge, and the internal checking.

6) The air chamber has impurities

If the air chamber has metal particles, powders or other impurities, it will seriously distort the local electric field, causing the internal discharge, at the time of the shake or airflow, which make them move to some particular place. We need to disassembly for further judgement, according to the location and traces of the discharge, and the internal particle detection.

Disassembly checking

According to the above cause analysis, we contrapose the last three causes, who need to disassembly for further judgement, carry out the targeted examinations and relevant tests. The disassembling the phase C of the 5053 interval, will be carried out in T company.

4.1 The appearance inspection of the parts

Found that:

(1) There are obvious traces of discharge on the inwall of the support insulating tube and the surface of two core insulating rods. The locations of them are mainly corresponding. And the surface of them are relatively smooth. As shown in Fig.2. The ambilateral fixed metal parts of the support insulating tube have obvious traces of discharge, too. And their locations are mainly corresponding as well, so it should be the discharge channel, as shown in Fig.3.

(2) The fixed bolts near the discharge area are not loose or fractured. The contacts and other parts are in good condition, without displacement.

(3) There are not obvious impurities (metal particles, etc.) on the bottom of the air chamber, flanges and bolts.

(4) The greases on the spindle of the crankcase have obvious overflow. There are oily matter on the bottom of the crankcase and the surface of the spindle, as shown in Fig.4.

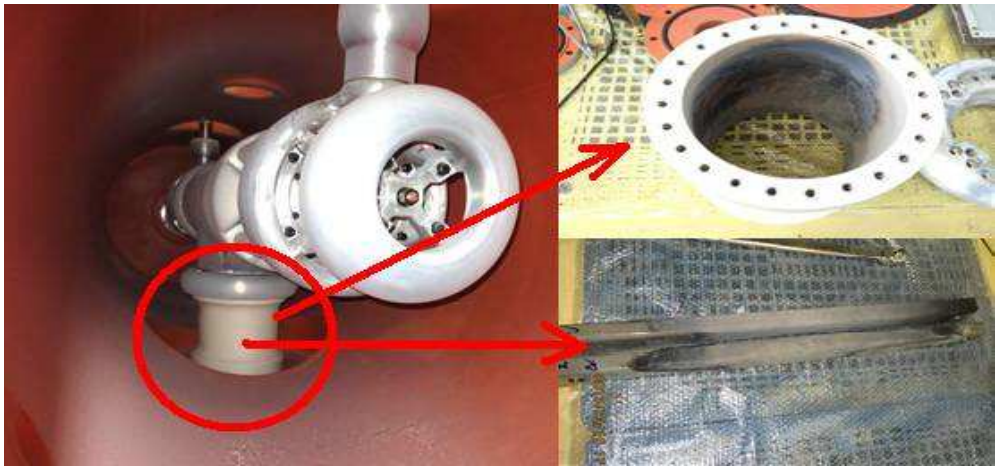

Fig.2 The empyrosis of the support insulating tube and the core insulating rods

Fig.3 The empyrosis of the ambilateral fixed metal parts of the support insulating tube

Fig. 4 The oily matter in the crankcase

4.2 test

Manufacturer have carried out the X-ray examination, material analysis and measuring vitrified temperature (Tg) to the support insulating tube and the core insulating rods, do not find any internal defects. Composition analysis of the residues in the tank shows that they are gray powders, main ingredients include C, F and O elements. Among them, C and O element mainly come from insulating tube and insulating rod. F element is mainly derived from SF_6. Mg, Si, Fe and zinc element come from the shield ring. There are no other suspicious components.

Determine the cause of the fault

According to the injury of the insulation materials, we can determine the discharge is not outward development from the inside insulating parts. If it develops from inside to outside, the surface should be crack or bulge, rather than flat, but the reality is on the contrary, as shown in figure 2. The test data of the manufacturer indicates that the internal insulating parts have not air gap or impurities, proves the previous view. So the fourth possible cause (The internal insulation materials have defects) could be eliminated.

According to the internal inspection, the fixed bolts near the discharge area are not loose or fractured. The contacts and other parts are in good condition, without displacement. So we can eliminate the fifth possible cause (The internal parts are loose or fractured).

The test results show that there are not obvious impurities (metal particles, etc.) on the bottom of the air chamber. However based on the analysis of the location, traces and channel of the discharge, combined with the exclusive method, it can be identified as the sixth possible cause (The air chamber has trace metal particles or other impurities, causing the discharge)

There are four conditions, the air chamber has impurities. (1) The dust-free environment of the GIS/H-GIS manufacturing workshop does not meet the requirements, especially in the final assembly workshop, the metal particles, powders or other impurities are easy to entrance into it; (2) in the process of assembly, friction between the conductors will produce metal powders or debris, left in some covert places; (3)The factory did not complete more than 200 times mechanical operations, according to the anti-accident measure. The contacts are not getting enough mechanical break-in, so it is easy to produce metal powders in the normal operations.(4) The metal powders, produced in the mechanical break-in, are not clean thoroughly.

The location of the metal particles, powders and other impurities in the air chamber is random. They are usually located at the bottom of the air chamber. When there are inflation, deflation or operations, it will produce the shake or airflow, changing their location. The residual trace metal particles or impurities in the air chamber, may move to the inwall of the support insulating tube. The greases in the crankcase (as shown in figure 4) volatilize in the long term, it will come into

being the trace oil film on the inwall, making them sticking on it.In the specific strong electric field, metal particles will distort the local electric field seriously[5]. The high field strength makes the ionization zone arising on the cutting-edge of the metal particles. There are processing the electron avalanche endlessly, producing a lot of space charge. It forms an avalanche of electron gradually, and leads to the disruptive discharge eventually, as shown in figure 3.

The preventive measures and suggestions

Combined with the H-GIS internal discharge fault, and puts forward some preventive measures and suggestions, for reference only.

1. The advice for the manufacturer and installation unit :

(1) Make sure the dust-free environment meet the requirements in the assembly workshop;

(2) Ensure completing more than 200 times mechanical operations, according to the anti-accident measure, to make the contacts get enough mechanical break-in. And clean the metal particles thoroughly during the operations.

(3) The greases or sealing greases, used in assembly, should be appropriate;

(4) In the assembly process, should keep the environment clean, and equip a vacuum cleaner to remove impurities thoroughly.

2. The advice for the equipment operation unit:

(1) The operation personnel should strengthen the monitoring, especially in the first year after the installation or overhaul. According to the statistical data of countries such as Canada, in the first year after the installation or overhaul of GIS/H-GIS, the equipment failure rate is 0.53 times/interval, and reduce to 0.06 times/interval in the second, reduced 8.83 times, and then tends to be stable. GIS/H - GIS is the most prone to failure in the first year.

(2) Install the UHF partial discharge on-line monitoring device, to real-time monitoring the running status of the equipment.

References

[1] G. Schoeffner, T. Neumann: Application of Gas Insulated Transmission Lines (GIL) and Gas Insulated Swithgear (GIS) for Power Plants[J]. Electric Power Construction, 2004, 25 (6): 4-7.(in Chinese)

[2] Xiaoqing Chen, Huadong Peng, Ming Ren, Qiang Sun, Ming Dong: Detection Techniques of SF_6 Decomposition and Application [J]. HIGH VOLTAGE APPARATUS, 2010, 46 (10) : 81-84. (in Chinese)

[3] Xiaoxing Zhang, Yao Yao, Ju Tang, Caixin Sun, Lingyun Wan: Actuality and Perspective of Proximate Analysis of SF_6 Decomposed Products Under Partial Discharge [J]. High Voltage Engineering, 2008, 34(4): 664-669. (in Chinese)

[4] Junkun Yang, Yongtao Peng, Xiangyu Tan, Ke Wang: GIS Device's Discharge Type Measured by SF_6 Decomposition Product [J]. INSULATING MATERIALS, 2012, 45(2) :61-64. (in chinese)

[5] Changyuan Feng: The operation experience and field test of GIS [J]. HIGH VOLTAGE APPARATUS, 2000 ,1: 49-53. (in Chinese)

Advanced Materials Research Vols. 960-961 (2014) pp 877-880

doi:10.4028/www.scientific.net/AMR.960-961.877

Analytic Theory and PIC Simulation of Electron Beam Generation under High Voltage

Hai Zhang[1, a], Wei-guo Zhang[1], Yang-zhou Shao[1] and Jian-guo Wang[2]

[1]College of Information Science and Engineering, Huaqiao University, Xiamen, 361021, China

[2]School of Electronic and Information Engineering, Xi'an Jiaotong University, Xi'an, 710049, China

[a]Email: xjtuzhanghai@163.com

Keywords: Electron beam; high current; high voltage; theoretical model; foil-less diode; PIC simulation.

Abstract. The theoretical analysis and numerical simulation of electron beam generation in foil-less diode are presented. The theories of OAL, CL, and equilibrium beam model are briefly compared. All the theoretical models can give a relatively accurate solution of electron gun, and the equilibrium beam model is more appreciated. A PIC simulation tool UNIPIC is introduced and is used to analyze the behaviors of a foil-less diode. Under the conditions of 180 kV incident voltage wave and 2.5 T axial magnetic fields, we obtained the 250 kV, 1.5 kA output beam current which can be used in high power microwave generators.

Introduction

Microwave vacuum electronic device is an important kind of electronic device which are widely used in contemporary defense equipments and national economic areas. In national defense equipment, It's the heart of radar, communication, electronic countermeasure, remote sensing and precision guided equipment; In information system, as the source of radio or television station, microwave and satellite communication forwarder, receiver and the display of color TV set, even all kinds of display devices have been widely used in our work and life already. Electron gun is an important part of vacuum electronic devices such as travelling wave tube and backward wave oscillator. Foil-less diode is one of the vacuum electron gun which can generate intense electron beam [1].

The uniform linear electron beam can be produced in a foil-less diode which consists of a coaxial transmission line of outer conductor radius, whose centre conductor is truncated to form a cathode. Both the anode (outer conductor) and the cathode can be shaped to vary the beam characteristics [2]. This “foil-less diode”, as shown in Fig.1, employs a large axial magnetic field to provide insulation and to guide the electrons into a beam. Foil-less diodes produce highly annular beams which possess high current density [3]. The earliest electron guns were designed using electrolytic tank experiments coupled with analytic theory. Over time, advances in synthesis techniques and computational abilities have significantly enhanced capabilities for interpolation, extrapolation, and even complete redesign of such electron guns. Virtual computer simulation is fast becoming the design tool of choice [4].

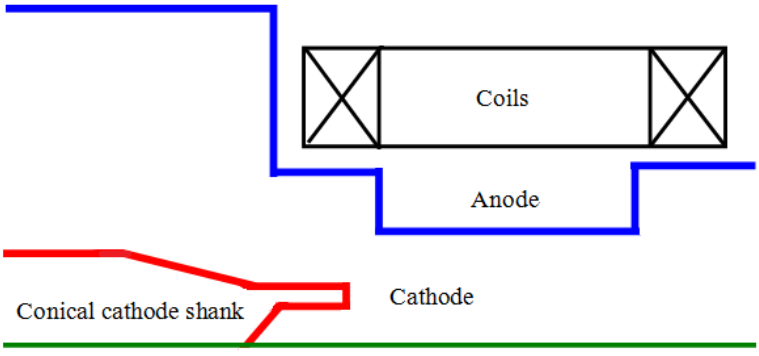

Figure 1. Structure of foil-less diode

THEORETICAL MODEL OF FOILLESS DIODE

2.1 OAL model

The model of OAL is essentially a "corner diode" [5]. As an idealized geometry, the anode is a semi infinite cylindrical conductor at potential $\phi = 0$ and the cathode surface is maintained at a constant potential $\phi = -\phi_0$ at the end of the anode cylinder. For the diode, the cathode outer radius is r_2 while the inter is r_1, the beam thickness is Δ and its distance to the anode wall is δ. In OAL model, the electron motion is constrained to be one dimensional by a very strong applied axial magnetic field and the voltage is assumed to be ultra relativistic. Based on the assumes, when $\Delta \ll \delta$, according to OAL model the diode total current and impedance are given approximately by

$$I_{OAL} = \frac{1700(\gamma_0^{2/3} - 1)^{3/2}(r_b / \delta)}{\ln(8\delta/\Delta)} \tag{1}$$

$$Z = 30\frac{\delta}{r_b}\ln(\frac{8\delta}{\Delta}) \tag{2}$$

where $\gamma_0 = 1 + e\phi_0 / mc^2$, is the constant of relativity, and $r_b = (r_1 + r_2)/2$.

2.2 CL model

The model of CL is similar to OAL model except that the electric potential is allowed to vary over an arbitrary boundary. In principle it gives a more accurate representation of experimental cathode geometries [6]. The solution for the potential of the cathode surface is not a constant but is a function of both r and z, which is may be written as

$$\phi(r,z) = \frac{2}{\varepsilon_0 R^2}\sum_{n=1}^{\infty}\frac{\rho_n}{k_n^2}(1 - e^{-k_n z})\psi_n(r) + \frac{1}{2\pi\varepsilon_0 R^2}\sum_{n=1}^{\infty}\phi_n e^{-k_n z}\psi_n(r) \tag{3}$$

where $\psi_n(r) = J_0(k_n r)(J_1(k_n R))^{-2}$, and $k_n = \lambda_n / R$ in which the λ_n are the roots of the J_0 Bessel function. Finally the diode current can be given approximately according to CL model by

$$I_{CL} \approx 4\pi\varepsilon_0 \frac{(\gamma_0^{2/3} - 1)^{3/2}(mc^3 / e)}{2\ln(\mathrm{R/r_b})} \tag{4}$$

where R is the anode radius of the diode. Obviously, the CL model is close to the fact compared with the OAL model, but more complex, so the model is not much applied in studies.

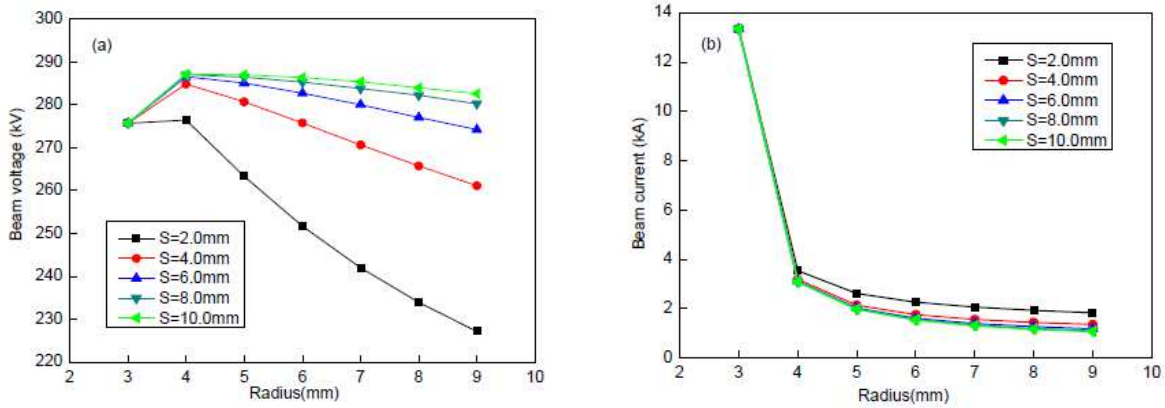

Figure 2. Dependence of output behaviors of electron gun on the anode radius

2.3 Equilibrium beam model

In OAL and CL models, the diode current is equal to the space-charge limited current. Indeed it was found in studies that only adapt to low voltage while at higher voltages the equilibrium of the beam yields a current substantially less than the space-charge limit. Thus, the equilibrium beam model was

put forward. In the model, to a good approximation, the beam can be modeled as a relativistic cold fluid [5-7]. The equilibrium equation in this model consists of the radial force balance equation together with Ampere's law and Poisson's equation. The model gives diode current formula as

$$I_{equ} = 3400((\gamma_0 /(1+4\ln(R/r_b))^2)-1)^{1/2} \quad (5)$$

where γ_0, R and r_b all have the same meaning above.

PIC SIMULATION OF FOILLESS DIODE

3.1 Simulation tool UNIPIC

From 1960, many useful codes were developed for simulating a variety of electron guns. Commercial software packages for electron gun design are available in various forms [8]. UNIPIC is a novel simulation program that can be configured at run time by selecting appropriate geometry, material properties, boundary conditions, field algorithms, particle algorithms, and output specifications [9]. Default configurations provide good accuracy in reasonable time for novice who does not wish to or may not know how to specify some aspects of an electromagnetic PIC simulation. The fields in Maxwell's equations are represented on a finite-difference grid.

3.2 Simulation results

We investigated the output behaviors of the electron gun by varying the anode radius, while the other parameters keep constant. The amplitude of incident voltage wave equals 180 kV, and the guiding magnetic field is equal to 4.0 Tesla. Fig.2 shows the results of parametric scanning. The two diagrams respectively represent: (a) Total diode voltage, and (b) Beam current. That is, the total diode voltage after superposition and the beam current generated in diode. Each category corresponds to 5 different longitudinal gap distances between cathode and anode, which is defined as S.

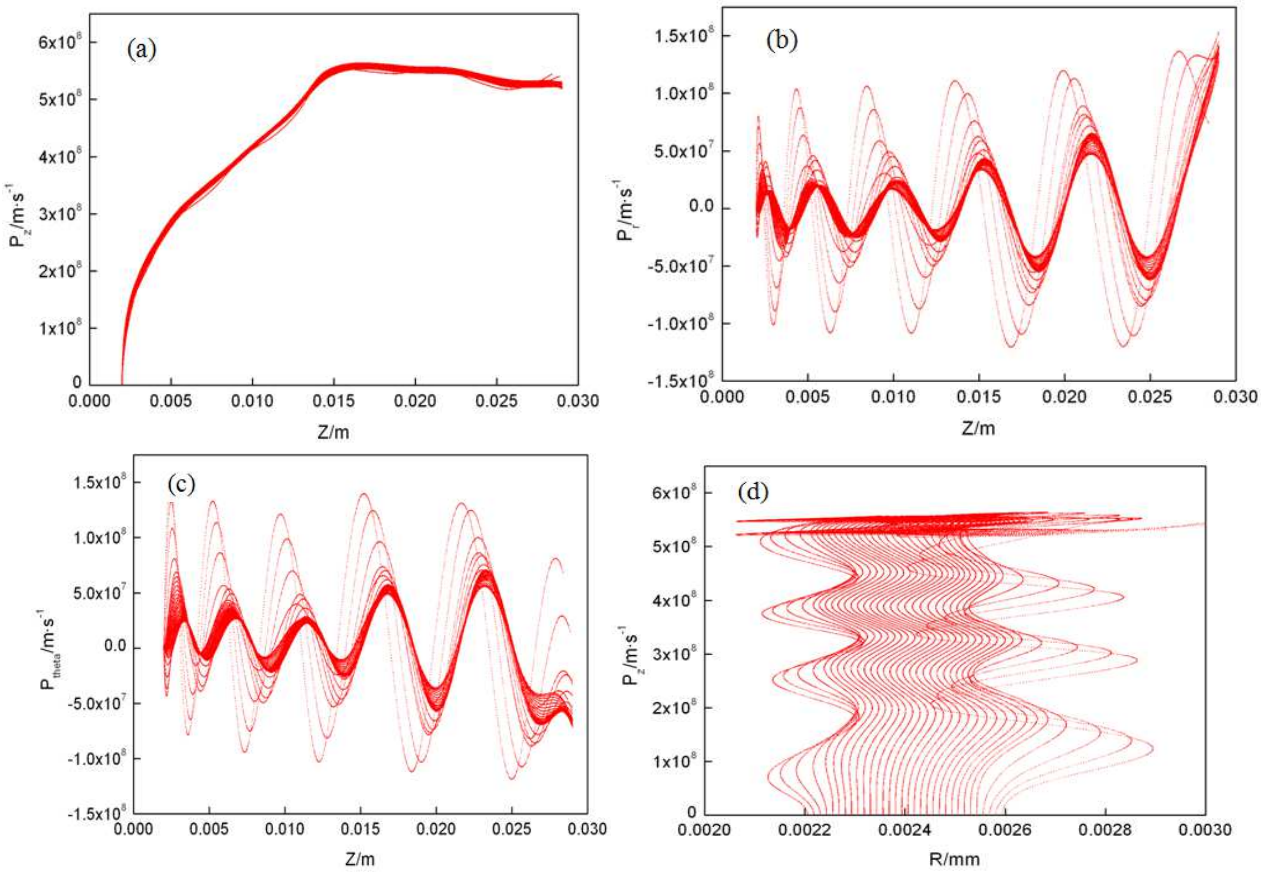

Figure 3. Phase space of electron beam (B=2.5 T)

Fig.3 shows the phase space of electron beam under the condition of 2.5 T magnetic fields. The four diagrams respectively represent: (a) Longitudinal momentum along z axis, (b) Radial momentum along z axis, (c) Angular momentum along z axis, and (d) Longitudinal momentum along r axis. It can be seen that the longitudinal momentum was increased along z axis because of the acceleration of electron beam under the high voltage; the radial momentum have the vibration characteristic because of the rotation effect of electron in magnetic field; and the angular momentum vibration are usually due to the Lamor rotation.

Conclusion

In this paper three main theoretical models of foil-less diode are reviewed. It is found that compared with basic OAL model, the CL model can carry electric potential which could vary over an arbitrary boundary. And the equilibrium beam model produces a current less than the space-charge limit at higher voltages, while the beam can be regarded as a relativistic cold fluid. Besides the analytic theory, the PIC simulations of the diode are also performed using a novel simulation tool UNIPIC. With 180 kV incident voltage and 2.5 T axial magnetic fields, the device can generate electron beam with the voltage of around 250 kV and current of 1.5 kA.

Acknowledgements

This work was financially supported by the Natural Science Foundation of Fujian Province, China (Grant No.2013J05093), and the Undergraduate Education and Teaching Reform Project of Huaqiao University, China (Grant No.2013JGYB36).

References

[1] Vlasov AN, Shkvaruntes AG, Rodgers JC, et al, Overmoded GW-class surface wave microwave oscillator [J]. IEEE Trans Plasma Sci, 2000, 28(3): 550-560.

[2] Miller RM, Prestwich KR, Poukey JW, et al. Production of annular electron beams by foilless diodes [J]. J Appl. Phys, 1980, 51(7): 3506-3515.

[3] Sheffield RL, Montgomery MD, Parker JV, et al. Generation of a cold, intense relativistic electron beam using a magnetized foilless diode [J]. Journal of Applied Physics, 1982, 53(8): 5408-5413.

[4] Robert J. Barker, John H. Booske, Neville C. Luhmann, Jr, and Gregory S. Nusinovich, Modern Microwave Millimetre Wave Power Electronics [M], New York: Wiley-IEEE Press, 2005.

[5] Ott E, Antonsen TM, Lovelace RV. Theory of foil-less diode generation of intense relativistic electron beams [J]. Physics of Fluids, 1977, 20(7): 1180-1184.

[6] Michael EJ, Mostrom MA, Thode LE. Analytical and numerical studies of foilless diodes [J]. Journal of Applied Physics, 1981, 52(8): 4942-4949.

[7] Michael E. Jones and Lester E. Thode. Intense annular relativistic electron in foilless diodes [J]. J Appl Phys, 1980, 51(10): 5212.

[8] Lawrence R, Bui T, David J, et al. Computer optimization of electron gun designs [C]. Proceedings of 32nd International Conference on Infrared, Millimeter Waves, and Terahertz Waves, Cardiff, England, 2007, pp.152-153.

[9] Wang JG, Zhang DH, Liu CL, et al. UNIPIC code for simulations of high power microwave devices [J]. Phys Plasmas, 2009, 16(3): 033108.

Advanced Materials Research Vols. 960-961 (2014) pp 881-884

doi:10.4028/www.scientific.net/AMR.960-961.881

Development of a Portable XLPE Cable Insulation Detection Device

Xiaoguang Xi[1, a], Yuyan Man[1, b], Chi Zhang[1, c], Minglei Wu[1], Yanwei Dong[1], Zhao Sun [1], Chen Xiaoxin[2, d]

[1] State Grid Tianjin Electric Power Research Institute, Tianjin, 300380, China

[2] Departments of Electrical Engineering, Shanghai Jiao Tong University, Shanghai, 200240, China

[a]kbreak@163.com, [b]manyuyan@yeah.net, [c]zc_zhangchi@163.com, [d]shawcine@gmail.com

Keywords: Partial Discharge; XLPE cable; HFCT sensor; UHF sensor; AE sensor; temperature sensor.

Abstract. In this article, a portable XLPE cable insulation detection device is introduced. Such a device utilizes electromagnetic coupling, UHF electromagnetic wave and acoustic emission to detect partial discharge signals in power cables. By analyzing the partial discharge signals and cable temperatures, the insulation status of XLPE power cables is judged.

Introduction

Since the introduction of XLPE cables, they are widely used in distribution power grids due to their good insulating performance, safety and reliability when supplying power, ease of manufacturing and installation convenience. However, XLPE cables are affected by electric fields, heat effects, mechanical stress, chemical corrosion and environmental conditions. Because of the important role XLPE cables play in power transmission and transformation, serious economic loss are often caused. [1,2]

Partial discharges are the main reason of XLPE cable insulation ageing, as well as an important sign and behavior of insulation deterioration. By detecting PD signals in cables, insulation problems in cables can be effectively discovered. Partial discharge detection usually represents partial discharge status by physical quantities, which are able to express phenomena caused by partial discharges. When partial discharges happen in XPLE cables, electric pulse, electromagnetic radiation and ultrasonic waves are generated, and there are means of detecting, namely electromagnetic coupling, UHF methods and ultrasonic methods, respectively. Besides, when severe deterioration happens in some part of a cable, partial overheat will occur. By measuring the temperature of such parts, the fault can be distinguished effectively. By analyzing XLPE cable temperature and the high frequency current pulse signals, high frequency electromagnetic wave signals and ultrasonic signals generated when partial discharges happen, cable insulation status estimations are performed.

Hardware Structure of the System

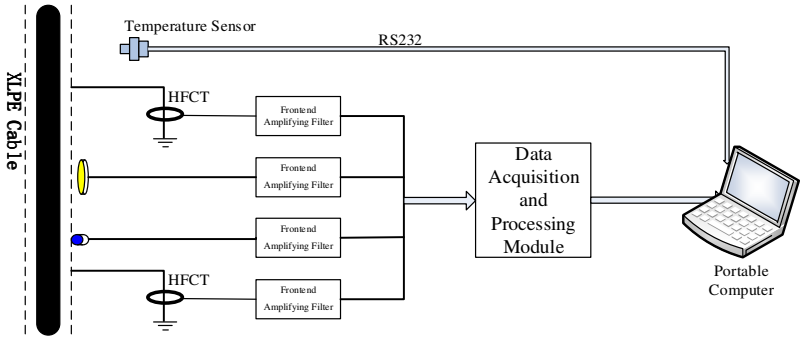

Fig. 1 Portable XLPE Cable Insulation Detection Device Schematic

Fig. 1 is the schematic of the portable XLPE cable insulation detection device. From the figure we can see that the device is composed of 2 major parts, namely sensors and detection terminal. The sensor part is composed of HFCTs (High Frequency Current Transformers), an UHF (Ultra-High Frequency) sensor, an AE (Acoustic Emission) sensor and a temperature sensor. It is mainly used for detecting pulse currents, electromagnetic radiations, ultrasonic waves and temperature generated by PDs in XLPE cables.

High Frequency Current Transformers (HFCTs）. HFCTs are commonly used in cable partial discharge detections. Based on electromagnetic coupling, the sensors are wide-band Rogowski coil current sensors with iron oxide cores.

It is required that HFCTs should be able to effectively filter interferences and extract PD signals. The sensors used in field detections are split-cored HFCTs with built-in amplifiers. Cable bodies are like inducting antennas. Cable detection experience shows that HFCT detection results contain a lot of radio interference [3]. To effectively extract PD signals, selectable amplification ratios of 20 dB and 40 dB are adopted in preposed amplifiers. Meanwhile, the amplifiers' sampling band is between 300 kHz and 25 MHz[4]. In field detections, install the split-cored HFCT around the grounding lead of the metal screen on the cable end. When PD occurs in the cable, pulse current will be inducted in the metal screen. The current will flow through the grounding lead and be detected by the HFCT.

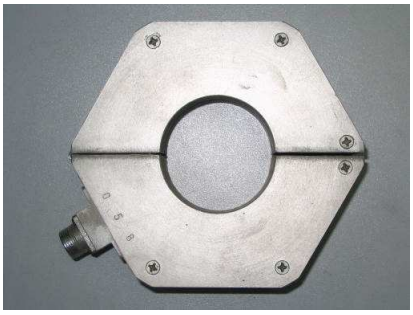

Fig. 2 High Frequency Current Transformer (HFCT)

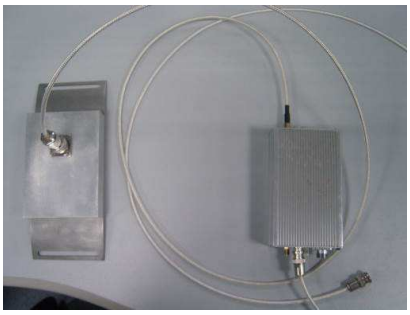

Fig. 3 Ultra-High Frequency (UHF) Sensor

Ultra-High Frequency (UHF) Sensor. UHF sensors' detected frequency bands are high. It means that they are far away from low frequency bands, which contains a great amount of noisy interference. UHF sensors are thus strongly anti-interference. Meanwhile, narrow-banded interferences (such as radio interference, cellular phone signals, etc.) can be recognized by methods like spectrum and waveform interference. Therefore, UHF detecting techniques are suitable for partial discharge detections[5,6]. Shown in Fig. 3 are the UHF sensor and its signal conditioning unit. The UHF sensor is a microstrip antenna with a bandwidth from 500 MHz to 1.5 GHz. UHF amplifier has 2 output channels, namely conditioned output and UHF output, which are used for PD signal detection and positioning, respectively [7] .

Ultrasonic Sensor. Shown in Fig. 4 is the combination of the ultrasonic sensor and its proposed amplifier. The ultrasonic sensor used in this device is a piezoelectric acoustic emission sensor. The maximum bandwidth of the sensor is 20 – 180 kHz. The sensitivity is 85 (-75) V/ (m/s) [V/ubar](dB). The output signal is a differential signal. The proposed amplifier is voltage type. It is composed of a 2-stage amplifier and a 4^{th}-order high-pass filter. It is mainly because that the detected signal is very weak, sometimes in microvolts or even less. So signals should go through such multistage amplification before they finally meet the requirement of data acquisition and processing.

Temperature Sensor. Temperature is the most obvious quantity in cable insulation detection. By measuring the temperatures of critical parts and vulnerable parts like XLPE cable bodies, joints, ends, etc., the condition of cable insulation deterioration can be effectively judged. This set system has an on-line infrared (IR) temperature sensor, which can measure temperatures without contacting the object being

measured. It is composed of a IR temperature converter and a box containing electronic components. The converter is used for sensing the temperature, while the box converts the sensed signal to digital signals that can be processed by industrial computers.

Fig. 4 Ultrasonic Sensor

Fig. 5 MID IR Temperature Sensor

Software Structure of the System

The software part is an important component of the system. The software unit is used for controlling sensor signal sampling, processing signals sampled, extracting PD features. It's expert system judges the insulation condition of XLPE cables by analyzing the data. The software part is mainly composed of the following modules: data acquisition, signal processing, feature extracting, diagnosis and interface display. The flow chart is shown in Fig. 6.

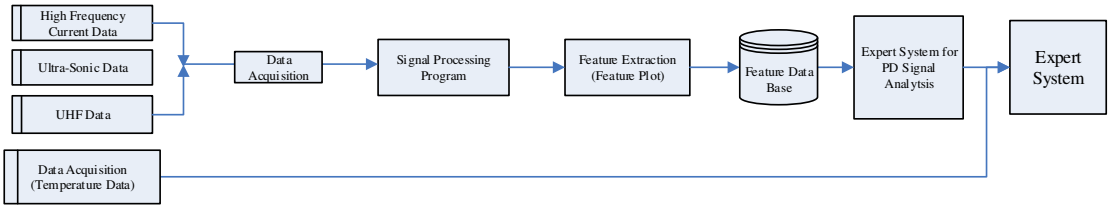

Fig. 6 System Software Flow Chart

Data Acquisition Program. The signals acquired by the system are PD signals and temperature signals. According to certain configured parameters, the data acquisition system controls signal acquisition from corresponding sensors. The acquired data will be saved to specified folders.

PD Signal Processing Program. Field detection will be effected by strong noisy interferences. The effective filtering such noises is the premise of accurately acquiring PD signal and analyzing cable insulation condition. The major function of the PD signal processing program is to filter these interferences in field. Due to that the forms of interferences in fields are diverse; it is very hard to use only one method to effectively filter all interferences. Thus different filtering methods should be applied to different interferences [8,9]. The PD signal processing program has adopted multiple filtering algorithms including FIR filtering, FFT filtering, wavelet filtering, etc.

Design of PD Feature Extracting Program and Feature Data Base. The PD feature extracting program is used for constructing the feature diagrams of PDs and extracting discharge fingerprints. PD feature diagrams include 5 kinds of 2-dimensional diagrams like maximum discharge to phase distribution, average discharge to phase distribution, etc. and the 3-dimensional φ-q-n diagram. Discharge fingerprints are extracted from 2-dimensional diagrams mainly includes kurtosis, skewness, etc.

For the convenience of future data comparison, analysis and research, a PD feature data base is constructed to store feature diagrams and discharge fingerprints of different types of discharges.

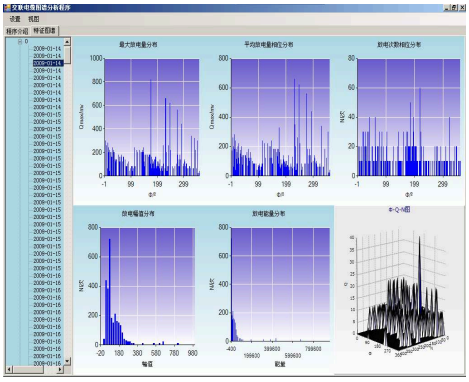

Fig. 7 Feature Diagrams

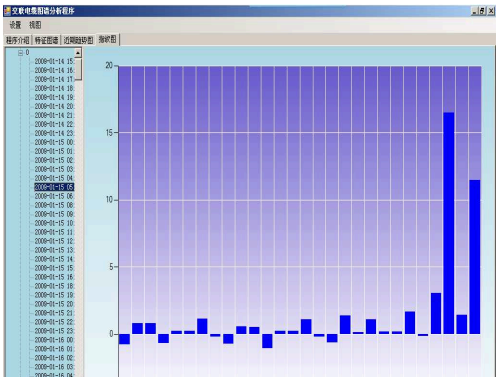

Fig. 8 A Fingerprint

Conclusion

The development scheme of portable partial discharge detection device for cable accessories is introduced in this paper. The paper mainly introduced the hardware structure and the software part. Field test results show that such device functions well.

Reference

[1] C.H.Li. Analysis and Comparison of Methods for Partial Discharge On-line Monitoring in XLPE Cable: Power System, Vol. 6(2005),p.29-33.

[2] X.C.Jiang. J.Cai. On-line Monitoring Techniques for 110kV and above XLPE Cable: Automatic Equipments of Electric Power, Vol. 25(2005), p.13-17.

[3] Y. Feng, Y.B. Fan, Y. Xu. Study on Anti-interference Technique of On-line Partial Discharge Detection for XLPE Power Cable Joints: High Voltage Technique, Vol. 32(2006), p.61-63.

[4] B. Wei, W. Wang. Partial Discharges On-Line Detection of 110kV XLPE Cables Using VHF Clamp Current Transducer: High Voltage Technique, Vol. 30(2004), p.37-39.

[5] J.H. Luo, J. Feng, J. Yuan. Study on Detection of Partial Discharge in XLPE Cable at High Frequency: Power System Technology ,Vol.25(2001), p.42-45.

[6] Shim et al. Digital signal processing applied to the detection of partial discharge, IEEE Electrical Insulation Magazine, Vol. 16(2000).

[7] S. Wang, X.H. Wu. Current Situation and Development of Calibration for UHF-PD(partial discharge) Detection System: High-Voltage Electrical Apparatus, Vol. 43(2007), p.59-61.

[8] R.J. Liao, J. Lv. Suppression of Periodic Narrowband Interference in Detection of Partial Discharges in Cable: Journal of Chongqing University, Vol. 9(2006), p.48-51.

[9] H.X. Fan, J.G. Cai. A Probe into the Background Interference of the Testing System for PD in Power Cables: Electric Wire, Vol. 2(2007), p.38-41.

Advanced Materials Research Vols. 960-961 (2014) pp 885-890

doi:10.4028/www.scientific.net/AMR.960-961.885

Suppression of Stochastic Pulses Interference in XLPE Cables Based on Fuzzy Clustering

Hong Mai[1, a], XiaoxinChen[2, b], YanranLi[2],ChongWei[2], YimingZhang[2]

[1] Foshan Power Supply Bureau of Guangdong power grid corporation, Foshan, 528000, China

[2]Departments of Electrical Engineering, Shanghai Jiao TongUniversity, Shanghai, 200240, China

[a]fs_mh@139.com,[b]shawcine@gmail.com

Keywords:adaptive fuzzy clustering partial discharge stochastic pulse interference

Abstract. To suppress the stochastic pulse interference in XLPE Cables, this paper uses equivalent time-frequency method to extract pulse feature values, adaptive fuzzy clustering to classify pulses, phase concentration as an index to distinguish PD and stochastic pulses. Analysis results of on-site data show that this method can effectively suppress stochastic pulse interference in the PD signal, providing a useful theoretical and practical basis to assess the state of XLPE cable insulation.

Introduction

Partial discharge (referred to as PD) is important factors and external performance causing cross-linked polyethylene (XLPE) cable insulation damaged [1]. Partial discharge test for XLPE cable is to assess the state of the cable insulation and an important means of preventing cable accidents [2]. In the field tests of PD, the random pulse interference has similar time domain and frequency domain characteristics with PD signal and is difficult to remove, so the suppression method has important practical significance in cable PD field testing.

In the current random pulse interference suppression studies, literature [3] proposed a suppression algorithm based on pulse waveform feature recognition; In the study of recognition algorithm, literature [4] proposed an algorithm to suppress random pulse interference based on PSO algorithm training neural network; Literature [5] did fuzzy clustering and gray clustering on the pulse, to achieve the removal of random pulse interference. This paper is based on the fuzzy clustering and theoretical results of random pulse interference suppression. For broadband partial discharge online detection of XLPE cable, we propose a randomized pulse interference identification method combining adaptive fuzzy clustering and phase concentration analysis. It is based on adaptive fuzzy clustering to get pulses categories, and calculates concentration of half-cycle for each pulse to determine the category of the pulse and achieve the random pulse interference removal.

Fuzzy C-Means clustering principle

Fuzzy C-Means clustering is classifying the samples by optimizing the iterative algorithm based on the distance between samples to obtain its membership degree. When the fuzzy C-means clustering algorithm process samples with unknown number of categories, the number of categories of clustering options is an important factor to determine the success of clustering algorithm. In the actual application, the number of clusters is often not directly determined. Therefore, this paper uses an adaptive fuzzy C-means clustering algorithm.

Suppose the data matrix $X=\{x_1,x_2,...,x_n\}\subset R^s$ and there are n samples which can be divided to c cluster (1<c<n). $V=\{v_1,v_2,...,v_c\}$ is the clustering central matrix, $U=[u_{ij}]_{c\times n}$ is the membership matrix and u_{ij} indicates the degree of j-th data elements x_j belonging to the i-th category. $u_{ij}\in\left\{u_{ij}\,|\,0\le u_{ij}\le 1,\sum_{i=1}^{c}u_{ij}=1,0<\sum_{j=1}^{n}u_{ij}<n\right\}$

The distance of sample x_j to the i-th clustering center v_i is:

$$d_{ij}=\|x_j-v_i\| \quad (1)$$

Objection function of clustering is:

$$J_m(U,V)=\sum_{i=1}^{c}\sum_{j=1}^{n}u_{ij}^m d_{ij}^2 \quad (2)$$

The central vector of the overall sample is:

$$\bar{x}=\sum_{i=1}^{c}\sum_{j=1}^{n}u_{ij}^m x_j / n \quad (3)$$

The adaptive function of the cluster numbers[6] is:

$$F(c)=\frac{\sum_{i=1}^{c}(\sum_{j=1}^{n}u_{ij}^m)\left\|\bar{x}-v_i\right\|^2/(c-1)}{\sum_{i=1}^{c}\sum_{j=1}^{n}u_{ij}^m\left\|x_j-v_i\right\|^2/(n-c)} \quad (4)$$

Adaptive fuzzy clustering algorithm steps [6] are as follows:

(a) Give the initial cluster numbers $c=2$ and the iteration criteria $\varepsilon>0$ .Initialize the clustering central matrix $V^{(0)}$, $F(1)=0$, $k=0$;

(b) Calculate the membership matrix of k-th iteration $U^{(k)}$:

$$u_{ij}^{(k)}=\frac{1}{\sum_{t=1}^{c}(\frac{d_{ij}^{(k)}}{d_{tj}^{(k)}})^{\frac{2}{m-1}}} \quad (5)$$

If $d_{rj}^{(k)}=0$, $u_{ij}^{(k)}=1$. If $i\ne r, u_{ij}^{(k)}=0$.

(c) Calculate the cluster center $V^{(k+1)}$ of $k+1$ -thiteration $V^{(k+1)}$:

$$v_i^{(k+1)}=\frac{\sum_{j=1}^{n}(u_{ij}^{(k)})^m x_j}{\sum_{j=1}^{n}(u_{ij}^{(k)})^m} \quad (6)$$

(d) Determine if $\| V^{(k+1)} - V^{(k)} \| \leq \varepsilon$ is correct. If it is correct, stop the iteration. Otherwise, $k = k+1$, repeat the iteration from step (a).

(e) Calculate $F(c)$. In the range of $2 < c < n$, if $F(c-1) > F(c-2)$ and $F(c-1) > F(c)$, c is the best cluster numbers and clustering process ends. Otherwise, add 1 to c and repeat iteration from step (a).

Fuzzy clustering based on pulse waveform characteristics

Pulse waveform extraction. Extract pulse waveform for pulse signal, and you will obtain a pulse waveform array and an array of pulse position. A pulse waveform array records amplitude of pulses in each sample point, pulse position array records sampling time of each point in the pulse. For a signal collected in a power frequency cycle, suppose there are N sampling points, K pulses, wherein, the p-th pulse signal includes n sampling points.

$t_p = \{t_p^1, t_p^2, ..., t_p^q, ..., t_p^n\}$ represents the sampling time of each point in p-th pulse

$s_p(t_p) = \{a_p^1, a_p^2, ..., a_p^q, ..., a_p^n\}$ represents amplitude function of p-th pulse in time domain.

Equivalent time-frequency analysis. In the time domain, the value describing a time-domain waveform pulse signal characteristic is equivalent time.

Time center of p-th pulseis:

$$T_p^0 = \frac{\int_1^n t_i \cdot s_i(t_i)^2}{\int_1^n s_i(t_i)^2} \tag{7}$$

Equivalent width of pulse waveform signal in the time domain is:

$$T_p = \sqrt{\frac{\int_{i=1}^n (t_p^i - T_p^0) \bullet s_p(t_p^i) dt}{\int_{i=1}^n s_p(t_p^i) dt}} \tag{8}$$

In the frequency domain, the value describing frequency domain waveform characteristic of a pulse signal is equivalent frequency.

Make FFT (Fast Fourier) transformation for the pulse and obtain the amplitude of the p-th pulse sequence in the frequency domain: $S_p(f_p) = \{A_p^1, A_p^2, ..., A_p^{n/2}\}$.

The frequency is: $f_p = \{f_p^1, f_p^2, ... f_p^q, ..., f_p^{n/2}\} = \{\frac{fs}{N}, \frac{2fs}{N}, ..., \frac{q \times fs}{N}, ..., \frac{nfs}{2N}\}$.

The frequency focus of p-th pulse is:

$$F_p^0 = \frac{\sum_{i=1}^{n/2} f_i \cdot S_i(f_i)^2}{\sum_{i=1}^{n/2} S_i(f_i)^2} \tag{9}$$

Equivalent width of pulse waveform signal in the frequency domainis:

$$F_p = \sqrt{\frac{\int_{i=1}^{n/2} (f_p^i - F_p^0) \bullet S_p(f_p^i) df}{\int_{i=1}^{n/2} S_p(f_p^i) df}} \tag{10}$$

From equation (7) - (10), the PD signal is converted to an equivalent T and F vectors. The dimension is reduced for the PD signal containing a high-dimensional information and domain and frequency characteristics of the PD signal are retained in a great extent, which provides a good clustering characteristics for fuzzy clustering of the pulse.

Removal of random pulse interference

Through broadband electromagnetic coupling method, collect five power frequency cycle (100ms) of XLPE cables PD signals in the substation site in 20M sampling rate. After noise cancellation of white noise, narrowband interference, periodic pulse interference, the discharge signal still has random pulse interference and high intensity, as shown in Fig. 1.

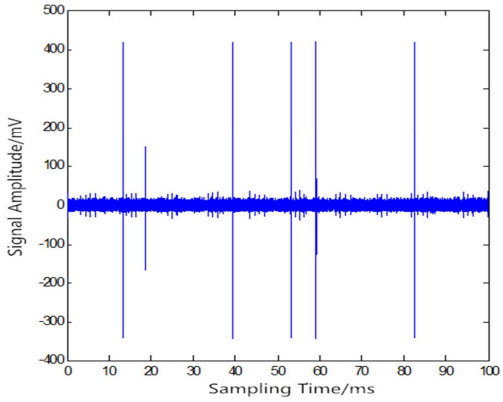

Fig. 1 PD signal before noise cancellation of random pulse interference signal

Since random pulse interference has random distribution in the whole power frequency cycle and PD pulses have a strong concentration in the positive and negative half-cycle power frequency cycle, design the following principles suppressing random pulse interference: First, take equivalent time frequency of a pulse the feature and use an adaptive fuzzy clustering algorithm to classify; second, take phase distribution concentration of various pulses as an indicator to distinguish whether it is random pulse interference.

Pulse adaptive clustering. Select 100 groups of PD data which didn't not eliminate random pulse interference, extract pulse waveform characteristic value TF using the equivalent time-frequency method, adaptive fuzzy C-means cluster for the pulses, and adaptive function of the number of clusters:

$F(2)=345.9$, $F(3)=1454.4$, $F(4)=2087$, $F(5)=2023.7$. Optimal number of classes is 4 and the pulse is divided into four clusters, as shown in Fig.2.

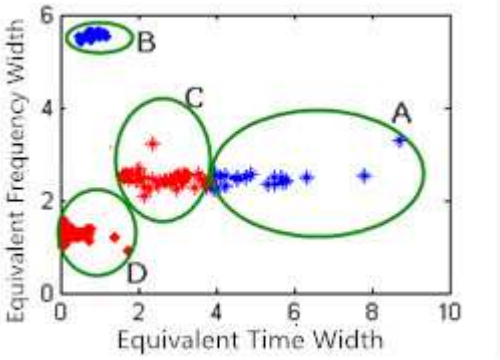

Fig.2 Adaptive fuzzy clustering diagram of the pulse

Pulses are clustered into A, B, C, and D four classes. But we still cannot determine which type is PD and which type is random pulse interference. In order to solve this problem, phase concentration analysis is used to identify the pulse.

Phase concentration analysis. In this paper, phase standard difference of various types of pulse is the index measuring the concentration density. As the standard difference is greater, the concentration is lower, the phase distribution is more widely, and the likelihood of being random interference is greater. Extract phases of four signals in the positive half-cycle (0-180 degrees) and negative half cycle (180 degrees to 360 degrees). Calculate phase standard differences of four pulse signals in the positive and negative half-cycle (Table 1).

Table 1 Phase Standard Difference for Signals of 4 types

Type	Standard Difference	
	0°-180°	180°-360°
A	55.6671	56.9703
B	57.7207	61.7910
C	59.2903	45.2781
D	14.2041	12.2675

As can be seen, phase standard difference of class D of signal is minimum.i.e. phase concentration of class D pulse is highest, and phase standard differences of A, B, C three classes of signals are larger. Based on the phase distribution knowledge of PD signal discharge pulse and random pulse interference, PD signals are mainly distributed in the first and third quadrants, focusing on near 90o and 270o and random pulse interference randomly is distributed from 0o to 360o. Thus the D class signal whose phase standard difference is minimum in positive and negative half-cycle is partial discharge signals; while A, B, C types of signals whose phase standard differences are larger are random pulses interference signals.

For the data in Figure 1, in the signal pulse sequence, remove the A, B, C three types of pulses, you can get a clear PD signals, as is shown in Fig.3.

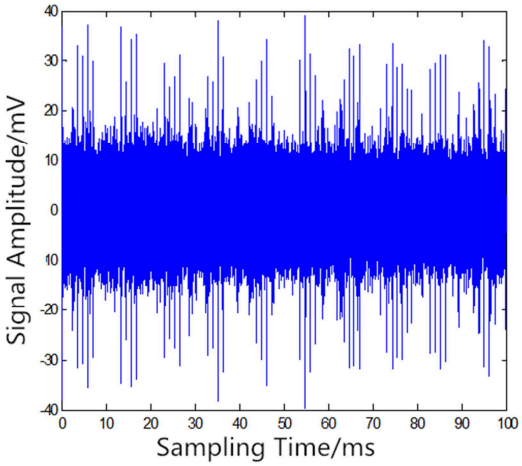

Fig.3 Adaptive fuzzy clustering eliminating noise results

Conclusion

This paper presents a new method for removing random pulse interference of XLPE cables partial discharge detection field signal. This method takes adaptive fuzzy clustering for the time-frequency characteristics of pulse signals which are collected in the field, and concentration of each class of pulse phase in the positive and negative power frequency half cycle is the index of distinguishing PD and random pulse. On-site data processing results show that this method can distinguish PD and random interference pulse.

Reference

[1] L. Yang，Y.S. Jin，W.S. Gao，Z. Yan．PD identification of HVDC equipment [J]: High Voltage Apparatus, Vol. 3(1998), p.48 ~ 51.

[2] X.C. JIANG, J. CAI, X.B. DONG.On-line monitoring techniques for 110KV and above XLPE cable［J］: Electric Power Automation Equipment，Vol. 25(2005), p.13 ~ 17.

[3] S. Happe, H.G.Kranz, W. Krause. Advanced suppression of stochastic pulse shaped partial discharge disturbances[J]: Dielectrics and Electrical Insulation, IEEE Transactions, Vol. 12(2005),p. 265 ~ 275.

[4] Z.Y. Shao, C.J. Huang, Y. Xiao. Application of PSO based neural network in suppression of stochastic pulse interference for partial discharge monitoring in large generators [J]: Automation of Electric Power Systems，Vol. 29(2005), p.49 ~ 52.

[5] Z.G. Tang, C.X. Wang, J.X. Chen. Pulse interferences elimination and classification of online UHF PD signals[J]: High Voltage Engineering，Vol. 35(2009), p.1026 ~ 1031.

[6] Y. Li, F.S. Yu. A New Validity Function For Fuzzy Clustering[C]: Proceedings of the 2009 IEEE 1st International Conference on Computational Intelligence and Natural Computing, Wuhan, China, 2009: 462 ~ 465.

Advanced Materials Research Vols. 960-961 (2014) pp 891-895

doi:10.4028/www.scientific.net/AMR.960-961.891

Impacts of UHV on Short Circuit Currents in China's Central 500kV Grid and Its Countermeasures

Zheng Xu[1,a], Wang Jianghong[2,b], Li Mei[3,c], Zhao Shuang[3,d] Zhang Buhan[3,e], Zeng Yuanfang[3,f], Zeng Ni[3,g], Zhu Ruoxi[3,h]

[1] School of Electrical Engineering Wuhan University, Wuhan, China

[2] State Grid Hubei Economic Research Institute, Wuhan, China

[3] State Key Laboratory of Advanced Electromagnetic Engineering and Technology

Huazhong University of Science and Technology, Wuhan, China

[a]hustzx987@163.com, [b]wangjianghong2008@126.com, [c]hnxnmeili@163.com, [d]525931413@qq.com [e]zhangbuhan@mail.hust.edu.cn, [f]zyf_jy@hust.edu.cn, [g]zengni@hust.edu.cn, [h]909706772@qq.com

Keywords: UHV; power grid; short circuit currents; limitation measures.

Abstract. Ultra-high voltage (UHV) projects are making power system growing lager and resulting in sharp increase of short circuit currents in some area especially in the vicinity of UHV access points. The paper presented the damage of short circuit current increases and common methods to limit fault current. Taking the construction and development of UHV grid in a province of central China as background, the over short circuit currents in 500kV Grid within UHV were showed and several countermeasures including choosing proper UHV access scheme, implementing UHV substation lower voltage bus partition running, installing reactors, optimizing power grid network based on UHV connection point were proposed and then verified by PSASP simulation. The results show those measures are useful to reduce the short circuit current to a reasonable level.

Introduction

UHV grid provides an effective solution to the energy and environmental problems that we are facing today, for it can allocate resources in a large scale with great efficiency and be a strong support for renewable energy power generation. According to the State Grid Corporation's development plan of UHV, by 2015, three vertical UHV lines from the north to south of China and three horizontal UHV lines from the west to east of China and all relevant DC project will be approved. By 2020, five vertical and five horizontal UHV lines and 20 UHVDC projects will be put into operation [1].

UHV projects have higher requirements for grid transmission capacity and reliability, making its scale to expand and reducing electrical distance gradually. The impedance of grid will decrease and short circuit currents will increase year by year which are more apparent in some 500 kV substations associated to UHV grid [2]. When the short circuit current exceeds the capacity of the circuit breaker, the fault can't be properly cut out, resulting in system instability and equipment damage. Therefore, balancing short circuit capacity of the power grid and limiting the short circuit current at a reasonable level should be put into first consideration when we build UHV projects.

In this paper, taking a province of central China as an example, short circuit currents of 500kV grid within UHV is simulated in PSASP6.28 software, which surpass the breaker capability in some area. Then several methods to limit fault current based on UHV construction are proposed and validated. Finally, some related countermeasures are suggested to guarantee the safety of power system.

Hazards of short-circuit current increases

The increase of short-circuit current makes circuit breakers, disconnecting switch, current transformers, buses and other equipment bear a large current surge. We have to choose larger capacity equipment which results in significant investment increment.

Temperature of transmission lines will rise according to short-circuit current increases, making the clamp portion of wires overheated and also intensifying the fault point damage, such as insulators broken, wires fused or other issues.

It constitutes a threat to gird safety if fault current grows too high that circuit breakers can't remove the failure effectively, causing the failure to expand in a larger area, endangering the operation of the whole power system.

Single-phase short-circuit current also increases. Asymmetrical short-circuit current will produce a strong unbalanced alternating magnetic field and then add hazards to communication lines [3].

Also, it results in the increase of step voltage and touch voltage near the tower, endangering neighboring humans and animals.

Comparative analysis of short circuit current limitation measures

Restructuring power grids, installing impedance equipment and adopting new technology are three common methods to suppress short-circuit current at home and abroad [4-6].

Restructuring power grids

Rationally allocate power source. By strictly controlling generator or UHV access point, it can balance grid short-circuit capacity and help limit short-circuit current. This method is sometimes limited by the energy supply or plant sites.

Substation bus partition running can increase system impedance, effectively reducing short-circuit currents. It is easy to operate but would lower grid safety margin and operation flexibility, even cause uneven load distribution.

Optimize network structure. Load centers are of high transient stability so we can untie some tight transmission loops, reduce substation in and out lines, use high-capacity transmission wires to meet the transmission requirements and increase electrical distance, maintaining reasonable impedance between power substations.

Operate power grids under district and voltage level classification. It is effective to reduce short circuit current but may also lower grid reliability, security, stability and capacity.

Installing impedance equipment

Using high impedance transformers or generators is an effective way to suppress the fault current. But they increase voltage angle difference, affect the quality of power supply, and also increase power losses under normal condition. Installing series reactor has the same disadvantage, but it can reduce the short-circuit current with small equipment investment. In addition, adopting low reactance at the neutral point of transformer has apparent effect on lowering single-phase to ground fault current but little effect on limiting three-phase short circuit current.

Adopting new technology

Using back to back device in the same place to divide AC system into sub running areas can limit the short-circuit current. It makes grid operation complex and has bad influence on system security. Besides, this equipment is very expensive.

Installing new generation current limiting devices is another way to lower fault current, including SFCL, FCL, FCL-TCSC, FCL-UPFC, etc [7-10]. Those devices have low impedance under normal condition and provide high impedance when fault occurs. But their application has the following problems: high cost, immature technique, small capability, control difficulty.

Application of limiting measures after the grid accessing UHV

Short-circuit current level without limiting measures

According to grid 2015 and 2018 plan of the province in the central China, three-phase short circuit currents of the 500kV bus node without any limitation measures are simulated in PSASP6.28 software and those buses that fault currents beyond the circuit breaker capacity are shown in Table 1, in which T stands for UHV substation lower voltage buses, N represents 500kV substation buses. The

circuit breaker capacity of 500kV grid in this province is 63kA. Fig.1 shows the grid network structure of the province in 2018.

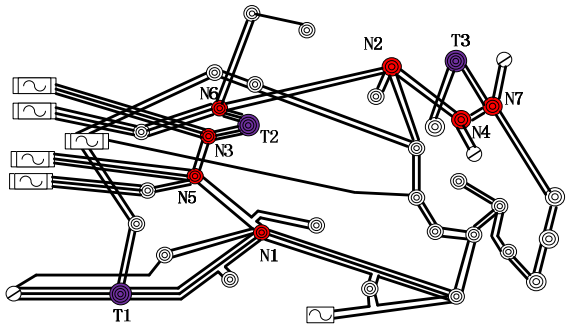

Fig.1. Grid network structure of the province in 2018

Table 1 Short circuit currents without limitation measures(kA)

Bus	2015	2018
T1a	—	**80.57**
T1b	—	**80.57**
T2a	**83.28**	**89.02**
T2b	**83.28**	**89.02**
T3a	60.72	**73.97**
T3b	60.72	**73.97**
N1	51.83	**69.13**
N2	**65.27**	**78.14**
N3	**69.53**	**73.76**
N4	59.91	**72.00**
N5	**72.85**	**80.52**
N6	**78.39**	**83.64**
N7	62.13	**69.79**

Table 2 Fault currents before and after UHV substation bus partition running(kA)

Bus	2015		2018	
	before	after	before	after
T1a	—	—	**80.57**	59.47
T1b	—	—	**80.57**	59.23
T2a	**83.28**	49.47	**89.02**	52.73
T2b	**83.28**	43.29	**88.98**	45.54
T3a	60.72	43.07	**73.93**	42.82
T3b	60.72	36.81	**73.97**	49.65
N1	51.83	50.83	**69.13**	**67.28**
N2	**65.27**	**64.51**	**78.14**	**76.97**
N3	**69.53**	49.28	**73.76**	52.13
N4	59.91	58.59	**72.00**	**70.09**
N5	**72.85**	**65.34**	**80.52**	**72.62**
N6	**78.39**	53.88	**83.64**	57.60
N7	62.13	57.91	**69.79**	**64.69**

The calculation shows that sites of short circuit currents that excess the regulation standard are mainly near the UHV access point, and there are 4 substations including 5 buses in 2015. And in 2018, the short circuit current level of 500 kV grids will continue to increase with new UHV projects put into operation. Those sites that fault currents surpass the breaker capability will increase from the original 4 to 10 including 13 buses.

Fault current limitation measures for UHV access

Determine proper UHV access schemes, such as adopting high impedance transformer in UHV substation, choose suitable connection method and access point according to the power balance requirements and former flow distribution to avoid lines and transformers overloading.

Implementing UHV substation lower voltage bus partition running is useful to suppress fault circuit of UHV substation and their connection substation. Results are compared in Table 2.By taking this method, short-circuit currents has been effectively controlled, less than switches capacity except N2 and N5 in 2015. Short circuit current of N2 is still 64.51kA, through load flow calculation, its highest value is 62.02kA.We need not to consider any other limitation method. N5 substation's short circuit current value is 65.34kA. Adopting series reactors on its exports double lines can reduce short-circuit current by 6.08kA, down to 59.26kA. However in 2018, this method can only solve part

of over fault current problem. Short-circuit currents of N1, N2, N4 and N5 substation are still far more than their switching capacity. Those problems need to be solved in the planning stage by grid network optimization according to the construction of UHV.

For limit short circuit currents of N1 and N5 substation, based on the T1 UHV construction, implement 500kV network optimization by reducing the N1 substation transmission lines and adding a new wire, shown in Fig.2 and Fig.3. Recheck fault currents after network optimization, their values of N1, N5 station are decreased to 64.89kA and 43.93kA. N5 station's short circuit current can be controlled also by adding series reactors in its connection transmission lines.

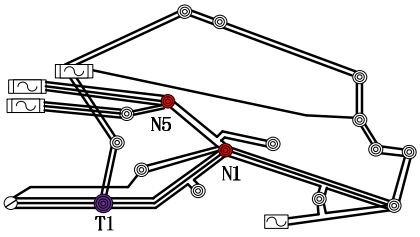

Fig.2. Network before optimization

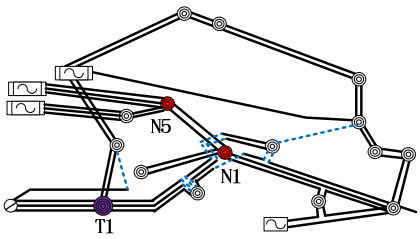

Fig.3. Network after optimization

In order to limit short-circuit currents of bus N2, N4, N7, expand the electromagnetic loop and weaken the function of each station. With new UHVDC accessing in, we can untie N4-N7 double lines, using UHVDC access point to form a network ring; simultaneously untie N2-N6 double lines, create a new substation, increase two transmission lines and use original N2-N6 wires to develop a larger loop. Grid structure before and after optimization near T3 are shown in Fig.4.and Fig.5. After optimization, short circuit currents of N2, N4, N7 are down to 62.89kA, 54.72kA, 49.57kA, below the switch breaking capacity.

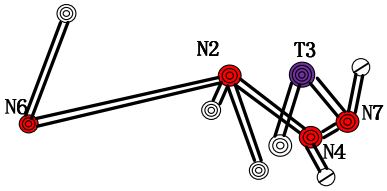

Fig.4. Network before optimization

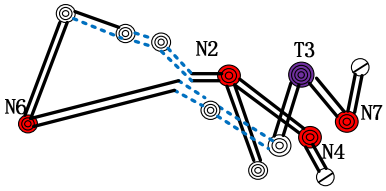

Fig.5. Network after optimization

N-1 check shows that the grid of this province after network optimization has reasonable flow distributions and can maintain transient stability.

Ways to deal with problems of fault current increases

Limiting measures are useful to control short-circuit current. But their level increases with the grid size year by year. For the security and stability of power system, improving operational management and control technologies are just as important as building strong power grid.

First, retain untied lines if possible to obtain support from the surrounding grid when the fault occurs. Secondly, install security and stability control devices in case that grid sub area running reduces power supply reliability. Finally, strengthen analysis of power grid operation to insure power equilibrium on the bus when implement UHV substation lower voltage bus partition running.

Conclusions

With construction of UHV grid and expansion of power system, the problem of short-circuit currents of 500kV grid exceeding the standard value will be exacerbated, especially in UHV access area. Several measures need to be taken from the long-term development of power grids, in which a rational network structure plan is the fundamental one. Appropriately adjusting the power grid operation mode is a more convenient way to reduce short circuit currents if the system is strong

enough. And installing series reactors can suppress the short circuit current with a little increase in investment. By reasonably selecting UHV access scheme, implementing UHV substation lower voltage bus partition running, installing reactors, optimizing power grid network based on UHV construction ,short circuit currents are successful controlled in the province of central China after UHV projects accessing in according to PSASP simulation. Results show those measures are useful to reduce the short circuit current to a reasonable level, which can provide a reference for network planning and the implementation of UHV projects.

Acknowledgements

This work was supported by State Grid Hubei Electric Power Company (Impacts of Mengxi UHVDC project on Hubei grid).

References:

[1] Information on http://www.chinasmartgrid.com.cn/news/20120813/379912.shtml

[2] HUANG Juan-juan, ZHENG Ying-fen. “Analysis of effect of 1 000 kV UHV grid on the short circuit current of the Central China Grid and research on limiting measures of short circuit current”, *Electric Power*, vol.40, no.3, pp.49-52, 2007. (In Chinese)

[3] He Yangzan,Wen Zengyin.Power System Analysis, pp.95-97(Huazhong University of Science and Technology Press,China 2011) (In Chinese)

[4] YUAN Juan，LIU Wen-ying，DONG Ming-qi，SHI Ke-qin,FAN Yue. “Application of Measures Limiting Short Circuit Currents in Northwest China Power Grid”, *Power System Technology*, vol.31, no.10, pp.42-45, 2007. (In Chinese)

[5] Ruan Qiantu．”Present situation of short circuit current control inShanghai power grid and countermeasures”, *Power System Technology*， vol.29, no.2, pp.78-83, 2005. (In Chinese)

[6] SUN Qizhen, CAI Zexiang, LI Aimin.”A Short circuit Current Over-limited Mechanism of 500 kV Power System and the Adaptability of Limiting Measures”, *Automation of Electric Power Systems*, vol.33, no.21, pp.92-96, 2009. (In Chinese)

[7] K. Hongesombut Y M K T. “Optimal Location Assignment and Design of Superconducting Fault Current Limiters Applied to Loop Power Systems “, *IEEE Transactions On Applied Super Conductivity*, vol.13, no.2, pp.1828-1831, 2003.

[8] Teng J H, Lu C N. “Optimum fault current limiter placement with search space reductiontechnique”, *Generation, Transmission & Distribution, IET*, vol.4, no.4, pp.485-494, 2010.

[9] WU Feng, ZHENG Jianyong, MEI Jun, WANG Lifeng.” Theoretical Study and Simulation of TCSC Based Fault Current Limiter”, *Power System Technology*, vol.36, no.2, pp.53-57, 2012. (In Chinese)

[10]GUI Fan, JIANG Daozhuo, LIN Zhiyong, LÜ Wentao, WU Zhaolin.” Design and Research of a Novel Unified Power Flow Controller With Fault Current Limiter”, *Power System Technology*, vol.37, no.8, pp.2187-2193, 2013. (In Chinese)

Advanced Materials Research Vols. 960-961 (2014) pp 896-899

doi:10.4028/www.scientific.net/AMR.960-961.896

Extreme Learning Machine in the Breaker Fault Diagnosis

Dan Jiang[1, a], Shutao Zhao[1,b], Jianfeng Ren[1,c], Yutao XU[1,d]

[1]North China Electric Power University, Baoding, Hebei, 071003, China

[a]jiangdan1015@163.com, [b]626919972@qq.com, [c]869941806@qq.com, [d]905011351@qq.com

Keywords: Vibration Signal, High Voltage Circuit Breakers, Fault Diagnosis, Extreme Learning Machine

Abstract. In order to improve the diagnosis method of the existing high-voltage circuit breaker fault, demonstrated a new diagnosis methord of mechanical failure of high voltage circuit breaker based on vibration signal. According to the factors of high voltage circuit breaker failure and the features of Single-hidden Layer Feedforward Neural Network, SLFN, a method of high voltage circuit breaker fault diagnosis proposed based on Extreme Learning Machine (ELM). Finally, the experiment proves the effectiveness of this method for breaker fault diagnosis based on vibration signal analysis and ELM.

Introduction

High voltage circuit breaker plays an important role in the control and protection of power system, its safe and reliable operation becomes one of the common concerns in the research field. Once breakdown it will cause huge losses, even threat the safety of personnel [1-2]. Breaker moving process will produce severe vibrations, the vibration of the vibration signal contains a wealth of information about the state of the circuit breaker, so breaker status will be reflected in the vibration signal, we need to study the vibration signal of the circuit breaker to diagnose the mechanical operation of high voltage circuit breaker status [3].

Extreme Learning Machine is a newly proposed method in recent years, based on Single Hidden Layer Feedforward Neural Networks. ELM algorithm generated threshold connection weights between the input layer and the hidden layer and the hidden layer neurons randomly, and no adjustment in the training process, just need to set the number of hidden layer neurons, we can obtain the optimal solution; it can learn fast and has the good generalization performance. Currently, ELM has been used in long-term load forecasting of power systems and power line construction cost estimates and other fields [4]. However, application in high-voltage circuit breaker fault diagnosis method need to be expanded.

In this paper, the history of engineering samples and laboratory testing data is used in the research of breaker fault diagnosis based on ELM, provide new ideas in the future for the study of fault diagnosis and monitoring of circuit breaker.

Theory of Extreme Learning Machine

For n different samples (x_i, t_i), there is $x_i = [x_{i1}, x_{i2}, \cdots, x_{in}]^T \in R^n$, $t_i = [t_{i1}, t_{i2}, \cdots, t_{im}]^T \in R^m$

The number of hidden layer nodes is N, the unified model of former single hidden layer feedforward neural networks which has a stimulate function $g(x)$ is:

$$\sum_{i=1}^{N} \beta_i g_i(x_j) = \sum_{i=1}^{N} \beta_i g(w_i \cdot x_j + b_i) = o_j \qquad j = 1, \cdots, N \tag{1}$$

w_i is the weights connected to the i-th hidden node and the input node, β_i is the weights connected to the i-th hidden node and the output node, b_i is the threshold of the i-th hidden layer node. The option -al excitation function is Sigmoid, radial basis function and so on.

β_i, w_i and b_i satisfies the following formula: $\sum_{i=1}^{N} \beta_i g\left(w_i \cdot x_j + b_i\right) = t_j \quad j = 1, \cdots, N$ (2)

The formula matrix is: $H\beta = T$ (3)

Matrix H is called the Output matrix of the neural network. From the above, w_i, b_i is fixed, so training a single hidden layer neural network is equivalent to seek a least squares solution $\hat{\beta}$ of linear systems $H\beta = T$ simply. However, in common applications, the number of hidden nodes N is much less than the number of training samples n, H matrix is not square, there is no w_i, b_i, $\beta(i = 1, \cdots, N)$ to make $H\beta = T$. The minimal norm least squares solution of linear systems described above are:

$$\hat{\beta} = H^{-1}T \tag{4}$$

H^{-1} is a Morre-Penrose generalized inverse matrix of matrix H.

Circuit Breaker Fault Diagnosis Model Based on ELM

Extracting Eigenvectors. (1) Use point-by-point filtering in Lab VIEW for filter based on circuit breaker vibration signal in the normal state. The waveform before and after filtering shown in Figure 1.

(2) Decompose the filtered signal in each state by EEMD. IMF component of the normal state of brake vibration signal decomposed by EEMD is shown in Figure 2; take the first 5 for example. Extract the energy entropy of each IMF component functions as shown in Table 1.

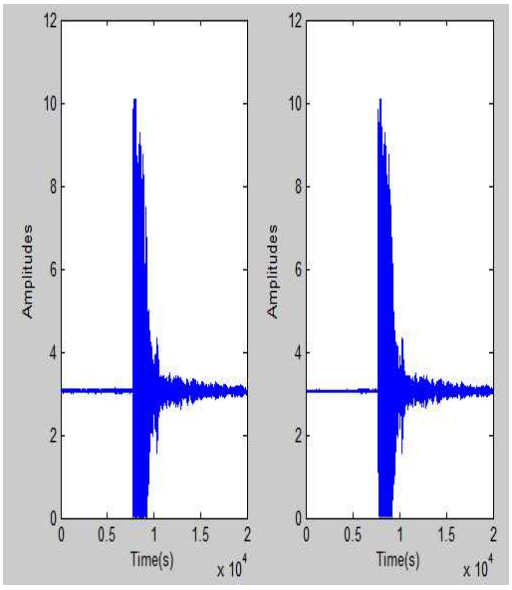

Figure 1. Point-by-point filtered waveforms before and after

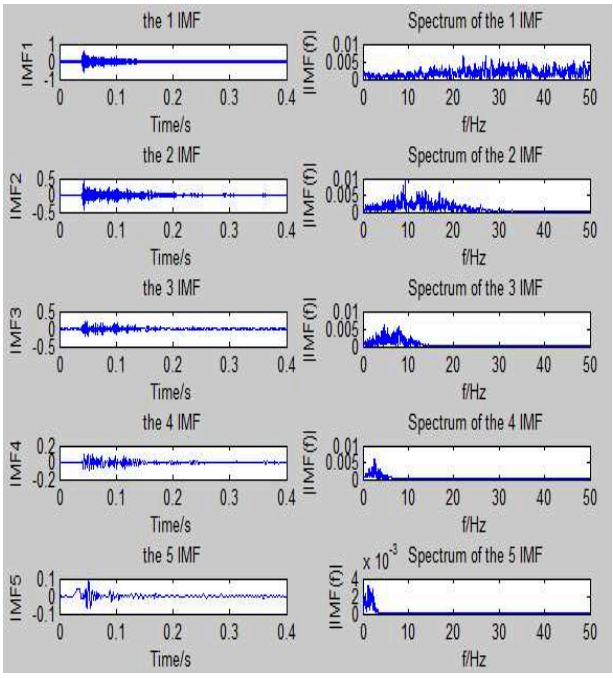

Figure 2. EEMD decomposition results

Table 1. Energy entropy of each component of the IMF

signal	E0	E1	E2	E3	E4	E5	E6	E7
Normal state	1.3375	1.5062	1.9116	2.2603	1.7260	2.0715	2.7317	3.0571
Fault state 1	1.8643	2.8030	2.7890	3.2948	3.1103	2.9971	3.2677	3.5595
Fault state 2	1.6870	1.7737	2.5444	2.5195	2.9480	2.8237	3.4730	3.6349
Fault state 3	1.5260	1.8367	1.8932	2.4591	2.8670	2.8917	3.0125	3.2593

(3) The energy entropy in (2) constitutes the characteristic quantity for each sample, which will be used as the input features of extreme learning machine. ELM input feature quantity can be expressed as:

$$e=(e_0,e_1,e_2,e_3,e_4,e_5,e_6,e_7)=\left(\frac{E_0}{E_\Sigma},\frac{E_1}{E_\Sigma},\frac{E_2}{E_\Sigma},\frac{E_3}{E_\Sigma},\frac{E_4}{E_\Sigma},\frac{E_5}{E_\Sigma},\frac{E_6}{E_\Sigma},\frac{E_7}{E_\Sigma}\right) \tag{5}$$

Wherein: $E_\Sigma=\sum_{i=0}^{7}E_i$. The number of neurons in the input layer of ELM is $n=8$.

(4) Determine the excitation function of Extreme Learning Machine model. The sigmoid function is selected for this experiment.

Fault Diagnosis Model Based on ELM. Breaker troubleshooting flowchart is showed in Figure 3.

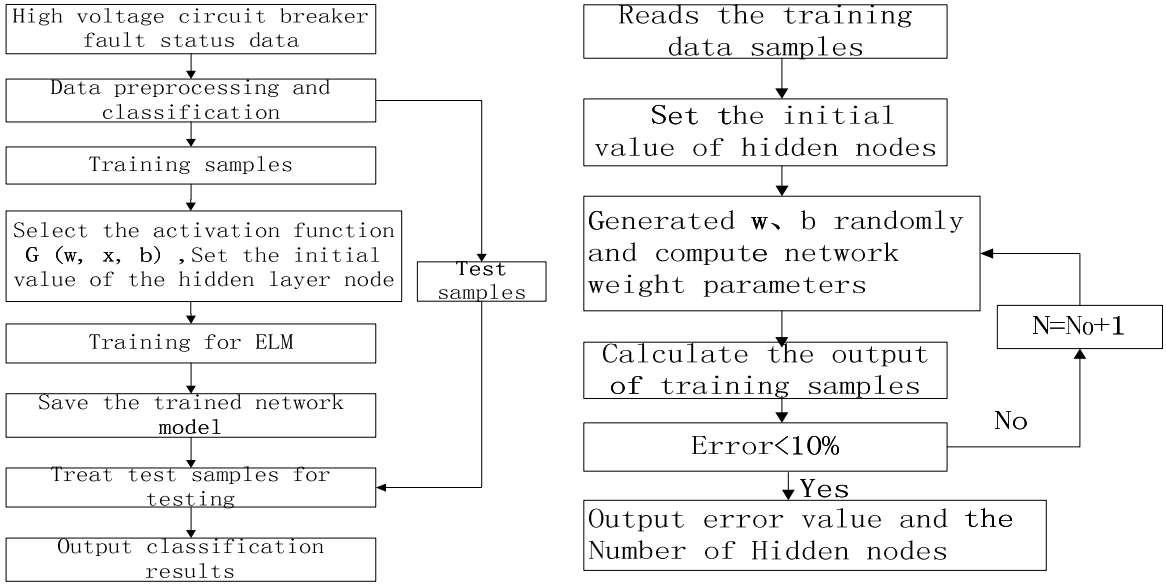

(a) ELM diagnostic process model (b) ELM training process

Figure 3. Breaker troubleshooting flowchart based on ELM

Experimental Analysis

Using ZN28A vacuum circuit breaker simulates normal, opening lock hook insufficient lubrication, operating coil faults and fault buffer failures. Using L0102T piezoelectric acceleration sensor gets vibration signals. Vibration signals were collected 100 groups of four states, 60 groups for training ELM, 40 groups for testing (10 groups of normal, 30 groups of fault).

(1) Set the initial hidden nodes, through training single hidden layer feedforward neural network, when the network learning ability and accuracy meet the requirements, determine the neural network weights parameter according to the formula (3) and (4) .

(2) Input the test sample to the trained network to obtain experimental estimation results.

(3) Input the under test 30 groups of fault signal to the diagnosis network, the test results shown in Figure 4. Visible, NO.11 groups of data is determined error; the classification accuracy was 96.67%.

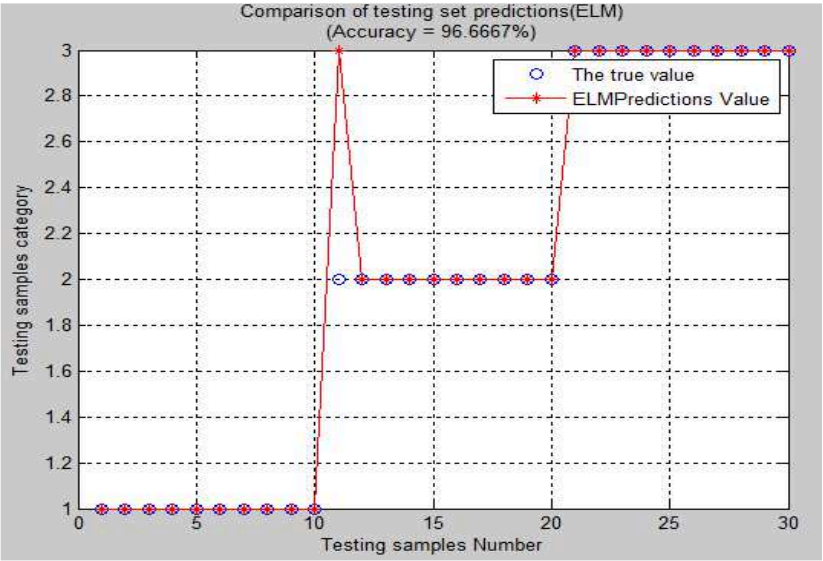

Figure 4. Analysis the classification results of ELM

Conclusion

Analyzing the collected vibration signal through point by point filtering, filter the mixed invalid signal during the measure process, then through EEMD decomposition, acquire the IMF components and its energy eigenvalues as the extreme learning machine input. By classifying the test sample to verify the results proved the extreme learning machine can be used to identify the circuit breaker failure, but, ELM training requires a lot of data, online status is still insufficient to meet this condition, so this method need for further improvement.

References

[1] CHEN Weigen, DENG Bangfei, YANG Bin. Fault recognition for high voltage circuit breaker based on EMD of vibration signal and energy entropy characteristic[J]. High Voltage Apparatus, 2009, 45(2):90-96, in Chinese.

[2] WU Zhensheng，WANG Wei，HUANG Mei，et al. Analysis of characteristics of vibration signals in high-voltage circuit breakers based on phase space reconstruction [J]. Modern Electric Power，2006，23(1)：10-14 , in Chinese.

[3] MA Qiang, RONG Mingzhe, JIA Shenli. Study of switching synchronization of high voltage breakers based on the wavelet packets extraction algorithm and short time analysis method [J]. Proceeding of the CSEE, 2005, 25(13):149-154, in Chinese.

[4] SHU Juan, GAN Lei. Research on cost estimation of power lines construction projects based on extreme learning machine method [J]. Modern Electric Power, 2011, 28(04):78-83, in Chinese.

[5] CHANG Guang, ZHANG Zhenqian, WANG Yi. Review on Mechanical Fault Diagnosis of High-voltage Circuit Breakers Based on Vibration Diagnosis[J]. High Voltage Apparatus, 2011, 8(8): 85-89, in Chinese.

Advanced Materials Research Vols. 960-961 (2014) pp 900-904

doi:10.4028/www.scientific.net/AMR.960-961.900

Based On EEMD And Multiclass Relevance Vector For High Voltage Circuit Breaker Mechanical Fault Diagnosis

Shang Chen[a], Weihua Niu[b] ,Baoshu Li[c] and Jie Yu[d]

Department of Electrical Engineering,North China Electric Power University, Baoding,Hebei,071000,China

[a]83329995@163.com,[b]tusiniuweihua@163.com,[c]libshu@263.net,[d]y824042101@126.com

Keywords: EEMD; Relevance vector machine; High voltage circuit breaker; Fault diagnosis

Abstract.Mechanical failure of high voltage circuit breaker accounted for the largest percentage of, it is necessary to diagnosis the mechanical fault .The acoustic signal of high voltage circuit breaker contains a large number of mechanical state information, can put the acoustic signal characteristics as a basis for high voltage circuit breaker fault diagnosis. M - RVM expanding traditional RVM to multiple categories, very suitable for fault diagnosis of high voltage circuit breaker.In this paper, the M-RVM combined with EEMD method for high voltage circuit breaker mechanical fault diagnosis, the experimental results show that the method has a good diagnosis effect.

Introduction

According to CIGRE for high voltage circuit breaker reliability the investigation and statistical analysis of the high voltage switch incidents in China show that in 80% of all high voltage circuit breaker fault fault belongs to the mechanical properties[1], to improve the running reliability of high voltage circuit breaker and ensure the quality of power grid is necessary for the mechanical fault diagnosis. In the high-voltage circuit breaker open or closing will occur during mechanical friction and impact and is accompanied by a loud noise, the resulting acoustic signal contains a large amount of machinery in the state information and sound waves through the non-contact measurement method, it is suitable for application in high voltage and strong electromagnetic environment characteristics, thus high voltage circuit breaker mechanical fault diagnosis can based on the acoustic signals of high voltage circuit breaker open or closing process[2].

In the past, the most frequently fault diagnosis method is artificial neural network (Artificial Neural Network, ANN) and support vector machines (Support Vector Machine, SVM), but the inherent defects exist in some aspects[3]: Local optimal problem and the problem of dimension disaster affect the accuracy of ANN algorithm, at the same time, ANN has a slow convergence speed, easily trapped in local minimumdefects;the SVM regularization coefficient determined difficulties, kernel function must satisfy macy's theorem and so on inherent limitations .Multiclass Relevance Vector Machine as a structural model using hierarchical Bayesian statistical learning algorithm proposed by the Damoulasy in 2008,compared with ANN and SVM[4]:M-RVM sparse stronger, low computational complexity, test time is short; direct multi-classification, and output membership probabilities for each category, and therefore can provide more information for decision making.

EEMD as a new signal processing method can handle nonlinear and non-stationary signals is well suited for acoustic signal processing and analysis. This article through the EEMD method for high voltage circuit breaker break-brake acoustic signal is decomposed, calculate the order of the intrinsic mode function energy and entropy as acoustic signal energy feature vectors, and enter into the M-RVM in high-voltage circuit breaker mechanical fault diagnosis.

M-RVM mode

In contrast with the original RVM, multiclass relevance vector employ the multinomial probit likelihood and provide probabilistic outputs for class membership.The M-RVM model structure is shown in figure1.

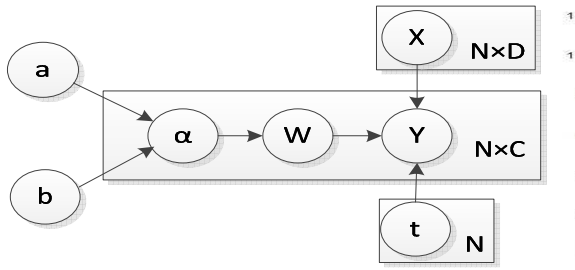

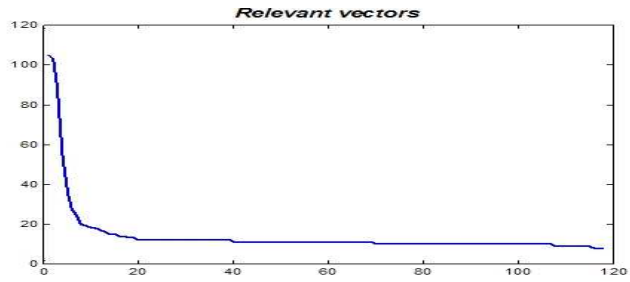

Fig.1 M-RVM model structure Fig.2 Iterative process

Training set is $X=\{x_i,t_i\}_{i=1}^{N}$, x_i $R^{N\times D}$, the category labels t $\{1,\cdots,C\}$, N is the total number of samples, D is the number of features , C is the number of categories. We apply kernel function K $R^{N\times N}$ in each feature space ,each row k_n of the kernel K expresses the tightness of the nth observations with other observed values.The learning process involves the inference of the model parameters $W^{N\times C}$, which by the quantity $W^T K$ act as a voting system to express which relationships of the data are important in order for our model to have appropriate discriminative properties.

Multiclass relevance vector by introducing auxiliary variables Y $R^{N\times C}$ that act as the regression targets of $W^T K$,we regress on Y with a standardized noise model[5],

$$y_{cn}|w_c,k_n \quad N_{y_{cn}}(w_c^T k_n,1) \tag{1}$$

The auxiliary variables are endowed with independent standardized Gaussian probability distributions to ensure statistical identifiability and enable closed-form iterative inference. The regressors W express the weight with which a data point "votes" for a specific class, the auxiliary variables Y express a class membership ranking system, given a sample n,we assign it to the class c with the highest y_{cn} . The continuous nature of Y allows not only multiple class discrimination via the multinomial probit link $t_n=i$ if y_{in} y_{jn} $j\neq i$ but also a probabilistic output for class membership via the resulting multinomial probit likelihood function ,

$$P(t_n=i|W,k_n)=\varepsilon_{p(u)}\left\{\prod_{j\neq i}\Phi\left(u+(w_i-w_j)^T k_n\right)\right\} \tag{2}$$

Where u~ N(0,1) and Φ the Gaussian cumulative distribution function. w_{nc} $N(0,\alpha_{nc}^{-1})$, α_{nc} priori parameter matrix elements in α and α_{nc} obey super-parameters *a, b* of the Gamma distribution[6].

Here we use a "top down"M-RVM model, first load the entire training set to the model and then continuously removed the sample which has no information from the entire training set,the iterative process as shown in figure2.

The training procedure involves consecutive updates of the model parameters based on a standard expectation maximization(E-M)scheme.First, according to E-step and Fig1 carried out α priori parameters update:

$$P(\alpha|W,a,b)\propto P(W|\alpha)P(\alpha|a,b) \tag{3}$$

Due to w_{nc} $N(0,\alpha_{nc}^{-1})$,and $\alpha\sim G(a,b)$, thus $\alpha_{nc}|w_{nc},a,b\sim G(1+a,w_{nc}^2+b)$ .So in E-step to update α by using the expectations of the Gamma distribution ,

$$\alpha_{nc}=\frac{1+a}{w_{nc}^2+b} \tag{4}$$

If for the *ith* sample we have α_{ic} 10^6 , then it is removed from A ,and update W_i,K_i,α_i . The weight parameters are updated based on the M-step.

$$\hat{W}=(K^T K+\alpha)^{-1}K^T Y \tag{5}$$

Finally,by using E-step and according to formula (6), (7) we update the auxiliary variable Y .If $c\neq i$,then

$$\tilde{y}_{nc} \leftarrow \hat{w}_c^T k_n - \frac{\varepsilon_{p(u)}\{N_u(\hat{w}_c^T k_n - \hat{w}_i^T k_n, 1)\Phi_u^{n,i,c}\}}{\varepsilon_{p(u)}\{\Phi(u + \hat{w}_i^T k_n - \hat{w}_c^T k_n)\Phi_u^{n,i,c}\}} \tag{6}$$

and $\Phi_u^{n,i,c} = \prod_{j \neq i,c} \Phi(u + \hat{w}_i^T k_n - \hat{w}_j^T k_n)$ .For class i have

$$y_{in} \leftarrow \hat{w}_i^T k_n - (\sum_{j \neq i} y_{in} - \hat{w}_j^T k_n) \tag{7}$$

According to equation (4) (5) (6) (7) at each iteration of the model parameters are updated.

Experimental Analysis

During the experiment, we use acoustic sensor for a ZN28A type vacuum circuit breaker were collected from normal state and fault simulation state in case of no-load break-brake acoustic signals (acquisition time of about 0.3s), simulated fault status including the base of a slightly loosen bolts base bolt looseness fault fault (I) and delay caused by insufficient lubrication fault fault (II), and use vector $[001]^T$,$[010]^T$,$[100]^T$ represents each state. Selection of acoustic sensors 502A-type pickups, this model pickups with high sensitivity, wide operating voltage range, low noise, low distortion, small features, built-in power supply reverse protection circuit, the connection is simple and convenient.

Feature Extraction. Based on the condition of high voltage circuit breaker break-brake acoustic signals(Fig.3) and ambient noise(Fig.5) power spectrum analysis(Fig.4,Fig.6) found that above 3000 Hz acoustic signal have with low energy, the 500 ~ 3000 Hz acoustic signals lasted for about 10 ms and are mainly concentrated in 0.02 s around, and contains a large number of high-voltage circuit breaker mechanical status information,below 500Hz low frequency components exist in the entire opening process.

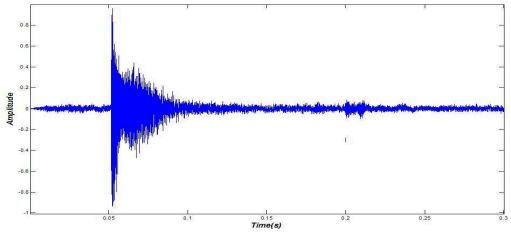

Fig.3 Acoustic signals in the process of high voltage circuit breaker points brake

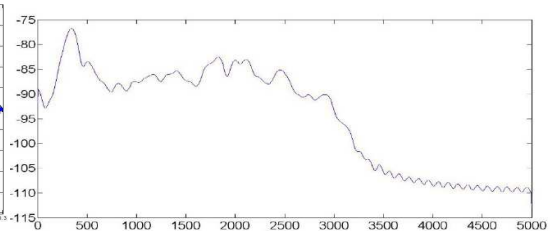

Fig.4 High voltage circuit breaker break-brake acoustic signal power spectrum

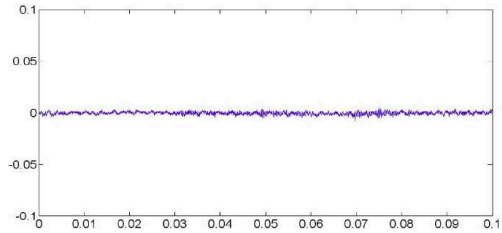

Fig.5 Points in the process of the brake environmental noise signal

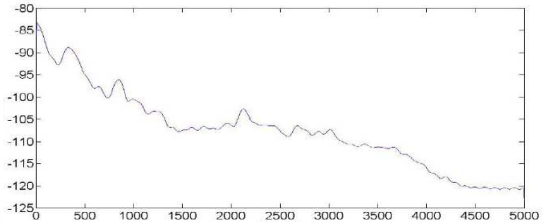

Fig.6 Environment in the process of high voltage circuit breaker points brake noise signal power spectrum

We here by EEMD method of 500 ~ 3000 Hz acoustic signal decomposition, the decomposed each IMF energy entropy as a high voltage circuit breaker fault diagnosis signal feature vector T.Due to the T value is bigger, in order to facilitate analysis and processing for normalized T. Some energy entropy is shown in table 1.

Tab.1 Some Energy Entropy

State	Energy entropy
Normal	0.9081 0.9695 0.9006 0.8986 0.9172 0.9357 0.9404 0.9452 0.7983 0.9925
Fault I	1.2240 1.2917 1.2004 1.2086 1.2153 1.2158 1.3374 1.2390 1.2475 1.2536
Fault II	1.1843 1.0832 1.0524 1.1516 1.1458 1.1821 1.0750 1.2301 1.1647 1.1368

Based On High-voltage Circuit Breaker Status M-RVM Classification. Experiments, we got 150 groups of experimental data(each state has 50 groups), in order to avoid skewed data problem, among them the 105 group as the training sample(each state has 35 groups),the remaining as test sample.

In order to prove the M - RVM can be used in fault diagnosis and has a good diagnosis effect at the same time, we put the M - RVM and nu - SVC support vector machine (SVM) is used for high voltage circuit breaker mechanical fault recognition, and compare the result.Two kinds of kernel function of the model adopts the radial basis function (RBF),For nu - SVC we adopt cross validation and PSO method of penalty factor C and kernel parameter g optimization, optimal parameters $c = 4.77$, $g = 1.41$ is shown in figure8.

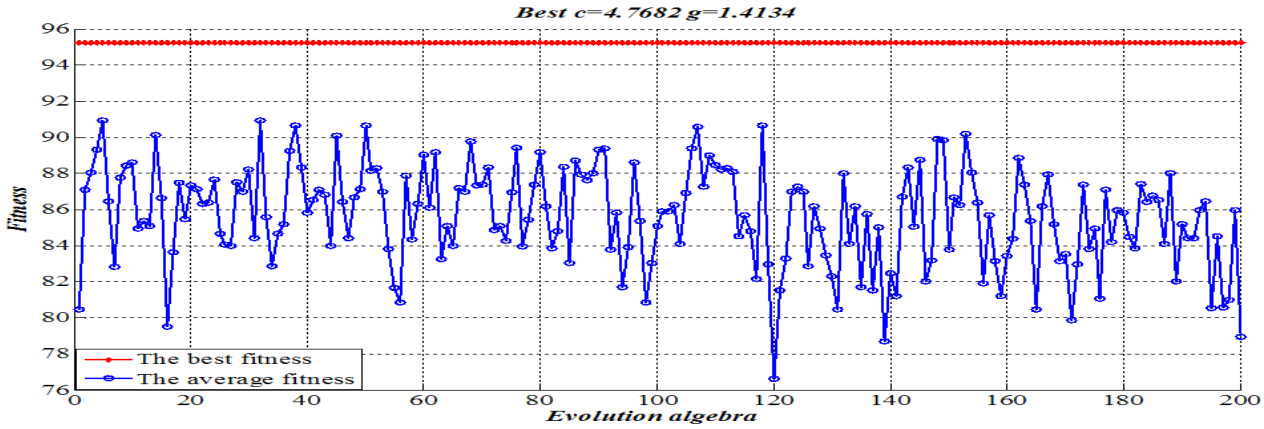

Fig.8 PSO parameters optimization

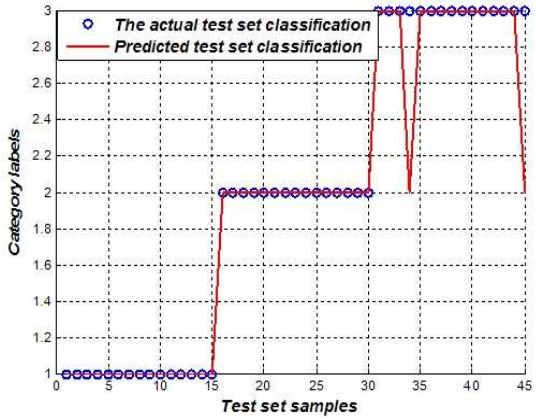

Fig.9 Result of SVM

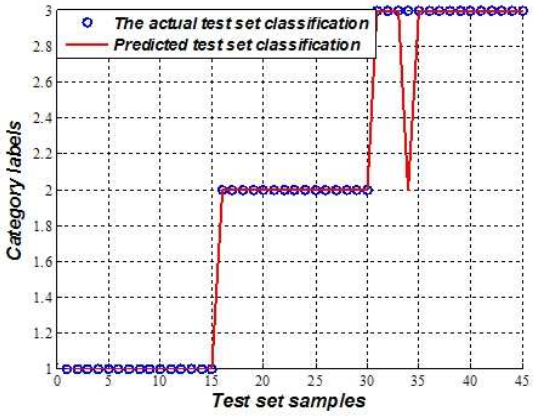

Fig.10 Result of M-RVM

The result of SVM and M-RVM are shown in figure 9 and figure10.Table 2 lists the high voltage circuit breaker mechanical fault diagnosis accuracy. Through the analysis of table 2 shows the method proposed in this paper can well used in high voltage circuit breaker mechanical fault diagnosis.

Tab.2.Results Are Different Methods To Test Set .

Failure type	Training sample	Test sample	Accuracy%	
			SVM	M-RVM
Normal	35	15	100	100
Fault I	35	15	100	100
Fault II	35	15	86.7	93.3
Counter	105	45	95.6	97.8

Not only M-RVM gives the diagnosis, but also the output of the circuit breaker corresponding probability P of each state, which provides the basis for further inspection for the circuit breaker. Part of the probability P as follows:

$$P = \begin{bmatrix} 1.0000 & 0.0000 & 0.0000 \\ 0.3575 & 0.3215 & 0.3210 \\ 0.2369 & 0.5264 & 0.2367 \\ 0.1142 & 0.7218 & 0.1640 \\ 0.1461 & 0.2144 & 0.6395 \\ 0.0006 & 0.3611 & 0.6384 \end{bmatrix}$$

Conclusion

This paper EEMD method is applied to decompose the brake process of high voltage circuit breaker acoustic signals, the decomposed each IMF energy and its energy entropy as a state of high voltage circuit breaker different feature vector.Then combined with M - RVM is applied to high voltage circuit breaker mechanical fault diagnosis, and gives the concrete realization method of the model and diagnostic process, through the experimental analysis of the fault diagnosis model has a good diagnosis effect.

References

[1] Yafang Liu. High voltage circuit breaker accident investigation [J]. Journal of international power. 1997, 1 (3) : 12-15.In Chinese.

[2] Liangliang Pan etc. Electrical equipment fault diagnosis method based on acoustic signal analysis [J]. Electric Power Automation Equipment, 2009,29 (8) :87-90.In Chinese.

[3] Dengwu Ma etc. Relevance vector machine and its application in fault diagnosis and prediction [J]. Journal of naval aeronautical engineering institute, 2013, 28 (2) : 154-160.In Chinese.

[4] Jinliang Yin etc. The new transformer fault diagnosis method for multi-class relevance vector machine [J] Based Power System Protection and Control, 2013,41 (5) :77-82.In Chinese.

[5] Psorakis I, Damoulas T, Girolami M A. Multiclass relevance vector machines: sparsity and accuracy[J]. IEEE Trans on Neural Networks,2010,21(10):1588-1598.

[6] Damoulas T, Ying Y etc. Inferring sparse kernel combinations and relevance vectors: an application to subcellular localization of proteins[C] // Proceedings of the 7th International Conference on Machine Learning and Applications (ICMLA2008), San Diego, USA, 2008.

Advanced Materials Research Vols. 960-961 (2014) pp 905-909

doi:10.4028/www.scientific.net/AMR.960-961.905

The Role of Improved K-means Clustering Algorithm in the Motion Parameters Determination of Breaker's Moving Contact

Yutao Xu[1, a], Shutao Zhao[1,b] , Dan Jiang [1,c] and Jianfeng Ren[1,d]

[1]Department of Electrical Engineering, North China Electric Power University,baoding,hebei,071000,China

[a]xuyutaocool@163.com, [b]shutaozhao@163.com, [c]jiangdan1015@163.com, [d]869941806@qq.com

Keywords: Motion Parameters of the Moving Contact, K-means Clustering Algorithm, Image Segmentation,

Abstract. High voltage circuit breaker's motion parameters of the moving contact is one of the key performance indicators in the evaluated of breaker. By means of extracting color features of *LW10B-252* circuit breaker by image segmentation, then determining its center point of the minimum circumscribed rectangle, getting the movement distance of center point and the use of time in adjacent images, realization motion parameter's measurement of the moving contact. This paper presents a algorithm based on improved k- means clustering algorithm to extract the color characteristics of the mechanical linkage of breaker, at the same time contrast with classical *OTSU* method and *RGB* color segmentation method. Experimental results show that the k- means clustering algorithm have a better segmentation result.

Introduction

In power system, the mechanical properties parameter of high voltage circuit breaker (*HV*) is an important basis of judgment and guarantee the normal work of the circuit breaker, it has a close relationship with safe and reliable of power grid [1]. In the test of high voltage circuit breaker's mechanical characteristic parameters, the parameters about breaker's moving contact is very important. So far, the measurement of the parameters is adding sensor, the way of 'contact' measurement is inevitable fixture installation, it is time-consuming and tedious, the most important thing is the installation been fixture affect the accuracy of the test results directly. At the same time because of variety of sensor type, its standard is not unification, the application of these methods can't be universal. So looking for a reliable, stable, convenient, rapid and accurate testing method is necessary.

At present, computer vision is widely used in the field of the electric power system fault and had get fruitful results [2].However It has a less application in the parameters testing of high voltage breaker's moving contact, and such way is not systematic and normalized, at the same time the key points in the selected aspects of measuring target is not too much introduction. This paper proposes a systematic way based on k-means clustering algorithm image segmentation. The first is get movement image of mechanical linkage by precise camera, to extract the study area of the mechanical linkage through improved k-means clustering algorithm image segmentation, calculating the external rectangular, with its center as a measurement of punctuation, finally determine the position of the center coordinates and the corresponding time, getting the coordinates and the change of the time, at last determine the trajectory by mathematical fitting method.

Image segmentation based on improved k-means clustering algorithm

The choice of the coordinate space

K- means clustering algorithm is a real-time unsupervised clustering algorithm ,it is put forward by Mac Queen, it has a simple principle and easy to deal with large amounts of data. Before using K-means clustering algorithm image segmentation we should to specify the number of clustering, the initial value of initial clustering center, the number of iterations or convergence condition, according

certain similarity measure criteria to assign each data to recently or similar clustering center, then formation of class, choose clustering center again, through the repeated iteration until convergence or end when the largest number of iterations is reached.

The color image obtained by the camera is belongs to *RGB* color space. *RGB* color space has a larger defect, it is that the brightness of the color cannot be separated with the chromaticity measurement. Although the color of the study area is fixed, but the change of light intensity can lead to the change of chromatic spaces, it's a certain effects on the image segmentation based on color. But the *L * a * b* color space is good to avoid the defect. *L * a * b* color space separate color and brightness thoroughly so that it overcome the influence of illumination of color differentiation. At the same time, the experiment of the study area is red, Match with magenta in *+a** axis.

The choice of initial clustering center and the way of distance measure

K-means clustering are for image segmentation, the algorithm process:

(1) Selecting a picture of a size of *m * n*, and *k* pixel as a kind of initial cluster centers of the clusters, *k = 1, 2, 3...k*;

(2) Calculating distance each pixel point with cluster center *s= 1, 2, 3...m t= 1, 2, 3...n, j=1，2, 3…k*

$$d(x_{(s,t)}, \mathrm{c}_j(I)) = \min\left\{d(x_{(s,t)}, c_j(I)), j = 1,2,...,k\right\} \tag{1}$$

(3) Calculate new clustering center

$$c_j(I+1) = \frac{1}{N_j}\sum_{i=1}^{N_j} x_{(s,t)} \tag{2}$$

(4) Judge: if $c_j(I+1) \neq c_j(I), j = 1,2,3,...,k,$, returned; Otherwise, the end of the algorithm.

K-means clustering algorithm is a continuously iterative process, the main factors of influencing the clustering results are as follows: number of clustering *k*, the initial clustering center c_j and the distance between objects $d(x_{(s,t)}, c_j(I))$. By the actual visual characteristics of the human eye, the color order of human eye can distinguish generally less than 60, but the number of class of color image segmentation has a lot smaller than this value. Actual class number is determined according to the specific application environment and the aim of segmentation. Due to the objective function minimization as a condition of the end of the clustering in k-means clustering, if random selection the initial clustering center, the k-means clustering algorithm is easy to get into the local optimum or has a wrong clustering results. The algorithm has a strong sensitivity to the initial clustering center, different initial clustering center could lead to a completely different effect. So the choice of initial clustering center and the size of object's distance is a key to the success of the k-means clustering algorithm.

The characteristics of the k-means clustering algorithm shows that the effect of clustering quality mainly depends on the initial clustering center and distance between the selected object, based on the circuit breaker image characteristics, from the initial clustering center and the optimal selection of weighted Euclidean distance $d(x_{(s,t)}, c_j(I))$ two aspects to improve k-means clustering algorithm.

There are many way to choice initial clustering center ,such as experienced selection method, the classification of the stochastic averaging, data sampling method, the density method, and the genetic algorithm, simulated annealing algorithm and particle swarm optimization [3]. Such ways solve the problem of the initial clustering center optimization to a certain extent, but at the same time there are some problems such as the algorithm complexity, it lead the algorithm has a very slow convergence speed, sometimes even no convergence. So above methods is not appropriate color image segmentation. But if the selection of the initial clustering center can satisfy the following two conditions. It is a very good solution to solve the problem of clustering center selection.

(1) There is one and only one cluster centers in each class;

(2) The choice of initial clustering center distance color as far as possible big and should be close to the center of the class.

In view of the above two conditions and the features that it is easy to distinguish image color, under the premise of class number *k* has been determine, order to extract each regional color target classification statistics of every image as the initial clustering center. In order better to solve the problem of color difference because of visual perception, difference illumination and natural conditions. At the same time in order to improve the accuracy of recognition, it should be further enlarge sample target classification and statistics calculate the initial clustering center in color area.

First of all, it necessary to establish an image library, the image library contains a variety of color classification. Combination *L *, a *, b ** coordinate characteristics with circuit breaker image characteristics to improve the clustering center. Classification of color image library is established, image library is the clustering center, among them

$$l_i = \frac{1}{\sum_{j=0}^{p_i} M_{i,j} * N_{i,j}} \sum_{j=0}^{p_i} \sum_{y=0}^{N_{i,j}-1} \sum_{x=0}^{M_{i,j}-1} f_l(x,y) \tag{3}$$

$$a_i = \frac{1}{\sum_{j=0}^{p_i} M_{i,j} * N_{i,j}} \sum_{j=0}^{p_i} \sum_{y=0}^{N_{i,j}-1} \sum_{x=0}^{M_{i,j}-1} f_a(x,y) \tag{4}$$

$$b_i = \frac{1}{\sum_{j=0}^{p_i} M_{i,j} * N_{i,j}} \sum_{j=0}^{p_i} \sum_{y=0}^{N_{i,j}-1} \sum_{x=0}^{M_{i,j}-1} f_b(x,y) \tag{5}$$

Among them： p_i as belonging to the number of the *i* samples, $M_{i,j}$ $N_{i,j}$ as belonging to the *i* classification of the size of the j sample; $f_l(x,y)$， $f_a(x,y)$， $f_b(x,y)$ as belonging to the values of corresponding samples pixels $f(x,y)$ in the space of *L * a * b.*

K-means clustering algorithm use Euclidean distance function to measure similarity between data points commonly. The calculation method of the traditional Euclidean distance think that all attributes of the data set in the clustering effect is the same, using this method to calculate the Euclidean distance can not accurately reflect the similarity between samples. According to human visual characteristics, tonal information is the main reason of the human eye to distinguish different colors, and then is the degree of saturation and brightness information. Therefore when using Euclidean distance as the distance criteria, actually neglected the role of the object component, after we are introduction of the weighted coefficient, on the one hand, it can give full play to the role of the correlation $d(Y_j, c_i)$, on the other hand can optimize clustering results by adjusting relevance weights. Weighted Euclidean distance measurement of correlation is:

$$d(Y_j, c_i) = \sqrt{[\alpha(l_j^y - l_i^c)]^2 + [\beta(a_j^y - a_i^c)]^2 + [\gamma(b_j^y - b_i^c)]^2} \tag{6}$$

Among them: $i = 1,...,k, j = 1,...,n$； Y_j as belonging to the image of a pixel； c_i as belonging to the cluster center； α, β and γ as belonging to the weights of three components； l_j^y, a_j^y, b_j^y, l_i^c, a_i^c and b_i^c as belonging to the three color component respectively [3].

Due to the *L * a * b* color space separate color and brightness thoroughly, it overcome influence of illumination of color differentiation, the factors affecting the size of the weighted Euclidean distance is mainly on the **a* and **b*, the weighted of and **b* should as far as possible big, and because the object of study mainly distributed on **a* coordinates, so it should have a maximum value, after repeated experiments, the best values are: 0.01, 1.00, 0.1.

Computer simulation results and analysis

According to the above model and algorithm, this paper uses the *Matlab* programming to illustrate the effectiveness of the k-means clustering algorithm, comparing it with classical *OTSU* segmentation algorithm and segmentation algorithm based on *RGB* respectively. We use a *LW10B - 252* type circuit breaker image as the research object. The image size of it is 2300 * 3880, the results as shown such Fig. 1.

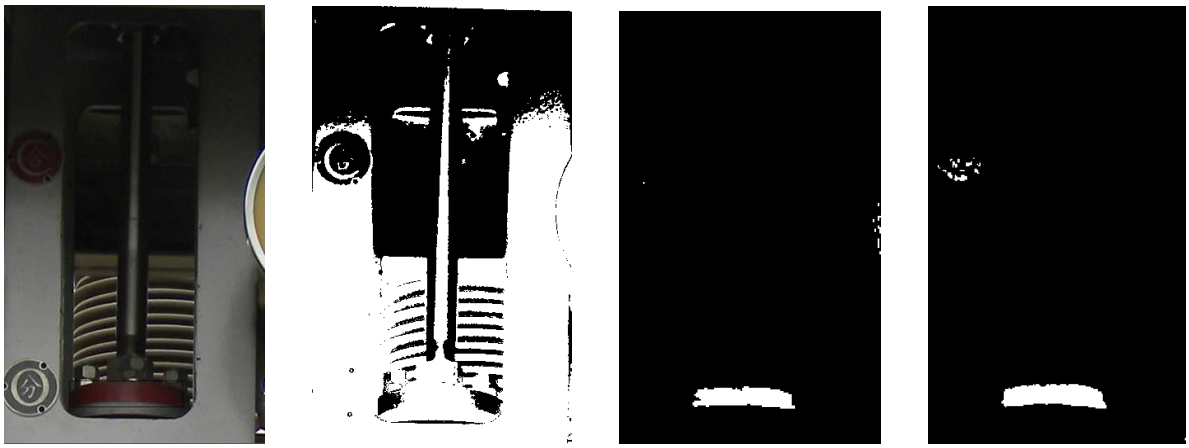

(a) original image (b) the classical *OTSU* (c) *RGB* (d) this paper

Fig.1 :The segmentation result of different methods

Fig.1(a) is mechanical connecting rod image which is connect to the moving contact, Fig.1(b) is the classic *OTSU* segmentation results, due to the complexity of the background color, the image segmentation effect is poorer. Fig.1(c) is a *RGB* segmentation results which is based on *RGB* color depth different. Fig.1(d) is the segmentation results of this paper. Form the figure we can find Fig.1(c) lose more pixels than Fig.1(d) in the target area, so that there is a bigger influence to measurement accuracy of the experimental data. Through the above analysis can know, k-means clustering algorithm has a better image segmentation in complex background, at the same time better retain the image edge details.

The determination of segmentation evaluation index

In this paper, by measuring the mechanical movement of the connecting rod to indirect gain movement parameters of the moving contact, thought above method to segment the target area, to calculate the target area of the minimum circumscribed rectangle, with the center of the rectangle as the target, by measuring the displacement of the target to determination motion parameters of the moving contact. For this purpose, the segmentation result affects the final experiment results directly, in view of the different types of images, the final segmentation quality evaluation indexes are different. In order to obtaining minimum circumscribed rectangle by the segmentation algorithm, this paper proposes a new evaluation criterion, to judge a good segmentation effect, the result as shown.

We can get a rectangular angle of each pixel location by the experiment, in the upper left corner as the origin of coordinates, the rectangular coordinates of original image and the result map as follows

Table 1 Rectangular coordinate point coordinate

	Upper left corner coordinates of rectangular	Bottom right corner coordinates of rectangular	Rectangular center coordinates
Original image	（631.3331）	（1595.3563）	（1113.3447）
RGB	（645.3387）	（1544.3597）	（1095.3492）
This paper	（648.3358）	（1590.3587）	（1119.3473）

Their corresponding coordinates are painted by the same proportion in the coordinate system is shown in Fig.2. The red rectangle is correspond to Fig.1(a) rectangular area, it is the original image area, blue rectangle is correspond to Fig.1 (c) rectangular area, the green rectangle is correspond to Fig.1 (d) rectangular area.

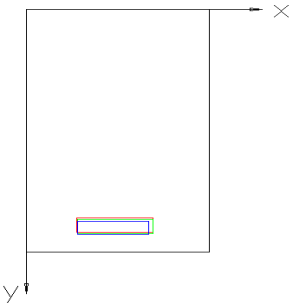

Fig.2 The projection of the axis of Fig.1

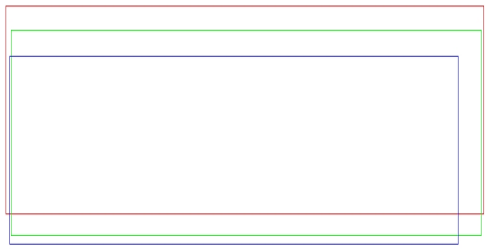

Fig.3 Rectangular area enlargement results of Fig.2

The Fig.3 shows the k-means clustering algorithm has a better result, rectangular area is closer to the original image, it mean than the loss of pixel is less, and the rectangular center is closer to the original image, so it has a small effect on the experimental results.

Conclusions

Experiments show that k-means clustering algorithm in the process of computer vision measure circuit breaker parameters play a key role, it ensures the accuracy of the results and provides important data support for the subsequent circuit breaker on-line monitoring and diagnosis. Although the function and structure of circuit breaker in the actual has a big difference, the circuit breakers have similar mechanical linkage structure connecting to the moving contact. We can add appropriate red rectangle icon or *LED* lighting with a rule shape on the mechanical linkage structure，this provides universality for k-means clustering algorithm.

References

[1] Shen Li, Yulong Huang: by Proceedings of the CSEE Vol. 17 (1997), p. 113-117. In Chinese.

[2] Feng Zhou, Aiguo Wu: Automation of electric power systems Vol. 23 (2005), p. 89-91. In Chinese.

[3] Zhonglin Zhang，Zhiyu Cao: Journal of zheng zhou university Vol. 31 (2010), p. 89-92. In Chinese.

[4] J.Liu, Y.H.Yang: Analysis and Machine Intelligence Vol. 26 (1994), p. 689-700

[5] K.S.Deshmukh, G.N.Shinde: Electronic Letters on Computer Vision and Image Analysis Vol. 5 (2005), p. 12-23

[6] Gexian Hou, Duyan Bi, Chengke Wu: Chinese journal of image and graphics Vol. 01 (2000), p. 42-46. In Chinese.

Advanced Materials Research Vols. 960-961 (2014) pp 910-915

doi:10.4028/www.scientific.net/AMR.960-961.910

A Novel PWM Technology based on High-power Current Source Inverter

Jing Bai, Shiqi Lu and Jian Liu

Beihua University Jilin 132021 China

bhdq2012@163.com

Keywords: Current source inverter, CSI-SPWM, CSI-TPWM, CSI-HVUSSPWM

Abstract. This paper presents a new *csi-hvusspwm* technology with many advantages such as the better output waveforms and the high utilization ratio of dc voltage based on the study of the *csi-spwm* technology and *csi-tpwm* technology. Theoretical derivation and modulation principle of *csi-hvusspwm* technology are described in detail. Finally, the simulation results validate the feasibility and effectiveness of this novel technology.

Introduction

With the development of the superconducting magnetic energy storage technology, current source inverter has become one of the most widely used inverter topology in AC drive and renewable energy power generation and other fields due to its advantages such as simple topology structure and reliable short-circuit protection [1-7]. At present, the mature modulation methods usually have selective harmonic elimination (*she*) technology, trapezoidal pulse width modulation (*tpwm*) technology, sinusoidal pulse width modulation (*spwm*) technology and so on [8]. However, sinusoidal pulse width modulation technology can produce a better output waveform, but requires a higher sampling frequency, so that the switching frequency of inverter is higher. Generally, the switching frequency is low for high-power inverters, and spwm-inverter with low switching frequency will produce huge amounts of low-order harmonics and a narrow pass-band, greatly reduce the performance of the control system [9]. Compared with SPWM technology, the output waveform of *tpwm* technology is not good, but the utilization ratio of the dc current is high and the switching frequency is low. In order to make *csi* has the better modulation output waveform, this paper presents a new modulation method which is high voltage utilization similar sinusoidal pulse width modulation (*hvusspwm*) technology. *Hvusspwm* technology has the advantage of *tpwm* and *spwm*.

Current Source Inverter Circuit

Fig. 1 shows the topology of a typical three-phase current source inverter, which consists of a current source, the load for star connection, six *gto* power switching elements. Three-phase *csi* principles: the state of the power switches $s_1 \sim s_6$ is expressed with bi-logic variables 0 and 1, which 0 for off and 1 represents conduction. Compared to the voltage source inverter (*vsi*), the working mode of *csi* requires one and only one switch is turned on at the same time in upper and lower half-bridge. The switch state variables satisfy the following constraints: $s_1+s_3+s_5=1$, $s_4+s_6+s_2=1$. This paper introduces the trio-logic phase switch status variables for describing the working state of *csi*.

$$S_j = \begin{cases} 1 & \text{The upper bridge arm switch turn-on; the lower bridge arm switch turn-of} \\ 0 & \text{The upper and lower bridge arm switches turn on or turn-off} \\ -1 & \text{The lower bridge arm switch turn-on; the upper bridge arm switch turn-off} \end{cases}$$

Where j=a, b, c

The relationship of phase switch status variables and a single switch state meet: $S_a=S_1-S_4$, $S_b=S_3-S_6$, $S_c=S_5-S_2$.

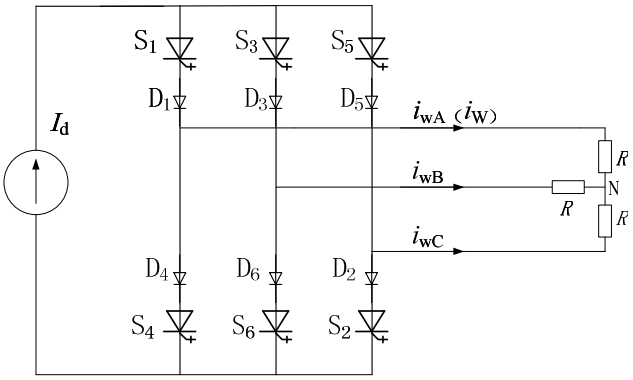

Fig. 1 Circuit topology of current source inverter

Current Source Inverter Modulation Technique

The requirements of three-phase *csi* for three-phase *pwm* signal is only two switches turn-on, which one lies in the upper bridge arm and the other lies in the lower bridge arm at any time (except during commutation). If only one switch is turned on, the current will lose the continuity and the current source will produce an extremely high voltage which will damage to the switches. If more than two switches are simultaneously turned on, *pwm* current will no longer meet the defined switching waveform. This is the important reason that the three-phase *csi-pwm* control becomes more complex than voltage-type [10].

Trapezoidal PWM. Trapezoidal pwm (*tpwm*) technology is a relatively common modulation method of *csi*. Fig. 2 shows *tpwm* schematic. Trapezoidal pwm technology obtains the symmetrical pwm waveform of the gate driving signal v_{g1} of the power switch S_1 in the first half cycle by comparing the trapezoidal modulating reference waveform v_m with the triangle carrier waveform v_{cr} in the oblique section of 0^0-60^0 and 120^0-180^0. The pwm waveforms of the power switches S_1~S_6 gate driving signal are queued in order delay 60^0. Then the pwm waveform of the current i_w is obtained by comparing the pwm waveforms of the gate driving signals v_{g1}~v_{g6}.

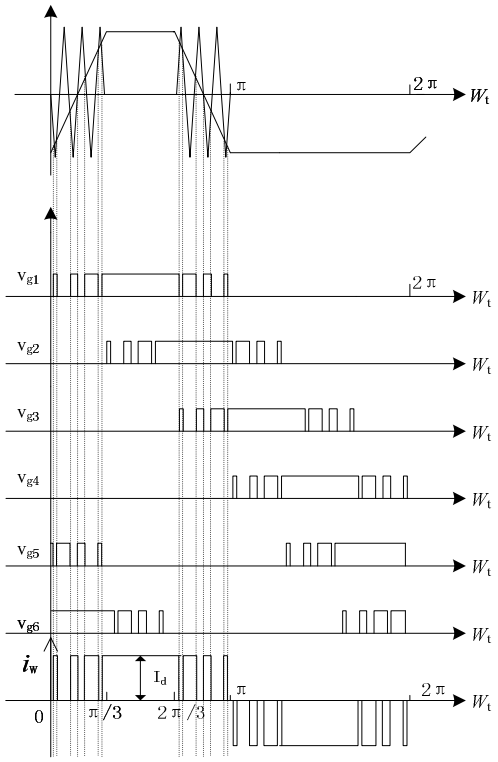

Fig. 2 Trapezoidal pwm modulation schematic

Sinusoidal PWM. As is shown in Fig. 3, *csi-spwm* technology adopts the control strategy of dynamic trio-logic *spwm*, which transforms the bi-logic *spwm* signals F_a, F_b, F_c into the trio-logic signals Y_a, Y_b, Y_c. Transform relations as follows[11]:

$$\begin{bmatrix} Y_a \\ Y_b \\ Y_c \end{bmatrix} = \frac{1}{2}\begin{bmatrix} 1 & -1 & 0 \\ 0 & 1 & -1 \\ -1 & 0 & 1 \end{bmatrix}\begin{bmatrix} F_a \\ F_b \\ F_c \end{bmatrix} \tag{1}$$

The control strategy meets the requirements of three-phase *csi* for three-phase pwm control signal, so the relationship between the output current and the input modulation signal is a linear, which to ensure the normal operation of three-phase *csi*.

HVUSSPWM. The comparative analysis of *tpwm* and *spwm* shows that the output current waveform of *csi* using *spwm* is better, but the switching frequency is higher and the *dc* current utilization is lower; while the *dc* current e utilization of *csi* using *tpwm* is higher and the switching frequency is lower, but the output current waveform is worse. A new *hvusspwm* modulation method is proposed for achieving better waveform output and higher utilization ratio of *dc* current based on the above analysis. As is shown in Fig. 4, *spwm* is used within 0^0~60^0, 120^0~240^0, 300^0~360^0 and Similar *tpwm* is used within 60^0~120^0, 240^0~300^0 in each cycle of the reference waveform.

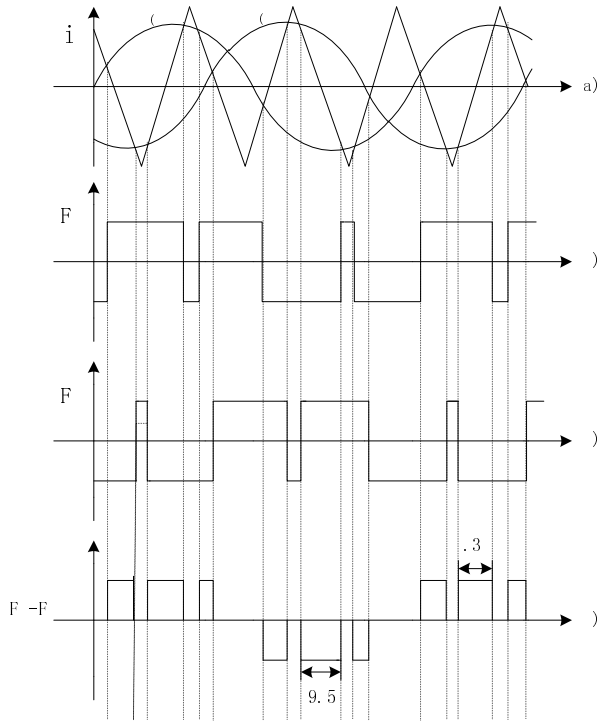

Fig. 3 SPWM modulation schematic

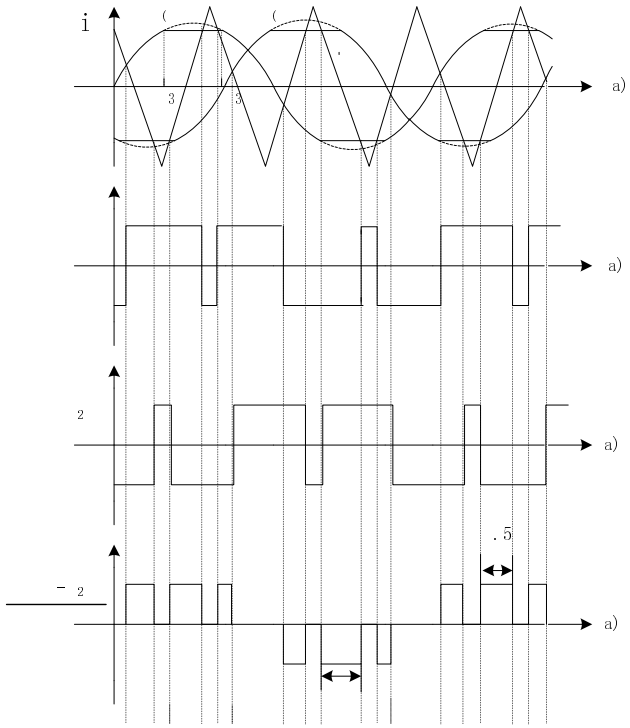

Fig. 4 HVUSSPWM modulation schematic

By comparing Fig. 2, Fig. 3 and Fig. 4, we can know that the switch sampling of *hvusspwm* technology is more uniform than one of *tpwm* technology; the dc current utilization rate of *hvusspwm* technology is higher than one of *spwm* by comparing the pulse width of the same position (10> 9.5,4.5> 4.3) in Fig. 3 and Fig. 4. Therefore, *hvusspwm* technology is a better modulation method in *csi*.

Simulation results and Experiment results

In the paper, simulation experiments are carried out in accordance with three-phase *csi* topology of Fig. 1. Because the *csi* current and the load don't matter, for the sake of discussion, the load in the simulation is purely resistive load. Parameters of simulation system are set as follows: I_d=1000A，

R=1 Ω, output current frequency is 20 Hz, Triangular carrier frequency is 500Hz, M=1. The simulation waveforms (A phase) and the spectrum (A phase) of *tpwm*, *spwm* and *hvusspwm* are respectively shown in Fig. 5, Fig. 6, Fig. 7. The experimental data of *tpwm*, *spwm*, and *hvusspwm* are shown in Table 1.

Table 1 The data sheet of simulation experiments

Modulation technique	Fundamental amplitude(V)	% of Fundamental									
		5	7	11	13	17	25	29	31	35	37
TPWM	1052	0.39	0.2	0.03	0	0.12	1.06	2.33	2.34	1.06	0.43
SPWM	868	0.03	0.13	0.03	0.02	0.02	0.06	0.05	0.14	0.07	0.06
HVUSSPWM	943	0.28	0.09	0.1	0.02	0.04	0.01	0.07	2.9	0.04	0.02

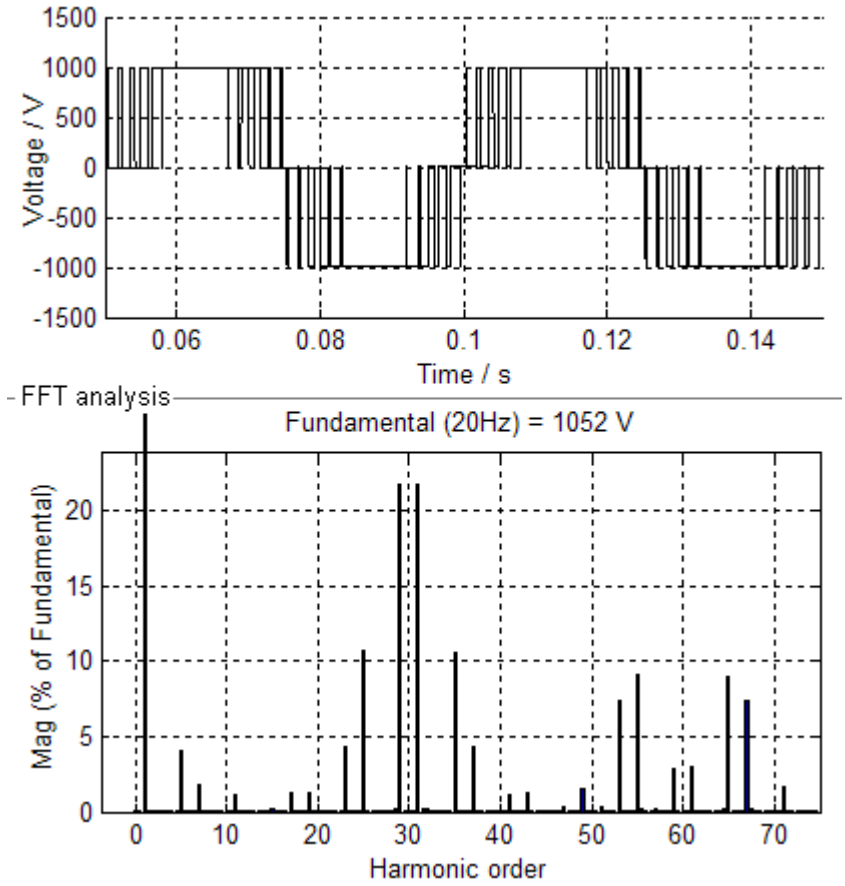

Fig. 5 Output current waveform and the spectrum of TPWM at 20 Hz

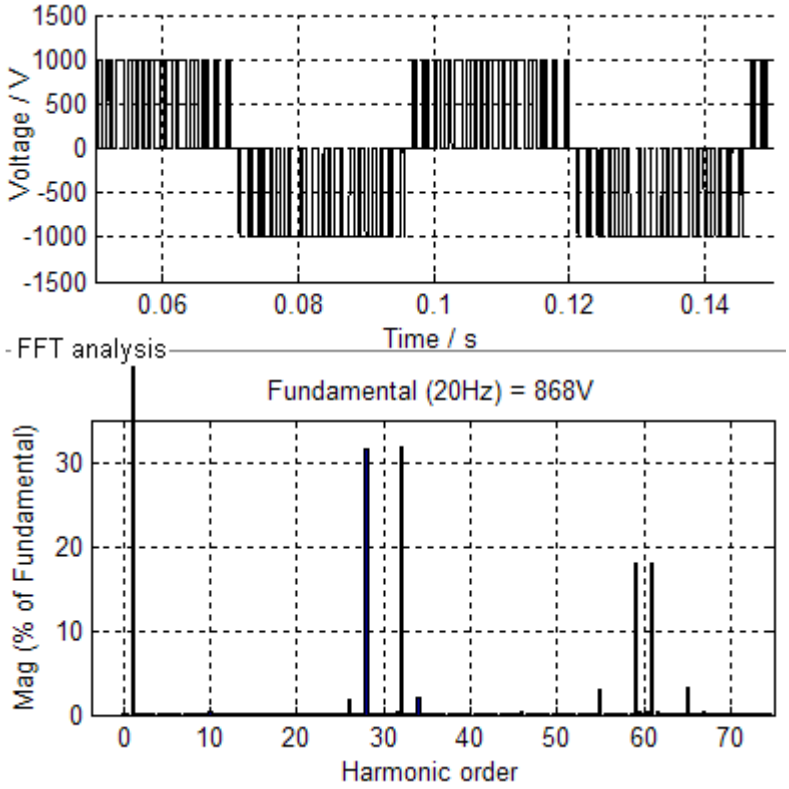

Fig. 6 Output current waveform and the spectrum of SPWM at 20 Hz

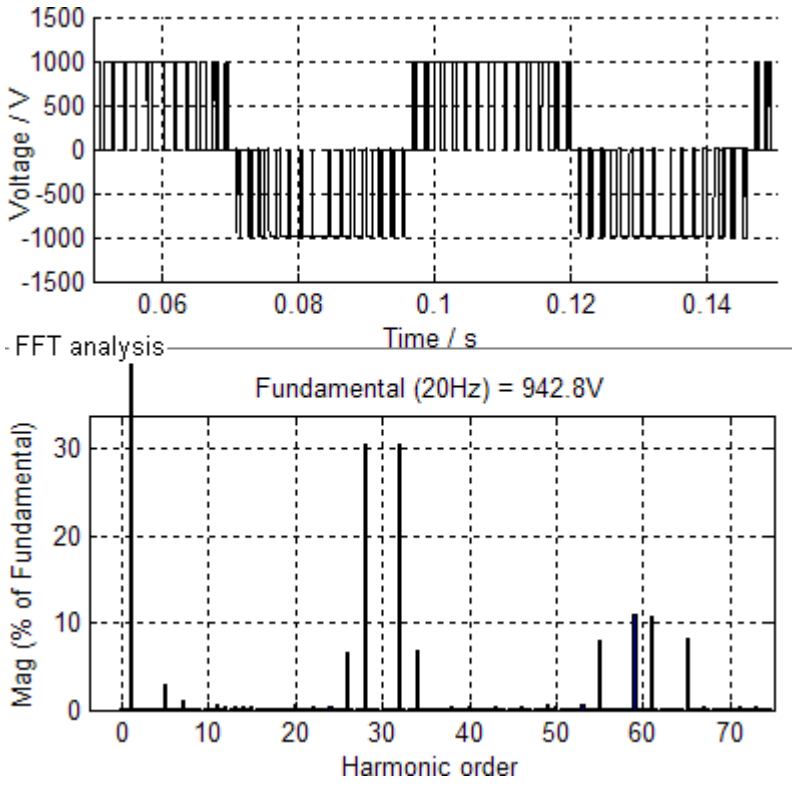

Fig. 7 Output current waveform and the spectrum of HVUSSPWM at 20 Hz

By the comparative analysis of the experimental data, we know that the relative content of 25th harmonic and the following harmonics of *hcusspwm* technology are so small that the output current waveform is better, and the utilization ratio of *dc* current is high. Therefore, *hvusspwm* technology is a better *csi-pwm* technology.

Summary

Hvusspwm technology achieves the output of the high utilization ratio of *dc* current and the good waveform in a relatively lower switching frequency, so that it is a better modulation method for the application of *csi* in the field of high-voltage and large-capacity variable frequency drive.

References

[1] Dan. Wang, Zhen-hui. Wu, Gang. Xu, Da-da. Wang, Meng. Song, Xiao-tao. Peng: *Real-time power control of superconducting magnetic energy storage*, in IEEE International Conference on Power System Technology, 2012, pp. 1-5.

[2] H. Komurcugil: *Steady-state analysis and passivity-based control of single-phase PWM current-source inverters*, IEEE Trans. Ind. Electron., vol. 57, no. 3, pp. 1026–1030, Mar. 2010.

[3] Zhihong Bai, HaoMa, Dewei (David) Xu and Bin Wu: "*Control Strategy With a Generalized DC Current Balancing Method for Multimodule Current-Source Converter*", IEEE Transactions on Power Electronics, vol 29, no 1, pp. 366-373, 2014.

[4] J. Dai, D. Xu, B.Wu, and N. R. Zargari: "*Unified DC-link current control for low-voltage ride-through in current-source-converter-based wind energy conversion systems*", IEEE Trans. Power Electron, vol 26, no 1, pp. 288-297, Jan. 2011.

[5] Popat Miteshkumar, Wu Bin, Zargari Navid R: "*Fault ride-through capability of cascaded current-source converter-based offshore wind farm*", IEEE Transactions on Sustainable Energy, vol 4, no 2, pp. 314-323, 2013.

[6] Jingya Dai, Sang Woo Nam, Manish Pande, Ghodrat Esmaeili: "*Medium Voltage Current Source Converter Drives for Marine Propulsion System using a Dual-Winding Synchronous Machine*", 2013 IEEE Energy Conversion Congress and Exposition, ECCE 2013, pp. 7-12, 2013.

[7] Jing Bai, Shi Qi Lu, Jian Liu: "*Study and Application of Sliding Mode Control Strategy for High-power Current Source Inverter*", Applied Mechanics and Materials, vol 527, no 1, pp. 259-266, Feb. 2014.

[8] Haixian. Yu: *Study of current source high--voltage converter using IGCT*, MA thesis, HeFei University of Technology, 2010, pp.31-40.

[9] Changyong. Wang, Mao. Liu, Zhongchao. Zhang: *Research on phase-shifted SPWM technique in current-source multi-converter*, power electronic technology, 1999(4):43~45.

[10] Zhaokai. Yuan: *Study on PWM control method of three-phase current source inverter*, MA thesis, China University of Petroleum (East China), 2008, pp.11-13.

[11] Yu. Xiong, Danjiang. Chen, Changsheng. Hu, Zhongchao. Zhang: *Analysis and experi ment of carrier phase-shifted SPWM technique based on current-source multi-converter*, power electronic technology, 2003, 37(4):39~41.

Advanced Materials Research Vols. 960-961 (2014) pp 916-920

doi:10.4028/www.scientific.net/AMR.960-961.916

Study on High-Voltage DC Power Supply for Electron Beam Furnace Based on Series Resonance

Sheng Wen Fan [1, a], Jun Du [2,b], Ze Ting Wang [3,c], Peng Wang [4,d]

[1] Beijing Higher Institution Engineering Research Center of North China Univ. of Tech.，Beijing 100144，China）

[2] Beijing Higher Institution Engineering Research Center of North China Univ. of Tech.，Beijing 100144，China）

[3] Beijing Higher Institution Engineering Research Center of North China Univ. of Tech.，Beijing 100144，China）

[4] Beijing Higher Institution Engineering Research Center of North China Univ. of Tech.，Beijing 100144，China）

[a] fsw@ncut.edu.cn, [b]dujun_vip@163.com, [c]wangzeting@ncut.edu.cn, [d]wangpeng2011@ncut.edu.cn

Keywords: high voltage power supply　series resonance　Electron Beam Melting　SRC.

Abstract.The high-voltage DC power supply for electron beam furnace belongs to Special Power Supplies. It has the characteristics of high voltage and high power. At present, the high voltage DC power supplies for electron beam furnace are mostly controlled by the silicon controlled rectifier operated by power frequency, which not only has the disadvantages of large volume but also doesn't has the characteristics of anti-short circuit capacity, rapid protection and restart. This characteristic affects the service life of the electron gun and the quality of the smelting. To solve the above problems, a high frequency resonant converter has been used in high voltage power supply, reduced the volume of power supply and the switching loss, and achieved rapid protection and restart. Simulation and experimental research show that the power supply can meet the requirement of smelting.

Introduction

The electron beam (EB) furnace is a device used for smelting high-reactivity metal under low vacuum. It mainly consists of furnace body, the electron gun, high-voltage DC power supply and control system, etc. [1] The high-voltage DC power supply is for accelerating electrons produced by electron gun. Electrons are accelerated in the electric field formed by high-voltage DC power supply, and electron beam is formed by the focusing and deflection coil. The electron beam with high-speed hits the metal surface, and the electrons'kinetic energy converts thermal energy, which can melt metals. Traditional Boost converters with industrial frequency transformer control the output voltage by controlling the thyristor conduction angle, which not only have large volume of transformer and filter but also have large voltage ripple. This study is based on the DSP control digital high-frequency high-voltage power supply. It is composed by thyristor rectifier and IGBT inverter. The structure of the inverter is full-bridge series resonance. Inverter works with constant frequency. High voltage controlled by DC-bus voltage.

Circuit Topologies and Working Principles.

Topology Structure of High Voltage DC Power Supply.

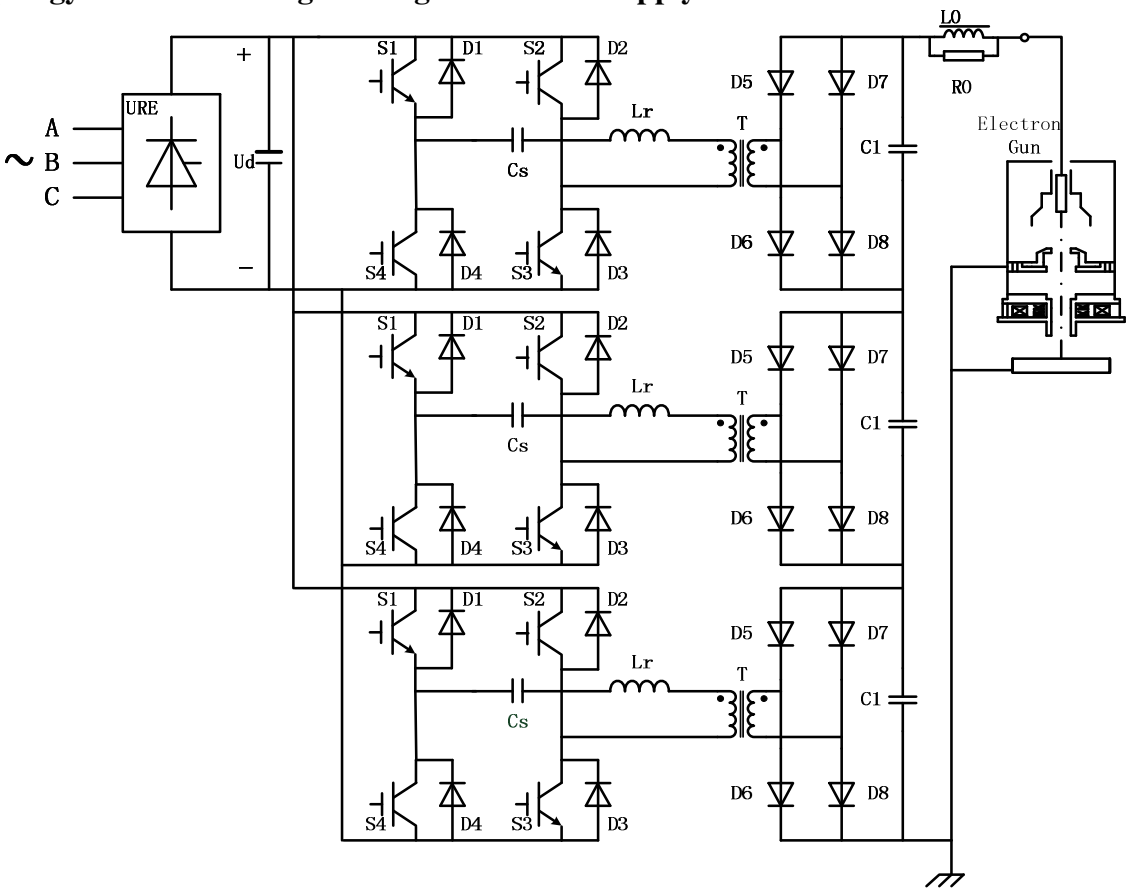

Fig. 1 The main circuit topology structure

The topology structure shown in figure 1 is mainly composed of three-phase thyristor controlled rectifier (URE), high-frequency inverter, high-frequency high-voltage transformer, high voltage silicon stack, high-voltage filter capacitor, high-voltage current-limiting inductor and electron gun. It has the energy delivered mode of AC-DC-AC-DC. We get the DC bus voltage U_d by thyristor controlled rectifier, which input is Three-phase 50Hz AC voltage（AC-DC）. High frequency inverter converts the DC power into the low-voltage AC power（DC-AC）. High-frequency high-voltage transformer takes the low voltage and changes it to high voltage. High voltage silicon stack connected to the output terminals of transformer, and converts high-voltage AC power to high-voltage DC power（AC-DC）. Take the input-parallel output-series based on full-bridge topology for reducing the transformer ratio, which can reduce the distributed capacitance of transformer. L_0 is the choking-winding for limiting the di/dt value at the time of short-circuited.

Operation Principles of the Inverter.

According to the relationship of the resonance frequency of the inverter f_r and switching frequency f_s, there are three operating modes of series resonant inverter[2][3]:

(a) $f_s < 1/2\, f_r$

The inverter works in discontinuous current mode (DCM). Switches turn on and off under ZCS condition. It can easily achieve soft-switch in all range, and has the constant-current characteristics.

The disadvantage of this mode is:

(1). The DC-bus voltage utilization ratio is low, which can lead to the increase of transformer ratio.

(2) Peak current through switches is high under the condition of the same power output.

(b) $1/2\, f_r < f_s < f_r$

The inverter works in current continuous mode (CCM1). Switches can turn off at zero voltage, but hard-opening.

(c) $f_s > f_r$

The inverter works in current continuous mode (CCM2). Switches can turn on at zero current, but hard-off.

Steady-State Analysis of High-Frequency Inverter

For the convenience of analysis, assume that the following conditions are established [4].

1. The resonance frequency f_r is equal to the switching frequency f_s.
2. Regardless of the dead zone, Duty ratio D = 50%.
3. Turn off one couple of switches and turn on another couple（S1, S3 or S2, S4）at the same time, when the resonant current reaches zero at the end of the half resonant period. the after-flow diode keeps closed.

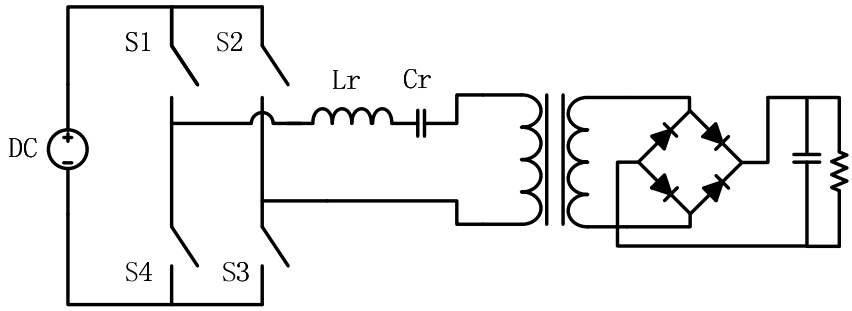

Fig. 2 A series resonant converter incorporanting a full-bridge switch network.

From the perspective of the energy transfer, resonant converters transfer energy relying on fundamental wave. Thus, the fundamental wave method can be used for steady-state analysis.

The input voltage of the L-C resonant network is square wave voltage (frequcncy is switching frequency f_s, amplitude is DC-bus voltage U_D, duty cycle is 50%). its input voltage waveform can be expressed in the Fourier series:

$$v_s(t) = \frac{4U_{in}}{\pi} \sum_{n=1,3,5} \frac{1}{n} \sin(n\omega_s t) \tag{2-1}$$

The fundamental component is (showed in Fig.3):

$$U_{base} = \frac{4U_{in}}{\pi} \sin \omega_s t \tag{2-2}$$

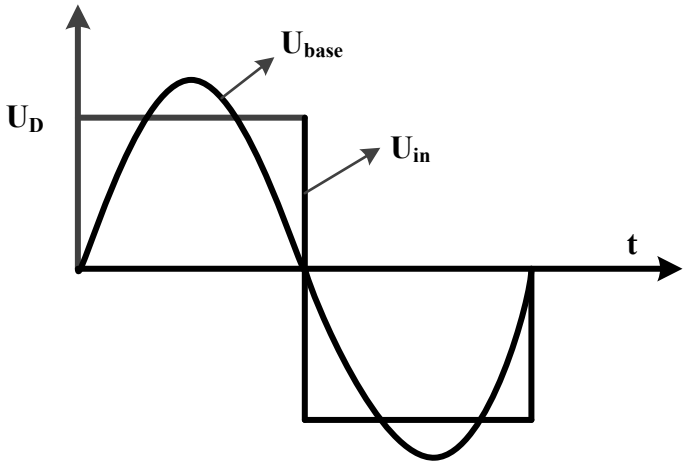

Fig. 3 Switch network output voltage U_{in} and its fundamental component U_{base}

Where $\omega_s = 2\pi f_s$, and the amplitude of U_{base} is $\frac{4U_{in}}{\pi}$.The transfer function of the resonant network can be described as:

$$H(j\omega) = \frac{1}{\sqrt{1+Q^2\left(\frac{\omega_s}{\omega_r}-\frac{\omega_r}{\omega_s}\right)^2}} \qquad (2-3)$$

Where $Q = \frac{\omega_r L_r}{R_e}$, $\omega_r = \frac{1}{\sqrt{L_r C_s}}$, $\omega_s = 2\pi f_s$, $R_e = \frac{8}{\pi^2}R_0$. R_e is the equivalent load of the transformer and rectifier-filter network. R_0 is the equivalent load Converted to the primary winding of transformer.

When $\omega_s = \omega_r$, The resonant network has the biggest voltage gain that equals 1. Resonance current is:

$$i_R(t) = \frac{U_{base}}{R_e} = \frac{\pi U_{in}}{2R_0}\sin\omega_s t \qquad (2-4)$$

Voltage Regulating Methods

There are three basic control methods (PWM, PAM, and PFM) and their combined methods. Take the PAM method in this paper. The inverter works with constant frequency. High voltage controlled by DC-bus voltage. Switching frequency is close to resonance frequency, which is Slightly smaller than the resonant frequency. Switches can turn off at zero voltage, and turn on at very low resonant current.

Simulation research and analysis

Simulation Conditions

DC-bus voltage U_{in}=400V. Resonant capacitance Cs=5.23uF. Resonant inductance L_r=10uH. Resonant frequency f_r=22kHz. Resonant period T_r=45us. Switching frequency f_s=21.27k. Switching period T_s=47us. Duty ratio D=49%. Transformer ratio n=25. Load resistance R_L=2000Ω.

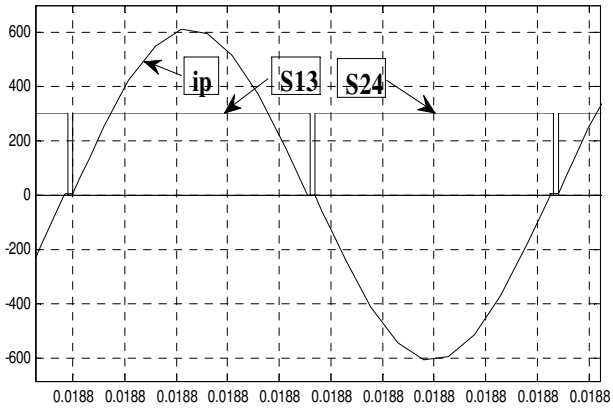

(Fig. 4 Ip is resonant current; S13and S24 is the driving waveform of switches)

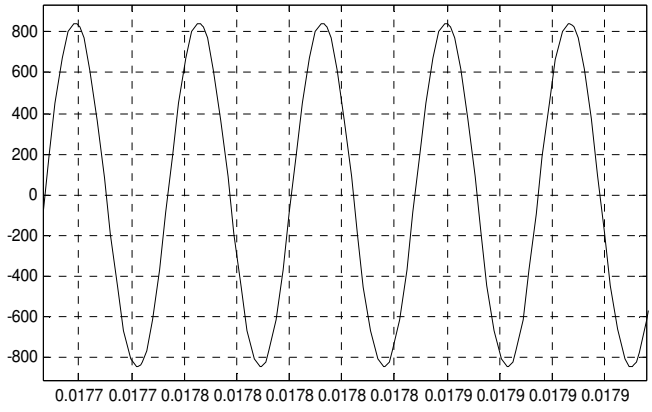

(Fig. 5 The voltage waveform of resantant capacitor)

The output high voltage is -30kV, and output power is 450kW. The peak current is 600A (showed on Fig.4). The peak voltage of the two end of resonant capacitor is 840V (showed in Fig.5). Switches turned off at zero current.

Experimental Result

At present, the power systerm only works in lower load restricted by experimental conditions. Waveforms in Fig.7 are high voltage output, driving waveform, and resonant current respectively. Current and driving waveform only shows its envelope. Fig.8 shows the high voltage output with light load. High voltage output can be Adjusted linearly in full range by controlling the output voltage of the rectifier. Series resonant converter has the characteristic of constant current,and it takes advantage of the leakage inductance of the transformer. Additional resonant capacitor has the function of avoiding the magnetic flux imbalance. It's a good choice for high-voltage high-power switching power supply.

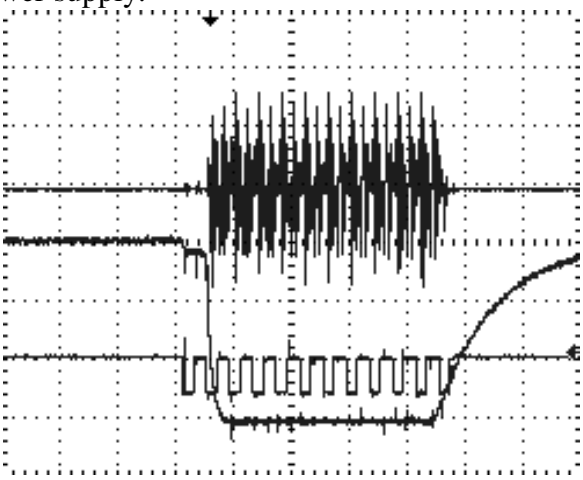

(Fig. 7 High voltage output, the transformer primary winding current, driving waveform. horizontal axis: 250ms/DIV vertical axis: 10kV/DIV)

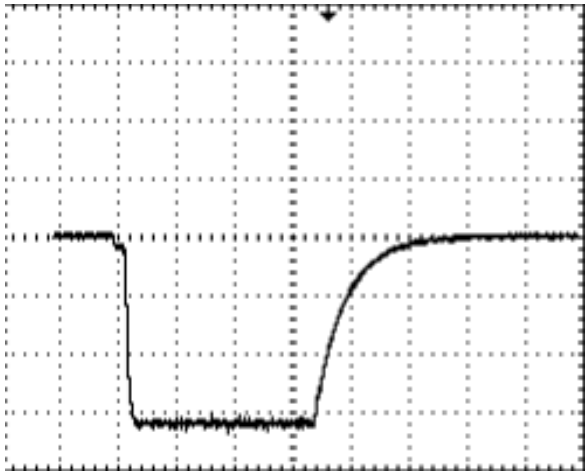

(Fig. 8 High voltage output waveform horizontal axis:250ms/DIV vertical axis: 10kV/DIV)

References

[1] B.E. Paton, M.P. Trygub, S.V. Akhonin: Electron Beam Melting of Titanium, Zirconium and Their Alloys. Kyiv, Ukraine, 2011.

[2] McQuage M M,McDowell V P,Peterkin F E,et al: High Power Density Capacitor Charging Power Supply Development for Repetitive Pulsed Power. Conference Record of the 2006 Twenty-Seventh International Power Modulator Symposium. 2006:368 -371.

[3] Bowles E E, Chapelle S, Ferguson G X, et al: A high power density, high voltage power supply for a pulsed radar system.Power Modulator Symposium Conference. California, USA: [s. n.]. 1994: 170-173.

[4] Robert W. Erickson, Dragan Maksimovic: *Fundamentals of Power Electronics* （Second Edition）.(Kluwer academic publishers, New York 2001).

[5] Zhang,Weiping: *Modeling and control of switching converters*(China Electric Power Press, Beijing 1987).

Advanced Materials Research Vols. 960-961 (2014) pp 921-924
© (2014) Trans Tech Publications, Switzerland
doi:10.4028/www.scientific.net/AMR.960-961.921

Effect of Phase Sequence Layout on Electric Field under Overhead Lines

Yuze Jiang[1, a], Zhenguang Liang[2, b], Can Li[2, b], Binxiang Du[3]

[1]State Grid Shandong Electric Power Research Institute, Jinan, China

[2]School of Electrical Engineering, Shandong University, Jinan, China

[3]State Grid Dezhou Power Supply Company, Dezhou, China

[a]jiangyuze@163.com, [b]lzg@sdu.edu.cn

Keywords: Electric field; phase sequence layout; overhead line; charge simulation method.

Abstract. This paper discusses effect of phase sequence layout on electric field under overhead lines. Charge simulation method is used. Examples of two circuit overhead lines and four circuit overhead lines show that phase arrangment of lowest height conductors has major influence and phase arrangment of middle height conductors has lesser influence on electric field under overhead lines. Interlacing placed lowest height conductors with different phase and phase arrangement of middle height conductors different from that of lowest height conductors help to reduce electric field.

Introduction

Extra high voltage overhead lines produce intense electric field above the ground. It may be harzard to health of human bodies and attracts public concerns. Several factors such as height of overhead lines, space between conductors, conductor arrangements and use of shielding lines have been studied to show their influences on electric field under overhead lines [1]-[3]. And a few methods have been used in calculation of electric field produced by overhead lines. This paper will analyze the influence of phase sequence layout on electric field under overhead lines by charge simulation method.

Charge simulation method used in calculation of electric field under overhead lines

Charge simulation method is an often used method in calculation of electric field. It's based on the Uniqueness Theorem of electromagnetic fields. Discrete simulation charges are used to replace continuous distributed free charges on surface of conductor and bound charges on interface of different dielectric. Electric field can be calculated by superposing electric field generate by these discrete simulation charges.

Setting simulation charges q_j (j=1,2,…,n) and selecting equal number of matching points at surfaces of conductors with their potential values being known φ_i(i=1,2,…,n), equations of potential on matching points can be expressed by simulation charges as

$$\left.\begin{aligned} \varphi_1 &= p_{11}q_1 + p_{12}q_2 + \cdots + p_{1n}q_n \\ \varphi_2 &= p_{21}q_1 + p_{22}q_2 + \cdots + p_{2n}q_n \\ &\vdots \\ \varphi_n &= p_{n1}q_1 + p_{n2}q_2 + \cdots + p_{nn}q_n \end{aligned}\right\} \tag{1}$$

where p_{11}, p_{12}, … , p_{nn} denote electric potential coefficients. p_{ij} denotes the electric potential coefficient of the j-th simulation charge to the i-th matching point and is affected by dielectric constant and relative position between the j-th simulation charge and the i-th matching point.

Values of simulation charges can be calculated by solving (1). Electric potential and electric field strength at any point can then be calculated by these simulation charges.

Overhead line is not infinite straight line, so its electric field is a three dimension problem. A overhead line is divided into sections of finite length straight lines. Line charges are are used to model conductor sections. Electric field of overhead line is superposition of that by decomposed finite length

straight line charges. Setting local z axis on a finite length straight line, electric potential produced by the finite length straight line charge can be expressed as

$$\varphi = \int_{z_0'}^{z_l'} \frac{\tau}{4\pi\varepsilon_0\sqrt{\rho^2+(z-z')^2}}\,\mathrm{d}z' = \frac{\tau}{4\pi\varepsilon_0}\ln\frac{z_0'-z+\sqrt{\rho^2+(z_0'-z)^2}}{z_l'-z+\sqrt{\rho^2+(z_l'-z)^2}} \tag{2}$$

where z'_0 and z'_l denote z coordinates of two end points of the finite straight line, (ρ, z) denote coordinates of field point, τ denotes line charge density, ε_0 denotes dielectric constant of air.

The ground is a conductor. Influence of infinite large plane ground is taken into account by use of method of images.

Electric field under overhead lines with different phase sequence layout

To study the influece of phase sequence layout on electric field under overhead lines, two examples are calculated. One is two circuit overhead lines. The other is four circuit overhead lines.

Electric field of the two circuit overhead lines. Line voltage of the two circuit overhead lines is 330kV. Conductor arrangement is shown in Fig.1. In order to analyze influence of phase sequence layout on electric field, six phase sequence arrangements shown in Table 1 are calculated.

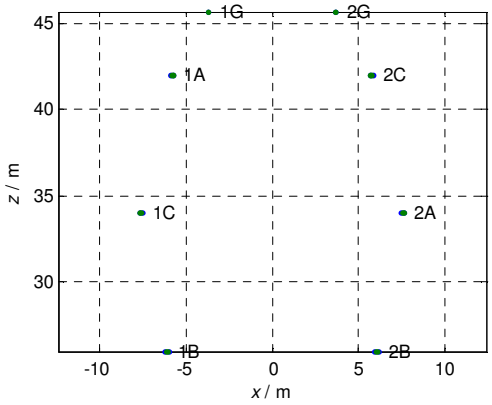

Fig. 1. Configuration of conductors of the two circuit overhead lines

Table 1. Phase sequence arrangements of the two circuit overhead lines

1	2	3	4	5	6
1A 2A	1A 2C	1A 2B	1A 2A	1A 2C	1A 2B
1B 2B	1B 2A	1B 2C	1B 2C	1B 2B	1B 2A
1C 2C	1C 2B	1C 2A	1C 2B	1C 2A	1C 2C

Distribution of electric field 1.5m above the ground at the lowest position of overhead lines and along direction vertical to overhead lines is shown in Fig. 2. It shows difference of electric field of the six arrangements. Maximal electric field of arrangement 1 is the biggest. Maximal electric field of arrangement 5 is the smallest. Arrangements 2 and 3 also have smaller values of maximal electric field. To the two circuit overhead lines, electric field is mainly influenced by two lowest height conductors. In arrangements 1 and 6, two lowest height conductors are in same phase. And they have larger maximal electric field than other arrangements. In arrangements 2 to 5, two lowest height conductors are in different phases, so they have smaller maximal electric field. Two middle height conductors also influence electric field. If their phases are different from that of lowest height conductors, there will be less values of maximal electric field. Arrangement 5 is in this case. Its lowest height conductors are in phase C and phase A which are different from each other. And its middle height conductors are both in phase B which are different from phase C and phase A.

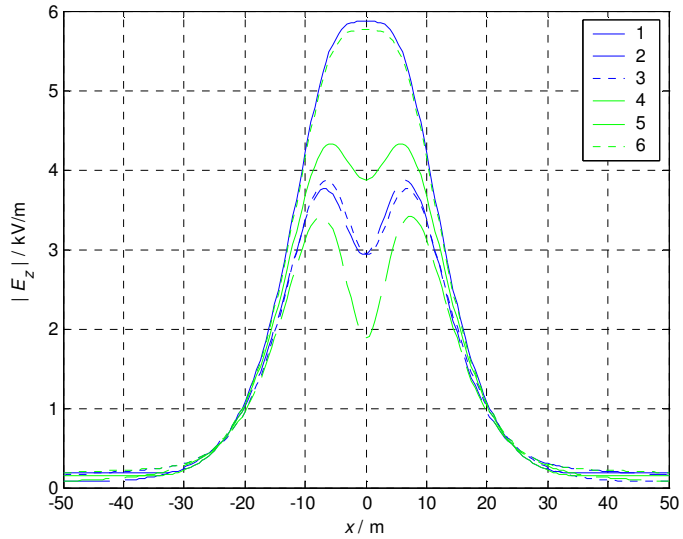

Fig. 2. Electric field of the two circuit overhead lines at 1.5m above the ground

Electric field of the four circuit overhead lines. Line voltage of the four circuit overhead lines is 500kV. Conductor arrangement is shown in Fig.3. In order to analyze influence of phase sequence layout on electric field, six phase sequence arrangements shown in Table 2 are calculated.

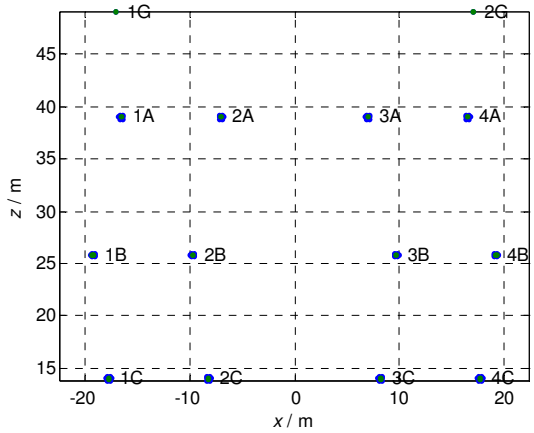

Fig. 3. Configuration of conductors of the four circuit overhead lines

Table 2. Phase sequence arrangements of the four circuit overhead lines

1	2	3	4	5	6
1A 2A 3A 4A	1A 2C 3A 4C	1A 2A 2C 4C	1A 2C 3C 4A	1C 2A 3A 4A	1A 2C 3A 4A
1B 2B 3B 4B	1B 2B 3B 4B	1B 2B3B 4B	1B 2B 3B 4B	1B 2B 3B 4B	2B 2B 3B 4B
1C 2C 2C 3C	1C 2A 3C 4A	1C 2C 3A 4A	1C 2A 3A 4C	1A 2C 3C 4C	3C 2A 3C 4C

Distribution of electric field 1.5m above the ground at the lowest position of overhead lines and along direction vertical to overhead lines is shown in Fig. 4. It also shows influence of phase sequence layout on electric field. Arrangements 1 and 5 have the biggest values of maximal electric field because at least three adjoining lowest height conductors are in same phase. Arrangements 3 and 6 also have bigger values because they have adjoining lowest height conductors of same phase. Arrangement 2 has the smallest value of maximal electric field because its lowest height conductors are interlacing placed with different phase.

Electric field influenced by phase sequence layout. Results of Fig.2 and Fig.4 all show that interlacing placed lowest height conductors with different phase can produce less electric field.

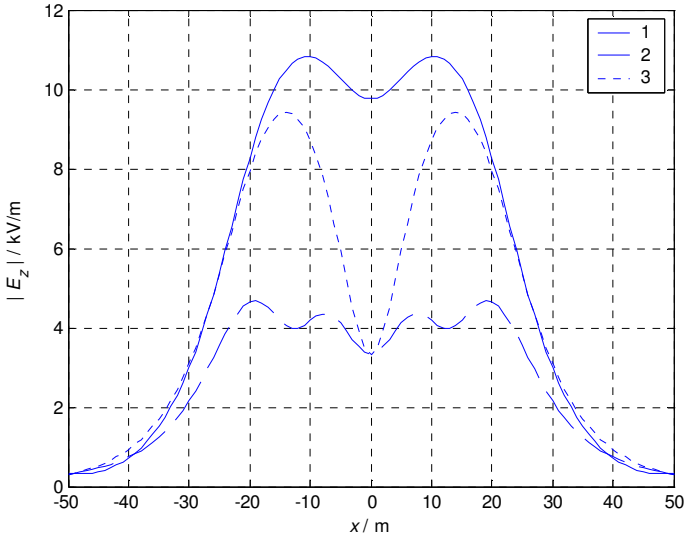

(a) Arangments of 1, 2 and 3

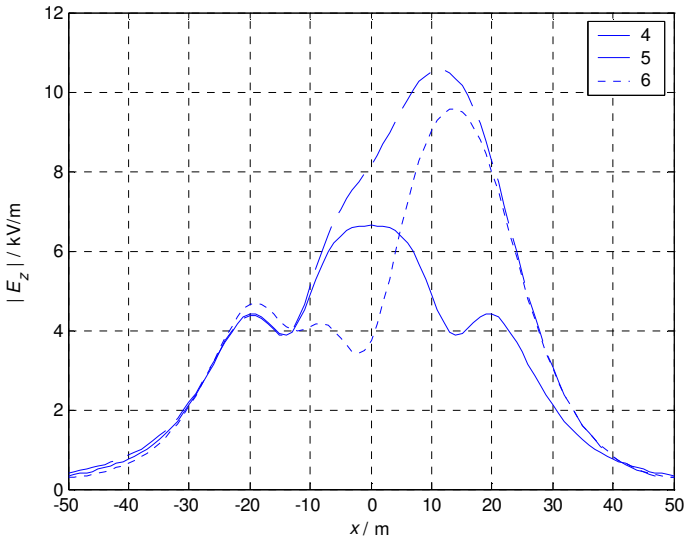

(b) Arangments of 4, 5 and 6

Fig. 4. Electric field of the four circuit overhead lines at 1.5m above the ground

Conclusions

In the paper, influence of phase sequence arrangement of conductors on electric field of overhead lines is studied. Electric field is calculated by charge simulation method. Results show that phase arrangment of lowest height conductors has major influence on electric field under overhead lines. And middle height conductors have also certain influence. Interlacing placed lowest height conductors with different phase help to reduce electric field.

References

[1] Olsen R.G. and Wong P.S.: IEEE Trans. on PD, Vol. 7, No. 4 (1992), p. 2046

[2] A.E. Tzinevrakis, D.K. Tsanakas and E.I. Mimos: IET Gener. Transm. Distrib., Vol. 3, iss. 6 (2009), p. 509

[3] Tadasu Takuma, Tadashi Kawamoto, Mitsuru Yasui, et al: IEEE Trans. on PAS, vol. 104, no. 9 (1985), p. 2612

Advanced Materials Research Vols. 960-961 (2014) pp 925-928

doi:10.4028/www.scientific.net/AMR.960-961.925

High Voltage Power Supply Designed for Electronic Beam Welder Based on LC Series Resonance

Ze-ting WANG[1, a], Hong-yin ZHANG[1,b] and Sheng-wen FAN[1,c]

[1]North China Univ. of Tech., 100144, Beijing, China

[a]wangzeting@ncut.edu.cn, [b]zhanghongyin895195@163.com, [c]fsw@ncut.edu.cn

Keywords: electronic beam welder; high voltage power supply; ZCS

Abstract. A 60kV/6kW high voltage power supply for electronic beam welder (EBW) based on LC series resonance is designed. It adopts pulse frequency modulation (PFM) way to adjust the output voltage, and it has over-current and over-voltage protection. The test proves that high voltage power supply has reached zero current switching (ZCS) on and ZCS off, and satisfied the actual requirements of welding technology.

Introduction

Electronic beam welding is a kind of technology which uses electronic beam as heat source. When the cathode filament of electronic gun is heated to a certain temperature, it will outcome electron. Electrons are accelerated in electronic gun and focused by electromagnetic lens to the beam of high intensity and high energy. When the beam bombards welding surface, its strong kinetic energy turns to heat energy flashily. It can molten metals to achieves the welding purpose[1].

The electron beam welding has high energy density, and EBW has been widely applied in air space, the car and shipping industry. Traditional electron beam welding machine power supply system adopts the technology of the power frequency or medium frequency, with high volume, low efficiency and poor stability of electron beam. To solve these problems, we developed a 60kV/6kW high voltage power supply with high efficiency and stability for electronic beam welder.

The Principle and Circuit Design of High Voltage Power Supply

A. The Principle of High-voltage Power Supply

The main circuit of high voltage power supply system is shown in Fig. 1. The smooth DC voltage can be obtained after three-phase AC is rectified and filtered. Full-bridge (FB) inverting circuit completes DC/AC transformation. AC square-wave boosts to about 60kV by high-frequency transformers in oil tank, then the output is rectified and filtered by the inductor to ensure a stable DC high voltage output. High voltage feedback signal is obtained by precision resistance network. After A/D data acquisition and DSP adjustment operations, we only need to change the frequency of pulse and it can change the output high voltage to achieve closed-loop control purpose.

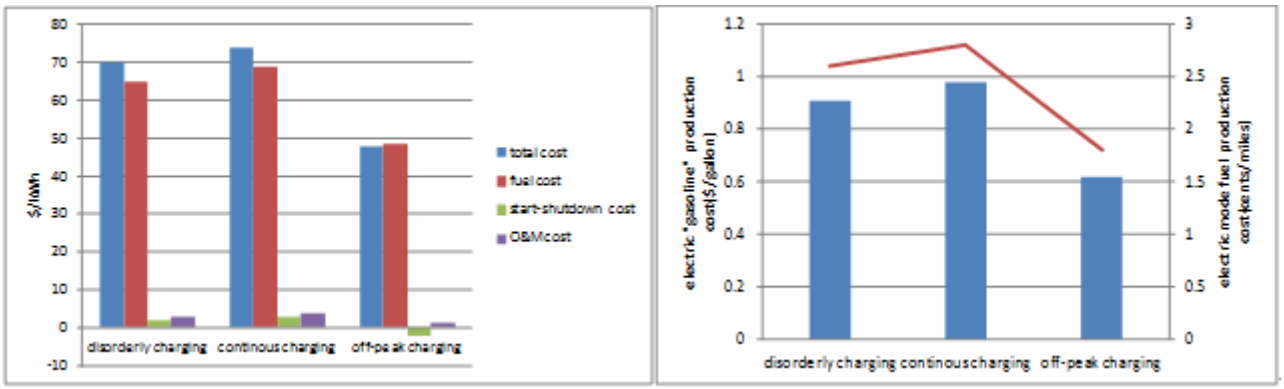

Fig. 1. Main circuit of high voltage power supply

B. Full-brige Series Resonant Inverting Circuit

According to the relationship between switching frequency and resonant frequency , power supply which is adopted series resonant inverting circuit has three working modes. ① < , discontinuous current mode (DCM). In this mode, switch works in soft switching condition which is zero-current turning on, zero -current/zero-voltage turning off. So it is suitable for small power supply. ② 2 < $_s$ < , continuous current mode (CCM). In this mode, resonant circuit is rendered capacitive, and switch works in soft turning off and hard turning on. So it is very suitable for large power supply. ③ f > f , CCM, this mode is generally adopted rarely[2].

The basic full-bridge series resonant circuit is shown in Fig. 2. The transformer T is used to transform energy and isolate.

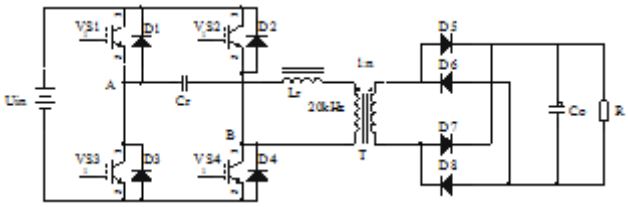

Fig. 2. Basic full-bridge series resonant circuit

In basic series resonant circuit which is composed of DC supply $_i$, resonant inductor and resonant capacitor , we assume that the initial time is , the initial current of is , and the initial voltage of is . According to L + U = and $_u$ = i_L , the expressions of resonant inductance current and resonant capacitor voltage are shown as follows[3,4].

$$i_{Lr}(t) = I_{L0}\cos\omega_r(t-t_0) + \frac{U-U_{C0}}{Z_r}\sin\omega_r(t-t_0) \tag{1}$$

$$u_{Cr}(t) = U - (U-U_{C0})\cos\omega_r(t-t_0) + Z_r I_{L0}\sin\omega_r(t-t_0) \tag{2}$$

Where ω is inductance angular frequency ω = , is characteristic impedance, = .

The main waveforms are shown in Fig. 3. The full-bridge series resonant converter works in < $_r$ working mode. A switching cycle includes two resonance cycle and six working modes . Because the article length is limit, this article does not describe six working modes in detail and the detailed description is available in reference.

The series resonant converter has the following advantages[5].

(1) Switch is zero-current turning on, zero-current or zero-voltage turning off, and anti-parallel diode turns on and off naturally, which greatly reduces the switching loss.

(2) Due to the presence of resonant capacitor C, it is ability to effectively protect power transformer from burning when it takes place biasing magnet.

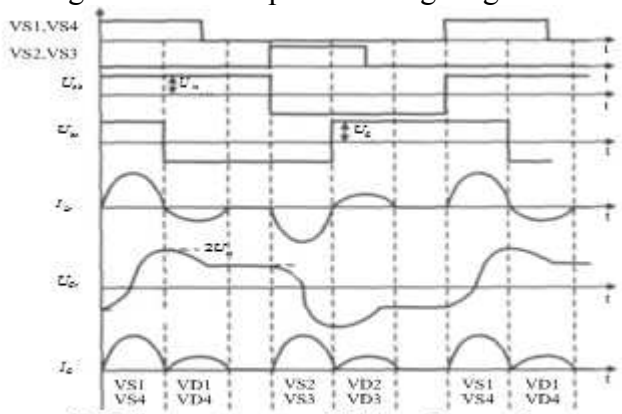

Fig. 3. Resonant current and driving pulse waveform.

C. High-voltage rectification and signal feedback

The high-voltage rectifying circuit is composed of high-voltage silicon stack, the output filter inductor, the protection circuit and the sampling circuit. The high voltage feedback and beam current feedback signals are obtained through using precise resistance network. There has electrical isolation between main circuit and control circuit, so DSP control board can be well protected.

D. DSP control board

Control circuit includes DSP(TMS320F28335), CPLD, and driver circuit. AD converter changes analog feedback signals into digital data. After DSP uses digital data gathered by AD to operate and adjust, DSP outputs the corresponding PWM signal impulse. Driver circuit mainly completes PWM signal isolation and amplification. CPLD mainly completes comprehensive fault, logic judgment and prohibition of PWM pulse. As long as there is any fault, it can quickly prohibit PWM output and cut off high voltage power supply, which achieves the purpose of protection.

Control Strategy and Implementation of Software

System software includes DSP procedure and CPLD procedure. DSP mainly completes algorithms, generates PWM pulses and communicates with touch-screen. CPLD mainly completes comprehensive fault, logic judgment and prohibition of PWM pulse.

DSP software program is composed of the main procedure and numbers of subroutines. Such as procedure of communication with touch -screen, sampling subroutine, welding logic procedure, PWM interrupt procedure, etc. Programming languages adopts C language [6].

After entering the PWM interrupt, the flowchart shown in Fig. 4, firstly, feedback from various signals are sampled and processed. And then it will produce respective PWM pulses after high-voltage supply, filament supply, gate bias supply and beam PI operation respectively. The PWM pluses is amplified and isolated by the driver circuit to drive IGBT, which realizes closed-loop control of the entire power supply system.

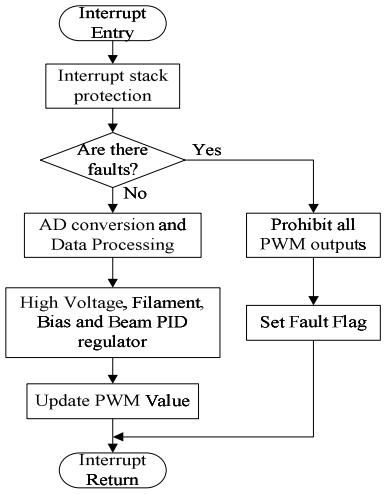

Fig. 4. Interrupt function flowchart

The power supply adopts full-digital interface. All parameter settings set up directly through the touch-screen, which has realized full-digital operation of high voltage power supply. What's more, touch-screen can display the main real -time parameters of high-voltage supply system, such as output voltage, running state, fault information etc.

The analysis of experimental results

The experimental waveforms are shown in Fig. 5. Where Vo is the high voltage feedback ,iR is the high voltage transformer primary current ,and up is the PWM signal with low active. the high voltage sampling ratio is 1:20,000. Figure 5a shows that high voltage can quickly boost to 60kV

within 10ms without overshoot, and it has very stable with small ripple. From the Figure 5b we can know that IGBT operates at ZCS on and ZVS/ZCS off mode with very high efficiency and low harmonic. So it can be able to achieve very good welding effect.

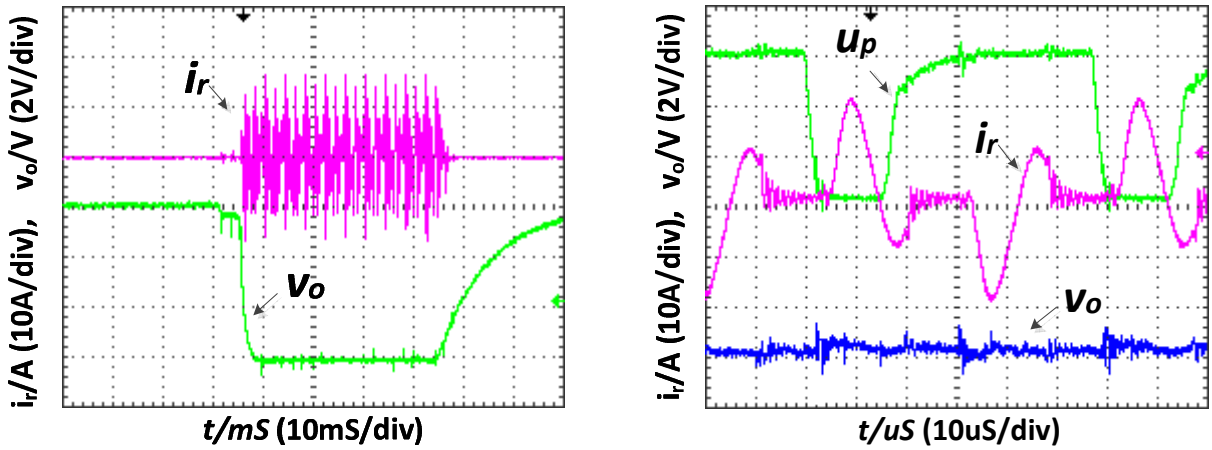

(a) 60kV high voltage without load (b)High voltage and beam current welding waveform

Fig. 5.Actual high voltage waveforms

Conclusion

The inverting high voltage power supply for EBW based on DSP (TMS320F28335) has high accuracy, small volume, all-digital etc, and it's all parameters can be set and stored directly through the touch-screen, What's more, all IGBTs operate at ZCS on and ZVS/ZCS off mode with very high efficiency and low harmonic . Experiments prove that the high voltage power supply has very high performance and it can be able to directly replace existing high voltage power supply system for EBW.

References

[1] LI Zheng-xi, WANG Lei, ZHAO Ren-tao. A New H-bridge Inverter of HV Power Source for Electron Beam Welder. Automation & Instrumentation, Vol. 3(2008), p. 15-17

[2] LIN Wei-xun. Modern Power Electronic Circuit. Zhejiang: Zhejiang University Press, 2006:98-102

[3] Xinbo Ruan, Yangguang Yan. Soft-switching Technology of DC Switching Power Supply. Beijing: Beijing Science and Technology Press, 2000

[4] WANG Zhao-an, HUANG Jun. Power ElectronicTechnolog. 4th ed.Beinjing: Machine Press,2008

[5] FENG De-ren1, SUN Jian-kun, HE Si-mo, XU Hai-bo. Design of High-voltage DC Power Supply Based on Series Resonant Constant-current Charging. Power Electronics, Vol. 3(2010), p. 60-62

[6] SUN Kui-feng.TMS320x28xxx Principles and Development. Beijing: Publishing House of Electronics Industry, 2009

Advanced Materials Research Vols. 960-961 (2014) pp 929-934

doi:10.4028/www.scientific.net/AMR.960-961.929

Analysis and Prevention of Grid Over-voltage Ferromagnetic Resonance

Mingjun Lv[1],Xin Zhao[2,a],Xiangdong Zhao[1],Jianguo Liu [1],Fengzhen Liu [1]

and Yanhui Sun[1]

[1]State Grid Liaoning Chaoyang Power Supply Company, Chaoyang, Liaoning,122000, China

[2]State Grid Beijing Tongzhou Power Supply Company,Beijing,101100,China

[a]tsustar@126.com

Keywords: ferromagnetic resonance, measures, harms, reasons

Abstract. Over-voltage in the power system can be caused by a lot of reasons , including higher frequency ferromagnetic resonance overvoltage which occurs in normal operation and causes great harm. Overvoltage events often result in damages to electrical equipment or even power outages . In this paper, ferromagnetic resonance is analyzed to study harm , causes, conditions , and phenomena and to handle resonance and develop practical preventive measures. The related analysis is important to work for the future operation of the power grid to prevent and limit the ferromagnetic resonance over voltage which provides some help to further ensure the safety and stable operation of the power grid .

Introduction

Ferromagnetic resonance over-voltage is essentially due to grid neutral point of instability caused by the ferromagnetic nonlinear magnetizing inductance capacitance of the system's resonant electromagnetic voltage transformer . Ferromagnetic resonance is one of the power system common phenomenon[1][2] , and resonance overvoltage incidents sometimes accompanies with it . Since many inductive and capacitive elements exist in the power system , when the operating system fails, the inductance and the capacitance elements constituting the various oscillation circuit may , under certain conditions, cause a resonance phenomenon , resulting in some parts of the system with severe over-voltage components . It endangers the safety of electrical equipment and impacts protection device reliability. If certain conditions are met ,it may also stimulate the longer duration of ferromagnetic resonance over-voltage , resulting in large-scale power grid stability destruction and damage to the equipments .

Ferromagnetic Resonance Over-voltage Hazards

Resonance voltage transformer primary winding is with large current , yet when one side of the fuse blows, the injection may cause voltage transformer coil burning or explosion , causing the switch to trip causing widespread blackouts work , destroy the system, the safe operation of the power grid to bring great threat.

Caused the bus three phase, two -phase and single-phase ground voltage increases , the formation of over-voltage , so that the bus insulating sleeve or other device flashover and damage , lightning or explosion .resonance voltage transformer primary side bus blown fuse may cause the malfunction of the low -voltage protection , nuisance tripping or system bus load solution crack, collapse of the power grid and other serious accidents .

Organization of the Text Reasonsof Ferromagnetic Resonance

Many of the power system components are part of inductive or capacitive in nature, such as power transformers, transformers , generators, Petersen coil for inductive components, or series compensation and the parasitic capacitance capacitors , high voltage equipment for the capacitive element , and the line between the ground conductor and the conductor for the presence of both the horizontal longitudinal inductance and capacitance exist , these elements form complex LC oscillation circuit , the energy in a certain role , with the specific parameters of the resonant circuit phenomenon occurs .

Pairs of load bus charging overvoltage caused by ferromagnetic resonance

Before transmission operation to load the bus , if the first input bus voltage transformers , power transformers and enable charging for the bus , because the bus to ground capacitance and voltage transformer inductance constitute oscillation circuit . Capacitance and inductance values will cause a near equal ferromagnetic resonance over-voltage phenomenon , resonance over-voltage .

Single-phase voltage to generate magnetic resonance

In ungrounded system, bus load outlet due cause insulation breakdown flashover occurred arc grounding wires blown, close to the power side of a take away on the ground , qualifying two-phase operation. Then the connected outlet and transformer magnetizing impedance circuit capacitance changes, form a series resonant circuit . When the equivalent inductance and capacitance in parallel with non- capacitive two-phase fault , the entire power supply system does not produce series resonance. And when the equivalent inductance and capacitance in parallel two-phase non-fault is

inductive and capacitive parameters and fault relatively close , then passed to the resonance over-voltage on the bus , causing the bus voltage transformers generate magnetic resonance voltage.

Voltage transformer core saturation resonance overvoltage

Ferromagnetic resonance and core saturation , generally TV core premature saturation voltage characteristics deteriorate , more prone to use the neutral ground of ferromagnetic resonance , particularly in ungrounded systems TV time .

Switching operation caused by ferromagnetic resonance overvoltage

When the process of switching operation in run mode resonance conditions exactly constitutes a vote of three-phase circuit breaker or a different period , will cause the voltage and current fluctuations caused by ferromagnetic resonance . When equipped with a shunt capacitor circuit breaker disconnect fracture , such as capacitance and inductance of the loop parameters TV capacitors in parallel can also occur when the ferromagnetic resonance over-voltage match .

Ferromagnetic resonance caused by the sudden closing Overvoltage

Equipment reactance ωL, series and parallel capacitance 1/ωC form loops. When ωL = case 1/ωC loops appear , this will be a resonant circuit . Since the capacitance in the circuit is basically the same frequency invariant constant ; generally by the inductive coil with a core , in the voltage generating mutations rapidly saturated core , the core saturation inductance becomes small, and generate magnetic resonance voltage suddenly appeared ωL = 1/ωC after closing.

Common Power System Harmonic Elimination Program

Installation harmonic elimination device

Harmonic elimination device[3][4] , also known as the second harmonic elimination , is mounted on the voltage transformer (PT) in open delta winding. Normal operation or single-phase ground fault occurs when the device does not operate , while ferromagnetic resonance occurs when determining the grid , it will make the positive and negative ends of the triangular openings in parallel in two alternating zero trigger thyristor conduction ferromagnetic resonance and damping to limit when the self- resonant eliminate thyristor deadline , you can repeat the action if necessary. During the start-harmonic elimination device ,thyristor full conduction , low resistance state , the resistance of a few to tens of mΩmΩ. Such a small high-frequency damping resistor value is sufficient , baseband and divide three kinds of resonance , but for the entire grid is valid, that is, a system simply select a station transformer harmonic elimination device can be installed .

Installation harmonic elimination damper

Harmonic elimination damper , as LXQ damper is actually a non-linear harmonic elimination resistor R0 connected in series between the voltage transformer primary side neutral point , it uses neutral damping resistor to eliminate resonance. Grid during normal operation, the voltage harmonic elimination <500V, R0 showed high resistance values ??(up to several hundred kΩ), a large damping effect, so that the resonance is not easy to develop in the initial stage ; When the grid of single phase , the harmonic elimination the higher voltage (10kV grid and its value about 1.7 ~ 1.8kV), R0 was low (tens of kΩ), to meet the PT open delta voltage insulation monitoring requirements no less than 80V , but still damped harmonic ; when the power grid when arc grounding , R0 can still maintain a certain resistance , transformer inrush current limiting . The device has a resonance and eliminating PT saturation limit inrush two functions.In the installation of the secondary side of the transformer zero-sequence voltage harmonic elimination -type PT retrofit harmonic elimination device

In the installation of harmonic elimination device

For the installation of the zero-sequence voltage transformer harmonic elimination -type PT, will be installed in the computer harmonic elimination of its zero- sequence voltage transformer secondary side TV0 , when the system ferromagnetic resonance occurs other transformers , harmonic elimination will under the action of the zero -sequence voltage action , TV0 almost secondary side is shorted , TV0 and TV1 are reflected in the high voltage winding leakage reactance , zero sequence impedance transformer leakage inductance becomes a small value , equivalent to a temporary network neutral point directly to ground resonance will disappear. TV0 secondary harmonic elimination in this type of installation PT computer harmonic elimination device helps the entire harmonic elimination grid. Intelligent scheduling for grid , the grid is lost brain center , the integrated use of a variety of advanced technology and intelligent means of the transmission grid be active , intelligent monitoring , analysis, early warning , decision support , and self-healing controls for dispatch center Yun Fang , following intelligence business support means security, scheduling , planning, automation, and other full-service professional, provides for the transmission grid to provide strong technical support. Several intelligent application for the professional needs is the key to building support systems integration technology is the foundation .

Installation of automatic tuning system neutral Petersen Coil

The principle of automatic tuning grounding compensation device , through lump sum , full complement of running up and under way , can solve resonance problems. Currently automatic tuning grounding compensation device mainly consists of five major components : ground transformers, electric arc suppression coil , computer control section , damping resistor section dedicated transformer neutral point and non-linear resistors. Artificial neutral grounding transformer is used as

an access point arc suppression coil . Petersen coil current through the load switching regulator and implement remote automatic control , using pre-conditioning methods, namely, in the normal operation mode , the network parameters according to changes at any time to adjust Petersen coil tap into the best position. Use of computer controller for automatic tracking and automatic tuning. By measuring the displacement of the main phase voltage and current and the voltage between the neutral point , it is possible to calculate an accurate judgment , issued a directive automatically adjusted to show the relevant parameters: capacitive current , the inductor current , residual current and voltage offset . Recall , alarm , automatic printing and signal sent away to meet the needs of unattended substation .

Common Power System Harmonic Elimination ProgramGrid Operationto Preventthe Ferromagnetic Resonance Measuresand Methods

Resonance , should be immediately put into a standby equipment , such as transformers, etc. into spare change network parameters to eliminate resonance.Resonance , as a standby power supply bus can be switched to the backup power to the system parameters change , eliminate resonance.Resonance , a voltage transformer fuse is blown, eliminate resonance itself ; voltage transformer fuses in the fuse yet , you should stop using them immediately about the loss of pressure protection device easily mistaken move ; shall promptly replaced after the fuse , recovery voltage transformer running.Resonance method , due to the voltage transformer primary winding current is large , you should pull the voltage transformer or prohibit the use of direct access to a fuse to eliminate resonance.It can be used to change the sequence of operations necessary to avoid resonance conditions during operation. As the charge generated in the resonant load bus , the load line can be put in the methods used to change the resonance conditions.Reducing the voltage transformer stations, in the same system should minimize the number of voltage transformer station , especially limiting voltage transformer neutral grounding several .To improve the quality of the circuit breaker maintenance to ensure the same period of the closing operation.Maintaining good plant , station equipment, to avoid flashover or grounding accidents caused by resonance over- voltage.Changing the operation mode to avoid an empty bus and load transformer operation.

Summary

Many inductive core elements exist in the power system ,and under certain conditions , they may induce ferromagnetic resonance over-voltage ,which endangers the safe operation of the power grid and equipment. Based on analysis of the ferromagnetic resonance over-voltage hazards,the paper talks about arising events due to ferromagnetic resonance, the common power system harmonic elimination program , comprehensive introduction in grid operation and measures to prevent the ferromagnetic resonance method. This paper trys to further the work of the future grid operation

preventing and limit the generation of ferromagnetic resonance overvoltage. It provides some help to further ensure the safe and stable operation of the power grid . There are some limitations in terms of this analysis inevitably which need further research.

References

[1] Chen Weixian, Grid overvoltage tutorial, Beijing ,China Electric Power Press , 1999.

[2] Xie Guangrun,Power System overvoltage, Beijing : Water Power Press , 1985

[3] Zhou Ze, kept high voltage technology , Beijing: China Water Power Press , 1993

[4] Xie Guang-run, over-voltage and protection , Beijing: China Electric Power Press , 1987

Advanced Materials Research Vols. 960-961 (2014) pp 935-940

doi:10.4028/www.scientific.net/AMR.960-961.935

Nanometer Interconnect Test Structure for Modeling of Process Variation

Yonghong Zhang[1,a], Wei Jin[1,b],Tao Feng [1,c]

[1]Practicing and Training Center,Shanghai Second Polytechnic University,Shanghai,China

[a]yhzhangsspu@gmail.com, [b]jinwei@sspu.edu.cn, [c]fengtao@sspu.edu.cn

Keywords: Process Variation.Interconnect. SIPPs parameters. Test structures Design. Automatically realized.

Abstract. With the interconnection density and doubling the number of layers in VLSI, Interconnect line width,pitch,and the thickness of the dielectric layer will changed within the same chip caused by the process variation. and the interconnect parasitics changes ultimately affect circuit performance and yield.IC designers need an accurate BEoL corner model to help circuit design. Standard Interconnect Performance Parameters (SIPPs) is standard method to measure ultra-large scale integrated circuit BEOL performance. Designed parallel plate, layer-skipping parallel plate, comb meander, comb meander for via resistance test structures to extract SIPPs according to their sensitivity differences to different test structures, and realized them in CIF format file with High-level Perl language automatically. Then change to GDSII format file that wafer used widely by Cadence layout software, and pass electrical rule checks. Greatly improved the efficiency of test structure's design and realized. Lay the foundations for formulation of Design for Manufacturability physical design rules and further research interconnection statistical models under nanometer technology with more unique physical phenomena.

Introduction

With the application of dual Damascus process and copper interconnect technology, IC manufacture technology scales to the nanometer region, number of transistors on circuit becomes more and more, interconnect layers increase to ten layers or more. Manufacture process becomes more and more complicated accordingly. It include lithography, etching, deposition, chemical mechanical polishing Alternately during interconnect manufacturing process, and some parasitic effects or defects caused by theses process steps are the main issues for IC yield decrease [1,2,3]; As the production quantity of very large scale integrated circuit (VLSI) is fairly large, process variation will be raise during any manufacturing process, In order to analyze a process technology Really, must do a certain number of statistics to the chips [4,5]. Due to the effects of the interconnect manufacture is the main influence to the IC manufacture yield, so we need to quickly and accurately know the present situation of the manufacture process as it rapidly development, and use this information to establish accurately process model to increase IC manufacture yield.

How to quickly generate a large number of interconnect test structures for detecting Back End of the Line (BEOL) conditions during chip manufacturing, is issues faced by most people. In order to analysis the process statistically, the designers often generate a huge number of test structures manually in the former, The efficiency in this way is very low, and increased risk of structural errors as manual intervention. In this paper, we use High-level Perl language to generate interconnect test structures automatically in CIF format files, and then convert to GDSII format files which accepted widely in the industry by other electronic design automation (EDA) tools, and use the layout tools to do electric rule check. This can quickly reduce the time to design and generate test structures, achieve faster and more production efficient, and also have some stability and accuracy.

Nanometer Interconnect Test Structures Generation for process parameters monitor

SIPPs is the abbreviation for Standard Interconnect Performance Parameters, This standard is formulated by an international organization of Silicon Integration in 1998, which participated by

many industry leading companies. It's current version has been developed to V1.06. It is designed to provide a standard method of BEOL performance; it provides a parametric representation to almost all factors in BEOL process, simplifying the overly complex factors.

The test structures we designed, which goal is BEOL process of the interconnection. As to these interconnections, the method industry most commonly used is parametering of them, that's to find some parameters which can represent the majority nature of interconnect features. they are Low-K-A thickness, Low-K-A permittivity, Via resistance, Via diameter, Nitride-A thickness, Nitride-A permittivity, Metal thickness, Sheet resistivity, CD (Critical Dimension) bias, Low-K-B permittivity, Nitride-B thickness, Nitride-B permittivity. When wafer fabs get standard format SIPPs through measured some test structures, use industry Precise Field Solver tools to build a set of all possible situations, and then they stored the calculated results in a database [6, 7]. In order to estimate delay, crosstalk of design, the users can use the database to extracted their own electricity-related parasitic by EDA tools. It mostly use this method in present EDA tools of industry, such as commonly used Synopsys Star-RCXT and Mentor xCalibre,and so on [8,9].

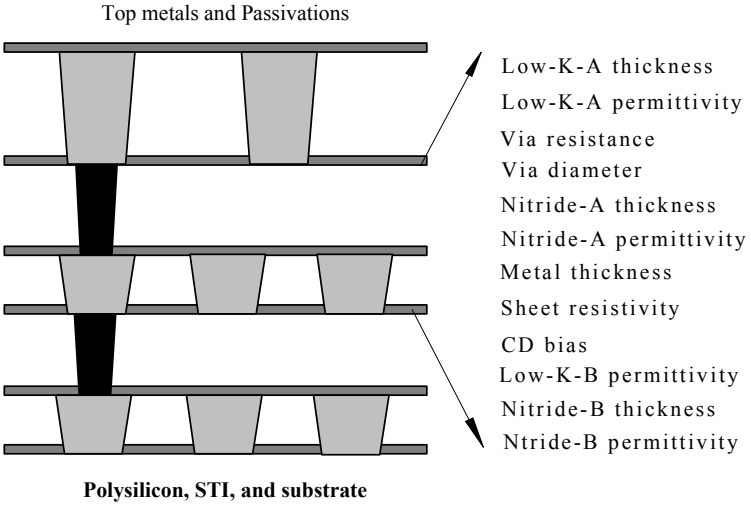

Fig.1 SIPPs parameters and copper interconnect

The Figure 1 is a total of 12 parameters; they can be divided into two categories. One is not easily change; they are mainly on the Nitride and via diameter, including five parameters: Nitride-A thickness, Nitride-A Permittivity, Nitride-B thickness, Nitride-B Permittivity, via diameter. The role of these parameters to the result is not as important as others during extracting electricity-related parasitics. The other parameters are seven necessary parameters of SIPPs which are easily to change. These parameters can be used to estimate the process variations during VLSI chip manufacture. In addition to two parameters related with permittivity, the other five parameters have more than ten percent greater variations during manufacture, which will be a very huge challenge to the Corner analysis and modeling,and this also affect chip yield ultimately.

Major Test structures design

In order to extract SIPPs as shown in Table 1, we designed parallel plate, layer-skipping parallel plate, comb meander, comb meander for via resistance test structures orderly. Each type test structure has its specific purpose, it use the sensitivity that every parameter has different sensitivity to different type test structure. It increases the effection of specific parameters and reduces the effection sensitivity of non-test parameters during test structure design. This will make the test structure has very high sensitivity to a particular parameter.

Tab.1 SIPPs and corresponding test structures

Test structures	First Order	Second Order
Parallel Plate	Low-K-A permittivity	Low-K-A thickness
Layer-skipping Parallel Plate	Metal thickness	Low-K-B permittivity
Comb Meander	Sheet resistivity CD bias Metal thickness Low-K-B permittivity	
Comb Meander For Via Resistance	Via resistance	Via capacitance

Parallel plate test structure mainly used to extract Low-K-A permittivity and Low-K-A thickness of SIPPs. This test structure is used to observe the characteristics of dielectric layer that between metal layers, and most affected the characteristics of dielectric layer is its thickness and permittivity.

When design Layer-skipping Parallel Plate test structure, the middle metal layer is ignored. In general, it is similar with the parallel plate test structure; the only difference is that it skipped a metal layer. For example, if the test structures designed mainly to extract second metal layer M2 parameters, it will include all the other parallel plate layers except M2. Combined with the following Comb Meander test structures, it can extract interconnect thickness parameter of SIPPs.

Comb Meander test structure is a special test structure, it can be used to measure two electrical properties, capacitance, and resistance. Moreover, As the measurement of resistance and capacitance is at the same time, so both of them have the same process variations, which is more conducive to Corner model accuracy. Figure 2 is Comb Meander test structure diagram, the main test structure is placed in metal layer i and (i +1), other layers are placed metal plate except these two metal layers. The lower left corner is the interconnection of upper and lower comb, In order to avoid short-circuit, this part is connected by via to another metal layer. As it is very short compared to the total length of comb, it's influence to SIPPs error can ignore. Moreover, in order to reflects the CD bias directly, it has placed ruler test structure which has same width and spacing in Layer (i +2) or (i-2).

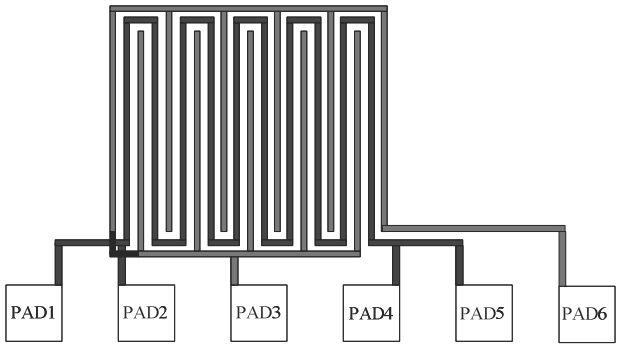

Fig.2 Comb Meander test structure

This test structure has width that of 6 PAD, It measured the meander resistance of the test structure, It is a 4-points Kelvin resistance test structure, we get the meander resistance by poured into a current between PAD1 and PAD5, and then measured the voltage between PAD2 and PAD4; Then get the sheet resistance of SIPPs. we can obtain two capacitance in this test structure, one capacitance is between upper and lower comb and the meander placed between them, the other capacitance is between comb-meander and upper parallel plate metals. We can obtain Metal thickness, CD bias, Low-K-B permittivity of SIPPs by using both capacitances. In order to extract the parameters of SIPPs, PAD1, PAD2, PAD3, PAD4, PAD5 should connect to sense when measuring,

and PAD6 should connect with drive; The other way is that PAD1, PAD2, PAD4, PAD5 connect to sense, PAD3, PAD6 connect to drive. Figure 3 is the layout result generated by Perl language.

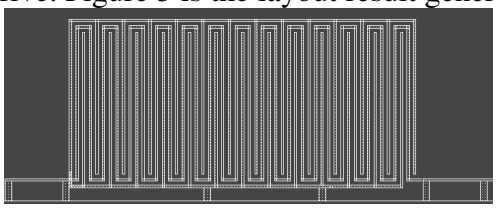

Fig.3 Layout of Comb Meander test structure

Comb Meander for via Resistance is another test structure, It's only different with comb meander test structure is that the meander is changed into via chain, as Fig 4 shows. As the meander is changed to via chain as more as possible; we will get a total resistance linked up by many via resistance when using Kelvin 4-point test method, and then get via resistance of SIPPs. We can also get a capacitance by this test structure, it also can extract Metal thickness, CD bias of SIPPs which extracted by former comb meander test structure. Figure 5 is part of the test structure layout generated automatically.

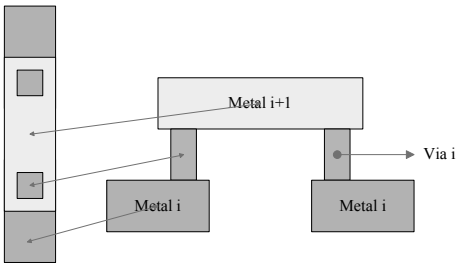

Fig.4 Comb Meander For Via Resistance test structure

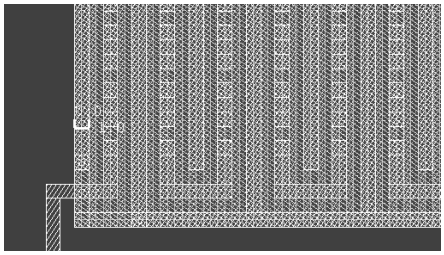

Fig.5 Layout of Comb Meander for Via Resistance test structure

Test structures Realization

The test structures realization flow as fig 6 shows. We need to prepare some relevant information Firstly; there is layer information of layout, which includes the GDSII layer numbers. Only with it, we can get the correct layer when generating the layer by Perl language. The other is the information of test structures, it include layer name, metal width, metal space and so on. These datas should decide when design the test structure according to parameters extracted. At last, generate all the test structures according to the following flow chart by Perl language.

```
#!/usr/bin/perl
if ($#ARGV != 2) {
  print "usage: perl sample.pl struct_file layer_map out_cif_dir \n";
  exit; }
print "usage OK \n";
# Some fixed key words
$struct_key_word = "S65";
$parallel_plate_type = "pp3D";
$comb_meander_type = "comb3D";
$via_resistance_type = "via";
# Declare a CIF file name's prefix
$cif_file_prefix = "dummy";
```

```
# Let Perl's memeory start to manage
# the input arguments
$struct_file = $ARGV[0];
$layer_map = $ARGV[1];
$out_cif_dir = $ARGV[2];
# An overall CIF output file dir is good
system ("mkdir -p -m 777 ./$out_cif_dir");
# Initialize some indices and parameters
$total_gds_layer_count = 0;
$total_metal_layer_count = 0;
$width = 0.0;
$spacing = 0.0;
……
```

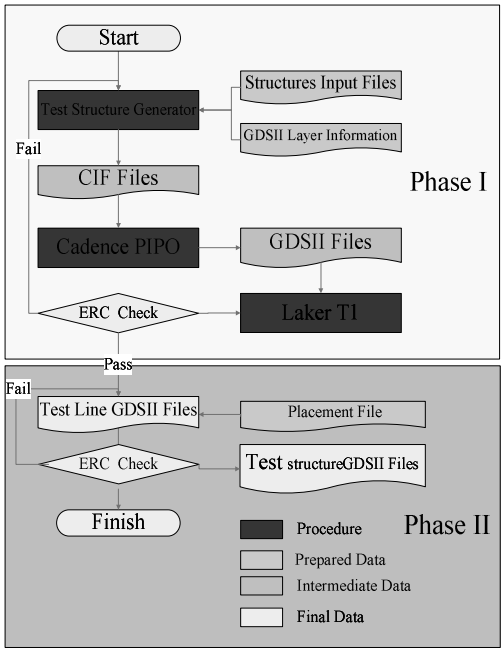

Fig.6 Test structure realize Flow chart

Results and discussion

The platform we realized all test structures is Sun's FireV490 machine, the operating system is under SunOS 5.8, Perl language version is v5.6.0, Cadence IC version is 5.10.41. We generate all the test structures targeted to extract 8 metal layers parameters of SIPPs according to design rule(0.065um Logic 1P8M Salicide 1.0(G) or 1.2(LL)/1.8/2.5.or 3.3V Design Rule, Version 1.0)during experiment. For each layer interconnection, we have designed 16 different metal width and space, a total of 152 test structures. Then estimate time and resources spent during whole experiment and the results of experiment.

First, it reads all the test structures and generate appropriate CIF format file, it took 50 seconds of CPU time, and Then Translate the CIF format file into DFII format file that Cadence's layout stander format file and read, a total of 15 minutes and 42 seconds was spent. Then put all of the test lines into a unit, do electric rule check of all structures again, The results is as Figure 7 shows :both short or open check of test structures have passed. Finally, translate all test structures into GDSII forma filets that wafer use widely. The GDSII file size is 216.4M. It took a total of 18 minutes 6 seconds during second phase.

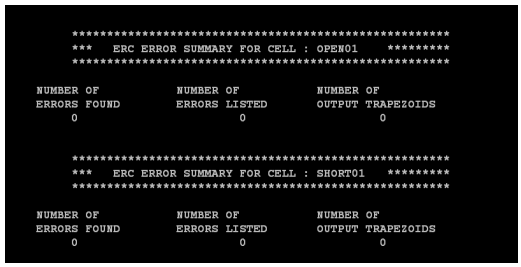

Fig.7 Electric Rule Check result of test structures

We have designed a set of test structures and realized them by High-level Perl language automatically. It includes parallel plate, layer-skipping parallel plate, comb meander, comb meander for via resistance test structures and test structures to eliminate their error. It saved all test structures and GDSII layers numbers of layout information Correspond with these test structures into text file, then realized with High-level Perl language automatically by transferring the two files.

The test structure kits designed mainly for nanometer process node, to get standard interconnect performance parameters SIPPs of nanometer process, then have accurate assessment of current technology level. And establish process Corner modeling and provide design for manufacturability (DFM) physical design rules and nonlinear resistance SPICE models of Interconnect to designers. It Not only makes Just taking a short time to prepare the input files when needed a large number of test structures to do statistical analysis to generate the test structures, but also reduce errors Generated due to human intervention. Moreover, the test structures can track process nodes automatically, as long as modify the input files; the program can generate new test structures to evaluation the next process node performance automatically.

Acknowledgements

This work was financially supported by the Shanghai Young College Teacher Training Subsidy Scheme(Contract No.egd110015).

References

[1] R M Geffken, W T Motsiff. INTERNATIONAL TECHNOLOGY ROADMAP FOR SEMICONDUCTORS [EB/OL]. .http://www.itrs.net/Links/2010ITRS/Interconnect2010.pdf.(2010)

[2] N S Nagaraj, T Bonifield, A Singh. Benchmarks for interconnect Parasitic resistanee and capacitanee[C].International SymPosiumonQualityEleetronieDesign:(2003),P.24-26.

[3] R Jiang. Three-Dimensional Interconneet Modeling for Nano-Seale VLSI Teehnologies[D],University of wiseonsin-Madison.(2006).

[4] Y H Cheng. A glance of technology efforts for design-for-manufacturing in nano-scale CMOS processes [J] Science in China, 51(6): 807-818:(2008).

[5] A Husain, Models for Interconnect capacitanee Extraction[C].International SymPosium on Quality Eleetronic Design,167—172: (2001).

[6] http://archives.si2.org/si2_publications/SIPPs/pdf/sipps_spec.pdf [R]. version 1.06. USA: Austin ,(2010).

[7] W Shi, J Liu, N Kakani. AFastHierarchiealAlgorithmforThree-Dimension Capacitance Extraction[J]. IEEE Transactionson ComPuter-Aided Design of Integrated Cireui and Systems: 21(3),330-336:(2002).

[8] Cadence Design Systems. Dracula Reference[R]. version 4.9, USA,San Jose, (2012).

[9] Cadence Design Systems. Design Data Translator's Reference[R] version 5.1.41, USA, San Jose, (2012).

CHAPTER 9:

Power System, Control and Automation

Advanced Materials Research Vols. 960-961 (2014) pp 943-951

doi:10.4028/www.scientific.net/AMR.960-961.943

A Novel Genetic Algorithm Based on All Spanning Trees of Undirected Graph for Distribution Network Reconfiguration

ZHANG Jian[1,a], YUAN Xiaodong[2,b]

[1,2]Jiangsu Electric Power Company Research Institute, Nanking, 211103, China

[a]z_jj1219@sina.com, [b]lannyyuan@hotmail.com

Keywords: network reconfiguration, genetic algorithm, paralleling computing, all spanning trees of undirected graph, decimal coding, distribution network.

Abstract. Network reconfiguration is of theoretical and practical significance to guarantee safe and economical operation of distribution system. In this paper, based on all spanning trees of undirected graph, a novel genetic algorithm for electric distribution network reconfiguration is proposed. Above all, all spanning trees of simplified graph of distribution network are found. Tie branches are obtained with spanning tree subtracted from simplified graph. There is one and only one switch open on each tie branch. Decimal identity number of open switch on each tie branch is taken as the optimization variable. Therefore, length of chromosome is very short. Each spanning tree corresponds to one subpopulation. Gene operations of each subpopulation are implemented with parallel computing method. Individuals of offspring after gene operation automatically meet with radial and connected constraints for distribution network operation. Disadvantages of conventional genetic algorithm for network reconfiguration that a large amount of unfeasible solutions are created after crossover and mutation, which result in very low searching efficiency, are completely overcome. High calculation speed and superior capability of the proposed method are validated by two test cases.

Introduction

In order to improve the reliability of power supply, urban distribution network is designed to be a looped net structure. For the sake of reducing short circuit current and facilitating protection relay settings, distribution network takes open loop operation mode. On distribution network, there are a large number of sectionalizing switches and a small amount of tie switches. By adjusting switches state, distribution network reconfiguration can reduce power loss, isolate fault, balance load, and improve voltage. At present, distribution automation demonstration projects is in full swing in many large and medium sized cities in China. Distribution Automation System (DAS) can manually, interactively or automatically adjust switches state which lay a solid foundation for the application of distribution network reconfiguration.

Network reconfiguration is a large scale, nonlinear, mixed integer programming problem, mainly including branch-exchange method[1-3], optimal flow method [4-5], genetic algorithm[6-15], heuristic method[16-18], mixed method[19], etc. Because genetic algorithm has the merits of independency of initial values, good robustness, capabilities of finding global solutions, it wins many scholars' attention.

In the early genetic algorithm for network reconfiguration, binary coding scheme is widely used, in which, each gene of chromosome corresponds to one switch. If gene is 0, then it indicates switch open. While if gene is 1, it indicates switch closed. This coding scheme is easy to implement and understand. However, a large amount of switches that cannot be opened in practice participate in coding. Therefore, the chromosome is too long, and in the process of crossover and mutation, too much unfeasible solutions are brought about, which result in extremely low search efficiency.

In [7], an improved genetic algorithm for network configuration is proposed, in which, only the switches located on a loop of distribution network participate in binary coding, unfeasible solutions after crossover and mutation are ameliorated. Nevertheless, the ameliorating process is time

consuming. In [8], coding genes of switches located on same loop are in one block, and coding genes of adjacent switches adjoin are proposed. But in this method, at each generation, crossover operation can only be implemented on one gene block, and mutation operation can only be done on one gene. Furthermore, in the process of mutation, unfeasible solutions are brought about. Consequently, the search efficiency of this method is comparatively low. In [9], a decimal coding scheme that the identity number of open switch located on loop is coded with an integer is proposed. In this method, if there is not any one switch located on more than one loops, then no unfeasible solutions are produced in the process of gene operation. Unfortunately, if there is switch located on more than one loops, many unfeasible solutions are produced.

In this paper, a novel genetic algorithm based on all spanning trees of undirected graph for distribution network reconfiguration is proposed. Above all, in the graph of distribution network, branches not located on any loop are removed, and adjacent branches whose crossing points have a degree of two is incorporated into one edge. Thus, an undirected simplified graph of distribution network is obtained. All spanning trees of this simplified graph are found with a program using backtracking and a method for detecting bridges based on depth-first search. Tie branches are obtained with spanning tree subtracted from the simplified graph. There is one and only one switch open on each tie branch. Once the switch on each tie branch is open, all other switch must be closed so as to meet the radial and connected constraints for distribution network operation. Which tie branches and which switch on each tie branch is chosen to be open are determined by genetic algorithm.

In this paper, a decimal coding scheme that the whole switch number of each tie branch constitutes the base vectors, and identity number of open switch on each tie branch is taken as the optimization variables are proposed. With such a coding scheme, the length of chromosome is equal to the number of independent meshes on the graph of distribution network. Therefore, it is very short. In the genetic algorithm, one sub-population corresponds to one spanning tree. Selection, crossover, mutation, reinsertion operations are all taken in sub-population with paralleling computing method. Individuals of offspring after gene operation automatically meet radial and connected constraints for distribution network operation. None unfeasible solutions are produced and none ameliorating operation is need. The disadvantages of conventional genetic algorithm for distribution network reconfiguration that a huge number of unfeasible solutions which result in very low search efficiency brought in the process of crossover and mutation operation are completely overcome. When the specified number of evolution generation is reached, the chromosome whose objective function value is minimal in the whole population is output as the global optimal solution. Two simulation cases indicate the proposed algorithm greatly improve calculation speed.

Model of Network Reconfiguration

The objective is that power loss is minimal after network reconfiguration under necessary constraints for distribution network operation. The objective function is formulated as Eq.1.

$$\min\ f = \sum_{i=1}^{n} \frac{P_i^2 + Q_i^2}{U_i^2} r_i k_i \tag{1}$$

Where P_i, Q_i are active and reactive power flowing through the terminal of branch i, respectively; U_i is the terminal node voltage of branch i; n is the total number of branches; r_i is the resistance of branch i; k_i is the switch state of branch i, which is a 0 or 1 discrete variable, with 0 indicating switch open, and 1 indicating switch closed; f is the active power loss of network, which can be obtained by power flow calculation.

Node voltage and branch power must meet the following constrains.

(a) Node Voltage Constraint

$$U_{i\min} \le U_i \le U_{i\max} \tag{2}$$

Where $U_{i\min}$, $U_{i\max}$ are the upper and lower voltage constraints for node i, respectively.

(b) Branch Power Constraint

$$S_i \le S_{i\max} \tag{3}$$

Where S_i , $S_{i\max}$ are the calculated and allowed maximal power value flowing through branch i respectively.

When node voltage or branch power exceeds constraint, a penalty function will be taken into account in f . The more is the constraints being exceeded, the more is penalty function.

All Spanning Trees of Simplified Graph and Relevant Concepts

All Spanning Trees and Tie Branches of Simplified Graph.

In order to decrease the number of spanning trees and reduce calculation complexity, adjacent branches located on a loop whose crossing point have a degree of 2 are incorporated into one edge, and branches not located on any loop can be removed from the graph of distribution network. Thus, the graph of distribution network can be simplified to a graph G . Spanning tree of G is a sub-graph of G , in which, any two nodes have one and only one simple path. Spanning tree of G has all nodes of G , but do not have all edges of G . Different spanning trees are composed of different edges. Tie branches are supplementary set of spanning tree. That is, tie branches equal to spanning tree subtracted from G. The number of edges in tie branches equals to the number of independent mesh in G . In this paper, we introduce the method in [20] to find all the spanning trees and corresponding tie branches of G .

Fig.1 is IEEE typical three feeder test system, in which, dotted line are the branches on which tie switches located. In order to facilitate finding all the spanning tree, bus 1, 2 and 3 are connected together. With adjacent branches located on a loop whose crossing point have a degree of 2 incorporated into one edge, and branches not located on any loop removed Fig.1 is simplified to Fig.2. It can be seen from Fig.2, edges (1), (3), (4), (5) constitute a spanning tree while edges (2), (6), (7) are the corresponding tie branches. Edges (1), (2), (4), (5) constitute another spanning tree while edges (3), (6), (7) are the corresponding tie branches. All spanning trees and the corresponding tie branches of Fig.2 are listed in 2th and 3th column of Table 1.

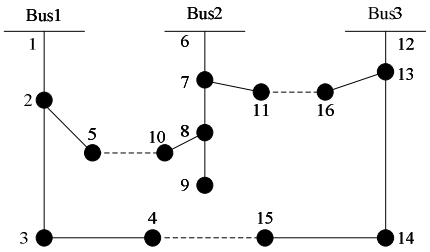

Fig.1 IEEE typical three feeder test system

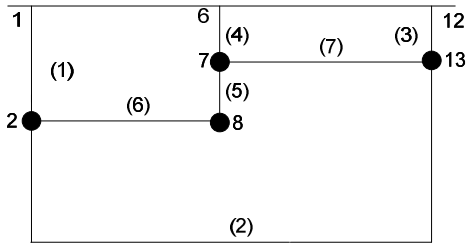

Fig.2 Simplified system

Base Vector of Tie Branches.

Base vector is composed of total switch number on each tie branch. Taking tie branches (1), (2), (4) for example, as shown in the second row, third column of Table 1, there is 1 switch on edge (1), 5 switches on edge (2), and 1 switch on edge (4). Thus, the base vector of this tie branches is $(1\ 5\ 1)$. All the base vectors of Fig.2 are listed in 4th column of Table 1.

Candidate Solutions.

Any combination of open switches that meet the radial and connected constraints for distribution network operation is defined as a candidate solution for network reconfiguration. The optimal solution can only be one of the candidate solutions. One candidate solution can be created if and only if open one switch on each tie branch. As to each spanning tree, the number of candidate solutions equals to the product of each component of the corresponding base vector. For example, shown as the 2^{th} row, 5^{th} column of Table 1, number of candidate solutions corresponding to 1^{th} spanning tree is $1\times5\times1=5$. That is, there are 5 combinations of open switches meeting the radial, connected constraints for distribution network operation. The total number of candidate solutions of network reconfiguration equals to the sum of candidate solutions corresponding to each spanning tree. Shown as the 26^{th} row, 5^{th} column of Table 1, there are 190 candidate solutions for the IEEE typical 3 feeder test system.

Table 1 Spanning trees, tie branches and base vectors

NO.	spanning tree	tie branches	base vector	candidate solutions
1	(3) (5) (6) (7)	(1) (2) (4)	(1 5 1)	5
2	(2) (3) (5) (7)	(1) (4) (6)	(1 1 3)	3
3	(1) (3) (5) (7)	(2) (4) (6)	(5 1 3)	15
4	(2) (3) (6) (7)	(1) (4) (5)	(1 1 1)	1
5	(1) (3) (6) (7)	(2) (4) (5)	(5 1 1)	5
6	(2) (3) (5) (6)	(1) (4) (7)	(1 1 3)	3
7	(2) (3) (4) (6)	(1) (5) (7)	(1 1 3)	3
8	(2) (3) (4) (5)	(1) (6) (7)	(1 3 3)	9
9	(3) (4) (5) (6)	(1) (2) (7)	(1 5 3)	15
10	(1) (3) (4) (5)	(2) (6) (7)	(5 3 3)	45
11	(1) (3) (4) (6)	(2) (5) (7)	(5 1 3)	15
12	(1) (3) (5) (6)	(2) (4) (7)	(5 1 3)	15
13	(2) (4) (6) (7)	(1) (3) (5)	(1 1 1)	1
14	(2) (4) (5) (7)	(1) (3) (6)	(1 1 3)	3
15	(4) (5) (6) (7)	(1) (2) (3)	(1 5 1)	5
16	(1) (4) (5) (7)	(2) (3) (6)	(5 1 3)	15
17	(1) (4) (6) (7)	(2) (3)(5)	(5 1 1)	5
18	(2) (4) (5) (6)	(1) (3) (7)	(1 1 3)	3
19	(1) (2) (4) (5)	(3) (6) (7)	(1 3 3)	9
20	(1) (2) (4) (6)	(3) (5) (7)	(1 1 3)	3
21	(1) (5) (6) (7)	(2) (3) (4)	(5 1 1)	5
22	(1) (2) (5) (6)	(3) (4) (7)	(1 1 3)	3
23	(1) (2) (6) (7)	(3) (4) (5)	(1 1 1)	1
24	(1) (2) (5) (7)	(3) (4) (6)	(1 1 3)	3
total	-	-	-	190

Coding Scheme and Gene Operation

Coding Scheme.

In this paper, decimal coding scheme is introduced. Subpopulations are one-to-one relevant to spanning trees. The length of chromosome is equal to the number of tie branches, which is equal to the number of independent meshes of distribution network. In contrast to conventional binary coding scheme, the proposed decimal coding scheme can greatly shorten the length of chromosome. The value of each gene is a non negative integer, indicating the open switch identity number on corresponding tie branch. The value of each gene is smaller than corresponding component of corresponding base vector. When we talk about a chromosome, we must point out the subpopulation it belongs to. If two chromosomes have the same genes but belong to different subpopulations, they have different meanings. For example, if chromosome $(0\ 0\ 0)$ belongs to 1^{th} subpopulation corresponding to 1^{th} spanning tree in Table 1, it implies the 0^{th} switch of tie branch (1), (2), (4) are

open. Otherwise, If chromosome $(0\ 0\ 0)$ belongs to 2^{th} subpopulation corresponding to 2^{th} spanning tree in Table 1, it implies the 0^{th} switch of tie branch (1), (4), (6) are open.

Creation of Initial Population.

Number of individuals in each subpopulation can be different according to the candidate solutions for the corresponding spanning tree. For example, because there are 15 candidate solutions correspondent to the 3^{th} spanning tree in Table 1, individuals number of the 3th subpopulation can be chose to be 2. While there are 45 candidate solutions correspondent to the 10^{th} spanning tree in Table 1, the individuals number of the 10^{th} subpopulation can be chose to be 6.

Fitness Value of Chromosome.

The open switches in the distribution network can be obtained by decoding the chromosome in each subpopulation. Network power loss is calculated with parallel back forward sweep power flow calculation method introduced in [21]. Power losses, with their corresponding chromosomes are sorted in ascending order. Order numbers in descending order are uniformly spaced mapped to real numbers 0~2. That is, the fitness value of chromosome with biggest power loss is mapped to 0, while the fitness value of chromosomes with smallest power loss is mapped to 2. The intervals of fitness value between any two adjacent chromosomes after sorted are equal.

Gene Operation.

Gene operation includes selection, crossover, mutation, and reinsertion, all of which are implemented in each subpopulation with parallel computing. After specified number of evolution generation, the individual whose objective value is minimal in the whole population (not in subpopulation) is output as the optimal solution.

(a) Selection

In each subpopulation, because numbers of individuals are different, numbers of individuals are selected to perform gene operation are different. Roulette method are introduced for selection.

(b) Crossover

Crossover is to exchange the number at the same position of parents, with a specified probability. For example, shown as Table 2, if the crossover probability is specified to 0.7, the offspring of parents chromosomes $(4\ 2\ 1)$, $(2\ 1\ 2)$ may be $(2\ 1\ 1)$, $(4\ 2\ 2)$.

Table 2 Crossover operation

parents			offspring		
4	2	1	2	1	1
2	1	2	4	2	2

(c) Mutation

Mutation is to replace the gene of parent with a non negative integer smaller than the corresponding component of base vector. For example, shown as Table 3, if the mutation rate is specified as 0.01, and the base vector is $(5\ 3\ 3)$, the chromosomes $(4\ 2\ 1)$, $(2\ 1\ 2)$, after mutation may be $(3\ 2\ 1)$, $(2\ 2\ 2)$.

Table 3 Mutation operation

parents			offspring		
4	2	1	3	2	1
2	1	2	2	2	2

(d) Reinsertion

As to each subpopulation, after crossover and mutation, specified numbers of individuals whose fitness values are smallest are removed from the parents. Then, the offspring are inserted into the

parents. Thus, in each subpopulation, new individuals are created while multiple old elite individuals are retained and population sizes are kept constant.

Parallel computing.

Coding, creation of initial population, calculation of fitness values and gene operations are all implemented in subpopulation. There is little coupled calculation between subpopulations. Therefore, it is very suitable for parallel computing. The calculation speed is highly improved, with parallel computing.

Flow chart of the proposed algorithm.

The flow chart of the proposed algorithm is shown as Fig.3. When the specified number of evolution generation is reached, the individual whose objective value is smallest in the whole population (not in the subpopulation) is output as the optimal solution of the network reconfiguration problem.

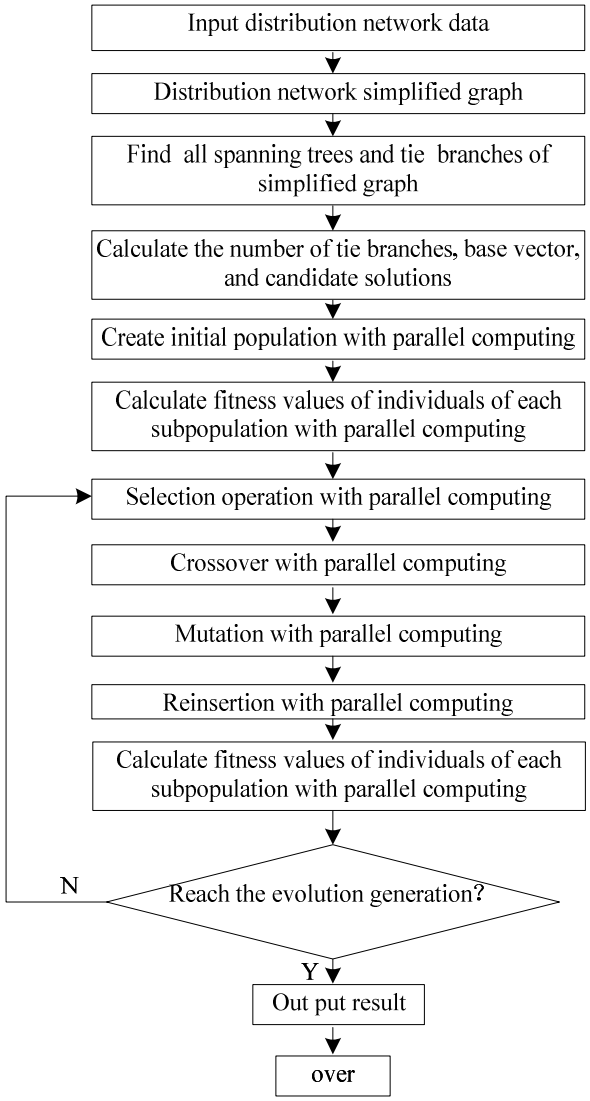

Fig.3 Flow chart of the algorithm

Simulation Case

Two simulation cases are taken to test the capability of the proposed method under the condition that there is single power supply and multiple power supply. In order to facilitate recording data, the optimal solution is determined with the proposed method. Then the optimal solution is taken as the program termination condition. All the relevant programs are written by MATLAB language.

Case 1: shown as Fig.1, there are the 3 feeders, 16 nodes, 3 independent meshes in this distribution network. Fig.2 is the simplified graph of Fig.1. There are 24 spanning trees and total 190 candidate solutions for Fig.2. The length of each chromosome is 3. Because the total amount of candidate solutions is very small, in each subpopulation, chromosomes are chosen to be one-to-one relevant to candidate solutions. That is, method of exhaustion is introduced to directly find the optimal solution.

Case 2: shown as Fig.4, there are 69 nodes, 73 branches, 5 independent meshes in this distribution network. Fig.5 is the simplified graph of Fig.4. There are 463 spanning trees and 377417 candidate solutions for Fig.5. The length of each chromosome is 5. The number of subpopulations equals to that of spanning trees. In the 37 subpopulations which correspond to the most candidate solutions, there are 4 individuals for each population. While in the rest 426 subpopulations, there are 2 individuals for each subpopulation. Therefore, there are 1000 individuals for the whole population. The crossover rate is 0.7, and the mutation rate is 0.01. The program is performed 50 times.

Reconfiguration results and relevant statistical data for case 1 and 2 are shown as Table 4 and Table 5.

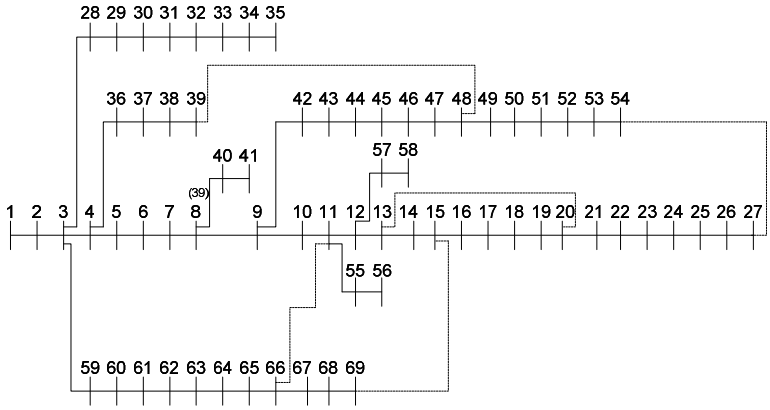

Fig.4 American PG&E69 nodes distribution network

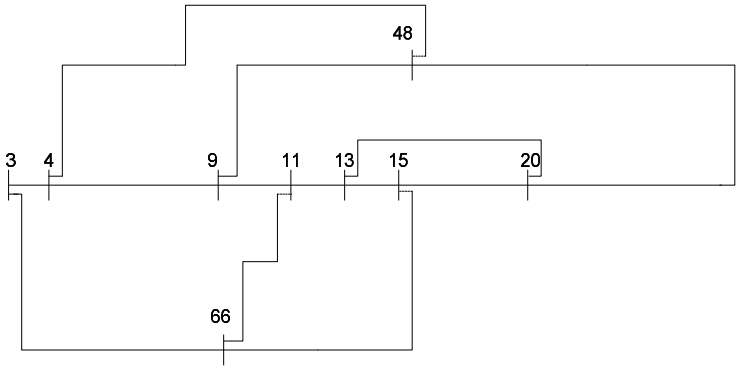

Fig.5 Simplified graph of Fig.4

As for the 16 nodes system, it takes 0.012s to find the optimal solution. As for 69 nodes system, it takes 6.22 times of average evolution generation and 0.534s to find the optimal solution, much better than the results of reference [8]. The reason why the reconfiguration results of the proposed method are different from that of reference [8] is that because there are no loads at nodes 45, 46, 47, open switches on the branches 44-45, 45-46, 46-47, 47-48 have the same effect.

It can be seen from the cases that the proposed method has very high search efficiency and calculation speed.

Table 4 Reconfiguration results of the two distribution network

Distribution system	Open switches before reconfiguration		Open switches after reconfiguration	Power loss before reconfiguration [kW]	Power loss after reconfiguration [kW]	Power loss descent rate
16nodes	5-10, 11-16, 4-15		4-15, 8-10, 7-11	511.4	466.1	8.85%
69nodes	11-66, 15-69, 27-54, 13-20, 39-48	Results in[8]	11-66, 14-15, 50-51, 13-20, 47-48	229.5	102.10	55.5%
		Results in this paper	11-66, 14-15, 50-51, 13-20, 46-47	229.5	101.01	56.0%

Table 5 Evolution statistics

Distribution system	Minimal generation to get global optimum results [generation]	Maximal generation to get global optimum results [generation]	Average generation to get global optimum results [generation]	Average calculation time[s]
16nedes	1	1	1	0.012
69nodes	Results in[8] 21	32	22.40	25.423
	Results in this paper 1	16	6.22	0.534

Conclusions

In this paper, a genetic algorithm based on all spanning trees of simplified graph of distribution network for network reconfiguration is proposed. The total candidate solutions and their distribution can be precisely calculated, which can supply information for determining the numbers of subpopulations and individuals in each subpopulation. The disadvantages of conventional genetic algorithm for distribution network reconfiguration that a large amount of unfeasible solutions are created in the process of crossover and mutation is completely overcome. Therefore, search efficiency of the proposed algorithm is highly improved. The identity number of open switch on each tie branch is taken as the optimization variable and decimal coding scheme is introduced. As a consequence, the length of chromosome is greatly shortened and storage space is minimized while calculation speed is improved. There is little calculation coupled between subpopulations. So it is very suitable for parallel computing. Two cases indicate the proposed algorithm has the merits of high calculation speed and superior capabilities.

References

[1] He Yuqing, Peng Jianchun, Wen Ming, Zhou Yangxi, Li Jianying, Li Peng. Minus feasible analysis unit and fast algorithm for distribution network reconfiguration. Proceedings of the CSEE, Vol.30 (2010), p.50.

[2] S. Civanlar, J.J. Grainger, H. Yin, S.S.H. Lee. Distribution feeder reconfiguration for loss reduction. IEEE Transactions on Power Delivery, Vol.3 (1988), p.1217.

[3] Bi Pengxiang, Liu J ian, Zhang Wenyuan. A refined branch exchange algorithm for distribution network reconfiguration. Proceedings of the CSEE,Vol.22 (2001), p.98.

[4] Lei Jiansheng, Deng Youman, Zhang Boming. Hybrid flow pattern and its application in network reconfiguration. Proceedings of the CSEE, Vol.21(2001), p.57.

[5] Liu Wei, Han Zhenxiang. Distribution network reconfiguration based on optimal flow pattern algorithm and genetic algorithm. Power System Technology, Vol.28 (2004), p.29.

[6] Liu Jian, Bi Pengxiang, Dong Haipeng. Analysis and simplification of complicated distribution network. China Electric Power Press, 2002, Beijing.

[7] Bi Pengxiang, Liu J ian, Zhang Wenyuan. Study on algorithms of distribution network reconfiguration. Automation of Electric Power Systems, Vol.10 (2001), p.54.

[8] Li Xiaoming, Huang Yanhao, Yin Xianggen. A genetic algorithm based on improvement strategy for power distribution network reconfiguration. Proceedings of the CSEE, Vol.24 (2004), p.49.

[9] Bi Pengxiang, Liu Jian, Liu Chun Xin, Zhang Wenyuan. A refined genetic algorithm for power distribution network reconfiguration. Automation of Electric Power Systems, Vol.2 (2002), p.57.

[10] Ma Xiufan, Zhang Lizi. Distribution network reconfiguration based on genetic algorithm using decimal encoding. Transactions of China Electro- technical Society, Vol.19 (2004), p.65.

[11]Koichi Nara, Atsushi, Shiose, Minoru Kitagawa,Toshihisa Ishihara. Implementation of genetic algorithm for distribution system loss minimum reconfiguration. IEEE Transactions on Power System, Vol.7 (1992), p.1044.

[12] Xu Kui. A study of reconfiguration network based on improved adaptive genetic algorithms. Master's dissertation of Guangxi University, 2008.

[13] Wang Yansong， Chen Guoming， Zhang Jiasheng， et al． Optimal switching device placement based on niche genetic algorithm in distribution networks. Transactions of China Electro- technical Society, Vol.21 (2006), p.82.

[14] Liu Li, Cheng Xueyun. Reconfiguration of distribution network based on fuzzy genetic algorithm. Proceedings of the CSEE,Vol.20 (2000), p.66.

[15] Yu Yixin, Duan Gang. Shortest path algorithm and genetic algorithm based distribution system reconfiguration. Proceedings of the CSEE, Vol.20 (2000), p.44.

[16] Ge Shaoyun, Liu Zifa, Yu Yixin. An improved Tabu search for reconfiguration of distribution systems. Power System Technology, Vol.28 (2004), p.22.

[17] Wang Shouxiang, Wang Chengshan. A novel network reconfiguration algorithm implicity including parallel searching for large scale unbalanced distribution systems. Automation of Electric Power Systems, Vol.24 (2000), p.34.

[18] Kubin Taleski, Dragoslav Rajicid. Distribution network reconfiguration for energy loss reduction. IEEE Transactions on Power Systems, Vol.12 (1997), p.398.

[19] Chen Genjun, Li Jiguang, Tang Guoqing. A tabu search approach to distribution network reconfiguration for loss reduction. Proceedings of the CSEE, Vol. 22(2002), p.28.

[20] HAROLD N. Gabow, EUGENE W. Myers. Finding All Spanning Trees of Directed and Undirected Graphs[J]. Society for Industrial and Applied Mathematics, Vol.7 (1978), p.280.

[21] Yan Wei, Liu Fang, Wang Guanjie, et al. Layer-by-layer back/forward sweep method for radial distribution load flow. Proceedings of the CSEE, Vol.23 (2003), p.76.

Advanced Materials Research Vols. 960-961 (2014) pp 952-959

doi:10.4028/www.scientific.net/AMR.960-961.952

Aggregation of Loads with Distribution Network Considered

ZHANG Jian[1,a], YUAN Xiaodong[2,b]

[1,2]Jiangsu Electric Power Company Research Institute, Nanking, 211103, China

[a]z_jj1219@sina.com, [b]lannyyuan@hotmail.com

Keywords: power system, load model, induction motor, static load, distribution network, load aggregation.

Abstract. This paper proposes a methodology for the aggregation of distribution network, induction motors and static loads. This methodology can aggregate induction motors and static loads model into one composite load model with distribution network considered. The absence of simplifications, the proper aggregation of distribution network and the adequate handing to motor mechanical load allow this methodology shows pretty good accuracy. A simple simulation test is also taken to validate the proposed methodology.

Introduction

In power system, The model of each component is the base of simulation. Load model plays one of the key roles on power system dynamics[1-3]. Because of its time variability, randomness and complexity, load model is the bottle beck of improving the accuracy of simulation. In practice, thousands of induction motors loads and static loads scatter in a large distribution network. The distance from induction motors loads and static loads to the 220kV bus of substation is different. How to precisely simulate the overall effect of induction motors loads and static loads is a challenge. Limited by memory capacity and speed of computer, it is not practical to simulate substation in detail. In load modeling, component-based approach is adopted widespread[4]. In component-based load modeling approach, aggregation algorithm is crucial to the accuracy of the load model. Because parameters of induction motor have extraordinary impact on power system dynamics, aggregation of induction motors is focused on. So as far, there are kVA-weighted averages aggregation method, no-load and block-up-roll based aggregation method, static equivalent circuit of induction motor based aggregation method and dynamic equivalent circuit of induction motor based aggregation method. In [5], with the impact of loading factor and critical slip of induction motor on the transient stability of system analyzed, a improved MVA-weighted averages aggregation method is proposed. But this method is still a heuristic method, lack of strict theoretic basis. In [6], with the skin effect considered, leak reactance of stator and rotor are divided to two parts respectively. Thus, the impedance parameters of induction motors add to seven ones. In [7], a no-load and block-up-roll based induction motor aggregation method is proposed. In [8], based on electromechanical model of induction motor, a static aggregation method is proposed, with the assumption that the stator resistance is zero, the mechanical torque is constant and the leak reactance of stator is equal to the leak reactance of rotor. In [9] and [10], the steady equivalent circuit of induction motor is transformed to a three impedances paralleled form, resulting in the aggregation complexity of motors is drastically reduced, but because the steady slip of motors are not considered, active and reactive power absorbed by induction motors is not equal before and after aggregation.

In the load aggregation method mentioned above, the induction motors are assumed to connect to the same bus, that is, the effect of distribution network is not considered. But in practice, induction motors and static loads scatter in a large distribution network. The value of equivalent distribution reactance plays significant influence on the transient and voltage stability of power system. With the distribution network considered, this paper propose a strict load aggregation method. The absence of simplifications, the proper aggregation of distribution network and the adequate handing to motor

mechanical load allow this methodology shows pretty good accuracy. A simulation test is also taken to validate the proposed method.

Shown as Fig.1, a substation is composed of transmission lines, transformers, capacitors, induction motors loads and static loads. Simulation achieves computationally feasible only if the substation be equivalent to a simple model. Shown as Fig.2, the synthesis load model (SLM) that takes the distribution network into account, is a proper load model structure.

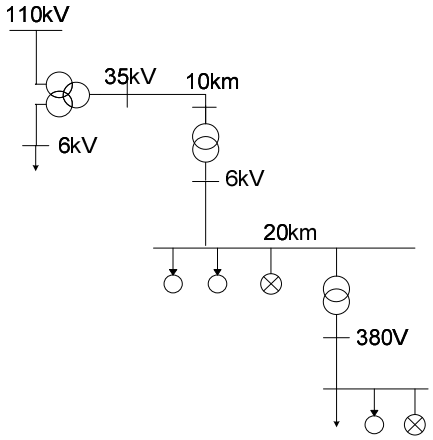

Fig.1 Distribution network diagram

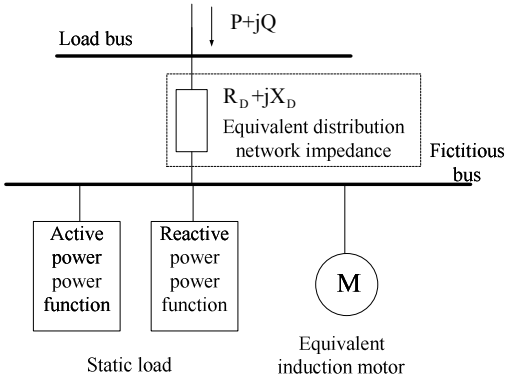

Fig.2 SLM model

Aggregation of Distribution Network

Suppose the number 0 bus is the main bus of substation; number 1～k buses are load buses; k+1~m are connection buses. The buses voltage equation of distribution network is:

$$\begin{bmatrix} \dot{I}_A \\ \dot{I}_B \end{bmatrix} = \begin{bmatrix} Y_{AA} & Y_{AB} \\ Y_{BA} & Y_{BB} \end{bmatrix} \begin{bmatrix} \dot{U}_A \\ \dot{U}_B \end{bmatrix} \tag{1}$$

where, $\dot{I}_A$ is the steady current vector injected into the main bus and the load buses; $\dot{I}_B$ is the steady current vector injected into connection buses; $\dot{U}_A$ is the steady voltage vector of the main bus and the load buses; $\dot{U}_B$ is the steady voltage vector of connection buses; Y_{AA} is the self- admittance matrix of 0 ～k buses; Y_{AB} , Y_{BA} are mutual admittance matrixes between 0～k buses and k+1~m buses; Y_{BB} is the self-admittance matrix of k+1~m buses. Eq.1 can be expanded to the following two equations:

$$\dot{I}_A = Y_{AA}U_A + Y_{AB}\dot{U}_B \tag{2}$$

$$\dot{I}_B = Y_{BA}\dot{U}_A + Y_{BB}\dot{U}_B \tag{3}$$

Because the current injected into the connection buses are zeros, we have:

$$\dot{U}_B = -Y_{BB}^{-1}Y_{BA}\dot{U}_A \tag{4}$$

Substituting for $\dot{U}_B$ from Eq.4 in Eq.2, one deduces:

$$\dot{I}_A = (Y_{AA} - Y_{AB}Y_{BB}^{-1}Y_{BA})\dot{U}_A \tag{5}$$

Thus, the connection buses is eliminated. The distribution network can be simplified to the form shown as Fig.3.

According to the principle of equivalence of active and reactive loss on the distribution network before and after aggregation, the equivalent impedance of distribution network is:

$$Z_{D,eq} = \left[\sum_{i=1}^{k} U_i^2 \hat{y}_{i0} - \sum_{i=1}^{k-1} \sum_{j=i+1}^{k} \dot{U}_i \left(\hat{\dot{U}}_i - \hat{\dot{U}}_j \right) \hat{Y}_{ij} \right] / I_s^2 \tag{6}$$

where, $\dot{U}_i$ is the steady voltage phasor of the i^{th} load bus; $\hat{\dot{U}}_i$ is the conjugate complex of $\dot{U}_i$; $\hat{\dot{U}}_j$ is the conjugate complex of the steady voltage of the j^{th} load bus; $\hat{y}_{i0}$ is the conjugate complex of to-ground-admittance of the i^{th} bus; $\hat{Y}_{ij}$ is the conjugate complex of the mutual admittance between i^{th} and j^{th} load bus; I_s is the steady current injected to the main bus from transmission system. The steady voltage of the fictitious bus is:

$$\dot{U}_f = \dot{U}_s - Z_{D,eq}\dot{I}_s \tag{7}$$

where, $\dot{U}_s$ is the steady voltage of the main bus; $\dot{I}_s$ is the steady current phasor injected into the main bus. Thus, shown as Fig.4, each load bus can be connected to fictitious bus through an ideal phase shift transformer. Then all induction motor loads and static loads can be transferred to the fictitious bus according to their per unit parameters. Therefore, the aggregation of loads can be done in such a way that all loads is under the same bus.

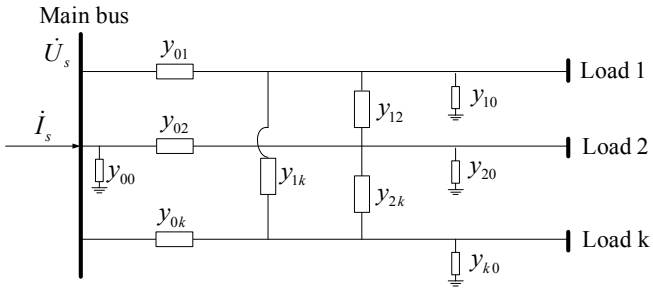

Fig.3 The implied figure of computing distribution network

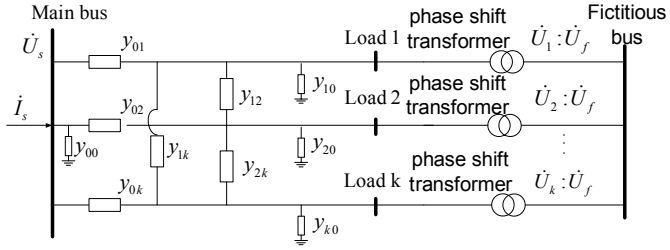

Fig.4 The implied figure of displacing load

Aggregation of Induction Motors

Equivalent Circuit of Induction Motor.

Steady equivalent circuit of induction motor is shown as Fig.5 and the dynamic one is shown as Fig.6.

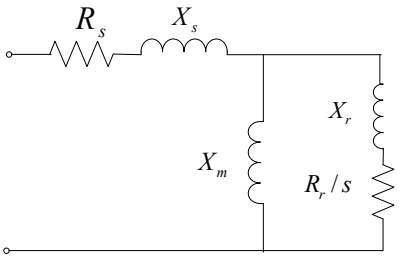

Fig.5 Steady equivalent circuit of induction motor

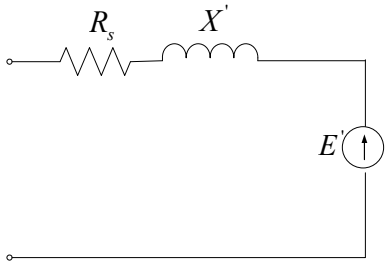

Fig.6 Transient equivalent circuit of induction motor

In steady state, according to Thevenin theorem, seen from the rotor resistance of induction motor, the steady equivalent impedance of induction motor is:

$$Z_e = R_e + jX_e = (R_s + jX_s)//jX_m + jX_r = (R_s X_{sm}^2 - jX_p X_{rm})/(X_P^2 + R_s^2 X_{sm}^2) \tag{8}$$

where $X_{sm} = X_s + X_m \quad X_{rm} = X_r + X_m, X_p = X_s X_m + X_r X_m + X_s X_r$.

The steady equivalent voltage is:

$$U_e = X_m / \sqrt{R_s^2 + X_{sm}^2} U_f \tag{9}$$

The steady electric torque of induction motor is:

$$T_e = \frac{U_e^2 (1-s) R_r / s}{\omega_s [(R_r / s + R_e)^2 + X_e^2]} \tag{10}$$

The mechanical torque of induction motor has the following form:

$$T_m = T_0 [a(1-s)^2 + b(1-s) + c] \tag{11}$$

where, $a+b+c=1$ and T_0 is a constant. According to $T_e=T_m$, the steady slip of induction motor can be calculated. From Fig.6, the steady electromotive is:

$$\dot{E}^{'}=j(X-X^{'})\dot{U}_f/[jsZ^{'}T_{d0}^{'}+Z^{'}+j(X-X^{'})] \tag{12}$$

Aggregation Method.

The dynamic model of induction motor is:

$$d\dot{E}^{'}/dt=-js\dot{E}^{'}-[\dot{E}^{'}-j(X-X^{'})\dot{I}]/T_{d0}^{'} \tag{13}$$

$$\dot{U}_f=\dot{E}^{'}+(R_s+jX^{'})\dot{I} \tag{14}$$

$$T_j ds/dt=T_m-T_e \tag{15}$$

$$T_e=\mathrm{Re}(\dot{E}^{'}\hat{\dot{I}}) \tag{16}$$

where $T_m=(A\omega^2+B\omega+C)T_0$ $A\omega_0^2+B\omega_0+C=1$ $\omega_0=1-s_0$; $T_{d0}^{'}=(X_r+X_m)/(\omega_s R_r)$ is the open circuit time constant; $X=X_s+X_m$ is the open circuit reactance of stator of induction motor; $X^{'}=X_s+X_r X_m/(X_r+X_m)$ is the transient reactance of induction motor; T_j is rotor inertia time constant of induction motor.

Let $\dot{E}^{'}=Ee^{j\delta}, \dot{U}_f=Ue^{j\theta}$, $j(X-X^{'})/(R_s+jX^{'})=Z=Ke^{j\alpha}$ $R_s+jX^{'}=Z^{'}=\left|Z^{'}\right|e^{j\beta}=\left|Z^{'}\right|e^{j(90^{\circ}-\alpha}$, substituting them into Eq.13, Eq.15 the dynamic model of induction can be transferred to the following form:

$$dE/dt=-[E-KU\cos(\theta+\alpha-\delta)+KE\cos\alpha]/T_{d0}^{'} \tag{17}$$

$$d\delta/dt=-s+[KU\sin(\theta+\alpha-\delta)/E-K\sin\alpha]/T_{d0}^{'} \tag{18}$$

$$T_j ds/dt=[EU\cos(\delta-\theta-\beta)-E^2\cos\beta]/\left|Z^{'}\right|-T_m \tag{19}$$

There many induction motors connected to the fictitious bus, the Norton equivalent circuits are shown as Fig.7. The equivalent transient impedance is:

$$Z_{eq}^{'}=1/(\sum_{i=1}^{n}1/Z_i^{'}) \tag{20}$$

The equivalent steady electromotive is:

$$\dot{E}_{eq}^{'}=\sum_{k=1}^{n}\left(\dot{E}_k^{'}/Z_k^{'}\right)Z_{eq}^{'} \tag{21}$$

From Eq.20, it has:

$$\left|Z^{'}\right|=\left|Z_{eq}^{'}\right| \tag{22}$$

$$\beta_{eq}=Ang\left(Z_{eq}^{'}\right) \tag{23}$$

$$R_{s,eq}=Re(Z_{eq}^{'}) \tag{24}$$

$$X_{eq}^{'}=\mathrm{Im}(Z_{eq}^{'}) \tag{25}$$

From Eq.21, it has:

$$E_{eq}=\left|\dot{E}_{eq}^{'}\right| \tag{26}$$

$$\delta_{eq}=Ang\left(\dot{E}_{eq}^{'}\right) \tag{27}$$

$$\alpha_{eq}=90^{\circ}-\beta_{eq} \tag{28}$$

In steady state, the left side of Eq.17 is zero, the equivalent impedance is:

$$K_{eq}=E_{eq}/[U\cos(\theta_0+\alpha_{eq}-\delta_{eq})-E_{eq}\cos(\alpha_{eq})] \tag{29}$$

According to the definition of Z_{eq} ,the equivalent reactance is:

$$X_{eq}=X_{eq}^{'}+K_{eq}\left|Z_{eq}^{'}\right| \tag{30}$$

$$X_{m,eq}=1/\left(\sum_{k=1}^{n}\frac{1}{X_{m,k}}\right) \tag{31}$$

$$X_{s,eq}=X_{eq}-X_{m,eq} \tag{32}$$

$$X_{r,eq}=\left(X_{eq}^{'}-X_{s,eq}\right)X_{m,eq}/\left(X_{eq}-X_{eq}^{'}\right) \tag{33}$$

According to [6], the transient electromagnetic torque of each motor reaches its peak value after it starts for 13 ms. The peak transient electromagnetic torque is:

$$T_p = V_t^2 R_r [1+\sqrt{1+(X_s+X_r)^2/R_r^2}]/[R_r^2+(X_s+X_r)^2] \quad (34)$$

The peak transient electromagnetic torque of the equivalent motor is equal to the sum of that of the individual motor:

$$T_{p,eq} = \sum_{i=1}^{n} T_{p,i} \quad (35)$$

According to Eq.35, the rotor resistance of the equivalent motor can be obtained. Therefore, the time constant of rotor circuit is:

$$T'_{d0,eq} = (X_{meq} + X_{req})/(\omega_s R_{r,eq}) \quad (36)$$

In steady state, the left side of Eq.18 is zero. Substituting Eq.36 into Eq.18, the steady slip of the equivalent motor is:

$$s_{eq} = [K_{eq} U \sin(\theta_0 + \alpha_{eq} - \delta_{eq})/E_{eq} - K_{eq}\sin\alpha_{eq}]/T'_{d0,eq} \quad (37)$$

In steady state, the left side of Eq.19 is zero. The steady mechanical torque of the equivalent motor is:

$$T_{m0} = [E_{eq} U \cos(\delta_{eq} - \theta_0 - \beta_{eq}) - E_{eq}^2 \cos\beta_{eq}]/|Z'_{eq}| \quad (38)$$

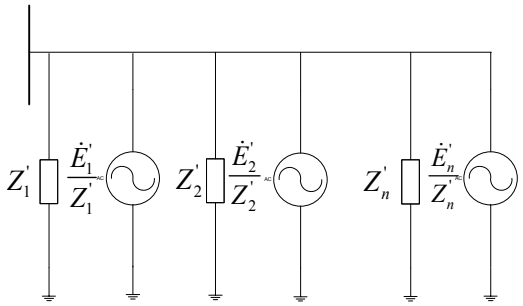

Fig.7 Steady equivalent circuit of manyinduction motors under the same bus

In steady state, the kinetic energy should be equal to the sum of that of individual motor. The inertia time constant can be obtained as follows:

$$H_{eq} = \sum_{i=1}^{n} H_i (1-s_i)^2/(1-s_{eq})^2 \quad (39)$$

The aggregation of mechanical load is as follows:

1) Choose the fictitious bus voltage with a series of discrete values equidistantly in a certain range (such as 1.2-0.1 p.u.).
2) As to every discrete voltage value, calculate the steady slip of every motor.
3) Calculate the active power absorbed by every motor.
4) According to that the active power absorbed by the equivalent motor is equal to the sum of that of the individual motor, calculate the steady slip of the equivalent motor.
5) Calculate the electromagnetic torque of the equivalent motor according to Eq.4.
6) In steady state, the mechanical torque is equal to the electromagnetic torque, therefore, a pair of slip -mechanical torque $(s_{eq}, T_{m,eq})$ can be obtained.
7) The complete mechanical torque characteristics can be obtained by Interpolation and fitting method.

Aggregation of Static Loads.

Generally, the power function model of static load is as follows:

$$P = P_0 \left(\frac{U}{U_0}\right)^{p_u} \quad (40)$$

$$Q = Q_0 \left(\frac{U}{U_0}\right)^{q_u} \quad (41)$$

The model of the equivalent static load should be:

$$P_{eq} = \sum_{k=1}^{n} P_k \quad (42)$$

$$Q_{eq} = \sum_{k=1}^{n} Q_k \tag{43}$$

To get the power function model of the equivalent static load, it has:

$$P_{0,eq} = \sum_{k=1}^{n} P_{0k} \tag{44}$$

$$Q_{0,eq} = \sum_{k=1}^{n} Q_{0k} \tag{45}$$

$$p_{u,eq} = \sum_{i=1}^{n} \rho_{pi} p_{ui} \tag{46}$$

$$q_{u,eq} = \sum_{i=1}^{n} \rho_{qi} q_{ui} \tag{47}$$

Where, $\rho_{pi} = P_{0i} / P_{0,eq}$, $\rho_{qi} = Q_{0i} / Q_{0,eq}$.

Validation Test

The proposed methodology has been tested on a simple distribution network. Shown as Fig.8, four induction motors , a electric arc furnace and a fluorescent ramp scatter in a distribution network. The model of the electric arc furnace and a fluorescent ramp are the ones recommended by IEEE. The inner impedance of the voltage resource is 0.00527+j 0.0378.

The parameters of the four individual motors and of the equivalent motor is shown in the appendix. Impedance between bus 6 and 5 and that between bus 6 and 4 have been incorporated into M4 and M3 respectively. The equivalent impedance of distribution network is 0.0158+j0.0567. The index of active and reactive power of equivalent static load is 4.0649 and 1.65. All parameters are in per unit on base power of 10 MVA.

The simulation is taken in such a way that at 0.05s , a voltage dip of 20% of bus 1 takes place and is cleared at 0.35s. Fitting results of active and reactive power is the criterion to judging the effectiveness of this methodology. Voltage curve of bus 1 is shown in Fig.9. Active and reactive curves before and after aggregation are shown as Fig.10 and Fig.11. It can be seen from Fig.10 and Fig.11 that the fitting result is pretty good.

Shown as Fig.8, four induction motors , a electric arc furnace and a fluorescent ramp scatter in a distribution network. The model of the electric arc furnace and a fluorescent ramp are the ones recommended by IEEE. The inner impedance of the voltage resource is 0.00527+j 0.0378.

The parameters of the four individual motors and of the equivalent motor is shown in the appendix. Impedance between bus 6 and 5 and that between bus 6 and 4 have been incorporated into M4 and M3 respectively. The equivalent impedance of distribution network is 0.0158+j0.0567. The index of active and reactive power of equivalent static load is 4.0649 and 1.65. All parameters are in per unit on base power of 10 MVA.

The simulation is taken in such a way that at 0.05s , a voltage dip of 20% of bus 1 takes place and is cleared at 0.35s. Fitting results of active and reactive power is the criterion to judging the effectiveness of this methodology. Voltage curve of bus 1 is shown in Fig.9. Active and reactive curves before and after aggregation are shown as Fig.10 and Fig.11. It can be seen from Fig.10 and Fig.11 that the fitting result is pretty good.

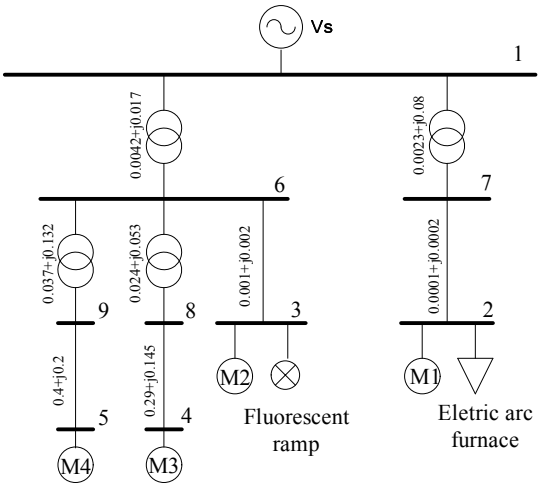

Fig.8 A simple distribution system

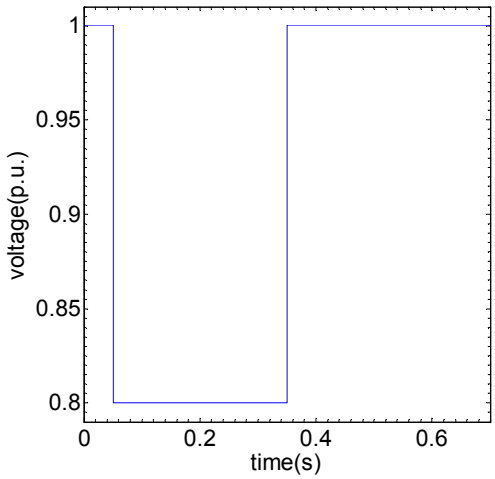

Fig.9 Curve of interrupted voltage

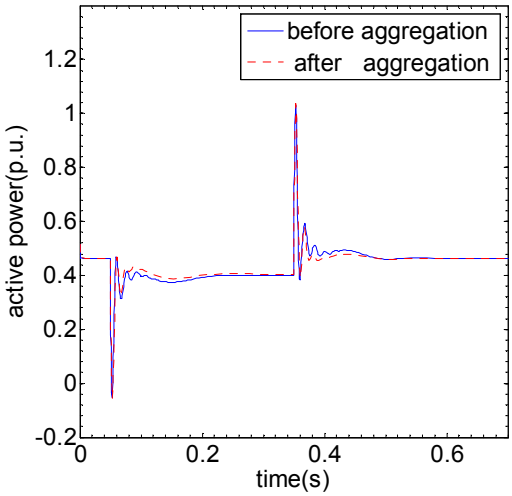

Fig.10 Sum of active power before and after aggregation with SLM model

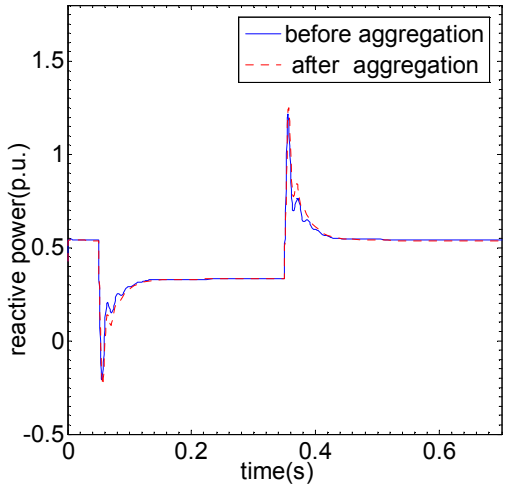

Fig.11 Sum of reactive power before and afteraggregation with SLM model

Conclusions

This paper propose a static methodology of aggregation induction motors and static loads, with distribution network considered. The accuracy of fitting result before and after aggregation is validate by an example.

References

[1] CIGRE Task Force. Load modeling and dynamics. Electra, Vo1.130 (1990), p.124.
[2] IEEE Task Force. Load representation for dynamic performance analysis. IEEE Trans. on Power Systems, Vol.8 (1993), p.472.
[3] IEEE Task Force Standard load models for power flow and dynamic performance simulation. IEEE Trans. on Power System, 1995, Vol.10 (1995), p.1302.
[4] Ju Ping, Ma Daqiang. Load modeling of power system (second edition) . Beijing: China Electric Press, 2008.
[5] Guo Jinchuan, Yu Yixin, Ni Peng, Zeng Yuan. An improved weighting mean aggregation method of induction motors considering load rates and critical slips. Automation of Electric Power Systems, Vol.32(2008), p.6.

[6] M. Akbaba, S.Q. Fakhro. New model for single-unit representation of induction motor loads, including skin effect, for power system transient stability studies. IEE Proceedings-B, Vol. 139, NO. 6, November 1992.
[7] Zhang Hongbin，Tang Yong，Zhang Dongxia，et al．Equivalent model for induction-motor load connected to high voltage bus. Proceedings of the CSEE, Vol.26 (2006), p.1(in Chinese)．
[8] M.Taleb, M. Akbaba, E. A. Abdullah. Aggregation of induction machines for power system dynamic studies. IEEE Transactions on Power systems, Vol.9, No.4, November 1994.
[9] Zhang Jinchao, Zhang Chenxue, Yan Anhe, Zhang Pengfei, Li Kui. Aggregation of multi induction motors based on the self-organized neural network and steady state model. Automation of Electric Power Systems, Vol.31(2007), p.44.
[10] D.C. Franklin, Amorelato. Improving dynamic aggregation of induction motor models. IEEE Transactions on Power Systems. Vol. 9, No. 4, November 1994.
[11]Tang Yong, Hou Junxian, Liu Wenchuo. The modeling of distribution network and var compensator and induction motor in the Load model for power system digital simulation. Proceedings of the CSEE, Vol.25 (2005), p.8.
[12] Ni Yixin, Chen Shousun, Zhang Baoling, Theory and analysis of dynamic power system, Tsinghua University press, 2002.

Advanced Materials Research Vols. 960-961 (2014) pp 960-963

doi:10.4028/www.scientific.net/AMR.960-961.960

Design of a Wide-Area Damping Controller Based on Fuzzy Control

Lin Sun[1, a], Wei Cai[1, b], Tianran Li[1, c] and Huaren Wu[1, d]

School of Electrical and Automation Engineering, Nanjing Normal University, Nanjing 210042, China

[a]sunlin0105@yeah.net, [b]caiwei-789@163.com, [c]litianran@njnu.edu.cn, [d]huarenwu@yahoo.com

Keywords: fuzzy control; wide-area damping control; time delay; power system stability

Abstract. A method is proposed to design a wide-area damping controller (WADC) based on fuzzy control to dampen the low-frequency oscillations of interconnected power systems. First, the inputs and expected outputs of a fuzzy logic controller are analyzed. Then, a universe of fuzzy sets, membership functions and fuzzy rules are determined based on the relationship between inputs and outputs, and the fuzzy logic controller is constituted. The WADC consists of a fuzzy logic controller and a gain. The gain is obtained using particle swarm optimization. A four-machine two-area power system is simulated using the Matlab/Simulink software to test the performance of the fuzzy-based WADC. The simulation results indicate that the designed controller can compensate for communication delay and improve interconnected power system damping.

Introduction

With the expansion of the power system, the inter-area low frequency oscillation between power grids has become a significant problem in power system stability. Traditional power system stabilizers, which use local variables as input signals, cannot suitably solve this problem [1]. A wide-area measurement system (WAMS) can provide wide-area feedback signals. These signals can be used in excitation control to enhance multimachine system damping and to restrain low frequency oscillations. In practical engineering, a time delay inevitably exists during the communication of a wide-area signal. This delay will reduce the control effects [2].

A few methods are used to reduce the negative impact of the time delay. Reference [2] developed a switched control algorithm for an excitation control using a wide-area signal with a time delay. This algorithm can reduce the impact of time delays. Reference [3] investigated an adaptive wide-area damping control based on federated Kalman filters. Reference [4] proposed a stability criterion for a wide-area damping controller (WADC) based on the Padé approximation.

Fuzzy control is a type of nonlinear control that does not require a complicated mathematical model. Furthermore, it has good robustness and adaptability. Reference [5] designed a fuzzy logic WADC to compensate for the continuous latency and damp the inter-area oscillations. The oscillatory signal $\Delta\omega$ is a hypothetical sine wave, and it is analyzed in a period of oscillation when fuzzy rules are determined. However, the actual oscillatory signal is not a sine wave.

This report applies fuzzy control to wide-area damping control to compensate for a communication delay in the wide-area measurement system. The method of designing the fuzzy wide-area damping controller (FWADC) is described. Based on a power system toolbox and the fuzzy logic toolbox of Matlab, a four-machine two-area power system is simulated to analyze the performance of the designed controller with different time delays.

Design of FWADC

Modern generators are typically equipped with a high initial response excitation system with high-ceiling voltage to enhance the transient stability of power systems. An excitation system with a PSS can improve the dynamic stability of a power system. Wide-area signals provided by the

WAMS, such as the rotor speed of the generator, the power angle and the tie-line power, can be used in additional excitation control to increase the interconnected power system damping. This report selects different generator speeds as the inputs for wide-area damping control and applies fuzzy control to compensate for the communication delay. A block diagram of the automatic voltage regulator (AVR), PSS, and WADC of generator *i* is provided in Fig. 1.

In Fig. 1, $G_{PSS}(s)$ is the transfer function of the traditional PSS, and $\Delta\omega_i(t)=\omega_i(t)-1$ is its input, where $\omega_i(t)$ is the speed of generator *i*. The input of FWADC is $\omega_{ij}(t-T_d)=\omega_i(t-T_d)-\omega_j(t-T_d)$, where $\omega_j(t-T_d)$ is the wide-area signal from generator *j*. T_d is the communication delay. A block diagram of the FWADC is provided in Fig. 2. The inputs for the fuzzy logic controller are $e=\omega_{ij}(t-T_d)$ and $ec=\dot{\omega}_{ij}(t-T_d)$, where u is the output of the fuzzy logic controller.

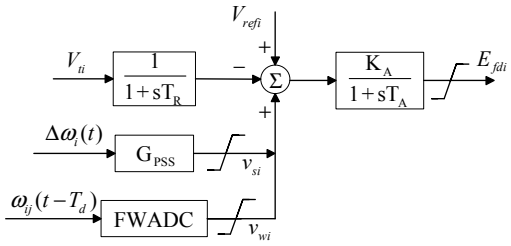

Fig. 1 AVR, PSS and FWADC

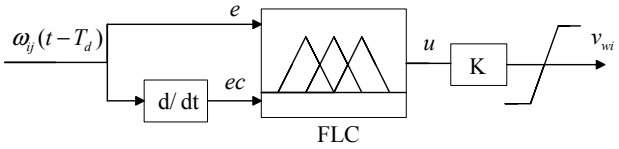

Fig. 2 Block diagram of FWADC

As provided in Fig. 3 [6], a four-machine two-area power system is used to illustrate the design method of the FWADC.

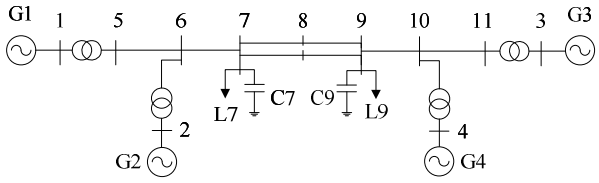

Fig. 3 Four-machine two-area power systems

All four generators are equipped with the local PSS. The transfer function of the PSS is given as follows: $G_{PSS}=20\frac{10s}{1+10s}\left(\frac{1+0.05s}{1+0.03s}\right)\left(\frac{1+3.0s}{1+5.4s}\right)$.

In Fig. 1, the output limit of PSS is ±0.2 pu. The output limit of E_{fdi} is ±5 pu; T_R=0.02; K_A=200; and T_A=0.001. Other parameters can be obtained in reference [6]. Generators 1 and 2 have wide-area damping controllers with inputs $\omega_{14}(t-T_d)$ and $\omega_{24}(t-T_d)$, respectively.

A three-phase short-circuit fault was applied to bus 7 in Fig. 3, and the short-circuit fault lasted for 0.12 s. The results of the time domain simulation are provided in Fig. 4. Curves 1 and 2 in Fig. 4 are the angle differences $\delta_{14}(t)$ and $\delta_{24}(t)$, respectively, when the generators are equipped with only PSSs and no WADCs. Curves 3 and 4 are the angle differences $\delta_{14}(t)$ and $\delta_{24}(t)$, respectively, when generators 1 and 2 are equipped with WADCs without time delay. The WADCs use a conventional proportional control strategy. Fig. 4 indicates that the WADC can obtain a good control effect without time delay when a conventional proportional control strategy is applied. In this condition, the input of WADC is $K\omega_{ij}(t)$, which indicates that the WADC's output v_{w1} is essentially in phase with its input $\omega_{14}(t)$ while v_{w2} is essentially in phase with $\omega_{24}(t)$. Thus, when

the input of the FWADC is $\omega_{ij}(t-T_d)$, the FLC must have the ability to compensate for time delay so that the FLC's output u is in phase with $\omega_{ij}(t)$ to achieve a control effect as good as that without time delay.

Fig. 5 is used to demonstrate the method of determining fuzzy rules [5]. Curve 1 in Fig. 5 is $\omega_{14}(t)$ when only the PSS is applied. Curve 2 is $\omega_{14}(t-0.3)$, and curve 3 is $\dot{\omega}_{14}(t-0.3)$.

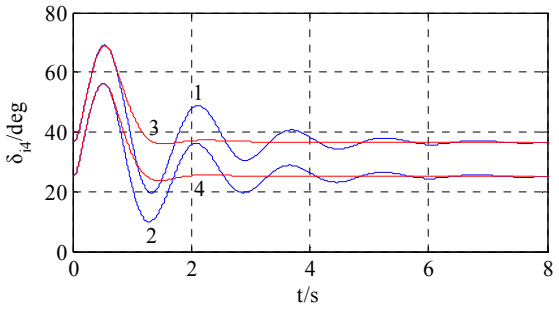

Fig. 4 Curves of rotor angles for T_d=0 s

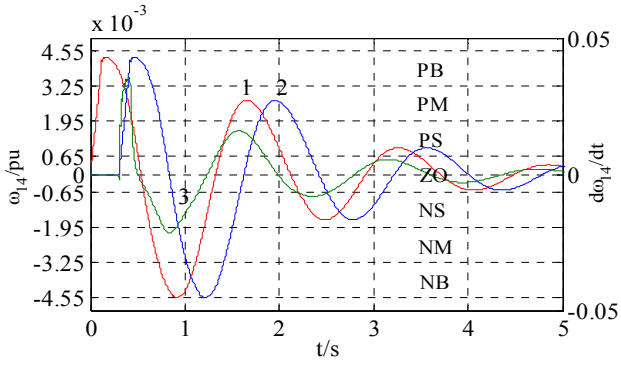

Fig. 5 Determination of fuzzy rules

The universe of fuzzy input and output variables e and u includes seven fuzzy subsets: NB (negative big), NM (negative medium), NS (negative small), ZO (zero), PS (positive small), PM (positive medium) and PB (positive big). The universe of fuzzy input variable ec includes two fuzzy subsets: N (negative) and P (positive).

The fuzzy input and output variables select a triangular function as their membership function. The membership functions of fuzzy input variable e and output variable u are provided in Fig. 6. The membership function of fuzzy input variable ec is presented in Fig. 7.

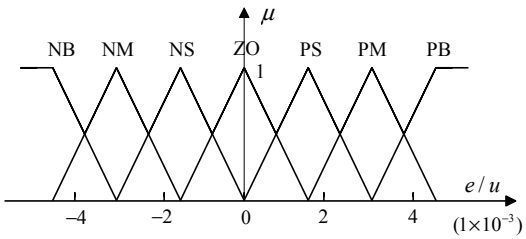

Fig. 6 Membership function of e and u

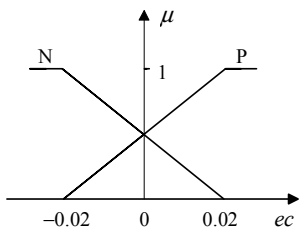

Fig. 7 Membership function of ec

For a four-machine two-area system, the objective of determining fuzzy rules is to ensure that the FLC's input u is in phase with $\omega_{ij}(t)$. The fuzzy rules for generator 1 at T_d=0.3 s are provided in table 1.

Table 1 Fuzzy rules of generator G1

u		e						
		NB	NM	NS	ZO	PS	PM	PB
ec	N	NB	NB	NB	NM	NB	NM	NS
	P	PS	NS	PM	PM	PM	PM	PM

Simulation analysis

The four-machine two-area power system is tested to analyze the performance of the FWADC.

The appropriate universe of variables is determined according to Fig. 5. The universe of input variable e and output variable u is [-0.00455, 0.00455], and the universe of input variable ec is [-0.02, 0.02].

The time delay is approximately 0.1 s for a fiber-optic link [7]. As for the small time-delay, the designed FWADC in this report can easily achieve a good performance. Thus, the details are ignored at T_d=0.1 s.

The time delay is approximately 0.3 s for a telephone link [7]. The fuzzy rules at T_d=0.3 s are provided in Table 1. Details of the FLC are set based on the analysis above. The four-machine two-area power system is simulated, and the results are provided in Figs. 8 and 9.

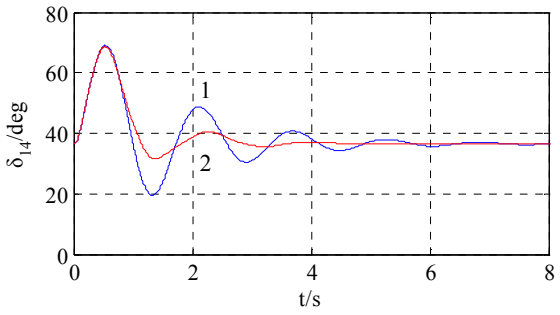

Fig. 8 Curves of rotor angle δ_{14} for T_d=0.3 s

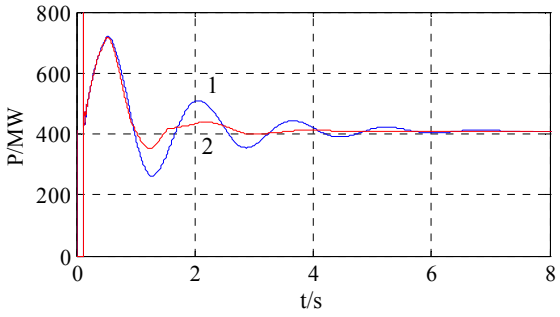

Fig. 9 Tie-line power for T_d=0.3 s

Curve 1 in Figs. 8 and 9 shows the simulation results with PSS and without WADC. Curve 2 in Fig. 8 and Fig. 9 is the results with FWADCs equipped in generators 1 and 2 at T_d=0.3 s. The two figures indicate that the designed FWADC can clearly improve power system damping.

Conclusion

In this report, the communication delay of the WAMS is considered, and fuzzy control is applied to compensate for the delay. The process of determining the universe of fuzzy sets, membership functions and fuzzy rules are analyzed. A simulation of the four-machine two-area power system indicates that the presented method can suppress the adverse effects of time delay, enhance interconnected power system damping and restrain low frequency oscillations.

Acknowledgements

This study was financially supported by the National Natural Science Foundation of China (51177074).

References

[1] J. Liu, H. Wu, J. Zhu: Power Engineering and Automation Conference Vol. 1 (2011), p.315.

[2] H. Wu, D. Wu, Q. Wang, X. Li: International Conference on Sustainable Power Generation and Supply Vol. 1(2009), p.1.

[3] J. Ma, T. Wang, Z. Wang, J. S. Thorp: IEEE Trans. on Power Systems Vol. 28 (2013), p.1627.

[4] J. Bo, C. Lu, X. Jin, P. Li: IEEE Asia Pacific Conference on Circuits and Systems Vol. 1 (2008), p.758.

[5] M. Mokhtari，F. Aminifar，D. Nazarpour，S. Golshannavaz: IEEE Trans. on Power Systems Vol. 28(2013), p.1997.

[6] P. Kundur: *Power system stability and control* (McGraw-Hill Education Company, New York 1994).

[7] B. Naduvathuparambil, M. Valenti, A. Feliachi: Proceedings of the Thirty-Fourth Southeastern Symposium on System Theory Vol. 1(2002), p.118.

Advanced Materials Research Vols. 960-961 (2014) pp 964-968

doi:10.4028/www.scientific.net/AMR.960-961.964

Distribution Network Planning Based on Multi-island Group Strategy Genetic Algorithm

Siqing Sheng[1, a], Shaobo Yang[2,b]

[1] North China Electric Power University, Baoding 071003, Hebe Province, China

[2] North China Electric Power University, Baoding 071003, Hebe Province, China

[a]hdbdssq@163.com, [b]yangshaobobdhd@163.com

Keywords: Distribution network; Genetic Algorithm; Yearly comprehensive costs; Multi-island group strategy

Abstract: In view of faults which the traditional genetic algorithm (GA) have such as slow convergence speed and easy to fall into the local optimum. This paper put forward a genetic algorithm which is based on the multi-island group strategy, and applied it to the distribution network planning. The paper has established a planning model which takes the yearly comprehensive cost as objective function and discusses the repair methods of islands, solitary chain and closed-loop to meet with the requirements of grid radial. Finally, the proposed method is planning on a 54-node grid to prove the effectiveness of the algorithm and model.

Introduction

Distribution network planning is based on the existing network structure, power distribution network planning and load forecasting, according to the existing power grid structure and the economic development, to make the working economy of the power distribution network to achieve the optimal, and to have a higher quality of power supply and power supply reliability by reasonably choosing new circuits such as transformer and other electric equipment[1].

With the increasing of the distribution network scale, using the traditional mathematical programming method to solve the distribution network planning problem is becoming harder and harder. Therefore, a large number of intelligent algorithms have sprung up in recent years including genetic algorithm [1], the ant colony algorithm[2], the tabu search algorithm[3], etc. The ant colony algorithm[2]determine the upward node of each new node by transition probability, but you must generate new expression if you want to add new options factors in the transformation probability, which will heavily affect the stability of the planning results and are not suitable for flexible application. The tabu search algorithm[3]often lead to phenomenon of coding too long and the planning result change along with experience, which will lead to low optimization efficiency . The genetic algorithm has considered the nonlinear characteristic of the optimization problem and the discontinuous characteristics of the constraint and can provide multiple sets of optimization solutions, which are more suitable for solving the distribution network planning problem.

This paper established a model of distribution network planning which take the minimum comprehensive yearly cost as the objective function and adopt the genetic algorithm (GA) based on the multi-island group strategy to solve the model. Then through comparing with the mode only considers the initial investment and other algorithms, the paper uses a 54-node case to have proved the effectiveness of the model established in this paper.

The mathematical model of distribution network planning

The objective function. The distribution network planning model in this paper take minimum yearly comprehensive cost of the power grid as the objective function [4], namely

$$\min f(X) = \sum_{i=1}^{n} (C_{1i} T_i x_i + C_{2i} \tau_{\max i} \Delta P_i) \tag{1}$$

where f(X) represents yearly comprehensive cost of power grid and n represents the number of the erection line; $C_{1i}=\gamma_i+\alpha_i$， γ_i is the return on investment, and αi is the depreciation maintenance fee of equipment; T_i is the cost of new branch *i* cost (yuan). As n decision variables, X=(x1,x2,...,xn) on behalf optional *n* lines in the distribution network planning problem and when i are being built, xi takes 1, otherwise xi takes 0 ; C_{2i} represents the unit electricity price (yuan/kWh) ; τ_{maxi} is the maximum load availability hours(h),ΔP_i is the active power loss of the branch(kW);C_{1i}Tixi is the investment cost of the grid.$C_{2i}\tau_{maxi}\Delta P_i$ is the the cost of power grid loss。

The constraints. Line constraints:

1) power balance constraint

$$\sum P_{ij} = P_{Gi} - P_{Di} (i, j \in N) \tag{2}$$

2) power flow constraint

$$-P_i^{\min} \le P_i \le P_i^{\max}, i \in m + m_0 \tag{3}$$

3) number constraint of Line corridors that allow to wire

$$0 \le x_i \le x_i^{\max}, x \in Z, i \in m \tag{4}$$

Spatial constraint:

1) all the nodes have power supply

2) the ring network is not allowed

Genetic algorithm on the base of multi-island group strategy.

The basic principle of multi-island group strategy. This paper scatter all creatures participating in the evolution in two island groups. Individuals in one island group evolution by the mutation strategy same with traditional genetic algorithm, which is known as gentle island group D_m. The mutation rate threshold of individuals on another island group can be changed dynamically to simulate that the natural environment as a whole is rapidly changing, and this island group is called turbulent island group D_n. Principle of double island swarm is shown in Figure 1.

In order to reserve the optimal solution during evolution of the species, the improved algorithm has taken elitist strategy, where elite individuals from the two island groups will be compared each generation and the best h species will be selected to save in another island group, called elite island group D_h. The individuals in D_h are saved to replace h individuals which have the worst fitness value in the two island groups D_m and D_n in the next generation. Individuals in elite island group have without crossover and mutation, and the island is only used to retain the elite individuals in the other two island groups and to make mutual transmission.

The maximum variation rate setting mode. (1)When aggregation phenomena appears among better solutions, the mutation rate increases.
(2) when the number of the elite individuals in D_n transfer to D_h increases, the mutation rate should reduce.

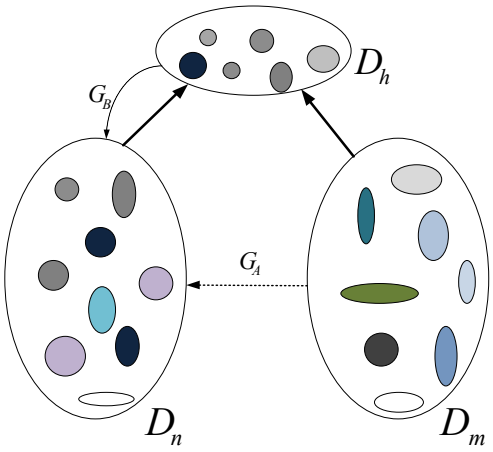

Fig.1 Principle of multi-island algorithm

Combined with the principles above, the largest mutation rate formula is as follows:

$$P'_{m\max} = P_m + \alpha_1 G_A + \alpha_2 G_B \tag{5}$$

Where Pm is the original mutation rate of turbulent island group and α_1,α_2 is the clustering coefficient and strength coefficient, characterizing the influence of aggregation phenomenon in D*m* and the increase of elite individuals in D_n to the variation rate. G_A and G_B are variables which are expressed by 0 and 1 corresponding to the phenomena of aggregation in D_m and the increase of the individual number D_n transferring to D_h.

Network repair program

For the three kinds of problems generates in initialization and genetic operation, namely solitary chain and ring network[5], The repair plan is as follows.

Solitary chain repair. Solitary chain refers to that two or more load nodes connect to each other (it may constitute a loop), but there's no pathway between any node and the power supply, causing the solitary chain can't electricity. Repair method: select any one line to be built that connect load node in solitary chain and the powered grid, so that the entire solitary chain are supplied with power.

Ring repair. When a series of load nodes are linked end to end, a closed-loop is formed, which will bring great inconvenience to the power flow calculation of radial distribution. Repair method is as follows: disconnecting a feeder in a closed network loop, or a feeder that connects pairwise multiple power make each network a radiation network supplied with single power.

Island restoration. A load node without power supply in distribution network is called island. The repair of Island is similar to the method of island chain, the only difference is that every load node must be connected with a network that has been supplied with power by a feeder to get power in Island repair[6].

Cases analysis

The initial network frame and its parameters .The initial network frame is shown in figure 2. The solid line shows the existing network and node, and the dotted line is the extend node network.

The case results and analysis. After the analysis of distribution network planning by improved genetic calculation, the yearly minimum comprehensive cost scheme is shown in figure 3:

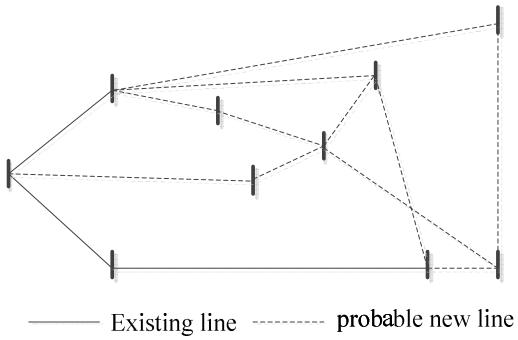

Fig.2 Initial network frame diagram

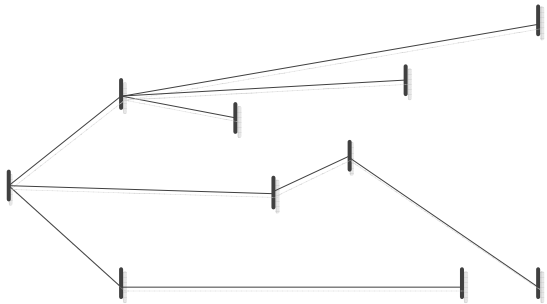

Fig.3 The yearly minimum comprehensive cost solution circuit diagram

The specific circuit connection and circuit parameters of the optimal scheme is shown in the following table 1.

By the data available in the table2, the initial investment of the initial investment model is smaller than that of the yearly comprehensive cost model, but the yearly running cost of the former are much higher than that of the latter, and clearly the final total cost of the model in this paper is much less, which fully shows the advantage of the model in this paper.

Tab.1 Year minimum comprehensive cost

Sending node	Receiving node	R[Ω]	X[Ω]	Active of Sending node[MV]	Active of receiving node [Mvar]
0	1	0.246	0.463	1.20	0.90
1	2	0.898	0.931	1.50	1.13
2	5	0.633	0.515	1.20	0.90
2	8	0.422	0.333	0.50	0.38
2	4	0.868	0.760	0.40	0.30
5	6	0.456	0.354	0.75	0.55
4	3	0.726	0.613	0.60	0.45
4	9	0.112	0.150	0.55	0.41
6	7	0.754	0.556	0.80	0.60

Tab.2 Comparison of two kinds of model

Cost model	Initial investment [wanyuan]	Operation cost [wanyuan]	Yearly Comprehensive cost [wanyuan]
model in this paper	10.05	33.42	43.47
the initial investment model	7.81	56.44	64.25

In this paper, the minimum comprehensive cost model has considered the initial investment and the yearly operation cost, the following table is the comparison of case result of the model in this paper and the model only considering the initial investment.

In this paper, a standard Ackley is used to compare the improved genetic algorithm, traditional genetic algorithm and particle swarm optimization (PSO). The comparison result shown in Fig.4 shows that the convergence speed of improved genetic algorithm is more quickly and search capability is stronger.

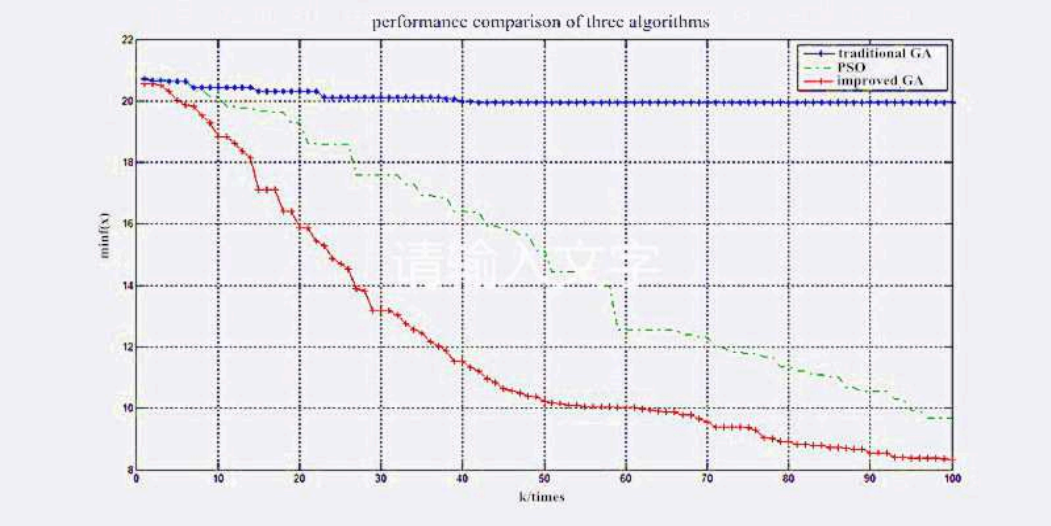

Fig.4 Performance comparison of three algorithms

Conclusions

This paper has established a distribution network planning model which takes the comprehensive annual cost as the objective function and has applied the improved genetic algorithm to solve the model. The multi-island group strategy has been proposed in this paper many islands strategy, which can automatically adjust the evolution strategy by the dynamic change of variable rate threshold. Compared to the traditional algorithm, the improved genetic algorithm has faster convergence speed and stronger optimization ability. Compared to the distribution network planning model only considering the initial investment cost, the optimal scheme under the model put forward in this paper has less operation cost and lower yearly comprehensive cost.

References

[1] Wang Jikui. Chaos genetic hybrid algorithm in the application in power distribution network reconfiguration. Shanxi Electric Power,2012,5:5-7(in Chinese)

[2] Xu He,Li Xin,Wang Hai,Yang Na,Hong Jingya. Distribution network planning based on the improved genetic algorithm.Guangdong Electric Power,2010,23(6):6-9(in Chinese)

[3] Wang Lei,Gu Jie. Medium voltage distribution network optimal planning based on the improved genetic algorithm. Relay,2006,34(7):43-50(in Chinese)

[4] Ni Qiulong, Huang Minxiang. The simulated annealing algorithm based on branch exchange in the application of the power distribution network planning. Power System Technology,2000, 12(4):31-35(in Chinese)

[5] Chen Genjun, Wang Lei,Tang Guoqing. The optimal method of distribution network planning based on ant colony. Power System Technology,2003,27(3):71-75(in Chinese)

[6] Kang Qingping, Zhou Lei. A practical method of power network planning. Power System Technology,1996,18(6):39-43(in Chinese)

Advanced Materials Research Vols. 960-961 (2014) pp 969-973

doi:10.4028/www.scientific.net/AMR.960-961.969

Experimental Investigation of Static Load Characteristics

Tavlintsev Alexander[1, a], Pazderin Andrey[2,b] , Suvorov Anton[3,c] ,
Chusovitin Pavel[4,d] , Malozemova Olga[5,e]

[1] 620002, 19 Mira street, Ekaterinburg, Russia

[a] winddaes@gmail.com, [b] AVPazderin@gmail.com, [c] saa@daes.ustu.ru, [d]pvchus@gmail.com, [e]malozemovao@yandex.ru

Keywords: Static Load Characteristics, Experiment, Derivatives, Analysis of voltage fluctuations.

Abstract. It is common practice to use 2nd order polynomial load model for steady-state power flow calculation. The paper describes the experiment for obtaining static load characteristics and the technique for identifying coefficients of the load model based on remote metering system data.

Introduction

There are two most common ways of load representation in mode calculation, namely, constant value of power and static load characteristics.

Presently, the first method is used more often, as obtaining of static load characteristics is a very complicated problem. This assumption is acceptable, but it can result in large error in some situations. Moreover, more accurate static load characteristics allow reducing error in power flows limited by stability conditions [1].

Large load nodes consist of different consumer types. Different consumer types have various static load characteristics. It is usual practice to use 2nd order polynomial as model, because $P(U)$ and $Q(U)$ dependences of the most widespread consumer types is closed to quadratic dependences:

$$Q(U) = Q_n(x)\left(a_0 + a_1\frac{U}{U_r} + a_2\left(\frac{U}{U_r}\right)^2\right). \quad (1)$$

Generalized static load characteristics can only be obtained by experiments: load supply conditions are changed, and then corresponding power changes are fixed. The main power system parameters affecting the load power are frequency and voltage. Frequency fluctuations are negligible, therefore static load voltage characteristics will be referred to as simply static load characteristics.

The problem is that static load characteristics can be obtained if load structure is constant. It means that technical process intervention in power changes should be excluded. However, it is connected with technical complexity and quite often, it is impossible to conduct such experiment. Therefore special algorithms of experiment conducting and data processing should be developed.

Automated electrical systems department of the Ural Federal University has been working on the problem in recent years. As a part of the study, some methods of characteristics definition based on measurement data were developed.

For the purpose of testing developed methods, some experiments were conducted in the node of Russia power system. The task was to obtain static load characteristics for two large enterprises. Data obtained as a part of the experiment were processed by means of developed methods.

Preparation to the experiment

Firstly, a number of steady modes were calculated based on the network diagram. This diagram is shown below. It consists of two power plants (power plant 1, power plant 2) and three substations (substation 1, substation 2 and substation 3).

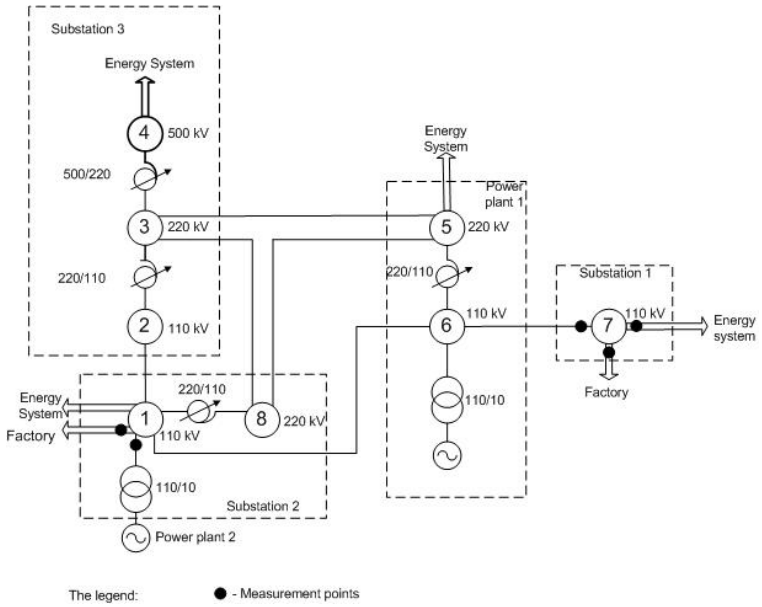

Figure 1 Scheme of investigating node

As a part of calculation results analysis, it was founded that the desired range of voltage fluctuation can be reached using following regulating means: excitation system of synchronous generator in power plant 1, excitation system of synchronous generator in power plant 2, tap-changer of 500/220 kV autotransformer in 500 kV neighboring substation, static capacitor bank 110 kV in neighboring substation.

The Experiment

The Experiment involved sequential voltage changes on the 110 kV buses of substation 1 and 110 kV buses of the substation 2 by regulating means mentioned above.

Due to a great number of measuring points and lack of opportunity to connect directly to the substation current circuits, telemetering data were used.

Voltage changes were the following:

$$U_r \to U_{\max} \to U_r \to U_{\min} \to U_r . \quad (2)$$

Voltage changing step in regulation points should be more than quantum of telemetering, it has been achieved by step size more than 0,5-1 kV. Retracing of control voltage values is necessary to identify opportunity of using the data by means of rapid assessment (fig.2).

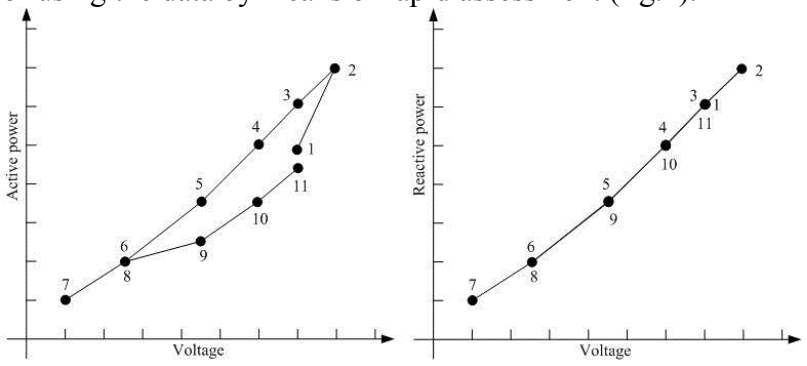

Figure 2 Active and reactive power as a function of voltage. Numbering corresponds to the order of measurements.

Significant load changing could happen for reasons beyond the control. Rapid assessment identifies whether the change was significant. Load changing can be concerned as significant, if the difference between total capacity in the beginning of experiment (point 1, fig. 2) and in the end (point 11, fig. 2) is more than 10 %. In this case, experiment should be repeated. If dispersion of experimental data is negligible, then obtained arrays of voltage, active and reactive power are handled by developed methods.

The maximum voltage value on 110 kV bus was 124 kV, the minimum voltage value was 106 kV. However, actual range was less.

As a part of experiment, it was obtained: values of active and reactive power of incoming line, voltage values of upper (110 kV) and low (10 kV) voltage buses, values of active and reactive power of outgoing lines.

Dynamics of the controlled mode parameters (voltage and active power) on the upper voltage buses is pictured on fig. 3-4.

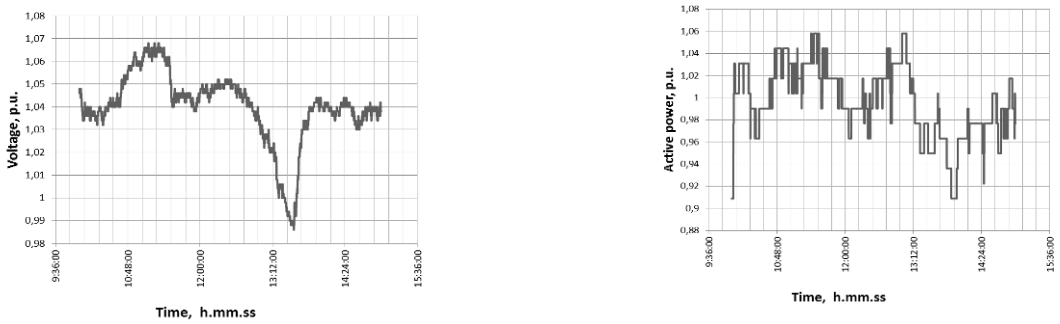

Figure 3 Dynamics of the controlled mode parameters (voltage and active power)

Experimental voltage-power dependence is shown on figure 4.

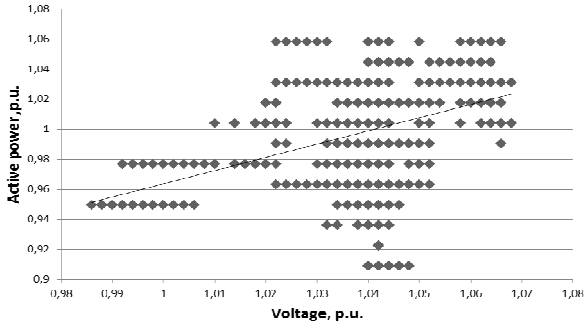

Figure 4 Experimental dependance active power to voltage

It is clear from the picture that one value of voltage corresponds to different values of active power. It means that changes of customer's load have occurred during the experiment. Also other factors could have an influence on the voltage, such as an error of measurement tools, quantization error and so on.

The analysis shows that experimental data should be pretreated with the purpose of elimination of the technological process effect. Arrays of voltage, active and reactive power for each low voltage bus system are initial data.

Data processing

Data processing was carried out by three methods: based on investigation of derivatives, based on the analysis of voltage fluctuations on the adjacent buses, based on the computational simulation experiment.

Method based on investigation of derivatives. The technique is to find the slope of the polynomial curve. At the first stage, a small interval, for instance 10 points, is adopted. As power and voltage increments are small, then it is possible to equate the ratio of the power increment to voltage increment and slope of the tangent. Thus, the slope of the tangent can be determined as derivative of polynomial Eq.1:

$$\tan\varphi = a_1 + 2a_2 U'_{p.u.}, \quad (3)$$

where $\tan\varphi$ - slope of the tangent

$U'_{p.u.}$ -average voltage in the interval

a_1, a_2 –coefficients of polynomial.

On the other hand, taking into account small of increments:

$$\tan\varphi = \frac{P_1 - P_2}{U_1 - U_2}, \tag{4}$$

where P_1 and P_2 are maximum and minimum values of the power respectively, in the time interval under study.

Then the interval is moved by one point and calculation is repeated. There can be runouts in the experimental data, therefore some filtration algorithms should be used.

As a result, overdetermined system will be obtained:

$$\begin{cases} a_1 + 2a_2 U'_{p.u.}(1) = (\tan\varphi)_1 \\ < \ldots > \\ a_1 + 2a_2 U'_{p.u.}(m) = (\tan\varphi)_m \end{cases}, \tag{5}$$

where m- the number of equations after filtering.

In matrix form, Eq.5 can be written according to the Eq.6:

$$\overline{U}\,\overline{A} = \overline{T},$$

$$\overline{U} = \begin{pmatrix} 1 & 2U'_{p.u.}(1) \\ < \ldots > & < \ldots > \\ 1 & 2U'_{p.u.}(m) \end{pmatrix}; \tag{6}$$

$$\overline{A} = \begin{pmatrix} a_1 \\ a_2 \end{pmatrix}; \overline{T} = \begin{pmatrix} (\tan\phi)_1 \\ < \ldots > \\ (\tan\phi)_m \end{pmatrix}.$$

The system solution by means of the least square methods can be represented as:

$$\overline{A} = \left[\overline{U}^T \overline{U}\right]^{-1} \overline{U}^T \overline{T}. \tag{7}$$

Coefficient a_0 can be founded from relation:

$$a_0 = 1 - a_1 - a_2. \tag{8}$$

Method based on the computational simulation experiment. The method is based on mathematical models, which include separate electrical receivers in the form of different equivalent electrical circuits. Also the method relies on the systems of equations which describe the behavior of an object in steady states.

Model is compiled in the software, and then a series of calculations of steady states is made. Polynomial coefficients are indicated using the method of the least squares.

The features of this method are:

- the absence of necessity in full scale tests;
- the inaccuracy of the statistical characteristics of loads depends on the degree of the mathematical model specification and adopted assumptions. The structure of the model and the typology of the analytical scheme also depend on structure, quality and availability of input data on the object of study.

Method based on the analysis of voltage fluctuations on the adjacent buses . This method as well as the method based on investigation of derivative deals with telemetry data.

The basic idea of this method is the following: each of the low voltage bus section is connected with high voltage buses, which are joined by a parallel job. During voltage changes on the high voltage bus, the voltage and load changes on one bus section will have the same direction as the voltage and load changes on another. Consequently, if we consider the two bus sections and take only the points where the voltage and power of both sections are changed in the same direction. Then on the remaining points static load characteristics can be obtained by method of the least square method.

These methods are described in [2].

The results are shown on fig.7.

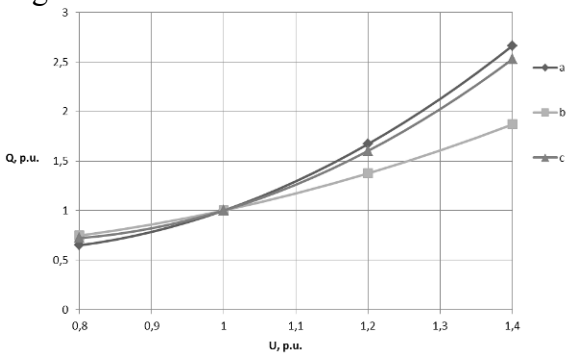

Figure 7. Static load model for the industrial factory

a- Method based on the investigation of derivatives;
b- Method based on the computational simulation experiment;
c- Method based on the analysis of voltage fluctuations on the adjacent bus

As it can be seen, the obtained curves are quite close to each other in the range around nominal value. Hence it can be assumed that the proposed algorithm identifies coefficients of static characteristics of the load voltage with sufficiently low inaccuracy.

It should be noted, that data were obtained around nominal value, therefore it is impossible to accurately determine static load characterisics for low and high values. To solve this problem practical data should be obtained for a wider range of values. But it is impossible to conduct this experiment for technical reasons.

Summary

Method based on computational simulation experiment is effective, but rather time-consuming. Method based on investigation of derivatives and method based on the analysis of voltage fluctuations are rather low work content. Moreover the last method can be used for automated analysis of static characteristics of major load centers.

It should be noted that characteristics obtained by three methods are rather close to each other.

References

[1] A.V. Pazderin, A.A. Suvorov, A.S. Tavlintsev, P.V. Chusovitin, A.V. Yudin. Identifiication of the static characteristics of large load centers. Scientific Review # 7, 2013, ISSN: 1815-4972.

[2] A.Tavlincev, A.Pazderin, P.Chusovitin, O.Malozemova.Identification of Static Polynomial Load Model Based on Remote Metering Systems Information. 13th International Conference on Environment and Electrical Engineering, EEEIC'13, Wroclaw, Poland, 1-3 november, 2013. ISBN 978-1-4799-2802-6. CFP1353W-CDR.

[3] A.A. Rahim, M.F. Hashim, M.F.M.Siam. Load model derivation based on load response to actual disturbances in Malaysia power system, 5th IASTED Asian Conference on Power and Energy Systems, AsiaPES 2012; Phuket; Thailand; 2 April 2012 through 4 April 2012; Code 90023 Pages 128-133

[4] A.I.Khalyasmaa, S.A. Dmitriev, S.A. Eroshenko. Membership functions for the formation of the electrical equipment state estimation for power stations and substations. ICAEES 2013; Guangzhou; China; Code 100428.

Advanced Materials Research Vols. 960-961 (2014) pp 974-977

doi:10.4028/www.scientific.net/AMR.960-961.974

Research and Application of Medium-speed Pulverizer Control Based on AGC Mode

Jun Li[1, a], Weiwei Li[2,b] ,Huicong Li[3,c]

[1]Shandong Electric Power Research Institute, Jinan 250002, China

[2]Network Center, Shandong University of Arts, Jinan 250014, China

[3]Shandong Electric Power Corporation, Jinan 250001, China

[a]lijun_sdu@hotmail.com, [b]liweiwei@sdca.edu.cn, [c]lhc_111@163.com

Keywords: medium-speed pulverizer, large delay, AGC, energy saving and consumption reducing

Abstract. Large delay is the main characteristics of medium-speed pulverizer system which used in subcritical and supercritical unit. By introducing and analyzing the operating principle and working process, considering energy saving and consumption reducing, and combined with the performance requirement of AGC (Automatic Generation control), recommend solutions were put forward. It can effectively solve AGC control problems of load and pressure control accuracy and ensure frequency stability of the grid, provide a reference for similar units.

Introduction

Power grid frequency is one important indicators of power quality, it reflects the balance between the generation of active power and actual electricity usage, and it is an important control parameter of the power system operation. Currently, frequency compensation is mainly used for thermal power.

The safety and efficiency of the majority of users of electrical equipment and power equipment have a close relationship with power grid frequency. Equipment of users is generally driven by the motor, the same as equipment of power plant. The frequency fluctuation has a critical influence over them. With the development of science and technology, some new electronic equipment and precision processing equipment put forward higher request to power grid frequency, the frequency fluctuations will lead to lower product quality or equipment damage. According to the IEEE 446-1995 standard and BS EN50160:1995 standard, ±0.5Hz is the maximum tolerance of the frequency fluctuations of many devices. The occurrence of unexpected failures in the power grid will break the balance between the generation of active power and load. With the development of the power system, single device failures bring a growing loss of generating power grid. Only relying on manually adjust the power generation output will require a longer time to achieve a new balance. Solve these problems, the way is only one that is the techniques of primary frequency compensation and automatic generation control (AGC, the equivalent of secondary FC). It's a good idea to use different logical controls according to its own regulation performance, to maintain the balance of power system supply and demand automatically, thus ensuring the quality of the power system frequency.

To meet the power requirements of power quality and according to the latest standards, unit power and pressure control has been redesigned and verification. Especially, the large delay problem of widely used medium-speed pulverizer system has been analyzed and proposed effective solutions.

Status of AGC Control

Traditional AGC in the power plant control structure is shown as Fig.1. The standalone AGC commands from energy manage system(EMS) will be sent to remote terminal unit(RTU) of power plant side, then by the RTU via I/O hard-wired to send to unit coordinated control system (CCS), to complete the adjustment task of unit's AGC system.

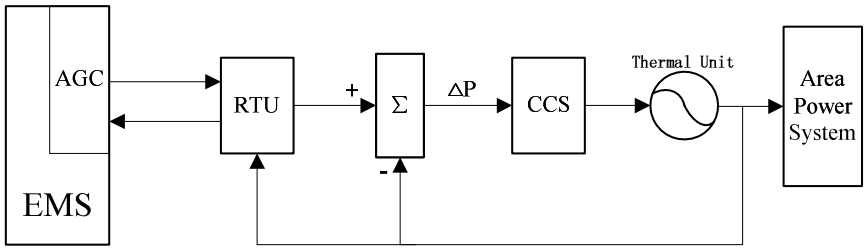

Fig.1. Dispatch center control schematic diagram of a single thermal power unit

According to the rules of Dispatch center, the operation of AGC must to be run in accordance with the scheduling curve, it put forward higher requirements on control system of the unit. The full load of power generation is the test of the device; the variable load is the test of the whole control system. How to on the basis of existing equipment, optimize the control strategy, realize the load control requirements, and ensure stable operation of the unit, is a problem that must be considered.

Adjustment rate, adjustment accuracy and response time is three main criteria of AGC assessment. As shown in Fig.2, it is a set point control process of a typical AGC unit. $P_{\min,i}$ is the lower limit of the unit adjustable output, $P_{\max,i}$ is the upper limit of its adjustable output, P_{Ni} is its rated output, P_{di} is a critical power point of its start and stop grinding. The whole process can be described as, T0 time ago, the unit work stably near the output P1. T0 time, AGC control program sent power command P2 to unit, the unit start up. To the time T1, unit reliable across the P1 adjustment dead zone, and to the T2 time, unit work into the rev grinding range. Until T3 moment, the rev grinding process is over; the unit continues to raise its power. To T4 time, unit first time work into the dead zone adjustment range, then near P2 unit adjust slightly and has a stable value. Until T5 time, AGC control program sent a new unit set point command, the power is P3, unit began to a new work.

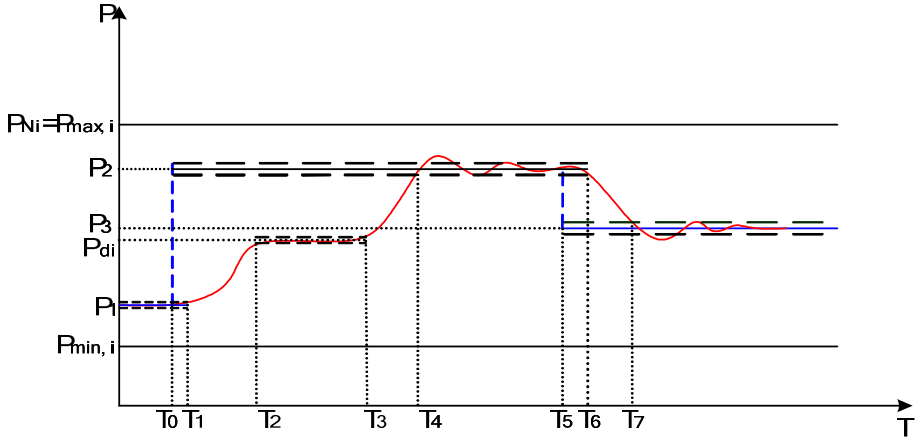

Fig.2. Typical AGC unit set point control process

Adjustment rate. According to the requirement of Dispatch center, In general, the rate of Pulverizing System and drum boiler unit is 1.5% of unit's rated active power, thermal power units with intermediate storage pulverizing system is 2% of unit's rated active power, circulating fluidized bed coal-fired units is 1%, supercritical once-through boiler unit is 1.0%.

Adjustment accuracy. It is the difference between the actual output of unit and the set point of EMS when unit work stably after a response, permissible deviation is 1% of unit's rated active power.

Response time. Response time refers to, after the EMS system send commands, on the basis of the original output point, the time that the output of generating unit reliably adjust to across adjusting dead zone to need. AGC response time of thermal power unit should be less than 1 minute.

Characteristics and Main Problems of Coal Pulverizing System

300MW and more than 300MW units mostly used pulverizer system. For example, the work process of medium-speed pulverizer system is as follows, boiler demand to be sent to coal feeder, the coal from the coal bucket conveyor to the mill and the mill to be ground into the pulverized coal. The

advantage is that the system is simple, less equipment, coal is no intermediate stop, air temperature is not too high, dangerous explosion is appear rarely. But, there are two main disadvantages. One is output required to run the mill with the boiler load change, therefore, can not run often in economic output. Two, when the boiler load changes need to adjust the amount of coal by coal feeder, so time delay is bigger.

Main control way of system is to guarantee to the amount of coal following the changes of coal feed rate command, to adjust the hot primary air damper opening control changes in the total amount of wind followed by the amount of fuel command (after line correction), to adjust the cold primary air damper opening degree control the export of wind mill flour mixture temperature is maintained constant.

Main Problems. For pulverizing system in the AGC mode, when the change range of load is small, generally does not need to start and stop coal mill, but when the load changes is in a wide range, it need to start and stop coal mill. In the process of start and stop coal mill, there are a series of operations and it will take some time. It will cause to fluctuations of coal, wind and first pressure. Sometimes it needs to change the load to absorb energy imbalance between the turbine and boiler, cause the unit's load fluctuation, and affect AGC adjustment control accuracy. Quality of coal drastically change sometimes make the tuned parameters not adapt to the control system, must to be adjusted again.

Solution Design and Effect

For example, 600MW supercritical unit are typically designed to six sets of pulverizing system, five sets is running and one is set aside. To solve the fluctuation problem of the mill start and stop process, we need to take a test to achieve the pure delay time of A, B, C, D, E and F pulverizer system. Because the analysis conclusion we have achieved that in the initial amount of coal pulverizing system starts with the load response is pure delay, there is the step response from the balance; therefore, we design a linear correction function according to the initial coal to solve the problem. When the system start with an initial amount of coal, the automatic coal pulverizing system remained coal unchanged in the pure delay time. After the delay time, when the initial amount of coal began to affect the heat load on the boiler, the effective amount of coal began to calculate according to the coal correction function. By taking this strategy, volatility problems of pressure and load when the mill systems start and stop are eliminated.

To improve the response speed of the load, the dynamic process air must be allowed to overshoot. For enhancing the air of feedforward action, a load variation feedforward signal is introduced into the air volume control circuit of primary air fan (PAF). It can make full use of the coal in the powder storage when unit need to quickly response to load and the boiler combustion rate change quickly, and shorten the boiler pure delay time. Block diagram is shown in Fig.3, generate a function curve F(x) of PAF setpoint pressure based on the actual load of the unit and adjust the pressure setting in real time. Meanwhile, by increasing the feedforward correction amount to PAF pressure, can shorten the delay time of 1.5-2.5 min, and can improve the AGC generator response speed.

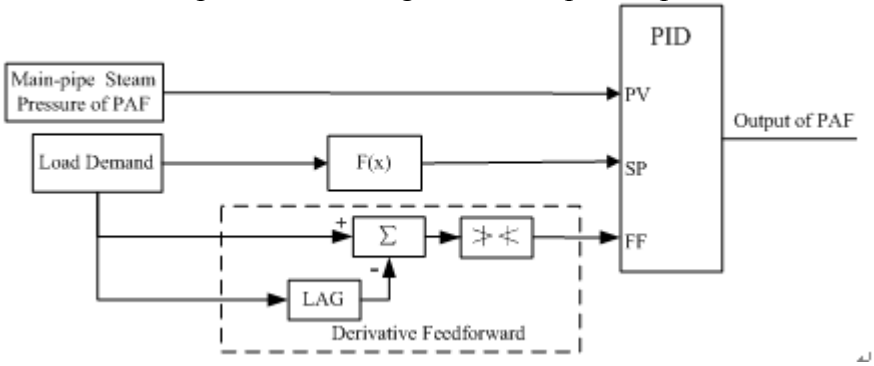

Fig.3. Block diagram of primary air fan control

In other words, the regulation of PAF is similar to the regulation of force draft fan (FDF), following up the principle that wind is to be increased before coal when unit's load is in growth stage and wind is to be reduced after coal when unit's load is in falling stage, so, due to the change of PAF pressure and air volume, we can take advantage of pulverized coal inside pulverizers to accelerate the response speed of load and shorten the boiler delays.

It was applied to a 600MW medium-speed pulverizer unit, when the load demand changes, the regulation of PAF will produce a dynamic differential feedforward output to accelerate the unit response speed in AGC mode. As Fig.3 shown, we can clearly see that the actual power tracking AGC demand in good condition, with an average deviation of less than 0.7MW.

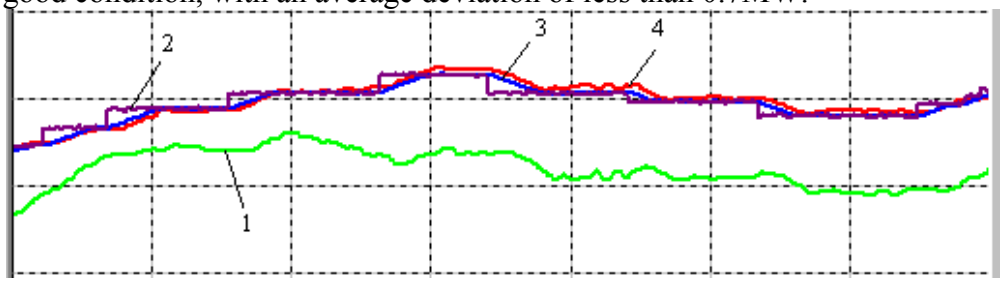

1-output of PAF, 2-AGC demand, 3-Rated load demand, 4-unit load

Fig.4. Load control curve of AGC mode

Conclusions

By analyzing the large delay of medium-speed pulverizer system which used in the thermal power unit, considering energy saving and consumption reducing, and combined with the performance requirement of AGC, recommend solutions were put forward. The practical application results show that it can effectively solve AGC control problems of load and pressure control accuracy, ensure frequency stability of the grid and the economic benefits of units can be further improved, provide a reference for similar units.

References

[1] Sigurd Skogestad. Simple analytic rules for model reduction and PID controller tuning. Journal of Process Control 13(2003)291-309.

[2] Svante, B., & Ljung, L, A survey and comparison of time-delay estimation methods in linear systems, Proc. of the 42nd IEEE Conf. Decision and Control, 2003, pp. 2502-2507.

[3] M. Zhuang, D.P. Atherton, Automatic tuning of optimum PID controllers, IEE ProcD, 140, 1993, pp. 216-224.

[4] Antonio Visioli, A new design for a PID plus feedforward controller, Journal of Process Control, 14, 2004, pp. 457-463.

[5] F.Shinskey, Process Control Systems Application Design Adjustment, McGraw-Hill, New York, 1996.

[6] D.R.Coyghanowr, Process Systems Analysis and Control, McGraw-Hill, New York, 1991.

[7] Silva, R.; Sbarbaro, D.; Barra, B.A.L. Closed-loop process identification under PI control: a time domain approach. Ind. Eng.Chem. Res. 2006, 45, 4671-4678.

[8] Lee, Y.; Lee, M.; Park, S.; Brosilow, C. PID controller tuning for desired closed-loop responses for SI/SO systems. AIChE J. 1998, 44(1), 106-115.

[9] Panda, R.C. Synthesis of PID tuning rule using the desired closed-loop response. Ind. Eng.Chem. Res. 2008, 47, 8684-8692.

Advanced Materials Research Vols. 960-961 (2014) pp 978-981

doi:10.4028/www.scientific.net/AMR.960-961.978

A Electronic Control Stirling engine Fuel Supply System Based on Real-time Operating System

Jianxin Liu[1, a], Dongwei Chen[1], Zhancheng Wang[1], Bin Xu[1]

[1]Vehicle&Traffic Engineering College, Henan University of Science and Technology, Luoyang 471003, China

[a]Ljx001@mail.haust.edu.cn

Keywords: uC_OS-II, Fuel Supply Systems, Electronic Control

Abstract. The uC_OS- II embedded real-time operation system is used to improve the original designed fuel supply system of a Stirling engine which governed by the electronic control system based on a rotating speed control method. Task modules for each level are built and the fail-safe modules are also improved in this paper. The developed fuel supply system is investigated through experiment, and test results show that the new real-time operating system works stably and realizes the fuel supply fast adjustment.

Introduction

Stirling engine is a piston engine of external heating (or combustion) which works by the way of a closed regenerative cycle, it uses gaseous as a working fluid [1]. Fuel injector of Stirling engine is continuously open, the accuracy and stability of the fuel injection quantity per unit time needs to be ensured in order to get a good atomization and combustion stability of the engine in various operating conditions.[2]. Conventional Stirling engine fuel electric control system changes the fuel supply by adjusting rack displacement of a high-pressure piston pump [3]. Here we provide a time-based speed regulator control mode, simulates and analyzes the pressure fluctuations under different operating rotation rate [4], proposes and implements some of the fail-safe control strategy [5]. But accompanied by the increase in fuel electric control system module, the control strategy is more complex. Continue to follow the traditional single-threaded, before desktop programming approach will lead to code complexity and increase development cycle, reduce the reliability and maintainability.

Based on the rotating speed control method, we design the fuel supply system module hardware, introduce the uC_OS-II embedded real-time operating system, and establish hierarchical modules according to the functional requirements of each task, carry out experiments under the control of real-time operating fuel supply system.

Establishment of experimental platforms

Platform structure. Stirling engine combustor fuel electric control system shall provide accurate, stable, continuous fuel, and can timely change depending on the engine air supply. Experimental platform built on uC_OS-II core embedded control systems. Fuel electric control system experimental platform is shown in Fig.1, including the fuel injection system based on rotating speed control method, uC_OS-II embedded control system (ECU), upper monitor (to send a signal of the required oil quantity to the ECU), acquisition and analysis system of output signal, analysis systems, mechanical connections and corresponding protection devices. The platform can achieve dynamic and static testing of various components and systems.

Main components of the platform. Experimental platform structures refer to the high pressure common rail diesel systems, using a three-phase rare earth permanent magnet AC servo motor system to drive the high-pressure pump to provide high-pressure fuel for the system, the high-pressure fuel is delivered to the injectors by accumulator regulator. Fuel injector is a swirl atomizing injector produced by the DELAVAN Company, with the pressure difference at both ends of the injectors, the fuel rotates high-speed in the vortex oil tract and ejects from the nozzle atomization.

The injection rate which is decided by the injection pressure determines the atomization quality of the nozzle [2]:

$$\text{Flow rate}=CA\,(2gh)^{0.5} \quad (1)$$

Among them: Flow rate is described as the injection rate(kg/s), C as the dimensionless coefficient of swirl atomizing nozzle, A as the nozzle area for swirl atomizing nozzle(m^2), g as the acceleration due to gravity, h as the pressure head(m).

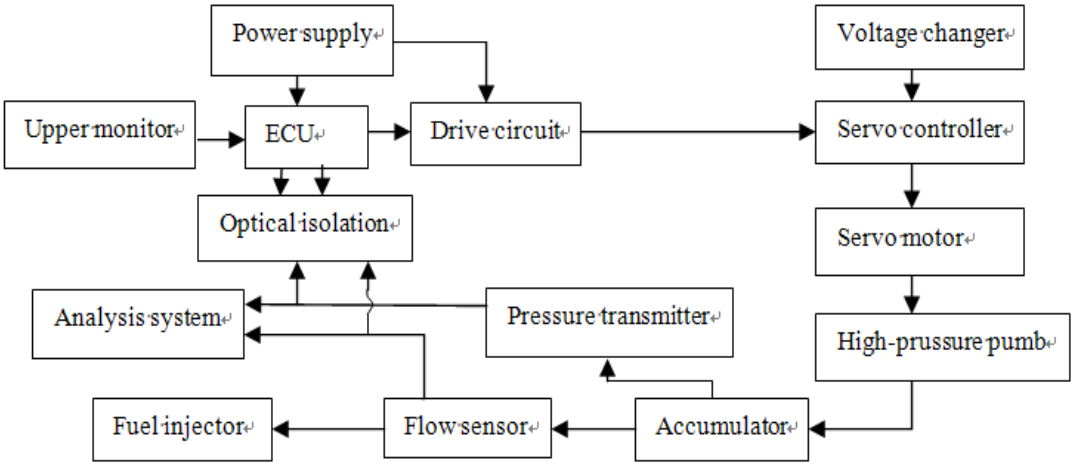

Fig.1 Test platform of fuel electric control system

A Model213 piston type flow sensor based on volumetric measurement principle which is produced by MAX company is used as the flow sensor, it outputs 112 square wave pulse signal with the frequency in proportion to flow for per ml fuel. The Kistler 4262A pressure transmitter outputs a pressure signal. Data acquisition system is composed of high-speed data acquisition box WaveBook/512 and DasyLab configuration software. Servo controller needs a 0-10V DC analog input for speed control. The PWM microcontroller output is a square wave, needs to be converted to DC analog, a servo motor drive circuit is shown in Fig.2.

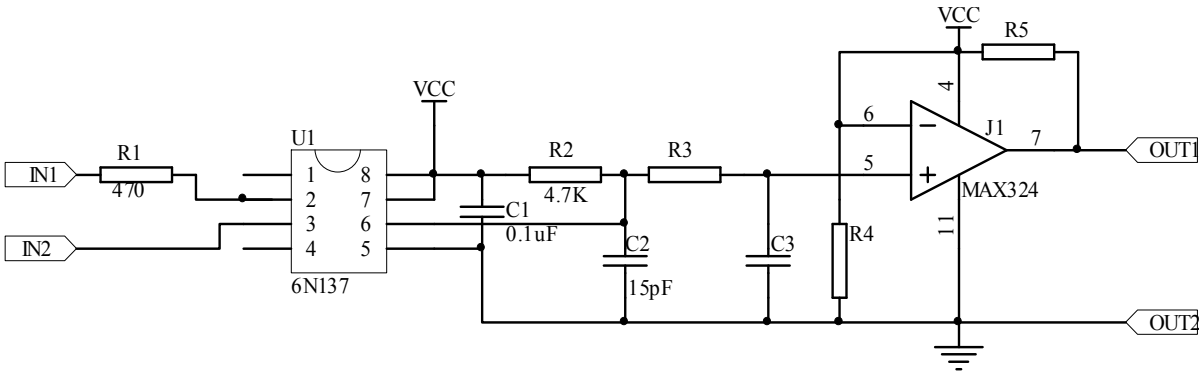

Fig.2 Servo motor drive circuit

Division of tasks and analysis based uC_OS-II nuclear.uC_OS-II is a complete, portable, curing, cutting preemptive real-time multitasking kernel [6]. Its core is stable, reliable, has been implemented to run on 8-64 from more than 40 different microprocessor architectures. Most

programs using ANSI C language, 64 tasks can be run at most, each task gets a different priority, and the system is always running in the ready state with the highest priority task. Here we use Freescale's MC9S12DG128 processor [7], transplant uC_OS-IIV4.51 in codewarrior 4.6 development environment.

System involves the following 10 tasks: 1 startup and hardware initialization task; 2 flow acquisition task; 3 accumulator pressure acquisition task; 4 flow control signal acquisition task; 5.PID control task; 6 digital tube display refresh task; 7 upper monitor communication task; 8 system status monitoring task; 9 error code acquisition record task; 10 fail-safe protection task.

Depending on the different requirements of real-time control system, all tasks can be divided into four levels, namely: initialization tasks, real-time tasks, time-sharing tasks and hidden tasks. Initialization tasks began to run when the system is powered and delete themselves after running, In this process, hardware resources are initialized and other tasks are established; Real-time tasks run higher priority tasks, including flow acquisition tasks; accumulator pressure acquisition task; flow control signal acquisition task and PID control task; time-sharing tasks run lower priority tasks, such as task 6-8; hidden tasks which run security tasks work only when system status monitoring task detects abnormal state of the system, Otherwise it's dormant. For example, when the flow sensor is detected fault, fail-safe protection task will start to detect flag and trigger the following three functions: 1 set PID control value as the pressure signal to replace the flow signal; 2 raise the priority of the accumulator pressure collection task, reducing priority of the flow acquisition task; 3 mark the corresponding error code, lit the error warning lights.

Experiment results. Flow signal is collected under steady-state operating conditions, with 100 kHz sampling rate in 100 seconds, MATLAB is used to convert square wave pulse signal into waveform. Flow set values for the measured value of 31.2kg/h is given in Fig.3, The measured mean value is 31.2149kg/h, variance is 0.0037kg/h, flow range is 0.3865kg/h, and deviation is ± 0.47% relative to the rated working flow (40kg/h). Fig.4 gives flow changing amplitude under different rotating speed in steady working condition.

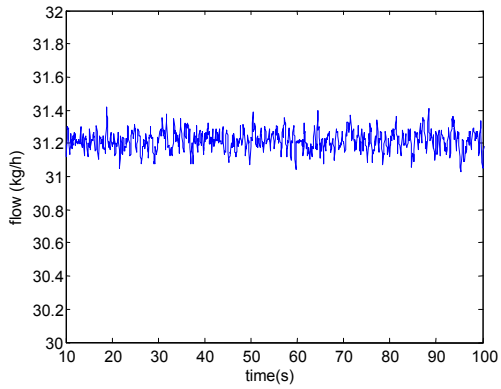

Fig.3 Stable Flow (preset value is 31.2kg/h)

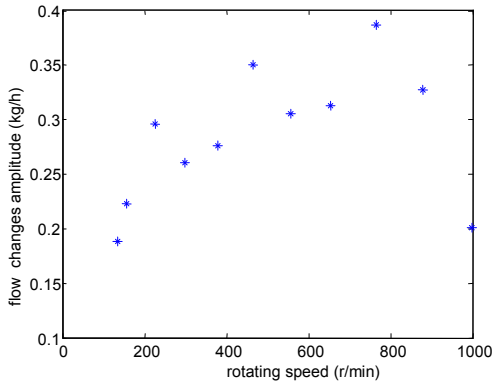

Fig.4 Flow fluctuation in stable condition

Corresponding gear is set for pre-set operating point, a gear correspond to a rotating speed from low to high, shifting different gears to change the rotating speed and collecting flow signal can detect the dynamic response ability of the system. Fig.5 is a gear shifting from 4 to 5, a vertical line stands for the shift points, and measured adjustment time is about 632ms in the condition so that gear shifts rapidly with no overshoot. Fig.6 gives adjustment time for shifting each gear. High and low gear shifting needs a long adjustment time, the middle gear adjustment time is short. The reason is that the pressure fluctuation is influenced by the rotating speed especially when rotating speed is low. With the increase of the rotating speed, the pressure fluctuation decreases, so is the adjustment time. Pressure and speed is a power relationship

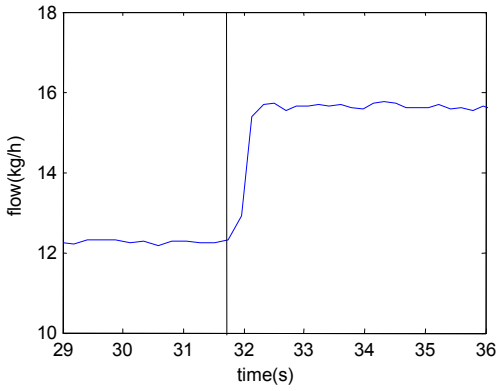

Fig.5 Flow response of gear-shifting (from 4 to 5 gear)

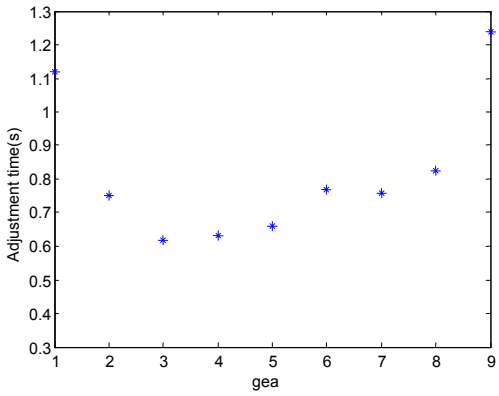

Fig.6 Flow response time for gears-shifting

Conclusion

Based on a rotating speed control method, introducing a uC_OS-II embedded operating system, we build a new Stirling engine combustor fuel electric control system, establish task module of different levels and priorities, improve the hardware and software unit, test the improved system work condition. After using uC_OS-II, the system adds support for time-sharing tasks and makes the fail-safe protection task more modular, the test results show that the new real-time operating system can adjust fuel supply quickly and stably.

Acknowledgements

This work was financially supported by the Henan Province Outstanding Talent Innovation Foundation Project (104200510006).

References

[1] Donghan Jing: Stirling engine technology [M] Harbin: Harbin Engineering University Press, 2009:266(in Chinese).

[2] E.O.Olson: Fuel Nozzles for Oil Burners [Z].2003.

[3] Zhijian He, Mengliang Shen: Stirling engine Combustion System [J] control. Control Technology, 2001 (09),49-50(in Chinese).

[4] Jianxin Liu, Jiang Zhu, Huiyong Du etc:Stirling engine fuel system pressure fluctuations simulation [J]. Henan University of Science and Technology (Natural Science), 2009 (5),24-27(in Chinese).

[5] Kun Stirling engine fuel system control device fail-safe strategy research: (Master Thesis) Luoyang: Henan University of Science and Technology, 2010:5(in Chinese).

[6] Jane J.Labrosse embedded real-time operating system uC_0S-II (Second Edition) [Z] Beijing: Beijing University of Aeronautics and Astronautics Press, 2003:8.

[7] Tongjing Sun, Guiyou Chen: Freescale 9S12 sixteen SCM principles and embedded development technology [M] Beijing: Mechanical Industry Press, 2008:5(in Chinese).

Advanced Materials Research Vols. 960-961 (2014) pp 982-988

doi:10.4028/www.scientific.net/AMR.960-961.982

Research on Flow Transferring Identification Method Based on WAMS

Yan Xu[1, a], Ping Han[1,b]

[1]State Key Laboratory of Alternate Electrical Power System with Renewable Energy Sources, North China Electric Power University, China

[a]xy19761001@aliyun.com, [b]hanping_1991@sina.com

Keywords: Flow Transferring Identification; Overload; Distance Relay

Abstract. In power system, flow transferring can cause non-fault overload. Traditional zone 3 distance relays cannot distinguish overload caused by faults or by transferred power flow and may operate incorrectly, thus cause cascading trips, even blackout. Based on wide area measurement system (WAMS), this paper proposes two criteria to realize flow transferring identification function. First, three-phase voltages and currents are measured and compared with those calculated before fault, which should be applied to the given identification criteria. Then, the logical relationship for flow transferring identification are put forward to prevent distance relays from incorrect behavior caused by non-fault overload and unblock zone 3 distance relays when fault occurs. Through the simulation results, the effectiveness of the proposed method is verified.

Introduction

Power system relay protection is of great significance to the security and stability of power system. Once there is any fault in the system, if protective devices can operate correctly, rapidly and reliably, fault can be cleared on time to be stopeped worsening system's operating condition. Otherwise, the process of system collapse may be promoted and cascading trips will lead to large-scale blackouts. When power system is heavily loaded, blackouts will occur as a result of flow transferring after a faulted line is cleared. The clearance of a faulted line might cause flow transferring, which results in overload on other transmission lines. Zone 3 distance relays will trip to remove these lines and then overload will become more severe; eventually will lead to blackouts [1-2]. When the main protection of a transmission line fails to trip, the backup protection plays a key role to clear the fault. Unfortunately, the existing protections only utilize local data to determine whether eliminating the faulted element or not and do not have the capability to distinguish between overloads caused by faults and by flow transferring. Although the protective relays operate correctly, the process of system collapse is promoted.

In recent years, scholars at home and abroad have raised some methods to avoid distance relays of backup protection operating incorrectly when other transmission lines overload after the faulted line is cleared. *Y. Serizawa et al.* have proposed a system of current differential backup protection for a bus bar and transmission circuits connected to that bus bar on an inter-station or wide-area basis [3]. Since the wide-area system consists of too many components such as terminal equipment and telecommunication equipment, the reliability and availability of the system may become a major concern. Conventionally, the overload caused by transferring flow is calculated by existing method AC power calculation. However, with the number of nodes increasing in modern power grid, there is hardly enough time to analyze the whole network by AC power calculation in case of emergency [4]. *X. Z. Dong et al.* have proposed a system protection scheme based on local information [5], but the availability of the proposed flow transferring identification is not verified through final simulation.

Recently, the advent of WAMS (Wide Area Measurement System) opens a new gate for power system wide area backup protections, because it makes synchronous data acquisition, exchange and analysis possible [6-7]. In this paper, a new flow transferring identification method based on WAMS is presented. First, the functions of wide area measurement system (WAMS) are introduced shortly. Then, two identification criteria are given in detail and logical relationship to prevent distance relays from incorrect behavior caused by non-fault overload are listed. Finally, the simulation results show that the proposed method works well. The advantages are summarized.

Structure and Functions of Wide Area Measurement System

Wide area measurement system consists of three parts: phasor measurement units (PMU) installed at power plants and substations, grid-covered communication network, and the control system of the EMS and SCADA [8]. After measured by PMU, the electrical quantities such as three-phase voltages and currents will be transmitted to scheduling control center through communication network, as is shown in Fig. 1.

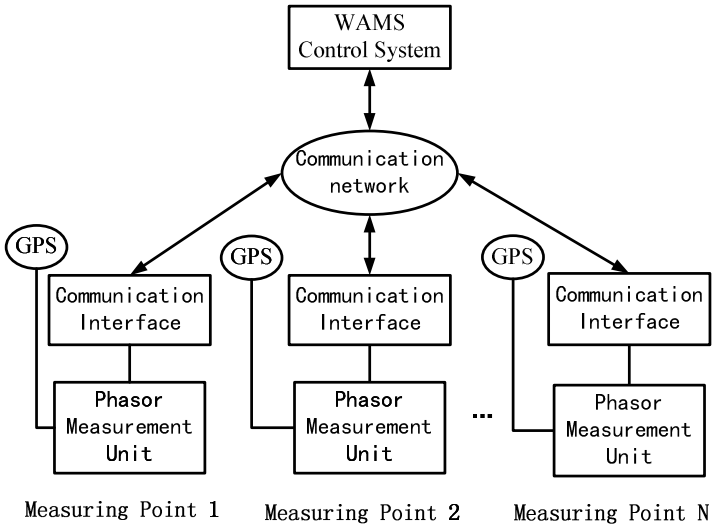

Fig. 1. Structure of Wide Area Measurement System

The key of the data validity of the phasor measurement unit is the synchronization. GPS-based synchronized phasor measurement unit can provide accurate measurement of node voltage phasor, branch current phasor, the power angle, and can provide fast calculation and transmission of power flow and phase angle information. The power system information at scheduling control center can be updated every 20-50 ms, so the supervisory center can deal with synchronous data taking the whole system status into account and make real-time control strategies [8].

Flow Transferring Identification Method

Identification Criterion 1. Three-phase currents will keep symmetric when overload occurs, and the current increments are equal. While when an asymmetric short circuit fault occurs, fault component of three-phase currents are not equal. Using linear transformation, currents can be divided into three symmetric components: positive sequence, negative sequence and zero sequence components. If it is an earth fault at the same time, zero-sequence current will exist. According to Superposition Theorem, the positive sequence component of the post-fault current can be divided into two parts: the pre-fault current and fault component. The pre-fault current is considered as normal component and it does not own fault features. The fault component has nothing to do with the pre-fault current, so it can be calculated through subtracting the pre-fault current from the current at the measuring point after fault occurs, as is shown in Equation (1):

$$\Delta \dot{I}_1 = \dot{I}_1 - \dot{I}_0 \tag{1}$$

where $\Delta \dot{I}_1$ represents the fault component current phasor; $\dot{I}_1$ and $\dot{I}_0$ represent the post-fault and pre-fault current phasors measured by WAMS at measuring point, respectively.

Based on formula (1), identification criterion 1 is given to distinguish between fault and overload:

$$\left|\dot{I}_0\right| + \left|\dot{I}_2\right| \geq m\left|\Delta \dot{I}_1\right| \tag{2}$$

where $\Delta\dot{I}_1$ is the positive sequence current increment measured by WAMS at the measuring point; $\dot{I}_2$ and $\dot{I}_0$ are negative sequence and zero sequence current phasors measured by WAMS at the measuring point, respectively. Taking the uncertainty of the measurements into consideration, the value of *m* should be about 0.8. This identification criterion will not be influenced by the differences between phases or fault impedance, and it can work well in case that power flow swings.

The positive sequence current increment $\Delta\dot{I}_1$ can be obtained through subtracting stable current before protection starts from the positive sequence current measured by PMU at the measuring point after zone 3 distance relays starts. Since current increases gradually when overload occurs, the stable current before protection starts can be obtained by calling back the measured pre-fault current from WAMS control system.

Analysis is in detail:

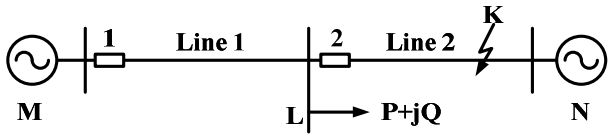

Fig. 2. Power System

Seeing from Fig. 2, if an asymmetric fault occurs at point *K* on Line 2, the positive, negative and zero sequence fault components measured at protection 1 are represented by $\Delta\dot{I}_{Ma1}$, $\Delta\dot{I}_{Ma2}$ and $\Delta\dot{I}_{Ma0}$. The three sequence currents flowing out of fault point are represented by $\dot{I}_{ka1}$, $\dot{I}_{ka2}$ and $\dot{I}_{ka0}$. The current distribution factors at protection 1 are represented by C_{M1}, C_{M2} and C_{M0}. To simplify calculation, assume $C_{M2}=C_{M1}$. Thus, three fault components at protection 1 can be calculated as: $\Delta\dot{I}_{Ma1}=C_{M1}\dot{I}_{ka1}$, $\Delta\dot{I}_{Ma2}=C_{M2}\dot{I}_{ka2}$ and $\Delta\dot{I}_{Ma0}=C_{M0}\dot{I}_{ka0}$.

There are three cases that should be discussed in detail. If the fault is A-phase earth fault, according to symmetric component method, the amplitudes of three sequence currents flowing out of fault point are equal: $\dot{I}_{ka1}=\dot{I}_{ka2}=\dot{I}_{ka0}$. According to (2), there is:

$$\begin{aligned}\gamma^{(1)}&=\frac{\left|\dot{I}_{Ma2}\right|+\left|\dot{I}_{Ma0}\right|}{\left|\Delta\dot{I}_{Ma1}\right|}\\&=\frac{C_{M2}\left|\dot{I}_{ka2}\right|+C_{M0}\left|\dot{I}_{ka0}\right|}{C_{M1}\left|\dot{I}_{ka1}\right|}\\&=\frac{C_{M2}+C_{M0}}{C_{M1}}\\&=1+\frac{C_{M0}}{C_{M1}}\end{aligned}\tag{3}$$

If the fault is two-phase short circuit fault, assuming the fault occurs between B-phase and C-phase, the relationship of three sequence currents satisfy the equations $\dot{I}_{ka1}=-\dot{I}_{ka2}$ and $\dot{I}_{ka0}=\mathbf{0}$. So there is:

$$\gamma^{(2)}=\frac{\left|\dot{I}_{Ma2}\right|+\left|\dot{I}_{Ma0}\right|}{\left|\Delta\dot{I}_{Ma1}\right|}=\frac{C_{M2}}{C_{M1}}=1\tag{4}$$

If the fault is two-phase earth fault, also taking B-phase and C-phase as an example, the relationship of three sequence currents satisfy the equation $\dot{I}_{ka1}=-(\dot{I}_{ka2}+\dot{I}_{ka0})$. So there is:

$$\gamma^{(1,1)}=\frac{\left|\dot{I}_{Ma2}\right|+\left|\dot{I}_{Ma0}\right|}{\left|\Delta\dot{I}_{Ma1}\right|}=\frac{Z_{\Sigma0}+\frac{C_{M0}}{C_{M1}}Z_{\Sigma2}}{Z_{\Sigma0}+Z_{\Sigma2}}\tag{5}$$

Identification criterion 1 is also applicative when fault occurs in other phases. The same reasoning process is also applied to protection 2. The worst condition is that the fault occurs at Bus *N* adjacent to neutral grounding transformer. The value of C_{M0} will become so small that the ratio γ may be smaller than 1 to cause confusion when identification criterion 1 is in use. This problem will be solved by identification criterion 2 in the next section.

Identification Criterion 2. If a two-phase or three-phase short circuit fault or a two-phase earth fault occurs on a line, the voltage between two faulted phases at point *K*— the arc voltage— is no more than 6 percent of the rated voltage in general [9]. Taking advantage of this feature, identification criterion 2 is given as follow:

$$\left|U_{\varphi\varphi}\cos(\varphi+90°-\varphi_{line})\right|<kU_N \tag{6}$$

where $U_{\varphi\varphi}$ represents the amplitude of the phase-to-phase voltage measured by WAMS at the measuring point; φ represents the angle between current phasor and voltage phasor measured by WAMS at the measuring point; φ_{line} represents the positive-sequence impedance angle of the transmission line; U_N is the rated voltage. The value of *k* should be about 0.6.

Take two-phase earth fault as an example. Analysis is in detail:

Suppose that the fault occurs between B-phase and C-phase at point *K*. The arc resistance of each phase is represented by R_o. According to Ohm's law, the phase-to-phase voltage measured at protection 1 in Fig.2 can be calculated as:

$$\begin{aligned}\dot{U}_M &= \dot{I}_M Z_{l1} + \dot{U}_L \\ &= \dot{I}_M Z_{l1} + \dot{I}_L Z_{l2} + \dot{U}_{arc}\end{aligned} \tag{7}$$

where $\dot{U}_M$ and $\dot{I}_M$ represent the voltage and current phasors between B-phase and C-phase measured by WAMS at protection 1, respectively; $\dot{U}_L$ and $\dot{I}_L$ represent the voltage and current phasors between B-phase and C-phase measured by WAMS at protection 2; Z_{l1} represents the impedance of line 1 and Z_{l2} represents the impedance from bus *N* to the fault point *K*; $\dot{U}_{arc}$ represents the voltage phasor between B-phase and C-phase at fault point *K*, also called arc voltage. Phasor diagram in Fig. 3 shows the relationship between voltages and currents.

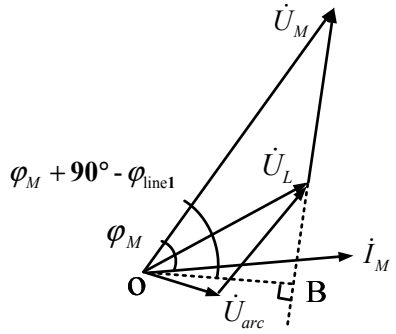

Fig. 3. Phasor diagram

In Fig. 3, φ_M represents the angle between $\dot{U}_M$ and $\dot{I}_M$ measured by WAMS at protection 1. φ_M represents the impedance angle of line 1. According to Ohm's law and Parallelogram Rule, the size of OB can be calculated by:

$$OB = U_M \cos(\varphi_M + 90° - \varphi_{line1}) \tag{8}$$

According to the geometric shortest perpendicular distance principle, the size of *OB* represents the smallest voltage possibly measured at protection 1. Based on different ranges of *OB* when fault or overload occurs, identification criterion 2 is proposed. If a transmission line overloads, the size of *OB* will keep no less than 80 percent of the rated voltage. Because zone 3 distance relays of protection 1 is the backup protection of line 2, when fault occurs, the size of *OB* is influenced by load on bus *L*. In order to get the maximum of *OB*, suppose three-phase short circuit fault occurs on bus *N*. Considering the greatest influence of load impedance, regard the load equivalent impedance as pure resistance. The size of *OB* is usually less than 30 percent of the rated voltage, even when load impedance is very large.

If the fault is two-phase or three-phase short circuit fault, analysis is similar and identification criterion 2 is also applicable.

Flow Transferring Identification Method. Both identification criteria discussed above can identify different types of fault, as is shown in Table 1.

Table 1. Types of fault that both criteria can identify

	Sing-phase earth fault	Two-phase short circuit fault	Two-phase earth fault		Three-phase short circuit fault
			$C_{M1} > C_{M0}$	$C_{M1} < C_{M0}$	
Criterion 1	√	√		√	
Criterion 2		√	√	√	√

From Table 1, the types of fault that can be identified through criterion 1 are sing-phase earth fault, two-phase short circuit fault and two-phase earth fault on condition that C_{M1} is smaller than C_{M0}. Similarly, the types of fault that can be identified through criterion 2 are two-phase short circuit fault, two-phase earth fault no matter C_{M1} is smaller than C_{M0} or not, and three-phase short circuit fault. Thus, the combination of these two identification criteria can distinguish between overload and all types of faults to prevent zone 3 distance relays from incorrect behaviors.

Logical relationship of the proposed identification criteria is shown in Fig. 4.

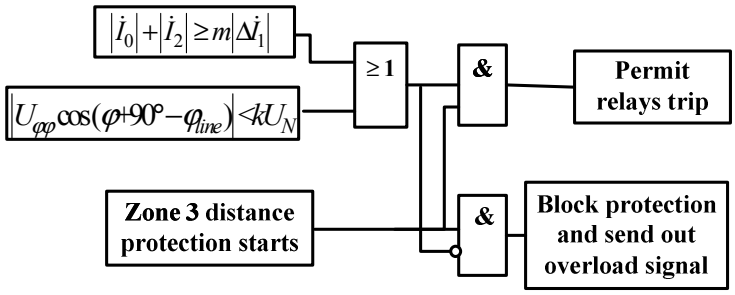

Fig. 4. Flow transferring identification strategies

From Fig. 4, if neither of the two criteria is satisfied, power flow transferring will be identified and zone 3 distance relays will be blocked reliably. Otherwise, protective relays will be permitted to trip until transmission line fault is cleared. For example, if a fault occurs on line 2, as shown in Fig. 2, zone 3 distance protection at protection 1 will start. Then relays at protection 2 will trip the line, which may result in overload on line 1. After the faulted line is removed, flow transferring identification will be in process to determine whether block zone 3 distance relays or not rather than permit them to trip when actuation time is up.

Simulation Results

The 3-nodes system in Fig.5 is set up to test the performance of the proposed power flow transferring method in this paper. The system frequency is 50Hz and the rated voltage is 500kV. All lines are installed with distance relays of directional impedance characteristics as their backup protection. Calculation results of the two ratios *m* and *k* in case of all faulted and transferring overloads are included.

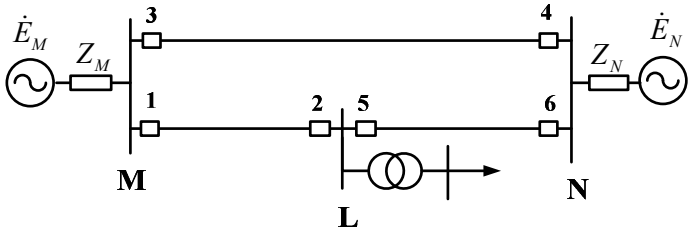

Fig. 5. Simulation system

Reliable Operation of Zone 3 Distance Relays When Fault Occurs. The case that fault occurs on the middle of the line from bus *L* to bus *N* is used to show the reliability of the identification method. 0.2 seconds later, relays at protection 5 and 6 trip to remove the line between bus *L* to bus *N*. From the fault occurring on, changes in voltage amplitude and current amplitude of A-phase measured at protection 1 are shown in Fig. 6.

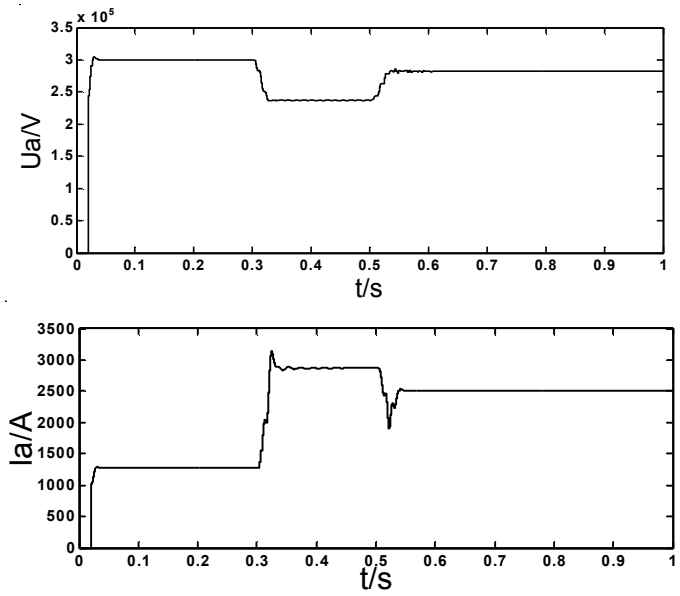

Fig. 6. Voltage and current curves

Seeing from Fig. 6, after the faulted line is removed, much flow is transferred to other lines such as the line from bus *M* to bus *L*, causing these lines overloaded. Through calculation, changes on the values of *m* and *k* are listed below. All the four types of fault are taken into consideration. Calculation results of the two ratios at protection 1 and 3 are shown in Table 2, where there are $m=\frac{|\dot{I}_0|+|\dot{I}_2|}{|\Delta\dot{I}_1|}$ and $k=\frac{U_{\varphi\varphi}\cos(\varphi_{\varphi\varphi}+90°-\varphi_l)}{U_N}$.

Table 2. Simulation results if fault occurs on bus 5

Protection	$m^{(1)}$	$m^{(2)}$	$k^{(2)}$	$m^{(1,1)}$	$k^{(1,1)}$	$k^{(3)}$
1	1.0386	1	0.0852	0.7204	0.0852	0.0852
3	2.0249	1	0.0946	1.0071	0.0946	0.0946

From calculation results of the ratios *m* and *k* in Table 2, if transmission line fault occurs, either of the two flow transferring identification criteria will be satisfied and zone 3 distance relays will be permitted to operate in case of main protection failure.

Reliable Blocking of Zone 3 Distance Relays When Non-fault Overload Occurs. After the relays trip to clear fault on the transmission line from bus *L* to bus *N*, much flow will be transferred to the line between bus *L* to bus *M*, resulting in measured impedance increasing to start zone 3 distance

protection. Calculated through the electrical quantities measured by WAMS at protection 1, the values of *m* and *k* can be obtained as 0 and 0.8379, respectively. Neither of the two identification criteria is satisfied, so zone 3 distance protection will be blocked reliably to prevent relays from incorrect behavior.

Conclusion

Non-fault overload caused by power flow transferring may lead to incorrect behavior of backup protective relays, which is considered as one of the main factors of cascading trips. Taking advantage of wide area measurement system (WAMS), this paper proposes a new flow identification method. The simulation results show that the proposed method works well with reliable operation in case that internal fault occurs. The identification criteria will not be influenced by the types of load or fault location, and it will not change the existing distance protection, either. The value of *m* and *k* can be set beforehand and small adjustments to them according to real scene are allowed.

References

[1] Y. S. Xue: Automation of Electric Power Systems Vol. 27(2003), p. 1-5.

[2] X. Gao, K. Q. Zhuang, Y. Sun: Power System Technology Vol. 31(2007), p. 25-31.

[3] Y. Serizawa, M. Myoujin, K. Kitarnura, et al: IEEE Trans. Power Delivery Vol. 13(1998), p. 1046-1052.

[4] Y. D. Zhang, B. C. Chen, H. Y. Xing, et al: Electric Power Automation Equipment Vol. 28(2008), p. 35-39.

[5] X. Z. Dong, L. Ding, K. Liu, et al: Proceedings of the CSEE Vol. 30(2010), p. 7-13.

[6] Q. X. Yang, T. S. Bi, J. T. Wu: Proc. IEEE Power Engineering Society General Meeting, 2007.

[7] R. Zivanovic and C. Cairn: Proc. IEEE 4th AFRICON Vol. 2(1996), p. 1006-1011.

[8] S. K. Xu, X. R. Xie, Y. Z. Xin: Power System Technology Vol. 29(2005), p. 44-49.

[9] B. H. Zhang, Xianggen Yin: *Power system protective relaying* (China Electric Power Press, China 2009).

Advanced Materials Research Vols. 960-961 (2014) pp 989-994
© (2014) Trans Tech Publications, Switzerland
doi:10.4028/www.scientific.net/AMR.960-961.989

Research on Setting Adjustment of Line Protection

Yufeng Gu[1, a *], Jianwen Ren[1, b]

[1]School of Electrical and Electronic Engineering, North China Electric Power University, Baoding, Hebei, 071003, China

[a]gyf31202@163.com, [b]rjw219@126.com

Keywords: Setting Adjustment Algorithm, Setting Detection, Setting Rectification, Interphase Current Protection, Coverage.

Abstract. In order to avoid incorrect setting from being a hidden fault source which threats the stable operation of power system, setting adjustment algorithm of line protection is proposed. Through setting detection and setting rectification the algorithm amends incorrect setting and reduces the number of mismatch protection to the greatest extent. A method of calculating high step coverage of interphase current protection based on node impedance matrix is also proposed in this paper. The example shows the proposed algorithm is practical.

Introduction

Relay protection is an important secondary system. It plays an important role on stable operation of the power system. Many serious power outages, such as "11.9" blackout accident in the northeast power grid of North America in 1965 and "8.14" blackout accident in America and Canada in 2003, are related to incorrect operation of relay protection device directly or indirectly [1]. Therefore it is urgent to improve reliability of relay protection.

Whether relay protection device could operate correctly largely depends on relay setting. Inaccurate relay coordination or change of operation mode may make relay setting incorrect under the current operation mode. In order to avoid incorrect relay setting from being a hidden fault source [2], efforts have been made on online check [3]. When an incorrect relay setting is checked, relay coordination workers should recalculate and work efficiency is low. If reference setting can be offered by software automatically after incorrect setting is checked, work efficiency will improve significantly. Based on online check, the paper makes further research and presents setting adjustment algorithm. Through setting detection and setting rectification, the algorithm could adjust incorrect relay setting. A method of calculating high step coverage of interphase current protection is also presented.

Concept of Setting Adjustment and Its Process

Setting adjustment refers to checking and correcting the relay setting which does not meet selectivity and sensitivity under the current operation mode. It includes setting detection and setting rectification. Setting detection checks whether all the protection in power system meets selectivity and sensitivity. For incorrect setting, setting rectification gives reasonable reference setting and reduces the number of mismatch protection to the greatest extent.

Setting adjustment involves in protection which needs coordination calculation, including zero sequence current protection, interphase current protection, interphase distance protection and ground distance protection. The flow chart of setting adjustment is shown in Fig.1.

Setting Detection

Setting detection is preparation stage of setting rectification. Setting detection can filter the protection whose setting does not need to change so as to avoid setting changing in large quantities. Setting

detection includes selectivity detection and sensitivity detection. If the protection passes all the detections, the setting does not need to change. Otherwise the setting needs to change.

The flow chart of setting detection is shown in Fig.2.

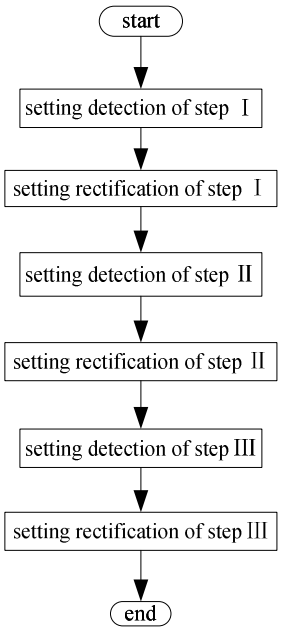

Fig.1 Flow chart of setting adjustment

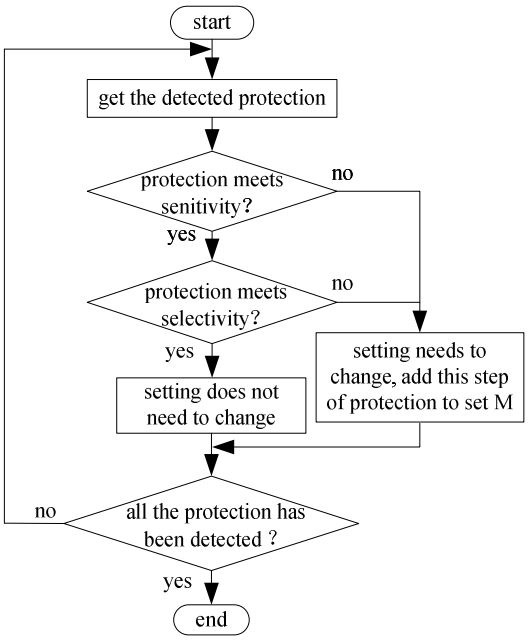

Fig.2 Flow chart of setting detection

The method of sensitivity detection is to calculate sensitivity of the original setting. If the sensitivity is no less than minimum requirement, the protection passes sensitivity detection. Otherwise the setting needs to change. There are two methods of selectivity detection, namely selectivity detection based on protection coverage and selectivity detection based on comparison.

Selectivity detection based on protection coverage contains the following steps.

(i) Search adjacent subordinate protection for step M-1 and step M whose operating time is nearest to the operating time of detected protection. Detected protection's operating time should be greater than step M-1's and less than step M's.

(ii) Calculate coverage of detected protection and step M of adjacent subordinate protection.

(iii) Compare the coverage and judge whether the detected protection meets selectivity. If the detected protection's coverage is greater than step M-1's, the protection passes selectivity detection. Otherwise the setting needs to change.

Traditional way of calculating coverage is golden section method or binary search method which needs much repeated calculation. In order to improve efficiency, researchers have made great efforts on fast coverage calculation [4,5]. However, a method of calculating high step coverage of interphase current protection is expected. A method proposed in this paper will be discussed in Chapter 3.

Selectivity detection based on comparison adopts comparison instead of quantitative calculation. Compare the original setting and the setting under the current operation mode and determine which detected protection meets selectivity. Taking distance protection as an example, the method contains following steps (Z_{set} is the original setting).

(i) For step I of distance protection, calculate the setting under the current operation mode. If $Z_{setI} < Z'_{setI}$ the detected protection passes selectivity detection; otherwise the setting needs to change.

(ii) For step II of distance protection, calculate the setting $Z'_{setII\cdot1}$, $t'_{setII\cdot1}$ and $Z'_{setII\cdot2}$, $t'_{setII\cdot2}$ under current operation mode which coordinates with longitudinal differential protection and step II of adjacent subordinate protection respectively. When $t_{setII} < t'_{setII\cdot2}$, if $Z_{setII} \le Z'_{setII\cdot1}$ the detected protection passes selectivity detection; otherwise the setting needs to change. When $t_{setII} \ge t'_{setII\cdot2}$, if $Z_{setII} \le Z'_{setII\cdot2}$ the detected protection passes selectivity detection; otherwise the setting needs to change.

(iii) For step III of distance protection, calculate the setting $Z'_{set\text{III}\cdot 2}$, $t'_{set\text{III}\cdot 2}$ and $Z'_{set\text{III}\cdot 3}$, $t'_{set\text{III}\cdot 3}$ under the current operation mode which coordinates with step II and step III of adjacent subordinate protection respectively. When $t_{set\text{III}} < t'_{set\text{III}\cdot 3}$, if $Z_{set\text{III}} \le Z'_{set\text{III}\cdot 2}$ the detected protection passes selectivity detection; otherwise the setting needs to change. When $t_{set\text{III}} \ge t'_{set\text{III}\cdot 3}$, if $Z_{set\text{III}} \le Z'_{set\text{III}\cdot 3}$ the detected protection passes selectivity detection; otherwise the setting needs to change.

Selectivity detection based on protection coverage can judge selectivity more intuitively and its calculation is more accurate. When difference between the coverage of detected protection and adjacent subordinate protection is small, messages can be sent to relay coordination workers. However, this method needs larger workload. Selectivity detection based on comparison can only judge selectivity qualitatively. Its principle is similar to relay coordination's and the workload is smaller.

Setting Rectification

Concept of line line's rank should be introduced firstly. Line of first rank is the detected protection's adjacent subordinate line. Line of second rank is line of first rank's adjacent subordinate line and the rest can be done in the same manner.

Step I's setting after rectification is the relay setting which is calculated under the current operation mode. The setting of other steps can be calculated as follows.

(i) Make the protection i whose setting is incorrect coordinates with protection's low step in the line of first rank and calculate the result. If the result meets sensitivity it can be regarded as protection i's new setting. Otherwise make the protection i coordinate with higher step until the result meets sensitivity. If protection i has several lines of first rank, make protection i coordinate with every line and select maximum (current protection) or minimum (distance protection) from all the results.

(ii) When protection i coordinates with the same step of protection in line of first rank and the result still can not meet sensitivity, the same step of protection's setting in line of first rank should be adjusted. The method is adjusting the cooperative relationship between line of first rank and its corresponding line of second rank.

According to different relay coordination plan, setting rectification's steps can be changed properly. However, setting rectification may not cut mismatch protection totally especially when long lines connect to short lines or complex ring exists in power grid. Manual regulation is in need sometimes.

Method of Calculating High Step Coverage of Interphase Current Protection

As shown in fig.3, side m in line mn installs interphase current protection. Dotted line in fig.3 can be any network structure. Suppose the end point of its high step coverage is node f whose distance to the line head is K of total line length. The impedance of line mn is z_{mn} and the impedance of line ij is z_{ij}.

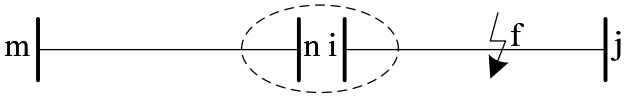

Fig.3 Circuit diagram

Unit current is injected into node f. $U_k^{(f)}$ is voltage of i when f is injected unit current and other expressions have similar meaning. According to the reciprocity theorem,

$$U_k^{(f)} = U_f^{(k)} = U_i^{(k)} - k(U_i^{(k)} - U_j^{(k)}) = (1-k)U_i^{(k)} + U_j^{(k)} = (1-k)U_k^{(i)} + U_k^{(j)} \quad (1)$$

Mutual resistance of fault point f is:

$$Z_{kf} = (1-k)Z_{ik} + kZ_{jk} \tag{2}$$

Current equation of fault point f is:

$$1 + \frac{U_i^{(f)} - U_f^{(f)}}{kz_{ij}} + \frac{U_j^{(f)} - U_f^{(f)}}{(1-k)z_{ij}} = 0 \tag{3}$$

$$1 + \frac{Z_{if} - Z_{ff}}{kz_{ij}} + \frac{Z_{jf} - Z_{ff}}{(1-k)z_{ij}} = 0 \tag{4}$$

Self-impedance of fault point f is:

$$Z_{ff} = (1-k)^2 Z_{ii} + k^2 Z_{jj} + k(1-k)(2Z_{ij} + z_{ij}) \tag{5}$$

When two-phase short circuit happens in the node f, positive sequence current and negative sequence current of fault point is:

$$I_{f(1)} = -I_{f(2)} = \frac{1}{Z_{ff(1)} + Z_{ff(2)}} = \frac{1}{2Z_{ff(1)}} \tag{6}$$

Positive sequence current and negative sequence current of node m and n is:

$$\begin{cases} U_{m(1)} = 1 - Z_{mf(1)} I_{f(1)} \\ U_{m(2)} = -Z_{mf(2)} I_{f(2)} = Z_{mf(1)} I_{f(1)} \\ U_{n(1)} = 1 - Z_{nf(1)} I_{f(1)} \\ U_{n(2)} = -Z_{nf(2)} I_{f(2)} = Z_{nf(1)} I_{f(1)} \end{cases} \tag{7}$$

Positive sequence current and negative sequence current of line mn is:

$$\begin{cases} I_{mn(1)} = \dfrac{U_{m(1)} - U_{n(1)}}{z_{mn(1)}} = \dfrac{Z_{nf(1)} - Z_{mf(1)}}{z_{mn(1)}} I_{f(1)} \\ I_{mn(2)} = \dfrac{U_{m(2)} - U_{n(2)}}{z_{mn(2)}} = \dfrac{Z_{mf(1)} - Z_{nf(1)}}{z_{mn(1)}} I_{f(1)} = -I_{mn(1)} \end{cases} \tag{8}$$

The current of line mn is:

$$I_m = \sqrt{3} I_{f(1)} = \sqrt{3} \frac{Z_{nf(1)} - Z_{mf(1)}}{2Z_{ff(1)} z_{mn(1)}} = I_{set} \tag{9}$$

where I_{set} is the setting of protection m. And we get the quadratic equation in one unknown

$$AK^2 + BK + C = 0$$

$$\text{where } \begin{cases} A = \dfrac{2}{\sqrt{3}} I_{set} z_{mn(1)} (Z_{ii(1)} + Z_{jj(1)} - 2Z_{ij(1)} - z_{ij}) \\ B = \dfrac{2}{\sqrt{3}} I_{set} z_{mn(1)} (2Z_{ij(1)} - Z_{ii(1)} + z_{ij(1)}) - (Z_{nj(1)} - Z_{ni(1)} + Z_{mi(1)} - Z_{mj(1)}) \\ C = I_{set} z_{mn(1)} \dfrac{2}{\sqrt{3}} Z_{ii(1)} + Z_{mi(1)} - Z_{ni(1)} \end{cases}.$$

When three-phase short circuit happens, the equation can be derived in the same way.

Example analysis

The local connecting diagram of a power grid is shown in fig.4, letters in the diagram is protection's name and number is the impedance of corresponding line. Taking distance protection as an example, availability of the algorithm proposed in this paper is discussed as follows.

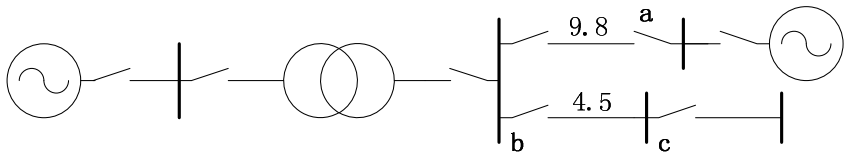

Fig.4 Local connecting diagram of a power grid

When the system operates normally, setting of protection a and b is shown in table 1. For some reason the transformer stops running. Protection a does not meet selectivity after setting detection as it's the coverage of step II stretches into protection b's step II and the operating time is the same. The setting of protection a is adjusted through detection rectification. When protection a coordinates with protection b's longitudinal differential protection the setting could not meet sensitivity. Therefore it coordinates with protection b's step II and the setting meets sensitivity. Setting after setting rectification is also shown in table 1.

Table 1 Setting before and after adjustment

protection's name	step	Setting before adjustment	Setting after adjustment
a	I	7.84 Ω , 0s	7.84 Ω , 0s
	II	16.68 Ω , 0.5s	13.24 Ω , 1s
b	I	3.60 Ω , 0s	3.60 Ω , 0s
	II	6.75 Ω , 0.5s	6.75 Ω , 0.5s

Conclusions

The paper presents setting adjustment algorithm. Through setting detection and setting rectification, the algorithm could adjust incorrect relay setting and reduce the number of mismatch protection to the greatest extent. The algorithm is easy to computer implementation and can improve working efficiency. The example shows the proposed algorithm is practical.

References

[1] Yang Cai: 'Review and brief analysis on power system accidents and suggestions on power system dispatching and management', Power System Technology, 2007, Vol.31, (11), p.6-10

[2] Liu Chenching, Jung Juhwan, Heydt G T, et al: 'The strategic power infrastructure defense system', IEEE Control System Magazine, 2000, Vol.20, (4), p.40-52

[3] Genghui Zeng, Yinhong Li and Xianzhong Duan: 'A discussion about on-line verifying of relay setting in power system', Relay, 2002, Vol.30, (1), p.22-24

[4] Li Cai, Xinghua Wang, Dongyuan Shi and Xianzhong Duan: 'Calculation coverage of zero sequence current protection based on node impedance matrix', Electric Power Automation Equipment, 2007, Vol.27, (3), p.49-52

[5] Pengfei Lv, Huaqiang Li, Junwen Zhang and Jian Wang: 'A new method for computing coverage of current protection in power network', Automation of Electric Power Systems, 2000, (6), p.42-44

Advanced Materials Research Vols. 960-961 (2014) pp 995-999

doi:10.4028/www.scientific.net/AMR.960-961.995

Simulation of Transformer Protection Based on an Embedded MATLAB Function

Wei Cai[1, a], Lin Sun[1, b] and Huaren Wu[1, c]

[1]School of Electrical & Automation Engineering, Nanjing Normal University, Nanjing 210042, China

[a]caiwei-789@163.com, [b]sunlin0105@yeah.net, [c]huarenwu@yahoo.com

Keywords: Relay protection, Differential protection, Transformer, Matlab function, Simulation.

Abstract. This paper establishes a simulation model of a simplified power system with transformer differential protection based on an embedded Matlab function block. The differential protection consists of percentage restraint differential protection, second harmonic restraint, differential current instantaneous trip protection and over-excitation protection. The model is able to correctly simulate the transformer's inrush current and internal and external faults. The results from the simulation show that the circuit breaker correctly operates for a transformer internal fault and provides a good braking effect for an external fault. In addition, the protection model is able to identify the inrush current of the transformer and avoid a protection mis-trip event.

Introduction

The embedded Matlab function block is an easy and convenient method used to write m-code that can be incorporated into a Simulink model [1]. In contrast to the s-functions block, m-code or C is more casual and simple to add in an embedded function block because the user is not required to strictly follow the function template rules. Most of the power system simulation can be constructed by combining an embedded Matlab function block and a SimPowerSystems block.

Electric power plays an important role in the economy and in our lives, and power system protection is used to ensure secure and stable operation of power systems. Simulation of relay protection contributes to the development of relay protection and analysis of relay protection operation. It is well known that the transformer is one of the most important pieces of equipment in power systems, and thus far, differential protection is still the primary protection scheme for power transformers. In this paper, a transformer protection model is developed in the Matlab/Simulink environment to evaluate the impact of faults on the differential relay. The model uses percentage differential protection to distinguish internal faults from external faults. Inrush current due to transformer energization can appear as a fault to the protection system. Therefore, the second harmonic restraint method is adopted to block the differential relay against inrush current. The concept of differential protection is briefly illustrated in Fig. 1 [2]. Generally, the current flowing into the transformer is compared with the current flowing out of the transformer. If the currents are in balance, the operating current will be zero, which indicates that the transformer is functioning in a healthy manner; the currents are not in balance, other methods are required to identify the transformer fault-type.

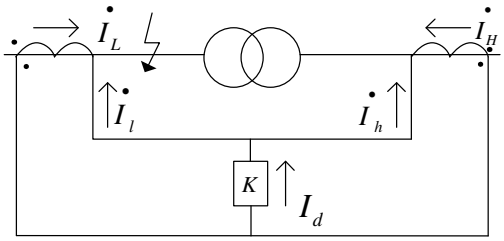

Fig. 1. Transformer differential protection

Structure of the Simulation Model

The transformer differential protection is simulated using Matlab/Simulink. Fig. 2 shows the simulation model of a simple system with the 20 MVA-110/10.5 kV YNd11 transformer. The parameters of the system are as listed follows:

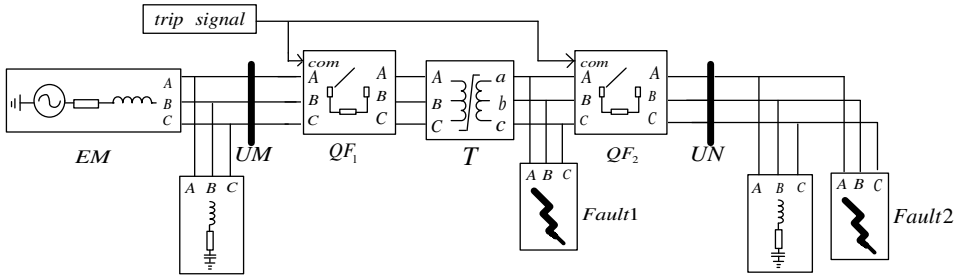

Fig. 2. Simulation model of a simple power system

a) Equivalent source: V=110 kV, Z=0.8929+j0.01658 Ω
b) Transformer: S_n=20 MVA, U_1=110 kV, U_2=11 kV, f=50 Hz, U_k%=10.5, ΔP_0=27 kW, I_0%=0.8, ΔP_k=104 kW, R_1=1.573 Ω, R_2'=0.1573 Ω, L_1=0.101 H, L_2'= 0.00101 H
c) Load 1: P=10 MW, Q_L=10 Mvar, Q_C=1 Mvar
Load 2: P=10 MW, Q_L=10 Mvar, Q_C=1 Mvar

Differential Protection Subsystem. The block diagram of differential protection is shown in Fig. 3. The figure demonstrates that the protection system consists of percentage differential protection, differential current instantaneous trip protection, second harmonic restraint and over-excitation protection. The gain block is used as a current converter. Using the Fourier block and the magnitude - angle to the complex block, we can easily identify the fundamental component, the second harmonic component, the fifth harmonic component and the three-phase current vector. In the embedded function block, the protection criteria are written directly according to the operation logic. The three-phase breaker block is set in external control mode. When the control signal turns to 0, the breakers are opened.

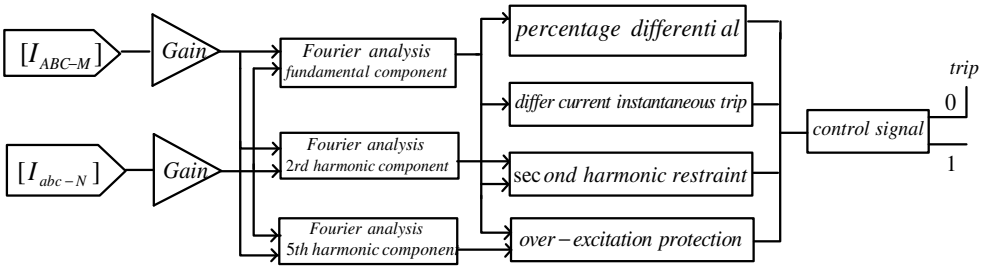

Fig. 3. Differential protection subsystem

The conventional differential protection calculates the differential current and the restraint current using the following equations:

$$I_d = |\dot{I}_A - \dot{I}_a'|. \quad (1)$$

$$I_r = (|\dot{I}_A| + |\dot{I}_a'|)/2. \quad (2)$$

$$\dot{I}_a' = (\dot{I}_a - \dot{I}_c)/\sqrt{3}. \quad (3)$$

where $\dot{I}_A$ and $\dot{I}_a$ are the vector current of phase A in the high-voltage and low-voltage side of the transformer, respectively, and $\dot{I}_a'$ is the vector current of phase *a* after phase shift compensation.

The percentage differential protection is a component of Fig. 3 and is used to explain the Matlab/Simulink simulation. The simulation model for percentage differential protection is presented in detail in Fig. 4. The differential current calculated block and the protection block are modeled using the embedded Matlab function block, and the embedded Matlab m-code is written directly according to the operational logic and equations (1), (2), (3) and (4).

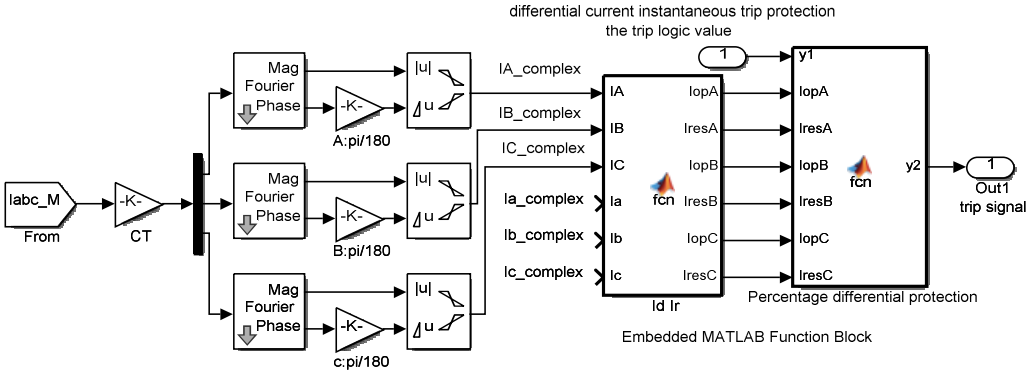

Fig. 4. Percentage differential protection

a) the differential current calculated block:

function [I_{opA},I_{resA},I_{opB}, I_{resB},I_{opC},I_{resC}]= fcn(I_A,I_B,I_C,I_a,I_b,I_c)
I_{aa}= (I_a-I_c)/sqrt(3); %phase shift compensation
I_{bb}= (I_b-I_a)/sqrt(3);
I_{cc}= (I_c-I_b)/sqrt(3);
I_{opA}= abs(I_A-I_{aa}); %differential current of phase A
I_{resA}= (abs(I_A)+abs(I_{aa}))/2; %restraint current of phase A
I_{opB}= abs(I_B-I_{bb});
I_{resB}= (abs(I_B)+abs(I_{bb}))/2;
I_{opC}= abs(I_C-I_{cc});
I_{resC}= (abs(I_C)+abs(I_{cc}))/2;

b) the percentage differential protection block:

function y_2 = fcn(y_1,I_{opA},I_{resA},I_{opB},I_{resB},I_{opC},I_{resC})
I_{r1}=2.0994; % 0.8*In
I_{r2}=7.87275; % 3*In
k_1=0.5;
k_2=0.7;
I_{opmin}=0.7873; % 0.3*In
y_2=10;
if y_1= =0
if
((I_{opA}>I_{opmin}&&(I_{opA}-I_{opmin})>k_1*(I_{resA}-I_{r1})&&(I_{opA}>k_2*(I_{resA}-I_{r2})+k_1*(I_{r2}-I_{r1})+I_{opmin}))||(I_{opB}>I_{opmin}&&(I_{opB}-I_{opmin})>k_1*(I_{resB}-I_{r1})&&(I_{opB}>k_2*(I_{resB}-I_{r2})+k_1*(I_{r2}-I_{r1})+I_{opmin}))||(I_{opC}>I_{opmin}&&(I_{opC}-I_{opmin})>k_1*(I_{resC}-I_{r1})&&(I_{opC}> k_2*(I_{resC}-I_{r2})+ k_1*(I_{r2}-I_{r1})+I_{opmin})))
y_2=1;
else
y_2=0;
end
end

Percentage differential protection is applied to distinguish between an internal fault and an external fault in the transformer. If the operating current exceeds a certain ratio of the restraint current, the

differential relay will operate [3, 4]. The algorithm for percentage differential protection is described by (4).

$$\begin{cases} I_d > I_{op.\min} & I_r \le I_{res1} \\ I_d > I_{op.\min} + K_1(I_r - I_{res1}) & I_{res1} < I_r \le I_{res2} \\ I_d > I_{op.\min} + K_1(I_{res2} - I_{res1}) + K_2(I_r - I_{res2}) & I_r > I_{res2} \end{cases}. \tag{4}$$

where K_1 and K_2 are constants.

Inrush current occurs during energization of a transformer and consists of a large transient current caused by saturation of the magnetic core [5]. The relay may mis-operate due to an inrush current. The second harmonic restraint method is the most commonly applied protection method in this case. Various studies have shown that the differential relay will not operate when

$$I_{op2} / I_{op1} > K_{2.\text{set}}. \tag{5}$$

where $K_{2.\text{set}}$ is a constant and I_{op2} is the second harmonic component of the operating current.

It is common practice to use the fifth harmonic of the operating current to avoid differential protection operation if the transformer experiences over-excitation [6, 7]. The differential protection operates if

$$I_{op5} / I_{op1} > K_{5.\text{set}}. \tag{6}$$

where $K_{5.\text{set}}$ is a constant and I_{op5} is the fifth harmonic component of the operating current.

Performance Evaluation

The performance of transformer differential protection can be examined in the Matlab/Simulink environment using the proposed model. If the differential current is eight times larger than the rated current, the differential current instantaneous trip protection will operate immediately; if not, the ratio restraint criteria are used to identify the fault-type. If the differential current enters the operation zone, second harmonic restraint and over-excitation protection are still required to discriminate the fault from the disturbances.

Fig. 5 shows the current waveforms for a healthy transformer, and the simulated currents agree well with the calculated results. Due to the star-delta winding connection of the transformer, the phase angle of the three-phase current in the high-side star winding lags behind the phase angle in the delta winding side [8]. The result of the phase shift compensation is depicted in Fig. 6.

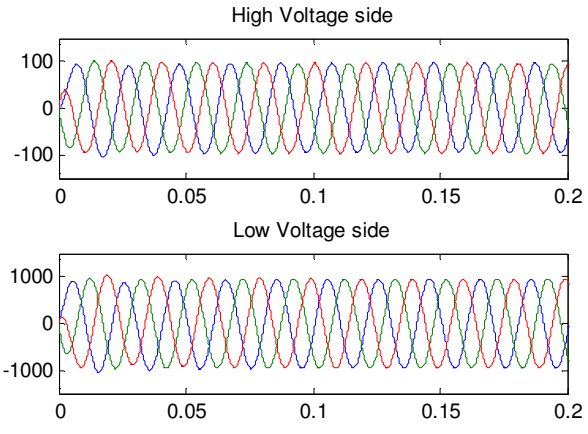

Fig. 5. Current waveforms

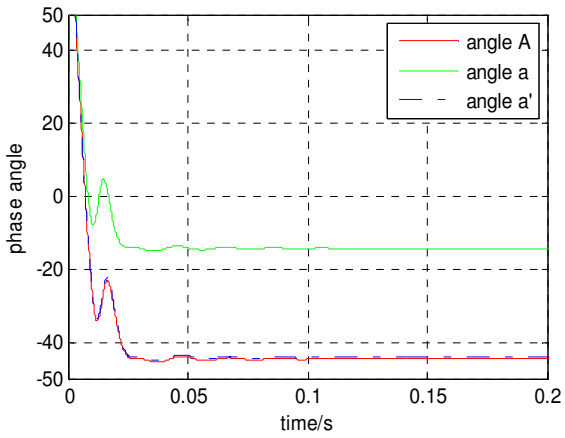

Fig. 6. Phase shift compensation

The currents in the transformer and the curve of the trip signal during a fault are shown in Fig. 7. A three-phase internal fault occurs at 0.1 s, and a trip decision is activated immediately.

To investigate the performance of the differential protection, the results of a three-phase external fault at 0.1-0.2 s are indicated in Fig. 8. Obviously, no trip signal is issued in the external fault case.

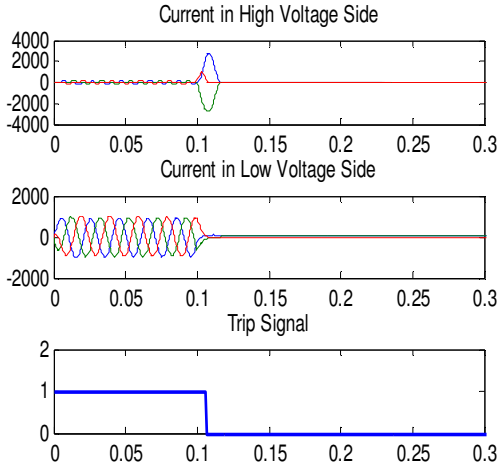

Fig. 7. Results of internal fault

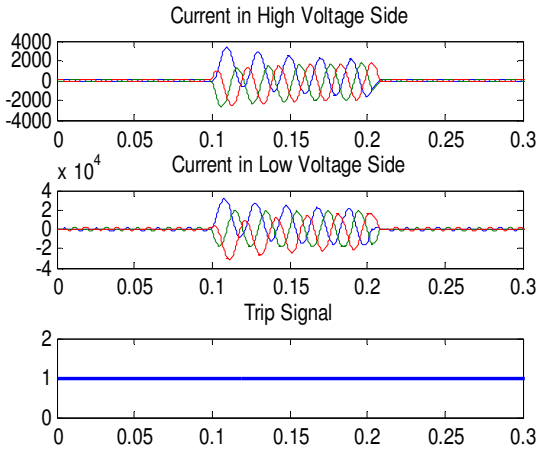

Fig. 8. Results of external fault

Conclusion

The paper proposes a simulation model of transformer differential protection using an embedded Matlab function block. The model is able to correctly discriminate an internal fault from an external fault. For an external fault, no trip signal is activated in this situation. In contrast, it is clear that a trip signal is activated during an internal fault. In the embedded function block, the protection criteria are written directly according to the operational logic, and the results validate the accuracy of the model.

Acknowledgements

This work was financially supported by the National Natural Science Foundation of China (51177074).

References

[1] Information on http://www.mathworks.cn/products/matlab-coder/

[2] R. Hamilton: IEEE Trans. on Industry Applications Vol.49 (2013), p. 1890.

[3] E.C. Segatto and D.V. Coury: IEEE Trans. on Power Systems Vol.21(2006), p. 1154.

[4] R.A. Habibabadi: Power Engineering and Automation Conference (PEAM), IEEE, Vol.3(2011), p. 50.

[5] B. Kasztenny, M. Kezunovic: Computer Applications in Power, Vol.11(1998), p. 39.

[6] R.P. Maheshwari and H.K. Verma: Electric Power Systems Research Vol.41 (1997), p. 175.

[7] L.L. Grigsby: *Power System Stability and Control* (CRC Press, USA2012)

[8] U.N. Khan and T.S. Sidhu: Electric Power Systems Research Vol.110 (2014), p. 31.

Advanced Materials Research Vols. 960-961 (2014) pp 1000-1005

doi:10.4028/www.scientific.net/AMR.960-961.1000

Studies on Improving the AC Outward Transmission Capacity of Sichuan Power Grid by Utilization of Phase-shifting Transformers

Gang Chen[1, a], Fan Tang[1,b], Yufei Teng[1,c],Hua Zhang[1,d], and Lijie Ding[1,e]

[1]State Grid Sichuan Electric Power Research Institute, Chengdu 610072, China

[a]gangchen08@gmail.com, [b]tangfance@163.com, [c]yfteng2011@163.com, [d]zhanghua0002@163.com, [e]ding_lijie@163.com

Keywords: Phase-shifting transformer; transmission capability; Sichuan power grid; power flow

Abstract. In this paper, the feasibility analysis of the utilization of phase-shifting transformers (PSTs) to improve the AC outward transmission capacity of Sichuan power grid (SCPG) is presented. Firstly, the authors analyze the working principle of PST, as well as the rules for selecting its location. Then, the AC outward transmission limit of SCPG is studied with PSASP software. Finally, the PST is used to change the power flow distribution of lines on border of SCPG. Simulations results show that the PST can significantly improve the AC outward transmission capacity of SCPG. At the same time, short-circuit current of SCPG is also reduced.

Introduction

Sichuan power grid (SCPG) is connected with Central China power grid (CCPG) merely through the border of Sichuan-Chongqing that is composed by Honggou–Banqiao double lines (simply called as Hongban lines) and Huangyan-Wanxian double lines (simply called as Huangwan lines). During the "Twelfth Five Year Plan" of China, the AC outward transmission capacity of SCPG will be extensively restrained by the transmission limit of the border of Sichuan–Chongqing power grid with the commissioning of some large hydropower stations, represented by Xiangjiaba hydropower station and Xiluodu hydropower station etc.. It has been one of the key issues to increase the outward transmission capacity of the border of Sichuan–Chongqing for SCPG, even for CCPG.

Phase shifting transformer (PST) is capable of controlling the power flow in certain power flowing towards certain direction and thus changes the distribution of power flow in loop grid. In turn, the overload on transmission lines or the main equipment of transformers can be avoided, enhancing the reliability. Moreover, a reasonable distribution of power flow is thereby realized to improve the transmission capacity of borders [1]. In addition, as mentioned in some literatures [2], PST also plays a certain role in reducing short circuit current. Authors in [3] points out that thyristor technology-based static PST improves the stability of power system, suppressing oscillations through proper controlling means.

1930s, American researchers firstly utilized PST to improve the distribution of power flow of electromagnetic loop in 66 kV and 132 kV [4]. In [5], PST was used to control the power flow of loop grid, in order to decrease loss and eliminate overload. In [6], PST was firstly realized on a power grid of 500 kV [7]. Holland, Italy and England also have the record of using of PSTs [7-9]. It can be concluded that PSTs are widely used in overseas power systems and application records can be observed on various voltage levels. Based on these engineering application experiences, IEEE has formed a standard for the application of PST, which provides guidance for formulating the application technology condition, equipment specification, and field test requirements of PST [10]. Relevant researches in China were initiated in 1980s. Chinese researchers and workers have profoundly investigated the principle, design method, and feasibility simulation etc. of PST [1-2]. In [11], an ultra-high voltage (UHV) PST was designed and its electromagnetic transient characteristics were analyzed. However, there is still no record of application of PSTs in China.

The AC outward transmission capacity of SCPG is fundamentally limited by the uneven distribution of power flows between Hongban lines and Huangwan lines. Under the current operation,

the ratio of power flow between the two lines reaches to 2:1. During the "Twelfth Five Year Plan" of China, this ratio may rise up to 5:1. With the operation of a large number of thermal power plant units in northern Chongqing, such uneven distribution is prone to be greatly widened. In adverse circumstances, the ratio might rise up to 7:1. This uneven power flow leads to the result that Hongban lines reach its stability limit untimely, while Huangwan lines cannot be fully utilized due to the over-small power flow. The AC outward transmission capacity of SCPG is thereby greatly limited. The pressure of outward transmission would be eased with the completion of the 1,000 kV Ya'an-Wuhan AC UHV. However, the difficulty of construction and other irresistible factors provide the project progress with great uncertainty. Therefore, in view of existing power grid resources, it is of great importance to study the utilization of PSTs to control the power flow distribution and improve the AC outward transmission capacity of SCPG.

In this paper, the basic principle of PST, methods of location selection, and design methods are briefly introduced. Then, the feasibility of application of PST on the border of Sichuan-Chongqing to increase the AC outward transmission capacity of SCPG is analyzed. Case studies based on PSASP suggested that PST significantly improved the transmission limit of border of SCPG. Moreover, the simulations also validates that the PST plays a role in reducing the short-circuit current of 500kV buses in SCPG.

The Basic Principle of PST

Principle of Phase Shifting. As shown in Fig. 1, a PST is generally composed by a series transformer and a parallel transformer. The series transformer is connected in Y/△ mode, while the parallel transformer is linked in Y/Y mode, with the neutral point connected with the ground. The primary winding of series transformer is connected in series with the line. The intermediate tap is linked to the primary winding of parallel transformer. Parallel transformer is in parallel with the line. The secondary winding of the parallel transformer, which is equipped with a polarity selector K_{ZF} and tap point control, is linked with the secondary winding of the series transformer in phase sequence relationship of A→C, B→A, and C→B.

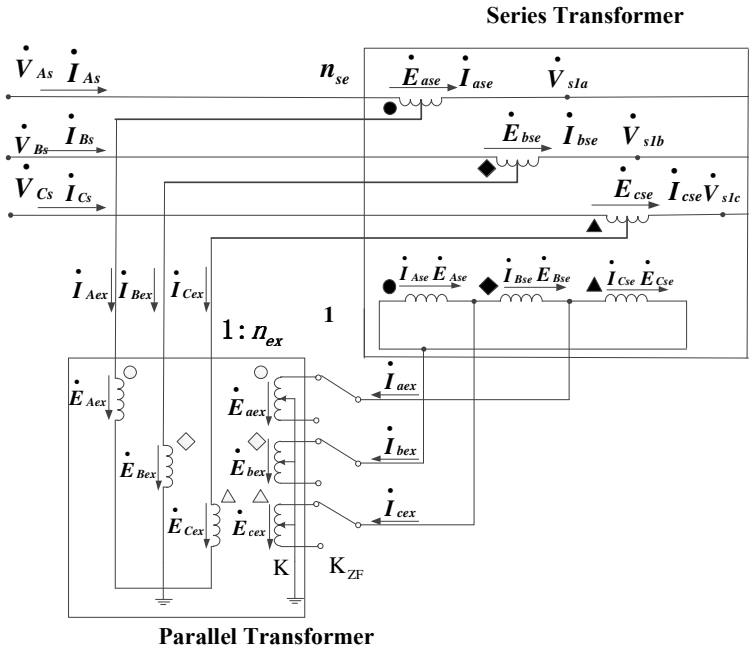

Fig. 1 Typical diagram of PST

During operation, the parallel transformer provides an exciting voltage for the series transformer. Under such exciting voltage, an additional voltage $\dot{E}_{ase}$ is accessed at the primary winding of the

series transformer. The additional voltage $\dot{E}_{ase}$ has 90 ° lead or lag, controlled by the polarity selector K_{ZF}, compared with the voltage $\dot{V}_{As}$ at the sending end system where the PST accesses. The phase relationship can be shown in Fig. 2. Therefore, a phase difference α between the output voltage $\dot{V}_{s1a}$ and input voltage $\dot{V}_{As}$ of PST is introduced, achieving the aim of adjusting the voltage phase, which is shown in Fig. 3.

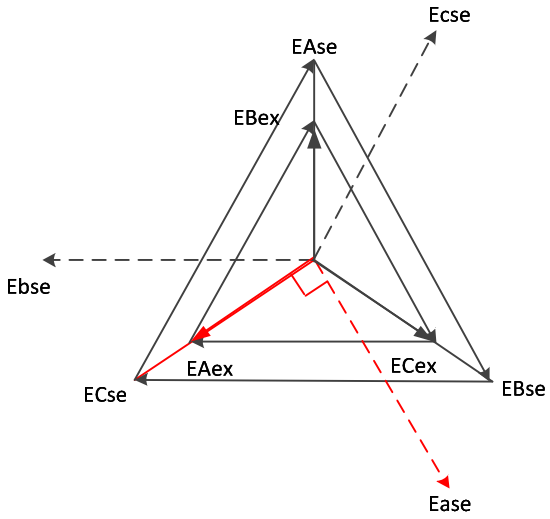

Fig. 2 Voltage phase relationships between the winding of PST

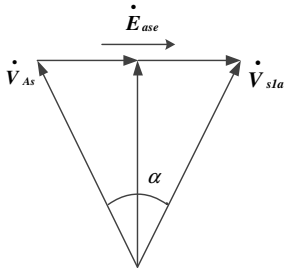

Fig. 3 The princple phase shifting

Model of PST. In simulations, a PST is modeled as a leakage reactance Z_{PST} connected with an ideal transformer, which could be expressed in Fig. 4. In Fig. 4, G_m and B_m are set to be infinite and R_{PST} is 0. In other words, the excitation conductance, excitation susceptance, and leakage resistance could be neglected. T_k is normally selected to be 1. The ideal control angle α is $\alpha = \alpha_J - \alpha_{I'}$, excluding the influence of the leakage reactance. In case of the leakage reactance $Z_{PST} = jX_{PST}$, the actual control angle $\alpha' = \alpha_J - \alpha_I$ of PST shows certain differences with the ideal α.

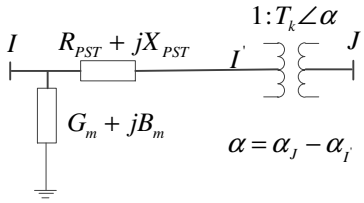

Fig. 4 Model of PST for simulation in PSASP

Control the Power Flows. Considering a single transmission system with between two nodes , if the phase angle of voltage on the receiving bus is set to be 0° , the active power transported over the transmission line is:

$$P = \frac{U_1 U_2}{X_L} \sin \delta \tag{1}$$

where, U_1 and U_2 are the voltage magnitudes on the sending and receiving ends, respectively; δ is the phase angle of voltage on the sending bus; X_L is the line impedance.

If the line is connected with a PST, the transmission power of the line changes to be:

$$P = \frac{U_1 U_2}{X_L + X_{PST}} \sin(\delta + \alpha) \tag{2}$$

As suggested by eq. (2), following results could be concluded: 1) A PST changes the transmission power between the sending and receiving ends. If there are other lines connected to the same sending and receiving ends, the distribution of the power flows between these lines are changed; 2) The PST enables transmitting the same power using a smaller phase angle difference between the sending and receiving ends. Moreover, the maximum transmitting power is reduced; 3) The leakage reactance X_{PST} introduced by PST can be seen as a series resistance, which increase the electrical distance between the installation bus of PST and the system. Therefore, the short circuit current on the installation bus of PST can be reduced.

The Design of PST

The capacity of a PST is the maximum transmission capacity of the line where the PST is placed. According to [3], the series transformer and parallel transformer have a same capacity. Assuming that the maximum transmission capacity of the line is S and the phase angle of the PST is adjustable in a range of $\pm\alpha$, the capacity of the series transformer and the parallel transformer could be obtained by:

$$S_S = S_P = S \sin \alpha \tag{3}$$

where S_S and S_P are the capacity of the series transformer and the parallel transformer, respectively. Since usually α is very small, it can be known that the capacity of series transformer and parallel transformer is far lower than the total capacity of PST.

Application of PST to Tmprove the AC Outward Transmission Capacity of SCPG

The AC Outward transmission path of SCPG, which is also called as the border of Sichuan and Chongqing, is composed by the 500 kV Hongban lines and Huangwan lines, as shown in Figure 5.

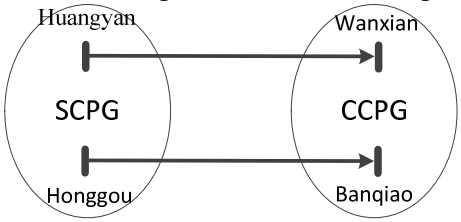

Fig. 5 Border of Sichuan and Chongqing Power Grid

Design of PST for the border of Sichuan and Chongqing. According to the limit capacity of 1900 MW for a single 500kV line, the rated power of PST in one of Hongban lines could be selected as 2,000 MVA.

Analysis reveals that the PST can achieve a desired power flow shifting by a smaller shifting angle. Thus the phase-shifting angle is designed to be ±10. The capacity of the series transformer and parallel transformer could be calculated by $2000 \times \sin 10^\circ = 347$ MVA thereby. As a result, the capacity of the transformers is 350 MVA. In the long-term, Hongban lines is possibly replaced by heat-resisting wires, the capacity of single line will rise to be 3,000 MW. In this condition, the

capacity of the series transformer and parallel transformer is 555 MVA, according to the design capacity of the PST (3,200 MVA). Thus the capacity could select as 560 MVA.

Verification for the designed PST. The designed PST is implemented as a model of Figure 4 and simulated in the software of PSASP based on the operation data of CCPG. The simulation results are summarized in Table 1.

As indicated in Table 1, without the PST, the power flow ratio after the N-1 contingencies of Hongban lines is 0.861. Moreover, under such operating mode, the power flow ratio of Hongban lines and Huangwan lines is 2:1. Based on the limit capacity of 1,900 MW for a single line of Hongban lines, the AC outward transmission capacity of SCPG is about 3,300 MW. With the installation of PST, the power flow ratio after the same fault of N-1 contingencies is significantly reduced. And the AC outward transmission capacity of SCPG increases to 5,090 MW, which is 1,800 MW larger than that without PST. In other words, the PST significantly improves the distribution of the power flow on the border and increases the transmission capability of SCPG.

Table 1 Simulation results after installation of PST for Hongban lines

Phase of Shifting	Power flow（MW）		N-1 of Hongban lines		Outward transmission capacity of SCPG （MW）
	Hongban lines	Huangwan lines	Hongban line （MW）	Power flow ratio	
0	2677	1327	2305	0.861	3300
-1°	2101	1873	1564	0.744	4830
-2°	2070	1902	1541	0.744	4900
-3°	2034	1938	1521	0.748	4960
-4°	2004	1970	1501	0.749	5030
-5°	1969	2001	1481	0.752	5094

During the “Twelfth Five Year Plan”, the short-circuit current of 500 kV buses in SCPG will have a remarkable increase, with the continuous strengthening of the structure of SCPG and the commissioning of large power stations, represented by Jinping power station, Xiangjiaba power station, and Xiluodu power station etc. Some breakers of 500 kV buses have approached to their breaking capacity and threatened the safe operation of power grid. According to the “Twelfth Five Year Plan” of Sichuan power grid, it would be urgent to suppress the short-circuit current in SCPG in the next 5 years.

As shown Fig. 4, in the equivalent circuit of the PST, the PST is equivalent to a series resistance connected to a transformer with a changeable phase. The connection of the series resistance X_{PST} has a good performance for reduce the short-circuit current. Table 2 shows the short-circuit current of 500 kV buses with short-circuit current exceeding 45 kA before and after installation the PST in Hongban lines. It can be seen that, the installation of PST significantly declines the short-circuit current of Honggou and those of other stations.

Table 2 The short-circuit currents of buses in SCPG before and after the installation of PST at Hongban lines

Bus name	short-circuit current（kA）		Bus name	short-circuit current（kA）	
	Before	After		Before	After
Honggou	54.13	49.51	Xufu	46.83	46.15
Dongpo	50.55	50.13	Ziyang	45.6	44.93
Taoxiang	48.64	48.42	Neijiang	45.16	43.25
Jianshan	48.55	48.34			

Summary

This paper provides an overview of the application of phase-shifting transformers around the world, analyzes the basic principle of PST, as well as the location and capacity of the phase-shifting transformer design. Finally, the PST is used to change the power flow distribution of lines on border of SCPG, and improve the AC outward transmission capacity of SCPG. Simulations with SCPG

using PSASP software show that: 1) the PST can increase the AC outward transmission capacity of SCPG by about 1800MW; 2) the short circuit current is also reduced, due to the leakage reactance of PST; 3) the transient stability after installation of PST needs to be further studied.

References

[1] Z. X. Xu, W. T. Zhang, G. Wang, et al. Application of phase-shifter for power flow control of parallel transmission lines. Power System Technology, 1996, vol. 20, no. 4, pp. 6-10.

[2] X. Q. Zhao, M. X. Guo. Study of installation of phase-shifting transformers for East China Power Grid. East China Electric Power，2006, vol. 34, no. 11, pp. 32-34.

[3] S. Q. Ni. Study on basic design and electromagnetic transient of UHV static phase shifter. Beijing: China Electric Power Research Institute, 2013.

[4] W. J. Lyman, J. R. North. Application of large phase-shifting transformer on an interconnected system loop. Transactions of the American Institute of Electrical Engineers, 1938, vol. 57, no. 10, pp. 579-588.

[5] R. Ogahara, Y. Kawaura, S. Iwamoto. Using phase shifters for power flow adjustment following large-scale generation loss. IEEE PES General Meeting, Canada, 2013, pp. 1-5.

[6] R. L. LEE, M. J. Beshir. Planning aspects of 525 kV phase shifters and static var compensators for the Mead-Phoenix and Mead-Adelanto transmission projects in the Southwestern U.S. ICPST’94, Beijing，China，1994, pp. 970-978.

[7] E. M. Carlini, G. Manuzio, D. Bonmann. Power flow control on the Italian network by means of phase-shifting transformers. CIGRE Session 2006，C2-206，Paris：CIGRE，2006, pp. 1-12.

[8] J. Verboomen, H. D. Van, P. H. Schavemaker, et al. Phase shifting transformers: principles and applications. 2005 International Conference on Future Power Systems, Amsterdam, 2005, pp. 1-6.

[9] M. Belivanis, K. R. W. Bell. Use of phase-shifting transformers on the transmission network in Great Britain. 2010 45th International Universities Power Engineering Conference (UPEC), Cardiff, Wales, 2010, pp. 1-5.

[10] IEEE Guide for the Application, Specification, and Testing of Phase-Shifting Transformers, IEEE Std C57.135-2011 (Revision of IEEE Std C57.135-2001).

[11] B. Zheng, Z. T. Xiang, L. G. Ban, et al. Electromagnetic transient analysis on static phase shift applied in UHV power grid. Power System Technology, 2013, vo. 37, no. 5, pp. 1373-1377.

Advanced Materials Research Vols. 960-961 (2014) pp 1006-1012

doi:10.4028/www.scientific.net/AMR.960-961.1006

Sub-module Controller and Sub-module Steady-state Test Platform Design for MMC-HVDC

Baoshun Zhang[1,a], Chengyong Zhao[1], Chunyi Guo[1], Lizhuan Zhou[2], Lin Li[2]

[1]Key Laboratory for Alternate Electrical Power System with Renewable Energy Sources (North China Electric Power University), Beijing, China

[2]Guangdong Mingyang Longyuan Power Electronics CO., LTD, Zhongshan, Guangdong, China

[a]zbs0516@163.com

Keywords: modular multilevel converter(MMC); sub-module controller (SMC) SM fault steady-state test platform

Abstract Compared with Line-Commutated-Converter High Voltage Direct Current (LCC-HVDC), the primary and secondary systems of modular multilevel converter based HVDC (MMC-HVDC) are more complicated. And control and protection function of sub-module controller (SMC) have great influence on the operation of MMC-HVDC system. This paper investigates the design method of SMC and sub-module (SM) steady-state platform. First, the structure of the primary system and the electrical parameters of the 21-level MMC-HVDC are designed. Second, the architecture of the control system and SM fault protection strategy are proposed, and the control program is developed and debugged. Then SM steady-state test platform and the relevant control and protection are designed. Finally, the steady-state test and the system test of the physical MMC-HVDC simulation system are conducted. The test result shows that the sub-module is of good property and SMC can communicate with upper control layer efficiently, control and protect the SM efficiently.

Introduction

Modular Multilevel Converter (MMC) is a multi-level voltage source converter (VSC) topology [1], [2]. High DC voltage is obtained by superposition of a number of sub-modules, which could avoid direct series press-packed connection of the semiconductor devices and hundreds of output voltage levels can be achieved. Compared with the 2- and 3-level VSC, the MMC output voltage harmonic contents and switching losses are reduced greatly and the voltage level can be changed flexibly[3], [4]. In VSC-HVDC applications, the use of MMC topology has become an international development trend.

So far, studies on MMC mainly concentrated on its modeling, modulation and control strategies, [5]-[9], etc. But almost no references did research on the design of MMC-HVDC physical device or control systems. In [10] MOSFET is integrated with sub-module controller (SMC) in designing SM and CompactRIO is taken as pole controller & protection system (PCP) to design MMC-HVDC dynamic simulation device which is fit for research application. Ref. [11] introduces dynamic simulation method for valve based controller (VBC) and put forward a capacitor voltage balance method. Ref. [12] and [13] mainly focus on the hierarchical structure of controller. Ref. [14] designs and develops hardware, software and protection strategy of VBC, which have already been applied in Shanghai Nanhui wind farm integration project.

MMC-HVDC physical simulation primary system is designed in this paper. Control system uses hierarchical controlled manner, from top to bottom the control system is made up of the operator control system (PC), PCP, VBC and SMC. Two types of SM faults are studied and the corresponding protection strategies are proposed. A steady-state test platform is designed for the SMC and SM. Results of SM steady-state test proved the validity of SMC. MMC-HVDC system experiment results verified that communication between SM with VBC, SM fault protection and other functions can be achieved.

MMC-HVDC physical system

***A*. MMC converter and SM structure**

As shown in Fig.1, the MMC contains six symmetrical arms, and each arm contains N SMs which were connected with a reactor L in series. An upper and a lower arm constitute a phase unit. The output voltage of converter can be adjusted by allocating the number of SMs in the inserted state of the upper and lower arms, and DC voltage can be maintained constant for the number of inserted SMs in 3 phase units are equal at anytime.

SM consists of two IGBT used as switches and a dc energy storage capacitor. A thyristor and a contactor are used as bypass switch. T1 and T2 represent IGBT, D1 and D2 represent the IGBT anti-parallel diode, C1 represents the DC side capacitor, S is mechanical bypass switch of SM, which can bypass SM for a long time, T is electronic bypass switch for fast protection of D2. According to switching states of T1 and T2, the state of SM can be divided into inserted, bypassed and blocked.

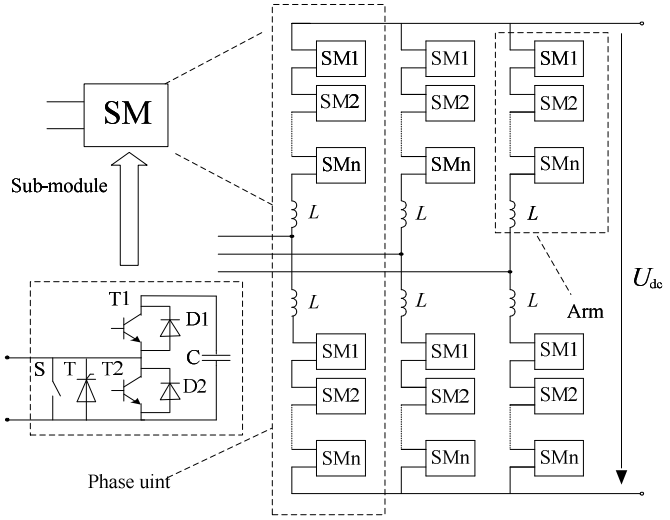

Figure 1. The topology of MMC

When the SM is transferred from inserted to bypassed state or from bypassed to inserted state, as characteristic of the IGBT are not identical, T1 and T2 may be switched on at the same time, so the capacitor is shorted. Therefore, it is necessary to set dead time for the two IGBTs, the setting method of dead time is adding blocked state into the SM switching operation. The output voltage is distorted, the fundamental component is reduced, and the harmonic component is increased by the dead time. It is more difficult for arm current direction detection. However, in order to prevent the SM capacitor form being shorted, dead time of the upper and lower IGBT is set in software in this paper.

***B*. Primary system of MMC-HVDC**

The rated power of MMC-HVDC physical system is 100kW, the rated DC voltage is ± 2kV. Each arm of converter has 22 sub-modules, and of which two SMs are used as spinning reserve. Main circuit of physical simulation system is depicted in Fig. 2.

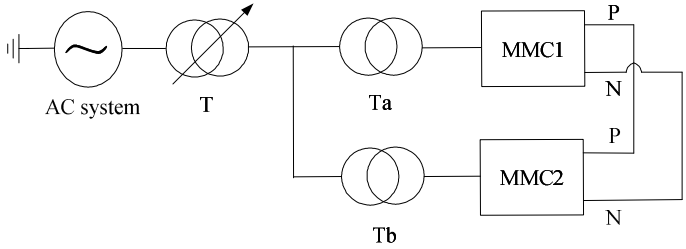

Figure 2. The primary system of MMC-HVDC physical simulation system

The rated input voltage of the regulator T is 380V, and the output voltage is raged from 0 to 430V. Rated capacity of converter transformer Ta and Tb is 120kVA, and the transformation ratio is 0.38/2 and the positive leakage inductance of the transformer is 0.1 p.u.. There is 50% taps on transformer

secondary side, and transformer connection group can be changed with power off. Fuses are equipped in the converter transformer secondary side, converter arms and DC lines. Current limiting resistor is 50Ω, and reactor of arm is 20mH. Three-phase PT and single-phase CT is used in main circuit. Active interfaces are reserved in the converter transformer primary side, secondary side and the DC side, so the filtering and fault simulation could be increased according to the need. Resistor is used to represent DC line and 1MΩ grounding resistors are set at both beside ends of the inverter. 15mH smoothing reactors are added at one end of the positive and negative DC bus. MMC-HVDC physical simulation system is shown in Fig. 3.

(a) (b)

Figure 3. MMC physical system (a) Two ends MMC (b) Three phase arm

C. Control system of MMC-HVDC

Hierarchical control method is used in control system. PC displays primary system voltage and current signals, and controls active and reactive power. PCP receives reference value of active and reactive power from PC, calculates modulation ratio M and phase angle δ. VBC completes sorting of capacitor voltages and distributes trigger signals of SMs to SMC. SMC triggers SM and protects the IGBTs. PCP processing functions are jointly implemented by digital signal processor (DSP) and field-programmable gate array (FPGA). FPGA is also used as processor of VBC and complex programmable logic device (CPLD) is used as processor of SMC. The hierarchical c ontrol system architecture is shown in Fig. 4.

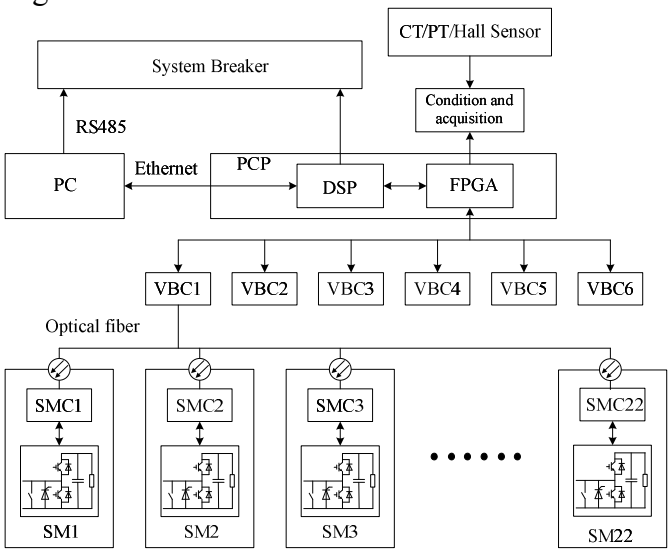

Figure 4. The architecture of control system

System status information is received by the host computer via an Ethernet from PCP, and the needs of human-machine interface displays and real-time control algorithms are taken into consideration. To ensure the rapidity of the protection system, breakers are controlled by PCP directly

and also operated by PC remotely. VBC communicated with SMC by a multiplexed pair of optical fibers for the asynchronous communication between VBC and SMC, which minimize the number of optical fibers and reduce the complexity of the control system.

Four operating states are set for the MMC-HVDC system: self-test, rectification, normal operation and shutdown. The main purpose of self-test state is checking whether control system hardware and communication between all layers of control system is normal when the primary system is power off. Under the coordination control, the MMC-HVDC can run at a stable state, with fixed DC voltage, fixed active power, fixed AC voltage and fixed reactive power.

Sub-module Controller

SMC is responsible for capacitor voltages conversion and SM status monitoring, and sending information to VBC through the fiber. Control information is received simultaneously from VBC to control IGBTs, and dead time of the two IGBTs is achieved in software. Mechanical bypass contactor and electronic thyristor are controlled. Hardware architecture of SMC includes AC power source, control chip, optical fiber, IGBT trigger voltage sampling and AD conversion, electronic bypass and mechanical bypass trigger, fault detection. Software features are displayed in the following Fig. 5. There are two types of SM fault: SMC communication fault and SM internal fault.

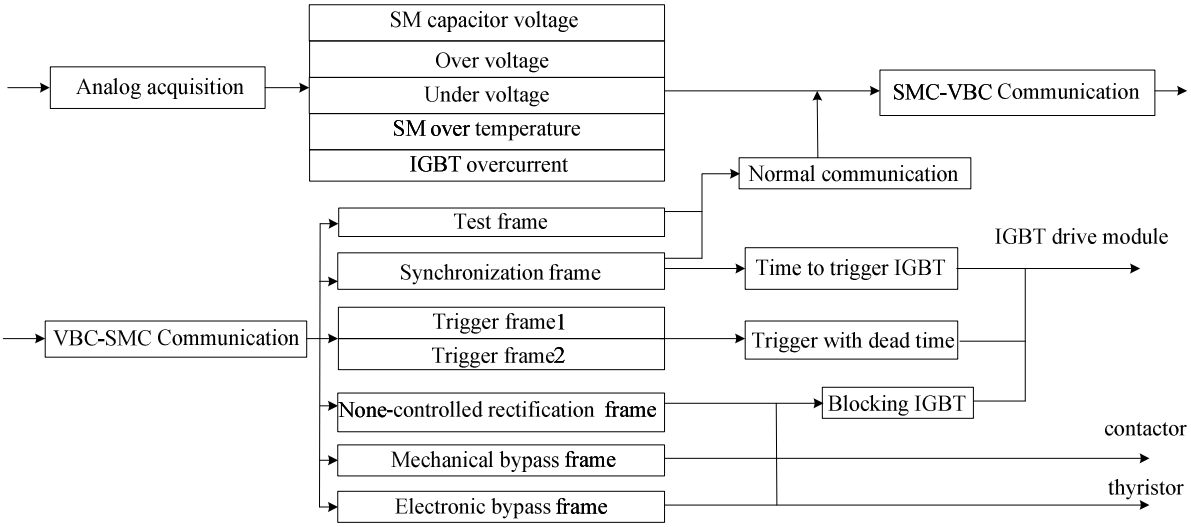

Figure 5. The program function of SMC

***A*. SMC communication fault**

Communication fault detection module detects the faults of received data, which includes overtime, the frame format error, and parity check error. Receiving data overtime refers to none of data or only a synchronous frame without any control frame is received from VBC in a control period. When receiving data overtime is detected, the fault is reported to VBC. Receiving frame format error means received data frame format of SMC does not match any normal frame. After a communication error is detected, fault is reported and the fault number is counted. SMC uses the correct control frame of last period for SM control.

***B*. SM internal fault**

After the control system is powered, SM status is monitored. Over voltage and under voltage is detected via SMC analog circuit. To prevent protection malfunction, SMC detects start time of over voltage or under voltage, the fault is confirmed only if the abnormal condition last for a certain time. Else, fault is ignored. Over temperature is achieved through the thermostat switch. Temperature switch is closed when over temperature fault occurs, so voltage level is changed to high by the conversion circuit to send fault to processor. When the IGBT over current fault occurs, the IGBTs are blocked by drive module quickly and fault information is sent to the processor.

At the start of one control period, capacitor voltage of SM and status of SM will be uploaded to the VBC, which will send control information to the SMC before the end of the control period. If a SM fails, the failure information in a period initial stage will be uploaded to the VBC, which will receive all fault information to determine whether the fault number of SM is less than the number of redundancy SM. If number of failed SM in the arm is less than or equal to two, bypass the corresponding SM, and insert redundancy SM. If the number of failed SM is greater than two, then upload a fault signal to PCP, and keep the open number of SM in the last control period before the PCP control the physical simulation system to stop. VBC sends stop request to the PCP, and PCP sends a stop command to the VBC. After receiving the stop command VBC to block all the SMs. Taking the VBC request to PCP the stop instruction time into accounts, SMC will receive control instructions of VBC in the next control cycle; SMC maintains the cycle state before stop instruction. When the SM fails, the control system can deal with failure in two control period.

SM steady-state test platform

A. Primary system of test platform

SM steady-state test platform consists of adjustable DC voltage source, a current limiting resistor, the DC capacitor and two IGBTs with anti-parallelled diodes. Test platform connect with the measured module through the right port, between which are the reactors. Since two SMs are packaged as a power unit, the two SMs are simultaneous measured in series. Fig. 6 shows the primary system of steady-state test platform.

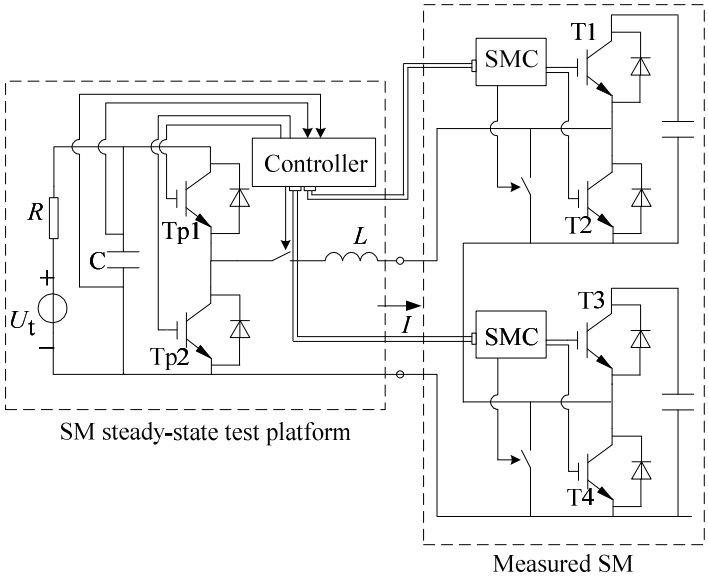

Figure 6. The primary system of SM steady-state test platform

Test platform and two SMs IGBT are controlled by SPWM, in which the test platform signal Tp1 and measured SM signal T1, T3 are the same; Tp2, T2 and T4 of measured SM control signal are the same. Two groups of signals are contrast.

When steady-state test platform is unloading, the test platform port output square wave. When TP1, T1 and T3 are switched on, the output voltage of the test port is Ut, otherwise when TP1, T1 and T3 are switched off, the output voltage is 0. After effection of smoothing reactor, the load current is sine wave with high frequency harmonics.

B. Controller design of test platform

The controller of steady-state test platform not only controls IGBT triggers of the test platform, but also controls the IGBTs of measured SM. In order to meet the different testing requirements of SM, different load currents can be adjusted by regulating DC output voltage and SPWM modulation.

A custom serial communication protocol is adopted for test platform controller to communicate with the measured SMC. IGBT trigger signal, bypass signal and other information are sent to SMC, which will then send capacitor voltages and SM states back. Communication data is exchanged between test platform controller and measured SM with a fixed period.

Experiment result

A. SMC steady-state test

Voltage of DC source Ut is regulated and the oscilloscope is connected to the output of the SM test platform to measure the output voltage. Fig. 7(a) shows the waveform of no-load test. Curve 1 is load voltage of the test platform. Curve 2 is Tp2 of the test platform. Curve 3 is inductive load current. The result is consistent with theory. And by adjusting the control button of testing platform to change SPWM modulation, the output voltage waveform modulation can be changed accordingly.

Switch on the load side, gradually increasing Ut, SM capacitor voltage and test platform voltage, and RMS of load current are displayed on the LCD screen of controller. The load current which is sine wave with high frequency harmonics and voltage waveforms of the measured SM are observed by oscilloscope. Fig. 7(b) shows voltage and load current of SM. Curve 1 is the output voltage waveform of the test platform. Curve 2 is Tp2 of the test platform. Curve 3 is the load current waveform. Curve 2 is T2 of the measured SM.

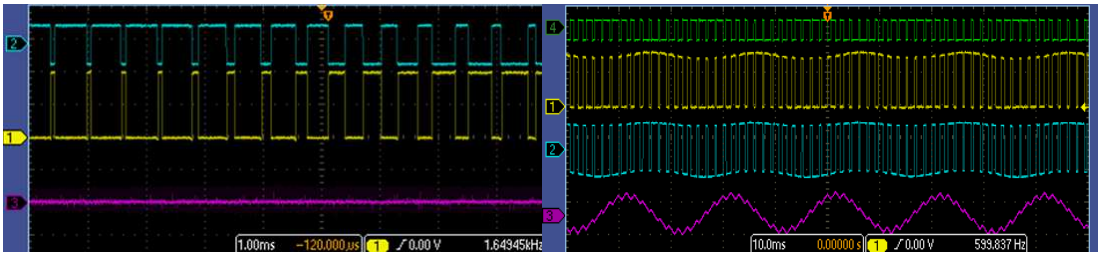

(a) (b)

Figure .7 Test voltage and current(a) Unload test(b) Load test

B. System test

To test the communication between SMC and VBC, SM fault protection, the system test of physical system of MMC-HVDC are done. Fig. 8 shows capacitor voltages of 22 SMs in upper arm of phase A recorded by PC at a low rate over an extended period, when the system is stable and DC voltage is 4kV. Fig. 8 shows that the capacitor voltages are maintained at about 200V.

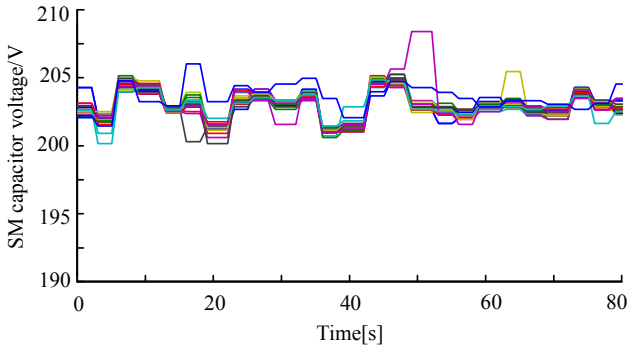

Figure 8. Capacitor voltages of upper arm in phase A

Experimental results also show that the SMC can protect the corresponding SM and send the fault information to VBC, when communication fault and over voltage or under voltage fault happened.

Conclusion

This paper introduces the primary system of MMC-HVDC physical system and the control system architecture. SMC and SM fault protection strategy are studied in details, and the SM steady-state test platform and MMC-HVDC physical simulation system are established. Experiment is done to test performance of the system. The conclusions are as following:

Hierarchical architecture is adopted for control system which is divided into PC, PCP, VBC and SMC, the communication between different control layers is determined, functions of the control layers are definited, respective control programs are developed.

The hardware and software of steady-state platform is reasonablely designed, which can ensure the efficient of SM test. The steady-state operating characteristic of SM is examined, which can verify the correctness of the SMC and SM.

Hardware architecture and software design of SMC have reference value for engineering applications.

This work was supported by National High Technology Research and Development Program of China (Program 863) (No.SS2013AA050105); National Science Foundation of China (51177042).

References

[1] Guanjun Ding, Guangfu Tang, Zhiyuan He, "New technologies of voltage source converter (VSC) for HVDC transmission system based on VSC", IEEE PES General Meeting. Pittsburg, USA：IEEE，2008：1-8.

[2] J.Dorn, H.Huang, D.Retzmann, "A new Multilevel Voltage-Sourced Converter Topology for HVDC Applications", CIGRE session, Paris, France, 2008.

[3] Lesnicar A, Marquardt R, "A new modular voltage source inverter topology", 10th European Conference on Power Electronics and Applications, Toulouse, France, 2003.

[4] Lesnicar A, Marquardt R, "An innovative modular multilevel converter topology suitable for a wide power range", Proceedings of IEEE Power Tech Conference, Bologna, Italy, 2003.

[5] Minyuan Guan, Zheng Xu, Qingrui Tu, "Nearest level modulation for modular multilevel converters in HVDC transmission", Automation of Electric Power Systems, 2010, 32 (2)： 48-52.

[6] P. M. Meshram, V. B. Borghate, "A Novel Voltage Balancing Method Applied to Direct control Strategy of MMC-HVDC System", International Conference On Advances In Engineering, Science And Management (ICAESM), 2012.

[7] A. Shojaei, G. Joos, "An Improved Modulation Scheme for Harmonic Distortion Reduction in Modular Multilevel Converter", Power and Energy Society General Meeting, 2012.

[8] Jaime Peralta, Hani Saad, Sébastien Dennetière, Jean Mahseredjian, "Dynamic Performance of Average-Value Models for Multi-terminal VSC-HVDC Systems", Power and Energy Society General Meeting, 2012.

[9] Jianzhong Xu, Chengyong Zhao, Wenjing Liu, Chunyi Guo, "Accelerated model of Modular Multilevel Converters in PSCAD/EMTDC", Power and Energy Society General Meeting, 2013.

[10] Yuebin Zhou, Daozhuo Jiang, Pengfei Hu, "A Prototype of Modular Multilevel Converters", Power Electronics, IEEE Transactions on，2013.

[11] Yang Gao, Dong Liu, Binjian Yang, "MMC based valve base controllers of HVDC flexible and their dynamic simulation experiment", Automation of Electric Power Systems, 2013, 30(15)： 53-58.

[12] Yuefeng Yang, Jie Yang, Zhiyuan He, Haitian Wang, "Research on Control and Protection System for Shanghai Nanhui MMC VSC-HVDC Demonstration Project", AC and DC Power Transmission (ACDC), 10th IET International Conference on, 2012.

[13] Shaojun Huang, Remus Teodorescu, Laszlo Mathe, "Analysis of Communication Based Distributed Control of MMC for HVDC", Power Electronics and Applications (EPE), 15th European Conference on, 2013.

[14] Xirui Jiang, Yuefeng Yang, Yang Gao, "Valve Base Controller (VBC) Used in HVDC Flexible System", Power and Energy Engineering Conference, Shanghai, 2012.

Advanced Materials Research Vols. 960-961 (2014) pp 1013-1016

doi:10.4028/www.scientific.net/AMR.960-961.1013

Accounting the second derivatives in the power flow calculation

Yuferev Sergey [1, a]

[1] Ural Federal University, E-309, Mira str. 19, Ekaterinburg, Russian Federation

[a] YuferevSV@gmail.com

Keywords: Convergence of iterative process, Hessian matrix, Static stability, Optimization, Power flow.

Abstract. In this paper, it is show how the second derivatives of the Hessian matrix influence on the convergence of the power flow calculation. Convergence conditions of the Combined Newton's method using 14 nodes IEEE testing schemes are investigated. The method can be used to determine the control actions to pull the operating point into the feasibility domain.

Introduction

The operting point of power electrical systems (PES) is subject to various disturbances - the fluctuation of the load, topology change, emergency (scheduled) off (on) of electrical equipment and so on - and you want to know the limits of change, both in terms of static stability of the power flow PES, and its existence.

In commercial programs, limiting regimes are usually repeated calculation of power flow in a given direction weighting. This approach is reliable and easy to implement, but because of the method used by the ideology of "trial and error" when calculating is largely determined by specifying the weighting step.Therefore, issues of improvement and development of new methods of power flow calculations are rather topical [1].

Theoretical background

Powert flow equations. The system of power flow equations are expressed:

$$\Delta W(X,Y) = 0, \tag{1}$$

where W(X,Y), X, Y are power unbalance vectors, dependent and independent variables, respectively. Separation of independent and dependent variables reflects the fact that the number of variables (parameters) exceeds the number of equations [2].

Second-order method of optimization. One way to find the minimum of thew objective function within the contrains [2, 3]:

$$F = [W\text{-}W(X,Y)]^T \cdot [W\text{-}W(X,Y)]. \tag{2}$$

The function minimum (2) is reached at the point where derivatives on all required variables are equal to zero:

$$dF/dX = -2dW/dX \cdot [W\text{-}W(X,Y)]^T. \tag{3}$$

The Hessian matrix, prepaid in the process of solving (2), contains two items:

$$H = [dW/dX]^T \cdot [dW/dX] - [d^2W/dX^2] \cdot [W\text{-}W(X,Y)]. \tag{4}$$

Jacobian and Hessian are different in form during the power flow calculation. This Hessian property is allows you to find the existing parameters of the operation point (power flows and voltages), even if the divergence of the Newton Raphson method for the initial conditions.

From (4) we see that the Hessian depends not only on the magnitude and angles of voltages, but also from the set of nodal capacities. The occupancy of the Hessian matrix is higher than the Jacobian matrix. This is due to the fact that the Jacobi matrix are non-zero elements - only the nodes of the first zone, that is, nodes that are directly connected. The Hessian matrix contains, besides the nodes of the first zone, nodes of the second zone, bringing the number of nonzero elements more. Figure 1 shows the nodes of the first zone (№ 8 and 11) and the second zone (№ 1, 2, 5 and 9) for node 6.

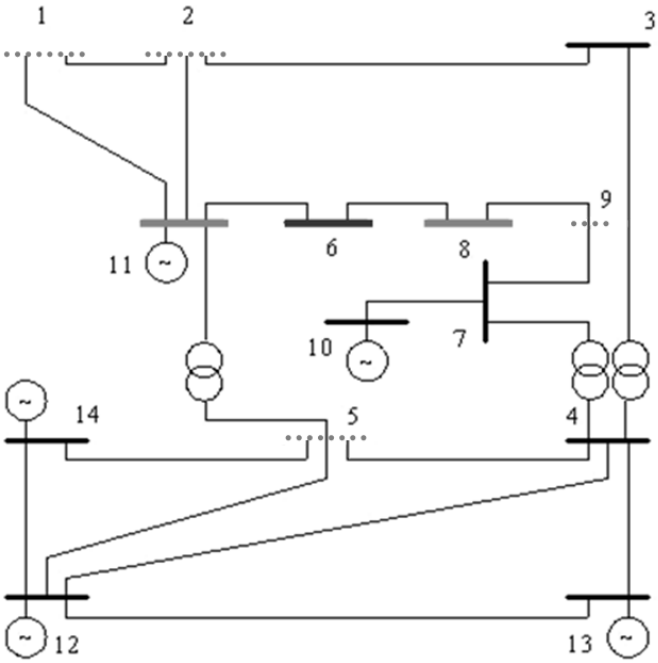

Figure 1. 14 nodes IEEE test scheme with marked first (—) and second (···) zones for node 6.

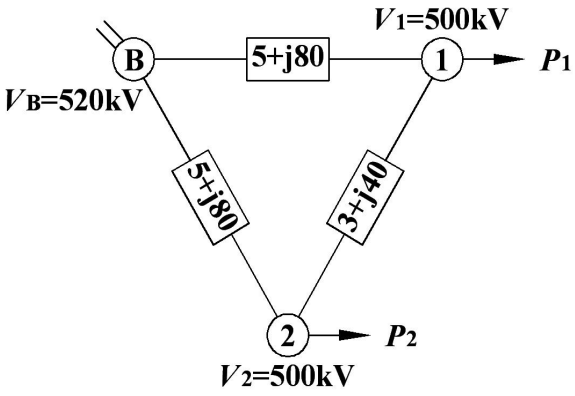

Figure 2. The test scheme

The term dW/dX2·[W-W(X,Y)] plays an important role in steady state calculation, when the operating point out of feasibility boundary. Due to this term, the Hessian matrix is not singular on the feasibility boundary of the solution [5].

Convergence of Combined Newton's method

Convergence of Combined Newton's method was investigated based on program MathCAD for 14 nodes IEEE test scheme (figure 1). The 14 node is infinity bus, nodes 10, 11, 12, 13 are active buses. Absolute values of voltage magnitudes are fixed at all buses. Initial nodal capacities (loading is positive value, generation is negative one) and voltage are shown in table I.

Table 1. Initial data

Bus number	1	2	3	4	5	6	7
P [MW]	90	80	70	100	40	50	70
V [kV]	115	115	115	230	230	115	115
Bus number	8	9	10	11	12	13	14
P [MW]	100	190	-350	-200	-800	-900	-
V [kV]	115	115	115	115	230	230	230

Results of power flow calculation are presented in table 2.

Table 2. Results of power flow calculation.

Scheme state	Combined Newton's method					Newton-Raphson method, № iters
	№ iters	P_{10}, MW	P_{11}, MW	P_{12}, MW	P_{13}, MW	
Normal	3	-350	-200	-800	-900	3
Off 4-13	3	-350	-200	-800	-604	Misconvergence
Off 12-13	5	-350	-200	-800	-742	Misconvergence
Off 4-7 and 4-9	6	-567	-70	-800	-900	Misconvergence

As you can see from the table 1, not all calculated nodal powers equal initial ones. This is due to the fact that initial nodal powers were outside of the boundary of existence domain. If we use Newton-Raphson method, we'll not get the solution, because N-R method with so initial data is misconvergence. Applying objective function (2) allowed us to find solution and this solution is the nearest to initial state point. Therefore Newton's method of optimization corrected nodal powers so, that difference between calculated and initial powers will be minimal.

Importance of the second derivatives s method

Influence of the full Hessian matrix has been investigated on the three-buses test scheme parameters of which are presented in Figure 2. Results of the power flow calculations are presented in the table 3. The term d2W/dX2·[W-W(X,Y)] of Hessian matrix designate as "The second component of the Hessian at the solution point".

Table 3. Results of power flow calculation.

Initial power, MW	Voltage phase, degree.	Calculated power, MW	Jacobian determinant at the solution point	Hessian determinant at the solution point	The second component of the Hessian at the solution point
P_1=0; P_2=0.	δ_1=0,0°; δ_2=0,0°.	P_1=0; P_2=0.	$5{,}073\cdot10^{7}$	$1{,}029\cdot10^{16}$	0 0 0 0
P_1=-1000; P_2=-1000.	δ_1=-18,0°; δ_2=-18,0°.	P_1=-1000; P_2=-1000.	$4{,}658\cdot10^{7}$	$8{,}679\cdot10^{15}$	0 0 0 0
P_1=-3040; P_2=-3040.	δ_1=-82,1°; δ_2=-82,1°.	P_1=-3040; P_2=-3040.	$3{,}080\cdot10^{6}$	$3{,}795\cdot10^{13}$	0 0 0 0
P_1=-3050; P_2=-3050.	δ_1=-86,4°; δ_2=-86,4°.	P_1=-3049; P_2=-3049.	0	$1{,}767\cdot10^{12}$	$7{,}363\cdot10^{3}$ $-1{,}644\cdot10^{3}$ $-1{,}644\cdot10^{3}$ $7{,}363\cdot10^{3}$
P_1=-4000; P_2=-4000.	δ_1=-86,4°; δ_2=-86,4°.	P_1=-3049; P_2=-3049.	0	$1{,}966\cdot10^{15}$	$7{,}942\cdot10^{6}$ $-1{,}773\cdot10^{6}$ $-1{,}773\cdot10^{6}$ $7{,}942\cdot10^{6}$
P_1=0; P_2=-4000.	δ_1=-32,1°; δ_2=-47,8°.	P_1=0; P_2=-4000.	$3{,}316\cdot10^{7}$	$4{,}398\cdot10^{15}$	0 0 0 0
P_1=0; P_2=-6000.	δ_1=-70,5°; δ_2=-99,0°.	P_1=-96; P_2=-5879.	0	$1{,}731\cdot10^{14}$	$9{,}226\cdot10^{5}$ $-3{,}226\cdot10^{5}$ $-3{,}226\cdot10^{5}$ $1{,}086\cdot10^{6}$

Influence of the initial approximations is shown in the table IV. There results of each iterations of power flow calculation are presented. The initial powers were P1=0 MW and P2 = -7000 MW.

Table 4. Influence of initial approximation.

№ iters	δ_1=0°; δ_2=0°	δ_1=-22,34°; δ_2=22,34°	δ_1=-22,34°; δ_2=45,26°
1	P_1= 392 MW, δ_1=-44,85° P_2= -5447 MW, δ_2=-69,39°	P_1= 4123 MW, δ_1=196,10° P_2= -275 MW, δ_2=773,76°	P_1= 6601 MW, δ_1=-25,82° P_2= -9855 MW, δ_2=84,43°
2	P_1= 555 MW, δ_1=-66,01° P_2= -6235 MW, δ_2=-98,39°	P_1= 4355 MW, δ_1=-193,85° P_2= -430 MW, δ_2=772,86°	P_1= 7038 MW, δ_1=-26,85° P_2= -9896 MW, δ_2=72,52°
3	P_1= 571 MW, δ_1=-67,70° P_2= -6250 MW, δ_2=-100,58°	P_1= 4355 MW, δ_1=-193,85° P_2= -430 MW, δ_2=772,86°	P_1= 7038 MW, δ_1=-26,85° P_2= -9896 MW, δ_2=72,52°
4	P_1= 571 MW, δ_1=-67,70° P_2= -6250 MW, δ_2=-100,58°	P_1= 4355 MW, δ_1=-193,85° P_2= -430 MW, δ_2=772,86°	P_1= 7038 MW, δ_1=-26,85° P_2= -9896 MW, δ_2=72,52°
5	P_1= 571 MW, δ_1=-67,70° P_2= -6250 MW, δ_2=-100,58°	P_1= 4355 MW, δ_1=-193,85° P_2= -430 MW, δ_2=772,86°	P_1= 7038 MW, δ_1=-26,85° P_2= -9896 MW, δ_2=72,52°
6	P_1= 571 MW, δ_1=-67,70° P_2= -6250 MW, δ_2=-100,58°	P_1= 4355 MW, δ_1=-193,85° P_2= -430 MW, δ_2=772,86°	P_1= 7038 MW, δ_1=-26,85° P_2= -9896 MW, δ_2=72,52°

Conclusions

Combined Newton's method is efficient to calculate the steady state of the EPS because of higher efficiency of the solution for the modes in the vicinity of the existence of solutions, as well as beyond it.

Accounting for the second derivatives of the area of the positive features of the Hessian of the Jacobian, which in turn allows the operating conditions are in negative values of the Jacobian.

The difference of the Hessian, in turn, leads to the need to analyze the primary approach, otherwise you can be either in the negative Hessian, either in a positive Hessian, but not the one where the point is the desired solution.

References

[1] V. I. Tarasov, Nonlinear minimization methods for calculating steady states of electric power systems, – Novosibirsk: Nauka, 2001, p. 214.

[2] V. M. Gornshtejn, B. P. Miroshnichenko, A.V. Ponomarev, Methods of power system mode optimization, Moscow: Energiya, 1981, p. 336.

[3] A.V. Pazderin, S.V. Yuferev “Pulling the operating point back onto the feasibility boundary”, Sustainable Power Generation and Supply, 2009 Nanjing, China, pp. 1-5.

[4] A. Pazderin, S. Yuferev “Steady-State Calculation of Electrical Power System by the Newton’s Method in Optimization” PowerTech, 2009 IEEE Bucharest, Romania, pp. 1-6.

[5] Sergey Yuferev, Andrey Pazderin / Combined Newton’s method for power flow calculation // Proceedings of the IASTED International Conference Power and Energy Systems (AsiaPES 2013) April 10 - 12, 2013 Phuket, Thailand. P. 104 – 107.

Advanced Materials Research Vols. 960-961 (2014) pp 1017-1021

doi:10.4028/www.scientific.net/AMR.960-961.1017

Design of HVDC Supplementary Subsynchronous Damping Controller

Qinlei Chen[1,a], Chunlin Guo[1,b], Han Chen[1,c], Jun Chen[1],
Ya'nan Li[2], Weiyong Jiang[2]

[1]State Key Laboratory for Alternate Electrical Power System with Renewable Energy Sources, North China Electric Power University ,Beijing 102206, China

[2]State Power Economic Research Institute, Beijing 102209, China

[a]hncql.ok@163.com, [b]799493057@qq.com, [c] chensheshijia@ncepu.edu.cn

Keywords: HVDC, subsynchronous oscillations (SSO), supplementary subsynchronous damping controller (SSDC)

Abstract. Supplementary subsynchronous damping controller (SSDC) is an effective countermeasure to damp the subsynchronous oscillation (SSO) caused by HVDC. On the basis of analyzing the mechanism of inducing SSO by HVDC, the principle of damping SSO by SSDC and SSDC design methods are expounded. A SSDC is designed for a practical power plant in China, and the correctness and validity of the SSDC control strategies are proved with time domain electromagnetic simulation results.

Introduction

As an extremely serious stability problem, Power system subsynchronous oscillation (SSO) first appeared in the long distance transmission system with series capacitance compensation, and then is founded in the HVDC system with steam-turbine generator shaft torsional oscillation caused by inappropriate control strategies [1-5]. With the rapid development of HVDC in China, the problem of SSO caused by HVDC became more and more prominent, so it is necessary to study damping measure of SSO caused by HVDC transmission.

A traditional method to overcome power system subsynchronous oscillation is using additional excitation control. However, its main drawback is that the response speed is not fast enough. Although using FACTS devices such as SVC, TCSC and filter to damp SSO can overcome shortcomings of additional excitation control, it requires additional equipment [6]. Additional subsynchronous oscillation damping controller (SSDC) was proposed by EPRI to damp SSO caused by HVDC system [7]. The basic principle of SSDC is to provide appropriate positive damping for steam-turbine generators in the subsynchronous frequency range. At present, there have been many scholars succeed in designing SSDC and obtained certain damping effect by using advanced control algorithm [6, 8-10]. On the basis of analyzing the mechanism of inducing SSO by HVDC, SSDC design and analysis methods are discussed in this paper. And then, a SSDC for a practical engineering is designed.

The mechanism of SSO caused by HVDC system

The change and interaction process of AC/DC system state variables can be shown in Fig.1. According to Fig. 1, the mechanism of SSO caused by HVDC system can be analyzed as follows [11]: If a small disturbance of electromagnetic torque is added to steam-turbine generator shaft, causing torsional modal rotation speed and angle fluctuate ($\Delta\omega$ and $\Delta\theta$), will lead to corresponding fluctuation of generator voltage amplitude and phase (ΔU and $\Delta\theta_U$), resulting in fluctuation of converter bus voltage amplitude and phase. Under an established DC control mode and operation condition, the HVDC trigger-delayed angle will fluctuate ($\Delta\alpha$), resulting in fluctuation of DC voltage (ΔU_{dr}), and then causing DC current or DC power fluctuate (ΔI_d, ΔP_d), This deviation will be fast corrected and adjusted by constant-current controller of HVDC rectifier, causing the generator electromagnetic torque fluctuate (ΔT_e), and eventually cause feedback on unit shaft. If the phase lag

(including additional phase lag caused by closed-loop control system) between the speed change and the resulting generator electromagnetic torque change exceeds 90 degrees, a torsional interaction with positive feedback characteristic will be formed to constantly help increasing perturbation amplitude, leading to unstable shaft torsional oscillation.

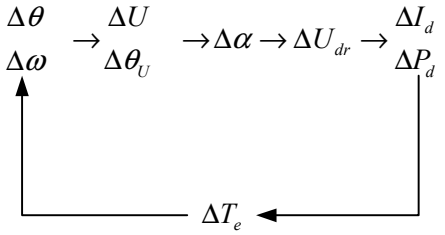

Fig. 1 Schematic diagram of SSO caused by HVDC

The principle of damping SSO by SSDC

According to complex torque coefficient method, power system electrical damping coefficient D_e can be expressed by Eq. 1

$$D_e = \mathrm{Re}\left(\frac{\Delta T_e}{\Delta\omega}\right) \tag{1}$$

Where ΔT_e is the variation of generator electromagnetic torque and $\Delta\omega$ is the deviation of generator speed. Power system electrical damping properties are determined by phase difference between ΔT_e and $\Delta\omega$. If the absolute value of this phase difference is less than 90 degrees, the power system electrical damping is positive and SSO will not occur. However, if the absolute value of this phase difference exceeds 90 degrees, the power system electrical damping is negative and the phenomenon of SSO may occur. The phase relationship between ΔT_e and $\Delta\omega$ is shown in Fig. 2.When the phase lag from $\Delta T_e$to $\Delta\omega$ is between 90 degrees and 270 degrees, namely when ΔT_e is located in third (or fourth) quadrant, the power system electrical damping coefficient (D_e) is negative, SSO may occur. At this point, if an additional electromagnetic torque in the first quadrant can be provided, making $\Delta T_e''$ which is the sum of phasor ΔT_e and phasor $\Delta T_e'$ located in the first quadrant, the power system electrical damping coefficient (D_e) is positive, SSO can be damped [12, 13].

As can be seen from Fig. 2, the effect of additional electromagnetic torque $\Delta T_e'$ provided by SSDC depends on magnitude of $\Delta T_e'$ and phase difference between $\Delta T_e'$ and $\Delta\omega$. The smaller the phase difference between $\Delta T_e'$ and $\Delta\omega$ or the bigger the magnitude of $\Delta T_e'$, the greater the effect of additional electromagnetic torque.

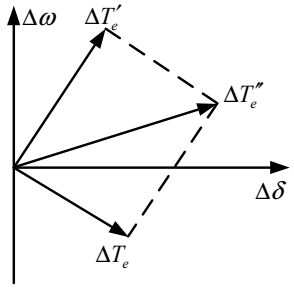

Fig. 2 The phase diagram of electromagnetic torque variation and speed deviation

SSDC design methods

SSDC design principle. According to DC system operation requirements, and considering using SSDC to participate in controlling SSO problem, SSDC design should follow basic principles as follows [14] :

(1)Be able to provide enough positive electrical damping for nearby steam-turbine generator under various operation modes.

(2) There is a certain gain margin and phase margin, and does not affect the regulatory function of DC control system.

(3) Does not affect the electromagnetic transient response characteristics of the DC system.

(4) Does not amplify characteristics and non-characteristic harmonics of AC/DC side in HVDC system.

(5) Its input signals should be easy obtained locally for DC converter station.

(6)Does not cause multiple interactions between DC rectifier stations or inverter stations

Input signal Selection. As for SSDC design, the input signal should have characteristics of the realizability and effectiveness. Realizability refers to using signal can be measured, and should try to avoid interference and noise attenuation caused by signal transmission process, making SSDC controller easier to realize. Effectiveness means the power system SSO characteristics can be accurately reflected by SSDC input signal, and the SSDC input signal has better controllability and observability, making controller play a better role. Therefore, converter bus voltage frequency and amplitude, AC current of converter transformer, DC current, DC voltage, DC power and generator rotating speed to be studied can reflect SSO characteristics. All of these can be used as SSDC input signal.

Control system Structure design. The SSDC control system can be designed by narrowband-pass mode-control method or broadband-pass optimal-design method. The SSDC designed by narrowband-pass mode-control method must be based on accurate modeling of shaft or accurate torsional natural frequency. Aiming at torsional natural frequency of steam-turbine generators which may have the possibility of SSO, this kind of SSDC designs narrowband-pass filter to carry out modal phase compensation and gain adjustment, thus realizes providing positive modal damping for generator. SSDC designed in this way can significantly improve the electrical damping of controlled modal, but may cause negative damping influence on other adjacent generators. The SSDC designed by broadband-pass optimal-design method designs a band-pass filter in a frequency range where units may have the possibility of SSO. The band-pass range is generally the low-pass band of HVDC. In this frequency range, this kind of SSDC provides common phase compensation for all oscillation modes. SSDC designed in this way needs to adopt optimization algorithm for parameter setting, and can provide strong positive damping for serious oscillation modes. Generally speaking, compared with narrowband-pass mode-control method, the positive damping it can provide is relatively small, but will enhance damping of all units in system.

As shown in Fig. 3, the control system of SSDC designed by narrowband-pass mode-control method consists of signal input, modal control, phase compensation, gain adjustment and amplitude limiting process.

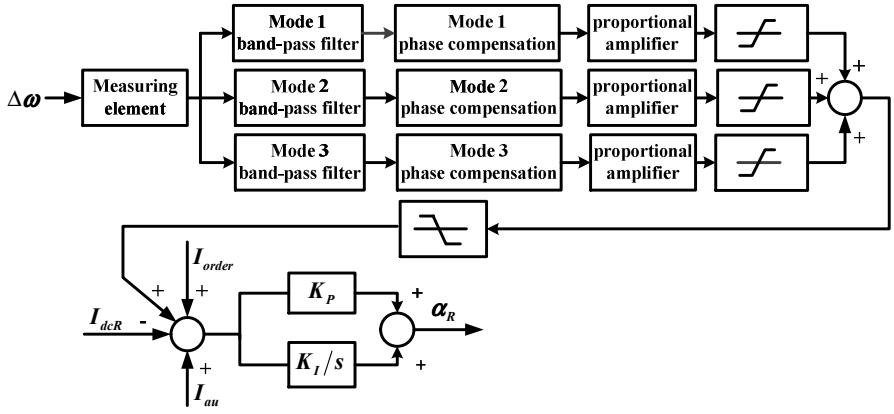

Fig. 3 The control system structure of SSDC designed by narrowband-pass mode-control method

In Fig. 3, I_{order} *i*s instruction value of HVDC constant current control; I_{dcR} is the DC current of HVDC rectifier; I_{au} is the additional control signal of HVDC; α_R is the trigger-delayed angle of HVDC rectifier.

Time domain simulation

The simulation system adopted in this paper is shown in Fig. 4.The two steam-turbine generators of plant A have the possibility of SSO. From previous shaft modeling and calculation, we can get the steam-turbine unit torsional natural frequency of 12.92 Hz, 22.50 Hz and 26.02 Hz.

According to SSDC design methods mentioned above, this paper designs a narrowband-pass SSDC for mode one of two steam-turbine generators in plant A. In order to validate the correctness of analyzing SSO mechanism and effectiveness of damping SSO by designed narrowband-pass SSDC, this paper simulated an operation condition that when HVDC is on double-pole operation condition, A phase to ground short-circuit fault occurs at Bus one in 18 seconds and the fault lasted 0.05 seconds. Figure 5 and Figure 6 respectively represent generator #1 shaft torque curve of each segment and mode one speed deviation under the condition with SSDC and without SSDC. In these figures, HP-IP represents high pressure cylinder to intermediate pressure cylinder, IP-LP represents intermediate pressure cylinder to low pressure cylinder, LP-G represents low-pressure cylinder to the generator and $d\omega$ represents speed deviation of mode one.

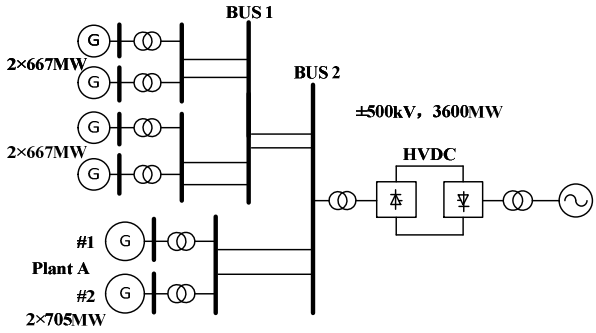

Fig. 4 AC/DC transmission system

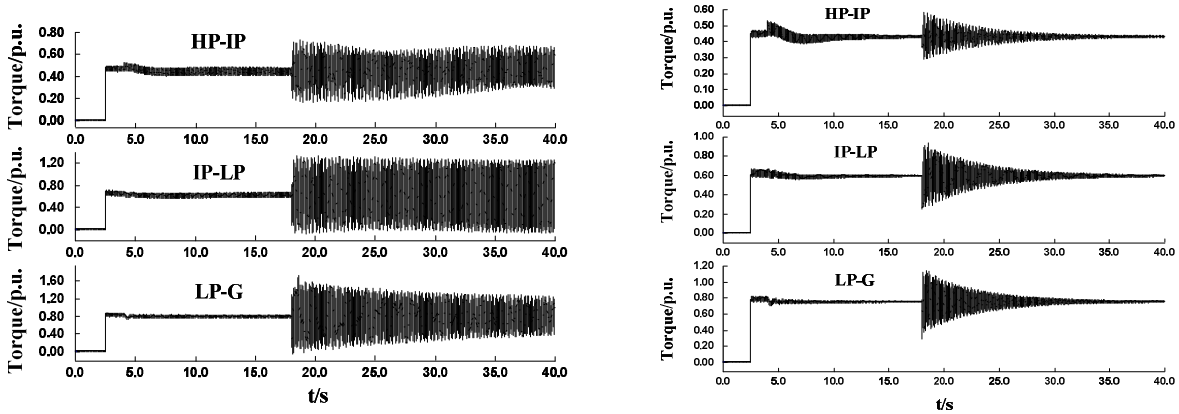

(a)Without SSDC (b) With SSDC

Fig. 5 Shaft torque curve of generator #1

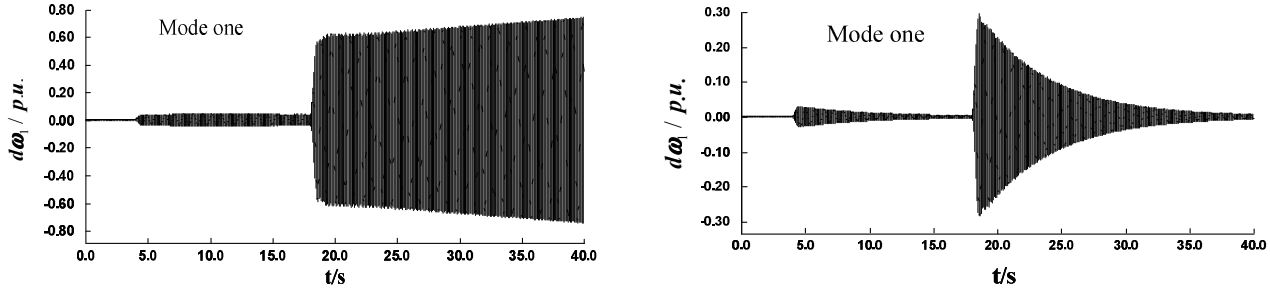

(a)Without SSDC (b) With SSDC

Fig. 6 Mode one speed deviation curve of generator #1

Conclusion

(1) This paper analyzed the mechanism of SSO caused by HVDC, expounded the principle of damping SSO by SSDC and discussed the selection of input signal, the controller structure in the process of designing SSDC and so on. Besides, the characteristics of different design methods are analyzed.

(2) Based on the above analysis, this paper designed a SSDC for a practical engineering. We can know that electrical damping of the system is significantly improved after the SSDC is put, the system SSO is damped obviously.

Acknowledgements

This work was financially supported by the National High Technology R&D Program of China (863 Program) (2012AA050804) and Fundamental Research Funds for the Central Universities (12ZX06).

References

[1] B. F. Gao, C. Y. Zhao, and X. N. Xiao et.a1: Design and implementation of SSDC for HVDC. High Voltage Engineering Vol. 36(2010), p. 501-506.

[2] F. Zhang and X. Zheng: Thyristor-controlled reactor used for damping subsynchronous resonance. High Voltage Engineering Vol. 34(2008), p. 43-46.

[3] R. J. Piwko, E.V. Larsen: HVDC system control for damping of subsynchronous oscillations. IEEE Trans on Power Apparatus and Systems Vol. 101(1982), p. 2203-2221.

[4] F. Zhang and X. Zheng: Study of SSR damping on a generator connected to TCSC. High Voltage Engineering Vol. 31(2005), p. 68-70.

[5] P. Kundur: *Power system stability and control* (China Electric Power Press, Beijing 2002).

[6] Q. Y. Jiang, S. J. Cheng, and Y. J. Cao: Design of HVDC supplementary subsynchronou5 damping controller genetic algorithms. Proceedings of the CSEE, Vol. 22(2002), p. 87-91.

[7] R. J. Piwko, E.V. Larsen: *HVDC System Control for Damping of Subsynchronous Oscillation*. EPRI EL-2708, Project 1425-1.1982.

[8] X. Yang, X. T. Wang, and C. Chen: Design of supplemental subsynchronous oscillation damping control based on roust control theory of HVDC system. Power System Technology Vol. 30(2006), p. 57-61.

[9] W. Fu, X. Y. Li and C. Hong et.al: Design of optimal supplementary sub-synchronous damping controller based on prony method. Proceedings of the CSU-EPSA Vol. 20(2008), p. 10-15.

[10] L. Y. Wu, X. Y. Li, and X. Gong: Design of subsynchronous damping controller based on fuzzy immune method. Automation of Electric Power Systems Vol. 31(2007), p. 12-16.

[11] Y. X. Ni, S. S. Che, and B. L. Zhang: *Theory and analysis of dynamic power system* (Tsinghua University Press, Beijing 2002).

[12] F. Zhang and Z. Xu: Theory and experiences of SVC for damping subsynchronous resonance. High Voltage Engineering Vol. 33(2007), p. 26-31.

[13] Z. Xu: *Dynamic analysis of AC／DC power systems* (China Machine Press, Beijing 2004).

[14] S. Svante, M. Karl: Damping of subsynchronous oscillations by an HVDC link and HVDC simulator study. IEEE Trans. on Power Apparatus and Systems Vol. 100(1981), p. 1431-1439.

Advanced Materials Research Vols. 960-961 (2014) pp 1022-1028

doi:10.4028/www.scientific.net/AMR.960-961.1022

Economical and Coordinated Dispatch of CHP Based Microgrid with Renewable Energy Resources

Xiaolong Jin[1, a], Haifeng Li[2, b], Tao Jin[2, c], Xiandong Xu[1,d], Mingshen Wang[1,e], Jian Meng[1,f]

[1] Key Laboratory of Smart Grid of Ministry of Education, Tianjin University, Tianjin 300072, China.

[2] State Grid Jiangsu Electric Power Company, Nanjing, 210024, China.

[1a] xljinresume@126.com, [2b] hptru64@163.com, [2c] lang80hua@126.com, [1d]xuxiandong@tju.edu.cn, [1e]wangmingshen@tju.edu.cn, [1f]mj9089@163.com

Keywords: Microgrid, Combined heat and power (CHP), Renewable energy resources, Coordinated optimal dispatch.

Abstract. The advantages of high energy efficiency and economic benefit promote the wide application of combined heat and power system (CHP) based microgrid. Firstly, a mathematical model of the CHP based microgrid is developed. Then, a cost function for the coordination of heat and electric load is proposed. Finally, an optimal dispatch model is developed to achieve the economical and coordinated operation of the CHP based microgrid system. Simulation results verify effectiveness of the proposed dispatch model, which is a powerful tool for the energy management of CHP based microgrid with renewable energy resources.

Introduction

The combined heat and power systems (CHP) are widely used in microgrids (MGs) due to the increasingly serious energy crisis and environmental pollution problems [1-4]. The CHP system utilizes waste heat to provide the thermal loads, which can improve the energy efficiency and decrease the production cost. Meanwhile, the MG not only can satisfy the requirements of a particular power quality of local loads, improve power supply reliability, but also can restore as much load as possible within the out-of-service area when a fault happens in the distribution network [5]. Therefore, the CHP based microgrid has the advantages of low pollutants emission, power quality improvement, and high reliability, *etc*.

Several studies have been carried out to investigate the CHP based microgrid system. A CHP based microgrid system was investigated in [7] and [8]. Ref. [9] optimized the operation of a fuel cell power plant with a CHP based microgrid system by using particle swarm optimization algorithm. In [10], different optimal power flow (OPF) models for the micro-sources in a CHP based microgrid system are constructed separately to minimize the total annual cost.

In this paper, a CHP based microgrid system is developed, which includes wind turbines (WTs), photovoltaics (PVs), micro-turbines (MTs), heat exchangers, gas fired boilers (GFBs), battery storage systems and thermal/electrical loads. Then, a coordinated optimal dispatch model of the CHP-based microgrid system is developed according to the power and load forecasting data over a 24-hour time interval with multi-objectives of the mimimum production cost and the minimum coordination cost.

CHP based Microgrid System with Renewable Energy Resources

The CHP based microgrid system with renewable energy resources developed in this paper is shown in Fig. 1.

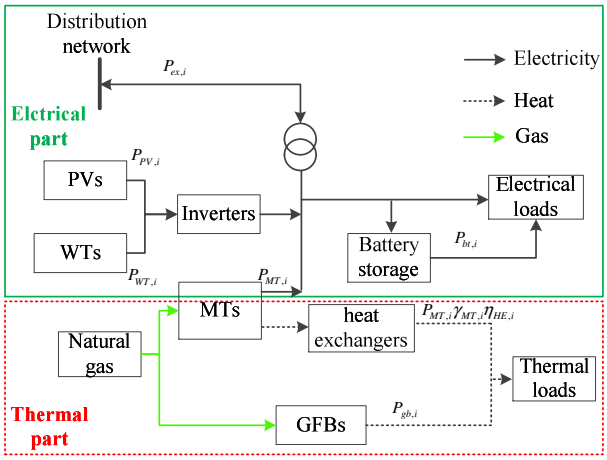

Fig. 1 A CHP based microgrid with renewable energy resources

The CHP based microgrid system consists of two parts:

1) The electrical loads are supplied by the electrical part, which consists of the WTs, PVs, battery storage systems and MTs. The WTs and the PVs utilize renewable energy sources to provide power for the electrical loads. The state of charge (SOC) of the battery storage system can be adjusted according to the operation status of the CHP based microgrid system in real time. The elecrical part can exchange power with the upstream distribution network. When the power output is larger than the eletrical loads, the power can be sold to the upstream grid, and when the outout power is lower than the eletrical loads, the system need to purchase power from the upstream grid.

2) The thermal loads are supplied by the thermal part, which consists of the MTs and GFBs. The MTs and the GFBs utilize natural gas to provide heat for the thermal loads. The MTs can provide both power and heat, which are responsible for the coordination of heat and power loads.

Modeling of the CHP-based Microgrid System

Production Cost. The production cost include the cost for providing power of the WTs and PVs, the cost for exchanging power with the upstream grid, the cost for purchasing natural gas for the MTs and GFBs and the maintenance cost for all the devices in the system. The function of the production cost is shown as follows:

$$C1=\sum_{i=1}^{24}[\frac{C_{ph,i}+C_{se,i}}{2}P_{ex,i}+\frac{C_{ph,i}+C_{se,i}}{2}\left|P_{ex,i}\right|+C_{gas}\left(\frac{P_{MT,i}}{\eta_{MT}}+\frac{P_{gb,i}}{\eta_{gb}}\right)+P_{MT,i}C_{MT\_om}+$$
$$P_{MT,i}\gamma_{MT}\eta_{HE}C_{HE\_om}+P_{gb,i}C_{gb\_om}+\left|P_{bt,i}\right|C_{bt\_om}+P_{WT,i}C_{WT\_om}+P_{PV,i}C_{PV\_om}] \quad (1)$$

where: $C1$ is the function of the production cost; $P_{ex,i}$ is the exchange power with the upstream grid in time i; $P_{MT,i}$ is the power output from the MTs in time i; $P_{gb,i}$ is the thermal power output from the GFBs in time i; $P_{bt,i}$ is the charging or discharging power of the battery storage system in time i; $P_{WT,i}$ is the power output from the MTs in time i; $P_{PV,i}$ is the power output from the PVs in time i; $C_{ph,i}$ is the price to purchase electricity in time i; $C_{se,i}$ is the price to sell electricity in time i; C_{gas} is the price for natural gas; C_{MT_om}, C_{HE_om}, C_{gb_ocm}, C_{bt_om}, C_{WT_om} and C_{PV_om} are the maintenance cost for MTs, heat exchangers, GFBs, battery storage systems, WTs and PVs separately; η_{MT}, η_{gb} and η_{HE} are the efficiency of the MTs, GFBs and heat exchangers; γ_{MT} is the thermoelectric ratio of the MTs.

Coordination Cost of Heat and Power. A cost function for the coordination of heat and power is proposed based on the different properties of the thermal and power loads and the different production states of generation units is developed in this section.

- **Definition of the Thermoelectric Ratio and Thermoelectric Load Ratio**

Definition 1: The thermoelectric ratio is defined as the ratio of the thermal production from the MTs to the power output from the MTs:

$$k = \frac{H}{P} \tag{2}$$

where: H is the thermal production from the MTs; P is the power output from the MTs.

Definition 2: The thermoelectric load ratio is defined as the ratio of the thermal loads to the power loads:

$$K_i = H_{Di} / P_{Di}, \quad i = 1, 2, 3, \ldots, 24 \tag{3}$$

where: H_{Di} is the thermal loads in time i; P_{Di} is the power loads in time i.

- **Modeling of the Coordination Dispatch of Heat and Power**

The cost for the coordination of heat and power is proposed to solve the different properties of the thermal and power loads based on the rated thermoelectric ratio under the condition of satisfying the thermal and power loads, thereby reaching the mimimum coordination cost for the CHP based microgrid system.

The function of the cost for the coordination of heat and power is shown as follows:

$$\begin{aligned} C2 = \sum_{i=1}^{24} [& C_{ph,i} \max\left\{ -\left[\sum_{m=1}^{N_p} P_m(i) + \left(1 - \frac{k}{k_i}\right) \sum_{k=1}^{Nc} P_k(i) - \sum_{n=1}^{N_h} H_n(i) \right], 0 \right\} - \\ & C_{se,i} \max\left\{ \left[\sum_{m=1}^{N_p} P_m(i) + \left(1 - \frac{k}{k_i}\right) \sum_{k=1}^{Nc} P_k(i) - \sum_{n=1}^{N_h} H_n(i) \right], 0 \right\}] \end{aligned} \tag{4}$$

where: $C_{ph,i}$ is the price to purchase electricity in time i; $C_{se,i}$ is the price to sell electricity in time i; k is the thermoelectric ratio and k_i is the thermoelectric load ratio in time i.

Optimization Problem of the CHP based Microgrid System. The mathematical formulation of the optimization problem for the CHP based microgrid system is mathematically expressed as:

- **The Multi-objective Optimization**

The multi-objective function is expressed as:

$$f = \min(C1, C2) \tag{5}$$

where: $C1$ is the production cost of the CHP based microgrid system in one day; $C2$ is the coordination of heat and power cost of the CHP based microgrid system in one day. So the objective function is to minimize the production cost and the coordination cost. If the individual objective is to minimize $C1$, the shortage of electricity can be purchased from the upstream grid, which makes $C2$ relatively high; and if the individual objective is to minimize $C2$, the system will improve the power exchange to the upstream grid to make profits, leading $C1$ greatly increased. Therefore, the multi-objective optimization taking both production cost and coordination cost into consideration can reach a comprehensive optimal dispatch scheme for the CHP based microgrid system.

- **Constraints**

1) Electrical power balance:

$$P_{ex,i} + P_{MT,i} + P_{WT,i} + P_{PV,i} + \frac{P_{bt,i}}{\eta_{ch}} - P_{D,i} = 0 \tag{6}$$

$$P_{ex,i} + P_{MT,i} + P_{WT,i} + P_{PV,i} + P_{bt,i}\eta_{dis} - P_{D,i} = 0 \tag{7}$$

where: P_{Di} is the power loads in time i; η_{MT} is the efficiency of the MTs; η_{ch} is the charging efficiency of the battery storage systems; η_{dis} is the discharging efficiency of the battery storage systems.

2) Thermal power balance:

$$P_{MT,i}\gamma_{MT}\eta_{HE} + P_{gb,i} - H_{Di} = 0 \tag{8}$$

where: H_{Di} is the thermal loads in time i.

3) Exchanging power with the upstream grid:

$$P_{ex,\min} \le P_{ex,i} \le P_{ex,\max} \tag{9}$$

where: $P_{ex,min}$ and $P_{ex,max}$ are the minimum and maximum exchanging power with the upstream grid in time i.

4) Operational constraints for the MTs, heat exchangers, GFBs and the battery storage system:

$$P_{MT,\min} \le P_{MT,i} \le P_{MT,\max} \tag{10}$$

$$P_{HE,\min} \le P_{MT,i}\gamma_{MT}\eta_{HE} \le P_{HE,\max} \tag{11}$$

$$P_{gb,\min} \le P_{gb,i} \le P_{gb,\max} \tag{12}$$

$$P_{bt,\min} \le P_{bt,i} \le P_{bt,\max} \tag{13}$$

$$\sum_{i=1}^{24} P_{bt,i} = 0 \tag{14}$$

$$W_{bt,\min} \le W_{init} - \sum_{i=1}^{24} P_{bt,i} \le W_{bt,\max} \tag{15}$$

where: $P_{MT,min}$ ($P_{MT,max}$) is the minimum (maximum) power output from the MTs in time i; $P_{HE,min}$ ($P_{HE,max}$) is the minimum (maximum) thermal power output from the heat exchangers in time i; $P_{gb,min}$ ($P_{gb,max}$) is the minimum (maximum) thermal power output from the GFBs in time i; $P_{bt,min}$ ($P_{bt,max}$) is the minimum (maximum) charging and discharging power of the battery storage systems in time i; $W_{bt,min}$ ($W_{bt,max}$) is the minimum (maximum) power storage of the battery storage systems. The equation (15) is formulated to make the finally power storage equal to the initial power storage in the battery srotage systems.

Simulation and results

Case Study. In this section, step controlled primal dual interior point method is implemented to optimize the operation of a CHP based microgrid over a 24-hour time interval [11]. The CHP based microgrid is shown in Fig. 1, and the WTs power output, PVs power output, the forecasting thermal and power loads over a 24-hour time interval are shown in Fig. 2 and Fig. 3. The parameters used during the simulation are summarized as follows: $P_{ex,min}$=-400kW, $P_{ex,max}$=400kW, $P_{MT,min}$=0kW, $P_{MT,max}$=150kW, $P_{bt,min}$=-10kW, $P_{bt,max}$=10kW, $P_{gb,min}$=0kW, $P_{gb,max}$=150kW, C_{gas}=0.2CNY/kWh, C_{MT_om}=0.04CNY/kWh, C_{HE_om}=0.025CNY/kWh, C_{gb_om}=0.03CNY/kWh, C_{bt_om}=0.02CNY/kWh, C_{WT_om}=0.11CNY/kWh, C_{PV_om}=0.08CNY/kWh, γ_{MT}=0.6801, η_{MT}=0.2716, η_{gb}=η_{HE}=η_{dis}=η_{ch}=0.9. The time-of-use price of the area are summarized in Table 1.

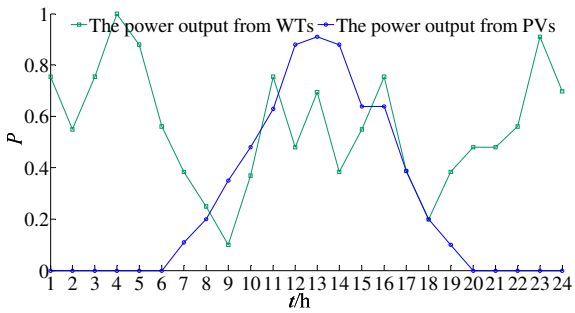

Fig. 2 WTs power output and PVs power output over 24-hour time interval

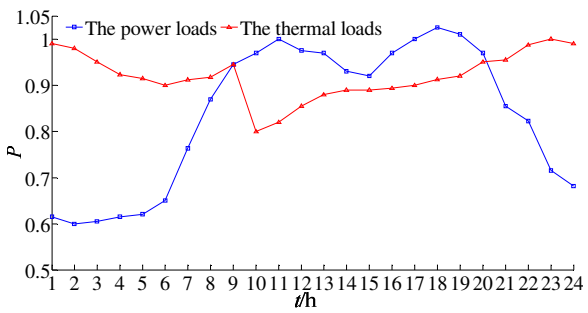

Fig. 3 Forecasting thermal and power loads over a 24-hour time interval

Simulation Results. The simulation results include two parts: the first part is the simulation results for the single-objective of minimizing the production cost and the coordination cost separatly; the second part is the simulation results for the multi-objective considering the production cost and coordination cost.

- **The simulation results for the single-objective optimization**

The optimal results by single-objective are shown in Table 2. The minus value in coordination cost represents that the CHP based microgrid system has made profit over 24-hour time interval.

The simulation results (shown in Table. 2) suggest that when the single-objective is minimizing the production cost, the heat and power production will cost lower (1801.6<2648.7) and the corresponding coordination of heat and power will cost higher (-912.4>-1257.6), and vice versa. The optimal dispatch of the CHP-based microgrid system based different single-objectives are shown in Fig. 4 and Fig. 5.

Table 1. Time-of-use price of the area

Time/h	C_{ph} /(CNY/kWh)	C_{se}/(CNY/kWh)
(10,15], (18,21]	0.7749	0.6150
(7,10], (15,18], (21,23]	0.4551	0.3567
(0,7], (23,24]	0.1599	0.1230

Table 2. Optimal results by single objectives

Objective	$C1$ /CNY	$C2$ /CNY
Production cost	1801.6	-912.4
Coordination cost	2648.7	-1257.6

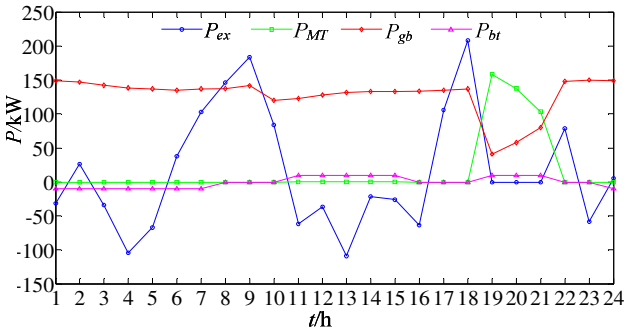

Fig. 4 Optimal dispatch of the system based on minimizing the production cost

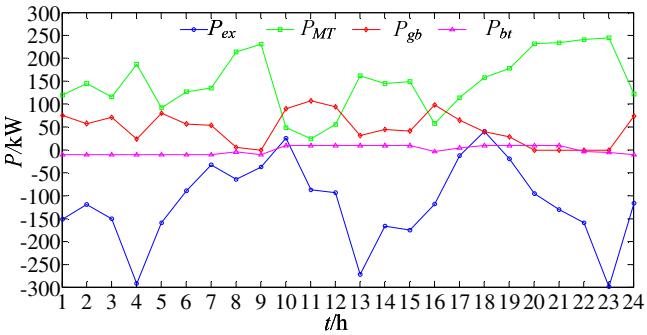

Fig. 5 Optimal dispatch of the system based on minimizing the coordination cost

- **The simulation results for multi-objective optimization**

The optimal results by multi-objective are shown in Table 3. The minus value in coordination cost represents that the CHP based microgrid system has made profit over 24-hour time interval.

The simulation results (shown in Table. 2 and Table. 3) suggest that if the individual objective is to minimize the production cost, the shortage of electricity can be purchased from the upstream grid, which makes the coordination cost relatively high; and if the individual objective is to minimize the coordination cost, the system will improve the power exchange to the upstream grid to make profits, leading the production cost greatly increased. Therefore, the optimal dispatch of the CHP based microgrid system can be obtained by applying the multi-objectives which taking both production cost and coordination cost into consideration. The results (shown in Table. 3) show that the CHP based microgrid system can find a optimal dispatch scheme, which not only has the relatcively low production cost, but also has relatively low coordination of heat and power cost.

Table 3. Optimal results by multi-objectives

Objective	$C1$ /CNY	$C2$ /CNY
Multi-objectives	1816.3	-1010.1

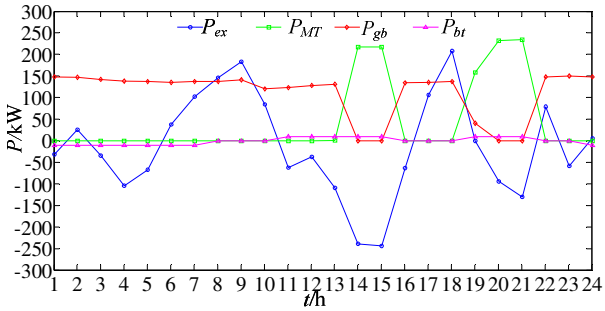

Fig. 6 Optimal dispatch of the system based on minimizing the coordination cost

Summary

This paper has developed a CHP based microgrid system model with renewable energy resources. Based on this developed model, a multi-objective optimal dispatch model for the CHP based microgrid is proposed in this paper taking both the production cost and coordination cost into account. The production cost is the operation cost for the system, while the coordination cost is led by the coordination for the unbalanced thermal and power loads, which have differnt control goals. Therefore, the multi-objective optimization can reach a comprehensive optimal dispatch scheme for the CHP based microgrid system. With the combination of time-of-use electricity price during the day, the constraints of equipment operation, balance of thermal and power loads, etc. are considered. Simulation results show that the multi-objective optimal dispatch model is able to provide a high efficient utilization of energy source and economic power dispatching scheme.

Acknowledgements

This work is supported by Science and Technology Projects of State Grid Corporation on the Key Technologies and Demonstration Project of Distributed Power Generation System with its Operation and Dispatching, National High Technology Research and Development Program of China (863 Program) (Grant No. 2014AA051901), National Natural Science Foundation of China (Grant No., 5137711 and 51307115).

References

[1] M. Houwing, R. R. Negenborn, B. Schutter: Proceedings of the IEEE, Vol. 99 (2011), p. 200

[2] R. Jablko, C. Saniter, R. Hanitsch, et al: Proceedings of International Conference on Future Power Systems (2005), p. 1

[3] M. Houwing, P. W. Heijnen, I. Bouwmans: Proceedings of 2006 IEEE International Conference on Networking, Sensing and Control (2006), p. 302

[4] H. J. Jia, Y. Qi, Y. F. Mu: SCIENCE CHINA Technological Sciences, Vol. 56 (2013), p. 693

[5] Y. F. Mu, H. J. Jia: SCIENCE CHINA Technological Sciences, Vol. 53 (2010), pp. 3232

[6] H. J. Jia, Y. F. Mu, Y. Qi: International Journal of Electrical Power& Energy Systems, vol. 54 (2014), p. 516

[7] C. Marnay, G. Venkataramanan, G. Stadler, A. Siddiqui, R. Firestone and R. Chandran: IEEE Trans. Power Syst. Vol. 23 (2008), p. 975

[8] B. Award, M. Chaudry, J. Wu, et al: Proceedings of the 20th International Conference and Exhibition on Electricity Distribution. Prague, Czech Republic, IEEE (2009)

[9] M. Shahverdi, SM. Moghaddas-Tafreshi: Proc. 3rd international conference on DRPT, (2008), p. 2542

[10] A. K. Basu, S. Chowdhury, S.P. Chowdhury: Proceedings of IEEE Power and Energy Society General Meeting (2009), p. 1

[11] M. Geev, S. Pierluigi: IET Generation, Transmission & Distribution, Vol. 8 (2014), p. 281

Advanced Materials Research Vols. 960-961 (2014) pp 1029-1033

doi:10.4028/www.scientific.net/AMR.960-961.1029

Influence Assessment of UHV Project on Jiangxi Power Grid

SU Yongchun [1, a] and Chang Kaixuan [2,b]

[1] JiangXi Electric Power Research Institute, NanChang 330096, China

[2] East China Jiaotong University, NanChang 330013, China

[a]suyongchun@126.com, [b]kxchang@126.com

Keywords: Ultra High voltage; Jiangxi power system; stability assessment

Abstract. In order to face the challenge of our economy and the environment, it is needed to speed up the energy structure transition and UItra High voltage (UHV) transmission has become an inevitable choice. Researches on the influence of UHV project to Jiangxi power grid are carried out in this paper. Using advanced digital power system simulator (ADPSS), the real-time simulation model of Jiangxi power grid is build up including the UHV project. Based on the simulation model, the problem of low frequency oscillation in Jiangxi power system is studied after the UHV power transmission project accessed. The influence of the UHV transmission line faults on system stability of Jiangxi grid is also researched.

Introduction

In modern society, the use of electricity is closely related to each person. With the development of economy and civilization, the power load is increasing, the power network is becoming bigger and bigger and the power network voltage is getting higher and higher. UItra High voltage (UHV) [1-4] can realize power transmission with long distance and large capacity, which can decrease the transmission cost. Therefore, the developed countries such as American, Japan, the former Soviet Union and Italy had dedicated UHV transmission technology. At present, the 1000kV UHV AC transmission line from Jindongnan to Jingmen has been run successfully which constructed by the State Grid Corporation of China (SGCC) as a demonstration project. Another UHV AC lines Huainan-Shanghai and Zhejiang-Fuzhou will be put into operation soon. These projects indicate that the application of UHV in China has entered a new stage. UHV transmission has become an inevitable choice.

There are the following reasons which urge UHV use in China:

(1) In China, the geographical distribution of energy and load is imbalance. The energy resources are mainly distributed in the north and northwest area, but power consumption is mostly in east and central area. These two places are far away from each other.

(2) UHV transmission can greatly ease the tense of coal transportation. For a long time in the future, the situation of coal dominated energy structure will not change fundamentally. Power generation needs lots of coal. Coal transportation need much transport capacity of road and railway. UHV transmission instead of coal transportation will be a better choice.

(3) Since 2013, China suffered the fog haze weather. Thermal power generation is one of the most important reasons. Increase clean energy supply in northwest can greatly reduce coal-burning pollution, which need UHV power platform.

(4) UHV transmission line will occupy less land than 500kV transmission line compared with the same capacity. At the same time, UHV transmission has less loss. So it has particularly advantage in China middle-east area which land resources is scarce.

It is short of energy resources in Jiangxi province. With the development society economy, the tension between power supply and demand will be gradually aggravated. Therefore, it is urgent for Jiangxi to build UHV power supply corridor which can realize electricity import from other province.

In this paper, the influence of UHV access to Jiangxi power grid is analyzed based on real-time digital simulation [5-6]. Using simulation device of ADPSS, the real-time simulation model of Jiangxi grid is constructed with UHV accessed. The problems such as the low frequency oscillation and transient stability are investigated.

UHV Transmission Planning

In period of the twelfth Five-Year planning, construction of UHV line in SGCC will be gradually accelerated. According to the 2015planning, three vertical and three horizontal and one ring UHV network will be built in Sanhua synchronized power grid.

By the end of 2020, strong and smart grid will be constructed in China by SGCC with five vertical and five horizontal UHV lines. This huge power network will connect with the major coal bases, large hydropower bases, large nuclear power base, and large-scale renewable energy bases. It will link China Southern Power grid by UHV transmission line as well.

Jiangxi power grid is located in the eastern end of central china power grid. It associates with central china power grid by Xianning-Mengshan parallel transmission lines and Cihu-Yongxiu line. Through these three lines, the max received power is 3000MW. With the release of the national "steady growth" policy effect and application of the original Central Soviet area revitalization planning, it is expected that in the future Jiangxi power grid electricity level will have a large growth. The peak load in 2020 will reach 34000MW and the power shortage well reach 12000MW.

At the beginning of the Thirteen Five Planning, UHV power transmission line will connect with Jiangxi power grid to solve power supply problem. In 2016, Wuhan-Nanchang UHV power transmission project will be built. A 1000kV UHV substation will be constructed in Nanchang with two UHV lines connected with UHV Wuhan substation. There will be four 500kV lines connected Nanchang UHV substation with Jinxian and Fuzhou 500kV substation.

In view of the UHV transmission capacity, detailed analysis must be carried out to ensure the safe and stable operation of Jiangxi power grid before UHV power transmission project accessed.

UHV Power Transmission Modeling

Using as a reference of the 1000kV Jindongnan-Nanyang demonstration project, LGJ-630x8 wire is chosen as the UHV line type of Wuhan-Nanchang. The wire parameters can be seen in table 1. Length of the UHV line is 310km. When choosing UHV line parameters, if the concentrated circuit model is used, it will reduce the simulation accuracy because of neglecting the wave propagation process of long distance lines. Therefore it is more accurate by using sectional circuit simulation. Three segment line models are adopted in this research.

Table 1 LGJ-630x8 line parameters

R(Ω/km)	L(Ω/km)	C(μF/km)
0.0082	0.26	0.014

The main transformer capacity of Nanchang UHV substation is 2*3000MVA. Referring to transformer parameters of UHV demonstration project, the specific parameters are shown in table 2.

Table 2 UHV transformer parameters

Rated capacity of high-voltage side	3000MVA
Rated capacity of mid-voltage side	3000MVA
Rated capacity of low-voltage side	1000MVA
Short-circuit voltage(high-mid)(%)	19
Short-circuit voltage(mid-low)(%)	40
Short-circuit voltage(high-low)(%)	63
Tap position	mid-voltage side
Voltage regulation level difference (%)	1.25
Voltage regulation range (%)	±5

Compensation capacity of shunt reactor on the transmission line can also refer to the UHV demonstration project. The shunt reactor is divided into two parts and hung on the two ends of the line. 40% and 60% of the compensation capacity is installed at the beginning and the end of one UHV line. On the other UHV line, 60% and 40% of the compensation capacity is installed at line two ends. Considering the steady state voltage level and economic point of view, compensation degree of the shunt reactor is preferred 70%.

Except the UHV related elements, other elements use the planning data model which North China Grid and Central China Grid are connected. By this way, the real-time simulation modeling is completed with consideration of UHV accessed Jiangxi power grid. The whole simulation model covers north and central China UHV, each 500kV and 220kV network node.

Influence of UHV on Jiangxi Grid

(1) Load Flow Analysis

After Nanchang UHV AC substation put into operation, there will be five power transmission line connected Jiangxi grid with Central China grid. These lines include two UHV lines and three 500kV lines. The power flow distribution is roughly as follows: the total received power by Jiangxi grid is 4280MW. The power supply by UHV Transformer is 2570MW, and other 1710MW power is burdened by three 500kV contact line. The power flow from the UHV transformer will supply the load of Nanchang and western area in Jiangxi. The power flow from 500kV tie line will supply the load of Jiangxi northern area.

(2) Small Disturbance Stability Analysis

Oscillation modes correlated with generator in Jiangxi are shown in table 3. The damping ratios shown in table 3 are less than 5%.

Table 3 Oscillation mode concerned with Jiangxi grid

No.	Characteristic Values	Frequency Hz	Damping Ratio (%)	mode
1	-0.018+j8.879	1.413	0.201	Oscillation mode between Shangyoujiang hydropower plants and Jiangxi main network
2	-0.066+j11.678	1.859	0.569	Oscillation mode between Shihutang hydropower plants and Jiangxi main network
3	-0.083+j11.202	1.783	0.739	Oscillation mode between Baozhishi and Zhelin hydropower plants

It is shown in table 3 that no negative damping oscillation modes exist in Jiangxi power grid after UHV line accessed. The weak damping mode associated with the Jiangxi grid are small hydropower relative oscillation mode between Jiangxi power grid or small hydropower, which belongs to the mode oscillations within the region. UHV transmission lines are tie lines, therefore the oscillation modes caused by UHV lines must be modes between Jiangxi grid and Central China grid. The newly increased mode corresponding frequency will below 1Hz. As no modes fit the conditions above, it means that the UHV power transmission will not bring low frequency oscillation to Jiangxi grid.

(3) Transient Stability Analysis

In research of UHV transmission line fault effect on system stability of Jiangxi, N-1 and N-2 fault types is considered on UHV transmission lines. Three-phase fault is selected as it is the most unfavorable to system stability. Output of Nanchang UHV substation is selected as the fault location. When N-1 fault on UHV transmission line occurs, voltage and power angle variations before and after the faults are shown in Fig. 1 and Fig. 2.

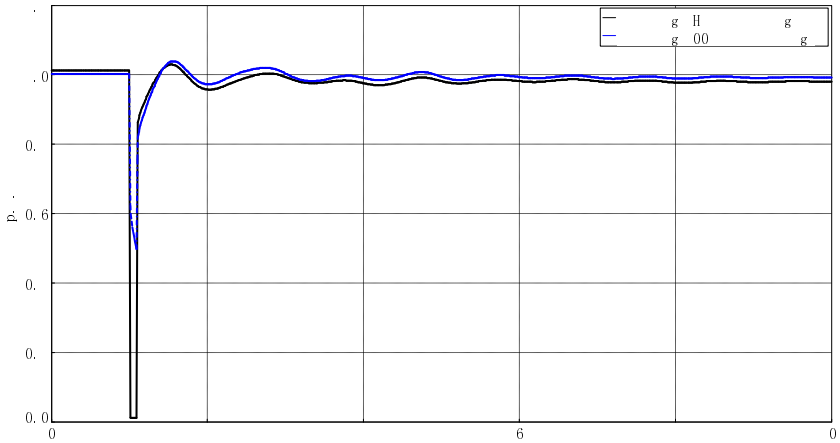

Fig. 1 Voltage variations curves when UHV lines N-1

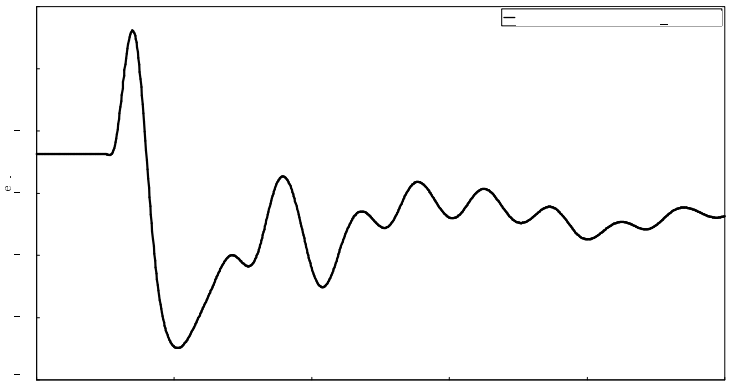

Fig. 2 Power angle variation curves when UHV lines N-1

It can be seen from Fig. 1 and Fig. 2 that the bus voltages quickly restore to more than 0.90p.u. after the fault is cleared. 1s later, the voltage restore more than 0.95p.u.. 10s later, the angle oscillations largely disappear, and the power system maintain the angle stability.

The process of N-2 fault on UHV double lines is as follows: two lines single-phase permanent short circuit of different phase on Nanchang side, single-phase tripping, and two lines three-phase jumped after single-phase reclosing failure. Voltage and power angle variations before and after the faults are shown in Fig. 3 and Fig. 4 when N-2 fault occurs.

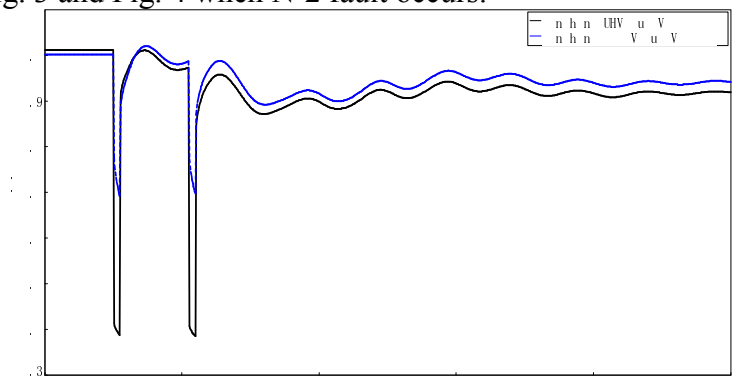

Fig. 3 Voltage variations curves when UHV lines N-2

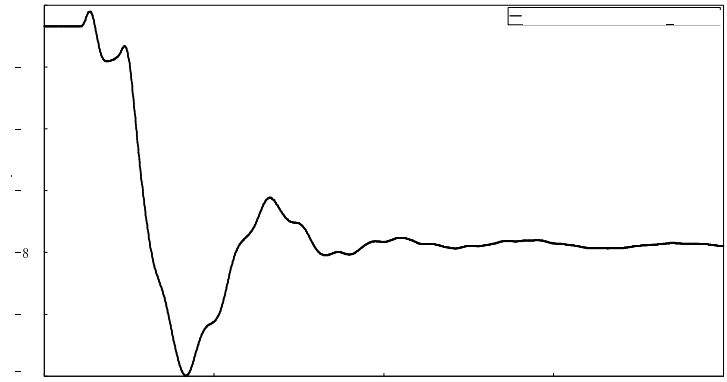

Fig. 4 Power angle variation curves when UHV lines N-2

It can be seen from Fig. 3 and Fig. 4 that the bus voltages quickly restore to more than 0.9p.u. after the fault is first cleared. After the fault is second cleared the voltage quickly restore more than 0.85p.u. and more than 0.9p.u. 3s later. 10s later, the angle oscillations largely disappear, and the power system maintain the angle stability.

Based on the above analysis, we can see that Jiangxi power system will not lose stability when N-1 or N-2 faults on Wuhan-Nanchang UHV transmission lines occurred.

(4) Short Circuit Current Calculation

After UHV transmission line connected to Jiangxi power grid, the network will link more closely. So the system short-circuit current level will increase. Effects of UHV lines connection on the short circuit current are studied in the following. Variations of 500kV and 220kV bus short-circuit current level in Jiangxi power grid is separately calculated considering UHV project accessed.

Table 4 Variation of 500kV bus current Short circuit [kA]

Bus	No UHV accessed	UHV accessed	Difference
Fuzhou	36.4	50.0	13.6
Jinxian	30.2	48.1	17.9
Nanchang	37.6	48.4	10.8
Yongxiu	43.0	48.2	5.2

Table 5 Variation of 220kV bus current Short circuit [kA]

Bus	No UHV accessed	UHV accessed	Difference
Changdong	39.5	42.4	2.9
Jinxian	38.2	43.0	4.8
Nanchang	42.9	46.2	3.3
Wugang	34.6	37.8	3.2
Xiangtang	31.8	34.9	3.1

It can be seen from table 4 and table 5 that UHV grid seriously affects short-circuits current level in Jiangxi power system. The increases of 500kV bus short-circuit current are larger than that of 220kV system. The buses with the largest short-circuit current increase are Fuzhou and Jinxian bus which are 500kV access points of UHV substation. Therefore, after UHV landing in Jiangxi, the short circuit current probably exceed the switch breaking capacity. At that time, limitation measures such as electromagnetic loop decoupling and lines breaking must be taken to decrease the short-circuit current.

Summary

UHV transmission is gradually applied in China with advantages of long transmission distance and huge transmission power capacity. Jiangxi as a province lack of energy resources, it is urgent to utilize UHV line accepting clean power supply from remote place. In this paper, the problems possible caused UHV access is analyzed in Jiangxi power grid. The results show that UHV transmission will bring no small disturbance and transient stability problems to Jiangxi power grid, but it will increase the short circuit current level and corresponding control measures should be taken in advance.

References

[1] J.H. Zhang, W.P. Jiang and Y.H. Yin: Security and stability study on Planned UItra High voltage Power Grid, *Proceedings of the CSEE*, Vol. 28-22 (2008), p. 64

[2] X.H. Qin, H. Shen and Q.Y. Zhou: Voltage Distribution along the Line and Disposition Scheme of Series Capacitors for UHV Transmission Lines with Series Capacitors, *Proceedings of the CSEE*, Vol. 31-25 (2011), p. 43

[3] H.Q. Liang, X. Wu and X.M. Liang: Operation Losses and Economic Evaluation of UHVAC and HVDC Transmission Systems, *High Voltage Engineering*, Vol. 39-3 (2013), p. 630

[4] H. CHEN, Y.M. ZHANG and Y. He: Impact assessment of UHVAC on multi-send HVDC systems of Sichuan power grid, *Power System protection and Contral*, Vol. 39-7 (2011), p. 136

[5] C. WANG, J.H. Li and Y.Y. Li: Low Frequency Oscillation Characteristics of East China Power Grid after Commissioning of Huainan-Shanghai UHV Project, *Automation of Electric Power Systems*, Vol. 37-18 (2013), p. 120

[6] X.D. LIU, Q.Y. JIANG and Y.J. Cao: Transient security risk assessment of power system based on risk theory and fuzzy reasoning, *Electric Power Automotion Equipment*, Vol. 29-2 (2009), p. 15

Advanced Materials Research Vols. 960-961 (2014) pp 1034-1038

doi:10.4028/www.scientific.net/AMR.960-961.1034

Orthogonal Transformation State Estimation Based on Generalized Tellegen's Theorem

Guihua Lin [1, a], Tao Wang [1,b] ,Yuying Wang [1,c],Meiying Cui[1,d] and Ting Guo[1,e]

[1] State Grid of China Technology College (SGTC),Jinan, Shandong 250002,China

[a]gh_lin@yahoo.cn, [b]wangtaogongzuo@126.com,[c]1363954640@qq.com,
[d]598279932@qq.com,[e]376121580@qq.com

Keywords: energy management system (EMS), orthogonal transformation, Generalized Tellegen's Theorem, state estimation.

Abstract. One of the most important ways to enhance the speed of state estimation is to establish the constant matrix Jacobian. This essay puts forward a new type of orthogonal transformation state estimation method based on Generalized Tellegen's theorem. This paper uses orthogonal transformation method to improve state estimation's numerical stability, and makes the algorithm enjoy an ideal convergence. Moreover, it has strong compatibility of various distribution measurements. The method put forward in this essay has been verified through IEEE-30 Node System, and the efficiency of it has been fully proved by the example results.

Introduction

With the development of China's extra-high voltage and smart grid construction, state estimation is becoming more and more important. Thus, it is of greater importance to acquire rapid, reliable and accurate state estimation.

Power system weighted least squares state estimation method brought forward by F.C.Schweppe et al in 1970 has relatively high estimated quality and convergence. For the ideal normal distribution measurement, this kind of method produces optimal and unbiased estimated results. There is no doubt that Power system weighted least squares state estimation method is the classical algorithm and theoretical basis, yet it is to be improved in its rapidity.

In recent years, the state estimation method based on equivalent current transformation has been widely studied[1-5]. The literature 6 discusses the relationship between research and training education. Through this method, the measured power measurement can be transformed into an equivalent current measurement, and the voltage obtained through iteration can be used to revise the equivalent current constantly till it converges. This algorithm has realized constant Jacobian matrix in a true sense, and the automatic decoupling of the information matrix can be achieved when the weights of the active and reactive power measurements are equal or more or less the same. However, when the slip current amplitude measurement is considered, there may be multiple solutions, and the number of iterations is greater than the least-squares method. It remains the focus of the study on how to improve the numerical stability.

Orthogonal transformation method can improve state estimation's numerical stability. This essay focuses on a new type of orthogonal transformation state estimation method based on Generalized Tellegen's theorem, and applies the thought of flow calculation based on Generalized Tellegen's theorem to the state estimation. This paper uses givens orthogonal transformation method to improve state estimation's numerical stability， and makes the algorithm enjoy an ideal convergence. Moreover, it has strong compatibility of various distribution measurements.

Givens orthogonal transformation method

Givens rotation transformation is one of the most commonly used method for determining the orthogonal matrix.

If the type shown in equation (1) exists.

$$Ax + B = 0 \tag{1}$$

In formula (1),A—— m×n dimensional matrix； B—— m×1 dimensional matrix.

Givens rotation transform is a sub- matrix transformation of coefficient matrix, defining the n × n matrix Q, In addition to its elements $Q_{pp} = Q_{qq} = \cos\theta$, $Q_{pq} = -Q_{pq} = \sin\theta$, $p < q$, the other elements are the same as the corresponding elements of the unit matrix.

Series of Givens matrix G is left multiplied by the formula (1). Formula (2) is established.

$$\begin{cases} G_m G_{m-1} \ldots . G_2 G_1 A = \begin{bmatrix} R & 0 \end{bmatrix}^T \\ G_m G_{m-1} \ldots . G_2 G_1 B = \begin{bmatrix} e & g \end{bmatrix}^T \end{cases} \tag{2}$$

As can be seen from the above analysis , Givens transformation to transform some of the elements of the coefficient matrix. Therefore, Givens transformation can be used for power system state estimation to improve convergence.

Orthogonal transform state estimation method

The main measurements of SCADA system are node injection power measurement $\dot{S}_{m,i}$,branch power measurement $\dot{S}_{m,ij}$. Its measurement equation is shown in formula(3) .

$$\begin{cases} \overset{*}{S}_i = \overset{*}{U}_i \sum_{j=1}^{n} Y_{ij} \dot{U}_j \\ \overset{*}{S}_{ij} = \overset{*}{U}_i Y_{ij} (\dot{U}_i - \dot{U}_j) + \overset{*}{U}_i \dot{U}_i Y_{i0} \end{cases} \tag{3}$$

In the formula(3), $\dot{U}_i$ is the node voltage; Y_{ij} is the branch admittance; Y_{i0} is half of the Line capacitance to ground susceptance; Lines and transformers both adopt equivalent circuit of type π.

After equivalent transformation, it can be transformed into:

$$\begin{cases} \overset{*}{S}_{m,i} / \overset{*}{U}_i = \sum_{j=1}^{n} Y_{ij} \dot{U}_j \\ \overset{*}{S}_{m,ij} / \overset{*}{U}_i = Y_{ij} (\dot{U}_i - \dot{U}_j) + \dot{U}_i Y_{i0} \end{cases} \tag{4}$$

Formula (4) is abbreviated as shown in formula(5).

$$\begin{cases} \dot{I}_{m,i}^{eq} = \overset{*}{S}_N / \overset{*}{U}_i = Y_N \dot{U} \\ \dot{I}_{m,B}^{eq} = \overset{*}{S}_B / \overset{*}{U}_i = Y_B \dot{U} \end{cases} \tag{5}$$

Differentiating formula (5), the obtained is shown in formula(6).

$$\begin{cases} \Delta \overset{*}{S}_N / \overset{*}{U} - \overset{*}{S}_N * \Delta \dot{U} / \overset{*}{U}^2 = Y_N \Delta \dot{U} \\ \Delta \overset{*}{S}_B / \overset{*}{U} - \overset{*}{S}_B * \Delta \dot{U} / \overset{*}{U}^2 = Y_B \Delta \dot{U} \end{cases} \tag{6}$$

In the formula(6),

$$\overset{*}{S}_N / \overset{*}{U}^2 = \left[P_N \left(e^2 - f^2\right) + 2efQ_N \right] / \left(e^2 + f^2\right)^2 + j\left[-Q_N \left(e^2 - f^2\right) + 2efP_N \right] / \left(e^2 + f^2\right)^2 \tag{7}$$

$$\overset{*}{S}_B / \overset{*}{U}^2 = \left[P_B \left(e^2 - f^2\right) + 2efQ_B \right] / \left(e^2 + f^2\right)^2 + j\left[-Q_B \left(e^2 - f^2\right) + 2efP_B \right] / \left(e^2 + f^2\right)^2 \tag{8}$$

Formula (6) can be collectively represented as:

$$\Delta Z_m^{eq'} = (H + D)\Delta \dot{U} \tag{9}$$

Of which, $\Delta Z_m^{eq'}$ is the variation of the equivalent current measurement corresponding to $\Delta \overset{*}{S}_N / \overset{*}{U}, \Delta \overset{*}{S}_B / \overset{*}{U}$, while matrix D is the coefficient matrix corresponding to $\overset{*}{S}_N / \overset{*}{U}^2, \overset{*}{S}_B / \overset{*}{U}^2$.

Introduce the formula (9) into the least squares objective function:

$$J(\dot{U}) = [\Delta Z_m^{eq'} - (H + D)\Delta \dot{U}]^T R^{-1} [\Delta Z_m^{eq'} - (H + D)\Delta \dot{U}] \tag{10}$$

The formula (10) treated accordingly into the form shown in the formula (11).

$$\begin{aligned} J(\dot{U}) &= \left[\Delta Z_m^{eq'} - (H + D)\Delta \dot{U} \right]^T M \left[\Delta Z_m^{eq'} - (H + D)\Delta \dot{U} \right]^* \\ &= \left[\Delta \tilde{Z}_m^{eq'} - \left(\tilde{H} + \tilde{D}\right)\Delta \dot{U} \right]^T \left[\Delta \tilde{Z}_m^{eq'} - \left(\tilde{H} + \tilde{D}\right)\Delta \dot{U} \right]^* \end{aligned} \tag{11}$$

In the formula (11), $\Delta \tilde{Z}_m^{eq'} = M^{1/2} \Delta Z_m^{eq'}; \tilde{H} = M^{1/2} H; \tilde{D} = M^{1/2} D$.

If there is an orthogonal matrix, the formula (12) is satisfied.

$$\begin{cases} Q\Delta \tilde{Z}_m^{eq'} = [\Delta I \quad b]^T \\ Q\left(\tilde{H} + \tilde{D}\right) = [A \quad 0]^T \end{cases} \tag{12}$$

The objective function can be further converted to the formula (13).

$$\begin{aligned} J(U) &= \left[\Delta \tilde{Z}_m^{eq'} - \left(\tilde{H} + \tilde{D}\right)\Delta \dot{U} \right]^T Q^T Q \left[\Delta \tilde{Z}_m^{eq'} - \left(\tilde{H} + \tilde{D}\right)\Delta \dot{U} \right]^* \\ &= \| Q\Delta \tilde{Z}_m^{eq'} - Q\left(\tilde{H} + \tilde{D}\right)\Delta \dot{U} \|_2^2 \\ &= \| \Delta I - A\Delta \dot{U} \|_2^2 + \| b \|_2^2 \end{aligned} \tag{13}$$

Because the norm is greater than or equal to zero, when the formula (14) is satisfied, $J(U)$ will reach the minimum $\|b\|_2^2$.

$$A\Delta \dot{U} = \Delta I \tag{14}$$

$J(U)$ will reach the minimum $\|b\|_2^2$.

Therefore, just follow the Givens transformation method to construct the matrix *Q* can transform *A* and *b*, the state vector can be got.

Orthogonal Transformation State Estimation Based on Generalized Tellegen's Theorem

The following formula (15) can be acquired according to the generalized Tellegen small perturbation theorem[7].

$$\delta \dot{U}_i = -\tilde{U}(i)^T \delta A \cdot \Delta \dot{U}_0 + \tilde{U}(i)^T \delta \Delta I \tag{15}$$

$\tilde{U}(i)$ can be acquired through the adjoint equation shown in the formula (16)

$$\tilde{A}(\tilde{U})\tilde{U}(i) = \tilde{B}(i)^T \tag{16}$$

$\Delta\dot{U}_0$ can be acquired through the following formula (17)

$$\Delta I_0 = A(U_0)\Delta U_0 \tag{17}$$

What has to be acquired during the whole computing process are ΔU_0 and $\tilde{U}(i)$.If $A(\dot{U})$ and $\Delta I(\dot{U})$ are nonlinear, ΔU_0 can be acquired by adopting numerical iterative method, but it is enough for the linear equation to be solved only once to get $\tilde{U}(i)$.During the whole process of state estimation, what needs to be done is to acquire $\tilde{U}(i)$ calculating the factor table on $\tilde{A}(\tilde{U})$ which is $A(U_0)^T$ only once. In the subsequent iterative process, only $\delta\Delta I(\dot{U})$ and $\delta T(\dot{U})$ are needed to be solved.

$\delta\Delta I$ is the difference value of the equivalent measurement ΔI in each iteration and equivalent measurement ΔI_0 in the first calculation, which is the variable quantity of the equivalent measurement. δA is the difference of the information matrix in each iteration and the information matrix corresponding to $\dot{U}_0$.

It can be concluded from the above analysis that the method put forward in this essay, compared with the traditional state estimation based on generalized tellegen's theorem, enjoys better convergence. Moreover, its calculation accuracy is improved compared with the traditional estimation method of equivalent transformation state.

Numerical example

This essay, taking IEEE 30 node system as an example, conducts a comparative analysis in three aspects. The example assumes a normal distribution in which the SCADA system measurement error distribution with mean is 0 and a standard deviation is 0.02; and convergence accuracy is 10−6 . Using state the amount of amplitude and the absolute error of the phase angle δ_V and δ_θ as computational performance indicators, the value achieved is equal to the absolute value of the estimated value and the corresponding true value difference. Numerical example 1 has respectively computed and compared the iterations, computing time, and performance indicators such as δ_V and δ_θ of the algorithm proposed in this essay, the method of least squares algorithm and the traditional equivalent current transformation state estimation method, and the results are shown in table 1.

Tab.1 The comparison of algorithm stated in this essay and other kinds of algorithm in performance

information	iteration	computatin time(ms)	δ_V/pu	δ_θ/pu
WLS method	4	193	0.0063	0.0102
the traditional state estimation based on generalized tellegen's theorem	4	127	0.006	0.0107
Method in this essay	3	121	0.0059	0.0100

It can be concluded from table 1 that the method has been improved in the convergence compared with the least squares method and the traditional equivalent current transformation state estimation method. the calculation time is shorter than the least-squares method. Moreover, the estimated accuracy is basically consistent with the least squares method. This further verifies the correctness and practicability.

Conclusions

This essay focuses on a new type of orthogonal transformation state estimation method based on Generalized Tellegen's theorem, and uses givens orthogonal transformation method to improve state estimation's numerical stability, and makes the algorithm enjoy an ideal convergence. And has the same calculation accuracy with the least squares state estimation method.

References

[1] F. C. Schweppe, J. Wildes. Power System Static State Estimation[J], Part I-III. IEEE Trans. PAS. 1970, 89: 120-135.

[2] L Roy, T A Mohammed. Fast Super Decoupled State Estimator for Power Systems[J]. IEEE Transactions on Power Systems. 1997, 12(4):1597-1603.

[3] A. Monticelli. Electric Power System State Estimation[J]. Proceedings of the IEEE.2000, 88(2): 262-282.

[4] Whei-Min Lin，Jen-Hao Teng. State Estimation for Distribution Systems with Zero-Injection Constraints[J]. IEEE Transactions on Power system. 1996,11(1):518-524.

[5] Abur A，Exposito A G. Detecting multiple solutions in state estimation in the Presence of current magnitude measurements[J]. IEEE Transactions on Power system. 1997，12(1)：370-374.

[6] Guihua Lin, Tao Wang. Function Analysis of the Enterprise Skills Training Center in the Engineering Education Field[J]. International Conference on Education Technology and Management Science. 2013, 1171-1174.

[7] Zhizhong Guo, Baochun Lu, Zhuo Liu. Generalized Tellegen's Theorem[J]. Journal of Yanshan University, 1999, 23(1):58-61.

Advanced Materials Research Vols. 960-961 (2014) pp 1039-1042

doi:10.4028/www.scientific.net/AMR.960-961.1039

State Estimation of Power System based on Taylor series method

Guihua Lin [1, a], Yuying Wang [1,b] and Tao Wang [1,c]

[1] State Grid of China Technology College (SGTC), Jinan, Shandong 250002,China

[a]gh_lin@yahoo.cn, [b]1363954640@qq.com, [c]wangtaogongzuo@126.com,

Keywords: energy management system(EMS),wide-area measurement system(WAMS),state estimation, Taylor series.

Abstract. Take full advantage of the PMU's accurate mass measurement data is the effective method to improve the calculation accuracy of power system state estimation. This essay puts forward the state estimation method of power system based on the Taylor series method. It analysis of power system operating conditions based on the real-time measurement of Wide area measurement system, divides the state time, establishes the equation of state of the measurement data by curve fitting method in the period of state time, creates a new state estimation calculation method by Taylor series method, constructs a new voltage characteristic curve calculation method, determines the system state and achieve the continuity of power systems steady-state analysis. The method put forward in this essay has been verified through IEEE-30 Node System, and the efficiency of it has been fully proved by the example results.

Introduction

The phasor measurement unit(PMU) provides accurate , high-precision phase angle information to the power system, and taking full advantage of PMU measurements can improve the estimation accuracy and processing speed of power system state estimation , it also can provide accurate, real-time grid data for subsequent advanced application software.

The current state estimation method [1-6] uses only a time or several sections of grid data, and gets a true reflection of the system state (the voltage phase of power system) taking numerical analysis method, but it unable to achieve the continuity analysis of power system steady state. PMU measured massive data will be subject to existing state estimation methods' the calculation speed and the limited use of the state time data. The voltage and current phasor measured by PMU have higher accuracy, but still there are some errors and it may still affect the analysis results in the direct use of the current technology level; Therefore, the study of a state estimation method can make full use of vast amounts of data PMU measurements, and can ensure rapid computational speed has very important practical significance.

This essay puts forward a new state estimation method of power system based on the Taylor series method. It analysis of power system operating conditions based on the real-time measurement of Wide area measurement system and divides the state time, then it establishes the equation of state of the measurement data by curve fitting method in the period of state time and creates a new state estimation calculation method by Taylor series method, constructs a new voltage characteristic curve calculation method. Finally, it determines the system state and achieve the continuity of power systems steady-state analysis.

State Time Divide

State time power system can be divided as follows. firstly, this paper set a fixed time interval as a state time according to the actual situation of power system operation. Then, it determines whether the occurrence of adverse circumstances within the state time such as topology changes , sudden load change and PMU data loss based on measured data. If the system does not have these adverse circumstances occur during this state time it is a state time. If any one or both adverse events occur

during this time the process, it is divided into two states to the adverse circumstances places the moment as the dividing line.

Voltage Characteristic Curve

Firstly, This paper uses curve fitting method to determine the time function of each measurement according to real-time information PMU measurements. The time function is represented by the following formula (1)-(4).

$$I_{ma} = a_0 + a_1 t + a_2 t^2 + ... + a_n t^n \tag{1}$$

$$I_{mb} = b_0 + b_1 t + b_2 t^2 + ... + b_n t^n \tag{2}$$

$$U_{ma} = c_0 + c_1 t + c_2 t^2 + ... + c_n t^n \tag{3}$$

$$U_{mb} = d_0 + d_1 t + d_2 t^2 + ... + d_n t^n \tag{4}$$

I_{ma}, I_{mb} are the real part and imaginary part of the transformed branch current measure. U_{ma}, U_{mb} are the real part and imaginary part of the transformed bus voltage measure. T is time variable.

For power systems, the measurement function is shown in formula (5).

$$Z(t) = h\left[\dot{U}(t)\right] + \xi \tag{5}$$

In formula (5), $\dot{U}(t)$ is voltage characteristic curve, $h\left[\dot{U}(t)\right]$ is the measurement function equation, ξ is random error.

Differentiating formula (5), the obtained is shown in formula (6).

$$Z^{(1)}(t) = H\left[\dot{U}(t)\right]\dot{U}^{(1)}(t) \tag{6}$$

In formula (6), $H\left[\dot{U}(t)\right] = \partial h\left[\dot{U}(t)\right] / \partial \dot{U}(t)$ is Jacobian matrix, $\dot{U}^{(1)}(t)$ is the first derivative of state quantity.

While getting the m-order derivative of formula (6) with respect to time *t*, formula (7) is acquired by binomial theorem.

$$Z^{(m)}(t) = \sum_{j=0}^{m-1} C_{m-1}^{j} H^{(j)}\left[\dot{U}(t)\right]\dot{U}^{(m-j)}(t) \tag{7}$$

In formula (7), C_{m-1}^{j} is the binomial coefficients, $H^{(j)}\left[\dot{U}(t)\right]$ is the j-order derivative of Jacobian matrix, $\dot{U}^{(m-j)}(t)$ is the (m-j)-order derivative of $\dot{U}(t)$.

According to formula (7)，the derivative binomial equation of the measurement data shown in formula (8) can be obtained.

$$Z^{(m)}(t) - \sum_{j=1}^{m-1} C_{m-1}^{j} H^{(j)}\left[\dot{U}(t)\right]\dot{U}^{(m-j)}(t) = H\left[\dot{U}(t)\right]\dot{U}^{(m)}(t) \tag{8}$$

Because of the linear relationship between branch current measurement, voltage measurement measured by the PMU and state. The measurement function can be written as formula (9).

$$Z = h\left[\dot{U}(t)\right] = H \cdot \dot{U}(t) + \xi \tag{9}$$

In formula (9), H is Jacobian matrix, ξ is random error.

So formula (10) can be acquired.

$$H^{(j)}\left[\dot{U}(t)\right] = O, j \geq 1 \tag{10}$$

In formula (10), O is zero matrix.

The derivative binomial equation of the measurement data can be further written as formula (11).

$$Z^{(m)}(t) = H \cdot \dot{U}^{(m)}(t) \tag{11}$$

The formula (12) can be got by multiplying $H^T R^{-1}$ both sides of the formula (11).

$$H^T R^{-1} H \dot{U}^{(m)}(t) = H^T R^{-1} Z^{(m)}(t) \tag{12}$$

In formula (12), R^{-1} is the coefficient matrix, H^T is the transposed matrix of Jacobian matrix.

The formula (13) can be got by multiplying $H^T R^{-1}$ both sides of the formula (12). While the voltage characteristic curve's all order derivatives can be calculated by formula (13).

$$\dot{U}^{(m)}(t) = \left(H^T R^{-1} H\right)^{-1} H^T R^{-1} Z^{(m)}(t) \tag{13}$$

Further expression of the voltage characteristic curve is determined as shown in formula (14).

$$\begin{cases} U_a(t) = e_0 + e_1 t + e_2 t^2 + ... + e_n t^n \\ U_b(t) = f_0 + f_1 t + f_2 t^2 + ... + f_n t^n \end{cases} \tag{14}$$

According to Taylor's formula, the voltage characteristic curve should satisfy formula (15).

$$\begin{cases} U_a(t) = U_{a0} + \frac{U_a'(t)}{\partial t}(t - t_0) + \frac{U_a^{(2)}(t)}{2!}(t - t_0)^2 + ... + \frac{U_a^{(n)}(t)}{n!}(t - t_0)^n \\ U_b(t) = U_{b0} + \frac{U_b'(t)}{\partial t}(t - t_0) + \frac{U_b^{(2)}(t)}{2!}(t - t_0)^2 + ... + \frac{U_b^{(n)}(t)}{n!}(t - t_0)^n \end{cases} \tag{15}$$

In formula (15), $U_a'(t)$, $U_a^{(2)}(t)$ …. $U_a^{(n)}(t)$ is 1-order , 2-order .... n-order derivative of $U_a(t)$. $U_b'(t)$, $U_b^{(2)}(t)$ …. $U_b^{(n)}(t)$ is 1-order , 2-order .... n-order derivative of $U_b(t)$.

Taking the initial time $t_0 = 0$, the formula (15) can be simplified to formula (16).

$$\begin{cases} U_a(t) = U_{a0} + \frac{U_a'(t)}{\partial t} t + \frac{U_a^{(2)}(t)}{2!} t^2 + ... + \frac{U_a^{(n)}(t)}{n!} t^n \\ U_b(t) = U_{b0} + \frac{U_b'(t)}{\partial t} t + \frac{U_b^{(2)}(t)}{2!} t^2 + ... + \frac{U_b^{(n)}(t)}{n!} t^n \end{cases} \tag{16}$$

The formula (17) can be got by the comparator (16) and formula (14).

$$\begin{cases} e_0 = U_{a0}, e_1 = \frac{U_a'(t)}{\partial t}, e_2 = \frac{U_a^{(2)}(t)}{2!}, ..., e_n = \frac{U_a^{(n)}(t)}{n!} \\ f_0 = U_{b0}, f_1 = \frac{U_b'(t)}{\partial t}, f_2 = \frac{U_b^{(2)}(t)}{2!}, ..., f_n = \frac{U_a^{(n)}(t)}{n!} \end{cases} \tag{17}$$

Numerical example

This essay, taking IEEE 30 node system as an example, assumes that all nodes are equipped with PMU, the simulation data takes flow results as the true value. The generation and load values for each

section of the overall grow 1%. The example assumes a normal distribution in which the SCADA system measurement error distribution with mean value is 0 and a standard deviation is 0.02; and convergence accuracy is 10e−6 . Using state the amount of amplitude and the absolute error of the phase angle δ_V and δ_θ as computational performance indicators, the value achieved is equal to the absolute value of the estimated value and the corresponding true value difference.

To verify the numerical properties of the proposed algorithm, the case analyzes the mutation case that important nodes of a sudden load from increase 1% to drop 3%, the Performance Characteristics of the algorithm proposed in this essay, the method of least squares state estimation and traditional linear dynamic state estimation method, and the results are shown in table 1.

Tab.1 The performance comparison of algorithm stated in this essay and other kinds of algorithm in mutation load

information	computatin time (ms)	δ_V/pu	δ_θ/pu
WLS method	483	0.0072	0.0131
Traditional dynamic state estimation	264	0.1370	0.5326
Method in this essay	179	0.0075	0.0130

As can be seen from Table 1, in the special case of a sudden change in load occurs, the accuracy of the proposed method is higher compared to traditional linear dynamic estimation. Mainly because of the linear dynamic state estimation accuracy greatly affected by forecasting state, the forecast accuracy is poor when sudden load change state take place, affecting the estimation accuracy of the dynamic state estimation. This algorithm overcomes the fault of traditional linear dynamic state estimation influenced by the forecasting state.

Conclusions

The new state estimation algorithm of this paper has fast computing speed characteristics , and realizes the full utilization of the massive PMU data, this algorithm has higher calculation accuracy in the special circumstances of load suddenly changes, ; It makes the continuous analysis of the power system static analysis.

References

[1] HUA Guo-dong, YING Jian-lie, Yaonian LIU, et al. State estimation with the least robustness square method based on distribution [J].Journal of Northeast Electrical.

[2] Yanglin LI, Zhinong WEI, Junbiao WAN. A new algorithm for the distributed state estimation of power system [J].Relay, 2007, 35(20):13-17 (In chinese).

[3] Li HAN, Xueshan HAN, Fang CHEN. Dynamic state estimation in power system based on integrated forecasting model and adaptive filter. Transactions of China Electrotechnical Society, 2008, 23(8):107-113.

[4] MANDAL J K, SINH A A K, ROY L, et al. Incorporating nonlinearities of measurement function in power system dynamic state estimation. IEE Proceedings: Generation, Transmission and Distribution, 1995, 142(3):289-296.

[5] Guihua Lin, Yanjun Zhang, Tao Wang, Yuying Wang. State Estimation of Equivalent Current Measurement Transformation Based on Generalized Tellegen's Theorem. Advanced Materials Research Vols.732-733 (2013) pp 941-947.

[6]Haozhong Cheng, Qingshan Yuan, Yihua Wang, etc. A state estimation method of power systems based on equivalent current measurement transformation, Automation of Electric Power System，2000，24(14)：25-29 (In chinese).

Advanced Materials Research Vols. 960-961 (2014) pp 1043-1047

doi:10.4028/www.scientific.net/AMR.960-961.1043

A new evaluation system method for small current grounding line selection device

Jinlong Zhou[1, a], Jinling Lu[1, b], Chao Xu[1, c]

[1]Department of Electrical and Electronic Engineering, North China Electric Power University, Baoding, Hebei, 071003, China

[a]814278610@qq.com, [b]Lujinling@126.com, [c]xuchao.21@163.com

Keywords: AHP, judgment matrix, evaluation for line selection device, weight vector.

Abstract: The evaluation of small current grounding line selection device plays an important guiding part in fault diagnosis and device promotion. But the current methods focus on the evaluation of individual indicator and can not form systematic evaluation of the programs.This paper firstly makes use of AHP method to evaluate small current grounding line selection device, and establishes the evaluation system of small current grounding line selection device. During the weight solution process, this paper uses three scale method to determine the comprehensive weight of individual indicator, and achieves a combination of expertise and quantitative, qualitative assessment of the results. The practical case analysis of small current grounding line selection device proves the validity and practicability of this method, which is of great theoretical and practical significance.

Introduction

At present, the operating mode of ungrounded or resonant grounding is usually used in 6~35kv medium and low voltage distribution network in China[1-2], which is also known as small current grounding. Single-phase ground fault is one of the common faults in small current grounding system. Due to small fault current, unstable arc and other factors, line selection of grounding fault is difficult, especially for resonant ground running mode, line selection problem has not been solved well.

With the development of the reliability and automation level of the distribution network, we urgently need to improve accuracy and reliability of the automation line selection technology and the corresponding automatic line selection device. Traditional evaluation of small current grounding line selection device is often focused on a single indicator, such as the accuracy of fault line selection, the economy, the applicability of the device. These indexes can evaluate the performance of small current grounding device from different sides and different levels, but lack the overall evaluation and do not have a strong guiding role in small current grounding line selection. So we require a systematic, scientific assessment method.

This paper presents a systematic method that can quantitatively assess the small current grounding line selection device overall—evaluation system of small current grounding line selection device. This method, which is based on the analytic hierarchy process (AHP) [2-3], can evaluate the comprehensive index of small current grounding line selection device, analyze small current grounding fault more scientifically and more effectively, and guide the development of small current grounding line selection device.

The basic idea of analytic hierarchy process

AHP is a multi-scheme or multi-objective decision-making method which does a quantitative analysis of non-quantitative incident and an objective analysis of the subjective judgment in the decision-making process. The method combines quantitative analysis with qualitative analysis, and judges the relative important degree of each measure by the experience of policy makers. It divides the elements that are closely related to decision into different levels, such as target, criteria, scheme, then on this basis, we can analyze it qualitatively and quantitatively.

First of all, the thought of AHP is that: the problems are broken into different constituent elements depending on the characters and requirements of the problem, and according to the

correlation between factors' influence and subordinately relations, factors are gathered in different chromatography. Secondly, by introducing measurement theory, people's judgment is quantified with a relative scale, and the judgment matrix is established layer by layer [4], then the weight of the judge matrix is solved. Finally, the comprehensive weight of the scheme is calculated. The steps of comprehensive evaluation based on AHP include:

(1)Establish the hierarchical structure model;
(2)Construct judgment matrix;
(3)Solve the weight of judgment matrix;
(4)Hierarchical ranking and consistency check;
(5)Calculate the comprehensive weight and rank;

Establish comprehensive evaluation system of small current grounding line selection device

The assessment system flow chart of the small current grounding line selection device is shown in Fig.1.

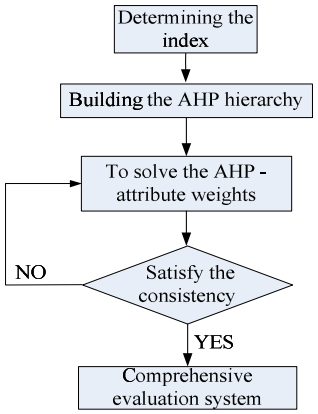

Fig.1 Assessment system flow chart of the small current grounding line selection device

The comprehensive assessment of the small current grounding line selection device is based on the scientific theory of systematic analysis, results of objective and quantitative are given according to the requirements of comprehensive, reasonable and rigorous, This paper establishes the comprehensive index evaluation system of small current grounding line selection device, the evaluation process includes the following four parts:

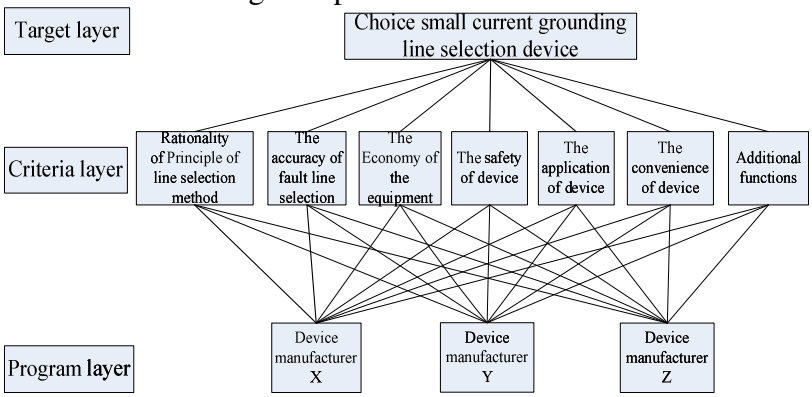

Fig.2 Hierarchy chart of small current grounding line selection device evaluation system

1）Establish a hierarchy: AHP is the key technology to establish the evaluation system when analyzing complex problems in the evaluation. Breaking down complex problem by establishing a clear hierarchy is its key. This paper uses the basic idea of analytic hierarchy process to propose the evaluation system of the small current grounding line selection device of Tianjin Power Grid by combining the actual situation in the area. Its hierarchical structure diagram is shown in Fig. 2.

2）Analysis, calculation and evaluation of single index: In the evaluation system of the small current grounding line selection device of Tianjin Power Grid, many factors need to be considered during the calculation and evaluation of each individual index, such as the determination of index evaluation standard, each index score standard， as well as the weight of single index. Among them, the evaluation standard is mainly based on the regulations of relevant guides and experts experience. Determining the score according to expert advice. The weight of single index is determined by feature vector of the judgment matrix .

3）Comprehensive score method: The score of single index reflects the specific situation of the small current grounding line selection device from different sides, but not enough to explain the overall situation. Therefore, we need to use the AHP method to calculate layer by layer until the comprehensive score of the line selection device is calculated. The calculation equation is:

$$W^{(3)} = \sum_{j=1}^{n=7} w_j^{(3)} w_j^{(2)} \tag{1}$$

In Eq.1, $W^{(3)}$indicates the score of the criteria layer to target layer in the hierarchy, the greater $W^{(3)}$ is the better the device is. n expresses the number of attribute j in the program layer. $w_j^{(3)}$ indicates the score of the program layer to criteria layer in the hierarchy. $w_j^{(2)}$ expresses the weight of criteria layer's attribute j to target layer.

4）Analysis of problems: This study proposes the comprehensive index evaluation system of small current grounding line selection device, the comprehensive analysis method combines the part with the whole. In the single index calculation process, whether there are any problems is automatically recognized by evaluating data, and the details of the existing problems are recorded. While the analytic hierarchy process (AHP) is used to calculate the comprehensive score, the existing problems in the line selection device are hierarchically counted, and the seriousness of problems is sorted. This provides a theoretical basis for the supplement and improvement of line selection device.

The example analysis

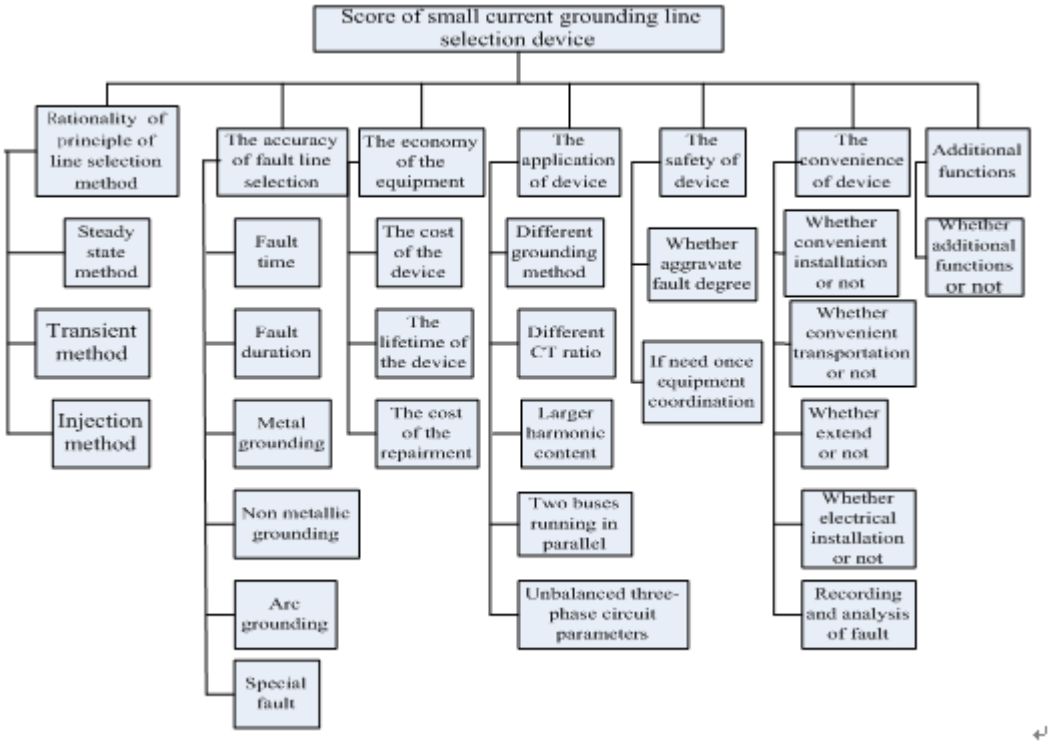

Fig.3 Small current grounding line selection device evaluation system

This paper uses the analytic hierarchy process to analyze the instance of solving weight value of each index. First of all, the process of solving the weight of the first layer is illustrated. Indicators of the layer include:c_1-rationality of principle of line selection method; c_2-the accuracy of fault line

selection; c_3-the economy of the equipment; c_4-the application of device; c_5-the safety of device; c_6-the convenience of device; c_7-additional functions[5]. As shown in the Fig. 3。

(1)Establish comparative matrix

According to the need of line selection, we can make the relative importance by combining with data analysis and expert opinion. In view of the seven level indicators, comparison matrix is constructed by using three scale method:

$$A_1=(a_{ij})=\begin{bmatrix} & c_1 & c_2 & c_3 & c_4 & c_5 & c_6 & c_7 \\ c_1 & 1 & 0 & 0 & 0 & 0 & 2 & 2 \\ c_2 & 2 & 1 & 2 & 2 & 2 & 2 & 2 \\ c_3 & 2 & 0 & 1 & 1 & 1 & 2 & 2 \\ c_4 & 2 & 0 & 1 & 1 & 1 & 2 & 2 \\ c_5 & 2 & 0 & 1 & 1 & 1 & 2 & 2 \\ c_6 & 0 & 0 & 0 & 0 & 0 & 1 & 2 \\ c_7 & 0 & 0 & 0 & 0 & 0 & 0 & 1 \end{bmatrix}$$

(2)Construct the judgment matrix by using pole ratio method[6].

$$A=(a_{ij})=\begin{bmatrix} & c_1 & c_2 & c_3 & c_4 & c_5 & c_6 & c_7 \\ c_1 & 1 & 0.4411 & 0.6044 & 0.6044 & 0.6044 & 1.5490 & 3.9698 \\ c_2 & 2.2671 & 1 & 1.3703 & 1.3703 & 1.3703 & 3.5118 & 9 \\ c_3 & 1.6545 & 0.7298 & 1 & 1 & 1 & 2.5628 & 6.5680 \\ c_4 & 1.6545 & 0.7298 & 1 & 1 & 1 & 2.5628 & 6.5680 \\ c_5 & 1.6545 & 0.7298 & 1 & 1 & 1 & 2.5628 & 6.5680 \\ c_6 & 0.6456 & 0.2848 & 0.3902 & 0.3902 & 0.3902 & 1 & 2.5628 \\ c_7 & 0.2519 & 0.1111 & 0.1523 & 0.1523 & 0.1523 & 0.3902 & 1 \end{bmatrix}$$

(3)Compute the weight vector and consistency check

1) Solve the eigenvector of judgment matrix from criteria layer to target layer：

$$\begin{aligned} w^{(2)} &= (w_1^{(2)}, w_2^{(2)}, w_3^{(2)}, w_4^{(2)}, w_5^{(2)}, w_6^{(2)}, w_7^{(2)}) \\ &= (0.1096, 0.2484, 0.1813, 0.1813, 0.1813, 0.0707, 0.0276) \end{aligned}$$

2) Solve the maximum eigenvalue of judgment matrix：

$$\lambda_{\max} = 7.00016$$

The consistency check of criteria layer to target layer can be calculated:

$$CI = \frac{(\lambda_{\max} - n)}{(n-1)} = \frac{0.00016}{6} = 0.000027 \tag{2}$$

Random consistency index:

$$RI = 1.32$$

The consistency ratio:

$$CR = \frac{CI}{RI} = \frac{0.000027}{1.32} = 0.0000202 < 0.1 \tag{3}$$

Thus, the non-consistence of the judgment matrix is within the permissible range. We can use the eigenvector as weight:

$$\begin{aligned} w^{(2)} &= (w_1^{(2)}, w_2^{(2)}, w_3^{(2)}, w_4^{(2)}, w_5^{(2)}, w_6^{(2)}, w_7^{(2)}) \\ &= (0.1096, 0.2484, 0.1813, 0.1813, 0.1813, 0.0707, 0.0276) \end{aligned}$$

Table 1 The weight vector and the consistency check of judgment matrix B1to B7

	B1	B2	B3	B4	B5	B6	B7
	0.637	0.540	0.136	0.279	0.467	0.547	0.122
$w_k^{(3)}$	0.105	0.297	0.625	0.649	0.067	0.345	0.320
	0.258	0.163	0.238	0.072	0.467	0.109	0.558
$\lambda_{\max}$	3.039	3.009	3.018	3.065	3.00	3.054	3.018
CI_K	0.019	0.005	0.009	0.032	0.00	0.027	0.009

According to the calculation method above, the weight vector and the consistency test of judgment matrix B1to B7 from scheme layer to criteria layer are calculated.

The table shows $RI = 0.58$, after calculation of B1- B7 and get $CR<0.1$, so all records satisfy the consistency test. Now we get weight vector of scheme layer to criteria layer:

$$W^{(3)} = (W_1^{(3)}, W_2^{(3)}, W_3^{(3)}, W_4^{(3)}, W_5^{(3)}, W_6^{(3)}, W_7^{(3)})$$

$$= \begin{bmatrix} 0.6370 & 0.5396 & 0.1365 & 0.2790 & 0.4667 & 0.5469 & 0.1220 \\ 0.1047 & 0.2970 & 0.6250 & 0.6491 & 0.0667 & 0.3445 & 0.3196 \\ 0.2583 & 0.1634 & 0.2385 & 0.0719 & 0.4667 & 0.1085 & 0.5584 \end{bmatrix}$$

So the weight vector of the scheme layer to the target layer is calculated:

$$W^{(3)} = W^{(3)} \times W^{(2)} = (0.4058, 0.3615, 0.2329)^T \quad (4)$$

The consistency ratio of total hierarchical order is:

$$CR = \frac{a_1 CI_1 + a_2 CI_2 + \ldots + a_7 CI_7}{a_1 RI_1 + a_2 RI_2 + \ldots + a_7 RI_7} = \frac{0.013}{0.58} = 0.02 < 0.1 \quad (5)$$

Therefore the total hierarchical order meets the consistency test. Then the weight of X, Y, Z device manufacturer is respectively 0.4058, 0.3615, and 0.2329. Device manufacturer X gets the highest weight, so the device manufacturer X is the best choice.

Conclusion

In this paper, the analytic hierarchy process (AHP) is used in the assessment of the small current grounding line selection device. And the structure detection and performance evaluation of the small current grounding line selection device in Tianjin Power Grid is set up. All attributes of evaluation index of line selection device are reflected comprehensively. In the process of solving weights, judgment matrix formed in this paper is different from the general judgment matrix which uses1-9 scale formation, the consistency and rate of convergence etc are more practical. The degree of the importance of relationship between two indexes is considered completely, and the consistency check is verified in detail. This evaluation system can be well applied in detection and performance assessment of the small current grounding line selection device in Tianjin Power Grid, and this system is of great theoretical and practical significance.

References

[1] Huannian Yao, Meiyue Cao. The Resonance Grounding of Power System [M], Beijing: Chinese Electric Power Press, 2000. (In Chinese)

[2] Lianfen Wang, Shubo Xu. AHP Introduction[M]. Beijing: Chinese People's University Press, 1990. (In Chinese)

[3] Xinhua Wang, Tangjun Li, Lili Ding. Complex system evaluation theory and technology [M]. Ji nan: Shandong University press, 1990. (In Chinese)

[4] Jun Zuo. AHP Judgment Matrix in the Indirect Method[J]. Systems Engineering, 1988, (6). (In Chinese)

[5] Xiao yong Yu, Like Gao, Yanliang Gao, Yongduan Xue. Study on Performance Evaluation Method for Small Current Grounding Line Selection Device[J]. Guang xi Electric Power, Vol.35(2012), p. 1-3, 20. (In Chinese)

[6] Xiaohui Li, Lai Zhang, Xiaoyu Li, Zhu Chen. The research on the evaluation system for existing network based on analytic hierarchy process and Delphi method[J]. Power System Protection and Control, Vol.36(2008), p. 57-61. (In Chinese)

Advanced Materials Research Vols. 960-961 (2014) pp 1048-1053

doi:10.4028/www.scientific.net/AMR.960-961.1048

Optimal Siting and Sizing of Distributed Generation Planning in a standalone Microgrid

Xiaoyue Cheng[1, a] ,Jinling Lu[2,b]

[1,2]Department of Electrical Engineering, North China Electric Power University, Baoding, Hebei 071003, China

[a]lingkong214@126.com, [b]644869425@qq.com

Keywords: offshore platforms, renewable resource, volatility of CO_2 emission price, low-carbon effect, latin hypercube sampling, optimal sizing of distributed generation.

Abstract. This paper introduces renewable energy to ensure offshore platforms as a stand-alone microgrid operate reliably economically in low-carbon environment, considering volatility of CO_2 emission price. A probability distribution model and economic model containing investment cost and low-carbon effect is established respectively, using latin hypercube sampling(LHS), meanwhile, the stochastic power is adopted to judge whether the built planning model can meet power flow constraint, Monte Carlo method is used to simulate characteristics of distributed generation(DG), a probabilistic power flow is made to illustrate reliability index. The model takes the types, sites and sizes of DG as decision variables, economy and environment as the objective function, particle swarm algorithm is proposed to solve the multi-objective optimization problem .A case study based on data from offshore oilfield is presented to verify the advantages of the improved optimal sizing method.

Introduction

Recently, most of the countries all over the world have paid great attention to CO2 emission. To meet its obligations to reduce CO2 concentrations under the Kyoto Protocol, the European Union(EU) established the first cap-and-trade system for CO2 emissions in the world starting in 2005.Our country proposes the target to save energy and reduce pollutant emission[1].

DG has conformed to the development of low-carbon in recent years. Microgrid technology provides a flexible and efficient platform for DGs and renewable energy .

At present, domestic and foreign scholars do researchs about DGs. In[2] bacterial foraging algorithm is proposed to solve the optimal sizing problem of hybrid solar-wind DG in microgrid. An optimal configuration model of microgrid power supply based on maximizing net benefits is proposed in[3]. Mohamed F, Koivo H present a generalized formulation to determine the optimal operating strategy and cost optimization scheme as well as the reduction of the emissions for a MicroGrid [4]. When solving the problem about distributed power optimization of microgrid ,economy, reliability, environment is all considered in works [2-4]. However, low-carbon model, carbon price fluctuations and other uncertainties about carbon emissions, which brings new challenges to optimize the allocation of microgrid, works above do not fully consider.

This paper firstly takes carbon price fluctuations into optimal sizing of distributed generation . In order to improve the effectiveness of sampling for wind speed and solar radiation, LHS is introduced innovatively.

Power Generation Modeling

Wind Turbine Generator (WG). Based on a large number of historical data ,the wind speed obeys two-parameter Weibull distribution approximately, the probability density function as fomula(1)

$$\varphi(v) = \frac{k}{c}(\frac{v}{c})^{k-1} e^{-(\frac{v}{c})^k} \tag{1}$$

Where v is wind speed, m/s. k is the shape parameter, k =1.8~2.3 in general; c is the scale parameter which reflects the average wind speed, distribution probability density function shows as fomula(2)

$$F(V) = p(v \le V) = 1 - \exp[-(\frac{v}{c})] \tag{2}$$

Where range of $F(V)$ is [0,1]，dividing it into N parts， generating random number from 0 to1,then convert it to random numbers as equation (3)

$$U_n = \frac{U}{N} + (n-1)/N \tag{3}$$

Where, n=1,2…N， U is a random number in the range (0,1), U_n is a random number in the n-th interval.

Use inverse function to convert these random numbers to random variable v, then latin hypercube sampling for the velocity is completed. Relationship about wind turbines between power output and actual wind speed can refer to work[5].

Photovoltaic power generation. Power output of photovoltaic varies as solar radiation conditions changes. First, sampling for solar radiation and skies coefficient, then simulating power output of photovoltaic[6]. Fomula is shown as

$$P_{PV} = \eta S I_\beta \tag{4}$$

Where, S is size of battery; I_β is solar radiation hourly accepted by PV panels in per unit area ; η is conversion efficiency of battery at the moment of t.

Gas Turbine Generator(GS). Adopting dual fuel generator set is a characteristic of power station at offshore platform, where uses oil associated gas as main fuel. Characteristics of energy consumption-power described as fomula(5)

$$V_f = \sum_{i=1}^{N} K_f E \tag{5}$$

Where, V_f is natural gas consumed per unit time, m^3. K_f is coefficient of natural gas.

Battery Storage (BS) and Super Capacitor(SC) Modeling. Cycle life of battery is short, power density is low, charging time is long, while volume of super capacitor is small, weight is light, power density is high, cycle life is long, therefore,BS and SC is adopted as hybrid energy storage.Models of BS and SC refer to work[7].

Objective Function

System Economic Model .Under low-carbon economy, it aims at achieving minimum economic cost annually, realizing new energy saving and emission reduction significantly, meanwhile ensuring system operate reliabily.

Initial investment cost, operation and maintenance costs, low-carbon effect, penalties and subsidies expenses are included in comprehensive economic cost, which is made as the objective function, formulated as(6)

$$E = E_{az} + E_{om} + E_{fuel} + E_{co_2} + E_{cf} + E_{sub} \tag{6}$$

Initial Investment Cost

$$E_{az} = \sum_{i=1}^{p} \frac{r(1+r)^{n_i}}{(1+r)^{n_i} - 1} \cdot C_{gi} \tag{7}$$

Where, E_{az} is equivalent cost of equipment investment every year, C_{gi} is installation costs of the i-th power, n_i is the life of the i-th power, r is interest rate.

Operation and Maintenance Costs

$$E_{om} = \sum_{i=1}^{p} K_{om_i} P_{gi} \tag{8}$$

Where, E_{om} is annual operating cost, K_{omi} is scaling factor between maintenance costs and capacity of the i-th power, RMB/kW.

Fuel costs
$$E_{fuel} = c(\sum_{i=1}^{p} K_{fi} E_i - E_{in}) \tag{9}$$

Where, E_i is power generation of the i-th gas turbine , K_f is fuel provided to the gas turbine（m^2/kWh ）,E_{in} is the total amount of natural gas that platform can be supplied, c is fuel price.

Low-carbon effect.Under emission trading scheme, CO2 emission is strictly restricted, CO2 emission index can participate in the market as a commodity trading, thus, influence brought by CO2 emission price can not be ignored. Based on historic date , the CO2 emission price is approximately by a Weibull PDF which can be expressed by (10) and whose curve is shown in Fig.1

$$f(x) = \frac{2.78}{19.56}(\frac{x}{19.56})^{1.78} e^{-(x/19.56)^{2.78}} \tag{10}$$

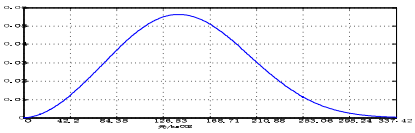

Fig.1 Weibull PDF modeling CO_2 emission price

From the environmental point of view, in order to achieve energy conservation, development and utilization of new energy sources and energy storage charging is promoted, carbon price is calculated step by step from formula (11) to (13)

$$X_i = K_{co_2 i} \cdot V_f - A_{WPC} - A_i \tag{11}$$

$$A_{WPC} = \beta_{CO_2} \sum_{t=1}^{8760} \sum_{i=1}^{m} N_i P_i \tag{12}$$

$$E_{co_2} = \sum_{i=1}^{N_g} \pi_{co_2} \cdot X_i + E_{PV} \tag{13}$$

Where, X_i is emissions of i-th generator per hour(tCO_2/h) , A_i is carbon emissions allowed every generator per hour, A_{WPC} is reduction of CO_2 emission due to renewable energy generating and storage charging . K_{CO2}i is CO_2 emission coefficients of natural gas. π_{co_2} is emission price, N_g is generator number, E_{pv} is costs of photovoltaic power generation.

In the model above, generators can sell their emission allowance surpluses or buy the shortage in allowance from the emission trading market.

Penalties and subsidies expenses.In order to ensure power supply reliably and avoid energy waste so as to optimize configuration, penalties and subsidies expenses is introduced as fomula(14)

$$E_{cf} = k_{pl} E_{lp} + k_{pw} E_{pw} \tag{14}$$

Where, k_{pl} is penalty coefficient due to power storage, E_{lp} is power shortage each year, k_{pw} is penalty coefficient due to energy waste**,** E_{pw} is electricity surplus each year.

Power subsidy.To encourage the development and utilization of renewable energy, the government gives subsidies to support .

$$E_{sub} = c_{sub} \sum_{t=1}^{8760} \sum_{i=1}^{m} N_i P_i \tag{15}$$

Where, C_{sub} is subsidy price, N is number of installations of turbine and solar panels, P is power supply of renewable energy.

Equality constraints.The main consideration is the balance of power system as fomula(16)

$$\begin{cases} \sum P_g = \sum P_l + \sum P_{loss} \\ \sum Q_g = \sum Q_l + \sum Q_{loss} \end{cases} \tag{16}$$

Inequality constraints
$$\mathrm{SOC}_{\min} \le \mathrm{SOC} \le \mathrm{SOC}_{\max} \tag{17}$$

Where, SOC is charge state of battery, SOC_{min}, SOC_{max} is lower and upper limits, which is usually set at 20%, 100%..

Voltage constraints
$$v_{i\min} < v_i < v_{i\max} \tag{18}$$

Where v_{imax}, v_{imin} is upper and lower voltage at Voltage node j.
Reliability of system.In this paper, load power shortage rate (loss of power supply probability, LPSP) characterized system reliability. To ensure system reliability, load power shortage rate is limited within a certain range[8] .

$$lpsp = \frac{\sum_{i=1}^{8760}(P_{li} - (P_{WTi} + P_{PVi} + P_{c1i} + P_{c2i})}{\sum_{i=1}^{8760} P_{li}} \le lpsp_{\max} \tag{19}$$

Where, P_{li}, P_{WTi}, P_{PVi}, P_{c1i}, P_{c2}i is the power of load, wind turbine, photovoltaics, batteries, capacitors.

Solution of Optimization Model

Option 1. In order to avoid oil associated gas waste, diesel-powered generators are used at first, when the oil associated gas supply is not enough, wind turbine, and photovoltaic cells are put into operation, if power generation exceeds or lacks, energy storage devices play a role of peak load shifting.
Option 2 In order to improve the utilization of renewable energy, wind turbines and photovoltaic cells are put into use firstly, diesel generators secondly, scheduling strategy energy storage is consistent with option 1.

Optimal allocation based on particle swarm optimization algorithm, PSO

PSO is adopted to solve the model of optimal allocation. Procedure is followed as below
1)Select the initial particle. Roughly determine the feasible region, generate a random initial population:
$[n_{PV}, n_{WG}, n_{bat}, n_{sc}, n_{WG}, n_{dis}]$.
2)Dealing with constraints.Using penalty function to handle particles that not meeting the constraints in iterative process, new objective function derived from orginal objective function and penalty terms. This article applys rate of node voltages off-limit δ as penalty term , fomula as (20), Process shows as Fig.2

$$f = \max E + K\sum_{i=1}^{m}\delta_i \tag{20}$$

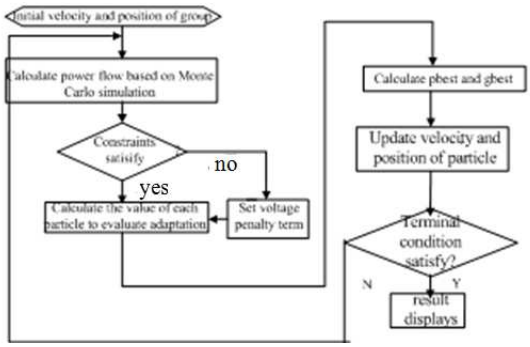

Fig.2Flow chart of sizing DG based on PSO algorithm

Results and discussion

Fig.3 is a simplified diagram of offshore oilfield, which is a 14-node system. The field includes five power centers, 1,2,3,12,13. Distributed generations locate at platform 2, 3, 12, 13.

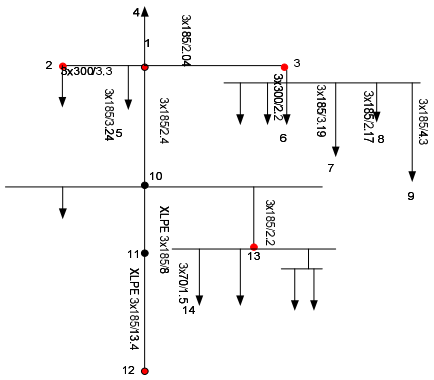

Fig.3 Diagram of offshore platforms microgrid system

Select typical months of offshore platforms microgrid to simulate weather condition, results of simulation show as Fig.5 and Fig.6.

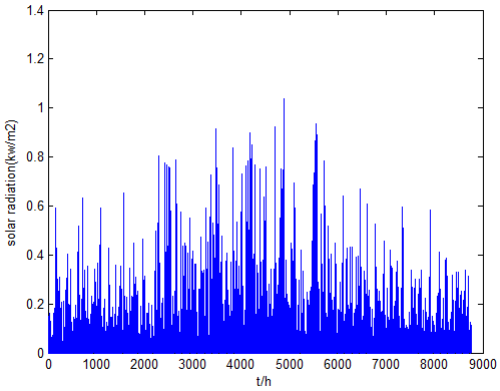

Fig.5 Simulation of annual solar radiation

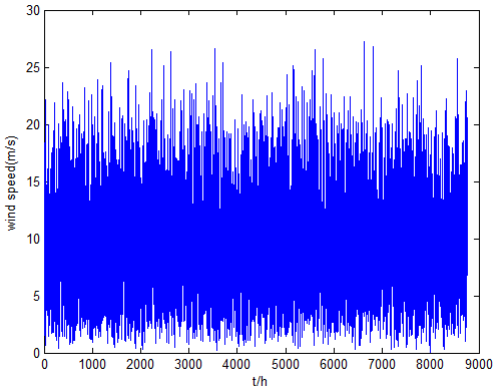

Fig.6 Simulation of annual wind velocity at the location of Microgrid

Results of optimal siting and sizing of distributed generation shows as Tab.1 and Tab.2.

Tab.1 Planning of schemes

DG types	option1	option2
PV	448,408,817,336	2063,736,383,2513
MT	8,6,1,4	10,43,18,25
GS	7	1
BS	218	1332
SC	176	275

Tab.2 Cost of planning schemes

option	Investment	Low-carbon effect	Punishment cost	Total cost
Option1	178369	9964	288	168693
Option2	247584	28645	2646	221585

Results above shows that initial investments and operating costs of renewable energy are higher than conventional units, great benefits bought by low-carbon can not be ignored, thus renewable energy generation has great potential, energy storage contributes to increase capacity of renewable accepted by grid. Further study will be needed.

Conclusion

In this study, considering carbon price volatility agrees to actuality, renewable energy can realize energy saving and emission reduction, PSO algorithm can obtain optimal solution to minimize the total cost .

References

[1] Huan Wei, Sun Xuhui, Wu Zipping, et al: Power System Technology.Vol.33(2009), No.9,p. 14.(in Chinese)

[2] Ma Xiyuan, Wu Yaowen, Fang Hualiang, et al: Proceedings of the CSEE. Vol.31(2011), No.25,p. 17.(in Chinese)

[3] LI Dengfeng, Xie Kaigui, Hu Bo,et al: Power System Protection and Control. Vol.41(2013), No.20,p. 21. (in Chinese)

[4] Mohamed F, Koivo H: 6th International conference on renewable energies and power quality (ICREPQ'07), Sevilla, Spain. 2007,p.26.

[5] Wang Xinzhi. Wind power technology of Offshore. Beijing:China Machine Press.2012. (in Chinese)

[6] Sun Rui, Liang Lu: Meteorological and Environmental technology. Vol.30(2007), No.1,p. 24. (in Chinese)

[7] Lu Yang. Optimal Siting and Sizing of Distributed Generation Planning in a Microgrid Considering Stochastic Characterastic. North China electric power University.2013. (in Chinese)

[8] Borowy B S, Salameh Z M:Energy conversion, ieee transactions on, Vol.11(1996), No.2,p. 367.

Advanced Materials Research Vols. 960-961 (2014) pp 1054-1057
© (2014) Trans Tech Publications, Switzerland
doi:10.4028/www.scientific.net/AMR.960-961.1054

Power System Transient Stability Analysis via Second-Order Non-Uniform Kuramoto Model

Liu Yang[1, a], Yufeng Guo[1, b *], Ning Chen[2, c], Minhui Qian[2, d], Xiaoping Xue[1, e] and Daren Yu[1, f]

[1]Harbin Institute of Technology, Harbin 150001, China

[2]China Electric Power Research Institute, Nanjing 210003, China

[a]yangliuhit@126.com, [b]guoyufengHIT@163.com, [c]chenning8375@163.com, [d]qianminhui@gmail.com, [e]xiaopingxue@263.net, [f]yudaren@hit.edu.cn

Keywords: second-order Kuramoto model, frequency synchronization, power system, transient stability, network topology, region of attraction

Abstract. Based on frequency synchronization theory of the second-order non-uniform Kuramoto model, a novel approach for power system transient stability analysis is put forward by establishing the correspondence between the classic power system model and the second-order non-uniform Kuramoto model. This method relates network parameters with the region of attraction of the disturbed system's stable equilibrium and thus the transient stability information of the disturbed system can be obtained by comparing the initial configuration with trapping region of the stable equilibrium of the disturbance-canceling system. The application of our approach to single machine infinite bus system shows that this method features a fast computation speed. It can determine the transient stability of the system when a certain perturbation acts on as well as offer the stability margin of the disturbed system, which is of great importance for practical use.

Introduction

Power system stability has been considered as a critical issue for secure system operation since 1920s. As one of the common forms in power system stability problems, transient stability never fails to draw the academic's and industry's attention [1]. Generally speaking, approaches for transient stability analysis essentially fall into such categories of time-domain simulation methods and direct methods which present advantages but also disadvantages [2]. As power grids integrate an increasing number of highly stochastic renewable energy sources, the transient stability of power systems turns to be more severe than anytime before. Therefore, an open problem is the quest for simple and practical criteria to investigate the transient stability of a disturbed system.

It is recognized that the second order non-uniform Kuramoto model is strikingly similar with the classic power system model employed in transient stability, and more importantly, the frequency synchronization in the Kuramoto model exactly equals to the transient stability in the power system [3,4]. Recently, Xue, one of the authors of this paper made a breakthrough in studying the frequency synchronization of the second-order non-uniform Kuramoto model. Using Lojasiewicz gradient inequality, Xue et al. studied the potential function of the coupled oscillator, and established the relation between network topological connection strength and trapping region of the system's synchronized solution, based on which, the synchronized solution's attraction domain can be conveniently estimated by network parameters (*cf. theorem 2.1 in [5]*), which open up a new way for investigating the region of attraction of the stable equilibrium with direct methods of power system transient stability analysis. This paper, applying the latest frequency synchronization theory of second-order non-uniform Kuramoto model to power system, provides a novel perspective for the research of transient stability.

Classic power system model and second-order non-uniform Kuramoto model

Classic power system model. Let $\delta_i = \delta_i(t)$ be the rotator angle of generator i. M_i, D_i, and P_{mi} stand for the inertia constant, damping constant and input active power of the ith generator separately, G_{ii} and $|Y_{ij}|$ are the self-conductance of the ith generator and modulus of mutual admittance between the ith and jth generators in the reduced network, and $|E_i|$, $|E_j|$ represent the magnitudes of voltage behind transient reactance of the ith and jth generators respectively. Then $P_i = P_{mi} - |E_i|^2 G_{ii}$ donates the injection active power of generator i and $P_{\max ij} = |E_i||E_j||Y_{ij}|$ depicts the maximum active power transferred between generators i and j. Under the common assumption of network-reduced model of power system, ignoring the transfer conductance, the swing equation of each generator for a disturbed power system containing n generators can be expressed as [6]:

$$M_i\ddot{\delta}_i + D_i\dot{\delta}_i = P_i + \sum_{j=1}^{n} P_{\max ij}\sin(\delta_j - \delta_i),\quad i = 1,2,\ldots,n \tag{1}$$

All parameters are given in per unit system, except for M_i, D_i which are given in s^2/rad and s/rad.

Second-order non-uniform Kuramoto model. Let $\theta_i = \theta_i(t)$ be the phase of the ith oscillator in the coupled nonlinear dynamic system, the second-order non-uniform Kuramoto model read as [5]:

$$m_i\ddot{\theta}_i + d_i\dot{\theta}_i = \Omega_i + \sum_{j=1}^{n} a_{ij}\sin(\theta_j - \theta_i),\quad i = 1,2,\ldots,n \tag{2}$$

Where m_i, d_i and Ω_i represent the inertia constant, damping constant and natural frequency of the ith oscillator respectively, and a_{ij} describes the interaction between the ith and jth oscillator.

Second-order non-uniform Kuramoto model based criteria for transient stability investigating

Under the assumption that the ratios of the damping constants to inertia constants of every generator in the system are identical ($\alpha_1 = \alpha_2 = \cdots = \alpha_i$), power system (1) turns into a homogeneous damped system. Let $\boldsymbol{\delta}(t) = (\delta_1(t),\ldots,\delta_n(t))$ and $\boldsymbol{\omega}(t) = (\omega_1(t),\ldots,\omega_n(t))$ be the ensemble of rotator angles and rotator angular velocities of all the generators respectively; while $\boldsymbol{\delta_0} = \boldsymbol{\delta}(0)$ and $\boldsymbol{\omega_0} = \boldsymbol{\omega}(0)$ donate the prescribed initial data of $\boldsymbol{\delta}(t)$ and $\boldsymbol{\omega}(t)$.

Define $\delta_m = \min\limits_{1\le i\le n}\delta_i$, $\delta_M = \max\limits_{1\le i\le n}\delta_i$, $D(\delta) = \delta_M - \delta_m$, $\dot{D}(\delta_0) = \dfrac{d}{dt}D(\delta(t))|_{t=0^+}$,

$$C(\delta_0,\omega_0,\alpha) = \max\left\{D(\delta_0), D(\delta_0) + \frac{1}{\alpha}\dot{D}(\delta_0)\right\},\ D(\overline{P}) = \max_{1\le i\le n}\{P_i/M_i\} - \min_{1\le i\le n}\{P_i/M_i\}$$

$$L = \min_{1\le i\ne j\le n}\left\{(\frac{1}{M_i} + \frac{1}{M_j})P_{\max ij} + \sum_{k\ne i,j}\min\{\frac{P_{\max ik}}{M_i}, \frac{P_{\max jk}}{M_j}\}\right\}$$

In the context of transient stability analysis, the frequency synchronization theory of second-order non-uniform Kuramoto model discussed in [5] (*cf. theorem 2.1*) can be adapted as following:

Lemma 1. Assuming that upon the removal of disturbance, the parameters of system (1) satisfy

$$L > D(\overline{P})/\sin D_c \tag{3}$$

Where D_c is determined by $\frac{\sqrt{2D(\overline{P})}}{\alpha}\frac{\sqrt{D_c-\tan(D_c/2)}}{\pi-2D_c}=1,\ \ D_c\in(0,\pi/2)$ (4)

If the initial configurations (the state variables' values at the instant of disturbance removal) meet

$$0<C(\delta_0,\omega_0,\alpha)<\pi-K \tag{5}$$

With K being determined by $\sin K=D(\overline{P})/L,\ \ K\in(0,D_c)$ (6)

Then, power system (1) can keep transient stability after disturbance canceling.

Example

The single machine infinite bus (SMIB) system is shown in Fig. 1. Circuit CCT 2 suffered a solid three-phase fault at point F which was cleared after the isolation of CCT 2.

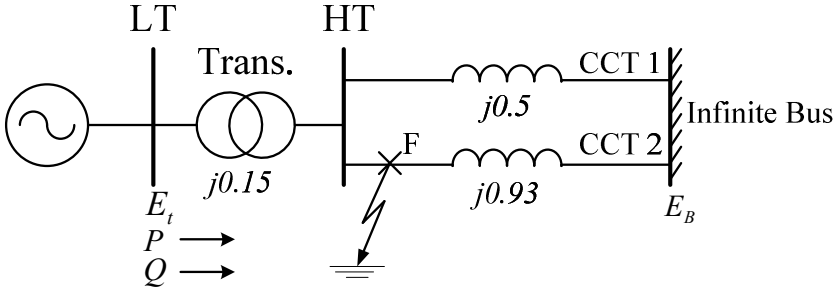

Fig. 1 SMIB system

Parameters of this SMIB system are in per unit on 2220MVA, 24kV base and the system's rated frequency is 60Hz.Other parameters of this SMIB system are listed in Table 1 bellow:

Table 1 SMIB system's parameters

parameter	P	Q	E_t	E_B	X'_d	M [s^2/rad]
value	0.9	0.436	1.0∠28.34°	0.90081∠0°	0.3	0.01857

Table 2 shows requisite parameters for Lemma 1 to determine the SMIB system's transient stability.

Table 2 Parameters of fault-cleared network

parameter	value	remark
L	59.3703	$D_c\in(0,\pi/2)$
$D(\overline{P})$	48.4703	$L>D(\overline{P})/\sin D_c=53.4304$
D_c	1.1365	Eq. 3 and Eq. 4 are satisfied
K	0.9552	region of attraction of stable equilibrium $\pi-K=2.1864$

The SMIB system's state variables at the moment of fault removal are obtained by solving the SMIB system's state equations during the time interval between fault-occurring and fault-clearing. Different fault clearing times t_c correspond to different parameter initial configurations $C(\delta_0,\omega_0,\alpha)$, which is illustrated in Table 3.

Table 3 Initial configurations of the fault-cleared network at different fault clearing time

initial configuration	Fault clearing time t_c [s]		critical fault clearing time obtained by Lemma 1[s]
	0.240	0.241	
$C(\delta_0,\omega_0,\alpha)$	2.1832	2.1864	0.240

To verify the accuracy of the critical fault clearing time obtained via Lemma 1, a time-domain simulation of the SMIB system was conducted in a four-second-duration from the moment of 1 second to 5 second with a step of 0.001s and then we got the critical fault clearing time as $t_{cr} = 0.267$ s. Swing curves of the generator rotor angle are shown in Fig. 3.

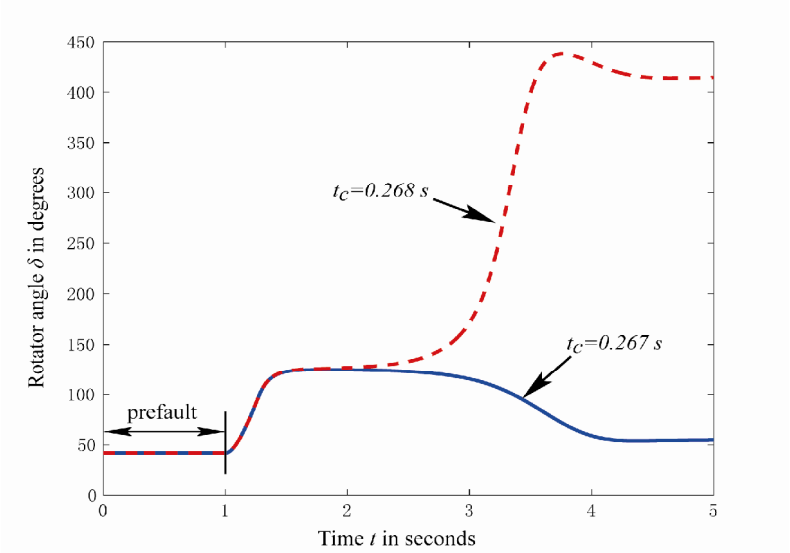

Fig. 3 Swing curves of the generator rotator angle at different fault clearing time

Contrasting the critical fault clearing time obtained by Lemma 1 to that solved by time-domain simulation method, it can be seen that Lemma 1 led to a conservative but acceptable result, it is a sufficient condition to determine the system's transient stability.

Conclusions

In this paper, we correlate the classic power system model to the second-order non-uniform Kuramoto model and then present a Kuramoto model based transient stability analysis methodology. Example given in the paper demonstrates the specific calculation procedure and computational accuracy of this method. Relative to traditional power system transient stability analysis approaches, our method reflects the transient stability of the system from the connection strength of the network's topological graph, provides a simple algebraic operation to estimate trapping region of the disturbed system's stable equilibrium, and exhibits the transient stability scenarios of the post-fault system by comparing initial configuration with the attraction domain. Our technical approach characterized by high computational efficiency which is beneficial to the guidance of power systems' on-line operation.

Acknowledgements

This work was financially supported by the National Basic Research Program of China (973 Program) (2012CB215201) and Technical Project of State Grid Corporation of China (2013320001510213).

References

[1] P. Kundur, J. Paserba et al.: IEEE Transactions on Power Systems Vol. 19 (2004), p. 1387.

[2] X. Wang, Y. Song and M. Irving: Modern Power Systems Analysis (Springer US, USA 2008).

[3] F. Dorfler and F. Bullo: SIAM Journal on Control and Optimization Vol. 50 (2012), p. 1616.

[4] F. Dorfler, M. Chertkov and F. Bullo: Proceedings of the National Academy of Sciences of the United States of America Vol. 110 (2013), p. 2005.

[5] Z. Li, X. Xue and D. Yu: submitted to SIAM Journal on Control and Optimization (2013).

[6] P. M. Anderson and A. A. Fouad: Power System Control and Stability (John Wiley, USA 2008).

Advanced Materials Research Vols. 960-961 (2014) pp 1058-1061

doi:10.4028/www.scientific.net/AMR.960-961.1058

Research of Distribution Network Reconfiguration Based on SFLGA

Zhu Kaifeng[1, a *], Wang Xue[1,b] and Cai Guihua[2,c]

[1]North China Electric Power University, Yonghua Street, Baoding city, Hebei Province China

[2]Baoding Power Supply Company, Yangguang Street, Baoding city, Hebei Province China

[a]6961307@qq.com, [b]wangxuedl@126.com, [c]caiguihuadl@126.com

Keywords: SFLA; genetic algorithm; multi-objective optimization; distribution network reconfiguration.

Abstract. The article studies on the application of the shuffled frog leaping algorithm (SFLA) in power distribution network reconfiguration, taking the minimum loss and voltage quality of distribution network as a multi-objective function. The article improves the initial solution generation strategy of traditional genetic algorithm, which ensures the initial solution is feasible solution. Shuffled frog leaping algorithm and genetic algorithms are combined and proposed as shuffled frog leaping genetic algorithm (SFLGA). The algorithm uses the efficient coding strategy based on the basic loop and initial solution generation strategy, improves the calculation efficiency. The algorithm is verified by simulation results from test case on IEEE 33-bus system with distributed generations.

Introduction

Power system contains electricity generation, electricity transmission and electricity distribution [1]. The safe and stable operation of the distribution network will have a direct impact on the users. In China, loss of distribution network accounted for more than 80% of power system loss, further reduce the loss of distribution network is of great potential [2]. Improvement and development of distribution network automation system can produce huge economic and social benefits. Distribution network reconfiguration is an important means to control and run the distribution network [3-5].

There are several algorithms to solve the distribution network reconfiguration problem [6]: traditional mathematical optimization, heuristic algorithms, artificial intelligence algorithm. Among many artificial intelligence algorithms, genetic algorithm stands out and has been widely applied on pattern recognition, adaptive control and combinatorial optimization because of its advantages such as its search strategy and optimization process does not depend on the characteristics of gradient information. But the traditional genetic algorithm appears to produce infeasible solutions and converge to local optimal solution, which means 'premature' problem.

Based on the characteristics of the above algorithms, this article combines the practical problems of distribution network reconfiguration, proposes shuffled frog leaping genetic algorithm. The algorithm is verified by simulation results from test case on IEEE 33-bus system with distributed generations, it's proved feasible and effective.

Multi-objective optimization model for distribution network reconfiguration

Distribution network reconfiguration is a multi-objective optimization problem. Researchers usually often take the minimum loss and voltage quality of distribution network as a multi-objective function.

This article uses sum of line loss to describe the loss of network and uses voltage-balance index to describe the quality of voltage, expressions show as blow:

$$L = \sum_{k=1}^{N_b} R_k (P_k^2 + Q_k^2) / U_k^2 \tag{1}$$

$$V_{bal} = \sum_{k=1}^{N_b} \frac{max[U_i, U_j]}{min[U_i, U_j]} \tag{2}$$

In the above expressions, L is the sum of network loss, N_b is the quantity of lines in the network, V_{bal} is voltage-balance index. This article uses a weighted approach to switch the network configuration into a single objective problem. Define a new variable:

$$C = \omega_1 V_{bal} + \omega_2 L \tag{3}$$

In the above expression, ω_1 and ω_2 are weighting factors of voltage quality and network loss, their sum is 1. In this way, variable C contains two kinds of information.

Distribution network reconfiguration need to meet the following constraints:(1)meet the power flow equations.(2) meet the power flow equations.(3)voltage and current does not exceed the limitation.(4)distribution network can not exist isolated node.(5) distribution network always have a closed loop in construction and a open loop in operation, so the structure of distribution network after reconfiguration must be radiated. Inequality constraints can be added via a penalty function to the objective function. According to the analysis above, we can construct the fitness function F:

$$f = C + \sum_{j=1}^{N_b} \alpha_j (I_j - I_{j\lim})^2 + \sum_{k=1}^{N_b} \beta_k (U_k - U_{k\lim})^2 \tag{4}$$

$$F = 1/f \tag{5}$$

f is objective function, F is fitness function, α_j, β_k are penalty coefficient. $I_{j\lim}, U_{k\lim}$ are limitations of node k.

Theory of SFLGA

SFLA is a metaheuristic evolutionary algorithm proposed by Eusuff and Lansey, it has fast convergence ability and strong ability to jump out of local optima. Genetic algorithm recombinant individuals that have some structural features, to seek out common ground between individuals and approach the optimal solution. This paper combines these two algorithms for solving distribution network reconfiguration.

2.1 Chromosome coding strategy

This paper argues that most of the distribution network breakers are closed, if we take the state of each breaker as a control variable causes that chromosome length is too long, which's unnecessary. Distribution network always have a closed loop in construction and a open loop in operation. Closing all breakers will form several loops in distribution network, and we define the loop as basic

loop when it contains the minimum number of branches. Using the number of basic loop as coding characteristics will improve coding efficiency. As demonstrated in the figure 1, there are five loops in the network, encoding in loops can reduce unnecessary coding and decoding step.

2.2 Frog generation strategy

Previous studies always generate initial individuals by random which have low proportion of feasible solutions. This paper proposes a method to generate the initial individual, which can ensure each individual is a feasible solution.

(1) Ensure that each basic loop has an open breaker.

(2) Loops that have cutting breakers will not cut a second breaker. This rule limits the infeasible solutions.

(3) This paper choose the loop to cut in random sequence, which ensures to take all feasible solutions.

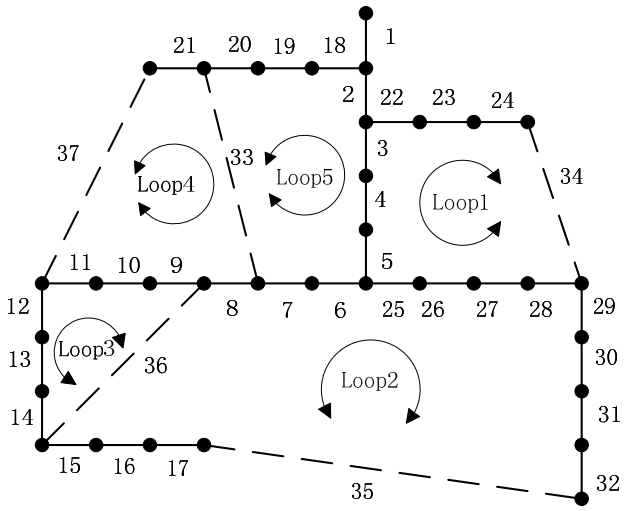

Fig.1 IEEE 33-bus system

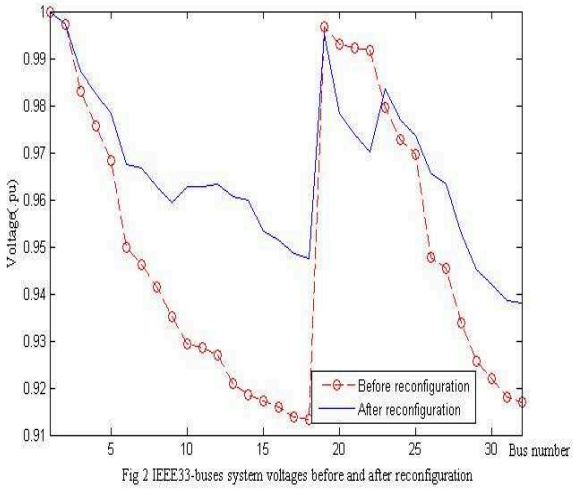

Fig 2 IEEE33-buses system voltages before and after reconfiguration

2.3 Process of SFLGA

SFLGA consists of two parts: the global information exchange and local search. Process of using this algorithm to solve distribution network reconfiguration problem is as follows:

Step 1: Set the initial parameters. The initial number of frogs is F , number of groups is m , global iterations N_g , local iterations N_1 ,crossover and mutation rate P_c and P_m .

Step 2: Produce F frogs as the initial population. Coding strategy and population generation strategy can guarantee that every frog is feasible solution.

Step 3: Calculate the fitness function. Do power flow calculation for each frog, get net loss, voltage quality and then calculate fitness value of each frog.

Step4: Divide the frogs into m groups in the rules below:

$$Y_s = \{X_s + m(h-1), h = 1,2,...,n\} \ (s = 1,2,...,m) \tag{6}$$

Step5: local search. Do local search in every group.

Step6: Mix all of the groups. Merge all frogs and repeat the step4, 5, 6 until the operation reaches the global iterations.

Test case calculation and analysis

This paper use IEEE 33-bus system as test case. This case has 37 branches, 33buses, rated voltage is 12.66kV. Parameters in the algorithm is set as $F=100$, $N_g=50$, $m=10$, $P_c=0.9$ $P_m=0.05$.

Table 1: Reconstruction program

Program	Branches to cut	Loss[kW]	Lowest voltage in system[.pu]
The initial structure	33,34,35,36,37	203.43	0.9128
Reconfigurated structure	34,32,14,9,7	139.35	0.9473

According to the results in Table 1 we can obtain that IEEE 33-buses system has a loss up to 233.43kW with its initial structure, after reconfiguration, system loss reduces to 139,35kW, reduced by 32%. Lowest node voltage has been increased from the initial 0.9128 to 0.9473 ,which is shown in figure 2. The effect of the algorithm is significantly.

Summary

This article combines SFLA and GA to solve distribution network reconfiguration. Using the encoding strategy according to the basic loop can guarantee all initial solutions are feasible. In this paper, frogs are sorted by fitness and initial population is divided into several groups, so that genetic algorithm is well used within the groups. This algorithm is of high efficiency and has a strong ability to jump out of local optima. The algorithm is verified by simulation results from test case on IEEE 33-bus system with distributed generations.

References

[1] J. Zhu, et aI. ,"A rule based comprehensive approach for reconfiguration of electrical distribution network", Electric Power Systems Research, No.79,(2009) pp.311-315.

[2] D. Das, "A fuzzy multi-objective approach for network reconfiguration of distribution systems", IEEE Trans. Power Delivery, VoI.21(2006) ,pp.202-209.

[3] B. Enacheanu, B. Raison, R. Caire, O. Devaux, W. Bienia, and N. HadjSaid, “Radial Network Reconfiguration Using Genetic Algorithm Based on the Matroid Theory”, IEEE Transactions On Power Systems, Vol. 23, No. 1(2008),pp. 186-195.

[4] R.S. Rao, S.V.L. Narasimham, M.R. Raju, and A.S. Rao,“Optimal Network Reconfiguration of Large-Scale Distribution System Using Harmony Search Algorithm”, IEEE Transactions on Power Systems, Vol. 26, No. 3, (2011), pp. 1080-1088.

[5] Tilak Thakur, Jaswanti Dhiman. " A Tabu search algorithm for multi-objective purpose of feeder reconfiguration". Journal of Electrical and Electronics Engineering Research, voI.3,No.4 (2011), pp. 71-79.

[6] D. P. Bernardon, L. Comassetto, L. N. Canha, and A. R. Abiade, “New methods for distribution network reconfiguration from multicriteria decision- making,” in Proc. IEEE Int. Conf. Power Engineering, Energy and Electrical Drives, (2007), pp. 225–230.

Advanced Materials Research Vols. 960-961 (2014) pp 1062-1067

doi:10.4028/www.scientific.net/AMR.960-961.1062

Research of Sub-synchronous Oscillations in HVDC and SSDC Designing

Han Chen[1,a], Chunlin Guo[1,b] , Qinlei Chen[1], Zheci Tang[1], Ya'nan Li[2], Weiyong Jiang[2]

[1]State Key Laboratory for Alternate Electrical Power System with Renewable Energy Sources, North China Electric Power University ,Beijing 102206, China

[2]State Power Economic Research Institute, Beijing 102209, China

[a]chensheshijia@ncepu.edu.cn, [b]chenhao0127@126.com

Keywords: HVDC, Sub-synchonous oscillations (SSO), Supplementary Sub-synchronous damping controller(SSDC), Phase compensation

Abstract. SSDC(Supplementary sub-synchronous oscillation damping controller) is one of effective measures to suppress the SSO(sub-synchronous oscillations) caused by HVDC. The article researched the phase compensation method of SSDC on the basis of studying the SSO and the SSDC mechanism in depth. We verified the validity of the method used by designing SSDC in an large domestic HVDC simulation model. And we find that the SSDC designed can effectively increase the positive electrical damping in the sub-synchronous frequency range with the sub-synchronous frequency scanning to suppress the SSO.

Introduction

With the rapid development of China's power industry, large-scale long-distance transmission is inevitable. SSO of the power system is a serious stability problem which first appeared in the long-distance transmission power project with series capacitor compensation . In 1977, the United States，a power plant named Square Butte first discovered the steam turbine shafting torsional oscillation caused by HVDC. In recent years, HVDC project is developing highly , SSO issue about it has become increasingly serious.

SSDC is the main efficient measure to suppress the SSO caused by HVDC. There is no agreed requirement so far at home and abroad about the SSDC control structure, phase compensation methods and so on. Article[4] has used the $H\infty$ robust control theory to design the SSDC in the HVDC transmission system , and made the SSDC designing to be a mixed sensitivity problem solving $H\infty$ robust control theory. Article[5] is based on the method of prony algorithm to compute the system transfer function, which is applied to SSO analysis and SSDC designing in the AC / DC hybrid transmission system. Article[6] designed the SSDC based on the complex torque coefficient principle and fuzzy immune method , which can adjust the controller parameters according to the control signal . Article [7] applied the genetic algorithm to solve the mini and max controller parameters optimization in value, so that SSDC can suppress the SSO effectively in a wide range of load conditions and the degree of compensation. Articles above had made a certain effect about SSDC design, but the principle of SSDC phase compensation is not so clear. In this paper, we have designed the single channel SSDC, and the phase compensation method is clear, simple, and finally through the domestic actual HVDC project we verified the practical value of the SSDC.

Through small signal testing method, we can obtain the phase frequency characteristics curve from constant current reference links ΔId to ΔTe. If the phase difference of ΔTe and $\Delta\omega$ is as small as possible ,the system can get the maximum electrical damping and this way is reasonable.

HVDC SSO mechanism and SSDC designing principles

SSO caused by HVDC. The direct reason of the occurrence of HVDC rectifier turbine SSO is the negative damping caused by HVDC current loop control system. The state change and interaction process of the variables in the AC-DC system[8] can be shown by Fig. 1 and Fig. 2.

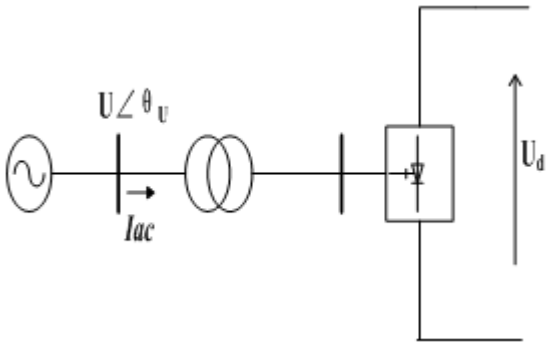

Fig. 1 HVDC Simplified Model

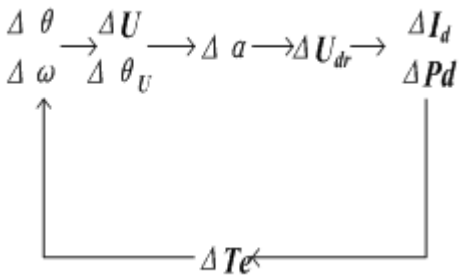

Fig. 2 SSO in HVDC Mechanism Simplified Diagram

If Turbine Shaft has a small disturbance by electromagnetic torque, this will result in fluctuations in the speed and angle of a torsional vibration modes（$\Delta\omega$ and $\Delta\theta$）. This will lead terminal voltage amplitude and corresponding phase fluctuations （ΔU and $\Delta\theta U$）, which leads to fluctuations in the amplitude of the converter bus voltage and phase and at last the amplitude and phase of commutation bus voltage will have a change. In the set current control mode and operating conditions, the trigger delay angle（$\Delta\alpha$）in HVDC will change and the DC voltage（ΔUd）changes as a result, which causes the DC current or DC power（ΔId, ΔPd） fluctuations. The HVDC rectifier current controller will be fixed quickly and adjusted correctly according to this bias, causing fluctuations in the electromagnetic torque of the generator（ΔTe）and, eventually, the feedback influences the generator shaft. If the phase lag of the generator speed changes and the resulting changes in the electromagnetic torque (including closed-loop control system additional phase lag) exceeds 90 °, it will form a positive feedback nature of the torsional vibration interaction and constantly increase vibration amplitude, leading to the shaft torsional vibration instability.

SSDC principle. According to the complex torque coefficient method $Dn = Dmn + Den$, Dn is the total damping of turbine generator at a generator, *Dmn* is the mechanical damping at this mode and Den the electrical damping. The mechanical damping is positive, when the electrical damping of the system in a mode is positive, the total system damping is positive too. If the system has series compensation capacitor or HVDC, it may produce negative electrical damping. And when $Dn = Dmn + Den < 0$,the system will be not stable. Under the disturbance effect, it will enhance the role of the turbine generator shaft torsional vibration, the system sub-synchronous oscillation will diverge. The electrical damping coefficient of the system is $De = Re(\Delta Te/\Delta\omega)$. ΔTe, $\Delta\omega$ are respectively the generators electromagnetic torque variation, speed error. Obviously, as shown in Fig.3,when the phase difference of ΔTe and $\Delta\omega$ between -90 ° to 90 °, the electrical damping is positive. Therefore, the phase difference between electromagnetic torque $\Delta Te'$of SSDC channel and $\Delta\omega$ is smaller（-90°~ 90°， it will take -45~45° in the project),and the amplitude of $\Delta Te'$is larger, the electrical damping may be larger, then, we can suppress the SSO.

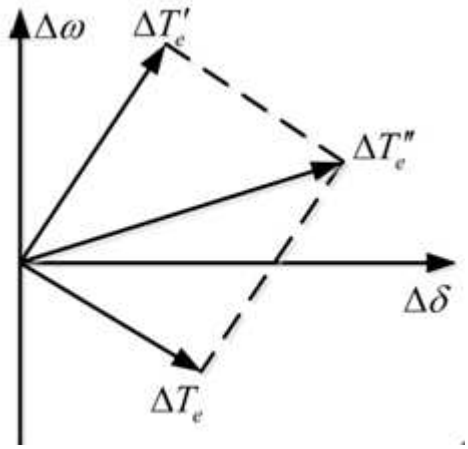

Fig.3. Electromagnetic torque vector diagram

Summary: The principle of the SSDC suppressing SSO is similar to PSS restraining the low frequency oscillation: taking the system signal $\Delta\omega$ or Δf, then through the appropriate proportion link and the phase link ,it can produce additional torque $\Delta Te'$ through the constant control circuit. At last, $\Delta Te'$ and the system old electromagnetic torque ΔTe will produce the new $\Delta Te''$,and enhance the system electrical damping. Therefore, the reasonable selection of SSDC parameters, s critical for suppressing sub-synchronous resonance effect.

SSDC control structure and parameters designing

Similar to PSS, SSDC includes DC link, filter, phase compensation, gain adjustment and limiter link. Control system architecture can be used through a multi-channel narrowband method and can also be used through a single channel broadband method. The multi-channel narrowband method must be based on the accurate shaft model or correct access on the natural shaft torsional vibration frequency. The single channel broadband method does not ,it has more universal and practical value and uses optimization method and provides better electrical positive damping of sub-synchronous frequency range (10-40Hz) . Considering the practical engineering, sub-synchronous frequency ranges from 10 to 30Hz . The different mode frequency phase compensation is not large, so we use broadband multi-channel control structure, as shown in Fig. 4:

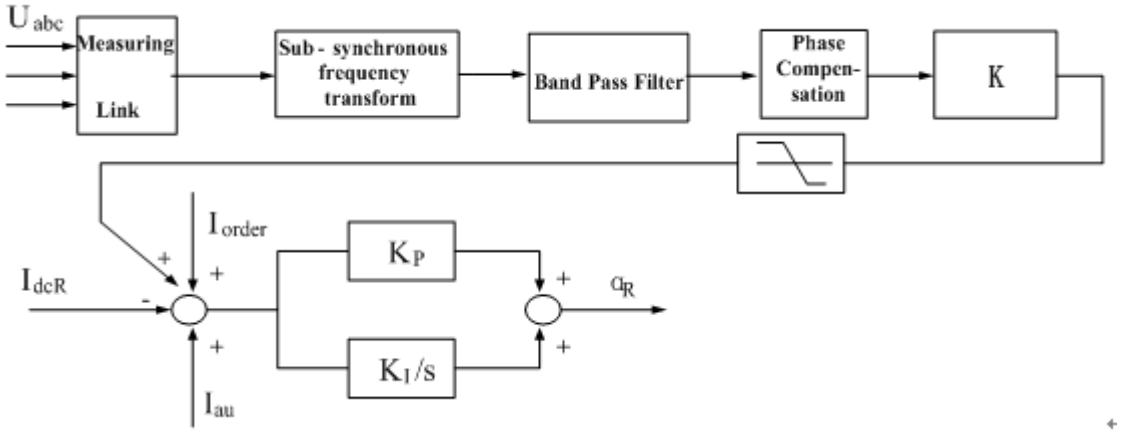

Fig.4 SSDC Control Structure

Designing the phase compensation link of broad band pass SSDC should take into account the most serious oscillation mode and the system operation ways. What's more, we should account the compensation parameter using the optimization and make the SSDC have certain robustness. According to the previous SSDC damping SSO principle and the analysis of controlling structure of broad band pass SSDC. Phase compensation link in the SSDC need compensate the sub-synchronous frequency converter phase-lag and the phase-lag caused by the converter bus voltage

sub-synchronous component and the generator rotor speed deviation. Through the analysis , when the electromagnetic transient state caused by the system fault is finished, the system entered into a stable sub-synchronous oscillation process, and the phase-lag in sub-synchronous generator component torsional oscillations and sub-synchronous component in converter bus voltage can be $\alpha=(180-\theta_0)$。And that θ_0 is the phase-lag between generator terminal voltage phase and converter bus voltage phase , associated with the generator output and system structure, which is the phase difference can be obtained by solving the steady-state flow, you can also get the measurements obtained by PMU in WAMS system. The phase compensation is mainly using the $((1+sT1)/(1+sT2))^n$ at the mode frequency, and the relevant parameters are shown in equation(1)-(3) :

$$a = T2/T1 = (1-\sin\varphi)/(1+\sin\varphi) \quad (1)$$

$$T1 = 1/\omega x\sqrt{a} \quad (2)$$

$$T2 = aT1 \quad (3)$$

ωx is modal angular frequency point which needs phase compensation ,φ is the compensated phase degree at this point. If the compensated phase degree is too large, we can use more links like this for compensation to get better feature.

SSDC gain is directly related to the damping it provides. Generally the gain is larger, the greater the electrical positive damping that SSDC can provide. In the premise of not affecting the stability of the system, the gain is chosen by the limiting requirements and the inhibition of SSO steady state amplitude. In general, the phase of SSDC correction is determined, we can regulate the SSDC by adjusting the proportion coefficient to provide electrical damping.

SSDC design and simulation in domestic HVDC system

First we design the famous HVDC/AC system in China with the PSCAD/EMTDC and the structure is shown in Fig. 5：

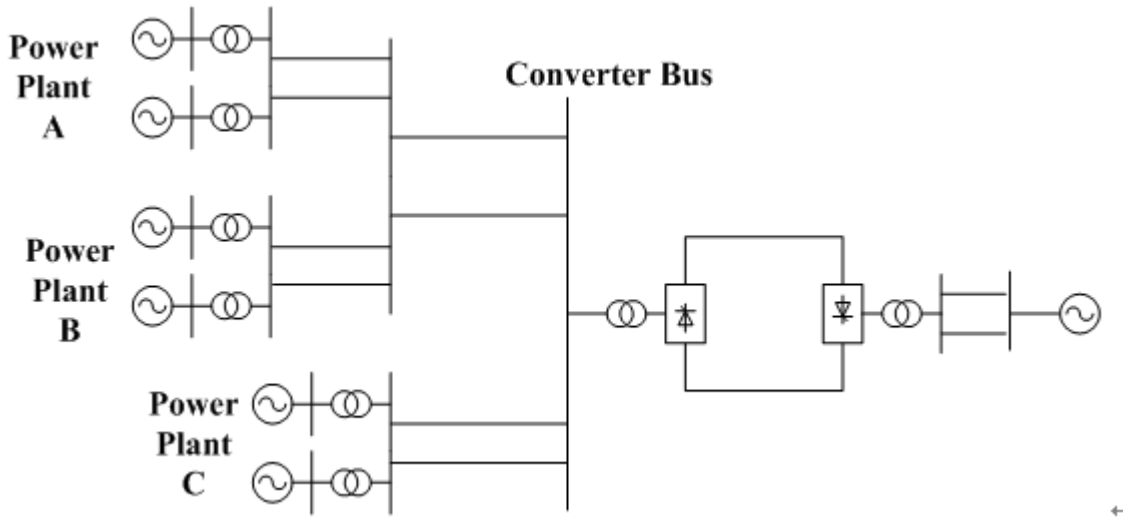

Fig.5 Simple Structure Diagram of a Domestic HVDC System

The actual operation of the HVDC system appears SSO problem in the turbine generator of C power plant. After calculating 3 mode shaft torsional oscillation frequencies of C power plant are 12.9132Hz, 22.5132Hz,26.0202Hz; Design the appropriate broad band pass SSDC according to the answers above for this problem. At last, we chose the pass band of the broad band-pass SSDC filter being 10-40Hz,and especially for the most serious mode, the phase to compensate of the system being 120° after measurement.

Set the 3 phase grounded fault at18s on the converter bus, and clear it at 0.05s, after the simulation, we found that the mode speed error dw, shaft torque T are as the following shown in Fig. 6 and Fig.7:

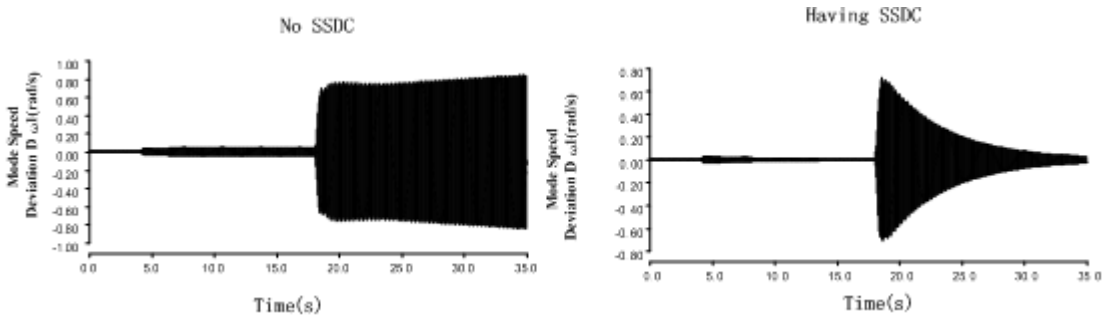

Fig. 6 Mode Speed error dw

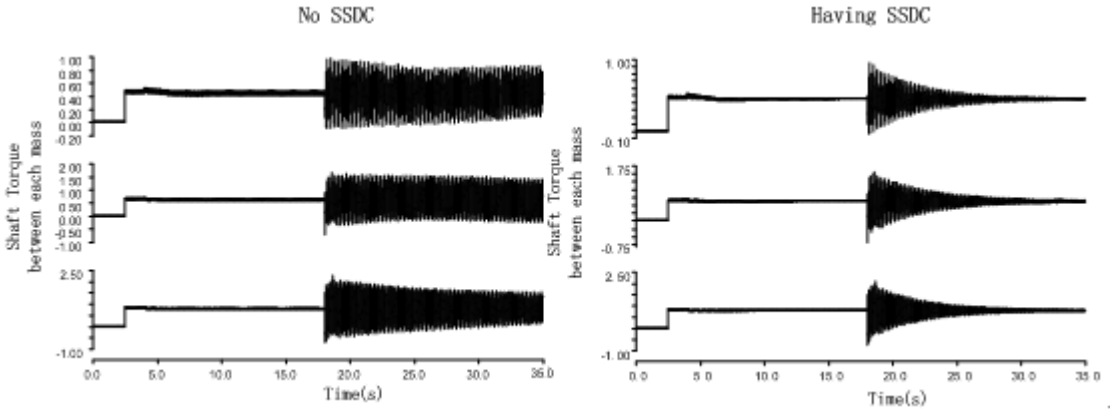

Fig. 7 Shaft Torque

After the simulation， we can know that electrical damping of the system is significantly improved after the SSDC is put, the system SSO is damped obviously. And the mode speed error dw and shaft torque fall into the reasonable value in 15s to ensure the safe and stable system generators operation.

Conclusions

1).We designed the appropriate SSDC and verified the validity by modeling using the PSCAD/EMTDC.

2).Through comparing with and without SSDC electrical damping Scanning, SSDC can effectively improve the system electrical damping and has a significant effect to suppress the SSO in HVDC.

Acknowledgements

This work was financially supported by the National High Technology R&D Program of China (863 Program) (2012AA050804) and Fundamental Research Funds for the Central Universities (12ZX06)..

References

[1] Changchun Zhou: Study of SSO damping in the HVDC power system, Hang Zhou, Zhejiang University(2004)

[2] Zheng Xu, Ruiqun Luo, and Ruijin Zhu : Review On method of analysis for sub-synchronous oscillations of power systems, Zhejiang University, Power System Technology , Vol .23(6) (1999),p. 36-39.

[3] Yixin Ni, Shousun Chen and Baolin Sun: Theory and analysis of dynamic power system[M]. Beijing, Tsing-hua University Press(2002).

[4] Xiu Yang, Xitian Wang, Chen Chen. Design of supplemental sub-synchronous oscillation damping control based on H∞ roust control theory of HVDC system[J].Power System Technology, Vol：30(9)(2006):57-61.

[5] Lingyun Wu, Xingyuan Li, Yu Yang, Chao Hong, Haiyang Liu and Fu We: Design of optional supplementary sub-synchronous damping controller based on prony method[J].Electric Power Automation Equipment. Vol 27(9), 2007.

[6] Lingyun Wu, Xingyuan Li, Yang Yu, Chao Hong, Dapeng Xu and Wei Li: Design of subsynchronous damping controller based on fuzzy immune method. Automation of Electric Power Systems, Vol 31(11),2007

[7] Quanyuan Jiang, Shijie Cheng and Yijia Cao: Design of sub-synchronous damping controller based on genetic algorithms. Proceedings of the CSEE, Vol 22(11),2007, 87~91.

[8] Dan Zhang :Eigen value analysis and control of sub-synchronous oscillation in HVDC system (2011)

[9] Niang Tang ,Xiangning Xiao, Wei Li, Benfeng Gao and Wei Zheng. Phase correction method of HVDC supplementary sub-synchronous multiple models damping controller ,High Voltage Engineering. 37(4):1015-1021

[10] Benfeng Gao, Chengyong Zhao, Xiangning Xiao, Weiyang Yin, Chunlin Guo and Yanan Li: Design and implementation of SSDC for HVDC. High Voltage: Engineering, Vol:36(2): p.502 -506.

[11] Fan Zhang and Zheng Xu: A method to design a sub-synchronous damping controller for ` HVDC transmission system. Power System Technology ,Vol :32（11）.

[12] Xiangning Xiao, Chunlin Guo, Benfeng Gao and Yang Lin. The power system sub-synchronous oscillation and the damping method. Machinery Industry Press , Vol :32（11).

[13] Shijie Cheng, Yijia Cao and Quanyuan Jiang: The Method and damping method of power system sub-synchronous oscillation ,Science Press

[14] Wanjun Zhao :HVDC engineering technology, China Electric Power Press

[15] Xuesheng Li :Modeling and Simulation of PSCAD, China Electric Power Press

[16] Zheng Xu: The complex torque coefficient approach's applicability analysis and its realization by time domain simulation, Proceedings of the CSEE, Vol: 20（6）

Advanced Materials Research Vols. 960-961 (2014) pp 1068-1072

doi:10.4028/www.scientific.net/AMR.960-961.1068

Research on intelligent building power monitoring system based on the Zigbee and GPRS

Liang Zhang [1, a], Xiaolu Sun [2,b] Aihua Qi [3,b]

[1,2,3]No.13,Chaoyang Street Zhangjiakou, Hebei Province,China

[a]miaopiao22@163.com, [b]sunny20008@ailiyun.com, [3] 308359879 @qq.com

(Hebei Institute of Architecture and Civil Engineering,Zhangjiakou Hebei 075000，China)

Key word Internet of things; Intelligent building; Power Minitoring; ZigBee; GPRS

Abstract: With the improvement of living standards, people want to have a comfortable, convenient, safe working and living environment. In this context, the traditional architectural forms has been unable to meet the basic needs of the people. Therefore, in recent years, the intelligent building has been rapid development in our country.

In the intelligent building, electrical equipment occupies a very important position. For reliability and safety considerations, the power requirements of various equipment in intelligent building is very high.

This paper designs a kind of intelligent building power monitoring system based on Internet of things. This system treating embedded hardware as the core, basing on ZigBee wireless communication technology for signal transmission, using GPRS communication technology to remote monitoring system, achieved the control of a variety of equipment in the power system in the intelligent building of local . The test result shows that this system runs stably, and has practical application value.

Introduction

The first intelligent building in the world is the City Place Building which was built in Hartford of America in 1984. While in our country, intellegent building has also entered a rapid development period since 1990s. These developments comply with people's basic requirements for comfortble, convenient and safe work and study environment. Therefore, intelligent building is the product of social development, its degree of intelligence certainly will be improved gradually with the development of science and technology.

The intelligent building is a kind of special buildings, it uses digital communication technology, control technology, computer networking technology, television technology, optical fiber technology, sensor technology, database and other high and new technologies. It is based on these technologies, makes use of all kinds of power electronic equipments to constitute corresponding intelligentized system and complete the function of intelligent control. For this reason, the power electronic equipment is the body equipment to constitute intelligent building. If we want to keep thess power electronic equipments' normal operation, we must ensure the security and reliability of power system[1].

Aiming at above probelems, the intelligent building power monitoring system based on Internet of Things is presented in this paper. This system utilizes Internet of things technology to build a

local and remote monitoring system, which treats embedded hardware as the core and bases on ZigBee wireless communication technology and GPRS communication technology for system communication. This system achieved effective monitoring to intelligent building power system.

The analysis of Internet of Things applied to intelligent building power monitoring system

The Internet of Things is a global attention and research hot technology in recent years. By RFID, infrared sensor, GPS, laser scanner and other information sensing equipments, according to promissory agreement ,it can connect any items with Internet to do information exchange and communication in order to achieve intelligent identification, location, tracking, monitoring and management.

Most Internet of Things application system are composed of sensor layer, transport layer and application layer. For intelligent building power monitoring system, the three-layer structure is also an essential basic structure.

The sensor layer of intelligent building power monitoring system is composed of all kinds of equipments with sensory ability, including camera, GPS, sensor, M2M terminal, sensor network, sensor gateway and so on. These equipments are installed in power equipment monitoring area, or embedded in power system equipment, to perceive and distinguish objects, collect and capture voltage ,electric current, temperature and other relevant information in all kinds of power system, and provide essential data for monitoring center. At the same time, these equipments also need to adjust the running status of power system according to monitoring center instruction. The transport layer is the solid structure which is responsible for the data transmission. This system utilizes two kinds of communication protocol, one of them is ZigBee wireless sensor network, the other one is GPRS wireless communication unit based on Ethernet. The ZigBee wireless sensor network builds the core of local control communication, and GPRS builds the remote one. Effectively combining these two forms can achieve the local and remote monitoring function of the power system. The application layer is the top of the whole monitoring system. Its main function includes displaying data, summarizing data, reporting status, giving command and so on. These functions can be achieved by related development tool, such as VC++.

The study of local power monitoring system structure based on ZigBee wireless sensor network

The ZigBee wireless sensor network is a multihop self-organizing network which is composed of a mass of deployed in monitoring area microsensor nodes and formed by means of wireless communication mode. It mainly includes four parts: sensor unit(composed of sensor and analog-digital conversion function modules), processing unit(composed of embedded system, including CPU, memorizer and so on), communication unit(wireless transmission module, etc) and power unit. The sensor unit is responsible for collecting environmental information and data conversion. The processing unit is the operation core which controls the whole sensor nodes, it processes data collected by itself and sent by other nodes, operates network protocol to make sensor nodes interconnect into network in order to work together. The communication unit is responsible for communicating with other sensor nodes and exchanging control message and data message. The power unit provides energy for every unit[2] .

The wireless sensor network is a new information acquisition platform, it can real time monitor and collect information of all kinds of detected object in the network distribution area. In this sense, the wireless sensor network can include sensor layer function and a part of communication layer

function of the power monitoring which is based on the Internet of Things. It can send these information to geteway note expediently in order to detect and track complicated objective in designated area, so it has the characteristic of rapid unwinding and strong invulnerability. At the same time, compared with traditional wired sensor network, the wireless sensor network has the advantage of less cost, easier installation, less maintenance and renewal charge. So the wireless sensor network is right for the design of intelligent building power monitoring system under the special conditions.

The intelligent building power system is a complicated system. In the use of it, most operating parameter of the electrical equipment need real-time monitoring. While the scheme of wireless sensor network can achieve these functions expediently. The general structure design is as shown in Figure 1.

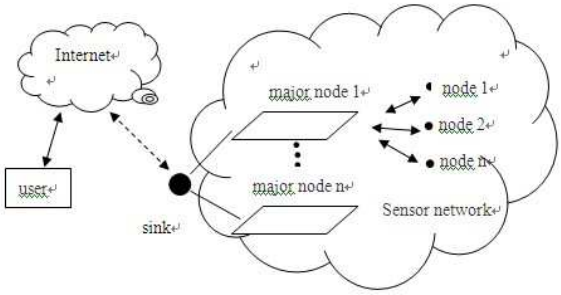

Figure 1 The structure of the overall system

Known from the figure, we can set a host node in every power system, and set several slave nodes at every monitoring points in every power system. Slave nodes collect local data and send to host nodes, and host nodes are linked to local monitoring center, thereby the local monitoring function can be realized.

The structure of every node is almost the same. They play roles of sensing, processing information, collecting and sending information. The concrete structure is as shown in Figure 2.

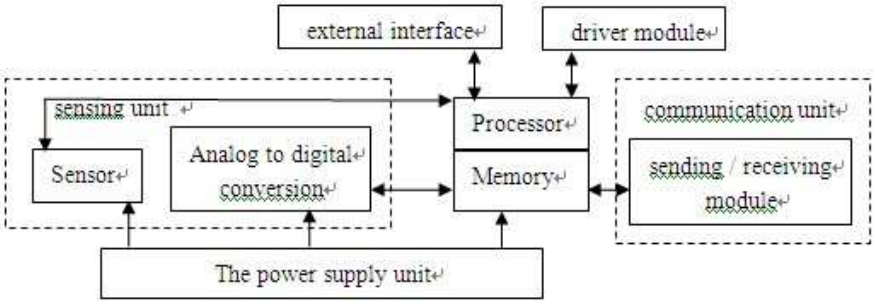

Figure 2 Wireless sensor network node structure

The sensor unit in the figure is composed of multiple voltage, electric current, temperature and humidity sensor, and it can collect data and convert analog data to digital data. The processing unit chooses TI's MSP430F149 as MCU to control the collecting, sending and processing of data of node. This MCU is power supplied by 3.3 V, its fundamental features include ultra-low power dissipation and high accuracy. The wireless receive/send module uses Chipcon's RF transceiver chip CC2430 which meets the standards of IEEE802.15.4.

The structure of telecommunication with GPRS communication module

The remote data transmission of this system uses GPRS technology and the specific module is ZTE's ZXGM18G. This GPRS module can support data, voice, SMS, fax and other communication

modes. Aftering doing level switch by chip MAX3245, this module can be linked to serial port RS232 and use General AT command complied with international standards to control. It has been widely used in wireless public telephone, industrial monitoring, automobile navigation, vehicle dispatching, emergency services, remote monitoring, banking and finance, commercial retail and other fields. This design takes MSP430F149 as the core, and provides two-channel port linked to GPRS. The UART is GPRSmodem and it can provide complete serial port for Dial-up. The structure of GPRS communication module can remotely transmit data, at the same time it can also locate error and judge operation status by chip status register.

The design of whole system structure and software

The whole structure of intelligent building power monitoring system is as shown in Figure 3. The middle layer is communication layer, the bottom layer is data collection layer composed of wireless sensor network and the top layer is application layer. The monitoring center is set up in the application layer and the software system developed by development tool VC++ is in the center. The software system is composed of five parts and it is used to remotely monitor the power electric parameter in intelligent building. Its main functions include: displaying, storing and printing the voltage, electric current, temperature and humidity data of every group of power; displaying and printing the operation normal data of power; displaying, storing and printing the fault information and maintenance information; contrastively analyzing the runtime value and standard value; alarming and recording the fault point; and so on. The concrete functional procedure is as shown in Figure 4. The power running status database is set up in the software system. The database uses SQL Server 2005 to store running status normal data, running status data and fault data in case of using when system monitoring and operating maintenance.

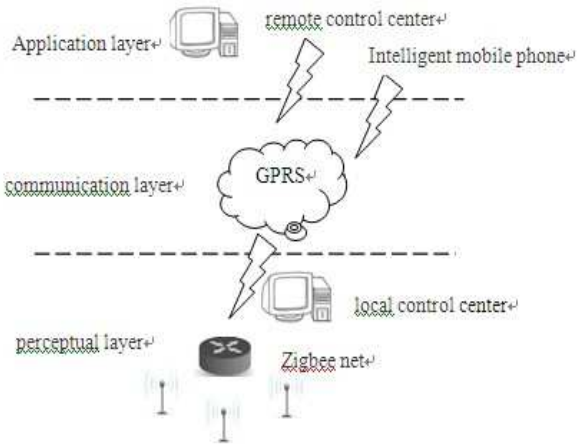

Figure 3 The structure of the overall system

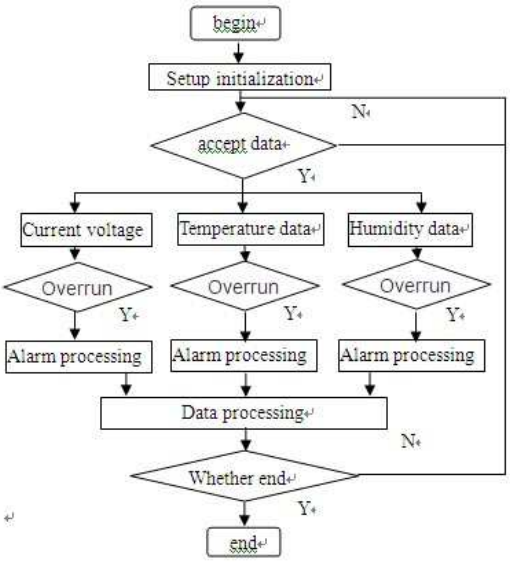

Figure 4 The software function flow chart

Conclusions

Along with the sociometric development, the intelligent building will show its superiority increasingly. The intelligent building power monitoring system, which is based on the Internet of Things technology, utilizes the way of the combination of wireless sensor network and GPRS, takes MSP430F149 microprocessor as control core, uses ZigBee technology to achieve local

communication of each subsystem and control center; and also achieves remote monitoring of the system by GPRS technology, real time monitors the intelligent building power system effectively, in order to grasp the power running state in time and alarm and report the fault point timely. The test shows that the power monitoring system which is researched in this paper can achieve communication among each node and ensure that the whole system operate stably and reliably, and has well practice guidance function.

References

[1] Wang Wen-liang,SHEN-Jian．Design and realization of monitoring and controlling system of power supply system for intelligent building, Chinese Journal of Power Sources,7(2010):7～9
[2] Sinha A, Chandrakasan A, Dynamic power management in wireless sensor networks. IEEE Design and Test of Computer, 2001, 18(2) :62-74

Advanced Materials Research Vols. 960-961 (2014) pp 1073-1076

doi:10.4028/www.scientific.net/AMR.960-961.1073

Study on Electrical Characteristics of Metal-oxide Surge Arresters in Medium Voltage Power System

Li Zhang[1,a], Kun Yang[2,b] and Limei He[2,c]

[1]School of Electrical Engineering and Information, Xihua University, Chengdu, Sichuan, China, 610039

[2]China Petroleum Engineering Co., LTD Southwest Company, Chengdu, Sichuan, China 610041

[a]zhangli_xhu@163.com, [b]ykcpe@163.com [c]helimei@cnpc.com.cn

Keywords: Metal-oxide Surge Arresters, Medium Voltage Power System, Electrical Characteristics, Selection and Application

Abstract. The index system for electrical characteristics of metal-oxide surge arresters is proposed and established, which is based on rated voltage (U_r), continuous operating voltage (U_c), nominal discharge current (I_n), overvoltage protection and insulation coordination including lightning overvoltage protection level, operating overvoltage protection level and coordination coefficient (K_s). The study considers both selection and application of overvoltage protection devices for the electrical equipments in 3-35kV medium voltage power system, and comparatively calculates and analyzes the main parameters between two types metal-oxide surge arresters (without gaps and containing series gapped structures), and illustrates their technical features and puts forward suggestions on how to improve the effective utilization. The results of 10kV power distribution system are simulated to show that the conclusions are feasible and available in the practical engineering application.

Introduction

In modern AC power systems, metal-oxide surge arresters have been gradually replacing the traditional silicon carbide arresters, which have become the more advanced overvoltage protection devices for the electrical equipments. The core parts of metal-oxide surge arresters is the metal-oxide resistors with nonlinear current-voltage characteristics: high resistance under the normal power frequency voltage, the leakage current is only microampere level; when withstanding overvoltage, the arresters have a low resistance in conducting state, releasing the overvoltage energy to limit the damages on the electrical equipments effectively. Comparatively, metal-oxide surge arresters changed the current-voltage characteristics to improve the flow capacity when overvoltage, so that the characteristics of arresters have undergone fundamental changes. According to the structures, they mainly divided into three types: without gaps, containing series gapped structures and containing parallel gapped structures [1].

In the paper, for the hidden dangers existed in the application of metal-oxide surge arresters, we take the electrical characteristics of two types (without gaps and containing series gapped structures) in 3-35kV MV power system to study, comparatively calculate and analyze the parameters for selection and application, and illustrate technical features to promote the correct usage of arresters, and further to improve the effective utilization for overvoltage protection of electrical equipments.

Electrical Characteristics

In addition to the basic conditions of environment, operating situation and mechanical strength, the index of electrical characteristics for metal-oxide surge arresters mainly include: rated voltage (U_r), continuous operating voltage (U_c), nominal discharge current (I_n), overvoltage protection and insulation coordination [2-3]. Where, U_r and U_c are associated with system neutral grounding modes.

Rated Voltage (U_r). U_r refers to the maximum effective value of power frequency voltage between terminals in the arrester, which is also known as the starting voltage of arresters [4]. The classification of U_r with different grounding modes is shown in Tab. 1, and where, U_m refers to the maximum work voltage of power system.

Tab. 1 Rated voltage of metal-oxide surge arresters

Grounding Modes	Arresters without gaps	Arresters containing series gapped structures
Low-resistance grounding	$U_r \geq 1.1U_m$	$U_r \geq 1.1U_m$ No distinction of the specific grounding modes [5].
Non-grounding or high-resistance grounding	$U_r \geq (1.25 \sim 1.3) \times 1.1U_m$	
Grounding via arc-suppression coil	$U_r \geq (1.25 \sim 1.3)U_m$	

Continuous Operating Voltage (U_c). U_c refers to the effective value of power frequency voltage between terminals in the arrester. The classification of U_c with different grounding modes is shown in Tab. 2.

Tab. 2 Continuous operating voltage of metal-oxide surge arresters

Grounding Modes	Arresters without gaps	Arresters containing series gapped structures
Low-resistance grounding	$U_c \geq U_m / \sqrt{3}$	$U_c \geq 0.8U_r$ No distinction of the specific grounding modes [5].
Non-grounding or high-resistance grounding	$U_c \geq 1.1U_m$	
Grounding via arc-suppression coil	$U_c \geq U_m$	

Nominal Discharge Current (I_n). I_n refers to the lightning impulse current peak values with 8/20μs shock wave, and are divided into three grades as the different operating conditions of arresters: 5kA, 2.5kA and 1.5kA. The classification of I_n is shown in Tab. 3.

Tab.3 Nominal discharge current of metal-oxide surge arresters

	Arresters without gaps			Arresters containing series gapped structures		
I_n	5kA	2.5kA	1.5kA	5kA	2.5kA	1.5kA
U_r	$Ur \leq 132kV$	$Ur \leq 36kV$	$Ur \leq 207kV$	$3kV \leq Ur \leq 52kV$	$3kV \leq Ur \leq 52kV$	$3kV \leq Ur \leq 52kV$

Overvoltage Protection and Insulation Coordination. The protection levels referring to the arresters residual voltage or discharge voltage should be lower than the insulation levels of the protected electrical equipments, and also have a certain margin. Different arresters have different protection levels, and therefore, they need to be checked with insulation coordination in selection and application. The index of overvoltage protection and insulation coordination is shown in Tab. 4.

Tab. 4 Overvoltage protection and insulation coordination of metal-oxide surge arresters

Overvoltage Protection and Insulation Coordination	Arresters without gaps	Arresters containing series gapped structures
Lightning overvoltage protection level	Taking the highest value in following: w The maximum residual voltage under 1/20μs steep impulse current / 1.15; w The maximum residual voltage under 8/20μs nominal discharge current.	Taking the highest value in following: w The maximum residual voltage under 1/20μs steep impulse current / 1.15; w The maximum residual voltage under 8/20μs nominal discharge current; w Lightning impulse discharge voltage; w Front of wave impulse sparkover voltage / 1.15.
Operating overvoltage protection level	The maximum residual voltage under 30-100μs operating impulse current.	No required.
Coordination coefficient (K_s)	K_s = Insulation level / Overvoltage protection level, and should be no less than the following values 1) K_s for lightning overvoltage ≥1.4; 2) K_s for operating overvoltage ≥1.15.	

Selection and Application

As 10*kV* power distribution system for example, taking $I_n = 5kA$ [2-3], we performed the selection and verification of U_r, U_c, overvoltage protection and insulation coordination, and compared the two types of metal-oxide surge arresters combined with the typical parameters.

Arresters without Gaps. For the different grounding modes, the calculation formulas of U_r and U_c are respectively shown in Tab. 1 and Tab. 2. The calculations and recommendations with different grounding modes are shown in Tab. 5.

Tab. 5 Calculations & Recommendations of arresters without Gaps

Grounding Modes	U_r (kV)		U_c (kV)	
	Calculations	Recommendations	Calculations	Recommendations
Low-resistance grounding	13.2	12	6.9	9.6
Non-grounding or high-resistance grounding	17.16	17	13.2	13.6
Grounding via arc-suppression coil	15	15	12	12

In Tab. 5, when it showed a big difference between calculations and recommendations, we could use Eq. 3 and Eq. 4 to determine whether U_r and U_c meet the requirements based on [2].

$$U_r \geq U_m \tag{1}$$

$$U_c \geq 0.8U_m \tag{2}$$

The typical residual voltages of arresters without gaps are shown in Tab. 6. Taking the corresponding value of lightning impulse withstand voltage and transient power frequency withstand voltage of 10*kV* electrical equipments separately to be equal to 75*kV* and 42*kV*, the results show that K_s for lightning overvoltage has met the requirement of insulation coordination with a slight margin of operating overvoltage by the calculation of Tab. 4, which are shown in Eq. 3 and Eq. 4.

Tab. 6 Typical residual voltages of arresters without gaps

The maximum residual voltage under steep impulse current (*kA*)	The maximum residual voltage under nominal discharge current (*kA*)	The maximum residual voltage under operating impulse current (*kA*)
51.8	45	38.3

$$K_s \text{ for lightning overvoltage} = 1.67 \geq 1.4 \tag{3}$$

$$K_s \text{ for operating overvoltage} = 1.1 \leq 1.15 \tag{4}$$

Arresters Containing Series Gapped Structures. For the different grounding modes, the calculations of U_r and U_c have none distinction, which are respectively shown in Tab. 1 and Tab. 2. The calculations and recommendations values with different grounding modes are shown in Tab. 7.

Tab. 7 Calculations & Recommendations of arresters containing series gapped structures

Grounding Modes	U_r (kV)		U_c (kV)	
	Calculations	Recommendations	Calculations	Recommendations
Low-resistance grounding Non-grounding or high-resistance grounding Grounding via arc-suppression coil	13.2	12.7	10.2	10.2

The typical residual voltages of arresters containing series gapped structures are shown in Tab. 8. Taking the corresponding value of lightning impulse withstand voltage of 10*kV* electrical equipments to be equal to 75*kV*, the result shows that the factor K_s for lightning overvoltage has met the requirement of insulation coordination [3] by the calculation of Tab. 4, which is shown in Eq. 5.

Tab .8 Typical residual voltages of arresters containing series gapped structures

The maximum residual voltage under steep impulse current (kA)	The maximum residual voltage under nominal discharge current (kA)	Lightning impulse discharge voltage (kA)	Front of wave impulse discharge voltage (kA)
47.2	41	45	56.5

$$K_s \text{ for lightning overvoltage} = 1.53 \geq 1.4 \quad (5)$$

Comparison and Discussion

Metal-oxide Surge Arresters without Gaps. There are many advantages of simple structure, excellent protection performance and effect. But also, their abilities to withstand transient overvoltage are weak, and the long-term repeated continuously actions easily accelerate aging. Therefore, they are mainly used in 110kV high-voltage power systems and above [6].

Metal-oxide Surge Arresters Containing Series Gapped Structures. Due to the increase of gaps, they can not only prevent resistance directly withstanding system voltage and transient overvoltage, effectively extending the service life, and also can reduce the number of metal-oxide resistors. They have excellent technical and economic performance, low residual voltage values, which are more suitable for MV power system.

Conclusions

According to the statistics, in the explosion of metal-oxide surge arresters, there are more than 60% accidents caused by manufacture quality and improper selection. Among them, the improper selection of rated voltage and continuous operating voltage of arresters without gaps, and the manufacture quality defects by structure design of arresters containing series gapped structures are the main reasons. Therefore, in the practical engineering application, it should be paid attention to the correct choice of metal-oxide surge arresters rated voltage and continuous operating voltage and the verification of frequency voltage withstand time characteristic curve, and the confirmation of overvoltage protection capacities. Meanwhile, the arresters should be checked with overvoltage protection and insulation coordination to ensure effective overvoltage insulation protection of the electrical equipments. In the MV power systems, it should be combined with the actual situation and operating experience to complete the corresponding selection and application [7].

Acknowledgements

This work was financially supported by the Scientific Research Key Fund of Sichuan Provincial Education Department (11ZA280) and Academic Research Fund of “Fluid and Power Machinery” Key Laboratory under the Supervision of Ministry of Education (SBZDPY-11-15).

References

[1] S.Q. Long: Electric Engineering Vol. 1 (1997), p. 10-16

[2] SAC/TC 81: *GB 11032-2010 Metal-oxide surge arresters without gaps for a.c. systems* (Standards Press of China, Beijing 2011).

[3] SAC/TC 81: *GB/T 28182-2011 Surge arresters containing series gapped structures with rated voltage 52 kV and less* (Standards Press of China, Beijing 2012).

[4] L. Li and T.W. Yang: Building Electricity Vol. 28 (2009), p. 44-46

[5] Y.M. Zhang and W.Y. Cheng: Insulators and Surge Arresters Vol. 5 (2011), p. 55-59

[6] S.G. Wang: Petrochemical Design, Vol. 25 (2008), p. 58-61

[7] M.H. Yu: Jiangsu Electrical Apparatus Vol. 3 (2007), p. 36-40

Advanced Materials Research Vols. 960-961 (2014) pp 1077-1080

doi:10.4028/www.scientific.net/AMR.960-961.1077

Study on large- scale distributed power access to distribution networks for the impact of the loss in the power

Bolun Wang[1,a]

Shandong University, Shizhong District, Jinan 250002, China

634420080@qq.com

Keywords: New energy access to distribution networks the network loss.

Abstract: Near the load of distribution network access distributed networks, the entire distribution network load distribution will change, system trend then change, then the trend of the distribution network can also be changed from the original "one-way flow" to "two-way flow". For synchronous generator connected to the power distribution network, the input active power and reactive power at the same time to the system, can reduce the loss and the voltage distribution network can play a supporting role, but for asynchronous induction generator connected to the power distribution network, the input to the system active power and reactive power absorption, reduce the power factor of the grid. By trend analysis found that introducing asynchronous induction generator to increase distribution network loss, deterioration in transmission line voltage level. Distributed generators after introducing the distribution network could reduce may also increase the system network loss.

Introduction

Entering the new century, with the development of world economy, the human face more serious problems such as population growth and environmental pressures. Clean and efficient power development, no doubt, is one of the important measures to solve these problems. Especially from the beginning of the last century, western developed industrial countries is emerging to develop new type high efficiency green independent power of the boom, since then the Distributed power supply (Distributed Generation) the term arises at the historic moment. Distributed power include: solar power stations, wind power, geothermal power plants, micro gas turbines, fuel cells, biomass power device and the energy storage device, such as a kw power to tens of megawatts. The power supply for electric power department, all electric power users or a third party. Its working mode is mainly to its close to the user side to install, make its can be directly with public independent power transmission and distribution network, provide power for a small amount of users, can also be incorporated into the power grid with public power grid power, to provide users with flexible working patterns can satisfy the specific requirements of power system and the user [1,2].

In addition, the emergence of the distributed power due to the following reasons: 1) the large-scale development of city, opening up new distribution line corridors, more and more difficult, and can be placed directly on the users nearby of distributed power supply device is a kind of feasible alternatives: 2) previous power system model is: concentrated power, long distance transmission and large power grid interconnection. In this system, the local accident can spread easily, for the whole power grid may be adversely affected, severe cases can cause blackouts and power grid collapse; In recent years in western countries several blackout accidents to a certain extent, reflects the traditional power system faults. In order to change this vulnerability, avoid a chain reaction, guarantee the safe and reliable power supply, spread power such as the configuration of distributed power supply device, can under the condition of the power grid collapse and unexpected disaster to maintain the supply to important users; 3) power supply for remote distributed user, close to the user configuration of distributed power supply measures with the existing distribution network than simply increase capacity to more economic, faster and more convenient to use, effective; 4) distributed power supply technology, many are environmental protection and energy saving, can satisfy the need of sustainable development; Especially the parallel operation mode has been a lot of energy experts say is the important direction of future power industry [3,4,5,6].

For distributed power supply and power grid operation problems, mainly has the following several aspects,it shown by Fig 1.

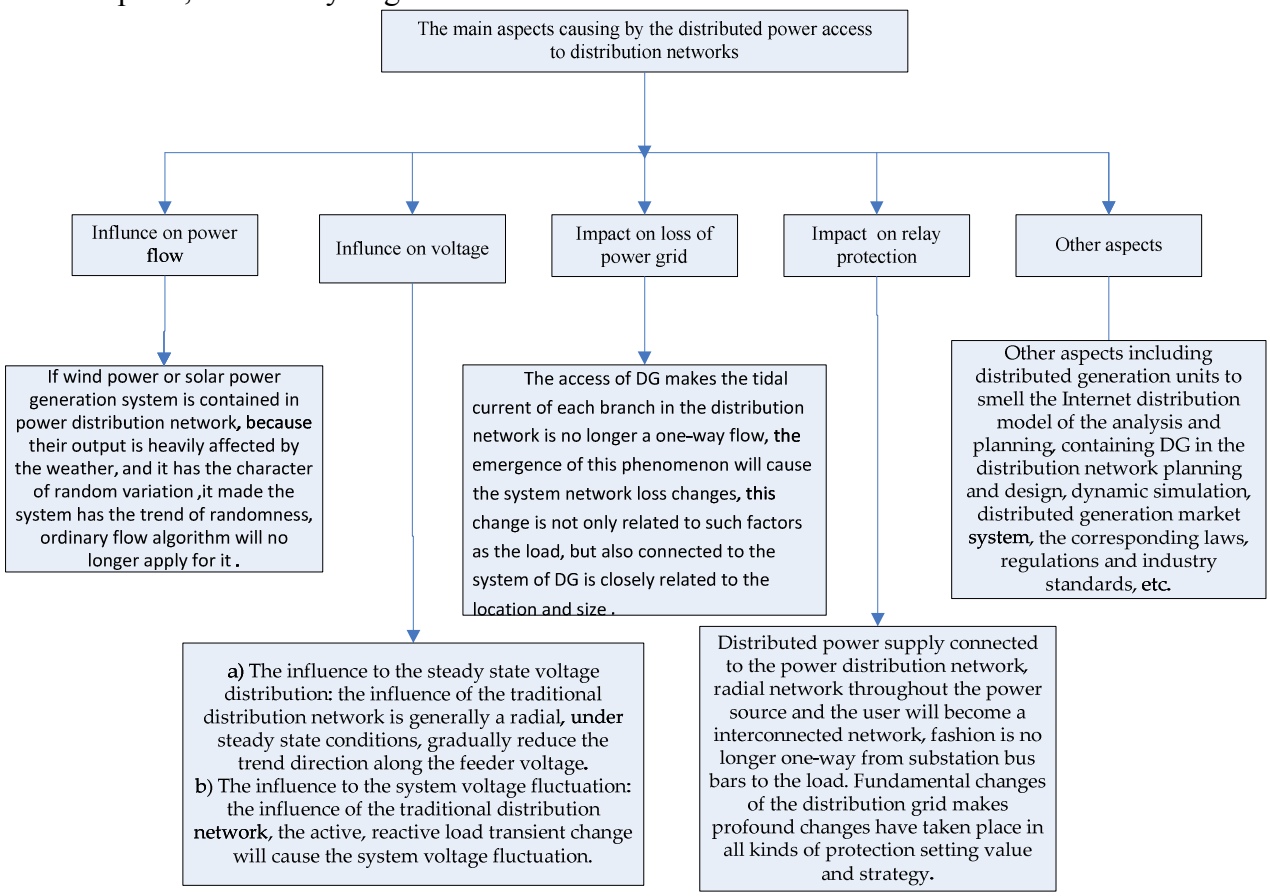

Fig 1 The main aspects causing by the distributed power access to distribution networks

Organization of the Text

DG access network loss changes after distribution network model analysis

1 The ideal model of the system

Compared two simple distribution network model: the model I system a not access distributed power (DG); Model II system connected to a distributed power supply. Both models in the end of the transmission line .

Containing the same load, assumes that the load with Y type access system and three-phase load balance, the power factor of load with a fixed from the system absorbs the active power and reactive power; On the transmission line is not long, can assume a power line voltage the same everywhere, and transmission line on voltage little change before and after the introduction of DG. Model I as shown in figure 2, model II as shown in figure 3.

In the articles ,used in the symbols of the instructions are as follows:

G : the distance from the power supply to the DG, unit of km

L : the distance from the power supply to the load, the unit of km

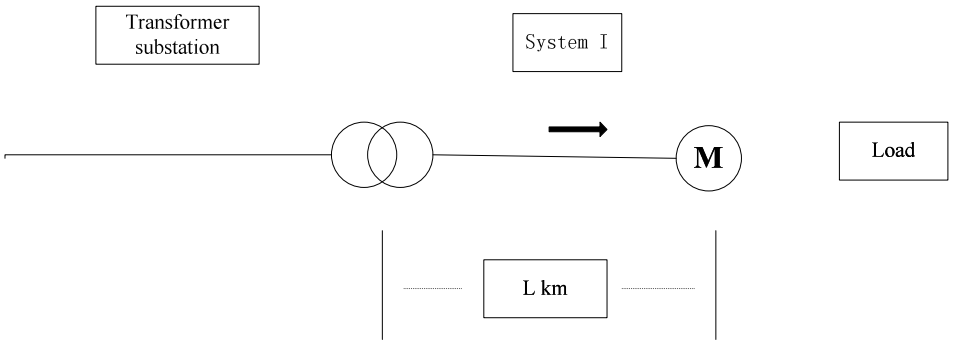

Fig 2 Model I (system I ,without DG)

I_g :single-phase current output from power DG, the unit of A

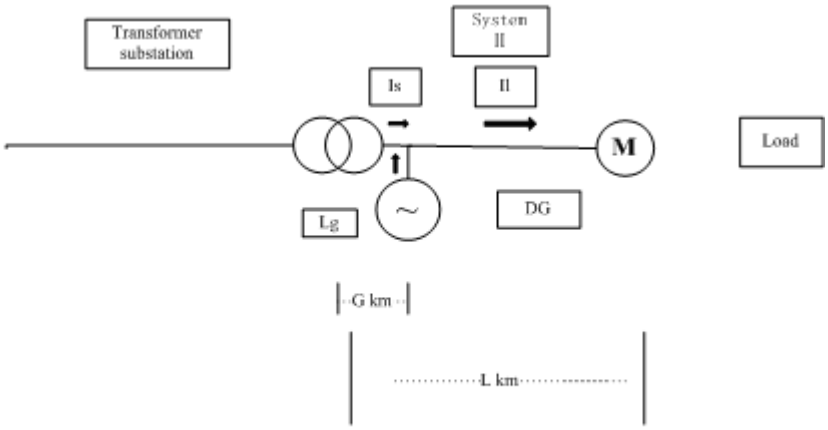

Fig 3 Model II (system II ,with DG).

I_l :single-phase current flows into the load, the unit of A

I_s : single-phase current output from power , the unit of A

2 The analysis of the loss changed after the DG in the model system access to distribution network

Load connected to the system inevitably produces the network loss. For system loss on one branch, its size depends on the current through the branch, and the branch resistance size, thus reducing the branch resistance and flow of electric current can achieve the purpose of reduce the loss. Distributed power supply is introduced on the load side, which can reduce system branch in the current, so can reduce the loss on the branch. The following from the simple model which can get the analysis of current changes in changes in the network loss.

System load for:

$$S_L = P_L + jQ_L \tag{1}$$

Type P_L ： the load active power consumption, unit w

Q_L ： the load reactive power consumption, unit Var

Single-phase current flows into the load:

$$I_L = \frac{P_L - jQ_L}{3V} \tag{2}$$

Type V the system transmission line voltage are, unit V

In model I，,the system loss is:

$$Loss_1 = \frac{rL(P_L^2 - jQ_L^2)}{3V} \tag{3}$$

Type r ： the system transmission line voltage are, unit Ω/km

In model II，,the system loss is:

$$I_G = \frac{P_G - jQ_G}{3V} \tag{4}$$

Type P_G ： the load active power consumption, unit w

Q_G ： the load reactive power consumption, unit Var

After the distributed power supply connected to the system, according to the DG access to the location of the power loss on the feeder can be divided into two parts: the first part is the power and power loss between the DG loss， here we call it $Loss_A$, the second part is the loss between the DG and load of power ,here we call it $Loss_B$.

$$I_L = I_S - I_G \tag{5}$$

$$Loss_A = 3rGI_S^2 = \frac{rG(P_L^2 + Q_L^2 + P_G^2 + Q_G^2 - 2P_LP_G - 2Q_LQ_G)}{3V^2} \tag{6}$$

On to the second part, due to the access to DG side load current before and after I_L change, so after the introduction into the DG network loss $Loss_B$ and before the introduction of DG is the same:

$$Loss_B = 3r(L-G)I_L^2 = \frac{r(L-G)(P_L^2 + Q_L^2)}{3V^2} \tag{7}$$

After the introduction of DG into the model Il ,the network loss in the transmission line L total amounts :

$$Loss_2 = Loss_A - Loss_B = \frac{rL}{3V^2}(2P_LP_Q + 2Q_LQ_G - P_G^2 - Q_G^2)\left(\frac{G}{L}\right) \tag{8}$$

From the above it can be seen that when $\Delta Loss > 0$, the introduction of DG can reduce network loss, on the contrary, when $\Delta Loss < 0$, While the introduction of DG increased the original line network loss.

Conclusion

The reasonable capacity of distributed power supply connected to the right place and with power factor operation is not only can largely reduce the network loss, but also suitable for distribution network and voltage support and safety and reliability of distribution network has a positive role in such aspects, the economic and reliable operation of the distribution network is very good.

References

[1] Lu Zhigang, Wang Ke, Dong Xuzhu. “Impact of consumer-side Distributed Generation on Power Grid.” Proceedings of the CSU—EPSA, 2012, 06(07): 23-27

[2] Gabriela Martin. “Renewable Energy Gets the “Green” light in Chicago.” IEEE power&energy magazine，2003，1(6)：34-39

[3] Frank C．Lambert. “Distributed Generation：semantic hype or the dawn of a new era.” IEEE power&energy magazine，2003，1(1)：22-29

[4] Zhang He. “Multichannel Wireless Fire Alarm System.” Modern Electronics Technique, 2007，30(5)：45-48

[5] Shen Hong. “Variable speed constant frequency wind generating set of the reactive power limit.” Grid Technology, 2003，27(11)： 60-63

[6] Wang Zhiqun. “The influence of distributed generation on distribution network voltage distribution.” ． Automation of electric power systems, 2004, 28(16)：56-61

Advanced Materials Research Vols. 960-961 (2014) pp 1081-1085

doi:10.4028/www.scientific.net/AMR.960-961.1081

The Steam Pipe Network Mathematical Modeling and Flow Field Analysis of Zibo Power Plant

Dong Yang[1, a], Xiao Lu[2,b]

[1] Key Laboratory of Renewable Energy Utilization Technologies in Buildings,Ministry of Education,Jinan, China

[2] School of Thermal Energy Engineering,Shandong Jianzhu University,Jinan 250101,China

[a]ydc1178@163.com, [b]kgluxiao514@163.com

Key Words: steam pipe network;transformation;mathematical mode;flow field analysis

Abstract. As Zibo power plant original steam pipes for a long time to run, the strength decreased and resistance was large, transformation was proposed to optimize. A mathematical model of the main steam pipe network was established to analysis changes of temperature, pressure and velocity vector before and after transformation. After transformation, the loss was significantly reduced,so transformation successfully achieve the optimization, adjustment and analysis functions of the main steam pipe network.

Introduction

Cogeneration is an important energy cascade utilization form. Because of its many advantages of energy-saving, environmental protection, economic and other domestic, it has become the main form of central heating in modern town international. The steam pressure is often more important than the temperature parameters in the turbine generate electricity, and power loss of temperature is greater than the pressure loss, it should try to avoid loss of pressure and temperature. In this paper, Zibo power plant main steam pipe network system, for example, conducted an investigation and computational analysis of its operation status and reduce pressure drop and temperature loss by energy-saving measures. Although the safety and reliability of the steam pipe network conducted many studies in many countries, mostly for the hot water pipe network, the steam pipe network system yet detailed algorithms. Irrationality steam pipe network layout, the difficulty of network operation and the lack of successful ways to learn from the experience, make this study practically significant[1,2].

An example of the steam pipe network transformation

Overview of Zibo Power Plant. Object of study is the Zibo thermal power plants, which now has six boiler rooms and 64 heat transfer stations, pipe network extending more than 420 km. Existing total heating area is 650 square meters, heating cover the entire scope of Zhangdian District of Zibo City,High Technology Development Zone and the New City.

Transformation range.(1) Transformation Cause: The original main steam pipe running for about three years, its creep is serious and strength is decreased. For the future operation to stay hidden danger, and the main steam pipe had greater resistance, an urgent need for reform.

(2) Transformation Content: 1 #, 2 # boiler and main steam pipe of 1 # turbine.

(3) Transformation principles: Try to go according to the original arrangement of pipes ,embedded originally reserved for the use of pipe hangers, while reducing the flow resistance losses.

Rehabilitation programs.(1) Change the original Φ193.7 * 22.2 main steam pipe to Φ219 * 18, the original Φ273 * 30 main steam pipe to Φ273 * 20, partial adjustment of Φ351 * 30;
(2) Adjust pipe material from 10CrMo910 to12Cr1MoVG;
(3) Take a single mother pipe program, remove the ring main pipe, pressure reducer to reduce the temperature of the main steam pipe leads directly from the mother, two manual segmentation reducing valves, electrical isolation to keep a door;
(4)Adjust diameter of 1 #, 2 # boiler and main steam pipe of 1 # turbine ment to DN250.Remove 1 #, segmented valve on the main pipe between the boiler # 2 (two), an increase of 3 # boiler with segmented valve.
(5) Valves can be approximated as 0.85 times the transformation of the main steam pipe diameter.

Numerical modeling of the main steam pipe network

In model building process, the steam pipe to model as a whole. Take y-axis is vertical, positive upward; x-axis direction is east-west, east is positive; z-axis direction is north to south, the south is positive, the established pipeline model diagram as shown in Fig 3.1[3,4].

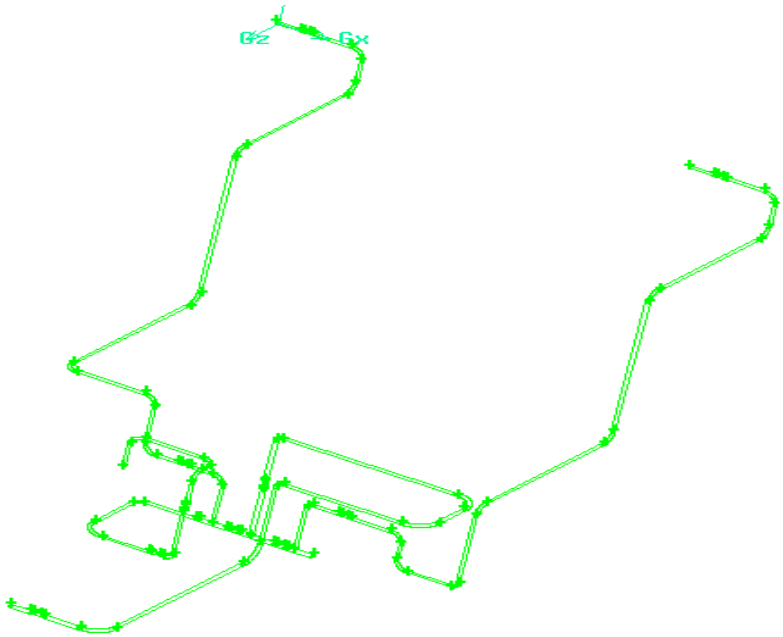

Fig 3.1 Pipeline model diagram

The main steam power plant boundary conditions of temperature and pressure pipe network settings are as follows:
(1) 1 #, 2 # steam import using pressure inlet boundary condition, its speed is determined by the inlet pressure and diameter;
(2) steam outlet using the default outflow boundary conditions;
(3) wall boundary conditions that no velocity slip wall, pipe wall is assumed to be adiabatic boundary;
(4) water vapor is a continuous medium, fluid flow is turbulent, incompressible Newtonian fluid.The vapor density is 0.5542 kg / m³, viscosity is 1.34kg/（m•s）, specific heat capacity is 2014 J / (kg • K), thermal conductivity is 0.0261W / (m • k). 1 # inlet pressure is 9730000Pa, inlet temperature is 811K; 2 # inlet pressure is 9810000Pa, inlet temperature is 809K.

The simulation results analysis

Using simulation software to establish the mathematical model of steam pipe network, entering the actual network operating parameters to accomplish simulation and analysis, together with the necessary shidechakan work, we can comprehensive, quantitative evaluation of pipe heat loss situation.

We used simulation software to establish a mathematical model of this power plant steam pipe network, entering the actual network operating parameters, together with a few necessary Shidechakan work, through simulation of different conditions, the simulation results obtained, then calculate, research and analysis, ultimately to achieve a comprehensive, quantitative evaluation of pipe heat loss situation[5]. The following is the simulation results and analysis.

Temperature Analysis. Through simulation software，drawing temperature distribution of the pipe network as shown in Fig 4.1-4.2.

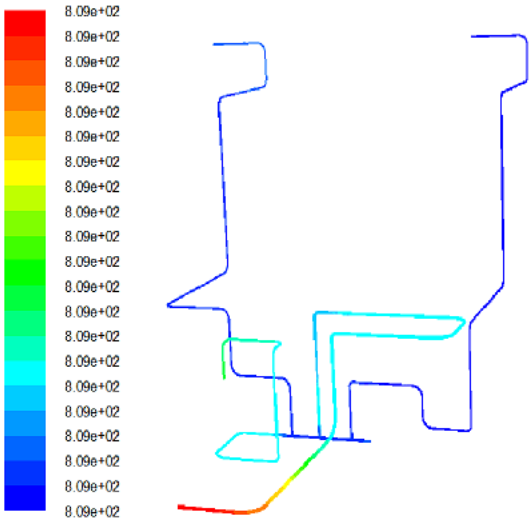

Fig 4.1 Befoer transformation

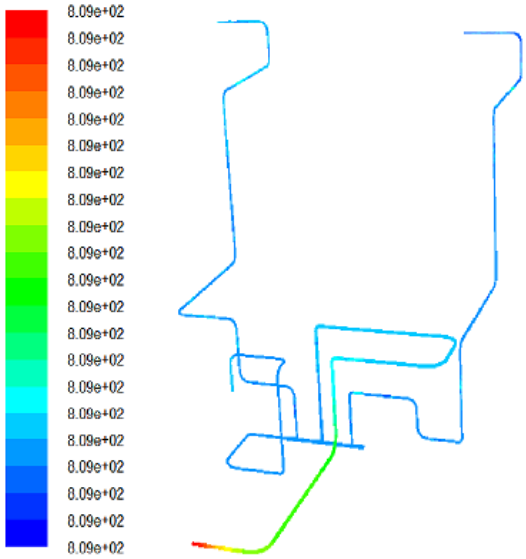

Fig 4.2 After transformation

As can be seen from the temperature distribution, steam mixture of the two different temperatures with the flow through a pipe, the temperature of the mixture is between two speeds, and the longer the pipe, the temperature dropped into the gradient. Close to the interface at a temperature close to the temperature of the fluid close.

Pressure Analysis. Through simulation software，drawing pressure distribution of the pipe network as shown in Fig 4.3-4.4.

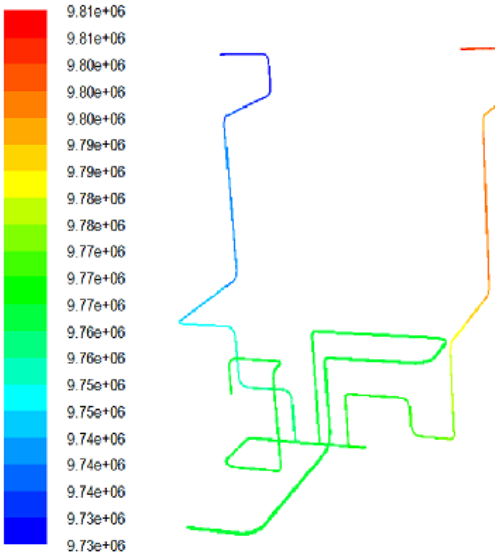

Fig 4.3 Befoer transformation

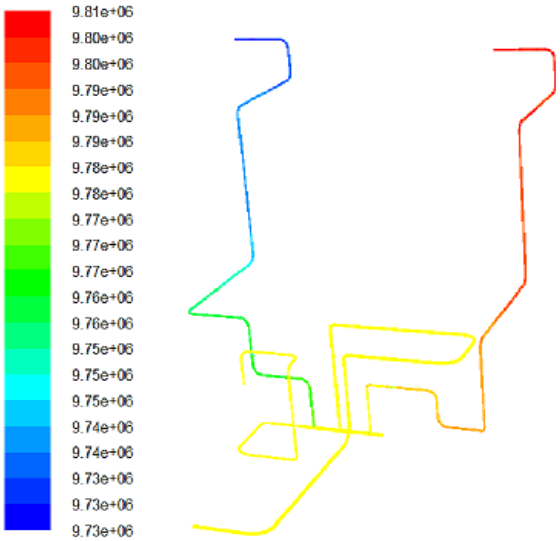

Fig 4.4 After transformation

As can be seen from the pressure distribution, the two strands of different vapor pressure of the mixed flow through the same pipe after the pressure in the pipeline at the junction is relatively large, but with the increasing distance pipeline, the pressure is gradually reduced, the mixing the end of the pipe fluid pressure to a minimum.

Velocity vector analysis. Through simulation software，drawing velocity vector distribution of the pipe network as shown in Fig 4.5-4.6.

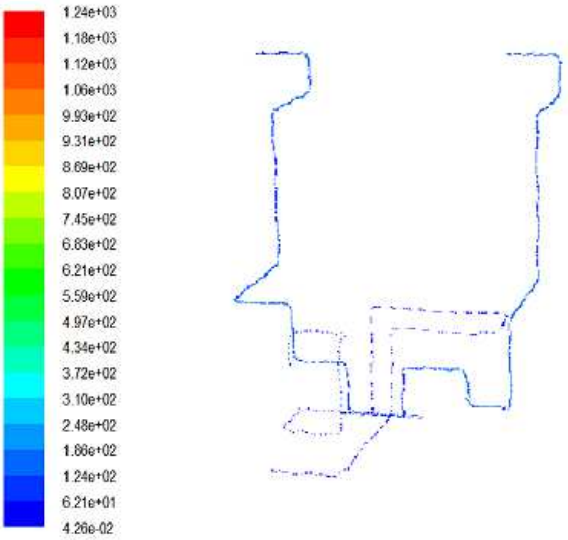

Fig 4.5 Befoer transformation

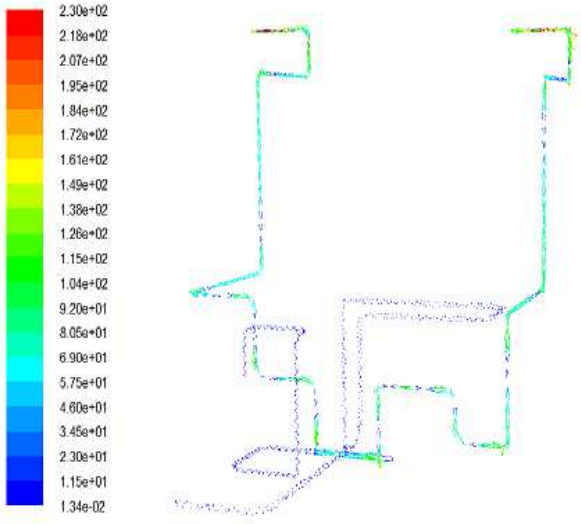

Fig 4.6 After transformation

As can be seen from velocity vector, when two fluids of different speeds after mixing flow through the same pipe, the pipe junction to get maximum speed and turbulence. As the distance becomes large pipeline velocity decreases, the distribution is similar to the temperature distribution.

Through simulation, the main steam pipe steam flow before and after the transformation, when the changes and export pipeline pressure loss including: Before transformation pressure drop is 41523Pa, after transformation pressure drop is 24137Pa; after transformation the outlet pressure is increased by 58.14% than that of the former, pressure losses are significantly reduced.

Conclusions

Zibo power plant operating conditions of the main steam pipe network to simulate multiple , based structural optimization of steam pipe network to provide a reference and basis through . Work done and conclusions are summarized as follows :

(1) By comparison, after transformation the outlet pressure is increased by 58.14% than that of the former. So the main steam pipe network, pressure losses are significantly reduced after transformation, the steam pipe network mathematical model established is reasonable, and it is successful transformation .

(2) Through simulation software, drawing velocity, temperature and pressure distribution of the pipe network, in practice, that the production of selected and appropriately selected to optimize the design diameter of the pipeline structure , according to the distribution pipe to these quantities, for software sampling can do a better theoretical basis for the practice.

(3)In technical analysis and balance adjustment process ,we can Conclusion, in the case that the heat source matches heat user, scientific and reasonable resistance to steam and heat pipe network comprehensive and systematic balance adjustment is to improve thermal efficiency and ensure steam pipe network security, improve plant efficiency is an important measure.

Acknowledgements:

This work was financially supported by the Doctor Foundation of Shandong Jianzhu University (XNBS1223) which is assumed by Prof. Dong Yang.

References:

[1] Kewu Zhu,Yuxing Wang,Yanqin Tang. Numerical analysis of five-tube flow field based on FLUENT[J]. Inner Mongolia Petrochemical. 2009(15):70-71.

[2]Yang Song,Fangzhen Chen,Xu Yang,et al. Dynamic simulation modeling of steam heating pipe network[J]. Journal of Tsinghua University (Natural Science).2008(10)

[3] Pei Wen. Valve Selection Guide[M]. Beijing Machinery Industry Press 2009

[4] Shunlong Liu. Computational Fluid Dynamics[M]. Harbin Engineering University Press 2008

[5] Huaping Liu,Fu Chen,Bo Ma. Numerical simulation of Valves flow field based on dynamic mesh technology with UDF[J]. Turbine Technology.2008(2):106-108

Advanced Materials Research Vols. 960-961 (2014) pp 1086-1090

doi:10.4028/www.scientific.net/AMR.960-961.1086

Torque Ripple Suppression of Switched Reluctance Motor Based on Torque Sharing Strategy

Qian Zhang[a], Ying Zhao[b], Hao Mu, Shuai Liu, Yiheng Li

Department of Power Engineering, Chongqing Communication Institute,

Chongqing, China

[a]479855782@qq.com, [b]zhaoying2666@163.com

Keywords: Switched reluctance motor; Torque sharing; RBF neural network; Current compensation

Abstract: The torque ripple is the main disadvantage of switched reluctance motor (SRM). In order to reduce the torque ripple of SRM, and improve the performance of the system, the torque sharing strategy was combined with RBF neural network for the purpose of torque ripple suppression by controlling the winding current of each phase. In consideration of the possible error of network, the real-time current compensation was taken to compensate the loss of torque which could suppress the torque ripple of the system in further. The results show that he torque ripple of SRM was suppressed effectively.

Introductions

SRM has a series of advantages such as simple structure, agile control, excellent capability of fault tolerance, etc. All these merits made it widely used in the fields of both military and civilian [1-3], however, the nonlinear characteristic of SRM will generate large torque ripple, which limits the popularization and application of SRM. Therefore, effective control strategy should be taken to reduce the torque ripple of SRM which is of great importance to improve the performance of the system.

Strategy of torque ripple suppression

Because of the nonlinear characteristics of torque, the change rates of torque of each phase are different during the commutation of current, which makes the total torque of SRM appears larger fluctuation. Therefore, realizing smooth transition of torque plays an important role to inhibit the torque ripple of SRM. The essence of Torque Sharing Function (TSF): Realizing smooth commutation of torque by distributing the total torque of SRM to each phase, and ensure that the total torque keeps a constant value [4]. Since it is difficult to control torque of SRM in direct, the torque of each phase distributed by TSF need to be transformed to the corresponding expected current by torque inverse model, the hysteresis comparator makes the winding current of each phase to follow the expected current with small error, so as to achieve the aim of indirect torque control. The general structure of the SRM control system as shown in Fig.1.

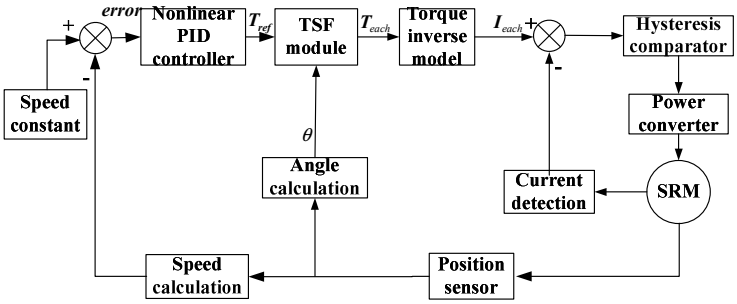

Fig.1. The structure of SRM TSF system

The system as shown in figure.1 adopts double closed loop control: speed loop and current loop. The expected torque T_{ref} was realized by PID speed controller, and the current I_{each} of each phase was realized by torque distribution module and torque inverse model.

Speed controller. The expected torque was realized by speed controller, and the relationship between torque and speed shown as formula (1):

$$T_e = J\frac{d\omega}{dt} + T_L + F\omega \tag{1}$$

Assume that the speed is a constant value, then there is an equation $d\omega/dt = 0$, and the formula (1) can be simplified as formula (2).

$$T_e = T_L + F\omega \tag{2}$$

The value of T_L and $F\omega$ is approximately remain unchanged when Δt takes a value small enough.

$$\begin{cases} \Delta T_e = J\dfrac{d\omega}{dt} \\ \dfrac{d\omega}{dt} = \dfrac{\Delta\omega}{\Delta t} \end{cases} \tag{3}$$

ΔT_e of expression (3) is the increment of torque within the time Δt.

$$\Delta T_e = K_P \Delta\omega \tag{4}$$

The choice of TSF. TSF describes the relationship between torque and rotor position angle of SRM, the form of the function is not unique, but must meet the need of function (5)[5]:

$$\begin{cases} T_j = T_{ref} f_j(\theta) \\ \sum_{j=1}^{n} f_j(\theta) = 1 \\ 0 \le f_j(\theta) \le 1 \end{cases} \tag{5}$$

The parameter of function (5) represented as follow: n is the phase number of SRM; θ is the relative position of phase winding and rotor; $f_j(\theta)$ represent torque distribution function; T_{ref} is the total expected torque of SRM; T_j is the expected torque of each phase.

There are some commonly used TSF such as trapezoidal function, cosine function, etc[6]. While there is no essential difference between each TSF, the only different between each function is just the shape of torque edge during commutation. The cosine function was used as the torque distribution function in this paper; the expression shown as function (6).

$$f_k(\theta)=\begin{cases} 0.5-0.5\cos\dfrac{\pi}{\theta_1-\theta_{on}}(\theta-\theta_{on}) & \theta_{on}\le\theta\le\theta_1 \\ 1 & \theta_1\le\theta\le\theta_{off} \\ 0.5+0.5\cos\dfrac{\pi}{\theta_1-\theta_{on}}(\theta-\theta_{off}) & \theta_{off}\le\theta\le\theta_2 \\ 0 & else \end{cases} \tag{6}$$

In equation (6), θ_{on} corresponding to opening angle of current electricity winding; θ_{off} represents the turn-off angle of current electricity winding; $\theta_1-\theta_{on}$ signify the overlapping conduction angle of two phase winding, θ_{on} meet the relationship as $\theta_{on}<\theta_1<\theta_{off}$, the best value of two phase overlap angle is 7.5°. The shape of TSF used in this paper shown as in Fig.2.

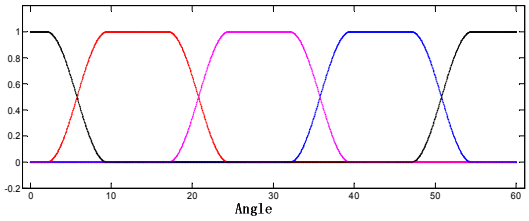

Fig.2. The shape of TSF

The torque inverse model based on RBF neural network. The expected torque of each phase was obtained by torque distribution function, while the essence of the torque control is the control of the current. Because of the strong nonlinear characteristics of SRM, it is difficult to obtain the expectations current match the corresponding torque of each phase by specific analytical solution. As a nonlinear network, Radial Basis Function Neural Network (RBF NN) can approximate any nonlinear Function with arbitrary precision [7], so that the relationship of torque, angle, and current could be expressed by RBF Network very well. The structure of RBF neural network as shown in Fig.3.

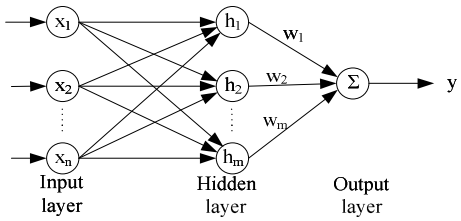

Fig.3. The structure of RBF neural network

The training sample data of RBF neural network were obtained by sampling the characteristic curve of angle and torque, the surface of training sample data as shown in Fig.4 and Fig.5.

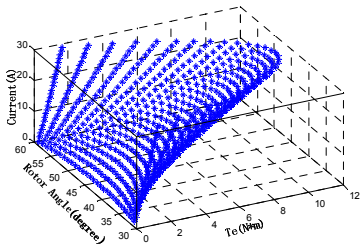

Fig.4. The surface of training sample data

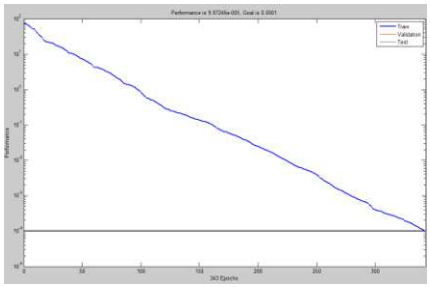

Fig.5. The network training process error curve

The network training process error curve as shown in figure 3.18, it can be seen that the error of the network is 9.98246 e-5 which is less than the pre-selected target 0.0001 when the network stop training, the output of the trained RBF neural network and the error curve between output of the trained RBF neural network and the sample data as shown in Fig.6 and Fig.7:

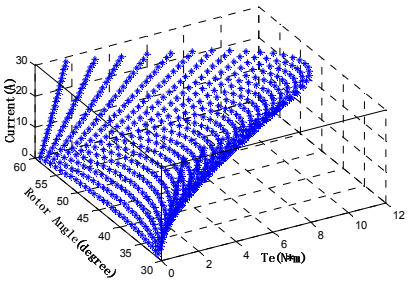

Fig.6. The output of RBF neural network

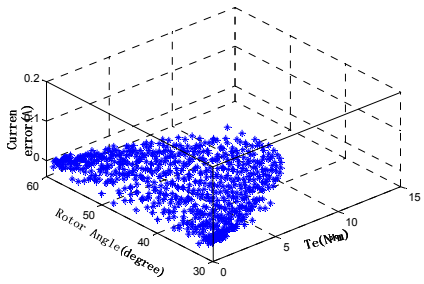

Fig.7. The error curve between output of RBF and sample data

Current compensation. There will be some errors inevitably during conversion from torque to corresponding expectations current because of the certain errors of RBF neural network， therefore， the torque of each phase cannot follow the expected torque very well which will cause torque ripple. Putting that in perspective, the segment of current compensation was proposed to compensate the losses of torque of each phase which will have a good effect for suppressing torque ripple. The simulink module of current compensation as shown in Fig.8.

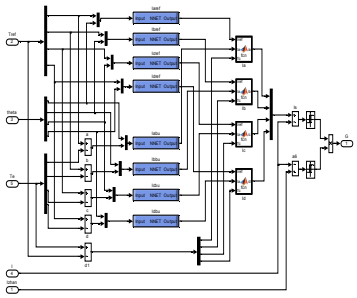

Fig.8. The simulink module of current compensation

Simulation analysis of TSF

The winding current is very small almost to zero under no-load cases, in order to observe the effect of current compensation for suppressing torque ripple of the system, the speed was set as 100 r/min, the load was set as 5N·m, the PI parameter was set as $K_p = 1, K_i = 0.1$, the simulation time was set as 0.5s. The simulation results as shown in Fig.9.

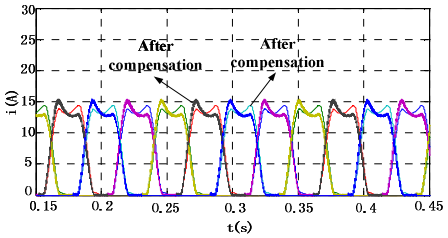

(a) Current contrast before and after current compensation

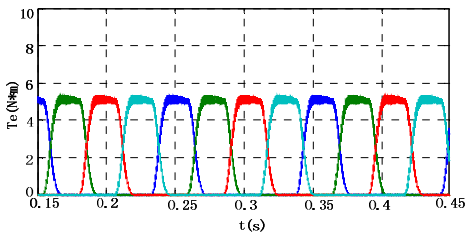

(b) The torque of each phase before current compensation

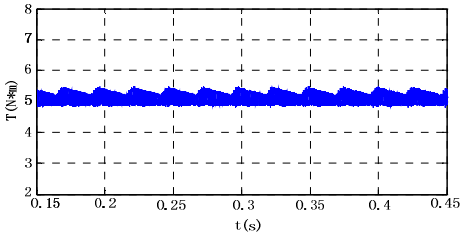

(c) The total torque before current compensatio

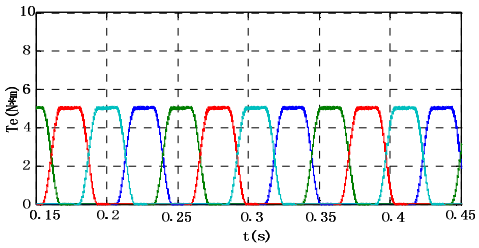

(d) The torque of each phase after current compensation

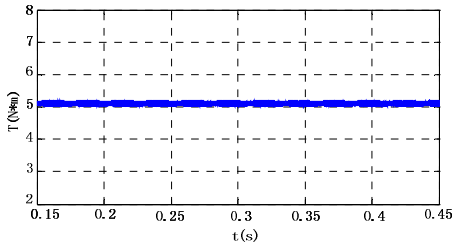

(e) The total torque after current compensation

Fig.9. The simulation results before and after current compensation

It can be seen from the diagram; the torque ripple decreased obviously by current compensation, and torque of each phase realized smooth commutation.

Summary

The torque distribution control strategy was adopts in this paper to distribute the total expected torque to each phase; since it is difficult to control the torque of SRM in direct, the RBF neural network was proposed to obtain the expected current corresponding to expected torque. The segment of current compensation was proposed to compensate the losses of torque of each phase for the possible errors of network. Researches have shown that the torque distribution control strategy can effectively reduce the torque ripple of SRM, and plays an important role in improving performance of the system.

References

[1] Hongxin Wu, Heng Ji, Baoquan kou. Summary of Switched Reluctance Motor Development[J]. MICROMOTORS, 2010, Vol. 44(1):78~83.

[2] C.Kamalakannan, V.Kamaraj, S.Paramasivam.Switched Reluctance Machine in Automotive Applications -A Technology Status Review. IEEE, 2011: 187~197.

[3] S.Gopalakrishnan, A.M.Omekanda, B.Lequesne. Classification and Remediation of Electrical Faults in the Switched Reluctance Drive[J]. IEEE Transaction on Industry Applications, 2006, 42(2): 479~486.

[4] Shi Zhong-lin, Huang Yun-sheng, Chen Xue. Research of Switched Reluctance Motor Control System based on Torque-sharing Strategy[J]. Coal Mine Machinery, 2010, 31(10): 59-61. (in Chinese)

[5] Kim C H, Ha I J. A new approach to feedback-linearizing control of variable reluctance motors for direct drive applications[J]. IEEE Transac tions on Control Systems Technology, 1996, 4(4): 348-362.

[6] Xu Zhen-wei. Switched Reluctance Motor Direct Torque Control Strategy Based on Torque Share Function[J].Tractor and Farm Transporter, 2010, 38(2): 61-67.(in Chinese)

[7] Wei Hai-kun. Structure Design Theory and Method of Neural Network[M]. Beijing: National defence industry press, 2005: 55-62. (in Chinese)

Advanced Materials Research Vols. 960-961 (2014) pp 1091-1094

doi:10.4028/www.scientific.net/AMR.960-961.1091

A Novel Shapley Solution for Power System Loss Allocation Under Hybrid Transaction Modes

Wu Xiaoteng[1, a], Qin Lijun[1,b]

[1]School of electrical and Electronic Engineering, North China Electric Power University, Changping District, Beijing 102206, China

[a]wuxiaoteng_vic@126.com

Keywords: electricity market; power system loss allocation; cooperate game; Shapley value; power flow; pool transaction; bilateral transaction

Abstract. The allocation of power system loss under hybrid transmission modes was investigated. First, a concept and method for converting a bilateral transaction into its two equivalents pool transactions were proposed. Then, a model based on Shapley value was designed to allocate the power system loss in the framework of equivalent pool transactions. The Shapley solution in cooperative game theory was employed to allocate the power system loss to each load pool transaction that includes the equivalent ones. The proposed method is applicable for electricity markets containing pool and bilateral transactions. It satisfies electric circuit laws and provides economic signals to users. The effectiveness of the proposed method is verified by the IEEE 5-bus test system.

Introduction

The current electricity market transaction model is divided into bilateral trading pattern and associated trading pattern. Other hybrid models are the expansion combined by bilateral and associated trade transactions. The transmission loss produced by all transactions in the system may account 5%-10% of the total generation [1]. Therefore, a fair and reasonable method to allocate the power loss is a problem cannot be ignored, but no method is widely accepted by now.

So far, many methods of power system loss allocation have been put forward. Using marginal cost theory in economics, a method based on marginal loss coefficient to allocate the network loss has been raised [2]. To solve the problem that marginal loss coefficient method cannot guarantee that the actual allocation of power system loss equal to the real allocation, paper [3] came up with a proportional method to adjust the unbalance. Paper [4] proves that node reactive power impacts the allocation result. The method based on marginal loss provides economic signals, but the different setting of slack bus lead to result divergence. Besides, this kind of methods is too sensitive to system data, and the result is also lack of feasibility and transparency [5]. In recent years, the concept of game theory are brought to power system, some researchers use game theory to solve the problem of loss allocation. Paper [6] proposes an approach of transmission cost allocation based on the Shapley Value, and paper [7] apply this method to system loss allocation. This approach can solve the problem that the allocation may lead to different results due to different sequences joining in the network, and it may also provide economic excitation signals. Paper [8] brings another method in cooperative game theory – Nucleolus. On a bilateral transaction mode, the result of system loss allocation is fair and effective. When the market consists of different types of patterns, paper [9] transforms bilateral trades into associated trades, and calculates the fixed transmission cost allocation using Nucleolus method.

Equivalent From Bilateral Transaction To Associated Transaction

In bilateral transaction mode, generators sign contracts directly with users and determine the trading volume and price. In associated transaction mode, the trades between generators and users transit through the power pool. Although at economic level, the two modes are different, in the physical level, all of electric power is generated by power plants, and conveyed to the users by

transmission network. Therefore, we can believe that both bilateral transaction and associated transaction can be treated as equal to the electric power flowing through the power grid.

Suppose generators at node i provide power P_{ij} to users at node j according to a bilateral contract stipulation, from the network point of view, the actual effect of the physical processes is to increase power P_{ij} in at node i and power P_{ij} out at node j. If thegenerating capacity of the original associated transaction at node i is G_i and the load capacity at node j is D_j, the value of generating capacity at node i and load capacity at node j after the equivalence from bilateral transaction to associated transaction are as follow:

$$G_i' = G_i + P_{ij}, D_j' = D_j + P_{ij}$$

Generators and users are the subscribers of the entire network. The essence of any transaction mode is power transmission from generators to users. Although on a bilateral transaction mode, the specific relationship between generators and users is clear, the order to join the network may lead to different net loss due to the presence of the cross item. The equivalent from bilateral transaction to associated transaction and allocation to each transaction is a more equitable allocation plan.

Power Loss Allocation Method Based On Shapley Value

Cooperative Game Theory

Cooperative game theory is an effective mathematical model that addresses benefits sharing issues in multi-party coordinating situations. If a problem deals with n (n>1) participants, they have the possibility to make an alliance, and all members of the league (the players) will take joint actions through full consultation in order to maximize the league benefit. It is the cooperative game of n participants.

A variety of methods can be used to solve cooperative game, such as the nucleolus, the nuclear, the bargaining sets, Shapley value, etc. Shapley value is used to solve the loss allocation problem.

Shapley Value Solution

Shapley value is a solution concept introduced by American researcher Shapley in 1953. Shapley value allocates the union total revenue by each player's marginal contribution to the alliance, which can ensure the fairness of the approach.

The Shapley value can be calculated by

$$\Phi_i(v) = \sum_{S:i\in S} \frac{(n-|S|)!(|S|-1)!}{n!} \times [v(S) - v(S-\{i\})], \quad i = 1,2,...,n \qquad S \subset I$$

where S represents all the coalitions containing participant i; $|S|$ is the number of transactions in coalition S; n is the number of transactions taking part in the allocation; $v(S)$ represents the function of coalition S; S-$\{i\}$ represents removing the player i from coalition S; $v(S)$-$v(S$-$\{i\})$ represents the contribution player i accedes to coalition S, namely, $v(S)$-$v(S$-$\{i\})$ is marginal profit of coalition S.

Power Loss Allocation Based On Shapley Value

Suppose in a regional electricity market, there are M bilateral transactions and N associated transactions. All bilateral transactions should be changed to associated transactions at certain nodes first. Then the equivalent associated transactions is now $n=M+N$, namely, there are n participants taking part in the loss allocation. Using Shapley value method to allocate the power loss to n transactions, the steps are as follows:1) List all the associations S of the transaction alliance. For n players, there are 2^{n-1} transaction associations.2) Calculate the active power loss $P_{Loss}(S)$ in each transaction association S.3) Calculate different Shapley value $\Phi_i(P_{Loss})$ for transaction i using Shapley value formula. $\Phi_i(P_{Loss})$ is the active power loss for transaction i. To calculate reactive power loss, replace all the $P_{Loss}(S)$ of the steps above to $Q_{Loss}(S)$. The result is reactive power loss for transaction i.

Numerical Examples

The diagram of the 5-bus power system is shown in Fig. 1. Two generators and five loads exist in the system. The branch parameters of the system are given in table 1.

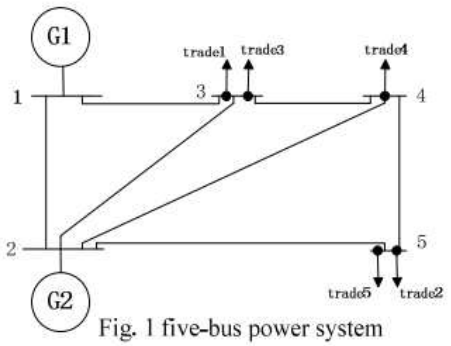

Fig. 1 five-bus power system

Tab. 1 Five-bus power system parameters of lines

Start Node	End Node	R/p.u.	X/p.u.	B/p.u.
1	2	0.02	0.06	0.0
1	3	0.08	0.24	0.0
2	3	0.06	0.18	0.0
2	4	0.02	0.18	0.0
2	5	0.08	0.12	0.0
3	4	0.01	0.03	0.0
4	5	0.03	0.24	0.0

There are five transactions in this market. Transaction 1 and 2 are bilateral transactions; transaction 3, 4 and 5 are associated transactions (pool transaction). The transaction data are given in table 2.

Tab. 2 Five-bus power system date of transaction

Trans No.	User	Supplier	Transaction Quantity	
			P/MW	Q/MVar
1	3	1	30	18.59
2	5	2	60	37.18
3	3	Pool	37.5	23.24
4	4	Pool	60	37.18
5	5	Pool	30	18.59

Tab. 4 Results of loss allocation

Trans No.	Active Power Loss /MW
1	1.0374
2	4.1086
3	1.2924
4	2.1688
5	2.1140
Total	10.7212

First the two bilateral transactions are equated to pool transactions. At node 1 there are *(30+j18.59) MVA* generating capacity increase, and node 2 *(60+j37.18) MVA*. At node 3 there are *(30+j18.59) MVA* load increase, and node 5 *(60+j37.18) MVA*. The whole system is equivalent to a regional power market with five pool transactions.

Computing the optimal power flow on the condition of minimum network loss using PSASP software, so each network loss of the transaction combinations is available. Only active power loss data are shown in table 3.

Tab. 3 Network losses of five-bus power system

Transaction Combination	Active Power Loss/MW	Transaction Combination	Active Power Loss/MW	Transaction Combination	Active Power Loss/MW	Transaction Combination	Active Power Loss/MW
1	0.1653	1&5	0.8056	1&2&4	4.7607	2&4&5	6.8531
2	1.8601	2&3	2.6462	1&2&5	5.2542	3&4&5	2.7847
3	0.2602	2&4	3.6089	1&3&4	2.7027	1&2&3&4	6.8013
4	0.622	2&5	4.4088	1&3&5	1.774	1&2&3&5	6.8629
5	0.4392	3&4	1.5285	1&4&5	2.4973	1&2&4&5	8.2925
1&2	2.4413	3&5	0.9523	2&3&4	5.1134	1&3&4&5	4.2001
1&3	0.8667	4&5	1.5966	2&3&5	5.5252	2&3&4&5	8.7201
1&4	1.2992	1&2&3	3.7091				

The loss transaction 1 should undertake using Shapley value is calculated by

$$\Phi_1(P_{Loss}) = \frac{4!\times 0!}{5!}P(1) + \frac{3!\times 1!}{5!}\{[P(1,2)-P(2)]+[P(1,3)-P(3)]+[P(1,4)-P(4)]+[P(1,5)-P(5)]\}+$$
$$\frac{2!\times 2!}{5!}\{[P(1,2,3)-P(2,3)]+[P(1,2,4)-P(2,4)]+[P(1,2,5)-P(2,5)]+[P(1,3,4)-P(3,4)]$$
$$+[P(1,3,5)-P(3,5)]+[P(1,4,5)-P(4,5)]\}+\frac{1!\times 3!}{5!}\{[P(1,2,3,4)-P(2,3,4)]+[P(1,2,3,5)-P(2,3,5)]$$
$$+[P(1,3,4,5)-P(3,4,5)]+[P(1,2,4,5)-P(2,4,5)]\}+\frac{0!\times 4!}{5!}[P(1,2,3,4,5)-P(2,3,4,5)]$$
$$=1.0374(MW)$$

Similarly, loss the rest transactions should bear can be calculated. The result is shown in table 4.

The allocation result shows that whether individual transaction or transaction coalition as well as the whole allocation, the result of the allocation method is rational. The reasons are as follow:1) The loss allocation result for individual transaction is greater than the loss of certain transaction working in the system alone. 2) For any of the transaction coalition, the sum of the loss allocation to every coalition member is greater than the loss of the transaction coalition. Because of the presence of cross item, the result is reasonable and capable of being accepted by the coalition member.3) For the power network of the entire region, the sum of all loss allocation to transaction coalitions is equal to the total loss of the major league. The loss allocation is consistent with the real loss.

Conclusion

Based on cooperative game theory, a novel Shapley value theory-based method for power loss allocation under hybrid transaction modes is introduced. With the method, the physical route of the transactions can be recognized, and sequences of transactions acceding to coalition are taken into consideration. Moreover, the impacts of different market participants on network power losses are also taken into consideration.

The idea of equivalent from bilateral transactions toassociated transactions considers the whole regional power market as an entirety formodeling and analysis. So the results are convincing.

In addition, after calculating the loss allocation, whether the results need to be fixed for bilateral transactions and associated transactions is under discussion.

References

[1] B Xu, X.J. Zhang and Z.X. Ti, “Loss Allocation Using Marginal Loss Coefficient Method”, East China Elect.Power, vol.01, pp.15-17, 2001.In Chinese.

[2] Z.C. Du and D.Z. Xia, “The Allocation of Power System Loss”, Autom. Elect. Power Syst., vol. 04, pp.18-22, 2002. In Chinese.

[3] Q.G. Wu, Z.H. Cheng and Z.H. Liu, “New Regulation Method of Marginal Loss Coefficient Loss Allocation of Power Market”, Proc. of Elect. Power Syst. andAutom., vol.03, pp.78-81, 2005. In Chinese.

[4] Z.H. Liu, Z.H. Cheng and X.D. Liu, “Influence of Node-injected Reactive Power on Loss Allocation in Electricity Market by Marginal Loss Coefficient Method”, Power Syst. Tech. vol.03 pp.51-54, 2004. In Chinese.

[5] G.M. Lu, “Research on Losses Allocation and Generation Bidding Price Modification in Electricity Market”, North China Elec. Power Univ.

[6] X Tan, T.T. Lie, “Application of the Shapley value on transmission cost allocation in the competitive power market environment generation”, Trans.&Dist., vol.49, pp15-20, 2002.

[7] Z.Y Hu, Z.X. Han, “A Shapley Value for Loss Allocation”, Autom. Elect. Power Syst., vol. 07, pp.32-35, 2003. In Chinese.

[8] X.H. Zhou, S.H. Du, “A Novel Nucleolus-Based Loss Allocation Methodin Bilateral Electricity Markets”, Proc. of the Csee, vol. 01, pp.63-68, 2005. In Chinese.

[9] X Gao, J.C. Peng and A Luo. “A Nucleolus Solution for Fixed Transmission Cost Allocation Under Hybrid Transactions Modes”, Proc. of the Csee, vol.23, pp.120-124, 2007.In Chinese.

[10] Z. Xie“Game Theory”, in press.

[11] RodicaBranzei, DinkoDimitrov, StefTijs, “Models of Cooperative Game Theory”, in press.

Advanced Materials Research Vols. 960-961 (2014) pp 1095-1099

doi:10.4028/www.scientific.net/AMR.960-961.1095

A Role Mengxi UHVDC Project Plays in Improving the Energy Demand in the Central China Power Grid

Zheng Xu[1,a], Wang Jianghong[2,b] , Zhao Shuang[3,c] , Li Mei[3,d], Zhang Buhan[3,e], Zeng Ni[3,f], Zhu Ruoxi[3,g] , Zeng Yuanfang[3,h]

[1] School of Electrical Engineering Wuhan University, Wuhan, China

[2] State Grid Hubei Economic Research Institute, Wuhan, China

[3] State Key Laboratory of Advanced Electromagnetic Engineering and Technology Huazhong University of Science and Technology, Wuhan, China

[a]hustzx987@163.com, [b]wangjianghong2008@126.com, [c]zhaoshuang@hust.edu.cn, [d]hnxnmeili@163.com, [e]zhangbuhan@mail.hust.edu.cn, [f]zengni@hust.edu.cn, [g]909706772@qq.com, [h]zyf_jy@hust.edu.cn,

Keywords: Mengxi UHVDC; Energy Demand; Power Flow; Access Point;

Abstract. A province in the central China faces the problem of energy shortage, 800kV Mengxi UHVDC project will effectively broaden the energy input channels of the province, enhance energy supply security, and reduce the pressure on coal transportation. This paper analyses the load, power supply and power shortage of a central province, and explored the role of Mengxi UHVDC project played in improving the energy demand in the Central China power grid. By comparing the different access plans to the grid, this paper demonstrated that it's more appropriate to divide the Mengxi UHVDC into 1000kV and 500kV at the inverter side for consuming the power of UHVDC and protecting the normal power supply.

Introduction

Hydropower resources have been fully developed in a central province. Backup power supply of thermal power has been less, and subject to coal supply. So far, the installed capacity of wind power, biomass and other new energy are small-scale. Nuclear power can't form the productive forces during the Twelfth Five-Year Plan Period [1-2]. However, the growth of installed power generation capacity, the per capital generated energy and outside delivery electric quantity in a northern province rank first in China.

The construction of Mengxi UHVDC project can well support the UHVAC project as a preparation, meet the urgent demand for the northern power resource electricity in central resource-poor province. What's more, it can also change the situation that North China grid and central China grid have remained one-way communication for a long time, enhance the level of security and stability, and improve the power transmission capacity from north to the central grid.

The placement of UHVDC project should fully consider the impact of landing position and access way on power flow, stability of the entire grid[3-7]. In article [8], it takes the 1000kV Jindongnan-Nanyang-Jingmen UHVAC project as an example to expound the Jingmen substation placement and access system solutions. In article [9], it analyzes the security and stability issues of UHVAC access of Jiangsu power grid. In article [10], it studied the Zhuzhou convert station access system solution of Xiluodu–Zhuzhou ±800kV UHVDC project from the perspective of geography, economy and so on. This article attempts to explore the access plan to the central province of Mengxi UHVDC project from the perspective of consuming the power flow.

An analysis of energy demand in Central China Power Grid

Figure 1 is a schematic diagram of the grid structure in a central province. In order to analyze the power flow conveniently, this paper divides the province into three regions - east, west and northwest.

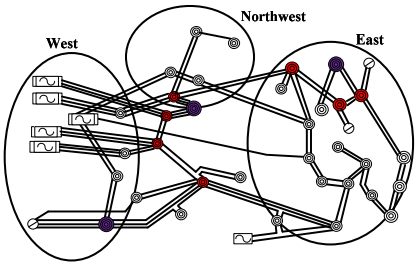

Fig.1 The schematic diagram of the grid structure in a certain central province

The electric power receiving space of the three regions is shown by Table 1. Loads are concentrated in East region, where the electric power receiving space account for more than 50% of the province's electricity demand. West is the power supply concentrated area; while the northwest is mountainous, and the load base is low. According to the results of load forecasting in Table 2, the electric power balance calculation result is shown in Table 3.

Tab.1 The electric power receiving space of the central province (Unit: million kw)

province	2015 wet	2015 dry	2020 wet	2020 dry
	810	950	2270	2230
East	660	490	1380	1080
West	70	280	570	740
Northwes	80	180	320	400

Tab.2 Electricity demand forecast of the central province (Unit: million kw, billion kwh)

project	2011	2015	2020
Total Consumption	1450.8	2150	3100
Arrangement Maximum Load	2483.4	3660	5200
Arrangement Installed Capacity	2633	3300	3550

Tab.3 The electric power balance calculation in 2015 and 2020(Unit: million kw)

Plan	2015		2020	
Electricity shortfall	**wet**	**dry**	**wet**	**dry**
	810	950	2270	2230

Role that Mengxi UHVDC project plays in improving energy demand in Central China Power Grid

Mengxi UHVDC project is the need for the energy development strategy in Central China Power Grid

The energy resources and its impact on electricity production

Less coal, less oil and less gas, these are the energy status of the province [3]. Hydropower resources development rate is over 90%, and the potential for further development is relatively limited [2-3]. Energy external dependency is higher .

Due to less resources and high load from Table 3, it indicates that the province's largest electricity shortfall is 900 million kilowatts in 2015, and by 2020, it will be up to 22.5 million kilowatts. So the province has to accept the transferred electricity from other province to keep co-ordination of supply and demand.

The solution of electricity shortfall

From Table 2, the load develops rapidly during the Twelfth Five-Year Plan Period. In 2015, the unified schedule maximum load will reach to 33.6 million kilowatts, while the average annual growth rate of electricity consumption will be 10.7%. With the economic development, electricity demand is bigger in the future. It must input a lot of energy from outside when the province is in the absence of sufficient resources.

(1) Import coal for power generation from other provinces. Input the coal from outside the province in long distance and large capability, will not only cause an increase in the cost of electricity production, but also bring a tremendous risk to the power supply in the province.

(2) Actively fight for the electricity share of the Three Gorges Dam. The electricity share allocated to the province by the Three Gorges Dam is only about 15%.

(3) Develop nuclear power. Development of nuclear power is not only the objective requirements to optimize the energy structure and safeguarding the economic and social sustainable development, but also is the requirement of adjusting structure of power source.

(4) Accept electricity from other province on a large scale. The province has achieved grid interconnection and exchange with some provinces through the AC lines.

From the above analysis, it indicates that under the condition of increasing pressure on coal transportation and limited ecological carrying capacity, except for optimizing the structure of power source on the basis of consuming hydropower in the priority, exploring sources of renewable energy, and developing the nuclear power, the most effective way to solve the electricity shortfall is to embrace electricity from other provinces on a large scale.

Mengxi UHVDC project is the guarantee of the grid's security and stability

The grid of the province is the center of the national grid, and become a hub and a trafficking corridor of optimizing allocation of resources between the three gorges hydropower station, the northern coal-fired power, and the southwest hydropower. Grid security is mattered [3]. North and Central grid still remains single transmission line connected by UHVAC project, once surrounding provinces emerge a big load shedding incidents, it will endanger the safe operation of the Central China Power Grid.

In order to improve the reliability of power transmission, construction of Mengxi UHVDC project should be accelerated, to form a support project with UHVAC project as a preparation to meet the province's urgent needs for the northern electricity resources, and change the single contact situation between the North China power grid and Central China power grid so as to enhance the level of security and stability, and improve the power transmission capacity from north to the central grid, ensure the province's energy security.

Analyze the placement of Mengxi HVDC project through Power flow

Taking 2020 as calculating level year, the largest electricity shortfall in east is about 13.8 million kilowatts, and the placement of Mengxi UHVDC project located in the east region of the province can ensure the power balance. The following discussion can be divided as two plans: access to the 1000 kv power grid and access to 500 kV power grid of Mengxi UHVDC project in 2020 wet season.

Mengxi UHVDC project access to 1000kV grid

In the abundance of hydropower, the electric power receiving space of west is 5.7 million kilowatts. Considering feeding in 2.3 million kilowatts of hydropower, 6.5 million kilowatts are from UHV substation, the power surplus of the west is about 3.1 million kilowatts. In the east, the electric power receiving space is about 13.8 million kilowatts, under the total consideration of 6.3 million kilowatts are from the UHV substation, 7.5 million kilowatts are from the UHVDC. the power of the eastern part is balanced. The electric power receiving space of the northwest is about 3.2 million kilowatts, and it is supplied by the surplus power of the west.

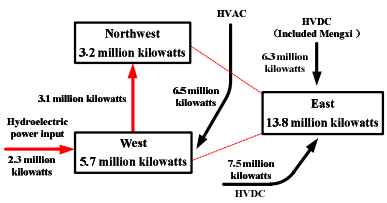

Fig.2 Mengxi UHVDC project access to 1000kV grid

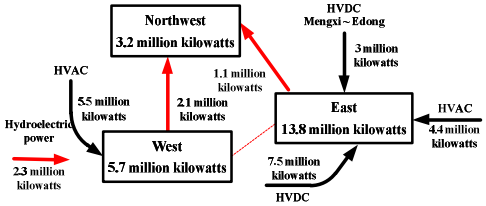

Fig.3 Mengxi UHVDC access to the 500 kV grid

Due to the Mengxi UHVDC Project access to the 1000kV grid, in order to meet the electricity demand, it needs to download large amounts of electricity from the grid before UHVAC to meet the normal power supply.

Mengxi UHVDC project access to 500kV grid

When access to 500kV grid, The electric power receiving space of west is 5.7 million kilowatts, considering feeding in 2.3 million kilowatts of hydropower, 5.5 million kilowatts are from UHV substation, the power surplus of the west is about 2.1 million kilowatts. In the east, the electric power receiving space is about 13.8 million kilowatts, under the total consideration of 4.4 million kilowatts are from the UHV substation, again 3 million kilowatts are from the UHVDC. the surplus electricity of the eastern part is about 1.1 million kilowatts. The electric power receiving space of the northwest is about 3.2 million kilowatts, and it is supplied by the surplus power of the west and east.

Based on the province's power flow analysis, the province need to download a lot of power from the UHVAC grid to meet the province's the normal power need when Mengxi UHVDC project access to 1000kV grid, and the AC UHV variable capacitance load ratio of the province is as low as 1.34. However when it access to 500kV grid, it is more appropriate to directly consume the power of UHVDC grid and protect the province's normal power supply.

According to the preliminary plans, Mengxi UHVDC project should access to 1000kV grid. However, the province's electricity shortfall will be more than 22 million kilowatts by 2020, at that time it needs to accept the external power to meet load demand. It it is bound to squeeze the main transformer capacity of UHV substation when Mengxi UHVDC electricity is consumed. Therefore, Mengxi UHVDC inverter side should be divided to 1000kV grid and 500kV grid to safeguard the security and stability.

Program analysis of Mengxi UHVDC project access system

Based on the power flow analysis, this paper proposes two 500kV access programs: two of the Mengxi DC outlets connect to the substation C and the other two DC outlets connect to the substation E; Mengxi DC outlets connect to the system by dual-π type from substation D-substation E with double-circuit line. The mode of connection is shown in Figure 4, 5.

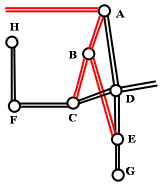

Fig.4 Wiring diagram of option 1

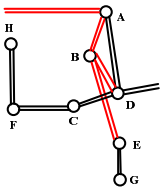

Fig.5 Wiring diagram of option 2

Option one and option two all access Mengxi UHVDC to the east power grid. Option one can reduce the pressure on evacuating the power flow from substation D ~ substation E to make the power flow of the east more reasonable. By analyzing, the short circuit current of substation C, substation D, and substation F will become overload in 2018. So this paper recommends option 1 and suggests disconnecting the double lines of substation C-substation D, use low-end access system of Mengxi UHVDC project to form the ring network of east.

Conclusions

The most effective solution to solve the electricity and resource shortfall is to input electricity from other province on a large scale. It also suggests continuing to enhance the size of the province's power grid interconnection with the grid outside the area, and improve the ability to accept power outside the region.

Mengxi UHVDC project access to the central province will bring new challenges. On one hand, it will solve the electricity shortfall effectively form a "strong DC-AC grid" with the UHVAC power grid project to meet the provincial demand for the power resources in the north. On the other hand, it can change the one-way communication situation between the north grid and central grid.

After a comprehensive analysis, this paper preliminary recommends Mengxi UHVDC invert side should have 1000kV and 500kV high-low side access options, high-end access to substation A, and the low-end side has four outlets - two access to substation C, other two access to substation E. By then the central grid will enter a new phase of DC outgoing, fed coexist and AC-DC hybrid. It creates the condition that the central province can consume the power delivered from the north province.

Acknowledgements

This work was supported by State Grid Hubei Electric Power Company (Impacts of Meng Xi UHVDC project on Hubei grid).

References

[1] Wang Jianghong. "Study on Substation Location for Planned UHV Power Grid in Hubei[J] ".*Hubei Power*,2009,04:47-49 +74.

[2] Wu Yaowen , etc. "The Twelfth Five-Year Plan on designing of Hubei grid" [Z] .2010.

[3] Zhang Wenliang，Zhou Xiaoxin，Guo Jianbo，et a1．Feasibility of ±1 000kV ultra HVDC in the power grid of China[J]．*Proceedings of the CSEE*，2007，27(28)：1-7(in Chinese)．

[4] ShenYangwu,Peng Xiaotao,Mao XunShi,Xing Jie. "Comprehensive Evaluation Indexes Framework and Evaluation Method on Location Layout of UHV Substations [J]". *Power System Technology*,2012,12:44 -53.

[5] Guo country Shen Shanshan, "Study on construction necessity and schemes connecting to power grid for Nanchang UHV AC transmission project [J]". *Electric Power*, 2010,08:40-44.

[6] Lu jing, "Study on Optimizing Configuration for Connecting Power Sources in Guangxi Power Grid into the Main Power System[J]". *Guangxi Electric Power Technology*,2002,01:1 -4 +12 .

[7] Peng Hui, Zhang Xin , Li Yajun , Tao Rin , "Influence of Selection of Connecting Position for UHVDC Transmission Line With Transmission Capacity of 10 GW on the Stability of Receiving-End System in Chongqing Power Grid [J]". *Power System Technology* ,2011,11:25 -28 .

[8] Zhou Li , the iron yuan , Kang Yi , Zheng Yingfen , Fang Xiaosong , Chen , Juan-Juan Huang, "Study on the location and system scheme of Jingmen substationin 1000kV Jindongnan-Nanyang-Jingmen UHVAC transmission project [J]". *Electric Power* ,2006,07:65 -69.

[9] LIU Jiankun , HU Ya Shan, Zhao Jingbo , "Prospects to the Influences of the Ultra High Voltage Grid on Jiangsu Power System [9] [J]". *Jiangsu Electrical Engineering* ,2010,01:1-3 .

[10] Fang Xiaosong , Zhong Sheng , Chen Zheng, CHEN Ling-yun , WANG , "System scheme study of Zhuzhou converter stationin ±800k VUHVDC transmission project From Xiluodu Left Bank to Zhuzhou [J]". *Electric Power*,2006,03:50 -54.

Advanced Materials Research Vols. 960-961 (2014) pp 1100-1103

doi:10.4028/www.scientific.net/AMR.960-961.1100

An Approach of Wavefront Identification for Traveling Wave Fault Location Based on Harris Corner Detector

Guangbin Zhang[1, a *], Hongchun Shu[2,b] and Jilai Yu[1,c]

[1] School of Electrical Engineering and Automation, Harbin Institute of Technology, China

[2] Faculty of Electric Power Engineering, Kunming University of Science and Technology, China

[a]guangbin85@gmail.com, [b]kmshc@sina.com, [c]yupwrs@hit.edu.cn

Keywords: wavefront identification, Harris Corner Detector, traveling wave, fault location, waveshape

Abstract. Wavefront identification is important for traveling based fault location. In order to improve its reliability, a novel wavefront identification method based on Harris corner detector has been proposed in this paper. The principle of single-ended traveling wave fault location was briefly introduced at first, and the features of wavefronts generated by faults on transmission lines were analyzed. The arrival of traveling waves' wavefronts is considered as corner points in digital image of waveshape. The corner points can be extracted precisely by Harris corner detector, and both false corner points and non-fault caused disturbance can be eliminated according to the calculated distance between two neighbour corner points and the angle of the corner point. The proposed method is proved feasible and effective by digital simulated test.

Introduction

Accurate fault location technique is essential for speeding up the determination of transmission line's trouble and restoration of power supply, and has been always attracted many studies for decades [1]. Traveling wave fault location technique has the advantage of high theoretical accuracy, immune to power swings and CT saturation, intensive to various fault conditions. Reliable detection of the available traveling wave forefront is the key technology for traveling based fault location. Many research works have been dong and many signal processing methods such as difference, correlation, matched filtering and wavelet transform have been applied in wavefront identification [2]. Nevertheless, it is still difficult to detect and identify fault reflected wave effectively and reliably at present, and this makes single-ended method difficult to be implemented automatically. In this paper, from the perspective of digital waveshape image processing, a new wavefront identification method is proposed, and is proved feasible and effective by digital simulated data test.

Feature analysis of wavefronts for single-ended traveling wave fault location

Single-ended traveling wave fault location calculates the fault distance according to the time required for the fault generated traveling wave traveling from the bus to the fault position and back, as is shown in Fig.1. The equation of computation is shown as Eq.1 [1].

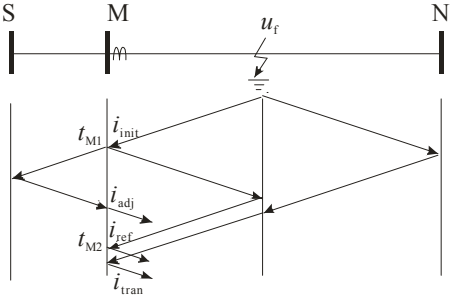

Fig.1 Lattice diagram for the propagation of the fault induced traveling waves

$$x_{\mathrm{M}} = \Delta t_{\mathrm{M1}} v / 2 = (t_{\mathrm{M2}} - t_{\mathrm{M1}}) v / 2 \tag{1}$$

where, t_{M1} and t_{M2} is the arrival time of the initial surge and the reflection wave from the fault point at terminal M; v is the velocity of propagation for traveling waves.

When a fault occurs on the transmission line, the transient current travelling wave recording device equipped at M busbar terminal senses four kinds of surges: initial surge, reflection waves from the fault point, transmitted waves from remote busbar reflection and reflected waves from the end of adjacent healthy line, as is shown in Fig.1. The derivation of the four kinds of traveling waves produce the expressions as is shown in Eq2~Eq5 [3]:

$$i_{\mathrm{init}} = (-1 + \beta_{\mathrm{M}}) e^{-\gamma x} u_f / (Z_{\mathrm{C}} + 2R_f) \tag{2}$$

$$i_{\mathrm{ref}} = (-1 + \beta_{\mathrm{M}}) \beta_{\mathrm{M}} \beta_f e^{-3\gamma x} u_f / (Z_{\mathrm{C}} + 2R_f) \tag{3}$$

$$i_{\mathrm{tran}} = (-1 + \beta_{\mathrm{M}}) \beta_{\mathrm{N}} \alpha_f e^{-\gamma(2l - x)} u_f / (Z_{\mathrm{C}} + 2R_f) \tag{4}$$

$$i_{\mathrm{adj}} = \alpha_{\mathrm{M}}^2 \beta_{\mathrm{K}} e^{-\gamma(x + 2l_K)} u_f / (Z_{\mathrm{C}} + 2R_f) \tag{5}$$

where u_f represents the initial faulted voltage source in superimposed network, l represents the length of faulted line MN, x represents the distance between fault point and monitored busbar, l_{K} represents the line length of shortest line connected with busbar, R_{f} represents the fault resistance， α_{M}, β_{M}, α_f, β_f, separately represents the voltage transmission and reflection coefficient at busbar M and fault point, γ, Z_{c} represents the attenuation and surge impendence of the line.

When traveling waves arrives at the mointored bus, the observed signal changes sharply. Thus, wavefronts of traveling waves can be represented by the corner points on digital image of waveshape. The busbar of critical substation equipped with transient current traveling wave recorders can be considered as a rich node, and this multi-line connection feature determines the polarity differ between the reflection waves from fault point and refraction waves of remote busbar, and also determines the low amplitude of disturbance caused by reflection waves from end of the healthy lines [3]. Therefore, the subsequent surges reflected from faulted point presents the regular change in amplitude and slope attenuation, this makes the distinction of fault reflection waves can be realized via extracting the corner points which meets certain constraint of angle and amplitude.

Harris corner detector

Harris corner detector is based on the local auto-correlation function of a signal, where the local auto-correlation function measures the local changes of the signal with patches shifted by a small amount in different directions [4]. It has strong invariance to rotation, illumination variation and image noise. The principle of Harris corner detector is stated as follow.

For a digital image I, given a shift (u,v), the auto-correlation function is defined as Eq.6.

$$E(u,v) = \sum_{x,y} w(x,y) \left[I(x+u, y+v) - I(x,y) \right]^2 \tag{6}$$

By approximating the shifted image using Taylor expansion, the function can be described as Eq.7 and Eq.8.

$$E(u,v) \simeq [u,v] \boldsymbol{M} \begin{bmatrix} u \\ v \end{bmatrix} \tag{7}$$

$$\boldsymbol{M} = \sum_{x,y} w(x,y) \begin{bmatrix} I_x^2 & I_x I_y \\ I_x I_y & I_y^2 \end{bmatrix} \tag{8}$$

where, $w(x,y)$ is the Gaussian window; I_x and I_y denotes the partial derivatives in x and y; Matrix $\boldsymbol{M}$ represents the intensity structure of the local neighborhood.

Invariant description can be made according to the eigenvalues of matrix $\boldsymbol{M}$. If both eigenvalues have large positive values, that is, the local autocorrelation function is sharply peaked, then shifts in any direction will increase, thus it means a corner is determined.

In order to avoid the direct computation of eigenvalues of $\boldsymbol{M}$, the cornerness measure is usually implemented as Eq.9.

$$R = \det(\boldsymbol{M}) - k\,\mathrm{trace}^2(\boldsymbol{M}) \tag{9}$$

where, $\det(\boldsymbol{M}) = \lambda_1\lambda_2$; $\mathrm{trace}(\boldsymbol{M}) = \lambda_1 + \lambda_2$; k stands for empirical constant, usually k=0.04~0.15.

Identification of wavefronts based on Harris corner detector

As analyzed before, when traveling wave arrives at the mointered bus, the obvious corner point occurs in the waveshpe. The wavefronts identification in traveling wave fault location can be considered as the detection of corner points on digital image of waveshape, and the corners can be judged by the cornerness measure. However, threshold must be set properly, in order to avoid the detection of false corners which may have a relatively large cornerness value due to noise. Considering the analyzed feature of attenuation in amplitude and slope of the successive waves, additional rules can be formed to eliminate the false corner points and preserve the corners related with initial surge and fault reflection waves. On the basis of this concept, the proposed method is composed by 3 procedures: pretreatment, Harris corner detection, and false corner points elimination.

Pretreatment. Select the faulty phase current and display the waveform in experienced window. The length of the displayed data can be determined according to the time interval of the wave propagates 5 times length of the faulty line. Flip the waveshape if the value of first surge peak is negative, in order to keep the slope of the initial surge always positive.

Harris corner detection. Form the primary corner points set via computing the cornerness measure by using Eq.9, and then calculate the distance and slope between each adjacent corner points.

False corner points elimination. Consider the fact that the initial surge has the strongest amplitude and steepest slope, elimination is implemented with following constraints: i) Length constraint. Preserve the corners of which the distance between two adjacent corners is exceeding the threshold. ii) Slope constraint. Eliminate the successive corners which are steeper than slope of initial surge, preserve the corners of which the angle is close to the initial surge. And then the set of the corner points ordered by horizontal coordinate of the points is finally formed.

Result and discussion

Taking a 220kV transmission system model in PSCAD/EMTDC shown in Fig.2 as an example, The length of the line MN is 100km. The frequency-dependent transmission line model is used and both calculation step and sampling step in simulation are set as 1μs.

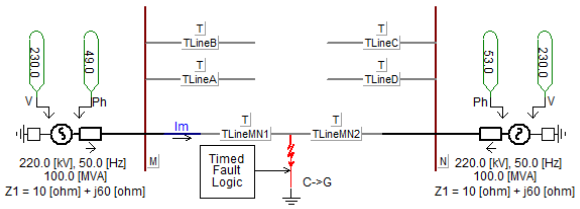

Fig.2 Diagram of simulated 220kV transmission systems in PSCAD/EMTDC

When a C-g fault occurs on the line MN 20km from the bus M, the simulated waveform of each phase current is shown in Fig.3a, and the faulty phase traveling wave current displayed in empirical window is shown in Fig.3b. By implementing Harris corner detection, 19 corner points was detected primarily, as is shown in Fig.4a. And 5 corner points was finally determined by performing false corner points elimination, according to the constraint of the length and slope between two neighbor corner points, as is shown in Fig.4b.

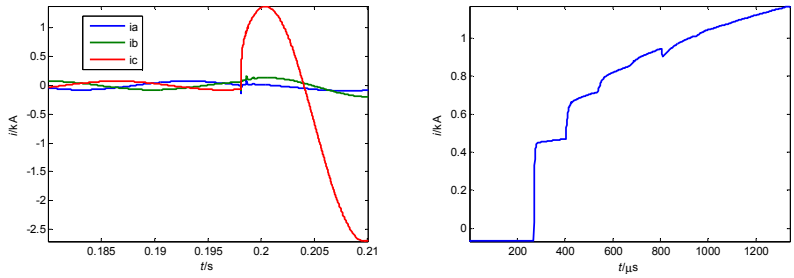

Fig.3: (a) Each phase current in large window (b) Faulty traveling wave current in emprical window

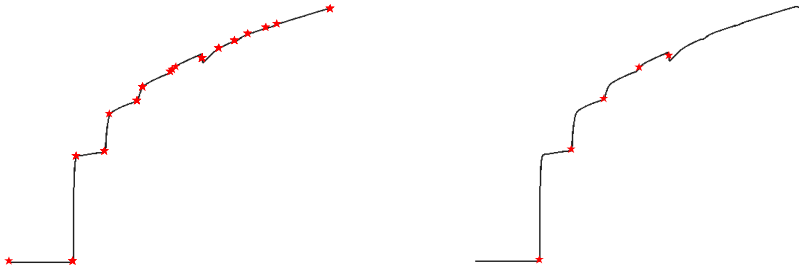

Fig.4: (a) Result of primary corner detection (b) Final result after false corner points elimination

The horizontal pixel of 5 detective corner points is 342,434,527,629,717. The total horizontal pixel of the waveshape is 930, and the total sample data of the wave shape is 1341. Convert the first interval between the two corner points into real time interval: Δt_{M1}=(434-342)/930*1341=132.66μs. Substituing Δt_{M1} and v=0.298km/μs into Eq.1, the calculated fault distance is 19.77km, which is highly close to the 20km simulated fault condition.

Conclusions

Multi-line connection feature determines the polarity differ between the reflection from fault point and refraction of remote busbar, and also determines the low amplitude of disturbance waves caused by refraction from healthy lines. Arrival of traveling waves' wavefronts can be represented by the corner points on digital image of waveshape, and the identification of wavefronts can be implemented by piecisely extracted the corner points via Harris corner detection. False corner points and disturbance waves can be eliminated according to the calculated distance between two neighbour corner points and the angle of the corner point. Digital simulation test shows that the result of fault location is available and reliable according to the wavefronts identified by the proposed method.

Acknowledgements

This work was financially supported by National Natural Science Foundation of China (U1202233).

References

[1] Murari Mohan Saha, Jan Jozef Izykowski and Eugeniusz Rosolowski: Fault Location on Power Networks. Springer, 2010.

[2] Fenado H. Magnago and Ali Abur: Fault Location Using Wavelets. IEEE Trans on Power Delivery, Vol.13(1998), p.1475.

[3] Guangbin Zhang, Hongchun Shu and Jilai Yu: Surge Identification for Travelling Wave Based on Straight Lines Detection Via Hough Transform. Proceedings of the CSEE, Vol.33(2013), p. 165 (in Chinese).

[4] C. Harris and M.J. Stephens: A combined corner and edge detector. Alvey Vision Conference, 1988, p.147.

Advanced Materials Research Vols. 960-961 (2014) pp 1104-1107

doi:10.4028/www.scientific.net/AMR.960-961.1104

Analysis and Simulation of Medium-frequency Power Supply Based on PSCAD

Jianfeng Ren[1, a], Shutao Zhao[1,b], Yutao Xu[1,c] and Dan Jiang[1,d]

[1] School of North China Electric Power University, Baoding 071000, China

[a]869941806@qq.com, [b] 626919972@qq.com, [c]446027120@qq.com, [d]905011351@qq.com

Keywords: Medium-frequency furnace. Rectifier circuit. Inverter circuit. Pulse Width Modulation(PWM) .

Abstract. The work process of medium-frequency power supply is complicated .Its waveform is complex and can not be measured conveniently. Therefore,This paper focuses on the analysis of operating principles and control methods of medium- frequency power supply, to determine its basic structural units.A simulation model of medium-frequency power supply which is controlled by pulse width modulation(PWM) is built with the electromagnetic transient analysis software PSCAD. The simulation and analysis of the medium-frequency power supply circuit are performed on the basis of the model.The simulation waveform can reflect the working process of medium-frequency power supply accurately. So this paper will provide a reliable basis for further research of medium-frequency furnace.

Introduction

In recent years, medium-frequency furnace is widely used in metallurgy, iron and steel industries .Modern and large-scale medium-frequency furnaces, because of its large capacity and high power consumption, have great influence on the electric net-work, especially in generating harmonics, voltage fluctuations and flicker. In addition to affecting stable operation of the thyristor devices and precision instruments, it will also endanger power distribution and a large number of users and itself yield and quality.

Accurate analysis of the electromagnetic working process of medium-frequency furnace is critical to solve a series of power quality problems which are caused by medium-frequency furnace. It also play an important part in analysis and control of power system. Therefore, this paper analyzes the working principle of medium frequency power supply in detail and establish an accurate medium-frequency power supply model. This model will provides a frame of reference for future research.

Medium-frequency Power Supply

Medium-frequency furnace is a "AC - DC - AC" frequency conversion equipment, medium-frequency power supply is a core part of the furnace. firstly, the rectifier circuit of medium-frequency power supply make the three-phase AC voltage which frequency is 50 HZ into a DC voltage. Then, using the smoothing filter to filter out clutter. At last, the DC voltage will be converted into medium-frequency voltage by inverter circuit. Generally ,the frequency of output power is $150 \sim 10000$HZ . The medium-frequency current is flowing though the metal ,at the same time ,electromagnetic induction is generated in internal of metal which will Heat and melt metal.

2.1 Circuit of rectifier and filter

The rectifier circuit of medium-frequency power supply generally adopts three-phase fully-controlled bridge rectifier circuit, which has many advantages ,such as high output voltage and small ripple, high frequency of ripple and fast dynamic response. So the rectifier circuit can help get smooth DC voltage. The three-phase AC voltage(50HZ) will be rectifier into a smooth DC voltage. Then , the DC voltage will be more smooth through the filter reactor. Filter reactor can not

only play the role of gentle pulsating DC voltage, can also have the effect of isolating interference and Impact resistance. When the inverter failed, filter reactor will resist the impact of the surge current and reduce impact damage to the internal circuit device .

The output voltage of three-phase fully-controlled bridge rectifier circuit,as follows:

$$U_d = 2.34 \times U_2 \times \cos\alpha \tag{1}$$

In the formula, U_d :Output DC voltage average; U_2 :Grid phase voltage; α : Trigger phase angle.

2.2 Serial inverting circuit

Generally ,the inverter circuit of medium-frequency power supply is single-phase full-bridge inverting circuit. In this paper, the medium-frequency power supply uses single-phase serial inverting circuit. Its inverter circuit and load circuit is in series form. The load of Inverter circuit can be thought of as L, R, C oscillation circuit, L for inductance oven's inductive coil , R for resistance (usually very small), C for compensating capacitance. Its natural frequency of the load circuit is f_0 , $f_0 \approx 1/2\pi\sqrt{LC}$ .The working frequency of the inverter circuit is higher than the inherent frequency of the load. The load is of low impendence to high frequency harmonic current which is existed in input medium-frequency trapezoidal current. But, it is of high impendence to medium-frequency harmonic current so that the output voltage is close to sine wave. The relationship between the load voltage and output DC voltage as follows: $U_L = 1.11 \times \frac{U_d}{\cos\varphi}$, φ for the load power factor angle.

Simulation Model Based on PSCAD

On the basis of above analysis, medium-frequency power supply model is established in PSCAD, which rectifier circuit is six-pulse rectifier , as shown in Fig. 1.The left part is rectifier circuit, which change three-phase electric power into DC voltage Udc and DC current Idc. The right part is inverting circuit, which change DC voltage Udc2 into AC voltage U0.

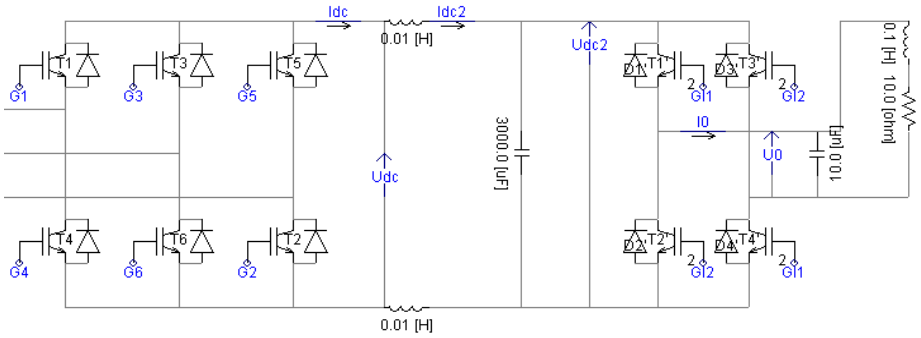

Figure 1. Simulation model of medium-frequency power supply

3.1 Simulation Model of rectifier circuit

The rectifier adopts six-pulse rectifier circuit and three-phase fully-controlled bridge rectifier. The bridge arms are form of serial full-control insulated gate bipolar transistor (IGBT) .IGBT can easily control the current on and off, so the converter bridge has the ability to turn off automatically. IGBT thyristor use default Settings.

The control circuit of rectifier adopts pulse width modulation(PWM) technology to control thyristor on and off .The park transformation converts input three-phase voltage equation into the model in a synchronously rotating reference frame, to realize the decoupling control of active power and reactive power. PWM pulse generating circuit is shown in Fig. 2.

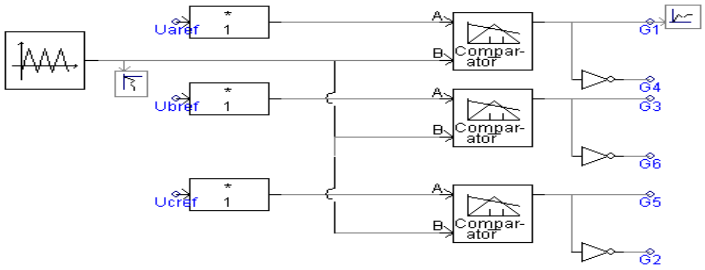

Figure 2. Pulse generating circuit

G1 and G4 are different control signals whose angle are difference of 180 degrees. They control VT1 and VT4 on and off, respectively .In the same way, the G3 and G6, G5 and G2 are two pairs of opposite control signals. The function of these control signals is to control trigger of the six thyristor according to the order of the 1-2-3-4-5-6 cycle. These opposite signals can guarantee that there is a thyristor conductive both in the group of common cathode and anode at the same time, to ensure that the circuit of the load and power supply are always keep open. Below for each other instead of G1 and G4 pulse signal.

Setting the AC line voltage is 380V and frequency is 50 HZ.AC current change into DC voltage though the rectifier circuit. The output DC current waveform is shown in Fig.3.

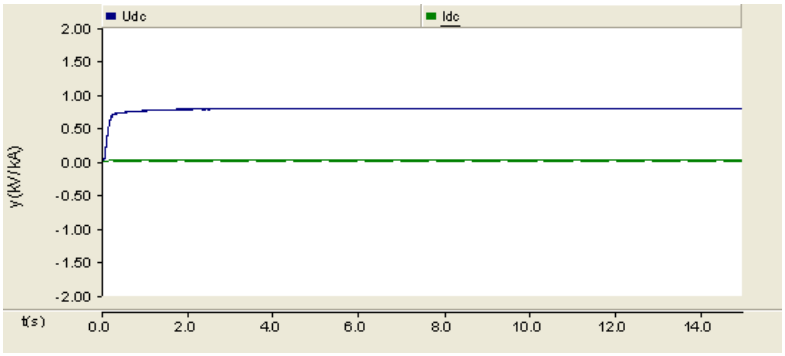

Figure 3. DC power waveforms

From the simulation results we can see that rectifier circuit convert sinusoidal AC voltage and sinusoidal AC current into DC voltage and DC current.The designed rectifier has fulfilled expected operation process successfully and got the eligible output waveform. The designed rectifier and control method is verified correctly.

3.2 Simulation model of inverting circuit

The inverter circuit of medium-frequency power supply is composed of four IGBT thyristors. $VT_1 \sim VT_4$ are controlled by two pairs of opposite control signals .So the frequency of the PWM signal is the work frequency of the inverter circuit.Changing the frequency of the PWM signal can control the frequency of load voltage waveform of medium-frequency furnace. Setting the frequency of the PWM control signal as 500 HZ. The output voltage waveform is shown in Fig. 4.

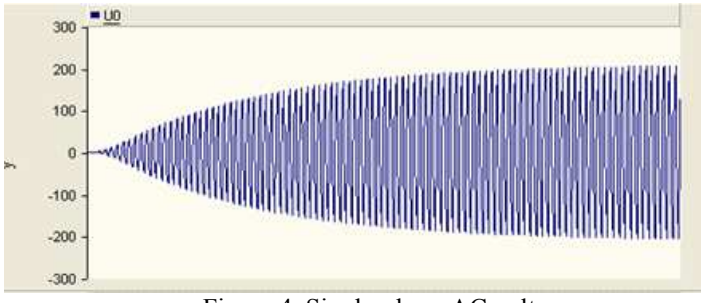

Figure 4. Single-phase AC voltage

When gate voltage on VT1'and VT4' is positive and the voltage on VT2' and VT3' is negative, the VT1' and VT4' is conductive and VT2' and VT3' is off. When VT1 'and VT4' begin to conduct ,IVT1 'and IVT4' will be a positive peak, as shown in Fig. 5. Then, the two currents is not increase gradually, but remains the same.The reason is that there is no serial inductance in inverter circuit.Similarly, when VT2 'and VT3' is off and IVT2' and IVT3 'will be a negative peak.Then the amplitude mutation to a stable value and remains the same, waiting for the arrival of the next peak.

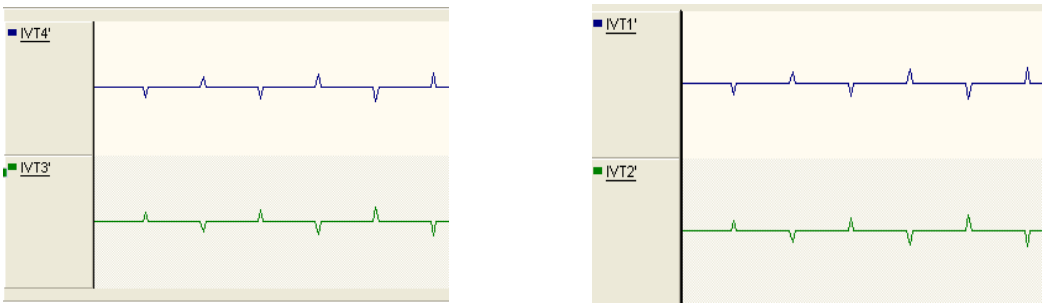

Figure 5. Current waveform of IGBT

Conclusion

In recent years, the use of medium-frequency furnace in China's metallurgy, iron and steel industries has been increasing in number and capacity.A series of power quality problems caused by medium-frequency furnace are increasingly serious.In this paper, the simulation model of six-pulse rectifier medium-frequency power supply is built in PSCAD simulation environment on the basis of analyzing the working principle of medium-frequency furnace. Simulation shows that the result is an accurate reflection of the working process of the medium-frequency power supply.It provides a reference for the later simulation and analysis of medium-frequency furnace .And it also has a certain practical significance.

References

[1] Bin Wu. High Power Inverter and AC Drive [M]. Beijing: China Machine Press, 2008-11-15 . In Chinese.

[2] Naigang Hong. Fundamentals of Electronics Power Technology [M]. Beijing:Tsinghua University Press, 2008 .In Chinese.

[3] Xinghua Tao, Yongdong Li, Min Sun.Research of Cascade PWM Rectifier Control Strategy [J].Electric Drive,2010,40(7):33-36 .In Chinese.

[4] Jianlin Li.Analysis of The Latest Progress in Modern and Large Power Inverter Topology. Inverter World, 2011, (60) : 55-61 .In Chinese.

[5] Peng Dai, Xiao Fu, Qingqing Yuan.A Novel Complex State Current Controller for PWM Rectifier at Very Low Switching Frequency[J].Proceedings of The CSEE, 2011, 31(21)25-31. In Chinese.

[6] Wenting Wang, Jincheng Zhao, Lin Zhang.Simulation of Inverter Circuit Based on PSCAD[J]. Modern Electronic Technology,2011,30(18)190-194 .In Chinese.

Advanced Materials Research Vols. 960-961 (2014) pp 1108-1111

doi:10.4028/www.scientific.net/AMR.960-961.1108

Analysis of UHV Power Grid Operation and Maintenance System Construction and Optimization Strategy----Taking Shan-xi UHV Grid as an Example

DUAN Ding-qiang [1, a], JIAO Li-ting [2, b]

[1] Wuhan Textile University, 1 Fangzhi Road, Wuhan, P. R. China
[2] Shan-xi Province Electric Power Company, 169 Fudong Street, Taiyuan, P. R. China
[a]ddq-tma@163.com, [b]jiaoliting@sx.sgcc.com.cn

Keywords: Shan-xi Province Electric Power Company, Ultra High Voltage, Operation and Maintenance

Abstract: Compared with the traditional power grid, UHV power grid has the characteristic of stronger system function, higher control requirement, and also set a higher request to the daily maintenance management. The operation and maintenance experience of Shan-xi province electric power company on the UHV power grid proved the importance of establishing the new mode of management, strengthen the application of automation technology, ensure the technology and resources guarantee. In order to improve the efficience and quality of UHV power grid operation and maintenance, we should speed up the formulation of operation guidelines for UHV live working and strengthen personnel training and reserve technical talents.

Introduction

Compared with the traditional equipment, great changes have taken place in the operation and maintenance of the UHV equipment, and those conventional methods of maintenance have been unable to meet the changes brought by new demand. At present, the operation of the UHV equipment and maintenance methods are lack of experiences in the world scope, need us to constantly explore and practice operation rules and characteristics, to achieve the upgrade of UHV operation and maintenance technology. This paper takes UHV operation practice of Shan-xi Province Electric Power Company as an example, analyzes operation characteristics of UHV power grid, summarizes experience, and puts forward the corresponding improvement measures.

Demonstration project of 1000kV Jindongnan-Nanyang-Jingmen UHV AC pilot, is China's first UHV power grid, is also the world's first commercial operation UHV transmission line. At present, Shan-xi Province Electric Power Company is responsible for operation and maintenance of 1000kV Changnan line (Shan-xi section), including a UHV electricity substation-Changzhi Substation.

Analysis of the characteristics of UHV power grid operation and maintenance

Compared with the traditional power grid, UHV power grid has the characteristic of stronger system function, higher control requirement, and also set a higher request to the daily maintenance management.

Compared with 500kV power grid, UHV power transmission system has realized bidirectional, full voltage, and high power operation, can suffer all kinds of operation tests, and shows the good dynamic operation characteristics and anti disturbance ability, its function has been enhanced significantly.

The UHV line power fluctuations will not only cause electric power wattless voltage fluctuation, occupy the stability margin, but also cause no power surging trend of nearby power grid and central point of grid voltage fluctuation, that will threat to the safe operation of UHV equipment and power grid, the impact is far from 500kV system can match, so, requirement of stability control on the UHV is much higher than that of 500kV system.

Because of bulk power transmission of UHV power line, once the fault it will have great influence on the whole power grid. For guaranteeing the safe and stable operation of UHV power grid, we must rely on deep technical supervision. If comprehensive technical supervision was adapted to the UHV equipment, we can find the problem earlier and avoid risk timely.

Main practices of Shan-xi Electric Power Company in constructing UHV power grid operation and maintenance system

1. Establish standardized management system

Since the UHV commissioning, Shan-xi Province Power Company follow the principle of "simple, practical and convenient", in accordance with the requirements of "Standardization, modularization and maneuverability", established and improved standardized work instructions of line operation, operation management standards for substation , standardized operating procedures of UHV operation, repair and test work.

2. Implement 1000kV UHV equipment support system

Investigate the hidden danger of equipments regularly. In order to ensure the quality of UHV equipment, Shan-xi Province Electric Power Company made standardized approval processes and procedures for UHV projects, implemented dynamic acceptance and technical data sampling to ensure that the UHV project operates with zero defect. Shan-xi Province Electric Power Company also carried out comprehensive, detailed equipment hidden danger investigation works, aiming to prevent blackouts, personal injury, malignant mis-operation, serious equipment damage, forced outage and so on.

Strengthen the "10+1" equipment monitoring mode. "10" refers to the 10 sets of on-line monitoring equipments, with which operation and maintenance personnel can analyze the running state of the equipment in the control room. "1" is to strengthen the off-line data analysis and management, by the regular manual oil chromatographic analysis, infrared temperature measurement, ultraviolet imaging, gas leakage detection, combined with the analysis of on-line monitoring data, Shan-xi Province Electric Power Company realized the real-time control of UHV equipment health status.

Monitor key operation data with "Hawkeye" device. With the operation data received from the background telemetry, remote, on-line monitoring and on-site inspections, Shan-xi Province Electric Power Company made key data monitoring pictures in the monitoring of the background, put the main data into a simple "Hawkeye" interface, showed the contrast of the measurement, monitoring and standard values in the monitoring interface. By setting the over limit alarm functions, Shan-xi Province Electric Power Company can guarantee the key data "do not go beyond the prescribed limit" and keep the equipment in control.

Carry out state evaluation and improve the operation efficiency. The state evaluation can be divided into regular evaluation and dynamic evaluation. Regular evaluation takes 3 months as a evaluation period, evaluates the UHV power line within the prescribed period. Dynamic evaluation is to revise the results of periodic evaluation dynamically base on the state of operation and power line protection work, so as to optimize the running state of UHV equipments.

3. Optimize 1000kV UHV operation support system

Construct a lean and efficient UHV transmission line patrol management mode. In order to adapt to the regional characteristics and technology characteristics of UHV in Shan-xi, Shan-xi Province Electric Power Company reformed the UHV patrol management mode, combined the expert field patrol and helicopter altitude patrol, established a three-dimensional(expert collaborative patrol line, the helicopter patrol line, cross Patrol) patrol management mode.

Implement the "1+3" substation equipment inspection mode. "1+3" substation equipment inspection mode means that the operation and maintenance personnel make full use of the fixed video camera system, PDA intelligent inspection system, robot intelligent inspection system and carry out a comprehensive, all-round inspection on the equipments of substation, based on regular on-site manual inspection. By this patrol mode, the daily inspection quality of the equipment can be improved.

4. Strengthen the 1000kV UHV emergency system

Establish the UHV "four in one" intensive care system. According to the principle of "cost savings and efficiency improving", Shan-xi Province Electric Power Company established the "four in one" special care system, which is composed of the operation companies, equipment manufacturers, technical supervision companies, engineering installation and construction companies. The special care system includes the normal interaction system with the construction team near the UHV transmission line, the priority supply system of emergency material with equipment factory, and the assistance mechanism of technology supervision with Shan-xi Electric Power Research Institute. By the special care system, Shan-xi Province Electric Power Company can integrate all emergency resources effectively, optimize the management of repair spare parts, and realize the emergency repair seamless docking and all-weather rapid reaction.

Create the "4+1" security system. 1000kV UHV Changzhi Substation security system is composed of "high voltage pulse electronic fence", "building and equipment access control system", "the 68 roads industrial video surveillance system", "24 security cameras" and "8 security personnels". The "4+1" security system can ensure 24 hours inspection and video without intermittent, besides that, its security cameras have the image capture function, can automatically alarm under abnormal circumstances. Such multiple means can ensure that the substation security work has no danger of anything going wrong.

Difficulties and problems in maintenance of UHV transmission line

Line environment is complex and maintenance is difficult. In southeastern of Shan-xi province, topography and micro meteorological areas are widely distributed, but special design was not applied to adopt to the significant characteristics of UHV running environment, so the equipments in UHV power grid cannot withstand natural disasters and external damage, risks of line fault caused by bad weather conditions and external damage still exists. Line construction and illegal coal-bed methane mining in 1000kV Changnan line area is increasing, especially, in the area that UHV line pass through, there are many large scale forest farm and the forest coverage rate has reached more than 40%, straw burning occurred from time to time raises the possibility of large area fire greatly, that may cause some threat to the stable operation of UHV power grid.

Lack standardized live working rules. The difficulty of live working on 1000kV UHV transmission line is the high voltage, high operational altitude and large weight of insulator string. At present, there is no live working rules for 1000kV UHV transmission line, no matter the electric field distribution, area of operation, safe distance, and the insulation of finite length, are to be determined through simulation of strict test, which cause delays and extra costs.

Conclusions

Although Shan-xi province electric power company has accumulated rich experiences in UHV power grid maintenance, but in order to improve the efficiency and quality of UHV transmission line operation, it still needs to further strengthen the construction of operation and maintenance system for UHV power system, optimize the operation management mode.

Investigate risks of UHV transmission line, revise state diagram of line channel dynamically, evaluate the line state, and determine the risk points about key time and key section. In addition, according to the seasonal characteristics, special state inspection for special areas should be organized and the state inspection should be differentiated.

Speed up the formulation of operation guidelines for UHV live working. In order to standardize the UHV power grid live working rules, standards for UHV should be developed as soon as possible, some related requirements need to be clear. Thus, we can save the operation cost, reduce the incidence of accidents in operation and improve the efficiency of maintenance.

Strengthen personnel training and reserve technical talents. With the UHV grid operation technology advances, electronic equipments will play a more important role in the operation and maintenance of UHV power grid, but the basic function of technical personnel will never change. Therefore, we should make full use of existing intelligent systems, such as robot intelligent inspection system, fixed infrared temperature measurement system, at the same time, we should pay more attention to the talent team construction, strengthen training of related professional knowledge and skills, reserve specialized personnel, aiming to meet the needs of operation and maintenance work.

Reference

[1] J. Arrillaga: High Voltage Direct Current Transmission (Peter Peregrines Ltd, London 1983)

[2] Naidoon, Ijumbanm: International Conference on Power System Technology (2004), p.1327~1332

[3] Liu Zhen-ya: Maintenance and Detection of UHV DC Transmission Line (China Power Press, Beijing 2009)(In Chinese)

[4] Shu Yin-biao, Zhang Wen-liang, Zhou Xiao-xin et al: Chinese Journal of Electrical Engineering, Vol. 34(2007), p.1~6 (In Chinese)

[5] Zhao Biao, Shi Xue-fei, Zheng Yan, Li Jing-ru, and Zhang Hao-yu: Proceedings of the International Conference of UHV Transmission Technology(2009) (In Chinese)

[6] Kang Yu-bin, Bian Yu-ping: East China Electric Power (2011), p.114-116 (In Chinese)

[7] Ye Meng, Cao Hai-yan and Ma Guo-peng:Southern Power System(2008), p.43-46 (In Chinese)

[8] Shu Yin-biao, Hu Yi: High Voltage Engineering, Vol. 33(2007), p.1~4 (In Chinese)

Advanced Materials Research Vols. 960-961 (2014) pp 1112-1115

doi:10.4028/www.scientific.net/AMR.960-961.1112

Estimation of significant number of simultaneously failed elements during power system security calculations

Sergey AleksandrovichGusev

Ural Federal University, 620002, Russia, Yekaterinburg, Mira, 19

sergeyalexgusev@gmail.com

Keywords: Power system reliability, security calculations, contingency analysis,simultaneous failures, combination of simultaneously failed elements,n-1 criterion, lost load damage.

Abstract. Nowadays contingency analysis being a part of a power system security calculations is a mandatory procedure for a short-term operational stage of the electrical power system (EPS). Nevertheless, there are still a lot of problems, concerning security calculations. For instance, recent studies have shown necessity to consider simultaneous failures of several power system elements during contingency analysis. This brings complexity and voluminosity of security calculations to the new level.On the one hand, analysis of all possible contingency combinations results in unreasonably high computing time. On the other hand, many contingency combinations, especially with verylarge number of simultaneously failed elements (SFE), have little impact on overall result of security estimation due to very low probability of such combinations. This paper presents novel mathematical algorithm allowing estimation of significant number of simultaneously failed elements (SNSFE). Proposed algorithm was tested on the 14-bus IEEE reliability test system. Results show adequate accuracy of the technique and also confirm the necessity to simulate simultaneous failures of several network elements.

Introduction

It is possible to point out three types of reliability, depending on the system of assumptions andapplied mathematical tool: diagram reliability (structural reliability), balance reliability (adequacy) and regime reliability (security).

In terms of structural reliability (SR), there is no failure if at least one conducting path connecting the power supplying node with the node under analysis exists [1]. In other words, it is assumed that tie capacities are unlimited. Also, security restrictions, such as voltage bounds, are ignored.Thus, diagram reliability allows analyzing reliability of power system network in general or, in other words, reliability of power system topology.

From mathematical point of view, the main goal of adequacy is to identify probabilistic characteristics (such as distributive function, frequency, expected value, variance) of power (or energy) shortage in a separated concentrated power system connected with other systems through tie lines with limited capacity [2]. Basing on these characteristics, it is possible to calculate lost load damage (LLD) expected value(EV), hence, to solve the investment problem. Therefore, balance reliability calculations are necessary to justify investments into power system.

Regime reliability (RR), in turn, defines capability of EPS to work without deviation of state parameters (SP), such as nodal voltages, power flows and thermal capacities out of permissible boundaries, after random disturbances, such as failure of transformer, power line or generator.As a result, RRaims to protect system from total outageand to minimize overall LLD EVas it will be noted further.

Security calculation problem

Security problem consists in simulation of possible failures and analysis of resulting post-contingency states. If the failure results in SP boundaries violation, in order to recover permissible SP, it is necessary to implement control actions (CA).These CA may include adjustment of transformer ratios, actual and reactive generation, and the state change of static capacitor banks, static compensators and hydro generators. In the absence of spare capacity, it is necessary to cut off

energy consumption. In this case, the optimal cutting problem is solved, according to the criterion of minimal LLD. Resulting damage, with a certain weighing coefficient defined by probability of the failure includes in EV of overall damage, which is one of the most important security indices.

As a matter of fact, RR problem results in multiple calculations of post-contingency states, where one or several elements are assumed to fail.The number of SFE depends on the calculating criterion $n-m$, where n is the total number of elements and m is the number of SFE. Global experience shows the necessity to analyze post-contingency states in accordance with $n-2$ or even $n-3$ criteria [3]. This is determined by the fact that maximum of LLD EV, generally, corresponds to 2 or 3 simultaneous failures.Recent studies have shown that in certain power systems number of analyzed SFE has to be even higher [4].

The key problem connected with the number of analyzed SFE is the extremely growing computational time.Simulation of simultaneous failures significantly complicates the security estimation procedure, due to the very rapidly increasing number of calculations. Indeed, the number of calculations increases in accordance with binomial coefficient:

$$C_n^k = \frac{n!}{k! \cdot (n-k)!}, \tag{1}$$

where$n$ is the total number of network elements, k is the number of SFE.

For instance,analysis ofpower system of a medium size containing about 100nodes and 150 branchesfor one, two and three SFEwould require 250, 31 125 and 2 573 000 computations correspondingly.

Thus, full contingency search results in impossibly high computing time. On the other hand, many contingency combinations have little impact on overall EV of LLD, due to the very low probability of such combinations. Therefore, it would be very useful to estimate significant number of SFE (SNSFE).

Significant number of simultaneously failed elements calculating technique

SNSFE value may be estimated, basing on maximum LLD criterion. EV of overall LLD is defined as follows:

$$D = \sum_{S_i \in S} \mathcal{P}_i D_i, \tag{2}$$

where $S = \{S_i\}$ is a set of all possible contingency combinations; $\mathcal{P}_i$ is the probability of combination S_i; D_i is EV of state i.

Let D^{max} is the maximum damage, corresponding to the most unfavorable combination of SFE. In this case, the following inequality is valid:

$$D < D^{max} \sum_{S_i \in S} \mathcal{P}_i. \tag{3}$$

In the idealized case, when all network elements have the same failure probability q, for instance $q = q^{max}$, each combination may be defined by the number of failed elements k. Probability of such state defines as follows:

$$\mathcal{P}_i = C_n^k q^k p^{n-k}, \tag{4}$$

whereC_n^k is binominal coefficient, defined according to eqn. (1).

Substituting of eqn. (3) to inequality (2) results in:

$$D < D^{max} \sum_{k=0}^{n} C_n^k q^k p^{n-k}. \quad (5)$$

The sum in the right part of inequality (5) may be presented as two sums, corresponding to significant and insignificant contingency sets:

$$D < D^{max} \left(\sum_{k=0}^{m} C_n^k q^k p^{n-k} + \sum_{k=m+1}^{n} C_n^k q^k p^{n-k} \right), \quad (6)$$

where$m$ is SNSFE in significant contingency set.

Inequality (6) may be presented as follows:

$$D < D^{max} \left(B(m,n,q) + \tilde{B}(m,n,q) \right) = D^{max} B(m,n,q) + \varepsilon, \quad (7)$$

where$B(m,n,q)$ is integral function of binominal distribution (IFBD); $\tilde{B}(m,n,q)$ is co-function of binominal distribution (CFBD); ε is permissible damage calculation error (PDCE).

According to inequality (7) PDCE determines as:

$$\varepsilon = D^{max} \tilde{B}(m,n,q). \quad (8)$$

Thus, permissible value of CFBD is defined as:

$$\tilde{B}(m,n,q) = \frac{\varepsilon}{D^{max}}. \quad (9)$$

Eqn. (9) allows finding SNSFE m as probability quintile, meeting eqn. (9).

Several rude assumptions, connected with LLD EV and probability of failure, have been made during development of eqn. (9). A more precise solution may be obtainediteratively.

The first approximation of maximum LLD D^{max} is calculated by the assumption that SNSFE m equals to two or three, depending on the analyzed network. This is based on the fact that, probably, maximum of LLD EV corresponds to two or three simultaneous failures. A new value of SNSFE obtained according to eqn. (9),corrects initial SNSFE and iterative calculating procedure runs again.

It's worth noting that branch failure probability is significantly higher than node failure probability. Thus, it may be reasonable to estimate SNSFE separately for nodes and branches and then find a weighted value of SNSFE, where the number of nodes (or branches) stands for the weight of node SNFSFE (branch SNSFE):

$$m = \frac{m^{nd} n^{nd} + m^{br} n^{br}}{n^{nd} + n^{br}}, \quad (10)$$

wherem^{nd} and m^{br} are the number of node and branch SNSFE correspondingly; n^{nd} and n^{br} are the number of nodes and branches in the network correspondingly.

Case study

The proposed technique was tested on the 14-bus IEEE reliability test system. Initial data was elaborated with element failure probabilities and node lost load damages. Failure probability was set to 0.01 and 0.1 for nodes and branches correspondingly. LLD for all nodes was set to 1 relative unit (r. u.). Initial approximation of SNSFE was 2.PDCE was set to 1% D^{max} and 0,1% D^{max} for branch and node calculations correspondingly. As a result, node SNSFE was 2 and branch SNSFE was

5.Weighted value of SNSFE was 3.76. Since SNSFE is calculated according to maximum criterion,fractional part of SNSFE may be ignored. Therefore, with high degree of accuracy, it is possible to say that maximum of LLD EV corresponds to 3 SFE. Since resulting SNSFE was different from the initial, second iteration was necessary. At the second iteration node SNSFE was 2 and branch SNSFE was 6. The weighted value of SNSFE was 4.35. The third iteration didn't change the resulting SNSFE. So, the final value of SNSFE was 4.

The proposed technique was verified by full contingency search. Its results are presented in table 1.

Table 1: The results of full contingency search.

Number of simultaneously failing elements	1	2	3	4	5
Lost load damage expected value,[r.u. per year]	270.98	839.21	1111.04	934.21	219.03
Computing time, [min.]	0.25	5.26	123.51	552.20	3709.87

As it is clearly seen from table 1 maximum of LLD EV corresponds to 3 SFE and SNSFE is 4. So resulting SNSFE totally corresponds to estimated SNSFE. Hence, it is possible to say that proposed technique is accurate enough.

Summary

Number of simultaneously failed elements is one of the key issues in security calculations.On the one hand, maximum of LLD EV, generally, corresponds to simultaneous failure of several power system elements. On the other hand, many contingency combinations have a little impact on overall EV of LLD, due to the very low probability of such combinations. Full contingency search results in unreasonably high computing time. This paper presents technique estimating significant number of simultaneously failed elements almost without additional computational load. The proposed technique was tested on the 14-bus IEEE reliability test system. Results show adequate accuracy of the technique and confirm the necessity to simulate simultaneous failures of network elements.

Acknowledgements

This research project has been supported by UrFU under the Framework Programme of development of UrFU through the «Young scientists UrFU» competition.

References

[1] V.P.Oboskalov: *Power systems structure reliability*(UrFU,Russia 2012).

[2] V.P.Oboskalov: *Power systems balance reliability*(USTU-UPI, Russia 2002).

[3] N.A.Manov, M.V.Hohlov, Y.J.Chukreev:*Meshed power system reliability estimation models and approaches*(Komi science center of Uro RAN, Russia 2010).

[4] S.A.Gusev, V.P.Oboskalov, in:Estimation of optimal simulation depth for simultaneously failing elements during security calculations. Proc. of the 4th Int. Conf. On Youth Point of View to Power Industry (2013), vol.1, pp. 127-130.

Advanced Materials Research Vols. 960-961 (2014) pp 1116-1119

doi:10.4028/www.scientific.net/AMR.960-961.1116

PFC Voltage Loop of Visual Design

Ping Liu[1, a], Wanyu Diao[2, b], Huanhuan Shi[3, c], Shengyan Huang[4, d]

[1]Xiamen University Tan Kah Kee College, Zhangzhou, Fujian 363105, China

[a]152638961@qq.com, [b]rob10085@gmail.com

Keywords: Power factor; Voltage loop parameter; Visualization

Abstract. Build a mathematical model by using the voltage loop of UCC28019 to get open loop transfer function. And use MATLAB to obtain variable range of voltage loop parameter when system is stable, in the mean time, use system time domain performance as objective function to optimize the parameter, based on system stability. The user can get better parameters on the three-dimensional image clearly and directly, for there is no complex formula and theoretical derivation in process of optimizing. Hardware circuit experiments verify the effectiveness of the proposed method.

Introduction

Improve the effective utilization of energy and green environmental protection is the theme of this century, and power electronic devices harmonic pollution and low power factor problem get more and more attention. In this paper, a power supply which output power is 72W is designed: the input AC voltage (*Uin*) range from 20*V* to 30*V*, the output DC voltage (*Uout*) is 36*V*±0.1*V*, the power factor is above 0.97.To get high output power, we select a PFC device--UCC28019.It can obtain the unity power factor with minimal harmonic distortion and employ double closed-loop structure of the voltage and current in the internal circuit. The parameter being set appropriate or not directly determine the performance of the system. By using three-dimensional (3D)visualization algorithm towards Power Factor Correction (PFC) voltage loop periphery parameter , the design in this paper can get the distribution of concerned information and degree of difficulty won't be raised while system order improve which is intuitive, simple and practical.

Control System Analysis

Switching mode power supply based on UCC28019 includes power circuit and control circuit.The parameters of the power circuit will not be discussed here. The function and implementation mechanism of control circuit are mainly analyzed as followed.

(1)The circuit can assure input current waveform and input voltages in same phase without distortion and harmonic. There is a current loop inside UCC28019 whose duty circle can be adjusted according to period quickly and can follow the input voltage sine wave changing when work in closed-loop.

(2)The circuit can keep the output voltage constant when load current changes. Compared sampling voltage with reference voltage of the internal operational amplifier inside voltage loop, UCC28019 can ensure the output voltage as a constant by adjusting amplitude of reference current sine waveform.

(3)The difficulty of the design as well as the focus of this paper is the input voltage compensation should be variational to keep input power being equal to the output power when input voltage changes by adjusting input current RMS. If the input voltage varies in a long period, there will be a changing trend for output power. Though the external voltage control loop will compensate this change, the parameter is not a simple linear control. In order to make the loop stability, unity gain crossover frequency must be kept lower than the zero frequency in right half plane. Therefore in the compensating network, large drift of unity gain crossover frequency need a slowly fall which may produce a poor transient response. In order to compensate for this effect, a very low band-pass filter is designed in the voltage loop to compensate input voltage RMS. As a result of correspondence

between frequency domain index and time domain index, compensation device parameters of voltage loop is designed in this paper aiming at time domain performance.

Model Voltage Loop

Look up the inside structure of UCC28019 [1], the voltage loop block diagram is shown in Fig.1.

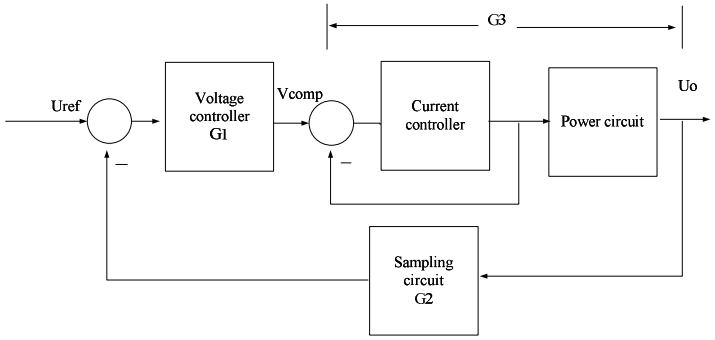

Fig.1 Voltage loop block diagram

Fig. 2 is voltage controller circuit, Fig. 3 is sampling circuit

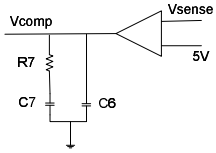

Fig.2 Voltage controller circuit

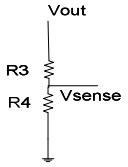

Fig.3 Sampling circuit

From Fig. 2, Fig. 3, calculate module transfer function

$$G_2 = Vsense / V_{out} = R_4 / (R_3 + R_4) = 50K / (50K + 310K) = 5/36 \quad (1)$$

$$G_1 = V_{comp} / V_{sense} = (1 + sR_7C_7)gmv / (C_6 + C_7)s(1 + sR_7C_6C_7 / (C_6 + C_7)) \quad (2)$$

gmv is a constant whose value is $42 \times 10^{-6} s$.

G3 is the inherent part of system. [1]

$$G_3 = (M_3 V_{out} / M_1 M_2) / (s / w_1 + 1) = 49.5 / (s / 10.7 + 1) \quad (3)$$

$$w_3 = K_{FQ} M_1 M_2 V_{inrms}^3 / K_1 R_2 V_{out}^3 C_{out}, M_3 = 0.512, M_1 = 0.484, M_1 M_2 = 0.372, K_1 = 7, V_{inrms} = 24, \mathrm{V}_{out} = 36$$

In order to be convenient for the analysis, here, take *Vsense* as the output of the system, then the voltage loop is unit feedback system and the open-loop transfer function is:

$$G = 6.875(1 + sR_7C_7)gmv / (s / 10.7 + 1)(C_6 + C_7)s(1 + sR_7C_6C_7 / (C_6 + C_7)) \quad (4)$$

The value of C_6 decides the length of the system boot time. Set the C_6 = 0.1 uf here.

Parameters Visualization Design

Use MATLAB to obtain variable range of voltage loop parameter when system is stable. Use time domain performance as objective function to draw 3D surface diagram and 3D contour diagram and find right parameter correspond to a nice system performance from diagram conveniently and directly. Parameter *R7, C7*optimization program block diagram is shown in Fig.4.

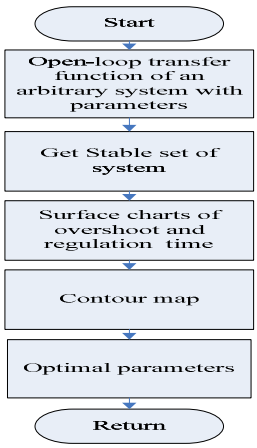

Fig.4 Program flow charts

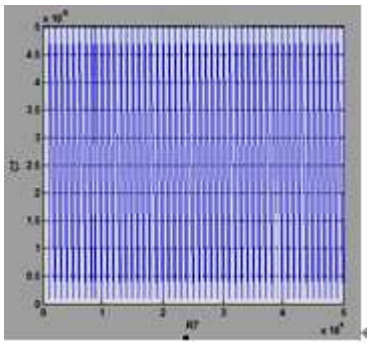

Fig.5 R6,C7 stable sets

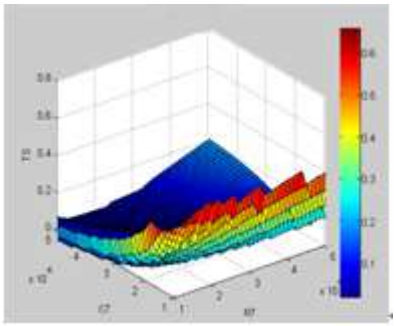

Fig.6 Regulation time 3D surface diagram

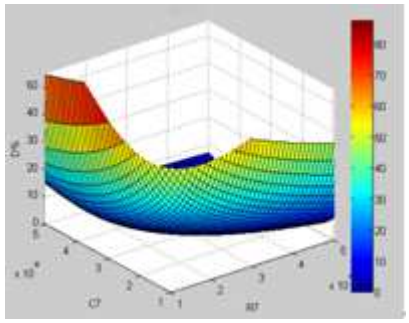

Fig.7 Overshoot 3D surface diagram

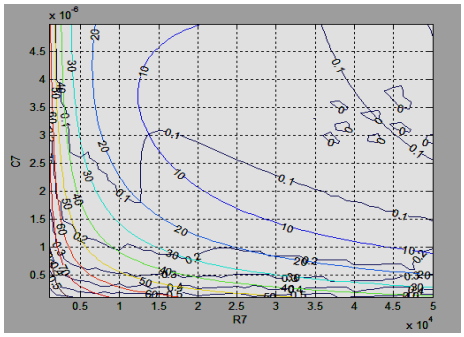

Fig.8 Regulation time and overshoot 3D contour diagram

(1) Parameter Stable Set

Get the system characteristic equation from system open-loop transfer function G and then getsystem characteristic root. Combined with judging condition of system stability, the range of R7, C7 when system is stable can be obtained rapidly. R6,C7 stable set is shown in Fig.5.

(2) Dynamic Performance Optimization

According to the system transfer function, the step response of the system can be obtained and then can acquire the relation of overshoot, regulation time and parameter R7, C7.These messages can be get from Fig.6, Fig.7, and Fig.8.

1) The result of optimization parameters often is not limited to a finite number of analytical solutions; instead, it is countless numerical solution of certain scope.

2) Using data visualization can clearly show cause-and-effect relation between the parameter and effect of the design in a global scope.

3) Taking different data sets can visualize the problems of Contradictory and restrict to each other.

Select parameters correspond to the crossing point when regulation time is 0.1 s and overshoot is zero in Fig.8:R7=4.2k, C7=3.4uf.select R7=4.2k, C7=3uf actually.

Experimental Results and Analysis

According to the power supply design requirements, the maximum input current RMS is $3.83A$. The input current RMS peak value is $5.41A$ .the input current maximum average value is $3.45A$ .Input inductance current maximum peak value is $5.95A$ .Then calculate related parameter based on the value showed above. Hardware circuit rectifier bridge output connect a low ESR 155 CBB capacitor to filter out high frequency components of the rectifier output voltage ; Boost inductance choose circular silicon aluminum iron core, select the inductance value as $128\mu H$;Select two 4700 μF capacitors in parallel as output filter capacitor C_{out} ;filter capacitor C_9 is $0.47\mu F$ .The value of the resistance R_9 on the input voltage VIN side is 10K. R_6 is *170K*. The capacitor C_8 on the input voltage side is $10\mu F$ .The capacitor of current loop C_5 is *1nF*.The hardware circuit is shown in Fig.9.The measured wave form of rectifier bridge output side is shown in Fig.10, it shows that current waveform synchronize with tracking voltage waveform, which achieve high power factor output, the power factor is above 0.987.

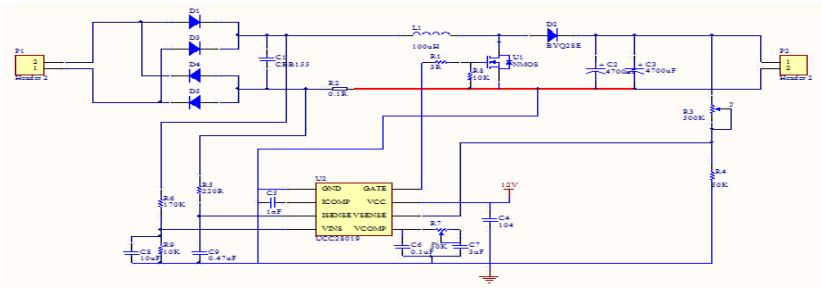

Fig.9 Hardware main circuit diagram

Fig.10 Rectifier bridge Voltage and current output

Conclusions

PFC voltage loop of 3 D visualization algorithm design in this paper based on stable set, use time domain performance as the objective function, is intuitive, simple, and practical. Hardware circuit experiments verify the effectiveness of the proposed method. The method can be transplanted to other circuit system by simple modification, therefore, it worth high application.

References

[1]TEXAS INSTRUMENTS.8-Pin Conduction Mode (CCM) PFC controller [EB/OL].(2007-12-01). http.//focus.ti.com/lit/ds/symlink/ucc28109.pdf.

[2] Hu Shousong:*Automatic Control Theory*.(Chinese Science Press, P.R.of China2007).

[3]Wu Jiaju, LiuWen.computer simulation, 2011, 28(7):272-275.

[4]IEC.Electromagnetic compatibility (EMC)-patr3-2: Limits for harmonic current emission (equipment input current≤16A per phase)[S].IEC 61000-3-2:2005.

Advanced Materials Research Vols. 960-961 (2014) pp 1120-1123

doi:10.4028/www.scientific.net/AMR.960-961.1120

Research of Power Flow Distribution Evenness Based on Entropy

Jin Bingjie[1,a], Zhang Buhan[1,b], Wang Ke[2,c], Deng Weisi[1,d], Zeng Dan[2,e], Zhang Kaimin[1,f], Shao Jian[1,g], Ge Tengyu[1,h]

[1]State Key Laboratory of Advanced Electromagnetic Engineering and Technology

Huazhong University of Science and Technology, Wuhan, China

[2]China Electric Power Research Institute (Nanjing), Nanjing, China

[a]loveice_2008@126.com,[b]zhangbuhan@mail.hust.edu.cn,[c]wangke@epri.sgcc.com.cn, [d]289041419@qq.com,[e]zengdan@epri.sgcc.com.cn,[f]565265960@qq.com, [g]hustceeeshao@gmail.com,[h]gety163@163.com

Keywords: power flow balance; entropy; power system static security assessment; limit violations.

Abstract. Research of power flow evenness has great significance for grid steady state analysis. This paper researched for a method for power flow evenness analysis through entropy theory. According to current power flow distribution and branch power limits, the branch load ratio distribution could be obtained, and the power flow entropy was calculated based on discrete information entropy theory. The study case indicates that the power flow entropy effectively describes the power flow evenness. With certain system load level, the system security level will be dramatically declined when power flow evenness reduces to a certain level, which is demonstrated in the case meanwhile. Power flow evenness analysis based on entropy theory is applicable in power system static security assessment.

Introduction

Modern large scale power system has the characteristics of interconnectedness, dynamic nature, nonlinearity, randomness and real time performance [1]. With the access of intermittent energy, power system in the environment of "source-grid-load" interactive operation [2] is exposed to more uncertainties. Under this circumstance, the various states of system power flow distribution in real time influences the security of power system operation. Consequently, research for power flow distribution evenness is necessary and significant. Power flow evenness analysis is an effective method for grid steady state analysis. Branch power off-limit is likely to appear at low power flow evenness, and large scale cascading failure might be caused further [3]. In power system static security assessment, power flow evenness analysis is conducive to optimizing the power flow distribution and reducing system operation risk. Extracting the power flow distribution characteristic quantity and establishing power flow evenness evaluation indicator is a great challenge for power system analysis. Research on methods for power flow evenness analysis is significant and impending.

With the development of the information theory, entropy is gradually applied in fields such as available transmission capacity evaluation, optimal power flow, probabilistic load flow and fault detection [4-7]. Entropy describes the degree of system disorder. The higher the degree of a system in order, the smaller the entropy is. It could serve as an important parameter for power flow evenness description. Therefore, the application of entropy to power system flow evenness analysis has practical significance and feasibility.

This paper researched for power flow evenness analysis through entropy theory. According to branch load ratio distribution, the power flow entropy index was calculated based on discrete information entropy theory. Power flow distribution evenness analysis could be used to power system static security assessment considering N-1 branch outage and node power injection disturbance.

Information Entropy Theory

Entropy describes the degree of system disorder. With the development of entropy theory, it leads in more specific definition and becomes an important parameter in various disciplines and fields.

Basic theory description. When entropy was led in information theory, the concept of information entropy was proposed, which solved the problem of information quantization. The more orderly a system, the less the information entropy is; conversely, the less orderly a system, the higher the information entropy is. On this basis, information entropy could be regarded as measurement of system ordering degree. The definition of discrete information entropy is shown in Eq. 1:

$$H = -C\sum_{i=1}^{N} p(x_i)\ln(p(x_i)) \tag{1}$$

Where, C is a constant; $p(x_i)$ is the probability when the value of information source x is x_i. As:

$$\lim_{p\to 0+} p\ln p = 0 \tag{2}$$

When $p(x_i) = 0$, $p(x_i)\ln(p(x_i))=0$.

Properties of entropy. The information entropy has the following properties.

Non-negativity: Entropy is greater than or equal to zero, namely $H_s \geq 0$;

Extremum: According to probability theory, $H \leq \ln N$. N is the total number of events within the system. Meanwhile, if and only if $p_1 = p_2 = ... = p_N$, the equal sign works, when the system has maximum entropy;

Symmetry: $H(p_1,...,p_n)$ is independent of the order of $p_1,...,p_n$.

Power Flow Distribution Evenness Analysis Based on Entropy

When the system is in a certain load level, may all line load ratios are near the average load ratio. May also some line load ratios are greater than the average and meanwhile some other line load ratios are far less than the average. Different power flow distribution evenness might lead to different results. Quantify the power flow evenness by entropy theory in the following steps.

Calculate the load ratio of each line: For a certain operating state of the system, calculate the load ratio of each line by Eq. 3:

$$\mu_i = \left|P_i^0 / P_i^{\max}\right| \quad i = 1,2,...,N_l \tag{3}$$

Where, $P_i^{\max}$ is the active power transmission capacity of line i; P_i^0 is the active power of line i in current operating state; μ_i is the load ratio of line i; N_l is the number of system lines.

Load ratio distribution statistics: Set a constant sequence $U=\{U_1,U_2,...,U_k,...,U_{N_l+1}\}$, n_k is the number of lines which $\mu_i \in (U_k,U_{k+1}]$. Obtain the probability for lines distributed in each load ratio intervals:

$$p(k) = n_k / \sum_{k=1}^{N_l} n_k \tag{4}$$

Where, $p(k)$ refers to the probability for the lines distributed in $\mu_i \in (U_k,U_{k+1}]$.

Calculate system power flow entropy by Eq. 1. Where, $p(k)$ is $p(x_i)$, and N_l is N.

Analysis for different system operation states: On account of the great influence of system load level on its safe operation, power flow evenness analysis should be processed in the same load level. Calculate the average load ratio for each operation states by Eq. 5.

$$\overline{\mu} = \sum_{i=1}^{N_l}\left|P_i^0\right| / \sum_{i=1}^{N_l} P_i^{\max} \tag{5}$$

Put the operations with similar load level in the same class, and analyze the influence of power flow entropy on system security under a certain load level.

When all line load ratios lie in the same interval, the power flow entropy is 0. This is the most orderly state of power flow distribution, when lines of large capacity take heavy load, and lines of small capacity take lesser load. When there are no 2 line load ratios in the same interval, the power flow entropy reaches maximum:

$$H_{\max} = -C \ln(1/N_l) \tag{6}$$

This is the most uneven state of power flow distribution. In this instance, lines of large load ratio will be overload in all probability when encounter disturbance, even cause cascading failure. And the capacity of lines in very low load ratio has not been fully used.

Case Study

In IEEE300 case, operating states in different system load levels and power flow entropies were studied. For each operating state, the average number of branch power limit violations under N-1 branch outage was calculated and displayed in Fig. 1. In this paper, $U=\{0,1/N_l,2/N_l,...,1\}$ and $C=\ln 10$.

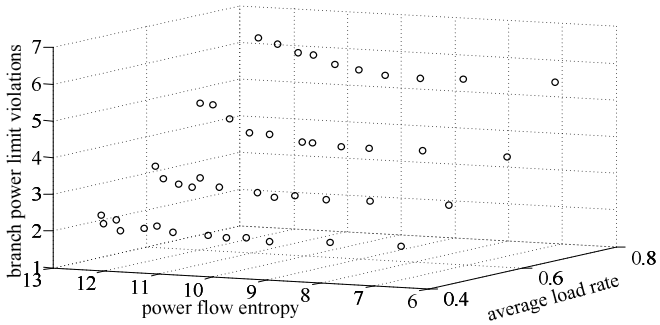

Fig.1. 3D figure of system security under N-1 branch outage in different power flow entropy

In Fig. 1, the average number of branch power limit violations under N-1 branch outage is related to the power flow entropy and system load level, and increases accordingly. In a certain system load level, when power flow entropy is less than a specific value (namely the power flow distribution is more even), the number of branch power limit violations basically remains unchanged. Otherwise, the system security will dramatically decline. Namely, the number of branch power limit violations will increase. This case study indicates that power flow entropy influences the system operating security.

In IEEE300 case, operating states in different system load levels and power flow entropies were studied. For each operating state, the average number of branch power limit violations under node power injection fluctuations (20%) was calculated and displayed in Fig. 2.

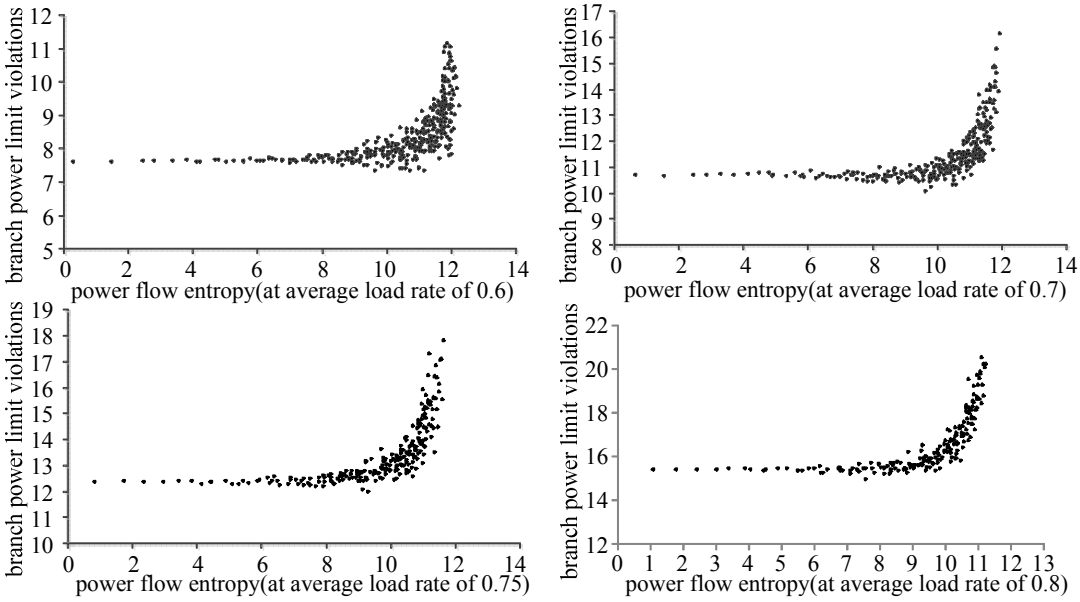

Fig.2. System security under node power injection fluctuations in different power flow entropy

From Fig. 2, similar conclusions to Fig. 1 could be received. The average number of branch power limit violations under node power injection fluctuations is related to the power flow entropy and system load level, and increases accordingly. In a certain system load level, when power flow entropy is less than a specific value, the number of branch power limit violations basicly remains unchanged. Otherwise, the system security will dramatically decline, which indicates that the power flow entropy influences the system operating security.

Conclusions

This paper proposed a method for power flow evenness analysis based on entropy theory. According to branch load ratio distribution, the power flow entropy index was calculated based on discrete information entropy theory. The study case indicates that power flow entropy effectively describes the power flow evenness and system security is related to the power flow entropy and system load level. Power system security will be likely to decrease with low power flow evenness.

Conclusions were received from this paper that power flow evenness analysis based on entropy theory is applicable in power system static security assessment. In certain system structure and load level, system operating security could be improved by optimizing the power flow distribution. In power system static security assessment, power flow evenness analysis is conducive to optimizing the power flow distribution and reducing system operation risk.

Acknowledgements

This work was supported by State Grid Corporation of China(the Study of Steady-state Analysis Method in the 'Source-Grid-Load' Interactive Environment) (dz71-13-036).

References:

[1] CAO Yijia, WANG Guangzeng. "Research on power system complexity and related topics", *Electric Power Automation Equipment*, vol.30, no.2, pp.5-9, 2010(In Chinese).

[2] YAO Jianguo, YANG Shengchun, WANG Ke, YANG Zhenglin, SONG Xiaofang. "Concept and Research Framework of Smart Grid "Source-Grid-Load" Interactive Operation and Control", *Automation of Electric Power Systems*, vol.36, no.21, pp.1-6, 2012(In Chinese).

[3] CAO Yijia, WANG Guanagzeng, CAO Lihua, DING Lijie. "An Identification Model for Self-organized Criticality of Power Grid Based on Power Flow Entropy", *Automation of Electric Power Systems*, vol.25, no.7, pp.1-6, 2011(In Chinese).

[4] ZHENG Yanan, ZHOU Ming, LI Gengyin. "An Information Entropy Based Contingency Enumeration Approach for Available Transfer Capability Assessment", *Power System Technology*, vol.35, no.11, pp.107-113, 2011(In Chinese).

[5] Li Zhimin, Li Weixing, Wang Yongjian. "Surrogate Constraint Algorithm fo Optimal Power Flow Based on the Entropy Theory", *Automation of Electric Power Systems*, vol.25, no.11, pp.28-31, 2001(In Chinese).

[6] Trevor Williams, Curran Crawford. "Probabilistic Load Flow Modeling Comparing Maximum Entropy and Gram-Charlier Probability Density Function Reconstructions", *IEEE Trans. on Power Systems*, vol.28, no.1, pp.272-280, 2013.

[7] HE Zheng-you, CAI Yu-mei, QIAN Qing-quan. "A Study of Wavelet Entropy Theory and its Application in Electric Power System Fault Detection", *Proceedings of the CSEE*, vol.25, no.5, pp.38-43, 2005(In Chinese).

Advanced Materials Research Vols. 960-961 (2014) pp 1124-1127

doi:10.4028/www.scientific.net/AMR.960-961.1124

Research on Dynamic Stability Improvement by Using STATCOM in Power System

Li Siyu[1,a], Huang Jiadong[1,b], Ma Cui[2,c]

[1]School of Electrical and Electronic Engineering, North China Electric Power University, Baoding 071003, China

[2]Power Supply Bureau of Yi County, Baoding 074200, China

[a]guojihuiyitougao@163.com, [b]huajd5188@sina.com, [c]ugao@163.com

Keywords: static voltage stability, SVC, STATCOM, reactive power compensation

Abstract. Nowadays, unbalanced loads or nonlinear loads produce a bad effect on the power quality of utility mains. Also, it is necessary for reactive power to be compensated because the most of industrial loads is inductive and make a lagging displacement power factor. Reactive power compensation utilizing STATCOM is one of the most important methods to improve power quality. In this paper, the technical feature of STATCOM is introduced and then a comparison with SVC is made. The effect of STATCOM on static voltage stability in power systems has been studied. Based on PSD-BPA software, effect of STATCOM is determined. Static voltage stability margin enhancement using STATCOM and SVC is compared in the modified IEEE 14-bus test system. Test results show very encouraging result.

Introduction

Recently, most of the critical loads in an industrial low voltage AC system have an unbalanced and/or nonlinear characteristic because it is a single-phase rectifier with a capacitor or thyristor-based three phase rectifier. The unbalanced and nonlinear characteristic of the load has an undesirable effect on the power quality of input utility mains and adjacent load side. Therefore, reactive power should be generated and compensated properly to improve the power quality of input utility mains.

Voltage instability is mainly associated with reactive power imbalance. The loadability of a bus in the power system depends on the reactive power support that the bus can receive from the system as the system approaches the maximum loading point (MLP) or voltage collapse point, both real and reactive power losses increase rapidly. Therefore, the reactive power supports have to be local and adequate.

Typically, the response time and the bandwidth of the closed voltage regulation loop of the STATCOM which is a shunt-connected synchronous voltage source are significantly better than those of the SVC which is a shunt-connected reactive admittance. Consequently, STATCOM can be more effective than SVC in an industrial low voltage AC system.

In this paper, operational principle and basic control loop of STATCOM are described. Also, control loop to compensate the unbalanced load and nonlinear load is discussed in detail. Its performance of the control loop of STATCOM in unbalanced and/or nonlinear load conditions is verified by PSIM simulation software. These results can be used for the software implementation in the prototype STATCOM system

System configuration of STATCOM

STATCOM based on VSI (voltage source inverter) is a synchronous voltage source connected to the utility mains in parallel through a link reactor (L1) as shown in Fig. 1(a).
Switching device can be GTO for high voltage, high power application or can be IGBT for low voltage, low power application. It is necessary to note that the size of dc capacitor in STATCOM is considerably smaller than the general ac capacitor for direct power factor compensation.

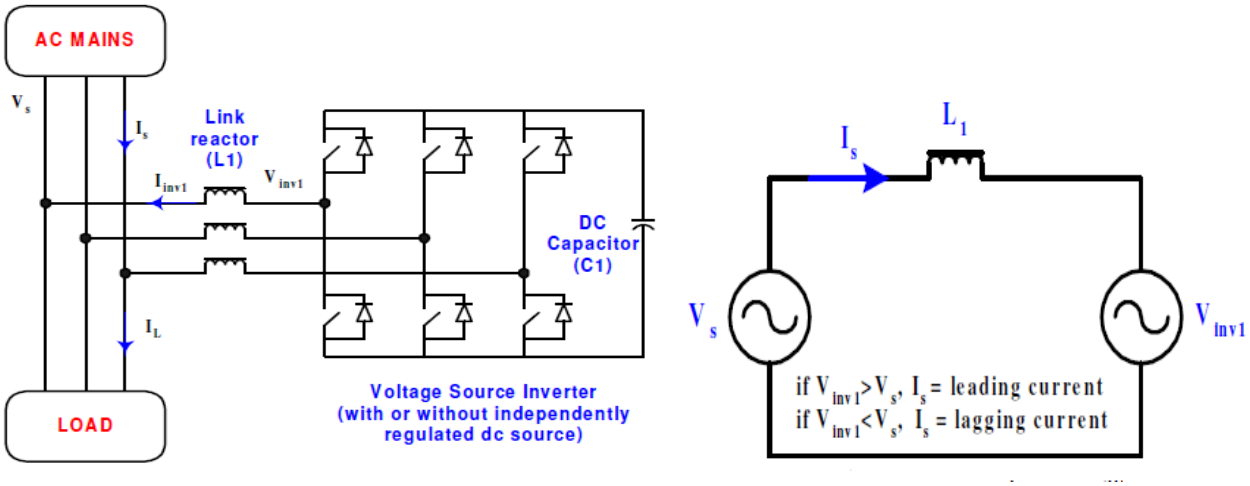

(a) Configuration (b) Single phase equivalent circuit

Fig.1 STATCOM system based on VSI

Comparison between STATCOM and SVC

There are two type of controllable reactive power (shunt) generator. One is a static var compensator (SVC) whose output is adjusted discontinuously to inject or absorb the reactive current. It can be treated as a shunt-connected reactive admittance. For example, thyristor-controlled reactor (TCR), thyristor-switched reactor (TSR) and thyristor-switched capacitor (TSC) are typical SVC system. The other one is a static synchronous compensator (STATCOM) whose output is adjusted continuously to inject or absorb the reactive current. It can be treated as a shunt-connected synchronous voltage source. Comparison results between SVC and STATCOM is shown in Table 1.

Tab.1 Comparison between SVC & STATCOM

Items	SVC	STATCOM
Continuity of control	Discontinuous	Continuous
Control	Phase control	PWM Control
Phase delay (max.)	0.5 ~ 1 cycle	Very few
Low-order harmonics	Much	Small
Installation space	Large.	Small
Size of reactive components	Bigger	Small
Loss	Bigger	Very small
Response	Slow	Very fast

Generally, STATCOM is more effective and more rapid compensator than SVC regarding to V-I characteristic, V-Q characteristic, transient stability and response time [1]. Many researches about the analysis and design method of STATCOM system had been already done at reference [2~4].

Simulation of Applying STATCOM

IEEE 14-bus test system as shown in Fig. 2 is used for voltage stability studies. The test system consists of 5 generators and 11 PQ bus (or load bus). The simulations use BPA simulation software. BPA is power system analysis software, which can be used to investigate voltage stability of the test power system.

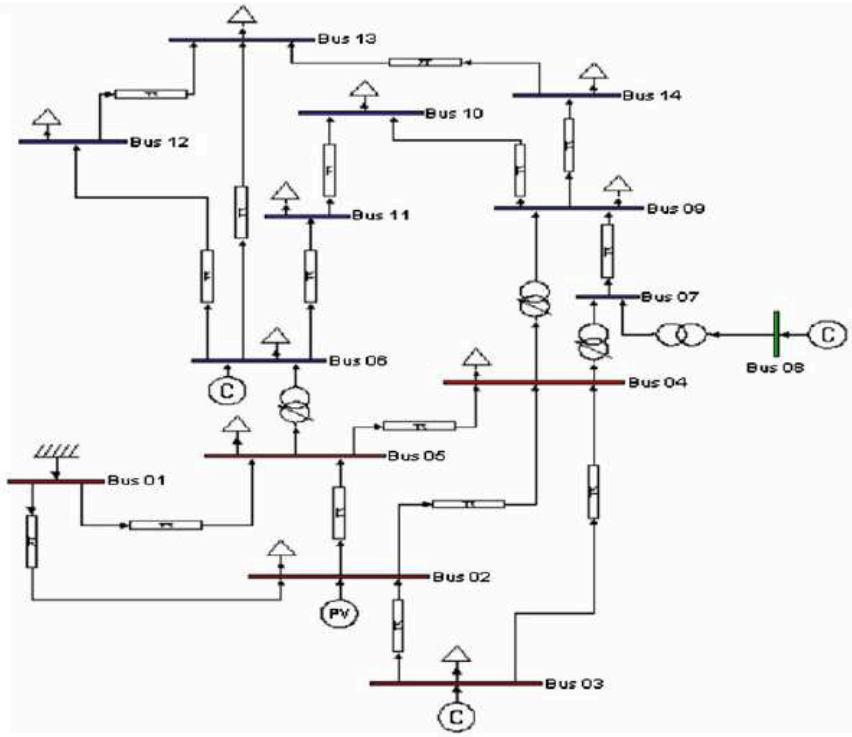

Fig. 2 IEEE 14-bus test system

The behavior of the test system with and without FACTS devices (SVC and STATCOM) under different loading conditions is studied. The location of the FACTS controllers is determined through bifurcation analysis. A typical PQ model is used for the loads and the generator limits are ignored. Voltage stability analysis is performed by starting from an initial stable operating point and then increasing the loads by a factor λ until singular point of power flow linearization is reached. The loads are defined as:

$$P_{\mathrm{L}} = P_{\mathrm{L0}}(1+\lambda) \tag{1}$$

$$Q_{\mathrm{L}} = Q_{\mathrm{L0}}(1+\lambda) \tag{2}$$

Loss of loads in system will happen after three-phase short-circuit faults. It is a serious threat to the system's normal production and causes great economic losses. In this section, a scheme of reactive power compensation is proposed that install SVC or STATCOM in low-voltage side of the transformer in power grid. A simulation is needed to research the effectiveness of reactive power compensation utilizing SVC and STATCOM and make a comparison between SVC and STATCOM. The installed location and capacity of STATCOM should be determined. Usually, placing adequate reactive power support at the weakest bus enhances static voltage stability margins.

Then, we replace SVC with STATCOM to do the same simulation experiment. It turns out that the needed capacity of STATCOM is less than SVC. A comparison between SVC and STATCOM can be made. Voltage changes of 'Bus 7' with the same capacity of SVC or STATCOM is shown in Fig. 3. Obviously, the bus has a faster rate of voltage recovery by installing STATCOM than SVC.

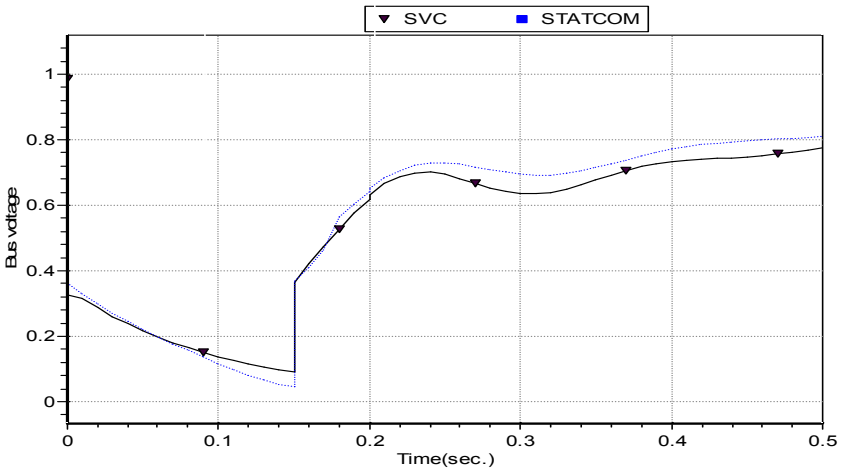

Fig. 3 Voltage changes of 'Bus 7'

Conclusion

In this paper, voltage stability assessment of the modified IEEE 14-bus test system with STATCOM and SVC is studied. STATCOM provides higher voltage stability than SVC. Two types of controllable reactive power compensator discussed. A reasonable simulation experiment is established to test and verify the dynamic stability improvement by using STATCOM. Test results show very encouraging result. Generally, STATCOM is more effective and more rapid compensator than SVC regarding to Tab.1and Fig. 3.

Consequently, STATCOM can be more effective than SVC in an industrial low voltage AC system. However, it costs more by installing STATCOM than SVC.

References

[1] N. G. Hingorani and L. Gyugyi,, "Understanding FACTS", IEEE Press, 1999.

[2] Luis T. Moran, Phoivos D. Ziogas and Geza Joos, "Analysis and Design of a Three-Phase Synchronous Solid-state Var Compensator", IEEE Trans. Ind. Appl., vol. 25, no.4 , pp. 598-608, July/Aug., 1989.

[3] Hassan Ali Kojori, Shashi B. Dewan and J. Douglas Lavers, "A Large-Scale PWM Solid-State Synchronous Condenser", IEEE Trans. on Ind. Appl., vol. 28, no. 1, Jan./Feb., 1992.

[4] Sode-Yome A, Mithulananthan N (2004) Comparison of shuntcapacitor, SVC and STATCOM in static voltage stability margin enhancement. Int J Electr Eng Educ (UMIST) 41(2):158–171

Advanced Materials Research Vols. 960-961 (2014) pp 1128-1133

doi:10.4028/www.scientific.net/AMR.960-961.1128

The Coordinated Control Strategy for Generator-transformer's Voltage Regulation

Yuze Zhang [1, a], Wenying Liu[2, b], Shuxin Li[3], Weizhou Wang[4], Fuchao Liu[5] and Jingjing Zheng[6]

[1,2,3] School of Electrical and Electronic Engineering, North China Electric Power University, Beijing, China

[4,5,6] Gansu Electric Power Research Institute ,Gansu, China

[a]zyz100rcs@ncepu.edu.cn, [b]liuwenyingls@sina.com

Keywords: excitation control; OLTC; coordinated control; phase-advancement operation; smart grid.

Abstract. Nowadays the main electrical wiring in medium-size and large-size thermal power units is mostly unit wiring. In the quarter of small reactive power load, some generators need to work in phase-lag operation during the daytime and in phase-advancement operation at night to meet the demand of voltage quality of their plant's high-voltage side. This operation, however, will lower the voltage of auxiliary power and do harm to system's stability. This paper proposes a kind of coordinated control strategy for generator-transformer's voltage regulation. In this strategy, the main transformer should be on-load tap charger and the controller regulate the generator voltage and transformation ratio simultaneously when needed, thus the voltage quality of both high-voltage side and auxiliary power side can be insured and the generator no longer work in phase-advancement operation. This control strategy can be a meaningful proposal for AVC in smart grid in the future. Simulation result shows the stability and reliability of the proposed control strategy .

Introduction

Nowadays the main electrical wiring in medium-size and large-size thermal power units is mostly unit wiring. In the quarter of small reactive power load, some generators need to work in phase-lag operation during the daytime and in phase-advancement operation at night or even work in phase-advancement operation all-time to meet the demand of voltage quality of their plant's high-voltage side[1-3]. This operation can lower the voltage of the end of transmission lines, but also lower the voltage of auxiliary power and affect the normal operation of various types of auxiliar machines as a side effect. In addition, multiple units work in phase-advancement operation simultaneously can reduce the stability of the power system[4].

Since the 1950s, the excitation control strategy developed from classical control theory to modern control theory[5-7]. Many experts and scholars have proposed numerous control strategies based on different theories in recent years. However, their proposals can't solve the above-mentioned problem as the control objectives of their proposals are all to maintain the generator voltage[8-11]. This paper proposes a kind of coordinated control strategy for generator-transformer's voltage regulation. In this strategy, the main transformer in corresponding plants should be on-load tap charger and the controller regulate the generator voltage and transformation ratio simultaneously when needed. Regulating the transformation ratio is the process of coarse adjustment while regulating the generator voltage is precise adjustment. Two parties work together to meet the demand of voltage quality of both plant's high-voltage side and auxiliary power side under the condition that the generator no longer need to work in phase-advancement operation. The proposed control strategy makes full use of OLTC[12,13], and can be an meaningful proposal for AVC. Simulation result shows that the proposed control strategy is stable and effective.

Mathematical model

Consider the generator-transformer unit as shown in Fig.1, the transformer is elected to be on-load tap charger.

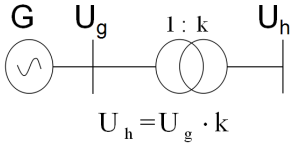

Fig.1 Simplified diagram of a generator-transformer unit

At present most generation units are equipped with static self-excitation system in China, which obtain power from the generator and transform it into field current by silicon controlled rectifier. The control loop of static self-excitation system consist of measuring part, excitation controller, power unit and generator, as shown in Fig.2[14].

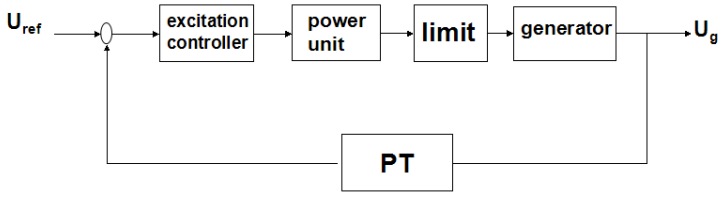

Fig.2 Control loop of static self-excitation system

The transfer functions of PT and static self-excitation controller are $G_t(s)=\frac{K_r}{T_r s+1}$, $G_e(s)=\frac{T_1 s+1}{T_2 s+1}\cdot\frac{T_3 s+1}{T_4 s+1}\cdot\frac{K_a}{T_a s+1}$ respectively while the restriction of exciting voltage can be represented as a limiting link. The process of generator voltage changing with field current can be considered as a gain link $G_g(s)=K_g$, as its transition time is shorter than the simulation step.

The mathematical model of OLTC can be established using mechanism modeling methods. For simple, the transfer function of tap position indicating is $G_l(s)=\frac{1}{T_l s+1}$ and the process of transformer's tap adjustment can be expressed as $G_w(s)=\frac{1}{T_w s+1}$.

Control Principle

Control objectives. The coordinated control strategy for generator-transformer's voltage regulation must insure the voltage quality of plant's high-voltage side under the condition that the generator won't work in phase-advancement operation. Refereeing to DL/T650-1998 <Specification for potential source static exciter systems for large turbine generators>, the control objectives of the proposed strategy can be formulated as follows: ①the generator won't work in phase-advancement operation all-weather; ②the response time of voltage of plant's high-voltage side should be lesss than 0.1s; ③the overshoot of step response should be less than 2%～4% of the setpoint while the damping ratio less than 0.1, regulating time less than 1s and the steady-state error less than 0.5kV.

Control scheme. During the process of adjusting the voltage of the plant's high-voltage side, regulating the transformation ratio is coarse adjustment for the sake that the transformer tap can't be adjusted continuously while regulating the generator voltage is precise adjustment as the generator voltage can be. For a given regulating process, assume that the initial value and setpoint of voltage of the plant's high-voltage side are U_{h0} and U_h, those of generator voltage are U_{g0} and U_g and those of transformation ratio are k_0 and k.Obviously $U_{h0}=U_{g0}\cdot k$ if ignore the voltage loss of transformer. The adjustable range of the stator voltage is (U_{gmin},U_{gmax}) when the generator works in phase-lag operation. In other words,if the generator works in phase-advancement operation, that

voltage will below U_{gmin}.The adjustable range of transformation ratio is $(k_{\min},k_{\max})$.In one case that the predetermined changing amount of voltage of the plant's high-voltage side is less than $(U_{\text{gmax}}\text{-}U_{\text{g0}})\cdot k_0$ or $(U_{\text{g0}}\text{-}U_{\text{gmin}})\cdot k_0$, regulating the generator voltage merely can achieve the control target and the generator won't work in phase-advancement operation.In the other case that the predetermined changing amount is greater than that, both the generator voltage and the transformation ratio should be adjusted to insure that the generator won't work in phase-advancement operation.To estimate the changing amounts of generator voltage and transformation ratio in the control loop preliminary, a coordination coefficient denoted as A can be used assuming that there is a positive correlation between that changing amounts. The size of A can be tunning according to the given control requirement. Obviously the equation has a unique solution

$$\begin{cases} U_{\text{g}}\cdot k=U_{\text{h}} \\ \dfrac{|k\text{-}k_0|}{|U_{\text{g}}\text{-}U_{\text{g0}}|}=A \end{cases}$$

which shows the rough changing amounts of generator voltage and transformation ratio.The controller select the transformer tap position which is closest to the above-mentioned solution, and then regulate the generator voltage precisely on that basis.

Construct a control loop as shown in Fig.3. Calculate the values of $(U_{\text{gmax}}\text{-}U_{\text{g0}})\cdot k_0$ and $(U_{\text{g0}}\text{-}U_{\text{gmin}})\cdot k_0$ first and dispose a logic trigger device in the control system. If the setpoint of voltage of the plant's high-voltage side is between $U_{g\min}\times k_0$ and $U_{g\max}\times k_0$, the controller trigger the small control loop and regulate the generator voltage merely while the transformation ratio is constant; if the setpoint is out of that range, the controller will trigger the large control loop and regulate the generator voltage and transformation ratio simultaneously. In the large loop, the circuit

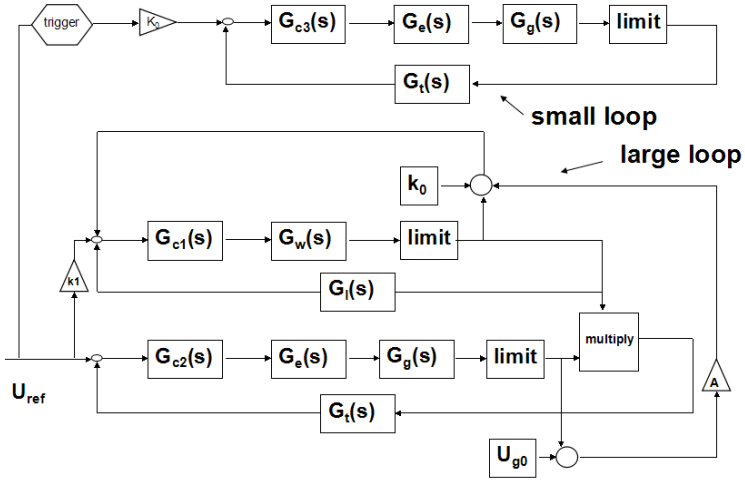

Fig.3 Control block diagram

that involves the excitation controller is main loop while that involve the transformer tap controller is vice loop. The small loop only include one controller. Those controllers are all proportional-integral controllers and successive approximation approach can be adopted to tunning the two controllers in the large loop. For simple, $G_g(s)=K_g$ in the main loop can be amalgamated into $G_e(s)$,so the generalized controlled object becomes to $G_e(s)=\dfrac{T_1s+1}{T_2s+1}\cdot\dfrac{T_3s+1}{T_4s+1}\cdot\dfrac{K_a}{T_as+1}$.

Stability analysis of control system. To calculate the input - output transfer function of this system, the control block diagram should be simplified as shown in Fig.4.

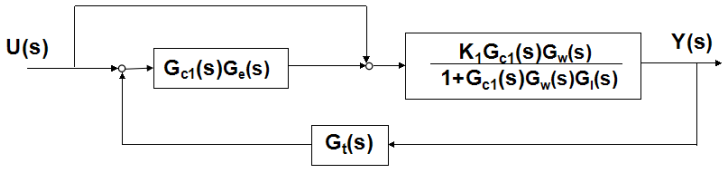

Fig.4 Simplified control block diagram

The input - output transfer function of this system is

$$H(s)=\frac{Y(s)}{U(s)}=[1+G_{c2}(s)G_e(s)]\cdot\left[\frac{\dfrac{K_1G_{c1}(s)G_w(s)}{1+G_{c1}(s)G_w(s)G_l(s)}}{1+\dfrac{K_1G_{c1}(s)G_{c2}(s)G_w(s)G_e(s)G_t(s)}{1+G_{c1}(s)G_w(s)G_l(s)}}\right]$$

$$=\frac{K_1G_{c1}(s)G_w(s)+K_1G_{c1}(s)G_{c2}(s)G_w(s)G_e(s)}{1+G_{c1}(s)G_w(s)G_l(s)+K_1G_{c1}(s)G_{c2}(s)G_w(s)G_e(s)G_t(s)}$$

It is not hard to verify that the whole system is stable if and only if the above transfer function is stable.

Illustrative examples

Consider a typical 300MW thermal power units, corresponding coefficients are

$T_1=T_2=T_3=T_4$=2.0s , K_a=20 , T_a=0.02s , T_t=0.03s , T_w=0.02s , T_l=0.02s

$U_{g\min}=19.5\text{kV}$, $U_{g\max}=20.5\text{kV}$

The scale of voltage tap of the main transformer is $\pm2\times2.5\%$ .The initial values of generator voltage and transformation ratio are $U_{g0}=20\text{kV}$ and k_0=12.1. Tuning the coordination coefficient and the three PI controllers as

$$A=0.32,\quad K_{c1}(s)=0.002+\frac{0.1}{s},\quad K_{c2}(s)=0.05+\frac{0.6}{s},\quad K_{c3}(s)=0.018+\frac{0.6}{s}$$

The simulation model of control system is shown in Fig.5

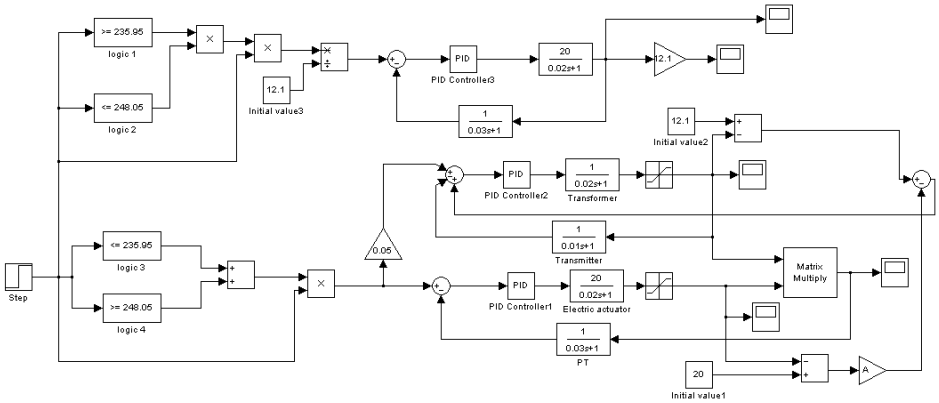

Fig.5 Simulation model

Firstly, consider the situation that the setpoint of voltage of the plant's high-voltage side is between 235.95kV and 248.05kV. The step response of generator voltage is shown in Fig.6 when

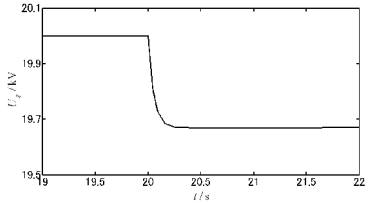

Fig.6 Step response when the setpoint is 238kV

the setpoint is set to be 238kV. The delay time and settling time are $t_d = 0.0389\text{s}$ and $t_s = 0.168\text{s}$ respectively. There is no overshoot, oscillation and any steady-state error. The adjustment process meets the control requirements as the damping ratio is larger than 1.

Then consider that the setpoint is lower than 235.95kV. The voltage tap of the main transformer should be adjusted to $235.95/20\text{kV}$ and the generator voltage should be 19.665kV if setting the setpoint to be 232kV. The step response of voltage of the plant's high-voltage side, generator voltage and transformation ratio is shown in Fig.7. The delay time and settling time of the

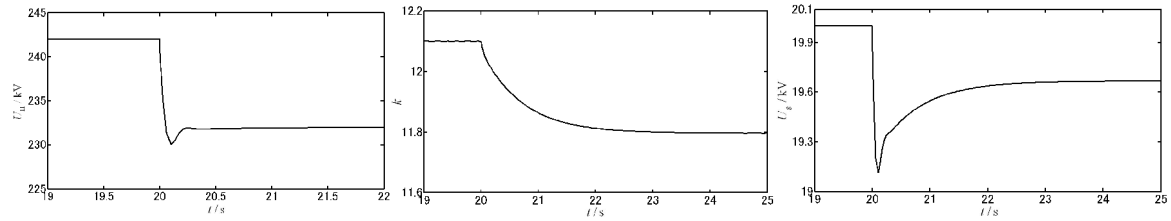

Fig.7 Step response when the setpoint is 232kV

response of voltage of the plant's high-voltage side are $t_d = 0.0193\text{s}$ and $t_s = 0.1815\text{s}$ respectively. The ratio of overshoot than the setpoint value is 1.05% .The steady-state values of transformation ratio and generator voltage are 11.7965 and 19.666kV respectively, which is consistent with the theoretical values. The adjustment process also meets the control requirements as the damping ratio is about 0.9.

The simulation result shows the good accuracy and rapidity of the proposed control system. Calculate the characteristic equation of the closed-loop transfer function as $Q(\text{s}) = 4.8\times10^{-7}\text{s}^7 + 1.36\times10^{-4}\text{s}^6 + 0.0149\text{s}^5 + 0.833\text{s}^4 + 24.5\text{s}^3 + 308.5\text{s}^2 + 121.6\text{s} + 12$

The Eigen values are $\lambda_1 = -1.1185$, $\lambda_{2,3} = -0.3554 \pm 0.3103i$, $\lambda_{4,5} = -0.5$, $\lambda_6 = -0.0023$, $\lambda_7 = -0.0018$ .Obviously the control system is stable as those close-loop poles are all locate in the left half of 's' plane.

Summary

This paper proposes a kind of coordinated control strategy for generator-transformer's voltage regulation. In this strategy, the main transformer should be on-load tap charger and the controller regulate the generator voltage and transformation ratio simultaneously when needed, thus the voltage quality of both high-voltage side and auxiliary power side can be insured and the generator no longer work in phase-advancement operation. This control strategy can be an meaningful proposal for AVC in smart grid in the future. Simulation result shows that the proposed control strategy is stable and effective.On the basis of this paper, bringing the circumstances of each power plant's transformer tap into AVC system is a worthy research topics in the reactive / voltage management area in the future.

Acknowledgements

This work was financially supported by the science and technology major project supported by Gansu Province (1203GKDA009) and the science and technology major project supported National Grid: The research on loss reduction of the power grid based on the coordinated control among source, net and load (National Grid Division [2014] 398).

References

[1] Li Qin,Wen Baijian: *Research of the construction of AVC substation of power plant of Guangdong power grid,* Power System Protection and Control,Vol. 36(2008), p. 38(In Chinese)

[2] LEI Chun-ming,ZHANG Xiao-dong: *The practice of AVC based on the DCS of Huaneng Yueyang power station,* Central China Electric Power,Vol. 3(2007), p. 57(In Chinese)

[3] TANG Jian-hui, ZHANG Li-gang, ZHAO Xiao-liang: *Application of the auto-voltage-control in power plants,* Power System Protection and Control, Vol. 4(2009), p. 32(In Chinese)

[4] LU Chunliang,Ye Lin,DAI Yan: *Influence of leading phase operation of generators in Zhejiang power grid on system stability,* East China Electric Power,Vol. 9(2006), p. 36 (In Chinese)

[5] CHENG Qiming,CHENG Yinman,XUE Yang,HU Xiaoqing: *Development and prospects of excitation control methods for synchronous generator,* Electric Power Automation Equipment,Vol.5(2012), p. 108(In Chinese)

[6] Li Lihua: *Design and Analysis of Synchronous generator excitation control system,* Inner Mongolia Science & Technology and Economy,Vol. 23(2006), p. 105(In Chinese)

[7] Han Yingduo, Xie Xiaorong, Cui Wenjin: *Status quo and future trend in research on synchronous generator excitation control,* J Tsinghua Univ(Sci&Tech),Vol. 41(2001), p. 142 (In Chinese)

[8] RUAN Yang, YUAN Rong-xiang, WAN Li: *Nonlinear robust voltage control for synchronous generators,* Transactions of China Electrotechnical Society,Vol. 9(2012), p. 9 (In Chinese)

[9] He hui: *A Dissertation Submitted in Partial Fulfillment of the Requirements for the Degree of Doctor of Engineering,* Huazhong University of Science and Technology doctoral Thesis(2011)(In Chinese)

[10] Tang Xiaojun: *Study of Intelligent Control for Synchronous Generator Excitation Control System,* Tianjin University master's degree thesis(2004)(In Chinese)

[11] Wang Xihuai, Zheng Tianfu, Xiao Jianmei: *Nonlinear robust excitation control strategy with voltage regulation,* Electric Power Automation Equipment, Vol. 8(2007), p. 38(In Chinese)

[12] WANG Guangliang: *A Survey on Effect of On-Load Tap Changer on the Voltage Stability,* Relay,Vol. 11(2008), p. 79(In Chinese)

[13] XUE Bao-xing: *Study on Impact of OLTC Transformer on Voltage Stability in Power System,* Zhengzhou:Zheng-zhou Univercity(2007)(In Chinese)

[14] Li JiChen: *Design and Application of Modern Synchronous Generator Excitation System,* Beijing:China Electric Power Press(2009)(In Chinese)

Advanced Materials Research Vols. 960-961 (2014) pp 1134-1141

doi:10.4028/www.scientific.net/AMR.960-961.1134

A Gas-turbine with Approximate General Carnot Cycle and Its Performance Prediction

Zhong LI[1], Dalong ZHANG[2, a], Jianfeng Li[3], Dinghua YANG[1, 2], Wenjun QIN[1], Gensheng YANG[1], Xiaolin WANG[1]

[1] Shenhua Group Co.Ltd, Beijing China

[2] Department of Thermal Engineering, Tsinghua University, Beijing, 100084, China

[3] Scientific and Technical Service Center, China Electricity Council, Beijing, 100038

[a]email: zhang_dalong88@163.com

Keywords: Gas-turbine; General Carnot Cycle; Combustion in the Turbine

Abstract. Based on polytrophic process of air compression and gas combustion inside the turbine isothermally, an approximate gas-turbine with General Carnot cycle and relevant implementing schemes are suggested. Its performance was predicted with mathematics model compared with traditional one. The results show that the heat efficiency of the suggested gas turbine is higher than the traditional one. The suggested cycle combines the gas cycle and steam cycle, of which the NOx emission can be easily decreased

Introduction

Advanced gas-turbine is the key equipment of the power equipment in 21 century. In order to improve the thermal efficiency of gas-turbine, conventional methods consist of improving the efficiency of the compressor and turbine, increasing the press ratio, using more advanced material and increasing inlet temperature of turbine. However, it is very difficult to improve the efficiency of compressor and turbine markedly under the existing art and craft of design and manufacture. Improving press ratio was mainly limited by material and power output. More high quality material used in the turbine will increase the cost of gas-turbine obviously. Improving the inlet temperature of turbine requires better thermal defend for gas-turbine, because it is not only need more high temperature endurably material but also increase the flux of the cooling air. Actually, in some aircraft engines, the flux of the cooling air could achieve 10-20% [1] of the whole air flux in the core engine, excessive cooling air will disadvantage for the thermal efficiency. On the other hand, excessive highly turbine inlet temperature caused higher temperature in the combustor, which could reach 2200K now. Under this temperature, the turbine NOx emission increase obviously.

In the cyclic process of the gas-turbine, consuming work will increase in the air compress process because air temperature increase. So spraying water into compressor could decrease the consuming work obviously in the process of air compress, and the air compress process changes into a polytrophic process. The advantage of this method could omit the huge middle-colder and relative system, and simplify the structure of gas-turbine. Li [2] gave an example of SIA-02 type gas-turbine feed on methane, and researched the cycle of the gas-turbine which was sprayed water into stage of compressor. The results showed that spraying water into compressor stages could reduce compressing work, decrease the outlet temperature of compressor, and increase the power output. In addition that, the variation of efficiency of the system related with the flux of spray water. If turbine inlet air temperature keeps unchanging, the efficiency had a maximum value with the increasing flux of spray water, and if power output was constant, the efficiency decreased with the increasing flux of spray water. In fact, there was no regenerator in Li's research, if the regenerator was taken into account, the results may be different.

When high-temperature and high-pressure air in the process of applying work inside the turbine, the air temperature decrease sharply, and this will reduce the air work capacity. But the air work capacity will enhance if air temperature keep constant in the process of applying work, and it will become an isothermal process. In actual gas-turbine, people hope the fuel could combustor rapidly

and completely in combustor, so the thermal-defense of combustion chamber is very difficult because the temperature in the combustion chamber is very high. If we properly decrease temperature of the combustion chamber and make partial fuel jet into turbine to keep combustion. In this situation, the air could expand in turbine and react with the fuel at the same time. The reaction heat could keep a constant air temperature in process of expanding, this will be another direction of increasing the thermal-efficiency of gas-turbine.

Sirignano W A [3][4] researched the affection of applying the combustion inside turbine technology in improving the thrust of unit windward area and dropping fuel consuming of aero-engine. They also compared the combustion inside turbine with conventional aero-engine with or without afterburners, their research indicated that combustion inside turbine could improve the aero-engine performance obviously.

Exhaust temperature of the turbine is very high because of combustion inside turbine, so the regenerator is necessary for the turbine. The temperature of air from compressor will increase after the pre-heating in regenerator and increase further in pre-combustion chamber that in order to satisfy work output and maintain rapid reaction.

From the analyses above, an approximate generality Carnot thermal cycle was proposed: in the air compression process, water was sprayed in at proper position for absorbing the heat quantity generated from compression, this will render air compression easily. After compression, the air pass through the regenerator and flow into pre-combustion chamber and turbine orderly. Then air expand and react with fuel in turbine simultaneously. The exhaust air flows into atmosphere after passing through regenerator to complete the whole thermal cycle. The cycle discussed above is the Approximation General Carnot Cycle (AGCC) which is proposed in this paper. The gas-turbine system applied AGCC is revealed in Fig.1. The key advantage of AGCC is even though the combustion temperature is lower than the conventional Brayton recycle, but the thermal efficiency of AGCC could be the same or higher than the Brayton recycle. Besides that, the lower combustion temperature could restrain the generation of thermal force NOx, so the whole emission of NOx was reduced.

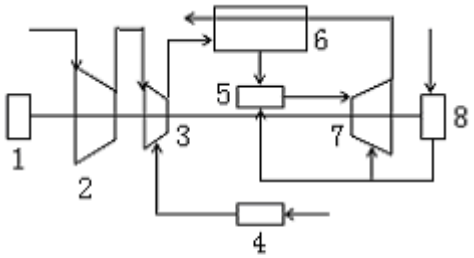

Fig.1 System of Gas-Turbine with an approximate Generality Carnot Cycle

Performance prediction model

According to calculation, the temperature of air arise up to nearly 406k when air is compressed from T_o=298K and P_o=0.1MPa to 0.3MPa after an isentropic compression process. And the water saturation temperature at 0.3MPa Tm is approximate equal to 406K as shown in Fig.2.

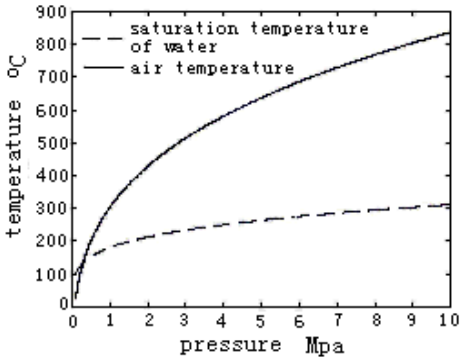

Fig.2 Comparison between saturation temperature of water and air temperature from isentropic compression in same pressure.

As we can see from Fig.2, it is proper to spray water into compressor when air pressure exceed 0.3MPa, because water in compressor change into boiling steam rapidly after 0.3MPa. While pressure is below 0.3MPa, water changes into steam depend on diffusion process mainly. At that condition, the water drop which evaporation incompletely would harm to the compressor blade. Therefore, mathematic model could be established to calculate maximum flux of spray water and the thermal efficiency of the system according to the analysis above. Some assumptions of the model is following:

1) Air and steam can be treated as ideal gas;
2) Air flows into compressor initially without steam.
3) The specific heat of air and steam were constant, and c_p=1.005kJ/(kg·K);
4) Air was compressed by low-pressure compressor from the initial condition of 298K and 0.1MPa, when air pressure exceeds 0.3MPa, high-pressure compressor was used and cooling water was sprayed in.

Fig.3 displays one stage of compress process. η_c is efficiency of compressor, h_a and h'_a are enthalpy of air at inlet and outlet of one stage of compressor. h_{wg} and h'_{wg} are enthalpy of steam at inlet and outlet of one stage of compressor respectively. Δw_i is shaft work that is consumed in one stage of compression, and h_{wl} is enthalpy of water sprayed into one stage compression.

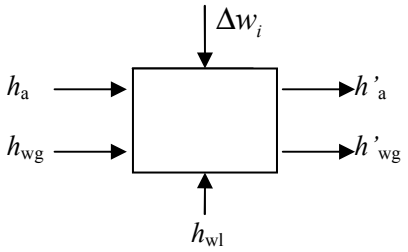

Fig.3 Calculation model of a stage compressor

According to energy conservation:

$$h_a^{'} + m_0 h_{wg}^{'} + q = h_a + m_0 h_{wg} + \Delta w_i \tag{1}$$

In the equation, m_0 is water flux which is sprayed in one kilogram dry air, q is the quantity of heat released from compression that will be absorbed by sprayed water in the process of evaporation:

$$q = \Delta m_i (h_{wg}^{'} - h_{wl}) \tag{2}$$

Supposed polytrophic coefficient is α because air compression is a polytrophic process:

$$T(\pi_1 P) = T(P)\pi_1^{\frac{\alpha-1}{\alpha}} \tag{3}$$

α can be expressed as:

$$\alpha = \ln \pi_1 / \ln \frac{\pi_1 T(P)}{T(\pi_1 P)} \tag{4}$$

Therefore:

$$\Delta w_i = (R + mR_w)\frac{\alpha}{\alpha - 1}T(P)\left(\pi_1^{\frac{\alpha-1}{\alpha}} - 1\right)/\eta_c \tag{5}$$

η_c is the efficiency of compressor.

Consider consuming work of low-pressure compressor which is:

$$w' = \frac{kRT_0}{k-1}\left(\left(P_m/P_0\right)^{\frac{k-1}{k}} - 1\right)/\eta_c \tag{6}$$

So the total work consumed in process of air compression is:

$$w = \sum_{i=1}^{n}\Delta w_i + w' \tag{7}$$

Extra water should be sprayed in before air spraying into high-pressure compressor in order to adjust air temperature at Tm, because the water can absorb part of heat, which come from losing work in the low-pressure compressor. And the extra water needed to adjust air temperature in the high-pressure compressor to Tm should be:

$$\Delta m = w'(1 - \eta_c)/\left(h_{wg|0.3} - h_{wl}\right) \tag{8}$$

$h_{wg|0.3}$ is saturation enthalpy of water at the pressure of P_m, so:

$$m = \sum_{i=1}^{n-1}\Delta m_i + \Delta m \tag{9}$$

After compression, air should pass through the regenerator before spray into pre-chamber. On one hand, the regenerator can increase air temperature to get a better combustion condition; on the other hand, it will decrease thermal loss of exhaust. Suppose P, T are pressure and temperature of compressor outlet, ε and δ are thermal ratio and pressure loss ratio of regenerator, T* is inlet temperature of turbine, respectively. So the quantity of heat should accede to pre-chamber is:

$$Q_1 = \left(c_p + mc_{pw}\right)\left(T^* - T\right)(1 - \varepsilon) \tag{10}$$

The work output quantity of turbine is equal to the heat quantity, because air temperature in turbine is constant:

$$Q_2 = (R + mR_w)T^*\eta_t \ln\frac{P(1-\delta)^2}{P_0} \tag{11}$$

R_w is gas constant of steam; η_t is efficiency of turbine, respectively.

The whole efficiency of system is expressed as:

$$\eta_1 = \frac{Q_2 - w}{Q_1 + Q_2} \tag{12}$$

If we define temperature rise ratio as:

$$\tau = T^*/T_0 \tag{13}$$

Define $n = \dfrac{1-k}{k}$ (14)

So the efficiency of conventional gas turbine with regenerator expressed as:

$$\eta_2 = \frac{\tau\eta_t\left(1 - \pi^n(1-\delta)^{2n}\right) - \left(\pi^{-n} - 1\right)/\eta_c}{\tau\left(1 - \varepsilon + \varepsilon\eta_t\left(1 - \pi^n(1-\delta)^{2n}\right)\right) - \left(1 + \left(\pi^{-n} - 1\right)/\eta_c\right)(1-\varepsilon)} \tag{15}$$

π is whole pressure ratio.

If there is no pressure loss in regenerator, then ε=0，δ=0， and the system without regenerator, this is the conventional brief cycle gas turbine. Equation (15) could be simplified as:

$$\eta_3 = \frac{\tau\eta_t/\pi^{-n} - 1/\eta_c}{(\tau - 1)/(\pi^{-n} - 1) - 1/\eta_c} \tag{16}$$

Results and Analysis

Some related data from literature [5][6]were used in calculation in this paper, the initial air temperature and pressure were 298K and 0.1MPa, temperature of water was 298K, respectively. The result is showed in Fig.4 to Fig.8.

Fig.4 compared efficiency of gas-turbine with an AGCC and conventional gas-turbine with or without regenerator influenced by overall pressure ratio. With pressure ratio increasing, efficiency of conventional gas-turbine with or without regenerator has a maximum, while the efficiency of gas-turbine with an AGCC increases rightly, although pressure ratio is bigger. Efficiencies of gas-turbine with an AGCC and gas-turbine with regenerator influenced by turbine inlet temperature are compared in Fig.5. We can see that the difference of efficiency of the two gas-turbine are decreasing with the inlet temperature increasing. The pressure ratio selected in Fig.5 is corresponding with the maximum efficiency pressure ratio of gas-turbine with regenerator in Fig.4. Because the work output of small pressure ratio gas-turbine is small, so its application will have some limit.

Efficiencies of gas-turbine with an AGCC and conventional gas-turbine influenced by turbine inlet temperature, efficiency of turbine and compressor were revealed in Fig.6~Fig.8. From the pictures, we can see that efficiency of gas-turbine with an AGCC is influenced smaller than the gas-turbine without regenerator by turbine inlet temperature, efficiency of turbine and compressor smaller. It implies that we can increase efficiency of gas-turbine distinctly based on fundamental of turbine and compressor existing manufacture.

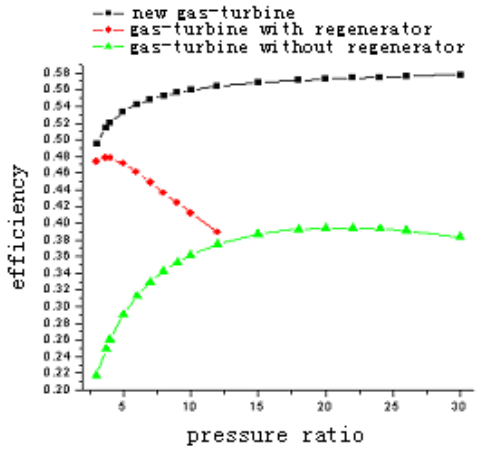

Fig.4 Relationships comparison of thermal efficiency of three types of cycle and pressure ratio. Efficiency of compressor: 0.88, efficiency of turbine: 0.90, thermal ratio: 0.90, pressure loss ratio: 0.05, turbine inlet temperature: 1300K.

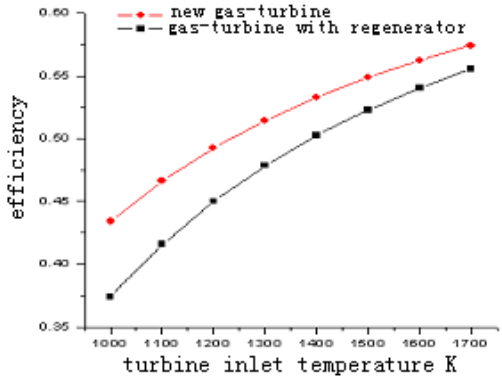

Fig.5 Relations between efficiencies of two types of gas-turbine and turbine inlet temperature change.
Efficiency of compressor: 0.88, efficiency of turbine: 0.90, thermal ratio: 0.90, pressure loss ratio: 0.05, pressure ratio: 3.7.

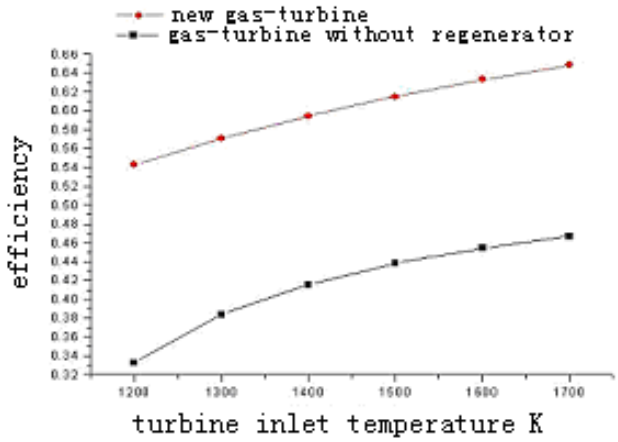

Fig.6 Relations between efficiencies of two types of gas-turbine and turbine inlet temperature change.
Efficiency of compressor: 0.88, efficiency of turbine: 0.90, thermal ratio: 0.90, pressure loss ratio: 0.05, pressure ratio: 30.

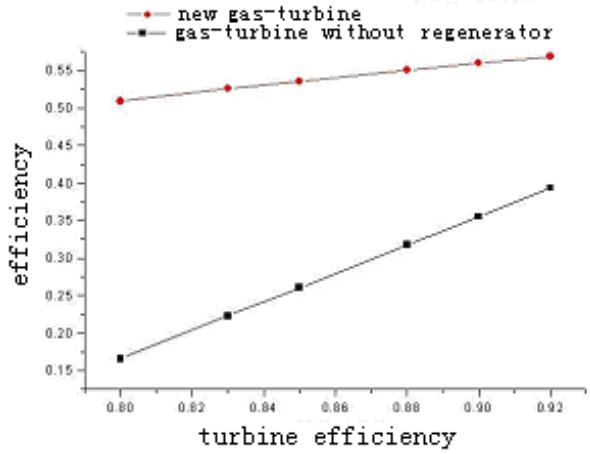

Fig.7 Relations between efficiencies of two types of gas-turbine and change of efficiency of turbine.
Efficiency of compressor: 0.88, turbine inlet temperature: 1300K, thermal ratio: 0.90, pressure loss ratio: 0.05, pressure ratio: 30, high pressure ratio: 10.

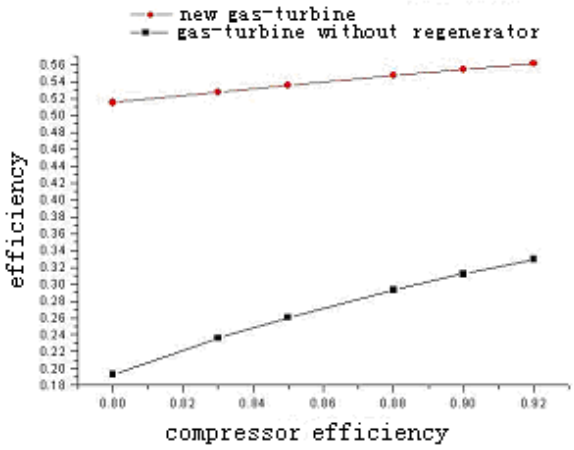

Fig.8 Relations between efficiencies of two types of gas-turbine and change of efficiency of compressor.
Efficiency of turbine: 0.90, turbine inlet temperature: 1300K, thermal ratio: 0.90, pressure loss ratio: 0.05, pressure ratio: 30, high pressure ratio: 10.

Discussion and Conclusion

Combustion is essentially a chemistry reaction under a given temperature region. If conditions are satisfied, it can be completed rapidly and spontaneously. Inside the turbine, temperature is very high and air is enough, so the reaction of fuel and air may continue even though there have no stabile burning region. Furthermore, air and fuel could contact sufficiently inside the turbine because of the stirring of the blades and the turbulence of air.

Based on the structure of gas turbine, fuel is sprayed into turbine might through the small hole bored on the immobile blades or the ejector nozzle lay between the immobile blades. This means the spaces between two blades becomes mini-type combustors. What we called combustion technology inside turbine might be a technology that heat released from sprayed fuel equaled to the work output of this stage. But this method would destruct flow field, make the structure and process control of turbine more complicated and occur partial overheat region. The structure of turbine blades is displayed in Fig.9.

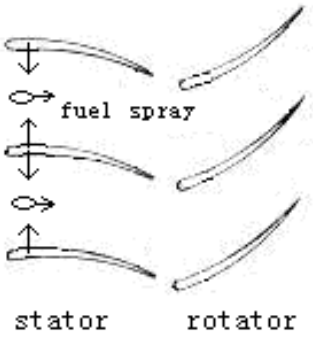

Fig.9: Combustion inside vane channel.

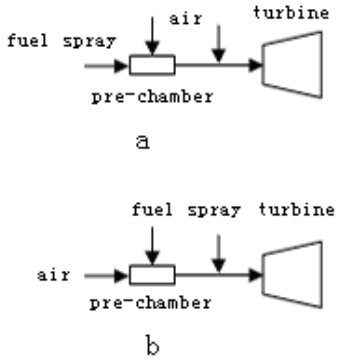

Fig10 Combustion inside the turbine.

On the other hand, we can divide the main airflow into two parts, one flows into pre-chamber with the whole fuel sprayed into, and could form a rich-fuel combustion state. So the high temperature gas with incomplete combusting fuel would flow into turbine and react with the other airflow continually when they are mixing, as the Fig.10 (a) displays.

Or the air flowed into pre-chamber wholly while fuel sprayed in two stages. One fuel-flow sprayed into pre-chamber and the remains sprayed into before turbine, this means that the fuel reacts with remained oxygen in the high temperature gas and export work, seen in Fig.10 (b).

The two models both make the turbine become a big combustor with stirrer. In order to avoid reaction much rapid or much slow, the position and flux of fuel spray, mixing process of fuel and high-temperature fume, concentration of reactors and temperature field of turbine must be think carefully, and the turbine might be redesigned. Both the two models have some analogies with the technology of high-temperature-air-combustion [7][8]. Thereby the process of combustion inside the turbine comes true.

The combustion process inside the turbine is very complicated. For liquid fuel, we hope the process of atomization, vaporization, mixing and combustion would be finished completely, on the other hand, the liquid fuel should avoid to spray onto the surface of blades in the small spaces, since it will be harm to turbine blades. Besides that the process of soot production is to be thought carefully. These need research systematically in serial problems such as: turbine structure, blade air-film defense, flow field and temperature field and process control. In present, the technology of combustion inside the turbine still is a conception, and application in practice has no report, therefore, the relative experiments should be necessary.

Compared to conventional gas-turbine, the efficiency of the AGCC gas-turbine have obvious improvement. Moreover, sensitivity of AGCC gas-turbine to the temperature, efficiency of turbine and compressor is lower than conventional one. So higher efficiency might be achieved even though low reaction temperature as long as the reaction could continue. And this low temperature is benefited for turbine thermal-defense and reducing NOx emission. Furthermore, efficiency of gas-turbine could be enhanced greatly based on existing technical foundation.

In addition that improving efficiency of modern gas-turbine would be influenced by increasing cooling air flux in gas-turbine, but apply technology of combustion inside the turbine could increase air utilization in maximum degree, because the cooling air flowed into turbine can occur re-burning action. This will be benefited to improve efficiency of gas-turbine. Although achieving the process of combustion inside the turbine has many big difficulties, it is deserved to research farther.

References：

[1] Wang Rugen, Gao Kunhua. New technology of aero-engine. Beijing: Aviation Industry Press. 2003.

[2] Li Shuying Zheng Qun et al. Cycle Analysis of Gas Turbine with Water Injection into Inter-Stage of its Compressor. Ship Engineering. 2001 .3，pp.28-33.

[3] Siregnano W A, Liu F. Performance Increases for Gas-Turbine Engines through Combustion inside the Turbine. Journal of Propulsion and Power. 15(1) No. 1, Jan-Feb 1999, pp.111-118.

[4] Liu F, Siregnano W A. Turbojet and Turbofan Engine Performance Increases through Turbine Burners. Journal of Propulsion and Power. Vol. 17, No. 3, May-June 2001, pp.695-705.

[5] Yan Jialu. Engineering Thermodynamics. Beijing: Higher Education Press. 2001.

[6] Shen Bingzheng. Device of Gas turbine. Beijing: China Machine Press. 1981.

[7] WU Guang2liang, LIU Run-zao, et al. Studing on High Temperature Air Combustion Using Reaction Engineering Method. Journal of Iron and Steel Research. Vol.16, No.2 Apr.2004.

[8] AI Yuan-fang, JIANG Shao-ji, et al. Experimental Study of High-temperature Air and Flameless Combustion and Its Flame Characteristic. Journal of Engineering for Thermal Energy & Power. 2001, 16(6). pp615~617.

Advanced Materials Research Vols. 960-961 (2014) pp 1142-1145

doi:10.4028/www.scientific.net/AMR.960-961.1142

Design of Magnet Power Supply Controller Based on DSP + FPGA

KeWang Pang

School of Electronic and Information, Jiangsu University of Science and Technology

Zhenjiang, Jiangsu 212003, P. R. China

E-mail: jskd1963@163.com

Key words: Ferromagnetic power ; DSP; controller; FPGA;SPI

Abstract: For the output requirements of low ripple voltage and high precision exciting current for ferromagnetic power, The combination of DSP and FPGA is put forward to the magnet power supply controller design scheme, First ,The power source controller hardware system is given, then the signal conditioning circuit, the intermediate link of data processing and the backend driver circuit of system is Introduced in detail, Finally gives control process of the program of the controller software design for the main program and PWM dead zone.

Introduction

Magnet power supply mostly as a special power supply offers specific exciting current for magnet to generate required magnetic field,it is widely used to apply for accelerator, mass spectrometer and so on equipment.The magnet power basic requirements from the magnetic field characteristic, so the magnet power supply based on digital power controller in order to output high precision and high stability exciting current provide an important guarantee[1-2]. This paper introduces magnet power supply controller adopt double CPU structure of DSP and FPGA, FPGA control the high-resolution converter AD7679 to sample the signal, the data acquired can be sent to DSP by SPI interface of DSP, then the output of DSP after operation processing to control the magnet power supply PWM wave with dead time.

General Structure of Controller

Magnet power controller is adopt DSP TMS320F2812 as digital processing module, Through the use of Altera's FPGA controls AD to sample data, data transmission can be realized through SPI interface of DSP and FPGA. The controller communicate with upper computer by the SCI serial port of DSP, it will display and control the running condition of magnet power supply, Main circuit and driver circuit implementation isolation by the backend drivers. General structure of controller is shown in Fig.1.

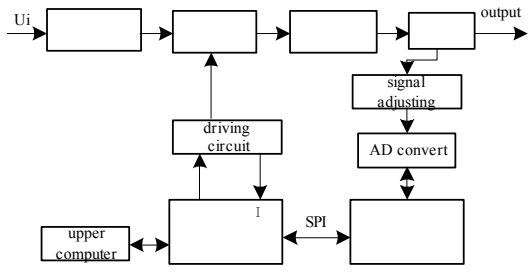

Fig.1 Structure diagram of the magnet power supply controller

Signal Conditioning Circuit

The main function of signal conditioning circuit is signal magnifying and low-pass filtering. To ensure the collection signal of the A/D converter limit between 0 to + 5V, prevent the large current

signal generated the high input voltage damage the port of A/D, level limit protection circuit is designed. A/D converter input adopts finite difference method, the single-ended signals is converted to differential signal, achieve proportional amplifier, Filtering the high frequency noise effectively, to facilitate high precision acquisition of the input signal of A/D. The circuit for the signal amplitude limit, isolation, filtering and amplifying is shown in Fig.2.

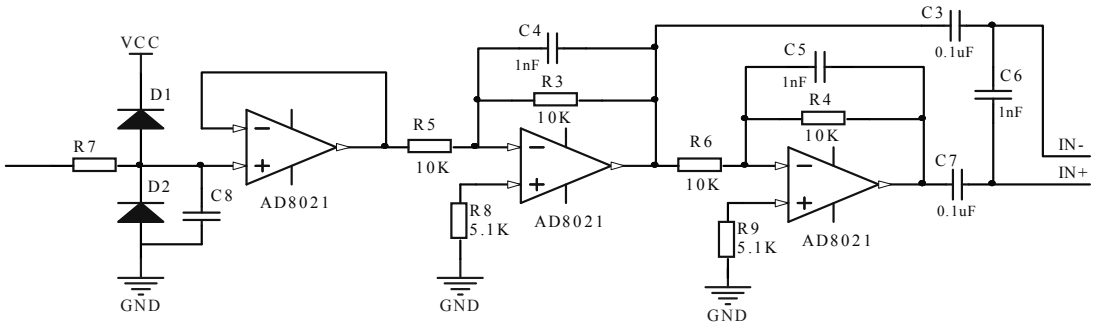

Fig.2 Signal conditioning circuit

The FPGA control of the AD

This design adopts the 18 bit completely differential successive approximation type ADC AD7679, with 570 Kbps sampling rate, at the same time, with 5V or 3V digital logic level compatible. In order to prevent the sample point on pulse switch enables the system oscillation, the DSP sends a switching impulse to FPGA a synchronous signal at the same time, make appropriate delay, FPGA give the ADC sampling command after signal spike pulse disappears. AD operation is divided into four states: idle, start the AD conversion, waiting for the results AD conversion and read the AD conversion. On the falling edge of CONVST signal open conversion process, BUSY will automatically set 1, keep the conversion. When the BUSY signal into a low level and CONVST keep high electricity, AD7679 in the stage of data collection. The FPGA control of the AD is shown in Fig.3. The actual circuit, Between FPGA and AD converter to join four channel magnetic separation device ADuM1412 for data isolation.

Communication Between DSP and FPGA

TMS320F2812 inside with a SPI interface, by defining the control registers, and set up the DSP as the main equipment, to provide the clock signal for communication, the FPGA as a from device. Because of the DSP and FPGA pin voltage to match the I/O interface (3.3V), Don't need level conversion circuit. Set the FPGA to send data in clock pulse rising along, when falling edge in the receive data. Since the FPGA always remove the highest data when sending data, the remaining data left one respectively, so The received data of DSP must be bit by bit left to realize data received. When the SPI STE pin for the lower levels, the FPGA bit by bit to send data; When the SPI CLK pins for high levels at ordinary times, DSP bit by bit to read data, and left after a wait for the next SPI CLK for high level; When SPI STE pin for high levels, DSP has been receiving the data of FPGA sending, after eight

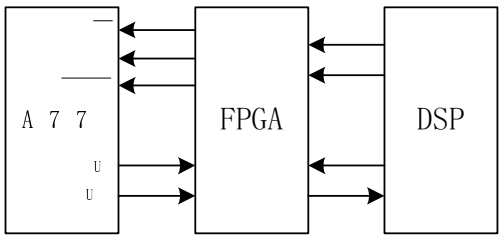

Fig.3 DSP control of the AD and circuit of communication between DSP and FPGA

clock, to complete a sequence of SPI , The received data will be stored in the defined array by DSP. DSP and FPGA communication pin connection is shown in Fig.3.

Driver Circuit Design

Drive circuit use high-speed photoelectric coupler HCPL-4503 to fast realize signal conversion and isolation. The fault signal be sent to PDPINTx pins after by photoelectric coupler isolation TLP521-1, the PWM output pins into a high impedance state, at the same time to generate an interrupt, blockade drive signal, shut down power devices. Driver circuit is shown in figure.4.

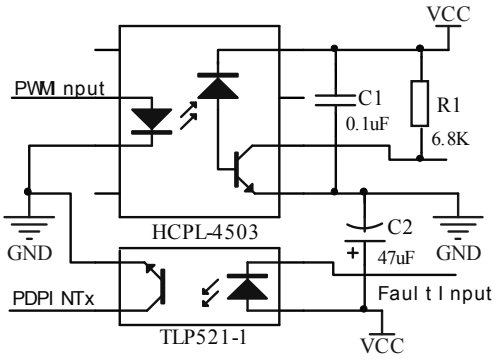

Fig.4 Backend driving circuit

Conteroller Software Design

When the interrupt occurs, DSP program will be jump to the corresponding scale judgment according to the priority of the interrupt response and interrupt subroutine, realize their respective functions. the main program flow chart is shown in Fig.5.

In order to prevent switching devices conduction at the same time of the converter bridge arm up and down, driving signal need to have a dead zone. Set (8-11)bit of dead zone control register DBTCONx of DSP for the dead zone of the timer, its time cycle is m, (2-4)bit for the dead zone of timer reserve scale factor x/p , if the general timer clock cycles is t, the dead band time $t_s = m \times p \times t$. Dead zone parts control process is shown in Fig.6.

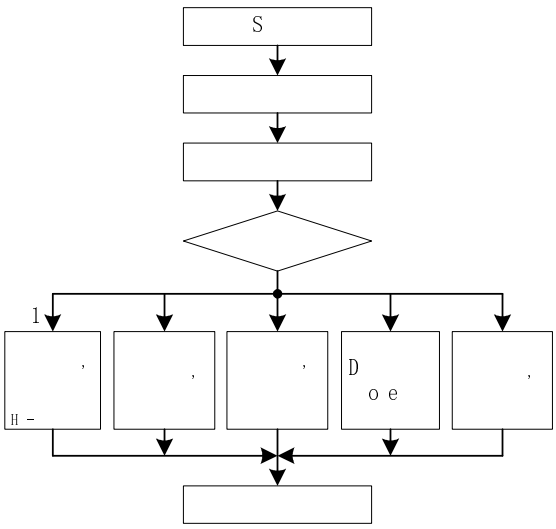

Fig.5 Flowchart of main program

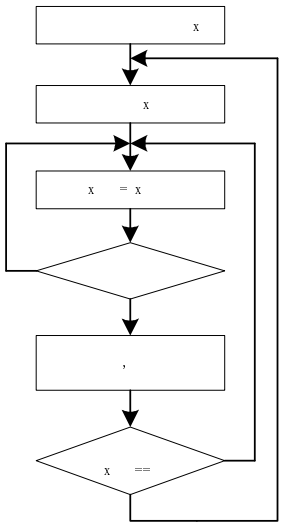

Fig.6 Control-flowchart of dead zone

The configuration of baud rate by SPIBRR registers programming implementation of DSP, Must be pay attention to use system clock synch realize SCLK signal, to reduce the SCLK cause communication error. The communication flowchart of SPI between DSP and FPGA is shown in Fig.7.

Summary

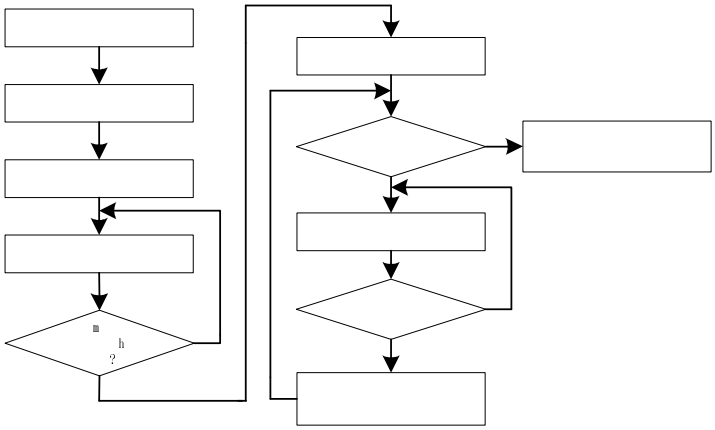

Fig.7 Flowchart of SPI communication between DSP and FPGA

The magnet power supply controller which adopted DSP+FPGA architecture has superiority of both signal processing chips, improve calculation speed and accuracy effectively. In the subsequent research,According to the need to set up the corresponding parameter, Select the appropriate control algorithm, In order to meet the magnet power supply low ripple output and high accurate current control requirements.

Reference

[1] MA Hong-xia, YAN Wei-kang, ZHAO Sheng. A magnet stabilized-current supply of high-stability soft switch accelerator[J]. Electric Drive Automation,2009,31(3):32-34.

[2] LIU Yong,ZHU Zhong-ming,LUO Wen-yuan, etal. Design of high-precision digital power data collecting system based on FPGA+DSP[J]. Electronic Components Applications, 2009,11(3):25-27.

[3] LI Xi-hong. The practical research of digital switching power supply Based on DSP and FPGA [D]. Chengdu university of technology,2008

[4] LIU Peng-peng, WANG Jing, YIN Xiao-jie, etal. Design of a genrral motion controller based on DSP and FPGA[J]. Electronic Design Engineering,2011,19(21):170-172.

[5] ZHANG Chun-lin, YAN Ping. Research of Digital High-Voltage DC Power Supply Based on DSP[J]. High Voltage Engineering,2008,34(10):2240-2243.

Advanced Materials Research Vols. 960-961 (2014) pp 1146-1150

doi:10.4028/www.scientific.net/AMR.960-961.1146

A Double Exponential Function Fitting Algorithm for Optimize Parameter of μH Curve

Jiao Du[1,2,a], Meng Song[1], Nannan Hu[1], Kunnan Cao[1],Wentao Huang[1,3], Peng Xu[1,2], Yiyang Li[1,2]

[1]Yunnan Electric Power Research Institute, Kunming City, Yunnan Province, P.R. China, 650217

[2]School of Electrical Engineering, Kunming University of Science and Technology, Kunming, P.R. China, 650500

[3]School of Electrical Engineering, University of Chongqing, Chongqing, P.R. China, 400044

[a] 921562872@qq.com

Keywords:electric power system security; iron-core saturation; double expontential function fitting algorithm

Abstract. Saturable magnetic circuit is a common phenomenon in power system. It can lead to waveform distortion, coefficient of self inductance decrease and measurement error increase. So establishing a mathematical model for saturable magnetic circuit and revealing the mathematical relationships in saturable phenomenon. It is helpful to reliable and safe operation of power system. This paper base on double expontential function fitting algorithm and simplex algorithm to establish the function relationship between relative permeability and magnetic field intensity. Applying for the model,we can obtain the waveform of magnetic flux in transformer core and transformer voltage waveform. The research has certain significance in the abstract and foreground in the application for the study of saturable phenomenon.

Introduction

BH curve is the key to studying saturable phenomenon. Generally speaking,the BH curve can be determined in laboratory. Therefore there is no simple formula for this kind of curve. But if you look at the mathematics of the problem, BH curve can be gotten according to the polynomial fitting, cubic spline interpolation and so on. The data of curve fitting would be in error. Because calculation of secondary voltage transformers and magnetic flux of iron core have many procedures, calculation error has the trend of becoming bigger. Therefore, in this paper a new method of fitting $\mu_r H$ (μ_r: relative permeability) curve is proposed.

Applying for the model, we can reduce the amount of calculation and lower the calculation error.

Model Building

It is well known that experimental BH curve of silicon steel sheet,as shown in figure(1).

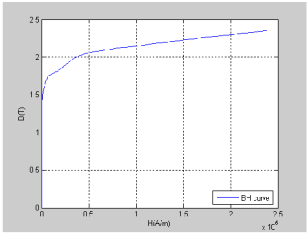

Fig. 1. BH curve of silicon steel sheet.

The relationship between relative permeability and magnetic field intensity, expressed by the simple equation(1). $\mu_r H$ curve shown in figiure(2).

$$\mu_r = \frac{B}{\mu_0 H} \tag{1}$$

In equation(1), the μ_0 is permeability of vacuum, μ_r is relative permeability, B is magnetic induction intensity,H is magnetic field strength.

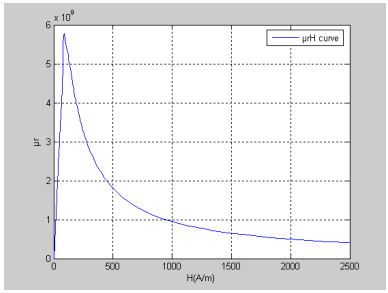

Fig. 2. $\mu_r H$ curve of silicon steel sheet.

Now, we utilized the curve-fitting to establish $\mu_r H$ fun-ction. $\mu_r H$ curve look like a impulse function. So double expontential function fitting algorithm can express $\mu_r H$ curve. The expression can be given as equation(2).

$$y = A(e^{-\alpha x} - e^{-\beta x}) \tag{2}$$

In equation(2). A, α , β is the fitting coefficient.

The basic ideas concerning curve fitting is that find the optimum solution of A, α , β , and make difference between the data of the curve fitting and the experimental data as small as possible. The error function can be given as equation(3).

$$E(A,\alpha,\beta) = [\mu_r - A(e^{-\alpha H_e} - e^{-\beta H_e})]^2 = \min \tag{3}$$

In ordor to find the optimum solution of A, α , β , we need solving the partial derivatives of E function. Then make partial derivatives of E function equal to zero,It can be shown as equation(4).

$$\begin{cases} \dfrac{\partial E(A,\alpha,\beta)}{\partial A} = 0 \\ \dfrac{\partial E(A,\alpha,\beta)}{\partial \alpha} = 0 \\ \dfrac{\partial E(A,\alpha,\beta)}{\partial \beta} = 0 \end{cases} \tag{4}$$

The simplex method is used to solve the system of algebraic equation(4). Since our prices are closely calculated, $A = 2.3584^{10}$, $\alpha = 0.0059429$, $\beta = 0.010769$. $\mu_r H$ curve as shown in figure(3).

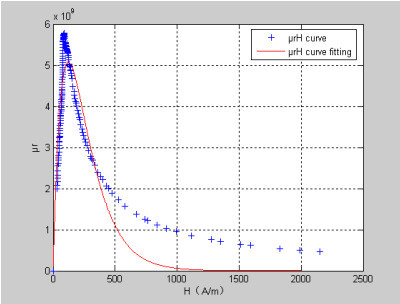

Fig. 3. $\mu_r H$ curve fitting.

From the $\mu_r H$ curve (figure 3), the fitting data accords with the experiment data basically. Fitting function can be shown as equation(5).

$$\mu_r = 2.3584^{10}(e^{-0.006H} - e^{-0.011H}) \tag{5}$$

The function relation between exciting current and magnetic field strength in transformer can be shown as equation(6).

$$H = \frac{NI_e}{l} \tag{6}$$

In equation(6). I_e is exciting current, N is turns,l is loop length.

Eq.(6) substituted in Eq(5), The function relation between relative permeability and exciting current can be express as equation(7).

$$\mu_r = 2.3584^{10}(e^{-0.006\frac{NI_e}{l}} - e^{-0.011\frac{NI_e}{l}}) \tag{7}$$

Model Application

Using the model(7), the magnetic flux and induced electromotive force in transformer core can be calculated. Model of power transformer as shown in the figure(4). Coil(1) is primary winding. The parameters as shown in the Table Ⅰ.

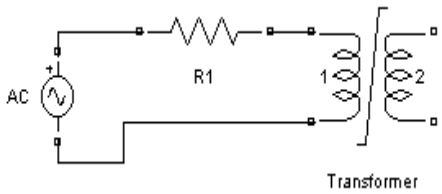

Fig. 4. Model of power transformer.

Table 1. Transformer Parameter

The capacity / frequency of transformer : 150MVA/ 50Hz					
Loss resistance / remanence flux of iron core:1.0805e+006ohm/ 0T					
Loop length / sectional area of iron core: 2m/ 1 m^2					
	Coil resistance R1	Coil leakage inductance L1	Nominal voltage peak	Nominal current peak	Turns of coil
Coil(1)	1.1111 ohm	0.11789H	500kV	300A	500
Coil(2)	1.1111 ohm	0.11789H	230kV	500A	300

According to Faraday law of electromagnetic induction, Induced electromotive force at primary winding can be expressed as equation(8).

$$e = \mu_r \mu_0 N(\frac{dH \cdot S}{dt}) \tag{8}$$

Suppose exciting current equals rated current. Using the model(7), the iron core magnetic flux-time function picture as shown in the figure(5).

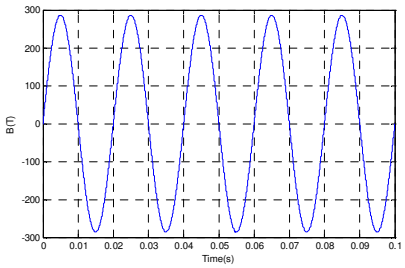

Fig. 5. Iron core magnetic flux-time function picture.

When iron core is not saturated,the magnetic flux-time function is a sine function. So using the model(8), the induced electromotive force at secondary winding is a sine wave as shown in the figure(6).

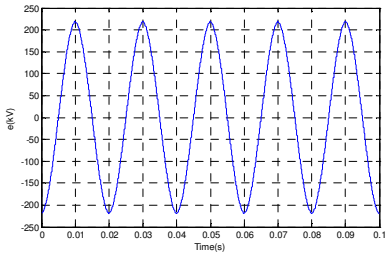

Fig. 6. Induced electromotive force -time function picture.

Suppose exciting current is greater than rated current. Using the model(7), the iron core magnetic flux-time function picture as shown in the figure(7).

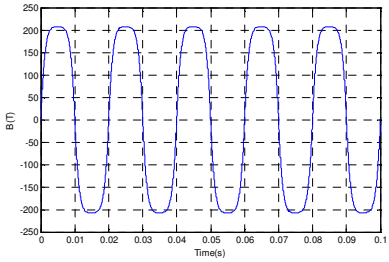

Fig. 7. Iron core magnetic flux-time function picture.

Because of core saturation, magnetic induction intensity in the iron core is a flat wave. Using the model(8), the induction electromotive force at secondary winding is a peaked wave. It shown in figure(8).

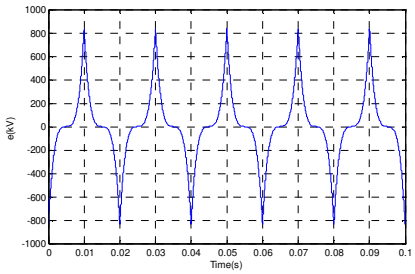

Fig. 8. Iron core induction electromotive force -time function picture.

Conclusion

Detailed calculations shows that it the result of the model(7) is in accordance with the theoretical analysis. So the model is feasible and available. These research and practices are useful references to us.

References

[1] QianSheng Hu,MinQiang Hu, ”Electromechanics,” Beijing:China Electric Power Press,2009.

[2] William H.Hayt, John A.Buck, ”Engineering Electro- magnetics,” XiAn: XiAn JiaoTong University Press,2009.

[3] DeXin Xie,ShiYou Yang, ”Numerical Analysis of Engineering Electromagnetic Field,” Beijing:China Machine Press,2008.

[4] Qian Li,TianBi Tu,XiaoYu Wang, ”An Improve Method for the Fitting of Excitation Curve of Electromagnetic Voltage Transformer,” Transformer, vol.35,pp.28-30,march.1998

[5] YanPeng Hao,GuoLi Wang,YanMing Li,Heng,Xie, ”A Double Exponential Function Fitting Algorithm for Impulse Parameter Evaluation,” High-Voltage Technology,vol.26,pp.31-35, June.2000..

Advanced Materials Research Vols. 960-961 (2014) pp 1151-1155

doi:10.4028/www.scientific.net/AMR.960-961.1151

Analysis and Modeling of Droop Control in Micro-source for Islanded Micro-grid

Weilin Zhang[1,a], Jing Xiong[1,b], Yujiong Gu[1,c] and Ping Zhu[1,d]

[1] School of Energy Power and Mechanical Engineering, North China Electric Power University, Beijing, 102206, China

[a]zhangweilin0616@126.com, [b]xiongjing@163.com, [c]guyujiong@263.net, [d]zp@ncepu.edu.cn

Keywords: Micro-grid, Micro-source, Droop Control, PWM Control, Proportional Integral, Converter.

Abstract. Considering decentralization of the micro-source units and loads in the micro-grid and concentrating on generation types and models of the storage devices, *droop control* strategy is used in controller design for the distributed generation units. The generation units adopting droop control method based on the droop characteristics can facilitate load power sharing when the powers of loads vary, and can also maintain the system frequency when a unit fault occurs and the micro-grid islands. Then, the operation variations of the micro-grid are analyzed when it runs with load changes in islanding mode and runs with the load power of micro-source varied suddenly. The corresponding rules of the active power, voltage and current for each micro-source and the frequency for the micro-grid are obtained. The simulation data results show the correctness and validity of the droop control strategy.

Introduction

Micro-grid is an independently-controllable power system and the combination of micro-sources, loads, power electronic devices etc. It can fully use the advantage of distributed power generation and overcome the disadvantage of what distributed power generation brings in power distribution network. Micro-sources include Photovoltaic Cell, Fuel Cell, Micro gas turbine, wind power generator, storage battery, super capacitor, fly-wheel storage etc. Micro-grid can operate in grid-connection mode or islanded mode and switch seamlessly between the two modes [1].

Micro-source generates DC by DC converter or rectifier, then through inverter it produces AC, thus form a distributed micro-source which can be connected to micro-grid. Generally, the control strategy for inverter adopts constant PQ control, constant V/f control [4] or droop control. An inverter that adopts PQ control is equivalent to a current source, whose output power is determined by the initial power setting value and not affected by internal power change of micro-grid, applying to the micro-sources don't need the outside support of voltage and frequency. An inverter that adopts V/f control is equivalent to voltage source [5], whose output power is determined by the internal power change of micro-grid and can regulate power, applying to the micro-sources having power storage devices. For parallel-connected micro-source in micro-grid, when grid-connectedly operating, its voltage and frequency is supported by power distribution network. When islanded operating, because of the breaking of power distribution network, the system need a certain number of V/f controlled micro-sources to support the voltage and frequency of micro-grid. Or, all micro-sources adopt droop control to maintain the gird's voltage and frequency together.

For the island micro-grid which uses ocean wave and current as power sources, due to natural causes, the difference between actual condition and rated condition is very big, causing the actual output power of micro-grid is lower than the rated power, unable to set the main control unit of the system in advance, or the main control unit cannot meet the voltage and frequency requirements for the system. If all micro-sources use droop control strategy, it can make all the power involved in micro-grid's voltage support to ensure stable voltage and current, avoid power fluctuation in the main control unit causes the risk of instability.

Droop Control

Droop Control Principle. By imitating traditional generator's characteristics, droop control use the perceptual line impedance's droop character of paralleled active power with frequency, reactive power with voltage amplitude which are approximation of the droop curve to adjust the frequency and amplitude of output voltage. So the essence of droop control is: micro-source measures its own emitted power, according to droop character, then converts the power signal to output voltage amplitude and frequency control signal as instruction; According to the adjusted power, it reversely reacts on output voltage and frequency signal to realize self-adjusting and automatic power distribution.

Inverter's droop control principle is shown in Fig 1. For Fig 1(a), when a distributed power supply active output power increases, the operating point of the distributed power moves from A in Fig. 1(a) to B. So does Q-V droop control principle, which is shown in Fig. 1(b).

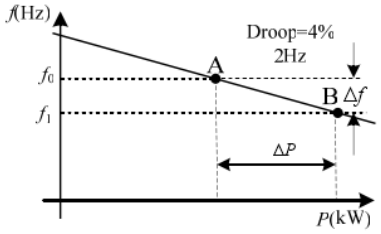

Fig. 1(a) P-f droop control principle

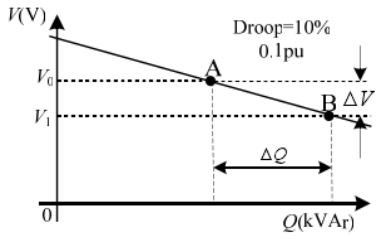

Fig. 1(b) Q-V droop control principle

Droop Character. For a micro-source controlled by inverter in micro-grid, the output power can be modeled as:

$$P_i = \left(\frac{UU_i}{Z} \cos \delta_i - \frac{U_i^2}{Z} \right) \cos \theta + \frac{UU_i}{Z} \sin \delta_i \sin \theta \tag{1}$$

$$Q_i = \left(\frac{UU_i}{Z} \cos \delta_i - \frac{U_i^2}{Z} \right) \sin \theta - \frac{UU_i}{Z} \sin \delta_i \sin \theta \tag{2}$$

U is the voltage of micro-grid, U_i is the output voltage of micro-source, δ_i is the phase difference between U_i and U, Z and θ are respectively the amplitude and phase of output resistant.

In micro-grid, because δ is very small, so $\sin \delta \approx \delta$ and the power calculations can be simplyfied as:

$$P_i \approx \frac{UU_i}{\omega L_i} \delta_i \tag{3}$$

$$Q_i \approx \frac{U(U_i - U)}{\omega L_i} \tag{4}$$

Micro-grid's voltage phase is determined by the line impedance, so it is considered as constant in the short term.And phase voltage of the inverter is determined by integration of frequency to time, So phase angle is proportional to the frequency, the relation between droop is below and shown in Fig. 2:

$$f^* = f_0 - m(P - P_0) \tag{5}$$

$$U^* = U_0 - n(Q - Q_0) \tag{6}$$

m and *n* are respectively the droop coefficent of frequency and voltage, f_0, U_0 are respectively rated frequency and voltage. P_0, Q_0 are respectively rated active output power and reactive output power. P, Q are respectively actual active output power and reactive output power. f^*, U^* are respectively referentce frequency and voltage at present.

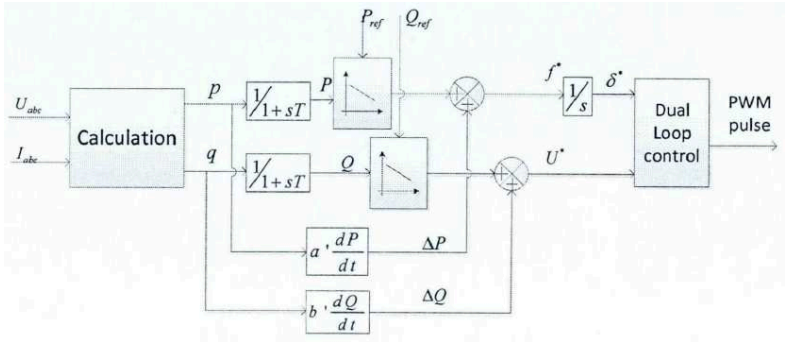

Fig. 2: Diagram of droop control for inverter

Voltage Output Control

Voltage-Current Dual Loop Control. Detect 3-phase load voltage U_{abc}, load current I_{abc} and inverter output current i_C, through the axis conversion shown in equations(7)(8) aquires values of d, q axis, voltage controller and output voltage feedback form voltage loop, corresponding currents are i_{Cdref}, i_{Cqref}. Assuming $U_d^* = U_R$, $U_q^* = 0$. Under the voltage loop control, output voltage can stabilise. Current controller and output current feedback form current loop, whose output vectors are u_d, u_q.

$$\begin{bmatrix} u_d \\ u_q \end{bmatrix} = \sqrt{\frac{2}{3}} \begin{bmatrix} \cos\omega t & \cos\left(\omega t - \frac{2\pi}{3}\right) & \cos\left(\omega t + \frac{2\pi}{3}\right) \\ -\sin\omega t & -\sin\left(\omega t - \frac{2\pi}{3}\right) & -\sin\left(\omega t + \frac{2\pi}{3}\right) \end{bmatrix} \begin{bmatrix} u_A \\ u_B \\ u_C \end{bmatrix} \tag{7}$$

$$\begin{bmatrix} i_d \\ i_q \end{bmatrix} = \sqrt{\frac{2}{3}} \begin{bmatrix} \cos\omega t & \cos\left(\omega t - \frac{2\pi}{3}\right) & \cos\left(\omega t + \frac{2\pi}{3}\right) \\ -\sin\omega t & -\sin\left(\omega t - \frac{2\pi}{3}\right) & -\sin\left(\omega t + \frac{2\pi}{3}\right) \end{bmatrix} \begin{bmatrix} i_A \\ i_B \\ i_C \end{bmatrix} \tag{8}$$

Using output voltage vector u_d, u_q and voltage vector SPWM control modulation, PWM pulse signals of 6 switched of inverter are aquired. Under the voltage-current dual loop control shown in Fig 3, inverter can output stable sinusoidal wave voltage.

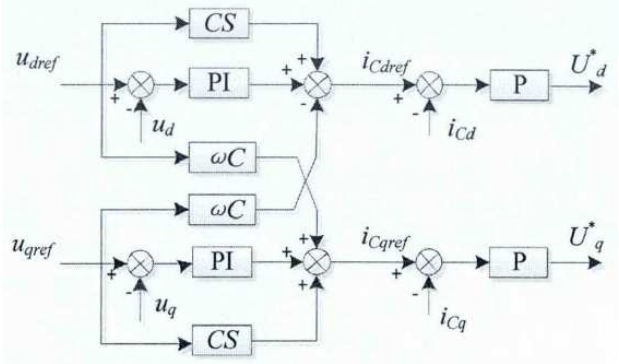

Fig. 3 Diagram of voltage-current dual loop control

Proportional Integral. Proportional Integral (PI) modulation combines negative voltage feedback to realize indifference regulation. Current internal loop controlling capacitor current is better than controlling inductive current as former can improve system response speed. When carrier frequency is far greater than system frequency, integral control is used.

Simulation Analysis

Simulation Parameters. In the simulation, system parameters are set as: Micro-source DC-side voltage V_{dc}=800V, PWM generator carrier frequency f_s=8000Hz, filter inductance L=3mH, filter capacitor C=1500uF, voltage loop PI controller K_p=10, K_i=100, current loop PI controller K_p=10, droop control coefficient $m=10^{-5}$, $n=3\times10^{-4}$, P_{ref}=15000W, Q_{ref}=0. Active power load of Load 1 is 10^4 kW, active power load of Load 2 is 5×10^3 kW. Simulation time is 0.4s, simulation discrete time is 5×10^{-5}s。 Load 1 is connected at first. Load 2 connect to micro-grid at 0.2s and break at 0.3s. Simulation results show in Fig. (4).

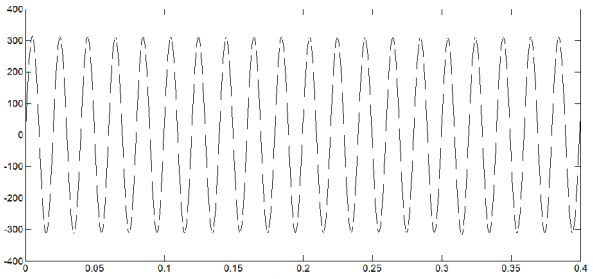

Fig. 4(a). Voltage of micro-grid system

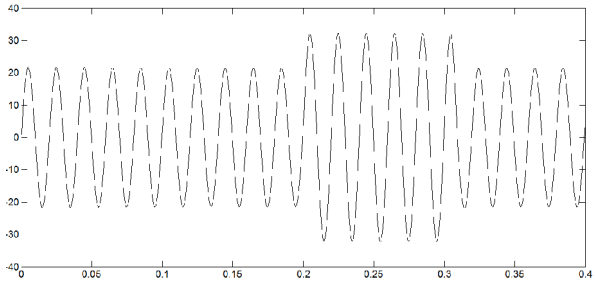

Fig. 4(b). Current of micro-grid system

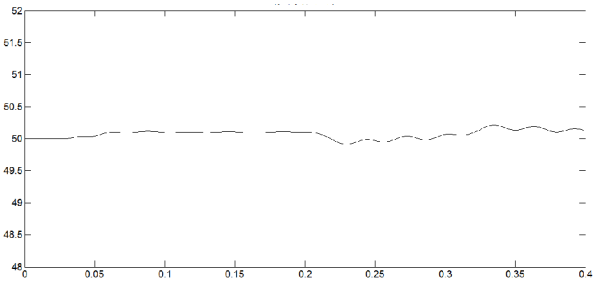

Fig. 4(c). Frequency of micro-grid system

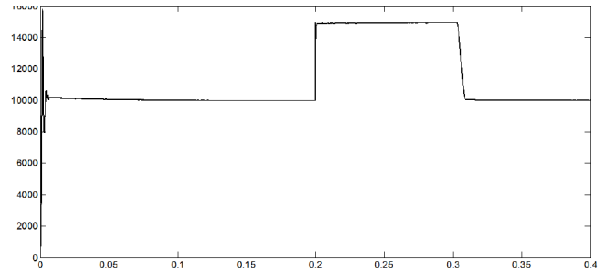

Fig. 4(d). Active output power of micro-grid

Result Analysis. Simulation results are shown in Fig. 4. For Fig. 4(a), AC peak voltage of system is 310V, which means AC V_{rms} is 220V. When breaking Load 2 at 0.3s, the voltage is still 310V, indicating the voltage control is effective.

For Fig. 4(b), between 0.2s and 0.3s, because load power increases from 10kW to 15kW, the output current increases to a multiple of 1.5.

For Fig. 4(c), the frequency of system declines after 0.2s and increases after 0.3s, and the values of declining and increase accord with the value of droop control principle, also range in the 50 ± 0.5Hz, demonstrating droop control adopts adjusting frequency to adjust active output power.

Fig. 4(d) shows the active output power of system, after the start of simulation, the miro-grid can output 10kW active power in a short time. At 0.2s, the system begins to output 15kW. At 0.3s, the system downs its output to 10kW. The output power can meet the load power.

Conclusions

By MATLAB/Simulink software, the simulation of the droop control for single Micro-source grid system is verified. The results manifest that droop control strategy can ensure power balance between micro-source and load when system's output power varies. And it keeps the stability of voltage and

frequency in islanded operation, which satisfies the requirements of system's power quality that the load demand. It proves the feasibility and reasonability of the application of droop control strategy in the island micro-grid.

Acknowledgement

The financial support of National High-Technology Research and Development Program of China (863 Program) (NO. SS2012AA052601) is gratefully acknowledged.

References

[1] Wang Chengshan, Wang Shouxiang. Study on Some Key Problems Related to Distributed Generation Systems [J]. *Automation of Electric Power Systems*. 2008,32(20):1-4.

[2] Lu Zongxiang, Wang Caixia, Min Yong. Overview on Microgrid Research [J]. Automation of Electric Power Systems. 2007,31(19):100-107

[3] Yang Qi, Ma Shiying, Li Sheng, Tang Xiaojun, Li Xiaojun. Design of Microgrid Operation Model and Control [J]. *TRANSACTIONS OF CHINA ELECTROTECHNICAL SOCIETY*. 2011,26(1):267-273.

[4] Wang Chengshan, Xiao Zhaoxia, Wang Shouxiang. Synthetical Control and Analysis of Microgrid [J]. *Automation of Electric Power Systems*. 2008,32(7):98-103.

[5] Mu Xiaochun, Bi Daqiang, Ren Xianwen. Study on Control Strategies of a Low Voltage Microgrid[J]. *Automation of Electric Power Systems.* 2010, 34(19):91-96.

[6] Li Gengyin;Xu Yuqin;Wang Xinwei;Wang Yaling. Research of active compensator PWM current waveform control methods [J]. *Journal of North China Electric Power University*. 1996, 23(3):7-12.

[7] C. E. Jones. Local control of Micro Grids using energy storage [D].University of Manchester, UK,PhD thesis, 2007.

[8] N. Jayawarna, X. Wut, Y. Zhangt, and et al. Stability of a Micro Grid [C]. The 3rd IET International Conference on Power Electronics, Machines and Drives, Ireland, 2006: 316-320.

[9] J. A. P. Lopes, C. L. Moreira, and A. G. Madureira, "Defining control strategies for analysing Micro Grids islanded operation," in Proc. IEEE.St. Petersburg PowerTech, St. Petersburg, Russia, 2005.

[10] J. M. Guerrero, N. Berbel, J. Matas, J. L. Sosa, de Vicuna G. Luis,"Droop control method with virtual output impedance for parallel operation of uninterruptible power supply systems in a Micro Grid," Applied Power Electronics Conference, APEC, pp. 1126-1132, 2007.

Advanced Materials Research Vols. 960-961 (2014) pp 1156-1161

doi:10.4028/www.scientific.net/AMR.960-961.1156

PID Parameter Optimization Based on Fuzzy Control

Wenwen Chen[1,2,a], Youkuan Liu[3], Xiangyu Tan[4], Jianping Sun[1],

Shaoquan Zhang[4], Jiao Du[2], Shuo Wang[2]

[1]North China Electric Power University, Baoding City, Hebei Province, P.R. China, 071000

[2]North China Electric Power University Graduate Student Workstations of Yunnan Power Grid Corporation, Kunming City, Yunnan Province, P.R. China, 650000

[3]Smart Grid Department of Yunnan Electric Power Research Institute, Kunming City, Yunnan Province, P.R. China, 650000

[4]Yunnan Electric Power Research Institute, Kunming City, Yunnan Province, P.R. China, 650000

[a]961689821@qq.com

Keywords: PID; Fuzzy Control; Fuzzy PID

Abstract. PID controllers are widely used in industrial process control. The determination of the conventional PID controller parameter tuning is based on obtaining the mathematical model of controlled objects and according to certain rules, which is difficult to adapt to complex control systems. In this paper ,against its adverse effect parameter tuning, long time debugging, defects and poor adaptability of the controlled object，the fuzzy control and PID control are combined and the fuzzy PID controller is proposed. Then, I combine the examples of thermal power units using MATLAB to simulate. The simulation results show that the fuzzy self-tuning PID controller not only has the advantages of fuzzy control such as fast, adaptability, etc, but also the characteristics of high accuracy PID control, which make the system has a good control effect.

Introduction

In industrial control, PID controllers are widely used for its advantages as simple device, easy parameter adjustment and etc. In PID control algorithm, parameter tuning is very important, which directly affects the control performance. For simple control objects or known models, the use of traditional PID control parameters tuning method generally can get good control performance. However, conventional PID control is mainly used to control linear controlled object with exact models, but for some time-varying and nonlinear systems, it is difficult to achieve desired control effects. The best parameters adjustment method of conventional PID control has not been automated, which rely on manual tuning method of trial and error requires not only a wealth of skills and experience, and very time consuming. Fuzzy control does not depend on precise mathematical model of controlled object, but a way of summarizing manual automatic control based on the experience. This article shows a fuzzy PID controller based on the fuzzy control theory. In this paper, PID control and fuzzy PID control are used for the actual thermal power system simulation, and their control effects are observed and compared.

PID control

PID control is proportional (P), integral (I), differential (D) controller, which is a linear control. Its role is to take the difference of the setpoint value r(t) and the actual output of the controlled parameter y (t) as the input of the controller, then the controller generates control volumes according to the percentage of deviation, proportional-integral and proportional integral derivative. The result of the sum of the three operators, we get the output of the PID controller. In the continuous-time domain, PID controller algorithm is expressed as equation (1):

$$Y(t) = K_p\left[e(t) + \int_0^t e(t)dt/T_i + T_d d\,e(t)/dt\right] \tag{1}$$

In equation (1), $Y(t)$ is the output, $e(t)$ is the deviation, K_p is the proportionality coefficient, T_i is the integral time coefficient, T_d is the derivative time coefficient.

PID algorithm schematics is shown in figure (1) .

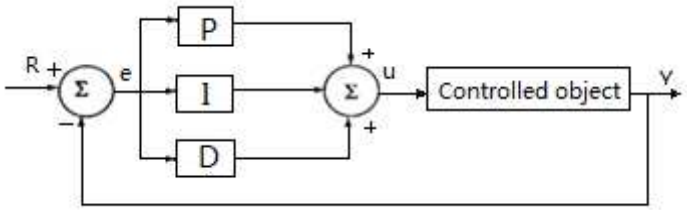

Fig. 1. PID algorithm schematics

In the computer control system, the digital PID controller is generally used. This controller is discretized using differential equations. At the sampling time t=KT (T is the sampling period), equation (2) can be obtained:

$$Y(t) = K_p\left\{e(t) + \frac{T}{T_i}\sum_{i=1}^{k} e(i) + \frac{T_d}{T}\left[e(k) - e(k-1)\right]\right\} \tag{2}$$

Under normal circumstances, PID controller in accordance with the control principle of steady, accurate and fast to adjust the three parameters. At the same time, PID controller needs to taking into account the diversity of object features, different control targets set and optimized in order to achieve satisfactory control effect. The PID controller parameter optimization problem is to use the algorithm to optimize the three parameters K_p, T_i, T_d in equation (2).

Conventional PID parameter optimization methods are generally single-objective approach, which is difficult to take into account of the three indicators, resulting in less than optimal parameters, poor performance and poor adaptability on the operating conditions, less than ideal control effect, so that the application of the PID controller is limited. Therefore, this article uses the Particle Swarm Optimization (PSO) on PID parameter optimization.

Fuzzy Control

Fuzzy control is the use of fuzzy set theory, which turns the human expert control strategy using natural language into algorithm language that a computer can accept in order to simulate human intelligence and achieve effective control of the production process. Fuzzy control system is a computer control system, generally similar to the composition of a digital control system, and only the digital controller is a fuzzy control algorithm operation. Fuzzy control system block diagram is shown in figure (2).

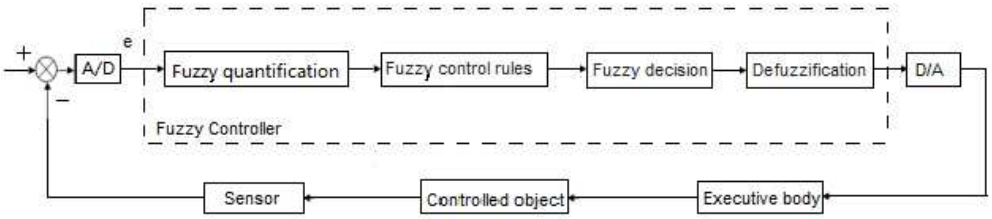

Fig. 2. Fuzzy control system block diagram

Fuzzy controller generally consists of the following four components:

(1) Fuzzy quantification (fuzzy interface): Fuzzy controller receives the exact digital amounts that represent the system deviation signal transferred from the digital A / D converter, therefore, the exact function of the part is converting the exact deviation amount into a digital amount of blur. If the fuzzy controller is a dual input, you should also calculate the deviation of the rate of change according to the deviation, and then convert it into a blur. This process makes the exact amount of input convert into the amount of blur represented by fuzzy set membership function.

(2) Fuzzy control rules: Also known as the knowledge base, which is used to store knowledge fuzzy reasoning required. Generally, we acquire knowledge according to the control experience of experts and the design of knowledge base is usually performed offline. However, with the increasing demand for the control, it also can be designed as online learning, such as changing the parameter of language value, control the number or form of rules and the like.

(3) Fuzzy decision: Also known as the fuzzy inference engine, which is the core part of the fuzzy controller. It uses knowledge of fuzzy control rule base to simulate human reasoning process, and gives the appropriate output. So it has the ability to simulate human reasoning fuzzy.

(4) Defuzzification (exact oriented interface): The output we've got is a fuzzy variable and we must use a exact amount to control. Thus, the task of defuzzification is to convert the fuzzy output obtaining by fuzzy calculation into the exact digital amount that can be received by actual systems, and use a D / A converter to convert it to a analog and then send it to actuators.

Fuzzy PID Control

About fuzzy controller design, it is not based on the mathematical model of controlled objects to set the parameters, thus, the fuzzy control has some adaptation to nonlinear and time-varying controlled objects, that is has a advantage of good robustness. In addition, as long as the system is stable, the desired control action frequency is very low, so that the actuator does not require frequent moves, which is a special project needed feature. However, the biggest problem of fuzzy control system is that it can't guarantee that the system no static error and it does not meet many of the needs of engineering problems. PID controller has characteristics such as a simple principle, easy to use, robustness, control quality of the process's lower sensitivity to process changes, the controller parameter tuning easier, no static droop characteristics, has been leading the field of industrial process control controller. Therefore, the combination of fuzzy control and PI control constitutes a complex controller to play the advantages of both controllers, which can expand the applications of fuzzy control.

Fuzzy control and PID control series

In the basic fuzzy control system, the output of fuzzy control table to go through a output link into actual control amount and then applied to the controlled object. There are two commonly used output links: output proportional and integral output. The proportion of the output is the basic fuzzy controller and its step response faster, but also have poor control. There are many forms integral output, such as series an integrator between the fuzzy controller and the controlled object. Static output allows the system integrator difference is small, but with slow corresponding, large overshoot, and the system is easy unstable. Therefore, this approach is not recommended.

Parallel fuzzy control and PID control

Compound fuzzy control system fuzzy controller with PID controller in parallel is shown in figure (3). In this control mode, it is equivalent to parallel a non-linear proportional link in the proportion links of PI controller in order to improve the speed of adjustment.

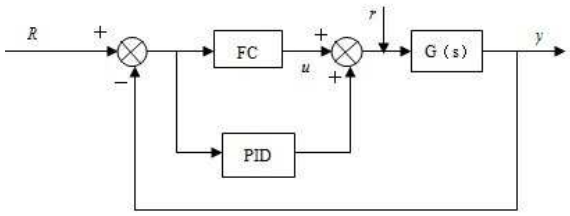

Fig. 3. Compound fuzzy control and PID fuzzy controller parallel system structure.

Fuzzy self-tuning PID control

PID control requires very precise model of the structure, but in practical applications, most industrial processes have different levels of nonlinear, parameter variability and model uncertainty and thus using conventional PID control cannot achieve precise control for industrial process. The fuzzy control has weak dependence on the mathematical model and the process does not need to establish precise mathematical model, just need to send the fuzzy rules and related information (such as evaluation, initial PID parameters) into the computer as a knowledge repository. Then the computer control system according to the actual situation takes the use of fuzzy reasoning can automatically adjust to the optimal PID parameters, and that is the fuzzy adaptive PID control.

Fuzzy PID parameters self-tuning control takes error *e* and error rate of change *ec* as fuzzy PID input, so can meet the different moments of *e* and *ec* on the PID parameter tuning requirements. Modify PID parameters K_p, T_i, T_d online use fuzzy control rules then it constitutes a self-tuning fuzzy PID controller. The control system architecture is shown in figure (4).

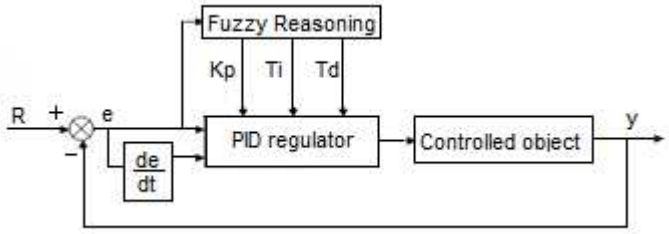

Fig. 4. Fuzzy PID control system structure.

The simulation results and analysis of a PID controller and a fuzzy PID controller

The article takes air volume furnace pressure transfer function and water volume main steam temperature transfer function of a thermal power plant as models, uses the traditional PID control and fuzzy PID control to optimize PID controller parameters and simulation.

The transfer function model of air volume furnace pressure of a thermal power plant is shown in equation (3):

$$G(s)=\frac{0.74}{(3s+1)^2} \quad \text{(System I)} \tag{3}$$

The transfer function model of water volume main steam temperature of a thermal power plant is shown in equation (4):

$$G(s)=\frac{-11.32}{(192.5s+1)^3}e^{-8.4s} \quad \text{(System II)} \tag{4}$$

The two systems are used in a single-loop control structure, and the same controller. These two systems are first with PID control and then with fuzzy PID control. Comparison and analysis of the effects of two control methods will be shown.

Simulation results and analysis. The simulation result is shown in figure(5).

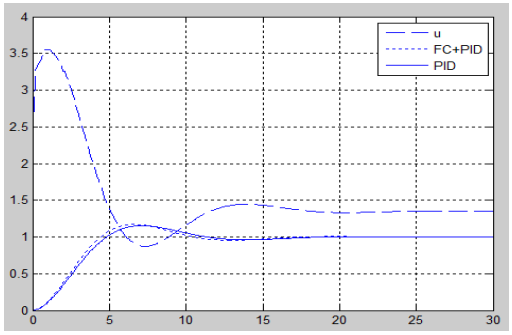

Fig. 5. Simulation of System I.

Shown as figure (5), the control effects of traditional PID control and fuzzy PID control basically meet the performance requirements (overshoot $\varphi < 15\%$, 0.75 <decay rate M_p <0.95, rise time, settling time, etc.), and the control effect is almost the same. Comparing the two methods, the rise time of fuzzy PID control is shorter than the traditional PID control, so the fuzzy PID controller responses faster. Generally speaking, for the system I: $G(s) = \dfrac{0.74}{(3s+1)^2}$, fuzzy PID control slightly better than the traditional PID control.

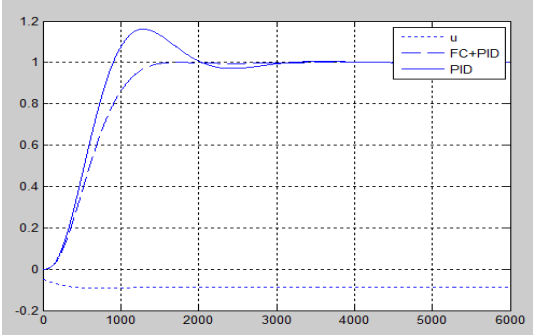

Fig. 6. Simulation of System II.

Shown as figure(6), System II using traditional PID control has overshoot, fast response, long time to adjust; using fuzzy PID control, there is no overshoot, response speed is slightly slower than the traditional PID and adjust time is shorter. Compared to the two methods shows that the fuzzy PID control enables the system without overshoot, but also greatly shorten the adjustment time and the adjustment is better than traditional PID control.

Compared the curve of the controller output u in Figure 5 and Figure 6, it shows that u in Figure 5 has a large output fluctuation and tends to balance in the final; u in Figure 6 has small output fluctuation and becomes more balanced quickly. That is fluctuations in the System II controller output is smaller than in System I. It can be seen that the fuzzy PID control has strong control ability for controller output of small inertia coefficient systems (such as System I) and poor control ability for big ones (such as System II). But for the system output 'y', the control effect is ideal.

Conclusion

In this paper, principles of traditional PID control, fuzzy control, fuzzy PID control are simply explained and based on examples of a thermal power plant uses traditional PID control and fuzzy PID control two methods to simulate with MATLAB, and then compare the control effects of the two methods.

From the simulation results in figure(5)and figure(6), it can be seen that the traditional PID control system has a large overshoot, long transition time and poor stability. However, Fuzzy PID controllers are better than conventional PID controller on overshoot and response time and the system stability is significantly improved. In the parameter tuning process, the PID parameters can be automatically adjusted according to error and error rate of change of the system so it has a better adaptability. This method can be applied to fuzzy control of complex systems, this kind of fuzzy

PID control has advantages of fuzzy control, such as flexibility, fast response, high control accuracy, high robustness; On the other hand, it can build a variety of complex fuzzy PID control systems and observe the results in a very intuitive SIMULINK environment so as to overcome the engineering practice blindness. Thus, combining the fuzzy control with PID control organically, you can achieve good control effects.

References:

[1] Pu Han, etc., "Intelligent Control Theory and Applications", Beijing: China Electric Power Press, 2013.

[2] Yunliu Shi, "Fuzzy-PID Temperature Control Applications in Industrial Furnaces", Non-ferrous metal processing, vol.36, No. 4, pp.60-62, 2007.

[3] Changju Ma, Boyuan Ma, "Design and Simulation of MATLAB Parameters based on Fuzzy Self-tuning PID Controllers", Electronic Test, pp.20-22, October, 2012.

[4] Rui Zhou, "Based Fuzzy Control PID Parameter Tuning", Computer and Digital Engineering, vol.33, No. 8, pp.166-168, 2006.

[5] An Wang, Qingqing Yang, Wenyu Yan, "Fuzzy Self-tuning PID Controller Design and Simulation", Computer Simulation, vol.29, No. 12, pp.224-228, 2012.

[6] Pu Han, Xiyan Zhu, "Automatic Control System Digital Simulation", Beijing: China Electric Power Press, 1996.

[7] Ping He, Hongxu Wang, "Design and Application of Fuzzy Controller", Beijing: Science Press, 1997.

[8] Wushan Cheng, "Intelligent Control Theory and Applications", Shanghai: Shanghai Jiaotong University Press, 2006.

Advanced Materials Research Vols. 960-961 (2014) pp 1162-1167

doi:10.4028/www.scientific.net/AMR.960-961.1162

Optimal Reactive Power Compensation Configuration in Distribution Power System Integrated with Small Hydro Power Plant

Hongliang Ma[1, a], Zhengmou Ren[1,b], Wenxin Lu[1,c], Yuxin Han[2,d], Zhaojian Wang[2,e],and Laijun Chen[2,f]

[1] Shaanxi Regional Electric Power Group Co., Ltd. Xi'an 710061, China

[2] State Key Laboratory of Control and Simulation of Power System and Generation Equipment, Department of Electrical Engineering, Tsinghua University, 100084 Beijing, China

[a]wangzhaojianjs@126.com, [b]zj-wang13@mails.tsinghua.edu.cn, [c]qiuzhuangthu@163.com, [d]hyx92@139.com, [e]wangzhaojiantj@163.com, [f]chenlaijun@tsinghua.edu.cn

Keywords: Small Hydro Power Plant, Magnetic Control Reactor, Optimization Model, Particle Swarm Optimization.

Abstract. Hydropower is the most widely used renewable energy for electricity generation in China, and small hydro power plant (SHPP) is a flexible way of electricity generation in water-rich remote area. Voltage at the end of distribution network may be increased over the acceptable range due to the connection of SHPPs. Magnetic control reactor (MCR) is usually used to reduce the voltage by consuming reactive power. A mathematical model for calculation of the optimal capacity of MCR is proposed in this paper, and particle swarm optimization (PSO) is adopted to solve the optimization problem. Two cases based on the IEEE 33-bus test system are used to validate the proposed method. In the given cases, system voltage is adjusted to the acceptable range.

Introduction

Electrical energy is important to the world and its production increases the carbon emission due to the use of fossil fuel [1, 2]. The increasing environment pressure facilitates the need of clean energy, such as solar energy, wind energy, hydropower, etc. Hydropower is the most widely used renewable energy for electricity generation in China, providing over 20% power consumption annually. Small hydro power plant (SHPP) is one of the most flexible and effective ways of electricity generation in remote area especially in water-rich region, which plays an important role in the improvement of the living standard [3, 4].

However, there are some problems when SHPP connected to the grid, one of which is the voltage violation. SHPP is usually connected at the end of low voltage distribution power system, and its capacity is much bigger than load demand, which results in the voltage increase. Sometimes, the voltage near SHPP connection bus is even beyond the acceptable range. To reduce the high voltage to an appropriate range around the rated value, a shunt reactor is needed. Magnetic control reactor (MCR) is a kind of capacity adjustable shunt reactors, which can be used to lower the voltage by absorbing reactive power. The capacity of MCR determines the bus voltage reduction value, so it is necessary to obtain the optimal MCR capacity. Many studies have been done on maximizing access power and introduction limits of distributed generation [5-7], and the reactive power is usually treated as means of improving the voltage [8-10], but few of them focus on the reactive power absorption. Background with the reality of SHPPs in the southern part of Shaanxi Province, this paper mainly focuses on the reactive consumption of the distribution power system with SHPPs.

A mathematical model is proposed to calculate the optimal capacity of MCR, and particle swarm optimization (PSO) is adopted to solve the optimization problem. Furthermore, two cases featured in single SHPP and three SHPPs are presented to get the optimal MCR capacity, and the method is proved effective.

METHODOLOGY

Mathematical Model. The optimal MCR capacity calculation for distribution power system integrated with multiple SHPPs is shown below.

Objective Function. The object of the SHPP owner is to minimize the total capacity of MCR, which is shown in Eq. 1.

$$\min \sum_{s=1}^{m} Q_{cs} \tag{1}$$

where m is the of number of MCR installation sites, Q_{cs} is the MCR capacity at bus s ($s = 1, 2, \cdots, m$).

Constraint Conditions. There are two kinds of constraints, equality constraints and inequality constraints. The former is power flow equation and the latter is the bound of variables, which is shown below.

Power flow equation:

$$\begin{cases} P_i = P_{Gi} - P_{li} = V_i \sum_{j=1}^{n} V_i \left(G_{ij} \cos\theta_{ij} + B_{ij} \sin\theta_{ij} \right) \\ Q_i = Q_{Gi} + Q_{ci} - Q_{li} = V_i \sum_{j=1}^{n} V_j \left(G_{ij} \sin\theta_{ij} - B_{ij} \cos\theta_{ij} \right) \end{cases} \tag{2}$$

where P_i, P_{Gi}, P_{li} is the active power injection, generation and consumption at bus i, $Q_i, Q_{Gi}, Q_{ci}, Q_{li}$ is the reactive power injection, generation, compensation and consumption at bus i, V_i and θ_i is the voltage and phase angle at bus i, G_{ij} and B_{ij} is the line admittance between bus i and j.

Power limits of SHPPs:

$$0 \le P_{Gs} \le P_{Gs\max} \tag{3}$$

$$Q_{Gs} = k_s P_{Gs} \tag{4}$$

where P_{Gs}, Q_{Gs} is the active power and reactive power of SHPP s, $P_{Gs\max}$ is the upper power limit of SHPP, k_s is a constant determined by power factor of SHPP.

Compensation capacity limits of MCRs:

$$0 \le Q_{cs} \le Q_{cs\max} \tag{5}$$

where $Q_{cs\max}$ is the upper power limit of MCR.

Voltage amplitude limits:

$$U_{i\min} \le U_i \le U_{i\max} \tag{6}$$

where $U_{i\min}, U_{i\max}$ is the lower and upper bound of voltage at bus i.

The optimization model can also be applied to distribution power system with single SHPP, and the objective function is shown in Eq. 7.

$$\min Q_c \tag{7}$$

where Q_c is the MCR capacity and all the constraints are identical.

Optimization Algorithm. Considering the complexity of the optimization problem, a particle swarm optimization algorithm is adopted to calculate the optimal MCR capacity [11], and the flowchart is shown in Fig. 1. In the following cases, the particle number and the iteration are both set as100.

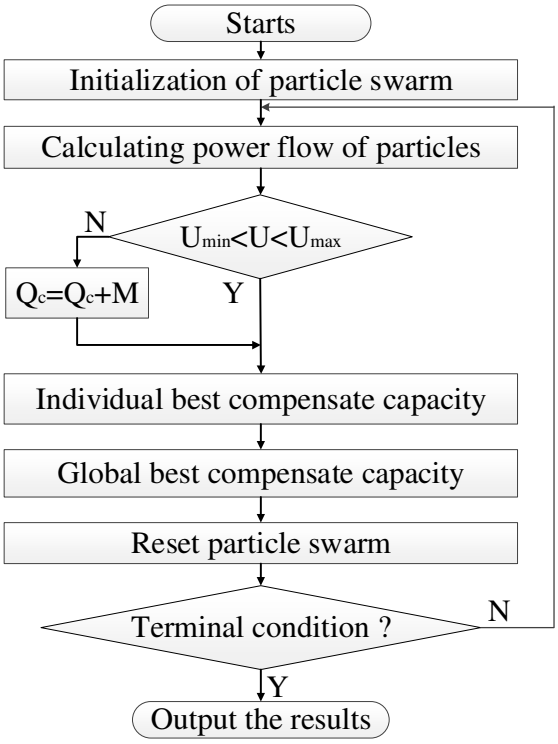

Fig. 1 Flowchart of PSO

Numerical Results

In this section, two cases based on the IEEE 33-bus test system is used to solve the proposed model and the results are provided. The voltage at bus one is set as 10.5kV, and the lower and upper bound of voltage is 0.93kV and 10.5kV respectively [5]. The power factor is 0.8, so k_s equals 0.75.

Case One: Single Small Hydro Plant. In this case, SHPP and MCR are connected at bus 18, and the SHPP capacity is $1600+j1200$ kVA, which is shown in Fig. 2.

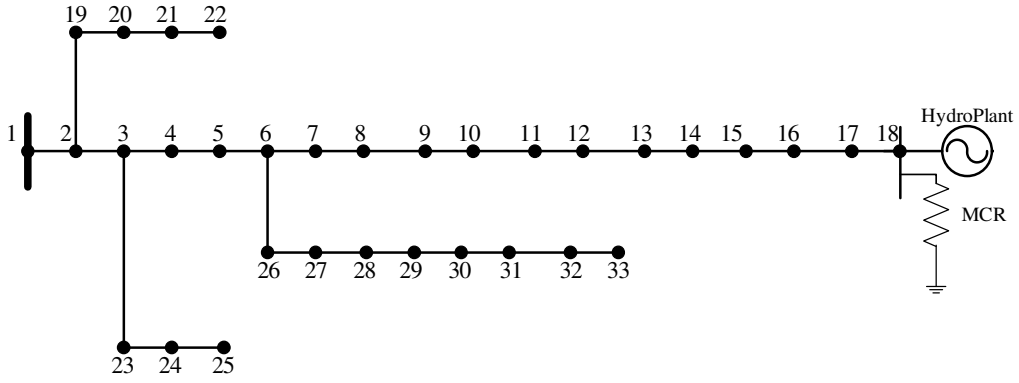

Fig. 2 Diagram of IEEE 33-bus system with single SHPP

The results of single MCR compensation is illustrated in Table 1.

Table 1 Results of single MCR compensation

Bus	Capacity（kVar）	Voltage without MCR（kV）	Voltage with MCR（kV）	Percentage（%）
18	1496	11.7	10.5	-10.25

In Table 1, the optimal capacity of MCR is 1496kVar, and voltage of bus 18 is 11.7kV without MCR, which is much higher than upper limit. By installing MCR, the voltage is reduced 10.25% to

10.5kV, which is within the voltage range. Voltage of all the buses in the system is illustrated in Fig. 3.

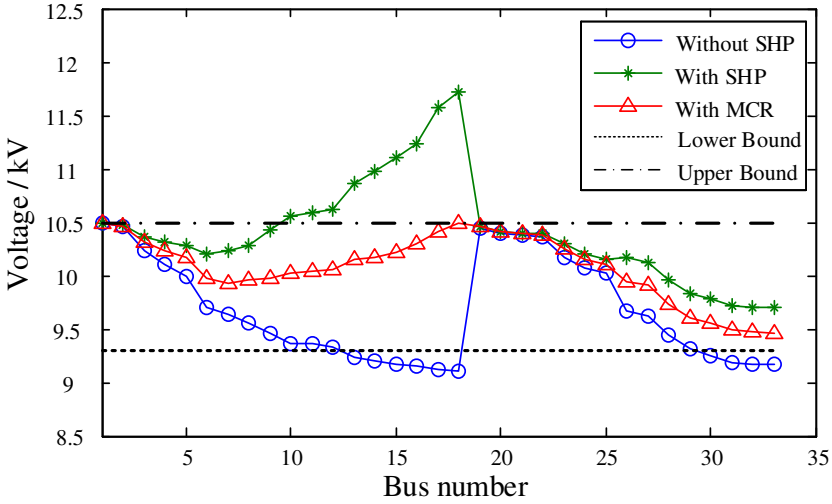

Fig. 3 All buses voltage of the system with single SHPP

Voltage from bus 10 to bus 18 is higher than the upper voltage limit before installing MCR, and the system voltage is reduced within the proper range after installing MCR.

Case Two: Three Small Hydro Plants. In this case, SHPPs and MCRs are connected at bus 18, 22, 33, and SHPPs capacity are $1600+j1200$ kVA, $800+j600$ kVA, $1600+j1200$ kVA respectively, which is shown in Fig. 4.

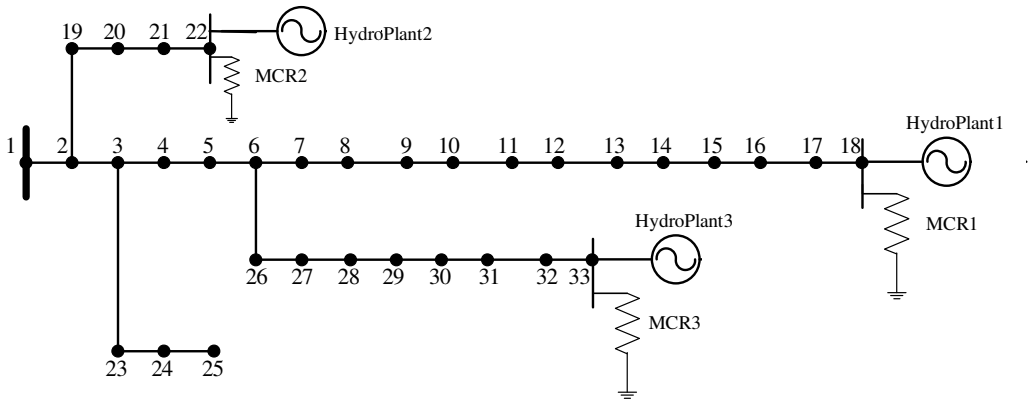

Fig. 4 Diagram of IEEE 33-bus system with three SHPPs

The results of multiple MCRs is illustrated in Table 1.

Table 2 Results of multiple SHPPs compensation

Bus	Capacity（kVar）	Voltage without Compensation（kV）	Voltage with Compensation（kV）	Percentage（%）
18	1837	12.2	10.5	-13.93
22	998	10.8	10.5	-2.78
33	1112	11.3	10.5	9.73

In Table 2, the optimal capacity of MCRs installed in bus 18, 22 and 33 is 1837kVar, 998kVar and 1112kVar respectively and voltage is 12.2kV, 10.8kV and 11.3kV without MCRs, which is much higher than upper limit. By installing MCR, the voltage is reduced to 10.5kV by 10.25%, which is within the voltage range. Voltage of all the buses in the system is illustrated in Fig. 3.

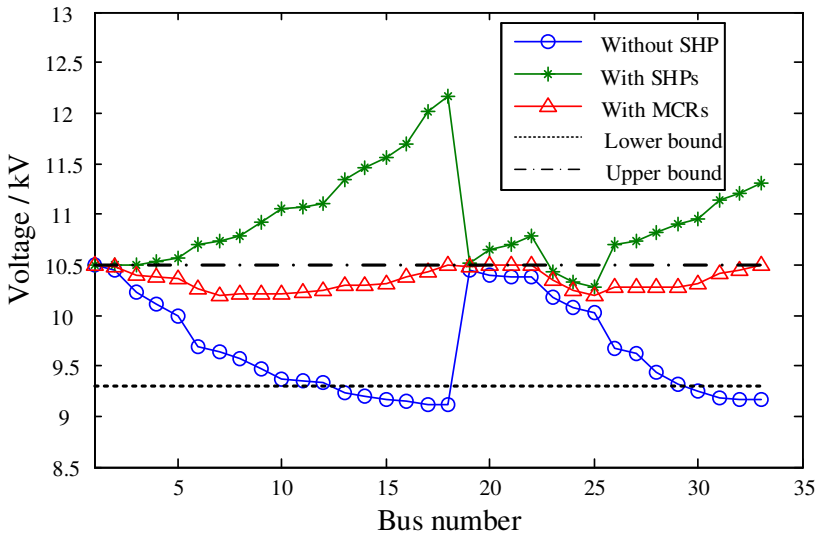

Fig. 5 All buses voltage of the system with three SHPPs

The system bus voltage is almost higher than the upper voltage limit before installing MCRs, and the voltage is reduced to the voltage range.

Conclusions

In order to mitigate the voltage problem in distribution power system integrated with small hydro power plant through reactive power compensation, an optimization model to calculate the optimal MCR capacity is proposed in this paper. From the results of two cases based on the IEEE 33-bus test system, voltage is reduced remarkably and is within the acceptable range. Transformer tap is fixed in the paper, and further studies will be continued with the consideration of adjustable transformer tap.

Acknowledgements

This work was financially supported by the Shaanxi Regional Electric Power Group Co., Ltd.

References

[1] Doolla S, Bhatti T S. Automatic generation control of an isolated small-hydro power plant [J]. Electric Power Systems Research. 2006, 76(9): 889-896

[2] Castronuovo E D, Peas Lopes J A. On the optimization of the daily operation of a wind-hydro power plant [J]. Power Systems, IEEE Transactions on. 2004, 19(3): 1599-1606

[3] Paish O. Small hydro power: technology and current status [J]. Renewable and sustainable energy reviews. 2002, 6(6): 537-556

[4] Kaldellis J K, Vlachou D S, Korbakis G. Techno-economic evaluation of small hydro power plants in Greece: a complete sensitivity analysis [J]. Energy Policy. 2005, 33(15): 1969-1985

[5] Hu Hua，Wu Shan，Xia Xiang，et al．Computing the maximum penetration level of multiple distributed generators in distribution network taking into account voltage regulation constraints [J]. Proceedings of the CSEE, 2006, 26(19): 13-17 (in Chinese)

[6] Xia Xiang, Huang Wei, Xu Xianghai, et al. Penetration level calculation taking into consideration the unit commitment of small hydro power [J]. Automation of Electric Power Systems, 2006, 30 (22): 48-52 (in Chinese)

[7] Kim T E, Kim J E. A method for determining the introduction limit of distributed generation system in distribution system [C]. Vancouver, BC: 2001

[8] GUO Jinming, LI Xinran, DENG Wei, et al. Comprehensive Optimal Allocation of Intermittent Distributed Generation and Reactive Power Compensation Based on Bi-level Planning [J]. Proceedings of the CSEE, 2013(28): 25-33 (in Chinese)

[9] YU Kun, CAO Yijia, CHEN Xingying, et al. Reactive power and voltage optimization of the district grid with distributed generation [J]. Automation of Electric Power Systems, 2011, 35(8): 1-5 (in Chinese)

[10] ZHANG Li, XU Yuqin, WANG Zengping, et al. Reactive power optimization for distribution system with distributed generators [J]. Transactions of China Electrotechnical Society, 2011, 26(3): 168-174 (in Chinese)

[11] Zhaojian W, Ying C, Shengzhou K, et al. Optimal design of isolated microgrid considering run-time load controllability [C]. Xi'an: 2013

Advanced Materials Research Vols. 960-961 (2014) pp 1168-1173

doi:10.4028/www.scientific.net/AMR.960-961.1168

Design and implementation of automatic test system of digital device

Juliang Zhang [1, a], QingChuang Deng [2,b], Yunhua HU [3,c]

[1,2,3]XJ Group Corporation XuChang, China

[a] juliangzh@xjgc.com,[b] dengqingchuang@xjgc.com,[c] keithy@ceptc.com

Key words: digital device test automatic testing; test system; IEC61580

Abstract: Aiming at the digital device test, design a automatic test system, introduced the concept, architecture and technology. The PC sends SMV to digital device based on IEC61850-9-2, Then receive real data from device through the PC serial based on IEC103, constructing a loop, then completed the test. Software static structure adopts the modular programming, dynamic data exchange uses multithread. According to the configured test case, test items can be completed automatically. The system is based on PC, compared with the traditional test instrument to save hardware cost. With the help of calculation and control capabilities of the PC, realize the automatic testing, make people liberation from repetitive work, more focused on the analysis of test results, improve test quality and efficiency.

Introduction

Digital device is an important part of power system, its normal work of great significance to ensure the safe and stable operation of power system. The digital device tested effectively, very important to ensure the normal and stable of the whole power system. With the development of science and technology make a spurt of progress and the coming of digital era, digital substation[1] has become the development direction of the future substation technology. The testing specification of digital device Based on the IEC61850 communication is not the same as usual. the digital device's sampling value, input/output value are based on the digital signal, so can simulated by PC, and digital relay protection testing automatically become possible.

Automatic measuring technique is introduced in this article, for measurement function of the digital device, realize the automatic test. Provides an automatic test scheme for the Testing personnel. Set the test case, automatic testing can be unmanned, and generate test results. In addition, the system provides debugging interface for test personnel, can by a single test case, also can set breakpoints to check and locate defects.

Test architecture

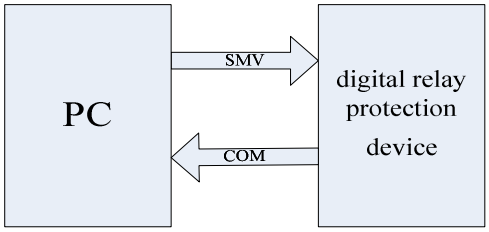

Fig.1 Simulating surroundings on test system

Figure 1 is a simulation environment of the automatic test system[2], it is a closed loop structure. In this system, the PC based on IEC61850-9-2 protocol send predetermined SMV messages to the digital Device and calculate the expected results, in the second time delay (customizable), PC call

data from digital Device through serial port based on IEC60870-5-103, and then put up the measured value and the expected values are compared, concluded that the results.

Test system software design

2.1 Software architecture

In order to facilitate code reuse, expansion and reduce the cost of maintenance, this system uses the development method of modular, hierarchical design. Between the various functional modules design idea of high cohesion, low coupling, in addition to the host program, all of other modules use dynamic link library in technology, module between synchronous multithread and signal mechanism. The test system software architecture is shown in figure 2.

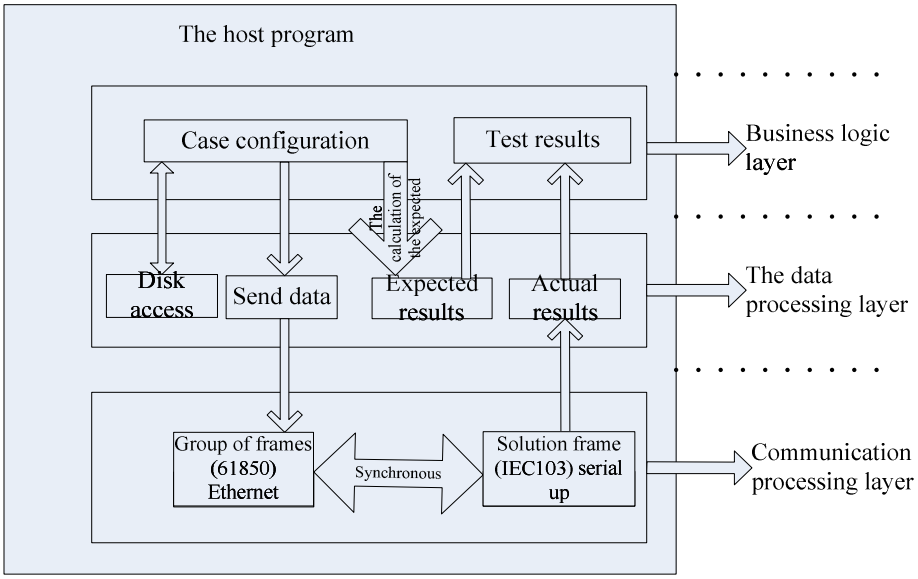

Fig.2 Software structure of test system

The host program is the main program of the system, Contain business logic layer, data processing layer, communication layer. To connection the hierarchy and module， realize the function of start and stop operation. In addition to providing global message processing and recording the running log operation. The following three levels: the system business logic layer, data layer, communication layer are introduced.

2.2 Business logic layer

Business logic layer mainly realizes the Processing of test configuration and results. Configured test case includes two parts，test instrument configuration and state sequence configuration.

The test instrument configuration to achieve communication and digital device, network configuration, serial configuration; channel analog correlation, channel number, channel packet types and ratings settings; group SMV frame related appid, priority, sampling points set[3].

State sequence configuration include the data source configuration, sending data source with the state sequence pattern, in order to make the sequence in each state or state combination simulation of a fault, the continuous playback of multiple faults in order to realize the automatic measurement, automatic testing unattended. Each state in the sequence contains not only to value information transmitted sample, also contains the current state of the actual results allowed error range.

Processing test results is in accordance with the error range of the fault condition of the requirements, the data processing layer to calculate the expected results and actual results data are compared, and finally generate test results and to submit the report. Test report is generated

automatically, in the test report in addition to each gives the conclusion on the measurement test content, test results are also with each dynamic test case, the test results contain "OK", "FAULT", "UNKNOWN" status, covering the test configuration used in all test cases project.

2.3 The data processing layer

Data processing layer consist of four function blocks. Access of test case，generation send data, calculate the expected results, deal actual results.

Access of test case to provide interface of test cases to save and read from disk, since the state sequence relates to the data quantity is relatively large and the structure is complex, the memory mapping technology, avoids the troublesome operation of the complex structure of disk reads and writes, in the test cases stored and read time showed superior performance.

Generation send data mainly completes to each channel test cases sampled values in discrete and harmonic superposition. discrete sampling values is based on amplitude, initial phase, the number of sampling points and other information which configured in case, using sine wave discrete algorithm[4]. Harmonic superposition of harmonic[5] according to the frequency, amplitude information configured in test cases . Each channel can be stacked 2 to 50 harmonic data[5].

Calculate the expected result is according to sampling and harmonic information, Based on the principle of digital device, to calculate the expected test results of measured values. The line voltage and line current can use results from channel sampling value configuration, the main phase voltage, active power, reactive power, apparent power and so on are need to calculate.

The actual result here is acquired from the IEC60870-5-103 frame which processing in layer solution frame.

2.4 Communication processing layer

SMV messages based on IEC61850-9-2, Serial messages based on IEC60870-5-103 were completed in Communication processing layer. The synchronization is to ensure that the measured data from the IEC60870-5-103 message and the sampling data of current state are Correspond, in order to protect the business logic layer processing test results when the expected value and the actual value of comparable.

2.4.1 SMV packet sending module

SMV message frame based on IEC61850-9-2 specification, frame content depends on the test configuration module configuration.

PC simulation of the SMV message sent is a problem of technology, digital device requires very high received SMV message real-time, 50HZ frequency, according to the sampling rate and ASDU numbers in frame, the transmission rate requirements are also different, as shown in table 1.

Tab.1 Sending speed rate and sampling rate at 50Hz

Sampling rate (points / Cycle)	ASDU numbers of one Frame （points/Frame）	The sending rate(frames per second)	Transmission interval(MS)	Maximum allowed message sending interval (MS)
200	2	5000	0.2	5
200	5	2000	0.5	5
200	10	1000	1	5
80	5	800	1.25	5
80	10	400	2.5	5

From table 1 we can see, when the sampling rate is 200, each frame of the message contains 2 ASDU, requirements on the transmission rate of 5000 frames per second, which is average every 0.2ms would send a message, the largest interval does not exceed 5ms. The PC in the data preparation and transmission timing control put forward higher requirements. The conventional PC based computing power, the cache technology, to continue to prepare the data to be transmitted is feasible, but due to the non real-time operating system PC is based on the message mechanism, the precision of time control in about 10ms under the general situation, be far from the transmission precision 0.2ms.

In this issue we through technology exchange preselected multimedia timer and system timer interrupt two schemes, finally through the practice of using the system timer interrupt to achieve timing control. System timer interrupt the use of 8253 PC in the programmable timer / counter chip, to meet the demand for control.

2.4.2 IEC60870-5-103 message up module

Digital device provides external serial port which follows the IEC60870-5-103 protocol, other device can get sampling values and other information via this serial port. Our automatic testing system is to grasp this point, first establish communication with device through the serial port, and then upload information in accordance with the IEC60870-5-103 standard. According to the demand of the system, the module is divided into three layers, as shown in figure 3.

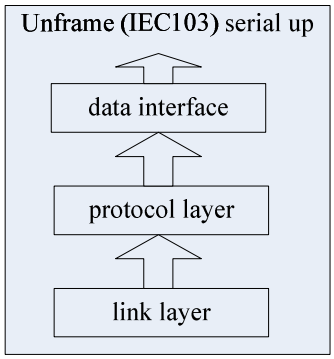

Fig.5 Relational heirarchical structure of IEC103

The link layer is responsible for establishing IEC103 communication, to ensure the general operation of communication link, and complete the command of receiving and sending message. Protocol layer based on IEC60870-5-103 protocol, is responsible for the formation of the device commands, analyzing information from the device callback. The data interface provide information for upper layer application(data processing layer), analysis out the real-time data information from protocol layer ， According to the need to provide to the upper application.

The serial code technology we adopted Microsoft stable MSComm control, combining with the multithreading technology, guarantee for real-time and reliability of receiving message processing.

Application

The system can play a big role in the test of the digital device, complete all test project configuration (Table 2).

Tab.2 Measurement items statistics of measurement system

Testing options		Test cases and requirements	Completion
Base options	Ia，Ib，Ic，Ua，Ub，Uc，Uab，Ubc，Uca，P，Q，f，S，COSφ	fundamental wave environmental testing	Automatic
		Superposition of harmonic (2-50) test	Automatic
Extend options	3I0 real，3I0 imaginary，3U0 real，3U0imaginary，3I0 real part of five harmonics，3I0 imaginary of five harmonics，3U0 real part of five harmonics，3U0maginary of five harmonics	fundamental wave environmental testing	Automatic
		Superposition of harmonic (2-50) test	Automatic

A friendly man-machine interface to the cases configuration was designed, convenient configuration input, including each channel phase voltage, current, superposition of multiple harmonic, the program automatically calculate the expected value according to the input cases, get actual results from the device, gives the test report by comparison.

After the completion of test case allocation, only need to click the test button, the test system can in the unattended condition, the maximum traversal algorithm, to complete test and gives test report. Its advantages in practical application process:

1) Can run on PC , Compared with the traditional test instrument, cost is lower than 5% (currently on the market a lot of testing algorithms are based on the tester ,not PC).

2) automatic test function based on the powerful computing ability and multi task processing characteristics of PC , greatly improves the test efficiency, this is the general testing instrument cannot handle.

3) To save human resources, avoid omission caused by long time repeated work paralysis.

4) Processing ability based on PC, human can't reach the depth and breadth of the testing procedure.

The product is put into use is important to the quality of protection device. In addition to a certain type of protection device, only need to configure a set of use cases, then we can reuse in the future.

Conclusion

This paper introduces the automatic test system of digital device ， which when doing the task, realize the automatic test of true. Enable testers get rid of complicated manual operation in the test time, dedicated to testing research and theory analysis, and make greater contribution to the development of testing field. In addition, the system only need a computer can, simple structure, reliable performance. The system carries out IEC61850-9-2 and IEC60870-5-103 standards, play a positive role for digital device to achieve interoperability of different manufacturers.

Author brief introduction:
Deng Qingchuang (1980-), male, electrical engineer, software engineer, Committed to the research of Digital and automation test.email:Dengqingchuang@xjgc.com

References

[1] LI Xian-mei, HUANG Jia-dong, TANG Bao-feng. Research on testing technology of relay protection for digital substation [J].Power System Protection and Control,2012,V40(3):105-108.

[2] LAI Qing, HUA Jian-wei, LV Yun, CHEN Yue-fei, XU Jian. Research on general relay protection auto-test system software[J]. Power System Protection and Control, 2010, 38(3): 90-94.

[3] WANG YE, LU Yu-ping, XU Yi-chao, XU Dan-xuan. A Novel Resampling Method for Differential Protection [J]. Transactions of China Electrotechnical Society, 2012, 27(11): 239-247.

[4] ZHANG PENG, LI Hong-bin. A Novel Algorithm for Harmonic Analysis Based on Discrete Wavelet Transforms [J]. Transactions of China Electrotechnical Society, 2012, 27(3): 252-259.

[5] HUI JIN, YANG Hong-geng. Harmonics and Interharmonics Separate-Detection Method Based on Estimation of Leakage Values Caused by Interharmonics [J]. Transactions of China Electrotechnical Society, 2011, 26(1): 183-190.

Advanced Materials Research Vols. 960-961 (2014) pp 1174-1179

doi:10.4028/www.scientific.net/AMR.960-961.1174

POWER SYSTEM VOLTAGE CONTROL USING WIND FARMS BASED ON A DOUBLY FED INDUCTION GENERATION (DFIG)

Sabir MESSALTI [1] Bilal.Boudjlal[2] Hichem Azli [3]

[1,2] University of M'sila, Faculty of Technology, 28000, M'sila , Algeria,

[3] University of Setif, Faculty of Technology, Setif 19000, Algeria

[1] messalti.sabir@yahoo.fr; [2] i.bilux@gmail.com, [3] az_hic@yahoo.fr,

Keywords: Voltage control, independent control of active and reactive power, DFIG, Field-oriented control, wind turbine, power system.

Abstract. This paper shows the modeling and the effectiveness of wind turbine for voltage improvement of power systems. The wind turbine is based on a doubly-fed induction generator (DFIG). A field-oriented control is used to control of the power flow exchanged between the DFIG and the power system. A simplified wind turbine model based on independent control of active and reactive powers is used in this paper. The proposed methodology is tested in the single machine power system connected to a wind farms in the case of sudden voltage variations.

Introduction

Power system is increasingly confronted with problems related to the production, transport and distribution of energy. Despite the multitude of strategies and means of protection, power systems are confronted by numerous constraints such as the increase in demand, disturbances, planning, interconnection and network complexity. It is imperative to provide detailed information for each option. An important study that should be included in the design of electrical networks is controlling and improving the voltage stability, the main causes for occurrence of voltage instability are: Voltage sources are too far from load centers; High Reactive Power Consumption at Heavy Loads; Poor coordination between multiple FACTS;…, etc [1-5].

Production of electricity from wind power, as a renewable energy source, is continually attracting the attention of investors, researchers and electrical utilities. Integration of wind power into the power system has been studied by many authors. Wind power influences several power system characteristics from economic dispatch to stability and quality issues.

Many types of generators have been used to convert wind power into electricity, especially the Doubly-Fed Induction Generators (DFIG) which is becoming increasingly popular in large wind power conversion systems due to their various advantages. [6,8]. A DFIG in a wind turbine has the ability to generate maximum power with varying rotational speed, to control active and reactive by integration of electronic power converters such as the back-to-back converter[9-11].

This paper is organized as follows: The first part studies wind park model and the dynamics of the DFIG model establishing the Field-oriented control strategy (FOC) with PI current and power controllers [12-14]. The second part shows the modeling of power system and reactive wind controller. The discussion and analysis are presented in the third part, which the equivalence modeling of a wind park involves combining all turbines with the same mechanical natural frequency into a single equivalent turbine.

2. Wind Generator Model

2.1 Wind Turbine Model

The mathematical relation for the mechanical power extraction from the wind can be expressed as follows:

$$P_{aer} = \frac{1}{2} C_p(\lambda, \beta) \rho S v_{wind}^3 \tag{1}$$

Where:

P_{aer} is the extracted power from the wind; ρ : is the air density (kg/m^3); S : is the turbine swept area (m^2); v_{wind} : is the wind speed (m/s); β : Blade pitch angle (deg); λ : is the ratio of blade tip speed to wind speed defined by:

$$\lambda = R\Omega_t / V_{wind} \tag{2}$$

C_p is the performance coefficient of the turbine, C_p is often given as a function of the tip speed ratio λ; Ω: the wind turbine rotational speed (rad /sec); R: the wind turbine radius.

The expression of the power coefficient Cp is given by the following equation [15]:

$$C_p(\lambda,\beta) = (0.35 - 0.0167(\beta - 2))\sin\left(\frac{\pi(\lambda + 0.1)}{14.34 - 0.3(\beta - 2)}\right) - (0.00184(\lambda - 3)(\beta - 2)) \tag{3}$$

The mechanical torque of the turbine is given by the following relationship

$$C_t = \frac{P_t}{\Omega_t} = \frac{1}{2\lambda}\rho\pi R^3 v^2 C_p(\lambda,\beta) \tag{4}$$

Knowing the speed multiplier G (coupling),the generator speed is given by:

$$\Omega_t = \Omega_{mecg} / G \tag{5}$$

The mechanical power available on the shaft of the electric generator is expressed by:

$$P_{mg} = \frac{1}{2} C_p\left(\frac{\Omega_{mec} R}{G v_{wind}}\right)\rho\pi R^2 v_{wind}^3 \tag{6}$$

2.2. Modeling and Stator Flux Oriented Control of DFIG

The DFIG wind turbines utilize a wound rotor induction generator. The concept is based on two back-to-back voltage source converters connecting the grid and the rotor windings. The stator windings are connected directly to the grid [12-14]. The general model of the DFIG obtained using Park transformation is given by the following equations [13-15].

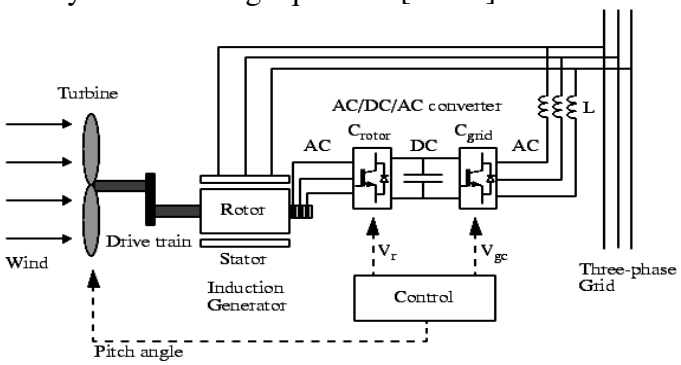

Fig. 1. The Wind Turbine and the DFIG System

$$\begin{cases} V_{ds} = -R_s.I_{ds} + \frac{d}{dt}\phi_{ds} - \omega_s\phi_{qs} \\ V_{qs} = -R_s.I_{qs} + \frac{d}{dt}\phi_{qs} + \omega_s\phi_{ds} \\ V_{dr} = R_r.I_{dr} + \frac{d}{dt}\phi_{dr} - \omega_r\phi_{qr} \\ V_{qr} = R_r.I_{qr} + \frac{d}{dt}\phi_{qr} + \omega_r\phi_{dr} \end{cases} \tag{7}$$

$$\begin{cases} \phi_{ds} = -L_s.I_{ds} + M.I_{dr} \\ \phi_{qs} = -L_s.I_{qs} + M.I_{qr} \\ \phi_{dr} = L_r.I_{dr} - M.I_{ds} \\ \phi_{qr} = L_r.I_{qr} - M.I_{qs} \end{cases} \tag{8}$$

The electromagnetic torque and its associated motion equation are expressed respectively by:

$$C_{em} = p\frac{M}{L_s}\left[\varphi_{qs} i_{dr} - \varphi_{ds} i_{qr}\right] \tag{9}$$

$$J\frac{d\Omega}{dt} = C_{em} - C_r - f\Omega \tag{10}$$

To achieve a stator active and reactive power vector independent control, by orienting the reference (d,q) so that the axis is aligned with the stator flux [13-15], the following solutions can be obtained:

$$\phi_{ds} = \phi_s \quad and \quad \phi_{qs} = 0 \tag{11}$$

$$C_{em} = -p\frac{M}{L_s}\varphi_{ds} I_{qr} \tag{12}$$

According to the adopted assumptions and mathematical substitutions, the voltage expressions are:

$$\begin{aligned} V_{dr} &= R_r.I_{dr} - g\omega_s\left(L_r - \frac{M^2}{L_s}\right)I_{qr} \\ V_{qr} &= R_r.I_{qr} + g\omega_s\left(L_r - \frac{M^2}{L_s}\right)I_{dr} + g\omega_s\frac{M\phi_s}{L_s} \end{aligned} \tag{13}$$

The active and reactive power expressions are:

$$\begin{cases} P_s = V_s I_{qs} = -\dfrac{\omega_s \phi_s M}{L_s} I_{qr} \\ Q_s = V_s I_{ds} = -\dfrac{\omega_s \phi_s M}{L_s} I_{dr} + \dfrac{\omega_s \phi_s^2}{L_s} \end{cases} \tag{14}$$

Figures 2 and 3 show the performance of the active–reactive power control.

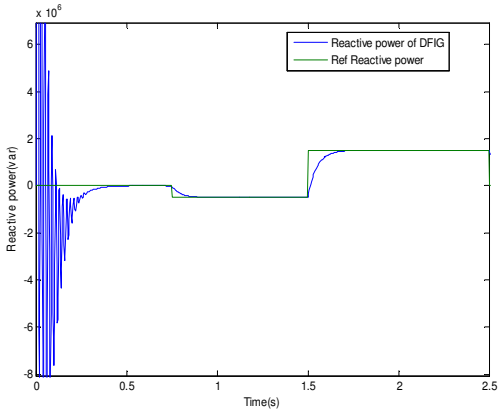

Fig. 2. Active power of DFIG using F.O.C

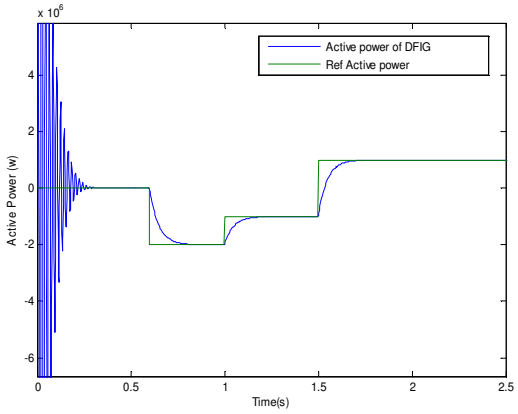

Fig. 3. Reactive power of DFIG using F.O.C

3. Modeling of Power system

A single machine power system is used to demonstrate the fundamental concepts and principles of voltage control using wind turbine when subjected to large disturbances (Fig. 4).

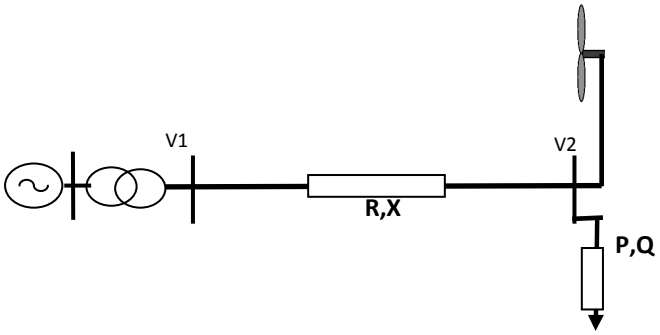

Fig. 4. A Single machine power system with wind generator

-P and Q are the active and reactive powers respectively of load, R and X are resistance and reactance line respectively, V_1 and V_2 are voltage of bus 1 and 2 respectively.

The voltage at the Bus 2 can be determined as follow:

$$V_2 = V_1 - \Delta V \tag{15}$$

The relationship between voltage gradient and the flow of active and reactive power on a radial distribution line can be expressed as follows:

$$\Delta V = (\mathrm{P}\, R + Q X)/V_n \tag{16}$$

The voltage can increase or decrease depending on the amount of the reactive and active power flux and on the network characteristics.

4. Modeling of Wind Power Controller

The rapid controllability of the DFIG can be used to significantly enhance the power system voltage control. The wind power controller used for this purpose is given in figure.5, where k_{wind} and T_{wind} are the gain and time constant of the wind power controller respectively, in which the output power controller ($C_{controller}$) will be used as specific or reference power to be produced by the DFIG.

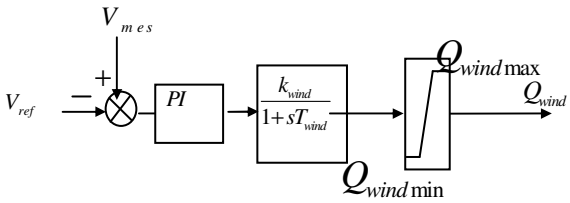

Fig. 5. Reactive wind power controller.

Where :

V_{ref} ,V_{mes} are the reference and the measured voltage bus respectively.

The proposed power modulation Q_{wind} has been incorporated in the power system in which any deficit or excess of voltage is compensated by the DFIG. The equation (22) can written by:

$$\Delta V = \mathrm{P}\, R + (Q - Q_{wind})\, X / V_n \tag{17}$$

5. Results Analysis

The feasibility and efficiency of the proposed controller have been tested on a single machine test system connected to a wind farms as shown in Fig.4, a sudden variation of voltage of generator is applied at t=3s (V_1= 0.9 V_{ref}) and at t=5s (V_1= 1.1 V_{ref}) .

Figure 6 shows the reactive wind power produced by DFIG after the disturbances in order to restore the voltage of bus N°2. Figure 7 shows the comparative bus voltage (N°2) with and without controller. It's clear that the proposed controller significantly improve the bus voltage rapidly.

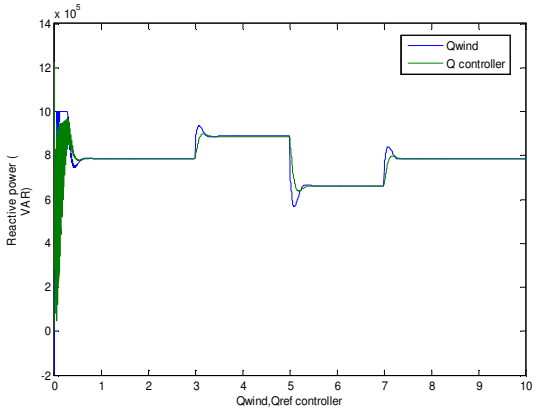

Fig. 6. Reactive power of wind turbine injected after disturbances

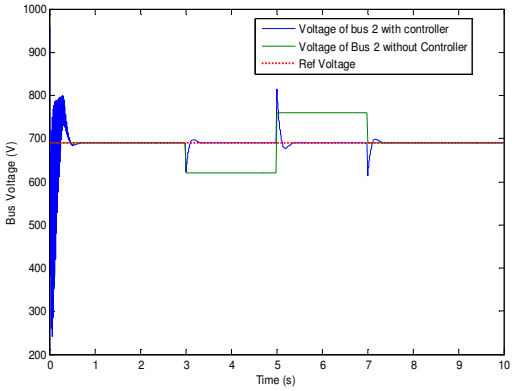

Fig. 7. Voltage control using reactive wind controller

6. Conclusion

In this paper, a new control strategy of reactive wind power has been successfully applied to improve the power system voltage. In which the wind turbine is based on a doubly-fed induction generator (DFIG). A field-oriented control is used to control of the power flow exchanged between

the DFIG and the power system. The rapid controllability of injected active provided by wind turbines are used to control and improvement of the voltage. Results indicate that the reactive wind power control can significantly improve the system performance, the efficiency of the wind farms is more important when the percentage of the installed wind power over the total production is higher.

Appendix

P_s , Q_s	Active and reactive stator power,
f	Coefficient of viscous frictions,
C_r	Load torque,
C_{em}	Electromagnetic torque.
I_{ds} , I_{qs}	Two-phase stator currents,
I_{dr} , I_{qr}	Two-phase rotor currents,
V_{ds} , V_{qs}	Two-phase stator voltages,
V_{dr} ,V_{qr}	Two-phase rotor voltages,
φ_{ds} , φ_{qs} ,	Two-phase stator fluxes,
φ_{dr} , φ_{qr}	Two-phase rotor fluxes,
Rs , Rr	Per phase stator and rotor resistances,
L_s , L_r	Per phase stator and rotor inductances,
M	Mutual inductance,
p	Number of pole pairs.

Parameters of DFIG:

3MW ; 690V/15KV ; 50Hz;Nm=1440; m=1;
Lfs=121e-6; Lfr=57.3e-6; Lm=12.12e-3;
Ls=Lfs+Lm; Lr=Lfr+m^2*Lm; M=m*Lm;
Rs=0.00297;Rr=0.00382;Jg=114;
fg=0.0071 p=2;

Parameters of wind turbine:

air_dens=1.225;R=45;Beta=2;G=100;
ft=0.0024;
Jt=(1.4e6/G^2+Jg);
lambda_max=7.07;cp_max=0.35;
c1=0.5176;c2=116;c3=0.4;c4=5;c5=21;
c6=0.0068;

References

[1] C.Taylor, Reactive power compensation and voltage stability: removing transmission limitations, Seminar Book, February (1997).

[2] P. Kundur, Power System Stability and Control: McGraw-Hill, (1994)

[3] P. M. Anderson , A. A. Fouad, Power System Control and Stability, IEEE Press, (1994)

[4] V.Ajjarapu, B.Lee, Bibliography on voltage stability, IEEE Trans. Power Systems, vol. 13(1), pp. 115-125 (1998).

[5] J. R. Shin, B. S. Kim, M. S. Chae, and S. A. Sebo, Improvement of the precise P-V curve considering the effects of voltage dependent load models and transmission losses for voltage stability analysis," Proc Inst. Elect. Eng., Gen., Transm., Dist., vol. 149(4), pp. 384–388,(2002)

[6] V. Akhmatov, Variable-speed wind turbines with DFIG. Part IV: Wind Energy, vol(27), pp. 519–529 (2003)

[7] S. Muller, M. Deicke, , R. W. De Doncker, Doubly fed induction generator systems for wind turbines, IEEE Ind. Appl. Mag, vol. 8(3), pp. 26–33 (2002)

[8] Y. Lei, A. Mullane, G. Lightbody, R. Yacamini, Modeling of the Wind Turbine with a DFIG for Grid Integration Studies, IEEE Trans. Energy Conversion, vol. 21, n. 1, pp. 257 – 264(2006).

[9] W . Leonard, "Field oriented control of a variable speed alternator connected to the constant frequency line", Proceedings of the IEEE Conf on control of power system, , pp. 149-153(1979)

[10] M. Yamamoto , O. Motoyoshi, Active and reactive power control for doubly-fed wound rotor induction generator", IEEE Trans. Power Electron., vol. 6, n. 4, Oct. 1991, pp. 624–629.

[11] R. Pena, J.C. Clare, G.M. Ashek , "Doubly-fed induction generator using back-to-back PWM converters and its application to variable-speed wind-energy generation", Electric Power Applications , IEE Proceedings, vol. 143, (3) ,pp. 231-241(1996).

[12] F. Poitiers, M. Machmoum, R. L. Doeuff, M. E. Zaim, "Control of a DFIG for wind energy conversion systems", Inte Jour Rene Energy Eng, pp. 373–378(2001).

[13] A. Naamane, N.K. Msirdi, "Doubly-fed induction generator control for an urban wind turbine", International Renewable Energy Congress , Sousse, Tunisia Nov(2010)

[14] Z. Boudjema, A. Meroufel , E. Bounadja, Robust Control Improvement of a Doubly Fed Induction Generator for Wind Energy Conversion, 4th *Int Conf* ICEE, Algiers (2012).

[15] A. GAILLARD : Système éolien basé sur une MADA : contribution à l'étude de la qualité de l'énergie électrique, Ph.D. dissertation University Henri Poincaré, Nancy, (2010).

CHAPTER 10:

Motor and Electrical Research

Advanced Materials Research Vols. 960-961 (2014) pp 1183-1188

doi:10.4028/www.scientific.net/AMR.960-961.1183

Design and Implementation of Sensorless Vector Control System for Permanent Magnet Synchronous Motor

Sheng wen Fan[1, a],Dong Liu[1, b],Zheng xi Li[1, c],Ze ting Wang[1, d],Peng Wang[1, e]

[1]Power Electronics & Motor Drivers Engineering Research Center,North China University of Technology,Beijing 100144,China

[a]fsw@ncut.edu.cn, [b]ncutliudong@126.com,
[c]lzx@ncut.edu.cn,[d]wangzeting@ncut.edu.cn,[e]catdapeng2008@163.com

Keywords: permanent magnet synchronous motor； sensorless； back electromotive force; TMS320F2808

Abstract. This paper will introduce the sensorless vector control system of permanent magnet synchronous motor,it adopts the PLL structure to correct motor back electromotive force for the motor rotor speed/position estimation and vector control algorithm to realize speed and current loop control of PMSM.This paper established a mathematical model of the PMSM,design of system software and hardware,the principle of speed/position estimation method and simulation of system in Matlab/Simulink.Finally,it introduces the experiment of whole system in TMS320F2808-based PMSM experiment platform,the simulation and experimental result verify feasibility,fast response and practicability of the system.

Introduction

Permanent magnet synchronous motor has the following advantages: low rotor losses and moment of inertia, good acceleration and deceleration performance, smooth torque, high efficiency[1]. Compared to the DC motor, it no mechanical commutator and brushes, which makes system maintenance of low cost, high reliability, compared with asynchronous motors, no reactive excitation current, high power factor[2]. Because of these advantages, making it has widely applied in various industrial applications.In conventional permanent magnet synchronous motor vector control system, commonly used optical encoder or resolver and other mechanical sensors to detect the rotor speed / position, but these mechanical sensors will lead to high system cost and poor reliability. To solve this problem, various sensorless control strategies has become a research focus in AC drive field.

Speed/position estimation method currently used in permanent magnet synchronous motor vector control system is mainly divided into two categories[3]:one is the high-frequency signal injection method, and the other is calculated based on the motor model and parameters, including state observer, flux observer and back electromotive force method. This paper will adopt the back-EMF observation and phase-locked loop (PLL) a combination of speed/position estimation algorithm[4] and also be introduce system software and hardware design, and ultimately the simulation and experimental result verify feasibility,fast response and practicability of the system.

The mathematical model of PMSM

The PMSM has the magnet on the rotor, and it is usually designed to generate sinusoidal back EMF. And there are no field winding and no damper windings either at the rotor. And the field flux is

constant because of the permanent magnet. The effective air gap is larger compared to the wound rotor synchronous machine because the relative permeability of the magnet is almost unity like air. By omitting damper winding circuits and by replacing the field winding circuit by a constant current source,the equivalent circuit can be modified as Figure 1.

Based on the equivalent circuit of permanent magnet synchronous motor, the mathematical model[5]in the d-q axis can be obtained, including voltage equation(Eq. 1, Eq. 2),flux equation(Eq. 3, Eq. 4), torque equation(Eq. 5)and the equation of motion(Eq. 6).

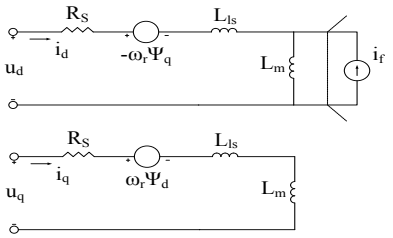

Fig.1 The equivalent circuit of permanent magnet synchronous motor in the d-q axis

$$u_d = R_s i_d + p\psi_d - \omega_r \psi_q \tag{1}$$

$$u_q = R_s i_q + p\psi_q + \omega_r \psi_d \tag{2}$$

$$\psi_d = \psi_f + L_s i_d \tag{3}$$

$$\psi_q = L_s i_q \tag{4}$$

$$T_e = \frac{3}{2} n_p L_m i_f i_q = \frac{3}{2} n_p \psi_f i_q \tag{5}$$

$$T_e - T_l = \frac{J}{n_p}\frac{d\omega_r}{dt} + B\omega_r \tag{6}$$

Overall design of the system

Hardware design of the system. Hardware circuit of sensorless vector control system for permanent magnet synchronous motor can be divided into two parts: the main circuit and control circuit. In the main circuit, the voltage inverter circuit uses intelligent power module (IPM), which integrates a 6-channel PWM output and fault alarm.Main circuit further includes a EMC filter circuit, a rectifying circuit, a pre-charge circuit, IPM drive circuit and phase current sampling circuit; Control circuit includes TMS320F2808 DSP chip and the peripheral circuit including the auxiliary power source, PWM driving circuits, communications circuits, E^2PROM memory circuit.Electric circuit and electronic circuit will be isolated by the optocoupler. Hardware block diagram is shown in Figure 2.

The principle of double closed loop vector control. Rotor field oriented control (ie vector control) of permanent magnet synchronous motor make the rotor flux as the stator and gap flux's reference frame.The purpose is the decoupling between the torque component and the excitation component of stator current,so that AC motor can be controlled like DC motor. As the air gap flux equal permanent magnet rotor flux and the armature reaction flux the stator currents generated, excitation current component i_{dref} should be set to zero, d-axis gas gap flux only equal to Ψ_f and d-axis armature reaction flux is zero for field-oriented control of constant torque mode. This article focuses on field oriented control under constant torque mode, Figure 3 shows the block diagram of the control system.

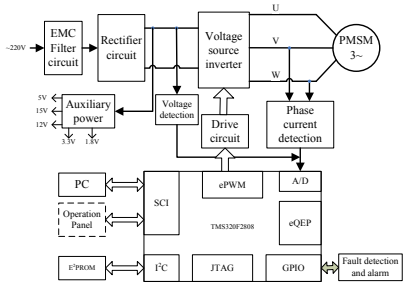

Fig.2 System hardware block diagram

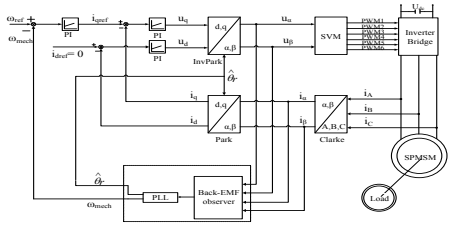

Fig.3 The block diagram of sensorless field oriented control for PMSM

Rotor velocity/position estimation method. In this paper, the velocity/position estimation algorithm based primarily on the mathematical model of the motor, the back electromotive force calculation and PLL. Since there will be inevitably error between the actual back-EMF and calculated back-EMF in the sensorless field-oriented control of PMSM,so the deviation of the rotor position angle will also appear. Figure 4 shows the relation of back electromotive force vector and estimated position angle[6].

Based on the above analysis, the d-axis component of the back-EMF is not zero would lead to the deviation of velocity/position estimated results, but it can be eliminated by PLL to correct q-axis component of the back-EMF. Voltage equations can be written as equation (5) and (6) in the estimated rotating coordinate system. θ_{err} is defined as equation (7).

Where θ_r is the actual rotor position angle, $\hat{\theta}_r$ is estimated rotor position angle. Equation (5) can be obtained when the system is running at steady state, if the angle of the estimated position and the actual position angle is consistent, then the d-axis component of the the back-EMF must be zero.The estimator is shown in Figure 5.

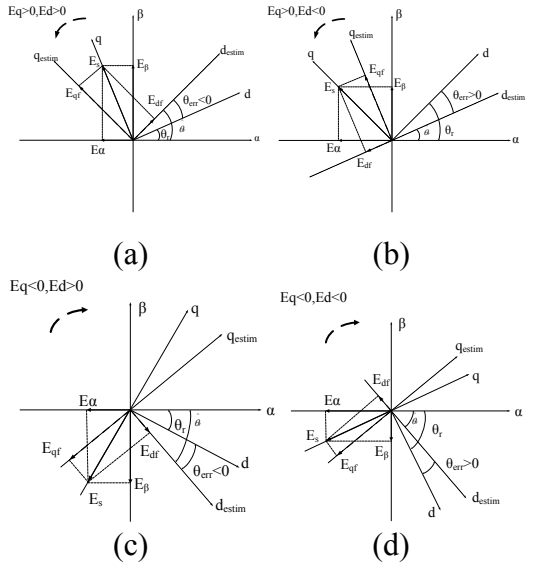

Fig.4 The relation of back electromotive force vector and estimatied position angle

$$u_d = R_s i_d + L\frac{di_d}{dt} - \omega_r L_s i_q - \omega_r \psi_f \sin\theta_{err} \tag{5}$$

$$u_q = R_s i_q + L\frac{di_q}{dt} + \omega_r L_s i_d + \omega_r \psi_f \cos\theta_{err} \tag{6}$$

$$\theta_{err} = \theta_r - \hat{\theta}_r \tag{7}$$

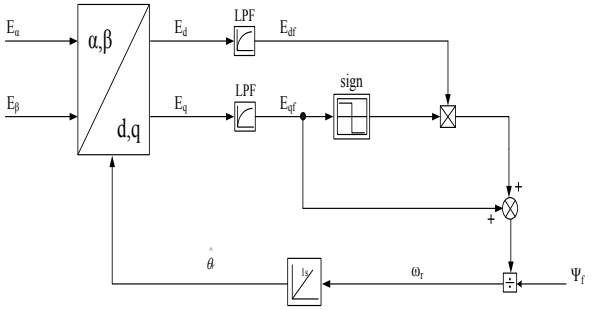

Fig.5 The block diagram of rotor speed/position estimation

In the two-phase stationary coordinate system, the back electromotive force α, β components can be obtained by detecting the stator voltage u_α, u_β and stator current i_α, i_β. It is calculated according to equation (8), (9).

According to Park transformation,the back electromotive force d, q components in the rotating coordinate system can be obtained.Then the back electromotive force d,q components are filtered through a low-pass filter, aims to reduce the noise introduced by the current differential.PLL correction part correct the back-EMF q axis component e_{qf} with the back-EMF d axis component e_{df} based on e_{qf} direction.Then the estimated angular velocity is obtained by dividing the permanent magnet flux Ψ_f and the estimated position angle is obtained through the integral operation.The principle see equation (10), (11).

$$e_\alpha = u_\alpha - R_s i_\alpha - L_s\frac{di_\alpha}{dt} \tag{8}$$

$$e_\beta = u_\beta - R_s i_\beta - L_s\frac{di_\beta}{dt} \tag{9}$$

$$\omega_r = \frac{1}{\psi_f}(e_{qf} - sign(e_{qf}) \bullet e_{df}) \tag{10}$$

$$\hat{\theta} = \int \omega_r dt \tag{11}$$

Software design of the system. The software design of system mainly composed of three parts: the initialization procedure, the main program and interrupt service procedure.The operating mode of peripheral resources in DSP chip as well as each variable is initialized in initialization process.Main program mainly execute keyboard scanning, status and parameters display, communication with computer.

The interrupt service routine is a core part of the software, mainly to complete the system control algorithms, data acquisition, protection and fault handling. In each PWM cycle interrupt service routine for the stator phase currents and bus voltage values are sampled, and the implementation of the current loop and speed loop, and then through the SVPWM modulation algorithm calculates a duty cycle of the next PWM cycle duty. System execute core algorithm in each PWM cycle interrupt service routine every 100us, Figure 6 is a flow chart of PWM period interrupt service routine.

Experimental Analysis

System Simulation and result Analysis. According to the theoretical analysis, in order to verify the feasibility and performance of this system, it was simulated on Matlab/Simulink platform, where the motor rated frequency was 150Hz, the inverter switching frequency of 10kHz, the system sampling frequency was 10kHz, the low pass filter was 100Hz in the speed feedback channel. Simulation block diagram is shown in Figure 7.

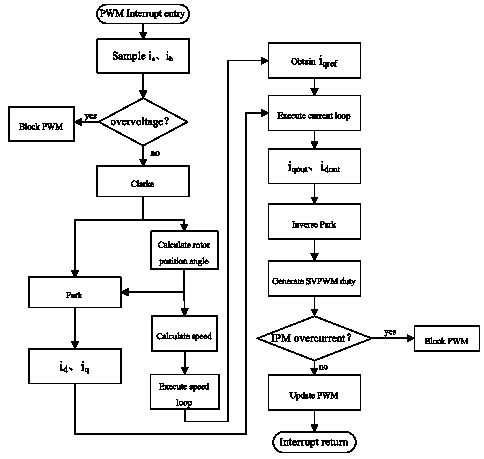

Fig.6 Flow chart of PWM period interrupt service procedure

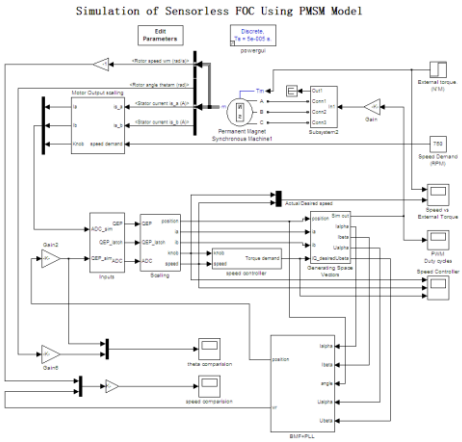

Fig.7 Simulation block diagram of the system

When given speed command was 1500rpm , the motor started from no load state,then suddenly gave rated load torque 2.39N • M at 1.5s.In this case simulation environment time was set 3s in order to observe the system performance . Figure 8 (a) shows the change of the estimated speed and the actual speed, (b) shows the waveform of the estimated and the actual rotor position angle.

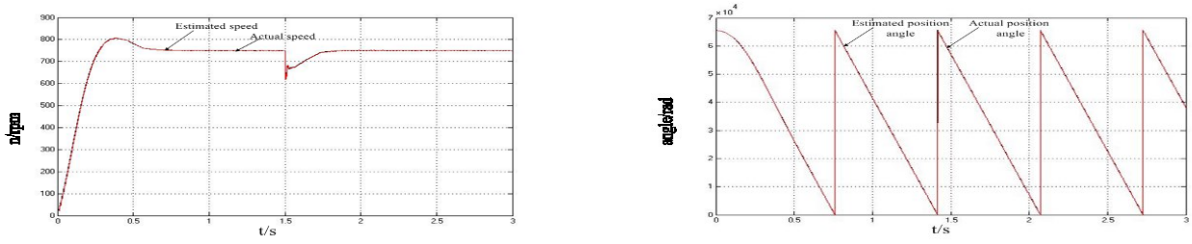

(a) (b)

Fig.8 The estimated, actual speed and angle waveform under 1500rpm

Due to data processing in the simulation experiment was simulated DSP data processing ,so the rotor position angle was unit16 in picture (b). As could be seen from Figure 8, the estimated results

were very close to the actual speed value and speed still converge to given speed with a small overshoot after sudden change of load.

System experiments and results analysis.PMSM parameters was shown in Table 1.The control circuit was based on TMS320F2808 DSP , the digital control period of 100us and the dead time of 3us. The power module used IPM of FSBB15CH60 in main circuit. In order to compare experiment results, the motor was mounted on the incremental encoder of 2500 lines.

Tab.1 The parameters of PMSM

parameter	value	parameter	value
Rated power/W	750	Line-Line R/Ω	1.4
Rated torque/N•M	2.39	Line-Line L/mH	7.5
Rated current/A	3.9	back-EMF constant /V/krpm	50
Rated frequency/Hz	150	poles	3
Rated speed/rpm	3000	DC bus voltage/V	300

To verify the performance of system, in view of the low speed motor operation quality is an important indicator of system performance, so the PMSM operated with 200rpm at no load[7].The experimental results is shown in Figure 9.

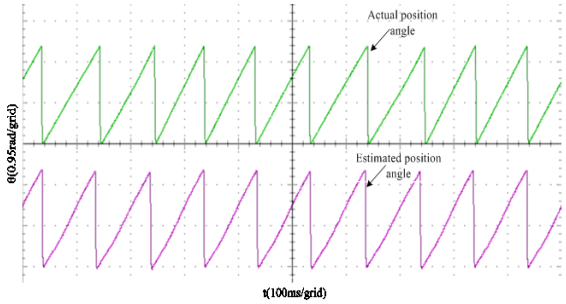

(a)Actual and estimated rotor position angle

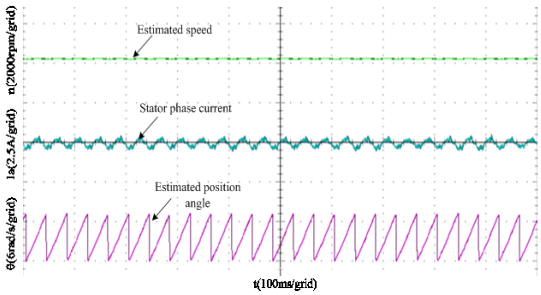

(b)Estimated speed/position angle and stator phase current

Fig.9 Steady-state experiments with 200rpm

Experimental results indicated:1)Estimation error of rotor position angle was small; 2) Stable position angle and current signal was able to ensure the operation of PMSM at low speed;

To verify the dynamic performance of system, given speed command changed from 200rpm to 3000rpm,then from 3000rpm to 200rpm.The result of dynamic response test is shown in Figure 10.Experimental results indicated that the system had good speed tracking,small overshoot and fast dynamic response.

To further test load capacity, the system run on MAGTROL HD-715-8NA-0100-type hysteresis dynamometer load platform at rated load 2.39N • M.The experimental result is shown in Figure 11.

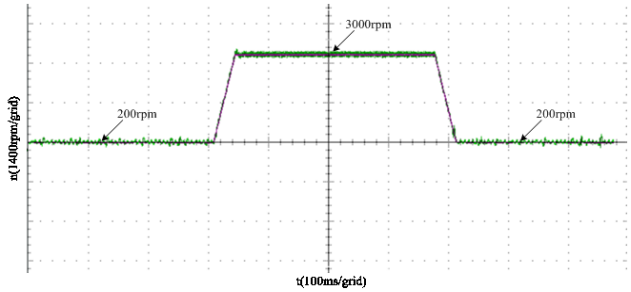

Fig.10 Dynamic response with speed command change

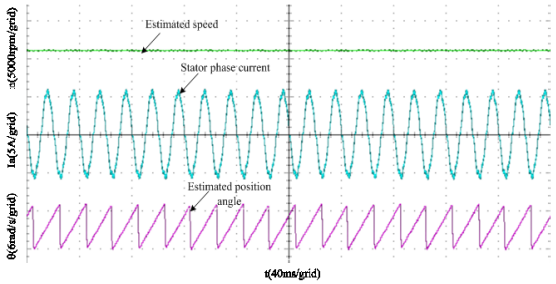

Fig.11 Experimental result with 2.39 N•M rated load

Conclusion

The sensorless vector control system of permanent magnet synchronous motor, using speed/position estimation algorithms a combination of the back-EMF observation and phase-locked loop (PLL) possess reliable structure,good feasibility and practicality in many occasions. Experimental results can be described as follows:

(1) This system using the estimation algorithm can effectively detect the rotor position and speed.

(2) In the no-load testing, the system had small steady-state error and estimation error of rotor position angle.

(3) In the load testing,the system possess strong load capacity and good dynamic performance.

References

[1] WANG Yu, DENG Zhi-quan, WANG Xiao-lin:A Novel Algorithm of Motor Flux Estimation[J]. Proceedings of the CSEE ,2007,27(6):39-43.(In Chinese)

[2] LI Yong-dong , ZHU Hao:Overview of Sensorless Control of Permanent Magnet Syncoronous Motors[J].Electric Drive,2009,39(9):3-10.(In Chinese)

[3] El Murr,G. Giaouris,D.Finch, J.W.Universal PLL Strategy for Sensorless Speed and Position Estimation of PMSM[C].*Industrial and Information Systems (ICIIS) 2008.Region 10 and the Third international Conference on IEEE*, 2008:1-6.

[4] Fabio Genduso,Rosario Miceli,et al.Back-EMF Sensorless Control Algorithm for High Dynamics Performances PMSM[J].IEEE Trans on Industrial Electronics,2010,57(6): 2092-2100.

[5] Seung-Ki Sul.Control of Electric Machine Drive Systems[M].NewYork:IEEE Press, 2011:116-324.

[6] Tong Li,Zou Xudong,Feng Shushuai,Huang Qingjun.A Sensorless Control Scheme for Permanent Magnet Synchronous Generators Using Predictive Dead-Beat Algorithm [J].TRANSACTIONS OF CHINA ELECTROTECHNICAL SOCIETY,2013,28(3):17-25.(In Chinese)

[7] Anton Dianov,Nam Su Kim,Seung Moo Lim.Sensorless starting of Horizontal Axis Washing Machines with Direct Drive[C].Electrical Machines and Systems(ICEMS),2013 International Conference on IEEE.

[8] WANG Hong-jia, YANG Ming, NIU Li, XU Dian-guo.Current Loop Bandwidth Expansion for Permanent Magnet AC Servo System[J].Proceedings of the CSEE,2010,30(12):56-62.(In Chinese)

Advanced Materials Research Vols. 960-961 (2014) pp 1189-1193

doi:10.4028/www.scientific.net/AMR.960-961.1189

Multi-function stepper motor design based on MCS

DongJin Yang[1,a], HaoDing Han[1,b] and Yan Zhang[1,c]

[1] College of Mechanical and Electrical Engineering, Hainan University, Haikou 570228, China

[a]493279963@qq.com [b]153347705@qq.com [c] z_yhs@163.com

College of Mechanical and Electrical Engineering, Hainan University, Haikou 570228, China）

Author: Yang Dongjin(1991-),male, undergraduate. Han Haoding(1990-),male, undergraduate.

Address: College of Mechanical and Electrical Engineering, 570228.

Corresponding author: Zhang Yan (1978-), female, Hubei Ezhou, Master, associate professor, Mechanical and Electrical Engineering University of Hainan. E-mail: z_yhs@163.com.

Key words: single chip microcomputer, multi-function, stepper motor

Abstract. The multifunctional stepper motor is built on the basis of ordinary stepper motor, combined with single chip microcomputer control system, dedicated driver chip STK672-040 and chip ULN2003A function, it can not only do the actual stepping motor testing but also can set out the particular function of stepper motor. In addition, the system can link an external circuit and cooperate with the external circuit to complete the work required.

Introduction

Stepper motor is a kind of servo motor. Stepping motor is controlled by electric pulse signal and converts electrical pulse signal into the motor controlled by corresponding linear displacement or angular displacement. Each pulse signal can make the stepping motor rotate a certain angle, namely interval angle. Pulse frequency determines the speed of motor rotation, the total number of pulse determines the angle of rotation, the change of winding current order can change the direction of motor rotation. The structure and control of stepper motor's open loop servo system is simple and easy to adjust. In the cases where precision and speed is not highly demanded it has certain use value. Stepper motor can be said to be the important member of the family of motor and has some significant advantages: a concise control circuit, high reliability, flexible software programming and strong logicality. As a executive component, motor has the characteristics of precise stepper and rapid start-up under rated load Step. Performing as an important element, stepper motor has been widely used in the automatic control system. Corresponding stepper motor extension model is shown in figure 1:

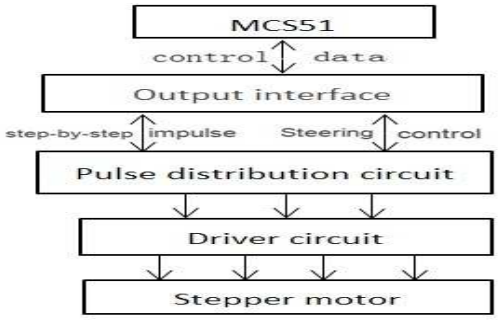

Fig 1 Stepper motor extension application mode

The drive of stepper motor

Principle of stepper motor driver. Although there are many kinds of stepping motor, but all their control modes are the same, all need to be driven by pulse current. if it is calculated by one turn with 20 excitation signal, the stepping motor each step forward in 18 degrees. In this way, pulse number is proportional to the Angle of rotation, and the positive and reverse of motor controlled by the pulse sequence.

Stepper motor excitation method is composed of half step excitation and whole excitation, specific content is as follows：

1 phase excitation method. Exactly the same time conduction a coil.Small torque, vibration but its consumption is small, high accuracy, every step forward in 18 degree. Positive rotation excitation sequence is shown in fig2:

STEP	A	B	C	D	STEP	A	B	C	D
1	1	0	0	0	3	0	0	1	0
2	0	1	0	0	4	0	0	0	1

Fig 2 Positive sequence: A→B→C→D→A

2 phase excitation method. Exactly the same time conduction two coils. Its most prominent feature is large torque, small vibration, 18 degree every step forward. Positive rotation excitation sequence is shown in fig 3:

STEP	A	B	C	D	STEP	A	B	C	D
1	1	1	0	0	3	0	0	1	1
2	0	1	1	0	4	1	0	0	1

Fig 3 Positive sequence: AB→BC→CD→DA→AB

1-2 phase excitation. The 1 phase and 2 phase alternate conduction.Its smooth operation, high resolution, each step forward 9 degrees. Positive rotation excitation sequence is shown in fig 4:

STEP	A	B	C	D	STEP	A	B	C	D
1	1	0	0	0	5	0	0	1	0
2	1	1	0	0	6	0	0	1	1
3	0	1	0	0	7	0	0	0	1
4	0	1	1	0	8	1	0	0	1

Fig4 Positive sequence: A→AB→B→BC→C→CD→D→DA→A→AB

Stepper motor driver chip. Integrated ULN2003A is a kind of High current-driven Darlington transistor array, usually used for PLC and single-chip microcomputer, digital output card, the control circuit of the intelligent instrument, and can be directly used to drive the relay load, etc. ULN2003A, it's features include high working voltage, wide temperature range, high current gain, Strong load capacity, etc. It is suitable for all kinds of high power drive system.

STK672-040 is produced by SANYO company is a hybrid integrated stepper motor driver chip, its internal consists of two parts, power and control. The control part is mainly composed of a sine wave generating circuit and current distribution switch, three input logic to control the electric mode. STK672-040 can realize the motor control system that can achieve low vibration, high speed, low noise, fast response and high efficient.

Control system and circuit design

The part of single chip microcomputer control circuit. MCU is the chip level of computer, which is a kind of integrated chip composed by CPU, RAM, ROM, timing/number, and a variety of I/O. It

has many advantages such as excellent performance price ratio, high integration, small volume, high reliability, strong control function, low voltage, low power consumption. The multi-function stepper motor controlled by MCU is very promising. The circuit is mainly based on MCU, stepper motor as the executive element, start chip, conversion chip as an assistant, which make the stepper motor function can be extended. This system is mainly aimed at four phase stepper motor design and control, the STK672-040 and ULN2003A driver chip are prepared for the system of the multi-function, their control mode is in the same way , So the two drive chip not contradictory. The single-chip computer peripherals input interface, which can finish all kinds of the specific needs of the stepper motor work mode. Single chip microcomputer control circuit is shown in fig 5.

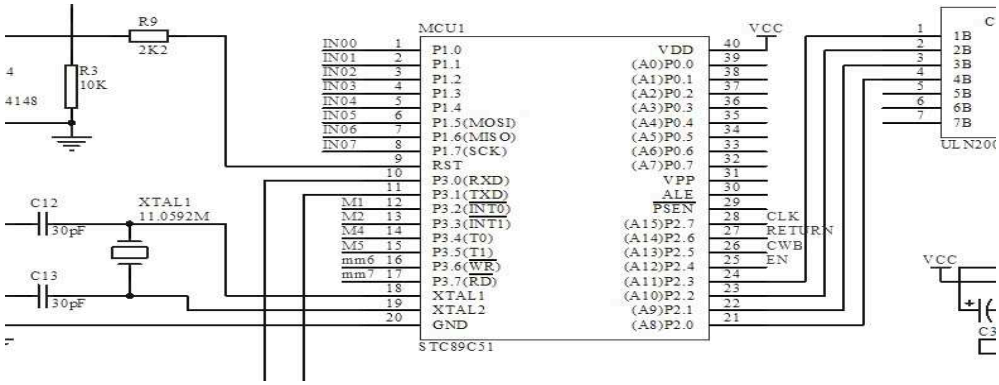

Fig5 SCM control circuit

Stepper motor control serial port. MAX232 belongs to the MAX220 - MAX249 series line of receiver / driver, designed for v. 28 / v. 24 and TIA - 232 - e/EIA communication interface, The drive cannot provide the supply of 12V power.Through the similar max232 chip to level conversion, making SCM match the serial port voltage.This part of the circuit controlled by single-chip microcomputer P2 feet, the main control is the signal of output and input. When D1 is lit, the motor forward transmission; and light emitting diode's D2 is lit, the motor rotates in the reverse direction; In D3 is lit, the motor stalling. Via serial port receives information, Data conversion by the chip ULN2003A, to Provide specific impulse, Drive the stepper motor rotation.Serial interface circuit is shown in figure 6:

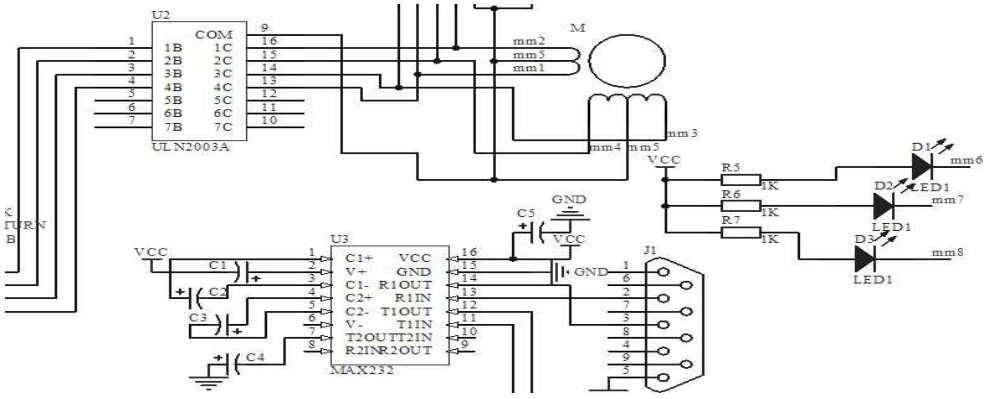

Fig 6 Serial interface circuit

Stepper motor control keyboard. STK672-040 chip is mainly complete the distribution of power and pulse signal, single chip microcomputer through the input signal of pressed key adjust the output signal of STK672-040 and control the rotation of the stepper motor. P3 interface in figure is mainly used for the data communication between single chip microcomputer and chip. M1, M2 is used to control the incentive mode of motor; M4, M5 is used to set the track of motor. The CLK pin is used to input pulse to STK672-040 chip.The circuit can simulate the specific pulse circuit and

applied to some experimental study on step motor system.Keyboard input circuit is shown in figure 7:

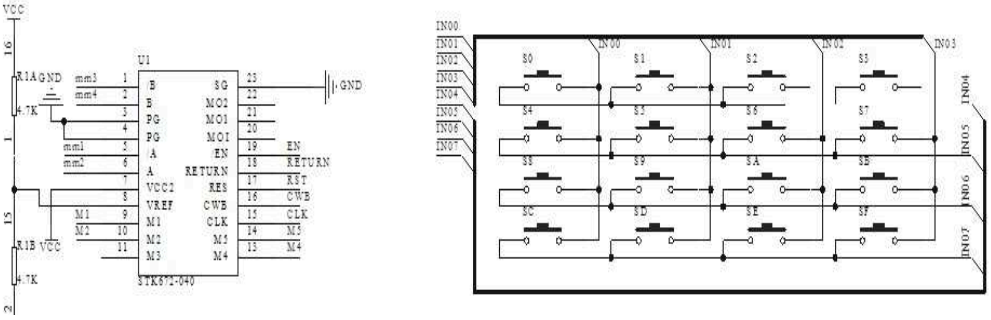

Fig 7 Keyboard input circuit

Stepper motor input circuit and I/O interface. In order to expand the application of stepping motor, this system design a stepper motor external entrance, by external signal directly supply MCU,Single chip microcomputer system analysis and signal processing, sending chip ULN2003A corresponding pulse signal, which can drive a stepper motor action is needed to complete in an external circuit. The external circuit is variously, but the start and driving of step motor is not much change. Setting the inherent system unit between step motor and MCU, no matter how complex the external circuit is, the function of stepper motor can be change according to the requirement of the circuit. Specific I/O interface is shown in fig 6.

The program design process

According to the design of this system, stepping motor as an objective element, when enter a program into the microcomputer, stepper motor execute the command according to the corresponding instruction. But for this system, the programming operation is very simple and fast, even in most cases, and can undertake simple adaptation according to established procedures, what's more, because this system adopts the chip are common multi-functional chip and the principle of design is simple and easy to understand. This paper separately explains the various functions of the module, according to the function of the module and the description of pin, according to the following programming flowchart can easily perform specific functions. The program flow chart shown in fig 8 .

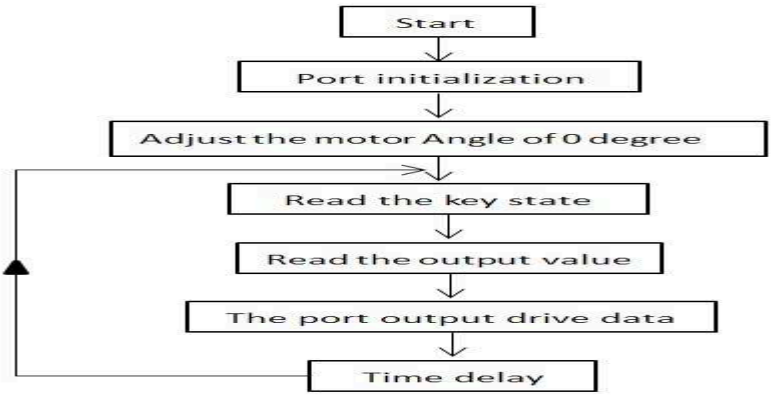

Fig 8 Program flow chart

Conclusion

The multi-functional stepper motor system introduced in the paper has the significant advantages: simple circuit structure, low cost, high reliability, simple and flexible software programming. It can realize the automatic control of productive process and have a good man-machine interface. Once the system is operated, it can have a strong anti-interference, reliable operation and less maintenance. Thus, it can obtain good effect. Nowadays, in the equipment with an automatic control system, the application of stepper motor is more and more, so the control of the stepper motor is to become a widespread but immature problem. Applying the single chip microcomputer to generally realize multi-function stepper motor, it will have the advantages like stable operation, simple control and short development cycle, which is a feasible scheme.

Reference

[1] Zhou Runjing. the design of single-chip microcomputer circuit, analysis and production. Beijing: mechanical industry press, 2010.5

[2] Peng Xuange, Huang Chuanlian, zhubing. A method of using single chip microcomputer direct control of stepping motor[J].Journal of jinggangshan normal college, 2004, 25 (5) : 70-71.

[3] Wang xiaoming. The single-chip microcomputer control of the motor [M]. Beijing: aeronautics and astronautics press, 2002.

[4] Peng Shusheng. The design of PIC microcontroller practice and system [M]. Beijing: electronic industry press, 2008.

[5] Li Yongcheng. Stepper motor control based on PLC application in industrial manipulator [J]. Journal of information science and technology, 2008 (18) : 30, 31.

[6] Cheng Guogang, Chen Yueqin, Cui Li. 51 MCU typical query template development manual. Beijing: electronic industry press, 2012.5

[7] Wu Hongxing. Motor drive and control application-specific integrated circuit and application [M]. Beijing: China power press, 2006.

Advanced Materials Research Vols. 960-961 (2014) pp 1194-1197

doi:10.4028/www.scientific.net/AMR.960-961.1194

Double Fault Parameters Estimation of Motor Based on Four-order Cumulate of MUSIC

Wei Tian[1, a], Jingzhi Wang[2,b] and Yutian Wang[3,c]

[1] Electric Information Engineering College Beihua University Jilin City, China

[2] Automation Dept Jilin Vocational College of Industry and Technology Jilin City, China

[3] Petro-China Jilin Petrochemical Company Refinery Jilin City, China

[a]twei71@163.com, [b]2006wjz-117@163.com, [c]zhao197329@163.com

Keywords: MUSIC. four-order-cumulat. rotor broken-bar. stator winding inter-turn short circuit.

Abstract. In this thesis, fault characteristic frequency can not be accurately detected if they are drowned by noise. A novel method which is Multiple Signal Classification(MUSIC) based on four-order cumulate is provided to diagnose motor broken rotor bars and stator winding inter-turn short circuit. Because four-order accumulation is able to depress noise meanwhile fault information can be obtained accurately through this way presented even with small samples. Simulation results shown that the method were higher in resolution of frequency, more accurately in fault detection and less in computational complexity.

Introduction

As motor fault cause loss of production. In all of the motor fault it was approximately 10%and 15% for motor broken rotor bars and stator winding inter-turn short circuit[1].

Now we used diagnostic methods to solve the equation which is established by the physical and mathematical model. But this way is failed for complexity relationship of electromagnetic in the failure motor[2.3]. At the same time the method of artificial neural network could effectively classify and identify the characteristics[4]. This way can avoid the complicated analytical techniques but it can not be used directly to the site.

If the motor rotor was breakdown, the symmetrical current is damaged. There appears sideband in the stator fundamental frequency. Its characteristic frequency is $f_b = (1 \pm 2s)f$, f is current base-band, s is slip. When it is short circuit between stator winding there is higher harmonic and their frequencies are away from the fundamental. The fault feature is found out by detecting the harmonic components of the stator current.

In this paper, MUSIC method which is based on cross-high-order cumulate is provided for diagnosing stator inter-turn short circuit and rotor broken-bar because this way can depress non-correlative noise and correlative gauss noises by Cross high order accumulation. The fault signal space can be decomposed into signal and noise signal subspace.

MUSIC Method Based on Four-order Cumulate

Commonly this ways which diagnose induction motor broken rotor bars is stator current spectrum analysis. Generally the normal asynchronous motor is passed on symmetrical three-phase coupled voltage. When the motor fault, the rotor will flow symmetrical three-phase current with frequency sf_1 (where s is the slip). There will be fundamental frequency band around the edges in the current in the stator. Its characteristic frequency is $f_b = (1 \pm 2s)f_1$,where f_1 is the fundamental frequency; s is slip. The number of broken rotor bars can be predicted if the composition and the frequency f_1 of the difference between the sizes of the current amplitude can be known. The motor load and the power provided voltage were fluctuation so causing s is volatility. Then broken rotor bars characteristic frequency f_b is changing. Because the fundamental frequency f_1 and f_b are very closely. The f_b can

easily be fundamental frequency f_1 side-lobe "annihilation". When the motor load changes frequently, using the traditional method of spectral analysis should be significantly affected, or even impossible to accurately extract the characteristic frequency f_b.

When the stator winding inter-turn short circuit occurs, it will generate current frequency $f_{st} = f_1[k \pm \frac{n}{p}(1-s)] = nf_r \pm kf_1$ (where f_1 is the frequency of power, s is lisp, p is Number of pole pairs, $k = 1,3,5\cdots$, $n = 1,2,3,\cdots,(2p-1)$, f_r is Rotor rotational frequency $f_r = (1-s)f_1 / p$).By detecting spectral components occurs the stator fault can be distinguished. The f_r and ksf_1 is constantly changing. Therefore the diagnosis of short circuit of stator significantly was affected by using the spectral analysis of traditional method. Even around the edges can not be accurately extracted frequency nf_r component.

Therefore, people put forward the diagnostic method which is f_b and f_{st} -characteristic frequency signals from the original "stripping" out. This paper presents MUSIC method based on cross-high-order cumulate based. The high-order cumulate include more wealth of information, and depress the unknown spectrum of non-correlative noise and correlative noise.

Cross high order accumulation can depress non-correlative and correlative noise. In the literature [5]and [6]has been proven.

Among MUSIC method based on cross-high-order cumulate, cross-high-order cumulate was adopted and decomposed signal SVD. Fault signal space will be divided into two orthogonal sub-space, space-signal and noise-space. We use the noise-space-based signals to estimate the parameters. This part is smoothing the noise impact. And in the detection of the motor broken bars, the voltage or current can be seen as "signal" to transform and handling.

The fault signal $x(n)$ and $y(n)$ established are stator current which were mixed with additional color-noise sine signal, namely:

$$\begin{aligned} x(n) &= \sum_{i=1}^{q} a_i \exp[j\omega_i n + \varphi_x] + \xi_x(n) + \eta_x(x) \\ y(n) &= \sum_{i=1}^{q} \beta_i \exp[j\omega_i n + \theta_i + \varphi_y] + \xi_y(n) + \eta_y(n) \end{aligned} \tag{1}$$

Which: α_i, β_i were harmonic signal amplitude; θ_i was phase difference of the signal $x(n)$ and $y(n)$; ω_i was signal frequency; φ_x and φ_y were random initial phase and range evenly distributed between $(-\pi, \pi)$; ξ_x, ξ_y, η_x and η_y were spectral density were unknown and zero mean color noise that in Which η_x and η_y were correlative non-Gaussian noise; $\xi_x; \xi_y$ were non-correlative non-Gaussian noise; ξ_x *and* ξ_y and η_x *and* η_y were independent.

It is the four order-cumulate for $x(n)$ and $y(n)$:

$c_{xyyy}(k_1, k_2, k_3) = cum_4\{x(n), y(n+k_1), y^*(n+k_2), y^*(n+k_3)\}$, $c_{xyyy}(m,0,0) = E[x(n)y(n+m)y^*(n)y^*(n)] = -\sum_{i=1}^{q} \alpha_i \beta_i^3 e^{-j\theta_i} e^{-j\omega_i m}$,order $c_{xyyy}(m) = c_{xyyy}(m,0,0)$.While its corresponding $h \times h$ Victoria expansion order among the four accumulated matrix is:

$$c_{xyyy} = \begin{vmatrix} c_{xyyy}(0) & c_{xyyy}(-1) & \cdots & c_{xyyy}(-h+1) \\ c_{xyyy}(1) & c_{xyyy}(0) & \cdots & c_{xyyy}(-h+2) \\ \vdots & \vdots & & \vdots \\ c_{xyyy}(h-1) & c_{xyyy}(h-2) & \cdots & c_{xyyy}(0) \end{vmatrix} \tag{2}$$

Available: $c_{xyyy} = FE^{j\theta}PF^H$, In the formulas:

$F_i = \begin{bmatrix} 1 & e^{j\omega_1} & e^{j\omega_2} & \cdots & e^{j(q-1)\omega_1} \end{bmatrix}^T$ $F = [F_1 F_2 .. F_q]$ is Victoria complex matrix of $h \times q$

$E^{j\theta} = diag\left[e^{-j\theta_1} \quad e^{-j\theta_2} \quad \cdots \quad e^{-j\theta_q}\right]$, $P = diag[-\alpha_1\beta_1^3 \quad -\alpha_2\beta_2^3 \quad \cdots \quad -\alpha_q\beta_q^3]$(q is c_{xyyy} Rank).

It shows that C_{xyyy} is non-conjugate symmetric matrix and its SVD type:

$$C_{xyyy} = U\Sigma V^H \tag{3}$$

Where U and V were left and right singular vector of matrix C_{xyyy} ; $\Sigma = diag(\sigma_1, \cdots \sigma_i)$, where $\sigma_i (i = 1,2, \cdots, n)$ is all non-zero singular value and according to descending order (that is $\sigma_{i+1} \le \sigma_i$).

In the formula: $V = [V1, V2]$, $V1$ is a singular vector composed of q which is in the former composed of V ; $V2$ is a singular vector composed of $(h-q)$which is in the last composed of V ;namely left singular vector matrix U express block into $U = [U1, U2]$.

The matrix has sinusoidal harmonic component which are ; while characteristic equation for the root is, $v_i(0) + v_i(1)z^{-1} + \cdots + v_i(h-1)z^{-(h-1)} = 0$ $(i = q+1, \cdots, h)$.In formula (3), the root of $(h-q)$ characteristic equation have one and only q which are $e^{j\omega_1}, e^{j\omega_2}, ..., e^{l\omega_q}$.

When using $h >> q$ -order the expansion equation, this method greatly improve the accuracy of the estimated harmonic frequency and resolution, the failure is in the estimated harmonic frequency signal. But it produced (h-q)-by-Kan. As the root is corresponding to the peaks, pseudo-peak will be inevitably [7] meanwhile this is the cause of pseudo-peak. The various existing modern spectrum estimation algorithm that can not removed the roots, so there are different levels of the pseudo-phenomenon. This is calculation pseudo-spectral:

$$S(f) = \frac{1}{\left| A^H L \right|^2} \tag{4}$$

Which $A = \left| \sum_{i=q+1}^{h} v_i(0) \sum_{i=q+1}^{h} v_i(1) \cdots \sum_{i=q+1}^{h} v_i(h-1) \right|^T$, $L = \left[1 \quad e^{2\pi f} \quad \cdots \quad e^{2\pi(p-1)f} \right]^T$.

q -frequency harmonics were chose as a sine frequency estimates which $S(f)$ obtain the maximum. This is MUSIC method based on cross-high-order cumulate for the parameters estimated.

Simulation and Experimental

Motor main data:Model is Y100L1-4; Power:2.2kw; Voltage: 380V;Current: 5A; Speed: 440r/min; $s = 0.04$;Stator Turns:86,Sampling Frequency: 1000 Hz. The load is furnace: Voltage:250V, Current:10A.

The fault detection scheme is fig.1. In the system there is a single signal which is a sinusoidal sequence. Then we use the reference signal according to the actual situation. The original signal can be equivalently represented by the formula (1), in practical application is very easy to implement[8-10].

As well as the short circuit which is the stator inter-turn short circuit fault at 2.3%. And we can obverse the broken bars at changing load.

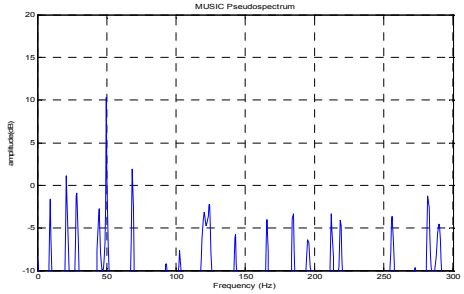

Fig.1 Spectrum of stator circuit(A-phase)

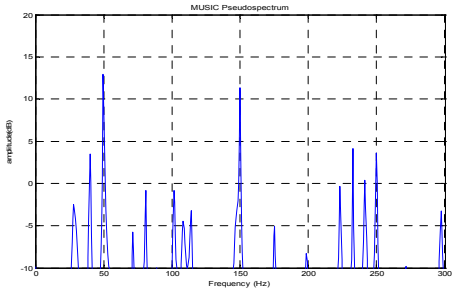

Fig.2 A-phase winding inter-turn short circuit(2.3%)

There is the frequency spectrum when the motor operates normal(fig.1).We can seen the maximum peak at f=50Hz and the peaks large changes of the third harmonic at 2.3%. In figure 2 there is the fifth harmonic in the biggest change. This is obtained fault frequency by calculating. The results consistent (150 ± 12) Hz in line.

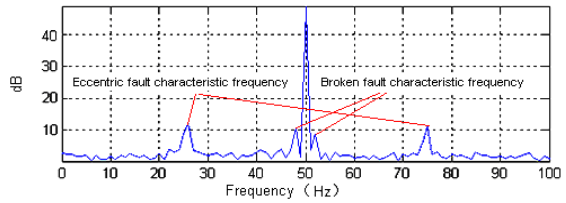

Fig.3 An eccentric + current spectrum (full)

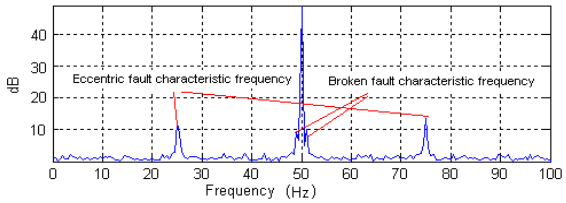

Fig.4 An eccentric + current spectrum (67% load)

Motor fault characteristic frequency component will increase as the load increased correspondingly for example fig.3and fig.4. With the increasing in the number of broken bars, the degree of fault is heavier correspondingly.

In literature [4]put forward a number of broken bars of the prediction formula:

$$n = \frac{2R}{10^{\frac{N}{20}} + 2P} \tag{5}$$

In the formula(5): n -Prediction of the number of broken bars; R -Core rotor slot number; N -DB difference peak is between $(1-2s)f_1$ frequency components and the fundamental frequency spectrum; P -the number of motor pole pairs.

Summary

Broken rotor bars and stator winding inter-turn short circuit fault are multiple failure for cage asynchronous motor. In practice, it is possibility for double fault. So using a single fault diagnosis method may make false. Therefore it is essential for rotor bar breaking and stator windings double fault characteristics being studied. In the paper, it is the biggest feature for the MUSIC method based on cross-high-order cumulate that is based on the original signal extrapolation and has inhibitory effect on the noise; Frequency estimation of fault signals has higher resolution. The simulation showed that the fault characteristics summed up for systematically the cage induction motor rotor bar breaking and Stator Windings. Clearly reveals the relationship between the two and provides an important theoretical basis for the realization of rotor bar breaking and stator winding short circuit.

References

[1] WANG Xu-hong, CHEN Yan. High Voltage Engineering, Vol. 29 (2003),p. 28-30 (In Chinese)

[2] ZHANG Jian-wen. High Voltage Engineering, Vol. 29 (2007),p. 114-117 (In Chinese)

[3] Tallam R M, Sang Bin Lee, et al. IEEE Trans on Ind Appl, Vol. 42 (2007),p. 920-933

[4] LIU Zhen-xing,YIN Xiang-gen, et al. Procedings of the CSEE, Vol. 23 (2003),p. 158-161.

[5] SHI Yao-wu,DAI Yi-song.Journal of Electronics, Vol. 17 (1995),p. 13-19 (In Chinese)

[6] SHI Yao-wu,DAI Yi-song,GONG.Acta Electronics Sinica, Vol. 24 (1996),p. 46-50 (In Chinese)

[7] Douglas H, Pillay P, Ziarani A K. IEEE Trans on Energy Conversion, Vol. 20 (2005),p. 135-141

[8] Liu Zhenxing, Yin Xianggen, etal. Procedings of the CSEE, Vol. 23 (2003),p. 158-161.

[9] Zhang Jianwen, Wang Chunsheng. High voltage engineering, Vol. 32 (2006),p. 25-28.

[10] Niu Fa-liang, Huang Jin, Yang Jia-qiang. Procedings of the CSEE, Vol. 24 (2005),p. 122-127.

Advanced Materials Research Vols. 960-961 (2014) pp 1198-1202

doi:10.4028/www.scientific.net/AMR.960-961.1198

Research on Application of Multi-Agent System in the Concentration Forecast of Dissolved Gases in Transformer Oil

Bin Li[1, a], Xuebin Li[1,b] , Zaiming Yu[1,c]

[1] Electric Power Research Institute of State Grid Liaoning Electric Power Co., Ltd., Shenyang 110006, Liaoning Province, China

[a]tflb@qq.com, [b]lixuebin1985@163.com, [c]yuzaiming007@163.com

Keywords: multi-Agent system, intelligent forecast, DGA, blackboard model, SVM.

Abstract. In view of the research in the existing forecast model and transformer DGA methods, this paper presents the collaborative model of intelligent concentration forecast of dissolved gases in transformer oil based on multi-Agent system, for improving the predictability of transformer fault. It presents the main function of each Agent, blackboard and JADE bus in this model, discusses the collaborative process of intelligent concentration forecast of dissolved gases in transformer oil based on multi-Agent system, and designs a combination forecasting architecture and a method of composition forecasting. Finally it indicates the feasibility and effectiveness of the intelligent concentration forecast model of dissolved gases in transformer oil based on multi-Agent system according to the application examples.

Introduction

Currently transformer fault diagnosis system is used to judge whether the transformer fault or not, or Diagnosis of failure positions and failure causes after the failure. Dissolved gas analysis(DGA) is one of the widely used methods [1-2] . The method is through the detection and diagnosis of collection sample to evaluate the running situation of transformer. The evaluation method is adopted by the single forecast model and combined forecasting model [3-4]. Because of many factors that affect the concentration of dissolved gases in transformer oil, when with a single forecasting model to forecast, as its own limitations, the prediction accuracy and stability is not high. And combination forecast research is predicted variable weight values, a lot of evidence that combination forecast is often better than its individual forecast [5]. But the existing combination forecasting results are in the training stage of the model realizes the variable weight value, and at the time of the actual forecast model, weights of each model is the same, it would limit the accuracy of prediction model and the suitability. Therefore, in order to realize the true meaning of variable weight combination forecasting, to increase the ability of transformer fault prediction, this paper introduces a multi Agent system in the field of artificial intelligence.

Multi Agent system (MAS) [6] is a branch of distributed artificial intelligence (DAI); it can make logically and physically dispersed system parallel to solve the problem coordinately. Adopt multi Agent control, not the pursuit of a single large and complex system, but, according to the requirement of the control system is divided into multiple Agent from the function, multiple Agent communication each other, coordinate each other, together to complete a large complex system control task. This system not only has the characteristic such as the resources to be Shared reliability Strong real time Easy to expand, etc as the general distributed system, but also through the coordination and collaboration between each Agent can solve the problem of large-scale complex, make the system has the very strong flexibility and robustness. Until now, the literature on multi Agent system in the transformer oil dissolved gas concentration prediction has not found yet. This article through to the existing intelligent forecast method research based on the basic structure and characteristic of the Agent, this paper puts forward a more Agent concentration of dissolved gas in transformer oil intelligent prediction model.

Based on multi Agent system of transformer oil dissolved gas concentration in the intelligent forecasting collaboration model

Based on multi Agent system of transformer oil dissolved gas concentration in the intelligent forecasting collaboration model is as Fig. 1 shows. The model is divided into five layers: display layer, intelligent agent application layer, intelligent agent core layer, data access layer, data resource layer.

(1) display layer: The user interface is based on JAVA technology with the characteristics of traffic ability, portable, and cross-platform. Take advantage of visual and various chart technology, provides the transformer monitoring and maintenance staff are very friendly interactive interface At the same time also provide personalized service for users of the system interface.

(2) Intelligent agent application layer: This layer is mainly consist of the blackboard, control management Agent, intelligent user Agent, data pre-processing Agent, forecast expert Agent management, combined forecast Agent, and self-learning Agent.

(3) Intelligent agent core layer: Consist of Agent public facilities and JADE [7] platform bus. JADE platform bus offer a basic services collection for different Agent, including control management Agent, (AMS), Agent communication channel (ACC), directory query device (DF), and Agent security, consistent persistence, communication and naming, etc. Agent Public facilities for various Agents in and out of the system, management of safety certification, registered, generate and recall migration.

(4) Data access layer: The data access layer provides intelligent agent core layer of the access control of data resources. Different business logic to database have different levels of access, to ensure the security of data access The layer of communication between various Agent and JADE platform adopts the ACL communication through a JDBC connection.

(5) Data resource layer: Adopt SQL Server XML database to store all kinds of information. Data resource layer includes: Oil gas in the database, to store the basic information of the gas content in transformer oil, such as H_2, CH_4, C_2H_6, C_2H_4, C_2H_2, CO, CO_2; Knowledge base; Depositing a prediction model for transformer fault diagnosis knowledge, such as expert experience and solving process, etc; At the same time also deposit Agent related knowledge, such as semantic, perception and reasoning, etc.; Predict library deposit forecast result of each prediction expert and combination forecast Agent; Error library: deposit each time prediction error of various experts and combination forecast Agent.

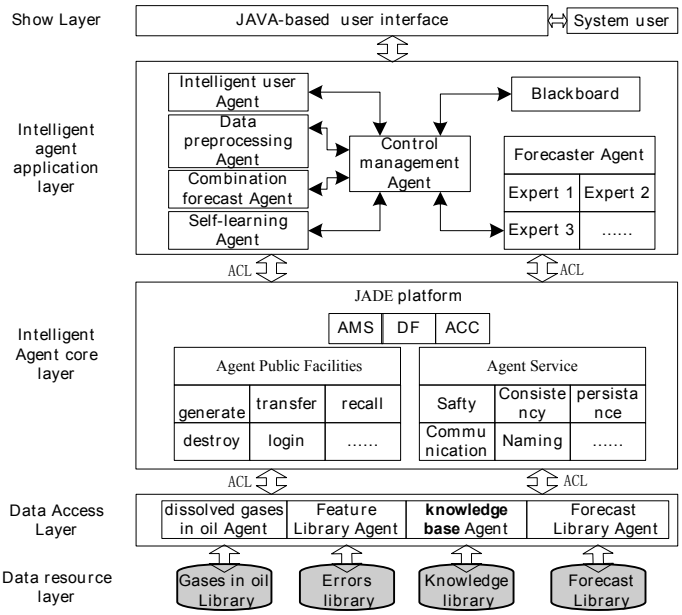

Fig.1 Collaborative model of intelligent concentration forecast model of dissolved gases in transformer oil based on multi-Agent

The collaborative process of intelligent concentration forecast model of dissolved gases in transformer oil based on multi-Agent

The collaborative process of intelligent concentration forecast model of dissolved gases in transformer oil based on multi-Agent, as shows in Fig.2. The collaborative process adopts the Agent technology in classic blackboard model, interaction between multi Agent are as follows

(1) First, Data pretreatment Agent will come from the transformer DGA data in standardizing, Standardized values in the range of [0, 1], offer characteristic data for Each forecasters as they need, And send the data to the blackboard corresponding layer. Then control Agent post the task to the blackboard, and request the domain experts to predict together.

(2) This article main forecasters include linear model, index model, power model, GM(1,1) model, and Verhulst model, According to their own experience, They together make predictions in a moment and the same DGA data, then the predicted results sent to the prediction results layer of blackboard.

(3) Combination forecast Agent obtain the prediction results of experts in the field from the blackboard, through the SVM (support vector machine) algorithm for combination forecasting get the final prediction results.

(4) Since the learning Agent will point to the forecast as a process of experience, deposited in the knowledge base, adjust the predicting model according to predicting the actual value. Then update each expert credibility and priority access to resources.

(5) Finally, the intelligent user Agent transmutes the result on the blackboard layer to the users in a friendly way.

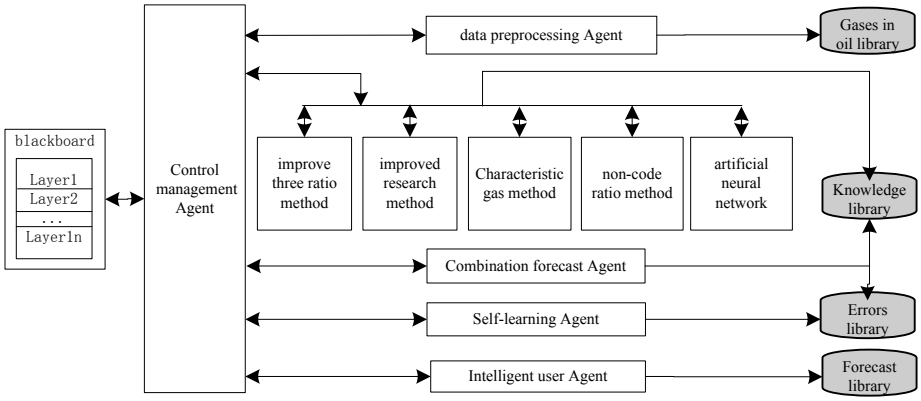

Fig.2 The collaborative process of intelligent concentration forecast model of dissolved gases in transformer oil based on multi-Agent

Combination forecast Agent architecture and prediction methods

(1) Architecture

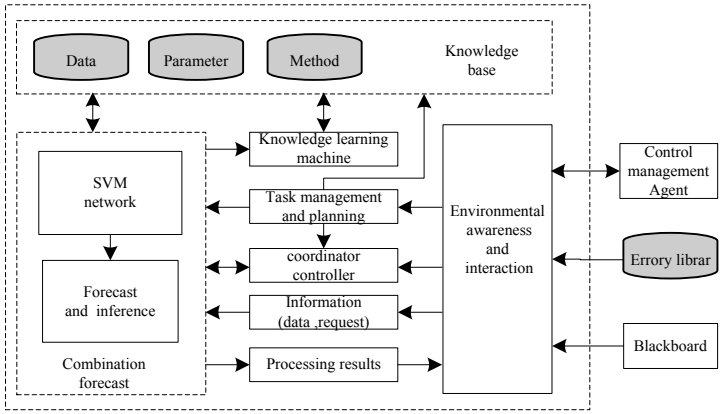

Fig.3 The architecture of combination forecasting agent

Combination forecast Agent mainly consist of environmental perception, learning machine, task management and planning, coordinator controller, information, result and the knowledge base, as shown in Fig 3.

First through combination forecast Agent interact with control management Agent, get the Combination forecast demand, and perceive the change of the blackboard, in order to get the experts at the beginning of the prediction results, then carries on the task management and planning work. Through coordinating the relationship between each function module, will have to deal with information input combination forecast machine. This article adopts the SVM algorithm to forecast

twice, finally through the environment interaction to transfer prediction results to the blackboard. The learning machine can dynamic update SVM network according to the prediction error every time, and form changeable weight combination forecast.

(2) Combination forecast method

Base on SVM regression of Non-linear combination forecast theory is to input the forecast result of forecast expert at a certain moment as the SVM sample. Take the actual Data capacity of solution gas in the transformer oil at the moment as exportation, Adjust the relevant parameters and through study and test for different input vectors corresponding output values. So by a certain samples training this model, nonlinear combination forecasting can be achieved. In this paper, model and standard error of each model, adopt mean absolute percentage error as evaluation index of model prediction accuracy [8]:

$$E_{Tr} = \frac{1}{n_{Tr}} \sum_{i=1}^{n_{Tr}} \frac{|\hat{y}_{Tri} - y_{Tri}|}{y_{Tri}} \times 100\% \quad (1)$$

$$E_{Te} = \frac{1}{n_{Te}} \sum_{i=1}^{n_{Te}} \frac{|\hat{y}_{Tre} - y_{Tre}|}{y_{Tre}} \times 100\% \quad (2)$$

$$E_s = E_{Tr} + E_{Te} \quad (3)$$

1) in formula: $\hat{y}_{Tri}$, y_{Tri}, n_{Tr} as the training set fitting values, actual value and sample capacity; E_{Tr} as fitting error; i as a certain moment.

2) in formula: $\hat{y}_{Tre}$, y_{Tre}, n_{Te} as Test data fitting values, value and sample capacity; E_{Te} as forecast error.

3) in formula: : E_s as the sum of error of fitting and extrapolation, It as a comprehensive index for measure of the precision of forecast model.

Application example

In this paper, it adopts five kinds of methods to forecast transformer oil dissolved gas concentration and Instance to forecast prediction model. The corresponding relation between serial number and model name is as follows: E1 express linear model, E2 express exponential model, E3 express power model, E4 express GM(1,1)model, E5 express Verhulst model, E6 express present model, according document [8]and present model, list three groups of actual data for H_2 gas dissolved in transformer oil and forecast data and error data from each forecast model, as Tab.1 and Table 1 show.

Table.1 Comparison of various forecasting methods on the H_2 sample value

model\year	1993	1994	1995
actual value	22.4	23.7	24.8
E1	23.60	24.97	26.33
E2	23.50	25.08	26.77
E3	23.79	24.77	25.60
E4	24.23	24.30	24.39
E5	22.47	23.81	25.73
E6	22.81	23.67	24.51

Table 1 illustrates that, the forecast result from the forecast model mentioned in this paper much more approach the actual value than single forecasting model. Table 2 illustrates that, minimized error to sample data fitting error E_{Tr}, is GM(1,1) model E4, the error is 4.47%., the minimized error to extrapolation error fitting E_{Te} is thesis forecast model E6, the error is 1.17%. According to the precision comprehensive index of thesis forecast model E_S can be see, the error of thesis forecast is 5.66%, the single forecasting model have lower error than single forecast model.

Table.2 Comparison of forecast errors

model\ error (%)	E_{Tr}	E_{Te}	E_s
E1	8.59	6.17	14.76
E2	8.30	7.95	16.25
E3	7.37	3.23	10.60
E4	4.47	1.67	6.14
E5	5.03	3.75	8.78
E6	4.49	1.17	5.66

Conclusion

To predict the dissolved gas in transformer oil can help predict transformer fault in time, on the basis of the research on the existing prediction system and transformer DGA method, design transformer oil dissolved gas concentration in the intelligent prediction model based on multi Agent system. In the examples of application, base on DGA data, the system require linear model, index model, power model, GM(1,1) model, and Verhulst model, Five forecasters independent forecasts on the concentration of dissolved gas in transformer oil. On the basis of the forecast results, the combination forecast Agent trough the SVM network algorithm, and gives the final prediction results. Finally comparing the actual results show that feasibility and effectiveness of intelligent concentration forecast model of dissolved gases in transformer oil based on multi-Agent system.

References

[1] DONG Zhuo, ZHU Yongli, ZHANG Yu, SHAO Yuying: Power System Protection and Control. Vol. 40 (2012), p. 94. In Chinese

[2] Su Q, Mi C, et al: IEEE Transactions on Power Systems. Vol. 15 (2000), p.593.

[3] YANG Tingfang, LI Jinglu, ZENG Xiangjun, ZHOU Lixing: Automation of Electric Power Systems. Vol. 33 (2009), p. 92. In Chinese

[4] WANG Xiao-ming, HE Ping, WU Hua, CHEN Zhen-gang: High Voltage Apparatus. Vol. 44 (2008), p. 543. In Chinese

[5] YANG Ting-fang, LIU Pei, LI Zhe, ZENG Xiang-jun: Proceedings of the CSEE. Vol. 28(2008), p.108. In Chinese

[6] Michael Wooldridge: An Introduction to Multi-agent Systems. John Wiley, 2003.

[7] Te.S.C.He.T.Project. Java Agent Development Framework is an open source platform for peer-to-peer agent based applications [EB/OL]. http://jade.cselt.it/，2004.

[8] ZHAO Wen-qing, ZHU Yong-li, ZHANG Xiao-qi: Proceedings of the CSEE. Vol. 28 (2008), p.14. In Chinese

Advanced Materials Research Vols. 960-961 (2014) pp 1203-1206

doi:10.4028/www.scientific.net/AMR.960-961.1203

Simulation of the Speed-sensorless Vector Control System Based On MRAS

ShenZhou , WenYanChen

(Electrical Control Engineering, Xi'an University of Science and Technology, Xi'an 710054,P.R.China)

zhoujimen@163.com ch_w_y@163.com

Key words:speed-less sensor; vector control; MRAS; simulation

Abstract: Aimed at the problem of speed identification for the asynthetic motor speed-less sensor vector control system, based on basic equations of vector control and centered by the current model and voltage model of rotor flux linkage, after the establishment of the rotor speed identification module by module reference self- adaptation theory(MRAS), this paper builds the MRAS speed-less sensor vector control system and establishes the system simulation model in Simulink software environment. Simulation results show that: the system has good dynamic and static characteristics and stability.

CLC: TM343.2 **Document Code:**A

Introduction

Asynchronous motor vector control (vector control, VC) with dynamic and static performance suchas high control accuracy, good low-frequency characteristics and quick torque response is widely applied in high-performance AC motor drive field. But the speed feedback signal with conventional vector control gets speed information through speed sensor. As a result, the cost of the system is increased, but the reliability of the system is reduced, the application of the system is limited and the performance of the speed control system is affected. Vector control without speed sensor technology gets physical quantities such as voltage and current from the motor side. This technology estimates the motor speed by calculation, which eliminates the hassle of speed sensor hardware detection, reduces system cost and improves system stability. Have a simple algorithm, small calculation, real-time speed and good stability of model reference adaptive system of nonlinear time-varying system based in many fields has been widely used. So I used MRAS to estimate the motor speed.

Vector Control

1.1. Fundamental

Asynchronous motor vector control principle simulates asynchronous motors as DC motors to get better control performance, according to the dynamic mathematical model of the motor, and taking advantage of PARK transformation and CLARK transformation. Under the premise producing the same rotation MMF, stator currents i_A, i_B, i_C in the ABC three-phasecoordinate system can be converted to currents iα,iβ in α β two phase static coordinate system,through CLARK transformation(3s/2s), and then α β two phase static coordinate system can be convertered to dq two phase rotating coordinate system through PARK Transform (i.e. 2s / 2r transform), as a result, the stator current of the motor is decomposed into orthogonal excitation current id and the torque

current i_q. In this way, when observer rotates with the coordinate standing on the core, the AC motor can be equivalent to a DC motor . Therefore, we can control the AC asynchronous motor with the method of controlling the DC motor. The schematic diagram is shown in Figure 1. i_A, i_B, i_C is the three-phase AC input current, ωr is the output speed.

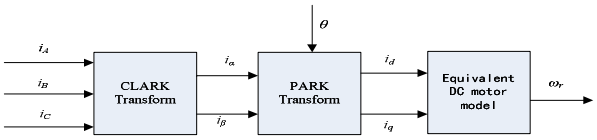

Figure 1. Vector control schematics

1.2.Current model of rotor flux

The mathematical model of the asynchronous motor shows that the motor is a multivariable, nonlinear and strongly coupled system. So if we want to control AC motorsas controllingDC motors, the vector must be transformed.

By vector transformation, we can get the voltage equation of the motorin the dq coordinate system:

$$\begin{bmatrix} u_{s\alpha} \\ u_{s\beta} \\ u_{r\alpha} \\ u_{r\beta} \end{bmatrix} = \begin{bmatrix} R_s + L_s p & 0 & L_m p & 0 \\ 0 & R_s + L_s p & 0 & L_m p \\ L_m p & \omega_r L_m & R_r + L_r p & \omega_r L_r \\ -\omega_r L_m & L_m p & -\omega_r L_r & R_r + L_r p \end{bmatrix} \begin{bmatrix} i_{s\alpha} \\ i_{s\beta} \\ i_{r\alpha} \\ i_{r\beta} \end{bmatrix} \tag{1}$$

In the two-phase stationary coordinate system, the component quantity of the rotor flux on αβ axis is:

$$\psi_{r\alpha} = L_m i_{s\alpha} + L_r i_{r\alpha} \tag{2}$$

$$\psi_{r\beta} = L_m i_{s\beta} + L_r i_{r\beta} \tag{3}$$

Therefore, corresponding current equation is:

$$i_{r\alpha} = \frac{1}{L_r}(\psi_{r\alpha} - L_m i_{s\alpha}) \tag{4}$$

$$i_{r\beta} = \frac{1}{L_r}(\psi_{r\beta} - L_m i_{s\beta}) \tag{5}$$

According to related derivation , the current model equation of the asynchronous motor rotor flux is:

$$\psi_{r\alpha} = \frac{1}{T_r \rho + 1}(L_m i_{s\alpha} - \omega T_r \psi_{r\beta}) \tag{6}$$

$$\psi_{r\beta} = \frac{1}{T_r \rho + 1}(L_m i_{s\beta} - \omega T_r \psi_{r\alpha}) \tag{7}$$

Thus, the current model equation of the rotor flux in the rotating two-phasecoordinate systemis:

$$\psi_r = \frac{L_m i_{sm}}{T_r \rho + 1} \tag{8}$$

Motor slip formula is:

$$\omega_s = \omega_1 - \omega = \frac{L_m i_{st}}{T_r \psi_r} \tag{9}$$

1.3 The voltage model of rotor flux

The voltage equation of the rotor flux can be got according to the ordinal transformation in the α β two-phase static coordinate system of asynchronous motor is:

$$\psi_{r\alpha} = \frac{L_r}{L_m}[\int (u_{s\alpha} - R_s i_{s\alpha})dt - \sigma L_s i_{s\alpha}] \quad (10)$$

$$\psi_{r\beta} = \frac{L_r}{L_m}[\int (u_{s\beta} - R_s i_{s\beta})dt - \sigma L_s i_{s\beta}] \quad (11)$$

MRAS speed identification based on rotor flux

Basic principle of MRAS: for a system which the mathematical model can be built and parameter or variable can not be fully measurable, a self adaptation structure which can change a certain or some parameters in the system can be designed by using the input deviation between a reference model and an adjustable model. In this structure, through parameters or variable, the output value of the adjustable model can be changed to make the output deviation between the reference model and the adjustable model be zero.[3]

The voltage model and current model formula of the rotor flux (8) (10) (11), and the motor slip formula (9) show that current model contains speed entry, but voltage model does not, so we take the voltage model of the rotor flux as reference item, the current model of the rotor flux as adjustable item, and then design self adapatation control system based on Popov stability theory. Adaptive law formula of the Speed Identification is:

$$\omega_r = (K_p + \frac{K_i}{s})(\psi_{\alpha r}\psi^*_{\beta r} - \psi_{\beta r}\psi^*_{\alpha r}) \quad (12)$$

System Simulation

3.1 Simulation Model

Based on Matlab/Simulink7.11.0 (R2010b), this paper simulate the MRAS speed calculation system of the asynchronous motor. Simulation motor parameters are: u=260v，f=50Hz，n_p=2，R_s=0.435Ω，L_{ls}=0.002mH，R_r=0.816Ω，L_{lr}=0.002mH，L_m=0.069 mH，J=0.19kg.$m^{2\circ}$. Stator and rotor winding resistor inductance is 0.071mH, leakage coefficient is 0.056, the rotor time constant is 0.087. Emulation circuit is shown in Figure 2

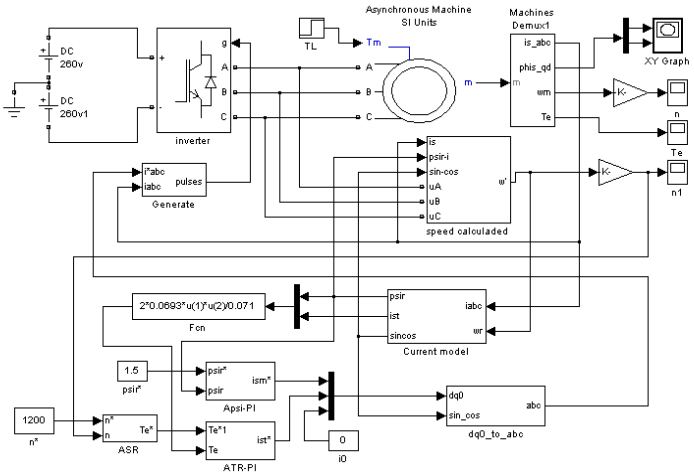

Figure 2 System Simulation Model

3.2 Simulation results

Simulation parameters: Motor starts with no-load, the given speed is 1200r/min, when t = 0.6s, the motor plus load torque TL = 55N.m. Figures 4, 5, 6, 7 are the actual motor speed, the estimated speed, the motor output torque and the stator flux. Figure 3and Figure 4 shows that the speed

difference between the measured motor speed and estimated speed is small, the system can get the same control effect as the speed sensor vector control. Figure5, the motor output torque response curve shows that, the torque responses rapidly and accurately, ripple is small, when the speed reaches the set value, the torque rapidly converges to the vicinity of the load torque stably, which gives the motor a higher speed adjustment performance. Figure 6shows that the stator flux trajectory is approximately similar toa circular flux.In the entire speed adjustment process, the motor load flux fluctuations are small when the motor load speed changes, which reflects that the system can realize excitation and torque decoupling of asynchronous motors, to reach the speed adjustment performance of the DC motor approximately .

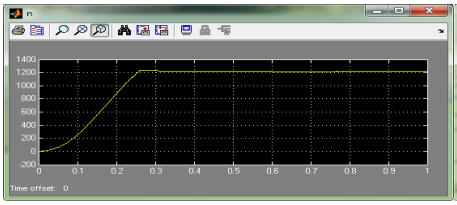

Figure 3. Actual speed

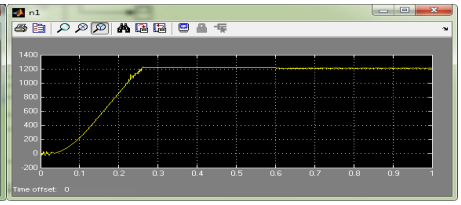

Figure 4. Speed Estimation

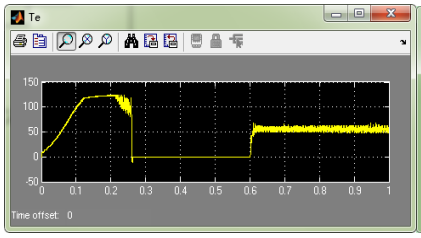

Figure 5. Motor output torque

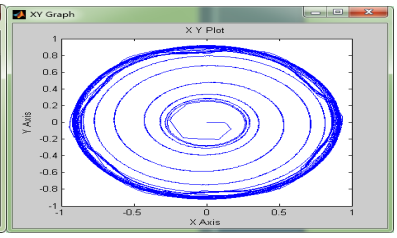

Figure 6. Motor stator flux

Conclusion

Simulation results show that: speed-lesssensor vector control system with good dynamic and static performance and stability, has a certain robustness, which can identify motor speed fast and accurately and guide practical engineeringsignificantly in theory.

References

[1] Li D H, Bai Jing, Li Z M, Li Qing, AC Speed Control System, Beijing, Electronic Industry Press, 2002. 92-150.

[2] Xia C Y, Adaptive control of AC and DC transmission system, Beijing; Machinery Industry Press, 2005,100-120.

[3]Li Zhen. Sensorless field orientation control of induction machines based on a mutual MRAS scheme [J].IEEE Trans on IE ,1998,45(5).

[4] Hong N G , Power electronics, motor control system modeling and simulation, Beijing, Machinery Industry Press,2010;178-207.

Advanced Materials Research Vols. 960-961 (2014) pp 1207-1213

doi:10.4028/www.scientific.net/AMR.960-961.1207

Application of Discrete Spectrum Correction Technology for Induction Motor Rotor Fault Diagnosis

HOU Xin-guo [1, a] , LI Yu[1,b] , Yang Zhong-lin[1,c] , BU Le-ping[1,d]

[1]college of Electronic Engineering, Naval Univ.of Engineering,Wuhan 430033, China

[a]hxinguo2008@126.com, [b]liyu@126.com, [c]yzlin@126.com, [d]bulp@126.com

Keywords: induction motor; fault diagnosis; rotor fault; spectrum correction

Abstract. The extraction method of induction motor's fault character based on coordinate transformation could restrain the influence of fundamental component leakage by translating fundamental component into DC component. The amplitude of the fault character frequency component was inaccurate by spectrum analysis taking no account of the leakage of itself. So rotor fault diagnosis method of induction motor based on discrete spectrum correction technology is proposed. This method which did not depend on spectral function of the window function improved the traditional phase difference correction method, and the stator current signal analysis by means of an appropriate window function is performed to reduce the interference between each frequency. The proposed method could detect the existence of fault character frequency component and its frequency and amplitude. The simulation and experimental results indicated that using this method could get better precision of frequency and amplitude of the fault character frequency component.

Introduction

Rotor fault is a common fault of the induction motor. At present, there are many methods used to detect rotor fault[1-7]. Stator current signal monitoring can be made into non-intrusion style, and has a wide prospect. When the rotor of induction motor broke down, the fault character frequency component $(1\pm 2ks)f_0$ appeared in stator current signals. However, because the slip ratio is very small when the motor runs steadily, it caused that the strongest fault character frequency component is very close to the fundamental component and the amplitude of the fault character frequency component is relatively smaller than that of fundamental wave. Documents now available usually describe the translation of fundamental component into DC component through a variety of methods (e.g. expanding Park translation method[1-2], Synchronous rotational coordinate system translation method[3], Hilbert translation method[4, 5], etc.). Operating like this belongs to qualitative analysis of fault discrimination. To realize the quantization of the fault degree, the amplitude of the fault character frequency component must be accurately measured.

When FFT and spectrum analysis are applied practically, the exact amplitudes and phases of all components can be obtained by correcting the components of frequency spectrum. At present, scholars have done a lot of research work in discrete spectrum correction[8]. Among them, the phase difference correction method is applied widely in engineering fields because it is convenient to realize, has higher precision and the good ability to overcome the noise[9-11]. This thesis researched a kind of improved phase difference correction method to correct the frequency spectrum of the stator current signals, count the amplitudes of the fault character frequency component accurately, and provided the algorithm theoretical basis for the quantitative evaluation of rotor fault.

Phase difference correcting method and its improvement

Assume harmonic signal $x(t) = A\cos(2\pi f_0 t + \theta)$, its Fourier transform is transformed into

$$X(f) = \frac{A}{2}e^{-j\theta}\delta(f + f_0) + \frac{A}{2}e^{j\theta}\delta(f - f_0) \tag{1}$$

In the equation: $f = kf_s / N = k\Delta f$, N is the sampling numbers, f_s is the sampling frequency, Δf is frequency resolution ratio.

Adding the window $w_T(t)$ (the length is $T(T=(N-1)/f_s)$) to the signal $x(t)$. $w_T(t)$ is obtained by moving the symmetrical window $T/2$ to the right. the window spectrum function of $w(t)$ is $W(f)$, the window spectrum function $W_T(f)$ of $w_T(t)$ relative to $W(f)$ has a Phase shift factor $e^{-j\pi fT,}$ that is

$$W_T(f) = W(f)e^{-j\pi fT} \tag{2}$$

According to the convolution theorem, the Fourier transforms of the signals adding window $x(t)w_T(t)$ is

$$X_w(f) = \frac{A}{2}W(f + f_0)e^{-j[\pi T(f+f_0)+\theta]} + \frac{A}{2}W(f - f_0)e^{-j[\pi T(f-f_0)-\theta]} \tag{3}$$

FFT analysis of N point is done on $x(t)w_T(t)$, assuming $f_0=(k-\Delta k)\Delta f$, wherein k is integer, and $\Delta k \in [-0.5, 0.5]$ is normalized frequency correction. then the peak value of discrete frequency spectrum should appear at the k spectral line, and its corresponding phase is

$$\varphi_0 = \theta - \pi T(k\Delta f - f_0) = \theta - \pi\Delta k \tag{4}$$

Move the center of the window function $w_T(t)$ to the right again for uT, now the phase shift is $e^{-j2\pi ufT}$, and similarly, FFT analysis of N point is done and then phase of the signal after adding the window is

$$\varphi_1 = \theta - \Delta k\pi - 2\pi u\Delta k = \theta - (\pi + 2\pi u)\Delta k \tag{5}$$

phase difference calculated from equations （4） and （5） is

$$\Delta\varphi = \varphi_1 - \varphi_0 = -2\pi\Delta k \tag{6}$$

in above equation, value of $\Delta\varphi$ is in the range of （-2π，2π）, and its main value range is （$-\pi$，π）. Therefore, the phase difference $\Delta\varphi$ is properly adjusted:

$$\Delta\varphi = \begin{cases} \Delta\varphi + 2\pi & \Delta\varphi < -\pi \\ \Delta\varphi - 2\pi & \Delta\varphi > \pi \end{cases} \tag{7}$$

Then the normalized frequency correction is $\Delta k = -\frac{\Delta\varphi}{2\pi u}$. Assuming that the coefficient of the k *spectral line* at which the peak value appeared is $X(k)=R_k+jI_k$, then the respective correcting formulae of both amplitude of the signals and the phase is $A = \frac{2|X(k)|}{W(\Delta k)}$ and $\theta = tan^{-1}(\frac{I_k}{R_k}) + \Delta k\pi$. The above is based on the time shift's phase difference method[7].。Besides the time shift's phase difference method[8-11], there are still other phase difference methods based on

adding different length or different types of symmetrical window function. Essentially speaking, all of the methods take the advantage of the character that both of the phase and the frequency correcting quantity have the linear relation in the main lobe of the window function, through counting FFT twice to get the phase difference of the spectrum peak to count the frequency correcting quantity and further correct the frequency and phase.

The correction of amplitude completely depends on the spectrum function $W(f)$ of the window function. Adding different windows, the spectrum function $W(f)$ of the window function is different, the amplitude correction formula is also different. Actually, even if it is commonly used window function, its spectrum functions are complex, and can only be approximately manipulated when counting. And some window functions themselves are rather complex and hard to extract the analytic expression of the spectrum function from them. That greatly limited the flexibility of window function selection in different applications, so the amplitude correction must be improved.

By multiplying the signal $x(t) = A\cos(2\pi f_0 t + \theta)$ with a complex signal $e^{j2\pi\Delta k\Delta ft}$, a complex signal $x_e(t) = A\cos(2\pi f_0 t + \theta)e^{j2\pi\Delta k\Delta ft}$ is obtained, then the Fourier transform with $x_e(t)$ is

$$X_e(f)=\frac{A}{2}e^{-j\theta}\delta(f+f_0-\Delta k\Delta f)+\frac{A}{2}e^{j\theta}\delta(f-f_0-\Delta k\Delta f)=\frac{A}{2}e^{-j\theta}\delta(f+k\Delta f-2\Delta k\Delta f)+\frac{A}{2}e^{j\theta}\delta(f-k\Delta f) \tag{8}$$

Add the window $w_T(t)$ with the length of T(T=（N-1)/f_s, f_s is the sampling frequency) to the signal $x_e(t)$, then the Fourier transform of the signal with window added $x_e(t)w_T(t)$ is

$$\begin{aligned} X_{ew}(f) &= X_e(f)*W_T(f) \\ &= \frac{A}{2}W(f+k\Delta f-2\Delta k\Delta f)e^{-j[\pi T(f+k\Delta f-2\Delta k\Delta f)+\theta]}+\frac{A}{2}W(f-k\Delta f)e^{-j[\pi T(f-K\Delta f)-\theta]} \end{aligned} \tag{9}$$

Obviously, if overlap of minus frequency is not considered, then when f=$k\Delta f$, the following formula is obtained

$$X_{ew}(k\Delta f)=\frac{A}{2}W(0)e^{j\theta} \tag{10}$$

that is the coefficient of the k spectral line of discrete spectrum for window added signal $x_e(t)w_T(t)$.

$$X_{ew}(k)=\frac{A}{2}W(0)e^{j\theta} \tag{11}$$

Amplitude equation and phase correction equation for $x(t)$ are $A=\frac{2|X_{ew}(k)|}{W(0)}$ and $\theta=\tan^{-1}(\frac{I_k}{R_k})$.Wherein: R_k and I_k are solid part and void part of X_{ew}（k）respectively. $W(0)$ is DC component of $w_T(t)$. It is not necessary to know expression of the window spectrum function, and it can be obtained by just taking average value of the window at N point.

Therefore, the calculation steps of spectrum correction method based on improved phase difference correction are: First step: to get normalized frequency correction quantity Δk of the signal $x(t)$ by utilizing phase difference method. Second step: Multiply signal $x(t)$ with a complex signal $e^{j2\pi\Delta k\Delta ft}$, to get a complex signal x_e(t).

Third step: Add window to complex signal x_e(t), calculate X_{ew}（k）by using DFT and then, correct amplitude and phase as above equations.

Simulation study

If the frequency of power supply of the induction motor is f_0=49.72Hz，$2sf_0$=1.64Hz，then when the rotor runs wrong, the stator current of the induction motor phase-A can be expressed as:

$$i_a = 10\cos(2\pi 49.72t + 32\pi/180) + 0.15\cos(2\pi 48.08t + 73\pi/180) + 0.11\cos(2\pi 51.36t - 13\pi/180) \quad (12)$$

Wherein: 48.08Hz component and 51.36Hz component are components of $(1\text{-}2s)f_0$ and $(1+2s)f_0$ respectively.

Because the stator current signal i_a is generated by mixing frequency-closed signals, its frequency is the intensively distributed frequency spectrum. In order to remove the interference of each frequency component, the choice of window function is very important, and the window function of which the side lobe decays fast must be selected.

Kaiser window is a group of self-defined adjustable window functions, composed by zero order Bessel function. The ratio of its main lobe energy to that of its side lobe is nearly the largest, and the ratio of the width of the its main lobe to the height of its side lobe can be freely chosen, and it has the character that the peak value of the side lobe is small and the rate of decay is large. Its time domain expression is:

$$w(n) = \frac{I_0\left[\beta\sqrt{1-\left(\frac{n}{N/2}\right)^2}\right]}{I_0(\beta)} \quad 0 \le |n| \le \frac{N}{2} \quad (13)$$

Wherein: $I_0(\beta)$ is modified zero-order Bessel function of the first kind, β is shape parameter of the window function, and N is length of the window function. The larger the shape parameter β, the smaller the peak value of the side lobe of Kaiser window function frequency spectrum, and the larger the rate of decay.

Based on adjustable feature of Kaiser window, this paper selects Kaiser window when adding window to stator current signal.

From simulation current signal of equation (17), the sampling frequency is 1024Hz，and make the spectrum point as 4096 points. Adding Kaiser window of β=10 to sampled data, and process with the improved phase difference correction method as mentioned previously. Simulation results are shown in Table 1 below.

Table 1 Correction results of the stator current simulation signal

Actual value	Actual frequency	48.02	49.72	51.36
	Actual amplitude	0.15	10	0.11
	Actual phase	73	32	-13
Corrected value	Correction frequency	48.07800	49.71998	51.36239
	Correction amplitude	0.14790	9.99993	0.10794
	Correction phase	73.58594	32.00894	-13.76456
Error	Relative error of frequency	0.00399	0.00005	0.00479
	Relative error of amplitude (%)	1.399	0.0006	1.873
	Error of phase (degree)	0.58594	0.00894	0.79456

Table 1 shows that after correcting, the respective relative errors of the amplitudes of the 48.08Hz frequency component and the 51.36Hz frequency component are 1.399% and 1.873%, while the respective phase errors are 0.58594° and 0.79456°. It is mainly because the foundation

component is excessively strong, and its amplitude is nearly 100 times of those of the 48.08Hz and 51.36Hz components, and the frequency spectrum leakage has effects on the 48.08Hz and 51.36Hz components. In contrast, because the amplitudes of the 48.08Hz and 51.36Hz components are smaller, and have less effect on foundation component, the correcting precision of the foundation component is higher.

To further improve the correcting precision of the fault character frequency component, we can use the frequency, amplitude and phase after the fundamental component is corrected to generate a sine sequence, and then minus the sine sequence from original sampling sequence to filter out the fundamental component in the signals completely, and then correct it to obtain an higher precision. The correction result is illustrated in Table 2: obviously after the fundamental component is filtered out, the 48.08Hz and 51.36Hz fault character frequency components both reached to a highest correction precision.

Table 2 Correction results of the stator current simulation signal filtered out fundamental component

Actual value	Actual frequency	48.08	51.36
	Actual amplitude	0.15	0.11
	Actual phase	73	-13
Corrected value	Correction frequency	48.08010	51.36014
	Correction amplitude	0.14998	0.109998
	Correction phase	72.99474	-13.00894
Error	Relative error of frequency	0.00019	0.00028
	Relative error of amplitude (%)	0.0106	0.0019
	Error of phase (degree)	0.00526	0.00894

Analysis of measured data

The experiment platform used the frequency conversion timing system as shown in figure 1. The motor drove the AC synchronization generator and the resistive loads. The motor is the Y132M-4 induction motor. The output frequency of the inverter f_0 is 45Hz, and the data sampling frequency is 25kHz.

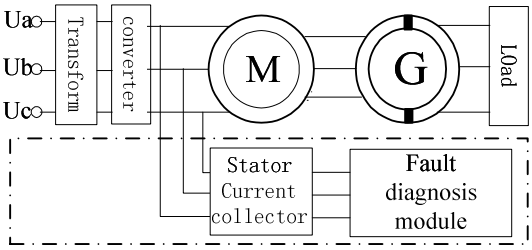

Fig. 1 The experiment scheme of detecting faults

The experiment is carried on when the rotor bar 1 was broken, after the motor ran steadily, the measured stator current wave shape and frequency spectrum of motor phase-A is shown in Diagram 2. Now $2sf_0$=2.2Hz is counted out according to the measured motor rotary speed. Diagram 2(b) is from adding rectangular window to 10s data and do FFT directly on it. In the diagram, a peak point appeared at 42.8Hz fault character frequency, while a sinking gap appeared at 47.2Hz , which was caused by the leakage of the frequency spectrum of the fundamental component, so all the

measured amplitudes were not correct. Even if the 45Hz fundamental component was close to 20dB as shown in diagram 2(b), that is 10A or so, while from diagram 2(a), the amplitude of the fundamental component should be about 15A, which means the leakage was quite serious.

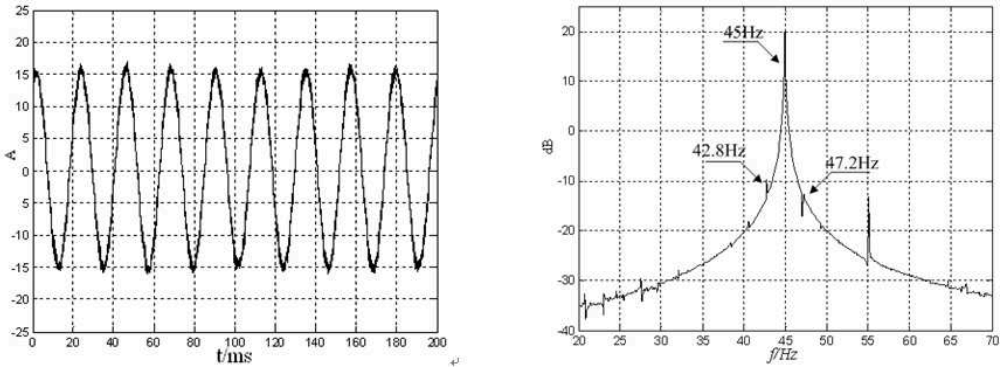

(a) A phase stator current shape (b)The frequency spectrum of A phase stator current

Fig.2 A-phase stator current

Extract a data with 7.5s length, and respectively count the data of the former 5s and latter 5s by adding Kaiser window, and firstly, correct the fundamental component with the improved phase difference method presented in this thesis to get accurate information of the frequency, amplitude and phase of the fundamental component, and then use the obtained information to form a sine sequence. Using the stator current signals minus the sine sequence could filter out the fundamental component in the stator current signals. Then, correct the frequency components of $(1\text{-}2s)f_0$ and $(1+2s)f_0$ in sequence, a better effect was obtained. The correction results are shown in table 3 below.

Table 3 Correction results of fundamental component and fault characteristic frequency components

	f_0	$(1\text{-}2s)f_0$	$(1+2s)f_0$
Frequency (Hz)	44.95	42.79	47.11
Amplitude (A)	15.355	0.129	0.151

Conclusion

The detection of induction motor's rotor fault based on stator current signals could avoid the influence of fundamental component leakage by translating fundamental component into DC component with coordinate transformation. However, the leakage may happen on the fault character frequency component itself , if it is ignored, the detected amplitude of the fault character frequency component is still inaccurate. This thesis improved the traditional phase difference correcting method first to make it never rely on the spectrum function of the window function when it is correcting the amplitude value, and then reduced the interference between the frequency components by choosing the proper window function to process the induction motor's stator current signals, and then corrected the frequency spectrum of the stator current with the improved phase correcting method, in this way, we could not only detect the existence of the fault character frequency component, but also obtained the exact information of the frequency and the amplitude of the fault character frequency component, and provided the algorithm support for further quantizing the fault severity。The simulation and experiment results proved：with the introduced research method in this thesis, by choosing proper window function, the frequency and amplitude of the fault character frequency component obtained by counting have higher precision.

References

[1] Cruz S M A, Cardoso A J M. Stator winding fault diagnosis in three-phase synchronous and asynchronous motors by the extended Park's vector approach[J]. IEEE Trans. On Industry Applications, 2001, 37(5): 1227-1233.

[2] Hou Xin-guo, Wu Zheng-guo, Xia Li. A method for detecting rotor faults in asynchronous motors based on the square of the Park's vector modulus[J]. Proceedings of the CSEE, 2003, 23(9): 137-140.

[3] Cruz S M A, Cardoso A J M, Toliyat H A. Diagnosis of stator, rotor and airgap eccentricity faults in three-phase induction motors based on the multiple reference frames theory[C]. Conference Record of The 2003 IEEE Industry Applications Society Annual Meeting, Salt Lake City, USA, 2003, Π: 1340-1346.

[4] Ma Hong-zhong, Yao Hua-yang, Li Hua-min. Study on rotor broken-bar fault in induction motors based on spectrum analysis of Hilbert modulus[J]. Electric machines and control, 2009, 13(3): 371-376.

[5] Niu Fa-liang, Huan Jin, Yang Jia-qiang, et al. Rotor broken-bar fault diagnosis of induction motor based on Hilbert-Huang transformation of the startup electromagnetic torque[J]. Proceedings of the CSEE, 2005, 25(11): 107-112.

[6] SHAO Ying, LI Xiao-ming,ZHANG Xiao-ming. Interharmonics parameter detection based on interpolation FFT and multiple signal classification algorithms[J]. Journal of Naval University of Engineering,2011，23（4）：53-59.

[7] HU Wen-biao,XIA Li,XIANG Dong-yang et al. An improved frequency spectrum correction method based on phase difference correction method[J]. Journal of vibration and shock, 2012, 31(1):162-166.

[8]Ding Kang, Chen Jianlin, Su Xiangrong. Development in vibration signal analysis and processing methods[J]. Journal of Vibration engineering, 2003, 16(1): 1-10.

[9]Xie Ming, Zhang Xiaofei, Ding Kang. A phase difference correction method for phase and frequency correction in spectral analysis[J]. Journal of Vibration engineering, 1999，12(4)：454-459.

[10] Ding Kang, Zhong Shun-cong. A universal phase difference correcting methods on discrete spectrum[J]. ACTA ELECTRONICA SINICA, 2003，31(1)：142-145.

[11] Ding Kang, Yang Zhijian. Improvement and anti-noise performance analysis of window-length changing phase difference correction[J]. Journal of South China University of Technology, 2007，35(10): 210-213.

Advanced Materials Research Vols. 960-961 (2014) pp 1214-1224

doi:10.4028/www.scientific.net/AMR.960-961.1214

Dynamic Aggregation Method of Induction Motors Based on Coherent Characteristics

ZHANG Jian[1,a], YUAN Xiaodong[2,b]

[1,2]Jiangsu Electric Power Company Research Institute, Nanking, 211103, China

[a]z_jj1219@sina.com, [b]lannyyuan@hotmail.com

Keywords: load modeling, induction motor, power system simulation, fuzzy C-means clustering, dynamic aggregation.

Abstract. Parameters of induction motors have crucial effects on power system simulation. This paper proposes a dynamic aggregation method of induction motors. In this method, firstly, starting off the electromechanical models of induction motors, taking the coefficients of the electromechanical equations and steady state slips of motors as the characteristic vectors, motors are grouped with fuzzy C-means clustering method. Then, electromechanical equations of the equivalent motor are obtained by averaging that of the individual motors in the same group. Finally, parameters of equivalent motors are calculated based on the relationship of transient impedance before and after aggregation, and the principle that active and reactive power loads are equal before and after aggregation. Simulation results show that the proposed method can improve the precision of simulation

Nomenclature

R_s	Stator winding resistance of motor (p.u.).
X_s	Stator leakage reactance of motor (p.u.).
X_m	Magnetizing reactance of motor (p.u.).
R_r	Rotor resistance of motor (p.u.).
X_r	Rotor leakage reactance of motor (p.u.).
H	Rotor inertia constant (s).
a	Torque coefficient in proportion to square of speed.
b	Torque coefficient in proportion to speed.
ω	Rotor speed (p.u.).
ω_s	Angle frequency of power system(rad/s).
I_d , I_q	d -axis and q -axis stator current.
V	Bus voltage.
$E_d^{'}$, $E_q^{'}$	d -axis and q -axis transient EMF.
eq	Subscript denoting constant or variable of equivalent motor.
i	Subscript denoting constant or variable of the i^{th} motor.
T	Superscript denoting the transpose of a matrix.
0	Subscript denoting steady state variable value.

Introduction

Model of each component is the base of power system simulation. Load model is the bottleneck of improving the precision of power system simulation due to its complexity. In load model, parameters of induction motors have crucial effects on voltage stability and angle stability [1-4].

In practice, thousands of induction motors scatter in a large distribution network. Simulation studies cannot be computationally feasible unless groups of individual induction motors are aggregated into a single equivalent one.

There are mainly two approaches to build load model: the component-based approach and the measurement-based approach. The component-based method from the investigation information, adopts aggregation algorithm to obtain the composite load model of a substation. There exist mainly four aggregation methods of induction motors: kVA weighted average method [4, 5], power invariance method [6,7], no load and block up working conditions of motor based method [8,9], dynamic equivalent circuit of induction motor based method [10].

In [4], based on the steady state equivalent circuit of induction motors, the parameters of the equivalent motor are obtained by kVA weighted averaging that of individual one. This method can easily obtain parameters of the equivalent motor, but reactive power load cannot be equal before and after aggregation. In [5], Guo et al believe that load factor and critical slip have notable impact on transient stability of power system and an improved kVA weighted average aggregation method of induction motor is proposed. In [6,7], the steady state equivalent circuit of individual induction motor is transformed to the form of three paralleled impedances, based on which groups of motors are aggregated to a single one. This method is strict based on the steady state equivalent circuit of motors. As opposed to kVA weighted average method, this method does not discriminate big motors from small ones, as a result, dynamic characteristics dominated by big motors is not retained. In [8], with the skin effect of motor taken into account, leakage inductance of stator as well as that of rotor is separated into two parts. Thus, electric parameters of motor reach to seven. In [8, 9], an aggregation method of motors is proposed based on no load and block up working conditions of motors. Because this method does not take the steady state working slip of individual motor into consideration, the dynamic errors of active and reactive power loads are comparatively large.

All the methods mentioned above, belong to static aggregation method. The dynamic error is comparatively large. In this paper, motors connected to the same bus are grouped by fuzzy C-means clustering method based on their coherency and a dynamic aggregation method of motors is proposed. The effectiveness of this method is also validated by a simulation case.

Model of Induction Motor

Equivalent Circuit of Induction Motor.

The steady state equivalent circuit of induction motor is shown as Fig.1, while the transient equivalent one is shown as Fig.2 [10].

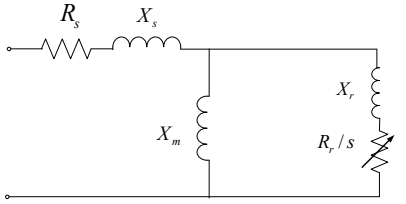

Fig.1 Steady equivalent circuit of induction motor

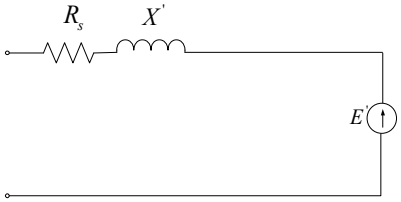

Fig.2 Transient equivalent circuit of induction motor

According to [11], with the stator resistance neglected, the simplified electromechanical model of induction motor is

$$T' \frac{dE'_q}{dt} = -E'_q + \frac{X - X'}{X} V + T' \omega_s (\omega - 1) E'_d \tag{1}$$

$$T^{'}\frac{dE_d^{'}}{dt}=-E_d^{'}-T^{'}\omega_s(\omega-1)E_q^{'} \tag{2}$$

$$2HX^{'}\frac{d\omega}{dt}=VE_d^{'}-T_{m0}\left(a\omega^2+b\omega+1-a-b\right)X^{'} \tag{3}$$

Where,

$T^{'}=T_0^{'}X^{'}/X$

$T_0^{'}=(X_r+X_m)/(\omega_s R_r)$

$X=X_s+X_m$

$X^{'}=X_s+X_rX_m/(X_r+X_m)$

Initialization of Induction Motor.

According to Thevenin Theory, seen from rotor resistance to stator, the equivalent impedance of induction motor on steady state is

$$Z_e=R_e+jX_e=(R_s+jX_s)//jX_m+jX_r=\frac{R_sX_m^2+j(X_pX_{sm}+R_sX_{rm}^2)}{R_s^2+X_{sm}^2} \tag{4}$$

Where

$X_{sm}=X_s+X_m$

$X_{rm}=X_r+X_m$

$X_p=X_sX_m+X_rX_m+X_sX_r$

$R_e=\frac{R_sX_m^2}{R_s^2+X_{sm}^2}$

$X_e=\frac{X_pX_{sm}+R_sX_{rm}^2}{R_s^2+X_{sm}^2}$

The equivalent voltage is

$$V_e=\frac{X_m}{\sqrt{R_s^2+X_{sm}^2}}V \tag{5}$$

The electromagnetic torque of induction motor on steady state is

$$T_e=\frac{V_e^2(1-s)R_r/s}{\omega_s\left[(R_r/s+R_e)^2+X_e^2\right]} \tag{6}$$

The steady state slip of rotor s_0 can be obtained according to Eq.7.

$$T_e=T_{m0}\left[a(1-s)^2+b(1-s)+1-a-b\right] \tag{7}$$

The active and reactive power loads of motor are

$$P=real\left(\frac{V^2}{R_s+jX_s+\frac{(R_r/s_0+jX_r)*jX_m}{(R_r/s_0+jX_r+jX_m)}}\right) \tag{8}$$

$$Q=imag\left(\frac{V^2}{R_s+jX_s+\frac{(R_r/s_0+jX_r)*jX_m}{(R_r/s_0+jX_r+jX_m)}}\right) \tag{9}$$

Motor Grouping Based on Fuzzy C-Means Clustering Method

Introduction of Fuzzy C-Means Clustering Method.

The idea behind fuzzy C-means clustering method is that it introduces the concept of membership from fuzzy mathematics. As opposed to hard C-means clustering method, fuzzy C-means clustering

method can obtain the membership of each class for every sample. The advantage of fuzzy C-means clustering method relies on that it reflects better the real world by expressing the intermediary property of samples.

The procedure of fuzzy C-means clustering method is as follows.

P1) According to the number of classes pre-specified, c clustering centers are produced at random.

P2) Square of distance d_{ik}^2 between each characteristic vector of sample x_k and each clustering center w_i is calculated as Eq.10.

$$d_{ik}^2 = \|x_k - w_i\|^2 = (x_k - w_i)^T (x_k - w_i) \tag{10}$$

P3) Suppose u_{ik} is the membership of i^{th} class for k^{th} sample and N is the number of samples, u_{ik} satisfies Eq.11.

$$\sum_{i=1}^{c} u_{ik} = 1, u_{ik} \in [0,1], \forall k = 1,2,\cdots N \tag{11}$$

Objective function is formulated by Eq.12.

$$J(U,W,\lambda) = \left\{ \sum_{k=1}^{N} \sum_{i=1}^{c} (u_{ik})^m (d_{ik})^2 + \sum_{k=1}^{N} \lambda_k \left(\sum_{i=1}^{c} u_{ik} - 1 \right) \right\} = \sum_{k=1}^{N} \left\{ \sum_{i=1}^{c} (u_{ik})^m (d_{ik})^2 + \lambda_k \left(\sum_{i=1}^{c} u_{ik} - 1 \right) \right\} \tag{12}$$

Where $\lambda_k (k = 1,2,\cdots N)$ is Lagrange multiplier, and real number $m \in [0,2]$ is a weighting index. According to Kuhn-Tucker Theory, the necessary conditions of the objective function minimization are

$$u_{ik} = \frac{1}{\sum_{j=1}^{c} \left(\frac{d_{ik}}{d_{jk}} \right)^{2/(m-1)}} \tag{13}$$

$$w_i = \frac{\sum_{k=1}^{N} (u_{ik})^m x_k}{\sum_{k=1}^{N} (u_{ik})^m} \tag{14}$$

By iteration, memberships and clustering centers are updated until difference between the latest two objective function values is lower than a threshold value or the most iteration number is reached.

Choice of Characteristic Vector.

Suppose there are n induction motors connected to the same bus. If the steady state slip s_0, initial transient EMF E_0' and the coefficients of the electromechanical equations of individual motor T', $2HX'$, $(X - X')/X$, $aT_{m0}X'$, $bT_{m0}X'$, $(1-a-b)T_{m0}X'$ are the same, then the n motors can be seen as only one motor. In practice, this condition cannot be satisfied, but motors with close parameters and initial states values can be classified into the same group and be seen as one motor. In this paper, for convenience, we choose $(T', HX', (X - X')/X, aT_{m0}X', bT_{m0}X', (1-a-b)T_{m0}X', s_0)$ as the characteristic vector for motor grouping. Difference of rotor speed ω for motors in the same group is thought to be trivial and neglected, that is, motors in the same group are considered as coherent.

Normalization of Characteristic Vectors.

To eliminate overshadows from big numbers on small ones, characteristic vectors must be normalized. Suppose row vector y_i is the characteristic vector of i^{th} sample, $Y = (y_1^T, y_2^T \cdots y_n^T)^T$ is the characteristic matrix, y_{ij} is the j^{th} coordinates of y_i and the i^{th} row, j^{th} column element of Y, row vector $y_{i,nom}$ is the normalized characteristic vector, $y_{ij,nom}$ is the j^{th} coordinates of $y_{i,nom}$, then $y_{ij,nom}$ can be calculated as Eq.15.

$$y_{ij,nom} = \frac{y_{ij} - \min_i(y_{ij})}{\max_i(y_{ij}) - \min_i(y_{ij})} \tag{15}$$

Aggregation of Induction Motors

Aggregation of the Simplified Electromechanical Equations of Motors in the Same Group.

Averaging the simplified electromechanical equations of individual motors in the same group, we can obtain the simplified electromechanical equations of the equivalent motor as Eq.16~Eq.18.

$$\frac{1}{n}\frac{d(\sum_{i=1}^{n}T_i^{'}E_{qi}^{'})}{dt}=-\frac{1}{n}\sum_{i=1}^{n}E_{qi}^{'}+\frac{V}{n}\sum_{i=1}^{n}\frac{X_i-X_i^{'}}{X_i}+\frac{1}{n}\omega_s(\omega-1)\sum_{i=1}^{n}T_i^{'}E_{di}^{'} \tag{16}$$

$$\frac{1}{n}\frac{d(\sum_{i=1}^{n}T_i^{'}E_{di}^{'})}{dt}=-\frac{1}{n}\sum_{i=1}^{n}E_{di}^{'}-\frac{1}{n}\omega_s(\omega-1)\sum_{i=1}^{n}T_i^{'}E_{qi}^{'} \tag{17}$$

$$\frac{1}{n}\sum_{i=1}^{n}2H_iX_i^{'}\frac{d\omega}{dt}=\frac{V}{n}\sum_{i=1}^{n}E_{di}^{'}-\frac{1}{n}\sum_{i=1}^{n}T_{m0,i}\left(a_i\omega^2+b_i\omega+1-a_i-b_i\right)X_i^{'} \tag{18}$$

Eq.16~Eq.18 can be simplified to Eq.19~Eq.21.

$$T_{eq}^{'}\frac{dE_{q,eq}^{'}}{dt}=-E_{q,eq}^{'}+\frac{X_{eq}-X_{eq}^{'}}{X_{eq}}V+T_{eq}^{'}\omega_s(\omega-1)E_{d,eq}^{'} \tag{19}$$

$$T_{eq}^{'}\frac{dE_{d,eq}^{'}}{dt}=-E_{d,eq}^{'}-T_{eq}^{'}\omega_s(\omega-1)E_{q,eq}^{'} \tag{20}$$

$$2H_{eq}X_{eq}^{'}\frac{d\omega}{dt}=VE_{d,eq}^{'}-T_{m0,eq}\left(a_{eq}\omega^2+b_{eq}\omega+1-a_{eq}-b_{eq}\right)X_{eq}^{'} \tag{21}$$

Where

$$E_{q,eq}^{'}=\frac{1}{n}\sum_{i=1}^{n}E_{qi}^{'} \tag{22}$$

$$E_{d,eq}^{'}=\frac{1}{n}\sum_{i=1}^{n}E_{di}^{'} \tag{23}$$

$$\frac{1}{n}\frac{d(\sum_{i=1}^{n}T_i^{'}E_{qi}^{'})}{dt}\approx T_{eq}^{'}\frac{dE_{q,eq}^{'}}{dt} \tag{24}$$

$$\frac{1}{n}\frac{d(\sum_{i=1}^{n}T_i^{'}E_{di}^{'})}{dt}\approx T_{eq}^{'}\frac{dE_{d,eq}^{'}}{dt} \tag{25}$$

$$T_{eq}^{'}=\frac{1}{n}\sum_{i=1}^{n}T_i^{'} \tag{26}$$

$$\frac{X_{eq}-X_{eq}^{'}}{X_{eq}}=\frac{1}{n}\sum_{i=1}^{n}\frac{X_i-X_i^{'}}{X_i} \tag{27}$$

$$H_{eq}X_{eq}^{'}=\frac{1}{n}\sum_{i=1}^{n}H_iX_i^{'} \tag{28}$$

$$a_{eq}T_{m0,eq}X_{eq}^{'}=\frac{1}{n}\sum_{i=1}^{n}a_iT_{m0,i}X_i^{'} \tag{29}$$

$$b_{eq}T_{m0,eq}X_{eq}^{'}=\frac{1}{n}\sum_{i=1}^{n}b_iT_{m0,i}X_i^{'} \tag{30}$$

Approximation effects caused by Eq.24, Eq.25 can be estimated by Eq.31, Eq.32.

$$\left|\frac{1}{n}\sum_{i=1}^{n}T_i^{'}E_{qi}^{'}-T_{eq}^{'}E_{q,eq}^{'}\right|\le\sqrt{\frac{\sum_{i=1}^{n}\left(T_i^{'}-\frac{1}{n}\sum_{k=1}^{n}T_k^{'}\right)^2}{n}}\sqrt{\frac{\sum_{i=1}^{n}E_{qi}^{'2}}{n}} \tag{31}$$

$$\left|\frac{1}{n}\sum_{i=1}^{n}T_i^{'}E_{di}^{'}-T_{eq}^{'}E_{d,eq}^{'}\right|\le\sqrt{\frac{\sum_{i=1}^{n}\left(T_i^{'}-\frac{1}{n}\sum_{k=1}^{n}T_k^{'}\right)^2}{n}}\sqrt{\frac{\sum_{i=1}^{n}E_{di}^{'2}}{n}} \tag{32}$$

It can be seen from Eq.31, Eq.32 that the variance of $T^{'}$ in the same group smaller, the better of the approximation effects. The small variance of $T^{'}$ in the same group can be guaranteed with the fuzzy C-means clustering method, by optimization of the objective function.

Calculation of Parameters for the Equivalent Motor.

According to Norton Equivalent Theory, transient equivalent circuit of motors connected to the same bus is shown as Fig.3.

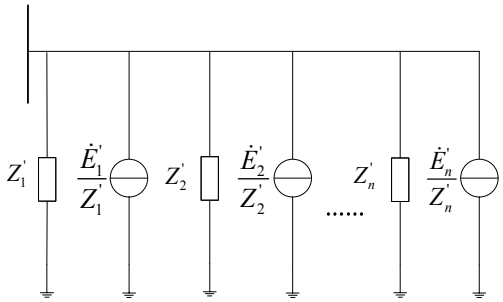

Fig.3 Transient equivalent circuit of induction motors

The transient impedance of the equivalent motor can be obtained by Eq.33.

$$R_{s,eq}+jX_{eq}^{'}=\frac{1}{\sum_{i=1}^{n}\frac{1}{R_{si}+jX_i^{'}}} \tag{33}$$

Substituting $X_{eq}^{'}$ from Eq.33 into Eq.26~Eq.28, the values of H_{eq}, $T_{0,eq}^{'}$, X_{eq} can be obtained, and Eq.34~Eq.36 holds.

$$\frac{X_{r,eq}+X_{m,eq}}{\omega_s R_{r,eq}}=T_{0,eq}^{'} \tag{34}$$

$$X_{s,eq}+X_{m,eq}=X_{eq} \tag{35}$$

$$X_{s,eq}+\frac{X_{r,eq}X_{m,eq}}{X_{r,eq}+X_{m,eq}}=X^{'}_{eq} \tag{36}$$

Generally, magnetizing inductance $X_{m,eq}$ is much larger than leakage inductances of stator and rotor $X_{s,eq}$, $X_{r,eq}$. Thus, $X_{s,eq}$, $X_{r,eq}$, $R_{r,eq}$ can be approximately calculated by Eq.37~Eq.39.

$$X_{s,eq}=X_{eq}-\sqrt{X_{eq}(X_{eq}-X_{eq}^{'})} \tag{37}$$

$$X_{r,eq}=X_{eq}^{'}-X_{s,eq} \tag{38}$$

$$R_{r,eq}=\frac{X_{eq}}{\omega_s T_{0,eq}^{'}} \tag{39}$$

Shown as Eq.40, Eq.41, the magnetizing inductance $X_{m,eq}$ and steady state slip $s_{0,eq}$ of the equivalent motor can be obtained according to principle that the active and reactive power absorbed by motors before and after aggregation are equal.

$$P_{eq}=\sum_{i=1}^{n}P_i \tag{40}$$

$$Q_{eq}=\sum_{i=1}^{n}Q_i \tag{41}$$

Substituting $s_{0,eq}$ into Eq.6, and $T_{m0,eq}$ can be obtained by Eq.42.

$$T_{m0,eq}=T_{e0,eq} \tag{42}$$

Substituting $T_{m0,eq}$ and $X_{eq}^{'}$ into Eq.29, Eq.30, a_{eq}, b_{eq} can be obtained.

Simulation Case

A simple simulation case is taken to validate the proposed method. Shown as Fig.4, three motors M_1 to M_3 are connected to bus B_2 through an ideal transformer, while six motors M_4 to M_9 are directly connected to bus B_2. Impedance parameters of the nine motors are cited from [13]. The chosen base power value is 373 kVA. The impedance of Z is $0.03 + j0.142$ ohm. The torque-speed characteristics of the nine motors are assumed to be constant, that is to say, a and b are zeros. Voltage disturbance is done on bus B_1 and active and reactive power response are measured on bus B_2.

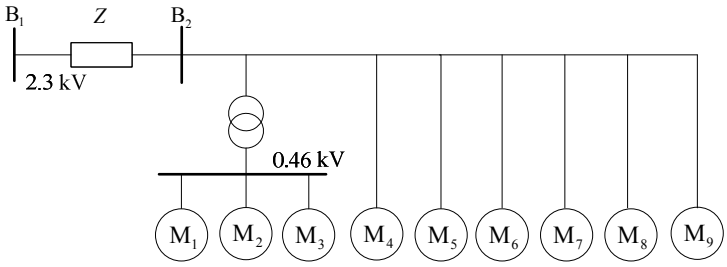

Fig.4 Simulation system

Grouping of Motors and Aggregation Results.

Table 1 lists the characteristic vectors of the nine motors. The results of fuzzy C-means clustering are shown as Table2. Obviously, the memberships of class one for motors M_1 to M_3 overwhelm that of class two. On the contrary, the memberships of class two for motors M_4 to M_9 overwhelm that of class one. So motors M_1 to M_3 are divided into group one, while motors M_4 to M_9 are divided into group two.

Table 1 Characteristic vector of each motor

Motors	T'	HX'	$(X-X')/X$	s_0	$T_{m0}X'$
1	0.00552728	0.103897	0.950787	0.03427	0.0611
2	0.00693847	0.166436	0.955437	0.02358	0.0538
3	0.00590828	0.22297	0.958979	0.01903	0.0375
4	0.0319691	0.22456	0.945262	0.003256	0.0342
5	0.0338508	0.177305	0.956791	0.001785	0.0202
6	0.040032	0.20259	0.961445	0.001113	0.0150
7	0.043005	0.240701	0.978083	0.001729	0.0254
8	0.0535508	0.223498	0.963103	0.001167	0.0211
9	0.0540806	0.192412	0.966200	0.001559	0.0284

Table 2 Membership of each motor

Motors	Class One	Class Two
1	0.9232	0.0768
2	0.9905	0.0095
3	0.6938	0.3062
4	0.0816	0.9184
5	0.0647	0.9353
6	0.0241	0.9759
7	0.0261	0.9739
8	0.0292	0.9708
9	0.0431	0.9569

Parameters of the equivalent motors are shown as Table 3, where, $M_{1,eq}$ is the equivalent motor of the first three motors, $M_{2,eq}$ is the equivalent motor of the later six motors, and M_{eq} is the equivalent motor of the total nine motors.

Table 3 Parameters of equivalent motors

Motors	$M_{1,eq}$	$M_{2,eq}$	M_{eq}
R_s	0.0397	0.0009818	0.00096767
X_s	0.1508	0.0062	0.0060
X_m	6.7153	0.3467	0.3295
X_r	0.1291	0.0007667	0.0010

R_r	0.1473	0.0061	0.0058
H	0.2759	8.5472	8.2545
T_{m0}	0.1536	1.9731	2.1267
a	0	0	0
b	0	0	0
s_0	0.0226	0.0017	0.0024

Simulation Results.

Shown as Fig.5, the first simulation is done in such a way that a voltage dip of 50% occurs at $t = 0.1$ second, and is cleared later at $t = 0.7$ second. Curves of active and reactive power absorbed by motors before and after aggregation are judging criteria of aggregation effects. Figures 6-11 show the dynamic response of different machines. The solid lines represent active or reactive power load before aggregation and the dashed lines represent active or reactive power load after aggregation.

Seen from Figs.6-7, it is observed that fitting effects with two equivalent motor are remarkably superior to that with only one equivalent motor. This observation leads to the conclusion that it is not always advisable to represent all motors with a single equivalent one.

Curves of active and reactive power load of the first and second group of motors before and after aggregation are shown as Figs.8-11. It can be observed that the curves of active and reactive power of each group before and after aggregation agree well.

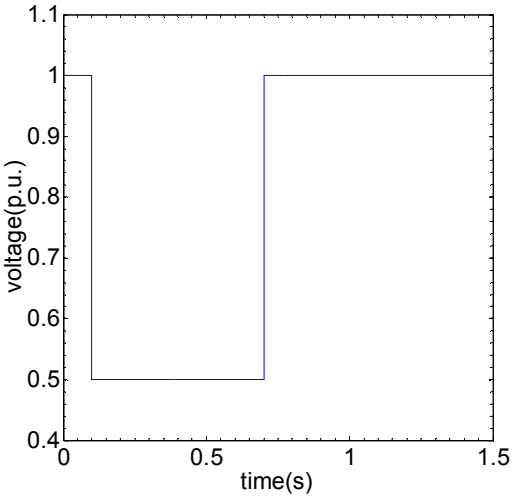

Fig.5 Curve of interrupted voltage

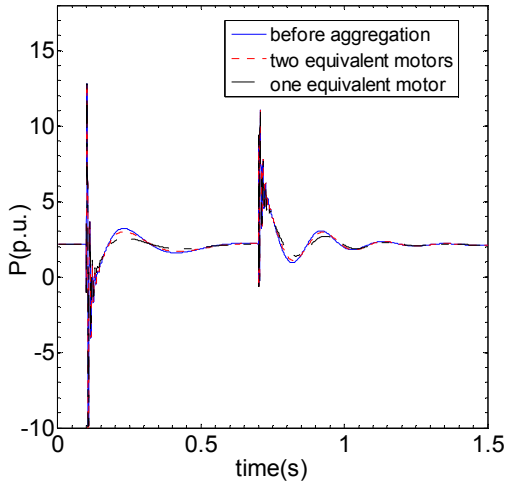

Fig.6 Sum of active power of the 9 induction motors before and after aggregation

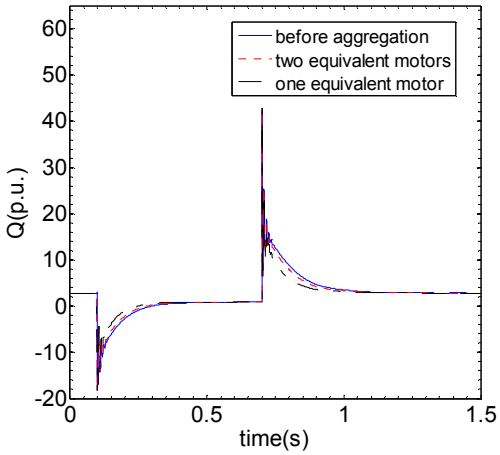

Fig.7 Sum of reactive power of the 9 induction motors first before and after aggregation

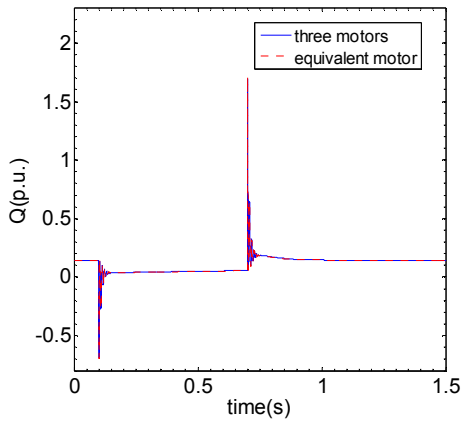

Fig.8 Sum of active power of induction motors of the group and before and after aggregation

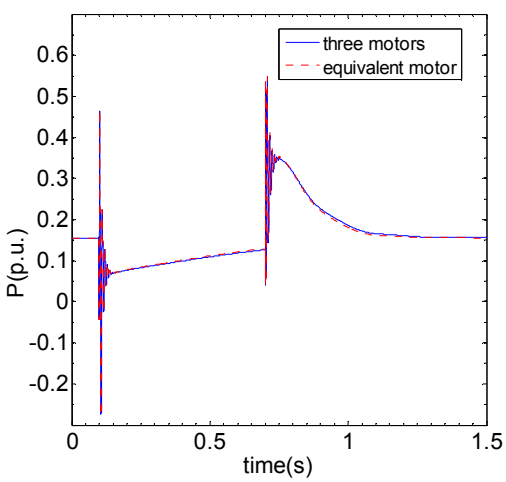

Fig.9 Sum of reactive power of induction motors of the first group before and after aggregation

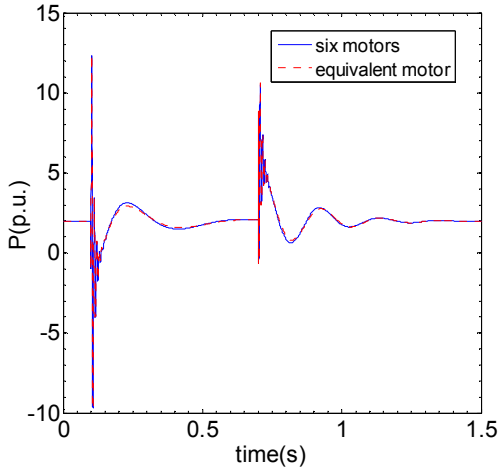

Fig.10 Sum of active power of the second group of motors before and after aggregation

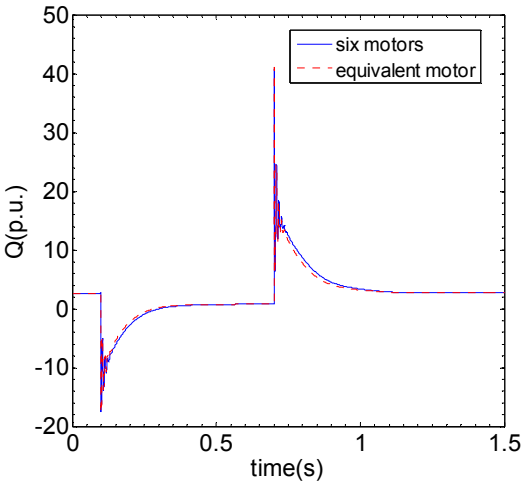

Fig.11 Sum of reactive power of the second group of induction motors before and after aggregation

Comparison with Selected Methods.

Shown as Fig.12, the second simulation is done in such a way that a voltage dip of 10% occurs at $t = 0.1$ second, and is cleared later at $t = 0.7$ second. Curves of active and reactive power of motors before and after aggregation with proposed method, with kVA weighted average method [4] and with power invariance method [7] are shown as Figs.13-14. From Figs.13-14, it is easy to observe that the dynamic errors of active and reactive power with power invariance method are quite noticeable. Figure 15 is the local amplified figure of Fig.14, from which we can observe that the steady state reactive power of the equivalent motor with kVA weighted average method is not equal to that of motors before aggregation.

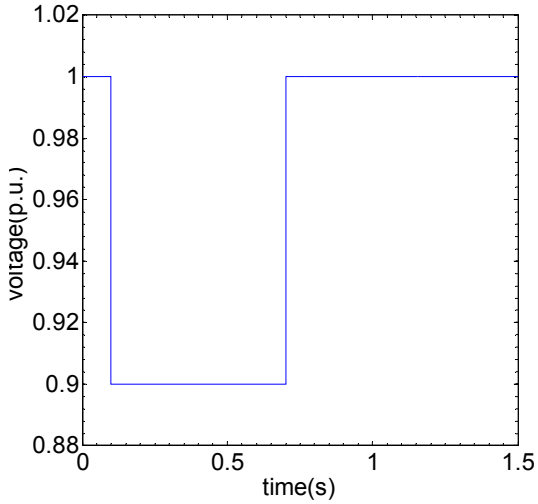

Fig.12 Curve of interrupted voltage

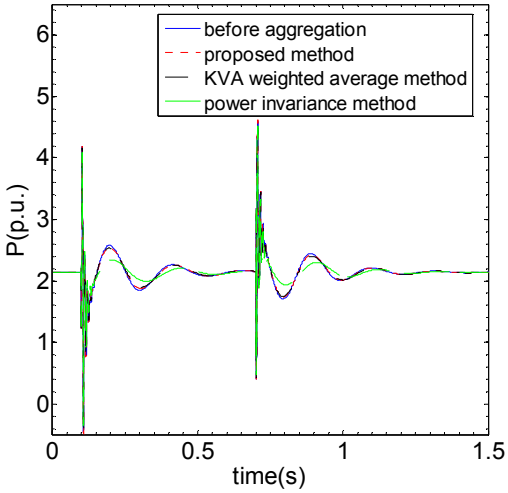

Fig.13 Active power comparison with other methods

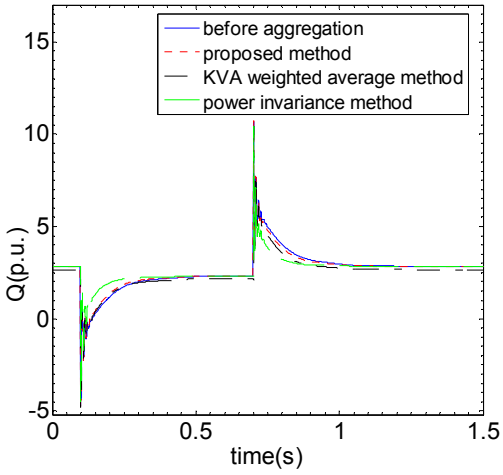

Fig.14 Reactive power comparison with other methods

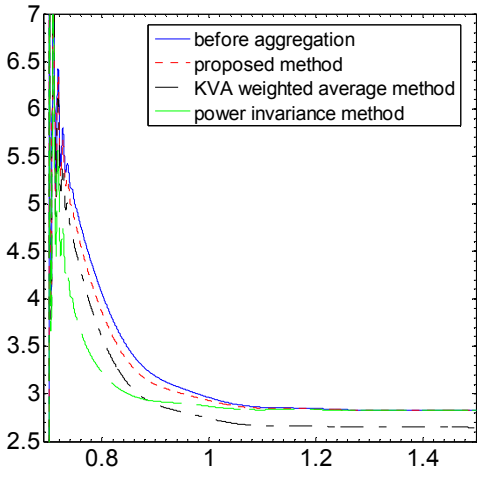

Fig.15 Local amplified figure of Fig.14

To evaluate the accuracy of different methods quantitatively, the relative root mean error between active and reactive power of motors before and after aggregation can be formulated as Eq.42, Eq.43.

$$E_p = \sqrt{\frac{\sum_{l=1}^{L}\left[\hat{P}(l)-P(l)\right]^2}{\sum_{l=1}^{L}P^2(l)}} \tag{42}$$

$$E_q = \sqrt{\frac{\sum_{l=1}^{L}\left[\hat{Q}(l)-Q(l)\right]^2}{\sum_{l=1}^{L}Q^2(l)}} \tag{43}$$

Where L is the sample points of simulation, $P(l)$ and $Q(l)$ are respectively the active and reactive load at the l^{th} step before aggregation, while $\hat{P}(l)$ and $\hat{Q}(l)$ are respectively the active and reactive load at the l^{th} step after aggregation. The relative root mean square errors of active and reactive power by different methods are shown as Table 4.

Table 4 Comparison of fitting errors with selected methods

Different Methods	E_p	E_q
kVA Weighted Average Method	0.0098	0.0743
Power Invariance Method	0.0404	0.1392
Proposed Method	0.0063	0.0282

From Table 4, it is appropriate to reach the conclusion that the proposed method reduces the fitting errors of active and reactive power sharply.

Conclusions

This paper directly starts off the electromechanical equations of induction motor. With coefficients of electromechanical equations and steady state slip chosen as the characteristic vector, motors are grouped by fuzzy C-means clustering method. Motor in the same group are aggregated with dynamic aggregation method. By the simulation case, the relative root mean errors of active and reactive power respectively reduce from 0.0098, 0.0743 of kVA weighted average method and, 0.0404, 0.1392 of power invariance method to 0.0063 and 0.0282.

References

[1] He Yuqing, Peng Jianchun, Wen Ming, Zhou Yangxi, Li Jianying, Li Peng. Minus feasible analysis unit and fast algorithm for distribution network reconfiguration. Proceedings of the CSEE, Vol.30 (2010), p.50.

[1] CIGRE Task Force, "Load modeling and dynamics," Electra, vol.130, pp. 124-141, 1990.

[2] IEEE Task Force, "Load representation for dynamic performance analysis," IEEE Trans. on Power Systems, Vol. 8(1993), p. 472.

[3] IEEE Task Force, "Standard load models for power flow and dynamic performance simulation," IEEE Trans. on Power Systems, Vol.10(1995), p.1302.

[4] Ju Ping, Ma Daqiang, Load modeling of power system (second edition), China Electric Press, 2008.

[5] Guo Jinchuan, Yu Yixin, Ni Peng, Zeng Yuan, "An improved weighting mean aggregation method of induction motors considering load rates and critical slips, " Automation of Electric Power Systems, Vol.32(2008.), p.6-10.

[6] Zhang Jinchao, Zhang Chenxue, Yan Anhe, Zhang Pengfei, Li Kui, "Aggregation of multi-induction motors based on the self-organized neural network and steady state model," Automation of Electric Power Systems, Vol.31(2007), p.44-48.

[7] D.C. Franklin, Amorelato, "Improving dynamic aggregation of induction motor models," IEEE Transactions on Power Systems, Vol. 9(1994), p.1934.

[8] M. Akbaba, S.Q. Fakhro, "New model for single-unit representation of induction motor loads, including skin effect, for power system transient stability studies," IEE Proceedings-B, Vol. 139(1992), p.521.

[9] Zhang Hongbin, Tang Yong, Zhang Dongxia, et al, "Equivalent model for induction-motor load connected to high voltage bus, " Proceedings of the CSEE, Vol.26(2006), p.1-4.

[10] M.Taleb, M. Akbaba, E.A. Abdullah, "Aggregation of induction machines for power system dynamic studies," IEEE Transactions on Power systems, Vol.9(1994), p.2042.

[11] Tang Yong, Hou Junxian, Liu Wenchuo, "The modeling of distribution network and var compensator and induction motor in the Load model for power system digital simulation, " Proceedings of the CSEE, Vol.25(2005), p. 8-12.

[12] S. Ahmed-Zaid, M. Taleb, "Structural modeling of small and large induction machines using integral manifolds," IEEE Transactions on Energy Conversion, Vol. 6(1991), p.529.

[13] Jimnmie J. Cathey, Rglph K. Cavin, A. K. Ayoub, "Transient load model of an induction motor, " IEEE Transactions on Power systems and Apparatus, Vol.PAS-92(1973), p.1399.

Advanced Materials Research Vols. 960-961 (2014) pp 1225-1229

doi:10.4028/www.scientific.net/AMR.960-961.1225

Study of Vehicle Power Supply With AC and DC Mixed Output

Yang Xingwu[a], Ji Hongchao[b], Gan wei[c]

Shanghai University of Electric Power, Yangpu District in Shanghai, Changyang road 2588,China

[a] yxw790930@sohu.com, [b]jihongchao@shiep.edu.cn, [c]ganwei@shiep.edu.cn

Keywords: vehicle power supply, AC and DC mixed output, double-loop PWM control,

Abstract. The paper proposes a AC and DC mixed output VPS(vehicle power supply). It is composed of a two-stage circuit with the input stage and the output stage. The input stage contains a single-phase PWM inverter, a HFT (high-frequency transformer) and an uncontrolled rectifier. The single-phase PWM inverter adopts the open-loop control strategy to convert the low DC voltage into a high-frequency one with square wave. The HFT enhances the voltage and insulates the low-voltage side from the high-voltage side. The uncontrolled rectifier transforms the square voltage into DC voltage. In the output stage, one output uses single-phase PWM inverter and the other uses a DC chopper, both of which adopt the double-loop PWM control mode. The mode consists of an outer voltage loop and an inner current loop to produce desirable voltage and power. With the two-stage control strategy, ideal output currents and the output voltages are obtained, and the input power factor is controllable. The VPS model is established on MATLAB/SIMULINK, and this system is also implemented in laboratory based on DSP TMS320F28335. The results of simulation and experiment verify the proposed VPS system.

Introduction

The electrical systems in the early automobiles are introduced mainly for lighting, cranking, and battery charging purposes. But, in the recent years, electrical and electronic system components, circuits, and accessories in the automobiles have steadily increased, both in complexity and quantity. This has motivated the research in restructuring the entire power system architecture in the vehicle. As a DC-AC or DC-DC conversion device, vehicle power can be connected directly between battery and all kinds of electrical drives, such as laptops, GPS navigator, and car refrigerator. VPS has brought a lot of convenience to people's life and is a kind of regular automobile electronic product. The traditional vehicle power supply, where it takes inverter and power frequency transformer, is big and low efficiency. With the development of power electronic devices and power electronic technology, the efficiency of the inverter circuit which adopt high frequency transformer is higher than before[1]-[4]. When used in automobiles, the VPS can not only enhance the voltage, but also improve the power quality, which leads to a wide application prospect[5]. Currently, the study of the VPS have focused on the topologies and control strategies[6].Reference[7] introduces the control strategy of typical VPS, where it takes single-loop control in the output side. It is difficult to obtain a good effect of current control.This paper adopt the double-loop control in the output side to get ideal waveforms.Traditional VPS only gives one output, and obviously it cannot adjust to variable loads. Therefore, this paper presents a new type of VPS-AC And DC mixed output VPS. The paper analyzes the basic principle and control strategies of the proposed system, and accomplishes the dynamic simulations and experiments to verify the proposed VPS system.

Construction of VPS system

The VPS is composed of the primary side converter and the secondary side converter, with the HFT. The input DC voltage is modulated into the high-frequency square waveform by the primary side converter, and then coupled to the secondary side. The high-frequency square waveform of the secondary side is converted into the waveform required by secondary side converter. Its Realization is DC-AC-DC-AC and DC-AC-DC-DC converter, which is shown in Fig.1.

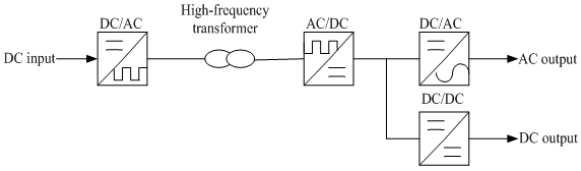

Fig.1 Principle diagram of VPS

The structure of DC-AC-DC-AC and DC-AC-DC-DC converter is more complex than the tradition DC-AC-AC converter. But the control performance of the former is better. The output current and the output voltage can be controlled by the PWM[8].The proposed DC-AC-DC-AC and DC-AC-DC-DC converter topology is shown in Fig.2. This topology is composed of two-stage power circuits. The input stage contains three parts, namely the single-phase PWM inverter, the HFT and the uncontrolled rectifier. The single-phase PWM inverter adopts the open-loop control strategy to convert the low DC voltage into a high-frequency one with square wave. The HFT enhances the voltage and insulates the low-voltage side from the high-voltage side. The uncontrolled rectifier transforms AC into DC. In the output stage, one output uses single-phase PWM inverter and the other uses a DC chopper, both of which adopt the double-loop PWM control mode. The mode consists of an outer voltage loop and an inner current loop to produce desirable voltage and power. With the two-stage control strategy, the VPS's output currents and the output voltages have ideal waveforms, and the input power factor is controllable.

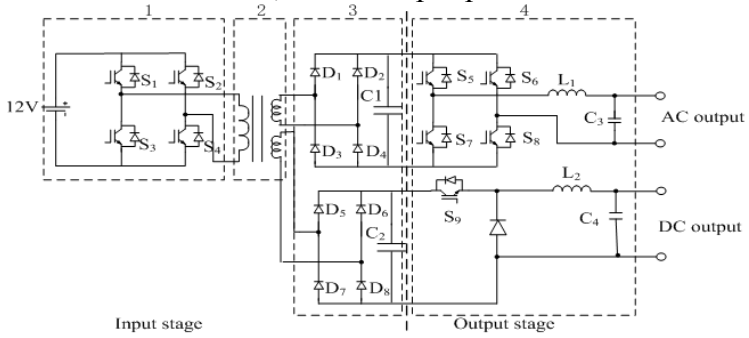

Fig.2 DC-AC-DC-AC and DC-AC-DC-DC converter topology of VPS

Principle of VPS

A. Control Strategy of Input Stage

According to the relevant knowledge of circuit and motor, we know that the high switching frequency is the most direct and effective way to reduce the volume and the weight. So we take the single-phase PWM inverter to enhance the frequency of primary side voltage, where it takes open-loop control to modulate the DC voltage into the high frequency square waveform with duty cycle of 50%. The open-loop control block diagram is shown in Fig.3. We compare zero and bipolar triangle carrier wave to get the switch signal.

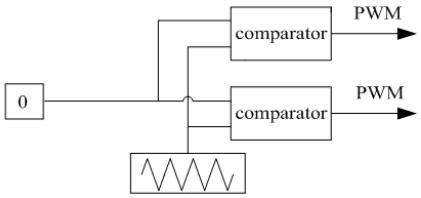

Fig.3 Control principle diagram of single-phase PWM inverter

B. Control Strategy of Output Stage

In output stage, one output takes single-phase PWM inverter, another output takes DC chopper, where they all adopt double loop PWM control mode which consists of outer voltage loop and inner current loop, to outputs the desired voltage and power to the load. The double-loop control block diagram is shown in Fig.4.

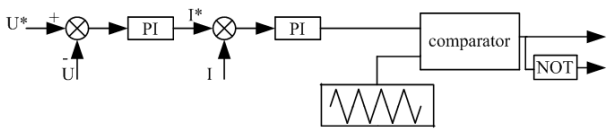

Fig.4 Double-loop control block diagram

Simulation results

The VPS model applied to automobile is established in Matlab/Simulink, as shown in Fig.5.The model parameters are as follows: ①input side: battery voltage 12V. ②High-frequency transformer: ratio of transformation is 1:50, frequency 5 kHZ ③DC voltage side: capacitance 500 μF(AC output side) and 300 μF(DC output side), ④AC output side: filter inductance 3 mH, filter capacitance 15 μF, the reference value of peak voltage is 311V, load resistance 100Ω and 0.05mH. DC output side: filter inductance 0.5 mH, filter capacitance 470 μF, the reference value of voltage is 50 V, load resistance 100 Ω and 0.005 mH.Fig.6 shows the simulation waveforms, including the input voltage, the primary voltage, and the secondary voltage of HFT, DC voltage, load voltage, and load current. Fig.7give the FFT analysis of the AC output current. According to the FFT analysis, we get the THD of output current is 0.90%. So the waveforms of output current is perfect to adjust to the load.

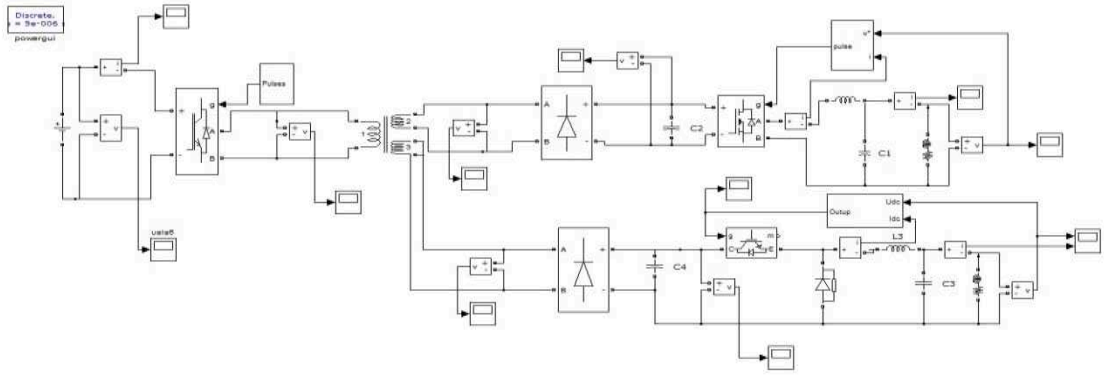

Fig.5 Simulation model of VPS applied to automobile

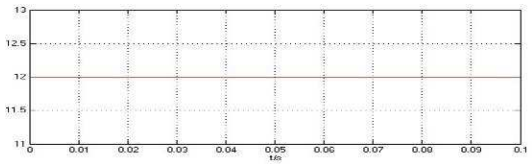

(a) Input voltage

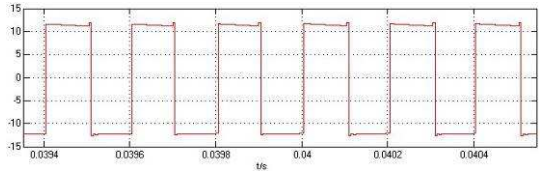

(b)Primary voltage of HFT

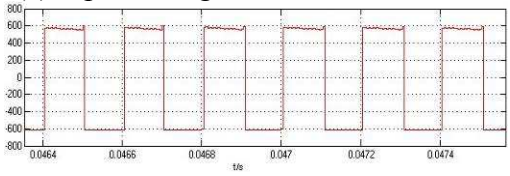

(c)Secondary voltage of HFT

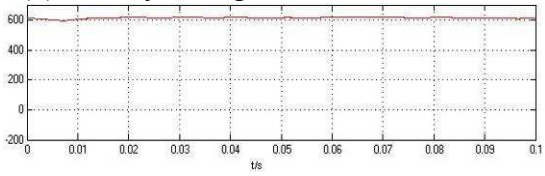

(d)Voltage in DC side (AC ouput side)

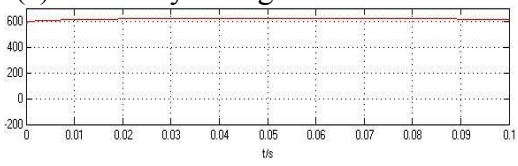

(e)Voltage in DC side (DC ouput side)

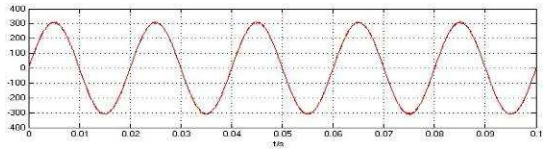

(f) Output voltage(AC side)

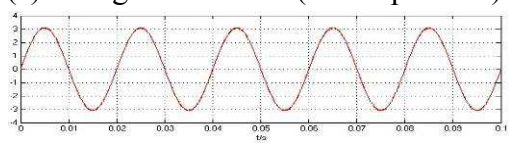

(g) Output current(AC side)

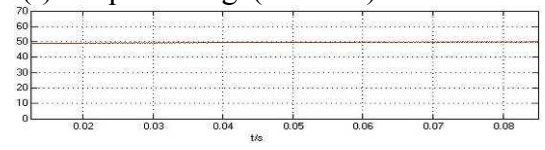

(h) Output voltage(DC side)

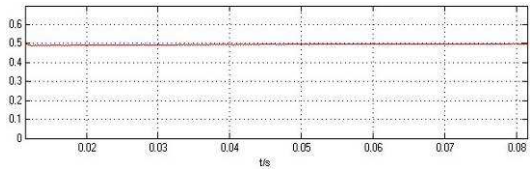

(i) Output current(DC side)

Fig.6 Simulation results of the VPS system

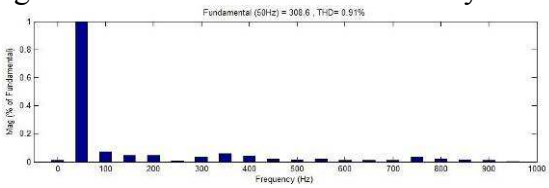

Fig.7 FFT analysis of output current (AC output)

Experimental results

This system is also realized in the laboratory based on DSP TMS320F28335, where is in charge of collecting and processing data, and compiling control algorithms. There are a total of 4 IGBT modules and the corresponding drive modules in the VPS experimental system. The system is shown in Fig.8. The system parameters are as follows: ①input voltage 12V. ②High-frequency transformer: ratio of transformation is 1:50, frequency 5kHz ③DC voltage side: capacitance 500 μF(AC output side) and 300 μF(DC output side)④ AC output side: filter inductance 3mH, filter capacitance 15μF, load resistance 100Ω , DC output side: filter inductance, filter capacitance 470 μF, load resistance 100 Ω . We set the reference value of peak voltage in AC output side at 330V and 50V separately. We get the corresponding waveforms as shown in Fig.9. We set the reference value of voltage in DC output side at 50V and 20 V separately. We get the corresponding Waveforms as shown in Fig.10.

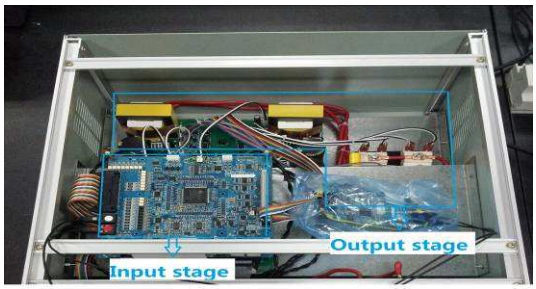

Fig. 8 Experimental system

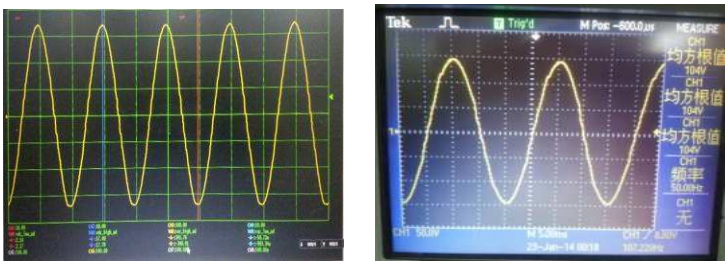

Fig.9 Output voltage(AC side)

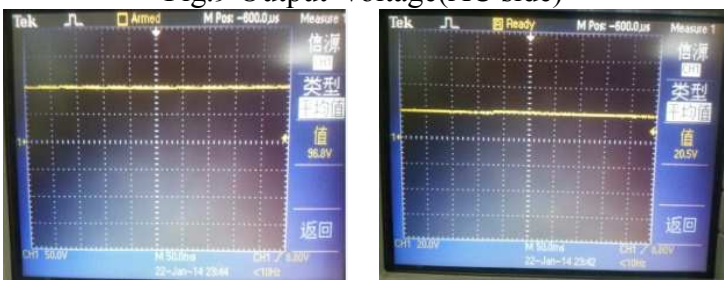

Fig.10 Output voltage(DC side)

Conclusion

In order to adjust to a variable load, this paper presents a new type of Multiple Output VPS. The efficiency of this type of VPS is high and the THD of output current is low. This paper analyzes the basic principle and control strategies of the proposed system, and finishes the dynamic simulations and experiments to verify the proposed VPS system. The results of simulation and experiment show that the output voltages have ideal waveforms, and verify the proposed power electronic transformer system.

Acknowledgements

This work was financially supported by the Natural Science Foundation of China(No.51207086), Innovation Program of Shanghai Municipal Education Commission(No.14YZ126), The Excellent Young Teachers Program of Shanghai Municipal Education Commission (No.sdl12004). Shanghai Green Energy Grid Connected Technology Engineering Research Center(No. 13DZ2251900)

References

[1] Huang Yi-yu, Mao Cheng-xiong, Lu Ji-ming, Fan Shu. Study on control strategy for power electronic transformer in power system. Relay, 2004, 32(6): 35-39.

[2] Mao Cheng-xiong, Fan shu, Wang Dan. Theory of Power Electronic Transformer and Its Applications. High Voltage Engineering, 2003, 29(10): 4-6.

[3] Deng Wei-hua, Zhang Bo, Hu Zong-bo. Research on the topology and control scheme of power electronic transformer. Automation of Electric Power System, 2003, 27(20): 40-44,48.

[4] Cheng Jian-peng, Mao Cheng-xiong, Fanshu. Principle of electronic power transformer and its simulation study. Electric Power Automation Equipment, 2004 , 12(24): 23-26.

[5] Cui Yan-yan, Mao Cheng-xiong. Voltage and reactive power synthetic optimization in the distribution system based on electronic power transformer. Relay, 2006, 34(6): 24-28, 43.

[6] Wang Dan, Mao Cheng-xiong, Lu Ji ming, Fan Shu. Electronic Power Transformer-Based Power Quality Control Method. High Voltage Engineering, 2005, 31(8): 63-65, 82.

[7] Wang Dan, Mao Cheng-xiong, Lu Ji-ming, Fan Shu, Cao Jie-wei. Simulation research on imbalance loads of electronic power transformer in distribution system. Electric Power, 2005, 38(11): 21-26.

[8] Shi Sai-mei. Dynamic simulation of power electronic transformer in parallel operation. Power System Protection and Control, 2009, 2(17): 20-23.

Advanced Materials Research Vols. 960-961 (2014) pp 1230-1236

doi:10.4028/www.scientific.net/AMR.960-961.1230

Speed Regulation Analysis of a Magnetic Gear Integrated Permanent Magnet Synchronous Motor Using Finite Element Method Coupled With Vector Control

Xiaoqin Xu[1, a], Qingqing Ding[1, b] and Jinghua Ji[2, c]

[1]Department of Electrical Engineering, Tsinghua University, Beijing 100084, China

[2] Department of Electrical Engineering, Jiangsu University, Zhejiang Jiangsu 212013, China

[a]xuxiaoqin8722@163.com, [b]d-qq00@mails.tsinghua.edu.cn, [c]jjh@ujs.edu.cn

Keywords: magnetic gear, compacted machine, finite element method, vector control, coupling

Abstract. This paper describes the speed regulation of a magnetic gear integrated permanent magnet synchronous motor. The operating principle of the motor is discussed and the torque transmission is analyzed using finite element method; hence the motor model is established. The speed regulation is analyzed under vector control, and the simulated results verify the feasibility of speed regulation control.

Introduction

Magnetic gear has good potential for torque and speed transmission in industrial applications with some advantages such as no mechanical loss and maintenance-free operation that are not achieved using conventional mechanical gear. Furthermore, its instinct overloading protection feature can avoid many mechanical problems, such as broken teeth and backlash. A variety of magnetic gears have been proposed, and magnetic gears employing magnetic flux harmonics is drawing attention with useful torque transmission obtained[1].

A novel structure in which the magnetic gear is integrated with a brushless motor was reported. Torque can be transmitted between a low-speed rotor and a high-speed rotor through the modulation of ferromagnetic pole pieces [2]. The high-speed rotor is driven by the electromotive force generated by the coils of stator, and the low-speed rotor rotates in accordance with the gear ratio. Therefore, the magnetic-geared motor is a type of low-speed, high-torque actuator.

However, the brushless permanent magnet (PM) motor has such problems as torque ripple and current ripple. In order to solve these problems, a magnetic gear integrated permanent magnet synchronous motor is proposed. Besides, its smooth speed regulation can broaden the range of the application.

This paper describes the operating principle of the motor and analyzes the electromagnetic and mechanical transmission using finite element method (FEM). The steady-state and transient performances of motor are studied to obtain the motor model for speed regulation. The speed regulation system is established under vector control, and the speed adjusting characteristics is simulated and analyzed.

Motor Structure and FEM Analysis

Fig.1 gives the configuration of the magnetic gear integrated motor. This motor is designed with 3 pole-pair PMs in the high-speed rotor, 22 pole-pair PMs in the low-speed rotor. Between the high-speed rotor and low-speed rotor is 25 modulating ferromagnetic pieces. These ferromagnetic modulation pole pieces are used to modulate the space harmonics of the air gap flux density. The stator is inside the motor carrying a set of three-phase, 3 pole-pair concentrated windings.

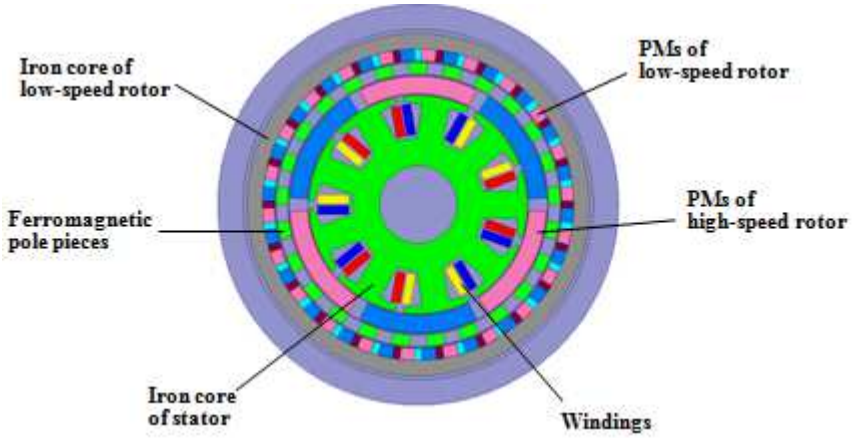

Fig.1. Magnetic gear integrated permanent magnet synchronous motor.

According to [3], the number of pole pairs in the space harmonics of the flux density distribution and the speed of the space harmonics produced by PMs of either rotor is given by

$$p_{m,k} = |mp + kn_s| \quad (1)$$

$$\Omega_{m,k} = \frac{mp}{mp + kn_s}\Omega_r + \frac{kn_s}{mp + kn_s}\Omega_s \quad (2)$$

where m=1,3,5, ⋯, ∞, k=0,±1, ±2, ±3, ±∞, p is the pole pair number of the high-speed rotor, n_s is the number of the ferromagnetic pole pieces, and Ω_r is speed of the high-speed rotor. $p_{m,k}$ is the pole pairs of the low-speed rotor, Ω_s is speed of the ferromagnetic pole pieces, and $\Omega_{m,k}$ is the speed of the space harmonics of the low-speed rotor. The largest space harmonic component is obtained when m=1, k=-1. When the ferromagnetic pole pieces is static, the speed of the low-speed rotor is

$$\Omega_{1,-1} = \frac{p}{p - n_s}\Omega_r \quad (3)$$

For this motor, the gear ratio is G_r=Ω_r/$\Omega_{1,-1}$=-22/3=-7.33. The stator windings with three-phase current produced electromagnetic torque that drives the high-speed rotor, and the torque is transmitted through the ferromagnetic gear to the low-speed rotor. In this case, the rated speed is 700 rpm for the low-speed rotor and 700*7.33=5133 rpm for the high-speed rotor.

FEM is employed to analyze the electromagnetic and mechanical transmission of the motor. The motor has three air gaps. Fig.2 shows the magnetic flux density and their corresponding harmonic spectra in the air gap between the stator and the high-speed rotor. It can be seen that the harmonics component with 3 pole pairs is the major component, due to the PMs of the high-speed rotor. Fig.3 shows the magnetic flux density and their corresponding harmonic spectra in the air gap between the high-speed rotor and the ferromagnetic pole pieces, and the main component is also 3 pole pairs. After the modulation, the main component becomes 22 pole pairs (Fig.4).

In order to get the static performance of the magnetic gear, set the high-speed rotor rotating at the rated speed while the ferromagnetic pole pieces and the low-speed rotor fixed. Fig. 5 shows the corresponding static torque obtained by conducting the simulation. It can be seen that the transmitted torque versus electrical angle is a sinusoidal wave, and the torque ratio of the low-speed rotor with respect to the high rotor is 7.33.

The theoretically expected transmitted torque versus angle characteristic can be described by

$$T_{G1} = T_{G1peak}\cos(\theta_H + \theta_L) \quad (4)$$

$$T_{G2} = T_{G2peak}\cos(\theta_H + \theta_L) \quad (5)$$

where T_{G1} and T_{G2} is respectively the gear coupling torque on the high-speed and low-speed rotors. θ_H and θ_L is respectively the electrical angle of the high-speed and low-speed rotors. The simulation gives the peak of gear coupling torque, as T_{G1peak}=17.7 Nm and $T_{G2\,peak}$=130 Nm, and the torque ratio agrees with the gear ratio.

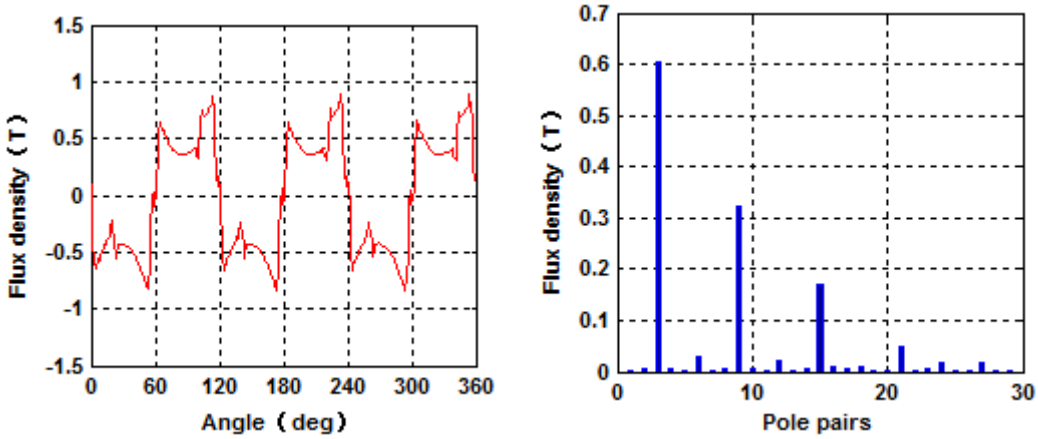

(a) (b)

Fig.2. Flux density in the air gap between the stator and the high-speed rotor. (a) Waveform. (b) Spectrum.

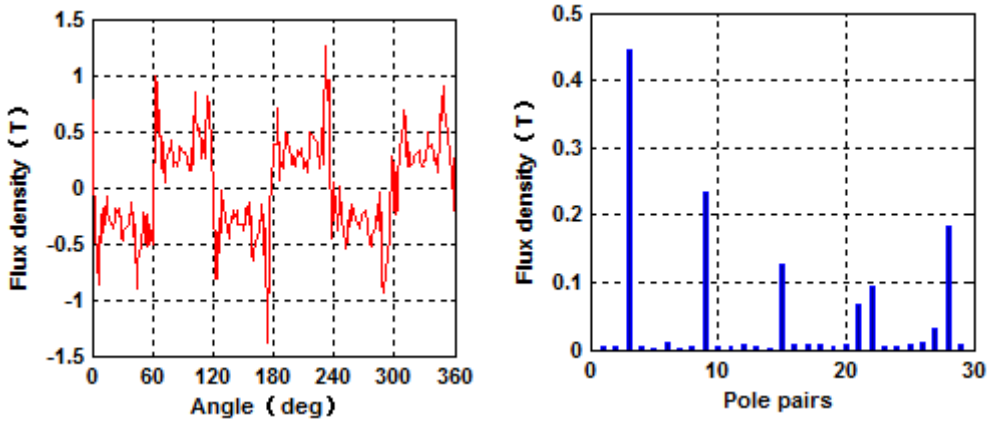

(a) (b)

Fig.3. Flux density in the air gap between the high-speed rotor and the ferromagnetic pole pieces. (a) Waveform. (b) Spectrum.

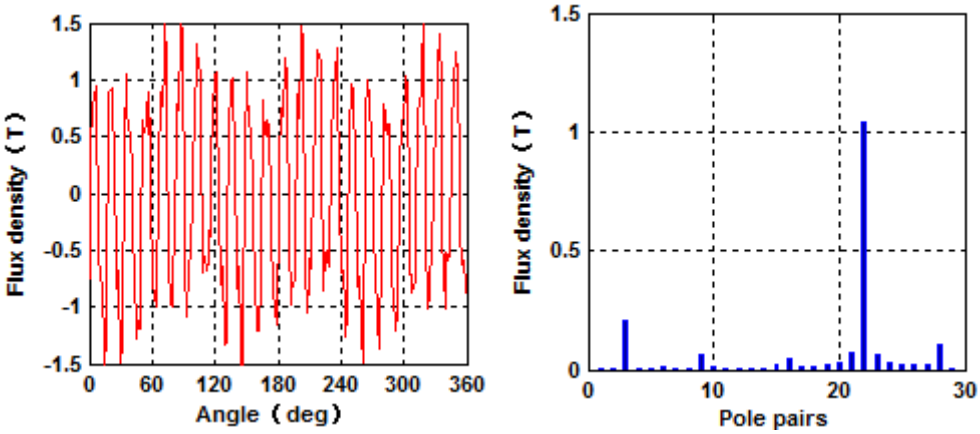

(a) (b)

Fig.4. Flux density in the air gap between the ferromagnetic pole pieces and the low-speed rotor. (a) Waveform. (b) Spectrum.

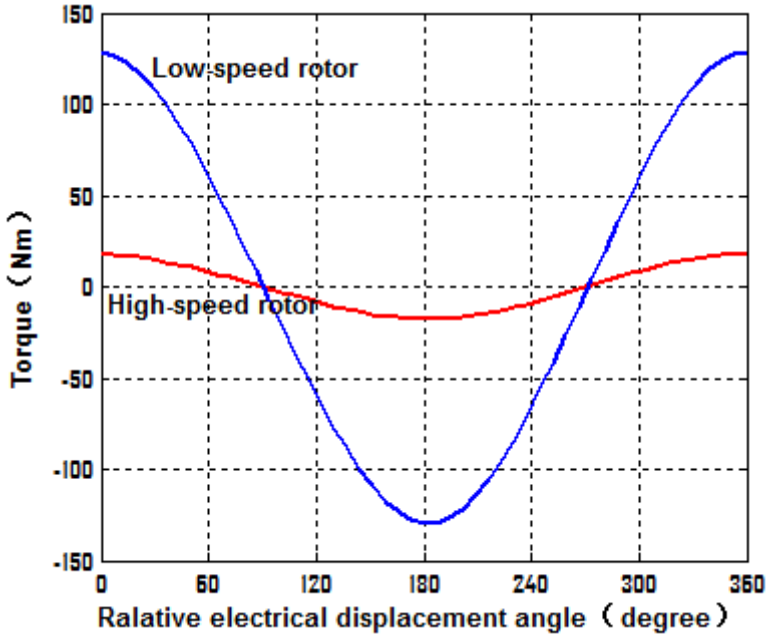

Fig.5. Static holding torque versus electrical displacement angle.

Motor Modeling and Control System

With the ferromagnetic pole pieces fixed, the electromechanical characteristic can be described by

$$\frac{J_H}{p_H}\frac{d^2\theta_H}{dt^2} = T_{EM} - T_{G1} \tag{6}$$

$$\frac{J_L}{p_L}\frac{d^2\theta_L}{dt^2} = T_L - T_{G2} \tag{7}$$

where T_{EM} is the electromagnetic torque produced by the stator windings, and T_L is the load torque. p_H and p_L represent the pole pair number of the high-speed and low-speed rotors. J_H is the inertia of the high-speed rotor, while J_L is the equivalent inertia of the load and low-speed rotor [4].

For this magnetic gear integrated PM synchronous motor shown in Fig.1, it can be shown that the motor can be divided into two parts. One is a PM synchronous motor with the load torque T_{G1}, which changes with the position of both rotors, and another is a magnetic gear driven by the transmitted torque T_{G2} and the real load torque T_L. In this way, the motor can be represented by the equivalent model shown in Fig.6.

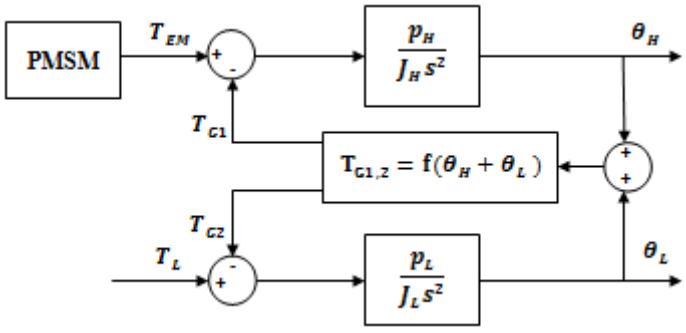

Fig.6. Equivalent model of the motor.

In order to adjust the speed, the high-speed rotor is rotated under vector control with the model of motor in Fig.6. The control block diagram is shown in Fig.7. In this control system, two closed loops are conducted and the current control loop use one feed forward loop and two feedback loops to get the reference of voltage. The target d-axis current is set as 0 A, while the target q-axis current varies with the load torque.

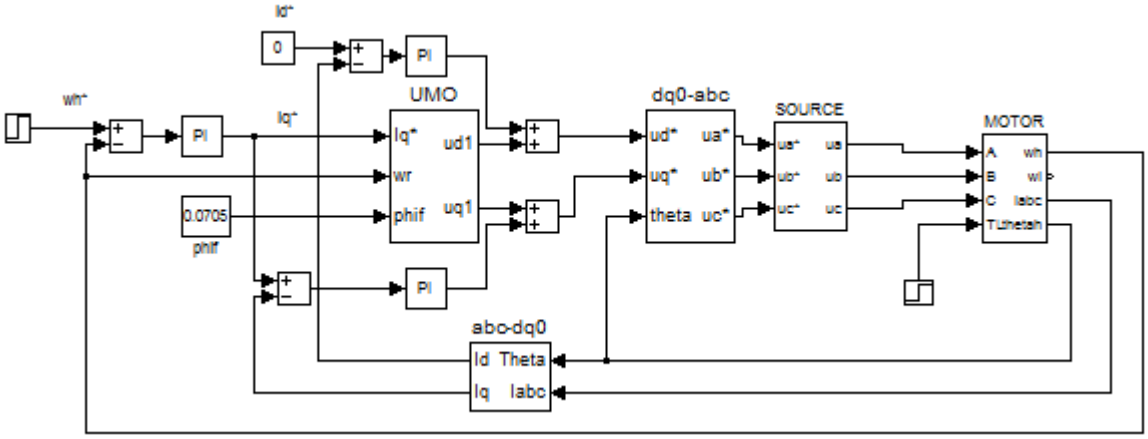

Fig.7. Control system of the motor.

Speed Regulation Analysis

In this simulation, the load torque is 50Nm, and the speed regulation range is from 300 rpm to 700rpm. Fig.8 shows speed waveform of the motor starting process. Reference speed of high-speed rotor is 300*7.33=2200 rpm. The speed volatility rises and stay stable after t=0.4 s. Speed in steady state is respectively 2200 rpm for high-speed rotor and 300 rpm for low-speed rotor, which agrees with the gear ratio.

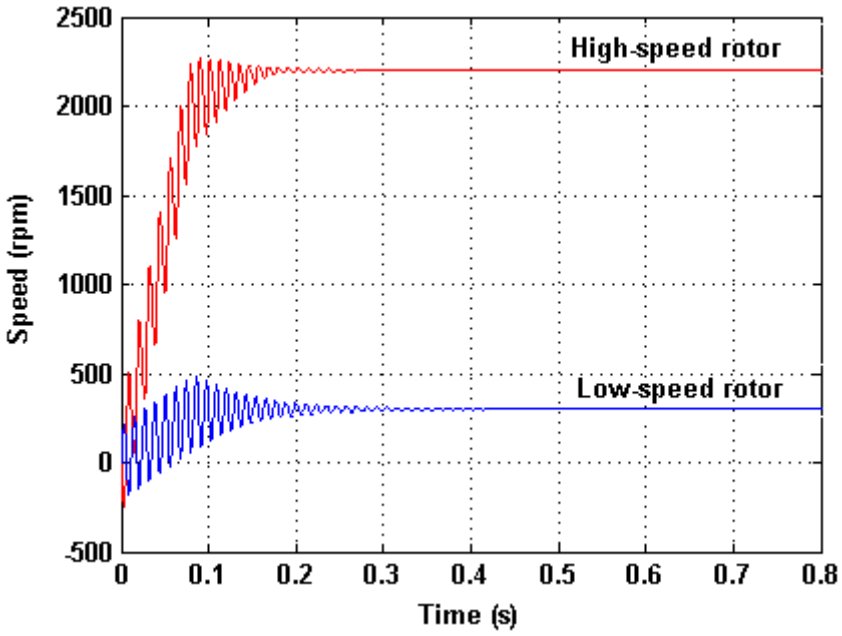

Fig.8. Speed waveforms for the starting process.

The speed reference of high-speed rotor is changed from 2200 rpm to 700*7.33=5133 rpm at t=3 s. Fig.9 shows speed waveform of speed adjusting process when reference speed of low-speed rotor changes from 300 rpm to 700rpm. It can be seen that the speed rises less volatility than the starting

process and stay stable after t=3.5 s. Speed in steady state is respectively 5133 rpm for high-speed rotor and 700 rpm for low-speed rotor, which verifies the effectiveness of the speed regulation strategy.

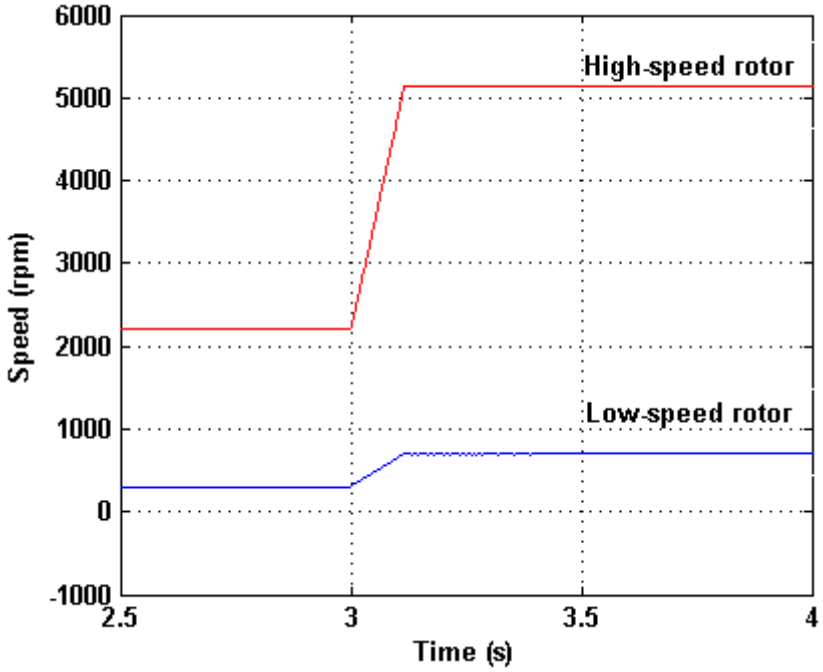

Fig.9. Speed waveforms of rotor for speed adjusting process.

The coupling torque of the magnetic gear on high-speed side is shown in Fig.10. The coupling torque changes versus the displacement of two rotors, and stay stable when the speed ratio remains 7.33. The couple torque influence the adjusting of speed, especially in the starting process. In the steady state the coupling torque on high-speed side is 6.82 Nm and 50 Nm on low-speed side, which consist with the gear ratio.

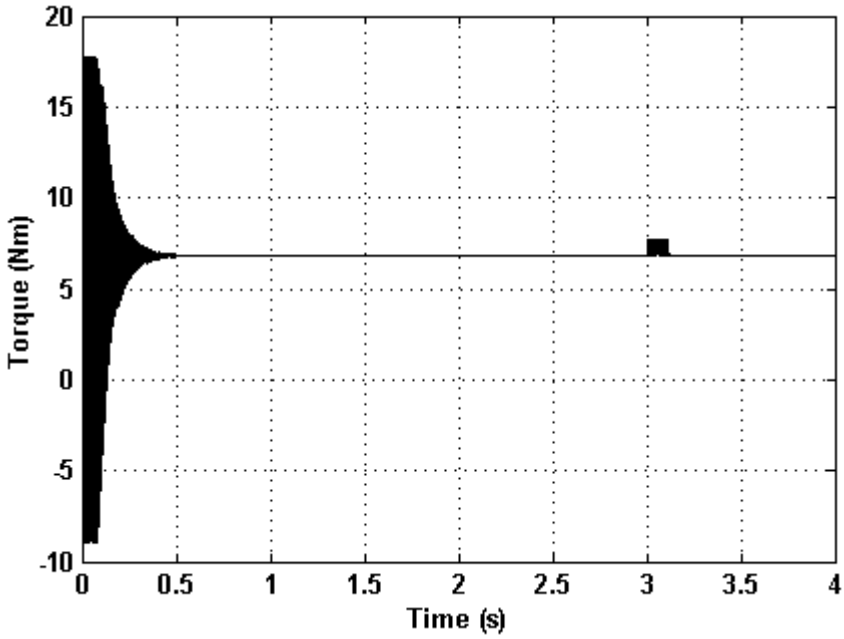

Fig.10. The coupling torque of the magnetic gear on high-speed side.

Conclusion

A magnetic gear integrated with PM synchronous motor is analyzed with FEM. The equivalent model of this motor is established though detailed dynamic analysis. The speed regulation and transmission torque characteristics are analyzed with vector control applied to the equivalent motor model. The simulation results verify the effectiveness of the speed regulation strategy.

References

[1] K.Atallah and D. Howe, "A novel high-performance magnetic gear," IEEE Trans. Magn., vol. 37, no. 4, pp. 2844-2846, Jul. 2001

[2] K.Atallah, J. Rens, S. Mezani and D. Howe, "A novel 'Pseudo' direct drive brushless permanent magnet machine," IEEE Trans. Magn., vol. 44, no. 11, pp. 4349-4352, Nov. 2008

[3] K.Atallah, S. D. Calverley, and D. Howe, "Design, analysis and realization of a high-performance magnetic gear," Inst. Electr. Eng. Proc. Elect. Power Applicat., vol. 151, no. 2, pp. 135-143, Mar. 2004

[4] R.Montague, C. Bingham, and K.Atallah, "Servo control of magnetic gears," IEEE Trans. Mech., vol. 17, no. 2, pp. 269-278, Apr. 2012

Advanced Materials Research Vols. 960-961 (2014) pp 1237-1240

doi:10.4028/www.scientific.net/AMR.960-961.1237

The research of servo motor control strategies for the mobile gantry milling machine

Fangyuan Li[1, a]

[1] Zhejiang Business Technology Institute, Ningbo, Zhejiang, 315012, China

[a]muzi_woody@163.com

Keywords: Servo Motor, Mobile Gantry Milling Machine, Master-slave Control, Adaptive-Neuro Fuzzy, ANFIS Architecture.

Abstract. It is known for the traditional milling machine in operation at low speed and efficiency. This paper describes the research of servo motor control strategies for the mobile gantry milling machine. The principles of AC servo motor dynamics, master-slave servo control, and adaptive -neuro fuzzy inference system based on controller are illustrated. Using these strategies when the master servo motor is interference by the external signal, the reference speed of the slave servo motor can follow just like the master motor. Finally the mechanical coupling can be eliminated and the mechanical damage can be avoided.

Introduction

The columns of the traditional milling machine are fixed and the table containing the work piece is fed along the rail longitudinal. Due to the large weight of the machine moving parts, it is difficult to obtain the high acceleration. At the same time due to the length of the table limit and saving footprint workplace requirements, the structure of the fixed goalposts can not meet the requirements for the high-speed milling machining of the large work pieces.

Under the condition of the dynamic, static rigidity, as for the high-speed mobile gantry milling machine, the table and the work piece remain stationary, the goalposts move along the longitudinal rail. Because of the relatively small mass movement of the columns, the high acceleration characteristics can be obtained.

The moving parts which are composed of the large beams, the matched holder, the gantry, and so on, do not always form a symmetrical structure and symmetry force. Although exactly the goal posts on both sides are same, eventually the gantry frame on both sides of the column can not guarantee the consistency of the movement which may cause the inconsistency of the gantry frame and damage the driving part and the work piece. So keeping both sides of the columns synchronous driving is a key technology to eliminate the mechanical coupling and avoid the mechanical damage in order to ensure the machining accuracy.

In the recent years, the development of the intelligent control is very quick, especially the fuzzy control which is not entirely dependent on the object's mathematical model, is suitable for uncertain systems and nonlinear systems to solve many difficult problems for the classical control. This paper introduces the fuzzy PID controller as a speed regulator, using the dynamic compensation method for adjusting the proportional gain, so that the two motors are synchronized.

AC Servo Motor Dynamics

Fig. 1 is the mobile gantry milling machine driven by double servo motor [1]. The model of the system consists of a motor coupled to a gear box and an inertia load rigidly fixed to output shaft. The control torque (Tc) for the AC servo motor is described as

$$T_C = \mathrm{k}_1 \mathrm{E(t)} - \mathrm{k}_2 \dot{\theta}(\mathrm{t})$$

Where Tc = Control torque (Nm)
k1 & k2 = motor constants (Nm/V, Nm/rad/s) - identified parameters from experimental test.
$\dot{\theta}$ = angular velocity of the AC servo motor (rad/s)
E = rated input voltage (v)
The dynamic equation of the mechanical system is given by

$$T_C = J\ddot{\theta} + B\dot{\theta} + T_L$$

Where θ = angular position of the AC servo motor (rad)
$\ddot{\theta}$ = angular acceleration of the AC servo motor (rad/s^2)
B = Friction coefficient
J = Moment of inertia (Kg.cm^2)
Taking laplace transform the above equations becomes

$$K_1E(s) - k_2s\theta(s) = Js^2\theta(s) + Bs\theta(s) + T_L(s)$$

The master and slave motor can adopt the same equation except the constant factors are different, such as Moment of inertia (J), Friction coefficient (B).

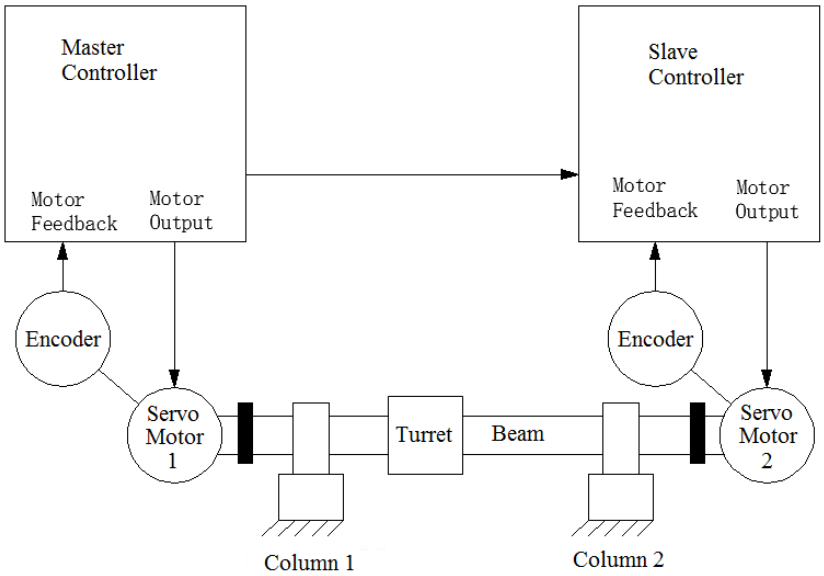

Fig. 1 Mobile gantry milling machine driven by a double servo motor

Master-Slave Servo Control

In the Synchronous Servo System of the mobile gantry milling machine, two servo subsystems move according to the same speed for a given signal. One of the servo systems is defined as the driving shaft which is called as master [2]. And the other is defined as driven shaft which is called as slave. So that a separate master-slave drive is constituted.

Among the master-slave control structure, only the master motor adopts the position control and the speed command signal of the slave motor is from the output of the position controller of the master motor. When the master is interference by the external signal, the position feedback changes, and the slave motor reference speed also changes just like the master motor. So that it will improve safety factor of the control system's coupling structure. The synchronous control system structure diagram is shown in Fig. 2.

In Fig. 2, P2 is the position feed-forward controller and P1 is the position proportional controller. Fuzzy PID controller is the speed controller in order to achieve the fast and accurate response to the input signal. PI controller is the force compensation of the dynamic deformation. Using PI controller too large synchronization error of the biaxial can be avoided among the high-speed operation.

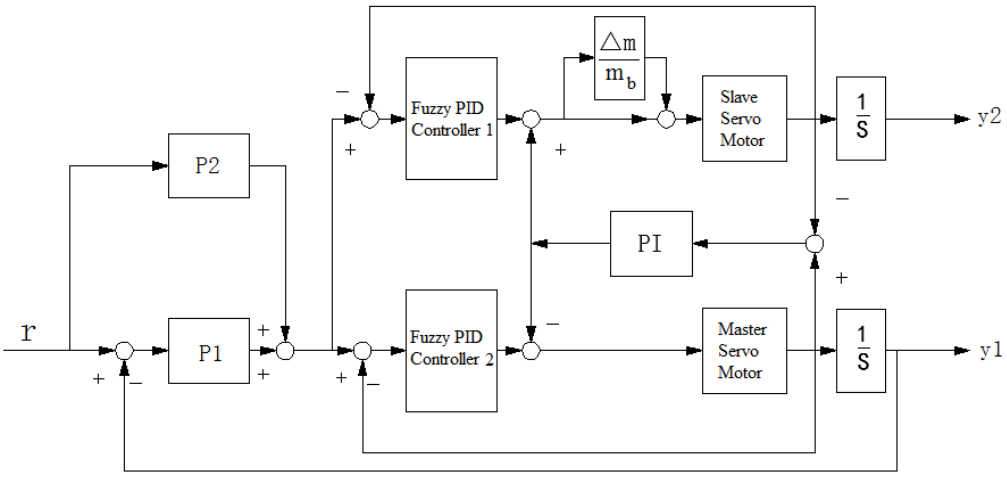

Fig. 2 Synchronous control system structure diagram

The purpose of the synchronous control system is to correct any angular error of the columns. Two drives are used in a master-slave setup. Through torque and speed control of the servo motors, the two columns are synchronized.

When the mobile gantry milling machine achieves the two-dimensional motion control, the turret position change of Y-axis servo motor often leads to the equivalent inertia change of X-axis servo motors. So the extra dynamic load compensation should be adopted, that is the function of $\triangle m/m_b$ shown in Fig. 2.

Adaptive -Neuro Fuzzy Inference System Based On Controller

Adaptive Neuro-Fuzzy Inference Systems are fuzzy Sugeno models put in the framework of adaptive systems to facilitate learning and adaptation. Such framework makes FLC more systematic and less relying on expert knowledge [3]. To present the ANFIS architecture, two-fuzzy rules are based on a first order Sugeno model:

Rule 1: if (x is A1) and (y is B1) then (f1 = p1x + q1y + r1)

Rule 2: if (x is A2) and (y is B2) then (f2 = p2x + q2y + r2)

One possible ANFIS architecture to implement these two rules is shown in Fig. 3. Note that a circle indicates a fixed node whereas a square indicates an adaptive node (the parameters are changed during training). In the following presentation *OLi* denotes the output of node *i* in a layer *L*.

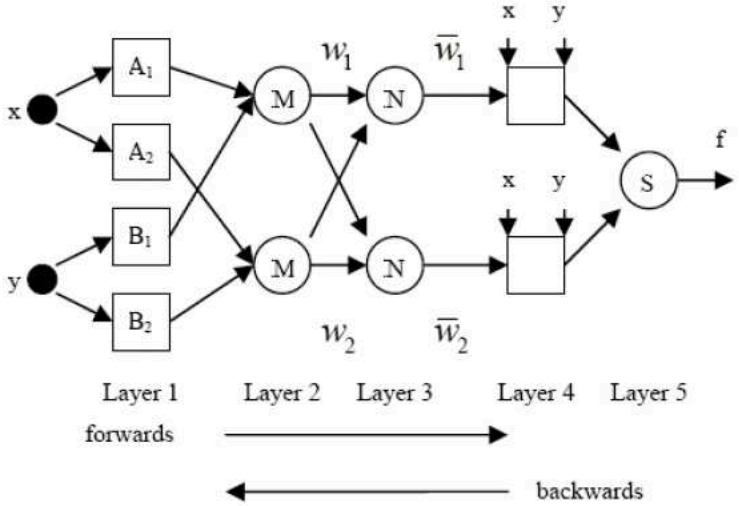

Fig. 3ANFIS architecture

ANFIS algorithm is composed of fuzzy logic and neural networks with 5 layers [4]. Properties of layer described for x, y as an input variables. The ANFIS architecture is not unique. Some layers can be combined and still produce the same output.

The following formulas are listed from layer 1 to layer 5.

$$O_{1,i} = \mu_{Ai}(x) = \frac{1}{1+\left[\left(\frac{x-c_i}{a_i}\right)^2\right]^{b_i}}$$

$$O_{2,i} = \omega_i = \mu_{Ai}(x).\mu_{Bi}(y)$$

$$O_{3,i} = \overline{\omega}_i = \frac{\omega_i}{\omega_1 + \omega_2}$$

$$O_{4,i} = \overline{\omega}_i f_i = \overline{\omega}_i (p_i x + q_i y + r_i)$$

$$O_{i,5} = f = \sum_i \overline{\omega}_i f_i = \frac{\sum_i \omega_i f_i}{\sum_i \omega_i}$$

In this ANFIS architecture, there are two adaptive layers[4]. Layer 1 has three modifiable parameters (*ai*, *bi* and *ci*) pertaining to the input MFs. These parameters are called premise parameters. Layer 4 has also three modifiable parameters (*pi*,*qi* and *ri*) pertaining to the first order polynomial. These parameters are called consequent parameters.

Fig. 4 shows the curves of the slave motor using ANFIS controller about the current-time response under the 300 Nm load and 50 radian/s reference velocity. As for the master motor, the response is same.

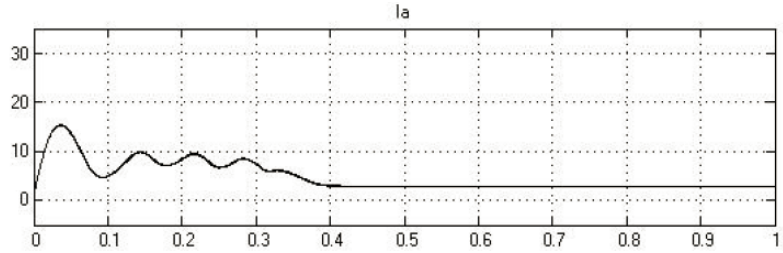

Fig. 4 ANFIS controller current-time response

Conclusion

Based on the analysis of the main reasons among the mobile gantry milling machine where the dual X-axis servo motor drives are not synchronized, the dynamic load compensation the adaptive-neuro fuzzy PID control are proposed. From the simulation curve it can be seen that the accuracy of double motor synchronization can be achieved.

References

[1] R.N.Conte, L.F.A.Pereira, J.F.Haffner. "Parameters Identification of Induction Machines Based on Frequency Response and Optimization Techniques"[J], The 29th Annual Conference of the IEEE.Vol.1, November 2003: 596-599

[2] Cui Naxin, Zhang Chenghui, Li Ke, Zhang chengjin, "Efficiency optimization control of induction motor drives based on online parameter estimation", Transactions of China Electroe Chncal Society,v22,n9,September,2007: 80-85.

[3] H. M. Kojabadi, L.Chang, R. Doraiswami. "A novel adaptive observer for very fast estimation of stator resistance in sensorless induction motor drives"[J], Proceedings of IEEE 34th Annual Power Electronics Specialist Conference, 2003, 3:1455-1459.

[4] Z. Hímer, V. Wertz, J. Kovács, U. Kortela Neuro- fuzzy model of flue gas oxygen content Proccedings of IASTED International Conference on Modelling Identification and Control, Grindelwald, Switzerland 2004

CHAPTER 11:

Power Electronics and Power Drives

Advanced Materials Research Vols. 960-961 (2014) pp 1243-1247

doi:10.4028/www.scientific.net/AMR.960-961.1243

Analysis of Sub-synchronous Oscillation (SSO) Caused by HVDC Transmission System

Yangchengxiang Song [1,a], Jun Luo [1], Shujun Yao [1,b]

[1] Institute of Electrical and Electronic Engineering, North China Electric Power University, Beijing, 102206, China

[a]email: hbdl_songyangcx@126.com, [b]email: Open2000@sina.com.cn

Keywords: Sub-synchronous oscillation(SSO), HVDC, Damping characteristic, Digital time-domain simulation

Abstract. Sub-synchronous oscillation (SSO) caused by highly non-linear HVDC devices can lead to shaft failure and electrical instability of a turbo-generator at oscillation frequency lower than power grid frequency. With increasing HVDC installed in power systems, analysis of SSO becomes a great concern of electrical engineers. In this paper, the reason and process of the SSO are presented by analyzing equations of the mass-springs model. Research methods of SSO are reviewed in HVDC system. And advantages of digital time-domain simulation are demonstrated through combining with algorithm of Prony.

Introduction

High voltage direct current(HVDC) is an application of power electronics technology in the field of power system. HVDC system consists of three parts which are rectifier station, DC transmission line and inverter station. The structure of HVDC system is essentially an AC-DC-AC current conversion system. The typical HVDC system, bipolar HVDC transmission system, is shown in Fig. 1.

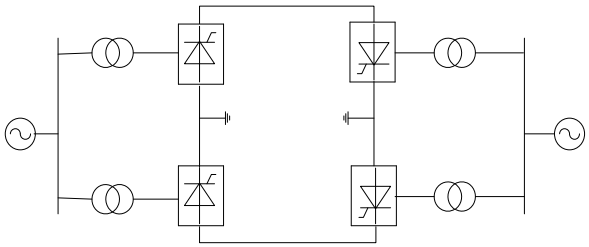

Fig. 1 The diagram of bipolar HVDC transmission system

The HVDC system has significant advantages in long-distance, large-capacity, underground and submarine cable transmission. It also plays an important role when two non synchronous systems are connected. However, because of the fast power control, HVDC system may cause the interaction between turbo-generator shaft and hybrid AC-DC system, and even sub-synchronous oscillation(SSO)[1,2,3] . Traditional AC system uses series capacitor compensation to improve the performance of stability and transmission capacity. The line inductance and compensation capacitor constitute a resonant circuit with a LC resonant frequency. And generator shaft has a natural torsional frequency. System suffers turbulence when two frequencies are complementary or approximately. There will be large-scale power exchange with frequency lower than grid frequency. This power oscillation, between the generator and power transmission system, will cause the generator shaft damage, named sub-synchronous resonance (SSR). Compared to AC system, the oscillation of AC-DC-AC system is due to the application of convertor station. Therefore, oscillation in HVDC system is called SSO instead of SSR[4].

Researches on SSO mainly focus on two aspects below now. Some papers is committed to novel methods to gain more accurate mechanical and electrical damping characteristics of SSO. In [5], author applies time-varying dynamic vector method to analyze the SSO of HVDC system, giving the relationship between characteristic value of HVDC system and parameters' variety of control system.

Another literatures work on inhibitory methods of SSO. In [6], thyristor controlled series compensation (TCSC) is added to the traditional supplementary excitation damping controller(SEDC) to restrain SSO. And the parameters of suppressors are designed newly. The rest of this paper is arranged as follows. Next section mainly describes the mechanism of SSO in HVDC. Then two detailed methods solving problems of SSO are illustrated. Finally, The concluding remarks are given.

Mechanism of SSO in HVDC System

Oscillation Problems in Power System. Power system has two types of oscillation problems, the SSO and low-frequency oscillation (LFO). SSO is caused by the electromechanical coupling interaction. LFO is a continuous low-frequency power oscillation owing to small disturbance and insufficient damping between generator rotor and transmission system. This paper mainly studies the SSO caused by HVDC.

Torsional Vibration of Shaft System of Large-Capacity Generator. SSO is a complex oscillation owing to the electromechanical coupling effect between shafting mass-springs system(Fig. 2) and hybrid AC-DC power system. To transmit higher power at longer distance, the large-capacity turbo-generators' shafts have unique characteristics. With increasing capacity of single turbo-generator and corresponding increase in power density, length of the shaft is greatly extended. So the shaft's cross-sectional area declines in relatively. Entire shaft can no longer be regarded as a rigid body. It is a mass-springs system with two ends freeing.

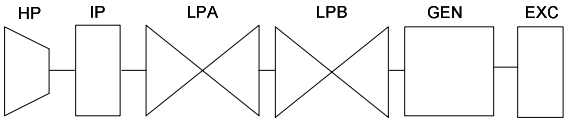

Fig. 2 The model of turbo-generator shafting

The principle of torsional vibration is given below using the model of two-mass-springs shaft. In this model, M_1 and M_2 are time constant of rotatory inertia. ω_1, ω_2 are rotor speed. δ_1, δ_2 are rotor angle. Assumptions are that no mechanical damping and external force when vibrations occurring. And K_{12} is elastic coefficient of model. Normalized value equation of motion is given below.

$$\begin{cases} M_1 \dfrac{\mathrm{d}^2\delta_1}{\mathrm{d}t^2} + K_{12}(\delta_1 - \delta_2) = 0 \\ M_2 \dfrac{\mathrm{d}^2\delta_2}{\mathrm{d}t^2} + K_{12}(\delta_2 - \delta_1) = 0 \end{cases} \tag{1}$$

Linearized form of (1) is given (2).

$$\begin{pmatrix} M_1 p^2 & 0 \\ 0 & M_1 p^2 \end{pmatrix} \begin{pmatrix} \Delta\delta_1 \\ \Delta\delta_2 \end{pmatrix} + \begin{pmatrix} K_{12} & -K_{12} \\ -K_{12} & K_{12} \end{pmatrix} \begin{pmatrix} \Delta\delta_1 \\ \Delta\delta_2 \end{pmatrix} = 0 \tag{2}$$

(3) is characteristic equation of (2).

$$\begin{vmatrix} M_1 p^2 + K_{12} & -K_{12} \\ -K_{12} & M_2 p^2 + K_{12} \end{vmatrix} = 0 \tag{3}$$

Assuming $\lambda = p^2$, (3) can be expressed as (4).

$$(M_1\lambda + K_{12})(M_2\lambda + K_{12}) - K_{12}^2 = 0 \tag{4}$$

The solution of the equation (4) is (5).

$$\begin{cases} \lambda_1 = 0 \\ \lambda_2 = -\dfrac{K_{12}(M_1 + M_2)}{M_1 M_2} \end{cases} \tag{5}$$

P can be obtained in (6) from (5).

$$\begin{cases} p_{1,2} = 0 \\ p_{3,4} = \pm j\sqrt{\dfrac{K}{M}} = \pm j\omega_n \end{cases} \tag{6}$$

In (6), $K=K_{12}$, $M=M_1M_2/(M_1+M_2)$. (6) shows that $P_{3,4}$ is a pair of conjugate complex roots. When subjected to disturbance, shaft may suffer the torsional oscillations at relative frequency ω_n. And the oscillations will decay if there exists damping. Actually each mass-spring have instantaneous velocity at different magnitude and phase. Interaction of two mass-springs results in rotating torque along the direction of rotation. The rotating torque is the reason for fatigue accumulation of shaft. Crack or even shaft fracture will appear for a long time.

Process of SSO in HVDC System. Electrical disturbances of generator and mechanical disturbances of turbine, as the incentives, can cause torsional vibration of shaft system. Torsional vibration may results in fluctuations of AC voltage. Commutation voltage and phase will change because of the fluctuations. Then the normal operating point, voltage, current, power of DC and trigger angle, will deviate.

HVDC system will try to eliminate the deviation by closed loop control. This will affect the output of DC power. The balance is broken down between electromagnetic torque and shaft. And perturbation is occurring. When the error of phase is greater than 90° between speed changes of generator($\Delta\omega$) and electromagnetic torque perturbation(ΔT_e), it will lead to negative damping. Once the negative damping is stronger than the mechanical positive damping, the shaft of generator will occur torsional vibration. Power transmission with a constant current(or constant power) control is independent of the AC system frequency. So HVDC system has not damping effect on frequency oscillation. When the following negative factors occur simultaneously, it is possible to produce SSO. These negative factors, including:

1) The distance is very near between turbine and rectifier station of HVDC.
2) The steam turbine and the AC network is a weak link.
3) The rated power of turbine and transmission are in the same order of magnitude.

The mechanism of SSO in HVDC system is shown in Fig. 3.

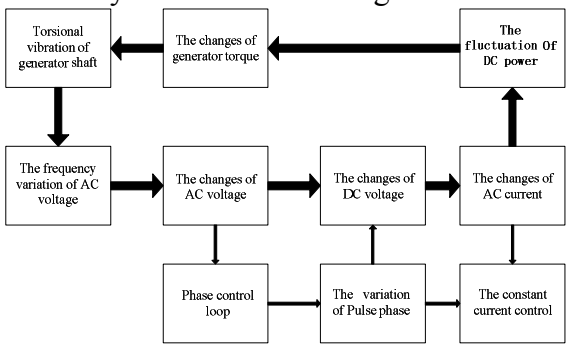

Fig. 3 The mechanism of SSO in HVDC system

Analysis methods of SSO

Traditional analysis methods of SSO are based on the linear system model, including: analysis of characteristic roots method, sweep frequency and equivalent impedance method, Sweep and complex torque coefficient method, sweep and multivariate Nyquist criterion method. When nonlinear and coupled characters of devices considered, the SSO analysis method will be different.

To solve this problem, an essential method is that establishing HVDC system mathematical model considering the nonlinear and coupling characters. In [7], two models are established by Dong-Joon Kim, a static mathematical model for studying of HVDC power flow, and a dynamic mathematical model for analysis of characteristic roots in SSO problem. Establishing mathematical model is strict, accurate and logical. But model is complicated. And according to the different emphasis of the research, simplifications and assumptions must be done. It may influence the accuracy of the this method. So method based on digital time-domain simulation is an another effective choice in the case where the exact expressions are not needed.

Digital time-domain simulation solves differential equations which describe the state of the system essentially. Since the method based on a rigorous mathematical deduction, there is no restriction on

the parameters of the model. Thus, the shaft of the generator can expressed by mass-springs model with finer division of the distribution parameters. So a more detailed description of the generator, control method, switching operation and fault conditions can be given. Because the SSO issues involving electromagnetic and electromechanical transient process, time-domain electromagnetic transient simulation model should be adopted. Fig. 4 shows the waveform of electromagnetic torque variation of generator appearing in SSO by PSCAD / EMTDC.

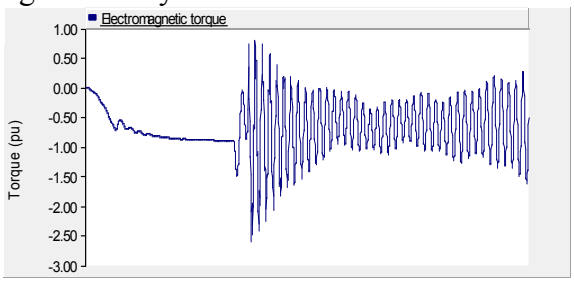

Fig. 4 The wave of electromagnetic torque in SSO

From the simulation, failure results in SSO at 1s. Electromagnetic torque of turbo-generator, suddenly oscillates viciously from the stable value. The simulation waveform is analyzed by algorithms of Prony or TLS-ESPRIT in method of digital time-domain simulation.

In 1957, Prony put forward a mathematical model based on a set of complex exponential functions to describe the equidistant sampling data combinations. This is named algorithms of Prony later. Prony algorithm can be applied directly in analysis of equidistant sampling data to estimate the signal frequency, initial phase and a series of informations. The analysis of simulation data based on Prony algorithm avoids the inaccuracy of linear model and complicacy of nonlinear model. And the sampling period is 1s. The sampling interval is 2ms. The results of Prony algorithm in Fig.4 are that the oscillation frequency 21.170Hz and damping ratio 5.870. The detailed calculations and steps refer to [8]. Although digital time-domain simulation method cannot directly obtain the influence of the parameters and the control methods, important parameters concerned in SSO analysis, such as oscillation frequency, damping ratio and the characteristic values, can be obtained by algorithm of Prony or TLS-ESPRIT.

Summary

In the HVDC connected hybrid AC-DC parallel system, the generator is especially vulnerable to SSO owing to large-scale applications of nonlinear devices. The SSO occurs for two main reasons below. One is that the shaft model of large-capacity steam turbine generator is different from the traditional rigid shaft system, putting up the characteristics of mass-springs system. The another main reason is the negative damping characteristics of generator because of fast power control relying on the nonlinear converter devices. The research methods of SSO in HVDC system, is different from the one of traditional AC transmission system owing to its nonlinearity, coupling. The digital simulation method is an effective, intuitive and simple one.

References

[1] Svensson S.Mortensen K.Damping of sub-synchronous oscillations by an HVDC link, an HVDC simulator study [J].IEEE Trans. on Power Apparatus and Systems.1981.100(3):1431-1437.

[2] Electric Power Research Institute .HVDC system control for damping of sub-synchronous oscillations[R]. New York EPRI. 1982.

[3] Canay I M. A new approach to the torque interaction and electrical damping of the synchronous machine, part I and part II [J]. IEEE Trans. on Power Apparatus and Systems .1982. 101(10) 3630-3647.

[4] Huang Beijun, Analysis and control of sub-synchronous oscillation in HVDC transmission system[D], Southwest Jiaotong University,2005.

[5] Huang Shengli, Song Ruihua, et al. Analysis and simulating the SSO caused by HVDC using the time-verying dynamic phasor [J]. Proceedings of CSEE，2003，23（7）： 1-4.

[6] Wu xi, Jiang Ping. Research on Sub-Synchronous Oscillation Mitigation Using Supplementary Excitation Damping Controller and Thyristor Controlled Series Capacitor[J]. Transactions of China Electrotechnical Society, 2012, 27(4): 179-184.

[7] Dong-Joon Kim.Hae-Kon Nam,et al. A Practical Approach to HVDC System Control for Damping Sub-synchronous Oscillation Using the Novel Eigenvalue Analysis Program[J].IEEE Trans.on Power Systems.2007.22(4):1926-1933.

[8] Dong Hang ,Liu Dichen,et al. Analysis of Power System Low Frequency Oscillation Based on Prony Algorithm [J]. High Voltage Engineering,2006,32（6）：97-98.

Advanced Materials Research Vols. 960-961 (2014) pp 1248-1253

doi:10.4028/www.scientific.net/AMR.960-961.1248

Hall Effect Sensor Based Field Oriented Control of Permanent Magnet Synchronous Machine Using in Electric Vehicle

Yu-Min Wang[1,2, a], and Qing Fan[2,b]

[1]Wuhan University of Technology, Wuhan, Hubei, China

[2] Zhengzhou Nissan Automobile Co. Ltd., Zhengzhou, Henan, China

[a]wangyumin2012@hotmail.com, [b]fanqing2012@hotmail.com

Keywords: permanent magnet synchronous machine, field oriented control, Hall effect sensor.

Abstract. Field oriented control (FOC) of permanent magnet synchronous machine (PMSM) is of very importance in electrical vehicle (EV) applications due to low acoustic noise and smooth operation. Nowadays the resolver is most widely used to predict the PMSM rotor position. However, with cost consideration this paper proposes a FOC of PMSM based on Hall effect sensor, , which is very useful in practical applications because of low price and high reliability. Since the Hall effect sensor is an absolute position sensor with 60-degree resolution, the position initialization process is not needed and the reversal rotation risk can be avoided. To improve resolution the interpolation method implemented by software is employed. And the high performance of this proposed method is validated by some experimental results.

Introduction

In electric vehicle (EV) applications permanent magnet synchronous machine (PMSM) is widely used according to some advantages, such as simple structure, high power factor, high efficiency, good dynamics, relative small size, low acoustic noise, and easy maintenance. These high performance of PMSM can be performed by means of field oriented control that requires information of rotor position. Therefore, the position sensor is used to obtain the absolute rotor position information to exactly control the motor torque. Generally a resolver is widely used in EV applications. These sensors increase not only the machine size but also the cost of drive [1,2].

To solve these problems many authors proposed sensorless control algorithms using different control methods that are mainly divided into two groups: 1) control strategies based on the voltage equation of machine and 2) control strategies based on signal injection techniques [3]. Control strategies based on the voltage equation can be only applied into the medium and high-speed operation due to the concern with the magnitude of back-EMF. Control strategies based on signal injection have no lower limitation. However, it is difficult to apply the control strategies to practice easily due to machine parameters sensitivity or complex calculations. So far most results in sensorless control method have remained at the theoretical level or still in the laboratory.

This paper proposes a FOC of PMSM based on Hall effect sensor with software interpolation, which can be considered as an intermediate stage of development between the general incremental encoder based and sensorless based PMSM control methods. The hardware of this proposed method is exactly same as that of general brushless DC (BLDC) machine. In comparison with the general incremental encoder and resolver the price of Hall effect sensor is very low and can be neglected. The size of Hall effect sensor is also rather smaller. Moreover, this proposed Hall effect sensor based PMSM is of high reliability without the reversal rotation risk and can easily be implemented in practical applications.

FOC of PMSM Based on Hall Effect Sensor

A permanent magnet brushless machine generally consists of a wound stator, a permanent magnet rotor assembly, and an internal or external device to sense rotor position. The sensing device provides logic signals for electronically switching the stator windings in the proper sequence to maintain

rotation of the magnet assembly. Two configurations of permanent magnet brushless machine are usually considered: one is the trapezoidal type; the other is the sinusoidal type. Depending on how the stator is wounded, the back-electromagnetic force (BEMF) will have a different shape. To obtain the maximum performance from each type of permanent magnet brushless machine, an appropriate control strategy has to be implemented. The trapezoidal BEMF motor called BLDC uses a two phases on strategy, whereas the sinusoidal BEMF motor called brushless AC (BLAC) offers its best performances by using three phase on strategy with sinusoidal currents [4]. Usually the BLAC is also called PMSM.

The power circuit of a three-phase voltage source inverter (VSI) with star-connected permanent magnet brushless machine is shown as Fig. 1. Each phase winding is connected to one inverter leg. The dc link voltage V_{dc} can be applied to the phase winding by switching on some semiconductors (S_1 to S_6) of inverter. The amplitude of the voltage applied to phase winding is controlled by the PWM technique.

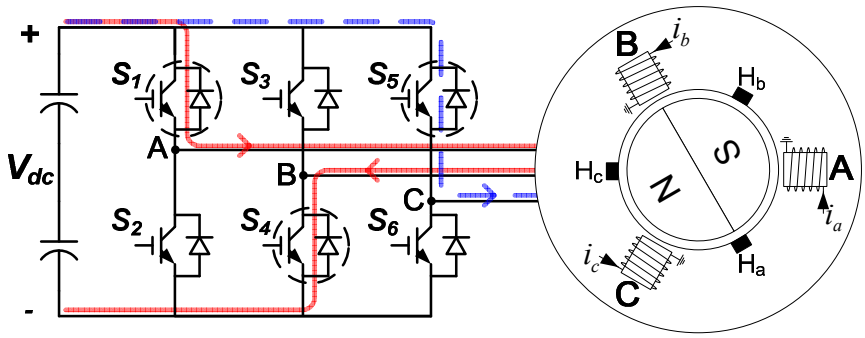

Fig. 1. Three-phase VSI bridge circuit with permanent magnet brushless machine.

BLDC mode operation. As shown in Fig. 1 three Hall effect sensors are embedded into the stator on the position with a 60º phase shift from the phase windings. Whenever the rotor magnetic poles pass near the Hall effect sensors, they give a high or low signal, indicating the N or S pole is passing near the sensors. Therefore, the exact sequence of commutation that is shown as Fig. 2(a) can be determined based on the combination of these three Hall effect sensor signals (H_{cba}). Within 360º, one electrical revolution, the communication sequence is 5, 1, 3, 2, 6, 4 in decimal form. Then the windings are energized following the sequence using a two phases on strategy. In the analysis we assume that the rotor is rotating in a counterclosewise (CCW) direction. The rotor position that is rotating from the starting point 210º to 270º is considered in the first sector 5 because the Hall effect sensor value keeps the value of 5. In this region the stator magnetic field F_{ab} shown in Fig. 2(b) is generated by switching the semiconductors S1 and S4 on shown in Fig. 1. The current will be following from phase-A to phase-B (A to B in the rightmost column in Table 1). The corresponding phase magnetic fields F_a and F_b are generated in the directions of 0º and 300º with same amplitude. Therefore, the resultant magnetic field F_{ab} is in the direction of 330º. Torque is produced because of the interaction between the magnetic field generated by the stator coils and the permanent magnets. Ideally, the peak torque occurs when these two fields are at 90° to each other. The phase difference between the two magnetic fields is between 120º and 60º in which region the generated average toque is largest. In order to keep the motor running, the magnetic field produced by the windings should shift position, as the rotor moves to catch up with the stator field. For example the energized currents should be from phase-A to phase-C in the next communication sequence (sector 1). It means that the resultant stator magnetic field rotates 60º forward in CCS direction. This magnetic field rotation is repeated for the following sequences. What is known as six-step commutation defines the sequence of energizing the windings. The relationship among the Hall effect sensor value, electrical angle, and energized current is shown in Table 2.

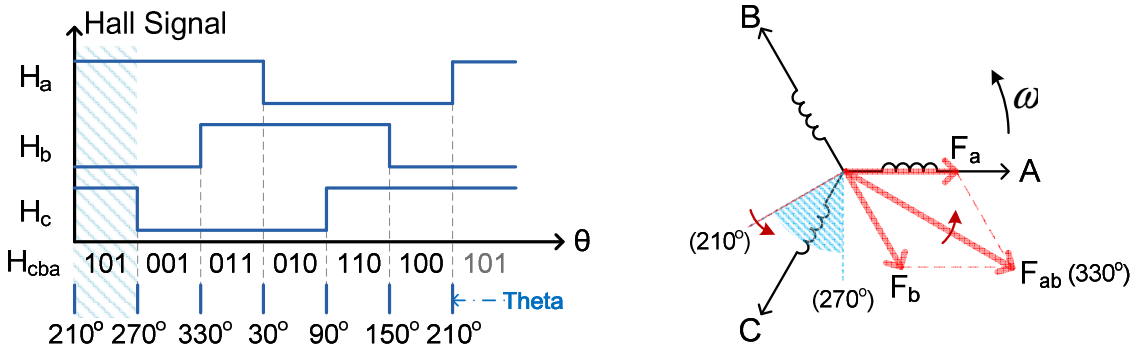

Fig. 2. Hall signals and magnetic field vectors, (a) Hall signal commutation sequence, (b) magnetic field vectors.

Table 1
Six-step commutation of BLDC motor

H_{cba} value		Electrical angle	Electrical	Energized current
binary	decimal	on entering edge	angle section	
101	5	210	210-270	A to B
001	1	270	270-330	A to C
011	3	330	330-30	B to C
010	2	30	30-90	B to A
110	6	90	90-150	C to A
100	4	150	150-210	C to B

PMSM mode operation. From the viewpoint of control there are three main differences between the BLDC mode operation and PMSM mode operation. One is the position refresh time, the second is the control strategy, and the third is the dead-time consideration. The detail comparisons of these three aspects are listed in Table 2. The position information of PMSM requires much more accurate than that of BLDC. The high precision position sensors, such as incremental or absolute encoder, and resolver, are used in PMSM control system. These high precision sensors increase not only the machine size but also the cost of drive. Therefore, to overcome the above drawbacks of the general PMSM in this paper we propose a novel and simple FOC of PMSM based on Hall effect sensor. The hardware of this control system and the positions of Hall effect sensors mounted on PMSM, together with the Hall signals, are exactly same as those of BLDC machine shown as Fig. 1. Because the values of the absolute positions, 210º, 270º, 330º, 30º, 90º, and 150º, obtained by Hall effect sensors shown as Fig. 2(a) are always correct. How the positions between these every 60º can be obtained is the key to the solution of achieving the FOC of PMSM.

To obtain the position information, the interpolated signals are software generated by digital signal processor (DSP) every period of PWM. Fig. 3 illustrates Hall signals together with software interpolation and corresponding predicted rotor positions. The time interval of two adjacent interpolated signals is the PWM period T_{PWM}. Therefore, the total number of the interpolated signals in every sector represents the 60 electrical degrees. In the next sector this total number is considered as a reference of 60º. The count number in the next sector will be used to compare with the 60º reference to predict the present position of the rotor. Then the FOC of PMSM can be executed. Corresponding to the rotor position of PMSM in Fig. 1 the semiconductors S1, S4, and S5 are switched on, and the stator magnetic field F_{abc} generated by three phases energizing windings shown in Fig. 4 is in the direction of 300º which is perpendicular to rotor permanent magnet.

The number of the interpolated signals is different in every 60 electrical degrees under different speed. Although the error of estimated rotor position based on the interpolated signals may exist, especially in the transient process, it can be corrected on every rising or falling edge of Hall signals.

Table 2
Main difference between BLDC and PMSM from the viewpoint of control

Difference	BLDC mode operation	PMSM mode operation
Position refresh	Every 60-degree	Every PWM interrupt
Control strategy	Two phase on	Three phase on
Dead-time consideration	No consideration	consideration

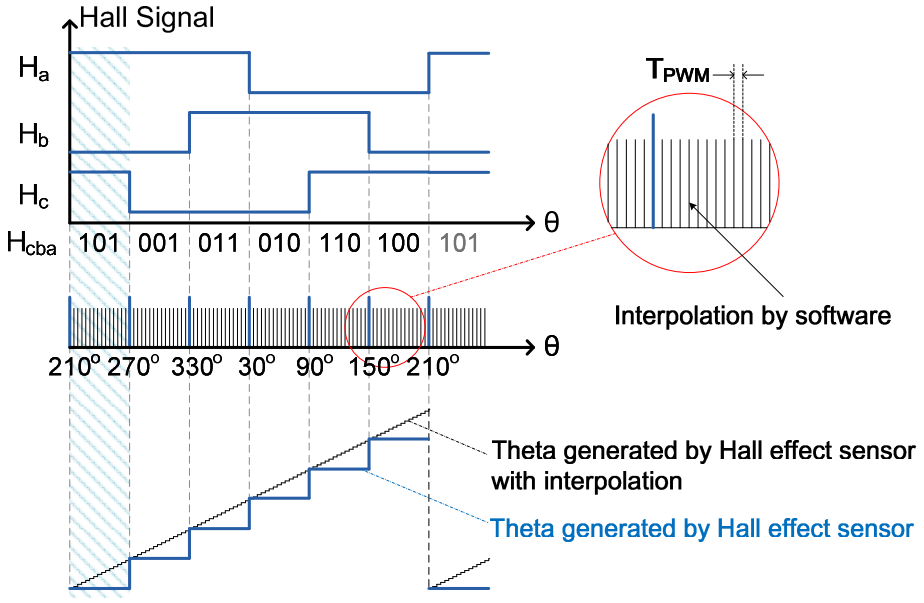

Fig. 3. Hall signals together with software interpolation and corresponding rotor position.

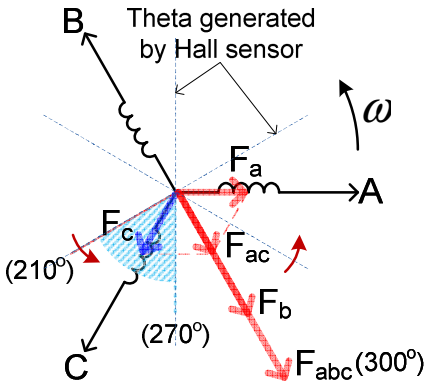

Fig. 4. Magnetic field vectors in PMSM.

Experimental Results. To validate this proposed method, we construct the control system of PMSM illustrated as Fig. 5. The proposed FOC of PMSM based on Hall effect sensor is implemented, together with the dead-time compensation [5]. The experimental results of the rotor position and phase-A current waveforms of PMSM are shown in Fig. 6.

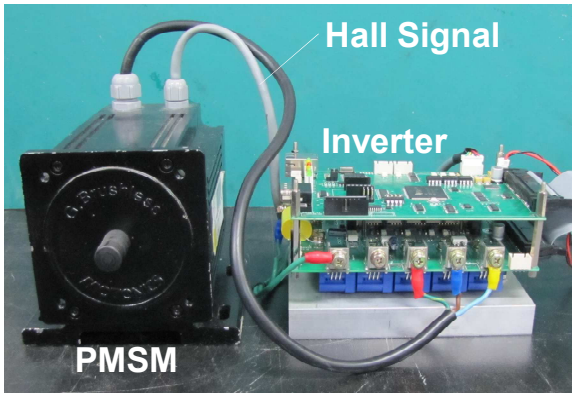

Fig. 5. Detent forces of two different winding types of PMLSMs.

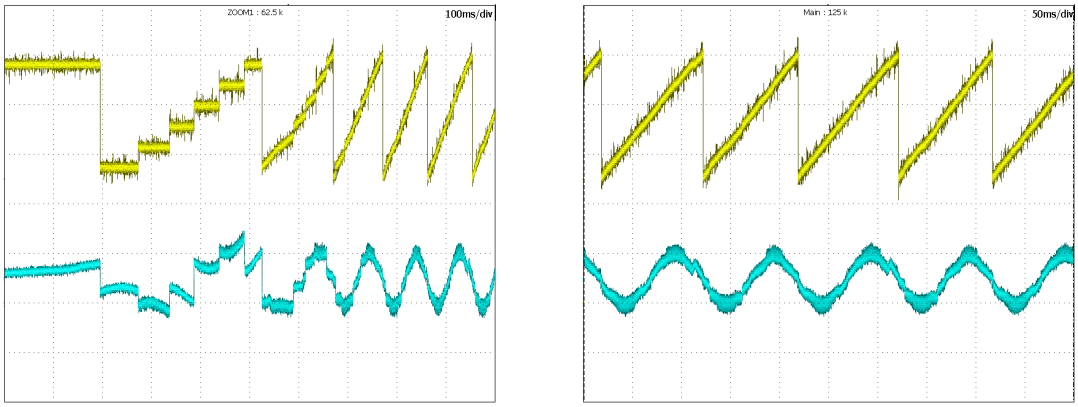

(a) (b)

Fig. 6. Rotor position and phase-A current waveforms, (a) starting waveforms of PMSM with Hall effect sensor with/without interpolation, (b) steady-state waveforms of PMSM with interpolated Hall effect sensor.

The start procedure waveforms are illustrated as Fig. 6(a). During the first electrical revolution the rotor position of which the resolution is 60 electrical degrees is only generated by Hall effect sensor. The current waveform is also changing every 60 electrical degrees interval. From the next revolution the rotor position is generated by Hall effect sensor with interpolation. In the second and third revolutions the predicted rotor position contains a large position error as the rotor speed is increasing in the transient-state. And these predicted position errors can be corrected on every rising or falling edge of Hall signals. In these two revolutions the phase-A current is also distorted because of the predicted rotor position errors. The steady-state waveforms are shown as Fig. 6(b). It also contains some rotor position errors that are caused by the position precision of the mounted Hall effect sensors. The higher the position precision of mounted Hall effect sensor is, the more sinusoidal the current is.

Conclusion

The proposed method of FOC of PMSM based on Hall effect sensor is very useful in practice. The estimated rotor position is predicted by using the interpolated signals which are generated by software every period of PWM. The hardware is exactly same as that of BLDC. In comparison with general sensor based PMSM system the cost is much lower. Moreover, this method can be extended to the position sensorless control of PMSM because the 60-degree information can be very easily obtained according to the back EMF waveforms. Compared with general position sensorless control method the advantage of this one is that the algorithm is more simple and easily implemented.

References

[1] P.J. Hor, Z.Q. Zhu, D. Howe, J. Rees-Jones: *Minimization of cogging force in a linear permanent magnet motor,* IEEE Transactions on Magnetics Vol. 34 (1998), p. 3544-3547

[2] S. Nakashima, Y. Inagaki, and I. Miki: *Sensorless initial rotor position estimation of surface permanent-magnet synchronous motor,* IEEE Transactions on Industry Applications Vol.36(2000) p. 1598-1603.

[3] J.K. Seok, J.K. Lee, and D.C. Lee: *Sensorless speed control of nonsalient permanent-magnet synchronous motor using rotor-position-tracking PI controller,* IEEE Transactions on Industry Electronics Vol. 53 (2006) p. 399-405.

[4] E. Simon: *Implementation of a speed field oriented control of 3-phase PMSM motor using TMS320F240*, Texas Instruments, (1999).

[5] J.S. Choi, J.Y. Yoo, S.W. Lim, and Y.S. Kim: *A novel dead time minimization algorithm of the PWM inverter,* Conference Record of the 1999 IEEE, Industry Application Conference Thirty-Fourth IAS Annual Meeting, Vol. 4 (1999) p. 181-186.

Advanced Materials Research Vols. 960-961 (2014) pp 1254-1257

doi:10.4028/www.scientific.net/AMR.960-961.1254

Investigation on Type-4 and Type-11 Mixed Topology of LLC Resonant Converter

Xiangwu Yan[1, a] Lei Sun[1, b*] Bo Zhang[1, c], Zheng Lv[1,d]

[1] State Key Laboratory of Alternate Electrical Power System with Renewable Energy Sources North China Electric Power University, Beijing 102206, China

[a]xiangwuy@163.com, [b]slslsl0811@126.com, [c]adam166@163.com, [d]lvzhengshibai@126.com

Keywords: LLC; Topological Group; Resonant converter

Abstract. LLC resonant converter can adjust the output for a wide range of source and load with a small fluctuation of switching frequency, so it is used widely. This paper introduces all arrangements of LLC topological group, then proposes a new topology which is consist of Type-4 and Type-11 that used widely，in this paper we also give its calculate method of resonant frequency. Lastly we get gain characteristics of the topologies in the PSpice simulation environment and analyse the influence factors on adjustment ability in certain load range .

Introduction

The series resonant converter (SRC) and the parallel resonant converter (PRC) which have two resonator components have been studied thoroughly [1]. The structures of SRC and PRC are simple, but their defects limit their industry developing. For improve the performance of resonant converter, Rudy Severns gived exhaustive topological groups of three resonator components according to their arrangements [2]. The topological groups include 18 kinds of LLC topologies. Type-4 [3], Type-10, Type-11, Type-13 and Type-17[4,5] have been studied, but no detailed analysis have been published yet. This paper give the 18 kinds of LLC topologies, and analyses three kinds of quasi-isometric topologies which are consist of Type-4 and Type-11, then give their calculate method of resonant frequency and gain characteristics.

LLC Resonant Topological Group

Fig. 1 is the exhaustive topological group of LLC resonant:

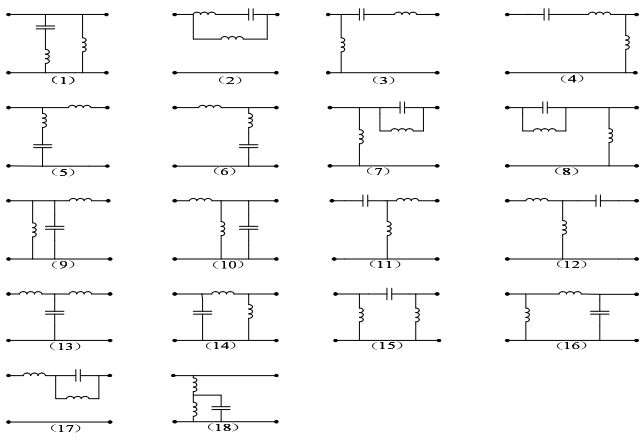

Fig. 1 LLC resonant topological group

Topological isomorphism in power electrics is the topologies have same mapping graph node, in the actual circuit is the circuits have same kind and quantity of components with same electrical properties. In Fig.1 each topology has different characteristics, but their common points is the additional resonator component would not destruct the characteristics of SRC or PRC while it is only used to improve them, so it can be treat as isomorphism or quasi- isomorphism.

Type-4 and Type-11 in The Bi-directional LLC Resonant Converter

Take full bridge topologies for instance as Fig.2

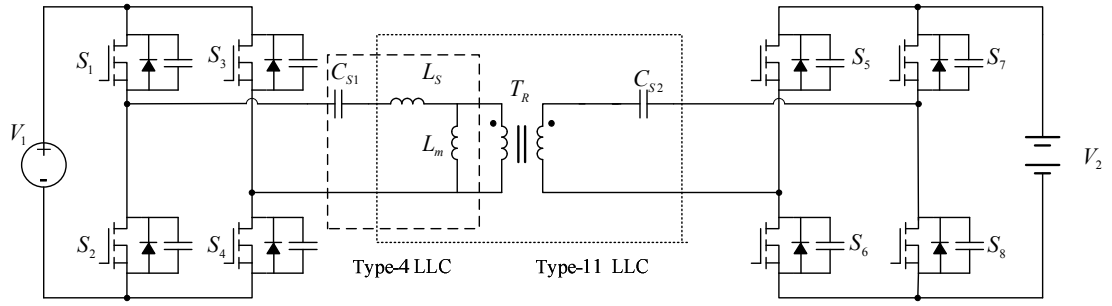

Fig. 2 Type-4 and Type-11 LLC Bi-directional resonant topology

In the forward direction mode the resonant circuit can be treat as Type-4 resonant circuit, and in the backward direction mode the resonant circuit can be treat as Type-11 resonant circuit. In order to analyse the characteristics of the two directions mode, we can use their AC equivalent circuits as the forward direction mode shown in Fig.3 and the backward direction mode shown in Fig.4.

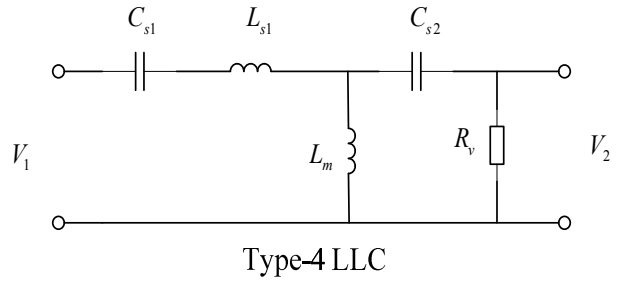

Fig. 3 Forward direction mode

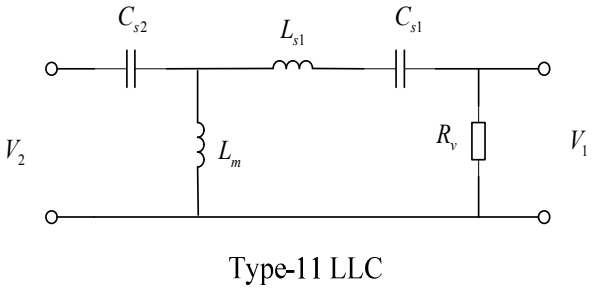

Fig. 4 Backward direction mode

In order to calculate the resonant frequency of heavy load in forward direction, it should meet

$$\begin{cases} -j\dfrac{1}{\omega C_{S1}} + j\omega L_{S1} + \dfrac{j\omega L_m \cdot \left(-j\dfrac{1}{\omega C_{S2}}\right)}{j\omega L_m - j\dfrac{1}{\omega C_{S2}}} = 0 \\ f_1 = \dfrac{\omega}{2\pi} \end{cases} \tag{1}$$

The second resonant frequency can be calculated by simplified Eq.1 as shown in Eq.2

$$\begin{cases} \omega^4 \cdot \left(C_{S1}C_{S2}L_m L_{S1}\right) - \omega^2\left(L_{S1}C_{S1} + L_m C_{S1} + L_m C_{S2}\right) + 1 = 0 \\ f_1 = \dfrac{\omega}{2\pi} \end{cases} \tag{2}$$

The first resonant frequency in light load mode is equal to Type-4 as shown in Eq.3

$$f_2 = \frac{1}{2\pi\sqrt{\left(L_{S1} + L_m\right)C_{S1}}} \tag{3}$$

In order to calculate the resonant frequency of heavy load in backward direction, it should meet

$$\begin{cases} -j\dfrac{1}{\omega C_{S2}} + \dfrac{j\omega L_m \cdot \left(j\omega L_{S1} - j\dfrac{1}{\omega C_{S1}}\right)}{j\omega L_m + j\omega L_{S1} - j\dfrac{1}{\omega C_{S1}}} = 0 \\ f_1 = \dfrac{\omega}{2\pi} \end{cases} \tag{4}$$

The second resonant frequency can be calculated by simplified Eq.4 as shown in Eq.5

$$\begin{cases} \omega^4 \cdot \left(C_{S1}C_{S2}L_m L_{S1}\right) - \omega^2\left(L_{S1}C_{S1} + L_m C_{S1} + L_m C_{S2}\right) + 1 = 0 \\ f_1 = \dfrac{\omega}{2\pi} \end{cases} \tag{5}$$

The first resonant frequency is

$$f_2 = \frac{1}{2\pi\sqrt{L_m C_{S2}}} \tag{6}$$

Analyse Eq.2 and Eq.5 we can know the resonant frequency in heavy load mode of this topology is equal, so the topology can realize bi-direction work in the same frequency.

Simulation Analysis of Gain characteristics

Analyse the fundamental-wave gain characteristics of the topology in the PSpice simulation environment and design parameter as following

The input voltage is 200V-400V, output voltage is 200-400V, output current is 0-20A, $L_S = 30uH$, $L_m = 130uH$, $C_{S1} = 200nF$, $C_{S2} = 200nF$, $n = 1$,and using the method of calculation we build can get the second resonant frequency is 64.926KHz, then normalize them.

The gain characteristics of the topology are shown in Fig.5, Fig.6.

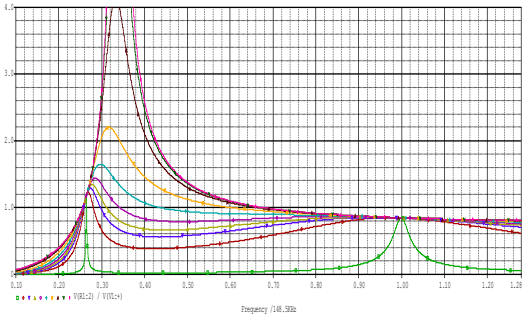

Fig. 5 Gain Characteristic of Type-4 and Type-11 Mixed Bi-direction LLC Resonant Converter in Forward Direction Mode

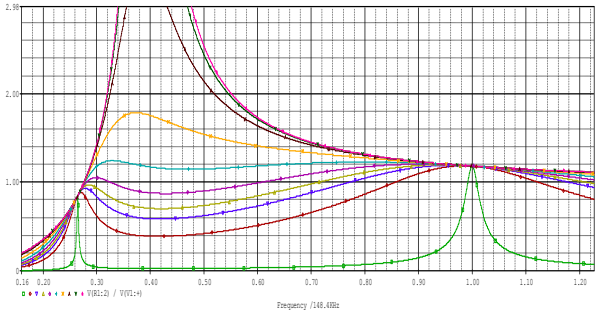

Fig. 6 Gain Characteristic of Type-4 and Type-11 Mixed Bi-direction LLC Resonant Converter in Backward Direction Mode

We know via the simulation analysis that the gain value of Type-4 and Type-11 mixed bi-direction LLC resonant converter in forward direction mode is less than 1, the gain value of Type-4 and Type-11 mixed bi-direction LLC resonant converter in backward direction mode is much more than 1, but it adjustment range of load is small, because the secondary capacitor participates in the resonance, then make frequency sweep of the secondary capacitor to learn its influence in Fig.7,and Fig.8

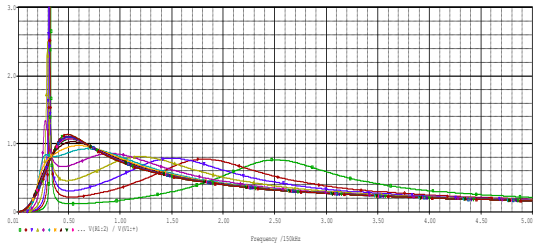

Fig. 7 Gain Characteristic of Type-4 and Type-11 Mixed Bi-direction LLC Resonant Converter in Forward Direction Mode By frequency sweep of the secondary capacitor

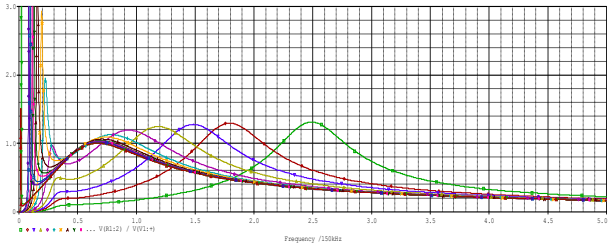

Fig. 8 Gain Characteristic of Type-4 and Type-11 Mixed Bi-direction LLC Resonant Converter in Backward Direction Mode By frequency sweep of the secondary capacitor

We can know the gain is in inverse proportion to the secondary capacitance, and the resonant point move to right with the reducing of the secondary capacitance. So the secondary capacitance value should be large in order to make the circuit meet the requirements of large load range.

Conclusions

LLC resonant converter can adjust the output for a wide range of source and load with a small fluctuation of switching frequency, so it is used widely. In this paper we talk about the theory of LLC resonant groups and exhaustively give the arrangements of LLC topological groups, then propose a new topology which is consist of Type-4 and Type-11 that used widely and build its mathematic models. Finally we prove its correctness and get gain characteristics of the topologies in the PSpice simulation environment, prove the adjustment ability of Type-4 and Type-11 mixed bi-direction LLC resonant converter has a good gain characteristic but can be effected by the secondary capacitance.

Acknowledgements

This work was financially supported by the Independent Research and Development project of State Key Laboratory of Alternate Electrical Power System with Renewable Energy Sources North China Electric Power University.

References

[1] Steigerwald.R: Acomparison of half-bridge resonant converter topologies[J],IEEE Transactions on Power Electronics,988,3(2):174-182.

[2] Severns. R: Topologies for three element resonant converters[C], IEEE APEC 1990, Los Angeles, California, USA,1990.

[3] Schmidtner E G: A high frequency resonant converter topology[C], High Frequency Power Conversion 1988,San Diego,California, USA,1988.

[4] Liu R, Batarseh I, Lee C.Q:The LLC-type and the class-E resonant converters[C], High Frequency Power Conversion 1989,Naples,Florida,USA,1989.

[5] Chakraborty C,Ishida M: Performance design and control of aseries-parallel(CL2-type) resonant DC/DC converter[J], IEE Electric Power Applications,2002,149(5):360-368.

Advanced Materials Research Vols. 960-961 (2014) pp 1258-1263

doi:10.4028/www.scientific.net/AMR.960-961.1258

Study of a Small-scale Controllable Reactor and Conceptual Design of a 35kV/5Mvar HTS Reactor

Ying Xu[1,a], Li Ren[1,b*], Yuejin Tang[1], Meng Song[2], Jingdong Li[1], Jing Shi[1], Hongda Dong[1], Kunnan Cao[2]

[1]State Key Laboratory of Advanced Electromagnetic Engineering and Technology, Huazhong University of Science and Technology, Wuhan City, Hubei Province, P.R. China, 430074

[2]Yunnan Electric Power Test & Research Group Co., Ltd. Electric Power Research Institute, Kunming City, Yunnan Province, P.R. China, 6502172

[a]xuyinghust@163.com, [b]renli@mail.hust.edu.cn

Keywords: HTS reactor, conceptual design, harmonics analysis, FEM

Abstract. Since Ultra High Voltage (UHV) transmission lines have the high charging capacitance, continuous reactive power compensation is vital for efficient operation of long transmission power lines or cables. A continuous reactive compensation will reduce the transmission losses and increase the transmission capacity of active power. In order to achieve the continuous reactive power compensation, we choose the magnetic saturable type reactor. The principle of a magnetic saturable reactor requires a high current ampere-turn coil as its dc bias, and this coil is necessary to use a high temperature superconducting (HTS) winding. As the first stage of the study, we have constructed a 220V small-scale prototype which the dc bias is made of copper coil instead of the HTS coil. The copper coil of the dc bias in small-scale reactor has the same ampere-turn with a 220V HTS controllable reactor (HCR), so its performance keeps the same except the HTS part. Based on this, we made a conceptual design for a 35kV/5Mvar HCR. The output property and harmonic property have been studied by simulation and experiment. The results prove that it can obtain a continuous controllable reactive power output.

1. Introduction

With the development of modern industry, the stability of power system and improvement of power quality are becoming more and more important. The control of the reactive power is a crucial subject to hit the mark for a transmission network, especially for excessively-high voltage long-distance transmission lines. To meet such demand, many kinds of devices are developed, such as, synchronous condensers, conventional shunting reactors, static var compensators and controllable reactors. Each of them has their own advantages and disadvantages. There are some types of controllable reactors available: the thyristor controlled reactor [1,2], the transformer type controlled reactor [3] and the magnetic saturable reactor [4-8]. Our research concentrates upon the magnetic saturable reactor. The reactor studied in this paper combined the superconducting technology with the magnetic saturation technology. It can automatically and smoothly adjust its inductance. It can provide a continuous reactive power compensation to suppress system over voltage, reduce the transmission losses and increase the transmission capacity of active power. However it requires a high current ampere-turn coil as its dc bias, and this coil is necessary to use a HTS winding.

In this paper, a series of experiments of a 220V small-scale prototype are conducted to validate the design and simulation results. A conceptual design of 35kV/5Mvar HTS controllable reactor is presented.

2. Structure and Working principle

The simplified structure of HCR is shown in figure 1. Its working principle is like a saturable type superconducting fault current limiter (SFCL). It is made up of two same racetrack shape iron cores and three windings, including one control winding and two working windings. The two working windings are constructed on the left and right limbs separately and connect in subtractive series so that their magnetic flux is offset by each other in the middle iron core limb. A dc bias winding, made of HTS tapes, is arranged on the middle iron core limb as the control winding.

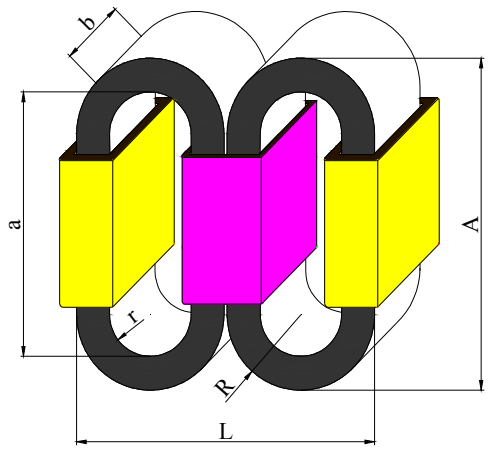

Fig .1 Schematic structure of the HCR

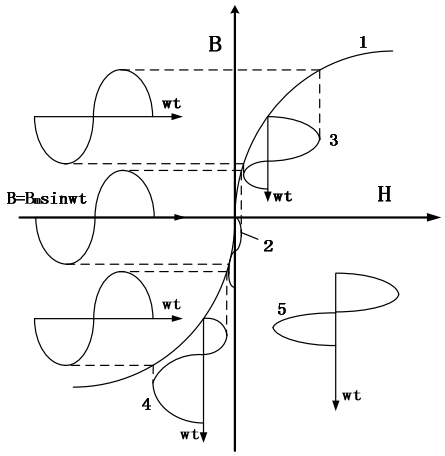

Fig. 2 Principle of the saturation core

As shown in figure 2, the saturation of HCR is changed by the value of the DC component which makes the magnetic flux of the iron core raise or decrease. The working current of HCR is controlled by regulating the DC voltage. Based on this, the capacity of HCR can be smoothly regulated. When the excitation current is 0A, the magnetic field intensity of the HCR is the curve 2. When regulating the DC voltage, the excitation current rise, curve 3 and 4 denote the magnetic field intensity of the HCR's left limb and right limb, respectively. So curve 5 denotes the magnetic field intensity which is the sum of the curve 3 and 4.

3 Simulation Model and Test results of a small-scale single phase HCR

The output current should be accurately simulated in the model, and the fundamental magnetic circuit equation is used to establish the simulation model of HCR. The simulation model is established on the assumption that: (1) the AC and DC voltage source is ideal which means voltage source has no harmonic component; (2) since the racetrack shape iron core has almost no leakage magnetic field, the leakage inductance is negligible.

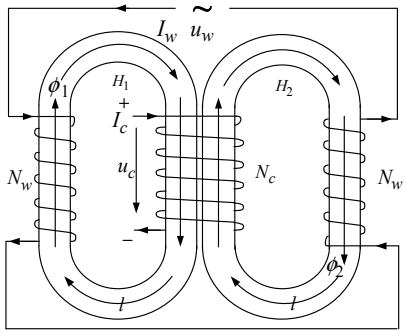

Fig.3 Physical quantities and forward directions in HCR

As shown in figure 3, for a single turn coil, the main magnetic flux Φ_1 and Φ_2 can be determined by

$$\phi_k = B_k \cdot S \quad (k = 1, 2) \tag{1}$$

The DC and AC circuit should meet Kirchhoff's Voltage Law, which has a relation as

$$\begin{cases} u_w = I_w r_w + N_w \, d\phi_1 / dt + N_w \, d\phi_2 / dt \\ u_c = I_c r_c + N_c \, d\phi_1 / dt - N_c \, d\phi_2 / dt \end{cases} \tag{2}$$

Based on Ampere circuital theorem in magnetic circuit, the fundamental magnetic circuit equation can be expressed as below

$$\begin{cases} N_w I_w + N_c I_c = H_1 l \\ N_w I_w - N_c I_c = H_2 l \end{cases} \tag{3}$$

Where N_c is control winding turns and N_w is working winding turns, I_c and I_w are winding current and control current respectively, u_w and u_c are working winding voltage and control winding voltage respectively, Φ_n (n=1,2) is main magnetic flux of winding, r_c and r_w are winding resistance. l is the length of the equivalent magnetic circuit, S is the cross-sectional area of the iron core, B_n (n=1,2) is magnetic flux density, H_n (n=1,2) is magnetic field intensity.

The combination of equations (1)–(2) results in magnetic flux density's equation:

$$\begin{cases} B_1 = \int_0^t 1/2\left(\dfrac{u_w - I_w r_w}{N_w S} + \dfrac{u_c - I_c r_c}{N_c S}\right)dt \\ B_2 = \int_0^t 1/2\left(\dfrac{u_w - I_w r_w}{N_w S} - \dfrac{u_c - I_c r_c}{N_c S}\right)dt \end{cases} \tag{4}$$

From formula (3), we can obtain the HCR's output current i_w,

$$I_w = l/2N_w(H_1 + H_2) \tag{5}$$

Therefore the relationship between magnetic flux density B and magnetic field intensity H can be represented by

$$\begin{cases} H_1 = f(B_1) \\ H_2 = f(B_2) \end{cases} \tag{6}$$

The formula (1)-(6) give the mathematical model of the HCR. The Specifications used in the simulation are shown in Table 1. In the model, if the working voltage U_w and control voltage U_c are given, the output current of the main coil, the magnetic flux density and the magnetic field intensity can be obtained. In this paper, we care about the output current of the main coil.

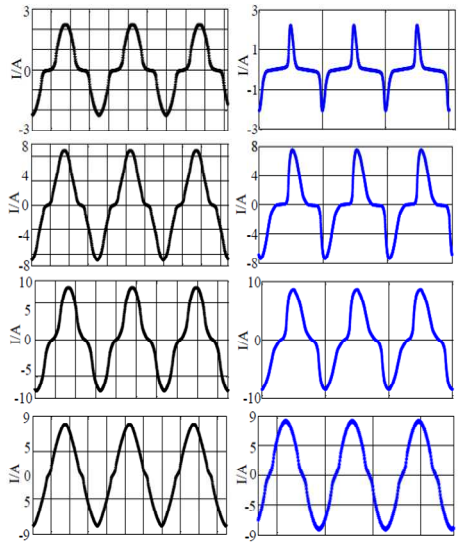

Fig.4 The wave form of I_w, test results (blue solid line) versus simulation results(black solid line), from top to bottom, the excitation currents are 0.5A, 3A, 9A, 18A ,respectively)

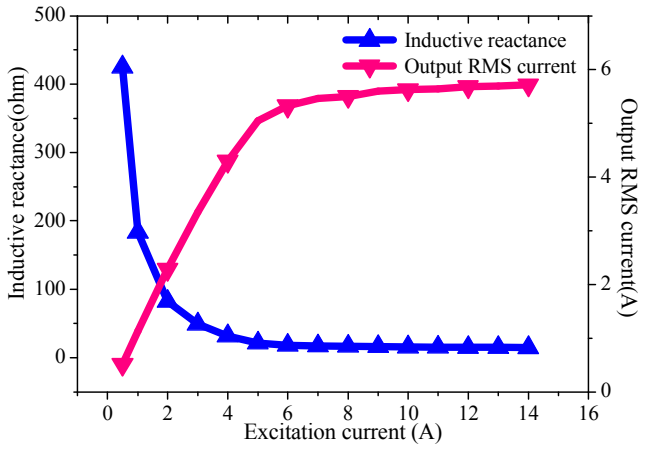

Fig.5 Output inductive reactance and output RMS current as a function of excitation current

Table 1 Specifications of the small-scale prototype used in the simulation

Voltage of working winding u_w	220 [V]
Number of control winding turns N_c	1350
Number of working winding turns N_w	650
resistance of control winding r_c	6 [Ω]
resistance of working winding r_w	0.4 [Ω]
length of the equivalent magnetic circuit l	0.614 [m]
cross-sectional area of the iron core S	0.00378 [m^2]

The working winding is fed by a variable voltage regulator operating at frequency of 50 Hz. The control winding is fed with a direct current source. The DL750 type oscillographic recorder is used to record the working current Iw and voltage uw in the working winding. Figure 4 shows the working current Iw as functions of time when Ic is held constant at 0 A, 3 A, 9 A, and 18A. Figure 5 shows the root mean square (RMS) values of output Iw after filtering harmonic component and the output inductive reactance as a function of control current.

As shown in figure 5, a little current variation will lead to a sharp decline in the inductance of HCR when the excitation current is between 0.5A and 4A. When the excitation current is over 8A, the inductance variation curve becomes flattened, and the core goes gradually into a deep magnetic saturation state.

4 Harmonic analysis of HCR

The induct electric potential in control winding e_c and working winding e_w can be obtained by the equation

$$\begin{cases} \mathrm{e}_w = \mathrm{e}_{w1} + \mathrm{e}_{w2} = SN_w(dB_1/dt + dB_2/dt) \\ \mathrm{e}_c = \mathrm{e}_{c1} - \mathrm{e}_{c2} = SN_c(dB_1/dt - dB_2/dt) \end{cases} \tag{7}$$

Since the two racetrack shape iron cores are axis symmetric and the magnetization curve of iron core is odd symmetric, the magnetic flux density in iron core 1 and 2 has a relation as

$$\begin{cases} B_1(\omega t) = -B_2(\omega t + \pi) \\ B_2(\omega t) = -B_1(\omega t + \pi) \end{cases} \tag{8}$$

In general, the magnetic flux density in iron core is not sinusoidal. Based on Fourier analysis, the magnetic flux density in iron core 1 and 2 can be formulated as

$$B_1(\omega t) = B_\mathrm{d} + B_{1m}\sin(\omega t - \phi_1) + B_{2m}\sin(2\omega t - \phi_2) + \ldots + B_{km}\sin(k\omega t - \phi_k) \quad (k = 1, 2\ldots) \tag{9}$$

$$B_2(\omega t) = -B_\mathrm{d} + B_{1m}\sin(\omega t - \phi_1) - B_{2m}\sin(2\omega t - \phi_2) + \ldots + (-1)^{n+1}B_{km}\sin(k\omega t - \phi_k) \quad (k = 1, 2\ldots) \tag{10}$$

The combination of equations (7) and (9) results in induct electric potential in control winding and working winding

$$e_c = 2B_d + \omega N_c S[4B_{2m}\cos(2\omega t - \phi_2) + \ldots + 4kB_{2km}\cos(2k\omega t - \phi_{2k}) \quad (k = 1, 2\ldots) \tag{11}$$

$$e_w = 2\omega N_w S[B_m\cos(\omega t - \phi_1) + \ldots + (2k+1)B_{2km}\cos[(2k+1)\omega t - \phi_{2k+1}] \quad (k = 1, 2\ldots) \tag{12}$$

Through above analysis, the voltage and current in control winding only have even-order harmonic component, while the output voltage and current in working wording only have odd harmonic component theoretically. In order to verify the validity of the theoretical analysis, we have carried through harmonic analysis of the actual output I_w and the voltage of the main coil.

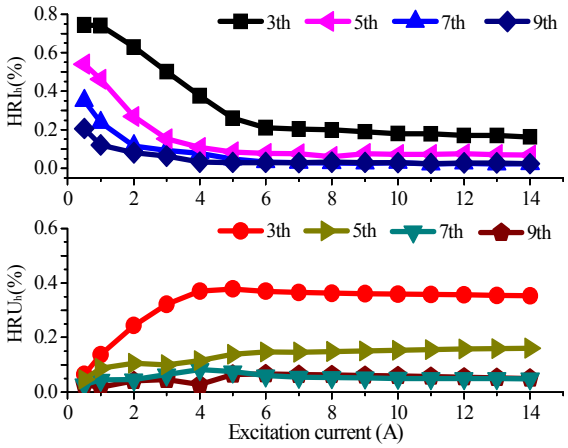

Fig.6 The odd order harmonic ratio of current HRIh and voltage HRUh as a function of excitation current

Figure 6 illustrates that the odd harmonic component of the output current and voltage of the main coil are remarkable, which is a prominent disadvantage of saturable type reactor. So some improvements are needed to decrease the harmonic component. To a three Phase HCR, the 3th

harmonic component is easy to be dispelled by circuit connection, and higher harmonic component can be decreased with a filter. Another way to decrease the harmonic component is to improve the design of the iron, for instance, inserting virtual air gap to the core [9], using the multi-Stage iron et al [10].

5 Design of a 35kV/5Mvar HTS controllable reactor

In this section, the design procedure of the HCR is presented. This procedure consists of determination of core dimensions, determination of winding quantities and dimensions.

The rated voltage U_n and rated output capacity of the single-phase HCR are $35/\sqrt{3}$ kV and 5 Mvar, respectively. The specification of HCR is shown in Table 2.

Table 2 Specification of HCR

Q_n (Mvar)	U_n (kV)	I_n (A)	η(%)	L (H)	X (Ω)
5	$35/\sqrt{3}$	247	50% ~ 100%	0.52~0.26	163.2~81.6

η is the regulating range of the output reactive power; L and X are the variation range of the output inductance and reactance, respectively. According to the design requirement, the core material selects cold-reduced silicon sheet in the thickness of 0.35 mm. The AC main coils use conventional metal copper conductors. The DC control coils use YBCO HTS tapes, which are cooled by liquid nitrogen. The wire type is Amperium 12 made by AMSC. Its critical current at 77 K is 175 A. The thickness and width are 0.2 mm and 12 mm, respectively.

The design procedure of HTS's main parameters is as follow: the core diameter of left/right main coil can be obtained by $D = K_D \sqrt[4]{Q_n} / 2$ .The lamination factor K_D is 0.95. Before calculating the quantities of the main coil W, the magnetic flux density B'_m of the main coil is selected as 1.5T. Then, W can be determined as $W = U / (\sqrt{2}\pi f B'_m A_z)$, where f is frequency of AC current; A_Z is effective cross-sectional area of the core. Details of the core structure are given in Table 3. The parameters of the coil are listed in Table 4.

Table 3 Details of HCR structure

a (mm)	b (mm)	r (mm)	R (mm)	A (mm)	L (mm)
1560	410	260	470	1980	1890

Table 4 Parameters of HCR coils

Quantity	DC coil	AC coil 1	AC coil 2
Inner size (mm×mm)	445×425	225×425	225×425
Outer size (mm×mm)	455×435	297×497	297×497
Height (mm)	600	910	910
Number of turns	1000	244	244

Based on the design specification of the HCR, the inductance variation is numerically solved by Finite Element Method (FEM) analysis. The inductance of the main coil is calculated corresponding to increasing steps of current from 1A to 55A.

From figure 7, it can be seen that a little current variation will lead to a sharp decline in the inductance of HRC when the excitation current is between 1 A and 5 A. When the excitation current is over 6 A, the inductance variation curve becomes flattened, and the core goes gradually into a deep magnetic saturation state. When the excitation current are 7A and 14 A, the corresponding inductance are 0.52 H and 0.26 H, respectively. The magnetic flux density distribution of the core is shown in figure 8.

In the current range of 7 A~14 A, the core center column goes gradually into the magnetic saturation state, and magnetic flux density in the core side yokes also increased gradually. When excitation current is 7 A, the maximum and minimum magnetic flux density are 1.73 T and 1.51 T, respectively. When excitation current is 14 A, the maximum and minimum magnetic flux density are 1.82 T and 1.56 T, respectively. The gap between the maximum and minimum values is not large.

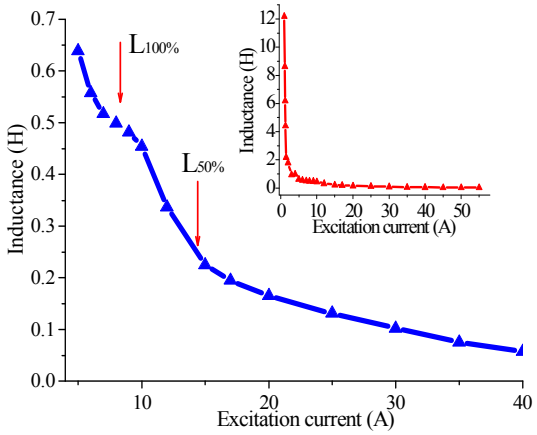

Fig.7. HCR reactor inductance versus DC excitation current

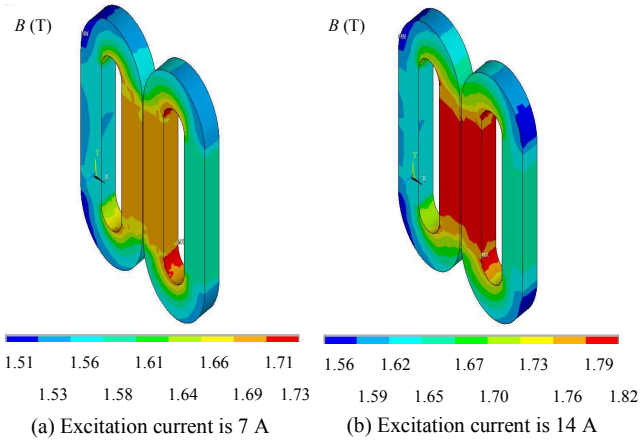

(a) Excitation current is 7 A (b) Excitation current is 14 A

Fig.8. Magnetic flux density distribution of the RC core

6 Summary

A detailed procedure of establishing the small-scale HCR's mathematical model is proposed. Test and simulation results of the small-scale HCR indicate that the reactor can smoothly regulate the output inductive reactance and the range of regulation is large. Beyond that the harmonic component of the HCR needs to be controlled. Then a basic conceptual design of a 35kV/5Mvar has been presented. Based on the design, FEM simulation has been carried out to verify the validity of the design.

7 References

[1] S. Torseng, Shunt-connected reactors and capacitors controlled by thyrisors, Inst. Elect. Eng. Proc., vol. 128, no. 6, pp. 366, Nov. 1981.

[2] M. Yu, B. Chen, Z. Cao, C. Tian, and H. Qiu, A novel 110 kV shunt controllable reactor and its application, Automation of electric power system, vol. 32, pp. 87, Feb. 2008.

[3] M. Tian, Q. Li, Q. Li, A Controllable Reactor of Transformer Type, IEEE transactions on power delivery, vol. 19, pp. 1718, Oct. 2004.

[4] M. Tian, and Q. Li, An equivalent circuit and simulation analysis of magnetically-saturated controllable reactors, Transactions of China electrotechnical society, vol. 18, pp. 64, June 2003.

[5] Z.Q. Wang, Z.D. Yin, L.X. Zhou, Z.J. Wang and L.R. Ma, Study on Controllable Reactor Magnetic Structure and Loss Based on ANSYS, Industrial Electronics and Applications, pp.201, May 2009.

[6] G. Feng, F. Wang, J. Wang, Design Principles of Magnetically Controlled Reactor, Electrical Machines and Systems, vol.1, pp. 212, 2001.

[7] G. Feng, F. Wang, B. Zhang, Modeling and Characteristics of A Novel Magnet Saturation Controllable Reactor, Power Electronics and Drive Systems, vol.1, pp. 313, Nov. 2003.

[8] T. Wass, S. Hörnfeldt and S. Valdemarsson, Magnetic Circuit for a controllable reactor, IEEE Transactions on Magnetics, vol. 42, pp.2196, Sept. 2006.

[9] Dale S.L. Dolan, P.W. Lehn, Analysis of a Virtual Air Gap Variable Reactor, Power Electronics Specialists Conference, pp. 1182, June 2007.

[10] X. Chen, C. Tian, B. Chen, Y. Liu, J. Yuan, Mathematical Model for Harmonics Analysis of the Multi-Stage Saturable Magnetic-Valve Controllable Reactor, Transactions of China electrotechnical society, vol. 26, pp. 57, Mar. 2011.

Advanced Materials Research Vols. 960-961 (2014) pp 1264-1267

doi:10.4028/www.scientific.net/AMR.960-961.1264

A flyback switching power supply based on L6561for LED

Zhu Lei Shao[1, a]

[1] College of Electrical and Information Engineering, Xuchang University, Xuchang 461000, China

[a]cyzyszl2@163.com

Keywords: Single-ended flyback; switching power supply; LED driver.

Abstract. A flyback switching power supply was designed, which can drive LED stability. The switching power supply is the single-ended flyback structure, and based on PWM driver chip L6561. The input voltage range of the switching power supply is 85V to 265V. The output voltage is 15V and the maximum output current is 2A. The switch power supply is suitable for mobile phone, office equipment and LED. According to experiment, the switching power supply can steadily drive 5 LED, the ripple factor of output is 1.33%, the power efficiency is 85.7%.

Introduction

With the development of technology, the switching power supply is playing a more and more important role in the electronic equipments. The switching power supply is often used in special equipments, which provides necessary voltage and current for the normal operation of the circuit. The more complicated the equipment is, the less weight the switching power supply is required. Because the operation of some equipments require stable direct current, the switching power supply must own the ability of transforming current. At the same time, the Switching power supply should own high efficiency for saving energy. Based on the current-mode PWM controller L6561, a new type of single-ended flyback switching power supply is designed.

Working principle of circuit

The switching power supply is the core device of the power electronic equipment, which can output stable voltage and current by feedback control. The switching power supply has some common topologies, such as, forward, flyback, push-pull, half-bridge and full-bridge. The design of switching power supply for LED adopt flyback, it is shown in Fig. 1.

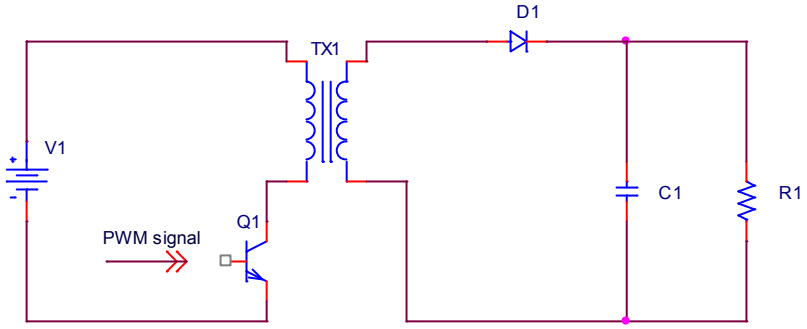

Fig. 1 The schematic of flyback switching power supply

The flyback switching power supply has the characteristics of reverse polarity converter. It has the advantage of fast response and simple structure of compensation circuit. The flyback switching power supply is made up with the power switch Q1， the high-frequency transformer TX1, the rectifier tube D1, the filtering electric C1, the feedback control circuit and PWM drive.

When the power switch Q1 turns on, the primary side of the transformer TX1 begins to store energy, the current of primary side increases gradually, the rectifier tube D1 cut off, the capacitor C1 provides current to the load R1. When the power switch Q1 turns off, the rectifier tube D1 is on, the energy of transformer TX1 charges the capacitor C1, and provides current to the load R1. The formula of output voltage is shown in formula (1).

$$V_o = \frac{N_2}{N_1}\frac{DV1}{1-D} \tag{1}$$

In formula (1), V_o is the output voltage, N_1 is the winding number of primary side, N_2 is the winding number of secondary side, D is duty ratio of PWM signal.

Design of switching power supply

The flyback switching power supply system is composed of the rectifier filter circuit, L6561 drive circuit, the voltage feedback circuit and the current feedback circuit. The function of the system is converting alternating current to steady direct current, and drives the load. L6561 will change the open time of power switch by sampling the output voltage and the current of the primary side of the transformer. L6561 is the core of feedback control circuit, which makes output voltage steady in 15V. The advantages of the design circuit are fast reaction speed, simple control circuit and steady output. The circuit topology of flyback switching power supply is shown in Fig. 2.

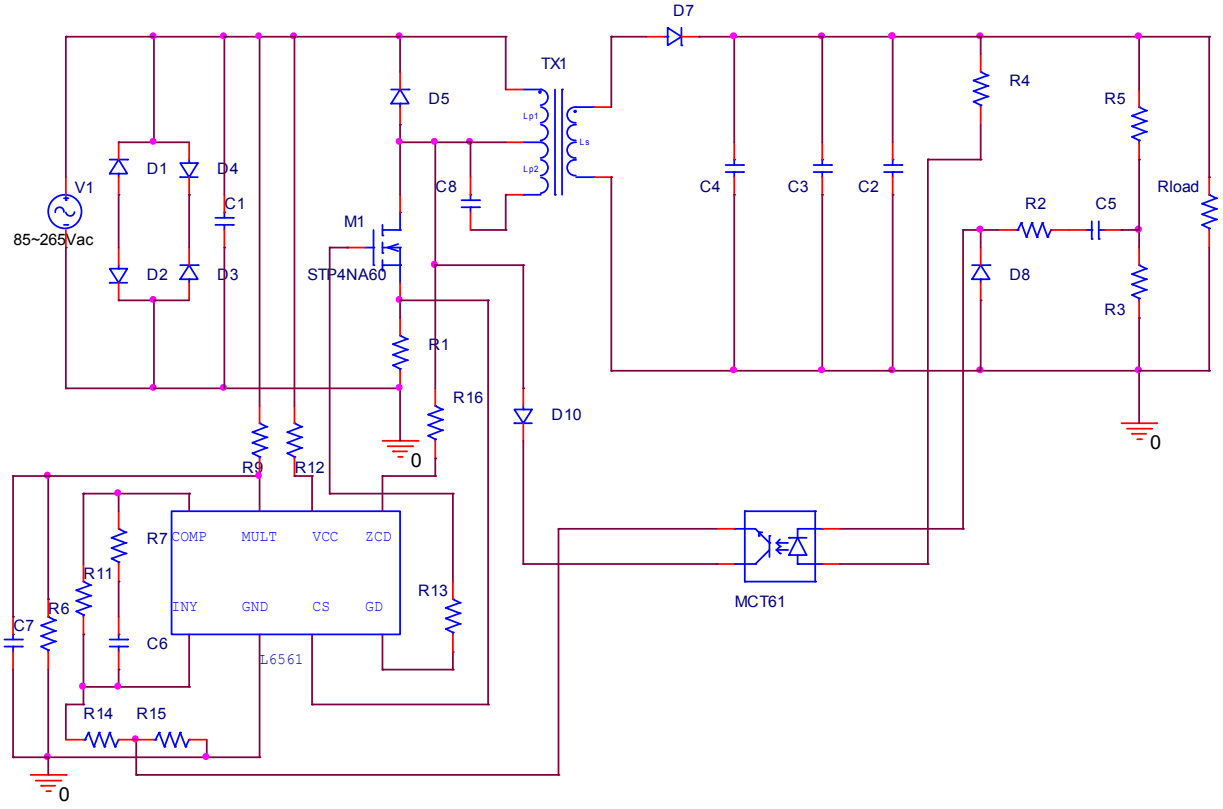

Fig. 2 The circuit topology of flyback switching power supply

TX1 is the transformer of flyback switching power supply, which can store electric energy and separate electric grid. While the output voltage is minimum, the output frequency is the largest. According to faraday law of electromagnetic induction, the formula (2) can be get.

$$\frac{V_{in(\min)} D_{\max}}{L} = \frac{V_{or}(1 - D_{\max})}{L} \tag{2}$$

In the formula (2), V_{or} is refraction voltage of secondary to elementary, L is elementary inductor, $D_{\max}$ is the maximum duty ratio of PWM signal, it can be get in formula (3).

$$D_{\max} = \frac{V_{or}}{V_{or} + V_{in(\min)}} \tag{3}$$

The current of the primary side of the transformer can be get in formula (4).

$$I_p = \frac{2p_{0(\max)}}{V_{in(\min)}\eta D_{\max}} \tag{4}$$

The inductance of primary side of the transformer can be get in formula (5).

$$L_p = \frac{V_{in(\min)}^{\ 2} D_{\max}^{\ 2}}{2P_{in(\max)}} = \frac{V_{in(\min)}^{\ 2} D_{\max}^{\ 2} \eta}{2P_{o(\max)}} \tag{5}$$

The winding number of primary side of the transformer can be get in formula (6).

$$N_p = \frac{LI_p}{B_{\max} A_c} = \frac{V_{in(\min)} D_{\max}}{F B_{\max} A_c} \tag{6}$$

By calculating, the transformer parameters can be get. The winding number of primary side of the transformer N_P=41, The inductance of primary side of the transformer L_p=510uH, The winding number of secondary side of the transformer N_s=8, The winding number of auxiliary N_f=8.

Analysis of experimental results

In order to verify the performance of the switching power supply, the flyback switching power supply is established in PSPICE. The circuit parameter settings are as follows. The input voltage range is 85v to 265V. The output voltage is 15V. The maximum output current is 2A. The ripple factor of output is 5%. The power switch adopts MOSFET STP4NA60. The drain source voltage waveform of MOSFET is shown in Fig. 3. The output voltage waveform of switch power supply is shown in Fig. 4.

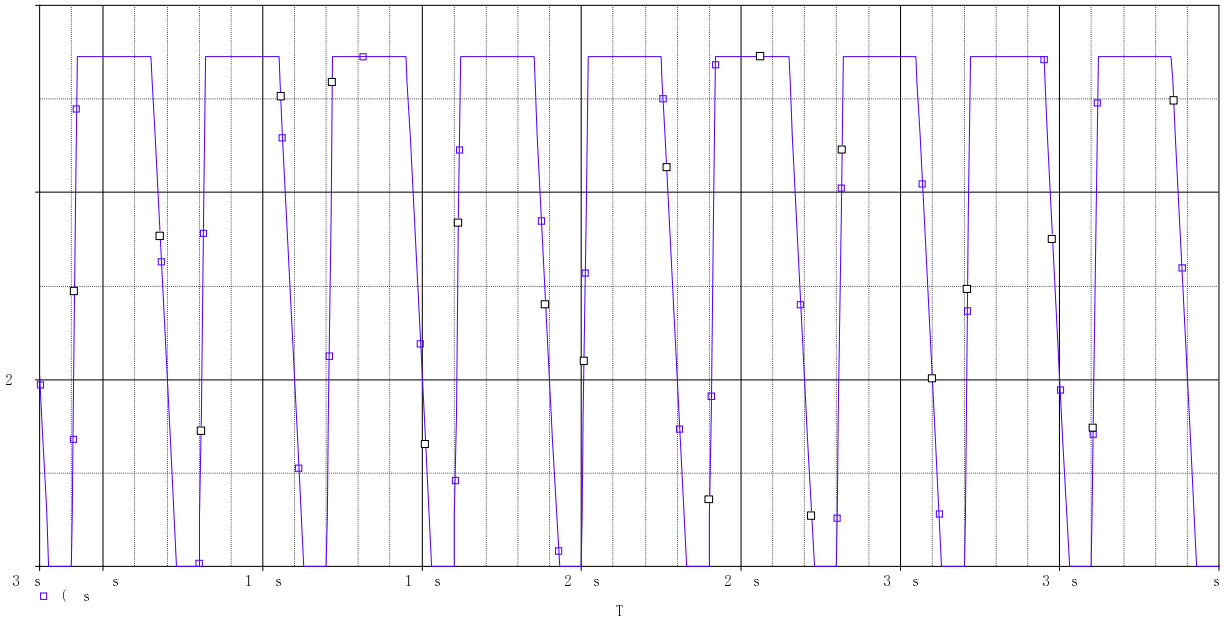

Fig. 3 The drain source voltage waveform of MOSFET

As shown in Fig. 3, the maximum drain source voltage of MOSFET V_{ds} is 545V, which includes the maximum input peak voltage V_P, the transformer primary side to the secondary side refraction voltage V_T, and The primary side of the transformer leakage inductance voltage V_L. V_P is 375V. V_T is 100V. V_L is 70V. $V_{ds} = V_P + V_T + V_L$ =545V. The working frequency of MOSFET is 25 kHz.

As shown in Fig. 4, the output voltage of flyback switching power supply is 15V. When the output voltage is stable, the ripple wave of output voltage is 0.2V, so the Ripple factor of output voltage is 1.33%, which meets the design requirements of the Ripple factor less than 5%. The output voltage can be long-term stable in 15V, so the flyback switching power supply is suitable for driving LED.

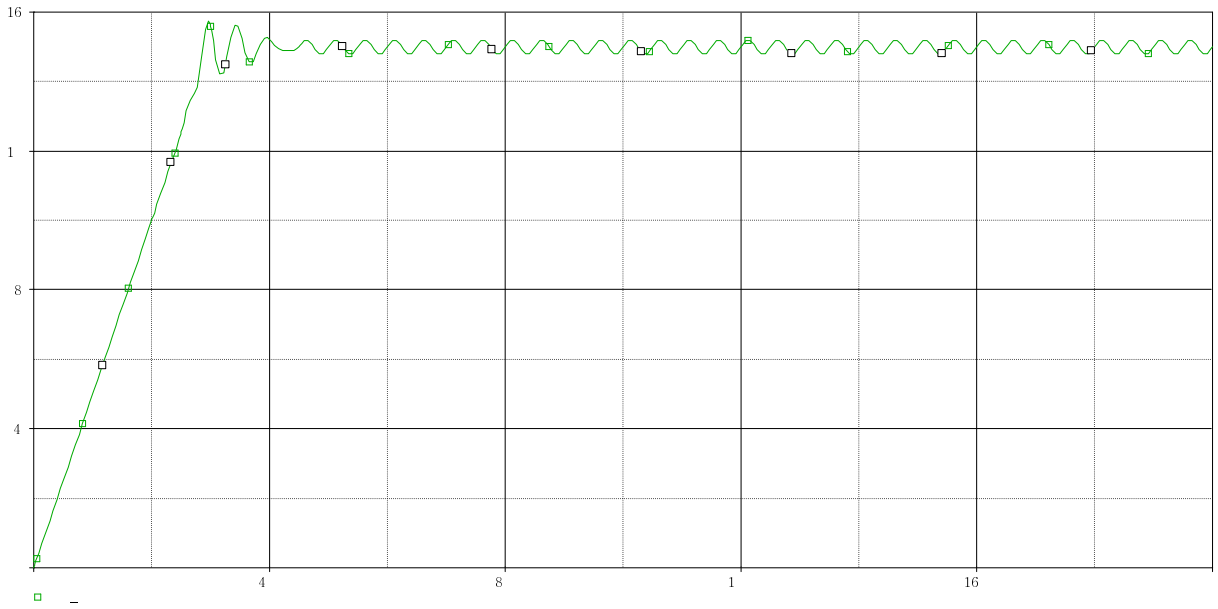

Fig. 4 The output voltage waveform of switch power supply

Conclusions

A new type flyback switching power supply based on L6561 is designed. According to experiment, The output voltage can long-term stable in 15V, while the input voltage is 85~265V. The Ripple factor of output voltage is 1.33%, which meets the design requirements of the Ripple factor less than 5%. The largest output current can be 2A. The flyback switching power supply meets the design requirements, which can stable drive LED.

References

[1] FAN Qiang, FU Xiansong, LIU Yili. A Novel high efficiency solution of high power LED lighting [C]. 2011 International Conference on Intelligent Control and Information Technology ，2011, 14(7): 213-216.

[2] Sanghoon , HaeK Y, Youl K S. Circuit-model based analysis of a wireless energy transfer system via coupled magnetic resonances [J]. IEEE Transactions on Industrial Electronics, 2011, 58(7) : 2906-2914.

[3] JX Xu, W B Croft. Improving the effectiveness of information retrieval with local context analysis [J]. ACM Transactions on Information Systems, 2000, 18(1): 79-112.

[4] Sheng Ye, Wilson Eberle. A novel EMI filter design method for switching power supplies [J]. IEEE Transactions on Power Electronics, 2004, 19(6): 1668-1677.

[5] Liu Yan-tao, Liu Yu-bei, Yin Wei. Introduction of Design Methods of LC Filter and Simulation of Responding Characteristics [J]. Electronic Measurement Technology, 2010, 5(5): 17-21.

Advanced Materials Research Vols. 960-961 (2014) pp 1268-1271

doi:10.4028/www.scientific.net/AMR.960-961.1268

Design of CMOS Sawtooth Wave Oscillator for Switching Power Supply

Zhu Lei Shao[1, a]

[1] College of Electrical and Information Engineering, Xuchang University, Xuchang 461000, China

[a]cyzyszl@163.com

Keywords: Oscillator; Switching Power Supply; Sawtooth Wave

Abstract. Based on the CMOS technology, the sawtooth wave oscillator used in switching power supply is designed. In the condition of 27 ˚C and 4 V power supply voltage, the oscillation frequency of sawtooth wave oscillator is 246.61 KHz. The oscillation frequency of sawtooth wave oscillator changes between 245.94 KHz and 247.89 KHz when the power supply voltage changes between 3V and 6V. The maximum deviation is ±0.52%. From the experimental results, the sawtooth wave oscillator has good linearity, the effect of temperature and power supply to the oscillation frequency of sawtooth wave oscillator is very little. The CMOS sawtooth wave oscillator is suitable for switching power supply.

Introduction

The switching power supply has the advantages of small volume and high efficiency, which is widely used in electronics, telecommunications and aerospace fields. At present, the switching power supply adopts the technology of pulse width modulation control, while the sawtooth wave oscillator is the core module of pulse width modulation circuit. The performance of Sawtooth wave oscillator directly affects the performance of switching power supply. So the sawtooth oscillator must be stable output in the environment of voltage and temperature changes. A sawtooth wave oscillator for switch power supply is designed, which adopts the structure of RC oscillator.

Working principle of sawtooth wave oscillator

The schematic diagram of the sawtooth wave oscillator is shown in Fig. 1. The circuit consists of current source I_1, capacitance C_1, switch K and control circuit. The switch K turns off when the output voltage is low level. The current source I_1 charges the capacitor C_1, and voltage V_s rise. The control circuit makes the output voltage V_m is high level when the voltage exceeds the threshold. The high level voltage V_m makes the switch K turn off, the capacitor C_1 discharge by switch K, and the voltage V_s is changed into low level. The circuit circle works that produces sawtooth wave V_s.

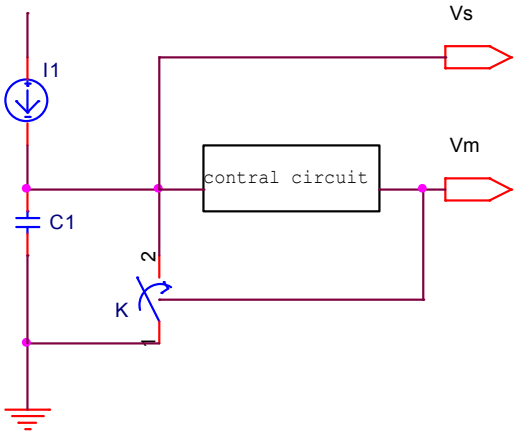

Fig. 1 The structure of sawtooth wave oscillator

Design of sawtooth wave oscillator

The circuit topology of sawtooth wave oscillator is shown in Fig. 2. The reference signal V_{ref} is 1.25V. Sawtooth wave output signal is V_S. The current source consists of the error amplifier A_1, the CMOS transistor M_1, M_2, M_5 and the resistor R_1. The negative feedback system is composed by the error amplifier A_1, the CMOS transistor M1 and the resistor R_1.

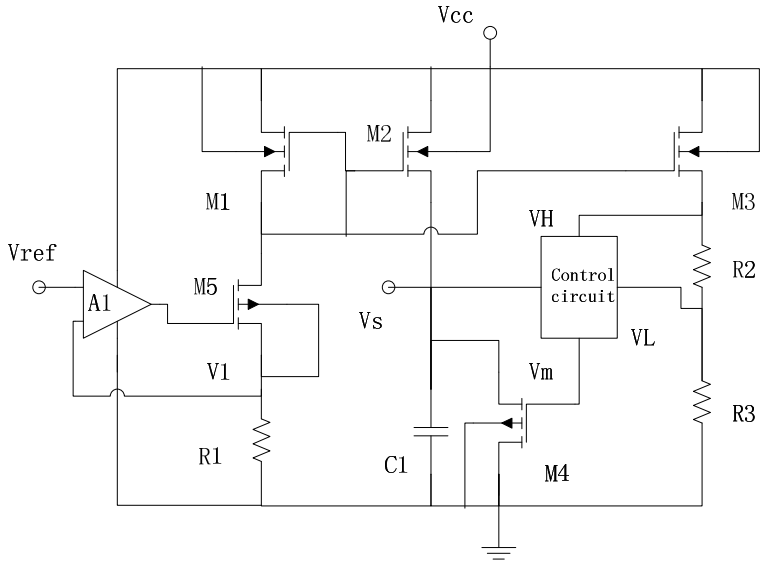

Fig. 2 The circuit of sawtooth wave oscillator

The error amplifier A_1 makes V_{ref} equal to V_1, the current I_{R1} of R_1 can be got in the formula (1).

$$I_{R1} = \frac{V_{ref}}{R_1} \tag{1}$$

The CMOS transistor M_1 and M_2 construct current mirror, the charging current I_1 can be got in the formula (2)

$$I_1 = \frac{(W/L)_3}{(W/L)_2} I_{R1} \tag{2}$$

In the formula (2), $(W/L)_2$ is length-width ratio of the CMOS transistor M_2, $(W/L)_3$ is length-width ratio of the CMOS transistor M_3.

The CMOS transistor M_4 and M_2 construct another current mirror, The leakage current I_{M4} of M_4 can be got in the formula (3)

$$I_{M4} = \frac{(W/L)_4}{(W/L)_2} I_{R1} \tag{3}$$

The current I_{M4} creates the threshold voltage V_H and V_L by R_2 and R_3, the threshold voltage V_H and V_L can be got in the formula (4) and the formula (5).

$$V_H = I_{M4}(R_2 + R_3) \tag{4}$$

$$V_L = I_{M4} R_3$$

Analysis of experimental results

In order to verify the performance of the sawtooth wave oscillator, the sawtooth wave oscillator was built in Pspice. The power supply voltage is 4V. The charge and discharge capacitance C_1 is 50pF. The environmental temperature is 27 ˚C. The sawtooth wave signal V_s and the charge and discharge

control signal V_m are shown in the Fig. 3. As can be seen from the waveform, the frequency of sawtooth wave signal is 246.61KHz. When the control signal V_m is low level, the CMOS transistor M_4 turn off, the current source charge the capacitor C_1 , and the voltage V_s liear rise. When the control signal V_m is high level, the CMOS transistor M_4 turn on, the capacitor C_1 discharge, and the voltage V_s drop rapidly.

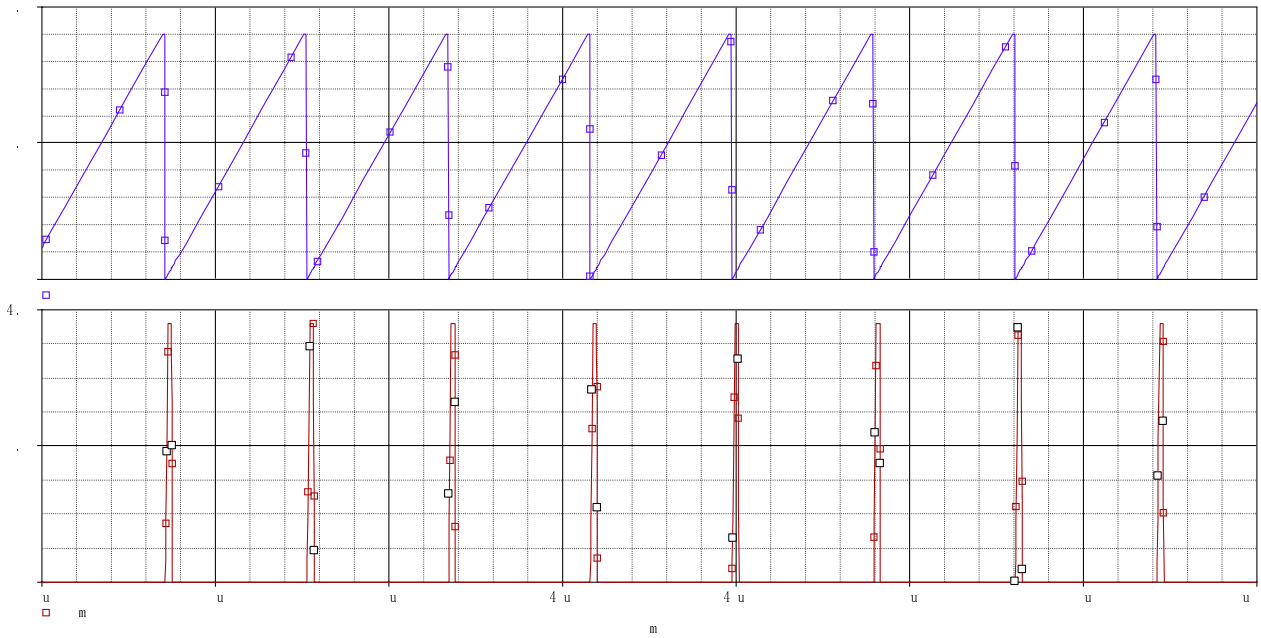

Fig. 3 The sawtooth wave signal Waveform and the charge and discharge control signal Waveform

It is shown in table 1 and table 2 that the changes of sawtooth wave frequency in different temperature and power supply voltage. The sawtooth wave frequency increase gradually when the power supply changes from 3V to 6V. The sawtooth wave frequency also increase gradually when the temperature changes from 0˚C to 70˚C.

Table 1 The relationship of sawtooth wave frequency and power supply voltage

Power supply voltage/V	Period/us	Frequency/KHz
3	4.006	245.94
3.5	4.057	246.49
4	4.055	246.61
4.5	4.051	246.85
5	4.049	246.97
5.5	4.046	247.16
6	4.034	247.89

Table 2 The relationship of sawtooth wave frequency and temperture

Temperature/˚C	Period/us	Frequency/KHz
0	4.096	244.14
10	4.072	245.58
20	4.084	246.06
27	4.055	246.61
30	4.053	246.73
40	4.051	246.91
50	4.045	247.22
60	4.043	247.34
70	4.042	247.40

Although the sawtooth wave frequency changed, the change is very small. The sawtooth wave oscillator owns high precision. The changes of temperature and power supply voltage have very little influence on the output of the sawtooth wave oscillator, which meets the requirements of the switching power supply.

Summary

A sawtooth wave oscillator for switching power supply is designed. The constant current source technology is adopted in the circuit, which effectively improves the linearity of the sawtooth wave oscillator. From the experimental results, the output of sawtooth wave oscillator is least affected by the changes of temperature and power supply voltage. The performance of the sawtooth wave oscillator meets the requirements of the switching power supply.

References

[1] TAO Chengwu, FAYED Ayman A. Spurious-Noise Buck Regulator for Direct Powering of Analog / RF Loads Using PWM Control with Random Frequency Hopping and Ran-dom Phase Chopping [C]. IEEE, International Solid-State Circuits Conference, San Francisc, CA, USA:IEEE Press, 2011: 396-397.

[2] DEMIR A, MEHROTRA Amit. Phase Noise in Oscillators: A Unifying Theory and Numerical Methods for Characterization [J]. IEEE Trans-actions on Circuits and Systems-I: Fundamental Theoryand Applications. 2000, 47(5) : 655-674.

[3] DAVID Suo, SUO Zhouchao, CHIUNG A K. A Buck Con-verter with Sawtooth Voltage Feed Forward Control [C]. IEEE. International Solid- State and Integrated Circuit Technology. Shanghai, China: IEEE Press, 2010: 147-149.

[4] YAN Gangfeng, HUANG Xianhe. Research on Phase noise of Oscillators: A Survey [J]. Journal of Astronautic Metrology and Measurement, 2009, 29(4) : 74-78.

[5] TAN Min, ZHOU Qianneng. A End-Point Prediction Scheme with Constant Amplitude Ramp Signal Suitable for High Voltage Applications [C]. IEEE. International Conference of Electron Devices and Solid-State Circuits, HongKong, China: IEEE Press, 2010: 1-4.

[6] HAJIMIRI A, LEE T. A general theory of phase noise in electrical oscillators [J]. IEEE Solid State Circuits, 1998, 33 (2) : 179-194.

Advanced Materials Research Vols. 960-961 (2014) pp 1272-1276

doi:10.4028/www.scientific.net/AMR.960-961.1272

Micro-grid Inverter AC Side Load Voltage Stability Control Based on SVPWM

Weilin Zhang[1,a], Pengfei Shi[1,b], Yujiong Gu [1,c] and Ping Zhu[1,d]

[1]School of Energy Power and Mechanical Engineering, North China Electric Power University, Beijing 102206, China

[a]1015510254@qq.com, [b]shipengfei@163.com, [c]guyujiong@263.net, [d]zp@ncepu.edu.cn

Keywords: SVPWM, Inverter, Dual loop control, Voltage Stability.

Abstract: Space vector pulse width modulation (SVPWM) technology can significantly reduce the harmonic content of the inverter output voltage and increase voltage stability compared to other modulation techniques. This paper apply the SVPWM technology in the micro-grid inverter side load voltage stability control, on the basis of dual loop vector inverter control and the basic principles and algorithms of SVPWM. The MATLAB/Simulink simulation show that the response based on SVPWM inverter system changes very rapid load ,the AC side load voltage and frequency control is also very stable.

Introduction

Micro-grid is an independent power supply system composed of a set of distributed generation device, in Fig. 1, in the microgrid the energy storage device is battery, and in the system battery as energy storage devices, the inverter has connected the DC side power supply to the AC side, the AC side load voltage quality depends on the DC side voltage and inverter capacity, when the DC side voltage is stable, the inverter control algorithm determines the quality of the AC voltage. There were two typical ways to inverter control algorithm: the traditional method of sine pulse width modulation (SPWM) and the space voltage vector pulse width modulation (SVPWM), the existing literature[1] is pointed out that the SVPWM can significantly reduce the harmonic components of inverter output voltage, and the control methord is simple and digital realization is easy , it has greatly trend to take place of the traditional SPWM. Literature[2]-[4] describes the control of wind power grid-connected inverter. This paper apply the SVPWM technology in the micro- grid inverter side load voltage stability control, on the basis of dual loop vector inverter control and the basic principles and algorithms of SVPWM,in order to research the ability of SVPWM technology to control the AC voltage.

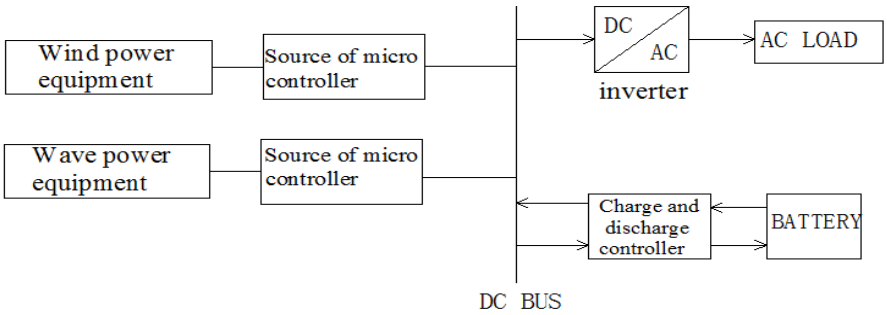

Fig. 1 OES(Ocean Energy Source) integrated power supply system structure

Inverter double closed-loop vector control strategy

Fig. 2 is three-phase voltage type inverter main circuit structure, according to the circuit principle，three phase inverter circuit model is analyzed.Through the CLARK transform and PARK transform,we can get the direct-axis component and quadrature-axis component of AC-side voltage and current, through decoupling control to the direct-axis and quadrature-axis of the AC component, and then through the PARK, deliver inverse transformation of the two phase voltage parameters of static coordinates to SVPWM controller. Voltage and current double closed loop control based on vector coordinate transformation model [3] has shown in Fig. 3:

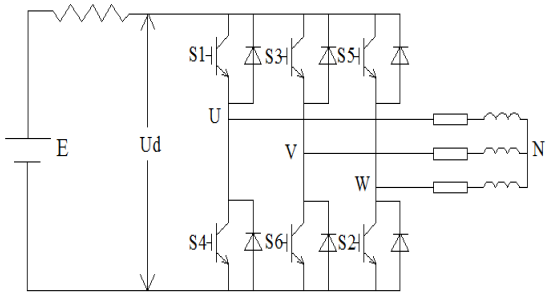

Fig. 2 3-phase voltage type inverter structure

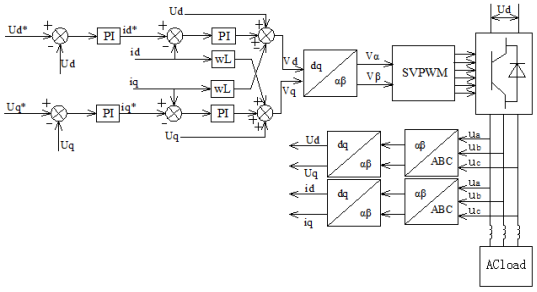

Fig. 3 Dual loop control mode

Set a three-phase sine wave electricity ideal reference voltage as follow:

$$\begin{cases} U_a = 220\sqrt{2}\cos(\omega t) \\ U_b = 220\sqrt{2}\cos(\omega t - 2\pi/3) \\ U_a = 220\sqrt{2}\cos(\omega t + 2\pi/3) \\ \omega = 2\pi f = 100\pi \end{cases} \quad (1)$$

Make CLARK transformation and PARK transformation to the Ua, Ub, Uc:

$$\begin{cases} U_{d^*} = 220\sqrt{2} \\ U_{q^*} = 0 \end{cases} \quad (2)$$

Compare the dq- axis component of the voltage reference Ud^*, Uq^* to the actual dq-axis voltage component Ud, Uq ,the result work as the reference voltage id^* iq^*, id^* iq^* is adjusted through the PI regulator,compare with the actual dq -axis voltage component, obtained vd, vq, vd, vq and then through the PARK inverse transform get v_α, v_β, finally sent v_α, v_β into SVPWM , get six switching signals of PWM wave.

The Principle of SVPWM

SVPWM is a circular magnetic field which start from the perspective of three phase AC motor, induction motor input continuous three-phase sine voltage to obtain the constant amplitude. In the case of voltage source inverter supply power, with balanced three-phase sine voltage produced by the circular magnetic field as a benchmark, PWM waveforms produce by the choice of the inverter switch state, makes the actual flux trajectory approximate to circle flux trajectory. Space vector modulation is based on the combined action of a finite space vector generation process to determine the location of the space to meet anywhere and a certain amplitude range required vector. In the PWM cycle formation the needed space vector by changes the distribution of each phase conduction time. General civil load is balanced load and three-phase needs to power supply in the same time, and voltage is sinusoidal, In order to obtain a symmetrical three-phase voltage parameters ,we can be modeled AC motor control methord to control the switching state of battery back-end inverter.

Three-phase Phase-Locked Loop of Inverter

The amplitude of three-phase voltage output can be directly calculated, but the phase and frequency of the output waveform and the phase angle of PARK transformation, need to be determined by phase-locked loop, phase-locked loop model [5] has shown in Fig. 4.

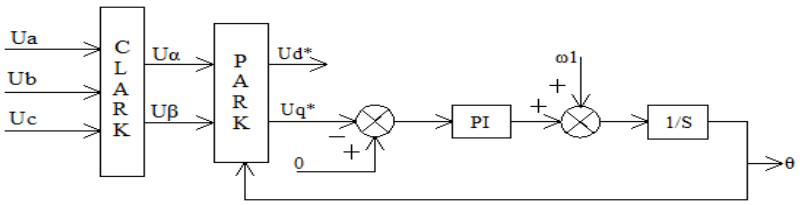

Fig. 4 Three-phase phase-locked loop control flow chart

Three-phase phase-locked loop using the synchronous rotating coordinate system to detect angular frequency and phase information, and then compare to the synchronous signal in the phase-locked loop, the frequency and phase of internal signal phase locked loop can be adjusted to the comparison results, when the angular frequency ω^* of the phase-locked loop output is equal to actual angular frequency ω, and their phase is same, the phase-locked loop being locked, $U_q = 0$.

Inverter control algorithm simulation and analysis

According to the inverter double closed-loop vector control strategy and SVPWM algorithm, each simulation module of the design of inverter control program has shown in Fig. 5.

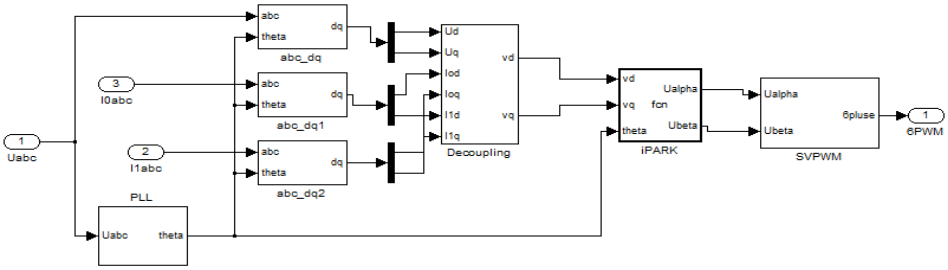

Fig.5 Double closed-loop decoupling and SVPWM control module

The input signal inculde the load voltage,current vector and AC-side current vector, the load voltage get the system voltage angular frequency through three-phase phase-locked loop module, to transform the voltage angular frequency by three vector coordinate respectively, obtained dq axis component of each vectors, and then through decoupling control module and PARK inverse transformation get voltage components in two-dimensional coordinates, finally sent voltage components into SVPWM control module will get six PWM switch signals.

To rule out the battery performance impact on the process of simulation, the simulation used DC voltage source to replace batteries, set DC side voltage at 600V, three-phase load is pure impedance load, set both load for 10 kw, at the start of the simulation, only load 1 access, in 0.5s, load 2 cut in, when it is 1s, load 2 cut out. Fig. 6 is inverter vector control simulation program block diagram.

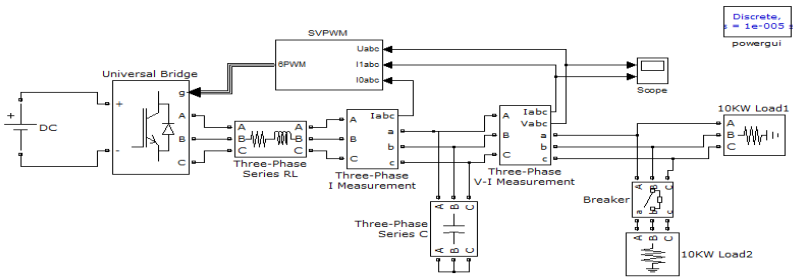

Fig. 6 Inverter vector control simulation program block diagram

By the Fig. 7 and Fig. 8, you can see that at the beginning of the program ,three-phase AC voltage is running at small fluctuations, but then quickly reach the set three-phase sine wave, when load increase at 0.4s, the AC voltage is almost no change, current doubles, when load decrease at 0.8s, voltage does not change, current drop to the initial value, it is visible that in the case of DC side capacity is enough, t SVPWM control strategy has the very good effect o maintain the stability of the load voltage, also can be seen from Fig. 9 that during the whole operation process, the frequency of the ac voltage has slight fluctuations near 50 Hz, frequency deviation limits within ± 0.2 Hz, meet the requirements of power system frequency deviation limits.

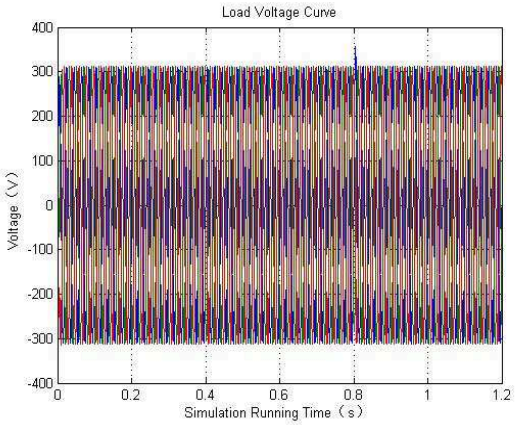

Fig. 7 The curves of load bus voltages

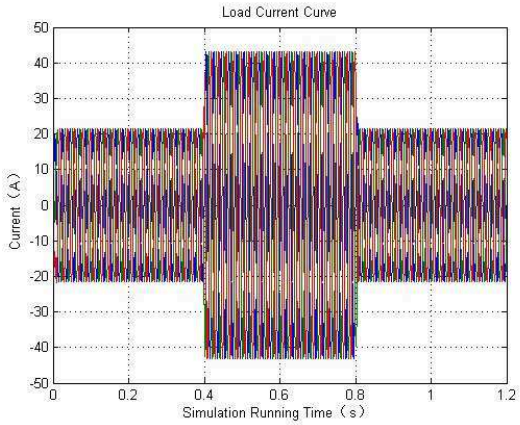

Fig. 8 The curves of load current

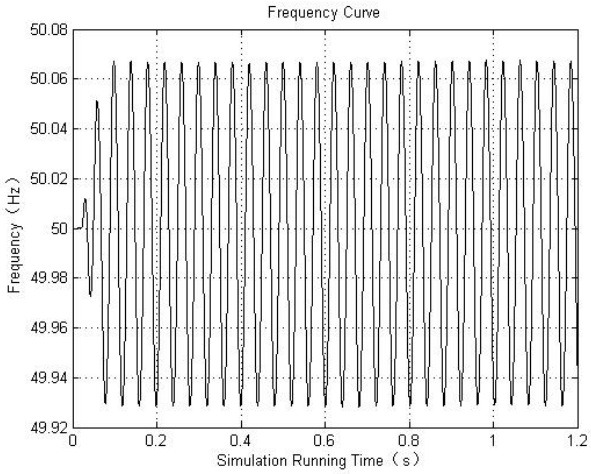

Fig. 9 Frequency curve

When run time and load parameter is set at the same situation, the single inverter SVPWM control process also implements that using SPWM realizing master-slave control the function of the double inverter like the literature [6], visible under the conditions that inverter DC side capacity is same to the system capacity, this design is better than double inverter design in the document [6] on the cost, and the SVPWM is easy to realize digital realization compared with SPWM, and has higher practicality.

Conclusion

This paper introduces the principle of voltage and current double closed-loop inverter based on SVPWM vector control technology, and simulation to the control process through MATLAB/Simulink software, the output waveform of simulation indicate that when the control algorithm put into operation, can quickly stable voltage, timely response to load changes, to maintain the stability of the AC voltage, and with less harmonic components at the same time. Prove that the voltage and current double closed-loop SVPWM control technology can be applied in the control of microgrid inverter AC side voltage stability.

Acknowledgement

The financial support of National High-Technology Research and Development Program of China (863 Program) (NO. SS2012AA052601) is gratefully acknowledged.

Reference

[1] Hou Limin, Li Hongzhu, Wang Wei. The principle of space voltage pulse width modulation SVPWM and the realization of DSP [J]. Journal of da lian university of technology, 2007, 26 (6), 898-900.

[2] Lu Zongxiang, Wang Caixia, Min Yong. Overview on Microgrid Research [J]. Automation of Electric Power Systems. 2007,31(19):100-107

[3] Chen Chuna. New energy distributed micro power grid dispatching management independent research [D]. Hunan: hunan university, 2011.

[4] XiaoChunYan. Voltage space vector pulse width modulation technology research and its implementation [D]. Jiangxi, nan chang university, 2005.

[5] Huang Shoudao Wang Dejiang etc. Based on the theory of instantaneous reactive power single-phase phase-locked loop [J]. Power electronics technology, the lancet, 2009 (10) : 89-90.

[6] Zhang Yuanfei, Du Wei, Gu Yujiong, Zhu Ping. Based on the oceanic island power supply technology research [J]. Journal of east China power, 2013, 9 (1) : 185-189.

Advanced Materials Research Vols. 960-961 (2014) pp 1277-1284

doi:10.4028/www.scientific.net/AMR.960-961.1277

Research on Fuzzy PI Compensating Current Control of Three Level Active Power Filter

Yanqing Peng[1, a], Jia Li[1, b], Ji Zhang[1, c], Damin Zhang[1, d], Hu Deng[1, e]

[1]School of Electrical Engineering and Automation, Xiamen University of Technology, Fujian, Xiamen, 361024, China

[a]pyqxm@163.com, [b]alexlij@163.com, [c]221zhangji@163.com, [d]hqxmzju@xmut.edu.cn, [e]ilovehuzi@2008.sina.com

Keywords: Active Power Filter, Fuzzy Control, PI Control, Three Level.

Abstract: This paper presents a new method which combines the fuzzy theory with the traditional PI control to obtain the accurate tracking of the compensating current of the active power filter (APF) in full frequency range. Online adjustment of the parameters of the controller is realized by using fuzzy reasoning and defuzzication, so as to achieve the accurate tracking of the compensating current and thereby improve the capabilities of the APF to suppress the harmonics effectively. Simulation analysis and experiment results verify the effectiveness of the presented method.

Introduction

With the wide application of power electronic devices, such as nonlinear loads, the problem of harmonic pollution in power system is increasingly serious, which caused great influence on safe and economic operation of power system [1]. So we must take effective measures to improve it. As a new compensation device, active power filter (APF), which was capable of track complex harmonic both frequency and amplitude changes, and its compensation characteristics were affected little by changes in grid parameters, thus received wide attention [2].

Timely and effective control of the compensation current is a key link of APF, due to the current signal of harmonic current detection link get instruction current, compensation current must quickly and accurately track the signal, which is hard to do in the general case [3]. For this, many scholars have done a lot of work to study the compensation current control problem, to ensure to achieve the ideal compensation effect of APF. [4] using the upper and lower limits of instruction signal to form the hysteresis loop, hysteresis control on the difference of output current and the compensation current reference value. This method has advantage of quick response, does not contain specific times harmonic but defects exist in uncertainty of the switching frequency. [5] used the state information of the current sampling time, estimated next sampling period for compensation current, calculate the power switching device turn on and turn off pulse, deadbeat control on the compensation current. The method has fast dynamic response, but more dependent on the system parameters and has poor anti-interference ability. Specific to the disadvantage of the traditional PI control, which bandwidth is limited and cannot effectively track all frequencies of APF compensation current, this paper combines fuzzy control with PI control to constitute a composite control, which combines the advantages of both, and can compensate for lack of another, not only has rapid system response, but also ensures the control accuracy of the system. Finally, the effectiveness of the proposed composite control strategy is verified based on the MATLAB/SIMULIK simulation and hardware experiment platform.

The mathematical model of active power filter

The research object of this paper is shunt diode clamped three level active power filter, to simplify the analysis, introducing the concept of switching function, the bridge arm of each phase is equivalent to a single pole three throw switch, then the simplified circuit of the APF main circuit as shown in Fig. 1.

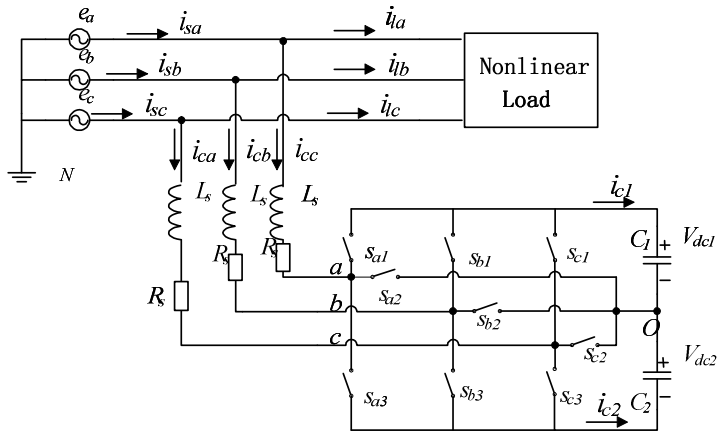

Fig. 1 Three level APF simplified circuit diagram

The switching function [6] $s_{ij}(i=a,b,c;\ j=1,2,3)$ is defined as Eq. 1:

$$\begin{cases} s_{ij}=1, & \text{the switch is closed} \\ s_{ij}=0, & \text{the switch is off} \end{cases}, \tag{1}$$

and s_{ij} satisfy the constraints of Eq. 2:

$$\sum_{j=1}^{3} s_{ij}=1 \qquad (i=a,b,c). \tag{2}$$

When $S_{j1}=1$, the above two switch tubes conduct, when $S_{j2}=1$ the middle two switch tubes conduct, when $S_{j3}=1$ the underneath two switch tubes conduct.

Through coordinate transformation, available mathematical model of the three level APF under the dq rotating coordinate system is shown in Eq. 3:

$$\begin{cases} L_s\dfrac{di_{cd}}{dt}=-R_s i_{cd}+\omega L_s i_{cq}+e_d-u_{cd} \\ L_s\dfrac{di_{cq}}{dt}=-R_s i_{cq}-\omega L_s i_{cd}+e_q-u_{cq} \\ C_1\dfrac{du_{dc1}}{dt}=S_{d1}i_{cd}+S_{q1}i_{cq} \\ C_2\dfrac{du_{dc2}}{dt}=-S_{d3}i_{cd}-S_{q3}i_{cq} \end{cases} \tag{3}$$

Three level APF switch function, the ac output voltage, the dq transform of three-phase grid voltage is shown in Eq. 4 and Eq. 5:

$$\begin{cases} \begin{bmatrix} S_{d1} & S_{q1} \end{bmatrix}^T = T_{abc/dq} \begin{bmatrix} S_{a1} & S_{b1} & S_{c1} \end{bmatrix}^T \\ \begin{bmatrix} S_{d3} & S_{q3} \end{bmatrix}^T = T_{abc/dq} \begin{bmatrix} S_{a3} & S_{b3} & S_{c3} \end{bmatrix}^T \end{cases} \tag{4}$$

$$\begin{cases} u_{cd} = S_{d1} u_{dc1} - S_{d3} u_{dc2} \\ u_{cq} = S_{q1} u_{dc1} - S_{q3} u_{dc2} \end{cases} \tag{5}$$

In the formula, there is:

$$T_{abc/dq} = \sqrt{\frac{2}{3}} \begin{bmatrix} \cos\theta & \cos(\theta - 2\pi/3) & \cos(\theta + 2\pi/3) \\ -\sin\theta & -\sin(\theta - 2\pi/3) & -\sin(\theta + 2\pi/3) \end{bmatrix},$$

$\theta = \omega t = 2\pi ft$, θ is synchronous rotary angle, $\omega = 2\pi f$ is spatial vector synchronous rotational angular frequency. After simplification, we get:

$$\begin{cases} L_s \dfrac{di_d}{dt} = -R_s i_d + \omega L_s i_q - u_d + e_d \\ L_s \dfrac{di_q}{dt} = -R_s i_q - \omega L_s i_d - u_q + e_q \end{cases} . \tag{6}$$

It can be seen from Eq. 6, APF is a system of strongly coupled, nonlinear characteristics, which need a high performance dynamic static controller to compensation current control.

Fuzzy PI control

Fuzzy PI control block diagram is shown in Fig.2, its basic principle is to develop "if-then" fuzzy rule form, and these results and system parameters are stored, the *e* is error between compensate current and harmonic current, the *ec* is the variety rate of error, then put them into fuzzy PI controller, after processing, get the ΔK_p , ΔK_i in that situation, online adjust the original PI parameters.

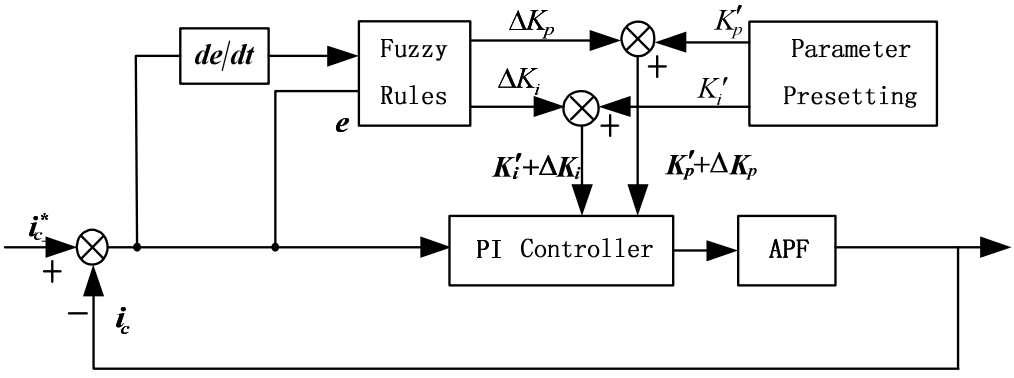

Fig. 2 Fuzzy PI controller structure diagram

Fuzzy inference of fuzzy control can only deal with fuzzy variables, so the input values should be changed into fuzzy values. The fuzzy language of input values is: negative big (NB), negative medium (NM), negative small (NS), zero (ZO), positive small (PS), positive medium (PM), positive big (PB). The fuzzy rules are the cores of the fuzzy control, the proportion gain K_p can reflect the error e, if the error e is large, in order to quickly suppress, the value of K_p will be larger; conversely, if the error is small, to prevent large overshoot that will leads the system oscillation, the value of K_p will be smaller. Considering the error variety rate ec, when ec and e are the same sign, the output value will deviate from the stable value, at this time the value of K_p should be increased; conversely, the value of K_p should be reduced. The fuzzy control regulation of ΔK_p is shown in Table 1.

Table 1 Fuzzy regulation control table of ΔK_p

e	ec						
	NB	NM	NS	ZO	PS	PM	PB
NB	PB	PB	PM	PM	PS	ZO	ZO
NM	PB	PB	PM	PS	PS	ZO	NS
NS	PM	PM	PM	PS	ZO	NS	NS
ZO	PM	PM	PS	ZO	NS	NM	NM
PS	PS	PS	ZO	NS	NS	NM	NM
PM	PS	ZO	NS	NM	NM	NM	NB
PB	ZO	ZO	NM	NM	NM	NB	NB

The function of the integral gain K_i is to reduce the static error. If its value is too large will increases the system's overshoot. In order to prevent the integral saturation, when the value of error e is large, make K_i=0; when the value of error e is small, let K_i effect, and take it greater when error e is smaller, to reduce the steady state error. The fuzzy control regulation of ΔK_i is shown in Table 2.

Table 2 Fuzzy regulation control table of ΔK_i

e	ec						
	NB	NM	NS	ZO	PS	PM	PB
NB	NB	NB	NM	NM	NS	ZO	ZO
NM	NB	NB	NM	NS	NS	ZO	ZO
NS	NB	NM	NS	NS	ZO	PS	PS
ZO	NM	NM	NS	ZO	PS	PM	PM
PS	NM	NS	ZO	PS	PS	PM	PB
PM	ZO	ZO	PS	PS	PM	PB	PB
PB	ZO	ZO	PS	PM	PM	PB	PB

In the fuzzy inference, the output value defuzzification, transform into the accurate value, and then output ΔK_p, ΔK_i, available online modified PI formula are shown in Eq. 7:

$$\begin{cases} K_p = K_p' + \Delta K_p \\ K_i = K_i' + \Delta K_i \end{cases} . \tag{7}$$

The simulation and experimental analysis

In order to verify the feasibility of the fuzzy PI control strategy for three level active power filter, the above scheme is validated on the MATLAB / SIMULINK simulation platform and hardware test platform. The simulation parameters and experimental parameters are the same: the three-phase power supply voltage is 220V, frequency is 50Hz, the system impedance is negligible. Harmonic source is the three-phase uncontrolled rectifier bridge with a resistance-inductance load, the resistor R=12Ω, inductor L=1mH. Inductance of incoming line of the APF is 1.2mH, switching frequency is 5KHz.

Fig.3 shows the current and harmonic analysis waveform of the uncontrolled bridge rectifier with a resistance-inductance load before compensation, there are a lot of harmonic before compensation, for example in phase A current, total harmonic distortion THD=23.65%. Simulation waveforms of traditional PI control after compensation is shown in Fig.4. Fig.4(c) shows the waveforms of the tracking current and instruction current, both almost consistent in the waveform curve trend, but the amplitude and phase have error, this is due to the traditional PI control can not achieve tracking without steady-state error.

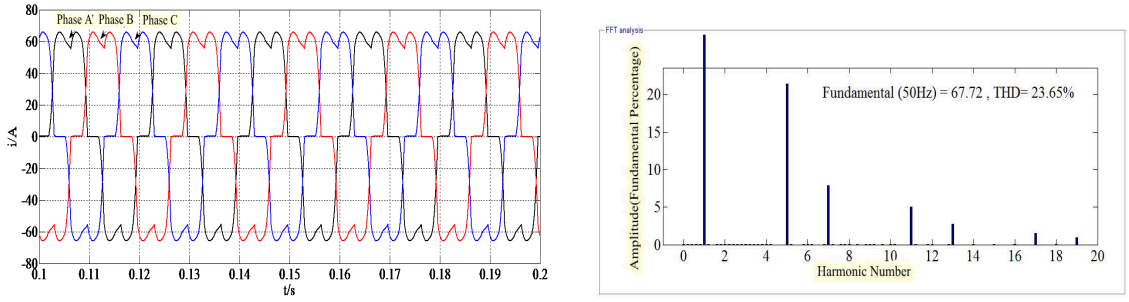

(a) (b)

Fig. 3 System's current waveform and harmonic analysis before compensation, (a) current waveform before compensation and (b) phase A current harmonic before compensation

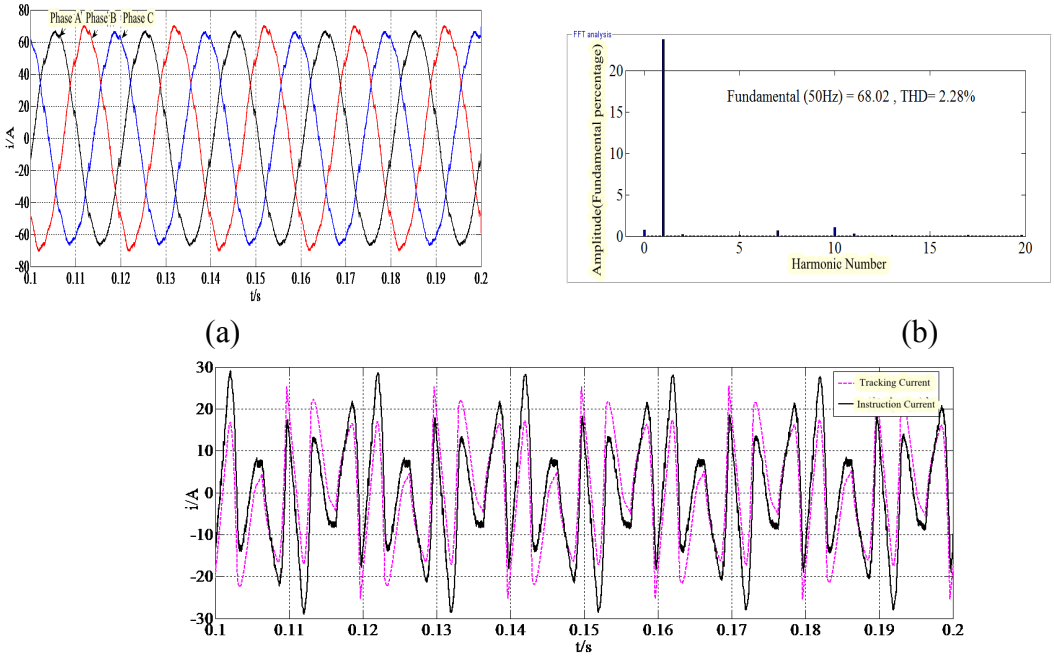

(a) (b)

(c)

Fig. 4 Simulation of traditional PI control compensation effect, (a) Current waveform after compensation; (b) Phase A current harmonic after compensation; and (c) Current tracking waveform

Fig.5 shows the simulation of fuzzy PI control compensation effect, Fig. 5(a) shows the current waveform after compensation, Fig. 5(b) shows the phase A current harmonic after compensation, Fig. 5(c) shows the waveforms of the tracking current and instruction current. The figures show that current waveform have a high sinusoidal after compensation, the total harmonic distortion THD=1.20%, and the tracking current can track the instruction current rapidly and accurately, compensation effect is much better than the conventional PI control.

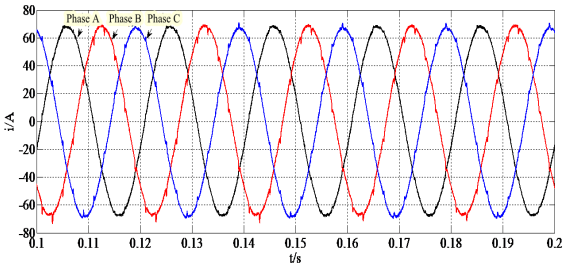

(a)

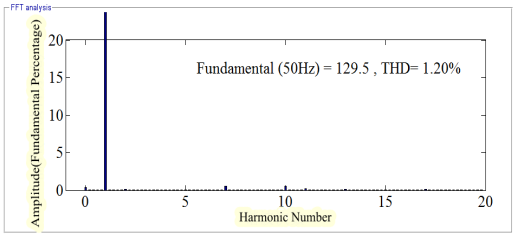

(b)

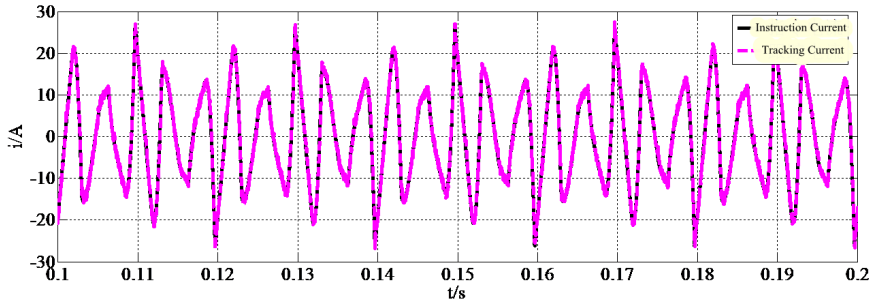

(c)

Fig. 5 Simulation of fuzzy PI control compensation effect, (a) Current waveform after compensation; (b) Phase A current harmonic after compensation; and (c) Current tracking waveform

Three level active power filter fuzzy PI control experiment platform is set up based on DSP and FPGA control chip. The TMS320F28335 chip is chosen for the DSP, the XC2S200FPGA of XILINX chip is chosen for the FPGA. The DSP is mainly used for double closed loop control and SVPWM arithmetic processing [7], FPGA is used to achieve pulse generation of each arm. The 8 channel, 16 bit AD7606 is used for sampling. The 7MBP150RA120 of Fuji IGBT-IPM is adopted for main circuit.

Fig.6 shows the grid voltage and current waveforms before compensation when no controlled rectifier bridge is with a resistance inductance load. From the figure, the current harmonic content is high, and distortion is serious, which will cause serious harmonic pollution to power grid. Fig.7 shows the grid voltage and current waveforms after compensation when use the fuzzy PI control of APF. From the figure, a high sinusoidal current waveform is achieved after compensation. The current harmonic content is small, a well harmonic governance capabilities is achieved. Fig.8 shows the grid current and DC side voltage waveforms before and after the APF is put into. When the APF is put into, the intended effect of compensation can be achieved after a period of transient process. The system has rapid dynamic response and high precision of harmonic detection and compensation control. It has a good dynamic and static performance.

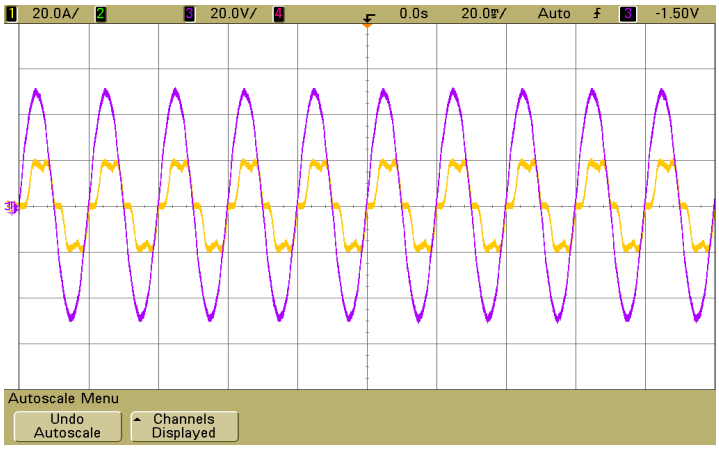

Fig. 6 Grid voltage and current waveforms before compensation

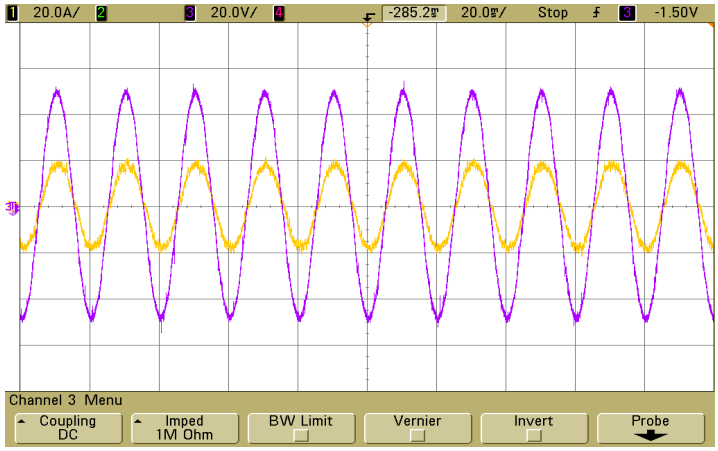

Fig. 7 Grid voltage and current waveforms after compensation

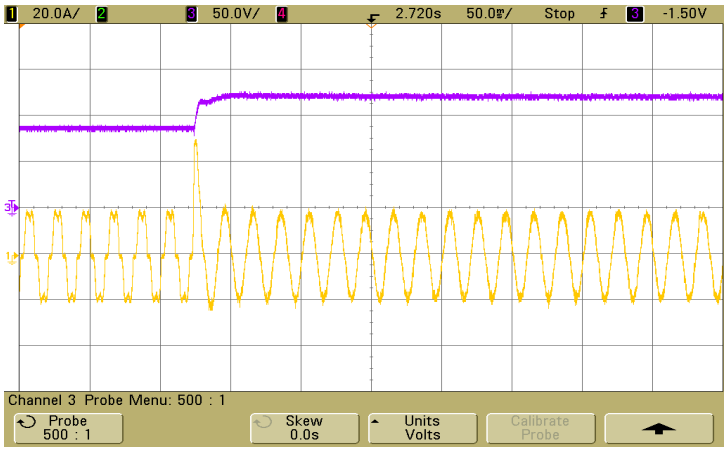

Fig. 8 APF input process grid current and DC side voltage waveforms

Conclusions

1. This paper constitutes a new hybrid control strategy by combining fuzzy control with PI control. The novel method can improve the traditional PI control, which has the disadvantage of cannot effectively track all frequencies of APF compensation current because of the bandwidth limit.
2. Through fuzzy reasoning and defuzzification, online adjustment of the PI parameters is achieved, which can improve the regulator full frequencies tracking performance to instruction current, and optimize the response ability of the harmonic compensation current.
3. Finally, based on the MATLAB/SIMULIK simulation and DSP+FPGA experiment results verify the effectiveness and feasibility of the proposed method.

Acknowledgment

This work was financially supported by the Science and Technology Key Program of Fujian Province, China (2012H0040), the Science and Technology Program of Xiamen, China (3502Z20133039), the Science and Technology Program of Zhangzhou, China (ZZ2013022).

References

[1] Mekri F, Mazari B, Machmoum M. Canadian Journal of Electrical and Computer Engineering, Vol. 31(3) (2006), p. 127-134.

[2] Jinwu Gong, Xiaoming Zha, Baifeng Chen. Transactions of China Electro technical Society, Vol. 26(10) (2011), p. 110-117.In Chinese.

[3] Sasaki H, Machida T. IEEE Transactions on Power App. & Syst., Vol. 90(5) (1971), p. 2009-2019.

[4] Ziyong Guo, Youqing Zhou, Hongchao Liu, et al. Proceedings of the CSEE, Vol. 27(1) (2007), p. 112-117. In Chinese

[5] Jian Tang, Xiang Wang, Yingjie He, et al. Automation of Electric Power Systems, Vol. 31(19) (2007), p. 59-64. In Chinese

[6] Zhang Jianliang, Tan Guojun, Han Yaofei. Power Electronics, Vol. 5(43) (2007), p. 7-9. In Chinese

[7] Texas Instruments Inc. TMS320F28335/ F28334/ F28332/ F28235/ F28234/ F28232 digital signal controllers [EB/OL]. Texas: 2010.

Advanced Materials Research Vols. 960-961 (2014) pp 1285-1289

doi:10.4028/www.scientific.net/AMR.960-961.1285

Research on single-phase inverter dual loop control technology with feed-forward compensation

Shujun Yao [1, a], Jun Luo [1, b], Minxiao Han[1], Yangchengxiang Song [1]

[1] Institute of Electrical and Electronic Engineering, North China Electric Power University, Beijing, 102206, China

[a]email: Open2000@sina.com.cn, [b]email: armyluojun@gmail.com

Keywords: inverter, nonlinear loads, dual loop control, current feed-forward, pole assignment

Abstract. A new approach of dual closed-loop control strategy is proposed, and the internal cause of the inverter output voltage waveform distortion is analyzed in this paper. The ability to resist load disturbance is improved by load current feed-forward compensation in the approached scheme. With inner current loop improving the speed of dynamic response, nonlinear load adaptability is enhanced. Pole assignment method is used to design controller parameters, the control scheme is simulated in PSCAD/EMTDC, the nice performance of the proposed control strategy is verified by the simulation results.

Introduction

Single phase inverters have been widely used in UPS and other industrial equipment. The control methods of inverter including single closed-loop control, dual closed-loop control, deadbeat control, repetitive control, fuzzy logic control, etc [1,2]. The dual closed-loop control is one of the developing directions of high performance inverters.

A single phase inverter applying dual closed-loop with load current feed-forward compensation control technique is researched. Controller parameters are obtained with pole assignment technique [3,4]. The principle for the control system can improve the adaptability of nonlinear load is illustrated in terms of equivalent output impedance. The simulation results verified the designed inverter can achieve good static characteristics with nice dynamic response even with nonlinear loads.

Mathematical model of single-phase inverter

The main circuit structure of a single phase full bridge inverter is shown in Fig.1.

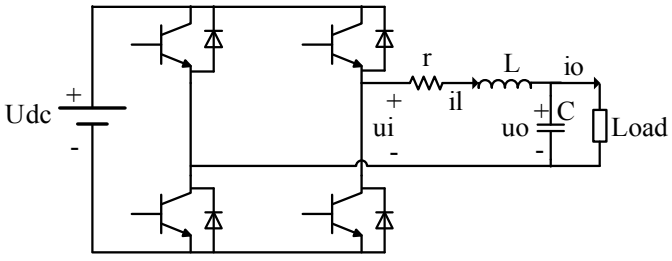

Fig.1 Schematic diagram of single phase full bridge inverter main circuit

In Fig.1, U_{dc}, u_i and u_o indicate the DC bus voltage, filter input voltage and output voltage of inverter. i_l, i_c and i_o indicate inductor current, capacitor current and load current. r indicates parasitic resistor and dead time effect equivalent resistance. L,C indicate Filter inductance and capacitance respectively. Choosing the u_o and i_l as state variables, the state equation becomes as:

$$\begin{bmatrix} \dot{u}_o \\ \dot{i}_l \end{bmatrix} = \begin{bmatrix} 0 & \frac{1}{C} \\ -\frac{1}{L} & -\frac{r}{L} \end{bmatrix} \begin{bmatrix} \dot{u}_o \\ \dot{i}_l \end{bmatrix} + \begin{bmatrix} 0 \\ \frac{1}{L} \end{bmatrix} u_i + \begin{bmatrix} -\frac{1}{C} \\ 0 \end{bmatrix} i_o \qquad y = \begin{bmatrix} 1 & 0 \end{bmatrix} \begin{bmatrix} \dot{u}_o \\ \dot{i}_l \end{bmatrix}. \tag{1}$$

According to (1), the transfer function is derived as:

$$U_o(s) = \frac{U_i(s)}{LCs^2 + rCs + 1} + \frac{-(Ls + r)}{LCs^2 + rCs + 1} I_o(s) = G_i(s) \cdot U_i(s) - Z_o(s) \cdot I_o(s). \tag{2}$$

Internal cause of output voltage waveform distortion

The nonlinear load model. Due to the nonlinear load contains the nonlinear components such as diodes, silicon controlled rectifier, even if the load voltage is standard sine wave, load current still contains a lot of harmonics. Diode uncontrollable rectifier circuit is a sort of commonly used nonlinear load, it serves as an important means of testing the performance of power source. The typical nonlinear LCR single-phase load is shown as Fig.2.

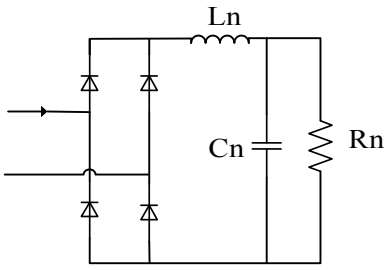

Fig.2 Typical model of nonlinear load

Open loop characteristic of single phase inverter. According to (2), inverter output voltage consists of two parts, thus the inverter can be regarded as the series of an ideal voltage source and the equivalent output impedance of the inverter. $Z_o(s)$ can be taken as the equivalent output impedance. Taking the inverter designed in this paper as an example, with main parameters as: L=0.8mH，C=90uF，r=0.1Ω，the frequency characteristics of inverter output impedance can be derived as Fig.3.

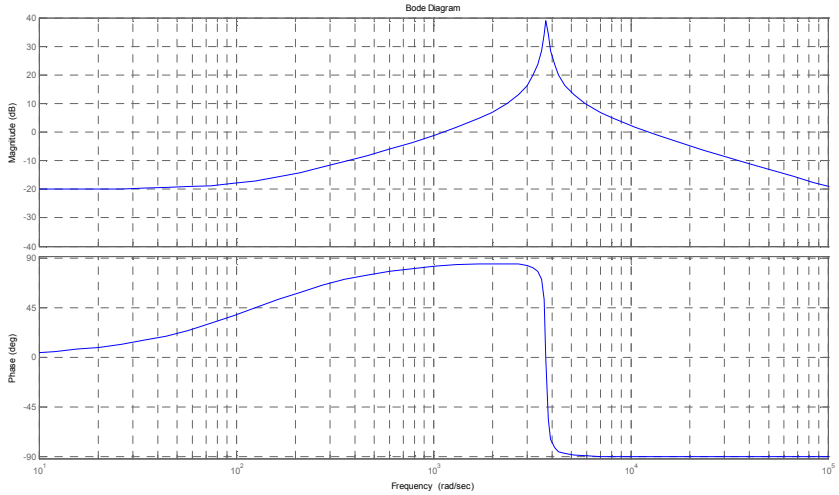

Fig.3 The bode diagram of inverter output impedance

According to Fig.3, the amplitude of output impedance increases with the rising of frequency at low-frequency stage. For nonlinear load, the harmonic current shock is huge, the output impedance causes larger harmonic voltage drop, thus lead to output voltage distortion. That is the internal reason of voltage waveform distortion caused by nonlinear load.

Control system design

The dual closed-loop with load current feed-forward compensation control scheme is shown as Fig.4. The load current feed-forward can enhance the ability to resist load disturbance, the inner current loop increases bandwidth of the inverter control system to achieve faster dynamic response and strengthen the adaptability for nonlinear load [5-7].

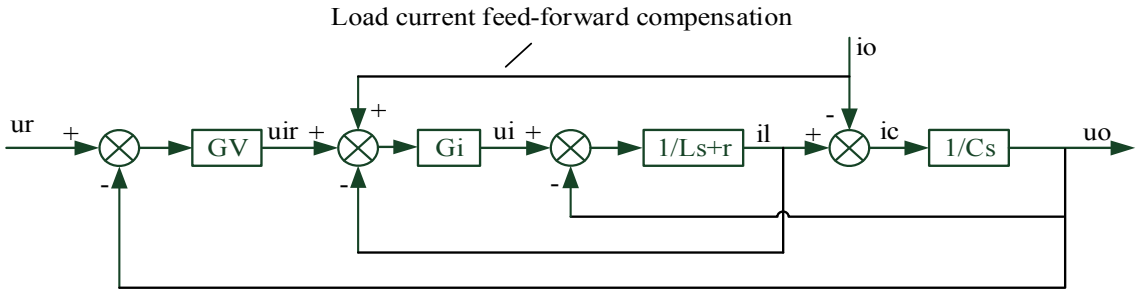

Fig.4 The block diagram of dual loop with feed-forward control scheme

Design of parameters. The proportion-integral control is adopted to regulate the output voltage in the outer loop and the inductor current in the inner loop. The regulator becomes as:

$$G_v(s) = k_{1p} + \frac{k_{1i}}{s} \quad , \qquad G_i(s) = k_{2p} + \frac{k_{2i}}{s} \quad . \tag{3}$$

According to (3) and Fig.4, we can get the dynamic characteristics of closed-loop output voltage as:

$$U_o(s) = \frac{\frac{k_{1p}k_{2p}}{LC} + \frac{k_{1p}k_{2i+}k_{1i}k_{2p}}{LC}s + \frac{k_{1i}k_{2i}}{LC}}{D(s)} U_r(s) - \frac{\frac{1}{C}s^3 + \frac{r}{LC}s^2}{D(s)} I_o(s) = G_{ur}(s)U_r(s) - Z_o(s)I_o(s) \, , \tag{4}$$

with

$$D(s) = s^4 + \frac{r + k_{2p}}{L}s^3 + \frac{k_{1p}k_{2p} + Ck_{2i} + 1}{LC}s^2 + \frac{k_{1p}k_{2i} + k_{2p}k_{1i} + 1}{LC}s + \frac{k_{1i}k_{2i}}{LC} \, . \tag{5}$$

Set the dominant pole of the fourth order system as $s_{1,2} = -\zeta_r\omega_r \pm j\omega_r\sqrt{1-\zeta_r^{\,2}}$, the non-dominant pole as $s_3 = -m\zeta_r\omega_r$, $s_4 = -n\zeta_r\omega_r$, the expected characteristic equation becomes as:

$$D_r(s) = (s^2 + 2\zeta_r\omega_r s + \omega_r^{\,2})(s + m\zeta_r\omega_r)(s + n\zeta_r\omega_r) \quad . \tag{6}$$

Set m=n=10, expected damping ratio as $\zeta_r = 0.8$, natural frequency as $\omega_r = 3000 \mathrm{rad/S}$, comparing (5) with (6), we can get:

$$G_v(s) = 0.4496 + \frac{866.6481}{s} \qquad G_i(s) = 42.14 + \frac{430680}{s} \tag{7}$$

Analysis of output impedance frequency response characteristic. According to (4) and (5), the equivalent output impedance of the inverter can be characterized by

$$Z_o(s) = \frac{Ls^3 + rs^2}{LCs^4 + (r + k_{2p})Cs^3 + (k_{1p}k_{2p} + Ck_{2i} + 1)s^2 + (k_{1p}k_{2i} + k_{2p}k_{1i})s + k_{1i}k_{2i}} \, . \tag{8}$$

Controller parameters are given in (7), the Bode diagram of output impedance can be shown as Fig.5.

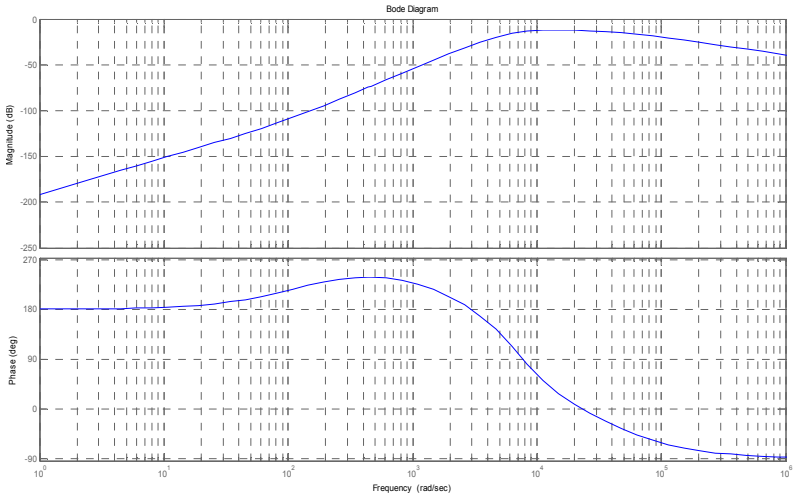

Fig.5 The bode diagram of inverter output impedance

Comparing Fig.5 with Fig.3, the output impedance in each frequency band is largely damped due to the designed control scheme, so nonlinear load adaptability is reinforced.

Simulation test

The parameters used for the simulation are shown below.

DC voltage: $U_{dc} = 400V$, Output AC voltage: $U_o = 220V$, f=50HZ, Filter inductance: L=0.8mH, Filter capacitor: C=90uF, Equivalent resistance: r=0.1Ω, Switching frequency: $f_s = 8kHZ$.

The waveforms of load current and output voltage in the case of sudden increase of load are shown as Fig.6 and Fig.7, respectively. In the case of sudden decrease of load, the waveforms are shown as Fig.8 and Fig.9. Under the condition of rectifier nonlinear load, the waveforms of load current and voltage are shown as Fig.10 and Fig.11. The nonlinear load model adopted in the simulation is shown as Fig.2, with the parameters as: $L_n = 1.0mH$, $C_n = 400uF$, $R_n = 10\Omega$.

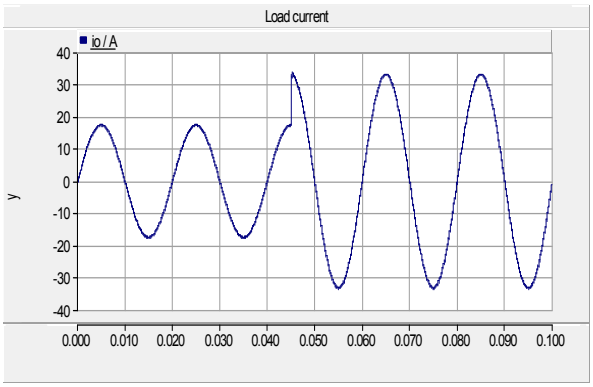

Fig.6 Load current for sudden increase of load

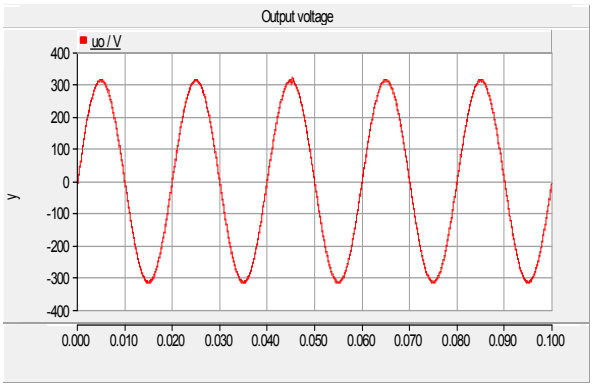

Fig.7 Output voltage for sudden increase of load

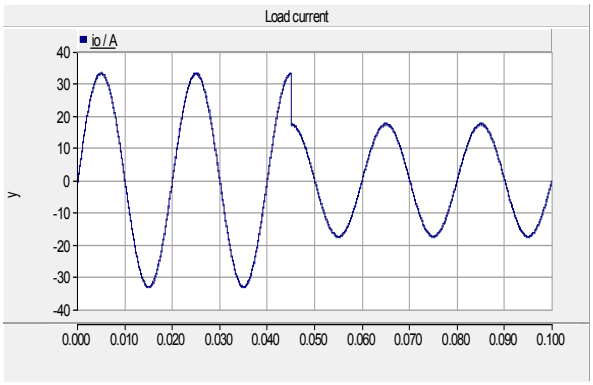

Fig.8 Load current for sudden decrease of load

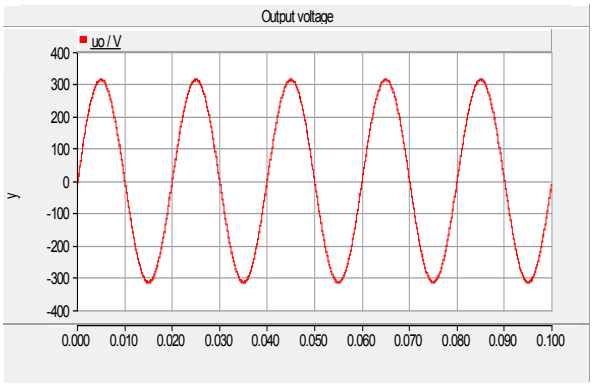

Fig.9 Output voltage for sudden decrease of load

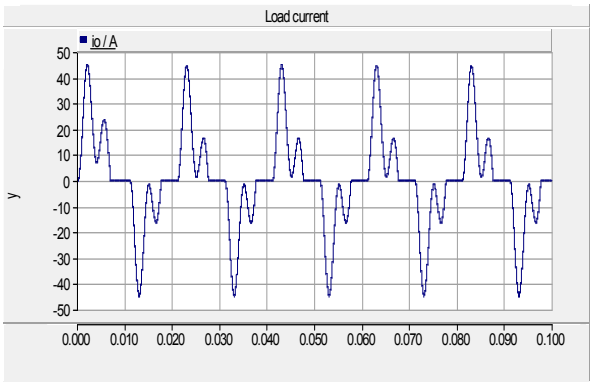

Fig.10 Load current for nonlinear load

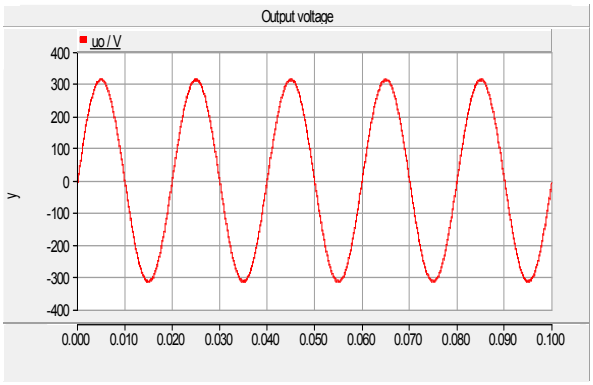

Fig.11 Output voltage for nonlinear load

From Fig.6 to Fig.9, we can get that the load current can be changed instantly during the load mutation with little output voltage fluctuation. The output voltage variation is not more than 3.76%, and the recovery time is less than 0.5ms, the dynamic response is fast. The THD is only 0.0754% under the condition of resistance load. According to Fig.10 and Fig.11, the load current is seriously distorted under the condition of nonlinear load, while the output voltage is a good sinusoidal wave with the THD is only 0.6461%.

Conclusions

Due to the inverter output impedance, nonlinear load current harmonics lead to output voltage wave distortion. In virtue of the proposed dual loop with feed-forward control scheme, the output impedance is damped and dynamic response accelerated. The simulation results show that the presented control scheme can obviously improve dynamic characteristics. The output waveforms under the condition of nonlinear load are satisfied for the low THD.

References

[1] Kun Cai, Yaohua Li, et al. Output Control of the High Performance Single-Phase Voltage-Source Inverters [J]. Transactions of China Electrotechnical Society, 2005, 20(1):104-107.

[2] Loh P C, Newman M J, Zmood D N, et al. A Comparative Analysis of Multi-loop Voltage Regulation Strategies for Single and Three Phase UPS Systems [C]. IEEE Trans on Power Electronics, 2003, 18 (9) : 1176-1185.

[3]Jun He. Research on PWM Inverter Dual Loop Control Technology [D].Huazhong University of Science and Technology, 2007.

[4] Shuhui Wang, Li Peng, Yong Kang. The Research of PI Digital Dual-Loop Control Method for PWM Inverter Based on Pole Assignment [J]. Power Supply Technologies and Applications, 2008,11(9):34-39.

[5] Wei Song, Taiqiang Cao, Xingmin Liu. Design of Single-phase Inverter with Inductance Current Inner Loop [J]. Electronic Component & Device Applications, 2010, 12(10):73-75.

[6] Zhijian Guo, Shaojuan Yu, et al. Simulation Study on PWM Inverter with Dual Loop Control [J]. Industrial Control Computer, 2013, 26(8):77-78.

[7] Liangliang Chen, Lan Xiao, Yangguang Yan. Research on Output Characteristics of Double Close-loop Control Voltage Source Inverter [J]. Power Electronics, 2004, 38(3):6-7.

Advanced Materials Research Vols. 960-961 (2014) pp 1290-1294

doi:10.4028/www.scientific.net/AMR.960-961.1290

A Coordinated Controlled PV Three-ports Converter Based on Magnetic Coupling

Liwei Tao [1,a*], Jingcao Chen [1,b] and Jianhu Yan [1,c]

[1]School of Energy and Power Engineering, Nanjing University of Science and Technology, China

[a] tao90@ 21cn.com, [b]joyjay3366@sina.com, tzpp90@163.com

Keywords: Coordinated control, MPPT, Multiport converter, Matlab, Simplorer

Abstract. According to the requirements on multiport and power flow in the application of renewable energy, a novel multiport converter based on magnetic coupling is proposed in this paper. This multiple converter is capable of charging and discharging the battery while supplying the load. Theoretical method for the analysis of a three-port converter based on magnetic coupling is presented. The principle of the control loop for the converter is given that the maximum power point tracking (MPPT) is applied for the Photovoltaic (PV) part and the independent control is for the power flow part respectively. In addition, this proposed control method is also available for multiple modules. The simulation model is built by Simplorer-Matlab software and the simulated results demonstrate that this proposed converter can realize the power distribution very well. The control strategy proposed is of great isolation and low mutual interference between different ports so that the converter can reliably operate.

Introduction

With the rapid development of renewable energy, various new types of converters are developed in order to combine multiple energy sources to meet the requirement of power flow between each unit. Comparing with traditional ones, most converters applied in renewable energy system have the characteristics of multiport with bidirectional power flow. And the control methods are also simple and effective as well [1-3].

Multiport converter is applied to convert power or voltage among ports by using only one converter. Electric coupling and magnetic coupling, as shown in Fig.1, are the most commonly used for connecting different ports in a multiport converter. Electric coupling is mainly achieved by the DC bus while magnetic coupling by a transformer. Ref [4] presents the fundamental form of a multiport converter based on electric coupling that a switch module is used for putting into the multiple low-power energy harvesting sources while a Boost circuit following is applied for supplying the load. Ref [5] changed the single switch that described in [4] into two parallel-connected switches in the pre-stage and the bidirectional power flow is achieved in the followed stage by applying a bidirectional Buck-Boost circuit. Ref [6] utilizes a transformer as a unit for energy storage and transformation. The input ports which are connected to the Photovoltaic (PV), the grid and the battery respectively supply the two output ports on the load side by a multi-winding transformer. Besides, the battery can be charged or discharged. However, the multiple-input boost converter proposed in Ref [4] cannot extract power from multiple low-power energy harvesting sources simultaneously due to its parallel structure, resulting in the low use efficiency. In the Ref [6], it can operate bi-directionally without any need for additional converters, but a five-port transformer is difficult to design undoubtedly. Hence, a simultaneous power-feeding converter with a three-port transformer is proposed in this paper.

The main advantage of an electric coupling multiport converter is simple to achieve and easy to control. However, the limitation of these topologies is that only one power source is allowed to transfer energy into the load at a time to prevent power coupling effects and without the isolation leads to low reliability [7]. A magnetic coupling multiport converter is more capable of controlling the power flow of each port, but the transformer in this converter is complex in structure. Along with the operating principle and the power control strategy, a coordinated controlled three-port converter

based on the magnetic coupling is proposed in this paper to achieve the power flow by isolating the electric circuit, which has a simpler structure than the traditional multiport magnetic coupling converters. Besides, the extension of multi-module PVs is more achievable.

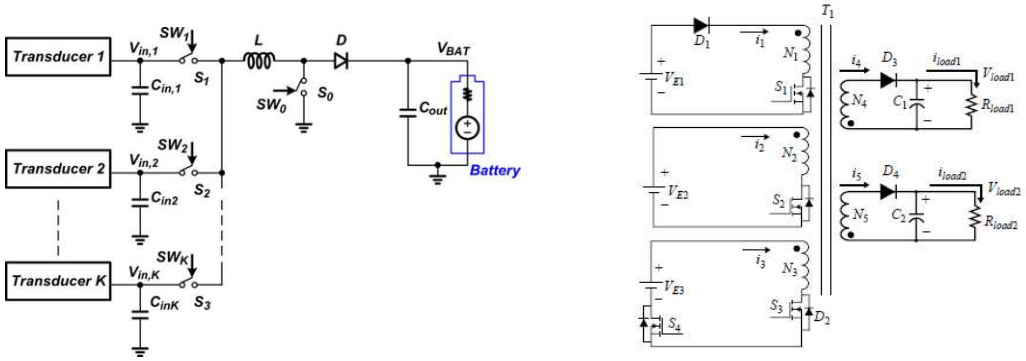

Fig.1 a) Multiple-input boost converter b) Multiple-input multiple-output converter

Operation Principle

The proposed multiport converter is illustrated in Fig.2. The converter, which contains three ports (PV port, battery port, load port respectively) is mainly constituted by a three-winding isolated transformer. The two input ports which connect to PV array and battery both adopt the fundamental full-bridge circuit to realize the bidirectional power flow easily. The output port which connects to the load obtains power by rectifying from secondary wingding of the transformer. Moreover, the converter can successfully transfer power from the different voltage sources to the load individually or simultaneously, and the PV array is capable to supply the load and battery at the same time when the battery is out of charge.

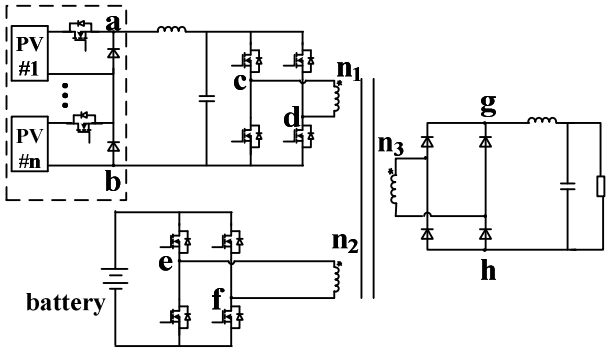

Fig. 2 Topology of proposed converter

The basic PV parallel module or serial module is adopted by coordinated control according to the power requirement. The parallel module need a current divergence control strategy, which is quite complex when the number of module increases. The serial module control is relatively simple, because the total PV array voltage (V_{ab}) changes little when the number of modules is larger than 15. In this paper, the circuit of Buck is chosen as the module unit due to its simple structure and control method.

According to the analysis above, the converter can operate in four modes: I. Both PV port and battery port supply the load. II. PV port supplies both the battery and load. III. Only battery port supplies the load. IV. Only PV port supplies the load

In the mode III and mode IV, only one port supplies the load, and the other port operates without control, so the paper focuses on the former two modes. Mode I and mode II are of the same operation state in state II and state IV.Besides, there are just the switch pairs S_7/S_{10} and S_8/S_9 work the other way around, so this part shows operation state in mode I only. Assuming all the switches and the transformer are ideal, the following part demonstrates the operating state of the mode I and mode II with the only PVs at the head and the tail.

On the basis of the operating condition of each switch, it can be divided into four states in the Mode I.

State I: As shown in Fig.3 (a), with S_1, S_2, S_3 and S_6 turned ON for a span, the total voltage of PV array puts on the primary winding, which values V_{ab}. Meanwhile, the battery port also supplies the load through the switches of S_7 and S_{10}. The secondary rectifier diodes of D_3 and D_6 persistently conduct, resulting in the voltage of the rectifier rising to (n_3/n_1) $V_{ab.}$ Energy of the primary side is transmitted to the secondary side, and windings of transformer storage power at this phase.

State II: As shown in Fig.3 (b), with S_3 and S_6 turned ON for a span, the total voltage of PV array values 0. Meanwhile, the voltage of the battery port changes to 0 as well, and the diodes in parallel to the switches offer an access for the power releasing of transformer. The secondary rectifier diodes of D_3, D_4, D_5 and D_6 conduct, leading to voltage rectified also changing to 0. Windings of transformer release power at this phase. When the windings release its stored energy completely, and the secondary rectifier diodes turned OFF, this state ends.

State III: As shown in Fig.3 (c), with S_1, S_2, S_4, S_5 turned ON for a span, the total voltage of PV array puts on the primary winding, which values $-V_{ab}$. Meanwhile, the battery port also supplies the load through the switches of S8 and S9. The secondary rectifier diodes of D_4 and D_5 persistently conduct, resulting in the voltage of the rectifier rising to (n_3/n_1) $V_{ab.}$ Energy of the primary side is transmitted to the secondary side, windings of transformer storage power at this phase.

State IV: As shown in Fig.3 (d), with S_4 and S_5 turned ON for a span, the total voltage of PV array values 0. Meanwhile, the voltage of the battery port changes to 0 as well, and the diodes in parallel to the switches offer an access for the power releasing of transformer. The secondary rectifier diodes of D_3, D_4, D_5 and D_6 conduct, leading to voltage rectified also changing to 0. Windings of transformer release power at this phase. When the windings release its stored energy completely, and the secondary rectifier diodes turned OFF, this state ends.

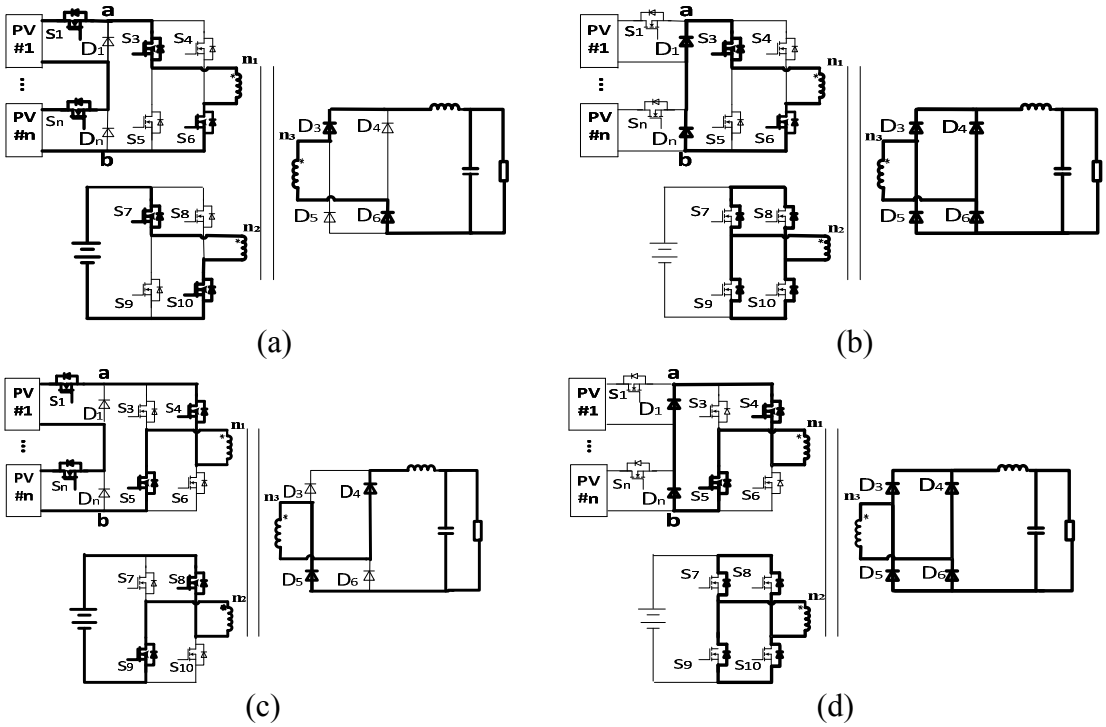

Fig. 3 a) Stage I b) Stage II c) Stage III d) Stage IV

Control Strategy

The converter is consists of numerous switches, so a coordinate control strategy is indispensable. The principle is that switches of Buck are controlled to adjust the total voltage of the PV array for MPPT, while switches of full-bridge inverter are regulated to realize the power flow. In order to obtain the maxim efficiency in the PV port, each module demands for MPPT control respectively. The symmetric alternating voltage of primary winding is essential to avoid the magnetic saturation in the transformer [8]. Thus, the following requirements are necessary:

I. The switch pairs, S_7/S_{10} and S_8/S_9, which belong to identical full-bridge inverter are supposed to share the same duty-cycle; the same with the switch pairs, S_3/S_6 and S_4/S_5.

II. Power storage and release should be achieved in half cycle by the full-bridge inverter of battery port.

III. The switching frequency of the Buck is required to be an even multiple than that in the inverter.

To simplify the control loop, settings are defined as follows. The switching frequency of S_l and S_n is double than that in the inverter. Switch pairs S_3/S_6 and S_4/S_5, which are in PV port, complementarily conduct with the duty-cycle maintaining 50%. The duty-cycle of switch pairs S_7/S_{10} and S_8/S_9, values 25%. Control signal in mode I is illustrated in Fig.4. When the converter changes to mode II, signals of switch pairs S_7/S_{10} and S_8/S_9 turn in opposite and other signals remain the same correspondingly, which is not repeated here.

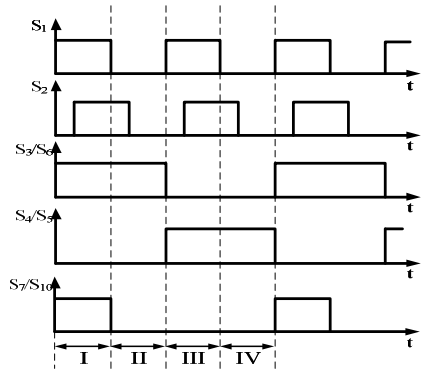

Fig. 4 Proposed control strategy

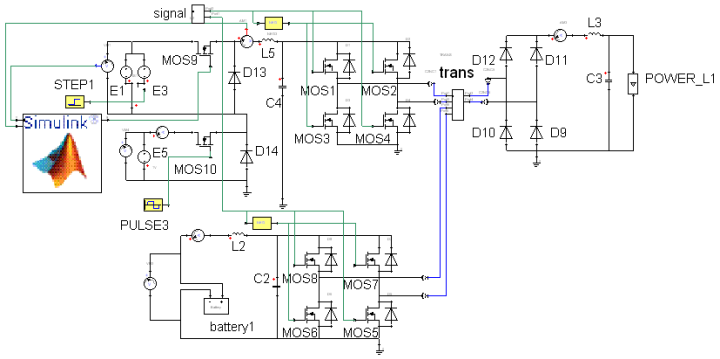

Fig. 5 Converter model in sim2sim simulation platform

Simulation

The simulation presents both steady-state and dynamic-state performance. The converter is modeled with two PVs by Simplorer.

Steady-state Simulation. Power flow is demonstrably verified in this part. The converter model is shown in Fig. 5. Given different input voltages of PV port, assume two groups to research mode I and mode II: i. Total PV voltage (Vin_1) =12V, the voltage of battery (Vin_2) =12V. ii. Total PV voltage (Vin_1) =16V, the voltage of battery (Vin_2) =12V

The Fig.6 and Fig.7 show the performance under two conditions above. Each one illustrates concern on the power flow of the converter. In the figure, P_{out} represents output power; P_{in1} represents input power of PV port and P_{in2} represents input power of battery port.

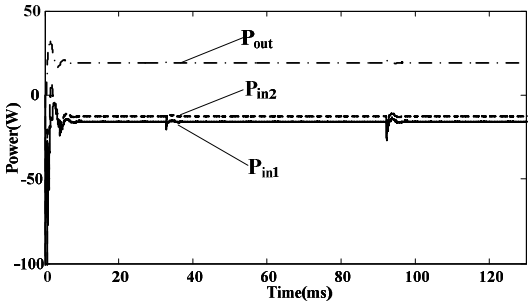

Fig.6 Power in Vin_1=12V, Vin_2=12V.

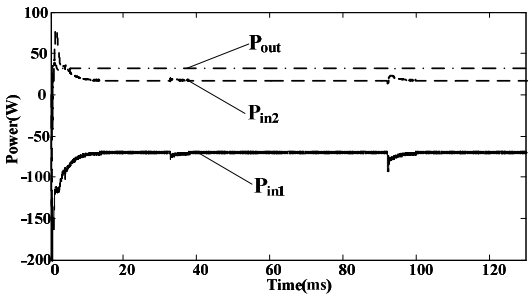

Fig.7 Power in Vin_1=16V, Vin_2=12V

It can be observed that, in the Fig.6, P_{in2} is below 0, showing that the battery is discharging at this circumstance. Conclusion can be drawn that the converter operates in mode I. Fig.7, on the contrary, shows that the converter operates in mode II with the same analysis. The two figures all together reveal that the proposed converter can be shifted between the two modes, supplying the load and achieving the bidirectional power flow.

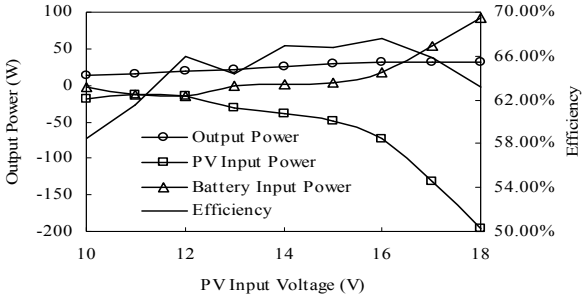

Fig.8 Efficiency curve

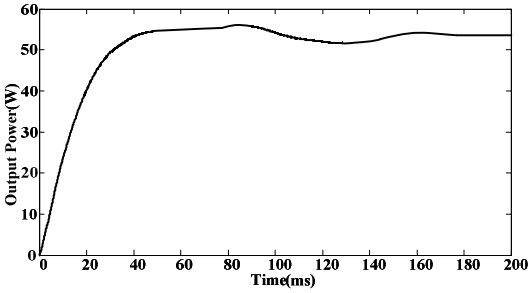

Fig.9 Waveform of power in the dynamic-state

In addition, assuming Vin_2 is constant, which values 12V, changing Vin_1, an efficiency curve can be drawn, as shown in Fig.8. It shows that when Vin_1 reaches 15V, the converter shifts to mode II from mode I. Meanwhile, the battery port changes to absorb power instead.

Dynamic-state Simulation. The output voltage of PV may change slightly due to the variation of light, temperature and other integrated factors. Dynamic-state simulation is used to test the performance of the system in the presence of such small disturbance. The simulation model is constructed on the Sim2sim which is a union simulation platform based on Matlab/Simulink and Simplorer. Perturbation and observation method is applied in the MPPT control of the Buck circuit in the head of PV module. The input voltage of the Buck circuit in the tail of PV module is V_{i2}=36V. The battery voltage V_{i3}=13.8V and the load power is 200W. Simulation results when the input voltage of the first Buck circuit Vi_1 falls from 36V to 30V are plotted in Fig.9.

The disturbance is exerted at t=80ms. As shown in Fig.9, the load becomes stable after about 100ms. This dynamic-state simulation has demonstrated that the system can effectively suppress the output voltage disturbance of the PV array and stabilize the load within a reasonable range after adding MPPT control to the ports of the PV array.

Conclusions

The three-port converter discussed in this paper has overcome the problems that the energy flow rarely achieve as an electric coupling converter and the multiple-winding transformer is difficult to manufacture as a magnetic coupling converter. By coordinating each switch, energy can flow between the three ports. Such a converter is mainly supplied by the PV array. Meanwhile, the battery port can provide or absorb energy according to the actual operating conditions. The operating principle and control strategy of this novel three-port converter is analyzed in this paper and the simulation shows the validity and effectiveness of the new topology.

References

[1] K. Kobayashi, H. Matsuo, and Y. Sekine, in: *IEEE Transaction on Industrial Electronics*. 2006, 53(1): 281-286.

[2] C. N. Onwuchekwa, and A. Kwasinski, in: *IEEE Transaction on Power Electronics*. 2012, 27(11): 4492-4502.

[3] A. Kwasinski, in: *IEEE Transaction on Power Electronics*. 2009, 24(3): 856-861.

[4] C. Shi, B. Miller, K. Mayaram, and T. Fiez, in: *IEEE Transaction on Circuit and System*. 2011,58(12):827-831.

[5] A. Khaligh, J. Cao, and Y.-J. Lee, in: *IEEE Transaction on Power Electronics.* 2009, 24(3): 862-868.

[6] Y. Li, X. Ruan, D. Yang, F. Liu, and C. K. Tse in: *IEEE Transaction on Power Electronics*. 2010, 25(9): 2372-2385.

[7] Y. Chung, D. Lin, K. Tseng, and C. Wang, in: *Journal of the Chinese Institute of Engineers*. 2007, 30(7):1277-1286.

[8] Q. Wang, J. Zhang, X. Ruan, and K. Jin, in: *IEEE ECCE*. 2010, 1938-1944.

Advanced Materials Research Vols. 960-961 (2014) pp 1295-1299

doi:10.4028/www.scientific.net/AMR.960-961.1295

Low Frequency Oscillation Analysis of Microgrid Using Perturbation Theory

Bingyang Xia[1, a], and Jing Ma[1, b]

[1] State Key Laboratory of Alternate Electrical Power System with Renewable Energy Sources, North China Electric Power University, Beijing 102206, China

[a]hdmajing@aliyun.com [b]hdmajing@ncepu.edu.cn

Keywords: small-signal stability; microgrid; eigenvalue; perturbation; damping ratio; modal analysis

Abstract. This paper presents a perturbation based method for small-signal stability analysis in microgrid based on the uncertainty of microgrid parameters. The small-signal state-space model is built including the dynamic characteristics of the controllers, the power measurement and the system circuit and load dynamics model. The system eigenvalues of operating point at a steady-state in microgrid are obtained by the model. Based on perturbation theory, the corresponding low-frequency eigenvaluea and damping ratio of the microgrid system are calculated when the microgrid parameters changing in the range. Then the relationship between small-signal frequency stability and parameters changes can be determined. The validity of the proposed method and the importance of the stablility analysis of the microgrid small-signal are proved by the simulation results.

Introduction

The microgrid which is under performance of island mode, must be able to maintain its own voltage and frequency. In traditional power grid, frequency can be maintained by large inertia generator which existed in large-scale power plants, voltage can be maintained by adjusting the reactive power. In microgrid, due to the application on a large number of interface inverters, the system has very small or no inertia and poor overload ability, intermittent of output power in distributed power supply which generated by renewable energy and variation of load power, have increased the difficulties of conformity for microgrid frequency and voltage, this may lead to oscillatory instability when microgrid received disturbance.

So far, there is no systematic and complete stability analysis model and method for small-signal in microgrid due to the late development of the distributed generation technologies. The system overall modeling for network, load and inverter in microgrid is performed in[3].The ideal modeling is adopted for inverter, i.e. assume that the bandwidth of closed cycle controller inside inverter is larger than the bandwidth of power controller, current and voltage references can be traced quickly and precisely by closed cycle controlling in inverter, for inverter with smaller capacity, the switching frequency is high, and aforementioned assumption is feasible, but for inverter with large capacity, the bandwidth of the internal controller are limited by the reduction of switching frequency, this will lead to ignorance of some important dynamic properties if the ideal model of the invertered is still applied. Modeling for grid and load has considered the dynamic charateristics of the integrated circuit. Finally the model is applied for analyzing the variation of the eigenvalue of state matrix A in microgrid when the specific parameters changed, then the influence situations of stability on small signal which is impacted by specific parameters in microgrid are obtained. It shows that this kind of stability analysis for small signal is reasonable, however, uncertainty of operation which is caused by uncertainty of parameter variations in microgrid has not taken into account.

The system eigenvalues at a operating point in steady state are obtained in the first place in this paper, then the uncertainty of operation which is caused by uncertainty of parameter variations in microgrid has taken into account, the perturbation theory are applied for the new eigenvalues and eigenvectors under possible operating mode in microgrid and the modeling analysis is performed. Finally the effectiveness of the proposed method is verified by MATLAB simulations.

Space Model of Small Signal in Microgrid

The structure of microgrid is shown in Fig. 1. Micro-source 1 and Micro-source 2 are both connected with power system by inverters, which are controlled in mode of droop control of P-f and Q-V. Microgrid frequency is determined by power system when microgrid is in-grid, therefore the islanding situation is analyzed.

The principle of P-f and Q-V droop controlling is shown in Fig. 2. Instantaneous active power and reactive power of micro-source output are calculated by measured voltage and current. Then average power is obtained from low-pass filter, which is compared with reference power. Micro-source output frequency and voltage amplitude are made out by droop control.

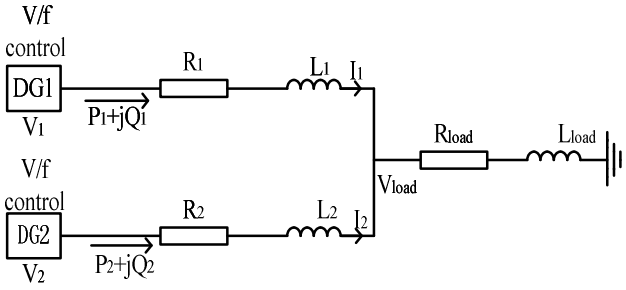

Figure 1. Equivalent circuit model

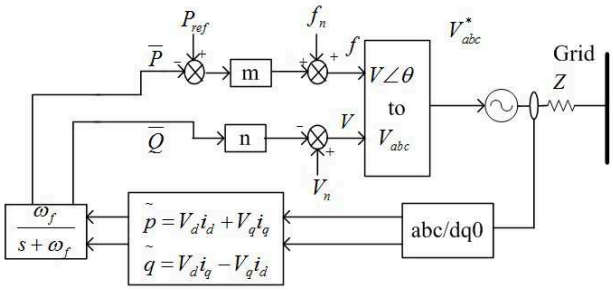

Figure 2. Structure ofP-f&Q-Vdroop controller

The instantaneous power calculation and the low-pass filter model are shown as follows.

The instantaneous power of distributed generation output can be obtained by the following formula:

$$\begin{cases} p_i = V_{di} i_{di} + V_{qi} i_{qi} \\ q_i = V_{di} i_{qi} - V_{qi} i_{di} \end{cases} \tag{1}$$

Linearization of Equation (1) is shown as follow:

$$\begin{cases} \Delta p_i = \Delta V_{di} i_{di0} + V_{di0} \Delta i_{di} + \Delta V_{qi} i_{qi0} + V_{qi0} \Delta i_{qi} \\ \Delta q_i = \Delta V_{di} i_{qi0} + V_{di0} \Delta i_{qi} - \Delta V_{qi} i_{di0} - V_{qi0} \Delta i_{di} \end{cases} \tag{2}$$

where Vdi0, Vqi0, idi0, iqi0 are voltages and currents of output axis d and axis q in distributed generation at steady state operating point, respectively.

The values of average power P and Q through low-pass filter when real-time active or reactive power is obtained by power calculation are shown as follow:

$$\begin{cases} \overline{P_i} = \dfrac{\omega_{fi}}{s+\omega_{fi}} p_i \\ \overline{Q_i} = \dfrac{\omega_{fi}}{s+\omega_{fi}} q_i \end{cases} \tag{3}$$

The linearization model for controller is shown as follows.

For each distributed power supply which is applied by droop controller, the mathematical expression for controller can be described by the following equations:

$$\begin{cases} \omega_i = \omega_{ni} - m_{pi}(\overline{P_i} - P_{refi}) \\ V_i = V_0 - n_{qi}(\overline{Q_i} - Q_{refi}) \end{cases} \tag{4}$$

Embedded (3) into (4), linearize at one point which is implemented by Taylor seried, the constant and one-time term are reserved, assume that $\Delta\omega ni=0$， $\Delta V_0=0$, then:

$$\begin{cases} \dot{\Delta\omega_i} = -\omega_{fi}\Delta\omega_i - m_{pi}\omega_{fi}\Delta p_i + m_{pi}\dot{\Delta P}_{refi} + m_{pi}\omega_{fi}\Delta P_{refi} \\ \dot{\Delta V_i} = -\omega_{fi}\Delta V_i - n_{qi}\omega_{fi}\Delta q_i \end{cases} \tag{5}$$

The value of δi can be obtained by following equation:

$$\delta_i = \arctan\frac{V_{qi}}{V_{di}} \tag{6}$$

where： $V_{di} = V_i\cos\delta_i$; $V_{qi} = V_i\sin\delta_i$ 。

Linearized Equation (6), the result is shown as follow:

$$\Delta\delta_i = k_{di}\Delta V_{di} + k_{qi}\Delta V_{qi} \tag{7}$$

where $k_{di} = -V_{qi0} / (V^2{}_{di} + V^2{}_{qi})$; $k_{di} = V_{di0} / (V^2{}_{di} + V^2{}_{qi})$.

Due to:

$$V_i = \sqrt{V^2{}_{di} + V^2{}_{qi}} \tag{8}$$

Linearization of Equation (8) is shown as follow:

$$\Delta V_i = l_{di}\Delta V_{di} + l_{qi}\Delta V_{qi} \tag{9}$$

where $l_{di} = V_{di0} / \sqrt{V^2{}_{di} + V^2{}_{qi}}$ $l_{qi} = V_{qi0} / \sqrt{V^2{}_{di} + V^2{}_{qi}}$.

Perturbation Theory and Modal Analysis Theory

The eigenvalues of system state matrix A and the relationship of the left and right eigenvectors are shown as follow:

$$\begin{cases} \mathrm{A}\varphi = \lambda\varphi \\ \phi^{\mathrm{T}}\mathrm{A} = \lambda\phi^{\mathrm{T}} \end{cases} \tag{10}$$

where A is state matrix of the system, λ is eigenvalue, φ and ϕ are corresponding left and right eigenvector, respectively;

There exist a variable ΔA in state matrix when a parameter changes, the relationship of the eigenvalues and eigenvector become:

$$(\mathrm{A}+\Delta\mathrm{A})(\varphi+\Delta\varphi)=(\lambda+\Delta\lambda)(\varphi+\Delta\varphi) \tag{11}$$

The values of system eigenvalues and right eigenvector after disturbance are shown as follow:

$$\begin{cases}\lambda^{'}=\lambda+\Delta\lambda\\ \varphi^{'}=\varphi+\Delta\varphi\end{cases} \tag{12}$$

According to perturbation,

$$\begin{cases}\Delta\lambda=\phi^{\mathrm{T}}\Delta\mathrm{A}\varphi\\ \lambda^{'}=\lambda+\Delta\lambda\end{cases} \tag{13}$$

A is seen in the afore-equation: the eigenvalues of $\mathrm{A}^{'}$=A+ΔA can be obtained by left and right eigenvectors and variable ΔA of matrix A which A has not been transformed.

Simulation Analysis

As is shown in Figs.1 and 2, the controller and circuit parameters of microgrid are shown as follow: the value of R_1+X_1 is (0.001+j0.0628) Ω, the equivalent circuit impedance R_2+X_2 is(0.001+j0.1256) Ω; the load impedance R_{load}+X_{load} is (2+0.314) Ω ;low-pass filter cutoff frequency ω_{f1} and ω_{f2} are 40 rad/s; frequency droop gain m_{p1} and m_{p2} are1.256 × 10^{-4}rad/(s • W) and 3.14 × 10^{-4} rad/(s • W) ,respectively; voltage droop gain n_{q1} and n_{q2} are 1×10^{-4} V/var and 5×10^{-4} V/var, respectively; regular operating frequency ω_n is 314 rad/s; voltage amplitude $V_0$is 311 V when there is no reactive power; rated active power P_{ref1} and P_{ref2} are 50 kV and 20 kW, respectively.

The eigenvalues of system at steady-state operating point when microgrid operated stably are calculated, -1.7653±0.3144i; -0.0235±0.2969i; -0.0199±0.0983i; -0.0001± 0.0096i; -0.0396±0.0013i; the electromechanical oscillation mode are the most commonly concern in stability analysis for small-signal in power system, i.e. low-frequency oscillation mode which rated at $0.2H_z$ ~$2.5H_z$. Therefore, main low-frequency eigenvalues -0.0190±0983i which real part close to imaginary axis are analyzed for eigenvalues of state matrix A of microgrid.

The uncertainty interval of equivalent circuit impedance in the system distributed at [0.85, 1.15] X_1 , [0.85, 1.15] X_2,i.e.X_1~[0.055264,0.072200],X_2~[0.011053,0.14440].Perturbation are used for calculating variations of main low-frequency eigenvalues of the system when the equivalent line impedance changes.

Conclusion

A small-signal state-space model of microgrid is built in this paper. This model concludes the inverter model and the dynamic network and load model. With this model, taking the parameter uncertainty into account, the low-frequency eigenvaluea and damping ratio of the microgrid system are calculated based on the perturbation when the microgrid parameters changing in the range. The analysis result of the low-frequency eigenvalues shows that the system may be unstable when the equivalent line impedance between distributed generations is very small. Increasing of the power controller droop gain will make the stability of the system worse. The system is less stable when the load impedance is much large. Time-domain simulation results verify the correctness of the eigenvalues calculation.

References

[1] ZHANG Jianhua; SU Ling; LIU Ruoxi; WANG Li; CHEN Yong, "Small-signal Dynamic Modeling and Analysis of a Microgrid Composed of Inverter-interfaced Distributed Generations". Automation of Electric Power Systems, vol.34, no.22, pp. 97-102, Nov.25, 2010.

[2] WANG Chengshan; XIAO Zhaoxia; WANG Shouxiang. "Synthetical Control and Analysis of Microgrid". Automation of Electric Power Systems, vol.32, no.7, pp. 98-103, Apr.10, 2008.

[3] XIAO Zhaoxia; WANG Chengshan; WANG Shouxiang. "Small-signal Stability Analysis of Microgrid Containing Multiple Micro Sources" Automation of Electric Power Systems, vol.33, no.6, pp. 81-85, Mar.25, 2009.

[4] LASSETEL R, AKHIL A, MARNAY C, et al. White paper on integration of distributed energy resources—the CERTSmicrogrid concept [R/OL]. [2008-06-06].

[5] ENGLER A. Applicability of droops in low voltage grids.International Journal of Distributed Energy Resources, 2005,1(1): 1-6.

[6] XING Jie; CHEN Chen; WANG Jie ,"A Small-signal Stability Analysis Method Under Interval Uncertainty." Automation of Electric Power Systems, vol.34, no.6, pp. 12-16, Nov.25, 2010.

[7] WANG Zhiqun, ZHU Shouzhen, ZHOU Shuangxi. Controller design for inverter-based distributed generation. Automation of Electric Power Systems, 2004, 28(24): 61-66.

[8] POGAKU N. Analysis, control and testing of inverter-based distributed generation in stand alone and grid-connected applications [D]. London, UK: Imperial College, London,2006.

[9] WANG Kang, JIN Yuqing, GAN Deqiang, et al. Survey of power system small signal stability and control. Electric Power Automation Equipment, 2009, 29(5): 10-19.

[10] WANG K W,TSE C T,TSANG K M. Algorithm for power system dynamic stability studies taking account of the variation of load power. Electric Power Systems Research, 1998, 46(3).

Advanced Materials Research Vols. 960-961 (2014) pp 1300-1303

doi:10.4028/www.scientific.net/AMR.960-961.1300

Development of Cathode Filament Power Supply for EBW Based on ARM

Ze-ting WANG[1, a], Peng LIU[1,b] and Sheng-wen FAN[1,c]

[1]Full address of first author, China

[a]wangzeting@ncut.edu.cn, [b]799325487@qq.com, [c]fsw@ncut.edu.cn

Keywords: electron beam welder, STM32, Digital, The cathode filament.

Abstract. The electron beam welding has high energy density, and has been widely applied in air space, the car and shipping industry. Traditional electron beam welding machine power supply system adopts the technology of the power frequency or medium frequency, with high volume, low efficiency and poor stability of electron beam. I put forward a digital filament power control scheme based on STM32, and introduce the hardware and software implementation method in detail. Experiments show that it can realize soft-start and soft-down process, and also be quickly identified and promptly forbid the output when filament fracture, which realize the intellectualization of filament power supply.

Introduction

Electronic beam welding is a kind of technology which uses electronic beam as heat source and it`s working principle is shown in Fig. 1. When the cathode filament of electronic gun is heated to a certain temperature, it will outcome electron. Electrons are accelerated to or close to the speed of light in electronic gun and focused by electromagnetic lens to the beam of high intensity and high energy. When the beam bombards welding surface, its strong kinetic energy turns to heat energy flashily. It can molten metals to achieves the welding purpose [1].

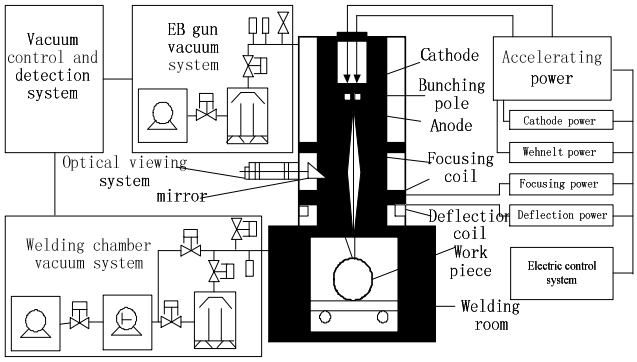

Fig. 1. The working principle of electron beam welder

Filament power is mainly used for heating the filament, which make its heat emission electrons, after controlling the filament heating power supply output voltage or current can achieve the goal of control overflow electronic, thereby indirectly control the electron beam size. In the process of actual welding, need the cathode filament can stable transmission electron and electron density within the electron gun is almost maintained constant, so it has a high requirement on the filament heating power.

The Existing Problems

In-depth study on the cathode filament heating power of the relevant literature, this paper [2] points out that the resistance of the filament in a cold only about one over ten of the thermal state, if use the primary side voltage control, power supply will have a great impact current on the cathode

filament, this will affect the service life of the filament and working state of the electron gun. And is described in the literature [3] if the filament transformer primary side adopts steady flow method, if burning filament in work break, second side current is almost zero, as a result of the action of a closed-loop controller will be the primary side current increase, making the original side voltage to maximum, so easy to damage the inverter circuit. Aiming at the problems mentioned in the above literature, I put forward a kind of limiting filament power supply output voltage is out of control.

System Structure and Design

Fig. 2 shows that the filament power is mainly composed of EMC filter, rectifier circuit, Buck circuit, full bridge inverter circuit, signal processing circuit, control circuit, fault protection circuit and high frequency transformer rectifier circuit, etc. Buck circuit is to realize the regulation of dc voltage amplitude and the full bridge inverter circuit is to complete DC/AC conversion. So we only need to change the duty cycle of IGBT of Buck circuit and it can change the output voltage or current to achieve closed-loop control purpose.

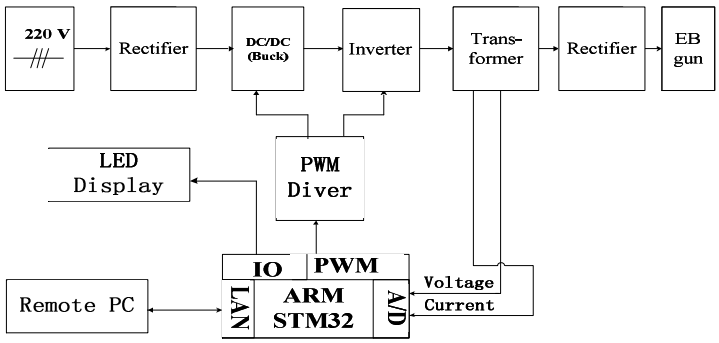

Fig. 2 The filament power supply block diagram

A. The Key Parameter Computation of Buck Circuit

Typical Buck circuit is shown in Fig. 3. The switching frequency is selected at 20,000Hz. Due to adopt a square wave full-bridge inverter and, don't change the duty cycle of PWM wave, so the full-bridge inverting circuit, transformer, rectifying and filter circuit can be equal to a DC voltage amplifier whose voltage gain is K. It only has a tiny lag which we don't have to consider.

Filament heating power supply is used for heating filament, and it can control the current through the filament which indirectly control the beam current when jointing.

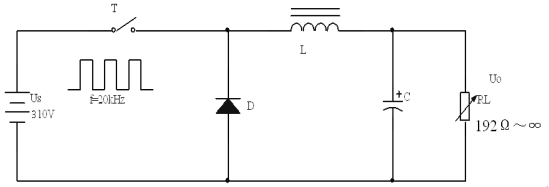

Fig. 3 Buck equivalent circuit of filament power

According to technological requirements, filament power whose maximum output voltage about 6 volt (corresponding to the filament transformer primary side input voltage is about 240 volt), and the output current is adjustable from 0 to 30 ampere, so the filament power supply output power changes form 0 to180 watt. In consideration of full bridge inverter circuit efficiency around 80%, the output power of Buck circuit is from 0 to 300 watt, which is equal to a load variable resistance from 192Ω to ∞.

The current ripple of Buck circuit is decided by the filter inductance, and the voltage ripple is decided by filter capacity [4]. The selection of capacity is relatively easy. The design of power inductance and filter capacitor is introduced as follows.

Inductance calculation formula $L=\frac{U_d-U_o}{\Delta I_L}DT$ (1)

Capacitance calculation formula $C=\frac{D_0}{8L_0f^2}\cdot\frac{U_0}{\Delta U_0}$ (2)

Where, U_d = = . 5 = 5 μ , current ripple ΔI_L=0.2I_d. Put these parameters into formula (1) and get the inductance value L=3.84mH. Consider actual situation, and finally choose the output filtering inductance L=4.5mH. Also Put the parameter into the formula (2) and get the minimum output capacitance C=5.6uF.The actual selection of output capacitance is C=10uF.

B. The CPU Control Circuit

CPU is the core part of the filament power supply, which mainly responsible for data acquisition, PI closed-loop control, PWM wave output, abnormal protection, parameter setting and external communication. CPU is selected as STM32F107 by ST company [5]. The chip adopts ARM 32-bit Cortex M3 as the core, and the highest frequency is up to 72 MHz. The chip has rich communication unit, including Ethernet interface, the asynchronous serial interface, USB devices, CAN devices, SPI and I2C module. Filament power also includes drive circuit, signal modulation circuit, protection circuit, communication circuit, display circuit and so on.

C. Filament Power Digital PI Closed Loop Control

With the output power gradually increasing of Buck circuit, the working mode of Buck circuit will change from DCM into CCM state. Therefore, the controlled system is a typical nonlinear control system [6].The digital PI control is adopted in the filament power supply.

When the filament in the cold state, if we adopt feedback voltage control and open filament power, which is bound to make a big impact current on the filament and it will affect the service life of cathode filament .To avoid this situation, the filament transformer primary side current control mode is adopted. If using current control, when the filament fracture, the inverter would output the high voltage that device is easily damaged. In order to solve those problems, it is necessary to limit the output voltage, and prompt the user filament fracture failure in time, then automatically output voltage down to zero.

The system software design

CPU mainly completes algorithms, generates PWM pulses, fault protection, data display and remote communication. System software is mainly to the STM32 chip programming. Programming languages adopts C language .

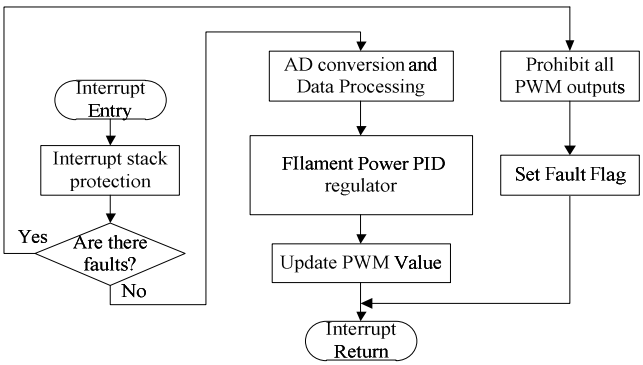

Fig. 4 Interrupt function flowchart

After entering the PWM interrupt, the flowchart shown in Figure 4. Firstly, feedback from various signals are sampled and processed. And then it will produce PWM pulses for filament supply. The PWM pluses is amplified and isolated by the driver circuit to drive IGBT, which realizes closed-loop control of the entire power supply system.

The Experimental Results

Very thin slices of tungsten filament is usually used for Electron beam welder cathode filament, and its resistance is usually extraordinary small .It is usually need to add adjustable voltage from 0 to 6 volt on both ends of the filament, and the maximum current through filament can be up to 30 ampere . We use the filament power on an electron beam welding machine by a well-known manufacturer, and some working waveforms of filament power are shown in Fig. 6.

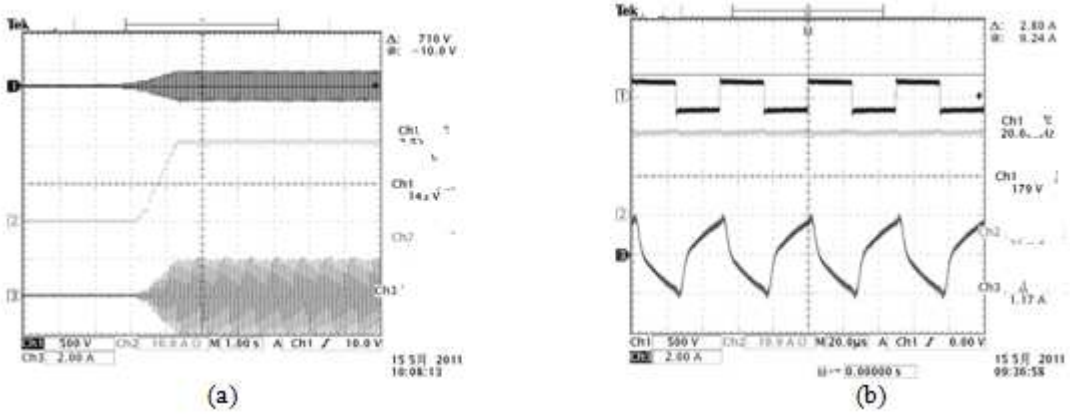

Fig. 6 (a) is filament power starting waveform and (b) is filament power steady-state waveform at 20 A

Ch1, Ch3 are filament transformer primary side voltage and current waveforms, and Ch2 is filament current waveform. We can see that filament power can well realize the soft start in fig 7 and almost no overshoot. And also we found that filament current ripple is very small in fig 8, which is controlled within 5%. These prove filament power has achieved good control effect.

Summary

Digital filament power based on Arm (STM32F107) has high precision, small size, full digital etc. All parameters can be set directly through the HMI or remote PC. It can realize soft-start and soft-down process, and also be quickly identified and promptly forbid the output when filament fracture.

References

[1] Shengwen Fan, Zeting Wang and Zhengxi Li: Development of High Voltage Source for Electronic Beam Welder Based on Phase Shift Control. Automation & Instrumentation, Vol. 12 (2010), p. 62-64

[2] Zhi Zhang: Constant Power Supply for the Filament of High-power Transmitting Tube. Radio & TV Broadcast Engineering, Vol. 1 (1990), p. 23-25

[3] Qiang Hai: The Electron Gun of Electron Beam Welding Machine of High Stability and Its Measuring Method, Vol. 12 (1999), p. 21-23

[4] Weixin Lin: Modern Power Electronic Circuit. Hangzhou: Zhejiang University Press, 2006

[5] Xiaoxue Wang, Jianming Liu: Design of Intelligent Motor Protector Based on ATM32. Resistor Technology, Vol. 10 (2009), p. 23-25

[6] Xinbo Ruan, Yangguang Yan: Review on Soft-switching Technique in DC/DC Power Supply. Beijing: Beijing science and Technology Press, 2000

Advanced Materials Research Vols. 960-961 (2014) pp 1304-1307

doi:10.4028/www.scientific.net/AMR.960-961.1304

Study on Buck-Boost Integrated Type Three-Port Converter

Zhu Lei Shao[1, a]

[1] College of Electrical and Information Engineering, Xuchang University, Xuchang 461000, China

[a]cyzyszl@163.com

Keywords: DC-DC converter; buck-boost integrated type; three port converter

Abstract. Aiming at simplifying the structure of power supply system of new energy, a buck-boost integrated type three-port converter is designed in this paper. The three-port converter can replace three separate converters, which makes the system structure is simplified and manufacturing cost is reduced. The three-port converter realizes the current expansion and ripple suppression by adopting inductor interleaved parallel bridge arm structure. The topology and control strategy of the three-port converter are analyzed in this paper. From the experimental results, the inductor current ripple and realization of soft switch meet the design requirement. The buck-boost integrated type three-port converter is applicable to the new energy power supply system.

Introduction

With the development of new energy application technology, the converter is more and more applied in new energy power supply system. All kinds of new energy power supply system include energy storage module and power conversion module, which contains a plurality of converters. With the increase of the number of converters, the structure of system becomes complex, and the manufacturing cost becomes high. The multi-port converter can replace multiple independent converters, and it can control the input power, the energy storage module and the load at the same time. The application of three-port converter makes the system structure is simplified and manufacturing cost is reduced.

A buck-boost integrated type three-port converter is designed in this paper, which can realize the free energy transmission between three ports. Comparing with the traditional three-port converter, the buck-boost integrated type three-port converter has a simpler circuit structure, and power switch can turn on in zero voltage. The adopting of coupling inductor makes symmetric bridge arm structure and reduces the inductor current ripple. The buck-boost integrated type three-port converter is suitable for large current power supply system.

Circuit topology and control strategy

The ports of three-port converter are defined as port1, port2 and port3. The full bridge structure unit and half bridge structure unit are respectively arranged at both sides of the transformer TX1. The buck-boost bidirectional conversion and the full bridge structure unit are integrated together. The buck structure unit and the boost structure unit share a group of bridge arm of full bridge structure unit. The connection point of the high voltage port of buck-boost structure unit and the full bridge structure unit are port1. The low voltage port of buck-boost structure unit is port2. The port3 transmit energy to port1 and port2 by transformer and half bridge structure unit. The circuit topology of the buck-boost integrated type three-port converter is shown in Fig. 1.

In order to control the voltages and currents of ports, PWM phase shift control strategy is adopted in three-port converter. The power switches of bridge arm alternately conducted for avoiding short circuit of voltage source. The power switch M1 and M2 control voltages and currents of port1 and port2, and the duty ratio of M1 and M2 is D and 1-D. The driving signal of M1 ahead of driving signal of M2 about half cycle for getting AC voltage of no DC component in the middle of the bridge. In order to transfer energy between the ports, the circuit units of both sides of the transformer adopt phase shift control strategy. The shifting-phase angle is φ, which is the phase angle of driving signal of M5 advancing driving signal of M1. The duty ratio of M5 and M6 are 0.5. The direction and amount of energy transmission between ports is controlled by adjusting the phase angle.

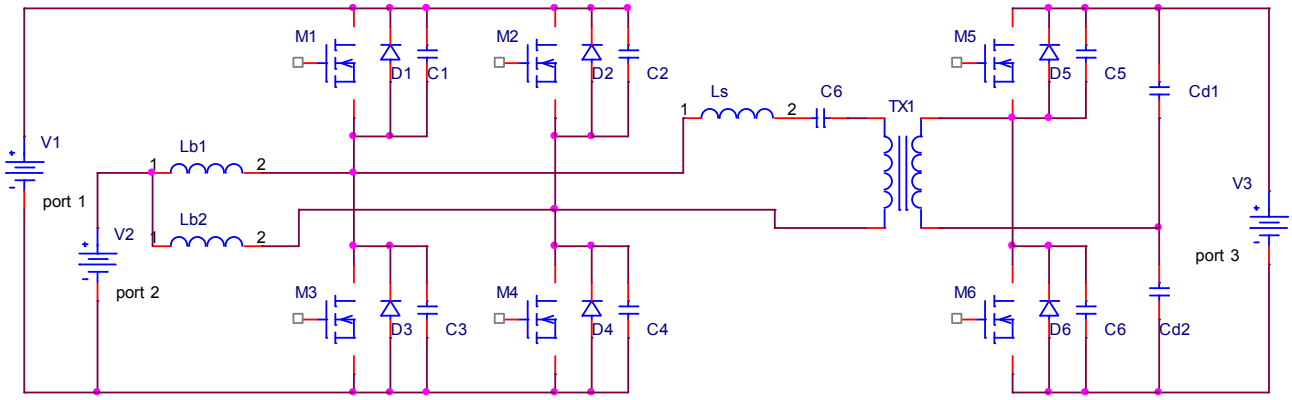

Fig. 1 The circuit topology of buck-boost integrated type three-port converter

Analysis of inductor current and port current ripple

The reverse coupling inductor can obtain bigger equivalent inductance, which can make the volume of magnetic core be reduced. The inductive coupling coefficient is k, which indicates the close degree of coupling. When the duty ratio is less than 0.5, the inductor current ripple Δi_{Lb1} and Δi_{Lb2} can be got in formula (1).

$$\Delta i_{Lb1} = \Delta i_{Lb2} = \left(\frac{V_1}{1+k} - V_2 \right) \frac{DT_s}{(1-k)L_b} \tag{1}$$

In the formula (1), V_1 is the voltage of port1, V_2 is the voltage of port2, and D is the duty ratio of power switch. T_s is the period of driving signal, and L_b is the value of L_{b1} and L_{b2}. When $(1-k)L_b$ is a constant, the bigger the inductive coupling coefficient k is, the smaller the inductor current ripple is. When the duty ratio is bigger than 0.5, the conclusion is similar to formula (1).

To make the comparison, the different topologies of inductor current ripple in port2 can be got in formula (2), formula (3) and formula (4).

$$\Delta i_2^{(1)} = \frac{V_1 - V_2}{L_b^{(1)}} DT_S \tag{2}$$

$$\Delta i_2^{(2)} = \frac{V_1 - 2V_2}{L_b^{(2)}} DT_S \tag{3}$$

$$\Delta i_2^{(3)} = \frac{V_1 - 2V_2}{(1-k)L_b^{(3)}} DT_S \tag{4}$$

$\Delta i_2^{(1)}$ is the inductor current ripple of a single inductor, $\Delta i_2^{(2)}$ is the inductor current ripple of parallel inductance, and $\Delta i_2^{(3)}$ is the inductor current ripple of coupling inductance. From the formula (2), (3) and (4), reducing current ripple of port2 should satisfy the condition as formula (5).

$$\lambda \geq 1 - \frac{1}{1/D - 1} \tag{5}$$

In the formula (5), $\lambda = L_b^{(2)} / L_b^{(1)}$, D is the duty ratio of power switch. If $(1-k)L_b^{(3)} = L_b^{(2)}$, $\Delta i_2^{(2)} = \Delta i_2^{(3)}$. When three-port circuit meet the formula (5) and $L_b^{(3)} = L_b^{(2)} / (1-k)$, the current ripple can be effectively reduced.

Analysis of soft switching condition

The soft switching technology can reduce the power consumption of converter. When the duty ratio is less than 0.5, the condition of soft switching is analyzed. The condition of soft switching of M1 to M4 can be got in formula (6) and formula (7)

The condition of soft switching of M1 and M2 is formula (6)

$$i_1(t)-(I_{Lb}-\frac{1}{2}\Delta i_{Lb}^{(1)})-\frac{1}{2}\Delta i_{Lb}^{(2)}>0 \tag{6}$$

The condition of soft switching of M3 and M4 is formula (7)

$$i_1(t)+(I_{Lb}+\frac{1}{2}\Delta i_{Lb}^{(1)})-\frac{1}{2}\Delta i_{Lb}^{(2)}>0 \tag{7}$$

In the formula (6) and (7), $i_1(t)$ is the current transformer, I_{Lb} is the DC component of the inductor current, which can be got in formula (8). $\Delta i_{Lb}^{(1)}$ is the inductor current ripple of L_{b1}, $\Delta i_{Lb}^{(2)}$ is the inductor current ripple of L_{b2}.

$$I_{Lb}=\frac{P_2}{2DV_1} \tag{8}$$

In the formula (8), P_2 is transmission power of port2, V_1 is the power supply voltage of port2. D is the duty ratio of power switch.

The inductor current ripple $\Delta i_{Lb}^{(1)}$ and $\Delta i_{Lb}^{(2)}$ can be got in formula (9) and (10).

$$\Delta i_{Lb}^{(1)}=\frac{DV_1}{L_b^{(1)}}(1-D)T_S \tag{9}$$

$$\Delta i_{Lb}^{(2)}=\frac{DV_1}{L_b^{(2)}}(1-D)T_S \tag{10}$$

In the formula (9) and (10), $L_b^{(1)}$ is the value of L_{b1}, $L_b^{(2)}$ is the value of L_{b2}. T_S is the period of power switch driving signal.

Experimental verification

In order to verify the circuit performance, the buck-boost integrated type three-port converter is built in PSpice. The circuit parameter settings are as follows. The port1 voltage V_1 is in 200V to 260V, the port2 voltage V_2 is in 100V to 120V, and the port3 voltage V_3 is in 200V. The power switching frequency f_S is 50kHz. The DC isolation capacitor C_b is 8uF. The series inductance L_S is 94uH. The transformer turns ratio n is 2. The divider capacitor C_{d1} and C_{d2} are both 1000uF. The coupling coefficient k is 0.5. The coupling inductance L_b is 67uH. When three-port converter is in full load condition, the waveforms of circuit nodes were shown in Fig. 2.

As shown in Fig.2, the transformer primary voltage Vab is shown on the top of the figure, the transformer secondary voltage Vcd is shown in the middle of the figure, and the coupling inductor current ILb is shown in the bottom of the figure. Because Vab is ahead of Vcd, port1 transmits energy to port2 and port3. The transformer primary voltage range is from -320V to 320V, and the transformer secondary voltage range is from -160V to 160V. When the port1 does not work, Vcd will be ahead of Vab. The port2 transmits energy to port3. With the increase of the inductance coupling coefficient, the current effective value of power switch will decrease gradually. So increasing inductance coupling coefficient can effectively reduce the current stress of power switch, and the power consumption of the circuit is reduced. But the inductance coupling coefficient should be small for getting a wide range of soft switching. So the selection of the inductance coupling coefficient should consider the efficiency of circuit and soft switching conditions at the same time. Three-port converter can transmit energy between three ports normally, and the power switches are working in the soft switching conditions.

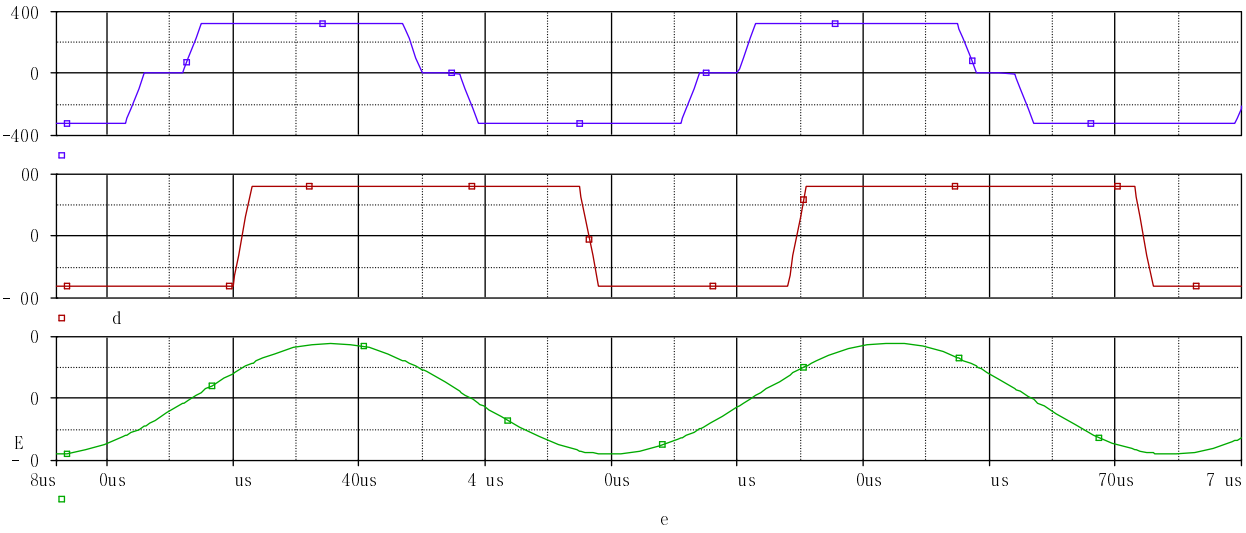

Fig. 2 The waveforms of circuit nodes in full load condition

Conclusions

A buck-boost integrated type three-port converter is designed in this paper, which can simplify the structure of power supply system. The three-port converter has the advantages of simple structure. The two bridge arms of three-port converter are symmetrical and inductor is in interleaved parallel connection state, which realizes the current expansion and ripple suppression at the same time. By reasonably selecting coupling coefficient, inductor current ripple is effectively reduced, and soft switching range is enlarged. From the experimental results, the buck-boost integrated type three-port converter has high efficiency, and the design of three-port converter meets the design requirements.

References

[1] Liw, Xiao J, HE X. PWM plus phase angle shift (PPAS) control scheme for combined multi-port DC/DC converters[J]. IEEE Trans on Power Electronics, 2012, 27(3): 1479-1489.

[2] KHANH L, SEO J, KIM Y. Power-management strategies for a grid-connected PV-FC hybrid system[J]. IEEE Trnns on Power Delivery, 2010, 25(3): 1874-1882.

[3] JIANG W, FAHIMI B. Active current sharing and source management in Fuel cell-battery hybrid power system[J]. IEEE Trans on Industrial Electronics, 2010, 57(2): 752-761.

[4] BENAVIDES N, CHAPMAN P. Power budgeting of a multiple-input Buck-Boost converter[J]. IEEE Trans on Power Electronics, 2005, 20(6): 1303-1309.

[5] KOTSOPOULOS A, DUARTE J, HENDRIX M. Transformer-coupled multiport ZVS bidirectional DC-DC converter with wide input range [J]. IEEE Trans on Power Electronics, 2008, 23(2): 771-781.

[6] YANU Fei, RUAN Xinbo, YANU Yang. Interleaved critical conduction mode Boost PFC converter with coupled inductor[J]. Transactions of China Electrotechnical Society, 2013, 28(1): 215-224.

Advanced Materials Research Vols. 960-961 (2014) pp 1308-1311

doi:10.4028/www.scientific.net/AMR.960-961.1308

The DMT power line channel sparse Bayesian regression estimation based on communication system

Yipei Huang[1, a], Yajun Han[2] and Baofan Chen[3]

School of Mechanical and Electrical Engineering, Chongqing Creation Vocational College, China

[a]email: 18811778@qq.com

Keywords: SBL, DMT, RVM, channel estimation, regression analysis

Abstract. This paper introduces the power line communications channel estimation method based on sparse Bayesian regression, it is through the use of Bayesian learning framework that provides a sparse model in the presence of noise accurate channel estimation model. Improved channel estimation using the power line for the system to consider the frequency domain equalization (FREQ) transmitter and receiver, the bit error rate and comparing the two methods for generating various channel estimation techniques, and (BER) performance curves simulation the results show that the performance of the method is better than the previous method of least squares technique.

Introduction

Power Line Communication (PLC) and more attention, because they represent two LAN access and efficient and economical solutions. Multi-Carrier (MC) based system is popular for wireline and wireless communications because of its many advantages, the use of DMT is well suited PLC channel [4] which has the advantage of flexibility and without regard to the loading position of signal to noise ratio (SNR). During modem initialization phase, the frequency response of the channel SNR estimate is usually performed measurements. When this paper, we use Bayesian regression and sparse mode, channel estimation, reducing the signal to noise ratio is low.

System Model

System block diagram of Figure 1, showing a discrete multitone (DMT) link, comprising: a DMT modulation, channel model, DMT demodulator, and the frequency domain equalizer.

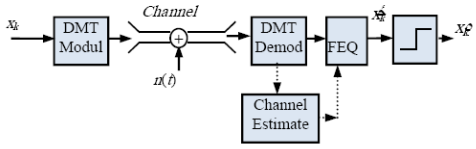

Fig.1-1: DMT system block diagram with FEQ at receiver

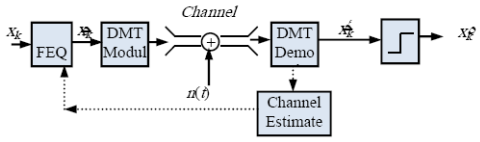

Fig.1-2: DMT system block diagram with FEQ at transmitter

DMT-speed transfer [3] data stream, while the R, N low-rate stream to a subcarrier. For any data stream using N R / N indicates that it is sent to a 2N-point Fast Fourier Transform (IFFT) block, the N complex frequency domain to the time domain data conversion, as shown in Figure 2. V is an extended cyclic data to 2N time domain samples of the formation of cyclic extension DMT.

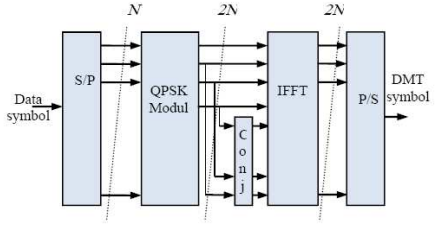

Fig.2: Block diagram of the DMT modulator

The use of DMT which is similar to the asymmetric digital subscriber line (ADSL) configuration, but is fixed for each subchannel modulation (i.e., QPSK). V cycle length of the data included in the

selection channel interference (ISI) and inter-channel delay spread such that the maximum time span cyclical DMT.

The PLC Channel Model

Power line network and the traditional media, such as topology and physical properties of different twisted pair, coaxial or fiber optic cables, the complexity PLC so that when high frequency signals [2], the first is caused by attenuation of the line length and increasing the frequency of the transmitted signal low-pass behavior, the second is caused by impedance mismatch at the branch multipath propagation. In this article, we will use the access domain measurement model is used for signal transmission [2] to simplify the PLC channel model is described as follows:

$$H(f)=\sum_{i=1}^{M} g_i e^{-(a_0+a_1 f^k)d_i} e^{-j2\pi f\frac{d_i}{v_p}} \quad (1)$$

Where M is the total number of paths, gi is the weighting factor of the corresponding path, di is the path length, vp is the phase velocity. Parameters a0, a1, and k low-pass characteristic described channel. PLC channel noise can be colored Gaussian noise with a high-power low-frequency modeling. Noise power spectral density N (f) = N0 + N1e-f/f0 [8], where N0, N1, and F0 are equal -140dB/Hz, -38dB/Hz, and 0.7MHz. The PLC channel model is simple, suitable for simulation and analysis of system performance PLC.

Linear System Representation of Signal Transmission

We will consider in the PLC channel has a CIR does not exceed the CP. Thus, the inserted sample V CP and dropping the first transmitter receiver provides real-valued time domain samples sampled (baud) of the received DMT is more than one data block:

$$r = Cx + n \quad (2)$$

Where the vector r= [R0，R1，R2，...，R2N-1]Tcontaining the time domain samples of the received vector x= [X0，X1，X2，...，X2N-1]T containing the transmitted the time-domain samples and the vector n= [N0，N1，N2，...，N2N-1]T containing the sample is limited to the average frequency power (variance) of the additive noiseσN2. Matrix multiplication operator in (2) circular convolution is no inter-symbol interference (ISI). The cyclic matrix is expressed as

$$C=\begin{bmatrix} h_0 & 0 & \cdots & 0 & h_L & \cdots & h_1 \\ h_1 & h_0 & & & & & \vdots \\ \vdots & & \ddots & & & & h_L \\ h_L & & & & & & \\ 0 & h_L & & & & & \\ \vdots & \ddots & \ddots & & \ddots & \ddots & \vdots \\ 0 & \cdots & 0 & h_L & \cdots & h_1 & h_0 \end{bmatrix} \quad (3)$$

$$\begin{bmatrix} R_0 \\ \vdots \\ R_{2N-1} \end{bmatrix}=\begin{bmatrix} H_0 & \cdots & 0 \\ \vdots & \ddots & \vdots \\ 0 & \cdots & H_{2N-1} \end{bmatrix}\begin{bmatrix} X_0 \\ \vdots \\ X_{2N-1} \end{bmatrix}+\begin{bmatrix} N_0 \\ \vdots \\ N_{2N-1} \end{bmatrix} \quad (4)$$

When in the frequency domain（X = W2N-1 [X0，X1，X2，...，X2N-1] T）of the transmission data generation, and the received samples are converted into the frequency domain（W2N1= [R0, R1, R2，...，R 2 N-1] T）, the resulting input-output relationship is very simple:

W2Nn=[N0，N1，N2，……N2N-1] T. From (4) we can see that the symbols for each frequency-domain symbols received in each subchannel is simply a scaled version of the transmission frequency domain plus Gaussian colored noise. Furthermore, each subchannel can be processed independently of the other subchannels. In other words, the CP and the converted block transmission time dispersive channel is 2N parallel flat narrow-band channels, each channel gain Hk or tone additive Gaussian noise with so called discrete multitone transmission (DMT).

Channel Estimation

When initialization channel estimation, using a pseudo-random sequence of frequency-domain

$$R_b = X_b H + N \quad (5)$$

$$H_k=\sum_{n=0}^{L-1} h_n e^{-j2\pi n/2N} \quad (6)$$

In (5), R b is the received signal vector 2N × 1 times, the transmission signal of the diagonal matrix Xb, N is the noise vector of 2N complex comprising subcarriers, H is a complex vector containing the entire transmitter and receiver channel gain between.

The current problem is that the frequency domain channel estimate vector, Hk, (K = 0,1,2,3, …, n-1) time-domain FFT L tap gains unknown sample interval, which contains the desired selection L the maximum delay spread, and does not exceed the CP length, V. tone of each of the 2n channel frequency domain model:

Where h is the channel taps in discrete time n. From (5) to perform channel estimation, we first training symbol by the conjugate of each frequency domain to produce a vector is [7]:

$$T_b = X_b^H R_b = X_b^H X_b H + X_b^H N \quad (7) \qquad t_b = h + n' \quad (8)$$

Where the superscript H, said conjugate transpose.

In the noise free case, the frequency domain channel gain in type 7 Tb contains the complete. When the channel impulse response values for the duration of compulsory sample number zero is larger than the cyclic prefix, so it will need to modify the LS estimation [11]. We will use a similar to that used for the relevance vector machine (RVM) model, the inverse Fourier transform of the DMT channel estimation (10) fitted regression model as follows:

tb =[t0，t1，t2，...，t2N-1] T, is a time-domain signal, target vector of h =[h0，h1，h2，..., hV, 0，...，0] T 2N x 1 channel vector, and the vector N' = [h0, H1, H2,..., h2N-1] T contains the band limited Gauss the noise variance σ'2

In order to avoid the influence of noise to observe the formula in the H model (8) in the TB, will use the sparse Bayesian regression, it has set the regression weight appropriate for automatic performance of zero, to avoid fitting in signal noise. Assume that the channel can use the function y (n) approximation is a linear combination of functions:

$$y(n) = \sum_i w_i \varphi(n - i) \quad (9)$$

Simulation Results

In the MATLAB simulation is used to evaluate the performance of DMT/ RVM system. The simulation parameters were: DMT 2N= 512 FFT size, cyclic prefix length. =64. Sub channel tones used for 6-255, which uses QPSK modulation scheme, each sub carrier. The additive channel noise is band limited Gauss color and power Delta n2. Channel in the actual power line length to generate the L=43. model parameters of the model: k = 1, a0=0, a1=7.8 * 10-10 s/ m and the path parameter gi={0.64, 0.38, -0.15, 0.05} and the corresponding DI / M ={200222.4244.8267.5}.

In Figure 3, we present an example, the target vector equation of time domain samples (8), in the noise free case, the channel impulse response and superimposed in the same product.

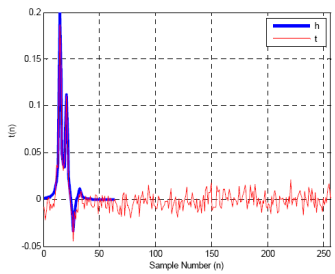

Fig.3: An example target vector

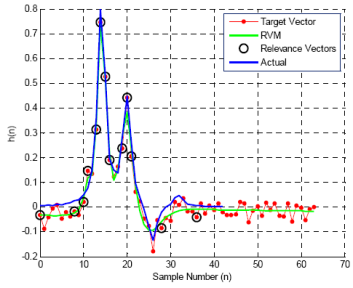

Fig.4. Channel impulse response and its estimate obtained using the RVM method

These channels are assumed to remain constant guide each detection frequency sequence in the. Figure 4 depicts the actual in cyclic prefix range of sampling channel if it is equal to zero time values larger than the cyclic prefix. The target vector is drawn at the same time range equivalent to least square channel estimation (LS). Bias sparse regression algorithm to deal with the target vector

samples, to filter out noise at 5 dB snr. Non zero regression weight position determination and circular plot. In 65 weight, defines 13 nonzero weights, from a total of 65, the remaining 52 are sparse mode is set to zero.

That estimate the impact on each sub carrier frequency attenuation of channel impulse response (equilibrium), from Figure 5 we see model, sparse channel estimation in the frequency domain of the adjacent smooth with changes between tone and closer to the ideal frequency response.

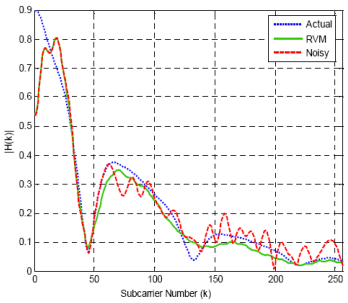

Fig.5. Frequency response of actual and estimated channel

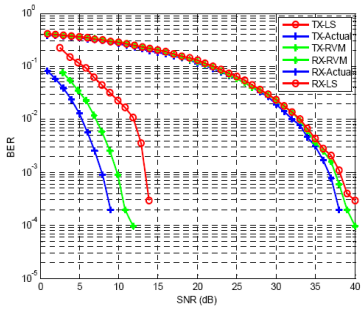

Fig.6. BER curves with equalization at transmitter and receiver

At the same time, based on the curve of bit error rate performance of the actual channel (perfect estimation) is added as a reference marker for the performance of the same plot in figure 6. We also compare the map accurate channel estimation is achieved when the 6 letter in the receiver, the transmitter. We can make two suggestions: first, this is obviously, the letter in the transmitter receiver is much better than that in the same channel estimation. Second, when the signal at the receiver in the channel estimation error rate performance has a limited effect on accuracy improvement (Rx marker), and bit error rate curve is almost the same channel, the channel estimation, sparse regression, and LS channel estimation. Equilibrium process of fading in low signal to noise ratio in this case, the channel for improved accuracy is not important.

Conclusion

In order to achieve the full utilization of the available bandwidth of DMT data transmission system of power line, channel equalization is a prerequisite. In this paper, we propose an improved channel estimation method, the sparse Bayesian regression method based on DMT communication system by RVM. The method in the accuracy of channel estimation to improve frequency equalization. Frequency domain equalization in the transmitter at the receiving end to estimate curve than the BER performance of precision is more sensitive and has a better channel. The least square method of sparse proposed regression method is superior to the traditional.

References

[1] H. Hrasinca, A. Haidine, and R. Lehnert, Broadband Powerline Communications Networks. West Sussex, England: Wiley & Sons, 2004.

[2] A. Tahat, and N. Galatsanos, “Relevenace Vector Machines for Enhanced BER in DMT Based Systems,” Journal of Electrical and Computer Engineering, vol. 2010, pp. 1-8, July 2010.

[3] D. Love et. al., “An overview of limited feedback in wireless communication systems,” IEEE J.Sselected areas in Communications, vol. 26 , pp. 1341–1366, October 2008.

[4] WANG Lin-sheng,” Theory and Practice Based on the DMTand DWMT Broadband Access,” RESEARCH AND EXPLORATION IN LABORATORY, vol. 25 , pp. 67–69, Jan. 2006.

[5] XIAO Xiao-chao ZHENG Bao-yu XU Xiao-rong,”Research of distributed Space-Time Coding techniques in Co-MIMO system,” Signal Processing ,vol. 27 , pp.340-345, Mar. 2011.

Advanced Materials Research Vols. 960-961 (2014) pp 1312-1318

doi:10.4028/www.scientific.net/AMR.960-961.1312

Anti- islanding detection for single-stage photovoltaic system based on Passivity

Lide Ji[1, a], Jianquan Yi[2, b]

[1]Jilin Jianzhu University, Changchun, 130000, China

[2]Architectural Design Limited Company of Jilin, Changchun, 130000, China

[a] jilide007@126.com , [b] 525876797@qq.com

Key words: anti-islanding detection, passivity, EL model, grid-connected inverter.

Abstract. Based on the basic principles of anti-islanding detection, this paper puts forward an anti-islanding(AI) detection method which combined/q-axis voltage decoupling and positive feedback with Euler-Lagrange(EL) model .The proposed method is classified as an passive islanding detection method and it is based on the voltage change at the point of common coupling (PCC) that occurs in islanding .In the method, Add the d-axis decoupling voltage of PCC to the d-axis reference current of the EL model. A simulation study shows that the method is simple and feasible.

Introduction

Single-stage photovoltaic (PV) system has the advantages of not having geographical constraints and sustainable development. PV becomes an important electricity generation which to replace the traditional generation and to ease the energy shortage situation. Since the connected-grid photovoltaic system becomes more and more available in our daily lives, we must focus on the problem of anti-islanding detection.

The meaning of Islanding phenomenon is that the grid turns on electrical failure or interrupts the power supply of natural factors and other reasons, the grid-connected PV system is still supplying the load to the surrounding, thus forming a self-contained power supply company uncontrollable island [1]. Reclosing islanding can cause problems; against normal power supply automatic or manual recovery interference and bring to the relevant personnel shock-hazard [2]. Researching islanding detection is significance.

Anti-Islanding detection method consists of detection grid side and detection inverter-Side. Grid side detection can be divided into detection which based on power line carrier communication, based on monitoring and data collection methods law and so on. Inverter side detection methods are divided into passive detection and active detection [3]. Passive detection which includes: voltage / frequency detection, voltage harmonics detection, voltage phase mutation detection, critical power change rate detection. Active detection includes: active power perturbation method, reactive power compensation method, active frequency offset method, sliding mode frequency shift method, specific frequency impedance measurement method, Sandia voltage shift method [4,5].

Passive detection methods are directly measuring the output power of the inverter or the changes of voltage and frequency in the PCC to determine whether the islands happen. Proactive detection method without detecting blind spots, no non-detection zone (NDZ), but larger output harmonics and the control algorithm is more complex, which is difficult to achieve practical application [6,7].

As a result, this article puts forward an anti-islanding detection method which combines d/q-axis voltage decoupling and positive feedback with Euler-Lagrange (EL) model.

The topology and modeling of photovoltaic inverter system

The single-stage photovoltaic grid-connected inverter topology is shown in Fig. 1.

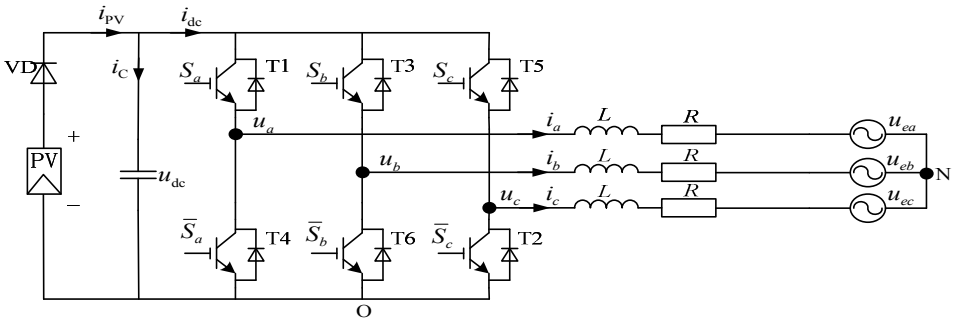

Fig.1. Grid-connected PV inverter topology.

Fig. 1 is the PV grid-connected inverter topology, in the case of three-phase balanced grid voltage, PV grid-connected inverter mathematical model of the three-phase abc coordinates is [8]:

$$\begin{cases} L\dfrac{di_a}{dt} = -Ri_a + u_{dc}\left(S_a - \dfrac{1}{3}\sum_{j=a,b,c} S_j\right) - u_{ea} = -Ri_a + u_a - u_{ea} \\ L\dfrac{di_b}{dt} = -Ri_b + u_{dc}\left(S_b - \dfrac{1}{3}\sum_{j=a,b,c} S_j\right) - u_{eb} = -Ri_b + u_b - u_{eb} \\ L\dfrac{di_c}{dt} = -Ri_c + u_{dc}\left(S_c - \dfrac{1}{3}\sum_{j=a,b,c} S_j\right) - u_{ec} = -Ri_c + u_c - u_{ec} \\ C\dfrac{du_{dc}}{dt} = -i_{pv} - S_a i_a - S_b i_b - S_c i_c \end{cases} \tag{1}$$

In Eq. 1, S_a, S_b, S_c is the inverter switching function respectively, S_j is defined as unipolar binary logic switch function, when the $S_j(j=u,v,w)=1$, it should turn on the up bridge arm, turn off the down bridge arm, when the $S_j=0$, it should turn off the up bridge arm, turn on the down bridge arm. L is the inverse output reactors, R is the internal resistance of the equivalent resistance of resistor and u_{dc} is the inverter system for the DC-side bus voltage, i_{pv} is the DC current supplied by the PV array for, i_{dc} is the current flowing to the inverter, i_a, i_b, i_c is the inverter output phase current, u_a, u_b, u_c is the variable-side three-phase AC phase voltage, u_{ea}, u_{eb}, u_{ec} phase grid side three-phase AC voltage.

Due to time-varying three-phase sinusoidal ac voltage exists in the mathematical model of three-phase ABC coordinate system, in order to facilitate the design of the controller, through the transformation matrix:

$$\boldsymbol{Q}_{abc/dq0} = \frac{2}{3}\begin{pmatrix} \cos\omega t & \cos(\omega t - 120^\circ) & \cos(\omega t + 120^\circ) \\ \sin\omega t & \sin(\omega t - 120^\circ) & \sin(\omega t + 120^\circ) \\ \dfrac{1}{2} & \dfrac{1}{2} & \dfrac{1}{2} \end{pmatrix}$$

To convert it to the mathematical model of the two-phase synchronous rotating d/q-axis coordinates system

$$\begin{cases} L\dfrac{di_d}{dt} = -Ri_d + \omega L i_q + u_d - u_{ed} \\ L\dfrac{di_q}{dt} = -Ri_q + \omega L i_d + u_q - u_{eq} \\ \dfrac{2}{3}C\dfrac{du_{dc}}{dt} = -\dfrac{2}{3}i_{pv} - i_{dc} = -\dfrac{2}{3}i_{pv} - S_d i_d - S_q i_q \\ u_d = S_d u_{dc},\ u_q = S_q u_{dc} \end{cases} \tag{2}$$

The above formula, i_d and i_q are in the d/q-axis component of the current output terminal, u_{ed} and u_{eq} are the output terminal voltages in the d/q-axis component, S_d and S_q are the switching functions in the d/q-axis component.

Islanding detection methods and passivity control algorithms

Islanding detection methods

For RLC load, as defined in standards, is assumed. The relationships between the RLC load active/reactive power and the voltage/frequency are [4, 5]:

$$P = V^2 / R \quad (3)$$

$$Q = V^2 (\omega C - 1/\omega L) \quad (4)$$

For voltage feedback, the mechanism is described as in Fig. 2. When the inverter-sensed output voltage is increasing, the AI feedback will command the inverter active-power output to be increased. Due to the load characteristic in (3), the voltage will keep increasing in order to balance the active power. The increased voltage will further drive the inverter active power up due to the AI feedback. As a result, the voltage will be eventually out of the nominal ranges so that the islanding can be detected. Similar but opposite destabilization occurs when the sensed voltage is decreasing initially.

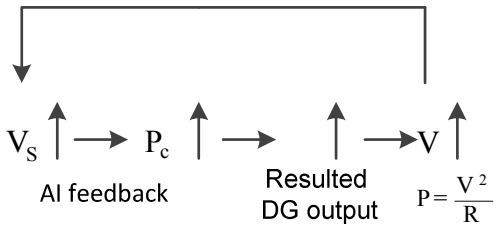

Fig. 2. Voltage positive feedback concept.

Fig. 3 illustrates a d-axis voltage-feedback scheme. When the inverter-sensed and computed d-axis voltage are increasing, the AI feedback will command the inverter d-axis current reference to be increased.It will result in increasing active-power output. Due to the load characteristic in (3), the voltage will keep increasing in order to balance the active power. The increased voltage, and thus d-axis voltage, will further drive the inverter active power up due to the Anti-islanding feedback. As a result, the voltage will be eventually out of the nominal range so that the islanding can be detected. Similar but opposite destabilization occurs when the sensed voltage is decreasing initially. Flow chart of the algorithm is as Fig.3:

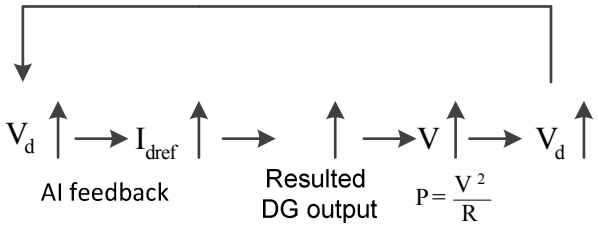

Fig. 3. Voltage positive-feedback in d-axis.

According to the principle of voltage feedback and d/q –axis decoupling, the flowchart of the anti-island detection is showing as in Fig. 4:

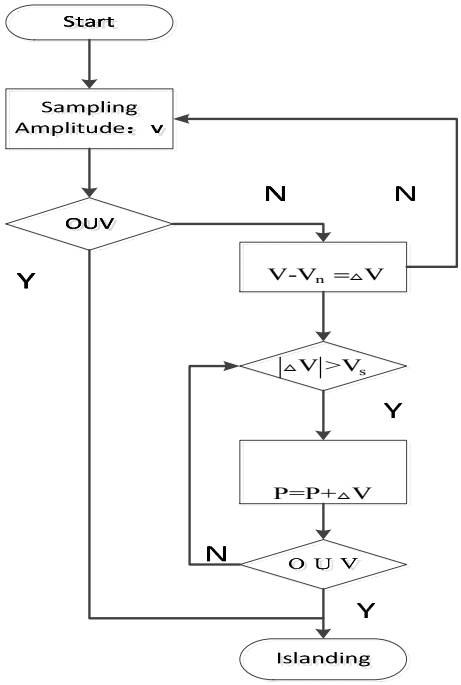

Fig. 4. Islanding detection flow chart.

Passive control algorithm

The EL form of (1) is [9, 10]

$$\boldsymbol{M}\ \dot{\boldsymbol{x}} + \boldsymbol{J}\,\boldsymbol{x} + \boldsymbol{\Re}\ \boldsymbol{x} = \boldsymbol{u} \tag{5}$$

Where $\boldsymbol{M}$ is Positive definite diagonal matrix, $\boldsymbol{J}$ is anti-symmetric matrix and reflecting the internal interconnection structure for symmetric, $\boldsymbol{\Re}$ is positive definite matrix which is reflecting the dissipation characteristics of the system, $\boldsymbol{u}$ is the energy exchange between the system and external. The Matrix expression is shown in *M.x.u.J.R*:

$$\boldsymbol{M}=\begin{pmatrix} L & 0 & 0 \\ 0 & L & 0 \\ 0 & 0 & 2C/3 \end{pmatrix},\boldsymbol{x}=\begin{pmatrix} i_{\mathrm{d}} \\ i_{\mathrm{q}} \\ u_{\mathrm{dc}} \end{pmatrix}=\begin{pmatrix} x_1 \\ x_2 \\ x_3 \end{pmatrix},\boldsymbol{u}=\begin{pmatrix} -u_{\mathrm{od}} \\ -u_{\mathrm{oq}} \\ 0 \end{pmatrix}$$

$$\boldsymbol{J}=\begin{pmatrix} 0 & -L\omega & -S_{\mathrm{d}} \\ L\omega & 0 & -S_{\mathrm{q}} \\ S_{\mathrm{d}} & S_{\mathrm{q}} & 0 \end{pmatrix},\boldsymbol{\Re}=\begin{pmatrix} R & 0 & 0 \\ 0 & R & 0 \\ 0 & 0 & \dfrac{i_{\mathrm{pv}}}{u_{\mathrm{dc}}} \end{pmatrix}$$

When the system operating steady-state and the expect power factor is 1, the DC voltage is equal to the maximum power point of the output voltage, so the expectation equilibrium point is $x_1^* = i_{\mathrm{d}}^*$ (i_{d}^* which is desired AC side of the line current d-axis value) $x_2^* = i_{\mathrm{q}}^* = 0$ (i_{q}^* is the desired AC side of the line current q-axis value), $x_3^* = u_{\mathrm{dc}}$ (u_{dc} is the desired voltage value across the capacitor).

Selection system error memory functions as follow:

$$H_{\mathrm{e}} = \frac{1}{2} x_{\mathrm{e}}^{\mathrm{T}} \boldsymbol{M}\ x_{\mathrm{e}}, \qquad x_{\mathrm{e}} = x - x^* \tag{6}$$

Where x^* is expectation equilibrium which points of the system .In order to accelerate the convergence speed, added damping to the system, making dissipation term is $\boldsymbol{\Re}_{\mathrm{d}} x_{\mathrm{e}} = (\boldsymbol{\Re} + R_{\mathrm{a}}) x_{\mathrm{e}}$. Rewrite (5) to:

$$\boldsymbol{M}\dot{x}_{\mathrm{e}} + \boldsymbol{\Re}_{\mathrm{d}} x_{\mathrm{e}} = u - \left[\, \boldsymbol{M}\dot{x}^* + \boldsymbol{J}(x^* + x_{\mathrm{e}}) + \boldsymbol{\Re} x^* - R_{\mathrm{a}} x_{\mathrm{e}} \,\right] \tag{7}$$

$$\dot{H}_e = -\frac{1}{2} x_e^T (\mathfrak{R} + R_a) \dot{x}_e < 0$$

Select the control law Eq. 8:

$$\boldsymbol{u} = \boldsymbol{M}\dot{x}^* + \boldsymbol{J}x + \mathfrak{R}\, x^* - R_a x_e \tag{8}$$

Because $\boldsymbol{M}\dot{x}^* = 0$. The switching function of the system is:

$$\begin{cases} S_d = \dfrac{u_{ed} - \omega L i_q + i_d^* (R + R_{a1}) - R_{a2} i_d}{u_{dc}} \\ S_q = \dfrac{u_{eq} + \omega L i_d - R_{a2} i_q}{u_{dc}} \end{cases} \tag{9}$$

Substituting (9) into equation (5) can be obtained equation (10)

$$\begin{cases} \dfrac{L}{R + R_{a1}} \dfrac{d i_d}{d t} + i_d = i_d^* \\ \dfrac{L}{R + R_{a2}} \dfrac{d i_q}{d t} + i_q = 0 \\ C u_{dc} \dfrac{d u_{dc}}{d t} = \dfrac{3}{2} u_{ed} i_d^* - \dfrac{3}{2} R i_d^{*2} - \dfrac{u_{dc}^2}{R} \end{cases} \tag{10}$$

Eq. 10 Show that the control law (9) can achieve good dynamic and static decoupling of the system and improve the static and dynamic performance of the system.

According to above control theory of PV system based on voltage feedback and passivity, System structure of anti-islanding detection can be obtained as shown in Fig. 5.

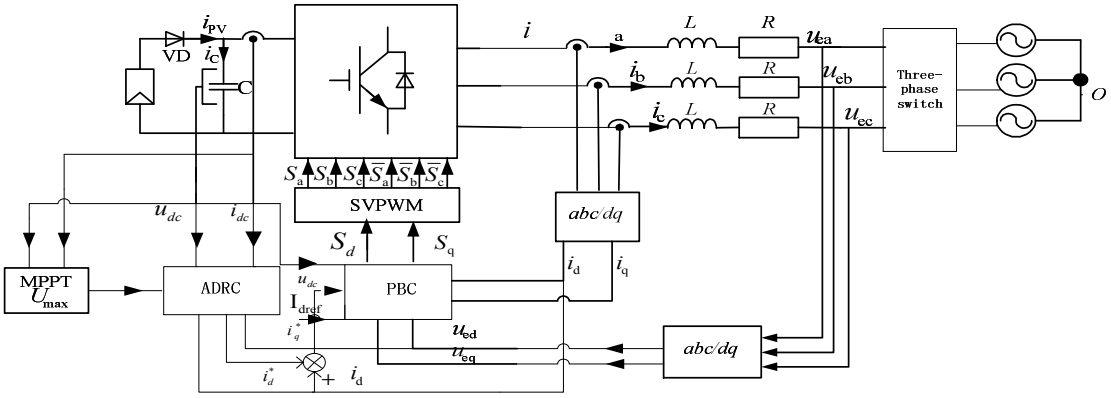

Fig. 5. Anti-islanding detection system structure.

Using Matlab / Simulink software simulation system is shown in Fig. 5. Where in the three-phase grid-equilibrium phase peak voltage 220V, the inverter output inductance of the reactor 15 μF , the reactor internal resistance resistor and inverter system is 0.2 Ω, the capacitor capacitance of 2200 μF , taken as 20 Ω. Fig. 6 and Fig. 7 illustrate the simulation waveforms when the load is only R load. Fig. 8 and Fig. 9 illustrate the simulation waveforms when the load is RLC load. As can be seen from Fig. 6, without using any islanding detection method and turning off the network side 0.15s, disconnect the power generation system is a remote island, the output side voltage hardly changed. As can be seen from Fig. 7, the use of the text islanding detection method proposed in 0.15s

network side is disconnected and the power generation system is islanding state, we can see the system at 0.154s, the voltage exceeds the detection voltage and detects the islanding.

Fig. 8 indicates that without any anti-islanding method when it breaks the three-phase switch at 0.15s, the output voltage is nearly unchanged. Fig. 9 indicates that the anti-islanding method when it breaks the three-phase switch at 0.15s, the islanding can be detected at 0.155s.

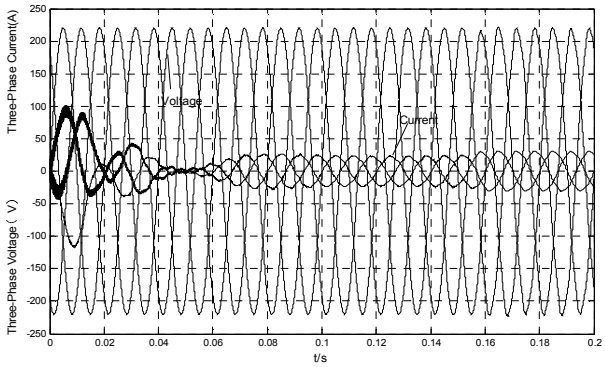

Fig. 6. Without anti-islanding(R Load).

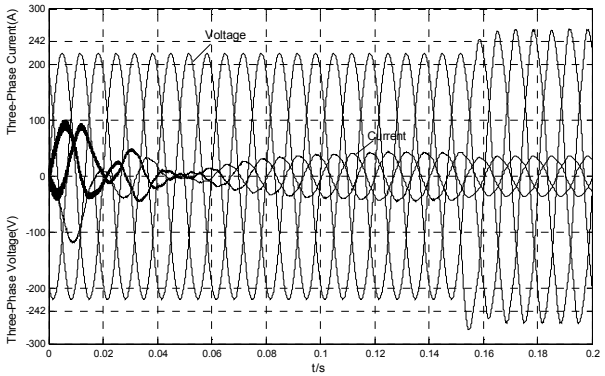

Fig. 7. With anti-islanding(R Load).

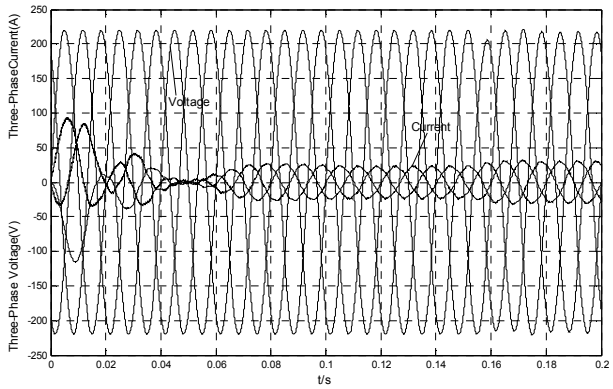

Fig. 8. Without anti-islanding (RLC Load).

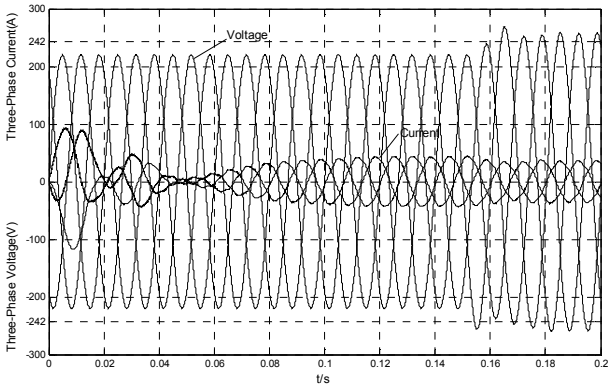

Fig. 9. With anti-islanding (RLC Load).

Conclusions

This paper presents anti-islanding detection method which consists of voltage positive feedback and passivity based on control strategy. The grid voltage of PCC through d/q-axis decoupling and then add into the d-axis reference current of the EL model consist a voltage positive feedback. This anti-islanding method which only uses voltage positive feedback has characteristics of simple structure and small input costs. What's more, this method can quickly detect the island, play a protective effect on the devices and have a certain application prospects in the actual project.

Acknowledgments

This work was financially supported by the National Natural Science Foundation of China (51077005)/by funding project for academic human resources development in institutions of higher learning under the jurisdiction of Beijing municipality (PHR201007130)

References

[1] IEEE recommended practice for utility interface of photovoltaic (PV) systems[S]. IEEE Std. 929-2000.
[2] Zhang, Cao Ren-xian etc. solar photovoltaic power generation and inverter controlling [M]. Beijing: Mechanical Industry Press, 2011
[3] W. Xiwei, X. Wei. Distributed grid system islanding analysis and detection method [J]. Electrician electrical,2012.6:47-52
[4] R. Teodorescu, M. Liserre, P. Rodriguez. Grid Converters for Photovoltaic and Wind Power Systems[M] .America: Wiley Press,2011
[5] S. Meining, Islanding detection Based on the positive feedback for inverter[D],He Bei: Yan Shan University
[6] Z. yi, W. Zhengqiu, L. Yanghua, L. Jianzhong, G. Lei, Z. Chao, islanding detection technology for Distributed power system [J], Power System and Automation 2009.21 (6) :106-110
[7] M. Xiaobin, W. Jiuhe and, G. Wen, X. Shengsheng. Nonlinear Current Control Strategy Based on Passivity of Photovoltaic Grid-Connected Inverter [J]. Supply Sinica, 2011, (04): 83-87.
[8] Z. Ye, R. Walling, L. Garces, R. Zhou, L. Li, and T. Wang .Study and Development of Anti-Islanding Control for Grid-Connected Inverters [J]. The US Department of Energy Office of Energy Efficiency and Renewable Energy by Midwest Research Institute.2004
[9] H. Jingqing Nonlinear state error feedback control law-NLSEF [J]. Control and Decision .1995, 10 (03):221-225.

Advanced Materials Research Vols. 960-961 (2014) pp 1319-1324

doi:10.4028/www.scientific.net/AMR.960-961.1319

Islanding Detection for multiple PV Grid-connected inverters Based on AFDPF and SMS

Yujie Shi[1,a], Xinyu Tan[2, b], Qinqin Liu [2, c]and Yuanjun Mao[1, d]

[1]College of Electrical Engineering & New Energy, China Three Gorges University, Yichang. China

[2]College of Materials & Chemical Engineering, China Three Gorges University, Yichang. China

[a]jj89757syj@163.com, [b]husttanxin@mail.tsinghua.edu.cn, [c]1009701424@qq.com, [d]390009967@qq.com.

Keywords: AFDPF, SMS, Islanding Detection, Grid-Connected inverter

Abstract. Due to the perturbation between multiple PV Grid-connected power system can't be synchronized easily, the islanding detection often lose efficacy when multiple PV Grid-connected inverters are running simultaneously. The paper show the in-depth analysis of the principle and the advantages and disadvantages of the detection method of AFDPF and SMS, a composition controller is designed aim at the non-detection zone in multiple PV Grid-connected system in the practical application. Through the software simulation, it shows that the method mentioned in the paper practically improves the effect of the islanding detection.

Introduction

When the grid switches off, the photovoltaic power generation system maintains power supply to the local load as an isolated power, consequently, creating an "islanding effect". Islanding effect not only can cause damage to the user's devices, may also make the photovoltaic power generation system overload operation and get burned when the load capacity is greater than the PV's. At the same time the safety of the maintenance staffs are also subjected to great hidden danger, and the grid is not safe because of the current surge when it recover after fault repair. Therefore, grid-connected PV system must have ability of timely detect the islanding and stop running automatically in a short time.

At present, the islanding detection has two kinds of method based on the changes of the detection object, namely, passive and active detection. Passive detection method checks whether the voltage amplitude, frequency and harmonic content at the grid-connected interconnection deviate from the range set by the standard of grid connection. Its working principle is simple, easy to implement, but detection blind area would be produced if the output power of inverter is similar to load power. Active detection method is to give a small disturbance to inverter (such as voltage amplitude). The effect brought by the disturbance is very small when network works in normal because of its clamp effect, so it can be neglected. However, once the grid failures happen, the disturbance will accumulate rapidly and exceed the allowed scope, triggering islanding protection circuit. Active detection method detection has small blind area, and it's more precise, but its control is more complicated, and reduces the quality of the inverter output power to a certain extent.

In the practical engineering, when multiple sets of PV grid –connected inverter are running at the same time, due to the possible disturbance between multiple photovoltaic power generation system are not synchronized, the effects of an island detection will be affected seriously. This paper analyzes the advantages and disadvantages of the AFDPF and SMS islanding detection method. Their compound was applied to more than one inverter grid case, thus to provide guide to the actual photovoltaic power generation systems engineering method.

Island detection principle

When the power grid work in normal, photovoltaic power generation system connects to power grid in public point A, they together supply power to RLC load, as is shown in figure 1.

When network work in normal, photovoltaic power generation system output active power (P) and reactive power (Q)to the load, and grid output power to the common point A, active power(ΔP), reactive power(ΔQ) , and the active power (P_{load})and reactive power(Q_{load}) of load, so the power balance equation of A point can be written as:

$$P_{load} = P + \Delta P \quad , Q_{load} = Q + \Delta Q$$

If the power outputted by photovoltaic power system is balanced with load power, namely ΔP =0, ΔQ =0, in this case, the voltage amplitude, frequency of the common point barely change. PV generation system continue to provide power to the load, thus a state of islanding effect without monitoring is generated at the common point.

If ΔP or ΔQ is big enough, and when the grid disconnect, only the inverter supply to the load as a current source, the inverter output power and load power do not match at this moment, so the common point voltage amplitude or frequency would change, and when exceed the normal scope, the inverter voltage amplitude frequency protection circuit detects islanding and take an action, so as to realize an islanding protection.

Commonly detection method

Active frequency drift detection. AFD detects islanding through importing a zero time to the signal of the inverter output current. If the half wave of a given current by PV generation system has been completed, but the common point half-wave voltage has not, the given current should be forced to be zero and keep a time length of t_z .Once the voltage of common point reaches zero, the given current of PV generation system immediately start the next half wave, as shown in figure 2, so that the frequency of the PV generation system is always slightly lower or higher than the common point's of previous period.

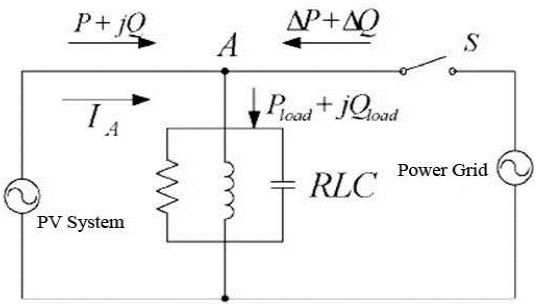

Fig.1 The equivalent circuit of island effect.

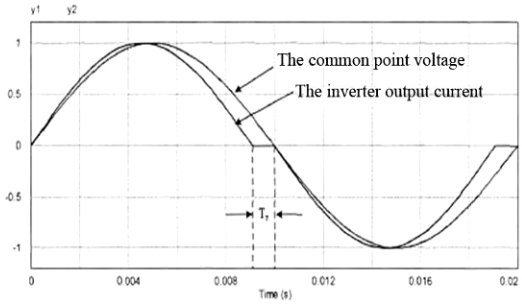

Fig.2 The oscillograph of the given current and the common point voltage

When the network works normally, the grid controls the magnitude of the common point's voltage frequency; when the grid blackout happens, the output current of inverter flows the resistive load, leading the voltage response of the load following the current wave distortion and reaching

zero in a shorter period of time, causing phase error between output voltage and current. To eliminate phase error the inverter will increase the frequency of current output, causing the voltage of resistive load passing zero in advance, then Inverter test phase error and increase the current frequency again until the frequency offset is beyond the scope set so that can be detected.

AFDPF introduce a positive feedback of frequency based on the frequency deviation of AFD, thus speeding up the common point voltage frequency deviation from normal, further reducing the measuring blind area. There is a 0.5 wt_z phase error between AFDPF current waveform and the base wave. If t_z is small enough, the current harmonic would be very small. The inverter output current and common point voltage phase can be represented as:

$$\theta_{AFDPF} = \frac{wt_z}{2} = \frac{\pi cf}{2} = \frac{cf_0 + k(f - f_g)}{2}\pi \tag{1}$$

In this expression, cf_0 is truncation coefficient under no frequency error; f is the voltage frequency of the common point; f_g is the rated grid frequency, k is feedback gain. In the case of ignoring the harmonic, the AFDPF current can be represented as:

$$i_{AFDPF} = I_{AFDPF}\sin(2\pi ft + \theta_{AFDPF}) \tag{2}$$

For RLC load in parallel, the disadvantages of active frequency drift method is the detection blind area exists when capacitive load is large. Because the load impedance angle of capacitive load less than zero would partly offset the phase advance effects brought by frequency deviation method, slowing down the speed of system frequency deviation, so that the system can not be able to quickly and accurately determine islanding.

Slip-Mode Frequency Shift Method. Slip-Mode Frequency Shift Method (SMS) is a kind of islanding detection method based on the common point voltage phase error. Figure 3 is the schematic diagram of SMS, its principle is taking the common point voltage frequency of last time cycle on the phase-locked loop as the current frequency in the next cycle of PV generation system, the starting moment of the next cycle is determined by the rise time of the common point voltage passing zero.

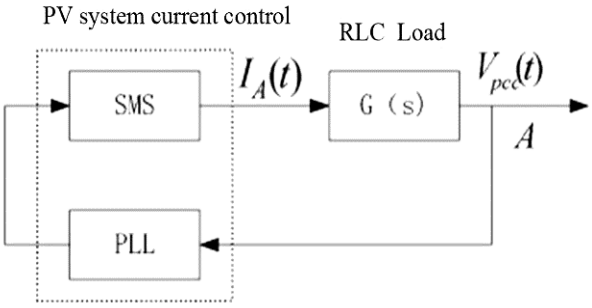

Fig.3 Schematic plot of the SMS

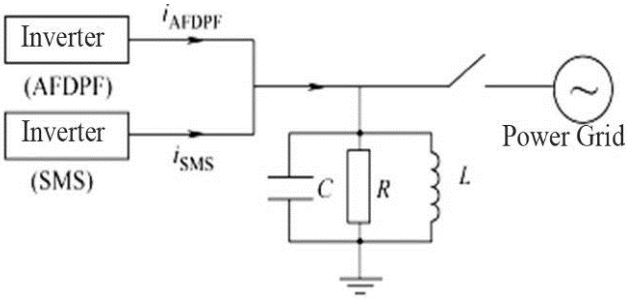

Fig.4 Schematic plot of multiple PV Grid-connected system

The SMS algorithm controls the initial phase of current, and generally takes:

$$\theta_{SMS} = \theta_m \sin\left(\frac{\pi}{2} \times \frac{f - f_g}{|f_m - f_g|}\right) \tag{3}$$

Among them, θ_{m} is the maximum phase shift angle, f is the common point voltage frequency, f_g is the rated power grid frequency, f_m is the maximum frequency when the maximum phase shift.

The output reference current of Inverter can be represented as:

$$i_{SMS} = I_{SMS}\sin(2\pi ft + \theta_{SMS}) \tag{4}$$

Once the grid interrupts, due to the phase of the current IA is always lead (or lag) the common point's voltage phase, and because of the effect of the phase lock loop, the frequency gradually increase (or decrease) until beyond the normal range at last and the islanding is detected. The SMS algorithm is simple in implementation, and has outstanding ability to detect islanding, etc. But if the phase offset got by SMS algorithm is zero, islanding may not be detected, resulting in a blind detection area, and the blind can not be eliminated but to shrink it.

AFDPF and SMS composite detection method

In order to overcome the blind detection area problem that multiple sets of inverter are running at the same time, we can combine AFDPF and SMS their respective characteristics. This article adopts this way, in order to facilitate analysis, choosing two PV grid inverters to supply power as is shown in figure 4.

The resultant current expressions has been given in reference [3]:

$$i = I_{SMS}\sqrt{1+m^2+2m\cos(\theta_{AFDPF}-\theta_{SMS})}\sin(2\pi f+\varphi) \tag{5}$$

Among them, m is the ratio of i_{AFDPF} and i_{SMS}, φ can be represented as:

$$\varphi = \arctan\left(\frac{m\sin\theta_{AFDPF}+\sin\theta_{SMS}}{m\cos\theta_{AFDPF}+\cos\theta_{SMS}}\right) \tag{6}$$

It is observed that：

$$\min(\theta_{AFDPF},\theta_{SMS}) < \varphi < \max(\theta_{AFDPF},\theta_{SMS}) \tag{7}$$

When an AFDPF inverter and a SMS inverter connect to the grid, the phase angle of resultant current is between the angle of two inverters' output current. In AFDPF method, the change direction of phase angle is kept for the existence of positive feedback. in other words, the two inverters' phase disturbance directions caused by frequency change are in the same direction. Therefore, as long as each inverter can effetely detect islanding when work alone, islanding could still be detected after they connect to the grid. But if the resonance frequency of RLC load in parallel is close to the grid's frequency, islanding effect will be difficult to be detected when the grid switches off for the system's frequency changes little. Thus, a factor, if we want to detect islanding precisely in extremely hard operating conditions, is required, which is the growth rate of phase angle of inverter output current is faster than the RLC load in parallel. For AFDPF method, the feedback gain should satisfy the following condition:

$$k \geq \frac{4Q_f}{\pi f_g} \tag{8}$$

In this formula, Q_f is the quality factor of load, generally $Q_f < 2.5$, to make it better compatible with SMS method, the truncation coefficient in SMS algorithm formula (2) can be improved as:

$$cf = \begin{cases} k(f - f_g) - cf_0 & f \geq f_g \\ k(f - f_g) + cf_0 & f \leq f_g \end{cases} \tag{9}$$

According to this formula, phase disturbance directions of AFDPF and SMS method are the same for any common point frequency and any RLC load, the positive and negative values are consistent as well.

Model simulation

In this paper, a PV generation system model is built on the basis of above analyze. The grid blackout happens at 0.1s, the model simulation monitors the voltage, current and islanding signal after the grid switches off. The model is shown in figure 5 and the system's parameters are shown in table 1.

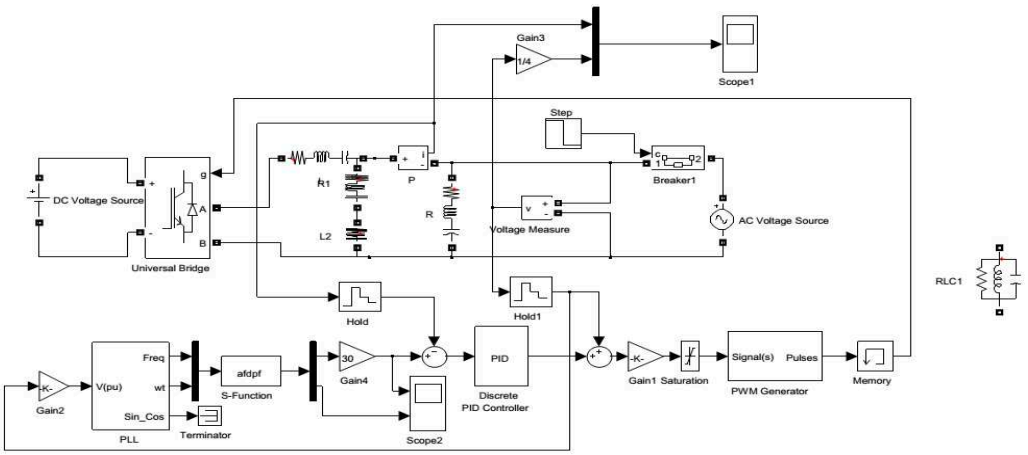

Fig.5 The simulation model of islanding detection

Table 1: System simulation specifications

Parameters	Value
Public grid	220V/50 Hz
Frequency protection threshold	50 ± 0.5 Hz
SMS parameters	$\theta_m = 10°$, $f_m = 53$Hz
Load quality factor	$Q_f = 2.5$
Load active power	10 kW

The simulation results is shown in figure 6, seeing from the figure, the power grid power switches off at 0.1s, and the system frequency exceeds the upper limit frequency 50.5Hz after 0.18s later, islanding is detected immediately, then the inverter driving signal is blocked. Test results meet the standard testing time of IEEE Std. 2000-929 . According to formula (6), (7), the method is also suitable for more than two inverters parallel operation.

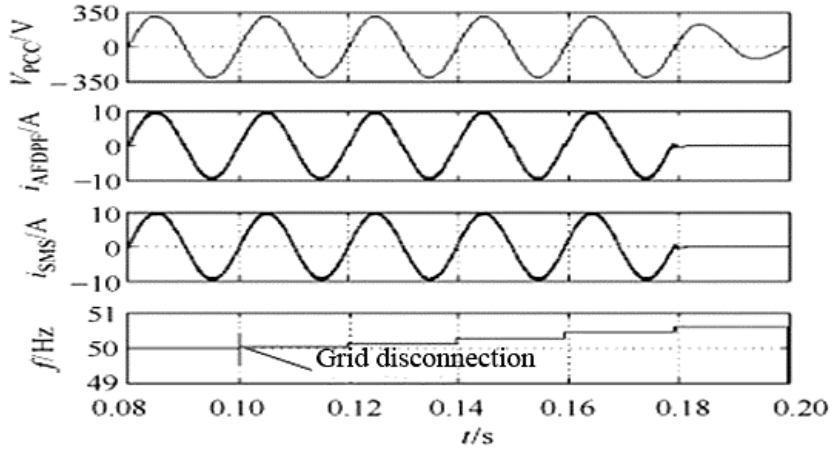

Fig.6 The result of simulation

Conclusion

This article has deeply analyzed AFDPF detection method and SMS detection method, aiming at the problem that the disturbance synchronism is difficult to realized to detect islanding when multiple inverters running at the same time, combined AFDPF with SMS and simulated in MATLAB, and the result shows its fast and precise performance in detecting islanding, accordingly providing a guided way for multiple sets of inverters' parallel operation.

Acknowledgements

This work was financially supported by the National Natural Science Foundation of China (Grant Nos. 11374181 and 51177088), the Natural Science Foundation of Hubei Province(Grant No. 2013CFB217).

Reference :

[1] Chunling Li: Islanding Detection Based on Phtovolotaic Grid-connected System. Tinjin University, 2008.

[2] Furong Liu, Hui Wang, Yong Kang and Shanxu Duan: Non-Detection Zone of Slip-Mode Frequency Error Method. TRANSACTIONS OF CHINA ELECTROTECHNICAL SOCIETY,2009，24(2): 178-182.

[4] Xiaoqiang Guo,Qinglin Zhao and Weiyang Wu: Islanding Detection Method for Photovoltaic Grid-Connected Power System. TRANSACTIONS OF CHINA ELECTROTECHNICAL SOCIETY, 2007, 22(4): 157-162.

[5] Minglian Zhu ,Zhengyou Yu and Chunying Gong: A Novel Active Frequency Drift Islanding Detection Method . Power Electronics, 2009, 43(11): 31-32.

[6] Hudson RM: Implementation and testing of anti-islanding algorithms for IEEE 929-2000 compliance of single phase photovoltaic inverters . Photovoltaic Specialists Conference，2002.

[7] Furong Liu , Hui Wang, Yong Kang and Shanxu Duan: The Application Of SMS in Household Island Detection .The Word of Power Supply,2008, (8):40-43.

[8] M.Hamzeh: Power Quality Comparison of Active Islanding Detection Methods in a Single Phase PV Grid Connected inverter,The Center of Excellence in Power System Management, IEEE International Symposium on Industrial Electronics (ISLE 2009),July 5-8,2009.

Advanced Materials Research Vols. 960-961 (2014) pp 1325-1330

doi:10.4028/www.scientific.net/AMR.960-961.1325

Design of Locomotive Energy Consumption Monitoring System

Yu Huijun [1,2,a] Zhou Zhiwei [1,b] Chen Caibiao[1,c] and Gu Juhui[1,d]

[1]Hunan University of Technology, china

[2] Central South University, china

[a]arejunyu@foxmail.com, [b]m12085207002@163.com , [c]05biao@sina.com, [d]gujuhui.cool@163.com

Keywords: Electric locomotive; Electric energy metering; STM32F103R8T6

Abstract: The paper introduces the structure of locomotive energy consumption monitoring system, technical parameters and the method of software design. The system uses electric energy metering chip CS5463, ARM kernel STM32F103R8T6, GPRS wireless communication module and RS485 communication interface to realize the multi-system locomotive AC and DC measurement, remote meter reading and other devices and locomotive communication connection. The liquid crystal display LCD stores the locomotive power information, the current, voltage, power and energy data with their own real-time clock time-sharing data fragmentation such as type test on the system, the system of high precision, strong anti-interference ability, low power consumption, safety etc.

Introduction

With the rapid development of electronic technology , energy metering energy monitoring device as a tool widely used in the national economy , especially in the electric locomotive .However,China 's energy resources are relatively tight, energy consumption monitoring system is not yet mature , reasonable ,so effective measure for energy is becoming increasingly important.Currently, electric locomotives measure energy consumption is often used mechanical energy monitoring devices and electronic monitoring devices,mechanical devices has low accuracy, weak immunity, low efficiency, mechanical loss.while high-precision electronic devices ,efficient use big,stability,security and high overload capacity and strong.

Therefore, as for the comparison between the mechanical energy consumption monitoring device and electric energy consumption monitoring device , this paper designs a kind of energy consumption monitoring system based on embedded system. It can detect electric locomotive real-time electricity information and remote wireless meter reading. the System consists of a dedicated high-performance energy measurement chip (CS5463), the power supply circuit and ARM microprocessors (STM32F103R8T6) etc. By high isolation, high-precision voltage transformers and current transformers or sensors to detect locomotive voltage, current, real-time calculation of electric power, and accumulated power consumption and locomotive traction regenerative braking power fed back into the grid.

The overall structure of a system

System composition

Electric locomotive energy consumption monitoring system shown in Figure 1, mainly by the energy measurement chip CS5463 [1], microprocessor STM32F103R8T6, clock circuits,

programmemory, display driver circuit, RS485 communication module, RS232 communication module, power supply circuit. Energy measurement chip CS5463 mainly to the acquisition of electric locomotives input current and voltage signals, information and computing power to get the locomotive, its information stored in FLASH memory. Microprocessor STM32F103R8T6 CS5463 collected primarily for computing power locomotives and locomotive power of information processing and display, cumulative feedback power locomotives, locomotive cumulative power consumption; and the locomotive current, grid voltage, locomotive power and consumption data combined with its own real-time bell to store data sharing segment, primarily in order to provide real-time clock chip for real-time display current battery information; metering system provides an RS485 communication interface to connect energy monitoring devices and other devices in the car. RS232 interface is mainly used for debugging the factory.

In order to ensure that the system electromagnetic compatibility [2], anti-jamming capability, the system should have three-way power input of certain protective measures should be taken so that the output power (energy measurement mode, the microprocessor module, wireless communication module) correctly isolation.

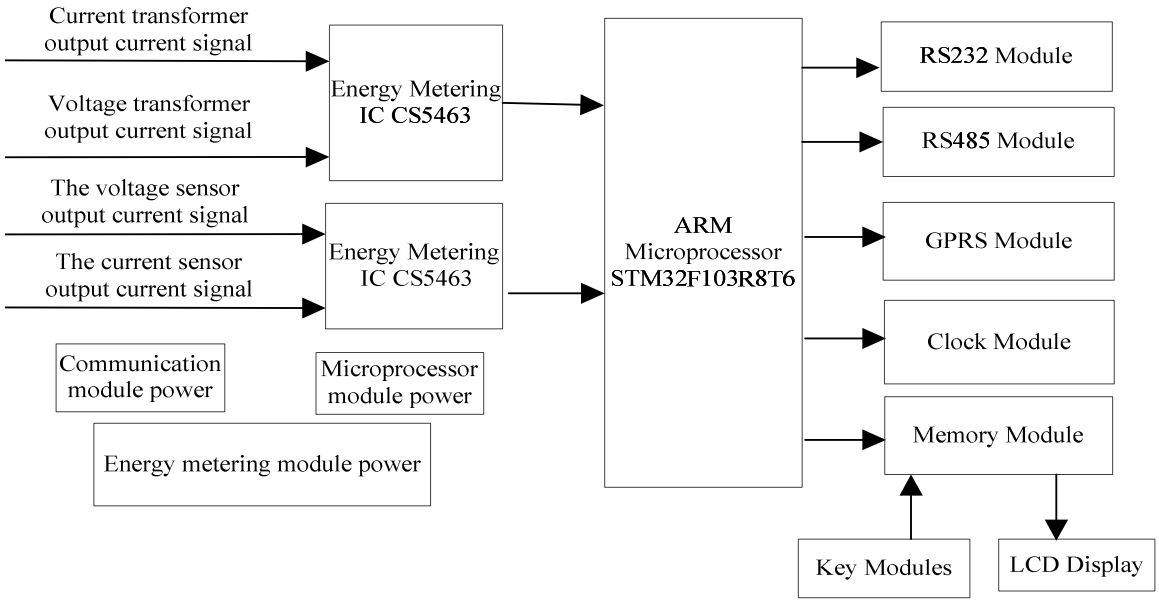

Fig. 1 Electric locomotive structure of energy consumption monitoring device

Sampling module power

Electric energy sampling module composed of electric energy metering IC CS5463 and current,voltagesamplingcircuit. CS5463 using current transformer for high current transform locomotive input for the current signal is small, the voltage transformer high voltage locomotive entered into a low voltage signal. The bidirectional serial communication with the microprocessor communication, with phase compensation, temperature sensor, and correction calibration functions.

The current sampling circuit and voltage sampling circuit uses the differential input circuit, when the locomotive DC voltage sampling, voltage sensor input rated voltage to the DC current through the shunt50mA,sampling circuit, resistance(R40 , R43) voltage sampling circuit output voltage value UIN (165mV), as the CS5463 of VIN+ and VIN--, the specific circuit as shown in figure 2.

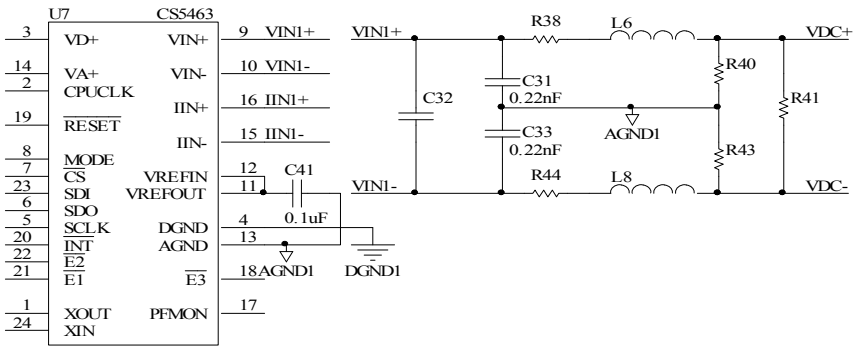

Fig.2 DC voltage sampling circuit

When direct current locomotives sampling, the current sensor rated current into DC current 400mA, through a resistor (R50, R51, R52) output voltage signal UIN (140mV), as CS5463's IIN1 + and IIN -. The CS5463 is connected with the microprocessor, the voltage and current signals inputted data operation to get the power of information Specifically, as shown in figure 3

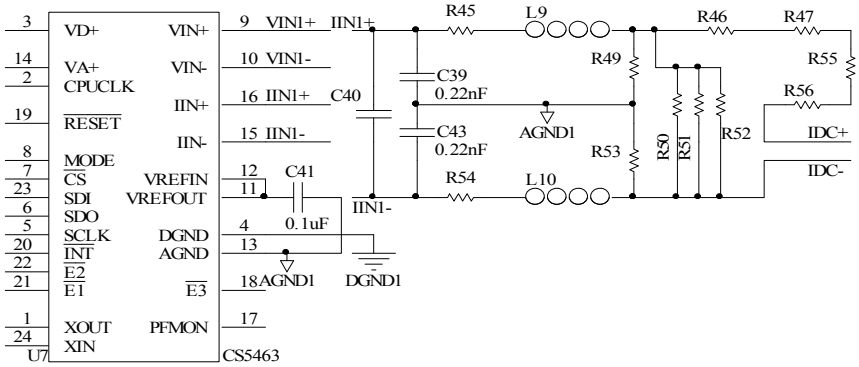

Fig.3 DC current sampling circuit

When the locomotive AC voltage sampling, voltage transformer output voltage signal 150V through the resistor divider (R26, R18, R22), filter (R17,C16, C18) is transformed into a 100mV voltage signal; when the current AC locomotive sampling, current transformer through the divider circuit, filter circuit converts the current signal into voltage signal output of locomotive. Specific AC voltage and AC current sampling circuit as shown in Figure 4.

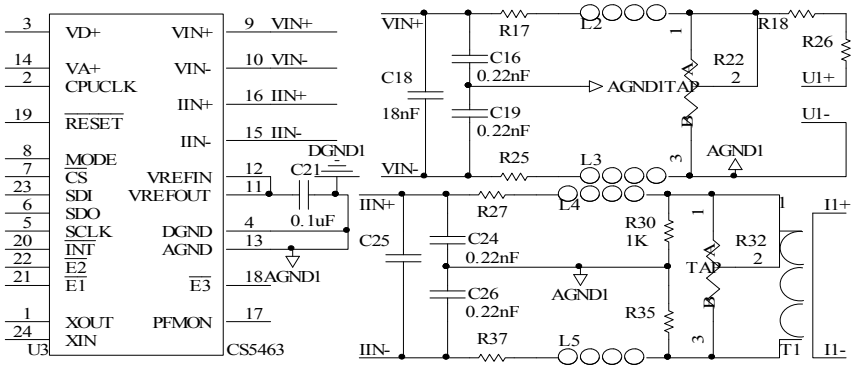

Fig.4 The sampling circuit of AC voltage and current

central processing module

The central processing module consists of 32 bit high performance ARM series microprocessor STM32F103R8T6, keyboardcircuit, RS48 communication module, 12864 display module,the SD2404 clock module, power module and GPRS wireless communication module, the microprocessor STM32F103R8T6 with measurement chip CS5463 by SPI interface, two keys are connected with the microprocessor I/O, microprocessor working in the range of -40 ℃—— +85 ℃, and has the advantages of strong anti-interference ability, high reliability, strong

function. The embedded microcontroller as the electric energy metering chip, mainly to complete the electric energy data processing, display and storage. Power supply circuit adopts double power supply, a spare battery and power supply(AC/DC) function, ensure the locomotive uninterruptible power supply, prevent the loss of information for electric locomotive.

power module

According to the requirements of power metering device, a power supply system and auxiliary power supply in two ways, the two kinds of power supply through the rectifier, filter are connected in parallel, the rectifier and filter two ways to isolate two kinds of power supply, so that the two power supply is not influence. and the power supply circuit measurement module and communication module needs mutual isolation, the DC-DC mode to achieve mutual isolation between the power:the input voltage regulator module 110V, can realize the mutual adaptive AC and DC, from interference at the input of the power access varistor protection power supply.

Wireless communication module

RS485 module

RS485 communication interference, power supply module, RS485 signal input and signal output should take certain measures [3] isolation. Among them, power supply using DC-DC magnetic isolation, input signal using optocoupler isolation, transceiver with strong anti-interference capability, low power MAX487, with magnetic isolation output signal. RS485 uses standard electrical standard interface, communication baud rate to 19200, mainly composed of MAX487 module, optical module and the external resistor.MAX487 can send data, and can receive data.

GPRS module

In order to ensure the energy consumption monitoring system of locomotive all-weather monitoring center and ground communication, power consumption has become a key factor in the GPRS module selection ,therefore, instinct consumption monitoring device based on MC55[4] wireless communication module Siemens production company, MC55 built in TCP/IP protocol, has not only the general voice, SMS, GSM module, MODEM wireless data service connect function, also has the data transmission of TCP/UDP and FTP, SMTP, protocol. Users only need to edit the AT instruction can check GPRS network, remote communication vehicle and the ground monitoring center. The MC55 range of working voltage is 3.3-4.8V, maximum current of 2A, and has the advantages of high integration degree.

System Specifications

Display range: LCD display, power 8-bit data, before the decimal point 5, after three;
consumption: less than 5W; Voltage channels: input AC voltage: 100 ~ 300V, rated 150V; input DC voltage: -71.4 ~ 71.4 mA, nominal 50mA; auxiliary supply voltage: DC110V (-30% ~ +25%); Accuracy: Active ± 0.5, reactive power ± 2.0; current channel: Input AC Current: 0 ~ 1.5A, rated 1A; input DC Current: -700 ~ 700 mA, rated 400mA ;Communication Interface: RS485 interface, GPRS interfaces; storage depth: stored once per minute,the capacity to store 30 days.

system software design

The system every 10 seconds to refresh the cumulative traction power consumption and regenerative braking feedback to grid electricity, which showed forward active，forward reactive power, Reverse reactive power，and the voltage, current. So the display using 3 seconds timer interrupt to update the data, followed by cycle display locomotive power information.

System uses Keil4 as development environment, based on the embedded μC/OS II operating system [5], using C language programming, modular approach to design. The main program is shown in Figure 5,it is the core of the system. Power on reset, the system into the main program, the program is first initialized to operation, including variable initialization for all sub components and global initialization, judging if power supply is power off, if the power supply powerdown, calling the data storage module, the information storage locomotive power letter letter to FLASH memory, at the same time the system into a low power state, effectively extend the standby battery time. Since the system uses two kinds of remote communication party tried to realize remote wireless meter reading, Therefore, the program uses RS485 bus communicating with TAX2 module, Using interrupt timer count way to achieve power information collection, display.

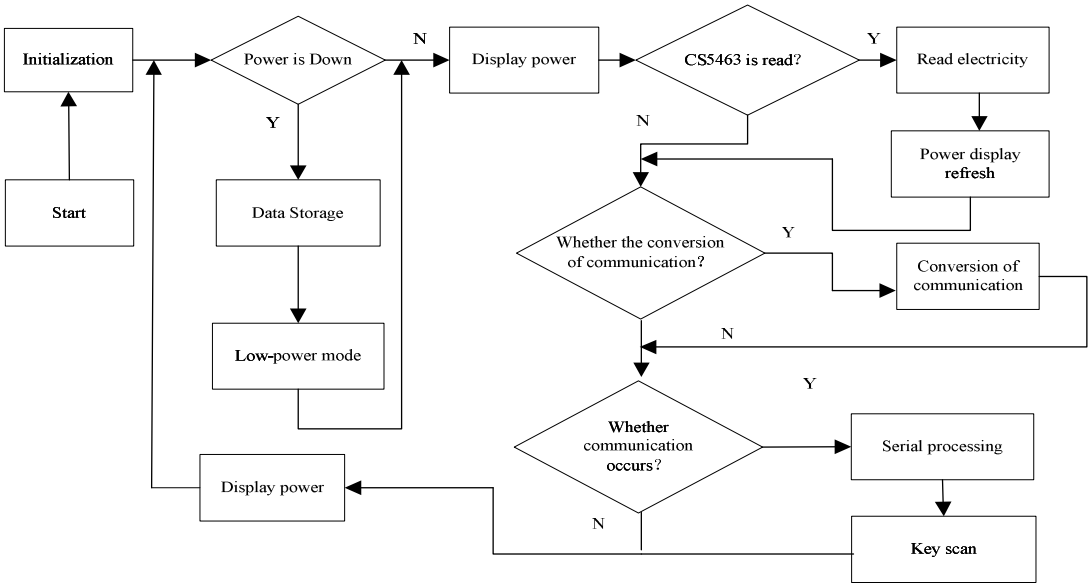

Fig.5 The main program flow chart

prototype testing

Detection accuracy

Electric locomotive monitoring system to measure the energy consumption of the core, but also to ensure the accuracy of measurement of the primary condition for the normal operation of the locomotive, mainly in order to measure the accuracy of the test locomotive voltage, current, active power, reactive power and power factor, to the national standard GB / T 17215.322-2008 as the standard for precision testing.

Developed by Zheng zhou Huate Control Technology Co.Ltd. precision test station of WT-T160 on locomotive energy consumption device parameters testing, accuracy class 0.2. Loading metering chip (CS5463) program can be done after the locomotive energy consumption monitoring device precision test, the choice of two locomotive energy consumption monitoring device prototype to verify the analysis, as shown in table 1.

Table 1 Locomotive energy precision test results

Phase			Forward active %			Positive Reactive %		
U/I	number	Load current	Error	average	entire value	Error	average	entire value
rated	1	Imax(1.2)	0.1251	0.0625	+0.1	0.00375	0.0125	+0.0
current	2	Ib(1.0)	0.1376	0.0813	+0.1	-0.0249	-0.0499	-0.0
1A	3	0.5Ib(1.0)	0.0125	0.0094	+0.0	-0.0312	-0.0406	-0.0

Rated	4	Imax(0.5L)	-0.0874	-0.0936	-0.1	0.2631	0.2505	+0.2
voltage	5	Ib(0.5L)	-0.0499	-0.0561	-0.1	0.2631	0.2569	+0.2
150V,	6	0.5Ib(0.5L)	0.0000	-0.0094	-0.0	0.2317	0.2254	+0.2
	7	Imax(0.8C)	0.1251	0.0938	+0.1	-0.3611	-0.3549	-0.4
	8	Ib(0.8C)	0.1126	0.0688	+0.1	-0.1248	-0.1186	-0.2
	9	0.5Ib(0.8C)	0.0437	0.0437	+0.0	-0.0687	-0.0718	-0.0

Table 1 shows: Input AC rated voltage 150V, rated current of 1A, adjust system output current 1.2Ib, ib, 0.5Ib, record voltage, current and power factor. Under current output unchanged, adjust the power of 0.5L, 1.0,0.8 C, record the voltage, current and power factor. By contrast with the standard measurement system to obtain accuracy of the system, the experimental results showed that: active energy measurement accuracy is 0.5 and reactive energy measurement accuracy 2, which have achieved the desired effect.

Conclusions

The electrical energy special-purpose chip CS5463 and ARM core chip STM32F103R8T6 are combined with operating system C/OS II to design energy consumption monitoring system of locomotive. The system can display real-time locomotive voltage, current, power, power factor, power consumption of locomotive traction , regenerative braking feedback to the electricity grid and to wireless remote meter reading. The system satisfies the GB/T17215.322-2008 international standard. The software uses the modular thought and the DL/T 645 communication protocol. Energy consumption monitoring device accuracy grade of this design: active power level 0.5 and reactive power level 2, widely used in electric locomotive, electric automatic meter reading, remote monitoring and management system.

Project supported by the Science and Technology Plan Projects of Hunan Province (Grant No.2012FJ4265), China.
Yu Huijun: Associate Professor, Research direction: detection and automatic control technology;
Corresponding author: Zhou Zhiwei, graduate, research direction: detection and electrical control technology

References

[1] Wei Huang. The electric energy measurement technology second edition [M]. Chinese electric power press, 2007(in chinese).

[2] People's Republic of China power industry standard DL / T 614-2007 multifunction energy meter(in chinese).

[3] Qiang Miao,Fengyou He, Shijian Deng and Yanbo Xue. Design of monitoring substation system based on RS485[J]. Chinese Journal of Scientific Instrument,2006(in chinese).

[4] Junfeng Hao. Remote Verification and Monitoring System for Electric Energy Measuring Device Study[D].Bei Jing: School of Electrical and Electronic Engineering,2012(in chinese).

[5] Ligong Zhou edited. embedded system based on ARM tutorial [M]. Beijing:Beihang University press, 2005(in chinese).

Advanced Materials Research Vols. 960-961 (2014) pp 1331-1335

doi:10.4028/www.scientific.net/AMR.960-961.1331

Research on Governor-side Power System Stabilizer

Fengping Pan[1,a], Min Zhong[2,b], Yuzhen Chen[2,c], Yaqing Zhu[1,d], Shihe Chen[1,e], Xi Zhang[1,f] and Jia Luo[1,g]

[1]Guangdong Electric Power Research Institute, Guangzhou, Guangdong, 510080, China

[2]Department of Energy Science and Engineering, Harbin Institute of Technology, Harbin, Heilongjiang, 150001, China

[a]panfpwxh@163.com, [b]zm759405760@sina.cn, [c]bigbaojiao@126.com, [d]zhuyaqing@163.com, [e]chen_shi_he@163.com, [f]zhangxi_sjtu@163.com, [g]jialuo@126.com

Keywords: GPSS, State feedback, Low-frequency oscillation

Abstract: By analyzing the control principle of power system stabilizer (PSS)，shows that the robustness of PPS is not ideal. Using the methods of state-space pole placement designed the governor-side power system stabilizer GPSS,and built a simplified model of the power system with simulink. The simulation experiment results made in the MATLAB shows that GPSS has good inhibitory effect of low-frequency oscillations.

Introduction

The continuous expansion of the scale of the power system, large capacity units, especially fast excitation device into operation, result in deterioration of the damping characteristics of the power system, causing low-frequency oscillation. The low-frequency oscillation is that under certain circumstances, negative damping system provided offset the original positive damping of system turbine, field winding, and mechanical, the damping is too small or the total result is negative, then if the system is disturbed, the disturbance will continues to enlarge in the negative damping effect, forming a low-frequency oscillation. Low-frequency oscillations will seriously affect the safe operation of the power system stability and generators, and may even cause damage to the power system blackouts.

Currently, the power system stabilizer (PSS) is the most common method of suppressing low-frequency oscillations. PSS is a kind of additional excitation controller, using generator speed deviation, frequency deviation, power or linear combination of the three as an input signal to compensate for the phase lag generated by the excitation system.

PSS is designed primarily for the exciting side of the phase compensator, and the study of the governor-side power system stabilizer GPSS has also been conducting. HAO Yushan et al analyzed and verified the feasibility of GPSS, Concluded that governor time constant and the gap dead-band do not affect the function of GPSS, and GPSS has good robustness of the system operation mode and working conditions[1-2]. Gu Gendai presented that using additional high-frequency periodic signal ‘rolling’ governor gap to realize linearization for eliminating the self-oscillation caused by the nonlinear governor gap[3]. Lin Qiyou, Chen Xingying et al designed GPSS for multi-machine system[4]. GPSS brought positive damping to local machine, while not giving negative damping to others, thus, GPSS has better robustness than PSS.

Analysis of power system stabilizer PSS

PSS achieves phase compensation by a lead - lag element, Fig.1 shows the model of phase compensation. According to the single - infinite system Philips-Heffron model, we can derive the generator speed, power angle and electromagnetic power phase diagram, Fig.2 shows the principle of PSS phase compensation.

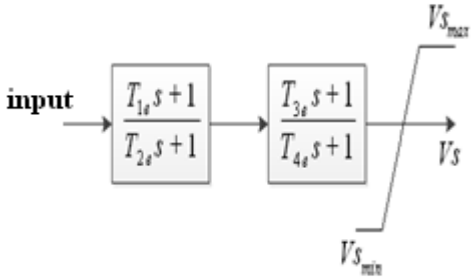

Fig.1 Model of PSS phase compensation

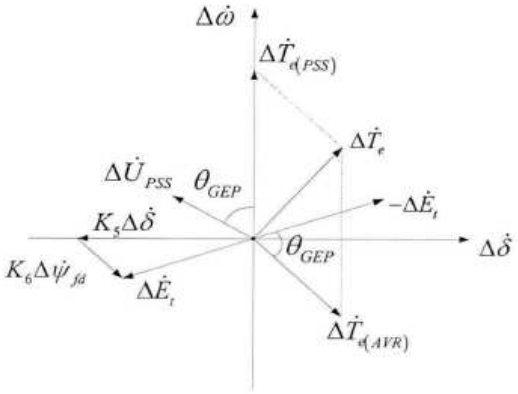

Fig.2 Damping torque synthesis principle

When the Synthetic phasor of electromagnetic torque generated by the excitation device and PSS appears in the first quadrant of the plane, the total system damping torque is positive. By tuning parameters in phase compensation aspects of PSS and compensating the phase between the electromagnetic torque generated by PSS and speed deviation, PSS can produce pure positive damping torque, thereby increasing the system damping.

PSS is widely used, and is also the most mature technology of low frequency oscillation suppression device by far. However, due to the generator excitation system is closely related to the power system operation mode and working conditions, PSS is difficult to be extended to multi-machine system. In addition, PSS control performance is largely determined by the mounting position of the stabilizer, the robustness of the system is not ideal.

Design of GPSS

In fact, research on GPSS began in the early time, However, due to the oil motive response was too slow, cannot keep control instructions at that time, control effect of GPSS has been unsatisfactory, thus affecting its application. But, with the gradual development of manufacturing technology, the time constant of the oil motive got smaller and smaller, have been able to keep control instructions and timely response.

Fig.3 shows the influence of the oil motive's time constant on the output.According to Fig.3, we know: Smaller time constant of the oil motive, more responsive output, greater adjustment range.

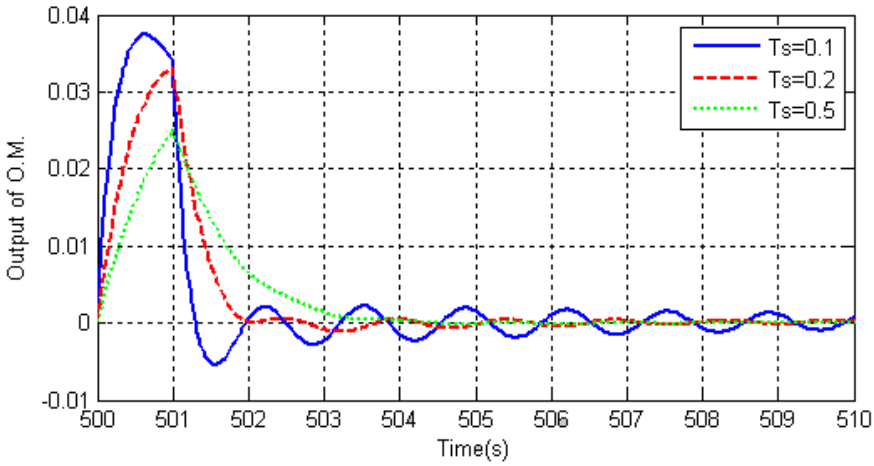

Fig.3 The influence of time constant on oil motive output

GPSS also generates a pure damping torque by the controller, like PSS, to suppress low-frequency oscillation. Let the system state space expression for: $\dot{\boldsymbol{x}} = \mathrm{A}\boldsymbol{x} + \mathrm{B}\boldsymbol{u}$, By configuring the desired poles to determine the state feedback control law: $\boldsymbol{u} = -\boldsymbol{k}\boldsymbol{x}$. In the entire system, we choose the output of oil motive, the output of high-pressure cylinder, generator speed and power of grid as State variables. Considering the system's need for additional damping, when configuring poles, the damping factor of dominant poles may be appropriate to some large. In this context, Let dominant pole be $-2 \pm \mathrm{j}2$ and vice pole be $-10, -10$, then we can obtain feedback gain matrix $\boldsymbol{k}$ by solving the state space expression.

Simulation of GPSS

Fig.4 shows the overall structure of the system simulation model.

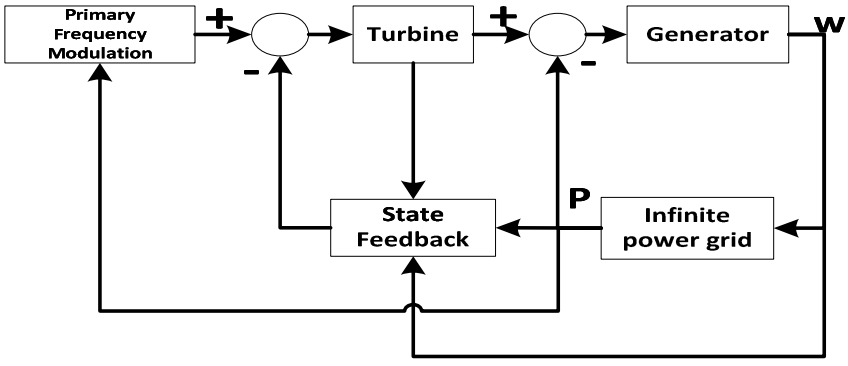

Fig.4 Simplified structure of the power system

Among it , the turbine including oil motive, high-pressure cylinder and reheat links. The oil motive and high-pressure cylinder simplified into first order damp elements, the time constants is Ts and Th:

$$G_1(s) = \frac{1}{T_s \cdot s + 1} \tag{1}$$

$$G_2(s) = \frac{1}{T_h \cdot s + 1} \tag{2}$$

The reheat links is described by the transfer function $G_{rh}(\mathrm{s})$:

$$G_{rh}(\mathrm{s}) = \frac{\alpha T_{rh} \cdot s + 1}{T_{rh} \cdot s + 1} \tag{3}$$

The generator is represented by an integration element with a gain $\frac{1}{T_a}$:

$$G_r(\mathrm{s}) = \frac{1}{T_a \cdot s} \tag{4}$$

The infinite grid is represented by $G_R(s)$:

$$G_R(s) = C_D + \frac{1}{T_R \cdot s} \tag{5}$$

Then we built a simulation model using the Simulink of MATLAB and did the simulation experiments.

Results of Simulation

After 500 seconds at the stable operation of the system, set an impulse interference with a per unit value 0.05, getting the simulation curve of generator speed, output of oil motive and grid power fluctuations versus time, the simulation results as shown in Fig.5:

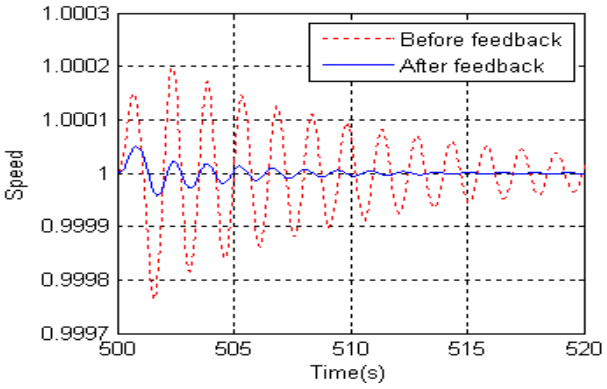

(a) Speed versus time

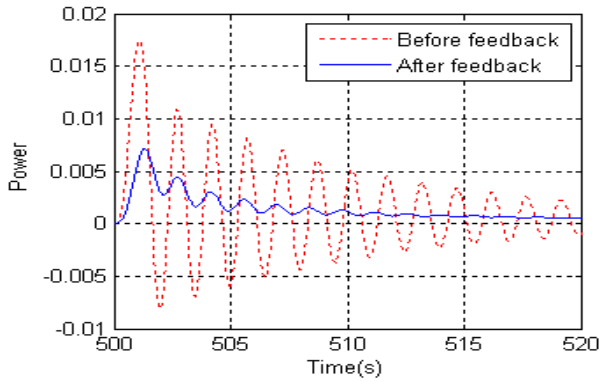

(b) Power versus time

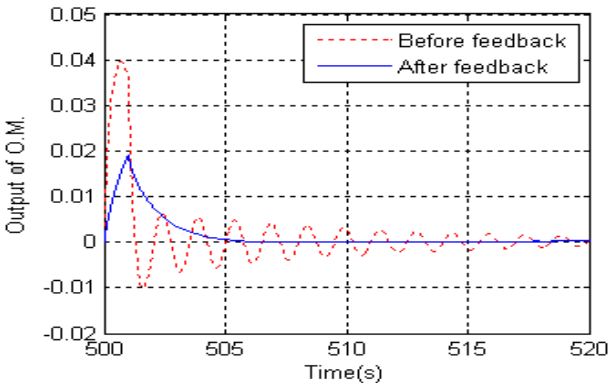

(c) Oil motive output versus time

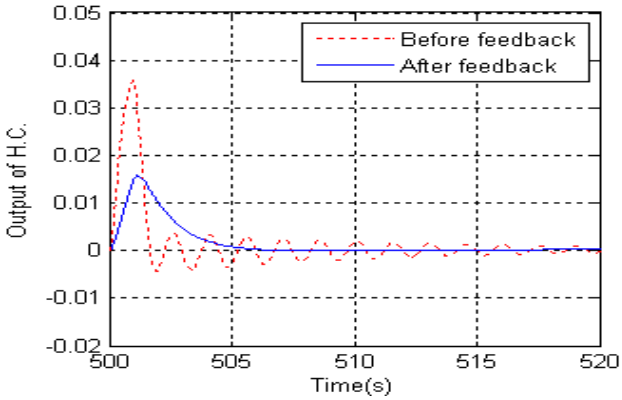

(d) High-pressure cylinder output versus time

Fig.5 Simulation results

Conclusions

Due to the state feedback control by the configuration desired poles, governor-side power system stabilizer has a good inhibitory effect for low-frequency oscillations. Also, due to the multi-machine decoupling, the system robustness of GPSS is better than PSS, GPSS can be used as a new power system stabilizer to promote application.

References

[1] Yushan Hao, HaiFeng Wang, Zhenxiang Han, Yihan Yang, B.W. HOGG: Automation of Electric Power Systems Vol. 16 (1992), p. 36-42(in Chinese)

[2] Yushan Hao, HaiFeng Wang, Z. X. Han, Yihan Yang, B.W. HOGG. Automation of Electric Power Systems Vol. 17 (1993), p. 26-32(in Chinese)

[3] Gendai Gu, Yushan Hao. Automation of Electric Power Systems Vol. 18 (2001), p. 45-47(in Chinese)

[4] Qiyou Lin, Xingying Chen, Zhifeng Cao. Power System Technology Vol. 31 (2007), p. 54-58(in Chinese)

Advanced Materials Research Vols. 960-961 (2014) pp 1336-1341

doi:10.4028/www.scientific.net/AMR.960-961.1336

Manufacture and experimental investigation of a multi-layer generator based on dielectric elastomer

Xuejing Liu [1,a] Gong Zhang [2,b] Yongquan Wang [*3,c] and Shuhai Jia [4,d]

[1-4]School of Mechanical Engineering, Xi'an Jiaotong University, Xi'an 710049, China;

[a]lisa890329@stu.xjtu.edu.cn, [b]dobby01@stu.xjtu.edu.cn, [c]yqwang@mail.xjtu.edu.cn, [d]shjia@mail.xjtu.edu.cn

[*] yqwang@mail.xjtu.edu.cn

Keywords: Dielectric elastomer, multi-layer, generator, harvesting circuit

Abstract. As a member of Electroactive Polymers (EAPs), dielectric elastomer (DE) has shown considerable potential for energy harvesting applications. After the basic principle of DE energy harvesting is studied, a multi-layer DE generator using VHB 4910 (3M, USA) is specially designed and fabricated. Then, an improved energy harvesting circuit is designed to make use of harvested electrical energy. Finally, energy harvesting experiments are implemented under the constant charge (open-circuit) condition and the results prove that the multi-layer DE generator fabricated can produce enough energy to constantly drive a light emitting diode. The harvested electrical energy has good consistent with generated electrical energy and the maximum energy harvesting efficiency η_h can reach 89%.

Introduction

Dielectric elastomers (DE), a member of electroactive polymers (EAPs), are capable of exhibiting large strains under an electric stimulus [1]. Dielectric elastomers have drawn much academic attention as actuating materials due to their advantages, such as low cost, light weight, fast respond speed, high efficiency, large deformation and long fatigue life [2-3].

As we all know, the generator mode of dielectric elastomers is the reverse process of the actuator mode, firstly discovered by Pelrine *et al.* in 2001 [4]. Different designs of dielectric elastomer generators (DEGs) have been put forward by scholars worldwide. DEGs have been demonstrated capable of harvesting energy from environmental sources including water current [5], ocean waves [6], and wind [7], as well as human motion such as heel striking [8] and knee bending [9]. The maximum harvested energy of above designs are mostly within a range of 0.02~0.4 J/g, far less than the theoretical prediction given by Koh A *et al.* [10] (nearly 2.7J/g per energy cycle). In 2010, McKay *et al.* [11] proposed a "self-priming" circuit which can be used as an inverse charge pump.

In this paper, based on the analysis of an energy harvesting cycle, an annular multi-layer DEG device is designed and fabricated. In addition, an improved harvesting circuit is presented and simulated. Then energy harvesting experiments are implemented to drive a light emitting diode continuously. Finally the results prove the feasibility of multi-layer DEG and the improved harvesting circuit. Since the complexity of multi-layer DEG, the results may be not the optimal one, still and all, it can provide a new direction in improving the performance of DE energy harvesting devices.

Basic principle of DE energy harvesting

The DE energy harvesting is a cycle process converting the mechanical energy into electrical energy. Before entering the operating cycle, the DE membrane is usually pre-stretched to a certain ratio.

To illustrate the DE energy harvesting process, a simplified working cycle which can be divided into four working phases is shown in Figure 1. Tensile Phase (from a to b): the DE membrane is mechanically stretched to a certain location, mechanical energy converted into the elastic potential

energy of the material. Charge Phase (from b to c): the membrane is charged by a bias voltage. Recovery Phase (from c to d): since the external load reduces, the membrane is relaxed with the combined effect of the elastic restoring force and the Maxwell stress, the capacitance decreased, converting the strain energy to electrical energy. The last is Discharge Phase (from d to a), the charges are removed and the membrane completely recovers to its initial working state.

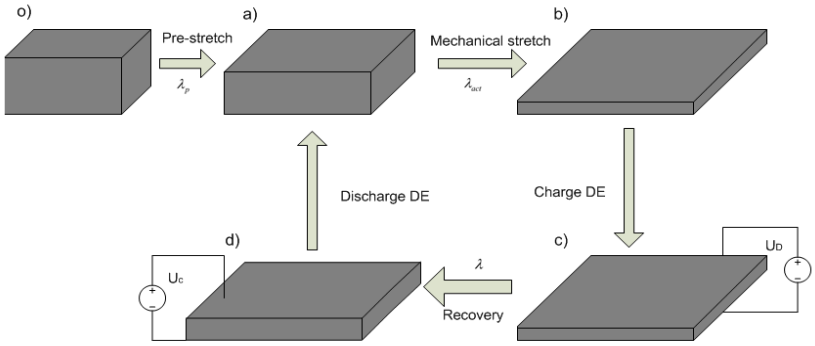

Figure 1 Schematic of the DE membrane energy harvesting cycle

Dielectric elastomers, in essence, are a type of variable capacitors. The capacitance C, can be expressed by equation (1) as follows

$$\mathrm{C} = \frac{\varepsilon \mathrm{A}}{\mathrm{z}} = \frac{\varepsilon P}{z^2} \tag{1}$$

where ε is the permittivity of DEG, A is the area of electrode, z is the thickness of DE membrane and P is the volume of the membrane.

Since the DEG works under constant charge condition, namely $\mathrm{Q} = C_C U_C = C_D U_D$, the capacitance and voltage at state c and d can be either measured or calculated according to the above formula. The electrical energy generated in each cycle can be obtained, namely

$$\Delta \mathrm{W}_E = \frac{1}{2}(\mathrm{C}_D U_D^2 - C_C U_C^2) = \frac{1}{2} C_D U_D (U_D - U_C) \tag{2}$$

where C_C and C_D denote membrane capacitance at states c and d, while U_C and U_D are voltages across the membrane at the two states accordingly.

Preparation of a multi-layer DEG

The dielectric elastomer used in this study is VHB 4910 (3M, USA). In our design, a pre-stretched DE membrane is fixed by two annular frames and the active working area of the DE membrane is an annular region with an inner diameter of 30 mm and an outer diameter of 80 mm.

A multi-layer DE generator contains several units and each unit consists of two layers of DE membrane. The fabrication process of the two-layer unit is shown in Figure 2, which mainly includes the following steps: 1) Prestretching. The DE membrane VHB4910 is equi-biaxially pre-stretched to a certain ratio. 2) Boundary Fixing. Put the two frames (made of lightweight ABS plates with thickness of 1mm) at the center and the edge of the membrane respectively, note that frames is attached only to one side of the membrane. Two copper foils are spliced on the two sides of DE membrane as electrode connectors. 3) Coating electrodes. 846 type conductive carbon grease (MG Chemicals) is coated on both surfaces of DE membrane as compliant electrodes. 4) Assembling. The above procedures are repeated on another DE membrane. Then put two single DE

membranes together, insure that the membranes are sandwiched between two pairs of frames. Finally we cut off the redundant membrane outside the frame.
To fabricate a multi-layer DEG which contains more than two layer membranes, we only need to stack up several units and make sure they are connected to each other in parallel.

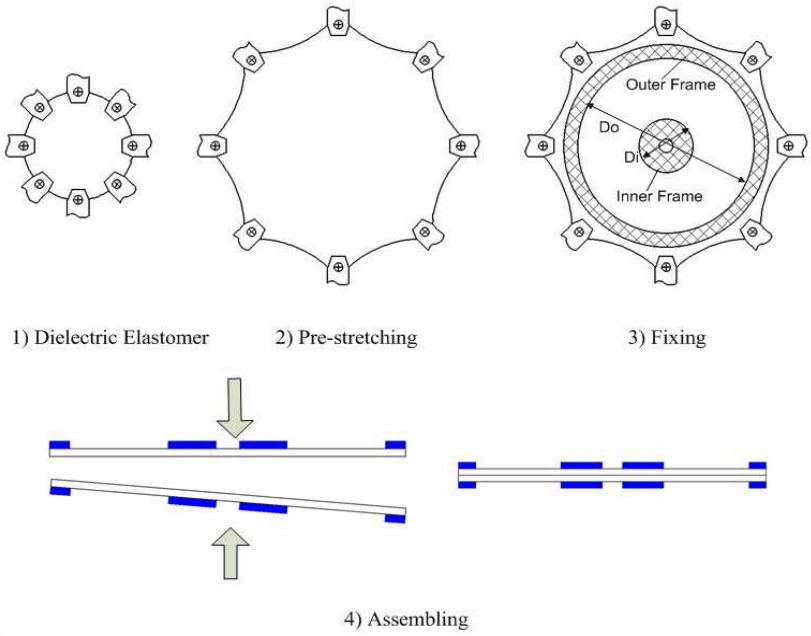

Figure 2 Fabrication process of a two-layer unit

Improved energy harvesting circuit

Considering the special energy generating mode, we designed a simple but useful circuit for energy harvesting. It consists of two capacitors and a rectifier bridge, shown in Figure 3.
Capacitor C1 is used to filter out the AC component caused by DE generated energy and keep the voltage of DEG on a relative steady value. In other words, we only make use of the generated electrical energy and remain the initial electrical energy on the device. Capacitor C1 is required to be a high voltage capacitor with relative high capacitance comparing with DEG. In our experiment, we use a 2000V/1μF and a 2000V/0.1μF capacitor respectively and the result shows that the 1μF capacitor can harvest more energy. The capacitor C2 is used to harvest electrical energy, which required to have a large capacitance value. In our experiment, a 50V/10μF capacitor is used. The energy can drive the load R directly or be stored into a battery for further usage.

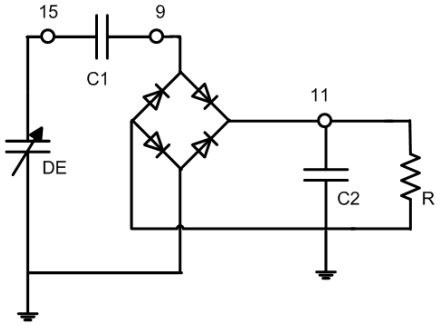

Figure 3 Improved energy harvesting circuit

Assume that the capacitance of DEG changes in sine form, the frequency is 4Hz and the capacitance varies from 2.84~6.31nF. The capacitance of DEG should be $C(t) = 1.735\cos(4 \cdot 2\pi t - \pi) + 4.575\text{nF}$. NI Multisim software is used to do the electrical analysis. In the analysis, we set the load R to ∞ so that the voltage increment on capacitor C_2 is exactly the energy harvested by the circuit. First we add an initial voltage of 1000V on DEG. A Zener diode can be introduced into circuit to control the maximum voltage value at 10V. The output voltage wave form in 10 seconds, is shown in Figure 4.

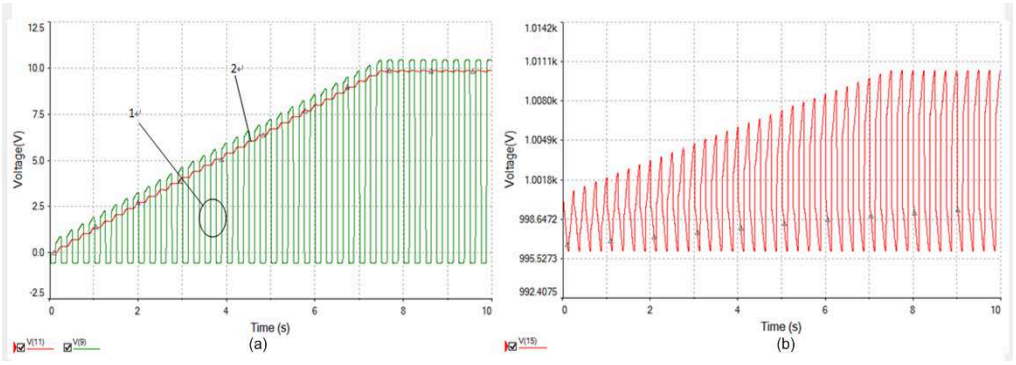

Figure 4 Output voltage wave form on node (a) 9 and 11 (b) 15 with a Zener diode in circuit

Curve 1 in Figure 4(a) shows the voltage on node 9, which is the AC component filtered by C1. Curve 2 shows the voltage on node 11, which is the harvesting voltage across capacitor C2. Figure 4(b) shows the voltage on node 15, which illustrates voltage fluctuation on DEG. It can be seen that the remaining energy on DE generator will keep stable and only change slightly with the harvest energy. We can obtain the voltage fluctuate on DEG is about 1.3%, which can be neglected.

Experimental tests

1.1. Experimental Setup

Figure 5 illustrates the experimental setup for energy harvesting tests, which consists of an annular multi-layer DEG, an oscilloscope (JC1062CA), a high-voltage probe(TREK P6015A, 1000:1) and a voltage amplifier (TREK MODEL 610E) which is controlled by a signal generator(Agilent 33220A).

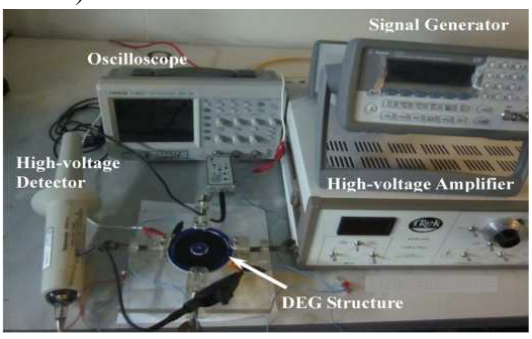

Figure 5 DEG energy harvesting experimental setup

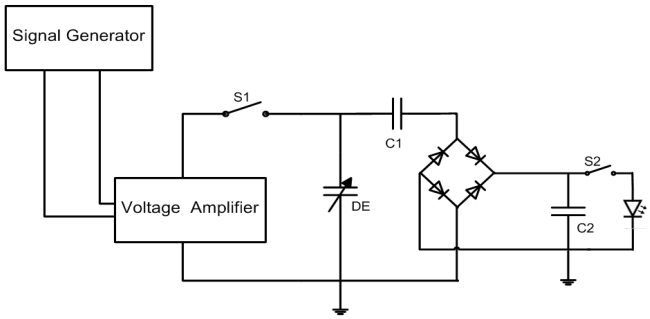

Figure 6 Schematic diagram of experimental circuit

Figure 6 shows schematic diagram of experimental circuit. The constant charge condition is easily achieved by switch S1 in practice. In the experiments, after the DEG is stretched to the certain stretch displacement, switch S1 is connected to charge the DEG. After DEG is charged, switch S1 is disconnected to ensure that the device recovers under the open-circuit condition. Then DEG device is stretched and recovered repeatedly by hand/motor, constantly converting mechanical energy into electrical energy and stored in the capacitor C2. Switch S2 is used to control whether the generated electrical energy is accumulated in capacitor C2 or consumed to drive the light emitting diode.

1.2.Experimental results and discussion

1.2.1. Generated electric energy

In order to obtain the amount of electrical energy generated (increased), the initial capacitance of a single unit need to be measured, combined with output voltage which can directly read from the oscilloscope. Generated energy of single unit per cycle can be calculated through Eq. (2). Since the units of a multi-layer DEG are connected in parallel, the total generated electrical energy can be calculated as

$$\Delta W_{Et} = n\,\Delta W_{Eu} \tag{3}$$

where n denotes the number of units in a multi-layer DEG.
In our investigation, a ten-layer DEG is fabricated, the bias voltage, pre-stretch ratio λ_p and stretch displacement h are 400V, $\lambda_p = 3$ and $h = 30\text{mm}$ respectively. The total electrical energy generated per cycle equals 1.29 mJ. (where corresponding output voltage is 860V, initial capacitance is 2.8nF and number of units in DEG is n=5).

1.2.2. Harvested electric energy

To evaluate the performance of the multi-layer DEG and harvesting circuit, the amount of harvested electrical energy should be paid more attention. As mentioned in Section 4, a capacitor of 50V/10μF is used to store electrical energy, thus harvested electric energy can be obtained through the measurement of the voltage across capacitor C2 (harvesting voltage), namely

$$\Delta W_h(i) = \frac{1}{2} C_h U_h^2(\mathrm{i}) \tag{4}$$

where C_h is capacitance of capacitor C2, i is the number of working cycles, $\Delta W_h(i)$ and $U_h(i)$ denote the harvested electrical energy and harvesting voltage after i working cycles, respectively.
Figure 7 shows the relationship between harvesting voltage U_h and number of working cycles. It can be seen obviously that harvesting voltage increases approximate linearly with the number of working cycles.

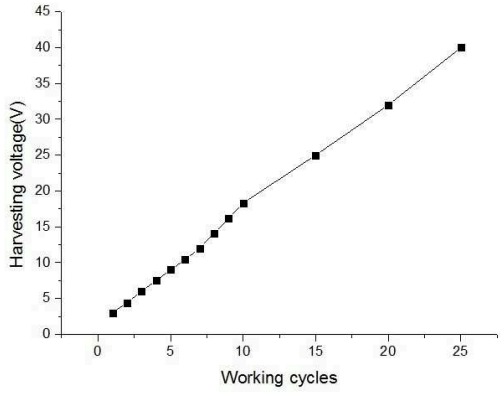

Figure 7 Harvesting voltage at different working cycles

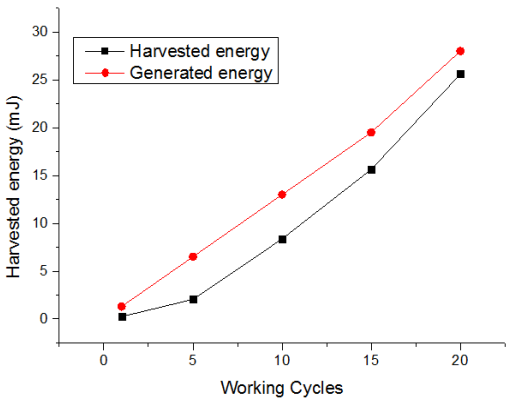

Figure 8 Comparison between harvested and generated energy vs. working cycles

Figure 8 shows comparison between harvested electrical energy and generated electrical energy at different working cycles. It can be observed that the generated electrical energy and harvested electrical energy results are comparable each other. The maximum energy harvesting efficiency η_h

can reach 89% (where η_h is the ratio between harvested energy and generated energy). This is possibly because the energy consumed by the components in harvesting circuit. What's more, a multi-layer DEG has a thickness of about 10mm, which result in a little error in the parameter of stretch displacement h.
In energy harvesting experiments, it can be observed that an annular ten-layer DEG can harvest enough electrical energy to drive a light emitting diode continuously.

Conclusion

In this paper, an annular ten-layer DEG device is specially designed and fabricated. Then an improved energy harvesting circuit is presented to make use of harvested electrical energy. Energy harvesting experiments are implemented to investigate its energy harvesting performance under the charge-constant condition. The experiments indicate that through stretch-recover the DEG device repeatedly, mechanical energy can convert into electrical energy and effectively drive a light emitting diode. In addition, The maximum energy harvesting efficiency η_h can reach 89%. Energy harvesting efficiency η_h can be further improved by increasing the active working area of DE membrane and enhancing the performance of energy harvesting circuit.

Acknowledgements

This research has been supported by the project of National Natural Science Foundation of China (Grant No. 51375367, U1233116) and the Research Fund for the Doctoral Program of Higher Education of China (Grant No. 2010020112004)

References

[1] R Pelrine, R Kornbluh, Q Pei and J Joseph. High-Speed Electrically Actuated Elastomers with Strain Greater Than 100% [J]. Science, 287: 836-839 (2000).
[2] Y. Bar-Cohen, Electroactive polymer (EAP) actuator as artificial muscles, SPIE publication, Washington (2001).
[3] B Chu, X Zhou, K Ren, et al. A Dielectric Polymer with High Electric Energy Density and Fast Discharge Speed [J]. Science, 313(5785): 334-336 (2006).
[4] Pelrine, R., Kornbluh, R., Eckerle, J., Jeuck, P., Oh, S. J., Pei, Q. B., and Stanford, S., Dielectric elastomers:Generator mode fundamentals and applications, P Soc Photo-Opt Ins, 4329, 148-156 (2001).
[5] Chiba, S.Waki, M., Masuda, K., and Ikoma, T., Current Status and Future Prospects of Electric Generators Using Electroactive Polymer Artificial Muscle, eds., Sydney, NSW, Australia (2010).
[6] Pelrine, R., Kornbluh, R., Eckerle, J., Jeuck, P., Oh, S., Pei, Q. and Stanford, S., Dielectric Elastomers: Generator Mode Fundamentals and Applications, Proc. SPIE 4329, pp. 148-156 (2001).
[7] Anderson, I. A., Mckay, T., O'brien, B., and Melhuish, C., Power for Robotic Artificial Muscles, IEEE/ASME Transactions on Mechatronics, 16(Compendex), pp.107-111(2011).
[8] Kornbluh RD, Pelrine R, Prahlad H, et al., From boots to buoys: promises and challenges of dielectric elastomer energy harvesting. In: Electroactive polymer actuators and devices (EAPAD), Proc.SPIE 7976, 797605(2011).
[9]Jean-Mistral, C., Basrour, S. and Chaillout, J.-J., Dielectric polymer: scavenging energy from human motion, Proc. SPIE 6927, 692716 (2008).
[10] Koh, S. A., Zhao, X. H., Suo, Z. G., Maximal energy that can be converted by a dielectric elastomer generator, Appl. Phys. Lett. 94, 262902 (2009).
[11] McKay, T. G., O'Brien, B. M., Calius, E. P. and Anderson I. A., Self-Priming dielectric elastomer generator design", Proc. SPIE, 8340, 83401Y (2012)

Advanced Materials Research Vols. 960-961 (2014) pp 1342-1346

doi:10.4028/www.scientific.net/AMR.960-961.1342

Detection of Systematical Errors of AMR System Complexes

Egorov Alexandr[1, a], Kochneva Elena[1,b] and Pazderin Andrew[1,c]

[1]620002 Russia, Ekaterinburg, 19, Mira street

[a]eao@daes.ustu.ru, [b]et-85@mail.ru, [c]pav@daes.ustu.ru

Keywords: automated meter reading system, bad data detection, state estimation, energy flow problem, accuracy class, metering error, observability, measurements.

Abstract. Reliability of measurements received from automatic meter reading (AMR) systems is important. This paper presents method of bad data detection. The method allows to estimate the value of systematical error of each AMR complex in case of sufficient statistical sampling.

Introduction

All measurements of the electric energy EE) contain mistakes. In a general EE measurement can be presented as a sum of true, but unknown meaning of the measured magnitude W_i^{true}, a systematical component of error δ_{Wi} and a random error σ_{Wi} which has a zero expectation and nonzero dispersion:

$$W_i^{msm} = W_i^{true} + \delta_{Wi} + \sigma_{Wi}\,. \tag{1}$$

Maximum permissible measuring error for the i-th energy complex is defined by[1]

$$\delta_i = 1{,}1\sqrt{\delta_{Ii}^2 + \delta_{Ui}^2 + \delta_{EMi}^2 + \delta_{link\_i}^2}\,,\ \% \tag{2}$$

where δ_I, δ_U, δ_{EM} are accuracy ratings of a current transformers, voltage transformers and an energy meter, correspondingly; δ_{link} is a drop of voltage in a cable line.

However, during operation, the actual EE measurement error can exceed permissible limits defined (2). Another way of researches is equipment functional state assessment system [2]. In state estimation (SE) theory incorrect measurements are called bad data. Bad data are to be revealed and eliminated as quick as possible. Analytical methods of bad data detection are least expensive.

Theoretical Background

Within frameworks of SE theory the equations containing all measured variables refer to as testing TE. [3-5] describes bad data detection method based on solving the testing equations system. TE technique is built on the fact that equations of state have small connection. Thus the measured EE flow clearly depends on few other flows. Sizable mismatches (imbalances)likely will correspond to equation containing bad data. Obviously it is necessary just to compare energy flows at the beginning and at end of the branch to validate them. The correct nodal balance or balance in separate circuit fragment indicates the correctness of measurements included into the balance equation.

The TE method also allows to form system of validating equations for each measurement. Dimension of this system is defined by total number of TE. That is each measurement can be recalculated using linear combinations of other measurements.

Reliability of measurement is rated according to difference between its recalculated value and measurement itself. Total variance is calculated for each validating equation D_i. The expression for determining the calculated value for measurement can be obtained from minimized objective function:

$$F = \sum_{i=1}^{N} \frac{1}{D_i} (W^{calc} - W_i^{calc})^2, \quad (3)$$

where D_i is the total variance if the i-th validating equation, W^{calc} is desired value of energy flow, W_i^{calc} is value of energy flow obtained by calculation the i-th validating equation.

Calculated value for measured energy flow is counted upon the formula:

$$W^{calc} = \sum_{i=1}^{N} \frac{1}{D_i} W_i^{calc} \cdot (\sum_{i=1}^{N} \frac{1}{D_i})^{-1} \quad (4)$$

Calculated EE flows values W_i^{calc} are determined on the input data basis which is measured flows W_i^{meas}. Accounted parameters completely match state equations system in contrast of measurements.

Computing of calculated EE flow value corresponding to the measurement using the system of verification equations allows to determine measurement error during each measurement interval under consideration.

The higher the precision of AMR complexes, the smaller the difference ΔW_i between measured W_i^{meas} and calculated W_i^{calc} values of EE flow. Thus, the relative value of the estimated error corresponds to the actual error of AMR complex:

$$\delta_W = (\Delta W_i / W_i^{meas}) \cdot 100 \ \% \quad (5)$$

Availability of numerous time intervals for calculation allows collecting statistical information about calculated errors of each AMR complex. Further processing of these data can help to detect presence and determine the magnitude of systematical error of corresponding AMR complex.

The expectation value of calculated errors series corresponds to the constant component of AMR complex error, i.e. systematical error. Accordingly, carrying out such calculations allow to distinguish AMR complexes in need of immediate metrological verification.

The results of calculations for each AMR complex can conveniently be presented as dynamic error distribution graph and histogram of error deviation from its expectation. The form of diagrams would show the presence of systematic error.

Calculation of Systematical Error

Calculations for part of Russia energy system are produced to demonstrate the effectiveness of the method under discussion. The considered network consists of four nodes ring and three radial branches. Calculations are carried out for 792 hour intervals.

Parameters of transmission lines and transformers are used as initial data for equivalent circuit construction. The source of 792 measurement intervals is AMR system. Losses in each network fragment are taken into account.

The system of TE is formed by excluding all unmeasured variables from system of state equations of EFP [6], i.e. system of balance equations in nodes and branches of equivalent circuit.

Initial EFP state equations system for equivalent circuit under consideration can be presented as:

$$\begin{aligned}
&W_2 + W_4 + W_5 + W_{12} + W_{13} + W_{14} + W_{15} + W_{16} + W_3 + W_{11} + W_{10} = 0 \\
&W_{23} + \overline{W_{3-31}} = 0 \\
&\cdots \\
&W_{40} + \overline{W_{7121-712}} = 0 \\
&W_{14} + W_{18} + \Delta W_{1-2mex} = 0 \\
&\cdots \\
&\overline{W_{712-7121}} + \overline{W_{7121-712}} + \Delta W_{712-7121mex} = 0
\end{aligned} \quad (6)$$

Configuration of equivalent circuit is presented on Fig. 1.

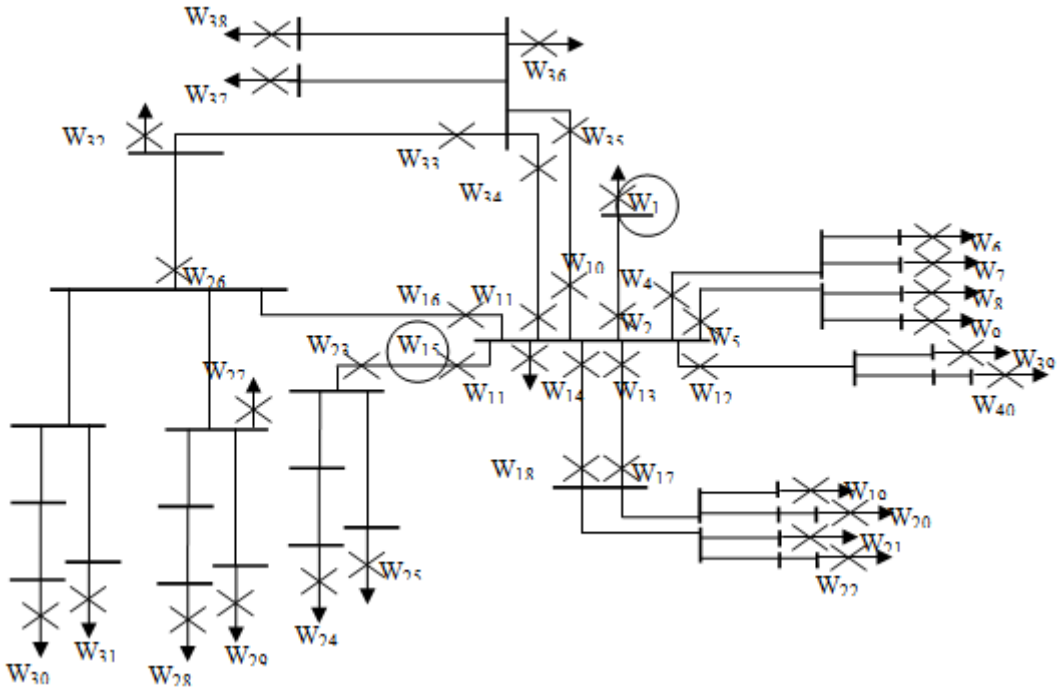

Fig.1 Configuration of equivalent circuit

Next step is to draw up a series of verifying equations for each measurement. Energy complexes errors determined by the formula (1) and error of technical losses calculation are assumed 1%and 10% correspondingly.

This system for measurement W_1 is**:**

$$
\begin{aligned}
&W_1 = W_2 - \Delta W_{1-13}\\
&W_1 = -(W_4 + W_5 + W_{12} + W_{13} + W_{14} + W_{15} + W_{16} + W_3 + W_{10} + W_{11}) - \Delta W_{1-13}\\
&W_1 = -(W_6 + W_7 + \Delta W_{1-111-112} + W_5 + W_{12} + W_{13} + W_{14} + W_{15} + W_{16} + W_3 + W_{10} + W_{11}) - \Delta W_{1-13}\\
&W_1 = -(W_4 + W_8 + W_9 + \Delta W_{1-121-122} + W_{12} + W_{13} + W_{14} + W_{15} + W_{16} + W_3 + W_{10} + W_{11}) - \Delta W_{1-13}\\
&W_1 = -(W_4 + W_5 + W_{39} + W_{40} + \Delta W_{1-7} + \Delta W_{7-711-7121} + W_{13} + W_{14} + W_{15} + W_{16} + W_3 + W_{10} + W_{11}) - \Delta W_{1-13}\\
&W_1 = -(W_4 + W_5 + W_{12} + W_{17} + \Delta W_{1-2(1)} + W_{14} + W_{15} + W_{16} + W_3 + W_{10} + W_{11}) - \Delta W_{1-13}\\
&\ldots
\end{aligned}
\qquad (7)
$$

Series of calculated values for each measurement is computed from the verification equations system. Table 1 presents computing results for the first four time intervals for measurement W_1 .

Table 1. Calculated values of W_1

Time interval PArameter	01.11.12 00.00-01.00	01.11.12 01.00-02.00	01.11.12 02.00-03.00	01.11.12 03.00-04.00
W_1 [kWh]	257600	268000	281400	291800
$W_1^{расч}$ [kWh]	253894	264517	277355	287806
$W_2^{расч}$ [kWh]	256446	267025	279819	290270
$W_3^{расч}$ [kWh]	256969	267649	280330	290826
$W_4^{расч}$ [kWh]	256619	267267	280004	290477
$W_5^{расч}$ [kWh]	256540	267227	280020	290505
$W_6^{расч}$ [kWh]	239500	250833	264334	274270
…				

Errors of measurements on each time interval are calculated according to the formula (5) using calculated values. Table 2 presents results for the same four time intervals for W_1 .

Table 2. Errors of measurement W_1

Time interval Parameter	01.11.12 00.00-01.00	01.11.12 01.00-02.00	01.11.12 02.00-03.00	01.11.12 03.00-04.00
W_1 , [kWh]	257600	268000	281400	291800
W_1^{calc} , [kWh]	254623	265341	278223	288625
δ_W , [%]	1,16	0,99	1,13	1,09

Error distribution and histogram for AMR complex W_1 are presented on Fig. 2a and 2b.

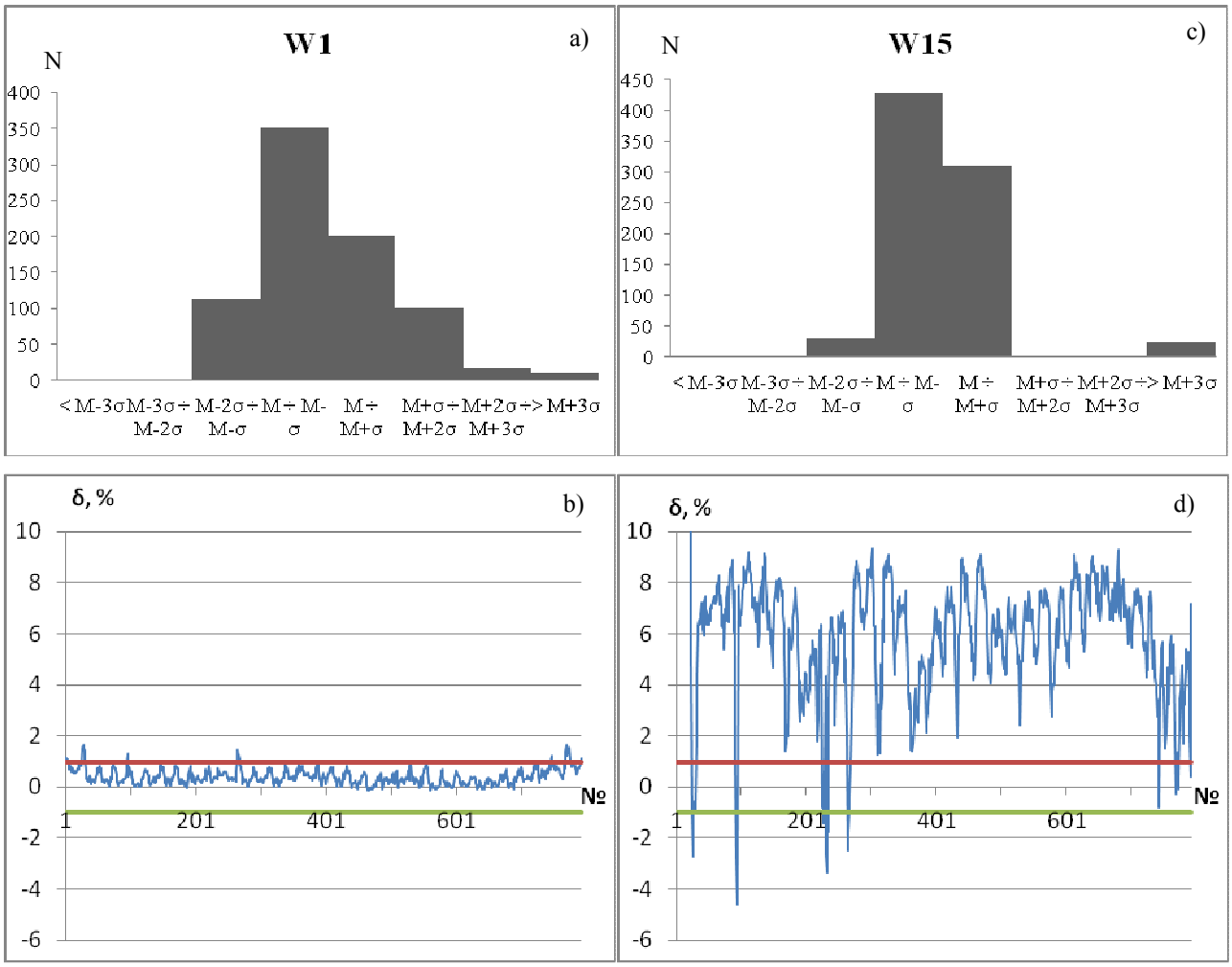

Fig 2. a, c – Histogram for measurements W_1 and W_{15} correspondingly, b, d – error distribution for W_1 and W_{15} correspondingly.

Serviceability criterion for any AMR complex is defined according to formula:

$$M_{W_i} \le \delta_{\lim_i}, \tag{8}$$

where M_{W_i} is the expectation of calculated errors series for W_i , $\delta_{\lim_i}$ is the maximum permissible error of AMR complex defined by (2).

The magnitude of calculated error expectation is 0.4% which does not exceed the limiting meaning of AMR complex error (which is 1%), so this AMR complex considered serviceable.

Similar calculations were performed for AMR complex W_{15}. The expectation is 5.8% that exceeds the maximum permissible margin of error. It should be recommended to carry out immediate metrological verification of this complex.

Summary

1. Ensuring the reliability of AMR system metering information is important. Only metrological methods are not sufficient to provide verification of measurements. Mathematical approaches require the least cost.
2. Bad data detection methods developed in frameworks of SE theory are the most effective methods of measurement reliability control.
3. Analytical methods based on TE along with verification allow to produce estimations of measurements. If there are sufficient retrospective it is possible to estimate systematical error of AMR complexes. Thus analytical approaches allow to excersize self-diagnosis of AMR system during metrological verification intervals.

Acknowledgements

This research project has been supported by UrFU under the Framework Programme of development of UrFU through the «Young scientists UrFU» competition.

References

[1] RD 34.09.101-94. Typical instruction for electricity metering in its generation, transmission and distribution. M. ORGRES, 1995.S. (in Russian).

[2] Dmitriev S.A., Khalyasmaa A.I. Power equipment technical state assessment principles. Applied Mechanics and Materials. Vol. 492, 2014, Pp. 531-535.

[3] Abur Ali, Exposito Antonio Gomez. Power System State Estimation. Marcel Dekker inc., New York

[4] Gamm A.Z, Kolosok I.N. Bad data detection in measurements in electric power system. Nauka, Novosibirsk, Sib. Enterpr. RAS 2000. (in Russian)

[5] Monticelly. State Estimation in Electric Power Systems – a Generalized Approach. Norwell, M A: Kluwer, 1990.

[6] Pazderin A.V., Kokin S.E., Egorov A.O., Kochneva E.S., Solution of energy flow problem using state estimation technique. 35th Annual Conference of the IEEE Industrial Electronics Society, Porto, Portugal. November 2-5 2009, pp:1750 - 1755.

Advanced Materials Research Vols. 960-961 (2014) pp 1347-1351

doi:10.4028/www.scientific.net/AMR.960-961.1347

Development of 110-220 kV power transformer model for equipment functional state assessment system

Alexandra I. Khalyasmaa[1,a], Stepan A. Dmitriev[2,b], Sergey E. Kokin[3,c], Daniil A. Glushkov[4,d] and Pavel A. Kuzin[5,e]

Ural Federal University named after the first President of Russia B.N. Yeltsin, 620002 Russia, Ekaterinburg, 19, Mira street

[a]lkhalyasmaa@mail.ru, [b]dmstepan@gmail.com, [c]kokinser@list.ru, [d]daniil.glushkov@yandex.ru, [e]pavel.a.kuzin@gmail.com

Keywords: power transformer, functional state, test, diagnostics, hybrid neural networks, Takagi-Sugeno fuzzy method.

Abstract. This paper addresses the problems, connected with implementation of 110-220 kV power transformer structural model for automated equipment functional state assessment system based on test and technical diagnostics data. This article describes the basic construction principles of hybrid neural network using Takagi-Sugeno fuzzy method. The paper also provides the statistical data analysis results for power transformers (of real energy grid part) to define fuzzy neural network criteria (layers).

Introduction

Today failure statistics analysis shows that the main causes limiting the electricity consumer's power supply are the equipment deterioration high degree, operation and repair errors, defects of manufacture and equipment installation. But the decision to replace or electrical substations equipment upgrades must be justified by its actual state, potential risks and economic expediency. Therefore the equipment functional state assessment system is one of the key issues in modern Grid Enterprise Asset Management (EAM).

Problem definition and solution

The modern Grid Enterprise Asset Management (EAM) is constructed on the principles of installing additional sensors and equipment monitoring systems at substations. But today the enterprise, on the balance of which there are a large number of substations, have neither technically or economically possible to install additional equipment functional state assessment system for each equipment at substations, particularly in remote areas. In turn each company must properly manage its technical assets (including repair, replacement, retrofit, renovation, maintenance of equipment, etc.) and the correct and timely identification of system bottlenecks (at substations or some substations) depends on the distribution of financial flows.

Thus the effective management of technical assets is provided a minimum of costs and therefore to make maximum use existing equipment technical state assessment methods, which in modern Russian power industry technical diagnostics methods and equipment test methods are presented. Therefore the authors in this paper proposed for the automated control system to realize the technical assets based on test data and technical diagnostics, which in turn are regulated by regulatory documents and are required at the moment.

It should be noted that this method is not appropriate for the assessment of equipment each part separately and only for the integrated (complex) substations assessment and only to solve the EAM task is effective. For the modeling of such systems in this case possible to use the hybrid neural networks, those combine the methods of fuzzy logic and artificial neural networks. In this paper, the Takagi-Sugeno fuzzy control method is used.

Power transformer model

This article presents the example of actual state system realization for 110-220 kV power transformer for the integrated substation assessment. The model consists of two main objects: "passport data" equipment and "technical components" (it is possible to use regime parameters as in [1]). If the object "passport data" includes manufacturer's data and the represents a simple object then the object "technical components" is a complex subject and consists of 9 simple sub-objects:

1. core;
2. winding;
3. solid insulation;
4. oil;
5. cooling system;
6. high-voltage bushing;
7. tank and auxiliary systems;
8. on load tap changer (OLTC);
9. contact connection.

Each of sub-object is characterized by different defects (possible) types each of them can be determined using different test methods shown in Table. 1. In this case, the model mathematical formulation is performed using the Takagi-Sugeno fuzzy method. Simulation of hybrid systems of this type in the software package Matlab is realized.

Proposed approach firstly results in the creation of neural network specific construction and secondly - in network connections' weights determination. This fuzzy neural network forms a fuzzy rules and membership functions adapts in the learning process by modification of connections' weights [2]. In Takagi-Sugeno fuzzy method the rules presented in the form functional binding (1) rather than as an output variable membership to the fuzzy sets

$$R^{(k)}: IF(x_1 \ is \ A_1^k \ AND \dots AND \, x_n \ is \ A_n^k) \ THEN \ y = f^{(k)}(x_1,...,x_n) \quad (1)$$

where $R^{(k)}$ - fuzzy rules ($k = 1,...,N$,where N - number of fuzzy rules); A_i^k - fuzzy sets (where $i = 1,...,n$); $x_1,...,x_n$ - input variables; y - system output is a input variables function. Each rule will produce its own numerical value of the control action [3].

There are a number of curves typical forms to define the membership functions. In this case for each input variable by the degree of membership for each of the states using membership functions LR-type is determined [4]: $\mu_i(x) \in R \to [a;c]$, where R - set of real numbers, $[a,c]$ - range of the variable, b - the most possible value of the variable.

$$\mu_i(x) = \begin{cases} 0, & x \le a \\ \dfrac{x-a}{b-a}, & a \le x \le b \\ \dfrac{c-x}{c-b}, & b \le x \le c \\ 0, & c \le x \end{cases} \quad (2)$$

Membership functions in this case are the linguistic functions "state" includes four possible states in terms of technical operability:

- good condition D_1, when the equipment meets all technical requirements. Good condition is always an operable one;
- fault and operable condition D_2, when technical requirements are met for object properties, which characterize the ability to perform predetermined functions;
- fault and inoperable condition (repairable) D_3, when the equipment is unable to perform the predetermined function, but it is possible and economically feasible to carry out service works;

– inoperable and non-repairable D_4, when service is technically impossible or economically unfeasible [5].

General view of membership functions in Fig.1 is shown. It is necessary to determine the memberships of parameters to following criteria set are presented in Table 1.

These criteria are defined on the basis of statistical data (analysis of 92 substations of Sverdlovsk region from 2000 to 2013 years) by selecting the direct related factors and determining correlations.

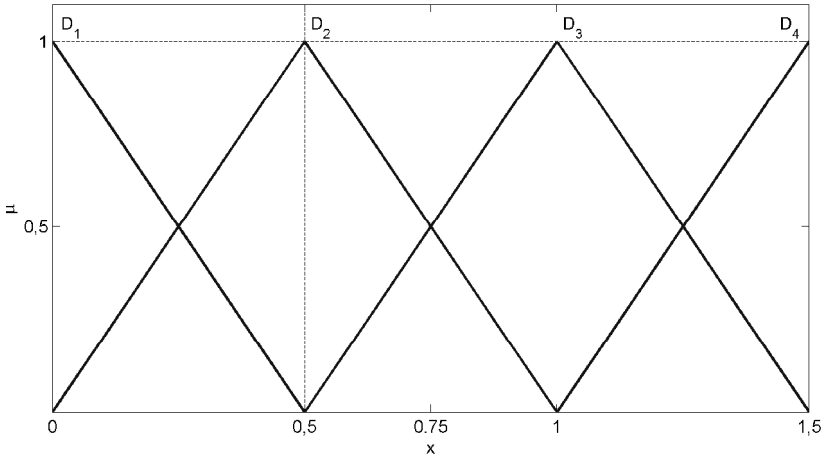

Figure 1 - Membership function

Table 1
Membership criteria for the input parameters

№	Transformer part	Defect type	Diagnostic and tests methods
1.	Core	a. varnish insulation defect between the magnetic plates; b. insulation defect between the core and fastenings elements; c. insulation defect between the core and LV winding; d. defect of core grounding; e. asymmetry of the core due to winding defect.	a. load losses test; partial discharges test; b. load losses test; partial discharges test; c. insulation resistance test and capacitance test by zones; d. insulation resistance test capacitance test by zones; e. load losses test.
2.	Winding	a. displacement and deformation of coil windings; b. defect connections of tap windings; c. defect connections between winding.	a. short-circuit resistance test; vibroacoustic test b. DC resistance test; c. DC resistance test.
3.	Solid insulation	a. breakdown longitudinal insulation; b. deterioration of the insulation; c. wetting insulation; d. partial discharges in insulation; e. decrease of the polymerization index.	a. induced high frequency voltage test; no-load test; b. opacity oil test c. wetting insulation assessment; d. chromatographic analysis; e. assessment of availability of furan compounds in the oil and degree of polymerization.

Table 1 Continuation

№	Transformer part	Defect type	Diagnostic and tests methods
4.	Oil	a. oil humidity; b. contamination; c. sludge; d. variation in electrical characteristics; e. variation of acid value; f. variation of closed cup flash point; g. variation of dielectric loss tangent; h. variation of water-soluble acids and alkalis; i. availability of ionol; j. gas oil ratio.	chromatographic analysis and physico-chemical analysis of oil
5.	Cooling system	a. stator windings insulation defect; b. bearing damage of electric pump; c. pollution of tubes coolers.	a. insulation resistance test; b. listening and measuring levels of noise and vibration; c. oil differential temperature test at the cooler.
6.	High-voltage bushing	a. cracks and chips of porcelain insulators; b. pollution of the insulator external surface; c. oil leak; d. variation of composition and oil content; e. variation in electrical characteristics; f. partial discharges; g. capacity increase of basic insulation.	a. thermal imaging control; b. thermal imaging control; c. overpressure test; thermal imaging control; d. chromatographic analysis and physico-chemical analysis of oil. e. control under operating voltage.
7.	Tank and auxiliary systems	a. leak of tank; b. increased heating of component parts; c. availability of short circuit loops; d. corrosion, paint coating defect; e. defects of protective circuits and control equipment.	a. tank density test; b. thermal imaging control; c. insulation resistance test between components and tank; d. external inspection; e. protective circuits and control equipment tests
8.	OLTC	a. oil leak; b. variation in electrical characteristics of oil and wetting insulation c. contact defects.	a. thermal imaging control; oil level measuring; b. oil humidity test; c. DC resistance test;
9.	Contact connection	a. heatings contacts in places of fastening to bushing.	a. thermal imaging control.

Afterwards, one should define the linear relation between the input and output parameters and specify production rules, basing on Table 1 data and specific boundary values for each test method and parameter rules, basing on Table 1 data and specific boundary values for each test method and parameter.

Summary

This article presents the model of the power transformer functional state by using fuzzy characteristic functions LR-type. Based on the statistical data of the power equipment failures and transformers diagnostics and tests are formed correlation dependences between the defects types and diagnosable parameters. These connections form the basis of power equipment assessment. This paper describes the model of automated control system, which is used for power equipment technical state assessment, based on diagnostics and test data, and can be considered as one of the main ways of power industry enterprise cost cutting.

References

[1] A. V. Pazderin, S. E. Kokin, A. O. Egorov, E. S. Kochneva: *Solution of energy flow problem using state estimation technique.* Source of the Document IECON Proceedings (Industrial Electronics Conference) 5414817, pp. 1736-1741.2009.

[2] D. Rutkovskaya, M. Pilinsky, L. Rutkovski: *Neural networks, genetic algorithms and fuzzy systems* (Hotline Telecom, Russia 2006).

[3] N. N. Nam: *Self-evolving Takagi-Sugeno-Kang fuzzy neural network* (NTU-School of Computer Engineering (SCE), China 2012).

[4] A. I. Khalyasmaa, S. A. Dmitriev, S. A. Eroshenko: *Membership functions for the formation of the electrical equipment state estimation for power stations and substations*. Advanced Materials Research. Vol. 694-697. P. 1329-1333. 2013.

[5] I. V. Davydenko, V. N. Osotov: *Systems for the diagnosis of high-voltage oil-filled electrical power* (UrFU, Russia 2013).

Advanced Materials Research Vols. 960-961 (2014) pp 1352-1355

doi:10.4028/www.scientific.net/AMR.960-961.1352

Research on Classification Performance of Circuit Breaker Vibration Signal based on Fuzzy C-means Clustering Analysis

Bin Li[1, a], Shuang Li[1,b] , Xuchen Lu[1,c]

[1] Electric Power Research Institute of State Grid Liaoning Electric Power Co., Ltd., Shenyang 110006, Liaoning Province, China

[a]tflb@qq.com, [b]lishuang_2006@126.com, [c]luxuchen@qq.com

Keywords: circuit breaker, mechanical vibration signal, fuzzy C clustering analysis, classification performance.

Abstract. With permanent magnetic actuator monostable circuit breaker as the research object, it gets three different running status signal data, normal circuit breaker closing state , break-brake spring single loss and Institutions unsmooth Through constructing data acquisition platform. The performance of the three methods of feature extraction is compared, short-time Fourier transform, wavelet packet energy entropy and Hilbert huang transform, through fuzzy c-means clustering analysis algorithm. Through the comparative study, it is concluded that adopt wavelet packet transform method to get the best classify performance of time-frequency entropy vector .

Introduction

Circuit breaker mechanical vibration signal is a typical non-stationary signal, the signal contains information of abundant working status and fault characteristic. The signal characteristic value can be extracted by time-frequency analysis method. The typical time-frequency analysis contains short-time Fourier transform, wavelet transform and Hilbert huang transform, etc. And signal feature extraction result affect much the performance of state classifier equal with the diagnostic method, the characteristics extracted is very different through different categories. It is easier to design a better performance classifier. On the contrary, if the characteristics extracted is little different through different categories, the training of the classifier and the study take a long time, the precision of design is also difficult to guarantee. Therefore, it need to analyze the classification performance of feature vector, to choose the optimum method of feature extraction, provide characteristic data basis for fault diagnosis of the next step[1~3].

With permanent magnetic actuator monostable circuit breaker as the research object, it gets three different running status signal data, normal circuit breaker closing state , break-brake spring single loss and Institutions unsmooth Through constructing data acquisition platform. The performance of the three methods of feature extraction is compared, short-time Fourier transform, wavelet packet energy entropy and Hilbert huang transform, through fuzzy c-means clustering analysis algorithm.

Circuit breaker mechanical vibration signal acquisition

In view of the vibration signals of circuit breaker, it designed and developed the data collection system. The system consists of sensor, communication unit and upper machine. lower machine adopts DSP28335 microcontroller and ADS8364 analog-to-digital conversion chip. communication unit adopts RS485 serial communication bus. upper machine adopts VC++ application development environment and MS SQL Server relational database. Mechanical vibration signal sensor adopts LC0159 type piezoelectric acceleration sensor, which sensitivity is 10mV/g, range is 500g, frequency range is 1-12000Hz and is directly installed in the B phase outside of circuit breaker shell with persistence flow power module. The actual measurement figure collection as shown in Fig.1.

The acquisition system is a total of 6000 data in 150ms, through sampling frequency of 40 kHz. Under the condition of no-load closing, it analyzes three signal of each state, the circuit breaker normal, the operation and the transmission mechanism unsmooth and break-brake spring single off. The measured data diagram as shown in Fig.2-4. the measured data of vibration signal needs to be done to eliminate trend before the eigenvalue extraction processing.

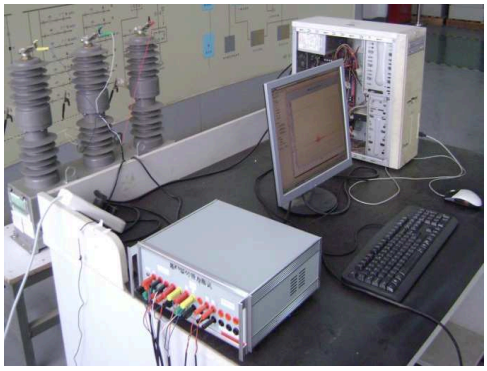

Fig.1 Acquisition field of circuit breaker mechanical vibration data

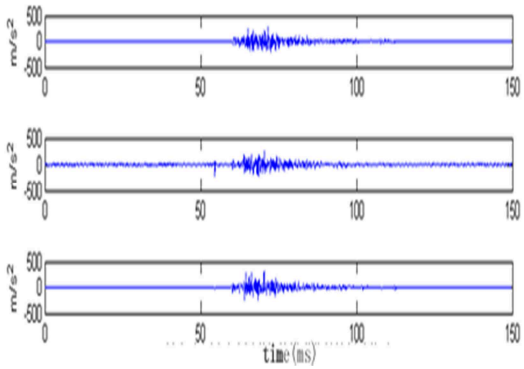

Fig .2 Mechanical vibration signal of normal closing

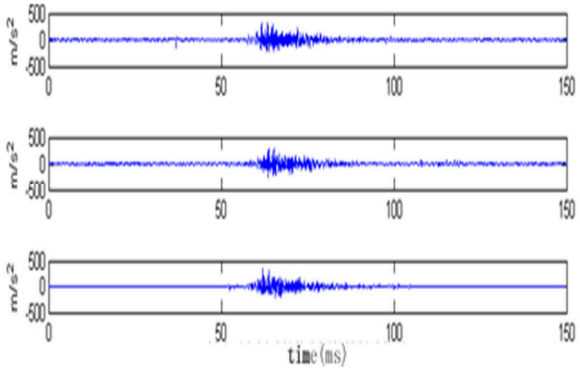

Fig.3 Mechanical vibration signal of break-brake spring single shed

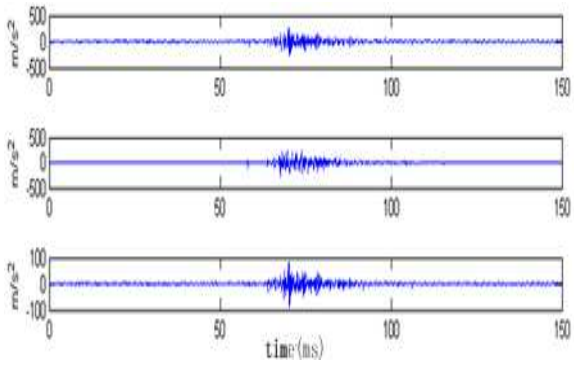

Fig.4 Mechanical vibration signal of mechanism unsmooth

Eigenvalue extraction of three kinds of time-frequency entropy vector

(1) vibration signal characteristic value is extracted by Short time Fourier transform

Principle of short time Fourier transform (STFT) is the non-stationary signal add a time window, which approximate consider the signal is smooth in small section time[4]. Such short transient time domain signal can be treated by Fourier transform. According to the vibration data in Fig.2-4, it establish characteristic data of length 256, the energy spectrum of the signal is extracted by short time Fourier transform as shown in Fig.5.

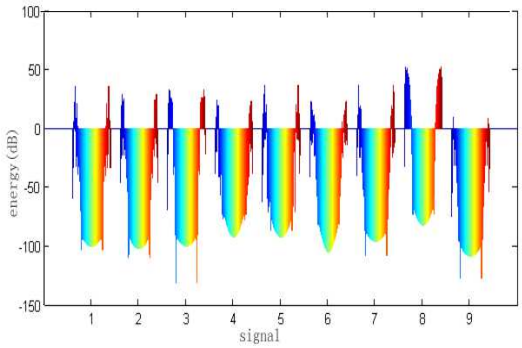

Fig.5 Short FFT energy spectra of circuit breaker vibration signal

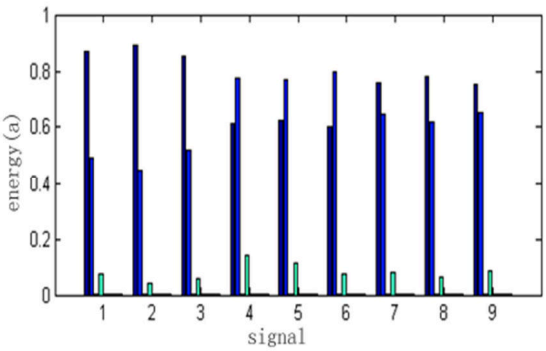

Fig.6 Wavelet packet energy spectrum of circuit breaker vibration signal

(2) vibration signal characteristic value is extracted by wavelet packet energy entropy method

Wavelet transform has the ability of denoting local signal characteristics in the time-frequency domain, but only decompose the low frequency part of signal, not decompose the high frequency part of signal[5]. And wavelet packet decompose the part of low frequency and high frequency signal at the same time. In fault diagnosis of circuit breaker, when the circuit breaker operation state is abnormal, the energy of each frequency components of circuit breaker vibration changed corresponding, the change of one or several frequency components maps the fault mode of circuit

breaker. According to the vibration data in Fig.2-4, it extract the energy spectrum of the signal through three layers db10 wavelet packet transform, as shown in Fig. 6.

(3) vibration signal characteristic value is extracted by Hilbert huang transform

Hilbert - Huang Transform (HHT) mainly includes two parts, the Empirical Mode Decomposition (EMD) and Hilbert spectrum analysis[6]. According to the vibration data in Fig.2-4, the energy spectrum of the signal is extracted through Hilbert - huang transform, as shown in Fig.7.

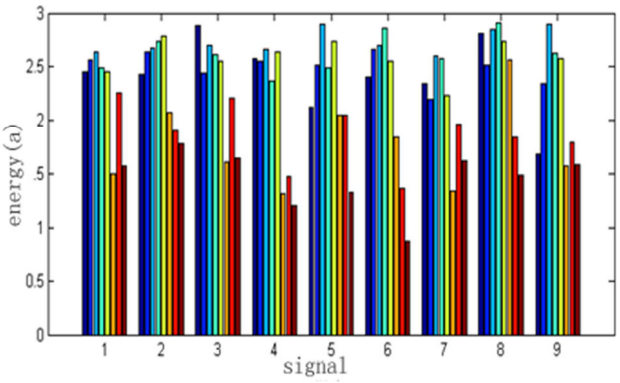

Fig.7 HHT energy spectra of circuit breaker vibration signal

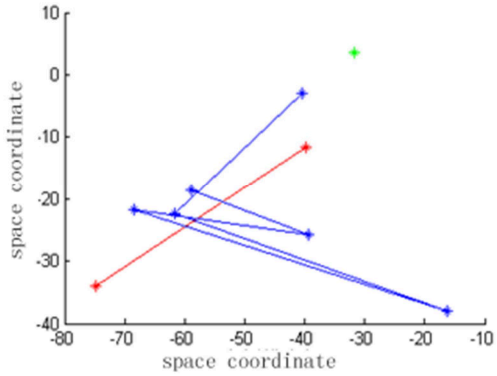

Fig.8 FCM clustering analysis diagram of the characteristics data of short-time FFT

Effectiveness analysis of the three kinds of time-frequency entropy vector

Clustering is understood as a collection of similar objects. Clustering analysis is an unsupervised learning method, and find the data underlying similarities[7].

Fuzzy c-means clustering (FCM) is a very typical fuzzy clustering method, it determine the best classification through the goal function iterative optimization. It define A data set $\{X_k\}_{k=1}^n$, and divide into class C by FCM algorithm. Its goal function express as follows.

$$J(U,V)=\sum_{i=1}^{c}\sum_{k=1}^{n}u_{ik}^{m}\|x_k-v_i\|^2 \tag{1}$$

It satisfies the following conditions：

$$\sum_{i=1}^{c}u_{ik}=1\,|\,0\le u_{ik}\le 1,\forall k=1,2,\cdots,n \tag{2}$$

$$0<\sum_{k=1}^{n}u_{ik}<n \tag{3}$$

In formula, U as the membership degree matrix, u_{ik} as membership degree of data points x_k to cluster center points v_i, m as membership weighting coefficient, V as matrix of clustering center. According to the Lagrange algorithm to get the iterative formula:

$$u_{ik}=\frac{1}{\sum_{j=1}^{c}\left(\frac{\|x_k-v_i\|}{\|x_k-v_j\|}\right)^{2/(m-1)}} \tag{4}$$

$$v_i=\frac{\sum_{k=1}^{n}u_{ik}^{m}x_k}{\sum_{k=1}^{n}u_{ik}^{m}} \tag{5}$$

FCM algorithm clusters data through the iteration formula (4) and (5).

According to the fuzzy c-means clustering analysis theory, it compares the three methods of feature extraction of vibration signal analysis under different condition of circuit breaker. its results of the clustering analysis through Short time Fourier transform is shown in Fig.8. its results of the clustering analysis through Wavelet packet transform is shown in Fig.9. its results of the clustering analysis through Hilbert huang transform is shown in Fig.10.

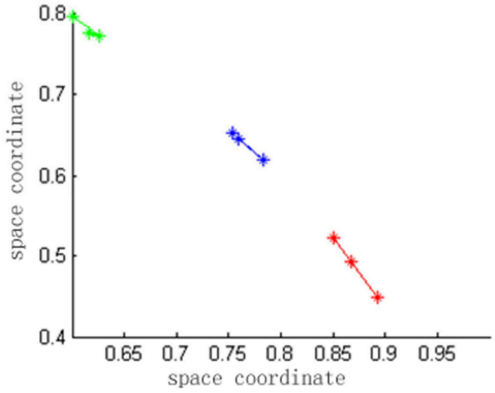

Fig.9 FCM clustering analysis diagram of characteristics data of wavelet packet

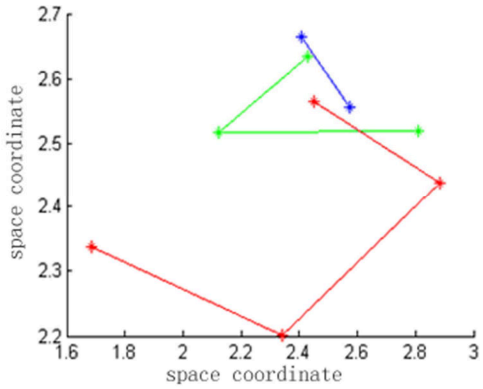

Fig.10 FCM clustering analysis diagram of HHT characteristics data

It concluded from the above figure, the characteristic value of circuit breaker vibration signal extracted through wavelet packet energy entropy, that achieve the best classification effect. Clustering results are consistent with implementation classes, the energy entropy vector clustering results are very different with implementation classes through the other two methods.

Conclusion

With permanent magnetic actuator monostable circuit breaker as the research object, it gets three different running status signal data, normal circuit breaker closing state , break-brake spring single loss and Institutions unsmooth Through constructing data acquisition platform. The performance of the three methods of feature extraction is compared, short-time Fourier transform, wavelet packet energy entropy and Hilbert huang transform, through fuzzy c-means clustering analysis algorithm. Come to the following conclusions:

(1)It gets the best classify performance of time-frequency entropy vector obtained Through Wavelet packet transform method. Clustering results are consistent with implementation classes

(2)The energy entropy vector clustering results are very different with implementation classes through Short-time Fourier transform and Hilbert huang transform.

References

[1] CHANG Guang, ZHANG Zhenqinan, WANG YI: High Voltage Apparatus. Vol. 47 (2011), p. 85. In Chinese

[2] ZHAO Yang, LIU Han-yu, ZENG Qingjun: High Voltage Apparatus. Vol. 46 (2010), p.46. In Chinese

[3] Jianyuan, ZHANG Bin, LIN Xin, LI Bin,TENG Yun: High Voltage Engineering. Vol. 38 (2012), p. 1299. In Chinese

[4] Zhang Dong, Wu Xiaolin: Computer & Dig ital Engineering. Vol. 39 (2011), p. 154. In Chinese

[5] OCAKA H，LOPAROB K A，DISCENZOC F M: Journal of Sound and Vibration. Vol. 302(2007), p.951.

[6] HUANG Jian, HU Xiaoguang, GONG Yunan: Proceedings of the CSEE. Vol. 31(2011), p. 108. In Chinese

[7] LIU Rui jie, ZHANG Jinbo, LIU Rui: Journal of Chongqing Institute of Technology(Natural Science). Vol. 22 (2008), p. 139. In Chinese

Advanced Materials Research Vols. 960-961 (2014) pp 1356-1360

doi:10.4028/www.scientific.net/AMR.960-961.1356

Power Control of Photovoltaic Inverter under Unbalanced Grid Faults Considering Limits of Its Current Harmonics

Yu Zhou[1, a], Zhiyong Dai[2, b], Qianggang Wang[3, c *], Ling Ye[3, d] and Niancheng Zhou[3, e]

[1]Guiyang Power Supply Bureau, Guiyang, 550002, Guizhou, China

[2]Planning center of Shenzhen Power Supply, 518001, Shenzhen China

[3]State Key Laboratory of Power Transmission Equipment & System Security and New Technology, Chongqing University, Chongqing, 400044, China

[a]yitagou@qq.com, [b]dzy13808800925@163.com, [c]qianggang1987@cqu.edu.cn, [d]809185007@qq.com, [e]cee_nczhou@cqu.edu.cn

Keywords: Photovoltaic inverter, unbalanced grid fault, distribution grid, power control, current harmonics.

Abstract. This paper studies the instantaneous output power characteristics of photovoltaic inverters and its flexible power control strategy under unbalanced grid faults. Then the optimal parameters model of the power control is established with minimum integrated fluctuation amplitude of the active and reactive power as a goal when the constraint of the output current harmonic distortion of photovoltaic inverters is taken into account. Finally, the optimal power control of photovoltaic inverters based on dead-beat current tracking is realized and the feasibility of the proposed control strategy is verified with the power system transient software PSCAD/EMTDC.

Introduction

More distributed generators (DG) has been embedded in distribution networks with increased penetration of renewable power [1, 2]. Photovoltaic (PV) has played a vital roll in DG systems for its easy installation and proven technique. In the actual operation of power grid, unbalanced faults happen more frequently than balanced faults, which will lead to oscillation of output power and output current increasing which will further bring about harmonic distortion of PV inverters. Hence, it is of necessity to study on PV inverter operation characteristics under unsymmetrical voltage and analyze the improved control in allusion to unbalanced faults.

Photovoltaic inverter control strategy under unbalanced grid faults includes two parts: reference current calculation and current tracking control. A dual control strategy was proposed to calculate positive and reactive current reference while keeping the DC voltage constant [3]. Resonant control could be added to proportional integral (PI) and improved current reference algorithm considering power oscillation caused by filter inductor [4, 5]. However, the research mentioned above has improved control strategy by considering only operation restrain but without the impact caused by injection current in the presence of faults. In allusion to active power control, reference [6] has proposed five kinds of control strategies and compared their characteristics of inverter output power oscillation and current harmonics with each other. According to the above, [7, 8] proposed the control strategy in which the amplitude of output double-frequency power oscillation of inverters is continuously adjustable within the limit value of DC voltage fluctuation.

This paper proposes a power control strategy of PV inverter under unbalanced grid faults and derivates the total harmonic distortion (THD) formula of reference current. In addition, establishes an optimal model of power control parameters. The current tracking part of PV inverter is designed based on the strategy of deadbeat control and the feasibility of the proposed control strategy has been verified by the power system transient software PSCAD/EMTDC.

Power Control of PV Inverter under Unbalanced Grid Faults

The structure of three phase PV generation system, which consists of PV array, single polarity inverter and control, is shown in Fig. 1.

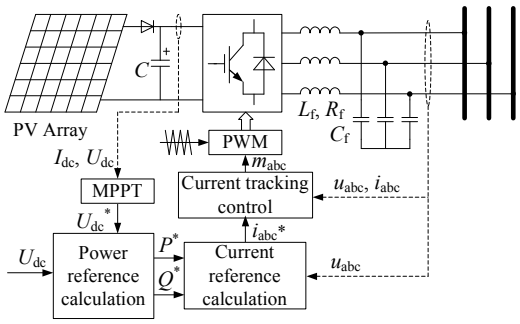

Fig. 1 Grid-connected PV generation system structure

The terminal voltage and current of PV inverter only contain positive and negative components under unbalanced faults which can be written in space form like $\boldsymbol{u}=\boldsymbol{u}^+ + \boldsymbol{u}^-$ and $\boldsymbol{i}=\boldsymbol{i}^+ + \boldsymbol{i}^-$, where $\boldsymbol{u}^+=[u_a^+, u_b^+, u_c^+]^T$, $\boldsymbol{u}^-=[u_a^-, u_b^-, u_c^-]^T$, $\boldsymbol{i}^+=[i_a^+, i_b^+, i_c^+]^T$ and $\boldsymbol{i}^-=[i_a^-, i_b^-, i_c^-]^T$. The terminal voltage is,

$$u(t)|_{a,b,c}=\sqrt{2}U^+\cos[\omega t-(m-1)\frac{2\pi}{3}+\varphi_u^+]+\sqrt{2}U^-\cos[\omega t+(m-1)\frac{2\pi}{3}+\varphi_u^-] \tag{1}$$

Set voltage vector $\boldsymbol{u}_\perp=[u_{\perp a}, u_{\perp b}, u_{\perp c}]^T=[u_b-u_c, u_c-u_a, u_a-u_b]^T/\sqrt{3}$, and $\boldsymbol{u}_\perp=\boldsymbol{u}_\perp^+ + \boldsymbol{u}_\perp^-$. Then the three phase instantaneous active power and reactive power of PV inverter can be written as ,

$$\begin{cases} p=\boldsymbol{u}\cdot\boldsymbol{i}=\boldsymbol{u}^+\cdot\boldsymbol{i}^+ + \boldsymbol{u}^-\cdot\boldsymbol{i}^- + \boldsymbol{u}^+\cdot\boldsymbol{i}^- + \boldsymbol{u}^-\cdot\boldsymbol{i}^+ \\ \quad =3[U^+I^+\cos(\varphi_u^+-\varphi_i^+)+U^-I^-\cos(\varphi_u^--\varphi_i^-)+U^+I^-\cos(2\omega t+\varphi_u^++\varphi_i^-)+U^-I^+\cos(2\omega t+\varphi_u^-+\varphi_i^+)] \\ q=|\boldsymbol{u}\times\boldsymbol{i}|=\boldsymbol{u}_\perp\cdot\boldsymbol{i}=\boldsymbol{u}_\perp^+\cdot\boldsymbol{i}^+ + \boldsymbol{u}_\perp^-\cdot\boldsymbol{i}^- + \boldsymbol{u}_\perp^+\cdot\boldsymbol{i}^- + \boldsymbol{u}_\perp^-\cdot\boldsymbol{i}^+ \\ \quad =3[U^+I^+\sin(\varphi_u^+-\varphi_i^+)+U^-I^-\sin(\varphi_u^--\varphi_i^-)+U^+I^-\sin(2\omega t+\varphi_u^++\varphi_i^-)+U^-I^+\sin(2\omega t+\varphi_u^-+\varphi_i^+)] \end{cases} \tag{2}$$

In order to maintain the active and reactive power of PV and consider the limit of the harmonic distortion of output current under unbalanced faults, the current reference can be obtained from (2)

$$\boldsymbol{i}^*=P^*(\boldsymbol{u}^+ + \alpha\boldsymbol{u}^-)\Big/\left(|\boldsymbol{u}^+|^2+(1+\alpha)\beta\boldsymbol{u}^+\boldsymbol{u}^- + \alpha|\boldsymbol{u}^-|^2\right) \tag{3}$$

Then the output current harmonics and the amplitude fluctuation of active and reactive power can be adjusted by means of changing the coefficient α and β ($\alpha\in[0, 1]$ and $\beta\in[-1, 1]$) in (3).

Formula Derivation of Current Harmonics of PV Inverter

Suppose the ratio of negative sequence voltage to positive sequence voltage is $U^-/U^+=n$, and based on (1) and (3), we can get the currents of three phases,

$$^*(t)|_{a,b,c}=\frac{\sqrt{2}}{3[1+\beta(1+\alpha)n\cos(2\omega t)+\alpha n^2]U^+}\left\{P^*[\cos(\omega t-(m-1)\frac{2\pi}{3})+\alpha n\cos(\omega t+(m-1)\frac{2\pi}{3})]\right\} \tag{4}$$

Set $A=\beta(1+\alpha)n$, $B=\alpha n^2$, $C=\sqrt{(1+B)^2-A^2}$, $T=1/f$. Take the current of phase a in (4) as an example, the root-mean-square value of fundamental current and of the full-wave current are I_{1rms} and I_{rms}, and then we can get the THD of phase a current reference in (4),

$$THD=\sqrt{\frac{I_{rms}^2}{I_{1rms}^2}-1}=\sqrt{\left(\sqrt{\frac{1}{T}\int_0^T[i_a^*(t)]^2dt}\right)^2\Big/\left(\frac{1}{2T}\int_0^T i_a^*(t)\cos(\omega t)dt\right)^2-1}=\sqrt{\frac{A^2}{2C(1+B-C)}-1} \tag{5}$$

Fig. 2(a) has shown the characteristics of current harmonics distortion with coefficient n and β (when P^*=1.0pu and α=0.2). The harmonics distortion will decrease as the coefficient n and β decrease. Fig. 2(b) has shown the contour lines of the total current harmonics distortion of 5%, 8%,

10% and 12%. When n=0.3 caused by grid unbalanced faults, current reference harmonics distortion will exceed the rules limit 5% if β>0.26, and current harmonics injecting into grid from the inverter can be reduced by decreasing the coefficient β.

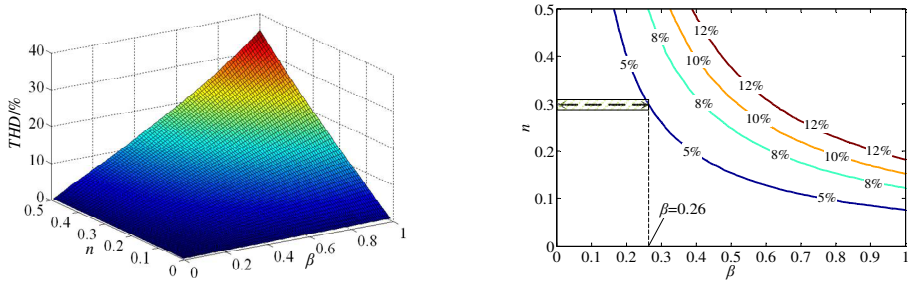

(a) Three-dimensional mesh (b) Contour lines

Fig. 2 Three-dimensional mesh and contour lines of total current harmonic distortion

Optimal Parameters of PV Power Control and Its Implementation

Power Control Parameters Optimization. Substituting (3) into (2), we can get the instantaneous active and reactive power of the PV inverter, and then the maximum value of the active and reactive power fluctuation can be obtained,

$$\tilde{p}_{\max} = P^* \frac{(1-\beta)(1+\alpha)n}{1-\beta(1+\alpha)n+\alpha n^2} \quad , \quad \tilde{q}_{\max} = P^* \frac{(1-\alpha)n}{1+\alpha n^2} \tag{6}$$

According to (6), the reactive power fluctuation is only related to α, and its amplitude fluctuation will increase with the decrease of the coefficient α. However, the fluctuation of active power is determined by both α and β. Hence, the active and reactive power fluctuation amplitude of PV inverter is effectively adjustable through the control of the coefficient α and β on the premise that all the coefficients are in the feasible region limited by harmonic distortion. This paper has built the optimal selection model of the coefficient α and β, aiming at getting the minimum synthesis power fluctuation with the constraint condition of current THD limit. The model is,

$$\begin{aligned} &\min f = \omega_p \frac{(1-\beta)(1+\alpha)n}{1-\beta(1+\alpha)n+\alpha n^2} + \omega_q \frac{(1-\alpha)n}{1+\alpha n^2} \\ &s.t. \quad 0 < \sqrt{\frac{A^2}{2C(1+B-C)} - 1} < THD_{\max} \end{aligned} \tag{7}$$

where ω_p and ω_q are the weight coefficients of active and reactive power fluctuation, and $\omega_p+\omega_q=1$. $THD_{\max}$ is the maximum limit value of PV current THD. We take $THD_{\max}$=5% in the study and solve the optimization problem of α and β with constrained cyclic coordinate descent method [9].

Implementation of PV Power Control Based on Deadbeat Current Tracking. The structure of the power control system for PV inverter is shown in Fig. 3. The optimal coefficient α and β can be calculated by (7). The three phase current reference i_{abc}^* of the dead beat current tracking inner loop, whose structure is shown in Fig. 3(b), can be obtained by (3).

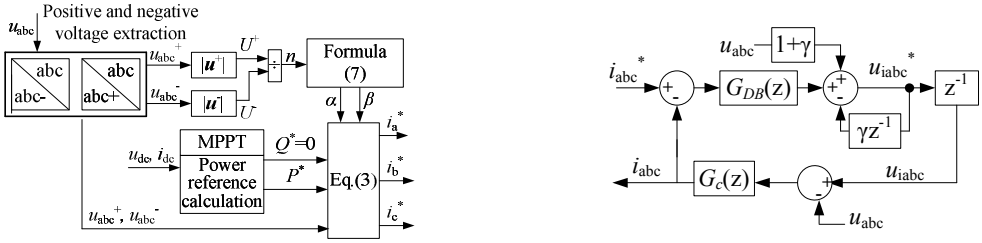

(a) Power control outer loop (b) Dead beat current tracking inner loop

Fig. 3 Power control outer loop and current control inner loop of photovoltaic inverter

The function of dead beat current control in Fig. 3 is $G_{DB}(z)=(1-\gamma z^{-1})/[\lambda(1-z^{-2})]$ where $\gamma=e^{-(Rf/Lf)Ts}$ and $\lambda=[1-e^{-(Rf/Lf)Ts}]/R_f$ are the current control parameters, T_s is the sampling period, z^{-1} is unit delayed in discrete system and the transfer function of the inverter is $G_c(z)=\lambda/(1-\gamma z^{-1})$. The Z function of the output current i_{abc} of the PV inverter can be expressed as,

$$i_{abc}=\frac{z^{-1}}{1+(1+\gamma)z^{-1}-z^{-2}-\gamma z^{-3}}i^{*}_{abc}-\frac{\lambda(1-z^{-1}-z^{-2}+z^{-3})}{1+z^{-1}-(1+\gamma+\gamma^{2})z^{-2}+\gamma^{2}z^{-4}}u_{abc}=G_i(z)i^{*}_{abc}+G_u(z)u_{abc} \tag{8}$$

Simulation Results and Analysis

In order to test the feasibility of the method, proposed in this study, namely power control of PV inverter under unbalanced grid faults, we have built a PV generation system model in PSCAD/EMTDC as is shown in Fig. 1. In the model, the ac and dc nominal voltages are 220V and 1000V, the rated apparent power is 2.5kVA, the carrier frequency is 16kHz,and L_f=12mH, R_f=0.4Ω, C_f=0.7μH, T_s=31.25μs.

Analysis of Current Harmonics Characteristics. Suppose that the output active power P_0=2kW under normal operation, and the grid unbalanced fault at t=0.5s leads to n=0.2, set α=0.5.

In Fig. 4 the power fluctuation and current THD of the PV inverter under different coefficient β before and after the grid faults are shown. The current THD of inverters will rise with the increase of β while the active power fluctuation will decrease, and the reactive power fluctuation is only related to α. The current THD in Fig.4 is 14.94%, 7.46% and 0.61% as β=1, 0.5 and 0, and the calculated value of (4) of current THD are 15.21%, 7.41% and 0 which basically fit the simulation value.

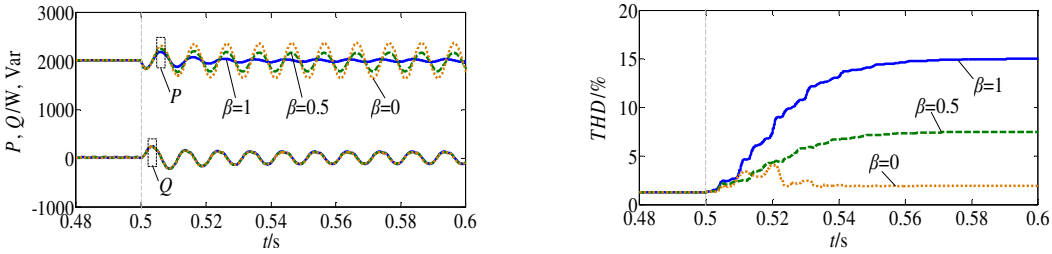

(a) Active and reactive power (b) Current total harmonic distortion

Fig. 4 Output powers and current harmonics of photovoltaic inverter for different coefficient β

The current THD goes beyond the limit 5% when β=1 and 0.5. When β=0, the active power fluctuation is still large though the current THD is tiny, so that under such condition, only by combining power fluctuation with current THD can we choose reasonable parameters.

Parameter Optimization of Power Control. Suppose n=0.4 and α=-1, β=0, and then test the two conditions under ω_p=0.6, ω_q=0.4 (case 1) and ω_p=0.2, ω_q=0.8 (case 2). Fig. 5 shows the changing trajectory of power control parameters under different weight coefficients. From the optimization model of (7), we can obtain the optimal control parameters of case 1 and 2 are separately α=-0.782, β=1 and α=1, β=0.144. Both the two sets of control parameter will enable the current THD of the PV inverter to get close to the limit 5%.

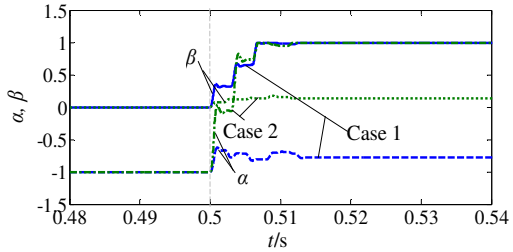

Fig. 5 Power control parameters in case 1 and case 2

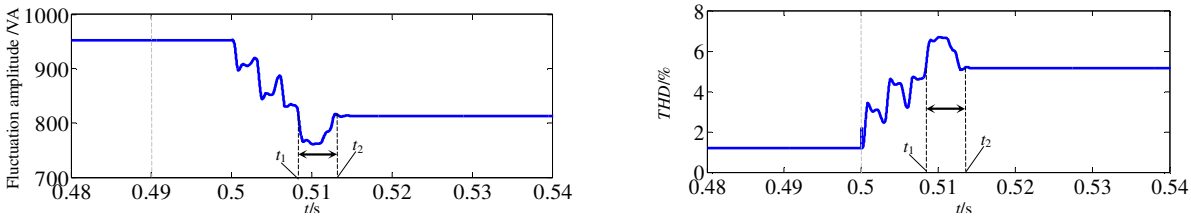

(a) Integrated power fluctuation (b) Current THD

Fig. 6 Integrated power fluctuation and current THD in case 1

Fig. 6 has shown the changing curves of integrated power fluctuation and current THD when the control parameters are being adjusted in case 1. Integrated power fluctuation drops fast after grid faults and the current THD of PV inverter will exceed the limit 5% even though the amplitude of power fluctuation is small among the interval t_1 and t_2. The operation point of control parameters can stabilize at the optimal operation point at last by the optimization method of power proposed above.

Conclusions

This paper has proposed a kind of power control strategy of PV inverter considering the current harmonics constraint of PV system under unbalanced grid faults. As is demonstrated in the test result, the parameter optimization method proposed above can ensure that the PV output current THD be constrained within the limit 5% and that the integrated power fluctuation of active and reactive power reduce to the minimum. It has realized a flexible active and reactive power control of PV under grid faults by bringing in power-regulation coefficients.

References

[1] J. Rocabert, A. Luna, F. Blaabjerg and P. Rodríguez: *IEEE Trans. Power Electron*. vol. 27(2012), p. 4734.

[2] F. Blaabjerg, R. Teodorescu, M. Liserre and A.V. Timbus: *IEEE Trans. Ind. Electron*. vol. 53(2006), p. 1398.

[3] H. Song and K. Nam: *IEEE Trans. Ind. Electron*. vol. 46(1999), p. 953.

[4] Y. Suh and T.A. Lipo: *IEEE Trans. Ind. Appl*. vol. 42(2006), p. 825.

[5] C.H. Ng, L. Ran and J. Bumby: *IEEE Trans. Ind. Appl.* vol. 44(2008), p. 845. 2008.

[6] P. Rodriguez, A.V. Timbus, R. Teodorescu, M. Liserre and F. Blaabjerg: *IEEE Trans. Ind. Electron.* vol. 54(2007), p. 2583.

[7] F. Wang, J.L. Duarte and M.A.M. Hendrix: *IEEE Trans. Power Electron.* vol. 26(2011), p. 1511.

[8] D.G. Luenberger and Y. Ye, *Linear and nonlinear programming*, New York, USA: Springer, 2008.

[9] F. Wang, J.L. Duarte and M.A.M. Hendrix: IET Gener. Transm. Distrib. vol. 4(2010), p. 905.

Advanced Materials Research Vols. 960-961 (2014) pp 1361-1366

doi:10.4028/www.scientific.net/AMR.960-961.1361

Modeling and Simulation of MMC-HVDC Energy System

Guanghao Yang [1, a], Youbing Zhang [1,b], Jiyun Yu [1,a] and Huiyong Liu [2,a]

[1]Zhejiang University of Technology, Hangzhou, China

[2]Zhoushan Electric Power, Zhoushan, China

[a]yangguanghao0824@163.com, [b]youbingzhang@zjut.edu.cn

Keywords: Modular Multilevel Converter, MMC-HVDC, PSCAD/EMTDC.

Abstract. In order to study the steady-state performance of modular multilevel voltage source converter (MMC-HVDC), a 21-level MMC-HVDC system is modeled by PSCAD/EMTDC software. This system uses the DC voltage and active power controls, which are designed by the fundamental operation principles and mathematical models of MMC-HVDC. By analyzing the steady-state performance of MMC-HVDC, the corresponding simulation waveforms verify the correctness and validity of the simulation model.

Introduction

HVDC (high voltage direct current) has received increasing attentions in recent years due to the requirement of high power and voltage level in power industrial applications. VSC (voltage sources convert) -HVDC has shown that it is possible to combine excellent output voltage waveforms with very high efficiencies[1,2]. VSC-HVDC is probably the most promising converter topology for applications such as grid access for regenerative energy sources, supply of passive loads and power supply of megacities[3].

So far, the realized VSC converters for HVDC applications are main based on 2 or 3-level technology, which with the drawbacks of a low-voltage level, high switching frequency and a distortion of voltage waveform has to be filtered. To solve the aforementioned problems, a modular multilevel converter (MMC) topology has been proposed[4]. Fig.1(a) shows a circuit configuration of a three phase MMC, each of which is a stack of cascaded multiple bidirectional sub-modules shown in Fig. 1(b). This technology makes the individual semiconductors have much lower switching frequency resulting in lower switching losses, and consequently, lower total losses of the transmission system compared to 2 or 3-level VSC[5]. In addition, MMC is consist of the same sub-modules, simplifys the control methods and reduces the manufacturing cost.

This paper deals with a modular multilevel converter with focus on working principle, mathematical model, control methods, using PSACD/EMTDC to simulate, analyzing steady-state characteristics.

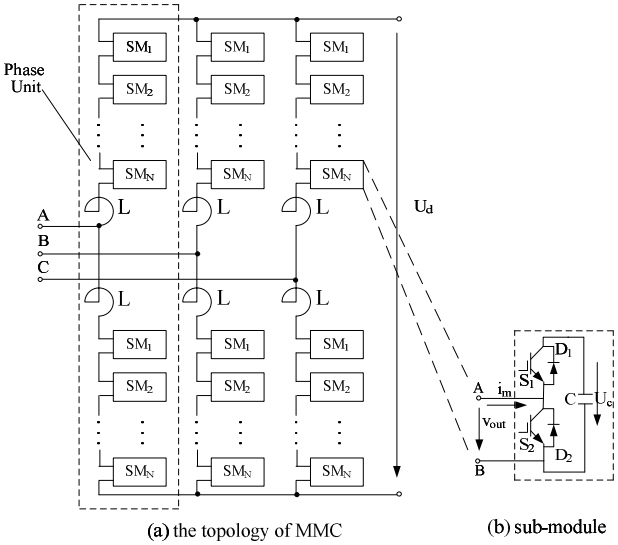

(a) the topology of MMC (b) sub-module

Fig.1 The topology of MMC

Fundamental Operation Principle and Mathematical Model

Fig.1(b) shows the topology of sub-modules. Sub-modules are equipped with capacitors C . By using IGBTs S_1 and S_2, each sub-module can be switched between a state with full module voltage and a state with zero module voltage in both current directions. Table 1 lists all states of a sub-module.

Table 1 States of a sub-module

Mode	S1	S2	Current Direction	V_{out}	State
1	0	0	A to B	U_s	Lock (charge)
2	0	0	A to B	U_s	full (charge)
3	0	1	A to B	0	zero (bypass)
4	0	0	B to A	0	Lock (bypass)
5	1	0	B to A	U_s	full (discharge)
6	0	0	B to A	0	zero (bypass)

In order to keep MMC operating in stable-state，there are three constraints should be subject to:

1. To maintain a stable DC voltage, the amount of sub-modules working in a state with full module voltage in each phase must be equal.
2. In each phase, the total number of sub-modules working in a state with full module voltage in upper and lower legs is always constant. For example, the number of upper legs increases 1, lower legs should be decreases 1.
3. Weather charge or discharge, the voltage of sub-modules capacitance value should always close to the initial value. An algorithm was introduced to balance voltage of each sub-module capacitance[6].

An equivalent circuit is presented in [7]. The equivalent circuit is a virtual equivalent model, rather than an actual circuit.

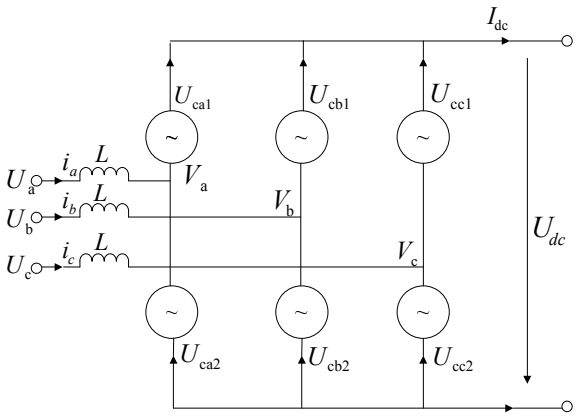

Fig.2 MMC simplified equivalent circuit

The circuit equation can be obtained from Fig.2:

$$\begin{cases} L\dfrac{di_a(t)}{dt} = u_a(t) - v_a(t) \\ L\dfrac{di_b(t)}{dt} = u_b(t) - v_b(t) \\ L\dfrac{di_c(t)}{dt} = u_c(t) - v_c(t) \end{cases} \tag{1}$$

It's hard to control active and reactive power independently, as variables of three-phase stationary coordinate system change with time. So it should be conversed to the synchronous rotating coordinate system with Clark transformation and Park transformation.

Clark transformation (abc -axis to $\alpha\beta$ -axis)

Park transformation ($\alpha\beta$ -axis to dq -axis)

$$\begin{bmatrix} f_\alpha \\ f_\beta \end{bmatrix} = \frac{2}{3}\begin{bmatrix} 1 & -\frac{1}{2} & -\frac{1}{2} \\ 0 & \frac{\sqrt{3}}{2} & -\frac{\sqrt{3}}{2} \end{bmatrix}\begin{bmatrix} f_a \\ f_b \\ f_c \end{bmatrix} \quad (2) \qquad \begin{bmatrix} f_d \\ f_q \end{bmatrix} = \begin{bmatrix} \cos wt & \sin wt \\ -\sin wt & \cos wt \end{bmatrix}\begin{bmatrix} f_\alpha \\ f_\beta \end{bmatrix} \quad (3)$$

f can be any electrical quantities, like current, voltage etc. Substituting f_α, f_β in Eq. 2 by Eq. 3:

$$\begin{bmatrix} f_d \\ f_q \end{bmatrix} = \frac{2}{3}\begin{bmatrix} \cos wt & \cos(wt-\frac{2\pi}{3}) & \cos(wt+\frac{2\pi}{3}) \\ -\sin wt & -\sin(wt-\frac{2\pi}{3}) & -\sin(wt+\frac{2\pi}{3}) \end{bmatrix}\begin{bmatrix} f_a \\ f_b \\ f_c \end{bmatrix} \quad (4)$$

Hence, i_{sd}, i_{sq} can be given by:

$$\begin{cases} L\frac{di_{sd}}{dt} + Ri_{sd} = U_{sd} - V_d + wLi_{sq} \\ L\frac{di_{sq}}{dt} + Ri_{sq} = U_{sq} - V_q - wLi_{sd} \end{cases} \quad (5)$$

V_d, V_q, d-axis and q-axis component of voltage from converters arm midpoint; i_{sd}, i_{sq}, d-axis and q-axis component of current from AC side.

Eq. 6 is derived from Instantaneous Power Theory [8]:

$$\begin{cases} P = 1.5(U_{sd}i_{sd} + U_{sq}i_{sq}) \\ Q = 1.5(U_{sq}i_{sd} - U_{sd}i_{sq}) \end{cases} \quad (6)$$

When system operates in steady-state, U_{sq}=0 and $U_{sd} = U_s$, so $P = 1.5U_s i_{sd}$, $Q = -1.5U_s i_{sq}$. Active power and reactive power are decoupled in synchronous coordinate system, and are proportional to i_{sd}, i_{sq} respectively.

MMC Control Strategy

Current loop controller

Eq. 5 presents i_{sd} is influence on V_d, wLi_{sq} and U_{sd}. Also, i_{sq} is influenced on V_q, wLi_{sd} and U_{sq}. V_d' and ΔU_q are defined to keep i_{sd} from the impact of wLi_{sq}. Similarly, V_q' and ΔU_d are defined.

$$\begin{cases} V_d = U_{sd} - V_d' + \Delta U_q \\ V_q = U_{sq} - V_q' + \Delta U_d \end{cases} \quad (7)$$

$V_d' = L\frac{di_{sd}}{dt} + Ri_{sd}$, $V_q' = L\frac{di_{sq}}{dt} + Ri_{sq}$, $\Delta U_d = wLi_{sq}$, $\Delta U_q = wLi_{sd}$. V_d' and V_q' are first-order differential voltage components that can be presented as PI parts.

$$\begin{cases} V_d' = K_{p1}(i_{sd}^* - i_{sd}) + K_{I1}\int(i_{sd}^* - i_{sd})dt \\ V_q' = K_{p2}(i_{sq}^* - i_{sq}) + K_{I2}\int(i_{sq}^* - i_{sq})dt \end{cases} \quad (8)$$

i_{sd}^*, i_{sq}^*, active and reactive current reference value. Substituting Eq. 7 and Eq. 8 into Eq. 5 yields:

$$\begin{cases} \frac{di_{sd}}{dt} = \frac{1}{L}\left[K_P(i_{sd}^* - i_{sd}) + K_I\int(i_{sd}^* - i_{sd})dt\right] \\ \frac{di_{sq}}{dt} = \frac{1}{L}\left[K_P(i_{sq}^* - i_{sq}) + K_I\int(i_{sq}^* - i_{sq})dt\right] \end{cases} \quad (9)$$

Eq. 9 indicates i_{sd} and i_{sq} can be decouple controlled. Eq. 10 is transformed from Eq. 9 by Laplace formula:

$$\begin{cases} i_{sd} = \dfrac{1}{sL}(K_P + \dfrac{K_i}{s})(i_{sd}^{\ *} - i_{sd}) \\ i_{sq} = \dfrac{1}{sL}(K_P + \dfrac{K_i}{s})(i_{sq}^{\ *} - i_{sq}) \end{cases} \tag{10}$$

According to Eq. 10, the current loop control is designed as shown in Fig.3.

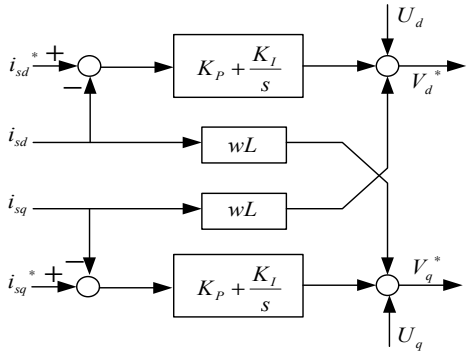

Fig.3 Current loop control

Voltage loop control

As shown in Fig.4, Δi_d is the difference between measured value and reference active power, and after a PI part. The reference value $i_{sd}^{\ *}$ is the sum of Δi_d and the estimated value $i_d^{'}$. Also $i_{sq}^{\ *}$ is sum of Δi_q and $i_q^{'}$ in Fig.5.

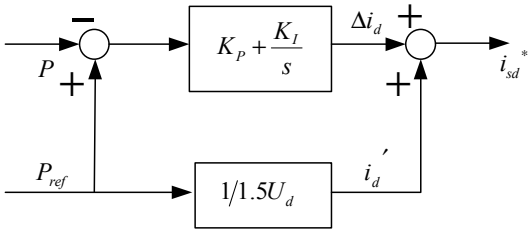

Fig.4 Active power control

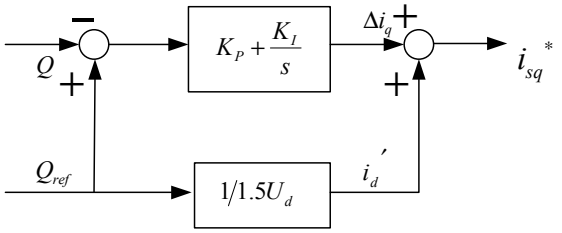

Fig.5 Reactive power control

DC voltage control

Fig.6 shows the topology of DC voltage control. The part of active power compensates the fluctuations of reactive power. The comparision between DC voltage (U_{dc}) and the reference value (U_{dcref}), and the PI part are used to make U_{dc} track U_{dcref}.

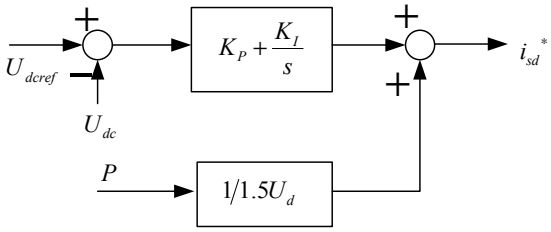

Fig.6 DC voltage control

Modeling of MMC-HVDC

According to the above control methods, a three-phase, 21-level MMC-HVDC energy system is developed based on PSCAD/EMTDC in Fig.7. In the model, there are 20 identical sub-modules and a converter reactor connected in per phase arm. MMC-1 uses the active and reactive power control (P_{1ref}=400kVA, Q_{1ref}=0). MMC-2 has the same structure, using the reactive power and DC voltage control (U_{dcref}=400kV, Q_{1ref}=0). Table 2 presents the simulation parameters.

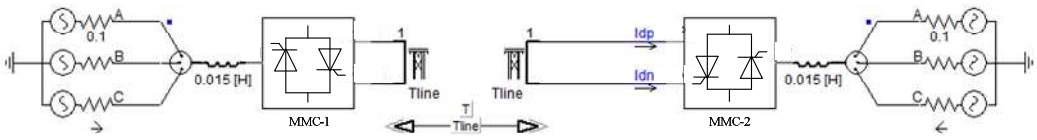

Fig.7 MMC-HVDC

Table 2 CIRCUIT PARAMETERS ON EXPERIMENT

AC side Line-to-Line voltage	$110\,kV$
DC bus voltage	$400\,kV$ ($\pm 200\,kV$)
Submodule capacitors	$3000\,\mu F$
The initial value of capacitor voltage	$20\,kV$
Overhead line length	$20\,km$
AC inductor	15 mH
Transformer ratio	$110/220\,kV$ (Y/Δ)

Simulation and Analysis

Stable operation

The system operates in initial state. When t=0.5s, set P_{1ref}=240 kVA; t=0.8s, set Q_{1ref}=80 $kVar$; t=1.0s, set Q_{2ref}=-80 $kVar$. Subscript 1, 2 present MMC-1 and MMC-2 electrical quantities.

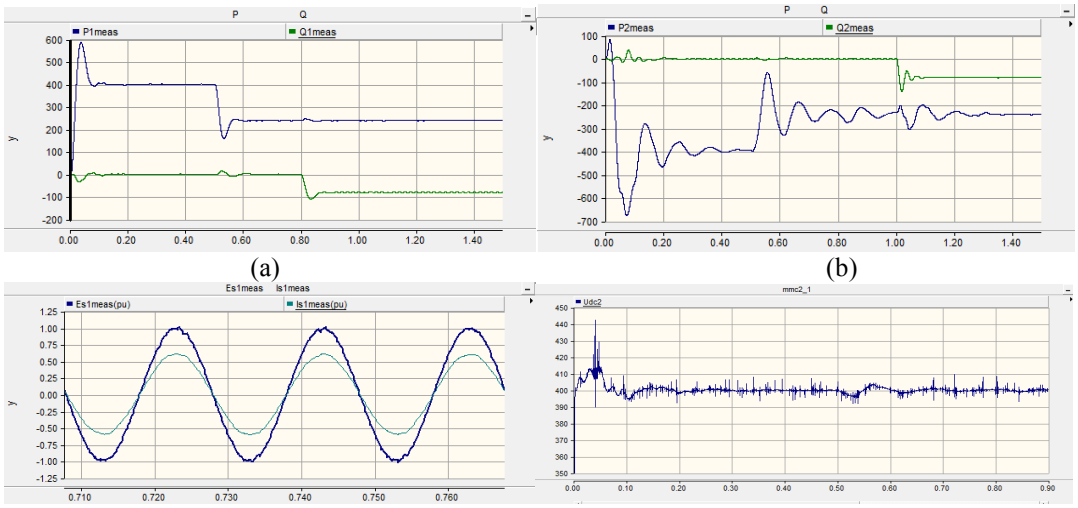

(a) (b)

(c) (d)

Fig.8 Stable opertion

Fig. 8(a) and (b) show MMC-1 and MMC-2 active and reactive power value track the changes of P_{ref} and Q_{ref}. When active or reactive reference values is changed, the other is unaffected. As shown in Fig. 8(c), MMC-1's AC side output phase voltage waveform is approximately sinusoidal. Fig. 8(d) presents DC bus voltage remains around 400 kV throughout the process.

Reverse active power

When t=0.5s, the direction of active power transmission is from MMC-2 to MMC-1.

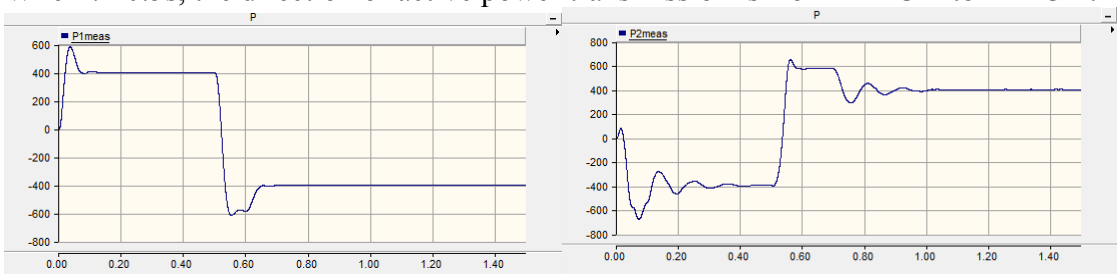

(a) (b)

Fig.9 Active power reversion

Compared with Fig. 9(a) and (b), active power of MMC-1 and MMC-2 are almost symmetrical. And process of reversion is quick and smooth.

Asynchronous interconnection

Set frequency of MMC-1 to 50Hz, frequency of MMC-2 to 60Hz.

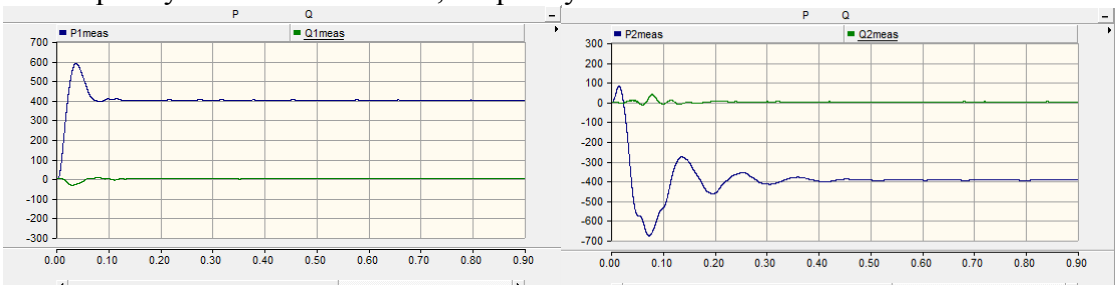

(a) (b)

Fig.10 Asychronous association

As shown in Fig. 10(a) and (b), the controllers can connect two ends of asynchronous grids smoothly.

Conclusions

This paper has described fundamental operation principle, mathematical model and control methods including current loop, voltage loop and DC voltage controls. To validate the performance and advantages of MMC, a 21-level MMC is constructed on PSCAD/EMTDC program. MMC-1 uses the active and reactive power control, while MMC-2 using the active power and DC voltage control. The simulation shows that the designed controller can effectively control the steady-state process. With all above detailed analysis and demonstration, it is not difficult to get the conclusion that MMCs will play an important role in power electronics application.

References

[1] Philipp Munch, Steven Liu and Mike Dommaschk: *Modeling and Current Control of Modular Multilevel Converters Considering Actuator and Sensor Delays*, 35th Annual Conference of IEEE Industrial Electronics, Vols.1-6 (2009), p.1520-1525.

[2] S. Rohner, S. Bernet, M. Hiller and R. Sommer: *Modulation, losses, and semiconductor requirements of modular multilevel converters*, IEEE Transactions on Industrial Electronics, Vol.5(2010), p.2633-2642.

[3] M. Hiller, D. Krug, R. Sommer and S. Rohner: *A new highly modular medium voltage converter topology for industrial drive applications*, 13th European Conference on Power Electronics and Applications, Vols.1-9(2009), p.5824-5833.

[4] Kui Wang, Yongdong Li and Zedong Zheng: *Voltage Balancing Control and Experiments of A Novel Modular Multilevel Converter*, Energy Conversion Congress and Exposition (ECCE), 2010 IEEE, p. 3691 – 3696.

[5] Ke Li and Chengyong Zhao: *New Technologies of Modular Multilevel Converter for VSC-HVDC Application*, Power and Energy Engineering Conference (APPEEC), 2010 Asia-Pacific, p.1-4.

[6] Glinka M, Marquardt R: *A new AC/AC multilevel converter family*, 5th International Conference on Power Electronics and Drive Systems, Vol.1, p.16-23.

[7] Minyuan Guan and Zheng Xu: Modeling and Control of Modular Multilevel Converter in HVDC Transmission, Automation Of Electric Power Systems, 2010, 34(19).

[8] Dairun Zhang, Nianci Huang: *Universal instantaneous power theory for DC, single-phase AC sinusoidal and nonsinusoidal circuits*, Power Electronics and Motion Control Conference, Vol.3(2000), p. 1442 - 1447.

Advanced Materials Research Vols. 960-961 (2014) pp 1367-1370

doi:10.4028/www.scientific.net/AMR.960-961.1367

Research on the system modeling and control of single-phase PV flexible grid-connected

Bo Hu[1, a], ZaiLin Piao[2,b]

[1,2] Shen yang agricultural university , Shen Yang

[a]boer5109@sohu.com, [b]piaozl@china.com,

Keywords: Maximum Power Point Tracking;Flexible grid-connected;Control Strategy; Power decoupling.

Abstract: Photovoltaic systems can not meet the needs in the power grid without the impact, due to its penriodicity, intermittent and randomness, thus the key to solve the core technology of photovoltaic power generation system is important to achieve PV grid-connected. This article explains the two-stage topology system control and modeling of single-phase PV grid-connected: Modeling of DC / DC converter provides basis for maximum power point tracking; DC / AC inverter in grid-connected modeling offer efficient communication basis for grid-connected, it research on the control strategies for DC / DC and DC / AC circuit: that PV grid-connected complete alternating current of unit power factor using the booster circuit and inverter control structure, in order to offer photovoltaic systems flexible grid-connected the foundation.

Introduction

Solar energy as a major clean energy, provides a sufficient condition for main grids supplement, but due to the affect of different seasons and alternaton of day with night .photovoltaic system gives expression to its own periodicity, intermittent and randomness, as the future primary energy supply resources, it only provide power value at the current stage, but because of their own shortcomings it can not offer sufficient capacity value, therefore that PV flexible grid-connected comes true has practical significance.

Single-phase photovoltaic systems of flexible grid-connected and control

In the photovoltaic power generation systems, photovoltaic maximum power point tracking and grid-connected technology strategy is the key of photovoltaic systems interconnection thchnology, during self-optimizing process at the maximum power point tracking how timely and accurate capture of the maximum power point , which provide efficient conversion effective protection for solar panels . and photovoltaic grid-connected project, which need bring DC photovoltaic panels into alternating current by an inverter into the grid, which will require boost circuit and full-bridge inverter circuit structure and network to complete. Thus, two-stage topology exists in the china's photovoltaic power generation systems, DC / DC link achieves maximum power point tracking and timely boosts voltage, DC / AC link transforms solar energy into alternating current output, which ensure that the grid same frequency and phase voltage and unity power factor grid-connected. Figure 1 is single-phase photovoltaic grid-connected systems

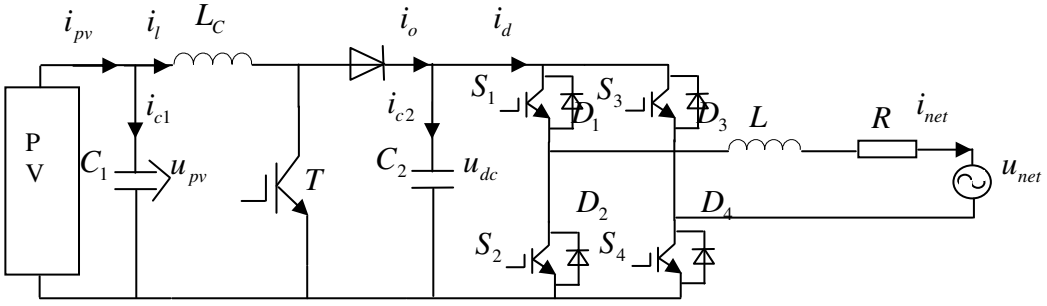

Fig.1 Single-phase PV grid-connected

Topology photovoltaic grid system using the two-stage topology , as shown in this article, the DC / DC boost circuit completes to the maximum power point tracking, and to inverter DC / AC dual loop device session accomplishs stability control of Dc voltage and unity power factor non-impact on the grid-connected. i_{pv} is the output current of the PV array, i_l is the inductor current, i_{c1} is the capacitor current of the photovoltaic array output; i_{net} is the current of photovoltaic grid systems; u_{net} is the grid voltage; L is inverter filter inductor; R is filtering resistor and the inverter equivalent impedance of the external circuit.

The mathematical modeling of DC/DC converter

According to the topology of photovoltaic grid systems, DC / DC converter mathematical modeling:

Switching function are indicated $S_{k1}: S_{k1} = \begin{cases} 0 & Ton \\ 1 & Toff \end{cases}$ .Mathematical model based on the switching function is turned on and off: $\begin{cases} \dfrac{du_{pv}}{dt} = \dfrac{i_{pv}}{C_1} - \dfrac{i_l}{C_1} \\ \dfrac{di_l}{dt} = \dfrac{u_{pv}}{L_C} - \dfrac{S_{k1}u_{dc}}{L_C} \end{cases}$ .Select the state variables $X = [i_l \ u_{pv}]^\tau$; Input variables $U = [i_{pv} \ u_{dc}]^\tau$; The output variables $Y = [i_l \ u_{pv}]^\tau$ State equation can be written as:

$$\dot{X} = AX + BU$$

$$Y = CX + DU$$

$$\frac{d}{dt}\begin{bmatrix} u_{pv} \\ i_l \end{bmatrix} = \begin{bmatrix} -\frac{1}{C_1} & 0 \\ 0 & \frac{1}{L_C} \end{bmatrix}\begin{bmatrix} i_l \\ u_{pv} \end{bmatrix} + \begin{bmatrix} \frac{1}{C_1} & 0 \\ 0 & -\frac{S_{k1}}{L_C} \end{bmatrix}\begin{bmatrix} i_{pv} \\ u_{dc} \end{bmatrix} \quad A = \begin{bmatrix} -\frac{1}{C_1} & 0 \\ 0 & \frac{1}{L_C} \end{bmatrix} \quad B = \begin{bmatrix} \frac{1}{C_1} & 0 \\ 0 & -\frac{S_{k1}}{L_C} \end{bmatrix} \quad C = \begin{bmatrix} 1 & 0 \\ 0 & 1 \end{bmatrix} \quad D = 0$$

The transfer function $G(s) = \dfrac{Y(s)}{U(s)} = -\dfrac{S_{k1}}{C_1 L_C S^2 + (L_C - C_1)S - 1} = \dfrac{1}{SC_1 + 1} \cdot \dfrac{-S_{k1}}{SL_C - 1}$

DC/DC converter to achieve maximum power point tracking

In the DC bus side increases PI controller，which controls deviation of the actual value of its reference value of the DC bus voltage control, in order to ensure that the DC bus side voltage stability.which to achieve the maximum power point of the PV array output using regulating DC / DC converter duty cycle by the PWM generator. MPPT controller uses self-optimizing control method itself by constantly detecting the output voltage of the PV array to determine the maximum power point. G1 (s), G2 (s), G3 (s) is respectively a PI controller, the boost circuit, MPPT controller transfer function.

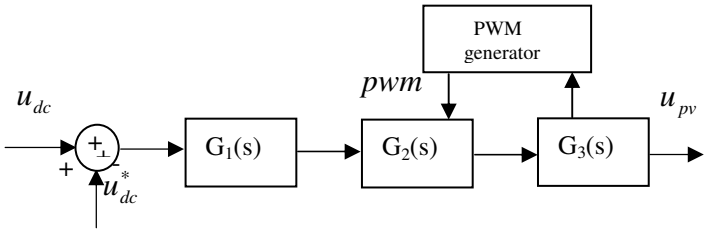

Fig2 Based on the dc bus voltage stability of MPPT control principle diagram

Mathematical modeling of inverter grid-connected

As the full-bridge inverter bipolar modulation leakage current is very small, which decreases the efficiency is not suitable for the grid-connected inverter that there is no transformer, so using single polarity modulation, single-phase grid-connected inverter switching states are, S_1 and S_4 equal to

begin; S_2 and S_3 equal to begin; S_1, S_2 and D_3 equal to begin; S_1, S_3 and D_1 equal to begin; S_2, S_4 and D_2 equal to begin; S_2, S_4 and D_4 equal to begin; however S_1 and S_3 equal to begin and S_2 and S_4 equal to begin, when the output voltage of the existence of two zero voltage state, so in DC / AC inverter switching
function:

$$S_{k2}=\begin{cases}1 & S_1 \text{ and } S_4 on\\ 0 & S_1 \text{ and} S_3 or S_2 \text{and} S_4 on\\ -1 & S_2 \text{and} S_3 on\end{cases} \qquad \begin{cases}\dfrac{di_{net}}{dt}=\dfrac{S_{k2}}{L}u_{dc}-\dfrac{Ri_{net}}{L}-\dfrac{1}{L}u_{net}\\ \dfrac{du_{dc}}{dt}=-\dfrac{S_{k2}}{C_2}i_{net}+\dfrac{S_{k1}i_l}{C_2}\end{cases}$$

Select the state variables $X=[i_{net}\ u_{dc}]^{\tau}$, Input variables $U=[i_l\ u_{net}]^{\tau}$, The output variables $Y=[i_{net}\ u_{dc}]^{\tau}$

$$A=\begin{bmatrix}-\dfrac{R}{L} & \dfrac{S_{k2}}{L}\\ -\dfrac{S_{k2}}{C_2} & 0\end{bmatrix} \quad B=\begin{bmatrix}0 & -\dfrac{1}{L}\\ \dfrac{S_{k2}}{C_2} & 0\end{bmatrix} \quad C=\begin{bmatrix}1 & 0\\ 0 & 1\end{bmatrix} \quad D=0$$

The transfer function $G(s)=\dfrac{Y(s)}{U(s)}=\dfrac{S_{k2}^3+S_{k2}RC_2S+S_{k2}LS^2}{LC_2S^2+RC_2S+S_{k2}^2}$

Achievement of DC/AC innverter grid-connected

Single-phase grid-connected inverters adopts double loop PI control algorithm, which to achieve voltage outer control and current inner control combined. Outer voltage control mainly effects DC voltage stability, and ensures maximum output power point boost circuit. If the outside temperature rises, the output power of the PV array is increased, the DC voltage also increases, so the outer ring under the influence of PI controller, so the amplitude is increased, while the lower inner PI control, will soon follow, so into the grid voltage increases, the voltage fed to the outer ring to adjust again.

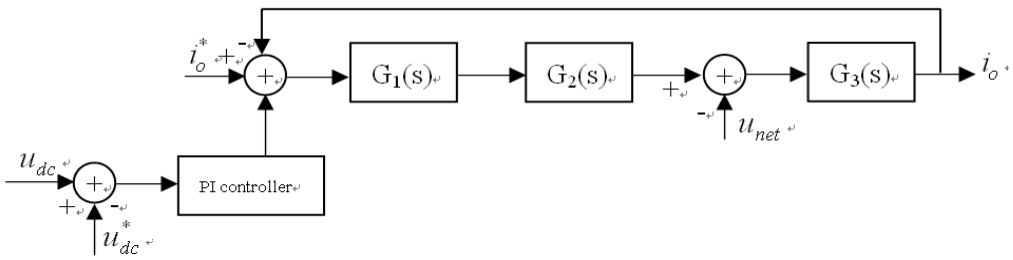

Fig3 Based on unit power factor grid-connecte inverter control principle diagram

Thus it can be seen that the inverter grid-connected current is influenced by the power grid voltage disturbance variable $u_g(s)G_3(s)$, which brings the grid voltage feed-forward into inverter input side, can counteract the effects of grid current from that power grid voltage, so the grid current closed loop control system increases power grid voltage feed-forward link.

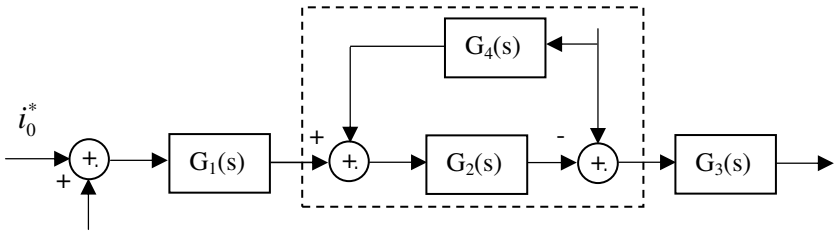

Fig4 Power grid voltage feed-forward control system block diagram

The single-phase flexible photovoltaic grid-connected system simulation

To verify the control algorithm of maximum power point tracking and grid current, with Matlab / Simulink simulation conducted photovoltaic grid system. The picture shows the simulation waveform.

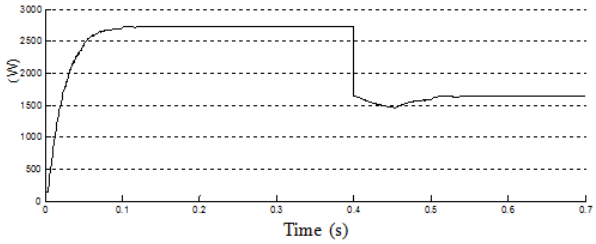

Fig 4 Photovoltaic array output waveform

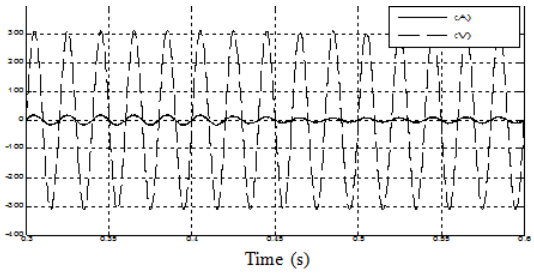

Fig 5 Inverter grid current voltage waveform

Parameters are as follows: u_{dc} total range is 380 ~ 450V, RMS voltage grid $U_{net} = 220V$, set the reference current and the same frequency and phase grid voltage, grid current waveform simulation with the same frequency and grid voltage sine wave phase to meet the design requirements, while maximum power point tracking simulation, assuming constant temperature, light intensity determines the maximum power output of photovoltaic panels. Simulation results show that the output power can be an effective real-time tracking.

The conclusion

In this paper, two-stage double-loop control structure to complete the single-phase photovoltaic flexible topology and network control strategy research, meet and network with current and the main power grid between the frequency and phase. Simulation results show the effectiveness of the method, and net

current real-time. Photovoltaic power generation system, there are still many technical problems to be solved, and the maximum power point tracking and grid inverter is the crux of the problem, of which there are island effect to prevent, and also need to find a more reliable, more accurate detection method, this article describes two topology control systems, the main relationship of the two topologies mutual decoupling detailed analysis for the realization of photovoltaic grid, a smooth switching off-grid, as well as network functions to achieve fast and opened up broad prospects.

Acknowledgements

This work was financially supported by the National Science and Technology Support program sub-topics: The micro grid control system for energy supply for low-carbon housing courtyard.(Contract number:2012BAJ26B01-6)

References

[1] Femia N，Petrone G，Spagnuolo G，et al.IEEE Transaction on Industrial Electronics，2009，

[2] L.Piegari, R.Rizzo. RenewablePowerGeneration,IET.2010,4(4):317-328.

[3] Emad M.Ahmed,Masahito Shoyama.TEN－CON 2010–2010 IEEE Region 10 Conference.

[4] LI Ran, LI Guang-min.Electric Power, 2008，41(2)：74—78．

[5] A. Vazquez-Blanco, C. Aguilar-Castillo, Power Electron. Conf. Expo.,Feb. 2009, pp. 452–458

[6] M. Jang and V. G. Agelidis, Power Electron., vol. 26, no. 5, pp. 1568–1577, May 2011.

[7] T. Zhou and B. Francois, Ind. Electron., vol. 58, pp. 95–104,Jan. 2011.

Advanced Materials Research Vols. 960-961 (2014) pp 1371-1375

doi:10.4028/www.scientific.net/AMR.960-961.1371

Study on VSC-HVDC Connecting to Passive Network and its Control Strategies

Weidong Qu[1, a *], Jianwen Ren[1, b], Xianchao Liu[1, c]

[1]School of Electrical and Electronic Engineering, North China Electric Power University, Baoding, Hebei, 071003, China

[a]qwdgeg@163.com, [b]rjw219@126.com, [c]imyelifu@sina.com

Keywords: HVDC, VSC, Control Strategy, Passive Network, MATLAB Simulation.

Abstract. The mathematical model VSC-HVDC system in dq reference frame is derived.For the VSC-HVDC system of transmitting power to passive network ,a constant DC voltage is used in the rectifier-side;a constant AC voltage controller is used in the inverter-side.Digital simulation models are set up by MATLAB/Simulink. Simulation results verify that VSC-HVDC has a independent control of active and passive power,and demonstrates superiority of transmitting active and passive power simultaneously when connecting to passive network.

Introduction

Based on the self-commutation devices and the technology of PWM, VSC-HVDC system has a flexible and quick control on both active and reactive power. And the system is furnished with SCC(self-commutated converter), which enables it to power passive nerwork even without external power supply. Therefore, VSC-HVDC promises to develop greatly in the field of transmission and distribution [1,2].

The rectangular coordinate form of VSC-HVDC system equations is deduced. A steady state model is put forward as well [3,4].Corresponding contol strategies are discussed in detail in both discrete time state space and continuous time state space [5,6].

Under the DQ synchronization reference frame, the mathematical model of VSC-HVDC system is established. And the control strategy is proposed, which consists of inner-loop current control and outer-loop voltage control. A constant AC voltage control unit is designed for supplying power to passive network. FInally,the simulation model of VSC-HVDC power to passive network is set up with the help of MATLAB / Simulink. When simulating different transmission conditions,the superiority of VSC-HVDC is obvious.

Mathematical Model of VSC-HVDC

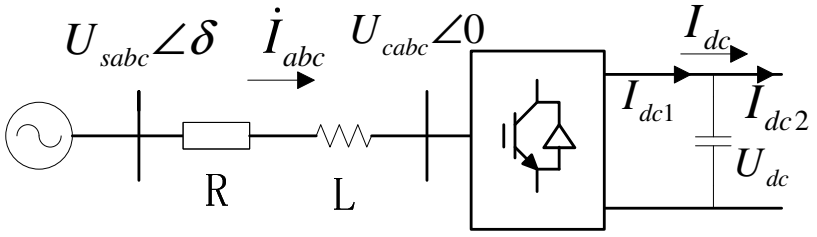

Fig.1 Structure of Voltage Source Control

As is shown in Fig.1, u_{sa}, u_{sb} and u_{sc} represent bus voltage of the AC power system side,and u_{ca}, u_{cb} and u_{cc} represent bus voltage of the converter side. C is a parallel capacitor in DC side. u_{dc} and i_{dc} respectively represent the DC voltage and DC current. i_a, i_b and i_c represent AC current of the converter side. L is the equivalent inductance and R is the equivalent resisitance.

The voltage function of AC power side can be given in the form

$$\begin{bmatrix} u_{sa} \\ u_{sb} \\ u_{sc} \end{bmatrix} = \begin{bmatrix} u_{ca} \\ u_{cb} \\ u_{cc} \end{bmatrix} + R \begin{bmatrix} i_a \\ i_b \\ i_c \end{bmatrix} + L \frac{d}{dt} \begin{bmatrix} i_a \\ i_b \\ i_c \end{bmatrix} \tag{1}$$

Through PARK transformation ,the quadrature axis and direct axis component of voltage and current under The two-phase synchronous rotating coordinate system can be obtained as follows.

$$\begin{cases} u_{sd} = u_{cd} + Ri_d + L\dfrac{di_d}{dt} - \omega L i_q \\ u_{sq} = u_{cq} + Ri_q + L\dfrac{di_q}{dt} + \omega L i_d \end{cases} \tag{2}$$

The function of switching power between the converter and the network can be written as follows.

$$\begin{cases} P = \dfrac{3}{2}(u_{sd} i_d + u_{sq} i_q) \\ Q = \dfrac{3}{2}(u_{sq} i_d - u_{sd} i_q) \end{cases} \tag{3}$$

Where

$$\begin{cases} u_{sd} = u_s \\ u_{sq} = 0 \end{cases} \tag{4}$$

Then The function of switching power can be rewritten in the form

$$\begin{cases} P = \dfrac{3}{2} u_s i_d \\ Q = -\dfrac{3}{2} u_s i_q \end{cases} \tag{5}$$

Therefore,P and Q and be controlled respectively by i_d and i_q ,which means the successful implementation of the decoupling control of active and reactive power.

Design of Controller

According to the engineering experience,there are four basic control modes: constant DC voltage control, constant power control, constant AC voltage control and variable frequency control [7].

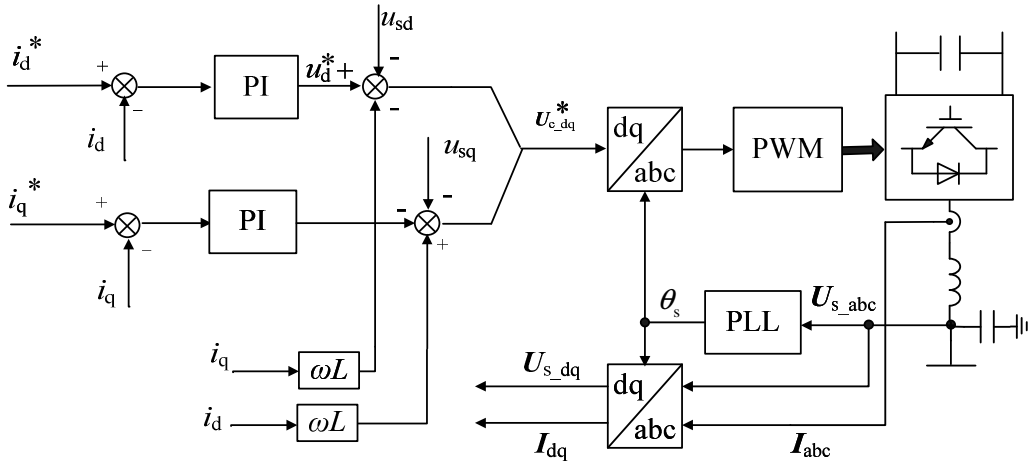

Fig.2 Block Diagram of Inner Current Control

Block Diagram of Inner loop current control is shown in Fig.2,PI regulator are used,and its output can be given as follows.

$$\begin{cases} u_{\mathrm{d}}^{*} = -(L\dfrac{\mathrm{d}\,i_{\mathrm{d}}}{\mathrm{d}\,t} + Ri_{\mathrm{d}}) = \left(K_{\mathrm{p}} + K_{\mathrm{i}}/s\right)\left(i_{\mathrm{d}}^{*} - i_{\mathrm{d}}\right) \\ u_{\mathrm{q}}^{*} = -(L\dfrac{\mathrm{d}\,i_{\mathrm{q}}}{\mathrm{d}\,t} + Ri_{\mathrm{q}}) = \left(K_{\mathrm{p}} + K_{\mathrm{i}}/s\right)\left(i_{\mathrm{q}}^{*} - i_{\mathrm{q}}\right) \end{cases} \tag{6}$$

Where u_d^* and u_q^* are the outputs of the PI regulator. i_d^* and i_q^* are the reference values of the inner loop current conntrol, which are given by outer loop voltage control.

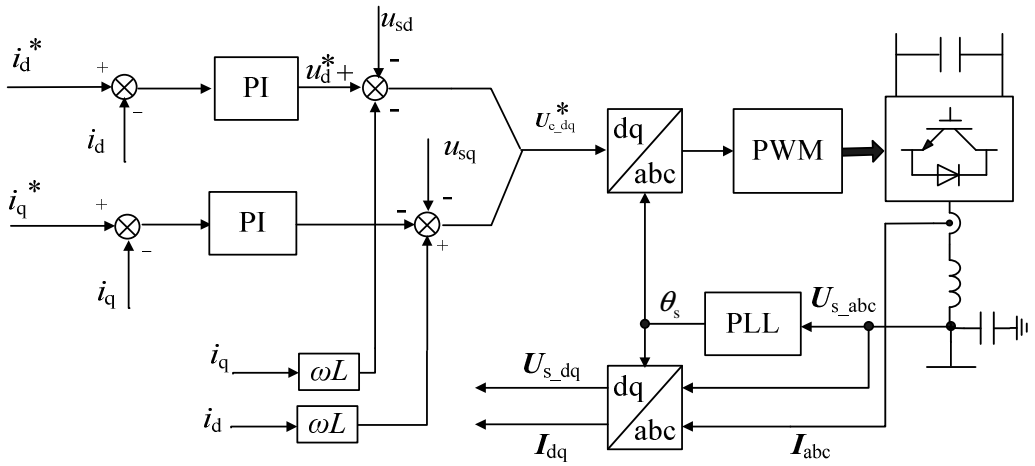

Fig.3 Block Diagram of Constant DC Voltage Control

Block Diagram of Constant DC Voltage Control is shown in Fig.3, PI regulator is used to eliminate the steady state error.Compare u_{sd} and u_{sq} with $[1,0]^{\mathrm{T}}$. And the error need regulating by PI regulator according to the formula (2).

Simulation of Supplying Power to Passive Network

In the model established by Matlab / Simulink,the main parameters are as follows. The rectifier parameter is 150kv/50Hz. The low pass filter parameter is 3Mvar. The PWM switching frequency is 2500Hz, and SPWM is adopted. The voltage in DC side is 300kv,and the capacitor in this side is 200 μF. Line length is 75 km. The resistance is 0.0130 Ω/km,and the inductance is 0.159mH/km. The

capacitance is 0.231 μ F/km. In the inner current control,Kp=5 and Ki=20. In the outer voltage control,Kp=0.4 and Ki=500. The sampling time is 5 μ s.

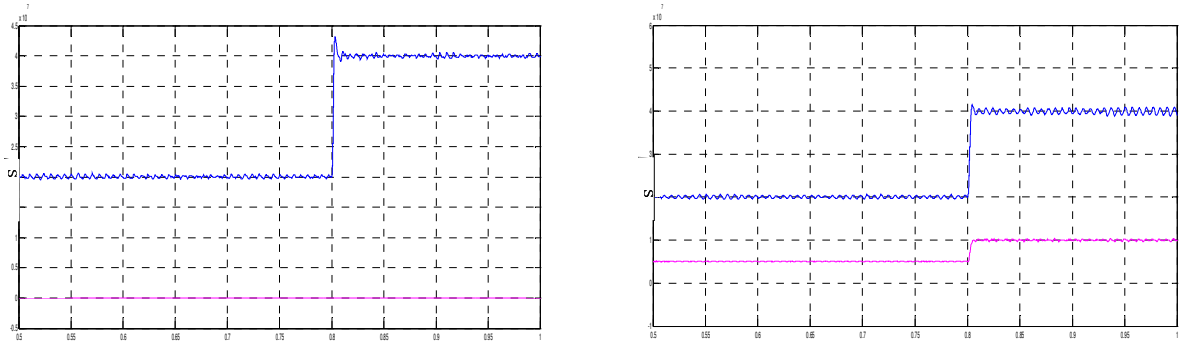

(a)load increased by 20MW (b)load increased by 20MW+5MVar

Fig.4 Simulation waveform for load change at the passive side

(i)Change of load in the passive network

As is shown in Fig.4(a), the load was 20MW at the begining , and it increased by 20MW at 0.8s. The simulation waveform is shown in Fig.4(b), the load is 20MW+5MVar, and it increased by 40MW+10MVar at 0.8s. Load can be controlled independently through this control strategy. Reactive power can be transmitted as well as active power at the same time.

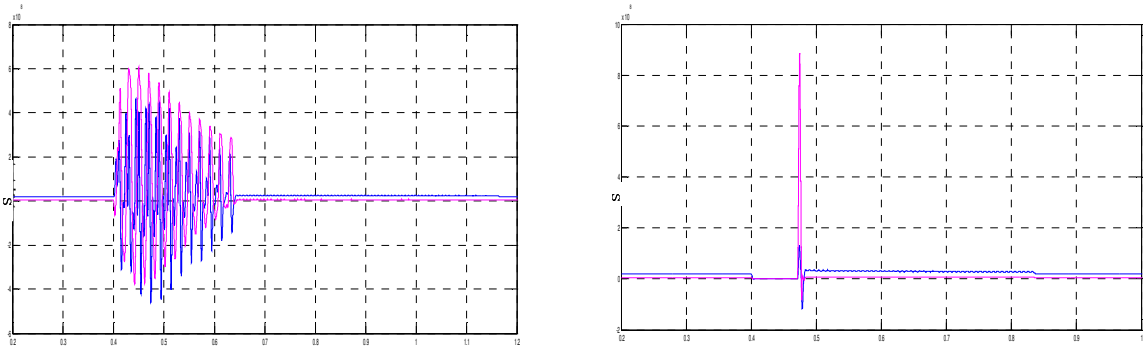

(a)single phase grounding fault (b)three-phase short circuit fault

Fig.5 Simulation waveform for short curcuit faut at the passive side

(ii)Short circuit faults

The load in the passive network was 20MW+5MVar at the beginning,and a short circuit fault happened at 0.4s, which lasts 1/15s. When a single phase grounding fault happens, the simulation waveform is shown in Fig.5(a). And when a three-phase short circuit fault happens, the simulation waveform is shown in Fig.5(b). As far as the VSC-HVDC is concerned, a steady state will return in a period of time.

Conclusions

Through the analysis on the VSC-HVDC mathematical model,a conclusion can be drawed that active and reactive power can be respectively controlled by i_d and i_q. MATLAB/Simulink was utilized to establish the simulation model of supplying power to the passive network, where constant DC voltage control and constant AC voltage control strategies are designed. The results show that VSC-HVDC can well satisfy the requirements of supplying power to passive network, and show the superiority of power transmission.

References

[1] LI Gengyin, Lü Peng-fei, LI Guangkai, et al: 'Development and prospects for HVDC light', Automation of Electric Power Systems, 2003, Vol.27, (4) p.77-81

[2] ZHANG Guibin, XU Zheng, WANG Guang-zhu: 'Steady-state model and its nonlinear control of VSC-HVDC system', Proceedings of the CSEE, 2002, Vol.22, (1) p.17-22

[3] YAO Weizheng, DENG Xiangchun, YI Yingping, et al: 'Research on modeling and simulation of VSC-HVDC based on dq0 synchronous coordinate', Power System Protection and Control, 2009, Vol.37, (22) p.71-76.

[4] WEI Xiaoguang, TANG Guangfu, ZHENG Jian-chao: 'Study of VSC-HVDC discrete model and its control strategies', Processdings of the CSEE, 2007, Vol.27, (28) p.6-11

[5] YANG Hao, ZHANG Nan, YE Ming-jia: 'Study of VSC-HVDC connected to passive network discrete model and its control strategies', Power System Protection and Control, 2012, Vol.40,(4) p.37-42

[6] LIANG Hai-feng, LI Gengyin, LI Guangkai, et al: 'Simulation study of VSC-HVDC system connecting to passive network', Power System Technology, 2005, Vol.29, (8) p.45-50

[7] Blasko V: 'Analysis of a Hybrid PWM based on modified space-vector and triangle-comparisonMethods', IEEE Trans on IA, 1997, Vol.33,(3) p.756-764

Advanced Materials Research Vols. 960-961 (2014) pp 1376-1380

doi:10.4028/www.scientific.net/AMR.960-961.1376

Protection Scheme for Distribution Network with Distributed Generation

Chongxin Xu[1, a *], Yanjun Jiao[1, b]

[1]School of Electrical and Electronic Engineering, North China Electric Power University, Baoding, Hebei, 071003, China

[a]sdxuxin12354@163.com, [b]jiao_yanjun@263.net

Keywords:distributed generation; distribution network; PSCAD/EMTDC; protection scheme;.

Abstract. Power generation becomes a main way of using new energy. However, the access of distributed generation(DG) causes the ordinary protection system develop a series of problems. In this paper, the structure of distribution network with DG is introduced firstly.Secondly,it is analysed that the effect that DG brings to distribution network protection, and then a new protection scheme of distribution network with DG is put forward. The segment I, II of direction three-current protection on the line which is at the upstream of DG, and the next line's segment I, II consists of a simple communication unit. Through the comprehensive judgment of two protections' action results, fault can be isolated in minimum range quickly and accurately. Finally, the correctness and feasibility of the new protection principle are verified by simulating a 10KV distribution system.

Introduction

DG is generating unit with small capacity, in the user field or near field.It's constructed to reach the special needs of individual customers,or to support the economic operation of distribution network, or both of them. As a useful supplement to the centralized power generation, it is of great practical significance to develop DG industry, which mainly depends on its economical, environmental protection, flexibility and specific peaking function [1-2].

It has many advantages that distributed generation connects with distribution network, but the negative impact brought by DG can not be ignored. DG accessed to low voltage distribution network, makes the distribution system from a single supply radial network into two-terminal or multiport active networks. The topological structure,current size and direction of the distribution network will change. The existing protection devices, designed for single supply radial network, are unable to meet the requirements of reliability, rapidity, accuracy and so on [3].

The Structure of Distribution Network Containing DG

Because of DG's accessed, the topological structure and current direction of distribution network may change. The selectivity, sensitivity and reliability of distribution network protection may be affected. The structure of distribution network with DG mainly includes the following [4].

1) DG is connected to the distribution network feeder on the first bus, as shown in Fig.1. In normal conditions, DG and system power supply operate parallelly, can be equivalent to a power supply.

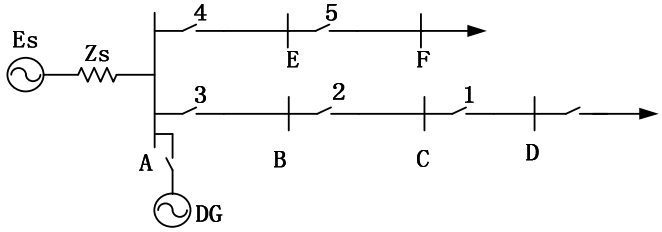

Fig.1 DG Accessed to Feeder on the First Bus

2) DG is connected to the distribution network feeder on non-end bus, as shown in Fig.2.DG supplies power to the load through the line BD.

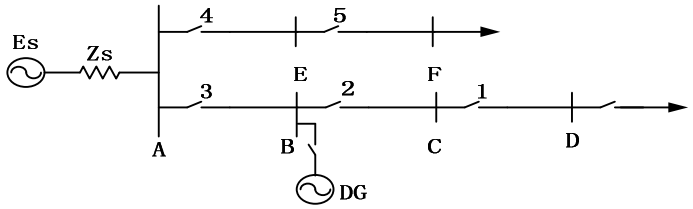

Fig.2 DG Accessed to the Feeder on Non-end Bus

3) The DG is connected to the distribution network feeder on the last bus, as shown in Fig.3. DG directly supply power to the load through bus D.

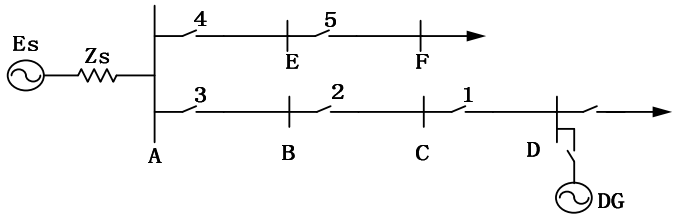

Fig.3 DG Accessed to the Feeder on the Last Bus

4) Multiple DGs access to distribution network feeder. DGs may be accessed differently,when a power distribution system has multiple DGs, but still can be divided into the above three categories according to the access point.

The impact of DG on distribution network protection

At present, the distribution network is mostly a single supply radial network. At the configuration of the existing protection, when DG accessed to distribution network ,there will have a great impact on the protection for the distribution network [5-6].

As is shown in Figure 4, the DG access to distribution network on the bus B.

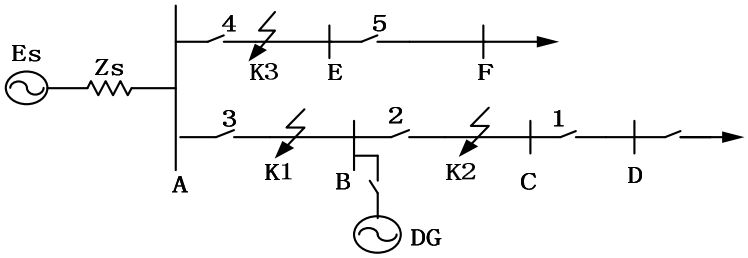

Fig.4 DG Accessed to Distribution Network on the Bus B

1) When a fault occurs at K1, protection 3 will act and separate the fault line from the system side. However, the fault still exists , and short circuit current will still be provided to the fault point by DG. In order to make the fault line resection, circuit breaker must be installed in bus B side,and line AB should be resected at both sides. Thereafter, due to the presence of DG, line BD can turn into islanded operation.

2) When short-circuit fault occurs at K2, because of the existence of the DG, there will have both the fault current flow from the system and the improving current from DG at the same time through protection 2. The scope of current quick-break protection of the protection 2 will extend.what's more, the scope may extend to the line CD,and then the conservation of protection 1 with 2 will be lost, also the selective can not be guaranteed, As for the limited current quick-break protection of protection 2 with 3. At the same time, the fault current flowed through protecting 3 will be weakened because of DG,and the scope of protection will be shortened. In some severe cases, limited current quick-break protection of protection 3 will cannot be as the backup protection of next line downstream.

3) When a fault occurs at K3, the fault should have be isolated only by protection 4. However, fault current with reverse direction which is provided by DG,will flow through the protection 3. When the fault current provided by DG is large enough, The protection 3 may misact and loss its selectivity.

New protection scheme for distribution network

There is no need to install protective devices on the other side of the line in the scheme. Only three-current direction protection should be installed on the original power supply side of each line which is on the upstream of DG. Then we can save the cost of circuit breaker, and avoid the problems caused by themselves [7].

The fixed value of section I of three-current direction protection should be set according to the principle that the protection can act reliably when short circuit happened at the end of the line with maximum operating mode, and the action time is 0. II, III segment action currents are still set by ladder time characteristic principle. Protection I, II segment of each line and protection I, II section of the next line constitute a communication unit. Protection I, II segment of this line will be unlocked when protection I, II section of the next line does't act. On the contrary, protection I, II segment of this line will be locked. Therefore, when fault happened in the line, the protection I or II segment will act, and cann't receive the locked message. Once this case is identified, remote control information will be sent to the next line's protection,and circuit breakers at two sides will trip at the same time, so as to cut off the fault line. The block diagram of action principle is shown in figure 5.

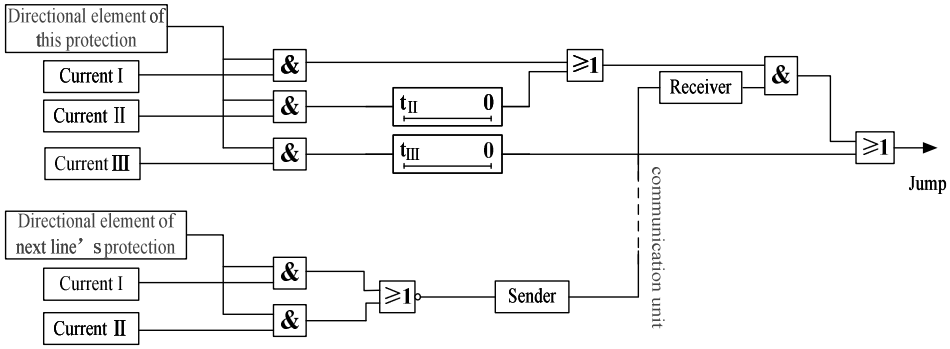

Fig.5 Current Protection Action Principle Diagram

However, for the last line on the upstream of DG, circuit breaker and directional element is need at the end of the line, because the communication unit is constituted only in this line. when protection I or II of the line acts and the power direction are positive direction both sides of the line, this line will be identified to be faulted, and then circuit breaker both sides should trip.

Because the lines at the downstream of DG don't change into two-terminal or multiport active networks, three-current protection is enough. in order to guarantee the protection selectivity, the influence of increasing current must be taken into account.

Protection action analysis

Figure 6 shows a distribution network system in a city, and let's take this system as the example to show the proposed protection scheme.

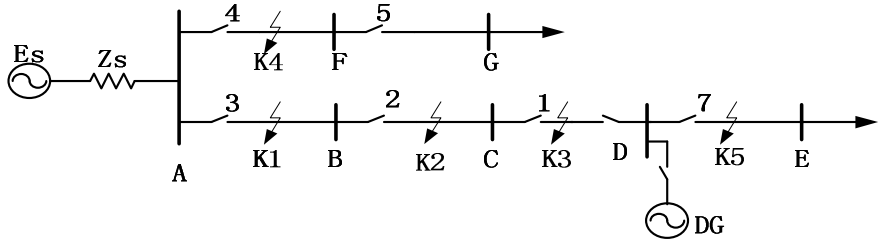

Fig.6 Distribution Network System Model

1) When a fault occurs at K1, direction element and current I or II of protection 3 will act, while the direction element of protection 2 does not act, because the power direction of protection 2 is "-". According to the protection scheme proposed in this paper, the protection 3 and 2 constituted a communication unit. Protection 2 will send the signal of unlocked to protection 3, and line AB will be judged as fault.Circuit breaker of protection 3 trips and sends the control information to protect 2, then circuit breaker of protection 2 trips,too.

2) When a fault occurs at K2, direction element and current I or II of both protection 3 and 2 act, but direction element of protection 1 does not acts. Therefore, protection 3 receives the signal of locked from protection 2, while protection 2 receives the signal of unlocked from protection 1.Circuit breaker of protection 2 trips and sends the control information to protect 1, then circuit breaker of protection 1 trips,too.

3) When a fault occurs at K3, current I or II of protection 1 acts, and the power direction of protection 1 and 6 were identified as "+". The fault will be judged on the line CD, and circuit breakers at two sides of line CD trips.

4) When a fault occurs at K4, directional element of protection 1, 2 and 3 was judged as negative direction, so the protections will not act. Protection 4 acts to isolation the fault feeder.

5) When a fault occurs at K5, requirements of selectivity and reliability can be achieved, because action value of protect 7 is set according to the capacity of DG.

Simulation

According to Fig. 4, distribution network simulation model is established. The reference capacity, S_B is 500MVA, the reference voltage, U_B is 10.5kV. The system impedances (maximum and minimum) are $x_{s\max}=0.126\Omega$ $x_{s\min}=0.091\Omega$.The load parameter is $Z_{LD}=(30+j15.7)\Omega$, equaling to a single feeder load about 4MVA. The capacity of DG is 5MVA. Each line's parameters as shown in the following table.

Tab.1 Impedance Parameters of Each Line

Line	Impedance	Line	Impedance	Line	Impedance
AB	0.54+j0.694	CD	1.813+j0.651	AF	1.08+j1.388
BC	0.54+j0.694	DE	3.626+j1.302	FG	1.554+j0.558

The simulation analysis is carried out, while the simulation model of this system is built by PSCAD/EMTDC. According to general configuration three-current protection, values of segment II of protection 3, 2 and 1 are calculated: I_{3dzII}=4375A, I_{2dzII}=2224A, I_{1dzII}=1093A; and the value of segment III of protection 7 is I_{7dzIII}=429A.

Short circuit current, that flows through the protection of the line, when three-phase fault occurs to a line's end, is shown in Table 2.

Tab.2 Short Circuit Current

Line	Fault current A	Line	Fault current A	Line	Fault current A
AB	6323	CD	1679	AF	3308
BC	3298	DE	814	FG	1817

The analysis of simulation results:

1) When a fault occurs to the end of line AB, the fault current of Protection 3 is detected: I3=6323A. Because of I3>I3dzII, according to rule (1), segment II of protection 3 acts,while the direction element of protection 2 does not act. Without locking signal, protection 3 trips, and send the remote control information to protection 2. Then protection 2 trips,too.

2) When a fault occurs to the end of line BC, the fault current of Protection 2 is detected: I2=3298A. Because of I2>I2dzII, according to rule (2), protection 3 receives locking signal 2 sent from protection 2 and does not trip, while protection 2 trips without locking signal. At the same time remote control information is sent to protect 1, and the circuit breaker of protect 1 act.

3) When a fault occurs to the end of line CD, the fault current of Protection 1 is detected: I1=1679A. Because of I1>I1dzII, according to rule (3), segment II of protect 1 acts, while direction elements of protection 6 and 1 act. Circuit breakers of protection 1 and 6 trip at the same time, while protection 3 and 2 receive locking signal.

4) When a fault occurs to the end of line DE, the fault current of Protection 7 is detected: I7=814A. Because of I7>I7dzIII, according to rule (5), segment III of protect 7 acts and the fault is isolated after circuit breaker of protection 7 tripped,while other protections receive locking signals.

As is shown in the simulation and analysis, the protection scheme advanced can absolutely meet the requirements of reliability, selectivity sensitivity.

Conclusions

With DG accessed to distribution network, traditional protection scheme can not meet the requirement of reliability, selectivity, sensitivity and quick-acting. This paper introduces a new protection scheme for distribution network with DG.The segment I, II of direction three-current protection on the line which is at the upstream of DG, and the next line's segment I, II consists of a simple communication unit. Through the comprehensive judgment of two protections' action results, fault can be isolated in minimum range quickly and accurately. The scheme proposed in the paper not only meets the requirements of relay protection, but also has three advantages. 1) The simple structure and reliable; 2) Don't need to change the fixed value,when a new DG accesses into; 3) For all the lines between the original power supply and DG, fault can be isolated quickly.

References

[1] Jian Wang , Xingyuan Li and Xiaoyan Qiu: 'Power system research on distributed generation penetration.' Automation of Electric Power Systems, 2005, Vol.29,(24), p.90-97.

[2] Wei Yang, Liang Hua: 'Based on multi-agent adaptive current protection research'. Relay, May.2008, Vol.36,(10), p.5-10.

[3] Xizhou Wang , Xin Chen , Deqiang Gan, et al: 'Distributed generation and study of coordination of distribution network protection.' Relay, 2006,Vol.34,(3), p.15-19

[4] Ping Wang , Ziqi Zhu, Jianxun Zhang, et al. 'Effect of distributed generation to distribution network protection.' Electric Automation, 2011,Vol.33,(4),p.43-45.

[5] Yongli Li, Shengwei Li, Sen Liu: 'Effects of inverter-based distributed generation on distribution feeder protection.' Proceedings of the 8th International Power Engineering Conference, December 3-6. 2007, Singapore.

[6] Kauhaniemi K， Kumpulainen L. 'Impact of Distributed Generation on the Protection of Distribution Networks.' Developments in Power System Protection,2004,p.315-318.

[7] Jingliao Sun, Yongli Li, Shengwei Li, et al. 'A protection scheme for distribution system with DG.' Automation of Electric Power Systems,2009,Vol.33,(1),p.81-84,89.

CHAPTER 12:

Power Machinery and Engineering

Advanced Materials Research Vols. 960-961 (2014) pp 1383-1388

doi:10.4028/www.scientific.net/AMR.960-961.1383

Dynamic Load Calculation of Mining Shovel Crowding System

LIN Gui-yu[1,a], LI Jie[2,b], LIAN Jin-hua[3,c], ZHAO Jun[4,d*]

[1]School of Mechanical Engineering & Automation, Northeastern University, Shenyang 110819, China

[2]AVIC Shenyang Liming Aero-Engine (GROUP) Corporation LTD, Shenyang 110819, China

[3]Technology Center, Taiyuan Heavy Industry Co., Ltd., Taiyuan 030024, China

[4]School of Mechanical Engineering & Automation, Northeastern University, Shenyang 110819, China

[a]GYlin@editor@mail.neu.edu.cn

[b]13555774933@163.com

[c] jszxljh2013@163.com

[d]zhaojunneu@163.com

Key words: Mining Shovel; Crowding system; Dynamics ; Vibration ; Dynamic load coefficient

Abstract. To highlight the main factors, only the crowding shaft was taken as elastic component, while the other crowding system parts, such as girth, driving shaft and swing arm were taken as rigid components; the effects of damping were ignored; the dynamical model of mining shovel's crowding system was simplified to a two degree of freedom model; mathematical and mechanical models were derived by Lagrange equation method; the locked rotor condition, when the bucket rod was perpendicular to the boom, was used as the calculation condition; the calculated dynamic load coefficient of the crowding system was compared with that in multi degree of freedom model and the result shows: to simplify calculation, it is practicable to replace multi degree of freedom models with two degree of freedom models in the preliminary design stage.

Introduction

Due to the complexity of the crowding system of mechanical mining shovel, static calculation methods are usually used in the present strength calculation of crowding systems, while actual dynamic loads when working are miscounted; the field test results proved：loads of crowding systems at work changed with soil properties；due to the frequent starting and braking, locked rotor could be arisen at any time and the dynamic loads were very obvious; therefore, in order to improve the reliability of structure parts and system performance , it is quite necessary to conduct dynamic research.

Derivation of differential equation of crowding system

For the sake of detailed dynamic calculation and analysis of crowding system [1], it was assumed as following:

1）The belt between crowding motor and reduction gearbox, transmission shafts of reduction gearbox, gears and boom were rigid components;

2）The final crowding shaft was elastic shaft and the effect of damping was neglected.

Then, the obtained model [2] was simplified to a two-freedom model. The rotation angle of motor (θ_0) and crowding smaller gears (θ_4) were selected as general coordinates and the

dynamic calculation of crowding system was obtained as illustrated in Fig.1. The kinetic and potential energy of crowding system were derived as following:

1）kinetic energy of the crowding system

$$T=\frac{1}{2}\cdot J\cdot\dot{\theta}_0^2+J_7\cdot\dot{\theta}_4^2+\frac{1}{2}\cdot\left(m_d+m_c\right)\cdot\dot{\theta}_4^2\cdot R_3^2 \quad (1)$$

where J is the whole moment of inertia of hoist and transmission system and can be expressed as

$$J=J_0+J_1+J_2+J_3+\frac{J_4}{i_1^2}+\frac{J_5}{i_1^2}+\frac{J_6}{i_1^2 i_2^2} \quad (2)$$

m_d is the mass of the bucket rod;
m_c is the mass of the empty bucket;
R_3 is the radius of the smaller crowding gear;
i_1 is the first transmission ratio of the crowding reducer;
i_2 is the transmission ratio of the crowding reducer;
J_0 is the moment of inertia of the crowding motor (J_0=53.100kg·m^2);
J_1 is the moment of inertia of the driver gear (J_1=13.475kg·m^2);
J_2 is the moment of inertia of the driven belt pulley (J_2=12.902kg·m^2);
J_3 is the moment of inertia of the gear No 1(J_3=0.617kg·m^2);
J_4 is the moment of inertia of the gear No 2(J_4=270.44kg·m^2);
J_5 is the moment of inertia of the gear No 3(J_5=2.007kg·m^2);
J_6 is the moment of inertia of the gear No 4(J_6=1153.073kg·m^2);
J_7 is the moment of inertia of the smaller crowding gear (J_7=31.157kg·m^2);
k_4 is the torsion stiffness of the crowding shaft (k_4=10960.00×10^{4}N·m/rad);
k_6 is the soil rigidity in crowding direction (k_6=40000.00×10^{4}N/m).

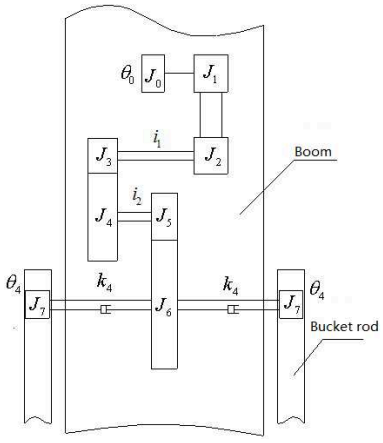

(a) Calculation diagram of crowding system

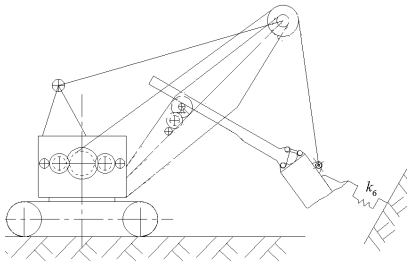

(*b*) Calculation diagram of whole mining shovel crowding system

Fig. 1 Dynamic calculation diagram of crowding system

2）The potential energy of crowding system [3]

$$V = k_4 \cdot \left(\theta_4 - \frac{\theta_0}{i_1 i_2} \right)^2 + \frac{1}{2} \cdot k_6 \cdot (\theta_4 \cdot R_3)^2 \quad (3)$$

The generalized force, that is, the kinetic moment ($Q_1 = Q_y(t)$) output by crowding motor acted on general coordinate θ_0 of the motor. There is no generalized force acted on the other general coordinates.

By substitution of the Eq. (1）,（2）and the generalized force into Lagrange equation, the below equations were derived:

$$\frac{d}{dt}\left(\frac{\partial T}{\partial \dot{\theta}_i}\right) + \frac{\partial V}{\partial \theta_i} = Q_i \qquad i=1, 2, 3 \quad (4)$$

The following two degree of freedom differential equations could be also obtained:

$$\frac{d}{dt}\left(\frac{\partial T}{\partial \dot{\theta}_0}\right) + \frac{\partial V}{\partial \theta_0} = Q_y(t)$$

$$J \cdot \ddot{\theta}_0 + 2k_4 \cdot \left(\frac{\theta_0}{i_1 i_2} - \theta_4 \right) \cdot \frac{1}{i_1 i_2} = Q_y(t) \quad (5)$$

$$\frac{d}{dt}\left(\frac{\partial T}{\partial \dot{\theta}_4}\right) + \frac{\partial V}{\partial \theta_4} = 0$$

$$2J_7 \cdot \ddot{\theta}_4 + R_3^2 \cdot (m_d + m_c) \cdot \ddot{\theta}_4 + 2k_4 (\theta_4 - \frac{\theta_0}{i_1 i_2}) + k_6 R_3^2 \theta_4 = 0 \quad (6)$$

The Eq. (4) ,（5）could be expressed by matrix:

$$[M] \cdot \{\ddot{X}\} + [K] \cdot \{X\} = \{Q\} \quad (7)$$

where $[M]$ is the mass matrix;

$[K]$ is the stiffness matrix；

$\{X\}$ is the displacement vector;

$\{Q\}$ is the column vector of the stimulating vibration loads;

$$[M] = \begin{bmatrix} m_1 & 0 \\ 0 & m_2 \end{bmatrix} \quad (8)$$

where $m_1 = J$；

$m_2 = 2J_7 + R_3^2 \cdot (m_d + m_c)$.

$$[K]=\begin{bmatrix} k_{11} & k_{12} \\ k_{21} & k_{22} \end{bmatrix} \tag{9}$$

where

$$k_{11}=\frac{2k_4}{i_1^2 i_2^2} \qquad k_{12}=-\frac{2k_4}{i_1 i_2}$$

$$k_{21}=-\frac{2k_4}{i_1 i_2} \qquad k_{22}=2k_4+k_6 R_3^2$$

$$\{X\}=\begin{Bmatrix} \theta_0 \\ \theta_4 \end{Bmatrix} \tag{10}$$

$$\{Q\}=\begin{Bmatrix} Q_y(t) \\ 0 \end{Bmatrix} \tag{11}$$

Dynamic loads calculation of the crowding system

2.1Calculation of exciting loads response

The eigenvalue question of the Eq.（6）is:

$$[K]\{A\}=\omega^2[M]\{A\} \tag{12}$$

where ω is the natural frequency;

$\{A\}$ is the natural vibration mode;

The eigenvalue equation is:

$$\Delta(\omega^2)=\begin{vmatrix} k_{11}-\omega^2 m_1 & k_{12} \\ k_{21} & k_{22}-\omega^2 m_2 \end{vmatrix} \tag{13}$$

$$=(k_{11}-\omega^2 m_1)(k_{22}-\omega^2 m_2)-k_{12}k_{21}=0$$

For the substitution of the related data, the natural frequency was obtained as follow:

$$\omega_1=13.1473 \text{ rad/s}, \qquad \omega_2=187.6364 \text{ rad/s}$$

ω_1, ω_2 was substituted into eigenvalue Eq.（12）and the natural vibration mode was under normalization process. Therefore, the following results were obtained:

$$\begin{Bmatrix} A^{(1)}{}_1 \\ A^{(1)}{}_2 \end{Bmatrix}=\begin{Bmatrix} 1.0000 \\ 0.0217 \end{Bmatrix}, \qquad \begin{Bmatrix} A^{(2)}{}_1 \\ A^{(2)}{}_2 \end{Bmatrix}=\begin{Bmatrix} 1.0000 \\ -0.5382 \end{Bmatrix}$$

For the sake of regularizing the natural vibration mode, the regularized vibration mode was obtained as follow:

$$\begin{Bmatrix} u^{(1)}{}_1 \\ u^{(1)}{}_2 \end{Bmatrix}=\begin{Bmatrix} 0.1059 \\ 0.0023 \end{Bmatrix}, \qquad \begin{Bmatrix} u^{(2)}{}_1 \\ u^{(2)}{}_2 \end{Bmatrix}=\begin{Bmatrix} 0.0213 \\ -0.0114 \end{Bmatrix}$$

The stimulating vibration load: $Q_1 = M_{\max y} \cdot \sin\left(\frac{\pi}{2.5} \cdot t\right)$.

The steady-state response of the system acted on the stimulating vibrationforce was obtained:

$$\{X\} = \begin{pmatrix} \theta_0 \\ \theta_4 \end{pmatrix} = \begin{pmatrix} 0.1608 \\ 0.0035 \end{pmatrix} \cdot \sin\left(\frac{\pi}{2.5} \cdot t\right) \quad (14)$$

2.2 Calculation of crowding shaft loads

Under the locked rotor condition when the bucket rod was perpendicular to the boom [8,9], the expression of dynamic load was :

$$M_4 = 2 \cdot k_4 \cdot \left(\frac{\theta_0}{i_1 i_2} - \theta_4\right) \quad (15)$$

The equation（13）was substituted into the Eq.（13） and the further result was obtained as:

$$M_4 = 2k_4 \left(0.0218 - 0.0214\right) \cdot \sin\left(\frac{\pi}{2.5} t\right) \quad (16)$$

The original data was substituted into the Eq.（15） and the change law with time of dynamic loads of the crowding shaft was calculated as illustrated in Fig.2.

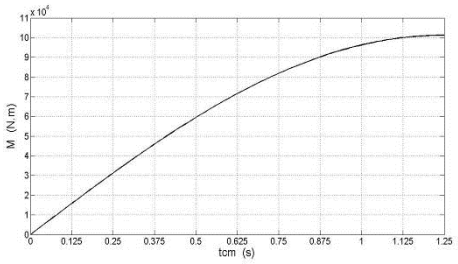

Fig. 2 Dynamic load of the crowding shaft change law with time

From the Fig.2, it could be deprived that : the maximum crowding dynamic load $M_{\max d}$ =10.1213×10^4 N·m ,the static load M_j=25.8441×10^4 N·m（based on the maximum power） and the coefficients of dynamic load were[10]:

$$K_{ye} = \frac{M_{\max d} + M_j}{M_j} \quad (17)$$

$$K_{ye} = \frac{M_{\max d} + M_j}{M_j} = \frac{10.1213 + 25.8441 \times 10^4}{25.8441 \times 10^4} \approx 1.392$$

They were compared with dynamic parameters derived from the multi degree of freedom model [11] as illustrated in Table 1.

Table 1 Comparison of dynamic parameters between two degree of freedom model and multi degree of freedom model

Terms	Multi degree of freedom model	Two degree of freedom	Comparisons
Coefficients of dynamic load K	1.408	1.392	1.408 1.392 /1.408≈1.14%
Maximum dynamic oad $M_{\max d}$ (N·m)	105105	101213	(105105 101213 /105105≈3.7%

From the Table 1: the gap between the obtained coefficients of dynamic load based on the above two model types is very narrow. Thus, it is practicable to replace multi degree of freedom models with two degree of freedom models in the preliminary design stage.

Conclusions

For the sake of above analysis and calculation，conclusions as follow are draw:

The calculation model and methods are correct and the obtained results are of great significance;

The analysis and calculation will become easier when multi degree of freedom models are replaced with two degree of freedom models.

Acknowledgement

The financial support of the National 863 Project (Grant No. 2012AA062001) is greatly appreciated.

References

[1] Li Jie. The Dynamics research of mechanical mining shovel's driving system [D], Northeastern University,2012

[2] Yan Shu-wen. The design of mechanical mining shovel[M]. Beijing: *China Machine Press*, 1983: 12-14

[3] Samuel Frimpong, Yafei Hu Hilary Lnyang. Dynamic Modeling of Hydraulic Shovel Mining shovels for Geomaterials[J]. *International Journal of Geomechanics*, 2008, 8(1): 20-29.

[4] Koivo A J, Thoma M, Kocaoglan E, et al. Modeling and control of mining shovel dynamics during digging operation[J]. *Journal of Aerospace Engineering*, 1996, 9(1): 10-18.

[5] Samuel Frimpong, Yafei Hu, Kwame Awuah-Offei. Mechanics of cable shovel-formation interactions in surface mining excavations[J]. *Journal of Terramechanics,* 2005, 42(1): 15-33.

[6] Awuah-offei K, Frimpong S. Numerical simulation of cable shovel resistive forces in oil sands excavation[J]. *International Journal of Mining, Reclamation and Environment ,* 2006, 20(3): 223-238.

[7] Vaha P K, Skibniewski M J. Dynamic model of mining shovel[J]. *Journal of Aerospace Engineering,* 1993, 6(2): 148-158.

[8] Halatchev R A, Knights P F. Spatial variability of shovel dig performance [J]. *International Journal of Mining, Reclamation and Environment ,* 2007,21(4) :244-261.

[9] Patnayak S, Tannant D D, Parsons I, et al. Operator and dipper tooth influence on electric shovel performance during oil sands mining[J]. *International Journal of Mining, Reclamation and Environment,* 2008, 22(2): 120-145.

[10] Kwame Awuah-Offei, Samuel Frimpong. Cable shovel digging optimization for energy efficiency[J]. *Mechanism and Machine Theory,* 2007, 42(8): 995-1006.

Advanced Materials Research Vols. 960-961 (2014) pp 1389-1393

doi:10.4028/www.scientific.net/AMR.960-961.1389

Effects of load ratio on dual-fuel engine operated with pilot diesel fuel and liquefied natural gas

Qiang shi[1, a *], Chunhua Zhang[1,b], Yanchao Cai[1,c], Juxiang Fang[1,d]

[1]School of Automobile, Chang'an University, Xi'an 710064, China

[a]623774939@qq.com,[b]zchzzz@126.com,[c]814161605@qq.com,[d]745046142@qq.com

Keywords: load ratio, diesel, liquefied natural gas, dual-fuel engine

Abstract. In order to study the application of the liquefied natural gas (LNG) on diesel engine, a turbocharged diesel engine was converted into a dual-fuel engine ignited by diesel fuel. The effects of load ratio on fuel economy and emissions of dual-fuel engine were compared and analyzed at engine speed of 1200 r/min, 1600 r/min and 2200 r/min. The experimental results show that, the specific fuel consumption is reduced with the increase of load ratio at different speeds. As the load ratio increases, CO emission of dual-fuel reduces, but it increases slightly at high loads and full load. When the load ratio is less than 40%, HC emission of dual-fuel is reduced significantly with the increase of load, but increases when the load ratio continues to increase, and finally HC emission is stable. When the load ratio is less than 40 %, NOx emission is relatively low, as the load ratio increases, increases sharply, but at high loads and full load, reduces slightly.

Introduction

The history of natural gas as automobile fuel could date back to the early development of internal combustion engine. Because of the inconvenience of storing and supplement, natural gas had been replaced by diesel fuel and petrol fuel. With the rapid development of the auto industry, our country's vehicle quantity is also increasing rapidly. Automobiles bring convenience while the environmental pollution and the shortage of petroleum. The demand of environmental protection and the shortage of petroleum resources have challenged the traditional petroleum fuels and its combustion forms of engines. So it is significant that clean alternative fuel is explored to promote auto industry continuously. Among the variety of alternative fuels, natural gas embraces the characteristics such as abundant resources, higher octane value, higher calorific value and lower pollution, and is regarded as a very promising cleaning vehicle fuel [1]. Therefore, it will be a new direction for developing the natural gas, and it is also an effective method to solve the petroleum crisis and environment problems.

The combustion process of LNG-diesel dual-fuel engines is complicated when compared with gasoline engines and diesel engines. The fuel injectors squirt a small amount of pilot diesel into cylinder while the piston is approaching to TDC in compression stroke. Millions of ignition sources come into being after the spontaneous combustion of diesel fuel, then ignite NG pre-mixture. Dual-fuel engines have the characteristics both premixed combustion of gasoline engines and diffusion combustion of diesel engines. LNG-diesel dual-fuel engine has been received more and more attention for its advantages such as good emission performance, convenient modification and flexible usage [2].

Experimental set-up

Experimental apparatus. Layout for tests on the engine is shown in Fig. 1. The dual-fuel engine is modified by YC6J270-30 diesel engine. The main characteristics of engine are shown in Table 1.

Electronically controlled LNG fuel delivery system is equipped on the original diesel engine, to control the injection parameters accurately. LNG delivery system is composed of cylinder for LNG, vaporizer, pressure regulator, buffer tank, safety valve, injector and mixer. Nature gas mixes with fresh air in the mixer and intake manifold, and finally enters into the engine cylinder. The pilot diesel to ignite the NG-air charge is injected to the cylinder before TDC and ignited in compression stroke, then the flame spread throughout all fuel-air mixture.

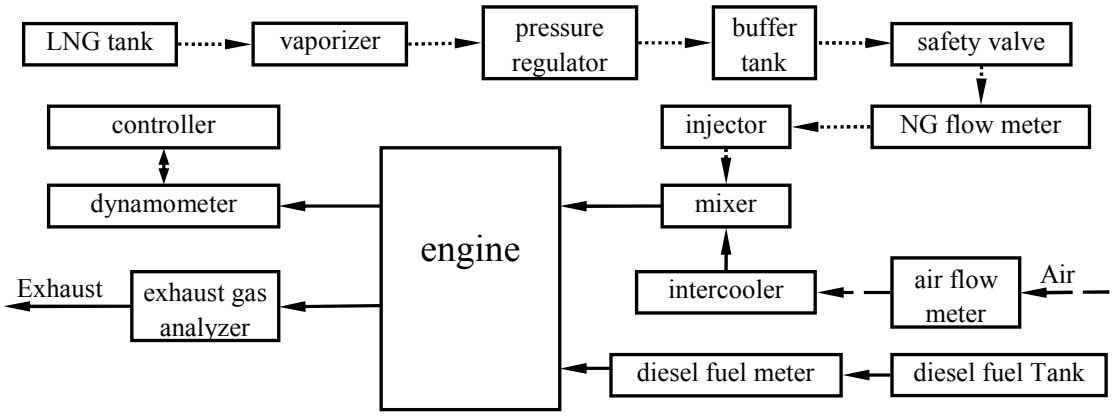

Fig. 1 Layout for the tests

Table 1 Engine characteristics

Model	YC6J270-30
Type	Vertical in-line, Water-cooled, 4 stroke, Electronic control, Direct injection
Bore [mm]×Stroke [mm]	105×125
Compression ratio	17.0:1
Number of cylinders	6
Displacement [L]	6.49
Intake way	Turbo-charging, Inter-cooling
Electronic control system	High pressure, Common rail
Rated power/speed [kW/r/min]	199/2500
Rated torque/speed [N·m/r/min]	950/1200-1700

Experimental procedure. Engine performance tests were conducted on a direct-injection dual-fuel engine with electronic control. The inlet air temperature is controlled at 40˚C. Measurements are taken at three different engine speeds of 1200 r/min, 1600 r/min and 2200 r/min, and twelve different engine loads corresponding to 10%, 20%, 25%, 30%, 35%, 40%, 50%, 60%, 70%, 80%, 90% and full load. At a constant engine speed, an effort has been made to keep the pilot diesel fuel constant, while the load ratio of dual-fuel engine is adjusted by the amount of LNG fuel until the desired load ratio is obtained. The values of load ratio, engine speed, consumption of LNG and diesel and the emissions of CO, HC and NOx were recorded at different operation conditions. By analyzing experimental data, the effects of load ratio on performance and emissions of dual-fuel engine can be studied.

Data processing. When the engine is fuelled with LNG-diesel dual-fuel, the fuel consumption consists of diesel consumption and LNG consumption. The LNG consumption is commuted to diesel consumption according to the low calorific value [3], so the overall dual-fuel consumption is given by:

$$m_{df} = m_d + \frac{H_{uNG}}{H_{ud}} \times m_{NG}. \quad (1)$$

where m_{df} is the consumption of dual-fuel, m_{NG} is the consumption of NG, H_{uNG} is the low calorific value of NG (49.54 MJ/kg), m_d is the consumption of diesel, and H_{ud} is the low calorific value of diesel (42.50 MJ/kg).

The specific fuel consumption of dual-fuel engine refers to the fuel consumption of unit effective power [4], given by:

$$b_e = \frac{m_{df}}{P_e} \times 10^3. \quad (2)$$

where P_e is the effective power.

Results and discussion

Fuel consumption. For the load characteristics at 1200r/min, 1600r/min and 2200r/min, the specific fuel consumption of LNG-diesel dual-fuel is shown in Fig. 2. When the load ratio is larger than 40 %, the specific fuel consumption of dual-fuel is reduced slightly with the increase of load, and its value is relatively low. However, when the load ratio is less than 40 %, the specific fuel consumption is increased significantly as the load ratio reduces.

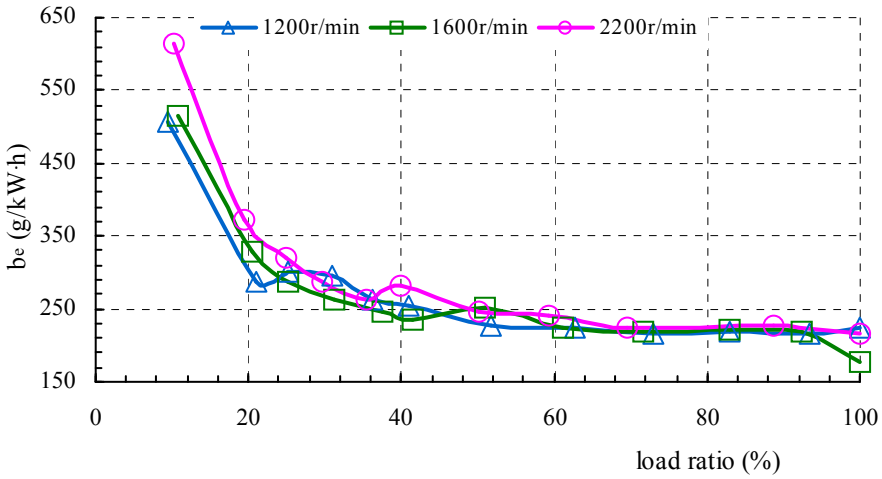

Fig. 2 The fuel consumption of the load characteristics

The concentration of NG-air mixture is low due to the less NG supply when the load ratio is less than 40 %. The NG-air mixture is not completely burned as the flame is missing in some places. Dual-fuel engine's combustion efficiency is low. The concentration of NG-air mixture is low due to the less NG supply when the load ratio is less than 40 %. The NG-air mixture is not completely burned as the flame is missing in some places. Dual-fuel engine's combustion efficiency is low. Therefore, the specific fuel consumption of dual-fuel increases rapidly with the reduction of load ratio. At middle and high loads, the reduction of the specific fuel consumption is determined by the mixture concentration and the high temperature in cylinder. As a result of the good quality of NG-air mixture and high efficiency of dual-fuel, the specific fuel consumption of dual-fuel is low at middle and high loads.

CO emission. For the load characteristics at 1200r/min, 1600r/min and 2200r/min, the CO emission of LNG-diesel dual-fuel is shown in Fig. 3. At middle and low loads, the CO emission of dual-fuel is reduced with the increase of load ratio. But at high loads and full load, the CO emission of dual-fuel is increased slightly.

CO is a kind of combustion intermediate product, and CO emission is mainly controlled by chemical reaction mechanism of fuel. The creation of CO is related to the mixture concentration and fuel composition. The change in CO emission is the result of the two factors that exert effects at the same time. When the engine is fuelled with dual-fuel, NG pre-mixture is too lean to burn completely at low loads, the flame can not spread throughout the whole combustion chamber because of the low flame spread speed. What is more, CO can not be oxidized as a result of the low combustion temperature in cylinder. In consequence, CO emission of dual-fuel is high at low loads. With the increase of load ratio, the NG-air mixture becomes richer, and so the possibility of incomplete combustion becomes less. Combustion process can be extended to the whole combustion chamber. On the other hand, exhaust temperature increases gradually as the load ratio increases, to oxidize CO into CO_2. Therefore, the LNG-diesel dual-fuel engine's CO emission is sharply reduced. At high loads and full load, the increase of CO emission of dual-fuel is due to the absent oxygen occurs in some areas during combustion period.

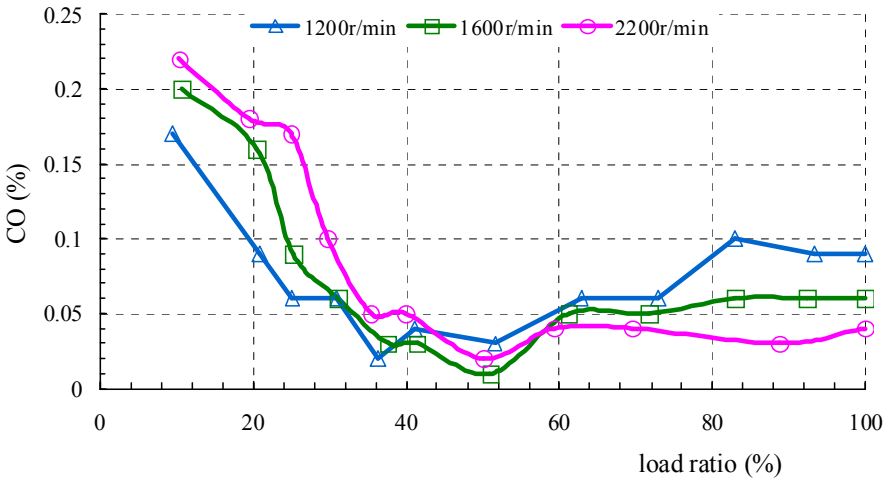

Fig. 3 The CO emission of the load characteristics

HC emission. For the load characteristics at 1200r/min, 1600r/min and 2200r/min, the HC emission of LNG-diesel dual-fuel is shown in Fig. 4. When the load ratio is less than 40 %, HC emission of dual-fuel is reduced significantly with the increase of load. But it increases when load ratio continues to increase, and finally HC emission is stable.

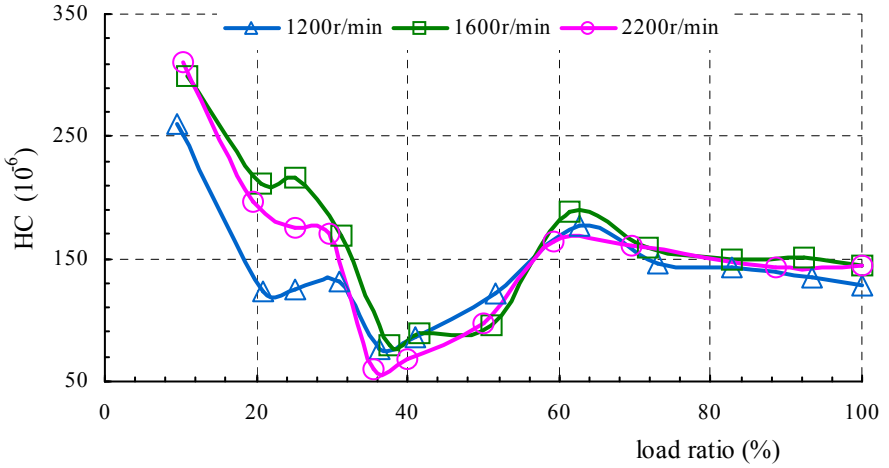

Fig. 4 The HC emission of the load characteristics

HC emission is mainly derived from incomplete combustion, quenching areas near the combustion chamber walls and the narrow crevices between piston top and cylinder. HC is a product of incomplete combustion. At low loads, NG and diesel gotten into the cylinder are few, mixture is too lean to make the flame rapidly spread throughout the combustion chamber, which leads to the high unburned HC emission of dual-fuel engine. With the increase of load ratio, HC emission of dual-fuel is reduced sharply, which is caused by three key factors: the first is that the mixture becomes richer, which improves the combustion conditions and gets high combustion efficiency; the second is that the thickness of quenching areas near the combustion chamber walls reduces slightly; and the third is that the rise of combustion temperature in cylinder makes the unburned HC completely oxidized. When load ratio is larger than 40%, HC emission increases because the NG-air mixture is directly scavenged to outside from cylinder in the overlap period, and the NG mixture can not be completely burned as the flame is missing in some places, what's more, the NG-air mixture in the narrow crevices between the piston top and cylinder and near the combustion chamber walls is difficult to burn [5].

NOx emission. For the load characteristics at 1200r/min, 1600r/min and 2200r/min, the NOx emission of LNG-diesel dual-fuel is shown in Fig. 5. When the load ratio is less than 40 %, the NOx emission of dual-fuel is relatively low. As the load ratio increases, NOx emission is increased sharply. But at high loads and full load, it reduces slightly.

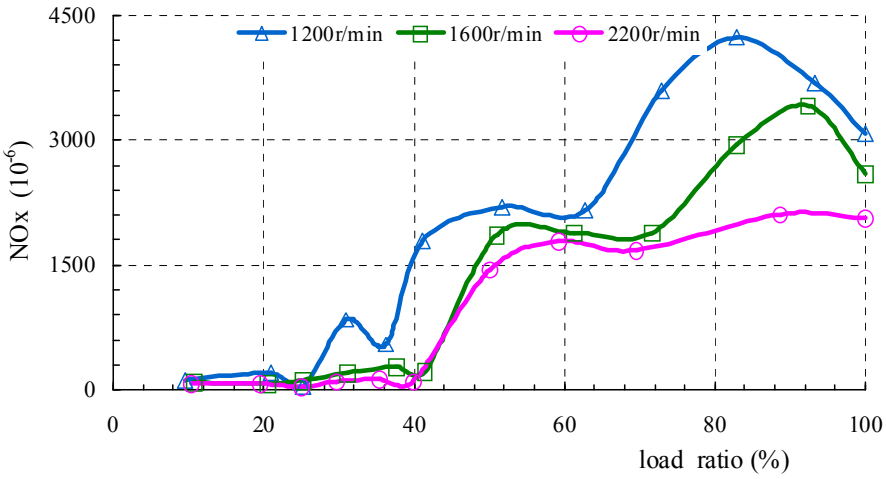

Fig. 5 The NO_X emission of the load characteristics

The formation of NOx is determined by the combustion temperature, the mixture concentration and the reaction duration. At low loads, excess air coefficient is large. Although there is plenty of oxygen in NG-air mixture, the combustion temperature in cylinder is low. Thus, the LNG-diesel dual-fuel engine’s NOx emission is low. As the load increases, the supply of LNG increases, resulting in good quality of the mixture and high combustion efficiency of dual-fuel. High pressure and combustion temperature in cylinder contribute to the formation of NOx. Therefore, NOx of dual-fuel is increased rapidly when the load ratio is larger than 40%. At high loads and full load, despite of the higher maximum combustion temperature, oxygen in mixture is too few to produce NOx. Therefore, the LNG-diesel dual-fuel engine’s NOx emission is reduced slightly.

Conclusions

1) With the increase of load ratio, the specific fuel consumption of dual-fuel reduces at different speeds.
2) At middle and low loads, the CO emission of dual-fuel is reduced with the increase of load ratio. But at high loads and full load, the CO emission is increased slightly.
3) When the load ratio is less than 40%, the LNG-diesel dual-fuel engine’s HC emission is reduced significantly with increase in the load. But it increases when load ratio continues to increase, and finally HC emission is stable.
4) When the load ratio is less than 40%, the NOx emission of dual-fuel is relatively low. As the load ratio increases, the NOx emission is increased sharply. But at high loads and full load, it reduces slightly.

References

[1] Carlucci. Antonio P., Laforgia. Domenico, Saracino. Roberto: Energy Conversion and Management. Vol.52 (2011), p.3004

[2] Mingfa Yao, Ning Huang, Jiaxiu Duan: Transaction of CSICE. Vol.4 (2003), p.211

[3] Chunhua Zhang: Journal of Chang’an University (Natural Science Edition). Vol.22 (2002), p.77

[4] Jinzhu Chen, Chunhua Zhang, Junzhi Liao: Journal of Chang’an University (Natural Science Edition). Vol.30 (2010), p.99

[5] Chunhua Zhang, Yaozhang Bian, Junzhi Liao: Proceedings of the Institution of Mechanical Engineers, Part D: Journal of Automobile Engineering. Vol.219 (2005), p.207

Advanced Materials Research Vols. 960-961 (2014) pp 1394-1399

doi:10.4028/www.scientific.net/AMR.960-961.1394

Experimental Study of the Spray Characteristics of n-Butanol/Diesel Blends

Jian Wu[1,2], Lili Zhu[1,a], Zhancheng Wang[1], Bin Xu[1,*] and Hongming Wang[1]

[1]College of Vehicle & Motive Power Engineering, Henan University of Science and Technology, Luoyang 471003, China

[2]State Key Laboratory of Motor Vehicle Biofuel Technology, Nanyang 473000, China

[a]zhulilihekeda2013@163.com

Keywords: Ambient pressure; Injection pressure; Spray penetration; Spray cone angle; Spray area

Abstract: we studied the spray characteristics of n-butanol/diesel fuel blends using a high-speed camera and schlieren system, and analyzed the effect of different fuels, ambient pressure and injection pressure conditions on the spray penetration, spray cone angle, spray area, et al. The results showed that, at the same injection pressure, as the increase of ambient pressure, the spray cone angle of the same volume of fuel increases gradually, the spray penetration and the spray area decreases; under the same ambient pressure, the spray penetration, spray cone angle and spray area increase gradually with the increasing injection pressure, but when the injection pressure increases enough, the parameters are roughly the same; and the parameters basically all increase with the adding of n-butanol.

Introduction

With the increase of car ownership, energy crisis and environment pollution are the main problems that we are facing. Recent years, alternative fuel in the aspect of energy conservation and emissions reduction aspect has made abundant research results [1]. Renewable alcohol fuel is considered to be one of the effective ways to reduce engine emissions, and n-butanol is more and more applied in experimental study [2]. Spray characteristics have a direct impact on engine combustion and emissions. The text is experimental study on spray characteristics of n-butanol/diesel blends through the spray penetration, spray cone angle and spray area [3].

Experimental Equipment and Process

The experimental equipment is shown in Fig.1. It includes fuel injection device, constant volume combustion bomb, schlieren system and a high-speed camera.

The experiment used n-butanol/diesel blends with volume scores of n-butanol are 5% (N5), 10% (N10) and 20% (N20); the motor

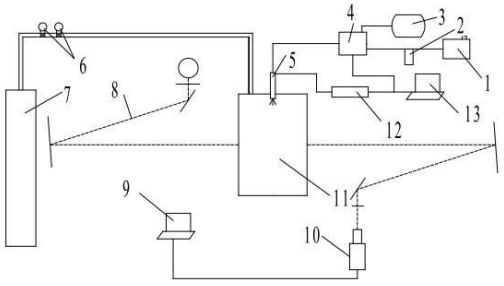

Fig. 1. Experimental device schematic diagram.
1.Oil tank 2.Filter 3.Motor 4.Fuel injection pump 5.Fuel injector 6.Pressure gauge 7.Nitrogen cylinder 8.Schlieren system 9.Computer 10.A high-speed camera 11.Constant volume combustion bomb 12.Fuel injection control unit 13.Computer

speed is 800r/min, the ambient pressure is 1MPa, 2MPa and 3MPa; the volume of the injected fuel is 14mm^3 and 24mm^3, and the corresponding injection pressure is 70MPa, 80MPa, 90MPa and 110MPa, 120MPa, 130MPa. The process of spray is recorded by a high-speed camera (the shooting speed is 1000 frames per second), we dispose the pictures through MATLAB program, and get the spray penetration, spray cone angle and spray area of each picture, then analyze the changing rule of spray characteristics at different conditions[4].

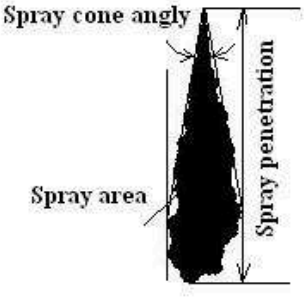

Fig. 2 The spray structure schematic diagram.

Experimental Results and Analysis

At present, the macroscopic parameters of spray characteristics have no unified standard in the word[5]. In this paper, in order to deal with spray images conveniently through using MATLAB program, the spray penetration, spray cone angle and spray area are definite as shown in figure 2 (the black region is the spray area).

The Influence of Ambient Pressure on the Spray Characteristics

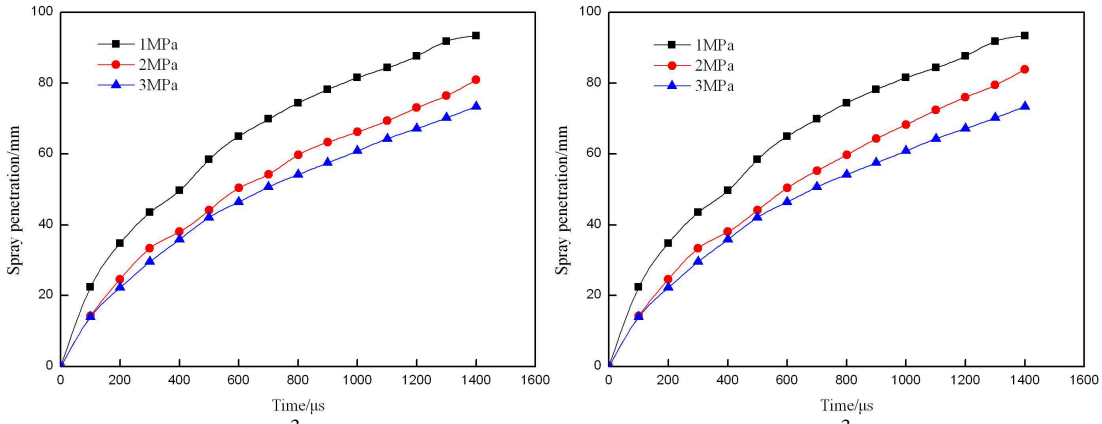

(a)14mm^3 80MPa (b)24mm^3 120MPa

Fig. 3 The spray penetration of N20 under different ambient pressure.

The changing curve of spray penetration of the same volume of N20 at different ambient pressure is shown in figure 3. As we can see from graph (a), when the injected fuel is 14mm^3 and the injection pressure is 80MPa, the spray penetration of spray evening as the ambient pressure is 1MPa is 12mm longer than that as the ambient pressure is 2MPa, and 17mm longer then that as the ambient pressure is 3MPa, obviously, the effect of ambient pressure on spray penetration is bigger. With the increase of ambient pressure, the spray penetration decreases gradually, and the trend is more obvious in the spray evening. It is because that, as the increasing ambient pressure, the density of environmental media is also increases, so the resistance that the spray faced is more larger[6]; as the spray beginning, the liquid drop is bigger and the speed is higher, so the resistance is relatively smaller, on the contrary, more closer to the spray evening, the effect of the resistance is more larger.

The changing curve of spray cone angle of the same volume of N20 at different ambient pressure is shown in Fig. 4. From graph (a) and (b), we can see that, under a certain injection pressure, the spray cone angle of the same volume fuel increases as the increasing ambient pressure, and this trend is more obvious in graph (b). Under the same condition, when the spray penetration is longer, the lateral average diameter is generally smaller. When the volume of injected fuel is 24mm^3 and the injection pressure is 120MPa, the pressure difference of the both ends of the injection nozzle is larger, the speed of spray beginning is higher, as the increasing ambient pressure, the density of

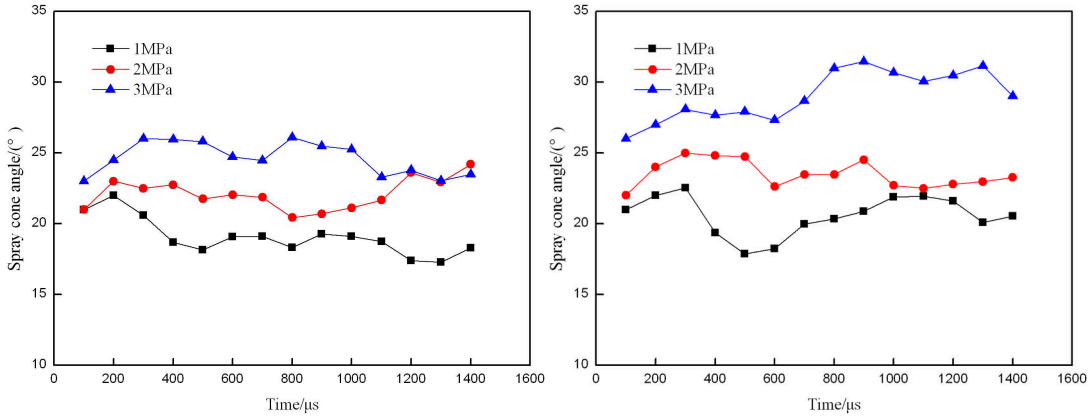

(a)14mm^3 80MPa (b)24mm^3 120MPa

Fig. 4 The spray cone angle of N20 under different ambient pressure.

environmental media is increases, the interaction of liquid drops and surrounding gas enhances, the entrainment effect caused at the external rim of the spray also enhances, so, the trend that the spray cone angle increases with the increasing ambient pressure is more obvious [7].

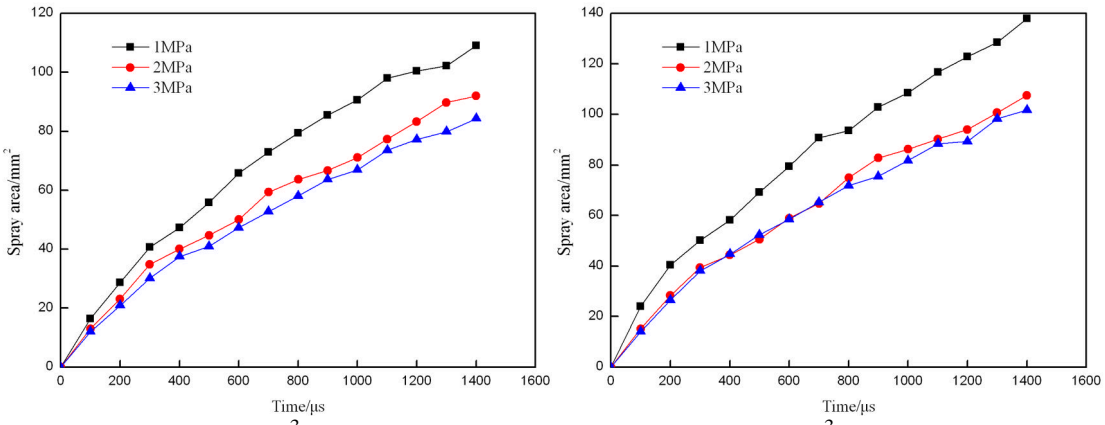

(a)14mm^3 80MPa (b)24mm^3 120MPa

Fig. 5 The spray cone area of N20 under different ambient pressure.

The changing curve of spray area of the same volume of N20 at different ambient pressure is shown in Fig. 5. When the injection pressure is 80MPa, the speed of spray beginning is lower, the kinetic energy exchanged with the surrounding gas is lesser, so the effect of the changing gas density is larger. When the injection pressure is 120MPa, the speed of spray beginning is higher, the exchange of kinetic energy with the surrounding gas increases, entrainment effect enhances, the spray cone angle increases and the spray area also increases, the phenomenon is shown in graph (b).

The Influence of Injection Pressure on the Spray Characteristics

Fig. 6 shows the changing of spray penetration of the same volume of N20 at different injection pressure as the ambient pressure is 2MPa. From the figure, with the increase of injection pressure, the spray penetration of the same volume of fuel increases and the changing trend is basically consistent; when the injection pressure increases enough, the spray penetration is roughly constant. As shown in graph (a), within a certain range, as the injection pressure increases, the speed of spray beginning also increases, the influence of the surrounding media is weaker, the spray penetration corresponding enlarges; when the injection pressure increases enough, the speed of spray beginning is higher, the exchange of kinetic energy with the surrounding gas increases, the influence of the surrounding media enhances, consequently, the increase of the spray penetration slows down, so the result is shown as in graph (b), the spray penetration of the same volume of fuel is roughly constant as the increase of injection pressure[8].

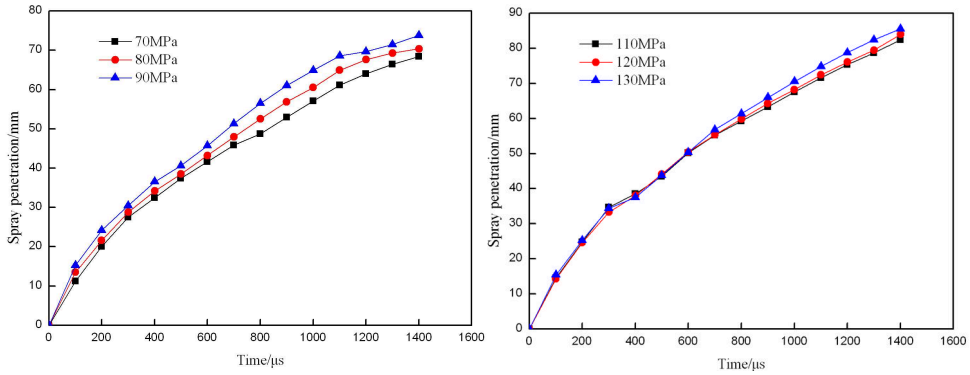

(a)14mm^3 (b)24mm^3

Fig. 6 The spray penetration of N20 under different injection pressure.

Fig. 7 shows the changing of spray cone angle of the same volume of N20 at different injection pressure as the ambient pressure is 2MPa. As shown in figure (a), the spray cone angle increases with the increase of injection pressure, but the difference is small; As shown in figure (b), the spray cone angle as the injection pressure is 120MPa is slight larger than that as 110MPa, but basically consistent with that as 130MPa. From the analysis in Fig. 6, within a certain range, as the injection pressure increases, the kinetic energy of liquid drops increases, the exchange of kinetic energy with the surrounding gas enhances, the atomization quality improves, the spray penetration corresponding enlarges; when the injection pressure increases enough, the entrainment effect caused at the external rim of the spray further enhances, the atomization quality further improves, the Sauter mean diameter (SMD) of liquid drops decreases, the drops are easy to evaporate, and the spray penetration decreases slightly [9].

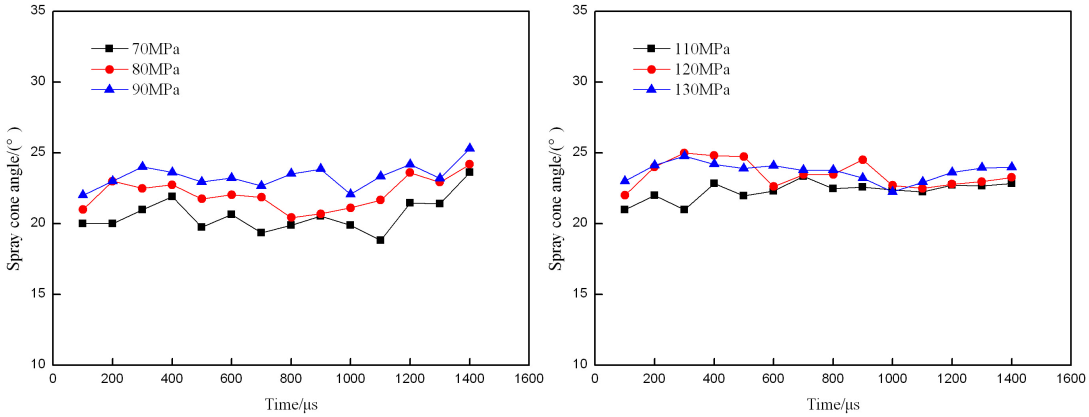

(a)14mm^3 (b)24mm^3

Fig. 7 The spray cone angle of N20 under different injection pressure.

Fig. 8 shows the changing of spray area of the same volume of N20 at different injection pressure as the ambient pressure is 2MPa. When the volume of injected fuel is 14mm^3, the spray area increases with the increase of injection pressure, but the difference is small; when the volume of injected fuel is 24mm^3, the changing trend of spray area under the different injection pressure is the same and the changing curve is basically coincident. From the analysis in figure 6 and 7, when the injection pressure is lower, the exchange of kinetic energy with the surrounding gas is lesser, the changing trend of spray area is basically consistent with that of spay penetration; when the injection pressure is higher, the entrainment effect is stronger, so the changing trend of spray area is basically consistent with that of spay cone angle.

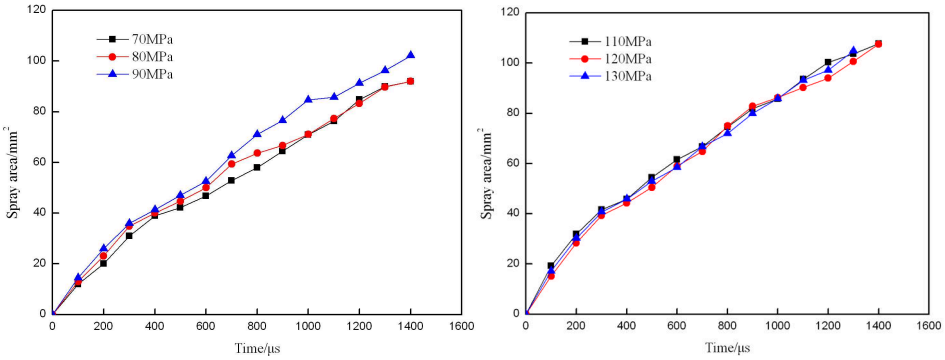

(a)14mm^3 (b)24mm^3

Fig. 8 The spray area of N20 under different injection pressure.

The Influence of Different Mixing Proportions of Fuel on the Spray Characteristics

To the different fuel, the difference of spray characteristics mainly depends on the difference of the physical property parameter, the parameters include density, surface tension, viscosity and volatility. The physical property parameter is shown in table 1. From the table, we can see that, with the adding of n-butanol ratio, the density, kinematic viscosity and surface tension of the mixing fuel decrease gradually, but the rangeability of density and surface tension is small.

The changing curve of spray characteristics of different fuel as the ambient pressure is 2MPa, the volume of injected fuel is 24mm^3 and the injection pressure is 120MPa is shown in Fig. 9. In the figure, with the adding of n-butanol ratio, the spray penetration and spray area increase gradually, the spray cone angle of N10 is larger than that of N5 and close to that of N20.

We know that the density difference of the three fuel is tiny, so the change of kinetic energy caused by density is small and the corresponding change of spray penetration is also small; but higher viscosity and surface tension make the resistence of the fuel received in the nozzle hole enlarge, the speed of the spray beginning decreases, then the spray penetration also decreases. So the spray penetration increases with the adding of n-butanol [10].

Tab. 1 The physical property parameter of each fuel

Items	N5	N10	N20
Density/×10^3·kg·m^{-3}	0.857	0.854	0.849
Kinematic viscosity(25℃)/ mm^2·S^{-1}	4.54	4.36	3.70
Surface tension(20℃)/ mN·m^{-1}	26.85	26.27	25.88

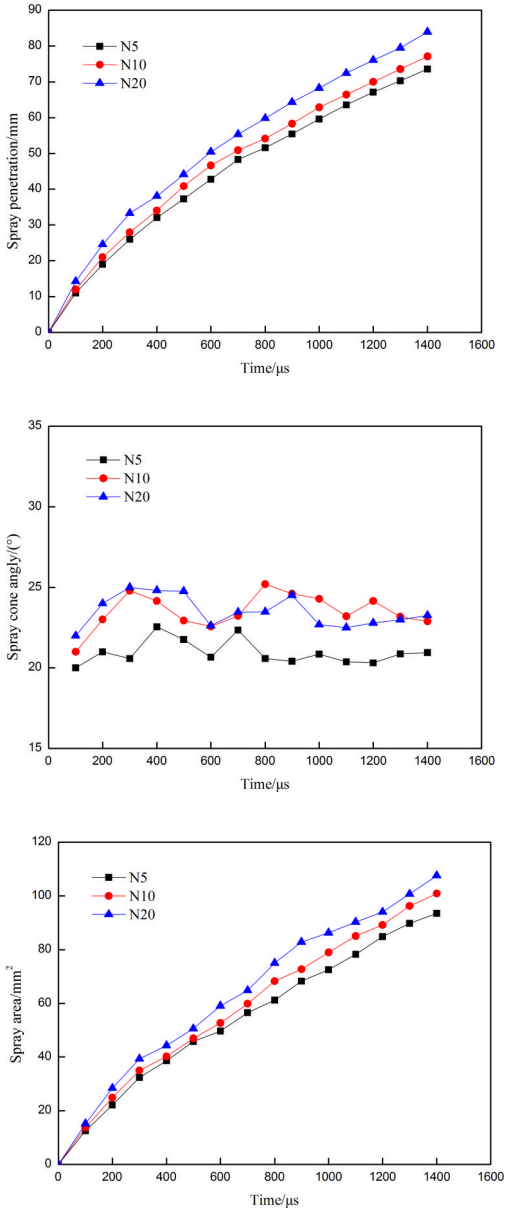

Fig. 9 The spray characteristics of different fuel.

In normal conditions, larger the viscosity and surface tension, the liquid drops will more hard break, the spray cone angle will be smaller. With the increase of n-butanol, the viscosity and surface tension decrease gradually, the drops break more easily, the mixture with surrounding gas is better, the spray cone angle is bigger; the atomization of N20 is better, the SMD is smaller, the drops is easier to evaporate, the spray cone angle corresponding decreases [11].

The spray area is the integrated embodiment of spray penetration and spray cone angle. From the analysis above, we know that, with the adding of n-butanol, the spray area increases, the mixture of spray and surrounding gas is better, the atomization quality is better.

Conclusions

(1) The influence of ambient pressure on the spray characteristics of N20 is larger. Under a certain injection pressure, as the increasing ambient pressure, the spray cone angle of the same volume of N20 increases gradually, but the spray penetration and spray area decrease gradually.

(2) The influence of injection pressure on the spray characteristics of N20 is smaller. Under the same ambient pressure, with the increasing injection pressure, the spray penetration, spray cone angle and spray area increase gradually, but when the injection pressure increases enough, the parameters are roughly the same.

(3) With the adding of n-butanol ratio, the spray penetration, spray cone angle and spray area basically increase gradually, but the spray cone angle of N10 is close to that of N20.

* Fund project: supported by the State Key Laboratory of Motor Vehicle Biofuel Technology (2013019) .

Reference

[1] Wu Jian, Xu Bin, et al. Experimental Analysis of Spray Performances of Ethanol-diesel Blends[J]. Journal of Agricultural Mechanization Research, 2010, 32(2): 195-198.

[2] ZHOU Tingbo. An Experimental Study on Diesel Engine Combustion and Emissions with Butanol-Diesel Blend Fuels. Changsha University of Science & Technology, 2009.

[3] Chen H, Shuai S J, Wang J X. Spray characteristics of ethanol, diesel and their blended fuels[J]. Journal of Combustion Science and Technology, 2005, 11(5): 46-469.

[4] DU Bao-guo, LONG Wu-qiang, et al. Study on Multi-Piece Spray Characteristics Based on Matlab Digital Image Processing Technology[J]. Chinese Internal Combustion Engine Engineering, 2008, 29(4): 1-5.

[5] LIU Jun-jie, WU Zhi-jun, et al. Research on Ethanol/Gasoline Spray Chatacteristics[J]. Journal of Jiamusi University, 2011, 29(3): 321-325.

[6] ZHAO Xiao-wei, HAN Xiu-kun, et al. Experimental Study on Spray Characteristics of Bio-Diesel Oil[J]. Chinese Internal Combustion Engine Engineering, 2008, 29(1): 16-19.

[7] Gao Jian D M, Huang Z H, "Spray Properties of Alternative Fuels: A Comparative Analysis of Ethanol-gasoline Blends and Gasoline." Fuel, vol. 86, pp. 1645-1650, December 2007.

[8] Zhao Luming, He Xu, et al. Spray Characteristics of Biodiesel under High Injection Pressure[J]. Transactions of the Chinese Society of Agricultural Machinery, 2012, 43(9): 6-10.

[9] ZHANG Deng-pan, YUAN Yin-nan, et al. Experimental Study on Bio-Diesel Free Spray[J]. Chinese Internal Combustion Engine Engineering, 2010, 31(6): 13-16.

[10] HE Bang-quan, DU Cheng-jun. Spray Characteristics of Various Alcohol-Gasoline Blends[J]. Journal of Combustion Science and Technology, 2012, 18(4): 301-308.

[11] ZHANG Xu-sheng, LI Li-guang, et al. An Experimental Study of Bio-Diesel Spray Characteristics[J]. Transactions of CSICE, 2007, 25(2): 172-176.

Advanced Materials Research Vols. 960-961 (2014) pp 1400-1403

doi:10.4028/www.scientific.net/AMR.960-961.1400

Extreme Learning Machine for Fault Diagnosis of Rotating Machinery

Rui Yu[1, a], Rui Xiang[1, b], Shiwei Yao[1]

[1]Lab. on Steam Power System, Wuhan Second Ship Des. & Res. Ins., Wuhan 430064, China

[a]yur04@163.com, [b]xiangrui_hit@163.com

Keywords: Rotating machinery, Fault diagnosis, Extreme learning machine

Abstract. The authors present extreme learning machine (ELM) as a novel mechanism for diagnosing the faults of rotating machinery, which is reflected from the power spectrum of the vibration signals. Extreme learning machine was originally developed for the single-hidden layer feedforward neural network (SLFN) and then extended to the 'generalized' SLFN. We obtained the fault feature table of rotating machinery by wavelet packet analysis of the power spectrum, then trained and diagnosed the fault feature table with extreme learning machine. Diagnostic results show that the extreme learning machine method achieves higher diagnostic accuracy than the probabilistic neural network (PNN) method, exhibiting superior diagnostic performance. In addition, the diagnosis of fault feature table adding noise signal indicates the extreme learning machine method provides satisfactory generalization performance.

Introduction

Extreme learning machine (ELM) is a new algorithm overcoming the inherent shortcomings of traditional single-hidden layer feedforward neural network (SLFN). The new algorithm randomly chooses the input weights and the thresholds without adjustment during the training process and tends to provide faster learning speed and better generalization performance than traditional training methods. In this study, we extract the feature vectors of rotating machinery faults by wavelet packet analysis and diagnose the faults with extreme learning machine, obtaining satisfactory diagnostic results.

Extreme learning machine

For N arbitrary distinct samples $(\boldsymbol{x}_i, \boldsymbol{t}_i)$, where $\boldsymbol{x}_i=[x_{i1}, x_{i2}, ..., x_{in}]^T \in \mathbf{R}^n$, $\boldsymbol{t}_i=[t_{i1}, t_{i2}, ..., t_{in}]^T \in \mathbf{R}^m$; standard SLFNs with L hidden neurons and activation function $g(x)$ are mathematically modeled as

$$\boldsymbol{o}_j = \sum_{i=1}^{L} \beta_i g_i(\boldsymbol{x}_j) = \sum_{i=1}^{L} \beta_i g(\boldsymbol{w}_i \cdot \boldsymbol{x}_j + b_i), \quad j=1, 2, ..., N. \tag{1}$$

where $\boldsymbol{w}_i=[w_{i1}, w_{i2}, ..., w_{in}]^T$ is the weight vector connecting the ith hidden neuron and the input neurons; $\beta_i=[\beta_{i1}, \beta_{i2}, ..., \beta_{in}]^T$ is the weight vector connecting the ith hidden neuron and the output neurons; b_i is the threshold of the ith hidden neuron; $\boldsymbol{w}_i \cdot \boldsymbol{x}_j$ denotes the inner product of $\boldsymbol{w}_i$ and $\boldsymbol{x}_j$.

That standard SLFNs with L hidden neurons and activation function $g(x)$ can approximate these N samples with zero error means, i.e., there exist β_i, $\boldsymbol{w}_i$ and b_i such that

$$\sum_{i=1}^{L} \beta_i g(\boldsymbol{w}_i \cdot \boldsymbol{x}_j + b_i) = \boldsymbol{t}_j, \quad j=1, 2, ..., N. \tag{2}$$

The above N equations can be written compactly as:

$$\boldsymbol{H}\beta = \boldsymbol{T}. \tag{3}$$

where

$$\boldsymbol{H}(\boldsymbol{w}_1,\cdots,\boldsymbol{w}_L,b_1,\cdots,b_L,\boldsymbol{x}_1,\cdots,\boldsymbol{x}_N)=\begin{bmatrix} g(\boldsymbol{w}_1\cdot\boldsymbol{x}_1+b_1) & \cdots & g(\boldsymbol{w}_L\cdot\boldsymbol{x}_1+b_L) \\ \vdots & \cdots & \vdots \\ g(\boldsymbol{w}_1\cdot\boldsymbol{x}_N+b_1) & \cdots & g(\boldsymbol{w}_L\cdot\boldsymbol{x}_N+b_L) \end{bmatrix}_{N\times L}. \tag{4}$$

$$\beta=\begin{bmatrix} \beta_1^T \\ \vdots \\ \beta_L^T \end{bmatrix}_{L\times m} \text{ and } \boldsymbol{T}=\begin{bmatrix} \boldsymbol{t}_1^T \\ \vdots \\ \boldsymbol{t}_N^T \end{bmatrix}_{N\times m}. \tag{5}$$

$\boldsymbol{H}$ is called the hidden layer output matrix of the SLFN; the ith column of $\boldsymbol{H}$ is the ith hidden neuron's output vector with respect to inputs $\boldsymbol{x}_1, \boldsymbol{x}_2, \ldots, \boldsymbol{x}_N$.

The gradient descent algorithms are generally used in traditional SLFNs to search the minimum of $\|\boldsymbol{H}\beta-\boldsymbol{T}\|$. However, it is clear that gradient descent based learning methods are generally very slow due to improper learning steps or may easily converge to local minimums [1]. To solve these problems, Huang et al. have proposed a simple learning algorithm for SLFNs called extreme learning machine (ELM) [2].

Unlike the traditional function approximation theories, which require to adjust input weights and hidden layer biases, the feedforward networks with arbitrarily assigned input weights and hidden layer biases and with almost all nonzero activation functions can universally approximate any continuous functions on any compact input sets. The input weights and the hidden layer biases of SLFNs need not be adjusted at all and can be arbitrarily given. For fixed input weights $\boldsymbol{w}_i$ and the hidden layer biases b_i, to train an SLFN is simply equivalent to finding a least-squares solution of the linear system $\boldsymbol{H}\beta=\boldsymbol{T}$:

$$\left\|\boldsymbol{H}(\boldsymbol{w}_1,\cdots,\boldsymbol{w}_L,b_1,\cdots,b_L)\hat{\beta}-\boldsymbol{T}\right\|=\min_{\beta}\left\|\boldsymbol{H}(\boldsymbol{w}_1,\cdots,\boldsymbol{w}_L,b_1,\cdots,b_L)\beta-\boldsymbol{T}\right\|. \tag{6}$$

The smallest norm least-squares solution of the above linear system is:

$$\hat{\beta}=\boldsymbol{H}^{\dagger}\boldsymbol{T}. \tag{7}$$

where $\boldsymbol{H}^{\dagger}$ is the *Moore–Penrose generalized inverse* of output matrix $\boldsymbol{H}$. This special solution have the properties of the minimum training error, smallest norm of weights and best generalization performance [3].

The learning speed of ELM can be thousands of times faster than traditional feedforward network learning algorithms like back-propagation algorithm while obtaining better generalization performance.

Extraction of Fault Features

The wavelet packet analysis, an improved method of wavelet transform, can decompose the signal into different frequency bands, belonging to band analysis techniques. As same as Fourier spectrum analysis, the theoretical basis of wavelet band analysis is Parseval energy integral equation. The energy of *f(x)* on the time domain is

$$\|f\|^2=\int_{-\infty}^{\infty}|f(x)|^2\,dx. \tag{8}$$

And the wavelet transform of *f(x)* is

$$C_{j,k} = W(2^j, 2^j k) = 2^{-\frac{j}{2}} \int_R \overline{\Psi}(2^{-j}x - k) f(x) dx \,. \tag{9}$$

According to Paseral identity,

$$\int_{-\infty}^{\infty} |f(x)|^2 \, dx = \sum_{k=1}^{n} |C_{j,k}|^2 \,. \tag{10}$$

From the above equation, the wavelet transform coefficients $C_{j,k}$ has the dimension of energy, and therefore can be used for energy analysis.

Current study on fault diagnosis of rotating machinery has been in-depth and comprehensive that the feature vectors of power spectrum from rotating machinery vibration signal can be easily and effectively extracted by multi-resolution analysis [4]. And the wavelet packet analysis is applied to the energy analysis on the common faults of rotating machinery.

The peak energy values of nine different frequency bands extracted from the vibration signals of rotating machinery are selected as the features [5]. We can obtain a variety of fault characteristics after a lot of experiments and establish the correspondence between the faults and features. The correspondence between the features and six common faults of rotating machinery, such as misalignment, is gathered as shown in Table 1.

Table 1 Fault feature table of rotating machinery

Fault Type	Vibration Frequency								
	0.01~ 0.39f	0.40~ 0.49f	0.50f	0.51~ 0.99f	1f	2f	3~5f	odd f	>5f
Imbalance	0	0	0	0	0.9	0.05	0.05	0	0
Rotor impact	0	0.3	0.1	0.6	0	0	0	0	0
Misalignment	0	0	0	0	0.4	0.50	0.10	0	0
Oil whirl	0.1	0.8	0	0.1	0	0	0	0	0
Radial rubbing	0.1	0.1	0.1	0.1	0.2	0.1	0.1	0.10	0.1
Pedestal looseness	0	0	0	0	0.2	0.15	0.4	0	0.25

Diagnostic results

To verify the diagnostic accuracy of ELM for common faults of rotating machinery, we adopt probabilistic neural networks (PNN) and ELM for training and judgment of fault features. First, the diagnostic models are trained with the fault feature samples. Then, we diagnose the faults by the trained models.

Let D_1 be the data matrix of fault samples before adding noise, and D_2 be the data matrix of fault samples after adding noise. The data matrix containing noise is obtained by the following formula

$$D_2(i, j) = D_1(i, j)\left(1 + \alpha \cdot \text{rand}(1)\right). \tag{11}$$

where α is the noise control coefficient; rands(1) is a function that generates a random number between -1 and 1. Five hundred groups of data samples are generated for each fault types by using the above formula such that we obtain a total of 3,000 groups of samples, including 1800 groups as the training set and 1200 groups as the test set.

The noise control coefficients are set in a range from 0 to 0.4 at intervals of 0.01. We train the ELM and PNN models with the training set at each α value, and then diagnose the test set by the trained models. The diagnostic results are shown in Fig. 1.

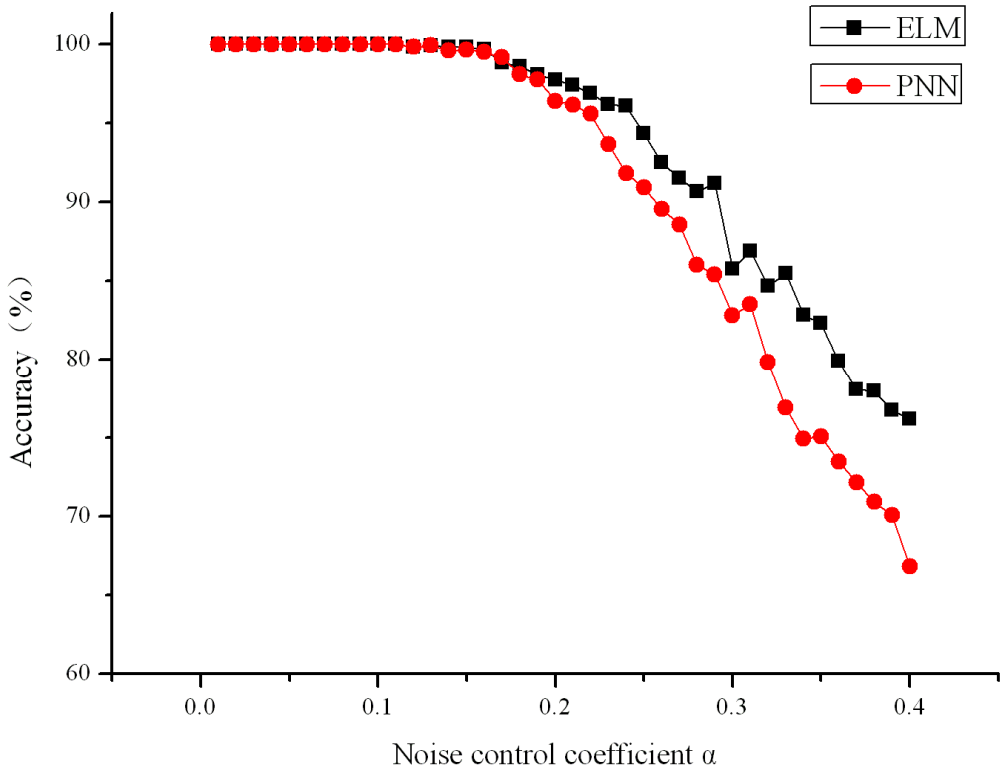

Fig. 1 Diagnostic accuracy of ELM and PNN

It can be seen from Fig. 1 that the diagnostic accuracy of both methods are affected by the noise control coefficient, and decrease with the increase of noise. The declining rate of accuracy in ELM model is significantly lower than PNN model. And the ELM model achieves a higher diagnostic accuracy under an identical noise sample and shows better generalization performance.

Conclusions

In this study, we propose a fault diagnosis method of rotating machinery by using wavelet packet analysis and extreme learning machine. We obtain the fault feature table from the wavelet packet decomposition of power spectrum in the vibration signals of rotating machinery. Then the fault feature table is noised to be the training and test samples. Diagnostic results show that the ELM method achieves higher diagnostic accuracy than the PNN method, exhibiting superior performance to effectively diagnose the faults of rotating machinery.

References

[1] K.Hornik: Neural Networks, Vol. 4 (1991), p. 251

[2] G.-B. Huang, Q.-Y. Zhu and C.-K. Siew, in: *Proceedings of International Joint Conference on Neural Networks* (2004), p. 985

[3] G.-B. Huang, Q.-Y. Zhu, and C.-K. Siew: Neurocomputing, Vol. 70 (2006), p. 489

[4] Yukio I, in: *JSME International Journal, Series C: Dynamics, Control, Robotics, Design and Manufacturing* (1994), p. 237

[5] Logan D, Mathaw J: Mechanical System and Signal Processing, Vol. 10(3) (1996), p. 241

Advanced Materials Research Vols. 960-961 (2014) pp 1404-1410

doi:10.4028/www.scientific.net/AMR.960-961.1404

Numerical Study of the Intake Temperature on Gasoline Engine

Lin-pei HAN[1,a], Wei HONG[1,b], Yan SU[1,c], Fang-xi XIE[1,d], Yun XU[1,e]

[1]State Key laboratory of Automobile Simulation and Control, Jilin University, Changchun, 130025，China

[a]hanlinpei1988@126.com, [b]hongw@jlu.edu.cn, [c]suyan@jlu.edu.cn, [d]xiefx2011@jlu.edu.cn, [e]xuyun@jlu.edu.cn

Keywords: intake temperature, combustion, pumping loss, emissions

Abstract . The optimum inlet temperature for different engine conditions was calculated based on the same knock probability with full load by CFD Fire software, and then the effects of inlet air heated on combustion，pumping loss and emissions of gasoline engine were also studied. The results showed that the highest intake temperature at intake pressure 50kPa operation can be 368K without knock, and that for 100kPa condition was 322K. Heating inlet air can enhance combustion, and the maximum combustion pressure was increased by 26.8% and IMEP by 4% at the case of 368K/50kPa condition compared with inlet pressure of 40.5kPa and temperature of 298K condition consuming same fuel. Pumping loss can also be reduced by increasing intake temperature. However, emissions of NO_X and CO were increased because of higher intake temperature.

Introduction

The most likely condition to exhibit knock for gasoline engine was heavy load. While, it was impossible for light load trapping less air flow to be auto-ignited, and the pressure wave produced after ignition was also not so strong to compress ignition the end un-burn mixture. Although knock can break the stability of engine operation and cause degradation of engine, some studies showed that critical knock condition can improve the power and economy performance of engine without damage[1]. So it is possible for the gasoline engine to get better fuel economy with all engine operation conditions approaching critical knock.

Knock tendency can be enhanced by heating intake in simple but effective ways. It can increase the temperature of mixture in combustion chamber and knock index during later compression stroke and improve combustion and thermal efficiency of engine. At the same time, heating inlet air can cause some abnormal combustion phenomena, such as knock or heavy knock and even HCCI once the inlet air was overheated[2,3]. Therefore, the work in this paper mainly studied the optimum intake air temperature of different engine condition and the effect of intake air temperature on combustion and emission performance by CFD software AVL-FIRE.

Numerical modeling approach

In this paper, the study was based on a 1.8L turbocharged gasoline engine with following geometry and parameters as showed in Table 1. The 3D-model without intake port used to calculate was prepared by reverse engineering and was meshed from intake valves closed timing 230°CA to exhaust valves opened timing 516°CA by the FAME Engine Plus function of FIRE software, which marks top dead centre at exhaust stroke as 0°CA. Figure1 shows the 3D computational mesh of the engine chamber at TDC. The maximum size was 1mm and the minimum was 0.5mm.

Table 1 Engine specifications

Engine	L4,16-valves	Stroke [mm]	84.2
Displacement [Liter]	1.798	Bore [mm]	82.5
Connecting rod length [mm]	148	Compression ratio	9.6

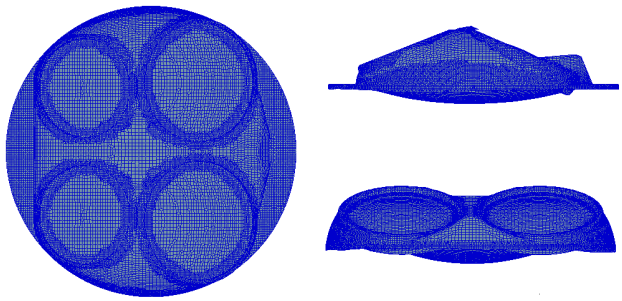

Figure1 Computational mesh for FIRE simulation

Usually, computational accuracy was significant affected by boundary conditions and initial conditions. The piston top was defined as moving wall, while other surfaces were defined as fixed wall. All the boundary valves and initial valves were showed in table 2 as follow.

Table 2 Boundary valves and initial valves

Intake valve temperature[K]	360	2000/4000rpm initial tumble ratio	0.7/0.85
Exhaust valve temperature[K]	580	2000/4000rpm initial TKE[m2/s2]	34/68
Chamber top temperature[K]	550	Equivalence ratio	1
Piston top temperature[K]	450	50/100kPa ignition angle[deg]	340/345
Liner temperature[K]	600	Fuel	Gasoline

In this modeling process, correlative flame model ECFM applied to homogeneous premixed combustion and Heywood original model used to calculate NO mass fraction were selected. Especially, knock model (shell model with temperature coupling) utilized to simulate auto-ignition. To explore the effect of intake temperature on different engine operating conditions such as speed at 2000rpm and 4000rpm and intake pressure of 50kPa and 100kPa, the optimum intake temperature of these conditions that exhibits the same knock probability with full-load at 2000rpm was computed at first. And then, the next work of this article mainly focused on the combustion and emission characteristics at 2000rpm with intake pressure of 50kPa and optimum intake temperature of 368K. Meanwhile, comparison with normal intake temperature condition but consuming the same air and fuel mass with the optimized condition was conducted to demonstrate the effect by means of heating intake air[4].

Computational results and analysis

Intake air temperature Optimization

Knock occurrence can not be calculated accurately by the present Fire software. Mean FQ reaction rate one of the intermediates in shell chain reaction or knock reaction rate were commonly used to evaluate knock probability. Due to slower flame-spreading speed and longer time for mixture heated in the edge of chamber, it was more easy to exhibit knock phenomenon at low speed and heavy load for gasoline engine[5,6]. The mean FQ reaction rate was calculated for 2000rpm and full load condition with intake temperature 306K and intake pressure 165kPa which did not appear knock phenomena according to experimental data. So the mean FQ reaction rate at 2000rpm and

full load was used as reference point. What was showed in figure 2(a) was the mean FQ reaction rate changing with crank angles at 2000rpm and full load, and the maximum was 1.33s^{-1} emerging at 403 CAD. Mean FQ reaction rate curves of 100kPa and 320K, 100kPa and 322K, 100kPa and 323K from 340 CAD to 440 CAD at 2000 rpm were showed respectively in figure (b) (c) (d). As you can see from figure 2(b), the mean FQ reaction rate was almost zero indicating knock happening unlikely. And the maximum mean FQ reaction rate showed in figure 2(c) was quite close to that of full load operation demonstrating the same knock probability with full load. While in figure 2(d), the maximum mean FQ reaction rate was 3.9s^{-1} that was almost triple the full load operation, so the knock probability was increased obviously. What were showed in figure 2 (e) (f) (g) were the mean FQ reaction rates for intake pressure of 50kPa with different intake temperature. The case with intake temperature of 368K whose mean FQ reaction rate was about equal with the full load operation was identified as the optimal temperature condition. Besides, mean FQ reaction rates equaling with full load operation of different cases at 4000rpm were illustrated in figure 2 (h) (i), and the optimizing temperatures were 374.5K and 413K for intake pressure of 100kPa and 50kPa respective.

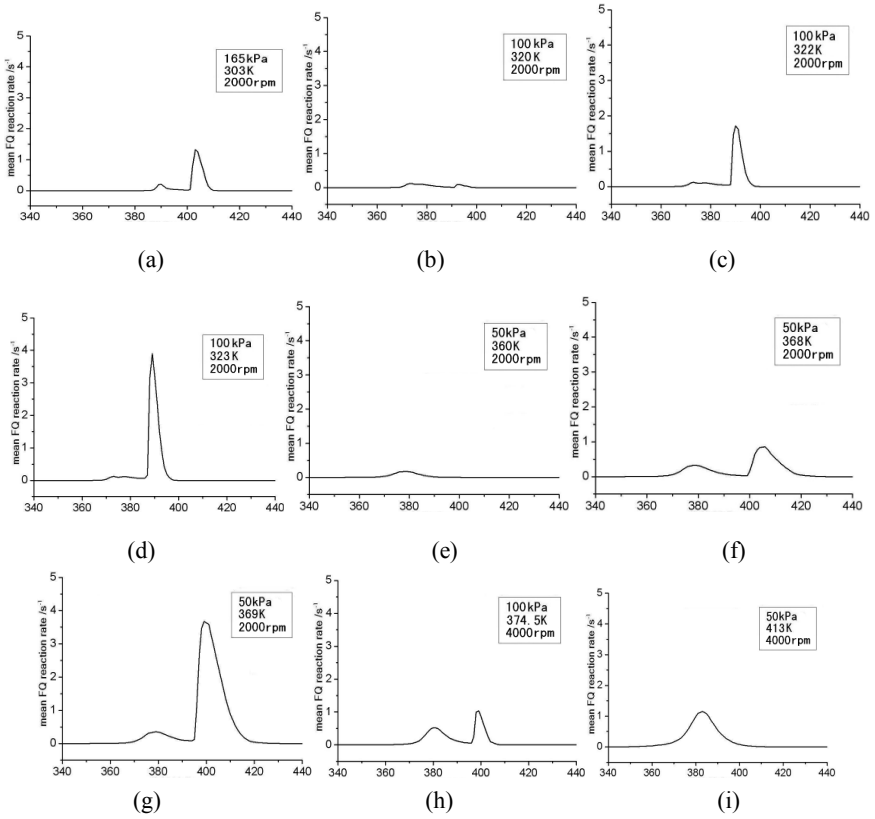

Figure 2. Curve of mean FQ reaction rate for different conditions

By contrasting figure 2 (b)(c)(d) and figure 2 (e)(f)(g), it can be come to the law that the higher intake temperature, the greater FQ reaction rate. In-cylinder temperature increased with intake temperature at the end of compression stroke, which was heated up to ignition points with high intake temperature. Combining stronger combustion pressure wave resulting from the enhancement of high intake temperature, the knock probability of end mixture was increased. Comparing figure 2(c) with figure 2(h) and figure 2(f) with figure 2(i), we concluded that the optimized temperature with higher speed could be increased, which also demonstrated low speed operations have much easier access to knock than high speed operations. So there is different optimized intake temperature for different engine conditions.

Combustion improvement

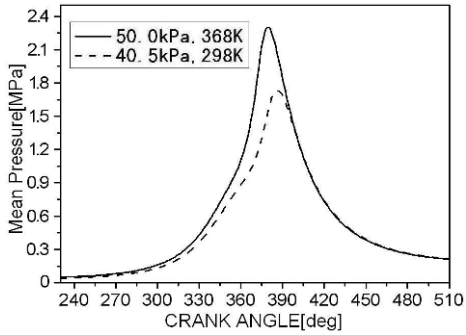

Figure 4. Mean cylinder pressure diagrams

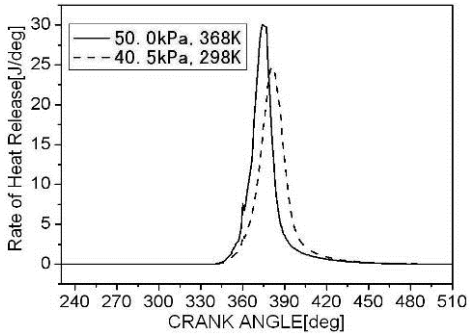

Figure 5. Heat release rate diagrams

In order to explain the effect of heating intake air on combustion process, cases at 2000rpm with intake temperature/pressure of 368K/50kPa and 298K/40.5kPa were calculated. Intake temperature 368K and pressure 50kPa was the case optimized in the upper portion of the paper and exhibiting same knock index with full load. Intake temperature 298K and pressure 40.5kPa was the case trapping air at room temperature and consuming same fuel mass with 368K/50kPa condition. Mean in-cylinder pressure curve and heat release rate curve of these two cases were showed in figure 4 and figure 5 respectively. For the case of 50kPa/368K, mean pressure rose more rapidly than that of 40.5kPa/298K condition, and the maximum pressure was 2.3MPa that was 32.9% higher. As shown in figure 5, the peak heat release rate of 368K/50kPa was 21.4% higher than 298K/40.5kPa operation, and the crank angle of peak heat release rate was also 7 deg earlier. Besides, the combustion duration was shortened by 12.6%. So it can be concluded that increasing the temperature of intake air helped to format flame kernel and develop initial flame stably so as to reinforce combustion and improve thermal efficiency. IMEP（indicated mean effective pressure）of 368K/50kPa and 298K/40.5kPa conditions can be known further by integrating cylinder pressure curve and then divided it by cylinder volume. The IMEP for 368K/50kPa condition was 0.514MPa and that of 298K/40.5kPa was 0.497MPa, which increased by 3.4%.

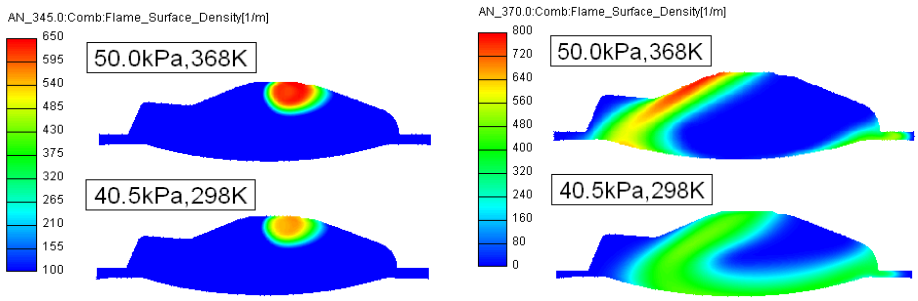

Figure 6. Slices of flame surface density at 345 CAD and 370 CAD

To further analyze the effect of increasing intake temperature on combustion at a micro level, the vertical slices of flame surface density for these two cases were showed in figure 6. It was obvious that the flame surface density around spark plug of 50kPa/368K was greater than 40.5kPa/298K at 345 CAD illustrating the improvement of flame formation and propagating. Furthermore, wider flame front was emerged for the case of 50kPa/368K at 370 CAD, which indicates faster flame-spreading speed with higher intake temperature too. Because temperature primarily affects molecule Brownian motion in combustion process, the higher temperature was, the more active molecule Brownian motion was. In a word, the mixing of burned fuel gas and un-burn fuel gas was enhanced.

The mean in-cylinder temperature of these two cases changed with crank angle was showed in figure 7. The mean in-cylinder temperature of 50.0kPa/368K was still higher than 40.5kPa/298K condition before 400 CAD. While, both of the mean in-cylinder temperature curves trended towards overlap after 400 CAD. Exhaust temperature was not increased though intake temperature was increased. That is because of shorter combustion during and faster heat release rate for intake heated condition. Instead, the case of 40.5kPa/298K had longer combustion during and longer heat release degrees. So the exhaust temperatures of these both were nearly equal at later stage.

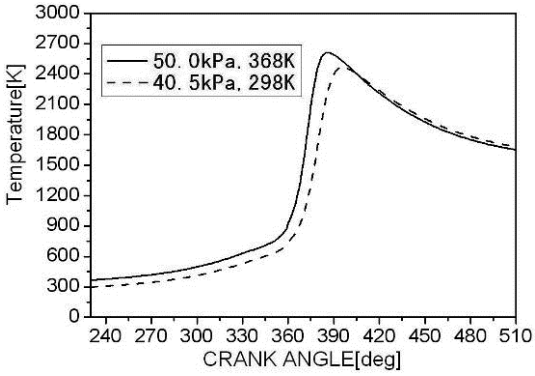

Figure 7. Mean in-cylinder temperature diagram

Pumping loss reduction

As we all know, gasoline engine load was regulated by throttle. Actually, it was volume flow adjusted by throttle instead of mass flow. Not only can heating intake air promote combustion, but also reduce air density to enlarge air volume under the same mass flow rate. Under the condition of stoichiometric burn, the higher the intake temperature was, the larger the intake air volume was needed with the same fuel consumption. As a result, pump loss could be reduced by wider throttle open resulting from intake air heated. Based on ideal gas state equation $PV=mRT$, intake temperature and intake pressure were proportional as engine displacement and air mass flow being constant. Intake pressure of 50kPa and intake temperature of 368K operation trapped the same air mass with 40.5kPa/298K condition. That is to say, the case heated to 368K at 50kPa achieves a 6 percent wider throttle open than 40.5kPa/298K operation in spite of consuming same fuel mass (setting intake pressure of 165kPa as WOT). As for the case of 100kPa/322K, the throttle was 4.5 percent wider than the case of 92.5kPa/298K.

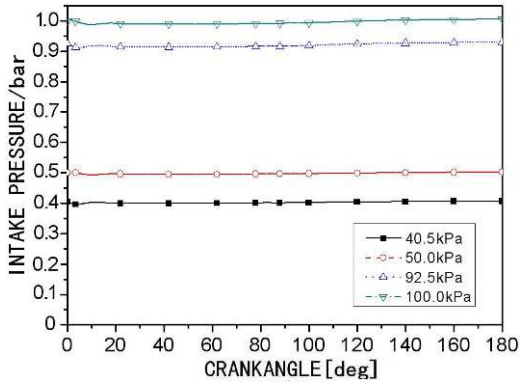

Figure 8. Intake pressure as a function of crank angle

In order to qualitative analysis the effect of heating intake air on pump loss, four cases of inlet port pressure 100kPa, 92.5kPa, 50kPa, 40.5kPa whose pressure changing as a function of crank angle during intake stroke were calculated by the same 3D-model but with intake manifold showed in

figure 8. The inlet pressure of these four cases kept nearly constant from TDC to BDC. Negative work was done when intake pressure was lower than one bar, which was known as pump loss. Pump loss during intake stroke of these four cases can be known by integrating the pressure curves. And the pump losses were 0J, 3.4J, 22.3J, 26.6J corresponding to intake pressure of 100kPa, 92.5kPa, 50kPa, 40.5kPa respectively. So as long as the intake air at part load operation was heated to the temperature value exhibiting same knock tendency with full load, it seems that very obvious improvement was obtained in reducing pump loss. For example in figure 8, the case of 322K/100kPa(intake temperature and pressure) had hardly any pump loss compared with that of 298K/92.5kPa condition which consumes same fuel mass but does not apply heating intake air. And for 368K/40.5kPa condition with intake air heated, 16.2% pump loss was reduced.

Emissions

The factor of generating nitrogen oxide for combustion is high temperature and enough oxygen, so the reaction of oxygen and nitrogen was enhanced by heating inlet air. The comparison that NO mass fraction at 2000rpm 368K/50.0kPa condition with 298K/40.5kPa (consuming the same fuel and air mass) condition were showed in figure9. We can see that the NO mass fraction arose sharply at about 380 CAD and the maximum for 368K/50.0kPa was 1.275% that was more than twice compared to the case of 298K/40.5kPa. This figure also indicated that the main reaction field for NO production was in the range of 380-410 CAD, and it was difficult to be eliminated before exhaust valves were opened once the NO was produced. The slices of temperature field for these two cases were showed in figure 11. It was obvious that the case of 368K/50.0kPa was higher than 298K/40.5kPa condition and the high temperature zone was wider too. This would state higher and wider temperature zone resulting from heating intake air was the major factor in NO production.

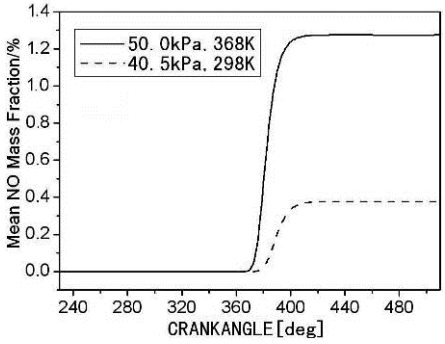

Figure 9. Mean NO mass fraction diagram

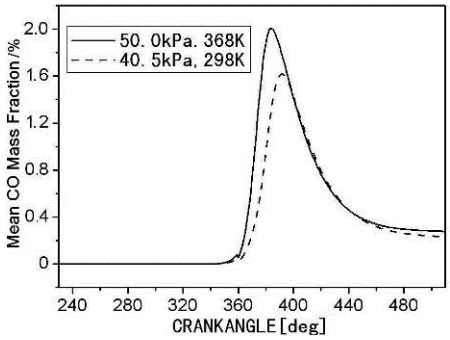

Figure 10. Mean CO mass fraction diagram

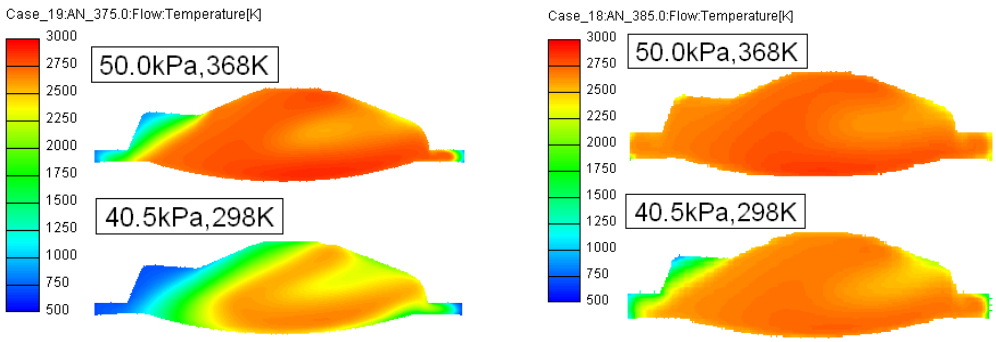

Figure 11. Slices of temperature field at 375 CAD and 385 CAD

When oxygen molecule is insufficient around carbon molecule in combustion process of fuel, the carbon molecule always reacts firstly to carbon monoxide and then the carbon monoxide reacts with excess oxygen brought by air motion in cylinder to carbon dioxide. And the carbon molecule can also react with carbon dioxide to carbon monoxide at high temperatures. So the trend of CO production with changing crank angle exhibited increasing first and then decreasing depicted in figure 10. At the later combustion process, high temperature became a more critical factor for carbon monoxide turned into carbon dioxide. The temperature in cylinder emerged a sharper fall for higher temperature condition due to faster combustion speed, so the production for NO was increased by heating intake air along with more NO production previous. As figure 10 showed, although these two cases consumed same fuel quality, there was a 19.5% increase in NO production for the case of 368K/50.0kPa than 298K/40.5kPa condition when exhaust valves were opened.

Conclusion

As changing of engine speed and load, the intake temperature should be adjusted for optimum engine performance. More specifically, higher intake temperature was applied for light load to promote combustion and reduce the pump loss, while lower intake temperature was kept for heavy load to increase airflow and reduce knock tendency.

a) Not only can heating intake air temperature improve combustion process, but also increase mean in-cylinder pressure and thermal efficiency, but also not increase exhaust temperature.
b) Increasing intake temperature can enlarge increase the air volume of a given mass flow rate, so the pump loss can be reduced resulting from the wider throttling.
c) Although it can increase mean in-cylinder temperature by higher intake temperature, it will bring the engine more production of CO and NO_X emissions.

Acknowledgments

This work was financially supported by the National 863 High Technology R&D Program (2012AA111702), the Natural Science Foundation of China (51276080), Jilin Province Science Foundation for Youths(20140520128JH), the China Postdoctoral Science Foundation (2013M540250) and Fundamental Research Funds for the Central Universities(450060481165).

References

[1] Qing Gao, Ying-ai Jin, Ming Li, in: Jilin University Engineering and Technology Edition in Chinese. 2003; 33(4): 7-11.

[2] Gregory E. Bogin Jr., J. Hunter Mack and Robert W. Dibble, “Homogeneous Charge Compression Ignition (HCCI) Engine”, SAE-Paper, 2009-01-1805.

[3] Wei-fei Yu, Hui Xie, in: Combustion Science and Technology. 2012; 18(3): 265-271.

[4] Yan-jun Xu. Experimental study on the SI-HCCI-SI Mode Transition with Intake Thermo Management System. MD Thesis. Changchun: Jilin university; 2006.

[5] Shiro Yamaoka, Hiromu Kakuya, Shinji Nakagawa, Takashi Okada, and Atsushi Shimada, “HCCI Operation Control in a Multi-Cylinder Gasoline Engine”, SAE-Paper, 2005-01-0120.

[6] James Szybist, Matthew Foster, Wayne R. Moore and Keith Confer, “ Investigation of Knock Limited Compression Ratio of Ethanol Gasoline Blends”, SAE-paper, 2010-01-0619.

Advanced Materials Research Vols. 960-961 (2014) pp 1411-1415

doi:10.4028/www.scientific.net/AMR.960-961.1411

Study of Combustion and Emission Characteristics of Gasoline Engine with Miller Cycle

Jian Wu[1,a], Wei Fan[1], Yang Hua[1], Yunlong Li[2], Shaozhe Zhang[2], Yiqiang pei[2]

[1]College of Vehicle and Traffic Engineering, Henan University of Science and Technology, Luoyang, 471003, China

[2] The State Key Laboratory for The Internal Combustion Engine Combustion Learn, Tianjin University, Tianjin, 300072, China

[a]wujian8402@163.com

Keywords: Variable valve timing, Miller cycle, Combustion characteristics, Emission characteristics

Abstract. On the basis of original engine, high compression ratio miller cycle can be realized, through perfecting the inlet cam profile, using higher geometry compression ratio, combining VVT control technology. The results indicate that the miller cycle achieved by VVT control technology can reduce pumping loss, and improve the effect utilization of energy. The combustion heat release rate is lower than the original engine, and combustion heat release are mainly concentrated on TDC later, lower the burning temperature. Compared with the original engine, NO_X emissions decrease significantly, but CO and HC emissions increase somewhat.

Introduction

Traditional otto cycle engine can't use the high compression ratio because of limitation of deflagration. Miller cycle can reduce the effective compression ratio by closing the inlet and exhaust valve behindhand, and improve thermal efficiency by high expansion ratios. Miller cycle engine can reduce pumping losses, fuel consumption rate and NO_X emissions [2-3]. Low effective compression ratio can prevent the deflagration and increase power, and also can reduce the institutions of engine and heat load, equivalent to improve the durability [3].

Through a comparative study of the otto cycle and miller cycle, it can be found that the purpose of low fuel consumption can be achieved by improving variable intake timing VVT and variable chamber volume [4-5]. The simple way of achieving miller cycle is to increase the compression ratio and inlet valve closed late [6]. This article realized miller cycle by controlling VVT on a motor gasoline engine, and also studied and analyzed the combustion and emission characteristics of engine.

Experimental facilities and research method

The experiment was conducted on a port fuel injection vehicle gasoline engine, with its compression ratio is 10.4. The specific parameters are shown in Table 1, and the bench experiment system is shown in Fig.1. The main equipments used in the experiment have YiKe hydraulic dynamometer, AVL7351CME type fuel consumption instrument, AVLZI31-Y5S type sensor, ETAS LA4 air-fuel ratio instrument. VVT is controlled by the Delphi MT22.1 open ECU, and emission characteristics is measured by HORIBA MEXA-7100DEGR type emission instrument.

On the basis of original engine, this paper makes the intake duration increase by replacing the inlet cam profile, increases geometry compression ratio by replacing piston, and achieves miller cycle of high compression ratio by combining with VVT control technology. Combined with the common working conditions of passenger vehicles, conduct a load characteristics experiment of 2000r/min on the original engine (otto cycle) and miller cycle. In the test, adjusting the inlet and exhaust VVT and ignition advance angle make specific fuel consumption and cycle fluctuation minimum, which keep excess air coefficient 1 and water temperature between 85oC to 90oC. In heavy load test, adjusting the air-fuel ratio makes the exhaust temperature below 850oC to protect

three-way catalytic converter and both fuel consumption. If there is deflagration, the ignition angle delay 1 to 2oCA. Because intake duration of miller cycle is longer than the original engine, inlet angle close later than the original engine, thus increase the throttle opening to maintain air input.

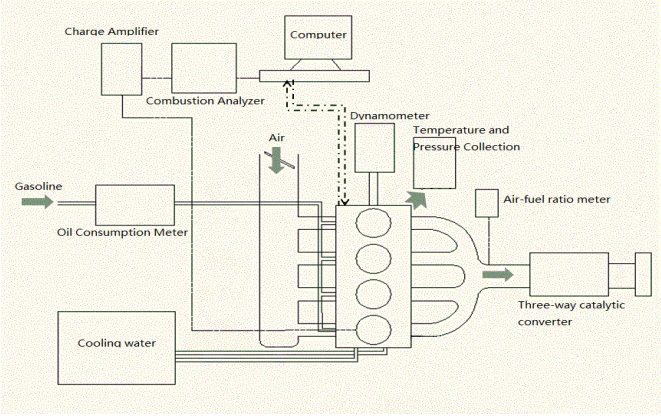

Fig.1. Schematic diagram of the test rig.

Table 1 Main technical parameters of gasoline engine

Model	Inline, DVVT
Bore / mm	78
Stroke / mm	83.6
Rod length / mm	134.7
Displacement / L	1.6
Compression ratio	10.4
Maximum torque / Nm	150
Power / kW	82/6000r/min

Experimental results and analysis

Variable valve timing (VVT). In the experiment, intake duration of the original engine (otto cycle engine) and the miller cycle engine are 265°CA and 285°CA, through the adoption of different inlet cam profile. The increase of intake duration of miller cycle is conductive to provide plenty of fresh impulse to cylinders, which can meet the needs of the combustion process in cylinder. At the same time, the original engine and miller cycle engine use different structure of pistons, and geometry compression ratio are 10.4 and 12.6. The adjusting of intake late closing angle and exhaust advance angle is combined with the variable timing VVT, the effective compression ratio and expansion ratio are shown in Table 2. Under the common effect of variable timing VVT and geometry compression ratio, the effective compression ratio of miller cycle reduce at low and middle loads, but the effective expansion ratio has an obvious increase in the entire loads. Effective compression ratio and effective expansion ratio will affect the cycle thermal efficiency and fuel economy collectively.

Table. 2 Comparison of effective compression ratio and effective expansion ratio

BMEP	Effective Compression Ratio		Effective Expansion Ratio	
/100kPa	Otto	Miller	Otto	Miller
2	5.95	5.52	8.77	11.37
4	6.45	5.05	9.45	11.4
6	7.24	6.05	9.45	11.4
8	8.14	8.61	8.6	9.75
9.5	8.95	9.52	8.35	9.33

Pumping loss is the main causes of poor fuel economy of otto cycle engine. In the experiment, in order to ensure adequate air inflow, according to different conditions to optimize the throttle opening. After optimization, the throttle opening of miller cycle is average 13.3% larger than that of original engine. The increase of throttle opening is helpful to decrease the throttling losses near throttle, and also can improve the intake pressure. Figure 2 shows that the intake pressure of miller cycle is about 12.7% larger than that of original engine. Under middle and low loads, the intake pressure increase quickly with the increase of loads. While in high loads, intake pressure increase gently. And the technology of late inlet valve close (LIVC) could part replace throttle to adjust the load. As shown in Figure 3, compared with the original engine, the pumping loss of miller cycle reduce obviously. Because the intake pressure increase, and the increase of expansion ratio also will lead to exhaust pressure reduce. Pumping loss of miller cycle engine is average 53.3% lower than that of original engine at 2000r/min.

Thus it can be seen that, miller cycle engine can reduce pumping loss significantly, improve the effective utilization of energy, and reduce the fuel consumption through using variable valve timing technology VVT.

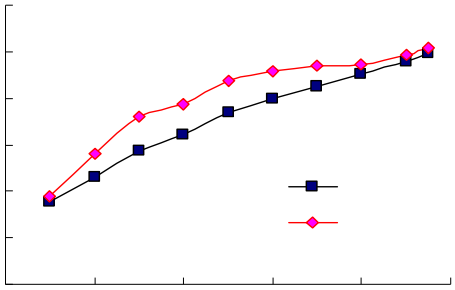

Fig. 2.Comparison of intake pressure

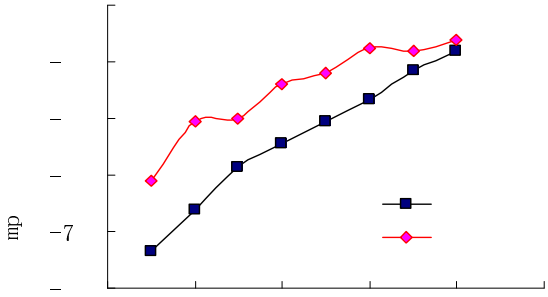

Fig. 3. Comparison of pumping loss

Combustion process analysis. Figure 4 shows that the combustion heat release rate changes with the crank angle under different loads of 2000r/min. Figure 5 shows the contrast of ignition advance angle under different loads of 2000r/min. As is shown in Figure 5, compared with original engine, the ignition advance angle reduce to avoid detonation combustion. And because the effective compression stroke of miller cycle is small, the air motion inside the cylinder is relatively weak, the burning speed slow, these lead to the combustion process of miller cycle focus after the top dead center.

As is shown in Figure 4, the heat release rate of miller cycle is slower under low loads. This is because that compared with the original engine, the effective compression ratio of miller cycle is low, and the throttle opening is bigger, thus the air motion inside the cylinder is relatively weak. These lead to that the burning speed slow and the peak heat release rate is lower. Under high loads, because of the increase in effective compression ratio, the air motion produced in compression process enhance, burning speed is accelerated, and the peak heat release rate increase.

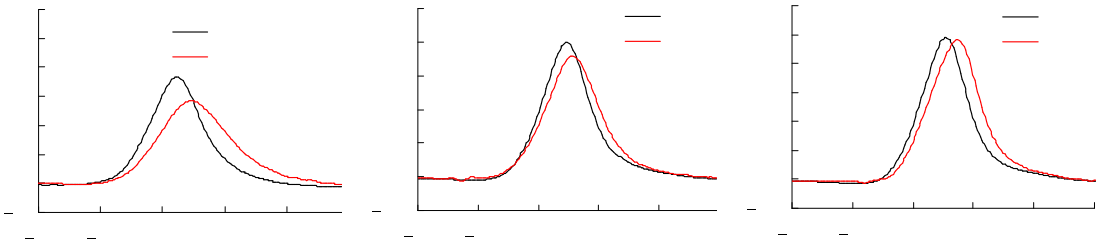

Fig. 4. Comparison of combustion heat release rate (dQ/dθ)

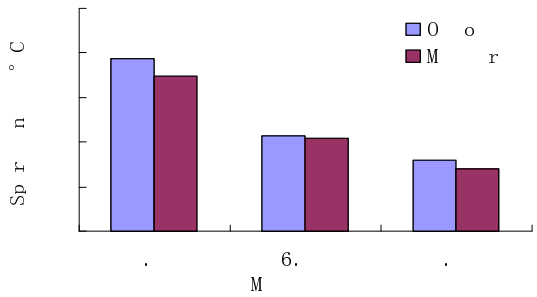

Fig. 5 Comparison of spark angle

Table. 3. Comparison of combustion temperature and exhaust temperature

BME P/kPa	combustion temperature/K		Exhaust temperature/K	
	Otto	Miller	Otto	Miller
200	2543	2398	699	666
600	2550	2418	735	719
800	2450	2380	759	732

Table 3 shows the contrast of maximum combustion temperature and exhaust temperature under different loads of 2000r/min. Because the combustion heat release rate of miller cycle is slower than original engine, and combustion focus on later top dead center, the combustion temperature

decrease somewhat. Because of the increase of expansion ratio, the exhaust temperature of miller cycle decrease somewhat, compared with original engine.

Emission analysis. The main source of NOx emissions is the nitrogen in the air which participated in combustion. The generation mechanism of NOx is Zeldvich mechanism[7]. NOx formation is mainly related to temperature and excess air coefficient. Excess air coefficient in this experiment keep 1, through regulating. So the combustion temperature has a great influence on NOx emissions. Figure 6 shows the contrast of NOx emissions. As is shown in the figure, compared with original engine, NOx emissions of miller cycle have obvious lower in the whole loads. NOx emissions of miller cycle reduce 50% at low load, and 30% in middle and high loads. This is because combustion temperature in cylinder of miller cycle reduce.

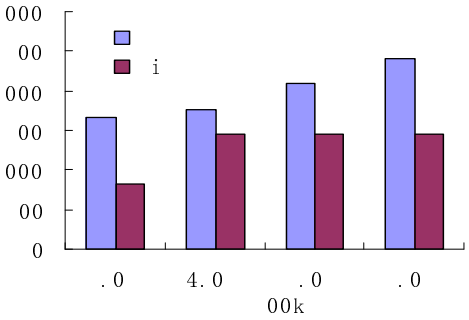

Fig. 6. Comparison of NOx emissions

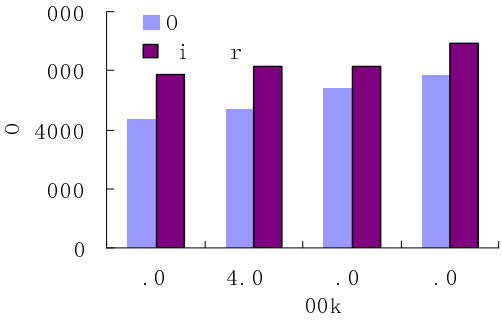

Fig. 7. Comparison of CO emissions

CO emissions is a result of incomplete combustion of fuel in cylinders, which is intermediate products caused by the lack of oxygen[8]. Figure 7 shows the contrast of CO emissions. As is shown in the figure, compared with original engine (otto cycle), CO emissions of miller cycle increase somewhat, especially in middle and low loads. Although the excess air coefficient is kept 1, there will be the phenomena of part hypoxia influenced by burned gases. And the combustion process of miller cycle mainly focus on the top dead center later, the combustion temperature is reduced, then the incomplete combustion increases, this lead to CO emissions increase.

HC emissions of gasoline engine is mainly the product of incomplete combustion, and the quality of mixed gas is one of the important factors that affect the combustion. Figure 8 shows the contrast of HC emissions. As is shown in the figure, compared with original engine (otto cycle), HC emissions of miller cycle increase somewhat in the whole loads. This is mainly caused by residual gas in the cylinder. The inlet and exhaust overlap angle of miller cycle engine is increased (Figure 9), through the regulation of variable timing VVT. This lead to residual gas in the cylinder increase, which would hinder the formation of flame center and flame spread, even interrupt the flame spread. This lead to the increase of HC emissions because of incomplete combustion.

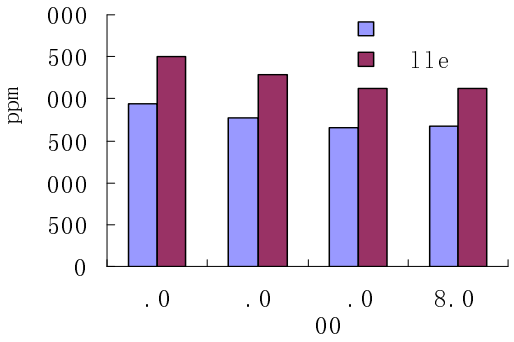

Fig. 8. Comparison of HC emissions

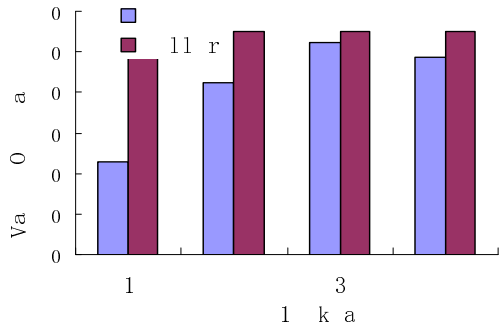

Fig. 9. Comparison of valve overlap

Conclusions

(a) By perfecting the inlet cam profile, using higher geometry compression ratio, and combining VVT control technology, the engine can achieves miller cycle of high compression ratio. The pumping loss can be reduced and the effective utilization of energy can be improved.

(b) The combustion heat release rate of miller cycle achieved by VVT control technology is slower than that of the original engine, and combustion heat release are mainly concentrated on TDC later. The combustion process can be improved through inlet pressurization and combustion system optimization.

(c) The miller cycle achieved by VVT control technology can reduces the combustion temperature, which can reduce NOX emissions effectively, but CO and HC emissions increase somewhat.

References

[1] Tuttle J H. Controlling engine load by means of late intake-valve closing[J]. SAE Paper 800794, 1980.

[2] Wang Y, Lin L, Roskilly A P, et al. An analytic study of applying Miller cycle to reduce NOx emission from petrol engine[J]. Applied thermal engineering, 2007, 27(11): 1779-1789.

[3] Xue Jun. Miller cycle gas engine[J]. Design and Manufacture of Diesel Engine, 1999(2): 28-33(in Chinese).

[4] Luria D, Taitel Y, and Stotter A. The Otto-Atkinson Engine- a New Concept in Automotive Economy[J]. SAE Paper 820352, 1982.

[5] Boggs D L, Hilbert H S, Schechter M M. The Otto-Atkinson cycle engine: fuel economy and emissions results and hardware design[J], SAE Paper 950089,1995.

[6] Zhao Jinxing, Xu Min, Li Mian, et al. Design and optimization of an Atkinson cycle engine with the Artificial Neural Network Method[J], Applied Energy, 2012, 92: 492-502(in Chinese).

[7] Georg Tinschmann, Marco Taschek, Mr. Heiner Haberland, et al. Combustion System Development for IMO Tier 2[C], CIMAC Congress 2007, Vienna, 2007, 148.

[8] Gong Jinke. Automobile emission and control technology[M]. Beijing: People's Communications Press, 2007:10-11(in Chinese).

Advanced Materials Research Vols. 960-961 (2014) pp 1416-1419

doi:10.4028/www.scientific.net/AMR.960-961.1416

Effect of Fuel Auto-ignition Quality on Particle Size Distribution and Particulates Morphology in a Direct Injection Diesel Engine

Jiakun Du[a], Wanchen Sun[b], Senlin Xiao[c], Guoliang Li[d], Manzhi Tan[e]

State Key Laboratory of Automotive Simulation and Control, Jilin University, Changchun, China

[a]email:jiakundu@126.com, [b]email:sunwc@jlu.edu.cn, [c]email:yimotechonolgy@gmail.com, [d]email:ligl@jlu.edu.cn, [e]email:tanmz@jlu.edu.cn

Keywords: Auto-ignition Quality; Particle Size Distribution; Morphology.

Abstract. The effect of fuel auto-ignition quality on particle size distribution and particulates morphology were investigated for the purpose of revealing the relationship between cetane number and particles emission. Experiments were conducted on common-rail direct injection engine under steady-state operating condition. Two basic diesel-like fuels were used in this study, hydrogenation diesel and straight-run diesel. The test fuels which have various cetane number were made up of these two basic ones. The results indicate that with increasing the fuel cetane number, a significant decrease of nucleation mode particles is found. For particle number size classification, the percentage of SOF has the same trend as the number of nucleation mode particles which size below 22nm and similar result is found between the percentage of dry soot and particles above 50nm.

Introduction

The diesel engine has a considerable advantage in regards to power output, durability and fuel economy when compared with other types of internal combustion engines. However, it is necessary to reduce exhaust emissions, especially NOx and PM. The use of Exhaust Gas Recirculation (EGR) offers areas of low combustion temperature inside the cylinder. Therefore NOx emissions decrease by reduction of production of thermal-NO. But particle emissions increase with the lack of oxygen. The emissions of exhaust diesel particles in the atmosphere are well known as hazardous substance for the human health. Therefore, more and more new technologies were applied on diesel engines, such as increasing fuel injection pressures, variable geometry turbochargers (VGT) and diesel particulate filters (DPF), particulate mass emission decreased with the increasing of particle number consequently [1]. Many toxicological and epidemiological studies established adverse health effects by PM, especially the ultra-fine particles with diameters below 100 nm [2].

Particles in diluted diesel exhaust are classified into three size modes, the nucleation mode (< 50 nm), the accumulation mode (50～1000nm) and the coarse mode (>1000 μ m) [3]. Many researchers have found that ultra-fine particles were sensitive to combustion parameters, such as fuel properties, injection strategies and EGR [4]. As is known to all, fuel auto-ignition quality is an important factor on combustion and emission, most of the studies were conducted with model fuel, such as n-paraffin, i-paraffin hydrocarbons and aromatic hydrocarbons. However, commercial diesel which actually used is consisted of hundreds of hydrocarbon components, studies based on model fuels cannot explain the authentic cause on combustion and emission [5,6]. Therefore, the aim of this work is to perform a comparative study on fuel auto-ignition quality in terms of particle emission and experimentally addresses the effect on particulates morphology. The diesel engine used in this study was equipped with a common-rail fuel injection system and without after-treatment devices.

Experimental Set-up

A four-cylinder four-stroke light-duty, intercooled diesel engine is chosen for the experiments. The engine is equipped with a Bosch high-pressure common-rail fuel system. Main parameters of the engine are listed in Table 1.

Table 1: Engine Specification

CATEGORY	PROPERTIES
Engine Type	Common Rail Turbo Charged with Intercooler
Bore	93 mm
Stroke	102 mm
Displacement	2.771L
Compression Ratio	17.2:1
Max Torque	260 N • m / 2000 rpm
EGR system	Disconnected

Table 2 shows a summary of the main properties. The hydrogenation diesel and straight-run diesel are main components in commercial diesel and have a distinct auto-ignition quality. Therefore, their blends, rather than model components (such as n-paraffin, i-paraffin hydrocarbons and aromatic hydrocarbons), could simulate the practical diesel properties well. CN44, CN55 and CN60, with different cetane number, are made by blending a hydrogenation diesel component and a straight-run diesel. In order to avoid the effect from the fuel used in previous tests, the engine was run at high load for half an hour before any new measurements were taken.

Table 2. Main Properties of Fuel

		Hydrogenation diesel	Straight-run diesel	CN44	CN55	CN60
Hydrogenation diesel		100%	--	100%	46%	25%
Straight-run diesel		--	100%	0%	54%	75%
Cetane number		44	66	44	55	60
Low heating value [MJ/kg]		42.6	43.05	42.6	42.84	42.93
Density(15℃) [g/L]		853.5	818.5	853.5	835	831
Sulfur content [ppm]		15	1350	15	736	1016
Distillation range [℃]	T10	208	263	208	230	239
	T50	260	298	260	288	294
	T90	338	342	338	345	348

The dilution system consisted of a partial-flow two-stage dilution system and particle filter sampling equipment. However, unlike Particle Measurement Program, the dilution system used in experiment did not have the CVS and heated evaporation tube. Instead, a cold partial-flow two-stage dilution system was used to dilute the raw exhaust gas. In order to avoid the raw exhaust components adsorbing unburned hydrocarbon and accumulating into particle groups, the dilution process should be rapidly. This also could prevent larger particles from diminishing during heated evaporation. By this way, the results will be close to actual environment. In our present work, the effect of dilution ratio (DR) on PSD had been discussed and a modest DR (about 200) might be benefit to rapid freezing which could terminate the particles' condensation. In this paper, the DR was kept constant at 200 by controlling the quantity of dilution air.

Test Conditions

In order to obtain a more repeatable result, the engine mode was selected at equivalence ratio=0.6 of the max torque speed, 1800r/min. The mode represents 75% of the max torque. The cooling water temperature and oil temperature were maintained at a constant range during the experiments. After fuel changing, residual fuels in the fuel supply line and fuel flow meter were completely drained by operating under heavy load for 30 minutes in order to prevent mixing of fuels. At the same time, residual volatile substance on inner wall of exhaust pipe will be removed because of the high temperature.

Results and Discussion

The influence of fuel auto-ignition quality on the exhaust particle size is shown in Figure 1(a). The majority of the particles with these three fuels are located in the diameter region of 5–300 nm and the peak value of nucleation mode is located between 10nm and 25nm. With increasing the fuel cetane number, a significant decrease of nucleation mode particles is found. This may be due to the short ignition delay which reduces the premixed burning portion and increases the diffuse portion. This will be benefit for producing more carbonaceous particles, these particles largen by accumulating and then carbonaceous agglomerates are formed. Due to large specific surface area of carbonaceous agglomerates, it is an excellent carrier for unburned hydrocarbon substance and hence the nucleation mode particle number is limited. Figure 1(b) and Figure 1(c) are volumetric distribution and superficial distribution. These two figures indicate that accumulation mode particles which take up more volume and superficial area would be more contributive to the adsorption of unburned substance.

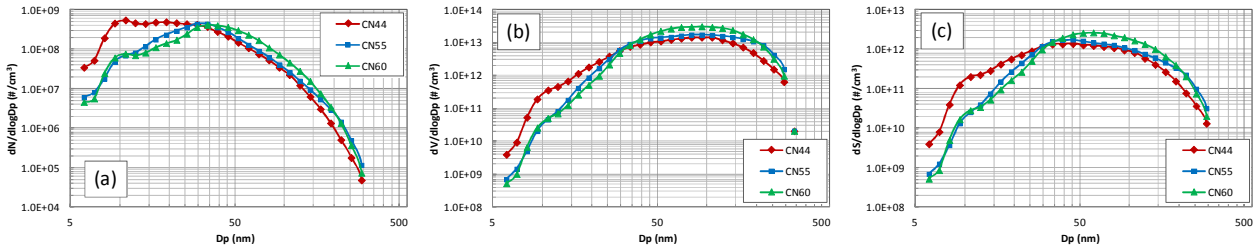

Fig.1: (a) Particle number distribution (b) Particle volumetric distribution(c) Particle superficial distribution

Figure 2(a) shows the influence of auto-ignition quality on particle sizes at the same operating condition. Just as mentioned above, high cetane number fuel tends to produce more accumulation mode particles with reducing the nucleation mode particles emission. Consequently, the percentage of nucleation mode particles decreases obviously with the cetane number becomes higher. The percentage of ultrafine particles, include nucleation mode particles and part of accumulation mode particles, is relatively stabilized. To study the effect of the auto-ignition quality on the PSD a bit further, the influence of cetane number on the particle size classification is shown in Figure2(b). The particle number of all the size classes below 22 nm is decreased with the cetane number increased. On the contrary, the number of particles above 22nm increase and the number of the particles located in the range of 15nm-22nm changes slightly. Figure2(c) indicates that the percentage of SOF has the same trend as the number of nucleation mode particles which size below 22nm. Meanwhile, similar result between the percentage of dry soot (DS) and particles above 50nm.

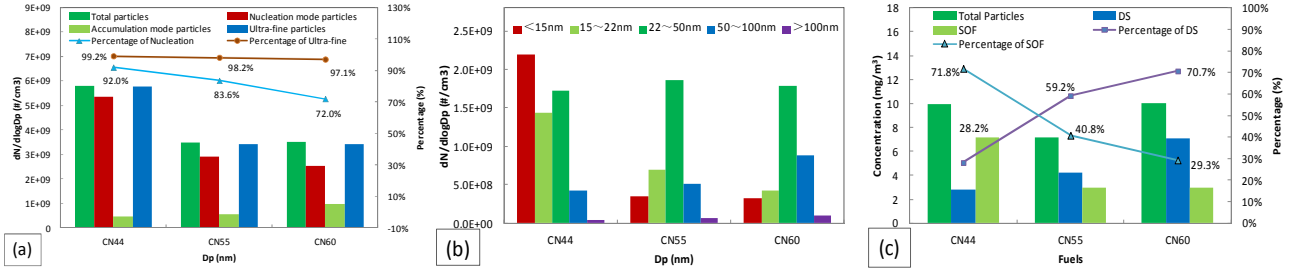

Fig.2: (a) Number of particles in different mode(b) Particle number size classification(c) DS and SOF mass concentration

Scanning electron microscope (SEM) images (Figure 3) were taken for the samples collected on the filter paper from the partial-flow dilution tunnel for different fuels. These samples were magnified by 8000 times. It can be seen from the images that most of the particles are nano-particles. Meanwhile, the agglomeratic particles number with CN60 is larger than that with CN44 and CN55. These results fall in line with the particle size distribution findings.

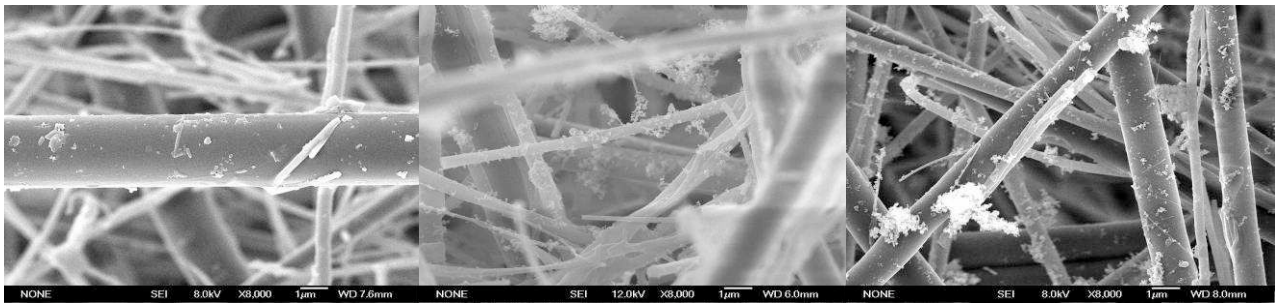

(a) CN44 (b) CN55 (c) CN60

Fig.3. Characteristic of particulates morphology

Conclusion

Present study explores the the effect of fuel auto-ignition quality on particle size distribution and particulates morphology in a common-rail direct injection engine under steady-state operating condition. On the basis of the results of present experiments, the conclusions were summarized as followed:

(1) With increasing the fuel cetane number, a significant decrease of nucleation mode particles is found. The results of volumetric distribution and superficial distribution indicate that accumulation mode particles which take up more volume and superficial area would be more contributive to the adsorption of unburned substance.

(2) High cetane number fuel tends to produce more accumulation mode particles with reducing the nucleation mode particles emission and the percentage of nucleation mode particles decreases obviously with the cetane number becomes higher. The percentage of ultrafine particles is relatively stabilized.

(3) The particle number of all the size classes below 22 nm is decreased with the cetane number increased. Besides, the number of particles above 22nm increase and the number of the particles located in the range of 15nm-22nm changes slightly. The percentage of SOF has the same trend as the number of nucleation mode particles which size below 22nm. Meanwhile, similar result between the percentage of dry soot(DS) and particles above 50nm.

(4) For particulates morphology, the results indicated that the agglomeratic particles number with CN60 is larger than that with CN44 and CN55 which fall in line with the particle size distribution findings.

Acknowledgement

In this paper, the research was sponsored by the National Natural Science Foundation of China (Project No. 51176064) and Science and Technology Development Plan of Jilin Province (Project No. 20140204012GX).

References

[1] Agarwal, A. K., Singh, A. P., Lukose, J., Gupta, T., J. Aerosol Sci. Vol. 58 (2013), p.71

[2] Brown, D. M., Wilson, M. R., MacNee, W., Stone, V., Donaldson, K., Toxicol. Appl. Pharmacol. Vol. 175 (2001), p. 191.

[3] N. Bukowiecki, D. B. Kittelson, W. F. Watts, H. Burtscher, E. Weingartner, U. Baltensperger, J. Aerosol Sci. Vol. 33 (2002), p. 1139.

[4] J.M. Desantes, V. Bermúdez, J.M. García, E. Fuentes, J. Aerosol Sci. Vol. 36 (2005), p. 1251.

[5] Z. Hong, D.F. Davidson, S.S. Vasu, R.K. Hanson, Fuel Vol. 88 (2009), p. 1901.

[6] Hellier, P., Ladommatos, N., Allan, R., Rogerson, J. Combust. Flame, Vol.160 (2013), p. 2141.

Advanced Materials Research Vols. 960-961 (2014) pp 1420-1423

doi:10.4028/www.scientific.net/AMR.960-961.1420

Modal Analysis of Two Wheels Scooter Based on Solidworks

Zhidong Huang[1, a], Guofei Li[1,b], Juan Cong[1,c], Yun Wang[1,d], Weina Yu[1,e] and Quan Gu[1,f]

[1]Dept. of Mechanical Engineering, Liaoning Institute of Science and Technology, Benxi, Liaoning, 117004, China

[a]hzdstarcraft@126.com, [b]1076950184@qq.com, [c]congjuan1125@126.com, [d]wyjhp@163.com, [e]bxyuweina@163.com, [f]guquanhao@aliyun.com

Keywords: scooter, modal analysis, finite element method, natural frequency

Abstract. Based on Solidworks software, the three-dimensional model of two wheels scooter is set up. The finite element model of two wheels scooter is generated. Modal analysis of driving system and telescopic mechanism of bar on two wheels scooter is investigated. The first five orders natural frequency and major modes of driving system and telescopic mechanism of bar are clarified. The method and the result can be used as a reference of dynamic design and lay foundation for calculation and analysis of dynamic response for the two wheels scooter.

Introduction

Nowadays, the scooters are rich in species numbers on the market such as two wheels scooter, three wheels scooter and four wheels scooter. Some scholars have devoted themselves to the research on scooter. Introducing scooter into floor cleaning is presented by Ref [1] and it can significantly shorten the housework time and reduce the work pressure. Adopting Fatigue/ANSYS, a software module is developed by Ref [2]. On the platform, visual analysis of fatigue life and design optimization can be carried out for the scooter. The 3D solid model and assembly of the scooter stepping on both feet is obtained with Pro/E software by Ref [3]. The simulation analysis on motion machanism of scooter is investigated and the displacement variation curve of scooter is given out. In a word, the two wheels scooter is the foundation of scooter. Therefore, this paper intends to set up the three-dimensional model of two wheels scooter. Modal analysis of driving system and telescopic mechanism of bar on two wheels scooter is obtained by Solidwoks software, which is significant for the dynamic design and dynamic response analysis of two wheels scooter.

Basic Theory of Modal Analysis

Based on the finite element theory of elasticity[4], the motion differential equations of system can be expressed as:

$$[\mathrm{M}]\{\ddot{q}\}+[C]\{\dot{q}\}+[K]\{q\}=\{Q(t)\} \tag{1}$$

Here [*M*] is mass matrix, [*C*] is damping matrix and [*K*] is stiffness matrix. $\{\ddot{q}\}$, $\{\dot{q}\}$ and $\{q\}$ are vectors of acceleration, velocity and displacement respectively. $\{q\}=\{q_1,q_2,\cdots,q_n\}^T$. $\{F(t)\}$ is the exciting force vector of system and $\{F(t)\}=\{f_1,f_2,\cdots,f_n\}^T$.

For undamped free vibration, Eq.(1) can be expressed as:

$$[M]\{\ddot{q}\}+[K]\{q\}=0 \tag{2}$$

The corresponding eigenvalue equation can be obtained:

$$([K]-\omega_i^2[M])\{q\}=0 \tag{3}$$

Here ω_i is the i order natural frequency, and i=1,2，…，n.

Three-Dimensional Model of Two Wheels Scooter

Based on the configuration of certain scooter, the three-dimensional model of the scooter is set up. The key components are shown in Fig.1 and the structure of two wheels scooter is shown in Fig.2.

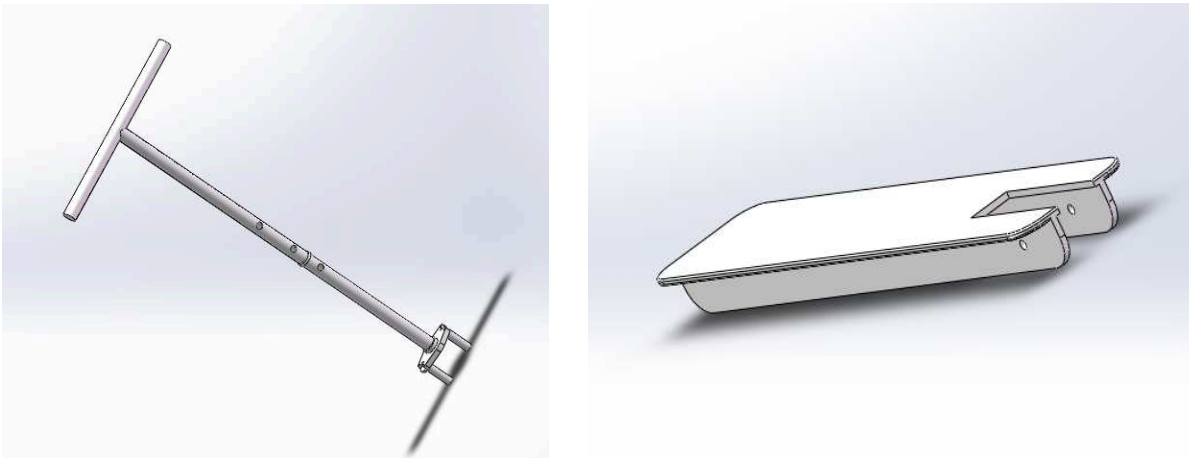

(a) Telescopic mechanism of bar. (b) Driving system.

Fig.1 The key components of two wheels scooter.

Fig.2 The structure of two wheels scooter.

Modal Analysis of Two Wheels Scooter

Based on the three-dimensional model of two wheels scooter, the finite element model of two wheels scooter is generated. And modal analysis of driving system and telescopic mechanism of bar on two wheels scooter is investigated.

Modal Analysis of Driving System. The mesh generation diagram of driving system and the first five orders major modes of driving system are shown in Fig.3.

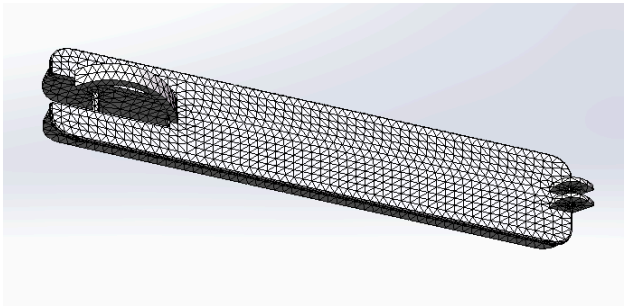

(a) The mesh generation diagram.

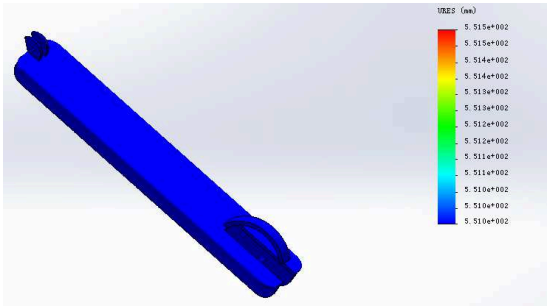

(b) one order mode.

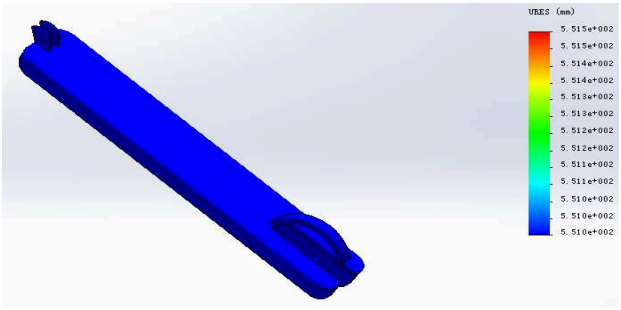

(c) two order mode.

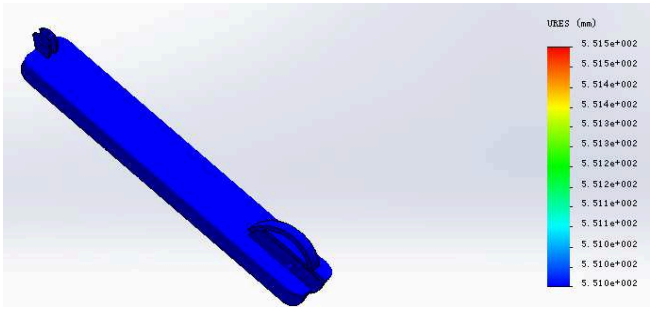

(d) three order mode.

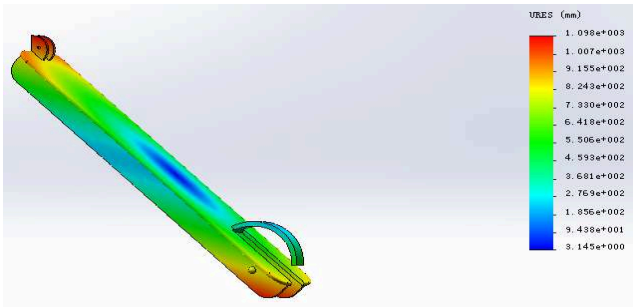

(e) four order mode.

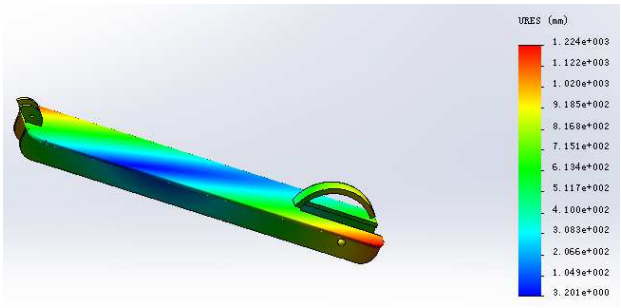

(f) five order mode.

Fig.3 The major modes of the first six orders for driving system.

Modal Analysis of Telescopic Mechanism of Bar. The mesh generation diagram of telescopic mechanism of bar and the first five orders major modes of telescopic mechanism of bar are shown in Fig.4.

(a) The mesh generation diagram.

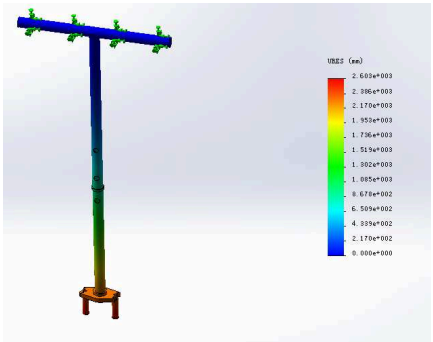

(b) one order mode.

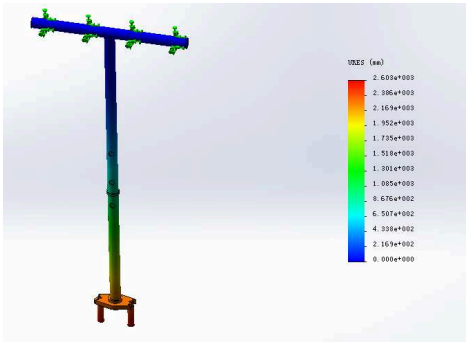

(c) two order mode.

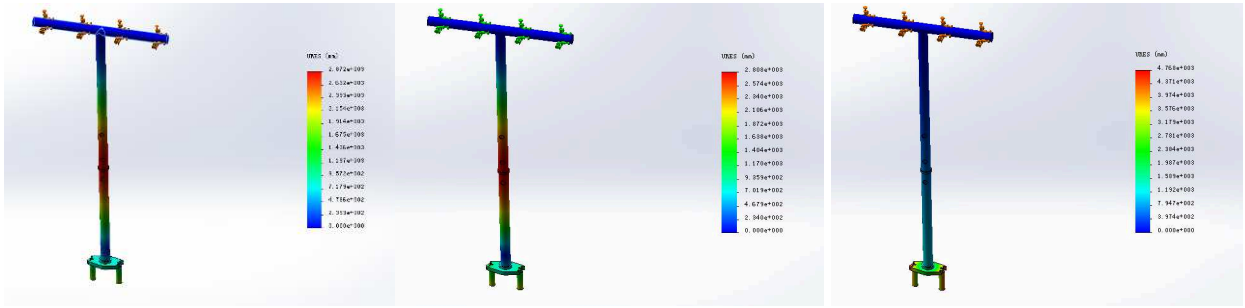

(d) three order mode. (e) four order mode. (f) five order mode.

Fig.3 The major modes of the first six orders for telescopic mechanism of bar.

Result of Modal Analysis. Analysis type is set to modal analysis and the order is set to 5. The natural frequency of the first five orders is listed in Table.1.

It is concluded in Table.1, Fig.3 and Fig.4 that for avoiding the resonance phenomenon in two wheels scooter, the response frequency of external-excitation should evade the natural frequency of driving system and telescopic mechanism of bar.

Table 1 The natural frequency of the first five orders.

Order	1	2	3	4	5
Driving System(Hz)	28.7	53.762	97.424	255.47	405.9
Telescopic Mechanism of Bar(Hz)	28.302	28.955	221.25	227.86	410.34

Conclusions

This paper focuses on three-dimensional model of two wheels scooter. Modal analysis of driving system and telescopic mechanism of bar on two wheels scooter is investigated by Solidwoks software. The natural frequency and major modes of the first five orders for driving system and telescopic mechanism of bar on two wheels scooter are clarified. The method and the result facilitate the dynamic design and dynamic response analysis of two wheels scooter.

Acknowledgements

This work was financially supported by Students' Innovation and Entrepreneurship Training Program of Liaoning Province (201311430003) and Key Undergraduate Specialty of Liaoning Province Ordinary College (ZD201245).

References

[1] F. Zhang, X.Z. Yang and T. Li: Journal of Hubei Polytechnic University Vol. 29 (2013), p. 13-16 (In Chinese)

[2] T.X. Tian, Y.G. Hu and H.J. Shen: Mechanical Engineer No. 9 (2005), p. 59-60 (In Chinese)

[3] P.P. Liu, D.D. Zhang: Development & Innovation of Machinery & Electrical Products Vol. 22 (2009), p. 67-68 (In Chinese)

[4] Y.M. Zhang: *Mechanical Vibration Dynamics*(Jilin Science and Technology Press, China 2000).

Advanced Materials Research Vols. 960-961 (2014) pp 1424-1428

doi:10.4028/www.scientific.net/AMR.960-961.1424

Research of Turbine Model Accuracy Based on Actual Data

Jin Ge[1,a], Shuchang Liu [2,b] and Ding Cai[2,c]

[1] Power Research Institute of Guangdong Power Grid Corporation, Guangzhou, China

[2]College of Energy Science and Engineering, Harbin Institute of Technology, Harbin, China

[a]happyjinge@163.com, [b]zoro1piece@live.cn, [c]cdhityou@163.com

Keywords: Turbine model, Model modify, BPA, Real data revise

Abstract. In the present power system stability analysis, BPA model for turbine and governor is commonly used. It simplifies the actual turbine system to a large extent, therefore the model simulation results may deviate from the actual conditions. In order to improve the actual data simulation accuracy, this paper compared the real and simulation data of power, high pressure cylinder (HPC) exhaust pressure and reheat pressure. Then calibrated and optimized the established model using the data of field operation. Meanwhile, the model modified method using actual data is given and guidance of parameters tests is offered.

Introduction

At present, the power system stability analysis often uses the model provided by "PSD-BPA Transient Stability Program User Manual" (referred to as: BPA model) as the turbine and governor model. It actually made a lot of simplifications on real turbine system and considered high, medium and low volume module, and the heat volume module etc. The natural power overshooting factor is also taken into consideration for enthalpy drop. However, the simulation results may deviate from the actual situation. To improve the accuracy of the simulation model, it needs to be verified and optimized with the actual operation data.

Min Luo et al.[1] proposed a practical load model well-integrated with the BPA, using the approach to load dynamic modeling during asymmetric disturbance to optimize the identification. And verified it with a simulation example. Peng Wei et al.[2] used the no—load test and other field measurements to get the model characteristics and dynamics characteristics of the excitation system therefore studied the stability of the generator in the BPA. Yunfeng Tian et al.[3] analyzed the thermodynamic process within reheating turbine and combined with the on-site test results, improved traditional steam turbine model for power grid stability calculation.

In this paper, the model modified method using actual data is given and guidance of parameters tests is offered.

Introduction of BPA model

According to the model provided by "PSD-BPA transient stability User's Manual (Version 4.15)" (hereinafter referred to as BPA), the turbine system model structure includes high, medium and low-pressure cylinder modules and reheater module etc., as shown in Fig.1. The parameters are shown in Table 1.

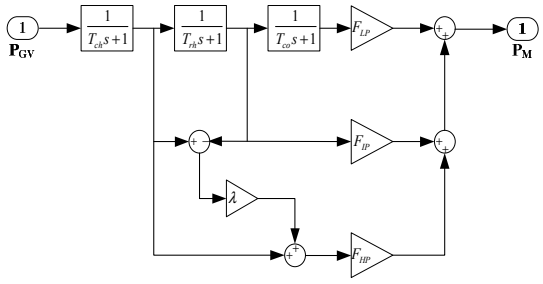

Fig. 1 Turbine model structure in BPA

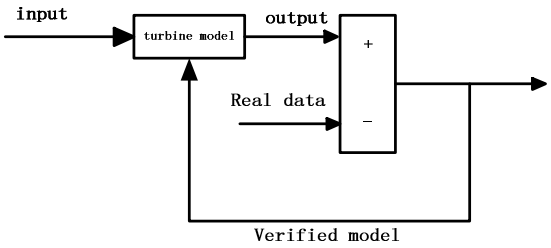

Fig. 2 Diagram of model validation method

Table 1 Parameters of turbine model

T_{CH}	Steam volume time constant[s]
F_{HP}	Ratio of power of high pressure cylinder(HPC)
T_{RH}	Time constant of reheater
F_{IP}	Ratio of power of intermediate pressure cylinder
T_{CO}	Time constant of cross-over steam line
F_{LP}	Ratio of power of low pressure cylinder
λ	Natural power overshooting coefficient of high pressure cylinder

Typical data：

F_{HP} = 0.3, F_{IP} = 0.4, F_{LP} = 0.3, T_{CH} = 0.1~0.4s，T_{RH} = 4~11s，T_{CO} = 0.3~0.5s

Verified methods and description of real data

To verify the accuracy and precision of the model, the actual data is needed. Verified method is to input the actual data to the turbine model. Based on the deviation of the model output and the actual data, the model is revised until the model output and the actual output are the same, as shown in Fig 2. This paper compared the actual value with simulation about power, HPC exhaust pressure and reheat pressure. The test data is from a 660MW supercritical coal-fired air-cooled generator. Test data is shown in Figure 3.

Contrast of real power and model simulation power. Turbine model can only get mechanical power, while the actual one is electric power. Through the rotor and the network model, can mechanical power obtains the electric power. Rotor time constant can be got by calculation, thus the stand-alone infinite grid model is needed, as shown in Fig. 4. The regulating stage pressure is as input and electric power is as output. The actual measured electrical power and electrical power of model can basically be the same by adjusting the infinite grid model frequency and damping ratio, as shown in Fig. 5.

As can be seen from Fig. 6, there is a certain lag between the simulation and actual measured electric power. This is because the measurement of regulating stage pressure is to use a very long pipe to lead steam and measures it at the end of the pipe. Due to the volume effect of pipeline and sensors' inertia, the experimental data lag behind the real pressure. Therefore, an advance correction module is added to amend the regulating stage pressure, as shown in Fig. 7.

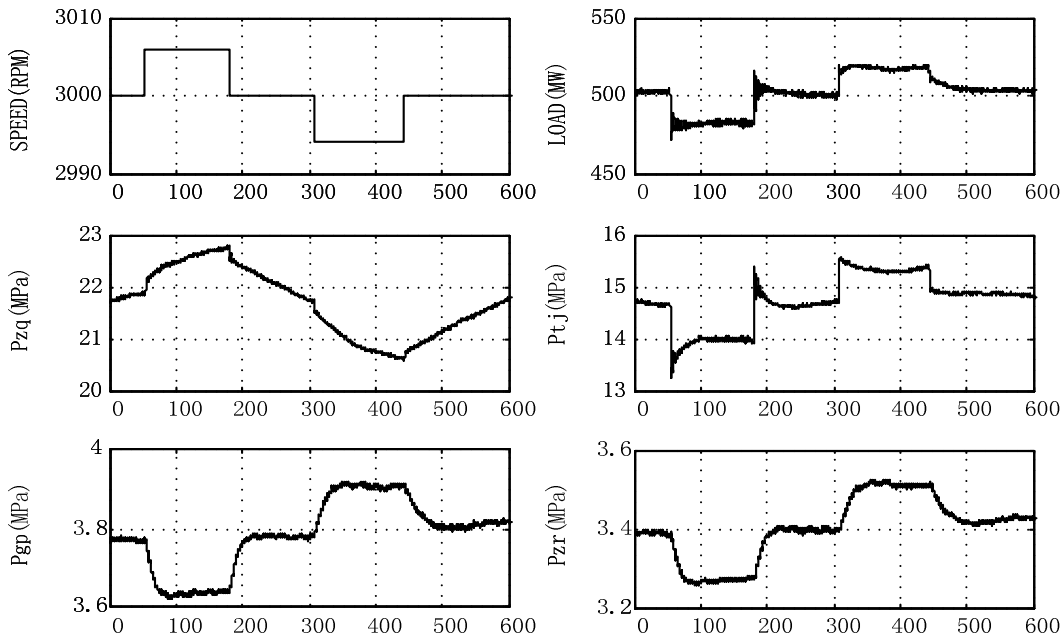

Fig. 3 Real testing data of parameters

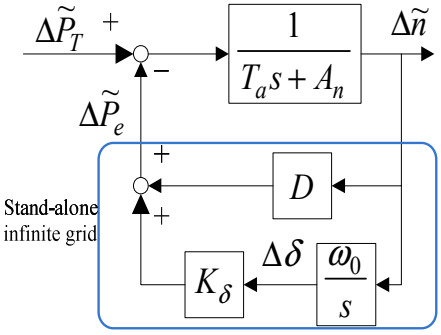

Fig. 4 Stand-alone infinite grid

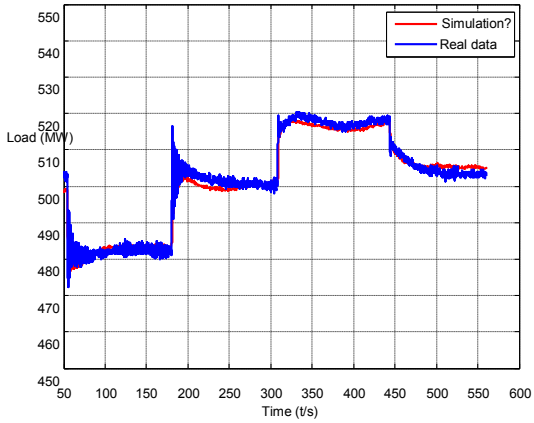

Fig. 5 Comparison of real and simulation power

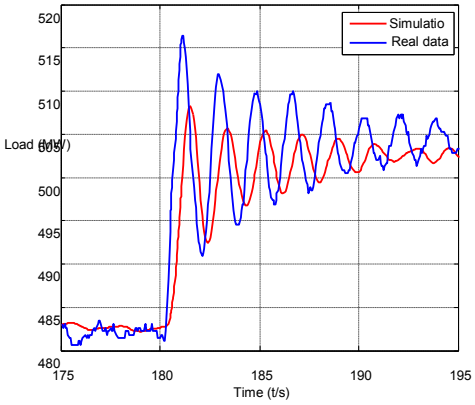

Fig. 6 Local map of the comparisons of real and simulation power

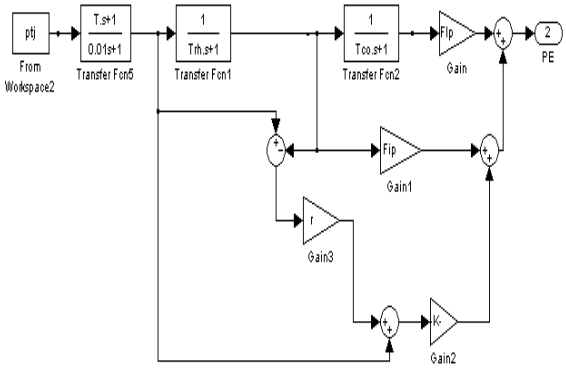

Fig. 7 Turbine modified model

Comparing the results obtained as a revised Fig. 8, Fig. 9, the frequency, amplitude and trend of electric power in the simulation results basically matches with the actual measured data.

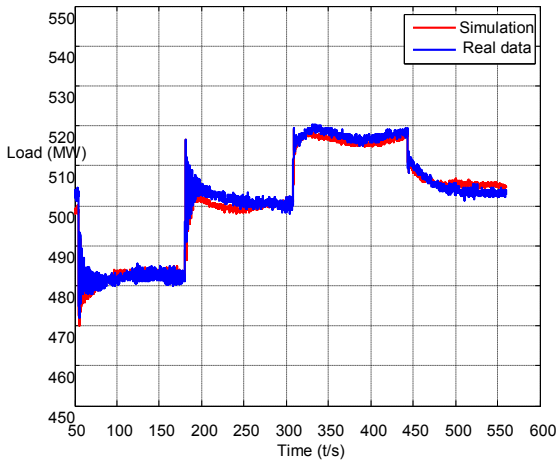

Fig. 8 Comparison of real and simulation power(modified)

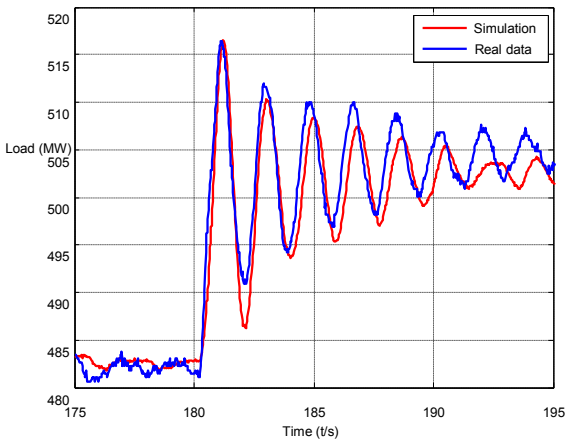

Fig. 9 Local map of Fig.8

Contract of real and simulation exhaust of HPC. The steam flow through flow path and enthalpy drop determines the turbine work jointly. But previous model does not consider the impact of enthalpy drop, so we introduced natural power overshooting factor[3].

From the perspective of turbine structure, from the high-pressure cylinder exports to the reheater outlet, pressure dynamic change has two main aspects. One is the volume effect, another is pressure loss. The volume effect can be described by reheat volume module, while the pure delay can show the pressure loss.

Therefore, in the actual HPC exhaust pressure simulation, a pure delay can be added before reheat volume to get the HPC exhaust pressure. From the actual data, the pure delay is 1.5s. Verification results is shown in Fig. 10 and local map is shown in Fig. 11.

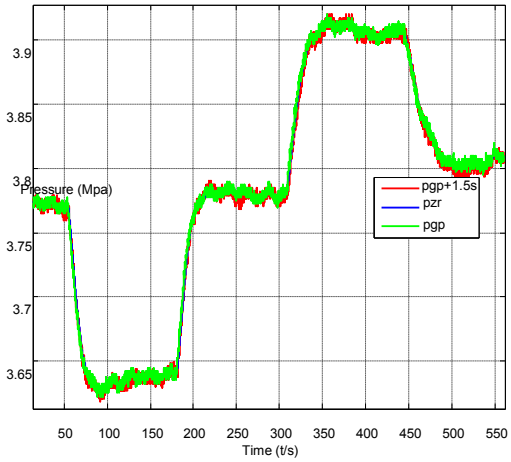

Fig. 10 Comparison of HPC exhaust pressure with reheat pressure before and after adjustment

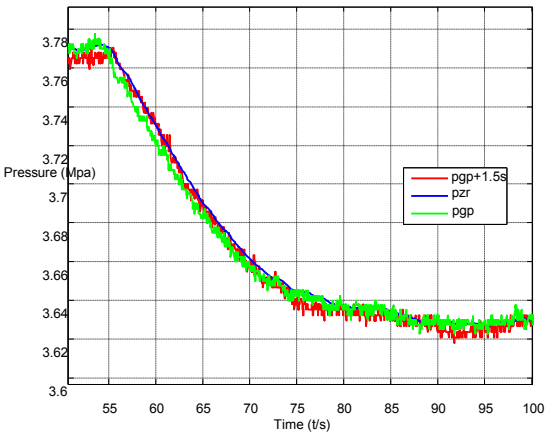

Fig. 11 Local map of Fig.10

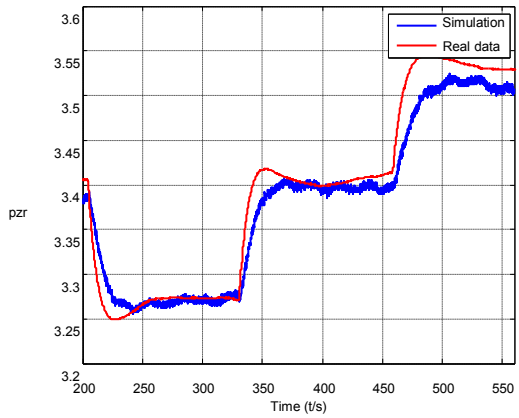

Fig. 12 Comparison of real and primary simulation reheat pressure

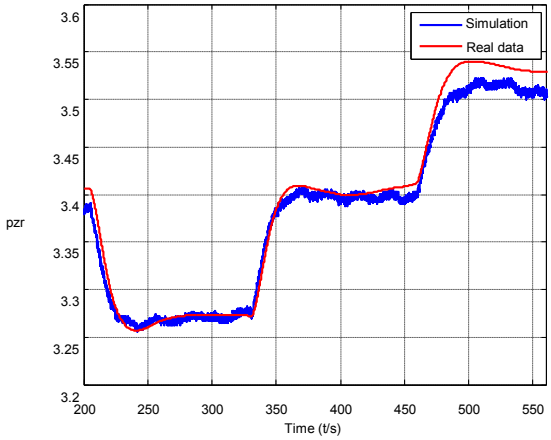

Fig. 13 Comparison of real and simulation with reheating system reheat pressure

Contrast of real and simulation reheat pressure. Using pressure from regulating stage as input and reheat pressure as output to verify the actual results with model simulation. There is a large variation between the original model simulation results and actual experimental data and real data responds more slowly, as shown in Fig. 12. This is because there is a big overshoot in input parameter simulation data. This is mainly because of the regenerator, a big inertia storage part, lies between the regulating stage and reheat pressure[4]. Therefore, the simulation result of reheat pressure for a model with regenerative system matches with the real data better, as shown in Fig. 13.

Conclusions

This paper compared the actual data of power, HPC exhaust pressure and reheat pressure with the BPA model simulation results and analyzed the causes of errors. Therefore calibrates and optimized the established turbine and governor. It proved the accuracy and advantages of the modified steam turbine and governor system mode and gave the correction model approach using actual data, thus provided guidance on the parameters for test trials.

For example, the lack of regenerative system is the cause for overshooting in reheat pressure calibration using conventional model. By comparing the real data and simulation model, it proves the importance of regenerative system in model.

When using the real data to validate the model, the phase problem needs to be considered and the problem is generally caused due to the sensor. So the data needs to be corrected according to the actual situation.

Reference

[1] Min Luo, Shangli Zhou et al.: Southern power system technology Vol.4, Supplement 1(2010), p.162-166 (in Chinese)

[2] Peng Wei, Ke Xu et al.: Power System and Clean Energy Vol.29 (2013), p.6-11 (in Chinese)

[3] Yufeng Tian, Jiayang Guo et al.: Power System Technology Vol. 31 (2007), p.39-44 (in Chinese)

[4] Daren Yu, Yufeng Guo et al: Proceedings of the CSEE Vol.25 (2005), p.84-88 (in Chinese)

Advanced Materials Research Vols. 960-961 (2014) pp 1429-1432

doi:10.4028/www.scientific.net/AMR.960-961.1429

Multifunctional Automatic Replacement Truck Design

Zhang Rong [1, a] Hu Jun [1, b]

[1]Wuhan Donghu University, Hubei Wuhan, 430212, China

[a] 55101725@qq.com, [b]1258622092@qq.com

Key Words： Solidworks,Multifunctional Automatic Replacement Truck,Design.

Abstract. This article from the market background and market current situation analysis, on the current market of forklift insufficiency and flaw analysis, found a multi-purpose vehicle is very suitable for the market current situation, so the multifunctional automatic change of engineering vehicle design. Then the main function are introduced, design, calculation, through modeling, error analysis and Solidworks analysis, design a reasonable multi-functional automatic replacement vehicle structure. finally introduced multi-function automatic change the character of engineering vehicles, introduce market prospect

Designing backgrounds

Traditional engineering vehicles according to the structural type of the main points of excavator, crane, grab, jumbo, normally use to do only one thing , such as in the same construction sections for different types of construction, it will require a different type of truck to construction waste greatly, a relatively new type of multifunctional truck has been exist , But excavator, crane, grab, jumbo need artificial replacement, such as great potential safety hazard, multi-functional automatic replacement truck is a kind of multifunctional device can automatically change the previous construction engineering vehicles, reduce the labor, reduces the construction cost, automatic replacement, convenient and quick.

Physical design

The design of construction equipment is placed. Multifunctional automatic replacement truck's rotating arm is the main work device, at the front of the activities arm plate can be equipped with many construction equipment, such as digging shake, crane, grab a car, such as jumbo, the articulated device at the front of activity board can be convenient and quick to complete construction equipment replacement, According to the different bodily form feature behind the respectively, to design different fixtures.

As shown in figure 1, behind the multifunctional automatic replacement truck with the placement of fixtures of drilling, respectively, asynchronous gripper, dig shaking and hook. According to their size, respectively fixed in the back of a multifunctional automatic replacement truck, can convenient to access at any time.

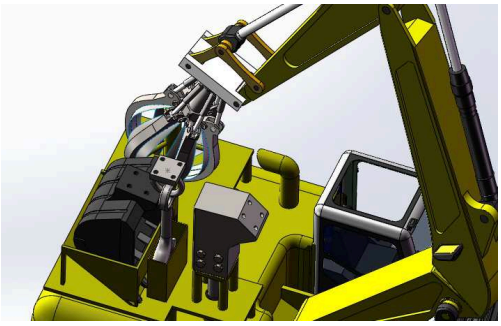

Figure 1. The construction unit is placed behind it

Multifunctional automatic replacement truck construction equipment installation. The automatic replacement truck is on the basis of ordinary excavator to be modified, ordinary excavator is only one scoop, and the dig shaking is fixed on the excavator arm, In addition to dig, we also increased the asynchronous gripper, drilling and hook. After the activity of the arm between the front-end and back-end, there is a small turntable to arbitrary Angle rotation, different construction equipment such as digging, asynchronous gripper, drilling and hook on the corresponding position behind the excavator, has activities in excavator arm on the front panel, activity board has four automatic screw bolt device, In the different construction device is equipped with four devices can be connected to activity on a board. As shown in figure 2, is hook and arm are connected through the board, as shown in figure 3,dig shaking and arm are connected through the board, Figure 4 for asynchronous gripper and arm are connected through the board, figure 5 for plate and arm are connected through activities board, The construction unit in active plate can fast connection and separation, greatly improve the speed and efficiency of the equipment replacement, and it does' t need artificial replacement at the same time, also more safety. Reduced the labor intensity and multi-usage function..

Figure 2 Hook

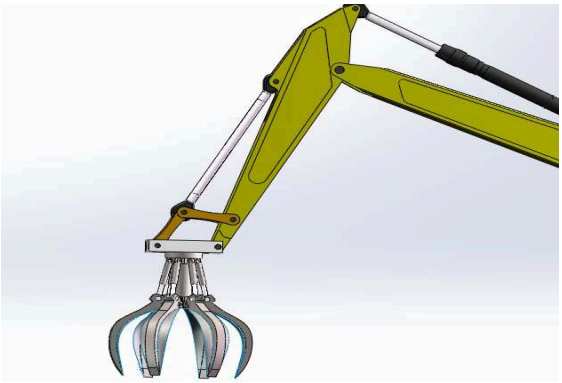

Figure 4 Asynchronous gripper

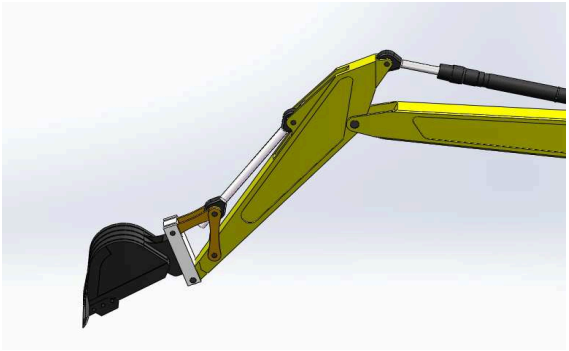

Figure 3 Scoop

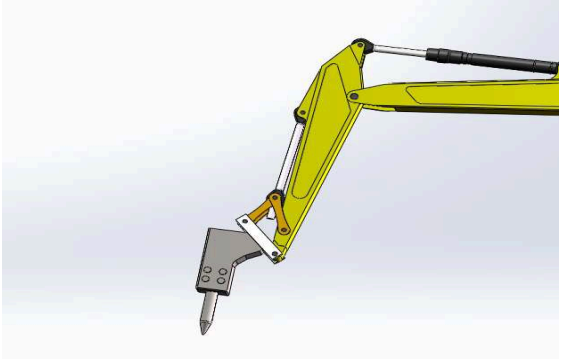

Figure 5 Bit

The automatic replacement process of multifunctional automatic replacement truck. Traditional excavator between car body and chassis can rotate, but the arm is not alone. a small turntable between front-end and back-end of the activities arm, can be to any Angle of rotation, Different construction equipment such as digging, asynchronous gripper, drilling and hook on the corresponding position, behind the excavator has activities board, activity board with four devices in excavator arm on the front panel, automatic screw bolt in the different construction device is equipped with four devices can be connected to activity on a board.

Such as the need to change different construction unit, just need to excavator arm after spin 180 degrees, and move to the corresponding required for the position of the construction unit, the activity board device and construction joint, the spin or device on the activity board began to spin, So that the construction unit change to the active arm up, and then rotating the small turntable that between front-end and back-end in the arm to move, which can carry out the construction. Device just need to change for different construction excavator arm after spin 180 degrees, then the movement to the corresponding construction set the required position, put down the construction unit, construction on the loosen activity board device, with the same way to change of other construction equipment.

Multi-functional automatic replacement truck automatic replacement system has following functions: free to change any set with construction, convenient and flexible, make the multifunctional automatic car replacement truck operation scope, further improve the work efficiency. Figure 6 is a multifunctional automatic replacement truck's arm rotated to the rear for asynchronous process of gripper construction equipment. Figure 7 for multi-function automatic replacement truck's arm rotated to the rear for digging shaking the process of construction equipment. Figure 8 is a multifunctional automatic replacement truck's arm rotation to the rear for hook the process of construction equipment. Figure 9 is a multifunctional automatic replacement truck's arm rotated to the rear is bit change process of construction equipment.

Figure 6 Rotate and gripper

Figure 8 Rotate with the hook

Figure 7 Rotate and scoop

Figure 9 Rotate and bit

The advantages of the multi-functional automatic change truck

Multifunctional automatic replacement truck can use a variety of auxiliary equipment, and automatic replacement device construction, can effectively to complete a variety of different assignments, truly become a multi-functional engineering machinery. The characteristics of the multifunctional automatic replacement truck are:

1. flexibility, Multifunctional automatic replacement truck after the activities of the arm between the front-end and back-end, there is a small turntable to arbitrary Angle of rotation, the flexibility of movement to different construction equipment such as digging, asynchronous gripper, drilling and hook the location, to achieve fast automatic replacement, which can replace any desired construction equipment.

2. versatility, Multifunctional automatic replacement truck wide range of uses, it can continuous operation for a long time. A series of quick replacement affiliated construction equipment to choose from, including digging shake, asynchronous gripper, drilling and hook, etc. Don't need to buy other models, the placement of the construction equipment on the truck's back position, construction equipment can be taken at any time, improve truck multi-usage, improve work efficiency.

3. Stability and security. Multifunctional automatic replacement truck construction equipment on the truck behind fixed place, uniform weight distribution, access at any time, convenient and quick

Through analysis to the multifunctional automatic replacement truck of design, modeling, multi-functional automatic car replacement truck is feasible. The market demand for multi-functional automatic replacement of engineering machinery, for multi-use of engineering machinery is in short supply. Multifunctional automatic replacement truck improve job performance, multi-usage, automatic replacement, without other auxiliary help, do not need artificial replacement of construction equipment, will bring a new revolution of the truck. With economic development, the growing construction industry, the demand for all kinds of loading and unloading machinery also continued to expand. For multifunctional automatic replacement truck is a multifunctional mechanical engineering vehicles, by replacement of construction equipment, automatic, jumbo can realize mining, crane, grab car free conversion. Multifunctional automatic replacement truck in the modern construction industry has an important significance.

References

[1] Liu Ruixin. Mastercam application tutorial [M]. Beijing: mechanical industry publishing house, 2005

[2]What full east. Mastercam X nc programming and machining examples about [M]. Beijing, 2007.

Advanced Materials Research Vols. 960-961 (2014) pp 1433-1436

doi:10.4028/www.scientific.net/AMR.960-961.1433

Real-time diagnosis of slide valve and oil servomotor's jam faults based on strong tracking filter

Yongxin Feng[1,a] ,Sun Cai [1,b] Ding Cai[2,c] and Chongming Song[2,d]

[1]Power Research Institute of Guangdong Power Grid Corporation, Guangzhou, Guangdong, 510600, China

[2]Department of Energy Science and Engineering, Harbin Institute of Technology, Harbin, Heilongjiang, 150001, China

[a]yonxingf@126.com, [b]pingguonothing@163.com,[c]cdhityou@163.com,[d]songchm_001@163.com

Keywords: slide valve and pilot valve, hydraulic servo system, jam fault, fault diagnosis, strong tracking filter, parameters estimation.

Abstract. Jam fault occurs most times in the hydraulic servo system, and is the one of the factors that mainly influences the reliability of the system. For parallel-operated turbine, the jam faults of regulating system are elusive and fatal. In order to monitor operation condition and improve the reliability of the system online, the model of jam fault had been built, the sizes of the dead zones which describe jam fault had been viewed as unmeasured parameters, which avoided the model uncertainty brought by the linearization of nonlinear system, and strong tracking filter had been used to estimate unmeasured parameter. Simulation and experimental results verified that, this technique could accurately, synchronously estimate respective degrees of jam faults of slide valve and pilot valve online whether in daily operation or moving test.

Introduction

Slide valve and oil servomotor is one of common structures of hydraulic servo system .It controls the turbine inlet through converting a given signal to a sufficient output power capability of the trip in order to manipulate the control valve. While the most frequently occurring fault is jam. It will seriously affect the reliability of the whole system if jam fault occurs. So it significances for online diagnosis and detection of oil motive spool jam fault，especially fault information is given in the early. But it is difficult to detect the jam fault reliably and feasibly because of concurrency fault sources and gradient of dry friction.

In order to detect the degree of jam fault of slide valve and oil servomotor, we build the mathematical model of slide valve oil motive, which parameterizes the jam fault directly and uses the dead zone to characterize the degree of jam fault. Then we use STF (Strong Tracking Filter) to joint estimate system status and parameters to be estimated. Thus we can achieve jam fault diagnosis of slide valve online. Simulation results demonstrate the effectiveness of this method.

Parameter estimation of nonlinear systems based on strong tracking filter

EKF(Extended Kalman Filter) is common used in the parameter identification of nonlinear models, There is often some uncertainty for the model of dynamic systems, but the robustness of EKF about the model uncertainty is poor, thus causing imprecise of identification, even divergent phenomena .STF is reformed from EKF. It has strong robustness about the model uncertainty

Discrete state-space models describe nonlinear time-varying stochastic system

$$x(k+1) = f(k,u(k),x(k)) + \Gamma(k)v(k) \tag{1}$$

$$y(k+1) = h(k+1,x(k+1)) + e(k+1) \tag{2}$$

Where $x \in R^n$ is the state variables, $u \in R^q$ is input vector, $y \in R^m$ is output vector. Process noise $v(k)$,observation noise $e(k)$ are separately p dimension and m dimension uncorrelated zero mean Gaussian white noise, and has the following statistical properties

$$E[v(k)v^T(j)] = Q_1(k)\delta_{k,j} \tag{3}$$

$$E[e(k)e^T(j)] = Q_2(k)\delta_{k,j} \tag{4}$$

Where $Q_1(k)$, $Q_2(k)$ are separately covariance matrix of process noise $v(k)$ and observation noise $e(k)$, $Q_1(k)$ is non-negative definite symmetric matrix，$Q_2(k)$ is symmetric positive definite matrix. $\delta_{k,j}$ is Kronecker delta function.

Model of slide valve and oil motor with jam faults based on strong tracking filter

2.1 State space description of jam fault model
We get

$$\begin{cases} T_h\dot{d} = f_1\left(u,d,y,C_h\right) \\ T_s\dot{y} = f_2\left(d,C_s\right) \end{cases} \tag{5}$$

Assuming the sampling interval is T, discrete state space can be described as：

$$\begin{bmatrix} d(k+1) \\ y(k+1) \end{bmatrix} = \begin{bmatrix} \frac{T}{T_h} f_1\left(k,u(k),d(k),y(k),C_h(k)\right) + d(k) \\ \frac{T}{T_s} f_2\left(k,u(k),d(k),C_S(k)\right) + y(k) \end{bmatrix} \tag{6}$$

The only that can be measured is the oil motive displacement output y,so the observation equation is:

$$y(k+1) = \begin{bmatrix} 0 & 1 & 0 & 0 \end{bmatrix} x(k+1)^T \tag{7}$$

2.2 Solving of jam fault model
State-space model can be expressed as:

$$x(k+1) = f\left(k,u(k),x(k)\right) \tag{8}$$

$$y(k+1) = h\left(k+1,x(k+1)\right) \tag{9}$$

The partial derivative term is:

$$F\left(k,u(k),x(k\mid k)\right) = \begin{bmatrix} \frac{T}{T_h}\frac{\partial f_1}{\partial d}+1 & \frac{T}{T_h}\frac{\partial f_1}{\partial y} & \frac{T}{T_h}\frac{\partial f_1}{\partial C_h} & \frac{T}{T_h}\frac{\partial f_1}{\partial C_s} \\ \frac{T}{T_s}\frac{\partial f_2}{\partial d} & \frac{T}{T_s}\frac{\partial f_2}{\partial y}+1 & \frac{T}{T_s}\frac{\partial f_2}{\partial C_h} & \frac{T}{T_s}\frac{\partial f_2}{\partial C_s} \\ 0 & 0 & 1 & 0 \\ 0 & 0 & 0 & 1 \end{bmatrix} \tag{10}$$

$$H\left(k+1,u(k+1),x(k+1\mid k)\right) = \frac{\partial h\left(k+1,x(k+1)\right)}{\partial x} = \begin{bmatrix} 0 & 1 & 0 & 0 \end{bmatrix} \tag{11}$$

Because f_1 and f_2 are piecewise functions, we think jam fault occurs at the cut-off point. The specific solving results are as follows:

$$\frac{\partial f_1}{\partial d} = \begin{cases} -1 & \left|u-y-d\right| > C_h \\ 0 & \left|u-y-d\right| \le C_h \end{cases} \tag{12}$$

$$\frac{\partial f_1}{\partial y}=\begin{cases}-1 & |u-y-d|>C_h\\ 0 & |u-y-d|\le C_h\end{cases} \tag{13}$$

$$\frac{\partial f_1}{\partial C_h}=\begin{cases}1 & u-y-d<-C_h\\ -1 & u-y-d>C_h\\ 0 & |u-y-d|\le C_h\end{cases} \tag{14}$$

$$\frac{\partial f_1}{\partial C_s}=0 \tag{15}$$

$$\frac{\partial f_2}{\partial d}=\begin{cases}1 & |d|>C_s\\ 0 & |d|\le C_s\end{cases} \tag{16}$$

$$\frac{\partial f_2}{\partial y}=0 \tag{17}$$

$$\frac{\partial f_2}{\partial C_h}=0 \tag{18}$$

$$\frac{\partial f_2}{\partial C_s}=\begin{cases}1 & d<-C_s\\ -1 & d>C_s\\ 0 & |d|\le C_s\end{cases} \tag{19}$$

Simulation results and analysis

In order to verify the jam fault diagnosis method of slide valve oil motive above is effective，we build simulation models on Simulink and analysis by simulation.

Initial state: $[0 \quad 0 \quad 0.01 \quad 0.2]^T$

The initial state estimate covariance matrix: $P(0|0)=diag[1000,1000,1000,1000]$

System noise covariance matrix: $Q_1=diag[0.1,0.1,0.1,0.1]$

Measurement noise covariance matrix: $Q_2=diag[0.1]$

Filters and other parameters in the model are shown as Table 1.

Table.1 Parameters of the simulation

Parameter	Value
Forgetting factor	0.95
Weakening factor	1
Spool death zone	0.01
Oil motive death zone	0.02
Sampling period	0.0001
Spool time constant	0.01
The time constant of oil motive	0.2

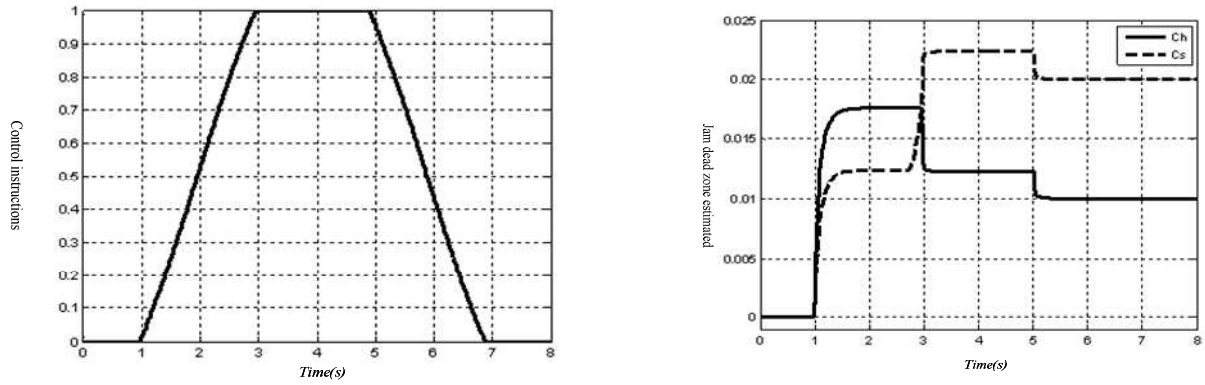

(a) (b)

Fig.1 a) Analog input signal b) Size of dead zone estimated

Fig.1 shows the simulation result of using STF when the excitation signal is the main steam valve activity test input signal. We get $C_h = 0.01$, $C_S = 0.02$,and their deviations are less than 0.1%.

After a lot of simulation experiments，we find:

1, the filter could not work effectively when no action of slide valve oil motive.

2, the filter can identify the size of dead zone only if the action of slide valve oil motive changes direction.

3, the filter can identify the size of dead zone only if the excitation signal is large enough.

Conclusions

This paper presents a accurate model describes slide valve oil motive jam fault in STF., which can avoid the uncertainty of the linearization of nonlinear systems .Only in the case of oil engine output can be measured，through joint estimating the state of the systems and the parameters describes jam fault, we can diagnose jam faults of slide valve and the oil motive. Simulation shows this method can detect and separate the jam fault of slide valve oil motive both in the daily operation of the unit or the main steam valve testing activities, it can even estimate jamming degree. What is more, it significances for online diagnosis and detection of oil motive spool jam fault，especially fault information is given in the early.

References

[1] Daren Yu, Qiang Liu: Proceedings of the CSEE.Vol.23(2003),p.179(in Chinese).
[2] Xuanyin Wang, Xiaoxiao Li, Fushang Li.: Journal of Shanghai Jiao tong University.Vol.43 (2009), p.1441 (in Chinese).
[3] Yunzhong Hu.: Aerospace Control.Vol.22(2004),p.10(in Chinese).
[4] Yang Guo, Shicheng Wang: Electronics Optics & Control.Vol.14(2007),p.49(in Chinese).
[5] Zhou D H, Frank P M:Aerospace and Electronic Systems.Vol.34(1998),p.420.
[6] Wenxing Fu, Supeng Zhu: Journal of Projectiles,Rockets,Missiles and Guidance Vol.27 (2007),p.182(in Chinese).
[7] B. Armstrong-Helouvry, P. Dupont:Automatica.Vol.30(1994),p.1083.
[8] Daren Yu: Submitted to Journal of Harbin Institute of Technology(1996).

Advanced Materials Research Vols. 960-961 (2014) pp 1437-1441

doi:10.4028/www.scientific.net/AMR.960-961.1437

Research of the Adaptation of Turbine Model Related to the Grid

Ge Jin[1,a], Shuchang Liu [2,b] and Yujia Ma[2,c]

[1] Power Research Institute of Guangdong Power Grid Corporation, Guangzhou, China

[2]College of Energy Science and Engineering, Harbin Institute of Technology, Harbin, China

[a]happyjinge@163.com, [b]zoro1piece@live.cn, [c]536087742@qq.com

Keywords: Turbine model, Characteristic parameters, Stability of grid

Abstract. With the rapid development of China's interconnected power grid, power system operation environment has become increasingly complex. The safety and stability of the power system requirements are also increasing. Turbine is an important basis for the analysis of power system stability. This paper studied the influence of turbine parameters related to network on the stability of the grid from the perspective of the frequency domain, and obtained the impact properties of turbine speed control system parameters related to different oscillation frequency of the power system. The conclusions are validated from time domain. So that when analyzing the stability of the power system, a more targeted turbine model according to different research purposes can be chosen because the parameters' importance can show the necessity of the modules.

Introduction

The power system operating environment has become increasingly complex, and the stability and security requirements of the power system have become more sophisticated. Random perturbations can cause power system's frequency, power and other parameters fluctuations or oscillations and have become a serious threat to the power system security and stability[1].Turbine model is an important foundation for analyzing the power systems' dynamic characteristics when various disturbances exists in the steady state. In current power system stability analysis, for turbine dynamic model, classical Cascade combination model is the mainstream. Because the model is too simplified, many problems appear in the application. Many scholars increased or improved part of the module on the basis of the classical model to improve the performance and made appropriate analysis.

Yunfeng Tian et al [2] improved the accuracy of the dynamic response of the turbine model by setting the high-pressure cylinder power natural overregulation factor. Xiaoqiang Liu et al [3] and Ge Jin et al[4] considered the impact of the main steam pressure model on unit primary frequency characteristics. Jiachuan Li[5], Rui Wang[6], Hui Liu et al[7]put emphasis on the boiler-turbine unit coordinated control of primary frequency characteristics.

Current situation shows that there exists no systematic analysis for the turbine model adaptation in power system simulation. Therefore, this paper established the steam turbine model, studied turbine characteristic parameters on the stability of the grid from the perspective of the frequency domain, and got the influence characteristics of a turbine combined with its speed control system related to network parameters on different oscillation frequencies of the power system.

Turbine model

This paper established a typical single reheat, single axle, four -cylinder exhaust steam turbine unit model, which mainly included steam volume effects module (describing the main dynamic characteristics at all levels of cylinders), rotor module, reheat system module, and heat recovery system module.

The volume time constant T_0 is:

$$T_0 = \frac{l\rho_0 A}{nAv_0\rho_0} = \frac{l}{nv_0} \tag{1}$$

Where the inlet pipe length is l, cross-sectional area is A, the designed flow rate of steam flow in the pipeline is v_0, rated conditions density is ρ_0.

Steam volume effect module is shown in Fig. 1:

Turbine generator unit rotor equation is

$$\chi_P - \chi_{NL} - \beta\chi_n = T_a \frac{d\chi_n}{dt} \tag{2}$$

While $\beta = (\frac{\partial N_f}{\partial \omega})_0 \frac{\omega_0}{N_{T0}}$, $T_a = \frac{J\omega_0^2}{N_{T0}}$

Where the rotor soaring time constant is T_a, self-balancing factor is β, a dimensionless quantity, which indicates a factor associated with the additional loss.

Have Laplace transform at both ends of Equ.2, then

$$\chi_P(s) - \chi_{NL}(s) = (\beta + Ta \cdot s)\chi_n(s) \tag{3}$$

According to Equ.3, the module is shown in Fig.2:

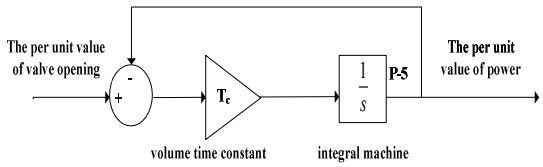

Fig. 1 Steam volume effect module

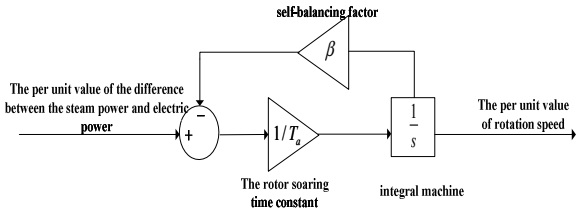

Fig.2 Turbine rotor simulation model

Reheat system model is mainly volume effect, the simulation module is shown in Fig.3.

Improved turbine characteristics related to network analysis model is shown in Fig.4.

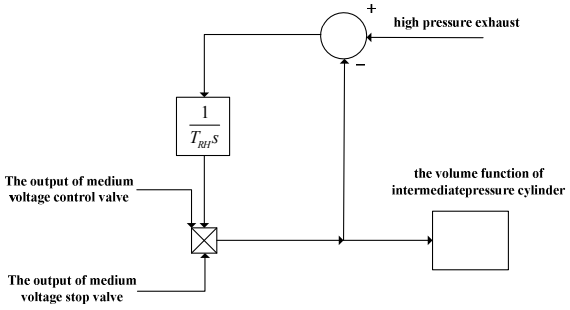

Fig.3 Reheat system model

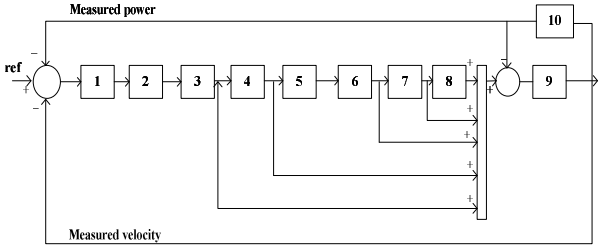

1. PID controller 2. Hydraulic servo-motor 3. Volume 4. High pressure cylinder backheating heater1 5. High pressure cylinder backheating heater2 6. Reheater 7. Intermediate and low pressure cylinder 8. Low pressure cylinder backheating heater 9. Rotor 10. Stand-alone infinite grid

Fig.4 Overall Schematic diagram Turbine

Frequency domain analysis for turbine characteristics related to network impact on the stability of grid

On the basis of the establishment of the turbine model, we carried out research on turbine parameters impact on the stability of the grid. Research method is to change a certain parameter, if it will cause changes in the frequency domain characteristics of the turbine system's specific band, then it indicates when the grid disturbance frequencies is in this band, this parameter's uncertainty will have an impact on the secure and stability of the grid.

Simulation results. Depending on the research objectives, actual measurement parameters tests are conducted, and the influence of disturbance of a particular frequency band is got, including where the parameter is to play a leading role in influencing and where are secondary. Turbine characteristic parameters related to network considered in this paper include steam volume time constant, reheat volume time constant, regenerator inertia time constant and the time constant of the hydraulic servo-motor. Simulation conditions and Bode plots are shown below.

Table 1 Values of main parameters

Serial number	Parameter	Symbol	Primitive value
1	Controller proportional element	Kp	1
2	Controller integration element	Ti	10
3	Normal regulation time constant of high pressure hydraulic servo-motor[s]	Tvh1	0.9
4	Volume time constant of high pressure cylinder[s]	TH	0.1279
5	Reheat volume time constant[s]	Trh	8.29
6	regenerator inertia time constant [s]	TrJG/TrJI/TrJD	20

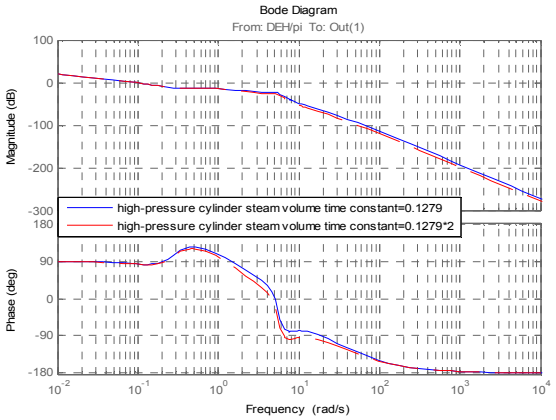

Fig. 5 Influence of high-pressure cylinder steam volume time constant on the system frequency domain characteristics

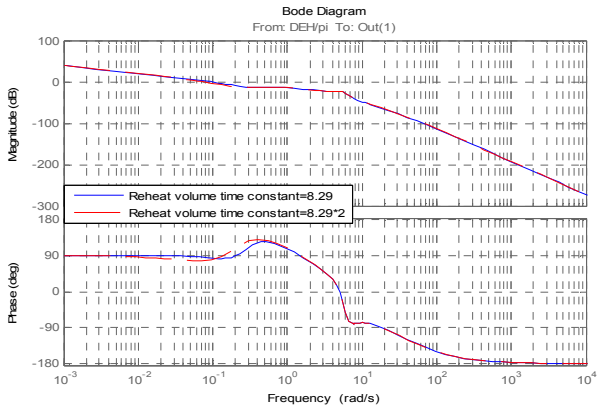

Fig. 6 Influence of intermediate-pressure cylinder steam volume time constant on the system frequency domain characteristics

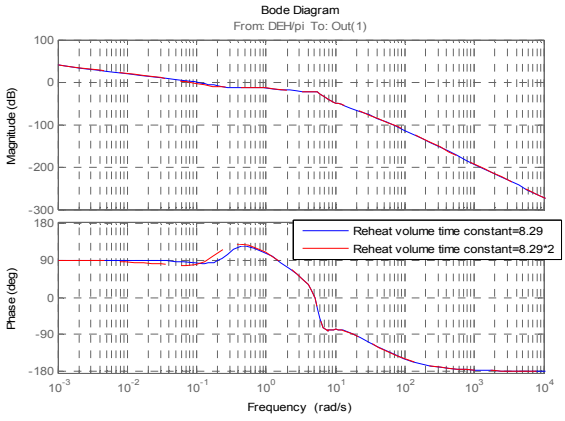

Fig.7 Influence of reheat volume time constant on the system frequency domain characteristics

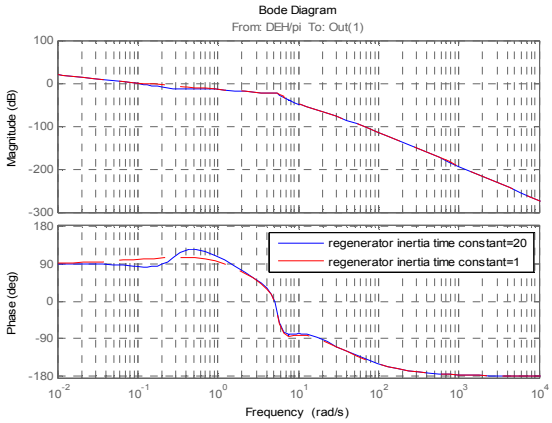

Fig.8 Influence of regenerator inertia time constant on the system frequency domain characteristics

As can be seen from Fig.5, the volume time constant of the high-pressure cylinder increases lead to the decrease of system bandwidth. When the system disturbance frequency is in the range of $\omega > 6rad/\sec$, the volume time constant of the high-pressure cylinder has an impact on the system's amplitude-frequency characteristics; when the system disturbance frequency in the range of $\omega = 0.02 \sim 2rad/\sec$, the volume time constant of the high-pressure cylinder has a rather large impact on the phase-frequency characteristics of the system. Considering the grid disturbances frequency is $f > 0.11Hz$, take the impact of the time constant of the high-pressure cylinder volume into consideration. From Fig.6, intermediate-pressure cylinder steam volume time constant generally has no impact on the system frequency domain characteristics.

As can be seen in Fig.7, reheat volume time constant has a big effect on the system low frequency region, particularly within the range $\omega = 0.01 \sim 0.5 rad/\sec$, i.e. $f = 0.0016 \sim 0.08 Hz$. So the grid frequency within this range need to consider the effect of reheat volume time.

As can be seen from Fig.8, within the range $\omega = 0.02 \sim 2 rad/\sec$, i.e $f = 0.003 \sim 0.318 Hz$, regenerator inertia time constant has a big effect on the system low frequency region.

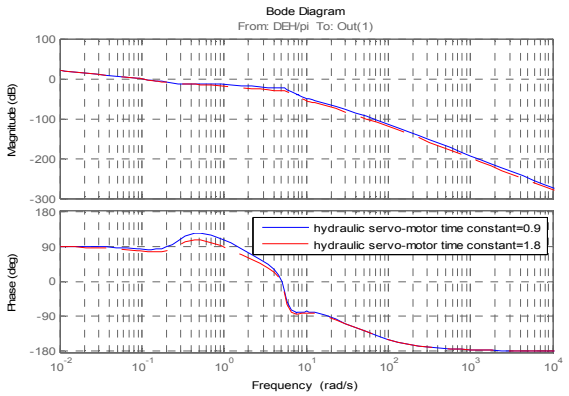

Fig.9 Influence of time constant of the hydraulic servo-motor on system frequency domain characteristics

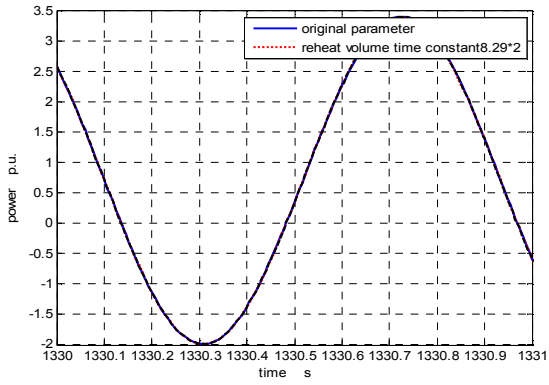

Fig.10 Influence of reheat volume time constant on the stability of grid

As can be seen from Fig.9, the system disturbance frequency $\omega > 1 rad/\sec$, the time constant of the oil motive influences the system amplitude-frequency characteristics greatly. When ω=0.1~3$rad/\sec$, the time constant of the oil motive effects the system phase frequency characteristics. When the grid disturbances frequency is $f > 0.016 Hz$, the time constant of the hydraulic servo-motor effect need to be considered.

Summary. This chapter considered turbine parameter uncertainty affecting the stability of the grid from the perspective of the frequency domain.

Time domain validation analysis

The influence of turbine power system network parameters on the different oscillation frequencies is obtained from frequency domain analysis. In order to more fully illustrate the problem, the conclusion is validated from time domain.

Effect of steam volume time constant and the volume time constant of high pressure cylinder.

Table 2 Simulation No. 1

Disturbance conditions	sinusoidal signal of frequency $f = 1.2 Hz$
Simulation results	Fig.10, Fig.11 and Fig.12

Table 3 Simulation No. 2

Disturbance conditions	sinusoidal signal of frequency $f = 0.04 Hz$
Simulation results	Fig.13 and Fig.14

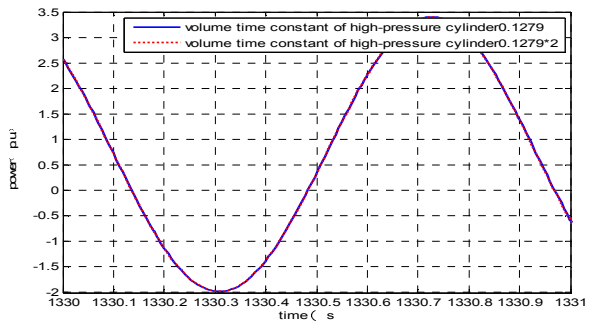

Fig.11 Influence of volume time constant of high-pressure cylinder on the stability of grid

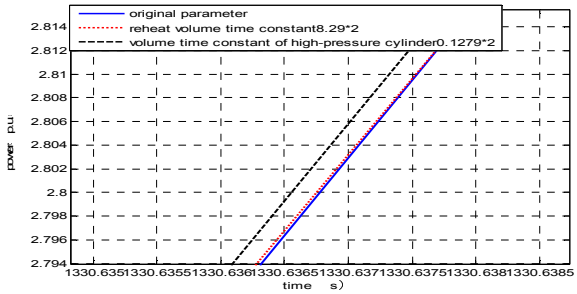

Fig.12 Comparison the influence of reheat volume time constant and volume time constant of high-pressure cylinder on the stability of grid

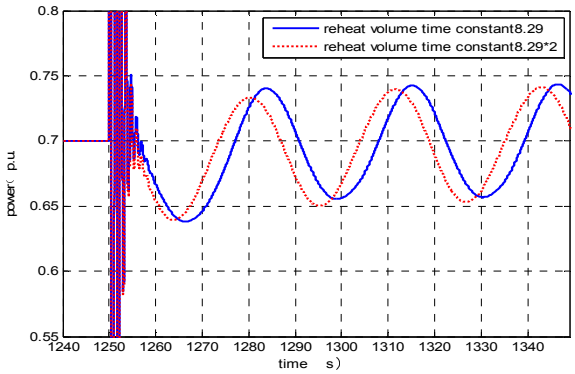

Fig.13 Influence of reheat volume time constant on the stability of grid

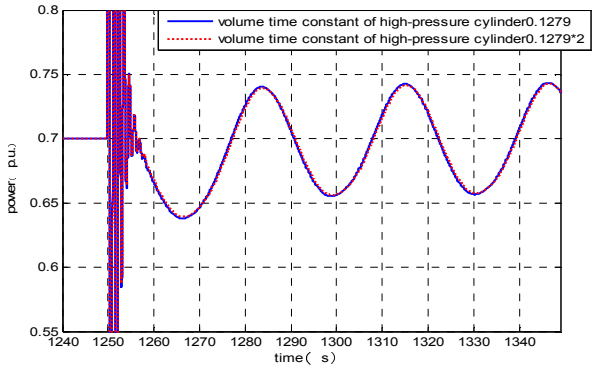

Fig.14 Influence of volume time constant of high-pressure cylinder on the stability of grid

Summary analysis. Take the high-pressure cylinder for example, when the grid disturbance is 1.2HZ, the analysis of the frequency domain shows that the reheat volume time constant changes have no effect on the stability of the grid, while changes in the volume time constant of the high-pressure cylinder influence the grid stability. The conclusion is verified from the time domain, but due to the stand-alone infinite power grid consideration and the controller design, the frequency is after the system cut frequency, thus the proven effect is not obvious. Therefore further demonstrate of this point is needed. When the grid disturbance is 0.04HZ, from the frequency domain analysis, changes in the reheat volume time constant have a great influence on the stability of the grid, while changes of the volume time constant of the high pressure cylinder do not impact the stability of the grid. For the frequency of the disturbance is in the vicinity of the shear frequency of the system, the difference between two parameters on the stability of the grid is obvious, which demonstrates our conclusion in the frequency domain analysis.

Conclusions

This paper established a revised turbine model as a basis to study turbine parameters' related to network influence on the grid stability from the perspective of the frequency domain, and obtained the turbine speed control system parameters related to the power system network effect of different characteristics of the oscillation frequency. The conclusion is validated from time domain. Therefore, when analyzing the stability of the power system, a more targeted turbine model according to different research purposes can be chosen because the parameters' importance can show the necessity of the modules.

For example, in the low-frequency oscillations (0.2Hz ~ 2.5Hz frequency disturbances), the establishment of the turbine should consider the module of hydraulic servo-motor, high-pressure cylinder, the rotor, while re-heater, the regenerator and other modules can be ignored. However, for long distance transmission case, re-heater and regenerator modules both need to be considered in the model.

References

[1] Pengchao Niu, Jitao Kang, Aiwu Li: Jiangxi Electric Power Vol.33 (2009), p.13-17 (in Chinese)
[2] Yunfeng Tian, Jiayang Guo, Yongqi Liu: Grid Technology Vol. 31(2007), p.39-44 (in Chinese)
[3] Xiaoqiang Liu, XitianWang: Thermal Power Engineering Vol. 23(2008), p.140-143 (in Chinese)
[4] Ge Jin, Shaoxiang Deng, Jin Tan: Guangdong Electric Power Vol. 24(2011), p.33-37 (in Chinese)
[5] Jiachuan Li, North China Electric Power University, 2008 (in Chinese)
[6] Rui Wang: Beijing Jiaotong University, 2009 (in Chinese)
[7] Hui Liu, Yunfeng Tian, Tao Wu: Automation of Power Systems Vol. 32(2008), p.103-107 (in Chinese)

Advanced Materials Research Vols. 960-961 (2014) pp 1442-1445

doi:10.4028/www.scientific.net/AMR.960-961.1442

The Simulation Study on Dynamic Characteristics of COGAG Engaging Process

Hui Meng[1, a], Zhitao Wang [1, b], Shuying Li [1], Ningbo Zhao[1],Gang Jin[1]

[1]College of Power and Energy Engineering, Harbin Engineering University, Harbin 150001, China

[a]menghuildj@126.com, [b]wangzhitao@hrbeu.edu.cn

Keywords: COGAG, Engaging process, Dynamic simulation

Abstract. This paper establishes the COGAG system simulation model in the environment of SIMULINK and ADAMS with the method of coupled simulation based on multiple simulation platforms; simulates and analyses the COGAG engaging process with the simulation model. Dynamic change rules of some key parameters such as speed, moment, power are obtained and analysed detailed, which plays an important role in development and application of COGAG device.

Introduction

Combined Gas turbine and Gas turbine (COGAG) system is widely used in ship machinery propulsion. It can effectively avoid the operation of gas turbine in low condition to improve the reliability and economy of the ship operation, compared with other power device. In order to reduce the test work, debase the risk of trial, save the cost and shorten the development cycle in the process of COGAG development , the comprehensive simulation on it is very necessary [1].

As the COGAG is a very complicated nonlinear system, the transmission device (especially SSS clutch) of COGAG is greatly simplified in the most simulations and analyses, the simplified model unable to fully reflect the dynamic characteristics and the specific engaging process. This paper adopts the method of coupled simulation based on multiple simulation platforms, establishes the simulation model of transmission device(SSS clutch, gear box) and other modules (gas turbine, engaging controller, propeller) in the environment of SIMULINK and ADAMS, and then take a systemic simulation and analysis on the engaging process and load distribution.

Simulation modeling

Introduction of COGAG. COGAG device is mainly composed of prime movers (double same gas turbine), transmission device(SSS clutch, gearbox, transmission shafts) and propeller, the typical arrangement is shown in Fig.1. The engaging process of COGAG can be summarized as follows: a gas turbine(1# gas turbine) is working with a certain load, another gas turbine (2# gas turbine) participates in the work and gradually maintains the same speed with the working gas turbine through the SSS clutch and gearbox; at the same time, the two gas turbine share the power together according to a certain proportion. When the ship need to improve the speed or increase the power, engaging process is necessary. The quality of engaging process directly affects the quality of COGAG as a power device, therefore, the study on the engaging process is important and necessary.

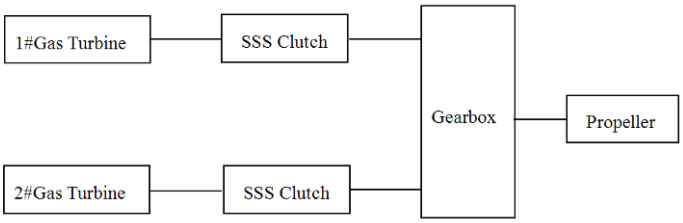

Fig.1 Typical arrangement of COGAG

The simulation model of COGAG system. The zero dimension variable specific heat simulation model of a gas turbine with three rotors was composed of compressor, combustor, turbine, volume, rotor, engaging controller and propeller, which were established in the environment of SIMULINK.

The simulation model as shown in Fig.2 took the outgassing process of compressor and the cooling process of turbine into account [2-5].

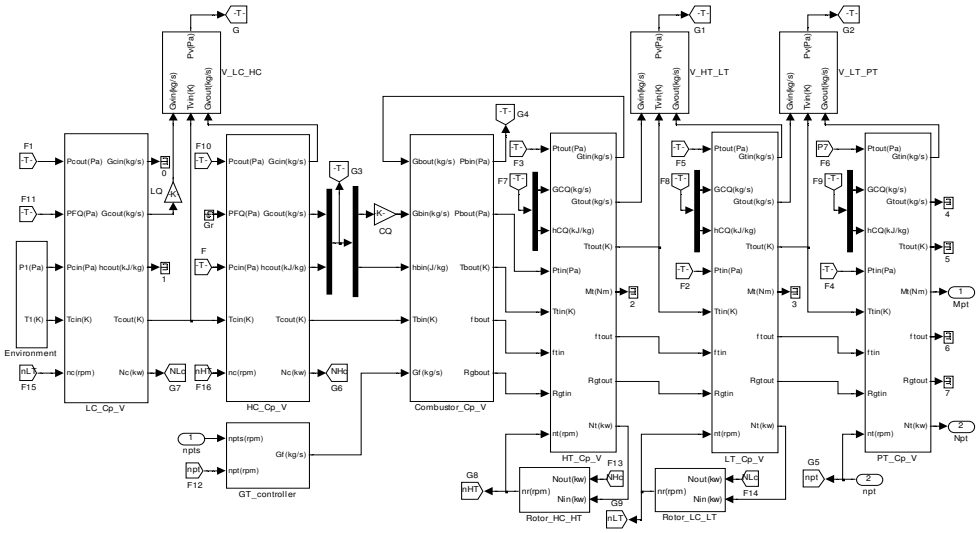

Fig.2 The model of a gas turbine with three rotors in SIMULINK

This paper established the model of the transmission device containing SSS Clutch and gearbox in the environment of ADAMS, according to the characteristic that the mathematic model of the transmission device was built based on the principle of mechanical system [6-9]. The simulation model was shown in Fig.3.

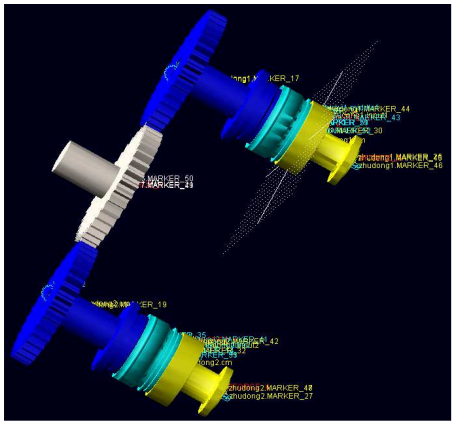

Fig.3 The model of transmission device in ADAMS

The whole COGAG model combined in the environment of SIMULINK was shown in the Fig.4. In the model, COGAG_controller and Propeller respectively represented the simulation model of engaging controller and propeller; SSS_clutch_and_Gearbox was the connector as a part of ADAMS between SIMULINK and ADAMS .

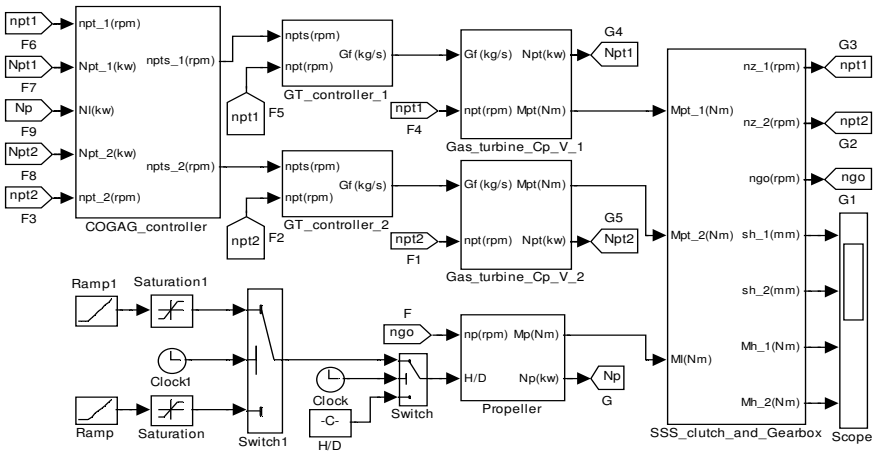

Fig.4 The whole COGAG model in SIMULINK

Results and analysis

The total simulation time was 20s, using ode14x fixed step algorithm, and the simulation step was 0.02s. Simulation process was summarized as follows:

(1) In the initial state, 1# gas turbine power turbine was running stable at speed of 2800rpm, the output power was 21000kw, of which 400kw was used to overcome resistance; 2# gas turbine power turbine was running stable at speed of 2800rpm, the output power was 400kw, all for overcoming resistance; 1# SSS clutch (connected to 1# gas turbine) was in engaged state; 2# SSS clutch (connected to 2# gas turbine) was in disengaged state; gearbox ratio was 19, the output shaft was connected directly to the propeller.

(2) Starting engaging at 10s, the power allocation coefficient of engaging controller was 0.5(1# gas turbine and 2# gas turbine had an average allocation of power after the engaging).

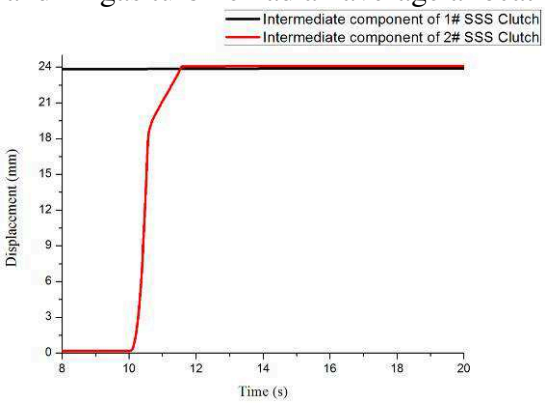

Fig.5 Displacement of middle ware

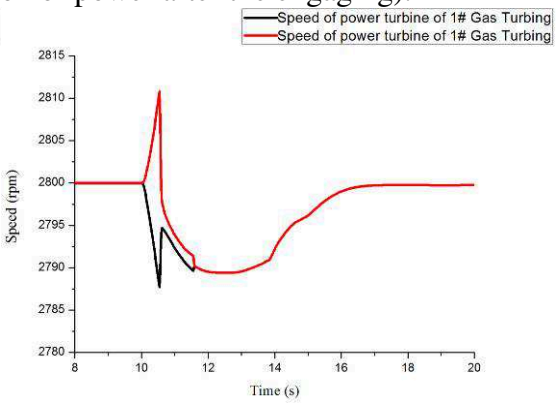

Fig.6 Speed of gas turbine

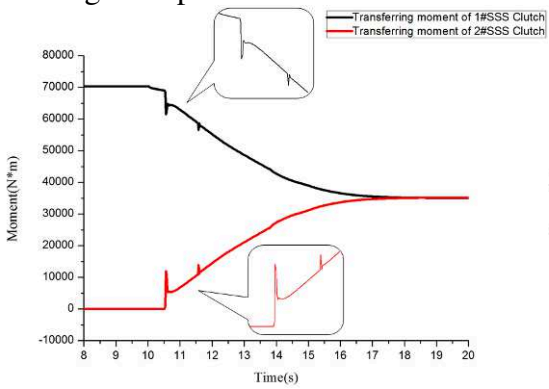

Fig.7 Moment of middle ware

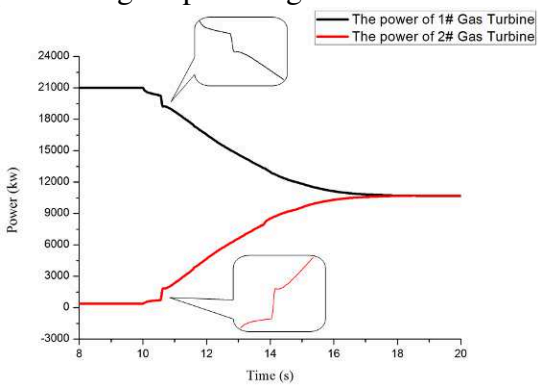

Fig.8 Power of gas turbine

The simulation results were analyzed as follows:

As shown in Fig.5, 2# SSS clutch middle ware started moving from 0mm displacement when starting engaging, gradually closer to the driving part along helical spline; within 0mm ~ 16mm distance range, the oil chamber damping almost did not work, and the axial movement of middle ware was fast; when the distance was greater than 16mm, the oil chamber damping started working, axial movement of middle was slowing down; and the time required of the engaging process was about 1.6s, finally the middle ware collided with the driving part, stopping axial movement and the engaging process was completed. During the engaging process, the displacement of the 1# SSS clutch was always 24mm, then the clutch always maintained engaged state.

As shown in Fig.7, the transferring moment of 2#SSS clutch increased gradually; When there was almost no effect of oil chamber damping, the transferring moment was very little; When the oil chamber damping had effect, transferring moment was increased suddenly; When the middle ware compacted the driving part, the transferring moment of middle ware increased suddenly again, but its amplitude was small; Subsequently, under the effect of engaging controller, the drive torque increased persistently, until the load distribution completed around 20s. The transferring moment of 1#SSS clutch middle ware decreased gradually, its change rule was basically opposite to 2#SSS clutch. As shown in Fig.8, the change rule of the output power of gas turbine was basically same as the above process, it was unnecessary to go into details here.

As shown in Fig.6, the speed of power turbine of 2# gas turbine was higher than power turbine 1# during the engaging process; After the oil chamber damping of 2#SSS clutch acting, the transferring moment of clutch middle ware increased suddenly and the speed of driving parts suddenly decreased; The moment transferred to 1# clutch driven parts via the gearbox, the speed of middle ware and driving parts increased suddenly under the effect of oil chamber damping; Although the output power of 2#gas turbine increased persistently, the effect of oil chamber damping was same, caused the speed of power turbine decreased slowly; Meanwhile, the output power of 1# gas turbine persistent decreased caused the speed of output shaft decreased slowly too; When the middle ware compacted the driving parts of 2# SSS clutch, the speed of output shafts of two gas turbines changed suddenly again, but the amplitude was small, the tendency and reasons of variation was same as the effect of oil chamber damping; Subsequently, under the effect of engaging controller, two gas turbines completed load distribution, and their output speed gradually stabilized at 2800rpm.

Conclusions

This paper simulated and analyzed the engaging process of COGAG based on coupled simulation method with SIMULINK and ADAMS, achieved relatively comprehensive dynamic change rules of the displacement of clutch middle ware, the transferring moment of clutch, the power and speed of gas turbine, and characteristics of other components. The results of simulation indicate that during the COGAG engaging process, the speed, moment, power, and other key parameters' variation were reasonable. The coupled simulation method can reflect the specific dynamic change rule of components during the engaging process further. It has very important effect to the research, production and application of COGAG.

References

[1] M. Altosole, G. Benvenuto, M. Figari. Real-time simulation of a COGAG naval ship propulsion system[J]. Proceedings of the Institution of Mechanical Engineers, Part M: Journal of Engineering for the Maritime Environment. 2009, 223(1): 47-61.

[2] T. S. Kim, S. H. Hwang. Part load performance analysis of recuperated gas turbines considering engine configuration and operation strategy[J]. Energy. 2006, 31(2-3): 260-277.

[3] S.M . Camporeale, B . Fortunato, M. Mastrovito. A Modular Code for Real Time Dynamic Simulation of Gas Turbines in Simulink[J]. Journal of Engineering for the Maritime Environment. 2006, 128(3): 506-517.

[4] W.T. Ma, Y. W. Liu, M. Su. New Scaling Method for Compressor Maps Using Average Infinitesimal Stage[J]. Chinese Journal of Mechanical Engineering. 2007, 20(6): 24-28.

[5] W.T. Ma, Y. W. Liu, M. Su. Multi-stage axial flow compressors characteristics estimation based on system identification[J]. Energy Conversion and Management. 2008, 49(2): 143-150.

[6] L.H. Morgan, B.Z.Michael. Experience With SSS (Synchronous-Self-Shifting) Clutches[C]. Turbo Expo 2008: Power for Land, Sea and Air. Berlin: ASME, 2008: 463-474.

[7] L.H.Morgan, G. H. Matthew. Development, Testing, and Implementation of a Gas Turbine Starting Clutch With Manual Turning Feature for U.S Navy Ships[J]. Journal of Engineering for Gas Turbine and Power. 2007, 129(3): 785-791.

[8] J.M. Jiang. The Study of The Dynamics Simulation for the SSS Clutch. [D]. Harbine: Harbin Engineering University，2010.

[9] G.J. Chen. Modern Marine Engineering[M]. Changshao: National University of Defense Technology press，2001: 372-376.

Advanced Materials Research Vols. 960-961 (2014) pp 1446-1449

doi:10.4028/www.scientific.net/AMR.960-961.1446

An Experimental Investigation of Cavitating Flow in Diesel Injector Nozzle under Different Back pressures

Xicheng Tao[a], Zhixia He[b*], Peng Zhao, Wenjun Zhong, Genmiao Guo

School of Energy and Power Engineering, Jiangsu University, Zhenjiang 212013, China

[a]769412989@qq.com, [b]zxhe@ujs.edu.cn

Key words: cavitating flow; diesel injector nozzles; visualization; back pressure.

Abstract: A study was carried out on the influence of different back pressures on internal flow of diesel injector nozzles. For this study, a flow visualization experimental system equipped with a pressurized chamber was setup. Experimental results show that, with the injection pressure remain constant and increase back pressure leading to the cavitation area diminished gradually and even disappeared. With a same pressure difference, higher back pressure test condition promoted the outlet mean velocity and inhibited the occurrence of cavitation inception, which demanded a larger pressure difference to make it happen. Moreover, it also resulted in a relatively large flow losses to the single phase flow compared to the cavitating flow.

Introduction

Recent studies have shown that the cavitating flow in diesel injector nozzles affect spray characteristics and therefore atomization behavior, which is decisive for diesel engine performance and pollutant formation[1]. Numerous researches have been carried out to investigate the formation mechanism and characteristics of internal cavitating flow[2-3]. However, most researches focused on the nozzle structures, with limited attention paid to the in-cylinder compression pressure(back pressure), which must have a strong influence on the cavitation distribution in nozzle orifices[4].

The Cavitation number (K) was defined as $K= (P_1-P_V)/(P_1-P_2)$.Where, P_1 is the injection pressure, P_2 the back pressure, P_v the saturated vapor pressure of the fuel. The value of K decreases as injection pressure increases or back pressure decreases. As K is smaller, the higher tendency to cavitate. Additionally, studies show that different nozzle structures have different critical Cavitation number K_{crit}, which indicates the start of cavitation. Another significant parameter is the discharge coefficient C_d. This parameter is defined as the relation between the real mass flow rate and the theoretical one, given by Bernoulli's equation: $C_d=\frac{Q_m}{A\sqrt{2\rho(P_1-P_2)}}$, where, Q_m is the actual flow rate, A the cross-sectional area, ρ the fuel density.

In this paper, a flow visualization experimental system equipped with a pressurized chamber was setup to investigate the effect of different back pressures on internal cavitating flow. The relationship between key parameters including K, Reynolds number Re, pressure difference ΔP, C_d were also discussed.

Visualization experimental setup

Fig.1 shows the basic experimental set-up. It was mainly consisted of the fuel injection system, the fuel supply system and the image acquisition system. It should be noted that the enlarged nozzle replica was designed and manufactured according to the similarity principle which ensured the internal structure and layout of nozzle unchanged. Bottled nitrogen is used to pressurize the fuel in the reservoir to supply fuel to the testing nozzle. A pressure gauge is located near the entrance of the injector to adjust and obtain the injection pressure. A flow rate meter is installed between the fuel tank and pressure gauge to provide flow rate value. The testing nozzle is placed between a light

source and a high speed camera, giving back lighting. All the captured images were digitally captured and stored in a computer. Table.1 shows the main parameters determined according to the similarity principle.

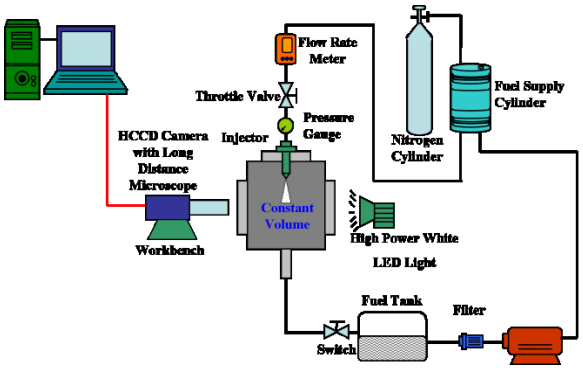

Fig.1 Schematic diagram of the nozzle flow visualization system

Table.1 Experimental parameters

Nozzle material	acrylic
Scaled-up times	5
Inclination of orifice（°）	70
Length of orifice（mm）	6.4
Orifice diameter（mm）	1.6
Working fluid	0# diesel
Fuel density（kg/m^3）	855
Fuel viscosity（Pa·s）	3.4

Experimental results and discussion

3.1 Analysis of cavitating flow development

Fig. 2 shows the cavitation variations happened during the experiments. These images were taken under the condition of keeping the injection pressure 0.7Mpa unchanged, while increasing back pressure P_2 from 0.2MPa to 0.45MPa.

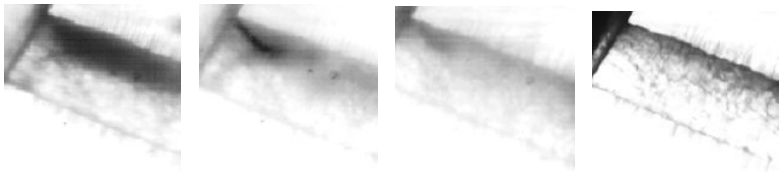

P_2=0.2MPa. P_2= 0.35MPa P_2=0.42MPa P_2=0.45MPa

Fig 2. The influence of different back pressures on cavitation distribution

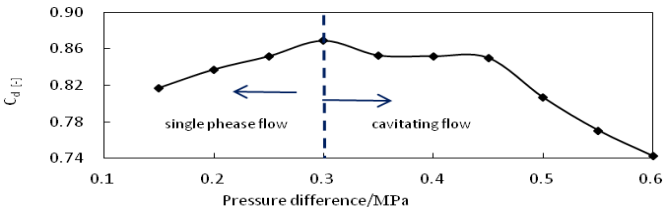

Fig.3 Correlation between C_d and ΔP

It can be seen from Fig. 2 that when P_2 was 0.2Mpa (i.e. maximum pressure difference), cavitation distribution area got most widespread. Then with the increase of back pressure, cavitation area diminished gradually. Moreover, when P_2 reached to 0.42Mpa, well developed cavitating flow faded to the critical condition of cavitation inception. Increase back pressure a step further, cavitation phenomenon completely disappeared. Fig.3 shows the correlation between ΔP and C_d for this experiment. It can be seen that in the single phase flow regime, C_d was not a constant value as Nurick proposed[5]. This was because that the flow resistance caused by the nozzle geometry was more prominent at small pressure difference, resulting in much more flow losses and smaller C_d.

With the increase of ΔP, internal disturbance increased and flow resistance diminished, leading to the raise of C_d. However, with the occurrence of cavitation phenomenon, discharge coefficient dropped sharply. This was because the mass flow choking effect in the orifice induced by the cavitation phenomenon. It is worth mentioning that there do exist hysteresis between the sharp diminishing start point of discharge coefficient and the cavitation inception.

3.2 Effect of back pressure on internal flow

Fig.4(left) shows the correlation between ΔP and C_d under different back pressures. It was obvious that with the increase of back pressure, the occurrence of cavitation inception became harder and called for a higher ΔP to make it happen. This was mainly because that the gas nucleus number of fluid is a key factor that affect cavitation inception, while large pressures at inlet and outlet effectively reduced the production of bubbles in the flowing liquid, therefore higher back pressure inhibited the cavitation phenomenon.

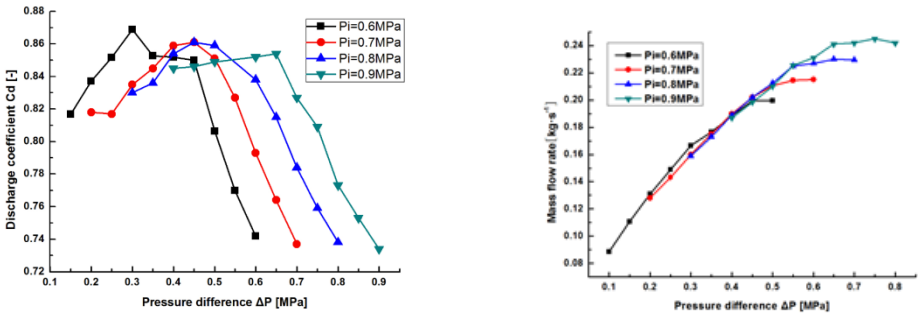

Fig. 4 Correlation between ΔP and C_d(left); correlation between ΔP and mass flow rate under different back pressures(right)

This can also be seen in Fig. 4(right) which shows the correlation between ΔP and mass flow rate. It was obvious that under the condition of same ΔP, higher back pressure leading to a larger flow rate, which can be interpreted as the area occupied by cavitaiton was very small under this condition.

In order to further investigate the effect of flow turbulence on flow losses, correlation between C_d and Re was obtained and drawn in Fig.5 (left). It can be seen that with the increase of Re, C_d decreased quickly after the cavitation phenomenon occurred. But Re corresponding to the blocking effect were different under different back pressure conditions, and higher back pressure meet with a higher Re. Therefore, it can be concluded that: under different back pressure conditions, flow losses of single phase regime was mainly caused by the flow turbulence and it was small; while in the cavitating flow regime, relatively large flow losses was produced by the occurrence of cavitation phenomenon.

Fig. 5(right) shows the correlation between K and outlet mean velocity. It can be seen that under the condition of sameΔP, after the occurrence of cavitation phenomenon, higher back pressure increased the mean velocity of fuel.

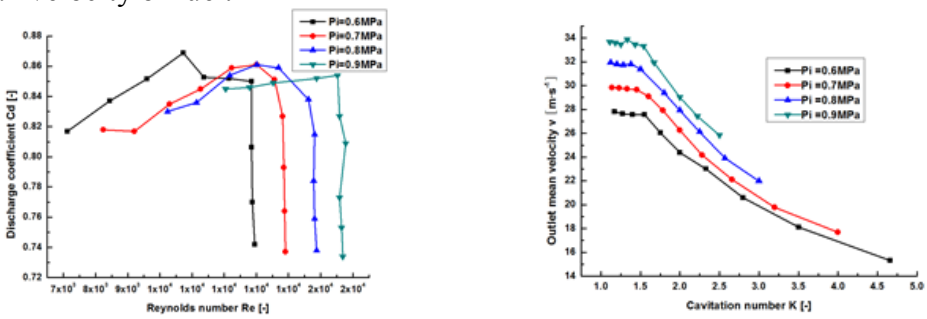

Fig. 5 Correlation between Re and C_d under different back pressures (left); correlation between K and mean velocity under different back pressures(right)

Conclusions

A flow visualization experimental system was setup to investigate the effect of different back pressures on internal flow. The main conclusions are as follows:

When injection pressure remains constant, the cavitation distribution area diminishes gradually and even disappeared as back pressure increases.

For cavitation inception phenomenon, higher back pressure condition calls for a larger ΔP between the nozzle inlet and outlet to make it happen, which indicates that higher back pressure condition inhibits the occurrence of cavitattion phenomenon. For cavitaing flow, under the condition of same ΔP, higher back pressure leads to a smaller cavitation distribution area. A hysteresis phenomenon exits between the sharp diminishing start point of C_d and cavitation inception.

In single phase flow regime, with a same ΔP, higher back pressure causes a larger flow losses due to the flow turbulences; while in cavitating flow regime, with a same ΔP, higher back pressure results in a smaller flow losses which was mainly caused by the occurrence of cavitation phenomenon. Additionally, flow losses cause by cavitation phenomenon is much larger than that cause by flow turbulences. Moreover, with a same ΔP, higher back pressure leads to a higher outlet mean velocity.

Acknowlegements

This research was supported by the National Natural ScienceFoundation of China (No.51176066, No.51276084) , Six Talent Peaks Project of Jiangsu Province (2013-JNHB-017) and Specialized Research Fund for the Doctoral Program of HigherEducation (No. 21033227110007)

References

[1] F. Payri, V. Bermudez, R. Payri, F. J. Salvador. Fuel, 83(2004)419-431.

[2] Schmidt D P, Rutland C J, Corradini M L. SAE Paper, 971587, 1997.

[3] Z.X. He, W.J.Zhong.. International Journal of Thermal Sciences 2013, 70: 132-143.

[4] R. Payri, F.J. Salvador, J. Gimeno, J. de la Morena. International journal of heat and fluid flow. 30(2009) 768-777.

[5] Nurick , W.H. Journal Fluids Engineering, 1976, Vo1.98.

Advanced Materials Research Vols. 960-961 (2014) pp 1450-1454

doi:10.4028/www.scientific.net/AMR.960-961.1450

Lifting force calculation and safty Analysis of hydraulic scissor lift platform

Leibo Sun [a], Renren wang[b] , Xinxin Li [c]

School of Mechanical & Automotive Engineering, Qilu University of Technology, Jinan, China, 250353

[a]842390767@qq.com, [b]wrr@qlu.edu.cn, [c]754559742@qq.com

Keywords: Hydraulic scissor lift platform; Design calculations; Component modules;

Abstract. Based on the structure, the hydraulic scissor lift platform can be divided into different component modules. The maximum lifting force is calculated in accordance with its structure features, and then the safty is analyzed.

The maximum thrust of the Hydraulic cylinder

The hydraulic scissor lift platform studied in this paper is SJPT-Series- mobile hydraulic lifting platform SJPT10-8 models. The main mechanical parts of the platform includes the platform, six scissor arms, chassis, five groups of inner frame and outer frame and other components. Maximum lifting height is 8m; Lifting capacity is 1000kg; Maximum overall dimension is length 2330mm x width1500mm x height 2700mm; Workbench size is length 1820mm x width 1200mm; Mating power is 2.2kw; Total weight is 2000kg[1] .

In accordance with the numbers of scissor arms which is pushed by hydraulic cylinder, it can be divided into three basic component groups: a hydraulic cylinder to promote a scissor arm, a hydraulic cylinder to promote two scissor arms, a hydraulic cylinder to promote three scissor arms[2].

The basic component groups of the hydraulic scissor lift platform studied in this thesis is a hydraulic cylinder promoting three scissor arms. The structure diagram is shown in Figure1.

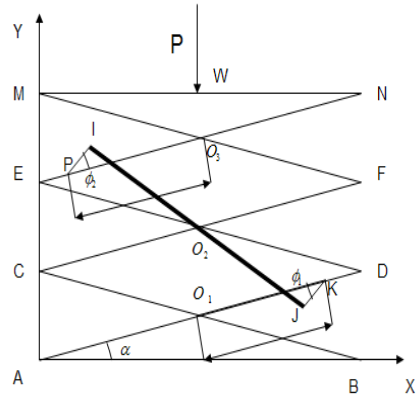

Figure 1 Structure diagram of the hydraulic scissor lift platform

l_1——The length of the lower hydraulic cylinder earrings

l_2——The length of the upper hydraulic cylinder earrings

K——The upper endpoint of the lower hydraulic cylinder earrings

P——The lower endpoint of the upper hydraulic cylinder earrings

J——The lower endpoint of the lower hydraulic cylinder earrings

I——The upper endpoint of the upper hydraulic cylinder earrings

L——Pin hole center distance of the scissor arm

l_1=210mm， l_2=210mm， L=1760mm， $\Phi_1 = \angle JKO_1 = 33^\circ$ ， $\Phi_2 = \angle O_3PI = 33^\circ$ ， a=O_3P=760mm，b=JK=760mm

In the same load, the position which the hydraulic scissor lift platform sufferes maximum thrust is the lowest position of the entire system, so the angle α between bottom scissor arm and the horizontal is taken as $\alpha=10^\circ$.

Considering the actual working conditions of the different staff operation and work-load, bias load issues may arise，therefore, calculation and check are carried out in accordance with unilateral weight, so under the condition of bias load the load which suffered by the hydraulic lift platform can be calculated as:

$$P = 0.5P_1 + 0.5P_2 \tag{1}$$

In the above,the P is the unilateral weight of the platform; P_1 is lifting weight; P_2 is the overall weight: P_1=1000kg, P_2=2000kg,So P=1500kg.

Here, the virtual displacement method is applied.

Them the virtual work formula can be calculated as:

$$\sum F_i \cdot \delta r_i = 0 \tag{2}$$

Analytical expression is:

$$\sum (F_{xi} \cdot \delta x_i + F_{yi} \cdot \delta y_i + F_{zi} \cdot \delta z_i) = 0 \tag{3}$$

Therefore, the thrust which is required by a single hydraulic cylinder can be drawn based on virtual displacement method. Firstly, list the coordinate equation of J point:

$$J_x = \frac{L}{2}\cos\alpha + b\cos\alpha - l_1\cos(\varphi_1 + \alpha) \tag{4}$$

$$J_y = \frac{(6i-5)}{2}L\sin\alpha + b\sin\alpha - l_1\sin(\varphi_1 + \alpha) \tag{5}$$

The coordinate equation of I point:

$$I_x = (\frac{L}{2} - a)\cos\alpha + l_2\cos(\varphi_2 + \alpha) \tag{6}$$

$$I_y = (3i-1)L\sin\alpha + (\frac{L}{2} - a)\sin\alpha + l_2\sin(\varphi_2 + \alpha) \tag{7}$$

The coordinate equation of J point can be divided into:

$$\delta_{jx} = [-\frac{L}{2}\sin\alpha - b\sin\alpha + l_1\sin(\varphi_1 + \alpha)]\delta_\alpha \tag{8}$$

$$\delta_{jy} = [\frac{(6i-5)}{2}\cos\alpha + b\cos\alpha - l_1\cos(\varphi_1 + \alpha)]\delta_\alpha \tag{9}$$

The coordinate equation of I point can be divided into:

$$\delta_{Ix} = [-(\frac{L}{2} - a)\sin\alpha - l_2\sin(\varphi_2 + \alpha)]\delta_\alpha \tag{10}$$

$$\delta_{Iy} = [(3i-1)\cos\alpha + (\frac{L}{2} - a)\cos\alpha + l_2\cos(\varphi_2 + \alpha)]\delta_\alpha \tag{11}$$

The coordinate equation of W point:

$$W_y = 3iL\sin\alpha \tag{12}$$

The coordinate equation of W point can be divided into:

$$\delta_{wy} = 3iL\cos\alpha \cdot \delta_\alpha \tag{13}$$

At the point of I, the angel between virtual displacement in the direction of Y and virtual displacement in the direction of X can be marked β; At the point of J, the angel between virtual displacement in the direction of Y and virtual displacement in the direction of X can be marked Ψ.

Therefore:

$$\tan\beta = \frac{\delta_{Iy}}{\delta_{Ix}} = \frac{(3i-1)\cos\alpha + (\frac{L}{2} - a)\cos\alpha + l_2\cos(\varphi_2 + \alpha)}{-(\frac{L}{2} - a)\sin\alpha - l_2\sin(\varphi_2 + \alpha)} \tag{14}$$

$$\tan\psi = \frac{\delta_{jy}}{\delta_{jx}} = \frac{\frac{(6i-5)}{2}\cos\alpha + b\cos\alpha - l_1\cos(\varphi_1 + \alpha)}{-\frac{L}{2}\sin\alpha - b\sin\alpha + l_1\sin(\varphi_1 + \alpha)} \tag{15}$$

Virtual work formula:

$$-P\delta_{wy} + F\sum_{i=1}^{n}\cos\beta\cdot\delta_{Iix} + F\sum_{i=1}^{n}\sin\beta\cdot\delta_{Iiy} - F\sum_{i=1}^{n}\cos\psi\cdot\delta_{jix} - F\sum_{i=1}^{n}\sin\psi\cdot\delta_{jiy} = 0 \tag{16}$$

Among them, When n = 1, stand for the case of a hydraulic cylinder promote three scissor arms;
When n = 2, stand for the case of a hydraulic cylinder promote six scissor arms;
According to the actual situation of this analytical study, take n=2.

Therefore, Virtual work formula can be changed:

$$-P\delta_{wy} + 2F\cos\beta\cdot\delta_{Ix} + 2F\sin\beta\cdot\delta_{Iy} - 2F\cos\psi\cdot\delta_{jx} - 2F\sin\psi\cdot\delta_{jy} = 0 \tag{17}$$

Simplify:

$$F = \frac{P\delta_{wy}}{2(\cos\beta\cdot\delta_{Ix} + \sin\beta\cdot\delta_{Iy} - \cos\psi\cdot\delta_{jx} - \sin\psi\cdot\delta_{jy})} \tag{18}$$

Substitute all the expressions:

$$F = \frac{6PL\cos\alpha}{2\left\{-\cos\beta[(\frac{L}{2} - a)\sin\alpha + l_2\sin(\varphi_2 + \alpha)]\right\} + \sin\beta\sum_{i=1}^{2}\left[(3i-1)\cos\alpha + (\frac{L}{2} - a)\cos\alpha + l_2\cos(\varphi_2 + \alpha)\right] - 2\left\{\cos\psi[-\frac{L}{2}\sin\alpha - b\sin\alpha + l_1\sin(\varphi_1 + \alpha)]\right\} - \sin\psi\sum_{i=1}^{2}\left[\frac{(6i-5)}{2}\cos\alpha + b\cos\alpha - l_1\cos(\varphi_1 + \alpha)\right]} \tag{19}$$

Substitute related data: $\tan\beta = -22.786^\circ$

So, $\beta = 93.7225^\circ$, Similarly too, $\Psi = 95.533^\circ$

Substitute related data into 2.23, the maximum thrust F can be drawn: 34282N.

Stress analysis in hinge joint of the hydraulic scissor lift platform

Considering the analysis is the instantaneous state at the initial position of the hydraulic scissor lift platform, therefore, the problem can be simplified as a issue which solving stress analysis in a system of static equilibrium. So, scissor arm force model can be simplified correspondingly: without considering the effects of inertia force , bias load as well as the weight of the hydraulic cylinder. For this model of a hydraulic cylinder promote three scissor arms, the hinge joint most bottom scissor arm has the maximum force. So the calculation should start from the very next level. If it meets the requirements of the stability and rigidity of other strengths, the other layers are bound to meet .As shown in Figure 2 and Figure 3.

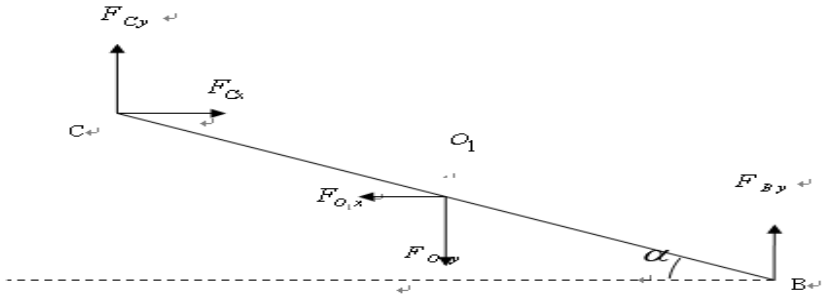

Figure 2 Force diagram of the bottom scissor arm BC

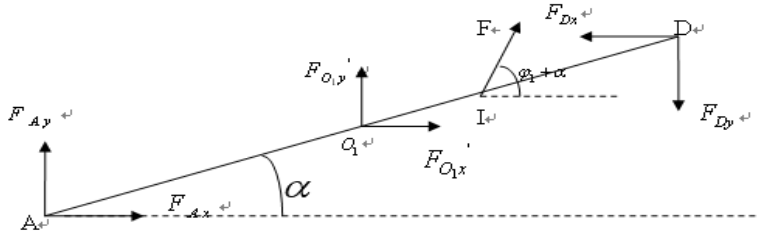

Figure 3 Force diagram of the bottom scissor arm AD

The Analysis of the Unilateral scissor arm

$$F_{Ax} = 0 \tag{20}$$

$$F_{Ay} = F_{By} = \frac{P}{2} = 7500N \tag{21}$$

The balance equation of BC

The balance equation of the direction force of X

$$F_{Cx} = F_{O_1x} \tag{22}$$

The balance equation of the direction force of Y

$$F_{Cy} + F_{By} - F_{O_1y} = 0 \tag{23}$$

Take moments of C Point

$$-F_{O_1x} \cdot CO_1 \cdot \sin\alpha - F_{O_1y} \cdot CO_1 \cdot \cos\alpha + F_{By} \cdot BC \cdot \cos\alpha = 0 \tag{24}$$

List the balance equation of AD

The balance equation of the direction force of X

$$F_{O_1x} + F\cos(\varphi_1 + \alpha) - F_{Dx} = 0 \tag{25}$$

The balance equation of the direction force of Y

$$F_{Ay} + F_{O'_1y} + F\sin(\varphi_1 + \alpha) - F_{Dy} = 0 \tag{26}$$

Take moments of O_1 Point

$$\begin{aligned} &-F_{Ay} \cdot AO_1 \cdot \cos\alpha - F\cos\alpha(\varphi_1 + \alpha) \cdot O_1I \cdot \sin\alpha \\ &+F\sin(\varphi_1 + \alpha) \cdot O_1I \cdot \cos\alpha + F_{Dx} \cdot DO_1 \cdot \sin\alpha - F_{Dy} \cdot DO_1 \cdot \cos\alpha = 0 \end{aligned} \tag{27}$$

Solve equations（20-27） can be obtained:

$F_{Dy} = 14591N$, $F_{Dx} = 32425N$, $F_{O_1x} = 7353N$, $F_{O_1y} = -16289N$, $F_{Cx} = 7353N$, $F_{Cy} = 23789N$

Stability analysis on the hydraulic cylinder piston of the hydraulic scissor lift platform

According to the hydraulic cylinder stroke and the actual working conditions and other conditions, the model chosen in this paper is CDL1MP5: AL- 40-125mm; Material is 45 steel; Piston rod diameter d=70mm;Piston rod length l=1132mm; Hydraulic cylinder length 1089mm;

Maximum force $F_{max} = 13.413KN$; Elastic modulus $E = 210GPa$; Proportional limit $\sigma_p = 280MPa$; Yield limit $\sigma_s = 350MPa$.

Calculate flexibility. Piston rod can be simplified into a rod which one end is fixed and the other is hinged, so the length factor $\mu = 2$.

Because the piston rod cross-section is circular, so

$$i = \sqrt{\frac{I}{A}} = \frac{d}{4} \tag{28}$$

Therefore the flexibility

$$\lambda = \frac{\mu l}{i} = \frac{\mu l}{\frac{d}{4}} = 129 \tag{29}$$

Among them, l——Piston rod length

D——Piston rod diameter

λ——flexibility

According to $\lambda_p = \sqrt{\frac{\pi^2 E}{\sigma_p}}$, Critical flexibility can be drawn $\lambda_p = 86$

$\lambda \geq \lambda_p$

Therefore Piston rod is greater flexibility piston rod, so the Euler formula can be used,

Calculation the critical force:

$$\sigma_{cr} = \frac{\pi^2 E}{\lambda^2} = \frac{\pi^2 \left(210 \times 10^9\right) Pa}{129^2} 1.244 \times 10^8 Pa \tag{30}$$

Critical load is:

$$F_{cr} = \sigma_{cr} \frac{\pi^2 d^2}{4} = \sigma_{cr} \frac{\pi^2 \left(70 \times 10^{-3} m\right)^2}{4} = 4.7859 \times 10^4 N \tag{31}$$

$F_{cr} = 4.7859 \times 10^4 N \geq 34282$

So the stability of the piston rod to meet requirements, which guarantees the stability of the lifting platform movement to some extent

Conclusion: SJPT10-8 types of hydraulic lift platform of maximum thrust of 34282 n, and SJPT10-8 types of materials also can meet the demand of application.

References

[1]shasha zhou Performance Analysis and Structure Optimization of Hydraulic Fork Lifting Platform, jinan Shandong Polytechnic University,2012 05

[2]wuping zeng．The Parametric design and structural analysis of the hydraulic scissor lift platform [D]．taiyuan：University of Science and Technology, 2009

[3] xiomei liu，lijie cao, zhiyi fan. Determine the sign and the size of the virtual work in Theoretical Mechanics [J]．Chinese Technology Expo 2010（1）: 224-225

[4]wuping zeng, liangbao wei Design calculation of Hydraulic Fork Lifting Platform taiyuan Taiyuan University of Science and Technology, 2010

Advanced Materials Research Vols. 960-961 (2014) pp 1455-1459

doi:10.4028/www.scientific.net/AMR.960-961.1455

Research for fuel common rail system about Marine Diesel Engine

Yuanqing Wang[1, a], Guang Ren[1,b] and Zhiqiang Zhou[1,c]

[1.]Marine Engineering College, Dalian Maritime University, Dalian 116026, China

[a]wangyqdmu@163.com, [b]reng@dlmu.edu.cn, [c]lanxiaocao@126.com

Keywords: diesel engine; fuel common rail; feedforward; rail pressure control.

Abstract. Wartsila RT- flex 60C diesel engine is selected as the object to research pressure control of fuel common rail system, building the system simulation model, and analyzing main factors influencing rail pressure in the system. it was concluded that they were diesel engine speed, load. In the process of MATLAB/Simulink simulation, the rail pressure control logic was designed by adopting maps with the two factors as independent variables to get theory feedforward quantity of fuel rack, feedback quantity of fuel rack is obtained by fuzzy PID control. The simulation experiments show that the improved control method reduces the rail pressure fluctuation, at the same time the overshoot volume of dynamic rail pressure control is greatly reduced, response velocity quickened. The control method has been used in a Marine simulator.

Introduction

Fuel common rail system controls the quantity of fuel injection, injection timing by using the way electronic control, makes the operation more flexible and accurate, becomes more and more popular in Marine diesel engine. Fuel rail pressure has a direct impact on injection timing, injection quantity.

Paper [1] established the steady-state simulation rail pressure, does not do dynamic simulation; Paper [2] established a dynamic simulation of marine fuel common rail pressure, but used the traditional PID control; Paper [3] established a control strategy that improve the fuel system of rail pressure, but the application object is car, therefore, it is necessary to make the further research of the Marine diesel engine fuel common rail pressure control [3].

The easiest way to adjust the rail pressure is that calculated directly the oil pump rack value with the rail pressure as input by the PID algorithm, it's just the feedback control, belong to the lag operation, it is difficult to avoid the overshoot, the control effect is limited, only rely on feedback lag operation, due to the marine diesel engine models and inertia very large. Marine fuel rail system specification stated that the rail pressure is regulated directly by the amount of fuel supply pump, making the amount of oil supply as another consideration, adopting the method of feedforward and feedback, the experiment proved to improve the response speed and accuracy of the rail pressure control. The specific calculation diagram is shown in Fig.1.

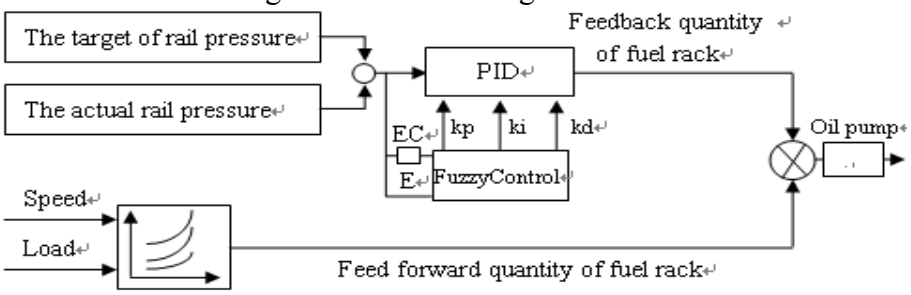

Fig.1. The control method of rail pressure

In this control method, got the real-time theory feedforward quantity of fuel rack with the speed and load as the feedforward input by the interpolation algorithm and look-up the MAP figure was produced by the bench experimental data was provided by the diesel engine manufacturers . In the feedback control, got feedback fuel rack with the rail pressure as input by the fuzzy control and adjusting the PID control parameters real-timely,. The more accurate the amount of feedforward rack

is, the smaller the amount of feedback rack would be, so as to achieve the control effect with faster and less overshoot. Finally, compare the control effect of the traditional PID control method with this article's the rail pressure control method by simulation experiments.

Fuel common rail system model of the RT-flex60C

Fuel common rail system of Marine diesel engine mainly consists of fuel pump, fuel rail, injectors, ECU electronic control unit and a variety of sensors, etc. From the control point of view, the key of the system is ECU electronic control unit which controls the oil supply of high-pressure fuel pump and the switch of fuel injector solenoid, so as to achieve these two critical control function that the fuel rail pressure and the width of fuel injection pulse.

Fuel rail system of diesel engine established mathematical model of the components according to the fluid mechanics and Newton's second law. In order to calculate conveniently, made the following assumptions during the modeling process the system: (1) the local loss of import and export are negligible, does not consider the system leakage; (2) does not consider friction resistance; (3) servo track the instantaneous equilibrium state and throughout the state are equal; (4) the system maintains a constant temperature liquid flow, and do the incompressible unsteady flow.

Model of the fuel injection system. Fuel injection system consists of rail valve, injection solenoid valve, injector and injection control unit ICU, etc. ICU control the fuel injector system, the 60-90Mpa fuel of fuel common rail is injected into the combustion chamber with the best injection timing, injection pulse-width. The quantity of fuel injection is related to the fuel common rail pressure and injection pulse-width. Their relationship is given as follows:

$$Q_p = \eta T_{WV} \sqrt{P_g} \tag{1}$$

In Eq. (1), Q_p denotes the fuel injection quantity; η denotes the constant of injection; T_{WV} denotes injection pulse-width; P_g denotes the common rail pressure.

The constant of injection η is a constant value from this formula; T_{WV} is related to the load, the greater the load is, the larger fuel injection pulse width is at the rail pressure under certain circumstances.

Model of the fuel rail pressure. A certain container, the amount of the liquid into the container is equal to the sum of the amount of liquid compression caused by pressure changes and the amount of the liquid out the container. It can be obtained mathematical models for each subsystem of the fuel common rail, the following is fuel common rail system mathematical model:

$$\frac{dP_g}{dt} = E(Q_b - Q_p)/V \tag{2}$$

In Eq. (2), E denotes elasticity modulus; Q_b denotes the supply oil from high pressure oil pump to the fuel rail oil; V denotes the volume of common rail.

From the paper [1] $E = 11.92p + 1230$, So we can find elastic modulus is only related to the rail pressure.

$$Q_b = A\frac{dh_z}{dt} = A \bullet \omega \bullet \frac{dh_z}{d\theta} \tag{3}$$

In Eq. (3), A denotes the area of oil pump plunger; ω denotes the speed of cam shaft; h_z denotes the stroke of plunger; θ denotes the angle of camshaft turned; $\frac{dh_z}{dt}$ denotes the speed of plunger movement; Plunger area A is constant value. Plunger velocity is controlled by the cam movement speed, the cam movement speed is controlled by the crankshaft speed； the crankshaft speed is determined by diesel engine load and speed. The volume of common rail V is constant value. Therefore, by formula (1) and formula (2), the fuel injection quantity is determined by the load and rail pressure, and the rail pressure is determined by diesel engine load and speed. So that we can find the decisive factor of the fuel rail pressure is determined by diesel engine load and speed.

The control method of rail pressure

Feedforward control. By the previous analysis, the decisive factor of the fuel rail pressure is the diesel engine speed and load, so get the real-time theory fuel rack values by look-up table with the two factors as input by interpolation algorithm and the MAP figure produced by the bench experimental data was provide by the diesel engine manufacturers.

Feedback control. Get quickly theoretical amount of fuel rack by feedforward control, but due to the intelligent diesel common rail system is very complicated, there is a certain rail pressure fluctuations, so that the control is fast and less overshoot to fine-tune the fuel rack by fuzzy control.

Fuzzy control adopts 2 × 3 Mamdani inference system, two inputs are e (system error) and ec (error rate), there outputs are three PID control parameters d_{k_p}, d_{k_i}, d_{k_d}. The change of the common rail pressure is between 0 and 90 MPa, so e and ec are in the range [0, 90], the value is 90 that it is greater than 90. Established fuzzy comprehensive domain to e, ec quantitative is {0,1,2,3,4,5,6,7,8,9} and their quantitative factor is 0.1. The domain of d_{k_p}, d_{k_i}, d_{k_d} is [0, 1]. E, ec corresponding input and output language variables and language values of d_{k_p}, d_{k_i}, d_{k_d} are Z, S, M and B four fuzzy subset, Z denotes Zero, S denotes Small, M denotes Medium, B denotes Big.

In this system, the membership functions of the variables are the triangular membership function. Output adopts the maximum membership degree method. PID parameters can be achieved self-tuning and the regulation characteristics of the system are improved. Adjustment may be expressed as:

$$K_p = K_p(0) + P_{K_p} \times d_{K_p} \tag{4}$$

$$K_i = K_i(0) + P_{K_i} \times d_{K_i} \tag{5}$$

$$K_d = K_d(0) + P_{K_d} \times d_{K_d} \tag{6}$$

In Eq. (4), Eq. (5), Eq. (6), $K_p(0)$, $K_i(0)$, $K_d(0)$ are the initialization values of the PID parameters; d_{K_p}, d_{K_i}, d_{K_d} are the change value of the PID controller parameters; P_{K_p}, P_{K_i}, P_{K_d} respectively are quantification factor d_{K_p}, d_{K_i}, d_{K_d}.

Simulation Models

The fuel system simulation model is divided into ECU control unit and fuel common rail system unit according to RT-flex60C machine structural characteristics and working principle, establish a simulation model of each system is based on the mathematical model by Matlab / Simulink simulation software and packaged each subsystem, the total simulation model is shown in Fig.2.

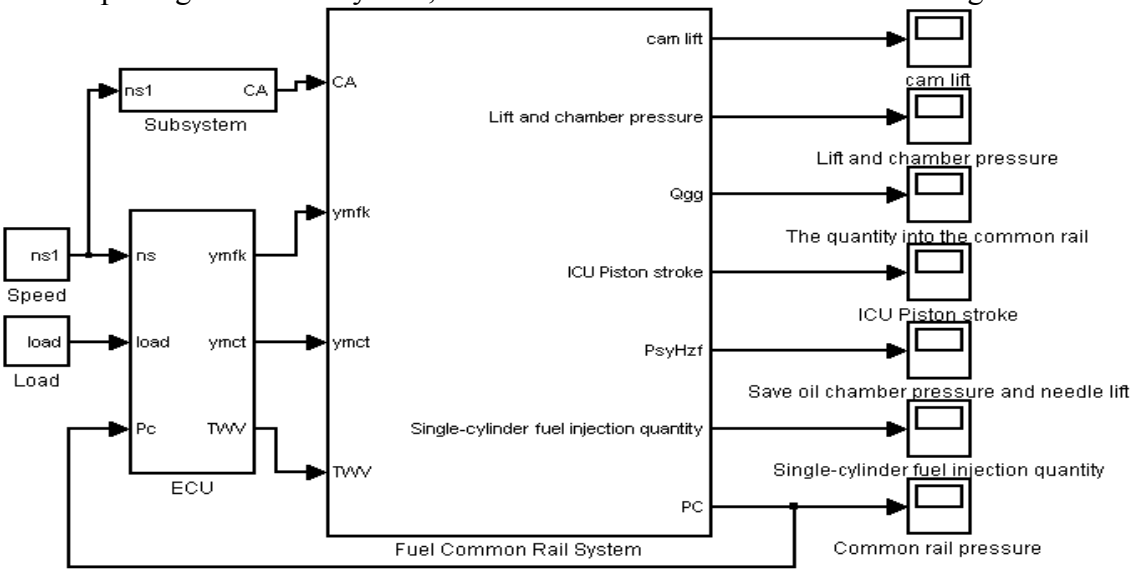

Fig.2. Common rail fuel system simulation model

Fig.3 is a package of ECU modules, included the target rail pressure look-up module, rail pressure fuzzy control module (get the fuel rack feedback value ymfk), theory of fuel rack look-up table module (ymct), fuel injection pulse-width look-up table module (TWV); the more accurate the feedforward fuel rack value is based on look-up table for diesel engine speed and load is, the smaller feedback fuel rack value is, the more stable rail pressure control would be.

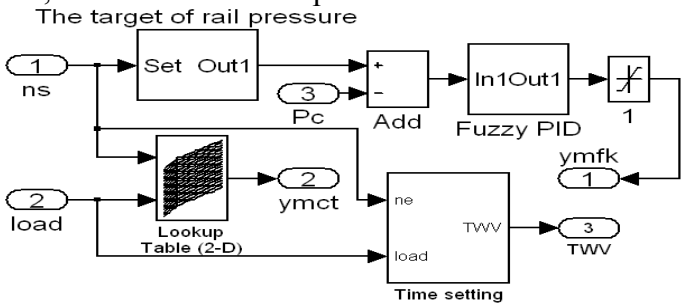

Fig.3 ECU control module

The simulation experiments and discussion

Use ode4 algorithm in MATLAB/Simulink simulation, the step length is 0.003. Common rail fuel pipe and intermediate reservoir volume are 0.5 and 0.25. The engine load is set to 99.9% and the speed is set to 114rpm at steady-state, the engine load is changed from 50% to 100% and the speed is changed from 91rpm to 114rpm at dynamic state. Respectively, do the simulation experiment by using the traditional PID control and that improved feedforward and feedback fuzzy PID control strategy. The following is the result of the experiment.

Figure 4 is the dynamic control effect contrast figure of the rail pressure that the diesel engine load and speed are changed, we can find that the response time of the rail pressure from 60 to 90 MPa is reduced and pressure to follow is faster from the improved control method; traditional PID control in rail pressure conversion has a certain overshoot, the feedback control is more precise, so overshoot is very small, rail pressure fluctuations is small, after the control is improved, getting a precise amount of pre-control by look-up table, and then optimizing the role by fuzzy PID control, so that this is very beneficial to the stable operation of diesel engine .

Fig.5 and Fig.6 are the steady-state rail pressure control, work only fuzzy PID feedback control at the steady-state. The traditional PID control rail pressure fluctuation is about 1.16 MPa that the load is 50% and the speed is 91rpm from Fig.5, but the improved rail pressure fluctuation is less than 0.11MPa. Figure 6 shows that the higher the load is, the greater the rail pressure is, the rail pressure fluctuation is increased, but it is a convergent fluctuation; Rail pressure fluctuation is less than 0.19 MPa after the control method is improved, volatility is far less than 5%, it meets the needs of actual situation.

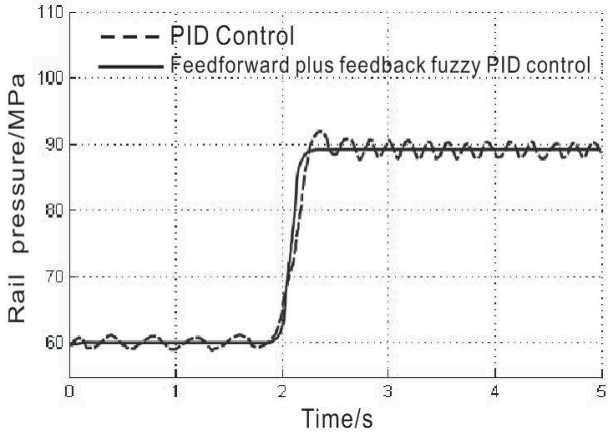

Fig.4. Dynamic simulation curve rail pressure

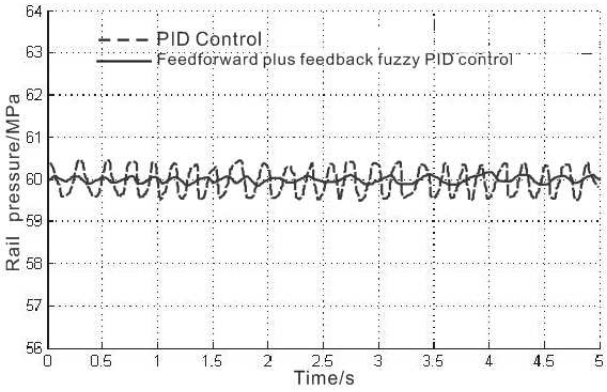

Fig.5. The rail pressure simulation curve when the load at 50% and the speed at 91 rpm

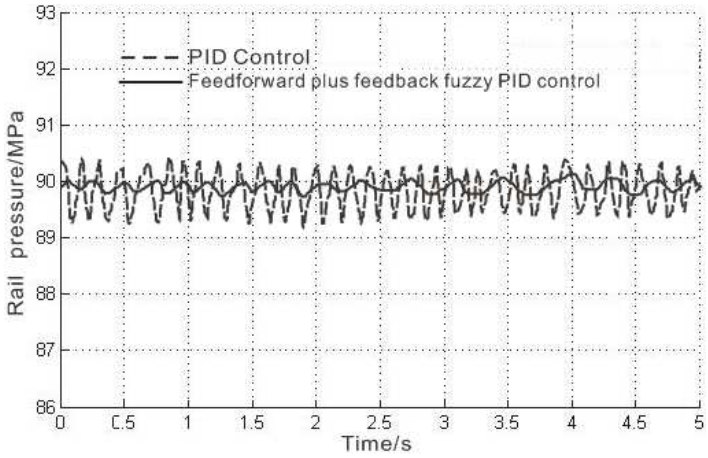

Fig.6. The rail pressure simulation curve when the load at 100% and the speed at 114 rpm

Conclusions

Fuel common rail system is an important part of intelligent Marine diesel engines, uses appropriate methods to improve its rail pressure control effect is an important reference for the independent research and development of common rail diesel engine fuel system. This article research conclusion is as follows: Established a MAP figure of feedforward fuel rack by the bench test data, feedforward fuel rack is obtained by look-up table with the engine speed and load as an input, the amount of feedback control is reduced, has greatly reduced the amount of system overshoot; makes the feedback control more precise with rail pressure as input in the feedback control by the method of fuzzy control and real-time self-tuning control parameters; the steady state rail pressure and dynamic rail pressure fluctuation are reduced and the response time is more faster by simulation experiments that the control method is improved, proved that the improved method is effectiveness.

Acknowledgments

The authors thank the financial support from the National Natural Science Foundation of China (Projects 51179102).

References

[1] Suhai Shen, Peili Wu, Hui Zhao. Modeling and simulation of common rail fuel system of electronically controlled marine diesel engine [J]. Journal of Shanghai Maritime University, 2013, 34(1):36-40 (in Chinese)

[2] Yongjian Wang, Guohao Yang, Siqin Li. Simulation for Fuel Common Rail Systems and Rail Pressure about Electronically Controlled Marine Diesel Engines[J].NAVIGATION OF CHINA, 2013, 36(2)：22-27(in Chinese)

[3] Tao Qiu， Yan Lei， Jing Peng, Xuchu Li. Research of rail pressure control strategy on common rail fuel system[J]. Chinese Internal Combustion Engine Engineering, 2013，34（2）：83-87(in Chinese)

[4] Mingzhi Chen, Huiru Guo, Haiyan Wang ,et al. Running simulation on electronically controlled marine two-stroke high pressure common rail diesel engine[J]. Journal of Shanghai Maritime University, 2013，34（1）：41-44(in Chinese)

[5] Tao Ping, Jianxin Xu, Wenchao Fang，et al. Dynamic Characteristics investigation of High Pressure Common Rail System for Marine Diesel Engine(I)[J].Ship Engineering, 2009, 31(3):7-10(in Chinese)

Advanced Materials Research Vols. 960-961 (2014) pp 1460-1464

doi:10.4028/www.scientific.net/AMR.960-961.1460

Study on the Impact of Distributed Generation on Distribution Power Losses

Haojie Shi[1, a], Xingying Chen[1], Kai Chen[2], Jian Liu[3] and Kun Yu[4, b]

[1]College of Energy and Electrical Engineering, Hohai University, Nanjing 210098, China

[2]Nanjing Power Supply Company, Nanjing 210019, China

[3]Shanxi Electric Power Research Institute, Xi'an 710054, Shanxi Province, China

[4]Nanjing Engineering Research Center of Smart Distribution Grid and Utilization, Nanjing 211100, China

[a]shihaojie1219@gmail.com, [b]kun.yu@vip.sina.com

Keywords: distributed generation (DG), distribution network, revised back/forward sweep method, power losses

Abstract. The impact of distributed generation (DG) on distribution power losses is closely related to DG technologies and load distribution. DG units are modeled as PQ, PQ(V) and PV nodes in power flow calculation. A revised back/forward power flow method is employed to calculate distribution power flow with various types of DG units. Power losses are computed when different types of DG units are connected to heavy load, general load and light load area apart. Simulation on IEEE 33-bus distribution network shows that connecting DG to heavy load area helps to maximize the loss reduction. And the installation of DG consuming reactive power will increase network losses unless reactive power compensation device is installed accordingly.

Introduction

With increasing penetration of DG connection, the distribution network power flow has changed a lot, thus changing the network losses. This is closely related to the DG technologies used and the load distribution of the DG access area [1].Several organizations in recent years have conducted research on the impact of DGs on distribution power losses. DG units are usually modeled as PQ node with constant active and reactive power output in power flow calculation [2].

However, for DGs which can't be modeled as PQ node, such as DGs with constant active power output and voltage control, and DGs with reactive power associated with output voltage, whether their impacts on power losses are similar to PQ model should be studied respectively. This paper considers the characteristics of different types of DGs, and models DG units as PQ, PQ(V) and PV node according to their constructive technology [3, 4]. Then a revised back/forward power flow method is employed to calculate distribution power losses with different kinds of DGs. Energy losses are computed and compared when different types of DG units are connected to heavy load, light load and general load area apart.

Distribution Power Flow Calculation with DGs

Traditional distribution network structure is radial or near radial. By using this feature, back/forward method is widely used in distribution power flow calculation. This algorithm includes a backward and a forward iterative processes. However, after DG units connecting to the distribution network, the original single-power supply system has changed into a multi-power supply system. The traditional back/forward method can't deal with various types of DG units [5]. Therefore, the traditional method needs to be revised for different types of DG model.

PQ node of DGs usually can be modeled as negative load and its active and reactive power are equal to the DG but have an opposite flow direction. Therefore, the current flow of the DG can be expressed as follows:

$$\dot{I} = [(-P - jQ)/(e + jf)]^{*}. \quad (1)$$

where e is the real part of the DG output voltage, f the imagine part of the DG output voltage, P the DG active power output, and Q is the DG reactive power output.

For some DGs with asynchronous generators, the active power is known and the reactive power is calculated as a function of the port voltage of the generators. This kind of DGs can be modeled as PQ(V) node in power flow calculation. The simplified model shown in Fig. 1 is assumed [6].

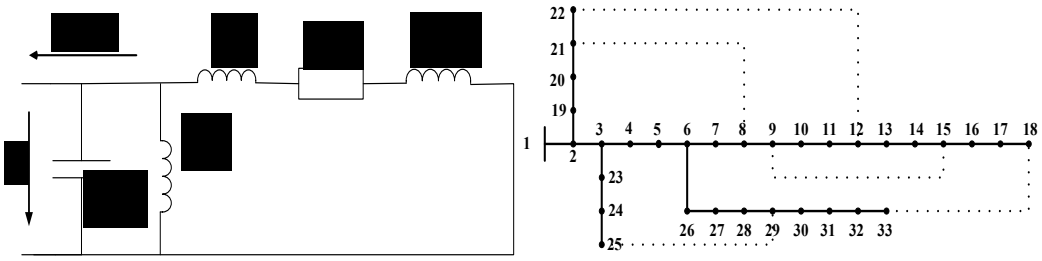

Fig. 1 Simplified model of asynchronous generator Fig. 2 IEEE 33 nodes test system

In Fig. 1, x_m represents the excitation reactance, x_1 the leakage reactance of stator, x_2 the leakage reactance of rotator, x_c the shunt capacitor reactance of DG port, R_2 the rotator resistance, and s is the slip rate of the generator. The stator resistance is ignored in this model.

According to Fig. 1, the injected reactive power of the asynchronous generator Q is described as a function of DG port voltage V:

$$Q = -\frac{V^2}{x_P} + \frac{-V^2+\sqrt{V^4-4P^2x^2}}{2x}. \tag{2}$$

where V is port voltage of DG, $x = x_1 + x_2$ and $x_P = \frac{x_c x_m}{x_c - x_m}$.

For DGs which take synchronous generator with the ability of excitation control as interface, there are generally two ways to control the excitation of the generator. They are voltage control and power factor control [7, 8]. DGs with voltage control can be treated as PV node while DGs with power factor control can be treated directly as PQ node in power flow calculation. However, for DGs which take synchronous generator without excitation as interface, they are modeled as PQ(V) nodes, and they need some special handling in power flow calculation. Consider a non-salient pole synchronous generator, the power output is expressed as follows:

$$P = \frac{E_{DGq}V}{X_d} sin\delta. \tag{3}$$

$$Q = \frac{E_{DGq}V}{X_d} \cos\delta - \frac{V^2}{X_d}. \tag{4}$$

where X_d represents the synchronous reactance, δ power angle, and E_{DGq} is no-load electromotive force of DG.

In power flow calculation, the output active power of DG is known. Therefore, the reactive power Q is described as a function of DG port voltage V:

$$Q = \sqrt{(\frac{E_{DGq}V}{X_d})^2 - P^2} - \frac{V^2}{X_d}. \tag{5}$$

Eq. 5 and Eq. 2 have similarities, but the reactive power Q in Eq. 2 is negative while in Eq. 5 is positive. This means that the asynchronous generator actually consumes reactive power.

When dealing with PQ(V) node in power flow calculation, the node voltage is amended after each iteration, and DG reactive power is computed based on this new voltage magnitude. Thus, in the first iteration, PQ(V) node is temporarily converted by Eq. 2 or Eq. 5 to PQ node in order to use

classical back/forward sweep algorithm. Then use Eq. 1 to simulate the DG node as injected current for power flow calculation. In the second iteration, the reactive power is computed based on the amended voltage. In this step, PQ(V) node is converted to PQ node again, and the reactive power is different from the last iteration. This iteration process is repeated until it converged.

For PV node, in order to guarantee the voltage magnitude and the active power unchanged in each iteration, a voltage source is introduced to inject a certain amount of current to the node. With this method, the voltage magnitude of PV node is set to the given value V'_{PV}. The added voltage source $\Delta\dot{V}_{PV}$ can be expressed as follows:

$$\Delta\dot{V}_{PV} = V'_{PV} - \dot{V}_{\mathrm{PV}}. \tag{6}$$

Whether to compensate PV node by injecting reactive current depends on the added voltage source magnitude. If $\left|\Delta\dot{V}_{PV}\right| < \varepsilon$ (ε as the convergence precision), the voltage of PV node converges to the given voltage magnitude V'_{PV}, else if $\left|\Delta\dot{V}_{PV}\right| \geq \varepsilon$, a certain amount of current injection is needed to ensure that the PV node will converge to the given voltage value. The Injected compensation current $\Delta\dot{I}_{PV}$ can be calculated as below:

$$\Delta\dot{I}_{PV} = Z_{ii}^{-1} \times \Delta\dot{V}_{PV}. \tag{7}$$

where $\Delta\dot{I}_{PV}$ is the injected compensation current of PV node, Z_{ii} the self-impedance of PV node. If there are more than one PV node in the network, Z_{ii} represents the input impedance matrix of the network port. Specifically, the diagonal entry of Z_{ii} is the self-impedance (the sum of all the impedance from PV node to the root node) of PV nodes, and the off diagonal element of Z_{ii} is the mutual impedance (the sum of all the impedance of the common path of two PV nodes) between PV nodes.

The problem of PV reactive power out-of-limit can be solved with the traditional method. That is, in iterative process, if the reactive power of PV node is out of limit after correction, it will be converted to PQ node with reactive power set to upper limit or lower limit of the PV reactive power limits.

Impact of DGs on Power Losses

When different types of DGs are connected to distribution network, their impact on the network losses differs as the load level of connection area changes from heavy load, general load to light load. Therefore, simulation is carried out respectively in the test distribution system shown in Fig. 2. System bus voltage is set to 1.02, the base power is 1MVA, the base voltage is 10kV, and the convergence precision is set to 10^{-6}. The parameters of different kinds of DGs are illustrated in Table 1.

Table 1 Parameters of different kinds of DGs

DG type	Parameters
PQ	$P = 0.424MW$ $Q = 0.220Mvar$
PQ(V)	$P = 0.424MW$ $E_{DGq} = 10.5kV$ $x_d = 14\Omega$ $x_p = 35.6\Omega$ $x = 1.38\Omega$
PV	$P = 0.424MW$ $V = 10.2kV$

Table 2 Network power losses before and after DG connection (in per unit)

Load level / DG type	Heavy load	General load	Light Load
Without DG	1.3463	0.5176	0.2916
PQ	1.1848	0.4435	0.2490
PV	1.2187	0.4590	0.2578
PQ(V) (consume reactive power)	1.5879	0.5633	0.3132
PQ(V) (produce reactive power)	0.8948	0.4024	0.2597

Assume that in the IEEE 33 nodes system shown in Fig. 2, heavy load, general load and light load is connected to node 11 to 18 separately. In these three load level, different types of DGs are connected to node 17. Network power losses are calculated before and after DG connection. The simulation result is shown in Table 2.

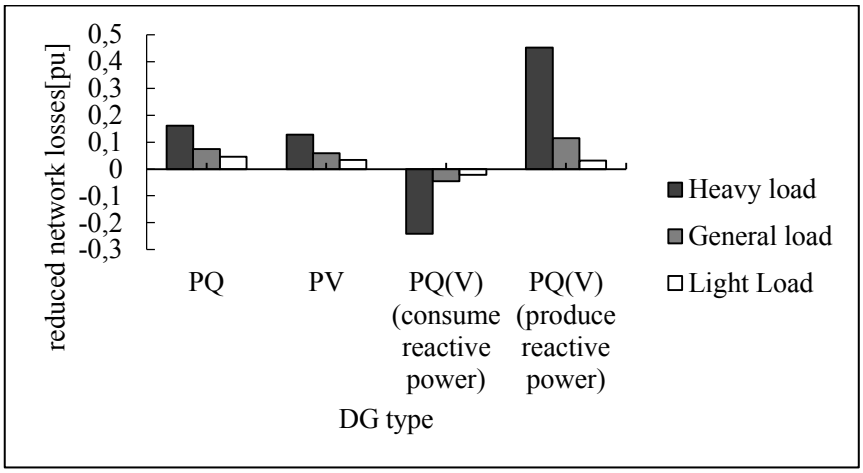

Fig. 3 Reduced network losses after DG connection

The network losses have been reduced after DG connection except PQ(V) type DG with reactive power consumption. The reduced network losses after DG connection are computed and plotted in Fig. 3. Negative value means that the network loss is actually increased after DG connection.

The result shows that the impact of DGs on distribution power losses is closely related to DG technologies and load distribution. Whatever the load level in DG connection area, the network loss can be reduced after connection of DGs with the type of PQ, PV and PQ(V) producing reactive power. However, the extent of loss reduction is closely related to the load level in connection area. Specifically, connecting DGs to heavy load area has the maximum loss reduction, then general load area, and connecting DGs to light load area has the least loss reduction. For DGs consuming reactive power, compensation device should be installed sufficiently, otherwise this type of DGs will increase network losses.

Conclusions

This paper fully summarizes and analyzes the impact of different types of DGs on distribution power losses. A revised back/forward power flow method for radial distribution system with DGs has been developed. Losses were computed and compared when different types of DG units were connected to heavy load, light load and general load area apart. Simulation result shows that connecting DG to heavy load area helps to maximize the loss reduction. And connection of DGs consuming reactive power will increase network losses unless reactive power compensation device is installed.

Acknowledgements

This research is supported by the National High Technology Research and Development of China 863 Program (2012AA050214), National Natural Science Foundation of China (51207047) and State Grid Corporation of China (the research and development for self-healing control technology in smart distribution grid).

References:

[1] V.H.M. Quezada, J.R. Abbad and T.G.S. Roman: IEEE Transactions on Power Systems, Vol. 21 (2006), No.2, p.533.
[2] P. Liu, M. Ma and J.F. Zhang: Modern Electric Power, Vol.25 (2008), No.6, p.27.
[3] L.M. Yan, M.X. Xie, J.J. Xu, et al: Power System Protection and Control, Vol. 41 (2013), No.5, p.17.
[4] H.Z. Chen, J.F. Chen and X.Z. Duan: Automation of Electric Power Systems, Vol. 30 (2006), No.1, p.35.
[5] X.Q. Lu and C.N. Wu: Power System Protection and Control, Vol. 40 (2012), No.21, p. 48.
[6] A.E. Feijoo and J. Cidras: IEEE Transactions on Power Systems, Vol. 15 (2000), No.1, p.110.
[7] W. Freitas, J.C.M. Vieira, A. Morelato, et al: IEEE Transactions on Energy Conversion, Vol. 20 (2005), No.2, p.474.
[8] P. Chiradeja and R. Ramakumar: IEEE Transactions on Energy Conversion, Vol. 19 (2004), No.4, p.764.

CHAPTER 13:

Power Systems Management

Advanced Materials Research Vols. 960-961 (2014) pp 1467-1472

doi:10.4028/www.scientific.net/AMR.960-961.1467

Electricity Competitiveness Evaluation Research Based on Principal Component Analysis

Dongxiao Niu[1, a], Qiong Wang[1,b], Peng Wang[1,c], Shuyi Zhou[1,d],
[2,e]Weidong Liu and [2,f]Xiaoyan Yu

[1]North China Electric Power University, Beijing,102206, China

[2]State Grid Zhejiang Electric Power Company Economic Research Institute, Hangzhou, 310008, China

[a]niudx@126.com, [b] wangqiong0890@163.com, [c]wangpeng.jiejie@163.com,[d]276703855@qq.com, [e]425795363@qq.com,[f]793908265@qq.com

Keywords: Electricity competitiveness, evaluation, PCA, compatibility degree

Abstract. This paper constructs the evaluation index system of electricity competitiveness in terminal energy consumption, evaluates the electricity competitiveness in Ningxia region from 2005 to 2011 using principal component analysis (PCA), and compares the evaluation results of PCA, the linear weighted method, the comprehensive index method and TOPSIS-grey correlation method. The compatibility degree and difference degree of each method are analyzed and calculated to verify the applicability of the PCA. The results show that PCA is the most scientific and appropriate evaluation method.

Introduction

By analyzing and evaluating the electricity competitiveness in terminal energy consumption, we not only can understand and grasp the competitive situation of electricity, will also be able to find the influence factors of electricity competitiveness and provide reference for the design of corresponding improvement strategy. How to evaluate the electricity competitiveness in terminal energy consumption more scientific and reasonable needs to be solved.

Throughout the research of the domestic and foreign scholars, the research on the competitiveness of power enterprise and competitiveness of energy is much more than the research of electricity competitiveness. Literature[1] uses the value chain to analyze the competitiveness factors of power generation enterprise. Literatures[2] evaluates the competitiveness of power supply enterprise by the entropy weight method. Considering the cost of long-term production, policy support and the cost of external factors, Georg Caspary assesses the likely competitiveness of different forms of renewable energy in Colombia over the next 25years. Scholars Fan Zhongqi analyses the competitiveness of China's coal industry with porter's diamond model[3]. Literature [4] evaluates and analyzes the competitiveness of Beijing's terminal energy price. Literature [5] analyzes the changes of energy consumption structure from the perspective of time. Literatures[6] builds the evaluation index system of power competitiveness in terminal energy consumption, providing a great help for the construction of index system in this paper.

Principal component analysis (PCA) is an effective multivariate statistical comprehensive evaluation methods, it can "regather" the data indicators through the linear transformation under the premise of information loss as little as possible. It gives up a small part of information at the same time to get the multidimensional index data well simplified. In addition, the PCA can effectively avoid the influence of human factors in the process of index weight determining and eliminate relevant effects between the index data. This paper evaluates the electricity competitiveness in Ningxia region from 2005 to 2011 with PCA. In order to verify the applicability of the method, this paper compares the evaluation results of PCA, the linear weighted method, the comprehensive index method and TOPSIS-grey correlation method. Finally, the compatibility degree and difference degree of each method are

analyzed and calculated to compare the pros and cons of each evaluation method. The results show that PCA is the most scientific and appropriate evaluation method.

The construction and pretreatment of the evaluation index

In order to reflect the changes of electricity competitiveness in terminal energy consumption in Ningxia region, describe and evaluate its variations objectively, this paper combines with their own situation and characteristics of Ningxia region, and constructs the evaluation index system of electricity competitiveness in terminal energy consumption as shown in Table 1.

Table 1 The evaluation index system of electricity competitiveness in terminal energy consumption

The evaluation target	The evaluation factors A	The child evaluation factors B	The evaluation index C
Electricity competitiveness in terminal energy consumption	The ability to occupy electricity market (A_1)	Terminal electricity consumption (B_{11})	Terminal electricity consumption of the whole society (C_{111})
			Terminal electricity consumption of the energy-intensive industries (C_{112})
			Terminal electricity consumption of residents living (C_{113})
		Terminal electricity consumption growth rate (B_{12})	Terminal electricity consumption growth rate of the whole society (C_{121})
			Terminal electricity consumption growth rate of the energy-intensive industries (C_{122})
			Terminal electricity consumption growth rate of residents living (C_{123})
		The proportion of electricity in terminal energy (B_{13})	The proportion of electricity in terminal energy consumption (C_{131})
			The proportion of electricity in energy-intensive industries (C_{132})
			The proportion of electricity in residents living (C_{133})
	Electricity products (A_2)	Electricity products quality (B_{21})	Supply voltage qualification rate (C_{211})
			Power supply reliability rate (C_{212})
			The proportion of new energy access (C_{213})
		Electricity products price (B_{22})	Average residents tariff (C_{221})
			Large industrial tariff (C_{222})
	The ability of power supply	The operation and management (B_{31})	The population of power supply (C_{311})
			Annual peak load (C_{312})

The evaluation target	The evaluation factors A	The child evaluation factors B	The evaluation index C
	enterprise (A_3)		Line loss rate (C_{313})
		Demand side management (B_{32})	The proportion of users performing TOU (C_{321})
	The competitive environment (A_4)	Level of economic development (B_{41})	GDP (C_{411})
			Per capita GDP (C_{412})
			The proportion of second industry output value in output value (C_{413})
			The proportion of tertiary industry output value in output value (C_{414})
		Level of social development (B_{42})	Per capita disposable income of urban residents (C_{421})
			Per capita net income of rural residents (C_{422})
			Urbanization rate (C_{423})
		Level of technological development (B_{43})	The proportion of R&D expenditure in GDP (C_{431})

Principal component analysis

2.1 The basic theory of principal component analysis

The basic principle of principal component analysis is that transforming the correlation matrix internal structure of the original index variable to converting many indexes into a handful of independent comprehensive index, namely the principal components, selecting a few principal components, constructing the comprehensive evaluation function with each variance contribution rates of the principal component as the weight, and. In this paper, the higher the score of synthetic evaluation function, the electricity competitiveness in terminal energy consumption of the corresponding year is better.

The basic steps of PCA：

(1)According to the specific index system, collect original data. The original data matrix can be

$$X = \begin{bmatrix} x_{11} & x_{12} & \cdots & x_{1n} \\ x_{21} & x_{22} & \cdots & x_{2n} \\ \cdots & \cdots & \cdots & \cdots \\ x_{m1} & x_{m2} & \cdots & x_{mn} \end{bmatrix}$$

Where, m is the number of years, n is the index number of index system, x_{ij}(i=1,2,…m; j=1,2,…,n) is the value of index j in i year.

(2) Process the original data to be consistent and dimensionless.

(3) Calculate the correlation matrix $R = (r_{ij})_{m \times n}$, r_{ij} is the correlation coefficient between index i and index j.

(4)Calculate the characteristic root and characteristic vectors of the correlation coefficient matrix, and order $\lambda_1 \geq \lambda_2 \geq ... \geq \lambda_n$. Characteristic value is the variance of the main component, reflecting the role of the various principal components playing in the description of the evaluation object.

(5)Calculate the variance contribution rate of each principal component.

$$\alpha_i = \frac{\lambda_i}{\sum_{i=1}^{n} \lambda_i} \quad (1)$$

(6)Select the principal component. Generally, the principal component of which characteristic root is greater than 1 will be taken. The principal component is a linear combination of the original index. The coefficients of the index are different and there are positive and negative. The absolute value of coefficient reflects the contribution of the principal component making to the property. If several variable coefficients are almost the same, the main component can be regarded as a combination of these indicators' characteristics.

(7)Calculate composite scores. With the contribution rate of each principal component as the weight, weighted average the main constituents.

2.2 Case study

In this paper, the hierarchy of index system is so many that the evaluation elements need to be layered when evaluating. Several principal components will be selected in each layer to participate in evaluation. In the end, the comprehensive score of each layer will be linear weighted to get the final total score which represents the electricity competitiveness in terminal energy consumption.

The scores of each evaluation factor and comprehensive evaluation value are shown in table 2. The ranking of electricity competitiveness in terminal energy consumption of Ningxia is: 2011>2010>2009>2008>2007>2006>2005, indicating that the electricity competitiveness in Ningxia region increases steadily year by year.

Table 2 Each evaluation factor's score and comprehensive evaluation value

Year	A_1	A_2	A_3	A_4	Comprehensive evaluation value	Ranking
2005	0.054	0.045	0.122	0.080	0.300	7
2006	0.066	0.036	0.132	0.085	0.319	6
2007	0.070	0.024	0.141	0.096	0.331	5
2008	0.065	0.025	0.144	0.113	0.347	4
2009	0.074	0.020	0.149	0.122	0.365	3
2010	0.099	0.019	0.156	0.140	0.415	2
2011	0.127	0.016	0.173	0.161	0.478	1

The change trend of each factor score can be visually seen from Fig. 1. The score of A_1 decreases first, and then increases, presenting "U" type trend. It's closely related to energy policy of Ningxia region and economic situation of the country in recent years. The score of A_2 reduces year by year. The scores of A_3 and A_4 increase year by year on the whole. As can be seen from the historical data, terminal electricity consumption of the whole society of Ningxia region continued to increase and the proportion of electricity in terminal energy consumption was growing in the past seven years. In 2006, terminal electricity consumption of the whole society increased by 23.98% from 2005, energy intensive industries terminal power consumption increased by 27.48%, and the growth was bigger compared with other years. The growth rate of terminal electricity consumption of the whole society and energy-intensive industries is not so high in 2007. In 2008, due to the global financial crisis, the growth rate of terminal power consumption was smaller and the ability of dominating the electricity market was weakened. Economy recovered gradually in 2009, and the score of A_1 increased, the ability of dominating the electricity market gradually began to recover. In 2011, the proportion of electricity in terminal energy reached 31.18%, reached the highest level in history. And it is the result of continuously adjustment the industrial structure and the transforming the mode of energy-using in Ningxia region. Also, it's reflecting that the achievement of energy policy in Ningxia region is significant. A_2 index declines, which is closely linked to the rise of electricity price in Ningxia region. It indicates the rise of electricity price has certain extent effect on electricity competitiveness in terminal energy consumption and related departments should pay attention.

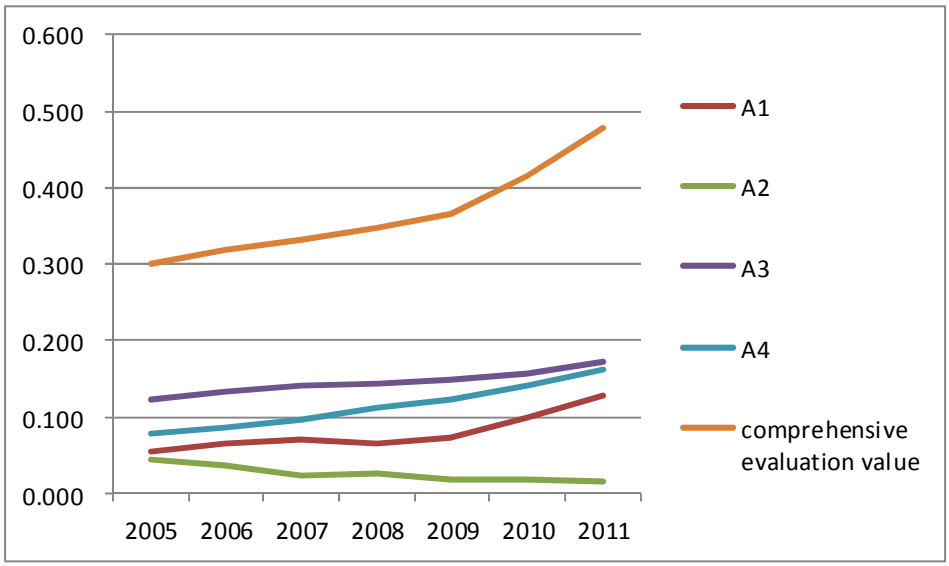

Fig. 1 Each evaluation factor's score and comprehensive evaluation value

2.3 The contrastive analysis with other algorithms

In order to verify the validity of PCA, linear weighted method, the comprehensive index method and TOPSIS-grey correlation degree are also used to evaluate the electricity competitiveness for the comparative analysis in this paper. The specific results of all the methods are shown in table 3. The results show that the ranking of different evaluation methods are various, but on the whole, the electricity competitiveness of Ningxia region presents growing trend.

Table 3 Ranking of each evaluation method

Year	Linear weighted method	Comprehensive index method	TOPSIS-grey correlation method	PCA
2005	7	7	7	7
2006	6	4	6	6
2007	4	3	4	5
2008	5	6	3	4
2009	3	5	5	3
2010	2	2	1	2
2011	1	1	2	1

Next, the compatibility degree and difference degree will be used to analyze the superiority and inferiority of each evaluation method.

Let $h+1$ be the number of evaluation methods and n be the number of years. The rank correlation coefficient of evaluation method i and evaluation method j can be calculated as follows, which reflects the related degree between them.

$$r_{ij} = 1 - \frac{6}{n(n^2-1)} \sum_{k=1}^{n} (a_k^{(i)} - a_k^{(j)})^2 \quad (i, j = 1, 2, \cdots, h+1) \tag{2}$$

Where, $\{a_k^{(i)}\}$, $\{a_k^{(j)}\}$ are respectively the year k' ranking of evaluation method i and evaluation method j.

The compatibility degree of a certain evaluation method refers to the weighted average of the rank correlation coefficient of the other evaluation methods. Therefore, the compatibility degree of a certain evaluation method $y = \{y_k\}$ with other methods can be calculated as follows.

$$r_y = \sum_{j=1}^{h} w_j r_{yj} \tag{3}$$

Where, $\sum_{j=1}^{h} w_j = 1$, $w_j > 0$ is the weight of evaluation method j which is usually $\frac{1}{h}$. Obviously, if each evaluation method is independent, the greater the compatibility degree is, the more representative the evaluation method is. The smaller the difference degree is, the better the evaluation method is.
From table 4, we can see that the compatibility degree of PCA is the biggest, and its different degree is the smallest. So the ranking of PCA is the most reasonable and scientific. Therefore, the PCA has strong applicability on the evaluation of electricity competitiveness.

Table 4 The compatibility degree and difference degree of each method

Evaluation method	Compatibility degree	Ranking	Difference degree	Ranking	Comprehensive ranking
Linear weighted method	0.845	2	0.419	2	2
Comprehensive index method	0.75	4	0.635	3	3.5
TOPSIS-grey correlation method	0.798	3	0.676	4	3.5
PCA	0.869	1	0.394	1	1

Summary

(1)This paper constructs the evaluation index system of electricity competitiveness in terminal energy consumption. And the principal component analysis is used to evaluate the electricity competitiveness in Ningxia region from 2005 to 2011. The evaluation results show that the rise of electricity price has a significant impact on the electricity competitiveness. In addition, the electricity competitiveness in Ningxia region increases steadily year by year and it reached the highest level in history in 2011. In a word, the electricity competitiveness in Ningxia region has great potential growth space in the future.
(2)This paper compares and analyzes the evaluation results of PCA, the linear weighted method, the comprehensive index method and TOPSIS-grey correlation method. And the applicability of the PCA is verified through the calculation of compatibility degree and difference degree of each method. The results show that PCA is the most scientific and appropriate evaluation method.

Acknowledgements
This research is supported by Technology Projects of State Grid Corporation of China.

References

[1]Zhang Lihui. Analysis on Power generation enterprise competitiveness[M]. Beijing: Economic management press, 2007.

[2]Wang Jingmin, Sun Yanfu, Kang Junjie. Evaluation of competitive of power enterprises based on entropy and improved TOPSIS[J]. Journal of North China Electric Power University(Natural Science Edition), 2010, 37(6): 61-64.

[3]Georg Caspary. Gauging the future competitiveness of renewable energy in Colombia[J]. Energy Economics, 2009, 31(3): 443-449.

[4]Fan Zhongqi. Coal Industry Competitiveness Evaluation Model and Advanced Path in China[D]. Sichuan: Southwest Jiaotong University, 2006.

[5]Zhang Ye, Niu Dongxiao. Comparison and Analysis of Terminal Energy Price Competitiveness in Beijing[J]. Journal of North China Electric Power University(Social Sciences), 2008, (7): 32-35.

[6]Liu Yuanyuan, Niu Dongxiao, Li Hanfang, etc. Construction of competence assessment systems for electricity in final energy[J]. East China Electric power, 2008, 36(5): 1-5.

Advanced Materials Research Vols. 960-961 (2014) pp 1473-1476

doi:10.4028/www.scientific.net/AMR.960-961.1473

Fuzzy Comprehensive Evaluation for Pumped Storage Capacity Determination Based on Entropy Weight Method

Zhan'an Zhang[1,a], Xingguo Cai[2,b]

[1,2]School of Electrical Engineering and Automation,Harbin Institute of Technology, Harbin 150001,China

[a]zza.163.com@126.com, [b]xingguo@hit.edu.cn

Keywords: pumped storage, fuzzy, entropy weight method, comprehensive evaluation,capacity

Abstract: To determine the pumped storage capacity is a comprehensive decision-making problem. This paper presents the entropy weight method to decide the weight in fuzzy comprehensive evaluation. Example analysis shows the effectiveness of the proposed methods.

Introduction

Pumped storage(P-S) is today viewed as the most suitable technology for accepting large amount wind power and meeting the peak load in power system[1-4]. However, how much P-S should be installed is worth to discuss[5].

In the past the optimum P-S capacity is often determined by individual factors, such as unit operating cost, power shortage time probability[6], peak-regulation proportion[7], wind and nuclear power capacity[8], generator utilization hours, etc.

To determine the P-S capacity is a comprehensive decision-making problem, at present the main methods are analytic hierarchy process(AHP)[9], fuzzy comprehensive evaluation and principal component analysis(PCA)[10]. The index weights are dependent on experts judgment in AHP, which is highly subjective and contingent. Athough PCA does not require subjective judgment, but it is based on the evaluation dimension reduction, using the cumulative variance contribution rate of more than 75% of the main ingredients to replace the original target, easy to lose the original information.

In this article, the entropy weight method is led into fuzzy comprehensive evaluation, such that the weights can be determined objectively[11,12]. Finally, case studies validated the correctness and rationality of the proposed method.

Pumped-storage capacity evaluation indexes

The benefits of P-S station can be divided into static and dynamic benefit[13-15], such as capacity benefit, peak-valley regulation, coal saving benefit, environmental benefit, spare capacity, frequency and phase modulation, load tracking and black start, etc. To simplify the analysis, here we select a few representative evaluation indexes:

2.1 Capacity benefit

P-S capacity benefit refers to equivalent thermal power capacity which can be replaced by P-S. The installed P-S capacity is not the more the better, too much P-S capacity will lead to waste. The equivalent coefficient of thermal will declined when the P-S capacity is over the demand capacity.

2.2 Coal saving benefit

Coal saving benefit refers to the difference of coal consumption in the case of P-S is involved in running and not running. Due to P-S can improved thermal units operation mode, the system's coal consumption rate will dropped. However, the P-S should be maintained the proper capacity, rather than the bigger the better.

2.3 LOLP

LOLP (Loss of Load Probability) is insufficient power load probability, it means that power generation system margin is less than zero probability in the system. The smaller value of LOLP, the higher reliability of power system.

$$LOLP = P(X \geq C_s - L) \tag{1}$$

where: X refers to system outage capacity; C_s is system installed capacity; L is the daily maximum load.

2.4 Peak-regulation proportion

System peak-regulation proportion is the ratio between adjustable units capacity and total system capacity. Assuming that all P-S capacity are in full use, and P-S unit can generate at rated full output.

$$R_G = \frac{P_{\max} - P_{\min} - 2P_{P-S}}{P_N} \times 100\% \tag{2}$$

where: R_G is the system peak-regulation proportion; P_{max} is maximum output of all units and P_{min} is minimum; P_N is all units rated output; $P_{P\text{-}S}$ is the required P-S capacity.

Only peak-valley difference accounted for the proportion of maximum load is less than or equal to the system peak-regulation proportion that the system's peak contradiction can be resolved.

Fuzzy comprehensive evaluation introduction

Establishing evaluation factors set $U=\{u_1, u_2, ..., u_n\}$, here it refers to the considerations to determin the optimal capacity of P-S, these factors are used to evaluate objects. Then establishing judgment set $V=\{v_1, v_2, \ldots, v_n\}$, here it refers to the various plans of P-S capacity. Finally, establishing a judgment matrix from U to $F(V)$ of fuzzy mapping.

$$f : U \to F(V), \forall u_i \in U$$

$$u_i \mapsto f(u_i) = \frac{r_{i1}}{v_1} + \frac{r_{i2}}{v_2} + \cdots + \frac{r_{im}}{v_m} \qquad 0 \leq r_{ij} \leq 1, 1 \leq i \leq n, 1 \leq j \leq m \tag{3}$$

The fuzzy matrix R can be induced by fuzzy relations , it is named as single factor judgment matrix, then a comprehensive evaluation model (U, V, R) is formed.

$$R = \begin{bmatrix} r_{11} & r_{12} & \cdots & r_{1m} \\ r_{21} & r_{22} & \cdots & r_{2m} \\ \cdots & \cdots & \cdots & \cdots \\ r_{n1} & r_{n2} & \cdots & r_{nm} \end{bmatrix} \tag{4}$$

the ith indicator entropy is defined as

$$H_i = -k \sum_{j=1}^{n} f_{ij} \ln f_{ij} \qquad (i = 1,2,...,n) \tag{5}$$

where: $f_{ij} = r_{ij} \Big/ \sum_{j=1}^{m} r_{ij}$, assume that when $f_{ij} = 0$, then $f_{ij} \ln f_{ij} = 0$; $k = 1/\ln m$.

The index weight set $A=\{a_1, a_2, ..., a_n\}$, where the entropy weight is

$$a_i = (1 - H_i) \Big/ (n - \sum_{i=1}^{n} H_i) \tag{6}$$

Take the vector A as the weight vector which reflects the various indicators' role in the decision-making process. Here, A is multiplied with the fuzzy matrix R to get the global evaluation vector $B = A \circ R$, which are the values of synthesis-evaluation scores.

$$b_j = \bigvee_{i=1}^{n}(a_i \wedge r_{ij}) \qquad j = 1,2,\cdots, \ m \tag{7}$$

According to the principles of maximum membership degree, that the maximum of B is the final result[16].

Example analysis

This paper takes the system in [17] as examples for analysis. Here we formed 5 P-S capacity plans, they are 400MW, 800MW, 1200MW, 1600MW, 2000MW. When different P-S are put into the system, the parameters are shown in Tab.1 and degrees table are shown in Tab.2 respectively. Where C_T is alternative capacity coefficient, F_C refers to the system annual coal consumption, S_C is the saving coal, R_G refers to the peak-regulation proportion.

Tab.1 The parameters corresponding to different pumped storage capacity

plan	P-S(MW)	C_T	F_C (10^4t)	S_C(10^4t)	R_G(%)	LOLP(h/y)
1	400	1.1	3029.38	29.62	34	6
2	800	1.0775	3012.35	47.9	38	5
3	1200	1.0617	3011.02	48.64	42	5
4	1600	1.0281	3014.98	45.26	46	5.5
5	2000	1.013	3019.65	40.54	50	8

Tab.2 Close to the degrees table of each index

plan	C_T	F_C	S_C	R_G	LOLP
1	1	0.9939	0.609	0.68	0.833
2	0.9795	0.9996	0.9848	0.76	1
3	0.9652	1	1	0.84	1
4	0.9346	0.9987	0.9305	0.92	0.909
5	0.9209	0.9971	0.8335	1	0.625

The evaluation set V={400,800,1200,1600,2000}, factor set U={ C_T , F_C , S_C , R_G ,LOLP}, experts evaluation matrix

$$R = \begin{bmatrix} 0.1 & 0.3 & 0.3 & 0.2 & 0.1 \\ 0.1 & 0.3 & 0.3 & 0.2 & 0.1 \\ 0.1 & 0.3 & 0.3 & 0.2 & 0.1 \\ 0.1 & 0.15 & 0.2 & 0.25 & 0.3 \\ 0.1 & 0.25 & 0.35 & 0.2 & 0.1 \end{bmatrix}$$

the weight matrix is A=(0.0127,0.0042,0.3856,0.2415,0.3559), B =(0.1,0.3,0.35,0.2415,0.2415).

The maximum value of option 3 is the best solution, that is, the system should be installed 1200MW P-S capacity. The result is consistent with literature[17], which shows that the approach is successful.

Conclusion

To determine the P-S capacity is a multi-index comprehensive evaluation problem. The entropy weight method is introduced into the fuzzy comprehensive evaluation to determine the index weights,

which can effectively avoid the influence of subjective factors in evaluation process. Example analysis proves that the method is feasible and practical.

References

[1] S.Papaefthimiou,E.Karamanou,S.Papathanassiou and M.Papadopoulos: IET Renewable Power Generation Vol.3 (2009),p.293-307
[2] Mingshun L,Chungliang C,Weijen L and Li W: IEEE Trans on Industry Applications Vol.45(2009), p. 2109-2115
[3] P.D.Brown,J.A.Pecas Lopes and M.A.Matos:IEEE Trans on Power Systems Vol.23(2008), p.523-531
[4] S.V.Papaefthymiou,E.G.Karamanou,S.A.Papathanassiou and M.P.Papadopoulos:IEEE Trans on Sustainable Energy Vol.1(2010),p.163-172
[5] Hongkun B and Gansheng L: Electric Power Construction Vol.22(2001),p.54-56(in Chinese)
[6] Wenge Y: Hydro Power Vol.4(2002),p.57-63(in Chinese)
[7] Fang C and Lizi Z:Eletric Power Automation Equipment Vol.27(2007),p.47-50(in Chinese)
[8] Wenxia P,Yongwei F,Li Z and Along G : Trans of China Electrotechnical Society Vol.23(2008), p.120-124(in Chinese)
[9] T. Kaya and C.Kahraman:Expert System with Applications Vol.38(2011),p.8553-8562
[10] A.Parente,J.C.Sutherland,B.B.Dally,T.Tognotti and P.J.Smith: Proceedings of the Combustion Institute Vol.33 (2011), p. 3333- 3341
[11] Jinying L, Jinchao L and Dongxiao N: RELAY Vol.36(2008),p.42-47(in Chinese)
[12] Huicheng Z, Gaihong Z and Guoli W: Shui Li Xue Bao Vol.38 (2007), p.100-106(in Chinese)
[13] Sujie G and Suhua L: Hydropower Automation and Dam Monitoring Vol.32(2008),p.11-15(in Chinese)
[14] Jichun C, Dianhai L, Weilie L,Feng X and Hongyu C: Electric Power Vol.40(2007),p.5-10(in Chinese)
[15] Jingcan D, Zongwen Z and Beiwen Z: Water Power Vol.36(2010),p.1-5(in Chinese)
[16] Hongzhan N, Pan L, Yi Q and Xiuping Y: Power System Technology Vol.33(2009), p. 60-64 (in Chinese)
[17] Dongpu G:Research on benefit's and economy for pumped storage station.A dissertation for master's degree submitted to Dalian University of Technology,(2001)(in Chinese)

Advanced Materials Research Vols. 960-961 (2014) pp 1477-1482

doi:10.4028/www.scientific.net/AMR.960-961.1477

Analysis of the Power Plant Security Management Capability Based on the ISM and AHP

Dongxiao Niu[1, a], Peng Wang[1,b], Qiong Wang[1,c], Fuyu Hua[1,d], [2,e]Feng Wang, and [2,f]Zhanghua Cai

[1]North China Electric Power University, Beijing,102206, China

[2]Hangzhou Yihe Electric Power Information Technology Co., Ltd., 310053, China

[a]niudx@126.com, [b]wangpeng.jiejie@163.com, [c] wangqiong0890@163.com, [d]825406374@qq.com, [e]553877009@qq.com, [f]1049417619@qq.com

Keywords: Thermal Power Plant, Security Management Capability, ISM, AHP

Abstract. This paper sets the thermal power plant security management system as the research object. First of all, with the application of the Interpretative Structural Modeling (ISM), we establish a multi-level hierarchical structure model on analysis of the influencing factors of thermal power plant security management. Furthermore, based on the structure model, we use the Analytic Hierarchy Process (AHP) to determine weights of all the influencing factors, in order to identify the main factors. Finally, according to the identified main factors, we provide several suggestions for security management of thermal power plant.

Introduction

The thermal power plant is one of the most basic entities in electric power industry, and the security of production is not only the most urgent requirement in the production process but also a prerequisite to ensure safe and stable operation of the power grid. Thus, for thermal power plants we need to stir our concern about the factors that affect security management capability, and explore the power plant's control force of its organizational structure and production security systems. Only in this way can we formulate targeted improvement measures for system's weaknesses and fundamentally avoid blindness management and traditional experience management. Ultimately, we can improve the security management level. Liu Tiezhong etc. [1,2] put forward that the so-called enterprise security management capability is one knowledge-accumulating collection of security management process with the factors including "employee ", " equipment ", " environment", " system" , and it's also the ability formed during the process of security management. Enterprise security management capability is the decisive force to the security management level, and ultimately manifests the performance of security production condition. Security management capability is the comprehensive result of numerous factors, the complex relationship between which will lead to the vague security management system structure. Based on the above understanding and aiming at the characteristics of enterprise security management capabilities, we use the Interpretative Structural Modeling(ISM) to establish interpretation chart for the influencing factors of security management combined with the actual situation of thermal power plant security management. Then we use Analytic Hierarchy Process (AHP) to analyze and identify the main factors and their weights to provide reference for thermal power plants implementing effective and targeted management.

1 Impact analysis of thermal power plant security management

1.1 Analysis of influencing factors

Liu Tiezhong etc. [1-2] put forward that the so-called enterprise security management capability is one knowledge-accumulating collection of security management process with the factors including "employee ", " equipment ", " environment", " system" , and it's also the ability formed during the process of security management. Luo Yun etc. [3] proposed that effective enterprise security

management is the use of human and material resources with wisdom of all staff, and through the joint efforts to achieve harmony between human and machine, equipment, technology, environmental condition during production process, finally to achieve the goal of security production. Therefore, it requires enterprise to have a thorough security management organization, systematic management means and approach and requires all levels of employees full of responsibility. Based on the reference to previous research, combining the characteristics of thermal power plants [4], we summarized that the factors that have an effect on the thermal power plant security management capability include the personnel quality, equipment status, environmental conditions and institutional conditions. Based on the above analysis, the specific security management influencing factors we conclude are shown in Table 1.

Table 1 Security Management Influencing Factors

	Influencing Factors	S_i
Personnel Quality	operation habits	S_1
	cultural knowledge and operation skills	S_2
	working attitude	S_3
Equipment Status	equipment operation specification	S_4
	maturity level of security equipment and facilities	S_5
Environmental Condition	enterprise security culture	S_6
	security working environment	S_7
Institutional Condition	emphasis of leadership	S_8
	healthiness degree of security management systems and procedures	S_9
	inspection and supervision of the department of management departments to monitor	S_{10}
	emergency disposal mechanism	S_{11}

1.2 Interpretative Structural Modeling (ISM) for thermal power plant security management system

Interpretative Structural Modeling (ISM) is put forward and developed by an American professor named Warfield in 1973, which is used to analyze complex issues related to the social and economic system [5,6]. The characteristic of ISM is that it can decompose the complex system into several subsystems (elements). With the advantage of people's experience and knowledge and help of computer technology, the system will eventually be constructed into a multi-level hierarchical structure model.

(1) Identification of the reachable matrix

According to the influencing factors shown in table 1, we can establish a reachable matrix M through expert interview advice, which can describe the final level that elements can reach after a length of access roads in system. Shown as follows, element 1 indicates that the row elements have a binary relationship with column elements directly or indirectly (including the elements' own auto-correlation), as element 0 indicates that the row elements have no direct or indirect binary relationship with column elements.

$$M=\begin{bmatrix}1&0&0&1&0&0&0&0&0&0&0&1\\0&1&0&1&0&0&0&0&0&0&0&1\\0&0&1&0&0&0&0&0&0&0&0&1\\0&0&0&1&0&0&0&0&0&0&0&1\\0&0&0&0&1&0&0&0&0&0&0&1\\1&0&1&0&0&1&0&0&0&0&1&1\\1&0&1&0&0&0&1&0&0&0&0&1\\1&1&1&1&1&1&0&1&1&1&0&1\\1&0&1&1&0&0&0&0&1&0&0&1\\0&0&0&1&1&0&0&0&0&1&0&1\\0&0&0&0&0&0&0&0&0&0&1&1\\0&0&0&0&0&0&0&0&0&0&0&1\end{bmatrix}$$

(2) Interstage division between elements

After obtaining the reachable matrix, next main procedure of establishing the structure model is the interstage division. Interstage division is used to divide all the elements into different levels (layers) based on criteria of reachable matrix. In the matrix, reachable set $R(S_i)$ indicates the set of all elements that S_i can reach, which includes all the column elements that equal to 1 in line i of matrix M ; Antecedent set $A(S_i)$ indicates the set of all elements of S_i , which includes all the row elements that equal to 1 in column i of matrix M . Results are shown in Table 2.

Table 2 Reachable set, antecedent set and their intersection

i	$R(S_i)$	$A(S_i)$	$R(S_i)\cap A(S_i)$
1	1,4,12	1,3,6,7,8,9	1
2	2,4,12	2,8	2
3	1,3,12	3,6,7,8,9	3
4	4,12	1,2,4,8,9,10	4
5	5,12	5,8,10	5
6	1,3,6,11,12	6,8	6
7	1,3,7,12	7	7
8	1,2,3,4,5,6,8,9,10,12	8	8
9	1,3,4,9,12	8,9	9
10	4,5,10,12	8,10	10
11	11,12	6,11	11
12	12	1,2,3,4,5,6,7,8,9,10,11,12	12

According to $R(S_i)\cap R(S_i)$, we can divide the influencing factors into different levels. Thus, the calculated factors that influent thermal power plant security management capability are divided into Level 1: $L_1=\{S_{12}\}$ .After redlining the rows and columns where S_{12} belongs to, we obtain Level 2: $L_2=\{S_4,S_5,S_{11}\}$ .Repeating the former procedure, we obtain Level 3: $L_3=\{S_1,S_2,S_{10}\}$, Level 4: $L_4=\{S_3\}$, Level 5: $L_5=\{S_6,S_7,S_9\}$ and Level 6: $L_6=\{S_8\}$.

(3) Establishment of structure model and interpretative structural model

According to interstage- arranged reachable matrix, we create a multilevel hierarchical structure diagram for the system of factors that influent thermal power plant security management capability in Figure 1. With the corresponding factors' names substituted into structure model, the interpretative structural model is established as shown in Fig. 1.

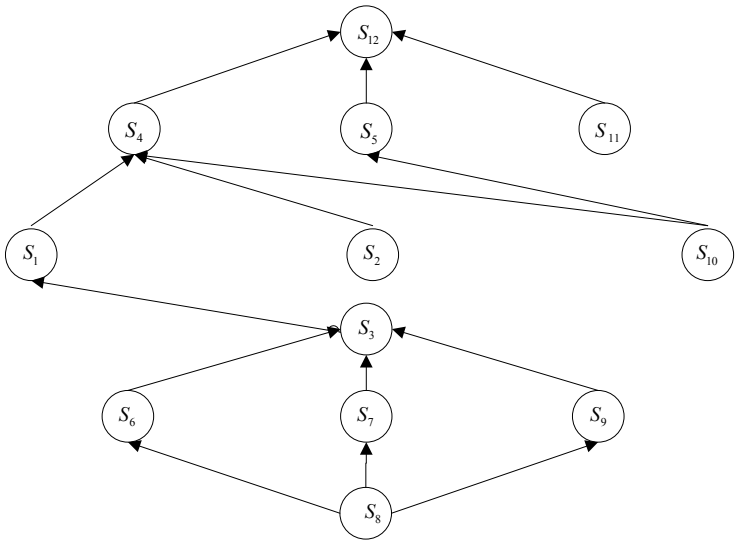

Fig. 1 Multilevel hierarchical structure diagram for influencing factors' system

(4) Determination of the weights of influencing factors

As a multi-criteria decision method, AHP method is able to integrate different subjective judgment so that it can simplify the complex system into pairwise comparisons and simple calculations between elements [7,8]. The main procedures of AHP method include the establishment of the index system, establishment of judgment matrix , calculation of the weight vector, consistency checking, calculation of comprehensive weights and so on. First, according to the ISM results, we select the elements in layered model as the index system. Secondly, based on the principles and procedures of AHP method and inviting relevant experts, we construct the comparison judgment matrix for the various factors which are in the same level and affect the factors in upper level. To complete this procedure we start from level 1(surface influencing-factor level) in hierarchical structure model with pairwise comparison method and 1-9 comparison scale. Thirdly, with similar method the judgment matrix of the middle and deep influencing-factor level can be constructed. The judgment matrix of surface influencing-factor level is shown in Table 3.

Table 3 Various factors weight table

type of table	judgment matrix $A=\{a_{ij}\}$				weight W	CR
weight table of second-level factors	S_{12}	S_4	S_5	S_{11}		
	S_4	1	3	3	0.6	0
	S_5	1/3	1	1	0.2	
	S_{11}	1/3	1	1	0.2	
weight table of third-level factors	S_4	S_1	S_2	S_{10}		
	S_1	1	4	3	0.63	0.09
	S_2	1/4	1	2	0.22	
	S_{10}	1/3	1/2	1	0.15	
weight table of fifth-level factors	S_3	S_6	S_7	S_9		
	S_6	1	1	4	0.46	0.01
	S_7	1	1	3	0.42	
	S_9	0.25	1/3	1	0.13	

2 Analysis of influencing factors for thermal power plant security management capability

According to Fig. 1 and Table 3, we analysis the relationship between each influencing factors as follows:

(1)The factors that have a direct influence on the security management capability of thermal power plant are: whether equipment operation conforms to the specification, maturity level of security equipment and facilities and emergency disposal mechanism. Among the above factors, equipment operation specification has a larger weight of 0.6, which indicates that the occurrences of thermal power plant accidents are often caused by violation operation of production line operators, on the other side, which also means the proper operation is of great importance for the security management capability of thermal power plant.

(2)The factors of operation habits, cultural knowledge and operation skills, inspection and supervision of the department of management have a direct influence on whether equipment operation conforms to the specification. Specifically, operation habits have the largest influencing weight of 0.63. In the practice, older employees who have longer length of service are always acting empirically. They believe that acting empirically is the safest way, and they tend to pass on their experience to young operators unconsciously when training them. Furthermore, the heavy operation tasks in thermal power plants are liable to cause employees' extreme fatigue, and in such condition people tend to act according to their experience, because acting empirically is often time-saving and caters to some employees' attitude of laziness. But they are not clearly aware of that their laziness may affect the normal use of equipment and even cause accidents. Among other mentioned factors, cultural knowledge of employees is weighted 0.22. Cultural knowledge level of employees will affect their security awareness and execution. Skills and experience of employees mainly emphasize the learning ability, analytical skills, security knowledge, operation skills, adaptive capacity for new knowledge, new equipment and new requirements. The above factors all have an impact on the equipment operation.

(3)Working attitude of employees directly affects the operation habits, which is influenced by enterprise security culture, security working environment and security management systems and procedures. The weight of security working environment is 0.42. The high temperature, strong noise and mess in workplace are liable to cause individual's psychological and physical discomfort which results in negative influence on employees' job morale and passive working attitude. The factor enterprise security culture is weighted 0.46. As the negative security environment directly affects employees' awareness and psychology of security, the enterprise security values could not root in employees' mind. The phenomenon reflects that employees are not authentically liable to approve of and participate in the construction of security culture, because most individuals tend to learn by imitation driven by psychology of conformity, which would lead to unsafe operation habits.

(4)Emphasis of leadership is a deep influencing factor towards capability of thermal power plant security management, as it affects enterprise security culture, security working environment and the construction of security management system directly.

3 Suggestions for thermal power plant security management

(1)Enhance employees' security training

From the analysis given above, operation and working attitude of employees have a greater impact on security management of thermal power plant. On one hand, enterprise should emphasis on training to employees' operation skills, on the other hand, enterprise should be responsible to carry out security education consistently. Scientific and effective security can not only correct and improve individual unsafe mental factors, but also improve the security quality of individuals in terms of the security of cognition, emotion and volition.

(2)Increase enterprise security investment

Increasing investment on security means the improvement of working condition, which indicates comfortable labor protection, reduced labor intensity and so on. Updating old equipment is another form of investment, which results in less machine failure as much as possible. As we all know,

superior security equipment and facilities can provide more efficient protection for personnel and production equipment in accidents and finally minimize losses.
(3)Construct a favorable security culture and improve security management system
Enterprise security culture potentially influences security awareness and psychology of employees, so a favorable security culture atmosphere is supposed to be constructed which requires total participation of all individuals. Along with the construction are the formation of security assessment mechanism and the establishment of the security system of rewards and penalties. The collective leadership of thermal power plant should pay particular attention to security management, making good examples by enforcing security regulations actively. The leading group is also responsible to establish a top-to-bottom security supervision system to ensure that enterprise security management concepts root into the heart of every employee.

Summary

(1) First of all, we build a security management system for thermal power plants' security-influencing factors on the basis of previous studies. The factors include: equipment operation specification, maturity level of security equipment and facilities, emergency disposal mechanism, operation habits, cultural knowledge and operation skills, inspection and supervision of the department of management, working attitude, enterprise security culture, security working environment, healthiness degree of security management systems and procedures, emphasis of leadership.
(2) Secondly, as the influencing factors of security management capability for thermal power plants are various and complex, we build a multi-level hierarchical structure model based on the Interpretative Structural Modeling (ISM). Then we analyze the hierarchy and relationships of various factors from a qualitative point of view, laying the foundation for quantitative analysis.
(3) Thirdly, we use Analytic Hierarchy Process (AHP) to analyze the factors' weights of each influencing layer, in order to clarify the importance of each factor and to improve the reliability and validity of analysis. Finally, we provide some suggestions for security management of thermal power plants on basis of the analysis results above.

Acknowledgements

This research is supported by Technology Projects of State Grid Corporation of China.

References

[1]Liu Tiezhong, Li Zhixiang, Wang Ziwei. Conceptual Framework Research on Enterprise Security Management Capability[J]. Commercial Age,2006,24:50-52.

[2]Liu Tiezhong, Li Zhixiang, Wang Ziwei, Liu Yafeng. Concept, Content and Level of Enterprise Security Management Capability[J]. Productivity Research,2007,14:116-118.

[3]Luo Yun, Luo Bo. Summary of Modern Safety Management Method[J]. Labor safety and health,1999,02:28-32.

[4]Wang Yajing. Research on Security Evaluation Method of Power Plant Management[D].North China Electric Power University(Beijing),2010.

[5]Bai Sijun, Systems Engineering[M].Beijing, Electronic Industry Press,2009:88-110.

[6]Li Naiwen, Xu Menghong, Niu Lixia. Research on the Influencing Factors for Inertial Violation of Miners based on the ISM and AHP[J]. China Safety Science Journal,2012,08:22-28.

[7]Zou Changcheng. Research on the Influencing Factors for Democratic Development of China's Nuclear Power Industry[J].Systems Engineering,2011,04:117-122.

Advanced Materials Research Vols. 960-961 (2014) pp 1483-1489

doi:10.4028/www.scientific.net/AMR.960-961.1483

Analysis on Losses of Distribution Network and Countermeasures to Reduce Losses

Qian Wang[1,a], Shang-ji Chen [2,b], Xiao-hui Han[3,c]

[1]Henan Electric Power Research Institute, Zhengzhou, Henan, 450000 China
[2]Henan Electric Power Corporation, Zhengzhou, Henan, 450000 China
[3]College of Information and Electrical Engineering of China Agricultural University, Haidian District, Beijing, 100083 ,China

[a]wangqian0523@163.com

Keywords: distribution network;loss analysis;saving energy and decreasing loss

Abstract: The thesis describes the loss model of distribution network and gives the transformer loss model and line loss model, Then it proposes some loss reduction measures at the stage of planning and design as well as operation and maintenance. Finally, according to the main problems about the loss reduction measures in China, it puts forward some countermeasures to reduce line loss .

Distribution network as part of the end for power configuration which is directly connected with the users of demand side. The loss of distribution network has been high because of feeder radius, complex voltage grade and a large number of devices on the network. The line loss of distribution network represents a major component of the line loss in the whole power system, the line loss of 10kv and below distribution network accounts for about 78% in it according to statistical analysis[1-2]. So, under the current energy shortage situation, there is a great economic and social significance to adopt the reasonable measures to save energy and decrease loss in distribution network.

Analysis of distribution network loss

Power loss of distribution network mainly includes the transformer loss and line loss[3], as shown in (1), saving energy and reducing loss needs to be optimized separately for each factor.

$$\begin{cases} \Delta W = \int_0^T \Delta P(t) d(t) \\ \Delta P = \Delta P_T + \Delta P_L \end{cases} \tag{1}$$

W ΔP_T is the transformer loss and ΔP_L is the line loss.

The active power loss of line

$$\begin{aligned} \Delta P_L &= 3 \times I_L^2 R_L \\ &= 3 \times (\frac{P}{\sqrt{3} U \cos\varphi})^2 \times R_L \\ &= \frac{P}{U^2 \cos\varphi^2} \rho l / A \end{aligned} \tag{2}$$

Where P is the line active power; U is the line operation voltage; $\cos\varphi$ is the line power factor; ρ is line resistivity;l is line length;A is line section area. As table 1 shows that the relationship between the energy consumption factor of line in distribution network and example for the saving energy and decreasing loss.

Table 1 Relationship between the energy consumption factor of line in distribution network and example for the saving energy and decreasing loss

Stage	Influence factors	Relationship	Example for the saving energy and decreasing loss
Equipment manufacturing	ρ	direct proportion	Replace aluminum conductor with copper wire
Planning and design	l	direct proportion	Industry substations and transformers planning to load centers, reduce line twists coefficient
	A	inverse ratio	Expand the line diameter
	U	inverse square	6kV high-voltage motor upgrading to 10kV
Operation and maintenance	P	proportional to the square	Using demand-side management to balance the load of each period
	$\cos\varphi$	inverse square	Devoting some compensators of reactive power

The active power loss of transformer

The total power loss of the transformer is composed of two main parts:the iron loss and copper loss, which can be given as follows:

$$\Delta P_T = P_{Fe} + P_{Cu} = (\frac{U}{U_N})^2 P_0 + (\frac{P}{S_N \cos\varphi})^2 P_k \tag{3}$$

Where P_{Fe} is the eddy current loss in the excitation branch; P_{Cu} is the resistance loss in transformer winding; U is the operating voltage; UN is the rated voltage; P0 is the no-load loss; Pk is the on-load loss. As table 2 shows that the relationship between the energy consumption factor of transformer in distribution network and example for the saving energy and decreasing loss.

Table 2 Relationship between the energy consumption factor of transformer in distribution network and example for the saving energy and decreasing loss

Stage	Influence factors	Relationship	Example for the saving energy and decreasing loss
Equipment manufacturing	P_0	invariable loss	Application of iron core transformer ,amorphous alloy transformer and other high quality transformer
	P_k	direct proportion	The original wire transformer into copper transformer
Planning and design	S_N	copper loss as the inverse square; Iron loss is directly proportional to S_N.	It runs in the economic load rate interval when the transformer planning

Operation and maintenance		proportional to the square	Using demand-side management to balance the load time and trying to make the transformer load rate operation on economic region
	$\cos\varphi$	inverse square	Switching capacitor

The main loss reduction measures of the distribution network based on the analysis of the loss model

The main loss reduction measures in the planning and design. The main loss reduction measures in distribution network planning and design is mainly reflected in the wires, transformers and power quality control.

Economic load levels of wire. The design of distribution line and the selection of cable type has many criteria. Usually , there are contradictions between the higher engineering design standards and the increased costs. So for a variety of design to meet technologies requirements, the relative economics of the program will be the most important determinant. The operation cost of large cross-section conductor (variable loss) is usually smaller than the relatively small cross-section wire, but it requires a higher initial investment. Since there are some accumulation losses in the line service period ,it should make trade-offs between the initial investment and operating costs during the planning period.

Factors affecting the total cost over the life of the power transmission lines include construction cost, operation and maintenance cost, power consumption cost and so on.

Economic load levels of transformer. Economic load levels of transformer also need to consider the initial cost and operation cost of the whole life cycle. Like the line, factors that affect the total cost of the whole life cycle include construction cost, operation and maintenance cost, power consumption cost and so on.

Experience shows that the economic load level of transformer should be in the ratings of around 75% on load saturation area or low growth area, while on the high load growth area the value should be in the ratings of around 50% [4].

Power quality control. All users want to get high-quality power ,but much non-linear load(such as thyristor rectifier, inverter, DC converter ,etc) in the users absorbs or injects harmonic current from the power grid, which causing distortion of the grid voltage. In addition, the power quality has deteriorated seriously by increased non-linear and impact load, power grid failure caused by unbalanced voltage, decreased dynamic voltage and so on ,as well as harmonic wave ,which reduces the reliability of power supply. Descending power quality makes the sensitivity power device of the user side is not working properly, resulting in huge economic losses. Therefore, the power quality problem is particularly outstanding and to improve the power quality for the economic operation of distribution network is significant.

Power quality control is the only means to improve power quality indicators. It is not only a necessary condition for high-quality power supply, but also the main means for saving energy and reducing loss. The main contents of power quality control include harmonic suppression, voltage adjustment, frequency regulation, three-phase voltage unbalance governance, flicker elimination, transient voltage control and so on. Commonly used power quality management and control measures have passive power filter,（PPF）, active power filter （APF）, active power line conditioner（APLC）, dynamic voltage restorer[5]. Commonly used power quality management and

control methods are not simply for a certain type of power quality indexes, but some means can achieve multiple power quality control purposes.

The main loss reduction measures in the operation and maintenance

Reactive power compensation technology. Reactive power compensation technology is to reduce power consumption and improve the quality of the grid voltage by means of reactive power compensation equipment provides additional reactive power to improve the power factor of the power system. When the reactive power compensation device is installed, the reactive power of transformers and all the connected lines from the point to the power point will be reduced, which can make the power loss of the point before the series element is reduced. The power factor of the load is lower , the reactive power of the load delivered from the power through line and the corresponding components in the power supply and distribution system is larger, thus the loss of the power supply and distribution system is also larger. After the reactive power of the distribution network is compensated, the current flowing through the line and transformer is reduced, which correspondingly decreases the reactive power loss on the line and transformers. Common reactive power compensation equipment includes synchronous compensator, capacitor compensation, static var compensator and so on.

Rationally adjusting the operation voltage. Rationally adjusting the operation voltage is to guarantee voltage quality by adjusting the generator terminal voltage and the tap changer of transformer and devoting capacitors on the bus line and regulating voltage with synchronous condensers. According to the equation (2) and (3) shows that the active power loss of power distribution equipment is inversely proportional to the square of the operating voltage U, so rationally adjusting the operating voltage can save energy and decrease loss.

Economic operation of transformer. To determine the economic operation of transformer should be calculated [7-8] that the power system operates by way of the minimum energy consumption in order to achieve the purpose of economic. Economic operation of transformer is classified into many ways: A single double-winding transformer economic operation, more than one of the same type of double-winding transformer economic operation, many different types of double-winding transformer economic operation and so on.

As a single double winding transformer economic operation, the efficiency of transformer is the highest and the operation of transformer is the most economic, when no-load loss is equal to the load loss .

As more than one of the same type of double-winding transformer economic operation, using n transformer parallel operation is economic when the maximum total load of the substation is greater than the value of critical load of n and n-1 transformer. Otherwise ,using n-1 transformer parallel operation is economic,

As many different types of double-winding transformer economic operation, It should be calculated the critical load tables for various combinations of mode, and then select the most economical combinations according to the load substation.

Using energy-efficient distribution transformer. Energy-efficient transformer is to save energy and decrease loss by reducing the iron loss of the transformer. It includes regulated capacity transformer, amorphous alloy transformer, single-phase distribution transformer and so on.

Regulated capacity transformer is a kind of regulating operation capacity transformer with a load capacity regulating switch according to the size of the actual load. Compared with the S9 transformer, the no-load loss of regulated capacity transformer can be decreased by 30%, the

no-load current can be decreased by 70%. For seasonal difference area, the annual operation cost of regulated capacity transformer can be decreased by about 45%.

Amorphous alloy transformer is to save energy and decrease loss through reducing no-load loss. Compared with the S9 transformer, the no-load loss of amorphous alloy transformer can be decreased by 70%-80%, the no-load current can be decreased by about 50%. Thus, it has low operation cost and obvious energy-saving result. Energy efficiency is the highest when the load factor of amorphous alloy transformer is in between 20% -30%.With the increase of transformer capacity, energy efficiency is also improved. Usually, selecting the capacity of amorphous alloy transformer should be more than 200kVA. But the application is limited because of its high price, low yield and special structure, it is only suitable for installation in areas with light load or no-load operation.

Single-phase distribution transformer is divided into single-phase three-wire transformer and single-phase two-wire transformer according to the different connection methods in low-voltage side of transformer. When the total transmission power of single-phase transformer is same, the single-phase three-wire connection mode can reduce by 1/4 length of low-voltage distribution line. When the two shunt load balancing, the single-phase three-wire connection mode can reduce by 1/2 power consumption of low-voltage line loss. Therefore, it is recommended that the use of single-phase three-wire power distribution technology. In the single-phase three-wire distribution mode, in order to avoid the user side voltage increase, it should be grounded in the neutral point of single-phase transformer low-voltage outlet (ground) and neutral point of the user side.

The problems about the loss reduction measures in China

In recent years, although China has developed many new technology of energy saving , but it did not focus on the long-term development and the overall economic benefits. In power supply and distribution system, there are still a great potential for energy saving and technology upgrade space, mainly as follows:

Cost-benefit analysis method of power network planning is relatively simple

Cost-benefit analysis method of investment for power grid planning in China is relatively simple, more attention to reliability, and can not achieve the coordinated development of economy and reliability of the whole power grid. Also, for a long time, conductor selection mainly based on the economic current density at planning stage, while the latest economic current density in China was issued in 1987 by the former Ministry of Water Resource and Electric Power, and now the metal material price, electricity price, the manufacturing process, load condition are changed, its effectiveness is not applicable to the present stage.

The economic operation level of the power grid needs to be improved

The load distribution is not balanced. The heavy and light load transformer contained within the same network leads to a serious deviation from the economic operation range, thus increasing the power loss. This imagination can be found to varying degrees at all the grid.

Reactive power compensation is difficult to meet the requirements. Low reactive power compensation and poor regulation ability increases the power loss and declines in the quality of power users. In addition, the power loss is also increased by the lack of users capacitor.

Have not been able to achieve the dynamic management of grid operation. Some areas invest blindly just to reduce the loss, can not be in the way of dynamic management of grid operation to achieve the purpose of saving energy and reducing loss.

High prevalence and obsolete equipment is universal

Due to the lack of funds,the distribution network construction is lagging behind and it is difficult to replace or modify the old equipment. A large number of high energy-consuming equipment is still used in the individual area, such as: S7-type and below S7-type distribution transformers. Even though some areas have used energy-saving transformer, they can not achieve the ideal results. For example, no load transfer capacity transformer has been applied in some areas, but many people do not grasp the correct way to use, thus resulting in distribution transformer capacity regulating function is underutilized, the large capacity operation mode is not adjusted as the load capacity increases and the burned accident of transformer capacity regulating is occured frequently.

Using some kind of isolated technological measures of loss reduction

In the energy-optimized of practical distribution network, it seems that only a "stop-gap" to take some kind of energy-saving measures and it do not focus on the long-term development and overall economic benefits. Such as: only a wire to replace or only in low-voltage reactive power compensation to change the line power flow to achieve the loss reduction effect is not enough, then, the former will influence the capacity or position of the reactive power compensation, the latter will influence the current carrying capacity and the cross-section selection of conductor. So, a few isolated measures do not have an ideal effect.

Countermeasures to reduce the line loss

Strengthening the cost-benefit analysis of the investment of distribution network planning. In the process of formulation and implementation to reduce line loss, we must consider the cost of investment and the loss reduction effect, let the investment income as an important basis for evaluation and carry out a comprehensive analysis of technical and economic, use the limited funds and create the best investment benefit.

Improving the economic operation level of the power grid. Adjusting the operation way of power grid according to the variation of load and outaging part of no-load transformer through the rational allocation of power flow and main transformer load rate, which can make the system in the economic operation way.

Strengthening the operation management of reactive equipment, improving automatic monitoring means and the operation rate of the reactive compensation device, and increasing evaluation efforts against reactive compensation device switching.

It is method to achieve the purpose of saving energy and reducing loss by strengthening the dynamic management of the power grid operation, optimizing the operation mode, shortening the cycle of adjustment operation mode according to the change of load level.

Intensifying the technological renovation of the power grid equipment. To reduce the loss of distribution network, the measures should be taken as follows: extension of high voltage power supply to the load center, increasing the wire section, shortening the supply radius of distribution network, reducing the bypass power supply, a planned step to change and eliminate the high loss distribution transformer, replacing the aging into the family line.

Strengthening the collaborative optimization of various energy saving measures. Energy saving and consumption reduction of distribution network is a system engineering and involves the aspects of power grid. To achieve the collaborative optimization in a variety of energy-saving

measures has a very important practical value for making the energy-saving modification plan of distribution network of global optimization. It should be plan the reasonable grid layout, evaluate energy saving measures of the distribution network and implement these measures according to actual condition of power network, formulate comprehensive renovation of energy saving optimization scheme in accordance with engineering practice, which ultimately achieve the goal of energy saving and loss reduction.

Conclusion

This paper mainly introduces some technique measures to reduce the loss of power system planning and operation. As can be seen, our measures in saving energy and reducing loss are still immature, It should be consider the reduction loss problem of power grid from long-term development, the economic operation, power grids, operation management and investment return and bring the power loss reduction index into all aspects of grid operation.

References

[1] Xueqi Liao: *Analysis and calculation of loss and countermeasures to reduce loss in rural power network* (China Water Conservancy and Hydropower Publications, Beijing, 2008)

[2] Ming Lei: *Handbook of loss reduction and energy saving in power network* (China Electric Power Publications, Beijing, 2005)

[3] Qing Yang: *Energy management and energy saving technology* (China Electric Power Publications, Beijing, 2011)

[4] Rui Li, Jian Su, Mingtian Fan, etc. Review of energy saving experience and measures in foreign distribution network. The second energy saving technique seminar of the industrial enterprises,2007

[5] Junling Lu: Series of books on Demand Side Management (China Electric Power Publications, Beijing, 2013)

[6] The research of line loss analysis and its reducing strategy for distribution power network[D]: Beijing, North China Electric Power University(2008)

[7] A.Bhuiya, N.Chowdhury, M.Huq. Optimum Market Strategy for An Independent Power Producer. Technology Driving Innovation, 2004, 1937-1942

[8] Steven T,Bruce A ,Kirchhoff and Scott Newber. Differentiating Market Strategies for Disruptive Technologies. IEEE Transactions on Engineering Management. VOL 49. NO.4. NOVEMBER 2002:341-350

[9] ZHANG Yong-jun, CHEN Chao, LIAO Min-chuan. Research on optimal model for energy saving reconstruction of distribution networks[J], Power System Protection and Control, Vol 38. No.15.2010:60-64.

Advanced Materials Research Vols. 960-961 (2014) pp 1490-1493

doi:10.4028/www.scientific.net/AMR.960-961.1490

Development Trends of Chinese Power Plants

Fangqin Li , Jiyong Liu, Xiaofeng Zhang, Jifa Zhang, Huan Liu

School of Energy and Mechanical Engineering, Shanghai University of Electric Power, Shanghai 200090, P.R. China

lf_q@163.com

Keywords: power plants; installed capacity; standard coal consumption rate; power supply; power generation; auxiliary power

Abstract: Through the analysis of some parameters of Chinese power plants operation in recent years, forecasting that at a certain period in the future, total installed capacity of 6000 kw or more units will have the growth rate of 7% - 8%.China's power supply coal consumption rate will continue to become lower by 3-5g/kwh every year.

Introduction

Nowadays, conventional coal or gas fired power plants are the dominant way to generate electricity in the world. However, the problems of pollution emissions, greenhouse gas emissions etc are getting more and more attention. The conventional power industry is under huge pressure with the renewable energy targets and carbon taxes set by various governments. A real technical revolution is needed to change the power industry into an environmentally friendly industry.

The growth of world energy consumptions and the need to meet the increasingly stringent environmental regulations make the repowering of existing coal-fired power plants an attractive option for boosting the generating capacity at competitive cost [1-3].

With the increasing depletion of fossil fuels, how to effectively use the heat released by fossil fuels has become the focus of current research. China is one of the countries which are heavily dependent on coal-based energy supply and coal- fired power generation ac-counts for 80% of the total electricity generation in China[4]. Due to many reasons such as design or operation, the temperature of the exhaust flue gas of a pulverized CFPP (coal-fired power plant) can be reached to 150℃ which makes the heat loss with the exhaust flue gas the biggest among the heat losses of a boiler. Preliminary estimates show that the waste heat resources contained in exhaust fl ue gas equals to 70 million tons of SCE (standard coal equivalent), in other words, there are almost 70 million tons of SCE in the form of waste heat released to atmosphere in China every year, causing energy waste and greenhouse effect[5-7].

With the great development of such fluctuant renewable energies as wind and solar power, more and more thermal power plants have been forced to compensate the loss of generation as the power source reserves for the grid stability.

Status of Chinese power plants

As is shown in Fig.1, in China, 6000 kw or more of the total installed capacity of the units is almost every year to increase around 100 million kw from the year of 2008 to 2013. The growth speed of the total installed capacity of the units is very great. About five years from the year of 2008 to 2013, 6000 kw or more of the total installed capacity of the unit increased from 793 million kw to 1.247 billion kw, added about 454 million kw, increased by 36.4%. The growth rate of 6000 kw or

more of the total installed capacity of the unit is between 8%-9% every year. This growth rate fits in the growth rate of China's national economy. So the power plant unit total installed capacity of annual growth can be reflected from the side of a country's economic development level. According to expert estimates, the level of economic growth in China in the future within a period of time, will still remain between 7% - 8%, therefore, can be estimated that China's total installed capacity of power plant, there will be 7% - 8% a year growth rate[8-9].

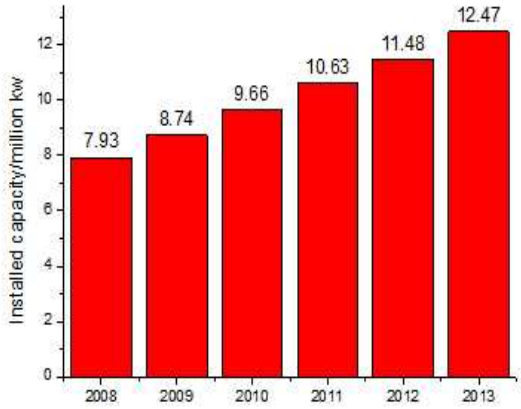

Fig.1 Situation of the total installed capacity from the year of 2008 to 2013 in China (more than 6000kw units)

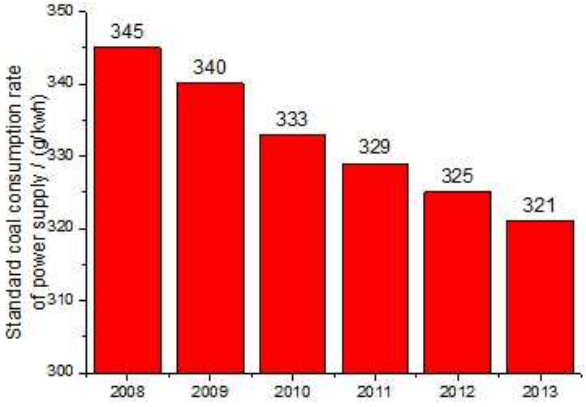

Fig.2 Standard coal consumption rate of power supply from the year of 2008 to 2013

Can be seen from the figure 2, more than 6000 kw of power supply coal consumption of units, from 2008 in 345 g/kwh, dropped to 2013 in 321 g/kwh, reduced about 24 g/kwh, reduced about 7.48%, the power supply coal consumption each year will have to reduce about 4-5 g/kwh. In December last year 1 - the national total capacity 5.24511 trillion kwh, compared with 2008, will save 1.259 billion tons of standard coal. In 2013, the total energy consumption in China reached 3.76 billion tons of standard coal, coal 3.5 billion tons (2.5 billion tons of standard coal), accounting for 33.48% of total consumption, made important contribution for our country's energy conservation and emissions reduction. National thermal power unit power supply coal consumption of 321 g/kwh, national 12th five-year plan for energy conservation and emissions reduction goals ahead of time (325 g/kwh), coal unit power supply coal consumption continues to the world advanced level. But China power plant energy conservation and emissions reduction potential is very big, there is a certain gap with the developed countries in the world. China's power supply coal consumption will continue to be a year there will be 3-5 g/kwh.

Can be seen from the Fig.3, more than 6000 kw power standard coal consumption rate of the unit from 322 g/kwh in 2008 dropped to 2012 in 305 g/kwh, every year there are 2-8 g/kwh. Contact with figure 2, be able to get power plant auxiliary power of standard coal consumption rate, as shown in figure 4.As can be seen from the Fig.4, 2008 to 2009, auxiliary power standard coal consumption rate fell sharply, later growth slightly, and then continue to decline. From then on, the auxiliary power standard coal consumption rate to maintain the low level. According to the report, the power plant by the original factory electricity accounts for about 10% of the total generating capacity, reduced to 5%, now that the energy consumption of the power plant level fell sharply, energy-saving effect is remarkable.

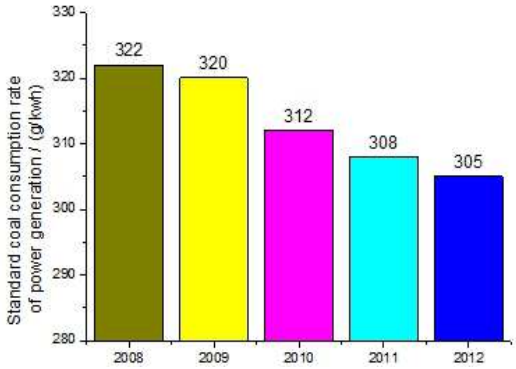

Fig.3 Standard coal consumption rate of power generation from the year of 2008 to 2012 in China

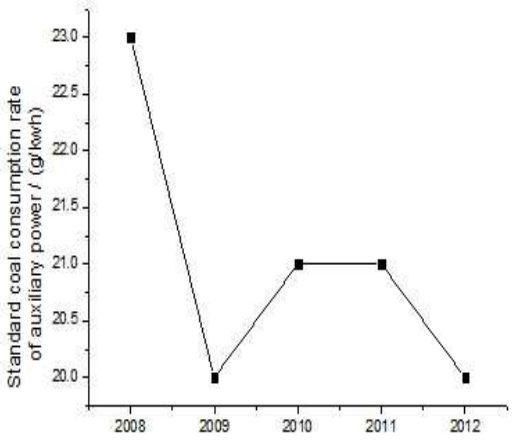

Fig.4 Standard coal consumption rate of auxiliary power from the year of 2008 to 2012 in China

Can be seen from the Fig.5, the proportion of thermal power unit capacity, it depends on China's energy structure, followed by water and electricity, and then the wind power and nuclear power. According to China's electric power network, by the end of December 2013, the whole caliber power equipment capacity of 1.24738 billion kilowatts, up 9.2% from a year earlier. The hydropower installed capacity of 280.02 million kilowatts, up 12.3%;Thermal power installed capacity of 862.38 million kilowatts, increased by 5.7%, compared to the clean energy capacity of continued ascension. In 2013, the national power of new production capacity (formal) with a 94 million kw, and among them, the hydropower 29.93 million mw, 36.5 million mw thermal power.

As is shown in Fig.6, in recent years by the new energy capacity of constantly improve and power supply and demand factors, such as the country's 6000 mw and above average power generation equipment utilization hour continues to decline, in 2013 to 2013 hours, compared with 68 hours.

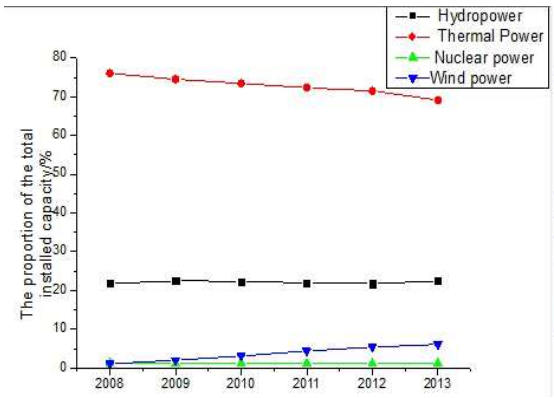

Fig.5 Proportion of some kinds of power plants as to the total installed capacity in China

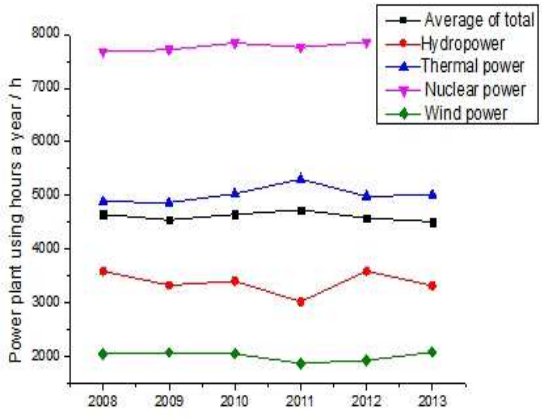

Fig.6 Power plant using hours a year in China from the year of 2008 to 2013

Summary and Conclusions

Through the analysis of some parameters of Chinese power plants operation in recent years, forecasting that at a certain period in the future, total installed capacity of 6000 kw or more units will have the growth rate of 7% - 8%.China's power supply coal consumption rate will continue to become lower by 3-5g/kwh every year.

New power plants will choose large capacity and high parameter unit equipment; in the energy-saving reconstruction of existing units, a press more than one batch of waste heat recovery equipment will be used, such as screw expander, heat pump, etc.; the automation level of power plant will be further improved, the frequency conversion technology will be more and more used in pump and fan and other equipment; renewable energy and traditional energy coupling, constitute a mixed heat power generation system, mixed with coal-fired units such as solar energy power generation system; all-round optimization operation mode change, such as no fan . Stop the pumps and downtime, unilateral, circulating pump and downtime, circulating water pump operation mode optimization, the optimization of open cooling water system, the coal pulverizing system operation optimization, optimization of constant pressure and sliding pressure operation mode, etc.; some other technology applications, such as the application of new type thermal insulation coating in power plant piping, etc.

Acknowledgements

This work was partially supported by Shanghai Engineering Research Center of Power Generation Environment Protection(11DE2281700) and by Scientific Problem Tackling Program of Science and Technology Commission of Shanghai Municipality (11dz2281700).

Reference

[1] Fränkle M. , SRS: the standarized repowering solution for 300 MW steam power plants in Russia. Si e mens Power Generation Germany. Report 2006.

[2] Electrical Power Research Institute (EPRI), Re powering Fossil Steam Plants with Gas Turbines and Heat Recovery Steam Generators : Design Considerations, Economics, and Lessons Learned, Technical report 2012.

[3] Bartnik R.,The Modernization Potential of Gas Turbines in the Coal-fired Power Industry: Thermal and Economic Effectiveness, Springer London, Limited, 2013.

[4] Simopoulos DN, Kavatza SD, Vournas CD. Energ Convers Manag 2007;48(11):3018-24.

[5] Yutang Fang, Weijun Wan: Materials Review. (2009), p.108, In Chinese

[6] Intergovernmental Panel on Climate Change. Climate Change: Synthesis Report. Intergovernmental Panel on Climate Change. 2007

[7] Dahowski RT, Li X, Davidson CL, Wei N, Dooley JJ, Gentiled RH. A preliminary cost curve assessment of carbon dioxide capture and storage potential in China. Energy Procedia

[8] Information on http://www.nea.gov.cn

[9] Information on http://www.cec.org.cn

Advanced Materials Research Vols. 960-961 (2014) pp 1494-1500

doi:10.4028/www.scientific.net/AMR.960-961.1494

Enchanted Multi-objective Differential Evolutional Algorithm for Economic/Environmental Dispatch

Peng Sun, Mingwu Luo, Chaoxia Sun

Adress:Qingnianlu No. 91, Zengdu District, Suizhou City, Hubei Province

Email: aptiva@126.com

Keywords: Security constrained economic/environmental dispatch,Constrained multi-objective differential evolution, Feasible region and infeasible region

Abstract. An enchanted multi-objective differential evolutional algorithm was proposed, and was applied to solve the environmental economic dispatch problem. Duo to the weakness of random initial population, the orthogonal method was used in the initialization. Based on survival of the fittest, improved differential operation was proposed, combined with the corresponding parameters control method proposed. With the combination of B-coefficient method and restrain dominance, the process of solving equation and selection operation were used to make the individuals meet the equality constrain. Then the algorithm was tested on the IEEE-30 test system, the results are compared with the results of non-dominated genetic algorithm-II, ulti-objective differential evolution and the known results in the papers, and the validity is verified.

Introduction

Due to the power generation of thermal units,the release of sulphur oxides（SO_x）, itrogen oxides（NO_x）and carbon dioxide (CO_2)has already caused high pollution and greenhouse effect. Under the background of energy conservation, power supply should be not only of high economy and reliability, but also to reduce the emission to the environment.

Common measures such as the installation of desulfurization equipment,building a carbon capture plant and its improvement and EED are taken to improve the operation of generation units. But the most effective method can be EED in a short term.

Fuel costs of thermal units and pollution emissions are mutually exclusive, which means pollution emissions are the highest when costs are lowest and pollution emissions are the lowest when costs are high. EED problem are proposed against this contradiction, which realize the system economy and satisfactionof emission index through optimizing the load distribution of units on the premise of system safety and stable operation. EED has been widely researched by scholar at home and abroad, in classic solution of EED problems, multi-objective problems are always converted to single objective problem to get the model solved, but the weight is difficult to determine and the Paretofront can't be achieved when the trade-off relationship of objective function isnonlinear[1]. Objective functions are linear decomposed and linear programming are applied in each part to simplify the calculation, but it can't express the trade-off relationship of objective functions[2], EED problems are converted to single objective problem under the constraint of emissions but only get an approximate solution after many times adjustments[3].

Heuristic algorithm is applied in EED problems in recent years, such as NSGA-II，evolutionary programming,multi-objective particle swarm algorithm, Multi-objective Differential EvolutionMODE [4-9]. MODE is widely used in EED problem solutions for its global search capability and easy implementation[8,12].

But of the classical EED problem does not take thetransmission linelosses constrain into consideration, and the solution got by those classical method may not satisfy the power balance constrain. And the value-point effect is not taken into consideration. So in this paper, all of these constrains are included. As the DEMO[10] method id used to solve unstrained multi-objective optimization problems, a newly EMODE based on DEMO andconstrained handle technique[11]was proposed to solve the security constrained EED problem.Experiments have been carried out on the standard IEEE 30-bustest system and the results are compared to different techniquesreported in literature. The effectiveness and potential of the proposedEMODE approach to solve the security constrained EED problemare demonstrated.

Problem statement

The EED problem is to minimize two competing objective functions,fuel cost and emission, while satisfying several equality andinequality constraints. Generally the problem is formulated as follows.

Problem objectives. 1.Minimization of fuel cost

When the value-point effect is taken into consideration, the total fuel cost $F_c(P_G)$ can be expressed as[5,7]:

$$F_c(P_G)=\sum_{i=1}^{N}(a_i+b_iP_{G_i}+c_iP_{Gi}^2+|d_i\sin(e_i(P_i-P_{\min,i}))|) \tag{1}$$

Where N represents the total number of generators;$a_i,b_i,,c_id_ie_i$arethe cost coefficientsof the i-th generator, and $P_{Gi}$is the real power output of the$i$-th generator.

2.Minimization of emission

The atmospheric pollutants such as SO_x, $O_x$andCO_2caused by fossil-fueled thermal generatorshould bemodeled separately. However, for comparison purposes, the total emission of these pollutants E(P_G) whichis the sum of a quadratic and an exponential function canbe expressed as[14]:

$$E(P_G)=\sum_{i=1}^{N}10^{-2}(\alpha_i+\beta_iP_{Gi}+\gamma_iP_{Gi}^2+\xi_i\exp(\lambda_iP_{Gi})) \tag{2}$$

where α_I, β_I, γ_I, ξ_I and λ_I are the emission coefficientsof the ith generator.

Problem constrains. 1.Generation capacity constraint

To maintain the generator operating stablely, the real and reactive power output of each generator is restricted by lower and upper limits as follows:

$$P_{Gi}^{min}\le P_{Gi}\le P_{Gi}^{max},i=1,...,N \tag{3}$$

where:$P_{Gi}^{min}$and P_{Gi}^{max} represent the lower and upper boundary of the ith generator's real power capacity respectively.

2.Power balance constraints

The total real power generated should meet the demand P_D and the real power loss in transmission lines P_{loss}:

$$\sum_{i=1}^{N}P_{Gi}=P_D+P_{loss} \tag{4}$$

There are two ways to calculate P_{loss}, such as B-matrix loss formula method[4,9] and power flow method[6-7]. And the B-matrix method is deployed here to calculate the real power losses:

$$P_L=\boldsymbol{P}_G^T\boldsymbol{B}\boldsymbol{P}_G+\boldsymbol{P}_G^T\boldsymbol{B}_0+\boldsymbol{B}_{00} \tag{5}$$

Where $\boldsymbol{P_G}$is the vector of all the generators' real power output,$[P_{G1}\ldots P_{GN}]$; **B**, $\mathbf{B}_0$, $\mathbf{B}_{00}$ are the coefficients of the B-matrix. Then the above equation can be re-written as:

$$\begin{aligned} P_L = &\sum_{i=1}^{N-1}\sum_{i=1}^{N-1} P_{Gi}B_{ij}P_{Gj} + 2P_{GN_G}(\sum_{i=1}^{N-1} B_{Ni}P_{Gi}) \\ &+ B_{NN}P_{GN_G}^2 + \sum_{i=1}^{N-1} B_{0i}P_{Gi} + B_{0N_G}P_{GN_G} + B_{00} \end{aligned} \tag{6}$$

Substituting （6）into （4），the power balance constrain can be formulated as：

$$\begin{aligned} &B_{NN}P_{GN_G}^2 + 2(\sum_{i=1}^{N-1} B_{Ni}P_{Gi} + B_{0N_G} - 1)P_{GN_G} + \\ &(P_D + \sum_{i=1}^{N-1}\sum_{i=1}^{N-1} P_{Gi}B_{ij}P_{Gj} + \sum_{i=1}^{N-1} B_{0i}P_{Gi} - \sum_{i=1}^{N-1} P_{Gi} + B_{00}) = 0 \end{aligned} \tag{7}$$

As shown in (7),the real power of N-th generator is an dependent variable of the other generators' outputs. So in our work, only N-1 generators' real power are taken as controllable variables, and the left one is obtained by (7).

EMODE

EMODE. Even DEMO can efficiently converges to the true Pareto front and uniformly spreadsindividuals along thePareto front, some weaknesses do exit, such as hard to choose the control parameters. What's more it is proposed for unconstrained problems, when it comes to constrained problems, how to handle the constrains is not yet proposed. So the newly algorithm called EMODE is proposed, canbe described in the following steps:

Step 1: Initialize

DEMO is a robust algorithm, and the final solution is not sensitive to initialization. But the computation timeis relatedto the distance between the initial guesses and the optimal solution. So theorthogonaldesign is used to generate a population of size $N_P$as the initial population.

Step 2:Mutation operation& Crossover operation

The traditional mutate operation is taken according to the following equation:

$$v_i^{G+1} = x_{r1}^G + F \bullet (x_{r2}^G - x_{r3}^G) \tag{8}$$

where r1, r2 and r3 are mutually different integers which are randomly selected with uniform distribution from the set{1,…,Np} ,and also different from the individual's index i,i=1,2,…Np; F is the mutation parameter.

As (8) shows, the searching ability of DE is mostly affected by F. To balance the global search and local search, the mutation strategy following is deployed in this paper:

$$v_i^{G+1} = \begin{cases} x_{r1}^G + F_l \bullet (x_{best}^G - x_{worst}^G) & if\ rand \le \tau \\ x_{r1}^G + F_g \bullet (x_{r2}^G - x_{r3}^G) & else \end{cases} \tag{9}$$

where rand is a uniform random number generation with [0,1]; τ is the control parameter to decided when to use the first kind of mutation strategy, in this paper it was set to 0.5; $F_l$and F_g are the mutation parameters , randomly generated from [0.4,0.6]and[-1,1] respectively;x_{best}^G and x_{worst}^G are the best and worst individual in the present population, respectively.

Following the mutation operation, crossover is applied to the individuals in the population.For each mutant vector, x_i^{G+1},an index of $rnbr_i \in$ {1,…,Np} is randomly chosen with a uniform distribution, and a trial vector is generated via:

$$x_{ij}^{G+1} = \begin{cases} v_{ij} & if\ rand \le CR\ or\ j = rnbr_i \\ x_{ij}^{G} & otherwise \end{cases} \tag{10}$$

where j=1,2,…,N is the parameter index; CR is a crossover rate in the range[0,1], and the strategy proposed in Ref[13] is deployed here to decide the value of CR in each generation:

$$CR_G = CR_{\max} + (CR_{\max} - CR_{\min})(1 - G / G_{\max})^k \tag{11}$$

Where CR_G is the crossover rate for the G-th generation;CR_{max} is the maximum crossover rate ,set to 0.95;CR_{min} is the minimum crossover rate, set to 0.5; G_{max} is the maximum iteration; k is the growth index, taken as 4 here.

Step 3:Selection operation

Even the power balance constrain(4) is transferred into a quadratic equation (7) ,the solution of (7) may be infeasible, as violation of the generator's capacity constrain (3).So the selection operation of EMODE is carried out after the one-to-one competition between the trial and parent individuals based on the concept of restrain dominance, unlike the MODE method proposed in Ref[12].

Definition 1: restrain dominance

$x_i$is said to restrain dominance x_j ,$x_i \prec_c x_j$,when:

1)$x_i$is feasible, and $x_i$is infeasible;

2)$x_i$is infeasible, and $x_i$is infeasible, and the total constrain violation of $x_i$is smaller than x_j's;

3)$x_i$is feasible, and $x_i$is feasible, and$x_i \prec x_j$.

where$x_i \prec x_j$ stands for the concept of dominance.

Definition 2: dominance

$x_i$is said to dominancex_j,$x_i \prec x_j$,when:

$$\begin{cases} f_i(x_i) \le f_i(x_j), \forall i \in \{1,2,...,N_f\} \\ f_i(x_i) < f_i(x_j), \exists i \in \{1,2,...,N_f\} \end{cases} \tag{12}$$

where $N_f$is the number of objectives, as proposed in this paper N_f was set to 2; $f_i(x_i)$ represents for the ith objective function value of individual x_i.

After the competition procedure, a population of size between Np and 2Np is formed. In Order to maintain the populationsize constant, the truncation based on non-domination and crowdingdistance calculation is carried out.

Step 4:non-domination and crowdingdistance calculation

In order to exploit the information the infeasible individuals carry and balance the search between feasible region and infeasible region, the constrain handling technique proposed in[11] is employed.

Because of that the non-domination and crowdingdistance calculation procedure is carried out on the population's objective functionvalues, to implement the constrain handling technique mentioned above, these values should be modified.The modified objective value hastwo components: distance measure and adaptive penalty.The details can be found in Ref[11].

After the objective functionvalues' adjustment, the non-domination and crowdingdistance calculation is carried out. The best $N_p$individuals are selected as theparent vectors for the next generationbasedon its ranking and crowding distance.

Step 5:Stopping Rule

The search can be interrupted after a givennumber of generations, or when no significant improvementin the solution occurs. Here EMODE is run for a fixed numberof generations; if the criterion is not satisfied then the procedureis repeated from step 2 creating the new populationfrom the parent population.

Step 6:Stop

Experiments

Having been applied for the first time, the proposed EMODEtechnique was tested on the standard IEEE 30-bus 6-generator testsystem as several techniques have been tested on this standard systemwithreported results in the literature. The single-line diagramof the IEEE test system and the detailed data aregiven in [2,7]. The values of fuel cost, emission coefficients and B coefficients are given in[14].

To demonstrate the effectiveness of the proposed approach,two cases with different complexity have been considered as follows:

Case 1：The value-point effect is not considered.

Case 2：The value-point effect is taken into consideration.

The parameters used for all cases were: Np were set to 36;the maximum number of generations$G_{max}$was set to 100, the total load P_D was set to 2.834pu on a 100MVA base.

To verify the effectiveness of our algorithm, the proposed uniform distribution index and coverage index were introduced:

$$S=\sqrt{\frac{1}{N_{PF}}\sum_{i=1}^{N_{PF}}(d_i-\overline{d})^2}\ /\ \overline{d} \tag{13}$$

$$I_c(A,B)=\frac{|\{b\in B;\exists a\in A:a\prec b\}|}{|B|} \tag{14}$$

Where S is the uniform distribution index, and the smaller of S means the better of the Pareto front;$d_i$is the Euclidean distance between the i-th non-dominated solution in the Pareto front and the nearest non-dominated solution;$\overline{d}$ is the average value ofd_i;N_{PF} is the number of non-dominated solutions in the Pareto front;I_c represents the percent of solutions in set B dominated by solutions in set A, and the higher of I_c means the better of A and worst of B.

Case 1

Tab 1 Comparison between best solutions of different algorithms without value-point effect

Method	Algorithmm	P_{G1}/pu	P_{G2}/pu	P_{G3}/pu	P_{G4}/pu	P_{G5}/pu	P_{G6}/pu	Fc:$	E:t	PL:pu	S	Ic
Best Economic	EMODE	0.1213	0.2855	0.5837	0.9919	0.5249	0.3523	605.9986	0.2207	0.0256	0.6272	——
	NSGA-II	0.1253	0.2848	0.5738	0.9871	0.5260	0.3628	606.0201	0.2200	0.0258	1.1002	0.1563
	DEMO	0.1205	0.2871	0.5795	0.9926	0.5272	0.3527	605.9998	0.2207	0.0256	1.2649	0.4333
	Ref[15]	0.1210	0.2860	0.5840	0.9930	0.5240	0.3520	606.0000	0.2217	0.0260	——	——
Best Emission	EMODE	0.4115	0.4651	0.5461	0.3907	0.5438	0.5121	646.1685	0.1942	0.0353		
	NSGA-II	0.4106	0.4642	0.5418	0.3891	0.5472	0.5164	646.3439	0.1942	0.0353		
	DEMO	0.4111	0.4638	0.5441	0.3904	0.5447	0.5152	646.2166	0.1942	0.0353		
	Ref[15]	0.3936	0.4683	0.5403	0.4040	0.5163	0.5466	645.3229	0.1943	0.0351		

The best economic dispatch solution and best emission dispatch solution of Case 1 are shown in Tab.1.Comapred to the results given in [15],the solutions in EMODE have the advantage in economic and emission, and the fuel cost and emission are reduced by 0.0012$/h and 0.001 t /h ,respectively. What's more, the uniform index *S* indicates that the EMODE obtain the most uniformly spread solutions. The convergence index I_c demonstrates the algorithm's convergence performance.

Case 2

The Pareto front obtained by the EMODE in Case 2 is shown in Fig.1,and the best economic dispatch solutions and the best emission dispatch solutions are shown in Tab.2.As shown in Fig.1,when the value point is taken into consideration, the Pareto front of EED is discontinuous.

When it comes to emission, EMODE obtains the best plan ,and dominates the other two. Further, compared to NSGA-II and DEMO, the fuel cost of the best economic plan in EMODE is reduced by 6.8789$/h and 1.2551$/h,respectively. What's more, 75.00% and 48.44% of non-dominated solutions in NSGA-II and DEMO are dominated by the solutions obtained by EMODE. Finally, *S*index indicates that EMODE always obtains the most uniformly spread solutions.

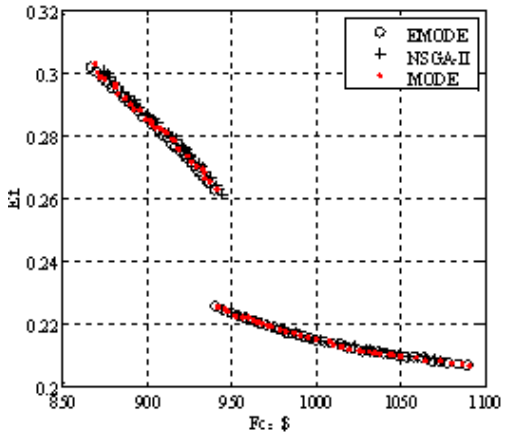

Fig 1 Pareto fronts under different cases

Tab 2 Comparison between best solutions of different algorithms with value-point effect

Method	Algorithmm	P_{G1}/pu	P_{G2}/pu	P_{G3}/pu	P_{G4}/pu	P_{G5}/pu	P_{G6}/pu	Fc:$	E:t	PL:pu	S	Ic
Best Economic	EMODE	1.5004	0.5218	0.5000	0.1178	0.1448	0.1308	867.4644	0.3021	0.0816	0.4363	——
	NSGA-II	1.4969	0.5214	0.4629	0.1359	0.1758	0.1218	874.3433	0.3006	0.0807	0.6176	0.7500
	DEMO	1.5005	0.5255	0.5000	0.1525	0.1064	0.1316	868.7195	0.3029	0.0825	0.5610	0.4844
Best Emission	EMODE	0.6784	0.7044	0.4999	0.3500	0.3000	0.4000	1089.8886	0.2071	0.0987		
	NSGA-II	0.7681	0.6168	0.4997	0.3500	0.2999	0.3989	1073.8157	0.2084	0.0994		
	DEMO	0.6796	0.7034	0.5000	0.3500	0.3000	0.4000	1090.0008	0.2071	0.0990		

Conclusion

In this paper, a novel enhanced multi-objective differential evolution algorithm has been proposed and applied to environmental/economic real power dispatch problem. The proposed EMODE technique presents a constrained version of the conventional DEMO technique and utilizes its effectiveness to solve the constrained multi-objective optimization problems. The EED problem is formulated with competing fuel cost and environmental impactobjectives.What's more, the real power losses and value-point effect are also taken into consideration.

The results show the efficiency of the proposed EMODE method to solve EED problemwith real power losses and value-point effect integrated.And the results also reveal proposed algorithm has the capacity to maintain the divergence of the population and converges to the true global Pareto front in the same iterations.

Reference

[1] Catalao J P S，Mariano S J P S，Mendes V M F，et al．Short-termscheduling of thermal units：emission constraints and trade-off curves[J].European Trans on Electrical Power,2008,18(1):1-14．
[2] FaragA, Al-BaiyatS, Cheng T.C.Economic load dispatch multi-objective optimization procedure susing linear programming techniques[J].IEEE trans on Power System,1995,10(2):731-738．
[3] Granelli GP,Montagna M,Pasini GL,Marannino P. Emission constraineddynamic dispatch. Electric Power System Research，2008，78(7)：1129–37．
[4] M. Basu. Dynamic economic emission dispatch using non-dominated sorting genetic algorithm-II[J]. Electrical Power and Energy Systems.2008,30:140-149．
[5] S. Dhanalakshmi , S. Kannan, K. Mahadevan, S. Baskar. Application of modified NSGA-II algorithm to Combined Economic and Emission Dispatch problem[J]. Electrical Power and Energy Systems.2011,33:992-1002．
[6] Tsay MT, Lin WM. Application of evolutionary programming for economicdispatch of cogeneration systems under emission constraints[J]. Electric PowerSystem,2001,23(8):805–12．
[7] M.A. Abido. Multi-objective particle swarm optimization for environmental/economicdispatch problem[J]. Electric Power Systems Research,2009,79: 1105–1113.
[8] YoulinLu,JianzhongZhou, HuiQin,YingWang,YongchuanZhang. Chaotic differential evolution methods for dynamic economic dispatch with valve-point effects[J]. Engineering Applications of Artificial Intelligence,2011,24:378-387．
[9] CelalYasar,SerdarÖzyön. A new hybrid approach for non-convex economic dispatch problemwith valve-point effect[J].Energy.2011,36:5838-5845．
[10] Robič T, Filipič B. DEMO. Differential evolution formulti-objective optimization[C]//EMO 2005.Heidelberg, Germany, Springer, 2005, 520-533．
[11] YonasGebreWoldesenbet, Gary G. Yen,Biruk G. Tessema. Constraint Handling in MultiobjectiveEvolutionary Optimization[J]. IEEE Transon EvolutionaryComputation, 2009,13(3):514:525.
[12] M. Basu. Economic environmental dispatch using multi-objective differential evolution[J]. Applied Soft Computing,2011,11: 2845–2853.
[13] Ali WagdyMohamed ,HegazyZaherSabry. Constrained optimization based on modified differential evolution algorithm[J]. Information Sciences,2012,194:71-208.
[14] CelalYasar, SerdarÖzyön. A new hybrid approach for non-convex economic dispatch problem with valve-point effect[J]. Energy.2011,36:5838-5845.
[15] Su Peng，Liu Tian-qi，Zhao Guo-bo,et al. An Improved Particle Swarm Optimization Based Multi-Objective Load Dispatch Under Energy Conservation Dispatching[J]. Power System Technology. 2009,33（5）：47—55. (in Chinese)

Advanced Materials Research Vols. 960-961 (2014) pp 1501-1507

doi:10.4028/www.scientific.net/AMR.960-961.1501

Site Selection Optimization for Thermal Power Plant Based on Rough Set and Multi-objective Programming

REN Feng

School of Business and Administration, North China Electric Power University, Baoding, China, 071003

renfeng2002@126.com

Keywords: Matter-element model Site selection optimization; Thermal power plant; Comprehensive evaluation; Rough set; Multi-objective programming

Abstract: The site selection optimization for thermal power plant will directly impact the economic operation and sustainable development. On the basis of constructing index system for site selection of thermal power plant, the method of rough set is applied to obtain the index weights, which are determined only by the system potential information. Through the method of expert decision-making, the quantitative and qualitative information is integrated, and the priority of the alternatives is obtained. The multi-objective model for site selection optimization is built up to balance the economical efficiency and the average comprehensive efficiency. In consideration of decision-makers' predilection and heat load demand, the two goals of cost minimum and average comprehensive efficiency maximum are achieved at the same time. Case analysis indicates that the method for site selection optimization of thermal power plant proposed in this paper possesses some advantages, such as scientificity and practicability.

Introduction

Along with the consciousness enhancement of people environmental protection, the issue of resource conservation and environmental protection has gradually become the focus of hot spots. There are many ways for city central heating, such as cogeneration, centralized coal-fired boiler, household gas boiler, heat pump heating, low temperature radiation heating, phase change thermal storage heating, geothermal heating, low temperature nuclear and solar heating, etc. Considering from China's national conditions, as well as from the perspectives of saving resource, reducing environment pollution and technical maturity, some studies concluded that the optimal model for central heating in China is still combined heat and power generation （CHP） within quite a period of time in the future [1-5].

The site selection issues related to energy mainly focus on the thermal power plant site selection[6-8], the nuclear power station site selection[9, 10], the solar energy power station site selection[11, 12], wind/solar hybrid power station site selection[13], the photovoltaic power station site selection[14-16], the wind wave energy power station site selection[17], etc. And the research methods are mainly stochastic dynamic programming [7], fuzzy set[9, 12], TOPSIS[8-10], AHP[9, 12, 14], entropy[10], ideal matter-elemnet extension[13], the Texel-Marsen-Arsloe Spectrum[17], et al. In particular, Barda, Ramos, KAI, et al. respectively studied the problems of site selection for thermal power plants in France, Brazil, and the United States [6-8]. The common problems in the

process of site selection are that the evaluation index system is not very reasonable, qualitative indexes and quantitative indexes are not well combined together, and the general evaluation function is only a single target, et al.

Unreasonable site selection for thermal power plant can cause heating costs increasing, resource wasting and environmental pollution, and bring great negative influences to society. Therefore, the site selection optimization for thermal power plant is of important practical significance.

Rough set operation system does not need any prior knowledge, can dig up the implicit information automatically, and completely avoid the human disturbance. In this paper, the exploratory study on the thermal power plant site selection optimization is discussed on the basis of constructing the index system of thermal power plant site selection using the methods of rough set theory and multi-objective programming.

Establishing index system

The main influencing factors of thermal power plant site selection are: (1) the availability of land(AL), (2) the construction cost(CC), (3) the heat pipe laying cost(HPLC), (4) the distance from the center of the heat load(DCHL), (5) the thermal load demand(TLD), (6) the grid access structure(GAS), (7) coal & water availability(CWA) and (8) environmental factors(EF), etc.

Modeling

Parameters and variable definition

Model parameters are as follows: $i \in I$: subscript of the central heating areas; $j \in J$: subscript of alternative locations; $m \in M$: subscript of thermal power plant heating capability levels; C_m : heating capacity of level m; F_j^m : construction and operation costs of the thermal power plant built at location j with the heating capability level m; a_i : the heat load of the central heating area i; D_{ij} : unit transportation cost from thermal power plant j to the central heating area i;

The decision variables are defined as follows:

$$X_j^m = \begin{cases} 1, \text{build a thermal power plant of level m at location j} \\ 0, \text{otherwise} \end{cases}$$

Z_{ij} : the percentage of the heat load in area i transported by thermal power plant j ;

The multi-objective optimization model

The multi-objective optimization mathematical model of site selection for thermal power plant is as follows:

$$\min \sum_{m}\sum_{j} F_j^m X_j^m + \sum_{i}\sum_{j} a_i Z_{ij} D_{ij} \tag{1}$$

$$\max \frac{1}{\sum_{m}\sum_{j} X_j^m} \sum_{m}\sum_{j} W_j X_j^m \tag{2}$$

$$\text{s.t.} \quad \sum_{j} Z_{ij} = 1, \forall i \in I \tag{3}$$

$$\sum_{m} X_j^m \le 1, \forall j \in J \tag{4}$$

$$\sum_{i} a_i Z_{ij} \le \sum_{m} C_m X_j^m, \forall j \in J \tag{5}$$

$$X_j^m \in \{0,1\}, \forall j \in J, m \in M \tag{6}$$

$$Z_{ij} \ge 0, \forall i \in I, j \in J \tag{7}$$

The objective function (1) is to minimize the total costs, including construction cost and transportation cost. The objective function (2) is to maximize the average comprehensive benefits of building thermal power plant. Where, W_j is the comprehensive evaluation value of the alternative sites. Formula (3) ensures that every district heating area's needs are met. Formula (4) ensures that only one thermal power plant at most is built at an alternative site. Formula (5) ensures that the heat load provided by a thermal power plant do not outnumber its maximum design capacity. Formula (6), (7) are the constraints of the variables.

Case analysis

There are four kinds of thermal power plant capacities, and the building costs of different capacities thermal power plants in different alternatives are shown in table 2.

Table 2. Building and operation costs (unit: one hundred million Yuan)

Alternatives	Capacity (MW)			
	125	250	300	375
1	6	11	16	21
2	5.5	10	15	20
3	5	10	15	20
4	6.5	12	17	22
5	5.8	11.5	16	20

There are four central heating areas. Assume that heat load will not change significantly in these areas in quite a long time in the future. Unit transportation costs (including heat loss) from each alternative to each central heating area are shown in table 3.

Table 3. Unit transportation costs (unit: ten thousand Yuan/ MW)

Load areas (demand)	Alternative sites				
	1	2	3	4	5
1（130MW）	132	141	130	136	125
2（120MW）	140	156	128	138	132
3（110MW）	128	154	152	159	142
4（110MW）	125	132	129	133	126

The objective functions (1) and (2) are integrated into the following form by the weighting method:

$$\min \omega_1(\sum_m \sum_j F_j^m X_j^m + \sum_i \sum_j a_i Z_{ij} D_{ij}) - \omega_2(\sum_m \sum_j W_j X_j^m)\ ,\quad \omega_1 + \omega_2 = 1$$

Different values are assigned to ω_1 and ω_2 to calculate the non-inferior solutions of the programming. Calculation results by lingo13.0 are shown in Table4:

Table4. The non-inferior solutions under different weightings

ω_1	0.0	0.1～0.3	0.4～0.5	0.6～1.0
ω_2	1.0	0.9～0.7	0.6～0.5	0.4～0.0
OBJ1	54.71	28.31	27.11	26.37
OBJ2	0.78	0.81	0.82	0.83
Amount	5	4	3	2

The explanations of the table above: OBJ1 and OBJ2 are these two objective functions, and respectively represent the thermal power plant construction costs and average comprehensive benefits. ω_1 and ω_2 can be viewed respectively as the importance of two goals. From table 4, we can see that goal 1 achieves the minimum, and goal 2 achieves the maximum when the weights of ω_1 and ω_2 changes respectively in the range of 0.6 ~ 1.0 and the range of 0.4 ~ 0.0. From Table4, the

conclusion can be drawn that the heat load demand of the four central heating areas can be met only by building two thermal power plants. At this point, the corresponding decision variables are as follows:

$$X=\begin{bmatrix}0&0&0&0&0\\0&1&1&0&0\\0&0&0&0&0\\0&0&0&0&0\end{bmatrix},\quad Z=\begin{bmatrix}0&0&1&0&0\\0&0&1&0&0\\0&1&0&0&0\\0&1&0&0&0\end{bmatrix}$$

That is to say, only two thermal power plants with capacity of 250 MW need to be built at the second and third alternative sites. The one at the second alternative site supplies heat to the third and the fourth central heating areas, and the other at the third alternative site supplies heat to the first and second central heating areas. In this way, the building cost reaches the minimum, and at the same time, the average comprehensive benefit reaches the maximum.

Conclusions

Site selection for thermal power plant is directly related not only to energy conservation and emissions reduction, but also to economic and stable operation of the power plant. It is more advantageous to make scientific decision for thermal power plant site selection optimization through the methods of rough set and expert group decision. It is a complex system engineering to evaluate thermal power plant site selection. In this paper, the evaluation index system is simplified with the purpose of illustrating the feasibility of this method. In the subsequent research work, we will intend to do further research to perfect the evaluation index system. In addition, it is a worth the effort direction to combine the rough set and other soft computing methods (such as fuzzy set and artificial neural network, genetic algorithm, etc.), play their respective advantages, and design hybrid intelligent evaluation system.

Acknowledgements

This work was supported by the Fundamental Research Funds for the Central Universities and the Soft Science of Hebei Province (12457301).

References

[1] Zhang S, Li H, Yang C. Study on Selecting Heating Equipment for Small Towns Based on Fuzzy Evaluation[J]. Journal of Shenyang JIanzhu University Natural Science. 2008, 24(03): 480-485.

[2] Zhao Y. A Study on Modes of Sustainable Development of Heat Supply in Cities[D]. Harbin: Harbin Institute of Technology, 2007.

[3] Meng Z. The Method Research of Optimizing of the Urban Heating Ways[D]. Tianjin: Tianjin University, 2004.

[4] Peng P, Tian Z. Economical Analysis on Heat Source Scheme of District Heat-supply[J]. Gas & Heat. 2004, 24(06): 333-336.

[5] S R D, S L W. Site selection and economic risks for thermal power plant projects under the new Brazilian regulatory framework[Z]. Perth, WA, Australia: 2000879-884.

[6] Barda O H, Dupuis J, Lencioni P. Multicriteria location of thermal power plants[J]. European Journal of Operational Research. 1990, 45(2–3): 332-346.

[7] Ramos D S, Fadigas E A A, Reis L B, et al. Important issues influencing thermal plant attractiveness in a large hydroelectric generation system[J]. International Journal of Electrical Power & Energy Systems. 2003, 25(10): 797-807.

[8] Kai T, Liang Y. Research on Site Selection of Thermal Power Plants Based on Improved TOPSIS[J]. 3rd International Symposium on Information Engineering and Electronic Commerce (IEEC 2011) Proceedings. 2011: 91-94.

[9] Ekmekcioglu M, Kutlu A C, Kahraman C. A Fuzzy Multi-Criteria SWOT Analysis: An Application to Nuclear Power Plant Site Selection[J]. International Journal of Computation Intelligence Systems. 2011, 4(4): 583-595.

[10] Huang Y J, Guo J Y, Yu Z T, et al. Application of Entropy-TOPSIS in Site Selection for Nuclear Power Station[J]. 2008 Proceeding of Information Technology and Environmental System Sciences, PT1. 2008: 1130-1134.

[11] Larraín T, Escobar R, Vergara J. Performance model to assist solar thermal power plant siting in northern Chile based on backup fuel consumption[J]. Renewable Energy. 2010, 35(8): 1632-1643.

[12] Kengpol A, Rontlaong P, Tuominen M. Design of a Decision Support System for Site Selection Using Fuzzy AHP: A Case Study of Solar Power Plant in North Eastern Parts of Thailand[J]. PICMET'12: Proceedings Tchnology Management for Emerging Technologies. 2012: 734-743.

[13] Wu Y N, Yang Y S, Feng T T, et al. Macro-site selection of wind/solar hybrid power station based on Ideal Matter-Element Model[J]. INTERNATIONAL JOURNAL OF ELECTRICAL POWER & ENERGY SYSTEMS. 2013, 50: 76-84.

[14] Xiao J H, Yao Z Y, Qu J J, et al. Research on an optimal site selection model for desert photovoltaic power plants based on analytic hierarchy process and geographic information system[J]. Journal of Renewable and Sustainable Energy. 2013, 5(0231322).

[15] Carrion J A, Estrella A E, Dols F A, et al. The electricity production capacity of photovoltaic power plants and the selection of solar energy sites in Andalusia (Spain)[J]. Renewable Energy. 2008, 33(4): 545-552.

[16] Carrion J A, Estrella A E, Dols F A, et al. Environmental decision-support systems for evaluating the carrying capacity of land areas: Optimal site selection for grid-connected photovoltaic power plants[J]. Renewable & Sustainable Energy Reviews. 2008, 12(9): 2358-2380.

[17] Lin Y H, Fang M C. An Integrated Approach for Site Selection of Offshore Wind-Wave Power Production[J]. IEEE Journal of Oceanic Engineering. 2012, 37(4): 740-755.

[18] Liu Q. Rough Sets and Rough Reasoning[M]. Beijing: Science press, 2003

Advanced Materials Research Vols. 960-961 (2014) pp 1508-1511

doi:10.4028/www.scientific.net/AMR.960-961.1508

Urban Power Supply System Risk Assessment

Qingmin Si, Xingbai Zhang, Xueying Jiang, Lei Tian, Gongxin Yu

School of Safety Engineering, Shenyang Aerospace University, ShenYang, China

siqingmin@163.com

Keywords: urban power supply system, urban public safety, risk assessment system, grey AHP

Abstract. Urban power supply system has close relationship with urban public safety. The main risk factors, accident types and the risk degree of failures or accidents in urban power supply system are analyzed. And, it has established the public safety risk assessment system of urban power supply system. In order to show that the assessment system has good applicability in the risk assessment of urban power supply system, the power supply system safety of one urban is assessed using established risk assessment system.

Introduction

Urban power supply system is the most basic urban municipal public facilities, and is the lifeline to ensure urban normal order. The power supply system which is safe and reliable has been the important factor to ensure the urban stability. However, urban power supply system is facing more and more risks. Correctly risk assessment for urban power supply system is the key to do well in urban electric power construction.

Risk identification and analysis of urban power supply system

The main risk factors which may cause failure or accident of urban power supply system are as followed: power transmission grid system, protection system, user system, safety management system and external environment system.

1) Power transmission grid system

The power transmission grid operation state has essential important impact on the urban power supply system safety, because it is constantly changing with the passage of time. Power transmission grid safety has a total of five criterias: power grid, scheduling and operation mode, relay protection, communication and scheduling automation, primary electric equipment[1].

The safety of power grid is affected by many factors, like electric source safety, power grid structure, stability, non-power compensation, short-circuit current, over voltage, current-carrying safety etc.

2) Protection system

It mainly includes: the automatic recovery system, automatic alarm device, lightning protection system, fire fighting system, typhoon and flood control, prevent freezing, seismic system and damage prevention system, etc.

Once the auto reply system does not exist or malfunction, it will have a great influence on production and residents' safety. The existence of the automatic alarm device for power grid failure or a certain area in danger, management personnel can timely access to information and for repair and processing. Influenced by a lightning strike, transmission line tripping circuit failure events occurred more frequently, seriously affect the stability of the power grid operation[2]. Due to power system fault caused by short circuit or insulation resistance is too small or breakdown caused power cables such as temperature, will make the cable caused by rapid burning fire. The seriousness of fire and secondary accidents occurred frequently makes us have a higher requirement for fire protection system. Once earthquake, typhoon, flood or freezing disaster happens, it will influence range, large losses, difficult recovery.The external force damage the common challenges facing the gradually become the major national power grid.

3) User system

It mainly reflects on the quality of the users and their interact.Power utilization nature is determined by the users' types. Different users' types will produce various influences on the safety of power grid. On the contrary, suddenly interruption of power supply for all kinds of users have different degrees of influence.User self-help ability but also the power grid safety goals setting, in the case of user self-help ability strong, power grid failure can avoid bigger losses.

4) Safety management system

Safety management institutions is essential.The system establishment regulate people's behavior, the good management system, can accurately identify risks, especially to find the weak link, objective assessment and release risk, to carry out the targeted prevention measures, control the risk in advance, reduce the risk to a minimum. Regular inspection of the assessment, you can find out equipment defects and inherent danger point and the environment, to further consolidate the safety of power grid. Grid emergency preplan for urban public safety can not be ignored, the influence of against blackouts and other major accident emergency drills, can in real time to reduce the loss caused by accident.

5) External environment system

The safety of the equipment itself, the design of the safe distance and the state of the surrounding environment makes different impact on the surrounding environment of power grid[3]. Protection and isolation measures can effectively prevent the electric shock accidents, ensure public safety grid runtime.Daily maintenance can reduce the incidence of accidents.Maintenance of equipment and the team from the accident point distance and time of arrival, indirect decide the progress of the accident, reasonable allocation of maintenance and rescue human, determines the urban power grid safety.

Urban power supply system of risk assessment system

Urban power supply system risk assessment system[4] is shown in Tab.1

Tab.1 Risk assessment system of urban power supply system

Target layer	Criterion layers	Index layers
Urban power supply system risk S	power transmission grid system U_1	power grid safety V_{11} scheduling and operation mode V_{12} relay protection system safety V_{13} communication and scheduling automation safety V_{14} primary electric equipment safety V_{15}
	protection system U_2	automatic recovery system V_{21} automatic alarm device V_{22} lightning protection system V_{23} fire fighting facilities V_{24} Seismic system V_{25} typhoon and flood control, prevent freezing V_{26} damage prevention system V_{27}
	user system U_3	users' types V_{31} self-help ability V_{32}
	safety management system[5] U_4	The establishment of safety management department V_{41} Safety risk management system V_{42} The safety risk assessment V_{43} anti-accident measure V_{44} Emergency preplan compiling [6]V_{45}
	external environment system U_5	Environmental state and establishment safety V_{51} safe distance V_{52} Protection and isolation measures V_{53} Maintenance and fire-fighting channel V_{54} Distence of maintenance equipment and staff V_{55}

For some complicated factors, the division of three level index is needed[7].

Application analysis

One urban is divided into five regional power, during normal operation of the grid, the load is 1014.5MW. In normal mode, the 220kV system, the total length is 453.7km,voltage is maintained at 231.1kV ~ 227.2kV, the maximumtransmission power flow dual loop is 2*161.2MW, 110kV system, the total length is 717.6km, voltage is maintained at 107.4kV ~ 117.1kV, the maximum transmission power is 2*75.6MW double loop. In the 220kV main substationmain transformer substation, a maximum overloadcapaurban ratio reached nearly 144%[8].

1) Determine the standard grade assessment index and weight

Using the AHP to determine the weight of U_i and V_{ij} [9]. As shown in *Tab*. 2.

2)Calculate the grey assessment coefficient, weight vector and weight matrix[10]

The assessment of the 4 grey classes. Grey number is e, e=1,2,3,4, said "excellent", "good", "bad". The assessment index of V_{ij}, grey assessment coefficient V_{ij} belongs to the eassessment grey types, denoted as X_{ije}. Total greyassessment of total ash belonging to the category of greyassessment of various number, denoted as X_{ij}. There are$X_{ije}=\sum f_e(d_{ijm})$，m∈[1，10]，$X_{ij}=\sum X_{ije}$，e∈[1，4].

All the assessment experts on the assessment index of V_{ij}, the rated objects that grey assessment e gray weight,denoted as r_{ije}, then, $r_{ije} = X_{ije} / X_{ij}$.

The vector can be composed of V_1,V_2,V_3,V_4, corresponding to matrix D_1, D_2, D_3, D_4.

As shown in Tab. 2.

Tab.2 Index score and gray weight vector

Experts / Index	1	2	3	4	5	6	7	8	9	10	r_{ij1}	r_{ij2}	r_{ij3}	r_{ij4}
V_{11}	3.5	2.5	4.0	2.0	3.5	2.5	2.0	2.5	2.5	2.0	0.3124	0.3693	0.3183	0
V_{12}	2.0	3.5	25	2.0	2.5	2.0	2.5	3.0	4.0	2.5	0.3124	0.3693	0.3183	0
V_{13}	2.5	2.0	3.0	3.5	2.5	2.0	2.0	2.5	3.0	4.0	0.3176	0.3765	0.3059	0
V_{14}	3.5	3.0	2.5	2.0	2.5	3.5	3.0	2.5	2.0	3.0	0.3023	0.3721	0.3256	0
V_{15}	3.5	3.0	2.5	2.0	2.5	3.5	3.0	2.5	2.0	3.0	0.3179	0.3931	0.2890	0
V_{21}	2.0	3.5	3.0	2.5	3.0	3.0	2.5	2.5	3.0	2.5	0.3156	0.3671	0.2905	0
V_{22}	3.0	3.5	2.5	3.5	3.0	3.5	3.0	2.5	4.0	3.0	0.3185	0.3764	0.3087	0
V_{23}	3.5	3.0	3.0	2.5	2.5	3.0	3.5	3.0	3.5	2.5	0.3186	0.3895	0.2867	0
V_{24}	2.0	2.5	3.5	2.5	3.5	2.5	2.5	3.5	4.0	3.0	0.3158	0.3853	0.3125	0
V_{25}	2.5	2.0	3.0	2.5	2.0	2.5	3.5	2.5	2.0	3.0	0.2925	0.3748	0.3327	0
V_{26}	2.5	3.0	2.5	2.5	3.0	3.0	2.0	2.0	4.0	2.0	0.3075	0.3792	0.3133	0
V_{27}	3.0	3.5	4.0	2.5	2.0	2.5	3.0	3.5	4.0	2.5	0.3291	0.4024	0.2485	0
V_{31}	2.5	3.0	3.0	3.0	2.0	2.5	4.0	2.5	2.0	2.5	0.3075	0.3792	0.3133	0
V_{32}	2.5	2.0	2.5	2.5	2.5	4.0	2.0	3.0	3.5	3.5	0.3333	0.3810	0.2857	0
V_{41}	3.0	2.5	2.5	3.0	3.0	3.5	2.5	3.0	3.0	2.5	0.3176	0.3865	0.2765	0
V_{42}	2.5	3.0	2.5	2.5	3.5	2.0	4.0	2.0	2.5	3.5	0.3333	0.3810	0.2857	0
V_{43}	3.0	2.5	2.0	2.5	3.5	2.0	4.0	2.0	2.5	3.5	0.3028	0.3886	0.3086	0
V_{44}	2.5	2.0	2.5	3.5	2.5	2.0	3.0	2.5	2.5	2.0	0.2874	0.3678	0.3448	0
V_{45}	3.5	2.0	3.0	2.0	2.5	2.5	2.5	2.5	2.5	3.0	0.2977	0.3816	0.3206	0
V_{51}	2.5	3.0	3.5	2.5	3.0	2.5	2.5	3.5	3.0	2.5	0.3126	0.3758	0.3312	0
V_{52}	3.0	2.5	3.0	3.5	2.5	3.0	3.0	3.0	2.5	2.5	0.2956	0.3568	0.3565	0
V_{53}	2.5	3.0	3.5	3.0	3.5	2.5	3.5	2.5	3.5	3.5	0.3033	0.3834	0.3216	0
V_{54}	2.5	2.5	3.0	2.5	2.0	2.0	3.0	2.5	3.5	2.5	0.3816	0.2978	0.3206	0
V_{55}	3.0	2.5	3.5	2.5	2.0	2.5	2.5	2.5	3.0	2.5	0.3028	0.3886	0.3086	0

3) Comprehensive assessment

Comprehensive assessment of index layer Vi, and the assessment results can be recorded as B_i, then: $B_i = U_{ij} \times D_i$ .By the comprehensive assessment index layer V_i results B_i, criterion layer U for grey assessment grey assessment weightmatrix R, comprehensive assessment criteria layer U resultsdenoted as B, are: $B=U\times R$.

Reference grey level evaluates the object system ofcomprehensive assessment. According to the comprehensive assessment results of B, the maximumprinciples for determining the rated objects belong to greylevel, and finally calculate the comprehensive assessment value. $S=B\times C^{T}$, where C^{T} is the grade of gray clusterassignment according to the "gray level" comprehensive assessment value. According to the corresponding interval is divided into corresponding levels as shown in *Tab.*3.

Tab.3 Index grade standard

Index	Comprehensive assessment value	Grade	Index	Comprehensive assessment value	Grade
One level	$3.3192\leq S\leq 3.5999$	excellent	Three level	$2.9435\leq S\leq 3.1108$	medium
Two level	$3.1108\leq S\leq 3.3192$	good	Four level	$2.7692\leq S\leq 2.9435$	bad

The assessment of urban V_{ij} are good indicators. Thecomprehensive assessment results of $S=B\times C^{T}=3.00672$. The whole urban power supply system of safety assessmentfor "the three level", "medium".

Conclusions

1) It give a comprehensive analysis of the five major risk factors which may lead to the urban power supply system failure or accident: power transmission grid system, protection system, user system, safety management system and external environment system..

2) Based on the risk analysis results, it has established the public safety risk assessment system of urban power supply system. The system consists of five indicators in criterion layer, twenty-four indicators in index layer.

3) The power supply system safety of one urban is assessed using established risk assessment system. The application results show that the assessment system has good applicability in the risk assessment of urban power supply system.

References

[1] Yin Changxin. Urban power grid safety Assessment [M]. China Power Press, 2011. In Chinese.

[2] Zhang Liying. The power plant synchronization operation safety Assessment [M]. China Power Press,2003. In Chinese.

[3] State Electricity Regulatory Commission Safety Supervision Bureau. Assessment basis of Wind power Synchronization safety [M]. China Power Press, 2012. In Chinese.

[4] Yang Weihong. Study of urban power grid planning risk assessment model and risk aversion methods [D]. North China Electric Power University, 2010. In Chinese.

[5] Huang An. The method of life cycle management of electric power of [J]. business culture, 2011, (05) . In Chinese.

[6] Li Rui, Chen Ying. Emergency early warning method of urban distribution grid based on outage risk assessment [J]. power system automation, 2010, (08) . In Chinese.

[7] Xue Dong. The construction of power system safety risk assessment system [J]. Technology Horizon, 2012, (10) . In Chinese.

[8] Liu Nan, Yuan Shun. Study of Shenyang urban power grid planning and optimization[J]. Heilongjiang Science and Technology Information, 2012, (01) . In Chinese.

[9] Xu Shubo. The principle of AHP [M]. Tianjin University press, 1988. In Chinese.

[10] Zhou Jiaqi, Zhao Xia. Power system risk assessment method and application [J]. Chinese Electric Power, 2006, (08) . In Chinese.

Advanced Materials Research Vols. 960-961 (2014) pp 1512-1515

doi:10.4028/www.scientific.net/AMR.960-961.1512

Supplied demand technique for power system balance reliability calculations

VladislavPetrovich Oboskalov[1,a], Irina Lvovna Kirpikova[1,b], S. Matugova[1,c], S. Gusev[1,d]

[1]Ural Federal University, 620002, Russia, Yekaterinburg, Mira, 19

[a]v.p.oboskalov@urfu.ru, [b]i.l.kirpikova@urfu.ru, [c]stanka.matuga@gmail.com, [d]sergeyalexgusev@gmail.com

Keywords: Power system reliability, adequacy, Monte-Carlo simulation, power pool, supplied demand technique, stochastic network reduction.

Abstract. This paper presents an iterative power system balance reliability calculating technique ensuring better convergence and faster calculations. The technique is called "supplied demand". Nodal power imbalance is considered as the primary stochastic value under analysis. An analytical solution does not contain probability density functions. It results in faster calculations. Results were verified by Monte Carlo Simulation and showed high accuracy of the technique.

Introduction

The main objectives and tasks for power pool reliability calculations in terms of ensuring the power and energy balances have been formulated and described in [1 – 4]. Electrical power system (EPS) balance reliability (BR) calculations are performed both in planning and operating stages of the EPS. The calculations are aimed at determining and allocating the distribution system real and reactive power reserves, justifying the integration of generation facilities and tie lines, scheduling the main equipment overhauls, pricing power and energy.

From mathematical point of view the key problem of BR calculations is to determine the probability characteristics, i.e. distribution function (DF), frequency, expected value (EV) and variance of the power and energy shortage in electrical power systems connected in power pool with limited capacity of tie lines. Basing on the received distribution functions it is possible to estimate expected value of lost load damage,hence to justify investments in EPS development [1, 3].

The structure of the initial data for BR calculations is presented in its reduced form in the description of Melentiev Energy Systems Institute test system [5]. Typically, initial data for BR problem is as follows:power pool topology, unit set and nodal load characteristics, tie line set and capacity probabilistic characteristics, power pool key element specifications and overhaul schedules, equipment commissioning and decommissioning plans.

In certain situations the generation subsystem of a concentrated EPS is presented as one equivalent unit [1]. More often it is presented as groups of similar units withbinomial probability distribution of their states. In further these groupsare combined in probabilistic series [3]. In addition, resulting probabilistic sequence is often approximated by certain continuous distribution, such as normal, gamma, etc. In general, the type of approximating distribution depends on load probability distribution, which is the most significant stochastic variable. This approximation causes a simulation error and should be substantiated for each calculation.

Tie lines are usually represented by capacity probabilistic series. In this case approximation of probabilistic series by continuous distribution is extremely inadvisable, due to a small number of line states (on and off).

A number of leading scientific organizations working on BR problem made a comparison of different BR calculation techniques [6]. The comparison showed a significant difference of the calculation results. In fact it is very difficult to point outmost accurate solution.However, as a general rule, Monte-Carlo simulation (MCS) is used as a reference technique.The key problem of MCS is associated with high computational load. As a result it is preferred for long-term calculations of network investments, when calculating time isn’t very important.

More recently, however, emphasis in adequacy calculations has been made on analytical methods. First of all, this is caused by extension of BR calculations to the sphere of operational calculations. In this case, BR calculations, on the one hand, allow optimizing commercial and operating reserves, but on the other hand, require a fast calculating technique [7].

Iterative approach for balance reliability problem

BR problem may be presented as a problem of supplying demand for a capacity margin (CM), when load L_i and spare capacity G_i have a stochastic nature. The power imbalance (PI) $N_i = L_i - G_i$ characterizes the power shortage in EPSi,which works separately from power pool (i.e. it isn't connected with other EPS). If $N_i < 0$ system has spare capacity, that could be provided to interconnected system j through tie line $i - j$. The tie line has capacity in the forward direction π_{ij} and capacity π_{ji} in the backward direction [7, 8].

Assume that each EPS has DF $F_i(x)$, EV $\overline{N}_i$ and variance D_i of stochastic variable N_i. Denote demand of EPS j for an spare capacity of EPS i by $N_{i(j)}$.Due to the impact of other interconnected systems, EPS i has a system demand$N_i^S = \sum_{j \neq i} N_{i(j)}$. The system demand has DF $F_i^S(x)$, EV $\overline{N}_i^S$ and variance $\overline{D}_i^S$. Taking into account the impact of other systems, summarized PI in EPS$i$is$N_i^\Sigma = N_i + N_i^S$.If capacity margin of tie $i - j$ is limited by the interval $(-\pi_{ji},\ \pi_{ij})$ then the PI reduced probability distribution function is defined as:

$$F_{i(j)}(x) = F_j^\Sigma\left(x, -\pi_{ji}, \pi_{ij}\right) = \begin{cases} 0, & x < -\pi_{ji}; \\ F_j^\Sigma(x), & -\pi_{ji} < x < \pi_{ij}; \\ 1, & x \geq \pi_{ij}. \end{cases} \quad (1)$$

Mutual aid or PI alternation results in the alternationof N_i^S. This alternation, in its turn, changes resulting probabilistic characteristics of all interconnected power systems. This fact determines correlation between all interconnected subsystems. Calculating $N_{i(j)}$ for every $i$and j, with account for subsystems interaction, gives a solution for BR problem. Nevertheless, at this moment, the problem in such a formulation may not be solved analytically.

In order to get a solution, it is possible to apply a capacity market model. According to this model, at the first stage, subsystems exchange spare capacity with near subsystems. Then exchanging capacity is being adjusted, due to the impact of distant subsystems. The transient process goes on until it results in a certain steady state. Changes in mutual aid in this steady state are caused only by fluctuations of PI. In terms of BR problem, such exchanging process is defined by the recurrence:

$$F_{i(j)}^{(k+1)} = \left(F_j^\Sigma(x)\Big|_{-\pi_{ij}}^{\pi_{ji}}\right)^{(k)}. \quad (2)$$

Convergence of the process in eqn. (2) depends on the way PI is redistributed. For instance, in a simple additive model, where, during calculation of $N_{i(j)}$, EPS j is presented by full PI N_j^Σ, positive feed-back should occur. Indeed, in a circular structure with three interconnected EPS i, j and k PI $N_{i(j)}$ increases PI N_i^Σ. It results in an increase of $N_{(k)i}$, therefore, an increase of $N_k^\Sigma, N_{j(k)}, N_j^\Sigma, N_{i(j)}$. At the same time, counter-current flow techniques, for instance, allocation of PI in proportion to the demand of the near systems enhances negative feedback, thus, convergence of the calculating process.However, these techniques don't ensure the desired robustness, due to different proportionality factors for load and generation. This fact brings up a necessity to account load and generation impact separately. Nevertheless, at the level of a single EPS these variables are united, which breaks down the regulating effect.

Supplied demand technique

The iterative procedure, presented by eqn. (2), results in the definition of PI in tie $i-j$. This PI is defined by the demand for a capacity margin both from EPS j ($N_{i(j)}$) and EPS i ($N_{j(i)}$). These variables form PI in tie $i-j$, but don't finally define it. PI in line is defined by the supplied demand, both from EPS j and EPS i.It is assumed that at each stage of multi-stage PI definition process DF $F_i^{\Sigma}(x)$ is known. In addition, it is necessary to know DF of the summarized power demand of EPS i without EPS $j$impact $F_{i/j}^{\Sigma}(x)$. This DF allows accounting impact of near subsystems in a proper way.

In order to decrease symbolic burden, PI distribution functions $F_{i/j}^{\Sigma}$ and $F_{j/i}^{\Sigma}(x)$ hereinafter are denoted as F_i and F_j correspondingly.

In a two-node network PI in tie $i-j$ is defined by a difference between the demand of EPS $j$supplied by EPS $iN_{ij(j)}$and the demand of EPS $i$supplied by EPS $N_{ij(i)}$:

$$N_{ij} = N_{ii(j)} - N_{jj(i)}. \tag{3}$$

Distribution function of PI N_{ij} is as follows:

$$F_{ii(j)}(x) = \begin{cases} V_i(-x)F_j(x), & x \geq 0; \\ R_i(-x)F_j(x), & x < 0, \end{cases} \tag{4}$$

where $R(x) = 1 - F(x)$ is an additional DF. In contrast with DF $F(x)$, function $V(x)$ indicatesthat stochastic variable ξ includes the right limit $V(x) = \mathcal{P}\{\xi \leq x\}$, when $F(x) = \mathcal{P}\{\xi < x\}$. This becomes important, when DF has a simple discontinuity, like DF of spare capacity. On the other hand, when DF is continuous $V(x) = F(x)$.Due to the smoothing effect of stochastic load,PI DF hereinafter is assumed to be continuous.

It is possible to represent PIEV in tie $i-j$as a sum of four components:

$$\overline{N}_{ij} = \overline{N}_{ij(j)} + \overline{N}_{ij(i)} + \overline{N}_{ij(\pi_{ij})} + \overline{N}_{ij(\pi_{ji})}, \tag{5}$$

where$\overline{N}_{ij(j)}$ and $\overline{N}_{ij(i)}$ are defined by supplied demand of EPS j and EPS i correspondingly; $\overline{N}_{ij(\pi_{ij})}$ and $\overline{N}_{ij(\pi_{ji})}$ are defined by tie line capacity π_{ij} and π_{ji}correspondingly.

Supplied demand from EPS j is defined as:

$$\overline{N}_{ij(j)} = \left[M_j F_j(x) - \sigma_j^2 f_j(x)\right]\Big|_{-\pi_{ji}}^{0} - \int_{-\pi_{ji}}^{0} xF_i(-x)dF_j(x) + \int_{0}^{\pi_{ji}} xF_i(-x)dF_j(x). \tag{6}$$

Equation (6) contains integrals. It is very useful to replace them by analytical expression. EPS load is usually described bynormal distribution, while generation subsystem is described by binomial distribution. It should be noted thatbinomial distribution asymptotically approaches normal distribution, when number of generators is growing. Therefore normal distribution is a good approximation of PI DF. Normal distribution has analytical expression of reduced EV.

After integration by parts eqn. (6) will be following:

$$J_{ij}(a,b) = \left\{F_i(-x)\left[M_j F_j(x) - \sigma_j^2 f_j(x)\right]\right\}\Big|_{a}^{b} + M_j \int_{-b}^{-a} F_j(-x)dF_i(x) - \\ -\sigma_j^2 \int_{-b}^{-a} f_j(-x)f_i(x)dx. \tag{7}$$

Equation (7) contains two integrals that are similar to convolutionsof PI DF and PI density function correspondingly. The only difference appears inintegration finite limits. However, if PI DF of EPS i is described by reduced normal distribution, the integrals define DF and density function of PI N_j and reduced PI$N_i|_{-b}^{-a}$. Then:

$$J_{ij}(a,b) = \{F_i(-x)[M_j F_j(x) - \sigma_j^2 f_j(x)]\}\Big|_a^b + \left[M_j F_{j+i_{-b}^{-a}}(0) - \sigma_j^2 f_{j+i_{-b}^{-a}}(0)\right] \times \\ \times [F_i(-a) - F_i(-b)] \quad (8)$$

As a result eqn. (6) is presented as follows:

$$\bar{N}_{ij(j)} = M_j\big(F_j(0) - F_j(-\pi_{ji})\big) - \sigma_j^2\left(f_j(0) + f_j\big(-\pi_{ji}\big)\right) - J_{ij}\big(-\pi_{ji}, 0\big) + J_{ij}\big(0, \pi_{ij}\big) \quad (9)$$

Power imbalance $N_{ij(i)}$ is calculated similarly:

$$\bar{N}_{ij(i)} = M_i\big(F_i(0) - F_i(-\pi_{ij})\big) - \sigma_i^2\left(f_i(0) + f_i\big(-\pi_{ji}\big)\right) - J_{ji}\big(-\pi_{ij}, 0\big) + J_{ji}\big(0, \pi_{ji}\big) \quad (10)$$

Resulting equations (9) and (10) were verified by MCS. Results show that analytical solution is the marginal result for MCS.Thus supplied demand technique it is accurate enough. Software based on the proposed technique calculated BR of test systemincluding 41 nodes [5] in 0.1 sec. Consequently the technique is also very fast.

Summary

This paper presents balance reliability calculation technique referred to as supplied demand. It calculates expected value of power imbalance in tie line without numerical integration. The technique was verified by MCS. Results show that the analytical solution is the marginal result for MCS. Moreover, the calculation speed is also very high. Hence supplied demand technique is recommended for power system balance reliability calculations.

References

[1] Y.N.Rudenko, M.B.Cheltsov.*Reliability and redundancy in power systems*(Nauka, Novosibirsk 1974).

[2] R.Billinton, R.Allan.*Reliability evaluation of electric power systems* (Energoatomizdat, Moscow 1988).

[3] M.N.Rozanov, in: *Reliability of energy system and equipment*, edited by Y.N. Rudenko. Energoatomizdat, Moscow(2000).

[4] N.A. Manov, M.V. Hohlov, Y.J. Chukreev: *Meshed power system reliability estimation models and approaches* (Komi science center of Uro RAN, Russia 2010).

[5] The test system№2. Methodical research questions of large-scale power system reliability (1984), vol. 28, pp. 31–44.

[6] G.F.Kovalev, in: Comparative analysis of reliability calculatingsoftware.Methodical research questions of large-scale power systemreliability (1991), vol. 41, pp. 53–62.

[7] S.A. Gusev, O.M. Kotov, V.P. Oboskalov, in: Meshed power system reliability estimation techniques. Energy Production and Management in the 21st Century (2014), vol. 190, pp. 235–250.

[8] V.P. Oboskalov: *Power systems balance reliability* (USTU-UPI, Russia 2002).

Advanced Materials Research Vols. 960-961 (2014) pp 1516-1522

doi:10.4028/www.scientific.net/AMR.960-961.1516

Application of Regression Analysis in Power System Load Forecasting

Chen Chen[1,a], Jiena Zhou[2,b]

[1,2]the College of Electrical Engineering, Guizhou University, Guiyang, Guizhou Province, China

[a]820540681@qq.com, [b]406073015@qq.com

Key words: Power system, load forecasting, regression analysis

Abstract: Power system load forecasting is an important job for power system scheduling, planning and planning departments. In the long run, the accuracy of load forecasting is closely related to reasonable extension and renovation of power grid development. On the basis of collecting historical load data of a region, considering the co-integration theory and error correction, the author adopts regression analysis to predict of the load development of the region in the next five years, then finally puts forward the new way of enhance load forecasting accuracy in the future.

Introduction

With the rapid development of power grid today, electricity workers are paying more and more attentions to load forecasting. As a traditional problem to research in the field of power system, considering its economic, social, weather and so on, load forecasting [1, 2] is used to estimate and speculate the development of load in advance, after analyzing and researching the historical data ,then exploring the internal relation and its development change rule.

So far, a variety of load forecasting methods are being used. In general, they can be divided into two types: classical forecasting method and modern load forecasting method. Among them, classic prediction method includes trend analysis, time series method and regression analysis; modern load forecasting methods includes grey mathematics theory, expert system method, neural network theory and fuzzy load forecasting. [3] In this article, the regression analysis method will be adopted.

Regression analysis

According to reference [4], in the premise of collecting and counting the historical data, regression analysis method is to obtain the function (or curve) which can describe the relationship between these related factors by using mathematical methods, then apply the function (or curve) for load forecasting at a certain moment of the future. The types of regression equation with one unknown are as follow:

type of equation	equation
general type (standard equation)	$y = a + bx$
Power function	$y = ax^b$
Exponential function	$y = ae^{bx}$
Logarithmic function	$y = a + b\ln x$

Via mathematical transformation: taking the logarithm on both sides of these non-standard equations, then they can be changed into standard linear equations as $y = a + bx$. After working out the estimated value of coefficients a ， b in the regression equation based on the samples, the value of the independent variable x can be calculated by the predictive value of the dependent variable in the regression equation.

If the regression equation is a standard one, assuming that a set of values (sample) (x_i, y_i) (I = 1, 2, 3，…n) is known, which is made up of the variables x and its corresponding random variables y, then the steps of calculating the standard equation coefficient a and b are as follows:

Calculating the average of x, y:

$$\bar{x} = \frac{1}{N}\sum_{i=1}^{N} x_i, \quad \bar{y} = \frac{1}{N}\sum_{i=1}^{N} y_i \tag{1-1}$$

Calculating the variance and covariance L_{xx}，L_{yy}，L_{xx}:

$$L_{xx} = \sum_{i=1}^{N}(x_i - \bar{x})^2, \quad L_{yy} = \sum_{i=1}^{N}(y_i - \bar{y})^2, \quad L_{xy} = \sum_{i=1}^{N}(x_i - \bar{x})(y_i - \bar{y}) \tag{1-2}$$

Calculating the coefficient:

$$\hat{b} = L_{xy} / L_{xx}, \quad \hat{a} = \bar{y} - \hat{b}\bar{x} \tag{1-3}$$

Obtained the regression equation:

$$y = \hat{a} + \hat{b}x \tag{1-4}$$

If the regression equation is a non-standard one, to the power function form, the form of exponential function and logarithm function form regression equation, it should firstly transform the original samples to the corresponding samples ((x'_i, y'_i), (x_i, y'_i) and (x'_i, y_i), (i=1, 2, 3,..., n), and then the corresponding coefficients can be determined, according to the above steps.

These established regression equation must be tested by correlation coefficient and standard deviation to confirm whether they can be used in load forecasting.

Correlation coefficient r:

$$r = \frac{\sum_{i=1}^{N}(x_i - \bar{x})(y_i - \bar{y})}{\sqrt{\sum_{i=1}^{N}(x_i - \bar{x})^2 \sum_{i=1}^{N}(y_i - \bar{y})^2}} = \frac{L_{xy}}{\sqrt{L_{xx} L_{yy}}} = \hat{b}\sqrt{\frac{L_{xx}}{L_{yy}}} \tag{1-5}$$

Standard deviation S*:

N>30: $$S^* = \sqrt{\frac{\sum_{i=1}^{N}(y_i - \hat{y}_i)^2}{N-2}} \tag{1-6}$$

N<=30: $$S^* = \sqrt{\frac{\sum_{i=1}^{N}(y_i - \hat{y}_i)^2}{N-2}} + \sqrt{1 + \frac{1}{N} + \frac{(x_0 - \bar{x})^2}{\sum_{i=1}^{N}(x_i - \bar{x})^2}} \tag{1-7}$$

In the above equations, N stands for samples, $\hat{y}_i$ is the estimated value of y_i, x_0 is the predicted value of year, for example, when predict the twelfth year, then x_0 equals twelve.

Correlation coefficient is always less than or equal to 1, its value reflects the relevance between x and y. The larger the value of r is, the more closely relevance between x and y is, therefore, using equation $y=a+bx$, more reliable results of load forecasting will be got. R=0 means x and y are uncorrelated, equation $y=\hat{a}+\hat{b}x$ can't be described the relationship between x and y. So the correlation coefficient is used to determine whether the corresponding regression equation is available. The smaller the standard deviation S is, the less prediction error will exist. That is to say, using the regression equation to get the prediction value is closer to the actual value. Therefore, standard deviation is used to choose the final regression equation from all the feasible regression equations.

Co-integration theory and error analysis

The traditional regression model ignores the non-stationary time series, so fitting equation may appear "spurious regression", finally due to an inaccurate prediction, although the process of applying the model to predict is simple[5]. So introducing co-integration theory and error correction model to deal with the non-stationary time series long-term equilibrium.

For a vector time sequence $\{X_t\}=(X_{1t}, X_{2t},..., X_{nt})'$, if all the components sequence is I(d) sequence, which is d order integration, there is a Nx1 order sequence β(β≠0):

$$\beta X_t = \beta_1 X_{1t} + \beta_2 X_{2t} + \ldots + \beta_n X_{nt} \tag{1-8}$$

If the equation above is (d-b) order integration, vector $\{X_t\}$ is d, b order co-integration, and vector β is a co-integration vector [6].

The purpose of the co-integration test is to determine whether a set of linear combination of the unsteady sequence have co-integration relationship. It can also determine whether the linear regression equation is reasonable[7]. Engle-Granger[8] co-integration test is an important method.

Co-integration theory consider that the dependent variable can be explained by a linear combination of the independent variables, there is a stable equilibrium relationship between them, the dependent variable can't be constitute a residual error sequence by the explained independent variable. The residual error sequence should be stable, namely, there is a co-integration relationship between dependent and independent variables, and this method is to test the unit root of residual error regression equation.

The steps of co-integration test are as follows:

(1) confirm the order of variable: using he unit root test to test whether variable X_t and Y_t have the same single order;

(2) Estimate the long-term equilibrium relationship: on the basis of step 1, the long-term equilibrium model can be set as $y_t = \beta_0 + \beta_1 x_t + u_t$;

(3) Check the residual sequence, whether it is smooth and steady.

Granger theorem shows that unless there is a co-integration relationship between non-stationary variables, it can inevitably establish error correction model; if the error correction model can be established, using non-stationary, variables, then there must be a co-integration relationship between these variables [9].

Autoregressive Distributed Lag model (Auto regressive Distributed Lag, ADL) is a common model, the expression of this model is a "long-term equilibrium" relationship between variables.

First-order autoregressive distributed lag model, ADL (1, 1):

$$y_t = \beta_0 + \beta_1 y_{t-1} + \beta_2 x_t + \beta_3 x_{t-1} + u_t \tag{1-9}$$

The load forecasting process

Based on the collected historical load data of a region, adopting monadic regression analysis method, and introducing association deals and error analysis, the article predict the total power consumption and maximum load in the next five years.

Basic steps of load forecasting program writing:

(1) Input samples, transform the samples;

(2) Calculate the average and variance of each sample;

(3) Get the coefficients of the regression equation;

(4) Calculate the correlation coefficient of the regression equation and determine the feasible regression equation

(5) Find the prototype of the feasible equation;

(6) According to the principle of minimum standard deviation, determine the final regression equation;

(7) Using the selected regression equation to do load forecasting;

(8) Output the load forecasting result.

According to the load forecasting process, the data flow diagram is as follows:

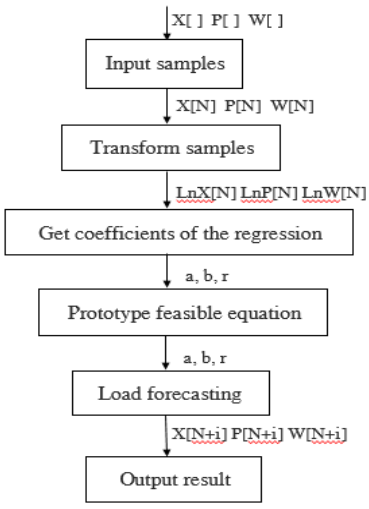

N: the number of sample data, in this program N = 6;

X[ ]: year;

P [ ]: power supply, (units: kWh);

W [ ]: the biggest power supply load, (units: MW);

a, b: the coefficient of function;

r: the correlation coefficient;

X[N+i]: the year of load forecasting, i=1,2,3,4,5;

P[N+i]: the power supply of load forecasting, (units: kWh);

W[N+i]: the biggest power supply load of forecasting, (units: MW);

The results of load forecasting

Collect and sort historical electricity load data of the region during year 2008 to 2013, including the total power consumption and the maximum power load in the region. The statistics are as follows in Table 1:

Table 1 2008～2013 historical electricity load data

year	total power consumption (1 Million kWh)	The maximum power load	
		（MW）	Growth Rate (%)
2008	3.0175	69.59	/
2009	2.9019	70.34	1.08
2010	4.0438	99.15	40.96
2011	5.5954	125.98	27.06
2012	7.8741	157.15	24.74
2013	10.2451	176.98	12.62

Using the load forecasting program, input historical electricity load data (samples) year by year, then run the program, the value of whole society power consumption and the maximum power load in the next five years (2014～2018) will be output, the load forecasting results are as follows in Table 2:

Table 2 2014～2018 load forecasting results

year	total power consumption (1 Million kWh)	The maximum power load	
		（MW）	Growth Rate (%)
2014	10.8551	197.16	/
2015	12.3660	221.48	12.33
2016	13.8769	245.79	10.98
2017	15.3880	270.11	9.89
2018	16.8989	294.43	9.00

The Growth trend of whole society power consumption and maximum power load are expressed in fig.1 and fig.2.

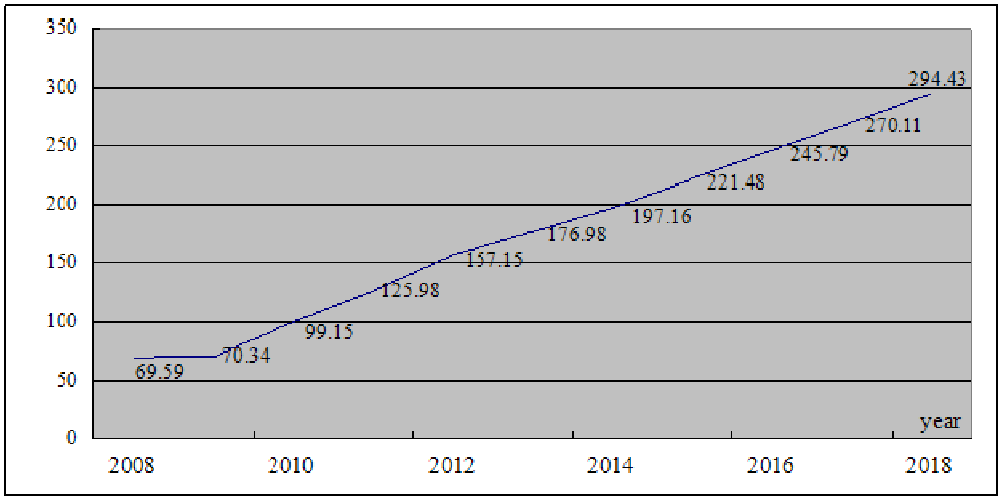

Fig.1 Maximum power load (MW)

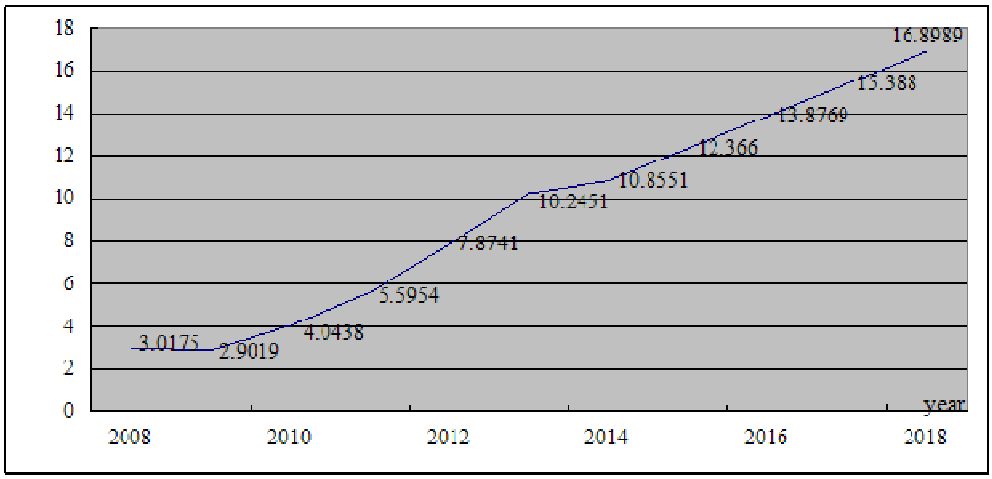

Fig.2 Whole society power consumption (1 Million kWh)

The load forecasting results indicate that both total power consumption and maximum power load are presented the Growth trend year by year, and their growth is relatively stable. The annual growth rate of total power consumption and largest power supply load are respectively about 12% and 10%, which shows that electric power industry is developing steadily.

Conclusions

Load forecasting is affected by the economic development, weather and other factors. In order to get a more accurate prediction results, the non-stationary time series of these factors need considering. So co-integration theory and error analysis are considered based on the traditional regression analysis to avoid "spurious regression" in this article.

In this article, there still have some deficiencies, which need to go deep into study in the future. Implementing the following principles [10]: The principle indicates that the power consumption and the trend of power supply load are more greatly affected by the development law in recent historical time. On the contrary, the development law of load long-time ago has a weak correlation with load forecasting. After introducing this principle, if analysis and correct the historical load data advisably, the accuracy of load forecasting results will be further improved. In conventional prediction, residual treated in each period is usually used.

References

[1] Liu Chen-hui. Theory and Methodology of Power System Load Forecasting [M]. Harbin: press of Harbin Institute of Technology, 1987.

[2] Niu Dong-xiao, Cao Shu-hua, Zhao Lei, etc. Power Load Forecasting Technology and Its Application [M]. Beijing: China Electric Power Press, 1998.

[3] Wu Man-hong, Yang Ji-wang. Several Electric Load Forecasting Methods and Comparison [J]. Guangdong Electric Power, 2004, 17(1):17-21.

[4] Power Industry Bureau of Hebei Province Planning Department. Applied Regression Analysis in Power Load Forecasting [J]. Hebei Electric Power Technology, 1987, 1:15-20.

[5] Yu Xuan, Cheng Zhong-hao, Wang Xu, etc. Long-term Power Load Forecasting Comprehensive Method Based on Related Analysis [J]. Relay, 2005, 33 (15) :49-52.

[6] Chen Hao, Wu Jie, Gao Shan. A New Method of Load Forecast Based on the Cointegration Theory [J]. China electric power, 2007, 40 (7) : 61-64.

[7] Yang Bao-chen, Zhang Shi-ying. Part of the Cointegration Model Cointegration Variable Structure Inspection [J]. Journal of Systems Engineering, 2005, 20 (3): 239-255.
[8]Liu Yin-xu, Zhang Shi-ying. Variable Structure Prediction Method of Nonlinear Cointegration System [J]. Statistics and Decision, 2007, (1): 4- 6.
[9] Chen Bei. Research on the Mid-long Term Load Forecasting in Power System [D]. Shanghai, Shanghai Jiaotong University, 2009.
[10] Kang Chong-qing, Xia Qing, Zhang Bo-ming. Review of Power System Load Forecasting Research and Development Direction [J]. Automation of Electric Power Systems, 2004, 9:1-9.

Advanced Materials Research Vols. 960-961 (2014) pp 1523-1526

doi:10.4028/www.scientific.net/AMR.960-961.1523

Review on Business Operation Mode and Technical Economy Evaluation of Micro-grid

Jie Liu [1, a], Nian Liu [1,b]

[1] North China Electric Power University, Beinong Road 2#, Changping District, Beijing, China

[a]liujie910125@163.com, [b]nian_liu@163.com

Keywords: smart micro-grid; business operation mode; technical economy evaluation.

Abstract. To make the advantages of smart micro-grid in economy and environment to the greatest extent, many countries choose to make detailed research on the business operation mode and technical economy of micro-grid. Based on the related research, this paper generalizes several typical user modes, and then provides a reasonable technical route to study the operation mode and technical economy of micro-grid. For its business operation mode, not only the existing proposals are analyzed, but also are its method of calculating the cost and benefits of this program. Finally, specific plans about how to assess the technical economy are also analyzed.

Introduction

During the primary development period of micro-grid, most attentions are put on the planning, control and operation of the micro-grid as well as research and development of related key technologies and devices [1, 2]. On the contrary, the attention on the input-output economy benefits and the application value of following promotions are obviously not enough. Meanwhile, it is also lack of reasonable policies and economic incentives, which leads to the low acceptance of micro-grid. Now the scope of micro-grid is also infinite and the business operation mode is not certain, leading to the confusion of the subjects of micro-grid establishment and business operation. Some enterprises even simply connect the distributed renewable energy sources to the power grid to operate as a micro-grid. To meet the requirements of user-side distributed generations connecting to the power grid, it is urgent to research the business operation mode and demand response strategies of micro-grid.

Technical route

For the business operation mode, several studies have been done as follows. Under the background of Chinese electricity market, an investment-benefits model to evaluate the balance between investment and benefits in different business operation mode for participants, including consumers, business operation organizer and government, is established. In paper [3], based on the investment-benefits model and the analysis on the inner relations among market participants, a business operation mode which is adaptable to the current situation of user-side micro-grid such as housing estate/ home, enterprise/ industry estate is proposed. Therefore, in the following work, we can analyze the application range and generalization performance of the typical business operation mode from multi-perspective, such as energy efficiency, energy consuming habits, load type, characteristics of distributed renewable energy sources and return of investment. Based on the characteristics of different user types, climate and areas, the optimal business operation mode for typical area and energy consumers can be further explored.

In paper [4], combined with the construction of demonstration engineering practice, the evaluation method of technological economy for user-side micro-grid is studied for the whole life circle. The input-output of this programme under different business operation mode is also assessed to provide a basis for the sustainable development of micro-grid. Paper [5] establishes a comprehensive index assesment and analysis model, which considers the reliability, security, quality of electric energy, ecomomical efficiency, environmental efficiency and business operation cost/benefits. Based on the model, a generalized index assesment and analysis method is proposed.

Therefore, it is advisable to evaluate the technological economy efficiency from the perspective of full life circle. According to analyzing the uer-side micro-grid in the developers, energy consumers and the whole interaction environment, the input-output model under typical business operation mode can be established. In the whole lofe circle of micro-grid programme, there are many aspects such as the assessment of manufacturability, cost evaluation, assembling ability and maintainability and so on. The indexes that can reflect and evaluate the business operation performance exactly are tobe selected to analyze with the consideration of demand response strategies and energy consuming efficiency . Finally, the influence of aspect, including the diversity of distributed energy resources, the energy composition and the ratio between distributed energy resources and energy storage system, on the cost and benefits of the system business operation performance can be analyzed.

Based on the above analysis and summary, the technical route of the research on business operation mode and technological economy evaluation is shown in Fig.1.

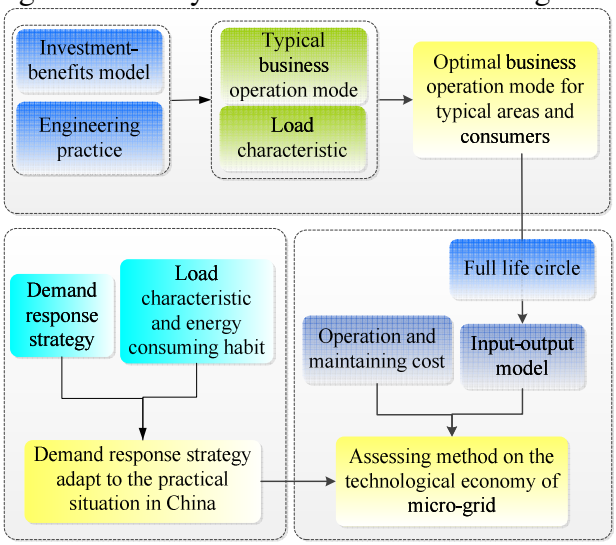

Fig.1 Technical route of business operation mode and technological economy evaluation

Business Operation Mode

In recent years, with the rapid development of distributed energy resources, developed countries such as United States, Japan, European countries and part of developing countries all concentrate on the practical application of micro-grid. Now they have achieved satisfactory performance by setting a series of standards, compensation mechanism to promote the development of micro-grid [15]. It can be found that all the program overseas has the following common characteristics: the construction of micro-grid is promoted by the joint efforts of enterprises and government; in order to guarantee the benefits of operation organizer, they all pay much attention to the setting a series of related policies such as the benefits distribution mechanism and cost compensation mechanism; during the period of initial development, the program relies on the support of related incentive policies. The operation organizers have some preferential policies for the close relationship with government; all the operation organizers concentrate on the application of new technologies and corresponding assessment of the operation performance.

According to the difference between the ownership and operation rights of housing estate micro-grid, paper [6] briefly introduces several business operation modes in this kind of energy consuming area and then provides the corresponding investments and economic benefits of energy consumers and electric companies. Based on the analysis of the current business operation development of micro-grid, paper [7] studied the investments and economic benefits in the independent business operation mode and then offered some advices to guarantee reasonable benefits of operation organizers. Safeguard mechanism such as electricity price mechanism, grid-connecting admission mechanism and cost compensation mechanism are suggested to establish. The influence of distributed generations, interruptible load and reactive power compensation on node capacitance on

the short-term business operation performance needs to be considered. Besides the fluctuations of energy demand and variation of the electricity price also need to be considered. Paper proposes a two-stage processing scheme and related mathematical model. The first stage of model is day-ahead operation mode and the second stage of model is real-time operation mode involving power distribution system. The day-ahead operation mode provides the decision results to the real-time operation mode, which means the real-time decision of power distribution system takes the day-ahead decision into consideration.

Based on the above research and analysis, we can summarize and conclude the typical business operation mode as for types under the special background and condition of Chinese electricity market. For the three participants of energy consumers, operation organizer and government, the four typical modes are “power grid company invest + power grid company operate”,” power grid company invest + energy consumers operate”,” power grid company incest + third party operate” and “energy consumers invest + energy consumers operate”. The influence on the benefits of program participants is evaluate from many aspects, including electricity mechanism, energy price, operation mode of micro-grid as well as difference between load demand and supply. Combined with the case study of actual projects, the optimal business operation mode for housing estate/home, enterprise/ industrial estate and other type of user-side micro-grid can be obtained respectively.

Technical Economy Evaluation

Fees lower than real cost produces serious financial balances, making operation and maintenance unfeasible and leading to the desertion of micro-grid projects by the local operator. To avoid this probelm, many countries have studied the technical economy evaluation of micro-grid in depth. Developed countries strats from the energy demand of electricity market and environment protection to promte the energy supply reliability and meet various requirements raised by different energy consumers. Furthermore, in order to reduce the cost, the economic policies of tax conssessions and finacial subsidies are set and enacted. Paper [3] takes Spain as example to make the technological economy evaluation on the PV rural electrification projects. The distribution of real costs (installation, operation and maintenance, management) is presented from the operational data of the energy service compancy during 5 years. The influence of some key aspects such as battery and geographical dispersion is also discussed.

Based on the summary and conclusion of the existing studies, for the whole life circle of this project, there are three periods in the business activities: installation period, operation and maintenance period and management period. And the cost structure of the micro-grid project is shown in Fig.2.

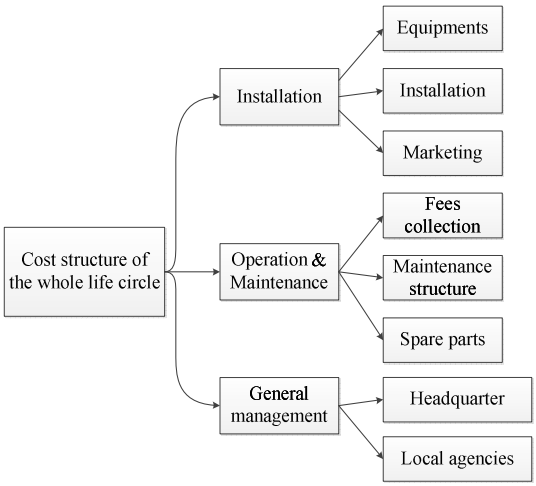

Fig.3 Cost structure of smart micro-grid project

The installation period contains both the fees of equipment and installation and the expenditure in marketing. The equipment cost is greatly influenced by the sell price of PV modules, batteries and son on. Considering the variation of the price of batteries and corresponding components in the

distributed energy resources (such as PV cells) in the market, the sensitivity analysis need to be conducted, which means to assess the effect of equipment prices on the total cost.

Operation cost mainly relates to the cost in fees collection. Maintenance includes both spare parts and the maintenance structure. For rural areas, it is not so convenient to collect fees as the urban areas. It demands a great effort in human capital and mobility, which justifies its high cost. The maintenance structure refers to the direct costs of this activity related to staff, offices, stores, vehicles, fuel, telephone, etc. Spare parts refers to the expenditure produced in the process of mantenance, including the repair and subsititute charges of devices (such as batteries, smart meters etc.).

The management period lasts from the end of installation period to the end of whole project. Take a project with 10 years life circle as example, if the first three years is the installation period, the remaining 7years is the management period. During the seven years, the management cost is relative even. For the operation and maintenance cost, it holds small share in the first three years while in the following seven years occupies a huge share in the annual year cost.

Conclusions

For the business operation mode, the realization method varies by the area and user type. This paper analyzes the evaluation method of technical economy from the perspective of whole life circle. In the following research, it is advised to combine the load characteristics and energy consuming habits of special area to study. To cater to the typical business operation mode, the demand response strategies and standards for certain areas are also need to be proposed.

References

[1] Zhao Bo, Zhang Xuesong, Hong Bowen. Energy penetration of large-scale distributed photovoltaic sources integrated into smart distribution network [J]. Electric Power Automation Equipment, 2012, 32(8): 95-100 (in Chinese)

[2] Wang Zhaoyu, Ai Qian. Muiti-objective allocation of micro-grid in smart distribution network [J]. Power System Technology, 2012, 36(8): 199-203 (in Chinese)

[3] Yang Qi, Ma Shiying, Li Sheng et al. Design of micro-grid operation model and control [J]. Transaction of China Electro Technical society, 2011, 26: 267-273 (in Chinese)

[4] L.M.Carrasco, L.Narvarte. E.Lorenzo. Operational costs of A 13,000 solar home systems rural electrification programme [J]. Renewable and Sustainable Energy Reviews, 2013,20:1-7

[5] Luo Yi, Wang Gang, Wang Longjun. Reliability Evaluation indices for micro-grid. Automation of Electric Power Systems, 2013, 37(5): 9-14 (in Chinese)

[6] Zeng Ming, Ma Shaoyin, Liu Yang et al. Investment cost-benefit analysis of regional micro-grid based on demand-side response [J]. Water Resources and Power, 2012, 30(7): 190-193 (in Chinese)

[7] Liu Yanru. Study on the business mode of smart power utilized district popularization and application [D]. Beijing, North China Electric Power University, 2011 (in Chinese)

Advanced Materials Research Vols. 960-961 (2014) pp 1527-1530

doi:10.4028/www.scientific.net/AMR.960-961.1527

Discussion on Price Settlement Policy Influence on the PV Power Generation Business Model

Hongzhuan Cai[1,a], Xiaohui Li[1,b]

[1] Xijing University, Xi'an, Shaanxi, 710123, China
[a] 175534337@qq.com, [b] lixh_spp@163.com

Keywords: PV (photovoltaic), Distributed, Electricity Subsidies, Feed-in Tariff, Net Metering, Self Consumption

Abstract. To support the development of the PV industry, the China National Energy Bureau has issued some policies to stimulate the domestic PV market consumption, such as the "Golden Sun Demonstration Project", "Building Integrated PV" policy. But these policies have some great vulnerability. Many developed countries, such as Germany, Japan, USA; they have some mature PV price settlement policies, such as Feed-in Tariff, Net Metering and Self Consumption. Therefore, according to the needs of domestic situation, China National Energy Bureau needs to refer to those developed countries' mature PV price settlement policies to formulate a PV price settlement policy. This policy must suit China PV market. And this policy should guide the development of domestic PV market correctly. Herein, I put forward some recommendations to improve our PV price settlement policy.

Instruction

China government began to implement the "golden sun demonstration project" from 2009 to support the development of domestic PV, which focuses on supporting user side of photovoltaic grid connected. This policy uses in accordance with the installation to subsidy every unit of electricity, which caused a lot of projects to use loopholes in the policy to obtain subsidies phenomenon. After the Chinese government learned the "golden sun demonstration project" lessons, according to the European experience, they take the electricity subsidy policy. This measure improves the utilization rate of fiscal funds. However, electricity subsidies are divided into several forms. In this paper, several forms of electricity subsidies are discussed. According to this discussion, we want to explore which kind of form is conducive to the development of Chinese photovoltaic power generation. [1]

European electricity subsidy policy

European electricity subsidy policy mainly has three forms. They are Feed-in Tariff, Net Metering and Self Consumption. [2]

Feed-in Tariff. The Feed-in Tariff policy is used in the form of two lines of revenue and expenditure. The form is that the electricity generated by PV power station is sold to the grid, and the electricity used by users is bought from the grid in retail price. Feed-in Tariff mainly has three forms: Standard FiT, Variable FiT and Premium FiT.

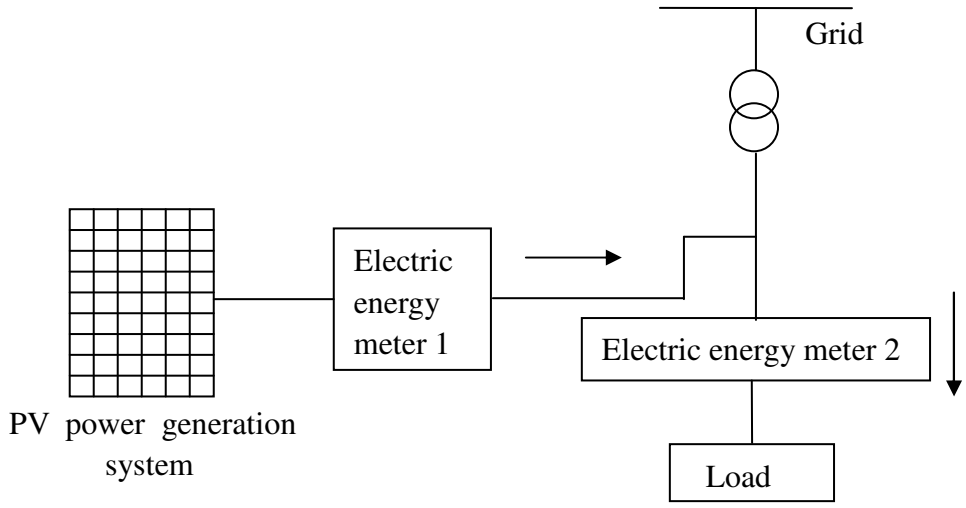

Fig. 1 Sketch of PV power generation system of Feed-in Tariff

In Fig. 1, electric energy meter 1: all of the electricity from PV power generation system, but also sold to grid electricity. Electric energy meter 2: the user purchase from the grid.

In the Feed-in Tariff, the point, which connect PV power system and grid, and electricity meters are mounted outside of users' electricity meters. [3]

The advantages of electricity price policy are: the PV power generation party can sign the purchase contract with the electric company, which can make the income of the power generation side security. It has no influence on the efficiency of Power Grid Corp. Disadvantages are: small power stations cannot issue formal invoices to Power Grid Corp. This will lead to some problems on the tax and business.

Net Metering. A part of power generate by PV power generation system are used by user, and remaining power are sold to grid, and then user buy a portion of electricity from grid to use. The part of spontaneous occupied don't be measured. Only calculate the difference between the power that is bought from power grid and electricity that is sold to power grid. This difference called net power. Money that should pay for net power to Power Grid Corp is calculated according to the retail price of electricity. Users can get subsidies of total amount of electricity that is generated by PV power generation system from the Power Grid Corp. The principle of design the PV power generation system is that the generating capacity throughout the year must be less than power consumption throughout the year.

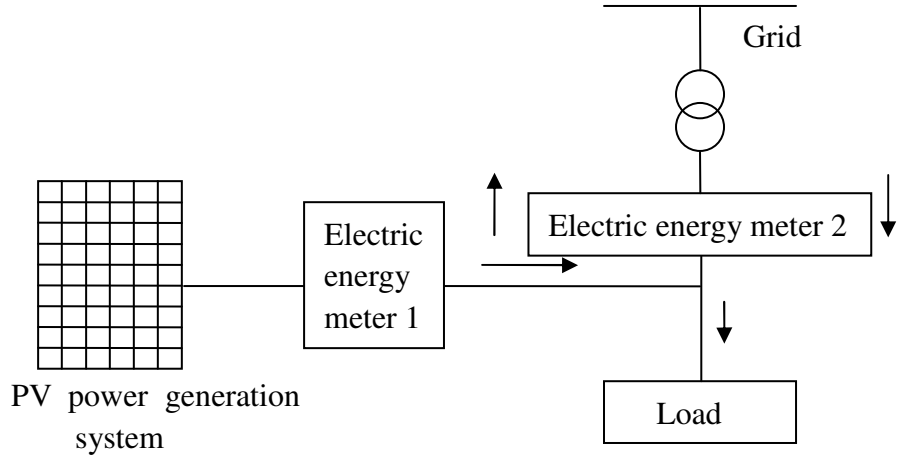

Fig. 2 Sketch of PV power generation system of Net Metering

In Fig. 2, electric energy meter 1: all of the electricity from PV power generation system. Electric energy meter 2: power that is bought from power grid and electricity that is sold to power grid.

The advantages of the Net Metering policy are followings. First, users needn't install energy storage device, so that the users can save some costs. Second, the power consumption is more than power generation. Therefore, users don't sell electricity to the Power Grid Corp. Problems on tax will not produce. The disadvantage is that PV power generation system will affects the efficiency of the Power Grid Corp.

Self Consumption. For power that is generated by PV power generation system, users can use a part of it, and the rest of the electricity can be sold to the grid. If power that users required is not enough, they can buy electricity from the grid by retail price. Electricity that is sold to grid can be settled by the published photovoltaic power tariff.

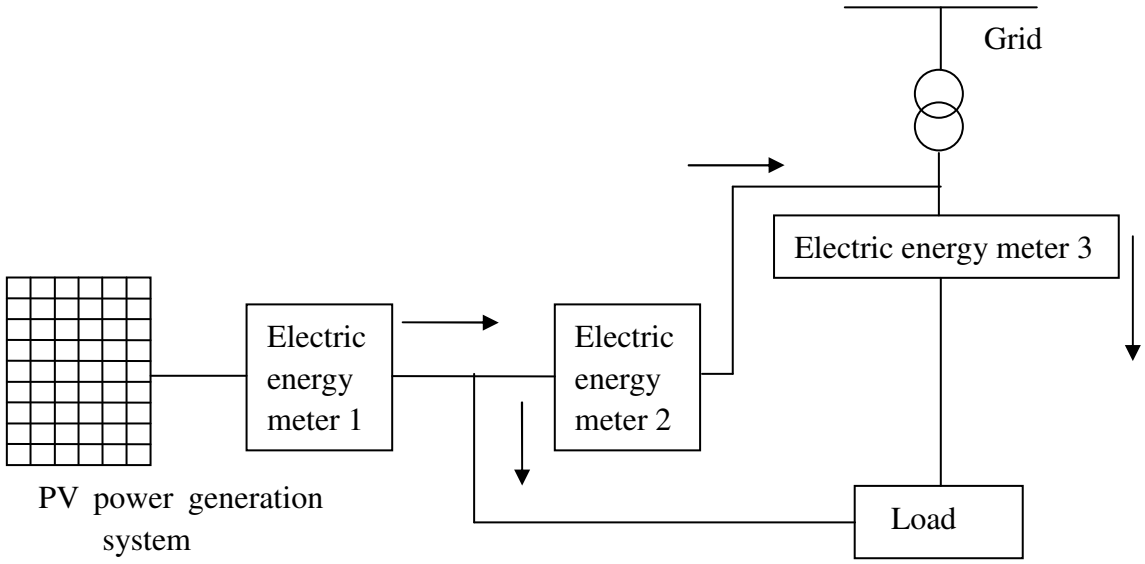

Fig. 3 Sketch of PV power generation system of Self Consumption

In Fig. 3, electric energy meter 1: all of the electricity from PV power generation system. Electric energy meter 2: electricity that is sold to grid. Electric energy meter 3: electricity that is bought from grid.

The advantage of self consumption policy: the electricity that is generated by PV power generation system and then directly used by user and power is bought from grid can offset each other, reducing the transaction between the user and the Power Grid Corp. Disadvantages are the followings. Electricity that is generated by PV power generation system and then directly used by user is not traded, so there will be some losses on tax for country. Electricity that is sold to grid will be traded with Power Grid Corp. It will produce some business and tax issues.

The current policies of PV in China

Although the price of electricity generated by PV power generation in China is not at the same level with the electricity of public grid, PV electricity used by industry and commerce will reach parity consumption level. So, it is necessary to investigate the policies of PV electricity.

In 2013 March, the National Development and Reform Commission issued a draft, which name is" *Notice about Perfecting PV Electricity's Price*". The draft regulates that current policy of PV electricity's price as follows.

(1) For the large PV power station, there are four type of price for four areas: class Ⅰ region is 0.75 Yuan/kWh; class Ⅱ region is 0.85Yuan/kWh; class Ⅲ region is 0.95 Yuan/kWh; class Ⅳ region is 1 Yuan/kWh.
(2) For the distributed generation system, electricity back into grid is purchased by Power Grid Corp for price of the coal-fired electricity. And each unit of electricity is given 0.35 Yuan additional.[4]

The Feed-in Tariff policy is used on large PV power stations, and the policy that used on distributed PV generation systems is similar to the Self Consumption. However, in some countries, such as Germany, electricity generated by PV power generation is inexpensive. No longer to give additional subsidies to the spontaneous occupied part. So the current PV power price policy implementing in China is more complex than in foreign.

Recommendations to model of Chinese PV power generation business

(1) In order to facilitate developers' intervention, the Feed-in Tariff policy can be used on PV station, which will make the developers' profit transparent and security.
(2) For distributed PV generation system under Self Consumption, according to the difference of solar energy resources in different areas, Power Grid Corp can make different subsidies. Whether how much does every unit of electricity cost, the revenue of PV power generation party can be controlled in the same level.
(3) With the rise of price of electric power in grid, electricity generated by PV power generation system for most users will be reach parity consumption level. Due to Net Metering is easy to be operated, I recommend that Net Metering can be used on distributed PV power generation system which are built when electricity generated by PV power generation system achieve parity consumption level.

Acknowledgments

This work is supported by 2012 the first batch of college level scientific research fund of Xijing university (serial No.:XJ120104), and 2012 the college students' innovation and entrepreneurship program of the shaanxi province.

References

[1] Lin Jiang: Jiangsu Electrical Engineering. Vol. 32, n°3 (2013), p. 66
[2] Sicheng Wang: Solar Energy. Vol. 08 (2013), p.8
[3] Yang Li, Zhiyan Xu: Technology Wind, (2010), 61-71
[4] "Notice about Perfecting PV Electricity's Price" draft, National Development and Reform Commission Press, 2013

Advanced Materials Research Vols. 960-961 (2014) pp 1531-1535

doi:10.4028/www.scientific.net/AMR.960-961.1531

Dual-Power PV-grid Energy System – an Alternative to the off-grid PV Energy System

Intan Rahayu Ibrahim[1,a], Ahmad Maliki Omar[2,b], Zakaria.Hussain[3,c], Mohd Najib Mohd Hussain[4,d], Siti Zaliha Mohammad Noor[5,e]

[1,2,3,4,5]Faculty of Electrical Engineering, Universiti Teknologi MARA (UiTM), Malaysia.

[a]intan121@ppinang.uitm.edu.my, [b] Maliki_omar@salam.uitm.edu.my, [c]zakaria183@salam.uitm.edu.my, [d]najib830@ppinang.uitm.edu.my, [e]sitizaliha@salam.uitm.edu.my.

Keywords: dual-power PV-grid system, PV energy system, off-grid power supply, solar hybrid system, dual-power system

Abstract. The Dual-power PV-grid energy system was initiated to reduce the capital installation cost of PV energy system and to make use the lower tariff rate offered at off-peak period. In this paper, the system configuration, architecture and operation of the system are described and discussed. The prototype has been developed and runs 24-hours to supply the load. Meteorological and electrical data collected prove the successful of such system. The system is expected to reduce 89% of electricity bill with estimated cost of energy (COE) of USD1.15/kWh. It is suggested that the dual-power PV-grid system is beneficial to serve as an alternative implementation of the off-grid PV energy system.

Introduction

A photovoltaic energy system is most promising renewable energy sources [1-4]. In fact, only about 0.1% of this energy has been utilized so far [5], indicating the potential in the future. Even though there has been a steady decline in the cost of PV generators in the past few years [6, 7], the installation cost is still considered as expensive with payback time of more than 20 years.

Furthermore, the PV energy system alone is not technically viable for continuous power supply [8, 9] an it is necessary to combine the system with other renewable energy sources or back-up with generators or battery system [10-12]. In the dual-power PV-grid energy system, the battery autonomy is reduce to a day, thus reducing the number of PV panels and batteries, consequently reducing the cost of installation [13-15]. The change over circuit is used to connect the load to the PV-battery system during the day (7.00am – 6.59pm) and change connection to the grid in the night time (7.00pm – 6.59am) or during unreliable solar energy. The system is also capable in manipulating low off-peak tariff offered during the night. This paper discusses system configuration, operation and cost evaluation of the proposed system. The discussion and analysis was done based on the prototype of 2.4 kW dual-power PV-grid energy system implemented at the guard house in Universiti Tenologi MARA (UiTM) Pulau Pinang.

System Configuration and Operation

System Design

The system comprises PV arrays, the inverter with a built-in charge controller and the switch-over circuit as depicted in Fig.1. The system operates 24 hours to supply power to the load consisting air-conditioning, CCTV and lighting system.

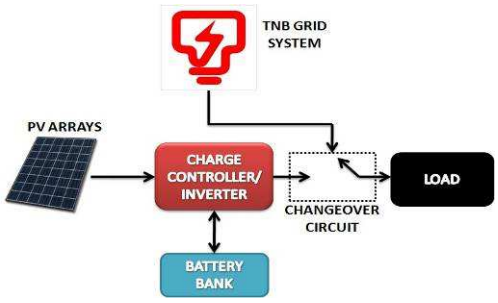

Fig.1: The dual-power PV-grid Energy system in UiTM Pulau Pinang, Malaysia.

A prototype system with below specification has been developed to meet the energy requirement:-

PV size : 14 X 175 W monocrystalline PV modules with a total rated power of 2.4 kW, 48 V
Battery Size : 24 X 2V/500 Ah connected in series to obtain 48 V/500 Ah
Load(s) : Air-conditioner, CCTV, computer, lamps
Converter : bi-directional, 3000 VA, 48 VDC ~ 230V SPWM AC, 50Hz, built-in charge controller

Mode of System Operation

During the day, the converter operates synchronously with the grid supply. A built-in PWM PV charge controller / regulator ensures that the batteries are charged at maximum power point. In the event of insufficient power supply from the PV, the battery will make up the shortfall. The battery charging process will automatically occur from the grid whenever the battery voltage falls below a preset value in order to maintain the battery bank at its float voltage. If no grid connection is provided, the inverter operates as a stand-alone inverter with the batteries being charge from the PV array. Meanwhile, during the off-peak, the utility grid supplies the energy from 7.00 pm until 6.59 am. The battery will be charged using grid current via bi-directional converter from 1.30am to 5am. The switch-over circuit comprises of relay timer which connect the load to the PV system during the on-peak demand and change connection to the grid in the off-peak demand.

Data Acquisition System

The data taker (DT80) collects the analogue data from analogue channels and converts the signals to digital signals and transmits to the data acquisition PC. The collected data are summarized in the Table 1.

Table 1: List of Measurements Data

Analogue sensor	
PV array current (DC), I_{PV}	Inverter PF
PV array voltage (DC), V_{PV}	Inverter Frequency
Battery current (DC), I_{bat}	Irradiance (W/m2), Irradiance
Battery voltage (DC), V_{bat}	Ambient temperature, T_{amb}
Inverter current (AC), I_{inv}	Ambient Rh, Rh_{amb}
Inverter voltage (AC), V_{inv}	

Fig.2 shows some of measured meteorological and electrical data of the system.

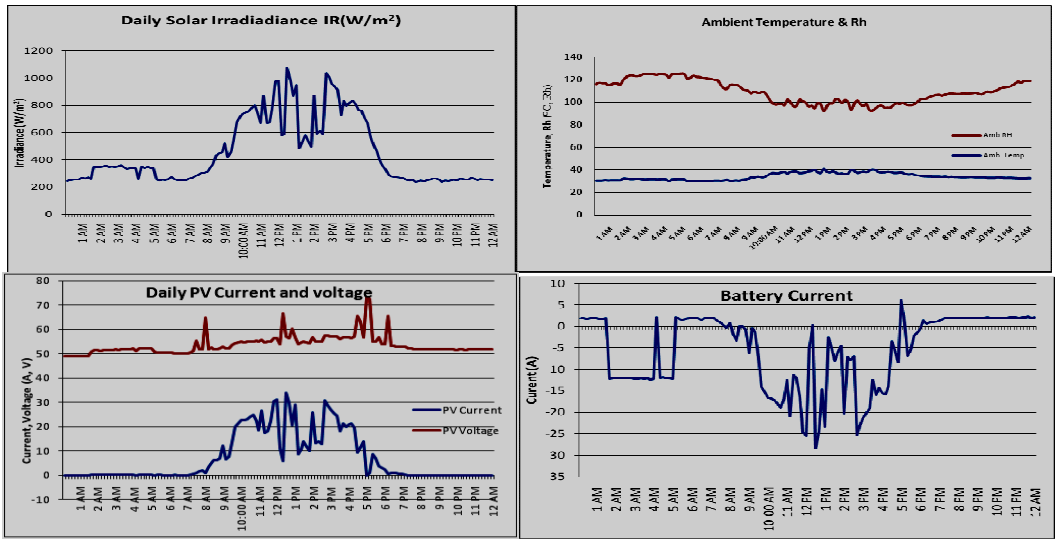

Fig.2: Some Meteorological and Electrical Data Monitored by the Data Logger.

Cost-benefit Evaluation

Hybrid Optimization Model for Energy Renewables (HOMER) software provided by National Renewable Energy Lab (NREL) was used to compute the cost analysis of the system. The radiation data, daily energy usage and an estimated cost of each component in the dual-power PV-grid plant were used as an input to the software. Table 2 shows the comparison between estimated number of batteries and PV panel and total capital cost for dual-power PV-grid energy system and standalone PV systems. The calculation was made based on the daily energy usage of 8.508 kWh/Day and market prices of the PV panel and battery.

Table 2: Number of Batteries and PV Panel and Estimated Cost for Dual-Tariff PV and Stand Alone PV Systems.

	Dual-power PV-grid Energy System	**Off-grid PV System**
Number of Batteries (500 Ah)	24	48
Number of PV Panels (175W)	20	26
Estimated Capital Cost (USD)	38,600	58,000

The software generates the net present cost and the cost summary as tabulated in Table 3 and Table 4 respectively. The cost of unit energy (COE) was estimated to be USD 1.15/kWh.

Table 3: Net Present Cost of the System (USD)

Component	**Capital**	**Replacement**	**O&M**	**Fuel**	**Salvage**	**Total**
PV Modules	25,000	7,903	0	0	-4,430	28,473
Battery	11,000	3,387	4,629	0	-1,898	17,118
Converter	2,600	755	771	0	-140	3,986
Overall System	38,600	12,045	5,400	0	-6,468	49,577

Table 4: Cost Summary of the System

Total Net Present Cost	USD 49,577
Levelized Cost Of Energy	USD 1.15/Kwh
Operating Cost	USD 858/Yr

Table 5: Electricity Bill for the Dual-power PV-grid System and the Normal System

	Dual-power PV-grid System	Normal System
Daily Energy Usage (kW/day)	1.632	10.104
Monthly Usage (kW/month)	48.96	303.12
Cost per Month (USD)	2.62	24.70
% reduced in electricity bill = 89.4%		

Conclusion

The dual-power PV-grid energy system promotes electrical energy usage during off-demand period and offers alternative solution to off-grid power generation. In this system, the load will be supplied by PV-battery system during on-demand higher tariff period and utilizes the grid supply including battery charging process during off-demand period. The successful implementation of such system is beneficial to the environment and lucratively cut the capital cost for PV system installation. The system expected to reduce the electricity bill by 89% with estimated COE of USD 1.15/kWh.

Acknowledgements

This work was financially supported by the Ministry of Science, Technology and Innovation(MOSTI) Malaysia, EScience Grant No: 03-01-01-SF0186 and Universti Teknologi MARA, Malaysia.

References

[1] S. Lalouni, et al., "Fuzzy logic control of stand-alone photovoltaic system with battery storage," *Journal of Power Sources*, vol. 193, no. 2, 2009, pp. 899-907.

[2] Y.L. Ke, et al., "Implementation of a solar power battery energy storage system with maximum power point tracking," *Proc. Conference Record - IAS Annual Meeting (IEEE Industry Applications Society)*, 2010.

[3] H. Wang and B. Li, "The cooperated MPPT control of stand-alone PV power generation system," *Proc. Proceedings of the World Congress on Intelligent Control and Automation (WCICA)*, 2010, pp. 2228-2231.

[4] T. Hiyama and e. al., "Evaluation of Neural Network Based Real Time Maximum Power-tracking Controller goes PV System," *IEEE* vol. 3, no. 10, September 1995.

[5] W. Hutzel and D. Goodman, "Remotely Accessible Solar Energy Laboratory for High School Students," *Book Remotely Accessible Solar Energy Laboratory for High School Students*, Series Remotely Accessible Solar Energy Laboratory for High School Students 3, ed., Editor ed.^eds., July 2004, pp. 18-22.

[6] B.M.T. Ho, et al., "An integrated inverter with maximum power tracking for grid-connected PV systems," IEEE, 2005, pp. 1559-1565.

[7] S. Kjaer, et al., "A Review of Single-phase Grid Connceted Inverters for Photovoltaic Modules," *IEEE Transactions on Industry Applications*, vol. 41, no. 5, 2005, pp. 1292-1306.

[8] S. Singh and A. Singh, "FPGA Based Sinusoidal Pulse Width Modulated Waveform Generation for Solar (PV) Rural Home Power Inverter," *Arxiv preprint arXiv:1002.3340*, 2010.

[9] I.R. Ibrahim, et al., "Control strategy of power converter system in the dual-power PV-grid system energy utilizing cascaded multilevel inverter," *Proc. 8th IEEE Conference onIndustrial Electronics and Applications (ICIEA), 2013*, 2013, pp. 848-853.

[10] P. Nema, et al., "A current and future state of art development of hybrid energy system using wind and PV-solar: A review," *Renewable and Sustainable Energy Reviews*, vol. 13, no. 8, 2009, pp. 2096-2103.

[11] J. Paska, et al., "Hybrid power systems-An effective way of utilising primary energy sources," *Renewable Energy*, vol. 34, no. 11, 2009, pp. 2414-2421.

[12] M. Sadikin, et al., "High-frequency link DC for power quality improvement of stand-alone PV system in cascaded multilevel inverter," *Proc. 2013 IEEE 10th International Conference on Power Electronics and Drive Systems (PEDS),*, 2013, pp. 597-601.
[13] International Energy Agency, "Management of Storage Batteries used in Stand-Alone Photovoltaic Power Systems - Report-IEA-PVPS-T3-10," *International Energy Agency (IEA) 2002*, 2002.
[14] D.B. CÃ¢ndido, et al., "Implementation of a stand-alone photovoltaic system based on decentralized DC-DC converters," *Proc. 2009 Brazilian Power Electronics Conference, COBEP2009*, 2009, pp. 174-180.
[15] I.R. Ibrahim, et al., "Dual-power PV-grid Energy System Utilizing Multilevel Inverter - An Overview and Alternative to PV Energy System in Malaysia," 2011.

Advanced Materials Research Vols. 960-961 (2014) pp 1536-1541

doi:10.4028/www.scientific.net/AMR.960-961.1536

Discussion on asset-backed securitization of PV power plants

Yifeng Wang[1, a]

[1]School of economics and management, North China Electric Power University,

[2] BeiNong Road, ChangPing District, Beijing, China

[a]598909473@qq.com

Keywords: PV power plant, financing channel, Asset-backed securitization

Abstract. At present, it universally exists that the financing problem confronts photovoltaic (PV) power plant construction in our country. The PV power plant construction in industry falls into the capital-intensive enterprises with the feature of long-time development, substantial investment needed but relatively fixed income. Thereby, it is greatly appropriate for solar securitization to address the financing needs of the industry with its characteristic and realize diversified financing channels. In this paper, firstly, the feasibility and necessity of ABS financing for PV industry is discussed. Then, we elaborate the current four construction modes of PV power plant, namely, transfer of beneficial interest of power charge, credit increment of financing platform company, BOT (build-operate-transfer), and financing leasing, according to which the financial institution designs the asset-backed securities supported by the beneficial interest of the power plant. Further, we analyze the main problems and challenges of carrying out the ABS business. Countermeasures and suggestion ns are put forward finally.

Introduction

The PV power plant construction is a capital-intensive project with great demand of capital investment in pre-construction. In 2012, the capacity of Chinese PV cell packs was about 23 GW, occupying 58% of total global capacity. At present, 10 billion Yuan of funds is required for the construction of 100MW PV power plant in China and we aim to create a PV industry with more installed capacity of 14GW in 2014 and a gross installed capacity of 50GW by 2020. Thereby, the widespread financing problem is increasingly acute, innovative means of financing and diversified financing channels are called for while traditional means of financing are far from enough to solve this problem.

The asset-backed securitization or ABS, one kind of emerging structured finances, relies on the capital markets to raise funds. The construction project of PV power station, however, with the feature of large investment and long construction period, is in line with the requirement of stable asset base and predictable cash flow of the ABS business. As a result, the ABS securitization business can be carried out to address the financing needs.

There lies great significance in exploring the ABS business of PV plant to crack the financing problems, accelerate the pace of constructing PV power plants, and provide valuable experience for the development of other renewable energy industry.

Overview of the ABS Business

The asset-backed securitization or ABS, as one kind of structured finances, means a technique or process enabling an array of assets (the “Assets” or “Underlying Assets”), which are capable of generating predictable and stable cash flows income in the future, to be converted into certain securitization products via particular structural arrangement and coupling with corresponding credit enhancement, and which products can be traded on the financial market and possess certain credit rating.

The ABS is an emerging product in the financial sector during the recent 30 years, and it evolved in the USA and developed rapidly in Europe, Japan, etc., and currently it spreads over worldwide in a quick speed. As to the ABS in China, since initially launched in 2004, it mainly consists of two systems: (i) one is the securitization of credit assets, which is originated by the banks and other financial institutions, and traded on the national inter-bank bond market upon the approval of the China Banking Regulatory Commission (the "CBRC"), and (ii) the other is the securitization of enterprises' assets (including the state-run institutions' assets), (the products of) which are issued by the securities companies through a Special Scheme and in the form of ABS, and traded and listed on the Shanghai Stock Exchange or the Shenzhen Stock Exchange upon the approval of the CSRC. In addition, the insurance companies, fund management companies, trust companies and other institutions are also allowed to conduct the ABS Business in accordance with the relevant rules regulating such business in their respective sectors.

Necessity and feasibility analysis of solar securitization

In the last decade, the PV industry in China has developed rapidly, with the joint promotion of the market and policies. China's PV modules' production is ranked top in the world, making a significant impact on the world's renewable energy development and solar PV industrial sector. Meanwhile, China's solar PV industry is facing several challenges, especially financial issues. Exploring new financing channels such as asset-backed securitization has become imperative of PV power plant construction. Currently, high cost, narrow financing channels, huge fund gap and a range of issues in PV industry are urgently calling for the ABS business to help to solve.

The financing status-quo of PV industry. Since 2013, the state has adopted a number of policies to support the development of PV industry and encourage the orderly construction of photovoltaic power plants. However, due to lack of capital, financing gap, and the long construction period of PV power stations, the process of PV plant construction has been seriously affected. There is still a large gap between the potential of PV market based on available resources and current levels of market development.

Currently, the main factors contributing to financing barriers for PV plant construction in China in existence are:

(1) There are limited financing channels, single way and backward means of financing, and dependence on national financing policies and commercial bank loan;

(2) Financing sources of funds are too focused on bank

(3) Financing structure is irrational, the ratio of indirect capital is too large, while direct financing takes up too small proportion

(4) Financing costs remain high and the PV industry is only now making the jump from niche markets, which are difficult and expensive.

Consequently, exploring new financing ways and improving financing structure to solve the financing problem of PV power plant construction are currently the primary task confronting China.

The necessity of the ABS in PV industry.

Large scale and huge financing needs of PV plant construction. In the national energy work conference in 2014, the National Energy Board finalize that the 2014 domestic PV installed capacity will be added by 14GW. According to the current average construction costs, capital needed to build 100MW PV power plant is about 10 billion Yuan, which means financing investment of about 140 billion is required with new added capacity by 14GW. Meanwhile, according to the "solar power development "second five" plan" issued by National Energy Board, China's PV gross installed capacity aims to reach 50GW by 2020. Faced with such a huge demand for funds, it is so tough to

meet the demand for PV power plant construction to merely rely on traditional means of financing. The construction layout of solar power is shown in Table.1.

Table .1 The construction layout of solar power [MW]

Solar Power System	2010	2015	2020
1.Solar power station	450	11000	23000
PV station	450	10000	20000
CSP station	0	1000	3000
2.Distributed PV system	410	10000	27000
Amount	860	21000	50000

Data source：《solar power development “second five” plan》

Urgent needs of broadening financing channels for PV station. The financing is a major problem in the process of PV plant construction, which is far too tough to be solved solely by current financing channel. Therefore, what should be done right now is, to actively expand financing channels, to diversify financing options, to optimize the capital structure and innovatively try to carry out the ABS mode, for finding new ways to solve the financing problem, under support of national policy.

The advantages of ABS . The asset-backed securitization is an innovative way of financing with the following special advantages compared with traditional financing:

(1) Ease of trade

One advantage of asset-backed securities for buyers and sellers is the ability to trade in assets that would otherwise be difficult to trade in primary existing form. And the financing process is relatively easy, short-period and low-cost.

(2) Abundant financing source and risk sharing, particularly for buyers, the ABS is able to spread risk over a number of investors.

(3) Increased Loans for Borrowers

For borrowers, asset-backed securities increase the availability of loans.

(4) It can expand the proportion of direct financing, decrease debt ratio of company, and vitalize high-quality solar power station assets.

The feasibility of ABS business for PV station.

The characteristic of PV station meets the requirement of ABS. The key to carry out ABS business is to provide predictable and stable cash flow from the underlying asset pool. It is more favorable when the industry served by the underlying asset pool is specially supported by the state. Despite the high cost of PV power plant construction and huge initial investment, once the PV network being built and kept in low-cost operation, considerable electricity and more fixed income annually (for 20 years or so) can be earned. The cash flow can be sufficient and stable, with strong product attributes of the "fixed income", which fully complies with the requirements of ABS thereby making it suitable for development of securitization products.

The environment for ABS business in PV industry is provided. The ABS is a direct financing in the capital markets, and reasonable capital market structure is a prerequisite for carrying out asset securitization. With the constant improvement of China's financial system, the establishment of a multi-level capital market provides a good opportunity for the ABS business in PV industry.

Related laws, regulations and policies with continuous improvement are promulgated, which both effectively controls the risks in the financial markets and provide conditions to carry out the ABS. In *the Administrative Provisions on the Securities Companies’ Asset-backed Securitization Business,* issued by CSRC in 2013, specific form of ABS is explicitly stipulated for PV power plants, which contributes to the development of solar securitization.

At the same time, all kinds of financing entities participating in the capital markets, with government's cultivation and their marketing experience, are getting more and more matured. Their professional quality and comprehensive ability have been greatly improved, which lead to the maturity of capitalized operation.

There have been successes in ABS in China. In December 2005, the China Development Bank successfully issued initial credit asset securitization, followed by several successful cases. In particular, in May 2006, Special Assets Management Scheme of Charges for Electricity of Huaneng Nancang River made a hit in the Shenzhen Stock Exchange. All the successful cases have accumulated a wealth of experience for China's power enterprises to carry out ABS business.

The ABS modes of PV station

Implementation of ABS business for PV power plants has already had its necessity and feasibility. And according to the specific requirements of the financing body and PV power plant construction, there are different ways of ABS to be chosen. Currently, there are four construction modes for China's PV power plants, namely, transfer of beneficial interest of power charge, credit increment of financing platform company, BOT (build-operate-transfer), and financing leasing.

Transfer of Beneficial Interest of Power Charge (TBIPC). The TBIPC model is the most basic model (Chinese-style transfer), in which securities companies and Financing Platform Companies (construction-operation company, namely, the installer) enter into a income beneficiary transfer contract about the power stations in the future, establish a Specific Asset Management Plan (SAMP), issue asset-backed securities by beneficial interests, and obtain transferee price beneficial interests. Investors make an inquiry and subscribe the shares of SAMP. The final gains of investors are power purchase price with the deduction of operating expenses for the installers and management fees for securities companies. The flowchart of TBIPC is shown in Figure. 1.

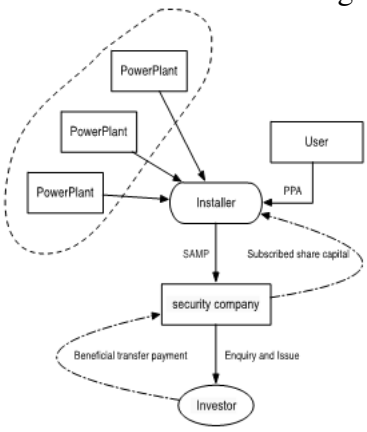

Figure.1: TBIPC

Credit Increment of Financing Platform Company (CIFPC). The most distinguishing characteristic of the CIFPC model from the TBIPC model is that PV power stations are acquired by Financing Platform Company, then realized asset transferring and withdrawing by ABS, and the purchase price are paid by the Financing Platform Company to the initial possessor of PV power stations. This mode is mainly applied to privately-owned and small and medium-sized enterprises, which can take advantage of high-quality credit standing and professional competence of financing platform to reduce financing costs against their own poor credit conditions. The flowchart of CIFPC is shown in Figure. 2.

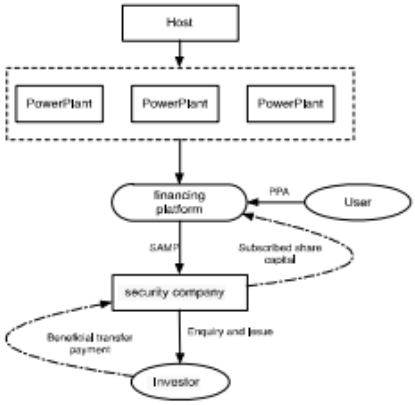

Figure.2: CIFPC

BOT (build—operate—transfer). There have been many large infrastructure projects, such as expressways and power plants, which are being constructed or have been operated by private firms under a procurement system called build-operate-transfer (BOT). Under the system, the franchisee (project sponsor) is responsible for financing, construction, and operating a facility and he, in return, has been granted a right to generate revenue from the facility for a specific period. After the concession period, the facility will be transferred at no cost to the franchiser, who usually is the government. The major motivator for the BOT system is that the host government need not spend any public funding but still can provide a public facility to her people. Meanwhile, the franchisees can enjoy a high potential profit from a successful BOT project. The flowchart of BOT is shown in Figure. 3.

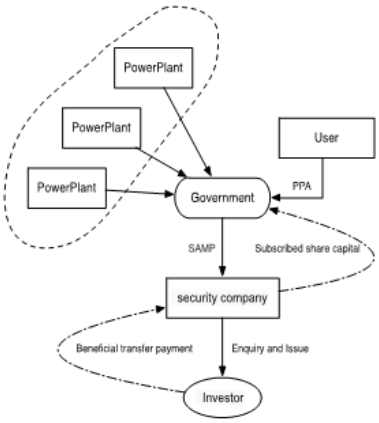

Figure.3: BOT

Financial leasing. Financial leasing is the activity in which the lessor:
Concludes a delivery contract with the supplier of the lease object whereby he/she obtains the ownership right of the lease object, with the lessee determining both the supplier and the lease object.

Concludes with the lessee the financial lease contract whereby he/she transfers to the lessee the authorization for keeping and using the lease object over a predetermined term and the lessee pays the agreed fee in agreed installments.

Advantages of lease financing: Less upfront cash needs to be outlaid; The risk of financing entity and project construction risk are diversified; There is typically an option to buy the equipment at the end of lease term; It offers fixed rate financing and potential tax benefits. The flowchart of Financial leasing is shown in Figure. 4.

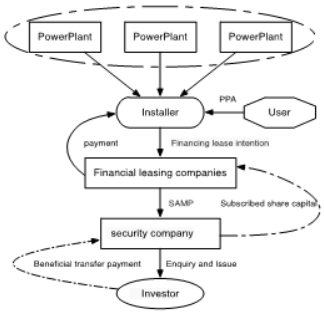

Figure.4: Financial leasing

Suggestions on implementing PV stations

Improving legal system. The further development of ABS depends on the support of appropriate corresponding laws and regulations. It is necessary to build up a complete legal system for SPV identification, the audit of ABS issuers and credit rating enhancement, the definition of bankruptcy isolation and a series of processes, in order to eliminate the obstacles to carry out the laws and regulations on asset securitization, improve operational efficiency, and reduce financing costs.

Encouraging the development of market intermediaries and promoting its operation standardization. The ABS, as a structured financing, needs participation and collaboration of investment banks, accounting firms, credit rating agencies and other intermediaries, to promote rationalization of the transaction structure, to reduce non-systematic risk, and to enhance confidence of investors. China should set up an ad hoc securities firm as soon as possible to specially conduct ABS business, and increase efforts to foster a number of widely recognized credit rating agencies and credit enhancement ones.

Completing accounting advice and tax system for ABS business. On the one hand, accounting standards should be amended as soon as possible, to make it clear for true sale, off-balance sheet and other accounting treatment. On the other hand, the existing heavy taxes of securitization business and the problem of double taxation need to be changed and replaced by providing tax support. Reduce stamp duty on securities transactions and tax rate of income taxes for investors, and give certain concessions to business tax, stamp duty for the promoters.

Fostering investor. It is the demand of investors that maintains the existence of any financial product. Financing PV plant construction through ABS business requires widening participation of investors in order to increase the total amount of financing, reduce financing costs, and further spread risk. However, the main investors in China's capital market are not diversified enough with low degree of specialization thereby making the market capacity not big enough and the transaction less active.

Reference

[1] Summary of asset securitization.http://blog.sina.com.cn/s/blog_5008228b010083pr.html
[2] Linping Zheng, Financing Options on Hydropower Project Asset Securitization [J]. Hydroelectric power, 2005(12) : 8-11. (In Chinese)
[3] Weimin Liao, Xiangjin Zhang. Hydroelectricity asset-backed securitization—financing innovation of Huaneng Nancang River. Hydropower co., Ltd. [J]. 2007(6): 42~43(In Chinese)
[4] Hegedus, L. (20 June 2013). “What Would a Solar Asset-backed Security look like?” Renewable Energy World. Accessed June 20, 2013:http://www.renewableenergyworld.com/rea/news/article/2013/06/what-would-a-solar-asset-backed-security-look-like.

Advanced Materials Research Vols. 960-961 (2014) pp 1542-1545

doi:10.4028/www.scientific.net/AMR.960-961.1542

Analysis of financing difficulties in Chinese PV industry

Yifeng Wang[1, a]

[1]School of economics and management, North China Electric Power University，

2 BeiNong Road, ChangPing District, Beijing, China

[a]598909473@qq.com

Keywords: PV industry; financing problem

Abstract. As China domestic photovoltaic (PV) policy forms a closed loop; PV subsidy, grid-connected and other issues have been solving gradually, PV financing problem, which becomes the greatest bottleneck of Chinese PV industry to restrict its development, is highlighted increasingly. In this paper, based on analyzing the current PV financing situation, we discuss the reasons for PV financing difficulties, and put forward some suggestions to help to solve it.

Introduction

The PV industry in China is one of the few strategic emerging industries with international competitive edge. There has published a number of policy measures to promote the healthy development of Chinese PV industry in 2013. At present, being in a world leading level, Chinese PV cell production accounts for 70% of global market share, the conversion efficiency of crystalline silicon photovoltaic cells reaches 20%. However, the PV industry is capital-intensive, which requires a lot of capital investment. As PV subsidy, grid-connected and other issues have been solved. Financing problem has become the biggest bottleneck of development of the photovoltaic industry.

Development and financing status quo of Chinese PV industry

Development status of Chinese PV industry. Chinese PV industry ushers in a historic turning point in 2013 with great support of a number of government policies. At present, China has become not only the world center of PV manufacturing, but the world's second largest PV market. As the data display in 2013, our polysilicon production is about 8 tons with year-on-year growth of 12.7%, and ranks first in the world for three consecutive years. Chinese PV modules production is approximately 26GW with year-on-year growth of 13% and ranks first in the world for seven consecutive years. The global PV added installed capacity is 36GW, while new installed capacity in China reaches 10GW with year-on-year growth of 122 percent ranking first in the world. According to the "Twelve-Five Planning", China's PV power generation capacity is aimed to reach 50GW by 2020. Chinese PV power-generating capacity is expected to add more than 14 GW in 2014, while distributed ones are added to 8GW accounting for about 60%. This series of data indicates that our PV industry has made great achievements, full of great prospects and potential.

However, in the case of Chinese PV industry ushering in a second take-off, some long-term restricting factors, such as the prominent contradiction of overcapacity; excessive dependence on international markets; the high cost of power generation; financing difficulties, etc., have not been properly addressed. It is urgently needed the multi-cooperation of the state, enterprises and other parties to work out these problems together.

Financing situations of Chinese PV industry. As the PV industry is capital-intensive, the process from polysilicon purification in industrial chain upstream to the construction of PV power generation system downstream requires a lot of capital investment. "Several Opinions of the State Council on Promoting the Healthy Development of Photovoltaic Industry", which mitigates PV subsidy and grid-connected and other problems, is promulgated in 2013 and highlights the financing difficulties shown below.

Large capital requirement and funding gap. Currently, under the impetus of various favorable policies, Chinese PV industry enters a second phase of rapid development, with substantial capital investment in need. According to the National Energy Board, domestic PV installed capacity is expected to add 14GW in 2014. While 10 billion Yuan is required for building a 100MW PV power plant in current cost level, there is 140 billion Yuan needed for 14GW. What is more, the "Solar industry 12th Five-Year plan" refers to that Chinese PV power generation capacity should reach 50GW by 2020. Faced with such a huge demand for funds in future, the PV industry is badly in need of finding a way to conquer the financing obstacle.

Limited financing channels and high dependence on subsidies. Due to the joint effect of various reasons, the current financing channel of PV market is very simple, which is mainly dependent on policy-type bank loans and government subsidies. There is statistics showing that Chinese PV enterprises in the start-up stage and growth stage rely on bank loans to obtain funds to a large extent, which accounts for about 80% of the total funds. In such a case, either the bank loan being not in the place or shift of national industrial policy can exacerbate the financing plight. It is necessary to pay more attention to explore innovative financing channels.

Unreasonable financing structure. The proportion of indirect financing is too large, while that of direct financing is too small, which may be partly blamed on the lack of enthusiasm for exploring innovative financing mechanisms under government subsidies. Moreover, multi-level capital market structure is still under construction; the relevant laws and regulations and institutional framework are deficient, making it tough for PV companies to use modern financial products to meet the fund requirement.

High financing costs. Chinese PV industry is currently in a transitional phase, with affects of production overcapacity and "double reverse". However, there are indeed certain limitations on loan size and loan conditions for PV business in most banks, except those favorable policies. Thus, a lower interest rate credit is unable to get for PV enterprises; collateral, guarantees, entrusted loans and other ways are used to obtain funds, lifting financing costs much higher.

Analysis on financing predicament of Chinese PV industry

Internal factors.

Higher business risk. PV industry is a new energy industry faced with higher business risk. Because of the two-out pattern of Chinese PV industry and excessive dependence for PV products on international markets, operating uncertainty is increased, which, furthermore, makes investors reluctant to provide funds to the PV business.

Non-standard management system. Financial system and internal supervision systems are not perfect in PV enterprise. The managers are lack in risk awareness and make business management not standardized. Moreover, less corporate assets, weak ability to withstand external shocks and so on are all making it a higher rate of PV business failure. As a result, the banks, a major provider of funds, are unwilling to bear the high "market risk" and "credit risk", making it much more difficult for PV ventures to rely solely on bank loan financing.

High technical costs. PV industry is high-tech with high degree of specialization. It requires certain knowledge about technical expertise for investment and financing analysis, which restricts investors to make rational investment decisions and adversely affects PV financing. Furthermore, PV companies have business information more non-transparent relative to other companies. For fear that core technology and trade secrets may be revealed. This information asymmetry results in higher investment risk and higher costs for investors.

External factors.

Domestic market is breaking the ice with international market downturn. Currently, European countries cut PV subsidies under economic downturn. The overall declines in market demand make Chinese PV companies that rely heavily on the European market have serious shock.

Besides, the EU and the U.S. have started anti-dumping, anti-subsidy investigations on the Chinese PV companies, which exacerbate the crisis of the entire PV industry. The ratio of liabilities to assets remains high, and financial risks are increasing. Although China is actively promoting the development of distributed PV industry, vigorously developing the domestic PV market, the effect is not yet apparent due to the short time.

Large gaps in PV subsidies and incomplete policies. Government subsidies are major funding source for Chinese PV business. The main subsidy is provided by the National Renewable Energy Development Fund, which has a funding gap of about 20 billion Yuan at presence, and will reach 80 billion in 2015, making it so difficult for the government subsidies to be in place. Moreover, the details of related policies need further improvement, and it is more important for regional departments to implement the requirements of policies well, to create a favorable environment for the development of PV industry.

Deficient financial system. From the perspective of the bank, the characteristics of high risk, large investment of PV industry contradict the principle of safety and profitability that commercial banks focus on, so the credit ceiling for PV business is very low. Meanwhile, policy-type bank loans have policy constraints, etc., making financing much more difficult, especially for small and medium private enterprises.

Tentative IPO makes those PV companies which have listed potential and want to be financed through the listing lose their opportunity. At the same time, financial service system for PV industry is not perfect, where limited financial support is mainly provided for large, state-owned enterprises, so that SMEs have no access to appropriate financial services. Moreover, asset securitization, debt financing and other innovative financial instruments are difficult to apply to PV business due to the underdeveloped capital markets in China.

Although venture capital (VC), with features of “high-risk, high-yield”, should have been an effective way to meet PV financing demand, due to its inadequate laws and incomplete withdrawal mechanism, venture capital investments in PV industry is rather limited.

Countermeasures and suggestions on solving financing dilemma

Improving self-financing ability of PV companies.

Improving enterprise managerial skill to ensure operating stability. Domestic PV industry is mainly dependent on the international market, so PV companies should pay close attention to international market dynamics, relevant policies; follow the rules of international trade and make timely response to market risks.

PV companies should improve internal management systems of their internal shareholder committee, board of directors, board of supervisors, etc.; establish effective power supervising mechanism, and form standardized modern enterprise management system. Meanwhile, perfecting internal control system and financial management and strengthening risk awareness of managers are also needed to be done right now.

Expanding financing channels. The market-led PV companies under government support should establish a diversified, multi-channel investment and financing mechanism; explore innovative financing methods; expand financing channels. Companies should actively use a variety of innovative financial products; learn from the experience of European countries; explore asset securitization, debt financing, lease financing and other business to increase the proportion of direct financing and improve financing structure.

Strengthening the construction of corporate credit. Good credit condition is the key for survival and development of modern enterprises. There exists that some PV companies have poor awareness of credit in China. Meanwhile, there are non-transparent operations, information asymmetry that adversely affect PV financing. Therefore, enterprises should strengthen their own credit construction; improve operational transparency; disclose management information and financial reports by qualified regularly, and consciously accept the supervision of investors, thereby

increasing investors' confidence for PV enterprise and obtaining financial support as much as possible.

Building sound financial service systems.

Strengthening financial support of bank credit. Bank credit is the most important source for PV companies funding. Currently, credit funds for PV business are mainly the policy-related bank loans from China Development Bank, while commercial banks invest a little in view of "credit risk", "market Risk" and other factors. Consequently, on the one hand, it is needed to increase bank credit funds to support PV enterprises; appropriately lower lending standards and to reduce the approval process. On the other hand, banks should give priority to support businesses with good operating conditions, huge potential and policy support. The post-lending management should also be done to timely prevent credit risks and guarantee credit safety.

Making full use of the capital market to raise funds. Making market-oriented operation based on modern financial instruments by the capital market is the fundamental way to solve the PV financing problem. China should timely restart IPO to make some PV companies with high-tech and broad market prospects have financing priority, to encourage PV enterprises to use the capital markets to raise funds.

China should accelerate the pace of financial reform and improve the market-oriented level of Chinese financial markets to provide support for innovative financial instruments and financial products. Furthermore, we are required to explore third-party financing platform, investment trusts equity financing, debt financing, crowd funds and many other modern financial products, following the tide of the Internet finance.

Improving VC mechanism. The characteristics of PV business meet the requirements of VC, so it is an effective way to bring VC into PV industry to solve the financial problems. China should improve the VC mechanism including exit mechanism as soon as possible; promulgate relevant laws to protect the interests of VC institutions and expand funding sources.

Promoting relevant policies to be nuanced and implemented.

Improving financial support system. Currently, financial support system of Chinese PV business has been basically formed, however, it needs to be further improved. Firstly, the funding gap should be resolved as soon as possible to make subsidies be in the place. At the same time, the government should reduce subsidies by more favorable guidance. Secondly, the PV industry is not only an emerging high-tech energy industry but environmental protection industry, so we can study on implementing preferential tax policy on it to gain certain tax breaks.

Improving relevant laws and regulations. It cannot be without the support of relevant national laws and regulations for PV companies to solve the financing problem, especially in the current situation of Chinese capital market imperfections. Based on the specific developing situation of PV industry, China should amend and promulgate timely relevant laws and regulations to provide protection for establishing a diversified, multi-channel PV financing system.

References

[1] Zhiping Zhang, Wei Yao; Financing innovation ability of PV industry under industry cluster context-- Guide to Business 2009(11)(In Chinese)

[2] Ge Yang; Discussion of PV companies on addressing the financial crisis-- Electric Power System Equipment 2009(1) (In Chinese)

[3] Xueqing Shao, Bingchuan Chen; Unconventional developing path of JiangXi Xinyu PV industry-- East China Science and Technology 2010(4) (In Chinese)

[4] Yuming Han; Thinking about financial support for the development of Qinghai solar energy industry. Qinghai Finance. 2010(01) (In Chinese)

Advanced Materials Research Vols. 960-961 (2014) pp 1546-1549

doi:10.4028/www.scientific.net/AMR.960-961.1546

Exergy Analysis and Improvement of the Thermal System of Power Plant

Bao Zhao[1, a], Li Yang[2,b] and Jiali Wang[3,c]

[1]Hebei university of Technology Beichen District Tianjin City China

[2]Hebei university of Technology Beichen District Tianjin City China

[3]Hebei university of Technology Beichen District Tianjin City China

[A]610699932@qq.com, [b]dyli1018@163.com, [c]458180320@qq.com

Keywords: hazy, exergy efficiency, steam cooler, temperature difference, optimalize.

Abstract. We took 600 MW sub critical unit of Taishan power plant as the research object and modeled. Analyzed the thermodynamic system by exergy method. Got the amount of exergy loss, the exergy efficiency of regenerative heater and so on. Found out the distribution of different kinds of exergy loss in the power plant with giving out the scientific and reasonable explanation and the weak point. Then increased the efficiency of thermal system by adding external steam coolers for high pressure heaters.

Introduction

Since 2013,The widespread haze occurred frequently in China[1-2].If we want to government atmospheric haze successfully, It can't do without the analysis and improvement of thermodynamic system in thermal power plant.Usually there are two kinds of method to analysis thermodynamic system, which are heat method and exergy method. The first method is based on the first law of thermodynamics which has been used a long time;The second method also consider the second law of thermodynamics.It main focus on how much energy can be used in a certain environmental condition.People have to pay more attention on developing and utilizing energy reasonably because of the energy tension.So the exergy method is increasingly seen as important in recent years. Today has been a consensus that must use the exergy method if people want to tap existing potential of energy saving deeply[3-4].Now most of the structures of the 600 MW steam turbine unit system are the same,This article selected the typical 600 MW subcritical unit of Taishan as the research object and modeling, and its principle thermal system structure is shown in Figure 1.

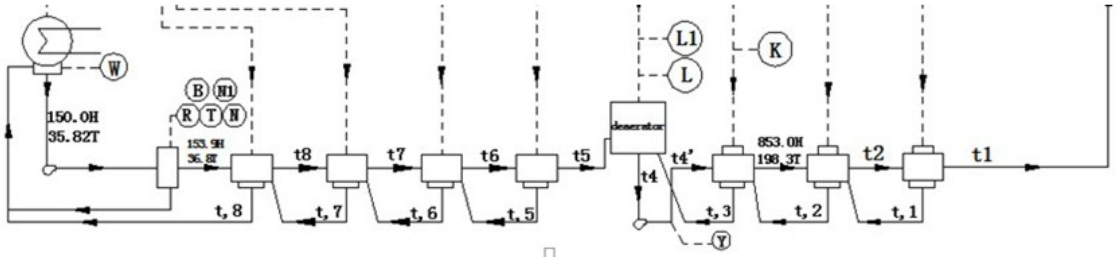

Fig. 1 The structure diagram of 600MW steam turbine of Taishan

The exergy analysis of the thermal system.

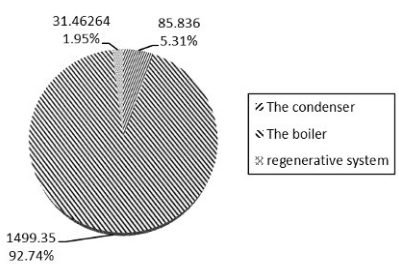

Fig. 2 The exergy loss distribution of boiler, condenser, regenerative heater of power plant

Exergy loss distribution of the thermal system. First collected raw data and calculated.Then drew the pie chart in order to show the loss distribution better.The Figure 2 shows that most of the exergy loss of power plant is in the boiler, the second is in the condenser. The conclusion of the traditional calculation method points out the efficiency of boiler of Taishan power plant is 93.75%, and most of the heat losses occurs in the condenser. It can completes and supplements the conclusion based on the first law of thermodynamics. Although the results of method of heat point out that the heat energy loss is small in the boiler, but it is overheating steam in the boiler, there is a big temperature difference of heat transfer,which causes a lot of energy loss. It is mainly exhaust gas which has been used in the condenser. Although the quantity is big, but quality is low.

Analysis of exergy loss of regenerative system. Firstly, Collected raw data, inquired the entropy of working fluids under different status. Secondly, Got the amount of the exergy loss, the exergy efficiency of regenerative heater and so on according to the formulas of exergy. The benchmark is 298.15K and 0.1Mpa in the process of calculation, which specified in the national standard guidelines for the analysis with exergy method(GB/T1490994). The results are shown in table 1.

Table 1. The exergy situation of each regenerative heater

	extraction factor	exergy drop of steam extraction	exergy rise of feedwater	exergy drop of drain	the amount of exergy loss	the amount of exergy enter	exergy efficiency	the rate of exergy loss
1	0.0722	964.8470	66.481	0	3.18095	69.66195	0.95434	0.00197
2	0.0829	929.8953	77.865	84.958	5.35729	83.22229	0.93563	0.00331
3	0.0385	1047.3910	47.565	51.958	6.12731	53.69230	0.88588	0.00379
4	0.0423	843.7798	39.695	18.876	8.70100	130.27800	0.93321	0.00538
5	0.0354	693.0598	27.602	63.456	3.17037	24.53432	0.87078	0.00196
6	0.0223	539.0534	14.165	15.044	1.58974	12.55345	0.87336	0.00098
7	0.0315	451.8340	17.152	18.531	2.04489	15.32054	0.86653	0.00127
8	0.0265	287.8353	9.304	9.369	1.29110	8.49239	0.84797	0.00080

Draw the line chart of each regenerative heater in order to be more intuitive to analyze, according to the data of table 1. The line charts are shown in Figure 3, 4, 5, and 6.

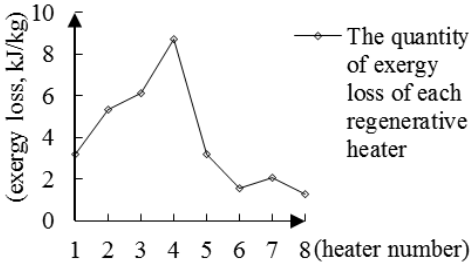

Figure 3. The quantity of exergy loss of each regenerative heater

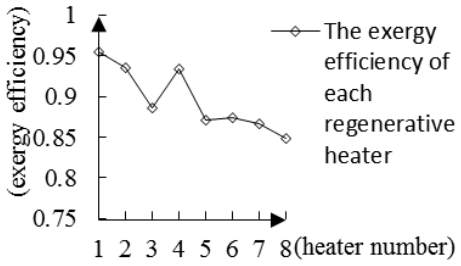

Figure 4. The exergy efficiency of each regenerative heater

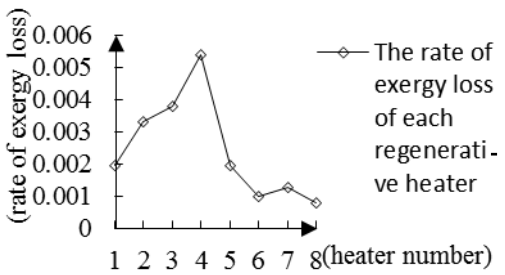

Figure 5. The rate of exergy loss of each regenerative heater

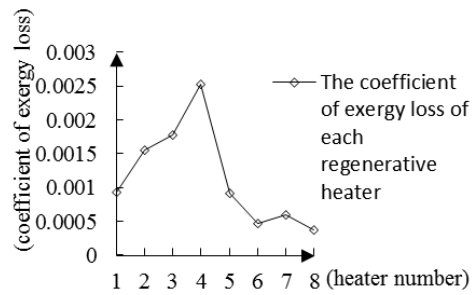

Figure 6. The coefficient of exergy loss of each regenerative heater

The Figure 3 shows that the exergy loss of high-pressure heater general higher than that of low-pressure heater in the regenerative system. The largest amount of exergy loss occur in the deaerator. Just consider the amount of exergy loss can't get the perfect degree of the device, also need to analyze its exergy efficiency. The Figure 4,5,6 show that though the exergy loss of deaerator 4 is the largest, but its exergy efficiency is higher than other heaters, which conform to the actual situation. The steam mixes with feedwater directly in the deaerator because of the deaerator is mixing heat exchanger. So the latent heat of vaporization of steam moves to feedwater entirely[5].

$$\triangle t=t,i-ti=0. \quad (1)$$

As shown in Eq.1. So compared with the surface heater, The exergy efficiency of mixing heater must be higher.

We can realize that the exergy loss of working fluids not only related to their own state, but also related to the state of environment by the calculation formula of exergy. The environmental status wich specified in the national standard is used to be a benchmark status usually.However, the actual environment status changes with the time and area. We inquired the relevant parameters under different temperature respectively for no.1, no. 2 high pressure heater and no.5, no. 6 low pressure heater. The results are shown in Figure 7.The Figure 7 shows that more loss with higher temperature. The influence of temperature change on the high-pressure heater is bigger than the low-pressure heater, which is consistent with the results in the literature8[6].

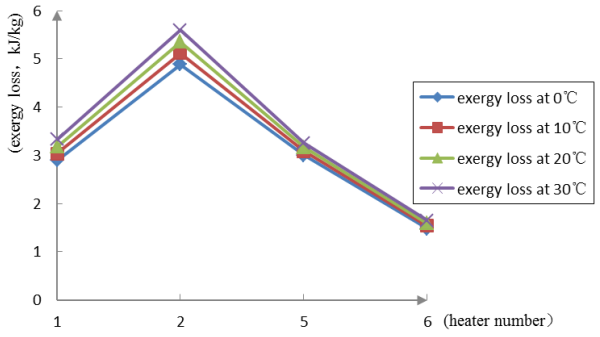

Fig. 7 The influence of temperature

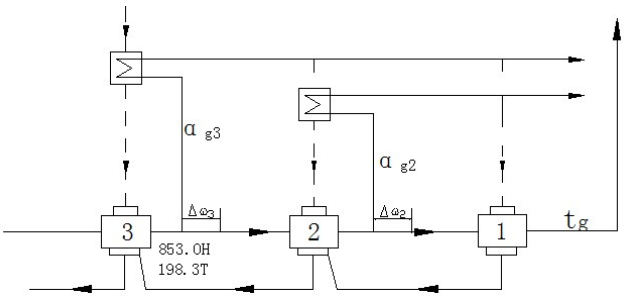

Fig. 8 The schematic of improvement

The improvement of the thermal system

From the analysis of previous section, we know that the most of exergy loss caused by heat transfer temperature difference.The figure 1 shows that all of bleeder heaters equipped with drain cooler in addition to the deaerator.These measures reduce heat transfer temperature difference effectively. But the extractive steam’s temperature is very high because it is high pressure steam.So we can further consider adding an outer steam cooler for no.2 and no.3 bleeder heater respectively.It is shown in Figure 8[7]. By passing a part of the feed water to steam cooling, it both reduces the temperature difference and can distributes to the appropriate level according to the quality of energy.

The effect of improvement mainly has four aspects. Taking no.3 heater as an example to analyze the effect. The first is because part of the feed water flow out, it make the quantity of extraction steam needed for the no. 1 and no. 2 heater is reduced, which can save energy of Eq. 2. Second, The additional equipment will increase the pressure loss of extraction steam inevitably. It make heating for feedwater is insufficient and loss energy of Eq. 3. Third,The feedwater takes away part of heat by steam cooler,which make the quality of the steam to reduce.So the quantity of extraction increase, it causes a energy loss of Eq. 4.The last affect is circulation heat changes, As shown in Eq. 5.

$$\alpha_{g3}(\tau_2\eta_2+\tau_1\eta_1). \quad (2)$$

$$\triangle\omega_3(\eta_2-\eta_1)(1-\alpha_{g3}). \quad (3)$$

$$\alpha_{g3}\eta_3(\tau_2+\tau_1+\theta_3). \quad (4)$$

$$\triangle Q = \alpha_{g3}\theta_3(\eta_i - \eta_3). \quad (5)$$

The sum of these four aspects is the variation of equivalent heat drop of new steam due to the improvement. The calculation results as shown in table 2.

Table 2. The analysis results of improvement program

heater number	fractional flow α_{gi}	the increment of equivalent enthalpy reduction△H[kJ/kg]	efficiency improvement△ η [%]	coal consumption rate savings△ b[g/kW • h]
2	0.042	0.248	0.173	0.213
3	0.042	0.541	0.198	0.244

The table2 shows, through using the outer steam cooler, We can use the energy gradient, reduces the irreversible loss in the process of heat transfer, achieve the effect of reducing coal consumption.

Conclusions

Study results are as follows:

1. Most of the exergy loss of power plant is in the boiler, the second is in the condenser, the last part is in the regenerative heaters. It is different from the traditional view and can completes the conclusion based on the first law of thermodynamics.

2. The exergy loss mainly occur in the heat exchange process, and it mainly caused by temperature difference.

3. More loss with higher temperature, So the energy loss under summer conditions is more than other seasons.The influence of temperature change on the high-pressure heater is bigger than the low-pressure heater.

4. We improve the efficiency of thermal system by adding an outer steam cooler for no.2 and no.3 bleeder heater respectively.

We have a new understanding about the energy loss, energy saving and system improvement by using the exergy method. It has very important practical significance, provides reference for energy conservation and emission reduction of power plant.

References

[1] Chengzhang Zhu. Countermeasures and Suggestions of preventing haze pollution in our country[J]. Sino-Global Energy,2013,18(6):1-4.

[2]Xiaozhuai Zhang, Junying Sun and Yaqiang Wang, et al.Thinking in haze formation and its governance[J]. Chinese Science Bulletin,2013,58(13):1178-1187.

[3]Danxing Zheng and Xianghong Wu. Research and revision of national standard of technical guidance of the exergy analysis[J]. Journal of North China Electric Power University,2005,32(2):103-107.

[4] Regulagadda P., Dincer I. and Natterer G.F. Exergy analysis of a thermal power plant with measured boiler and turbine losses[J]. Applied Thermal Engineering, 2010, 30: 970-976.

[5] Zhang Chao, Wang Yan and Chuguang Zheng,et al. Exergy cost analysis of a coal fired power plant based on structural theory of thermoeconomics[J]. Energy Conversion and Managem-ent, 2006,47:817-843.

[6]Li Yonghua and Liu Weiting. Influence of variety of different environmental reference temperature on exergy loss[J]. Turbine Technology,2011,53(4):257-263.

[7]Na An and Lanxin Zhou. The thermal system structure optimization research of coal-fired power plant[D]. depositary authority：North China Electric Power University, 2009.

Advanced Materials Research Vols. 960-961 (2014) pp 1550-1553

doi:10.4028/www.scientific.net/AMR.960-961.1550

Economic Analysis of a 660MW Supercritical Turbine for Steam Initial Parameters

Yu-Lin TANG[a], Shan TU[b *], Yang DU[c], Chao WANG[d], Hong-Juan WANG[e]

School of Energy and Power Engineering, Xi'an Jiaotong University, Shaanxi, China

[a]tangyulin@stu.xjtu.edu.cn, [b]tushan@mail.xjtu.edu.cn, [c]duyang@stu.xjtu.edu.cn

*Corresponding author: Shan TU

Keywords: Equivalent Enthalpy Drop; Variable Conditions; Economic Diagnosis; Steam Initial Parameters

Abstract. Economic diagnosis of thermal power units is to determine the economy of its operating parameters and operating modes by quantitative and qualitative analysis, which is significant to economic operation and energy saving of power plant. On the basis of equivalent enthalpy drop method and the theory of variable conditions, the economic diagnosis model of operating parameters was established. As main steam temperature and main steam pressure for example, economic diagnosis of a 660MW supercritical steam turbine unit was performed. The result demonstrates that improving the main steam temperature or main steam pressure can reduce heat consumption of the unit. The essence of improving the initial steam parameters is to improve the average temperature of the steam cycle endothermic process, thus improving the circulation efficiency and reducing heat consumption. The economic impact of main steam temperature is up to $0.61\ \mathrm{g\cdot(kW\cdot h)^{-1}}$, while which of main steam pressure is little. Therefore, by increasing the initial steam parameters, especially the main steam temperature, to improve the economy of the entire power plant is the main way to enhance the efficiency of power plant in the current.

Economic Diagnosis Model of Operating Parameters

Economic diagnosis of thermal power units is of great significance to economic operation and energy saving of power plant. As a way to determine the economy of operating parameters and operating modes, economic diagnosis can qualitatively analyze the rationality of operation modes and operation parameters, and quantitatively analyze the standard value of operating parameters and the economic influence of the deviation from standard value. On the basis of equivalent enthalpy drop method and the theory of variable conditions and considering the difference between the economic impact of the standard values and deviations of operating parameters, the economic impact of parameter deviations will be quantitatively calculated.

In this paper, a 660MW supercritical unit is the research object, and the economic diagnosis model of the operating parameters of the unit was established. In the case of main steam temperature and main steam pressure, the deviations were calculated between operation value and standard value of the main operation parameters and the size of economic impact of these deviations.

Equivalent enthalpy drop method is a new thermodynamic theory. The use of the theory for economic diagnosis of thermal system of power plants is simple, accurate and convenient. Equivalent enthalpy drop refers the real capacity for work of 1kg new steam of regenerative extraction turbine. Extraction equivalent enthalpy drop refers the real capacity for work after excluding 1kg heater extraction back to turbine [1].

The operating parameters of the turbine include main steam temperature, main steam pressure, reheat steam temperature, reheat steam pressure loss, etc. On the basis of equivalent enthalpy drop method and considering the difference between the economic effect of the standard value and the diviations of the operating parameters under different conditions and systems and interactions between multiple deviation factors, a quantitative method of calculating the economic impact of the deviations of operating parameters was proposed.

By using the theory of variable conditions, the mathematical model of economic dianosis of main steam temperature and main steam pressure are given as below [2].

$$\Delta b = f(\Delta x, N_d, t_{ob}, N) = b(x, N_d, t_{0b}, N) - b(x_b, N_d, t_{0b}, N) \quad (1)$$

On the type, Δb is standard coal consumption variation, x_b represents the standard value of operating parameters (calculated in accordance with variable conditions or check correction curve). x is the operating value (calculated in accordance with variable conditions or check correction curve).

Economic Diagnosis of Main Steam Temperature

In this paper, a 660MW supercritical unit is the research object. The unit is supercritical, once reheat, single shaft, 3-casing 4-exhaust, and direct air-cooled. Rated power: 643MW. Maximum power: 713MW. Rated main steam amount: 1874.1t / h. Maximum principal amount of steam: 2120t/h. Rated steam parameters: 24.2MPa/566 ˚C. Reheat steam parameters: 3.975MPa/566 ˚C. Rated back pressure: 15kPa. Ensure heat consumption: 7758 $kJ\cdot(kW\cdot h)^{-1}$. Rated speed: 3000r/min. The principled thermal system diagram in THA conditions is shown in Figure 1.

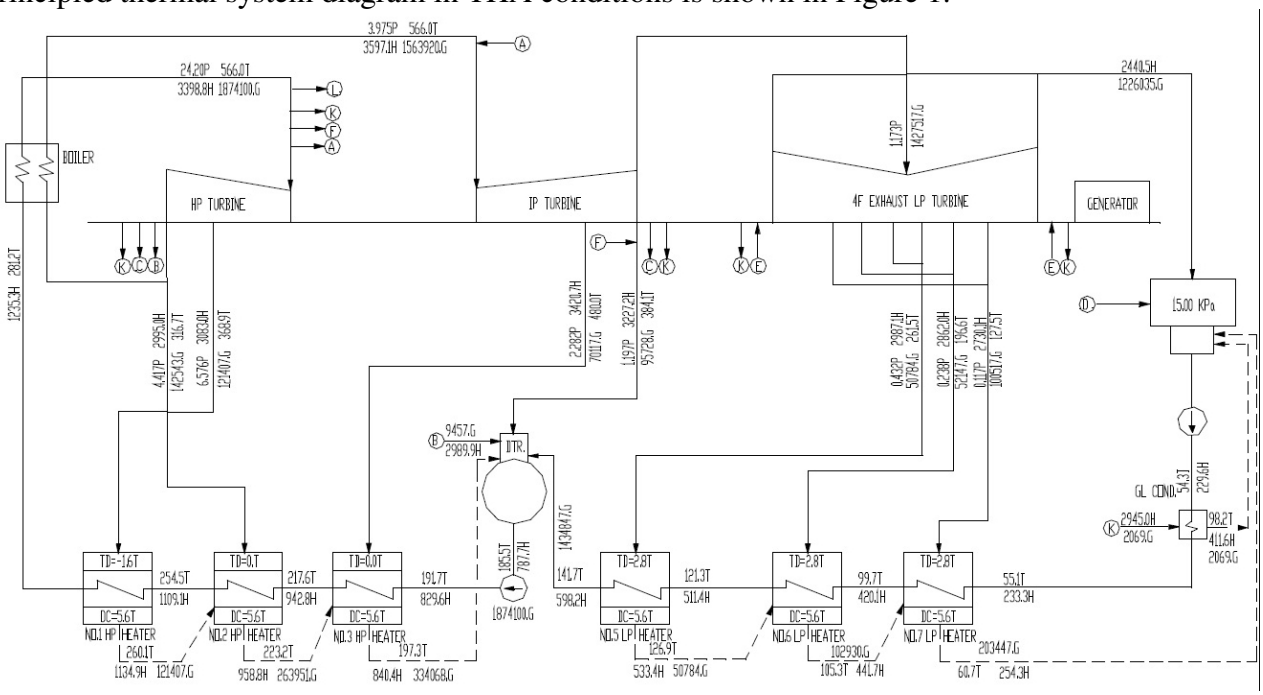

Figure1 Principled thermal system diagram in THA conditions

As initial steam parameters for example, economic diagnosis of the unit is performed. Initial steam parameters include main steam temperature and main steam pressure. According to the principle of the thermal system of power plant, the change of initial steam parameters will have a great impact to the efficiency of power plant. The essence of improving the initial steam parameters is to improve the average temperature of the steam cycle endothermic process, thus improving the circulation efficiency and reducing heat consumption.

The correcting curves of the changes of main steam temperature to the power and heat consumption of the unit are shown in Figure 2 and Figure 3. According to the correction curve and using the above calculation model, the results of economic influence of main steam temperature is shown in Table 1. Among them, heat consumption difference and coal consumption difference are respectively the difference of heat consumption and coal consumption between runtime value and standard value, in units of $kJ\cdot(kW\cdot h)^{-1}$ and $g\cdot(kW\cdot h)^{-1}$. When heat consumption difference or coal consumption difference is negative, the economy of operation parameters is ideal [3,4].

From the calculation results, heat consumption deduces as the main steam temperature rises. By increasing the initial steam parameters to improve the economy of the entire power plant is the main way to improve the efficiency of power plant in the current and future for a long period of time around the world. In the production stage, the combustion should be adjusted to rated new steam parameters. The impact on the economy of main steam temperature is up to $0.61\,g\cdot(kW\cdot h)^{-1}$.

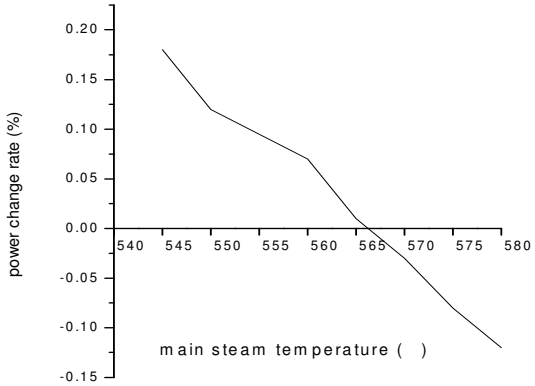

Figure2 Correcting curve of the changes of main steam temperature to power

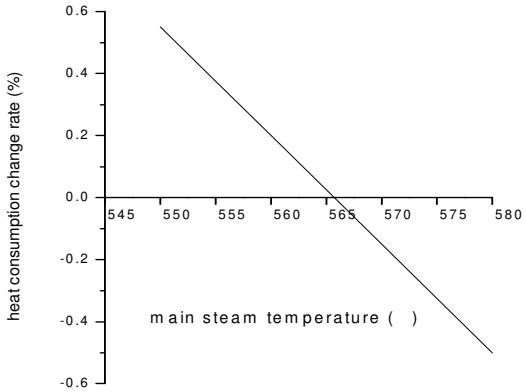

Figure3 Correcting curve of the changes of main steam temperature to heat consumption

Table 1 Economic influence of main steam temperature

Conditions	THA	VWO	TRL	TMCR	500MW	643MW
Runtime value of main steam temperature[°C]	562.8	560.4	561.1	562.5	561.39	564.25
Standard value of main steam temperature[°C]	566	566	566	566	566	566
Heat consumption difference[$_{kJ\cdot(kW\cdot h)^{-1}}$]/	5.82	14.92	13.67	9.26	10.90	6.95
Coal consumption difference[$_{g\cdot(kW\cdot h)^{-1}}$]	0.24	0.61	0.56	0.38	0.03	0.28

Increasing main steam temperature will increases exhaust steam dryness and reduces steam moisture loss of low-pressure cylinder. Meanwhile, increasing main steam temperature also increases the main steam specific volume, other things equal, the turbine blade height on high pressure side will increase, which will correspondingly reduce the steam leakage loss on high pressure side, thus improving the relative efficiency of the turbine.

Economic Diagnosis of Main Steam Pressure

The correcting curves of the changes of main steam pressure to the power and heat consumption of the unit is shown in Figure 4 and Figure 5, and the economic diagnosis of main steam pressure is shown in Table 2.

Within the range of engineering applications, for a sufficiently large steam volume flow, the increase of main steam pressure can improve the cycle efficiency. As shown in Figure 4, under the same conditions, the increase of main steam pressure makes larger unit power. Especially for heat supply units, as a result of the presence of heating steam flow, the volume flow of steam entering the turbine greatly increased, so the main steam pressure of heat supply units is higher than which of condensing unit under the same power. Improving the main steam pressure can significantly reduce heat consumption, as shown in Figure 5, main steam pressure increases 0.2MPa, heat consumption decreases by 0.1%.

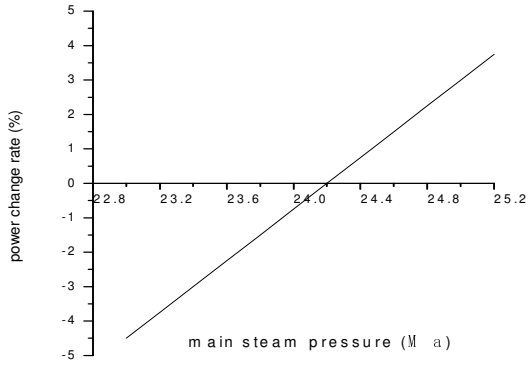

Figure4 Correcting curve of the changes of main steam pressure to power

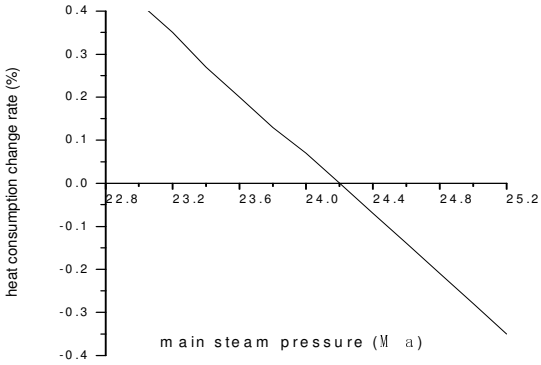

Figure5 Correcting curve of the changes of main steam pressure to heat consumption

Table 2 Economic influence of main steam pressure

Conditions	THA	VWO	TRL	TMCR	500MW	643MW
Runtime value of main steam temperature[°C]	23.94	23.9	24.29	23.96	21.22	24.28
Standard value of main steam temperature[°C]	24.2	24.2	24.2	24.2	21.15	24.2
Heat consumption difference[$_{kJ\cdot(kW\cdot h)^{-1}}$]/	6.58	7.51	-2.28	6.02	-1.73	-1.93
Coal consumption difference[$_{g\cdot(kW\cdot h)^{-1}}$]	0.27	0.31	-0.09	0.24	-0.09	-0.08

Conclusion

Improving the main steam temperature or pressure can both reduce heat consumption of the unit. The substance of improving the initial steam parameters is to improve the average temperature of the steam cycle endothermic process, thus improving the circulation efficiency and reducing heat consumption. Increasing main steam temperature will reduces steam moisture loss of low-pressure cylinder and improves the relative efficiency of the turbine. Improving the main steam pressure can significantly reduce heat consumption. When main steam pressure increases 0.2MPa, heat consumption decreases by 0.1%. For a sufficiently large steam volume flow, the increase of main steam pressure can improve the cycle efficiency. The main steam pressure of heat supply units is higher than which of condensing unit under the same power. The economic impact of main steam temperature is up to $0.61\ g\cdot(kW\cdot h)^{-1}$, while which of main steam pressure is little. By increasing the initial steam parameters, especially the main steam temperature, to improve the economy of the entire power plant is the main way to improve the efficiency of power plant in the current and future for a long period of time around the world.

References

[1] Junjie Yan, Qin'an Xing and Wanchao Lin, Theory and Application of Economic Diagnosis of Thermodynamic System in Power Plant, Xi'an Jiaotong University Press, Xi'an, 2000.

[2] Junjie Yan, Chunyu Zhang, Research on Thermo-economics Diagnostic Theory of Direct Air-cooled Devices, Journal of Test and Measurement Technology of NC IT. 14 (2000) 3-4.

[3] Chao Zhang, Sheng Chen, Chuguang Zheng, Thermo-economic Analysis of a Power/water Cogeneration Plant, Energy Conversion and Management. 48 (2007) 405-419.

[4] D.J. Smith, Market Competitiveness Requires Constant Control of Plant Operations and Maintenance Cost, Power Engineering. 7 (2003) 164.

Advanced Materials Research Vols. 960-961 (2014) pp 1554-1561

doi:10.4028/www.scientific.net/AMR.960-961.1554

Practical Analysis of State Estimation Based on Dispatching Simulation Platform

Ying Zhang[1, a], Shuhai Feng[2, b] and Jun Liu[2, c]

[1]8 Focheng west road, Nanjing, Jiangsu, China 211106

[2]8 Nari Road, Nanjing, Jiangsu, China 210003

[a]kixzay@126.com, [b]fengshuhai@epri.sgcc.com.cn, [c]liu-jun2@epri.sgcc.com.cn

Keywords: State estimation; Practical analysis; Simulation platform

Abstract: In the process of practical application of state estimation in the actual dispatching system, there are many factors that affect the accuracy of state estimation results. This paper based on the simulation platform of the dispatching system and used the operation data of the actual power grid to simulate the operation of power grid, then analyzed the various factors that have influence on the results of state estimation, which provided effective technical support for practical application of state estimation.

Introductions

State estimation is one of the key software of automatic dispatching system. From the application point of view, the basic goal of state estimation is to provide quasi real-time data, which is more accurate, complete and reasonable quasi than telemetry data, for online analysis.

The online application of domestic state estimation in Supervisory Control and Data Acquisition (SCADA) has gone through from the bad data check to the real-time cross-section data services. In recent years, automatic dispatching system is more goal-oriented at real-time cross-section services. However, there are many limitative factors in the process of practical application of state estimation in the actual dispatching system. In this paper, we used dispatching simulation platform to conduct a simulation experiment and analyzed the influence of the main factors that affect practical state estimation, it provided effective technology support for practical state estimation.

The main factors influencing the practical state estimation

State estimation of power system rely on the telemetry and remote signaling data communication information in SCADA, the network topology analysis and identification of remote communication to get connection model of the current power grid; exclude minority occasional bad data of the measured data through detection and identification of suspicious data; correct the parameters does not match the actual device through parameter identification; finally, conduct state estimation calculation to get more accurate data than the telemetry data. In state estimation calculation, the model and the telemetry data have greater impact on the results of state estimation.

1.1Model problems

The calculation model in state estimation is updated according to the real-time remote letter values in SCADA and parameter values of the network equipment in database. Model errors mainly in: (1) Remote letter error in SCADA. Although the state estimation have bad data detection and identification function, but there are “leakage identification” and “mistaken identification” phenomenon, which will lead to topological errors; (2) Parameter changes after the equipment is bound to run certain number of years, but the parameter values stored within the system are not updated in real-time, this result in equipment parameter error; (3) Wind, snow, lightning and other climate change makes equipment and circuit parameter changes will result in equipment outage, make

the connection of equipments is not timely update in the model base of dispatching system and lead directly to the grid model is not allowed.

1.2Telemetry problem

Telemetry data from the device to the dispatching system generally experienced data acquisition, data transmission and data processing. The telemetry problem reflected in the dispatching system can be attributed to data incorrect and inconsistent latency.

(1)Telemetry value incorrect

There are three main causes that lead to telemetry incorrect data of dispatching system, data acquisition error and error, data conversion and transmission error and data processing.

(2)Measurement of time-delay inconsistency

① Data delay

Measurement data from acquisition to the automatic dispatching system of the whole process needs to experience the prose of the substation sampling, substation data upload, master station receives data, master station processing the data and master station application and storage, etc. As shown in Fig.1, the time of the sampling data uploaded from the device to the sub-station is Δt_1 , which is less than two seconds, and from the sub-station to direct mining system master data is Δt_2 , which is less than three seconds, if the system is in better conditions, it will be less than one second, and the time from master-station receiving to the real-time database updates is $\Delta t_3 + \Delta t_4$ seconds. Under the current level of technology, in the case of uploading the data from the subordinate station to the superior master station, every transponder will increase about 5 seconds of delay.

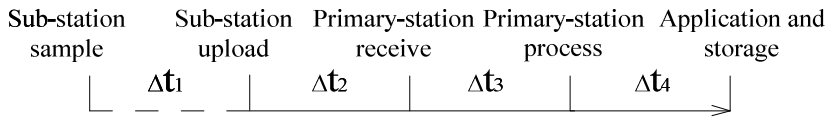

Fig.1 Key nodes of data transmission and processing

② Measurement inconsistency caused by the fluctuation of overall load

Due to the composition and characteristics of the various regions are identical, the load fluctuations of each region is also different. With the substantial increase of air conditioner, electric vehicles and other civilian load, a large number of institutions and schools and even some factory work concentrated in certain time periods, which lead to the overall load in many areas showing high volatility of periods, some areas in 10 to 30 minutes, its load fluctuations may reach 20 to 30% of its maximum daily load. Objectively, such a wide range of load fluctuations will be reflected in the power flow of volatility characteristics of the equipment, and different communication delay will also result in poor consistency of data used in state estimation.

③ Measurement inconsistency caused by the impact load and intermittent energy

Impact load (such as electric furnace steelmaking, heavy machinery, electric train, etc.) have a relatively clear variation characteristics, and its range can reach tens of mw, the change process can be completed in a few seconds, this leads to the section measuring data used in state estimation exist a few megabytes or even tens of megabytes of data inconsistency. And the intermittent and volatility the output of intermittent energy is very large. The fluctuations of the centralized access point power injection of impact load and intermittent power will cause a big change of the measured data of related equipment, and measurement time delay inconsistent will have great influence on the calculation results of state estimation.

④ Measurement inconsistency caused by equipment failures and improper operation

When equipment is in maintenance and failure, a large number of equipment in the power grid will outage or be put into operation. Lines, transformers, generators and other equipment breaking and put into operation, the change of parameter of the Direct Current(DC) system or the DC system lockout and the actions of automatic device etc., will make power flow redistribution in a short time (within one second) then cause large changes in the power flow. The change of power grid operation will

result in the data of rapid mutation and even the whole network data, and data transmission delay will lead to poor consistency of data used in state estimation. The accuracy of the results will also receive great influence.

Mathematical simulation of power grid operation

In good running condition of the power system should not contain system error, under normal circumstances, a measured value from remote sensing devices and power grid parameter values can be described by true value plus a random error:

$$V = V_t + V_{er} \tag{1}$$

Where V is the simulated values, V_t is the true value, V_{er} is a random error. The probability distribution law of random error is:

(1) The probability of different sizes error to occur is various, and the small error probability is larger than the big error probability, but maximal error probability is very small.

(2) The probability of positive and negative error is same, so its distribution curve is symmetric to zero.

The nature is well represented by a normal distribution and its value is subjected to:

$$V_{er} \sim \sigma \bullet N(0,1) \tag{2}$$

In the formula, σ is the standard deviation of random errors, $N(0,1)$ is standard normal distribution function with mean 0 and variance 1.

Normal random error simulation is divided into two steps:

Step 1) Produce uniformly distributed random numbers with mean 0 and variance 1 in interval $(-1,1)$.

If the probability density function of continuous random variable is:

$$p(x) = \begin{cases} \dfrac{1}{b \times a} & x \in (a,b) \\ 0 & x \notin (a,b) \end{cases} \tag{3}$$

And x is the uniformly distributed random variable in interval (a,b), its sampling value is subject to uniformly distributed random variable, the generating process is as follows:

First, put the initial x_0 into the equation $x_{n+1} = 5x_n$ to generate uniformly distributed random number ξ in the interval $(0,1)$, then, according to the equation $x = a + \xi(b-a)$ generate uniformly distributed random numbers in the interval (a,b).

Step 2) According to the central limit theorem, use the sum of uniformly distributed random numbers to form a normal distributed random noise.

The practical analysis of state estimation

Using disturbance simulation module in data simulation layer of experimental verification platform to simulated disturbance scenarios and achieving grid disturbance by means of software.

Take the various factors that affect the telemetry passing rate of state estimation, such as: measurement error of simulated power system, parameter fluctuations of transmission line device and measurement of time delay, and its probability distribution features into consideration. Under the condition of different disturbance, telemetry qualified rate and the objective function of state estimation is different .Then, analyze the tendency of the indicators of state estimation.

3.1 The introduction of the simulation platform of dispatching system

Build a complete experiment simulation system by using PSS/E software as a computational engine. Experimental verification platform use the realistic simulation data to drive dispatching system and organically integrated with dispatching system. Then, study the change of statistical indicators of

dispatching system state estimation after setting different disturbance cases. Experimental verification platform consist of simulation layer, data layer, and EMS analog emulation layer, whose architecture diagram is shown in Fig.2.

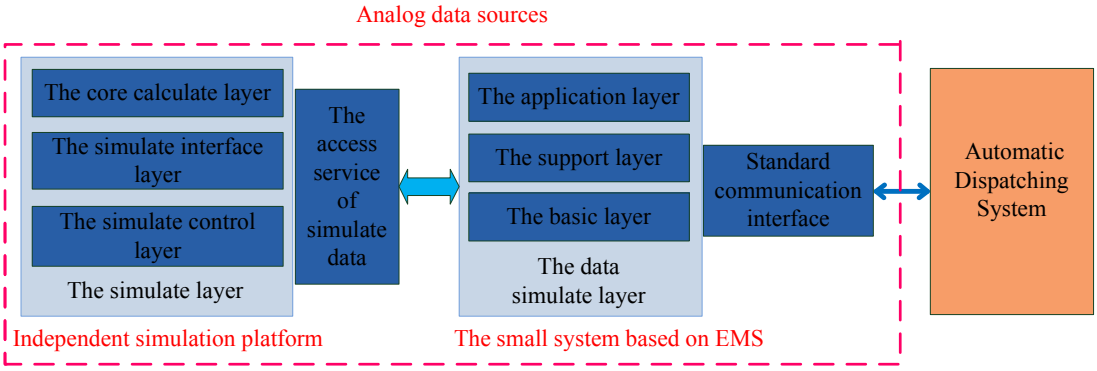

Fig.2 Architecture diagram of experimental verification platform

3.2 The implementation flow

The Automatic Dispatching system experiment platform use analog data to drive the data acquisition, data collection and other various application of the master system to realize the realistic simulation grid operation. Set various disturbances in actual simulation power grid and study the change of index in the master system state estimation.

The main steps are as follows:

Step 1) Simulation computer simulate the daily operation data of power grid;

Step 2) Data emulation layer to get the whole network operational data, simulate disturbance scenario and form various types of disturbance data;

Step 3) Send disturbance data, which is formed in data simulation layer, to the testing platform and the SCADA application;

Step 4) State estimation calculated according to the real-time data in SCADA. Compare and analyze the results of state estimations that based on power flow and many disturbance factors.

The example analysis of disturbance simulation

To verify the influence that the amount of random measurement error, parameters fluctuations of power transmission lines and measurement delay have on state estimation, this paper choose a regional dispatching support system of a smart grid to conduct the experimental verification. In the experiments, the number of the nodes calculated is 1079, the number of branches is 1949 and the number of stations is 530.

4.1 The measured perturbation data based on the normal distribution

The analog measurement value is described by the power flow calculation value and random error. According to the type of measurement and the data acquisition and accuracy requirements of substation, the specific method of calculating the values of active and reactive power and voltage of measured points. The method is shown in formula (4):

$$\begin{aligned} Value\ of\ measured\ point = Value\ of\ measured\ point + \frac{1}{3}k \quad Value\ of\ measured\ point \times a_m \\ + Full\ scale\ value\ of\ measured\ point \times b_m \end{aligned} \tag{4}$$

Where a_m is the error coefficient of measurement, b_m is the error coefficient of converter and transformer and k is a normal distributed random noise with mean 0 and variance 1. In this experiment, the histogram and fitting curve of the normal distributed random noise is shown in Fig.3, the mean is 0.0046, variance is 1.0168 and normal random points is 10373.

(1)When the error coefficient of power measurement is $a_m = 0.5\%$ and $b_m = 0.35\%$, the error coefficient of voltage measurement is $a_m = 0.2\%$ and $b_m = 0.3\%$.

(2)When the error coefficient of power measurement is $a_m = 0.2\%$ and $b_m = 0.35\%$, the error coefficient of voltage measurement is $a_m = 0.3\%$ and $b_m = 0.3\%$.

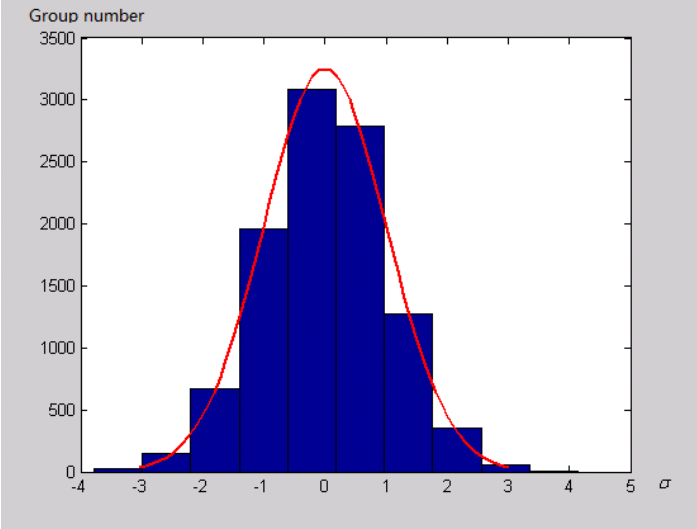

Fig.3 The normal random noise histogram and curve fitting

4.2 The simulation of parameter fluctuations

Experiment 1: According to the length of the transmission line simulate the fluctuations of reactance parameter of line

Take reactance value of every kilometer transmission line is 0.35 Ω, but for 100KM line, when the voltage level of transmission line is 220kV, its per-unit value of reactance is $X = (0.35 \times 100) / \frac{230^2}{100} \times 100 = 6.61$, when the voltage level of transmission line is 500kV, its per-unit value of reactance is $X = (0.35 \times 100) / \frac{525^2}{100} \times 100 = 1.27$.

Accordance with the rules that the fluctuation of the reactance of line longer than 100km is 1% and the line longer than 300km is 2%~4% to design reactance parameters, the specific method is as follows:

When the voltage level of transmission line is 220kV, the per unit value of reactance of 100km line is 6.7 and the line longer than 300km is 20. When the voltage level of transmission line is 500kV, the per unit value of reactance of 100km line is 1.3 and the line longer than 300km is 4. The fluctuation coefficient k is between -1 and 1 and in accordance with normal distribution. The formula to calculate is as follows:

$$X' = X_0 + X_0 \times coef_{flu} \times (\frac{k}{3.0}) \tag{5}$$

In the formula (5), $coef_{flu}$ is the fluctuation coefficient of reactance of the line, which is decided by the size of reactance.

It should be noted that the above per unit value refers to the reactance value, which is expanded after one hundred times, the same as follows.

Experiment 2: Analog the volatility of the reactance parameters of transmission line

For all the power transmission line parameters, the fluctuation of the reactance parameters rates is according to are 1%, 3%, 5%, 7%, 9%, 11%, the fluctuation coefficient of k is between -1 and 1 in accordance with normal distribution. In the formula (2), the reactance value of the parameter variation rate is from 1% to 11%.

Experiment 3: Analog the volatility of the resistance parameters of transmission line

In the formula $r_t = r_{20}[1+\alpha(t-20)]$, $\alpha = 0.00361/^{\circ}C$ (when t is less than seventy degrees Celsius) for aluminum conductor. When t equal to 20, 30, 40, 50, 60, 70, the change rate of resistance were 0%, 3.6%, 7.2%, 10.8%, 14.4%, 18%. Set the temperature of wire conductor, which is associated with the current load rate of the wire conductor, then conduct experiments of resistance volatility of transmission line, volatility coefficient is shown in formula (6).

$$k = 0.36\% \times \frac{i}{i_{\max}} \times 50 = 0.18 \times \frac{i}{i_{\max}} \tag{6}$$

In the formula (6), $i_{\max}$ is the limited value of the current flowing through the transmission line, i is the current of transmission line, which is calculated by power of line (active and reactive power) and bus voltage.

Experiment 4: The joint fluctuations of resistance and reactance

The resistance parameter of line is decided by the experiment of fluctuations in resistance. The reactance parameter of the transmission line is changing between 1% and 11% in accordance with the normal distribution characteristics.

4.3 The analysis of the impact of the measurement time-delay on state estimation

The load of system change in different ramp rate, in this situation, due to the different features of direct mining station and data forwarding station delay, we set different delay interval (0 second, 5 seconds, 10 seconds and 15 seconds), which means the measured data is divided into four periods. According to the station area partition delay range, the substation in 220 kV level, some is 15 seconds delay and some is 10 seconds delay; the substation in 500 kV level, some is 5 seconds delay and some is 0 second delay. Simulate the time-delay data of state estimation in master station system, and compare the change of the related indexes.

In the test platform, change the two time interval of the load curve in simulation layer to achieve the load with different ramp rates.

With different ramp rate of load, the change of eligible rate of state estimation is shown in Fig. 4 and the change value of the objective function in the state estimation is shown in Fig. 5.

Different ramp rate of load make the data obtained in state estimation is not consistent with the real-time data. It is obvious that when increase the ramp rate of the load gradually, the latency of measured data will result in the increase of the imbalance power of the computing nodes, the consistency of the time section will be destroyed, the imbalance power of measurement system become bigger, thus make the qualified rate of state estimation decrease and residual become larger.

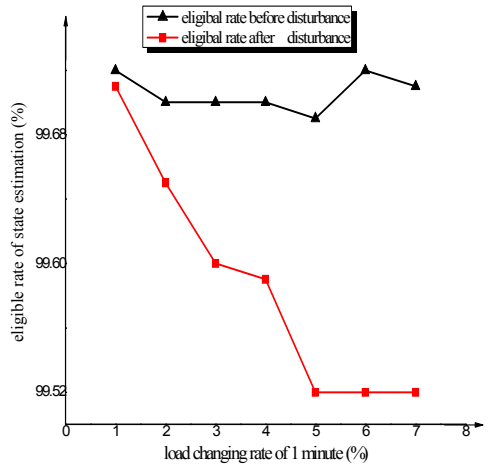

Fig.4 The change of eligible rate of state estimation under different load changing rate of 1 minute

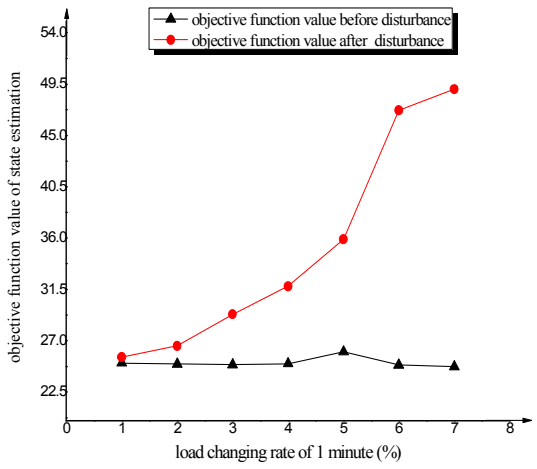

Fig.5 The change of objective function values under different load changing rate of 1minute

4.4 Comprehensive experiment of disturbance factors affected the indicators in state estimation

The setting table of comprehensive test case is shown in Tab.1, the experimental results are shown in Fig.6 and Fig.7.

Based on the analysis of the experiments, analyze the change trend between all kinds of statistical indicators of state estimation and disturbance factors, it is easy to see that the inevitable measurement error in the system, the change of environmental temperature of grid equipment, parameter error of transmission line and the ramp rate of load (without considering measurement system on the basis of gross error), the qualified rate indexes of state estimation fell to a certain extent, the objective function values, which is of one of the index to measure the precision of state estimation, gradually become larger. Under the action of these factors, residual error of the system increased, the reliability of calculation decreased.

Tab.1 The set table of comprehensive experiments

Experiment 1 of comprehensive factors	Random measured error of reactance parameters in system + the fluctuation of reactance parameters based on the length of line + fluctuation of resistance + 4% load fluctuation in one minute
Experiment 2 of comprehensive factors	Random measured error of reactance parameters in system + 3% fluctuation of reactance parameters + fluctuation of resistance + 4% load fluctuation in one minute
Experiment 3 of comprehensive factors	Random measured error of reactance parameters in system + 5% fluctuation of reactance parameters + fluctuation of resistance + 4% load fluctuation in one minute
Experiment 4 of comprehensive factors	Random measured error of reactance parameters in system + 7% fluctuation of reactance parameters + fluctuation of resistance + 4% load fluctuation in one minute
Experiment 5 of comprehensive factors	Random measured error of reactance parameters in system + 9% fluctuation of reactance parameters + fluctuation of resistance + 4% load fluctuation in one minute

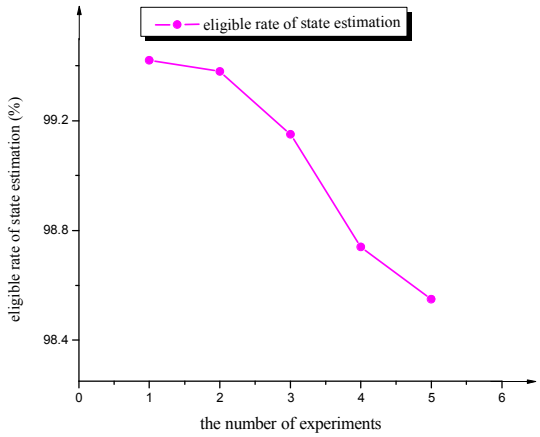

Fig.6 The change trend of eligible rate of state estimation under various disturbance factors work together

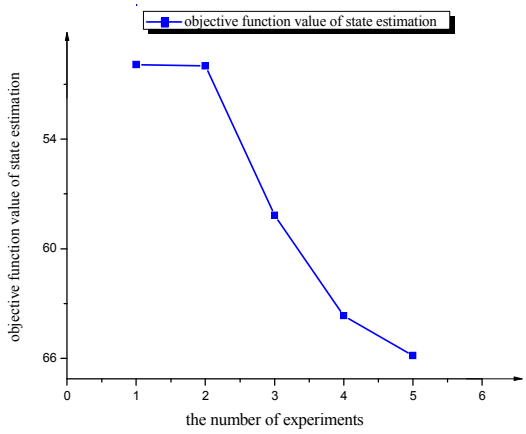

Fig.7 The change trend of objective function value of state estimation under various disturbance factors work together

Conclusions

With the expansion of the scale of power grid and the formation of UHV AC /DC hybrid power grid, the intermittent and randomness of renewable resources, the introduction of market mechanisms, the introduction and implementation of energy conservation and emissions reduction policy, which have made the operation mode of power grid become more and more complex and maintain the safe operation of the power grid is become more difficult. The influencing factors of state estimation are become more complex, the difficulties of the practical state estimation to overcome have become more and more. This paper analyzes the main factors affecting the results of state estimation, and through the simulation experiment of experimental verification platform analyzes the impact of various factors on the state estimation, provide strong technical support for practical functions of state estimation, such as the online analysis of power system and automatic dispatching system, and provide technical support for the improvement of safe and economic operation of the power grid.

Acknowledgements

This work was supported by the technology projects of state grid corporation of China(SGCC).

References

[1] Erkeng Yu. State estimation of power system[M], Hydraulic and electric power press, 1985.

[2] Schweppe F C, Wildes D B. Power System Static-State Estimation Part Ⅰ-Ⅲ[J]. IEEE Transactions on Power Apparatus and Systems, 1970, PAS-89(1): 120-135.

[3] Larson R E, Tinney W F, Peacta J, etc. al. State Estimation in Power Systems Part Ⅰ-Ⅱ[J]. IEEE Transactions on Power Apparatus and Systems, 1970, PAS-89(3): 345-352.

[4] Debs A S, Larson R E. A Dynamic Estimator for Tracking the State of a Power System[J]. IEEE Transactions on Power Apparatus and Systems, 1970, PAS-89(7): 1670-1678.

[5] Handschin E, Schweppe F C, Kohlas J, etc. al. Bad data analysis for power system state estimation[J], IEEE Transactions on Power Apparatus and Systems, 1975, PAS-94: 329-337.

[6] Bijun Li, Yusheng Xue, Jinwen Gu, etc. al. Weight function based power system state estimation algorithm [J]. Automation of Electric Power Systems, 1999, 23(8): 32-34(In Chinese).

[7] Guangyu He, Shufeng Dong. The evaluation of power system state estimation results based on the uncertainty of measurement (a) [J]. Automation of Electric Power Systems, 2009, 33(19): 21-35(In Chinese).

[8] Guangyu He, Shufeng Dong. The ecaluation of power system state estimation results based on the uncertainty of measurement (b)[J]. Automation of Electric Power Systems, 2009, 33(19): 21-35(In Chinese).

[9] Shufeng Dong, Guangyu He, Yingyun Sun, etc. a1. A new method of power system state estimation with the goal of maximizing the percent of qualified rate[J]. Automation of Electric Power Systems, 2009,33(16): 40-43(In Chinese).

[10] Tao Huang, Jiangang Lu, Hui Zhang. Adjustable measures to improve calculation precision of state estimation in Guangdong province[J]. Power System Technology, 2004, 28(16): 78-81(In Chinese).

Advanced Materials Research Vols. 960-961 (2014) pp 1562-1566

doi:10.4028/www.scientific.net/AMR.960-961.1562

Design of Microgrid Energy Management System based on LabVIEW

Ge Tengyu[1,a], Zhang Buhan[1,b], Wu Junli[1,c], Jin Bingjie[1,d], Zhao Shuang[1,e], Zhang Kaimin[1,f]

[1]State Key Laboratory of Advanced Electromagnetic Engineering and Technology

Huazhong University of Science and Technology, Wuhan, China

[a]gety163@163.com,[b]zhangbuhan@mail.hust.edu.cn,[c]wujunli_hust@126.com,

[d]loveice_2008@126.com,[e]525931413@qq.com,[f]565265960@qq.com

Keywords: microgrid; microgrid energy management system; structure design; LabVIEW

Abstract. Microgrid can be applied in different locations, relative to traditional power technology. It can improve the reliability of users of electricity and power system operation. Distributed power in microgrid needs real-time and multi-objective optimization management. This paper discusses functions and structure of microgrid energy management system(MGEMS) when connected with the main grid. Problems in long-term and short-term energy management of microgrid are discussed. From the point of view of the software platform, the system structure of MGEMS software are proposed. On this basis, this paper discusses the way to construct modules of MGEMS and their functions.

Introduction

Microgrid[1] is proposed by the Consortium for Electric Reliability Technology Solutions (CERTS) in the 90's of the last century. Distributed energy in the microgrid is called the microsource[2].

Microgrid consists of lager number and lager kinds of generating equipment, relative to traditional power technology. It can be used in large and medium-sized sports venues as power reserve, also be used in natural disaster reconstruction. So microgrid can improve the operation safety and reliability of power grid indirectly[3]. Therefore, the design of microgrid energy management platform becomes an urgent problem to be solved.

LabVIEW can manipulate the database using automation technology. The database has strong data management functions, such as data query. SQL query language is generally used for database application. By using Database Connectivity Toolkit of LabVIEW, the user don't need to consider the details of the database and understanding some common sense of the database is enough[4]. Powerful database operation function and convenient user interface creating function make the application convenient, which using LabVIEW software to build energy management system for microgrid.

From the point of view of system structure of the microgrid energy management system, the way to construct functions of each modules in microgrid energy management system are be introduced in this paper. Finally, this paper points out some issues about microgrid in islanding mode.

Key functions and control cycle of MGEMS

Energy management system(EMS)[5] is the general term for the modern power grid dispatching automation system. It provides real-time information, scheduling management and control of power grid for power grid dispatching management to ensure the safe operation of power grid and improve power quality and the economic operation of the power grid. Drawing on the existing EMS research results, in order to give full play to various distributed energy efficiency and achieve efficient, economic, safe, and reliable operation of the microgrid system, establishing a set of microgrid energy management system has become a problem to be solved.

Key functions of MGEMS MGEMS is the core of the microgrid system coordination control, which should achieve the following key functions[6]:

①Provides the power and voltage set point for each distributed energy controller in microgrid system; ②Ensure to meet the thermal load, electrical power load demand in microgrid system; ③Ensure that the microgrid system can meet the operating agreement between systems and microgrid; ④Try to make the minimum energy consumption and the system loss; ⑤Make distributed power supply the highest efficiency and try best to absorb renewable energy; The key function of MGEMS as shown in figure 1.

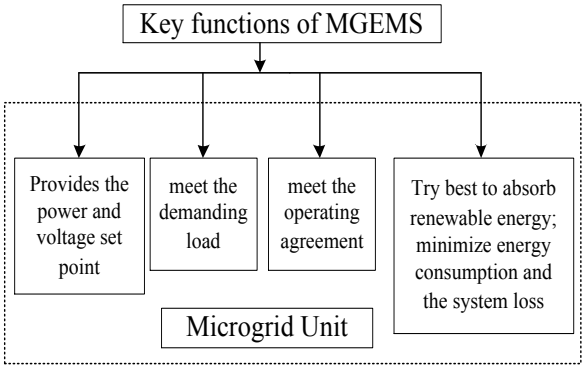

Fig.1 Key functions of MGEMS

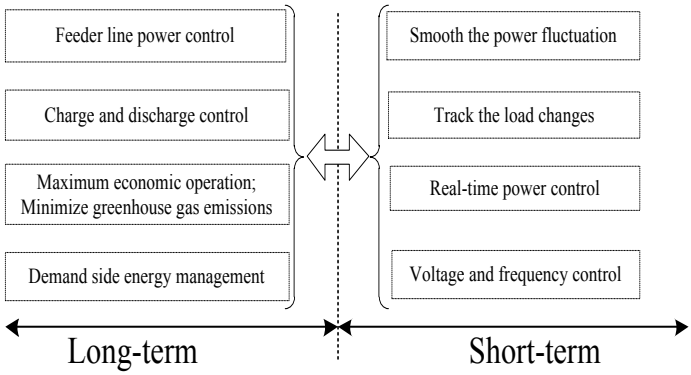

Fig.2 Control cycle classification of MGEMS

Control cycle of MGEMS According to the control cycle length, microgrid energy management platform can be divided into short-term and long-term management[7].

Short-term energy management includes: smooth the power fluctuation; track the load changes fastly and effectively; real-time power control of equipment in microgrid; voltage and frequency control. Long-term energy management includes: feeder line power control between microgrid and distribution network system; charge and discharge control according to the price mechanism of distribution network system; distributed power supply's maximum economic operation; minimize greenhouse gas emissions control; demand side energy management. Control cycle classification of MGEMS as shown in figure 2.

System structure of MGEMS

On the basis of computer operating system, MGEMS can be divided into three levels: software support platform, mathematical modeling and application function module. Scheme of MGEMS software configuration shown in figure 3.

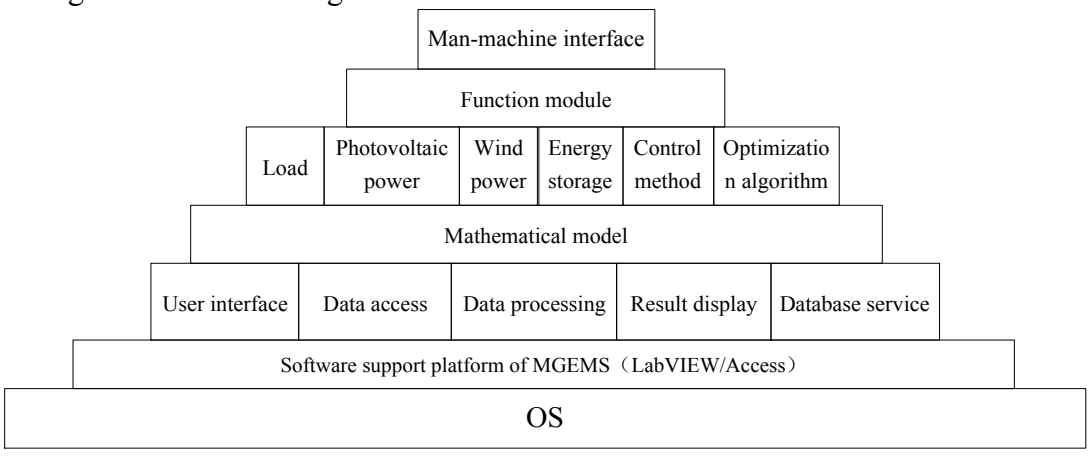

Fig.3 Scheme of MGEMS software configuration

On the basis of user interface, data access, data processing, result display and database service, MGEMS set up the mathematical model of the units in microgrid system, such as load, photovoltaic power generation, wind power, energy storage unit etc.. On the other hand, MGEMS sets up the control method and optimization algorithm for management of the microgrid system. MGEMS build the function module and man-machine interface for the related person to use, though the integration of relevant mathematical model, control method and optimization algorithm.

Modules of MGEMS

Microgrid energy management system mainly includes six modules: the database module, real time measurement and display module, renewable energy and load forecasting, micro economic scheduling module, capacity optimization module and flow analysis module.

Database module Database module includes the establishment, connection and operation of the database, which provides the following function:

①The MGEMS inquires about the basic information of the Access database, such as information contained in the database table, the types of the table data; ②The MGEMS operates on the access database tables, such as creating tables, deleting tables, inquiring specific table information; ③The MGEMS operates on data records, such as adding (delete, query) data records to the table.

We can see above, combining some access processing functions and MGEMS together is the main function. Some basic information and parameters of microgrid are stored in the database for MGEMS query and use in practical applications; and the data processed by the MGEMS can also be stored in the database for future reference.

Real-time measuring and displaying module The main function of this module is real-time measuring and displaying the microgrid status information and some power information on the primary node. This information includes: the active and reactive power of each load point, the real-time output of renewable energy, the switching power of the PCC(Point of Common Coupling) between microgrid and the main network, and the voltage size of the main network node, the frequency of the microgrid and so on.

Renewable energy and load forecasting module The main function of this module is to forecast the output of the renewable energy in microgrid and the power of the loads. Using the Neural Network method, by setting some parameters of neural network and training samples, to predict the wind speed, light intensity in the microgrid, and then to predict the output of wind turbine and other renewable energy generation like photovoltaic. Load forecasting similar.

Economic dispatch module After the access to energy supply and demand forecast information, Economic Dispatching Control(EDC) execute the optimization calculation of microgrid, combining with the information of distributed energy unit arrangement and microgrid's interaction program with the main network. Then the set point commands could be sent to related units in the microgrid[8,9].

During the real-time operating of microgrid, operation parameters and equipment state information, acquired by the monitoring equipment in microgrid, should be sent to EDC for decision making. At the same time, the results of microgrid EDC optimization provides basis for combination arrangement of DER unit and microgrid's interaction program with the main network. EDC can also takes the controllable load management into account. Information flow of EDC application as shown in figure 4.

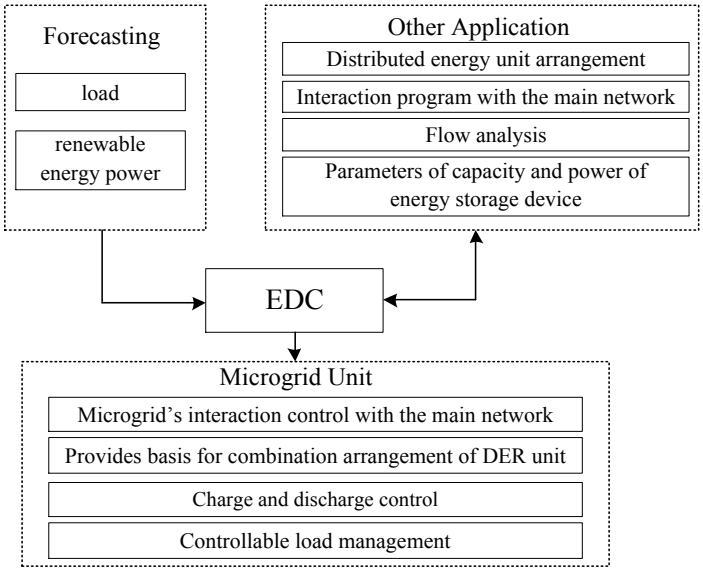

Fig.4 Information flow of EDC application

Capacity optimization module The main function of this module is to analyze configuration parameters of capacity and power of energy storage device that fit the best effect of smoothing wind power fluctuation. By setting power standard deviation of wind turbine and energy storage device as the optimization goal and setting characteristics of energy storage device as constraint conditions, the mathematical model of storage capacity optimization is established[10].

To optimize the model, we use typical daily active power turbine data. Then we get the configuration parameters of capacity and power of energy storage device, based on the calculation results. Finally, choose one group as the desired capacity and power of energy storage device by analyzing the effect of smoothing wind power fluctuation and the cost of energy storage device.

Flow analysis module Flow analysis module, taking the parameters of element in the microgrid from the database access, check the security of the microgrid system combined with the results of EDC. Flow analysis module applies the Newton-Raphson algorithm, and the calibration results can be fed back to the EDC for correction.

One block diagram window of MGEMS based on LabVIEW is shown in figure 5.

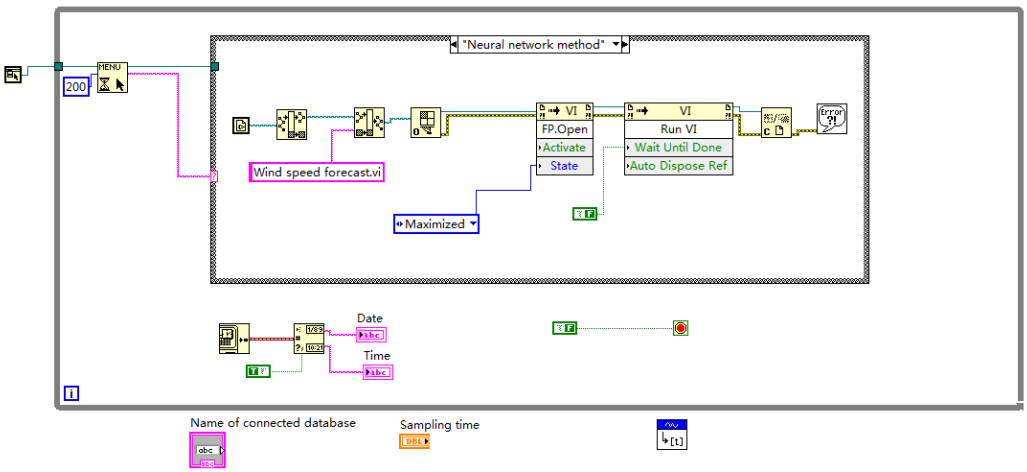

Fig.5 Block diagram window of MGEMS based on LabVIEW

Conclusions

The rapid development of distributed renewable energy and microgrid technology puts forward new requirement for EMS, which making the scheduling decision. The development of EMS, achieving safety, reliability, economic operation of the microgrid system, has a great significance.

This paper introduces the concept, characteristics and functions of microgrid, as well as the main problems facing in the development of micro grid. The feasibility to build the MGEMS using LabVIEW software is explained and the functions of MGEMS and its structure are made clear. Then the various MGEMS modules and their functions are explained in detail.

Functions of MGEMS in islanding mode, such as Optimized operation, synchronization and system splitting control, are the issues for further discussion.

Acknowledgements

This work was supported by National Basic Research Program of China (2010CB227206).

References:

[1] IEEE. IEEE standard for interconnecting distributed resources with electric power systems[S].2003

[2] Lasseter R. H, Akhil A, Marnay C, et al. Integration of distributed energy resources:the CERTS microgrid concept[R]: USA:Consortium for Electric Reliability Technology Solutions.2002.

[3] ZHANG Zhenchuan. “Design of Microgrid System Scheme and its Energy Management Platform[D]”, North China Electric Power University, 2012(In Chinese).

[4] CHEN Shuxue. “Bible of LabVIEW[M]”, Publishing House of Electronics Industry, 2011(In Chinese).

[5] YU Erkeng, LIU Guangyi, ZHOU Jingyang. “Energy Management System(EMS)[M]”, Science Press, 1998(In Chinese).

[6] ZHANG Yingyuan. “Study of Operation Optimization and Energy Management for Microgrids[D]”, Hefei University of Technology, 2011(In Chinese).

[7] Tsikalakis A G, Hatziargyriou N D. Centralized Control for Optimizing Microgrids Operation[J]. Energy Conversion, IEEE Transactions on, 2008, 23 (1): 241-248.

[8] DING Ming, ZHANG Yingyuan, MAO Meiqin, et al. “Economic Operation Optimization for Microgrids Including Na/S Battery Storage[J]”, Proceedings of the CSEE, vol.31, no.4, pp.7-14, 2011(In Chinese).

[9] ZHANG Lianqin, TAI Nengling. “Research of Energy Management System in Microgrid[J]”, Water Resources and Power, vol.31, no.4, pp.183-185, 2013(In Chinese).

[10] WEN Yi. “Optimal Configuration of Energy Storage Capacity in Wind Power Generation System[D]”, Huazhong University of Science and Technology, 2013 (In Chinese).

Advanced Materials Research Vols. 960-961 (2014) pp 1567-1574

doi:10.4028/www.scientific.net/AMR.960-961.1567

Research on Comprehensive Assessment Index System for Transmission Network PlanningAlternatives

Yong Lin [1, a], Zuohong Li[1,b], Meiling Dong[2,c], Dahai You[2,d], Gang Wang[2,e] and Weihua Chen[2,f]

[1] Guangdong Power Grid Development Research Institute Co., Ltd, Guangzhou 510000, Guangdong Prince, China

[2] State Key Laboratory of Advanced Electromagnetic Engineering and Technology(Huazhong University of Science and Technology), Wuhan 430074, Hubei Province, China

[a]linyong@gd.csg.cn,[b]zuohonglee@163.com,[c]tuoniaoyi@163.com, [d]youdahaihust@163.com,[e]1020311819@qq.com, [f]405078927@qq.com

Keywords:transmission network; planning alternatives; comprehensive assessment; index system

Abstract. In view of the lack of comprehensive and quantitative evaluation means for transmission network planning currently, a comprehensive assessment index system adapted to the characteristics of the transmission network planning is proposed, including6 strategic layer indices(safety and reliability, economic efficiency, flexibility and coordination, smart and green, controllable risk and social benefits), 16 target layer indices and 57 operating layer indices.And the assessment standard for each indexis determined to provide objective, comprehensive and systematic evaluation of transmission network planning alternatives as well as prepare for realization of the comprehensive evaluation of transmission network planning.

Introduction

Transmission network planning is the basic of the power system construction. A reasonable planning is necessary to ensure the power system security, stability and economy,as well as minimize wasted power system construction investment. Recently, with the economic and technological developmentin China, the grid plan should meet higher requirements for power quality and reliability put forward by power customers. So determining how to evaluate the planning and describe the result of the grid planning quantitativelybecomesa key problem. Therefore, a reasonable comprehensive assessment index system for alternative transmission network planning is needed to evaluate the pros and cons of the planning quantitatively.

Traditional evaluation of grid usually focuses on flow distribution,stability level,short-circuit level and economic evaluation of the planning alternative, including assessment of reliability, security, economy and other individual indices. Recently, researches on comprehensive evaluation have been emerging. Reference [1] proposes a comprehensive evaluation index system and method for distribution network planning, whichincludes 5 first grade indices: supply security, reliability, economy, flexibility and coordination, and contains a number of subordinate indices. However, as the transmission network and distribution network play different roles in the power system, the evaluation index system does not apply to the transmission network planning.Reference [2] evaluates the power system operating state from five aspects: safety, reliability, economy, stability and flexibility.However, the assessment index system focuses on the evaluation of power system operating state, whichcannot reflect the planning characteristics. Reference [3]divides the grid

assessment indicesinto transmission and distribution network, and makes further division in each category according to planning and running stage. Then a power network evaluation index system framework, including transmission network planning evaluation index system, transmission network after the evaluation index system, distribution network planning evaluation index system, and distribution network after the evaluation index system, is formed.But the transmission network planning evaluation index system is not comprehensive enough. There are other studies[4-7] about evaluation index system for the smart grid development. As forresearches on comprehensive evaluation of transmission network planning, reference[8] considers reliability, economy, social impact, adaptability and includes 12 indices such as line load rate; reference [9] evaluates the transmission network planningfrom four criteria layers:technology, economy, environmental impact and adaptability, including 15 indices such as load cut probability.

Transmission network planning is associated with the grid development strategy. Grid development should meet the social and economic development requirements and coordinate with the economy and reliability. Grid structure should be able to adapt to a variety of possible operating means, and ensure future needs of the load growth and network expansion. Power system should allocate resources optimallyand serve the low-carbon society and sustainable economic development as well as to be more intelligent, efficient, reliable and environment-friendly.

This paper studies the existing grid evaluation index system, focuses on the transmission network planning characteristics, and puts forward a comprehensive assessment index system, including safety and reliability, economic efficiency, flexibility and coordination, smart and green, controllable risk and social benefits to evaluate transmission network planning quantitatively.

Construction Principles of Index System

When establishing evaluation index system, each index should reflect the actual situation of the grid as comprehensively as possible, without missing any important indices. What's more, information validity, data collection and calculating complexity should also be considered. Therefore, the design of the index system needs to meet the following principles:(1) Consistency with the evaluation objectives;(2) Availability;(3) Comparability; (4) Mutual independence;(5) Overall completeness.

Contents of Index System

According to the construction principles of index system, a comprehensive evaluation index system for transmission network planning is established, combined with the actual characteristics and purpose of the transmission network planning.

Six strategic level indices is determined by the long-term development strategy of the power system,including safety and reliability, economic efficiency, flexibility and coordination, smart and green, controllable risk and social benefits. Then decompose the strategic levelhierarchically into target layer according tothe assessment purpose. The operating level indices are further division of the target level indices, which can be quantified and comparable.

Safety and Reliability.Safety and reliability is the basic requirement of electricity customers' demand. Security refers to the ability of power system to maintain the supply properly sectionfor a set of contingency at any time. Reliability refers to reliability of continuous supply under the premise that the power system meets the safety requirement. Safety and reliabilitylayer includesthree target layer indices: grid structure, power supply capacity and stability level.

Grid structure index reflects the ability to maintain normal power supply under a failure, and power contact tightness. It consists of five operating layer indices: N-1 passing rate, N-2 passing rate, average power supply radius, short-circuit current level, effective short-circuit ratio.

Power supply capacity index evaluates main transformer regional supply capacity, local power supply ability as well as the dependence of the regional power grid on external power. It consists of four operating layer indices: capacity-load ratio of each voltage level, power installed capacity ratio below 500kV, external input capacity ratio, station capacity variance of each voltage level.

Stability layer index assesses power system transient stability situation in the case of a certain fault. It consists of three operating layer indices:N-2 instability fault number, reactive power compensation, spinning reserve rate.

Economic Efficiency. Economic evaluation of network planning is an important mean to improve the economic efficiency of power grid construction projects. Economic efficiency indices evaluate utilization efficiency of equipment and investment efficiency.

Equipment utilization efficiency indices assess transmission lines and transformer load, reflecting the grid operating efficiency, including five operating layer indices: average line load rate of each voltage level, line voltage load rate distribution of each voltage level, average transformer load rate of each voltage level, transformer load rate distribution of each voltage level, utilization rate of annual maximum load.

Investment efficiency indices analyze supply satisfaction and economic benefits of power system investment, from the aspects such as capital investment, supply gain and loss reduction benefit, including increased electricity sales by unit investment, increased load by unit investment, line loss rate, decreasednetwork loss benefit, annual cost of unit load.

Flexibility and Coordination. Local overload or light load will affect the grid safety, reliability and economy tremendously, as power system is inseparable. Coordination is also needed between the high and medium voltage transmission network, otherwise the fragile part would weaken power supply level of the strong part. The load volatility requiresflexible changes of connection scheme after a certain fault. Flexibility and coordination indices reflectcoordination between installed capacity, load and grid equipment scale; substation capacity; as well as match of linescale and supply margin.

The coordination development between power grid and power supply target layer includes four operating indices: ratio of line length and generator capacity, ratio of line length's growth rate and generator capacity's growth rate, ratio of substation capacity and generator capacity, ratio of substation capacity's growth rate and generator capacity's growth rate.

The coordination development between power grid and power supply target layer includes three operating indices: ratio of substation capacity's growth rate and load's growth rate, ratio of line length increment and load increment, ratio of substation capacity increment and load increment.

The coordinated development between power grid in each voltage grade target layer includes five operating indices: ratio of outgoing line number of lower voltage and substation number of higher voltage, ratio of substation capacity between lower voltage and higher voltage, ratio of substation number between different voltages, ratio of substation capacity between different voltages, ratio of line length in different voltage grades.

The flexibility target layer includes five operating indices: ability to transfer power supply, extensible margin of substation capacity, transmission capacity margin of transmission section, line interval margin, channel margin.

Smart and Green. Smart and green indices evaluate intelligent devices and consumptive ability of new energy, including two target layer indices: intelligence level of transmission and transformation and ability to access new energy.

The intelligence level of transmission and transformation target layer includes six operating indices: intelligent substation's capacity ratio, compact-line' length ratio, large cross-section line' length ratio, reactive compensation capacity ratio of STATCOM, line' length ratio of flexible AC(DC) transmission, saved land amount.

The ability to access new energy target layer includes two operating indices: renewable energy' installed capacity ratio, renewable energy' generating capacity ratio.

Controllable Risk. Controllable risk indices assess accident risk, investment risk and ability to withstand natural disasters and otherrisks.

Accident risk indices analyzeaccident risks that should be checked in the power system planning stage, based on the document 'electrical safety accident emergency handling and investigation regulations' issued by the State Council (State Council Decree No. 599), including load reduction ratio of double and above circuit lines trip on the same tower (N-2 fault) andload reduction ratio of single HVDC bipolar latch (N-2 fault).

Investment risk indices focus on financial recovery ability and income level of grid projects, including two operating layer indices: dynamic payback period and internal rate of return(IRR).

Ability to withstand risks indices assess the ability of power system to withstand natural disasters and other risks like man-made or external damage based on the file 'grid security risk management (Trial)' (national energy security [2014] No. 123) 20140319) issued by the National Energy Board, consisting of two operating layer indices:ability to withstand natural disasters and ability to withstand other risks (human or external damage).

Social Benefits. Social benefits indices reflect the impact of grid development on the society, economy and environment, including new energy efficiency and energy-saving emission reduction efficiency.

New energy efficiency target layer consists of two operating indices: coal amount of reduced fossil energy consumption and treatment cost of reduced pollutant emissions.

Energy-saving emission reduction efficiency target layer consists of two operating indices: CO_2 emissions reduction and SO_2 emissions reduction.

Evaluation Standard of Indices

Evaluation standard(scoring criteria) of each underlying index (operating layer index)is necessary in the comprehensive evaluation process of the network planning program.

For quantitative indices, the evaluation standard can be divided into four basic types: cost type, benefit type, interval type and other type.

Cost-type index (inverse index) refers to indices of which the value the smaller the better, such as line loss rate, dynamic payback period, N-2 instability fault numberand so on. Linear function is used to score cost-type index, as Eq.1.

$$y = 100 \times \frac{X_{\max} - X}{X_{\max} - X_{\min}} . \quad (1)$$

Where, X represents the index value; *Xmax, Xmin* is the value bound of the index in accordance with relevant guidelines, conditions or experts constraints; y represents the index score(0-100).

Benefit-type index (positive index) refers to indices of which the value the bigger the better, such as N-2 passing rate, increased load by unit investment, internal rate of return, and so on. Linear function is also used to score benefit-type index, as Eq. 2.

$$y = 100 \times \frac{X - X_{\min}}{X_{\max} - X_{\min}} . \quad (2)$$

Interval-type index refers to indices of which the value falls within a rangeor on one point the best, such asaverage power supply radius, spinning reserve rate, channel margin and so on. Zigzag function is used to score the interval-type index, as Eq. 3.

$$y = \begin{cases} 100 \times \frac{X - X_{\min}}{a - X_{\min}} & X < a \\ 100 & a \le X \le b \\ 100 \times \frac{X_{\max} - X}{X_{\max} - b} & X > b \end{cases} . \quad (3)$$

Where, *a, b* represent the bound of the interval.

If the interval-type index value has no limit, which means it can be $[-\infty, +\infty]$.Then the scoring function can be replaced by mixed function,as Eq. 4.

$$y = \begin{cases} 100 \times e^{k_1(X-a)} & X < a \\ 100 & a \le X \le b \\ 100 \times e^{k_2(b-X)} & X > b \end{cases} . \quad (4)$$

Where, *k1, k2* represents the parameters of the exponential function selected according to the actual situation.

Other-type index refers to those that do not belong to the above three types, such as N-1 passing rate. Usually technical guidelines for network planning stipulate that the power system of key province and city must meet N-1 principle. That means N-1 passing rate must be 100 %, otherwise the index score would be 0.

Qualitative indices cannot be scored using correlative functions directly as quantitative indices. They can be grading scored according to experts' experience. The judgment is generally divided into 5-9 grades with vague language statements. For example, five grade evaluationcan be described as 'excellent', 'good', 'medium', 'poor' and 'terrible'. Indices like 'line voltage load rate distribution of each voltage level','transformer load rate distribution of each voltage level' and 'ability to withstand natural disasters'.etc. belong to this type.

Conclusions

This paper studies the evaluation of transmission network planning, establishes a systematic and comprehensive assessment index system for transmission network planning, and proposes a number of new indices, such as 'annual cost of unit load' based on Life Cycle Cost (LCC) theory, reflecting grid investment efficiency; 'line interval margin' highlighting the grid flexibility; 'intelligent substation's capacity ratio' reflecting the intelligence level of transmission network; 'dynamic investment recovery period', ' IRR' reflecting grid investment risk;'ability to withstand natural disasters', 'ability to withstand other risks (human or external damage)' reflecting the ability of power system to resist risks; 'treatment cost of reduced pollutant emissions' highlighting the benefits of the new energy.

The comprehensive assessment index system established in this paper can be used for longitudinal assessment about the development of the planning in different periods, helping planners grasp the trend of network development and enhance the target of network planning; as well as be used for horizontal assessment about various planning programs, highlighting features and pros and cons of different plans.

Work of the next step includes: 1) verify and improve the comprehensive assessment index system according to specific transmission network planning programs. 2)study grid evaluation methods[8-13], determine each index weight andintegrate multi-index scores into a composite score accurately, in order to evaluate different network plans comprehensively.

Acknowledgements

This work is supported by Guang Dong Power Grid Development Research Institute Co., Ltd (Research on Evaluation System Power Grid Planning Alternatives) (030000QQ00120020).

Appendix

Table 1 Structure of the assessment index system

Strategic layer	Target layer	Operating layer
Safety and reliability	Grid structure	N-1 passing rate
		N-2 passing rate
		Average power supply radius
		Short-circuit current level
		Effective short-circuit ratio
	Power supply capacity	Capacity-load ratio of each voltage level
		Power installed capacity ratio below 500kV
		External input capacity ratio
		Station capacity variance of each voltage level
	Stability	N-2 instability fault number
		Reactive power compensation
		Spinning reserve rate
Economic efficiency	Equipment utilization efficiency	Average line load rate of each voltage level
		Line voltage load rate distribution of each voltage level
		Average transformer load rate of each voltage level
		Transformer load rate distribution of each voltage level
		Utilization rate of annual maximum load
	Investment efficiency	Increased electricity sales by unit investment
		Increased load by unit investment
		Line loss rate
		Decreasednetwork loss benefit
		Annual cost of unit load
Flexibility and coordination	Coordination development between power grid and power supply	Ratio of line length and generator capacity
		Ratio of line length’s growth rate and generator capacity’s growth rate

		Ratio of substation capacity and generator capacity
		Ratio of substation capacity's growth rate and generator capacity's growth rate
	Coordination development between power grid and power supply	Ratio of substation capacity's growth rate and load's growth rate
		Ratio of line length increment and load increment
		Ratio of substation capacity increment and load increment
	Coordinated development between power grid in each voltage grade	Ratio of outgoing line number of lower voltage and substation number of higher voltage
		Ratio of substation capacity between lower voltage and higher voltage
		Ratio of substation number between different voltages
		Ratio of substation capacity between different voltages
		Ratio of line length in different voltage grades
	Flexibility	Ability to transfer power supply
		Extensible margin of substation capacity
		Transmission capacity margin of transmission section
		Line interval margin
		Channel margin
Smart and green	Intelligence level of transmission and transformation	Intelligent substation's capacity ratio
		Compact-line' length ratio
		Large cross-section line' length ratio
		Reactive compensation capacity ratio of STATCOM
		Line' length ratio of flexible AC(DC) transmission
		Saved land amount
	Ability to access new energy	Renewable energy' installed capacity ratio
		Renewable energy' generating capacity ratio
Controllable risk	Accident risk	Load reduction ratio of double and above circuit lines trip on the same tower (N-2 fault)
		Load reduction ratio of single HVDC bipolar latch (N-2 fault)
	Investment risk	Dynamic payback period
		Internal rate of return(IRR)
	Ability to withstand risks	Ability to withstand natural disasters
		Ability to withstand other risks (human or external damage)
Social benefits	New energy efficiency	Coal amount of reduced fossil energy consumption
		Treatment cost of reduced pollutant emissions
	Energy-saving emission re duction	CO_2 emissions reduction
		SO_2 emissions reduction

References

[1]XIAO Jun, CUI Yanyan, WANG Jianmin, et al. A hierarchical performance assessment method on the distribution network planning[J]. Automation of Electric Power Systems, 2008, 32(15): 36-40.
[2] LUO Dong, HU Lianghuan, XING Yuzhen. Investigation of assessment systems for operation of power grids[J]. Anhui Electric Power, 2009, 26（3）: 75-78.
[3]WANG Wei, WANG Chun, CHENG Hong, ZHAO Yan. Preliminary frame of index system for evaluating power network[J]. Power System Protection and Control, 2008, 36（24）: 14-18.
[4] ZHANG Jian, PU Tianjiao, WANG Wei, et al. A comprehensive assessment index system for smart grid demonstration projects[J]. Power System Technology, 2011, 35（6）:5-9.
[5] WANG Jingmin, SHI Ting. Construction of evaluation index system for smart grid[J].East China Electric Power, 2012,40（2）:193-197.
[6] YANG Lijun, WANG Shuo, LU Zhigang. Indices of distribution network intelligent planning evaluation[J]. Power System Technology, 2012,36（12）:83-87.
[7] SUN Qiang, GE Xubo, LIU Lin, et al. Review of smart grid comprehensive assessment systems[J]. Proceedings of the CSU-EPSA, 2011,23（6）:105-110.
[8] LI Yulong. Application and research on comprehensive assessment modeling method for alternative transmission network planning[D]. Beijing: North China Electric Power University, 2012.
[9] LIU Yali. Comprehensive evaluation and decision-making for transmission network planning alternatives based on DEAHP method[D]. Jinan, Shandong Province: Shandong University, 2010.
[10] CUI Yanyan. Study and application of comprehensive evaluation method for network planning[D]. Tianjing: Tianjing University, 2008.
[11] WANG Qin, WEN Fushuan, LIU Min, YI Su. Combined use of fuzzy set theory and analytic hierarchy process for comprehensive assessment of electricity markets[J]. Automation of Electric Power Systems, 2009,33(7):32-37.
[12] LIN Jikeng, LI Tongfei, ZHAO Ziming. Assessment on power system black-start schemes based on entropy-weighted fuzzy comprehensive evaluation model[J]. Power System Technology, 2012, 36(2):115-120.
[13] SUN Xiu dong, LlZong bin, CHEN Fumin. Research on multiple attribute synthetic evaluation methods based on artificial neural network[J]. Journal of Zhengzhou Institute of Light Industry (Natural science), 2003, 18(2):11-14.

Advanced Materials Research Vols. 960-961 (2014) pp 1575-1581

doi:10.4028/www.scientific.net/AMR.960-961.1575

Research on Comprehensive Evaluation Index System for Distribution Network Planning Alternatives

Lu Xun[1,a], Zhou Yang[1,b], Zhang Kaimin[2,c], Wu Jiasi[2,d], Yang Xueying[2,e], Zhang Buhan[2,f], Jin Bingjie[2,g], Shao Jian[2,h], Ge Tengyu[2,i]

[1]Guang Dong Power Grid Development Research Institute Co., Ltd, Guangdong, China

[2]State Key Laboratory of Advanced Electromagnetic Engineering and Technology Huazhong University of Science and Technology, Wuhan, China

[a]xunfeelings@163.com,[b]zhouy1115@foxmail.com.cn,[c]kmaixuexi@163.com,[d]wujiasi@hust.edu.cn, [e]yangxueying0209@sina.com, [f]zhangbuhan@mail.hust.edu.cn, [g]loveice_2008@126.com, [h]hustceeeshao@gmail.com,[i]gety163@163.com

Keywords: distribution network; planning alternatives; comprehensive evaluation; index system.

Abstract. In order to identify weaknesses in distribution network planning alternatives, providing a scientific basis for grid investment decisions, effective and comprehensive evaluation is needed. According to the related principles and objectives, this paper establishes a comprehensive evaluation index system based on hierarchy. This system is guided by the long-term development strategy of China southern power grid, including six strategic layer indices as safety and reliability, economic efficiency, coordination and flexible, smart and green, controllable risk and social benefits. The meaning and classification of every index is listed in details. According to different technical characteristics of every index different fuzzy membership functions are structured. Furthermore, in accordance with the relevant guidelines and specifications, this paper gives specific values of the membership function parameters to achieve standardization of indexes of different dimensions, laying the foundation for a comprehensive assessment.

Introduction

Located on the load side, the distribution network is an important part of distributing electric energy to the users. According to incomplete statistics, more than 80% of power failure is due to a fault caused by the distribution network therefore distribution network has the greatest impact on the users [1]. Distribution network planning alternatives can directly affect various aspects of the power grid construction such as reliability and economy.

Smart Grid is currently competing in the world to carry out, countries combining its own reality have been carrying out a comprehensive development and evaluation of grid to deal with the development of clean energy, climate changes and the need to control the risk of the power grid, on the basis of ensuring safety and economy. At present, the proposal of China's power grid construction projects and the priority of projects rely on experts' experience, therefore, the decision-making level is low and is with great blindness. This is not only a waste of limited investment, but also brings a lot of problems after rebuilding. The above situation is due to the lack of comprehensive knowledge and understanding of a network planning and a lack of clear quantitative criteria. Given the above situation, there is an urgent need to establish a more comprehensive, a wider range of multi-level evaluation system and to define a reasonable and scientific criterion.

About assessing indexes, extensive literature studies has found that the traditional power grid assessments mainly focus on individual assessment such as reliability[2-4], security[5] and the capacity of power supply[6-8]. Lacking a comprehensive evaluation system of technical and economic, these works don't have a strong direct guidance to the planning and construction of the power grid. Reference [9] establishes a comprehensive evaluation index system based on hierarchy, but it gives no consideration to the economic efficiency and environmental protection of the power grid.

About the index criteria, reference [10] invites many power experts to select evaluation criterion and scoring criteria to score the index, which is subjective and less practical. Reference [11] divides index into three basic types: cost type, benefit type and moderate type, giving each type a membership function, but it doesn't specify the value of the function parameters and gives no specific evaluation criteria, leaving the indicators rating lack of scientific basis.

Focus on the above problems, this paper takes a distribution network planning alternatives of a certain city from Guangdong Province for example. Guided by the long-term development strategy of China southern power grid, this paper establishes a comprehensive evaluation index system based on hierarchy, and the core of the system is safety, reliability, economy and coordination, besides it also takes the risk control and intelligent green into consideration. The system should fully reflect and guide the coordinated development among power grid, power source, society, and environment and so on. Meanwhile based on fuzzy theory and combined with relevant standards and regulations, the appropriate membership functions standardize different dimension indicators and objectively reflect the characteristics of each individual index, laying the foundation for the comprehensive assessment.

The Principles and Procedures of Establishing an Index System

The Basic Principles of Index System. The purpose of constructing the index system is to reflect the object of study comprehensively and profoundly, but it does not mean the more indexes, the better, it means increase the index which can provide useful information. So the establishment of comprehensive evaluation system needs to meet certain principles: (1) Consistency with the evaluation objectives; (2) Do not repeat and do not miss; (3) Availability; (4) A combination of qualitative and quantitative

The Procedures of Index System The purpose of the evaluation is to assess whether the index meets the planning guidelines constraint requirements before implementation of the project. Identifying weaknesses in planning alternatives to make adjustment in time, providing a scientific basis for grid investment decisions, the comprehensive assessment helps to make optimal allocation of power resources. Combining the front principles and purpose, the procedure of the construction of index system are as the following three steps:

Step one: Guided by the long-term development strategy of China southern power grid and closely integrated with the strategic objectives of network planning to get strategic layer indices.

Step Two: Target layer indices can be built on the basis of using analysis of hierarchical decomposition and combining with the purpose and effect of the evaluation.

Step three: Operating layer indices can be determined on the basis of absorbing domestic and foreign research results and adhering to related principles to screen indexes.

A Comprehensive Evaluation Index System Based on Hierarchy

The Hierarchy of Index System. The analysis of economical efficiency, reliability and security is requested in distribution network planning guidelines.On the basis of distribution network planning guidelines, coordination and flexible, smart and green, risk control and social benefits are considered in this paper. Meanwhile, hierarchy analysis model of technical and economic analysis are built. The result is shown in Table 1.

Two situations should be considered when judging whether power supply is safety or not. One is that grid occurs accident; the other one is that grid may occur accident. Two factors should be taken into account as follows: 1) whether the grid can guarantee the security of system or not when some equipments out of operation. 2) To what the extent can the power grid structure ensure system security.

The reliability of the distribution network can be measured by setting a series of index.Considering a large number of reliability indexes and simplify of state planning reliability evaluation, in this paper, reliability assessment only focus on the calculation of customer average interruption time and the

evaluation of power supply reliability rate. Meanwhile, reliability assessment of grid can be measured from the perspective of equipment by setting available modulus index and cable rate index.

Series of content should be considered when measuring the distribution network economy, such as long network planning projects duration cycle, different life of investment projects, expenses and incomes of grid construction and operation. Consequently, in order to evaluate the economics of the grid completer, Life-cycle-cost (referred to as LCC) management theory is introduced in this paper to evaluate the whole life cycle of power system.

Power system is an inseparable whole concept, generation side, transmission and the load side must be closely coordinate to ensure the safety and reliability of the grid. The grid coordination talking about here mainly refers to coordination development between grid and load and coordination development between different voltage levels.

In the process of assessing network planning project, power companies will confront many uncertainties, which will lead to risk. The existence of risk means loss, reducing risks and losses can be done through the identification and evaluation of risks. In the past, the evaluation of risk assessment is often overlooked for the grid assessment. According to the relevant guidelines[13, 14], this paper measures the controllable risk by three angles: accident risk, investment risk, ability to withstand risks.

Preliminary Research on the Index System According to the related principles and procedures, this paper establishes a comprehensive evaluation index system based on hierarchy, including 6 strategic layer indices, 15 target layer indices and 46 operating layer indices, which is listed in details in table 1.

Table 1 Comprehensive evaluation index system

Strategic layer	Target layer	Operating layer	Index Meaning	Index Classification
Safety and reliability	Power grid security	N-1 passing rate	Check the ability of power system to keep stable operating after any element out of operation	benefit type
		Ratio of single line and single transformer in high voltage distribution network	The ratio of a single into line and single main transformer substation, the larger the indicator, the poorer the security	cost type
		Interconnection ratio of medium voltage distribution lines	The ratio of lines met the interconnection structure, evaluating transferring ability and reliability of system after fault	benefit type
		Average number of transformer hooked into pubic line	Average number of transformer hooked into pubic line, the bigger the indicator, the more complicated the network ,the less the safety of the system	interval type
		Average transformer capacity hooked into pubic lines	Average transformer capacity hooked into pubic lines, the bigger the indicator, indicating the higher load rate, the less the safety of system	interval type
		Supply radius of high voltage distribution network	Evaluate the average power supply theoretical radius of substation of certain voltage level	interval type
		Average length of medium voltage distribution public lines	The ratio of the total length of main public lines and the number of the lines, reflecting the medium voltage distribution network power supply radius	interval type
		Typical connection ratio in high voltage distribution network	The percentage of number of lines meeting the typical connection mode and the total number of lines	benefit type
	Power grid reliability	Average interruption hours of customer	Average outage time for power users during statistics time (generally unit for years)	benefit type
		Electric reliability	The ratio of effective power supply hours regardless of planning outage and total statistics hours	benefit type

		Availability factor of transformer, circuit breaker, overhead line	Evaluate the accessibility of Transformer, circuit breaker, overhead line, reflecting the supply reliability of power grid	benefit type
		Cable rates	The ratio of length of cable lines and total lines, the bigger the indicator, the more reliable the system	benefit type
Economic efficiency	Equipment utilization efficiency	Maximum distribution line load rate of each voltage level	The ratio of maximum line operating current and long-term allowed current carrying capacity.	benefit type
		The distribution of Maximum distribution line voltage load rate	The distribution of Maximum distribution line voltage load rate, count according to below 50%, 50%~70% and above 70%.	benefit type
		Maximum distribution transformer load rate of each voltage level	The maximum annual load rate of each main transformer, access main transformer utilization of different voltage levels.	benefit type
		The distribution of distribution transformer load rate	The distribution of distribution transformer load rate, count according to below 50%, 50%~70% and above 70%.	benefit type
	Investment efficiency	Unit cost of distribution capacity	The ratio of power grid project total investment during accounting period and increased distribution capacity.	cost type
		Unit cost of line length	The ratio of total new transmission line investment and increased line length, access the construction cost of distribution lines.	cost type
		Distribution line loss rate	The ratio of system loss and grid electricity supply, evaluate the distribution operating economy.	cost type
		Annual cost of unit load	Calculate annual investment cost and operation and maintenance cost of grid unit load under different circumstances, guide the power grid planning construction and transformation economy.	cost type
Coordination and flexible	Coordinated development between grid and load	Ratio of substation capacity's growth rate and load's growth rate	The ratio of substation capacity's growth rate and the maximum load's growth rate	interval type
		Ratio of line length increment and load increment	The ratio of line length increment and load increment	interval type
		Ratio of distribution capacity increment and load increment	The ratio of distribution capacity increment and load increment	interval type
	Coordinated development between different voltage level	Ratio of substation number between different voltage level	Number of single higher voltage level substation supports lower voltage level substation	interval type
		Ratio of substation capacity between different voltage level	The ratio of substation capacity between different voltage level	interval type
		Ratio of line length between different voltage level	The ratio of line length between different voltage level	interval type
	Grid flexibility	Ability of transfer power supply	The ratio of the number of transferable line and the number of non-transferable line	benefit type
		Substation expansion margin	Statistics the ratio of substation expansion capacity and the total capacity	interval type
		Line interval margin	The ratio of the number of unused line interval and the total number of existing line interval and future expansion line interval	interval type
Smart and green	Intelligence level of	Proportion of smart distribution network	Statistics the ratio of smart distribution network capacity and the total distribution network	benefit type

	distribution network	capacity	capacity	
		The number of "plug and play" charging stations of end-use equipment	Statistics the number of "plug and play" charging stations of end-use equipment in the area	benefit type
		Proportion of smart meters	The ratio of smart meters and total meters in the area	benefit type
	Supply capacity of Distributed Energy	Capacity of Distributed Energy accessed to the system	Distributed Energy capacity	interval type
		Utilization ratio of Distributed Energy	The ratio of Distributed Energy average power and Distributed Energy capacity accessed to the system	benefit type
	Energy-saving emission reduction	CO_2 emission reduction	Calculate CO_2 emission reduction by converting the capacity of Distributed Energy accessed to the system	benefit type
		SO_2 emission reduction	Calculate SO_2 emission reduction by converting the capacity of Distributed Energy accessed to the system	benefit type
Controll-able risk	Accident risk	Load reduction ratio in N-1 faults	The ratio of load reduction in N-1 accident	interval type
		Load reduction ratio in N-1-1 faults	The ratio of load reduction in N-1-1 accident	cost type
	Investment risk	Dynamic investment pay-back period	Time that net earing of project consumes to counter the all investment, the smaller the indicator, the smaller the finance risk of the system investment	cost type
		Internal rate of return	Discount rate that makes the cash flow NPV of the series income and expenditure zero, the bigger the indicator, the stronger the system ability to resist economy risk	benefit type
	Ability to withstand risks	Ability to withstand natural disasters	Ability to withstand nature disaster in different nature disaster situation, including the design standard of important equipment, disaster protection and Repair resilience ability, etc.	qualitative index
		Ability to against other risk (human or external force damage)	Ability to withstand man-made or external damage(e.g., electric equipment damage, theft, etc. caused by line construction), important power plants, substations and equipment security, the secondary protection measures, etc.	qualitative index
Social benefits	The degree of popularity of rural electricity	Rural household energized rates	Count the proportion of electrical rural residents to the total number of residents	benefit type
		Each household each ammeter rate	Count the proportion of the number of rural residents achieved each household each ammeter to the total number of residents	benefit type
	The harmony power supply	Customer Evaluation Satisfaction	Measure the degree of customer satisfaction reduction caused by power failure	benefit type
		Comprehensive distribution voltage qualification rate	Measure qualified distribution voltage level comprehensively	interval type

A Comprehensive Evaluation Index System Based on Hierarchy

Previously described various quantitative and qualitative indicators reflect the technical and economic characteristics of different aspects in the distribution planning schemes, however there is no uniform measure standards, direct results' comprehensive assessment of indicators cannot be achieved. Quantitative indicators can be normalized by directly scoring method, there are many indicators scoring methods, currently the most widely used is fuzzy membership method, using the

membership function to reflect the membership degree of the investigated fuzzy object, that is to create a mapping from domain (all being investigated objects) to [0,1]. In practical applications, indicators can usually be divided into the cost, benefit and interval categories. Based on the characteristics of each index evaluation attributes, combined with expert recommendations for program simulation, get the membership function closest to the real situation. Qualitative indicators are normalized by fuzzy comprehensive evaluation method. Following, different categories of indicators are introduced combined with specific guidelines and constraints. Other indicators can refer to such methods to get.

Interval Type Indicator Interval type indicator refers to indicator of which values within a range of interval. Membership function is as Eq. (1):

$$Z_{ij}=\begin{cases} 1-\dfrac{q_{1j}-y_{1j}}{\max\left\{\left|y_{ij}-y_j^{''}\right|\right\}}, & y_{ij}<q_{1j} \\ 1, & y_{ij}\in[q_{1j},q_{2j}] \\ 1-\dfrac{y_{ij}-q_{2j}}{\max\left\{\left|q_{1j}-y_j^{\min}\right|,\left|y_j^{\max}-q_{2j}\right|\right\}}, & y_{ij}>q_{2j} \end{cases} \tag{1}$$

i=1,2,⋯,n; $j\in\Omega_4$. Where $[q_{1j}, q_{2j}]$ is the best stable range of indicator, y_j^{min}, y_j^{max} are the indicator's minimum and maximum values.

Taking "Average transformer capacity hooked into pubic lines" for example, when evaluate the indicator, although there is no clear guidance or constraints, according to relevant guidelines [15], considering 50% line load rate of various line types, the line load range is [4.11,5.27](MW). Consider the case: transformer capacity-load ratio is 100%, the reasonable range of indicator is [4.11,5.27] (MW), which is also consistent with the planning data.

Benefit and Cost Type Indicator Benefit indicator refers to indicator of which values the bigger the better, cost indicator refers to indicator of which values the smaller the better. Sine and cosine distribution membership function are used respectively, the mathematical expression are as Eq. (2,3):

$$\mu=\begin{cases} \sin\left(\dfrac{\pi}{2}\cdot\dfrac{x-x_0}{1-x_0}\right), & x_0\le x\le 100 \\ 0, & x<x_0 \end{cases} \tag{2}$$

$$\mu=\begin{cases} \cos\left(\dfrac{\pi}{2}\cdot\dfrac{y}{y_0}\right), & 0\le t\le t_0 \\ 0, & t>t_0 \end{cases} \tag{3}$$

Such as "electric reliability" is benefit type indicator, " average interruption hours of customer"is cost type indicators. where x_0 is the system minimum average rate of power supply reliability; y_0 is the maximum customer average interruption time, specific values can be selected under the relevant guidelines and specification[15]. Different load density regions are judged according to different standards.

Treatment to qualitative indicators The indicators of ability to withstand risks are qualitative indicators, which need assessment results given by relevant experts according to the power grid plan and design, and it can be divided to very high (1 point), high (0.75 points), medium (0.5 points), low (0.25 points), very low (0 points) five levels. In this paper, fuzzy comprehensive evaluation method is used to deal with such indicators, changing the qualitative indicators to quantitative to treat with.

Conclusions

Traditional comprehensive evaluation index system mainly focuses on evaluation of the status of the grid, this paper proposes a comprehensive evaluation index system suitable for planning grid. Compared with the traditional grid evaluation, this paper combines the characteristics of planning grid, simplifying some of the indicators which are not readily available in the planning grid programs,

such as the traditional "user interruption frequency" index is simplified as "cable rate" index, measuring the reliability of network planning from the perspective of the device. Guided by the long-term development strategy of China southern power grid, this paper proposes some new indicators in accordance with relevant standards and regulations, what's more this paper gives specific values of the membership function parameters to standardize index of different dimensions, laying the foundation for the comprehensive assessment.

Acknowledgements

This work was supported by Guang Dong Power Grid Development Research Institute Co., Ltd (Research on Evaluation System Power Grid Planning Alternatives) (030000QQ00120020).

References:

[1] HU Rong. "Study on Assessment of Medium Voltage Distribution Network Planning Method [D]". *Shanghai Jiaotong University Thesis*, 2008.

[2] WU Kaigui. WANG Shao, ZHANG Anbang, et al. "Power System Reliability Assessment Model Based on RBF Neural Networks [J]", *Proceedings of the CSEE*, 2000, 20(6):9-12.

[3] XIE Yinghua, WAGN Chengshan. "Reliability Assessment of medium voltage distribution system based on partition feeder [J]", *Proceedings of the CSEE*, 2004, 24(5):35-39.

[4] Li Weixing, Wang Peng, Li Zhimin et al. "Reliability evaluation of complex radial distribution systems considering restoration sequence and network constrains[J]". *IEEE Transactions on Power Deliver*, 2004, 19(2):753-758.

[5] LIU Wei, GUO Zhizhong. "Research on Distribution Network security indicators [J]". *Proceedings of the CSEE*, 2003, 23(8):85-90.

[6] LI Zhengkun, CHEN Xingying, Liu haoming, et al. "Real-time evaluation and analysis capabilities with the power grid [J]". *Automation of Electric Power Systems*, 2009, 33(6):36-39.

[7] Miu K N, Chiang H D. "Electric distribution system load capability：Problems formulation，solution algorithm，and numerical results[J]". *IEEE Trans. on Power Delivery*, 2000, 15(1): 436-442.

[8] Luo F Z, Wang C S, Xiao J, et al. "Rapid evaluation method for power supply capability of urban distribution system based on N-1 contingency analysis of main-transformers[J]". *Electrical Power and Energy Systems*, 2010, 32(10):1063-1068.

[9] XIAO Jun, GAO Hai-xia, GE Shao-yun, et al. "Evaluation Method and Case Study of Urban Medium Voltage Distribution Network [J]". *Power System Technology*, 2012, 36(8):95-99.

[10] XIAO Jun, CUI Yanyan, WAGN Jianmin, et al. "Comprehensive Evaluation Index System and Method of Distribution Network Planning [J]". *Automation of Electric Power Systems,* 2009, 32(15): 36-40.

[11] YE Yun." Research and Application of the grid with integrated assessment methods[D]". Chongqing: Chongqing University, 2011.

[12] People's Republic of China Electric Power Industry Standard: City power grid safety standards(DLT 256-2012) [Z]. Beijing: National Energy Board, 2010.

[13] State Grid Corporation of China: Urban Power Network Planning and Design Guidelines (Q / GDW 156-2006) [Z]. Beijing: State Grid Corporation of China, 2006.

[14] National Energy Board: grid security risk management (tentative) (country safe [2014] No. 123) [S] Beijing: National Energy Board, 2014.

[15] State Grid Corporation: Distribution Network Planning Design Technical Guidelines (Q / GDW 1738-2012) [Z]. Beijing: State Grid Corporation of China, 2012.

Advanced Materials Research Vols. 960-961 (2014) pp 1582-1587

doi:10.4028/www.scientific.net/AMR.960-961.1582

The Relationship among the Security, Efficiency and Adequacy of Electrical Power Grid based on the Novel Evaluation Method

Wangcheng Long[a,1], Feng Han[b,1], Xueming Zhang[c,2], Dong Peng[d,1] and Hui Li[e,1]

[1]State Power Economic Research Institute, Beijing China

[2] Department of Electrical Engineering Tsinghua University, Beijing, China

[a]longwangcheng@chinasperi.sgcc.com.cn, [b]hanfeng@chinasperi.sgcc.com.cn, [c]zhangxueming@mail.tsinghua.edu.cn, [d]pengdong@chinasperi.sgcc.com.cn, [e]lihui@chinasperi.sgcc.com.cn

Keywords: Electrical Power grid; Grid Security, Grid Efficiency; Grid Adequacy; Incidence Relationship; Power system evaluation.

Abstract: In order to study out the incidence relationship among security, efficiency and adequacy of Electrical Power Grid, a novel analyze model considering grid evolution and a relationship evaluation method is proposed in this paper. The model incorporates in fast dynamic and slow evolution. The former is based on an improved OPA model with low frequency load shedding control and the outage risk calculation. The latter is consists of increasing load, up-grading and constructing equipments including power plants, transformers and transmission lines, Using the model simulation the power grid development process. Based on the model, the customer outage risk caused by cascading failure is obtained in several times, the efficiency index and grid scale index are solved at the same times, these data are the basic data for analyze the incidence relationship among the security, efficiency and adequacy of electrical power grid. In this paper, the power grid of Kaifeng City in Henan Province, of China is used to simulate the evolution. The results show that the relationship among the security, efficiency and adequacy of grid is as exponential function, and a reasonable range of efficiency and adequacy of grid are proposed.

Introduction

At present, the electrical power becomes the lifeline of the national economy, which plays an extremely important role in social and economic development. At first, with the economic growing rapidly and living standard of the people enhancing quickly, the requirement of electricity power has been more and more, as a result, the construction of power system which include in power plant, transmission line, electrical transformer, ancillary facility and so on also has been constructed and put into operation more and more, the development of power grid should be ahead of the demand of power, on the other word, the power scale have to keep appropriate development margin. Secondly the security of power grid was becoming the highest priority-first matters because the grid security closely concerned the security of the economy, society people life and future. Thirdly, the power grid enterprise and the department of assets management request that the equipments must be effective.

Form the above three points, the power grid have to be secure, efficient and abundant. However, it is well known that the three aspects are conflicting opposing reciprocally. Study on the incidence relationship of the grid security, grid efficiency and grid adequacy become a important matter for government, electrical business, power enterprise and academia, it makes total sense to study a optimizing and coordinating developing way of power grid.

In this paper, a novel analyze model considering grid evolution and a relationship evaluation method is used to study on the relationship, and the key index of three aspects are proposed, the power grid of Kaifeng City in Henan Province of China is used to simulate the evolution. The results shows

that the relationship between the security and efficiency is increase exponential one, but the relationship between the security and adequacy is decrease exponential one.

Novel Evaluation Models

The power grid is continuous and quickly developing in China for match the requirements of power transfer, in order to calculate the data of the security, efficiency and adequacy of grid realistically, the process of grid development in long term is simulated in this paper. The upgrade of power grid in a long term has been studied by many academias, and different evolvement models have been proposed. Cao Y J and his colleges simulated the evolution based on a local-world evolving net-work model[1-2]; Mei S W and Ni X P did the same work based on BA scale free network model and compared the results with the real power grid through some indicators[4], such as clustering coefficient. However, the grid upgrade in the models above is quite different from the real one. For example, the upgrade of transmission lines only leads to larger capacity and smaller impedance, and N-1 criterion is not considered. So the evolution models cannot be used to estimate incidence relationship among the security, efficiency and adequacy of electrical power grid.

As we known, the proportion of satisfied N-1 criterion equipment and entire one of grid is necessary to achieve 100% in plan and operation. As a result, the proportion cannot measure the security of grid. Many blackout models are proposed to analyze power outage risks and grid safety [5-8], because blackout risk cannot be ignored [9-11]. Power outage risks caused by cascading failures are used to represent the security of grid in this paper.

The efficiency reflects the use ratio of electrical equipment, the transformer utilization efficiency (is average load ratio) and power line utilization efficiency is used to assess the efficiency of grid. The transformer utilization efficiency is related to power line load ratio in power grid with normal structure and function, therefore, The transformer utilization efficiency are used to represent the efficiency of grid in this paper.

The adequacy reflects the development of margin of the power grid, in other words, it shows that how much the newly increased electricity demand can be meet by the power grid. The transformer capacity-load ratio of power grid in an area is widely used to evaluate the adequacy and to guide the power system planning and construction. To accommodate the transformer utilization efficiency, the transformer capacity-load ratios are used to represent the efficiency of grid in this paper.

Based on the existing works about evolution simulation and risk analysis of cascading failure, this paper constructs a blackout model with evolution, which is driven by the N-1 criterion and load increasing. And power outage risks the security, efficiency and adequacy of electrical power grid will be obtained and the relationships are analyzed.

The Novel Evaluation Models inclued three parts, the frist is the strategy of evolution in slow dynamic, the second is the blackout model with evolution, the third is analyze the relationship based on the each stage data by simulation process . Then the power grid of Kaifeng city in Henan Province of China was used as an example to make analysis. Finally, the results show that the relationship among the security, efficiency and adequacy of grid is as exponential and some conclusions are given.

2.1 Evolution in slow dynamic

The development of power grid is driven by many factors. Among those factors, load growth is the essential incentive. When the load level is so high that power grid cannot meet the security needs of users, the system needs to be construct and upgrade. This construct and upgrade includes not only enhancing power generation capacity in the power supply side, but also increasing the transmission and capacity, under such condition, the power grid need keep high security in transmission of more enormous energy. The upgrade of generator, transformer and transmission line is particularly triggered by the three conditions: power reserve, load ratio and N-1 criterion. When there is a lack of power reserve in systems, generators will be built according to the distribution of resources to meet the power needs; In addition, in order to ensure the security, the components of system will be upgraded when it works with high load rate or the N-1 criterion is not satisfied. In order to complete

the upgrade of generators, transformers and transmission lines, a number of factors need to be considered, such as equipment capacity, voltage level, the access to network, etc. In this paper, we use a simplified strategy which is based on the actual situation of the grid's upgrade. The detail evolution strategy has been introduced clearly in before paper [12].

2.2 Black model with evolution in fast dynamic

Black model is used to simulate the process of cascading failure with initial faults and give assessment to blackout risk. This fast dynamic is based on the improved OPA model in this paper, and it is able to analyze low frequency load shedding [13]. The combination process of the fast dynamic and the slow dynamic is shown in Fig. 1. The slow dynamic is used to simulate the evolution of power grid in a long time frame, and the fast dynamic is used to calculate the power outage risks, the transformer utilization efficiency and the transformer capacity-load ratios.

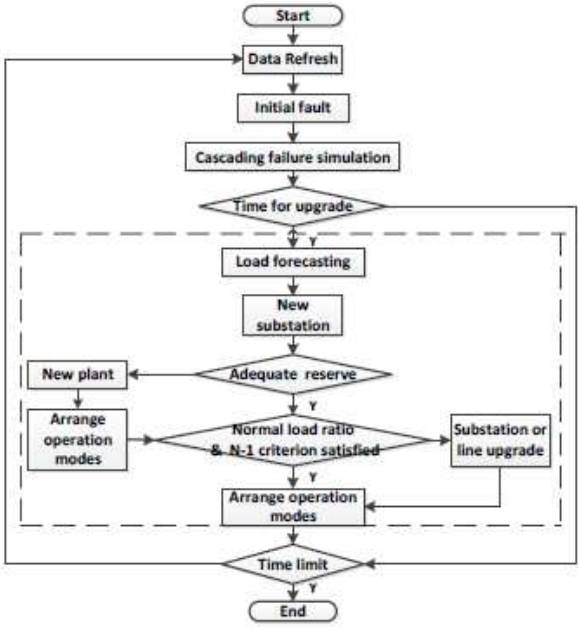

Fig. 1 Flow chart of blackout model

2.3 The relationship analysis method

The relationships of the three targets which represent the three aspects are analyzed by statistics, matching, regression analysis based on data from every time fast dynamic calculations. The equation of regression is utilized to study the reasonable range under acceptable power outage risks.

Empirical Analysis and discussions

The power grid of Kaifeng city in Henan Province of China was used as an example to make analysis in this paper. The power grid mainly contains 220kV and 500kV grade equipments, Power grid of Kaifeng city in Henan Province of China is shown in Fig. 2.

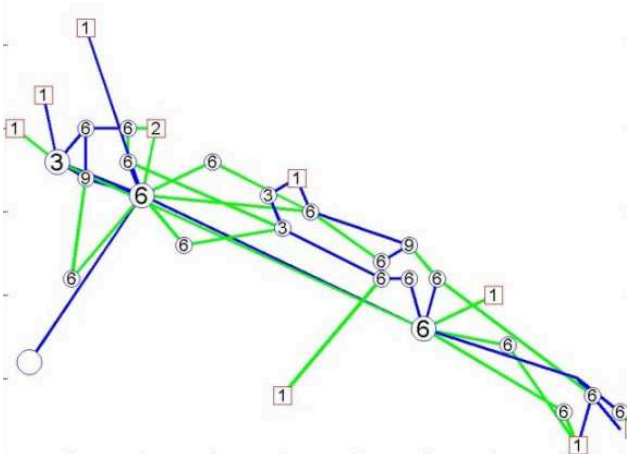

Fig. 2 Power grid of Kaifeng city in Henan Province of China

Two hundred times fast dynamic and tem times slow dynamic are calculated in simulations with power demand growth rate 6%, therefore, there are two hundred data arrays of the three targets are obtained to analyze the relationship. The relationship between the power outage risks and transformer utilization efficiency is shown in Fig. 3. With the transformer utilization efficiency increasing, the power outage risks increases correspondingly. There was an exponential relationship between the power outage risks and transformer utilization efficiency though regression analysis. The exponential equation is shown as Eq.1, with the variance is 0.7364. In equation, y is power outage risks, and x is transformer utilization efficiency.

$$y=0.0061e^{33.602x} \tag{1}$$

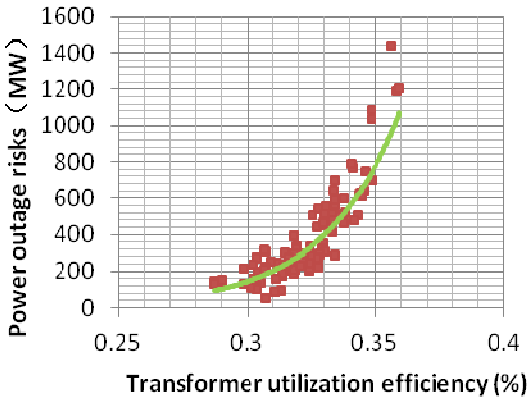

Fig. 3 The relationship between power outage risks and transformer utilization efficiency

The relationship between the power outage risks and the transformer capacity-load ratios is shown in Fig. 4. With the transformer capacity-load ratios increasing, the power outage risks decreases correspondingly. There was an exponential relationship between the power outage risks and transformer capacity-load ratios though regression analysis. The exponential equation is Eq. 2, with the variance is 0.6991. In equation, y is power outage risks, and z is transformer capacity-load ratios.

$$y=10^{6}e^{-1.8178z} \tag{2}$$

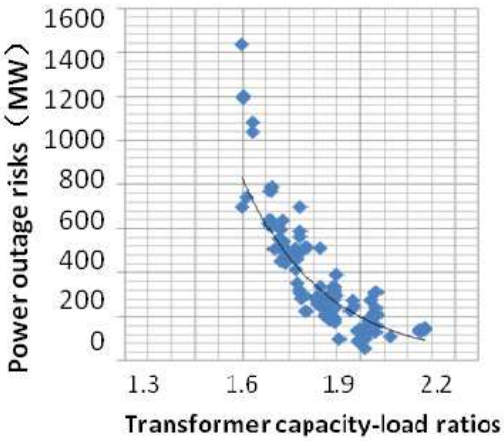

Fig. 4 The relationship between power outage risks and the transformer capacity-load ratios

We utilized the novel evaluation method simulating the power grid evolution. With the transformer utilization efficiency increasing, the power outage risks exponential increase, and with the transformer capacity-load ratios increasing, the power outage risks exponential decrease, those are reasonable as the common. As exponential equation, the independently variable *x, z* change a little, the dependent variable *y* will change greatly. Therefore, we consider controlling the power outage risks within certain limits, the independently variable *x, z* should limited in the value which avoid the power outage risks increasing greatly. Form the Fig.3, the power outage risks increasing sharply when the transformer utilization efficiency is greater than 35%. From Fig.4, the power outage risks increasing sharply when the transformer capacity-load ratios is less than 1.6, and the power outage risks increasing slowly when the transformer capacity-load ratios is more than 2.2, in other words, putting more cost to develop the power grid and increase transformer capacity-load ratios would do not assist to reduce the power outage risks and improve security of grid. Under that conditions, we can figure out that the reasonable transformer utilization efficiency is about 35% for the power grid, the reasonable transformer capacity-load ratios is range from 1.6 to 2.2.

Conclusions

Novel evaluation method which contained fast dynamic and slow dynamic was used to simulate the development process of the power grid. The power grid of Kaifeng city in Henan Province of China was used as an example to study the relationship among the security, efficiency and grid scale of electrical power grid., the calculation results were regressed as equation as exponential. And the reasonable transformer utilization efficiency is about 35% for the power grid, the reasonable transformer capacity-load ratios is range from 1.6 to 2.2 were concluded from the exponential function. The relationship among the security, efficiency and adequacy of electrical power grid are expression in quantitative equation to a certain extent.

Acknowledgements

This work was financially supported by the Technology Project of State Grid Shanghai Municipal Electric Power Company (NO.524400140003).

References

[1] Cao Y J, Wang G Z, Han Z X, Ding L J, Bao Z J,Cao L H, “A Cascading Failures Model in Power Grid Considering Topology Evolvement” Automation of Electric Power Systems,33(9), pp 5-10, May. 2009.

[2] Cao Y J, Wang G Z, Jiang Q Y, Han Z X, “A neighborhood evolving network model” Physics A, 349(6) pp. 462-466, Sep. 2006.

[3] Li X, Chen G R, “A local-word evolving network model” Physics A, 328(1/2) pp. 274-286, Jan. 2003.

[4] Mei S W , Ni X P, “Several new progresses on the complexity research of the interconnected power network” Journal of Changsha University of Science and Technology :Natural Science, 5 (2): pp. 128, Jun. 2008.

[5] Dobson I, Carreras B A, Lynch V E, Newman D E. “An initial model for complex dynamics in electric power system blackouts”. Proceedings of The 34th Annual Hawaii International Conference on System Science, Hawaii, USA, pp. 710-718, Jan. 2001.

[6] Mei S W, He F, Zhang X M, Wu S Y, Wang G, “An improved OPA model and blackout risk assessment” Power Systems, IEEE Transactions vol. 24, pp. 814-823, Apr. 2009.

[7] Mei S W, Yadana, Weng X F, Xue, A C, “Blackout model based on OPF and its self-organized criticality” Control Conference, 2006. CCC 2006. Chinese, pp. 1673-1678, Aug. 2006.

[8] Xia D M, Mei S W, Hou, Y H, “A Power System Blackout Model Based on OTS and Its Self-organized Criticality”, Automation of Electric Power Systems, 31(12), pp. 9-13, Jun, 2007.

[9] Dobson I, Carreras B A, Lynch V E, Newman D E. “Complex systems analysis of series of blackouts: cascading failure, criticality, and self-organization”. Proceedings of Bulk Power System, Dynamics and Control: Vol 6, Aug 22-27, 2004.

[10] Carreras B A, Newman D E, Dobson, Poole A B.“Evidence for self-organized criticality in electric power system blackouts”.IEEE Trans. on CASI, 51(9), pp. 1733-1740, Sep. 2004.

[11] Mei S W, Zhang X M, Cao M. “Power Grid complexity”, Bei Jing: Springer 2011.

[12] Guo J P, Zhang X M, Huang, S W, Long W C, Peng D , “A Novel Evaluation Method for Power Grid Evolution with Economy and Security Constraints”, Washington, DC PESGM IEEE 2014 , (To be published).

[13] Zhang Z A, Guo J P, Zhang X M, Mei S W, Li X M, Yao R. “Blackout Model Considering Frequency Stability and Applications”. Proceedings of the CSU-EPSA. (To be published).

Advanced Materials Research Vols. 960-961 (2014) pp 1588-1591

doi:10.4028/www.scientific.net/AMR.960-961.1588

Summary of the stability chanllenges and safe operation of power systems in view of dispatching

Xiangdong Zhao[1], Xin Zhao[2,a] ,Mingjun Lv [1] ,Jianguo Liu [1] ,Fengzhen Liu [1] and Yanhui Sun [1]

[1]State Grid Liaoning Chaoyang Power Supply Company, Chaoyang, Liaoning,122000, China

[2]State Grid Beijing Tongzhou Power Supply Company,Beijing,101100,China

[a]tsustar@126.com

Keywords: Power system ; Safe and stable operation ; Smart grid ; Intelligent scheduling

Abstract. The Internet and the gradual implementation of the continuous power grid market in recent years make the power system more complex under different operating environment. Safe and stable operation of power grids have become increasingly important . With the rapidf development of the grid and constant innovation, safe and stable operation also has a new requirement , because the rapid development of the power system brings more This paper analyzes the causes of blackouts and reviews security of the power system stability problems related to measures on the security and stability of the power system operation .

Introduction

In recent years, a wide range of power outages have occurred several times in the international community , causing huge losses to the economy of these countries , and seriously affect the social life. It is highly concerned by both governments and society . These incidents can be attributed to the damage events of the stability in the form of a variety of power system accidents , which are major disasters of the power system . Due to the complexity of the grid , once stable damage accidents occur , they tend to be in fast developments and the situation is more complex in the development process. There may be some automatic device failure, at which point the power grid control center is in a very nervous state among dispatchers ,it takes some time to ascertain the correct response to the accident. Therefore, it is difficult to find enough time to do the timely and correct treatment ,which is likely to disturb the control of the system , and to further expand the system collapse with serious consequences.

Blackout Analysis

By analyzing the major international incidents of the grid[1-7] , it can be concluded that the deep-seated causes of Blackouts are as follows :

Lack of overall planning of grid construction. Power grid structure is irrational , such as 345kV and 138kV lines high and low voltage lines operating in ring networks , lack of disconnecting methods between the low voltage side and high voltage side of the line of measures, untimely important information exchange between the regional power grid. Due to the hierarchy of dispatching system,the regional dispatcher can not the whole picture of the large system. Lack of unified management and coordination between the various power companies scheduling is another potential threat.

Problems in China's Power Grid

China's power grid is in a stage of rapid development. Although a lot of spectacular results has yielded , there still exists developing deficiencies. The foreign operating experiences provide good,

we have summarized the problems encountered in the development of the grid based on the current research results [8-10].

The characteristics of large interconnected power system and effectiveness of security and stability measures remain to be deeply studied ;

Unified planning and coordination of the power system during the power system (in particular, plants and networks) ;

The relationship between the grid margin and investment ; capacity issues under the electricity market ;

What is the condition of separating interconnected grid ;

The ratio of receiving power from the outside power grid and voltage support problems in the end of systems ;

Large power grids and emergency warning judgment method; Monitoring security and stability , evaluation and in-depth study of control theory ;Comprehensive assessment techniques

Power system of multiple data sources and cross- network real-time access to information issues ;

Configuration of protection relay devices and coordination of set value and level difference .

Measures to Ensure Safe and Stable Operation of the Power Grid

Three defense of security

"Guide on Security and Stability" (Chinese Standard for Power System, DL 755-2001)provides general rules of the security and stability of the power system to withstand disturbances ,where capacity is divided into the following three levels:

First-class standards : maintain stable operation and normal power grid ;

Second-class standards : maintain stable operation , but allow part load losses ;

Third-level standard : When the system can not maintain a stable operation , it is necessary to prevent system collapse and minimize loss of load .

To facilitate the analysis , we divided the state power system operation into normal, alert, emergency, extreme urgency (loss of synchronism) state and restoring state. Corresponding to the appropriate state, we set up three lines of defense to ensure that the power system in the face of various security incidents can stay stable operation :

The first line of defense : the rapid removal of faulty components with protection devices ,which is the most direct and effective way to ensure the power system transient stability ;

The second line of defense : The stability control system , cutting machine and generator , load shedding and other measures to ensure the stability of the power system in the event of large disturbances ;

The third line of defense : When the power system stability rans across multiple serious destroyed failures, relying step splitting device step- column grid solution by emergency frequency and voltage control device to maintain a balance of two parts after splitting power grid to prevent the accident and prevent blackouts .

Smart Grid

Strong smart grid is based on UHV power grid as the backbone[11-13] ,which calls for strong and coordinated development of grid power at all levels as the basis for communication and information platform for the support.It is with information technology, automation, interactive features , including power system generation, transmission, substation, distribution , consumption and scheduling of the six areas. The goal is to achieve a high degree of integration of integration covering all voltage levels , "power flow, information flow, business flow" , with a strong and reliable , cost-efficient , environmentally clean , transparent, open and friendly interactive connotation of modern grid.

Strong and smart are two basic development requirements of modern power grid. Strong are based on smart is the key. Strong emphasis is laid on highly integrated intelligent grid based on holistic, systematic approach to objectively describe the basic features of modern power grid development.

In terms of the optimal power source structure, strengthen coordination of plants and networks, smart grid is able to improve the safe operation of different power level and strengthen power system safety. Implementation of energy generation scheduling , the smart grid technology can be used to promote energy conservation . China now relies on the national wind power , solar power research and development (experimental) center to accelerate clean energy technology research and network operation and control , and to promote large-scale scientific and rational utilization of clean energy[14-16]. On the basis of national scenery storage demonstration projects, the modern clean energy technologies provide technical support and engineering potential of large-scale utilization of clean energy and flexible network operation . In order to promote the popularization and application of high-capacity storage technology it is important to adapt current guidelines to meet the needs of the rapid development of clean energy .

In terms of transmission on the basis of UHV power grid as the backbone[16] ,the development aims at the coordinated development of power at all levels of the strong grid with integrated application of new technologies, new materials , new processes to achieve the investigation digital, modular design, operation status , information standardization and application network. Full implementation of the transmission line, state-based maintenance and entire-life-cycle management.

Promoting the transformation of end-user energy use patterns is to improve energy efficiency by 2020 and strive to achieve final energy consumption in electricity accounted for more than 26.2% of the target[16] .

Intelligent scheduling

Today, large power grid to grid scheduling brings new challenges[17][18] , safe and stable operation of large power grids requires intelligent scheduling to provide technical support. National energy policy needs to access large-scale renewable energy and optimal allocation of resources , which is scheduled to run and control the grid presents new challenges. Constructed with Chinese characteristics strong smart grid . Smart Scheduling is an important part of the brain center of the smart grid . Comparing to non-adaptive scheduling , we need to build intelligent scheduling.

The overall technical route is to adhere to independent innovation , development and standardization and to carry out intensive management , research and development of intelligent scheduling technology support system as the core, around three main building and four categories applications[16] . The implementation of schedule management is through the integration of homogenization scheduling jobs . Around three main means ,sharing platform supporting is the integration of distributed , multi-dimensional coordinate security and defense and fine -optimized scheduling. Construction of four major categories of applications is the real-time monitoring and early warning applications with security check application , the application program scheduling and dispatch management applications.

Summary

Continuing to strengthen the construction of three lines of defense supporting while improving the stability control devices and a variety of automatic safety device is key to preventing a chain reaction of accidents and preventing serious damages to the master device and to avoid blackouts and ensure the rapid development of the national security, social stability and national economy.

References

[1] Xue Yusheng. The way from a simple contingency to system-wide disaster—Lessons from the Eastern interconnection blackout in 2003. Automation of Electric Power Systems，2003，Vol 27,No.18,pp.1-5,37(in Chinese).

[2] Fu Shuti. Summary on power system security problems on 2004 IEEE PES meeting and recommendation for developing defense measures. Automation of Electric Power Systems，2005，Vol 29,No.8,pp.1-4(in Chinese).

[3] SunYuanzhang，Mei Shengwei. Exploring the new advantages of the electric power system through international cooperation. Science Foundation in China，2003，Vol,17,No.3,pp.185-187(in Chinese).

[4] Amew. Power system operation corporation limited. New Delhi：National Load Dispatch Centre，2012.

[5] Tang Yong, Bu Guangquan, Yi Jun ,Analysis and Lessons of the Blackout in Indian Power Grid on July 30 and 31, 2012,Proceedings of the CSEE Vol.32 No.25 ,2012, pp.167-173

[6] Yin Yong-hua，Guo Jian-bo，Zhao Jian-jun，Bu Guang-quan,PRELIMINARY ANALYSIS OF LARGE SCALE BLACKOUT IN INTERCONNECTED NORTH AMERICA POWER GRID ON AUGUST 14 AND LESSONS TO BE DRAWN Power System Technology,2003, Vol. 27 ,No. 10 pp.8-11

[7] Gao Xiang，Zhuang Kan-qin，Sun Yong Lessons and Enlightenment from Blackout Occurred in UCTE Grid on November 4, Power System Technology, 2006, Vol. 31 No. 1,pp. 25-30

[8] Yuan Qingyun. Present state and application prospect of ultra HVDC transmission in China.Power System Technology，2005，Vol.29,No.14,pp.1-3(in Chinese).

[9] Shu Yinbiao，Liu Zehong，Yuan Jun，et al. A survey on demonstration of UHV power transmission by state grid corporation of China in the year of 2005. Power System Technology，2006，Vol.30,No.5,pp1-12(in Chinese).

[10] Yang Yihan，Zhang Dongying，Ma Qian，et al. Study on the architecture of security and defense system of large-scale power grid. Power SystemTechnology，2004，Vol.28,No.9,pp.23-27(in Chinese).

[11] Liu Zhenya. Innovation of UHVAC transmission technology in China . Power System Technology，2013，Vol 37,No 3,pp.1-8 (in Chinese).

[12] Xue Yusheng. Space-time cooperative framework for defending blackouts Part I From isolated defense lines to coordinated defending . Automation of Electric Power Systems，2006，Vol.30,No.1,pp,8-16(in zChinese).

[13] Wang Jianming，Sun Huadong，Zhang Jian. Stability characteristics and coordinated control strategy of interconnected grid integrated with UHVDC transmission line from Jinping to Sunan . Power System Technology，2012，Vol.32,No.12.pp.66-70(in Chinese).

[14] Shu Yinbiao. Current status and development of national grid in China, 2005 IEEE/PES T&D Conference. Dalian，China：IEEE，2005.

[15] Tang Yong. Framework of comprehensive defense architecture for power system security and stability [J]. Power System Technology，2012，Vol36,No8,pp.1-5(in Chinese).

[16] Liu Zhenya,"Smart grid technology.",China Electric Power Press,2010.

[17] Yang Shengchun，Yao Jianguo，Gao Zonghe，et al. Intelligentdispatching decision-making system based on integration of powerdispatching automation system. Power System Technology，2006，Vol 2,S2,pp.176-180(in Chinese).

[18] Chen Zhenyu，Wang Gang，Li Haifeng，et al. A MAS-based coordinated protection system for wide area power network,Power System Technology，2008，Vol.32,No.5,pp.42-45(in Chinese).

Advanced Materials Research Vols. 960-961 (2014) pp 1592-1596

doi:10.4028/www.scientific.net/AMR.960-961.1592

Classification Method of Galloping Region for Transmission Lines

Lichun Zhang[1, a *], Junhui Li[1, b], Jialun Yang[1, c], Bin Liu[1, d] and Kuanjun Zhu[1, e]

[1] China Electric Power Research Institute，Haidian District，Beijing 100192，China

[a]bkdzlc@126.com, [b]ljh@epri.sgcc.com.cn, [c]yangjialun@epri.sgcc.com.cn,
[d]liub1@epri.sgcc.com.cn, [e]zhukuanjun@epri.sgcc.com.cn

Keywords: galloping region, transmission line, frequency method, coefficient method, meteorological-geographical method.

Abstract. Transmission line galloping is self-excited vibration of iced conductor with low frequency and large amplitude, the countries almost all over the world have occurred transmission line galloping, which caused a great economic loss. Drawing the effective distribution map for galloping plays an important role in guiding the anti-galloping design, the key of this work is to establish a scientific method for galloping region division. In this paper, several methods for galloping region division were introduced: frequency method, coefficient method and meteorological-geographical method. This paper also compared the applicability of various methods and their advantages and disadvantages. It shows that the meteorological-geographical method is the best choice for us to divide galloping region at the present time. However, in the practical application, we should take all the applicability of the three methods into consideration to get a reasonable division for galloping region.

Introduction

Galloping region division is a complex work, which is based on the statistical data of galloping, the meteorology factor that affect galloping and the topographical data where the galloping occur [1-3]. After detailed analysis of the whole data above, determine a set of principle to describe the galloping strength, and then divide the galloping region according to this principle. At present, there are mainly three methods using to divide galloping region in China, which are: frequency method, coefficient method and the meteorological-geographical method.

To divide galloping region of transmission line, we must first clarify what is *galloping region*. Obviously, the so-called *galloping region* refers to the galloping prone areas of transmission lines, these areas are usually glaze prone areas. Lines are easily iced in winter when it is glaze and strong wind, if the angle between line direction and wind direction is larger (generally greater than 45 degrees), a self-excited vibration with low frequency and large amplitude will occur, that is conductor galloping. The probability and strength of galloping may vary greatly due to the weather and terrain conditions are different, especially there are micro-topography and micro-meteorological region at the same area, thus it is necessary to divide the galloping region rationally according to its strength level. The standard of classification for galloping region is not unified in the world at present. According to China's specific situation, it is divided into four grades, namely: strong galloping region (level 3), medium galloping region (level 2), weak galloping region (Level 1) and non-galloping region (level 0).

Frequency Method

On the basis of statistical analysis in some areas, galloping region was divided into different grades according to the strength and frequency galloping occurred, this can be referred to as: frequency method [4-5]. "Frequency" here means the average number of galloping occurred in a certain length of time. This method is influenced by the size and the number of lines, it is more appropriate to the areas which have a large number of lines in use. However, for the other areas which have no lines yet, it is not applicable or too rough. In addition, it is easy to underestimate the possibility of galloping with

frequency method because galloping not frequently occurs. The principles of classification are as follows.

*Strong(Level 3)*The area which galloping has occurred 5 times and above in recent 10 years; and galloping might occur much easily according to the comprehensive meteorological and geographical factors, such as the open areas which have a higher frequency of freezing weather.

*Medium(Level 2)*The area which galloping has occurred 3 to 4 times in recent 10 years; and galloping might occur easily according to the comprehensive meteorological and geographical factors, such as the open areas which have high frequency of freezing weather.

*Weak(Level 1)*The area which galloping has occurred 1 to 2 times in recent 10 years; and galloping is not easy to occur according to the comprehensive meteorological and geographical factors.

None (Level 0) The area where galloping has never occurred in recent 10 years; and galloping will never occur according to the comprehensive meteorological and geographical factors.

After the classification of galloping region, we can draw a distribution map of galloping region for a certain area. Fig. 1shows a distribution map of galloping region for Liaoning province in China.

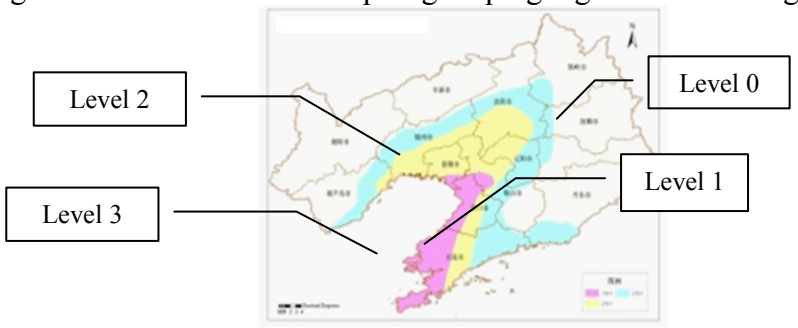

Fig.1 Galloping distribution map of Liaoning province

Coefficient Method

Based on the analysis of meteorological, geographical data when galloping occurs, use a certain coefficient to express galloping strength of different regions in a same area, this method was called coefficient method [6]. This method is relatively complicated, for it needs to estimate the galloping coefficients. The advantage of this method is that the galloping strength can be reflected more directly, and also has an instruction function to the areas which have no lines yet.

According to the analysis of the statistical data, the two parameters, thickness of ice and velocity of wind in galloping region, can be expressed by normal distribution function. The function expressions of these two parameters are shown in Eq. 1 and Eq. 2.

Ice thickness $X \sim N(\mu_X, \sigma_X^2) = N(14, 4^2)$, mm . (1)

Wind speed $Y \sim N(\mu_Y, \sigma_Y^2) = N(15, 3^2)$, m/s . (2)

The effect of topography for galloping can be represented as coefficient ξ, which ranges from 0~1, for the flat open areas, ξ values for 0.7~1, for the small part of flat areas in the mountain, ξ values 0.3~0.7, for hilly or mountain areas, ξ values below 0.3. These values are changeable; ξ can be revalued according to the actual situation in applications.

Transmission line galloping affected by ice thickness, wind speed and terrain together, and these three factors are independent of each other, then the probability of occurrence for galloping can be defined as Eq. 3.

$$P(\xi XY) = \frac{\xi}{24\pi} \iint e^{-\left(\frac{(X-14)^2}{32} + \frac{(Y-15)^2}{18}\right)} dXdY \quad (3)$$

Ice thickness of generic structure in an area was represented with x, and wind speed in winter was represented with y, according to many years'(generally not less than 20 years) statistics, these two parameters can be regarded as normal distribution, the expressions are: $x \sim N(\mu_x, \sigma_x^2)$, $y \sim N(\mu_y, \sigma_y^2)$.

According to the 3σ rule of normal distribution function, we can draw the following four intervals (Eq. 4 to Eq. 7).

3σ interval of ice thickness in galloping region,

$$X \in [\mu_X - 3\sigma_X, \mu_X + 3\sigma_X] = [2,26], \text{mm} . \quad (4)$$

3σ interval of wind speed in galloping region

$$Y \in [\mu_Y - 3\sigma_Y, \mu_Y + 3\sigma_Y] = [6,24], \text{m/s} . \quad (5)$$

3σ interval of annum ice thickness in a certain area

$$x \in [\mu_x - 3\sigma_x, \mu_x + 3\sigma_x], \text{mm} . \quad (6)$$

3σ interval of annum wind speed in a certain area

$$y \in [\mu_y - 3\sigma_y, \mu_y + 3\sigma_y], \text{m/s} . \quad (7)$$

Through the analysis of the statistical data, we can see that the annum ice thickness and wind speed intervals calculated according to the 3σ rule are often greater than the actual data intervals, therefore, the actual data (include ice thickness and wind speed) intervals should be considered in the application, the $[x_1, x_2]$ and $[y_1, y_2]$ are defined as the actual ice thickness interval and the actual wind speed interval respectively.

Intersect three intervals of ice thickness (3σ interval of ice thickness in galloping region, 3σ interval of annum ice thickness in a certain area and the actual interval of ice thickness), and then we can get a final interval of ice thickness which will be used in calculating the galloping coefficient. In the same way, a final interval of wind speed will also be obtained. They are shown in Eq. 8 and Eq. 9.

$$[2,26] \cap [\mu_x - 3\sigma_x, \mu_x + 3\sigma_x] \cap [x_1, x_2] = [\underline{X}, \overline{X}] . \quad (8)$$

$$[6,24] \cap [\mu_y - 3\sigma_y, \mu_y + 3\sigma_y] \cap [y_1, y_2] = [\underline{Y}, \overline{Y}] . \quad (9)$$

Then we can calculate the galloping coefficient η, which was shown in Eq. 10.

$$\eta = \frac{\xi}{24\pi} \int_{\underline{X}}^{\overline{X}} \int_{\underline{Y}}^{\overline{Y}} e^{-\left(\frac{(X-14)^2}{32} + \frac{(Y-15)^2}{18}\right)} dXdY . \quad (10)$$

According to the analysis above, galloping region can be classified as Table 1shows:

Table 1 Relationship between galloping strength and the coefficient

Strength of Galloping	Principles of classification
Strong (Level 3)	$\eta \geq 0.6$
Medium (Level 2)	$0.2 \leq \eta < 0.6$
Weak (Level 1)	$0.1 \leq \eta < 0.2$
None (Level 0)	$0 < \eta < 0.1$

Meteorological-geographical Method

It is easy to know that the meteorological-geographical method is to divide galloping region by analyzing meteorology and geography data. The first step is to get galloping meteorological days in 10 years through analyzing the historical meteorology data, second is to obtain galloping revising days in 10 years after studying on topographic feature, and then verify the result by experiences gathered from operating lines.

Concept involved in meteorological and geographical method.

Galloping days The day when transmission line galloping occur.

Daily minimum temperature The lowest temperature observed in 24 hours (Beijing time 08 am to 08 am of the next day)

Daily average relative humidity The average value of relative humidity observed in 24 hours (Beijing time 08 am to 08 am of the next day).

Daily maximum wind speed and corresponding direction The maximum wind speed and corresponding direction observed in 24 hours (Beijing time 08 am to 08 am of the next day).

Topographic prominence The difference between the highest and lowest altitude in a specific region.

Galloping meteorological days in 10 years Converting in 10 years period, the days that match the meteorological conditions for galloping.

Galloping revising days in 10 years Revised Galloping meteorological days in 10 years by terrain data.

Division of galloping region. To divide the galloping region by meteorological-geographical method, we must first determine which meteorology factors are intimately associated with galloping. After analysis and screening, four kinds of meteorology factors, the dominant wind direction, the maximum wind speed in the dominant wind direction, average relative humidity and daily minimum temperature, were selected as parameters for the model to decide galloping or not. Table 2 shows the threshold of the four meteorology parameters. If the weather satisfies the sum of these four threshold intervals in some day, transmission line galloping will probably occur, and this day will be regarded as a galloping meteorological day.

Table 2 Meteorological parameter threshold interval *

Parameters	Threshold interval
Dominate wind direction	north
Daily maximum wind speed in dominate wind direction (m/s)	4～15
Average relative humidity (%)	70～100
Daily minimum temperature(℃)	-5～3

*Note: The threshold interval above is just an example, the valuesare different in various areas, and they are determined by actual situation in a certain place.

The determination of meteorological days in 10 years. Collect the meteorological data in recent 10 years or more, calculate the number of days satisfying the four parameter thresholds in Table 2 at the same time, and convert them into meteorological days in 10 years (the sum of days *10/ total number of years). Using this method to do the calculation work for each meteorological station, and then get all the meteorological days in 10 years in a certain region by interpolation.

The revision work by topographic prominence. Take the digital elevation model (DEM) as background and 2000m as radius to calculate the topographic prominence, and then draw its distribution map. When the topographic prominence is larger than 100m, fit the meteorological days in 10 years and the topographic prominence, according to the function relationship between them, the meteorological days in 10 years will be revised. If the topographic prominence is less than 100m, it is not necessary to revise the meteorological days in 10 years.

The division of galloping region. Table 3shows the division result for galloping region using meteorological and geographical method.

Table 3 The division results for galloping region using meteorological and geographical method.

Strength of Galloping	Galloping revising days in 10 years
Strong (Level 3)	≥140
Medium (Level 2)	[90,140）
Weak (Level 1)	[50,90）
None (Level 0)	[0,50）

Summary

(1) The advantages of frequency method is simple and objective, it is applicable for the area which has detailed galloping observation data. For the areas which have no lines or lack of galloping observation data, frequency method is not applicable, because it will underestimate the possibility of the occurrence of galloping.

(2)The coefficient method is realized by probability and statistics, and it cannot be influenced by the transmission lines. Thus it is applicable for the areas which are lack of galloping observation data. However, it is difficult to obtain meteorological parameters which this method requires, and it is too theoretical to be popularization and application.

(3) Meteorological and geographical method is extended from coefficient method. The advantage is that this method is not affected by the transmission lines. And the meteorological and geographical data it requires is easy to obtain. So this method is applicable to all areas that no matter lines has been built or not. This method has been widely used in power system of China.
These three methods of galloping regional division have their own advantages and disadvantages respectively. In practical application, we should take all the applicability of the three methods into consideration to get a reasonable division for galloping.

Reference

[1] Jianguo Ma. Regional Division of Conductor Galloping of Power Networks in Hubei Province [J].Electric Power Construction.1995, (5), p. 39-40.

[2] Jianguo Ma. Hubei Power Grid Transmission Line Galloping Region and Anti-Galloping Method Research [J]. Hubei Electric Power.2002, 26(4) , p.100-104.

[3] Liang Liu, Hongbin Liu, Chun Deng et al. The Classification Principle of Galloping Probability Distribution Map in North China Power System[R].CIGRE 2012, B2-210-2012.

[4] Wei Zhang, Fei Wang, Zhongrui Zhang. Study on Partition for Transmission Line of Liaoning Grid Galloping Region and Drawing Rule of Galloping Distribution Map [J].Electric Power Technology of Northeast.2011, (1) , p.9-12.

[5] FufengRen, Ming Lu, Hongtao Zhang, et al. Henan Power Grid Transmission Line Galloping Region and Anti-Galloping Method Resesrch [J].Henan Electric Power. 2010, (4) , p.14-18.

[6] Ming Tu，LichunZhang，KuanjunZhu , et al. Zoning Method for Galloping of Transmission Lines [J].Electric Power Construction. 2011,32(4) , p.26-28.

Advanced Materials Research Vols. 960-961 (2014) pp 1597-1601

doi:10.4028/www.scientific.net/AMR.960-961.1597

Research on applying SDN technology to electric power data center

Jian Di [1, a], Bidan Liu[1, b]

[1]School of Control and Computer Engineering, North China Electric Power University,

Baoding 071003, China

[a] dijian6880@163.com ,[b] liubidan901115@163.com

Key words: electric power data center; SDN; OpenFlow; a multi-domain collaboration model

Abstract: In order to meet the developing demand of the new generation of data center, and to better satisfy the need of the smart grid, we introduce the OpenFlow-based SDN technology to electric power data center. Because there are many switches in electric power data center, it requires the use of a distributed multi-controller to manage, however there is currently no mechanism for these controllers to cooperate with the each other. Based on these questions this paper presents a collaborative model for multi-domains OpenFlow networks, which allows different network domains to collaborate with each other in an efficient way.

Introduction

Currently, electric power data center added more than 5000 thousand data records everyday. Especially with the access of renewable energy and distributed power, the amount of data in electric power data center will surge. This will propose higher demands for storage and process of massive smart grid information. However, the traditional data center network with scattered resources, limited bandwidth, low routing efficiency and other shortcomings; it is difficult to meet the power company's highly scalable, high robustness, flexible topology and other needs.

Due to the proposed of software defined network (SDN) technology and successfully applied in Google data center, a new solution has been provided to solve the bottleneck problem of electric power data center. SDN using OpenFlow protocol constitutes a control/forwarding separated networks to meet the intensive server requires centralized management in data center. This paper will research on applying OpenFlow-based SDN technology to electric power data center, to achieve efficient addressing, load balancing and other functions in data center.

OpenFlow-based SDN technology

In traditional internet, control and data forwarding are tightly coupled on network equipments, which result the management of control plane in network complicated and make the new technologies deploying on existing networks difficult. The core idea of SDN is decoupling traditional network architecture into the application layer, control layer, forwarding layer separated architecture and adopt standardization to achieve centralized management of network and make the network applications programmable [1].OpenFlow realizes the idea of SDN and represents the realization of a prototype and deploy instances of SDN technology. OpenFlow network consists of OpenFlow switches, FlowVisor and controller.

OpenFlow switch. OpenFlow switch is the core of the OpenFlow network, which mainly responsible for the data forwarding, representing the data forwarding plan. The structure is shown in Fig. 1. Each flow table in the OpenFlow switch contains a set of flow entries; each flow entry performs packet look-ups and forwarding. Data packets enter the switch to obtain the corresponding operation by querying the flow table. A secure channel is an interface between OpenFlow switch and controller .Controllers will configure and manage OpenFlow switches according to OpenFlow protocol through the interface.

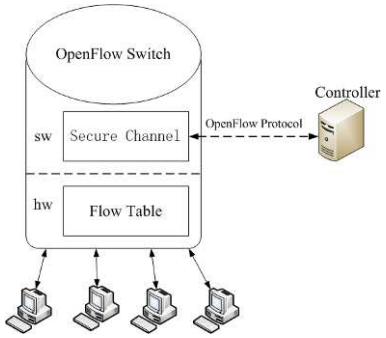

Fig.1 Structure of OpenFlow switch

FlowVisor. FlowVisor between controller and OpenFlow switch is used to realize the virtual layer of OpenFlow network. FlowVisor allows multiple controllers in an OpenFlow network but its mechanism is to slice the network into separate slices and let each slice managed by a controller.

Controller. Controller implements its functions through global topology view, and its control logic represents control plan. Controller controls the flow table in OpenFlow switches through OpenFlow protocol, in order to enable centralized control of the entire network.

In OpenFlow-based SDN, the underlying network devices are abstracted from the upper layer control and applications. So it may provide high performance, flexible management and granular traffic control for multiple vendors' network devices.

Analysis of characteristics and problems in electric power data center

Characteristics and problems in current electric power data center are as follows:

(1)Large data flow and many network devices. Data center is the core part of the smart grid. It achieves the distribution of data in production, scale, finance and other critical business. While the number of network devices is large and the management of the devices is difficult. Superposition of multiple application requirements led power information network requires higher performance.

(2)Network protocol to be improved. A typical electric power data center network topology is divided into core layer, import layer and access layer. All equipments are redundant cross-connect resulting multi-level network and complicated link [2].In data center, extensive of Transmission Control Protocol (TCP) is used. While the original TCP protocol is for the Internet, does not consider the low latency and high bandwidth characteristics in data center network.

(3)Due to strong smart grid construction needs, some information systems have been developed in order to guarantee the stable operation of the smart grid. These information systems need a strong network that almost uninterrupted. However, the current network still relies on Spanning Tree Protocol (STP) to protect link redundancy on layer 2 and Virtual Router Redundancy Protocol (VRRP) to protect equipment redundancy on layer 3. The fastest switching time is seconds or more, the network can't support the needs of the sensitivity of the information network of the smart grid.

Applying SDN technology to electric power data center

With the development of the cloud computing and SDN technology, applying OpenFlow-based SDN technology to data center has become a hot topic. Paper [3] first proposed applying OpenFlow technology into the data center. Paper [4] evaluated the usability of OpenFlow in different data center environments, such as $PRV2_1$, $PRV2_2$and EDU1. Based on the above researches, this paper proposes applying OpenFlow-based SDN technology to electric power data center.

The early design of OpenFlow implemented network management and control functions only through a single controller. Obviously, a single controller can't meet the need of large-scale electric power data center. This requires the use of multi-controller solutions. Paper [5] presented a distributed event-based control plane for OpenFlow, which allows network operators deploy any number of controllers in their networks. Paper [6] proposed two heuristic algorithms for the area

partitioning problem in a multi-controller controls. But there is no mechanism for cooperation between the controllers. When the controller received a cross-domain packet request but it didn't know the best transmission path, the controller used the flooding mechanism to route the data packets. This causes the controller can't deal with cross-domain data packets effectively. This paper proposes a collaborative model to build a multi-domain OpenFlow network, allowing for mutual cooperation through effective manner between different network domains.

Construction of the collaborative model for multi-domains OpenFlow networks

Each switch is connected to a nearest controller and directly controlled by the controller, so that each switch and the connected controller together compose a small OpenFlow network domain. Outside the network domains, a separate global controller is set and a communication channel between the controllers and the global controller is established, using a simple protocol to handle the exchange of specific information between the parties. The model is shown in Figure 2. Global controller maintains global topology view and has the global routing app, controlling the entire network on the basis of the overall. Main components of the model are shown in Fig.3.

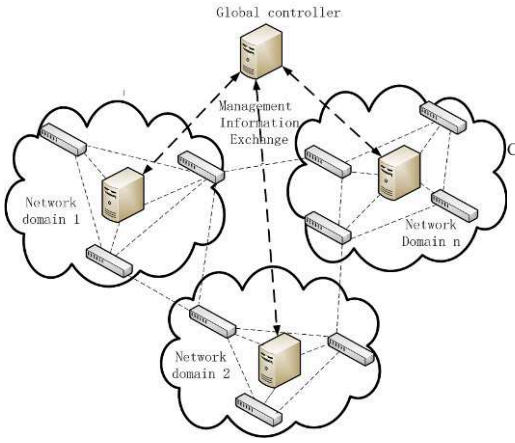

Fig.2 The collaborative model

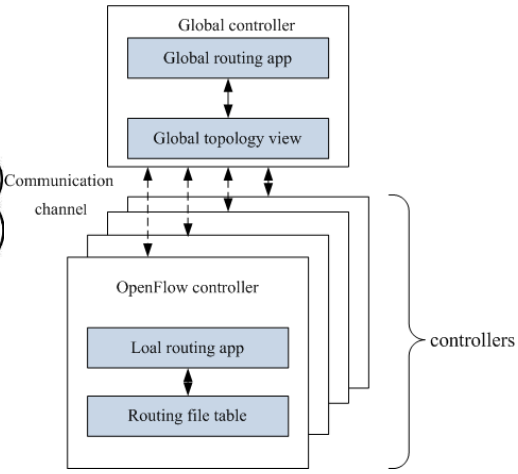

Fig. 3 Main components of the model.

Global topology view. Global topology view holds all the cross-domain routing network information and the estimated routing cost of the routing path between cross-domain switches in a network domain.

(1) Cross-domain connection table

A cross-domain connection is a link between two OpenFlow switches belonging to two different network domains. The fields contained in cross-domain connection table are shown in Table 1.As the role of source switch and destination switch in a cross-domain are equal, each cross-domain connection will be presented by only one entry in the table.

Table 1 Cross-domain connection table

Source Controller ID	Source Switch ID	Source port	Destination port	Destination Switch ID	Destination Controller ID

(2) Estimated routing cost table

In a network domain can be seen as two different types of switches: cross-domain OpenFlow switches which have a cross-domain connection; normal OpenFlow switches which have connection only in a domain. An estimated routing cost refers to the shortest routing path between cross-domain switches in a network domain. The shortest routing cost is calculated by the controller of that domain. The fields are shown in Table 2.

Table 2 Estimated routing cost table

Controller ID	Source Switch ID	Destination Switch ID	Estimated Routing Cost

All cross-domain switches and computed routing costs between these switches form each network domain together constitute the global topology view. The global topology view looks like a "weighted graph" as shown in Fig.4.In the "weighted graph", cross-domain switches are nodes(some normal switches in each network domain are not shown);connections between cross-domain switches are edges and the estimated costs between cross-domain switches are weights .

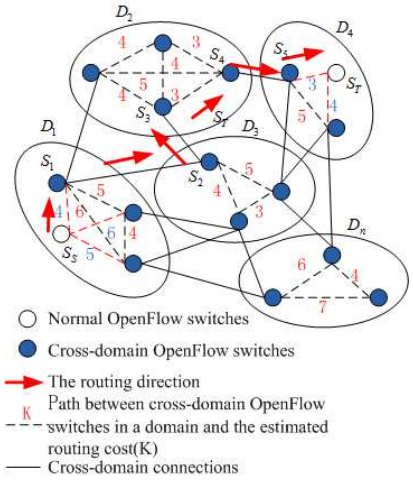

Fig.4 An image of the Global Topology View seen from Global controller

Routing file table. Each controller in the collaborative model has a learning routing file table. Each table entry is calculated on a global level. The fields are shown in Table 3. With the information, he controller can forward cross-domain data packets effectively rather than simply flood, greatly improving the efficiency.

Table 3 Routing file table

Local source switch ID	Terminal destination address	Terminal destination switch ID	Terminal destination controller ID	Local destination switch ID	Local destination output port	Estimated routing cost

Local destination switch ID, output port: In local domain, the ID of switch which the controller needs to route the packet to and the outgoing port number of the switch.

Estimated routing cost: The total estimated routing cost from the local source switch to packet's destination address.

Local routing app and global routing app. Local routing app placed in the controller side is responsible for discovering cross-domain connections in its domain and calculating the estimated routing cost between them. The information will transmit to the gable controller through the communication channel. It is also responsible for adding or deleting entries in the routing file, finding matches in the routing file to forward cross-domain packets. Global routing app placed in the global controller is responsible for building global topology view according to the collected topology information form each controller and using the shortest path algorithm to calculate cross-domain packets routing path.

Works of collaborative model for multi-domains OpenFlow networks

When the controller receives a packet request from one of OpenFlow switches it manages, extracts the destination address in packet header first. If the destination address of the packet within the network domain of the controller, the controller will process it according to OpenFlow1.3 specification [7].If there is no destination address information in the controller (that means destination address of the packet is outside the current controller domain), the controller sends the packet to the local routing app. The application will lookup in the routing file table. If a match is found, the application forwards the packet according to the instructions of the information. If no match is found, local routing app sends a routing instructions request to the global controller.

First, the controller calculates the routing cost between source OpenFlow switch (switch Ss shown in Fig. 4) and all cross-domain OpenFlow switches in the domain. Then the controller sent that information along with the destination address of the packet to the global controller. In global controller, the global routing app sends a route request of destination address to all domains addition to the domain which sending the request. Global controller will know the destination address (switch S_T shown in Fig. 4) according to the controller response and calculate the shortest path using the shortest path algorithm (as the path shown in Fig.4: Ss-S_1-S_2-S_3-S_4-S_5-S_T). Global controller sends routing instructions to the associated controller, these instructions helps to transmit cross-domain data packets effectively.

Conclusions

By analyzing the characteristics and problems the paper proposes applying OpenFlow-based SDN technology to electric power data center. A collaborative model in multi-domains OpenFlow networks is build. The model allows multiple controllers located in different network domains associate with each other so that it can deal with cross-domain data packets effectively. By analyzing the global topology view and adopt effective path computation methods to improve the performance of information exchange between multi-domain networks to provide a new solution for OpenFlow network scalability.

The next work we should do is test the efficiency, performance and scalability of this model. Then we should apply the model to electric power data center; improve the program in the practical application.

References

[1] Qingyun Zuo, Ming Chen, Guangsong Zhao, et al. Research on OpenFlow-Based SDN Technologies [J]. Journal of Software, 2013, 24(5): 1078-1097.

[2] Yongbo Ma. Research and implementation of electric power enterprise data center network via utilization [D]. Shanghai Jiao Tong University. 2012, 12.

[3]Tavakoli A, Casado M, Koponen T, et al. Applying NOX to the Datacenter [C]// HotNets. 2009.

[4]Pries R, Jarschel M, Goll S. On the usability of OpenFlow in data center environments [C]// Communications(ICC), 2012 IEEE International Conference on IEEE, 2012: 5533-5537.

[5]Tootoonchian A, Ganjali Y. HyperFlow: A distributed control plane for OpenFlow[C]// Proceedings of the 2010 internet network management conference on Research on enterprise networking. USENIX Association, 2010: 3-3.

[6]Tam A S W, Xi K, Chao H J. Use of devolved controllers in data center networks [C]// Computer Communications Workshops (INFOCOM WKSHPS), 2011 IEEE Conference on. IEEE, 2011: 596-601.

[7] “OpenFlow switch specification v1.3.0,” Open Networking Foundation, 2012.Available: https://www.opennetworking.org/images/stories/downloads/specification/openflow-spec-v1.3.0

Advanced Materials Research Vols. 960-961 (2014) pp 1602-1611

doi:10.4028/www.scientific.net/AMR.960-961.1602

A Study on Quantitative Methodology to Assess Cyber Security Risk of SCADA Systems

Pil Sung Woo[1, a*], Balho H. Kim[2,b]

[1]Power Economics Lab., Hongik University, Sandsu-dong 72-1 Mapo-gu Seoul, Korea

[2] Power Economics Lab., Hongik University, Sandsu-dong 72-1 Mapo-gu Seoul, Korea

[a]woopilsung@gmail.com, [b]bhkim0711@gmail.com

Keywords: Smart Grid, SCADA Systems, Cyber Security, Optimal Power Flow, Power Flow Tracing, Risk Assessment

Abstract. This paper aims to identify and clarify the cyber security risks and their interaction with the power system in Smart Grid. The SCADA system and other communication networks interact with the power system on a real time basis, so it is important to understand the interaction between two layers to protect the power system from potential cyber threats. In this study, the optimal power flow (OPF) and Power Flow Tracing are used to assess the interaction between the SCADA network and the power system. Through OPF and Power Flow Tracing based analysis, the physical and economic impacts from potential cyber threats are assessed, and thereby the quantitative risks are measured in a monetary unit.

Introduction

Presently power industry is facing diverse environmental changes internally and externally. The smart grid, one of them, is a core assignment promoted as a leading project of low-carbon green growth and a new power system for applying to environmental changes of power industry and enhancing the efficiency of energy use. But, power system needs real-time characteristics strongly and high-level availability (low failure frequency and fast restoration). These become factors making cyber threats of the power system more complicated and fatal than the IT system.

Therefore, this paper has the purposes in clearly defining more and more increasing problems in the security aspect of the smart grid and specifying connectivity with the power system. That is, through specific modeling on the information control system like SCADA and interaction with the power system, a methodology evaluating dangers was proposed, and specialized security measures that the smart grid could be operated stably were established.

Quantitative Methodology for Cyber Risk Assessment of SCADA in the Smart grid

In this section, problems of superficially stayed cyber risks of the smart grid are specified being connected with the physical power system, and the quantification methodology that those problems can be calculated in quantitative numerical values was suggested. Generally, cyber dangers in IT parts are defined as possible risks in occurrence actually from the mixture of vulnerability, threat, and assets.

Like Fig. 1, Vulnerability can be recognized as a parameter defining the relation between threats and assets. Threats mean cyber attacks and can be recognized as an independent variable. Lastly, assets mean a damage scale in case of the outbreak of threats from vulnerability. Namely, assets can be seen as a dependent variable.

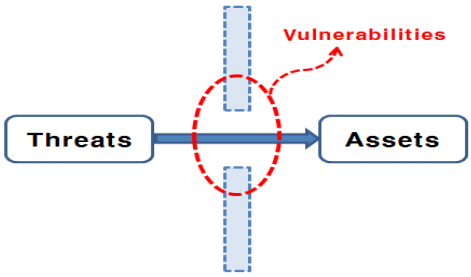

Fig. 1 Concept of Vulnerabilities

From this viewpoint, risks are defined as the possibility of real occurrence from being mixed with threats, vulnerability, and assets. That is, it can be expressed as Eq. l about R (risks) if we define T for threat, V for vulnerability and A for asset. The Eq. 1 means really credible damage scales in the power system.

$$R = T \times V \times A \tag{1}$$

Based on the above Eq. 1, by defining each element in detail, a system to quantify risks can be established. Among them, threats (T) and vulnerability (V) were defined as elements of an information layer and quantified on the basis of advanced study data [1]. In case of assets (A), it was quantified in an aspect of the power system.

Finally, to connect cyber risks with a reliability viewpoint of the power system organically, this paper proposed an evaluation method of synthetic reliability by quantitatively analyzing physical and economical effects which have on the power system based on Optimal Power Flow (OPF) and Power Flow Tracing as core technologies in operation of the power system.

2.1 Quantitative Modeling of the Information layer

In this paragraph, threats and vulnerability as elements of the information layer were quantified. In case of accidents and damage cases due to cyber attacks, because the information does not be opened well and each system has diverse cases and contexts, the quantification is not easy.

Hence, the quantification methodology referred to advanced studies [2,3]. The analysis result of the advanced studies defined attacks mostly through attack graphs in order to quantify cyber threats and vulnerability in the smart grid and tried to measure riskiness by applying generable probability by type of the pertinent attack.

For the quantification methodology of the information layer, some of the courses of AHP (Analytic Hierarchy Process) as one of quantitative methods considering multi-attributes which are often used in social science based on data of advanced studies were introduced in this study.

2.1.1 Quantification of Vulnerability (V)

According to the definition of SANA about the security vulnerability, vulnerability is like a passage to make external threats flow into systems [4]. In other words, vulnerability can be defined as security holes and plays a role of a parameter defining the relation of threats and assets.

This study selected 15 kinds of cyber threats and quantified the vulnerability in accordance with causal relationship between components of the power system and each individual cyber threat. Since the components of the power system are normally run through the control of the SCADA system, they were defined as components (EMS server, SCADA server, communication network, and RTU) of the SCADA system. In the info control system which was previously defined, based on the causal relationship between cyber threats and the components of the SCADA system, the vulnerability was arranged like Table 1.

Table 1 Vulnerablilty analysis of SCADA System

Types of threats \ Components		EMS server	SCADA server	Communication Network		RTU
				TCP/IP	Serial	
Confidentiality	Eavesdropping	V	V	V	V	V
	Traffic Analysis	0	0	V	V	0
	EM/RF Interception	0	0	0	0	V
	Indiscretions by Personnel	V	V	0	0	0
	Media Scavenging	V	V	0	0	0
mixed (Confidentiality +Integrity)	Trojan Horse	V	V	0	0	V
	Trapdoor(Backdoor)	V	V	0	0	V
	Service Spoofing	V	V	0	0	V
Integrity	Masquerade	0	0	0	0	V
	Bypassing Controls	0	0	0	0	V
	Authorization Violations	V	V	0	0	V
	Physical Intrusion	V	V	V	V	V
	Replay	0	0	0	0	V
	Theft &Illegitimate Use	0	0	0	0	V
Availability	Denial of Service	V	V	V	0	0

The shaded part (V) in Table 1 means that substantial risks occur by the relevant vulnerability. Probability of real occurrence and estimated numerable values by statistics are applied to it. Reversely, the non-shaded part (0) means rarity in the possibility of cyber threats. That is to say, because vulnerability can be said to be a probability concept that threats are realized against assets, it comes to have the value of $0 \leq$ vulnerability (V) ≤ 1. In here, 1 means that threats are passed and linked to assets according to Fig. 1. Since vulnerability cannot be defined absolutely, three predictions were made.

First, in case of the absence of the past data, probability of threats is 50%.

Second, because security strength is different according to the components of the SCADA system, after the order by each element is decided, 50% vulnerability is applied. Namely, it can be thought that as servers become stronger and the components are lower, the security strength is lower. Hence, vulnerability was defined as the level of server groups (EMS and SCADA) < TCP/IP section < Serial section < RTU.

Third, there is no differentiation by threat.

Based on already analyzed vulnerability, if an assumption is applied, quantitative numerical values can be calculated like the Table 2.

Table 2 Normalization of Vulnerability

	EMS sever	SCADA sever	TCP/IP	Serial	RTU
Vulnerability	0.057	0.057	0.051	0.057	0.278

2.1.2 Quantification of the Threat (T)

For quantitative numerical values against threats, based on the already analyzed vulnerability, about horizontal axis (by component of the SCADA) and vertical axis (cyber threats), according to latent damage capacity depending on each axis, relative ranking was given. About each axis that the order was given, normalization work was conducted. In here, the meaning of normalization means that if each individual threat exists and the size of threats is assumed to be 1, threat levels are given differentially to each element of the SCADA system.

Above all, as the components of the SCADA system of the horizontal axis, for server groups (EMS and SCADA), TCP/IP communication, Serial communication, and RTU, relative order like 4, 3, 2, and 1 was given according to the latent damage capacity.

The calculation standard of ranking is like the next. In case that server groups are breached by threats, since the latent damages are big, 4 is given. In case of RTU, because it is the lowest thing, the lowest 1 is given relatively. Also, based on the vulnerability analysis table (Table 1), in case that there is no relevance in the components of the SCADA system, 0 is given. Lastly, on the basis of the horizontal axis, assuming that the size of the pertinent threat is 1, normalization is applied. Table 3 is the result of normalization in accordance with potential damages by component of the SCADA.

Table 3 Normalization after Weights according to The Potential Damage Scale on The Horizontal axis

Components / Types of threats	EMS server	SCADA server	Communication Network		RTU	Normalization
			TCP/IP	Serial		
Eavesdropping	0.29	0.29	0.21	0.14	0.07	1
Traffic Analysis	0.00	0.00	0.67	0.33	0.00	1
EM/RF Interception	0.00	0.00	0.00	0.00	1.00	1
Indiscretions by Personnel	0.50	0.50	0.00	0.00	0.00	1
Media Scavenging	0.50	0.50	0.00	0.00	0.00	1
Trojan Horse	0.40	0.40	0.00	0.00	0.20	1
Trapdoor(Backdoor)	0.40	0.40	0.00	0.00	0.20	1
Service Spoofing	0.40	0.40	0.00	0.00	0.20	1
Masquerade	0.00	0.00	0.00	0.00	1.00	1
Bypassing Controls	0.00	0.00	0.00	0.00	1.00	1
Authorization Violations	0.40	0.40	0.00	0.00	0.20	1
Physical Intrusion	0.29	0.29	0.21	0.14	0.07	1
Replay	0.00	0.00	0.00	0.00	1.00	1
Theft & Illegitimate Use	0.00	0.00	0.00	0.00	1.00	1
Denial of Service	0.40	0.40	0.20	0.00	0.00	1

In a similar way, about each kind of threats, relative order was given according to vulnerable degrees. First, about 15 kinds of threats, they were divided into 4 areas such as confidentiality), mixture (confidentiality + integrity), integrity, and availability. Each threat was classified into the pertinent area.

In the purpose of the classification, because kinds of cyber threats are endless, there is somewhat hardness on the normalization. So, in this paper, by applying the concept of CIA as three elements of info security, threats were classified. In addition, regardless of same threats, according to IT and control systems, degrees of threats are different. This is because the capacity of lots of threats has the character of being filtered or amplified in the course of passing over through vulnerability.

This paper applied the security threat level of a control system, not the security threat level in accordance with the IT system. Normally, the power system is operated based on the control system. Therefore, on the control system, since the order of availability > integrity > mixture > confidentiality

is important; the relative order of 4, 3, 2, and 1 was given to each area orderly. Also, on the basis of the vulnerability analysis table (Table 1), in case that they are not applicable to the components of the SCADA system, 0 was given. The size of each individual threat level is assumed to be 1, they were normalized. Here, 1 means the level of a risk that each threat has. Table 4 is a result that the risk degree by each kind of threats was normalized.

Table 4 Normalization after Weights according to The Risk Scale on The Vertical axis

Components / Types of threats	EMS server	SCADA server	Communication Network		RTU
			TCP/IP	Serial	
Eavesdropping	0.04	0.04	0.13	0.20	0.04
Traffic Analysis	0.00	0.00	0.00	0.00	0.00
EM/RF Interception	0.00	0.00	0.00	0.00	0.04
Indiscretions by Personnel	0.04	0.04	0.00	0.00	0.00
Media Scavenging	0.04	0.04	0.00	0.00	0.00
Trojan Horse	0.08	0.08	0.00	0.00	0.08
Trapdoor(Backdoor)	0.08	0.08	0.00	0.00	0.08
Service Spoofing	0.08	0.08	0.00	0.00	0.08
Masquerade	0.00	0.00	0.00	0.00	0.12
Bypassing Controls	0.00	0.00	0.00	0.00	0.12
Authorization Violations	0.12	0.12	0.25	0.40	0.12
Physical Intrusion	0.12	0.12	0.25	0.40	0.12
Replay	0.12	0.12	0.00	0.00	0.12
Theft & Illegitimate Use	0.12	0.12	0.00	0.00	0.12
Denial of Service	0.16	0.16	0.38	0.00	0.00
Normalization	1	1	1	1	1

According to each axis, from executing normalization depending on potential damages and the risk degree, Table 3 and Table 4 were calculated.

If we define, potential damage effect by the system composition elements(horizontal axis) as I_T and risk level by the types of risk(vertical axis) as D_T, the final matrix equation on threat(T) can be expressed as the multiplication ($T = D_T \times I_T$) between the matrix elements of I_T and D_T.

2.2 Quantification of Assets (A)

Based on the concept of the smart grid, if assets are calculated, assets of the IT system and assets of the power system all come to be considered. The assets of IT system are commonly called tangible assets including network equipment and intangible assets like software and knowledge information, and so on. On the other hand, assets of the power system mean worth of all elements for constructing the SCADA system.

In this paragraph, to quantify the worth of assets, credible expected outage costs when loss value of communication facilities and pertinent facilities are exposed to threats was only considered.

$$A_n = \sum_{k=1}^{P}\left(LV_n^k(P) + OC_n^k(P)\right) \cdots LV_n^k + OC_n^k \approx OC_n^k \quad = \sum_{k=1}^{P}\left(OC_n^k(P)\right) \tag{2}$$

Here,
P : Power [MW]
k : Lower level compositions of nth SCADA system
A_n : Asset value of n number of SCADA system compositions
LV_n^k : Loss value of communication facilities [KRW]
OC_n^k : Outage cost [KRW]

In quantification of worth of assets defined above, communication facilities and economical worth of expected outage costs are calculated from combining them, normally, because the money of outage damage expenses is overwhelmingly higher than the worth of communication facilities, Eq. 2 presented the approximation into expected outage cost.

Related with quantitative numerical values of expected outage cost, a recently executed 2011 research report of Korea Electrotechnology Research Institute was referred [5].

Table 5 One hour Outage Cost according to the purpose

Region	Residential	Commercial	Industrial
Outage cost [KRW/kW]	2,800	32,365	127,420

2.3 Quantification of Modeling of the Power System

In this paragraph, to analyze the effect that special cyber threats have on the power system, based on optimal power flow calculation as core technology in operation of the power system, using the power flow tracing method, the power system was modeled quantitatively.

Due to physical features of electricity, in the power flow, how much the generation quantity of a special generator flows into a special load cannot be apprehended. Hence, to grasp it, using the optimal power flow calculation, net generation and power flow about a random system was calculated. About already calculated data, using the power flow tracing method, correlation of generation terminals and load terminals was grasped.

2.3.1 Formulation of the Optimal Power Flow (OPF)

The general OPF concept means economic dispatch plans under the technical, physical, and environmental restriction conditions. And conceptually, it is to conduct economic dispatch plans and power flow calculation simultaneously. Using this, the net generation and the power flow can be calculated. These calculated data are essential data to figure out correlation of generation terminals and load terminals. The formulation of OPF used in this paper is like the following.

Objective function $\underset{X_{i,g}}{\text{MINMIZE}} \sum_i \sum_g Cost_{i,g} \cdot X_{i,g}$ (3)

Constraints
$\sum_i Load_i = \sum_i \sum_g X_{i,g}$ (4)
$PF_{i,j,l} = \frac{\delta_i - \delta_j}{x_l}$ (5)
$X_{i,g} \leq CAP_g$ (6)
$PF_{i,j,l} \leq LTmax_l$ (7)

Here,

i, j	: Bus
l	: Transmission line
δ	: Phase angle
x_l	: Reactance of transmission line
$Cost_{i,g}$	: Generation cost
CAP_g	: Capacity of nth generator
Load	: Load of nth bus
LTmax	: Capacity of transmission line
$X_{i,g}$	: Generation of generator
PF	: Power flow

The objective function of Eq. 3 is the function of cost minimization. The constraint condition of Eq. 4 means supply-demand balances of systems. The constraint condition of Eq. 5 means the equation of electric supply-demand in each bus bar. Because of using the DC optimal power flow calculation, the power flow is directly proportional to phase difference and inversely proportional to the reactance of lines. The constraint condition of Eq. 6 is the restriction of generator capacity, and Eq. 7 means the restriction of line capacity.

2.3.2 Power Flow Tracing Method

The concept of power flow tracing is to grasp correlations of each individual generator and load terminals based on power flows linked between generation terminals and load terminals. By this, because how much each individual generator contributes to special loads can be apprehended, in case of disturbance occurrence in the power system, the capacity and damage of a latent outage can be predicted.

About the power flow tracing method, though there are lots of methods, this paper applied the method designed by Felix F. Wu and two people [6]. The power flow tracing method used in this paper was based on a graph theory. The graph theory is proper to solve controversial points on a system topology and can calculate contributiveness effectively between generation terminals and load terminals in the power flow.

Case Study

3.1 A Scenario and Diagram of SCADA System in the Smart Grid

In this study, the power system is composed of three generators and six bus bars. Also, loads are for commerce, industry, and residence. They have different attributes one another. The track capacity was assumed to be same of 100[MW]. This assumption was schematized like Fig. 2.

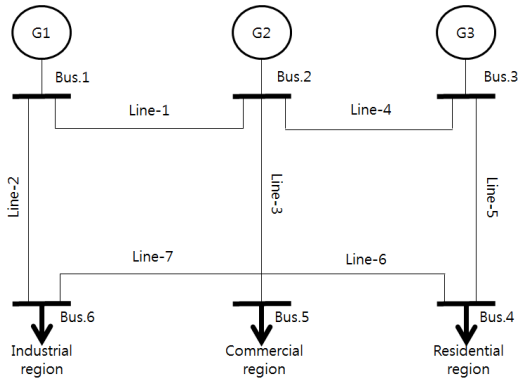

Fig. 2 6-bus power systems

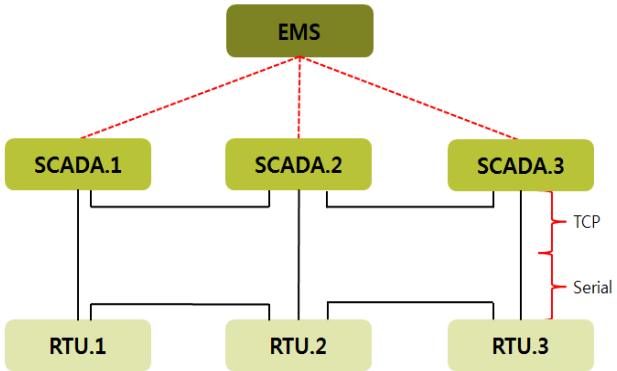

Fig. 3 Diagram of SCADA system in smart grid

On the basis of the simulated power system of six bus, hypothetical networks of the smart grid were modeled. In Fig. 3, the construction of a SCADA system model based on the simulated power system of six bus was schematized.

Table 6 Capacity and Cost of Generator

	Capacity[MW]	Cost[KRW/kW]
G1	100	8
G2	100	10
G3	100	15

Table 7 Load of Regions

	Load[MW]
Residential	50
Commercial	80
Industrial	100

3.2 Analysis of Case Study

Based on the above modeling and data, the result of the optimal power flow calculation is like the next. The red arrow in Fig. 4 means the direction of the power flow.

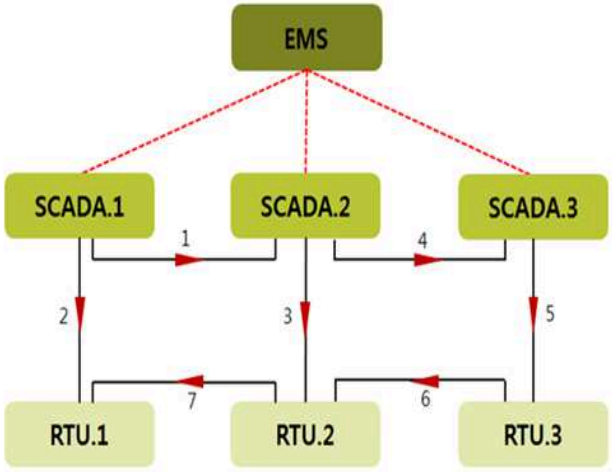

	OPF
	Net generation[MW]
G1	100
G2	100
G3	30
	Power Flow[MW]
1	6
2	94
3	82
4	24
5	54
6	4
7	6

Fig. 4 Result of Optimal Power Flow

On the basis of the result of the above optimal power flow calculation, if the power flow tracing method is used, generation quantity which each generator supplies can be calculated. The result is like Table 8.

Table 8 Result of Power Flow Tracing

	Residential	Commercial	Industrial
G1[MW]	1.257862	4.411292	94.33085
G2[MW]	20.96436	73.52152	5.514114
G3[MW]	27.77778	2.067183	0.155039

Based on one hour outage cost, in expected outage expenses (Table 5) defined by attribute of each load, the arranged result from adding generation quantities (Table 8) supplied by each region is like the following.

Table 9 Outage Cost according to SCADA Components and Regions

	EMS	SCADA.1	SCADA.2	SCADA.3	RTU.1	RTU.2	RTU.3
	Total	Industrial	Commercial	Residential	Industrial	Commercial	Residential
Outage cost	15,871	12,188	3,508	175	12,742	2,989	140
	L_TCP.1	L_TCP.2	L_TCP.3	L_TCP.4	L_TCP.5	L_TCP.6	L_TCP.7
	Commercial	Industrial	Commercial	Residential	Residential	Commercial	Residential
Outage cost	224	11,977	3,064	67	151	149	765
	L_Serial.1	L_Serial.2	L_Serial.3	L_Serial.4	L_Serial.5	L_Serial.6	L_Serial.7
	Commercial	Industrial	Commercial	Residential	Residential	Commercial	Residential
Outage cost	224	11,977	3,064	67	151	149	765
Outage cost : [1millon KRW]							

In Table 9, since EMS normally controls the whole region, outage expenses of all SCADA servers were calculated. Also, because transmission lines are composed of communication facilities (TCP and Serial), power flow values calculated from the optimal power flow calculation were added to elements of communication facilities. In conclusion, Table 9 means worth of assets in sample systems. The worth means only failure by direct cyber attacks. Lastly, the size due to cyber threats was calculated by the combination of threat (T) × vulnerability (V) × asset (A).

Table 10 Result of Risk

	EMS	SCADA.1	SCADA.2	SCADA.3	RTU.1	RTU.2	RTU.3
Threat(T)	0.29	0.29	0.29	0.29	0.58	0.58	0.58
vulnerability (V)	0.057	0.057	0.057	0.057	0.27	0.27	0.27
Asset (A)	15,871	12,188	3,508	175	12,742	2,989	140
Risk(R)	266	204	59	3	2,055	482	23
	L_TCP.1	L_TCP.2	L_TCP.3	L_TCP.4	L_TCP.5	L_TCP.6	L_TCP.7
Threat (T)	0.16	0.16	0.16	0.16	0.16	0.16	0.16
vulnerability (V)	0.051	0.051	0.051	0.051	0.051	0.051	0.051
Asset (A)	224	11,977	3,064	67	151	149	765
Risk (R)	2	95	24	0.53	1	1	6
	L_Serial.1	L_Serial.2	L_Serial.3	L_Serial.4	L_Serial.5	L_Serial.6	L_Serial.7
Threat (T)	0.09	0.09	0.09	0.09	0.09	0.09	0.09
vulnerability (V)	0.057	0.057	0.057	0.057	0.057	0.057	0.057
Asset(A)	224	11,977	3,064	67	151	149	765
Risk (R)	1	59	15	0.33	1	1	4
Unit of asset(A) : [1millon KRW] Unit of risk(R) : [1millon KRW]							

Table 10 is a result of a monetary unit of risks calculated finally based on data of this case study. The above table (Table 10) is represented. In the size of risks, RTU was represented to be the highest. Among them, it can be known that RTU in industrial regions is the most dangerous.

In the meanwhile, although the worth of assets of EMS and SCADA is high, since quantificational numerical values of threats and vulnerability are low, the risk capacity was calculated low relatively. As interpreted in a physical aspect, in case that cyber threats happen, it means that the possibility to be exposed to threats is low regardless of occurrence of great damages. On the other hand, in case of communication lines, it is shown that risk degrees are different according to power flows.

Conclusion

This paper established security evaluation items about an individual system element which is divided physically. About cyber security problems, the paper conducted interaction modeling between SCADA, power system, and power economy. The result of the above case study was proved to apprehend an index of security strength about the power system of future smart grids and also comprehend expected damage degrees in case of existence of cyber threats.

Namely, by evaluating cyber security risks, power system facilities were planned in the synthetic reliability viewpoint of a physical cyber aspect, and a framework to make an optimized decision economically in the pertinent course was provided.

This study is a start stage for quantifying cyber risk. So, by correctly defining and classifying security vulnerability of the smart grid which was not analyzed and perceived specifically, the study meaning is in preparing the foundation to develop future security measures and solutions.

Acknowledgements

This research was been supported by basic research of National Research Foundation of Korea (2012R1A1A2007953), which is funded by Ministry of Education in the 2013.

References

[1] Lawrence Carin, George Cybenko, “Quantitative Evaluation of Risk for Investment Efficient Strategies in Cybersecurity, The QuERIES Methodology”, 2007

[2] S. Massoud Amin, “Cyber and Critical Infrastructure Security – Toward Smarter and More Secure Power and Energy Infrastructures”, Canada-U.S. Workshop on Smart Grid Technologies at Vancouver, 2010

[3] Matias Negrete-Pincetic, Felipe Yoshida, George Gross, “Towards Quantifying the Impacts of Cyber Attacks in the Competitive Electricity Market Environment”, 2009

[4] Vulnerability Assessment, SANS Institute InfoSec Reading Room, http://www.sans.org/

[5] KERI, Seoul National University, A study on compensation amounts and risk hedging methods for damage or loss caused by power interruption, KEMCO, April 2011

[6] Felix F.Wu, Yixin Ni, Ping Wei, “Power Transfer Allocation for Open Access Using Graph Theory-Fundamentals and Applications in Systems Without Loopflow”, ieee transactions on power systems, VOL.15, NO.3, 2000

Advanced Materials Research Vols. 960-961 (2014) pp 1612-1619

doi:10.4028/www.scientific.net/AMR.960-961.1612

A Study on the Estimation of REC Weighting Value for ESS Introduction

Min Chul Kim[1,* a], Ji Yun Lee[2,b], and Balho. H. Kim[3,c]

[1,2,3]Power Economics Lab., Hongik University, Sandsu-dong 72-1 Mapo-gu Seoul, Korea

[a]alscjf03@hanmail.net, [b]jiyeoun486@naver.com, [c]bhkim0711@gmail.com

Keywords: ESS Introduction, Load leveling, RPS, REC market, LCCA, REC weighting value

Abstract. The governments of US, Japan, Europe are planning overall change of electrical power system by adapting Smart Grid as a solution of increasing demand of electricity every year. Especially, ESS have been actively studied to plan efficient use of electrical power and grid-connected. Korea government have been proceeding not only plan of renewable energy but also spread of smart grid. At the same time they have been discussing introduction of ESS which is effective solution of demand response and new growth power. In this study, according to K-ESS policy which is governmental policy of popularizing ESS. we suggest REC weighting value control among the a lot of supporting method that if renewable Genco apply ESS system they would not suffer from lose. It is meaningful because it could be referred to the way of offering governmental incentive for the purpose of decrease peak level and enhance the contribution level of peak.

Introduction

1.1 Research background and necessity

ESS can play a role of demand-side management resource through load leveling by using electricity at the point in time the peak occurs after storing electricity in the light load, and can reduce facility investment such as power plant construction cost and power transmission line construction cost through peak shaving and frequency regulation. In addition, electric power system can be effectively operated at the point in time of peak load of electricity in the winter, summer by securing electric power reserve. And it can play a role of emergency power supply also in case blackout occurs.

However, it is hard to push ESS enforcement considering current condition. First it is very difficult to induce investment of GENCO because of its high initial facility cost expense. Second of all, it's not profitable because current low electric charges make SMP difference between ESS charging and discharging. therefore, the government is required to build basement of ESS to popularize ESS.

This study is intended to present a method of giving aid to initial investment expenditure through a method of adjusting REC weight in case of installing ESS, which is a scheme of grafting RPS onto ESS as one of those. It is the objective of this study to calculate the unit cost recovery in consideration of initial installation cost of ESS and to find out at what level of REC weight the power producer at least doesn't suffer a loss through analysis.

1.2 The related research trends

1.2.1 Overseas trends

<Fig. 1> shows a prospect for the world ESS market size. The whole ESS market is at the level of 7.5 billion dollar as of 2013, and will be at the level of approximately 43.8 billion dollar as of 2020. And consumer and renewable energy-related demand is expected to account for 70% of total demand. And ESS market of 2~10-hour capacity is expected to form the mainstream.

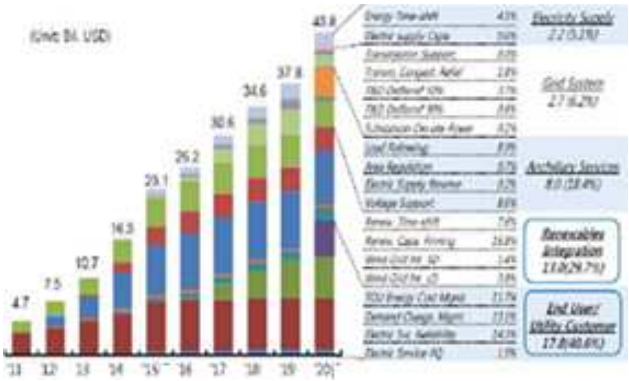

Figure.1 ESS market forecast

Japan pushes forward with a spread project in order to solve the problem of power shortage and in order to develop lithium-ion battery industry. The reason can be considered to be that ESS demand rapidly increased as household emergency power supply after Fukushima Nuclear Power Plant accident. Japan introduced the critical peak pricing with peak price difference of 5 times etc. on the basis of electric charges that are approximately 3 times as expensive as those of Korea. Therefore, the economical efficiency of ESS for consumer is relatively good in comparison with other countries.

U.S. is at the stage of carrying out commercial operation with frequency regulation and wind power ancillary resource, and is a country that first enforces mandatory ESS installation system in the world. A study on the introduction of ESS for frequency regulation is actively in progress in the areas under the jurisdiction of PJM, NYISO, CAISO, and MISO around the mainland of U.S.

In case of Germany among European countries, the purpose of pushing forward with spreading ESS is the same as that of other countries. A subsidy is granted to photovoltaic at the level of 30% in case of being connected with ESS, among main renewable energy resources.

1.2.2 Korean trends

Because Korea lacks production of renewable energy in comparison with advanced countries, there isn't sufficient motive of installing ESS. Therefore, Korean market is being slowly created. At present, it is mainly utilized for the purpose of load leveling at the transmission. distribution end, and consumer end, and is utilized as ancillary resource that compensate the output of wind power generation.

Korea focuses on preoccupying initial market. On the other hand, it is actively pushing forward with making inroads into foreign market such as U.S., Europe, and Japan. However, when considered in the aspect of technical level and demonstration experience of ESS, Korea shows inferiority in comparison with other countries. Because Lithium-ion batteries have reached the world's best level, these have been being exported overseas. On the other hand, it is the actual condition that the fundamental part and material technology of ESS is generally insufficient. The following <Table 2> shows the present technical level of Korean companies.

Table 1 ESS tecknology development status and compare technological level

	The world's best companies	Korea Companies	R&D Level	Technological level (The world's best, 100)		
				Sources	Materials	Manufacture
Li-ion	Mitsubishi	Samsung SDI, LG Chem	Apply	55	70	95
NaS	NGK	POSCO	Initial	35	35	30
Redox flow	Prudent Energy	LS. IS	Initial	40	40	45
Super capacitor	Panasonic	Nesscap, LS. Mtron	Apply	50	55	80
flywheel	Boeing	KEPRI	Product	70	60	70
CAES	PG & E	Samsung	Inicial	50	70	55

A scheme of assessing REC weight

This chapter would minutely explain a method of assessing REC weight in case of introducing ESS, which was presented as a method of the government giving aid to the initial investment expenditure of ESS, as already explained.

First of all, peak time slot is grasped through the analysis of system load pattern. And power generation pattern is analyzed according to each renewable energy resource. Through this, energy source having economical efficiency in installing ESS is selected. And scenario of each period is assessed. Peak time is fixed according to each assessed scenario. And a method of calculating REC weight at that time is explained in detail.

2.1 System load and power generation pattern analysis

2.1.1 System load pattern analysis

First of all, it is necessary to decide what time slot is regarded as peak by grasping the system load pattern. This will be more minutely explained in the case study. Load pattern analysis is meaningful in the respect that it is possible to find out the point in time of applying REC weight because peak period can be grasped.

2.1.2 Renewable energy source power generation pattern analysis

Economical power supply in introducing ESS means a energy source that has a lot of electric energy which can be stored owing to the relatively much energy generated in case of light load, and can obtain an incentive by discharging electricity in the peak time slot. Besides, in case of renewable energy source which has irregular output, the ability to respond to load change according to the demand variation increases. In other words, this means that the output of renewable energy source showing intermittent output can be changed into a high-quality energy source where the output of renewable energy source can be controlled.

2.1.3 Pattern analysis results

The pattern was analyzed on the basis of demand record and the generated energy in 2010~2012. The power generation pattern of renewable energy source was analyzed for 3 types such as wind power, photovoltaic, and fuel cell of which the output was judged to be irregular.

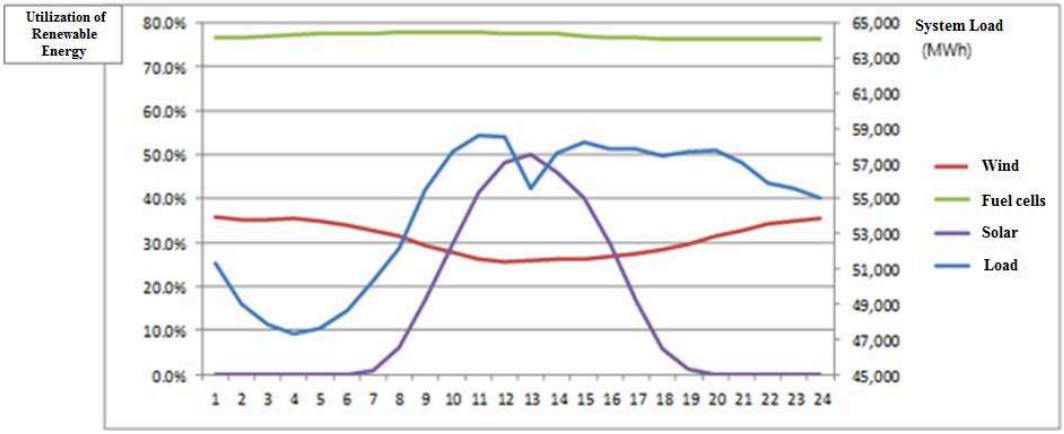

Figure.2 System load and generation pattern for renewable energy('10~'12)

Photovoltaic shows power generation pattern similar to average load curve. Therefore, we judge that there is no power to store in case of light load. Besides, fuel cell generates power on the basis of LNG and thermal power generation. Accordingly, it shows uniform power generation pattern regardless of demand curve. Therefore, it can be thought that the two power supplies under consideration don't have great effect on the mitigation of electricity demand. On the other hand, wind power generation has a characteristic that wind quantity increases owing to the difference in specific heat between land

and sea after sunset. Therefore, it is thought that the effect of ESS installation is excellent in the aspect of peak coincident factor because its share of power generation in light load is high.

2.2 REC weight assessment equation derivation

2.2.1 Renewable power producer profit calculation

The profit calculation method of renewable power producer was used in order to assess REC weight in case of introducing ESS.

$$P_t = X_t(SMP_t + REC \times w) \quad (1)$$

Where,
- t : Period
- P_t : Profit during period t
- X_t : Generation during period t (kWh)
- SMP_t : Average SMP during period t (KRW/kWh)
- REC : REC price (KRW/kWh)
- w : REC weight

The profit of renewable power producer is expressed in the form of the product of settlement part for SMP and settlement part for REC in the above Eq.1. Therefore those can be expressed, putting those together as follows. Dividing this equation by the generated energy X_t, it is changed into the equation for calculating a profit per kWh.

$$U_t = SMP_t + REC \times w \quad (2)$$

U_t : Profit per 1kWh during period t

2.2.2 ESS life cycle cost analysis

This study selected life cycle cost analysis as the method for calculating the initial installation cost of ESS. Life Cycle Cost (LCC) means total cost required in the total lifespan of specific asset or system. And it is useful for the evaluation of economical efficiency according to the change of capacity or size in the same system. There are many conventional economical efficiency analysis methods. However, the following method was selected because it is easy to consider electric charges, electricity consumption, interest rate, etc. for the corresponding period, assume that ESS life is regarded to b approximately 10 years at this point in time.

The following equation is an equation for calculating the life cycle cost of ESS.

$$LCC_{ESS} = \sum_{n=1}^{Life}\left[\left(EC^n + OM^n - OP^n_{benefit}\right)\left(\frac{1}{(1+r)^{n-1}}\right)\right] + C_0 \quad (3)$$

Where,
- n : Year
- r : Interest rates
- LCC_{ESS} : Life Cycle Cost
- EC^n : SMP
- OM^n : O&M Cost
- $OP^n_{benefit}$: Benefit due to Blackout Prevention
- C_0 : The initial construction cost
- $Life$: ESS life

Input data for calculating the cost incurred during ESS installation period is composed of SMP change, operation and maintenance cost, profit for blackout prevention, and initial investment expenditure.

2.2.3 REC weight derivation equation in case of introducing ESS

Putting the equations that have been already explained together, an equation for assessing weight in case of introducing ESS can be expressed as follows.

$$U_{t.ESS} = SMP_t + \Delta SMP_t + REC \times W \quad (4)$$

Where, $U_{t.ESS}$: Life cycle cost per kWh
ΔSMP_t : Difference between SMP
W : REC weight when ESS introduced

ΔSMP_t shows a difference between SMP and standard price according to the discharge of electricity stored in the ESS through power generation in light load. ESS life cycle cost calculated through LCC analysis is applied after being converted into kWh unit. And proper weight in case of introducing ESS is expressed in variable W, and then an equation for deriving final REC weight can be expressed as follows.

$$W = \frac{U_{t.ESS} - SMP_t - \Delta SMP_t}{REC} \quad (5)$$

Case study

Case study is carried out for onshore wind power generation equipment judged to be economically effective through the previous pattern analysis. Scenario is differently applied, being subdivided according to each season of which the heavy load continuance time slot is different.

Table 2 Estimate REC weighting value scenarios

*** Period	Note
Spring(March, April, May)	Period of '10~'12 data
Summer(June, July, August)	
Fall(September, October, November)	
Winter(December, January, February)	

3.1 System load pattern and power generation pattern analysis according to each scenario

First of all, the results of carrying out pattern analysis for deciding on peak time slot according to each scenario are as follows.

Table 3 Demand pattern & Wind generation pattern

	Demand pattern & wind generation pattern	Peak time
Scenario 1 Spring	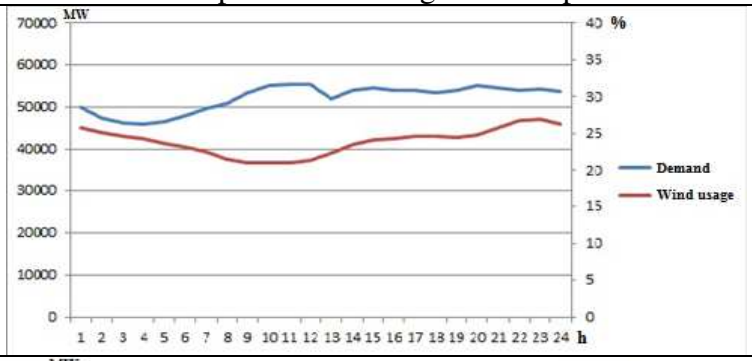	2~6p.m (4h)
Scenario 2 Summer	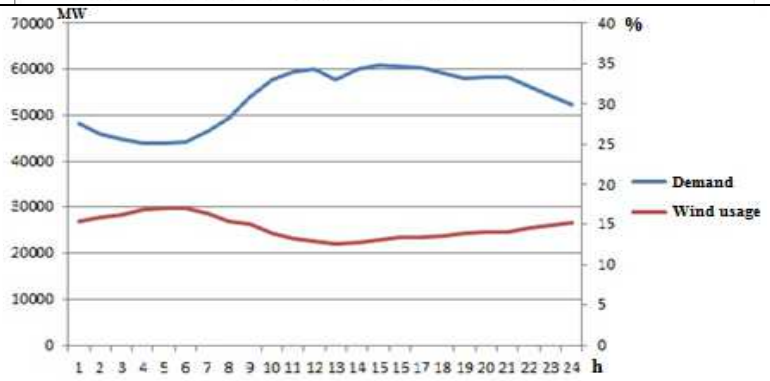	1~5p.m (4h)
Scenario 3 Fall	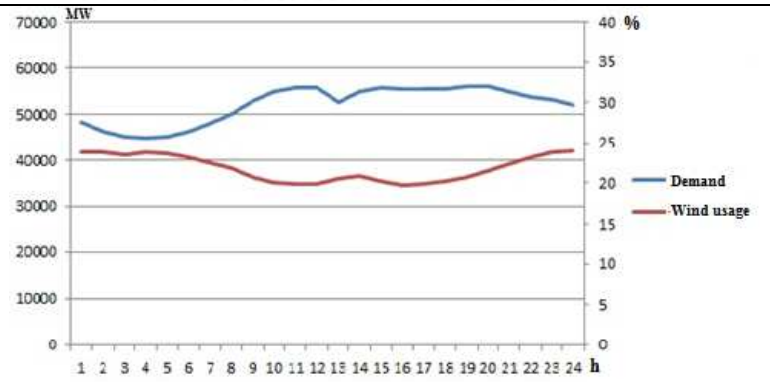	1~5p.m (4h)
Scenario 4 Winter	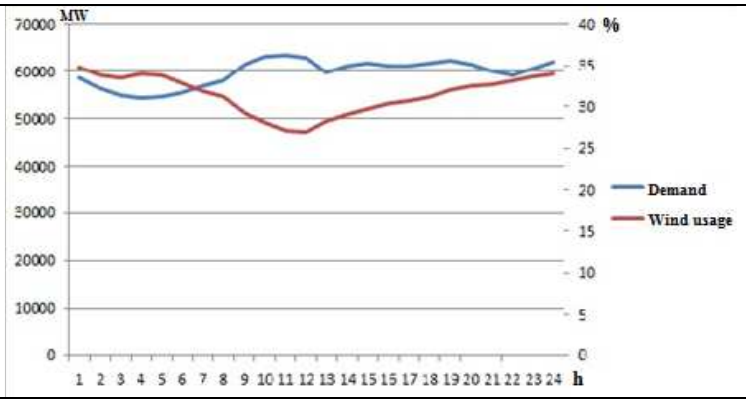	8~12a.m (4h)

3.2 Input data for carrying out case study

A chart of input data for carrying out REC weight analysis in the already selected peak time slot can be made as follows.

Table 4 Input data(SMP)

	SMP (24h, KRW/kWh)	On peak SMP (4h, KRW/kWh)	Difference: ΔSMP (KRW/kWh)
Spring	162.04	169.22	7.18
Summer	174.75	185.28	10.53
Fall	141.15	147.85	6.70
Winter	157.76	168.79	11.03

The following table 14 shows the main assumptions of ESS for the analysis of LCC. With regard to the items of ESS installation cost, when the life of wind power generation equipment is approximately 20 years in this point in time, the life of ESS is approximately 10 years, a half of wind power generation equipment life. As a result, it became necessary to install ESS 2 times during the life of wind power generation equipment. Therefore, KRW 500 million was reflected in the input data for the additional installation cost of ESS after 10 years.

Table 5 Initial condition for LCCA

	Input Data
ESS Life Span	10 yrs
ESS installation cost	1billion 5hundred million KRW/MWh 5hundred million KRW/MWh ()
Operation retention rate	2.5%
C-rate	90% fixed
SMP	'10~'12 years trend of SMP
REC Price	40,000KRW

3.3 Calculation result derivation according to each scenario

Calculation results of life cycle cost (LCC) in case of installing ESS are as follows.

Table 6 LCCA results

	$U_{t.ESS}$ (KRW/kWh)	(W × REC) (KRW/kWh)
Scenario 1	239.19	69.97
Scenario 2	257.95	72.67
Scenario 3	208.35	60.51
Scenario 4	232.86	64.08

Table 7 Estimated REC weighting value for ESS introduction

	Current sytem	Off peak (20h)	On peak (4h)
Scenario 1	1.75	1.47	3.06
Scenario 2	1.81	1.53	3.17
Scenario 3	1.51	1.27	2.65
Scenario 4	1.73	1.45	3.02

Table 7 expresses the final result values of REC weight assessment in case of introducing ESS. Here, the current system means weight in case of giving the same weight, not setting the preferential level of peak time slot. Calculation result values were marked, where the current system was divided into simultaneous equations for peak time slot of 4 hours and off-peak time slot of 20 hours. Application of different weight to peak time slot is meaningful in the respect that it is a factor that can motivate the renewable power producers to use ESS, and can be utilized as baseline data of incentive

provision method of government that aims at peak reduction and the peak coincident factor improvement of renewable energy source.

Conclusion

This study proposed a method of grafting the REC market of the currently enforced RPS system onto ESS, regarding ESS as one of renewable energy sources, which is a scheme of compensating for high initial investment expenditure as a scheme of laying the foundations of spreading ESS.

A method of adjusting REC weight in case of installing ESS was presented as a scheme of grafting RPS system onto ESS. And a method of giving aid to initial investment expenditure through this was explained. Peak time slot was determined through system load pattern and renewable power generation pattern analysis, and was utilized as input data for assessing REC weight through life cycle cost analysis according to each assessed scenario.

REC weight assessment is meaningful in the respect that it is a factor that can motivate the renewable power producers to use ESS, and can be utilized as baseline data of incentive provision method of government that aims at peak reduction and the peak coincident factor improvement of renewable energy sources.

We judge that a study on the application of ESS to other renewable energy sources is necessary as the future research. Besides, it is possible to carry out a study on REC weight quantification through the work of making more elaborate one for various ESS equipment.

Acknowledgements

This research has been supported by Korea Electrical Engineering & Science Research Institute funded by Korea Western Power Co., Ltd

References

[1] The 6th National Generation Expansion Planning. Ministry of Trade, Industry & Energy. (2013)

[2] RPS Management and Operating Instructions. Ministry of Trade, Industry & Energy (2011)

[3] Ministry of Economy, Trade and Industry. Home page. http://www.meti.go.jp Japan.

[4] Jin Su Kim. The study on the effect of wind generator during HVDC overlap period in JeJu (2011)

[5] Jong Hyun Lee, Young Woo Nam and Won Seok Ko. Calculating the Optimal Capacity of Battery Storage System for Power System in Je-Ju. 1229-4691. pp.8-14. KCI (2010)

[6] Jung Pyo Chun, Gwang Ho Kim. Estimation of the Optimal Capacity of Energy Storage System using LCC. The Korean Institute of Electrical Engineers. (2012)

[7] Information on http://www.kpx.or.kr/epsis/

Advanced Materials Research Vols. 960-961 (2014) pp 1620-1625

doi:10.4028/www.scientific.net/AMR.960-961.1620

3-D dynamic simulation system in the application of the power plant steam turbine overhaul

Shaohua Li[1, a], Yang Song[2,b],Tieying Wang[3,c]

[1.] China Datang Corporation Science and Technology Research InstituteCO, LTD, Changping District 102206, Beijing, China;

[2.] School of Energy and Power Engineering, Northeast Dianli University, Jilin 132012, Jilin Province, China

[3.] School of Energy and Power Engineering, Northeast Dianli University, Jilin 132012, Jilin Province, China

[a]shaohuali@263.net,[b]384656251@qq.com,[c]cw1988wc@163.com

Key words: steam turbine overhaul; dynamic simulation; 3-D model; visualization; the human-computer interaction

Abstract：With the rapid development of the power industry, there has been more and more large thermal power unit which is more than or equal to 600MW , steam turbine equipment gradually tend to be high parameter, large capacity, complicated, the overhaul maintenance to steam turbine is the main content of the power plant production activities, it directly affects the reliability of the coal-fired power plant production safety. Aimed at the complexity of thermal steam turbine overhaul, by the use of advanced interactive devices on the visual, do an auditory perception of the virtual environment for something, which is helpful to improve practical operation skills. This paper examines the necessity and superiority of this system applied in education and training. Taking 3-D dynamic simulation system of building as an example, this paper discussed how to utilize the SolidWorks2012 and VRP - SDK to build a virtual training system, realized the combination with virtual reality and education training ,also greatly promoted science and technology progress， equipment of the steam turbine overhaul industry.

Introduction

As of June 2012, China's thermal power installed capacity reached 787.44 million kilowatts, an increase of 7.3%. To 2015, national thermal power installed capacity will reach 990 million kilowatts [1]. With the increase of installed capacity , an increase in the number of large units , structures and more complex, making maintenance more difficult, the growth cycle maintenance , project management personnel for the entire overhaul is difficult to conduct an overall grasp of the construction progress from the macro . In the course of the entire power plant maintenance, overhaul the highest technical requirements of the turbine, the most difficult, the longest period. Turbine overhaul can be completed faster and better is a direct result of the safe operation of the plant.

In the repair process, the construction program tends to have diversity, variability and complexity, including a number of professional and technical standards, the repair process involves thermal, steam turbines, metal and management, standardize huge number. In this context, how to identify a

reasonable construction organization science, improve construction efficiency and training of qualified personnel and a high level of maintenance repair station become the goal.

In this paper, a genuine overhaul of domestic 600MW ultra-supercritical coal-fired power plant turbines for example. The three-dimensional simulation technology in turbine power plant maintenance construction, namely the use of three-dimensional visual simulation technology to simulate animation turbine power plant maintenance process. The construction involved in the construction process , technical standards and safety measures in the form of dynamic simulation to reflect, a true representation of the thermal power plant construction site maintenance , personnel training and maintenance of the power plant site construction and promote industry standardization has important significance.

Thermal steam turbine maintenance problems and needs

Problems. Through field research visits to the repair , overhaul process stage steam turbine power plant discovered the existence of the following main issues :

1) repair process guidance methods behind: Currently the main reference site maintenance programs and procedures to guide the construction drawings, this method is not intuitive, the impact of construction efficiency.

2) Maintenance standardization system is imperfect: turbine overhaul process, multi- certified cross-operation, maintenance personnel should reference multiple professional construction standards and specifications. There is no complete specification of the system [4].

3) maintenance technician training methods behind: Now turbine maintenance technician training is a combination of on-site inspection photographs and drawings, using on-site apprenticeship way, long approach this training period, and the risk is high.

Requirements Analysis

Through the above analysis of the problem , power plant maintenance needs are as follows :

1) the actual repair process for the host power plant simulation object, utilizing a three-dimensional moving images with pictures, text, sound and other multimedia scene mode for the entire site overhaul and repair processes and technology for three-dimensional visual simulation.

2) to establish a three-dimensional virtual engineering environment, maintenance technician for three-dimensional dynamic simulation training, so that by the trainers, without touching scene understanding overhaul the entire process.

3) the actual repair process in a 600MW domestic ultra-supercritical coal-fired power plant generating units is based on a large number of standards, norms carve professional categories other host repair process related standards, norms systematic collation, compilation, utilize three-dimensional pictorial expression dynamically.

Simulation system design and development

Three-dimensional dynamic simulation using three-dimensional computer software and programming languages , through the key elements of simulation construction job site equipment, environmental, construction methods and technology to create simulation scenarios, and as a platform to perform the job site intuitive layout, standardized deduction operating instructions for implementation. Meanwhile, the system can be invoked as specialized training, guidance on-site construction, shorten cycle time and improve corporate training staff efficiency.

Summary of design

System Design. The overall design of the system shown in Figure 2-1 :

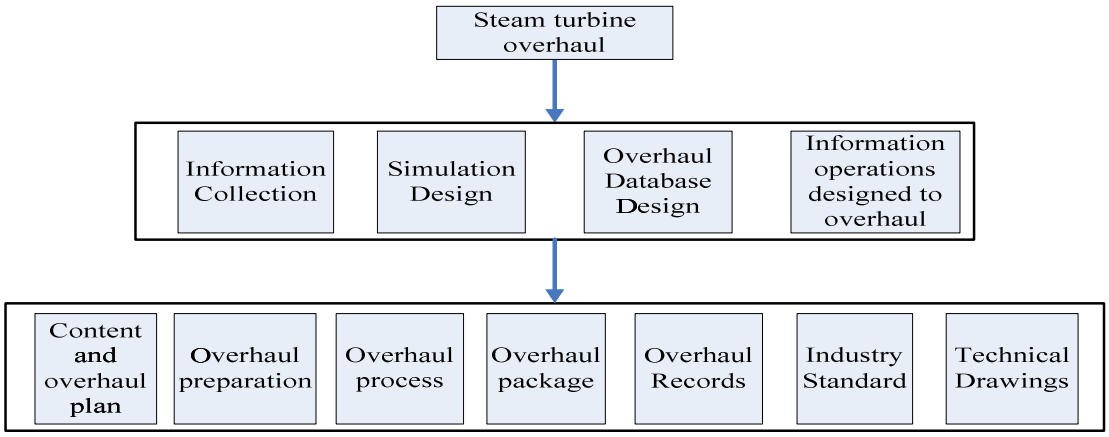

Figure 2-1 overall system design

System design framework. System design framework centered coding device, the device information, data measurement points, the technological transformation of data, maintenance data, equal to three-dimensional drawings related to the construction association model to achieve a three-dimensional model of the operation of the data. To provide users with an intuitive and vivid mode of operation. System framework design is shown in Figure 2-2:

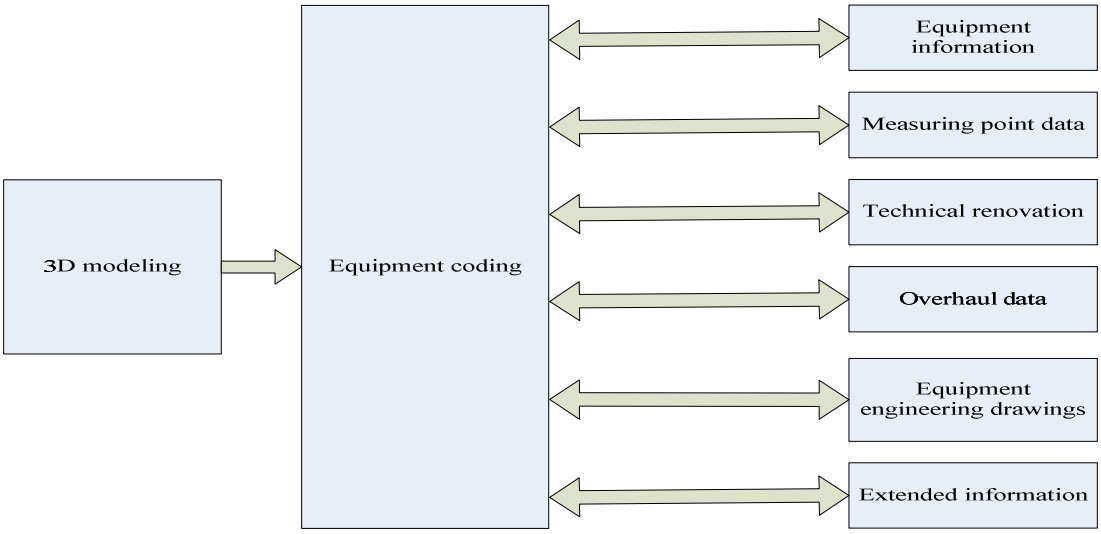

Figure 2-2 Simulation System Design Principles

System Design Principles. The system design should follow the following principles :

1)The system is a three-dimensional simulation system ;

2)To achieve a three-dimensional simulation of the real crew reproduction ;

3)Facilitate the training of operation and maintenance personnel ;

System development platforms and software selection

1)modeling software ;

The system uses SolidWorks2012 software for modeling, SolidWorks2012 modeling is characterised by simple operation, accurate modeling, dynamic simulation and image can be transmitted.

2) Plat

The system uses C # net as the system interface development software, which is easy to use, full-featured, is a painterly, object-oriented and event- driven approach structured high-level programming language;. VRP-SDK as a secondary development toolkit for scene roaming.

3)Other software

Access: database development tools ;

Photoshop: image editing tools ;

UleadVideoStudio: the simulation of dynamic simulation , sound files and subtitle files synthesis ;

Virtual reality platform editing tool system ;: VRP Builder

Coyote: audio processing tools.

Realization of three-dimensional dynamic simulation 2.3

The three-dimensional model. Turbine use SolidWorks2012 software for accurate modeling, modeling steps: select the drawing plane, according to the drawing sketch after sketch is completed, the feature to edit the generated three-dimensional models. All parts of the model generated by the above method turbine. A typical three-dimensional model of turbine parts shown in Figure 2-3:

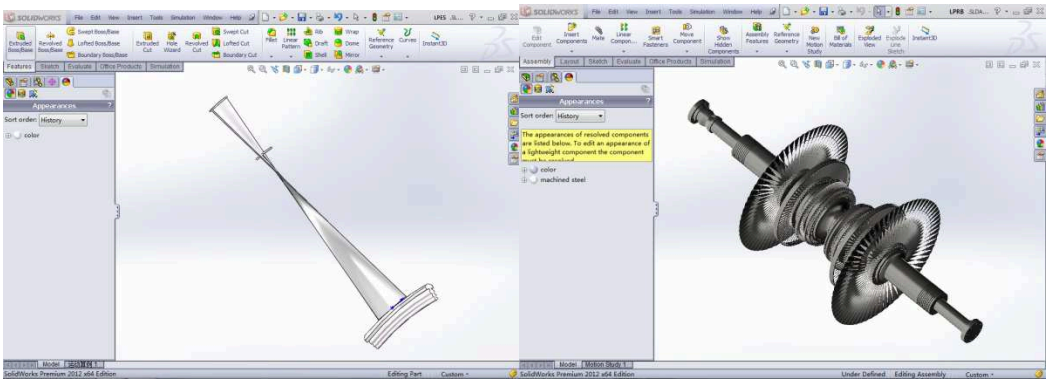

Low-pressure end stage Low-pressure rotor blades

Figure 2-3 Last stage low pressure and low rotor blades

Turbine virtual assembly. Virtual assembly is based on a computer assembly , that is a good three-dimensional part model has been painted by SolidWorks software to assemble it by drawing up, due to the complex structure of the turbine , a large number of parts required to assemble the model in the light of , but also to its interference checking, according to interfere with the results of the model changes, and re- assembly [6] . Assembly process is shown in Figure 3-4:

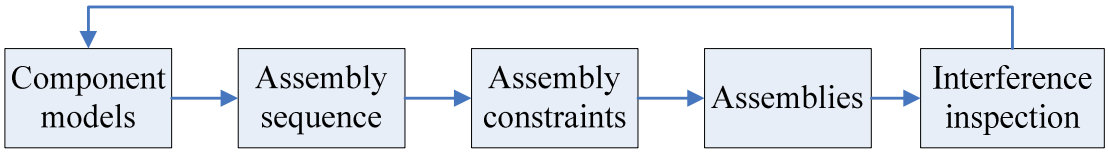

Figure 2-4 Flowchart assembly

Dynamic simulation overhaul. Dynamic simulation of a major overhaul, including maintenance processes and maintenance process demonstration. In this paper, a power plant 600MW steam turbine overhaul domestic ultra-supercritical coal-fired generating units , for example, includes eight parts : Turbine exposing large cap ; cylinder and sliding pin system overhaul ; separators and steam seal overhaul ; cylinder bolts and the center of the rotor inspection ; bearing and oil gear overhaul ; rotor blade reinforcement and repair ; deduction turbine large cap ; rotor shaft to find center.

Synthesis simulation animation, dubbing and subtitling files. The three-dimensional simulation system using Corel VideoStudio Pro X5 simulation animation, dubbing and subtitling files for synthesis. With this software, three-dimensional simulation animation, subtitles, voice synthesis, from a complete overhaul animated simulation, and finally into the system.

Systems to achieve human-computer interaction

The system requires a graphical form of human-computer interaction in the virtual dismantling, in the user interface of the three-dimensional scene model can move, rotate, hide and translucent display operation. As a consequence, users do not get too deep knowledge of computer knowledge can easily manipulate the model of the scene, to achieve the purpose of training. In the three-dimensional scene , trainees can have an intuitive understanding of the scene , in order to make trainees principles and processes for overhaul to better understand and grasp , but also the virtual scene HCI combination of three-dimensional animation and maintenance , so you can receive to good training and teaching effectiveness . Therefore, the system utilizes a three-dimensional program VRP-SDK interface to a three-dimensional scene and three-dimensional animation control. In a simulated environment, the user can utilise the mouse, keyboard, human-computer interaction. The human-computer interaction system is shown in Figure 2-5:

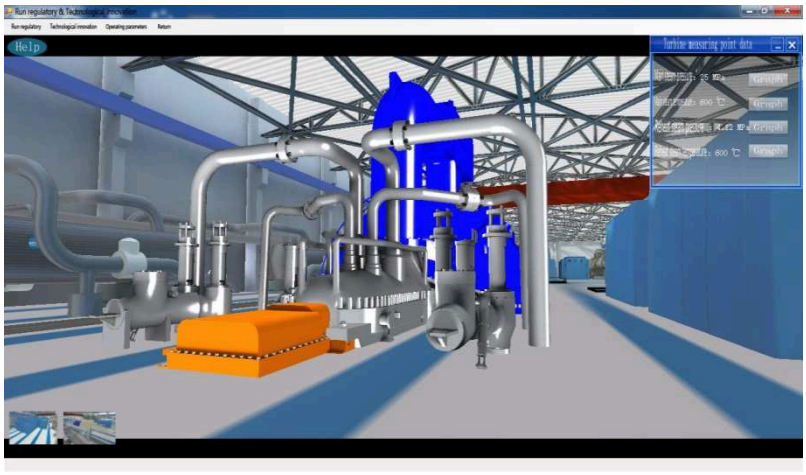

Figure 2-5 Demonstrates the human-computer interaction systems

Turbine repair industry to promote the role of science and technology

The completion of the system greatly facilitated the steam turbine overhaul the industry and technological progress, the power plant steam turbine overhaul significance of the following three aspects.

1) resolve a huge number of power plant steam turbine parts repair process three-dimensional model of light, system integration and other key technologies, reducing the demand for computer hardware, thereby reducing costs.

2) For the power plant steam turbine overhaul determine a reasonable construction organization plan, scientific construction methods to improve construction efficiency and promote technological advancement has enormous significance.

3) to assist the industry to develop high-quality turbine maintenance personnel, to promote electric power construction industry standardization process, reduce training costs, and improve the competitiveness of enterprises and promote the modernization of the plant maintenance industry.

Conclusions

This system will be applied to three-dimensional dynamic simulation technology turbine power plant maintenance process , to overcome the accurate modeling of three-dimensional simulation of the process , the system lighter , software integration and other technical problems, the first time the power plant turbine overhaul the entire process of three-dimensional visualization of dynamic simulation . Plan to build a standardized system of steam turbine power plant maintenance process will process the repair and overhaul of the standard three-dimensional dynamic simulation approach to reflect , to solve the two-dimensional display of complex environments and other security measures to analyze the situation and the danger point of reaction is not comprehensive questions , for the development of maintenance programs , security measures, layout, personnel division arrangements to provide a realistic simulation of the scene, while shortening the training cycle. The three-dimensional dynamic simulation technology used in power plant steam turbine overhaul, repair turbine power plant to promote the standardization process, digitization is important.

References

[1] Wang Liqiang.2010 country's electricity supply and demand analysis and forecast report [R] Beijing: China Electricity Council, 2010.In Chinese

[2] Liu Feng, Chen Xi, Virtual Reality and Education [J] Laboratory Research and Exploration, 1999,): 31-35. In Chinese

[3] Hung -Chi, etc. Virtual Maintenance Training System Review and discuss the development of key technologies, PLA University of Technology.2000 l (1) :63-67 In Chinese

[4] Wang Yulin turbine equipment operation and accident handling Beijing : Chemical Industry Press, 2005:34 page In Chinese

[5] Jiang Hong, Lu Lifeng, Wei Zheng solid works animation and motion analysis to resolve instances (M), Beijing: Mechanical Industry Press ,2006,6 -7. In Chinese

[6] Shen deep forest , Chen Ding-fang , based on solid works reducer design and virtual assembly of (J), Hubei University of Technology , 2007 (s) :56-55 In Chinese

[7] Dassault Systèmes (DS) SolidWorks Corp. Assembly Mates[Z]. SolidWorks Help.2010.

[8] Alan B A，Compilation of Simulation[J]．IEEE，1999，33(2)：61-63

[9] Hartholt Arno, Gratch Jonathan, Weiss Lori, et al. At the virtual frontier: Introducing Gunslinger, a multicharacter, mixed-reality,story-driven experience. Intelligent Virtual Agents [M]. Berlin: Springer Berlin Heidelberg, 2009: 500-501.

A

B

C

D

E

I

N

O

P

Q

R

T

U

V

W

X

Y

Z

E

F

G

H

I

J

K

M

N

O

T

W

X

Y

Z